Cover Picture

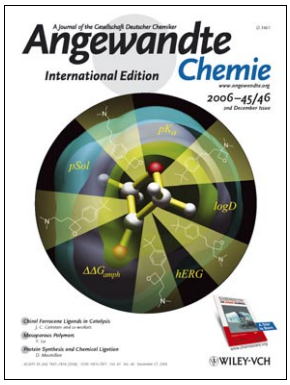

Georg Wuitschik, Mark Rogers-Evans,* Klaus Müller, Holger Fischer, Björn Wagner, Franz Schuler, Liudmila Polonchuk, and Erick M. Carreira*

The oxetane ring is an orphan heterocycle in medicinal chemistry. In their Communication on page 7736 ff., M. Rogers-Evans, E. M. Carreira, and co-workers show that this structural motif can improve key physico- and pharmacochemical properties of an underlying scaffold. An "oxetane scan" within a series of lipophilic tertiary amine derivatives was performed to probe the influence of the oxetane ring on selected compound properties.

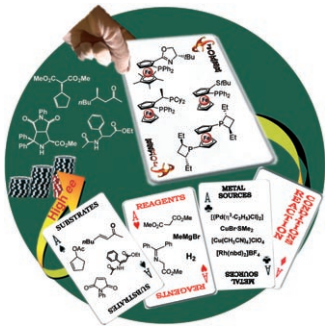

Asymmetric Catalysis
Chiral ferrocene ligands have emerged as versatile reagents for asymmetric catalysis. With an emphasis on newly developed ligands and reactions, the Review by J. C. Carretero and co-workers on page 7674 ff. details the progress of the last four years.

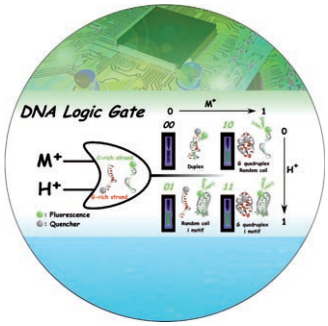

Molecular Devices
In their Communication on page 7716 ff., N. Sugimoto and co-workers discuss the development of simple DNA logic gates that are sensitive to two input signals, M^+ and H^+, and allow fast readout of the fluorescence output signal.

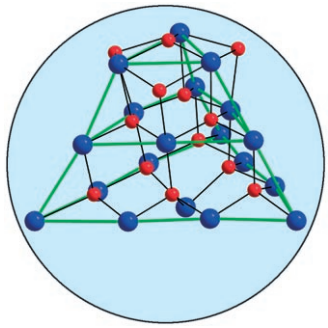

Mn_{19} Single-Molecule Magnets
G. Christou, A. J Tasiopoulos, and co-workers describe in their Communication on page 7722 ff. the open framework structures of two manganese carboxylate 3D coordination polymers with nanometer-sized cavities whose Mn_{19} units behave as single-molecule magnets.

Contents

VIP *The following Communications have been judged by at least two referees to be "very important papers" and will be published online at www.angewandte.org soon:*

*Y. Xiong, J. M. McLellan, Y. Yin, Y. Xia**
Synthesis of Palladium Icosahedrons with a Twinned Structure by Blocking Oxidative Etching with Citric Acid or Citrate Ion

*X. Liu, L. Shi, W. Niu, H. Li, G. Xu**
Environmentally Friendly and Highly Sensitive Ruthenium(II) Tris(2,2'-bipyridyl) Electrochemiluminescent System Using 2-(Dibutylamino)ethanol as Co-reactant

*Li-M. Yan, A. Velkova, M. Tatarek-Nossol, E. Andreetto, A. Kapurniotu**
Designed IAPP Mimic Blocks Aβ Cytotoxic Self-Assembly: Cross-Suppression of Amyloid Toxicity of Aβ and IAPP Suggests a Molecular Link between Alzheimer's Disease and Type 2 Diabetes

A. Rodríguez-Fortea, J. M. Campanera, C. M. Cardona, L. Echegoyen, J. M. Poblet**
Dancing with the Right Couple on a Fullerene Surface: Isomerization of N-Ethyl [6,6]Pyrrolidino-$Y_3N@C_{80}$ to the [5,6] Regioisomer

A. Corma, M. Renz**
A General Method for the Preparation of Ethers Using Water-Resistant Solid Lewis Acids

K. Banert, Young-H. Joo, T. Rüffer, B. Walfort, H. Lang*
The Exciting Chemistry of Tetraazidomethane

News

Bioinorganic Chemistry: Bertini honored ____ **7661**

Inorganic Chemistry: Krossing awarded ____ **7661**

Organic Chemistry: C.-H. Wong to Taiwan ____ **7661**

Books

Phosphorus World — Derek E. C. Corbridge — *reviewed by J. D. Woollins* ____ **7662**

Candid Science V — Balázs Hargittai, István Hargittai — *reviewed by G. B. Kauffman* ____ **7663**

Highlights

Mesoporous polymers

Y. Lu* ____ **7664 – 7667**

Surfactant-Templated Mesoporous Materials: From Inorganic to Hybrid to Organic

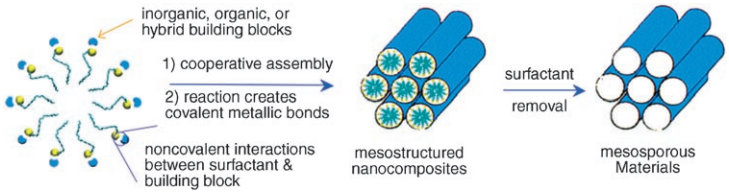

Poring over materials: Over the past decade, surfactant-directed self-assembly (see scheme) has led to numerous inorganic and hybrid mesoporous materials. Recently, this process was extended to organic materials: mesoporous polymers were prepared from oligomers by using Pluronic surfactants. This approach allows the design of novel and functional materials for broad applications.

Protein Synthesis

D. Macmillan* ____ **7668 – 7672**

Evolving Strategies for Protein Synthesis Converge on Native Chemical Ligation

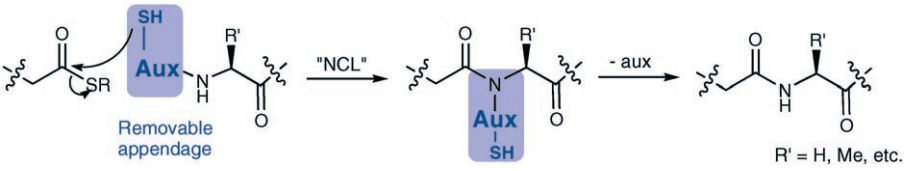

Build a bridge: Although used widely, certain limitations of popular protein assembly strategies such as native chemical ligation (NCL) have persisted. This highlight presents the results of recent reports that tackle these limitations (see picture). Aux = auxiliary.

InterScience

© 2006 Wiley-VCH Verlag GmbH & Co. KGaA, Weinheim

Reviews

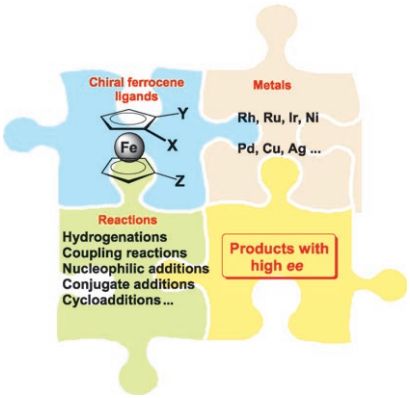

Pushing forward in asymmetric catalysis: Chiral ferrocene-based ligands have emerged as key structural motifs in transition-metal-mediated asymmetric catalysis because of their availability, unique stereochemical environment, and easy modulation of structural and electronic properties through a wide range of substituents and coordination modes. Recent results include novel types of ferrocene ligands and the development of innovative C–C and C–X bond-forming asymmetric processes.

Ferrocenes

R. Gómez Arrayás, J. Adrio, J. C. Carretero* ——— **7674 – 7715**

Recent Applications of Chiral Ferrocene Ligands in Asymmetric Catalysis

Communications

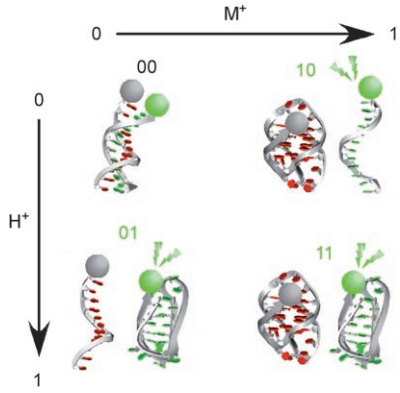

Environmentally sensitive: Structural polymorphism of telomere DNA molecules, which may be useful for the construction of molecular devices, is affected by environmental factors. Based on the conversion of the telomere DNA molecules among four states, simple and robust DNA logic gates that respond to two chemical input signals (M^+ and H^+) and generate a change in fluorescence intensity as the output signal were developed.

Molecular Devices

D. Miyoshi, M. Inoue, N. Sugimoto* ——— **7716 – 7719**

DNA Logic Gates Based on Structural Polymorphism of Telomere DNA Molecules Responding to Chemical Input Signals

Three "P"s in a pod: The polyanion P_8^{8-} in $Hg_4Ag_5P_8Cl_5$ has been stabilized by the combination of Ag^+ and Hg^{2+} ions, which are bound to the differently charged phosphorus atoms. Three different formal oxidation states of phosphorus are present in the structure.

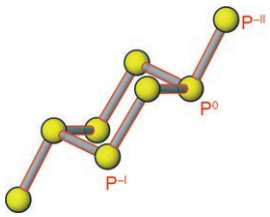

Phosphorus Chemistry

O. S. Oleneva, T. A. Shestimerova, E. V. Dikarev,* A. V. Shevelkov* ——— **7719 – 7722**

P_8^{8-} Polyanion with Phosphorus Atoms in Three Different Formal Oxidation States Stabilized by a Combination of Ag^+ and Hg^{2+} Cations

For the USA and Canada:
ANGEWANDTE CHEMIE International Edition (ISSN 1433-7851) is published weekly by Wiley-VCH PO Box 191161, D 69451 Weinheim, Germany. Air freight and mailing in the USA by Publications Expediting Inc. 200 Meacham Ave., Elmont, NY 11003. Periodicals postage paid at Jamaica NY 11431. US POSTMASTER: send address changes to *Angewandte Chemie*, Wiley-VCH, 111 River Street, Hoboken, NJ 07030. Annual subscription price for institutions: US$ 5685/5168 (valid for print and electronic / print or electronic delivery); for individuals who are personal members of a national chemical society prices are available on request. Postage and handling charges included. All prices are subject to local VAT/sales tax.

© 2006 Wiley-VCH Verlag GmbH & Co. KGaA, Weinheim

The best in chemistry –

for more than a hundred years

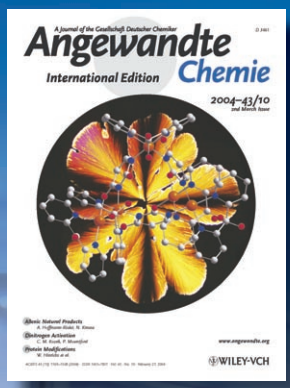

A Journal of the Gesellschaft Deutscher Chemiker

Angewandte
International Edition **Chemie**

www.angewandte.org

1888: ***The beginning of a success story***

Constant Innovations

1962: *First issue of the International Edition*
1976: *Graphical abstracts*
1979: *Cover pictures*
1988: *Centenary of Angewandte*
1989: *Routine use of color*
1991: *New section: Highlights*
1992: *Computerized editorial tracking system*
1995: *Internet service for readers*
1998: *Regular press service; full-text online*
2000: *New section: Essays; EarlyView: Communications available online ahead of the printed version*
2001: *New section: Minireviews*
2002: *Online submission of manuscripts*
2003: *Weekly publication; new section: News; new layout*
2004: *Backfiles (1962-1997); ManuscriptXpress: Online system for authors and referees*

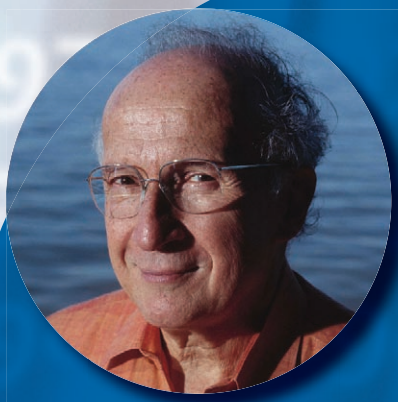

Angewandte's advisors...

Roald Hoffmann
Cornell University
(Photo: Lois Anshus)

» As an applied theoretical chemist, I love it that the best chemical journal in the world has „applied" in its title. It's history, I know. But there is also the implication in this adjective that these sterling accounts of the new, these just-in-time reviews, these incisive essays that ***Angewandte Chemie*** *contains – that they all are of true utility, and are really used, by the finest chemists of our time.«*

Angewandte Chemie International Edition *is a journal of the German Chemical Society (GDCh)*

GDCh

WILEY InterScience® DISCOVER SOMETHING GREAT

WILEY-VCH

1195104_gu

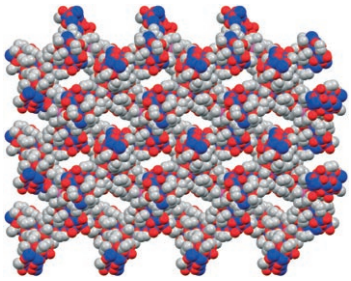

Singles networks: The use of 1,3-propanediol and of 2-methyl-1,3-propanediol in manganese carboxylate chemistry leads to two new 3D coordination polymers with an unprecedented Mn_{19} repeating unit. The polymers have open framework structures with nanometer-sized cavities (see picture; Na not visible, Mn blue, O red, C gray). The Mn_{19} units have a ground spin state of $S = 23/2$ and behave as single-molecule magnets.

Single-Molecule Magnets

E. E. Moushi, T. C. Stamatatos, W. Wernsdorfer, V. Nastopoulos, G. Christou,* A. J. Tasiopoulos* ——— **7722 – 7725**

A Family of 3D Coordination Polymers Composed of Mn_{19} Magnetic Units

Finger formation: Predictive all-atom folding of a DNA-binding αββ-zinc-finger motif in a free-energy forcefield has been demonstrated. The three models (shown in different shades of blue in the picture) show the lowest energy structures found in the simulation. The low-energy region of the free-energy surface and important steps of the folding pathway have been analyzed to help elucidate zinc-finger formation and function.

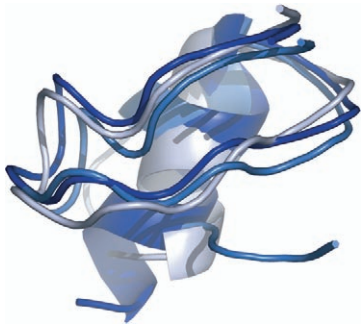

Protein Folding

S. M. Gopal, W. Wenzel* ——— **7726 – 7728**

De Novo Folding of the DNA-Binding ATF-2 Zinc Finger Motif in an All-Atom Free-Energy Forcefield

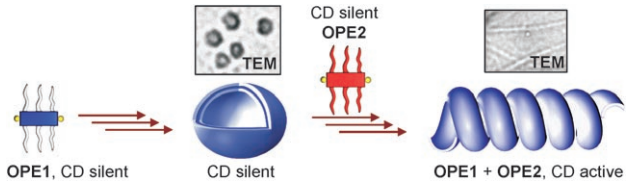

Coassembly of short molecular wires **OPE1** with chiral analogues **OPE2**, both of which are CD silent, exhibited a sergeant-and-soldiers effect that resulted in transformation of vesicular aggregates of **OPE1** into CD-active helical nanotubes (see schematic picture), as revealed by CD, dynamic light scattering, and atomic force and transmission electron microscopies (TEM). **OPE** = oligo(*p*-phenyleneethynylene).

Supramolecular Chemistry

A. Ajayaghosh,* R. Varghese, S. Mahesh, V. K. Praveen ——— **7729 – 7732**

From Vesicles to Helical Nanotubes: A Sergeant-and-Soldiers Effect in the Self-Assembly of Oligo(*p*-phenyleneethynylene)s

In full color: Ultrafine lanthanide-doped polyvinylpyrrolidone/$NaYF_4$ nanocrystals with narrow size distribution were synthesized and found to disperse well in water and many organic solvents. Silica was coated onto the nanocrystals to form a uniform thin layer. Highly efficient upconversion fluorescence was observed from both uncoated and silica-coated PVP/$NaYF_4$ nanocrystals doped with Yb/Er or Yb/Tm (see picture).

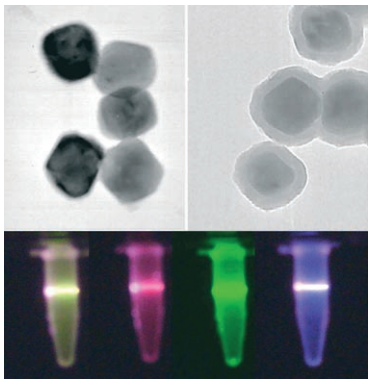

Fluorescent Labels

Z. Li, Y. Zhang* ——— **7732 – 7735**

Monodisperse Silica-Coated Polyvinylpyrrolidone/$NaYF_4$ Nanocrystals with Multicolor Upconversion Fluorescence Emission

© 2006 Wiley-VCH Verlag GmbH & Co. KGaA, Weinheim

Contents

Drug Design

G. Wuitschik, M. Rogers-Evans,* K. Müller, H. Fischer, B. Wagner, F. Schuler, L. Polonchuk, E. M. Carreira* ——— **7736 – 7739**

Oxetanes as Promising Modules in Drug Discovery

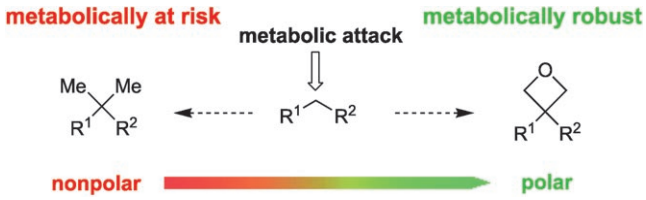

Ring the changes: Introduction of an oxetane ring results in remarkably improved physico- and biochemical properties of the underlying scaffold. The oxetane ring confers enhanced solubility, reduces the metabolic degredation, lipophilicity, and amphiphilicity, and modulates the basicity of a nearby amine group.

Lead Nanostructures

H. Tong, Y.-J. Zhu,* L.-X. Yang, L. Li, L. Zhang ——— **7739 – 7742**

Lead Chalcogenide Nanotubes Synthesized by Biomolecule-Assisted Self-Assembly of Nanocrystals at Room Temperature

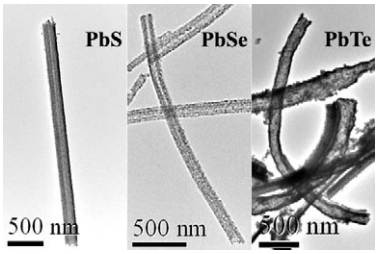

Natural help: PbE nanotubes (E = S, Se, Te; see picture) have been synthesized by a novel biomolecule-assisted method at room temperature. The precursor nanowires self-assembled from nanocrystals synthesized in the presence of cysteine play crucial roles as both the lead source and template in the formation of the nanotubes, which exhibit an obvious quantum confinement effect.

Encapsulated Oligonucleotides

A. N. Zelikin, Q. Li, F. Caruso* ——— **7743 – 7745**

Degradable Polyelectrolyte Capsules Filled with Oligonucleotide Sequences

To cap it all: A polycation-free encapsulation method is used to obtain high concentrations of uncomplexed, short oligonucleotide chains confined within monodisperse, degradable microcapsules. Oligonucleotide loadings of $>10^4$ chains per capsule are obtained, and more than 90% of the capsules are filled with DNA. These capsules also undergo degradation under reducing conditions (such as those that occur in cells), releasing the encapsulated DNA.

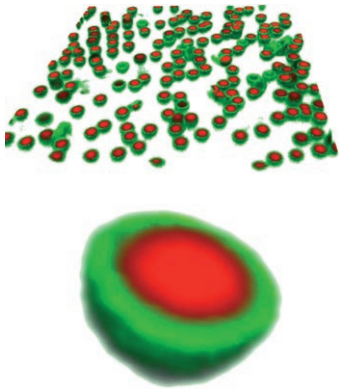

Directed Evolution

M. T. Reetz,* J. D. Carballeira, A. Vogel ——— **7745 – 7751**

Iterative Saturation Mutagenesis on the Basis of B Factors as a Strategy for Increasing Protein Thermostability

Efficiency counts: A new method of directed evolution for increasing the thermostability of proteins saves time and effort. In an illustrative study, iterative cycles of saturation mutagenesis were performed at those sites in a lipase that display high B factors.

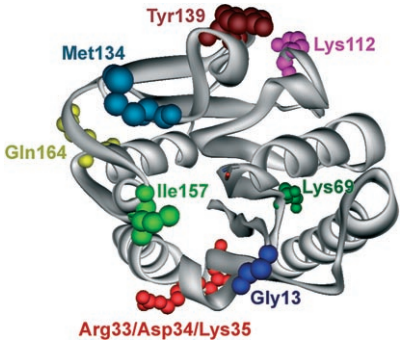

© 2006 Wiley-VCH Verlag GmbH & Co. KGaA, Weinheim

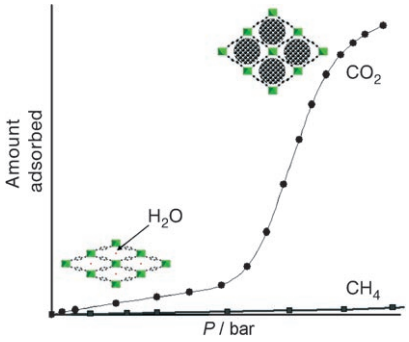

Taking a deep breath: The hydrated form of the microporous metal organic framework MIL-53(Cr) performs better than the dehydrated form for the selectivity binding of carbon dioxide over methane (see graph). The polarity of the adsorbed gas is thought to play a role in inducing framework flexibility and the breathing of the pores.

Selective Adsorption

P. L. Llewellyn,* S. Bourrelly, C. Serre, Y. Filinchuk, G. Férey ——— **7751 – 7754**

How Hydration Drastically Improves Adsorption Selectivity for CO_2 over CH_4 in the Flexible Chromium Terephthalate MIL-53

Targeting cancer: Multifunctional magnetic gold nanoshells (Mag-GNS) are prepared by coating silica spheres with gold nanoshells embedded with Fe_3O_4 nanoparticles. The Fe_3O_4 nanoparticles allow magnetic resonance imaging (MRI) for diagnosis, and the gold nanoshells enable photothermal therapy. By attaching an antibody to the Mag-GNS by a poly(ethylene glycol) (PEG) linker, cancer cells can be targeted.

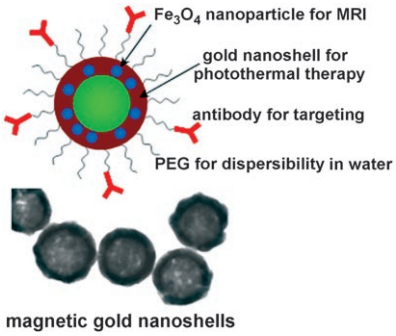

Nanomedicine

J. Kim, S. Park, J. E. Lee, S. M. Jin, J. H. Lee, I. S. Lee, I. Yang, J.-S. Kim, S. K. Kim, M.-H. Cho,* T. Hyeon* ——— **7754 – 7758**

Designed Fabrication of Multifunctional Magnetic Gold Nanoshells and Their Application to Magnetic Resonance Imaging and Photothermal Therapy

---

Te for two: A convenient method to prepare a series of tellurido-bridged mixed-metal clusters is demonstrated by the reactions of $[Cp^*Ir(CO)(TeTol)_2]$ (Tol = *p*-$CH_3C_6H_4$, $Cp^* = \eta^5$-C_5Me_5) with $[Pt(PPh_3)_3]$ and $[Pd(PPh_3)_4]$. The Group 10 metal center inserts itself into the Te–C bond (see scheme). This method may be applied to the synthesis of a wide range of mixed-metal telluride cluster compounds.

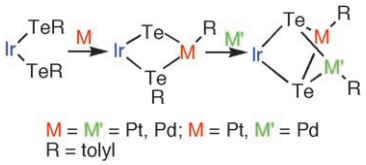

Cluster Compounds

T. Nakagawa, H. Seino, S. Nagao, Y. Mizobe* ——— **7758 – 7762**

Synthesis of Tellurido-Bridged $IrPt_2$, $IrPd_2$, and IrPtPd Clusters by Inserting Zero-Valent Pt and Pd Centers into Te–C Bonds

---

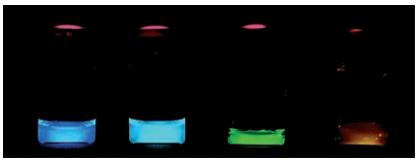

You light up my life! Antibodies, when bound to a donor–acceptor-substituted stilbene, strongly fluoresce with colors ranging from blue to green. Photophysical and structural analyses indicate that antibody binding alters the excited-state behavior of stilbene. Such complexes may find in vitro and in vivo application as fluorescent biosensors.

Antibody–Stilbene Complexes

F. Tian, E. W. Debler, D. P. Millar, A. A. Deniz, I. A. Wilson,* P. G. Schultz* ——— **7763 – 7765**

The Effects of Antibodies on Stilbene Excited-State Energetics

© 2006 Wiley-VCH Verlag GmbH & Co. KGaA, Weinheim

Contents

Protein Structures

B. D. Charette, R. G. MacDonald, S. Wetzel, D. B. Berkowitz,* H. Waldmann* ——— **7766 – 7770**

Protein Structure Similarity Clustering: Dynamic Treatment of PDB Structures Facilitates Clustering

In the family: The introduction of ligand docking, molecular dynamics, and the VAST algorithm into protein structure similarity clustering greatly streamlines the process and opens up otherwise unseen connections to new protein-cluster partners. VAST = vector alignment search tool.

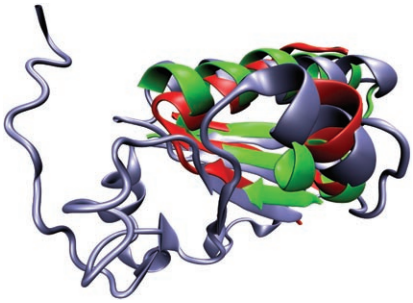

Solid-State Metal Hydrides

J.-N. Chotard, Y. Filinchuk, B. Revaz, K. Yvon* ——— **7770 – 7773**

Isolated $[Ni_2H_7]^{7-}$ and $[Ni_4H_{12}]^{12-}$ Ions in $La_2MgNi_2H_8$

Isolated and complex: $La_2MgNi_2H_8$ contains isolated dinuclear $[Ni_2H_7]^{7-}$ and tetranuclear $[Ni_4H_{12}]^{12-}$ anions (see picture). These are the first polynuclear solid-state nickel hydride complexes. Their formation upon hydrogenation of the intermetallic compound La_2MgNi_2 is associated with a metal–insulator transition.

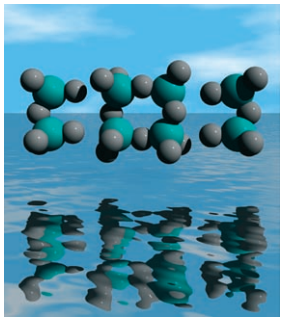

Nanostructures

Y.-L. Chueh, L.-J. Chou,* Z. L. Wang ——— **7773 – 7778**

SiO_2/Ta_2O_5 Core–Shell Nanowires and Nanotubes

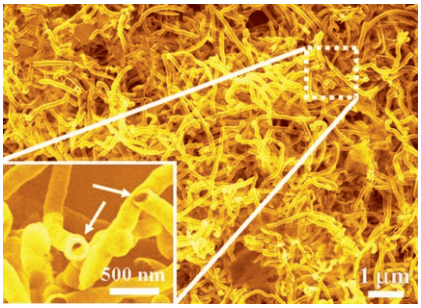

Tantalizing silica: SiO_2/Ta_2O_5 core–shell nanostructures were formed by reducing SiO_2 nanowires under a Ta atmosphere at 950 °C. The diameter of the SiO_2 nanowires inside the core–shell nanostructures could be manipulated by modifying the reduction time. Treatment of the core–shell structures in dilute HF solution yielded Ta_2O_5 nanotubes (see TEM image), whereas Ta_2O_5 nanowires were formed directly by increasing the reduction time.

Ionic Liquids

F. Maier,* J. M. Gottfried, J. Rossa, D. Gerhard, P. S. Schulz, W. Schwieger, P. Wasserscheid, H.-P. Steinrück ——— **7778 – 7780**

Surface Enrichment and Depletion Effects of Ions Dissolved in an Ionic Liquid: An X-ray Photoelectron Spectroscopy Study

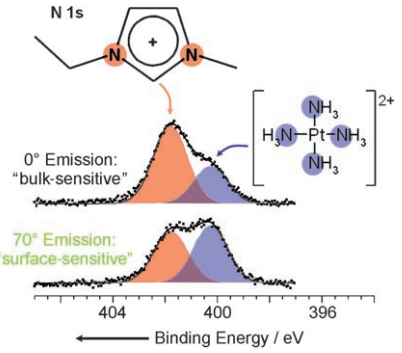

Surfaces of ionic liquids: Angle-dependent X-ray photoelectron spectroscopy (XPS) shows that the surface composition of a solution of $[Pt(NH_3)_4]Cl_2$ in the ionic liquid 1-ethyl-3-methylimidazolium ethyl sulfate ([EMIM][$EtOSO_3$]) deviates considerably from the bulk composition. The $[Pt(NH_3)_4]^{2+}$ cation is enriched on the surface at the expense of the [EMIM] cation (see picture), while the Cl^- anion is depleted to below the XPS detection limit.

© 2006 Wiley-VCH Verlag GmbH & Co. KGaA, Weinheim

New aspects of *N*-oxides: Pyrazine, pyridazine, and pyrimidine *N*-oxides are regioselectively arylated with aryl iodides, bromides, and chlorides in the presence of a palladium catalyst (see scheme). The resulting products can be deoxygenated in high yield or further functionalized by making use of the *N*-oxide functionality. FG = functional group.

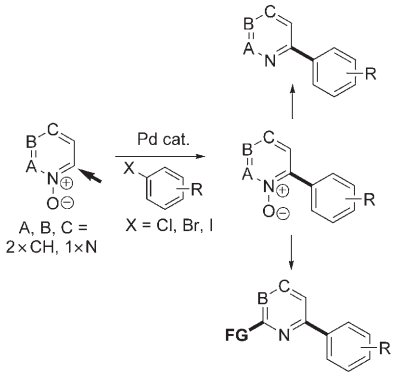

N-Oxide Arylation

J.-P. Leclerc, K. Fagnou* ____ **7781 – 7786**

Palladium-Catalyzed Cross-Coupling Reactions of Diazine *N*-Oxides with Aryl Chlorides, Bromides, and Iodides

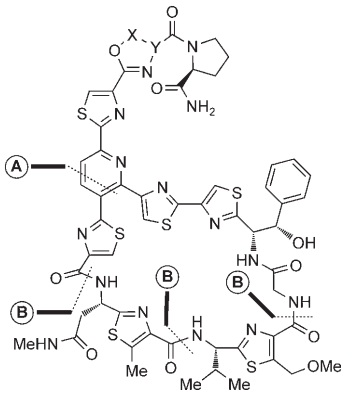

Beat the bugs: Total syntheses of the thiopeptide antibiotics GE2270A (X–Y = CH_2–CH) and GE2270T (X–Y = CH=C) have been accomplished. The modular approach featured a hetero-Diels–Alder dimerization Ⓐ to construct the trithiazolyl pyridine domain, and highly regioselective macrolactamizations Ⓑ to furnish the macrocyclic core.

Thiopeptide Antibiotics

K. C. Nicolaou,* B. Zou, D. H. Dethe, D. B. Li, D. Y.-K. Chen* ____ **7786 – 7792**

Total Synthesis of Antibiotics GE2270A and GE2270T

Tri-ed and tested: Ring expansion processes were observed in the novel three-component reaction of thiazolium salts **1**, 1,1-disubstituted ketenes **2** (generated in situ), and activated alkynes (see scheme, EWG = electron-withdrawing group). This protocol allows highly efficient assembly of unique furan-fused 1,4-thiazepine derivatives from simple and readily accessible starting materials.

Multicomponent Reactions

C. Ma,* H. Ding, Y. Zhang, M. Bian ____ **7793 – 7797**

A Ring-Expansion Methodology Involving Multicomponent Reactions: Highly Efficient Access to Polysubstituted Furan-Fused 1,4-Thiazepine Derivatives

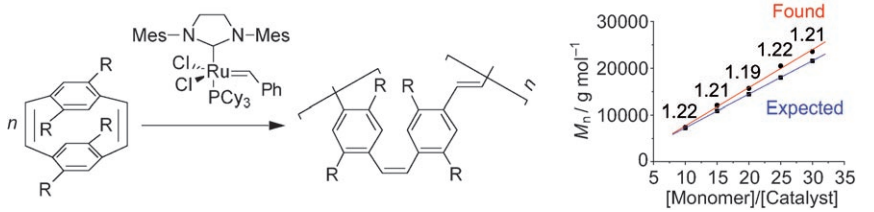

Ring opening of substituted cyclophanedienes by ruthenium-based metathesis catalysts gives soluble phenylenevinylene homopolymers of well-defined molecular weight with an alternating *cis-trans* microstructure (see picture, R = OC_8H_{17}). The living character of this polymerization is demonstrated by controlled chain extension.

Conjugated Polymers

C.-Y. Yu, M. L. Turner* ____ **7797 – 7800**

Soluble Poly(*p*-phenylenevinylene)s through Ring-Opening Metathesis Polymerization

© 2006 Wiley-VCH Verlag GmbH & Co. KGaA, Weinheim

Contents

Organic Light-Emitting Diodes

W.-Y. Wong,* C.-L. Ho, Z.-Q. Gao, B.-X. Mi, C.-H. Chen, K.-W. Cheah, Z. Lin ——— **7800 – 7803**

Multifunctional Iridium Complexes Based on Carbazole Modules as Highly Efficient Electrophosphors

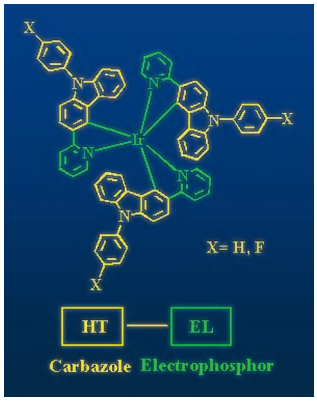

Getting the green light: Highly efficient organic light-emitting diodes (OLEDs) have been synthesized from robust green-electrophosphorescent Ir^{III} complexes based on carbazole derivatives (see picture, HT = hole transporting, EL = electroluminescence). The combination of short triplet lifetime, high emission efficiency, and improved charge-transporting properties allows these OLEDs to achieve peak efficiencies of 12% photons per electron and 38 cd A^{-1}.

Heterocycle Synthesis

A. M. Kearney, C. D. Vanderwal* ——— **7803 – 7806**

Synthesis of Nitrogen Heterocycles by the Ring Opening of Pyridinium Salts

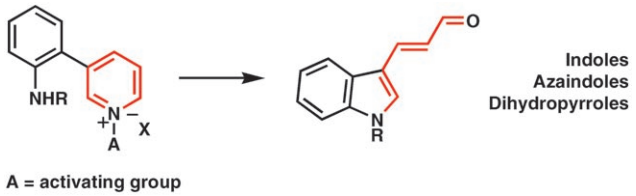

The century-old ring-opening reaction of pyridinium salts with tethered nucleophiles has been harnessed for a synthesis of substituted indoles and related nitrogen heterocyles. Extension of this method could lead to oxygen- and sulfur-containing heterocycles and carbocycles, as well as to applications in natural product synthesis and medicinal chemistry.

Photocatalysis

K. Maeda, K. Teramura, D. Lu, N. Saito, Y. Inoue, K. Domen* ——— **7806 – 7809**

Noble-Metal/Cr_2O_3 Core/Shell Nanoparticles as a Cocatalyst for Photocatalytic Overall Water Splitting

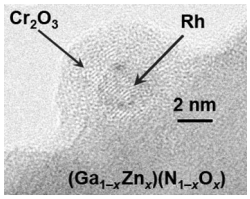

"Waterproof" coats: Rh/Cr_2O_3 (core/shell) nanoparticles supported on a $(Ga_{1-x}Zn_x)$-$(N_{1-x}O_x)$ solid solution are synthesized by an in situ photodeposition method. These nanoparticles (see picture) are used as a promoter for overall water splitting upon visible-light irradiation ($\lambda > 400$ nm). Without the Cr_2O_3 shell water is formed from H_2 and O_2 in an undesired back reaction.

Nonnatural Base Pairs

Y. Kim, A. M. Leconte, Y. Hari, F. E. Romesberg* ——— **7809 – 7812**

Stability and Polymerase Recognition of Pyridine Nucleobase Analogues: Role of Minor-Groove H-Bond Acceptors

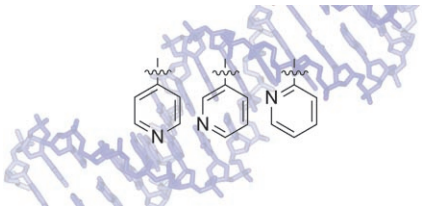

In the groove: In an effort to develop unnatural base pairs, pyridyl nucleoside analogues were synthesized and characterized (see structures). An α-glycosidic nitrogen atom provides an H-bond acceptor that does not significantly facilitate pairing with natural nucleobases. However, it forms minor-groove H-bonds with water molecules and DNA polymerases that optimize the stability and replication, respectively, of the unnatural base pair.

© 2006 Wiley-VCH Verlag GmbH & Co. KGaA, Weinheim

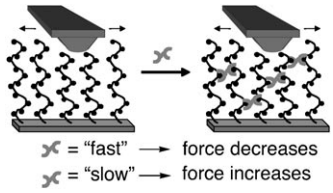

Detailed brushwork: Structurally and thermodynamically similar cross-linkers have opposite effects on the lateral resistance of grafted thin films of poly(4-vinylpyridine) brushes. The chemically reversible changes in mechanics are influenced by the dissimilar kinetics of the cross-linking interaction.

Polymer Brushes

D. M. Loveless, N. I. Abu-Lail, M. Kaholek, S. Zauscher,* S. L. Craig* — **7812 – 7814**

Reversibly Cross-Linked Surface-Grafted Polymer Brushes

Copper-sensitive cycle: A cyclic peptide nucleic acid (PNA) that does not bind DNA and RNA can be prepared by placing an optimized linker between the termini. Cu^{II} ions, but not other tested metal ions, catalyze the transformation of the cyclic PNA into the linear PNA, which is a strong binder of nucleic acids (see picture). This effect is used for the fluorimetric detection of Cu^{II}. ssDNA = single-stranded DNA

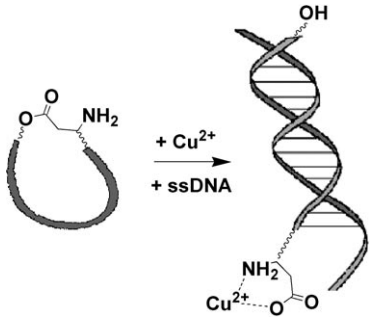

Peptide Nucleic Acids

J. Kovács, T. Rödler, A. Mokhir* — **7815 – 7817**

Chemodosimeter for Cu^{II} Detection Based on Cyclic Peptide Nucleic Acids

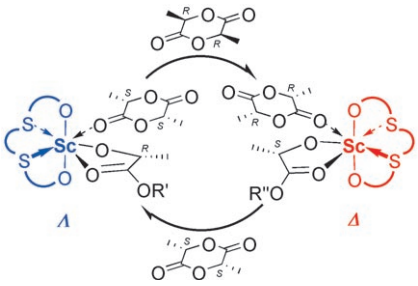

Tactical response: High heterotactic stereocontrol was observed from the ring-opening polymerization of *rac*-lactide on using a series of bis(phenolato)scandium complexes (see scheme). This stereocontrol appears to involve a dynamic monomer-recognition process as a result of the interconversion of the configuration from Λ into Δ.

Polymerization

H. Ma, T. P. Spaniol, J. Okuda* — **7818 – 7821**

Highly Heteroselective Ring-Opening Polymerization of *rac*-Lactide Initiated by Bis(phenolato)scandium Complexes

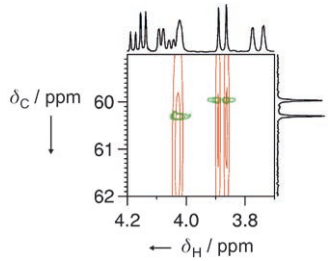

Double take: In the acquisition regime presented here, ^{1}H,^{13}C HSQC spectra are recorded twice with spectral widths of 5.8 and 6.2 ppm in the indirect dimension. The aliased signals are then unfolded to the full spectral width to yield an HSQC spectrum with 5 Hz per point in the ^{13}C dimension without additional time requirements (see example of strychnine).

NMR Spectroscopy

I. Baskyr, T. Brand, M. Findeisen, S. Berger* — **7821 – 7824**

Acquisition Regime for High-Resolution Heteronuclear 2D NMR Spectra

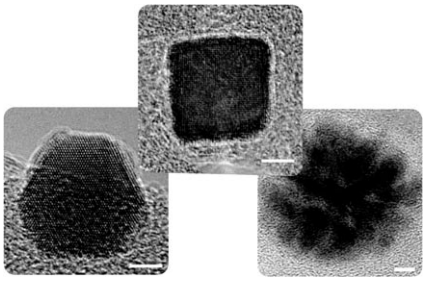

Activity revived: Platinum nanoparticles (cuboctahedra, cubes, and porous particles, see picture, from left to right) capped with alkylammonium ions are synthesized by manipulating the reduction kinetics. The catalytic activity of these nanoparticles is superior to that of nanoparticles whose shape was controlled with a polymeric capping agent and foreign metal ions.

Shape-Controlled Nanoparticles

H. Lee, S. E. Habas, S. Kweskin, D. Butcher, G. A. Somorjai, P. Yang* — **7824 – 7828**

Morphological Control of Catalytically Active Platinum Nanocrystals

© 2006 Wiley-VCH Verlag GmbH & Co. KGaA, Weinheim

Contents

Singlet Diradicals

M. Abe,* E. Kubo, K. Nozaki, T. Matsuo, T. Hayashi ——— **7828 – 7831**

An Extremely Long-Lived Singlet 4,4-Dimethoxy-3,5-diphenylpyrazolidine-3,5-diyl Derivative: A Notable Nitrogen-Atom Effect on Intra- and Intermolecular Reactivity

Life in the fast lane: An extremely long-lived singlet state of 4,4-dimethoxy-3,5-diphenylpyrazoline-3,5-diyl (**1**; $\tau = 9.67$ ms at room temperature) is reported, which affords intramolecularly the oxygen-migration product and reacts intermolecularly with 4-phenyl-1,2,4-triazoline-3,5-dione (PTAD) to give the cycloaddition product. The diradical intermediate was characterized by its absorption band at 645 nm.

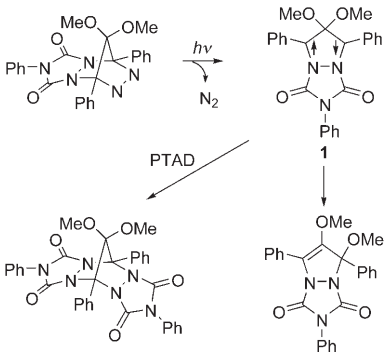

Organocatalysis

M. Rueping,* C. Azap ——— **7832 – 7835**

Cooperative Coexistence: Effective Interplay of Two Brønsted Acids in the Asymmetric Synthesis of Isoquinuclidines

A Mannich–aza-Michael reaction in which both an electrophile and a nucleophile are activated provides a simple, highly enantioselective route to isoquinuclidines (**1**) from imines (**2**) and cyclohexenone (**3**). A feature of the reaction is the interplay of an achiral and a chiral Brønsted acid, which enable the asymmetric reaction process by cooperative activation of the enone and the imine.

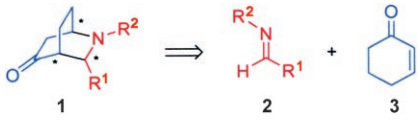

Natural Products

M. Müller, B. Kusebauch, G. Liang, C. M. Beaudry, D. Trauner,* C. Hertweck* ——— **7835 – 7838**

Photochemical Origin of the Immunosuppressive SNF4435C/D and Formation of Orinocin through "Polyene Splicing"

A splice from life: A photoinduced rearrangement cascade with alternating photochemical and thermal pericyclic steps leads to a novel pyrone compound with chain-contracted polyketide backbone (orinocin (**2**)). The excision of three propionate units from the polyene precursor, spectinabilin (**1**), proceeds via the immunosuppressive SNF4435C/D and yields an unusual triketide, mesitylene (see scheme).

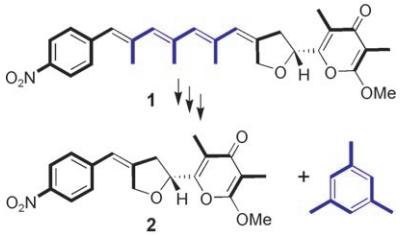

Amination

V. del Amo, S. R. Dubbaka, A. Krasovskiy, P. Knochel* ——— **7838 – 7842**

General Preparation of Primary, Secondary, and Tertiary Aryl Amines by the Oxidative Coupling of Polyfunctional Aryl and Heteroaryl Amidocuprates

A tolerant reaction: Functionalized tertiary amines have been prepared by the oxidative coupling of amidocuprates with chloranil used as the oxidant (see Scheme). A high tolerance of functional groups and insensitivity to steric hindrance characterize this general amination reaction.

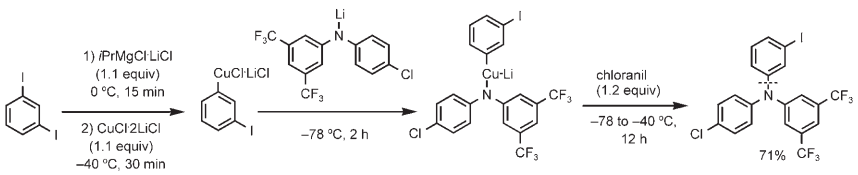

© 2006 Wiley-VCH Verlag GmbH & Co. KGaA, Weinheim

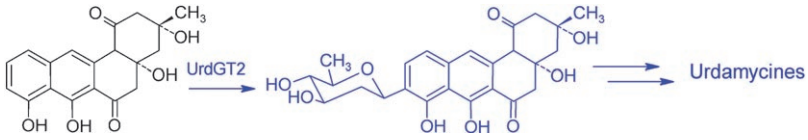

The transfer of the gene *urdGT2*, which encodes a C-glycosyltransferase in the urdamycin pathway, into the *lnd*-minus mutant of the landomycin (*lnd*) biosynthetic pathway indicates the difference in the first glycosylation step in the urdamycin and landomycin pathways. It also reveals indirectly the acceptor substrate of UrdGT2 (see scheme) and gives evidence of greatly relaxed substrate specificity of all *lnd* glycosyltransferases except LndGT2.

Combinatorial Biosynthesis

I. Baig, M. Kharel, A. Kobylyanskyy, L. Zhu, Y. Rebets, B. Ostash, A. Luzhetskyy, A. Bechthold, V. A. Fedorenko,* J. Rohr* _____ **7842 – 7846**

On the Acceptor Substrate of C-Glycosyltransferase UrdGT2: Three Prejadomycin C-Glycosides from an Engineered Mutant of *Streptomyces globisporus* 1912 Δ*lndE*(*urdGT2*)

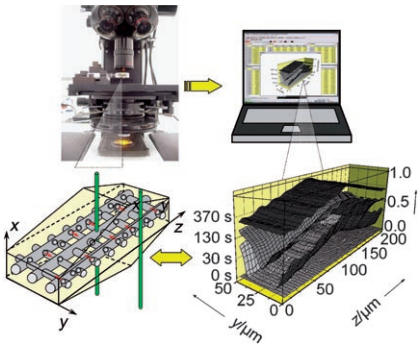

How many guests? Interference microscopy is used to monitor the concentration of guest molecules in a ferrierite zeolite. The micropore diffusivities are determined as a function of loading through the microscopic application of Fick's second law. This method can be used to study isotropic and anisotropic diffusion, as well as to locate and quantify surface barriers and internal defects.

Host–Guest Systems

J. Kärger,* P. Kortunov, S. Vasenkov, L. Heinke, D. B. Shah, R. A. Rakoczy, Y. Traa, J. Weitkamp* _____ **7846 – 7849**

Unprecedented Insight into Diffusion by Monitoring the Concentration of Guest Molecules in Nanoporous Host Materials

Supporting information is available on the WWW (see article for access details).

A video clip is available as Supporting Information on the WWW (see article for access details).

Sources

Product and Company Directory

You can start the entry for your company in "Sources" in any issue of ***Angewandte Chemie***.

If you would like more information, please do not hesitate to contact us.

Wiley-VCH Verlag – Advertising Department
Tel.: 0 62 01 - 60 65 65
Fax: 0 62 01 - 60 65 50
E-Mail: MSchulz@wiley-vch.de

Service

Keywords _____ ***7850***

Authors _____ ***7851***

Preview _____ ***7853***

© 2006 Wiley-VCH Verlag GmbH & Co. KGaA, Weinheim

Corrigendum

Switching On Cell Adhesion with Microelectrodes

C. Zhao, I. Witte,
G. Wittstock* _____ **5469–5471**

Angew. Chem. Int. Ed. **2006**, *45*

DOI 10.1002/anie.200601151

With sincere regret, we would like to inform the readers that our recent Communication quoted from Nishizawa and co-workers[1] without marking it as such. This refers in particular to the first two sentences of our paper. In addition, phrases in lines 20–30 and 66–71 are very similar to parts of references [1] and [2] without indication of their origin.

Moreover, we would like to emphasize that the scientific concept of the electrochemical drawing of cell-adhesive regions, which enables the multipatterning of different cells, was proposed and demonstrated for the first time by Nishizawa and co-workers in reference [2]. This statement was deleted in the process of shortening the manuscript and was not reinserted, and our claim of introducing an alternative strategy (lines 73–76) is misleading. References [1] and [2] were cited as reference [11] in our Communication only in the context of a side aspect of the study.

The reports by Nishizawa and co-workers in references [1] and [2] describe the local generation of HBrO (or Br_2) in a scanning electrochemical microscopy (SECM) configuration to alter a cell-repellent surface that consists of a physisorbed serum albumin layer on a glass support.[1] Subsequently, adhesion and motility of HeLa cells could be observed at these regions.[2] The method could be used for stepwise introduction of new HeLa cell populations.[2] The local oxidative treatment of surfaces by a bromide oxidation pulse in an SECM apparatus was already introduced much earlier by Mandler and Bard[3] and since then has been used for many surface modifications.

Our Communication described the use of chemisorbed oligoethylene glycol terminated alkanethiols that are bound as a self-assembled monolayer to a gold support. Such layers are frequently used as a standard surface that resists protein adsorption and cell adhesion. We demonstrated that the monolayer can be switched to allow protein adsorption and cell adhesion by local treatment with Br_2 as described in references [1] and [2]. We used the permeability change of the self-assembled monolayer during the patterning to characterize the modified surfaces by feedback imaging in SECM. In this way, we could characterize independently the extent of the modified area (which is not identical) after Br_2 treatment, after the adsorption of proteins, and after cell adhesion.

Finally, we reemphasize our regret at this oversight and wish to give full credit to Nishizawa and co-workers for the idea of using a local oxidative treatment to lift the cell-repellent properties of surfaces through the recent improvements and applications that they have described.[4–6]

[1] H. Kaji, K. Tsukidate, T. Matsue, M. Nishizawa, *J. Am. Chem. Soc.* **2004**, *128*, 15026–15027.
[2] H. Kaji, M. Kanada, D. Oyamatsu, T. Matsue, M. Nishizawa, *Langmuir* **2004**, *20*, 16–19.
[3] D. Mandler, A. J. Bard, *J. Electrochem. Soc.* **1990**, *137*, 2468–2472.
[4] H. Kaji, K. Tsukidate, M. Hashimoto, T. Matsue, M. Nishizawa, *Langmuir* **2005**, *21*, 6966–6969.
[5] H. Kaji, T. Kawashima, M. Nishizawa, *Langmuir*, DOI: 10.1021/la0610654, published on web 07/12/2006.
[6] H. Kaji, M. Hashimoto, M. Nishizawa, *Anal. Chem.* **2006**, *78*, 5469–5473.

 © 2006 Wiley-VCH Verlag GmbH & Co. KGaA, Weinheim

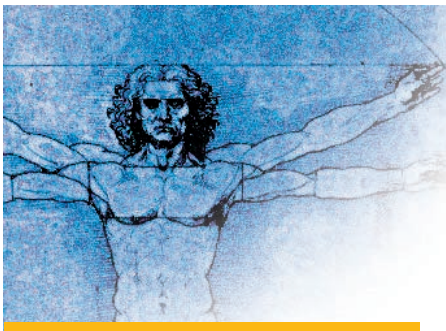

Awarded...

I. Bertini receives Basolo Medal

Ivano Bertini (University of Florence, Italy) received the Fred Basolo Medal for outstanding achievements in the area of inorganic chemistry. The prize is awarded by the Northwestern University (Evanston, IL, USA) and partly sponsored by the Chicago section of the American Chemical Society. The award lecture was titled "Metal Ions in the Proteome". For over 30 years, Bertini has researched structure–property relationships in metalloproteins by means of biophysical methods, especially NMR spectroscopy. Since 1990, he has dedicated himself increasingly to structural biology and is a pioneer in the use of genome databanks. He recently described the structural interplay between calcium and copper in binding to the protein S100A13 in *Angewandte Chemie*[1a] and discussed the possibilities of NMR spectroscopy of paramagnetic metalloproteins in *ChemBioChem*.[1b] He is on the advisory boards of *ChemBioChem* and *ChemMedChem*, and has served as Editor or Chairman of the Editorial Board of the *European Journal of Inorganic Chemistry* since its inception in 1998.

I. Bertini

Bertini completed his PhD in 1964 and his habilitation in 1969 at the University of Florence. In 1975 he became professor for general and inorganic chemistry and in 1999 he founded the Center for Magnetic Resonance of the University of Florence, which contains an impressive collection of NMR spectrometers. The Center is surrounded by many laboratories for biotechnology and drug discovery.

Otto Klung Weberbank Prize for I. Krossing

Ingo Krossing (University of Freiburg, Germany) received the Otto Klung Weberbank Prize for his outstanding work in the synthesis and application of novel, very weakly coordinating anions. The €50000 prize is awarded by the Free University of Berlin and Weberbank in alternate years for chemistry and physics. "Fact or fiction?" is the question Krossing asks in a recently published review article on weakly coordinating anions in *Angewandte Chemie*.[2a] The receipt of a highly endowed prize for young scientists is now a fact and will allow him to extend his research on weakly coordinating anions, their combination with reactive cations, and their applications. He recently reported in *Angewandte Chemie* on the synthesis and characterization of a donor-free silver(I) alkoxide and silyl oxide.[2b]

I. Krossing

Krossing received his PhD in 1997 in the group of H. Nöth at the Ludwig Maximilian University of Munich and subsequently worked as a Feodor Lynen Fellow at the University of New Brunswick in Saint John (Canada). As a recipient of a Liebig grant, he completed his habilitation in 2002 at the University of Karlsruhe, where he stayed until 2004 as a Heisenberg Fellow. He then took up an assistant professorship the Ecole Polytechnique Fédérale de Lausanne (Switzerland) and became professor for inorganic chemistry at the Albert Ludwig University of Freiburg in 2006.

... and announced

C.-H. Wong becomes President of Academia Sinica

Chi-Huey Wong (Scripps Institute, La Jolla, CA, USA) has become the new president of Academia Sinica in Taiwan, where he will have big shoes to fill as he replaces the chemistry Nobel laureate of 1986, Yuan-Tseh Lee. Wong studied chemistry at the Taiwan National University and received his PhD in 1982 from the Massachusetts Institute of Technology (Cambridge, MA, USA) in the research group of G. M. Whitesides. He moved, together with his doctoral advisor, within Cambridge to Harvard University to undertake postdoctoral research and in 1983 became an assistant professor at Texas A&M University. He rose to full professor there before answering the call in 1989 to the Scripps Institute. He has also led the Genomics Research Center of the Academia Sinica since 2003.

C.-H. Wong

Wong's research interests cover a broad spectrum of bioinorganic and synthetic chemistry, from interactions of small molecules with DNA, and the design and synthesis of inhibitors for receptors and enzymes, to the development of synthetic methods such as programmable one-pot reactions for the synthesis of oligosaccharides and glycoarrays, as well as the optimization of enzyme-catalyzed reactions such as for the synthesis of glycoproteins. This year he published articles on the one-pot synthesis of a tumor-associated antigen octasaccharide as well as the three-step synthesis of sialic acids and their derivatives in *Angewandte Chemie*.[3]

[1] a) F. Arnesano, L. Banci, I. Bertini, A. Fantoni, L. Tenori, M. S. Viezzoli, *Angew. Chem.* **2005**, *117*, 6499; *Angew. Chem.* **2005**, *44*, 6341; b) I. Bertini, C. Luchinat, G. Parigi, R. Pierattelli, *ChemBioChem* **2005**, *6*, 1536.

[2] a) I. Krossing, I. Raabe, *Angew. Chem.* **2004**, *116*, 2116; *Angew. Chem. Int. Ed.* **2004**, *43*, 2066; b) A. Reisinger, D. Himmel, I. Krossing, *Angew. Chem.* **2006**, *118*, 7153; *Angew. Chem. Int. Ed.* **2006**, *45*, 6997.

[3] a) J.-C. Lee, C.-Y. Wu, J. V. Apon, G. Siuzdak, C.-H. Wong, *Angew. Chem.* **2006**, *118*, 2819; *Angew. Chem. Int. Ed.* **2006**, *45*, 2753; b) Z. Hong, L. Liu, C.-C. Hsu, C.-H. Wong, *Angew. Chem.* **2006**, *118*, 7577; *Angew. Chem. Int. Ed.* **2006**, *45*, 7417.

DOI: 10.1002/anie.200604490

© 2006 Wiley-VCH Verlag GmbH & Co. KGaA, Weinheim

Mesoporous polymers

DOI: 10.1002/anie.200602489

Surfactant-Templated Mesoporous Materials: From Inorganic to Hybrid to Organic

*Yunfeng Lu**

Keywords:
mesoporous materials · organic–inorganic hybrid composites · polymers · self-assembly · template synthesis

Many fascinating materials in nature are composed of ordinary building components that are precisely defined with unique functions and properties. In recent years, rapid advances in bioinspired synthesis have been made by mimicking natural design. Self-assembly is emerging as one of the most promising approaches towards the synthesis of new materials with designed structures and functions.

Self-assembly, generally, refers to a spontaneous organization of building blocks driven by noncovalent interactions, such as hydrogen bonding, hydrophobic interactions, π–π stacking, and electrostatic interactions. The building blocks can range from predesigned molecules (for example, organic molecules, oligomers, and polymers), molecular clusters (for example, inorganic and hybrid organic–inorganic clusters), and low-dimensional objects (for example, nanoparticles, nanorods, and nanowires) to more complicated components. The existing assembled systems span two-dimensional systems, such as self-assembled monolayers (SAMs), three-dimensional systems, such as nanocomposites, and more complicated hierarchical systems. Similarly to building a machine from parts, an assembly process spontaneously arranges building blocks that carry intrinsic structural and functional information. Thus, the functionalities of the assembled systems greatly exceed those of the individual building blocks.

Among the existing assembled systems, the most cited over the past decade are probably the surfactant-directed mesostructured materials. Surfactants, generally known as soaps or detergents, are used extensively in industry and in daily life. Their unique functions arise from their amphiphilic molecular architecture and their capability to self-organize into micelles, rods, liquid crystals, and other supramolecular assemblies.[1] Until the discovery of the cooperative assembly of surfactants with silicates by Mobil scientists in 1992, which led to the synthesis of MCM-41 and the M41S family of mesoporous materials,[2,3] surfactants were almost exclusively used as surface and interface modifiers. This discovery sparked a decade of extensive research on surfactant-directed assembly, the use of surfactant to direct and assemble building blocks into mesoscopically ordered structures.[4] More specifically, noncovalent interactions between the surfactant and the building blocks drive the organization of the building blocks around supramolecular surfactant structures (Figure 1). Simultaneous or subsequent reactions (for example, a condensation of inorganic clusters, or an electrochemical reduction) create covalent or metallic bonds among the building blocks, resulting in a mesostructured nanocomposite containing liquid-crystalline surfactant. The removal of the surfactant by calcination or solvent extraction creates a mesoporous material with a templated pore structure. The size, shape, and intermolecular interactions of the mesoporous material can be tuned to produce hexagonal, cubic, lamellar, and other mesostructures.[5]

Experimentally, the synthesis of such materials is based on either a solution assembly[2,5–8] or an evaporation-induced self-assembly (EISA).[9–12] The solution-assembly approach involves the reaction of building blocks in a surfactant-containing solution, in which the surfactant concentration greatly exceeds the critical micelle concentration. The EISA approach utilizes precursor solutions containing building blocks and surfactant, in which the surfactant concentration is above or below the critical micelle concentration. Solvent evaporation during a coating, spraying, fiber-spinning, or microwriting process increases the surfactant and

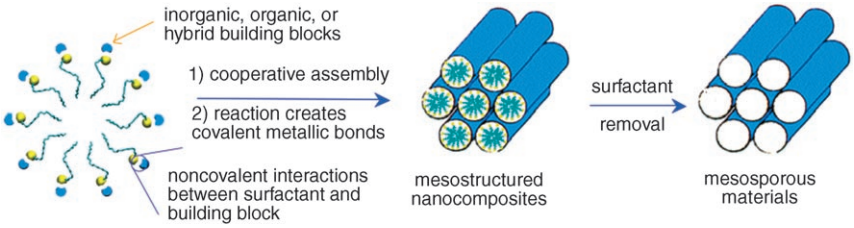

Figure 1. Surfactant-directed formation of mesoporous materials from inorganic, hybrid, or organic building blocks. See text for details.

[*] Prof. Y. Lu
Chemical and Biomolecular Engineering Department
University of California
Los Angeles, CA 90095 (USA)
Fax: (+1) 310-206-4107
E-mail: luucla@ucla.edu

InterScience
© 2006 Wiley-VCH Verlag GmbH & Co. KGaA, Weinheim

building-block concentrations and promotes their assembly into ordered mesostructures. Compared to the solution-assembly approach, the EISA approach allows a more rapid formation of mesostructured materials in the forms of thin films, particles, fibers, and arrays for device applications.

The judicious selection of building blocks allows the synthesis of mesoporous materials with desired chemical compositions. Inorganic mesoporous materials, such as mesoporous ceramics (for example, silica, titania, zirconia, alumina, niobium oxide, and metal phosphates), semiconductors (for example, metal sulfides), and metals (for example, platinum and palladium), can be successfully synthesized from inorganic complexes or clusters.[4] Similarly, hybrid mesoporous materials, such as mesoporous organosilicas, can be synthesized from hybrid silicate clusters containing covalently bonded organic ligands.[13] Extending the assembly process from inorganic and hybrid building blocks to organic building blocks, however, imposes great challenges.

Recently, a breakthrough in mesoporous polymer synthesis was achieved by Zhao and co-workers,[14,15] who used oligomers synthesized from the reaction of formaldehyde with phenol,[14,15] resorcinol,[16] or pholorglucinol[17] as building blocks. Phenolic oligomers, for example, can be readily prepared by heating phenol and formaldehyde in a molar ratio of 1:2 in a basic aqueous medium at 70 °C for 60 min. After the reaction, the solution is neutralized with hydrochloric acid, and the water is removed under vacuum, resulting in oligomers with molecular weights of less than 500 g mol^{-1}. Similarly, pholorglucinolic oligomers can be prepared by heating pholorglucinol with formaldehyde in acidic water–ethanol solution at room temperature. Like silicate clusters, these oligomers contain a large number of hydrophilic hydroxyl groups, which allow them to hydrogen bond with a Pluronic surfactant (a block copolymer of formula $EO_mPO_nEO_m$; EO = ethylene oxide, PO = propylene oxide). Pholorglucinolic oligomers afford stronger collective hydrogen bonding with the Pluronic surfactant than do phenolic oligomers, owing to the presence of three hydroxyl groups on pholorglucinol and only one on phenol.[17] Furthermore, the oligomers undergo thermopolymerization, which is comparable to silicate condensation, at intermediate temperatures to form cross-linked polymers.

Bakelite, a thermosetting phenol–formaldehyde resin, was the first plastic to be made from a synthetic polymer. The material is formed by the reaction of phenol and formaldehyde under heat and pressure, typically in the presence of wood flour. By following a similar scheme, mesoporous Bakelite can be readily prepared through the assembly of oligomers with surfactant, followed by polymerization and surfactant removal. More specifically, starting from an ethanol solution of phenolic oligomers and a Pluronic surfactant, EISA during a casting process leads to ordered surfactant–oligomer nanocomposite thin films (Figure 2).[15] Subsequent heating at 100 °C for 24 h polymerizes the oligomers and leads to mesostructured surfactant–polymer nanocomposites containing liquid-crystalline surfactant. Decomposition of the surfactant by heating at 350 °C for 5 h in nitrogen creates mesoporous polymer thin films.

Mesoporous polymers can also be prepared from phenolic oligomers and a Pluronic surfactant by the solution-assembly approach.[14] Interestingly, solution assembly only occurs at pH 8.5,

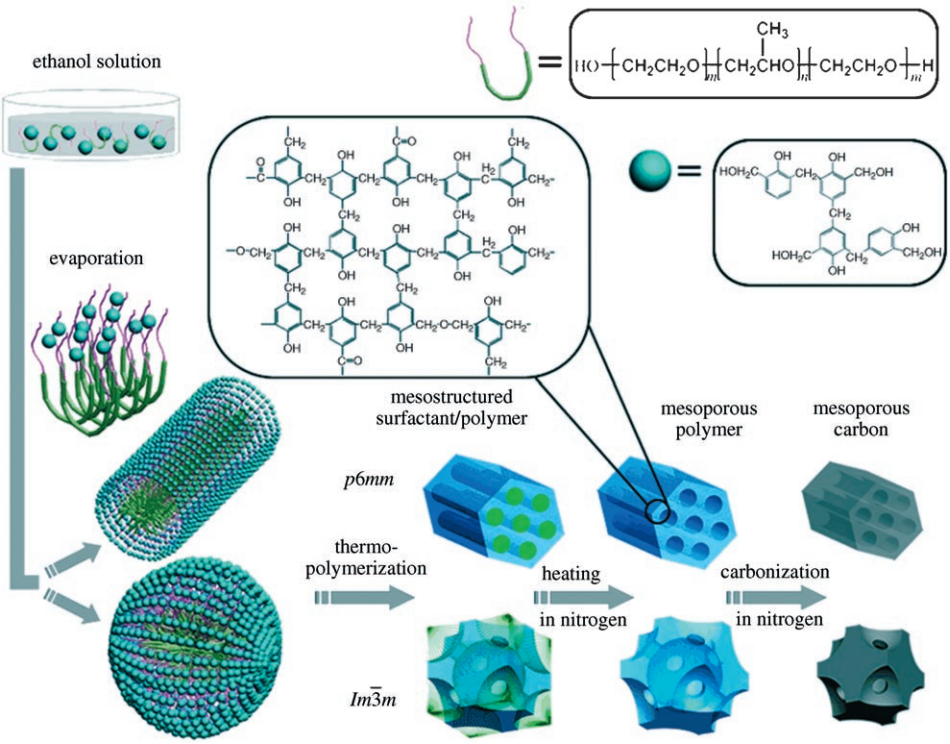

Figure 2. Surfactant-directed formation of a mesoporous phenol–formaldehyde polymer from oligomer building blocks. Mesoporous carbon is obtained after carbonization. See text for details. Adapted from reference [15].

© 2006 Wiley-VCH Verlag GmbH & Co. KGaA, Weinheim

since the phenolate anions formed at pH > 9 can destroy the hydrogen bonding between the surfactant and the oligomers, whereas a lower pH slows the polymerization dramatically.[14] As in the synthesis of inorganic or hybrid mesoporous materials, selection of the type and concentration of surfactant allows precise control over the resulting mesostructure. For example, mesoporous polymers with ordered two-dimensional hexagonal (*p6mm*),[15] three-dimensional cubic (*Im*$\bar{3}$*m* and *Ia*$\bar{3}$*d*),[14,15,17] or lamellar structures[15] can be synthesized using Pluronic surfactant F127 ($EO_{107}PO_{70}EO_{107}$) or P123 ($EO_{20}PO_{70}EO_{20}$).

Polymers are perhaps the most commonly used materials in our civilization. The production of polymeric materials with controlled structures and compositions is, therefore, of great importance. Prior to the development of self-assembly syntheses, mesoporous polymers were mainly synthesized by a hard-templating approach. In this approach, a monomer is infiltrated into a hard template (for example, an opal-like colloidal assembly of silica), which is removed after polymerization to give mesoporous polymer networks.[18] The self-assembly approach represents a breakthrough allowing the efficient synthesis of mesoporous polymers with controlled pore structures. More importantly, it refuels mesoporous materials research, as exemplified below.

Synthesis and Applications of Mesoporous Polymers. Over the past decade, research on mesoporous materials has led to advances in the control of pore structure and morphology, the tailoring of pore surface chemistry, and the design of framework composition. The application of this knowledge to the assembly of organic systems has allowed the synthesis of a new family of mesoporous materials with controlled structures and compositions. Such materials may be implemented in catalyst supports, sensors, optics, drug-delivery systems, and microelectronics.

The use of mesoporous polymers to synthesize mesoporous carbon is also noteworthy. Porous carbon materials have important applications as fuel-cell electrodes, catalyst supports, adsorbents, and hydrogen storage materials, among others. The synthesis of porous carbon often involves chemical or physical activation processes that create micropores with a broad size distribution. In addition, the relatively small pore size of the material produced in this manner prevents its use in applications where larger pore sizes are required. Although hard-template approaches have been developed to synthesize mesoporous carbon, these approaches are either time-consuming or produce carbon with a disordered pore structure.[19,20] The use of mesoporous polymers allows the efficient fabrication of mesoporous carbon with controlled pore structure by simply carbonizing the polymer template (Figure 2).[15–17]

Novel Mesoporous Nanocomposites through Multicomponent Assembly. Nanocomposites are of great interest for many applications, owing to their synergic properties. Multicomponent assembly, a process in which a surfactant and two or more other types of building blocks are simultaneously assembled, is a highly efficient approach for the synthesis of mesoporous nanocomposites. To date, the nanocomposites synthesized by this method have been limited to mesoporous organosilicas and hierarchical mesoporous silicas, which were prepared from mixtures of silicates or organosilicates, and other building blocks, such as polymers, surfactants, or inorganic salts.[21] The multicomponent assembly of mixtures of organic oligomers and other building blocks allows the efficient synthesis of mesoporous nanocomposites. This approach allows the pore structure to be controlled by the liquid-crystalline surfactant mesostructure and the composition to be controlled by the relative concentrations of the building blocks. By combining the oligomer building blocks with the vast library of inorganic and hybrid building blocks, numerous mesoporous polymer–inorganic nanocomposites can be synthesized. For example, we have recently reported the synthesis of mesoporous carbon–silica nanocomposites from silicates and phenolic oligomers.[22] The silica-cluster building blocks provide the nanocomposites with chemical stability, whereas the oligomer building blocks provide a high electronic conductivity after the polymerization and carbonization process. Such robust, conductive mesoporous nanocomposites are ideal candidates for fuel-cell electrocatalyst support materials, which could resolve the carbon-corrosion problem of current fuel cells.[23]

Novel Mesoporous Polymers beyond Bakelite. The recent breakthrough by Zhao and coworkers provides new building blocks for the synthesis of mesoporous polymers and nanocomposites. More importantly, it establishes a novel building-block design concept. As stated above, the successful synthesis of the mesoporous polymers is attributed to the hydrogen bonding between the surfactant and the oligomers, as well as to the thermopolymerization that crosslinks the oligomers. As learned from these oligomers, an ideal organic building block should contain moieties that can form strong noncovalent interactions with the surfactant; it should also contain reactive moieties that allow polymerization to form networks of building blocks. By following these criteria, novel organic building blocks may be designed and synthesized, leading to a new generation of mesoporous polymers beyond mesoporous Bakelite.

Looking back over a decade of mesoporous materials research, the field has experienced an evolution from the synthesis of inorganic to hybrid to organic materials. The design, synthesis, and assembly of building blocks with suitable shapes, sizes, interactions, compositions, and functionalities have been the main themes. The judicious selection of building blocks and the precise tuning of interactions between them afford an assembled system with the desired structure and composition. Building materials from simpler components, like a machine from its parts, according to molecular blueprints is still an ambitious goal; nevertheless, the innovative work presented herein has taken us one step further.

Published online: November 7, 2006

[1] J. Israelachvili, *Intermolecular and Surface Forces, 2nd ed.*, Academic Press, San Diego, **1992**.
[2] C. T. Kresge, M. E. Leonowicz, W. J. Roth, J. C. Vartuli, J. S. Beck, *Nature* **1992**, *359*, 710.
[3] J. S. Beck, J. C. Vartuli, W. J. Roth, M. E. Leonowicz, C. T. Kresge, K. D. Schmitt, C. T.-W. Chu, D. H. Olson, E. W. Shep-

 © 2006 Wiley-VCH Verlag GmbH & Co. KGaA, Weinheim

pard, S. B. McCullen, J. B. Higgins, J. L. Schlenker, *J. Am. Chem. Soc.* **1992**, *114*, 10834.
[4] J. Y. Ying, C. P. Mehnert, M. S. Wong, *Angew. Chem.* **1999**, *111*, 58; *Angew. Chem. Int. Ed.* **1999**, *38*, 56.
[5] Q. Huo, D. I. Margolese, G. D. Stucky, *Chem. Mater.* **1996**, *8*, 117.
[6] H. Yang, N. Coombs, G. A. Ozin, *Nature* **1997**, *386*, 692.
[7] Q. Huo, D. I. Margolese, U. Ciesla, P. Feng, T. E. Gier, P. Sieger, R. Leon, P. M. Petroff, F. Schüth, G. D. Stucky, *Nature* **1994**, *368*, 317.
[8] I. A. Aksay, M. Trau, S. Manne, I. Honma, N. Yao, L. Zhou, P. Fenter, P. M. Eisenberger, S. M. Gruner, *Science* **1996**, *273*, 892.
[9] C. J. Brinker, Y. Lu, A. Sellinger, H. Fan, *Adv. Mater.* **1999**, *11*, 579.
[10] Y. Lu, H. Fan, A. Stump, T. L. Ward, T. Reiker, C. J. Brinker, *Nature* **1999**, *398*, 223.
[11] Y. Lu, R. Ganguli, C. A. Drewien, M. T. Anderson, C. J. Brinker, W. Gong, Y. Guo, H. Soyez, B. Dunn, M. H. Huang, J. I. Zink, *Nature* **1997**, *389*, 364.
[12] H. Fan, Y. Lu, A. Stump, S. T. Reed, T. Baer, R. Schunk, V. Perez-Luna, G. P. López, C. J. Brinker, *Nature* **2000**, *405*, 56.
[13] B. Hatton, K. Landskron, W. Whitnall, D. Perovic, G. A. Ozin, *Acc. Chem. Res.* **2005**, *38*, 305.
[14] F. Hang, Y. Meng, D. Gu, Y. Yan, C. Yu, B. Tu, D. Zhao, *J. Am. Chem. Soc.* **2005**, *127*, 13508.
[15] Y. Meng, D. Gu, F. Zhang, Y. Shi, H. Yang, Z. Li, C. Yu, B. Tu, D. Zhao, *Angew. Chem.* **2005**, *117*, 7215; *Angew. Chem. Int. Ed.* **2005**, *44*, 7053.
[16] S. Tanaka, N. Nishiyama, Y. Egashira, K. Ueyama, *Chem. Commun.* **2005**, 2125.
[17] C. Liang, S. Dai, *J. Am. Chem. Soc.* **2006**, *128*, 5316.
[18] A. Stein, *Microporous Mesoporous Mater.* **2001**, *44–45*, 227.
[19] R. Ryoo, S. H. Joo, M. Kruk, M. Jaroniec, *Adv. Mater.* **2001**, *13*, 677.
[20] J. Pang, X. Li, D. Wang, Z. Wu, V. T. John, Y. Lu, *Adv. Mater.* **2004**, *16*, 884.
[21] J. Pang, H. Na, Y. Lu, *Microporous Mesoporous Mater.* **2005**, *86*, 89.
[22] Q. Hu, R. Kou, J. Pang, T. L. Ward, M. Cai, J. Tang, Y. L. Lu, *Chem. Commun.*, in press.
[23] L. M. Roen, C. H. Paik, T. D. Jarvi, *Electrochem. Solid-State Lett.* **2004**, *7*, A19.

 © 2006 Wiley-VCH Verlag GmbH & Co. KGaA, Weinheim

Protein Synthesis

DOI: 10.1002/anie.200602945

Evolving Strategies for Protein Synthesis Converge on Native Chemical Ligation

*Derek Macmillan**

Keywords:
native chemical ligation · peptides · protein synthesis · solid-phase synthesis · thiol auxiliaries

In recent years, there has been an explosion of interest in protein-assembly technologies such as native chemical ligation (NCL)[1] and expressed protein ligation (EPL).[2] NCL involves the chemoselective coupling of two protein fragments, one containing a C-terminal thioester and the other containing an N-terminal cysteine residue. The components combine to give a native peptide bond at the point of ligation (Scheme 1a) and the fact that they do this in aqueous solution, in the absence of protecting groups, has placed this powerful technology at the forefront of protein synthesis. In 1999, a modification of the Kenner sulfonamide safety-catch linker was reported that allowed peptides that had been prepared by using 9-fluorenylmethoxycarbonyl (Fmoc)-based chemistry to be cleaved as thioesters from the solid phase. This solved a long-standing problem in that peptide thioesters were traditionally prepared on a thioester resin by using *tert*-butoxycarbonyl (Boc)-based solid-phase peptide synthesis. The strongly acidic *N*-α-deprotection and resin-cleavage conditions were generally not compatible with many modified peptides such as glycopeptides. On the other hand, the Fmoc chemistry employed for the production of glycopeptides was not compatible with a thioester resin as thioesters were cleaved upon exposure to piperidine. The safety-catch linker therefore allowed access to glycopeptide thioesters for use in NCL by using Fmoc chemistry. This was first demonstrated by Bertozzi and co-workers in their synthesis of diptericin.[3] Since then, several other indirect methods have been reported for the production of peptide thioesters by using Fmoc chemistry. This advance, when combined with the development of EPL,[2] a reaction analogous to NCL but employing microbially generated thioester or N-terminal cysteine components, has delivered protein chemistry to the masses by overcoming the intolerance to posttranslational modifications and the size limitations of peptide fragments that can be efficiently synthesized (which is approximately 50 amino acid residues). This combination of developments has opened the door to new research opportunities in chemical biology and materials science. NCL has been particularly embraced by researchers pursuing posttranslationally modified (i.e. glycosylated or phosphorylated) proteins because sufficient homogenous material for analysis is not readily available from biological sources. NCL is particularly attractive as it also allows the construction of completely native structures through total chemical synthesis. In the case of glycosylated proteins, synthetic chemists can have complete control over the position, number, and type of oligosaccharides that are present within the sequence. Many methods that rely on targeting microbially derived proteins are not site specific (e.g. the targeting of lysine residues through reductive amination) or give rise to non-natural structures (e.g. proteins that are modified selectively on cysteine with α-haloacetamides).

Despite these advances, certain limitations of NCL and EPL have persisted. One limitation is the requirement for an N-terminal cysteine as cysteine residues are seldom conveniently distributed throughout a peptide sequence so as to facilitate NCL. Furthermore, the method is not fully convergent and multiple peptide fragments are joined in a linear fashion from the C terminus towards the N terminus. This is because the C-terminal thioester is not generally compatible with an N-terminal cysteine residue when present in the same molecule and under typical reaction conditions. Hence, multiple ligation and deprotection cycles are required to assemble very long peptide sequences. Some recent reports that address these limitations are highlighted below.

The first limitation (the requirement for cysteine residues) was initially addressed in the late 1990s through the development of thiol auxiliaries such as **1**[4] and **2**[5] (Figure 1), which, when attached to the N terminus of a synthetic peptide, can facilitate ligation and can be readily removed afterwards (Scheme 1b) upon treatment with trifluoroacetic acid (TFA). Surprisingly, thiol auxiliaries have not been successfully used widely and there has been considerable debate over their scope (which amino acids are tolerated as terminal residues on the thioester or the auxiliary-linked component), the size of the transition state, and the ease of cleavage. In a recent report, Danishefsky and co-workers employed the 4,5,6-trimethoxy-2-mercaptobenzyl (Tmb) thiol auxiliary (**2**), which was originally developed by Dawson and co-workers,[5] to unite glycopeptides that contain asparagine-linked saccharides

[*] Dr. D. Macmillan
Department of Chemistry
University College London
Christopher Ingold Laboratories
20 Gordon Street, London WC1H 0AJ (UK)
E-mail: d.macmillan@ucl.ac.uk

InterScience
© 2006 Wiley-VCH Verlag GmbH & Co. KGaA, Weinheim

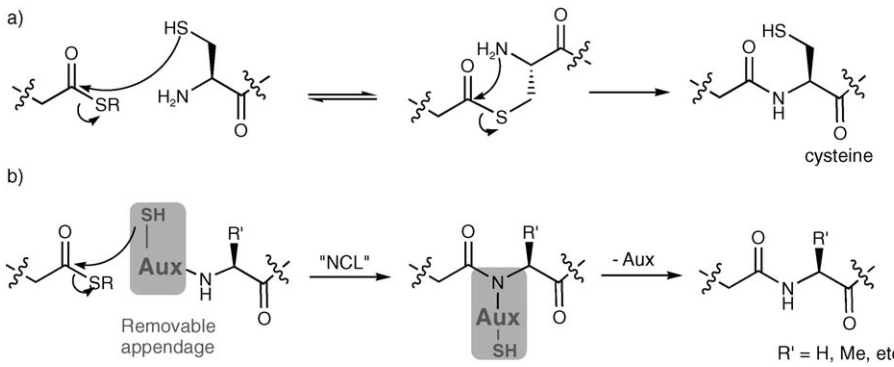

Scheme 1. NCL and auxiliary-mediated ligation compared. a) The commonly accepted mechanism of NCL, a rate-determining transthioesterification followed by a rapid S→N acyl shift, which occurs via a five-membered-ring transition state. b) Auxiliary-mediated ligation. A thiol appendage orchestrates the NCL-type reaction and is ultimately cleaved, permitting ligation at junctions other than X-Cys. Aux = auxiliary.

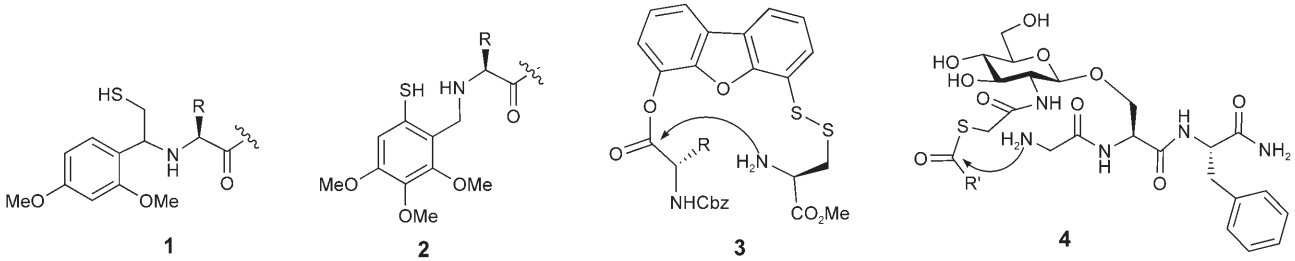

Figure 1. Auxiliaries for NCL (**1**), the 1-aryl-2-mercaptoethyl auxiliary class[4] (**2**), the Tmb auxiliary class[5] (**3**), dibenzofuran scaffold for studies of the prior thiol capture ligation developed by Kemp et al.[8] (**4**). "Carbohydrate-templated ligation" refers to the ligation that utilizes a carbohydrate template to facilitate a ligation as depicted in **4** and as reported by Wong and co-workers.[9] With the exception of **3**, all operate through a thiol/thioester/S→N acyl shift sequence and can be considered analogous to NCL. Cbz = benzyloxycarbonyl.

across a glycine–glutamine ligation junction.[6] The ligation was successfully achieved in over 58% yield. This further demonstrated that such auxiliaries are capable of joining peptides at ligation junctions other than glycine–glycine, but perhaps underscores the requirement that at least one of the residues should be glycine. Hence, this solution to the N-terminal cysteine requirement appears to come with a new collection of idiosyncrasies and limitations. When the α-carbon atom of the thioester or the auxiliary-linked amino acid component is substituted, then the acyl transfer (rather than the transthioesterification) appears to become rate limiting, and thioester hydrolysis competes more effectively. Interestingly, it was also noted that the Gly–Gln ligation product was contaminated with a species of identical mass after auxiliary cleavage. The resultant structure was assigned as thioester **5** (Scheme 2), which had presumably been formed through an N→S acyl shift, driven by the irreversible protonation of the benzylic amine under the acidic auxiliary cleavage conditions. Methylation of the thiol by using methyl-*p*-nitrobenzenesulfonate prior to auxiliary cleavage completely eradicated this deleterious (yet possibly rather prolific)[7] side reaction allowing a 17-residue glycopeptide containing two *N*-linked saccharides to be isolated (Scheme 3). Although it is certainly possible that use of this thiol capping procedure may reenamor this class of auxiliary to many users, a significant limitation remains for all auxiliaries in that they are currently only applicable to synthetic peptides. This is because an efficient method for the introduction of thiol auxiliaries to the N terminus of an expressed protein is yet to be reported. Early work by Kemp et al.[8] on the prior thiol capture ligation strategy suggested that "auxiliaries", such as the dibenzofuran scaf-

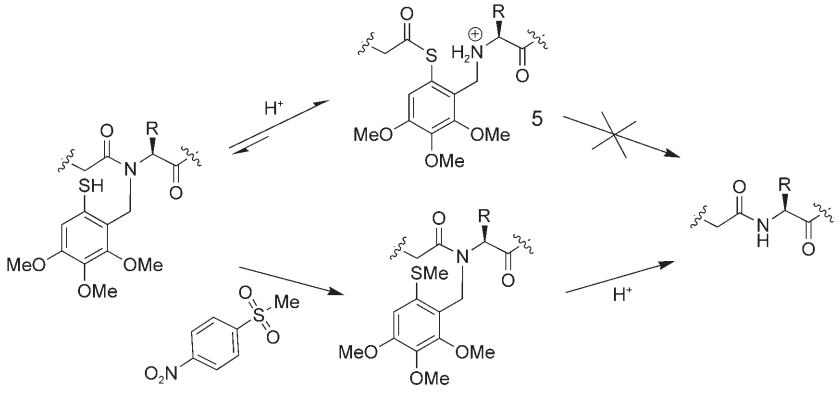

Scheme 2. Unanticipated N→S acyl shift to afford **5** results in inefficient cleavage of the trimethoxybenzyl auxiliary. Methylation of the free thiol prior to cleavage increases the yield of the isolated ligated peptide.[6]

© 2006 Wiley-VCH Verlag GmbH & Co. KGaA, Weinheim

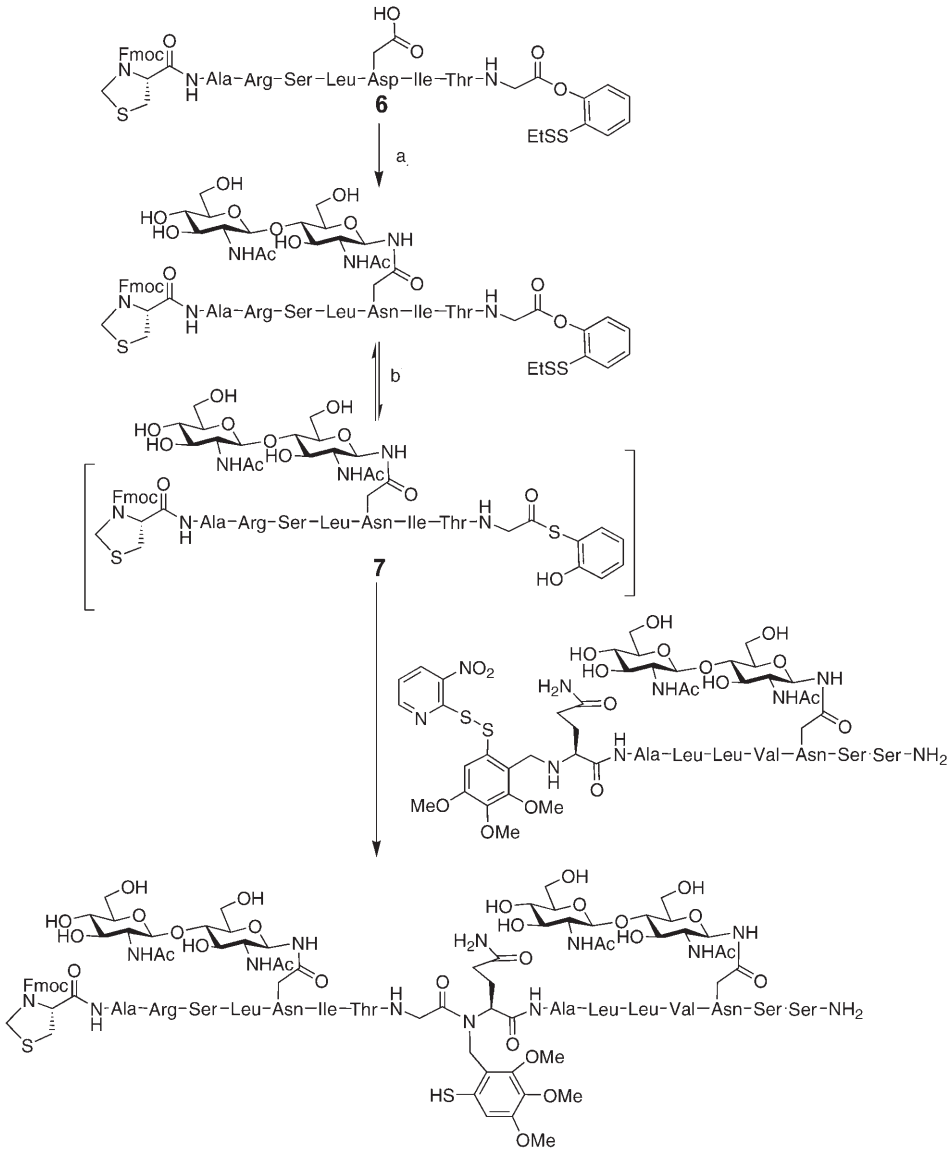

Scheme 3. A trifunctional peptide prepared by Danishefsky and co-workers.[6] The phenolic ester is stable while the glycosylamine is coupled to the selectively deprotected Asp residue. Reduction of the disulfide bond liberates the thiol, which, through an O→S acyl shift, ligates to an auxiliary-linked glycopeptide. Unmasking of the N-terminal cysteine residue enables further NCL reaction. Reagents/conditions: a) HATU, DIPEA, DMSO, 72%, b) TCEP, DMF, Na_2HPO_4, 58%. HATU = *O*-(7-azabenzotriazol-1-yl)-*N*,*N*,*N*',*N*'-tetramethyluronium hexafluorophosphate, DIPEA = diisopropylethylamine, DMSO = dimethyl sulfoxide, TCEP = tris(2-carboxyethyl)phosphane hydrochloride, DMF = *N*,*N*-dimethylformamide.

fold **3**, need only be employed to bring about a high local concentration of each component. It is not surprising that those auxiliaries that allow ligation to proceed by five- (as in NCL) or six-membered-ring transition states should be more efficient, and as a result, research has been focused on this area in recent years. Recently, however, Wong and co-workers reported a sugar-assisted glycopeptide ligation which proceeds via a 14-membered-ring transition state (**4**, Figure 1), which is a considerable deviation from this paradigm.[9] The ligation is facilitated by the presence of a thiol "handle" on the *N*-acetyl moiety of a 2-acetamido-2-deoxy sugar that is linked through a β-*O*-glycosidic linkage to a serine residue. The serine residue is positioned as the penultimate residue in the amino acid sequence. Ligation to model glycine, histidine, alanine, and valine thioesters was demonstrated. In each case, the N-terminal residue (adjacent to the glycoamino acid) was glycine, though the authors state that alanine and serine are tolerated in this position and predict that some templating effect of the carbohydrate is responsible for the efficiency of the ligation. Although this report describes an interesting and potentially traceless alternative to thiol auxiliaries (if used in conjunction with a glycosidase), many factors including the importance of the stereochemistry of the glycosidic linkage, the scope (do alternative glycopeptide linkages have similar templating ability?), and the importance of the N-terminal amino acid residue (the authors noted that the ligation was unsuccessful in the absence of the N-terminal

 © 2006 Wiley-VCH Verlag GmbH & Co. KGaA, Weinheim

residue) still need to be explored. It is likely that the method will not be generally applicable to glycoprotein synthesis as the thiol handle needs to be desulfurized to regenerate the carbohydrate *N*-acetyl group and this is not compatible with any side-chain thiols of cysteine residues that may be present in the target peptide sequence.

Recently, the issue of convergence and NCL has been tackled on two fronts by the Kent and Danishefsky laboratories. In 2004, Danishefsky and co-workers reported the use of a peptide C-terminal phenolic ester equipped with a disulfide protected *o*-thiol group for use in glycopeptide synthesis and chemical-ligation experiments.[10] By using this phenolic ester, short complex glycopeptide sequences could be prepared in solution, thereby avoiding exposure to the acidic cleavage conditions commonly encountered in solid-phase peptide synthesis protocols that may damage particularly labile glycosidic linkages. Oligosaccarides could then be coupled to selectively deprotected aspartic acid residues within the peptide sequence. This was significant as coupling of a glycosyl amine with side chain acids was unlikely to proceed efficiently in the presence of a C-terminal thioester while the phenolic ester remains intact. In more-recent work,[6] Danishefsky and co-workers have prepared the trifuctional peptide **6** (Scheme 3) for use in sequential chemical-ligation experiments. Following attachment of the disaccharide chitobiose, the glycopeptide was exposed to tris-carboxyethyl phosphine (TCEP), which reduced the disulfide bonds in both the acyl-transfer donor and auxiliary-linked acceptor. Through a subsequent O→S acyl shift, the thioester **7**, which participates in an NCL-type reaction, was transiently produced. A solid-phase method for the production of thioesters through an O→S acyl shift has also been reported.[11]

The Kent laboratory has focused on the inherent differences in reactivity between alkyl thioesters and aryl thioesters in the development of kinetically controlled ligations. This difference in reactivity can mainly be attributed to the pK_a of the thiol component of the thioester (pK_a thiophenol = 6.6, pK_a 2-mercaptoethanesulfonic acid (MESNA) = 9.2), hence, aryl thiols are better leaving groups. Aryl thioesters are more reactive but are often produced in situ by the addition of, for example, excess thiophenol to an alkyl thioester derived from solid-phase peptide synthesis. By using the new linker (**8**), which facilitates the quantitative preformation of aryl thioesters by using Boc-based solid-phase peptide synthesis, Kent and co-workers demonstrated that when peptide components containing an N-terminal cysteine residue and an alkyl thioester react with an aryl thioester fragment (in the absence of any aryl thiol additives), the ligation then proceeds in high yield leaving the alkyl thioester intact.[12] Interestingly, the 4-mercaptophenyl acetic acid **9** employed in the linker unit (**8**) was also recently observed to be the most efficient aryl thiol catalyst for use in regular NCL experiments.[13]

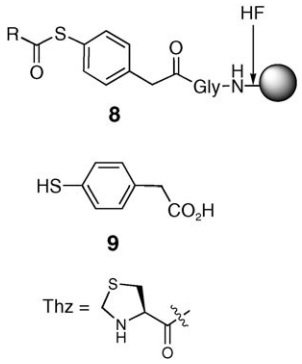

The difference in reactivity between alkyl and aryl thioesters has been applied to the assembly of a small 46-mer peptide called crambin. To demonstrate the principle, crambin was assembled by using six fragments and only two protecting groups.[14] In this report, the aryl thioesters were prepared through exchange of alkyl thioesters upon exposure to thiophenol (0.2% v/v; pH 6.8) for 12 h in approximately 90% yield. With the desired alkyl and aryl thioesters in hand, the peptide sequence was assembled by using five sequential ligation reactions (Scheme 4) at pH 6.8 in 6 M guanidine hydrochloride and in the absence of added thiophenol. The yield for ligation 1 was 71% (including the removal of the thiazolidine (Thz) protecting group, which was conducted in the same pot), ligation 2 proceeded in 50% yield, ligation 3 in 80% yield (or 40% overall when conducted in the same pot as ligation 4), and finally ligation 5 and folding to the native crambin structure was completed in 62% yield. Intriguingly, the N-terminal cysteine residues were unmasked by the

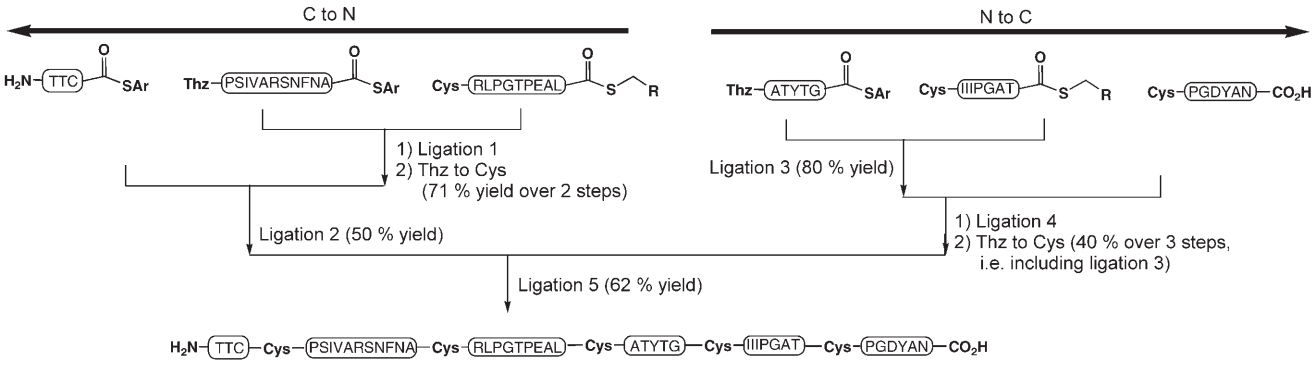

Scheme 4. Total synthesis of crambin employing five sequential chemical ligations.[14] Kinetically controlled ligations were conducted in 6 M guanidine hydrochloride in sodium phosphate buffer solution (pH 6.8) containing TCEP in either the N to C or C to N direction. Deprotection of the thiazolidine (Thz) protecting groups on the N-terminal cysteine residues was accomplished by addition of MeO-NH_2·HCl to the reaction mixture.

 © 2006 Wiley-VCH Verlag GmbH & Co. KGaA, Weinheim

addition of methoxylamine hydrochloride to the reaction mixture with no impact on the C-terminal thioester as the pH of the reaction was concomitantly reduced to pH 4. Cyclic peptides derived from the intramolecular reaction between the cysteine and thioester and the oligomeric products from the intermolecular concatenation of the bifunctional starting materials were observed only as trace species (< 2%) in the reaction mixture. It is important to note that there are factors at play in the kinetically controlled synthesis of crambin other than merely the thiol leaving group. The reactivity of the aryl thioesters was further enhanced by its placement at the position of sterically undemanding amino acids (Gly and Ala), whereas the reactivity of alkyl thioesters was further reduced by placement at bulky and β-branched amino acids (Leu and Thr), revealing a further layer of complexity in experimental design.

The addition of EPL and thiol auxiliaries to the NCL armory have allowed it to overcome the more-immediate challenges that have arisen as the demands on the chemistry have increased. An increased understanding of the workings of new and existing thiol auxiliaries should also widen their utility and permit more efficient cysteine-free NCL. Kinetically controlled ligation employing preformed aryl thioesters may allow very large proteins to be prepared more efficiently, but as the preformed aryl thioesters are currently prepared by using Boc-based chemistry, researchers will need to optimize an Fmoc-based alternative if glycosylated and phosphorylated proteins are to benefit from such an advance. The analogous direct synthesis of thioesters (i.e. on a thioester resin) by using Fmoc chemistry is not widely practiced despite some notable successes.[15] Further improvements in this technique will be required if an Fmoc-based synthesis of aryl thioesters is to be realized. When alternative ligation strategies,[16] such the traceless Staudinger ligation[17] and chemoselective decarboxylative peptide ligation,[18] are being developed, it is only appropriate that these limitations are addressed if NCL is to continue to enjoy widespread use.

Published online: November 8, 2006

[1] P. E. Dawson, T. W. Muir, I. Clark-Lewis, S. B. Kent, *Science* **1994**, *266*, 776; P. E. Dawson, S. B. H. Kent, *Annu. Rev. Biochem.* **2000**, *69*, 923.

[2] T. W. Muir, D. Sondhi, P. A. Cole, *Proc. Natl. Acad. Sci. USA* **1998**, *95*, 6705; C. J. Noren, J. M. Wang, F. B. Perler, *Angew. Chem.* **2000**, *112*, 458; *Angew. Chem. Int. Ed.* **2000**, *39*, 450; V. Muralidharan, T. W. Muir, *Nat. Methods* **2006**, *3*, 429.

[3] Y. Shin, K. A. Winans, B. J. Backes, S. B. H. Kent, J. A. Ellman, C. R. Bertozzi, *J. Am. Chem. Soc.* **1999**, *121*, 11684.

[4] P. Botti, M. R. Carrasco, S. B. H. Kent, *Tetrahedron Lett.* **2001**, *42*, 1831.

[5] J. Offer, C. N. C. Boddy, P. E. Dawson, *J. Am. Chem. Soc.* **2002**, *124*, 4642.

[6] B. Wu, J. Chen, J. D. Warren, G. Chen, Z. Hua, S. J. Danishefsky, *Angew. Chem.* **2006**, *118*, 4222; *Angew. Chem. Int. Ed.* **2006**, *45*, 4116.

[7] N. Ollivier, J.-B. Behr, Q. El-Mahdi, A. Blanpain, O. Melnyk, *Org. Lett.* **2005**, *7*, 2647.

[8] D. S. Kemp, N. G. Galakatos, B. Bowen, K. Tan, *J. Org. Chem.* **1986**, *51*, 1829.

[9] A. Brik, Y. Y. Yang, S. Ficht, C. H. Wong, *J. Am. Chem. Soc.* **2006**, *128*, 5626.

[10] J. D. Warren, J. S. Miller, S. J. Keding, S. J. Danishefsky, *J. Am. Chem. Soc.* **2004**, *126*, 6576.

[11] P. Botti, M. Villain, S. Manganiello, H. Gaertner, *Org. Lett.* **2004**, *6*, 4861.

[12] D. Bang, B. L. Pentelute, Z. P. Gates, S. B. Kent, *Org. Lett.* **2006**, *8*, 1049.

[13] E. C. B. Johnson, S. B. H. Kent, *J. Am. Chem. Soc.* **2006**, *128*, 6640.

[14] D. Bang, B. L. Pentelute, S. B. H. Kent, *Angew. Chem.* **2006**, *118*, 4089; *Angew. Chem. Int. Ed.* **2006**, *45*, 3985; D. Bang, S. B. H. Kent, *Angew. Chem.* **2004**, *116*, 2588; *Angew. Chem. Int. Ed.* **2004**, *43*, 2534.

[15] H. Hojo, Y. Matsumoto, Y. Nakahara, E. Ito, Y. Suzuki, M. Suzuki, A. Suzuki, Y. Nakahara, *J. Am. Chem. Soc.* **2005**, *127*, 13720; A. B. Clippingdale, C. J. Barrow, J. D. Wade, *J. Pept. Sci.* **2000**, *6*, 225.

[16] Reviewed by T. Kimmerlin, D. Seebach, *J. Pept. Res.* **2005**, *65*, 229.

[17] E. Saxon, J. I. Armstrong, C. R. Bertozzi, *Org. Lett.* **2000**, *2*, 2141; B. L. Nilsson, L. L. Kiessling, R. T. Raines, *Org. Lett.* **2001**, *3*, 9; L. Liu, Z.-Y. Hong, C.-H. Wong, *ChemBioChem* **2006**, *7*, 429.

[18] J. W. Bode, R. M. Fox, K. D. Baucom, *Angew. Chem.* **2006**, *118*, 1270; *Angew. Chem. Int. Ed.* **2006**, *45*, 1248.

 © 2006 Wiley-VCH Verlag GmbH & Co. KGaA, Weinheim

Ferrocenes

DOI: 10.1002/anie.200602482

Recent Applications of Chiral Ferrocene Ligands in Asymmetric Catalysis

*Ramón Gómez Arrayás, Javier Adrio, and Juan Carlos Carretero**

Keywords:
asymmetric catalysis · ferrocene ligands · metal-mediated reactions · nucleophilic catalysis · planar chirality

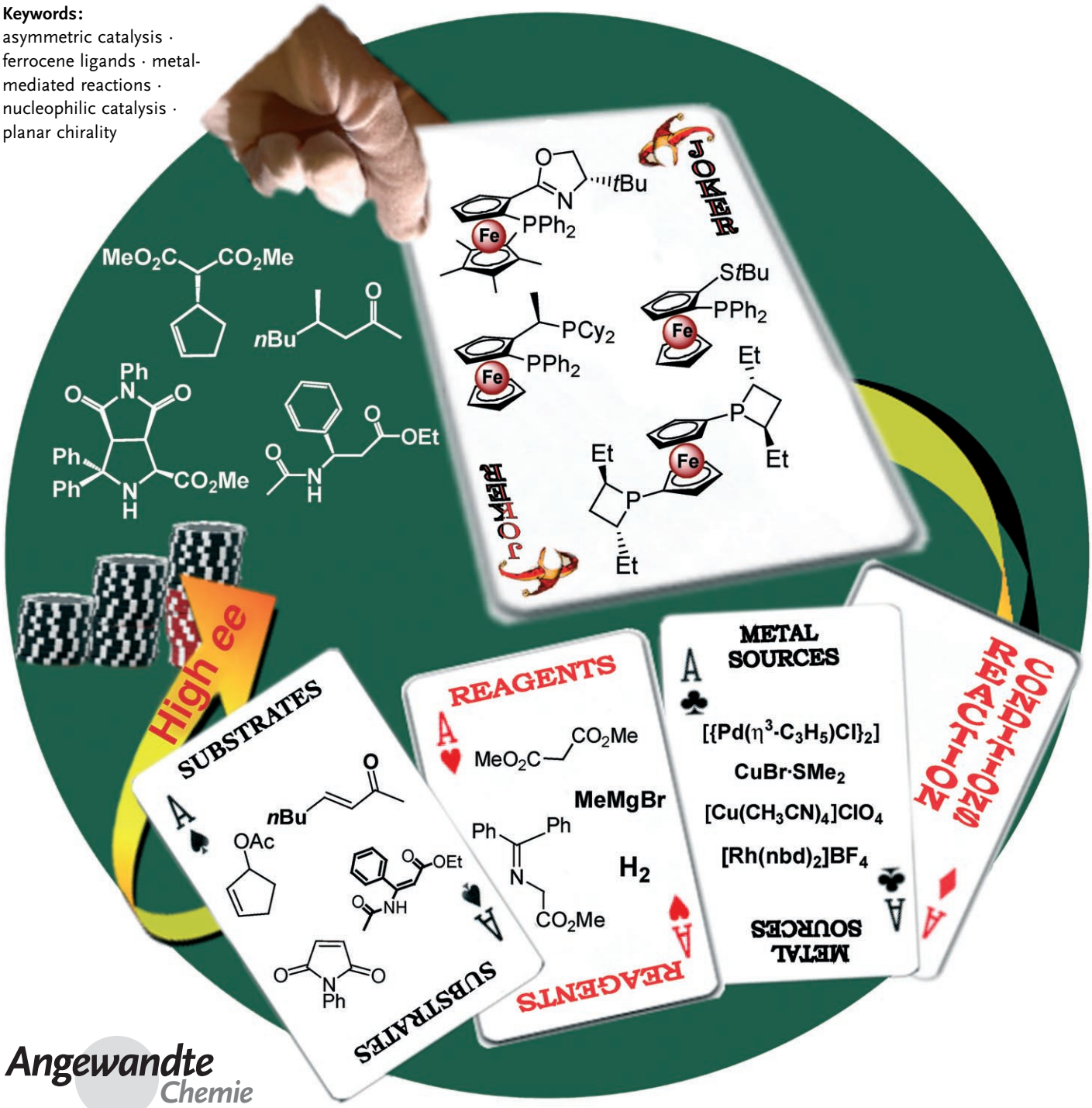

© 2006 Wiley-VCH Verlag GmbH & Co. KGaA, Weinheim

Despite the impressive progress achieved in asymmetric catalysis during the last decade, an increasing number of new catalysts, ligands, and applications are reported every year to satisfy the need to embrace a wider range of reactions and to improve the efficiency of existing processes. Because of their availability, unique stereochemical aspects, and wide variety of coordination modes and possibilities for the fine-tuning of the steric and electronic properties, ferrocene-based ligands constitute one of the most versatile ligand architectures in the current scenario of asymmetric catalysis. Over the last few years ferrocene catalysts have been successfully applied in an amazing variety of enantioselective processes. This Review documents these recent advances, with special emphasis on the most innovative asymmetric processes and the development of novel, efficient types of ferrocene ligands.

From the Contents

1. Introduction 7675

2. Structural Variety of Chiral Ferrocene Ligands 7676

3. Asymmetric Hydrogenation of Alkenes, Ketones, and Imines 7678

4. Asymmetric Addition of Hydrogen–Heteroatom and Heteroatom–Heteroatom Bonds to Alkenes 7689

5. Asymmetric Metal-Catalyzed Coupling Reactions and Related Processes 7690

6. Asymmetric Metal-Mediated Additions to Carbonyl Compounds and Imines 7697

7. Asymmetric Cycloaddition and Other Pericyclic Reactions 7702

8. Asymmetric Nucleophilic Catalysis 7706

9. Miscellaneous Reactions 7708

10. Summary and Outlook 7709

1. Introduction

Since the discovery of ferrocene in 1951,[1] its fascinating sandwich structure has captured the imagination of chemists, to the point of being nowadays among the most important structural motifs in organometallic chemistry, materials science, and, especially, catalysis. Furthermore, the applications of ferrocene compounds are not only a subject of increasing interest in academia, but also in industry. A quite remarkable example of the great utility of chiral ferrocene ligands in the industrial production of optically active compounds[2] is the synthesis of a precursor of the herbicide (*S*)-metolachlor by an Ir–Xyliphos-catalyzed asymmetric hydrogenation reaction. This process is extremely effective and presently constitutes the largest-scale enantioselective catalytic process in industry[3] (turnover numbers (TONs) of 2000000 and turnover frequencies (TOFs) of around 600000 h^{-1}, at more than 10000 tons per annum).

In addition to its unique structure, ferrocene has ideal properties such as low price, thermal stability, and high tolerance to moisture, oxygen, and many types of reagents. Interestingly, its behavior as an electron-rich aromatic compound in electrophilic aromatic substitutions, its facile lithiation and dilithiation (at the 1,1′-positions), and the extraordinary ability to stabilize carbocations at the benzylic-like position are key chemical properties that provide very practical ways for the synthesis of functionalized, substituted ferrocenes. For instance, the best-known ferrocene ligand, [1,1′-bis(diphenylphosphino)ferrocene] (dppf), was first described in 1965 by dilithiation of ferrocene with *n*-butyllithium and reaction with chlorodiphenylphosphine.[4] Since then, dppf and related achiral ferrocenyl phosphines have been successfully and extensively applied in transition-metal-catalyzed processes.[5]

Unlike 1,1′-disubstitution, a very interesting structural feature in ferrocene chemistry is that compounds substituted at positions 1 and 2 with different groups are chiral because of the loss of the plane of symmetry of ferrocene (planar chirality). The ligand ppfa (*N*,*N*-dimethyl-1-[2-(diphenylphosphino)ferrocenyl]ethylamine), synthesized by Hayashi and Kumada in 1974 by *ortho* lithiation of enantiopure (*R*)-*N*,*N*-dimethyl-1-ferrocenylethylamine (Ugi's amine) and reaction with chlorodiphenylphosphine, was the first reported example of a planar-chiral enantiopure ferrocenyl phosphine.[6] The discovery of ppfa and its high efficiency as a chiral ligand in some transition-metal-mediated reactions was a landmark in the development of chiral ferrocene ligands for asymmetric catalysis. Years later, in the 1990s, three breakthrough achievements were the synthesis of the Josiphos family of bisphosphine ferrocene ligands by S_N1-type reaction of the dimethylamino group on Ugi's amine-derived ligands with secondary phosphines (reported by Togni et al.),[7] the straightforward preparation of ferrocenyl phosphino–oxazolines (Fc-Phox ligands) by diastereoselective *ortho* lithiation/phosphinylation of chiral ferrocenyl oxazolines (independently reported by the groups of Richards,[8a] Sammakia,[8b] and Uemura),[8c] and the development of the 1,5-bisphosphine Taniaphos (Knochel and co-workers).[9]

[*] Dr. R. Gómez Arrayás, Dr. J. Adrio, Prof. Dr. J. C. Carretero
Departamento de Química Orgánica
Universidad Autónoma de Madrid
Facultad de Ciencias, Cantoblanco, 28049 Madrid (Spain)
Fax: (+34) 91-497-3966
E-mail: juancarlos.carretero@uam.es

© 2006 Wiley-VCH Verlag GmbH & Co. KGaA, Weinheim

Since the first monograph reported by Hayashi in 1995 on the synthesis and applications of chiral ferrocenes in asymmetric catalysis,[10] a set of reports by Kagan,[11] Richards,[12] Togni,[13] Santelli,[14] and Hou[15] covering different aspects of chiral ferrocene ligands have been published. Furthermore, the reviews of Lemaire[16a] and Guiry[16b,c] on chiral nitrogen-containing ligands include the case of ferrocenyl ligands bearing nitrogen donor atoms. The most recent authoritative reviews include a compilation on chiral ferrocenyl oxazolines reported in 2003 by Bryce and Sutcliffe,[17] a comprehensive review on chiral ferrocenyl phosphines disclosed by Colacot (also in 2003),[18] and a general report on the synthesis and catalytic applications of chiral ferrocene ligands presented by Gibson and Long in 2004.[19]

With this important background, the aim of this review is to provide the reader with a concise update on most of the recent applications of ferrocene ligands in asymmetric catalysis. To avoid a significant overlap with the previous reviews, we mainly focus on the results published in the last three years: from January 2003 to May 2006. It must be noted that, in spite of the shortness of this period of time, nearly 200 articles have been considered in the elaboration of this update which cover an astonishing variety of ligands and enantioselective processes. To highlight the great impact of ferrocene ligands in asymmetric catalysis, this review has been mainly organized according to the different types of asymmetric processes, rather than by structural families of ligands. Special focus is given to the most relevant applications, selected either because of the high enantioselectivities obtained or, especially, because of the chemical novelty of the enantioselective process. In this context the synthetic aspects of the ferrocene ligands will be treated only collaterally, since the main methods of functionalization of ferrocene have been appropriately discussed in previous reviews. For the sake of space constraints, the applications of chiral ferrocene ligands in the synthesis of achiral compounds have not been included.[20]

2. Structural Variety of Chiral Ferrocene Ligands

In recent years an amazing number and variety of chiral ferrocene ligands have been used in asymmetric catalysis. Part of these ligands were well-established before 2000, and very interesting novel enantioselective applications have emerged (for example, ppfa, Josiphos, Taniaphos, Fc-Phox, Trap, and FerroTANE), while others have been recently prepared and their asymmetric efficiency has started to be explored (for example, BoPhoz, Walphos, and Fesulphos). As a result of the high chemical stability of the ferrocene backbone and the existence of a variety of general methods for its functionalization, from a structural point of view a very wide array of substitution patterns have been applied in the preparation of chiral ferrocene catalysts, including 1-substituted, 1,1′-disubstituted, 1,2-disubstituted, 1,1′,2-trisubstituted, and 1,1′,2,2′-tetrasubstituted ferrocenes, as well as polysubstituted ferrocenes, bisferrocenes, and heterocyclic ferrocene-type compounds. On the other hand, the nature of the substitution can be also quite varied. Substituents with appropriately located metal-coordinating phosphorus and/or nitrogen atoms represent the most common alternative (P,P and P,N ligands), although sulfur (P,S ligands) and oxygen substituents (P,O ligands) are also known. In addition to this repertoire of bidentate metal-coordinating ligands, some interesting monodentate chiral ferrocenyl ligands and potentially tridentate ligands have also been developed in recent years. To help the reader in this jungle of structurally different ferrocene ligands and their current simplified names, in Figure 1 are shown some of the most relevant families of ferrocene ligands mentioned throughout this report, organized according to the substitution at the ferrocene backbone and nature of the coordinating heteroatoms.

Special attention is deserved by planar chiral ferrocenes with 1,2-substitution, which have emerged as a premier structural ligand motif in metal-catalyzed asymmetric reactions and are undoubtedly the most studied substitution pattern in ferrocene ligands. Since the pioneering work of Ugi et al. in 1970[6,21] on the C2 functionalization of enantiopure *N*,*N*-dimethyl 1-ferrocenylethylamine, the usual strategy for introducing planar chirality into the ferrocene backbone is based on the diastereoselective *ortho* lithiation of 1-substituted ferrocenes containing an appropriate chiral *ortho*-directing group and subsequent in situ trapping with an electrophile (for example, $ClPAr_2$). In addition to Ugi's amine, a good number of chiral *ortho*-directing groups have been progressively described, such as sulfoxides,[22] acetals,[23] oxazolines,[8] azepines,[24] pyrrolidines,[25] hydrazones,[26] sulfoximines,[27] *O*-methyl ephedrine derivatives,[28] imidazolines,[29] phosphine oxides,[30] and oxazaphospholidine.[31]

Juan Carlos Carretero, born in Madrid in 1960, received his Ph.D. from the Universidad Autónoma de Madrid (UAM) in 1985 with Prof. José L. García Ruano. After postdoctoral studies at the Université Catholique de Louvain (Belgium) with Prof. Léon Ghosez, he joined the Department of Organic Chemistry of the UAM and became Associate Professor in 1988 and Professor of Organic Chemistry in 2000. His research interests are focused on developing new chiral ligands for asymmetric catalysis and highly stereocontrolled metal-catalyzed processes using novel functionalized substrates.

Ramón Gómez Arrayás was born in Seville in 1969 and studied Chemistry in the Universidad Autónoma de Madrid (UAM), where he earned his B.S.(1992) and Ph.D. (1999) with Prof. Carretero. After postdoctoral research in the laboratory of Prof. Lanny S. Liebeskind at Emory University (Atlanta, USA), he became Ramón y Cajal Researcher of UAM in 2002, again in the group of Prof. Carretero, and was promoted to Assistant Professor in 2006. His current research interests include the development of new strategies for transition-metal-mediated reactions and asymmetric catalysis.

 © 2006 Wiley-VCH Verlag GmbH & Co. KGaA, Weinheim

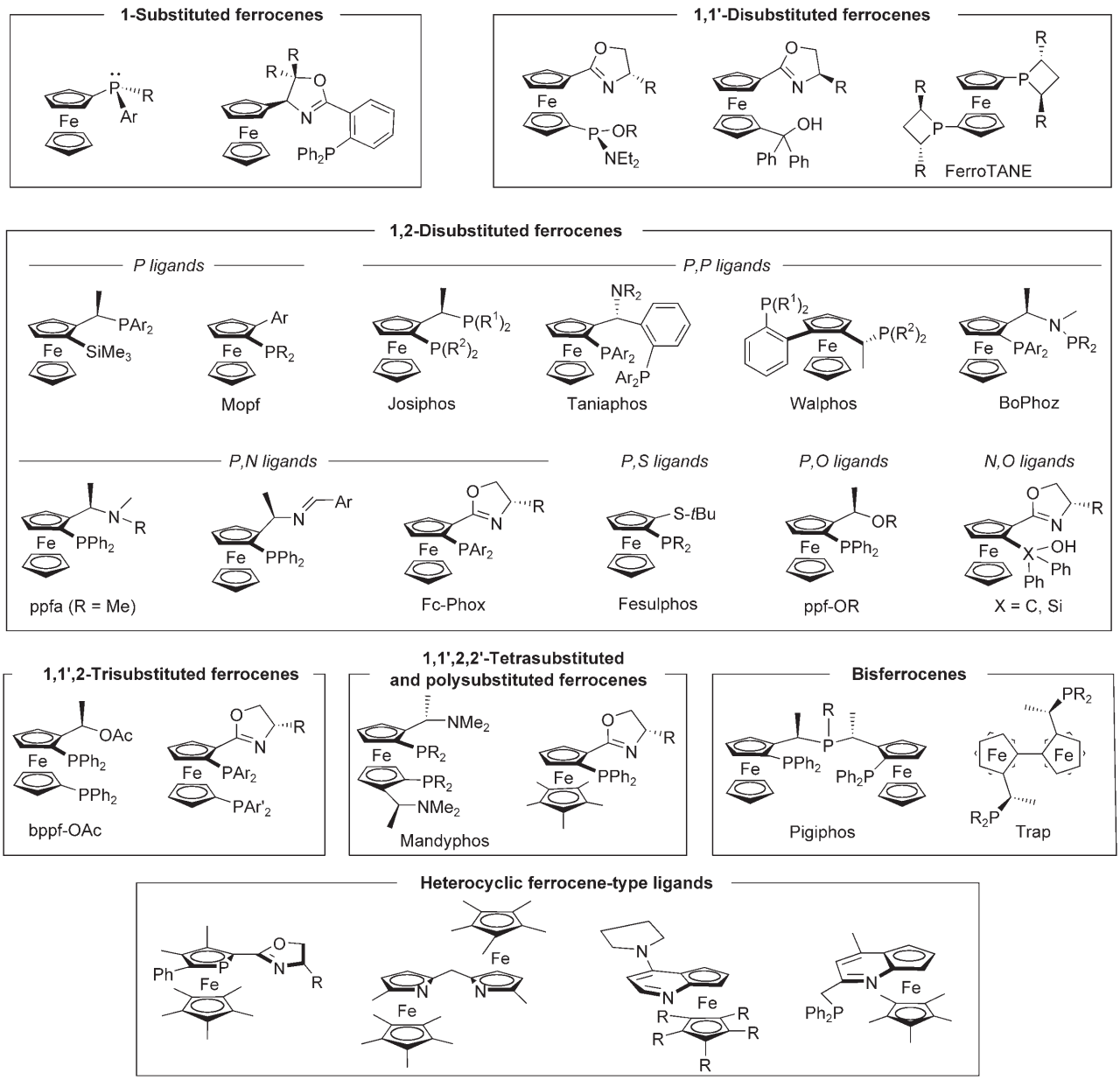

Figure 1. Representative families of chiral ferrocene ligands with outstanding applications in asymmetric catalysis.

Javier Adrio was born in Madrid in 1968 and received his B.Sc. in 1992 from the Universidad Autónoma de Madrid (UAM), where he completed his Ph.D. thesis in 2000 with Prof. Carretero. Until 2003 he worked as a senior scientist at PharmaMar S.A. and as a postdoctoral researcher (for one year) with Prof. Madeleine M. Joullié at the University of Pennsylvania. In 2003 he joined the Department of Organic Chemistry of the UAM as a Ramon y Cajal researcher. His research interests concern the development of novel metal-mediated alkyne cyclizations and transition-metal-catalyzed enantioselective processes.

Among them, up to now, the Ugi amine method, the oxazoline approach, and the sulfoxide approach described by Kagan are the most widely used strategies for the preparation of enantiopure 1,2-disubstituted ferrocene ligands.

The Ugi amine method allows, once the substituent at C2 has been introduced, a further stereospecific S_N1-type reaction of the dimethylamino moiety with different species (for example, Ac_2O, R_2PH, pyrazoles), which occurs with retention of configuration. This unique feature has led to the preparation of a large number of ligands with a wide variety of heteroatomic coordinating groups,[18] including the very recently reported synthesis of ligands having a sterogenic phosphorus atom at C2.[32] These ligands derived from Ugi's

© 2006 Wiley-VCH Verlag GmbH & Co. KGaA, Weinheim

amine usually possess the characteristic methyl group at the stereogenic carbon atom bonded to C1 (for example, ppfa,[6] BoPhoz,[33] Josiphos,[34] Xyliphos,[34] Taniaphos,[35] Walphos,[36] Trap,[37] and Pigiphos).[38] An important feature that makes this strategy particularly attractive is that both optical antipodes of Ugi's amine are equally available. As recent illustrative examples following this approach, in Scheme 1 are shown the syntheses of the ferrocene ligands BoPhoz[33] and Walphos.[36]

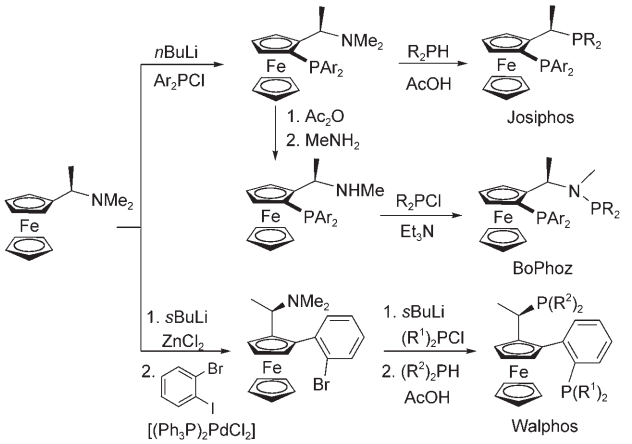

Scheme 1. Examples of synthesis of 1,2-disubstituted ferrocene ligands from Ugi's amine.

Parallel to the great interest of chiral oxazolines in asymmetric catalysis, the ferrocenyl phosphino–oxazolines (Fc-Phox ligands), readily prepared by *ortho* lithiation of ferrocenyl oxazolines, are an important type of P,N ligands. The modular approach in their synthesis has allowed the preparation of a great number of ligands, covering a very wide range of steric and electronic properties at the coordinating substituted phosphane and oxazoline moieties. The application of Fc-Phox ligands in asymmetric catalysis (up to 2002) has been extensively reviewed by Bryce and Sutcliffe.[17] As a pair of more recent examples of this approach, in Scheme 2 are shown Helmchen's Fc-Phox[39] and Bolm's organosilanol[40] ligands.

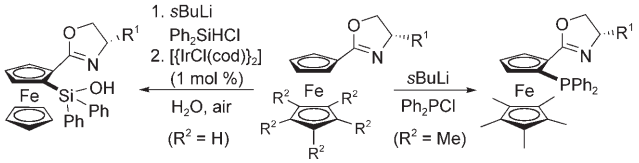

Scheme 2. Recent examples of 1,2-disubstituted ferrocene ligands prepared by *ortho* lithiation of chiral oxazolines.

In recent years the sulfoxide approach has significantly enlarged the possibilities for preparing structurally diverse 1,2-disubstituted ferrocenes, including ligands with planar chirality only (for example, Fesulphos[41] and aryl-Mopf)[42] or new Taniaphos-type ligands.[43] In this method, after the diastereoselective *ortho*-metalation/functionalization step, the sulfinylated *ortho*-directing group can be reduced to a metal-coordinating thioether (Fesulphos ligands) or can act as a removable group by *tert*-butyllithium-mediated C–S cleavage and further reaction of the resulting ferrocenyl lithium with an appropriate electrophile[44] (for example, synthesis of aryl-Mopf[42] and Taniaphos-type ligands;[43] Scheme 3).

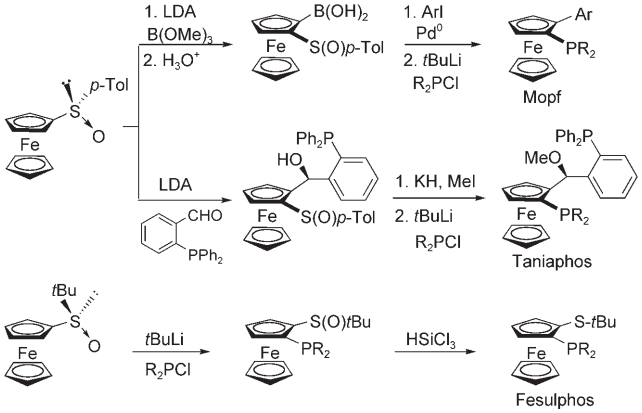

Scheme 3. Sulfoxide-mediated synthesis of 1,2-disubstituted ferrocene ligands. LDA = Lithium diisopropylamide

In addition to these approaches based on diastereoselective *ortho* metalation of ferrocenes that have a chiral directing group, the use of an external source of chirality for the enantioselective *ortho* lithiation of prochiral ferrocenes bearing a directing functionality constitutes another interesting conceptual alternative for the preparation of planar-chiral ferrocenes. The deprotonation with a combination of lithium bases and (−)-sparteine[45] or (1*R*,2*R*)-*N*,*N*,*N*′,*N*′-tetramethylcyclohexanediamine[46] as well as the use of chiral lithium amide bases[47] have been reported. In particular, the (−)-sparteine-mediated directed *ortho* metalation of tertiary ferrocenecarboxamides[45c] has proved to be very effective. However, to date, this strategy has found little application in the preparation of ferrocene ligands for asymmetric catalysis.

As a result of the predominance of methods for generating planar chirality based on chiral *ortho*-directing groups, the majority of chiral ferrocene ligands have both central and planar chirality. In some cases it has been proved that both chiral elements act synergistically (matched combination), which is essential for achieving a high asymmetric induction.[48] However, there is a growing number of ferrocene ligands with only planar chirality that provide excellent enantioselectivities in a variety of reactions, thus showing the key asymmetric role exerted by this stereogenic element.

3. Asymmetric Hydrogenation of Alkenes, Ketones, and Imines

Since the first studies reported in the late 1960s and early 1970s, the homogeneous asymmetric hydrogenation of C=C and C=O bonds has become the most studied process in asymmetric catalysis as well as the preferred catalytic method for the production of chiral compounds on an industrial

 © 2006 Wiley-VCH Verlag GmbH & Co. KGaA, Weinheim

scale.[2,49] During the period covered by this update (January 2003 to May 2006) a great number of new ferrocene ligands has been successfully tested in asymmetric hydrogenation reactions, thus showing that ligands based on the ferrocene framework can be considered as privileged structures for this kind of transformation.

3.1. Hydrogenation of Alkenes

3.1.1. Hydrogenation of Dehydro-α-Amino Acids, Itaconic Acid Derivatives, and Related Compounds

Owing to the long history and key biological relevance of α-amino acids, the Rh-catalyzed asymmetric hydrogenation of dehydro-α-amino acid derivatives and related two-point binding substrates, such as itaconates, are among the most employed processes in the screening of new chiral ligands for asymmetric catalysis.[50] In Scheme 4 are collected a selection of significant recent contributions involving ferrocene-based ligands.

On the basis of Ugi's methodology, Boaz and co-workers reported in 2002 the first family of bidentate phosphine–aminophosphine ligands to be used in asymmetric catalysis.[33] These readily available and air-stable compounds, known as BoPhoz ligands (**1**), have provided outstanding enantioselectivities (generally >95% *ee*) and high activities (substrate/catalyst ratio (S/C) of up to 10000) in the asymmetric hydrogenation of a wide variety of (*Z*)-dehydroamino acid derivatives, regardless of the nature of the protecting group at the nitrogen atom (Ac, Bz, Cbz, or Boc; Scheme 4A).[51] Similar levels of enantiocontrol (up to 99.8% *ee*) and catalytic activity were achieved in the hydrogenation of itaconate derivatives. A comparative study on the hydrogenation of methyl 2-acetamidocinnamate showed the superiority of the BoPhoz ligand **1a** over other well-established ligands such as Chiraphos, Dipamp, or Josiphos. The same BoPhoz ligand **1a**

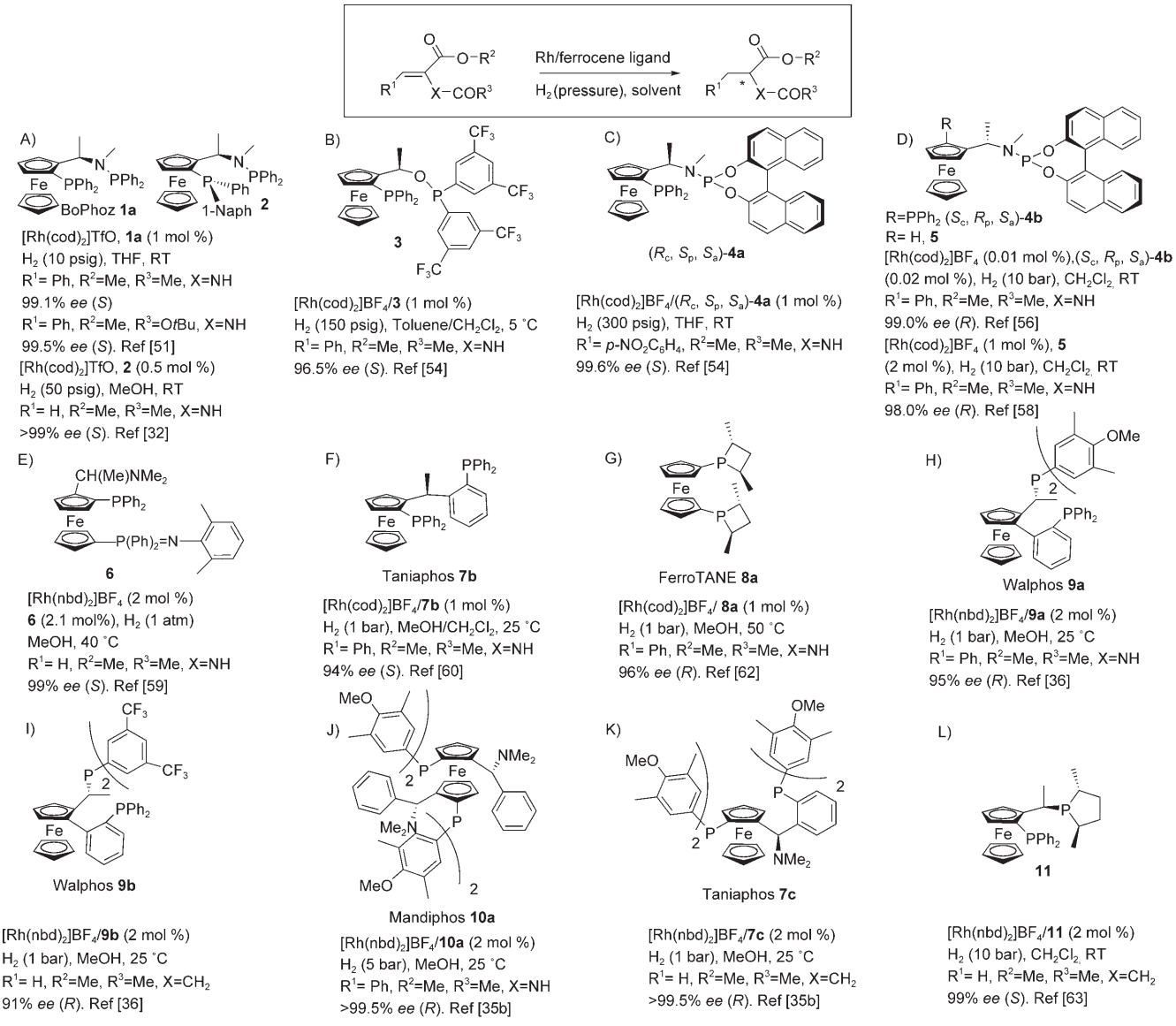

Scheme 4. Rh-catalyzed asymmetric hydrogenation of dehydro-α-amino acids and itaconic acid derivatives; 10 psig = 0.689 bar; cod = cyclooctadiene; nbd = norbornadiene.

© 2006 Wiley-VCH Verlag GmbH & Co. KGaA, Weinheim

has been efficiently applied to the synthesis of some non-natural α-amino acids, such as cyclopropylalanine[52] (up to 98% *ee* in the hydrogenation step) and 2-naphtylalanine.[53] In the latter case the asymmetric hydrogenation has been run on a multikilogram scale with an S/C ratio of 2000 and 97% *ee*.

Very recently, Chen and co-workers have developed an efficient stereoselective approach for the synthesis of BoPhoz-type ligands having a stereogenic phosphorus atom.[32] The procedure is based on the reaction of the *ortho*-lithiated Ugi amine with a dichlorophosphine and subsequent reaction with an organolithium or Grignard reagent. Preliminary comparative results demonstrate that P chirality improves the enantioselectivity when acting cooperatively with the planar chirality and the chirality at the carbon center. For instance, the activities and enantioselectivities provided by the ligand **2**, with matched chiral elements, are higher than those of the corresponding BoPhoz ligand **1a** (Scheme 4A).

Several phosphine–phosphinite, phosphine–phosphite, and phosphine–phosphoramidite ligands with the typical chiral ferrocenylethyl scaffold derived from the Ugi amine have been developed by Chan and co-workers.[54] The phosphinite ligand **3**, with the 3,5-bis(trifluoromethyl)phenyl substitution, and the phosphoramidite ligand (R_c,S_p,S_a)-**4**, derived from (*S*)-Binol, afforded the best results in the hydrogenation of dehydro-α-amino acids (up to 99.6% *ee*; Scheme 4B and C). The same research group has also prepared some phosphine–aminophosphine ferrocene ligands (for example, BoPhoz-type ligand **1b**), which are very efficient in the hydrogenation of α-aryl enamides (Scheme 5).[55]

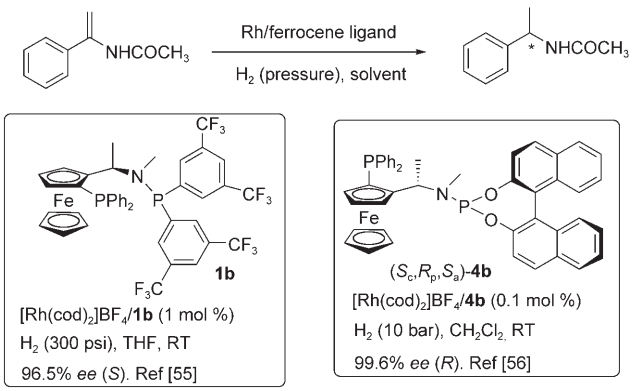

Scheme 5. Rh-catalyzed asymmetric hydrogenation of enamides.

Independently, Zheng and co-workers reported the same type of hybrid phosphine–phosphoramidite–Binol ligand (for example, (S_c,R_p,S_a)-**4b**) having the three stereogenic elements (central (c), planar (p), and axial (a) chirality). After preparing the four diastereomers of these ligands from the Ugi amine of (*S*) configuration, it was nicely demonstrated that the axial chirality of the binaphthyl moiety plays the dominant role in the asymmetric performance of the ligand. In the presence of 1 mol% of the ligand (S_c,R_p,S_a)-**4b**, impressive enantioselectivities were achieved in the Rh-catalyzed hydrogenation of dimethyl itaconate (up to 99.9% *ee*), methyl (*Z*)-α-acetamidocinnamate (up to 99.9% *ee*; Scheme 4D), and α-aryl acetylenamides (up to 99.6% *ee*; Scheme 5). This catalyst system is highly reactive and not significantly solvent-dependent, thus allowing the use of low catalyst loadings (up to S/C = 10000) with very little reduction in the enantioselectivity.[56] Very similar catalytic performances were later reported using the analogue H_8-Binol phosphine–phosphoramidite.[57] In another study it was demonstrated that related monodentate phosphoramidites **5**, lacking the phosphine moiety at the ferrocene backbone, also afford very high enantioselectivities in the catalytic hydrogenation of both enamides and dehydro-α-amino acid esters.[58] These results suggest that in this family of Binol-derived phosphoramidite ligands neither the planar chirality nor the bidentate coordination are essential to obtain high induction levels.

The first examples of chiral iminophosphoranyl ferrocenes as ligands for asymmetric catalysis have also been recently reported. For instance, the ligand **6**, readily available by reaction of (*R*,*S*)-bppfa with aryl azides, provided high enantioselectivities in the hydrogenation of methyl 2-acetamidocinnamate and methyl 2-acetamidoacrylate (up to 99% *ee*; Scheme 4E). With related iminophosphoranyl ligands high enantiocontrol has also been described for the hydrogenation of (*E*)-2-methylcinnamic acid. The isolation and structural characterization of a P,N-chelated rhodium complex of ligand **6** revealed that the iminophosphoranyl group seems not to be involved in the coordination with the metal.[59]

The group of Knochel has recently reported improved procedures for the preparation of new generations of Taniaphos[9,35a,43,60] ligands (1,5-diphosphine ferrocenes). These ligands have a carbon substituent or oxygen substituent at the stereogenic benzylic position instead of an Me_2N group as in previous Taniaphos ligands. Among the new ligands, the methyl-substituted ligand **7b** gave the best results in the hydrogenation of dimethyl itaconate (96% *ee*) and methyl 2-acetamidoacrylate (94% *ee*; Scheme 4F).[60] In accordance with the interest in C_2-symmetric 1,1′-bis(phosphetano)ferrocenes (FerroTANE ligands **8**) as ligands in asymmetric hydrogenations,[61] Marinetti and co-workers have isolated some rhodium and ruthenium complexes of such structures. High enantioselectivity (up to 96% *ee*) has been reported for the hydrogenation of methyl α-acetamidocinnamate in the presence of 1 mol% of the preformed complex of Me,Me-FerroTANE **8a** and Rh (Scheme 4G).[62]

The novel and easily modulable 1,5-diphosphine Walphos ligand family has been tested in the Rh- and Ru-catalyzed hydrogenation of α,β-unsaturated acid derivatives and carbonyl compounds, respectively. In a set of six Walphos ligands (**9**) it was demonstrated that the substitution at phosphorus has a very important effect on the enantioselectivity.[36] The ligand **9a** was the most efficient in the hydrogenation of methyl α-acetamidocinnamate (95% *ee*), while ligand **9b** provided the best results in the hydrogenation of dimethyl itaconate (91% *ee*) and (*E*)-2-methylcinnamic acid (82% *ee*; Scheme 4H and I). The same group at Solvias has reported a deep and systematic study on the catalytic properties of a set

 © 2006 Wiley-VCH Verlag GmbH & Co. KGaA, Weinheim

of eight Mandyphos (**10**) and three Taniaphos ligands (**7**) in Rh-, Ru-, and Ir-catalyzed hydrogenations of a variety of olefins, ketones, and imines (20 test reactions). Interestingly, in all these reactions relatively electron-rich aromatic substituents at the phosphorus atom usually led to the best enantioselectivities. In the case of the Rh-catalyzed hydrogenation of methyl 2-acetamidocinnamate most ligands showed good to excellent asymmetric performance. In particular, the Mandyphos ligand **10a** provided the highest *ee* values (up to > 99.5 % *ee*) and very high reactivities (S/C up to 20000; Scheme 4J), while the Taniaphos ligand **7c** was very effective in the hydrogenation of dimethyl itaconate (Scheme 4K).[35b] Among other recently developed ferrocene ligands, the Josiphos-type ferrocene, with a (*R*,*R*)-2,5-dimethylphospholane moiety at the stereogenic carbon atom (ligand **11**), has been successfully applied in the asymmetric hydrogenation of dimethyl itaconate (> 99 % *ee*), being far superior to the related ligand based on a planar chiral aryl chromium tricarbonyl scaffold (Scheme 4L).[63]

In the search for new reaction conditions in Rh-catalyzed hydrogenations, a screening of ferrocene ligands (Taniaphos, Josiphos, Walphos, and Mandyphos) using ionic liquids, or mixtures of ionic liquids and solvents, as reaction medium has been reported. In many cases the combination of an ionic liquid and water provided better results than conventional organic solvents with respect to catalytic performance and catalyst separation. Very high enantioselectivities (up to > 99 % *ee*) were obtained in the hydrogenation of methyl α-acetamidoacrylate.[64] As another strategy that facilitates catalyst recovery, the immobilization of a rhodium complex of the parent Josiphos ligand into the mesoporous material MCM-41 has been recently published. The chemical yields and *ee* values obtained in the hydrogenation of dimethyl itaconate (S/C = 500) are comparable to the corresponding homogenous catalyst (94 % versus 96 % *ee*), with the advantage that the heterogeneous catalyst can be readily recovered and reused several times without marked loss of catalyst performance.[65] The heterogenization of the rhodium complex of a ferrocenyl phosphine–oxazoline (Dipof ligand) on mesoporous silica has also been reported, providing 94 % *ee* in the hydrogenation of (*E*)-α-phenylcinnamic acid.[66]

3.1.2. *Hydrogenation of Dehydro-β-Amino Acids and Derivatives*

Enantiopure β-amino acids and derivatives are very important components in synthetic peptides with interesting biological properties. Although much less studied than the hydrogenation of α-dehydroamino acids, the asymmetric hydrogenation of β-dehydroamino acid precursors is one of the most efficient methods for the preparation of highly enantioenriched β-amino acids.

Among the most recent results using ferrocene-based ligands, the Rh-catalyzed hydrogenation of β-alkyl and β-aryl dehydroamino acid esters with commercially available Et,Et-FerroTANE was reported in 2003 by Heller and co-workers (ligand **8b**, Scheme 6). Very high enantioselectivities, up to > 99 % *ee*, were obtained in the hydrogenation of the *E* isomers, while the reduction of the *Z* diastereomers showed low enantioselectivity.[67] Interestingly, in a comparative study FerroTANE **8b** proved to be more efficient and active than classical ligands such as dipamp, diop, or DuPhos. Although the reasons for this high performance are yet unclear, it is interesting to note that the P-Rh-P bite angle found in an isolated Rh–FerroTANE complex (98.3°) is larger than the average bite angle in DuPhos ligands (84.8 ± 0.5°).

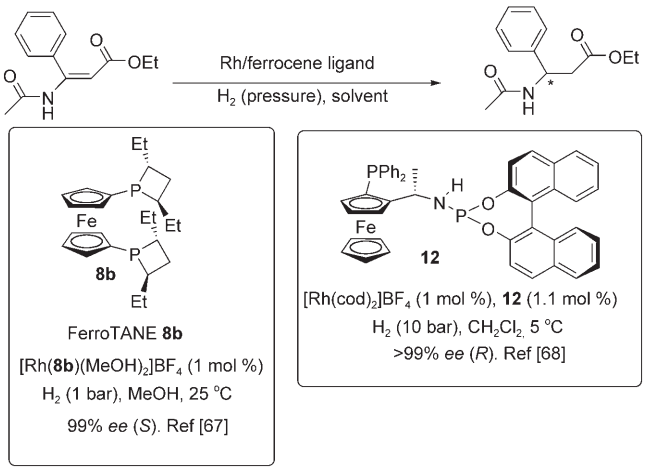

Scheme 6. Rh-catalyzed asymmetric hydrogenation of α,β-unsaturated (*E*)-β-acylamino esters.

Very recently Zheng and co-workers have studied the same hydrogenation reaction using the new ferrocenylphosphine–phosphoramidite Binol-based ligand **12** with (S_c,R_p,S_a) configuration. In the optimization of the ligand structure, the presence of the NH moiety (instead of NMe) proved to be crucial for achieving a high enantiocontrol (Scheme 6). Outstandingly, this ligand allowed a high enantiocontrol in the hydrogenation of both *E* (up to > 99 % *ee*) and *Z* isomers, although the latter substrates exhibited a somewhat lower enantioselectivity (up to 93 % *ee*). High turnovers (up to S/C = 5000) were described in some cases.[68]

An important limitation of the current methods for asymmetric hydrogenation of β-dehydroamino acid derivatives is the requirement of an acyl protecting group at the nitrogen atom (usually acetyl), presumably to assist in the chelation with the Rh atom. Unlike these precedents, a research group at Merck has reported the highly enantioselective hydrogenation of unprotected β-enamine esters and amides.[69] Among a variety of commercially available chiral ligands, the Josiphos ligand **13b** provided the best results in terms of conversion and enantioselectivity (up to 96.1 % *ee* in the hydrogenation of enamine esters and up to 97.1 % *ee* in the hydrogenation of enamine amides). The authors suggest that the reaction could proceed through the imine tautomer, making this reaction mechanistically analogous to β-ketoester hydrogenations. This methodology was later improved, thereby suppressing the observed amine-product inhibition and the low functional group compatibility in the case of β-amino esters, by performing the hydrogenation in the presence of Boc_2O (methanol as solvent). Under these conditions the corresponding Boc carbamates are isolated in good yields and high enantioselectivities (91–99 % *ee*; Scheme 7).[70] This strategy has been applied to the prepara-

 © 2006 Wiley-VCH Verlag GmbH & Co. KGaA, Weinheim

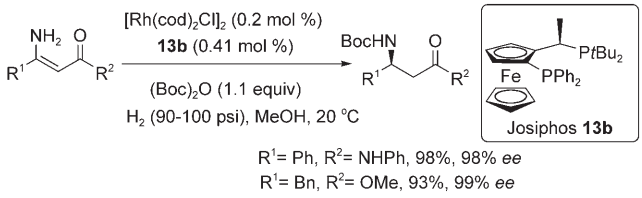

Scheme 7. Josiphos/Rh-catalyzed asymmetric hydrogenation of unprotected enamines. Boc = *tert*-butoxycarbonyl.

tion of derivatives of β-homophenylalanine with potential interest in the treatment of type II diabetes.[71]

3.1.3. Hydrogenation of Heteroaromatic Compounds

The asymmetric hydrogenation of heteroaromatic compounds is a challenging field that is receiving increasing attention. Kuwano and Ito described in 2000 the first examples of enantioselective hydrogenation of indolic compounds (*N*-acyl 2-substituted indoles). The catalyst system formed by $[Rh(nbd)_2]SbF_6$ as the metal source and the *trans* P,P-chelating bisferrocene ligand **14a** (Ph-Trap ligand) provided indolines with up to 95% *ee*.[72] In a further study this protocol has been successfully extended to the asymmetric hydrogenation of *N*-sulfonyl 3-substituted indoles (especially *N*-tosyl indoles), providing the indoline products in 95–98% *ee* (Scheme 8).[73] This methodology has been applied to the preparation of a key intermediate in the synthesis of the antitumor agent (+)-CC-1065.

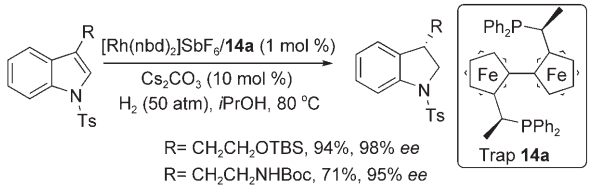

Scheme 8. Trap/Rh-catalyzed asymmetric hydrogenation of 3-substituted indoles. Ts = 4-toluenesulfonyl.

In another recent study, Zhou and co-workers have shown the usefulness of ferrocenyloxazolinylphosphines (Fc-Phox, **15**) as P,N ligands in the Ir-catalyzed asymmetric hydrogenation of 2-substituted and 2,6-disubstituted quinolines. The hydrogenation of 2-methylquinoline was chosen as a model reaction to assess the optimization of the ligand structure, whereby the *tert*-butyl-substituted ligand **15a** was the most efficient (90% *ee*; Scheme 9). The catalyst system $[\{Ir(cod)Cl\}_2]$/**15a**/I_2 has been employed at different S/C ratios (from 100 to 2000), evidencing a slight decrease of enantioselectivity at lower catalyst loadings.[74] The relative role of the planar and central chirality in the P,N ligands was also addressed, with the central chirality on the oxazoline group playing the dominant role in the enantiocontrol of the process. Within this context, the Ir–Xyliphos-catalyzed enantioselective hydrogenation of trimethylindoline in a variety of ionic liquids has been recently reported (*ee* values up to 86%).[75]

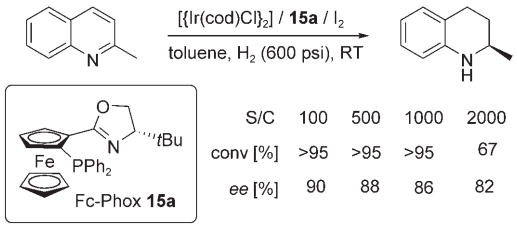

Scheme 9. Fc-Phox/Ir-catalyzed asymmetric hydrogenation of 2-methylquinoline.

For applications on medicinal chemistry, a research group at Solvias has developed some water-soluble chiral diphosphine ligands for the rhodium- and iridium-catalyzed hydrogenation of folic acid to L-tetrahydrofolic acid, which is an important cofactor in a variety of enzymatic reactions.[76] Diastereoselectivities up to 49% were obtained with the triacid Josiphos-type ligand **16** (Scheme 10). Although a good catalytic activity was achieved (TONs up to 334 h^{-1}), the diastereoselectivity is still too low for industrial application.

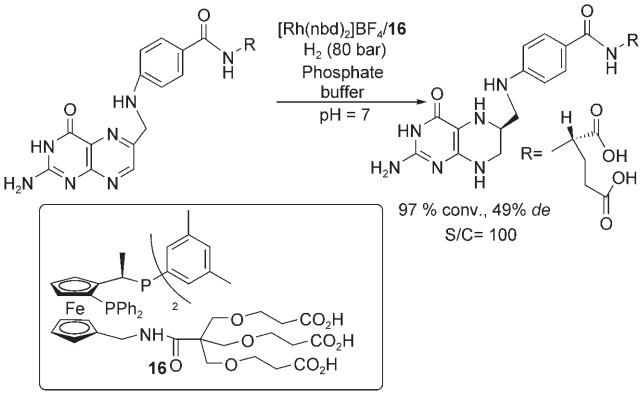

Scheme 10. Rh-catalyzed asymmetric hydrogenation of folic acid.

3.1.4. Other Asymmetric Hydrogenations and Synthetic Applications

Owing to the inherent atom-economy nature of the hydrogenation reactions, the reduction of vinyl metallic substrates is a very appealing method for generating stereogenic carbon–metal bonds. In this pioneering field, Morken and co-workers reported the highly enantioselective hydrogenation of vinyl 1,2-bis(boronates), readily available by Pt-catalyzed diboration of terminal alkynes, to afford enantiomerically enriched alkyl 1,2-bis(boronates), which can be converted to chiral 1,2-diols by further oxidation with H_2O_2/NaOH or to 1,4-diols by reaction with chloromethyllithium followed by H_2O_2/NaOH (Scheme 11).[77] After surveying different commercially available ligands (Binap, Phanephos, BoPhoz, and Walphos), the Walphos ligand **9b**, having the bis-(3,5-trifluoromethyl)phenyl substitution at the phosphorus on the stereogenic carbon atom, provided the best results. The stereoselectivity of the process proved to be highly dependent on the Rh/ligand ratio. The optimal results were found using 2 mol% of $[Rh(nbd)_2]BF_4$ and 4 mol% ligand. A

 © 2006 Wiley-VCH Verlag GmbH & Co. KGaA, Weinheim

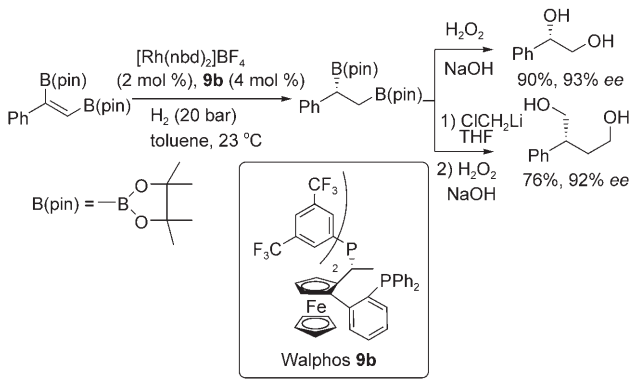

Scheme 11. Walphos/Rh-catalyzed asymmetric hydrogenation of vinyl 1,2-bis(boronates).

variety of 1,2-diols were isolated in 77–93% *ee* after oxidative work up. In a later study this procedure was extended to the hydrogenation of prochiral vinyl monoboronates.[78] Again the Walphos ligand **9b** was very effective, providing secondary organoborates that are not easily accessible from alkene hydroboration reactions.

A research group at Chirotech Technology and Pfizer has developed a robust synthetic approach to the imidazole δ-amino acid **I**, which is a potent inhibitor of thrombin fibrinolysis. The key step is the Rh-catalyzed hydrogenation of the enantiopure quinidine salt of its *N*-Boc derivative (Scheme 12). Although the best enantioselectivity was found with the Rh complex of the *t*Bu,*t*Bu-FerroTANE ligand **8c** (82% *ee*, S/C = 100), the 1,1′-bisphospholanoferrocene **17** displayed a much higher activity, thus allowing the reaction to be performed with a catalyst loading as low as 0.02 mol% (S/C = 5000).[79] After crystallization from ethyl acetate the *ee* value of the product was enriched from 62% to 94%. This procedure has been applied to the production of kilogram quantities of the product. The same group has also reported a

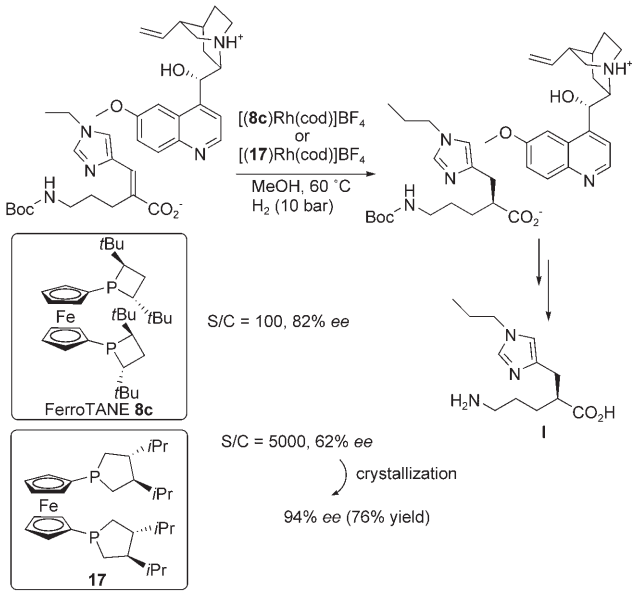

Scheme 12. Rh-catalyzed asymmetric hydrogenation of the enantiopure quinidine salt of an α,β-unsaturated acid.

concise enantioselective synthesis of the anticonvulsant pregabatin [(*S*)-3-aminomethyl-5-methylhexanoic acid] by hydrogenation of its α,β-unsaturated nitrile precursor.[80]

Regarding the synthesis of a promising sulfonamide lethal factor inhibitor (anthrax LFI), which is active against *Bacillus anthracis*, a research group at Merck has developed a highly enantioselective Ru-catalyzed hydrogenation reaction of *N*-sulfonylated α-dehydroamino acids (Scheme 13).[81] Screening experiments identified Josiphos **13b** as an efficient ligand, leading to high asymmetric inductions (up to 99.1% *ee*) in the reduction of a wide variety of substrates. These seem to be the first examples of Ru-catalyzed asymmetric hydrogenation of tetrasubstituted α-dehydroamino acid derivatives.

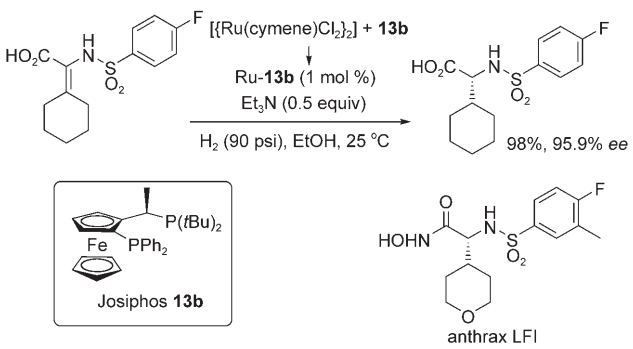

Scheme 13. Josiphos/Rh-catalyzed asymmetric hydrogenation of *N*-sulfonyl-α-dehydroamino acids.

In another recent application from the industry, a group at Takeda Chemical Industries studied the Rh-catalyzed asymmetric hydrogenation of a β,β-diaryl-substituted α,β-unsaturated acid (Scheme 14).[82] After an ample screening of ligands, Josiphos **13a** was the most enantioselective, providing the corresponding substituted propanoic acid in 93% *ee*, albeit with a high required catalyst loading (5 mol%). This product is a key intermediate in the synthesis of the naphthoquinone derivative **II**, a potential therapeutic drug for neurodegenerative deseases.

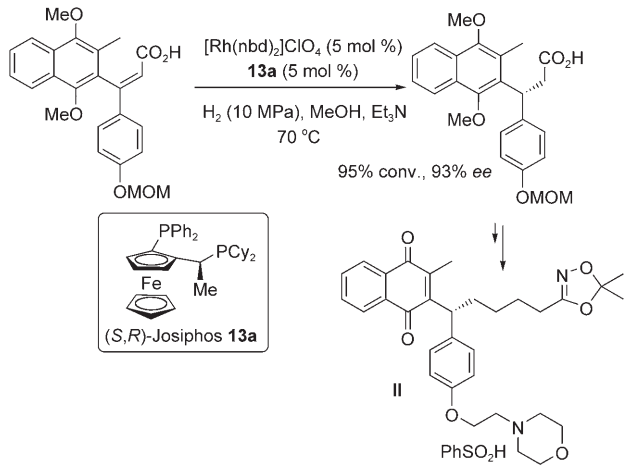

Scheme 14. Josiphos/Rh-catalyzed asymmetric hydrogenation of a β,β-diaryl-substituted α,β-unsaturated acid drug precursor. MOM = methoxymethyl.

 © 2006 Wiley-VCH Verlag GmbH & Co. KGaA, Weinheim

The synthesis of the peroxime proliferator activated receptor (PPAR) agonist **III** has been accomplished at Lilly by applying as the key step the Rh-catalyzed hydrogenation of a (*Z*)-2-ethoxycinnamic acid precursor.[83] A vast hydrogenation screening of over 250 ruthenium and rhodium catalysts and conditions, including ligands of the families Binap, DuPhos, Phanephos, Josiphos, and FerroTANE, revealed the Walphos ligand **9b** as the optimal choice. Upon optimization of the solvent (MeOH) and additives (NaMeO), this Rh–Walphos-catalyzed process provided the required product in 92% *ee* (Scheme 15). Interestingly, in the absence of NaMeO the yield was much lower, thus suggesting that the presence of the carboxylate is essential for the success of the process.

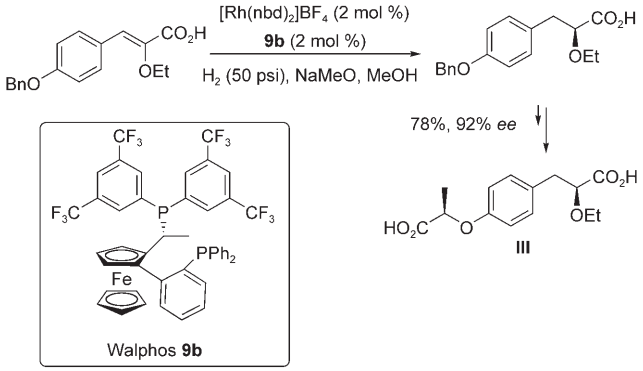

Scheme 15. Walphos/Rh-catalyzed asymmetric hydrogenation of a cinnamic acid derivative.

A research group at Dow Chemical has reported an efficient route to optically active 2-methylsuccinamic acid, an important building block for the synthesis of a number of biologically active compounds, by Rh-catalyzed asymmetric hydrogenation of 2-methylenesuccinamic acid. Although FerroTANE-type ligands proved to be promising ligands, affording high enantioselectivities (up to 93% *ee* at S/C = 100), Et-DuPhos was the only tested ligand to retain a high level of enantioselectivity at lower catalyst loadings (94% *ee* at S/C = 1000).[84]

3.2. Hydrogenation of Ketones

The Ru-catalyzed hydrogenation of 1,3-dicarbonyl compounds is a standard reaction for the screening of new chiral ligands for asymmetric hydrogenation of ketones. Since the first studies reported by Knochel and co-workers in 1999, Taniaphos ligands (**7**) have provided excellent results in the asymmetric hydrogenation of β-ketoesters.[9,35a,43] In this regard, some new Taniaphos ligands have also proved to be very useful. For instance, the methyl-substituted ligand **7b** led to 96% *ee* in the hydrogenation of ethyl benzoylacetate (Scheme 16A). A significant drop in the enantioselectivity was observed with the less bulky ethyl acetyl acetate (90% *ee*).[60] This effect was not observed with the first generation of Taniaphos (Me_2N-substituted ligand **7a**,

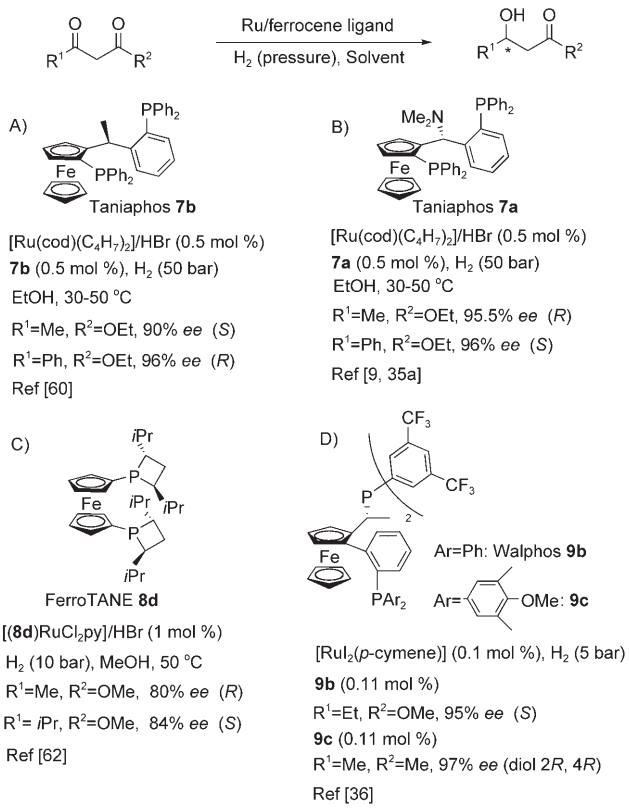

Scheme 16. Ru-catalyzed asymmetric hydrogenation of 1,3-dicarbonyl compounds.

Scheme 16B). High enantioselectivities have also been described in the hydrogenation of 1,3-diketones.[9,35a]

Moderate stereoselectivities have been achieved with the ruthenium complexes of the 1,1′-disubstituted FerroTANE family of ligands (**8**). The isopropyl ligand **8d** gave the best result (up to 84% *ee*; Scheme 16C).[62] The high efficiency of the 1,5-diphosphine Walphos ligand family (**9**) has also been reported in the Ru-catalyzed hydrogenation of 1,3-dicarbonyl compounds. After screening several Walphos ligands, the ligand **9c** bearing an electron-rich phosphine at the phenyl group directly attached to the ferrocene backbone and an electron-withdrawing phosphine substituent at the stereogenic carbon atom afforded the best enantioselectivity in the hydrogenation of methyl propanoylacetate (95% *ee*, S/C = 1000), while the related ligand **9b** was the most enantioselective in the hydrogenation of 2,4-pentanodione (97% *ee*; Scheme 16D).[36]

On the other hand, Boaz and co-workers have shown that the BoPhoz ligands (**1**) are very efficient in the Rh-catalyzed hydrogenation of α-ketoesters (Scheme 17). The enantiose-

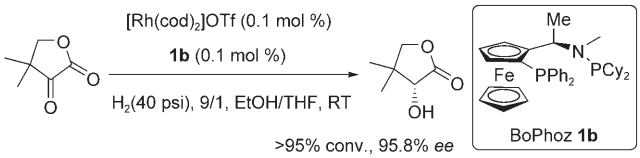

Scheme 17. BoPhoz/Rh-catalyzed hydrogenation of α-ketoesters.

 © 2006 Wiley-VCH Verlag GmbH & Co. KGaA, Weinheim

lectivity of the reaction proved to be highly solvent-dependent (EtOAc and THF were the best solvents). The optimal ligand **1b** provided *ee* values in the range 88–97% for a variety of acyclic and cyclic α-ketoesters, thus allowing to work at relatively low catalyst loadings (S/C = 1000).[51a] In a later study, the use of these ligands was successfully extended to the Ru-catalyzed hydrogenation of β-ketoesters and β-hydroxyketones.[85]

Regarding the hydrogenation of the more challenging simple ketones, in a very recent study at Solvias it was demonstrated that complexes prepared in situ from $[RuCl_2(PPh_3)_3]$ and the readily available ferrocenyl phosphine–oxazoline ligands (Fc-Phox, **15**) are extremely effective and reactive catalysts for the hydrogenation of aryl ketones with remarkable enantioselectivities (up to 99% *ee*) and excellent S/C ratios (up to 10000–50000).[86] Interestingly, in this robust catalyst system the performance of the Ru complexes does not depend very much on the substitution at the oxazoline group (for example, *t*Bu, Ph, or *i*Pr) or at the phosphine moiety. Enantioselectivities higher than 90% *ee* were achieved with most Fc-Phox ligands and substrates, and in many cases the stereoselectivity clearly exceeded 95% *ee* (Scheme 18). This catalyst system tolerates high substrate concentrations and has been scaled up to a pilot process in the case of the hydrogenation of 3,5-bis(trifluoromethyl)acetophenone (140 kg of substrate and 96% *ee*), which seems to be the first industrial catalytic process with a ferrocenyl oxazoline ligand. A research group at Merk has also employed Fc-Phox ligands in the enantioselective asymmetric hydrogenation of an α-alkoxy-substituted aryl ketone.[87]

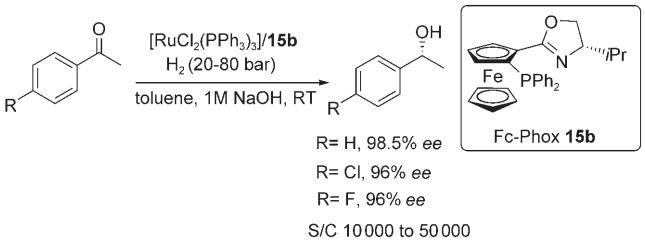

Scheme 18. Fc-Phox/Ru-catalyzed hydrogenation of aryl ketones.

Ru^{II} complexes of ppfa-type aminophosphine ligands have been recently shown to be effective catalysts in the hydrogenation of 1-acetonaphthone.[88] The influence of planar and central chirality on enantioselectivity was studied, the latter playing a decisive role. Up to 78.9% ee was achieved with the matched combination of both sources of chirality.

3.3. Hydrogenation of Imines

Unlike the asymmetric hydrogenation of alkenes and ketones, the hydrogenation of imines has been much less studied. For these substrates, Ir catalysts have frequently provided the best results.[89] In 2001, Zhang and co-workers developed a new 1,1′-diphosphino-substituted C_2-symmetrical ferrocene ligand, f-Binaphane (**18**), which showed excellent reactivities and enantioselectivities in the Ir-catalyzed asymmetric hydrogenation of acyclic imines.[90] Interestingly, under these reaction conditions ketones were not hydrogenated. More recently, this ligand has been applied to the asymmetric reductive amination reaction of a variety of aromatic ketones with *p*-anisidine, without isolation of the intermediate imines. The process is catalyzed by the Ir–f-Binaphane complex, generated in situ from $[\{Ir(cod)Cl\}_2]$ and the ligand, in the presence of $[Ti(OiPr)_4]$ and I_2 to accelerate the formation of the imine, which was found to be the rate-limiting step. High enantioselectivities, usually in the range of 92–96% *ee*, were obtained for most tested methyl aryl ketones using 1 mol% of catalyst.[91] Synthetically important, the further oxidative cleavage of the anisidyl group with cerium(IV) ammonium nitrate (CAN) leads to the corresponding enantioenriched primary amine (Scheme 19).

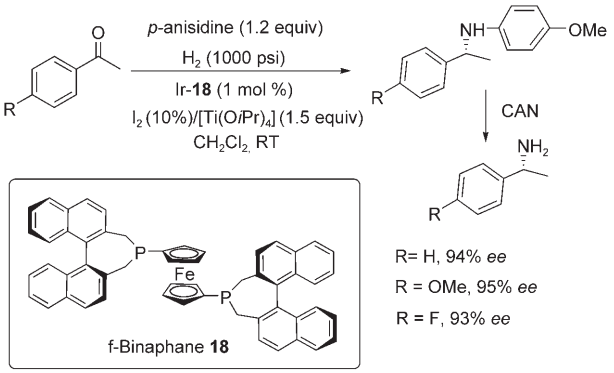

Scheme 19. f-Binaphane/Ir-catalyzed asymmetric hydroamination.

The key step in the industrial synthesis of the chiral herbicide (1*S*)-metolachlor (Syngenta) is the enantioselective hydrogenation of the imine **IV** catalyzed by a soluble chiral iridium ferrocene complex of the ligand Xyliphos (**19**), generated in situ by mixing $[Ir_2(\mu\text{-}Cl)_2(cod)_2]$, Xyliphos, iodide (sodium iodide or terabutylammonium iodide), and a Brønsted acid (for example, acetic or sulphuric acid), to provide the amine metholachlor precursor in 80% *ee* (Scheme 20). Outstandingly, this catalyst system is extremely reactive, being one of the fastest homogeneous systems known ($S/C = 10^6$) and nowadays the largest-scale enantioselective catalytic process in industry.[3] In a recent work, the preparation and characterization of some iridium complexes of *ent*-Xyliphos that contain all the catalyst ingredients in the coordination sphere of the iridium center (Xyliphos, cod, iodide, and hydride from a Brønsted acid, for example, in complexes **20** and **21**; Scheme 20) were described. These complexes were structurally characterized by single-crystal X-ray diffraction and proved to be very active in the asymmetric hydrogenation of the imine precursor.[92] Moreover, the isolation of several substrate–catalyst adducts confirmed the k^2 coordination mode of the imine to the Ir atom.

© 2006 Wiley-VCH Verlag GmbH & Co. KGaA, Weinheim

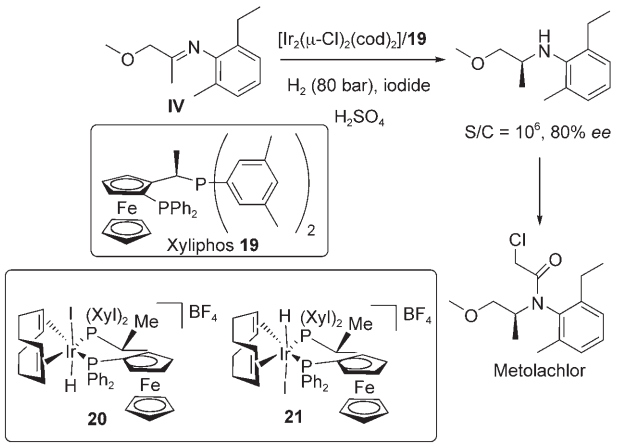

Scheme 20. Synthesis of metolachlor and isolated Ir–Xyliphos complexes **20** and **21**.

3.4. Asymmetric Transfer Hydrogenation of Ketones

The asymmetric hydrogenation of ketones employing small organic molecules as hydrogen donors (for example, formic acid and especially 2-propanol) constitutes a practical alternative to the enantioselective reduction of ketones. In this process Ru, Rh, and Ir chiral catalysts are particularly useful and have been intensively studied.[93] The process involves the participation of a metal hydride as a reducing intermediate species. However, unlike the asymmetric hydrogenation in which chiral diphosphines are usually the ligands of choice, in the transfer hydrogenation process nitrogen-based ligands hold a dominant role. The great efficiency of bidentate P,N Fc-Phox ligands (**15**) in the Ru-catalyzed reduction of aryl alkyl ketones was described ten years ago.[94] With the oxazoline **15c**, having a phenyl substituent at the stereogenic carbon, asymmetric inductions in the range 88–96% *ee* were achieved at a substrate/catalyst ratio of 500 (Scheme 21 A).

In recent years a variety of ferrocene ligands with nitrogen and/or phosphorus substituents have been tested in the reduction of acetophenone, although in many cases the enantiocontrol was moderate or low.[95] Among the best results, Zheng and co-workers have described good enantioselectivities with their novel P,N,O Schiff base ligands (Scheme 21 B). After a systematic screening of the effect of the substitution at the salicylaldehyde backbone, it was found that electron-withdrawing substituents resulted in significantly higher activity and enantioselectivity. With the optimal ligand **22a** a variety of substituted acetophenones were reduced with high enantioselectivity (usually 83–94% *ee*), albeit with a high required catalyst loading (2 mol% of ligand).[96] In an independent study, the same group described similar results using related ferrocene P,N,P-type ligands.[97]

Keeping in mind the pioneering work of Noyori on the impressive reactivity and stereoselectivity of [Ru(Binap)(diamine)(dihalide)] complexes in the hydrogenation of ketones,[98] the octahedral *trans*-substituted dichlororuthenium complex of Josiphos and pyridine has been recently isolated and characterized by X-ray analysis (complex **23**,

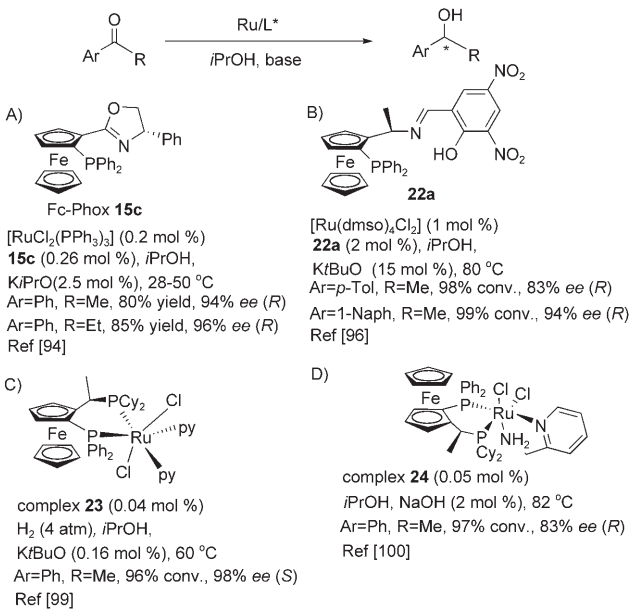

Scheme 21. Ru-catalyzed asymmetric transfer hydrogenation of ketones.

Scheme 21 C). This compound catalyzes the reduction of 1-acetonaphthone in 98% *ee* using a low catalyst loading (0.04 mol%) in the presence of a combination of hydrogen and 2-propanol/base.[99] Similarly, some related Josiphos dichlororuthenium complexes, in this case using the 2-(aminomethyl)pyridine as a bidentate N,N ligand (complex **24**), have also provided interesting results in the reduction of acetophenone under typical transfer–hydrogenation conditions (Scheme 21 D).[100]

On the basis of the known Ir-catalyzed α-alkylation of ketones with primary alcohols,[101] in a very recent study Nishibayashi and co-workers have reported the one-pot sequential Ir-catalyzed α-alkylation of ketones with alcohols and the Ru-catalyzed asymmetric transfer hydrogenation of the elongated ketone (Scheme 22).[102] Using the ruthenium complex of the oxazoline ligand *i*Pr-Fc-Phox (complex **25**), the resulting alcohols were obtained with high enantioselectivity (88–97% *ee*). This methodology is a nice example of sequential transition-metal-catalyzed reactions involving two compatible metal complexes.

Applying the reversibility of this metal-catalyzed redox reaction of ketones and alcohols, Uemura and co-workers have shown the usefulness of Fc-Phox ligands in the

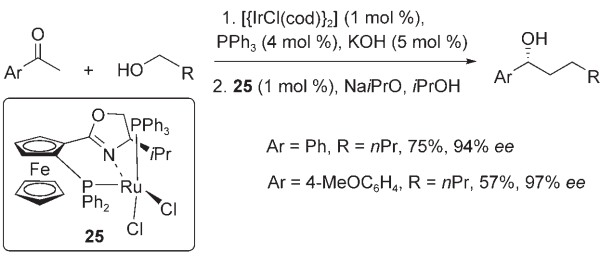

Scheme 22. Asymmetric α-alkylative reduction of ketones with alcohols by Ir- and Ru-catalyzed sequential reactions.

 © 2006 Wiley-VCH Verlag GmbH & Co. KGaA, Weinheim

ruthenium(II)-catalyzed oxidative kinetic resolution of racemic aryl alkyl alcohols.[103] Using acetone as both the solvent and oxidant (hydrogen acceptor) in the presence of a catalytic amount of sodium isopropoxide and the Ru complex **25** (0.1 mol%), the oxidative kinetic resolution of secondary benzyl alcohols was highly efficient and provided the unreacted alcohol in high yield and enantioselectivity (typically 41–53% yields and 85–99% *ee*). In particular, the oxidative kinetic resolution of 1-indanol proceeded quite rapidly, allowing the use of very high S/C ratios (up to 80000) with a small decrease in the enantioselectivity of the process (Scheme 23). This oxidative-resolution process has been applied on a 1-mol scale of substrate (134 g of racemic 1-indanol), thus highlighting its great practical applicability.

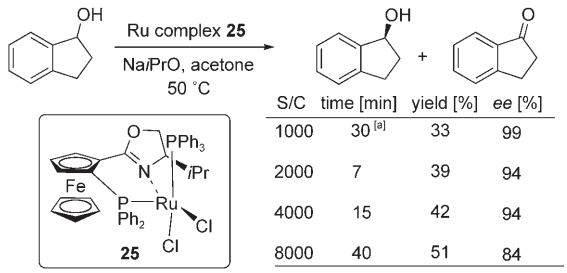

S/C	time [min]	yield [%]	*ee* [%]
1000	30 [a]	33	99
2000	7	39	94
4000	15	42	94
8000	40	51	84

[a] At 30 °C.

Scheme 23. Fc-Phox/Ru oxidative kinetic resolution of racemic indanol.

3.5. Asymmetric Hydrosilylation Reactions

The Rh-catalyzed hydrosilylation of ketones and final hydrolysis of the silyl ether is another practical alternative for the asymmetric reduction of ketones to alcohols.[104] The Trap ligands (**14**), developed by Ito and co-workers,[105] constitute a structurally outstanding family of chiral bisphosphines which form a *trans*-chelated nine-membered metallacycle. The interest in these ligands in the Rh-catalyzed hydrosilylation of ketones was first reported in 1994.[106] Unlike the previously tested Trap ligands, having both planar and central chirality, the Et-Trap-H ligand **14c** with only planar chirality has been recently prepared.[107] Interestingly, this ligand proved to be more stereoselective than the previous Trap ligands in the hydrosilylation of a varied set of ketones, including aryl alkyl ketones (88–94% *ee*) and the more challenging dialkyl ketones (76–89% *ee*; Scheme 24). These results show the dominant role of the planar chirality in Trap ligands in the stereocontrol of the process. In this regard it must be noted that the heterocyclic P,N ferrocene-type ligand **26** with only planar chirality, developed by Tao and Fu, is an excellent ligand in the Rh-catalyzed hydrosilylation of aryl alkyl ketones (95–99% *ee*) and dialkyl ketones (72–96% *ee*; Scheme 25).[108] An N,S-chelating zinc catalyst derived from a ferrocene oxazoline has also been recently tested in the hydrosilylation of ketones, although with low stereoselectivity (9–55% *ee*).[109]

Lipshutz and co-workers have developed the first general version of the catalytic asymmetric 1,4-reduction of β,β-disubstituted prochiral enones to give ketones with a stereo-

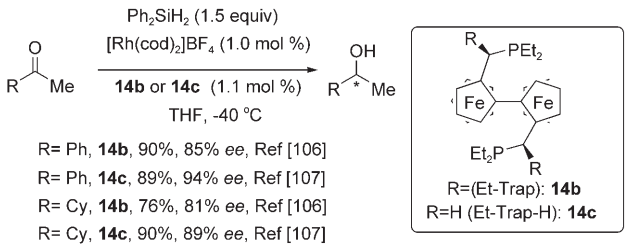

Scheme 24. Trap/Ru-catalyzed asymmetric hydrosilylation of ketones.

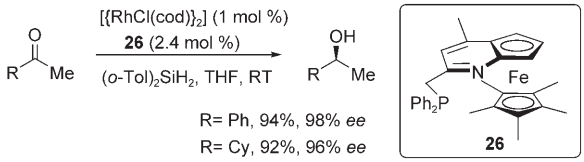

Scheme 25. Ru-catalyzed asymmetric hydrosilylation with the planar-chiral ligand **26**.

defined tertiary carbon center at the β position. This process is based on the asymmetric conjugate reduction with CuH, generated in situ from a catalytic amount of CuCl (typically 2 mol%) and stoichiometric polymethylhydrosiloxane (PMHS), in the presence of a chiral ligand (typically 1 mol%).[110] In the screening of a set of commercially available ligands, mainly ferrocene-based ligands, the Josiphos-type family proved to be the most efficient. In particular, the bulky (di-*tert*-butyl)phosphane **13b**, available in both enantiomeric forms, showed the highest enantiocontrol in the model reaction. With this ligand very high *ee* values (87–99% *ee*) were achieved in the reduction of a wide variety of *E*- and *Z*-substituted enones (Scheme 26). As expected, diastereomeric *E* and *Z* olefins led to opposite enantiomers. Interestingly, the amount of ligand can be substantially reduced without erosion of the enantioselectivity (an example is described with a ketone/ligand ratio of 1650:1).

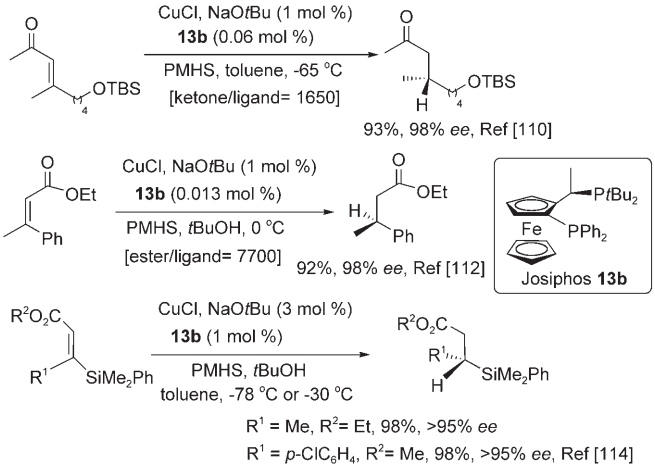

Scheme 26. Josiphos/Cu-catalyzed asymmetric conjugate reduction of α,β-unsaturated ketones and esters.

 © 2006 Wiley-VCH Verlag GmbH & Co. KGaA, Weinheim

This catalyst combination has also been successfully applied to the asymmetric 1,4-hydrosilylation of β,β-disubstituted α,β-unsaturated esters, originally reported by Buchwald and co-workers employing *p*-Tol-Binap as the ligand.[111] Using the Josiphos ligand **13b**, excellent enantioselectivities were achieved (93–99% *ee*).[112] Although ester/**13b** ratios are typically 500–1000, a lower ligand loading can be used (S/C up to 7700). In this reaction the axial chiral ligand Segphos proved also to be very efficient, as well as in the CuH-catalyzed asymmetric hydrosilylation of aryl ketones.[113] As a step further, this method has been very recently extended to the highly enantioselective conjugate reduction of (*E*)- and (*Z*)-β-silyl α,β-unsaturated esters[114] (*ee* values usually >90%), in which case the ligand **13b** is far superior to Segphos (Scheme 26).

As these reactions are proposed to proceed via a copper enolate intermediate, their trapping with a carbonyl compound is a very interesting approach to the stereoselective synthesis of aldol-type products.[115] In this area Riant and co-workers have investigated the conjugate reductive aldol reaction between methyl acrylate and aryl methyl ketones with phenylsilane as the reducing agent (Scheme 27).[116] Among several tested ligands, including MeO-Biphep, Binap, Josiphos, Mandyphos, Walphos, and Taniaphos ligands, the Taniaphos ligand **7c** was the most enantioselective. Thus, the catalyst system formed by $[CuF(PPh_3)_3]\cdot 2MeOH$ (1 mol%) and ligand **7c** (1 mol%) provided the *erythro* aldol product in good yield and high diastereoselectivity and enantioselectivity with a variety of aromatic and heteroaromatic ketones (82–95% *ee*).

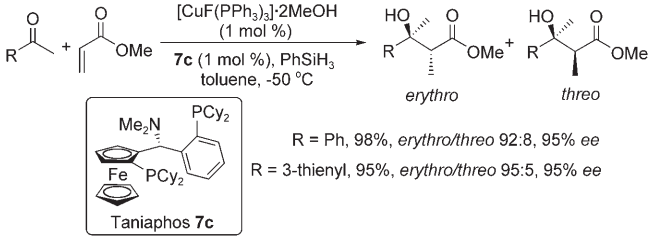

Scheme 27. Taniaphos/Cu-catalyzed asymmetric reductive aldol reaction.

Highlighting the broad structural scope of this type of Cu-catalyzed conjugate reduction, Carreira and co-workers have developed the highly enantioselective conjugate reduction of β,β-disubstituted nitroalkenes using the bulky *t*Bu-Josiphos ligand **13b** (Scheme 28). After screening different reaction conditions CuO*t*Bu proved to be a better copper source than typical CuCl as a result of the observed activity inhibition exerted by the chloride anion. Moreover, it was found that the highest reaction rates were achieved using a combination of phenylsilane (1.2 equiv) and PMHS (0.1 equiv) as a reducing Si–H source and a small amount of water (1.2 equiv) to suppress competitive overreduction processes. Under these optimized conditions an ample set of substituted nitroalkenes were reduced in good yields (55–89%) and enantioselectivities (68–94% *ee*).[117] Although 1 mol% of ligand **13b** is routinely employed, some examples have been successfully

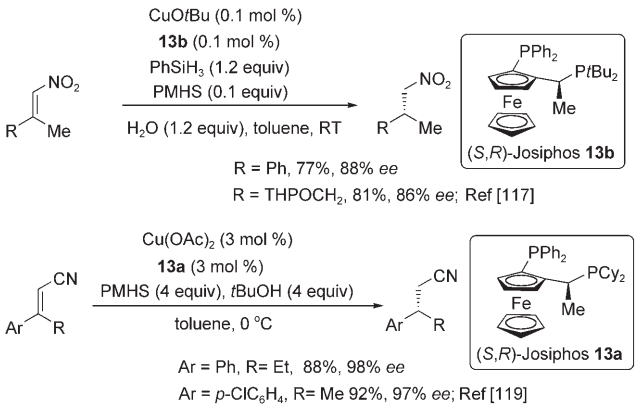

Scheme 28. Josiphos/Cu-catalyzed asymmetric conjugate reduction of nitroalkenes and α,β-unsaturated nitriles.

run at a lower catalyst loading (0.1 mol%). In a later study it was documented that commercially available CuF_2 can be employed instead of the oxygen- and moisture-sensitive CuO*t*Bu.[118]

Using a similar strategy, Yun and co-workers have described the enantioselective conjugate reduction of a variety of (*E*)- and (*Z*)-β-aryl-, β-methyl-disubstituted nitriles.[119] The optimized conditions involve the use of $Cu(OAc)_2$/Josiphos (**13a**) as the catalyst system (3 mol%). In this process Josiphos was found to be more efficient than Binap, Tol-Binap and other Josiphos-type ligands such as **13b**. The reduction process occurs with high enantioselectivity, usually in the range 94–99% *ee* (Scheme 28).

Concerning the hydrosilylation of multiple carbon–carbon bonds, in 2001 Hayashi and co-workers described the asymmetric Pd-catalyzed hydrosilylation of 1-buten-3-ynes with trichlorosilane (Scheme 29).[120] In the case of enynes

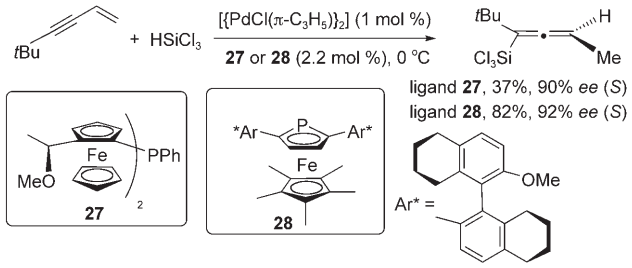

Scheme 29. Pd-catalyzed asymmetric hydrosilylation of 5,5-dimethyl-1-hexen-3-yne.

having a bulky substituent at the 4-position, allenyl silanes were obtained with high selectivity, presumably through the participation of a π-propargyl(silyl)palladium intermediate species. Initially, the highest enantioselectivity was obtained in the presence of the monodentate bisferrocene ligand bis-ppf-OMe **27**, affording the allene with up to 90% *ee*. This asymmetric induction has been recently improved with the structurally novel phosphaferrocene **28**, which has biaryl substituents with axial chirality at positions contiguous to the phosphorus atom (Scheme 29).[121]

 © 2006 Wiley-VCH Verlag GmbH & Co. KGaA, Weinheim

4. Asymmetric Addition of Hydrogen–Heteroatom and Heteroatom–Heteroatom Bonds to Alkenes

4.1. Hydroboration

Although the hydroboration of alkenes does not require any catalyst, it was reported in 1985 that the reaction is greatly accelerated by a rhodium–phosphine complex.[122] Since this report, great attention has been paid to the development of Rh-catalyzed asymmetric hydroborations using chiral phosphine ligands.[123] The resulting chiral boranes are very valuable precursors in the enantioselective synthesis of a variety of functional groups, such as alcohols, amines, and carboxylic acids. Traditionally, the model testing reaction has been the hydroboration of styrene with catecholborane, both the regioselectivity and enantioselectivity being highly dependent on the nature of the ligand. Concerning the use of ferrocene ligands, in the 1990s Togni described high enantiocontrol in the hydroboration of styrene with Josiphos[124] and pyrazol phosphino ferrocenes, such as **29** (Scheme 30).[125] More recently, in 2003, Knochel and co-workers described a new family of ferrocene P,N ligands having a coordinating nitrogen heterocycle at the 1-position. With the optimal ligand **30**, a maximum 92% *ee* was achieved, albeit with moderate regioselectivity.[126]

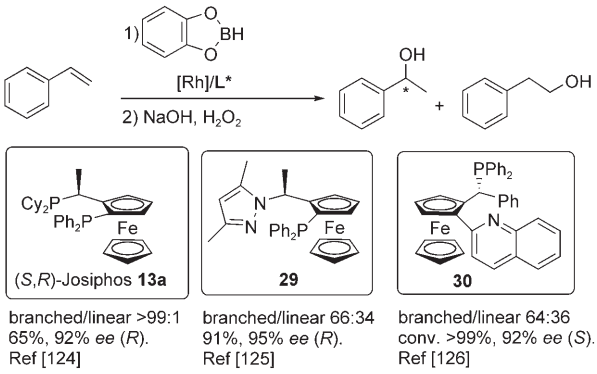

Scheme 30. Ferrocene ligands for Rh-catalyzed asymmetric hydroboration of styrene.

In a recent communication, Crudden et al. reported the utilization of pinacolborane (HBpin), which is more stable toward air and nucleophiles than the commonly used catecholborane, in rhodium- and iridium-catalyzed hydroboration reactions.[127] The use of cationic rhodium complexes in the presence of phosphines led to the branched product usually with high selectivity, while the iridium-catalyzed reaction afforded the linear compound as the only observable product. The asymmetric hydroboration reaction was studied using three well-established chiral ligands: Binap, Quinap, and Josiphos. The best yields and enantioselectivities were obtained with Josiphos (up to 88% *ee*). For instance, the hydroboration of styrene occurred with 84% *ee*, and the hydroboration of 6-methoxy-2-vinylnaphthalene (precursor of naproxen) with 88% *ee* (Scheme 31). Interestingly, inversion of the enantioselectivity was observed when pinacolborane was employed instead of catecholborane.

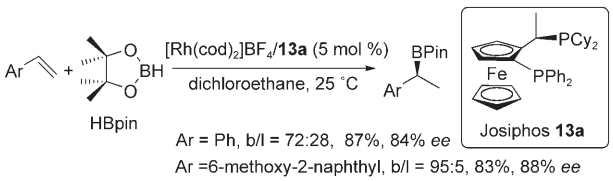

Scheme 31. Josiphos/Rh-catalyzed asymmetric hydroboration of vinyl arenes with pinacolborane.

The asymmetric bismetalation of carbon–carbon multiple bonds has not been extensively explored. Suginome, Murakami, and co-workers have described the Pd-catalyzed silaboration of terminal allenes to afford β-borylallylsilanes by regioselective addition of the Si–B bond to the internal double bond of terminal allenes. The use of [Cp(allyl)Pd] with tertiary monodentate phosphines allowed to carry out the reaction at room temperature. A series of silylboranes bearing chiral auxiliary groups on the boron atom, in combination with chiral monodentate phosphines, were used in the reaction.[128] High diastereoselectivities were achieved applying the appropriate matched combination of chiral auxiliary at boron and chiral monodentate phophine as ligand. Although a chiral axial binaphthyl monophosphine provided the best stereocontrol (up to 96% *de*), the monodentate silyl phosphine ferrocene **31** proved also to be very efficient (81% *de*; Scheme 32).

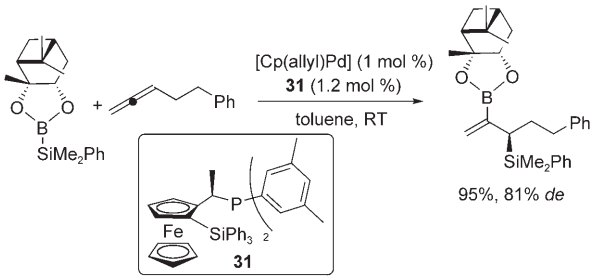

Scheme 32. Pd-catalyzed silaboration of allenes by double asymmetric induction.

4.2. Hydroamination, Hydrophosphination, and Hydrophosphorylation

Hydroamination of olefins constitutes a very appealing atom-economic approach to the synthesis of tertiary amines. However, the asymmetric version of this reaction is particularly challenging, and only a few enantioselective procedures are known, generally leading to moderate *ee* values.[129] An isolated example of asymmetric hydroamination of a vinylarene with ferrocene ligands is the Pd-catalyzed Markovnikov addition of benzyl methyl amine to 2-vinylnaphtalene in the presence of Et,Et-FerroTANE (**8c**), providing the tertiary amine in 36% yield and 63% *ee*.[130]

On the other hand, Togni and co-workers have reported that cationic Ni^{II} complexes of the potentially tridentate P,P,P ligand Pigiphos **32** are efficient catalysts for the hydroamina-

 © 2006 Wiley-VCH Verlag GmbH & Co. KGaA, Weinheim

tion of activated olefins (especially α,β-unsaturated nitriles) with both anilines and aliphatic amines with 1–5 mol% catalyst loading.[131] Disappointingly, the process occurs with low enantiocontrol, with the best result obtained in the amination of methacrylonitrile with morpholine (69% *ee*). In this reaction the related bidentate ligand Josiphos was unreactive. In a later report, the same chiral nickel catalyst, $[Ni(Pigiphos)(thf)](ClO_4)_2$, was successfully extended to the enantioselective hydrophosphination of methacrylonitrile.[132] After optimization of the reaction conditions, moderate to high enantioselectivities (32–94% *ee*) were achieved with a series of secondary phosphines in acetone at −25°C (Scheme 33). The best results were obtained with the bulkier

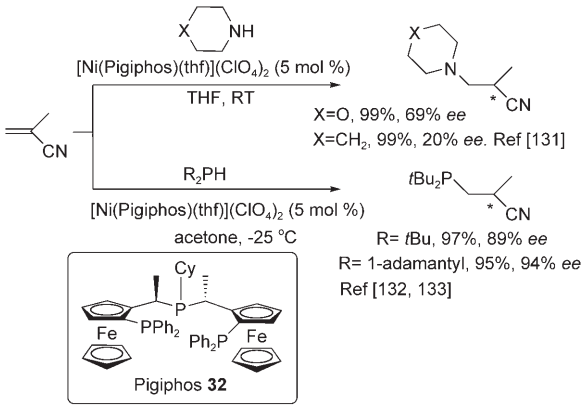

Scheme 33. Pigiphos/Ni-catalyzed asymmetric amination and hydrophosphination of methacrylonitrile.

nucleophiles, such as tBu_2PH (89% *ee*) and or $(adamantyl)_2PH$ (94% *ee*). Mechanistic investigations suggest the coordination of methacrylonitrile to the dicationic nickel catalyst, followed by 1,4-addition of the phosphine and subsequent rate-determining proton transfer.[133]

The palladium-catalyzed asymmetric hydrophosphorylation of norbornene has been reported very recently.[134] After screening a wide variety of chiral phosphines, the Josiphos family provided by far the best results. With the *tert*-butyl-substituted ligand **13c**, up to 88.5% *ee* was obtained in the reaction with dioxaphospholane 2-oxides (Scheme 34). Finally, several ferrocene ligands have been recently tested in the asymmetric hydroformylation[135] and hydroesterification[136] of styrene, albeit with very low enantioselectivity.

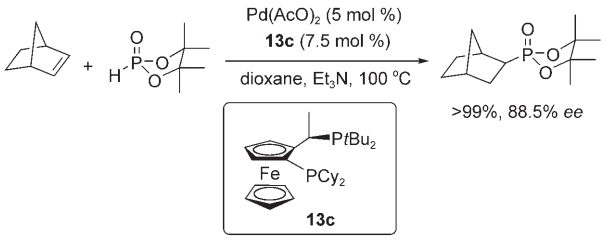

Scheme 34. Josiphos/Pd-catalyzed asymmetric hydrophosphorilation of norbornene.

4.3. Dihydroxylation and Aminohydroxylation

The osmium complexes of chinchona alkaloids, developed by Sharpless, for asymmetric dihydroxylation and aminohydroxylation of alkenes represents an outstanding contribution in the area of asymmetric catalysis.[137] In 2003 Muñiz and co-workers described the first examples of ferrocenoyl-substituted cinchona alkaloids (**33** and **34**) and their application in asymmetric oxidative double-bond transformations.[138] The dihydroxylation of (*E*)-stilbene under catalytic conditions afforded the corresponding diol in moderate enantioselectivity (up to 44% *ee*; Scheme 35). Similar asymmetric inductions were achieved in the catalytic aminohydroxylation of stilbene and cyclohexene using the bidentate ligand **34** and chloramine-T as terminal oxidant (42% and 48% *ee*, respectively). Under these optimized conditions the aminohydroxylation of cinnamic esters occurred with moderate regioselectivities (up to 5:1) and enantioselectivities (up to 61% *ee*). On the other hand, very low enantioselectivities have been described in the 1,4-diacetoxylation of 2-phenyl-1,3-cyclohexadiene with ferrocenyl–quinone ligands.[139]

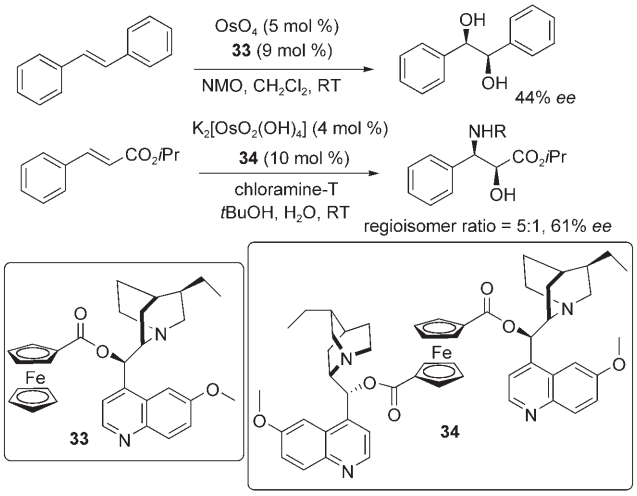

Scheme 35. Asymmetric dihydroxylation and aminohydroxylation by ferrocenoyl chinchona alkaloids; NMO = *N*-methylmorpholine *N*-oxide.

5. Asymmetric Metal-Catalyzed Coupling Reactions and Related Processes

5.1. Asymmetric Allylic Substitutions

In spite of its low interest from a synthetic-applicability point of view, the Pd-catalyzed asymmetric allylic alkylation (AAA) reaction[140] of 1,3-diphenylpropenyl acetate with soft nucleophiles has become a standard model reaction for the screening of newly designed ligand structures. Within the period covered by this review, more than twenty new ferrocene ligands with P,P,[141] P,N-,[126,142] P,S-,[41,142a,143] N,S-,[142a,n,144] S,S-,[143b] and P,P,N,N-coordination[145] modes have been tested in this benchmark reaction. Unfortunately,

 © 2006 Wiley-VCH Verlag GmbH & Co. KGaA, Weinheim

most of those ferrocene-based chiral ligands appear to be confined to this particular reaction, since only in very few cases their successful application to more challenging substrates has been documented.

Among the reported structures, three P,N ligands, one of which has only central chirality (ligand **35a**; Table 1) and the other two combine central and planar chirality (ligands **36** and **37**), and the Fesulphos ligands (**38**), with exclusively planar chirality, stand out for reaching enantioselectivities of 99% *ee* or higher in the asymmetric allylic alkylation reaction of 1,3-diphenylallyl acetate (Table 1). Moyano and co-workers have found that the Phox ligand **35a**, with a ferrocenyl group at C4 of the oxazoline ring led to 99.6% *ee* in the asymmetric allylic alkylation with dimethyl malonate (Table 1, entry 1).[142o] The same enantioselectivity was achieved in this transformation by Jin and co-workers with the phosphinoimidazolidine **36** (Table 1, entry 2).[142p] On the other hand, after exploring several phosphine–heteroaryl amine ligands, Zheng and co-workers have successfully applied the phosphine–triazine **37**[142l] in the asymmetric allylic alkylation reaction with dimethyl malonate (Table 1, entry 3). The novel P,S ligands with the structure of 1-phosphino-2-sulfenyl ferrocene (Fesulphos ligands), developed by our group, are also very effective in this transformation.[41] For instance, the ligands **38a** and **38b** with sterically demanding groups at both the sulfur (*tert*-butyl) and phosphorus [1-naphthyl (**38a**) and *o*-tolyl (**38b**)] coordinating atoms led to a 99.5% *ee* value in the asymmetric allylic alkylation with benzylamine (Table 1, entries 4 and 5).

Table 1: Ferrocene ligands in the asymmetric allylic alkylation of 1,3-diphenyl-2-propenyl acetate.

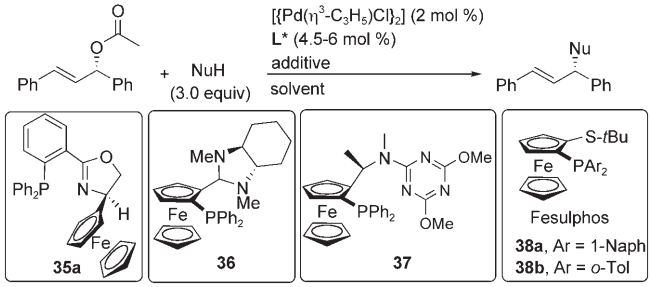

Entry	NuH	Conditions	L*	Yield [%]	*ee* [%]	Ref.
1	$CH_2(CO_2Me)_2$	CH_2Cl_2, RT[a]	**35a**	63	99.6	[142o]
2	$CH_2(CO_2Me)_2$	C_6H_6, RT[a]	**36**	99	99.6	[142p]
3	$CH_2(CO_2Me)_2$	CH_2Cl_2, 10 °C[b]	**37**	93	99.0	[142l]
4	$BnNH_2$	THF, RT	**38a**	82	99.5	[41]
5	$BnNH_2$	THF, RT	**38b**	93	99.5	[41]

[a] BSA (3.0 equiv; bis(trimethylsilyl)acetamide), LiOAc (cat.). [b] BSA (3.0 equiv), KOAc (cat.).

With few exceptions, most of ligands that perform well with the 1,3-diphenylallyl system typically lead to very poor results with more synthetically valuable substrates, such as cycloalkenyl esters or unsymmetrical allylic substrates. In fact, only a few ferrocene ligands proved to induce enantiomeric excesses of > 80% *ee* in the reaction of cyclic substrates (Table 2). Zheng and co-workers[142g,k] have evaluated their

Table 2: Ferrocene ligands in the asymmetric allylic alkylation of cyclic substrates.

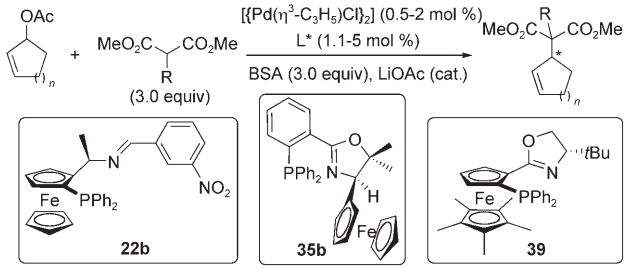

Entry	*n*	R	Solvent, *T* [°C]	L*	Yield [%]	Config.	*ee* [%]	Ref.
1	1	H	toluene, RT	**22b**	89	(*R*)	82	[142g]
2	2	Me	toluene, RT	**22b**	78	(*R*)	81	[142g]
3	3	H	toluene, RT	**22b**	95	(*R*)	89	[142g]
4	2	H	THF, RT	**35b**	60	(*S*)	58	[142o]
5	1	H	THF, −30	**39**	96	(*R*)	92	[39]
6	2	H	THF, RT	**39**	92	(*R*)	84	[39]
7	3	H	THF, RT	**39**	93	(*R*)	94	[39]

family of ferrocenyl phosphine–imine ligands in the asymmetric allylic alkylation reaction of 2-cycloalkenyl esters with dimethyl malonate. The best results were obtained with the *meta*-nitrophenyl imine **22b**,[142g] which provided the substitution products of cyclopentenyl, cyclohexenyl, and cycloheptenyl substrates with up to 89% *ee* (Table 2, entries 1–3).

Moyano and co-workers found that the Phox ligand **35b**, analogous to **35a** but with a geminal dimethyl group at the C5 position of the oxazoline ring, led to a significant enantioselectivity in the asymmetric allylic alkylation reaction of dimethyl malonate with 2-cyclohexenyl acetate (58% *ee*; Table 2, entry 4), while ligand **35a** provided the product in only 11% *ee*.[142o] The authors hypothesized that the geminal dimethyl group in ligand **35b** restricts the conformational mobility of the ligand, the ferrocene moiety becoming oriented towards the π-allylpalladium moiety.

A sterically highly demanding class of planar-chiral Phox ligands, possessing a pentamethylferrocene backbone, have been recently developed by Helmchen and co-workers.[39] In particular, ligand **39** with matched central and planar chirality has provided excellent yields and enantioselectivities (84–94% *ee*) in the Pd-catalyzed asymmetric allylic alkylation of cycloalkenyl acetates with dimethyl sodiomalonate (Table 2, entries 5–7) using 1 mol% of catalyst.

The research groups of Hou and Dai have devoted continuous effort in developing new methodologies of asymmetric allylic alkylation with chiral ferrocene ligands.[15] In 2001 they reported outstanding results in the asymmetric allylic alkylation of monosubstituted allylic acetates using newly designed chiral P,N-1,1′-disubstituted ferrocenes bearing a chirogenic phosphorus atom bonded to a key Binol unit.[146] As a step further, ligands **40** and **41** were more recently found to efficiently promote the allylic alkylation and amination of dienyl esters (Scheme 36).[147] In the reaction with dimethyl malonate, linear substrates gave better regio- and enantioselectivities (ligand **40**), while branched allyl acetates provided the best results in the amination with benzylamine (ligand **41**). The construction of chiral all-carbon

 © 2006 Wiley-VCH Verlag GmbH & Co. KGaA, Weinheim

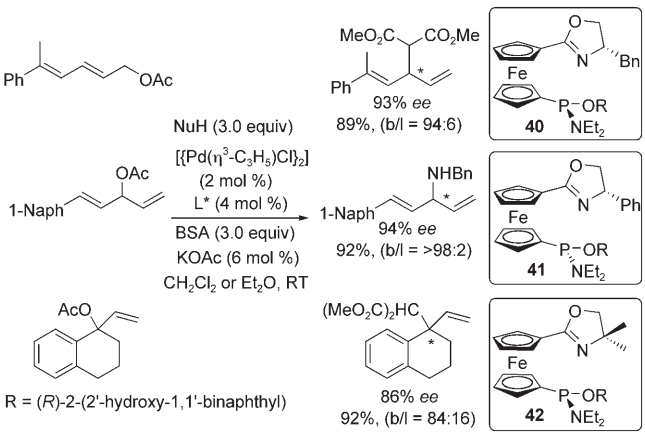

Scheme 36. Asymmetric allylic alkylation of unsymmetrical acyclic allylic substrates; * absolute stereochemistry not determined.

quaternary stereocenters by enantioselective nucleophilic addition on the geminal disubstituted terminus of the palladium π-allyl species, which is especially challenging because of the significant steric hindrance, has also been realized in the presence of ligand **42** (Scheme 36).[148]

The enantioselective nucleophilic addition of prochiral stabilized carbon nucleophiles to a π-allylpalladium complex represents a much less explored alternative of asymmetric allylic alkylation. In 1996 Sawamura, Ito, and co-workers found a novel alternative for stereochemical control in the asymmetric construction of quaternary carbon stereocenters: an allylation of cyanoesters catalyzed by a Pd/Rh two-component catalyst system.[149] While the palladium species activates the electrophile, the rhodium species can coordinate to the cyano group of the substrate to control the enantioselectivity. Up to 99% *ee* was achieved in the presence of the *trans*-chelating ligand *p*-$MeOC_6H_4$-Trap. This strategy has been recently applied in the allylation of methyl cyano(3,4-dichlorophenyl)acetate.[150] However, only 32% *ee* was attained with the catalyst system composed by Rh/Ph-Trap (**14a**) and Pd/dppb (1,2-bis(diphenylphosphino)benzene) in the allylation, while Trost's ligand promoted the reaction with 63% *ee* (Scheme 37).

Although traditionally the use of carbon nucleophiles was initially restricted to stabilized soft carbanions derived from 1,3-dicarbonyl compounds and analogues or heteroatom nucleophiles, Trost and Schroeder demonstrated in 1999 that simple ketones such as tetralone or cyclohexanone are also suitable nucleophiles, achieving high enantioselectivities with Trost's chiral-pocket ligand.[151] Hou and co-workers have recently reported the use of a similar ligand (**43**), which

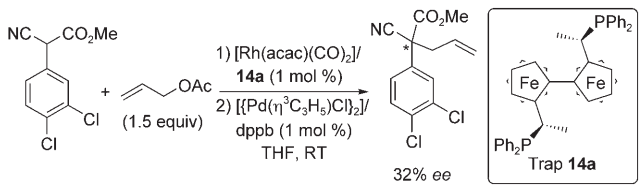

Scheme 37. Asymmetric allylic alkylation assisted by a bimetallic catalytic system; * absolute stereochemistry not determined.

incorporates the planar chirality of two ferrocene units as additional elements of asymmetry, in the asymmetric allylic alkylation of simple acyclic ketones (Scheme 38).[152] The choice of the bulky LiHMDS as base provided the best

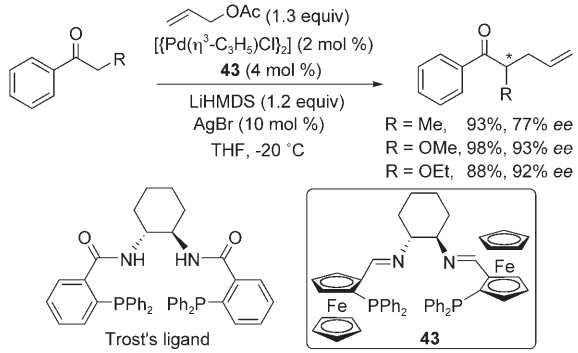

Scheme 38. Asymmetric allylation of prochiral nucleophiles; * absolute stereochemistry not determined.

results, while the addition of a catalytic amount of AgBr (10 mol%) as Lewis acid had a dramatic beneficial effect on both reactivity and enantioselectivity. The *Z*/*E* form of the enolate does also dramatically affect the enantioselectivity, the *Z* enolate affording the product with higher levels of asymmetric induction than that with *E* configuration. In accordance with this observation, ketones with an alkoxy group at the α position led to products with higher enantioselectivity compared to those with more sterically hindered α-alkyl groups.

While palladium and other metals, such as molybdenum and iridium for example, mostly require soft nucleophiles (that is, malonate-type anions or amines) for high regio- and stereocontrol, copper catalysts have emerged as a complementary strategy that allows the use of hard nucleophiles (for example, organometallic reagents).[153] Although the development of copper-catalyzed enantioselective asymmetric allylic alkylation is far behind that of palladium catalysts, remarkable progress has been achieved since the first report in 1995,[154] with most examples involving the use of organozinc reagents. Soon after the great success achieved by Alexakis and co-workers in the Cu–phosphoramidite-catalyzed asymmetric allylic alkylation with Grignard reagents,[155] Feringa and co-workers demonstrated that Taniaphos (**7a**) is a highly efficient ligand for the Cu-catalyzed asymmetric allylic alkylation of primary allyl bromides with Grignard reagents, providing the corresponding products with excellent enantiocontrol (94–98% *ee*) and good regioselectivities (Scheme 39).[156]

Some ferrocene ligands from the FerroTANE, Walphos, and Josiphos families have also been explored in a new Ni^0-catalyzed enantioselective intramolecular asymmetric-allylic-amination route to vinylglycinol derivatives.[157] Although a good asymmetric induction was attained with a Josiphos-type ligand (82% *ee*), very low conversion was observed (17%). The most practical results were obtained with ligands possessing axial chirality, such as MeO-Biphep (88% yield, 75% *ee*).

 © 2006 Wiley-VCH Verlag GmbH & Co. KGaA, Weinheim

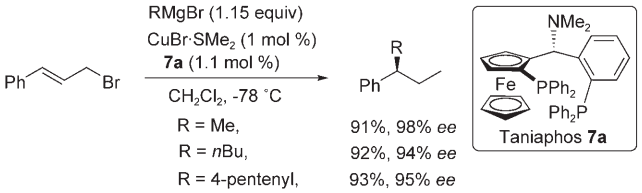

Scheme 39. Taniaphos/Cu-catalyzed asymmetric allylic alkylation with Grignard reagents.

5.2. Other Asymmetric Processes Involving Chiral Allylpalladium Intermediates

From a mechanistic point of view the palladium-catalyzed addition of stabilized nucleophiles to conjugated dienes is closely related to the allylic-substitution process, except for the fact that in the former the allylpalladium intermediate is formed by insertion of a chiral hydride palladium intermediate into the diene unit. Interestingly, this approach neither requires a leaving group nor an external base. The first intermolecular enantioselective version of this reaction was achieved by Hartwig and co-workers in 2004 using as chiral catalyst the combination of [CpPd(allyl)], as precursor to Pd^0, and the *tert*-butyl Josiphos ligand **13b**.[158] As the best result, the reaction of 2,4-pentadione with 1,3-cyclohexadiene occurred with 5 mol% catalyst to give the addition product in good yield (71%) and in 81% *ee* (Scheme 40). The addition of prochiral carbon pronucleophiles to acyclic dienes was also investigated as an alternative for asymmetric addition, but lower enantioselectivities were obtained (up to 57% *ee*).

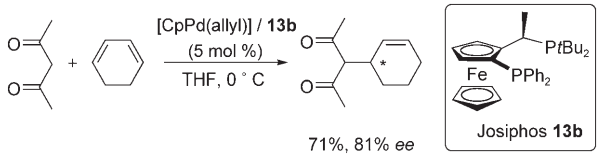

Scheme 40. Josiphos/Pd-catalyzed asymmetric nucleophilic addition to conjugated dienes; * absolute stereochemistry not determined.

The palladium-catalyzed carbopalladation of racemic allenes and subsequent nucleophilic substitution reaction of the transient allylpalladium intermediate with soft nucleophiles constitute another related route to functionalized alkenes. Hiroi and co-workers[159] have recently developed an asymmetric version of this one-pot reaction by using the chiral ferrocene ligand bppf-OAc (**44**, Scheme 41). The direct enantioselective 1,2-functionalization of racemic allenes was realized in the presence of iodobenzene and the chiral palladium(0) catalyst via carbopalladation of the allene with

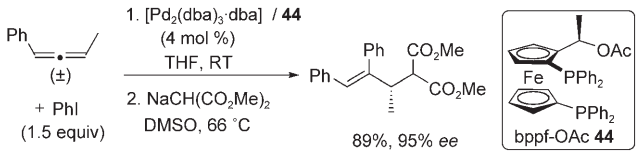

Scheme 41. Asymmetric 1,2-functionalization of racemic allenes.

the oxidative-addition species (that is, Ph-Pd-I), thermodynamic equilibrium between both diastereomeric allylpalladium intermediates, and final nucleophilic addition to the sterically preferred allylpalladium species. Very high enantioselectivity (95% *ee*) was attained in the reaction of (±)-1-phenyl-1,2-butadiene with iodobenzene and dimethyl sodiomalonate catalyzed by $[Pd_2(dba)_3{\cdot}dba]$/**44**. Similar levels of asymmetric induction were provided with some non-ferrocene ligands such as Binap and Mop-Diop.

5.3. Asymmetric Heck Reactions

High enantioselectivities have been documented in both inter- and intramolecular variants of the catalytic asymmetric Heck reaction, with Binap and Phox ligands occupying a prominent position.[160] For the intermolecular Heck reaction, the reaction of dihydrofuran with aryl or alkenyl trifates has become a standard test reaction for screening new ligands. In this reaction, a problem of double-bond isomerization is often observed, as the initial kinetic regioisomer **V** can experience double-bond isomerization to the more stable vinyl ether **VI**. While Binap and other diphosphine ligands typically produce compound **VI**, product **V** is usually favored in the presence of P,N-type ligands, such as Fc-Phox (**15**). As an extension of their initial success with 1,1′-P,N-ferrocenyl phosphinooxazoline ligands **45** (1,1′-Fc-Phox; Table 3, entry 1),[161] Hou and

Table 3: Asymmetric intermolecular Heck reaction.

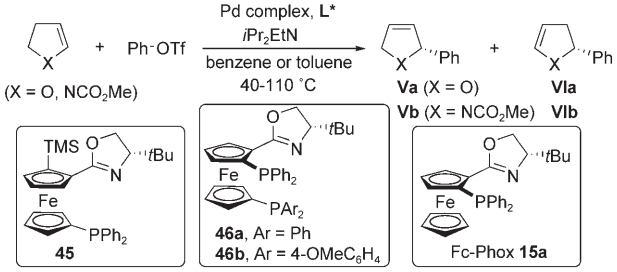

Entry	X	Pd complex (mol%)	L* (mol%)	V/VI	Yield V[%]	*ee* V [%]	Ref.
1	O	$[Pd_2(dba)_3{\cdot}dba]$ (3)	**45** (6)	<98:2	75[a]	92.1	[161]
2	O	$Pd(OAc)_2$ (1.5)	**46a** (3)	95:5	85[a]	97	[162]
3	NR	$Pd(OAc)_2$ (5)	**46a** (5)	95:5	68	98	[163]
4	O	$[Pd_2(dba)_3{\cdot}dba]$ (1.5)[b]	**46b** (3)	8:92	–	–	[162]
5	O	$[Pd_2(dba)_3{\cdot}dba]$ (3)	**15a** (6)	–	52[c]	99	[164]

[a] Conversion yield as determined by gas chromatography. [b] Reaction in CH_2Cl_2. [c] **VIa** was also isolated in 21% yield.

co-workers have reported that the 1,1′-diphosphine 2-oxazoline ferrocene **46a** provides high regio- (**V**/**VI** = 95:5) and enantioselectivity in the intermolecular Heck phenylation of 2,3-dihydrofuran (97% *ee*; Table 3, entry 2)[162] and *N*-methoxycarbonyl-2-pyrroline (98% *ee*, Table 3, entry 3).[163] In contrast to the P,N coordination of ligand **45**, diphosphinooxazolines **46** function as bidentate P,P ligands, as revealed by ^{31}P NMR spectroscopy and X-ray diffraction analysis. A dramatic variation of the regioselectivity was found, depend-

 © 2006 Wiley-VCH Verlag GmbH & Co. KGaA, Weinheim

ing on the palladium source, solvent, and the electronic nature of the phosphine units. Thus, reversed regioselectivity was observed when $[Pd_2(dba)_3 \cdot dba]$ was used instead of $Pd(OAc)_2$, especially in combination with electron-rich phosphines such as **46b** (Table 3, entry 4). Unfortunately, while the 2,5-dihydro derivative **V** is obtained with high a *ee* value (generally >90% *ee*), regardless of the palladium source or the electronic nature of the phosphine, that of **VI** was low in all cases (up to 48% *ee*). The authors hypothesized that when $Pd(OAc)_2$ is used as the palladium source, the nucleophilicity of the acetate anions with regard to the palladium atom facilitates dissociation of the metal–olefin complex to give product **V**. However, when $[Pd_2(dba)_3 \cdot dba]$ is used, such nucleophilic attack could not occur, so that insertion of palladium into the olefin, followed by β-hydride elimination, would produce product **VI**.

The group of Guiry has demonstrated the efficacy of 1,2-P,N-ferrocenyl phosphinooxazoline ligands (1,2-Fc-Phox) in inter-[164] and intramolecular[165] Heck reactions. The bulky *tert*-butyl-substituted ligand **15a** provided very high enantioselectivity in the phenylation of 2,3-dihydrofuran (99% *ee*; Table 3, entry 5), but with low regioselectivity and reactivity (14 days at 110°C). On the other hand, ligand **15a** afforded up to 85% *ee* in the intramolecular Heck reaction to form spirocyclic lactams and *cis*-decalins (Scheme 42). In both the inter- and intramolecular variants, higher reactivity of the *t*Bu-substituted ligand (**15a**) over the *i*Pr derivative was observed, a feature already pointed out by Pfaltz and co-workers in the original work with Phox ligands.[166]

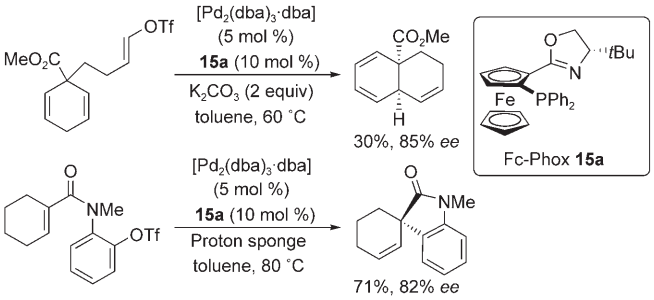

Scheme 42. Asymmetric intramolecular Heck reaction.

5.4. Asymmetric Suzuki–Miyaura Reaction and Other Asymmetric Cross-Coupling Reactions

5.4.1. Enantioselective Synthesis of Axial-Chiral Compounds

Owing to the importance of axially chiral biaryl compounds as key structural units in biologically active compounds, as well as chiral auxiliaries and chiral ligands, the development of catalytic enantioselective methods for their synthesis constitutes a topic of fundamental interest.[167] In spite of this, the direct asymmetric construction of the C–C biaryl bond from achiral substrates still remains challenging, likely because of the inherent difficulty in coupling two sterically hindered arenes. Hayashi, Ito, and co-workers, on the basis of initial investigations by the group of Kumada,[168] reported the first highly atropoenantioselective cross-coupling of aryl halides with aryl Grignard reagents (Kumada cross-coupling) using a combination of $NiBr_2$ (≤5 mol%) and the planar-chiral ferrocenyl phosphine ppf-OMe (**47**), providing axially chiral binaphthalenes such as **VII** in enantioselectivities up to 95% *ee* (Scheme 43).[169]

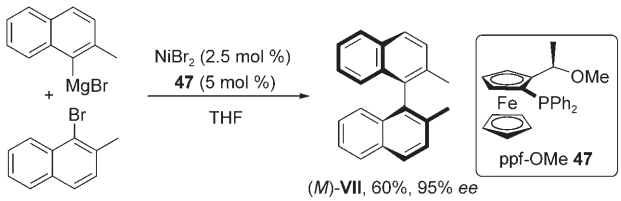

Scheme 43. Atropoenantioselective Kumada cross-coupling reaction.

This seminal work triggered subsequent developments in enantioselective biaryl coupling reactions. Within this context, the Suzuki–Miyaura cross-coupling has emerged as one of the most used methods for the construction of the C–C biaryl bond owing to its great versatility and relatively high environmental friendliness.[170] First investigations by Cammidge and co-workers in 2000,[171] recently accounted in its full extension,[172] showed that the Suzuki cross-coupling of 1-iodo-2-methylnaphthalene with the 2-methyl-1-naphthyl boronic ester **VIII** provided the C_2-symmetric binaphthalene **VII** with 85% *ee* in the presence of Hayashi's ligand ppfa (**48**, Scheme 44). In this case the ppf-OMe ligand (**47**) afforded

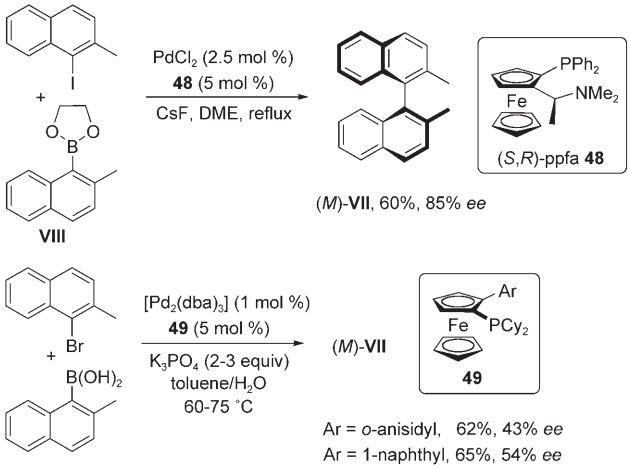

Scheme 44. Atropoenantioselective Suzuki cross-coupling reaction.

much lower enantioselectivities, which is in contrast to the results described for the Kumada coupling, in which **48** failed to promote the coupling. It was proposed that the stronger donor character of the NMe_2 group (compared to OMe) facilitates the coordination to the boron atom. Josiphos, bppfa, and other ferrocene P,P ligands proved ineffective, which reinforces the idea that P,N ligands are optimal in this transformation.

Johannsen and co-workers have applied the newly developed aryl ferrocenyl electron-rich phosphine ligands **49** (Mopf-type ligands) in the Pd-catalyzed synthesis of the

 © 2006 Wiley-VCH Verlag GmbH & Co. KGaA, Weinheim

binaphthyl compound (*M*)-**VII** (Scheme 44).[42a] The enantioselectivitiy slightly depends on the aryl substituent of **49**, typically within the range of 43–54% *ee*.

On the other hand, ppfa (**48**) has been used as a chiral ligand to improve the diastereoselectivity in the Suzuki cross-coupling between a chiral 5-iodoisoquinoline and a naphthylboronic acid for the synthesis of the antileishmanial alkaloids ancistroealaine A [(*P*)-**IX**] and ancistrotanzanine B [(*M*)-**IX**].[173] By using (*R*,*S*)-ppfa (**48**) an atropoisomeric ratio of 75:25 was observed in favor of (*M*)-**IX** (Scheme 45), a preference opposite to that obtained with an achiral catalyst. The enantiomer ligand (*S*,*R*)-ppfa (*ent*-**48**) did not provide any preference for one of the diastereomers (d.r. 51:49).

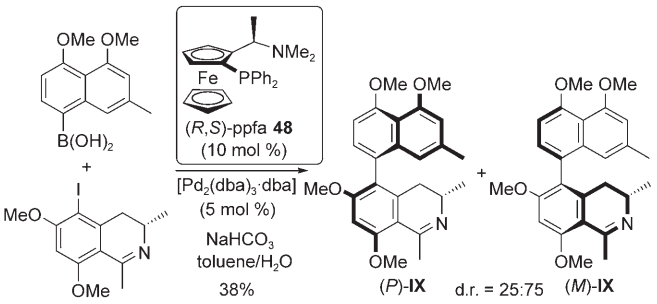

Scheme 45. Diastereoselective Suzuki cross-coupling.

5.4.2. *Enantioselective Synthesis of Planar-Chiral (Arene)chromium Complexes*

The generation of planar chirality by desymmetrization of *meso*-(arene)chromium complexes by cross-coupling reactions was pioneered by Uemura, Hayashi, and co-workers in 1993, achieving *ee* values of up to 31% in the Suzuki desymmetrization reaction of [(1,2-dichlorobenzene)$Cr(CO)_3$] in the presence of ppfa.[174] Subsequently, having shown that the desymmetrization of [(1,2-dichlorobenzene)$Cr(CO)_3$] can be efficiently achieved (in up to 95% *ee*) by enantioselective Pd-catalyzed methoxycarbonylation in the presence of the pyrrolidine ppfa-type ligand **50**,[175] Schmalz and co-workers have further extended this method to the catalytic enantioselective mono-methoxycarbonylation of [(1,3-dichloroarene)$Cr(CO)_3$] complexes **X** (Scheme 46).[176] The preformed complex [**50**·$PdCl_2$] (5 mol%) induced the reaction of **X** under 1 atm of CO pressure to produce the planar-chiral products **XI** in up to 90% *ee*. The presence of an alkyl substituent at C2 proved to be essential for an efficient discrimination of the two enantiotopic chlorine atoms, as the unsubstitued substrate **Xa** (R = H) gave rise to the product **XIa** with only 5% *ee*. The best results were obtained with the 2-methyl derivative **Xb**. The reaction generates a substantial amount of the bis-methoxycarbonylated product **XII**, the formation of which has a positive effect on the enantioselectivity. This result suggests that the initial reaction of methoxycarbonylation is followed by a kinetic resolution. In contrast, the catalyst [**50**·$PdCl_2$] failed to provide significant asymmetric induction (16% *ee*) in the Pd-catalyzed cross-coupling of [(1,2-dichlorobenzene)$Cr(CO)_3$] with stabilized vinylaluminium reagents.[177]

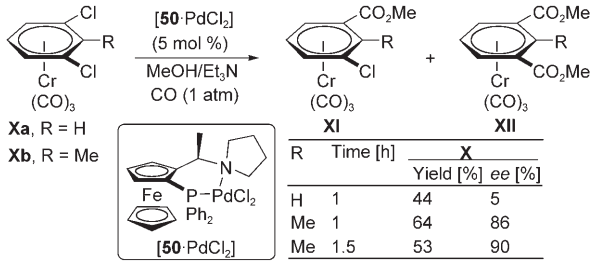

R	Time [h]	X	
		Yield [%]	*ee* [%]
H	1	44	5
Me	1	64	86
Me	1.5	53	90

Scheme 46. Pd-catalyzed asymmetric methoxycarbonylation of 1,3-dicholoroarene chromium complexes.

5.4.3. *Enantioselective Synthesis of P-Stereogenic Phosphines*

Despite the increasing interest in P-chirogenic ligands in asymmetric catalysis,[178] direct methodologies for producing such compounds in enantiomerically pure form remain scarce.[179] Recent efforts in this area led Helmchen and co-workers to develop a method for the enantioselective C–P cross-coupling of prochiral diarylphosphines with *ortho*-substituted iodoarenes (Scheme 47).[180] Up to 93% *ee* was achieved in the presence of a catalyst prepared in situ from Et,Et-FerroTANE (**8b**, 0.5 mol%) and [$Pd_2(dba)_3$]·HCl (1 mol%). LiBr as additive (1.1 equiv) was found to enhance the reaction rate and the enantioselectivity in most cases. Enantiomerically pure phosphine (*S*)-**XIII** (>99% *ee*) was obtained after reaction with sulfur, crystallyzation of the resulting phosphine sulfide, and subsequent desulfurization with Raney nickel. This methodology has also been successfully applied to the diastereoselective phosphination of a chiral *ortho*-iodoaryl oxazoline (d.r. up to 13:1 in the matched case), as a novel route to P-chirogenic Phox ligands.

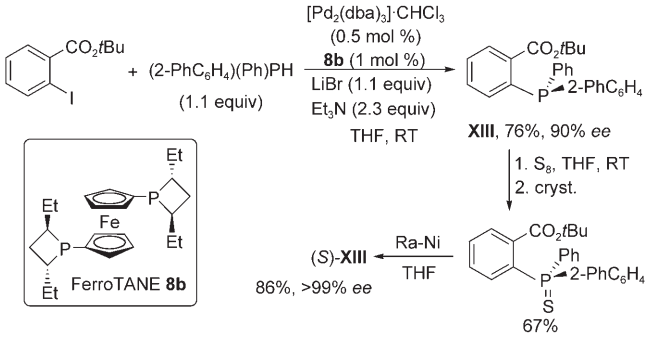

Scheme 47. FerroTANE/Pd-catalyzed enantioselective C–P cross-coupling.

Much lower enantioselectivities have been described in the palladium-catalyzed phosphination of aryl iodides using secondary phosphine–boranes with several ferrocene ligands such as Et,Et-FerroTANE (**8b**, 12% *ee*),[181] ppfa (**50**, racemic)[181] or *t*Bu-Josiphos (**13b**, 10% *ee*).[182]

 © 2006 Wiley-VCH Verlag GmbH & Co. KGaA, Weinheim

5.5. Desymmetrization of Prochiral meso Compounds

5.5.1. Desymmetrization of Anhydrides

Chiral ferrocene ligands have been applied to the asymmetric desymmetrization of prochiral *meso* compounds as a strategy for the expedient synthesis of products with two or more contiguous stereogenic centers in a single operation. Thus, using the commercially available Josiphos ligand (**13a**), Rovis and co-workers realized a palladium-catalyzed enantioselective alkylation of cyclic anhydrides with diphenylzinc (Scheme 48).[183] A variety of succinic anhydrides were subjected to the phenylation reaction in the presence of the catalyst system $Pd(OAc)_2$/**13a**, providing the corresponding desymmetrized γ-keto acids with 89–97% *ee*. Exploitation of dimethylzinc as a coupling partner required a catalytic amount of 4-fluorostyrene as promoter, affording the corresponding methyl ketone in up to 91% *ee*.

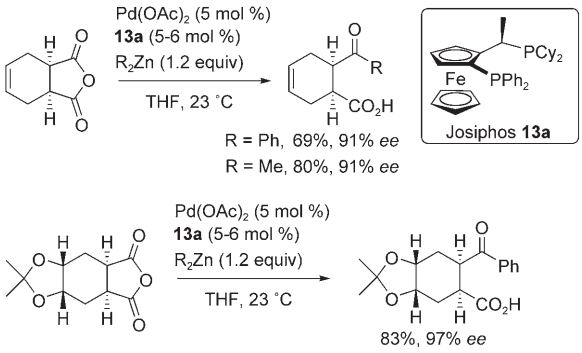

Scheme 48. Enantioselective alkylative desymmetrization of *meso*-succinic anhydrides.

5.5.2. Desymmetrization of Heterobicyclic Alkenes

The group of Lautens has been instrumental in the development of transition-metal-catalyzed strategies for the enantioselective ring opening of *meso* heterobicyclic alkenes.[184] For instance, the Pd-catalyzed nucleophilic ring opening with dialkylzinc reagents, first reported in 2000[185] using Tol-Binap and Phox as chiral ligands, is among the most outstanding C–C bond-forming desymmetrization reactions. Subsequent mechanistic work provided strong evidences for the participation of chiral cationic alkylpalladium(II) species $[L_2PdR]^+$ in the key enantioselective carbopalladation of the alkene.[186] Inspired by this mechanistic work, our group has developed well-defined cationic palladium catalysts with P,S coordination whose structures closely resemble the presumed active catalytic species.[187] After screening the effect of the substitution at phosphorus, methylpalladium(II) complexes of Fesulphos ligands proved to be extremely efficient catalysts in the enantioselective alkylative ring-opening reaction of a variety of *meso* oxabenzonorbornadienes, whereby the complex derived from the Fesulphos ligand **38c** having a dicyclohexylphosphino unit (Scheme 49) was especially reactive and enantioselective. The optimal cationic catalyst $[(\mathbf{38c})Pd(Me)]^+$, generated in situ from $[(\mathbf{38c})Pd(Me)(Cl)]$ by treatment with equimolar amounts of the Brookhart reagent $NaB(Ar^F)_4$ [$Ar^F = 3,5\text{-}(CF_3)_2C_6H_3$], afforded under very mild conditions (−25 °C to room temperature) and low catalyst loading (typically 0.5 mol%) the ring-opened products in good yields and excellent enantiocontrol (94–99% *ee*). Interestingly, the outstanding reactivity of this catalyst also allowed the highly enantioselective opening of much less reactive substrates, such as azabenzonorbornadienes and [2.2.1]oxabicyclic alkenes.

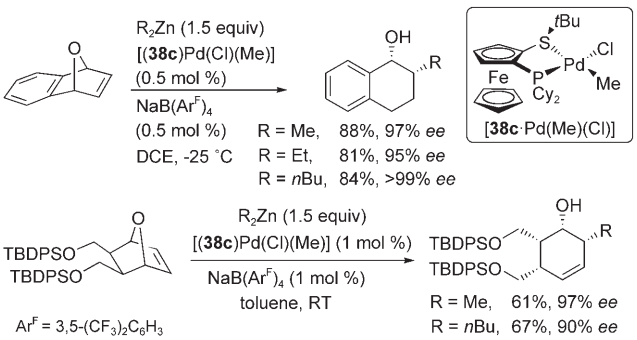

Scheme 49. Fesulphos/Pd-catalyzed asymmetric ring opening of bicyclic alkenes; TBDPS = *tert*-butyldiphenylsilyl.

A combination of DFT studies (B3LYP) combined with X-ray structural analysis of palladium complexes, including the presumed catalytically active cationic methyl Pd complex, suggested the coordination of the bicyclic alkene from its less hindered *exo* face *trans* to phosphorus on the palladium atom, thereby orienting the heteroatom bridge to the opposite side of the very bulky *tert*-butyl group (Scheme 50).[188] Therefore, the strong *trans* influence of the phosphine moiety, acting synergistically with the sterically demanding environment imposed by the stereogenic sulfur atom directly bonded to the palladium atom, seems to be responsible for the high asymmetric performance of Fesulphos ligands in this transformation.

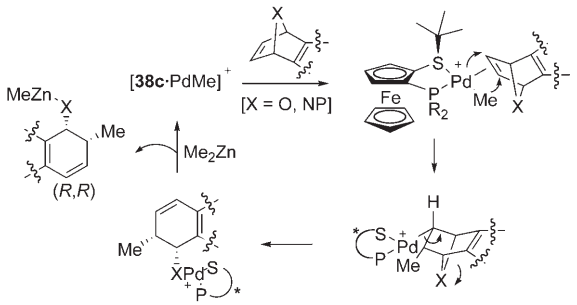

Scheme 50. Proposed mechanism for the Fesulphos/Pd-catalyzed enantioselective ring opening of heterobicyclic alkenes.

Hou and co-workers have described the Pd-catalyzed asymmetric ring opening of oxabenzonorbornadienes with organozinc halides as nucleophiles using a variety of chiral phosphino–oxazolines (Phox) as chiral ligands.[189] Among the tested ligands, the ferrocene-based Fc-Phox ligand (**15a**; see structure in Table 3) provided moderate levels of asymmetric induction (66% *ee*), while the non-ferrocene commercially

 © 2006 Wiley-VCH Verlag GmbH & Co. KGaA, Weinheim

available *i*Pr-Phox ligand was superior, affording the 1,2-dihydronaphthol product with the highest enantioselectivity (up to 96% *ee*).

The rhodium-catalyzed enantioselective ring opening of heterobicyclic alkenes with soft nucleophiles, described by Lautens in 2000, is another important asymmetric desymmetrization reaction.[190] The rhodium(I) complex of *t*Bu-Josiphos (**13b**) was reported to induce ring opening of oxa- and azabicyclic alkenes with alcohols, amines, malonates, and carboxylates to generate the corresponding 1,2-*trans* products as one regio- and diastereomer in high yields and excellent enantiocontrol. The application of halide effects[191] allowed to improve the enantiocontrol and overcome the catalyst poisoning associated with amine nucleophiles.[192] It was discovered that halide/proton additives make feasible the reaction with aliphatic amines in high yield and *ee* (Table 4, entry 1). In addition, simple replacement of the chloride ligand on the rhodium catalyst by iodide leads to dramatic improvements of the reactivity and enantioselectivity in the case of aromatic amines, malonate (Table 4, entry 2), carboxylate, and phenol (Table 4, entry 3) nucleophiles, thus permitting the reaction to be conducted with extremely low catalyst loadings (0.01 mol%).

Very recently, the extention of this methodology to the asymmetric ring-opening addition of aliphatic and aromatic amines to *N*-Boc-azabenzonorbornadienes has been achieved using the C_2-symmetric Ferriphos (**51**; Table 4) as the chiral ligand.[193] The nature of the chiral ligand and its use in excess amount (2.2 equiv based on Rh) play an important role in both reactivity and enantioselectivity (94–99% *ee*). In this case iodide additives produced enhanced reactivity, but lower enantioselectivities. Small amines such as dimethylamine and pyrrolidine (Table 4, entry 4), which may bind to the catalyst more tightly, require ammonium hydrochloride salts as additives for high enantioselectivity, although generally no additives are needed with other types of nitrogen nucleophiles (Table 4, entries 5 and 6).

Catalyst and substrate studies have also been recently performed to rationalize the stereochemical outcome and to get insights on the forces behind the high reactivities and enantioselectivities offered by the diphosphine ligands **13b** and **51**.[193,194] Thus, it was found that the two phosphine moieties in **13b** need to be electron-rich and of different size, with the larger phosphine located at the benzylic position, to maximize reactivity and enantioselectivity. Additionally, it was proved that the planar chirality of **13b** plays the main role in determining the absolute sense of induction. The proposed working model involves an oxidative insertion with retention into the C–Z bond to yield the rhodium(III) species **A** as the key enantiodiscriminating step (Scheme 51), which should be irreversible because of the release of ring strain. A proton transfer from the nucleophile to complex **A** to form **B** might activate both the allylrhodium intermediate, becoming more electrophilic as a result of the positive charge, and the nucleophile, which is made more nucleophilic upon deprotonation. Intermediate **B** then undergoes anti nucleophilic attack with inversion to yield the final product, thereby regenerating the rhodium catalyst (Scheme 51).

Table 4: Rh-catalyzed asymmetric ring opening of heterobicyclic alkenes with soft nucleophiles.

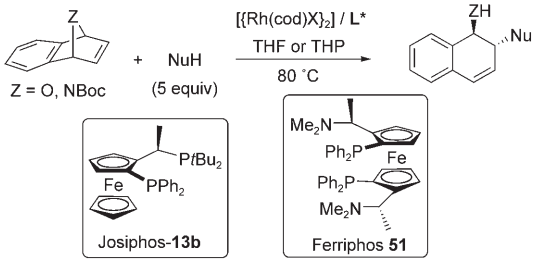

Entry	Z	NuH	[RhX] (mol%)	L* (mol%)	Yield [%]	*ee* [%]	Ref.
1	O	Bn_2NH[a]	RhI (1)	**13b** (1.5)	86	99	[192]
2	O	$CH_2(CO_2Me)_2$	RhI (1)	**13b** (1.5)	93	98	[192]
3	O	*o*-fluorophenol	RhI (1)	**13b** (1.5)	86	99	[192]
4	NBoc	pyrrolidine[b]	RhCl (5)	**51** (11)	78	>99	[193]
5	NBoc	piperidine	RhCl (5)	**51** (11)	83	97	[193]
6	NBoc	aniline	RhCl (5)	**51** (11)	96	96	[193]

[a] NH_4I (2.5 mol%) as additive. [b] Et_3NHCl (1 equiv) as additive.

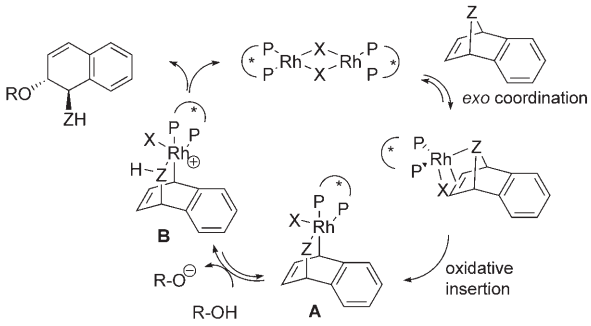

Scheme 51. Working model for the Rh-catalyzed asymmetric ring opening. Z = O, NBoc.

6. Asymmetric Metal-Mediated Additions to Carbonyl Compounds and Imines

6.1. Enantioselective Nucleophilic Addition to Aldehydes and Imines

6.1.1. Addition of Organozinc and Organoboron Reagents to Aldehydes and Aldimines

The addition of diethylzinc to aromatic aldehydes is by far the most studied type of catalytically asymmetric 1,2-addition of organometallic species to carbonyl compounds.[195] Since the finding by Oguni et al. in 1983[196] that (*S*)-leucinol catalyzes the reaction of diethylzinc to benzaldehyde and the impressive results described by Noyori in 1986 with 3-dimethylamino isoborneol ligand (daib),[197] literally hundreds of ligands have been tested, especially chiral aminoalcohols

© 2006 Wiley-VCH Verlag GmbH & Co. KGaA, Weinheim

and other bidentate N,O ligands. Among some recently developed ferrocene ligands,[144,198] the ferrocenyl aziridino alcohols **52** and **53** provided enantioselectivities higher than 90% *ee* in the reaction with aromatic aldehydes (Table 5). Both C_1- and C_2-symmetric ligands led to very similar results.

Table 5: Asymmetric addition of diethylzinc to aldehydes.

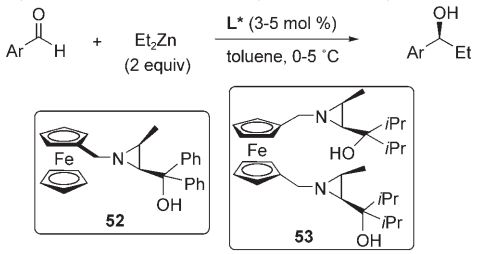

Entry	Ar	L* (mol%)	Yield [%]	*ee* [%]	Ref.
1	Ph	**52** (3)	97	92.7	[198b]
2	*m*-ClC_6H_4	**52** (3)	89	98.8	[198b]
3	Ph	**53** (5)	91	92.6	[198d]
4	*m*-ClC_6H_4	**53** (5)	84	99.5	[198d]

On the other hand, the enantioselective addition of phenylacetylene to aromatic and aliphatic aldehydes employing the combination phenylacetylene/diethylzinc, catalyzed by the 1,1′-disubstituted oxazoline–hydroxyalkyl ferrocene **54**, gave rise to the propargyl alcohols in 54–93% *ee* (Scheme 52).[199]

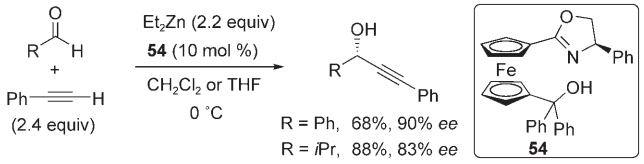

Scheme 52. Asymmetric phenylacetylene addition to aldehydes.

Unlike the addition of diethylzinc, aryl transfer reactions have been much less studied. Bolm and co-workers described in 2002 the zinc-promoted enantioselective addition of aryl boronic acids to aldehydes in the presence of the ferrocenyl–oxazoline carbinol ligand **55**, thereby allowing the synthesis of diarylmethanols with excellent yield and enantioselectivity (typically higher than 90% *ee*).[200] The presence of small amounts of dimethoxy poly(ethylene glycol) (DiMPEG) was found to drastically improve the *ee* values. This protocol was later adapted to the preparation of chiral diarylmethanols on a gram scale (10 mmol) while maintaining the high degrees of reactivity and enantioselectivity (Table 6, entries 1–2).[201] The beneficial effect of DiMPEG has also been found in the addition of diphenylzinc (in combination with diethylzinc).[202] Not only the enantiomeric excess of the product was improved by this "MPEG effect", but also it allowed a reduction of the catalyst loading by a factor of ten (up to 93% *ee* with 1 mol% of **55**).[203]

To avoid the use of expensive salt-free diphenylzinc, it has been reported that triphenyl borane is an interesting alternative phenyl source, low in cost and easier to handle, for the large-scale enantioselective preparation of arylphenylmethanols in the presence of ferrocene **55** as catalyst (Table 6, entries 3 and 4).[204] Continuing the search for new catalysts for this reaction, Bolm and co-workers have recently developed the chiral organosilanol **56**[40] (with the same oxazolinyl-substituted ferrocene backbone as **55**) and explored its catalytic properties in asymmetric phenyl transfer to aldehydes using both zinc- and boron-based aryl sources (Table 6, entries 5 and 6). However, in this first application of chiral organosilanols in asymmetric catalysis, the observed enantioselectivities were somewhat lower than those provided by carbinol **55** (typically 87–97% *ee* with **55** and 83–88% *ee* with **56**).

Table 6: Asymmetric synthesis of diarylmethanol derivatives.

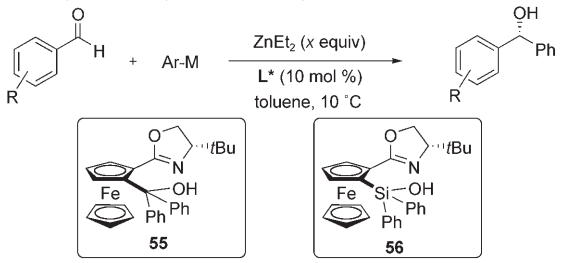

Entry	R	ArM (equiv)	*x* [equiv]	L*	Yield [%]	*ee* [%]	Ref
1	4-Cl	$PhB(OH)_2$ (2.4)[a]	7.2	**55**	93	96	[201]
2	4-Me	$PhB(OH)_2$ (2.4)[a]	7.2	**55**	94	96	[201]
3	4-Ph	Ph_3B (1)	3	**55**	88	98	[204]
4	4-Cl	Ph_3B (1)	3	**55**	98	97	[204]
5	4-Cl	Ph_3B (1)	3	**56**	73	88	[40]
6	2-Br	Ph_2Zn (0.65)	1.3	**56**	70	84	[40]

[a] DiMPEG (10 mol%) as additive.

In spite of the importance of chiral amines in organic chemistry, the organometallic addition to imines has not reached comparable success to that of aldehydes, owing in part to the markedly diminished electrophilicity of imines relative to aldehydes. Inspired by the pioneering work of Tomioka and co-workers,[205] who reported excellent yields and enantiocontrol (typically above 90% *ee*) in the Cu^{II}-catalyzed addition of diethylzinc to *N*-tosylimines of aromatic aldehydes with the proline-based amidophosphine ligand **XIV** (Table 7, entry 1), Wang and co-workers have developed a related proline-derived ferrocenyl amidophosphine ligand (**57**; Table 7, entries 2 and 3), but encountered inferior results (79–86% *ee*) in the same transformation.[206] On the other hand, moderate to high enantioselectivities (up to 97% *ee*) were attained in the addition of diethylzinc to *N*-phosphinoyl imines using $Cu(OTf)_2$/ppfa (**48**) as the catalyst system (Table 7, entries 4 and 5).[207]

6.1.2. *Aldol- and Mannich-Type Reactions*

In sharp contrast to the well-developed catalytic enantioselective aldol reaction to aldehydes,[208] the development of an efficient and general catalytic asymmetric aldol reaction to simple ketones represents a formidable challenge because of the lower reactivity and the lesser steric/electronic dissimilarity of ketones compared to those of aldehydes. On the

 © 2006 Wiley-VCH Verlag GmbH & Co. KGaA, Weinheim

Table 7: Asymmetric addition of Et_2Zn to imines.

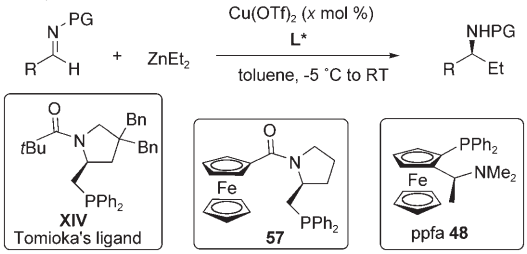

Entry	R	PG	*x* [mol%]	L* (mol%)	Yield [%]	*ee* [%]	Ref.
1	Ph	Ts	1	**XIV** (1.3)	94	90	[205]
2	Ph	Ts	3	**57** (4)	94	86	[206]
3	3-BrC_6H_4	Ts	3	**57** (4)	94	83	[206]
4	Ph	P(O)Ph_2	12	**48** (6)	85	92	[207]
5	2-furyl	P(O)Ph_2	12	**48** (6)	85	90	[207]

basis of mechanistic knowledge acquired in the previously reported CuF-catalyzed aldol reaction between ketones and trimethylsilyl ketene acetals,[209] Shibasaki and co-workers have very recently devised its extension to the first diastereo- and enantioselective catalytic aldol addition of silyl ketene acetals to ketones that relies on the use of the Taniaphos-type ligand **7d** (NBu_2-Taniaphos, Scheme 53).[210] The bulky amine

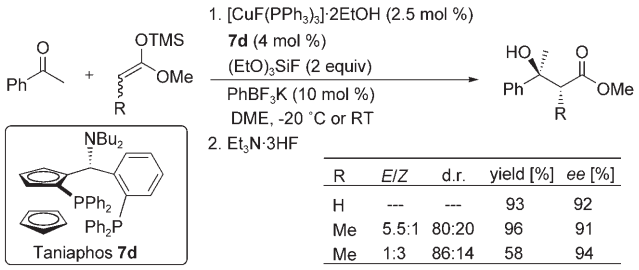

R	*E*/*Z*	d.r.	yield [%]	*ee* [%]
H	---	---	93	92
Me	5.5:1	80:20	96	91
Me	1:3	86:14	58	94

Scheme 53. Taniaphos/Cu-catalyzed asymmetric aldol reaction to ketones.

substituent (NBu_2) of **7d** proved to be essential for effective enantiocontrol. Very high enantioselectivities (78–94% *ee*) were obtained for a variety of aryl alkyl and dialkyl ketones. The diastereoselectivity was very high (usually >98:2) regardless of the *E*/*Z* ratio of the nucleophile. Having previously established that the actual nucleophile in the reaction is a copper enolate, generated in situ through transmetalation, and the necessity of a stoichiometric amount of $(EtO)_3SiF$ as additive for achieving high reactivity, they subsequently found that the addition of $PhBF_3K$ produced a significant further improvement in the reaction yield. This effect was explained by attributing to $PhBF_3K$ the role of a fluoride source to generate the highly electrophilic trapping silyl agent $(EtO)SiF_3$, which is presumably involved in the rate-determining catalyst turnover step.

Cationic copper(I) complexes of Fesulphos ligands proved to be effective Lewis acid catalysts in the Mannich-type reaction to *N*-sulfonyl imines (Scheme 54). The combination of the dimeric copper(I) bromide complex of the bulky

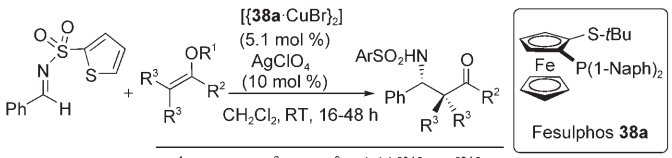

R^1	R^2	R^3	yield [%]	*ee* [%]
TBDMS	S-*t*Bu	H	80	91 (>99)[a]
TBDMS	OMe	Me	78	86
TMS	Ph	H	80	93

[a] After a single recrystallization.

Scheme 54. Fesulphos/Cu-catalyzed asymmetric Mannich-type reaction to *N*-sulfonyl imines; TBDMS = *tert*-butyldimethylsilyl.

dinaphthyl phosphine **38a** ([{**38a**·CuBr}$_2$]) and $AgClO_4$ promotes the addition of silyl enol ethers derived from ketones, esters, and thioesters to *N*-(2-thienyl)sulfonyl aldimines to afford the corresponding β-amino carbonyl derivatives in good yields (58–91%) and moderate to good enantioselectivity (61–93% *ee*). After considering different substitution at sulfur on the imine nitrogen atom, the 2-thienylsulfonyl group provided the highest levels of reactivity and enantioselectivity.[211] In the case of ester and thioester Mannich products the sulfonamide moiety was readily deprotected to the free amine by simple treatment with Mg in methanol.

6.2. Reductive Coupling of Alkynes and Carbonyl Compounds and Related Processes

The nickel-catalyzed coupling of alkynes with aldehydes, in both its reductive and alkylative variants, has emerged as an efficient and stereoselective method for the synthesis of synthetically useful allylic alcohols.[212] In this field the group of Montgomery has developed a very efficient procedure for aldehyde–alkyne reductive cyclization employing [Ni(cod)$_2$]/PBu_3 as catalyst and Et_3SiH as the reducing agent.[213] Despite the broad scope of this protocol, the corresponding intermolecular process proved not to be effective under these conditions. Jamison and co-workers found that the same catalyst system, but with the reducing agent replaced by Et_3B, allowed the intermolecular reductive coupling of alkynes and aldehydes.[214] This research group also achieved the first catalytic enantioselective version of this coupling reaction through the use of monodentate phosphines.[215] Subsequently, taking $FcPPh_2$ (Fc = ferrocenyl) as a lead structure, a novel class of P-chirogenic monodentate ferrocenyl phosphines (**58**) were developed, which proved to be very effective in a range of intermolecular couplings. For example, ligand **58a** was found to promote the Ni-catalyzed reductive couplings of aliphatic internal alkynes (alkyl-C≡C-alkyl′) and aldehydes to give the corresponding allylic alcohols with complete *E* selectivity in all cases, but moderate regioselectivity and enantioselectivity (Table 8, entry 1).[216] This process has been elegantly applied to complex natural product synthesis.[217] On the other hand, desymmetrization of $FcPPh_2$ by replacing a phenyl group by a 2-isopropylphenyl or a *o*-tolyl group (ligands **58b** and **58c**, respectively) were very effective in the reductive coupling of conjugated enynes with aldehydes (Table 8, entry 2)[218] and ketones (entries 3 and 4),[219] in

 © 2006 Wiley-VCH Verlag GmbH & Co. KGaA, Weinheim

Table 8: Ni-catalyzed enantioselective intermolecular reductive coupling of alkynes and 1,3-enynes with adehydes and ketones.

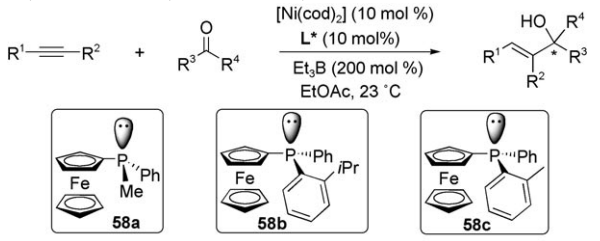

Entry	R^1	R^2	R^3	R^4	L*	Yield [%]	*ee* [%]	Ref.
1	Pr	Pr	*i*Pr	H	**58a**	80	55	[216]
2	2-propenyl	Et	*p*-Tol	H	**58b**	73	56	[218]
3	2-propenyl	Et	*p*-Tol	Me	**58c**	71	64	[219]
4	2-propenyl	Et	2-Naph	Me	**58c**	65	62	[219]

which the pendant alkene enhanced both the reactivity and regioselectivity of the process. These couplings afford synthetically useful 1,3-dienes possessing a stereogenic carbinol center (quaternary in the case of ketones) with high regioselectivity, complete *E* selectivity and moderate enantiocontrol.

The alkylative intermolecular coupling of alkynes and imines was developed by Jamison and Patel in 2003.[220] Interestingly, in contrast to the observed reductive coupling in the case of aldehydes, similar reaction conditions led to the alkylative manifold with imines (transfer of Et instead of H from Et_3B), methanol being a required cosolvent in imine couplings. Subsequently, the same authors developed the enantioselective variant of this three-component reaction by means of using the P-chirogenic ligand **58b** (Scheme 55).[221]

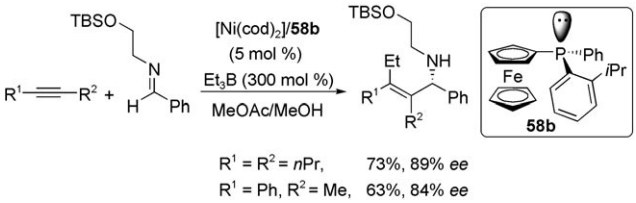

Scheme 55. Ni-catalyzed asymmetric alkylative coupling of alkynes with imines. TBS = *tert*-butyldimethylsilyl.

Good to excellent yields, high regioselectivitiy, complete *E* selectivity and high enantioselectivities (70–90% *ee*) were typically observed as long as the group on the nitrogen atom was aliphatic in nature. In particular, the $TBSOCH_2CH_2$ group on the imine nitrogen atom allows easy deprotection after the coupling reaction, thus providing direct access to primary allylic amines, whose maleic acid salts can be recrystallized to enhance the optical purity to >99% *ee*. Both symmetrical dialkyl acetylenes and unsymmetrical alkynes of the general formula Ar-C≡C-alkyl are suitable substrates for this asymmetric process.

The rhodium-catalyzed reductive coupling of conjugated enones, dienes, enynes, and diynes to carbonyl partners, described by the group of Krische, constitutes another fundamental catalytic reductive method for C–C bond formation.[222] Unlike other hydrometalative reductive couplings that utilize silanes or boranes as terminal reducing agents, Krische's procedure relies on elemental hydrogen as a terminal reductant, which enables such transformations to proceed with very high levels of atom economy. Having established that $[Rh(cod)_2]OTf$/Biphep efficiently catalyzed the intermolecular hydrogen-mediated reductive coupling of 1,3-enynes with α-keto aldehydes[223] and α-iminoesters,[224] the scope of the electrophile component has been recently expanded to α-ketoesters (Scheme 56).[225] Furthermore, it

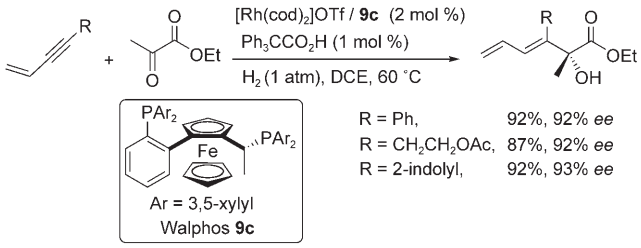

Scheme 56. Walphos/Rh-catalyzed asymmetric reductive coupling of enynes with α-ketoesters.

was found that replacement of the achiral Biphep ligand by (*R*)-xylyl-Walphos (**9c**) led to the development of the first catalytic enantioselective version of this reaction,[225] providing the corresponding α-hydroxyesters with complete regiocontrol and excellent levels of asymmetric inductions (typically ≥90% *ee*). In this case, the reaction rate and chemical yield were dramatically enhanced through the use of Brønsted acid additives, which were thought to activate the ketoester by protonation.

6.3. Conjugate Addition to α,β-Unsaturated Carbonyl Compounds

In accordance to the paramount importance of the conjugate addition as one of the most powerful and widely used synthetic tools for C–C bond construction, a number of efficient chiral catalyst systems have been developed in recent years for the enantioselective 1,4-addition of dialkylzinc reagents[226] and boronic acids[227] to Michael-type acceptors. In contrast, other organometallic reagents have remained reluctant to provide high stereoselectivities in this reaction. A breakthrough in this area came in 2004, when Feringa and coworkers focused on Grignard reagents as nucleophiles, demonstrating that it is no longer necessary to use dialkylzinc reagents to attain enantioselectivities of >95% *ee* in the copper-catalyzed asymmetric conjugate addition to a variety of activated cyclic and acyclic alkenes. The in situ prepared or preformed copper(I) complexes of the chiral ferrocenyl diphosphine Taniaphos or Josiphos-type ligands have been found to provide excellent enantioselectivities (typically in the range of 90–97% *ee*) and high regioselectivity (1,4- versus 1,2-addition) in the Cu-catalyzed asymmetric conjugate

 © 2006 Wiley-VCH Verlag GmbH & Co. KGaA, Weinheim

addition of Grignard reagents to cyclic[228] and acyclic[229] enones. In the addition to cyclohexenone Taniaphos (**7a**) was the most efficient (Scheme 57), while in the addition to

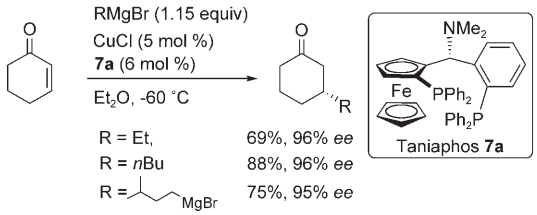

Scheme 57. Taniaphos/Cu-catalyzed asymmetric conjugate addition of Grignard reagents to cyclohexenone.

acyclic (*E*)-enones, Josiphos (**13a**) was the ligand of choice (Table 9, entries 1–3). The Josiphos/Cu^{I} catalyst system was later successfully extended to the conjugate addition of Grignard reagents to α,β-unsaturated esters (typically 86–98% *ee*; Table 9, entries 4–7)[230] and α,β-unsaturated thioesters (typically 85–96% *ee*; entries 8 and 9).[231] In the case of

Table 9: Josiphos/Cu-catalyzed asymmetric conjugate addition of Grignard reagents to acyclic α,β-unsaturated carbonyl compounds.

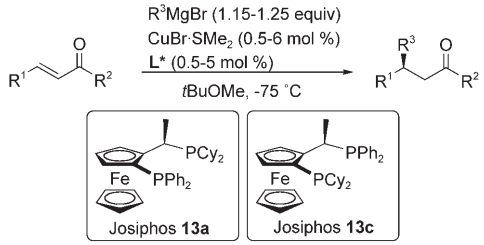

Entry	R^1	R^2	R^3	L*	Yield [%]	*ee* [%]	Ref.
1	Pr	Me	*n*Bu	**13a**	91	95	[229]
2	*n*Bu	Me	Me	**13a**	86	98	[229]
3	2-thienyl	Me	Me	**13a**	72	97	[229]
4	Me	OMe	Pr	**13a**	86	95	[230]
5	$PhCH_2$	OMe	Et	**13a**	75	95	[230]
6	*i*Pr	OMe	Et	**13c**	88	98	[230]
7	Ph	OMe	Et	**13c**	94	98	[230]
8	*n*-Pent	SEt	Me	**13a**	88	95	[231]
9	$BnO(CH_2)_3$	SEt	Me	**13a**	94	95	[231]

the Grignard addition to esters with bulky groups at the double bond (Table 9, entries 6 and 7), superior efficiency was observed with ligand **13c**, in which the positions of the alkyl and aryl phosphine groups have been interchanged. In the case of α,β-unsaturated thioesters the high yields and enantioselectivities in the conjugate addition of MeMgBr allowed the development of an iterative methodology for the preparation of enantiopure deoxypropionate subunits.[231] In all these conjugate-addition processes, as a general trend, the highest enantioselectivities are obtained with linear alkyl-chain Grignard reagents, although branching at the γ or β (but not α) position is well-tolerated. As a major limitation, aryl Grignard reagents such as PhMgBr provided much lower asymmetric induction, with a maximum of 76% *ee* obtained with acyclic enones.[229,232]

An important factor for the high efficiency of Josiphos ligands seems to be the robustness of their copper complexes, whose rapid formation avoids the presence of free copper salts that could promote the uncatalyzed background reaction. In fact, it has been demonstrated that the dinuclear complex [{Josiphos·CuBr}$_2$] ([{**13a**·CuBr}$_2$]) can be easily recovered from the reaction mixture by addition of pentane and reused without loss of reactivity or enantioselectivity.[230] A thorough exploration of the mechanism of this transformation considering kinetic, spectroscopic, and electrochemical analysis supports the model shown in Scheme 58, in which the monomeric complex **C**, formed by transmetalation

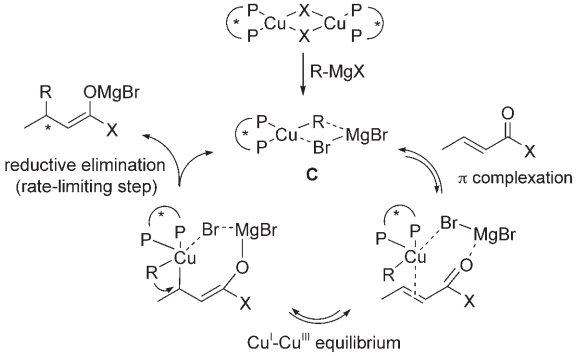

Scheme 58. Working model for the Cu-catalyzed asymmetric conjugate addition with Grignard reagents.

of [{**13a**·CuBr}$_2$] by a Grignard reagent, was identified as the active catalytic species.[233] The π complexation of **C** to the substrate leads to a fast equilibrium involving a Cu^{I} π complex and Cu^{III} σ complex, which is followed by the rate-limiting reductive-elimination step to afford the magnesium enolate of the final product. The presence of Mg^{2+} and Br^{-} ions is a necessary condition to achieve high selectivity and efficiency.

As in other recent results in conjugate additions using ferrocene ligands, moderate enantioselectivities have been reported in the $Cu(OTf)_2$-catalyzed addition of Et_2Zn to chalcones with either Mopf-type ligands[42b] or ppfa.[234] In the later case higher enantioselectivities were obtained for chalcones with an *ortho*-substituted aryl group at the β position (up to 92% *ee*). The enantioselective Rh-catalyzed conjugate addition of aryl boronic acids to α,β-unsaturated pyridyl sulfones has also been described.[235] A wide variety of ligands were tested, including members of the ferrocene families Josiphos, Taniaphos, Mandyphos, and Fesulphos, of which the last of these were the most enantioselective. However, for this transformation the non-ferrocene Chiraphos ligand showed the best profile in terms of both reactivity and stereoselectivity. Finally, a Cu-catalyzed conjugate addition of the organoaluminum reagents Et_3Al and [Me_2AlCH=C(Me)(Ph)] to cyclohexenone has recently been reported, occurring with good enantioselectivities (92% *ee* and 85% *ee*, respectively) in the presence of ferrocenyl phosphites combining planar and axial chirality.[236]

© 2006 Wiley-VCH Verlag GmbH & Co. KGaA, Weinheim

7. Asymmetric Cycloaddition and Other Pericyclic Reactions

7.1. Cyclopropanation Reaction

Zheng and co-workers have applied their P,N,N phosphine–heteroaryl imine ligands in the ruthenium(II)-catalyzed asymmetric cyclopropanation of styrene with ethyl diazoacetate.[237] The best results (*cis*/*trans* = 19:81, 95% *ee* for the *cis* isomer and 90% *ee* for the *trans* isomer) were achieved with the combination $[Ru(PPh_3)_3Cl_2]$/**22c** in DCE at 60°C (Scheme 59). Lower enantioselectivities were observed by either increasing or decreasing the reaction temperature.

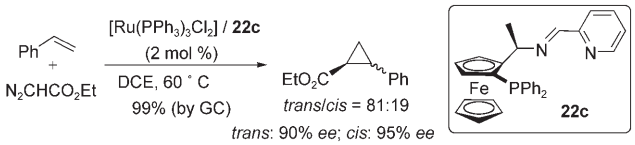

Scheme 59. Ru-catalyzed asymmetric cyclopropanation.

7.2. Diels–Alder Reactions and Other Metal-Catalyzed [4+2] Cycloadditions

7.2.1. Diels–Alder Reactions

The Diels–Alder cycloaddition between 3-alkenoyl-1,3-oxazolidin-2-ones as bidentate dienophiles and cyclopentadiene has become a standard test reaction for the evaluation of the efficiency of novel chiral Lewis acids, and very high levels of asymmetric inductions have been achieved with a large number of metal–ligand combinations.[238] However, few ferrocene-based Lewis acids have demonstrated high performance in this transformation. After exploring Fesulphos ligands (**38**) in this benchmark reaction,[239] our group reported that the dichloride complex of the *o*-Tol-Fesulphos ligand **38b** ([**38b**·$PdCl_2$], 10 mol%), in combination with $AgBF_4$ (20 mol%) as chloride scavenger, acts as an efficient chiral Lewis acid catalyst when *N*-acryloyloxazolidinone is used as the dienophile (Table 10, entry 1). The *endo* cycloadduct (*S*)-**XVa** was obtained in 95% *ee* at −78°C. Interestingly, the copper(I) complex of the same ligand, [{**38b**·CuCl}$_2$], led to the opposite enantiomer, (*R*)-**XVa**, in 54% *ee*. This reverse enantiodiscrimination displayed by Pd-Fesulphos and Cu–Fesulphos complexes was ascribed to the different geometry at the metal center (square-planar in the palladium complex and tetrahedral-like in the case of the copper complex).

Fukuzawa and co-workers[240] reported that the $Yb(OTf)_3$ complex of the bisferrocenyl oxazoline ligand **59**, readily accessed by diastereoselective pinacol homocoupling of the corresponding chiral oxazoline-substituted formylferrocene, provides moderate levels of enantioselectivity (up to 80% *ee*) in the reaction of *N*-acryloyl- and *N*-crotonyloxazolidinones (Table 10, entries 3 and 4).

Table 10: Asymmetric Diels–Alder reaction of cyclopentadiene with *N*-alkenoyloxazolidinones.

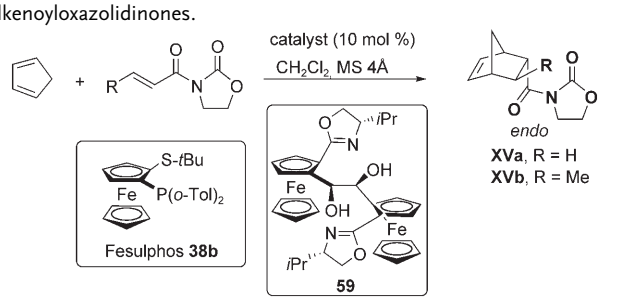

Entry	Catalyst	R	*T* [°C]	*endo*/*exo*	Yield [%]	*ee* [%] (config.)	Ref.
1	[**38b**·$PdCl_2$][a]	H	−78	98:2	91	95 (*R*)	[239]
2	[{**38b**·CuCl}$_2$][a]	H	−78	99:1	87	54 (*S*)	[239]
3	[**59**·$Yb(OTf)_3$]	H	0	80:20	95[b]	70 (*R*)	[240]
4	[**59**·$Yb(OTf)_3$]	Me	0	80:20	99[b]	80 (2*R*,3*S*)	[240]

[a] In combination with $AgBF_4$ (20 mol%). [b] Conversion.

7.2.2. Hetero-Diels–Alder Reactions

Copper(I) complexes of Fesulphos ligands (**38**) are very effective catalysts for the asymmetric formal aza-Diels–Alder reaction of *N*-sulfonyl imines with Danishefsky-type dienes,[241] which represents a convergent route to the highly valuable optically active 2,3-dihydro-4-(1*H*)-dihydropyridone intermediates (Scheme 60). The reaction affords predominantly the Mannich-type addition product, which is readily transformed into the Diels–Alder cycloadduct upon addition of trifluoroacetic acid to the reaction mixture. In particular, the copper bromide complex of the bulky 1-naphthylphosphine **38a** ([{**38a**·CuBr}$_2$], 5.1 mol%), in combination with $AgClO_4$ (10 mol%), provides good yields (usually 60–90%) and excellent enantioselectivities (typically above 90% *ee*) for a wide variety of substrates, including *N*-sulfonyl imines of aromatic, alkenyl, and enolizable aliphatic aldehydes.[241] This catalyst system also tolerates different aromatic substitutions at the *N*-sulfonyl group, which offers varied possibilities for the deprotection of the final cycloadducts.

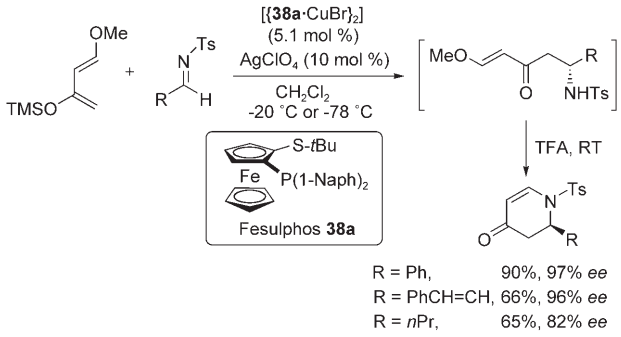

Scheme 60. Fesulphos/Cu-catalyzed enantioselective formal aza-Diels–Alder reactions of *N*-sulfonyl imines.

7.2.3. Rhodium-Catalyzed [4+2] Annulation of 4-Alkynals

Tanaka and Fu described in 2002 the rhodium(I)-catalyzed [4+2] carbocyclization of 4-alkynals with alkynes to afford 4-alkylidene cyclohexanones.[242] More recently, the enantioselective version of this [4+2] annulation was devel-

 © 2006 Wiley-VCH Verlag GmbH & Co. KGaA, Weinheim

oped with *N*,*N*-dialkyl acrylamides as a new route to enantioenriched cyclohexanones.[243] This procedure relies on the use of the cationic rhodium(I) catalyst system [Rh(cod)$_2$]BF$_4$/Walphos (5–10 mol %; Scheme 61). Compared to

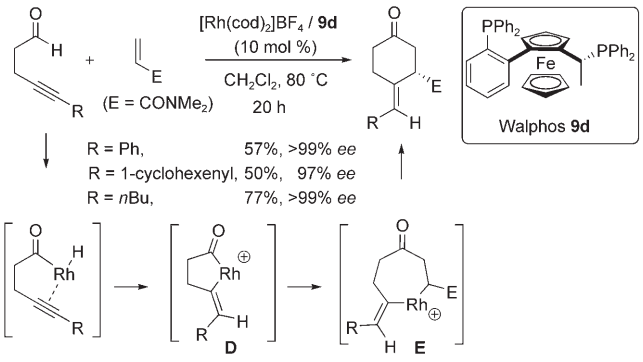

Scheme 61. Walphos/Rh-catalyzed asymmetric [4+2] annulation of 4-alkynals with *N*,*N*-dialkyl acrylamides.

other ferrocene ligands, such as Taniaphos and Josiphos, Walphos ligand **9d** dramatically increased the reactivity of the process. This effect has been attributed to its large P-M-P bite angle, which would facilitate the reductive-elimination step. Very high enantiocontrol was attained for a variety of 4-pentynals and 2-alkynylbenzaldehydes with aryl, alkenyl, and alkyl substituents at the alkyne, complete enantioselectivity (>99 % *ee*) being observed in a number of cases. The reaction is assumed to proceed through a five-membered acyl rhodium intermediate **D**, formed by intramolecular hydroacylation of the alkyne after insertion of the rhodium center into the aldehyde C–H bond, which undergoes complexation to the alkene and subsequent insertion to generate the metallacycle **E**, whose reductive elimination furnishes the cyclohexanone product, thereby regenerating the rhodium catalyst.

7.3. [3+2] Cycloadditions

7.3.1. 1,3-Dipolar Cycloaddition Reaction of Azomethine Ylides

In spite of its significance as one of the most powerful methods for the enantioselective construction of highly substituted pyrrolidine derivatives, the first catalytic asymmetric 1,3-dipolar cycloaddition of azomethine ylides to electron-deficient alkenes was not reported until 2002.[244] Since then, intense research in this field has resulted in the development of some very efficient procedures, in most cases involving ferrocene ligands.[245] Zhang and co-workers[244] found that the Ag^I complex of the bisferrocenyl P,P ligand **60** (Table 11, entries 1 and 2), structurally related to Trost's ligand, in the presence of the Hunig's base led to complete *endo* selectivity and very good enantiocontrol (70–97 % *ee*) in the cycloaddition of a variety of iminoesters derived from methyl glycinate with dimethyl maleate. More recently, Zhou and co-workers achieved slightly better levels of asymmetric induction using the catalyst system AgOAc/**15d** in the absence of any extra base, demonstrating that the reactive metal dipole can be generated by deprotonation with the

Table 11: Ag-catalyzed asymmetric 1,3-dipolar cycloaddition of azomethine ylides.

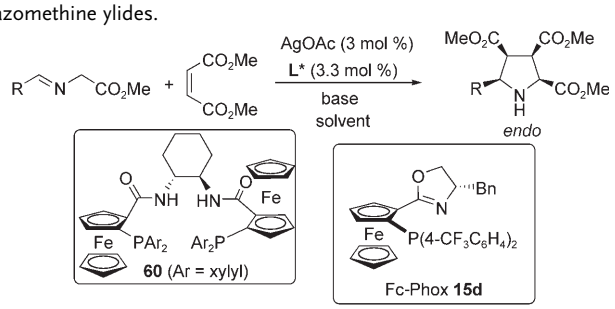

Entry	R	Base	Solvent	*T* [°C]	L*	Yield [%]	*ee* [%]	Ref.
1	4-ClC_6H_4	*i*Pr$_2$NEt	toluene	0	**60**	96	92	[244]
2	*i*Pr	*i*Pr$_2$NEt	toluene	25	**60**	82	70	[244]
3	4-ClC_6H_4	–	Et_2O	−25	**15d**	99	97	[246]
4	*i*Pr	–	Et_2O	−25	**15d**	56	88	[246]

acetate ligand of the precatalyst (Table 11, entries 3 and 4).[246] Other alkenes, such as *N*-phenylmaleimide (93 % *ee*), *tert*-butyl acrylate (88 % *ee*), and dimethyl fumarate (89 % *ee*) proved to be suitable dipolarophiles.

It has also been demonstrated that copper complexes of P,P-, P,N-, and P,S-ferrocene ligands are also successful chiral Lewis acids for this cycloaddition reaction. Thus, Zhang and co-workers have found that copper(I) complexes of the Fc-Phox ligand **15** promote the asymmetric 1,3-dipolar cycloaddition of a variety of iminoesters derived from methyl glycinate with acrylates in excellent enantioselectivity (typically above 90 % *ee*; Table 12, entry 1).[247] Et_3N was the base of choice for iminoesters bearing an electron-withdrawing aromatic substituent, while electronically richer substrates required a stronger base such as DBU. Interestingly, whereas the two previously mentioned Ag-based catalyst systems afford the *endo* adduct as either the major or the only

Table 12: Cu-catalyzed asymmetric 1,3-dipolar cycloaddition of azomethine ylides.

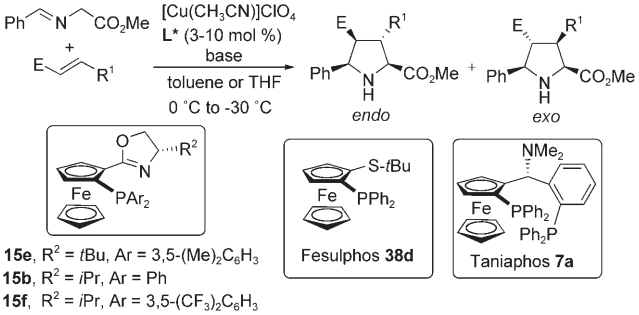

Entry	E	R^1	L*	*endo*/*exo*	Yield [%]	*ee* [%]	Ref.
1	CO_2tBu	H	**15e**	5:95	65	84	[247]
2	NO_2	Ph	**15b**	<2:98	87	95	[248]
3	NO_2	Ph	**15f**	86:14	85	98	[248]
4	CO_2Me	CO_2Me	**38d**	90:10	89	>99	[249]
5	CN	CN	**38d**	20:80	78	76	[249]
6	NO_2	Ph	**38d**	5:95	61	94	[249]
7	SO_2Ph	H	**7a**	<2:98	87	83	[251]

© 2006 Wiley-VCH Verlag GmbH & Co. KGaA, Weinheim

product, this Cu-catalyzed protocol proved to be highly *exo*-selective, with the *exo*/*endo* ratio exceeding 95:5 in most cases. Especially dramatic is the reverse diastereoselectivity observed in the reactions with the two Fc-Phox catalysts AgOAc/**15d** and $CuClO_4$/**15e** (Table 11 and Table 12).

Using the same copper(I) source and a very similar Fc-Phox ligand, Hou and co-workers[248] recently discovered that subtle variations on the nature of the aryl group on the phosphorus atom lead to dramatic changes on the *endo*/*exo* selectivity in the reaction of azomethine ylides with nitroalkenes, allowing a switch of diastereoselectivity (Table 12, entries 2–3). Thus, electron-rich phosphines such as **15b** gave the *exo* cycloadduct as the major or the only product with excellent enantioselectivities (typically 92–98% *ee*; Table 12, entry 2), while ligand **15f**, with two CF_3 substituents on each phenyl ring at phosphorus, afforded mainly the *endo* isomer with good diastereoselectivity and similarly high enantiocontrol (Table 12, entry 3). In this reaction the use of *t*BuOK as base proved to be essential, since weaker bases such as Et_3N provided significant amounts of the corresponding acyclic product from Michael addition of the ylide to the nitroalkene.

The copper(I)–Fesulphos catalyst system showed exceptional levels of reactivity and enantiocontrol with azomethine ylides (Table 12, entries 4–6, and Table 13), providing complete *endo* selectivity and enantioselectivity (> 99% *ee*) in the reaction of aryl imines of methyl glycinate with *N*-phenylmaleimide (Table 13, entry 1).[249] The catalyst system $CuClO_4$/**38d** (and Et_3N as base) tolerates α-substituted azomethine ylides, allowing the enantiocontrolled synthesis of pyrrolidines with a quaternary stereocenter at C2 with up to 92% *ee* (Table 13, entries 2 and 3). It is worth mentioning that this type of dipole species had only been previously studied with the AgOAc/Quinap catalyst system.[250] Remarkably, the previously unknown ketimine-derived azomethine ylides having two different groups at the ketimine moiety, such as those derived from acetophenones, also smoothly participated in the reaction, affording with virtually complete diastereoselectivity the corresponding pyrrolidines with a stereogenic quaternary center at C5, in up to > 99% *ee* (Table 13, entries 4 and 5).[249] Other dipolarophiles of varied nature, including mono- and diactivated alkenes such as methyl acrylate, dimethyl maleate, dimethyl fumarate, methacrolein, fumarodinitrile, and β-nitrostyrene also provided high enantioselectivities (for example, entries 4–6 in Table 12).

Our research group has also recently described the first general protocol for the catalytic enantioselective 1,3-dipolar cycloaddition of azomethine ylides to α,β-unsaturated sulfones.[251] Complete *exo* selectivity and high enantioselectivities (typically 65–85% *ee*) were attained with $CuClO_4$/Taniaphos (**7a**) as the optimal catalyst system (Table 12, entry 7). Interestingly, the enantiopurity of the resulting 3-sulfonyl cycloadducts can be enhanced to > 99% *ee* after a single recrystallization. These cycloadducts are versatile intermediates for the preparation of optically active 2,5-disubstituted pyrrolidines after reductive desulfonylation with Na(Hg), the vinyl sulfone acting as a synthetic equivalent of ethylene.

Table 13: Fesulphos/Cu-catalyzed asymmetric 1,3-dipolar cycloaddition of substituted azomethine ylides.

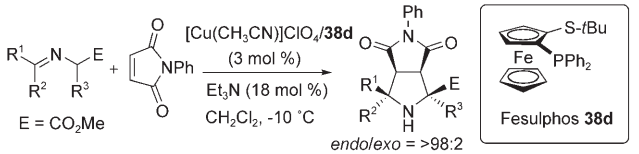

Entry	R^1	R^2	R^3	Yield [%]	*ee* [%]
1	Ph	H	H	81	> 99
2	Ph	H	Me	50	80
3	2-Naph	H	Me	78	92
4	Ph	Me	H	78	94
5	4-ClC_6H_4	Me	H	80	> 99

7.3.2. Cu-Catalyzed [3+2] Cycloadditions of Terminal Alkynes with Nitrones and Azomethine Imines

The copper(I)-catalyzed coupling of nitrones with terminal alkynes to afford β-lactams, known as the Kinugasa reaction, is assumed to proceed by 1,3-dipolar cycloaddition of the in situ generated copper acetylide to the nitrone. The resulting heterocycle **F** then rearranges to afford the copper enolate of a β-lactam (**G**), whose protonation furnishes the final product (Scheme 62). Driven by the wide-range significance of β-lactams in pharmacy and as synthetic intermediates, Fu and co-workers described in 2002 a catalytic enantioselective variant of this reaction using the bisazaferrocene **61** as the chiral ligand.[252]

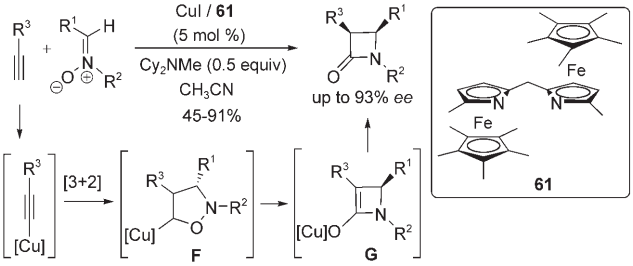

Scheme 62. Catalytic enantioselective synthesis of β-lactams by the Kinugasa reaction.

More recently the catalytic asymmetric intramolecular version of this reaction has been developed.[253] Although in this case the ligand **61** led to poor yields and low enantioselectivity, the new family of phosphaferrocene–oxazoline ligands **62** provided excellent results in terms of reactivity and stereoselectivity (Scheme 63). A range of tricyclic β-lactams containing a 6,4 or a 7,4 ring system were obtained with very good enantiocontrol under catalysis with the combination CuBr/**62** (5 mol%). The *i*Pr-substituted ligand **62a** was typically found to be the ligand of choice for the generation of a β-lactam fused to a six-membered ring (86–90% *ee*), whereas for seven-membered rings the *t*Bu-substituted analogue **62b** gave superior results (85–91% *ee*). Interestingly, the intermediate copper enolate **G** can be

 © 2006 Wiley-VCH Verlag GmbH & Co. KGaA, Weinheim

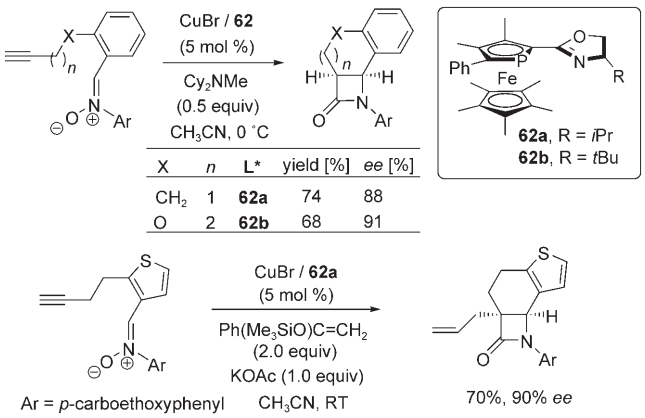

Scheme 63. Catalytic enantioselective synthesis of polycyclic β-lactams through intramolecular Kinugasa reaction.

trapped with an electrophile, thereby generating a quaternary stereogenic center. The competitive highly favorable protonation of **G** (for example, by the conjugate acid of the tertiary amine normally used as base) was minimized using a mixture of a silyl enol ether and KOAc as the base, thereby achieving α-allylation of the β-lactams with up to 90% *ee* (Scheme 63).

Fu and co-workers have also demonstrated that this type of P,N-phosphaferrocene ligands are very effective in other copper(I)-catalyzed [3+2] cycloaddition, such as the enantioselective reaction of terminal electron-deficient alkynes with azomethine imines,[254] which likely involves reaction of the dipole with a transient copper acetylide generated in situ. Initially CuI (5 mol%) was found to be an effective promoter for this reaction, affording the cycloadduct with very good yields. Additionally, high enantioselectivities (typically in the range of 81–96% *ee*) were obtained in the presence of the P,N-phosphaferrocene–oxazoline ligands **63** (Scheme 64). The scope of this method is fairly broad with respect to both the azomethine imine and the alkyne components, though the best yields and enantioselectivities were attained when the latter reaction partner bears an electron-poor substituent such as ester, amide, ketone, electron-deficient aromatic, or hetereoaromatic groups.

In an extension of this method, the same catalyst system has been applied to the kinetic resolution of racemic mixtures

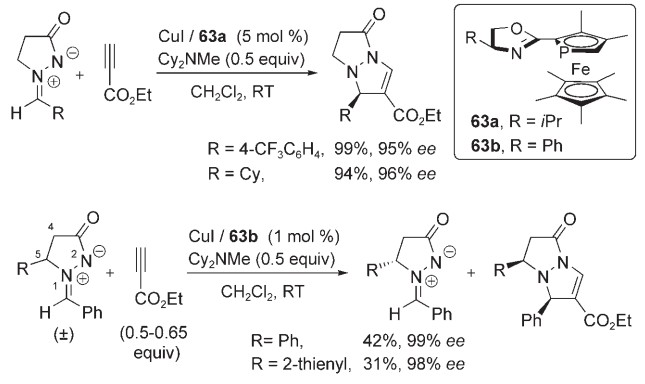

Scheme 64. Cu-catalyzed [3+2] asymmetric cycloadditions of terminal alkynes with azomethine imines.

of azomethine imines to yield enantioenriched dipole species, which were demonstrated to be versatile and synthetically useful compounds (Scheme 64).[255] A variety of electron-poor alkynes provided good selectivity factors ($s > 10$) in their reaction with azomethine imines possessing a variety of substituents at the N1 and C5 positions of the heterocycle (for example, alkyl, aryl, heteroaryl groups). In contrast, C4-substituted azomethine imines do not undergo kinetic resolution with useful selectivity ($s < 2$).

7.4. [3,3] Rearrangement of Allyl Imidates to Allylic Amides

Since the first catalytic asymmetric [3,3] rearrangement of allyl imidates to allylic amides, reported by Overman and co-workers in 1997[256] using chiral cationic palladium complexes, a number of palladium(II) catalysts have been reported. Among them, planar-chiral metalocene-derived palladacycle complexes have emerged as a premier class of catalysts for this synthetically important transformation. Overman and co-workers[257] have prepared and evaluated a small library of palladium(II) complexes based on a ferrocenyl–oxazoline palladacyclic scaffold, with compound **64** providing the best results (Table 14, entries 1 and 2). The cationic palladium species resulting upon activation of this type of dimeric complex (5 mol%) with an excess of silver trifluoroacetate catalyzes the allylic rearrangement of both *E* and *Z* prochiral primary allylic *N*-(4-methoxyphenyl)benzimidates to give the corresponding protected benzamides in high yield and good enantiocontrol (typically 81–95% *ee*).

Peters and co-workers found that structurally related complexes derived from pentamethylferrocenyl- and pentaphenylferrocenyl-2-imidazolines such as **65a** also provided

Table 14: Pd-catalyzed enantioselective [3,3] rearrangement of allyl imidates to allylic amides.

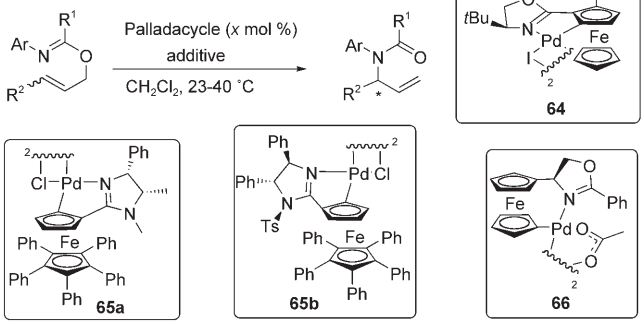

Entry	Ar[a]	R^1	R^2	*E*/*Z*	*x*	[Pd]	Yield [%]	*ee* [%] (config.)	Ref.
1	PMP	Ph	*i*Bu	*E*	5	**64**[b]	97	84 (*S*)	[257]
2	PMP	Ph	*i*Bu	*Z*	5	**64**[b]	89	96 (*R*)	[257]
3	PMP	CF_3	Me	*E*	5	**65a**[c]	93	88 (*S*)	[258]
4	PMP	CF_3	$(CH_2)_2Ph$	*Z*	5	**65b**[b]	95	95 (*S*)	[259]
5	PMP	CF_3	$(CH_2)_2Ph$	*E*	1	**65b**[b]	94	99.7 (*R*)	[259]
6	Ph	Ph	Ph	*E*	5	**66**	49	90 (*S*)	[260]

[a] PMP = *p*-methoxyphenyl. [b] $AgOCOCF_3$ (0.2 equiv) as additive. [c] $AgNO_3$ (0.3 equiv) as additive.

 © 2006 Wiley-VCH Verlag GmbH & Co. KGaA, Weinheim

excellent yields and good enantioselectivities (84–88% ee) in the aza-Claisen reaction of several trifluoroacetimidates (Table 14, entry 3).[258] Based on these initial results, the same research group has designed a less electron-rich catalyst (complex **65b**),[259] in which the bulky *N*-sulfonyl residue allowed its easy preparation through direct diastereoselective carbopalladation. Upon activation with Ag^{I}, this complex exhibits unprecedented activity (catalyst loading as low as 0.05 mol%), enantioselectivity (up to 99.7% *ee*), and tolerance toward a broad spectrum of substrates in the aza-Claisen rearrangement of *N*-*p*-methoxyphenyl trifluoroacetimidates. Interestingly, opposite absolute configurations of the major enantiomer of rearranged products were observed starting from (*E*)- or (*Z*)-acetimidate (Table 14, entries 4 and 5).

Moyano and co-workers[260] have reported a new structural type of ferrocenyl oxazoline palladacycle complex in which the palladium center is bonded to a carbon atom of the unsubstituted cyclopentadiene ring of the ferrocene backbone (for example, **66** in Table 14). These complexes were easily prepared from 4-ferrocenyl-oxazolines by direct cyclopalladation with $Pd(OAc)_2$. In contrast to the previous 2-ferrocenyl-oxazoline derivatives, in this case the most stable conformer is that in which the nitrogen atom is oriented towards the unsubstituted cyclopentadiene ring, thereby directing the metalation at this position. In particular, complex **66** provided moderate yields and up to 90% *ee* in the Pd^{II}-catalyzed aza-Claisen rearrangement of (*E*)-3-phenylallyl-(*N*-phenyl)benzimidate (Table 14, entry 6).

8. Asymmetric Nucleophilic Catalysis

As many examples presented along this update, the most developed and commonly used strategy for asymmetric catalytic nucleophile–electrophile reactions, especially processes involving substrates with C=O or C=N bonds, implies electrophile activation by metal-centered chiral Lewis acids. Complementarily, it is well-known that Lewis bases, such as nitrogen heterocycles and tertiary phosphines and amines, catalyze a variety of important chemical processes. Because of this nucleophilic reactive profile, the development of chiral Lewis bases for nucleophilic catalysis has attracted great attention in recent years.[261] In this field a limited number, but in some cases very efficient catalysts, having a ferrocene scaffold have been reported.

8.1. Planar-Chiral 4-(Dimethylamino)pyridine–Ferrocene-Type Catalysts

Owing to its high reactivity and chemical versatility, 4-(dimethylamino)pyridine (DMAP) is an excellent candidate for the design of chiral nucleophilic catalysts.[262] In this topic an array of outstanding contributions have been developed by Fu and co-workers from their fascinating nucleophilic planar-chiral ferrocene-type heterocycles.[263] Since the first report in 1996, this type of catalyst has proved to be quite effective in a variety of asymmetric transformations such as addition of alcohols and amines to ketenes, rearrangement of O-acylated enolates, and acylation of alcohols with anhydrides.[264]

More recently, in 2003, the first catalytic enantioselective C-acylation of silylated enols was described. Particularly, the reaction between silyl ketene acetals and acetic anhydride catalyzed by the chiral DMAP derivative **67a** was reported.[265] The proposed pathway for this nucleophile-catalyzed process is shown in Scheme 65, in which the formation of the highly reactive chiral acetylpyridinium ion is supposed to play a key role. In the presence of 5 mol% of catalyst **67a**, the acetylation at room temperature of the silyl ether of α-substituted butyrolactones provided the C-acylated product, with an all-carbon quaternary stereocenter, in high yield (typically 80–90%) and enantioselectivity (76–99% *ee*). Excellent results were also achieved in the case of acyclic esters.[266] Interestingly, since both *E* and *Z* silyl ketene acetals are converted into the same enantiomer product, *E*/*Z* mixtures of substrates can be directly employed (Scheme 66). This remarkable procedure of catalytic enan-

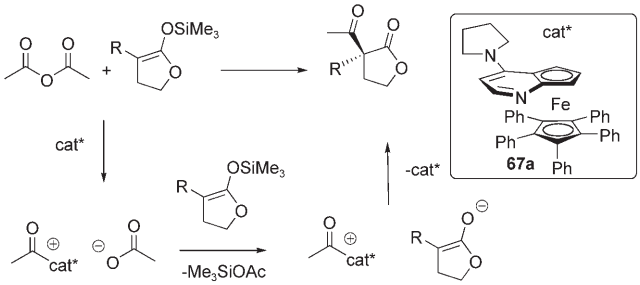

Scheme 65. Presumed pathway for the asymmetric C-acylation catalyzed by **67a**.

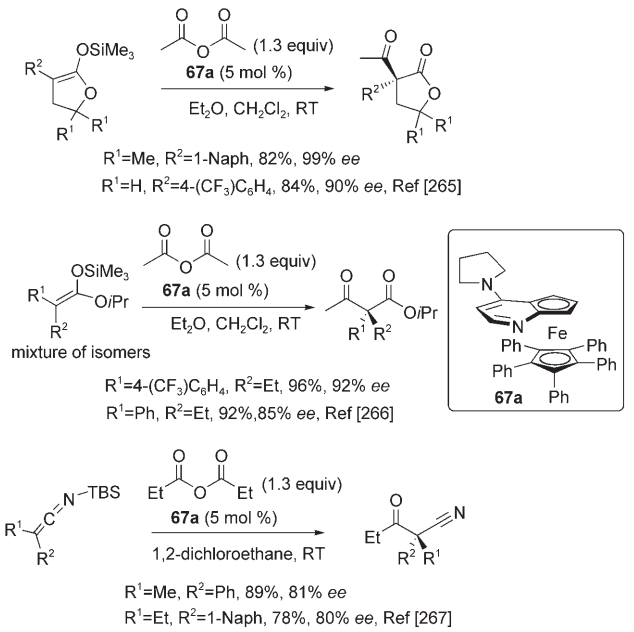

Scheme 66. Asymmetric C-acylation of silyl ketene acetals and silyl ketene imines.

 © 2006 Wiley-VCH Verlag GmbH & Co. KGaA, Weinheim

tioselective synthesis of all-carbon quaternary stereocenters has been recently expanded to the acylation of silyl ketene imines. Thus, in the presence of the same catalyst **67a** (5 mol%), the reaction of the readily available disubstituted ketene imines with anhydrides takes place in an efficient way, providing the corresponding α-cyano ketones with enantioselectivities in the range 77–83% *ee*. This procedure has been elegantly applied to the first catalytic asymmetric synthesis of the drug (*S*)-verapamil.[267]

The DMAP-catalyzed rearrangement of O-acylated benzofuranones to give their β-substituted C-acylated products was described in 1986.[268] Seventeen years later, the catalytic asymmetric version of this process and its extension to O-acylated oxindoles were developed.[269] In the presence of 5 mol% of the catalyst **67a** excellent yields (typically 80–95%) and asymmetric inductions (typically 90–99% *ee*) were achieved with a variety of substrates. It must be pointed out that for reaching this high enantiocontrol and reactivity it is essential the use of the bulky and electronically activated trichloro-*tert*-butyl group at the carbonate unit (Scheme 67). Typical carbonate substitutions led to low enantioselectivities (for example, methyl or ethyl carbonates) or were completely unreactive (for example, *tert*-butyl carbonates).

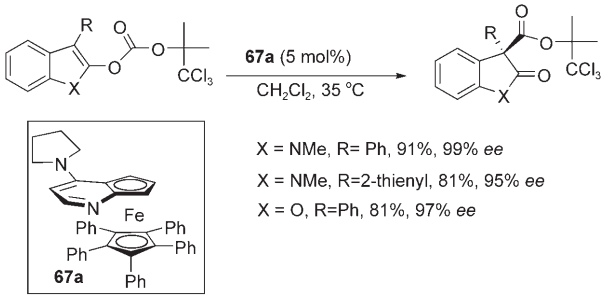

Scheme 67. Asymmetric rearrangement of oxindole and benzofuranone carbonate derivatives.

A quite attractive atom-economy approach to the synthesis of β-lactones is the stepwise [2+2] cycloaddition of ketenes and aldehydes.[270] Some reports on the asymmetric Lewis base catalyzed version of this reaction, sometimes with outstanding enantioselectivities, have recently been published.[271] However, only the ketene itself or monosubstituted ketenes had been employed in this process. On the basis of an earlier study on the highly enantioselective Staudinger-type cycloaddition of ketenes with imines to afford β-lactams,[272] catalyzed by the DMAP derivative **67b**, the group of Fu has further applied this catalyst in the enantioselective reaction between ketenes and aldehydes (Scheme 68).[273] Under very mild reaction conditions (−78°C) the reaction of dialkyl-substituted ketenes with aromatic aldehydes, catalyzed by **67b**, leads to α,α-disubtituted β-lactones with moderate to good yields (48–92%) and enantioselectivities (76–91% *ee*). In the case of unsymmetrically disubstituted ketenes two contiguous stereocenters are generated (one quaternary and one tertiary), usually with moderate *cis*/*trans* diastereoselectivity (4.1:1 to 4.6:1 isomer ratio).

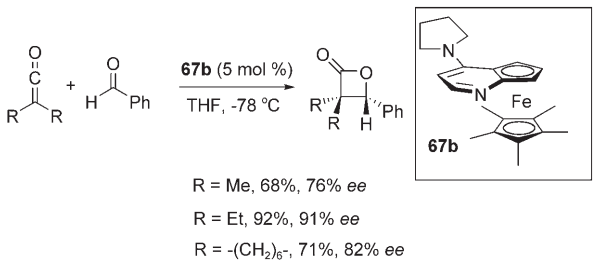

Scheme 68. Asymmetric overall [2+2] cycloaddition of ketenes and aldehydes.

A step further, which shows the versatility of planar-chiral DMAP-type catalysts, was reported in 2002, when the enantioselective addition of 2-cyanopyrrole to ketenes catalyzed by **67a** was investigated, providing the acylated pyrroles in up to 98% *ee*. Interestingly, in this study it was demonstrated that **67a** behaved as a Brønsted acid rather than a Lewis base as result of its in situ protonation with 2-cyanopyrrole (Scheme 69).[274] This concept has been recently

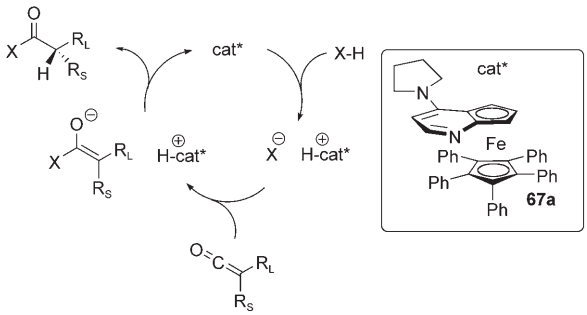

Scheme 69. Presumed asymmetric Brønsted acid catalysis pathway.

expanded to the enantioselective synthesis of phenolic esters by addition of phenols to aryl alkyl ketenes with ligand **67b** (Scheme 70).[275] Although moderate asymmetric inductions were achieved with phenol itself or *para*-substituted phenols (35–72% *ee*), a remarkable enhancement in the stereoselec-

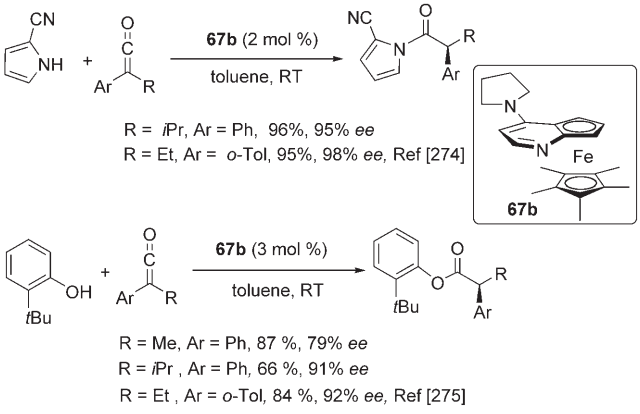

Scheme 70. Asymmetric addition of 2-cyanopyrrole and phenols to disubstiuted ketenes.

 © 2006 Wiley-VCH Verlag GmbH & Co. KGaA, Weinheim

tivity was obtained with the more sterically demanding *ortho*-substituted phenols, reaching the highest enantioselectivity with the bulky *ortho-tert*-butylphenol (79–94% *ee*).

8.2. Other Nucleophile-Catalyzed Reactions

The Baylis–Hillman reaction between Michael acceptors and aldehydes is one of the most studied Lewis base catalyzed processes, allowing the straightforward preparation of chemically versatile α-methylene-β-hydroxycarbonyl compounds.[276] In spite of the great progress achieved in recent years, much effort is still required for the development of structurally general and highly enantioselective protocols. Two reports on the use of chiral ferrocene catalysts in this reaction have been recently published (Scheme 71). Thus, a

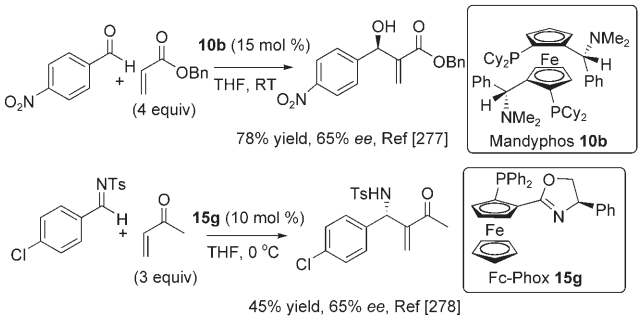

Scheme 71. Asymmetric Baylis–Hillman reaction catalyzed by ferrocenyl phosphines.

variety of planar-chiral ferrocenyl dialkylphosphines have been tested in the Baylis–Hillman reaction between aromatic aldehydes and acrylates, with the Mandyphos ligand **10b** providing the highest enantioselectivity (up to 65% *ee*).[277] Limited success has also been achieved when Fc-Phox ligands (for example, **15g**) were screened as nucleophilic catalysts in the aza-Baylis–Hillman reaction of the *N*-tosyl aldimine of *p*-chlorobenzaldehyde with methyl vinyl ketone (up to 65% *ee*). For this reaction axially chiral hydroxybinaphthyl phosphines were found to be more efficient catalysts.[278]

In 2003 Kobayashi and co-workers reported that chiral alkyl aryl sulfoxides effectively mediate the enantioselective reaction of *N*-acylhydrazones with allyltrichlorosilanes furnishing the corresponding homoallylic amines with high diastereo- and enantioselectivities.[279] Fernández, Khiar, and co-workers have recently reported the use of ferrocenyl sulfoxides as promoters in this reaction (Scheme 72).[280] Among several tested sulfoxides, the isopropyl derivative (**68**) was the most enantioselective (82% *ee*). Disappointingly,

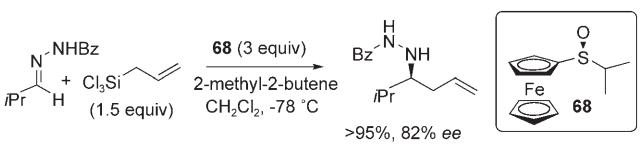

Scheme 72. Asymmetric allylation of hydrazones mediated by chiral sulfinyl ferrocenes.

this addition reaction requires a great amount of the sulfoxide promoter (3 equiv).

Metzner and co-workers have shown that ferrocenyl sulfides mediate the Johnson–Corey epoxidation of aldehydes via sufonium ylides. In the epoxidation of benzaldehyde to stilbene oxide, 67% *ee* was obtained using as catalyst the planar-chiral *tert*-butylsulfenylferrocene **69** (Scheme 73).[281] In a later study, the enantioselectivity was improved up to 94% *ee* by using the more rigid cyclic sulfide **70**, although in both cases the reaction time is very long (14 days).[282]

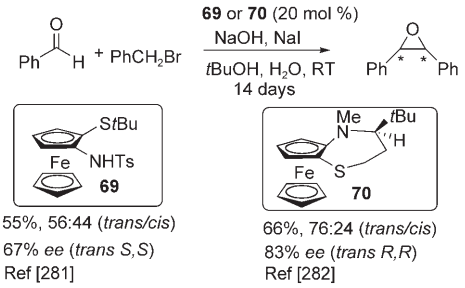

Scheme 73. Asymmetric epoxidation of aromatic aldehydes via chiral ferrocenyl sulfur ylides.

9. Miscellaneous Reactions

Uemura and co-workers reported in 1999 a novel palladium(0)-catalyzed arylation of *tert*-cyclobutyl alcohol to give γ-arylated ketones.[283] In the proposed mechanism for this reaction an arylpalladium intermediate, formed by oxidative addition of aryl bromide to a palladium(0) phosphine complex, undergoes a ligand exchange with *tert*-cyclobutyl alcohol to afford a palladium(II) alcoholate **H**, which evolves by β-carbon elimination to an alkylpalladium intermediate **J** (Scheme 74). This species **J** is prone to undergo reductive elimination to give the final γ-arylated ketones. Subsequently, the enantioselective variant of this reaction was developed by using ppfa-type ligands.[284] An initial chiral ligand screening demonstrated the superiority of bidentate P,N ligands over diphosphine or monophosphine structures, with the ppfa ligand **48** providing promising results. Further ligand optimization led to the discovery that ligands contain-

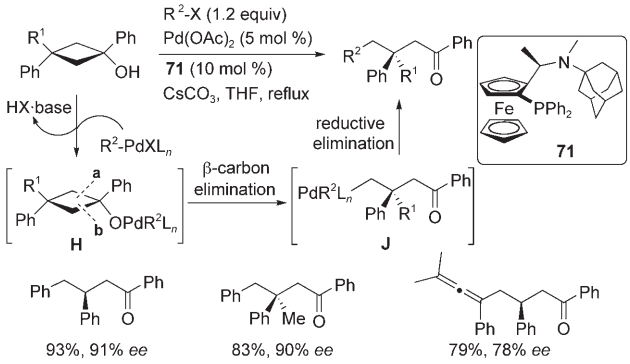

Scheme 74. Pd-catalyzed asymmetric arylation, vinylation, and allenylation of *tert*-cyclobutyl alcohol.

 © 2006 Wiley-VCH Verlag GmbH & Co. KGaA, Weinheim

ing nonsymmetrical amino groups produced a significant increase in enantioselectivity, the adamantyl derivative **71** providing the highest *ee* values. Under optimal conditions, a variety of 3-substituted *tert*-cyclobutyl alcohol undergo asymmetric arylation (73–91% *ee*) and vinylation (73–88% *ee*) with good enantioselectivity. Interestingly, 3,3-disubstituted cyclobutanols also participated in the reaction, providing the corresponding ketones with a chiral quaternary carbon stereocenter. The asymmetric allenylation reaction has also been accomplished (78–84% *ee*), albeit with a more limited scope. The required (σ-allenyl)palladium(II) species were generated in situ by oxidative addition of palladium(0) to propargylic acetates. The absolute configuration of the products reveals that the C–C bond **b** of the palladium(II) alcoholate is preferentially cleaved. Another factor affecting the enantioselectivity was the *cis*/*trans* ratio of the alcohols, with the *cis* isomer affording the product with higher levels of asymmetric induction than the *trans* isomer.

10. Summary and Outlook

Undoubtedly, asymmetric catalysis is one of the most active and challenging areas of research in current organic synthesis. In this field ferrocene-based ligands are becoming an extremely important alternative, especially in processes catalyzed by chiral metal complexes, rivalling other privileged ligand architectures such as bisoxazolines, phosphinooxazolines, salen complexes, DuPhos, or axially chiral ligands (for example, Binap, Segphos, Binol, Quinap). Key advantages of ferrocene as a scaffold for chiral ligands are its rigidity, its high availability and stability, and the existence of general methods for its functionalization at different positions of the sandwich structure, which allows the facile introduction of a vast variety of substituents, usually with coordinating phosphorus, nitrogen, or sulfur atoms, thus providing very different coordination modes and well-defined steric and electronic environments after chelation to the metal. From a stereochemical point of view, the methods for the selective generation of planar-chiral ferrocene ligands are particularly important. In this topic, although the diastereoselective *ortho* metalation of Ugi's amine continues to be the most used strategy, other chiral *ortho*-directing groups such as oxazolines, sulfoxides, and acetals are receiving increasing attention. In fact, this great chemical availability determines that chiral 1,2-disubstituted ferrocenes are by far the most common planar-chiral ligands employed in asymmetric catalysis. These ligands can have planar chirality only, but more frequently also possess central chirality.

In agreement with the excellent chemical and stereochemical features of ferrocene ligands, over the last few years a high number of relevant articles dealing with enantioselective applications have been reported, evidencing the growing impact of ferrocene ligands in the chiral-ligand toolbox for asymmetric catalysis. For instance, in the preparation of this update we have included 58 original publications from 2003, 52 from 2004, 55 from 2005, and 34 from 2006 (up to May). Overall, an amazing variety of asymmetric reactions have been studied, covering a very important portion of the general reactivity of organic compounds (for example, reduction of alkenes, ketones, and imines, 1,2-addition to carbonyl compounds and imines, conjugate additions, a diversity of metal-mediated coupling reactions, [4+2] and [3+2] cycloadditions). Part of the progress achieved concerns the development of structurally innovative chiral ferrocene ligands, which are frequently tested in known asymmetric reactions. Illustrative examples of this category are the steric and electronically modulable families of ligands Walphos, BoPhoz, Fesulphos, and P-chirogenic ferrocenylphosphines, which have provided good enantiocontrol in a variety of processes. It can be anticipated that new applications from these ligands, as well as other new interesting types of ligands, will be reported in the next years.

Another main area of research is the discovery of novel asymmetric processes from well-established ferrocene ligands, some of them commercially available. In this field, it must be mentioned that an ample set of impressive results has been achieved with members of the Fc-Phox, Ferro-TANE, Taniaphos, and Josiphos families. For instance, Josiphos ligands have taken the lead in the first described enantioselective versions of very important processes, such as the Cu-catalyzed conjugate addition of Grignard reagents to acyclic enones, esters, and thioesthers, the Cu-catalyzed conjugate hydrosilylation of α,β-unsaturated ketones, esters, nitriles, and nitro compounds, and the Pd-catalyzed desymmetrization of anhydrides. The commercial availability of many of these ligands (for example, the Solvias kit of ferrocene ligands), in some cases in both enantiomeric forms, is an excellent starting point for the discovery of innovative applications in the coming years. In this direction more detailed mechanistic studies and the characterization of the real ferrocene–metal species involved in the catalytic cycle are certainly needed. This progress in mechanism elucidation will help the more rational fine-tuning of the ligand and the development of ferrocene catalysts with higher turnover values, which is a crucial issue for developing industrial applications.

Unlike the plethora of chiral ferrocene ligands with heteroatomic substituents for coordination with transition metals (mainly phosphorus and nitrogen substituents), the application of nucleophilic ferrocene ligands as simple catalysts for asymmetric processes has been much less studied. In this field breakthrough results have been described with the fascinating planar-chiral 4-(dimethylamino)-pyridine–ferrocene-type catalysts developed by Fu and coworkers. Since this area of research seems to be underdeveloped, new contributions of chiral ferrocene compounds as direct catalysts in asymmetric processes are expected for the coming years.

Received: June 20, 2006

[1] T. J. Kealy, P. L. Pauson, *Nature* **1951**, *168*, 1039–1040.
[2] M. Breuer, K. Ditrich, T. Habicher, B. Hauer, M. Kebeler, R. Stürmer, T. Zelinski, *Angew. Chem.* **2004**, *116*, 806–843; *Angew. Chem. Int. Ed.* **2004**, *43*, 788–824.

 © 2006 Wiley-VCH Verlag GmbH & Co. KGaA, Weinheim

[3] a) H.-U. Blaser, *Adv. Synth. Catal.* **2002**, *344*, 17 – 31; b) H.-U. Blaser, W. Brieden, B. Pugin, F. Spindler, M. Studer, A. Togni, *Top. Catal.* **2002**, *19*, 3 – 16.

[4] G. P. Sollot, J. L. Snead, S. Portnoy, W. R. Peterson, Jr., H. E. Mertwoy, *Chem. Abstr.* **1965**, *63*, 18147b.

[5] a) K.-S. Gan, T. S. A. Hor in *Ferrocenes. Homogeneous Catalysis, Organic Synthesis, Materials Science* (Eds.: A. Togni, T. Hayashi), VCH, Weinheim, **1995**, pp. 3 – 104; b) T. J. Colacot, *Platinum Met. Rev.* **2001**, *45*, 22 – 30; c) U. Siemeling, T.-C. Auch, *Chem. Soc. Rev.* **2005**, *34*, 584 – 594.

[6] T. Hayashi, K. Yamamoto, M. Kumada, *Tetrahedron Lett.* **1974**, 4405 – 4408.

[7] A. Togni, C. Breutel, A. Schnyder, F. Spindler, H. Landert, A. Tijiani, *J. Am. Chem. Soc.* **1994**, *116*, 4062 – 4066.

[8] a) C. J. Richards, T. Damalidis, D. E. Hibbs, M. B. Hursthouse, *Synlett* **1995**, 74 – 76; b) T. Sammakia, H. A. Latham, D. R. Schaad, *J. Org. Chem.* **1995**, *60*, 10 – 11; c) Y. Nishibayashi, S. Uemura, *Synlett* **1995**, 79 – 81.

[9] T. Ireland, G. Grossheimann, C. Wieser-Jeunesse, P. Knochel, *Angew. Chem.* **1999**, *111*, 3397 – 3400; *Angew. Chem. Int. Ed.* **1999**, *38*, 3212 – 3215.

[10] T. Hayashi in *Ferrocenes. Homogeneous Catalysis, Organic Synthesis, Materials Science* (Eds.: A. Togni, T. Hayashi), VCH, Weinheim, **1995**, pp. 105 – 142.

[11] H. B. Kagan, O. Riant, *Adv. Asymmetric Synth.* **1997**, *2*, 189 – 235.

[12] C. F. Richards, A. J. Lock, *Tetrahedron: Asymmetry* **1998**, *9*, 2377 – 2407.

[13] A. Togni in *Metallocenes* (Eds.: A. Togni, R. L. Halterman), Wiley, New York, **1998**, pp. 685 – 721.

[14] D. Laurenti, M. Santelli, *Org. Prep. Proced. Int.* **1999**, *31*, 245 – 294.

[15] L.-X. Dai, T. Tu, S.-L. You, W.-P Deng, X.-L. Hou, *Acc. Chem. Res.* **2003**, *36*, 659 – 667.

[16] a) F. Fache, E. Schulz, M. L. Tommasino, M. Lemaire, *Chem. Rev.* **2000**, *100*, 2159 – 2232; b) P. J. Guiry, C. P. Saunders, *Adv. Synth. Catal.* **2004**, *346*, 497 – 537; c) H. A. McManus, P. J. Guiry, *Chem. Rev.* **2004**, *104*, 4151 – 4202.

[17] O. B. Sutcliffe, M. R. Bryce, *Tetrahedron: Asymmetry* **2003**, *14*, 2297 – 2325.

[18] T. J. Colacot, *Chem. Rev.* **2003**, *103*, 3101 – 3118.

[19] R. C. J. Atkinson, V. C. Gibson, N. J. Long, *Chem. Soc. Rev.* **2004**, *33*, 313 – 328.

[20] For instance, in recent years Hartwig and co-workers have described elegant and groundbreaking applications of palladium–Josiphos as a general and long-lived catalyst in the formation of aromatic carbon–heteroatom bonds. For recent references, see: a) M. A. Fernández-Rodríguez, Q. Shen, J. F. Hartwig, *J. Am. Chem. Soc.* **2006**, *128*, 2180 – 2181; b) Q. Shen, S. Shekhar, J. P. Stambuli, J. F. Hartwig, *Angew. Chem.* **2005**, *117*, 1395 – 1397; *Angew. Chem. Int. Ed.* **2005**, *44*, 1371 – 1375.

[21] a) D. Markarding, H. Klusacek, G. Gokel, P. Hoffmann, I. Ugi, *J. Am. Chem. Soc.* **1970**, *92*, 5389 – 5393.

[22] a) F. Rebière, O. Riant, L. Ricard, H. B. Kagan, *Angew. Chem.* **1993**, *105*, 644 – 646; *Angew. Chem. Int. Ed. Engl.* **1993**, *32*, 568 – 570; b) N. M. Lagneau, Y. Chen, P. M. Robben, H.-S. Sin, K. Tasaku, J-S. Chen, P. D. Robinson, D. H. Hua, *Tetrahedron* **1998**, *54*, 7301 – 7334.

[23] a) O. Riant, O. Samuel, H. B. Kagan, *J. Am. Chem. Soc.* **1993**, *115*, 5835 – 5836; b) O. Riant, O. Samuel, T. Flessner, S. Taudien, H. B. Kagan, *J. Org. Chem.* **1997**, *62*, 6733 – 6745; c) H. Wölfle, H. Kopacka, K. Wurst, K.-H. Ongania, H.-H. Görtz, P. Preishuber-Pflügl, B. Bildstein, *J. Organomet. Chem.* **2006**, *691*, 1197 – 1215.

[24] M. Wildhalm, K. Mereiter, M. Bourghida, *Tetrahedron: Asymmetry* **1998**, *9*, 2983 – 2986.

[25] a) Y. Farrell, R. Goddard, P. J. Guiry, *J. Org. Chem.* **2002**, *67*, 4209 – 4217; b) C. Ganter, T. Wagner, *Chem. Ber.* **1995**, *128*, 1157 – 1161.

[26] a) D. Enders, R. Peters, R. Lochtman, G. Raabe, *Angew. Chem.* **1999**, *111*, 2579 – 2581; *Angew. Chem. Int. Ed.* **1999**, *38*, 2421 – 2423; b) D. Enders, R. Peters, R. Lochtman, J. Runsink, *Eur. J. Org. Chem.* **2000**, 2839 – 2850.

[27] C. Bolm, M. Kesselgruber, K. Muñiz, G. Raabe, *Organometallics* **2000**, *19*, 1648 – 1651.

[28] L. Xiao, R. Kitzler, W. Weissensteiner, *J. Org. Chem.* **2001**, *66*, 8912 – 8919.

[29] R. Peters, D. F. Fischer, *Org. Lett.* **2005**, *7*, 4137 – 4140.

[30] U. Nettekoven, M. Widhalm, P. C. J. Kamer, P. W. N. M. Van Leeuwen, K. Mereiter, M. Lutz, A. Spek, *Organometallics* **2000**, *19*, 2299 – 2309.

[31] D. Vinci, N. Mateus, S. Wu, F. Hancock, A. Steiner, J. Xiao, *Org. Lett.* **2006**, *8*, 215 – 218.

[32] W. Chen, W. Mbafor, S. M. Roberts, J. Whittall, *J. Am. Chem. Soc.* **2006**, *128*, 3922 – 3923.

[33] N. W. Boaz, S. D. Debenham, E. B. Mackenzie, S. E. Large, *Org. Lett.* **2002**, *4*, 2421 – 2424.

[34] A. Togni, C. Breutel, A. Schnyder, F. Spindler, H. Landert, A. Tijani, *J. Am. Chem. Soc.* **1994**, *116*, 4062 – 4066.

[35] a) T. Ireland, K. Tappe, G. Grossheimann, P. Knochel, *Chem. Eur. J.* **2002**, *8*, 843 – 852; b) F. Spindler, C. Malan, M. Lotz, M. Kesselgruber, U. Pittelkow, A. Rivas-Nass, O. Briel, H.-U. Blaser, *Tetrahedron: Asymmetry* **2004**, *15*, 2299 – 2306.

[36] T. Sturm, W. Weissensteiner, F. Spindler, *Adv. Synth. Catal.* **2003**, *345*, 160 – 164.

[37] M. Sawamura, H. Hamashima, M. Sugawara, R. Kuwano, Y. Ito, *Organometallics* **1995**, *14*, 4549 – 4558.

[38] P. Barbaro, A. Togni, *Organometallics* **1995**, *14*, 3570 – 3573.

[39] F. M. Geisler, G. Helmchen, *J. Org. Chem.* **2006**, *71*, 2486 – 2492.

[40] S. Özçubukçu, F. Schmidt, C. Bolm, *Org. Lett.* **2005**, *7*, 1407 – 1409.

[41] O. García Mancheño, J. Priego, S. Cabrera, R. Gómez Arrayás, T. Llamas, J. C. Carretero, *J. Org. Chem.* **2003**, *68*, 3679 – 3686.

[42] a) J. F. Jensen, M. Johannsen, *Org. Lett.* **2003**, *5*, 3025 – 3028; b) J. F. Jensen, I. Søtofte, H. O. Sørensen, M. Johannsen, *J. Org. Chem.* **2003**, *68*, 1258 – 1265.

[43] M. Lotz, K. Polborn, P. Knochel, *Angew. Chem.* **2002**, *114*, 4902 – 4905; *Angew. Chem. Int. Ed.* **2002**, *41*, 4708 – 4711.

[44] O. Riant, G. Argouarch, D. Guillaneux, O. Samuel, H. B. Kagan, *J. Org. Chem.* **1998**, *63*, 3511 – 3514.

[45] a) M. Tsukazaki, M. Tinkl, A. Roglans, B. J. Chapell, N. J. Taylor, V. Snieckus, *J. Am. Chem. Soc.* **1996**, *118*, 685 – 686; b) R. S. Laufer, U. Veith, N. J. Taylor, V. Snieckus, *Org. Lett.* **2000**, *2*, 629 – 631; c) C. Metallinos, H. Szillat, N. J. Taylor, V. Snieckus, *Adv. Synth. Catal.* **2003**, *345*, 370 – 382.

[46] Y. Nishibayashi, Y. Arikawa, K. Ohe, S. Uemura, *J. Org. Chem.* **1996**, *61*, 1172 – 1174.

[47] D. Price, N. S. Simpkins, *Tetrahedron Lett.* **1995**, *36*, 6135 – 6136.

[48] a) C. Bolm, K. Muñiz, A. Seger, G. Raabe, K. Guenther, *J. Org. Chem.* **1998**, *63*, 7860 – 7867; b) K. Muñiz, C. Bolm, *Chem. Eur. J.* **2000**, *6*, 2309 – 2316; c) S.-L. You, X.-L. Hou, L.-X. Dai, Y.-H. Yu, W. Xia, *J. Org. Chem.* **1998**, *63*, 4684 – 4695.

[49] H.-U. Blaser, E. Schmidt, *Asymmetric Catalysis on Industrial Scale*, Wiley, New York, **2004**.

[50] J. M. Brown in *Comprehensive Asymmetric Catalysis*, *Vol. I* (Eds.: E. N. Jacobsen, A. Pfaltz, H. Yamamoto), Springer, Berlin, **1999**, pp. 121 – 182.

[51] a) N. W. Boaz, E. B. Mackenzie, S. D. Debenham, S. E. Large, J. A. Ponasik, Jr., *J. Org. Chem.* **2005**, *70*, 1878 – 1880; b) N. W. Boaz, S. E. Large, J. A. , Ponasik, Jr., *Tetrahedron: Asymmetry* **2005**, *16*, 2063 – 2066.

[52] N. W. Boaz, S. D. Debenham, S. E. Large, M. K. Moore, *Tetrahedron: Asymmetry* **2003**, *14*, 3575 – 3580.

 © 2006 Wiley-VCH Verlag GmbH & Co. KGaA, Weinheim

[53] N. W. Boaz, S. E. Large, J. A. Ponasik, Jr., M. K. Moore, T. Barnette, W. D. Nottingham, *Org. Process Res. Dev.* **2005**, *9*, 472 – 478.
[54] X. Jia, X. Li, W. S. Lam, S. H. L. Kok, L. Xu, G. Lu, C.-H. Yeung, A. S. C. Chan, *Tetrahedron: Asymmetry* **2005**, *16*, 2273 – 2278.
[55] X. Li, X. Jia, L. Xu, S. H. L. Kok, C. W. Yip, A. S. C. Chan, *Adv. Synth. Catal.* **2005**, *347*, 1904 – 1908.
[56] X.-P. Hu, Z. Zheng, *Org. Lett.* **2004**, *6*, 3585 – 3588.
[57] Q.-H. Zheng, X.-P. Hu, Z.-C. Duan, X.-M. Liang, Z. Zheng, *Tetrahedron: Asymmetry* **2005**, *16*, 1233 – 1238.
[58] Q.-H. Zheng, X.-P. Hu, Z.-C. Duan, X.-M. Liang, Z. Zheng, *J. Org. Chem.* **2006**, *71*, 393 – 396.
[59] T. T. Co, S. C. Shim, C. S. Cho, T.-J. Kim, S. O. Kang, W.-S. Han, J. Ko, C.K. Kim, *Organometallics* **2005**, *24*, 4824 – 4831.
[60] K. Tappe, P. Knochel, *Tetrahedron: Asymmetry* **2004**, *15*, 91 – 102.
[61] U. Berens, M. J. Burk, A. Gerlach, W. Hems, *Angew. Chem.* **2000**, *112*, 2057 – 2060; *Angew. Chem. Int. Ed.* **2000**, *39*, 1981 – 1984.
[62] A. Marinetti, F. Labrue, B. Pons, S. Jus, L. Ricard, J.-P. Genêt, *Eur. J. Inorg. Chem.* **2003**, 2583 – 2590.
[63] a) W. Braun, B. Calmuschi, J. Haberland, W. Hummel, A. Liese, T. Nickel, O. Stelzer, A. Salzer, *Eur. J. Inorg. Chem.* **2004**, 2235 – 2243; b) W. Braun, A. Salzer, F. Spindler, E. Alberico, *Appl. Catal. A* **2004**, *274*, 191 – 203.
[64] B. Pugin, M. Studer, E. Kuesters, G. Sedelmeier, X. Feng, *Adv. Synth. Catal.* **2004**, *346*, 1481 – 1486.
[65] W. P. Hems, P. McMorn, S. Riddle, S. Watson, F. E. Hancock, G. J. Hutchings, *Org. Biomol. Chem.* **2005**, *3*, 1547 – 1550.
[66] J. Rouzaud, M. D. Jones, R. Raja, B. F. G. Johnson, J. M. Thomas, M. J. Duer, *Helv. Chim. Acta* **2003**, *86*, 1753 – 1759.
[67] J. You, H.-J. Drexler, S. Zhang, C. Fischer, D. Heller, *Angew. Chem.* **2003**, *115*, 942 – 945; *Angew. Chem. Int. Ed.* **2003**, *42*, 913 – 916.
[68] X.-P. Hu, Z. Zheng, *Org. Lett.* **2005**, *7*, 419 – 422.
[69] Y. Hsiao, N. R. Rivera, T. Rosner, S. W. Krska, E. Njolito, F. Wang, Y. Sun, J. D. Armstrong III, E. J. J. Grabowski, R. D. Tillyer, F. Spindler, C. Malan, *J. Am. Chem. Soc.* **2004**, *126*, 9918 – 9919.
[70] K. B. Hansen, T. Rosner, M. Kubryk, P. G. Domer, J. D. Armstrong III, *Org. Lett.* **2005**, *7*, 4935 – 4938.
[71] M. Kubryk, K. B. Hansen, *Tetrahedron: Asymmetry* **2006**, *17*, 205 – 209.
[72] a) R. Kuwano, K. Sato, T. Kurokawa, D. Karube, Y. Ito, *J. Am. Chem. Soc.* **2000**, *122*, 7614 – 7615; b) R. Kuwano, M. Kashiwabara, K. Sato, T. Ito, K. Kaneda, Y. Ito, *Tetrahedron: Asymmetry* **2006**, *17*, 521 – 535.
[73] R. Kuwano, K. Kaneda, T. Ito, K. Sato, T. Kurokawa. Y. Ito, *Org. Lett.* **2004**, *6*, 2213 – 2215.
[74] S.-M. Lu, X.-W. Han, Y.-G. Zhou, *Adv. Synth. Catal.* **2004**, *346*, 909 – 912.
[75] a) R. Giernoth, M. S. Krumm, *Adv. Synth. Catal.* **2004**, *346*, 989 – 992; b) H.-U. Blaser, H.-P. Buser, R. Häusel, H.-P. Jalett, F. Spindler, *J. Organomet. Chem.* **2001**, *621*, 34 – 38.
[76] B. Pugin, V. Groehn, R. Moser, H.-U. Blaser, *Tetrahedron: Asymmetry* **2006**, *17*, 544 – 549.
[77] J. B. Morgan, J. P. Morken, *J. Am. Chem. Soc.* **2004**, *126*, 15 338 – 15 339.
[78] W. J. Moran, J. P. Morken, *Org. Lett.* **2006**, *8*, 2413 – 2415.
[79] I. Appleby, L. T. Boulton, C. J. Cobley, C. Hill, M. L. Hughes, P. D. de Koning, I. C. Lennon, C. Praquin, J. A. Ramsdem, H. J. Samuel, N. Willis, *Org. Lett.* **2005**, *7*, 1931 – 1934.
[80] M. J. Burk, P. D. de Koning, T. M. Grote, M. S. Hoekstra, G. Hoge, R. A. Jennings, W. S. Kissel, T. V. Le, I. C. Lennon, T. A. Mulhern, J. A. Ramsdem, R. A. Wade, *J. Org. Chem.* **2003**, *68*, 5731 – 5734.
[81] C. S. Shultz, S. D. Dreher, N. Ikemoto, J. M. Williams, E. J. J. Grabowski, S. W. Krska, Y. Sun, P. G. Dormer, L. DiMichele, *Org. Lett.* **2005**, *7*, 3405 – 3408.
[82] T. Ikemoto, T. Nagata, M. Yamano, T. Ito, Y. Mizuno, K. Tomimatsu, *Tetrahedron Lett.* **2004**, *45*, 7757 – 7760.
[83] I. N. Houpis, L. E. Patterson, C. A. Alt, J. R. Rizzo, T. Y. Zhang, M. Haurez, *Org. Lett.* **2005**, *7*, 1947 – 1950.
[84] C. J. Cobley, I. C. Lennon, C. Praquin, A. Zanotti-Gerosa, *Org. Process Res. Dev.* **2003**, *7*, 407 – 411.
[85] N. W. Boaz, J. A. Ponasik, Jr., S. E. Large, *Tetrahedron Lett.* **2006**, *47*, 4033 – 4035.
[86] F. Naud, C. Malan, F. Spindler, C. Rüggeberg, A. T. Schmidt, H.-U. Blaser, *Adv. Synth. Catal.* **2006**, *348*, 47 – 50.
[87] D. M. Tellers, M. Bio, Z. J. Song, J. C. McWilliams, Y. Sun, *Tetrahedron: Asymmetry* **2006**, *17*, 550 – 553.
[88] W. Chen, W. Mbafor, S. M. Roberts, J. Whittall, *Tetrahedron: Asymmetry* **2006**, *17*, 1161 – 1164.
[89] H.-U. Blaser, F. Spindler in *Comprehensive Asymmetric Catalysis, Vol. I* (Eds.: E. N. Jacobsen, A. Pfaltz, H. Yamamoto), Springer, Berlin, **1999**, pp. 247 – 264.
[90] D. Xiao, X. Zhang, *Angew. Chem.* **2001**, *113*, 3533 – 3536; *Angew. Chem. Int. Ed.* **2001**, *40*, 3425 – 3428.
[91] Y. Chi, Y.-G. Zhou, X. Zhang, *J. Org. Chem.* **2003**, *68*, 4120 – 4122.
[92] R. Dorta, D. Broggini, R. Stop, H. Rüegger, F. Spindler, A. Togni, *Chem. Eur. J.* **2004**, *10*, 267 – 278.
[93] a) R. Noyori, S. Hashiguchi, *Acc. Chem. Res.* **1997**, *30*, 97 – 102; b) S. E. Clapham, A. Hadzovic, R. H. Morris, *Coord. Chem. Rev.* **2004**, *248*, 2201 – 2237.
[94] T. Sammakia, E. L. Stangeland, *J. Org. Chem.* **1997**, *62*, 6104 – 6105.
[95] a) L. Schwink, T. Ireland, K. Püntener, P. Knochel, *Tetrahedron: Asymmetry* **1998**, *9*, 1143 – 1163; b) A. Patti, S. Pedotti, *Tetrahedron: Asymmetry* **2003**, *14*, 587 – 602; c) H. Seo, B. Y. Kim, J. H. Lee, H.-J. Park, S. U. Son, Y. K. Cheng, *Organometallics* **2003**, *22*, 4783 – 4791; d) P. Barbaro, C. Bianchini, G. Giambastini, A. Togni, *Eur. J. Inorg. Chem.* **2003**, 4166 – 4172; e) J. Cabou, J. Brocard, L. Pélinski, *Tetrahedron Lett.* **2005**, *46*, 1185 – 1188.
[96] H. Dai, X. Hu, H. Chen, C. Bai, Z. Zheng, *Tetrahedron: Asymmetry* **2003**, *14*, 1467 – 1472.
[97] H. Dai, X. Hu, H. Chen, C. Bai, *J. Mol. Catal. A* **2004**, *209*, 19 – 22.
[98] T Ohkuma, H. Ooka, S. Hashiguchi, T. Ikariya, R. Noyori, *J. Am. Chem. Soc.* **1995**, *117*, 2675 – 2676.
[99] C. G. Leong, O. M. Akotsi, M. J. Ferguson, S. H. Bergens, *Chem. Commun.* **2003**, 750 – 751.
[100] W. Barata, E. Herdtweck, K. Siega, M. Toniutti, P. Rigo, *Organometallics* **2005**, *24*, 1660 – 1669.
[101] K. Taguchi, H. Nakagawa, T. Hirabayashi, S. Sakaguchi, Y. Ishii, *J. Am. Chem. Soc.* **2004**, *126*, 72 – 73.
[102] G. Onodera, Y. Nishibayashi, S. Uemura, *Angew. Chem.* **2006**, *118*, 3903 – 3906; *Angew. Chem. Int. Ed.* **2006**, *45*, 3819 – 3822.
[103] Y. Nishibayashi, A. Yamauchi, G. Onodera, S. Uemura, *J. Org. Chem.* **2003**, *68*, 5875 – 5880.
[104] H. Nishiyama in *Transition Metals for Organic Synthesis*, 2nd ed. (Eds.: M. Beller, C. Bolm), Wiley-VCH, Weinheim, **2004**, pp. 182 – 191.
[105] M. Sawamura, H. Hamashima, Y. Ito, *Tetrahedron: Asymmetry* **1991**, *2*, 593 – 596.
[106] M. Sawamura, R. Kuwano Y. Ito, *Angew. Chem.* **1994**, *106*, 92 – 93; *Angew. Chem. Int. Ed. Engl.* **1994**, *33*, 111 – 114.
[107] R. Kuwano, T. Uemura, M. Saitoh, Y. Ito, *Tetrahedron: Asymmetry* **2004**, *15*, 2263 – 2271.
[108] B. Tao, G. C. Fu, *Angew. Chem.* **2002**, *114*, 4048 – 4050; *Angew. Chem. Int. Ed.* **2002**, *41*, 3892 – 3894.

 © 2006 Wiley-VCH Verlag GmbH & Co. KGaA, Weinheim

[109] S. Gérard, Y. Pressel, O. Riant, *Tetrahedron: Asymmetry* **2005**, *16*, 1889 – 1891.
[110] B. H. Lipshutz, J. M. Servesko, *Angew. Chem.* **2003**, *115*, 4937 – 4940; *Angew. Chem. Int. Ed.* **2003**, *42*, 4789 – 4792.
[111] D. H. Appella, Y. Moritani, R. Shintani, E. M. Ferreira, S. L. Buchwald, *J. Am. Chem. Soc.* **1999**, *121*, 9473 – 9474.
[112] B. H. Lipshutz, J. M. Servesko, B. R. Taft, *J. Am. Chem. Soc.* **2004**, *126*, 8352 – 8353.
[113] B. H. Lipshutz, K. Noson, W. Chrisman, A. Lower, *J. Am. Chem. Soc.* **2003**, *125*, 8779 – 8789.
[114] B. H. Lipshutz, N. Tanaka, B. R. Taft, C.-T. Lee, *Org. Lett.* **2006**, *8*, 1963 – 1966.
[115] J. Chae, J. Yun, S. L. Buchwald, *Org. Lett.* **2004**, *6*, 4575 – 4579.
[116] J. Deschamp, O. Chuzel, J. Hannedouche, O. Riant, *Angew. Chem.* **2006**, *118*, 1314 – 1319; *Angew. Chem. Int. Ed.* **2006**, *45*, 1292 – 1297.
[117] C. Czekelius, E. M. Carreira, *Angew. Chem.* **2003**, *115*, 4941 – 4943; *Angew. Chem. Int. Ed.* **2003**, *42*, 4793 – 4795.
[118] C. Czekelius, E. M. Carreira, *Org. Lett.* **2004**, *6*, 4575 – 4577.
[119] D. Lee, D. Kim, J. Yun, *Angew. Chem.* **2006**, *118*, 2851 – 2853; *Angew. Chem. Int. Ed.* **2006**, *45*, 2785 – 2787.
[120] J. W. Han, N. Tokunaga, T. Hayashi, *J. Am. Chem. Soc.* **2001**, *123*, 12915 – 12916.
[121] M. Ogasawara, A. Ito, K. Yoshida, T. Hayashi, *Organometallics* **2006**, *25*, 2715 – 2718.
[122] D. Männing, H. Nöth, *Angew. Chem.* **1985**, *97*, 854 – 855; *Angew. Chem. Int. Ed. Engl.* **1985**, *24*, 878 – 879.
[123] T. Hayashi in *Comprehensive Asymmetric Catalysis*, *Vol. I* (Eds.: E. N. Jacobsen, A. Pfaltz, H. Yamamoto), Springer, Berlin, **1999**, pp. 351 – 363.
[124] See reference [7].
[125] A. Schnyder, L. Hintermann, A. Togni, *Angew. Chem.* **1995**, *107*, 996 – 998; *Angew. Chem. Int. Ed. Engl.* **1995**, *34*, 931 – 933.
[126] R. J. Kloetzing, M. Lotz, P. Knochel, *Tetrahedron: Asymmetry* **2003**, *14*, 255 – 264.
[127] C. M. Crudden, Y. B. Hleba, A. C. Chen, *J. Am. Chem. Soc.* **2004**, *126*, 9200 – 9201.
[128] M. Suginome, T. Ohmura, Y. Miyake, S. Mitani, Y. Ito, M. Murakami, *J. Am. Chem. Soc.* **2003**, *125*, 11174 – 11175.
[129] P. W. Roesky, T. E. Müller, *Angew. Chem.* **2003**, *115*, 2812 – 2814; *Angew. Chem. Int. Ed.* **2003**, *42*, 2708 – 2710.
[130] M. Utsunomiya, J. F. Hartwig, *J. Am. Chem. Soc.* **2003**, *125*, 14286 – 14287.
[131] L. Fadini, A. Togni, *Chem. Commun.* **2003**, 30 – 31.
[132] A. D. Sadow, I. Haller, L. Fadini, A. Togni, *J. Am. Chem. Soc.* **2004**, *126*, 14704 – 14705.
[133] A. D. Sadow, A. Togni, *J. Am. Chem. Soc.* **2005**, *127*, 17012 – 17024.
[134] Q. Xu, L.-B. Han, *Org. Lett.* **2006**, *8*, 2099 – 2101.
[135] G. J. Clarkson, J. R. Ansell, D. J. Cole-Hamilton, P. J. Pogorzelec, J. Whittell, M. Wills, *Tetrahedron: Asymmetry* **2004**, *15*, 1787 – 1792.
[136] L. Wang, W. H. Kwok, A. S. C. Chan, T. Tu, X. Hou, L. Dai, *Tetrahedron: Asymmetry* **2003**, *14*, 2291 – 2295.
[137] K. B. Sharpless, *Angew. Chem.* **2002**, *114*, 2126 – 2135; *Angew. Chem. Int. Ed.* **2002**, *41*, 2024 – 2032, and references therein.
[138] K. Muñiz, M. Nieger, *Organometallics* **2003**, *22*, 4616 – 4619.
[139] H. K. Cotton, F. F. Huerta, J.-E. Bäckvall, *Eur. J. Org. Chem.* **2003**, 2756 – 2763.
[140] For recent reviews on asymmetric allylic alkylation, see: a) B. M. Trost, M. L. Crawley, *Chem. Rev.* **2003**, *103*, 2921 – 2943; b) T. Graening, H.-G. Schmalz, *Angew. Chem.* **2003**, *115*, 2684 – 2688; *Angew. Chem. Int. Ed.* **2003**, *42*, 2580 – 2584; c) B. M. Trost, *J. Org. Chem.* **2004**, *69*, 5813 – 5837.
[141] a) N. Oohara, K. Katagiri, T. Imamoto, *Tetrahedron: Asymmetry* **2003**, *14*, 2171 – 2175; b) M. M. Dell'Anna, P. Mastrorilli, C. F. Nobile, G. P. Suranna, *J. Mol. Catal. A* **2003**, *201*, 131 – 135; c) T. Tu, X.-L. Hou, L.-X. Dai, *J. Organomet. Chem.* **2004**, *689*, 3847 – 3852; d) M. Raghunath, W. Gao, X. Zhang, *Tetrahedron: Asymmetry* **2005**, *16*, 3676 – 3681.
[142] a) T. Tu, Y.-G. Zhou, X.-L. Hou, L.-X. Dai, X.-C. Dong, Y.-H. Yu, J. Sun, *Organometallics* **2003**, *22*, 1255 – 1265; b) X. Hu, H. Chen, H. Dai, X. Hu, Z. Zheng, *Tetrahedron: Asymmetry* **2003**, *14*, 2073 – 2080; c) P. Barbaro, C. Bianchini, G. Giambastiani, A. Togni, *Tetrahedron Lett.* **2003**, *44*, 8279 – 8283; d) T. Mino, T. Ogawa, M. Yamashita, *J. Organomet. Chem.* **2003**, *665*, 122 – 126; e) S. Mourgues, D. Serra, F. Lamy, S. Vincendeau, J.-C. Daran, E. Manoury, M. Guygou, *Eur. J. Inorg. Chem.* **2003**, 2820 – 2826; f) J. H. Lee, S. U. Son, Y. K. Chung, *Tetrahedron: Asymmetry* **2003**, *14*, 2109 – 2113; g) X. Hu, H. Chen, H. Dai, Z. Zheng, *Tetrahedron: Asymmetry* **2003**, *14*, 3415 – 3421; h) N. W. Boaz, J. A. Ponasik, Jr., S. E. Large, S. D. Debenham, *Tetrahedron: Asymmetry* **2004**, *15*, 2151 – 2154; i) H. Danjo, M. Higuchi, M. Yada, T. Imamoto, *Tetrahedron Lett.* **2004**, *45*, 603 – 606; j) T. Mino, H. Segawa, M. Yamashita, *J. Organomet. Chem.* **2004**, *689*, 2833 – 2836; k) X. Hu, C. Bai, H. Dai, H. Chen, Z. Zheng, *J. Mol. Catal. A* **2004**, *218*, 107 – 112; l) X.-P. Hu, H.-L. Chen, Z. Zheng, *Adv. Synth. Catal.* **2005**, *347*, 541 – 548; m) V. N. Tsarev, S. E. Lyubimov, O. G. Bondarev, A. A. Korlyukov, M. Y. Antipin, P. V. Petrovskii, V. A. Davankov, A. A. Shiryaev, E. B. Benetsky, P. A. Vologzhanin, K. N. Gavrilov, *Eur. J. Org. Chem.* **2005**, 2097 – 2105; n) J. C. Anderson, J. Osborne, *Tetrahedron: Asymmetry* **2005**, *16*, 931 – 934; o) A. Bueno, R. M. Moreno, A. Moyano, *Tetrahedron: Asymmetry* **2005**, *16*, 1763 – 1778; p) M.-J. Jin, V. B. Takale, M. S. Sarkar, Y.-M. Kim. *Chem. Commun.* **2006**, 663 – 664; q) R. J. Kloetzing, P. Knochel, *Tetrahedron: Asymmetry* **2006**, *17*, 116 – 123.
[143] a) J. Kang, J. H. Lee, K. S. Im, *J. Mol. Catal. A* **2003**, *196*, 55 – 63; b) S. Nakamura, T. Fukuzumi, T. Toru, *Chirality* **2004**, *16*, 10 – 12; c) L. Routaboul, S. Vincendeau, J.-C. Daran, E. Manoury, *Tetrahedron: Asymmetry* **2005**, *16*, 2685 – 2690; d) F. L. Lam, T. T. L. Au-Yeung, H. Y. Cheung, S. H. L. Kok, W. S. Lam, K. Y. Wong, A. S. C. Chan, *Tetrahedron: Asymmetry* **2006**, *17*, 497 – 499.
[144] B. F. Bonini, M. Fochi, M. Comes-Franchini, A. Ricci, L. Thijs, B. Zwanenburg, *Tetrahedron: Asymmetry* **2003**, *14*, 3321 – 3327.
[145] V. N. Tsarev, S. I. Konkin, A. A. Shyryaev, V. A. Davankov, K. N. Gavrilov, *Tetrahedron: Asymmetry* **2005**, *16*, 1737 – 1741.
[146] S.-L. You, X.-Z. Zhou, Y.-M. Luo, X.-L. Hou, L.-X. Dai, *J. Am. Chem. Soc.* **2001**, *123*, 7471 – 7472.
[147] W.-H. Zheng, N. Sun, X.-L. Hou, *Org. Lett.* **2005**, *7*, 5151 – 5154.
[148] X.-L. Hou, N. Sun, *Org. Lett.* **2004**, *6*, 4399 – 4401.
[149] M. Sawamura, M. Sudoh, Y. Itoh, *J. Am. Chem. Soc.* **1996**, *118*, 3309 – 3310.
[150] A. Nowicki, A. Mortreux, F. Agbossou-Niedercorn, *Tetrahedron: Asymmetry* **2005**, *16*, 1295 – 1298.
[151] B. M. Trost, G. M. Schroeder, *J. Am. Chem. Soc.* **1999**, *121*, 6759 – 6760.
[152] X.-X. Yan, C.-G. Liang, Y. Zhang, W. Hong, B.-X. Cao, L.-X. Dai, X.-L. Hou, *Angew. Chem.* **2005**, *117*, 6702 – 6704; *Angew. Chem. Int. Ed.* **2005**, *44*, 6544 – 6546.
[153] For a recent update, see: H. Yorimitsu, K. Oshima, *Angew. Chem.* **2005**, *117*, 4509 – 4513; *Angew. Chem. Int. Ed.* **2005**, *44*, 4435 – 4439.
[154] M. van Klaveren, E. S. M. Persson, A. del Villar, D. M. Grove, J.-E. Bäckvall, G. van Koten, *Tetrahedron Lett.* **1995**, *36*, 3059 – 3062.
[155] K. Tissot-Croset, D. Polet, A. Alexakis, *Angew. Chem.* **2004**, *116*, 2480 – 2482; *Angew. Chem. Int. Ed.* **2004**, *43*, 2426 – 2428, and references therein.
[156] F. López, A. W. van Zijl, A. J. Minnaard, B. L. Feringa, *Chem. Commun.* **2006**, 409 – 411.

 © 2006 Wiley-VCH Verlag GmbH & Co. KGaA, Weinheim

[157] a) D. B. Berkowitz, G. Maiti, *Org. Lett.* **2004**, *6*, 2661 – 2664; see also: b) D. B. Berkowitz, W. Shen, G. Maiti, *Tetrahedron: Asymmetry* **2004**, *15*, 2845 – 2851.
[158] A. Leitner, J. Larsen, C. Steffens, J. F. Hartwig, *J. Org. Chem.* **2004**, *69*, 7552 – 7557.
[159] F. Kato, K. Hiroi, *Chem. Pharm. Bull.* **2004**, *52*, 95 – 103.
[160] For a recent review, see: M. Shibasaki, E. M. Vogl, T. Ohshima, *Adv. Synth. Catal.* **2004**, *346*, 1533 – 1552.
[161] W.-P. Deng, X.-L. Hou, L.-X. Dai, X.-W. Dong, *Chem. Commun.* **2000**, 1483 – 1484.
[162] T. Tu, W.-P. Deng, X.-L. Hou, L.-X. Dai, X.-C. Dong, *Chem. Eur. J.* **2003**, *9*, 3073 – 3081.
[163] T. Tu, X.-L. Hou, L.-X. Dai, *Org. Lett.* **2003**, *5*, 3651 – 3653.
[164] T. G. Kilroy, A. J. Hennessy, D. J. Connolly, Y. M. Malone, A. Farrell, P. J. Guiry, *J. Mol. Catal. A* **2003**, *196*, 65 – 81.
[165] a) D. Kiely, P. J. Guiry, *Tetrahedron Lett.* **2003**, *44*, 7377 – 7380; b) D. Kiely, P. J. Guiry, *J. Organomet. Chem.* **2003**, *687*, 545 – 561.
[166] O. Loiseleur, P. Meier, A. Pfaltz, *Angew. Chem.* **1996**, *108*, 218 – 220; *Angew. Chem. Int. Ed. Engl.* **1996**, *35*, 200 – 202.
[167] For a recent review on the atroposelective synthesis of axially chiral biaryl compounds, see: G. Bringmann, A. J. P. Mortimer, P. A. Keller, M. J. Gresser, J. Garner, M. Breuning, *Angew. Chem.* **2005**, *117*, 5518 – 5563; *Angew. Chem. Int. Ed.* **2005**, *44*, 5384 – 5427.
[168] K. Tamao, H. Yamamoto, H. Matsumoto, N. Miyake, T. Hayashi, M. Kumada, *Tetrahedron Lett.* **1977**, *18*, 1389 – 1392.
[169] T. Hayashi, K. Hayashizaki, T. Kiyoi, Y. Ito, *J. Am. Chem. Soc.* **1988**, *110*, 8153 – 8156.
[170] For a review on asymmetric Suzuki coupling reactions to axially chiral biaryls, see: O. Baudoin, *Eur. J. Org. Chem.* **2005**, 4223 – 4229.
[171] A. N. Cammidge, K. V. L. Crépy, *Chem. Commun.* **2000**, 1723 – 1724.
[172] A. N. Cammidge, K. V. L. Crépy, *Tetrahedron* **2004**, *60*, 4377 – 4386.
[173] G. Bringmann, A. Hamm, M. Schraut, *Org. Lett.* **2003**, *5*, 2805 – 2808.
[174] a) M. Uemura, H. Nishimura, T. Hayashi, *Tetrahedron Lett.* **1993**, *34*, 107 – 110; b) M. Uemura, H. Nishimura, T. Hayashi, *J. Organomet. Chem.* **1994**, *473*, 129 – 137.
[175] B. Gotov, H.-G. Schmalz, *Org. Lett.* **2001**, *3*, 1753 – 1756.
[176] A. Böttcher, H.-G. Schmalz, *Synlett* **2003**, 1595 – 1598.
[177] H. Schumann, J. Kaufmann, H.-G. Schmalz, A. Böttcher, B. Gotov, *Synlett* **2003**, 1783 – 1788.
[178] For a review on P-chirogenic phosphine ligands in catalytic asymmetric reactions, see: K. V. L. Crépy, T. Imamoto, *Top. Curr. Chem.* **2003**, *229*, 1 – 40.
[179] M. J. Johansson, N. C. Kann, *Mini-Rev. Org. Chem.* **2004**, *1*, 233 – 244.
[180] C. Korff, G. Helmchen, *Chem. Commun.* **2004**, 530 – 531.
[181] S. Pican, A.-C. Gaumont, *Chem. Commun.* **2005**, 2393 – 2395.
[182] J. R. Moncarz, T. J. Brunker, J. C. Jewett, M. Orchowski, D. S. Glueck, *Organometallics* **2003**, *22*, 3205 – 3221.
[183] E. A. Bercot, T. Rovis, *J. Am. Chem. Soc.* **2004**, *126*, 10248 – 10249.
[184] For an overview, see: M. Lautens, K. Fagnou, S. Hiebert, *Acc. Chem. Res.* **2003**, *36*, 48 – 58.
[185] M. Lautens, J.-L. Renaud, S. Hiebert, *J. Am. Chem. Soc.* **2000**, *122*, 1804 – 1805.
[186] M. Lautens, S. Hiebert, *J. Am. Chem. Soc.* **2004**, *126*, 1437 – 1447.
[187] S. Cabrera, R. Gómez Arrayás, J. C. Carretero, *Angew. Chem.* **2004**, *116*, 4034 – 4037; *Angew. Chem. Int. Ed.* **2004**, *43*, 3944 – 3947.
[188] S. Cabrera, R. Gómez Arrayás, I. Alonso, J. C. Carretero, *J. Am. Chem. Soc.* **2005**, *127*, 17938 – 17947.
[189] M. Li, X.-X. Yan, W. Hong, X.-Z. Zhu, B.-X. Cao, J. Sun, X.-L. Hou, *Org. Lett.* **2004**, *6*, 2833 – 2835.
[190] a) M. Lautens, K. Fagnou, T. Rovis, *J. Am. Chem. Soc.* **2000**, *122*, 5650 – 5651; b) M. Lautens, K. Fagnou, M. Taylor, *Org. Lett.* **2000**, *2*, 1677 – 1679.
[191] For a review on halide effects in transition-metal catalysis, see: K. Fagnou, M. Lautens, *Angew. Chem.* **2002**, *114*, 26 – 49; *Angew. Chem. Int. Ed.* **2002**, *41*, 26 – 47.
[192] M. Lautens, K. Fagnou, D. Yang, *J. Am. Chem. Soc.* **2003**, *125*, 14884 – 14892.
[193] Y.-h. Cho, V. Zunic, H. Senboku, M. Olsen, M. Lautens, *J. Am. Chem. Soc.* **2006**, *128*, 6837 – 6846.
[194] M. Lautens, K. Fagnou, *Proc. Natl. Acad. Sci. USA* **2004**, *101*, 5455 – 5460.
[195] For reviews, see: a) L. Pu, H.-B. Yu, *Chem. Rev.* **2001**, *101*, 757 – 824; b) L. Pu, *Tetrahedron* **2003**, *59*, 9873 – 9886.
[196] N. Oguni, T. Omi, Y. Yamamoto, A. Nakamura, *Chem. Lett.* **1983**, 841 – 842.
[197] M. Kitamura, S. Suga, K. Hawai, R. Noyori, *J. Am. Chem. Soc.* **1986**, *108*, 6071 – 6072.
[198] a) M.-C. Wang, D.-K. Wang, Y. Zhu, L.-T. Liu, Y.-F. Guo, *Tetrahedron: Asymmetry* **2004**, *15*, 1289 – 1294; b) M.-C. Wang, L.-T. Liu, J.-S. Zhang, Y.-Y. Shi, D.-K. Wang, *Tetrahedron: Asymmetry* **2004**, *15*, 3853 – 3859; c) N. Faux, D. Razafimahefa, S. Picart-Goetgheluck, J. Brocard, *Tetrahedron: Asymmetry* **2005**, *16*, 1189 – 1197; d) M.-C. Wang, X.-H. Hou, C.-L. Xu, L.-T. Liu, G.-L. Li, D.-K. Wang, *Synthesis* **2005**, 3620 – 3626.
[199] M. Li, X.-Z. Zhu, K. Yuan, B.-X. Cao, X.-L. Hou, *Tetrahedron: Asymmetry* **2004**, *15*, 219 – 222.
[200] C. Bolm, J. Rudolph, *J. Am. Chem. Soc.* **2002**, *124*, 14850 – 14851.
[201] J. Rudolph, F. Schmidt, C. Bolm, *Synthesis* **2005**, 840 – 842.
[202] C. Bolm, N. Hermanns, J. P. Hildebrand, K. Muñiz, *Angew. Chem.* **2000**, *112*, 3607 – 3609; *Angew. Chem. Int. Ed.* **2000**, *39*, 3465 – 3467.
[203] J. Rudolph, N. Hermanns, C. Bolm, *J. Org. Chem.* **2004**, *69*, 3997 – 4000.
[204] J. Rudolph, F. Schmidt, C. Bolm, *Adv. Synth. Catal.* **2004**, *346*, 867 – 872.
[205] a) H. Fujihara, K. Nagai, K. Tomioka, *J. Am. Chem. Soc.* **2000**, *122*, 12055 – 12056; b) T. Soeta, K. Nagai, H. Fujihara, M. Kuriyama, K. Tomioka, *J. Org. Chem.* **2003**, *68*, 9723 – 9727.
[206] M.-C. Wang, C.-L. Xu, Y.-X. Zou, H.-M. Liu, D.-K. Wang, *Tetrahedron Lett.* **2005**, *46*, 5413 – 5416.
[207] M.-C. Wang, L.-T. Liu, Y.-Z. Hua, J.-S. Zhang, Y.-Y. Shi, D.-K. Wang, *Tetrahedron: Asymmetry* **2005**, *16*, 2531 – 2534.
[208] For a recent selected review, see: C. Palomo, M. Oiarbide, J. M. García, *Chem. Soc. Rev.* **2004**, *33*, 65 – 75.
[209] K. Oisaki, Y. Suto, M. Kanai, M. Shibasaki, *J. Am. Chem. Soc.* **2003**, *125*, 5644 – 5645.
[210] K. Oisaki, D. Zhao, M. Kanai, M. Shibasaki, *J. Am. Chem. Soc.* **2006**, *128*, 7164 – 7165.
[211] A. Salvador González, R. Gómez Arrayás, J. C. Carretero, *Org. Lett.* **2006**, *8*, 2977 – 2980.
[212] For a review, see: J. Montgomery, *Angew. Chem.* **2004**, *116*, 3980 – 3998; *Angew. Chem. Int. Ed.* **2004**, *43*, 3890 – 3908.
[213] X.-Q. Tang, J. Montgomery, *J. Am. Chem. Soc.* **2000**, *122*, 6950 – 6954.
[214] W.-S. Huang, J. Chan, T. F. Jamison, *Org. Lett.* **2000**, *2*, 4221 – 4223.
[215] K. M. Miller, W.-S. Huang, T. F. Jamison, *J. Am. Chem. Soc.* **2003**, *125*, 3442 – 3443.
[216] E. A. Colby, T. F. Jamison, *J. Org. Chem.* **2003**, *68*, 156 – 166.
[217] a) J. Chan, T. F. Jamison, *J. Am. Chem. Soc.* **2003**, *125*, 11514 – 11515; b) J. Chan, T. F. Jamison, *J. Am. Chem. Soc.* **2004**, *126*, 10682 – 10691.

© 2006 Wiley-VCH Verlag GmbH & Co. KGaA, Weinheim

[218] K. M. Millar, E. A. Colby, K. S. Woodin, T. F. Jamison, *Adv. Synth. Catal.* **2005**, *347*, 1533 – 1536.
[219] K. M. Miller, T. F. Jamison, *Org. Lett.* **2005**, *7*, 3077 – 3080.
[220] S. J. Patel, T. F. Jamison, *Angew. Chem.* **2003**, *115*, 1402 – 1405; *Angew. Chem. Int. Ed.* **2003**, *42*, 1364 – 1367.
[221] S. J. Patel, T. F. Jamison, *Angew. Chem.* **2004**, *116*, 4031 – 4034; *Angew. Chem. Int. Ed.* **2004**, *43*, 3941 – 3944.
[222] H.-Y. Jang, M. J. Krische, *Acc. Chem. Res.* **2004**, *37*, 653 – 661.
[223] H.-Y. Jang, R. R. Huddleston, M. J. Krische, *J. Am. Chem. Soc.* **2004**, *126*, 4664 – 4668.
[224] J.-R. Kong, C.-W. Cho, M. J. Krische, *J. Am. Chem. Soc.* **2005**, *127*, 11269 – 11276.
[225] J.-R. Kong, M.-Y. Ngai, M. J. Krische, *J. Am. Chem. Soc.* **2006**, *128*, 718 – 719.
[226] For a review, see: A. Alexakis, C. Benhaim, *Eur. J. Org. Chem.* **2002**, 3221 – 3236.
[227] For reviews: a) T. Hayashi, K. Yamasaki, *Chem. Rev.* **2003**, *103*, 2829 – 2844; b) T. Hayashi, *Bull. Chem. Soc. Jpn.* **2004**, *77*, 13 – 21.
[228] B. L. Feringa, R. Badorrey, D. Peña, S. R. Harutyunyan, A. J. Minnaard, *Proc. Natl. Acad. Sci. USA* **2004**, *101*, 5834 – 5838.
[229] F. López, S. R. Harutyunyan, A. J. Minnaard, B. L. Feringa, *J. Am. Chem. Soc.* **2004**, *126*, 12784 – 12785.
[230] F. López, S. R. Harutyunyan, A. Meetsma, A. J. Minnaard, B. L. Feringa, *Angew. Chem.* **2005**, *117*, 2812 – 2816; *Angew. Chem. Int. Ed.* **2005**, *44*, 2752 – 2756.
[231] R. D. Mazery, M. Pullez, F. López, S. R. Harutyunyan, A. J. Minnaard, B. L. Feringa, *J. Am. Chem. Soc.* **2005**, *127*, 9966 – 9967.
[232] D. Peña, F. López, S. R. Harutyunyan, A. J. Minnaard, B. L. Feringa, *Chem. Commun.* **2004**, 1836 – 1837.
[233] S. R. Harutyunyan, F. López, W. R. Browne, A. Correa, D. Peña, R. Badorrey, A. Meetsma, A, J. Minaard, B. L. Feringa, *J. Am. Chem. Soc.* **2006**, *128*, 9103 – 9118.
[234] L.-T. Liu, M.-C. Wang, W.-X. Zhao, Y.-L. Zhou, X.-D. Wang, *Tetrahedron: Asymmetry* **2006**, *17*, 136 – 141.
[235] P. Mauleón, J. C. Carretero, *Org. Lett.* **2004**, *6*, 3195 – 3198.
[236] V. E. Albrow, A. J. Blake, R. Fryatt, C. Wilson, S. Woodward, *Eur. J. Org. Chem.* **2006**, 2546 – 2557.
[237] H. Dai, X. Hu, H. Chen, C. Bai, Z. Zheng, *J. Mol. Catal. A* **2004**, *211*, 17 – 21.
[238] For a review, see: D. Carmona, M. P. Lamata, L. A. Oro, *Coord. Chem. Rev.* **2000**, *200–202*, 717 – 772.
[239] O. García Mancheño, R. Gómez Arrayás, J. C. Carretero, *Organometallics* **2005**, *24*, 557 – 561.
[240] S.-i. Fukuzawa, Y. Yahara, A. Kamiyama, M. Hara, S. Kikuchi, *Org. Lett.* **2005**, *7*, 5809 – 5812.
[241] O. García Mancheño, R. Gómez Arrayás, J. C. Carretero, *J. Am. Chem. Soc.* **2004**, *126*, 456 – 457.
[242] K. Tanaka, G. C. Fu, *Org. Lett.* **2002**, *4*, 933 – 935.
[243] K. Tanaka, Y. Hagiwara, K. Noguchi, *Angew. Chem.* **2005**, *117*, 7426 – 7429; *Angew. Chem. Int. Ed.* **2005**, *44*, 7260 – 7263.
[244] J. M. Longmire, B. Wang, X. Zhang, *J. Am. Chem. Soc.* **2002**, *124*, 13400 – 13401.
[245] For a review, see: C. Nájera, J. M. Sansano, *Angew. Chem.* **2005**, *117*, 6428 – 6432; *Angew. Chem. Int. Ed.* **2005**, *44*, 6272 – 6276.
[246] W. Zeng, Y.-G. Zhou, *Org. Lett.* **2005**, *7*, 5055 – 5058.
[247] W. Gao, X. Zhang, M. Raghunath, *Org. Lett.* **2005**, *7*, 4241 – 4244.
[248] X.-X. Yan, Q. Peng, Y. Zhang, K. Zhang, W. Hong, X.-L. Hou, Y.-D. Wu, *Angew. Chem.* **2006**, *118*, 2013 – 2017; *Angew. Chem. Int. Ed.* **2006**, *45*, 1979 – 1983.
[249] S. Cabrera, R. Gómez Arrayás, J. C. Carretero, *J. Am. Chem. Soc.* **2005**, *127*, 16394 – 16395.
[250] C. Chen, X. Li, S. L. Schreiber, *J. Am. Chem. Soc.* **2003**, *125*, 10174 – 10175.
[251] T. Llamas, R. Gómez Arrayás, J. C. Carretero, *Org. Lett.* **2006**, *8*, 1795 – 1798.
[252] M. M.-C. Lo, G. C. Fu, *J. Am. Chem. Soc.* **2002**, *124*, 4572 – 4573.
[253] R. Shintani, G. C. Fu, *Angew. Chem.* **2003**, *115*, 4216 – 4219; *Angew. Chem. Int. Ed.* **2003**, *42*, 4082 – 4085.
[254] R. Shintani, G. C. Fu, *J. Am. Chem. Soc.* **2003**, *125*, 10778 – 10779.
[255] A. Suárez, C. W. Downey, G. C. Fu, *J. Am. Chem. Soc.* **2005**, *127*, 11244 – 11245.
[256] M. Calter, T. K. Hollis, L. E. Overman, J. Ziller, G. G. Zipp, *J. Org. Chem.* **1997**, *62*, 1449 – 1456.
[257] a) Y. Donde, L. E. Overman, *J. Am. Chem. Soc.* **1999**, *121*, 2933 – 2934; b) C. E. Anderson, Y. Donde, C. J. Douglas, L. E. Overman, *J. Org. Chem.* **2005**, *70*, 648 – 657.
[258] R. Peters, Z.-q. Xin, D. F. Fischer, W. B. Schweizer, *Organometallics* **2006**, *25*, 2917 – 2920.
[259] M. E. Weiss, D. F. Fischer, Z.-q. Xin, S. Jautze, W. B. Schweizer, R. Peters, *Angew. Chem.* **2006**, *118*, 5823 – 5827; *Angew. Chem. Int. Ed.* **2006**, *45*, 5694 – 5698.
[260] A. Moyano, M. Rosol, R. M. Moreno, C. López, M. A. Maestro, *Angew. Chem.* **2005**, *117*, 1899 – 1903; *Angew. Chem. Int. Ed.* **2005**, *44*, 1865 – 1869.
[261] For recent reviews, see: a) S. France, D. J. Guerin, S. J. Miller, T. Lectka, *Chem. Rev.* **2003**, *103*, 2985 – 3012; b) S. E. Denmark, J. Fu, *Chem. Commun.* **2003**, 167 – 170; c) E. Vedejs, O. Daugulis, J. A. MacKay, E. Rozners, *Synlett* **2001**, 1499 – 1505.
[262] For a short review, see: A. C. Spivey, S. Arseniyadis, *Angew. Chem.* **2004**, *116*, 5552 – 5557; *Angew. Chem. Int. Ed.* **2004**, *43*, 5436 – 5441.
[263] A few chiral DMAP catalysts with ferrocene skeletons have recently been described by other research groups, although their asymmetric performance are, to date, much poorer than those obtained from Fu's catalysts. See a) S. H. Paeck, S. C. Shim, C. S. Cho, T.-J. Kim, *Synlett* **2003**, 849 – 851; b) J. G. Seitzberg, C. D. I. Søtofte, P.-O. Norrby, M. Johannsen, *J. Org. Chem.* **2003**, *68*, 8332 – 8337.
[264] a) G. C. Fu, *Acc. Chem. Res.* **2000**, *33*, 412 – 420; b) G. C. Fu, *Acc. Chem. Res.* **2004**, *37*, 542 – 547.
[265] A. H. Mermerian, G. C. Fu, *J. Am. Chem. Soc.* **2003**, *125*, 4050 – 4051.
[266] A. H. Mermerian, G. C. Fu, *J. Am. Chem. Soc.* **2005**, *127*, 5604 – 5607.
[267] A. H. Mermerian, G. C. Fu, *Angew. Chem.* **2005**, *117*, 971 – 974; *Angew. Chem. Int. Ed.* **2005**, *44*, 949 – 952.
[268] a) T. H. Black, S. M. Arrivo, J. S. Schumm, J. M. Knobeloch, *J. Chem. Soc. Chem. Commun.* **1986**, 1524 – 1525; b) T. H. Black, S. M. Arrivo, J. S. Schumm, J. M. Knobeloch, *J. Org. Chem.* **1987**, *52*, 5425 – 5430.
[269] I. D. Hills, G. C. Fu, *Angew. Chem.* **2003**, *115*, 4051 – 4054; *Angew. Chem. Int. Ed.* **2003**, *42*, 3921 – 3924.
[270] For an update, see: C. Schneider, *Angew. Chem.* **2002**, *114*, 771 – 772; *Angew. Chem. Int. Ed.* **2002**, *41*, 744 – 746.
[271] C. Zhu, X. Shen, S. G. Nelson, *J. Am. Chem. Soc.* **2004**, *126*, 5352 – 5353, and references therein.
[272] B. L. Hodous, G. C. Fu, *J. Am. Chem. Soc.* **2002**, *124*, 1578 – 1579.
[273] J. E. Wilson, G. C. Fu, *Angew. Chem.* **2004**, *116*, 6518 – 6520; *Angew. Chem. Int. Ed.* **2004**, *43*, 6358 – 6360.
[274] B. L. Hodous, G. C. Fu, *J. Am. Chem. Soc.* **2002**, *124*, 10006 – 10007.
[275] S. L. Wiskur, G. C. Fu, *J. Am. Chem. Soc.* **2005**, *127*, 6176 – 6177.
[276] For a review, see: D. Basavaiah, A. J. Rao, T. Satyanarayana, *Chem. Rev.* **2003**, *103*, 811 – 892.
[277] S. I. Pereira, J. Adrio, A. M. S. Silva, J. C. Carretero, *J. Org. Chem.* **2005**, *70*, 10175 – 10177.
[278] M. Shi, L.-H. Chen, C.-Q. Li, *J. Am. Chem. Soc.* **2005**, *127*, 3790 – 3800.

 © 2006 Wiley-VCH Verlag GmbH & Co. KGaA, Weinheim

[279] S. Kobayashi, C. Ogawa, H. Konishi, M. Sugiura, *J. Am. Chem. Soc.* **2003**, *125*, 6610 – 6611.
[280] I. Fernández, V. Valdivia, B. Gori, F. Alcudia, E. Álvarez, N. Khiar, *Org. Lett.* **2005**, *7*, 1307 – 1310.
[281] a) S. Minière, V. Reboul, R. Gómez Arrayás, P. Metzner, J. C. Carretero, *Synthesis* **2003**, 2249 – 2254; b) S. Minière, V. Reboul, P. Metzner, *Arkivoc* **2005**, *6*, 161 – 177.
[282] S. Minière, V. Reboul, P. Metzner, M. Fochi, B. F. Bonini, *Tetrahedron: Asymmetry* **2004**, *15*, 3275 – 3280.
[283] T. Nishimura, S. Uemura, *J. Am. Chem. Soc.* **1999**, *121*, 11010 – 11011.
[284] S. Matsumura, Y. Maeda, T. Nishimura, S. Uemura, *J. Am. Chem. Soc.* **2003**, *125*, 8862 – 8869.

GDCh

GESELLSCHAFT DEUTSCHER CHEMIKER

Deutsche Physikalische Gesellschaft DPG

STADT FRANKFURT AM MAIN

Otto-Hahn-Prize 2007

The Otto-Hahn-Prize is jointly administered by the city of Frankfurt am Main (Stadt Frankfurt am Main), the German Physical Society (DPG - Deutsche Physikalische Gesellschaft) and the German Chemical Society (GDCh - Gesellschaft Deutscher Chemiker). The prize is endowed with 50.000 Euro and a gold medal and is awarded every other year.

The prize promotes science by recognizing outstanding scientific achievements especially in the fields of chemistry, physics and applied engineering. One of the aims of the prize is to illustrate and promote the responsibility of science towards society as a whole.

In 2007 the prize should preferably honor an outstanding contribution in the field of chemistry. The prize will be awarded during a ceremony at the St. Paul's church (Paulskirche) in Frankfurt. Please submit your proposal including a letter of nomination, a curriculum vitae and a list of publications by **March 30, 2007** to

Gesellschaft Deutscher Chemiker
Barbara Köhler, Awards, Varrentrappstraße 40 – 42, 60486 Frankfurt am Main, Germany

Contact
Gesellschaft
Deutscher Chemiker
Abt. Preise und Auszeichnungen
P.O.Box 90 04 40
60444 Frankfurt a. M.
E-Mail: b.koehler@gdch.de
Tel. 069 79 17-323
Fax: 069 7917-307

© 2006 Wiley-VCH Verlag GmbH & Co. KGaA, Weinheim

Molecular Devices

DOI: 10.1002/anie.200602404

DNA Logic Gates Based on Structural Polymorphism of Telomere DNA Molecules Responding to Chemical Input Signals**

*Daisuke Miyoshi, Mamiko Inoue, and Naoki Sugimoto**

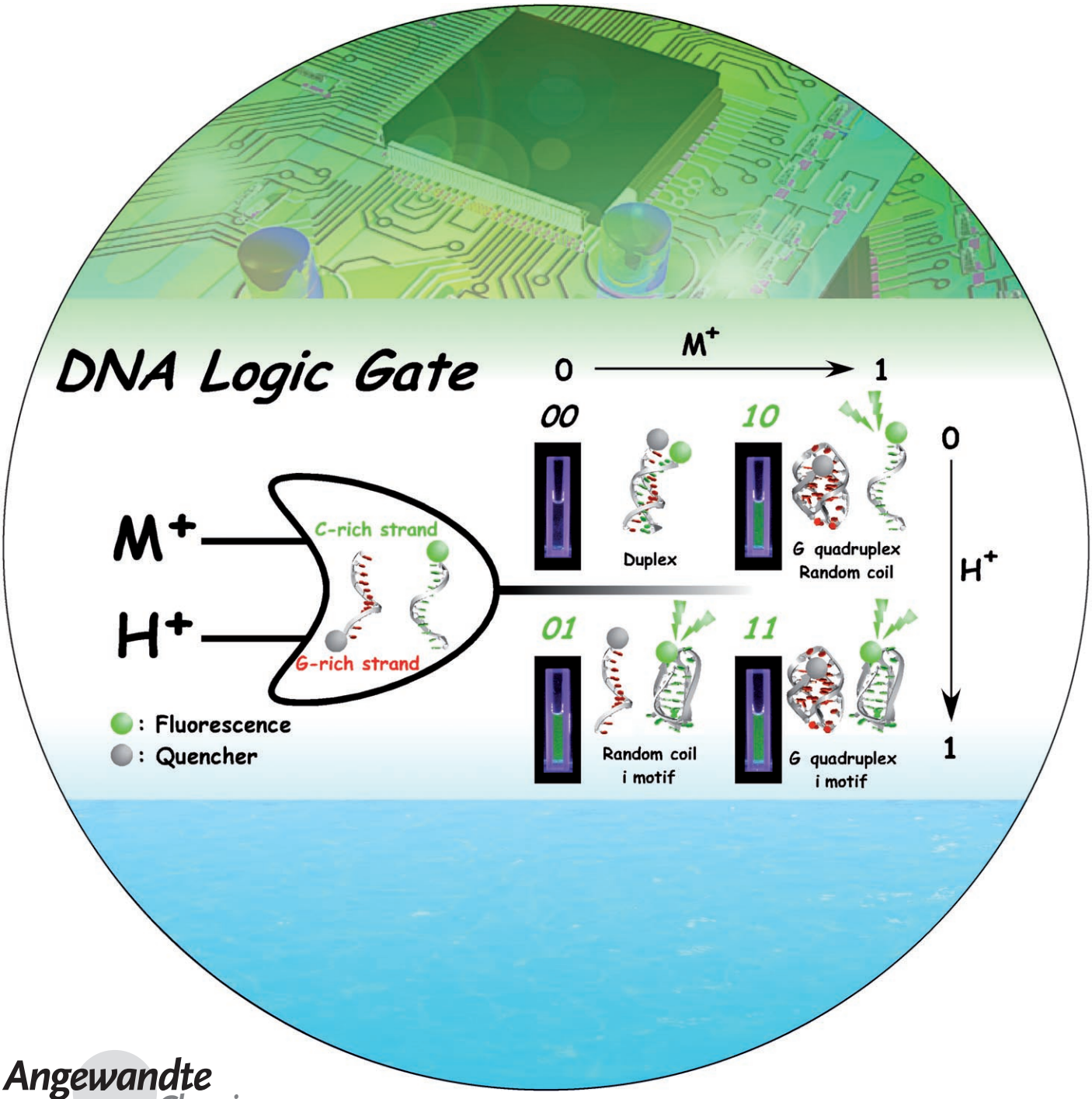

WILEY InterScience DISCOVER SOMETHING GREAT

© 2006 Wiley-VCH Verlag GmbH & Co. KGaA, Weinheim

Telomeres found at the termini of linear eukaryotic chromosomes may consist of double-stranded G- and C-rich sequences and 3′-single-stranded G-rich overhangs.[1] The G- and C-rich sequences can individually fold into four-stranded helices, namely, G quadruplexes and i motifs, respectively.[2] Furthermore, most telomere DNA molecules are thought to be made up of duplexes between G- and C-rich sequences, except for regions of G-rich overhangs. Whether G quadruplexes and i motifs are formed in living cells, however, remains unclear, although there is some evidences for the formation of G quadruplexes in cells.[3] We[4] and others[5] have shown that duplex–quadruplex conversion by telomere DNA molecules, which may be useful for the construction of molecular devices, is affected by environmental factors. In fact, several studies demonstrate that telomere DNA molecules can be used to construct nanomolecular machines.[6]

Systematic studies of the effects of multiple surrounding conditions on the structures of telomere DNA molecules are needed for the design of logic gates. Herein, we investigated the structure of two *Oxytricha* telomere DNA molecules, $d(G_4T_4)_3G_4$ (G strand) and $d(C_4A_4)_3C_4$ (C strand), under various conditions. Alone, the G strand folds into an intramolecular antiparallel G-quadruplex,[2a] whereas the C strand may fold into an i motif.[2b] Figure 1a shows the CD spectra of a 1:1 mixture of G and C strands (total strand concentration = 50 μM) in the presence of various concentrations of Li^+ at pH 8.0. The CD spectra had a positive peak and a shoulder at 260 and 290 nm, respectively, showing that the dominant structure is a B-form duplex at all concentrations of Li^+.[4] The CD spectra at the lower concentrations of K^+ at pH 8.0 showed that the dominant structure is a B-form duplex; however, at higher concentrations of K^+, the CD intensities at 260 and 290 nm decreased and increased, respectively, indicating that the mixture mainly folds into quadruplex(es) (Figure 1b). We further examined the structural conversion at pH 5.0. The CD spectra of the mixture in the presence of lower concentrations of Li^+ at pH 5.0 had a positive peak at 290 nm, showing that the mixture folds into quadruplex(es) (Figure 1c). In addition, the CD intensity at 290 nm decreased with increasing Li^+ concentrations, indicating destabilization of the G quadruplex by Li^+.[7] On the other hand, the CD spectra of the mixture in the presence of K^+ at pH 5.0 had a positive peak at 290 nm (Figure 1d), showing that quadruplexes dominate at all concentrations of K^+. Furthermore, the CD intensity at 290 nm in the presence of K^+ (200 mM) at pH 5.0 is twice that at pH 8.0 (Figure 1b), suggesting that the i motif structure is stabilized by acidic conditions.[2b] These results are consistent with the effects of pH and monovelant cations on the structures of human telomeric DNA molecules.[5a]

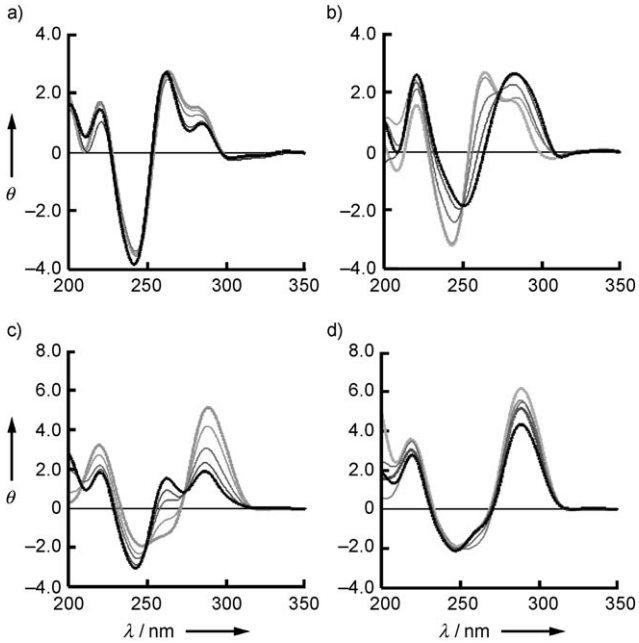

Figure 1. CD spectra (θ in 10^5 deg cm^2 dmol^{-1}) of a 1:1 mixture of $d(G_4T_4)_3G_4$ and $d(C_4A_4)_3C_4$ in the presence of various concentrations of a) Li^+ and Tris-HCl (50 mM; pH 8.0; Tris = tris(hydroxymethyl)aminomethane), b) various concentrations of K^+ and Tris-HCl (50 mM; pH 8.0), c) various concentrations of Li^+ and MES (50 mM; pH 5.0; MES = 2-(4-morpholinyl)ethane-sulfonic acid), or d) various concentrations of K^+ and MES (50 mM; pH 5.0). All measurements were carried out with a total strand concentration of 50 μM at 4 °C. The concentrations of monovalent cations (K^+ or Li^+) were 10, 20, 50, 100, and 200 mM (lines from the top to the bottom at 290 nm in panels a, c, and d and from the bottom to the top in panel b).

Characterization of the structures of the mixture by gel electrophoresis was found to be difficult as the equilibrium of the mixture between the duplex and the quadruplexes is shifted towards the duplex (data not shown). This may be due to changes in the pH of the buffer solution and/or other surrounding conditions during electrophoresis, although the mechanism of the structural changes of the mixture induced by the multiple surrounding conditions is not fully confirmed. Thus, we further characterized the structural conversion by isothermal titration calorimetry (ITC) in the presence of M^+ (Li^+ or K^+; 20 mM) at pH 8.0 or 5.0. Heat changes caused by the interaction between G and C strands were observed only

[*] Prof. Dr. N. Sugimoto
Frontier Institute for Biomolecular Engineering Research (FIBER), and
Department of Chemistry
Faculty of Science and Engineering
Konan University, 8-9-1 Okamoto, Higashinada-ku, Kobe 658-8501 (Japan)
Fax: (+81) 78-435-2766
E-mail: sugimoto@konan-u.ac.jp
Dr. D. Miyoshi
Frontier Institute for Biomolecular Engineering Research (FIBER)
Konan University (Japan)
M. Inoue
Department of Chemistry
Faculty of Science and Engineering
Konan University (Japan)

[**] This study was supported in part by Grants-in-Aid for Scientific Research and the "Academic Frontier" Project (2004–2009) from MEXT, Japan.

Supporting information for this article is available on the WWW under http://www.angewandte.org or from the author.

 © 2006 Wiley-VCH Verlag GmbH & Co. KGaA, Weinheim

in the presence of Li^+ at pH 8.0 (see the Supporting Information), demonstrating the formation of duplexes, although the ionic concentrations are slightly different from these for CD measurements. On the basis of these results, we conclude that the structural conversions of the G and C strands can be controlled by both M^+ and H^+ (dominant structures of the G and C strands are shown in Figure 2). We

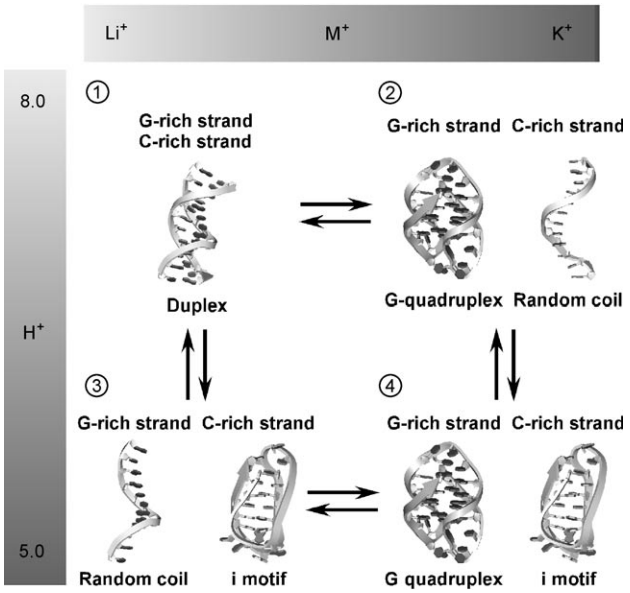

Figure 2. Schematic illustration of the structural conversion of the 1:1 mixture of G and C strands among duplex, quadruplex, and random-coil forms as controlled by M^+ (Li^+ or K^+) and H^+. 1) a duplex; 2) a G quadruplex and a random coil; 3) a random coil and an i motif; and 4) a G quadruplex and an i motif.

chose this ionic concentration (20 mM) to induce the random-coil state of the G strand in the presence of Li^+ at pH 5.0, which is required for functions of several logic gates as we will discuss later. Moreover, CD measurements confirmed that continuous structural conversions among the four states are induced by annealing the DNA structures after the conditions were changed (see the Supporting Information); however, we found that the conversions from the structural state 1 to 3 and 3 to 4 are very slow or do not occur (see the Supporting Information). These results suggest that the annealing process is required for the complete conversion of the mixture.

Based on the conversion of the telomere DNA molecules among these four states, we conceived a new concept for a DNA logic gate that responds to two chemical input signals (M^+ and H^+) and generates a change in fluorescence intensity as the output signal. As a proof of concept for the logic-gate function, we first built an OR logic gate by using a mixture that responds to two input signals, namely K^+ (20 mM; i_1) and acidic conditions (pH 5.0; i_2). Rhodamine Green, whose emission is independent of the pH,[6c] and 4-(4-dimethyl aminophenylazo)benzoic acid (Dabcyl) were attached to the strands as the fluorescent probe and quencher, respectively (see Figure 3a and b for the truth table and the positions of the fluorophores). Figure 3c shows the fluorescence spectra of the mixture (total strand concentration = 1 μM) excited at

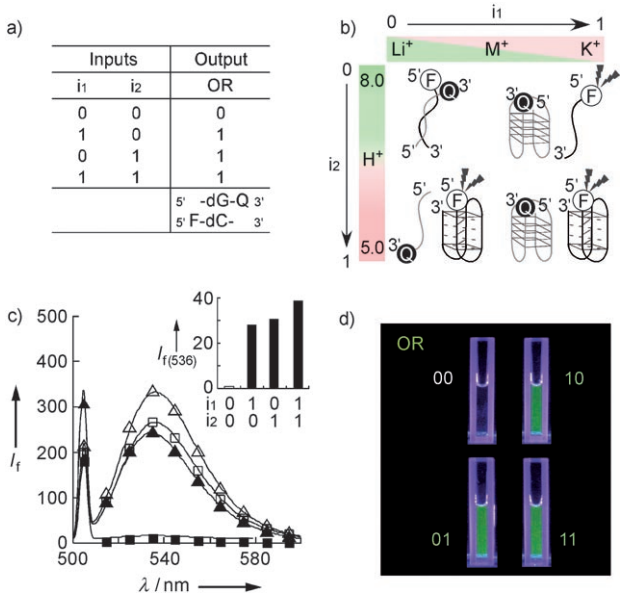

Figure 3. a) The truth table and design of the OR logic gate. b) Schematic illustration of the OR function of the 1:1 mixture of G and C strands and their response to M^+ and H^+. Gray and black lines indicate the G- and C-rich strands, respectively. c) Fluorescence spectra of the OR logic gate in the presence of Li^+ (20 mM; pH 8.0) ■, K^+ (20 mM; pH 8.0) ▲, Li^+ (20 mM; pH 5.0) □, or K^+ (20 mM; pH 5.0) △. All measurements were carried out at a total strand concentration of 1 μM and at 4 °C. Inset: normalized fluorescence intensities at 536 nm for the OR logic gate at 4 °C and ($i_1 = 0$, $i_2 = 0$), ($i_1 = 1$, $i_2 = 0$), ($i_1 = 0$, $i_2 = 1$), or ($i_1 = 1$, $i_2 = 1$). d) Fluorescence images of the OR logic gate. All measurements were carried out at a total strand concentration of 1 μM and at room temperature. F = Rhodamine Green, Q = Dabcyl. I_f = fluorescence intensity, $I_{f(536)}$ = fluorescence intensity at 536 nm.

504 nm in the presence of Li^+ (20 mM) at pH 8.0 ($i_1 = 0$, $i_2 = 0$), K^+ (20 mM) at pH 8.0 ($i_1 = 1$, $i_2 = 0$), Li^+ (20 mM) at pH 5.0 ($i_1 = 0$, $i_2 = 1$), and K^+ (20 mM) at pH 5.0 ($i_1 = 1$, $i_2 = 1$). The inset in Figure 3c shows the normalized fluorescence intensities at 536 nm of the mixture under the four listed conditions. The fluorescence intensities at the ($i_1 = 1$, $i_2 = 0$), ($i_1 = 0$, $i_2 = 1$), and ($i_1 = 1$, $i_2 = 1$) conditions were, respectively, 28-, 31-, and 39-fold higher than that of the ($i_1 = 0$, $i_2 = 0$) condition, confirming OR gate behavior, wherein the fluorescence signals can be recognized even by the naked eye (Figure 3d). In addition, these results are consistent with those from CD and ITC measurements, although the DNA strand concentrations used in CD, ITC, and fluorescence measurements are different. Moreover, we found that the structural conversion can be utilized to construct XOR (exclusive OR) and NOTIF logic gates, which generate fluorescence signals under either two or one conditions, respectively (see the Supporting Information). Notably, not only the logic gates developed here, but other logic gates as well can be created based on the structural conversion and incorporation of fluorophores in different combinations and at different positions (see the Supporting Information for molecular design of these logic gates).

In the current studies, we developed simple and robust DNA logic gates. Compared with DNA logic gates previously developed,[8] ours have a few potential disadvantages.

 © 2006 Wiley-VCH Verlag GmbH & Co. KGaA, Weinheim

Because the kinetics of folding and unfolding by G-quadruplex structures are very slow, conversion requires annealing (see the Supporting Information). Regardless, our system provides a simpler and faster readout of the output signals than systems employing gel electrophoresis. In addition, the kinetics of folding and unfolding can be controlled in our system by modulating the DNA sequences.[9] Thus, further optimization of the logic gates may be possible. On the other hand, only one type of logic gate can be made for each vessel because the solution conditions (input signals) affect all of the logic gates in the vessel and because we did not utilize sequence-specific hybridization as an input signal. The control of the structural conversion, however, can be extended to any telomere DNA. A previous report showed that the polymorphic structures of telomere DNAs can be controlled by their sequences and by surrounding factors such as divalent metal ions and molecular crowding as well as monovalent cations and pH.[4,5] Furthermore, a single base difference in the telomere sequences was reported to have a drastic effect on their structures.[4c] Therefore, further optimization should make it possible to individually control the behavior of multiple logic gates in a single vessel. These results demonstrate that it should be possible to employ the structural polymorphism of telomere DNA molecules in a broad spectrum of nanobiotechnological applications, such as logic gates under cell-mimicking conditions in which both the pH and concentration of monovalent cations control various biological events.

Received: June 15, 2006
Published online: October 10, 2006

Keywords: DNA · logic gates · molecular devices · nanomaterials · nanotechnology

[1] E. H. Blackburn, *Nature* **1991**, *350*, 569 – 573.
[2] a) Y. Wang, D. J. Patel, *J. Mol. Biol.* **1995**, *251*, 76 – 94; b) D. E. Gilbert, J. Feigon, *Curr. Opin. Struct. Biol.* **1999**, *9*, 305 – 314.
[3] a) C. Schaffitzel, I. Berger, J. Postberg, J. Hanes, J. H. J. Lipps, A. Pluckthun, *Proc. Natl. Acad. Sci. USA* **2001**, *98*, 8572 – 8577; b) A. Siddiqui-Jain, C. L. Grand, D. J. Bearss, L. H. Hurley, *Proc. Natl. Acad. Sci. USA* **2002**, *99*, 11593 – 11598; c) M. L. Duquette, P. Handa, J. A. Vincent, A. F. Taylor, N. Maizels, *Genes Dev.* **2004**, *18*, 1618 – 1629; d) K. Paeschke, T. Simonsson, J. Postberg, D. Rhodes, H. J. Lipp, *Nat. Struct. Mol. Biol.* **2005**, *12*, 847 – 854.
[4] a) W. Li, D. Miyoshi, S. Nakano, N. Sugimoto, *Biochemistry* **2003**, *42*, 11736 – 11744; b) D. Miyoshi, S. Matsumura, S. Nakano, N. Sugimoto, *J. Am. Chem. Soc.* **2004**, *126*, 165 – 169; c) D. Miyoshi, H. Karimata, N. Sugimoto, *Angew. Chem.* **2005**, *117*, 3806 – 3810; *Angew. Chem. Int. Ed.* **2005**, *44*, 3740 – 3744.
[5] a) A. T. Phan, J. L. Mergny, *Nucleic Acids Res.* **2002**, *30*, 4618 – 4625; b) N. Kumar, S. Maiti, *Nucleic Acids Res.* **2005**, *33*, 6723 – 6732; c) Z. Kan, Y. Yao, P. Wang, X. Li, Y. Hao, Z. Tan, *Angew. Chem.* **2006**, *118*, 1659 – 1662; *Angew. Chem. Int. Ed.* **2006**, *45*, 1629 – 1632.
[6] a) J. J. Li, W. Tan, *Nano Lett.* **2002**, *2*, 315 – 318; b) P. Alberti, J. L. Mergny, *Proc. Natl. Acad. Sci. USA* **2003**, *100*, 1569 – 1573; c) D. Liu, S. Balasubramanian, *Angew. Chem.* **2003**, *115*, 5912 – 5914; *Angew. Chem. Int. Ed.* **2003**, *42*, 5734 – 5736; d) W. U. Dittmer, A. Reuter, F. C. Simmel, *Angew. Chem.* **2004**, *116*, 3634 – 3637; *Angew. Chem. Int. Ed.* **2004**, *43*, 3550 – 3553.
[7] C. C. Hardin, A. G. Perry, K. White, *Biopolymers* **2001**, *56*, 147 – 194.
[8] a) M. N. Stojanovic, D. A. Stefanovic, *Nat. Biotechnol.* **2003**, *21*, 1069 – 1074; b) Y. Benenson, B. Gil, U. Ben-Dor, R. Adar, E. Shapiro, *Nature* **2004**, *429*, 423 – 429; c) A. Okamoto, K. Tanaka, I. Saito, *J. Am. Chem. Soc.* **2004**, *126*, 9458 – 9463.
[9] J. L. Mergny, A. De Cian, A. Ghelab, B. Sacca, L. Lacroix, *Nucleic Acids Res.* **2005**, *33*, 81 – 94.

 © 2006 Wiley-VCH Verlag GmbH & Co. KGaA, Weinheim

Phosphorus Chemistry

DOI: 10.1002/anie.200601155

P_8^{8-} Polyanion with Phosphorus Atoms in Three Different Formal Oxidation States Stabilized by a Combination of Ag^+ and Hg^{2+} Cations**

Olga S. Oleneva, Tatiana A. Shestimerova, Evgeny V. Dikarev, and Andrei V. Shevelkov**

Phosphorus is among the few elements that feature a large variety of allotropic modifications, polyanions, and clusters.[1,2] The discovery of elemental phosphorus lies far in the past but scientists continue to make exciting new experimental findings, among which the recent discovery of fibrous phosphorus ought to be mentioned.[3] Extensive research is also devoted to theoretical calculations of seemingly limitless varieties of phosphorus clusters.[4] Among these clusters, however, highly charged clusters and polyanions are poorly studied because of their lower stability. As a rule, the bonding in phosphorus clusters and polyanions is of two-center, two-electron type, and the formal oxidation states can be easily assigned to each phosphorus atom according to the number of homonuclear bonds it makes.[5] Typically, the clusters and polyanions are constructed by phosphorus atoms

[*] Prof. Dr. E. V. Dikarev
Department of Chemistry
University at Albany
Albany 12222, NY (USA)
Fax: (+1) 518-442-3462
E-mail: dikarev@albany.edu
Dipl.-Chem. O. S. Oleneva, T. A. Shestimerova,
Prof. Dr. A. V. Shevelkov
Inorganic Synthesis Laboratory
Department of Chemistry
Moscow State University
Leninskie Gory 1/3, Moscow 119992 (Russia)
Fax: (+7) 495-939-4788
E-mail: shev@inorg.chem.msu.ru

[**] This research was supported by the Russian Foundation for Basic Research and the European Commission 5th Framework Program. E.V.D. is grateful to the National Science Foundation for funding the CCD diffractometer (CHE-0130985) at the University at Albany.

Supporting information for this article is available on the WWW under http://www.angewandte.org or from the author.

© 2006 Wiley-VCH Verlag GmbH & Co. KGaA, Weinheim
InterScience

that have two different oxidation numbers. Polyanions with three different oxidation states are merely exceptions found only in the infinite branched chains of transition-metal polyphosphides.[6] Herein we report a highly charged phosphorus polyanion P_8^{8-} that features phosphorus atoms with three different oxidation numbers. This polyanion was stabilized in a framework of the new compound $Hg_4Ag_5P_8Cl_5$ by a combination of the Ag^+ and Hg^{2+} ions, which have the same coordination geometries but different charges and are linked to phosphorus atoms of different oxidation state.

The silver–mercury phosphide chloride $Hg_4Ag_5P_8Cl_5$ was obtained by an ampoule synthesis, and the crystal structures of two polymorphs (monoclinic from a low-temperature synthesis and orthorhombic from a high-temperature synthesis) were determined.[7] The P_8^{8-} polyanion in the fully ordered monoclinic structure consists of a six-membered ring in a chair conformation with two equatorial P atoms in 1,4-positions (Figure 1). The P–P bond lengths range from 2.18 to

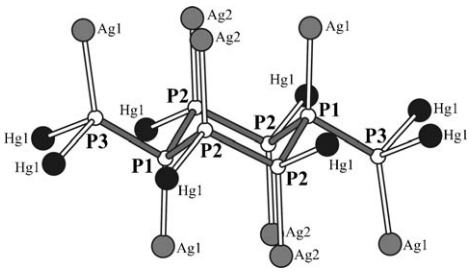

Figure 1. Geometry of the P_8^{8-} polyanion and its coordination by metal atoms in the monoclinic structure of $Hg_4Ag_5P_8Cl_5$: P1–P2 2.185(2) Å, P2–P2 2.200(3) Å, P1–P3 2.183(3) Å.

2.20 Å, which is typical for a single P–P bond.[1] All P atoms exhibit slightly distorted tetrahedral coordination geometries, although their formal oxidation states differ. The P1 atom of the six-membered ring forms three homonuclear bonds to two phosphorus atoms within the ring and to one equatorial phosphorus atom; thus, it is assigned a formal oxidation state of zero. The tetrahedral coordination geometry of this atom is completed by an additional bond to a silver atom. The P2 atom, which also belongs to the six-membered ring, is linked to two phosphorus atoms and two metal atoms (one silver atom and one mercury atom); hence, it has an oxidation state of −I. The equatorial P3 atom forms one homonuclear bond, is further connected to three metal atoms (two mercury atoms and one silver atom), and has an oxidation state of −II. Thus, phosphorus in a lower oxidation state of −II is preferentially linked to mercury, whereas phosphorus in the higher oxidation state of zero has only silver as a neighbor. Taking into account the typical oxidation states of mercury (with no Hg–Hg bonding), silver, and chlorine, one obtains the charge-balanced formulation $Hg_4^{2+}Ag_5^{+}P1_2^{0}P2_4^{-}P3_2^{2-}Cl_5^{-}$.

In the monoclinic structure, the P_8^{8-} polyanions are linked by mercury atoms to form layers within the *ab* plane, where they are produce a checkered pattern (Figure 2a). These layers are connected along the *c* axis through silver atoms (Figure 2b). One silver atom (Ag3) is disconnected from the

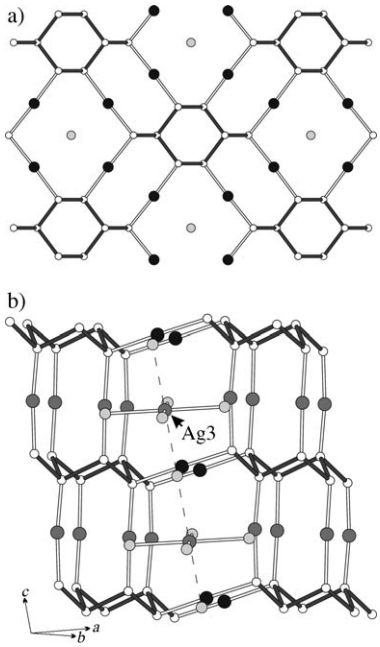

Figure 2. Crystal structure of the monoclinic structure of $Hg_4Ag_5P_8Cl_5$: a) projection of a layer along the (001) plane; b) general view. Black Hg, dark gray Ag, light gray Cl, white P.

phosphorus polyanion, and its coordination can be described as a 4+2 array of six chlorine atoms. The structure of the layer can be viewed as the result of disassembly of the corrugated 2D net from the structure of gray arsenic by insertion of mercury and chlorine atoms. Such a gray arsenic structure is unique. Another type of alternation is the structures of metal triphosphides MP_3 (M = In, Ge, Sn),[8] in which the metal atoms replace phosphorus atoms in such a way that the separated P_6 chairs retain the structural motif of gray arsenic. Many other compounds exhibit the black phosphorus, rather than gray arsenic, structure, which features buckled layers of atoms. In various binary and ternary pnictides, diverse modes of removing a fraction the phosphorus atoms from the buckled layer lead to various 2D and 1D substructures.[9]

The major difference between the two polymorphs of $Hg_4Ag_5P_8Cl_5$ is the packing of the phosphorus layers (Figure 3). Whereas the monoclinic structure features identical layers that propagate along the *c* axis, the orthorhombic structure has two types of layers that are mirror reflections of each other and alternate along the *c* axis. Another noticeable distinction between these two polymorphs is the occupancy of the metal-atom positions. The monoclinic structure is fully ordered: the silver and mercury atoms occupy different sites in the network as described above. Conversely, two of the metal positions in the orthorhombic structure are jointly occupied by silver and mercury, while one position remains fully occupied by silver only.

Band-structure calculations (Figure 4) performed for the fully-ordered monoclinic form show that, although the assignment of the oxidation states is merely a formality, the P1 atoms indeed possess the lowest negative charge, whereas the P3 atoms exhibit the highest negative charge, which is in accordance with their oxidation numbers. The analysis of the

 © 2006 Wiley-VCH Verlag GmbH & Co. KGaA, Weinheim

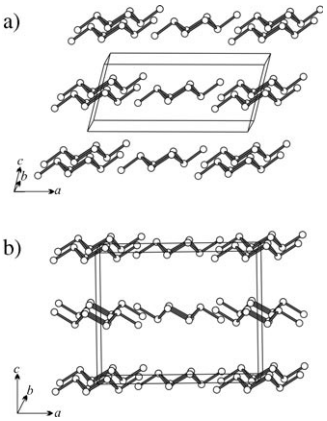

Figure 3. Interlayer ordering of phosphorus atoms in the monoclinic (a) and orthorhombic (b) forms of $Hg_4Ag_5P_8Cl_5$.

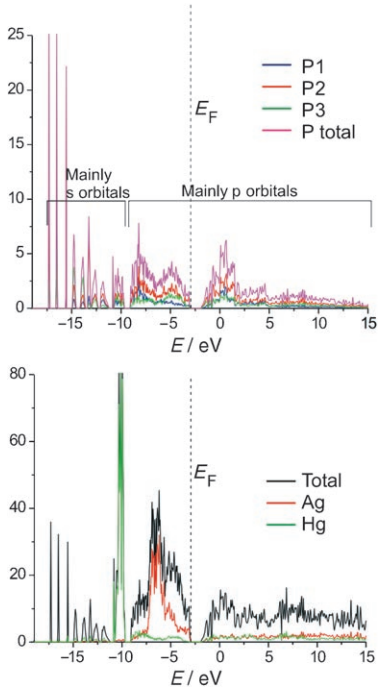

Figure 4. DOS plots for the monoclinic form of $Hg_4Ag_5P_8Cl_5$.

orbital interactions revealed that the P–M bonding involves mainly interactions of the phosphorus p orbitals with the mercury s and p orbitals and the silver d and s orbitals. However, the states in the vicinity of the Fermi level are composed mainly of chlorine p orbitals (not shown) and silver d orbitals. Therefore, the states of the P_8^{8-} polyanion should not contribute significantly to the electrical properties of the compound (calculated band-gap width E_g is 1.0 eV).

The crystal structures of three compounds reported earlier,[10] namely, $Hg_7Ag_2P_8I_6$, $Hg_7Ag_2P_8Br_6$, and $Hg_6Ag_3P_8AgBr_6$, have already provided examples of Ag^+ and Hg^{2+} ions linked to phosphorus atoms with different oxidation numbers. In particular, mercury is bound only to the P^{-II} atoms of the P_2^{4-} units, whereas silver prefers the P^{-I} atoms of the P_6^{6-} rings. In this work, the linking of Ag^+ and Hg^{2+} ions to differently charged phosphorus atoms has led to the stabilization of the P_8^{8-} polyanion in $Hg_4Ag_5P_8Cl_5$. The presence of phosphorus atoms in different oxidation states linked to different metal atoms seems to provide the stability for highly charged P_8^{8-} polyanion. It is expected that other combinations of cations that stabilize phosphorus atoms in different oxidation states will lead to the isolation of new phosphorus clusters and polyanions of even higher complexity.

Experimental Section

Mercury, red phosphorus, and silver chloride were mixed in the molar ratio 4:8:5 (1 g total), vacuum-sealed in quartz ampoules (inner diameter 8 mm), and heated for 5 days. The annealing temperature was set at 675 and 775 K for the monoclinic and orthorhombic forms, respectively. The X-ray diffraction patterns of the products (STADI-P (STOE), Cu$K_{\alpha 1}$ radiation) were identical to those calculated from the corresponding crystal data and did not reveal the presence of any impurities. Single crystals for the structural determination were selected from the respective samples. Band-structure calculations were performed for the monoclinic form of $Hg_4Ag_5P_8Cl_5$ by using the TB-LMTO-ASA approach with the TB-LMTO-47 code.[11] Before the calculation of the density of states (DOS), the self-consistent field (SCF) calculations were performed for 267 k-points in the irreducible wedge of the Brillouin zone.

Received: March 23, 2006
Revised: July 21, 2006
Published online: October 16, 2006

Keywords: mercury · phosphorus · polyanions · silver · structure elucidation

[1] H. G. von Schnering, W. Hönle, *Chem. Rev.* **1988**, *88*, 243–273, and references therein.
[2] a) X. Chen, L.-P. Zhu, S. Yamanaka, *J. Solid State Chem.* **2003**, *173*, 449–455; b) W. Jeitschko, A. J. Föcker, D. Paschke, M. V. Dewalsky, C. B. H. Evers, B. Künnen, A. Lang, G. Kotzyba, U. C. Rodewald, M. H. Möller, *Z. Anorg. Allg. Chem.* **2000**, *626*, 1112–1120; c) C. Hadenfeldt, F. Bartels, *Z. Anorg. Allg. Chem.* **1994**, *620*, 1247–1252.
[3] a) M. Ruck, D. Hoppe, B. Wahl, P. Simon, Y. Wang, G. Siefert, *Angew. Chem.* **2005**, *117*, 7788–7792; *Angew. Chem. Int. Ed.* **2005**, *44*, 7616–7619; b) A. Pfitzner, *Angew. Chem.* **2006**, *118*, 714–715; *Angew. Chem. Int. Ed.* **2006**, *45*, 699–700.
[4] a) P. Li, *Chin. J. Struct. Chem.* **2005**, *4*, 467–477; b) S. Böcker, M. Häser, *Z. Anorg. Allg. Chem.* **1995**, *621*, 258–286.
[5] For the application of the Mooser–Pearson rule and Zintl–Klemm formalism to phosphorus polyanions, see reference [1].
[6] a) W. Hönle, R. Kremer, H.-G. von Schnering, *Z. Anorg. Allg. Chem.* **1987**, *179*, 443–453; b) R. Rühl, W. Jeitschko, *Inorg. Chem.* **1982**, *21*, 1886–1891.
[7] Crystal data of the monoclinic form (**1**): space group *C*2/*m* (no. 12), $a = 14.490(2)$, $b = 10.9043(15)$, $c = 6.2863(9)$ Å, $\beta = 104.094(2)°$, $V = 963.4(2)$ Å^3, $Z = 2$, $\rho_{calcd} = 6.090$ g cm^{-3}; 4119 reflections, 1185 of which were independent ($R_{int} = 0.0215$), $T = 173$ K, ω scans (0.3° width, total 1850 frames), $Mo_{K\alpha}$ radiation, $\lambda = 0.71069$ Å, $2\theta_{max} = 56.58°$, crystal dimensions $0.07 \times 0.06 \times 0.04$ mm^3, empirical absorption correction (SADABS,[12a] min./max. transmission: 0.1759/0.3114, $\mu = 38.047$ mm^{-1}). Structure solution: full-matrix least-squares procedure on $|F^2|$ (Bruker SHELXTL Version 6.12,[12b] 1136 reflections with $F > 4\sigma(F)$) with 60 free parameters; $R1 = 0.0262$, $wR2 = 0.0639$; min./max. residual electron density 2.600/−2.854 e Å^{-3}; Crystal data of

 © 2006 Wiley-VCH Verlag GmbH & Co. KGaA, Weinheim

orthorhombic form (**2**): space group *Cmcm* (no. 63), $a=11.1426(6)$, $b=14.5064(8)$, $c=11.8444(6)$ Å, $V=1914.52(18)$ Å^3, $Z=4$, $\rho_{calcd}=6.129\,g\,cm^{-3}$; 8202 reflections, 1271 of which were independent ($R_{int}=0.0244$), $T=173$ K, ω scans (0.3° width, total 1850 frames), $Mo_{K\alpha}$ radiation, $\lambda=0.71069$ Å, $2\theta_{max}=56.52°$, crystal dimensions $0.15\times0.14\times0.13$ mm^3, empirical absorption correction (SADABS, min./max. transmission: 0.0690/0.0825, $\mu=38.291\,mm^{-1}$). Structure solution: full-matrix least-squares procedure on $|F^2|$ (Bruker SHELXTL Version 6.12, 1246 reflections with $F>4\sigma(F)$) with 72 free parameters; $R1=0.0216$, $wR2=0.0510$; min./max. residual electron density 1.944/−2.026 e Å^{-3}. Further details on the crystal structure investigation may be obtained from the Fachinformationszentrum Karlsruhe, 76344 Eggenstein-Leopoldshafen, Germany (fax: (+49) 7247-808-666; e-mail: crysdata@fiz-karlsruhe.de), on quoting the depository numbers CSD-416360 (**1**) and CSD-416361 (**2**).

[8] a) N. Kinomura, K. Terao, S. Kikkawa, H. Horiuchi, M. Koizumi, *Mater. Res. Bull.* **1983**, *18*, 53–57; b) J. Gullman, O. Olofsson, *J. Solid State Chem.* **1972**, *5*, 441–445.

[9] a) X. Chen, L.-P. Zhu, S. Yamanaka, *J. Solid State Chem.* **2003**, *173*, 449–455; b) M. M. Shatruk, K. A. Kovnir, A. V. Shevelkov, B. A. Popovkin, *Angew. Chem.* **2000**, *112*, 2561–2562; *Angew. Chem. Int. Ed.* **2000**, *39*, 2508–2509; c) W. Bauhofer, M. Wittmann, H. G. von Schnering, *J. Phys. Chem. Solids* **1981**, *42*, 687–695; d) W. Jeitschko, M. H. Möller, *Acta Crystallogr. Sect. A* **1979**, *35*, 573–579; e) K. Deller, B. Eisenmann, *Z. Naturforsch. B* **1978**, *33*, 676–677; f) W. Dahlmann, H. G. von Schnering, *Naturwissenschaften* **1973**, *60*, 518–518.

[10] O. S. Oleneva, A. V. Olenev, T. A. Shestimerova, A. I. Baranov, E. V. Dikarev, A. V. Shevelkov, *Inorg. Chem.* **2005**, *44*, 9622–9624.

[11] M. van Schilfgarde, T. A. Paxton, O. Jepsen, O. K. Andersen, G. Krier, Programm TB-LMTO; Max-Planck-Institut für Festkörperforschung, Stuttgart, **1994**.

[12] a) SADABS, Program for absorption correction based on the methods of Robert Blessing: R. H. Blessing, *Acta Crystallogr. Sect. A* **1995**, *51*, 33; b) SHELXTL, version 6.12, Bruker Analytical X-ray Systems, Madison, WI, **2001**.

 © 2006 Wiley-VCH Verlag GmbH & Co. KGaA, Weinheim

Single-Molecule Magnets

DOI: 10.1002/anie.200603498

A Family of 3D Coordination Polymers Composed of Mn_{19} Magnetic Units**

Eleni E. Moushi, Theocharis C. Stamatatos, Wolfgang Wernsdorfer, Vassilios Nastopoulos, George Christou, and Anastasios J. Tasiopoulos**

The current intense interest in polynuclear clusters stems not only from their aesthetically pleasing structures, magnetic interactions, and magnetostructural correlations, but also from the discovery that some function as nanoscale magnetic particles, or single-molecule magnets (SMMs).[1] Below their blocking temperature (T_B), such molecules behave as magnets and exhibit hysteresis in scans of magnetization versus dc field. This behavior results from the combination of a large ground spin state (S) with a large and negative (easy-axis type) magnetoanisotropy. SMMs have several potential applications, including high-density information storage, in which each bit of information is stored as the magnetization orientation of an individual molecule, and quantum computation, in which the molecules can serve as qubits.

Although there are many known species displaying SMM behavior,[1–5] most of which are manganese–carboxylate complexes,[3–5] there is a continuing need for new SMMs. One of the most successful synthetic approaches to new polynuclear clusters involves the use of chelating ligands containing alkoxide functions, since these are good bridging groups and, thus, favor the formation of polynuclear products.[4] Recently, we have been investigating the use of 1,3-propanediol (H_2pd) and 2-methyl-1,3-propanediol (H_2mpd) in manganese–carboxylate chemistry. Herein, we report the syntheses, crystal structures, and magnetic properties of two new 3D coordination polymers based on $[Mn_{19}Na(\mu_4\text{-}O)_9(\mu_3\text{-}$

[*] Dr. T. C. Stamatatos, Prof. Dr. G. Christou
Department of Chemistry, University of Florida
Gainesville, FL 32611-7200 (USA)
Fax: (+1) 352-392-8757
E-mail: christou@chem.ufl.edu

E. E. Moushi, Dr. A. J. Tasiopoulos
Department of Chemistry, University of Cyprus
1678 Nicosia (Cyprus)
Fax: (+357) 2289-2801
E-mail: atasio@ucy.ac.cy

Dr. W. Wernsdorfer
Laboratoire Louis Néel, CNRS, BP 166
Grenoble, Cedex 9 (France)

Dr. V. Nastopoulos
Department of Chemistry, University of Patras
26500 Patras (Greece)

[**] This work was supported by the University of Cyprus, the Cyprus Research Promotion Foundation (Grant: PENEK-ENISX/0505/18), and the USA National Science Foundation.

Supporting information for this article is available on the WWW under http://www.angewandte.org or from the author.

InterScience
© 2006 Wiley-VCH Verlag GmbH & Co. KGaA, Weinheim

O)(μ_3-OH)$_3$(O$_2$CMe)$_9$(pd)$_9$(H$_2$O)$_3$][OH] (**1**) and [Mn$_{19}$Na(μ_4-O)$_9$(μ_3-O)(μ_3-OH)$_3$(O$_2$CMe)$_9$(mpd)$_9$(H$_2$O)$_3$][OH] (**2**) repeating units. Compounds {**1**·0.5 MeCN·6 H$_2$O}$_\infty$ and {**2**·6 H$_2$O}$_\infty$, which are the first manganese complexes with the ligands H$_2$pd and H$_2$mpd, have open-framework structures with nanometer-sized channels and, in addition, behave as SMMs.[5]

The reaction of [Mn$_3$O(O$_2$CMe)$_6$(py)$_3$]·py (py = pyridine), H$_2$pd, and NaClO$_4$ in a 1:5:2 molar ratio in MeCN led to the isolation of {**1**·0.5 MeCN·6 H$_2$O}$_\infty$ in 23 % yield after several weeks (single crystals could be obtained as {**1**·3 H$_2$O}$_\infty$). When the same reaction was repeated with H$_2$mpd instead of H$_2$pd, with the reactants in a 1:5:1 molar ratio, {**2**·6 H$_2$O}$_\infty$ was isolated in 25 % yield (single crystals could be obtained as {**2**·3 H$_2$O}$_\infty$). As the crystal structures and magnetic properties of **1** and **2** are strikingly similar, only those of **1** will be described; structural figures and plots of dc and ac magnetic-susceptibility data for **2** are provided in the Supporting Information.

The crystal structure of {**1**·3 H$_2$O}$_\infty$, in the cubic space group $P2_13$,[6] reveals that **1** (Figure 1 a) is a mixed-valent complex, containing seven Mn^{II} ions and twelve Mn^{III} ions, as determined by bond-valence calculations,[7] charge considerations, and inspection of the metric parameters. The manganese–oxygen core of **1** (Figure 1 b) consists of three equilateral triangles stacked one above the other. The basal triangle contains ten manganese ions, nine on its edges, and the tenth near its center, whereas the middle and apex triangles contain six and three manganese ions, respectively, all of which lie on their edges. The manganese ions of the core are held together by nine μ_4-O^{2-}, one μ_3-O^{2-}, and three μ_3-OH$^-$ ions,[8] resulting in an overall triangular-pyramidal-frustum topology (Figure 1 b). The peripheral ligation of **1** is completed by nine bridging pd^{2-} ligands, nine bridging O$_2$CMe$^-$ ligands, and three terminal H$_2$O molecules.

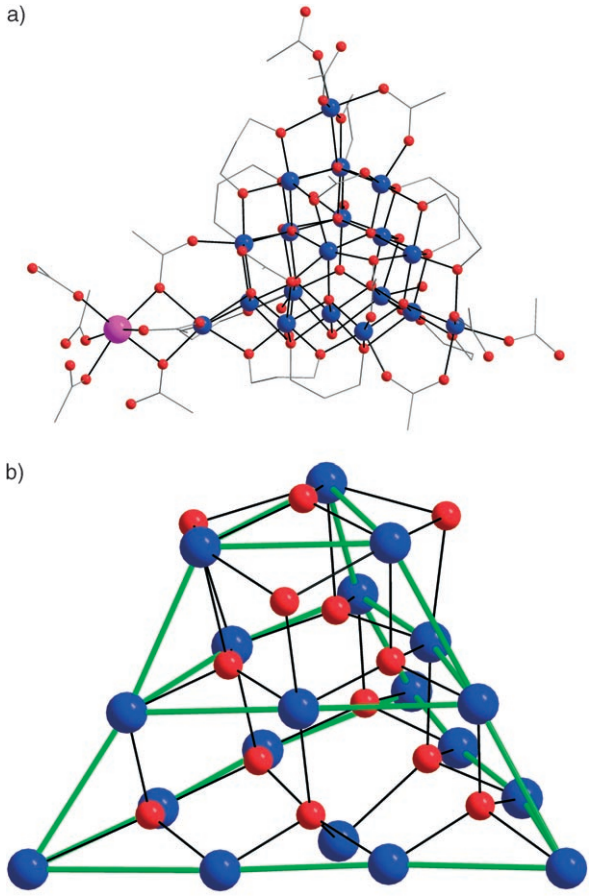

Figure 1. a) The molecular structure of **1**. b) The manganese–oxygen core of **1**; the green lines connecting the manganese ions emphasize the triangular-pyramidal-frustum topology. Na pink, Mn blue, O red, C gray. Hydrogen atoms and the free OH$^-$ ion are omitted for clarity.

Each Mn$_{19}$ aggregate is connected through three μ_3-O$_2$CMe$^-$ ligands to a Na$^+$ ion. One of the μ_3-O$_2$CMe$^-$ groups links Mn1 and Mn5 with the Na$^+$ ion, whereas the other two μ_3-O$_2$CMe$^-$ groups link Mn5 with the Na$^+$ ion and the symmetry-related Mn5 ions of two other Mn$_{19}$ units, resulting in a 3D coordination polymer (Figure 2 a). To our knowledge, Mn$_{19}$ is the highest-nuclearity repeating unit reported for a manganese coordination polymer. Note that although the Mn$_{19}$ units are bridged not only through the Na$^+$ ions, but also directly through μ_3-O$_2$CMe$^-$ ligands, the shortest Mn···Mn separation between the Mn$_{19}$ units is relatively large (5.52(1) Å). A close examination of the packing of **1** revealed a highly ordered 3D structure that contains large channels with dimensions of approximately 12 × 16 Å^2 (Figure 2 b,c). These channels are nearly empty, containing only a very small proportion of H$_2$O molecules and OH$^-$ counterions. In fact, approximately 44 % of the crystal structure of {**1**·3 H$_2$O}$_\infty$ is void space.

Measurements of the molar dc magnetic susceptibility (χ_M) of a microcrystalline sample of {**1**·6 H$_2$O·0.5 MeCN}$_\infty$ were made over the temperature range 5.0–300 K in an applied field of 0.1 T. The $\chi_M T$ value at 300 K is 54.15 cm^3 mol^{-1} K, and it increases with decreasing temperature to a maximum of 73.68 cm^3 mol^{-1} K at 15.0 K, before decreasing to 69.30 cm^3 mol^{-1} K at 5.00 K (see Supporting Information). The data indicate that **1** has a large ground spin state. Given the size of the molecule, it is not possible to apply the Kambe method to determine the individual pairwise exchange-interaction parameters between the manganese ions, and direct matrix-diagonalization methods are also computationally unfeasible. To determine the ground state, magnetization data were collected in the temperature range 1.8–10.0 K and the magnetic-field range 0.1–1 T (see Supporting Information). The data were fit by assuming that only the ground state is populated and by including axial zero-field splitting ($D\hat{S}_{z^2}$) and Zeeman interactions. A very good fit was obtained with $S = 23/2$, $D = -0.086(3)$, and $g = 1.99(1)$.

As described elsewhere,[3b,4d] reliable conclusions about the S value can be provided by ac magnetic-susceptibility measurements, which can also detect the slow magnetization relaxation suggestive of SMMs. Frequency-dependent out-of-phase ac susceptibility signals (χ_M'') were indeed detected for **1** below approximately 2.8 K (but no peaks were observed), along with a concomitant decrease in the in-phase signal (Figure 3). Extrapolation of the $\chi_m' T$ versus T plots to 0 K (from temperature ranges not affected by the decrease in χ_m' arising from slow relaxation) gives a value of approximately 70 cm^3 mol^{-1} K, which is consistent with that expected for an

 © 2006 Wiley-VCH Verlag GmbH & Co. KGaA, Weinheim

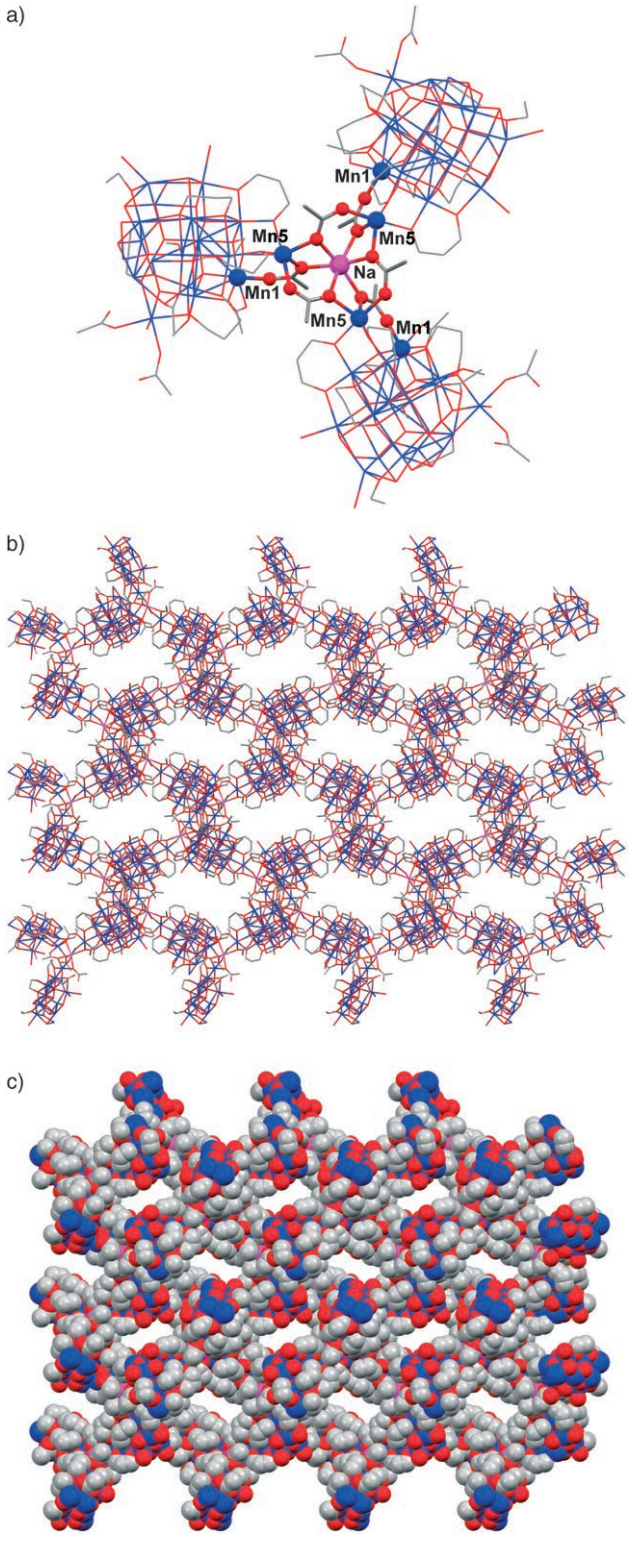

Figure 2. The polymeric structure of $\{\mathbf{1}\cdot 3\,H_2O\}_\infty$. a) View emphasizing the connectivity of the Mn_{19} units. b) Wire-frame and c) space-filling representations viewed along the *c* axis, emphasizing the large channels. Na pink, Mn blue, O red, C gray. Hydrogen atoms, free OH^- ions, and cocrystallized H_2O molecules are omitted for clarity.

$S = 23/2$ system (assuming $g \approx 1.98$). The ac susceptibility data, thus, support the $S = 23/2$ ground state determined from fits of the magnetization data.

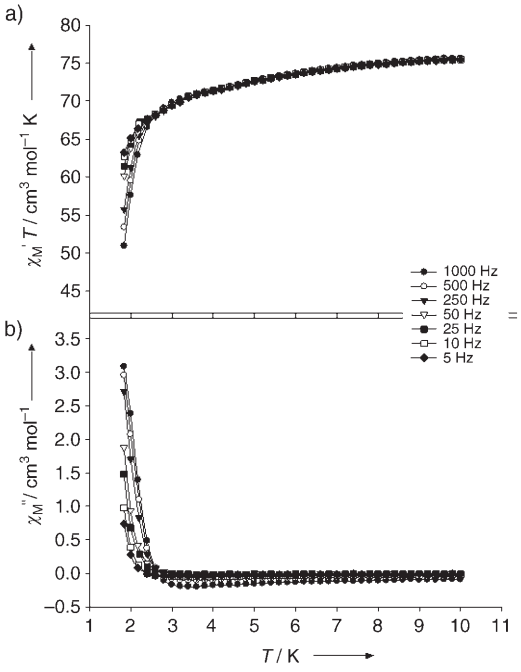

Figure 3. Temperature-dependence of a) the in-phase (χ_M') and b) the out-of-phase (χ_M'') ac magnetic susceptibility of $\{\mathbf{1}\cdot 0.5\,MeCN\cdot 6\,H_2O\}_\infty$ at the indicated ac frequencies.

Scans of magnetization versus dc field made on single crystals using a micro-SQUID (superconducting quantum interference device) setup confirmed that **1** is a SMM.[9] Below 1.1 K, hysteresis loops, the diagnostic behavior of magnets, were detected (Figure 4), their coercivity increases with decreasing temperature, as expected for SMMs. However, the hysteresis loops do not show steps characteristic of the quantum tunneling of magnetization (QTM); this behavior is typical for large SMMs, which are more susceptible to step-broadening effects associated with low-lying excited states, intermolecular interactions, and distributions of local environments due to ligand and solvent disorder.[3a,4e,f,5b]

In summary, the use of H_2pd and H_2mpd in manganese–carboxylate chemistry resulted in the isolation of two novel 3D coordination polymers based on an unprecedented Mn_{19}

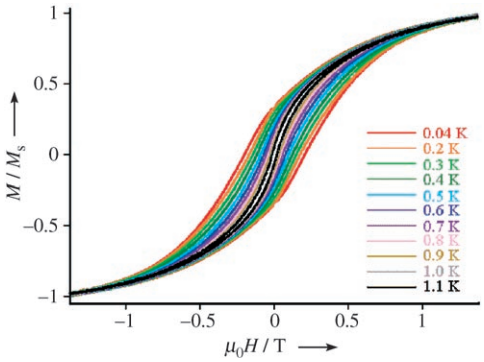

Figure 4. Field-dependence of the magnetization (hysteresis loops) of single crystals of $\{\mathbf{1}\cdot 3\,H_2O\}_\infty$ at the indicated temperatures; the magnetization (M) is normalized to its saturation value (M_s).

 © 2006 Wiley-VCH Verlag GmbH & Co. KGaA, Weinheim

repeating unit. These 3D networks were prepared under mild conditions (room temperature and atmospheric pressure) with self-assembly processes directed by metal–ligand coordination, and have open-framework structures with nanometer-sized channels. The Mn_{19} repeating unit has an aesthetically pleasing structure, in which the manganese ions have a triangular-pyramidal-frustum topology. The repeating unit also has a large ground spin state of $S = 23/2$ and displays SMM behavior (in-phase and out-of-phase ac magnetic susceptibility signals, and hysteresis loops in scans of magnetization versus dc field). Attempts to remove the cocrystallized solvent molecules from $\{\mathbf{1}\cdot 3H_2O\}_\infty$ and $\{\mathbf{2}\cdot 3H_2O\}_\infty$ are underway, as are studies of the thermal stability, permanent porosity, and N_2 sorption of the compounds; these investigations will be reported elsewhere in the near future. Finally, the supramolecular architecture of $\{\mathbf{1}\cdot 3H_2O\}_\infty$ and $\{\mathbf{2}\cdot 3H_2O\}_\infty$ offers a variety of possibilities for accessing interesting new materials, including the insertion (in the channels) of guest molecules (either organic or inorganic, paramagnetic or diamagnetic) that can affect the structural and magnetic properties.

Experimental Section

$\{\mathbf{1}\cdot 0.5\,MeCN\cdot 6H_2O\}_\infty$: H_2pd (0.085 mL, 1.176 mmol) and $NaClO_4$ (0.058 g, 0.470 mmol) were added to a solution of $[Mn_3O(O_2CMe)_6(py)_3]\cdot py$ (0.200 g, 0.235 mmol) in MeCN (10 mL). The reaction mixture was then stirred magnetically for 1 h, resulting in a dark brown slurry. After filtration, the dark brown filtrate was left undisturbed at room temperature. After several weeks, dark brown crystals appeared, and these were allowed to grow for a few more weeks to give X-ray quality crystals. The crystals were then separated by filtration, washed with MeCN and dried in vacuum (yield: 0.023 g, 23% based on total Mn content). Elemental analysis (%) calcd for $C_{46}H_{104.5}N_{0.5}O_{59}Mn_{19}Na$ ($\mathbf{1}\cdot 0.5\,MeCN\cdot 6H_2O$): C 20.65, H 3.94, N 0.26; found: C 20.90, H 3.76, N 0.18.

$\{\mathbf{2}\cdot 6H_2O\}_\infty$ was prepared by a similar procedure to that described for $\{\mathbf{1}\cdot 0.5\,MeCN\cdot 6H_2O\}_\infty$, except twice the amount of solvent was used (20 mL MeCN), and a 1:1, rather than 1:2, ratio of $[Mn_3O(O_2CMe)_6(py)_3]\cdot py/NaClO_4$ was used. The yield was 25%. Elemental analysis (%) calcd for $C_{54}H_{121}O_{59}Mn_{19}Na$ ($\mathbf{2}\cdot 6H_2O$): C 23.32, H 4.38; found: C 23.55, H 4.45.

Received: August 27, 2006
Published online: October 30, 2006

Keywords: cluster compounds · magnetic properties · manganese · O ligands · single-molecule magnets

[1] a) R. Sessoli, H.-L. Tsai, A. R. Schake, S. Wang, J. B. Vincent, K. Folting, D. Gatteschi, G. Christou, D. N. Hendrickson, *J. Am. Chem. Soc.* **1993**, *115*, 1804; b) R. Sessoli, D. Gatteschi, A. Ganeschi, M. A. Novak, *Nature* **1993**, *365*, 141; c) G. Christou, D. Gatteschi, D. N. Hendrickson, R. Sessoli, *MRS Bull.* **2000**, *25*, 66.

[2] a) D. Gatteschi, R. Sessoli, *Angew. Chem.* **2003**, *115*, 278; *Angew. Chem. Int. Ed.* **2003**, *42*, 268; b) E. K. Brechin, *Chem. Commun.* **2005**, 5141; c) G. Christou, *Polyhedron* **2005**, *24*, 2065.

[3] a) A. J. Tasiopoulos, A. Vinslava, W. Wernsdorfer, K. A. Abboud, G. Christou, *Angew. Chem.* **2004**, *116*, 2169; *Angew. Chem. Int. Ed.* **2004**, *43*, 2117; b) A. J. Tasiopoulos, W. Wernsdorfer, K. A. Abboud, G. Christou, *Inorg. Chem.* **2005**, *44*, 6324; c) C. J. Milios, C. P. Raptopoulou, A. Terzis, F. Lloret, R. Vicente, S. P. Perlepes, A. Escuer, *Angew. Chem.* **2004**, *116*, 212; *Angew. Chem. Int. Ed.* **2004**, *43*, 210; d) C. M. Zaleski, E. C. Depperman, C. Dendrinou-Samara, M. Alexiou, J. W. Kampf, D. P. Kessissoglou, M. L. Kirk, V. L. Pecoraro, *J. Am. Chem. Soc.* **2005**, *127*, 12862; e) C. M. Zaleski, E. C. Depperman, J. W. Kampf, M. L. Kirk, V. L. Pecoraro, *Angew. Chem.* **2004**, *116*, 4002; *Angew. Chem. Int. Ed.* **2004**, *43*, 3912; f) S. Maheswaran, G. Chastanet, S. J. Teat, T. Mallah, R. Sessoli, W. Wernsdorfer, R. E. P. Winpenny, *Angew. Chem.* **2005**, *117*, 5172; *Angew. Chem. Int. Ed.* **2005**, *44*, 5044.

[4] a) R. T. W. Scott, S. Parsons, M. Murugesu, W. Wernsdorfer, G. Christou, E. K. Brechin, *Angew. Chem.* **2005**, *117*, 6698; *Angew. Chem. Int. Ed.* **2005**, *44*, 6540; b) S. Piligkos, G. Rajaraman, M. Soler, N. Kirchner, J. van Slageren, R. Bircher, S. Parsons, H.-U. Gudel, J. Kortus, W. Wernsdorfer, G. Christou, E. K. Brechin, *J. Am. Chem. Soc.* **2005**, *127*, 5572; c) R. T. W. Scott, S. Parsons, M. Murugesu, W. Wernsdorfer, G. Christou, E. K. Brechin, *Chem. Commun.* **2005**, 2083; d) M. Murugesu, W. Wernsdorfer, K. A. Abboud, G. Christou, *Angew. Chem.* **2005**, *117*, 914; *Angew. Chem. Int. Ed.* **2005**, *44*, 892; e) D. Foguet-Albiol, T. A. O'Brien, W. Wernsdorfer, B. Moulton, M. J. Zaworotko, K. A. Abboud, G. Christou, *Angew. Chem.* **2005**, *117*, 919; *Angew. Chem. Int. Ed.* **2005**, *44*, 897; f) A. M. Ako, I. J. Hewitt, V. Mereacre, R. Clerac, W. Wernsdorfer, C. E. Anson, A. K. Powell, *Angew. Chem.* **2006**, *118*, 5048; *Angew. Chem. Int. Ed.* **2006**, *45*, 4926.

[5] a) A few examples of multidimensional coordination polymers that behave as SMMs exist, in which the repeating units are linked in a variety of different modes (through coordination bonds,[5b] a diamagnetic metal ion,[5c] or hydrogen bonds[5d]); the common feature is that the magnetic interactions between the repeating units are negligible: b) H. Miyasaka, K. Nakata, L. Lecren, C. Coulon, Y. Nakazawa, T. Fujisaki, K. Sugiura, M. Yamashita, R. Clerac, *J. Am. Chem. Soc.* **2006**, *128*, 3770; c) M. Murugesu, W. Wernsdorfer, K. A. Abboud, E. K. Brechin, G. Christou, *Dalton Trans.* **2006**, 2285; d) L. M. Wittick, K. S. Murray, B. Moubaraki, S. R. Batten, L. Spiccia, K. J. Berry, *Dalton Trans.* **2004**, 1003.

[6] Crystallographic data for $\{\mathbf{1}\cdot 3H_2O\}_\infty$: $C_{45}H_{97}O_{56}NaMn_{19}$, $M_r = 2601.05$, cubic, space group $P2_13$, $a = 24.0430(9)$ Å, $V = 13898.4(9)$ Å^3, $T = 100(2)$ K, $Z = 4$, $\rho_{calcd} = 1.275$ g cm^{-3}, 47607 reflections collected, 8117 unique ($R_{int} = 0.0724$), $R1 = 0.0720$, $wR2 = 0.1987$, for 5293 reflections with $I > 2\sigma(I)$. Crystallographic data for $\{\mathbf{2}\cdot 3H_2O\}_\infty$: $C_{54}H_{115}O_{56}NaMn_{19}$, $M_r = 2727.29$, cubic, space group $P2_13$, $a = 24.4332(6)$ Å, $V = 14586.2(6)$ Å^3, $T = 100(2)$ K, $Z = 4$, $\rho_{calcd} = 1.227$ g cm^{-3}, 76818 reflections collected, 8506 unique ($R_{int} = 0.0907$), $R1 = 0.0812$, $wR2 = 0.2062$, for 4214 reflections with $I > 2\sigma(I)$. CCDC-618951 ($\{\mathbf{1}\cdot 3H_2O\}_\infty$) and CCDC-618950 ($\{\mathbf{2}\cdot 3H_2O\}_\infty$) contain the supplementary crystallographic data for this paper. These data can be obtained free of charge from The Cambridge Crystallographic Data Centre via www.ccdc.cam.ac.uk/data_request/cif.

[7] Bond-valence sum calculations gave oxidation states of 2.82–3.09 (Mn^{III}) and 1.99–2.11 (Mn^{II}) for the manganese ions of **1**, and oxidation states of 2.65–3.13 (Mn^{III}) and 1.92–2.29 (Mn^{II}) for the manganese ions of **2**; W. Liu, H. H. Thorp, *Inorg. Chem.* **1993**, *32*, 4102.

[8] Bond-valence sum calculations for the oxygen atoms of **1** gave values of 1.52–1.92 for the O^{2-} ions, 0.63 for the OH^- ions, 0.33 for the H_2O molecules, and 1.83–2.06 for the RO^- groups of the pd^{2-} ligands. Bond-valence sum calculations for the oxygen atoms of **2** gave values of 1.66–1.80 for the O^{2-} ions, 0.60 for the OH^- ions, 0.49 for the H_2O molecules, and 1.81–2.24 for the RO^- groups of the mpd^{2-} ligands; a) I. D. Brown, R. D. Shannon, *Acta Crystallogr. Sect. A* **1973**, *29*, 266; b) G. Donnay, R. Allman, *Am. Mineral.* **1970**, *55*, 1003.

[9] W. Wernsdorfer, *Adv. Chem. Phys.* **2001**, *118*, 99.

 © 2006 Wiley-VCH Verlag GmbH & Co. KGaA, Weinheim

Protein Folding

DOI: 10.1002/anie.200603415

De Novo Folding of the DNA-Binding ATF-2 Zinc Finger Motif in an All-Atom Free-Energy Forcefield**

*Srinivasa M. Gopal and Wolfgang Wenzel**

Zinc fingers are among the most abundant proteins in eukaryotic genomes and occur in many DNA-binding domains and transcription factors.[1] They function in DNA recognition, RNA packaging, transcriptional activation, protein folding, and assembly and apoptosis. Many zinc fingers contain a Cys_2His_2 binding motif that coordinates the Zn ion in an αββ framework.[2–4] Much effort has been directed towards the engineering of novel zinc fingers.[5]

All-atom folding studies of the classical TFIIIa αββ motif may help elucidate the structural and functional properties of zinc finger proteins, but they tax the presently available all-atom folding methods. Recent improvements in simulation methods and forcefields have permitted the folding of several small helical proteins, hairpins, and β sheets from the unfolded ensembles.[6–14] The reproducible folding of proteins with mixed secondary structures, however, remains a significant challenge for the accuracy of the all-atom forcefield and the simulation method.[15]

Here we use the all-atom free-energy forcefield PFF02 to predictively fold a segment (amino acids 23–51) of the N-terminal subdomain of ATF-2 (Protein Data Bank (PDB) file 1BHI),[8,16] a 29 amino acid peptide that contains the basic leucine zipper motif. This peptide folds into the classical TFIIIa αββ conformation found in many zinc-finger subdomains. The fragment contains all the conserved hydrophobic residues (Phe25, Phe36, and Leu42) of the classical zinc-finger motif and the Cys_2His_2 zinc-binding pattern.

Starting with a completely unfolded conformation with no secondary structure (16-Å backbone root mean square deviation (bRMSD) from the native peptide), we performed 200 cycles of an evolutionary algorithm,[17] which speeds up the search of the conformational space by evolving an entire population (population size = 20), instead of a single conformation. The total simulation is split into many small steps, during which many closely related conformations are explored with fictitious dynamics to accelerate the search of the free-energy surface. New conformations are admitted into the active population according to a set of criteria that balance the free-energy gain and the structural diversity of the active population.

The distribution of the bRMSD versus the energy of all accepted conformations (Figure 1) demonstrates that the simulation explores a wide variety of conformations, with regard to their free-energy and their deviation from the native conformation. Among the 10 energetically lowest conformations, six fold into near-native conformations with bRMSDs of 3.68–4.28 Å, while four fold into conformations with a larger bRMSD. The three energetically best conformations are all near-native in character; an overlay with the experimentally determined conformation (Figure 2, top left) illustrates that the helix, the β sheet, and both turns are correctly formed. The hydrophobic residues, which determine the packing of the β sheet against the helix, are illustrated in orange in the figure. The helical section (Glu39–Glu50) and the β sheet (Phe25–Leu26 and Arg35–Phe36) deviate individually by bRMSDs of 1.6 and 2.4 Å, respectively, from the experimental counterparts. The overall deviation between the experimental and simulated folded conformations arises in the relative arrangement of the β sheet and the helix, which is controlled by unspecific hydrophobic interactions. All conserved hydrophobic side chains are also buried in the folded structure. The zinc-coordinating cysteine residues (Cys27 and Cys32) are within 2 Å of their native positions and are available for association with the Zn ion. We find many low-energy conformations in which much of the structure of the zinc finger is preformed. Binding of the metal ion is ultimately required to provide an important enthalpic contribution for the stabilization of the native conformation. These data demonstrate that the forcefield and simulation methodology are free of bias with respect to the formation of a particular type of the secondary structure and are able to describe the complex folding dynamics of at least small peptides/proteins with mixed secondary structures.

The partially folded low-energy conformations among the 10 energetically best (squares in Figure 1) all have a fully

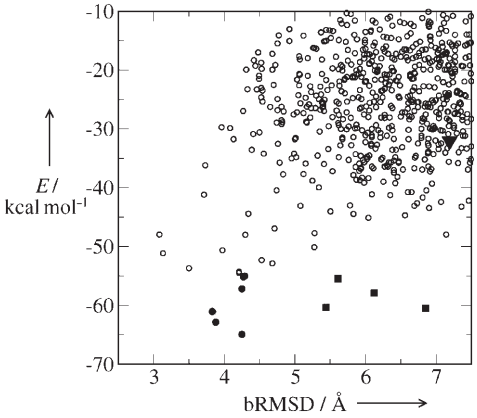

Figure 1. Internal free energy versus bRMSD of all accepted conformations in the simulation. Full circles/squares indicate the near-native and partially folded fractions of the 10 best conformations in the final population. The large triangle (▼) indicates the folding intermediate illustrated in the bottom right panel of Figure 2.

[*] S. M. Gopal, Dr. W. Wenzel
Institute for Nanotechnology
Research Centre Karlsruhe
Post Box 3640, 70621, Karlsruhe (Germany)
Fax: (+49) 724-7826434
E-mail: wenzel@int.fzk.de

[**] This work was funded by the Deutsche Forschungsgemeinschaft (WE 1863/10-2) and the Bode Foundation. We acknowledge the use of the computational facilities of the KIST Supercomputational Materials Lab.

InterScience
© 2006 Wiley-VCH Verlag GmbH & Co. KGaA, Weinheim

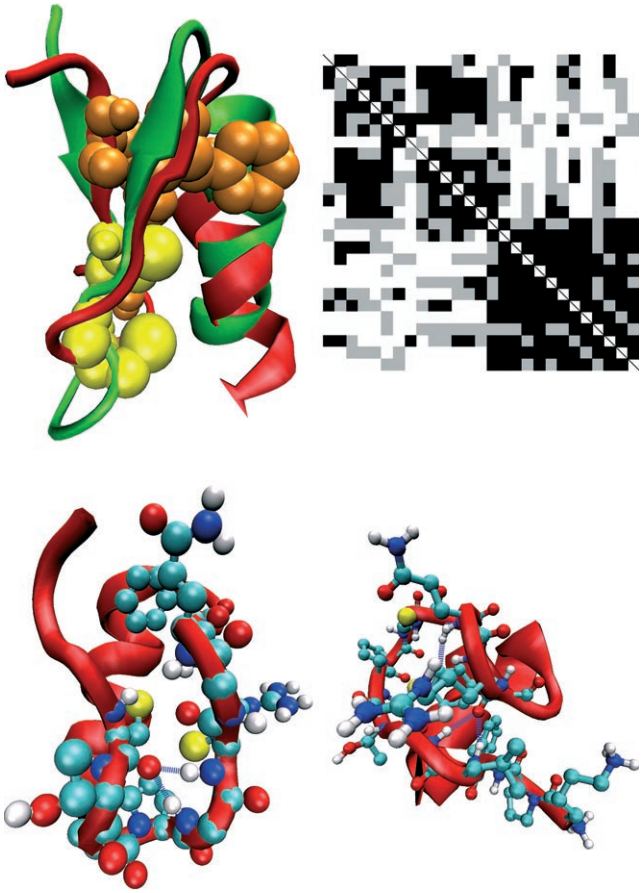

Figure 2. Top left: Overlay of the native (green) and folded (red) conformations of the peptide with the conserved hydrophobic residues shown in orange and the zinc-binding cysteine residues shown in yellow. Top right: C_β–C_β distance matrix of the folded conformation, which indicates the presence of 67% of the native contacts. Bottom left: Folding intermediate at the bottom of the free-energy surface with buried cysteine and stabilizing backbone hydrogen bonds (blue dashed lines; see text). Bottom right: Intermediate conformation with a partially formed helix and β sheet. Protein structures were drawn with VMD.[18] Red: backbone and oxygen; cyan: carbon; blue: nitrogen; yellow: sulfur; white: hydrogen.

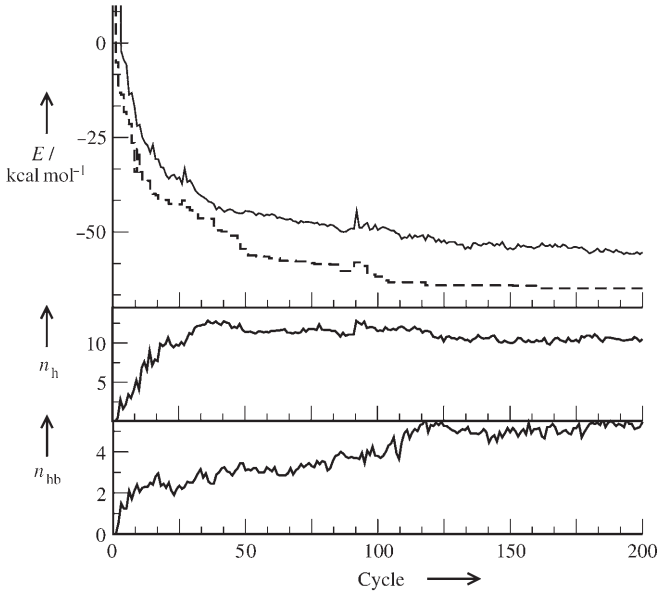

Figure 3. Average (solid line) and best (dashed line) energies, average number of amino acids (n_h) in a helical conformation (as computed by DSSP[20]), and number of hydrogen bonds (n_{hb}) as a function of the cycle number.

formed helical section in the right region of the amino acid sequence, a turn near Thr28–Pro30, and significant β content. The bottom left panel of Figure 2 shows the conformation furthest from the native one, with a partially unzipped β sheet. The hydrogen bonds near the turn are still present, while the native H-bonds at the end of the zipper have not yet formed.

Figure 3 shows the convergence of the energy: after about 120 steps per population member (3.5×10^8 function evaluations), the population converged with the native ensemble. According to the funnel paradigm for protein folding,[19] the tertiary structure forms as the protein slides downhill on the free-energy surface from the unfolded ensemble towards the native conformation. Here, each member of the active population of the evolutionary algorithm represents one point on this high-dimensional free-energy surface. Each cycle (simulated annealing with geometric cooling, number of steps $= 10^4 \sqrt{\text{cycle number}}$) generates a small perturbation on the existing conformation, which averages to a 0.5 Å bRMSD change (with a maximum of 3 Å initially). As new low-energy conformations replace old conformations, the population slides down the funnel of the free-energy landscape.

Ensemble averages as a function of free-energy over the moving population are thus associated with different stages of the structure-formation process, even though our method does not generate any kinetic information. The lower two panels of Figure 3 show the average helical content and the number of β-sheet H-bonds as a function of the cycle number. After a rapid collapse to a compact conformation, the helix forms first, and this is followed by formation of the β sheet. An analysis of the folding funnel upwards in energy illustrates that the lowest energy metastable conformations correspond to a partial unzipping of amino acids Phe25–Arg35, while the conserved cysteine residues are still buried (Figure 2, bottom left). Even much higher on the free-energy funnel (triangle in Figure 1), we find many structures that have a lot of residual secondary structure but few long-range native contacts. Figure 2 (bottom right) illustrates one such conformation where the preformed sheet region is stabilized by H-bonds (Leu26–Cys27, Arg35) and packs at a right angle to a broken helix. Here, the hydrophobic residues are only partially buried.

As the algorithm tracks the development of the population, it is possible to reconstruct a folding pathway by starting with the converged conformation and moving backwards to the completely unfolded conformation. Crucial steps along the continuous folding pathway are illustrated in Figure 4. (Note that there is no quantitative mapping onto the time axis.) The early folding process is characterized by helix nucleation and concurrent collapse into a globular conformation with a radius of gyration that is comparable to that of the native conformation. The simulation then explores confor-

 © 2006 Wiley-VCH Verlag GmbH & Co. KGaA, Weinheim

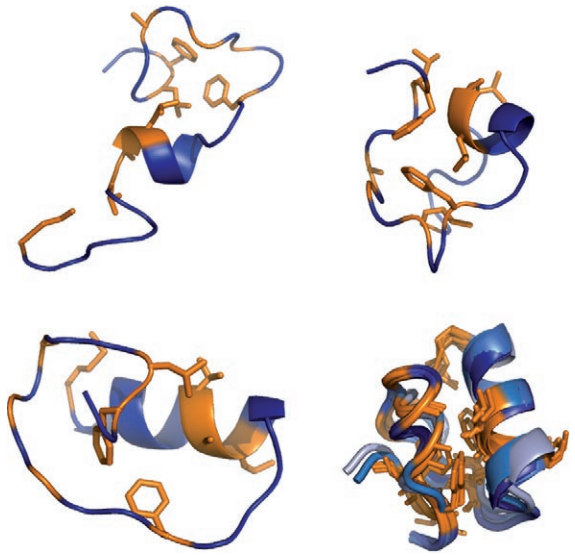

Figure 4. Key events in the folding process: helix nucleation (top left) with concomitant collapse into a globular conformation (top right), followed by helix growth. The fully formed helix (bottom left) acts as a template against which many partially formed beta-sheet conformations can pack (bottom right). The protein backbone is shown in blue, and the hydrophobic residues including side chains are shown in orange. In the bottom right panel, the shading of the backbone becomes darker as the simulation approaches the native conformation.

mations of the same spatial extent with increasing helical, but no β-sheet content. Lower on free-energy funnel, the simulation samples conformations in which partially formed β sheets pack against the helix.

De novo folding of the zinc-finger domain permits a direct sampling of the relevant low-energy portion of the free-energy surface as a first step towards the elucidation of the structural mechanisms involved in DNA binding.[5,21] On the basis of the free-energy estimate, conformations without the helix (at least 8 kcal mol^{-1} higher than the native conformation) cannot participate in DNA binding and transcription. By using the global optimization approach, which uses fictitious dynamics, we can rapidly explore the relevant free-energy region of the biologically active ensemble. Met51 packs in all low-energy conformations against the combined αββ scaffold and acts as a closure of the DNA-binding motif. It may thus provide an enthalpic contribution to a nonstandard helix-capping motif that differs from the TGEKP linker sequence observed in multifinger domains[1] in several zinc fingers.

We have thus demonstrated predictive all-atom folding of the DNA-binding zinc-finger motif in a free-energy force-field. This investigation offers the first unbiased characterization of the low-energy free-energy surface of the zinc-finger motif, which is unattainable in coarse-grained, knowledge-based models. We find that the helix forms first along the folding path and acts as a template against which a variety of near-native β-sheet backbone arrangements can pack. There are many zinc fingers with RMS deviations of less than 2 Å relative to the conformation illustrated in PDB file 1BHI;[16] thus, this investigation provides one important step in the theoretical understanding of zinc-finger formation and function.

Received: August 21, 2006
Published online: October 24, 2006

Keywords: evolutionary algorithms · protein folding · simulations · structure prediction · zinc-finger proteins

[1] J. H. Laity, B. M. Lee, P. E. Wright, *Curr. Opin. Struct. Biol.* **2001**, *11*, 39–46.
[2] M. S. Lee, G. P. Gippert, K. V. Soman, P. E. Wright, *Science* **1989**, *245*, 635–637.
[3] N. P. Pavletich, C. O. Pabo, *Science* **1991**, *252*, 809–817.
[4] S. A. Wolfe, L. Nekludova, C. O. Pabo, *Annu. Rev. Biophys. Biomol. Struct.* **2000**, *29*, 183–212.
[5] a) Y. Choo, M. Isalan, *Curr. Opin. Struct. Biol.* **2000**, *10*, 411–416; b) F. D. Urnov, J. C. Miller, Y.-L. Lee, C. M. Beausejour, J. M. Rock, S. Augustus, A. C. Jamieson, M. H. Porteus, P. D. Gregory, M. C. Holmes, *Nature* **2005**, *435*, 646–651.
[6] A. Schug, A. Verma, T. Herges, K. H. Lee, W. Wenzel *ChemPhysChem* **2005**, *6*, 2640–2646.
[7] a) J. Lee, H. A. Scheraga, S. Rackovsky, *J. Comput. Chem.* **1997**, *18*, 1222–1232; b) D. J. Wales, H. A. Scheraga, *Science* **1999**, *285*, 1368–1372; c) J. M. Carr, D. J. Wales, *J. Chem. Phys.* **2005**, *123*, 234901.
[8] a) T. Herges, W. Wenzel, *Biophys. J.* **2004**, *87*, 3100–3109; b) A. Verma, W. Wenzel, unpublished results.
[9] J. Chen, W. Wen, C. Brooks III, *J. Am. Chem. Soc.* **2006**, *128*, 3728–3736.
[10] a) C. Simmerling, B. Strockbine, A. Roitberg, *J. Am. Chem. Soc.* **2002**, *124*, 11258–11259; b) J. A. Vila, D. R. Ripoll, H. A. Scheraga, *Proc. Natl. Acad. Sci. USA* **2003**, *100*, 14812–14816; c) M. Khalili, A. Liwo, H. A. Scheraga, *J. Mol. Biol.* **2006**, *355*, 536–547.
[11] a) A. Schug, T, Herges, W. Wenzel, *Phys. Rev. Lett.* **2003**, *91*, 158102; b) T. Herges, W. Wenzel, *Phys. Rev. Lett.* **2005**, *94*, 018101; c) A. Schug, W. Wenzel, *J. Am. Chem. Soc.* **2004**, *126*, 16736–16737.
[12] a) C. D. Snow, L. Qiu, D. Du, F. Gai, S. J. Hagen, V. S. Pande, *Proc. Natl. Acad. Sci. USA* **2004**, *101*, 4077–4082; b) P. G. Bolhuis, *Proc. Natl. Acad. Sci. USA* **2003**, *100*, 12129–12134; c) D. A. Evans, D. J. Wales, *J. Chem. Phys.* **2004**, *121*, 1080–1090.
[13] W. Wenzel, *Europhys. Lett.* **2006**, *76*, 156–162.
[14] P. Ferrara, A. Caflisch, *Proc. Natl. Acad. Sci. USA* **2000**, *97*, 10780–10785.
[15] A. Abagyan, M. Totrov, *J. Comput. Phys.* **1999**, *151*, 402–412.
[16] A. Nagadoi, K. Nakazawa, H. Uda, K. Okuno, T. Maekawa, S. Ishii, Y. Nishimura, *J. Mol. Biol.* **1999**, *287*, 593–607.
[17] A. Schug, W. Wenzel, *Biophys. J.* **2006**, *90*, 4273–4280.
[18] W. Humphrey, A. Dalke, K. Schulten, *J. Mol. Graphics* **1996**, *14*, 33–38.
[19] J. N. Onuchic, Z. L. Schulten, P. G. Wolynes, *Annu. Rev. Phys. Chem.* **1997**, *48*, 545–600.
[20] W. Kabsch, C. Sander, *Biopolymers* **1983**, *22*, 2577–2637.
[21] J. H. Laity, H. J. Dyson, P. E. Wright, *J. Mol. Biol.* **2000**, *295*, 719–727.

 © 2006 Wiley-VCH Verlag GmbH & Co. KGaA, Weinheim

Supramolecular Chemistry

DOI: 10.1002/anie.200603238

From Vesicles to Helical Nanotubes: A Sergeant-and-Soldiers Effect in the Self-Assembly of Oligo(*p*-phenyleneethynylene)s**

Ayyappanpillai Ajayaghosh, Reji Varghese, Sankarapillai Mahesh, and Vakayil K. Praveen*

The past few years have witnessed significant progress toward the design of supramolecular architectures of nano- to micrometer dimensions with intriguing properties.[1,2] Of particular interest to chemists is the self-assembly of rigid π-conjugated molecules with controlled size and shape, as active components of organic electronic devices.[3,4] In this context, self-assembly of oligo(*p*-phenyleneethynylene)s (OPEs) has received considerable attention.[5] Control of the morphology of self-assembled structures requires rational design of molecular components.[6] For example, spherical to tubular or cylindrical assemblies are obtained by structural variation of the self-assembling units,[7] whereas nonhelical to helical transformation can be achieved by attaching chiral handles[8–11] or by the "sergeant-and-soldiers" coassembly approach.[12–14] However, transitions of linear π-conjugated molecules from vesicles to helical tubules or vice versa are rare.[15] Herein we reveal a spectacular chirality-amplification effect and an unprecedented transition from vesicles to helical tubules during the sergeant-and-soldiers coassembly of chiral and achiral OPEs.

We chose **OPE1** and its chiral analogue **OPE2** for our studies. These compounds were synthesized by palladium-catalyzed Sonogashira–Hagihara cross-coupling reactions[16] and characterized by ^{1}H NMR, ^{13}C NMR, and FAB-MS techniques.[17] Compound **OPE1** self-assembles in nonpolar hydrocarbon solvents to form nanoparticles, microspheres, giant superstructures, and blue-light-emitting organogels.[18] Surprisingly, **OPE2** failed to form aggregates in nonpolar hydrocarbon solvents, as evident from absorption, emission, and CD spectral features. This behavior of **OPE2** is different from that of an analogous chiral oligo(*p*-phenylenevinylene), OPV, for which formation of helical structures in decane leads to gelation.[19] These observations reveal the differences in the self-organization propensities of OPEs and OPVs, which reiterate that a subtle difference in π interaction is sufficient to induce a large difference in the morphological features.

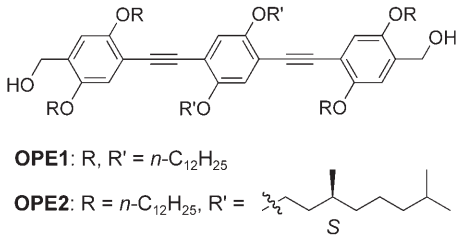

The UV/Vis absorption spectrum of **OPE1** in decane (1×10^{-5} M) at 25 °C exhibited a maximum at 384 nm with a shoulder at 420 nm. At this concentration, a decrease in the intensity of the π–π* transition band with first-order kinetics ($k = 47.41\ \text{min}^{-1}$) is observed over 6 h (Figure 1 a). Interestingly, addition of **OPE2** (5–30 mol %) to this solution at a total concentration of 1×10^{-5} M resulted in reversal of the absorption, which indicates probable destruction of the initial **OPE1** aggregates to form coassembled or molecularly dissolved species. On the other hand, addition of **OPE2** (5–30 mol %) to a fresh solution of **OPE1** in decane (without aging) at a total concentration of 0.7×10^{-5} M led to a decrease in the intensity of the aggregate band at 420 nm.[17] After heating to 80 °C and cooling to room temperature, this solution did not show any considerable change in the absorption spectrum, that is, the time-dependent process is arrested in this case (Figure 1 b).

Circular dichroism (CD) measurements on **OPE1** and **OPE2** in decane (1×10^{-5} M) did not show any detectable

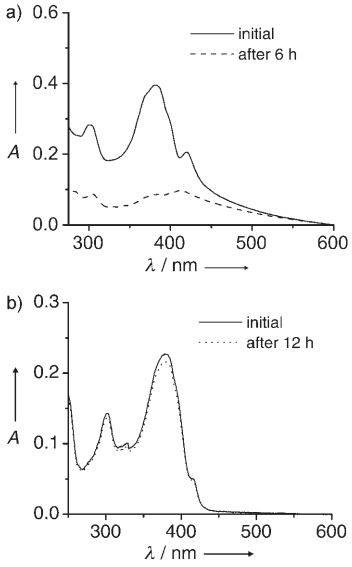

Figure 1. a) Time-dependent absorption changes of a) **OPE1** (1×10^{-5} M) and b) **OPE1** with 30 mol % of **OPE2** (0.7×10^{-5} M) in decane at 298 K.

[*] Dr. A. Ajayaghosh, R. Varghese, S. Mahesh, V. K. Praveen
Photosciences and Photonics Group
Chemical Sciences and Technology Division
Regional Research Laboratory, CSIR
Trivandrum 695019 (India)
Fax: (+91) 471-249-1712
E-mail: aajayaghosh@rediffmail.com

[**] We thank the Department of Science and Technology, New Delhi for financial support. R.V. and V.K.P. are grateful to CSIR and S.M. acknowledges UGC, Government of India for research fellowships. We acknowledge the help by the Biomedical Technology Wing of the Sree Chitra Tirunal Institute for Medical Sciences and Technology with DLS and the Rajiv Gandhi Centre of Biotechnology with TEM analyses. We thank the anonymous referees for critical comments which helped us in improving the quality of the work. This is contribution No. RRLT-PPG-232.

Supporting information for this article is available on the WWW under http://www.angewandte.org or from the author.

© 2006 Wiley-VCH Verlag GmbH & Co. KGaA, Weinheim

Cotton effect. Though this is expected for **OPE1**, the CD silence of **OPE2** was rather surprising and indicates that it is not able to form aggregates in decane. However, addition of **OPE2** (5–30 mol %) to a solution of **OPE1** (1×10^{-5} M) in decane, followed by heating and cooling, resulted in a positive Cotton signal and two negative signals (Figure 2a). Since both individual components are CD-silent, the observed CD of the coassembly is due to the induced chirality from **OPE2** in a

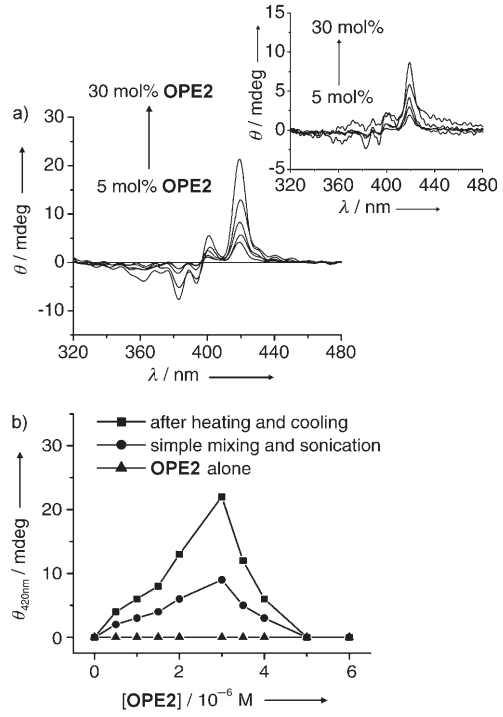

Figure 2. a) CD spectra of **OPE1** with different fractions of **OPE2** recorded after heating and cooling. The inset shows the corresponding spectra of sonicated solutions without heating and cooling. b) Plots of CD intensity at 420 nm against concentration of **OPE2**. All experiments were carried out in decane (1×10^{-5} M, $l=10$ mm) at 298 K.

helical sense. Interestingly, simple mixing of the two components in decane followed by sonication resulted in weak CD signals (Figure 2a, inset), that is, heating and cooling are crucial to the formation of helical coassemblies. The intensity of the induced CD (ICD) signals increases with increasing fraction of **OPE2** up to 30 mol %, then decreases, and finally disappears at 50 mol %, which is clear from the plots of the ICD intensity at 420 nm against the concentration of **OPE2** (Figure 2b). The increase in the ICD intensity reveals that up to 30 mol % **OPE2** is able to induce chirality in **OPE1**. Above this concentration, coassembly is destabilized, as indicated by the decreased ICD intensity, which finally disappears at higher concentrations of **OPE2** (50 mol %).

Dynamic light scattering (DLS) experiments on the aged solution of **OPE1** in decane (1×10^{-6} M) revealed the formation of particles with sizes in the range of 50–180 nm with peak intensity at 93 nm and a polydispersity of 0.24.[17] Tapping-mode atomic force microscopy (AFM) images of **OPE1** from decane (1×10^{-6} M) on a freshly cleaved mica surface showed characteristics of flattened spherical morphology (Figure 3a).[20] The histogram shows Lorentzian distribution ($R^2=0.9103$) with an average circular width of 94 nm (full width at half-maximum 34 nm) and height of 4 ± 1 nm after accounting for the tip-broadening factor.[21] The

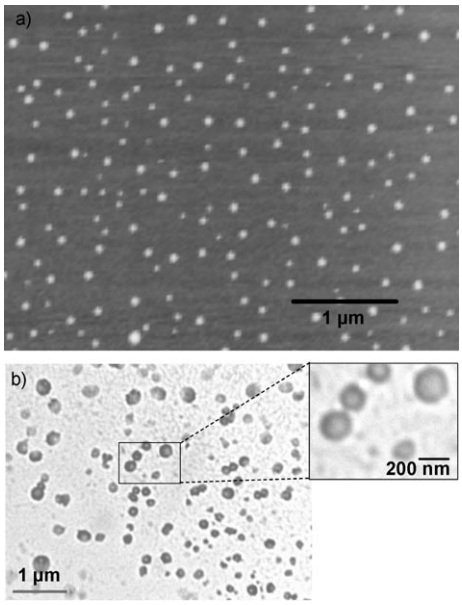

Figure 3. a) Tapping-mode AFM height (*z* scale = 20 nm) and b) TEM images (unstained) of **OPE1** from decane (1×10^{-6} M) under ambient conditions. The inset shows the zoomed portion of the marked area.

AFM analysis of **OPE1** from chloroform on a mica surface revealed significantly different morphology when compared to that from decane, that is, the solvent has some role in the formation of spherical aggregates.[17] The transmission electron microscopy (TEM) images of an evaporated decane solution of **OPE1** on carbon-coated grid revealed that the particles are vesicular with contrast difference between the inner part and the periphery (Figure 3b).

Interestingly, **OPE2** does not show any specific morphology from decane.[17] This observation is in agreement with the absorption and CD studies, which indicated that **OPE2** does not aggregate in decane. However, AFM pictures of the coassemblies of **OPE2** with **OPE1** revealed the formation of both nanoparticles and helical structures at 8 mol % of the former (Figure 4a). The width of the particles obtained under these condition varies in the range of 30–60 nm with average heights of 3–16 nm. However, at 25 mol % of **OPE2** almost all the spherical assemblies were transformed into helical structures (Figure 4b). Section analysis of the helical fibers revealed a width of 90 nm for the smallest fiber after accounting for the tip-broadening effect,[21] with almost uniform pitch of 140 nm. The height of the fibers varies between 6 and 25 nm, and this indicates considerable flattening of the fibers. However, TEM analysis of the coassembly revealed that the helical fibers are tubular in nature with diameters of 55–90 nm (Figure 4c). The width of the inner hollow tubular space is almost uniform in all cases. Above 50 mol % of **OPE2**, an ill-defined morphology could be seen, in agreement with the complete disappearance of the CD

 © 2006 Wiley-VCH Verlag GmbH & Co. KGaA, Weinheim

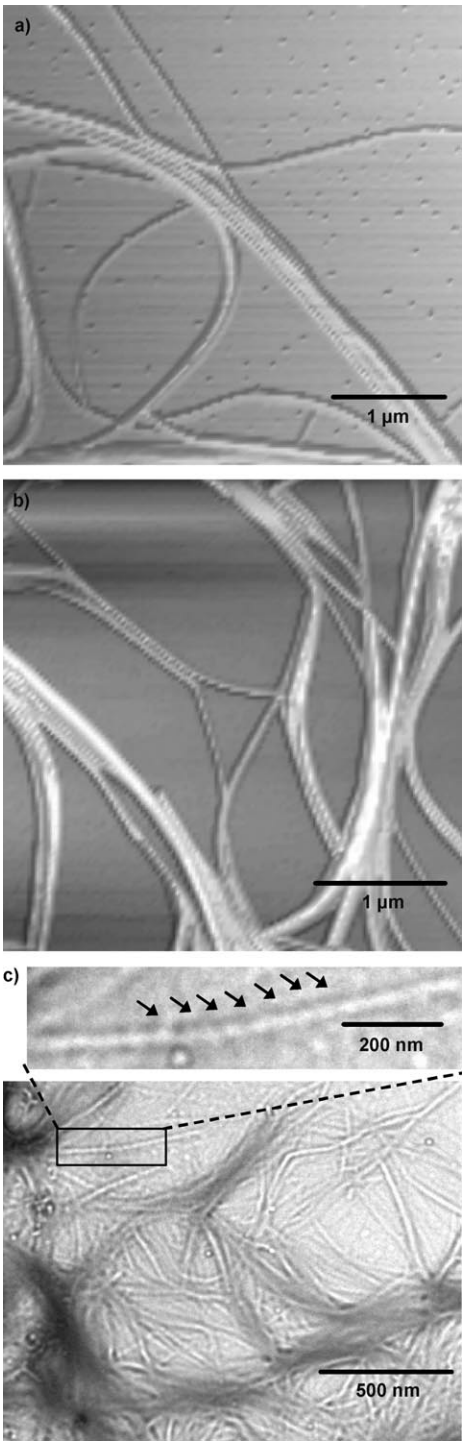

Figure 4. Tapping-mode AFM height images of the coassembly of **OPE1** with different concentrations of **OPE2** from decane (1×10^{-5} M). a) 8 mol% and b) 25 mol% under ambient conditions on freshly cleaved mica surface (*z* scale = 50 nm). c) TEM images (unstained) of 25 mol% **OPE2** with **OPE1** under ambient conditions. The inset is a zoomed image of the marked area showing the helical-tubular nature of the coassembly.

signal in Figure 2b.[17] Heating and cooling of the two components resulted in significant morphological differences in the AFM images when compared to those of samples prepared by simple mixing and sonication.[17]

A schematic representation of the coassembly processes of **OPE1** and **OPE2** is shown in Figure 5. In decane, **OPE1** forms vesicular structures, as indicated by DLS, AFM, and TEM studies. However, the coassembly of **OPE2** with **OPE1**

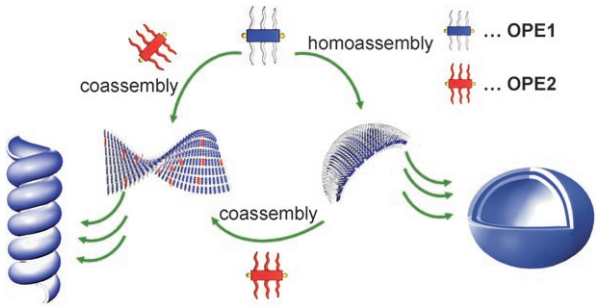

Figure 5. Self-assembly of vesicles and subsequent transformation into helical tubes in decane.

facilitates transcription of the molecular chirality of the former in a helical sense and results in transition from vesicular assemblies to helical tubular structures, as confirmed by CD, AFM, and TEM data. In summary, coassembly of **OPE1** with the chiral analogue **OPE2** retards the formation of vesicular assemblies and facilitates the evolution of helical structures. Though **OPE2** alone is unable to self-assemble, when mixed with **OPE1**, the former participates in coassembly and thereby transfers chiral information to the latter. To the best of our knowledge, this is the first report of the sergeant-and-soldiers approach to chirality-induced transformation from vesicles to helical tubules.

Received: August 9, 2006
Revised: September 11, 2006
Published online: October 25, 2006

Keywords: circular dichroism · helical structures · nanotubes · self-assembly · supramolecular chemistry

[1] a) J.-M. Lehn, *Supramolecular Chemistry, Concepts and Perspectives*, VCH, Weinheim, **1995**; b) J. W. Steed, J. L. Atwood, *Supramolecular Chemistry*, Wiley, Chichester, **2000**.
[2] For recent reviews, see a) S. I. Stupp, M. U. Pralle, G. N. Tew, L. Li, M. Sayar, E. R. Zubarev, *MRS Bull.* **2000**, 42–48; b) M. Lee, B.-K. Cho, W.-C. Zin, *Chem. Rev.* **2001**, *101*, 3869–3892; c) J. A. A. W. Elemans, A. E. Rowan, R. J. M. Nolte, *J. Mater. Chem.* **2003**, *13*, 2661–2670; d) S. I. Stupp, *Chem. Rev.* **2005**, *105*, 1023–1024.
[3] For a review, see F. J. M. Hoeben, P. Jonkheijm, E. W. Meijer, A. P. H. J. Schenning, *Chem. Rev.* **2005**, *105*, 1491–1546.
[4] a) J. M. Tour, *Molecular Electronics: Commercial Insights, Chemistry, Devices, Architectures and Programming*, World Scientific, River Edge, NJ, **2003**; b) M. van der Auweraer, F. C. De Schryver, *Nat. Mater.* **2004**, *3*, 507–508; c) A. P. H. J. Schenning, E. W. Meijer, *Chem. Commun.* **2005**, 3245–3258; d) A. C. Grimsdale, K. Müllen, *Angew. Chem.* **2005**, *117*, 5732–5772; *Angew. Chem. Int. Ed.* **2005**, *44*, 5592–5629.
[5] a) P. Samorí, V. Francke, K. Müllen, J. P. Rabe, *Chem. Eur. J.* **1999**, *5*, 2312–2317; b) P. Samorí, I. Sikharulidze, V. Francke, K. Müllen, J. P. Rabe, *Nanotechnology* **1999**, *10*, 77–80; c) U. H. F. Bunz, *Chem. Rev.* **2000**, *100*, 1605–1644; d) U. H. F. Bunz, *Acc.*

 © 2006 Wiley-VCH Verlag GmbH & Co. KGaA, Weinheim

Chem. Res. **2001**, *34*, 998 – 1010; e) S. Zahn, T. M. Swager, *Angew. Chem.* **2002**, *114*, 4399 – 4404; *Angew. Chem. Int. Ed.* **2002**, *41*, 4226 – 4230; f) J. Xu, C.-Z. Zhou, L. H. Yang, N. T. S. Chung, Z.-K. Chen, *Langmuir* **2004**, *20*, 950 – 956.

[6] For a review, see T. Shimizu, M. Masuda, H. Minamikawa, *Chem. Rev.* **2005**, *105*, 1401 – 1444, and references therein.

[7] B.-S. Kim, D.-J. Hong, J. Bae, M. Lee, *J. Am. Chem. Soc.* **2005**, *127*, 16333 – 16337.

[8] For reviews on helical structures, see a) "Supramolecular chirality": *Top. Curr. Chem.* **2006**, *265*; b) A. E. Rowan, R. J. M. Nolte, *Angew. Chem.* **1998**, *110*, 65 – 71; *Angew. Chem. Int. Ed.* **1998**, *37*, 63 – 68; c) J. J. L. M. Cornelissen, A. E. Rowan, R. J. M. Nolte, N. A. J. M. Sommerdijk, *Chem. Rev.* **2001**, *101*, 4039 – 4070; d) L. Brunsveld, B. J. B. Folmer, E. W. Meijer, R. P. Sijbesma, *Chem. Rev.* **2001**, *101*, 4071 – 4098; e) C. Schmuck, *Angew. Chem.* **2003**, *115*, 2552 – 2556; *Angew. Chem. Int. Ed.* **2003**, *42*, 2448 – 2452; f) E. Yashima, K. Maeda, T. Nishimura, *Chem. Eur. J.* **2004**, *10*, 43 – 51.

[9] a) E. D. Sone, E. R. Zubarev, S. I. Stupp, *Angew. Chem.* **2002**, *114*, 1781 – 1785; *Angew. Chem. Int. Ed.* **2002**, *41*, 1705 – 1709; b) P. Jonkheijm, F. J. M. Hoeben, R. Kleppinger, J. van Herrikhuyzen, A. P. H. J. Schenning, E. W. Meijer, *J. Am. Chem. Soc.* **2003**, *125*, 15941 – 15949; c) P. Jonkheijm, A. Miura, M. Zdanowska, F. J. M. Hoeben, S. De Feyter, A. P. H. J. Schenning, F. C. De Schryver, E. W. Meijer, *Angew. Chem.* **2004**, *116*, 76 – 80; *Angew. Chem. Int. Ed.* **2004**, *43*, 74 – 78; d) J. J. D. de Jong, L. N. Lucas, R. M. Kellogg, J. H. van Esch, B. L. Feringa, *Science* **2004**, *304*, 278 – 281; e) S.-i. Kawano, N. Fujita, S. Shinkai, *Chem. Eur. J.* **2005**, *11*, 4735 – 4742; f) A. Ajayaghosh, C. Vijayakumar, R. Varghese, S. J. George, *Angew. Chem.* **2006**, *118*, 470 – 474; *Angew. Chem. Int. Ed.* **2006**, *45*, 456 – 460.

[10] a) H. Engelkamp, S. Middelbeek, R. J. M. Nolte, *Science* **1999**, *284*, 785 – 788; b) F. Würthner, S. Yao, U. Beginn, *Angew. Chem.* **2003**, *115*, 3368 – 3371; *Angew. Chem. Int. Ed.* **2003**, *42*, 3247 – 3250; c) M. Kimura, T. Kuroda, K. Ohta, K. Hanabusa, H. Shirai, N. Kobayashi, *Langmuir* **2003**, *19*, 4825 – 4830; d) T. Yamaguchi, T. Kimura, H. Matsuda, T. Aida, *Angew. Chem.* **2004**, *116*, 6510 – 6515; *Angew. Chem. Int. Ed.* **2004**, *43*, 6350 – 6355; e) J. Wu, M. D. Watson, L. Zhang, Z. Wang, K. Müllen, *J. Am. Chem. Soc.* **2004**, *126*, 177 – 186; f) J. P. Hill, W. Jin, A. Kosaka, T. Fukushima, H. Ichihara, T. Shimomura, K. Ito, T. Hashizume, N. Ishii, T. Aida, *Science* **2004**, *304*, 1481 – 1483.

[11] a) T. Gulik-Krzywicki, C. Fouquey, J.-M. Lehn, *Proc. Natl. Acad. Sci. USA* **1993**, *90*, 163 – 167; b) A. P. H. J. Schenning, P. Jonkheijm, E. Peeters, E. W. Meijer, *J. Am. Chem. Soc.* **2001**, *123*, 409 – 416; c) J. Bae, J.-H. Choi, Y.-S. Yoo, N.-K. Oh, B.-S. Kim, M. Lee, *J. Am. Chem. Soc.* **2005**, *127*, 9668 – 9669; d) B. W. Messmore, P. A. Sukerkar, S. I. Stupp, *J. Am. Chem. Soc.* **2005**, *127*, 7992 – 7993; e) A. Lohr, M. Lysetska, F. Würthner, *Angew. Chem.* **2005**, *117*, 5199 – 5202; *Angew. Chem. Int. Ed.* **2005**, *44*, 5071 – 5074.

[12] a) M. M. Green, M. P. Reidy, R. D. Johnson, G. Darling, D. J. O'Leary, G. Willson, *J. Am. Chem. Soc.* **1989**, *111*, 6452 – 6454; b) M. M. Green, J.-W. Park, T. Sato, A. Teramoto, S. Lifson, R. L. B. Selinger, J. V. Selinger, *Angew. Chem.* **1999**, *111*, 3328 – 3345; *Angew. Chem. Int. Ed.* **1999**, *38*, 3138 – 3154.

[13] a) A. R. A. Palmans, J. A. J. M. Vekemans, E. E. Havinga, E. W. Meijer, *Angew. Chem.* **1997**, *109*, 2763 – 2765; *Angew. Chem. Int. Ed. Engl.* **1997**, *36*, 2648 – 2651; b) R. B. Prince, J. S. Moore, L. Brunsveld, E. W. Meijer, *Chem. Eur. J.* **2001**, *7*, 4150 – 4154; c) A. P. H. J. Schenning, A. F. M. Kilbinger, F. Biscarini, M. Cavallini, H. J. Cooper, P. J. Derrick, W. J. Feast, R. Lazzaroni, Ph. Leclère, L. A. McDonel, E. W. Meijer, S. C. J. Meskers, *J. Am. Chem. Soc.* **2002**, *124*, 1269 – 1275; d) A. J. Wilson, M. Masuda, R. P. Sijbesma, E. W. Meijer, *Angew. Chem.* **2005**, *117*, 2315 – 2319; *Angew. Chem. Int. Ed.* **2005**, *44*, 2275 – 2279; e) L. J. Prins, J. Huskens, F. de Jong, P. Timmerman, D. N. Reinhoudt, *Nature* **1999**, *398*, 498 – 502; f) L. J. Prins, P. Timmerman, D. N. Reinhoudt, *J. Am. Chem. Soc.* **2001**, *123*, 10153 – 10163.

[14] A. Ajayaghosh, R. Varghese, S. J. George, C. Vijayakumar, *Angew. Chem.* **2006**, *118*, 1159 – 1162; *Angew. Chem. Int. Ed.* **2006**, *45*, 1141 – 1144.

[15] J.-H. Ryu, H.-J. Kim, Z. Huang, E. Lee, M. Lee, *Angew. Chem.* **2006**, *118*, 5430 – 5433; *Angew. Chem. Int. Ed.* **2006**, *45*, 5304 – 5304.

[16] a) K. Sonogashira, Y. Tohda, N. Hagihara, *Tetrahedron Lett.* **1975**, *16*, 4467 – 4470; b) J.-F. Nierengarten, T. Gu, G. Hadziioannou, D. Tsamouras, V. Krasnikov, *Helv. Chim. Acta* **2004**, *87*, 2948 – 2966.

[17] See Supporting Information.

[18] A. Ajayaghosh, R. Varghese, V. K. Praveen, S. Mahesh, *Angew. Chem.* **2006**, *118*, 3339 – 3342; *Angew. Chem. Int. Ed.* **2006**, *45*, 3261 – 3264.

[19] S. J. George, A. Ajayaghosh, P. Jonkheijm, A. P. H. J. Schenning, E. W. Meijer, *Angew. Chem.* **2004**, *116*, 3504 – 3507; *Angew. Chem. Int. Ed.* **2004**, *43*, 3422 – 3425.

[20] M. Yang, W. Wang, F. Yuan, X. Zhang, J. Li, F. Liang, B. He, B. Minch, G. Wegner, *J. Am. Chem. Soc.* **2005**, *127*, 15107 – 15111.

[21] P. Samorí, V. Francke, T. Mangel, K. Müllen, J. P. Rabe, *Opt. Mater.* **1998**, *9*, 390 – 393.

 © 2006 Wiley-VCH Verlag GmbH & Co. KGaA, Weinheim

Fluorescent Labels

DOI: 10.1002/anie.200602975

Monodisperse Silica-Coated Polyvinylpyrrolidone/$NaYF_4$ Nanocrystals with Multicolor Upconversion Fluorescence Emission**

*Zhengquan Li and Yong Zhang**

Nanosized fluorescent labeling materials have been widely used for biological studies and clinical applications. Conventional downconversion fluorescent labels require an ultraviolet or blue excitation wavelength.[1,2] These single-photon

[*] Prof. Y. Zhang
Division of Bioengineering
Faculty of Engineering, Blk, EA-03-12
National University of Singapore
9 Engineering Drive 1, Singapore 117576 (Singapore)
Fax: (+65) 6872-3069
E-mail: biezy@nus.edu.sg
and
Nanoscience and Nanotechnology Initiative
National University of Singapore
9 Engineering Drive 1, Singapore 117576 (Singapore)
Dr. Z. Li
Singapore–MIT Alliance
National University of Singapore
4 Engineering Drive 3, Singapore 117576 (Singapore)

[**] The authors thank the Singapore–Massachusetts Institute of Technology Alliance (SMA) for a postdoctoral fellowship for Z.L. and the National University of Singapore for research funding.

Supporting information for this article is available on the WWW under http://www.angewandte.org or from the author.

WILEY InterScience DISCOVER SOMETHING GREAT
© 2006 Wiley-VCH Verlag GmbH & Co. KGaA, Weinheim

fluorescent labels emit one lower-energy photon after absorbing a higher-energy UV or visible photon. Their disadvantages include low light-penetration depth and possible severe photodamage to living organisms. Furthermore, many biological samples show autofluorescence under short-wavelength UV radiation, which decreases the sensitivity of detection. It is desirable to use fluorescent labels that can be excited in the near-infrared (NIR) region.[3] The IR-to-visible upconversion nanocrystal is a good choice.[4,5] The nanocrystal emits one higher-energy photon after absorbing two or more lower-energy photons. Different colors of visible light can be obtained from different upconversion phosphors when excited by the same IR laser.[4] In comparison with downconversion fluorescent materials, upconversion nanocrystals show very low background light as a consequence of their unique fluorescent properties. In addition, photodamage to biological tissues is minimal because the tissues are usually transparent to NIR light.[6] $NaYF_4$ has been reported as the most efficient host material for Yb/Er (or Yb/Tm) co-doped IR-to-visible upconversion phosphors.[7] Colloidal $NaYF_4$ nanocrystals co-doped with Yb/Er and Yb/Tm have been prepared, with strong upconversion fluorescence seven orders of magnitude higher than that of CdSe–ZnS quantum dots.[8,9]

Some efforts have been made to produce upconversion $NaYF_4$ nanocrystals with controlled size and shape.[5,8,10] Ethylenediaminetetraacetic acid (EDTA) was used as a chelating agent to control the growth of $NaYF_4$ nanocrystals, but the as-prepared nanocrystals tended to precipitate in solution as a result of the lack of both hydrophilic and hydrophobic chemical groups on their surface.[5,10] Colloidal solutions of $NaYF_4$ nanocrystals were prepared; however, toxic chemicals and laborious procedures were used. Furthermore, these nanocrystals were hydrophobic and could only be dispersed in certain organic solvents such as hexane and dimethyl sulfoxide (DMSO) under ultrasound sonication.[8,11,12] The use of these nanocrystals directly for biological applications is limited because of their very low solubility in water and unsuitable surface property. It is necessary to develop suitable methods for synthesizing upconversion $NaYF_4$ nanocrystals that are dispersible in water and many organic solvents, and also have some functional chemical groups on their surfaces for conjugation of biomolecules.[9]

The selection of a suitable chelating agent for controlling the growth of the nanocrystals and of a surfactant to stabilize the nanocystals and provide them with a desirable surface is the key to solving the above-mentioned problems. Polyvinylpyrrolidone (PVP) is an amphiphilic surfactant which can render the nanocrystals dispersible in water and organic solvents.[13] Furthermore, its pyrrolidone groups can coordinate with lanthanide ions.[14,15] As such it was used in this work as both the chelating agent and stabilizer to synthesize $NaYF_4$ nanocrystals with controlled size and shape, and with suitable surface property and solubility in water (Figure 1). The PVP-stabilized $NaYF_4$ nanocrystals could be directly coated with a uniform layer of silica to produce a surface for the conjugation of biomolecules.

Figure 2 shows TEM images of the PVP/$NaYF_4$:Yb,Er nanocrystals. The crystals are polyhedral in shape and very uniform in size with an average size of about 30 nm

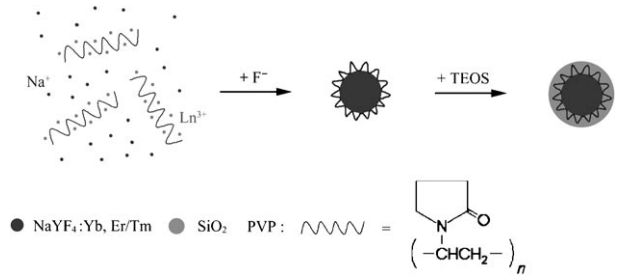

Figure 1. Synthesis of silica-coated PVP/$NaYF_4$ nanocrystals doped with lanthanide ions. TEOS = tetraethoxysilane.

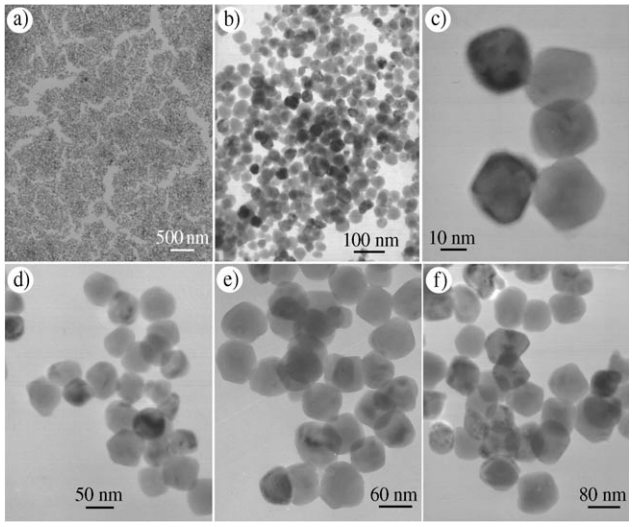

Figure 2. a–c) TEM images with different resolutions of PVP/$NaYF_4$:Yb,Er nanocrystals with a size of 30 nm. d–f) TEM images of nanocrystals with different sizes: d) 48; e) 65; f) 87 nm.

(Figure 2a–c). The black spots in the images result from PVP adsorbed on the surface of the nanocrystal, which was burnt out under exposure to the accelerated electron beam during the TEM measurement. The sizes of the PVP/$NaYF_4$ nanocrystals could be altered by changing the experimental conditions, such as concentrations of the reactants, and reaction temperature and time. The sizes could be adjusted within the range of 20–100 nm with a relatively narrow size distribution (Figure 2d–f). The XRD pattern of the nanocrystals (Figure S1 in the Supporting Information) agrees well with the data for pure cubic $NaYF_4$ nanocrystals, as reported in the JCPDS card (No. 77-2042, $a = 5.470$ Å), thus indicating a high purity of the $NaYF_4$ nanocrystals obtained. It was previously reported that in most cases a mixture of cubic and hexagonal $NaYF_4$ crystals was produced, although several methods for synthesizing pure cubic and hexagonal crystals have been developed.[6,8,16] The method presented herein seems to be efficient for producing pure-phase $NaYF_4$ nanocrystals in solution. The FTIR spectrum of the nanocrystals (Figure S2 in the Supporting Information) shows a peak at 1640 cm^{-1} that could be assigned to the C=O stretching vibration, which indicates the presence of PVP on the surface of the nanocrystals.

© 2006 Wiley-VCH Verlag GmbH & Co. KGaA, Weinheim

It has been demonstrated that only microsized $NaYF_4$ crystals can be formed if water is used as the solvent and no chelating agents are employed.[5,10] The strong chelating agent EDTA was used to form a complex with lanthanide ions to control the growth of the crystals and their size. According to LaMer's model, the formation of such a complex could control the concentration of lanthanide ions in the solution, and thus help to control the nucleation and growth of the crystals. In this work, lanthanide ions were complexed with the pyrrolidone groups of PVP and then released slowly to the solution to react with fluoride ions in the viscous and weakly polar solvent ethylene glycol, and thus small nanocrystals were formed.[14,15] Furthermore, PVP could also serve as a stabilizer of the nanocrystals.[17] As a result of the good solubility of PVP in water and many organic solvents, it is expected that the PVP/$NaYF_4$ nanocrystals can be well-dispersed in water and many organic solvents to form colloidal solutions. Especially, the nanocrystals should be dispersible in water and some polar solvents such as ethanol, otherwise their use in bio-related applications is very limited. The photograph in Figure 3 demonstrates that the PVP-

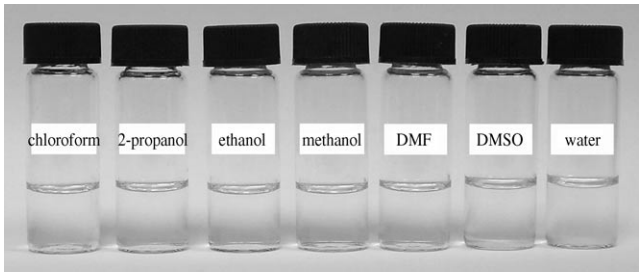

Figure 3. Photographs of colloidal solutions of the PVP/$NaYF_4$:Yb,Er nanocrystals dispersed in different solvents. DMF = *N*,*N*-dimethylformamide.

stabilized $NaYF_4$ nanocrystals are well-dispersed in some of the most commonly used solvents, from weakly polar chloroform to strongly polar water, to form transparent colloidal solutions. As for nonpolar solvents such as hexane, the solubility of the nanocrystals was about eight times lower than that in polar solvents. However, the nanocrystals could still be dispersed in a mixture of polar and nonpolar solvents, for example, a mixture of equal amounts of hexane and ethanol.

Fluorescence spectra of the lanthanide-doped PVP/$NaYF_4$ nanocrystals in ethanol solution are shown in Figure 4. The emission peaks of the PVP/$NaYF_4$:Yb,Er nanocrystals at 407, 521, 539, and 651 nm were a result of the transitions from $^4H_{9/2}$, $^4H_{11/2}$, $^4S_{3/2}$, and $^4F_{9/2}$ to $^4I_{15/2}$ of Er^{3+}, respectively. The emission peaks of the PVP/$NaYF_4$:Yb,Tm nanocrystals at 450, 479, and 649 nm were assigned to the $^1D_2 \rightarrow {}^3F_4$, $^1G_4 \rightarrow {}^3H_6$, and $^1G_4 \rightarrow {}^3F_4$ transitions of Tm^{3+}.[6] It is well-known that the crystallinity and surface property of the nanocrystals could alter the intensity of the fluorescence emission peaks of the doping lanthanide ions. For the $NaYF_4$ nanocrystals prepared using the co-precipitation method, the intensity of the green fluorescence emission peak is much higher than that of the red fluorescence emission peak,[5,10] while the emission peak of red fluorescence is much stronger

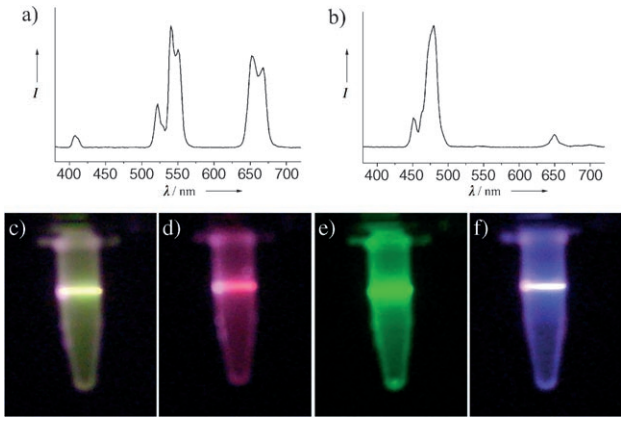

Figure 4. Fluorescence spectra of colloidal solutions of a) Yb/Er-doped and b) Yb/Tm-doped PVP/$NaYF_4$ nanocrystals (30 nm) in ethanol. c–f) Photographs of the PVP/$NaYF_4$:Yb,Er nanocrystals showing total fluorescence (c), fluorescence passing through filters (d, e) for red and green light, respectively, and PVP/$NaYF_4$:Yb,Tm nanocrystals (f), under excitation from a NIR laser (980 nm).

than the peak of green fluorescence for the nanocrystals stabilized by oleic acid.[12] For the PVP/$NaYF_4$:Yb,Er nanocrystals, strong green and red fluorescence were observed, which suggests that either green or red fluorescence can be seen selectively by using suitable filters for green or red light. Strong fluorescence with different colors from the PVP/$NaYF_4$ nanocrystals co-doped with Yb/Er or Yb/Tm can be seen under the excitation of a 980-nm NIR laser (see Figure 4 c–f). The color of the colloidal solution of PVP/$NaYF_4$ nanocrystals could be tuned by mixing the nanocrystals co-doped with Yb/Er and Yb/Tm at certain ratios.

Besides the good solubility in water and organic solvents, the PVP/$NaYF_4$ nanocrystals could be coated with silica directly, whereas other $NaYF_4$ nanocrystals without PVP generally required some surface modifications before coating.[18,19] The silica coating can improve the photostability and biocompatibility of the nanocrystals, and the protocol for conjugation of biomolecules to a silica surface is well established.[20–22] TEM images of the silica-coated PVP/$NaYF_4$:Yb,Er nanocrystals are presented in Figure 5. For the first time, we have demonstrated the formation of core–shell-structured silica/PVP/$NaYF_4$ nanocrystals with a very uniform layer of silica on the $NaYF_4$ nanocrystals. The TEM images showed that the thickness of the silica shell was about 10 nm and could be adjusted to 1–3 nm by adding a smaller amount of TEOS. After coating with silica, the nanocrystals can still emit strong upconversion fluorescence and are quite stable in water (Figure S3 in the Supporting Information).

In summary, ultrafine, pure cubic PVP/$NaYF_4$ nanocrystals co-doped with lanthanide ions such as Yb/Er or Yb/Tm were synthesized using PVP as a chelating agent and stabilizer. The nanocrystals are very uniform and the size is tunable by adjusting the experimental conditions. Furthermore, the nanocrystals are monodisperse in water and some of the most commonly used organic solvents, and strong multicolor upconversion fluorescence was observed from the clear colloidal solution of the nanocrystals under excitation from a 980-nm NIR laser. Moreover, a uniform layer of silica

 © 2006 Wiley-VCH Verlag GmbH & Co. KGaA, Weinheim

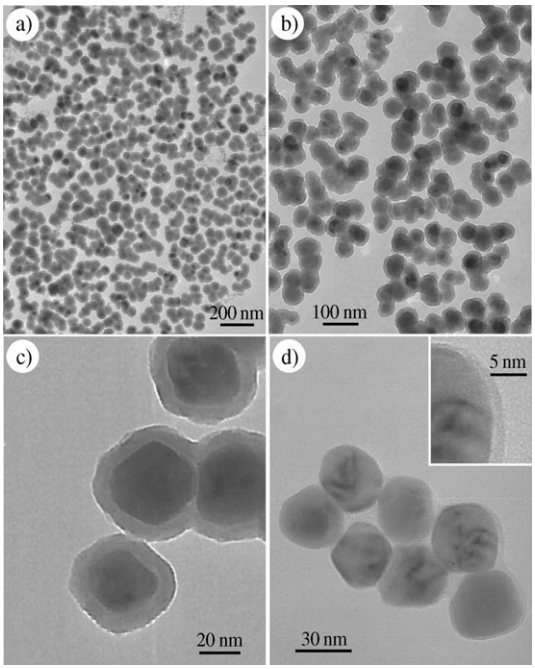

Figure 5. a–c) TEM images of silica-coated PVP/$NaYF_4$:Yb,Er nanocrystals. d) TEM image of PVP/NaYF4:Yb,Er nanocrystals coated with a very thin silica layer.

was coated onto the PVP/$NaYF_4$ nanocrystals to form a core–shell structure, with the silica thickness adjustable down to 1–3 nm. These upconversion nanocrystals have great potential for use as a fluorescent labeling material for biological applications.

Experimental Section

All the chemical reagents were purchased from Sigma-Aldrich and used without further purification. The PVP/$NaYF_4$:Yb(20%),Er(2%) nanocrystals were synthesized as follows. Y_2O_3 (88 mg, 0.78 mmol), Yb_2O_3 (39.4 mg, 0.2 mmol), and Er_2O_3 (3.9 mg, 0.02 mmol) were dissolved in 10% HNO_3 (10 mL), and then the solution was heated to evaporate the water completely. Ethylene glycol (10 mL) was added to dissolve the obtained $LnNO_3$ (Ln = Y 78%, Yb 20%, Er 2%). Polyvinylpyrrolidone (PVP 40, 0.5560 g) and NaCl (0.0588 g, 1 mmol) were subsequently added and the solution was heated to 80 °C until a homogeneous solution was formed. NH_4F (0.1482 g, 4 mmol) was dissolved in ethylene glycol (10 mL) at 80 °C and added dropwise to the $LnNO_3$ solution, which was maintained at 80 °C for 10 min under stirring. The solution was heated to 160 °C for 2 h and then cooled to room temperature. The product was isolated by centrifugation and washed twice with absolute ethanol. The PVP/$NaYF_4$:Yb(20%),Tm(2%) nanocrystals were synthesized using the same protocol except that Er_2O_3 was replaced by Tm_2O_3.

A typical procedure for coating silica onto the PVP/$NaYF_4$ nanocrystals was as follows. PVP/$NaYF_4$:Yb(20%),Er(2%) nanocrystals (0.05 mmol) were dispersed in ethanol (20 mL) and mixed with water (4 mL) and ammonia (30%, 0.5 mL). Tetraethoxysilane (TEOS, 0.06 mL) dissolved in ethanol (10 mL) was then added slowly to the solution with continuous stirring. The product was isolated by centrifugation and washed twice with water.

The samples were also studied with a JEOL 2010F transmission electron microscope. Fluorescence spectra were recorded on a Hitachi F-500 fluorescence spectrophotometer and fluorescence images were captured using an Axiostar plus fluorescence microscope, equipped with a NIR laser (980 nm).

Received: July 25, 2006
Published online: November 7, 2006

Keywords: crystal growth · fluorescence · lanthanides · nanocrystals · polyvinylpyrrolidone

[1] F. Wang, W. B. Tan, Y. Zhang, X. P. Fan, M. Q. Wang, *Nanotechnology* **2006**, *17*, R1.
[2] E. Beaurepaire, V. Buissette, M. P. Sauviat, D. Giaume, K. Lahlil, A. Mercuri, D. Casanova, A. Huignard, J. L. Martin, T. Gacoin, J. P. Boilot, A. Alexandrou, *Nano Lett.* **2004**, *4*, 2079.
[3] H. Sertchook, D. Avnir, *Chem. Mater.* **2003**, *15*, 1690.
[4] F. van de Rijke, H. Zijlmans, S. Li, T. Vail, A. K. Raap, R. S. Niedbala, H. J. Tanke, *Nat. Biotechnol.* **2001**, *19*, 273.
[5] G. S. Yi, H. C. Lu, S. Y. Zhao, G. Yue, W. J. Yang, D. P. Chen, L. H. Guo, *Nano Lett.* **2004**, *4*, 2191.
[6] J. F. Suyver, A. Aebischer, D. Biner, P. Gerner, J. Grimm, S. Heer, K. W. Kramer, C. Reinhard, H. U. Güdel, *Opt. Mater.* **2005**, *27*, 1111.
[7] K. W. Kramer, D. Biner, G. Frei, H. U. Güdel, M. P. Hehlen, S. R. Luthi, *Chem. Mater.* **2004**, *16*, 1244.
[8] S. Heer, K. Kompe, H. U. Güdel, M. Haase, *Adv. Mater.* **2004**, *16*, 2102.
[9] D. R. Larson, W. R. Zipfel, R. M. Williams, S. W. Clark, M. P. Bruchez, F. W. Wise, W. W. Webb, *Science* **2003**, *300*, 1434.
[10] J. H. Zeng, J. Su, Z. H. Li, R. X. Yan, Y. D. Li, *Adv. Mater.* **2005**, *17*, 2119.
[11] H. X. Mai, Y. W. Zhang, R. Si, Z. G. Yan, L. D. Sun, L. P. You, C. H. Yan, *J. Am. Chem. Soc.* **2006**, *128*, 6426.
[12] J. C. Boyer, F. Vetrone, L. A. Cuccia, J. A. Capobianco, *J. Am. Chem. Soc.* **2006**, *128*, 7444.
[13] Y. Yang, J. R. Li, J. Mu, H. L. Rong, L. Jiang, *Nanotechnology* **2006**, *17*, 461.
[14] D. M. L. Goodgame, D. J. Williams, R. E. P. Winpenny, *Angew. Chem.* **1988**, *100*, 266; *Angew. Chem. Int. Ed. Engl.* **1988**, *27*, 261.
[15] Q. Li, T. Li, J. G. Wu, *J. Phys. Chem. B* **2001**, *105*, 12293.
[16] A. Aebischer, S. Heer, D. Biner, K. Kramer, M. Haase, H. U. Güdel, *Chem. Phys. Lett.* **2005**, *407*, 124.
[17] R. Si, Y. W. Zhang, L. P. You, C. R. Yan, *J. Phys. Chem. B* **2006**, *110*, 5994.
[18] C. Graf, S. Dembski, A. Hofmann, E. Ruhl, *Langmuir* **2006**, *22*, 5604.
[19] C. Graf, D. L. J. Vossen, A. Imhof, A. van Blaaderen, *Langmuir* **2003**, *19*, 6693.
[20] T. Nann, P. Mulvaney, *Angew. Chem.* **2004**, *116*, 5511; *Angew. Chem. Int. Ed.* **2004**, *43*, 5393.
[21] D. K. Yi, S. T. Selvan, S. S. Lee, G. C. Papaefthymiou, D. Kundaliya, J. Y. Ying, *J. Am. Chem. Soc.* **2005**, *127*, 4990.
[22] T. J. Yoon, K. N. Yu, E. Kim, J. S. Kim, B. G. Kim, S. H. Yun, B. H. Sohn, M. H. Cho, J. K. Lee, S. B. Park, *Small* **2006**, *2*, 209.

 © 2006 Wiley-VCH Verlag GmbH & Co. KGaA, Weinheim

Drug Design

DOI: 10.1002/anie.200602343

Oxetanes as Promising Modules in Drug Discovery**

Georg Wuitschik, Mark Rogers-Evans, Klaus Müller, Holger Fischer, Björn Wagner, Franz Schuler, Liudmila Polonchuk, and Erick M. Carreira**

In drug discovery, it is common practice to block metabolically exposed sites in a biologically active molecule by the introduction of a *gem*-dimethyl unit (Figure 1). However, for a typical small molecule in medicinal chemistry, the replacement of hydrogen atoms by methyl groups leads to a significant increase in its lipophilicity, which in turn may adversely affect its metabolic and pharmacokinetic properties. Therefore, a stable, small, and less lipophilic molecular module with reduced susceptibility to metabolic attack would be a very desirable alternative. We have been interested in modules amenable to convenient synthesis and to facile incorporation into biologically active compounds, and have considered oxetanes to be of particular interest. Herein, we report the synthesis of discrete oxetane building blocks, which are readily prepared and attached onto molecular scaffolds. We show that incorporation of this motif results in remarkable improvements of key physicochemical characteristics and provides valuable opportunities for property-guided drug discovery.

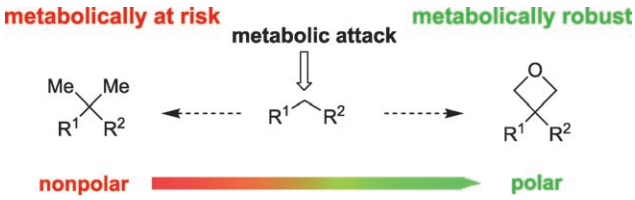

Figure 1. Comparison of gem-dimethyl and oxetane modules.

The analysis of the calculated van der Waals volumes reveals that an oxetanyl unit and a *gem*-dimethyl group occupy nearly the same volume. These calculations are in line with the experimental finding that the partial molar volumes of oxetane and propane in water are essentially the same.[1,2] We chose to incorporate oxetanes onto small molecules to make use of the polar nature of the oxetane to reduce the lipophilicity and metabolic liability. Little is known about the metabolic and chemical stability of oxetanes, and there are few synthetic methodologies of relevance to their incorporation and subsequent elaboration in compounds of pharmacological interest. Taxol,[3] oxetanocin,[4] and oxetin[5]—the best studied of oxetane containing biological actives—incorporate specifically 2,3-disubstituted oxetanes; however, the intrinsic chemical and pharmacological properties (or inherent advantages) of the oxetanes are far from clear.

To explore the utility of the oxetanyl moiety we selected *N*,*N*-dimethyl-4-(*p*-*tert*-butylphenyl)butylamine (**2**) as a model system. This compound contains a large hydrophobic unit, which renders it essentially insoluble in water in its neutral form, and also a polar head group, which makes it highly amphiphilic. Additionally, its readily accessible hydrophobic subunits may be perfect target sites for metabolic attack. For these reasons, **2** would most likely be designated an undesirable candidate in a medicinal chemistry program, thus making it a suitable starting point to probe the effect of introducing the oxetane unit at various positions. Several important synthetic aspects of the underlying oxetane chemistry targeted for development need to be considered for the assembly of oxetanyl analogues of **2**. This approach

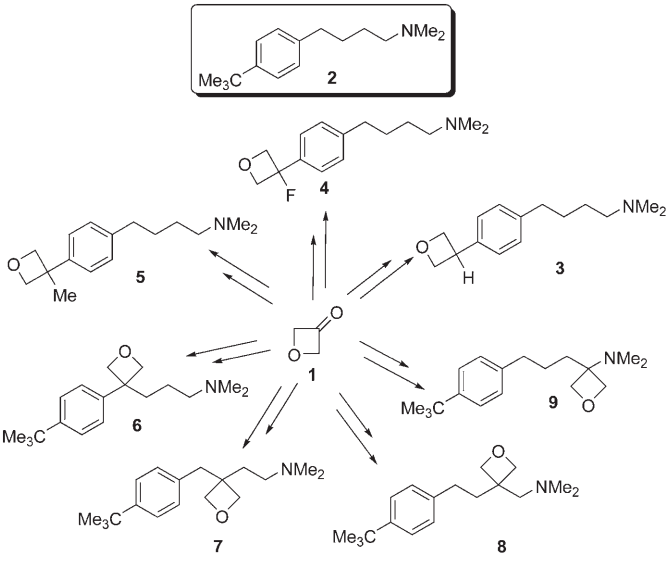

[*] G. Wuitschik, Prof. Dr. E. M. Carreira
Laboratorium für Organische Chemie
ETH Hönggerberg, HCI H335
8093 Zürich (Switzerland)
Fax: (+41) 44-632-1328
E-mail: carreira@org.chem.ethz.ch
Dr. M. Rogers-Evans, Prof. Dr. K. Müller
F. Hoffmann–La Roche AG
Pharmaceuticals Division
4070 Basel (Switzerland)
Fax: (+41) 61-688-6965
E-mail: mark.rogers-evans@roche.com
H. Fischer, B. Wagner
F. Hoffmann–La Roche AG, Basel
Pharmaceuticals Division, Molecular Properties & Structure Correlation Group
F. Schuler
F. Hoffmann–La Roche AG, Basel
Pharmaceuticals Division, DMPK Department
L. Polonchuk
F. Hoffmann–La Roche AG, Basel
Pharmaceuticals Division, Safety Pharmacology

[**] We thank the Swiss National Science Foundation and F. Hoffmann–La Roche AG for support of this research. We are very indebted to I. Parrilla, F. Senner, and P. Warga for their great dedication in measuring important physicochemical data described in this work.

Supporting information for this article is available on the WWW under http://www.angewandte.org or from the author.

InterScience
© 2006 Wiley-VCH Verlag GmbH & Co. KGaA, Weinheim

would involve the convenient preparation of oxetanes substituted with aliphatic, aromatic, and heterofunctional groups. Another structural feature of **2** is the *tert*-butyl group, which can be considered a special case of a *gem*-dimethyl group on a small aliphatic (ethyl) side chain. As the *tert*-butyl group is frequently encountered in medicinal chemistry,[6] its replacement by a 3-methyl-oxetan-3-yl unit and the study of concomitant property changes constitute a particularly interesting aspect of this work.

We chose structures **3**–**5** to examine the effect of replacing the *tert*-butyl group by an oxetane-containing unit. Structures **6**–**9** were prepared so as to carry out an "oxetane scan", in which the oxetanyl unit was placed at different topological distances from the basic amine. We focused on strategies in which an oxetane ring is conveniently introduced in a modular building block approach rather than built up de novo for each molecule.[7] The targeted oxetane derivatives were assembled using oxetan-3-one[8–10] (**1**) as the starting material (Scheme 1). The existing procedure for the preparation of oxetan-3-one[8,11] involves a five-step sequence, with preparative GC as a final purification step, and proceeds in 13% overall yield. Consequently, we developed an efficient and scalable route that could provide useful quantities of oxetan-3-one (**1**). The new route commences with the conversion of dihydroxyacetone into its dimethylacetal (MeOH, toluene *p*-sulfonic acid, trimethylorthoformate). Monotosylation of the isolated 1,3-dihydroxy-2,2-dimethoxypropane, followed by treatment with NaH, furnished 2,2-dimethoxyoxetane (37% overall yield).[12] Hydrolysis of the acetal proved difficult. However, heating a solution of 2,2-dimethoxypropane in the presence of Montmorillonite K10 at reflux provided the desired oxetan-3-one in 62% yield. This four-step sequence affords the target compound in an overall yield of 23% after purification by distillation.[13]

The addition of an aryl lithium compound to oxetan-3-one (**1**) furnished the 3-aryl-3-hydroxyoxetane **10**, which in turn was converted into the 3-aryl-3-fluorooxetane **4** by treatment with DAST (Scheme 1). Alternatively, the 3-hydroxy-oxetane **10** can be reduced to **3** in a one-pot procedure involving tosylation followed by reduction ($LiAlH_4$). These two protocols thus provide the simple aryl oxetanes.

We next developed routes to oxetanes bearing a quaternary center at C-3. Oxetan-3-one (**1**) undergoes reaction with stabilized ylides to furnish the α,β-unsaturated ester **11** and aldehyde **12**. The analogous nitroalkene **13** was obtained in 81% yield from condensation of **1** with nitromethane. It is worth noting that all of these unsaturated compounds, to the best of our knowledge, have not been previously reported and yet are easily handled and stored. Given the ease with which **11**–**13** were prepared, the stage was set to examine these as Michael acceptors. We were pleased to find that all three compounds readily undergo 1,4-addition by various nucleophiles, including amines, aryl and vinyl boronic acids (catalyzed by Rh complexes), as well as organocuprates, thus making them useful building blocks.

With compounds **3**–**9** in hand, we examined the physical and pharmacological properties imparted by the oxetane ring. The thermodynamic solubilities measured in buffered solutions at pH 9.9 are shown in Table 1. We chose these

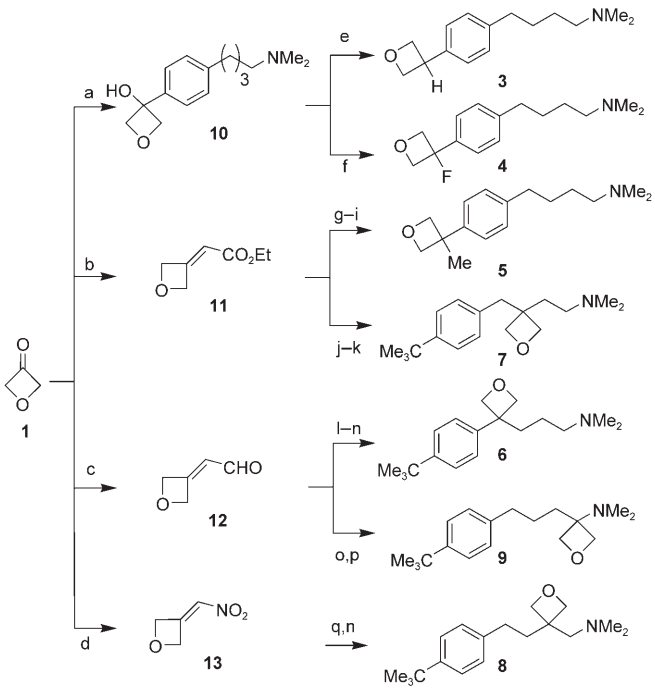

Scheme 1. a) $(Me_2N)(CH_2)_4(C_6H_4)$-*p*-Li, THF, −78 °C, 71%; b) Ph_3PCHCO_2Et, CH_2Cl_2, RT, 89%; c) $Ph_3PCHCHO$, CH_2Cl_2, RT, 81%; d) 1. NEt_3, $MeNO_2$, RT; 2. NEt_3, MsCl, CH_2Cl_2, −78 °C, 81%; e) 1. NaH, Et_2O, 0 °C; 2. TsCl, 0 °C; 3. $LiAlH_4$, −78 °C, 58%; f) DAST, CH_2Cl_2, −78 °C, 40%; g) $(Me_2N)(CH_2)_4(C_6H_4)$-*p*-$B(OH)_2$, cat. [{Rh(cod)Cl}$_2$], KOH, aq dioxane, RT, 83%; h) DIBAL-H, −78 °C; i) [$(Ph_3P)_3RhCl$], toluene, 105 °C, 33% (2 steps); j) 4-*t*BuBnMgBr, TMSCl, CuI, THF, −18 °C, 70%; k) Me_2NH, $NaCNBH_3$, MeOH, 28% (2 steps); l) 4-*t*BuPhB$(OH)_2$, cat. [{Rh(cod)Cl}$_2$], KOH, aq dioxane, RT, 78%; m) 1. $MeNO_2$, NEt_3, RT; 2. NEt_3, MsCl, CH_2Cl_2, −78 °C, 58%; n) 1. H_2, $Pd(OH)_2$/C, CH_2O, RT, MeOH; 2. $NaCNBH_3$, CH_2O, MeOH, 34% o) 1. $HNMe_2$, DBU, THF, −18 °C; 2. 4-*t*BuPhCHPPh_3; p) H_2, Pd/C, MeOH, 36% (3 steps); q) (*E*)-4-*t*BuC_6H_4CHCHB$(OH)_2$, cat. [{Rh(cod)Cl}$_2$], KOH, aq dioxane, RT; 34% (overall sequence). Ms = methanesulfonyl, Ts = toluene-*p*-sulfonyl, DAST = (diethylamino)sulfur trifluoride, cod = cycloocta-1,5-diene, DIBAL-H = diisobutylaluminum hydride, TMS = trimethylsilyl, DBU = 1,8-diazabicyclo[5.4.0]undec-7-ene, Bn = benzyl.

conditions to better differentiate the solubilities of amines with slightly different basicities, and to avoid complications resulting from the tendency of charged lipophilic compounds to form micelles under neutral pH conditions (a tendency observable for some of these compounds). At basic pH, **2** is essentially insoluble, whereas the oxetane derivatives **3**–**5** remain highly soluble (Table 1). The solubility data closely parallel the lipophilicity data represented by log*D* and log*P* values. The latter constitutes the intrinsic lipophilicity of the neutral base derived from the experimental pK_a and log*D* values, which correspond to the octanol/water distribution coefficients measured at pH 7.4. The replacement of the remote *tert*-butyl group by the 3-methyl-3-oxetanyl group results in a lowering of the log*D* (and log*P*) value by one unit. Interestingly, the magnitude of this decrease in lipophilicity is comparable with the increase in lipophilicity when going from ethylbenzene (log$P \approx 3.2$) to *tert*-butylbenzene (log$P \approx 4.1$).[14] The introduction of an oxetanyl module into a methylene unit thus constitutes a "liponeutral" bulk increase.

 © 2006 Wiley-VCH Verlag GmbH & Co. KGaA, Weinheim

Table 1: Physicochemical and biochemical properties.

Compound	Sol.[a]	hCL_{int}[b]	mCL_{int}[b]	$\log D$[c] ($\log P$[d])	pK_a[e]
2	<1	16	417	1.8 (4.3)	9.9
3	4000	2	27	−0.1 (2.4)	9.9
4	6100	6	50	−0.5 (2.0)	9.9[f]
5	4400	0	43	0.8 (3.3)	9.9
6	270	0	147	1.7 (3.9)	9.6
7	4100	6	13	1.7 (3.5)	9.2
8	25	42	383	3.3 (4.0)	8.0
9	57	13	580	3.3 (3.6)	7.2

[a] Thermodynamic solubility ($\mu g\,mL^{-1}$) in 50 mM phosphate buffer at pH 9.9 and 22.5 ± 1 °C. [b] Intrinsic clearance rates in $min^{-1}\,mg^{-1}\,\mu L$ measured in human (hCL_{int}) and mouse (hCL_{int}) liver microsomes (see text). [c] Logarithmic octanol/water distribution coefficients at pH 7.4. [d] Intrinsic lipophilicity of the neutral base, according to $\log P = \log D^{pH} + \log(1+10^{(pK_a-pH)})$. [e] Amine basicities in H_2O measured spectrophotometrically at 24 °C. [f] The pK_a value for **4** in H_2O is estimated on the basis that its pK_a value (9.2) measured in MeOH/H_2O (1:1) is identical to the pK_a values of amines **2**, **3**, and **5**, also measured under these conditions.

While it comes as no surprise that **3**, which lacks the 3-methyl group on the oxetane ring, is less lipophilic than **5**, the further decrease in lipophilicity upon H/F exchange at the 3-position (**4**) is noteworthy. Typically, the replacement of one hydrogen atom by fluorine in an otherwise identical molecule results in a slight increase in the lipophilicity ($\Delta\log P \approx 0.25$).[15]

The chemical stability of all compounds was tested by stirring solutions of these for 2 h at 37 °C in aqueous buffers at pH 1–10. Oxetane-containing compounds (**3**–**9**) proved stable over the range of acidic to alkaline conditions. Compound **3** is stable in the pH range 2–10, but shows partial decomposition at pH 1, although 84% of **3** is recoverable.

Reference compound **2** was designed to be amphiphilic, because it consists of a large apolar residue connected to a basic, polar amine. Amphiphilic behavior is known to correlate with the free energy of amphiphilicity $\Delta\Delta G_{amp}$, which is defined as the difference in the free energies in transferring a compound from the aqueous phase to the air/water interface and from the aqueous phase into a micelle.[16] Compounds displaying high absolute values for $\Delta\Delta G_{amp}$ are more likely to induce phospholipidosis in cells.[17] In our experience, a basic compound ($pK_a > 7$) with $\Delta\Delta G_{amp}$ values less than 7.0 $kJ\,mol^{-1}$ is likely to cause phospholipidosis in vivo. Model compound **2** exhibits a free energy of amphiphilicity of −8.3 $kJ\,mol^{-1}$, clearly showing its pronounced amphiphilic nature and thus raising concerns about potential phospholipidosis. By contrast, oxetane **5**, with an experimental value of −3.2 $kJ\,mol^{-1}$, is well below the critical threshold.

We next examined the susceptibility of the oxetane-containing compounds towards metabolic degradation in human and mouse microsomes by incubating the compounds at 2 μM for up to 30 minutes at 37 °C. The levels of non-metabolized compound were determined by calibrated HPLC/MS/MS at regular time intervals. The intrinsic clearance (CL_{int}, in $min^{-1}\,mg^{-1}\,\mu L$ microsomal protein) is the rate constant of the first-order decay of a given compound, normalized for the protein concentration in the incubations. Examination of the parent structure **2** reveals medium and high clearance rates from human and mouse microsomes, respectively (Table 1). By contrast, oxetane derivatives **3**–**5** show a significantly reduced susceptibility to microsomal attack. Compound **5** displays a marked increase in metabolic stability, with no detectable degradation in human microsomes, and a clearance rate an order of magnitude lower than that of **2** in mouse microsomes. Likewise, the replacement of the *tert*-butyl unit by an oxetane or fluorooxetane module, as in **3** and **4**, results in improved metabolic stabilities. It should be noted that **2**–**5** may suffer metabolic attack at various sites, and the substantial increase in metabolic stability found for the three oxetane-containing compounds **3**–**5** correlates with an overall reduction in lipophilicity. The enhanced stability of **5** is noteworthy given that **5** is more lipophilic than **3** or **4**.

We then decided to investigate the effect of oxetane incorporation on the hERG (*human ether-à-go-go*) potassium channel. Blockade of this channel may lead to a prolongation of the QT interval (electrophysiological heart parameter) and is therefore a fundamental test for in vitro safety.[18] It is known that lipophilic compounds containing a basic amine are often substrates of this channel, and that the introduction of polar functional groups into the extremity of the structure of such compounds can reduce their hERG liability. Indeed, this is confirmed by a comparison of the lipophilicity and hERG assay results for **2** and **5**. The marked reduction in lipophilicity by introduction of the oxetane unit resulted in a clear reduction of hERG liability for **5** (hERG $IC_{50} = 35$ μM) in comparison with **2** (hERG $IC_{50} = 7.5$ μM).

Finally, we prepared a series of compounds in which the distance between the amine and oxetane ring incrementally varied, thus giving rise to an "oxetane scan" (Scheme 1). The resulting series **6**–**9** allowed us to assess the influence of the oxetane unit on the basicity of the neighboring amine. The pK_a values for the various amines were determined spectrophotometrically by using a ProfilerSGA/Sirius Instrument. While an oxetane ring incorporated in a remote position from the amine (as in 3-5) did not affect the basicity of the compound, its incorporation α or β relative to the amine has a pronounced effect, lowering the basicity by nearly 3 and 2 pK_a units, respectively. The basicity-lowering effect of the compound may be diagnosed even when the oxetane is separated from the amine function by four single bonds (**6**). The remarkable power of an oxetane ring to reduce amine basicity renders it an interesting structural motif for the tempering of a nearby basic functional group.

The introduction of an oxetane moiety in the γ or δ position results in a marked increase in solubility. Its incorporation close to the amine group still results in reasonable solubility for **8** and **9**. Likewise, increased resistance towards metabolic attack, as assayed in human and mouse microsomes, can be diagnosed for **6** and **7**, in contrast to **8** and **9**, which display reduced metabolic stability probably because of their enhanced lipophilicity. Preliminary data (not shown) indicate that the primary metabolic attack occurs at the amine and *tert*-butyl groups, but not at the oxetane moiety.

In conclusion, we have demonstrated that, starting from the readily available building block oxetan-3-one, a prototypical set of compounds can be made, which contain the oxetane motif at different positions. These compounds

 © 2006 Wiley-VCH Verlag GmbH & Co. KGaA, Weinheim

improve remarkably the physico- and biochemical properties of the underlying scaffold. Enhanced solubility, reduced lipophilicity, amphiphilicity, and hERG liability, as well as pronounced modulation of the basicity of a nearby amine group are documented. The various oxetane-containing compounds display robust chemical stability under various basic and acidic conditions, as well as an improved resistance towards metabolic degradation in most cases. The synthetic routes outlined in this study illustrate the relative ease with which the key oxetane building blocks can be incorporated at various sites of a given lead structure. Taken together, our data make a case for a more general use of this under-represented structural motif in drug discovery and beyond.

Received: June 12, 2006
Published online: October 2, 2006

Keywords: drug design · metabolism · oxetanes · small ring systems · synthesis design

[1] J. C. Moore, R. Battino, T. R. Rettich, Y. P. Handa, E. Wilhelm, *J. Chem. Eng. Data* **1982**, *27*, 22.
[2] J. T. Edward, P. G. Farrell, F. Shahidi, *J. Chem. Soc. Faraday Trans. 1* **1977**, *73*, 705.
[3] M. Wang, B. Cornett, J. Nettles, D. C. Liotta, J. P. Snyder, *J. Org. Chem.* **2000**, *65*, 1059.
[4] N. Shimada, S. Hasegawa, T. Harada, T. Tomisawa, A. Fujii, T. Takita, *J. Antibiot.* **1986**, *39*, 1623.
[5] S. Omura, M. Murata, N. Imamura, Y. Iwai, H. Tanaka, A. Furusaki, T. Matsumoto, *J. Antibiot.* **1984**, *37*, 1324.
[6] A search in the World Drug Index (Version 2005/5, Thomson Derwent), revealed 714 entries for molecules containing a *tert*-butyl group and 69 such drugs that are currently on the market.
[7] For a similar approach involving click chemistry, see: Z. Radic, R. Manetsch, A. Krasinski, J. Raushel, J. Yamauchi, C. Garcia, H. Kolb, K. B. Sharpless, P. Taylor, *Chem.-Biol. Interact.* **2005**, *157*, 133.
[8] Y. Dejaegher, N. M. Kuz'menok, A. M. Zvonok, N. De Kimpe, *Chem. Rev.* **2002**, *102*, 29.
[9] J. A. Wojtowicz, R. J. Polak, *J. Org. Chem.* **1973**, *38*, 2061.
[10] K. Baum, P. T. Berkowitz, V. Grakauskas, T. G. Archibald, *J. Org. Chem.* **1983**, *48*, 2953.
[11] A. P. Kozikowski, A. H. Fauq, *Synlett* **1991**, 783.
[12] P. Picard, D. Leclercq, J. P. Bats, J. Moulines, *Synthesis* **1981**, 550.
[13] B.p. 50–56 °C/91 mbar, this process has been conducted on a 15 g scale; digital scanning calorimetry measurements show that samples should not be heated above 80 °C to avoid exothermal decomposition.
[14] Based on data retrieved from the MedChem Database (Version 04 (2005) of Daylight Chemical Information Systems Inc., Aliso Viejo, CA 92656, USA).
[15] Böhm et al. has noted that introduction of fluorine in beta-position to an oxygen functionality may cause a lipophilicity reduction, possibly due to increased local polarity or synergistic solvation effects; see: H.-J. Böhm, D. Banner, S. Bendels, M. Kansy, B. Kuhn, K. Müller, U. Obst-Sander, M. Stahl, *ChemBioChem* **2004**, *5*, 637.
[16] H. Fischer, M. Kansy, D. Bur, *Chimia* **2000**, *54*, 640.
[17] Phospholipidosis is an intracellular lipid storage disorder caused by cationic amphiphilic drugs (CADs) characterized by the lysosomal accumulation of phospholipids and drug.
[18] A. Cavalli, E. Poluzzi, F. De Ponti, M. Recanatini, *J. Med. Chem.* **2002**, *45*, 3844.

 © 2006 Wiley-VCH Verlag GmbH & Co. KGaA, Weinheim

Lead Nanostructures

DOI: 10.1002/anie.200602952

Lead Chalcogenide Nanotubes Synthesized by Biomolecule-Assisted Self-Assembly of Nanocrystals at Room Temperature**

Hua Tong, Ying-Jie Zhu, Li-Xia Yang, Liang Li, and Ling Zhang*

Since the discovery of carbon nanotubes in 1991,[1] extensive research has been carried out on one-dimensional nanostructures because of their unique properties.[2–6] Various methods have been developed for the synthesis of nanotubes.[7] In general, it is relatively easy for layered materials to form nanotubes directly under the appropriate experimental conditions.[8] For materials that do not have a layered structure, nanotubes may be synthesized by a variety of methods, such as decomposition of the precursor,[9] template-assisted growth,[8,10–14] self-assembly,[15,16] and vapor deposition.[17,18] However, these methods are still limited to the synthesis of specific kinds of nanotubes.

Lead chalcogenides (PbE, E = S, Se, Te) are important semiconductors with narrow band gaps that are showing great promise in the field of IR photoelectronic and thermoelectric devices.[19–21] Various nanostructures of lead chalcogenides, such as quantum dots,[22–24] nanorods,[25,26] nanowires,[27,28] and nanotubes,[14,15,29,30] have been reported over the past decade. However, to the our knowledge, little work has been reported on polycrystalline nanotubes of lead chalcogenides assembled from nanocrystals, although one key example is the formation of composite nanotubes consisting of PbS nanoparticles, sodium dodecyl sulfate, and poly(ethylene oxide).[15]

Herein we report a novel biomolecule-assisted route to the synthesis of lead chalcogenide polycrystalline nanotubes by the self-assembly of nanocrystals at room temperature. Cysteine ($HSCH_2CH(NH_2)COOH$, including L-cysteine, L-cysteine hydrochloride monohydrate, and DL-cysteine hydro-

[*] H. Tong, Prof. Y.-J. Zhu, L.-X. Yang, L. Li, L. Zhang
State Key Laboratory of High Performance Ceramics and Superfine Microstructure
Shanghai Institute of Ceramics
Chinese Academy of Sciences
Shanghai 200050 (P.R. China)
and
Graduate School of Chinese Academy of Sciences
Shanghai 200050 (P.R. China)
Fax: (+86) 215-241-3122
E-mail: y.j.zhu@mail.sic.ac.cn

[**] Financial support from the National Natural Science Foundation of China (50472014) and the Chinese Academy of Sciences under the Program for Recruiting Outstanding Overseas Chinese (Hundred Talents Program) is gratefully acknowledged. We also thank the Fund for Innovation Research of the Shanghai Institute of Ceramics and financial support from the National Basic Science Research Program of China (973 Program) (grant no. 2005CB522700).

Supporting Information for this article is available on the WWW under http://www.angewandte.org or from the author.

© 2006 Wiley-VCH Verlag GmbH & Co. KGaA, Weinheim

chloride monohydrate) biomolecules, lead nitrate, and ethanolamine (or ethanediamine or ammonia) are used to prepare nanowires of a precursor at room temperature. These nanowires, which self-assemble from nanocrystals, act as both lead source and template for the subsequent preparation of lead chalcogenide nanotubes. Note that the precursor nanowires are transformed into lead chalcogenide nanotubes by our synthetic route, and that L-cysteine was recently used in the synthesis of sulfide nanostructures, such as Bi_2S_3[31] and Sb_2S_3.[32]

The precursor nanowires were characterized by powder X-ray diffraction (XRD; Figure 1a), which showed that they

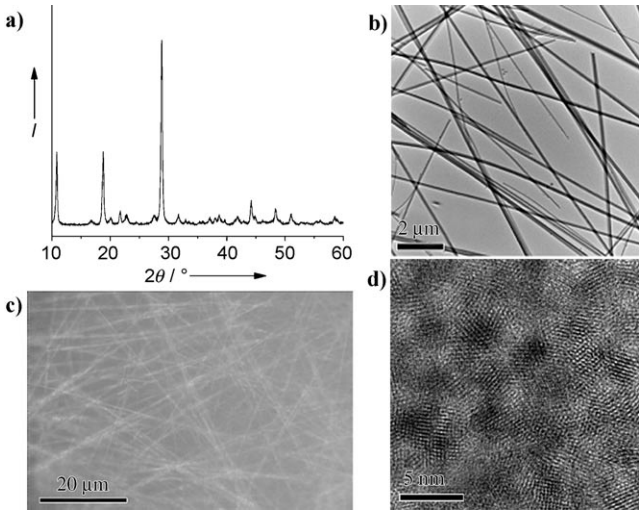

Figure 1. Characterization of the precursor nanowires prepared from $Pb(NO_3)_2$, L-cysteine, and ethanolamine: a) XRD pattern; b) TEM image; c) optical microscopy image; d) HRTEM image.

are well crystallized. On the basis of energy-dispersive spectroscopy (EDS) (see Supporting Information, Figure S1) and FTIR spectroscopy (Supporting Information, Figure S2), the likely chemical structure of the precursor nanowires is $HSCH_2CH(NH_2)COO{-}Pb{-}OH$. We chose cysteine for the synthesis because of its three functional groups (SH, NH_2, COOH). In the presence of a weakly basic additive, such as ethanolamine, which provides OH^- ions, the proton of the COOH group is removed and Pb^{2+} ions can react with cysteine to form the precursor.

TEM revealed that the precursor has a wirelike morphology. These precursor nanowires have a typical diameter of around 200 nm (Figure 1b) and a length of around 100 μm (Figure 1c). The high-resolution TEM (HRTEM) image in Figure 1d shows that the nanowires are formed by the self-assembly of nanocrystals smaller than 5 nm. The precursor nanowires can also be obtained by using L-cysteine hydrochloride monohydrate or DL-cysteine hydrochloride monohydrate instead of L-cysteine.

In addition to ethanolamine, we also tried other weakly basic additives, such as ethanediamine or ammonia with quite similar results (see Supporting Information, Figure S3 and Figure S4). However, no precursor nanowires were obtained in the absence of base, in the presence of a strong base such as NaOH, or in the presence of an acid.

A simple replacement route was designed to synthesize lead chalcogenide nanotubes using the precursor nanowires as both the lead source and the template. Figure 2 schematically outlines the synthetic route and the proposed mechanism for the formation of lead chalcogenide nanotubes. It includes three key points: a) PbE nanocrystals are formed on the surface of the precursor nanowire by an anion-replacement reaction that is the result of the lower solubility of PbE in solution; b) the wall of the PbE nanotube is built up on the surface of the precursor nanowire by the self-assembly of PbE nanocrystals; c) the tubular structure forms at the expense of the precursor nanowire. Herein we demonstrate the synthesis of PbS, PbSe, and PbTe nanotubes by using this simple synthetic route.

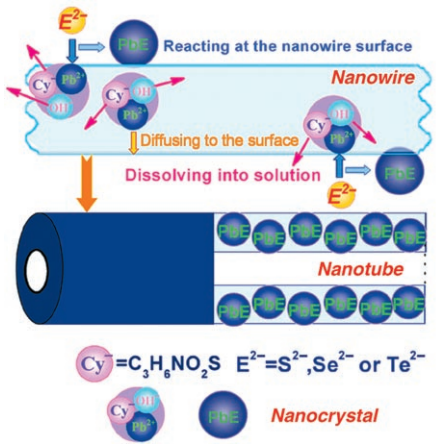

Figure 2. Schematic diagram of the synthetic route and proposed mechanism for the formation of PbE (E = S, Se, Te) nanotubes self-assembled from nanocrystals.

The XRD patterns (Figure 3) of the synthesized samples confirmed the formation of crystalline PbS (JCPDS no. 78-1901, Figure 3a), PbSe (JCPDS no. 78-1903, Figure 3b), and

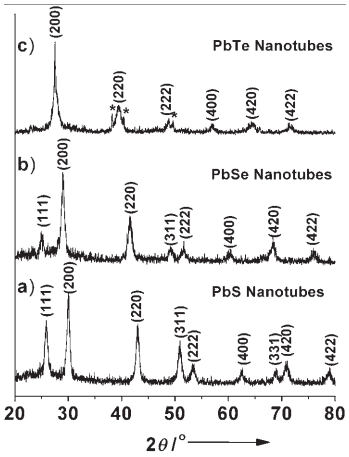

Figure 3. XRD patterns of synthesized lead chalcogenide nanotubes: a) PbS; b) PbSe; c) PbTe (* indicates peaks arising from Te).

 © 2006 Wiley-VCH Verlag GmbH & Co. KGaA, Weinheim

PbTe (JCPDS no. 78-1905, Figure 3c), all of which have a face-centered cubic structure. No diffraction peaks from the precursor nanowires were observed, thus indicating that the precursor nanowires are completely transformed into lead chalcogenide nanotubes. The total yields of lead chalcogenides were higher than 90%. The broadening of the diffraction peaks implies that the lead chalcogenide nanotubes consist of very small nanocrystals.

The TEM and SEM images (Figure 4) show that all the synthesized samples of PbS (Figure 4a–e), PbSe (Figure 4f–j), and PbTe (Figure 4k–o) consist of nanotubes. These

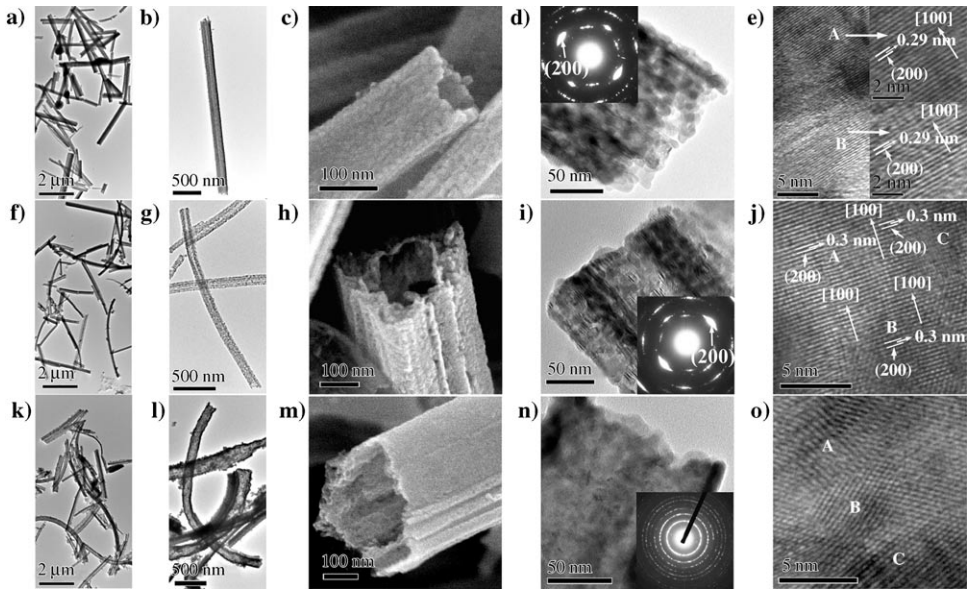

Figure 4. Characterization of PbE nanotubes: TEM (a,b,d,f,g,i,k,l,n; insets in d,i,n: ED pattern of a single nanotube), SEM (c,h,m), and HRTEM (e,j,o) of PbS (top), PbSe (middle), and PbTe (bottom), respectively.

nanotubes have similar sizes in terms of both diameter and length. The typical diameter is about 200 nm. They are several micrometers long—much shorter than the precursor nanowires—possibly because of breaking of the nanotubes by sonication during preparation. PbE nanotubes could also be obtained without using sonication, although it was frequently observed that several nanotubes grew together. From Figure 4 it can be seen that the PbE nanotubes are formed by the self-assembly of nanocrystals. The electron diffraction (ED) patterns (insets in Figure 4d, i, and n) show that the nanotubes are polycrystalline in nature. The HRTEM images (Figure 4e, j, and o) reveal that the PbE nanocrystals in the nanotubes are smaller than 10 nm.

The ED patterns of the PbS (inset in Figure 4d) and PbSe nanotubes (inset in Figure 4i) show discrete elongated bright dots for the (200) planes, unlike the usual polycrystalline diffraction rings, thus indicating that the nanocrystals aggregate into nanotubes with a highly oriented [100] crystallographic axis. This observation was supported by HRTEM. Figure 4e shows that two neighboring nanocrystals (A and B) in a PbS nanotube have the same orientation of the crystallographic axis along [100]. In Figure 4j, three nanocrystals (A, B, and C) in close contact in a PbSe nanotube have the same orientation along the [100] crystallographic axis.

No surfactant is used in our synthesis therefore the nanocrystals may aggregate together preferentially along a certain axis corresponding to a lower atom-density plane[33] and attach spontaneously through dipole–dipole attractions.[34,35] For face-centered cubic lead chalcogenides, a crystal unit has six equivalent [100] crystallographic axes and the (100) plane has the lowest atom density, thus making it more probable for nanocrystals to aggregate with their [100] crystallographic axis oriented in one direction. In contrast, the ED pattern (inset in Figure 4n) and HRTEM image (Figure 4o) of the PbTe nanotube clearly show a disorderly aggregation of the nanocrystals. The Pb/S and Pb/Se atomic ratios of the nanotubes were found to be about 1 by chemical composition analysis using EDS, whereas the Pb/Te atomic ratio was about 0.6. This excess of Te is due to the oxidation of Te^{2-} to elemental Te (Figure 3c, JCPDS no. 79-0736), which is responsible for the disordered aggregation of the PbTe nanocrystals.

The lead chalcogenide nanotubes described herein, which consist of nanocrystals smaller than 10 nm, in contrast to the Bohr exciton radii (bigger than 20 nm[23]) for bulk materials, exhibit a significant quantum confinement effect, as shown by the room-temperature absorption spectra (Figure 5). At the beginning of the absorption, a steep linear transition (absorption edge) can be seen, which is characteristic of direct band gap semiconductors. Based on the absorption edges,[36] the band gaps of the PbS, PbSe, and PbTe nanotubes were calculated to be 1.35, 1.13, and 0.75 eV, respectively, much larger than those of the bulk materials (0.2–0.4 eV[22]). These lead chalcogenide nanotubes, which are self-assembled from nanocrystals that display a quantum confinement effect as strong as that

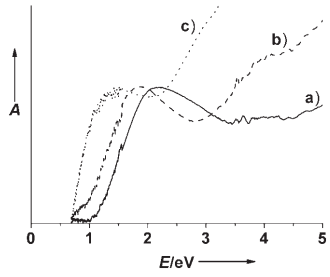

Figure 5. Absorption spectra of PbE nanotubes: a) PbS; b) PbSe; c) PbTe.

© 2006 Wiley-VCH Verlag GmbH & Co. KGaA, Weinheim

reported for quantum dots,[22–24] are presumed to be remarkably different from single-crystalline lead chalcogenide nanotubes.

In summary, lead chalcogenide nanotubes self-assembled from nanocrystals have been synthesized by a novel biomolecule-assisted method at room temperature. Polycrystalline precursor nanowires self-assembled from nanocrystals synthesized using cysteine play crucial roles as both the lead source and the template in the formation of lead chalcogenide nanotubes. These lead chalcogenide polycrystalline nanotubes display a definite quantum confinement effect. The biomolecule-assisted synthetic method demonstrated herein may also be extended to synthesize a variety of nanostructures assembled from nanocrystals.

Experimental Section

In a typical synthetic procedure for the precursor nanowires, a source solution was prepared by dissolving $Pb(NO_3)_2$ (0.033 g) and L-cysteine (0.012 g) in deionized water (30 mL) under magnetic stirring at room temperature. The reaction started when ethanolamine (0.2 mL) was quickly injected into the source solution at room temperature. A white product (precursor nanowires) formed immediately, and the solution was stirred for 20 min at room temperature. The product was separated by centrifugation and washed three times with deionized water and absolute ethanol. The precursor nanowires were then dispersed in ethanol (30 mL) to act as the lead source for the subsequent synthesis of lead chalcogenide nanotubes.

For the synthesis of the nanotubes, the chalcogenide source solution was prepared by dissolving $Na_2S{\cdot}9H_2O$ (0.050 g) or Se powder (0.015 g) and $NaBH_4$ (0.020 g) or TeO_2 powder (0.032 g) and $NaBH_4$ (0.050 g) in deionized water (5 mL). The reaction started and was allowed to proceed for 5 min by mixing the chalcogenide source solution and the precursor nanowire solution at room temperature whilst sonicating to ensure a homogeneous dispersion. The product was collected by centrifugation and washed three times with deionized water and absolute ethanol.

TEM was performed with a JEM-2100F field-emission transmission electron microscope (JEOL). SEM was carried out with a JSM-6700F field-emission scanning electron microscope (JEOL). X-ray powder diffraction patterns were recorded with a D/MAX 2200 (Rigaku) X-ray diffractometer with $Cu_{K\alpha}$ radiation ($\lambda = 1.54178$ Å) and a graphite monochromator. Absorption spectra were measured with a Cary-500 spectrophotometer (Cary).

Received: July 22, 2006
Published online: October 24, 2006

Keywords: chalcogens · lead · nanostructures · nanotubes · self-assembly

[1] S. Iijima, *Nature* **1991**, *354*, 56.
[2] L. Sun, F. Banhart, A. V. Krasheninnikov, J. A. Rodriguez-Manzo, M. Terrones, P. M. Ajayan, *Science* **2006**, *312*, 1199.
[3] A. B. Panda, G. Glaspell, M. S. El-Shall, *J. Am. Chem. Soc.* **2006**, *128*, 2790.
[4] D. Normile, *Science* **1999**, *286*, 2056.
[5] T. Hasobe, S. Fukuzumi, P. V. Kamat, *Angew. Chem.* **2006**, *118*, 769; *Angew. Chem. Int. Ed.* **2006**, *45*, 755.
[6] H. Tokudome, M. Miyauchi, *Angew. Chem.* **2005**, *117*, 2010; *Angew. Chem. Int. Ed.* **2005**, *44*, 1974.
[7] M. Remskar, *Adv. Mater.* **2004**, *16*, 1497.
[8] Y. G. Sun, Y. N. Xia, *Adv. Mater.* **2004**, *16*, 264.
[9] C. C. Tang, Y. Bando, B. D. Liu, D. Golberg, *Adv. Mater.* **2005**, *17*, 3005.
[10] Z. Y. Sun, H. Q. Yuan, Z. M. Liu, B. X. Han, X. R. Zhang, *Adv. Mater.* **2005**, *17*, 2993.
[11] K. S. Mayya, D. I. Gittins, A. M. Dibaj, F. Caruso, *Nano Lett.* **2001**, *1*, 727.
[12] W. Lee, R. Scholz, K. Niesch, U. Gosele, *Angew. Chem.* **2005**, *117*, 6204; *Angew. Chem. Int. Ed.* **2005**, *44*, 6050.
[13] T. Kijima, T. Yoshimura, M. Uota, T. Ikeda, D. Fujikawa, S. Mouri, S. Uoyama, *Angew. Chem.* **2004**, *116*, 230; *Angew. Chem. Int. Ed.* **2004**, *43*, 228.
[14] L. Li, Q. S. Wu, Y. P. Ding, *Nanotechnology* **2004**, *15*, 1877.
[15] E. Leontidis, M. Orphanou, T. Kyprianidou-Leodidou, F. Krumeich, W. Caseri, *Nano Lett.* **2003**, *3*, 569.
[16] N. Diaz, F. X. Simon, M. Schmutz, M. Rawiso, G. Decher, J. Jestin, P. J. Mesini, *Angew. Chem.* **2005**, *117*, 3324; *Angew. Chem. Int. Ed.* **2005**, *44*, 3260.
[17] E. Bakkers, M. A. Verheijen, *J. Am. Chem. Soc.* **2003**, *125*, 3440.
[18] X. G. Wen, Y. P. Fang, S. H. Yang, *Angew. Chem.* **2005**, *117*, 3628; *Angew. Chem. Int. Ed.* **2005**, *44*, 3562.
[19] H. Zogg, K. Kellermann, K. Alchalabi, D. Zimin, *Infrared Phys. Technol.* **2004**, *46*, 155.
[20] V. V. Shchennikov, S. V. Ovsyannikov, *Solid State Commun.* **2003**, *126*, 373.
[21] T. C. Harman, R. E. Reeder, M. P. Walsh, B. E. LaForge, C. D. Hoyt, G. W. Turner, *Appl. Phys. Lett.* **2006**, *88*, 243504.
[22] E. H. Sargent, *Adv. Mater.* **2005**, *17*, 515.
[23] F. W. Wise, *Acc. Chem. Res.* **2000**, *33*, 773.
[24] W. G. Lu, J. Y. Fang, K. L. Stokes, J. Lin, *J. Am. Chem. Soc.* **2004**, *126*, 11798.
[25] M. Chen, Y. Xie, J. C. Lu, Y. J. Zhu, Y. T. Qian, *J. Mater. Chem.* **2001**, *11*, 518.
[26] X. F. Qiu, Y. B. Lou, A. C. S. Samia, A. Devadoss, J. D. Burgess, S. Dayal, C. Burda, *Angew. Chem.* **2005**, *117*, 6005; *Angew. Chem. Int. Ed.* **2005**, *44*, 5855.
[27] W. H. Wang, Y. Geng, Y. Qian, M. R. Ji, X. M. Liu, *Adv. Mater.* **1998**, *10*, 1479.
[28] K. S. Cho, D. V. Talapin, W. Gaschler, C. B. Murray, *J. Am. Chem. Soc.* **2005**, *127*, 7140.
[29] G. F. Zou, Z. P. Liu, D. B. Wang, C. L. Jiang, Y. T. Qian, *Eur. J. Inorg. Chem.* **2004**, 4521.
[30] S. F. Wang, F. Gu, M. K. Lu, G. J. Zhou, A. Y. Zhang, *J. Cryst. Growth* **2006**, *289*, 621.
[31] B. Zhang, X. H. Ye, W. Y. Hou, Y. Xie, *J. Phys. Chem. B* **2006**, *110*, 8978.
[32] X. Y. Chen, X. F. Zhang, C. W. Shi, X. L. Lia, Y. T. Qian, *Solid State Commun.* **2005**, *134*, 613.
[33] Z. P. Zhang, H. P. Sun, X. Q. Shao, D. F. Li, H. D. Yu, M. Y. Han, *Adv. Mater.* **2005**, *17*, 42.
[34] Z. Y. Tang, N. A. Kotov, M. Giersig, *Science* **2002**, *297*, 237.
[35] C. Pacholski, A. Kornowski, H. Weller, *Angew. Chem.* **2002**, *114*, 1234; *Angew. Chem. Int. Ed.* **2002**, *41*, 1188.
[36] N. S. Pesika, K. J. Stebe, P. C. Searson, *Adv. Mater.* **2003**, *15*, 1289.

 © 2006 Wiley-VCH Verlag GmbH & Co. KGaA, Weinheim

Encapsulated Oligonucleotides

DOI: 10.1002/anie.200602779

Degradable Polyelectrolyte Capsules Filled with Oligonucleotide Sequences**

*Alexander N. Zelikin, Qi Li, and Frank Caruso**

Hollow polyelectrolyte capsules prepared by the layer-by-layer adsorption of polymers on sacrificial template particles[1] hold immense potential for drug delivery.[2] The capsules can be engineered with controlled sizes, composition, and functionality, and can be loaded with model therapeutics such as proteins[3,4] and low-molecular-weight drugs.[5] However, methods for loading such capsules with gene vaccines remain largely unexplored. Recent work has shown that DNA can be precipitated onto template particles with spermidine, coated with polyelectrolyte multilayers, and subsequently released into the capsule interior upon dissolution of the core particle.[6] Another approach is based on rehydration of capsules in a DNA-containing solution.[7] Although these earlier studies demonstrate the loading of large DNA molecules (e.g., calf-thymus DNA, DNA from herring testes), encapsulation of short oligonucleotides, such as small-interfering (si)RNA, is of particular importance as these molecules are highly susceptible to degradation and therefore need protection during storage and cellular delivery.[8]

Herein, we report a polycation-free encapsulation method to obtain high concentrations of uncomplexed, short oligonucleotide chains confined within monodisperse, degradable microcapsules. The encapsulation method exploits amine-functionalized silica (SiO_2^+) particles to adsorb oligonucleotides, followed by the assembly of thiol-functionalized poly(methacrylic acid) (PMA_{SH}) and poly(vinylpyrrolidone) (PVPON) multilayers.[9] Removal of the template particles produces degradable capsules filled with oligonucleotides (Scheme 1). The key advantages of this method include: 1) the ability to attain high loadings of oligonucleotides ($>10^4$ chains per capsule); 2) quantitative incorporation of oligonucleotides from the starting solution into the final formulation with more than 90% of the capsules filled with DNA; 3) avoiding the use of mechanical forces, such as those typically applied in emulsion encapsulation processes, which can cause DNA degradation; and 4) the ability to release DNA under reducing conditions (as occurs in cells) that degrade the capsules.

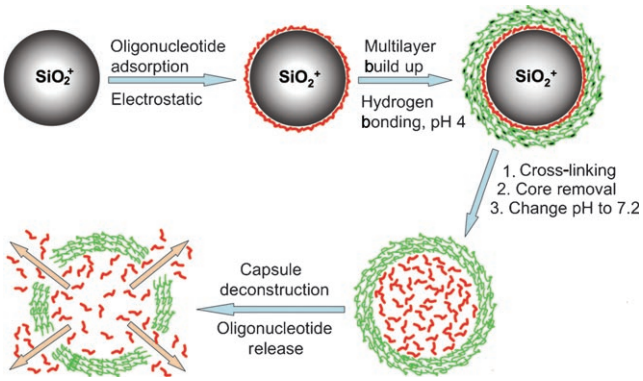

Scheme 1. Schematic representation of the encapsulation of short oligonucleotide sequences within polyelectrolyte capsules.

The 1-μm diameter amine-functionalized SiO_2 particles (ζ-potential of 62 ± 4 mV at pH 4) were exposed to solutions of varying concentrations of carboxytetramethylrhodamine (TAMRA)-labeled oligonucleotides containing 15 repeating thymidine (T) residues followed by 15 repeating cytosine (C) residues, TAMRA-poly$T_{15}C_{15}$. The electrostatic interaction between the negatively charged poly$T_{15}C_{15}$ and the SiO_2^+ particles results in adsorption of the oligonucleotides. By monitoring the fluorescence intensity of the supernatant before and after oligonucleotide adsorption, the saturation coverage of the particles was determined as $\approx 0.3\ mg\,m^{-2}$ (see the Supporting Information). In all subsequent experiments, we chose a TAMRA-poly$T_{15}C_{15}$ surface coverage below the saturation limit ($0.24\ mg\,m^{-2}$).

The PMA_{SH}/PVPON multilayer build up was initiated by exposing the particles with preadsorbed poly$T_{15}C_{15}$ to a PMA_{SH} solution at pH 4. At this pH value, the carboxylic groups of PMA_{SH} are largely uncharged ($pK_a \approx 6.5$), and as a result only minor displacement of DNA from the particles into the bulk solution ($\approx 2\%$) was observed (see the Supporting Information). Adsorption of the second polymer, PVPON, as well as subsequent assembly of the multilayers proceed through hydrogen bonding of the polymers and results in no measurable loss of DNA, as determined by fluorescence spectroscopy. These data provide evidence that more than 95% of the initially introduced DNA was retained on the particles during deposition of the multilayers (up to 16 layers). We note that although the oligonucleotides electrostatically interact with the amine binding sites on the silica particles, PMA_{SH} adsorption is most likely a combination of electrostatic interaction with accessible positive charges on the particles and hydrogen bonding with the particles and/or the poly$T_{15}C_{15}$.

To analyze the multilayer build up, we used PMA_{SH} labeled with 0.1 wt% Alexa Fluor 488 maleimide dye (AF488) and flow cytometry as this technique allows rapid and quantitative analysis of the particles and simultaneous monitoring of fluorescence from multiple fluorophores (Figure 1). The PMA_{SH}/PVPON build up is reflected by an increase in AF488 fluorescence and a similar amount of PMA_{SH} is adsorbed on bare SiO_2^+ particles (curve 1) and

[*] Dr. A. N. Zelikin, Q. Li, Prof. F. Caruso
Centre for Nanoscience and Nanotechnology
Department of Chemical and Biomolecular Engineering
The University of Melbourne
Parkville, Victoria 3010 (Australia)
Fax: (+61) 3-8344-4153
E-mail: fcaruso@unimelb.edu.au

[**] This work was supported by the Australian Research Council (Discovery Project and Federation Fellowship schemes). We thank A. P. R. Johnston for helpful discussions.

Supporting information for this article is available on the WWW under http://www.angewandte.org or from the author.

© 2006 Wiley-VCH Verlag GmbH & Co. KGaA, Weinheim

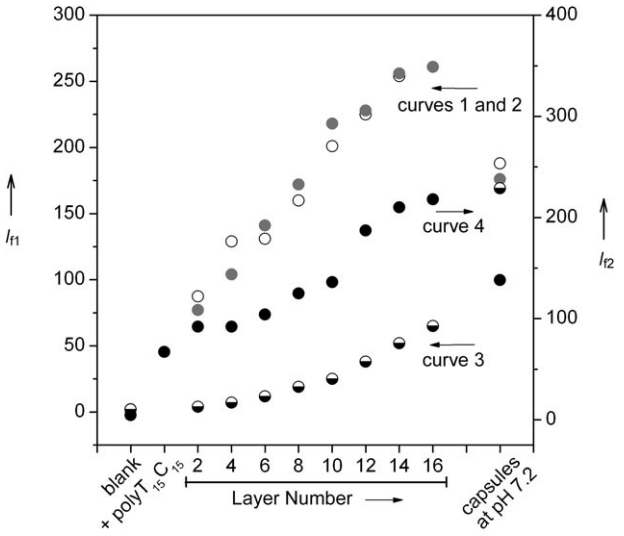

Figure 1. Flow cytometry data for the build up of PMA_{SH}/PVPON multilayers on 1 μm SiO_2^+ particles. Multilayer build up in the absence (curve 1) and presence (curve 2) of unlabeled $polyT_{15}C_{15}$ on SiO_2^+ particles, monitored through the fluorescence of the AF488 label (I_{f1}) on PMA_{SH}. Multilayer build up on particles with preadsorbed TAMRA-$polyT_{15}C_{15}$, monitored through the fluorescence of AF488 (I_{f1}) on PMA_{SH} (curve 3) and TAMRA (I_{f2}) on $polyT_{15}C_{15}$ (curve 4). The measurements were taken after the deposition of each PVPON layer.

those precoated with $polyT_{15}C_{15}$ (curve 2), including the deposition of the first PMA_{SH} layer. In contrast, when TAMRA-labeled $polyT_{15}C_{15}$ was used, we observed only a minor increase in AF488 fluorescence (curve 3) and a pronounced increase in TAMRA fluorescence (curve 4). This is readily attributed to the resonance energy transfer from AF488 to TAMRA and provides evidence that the PMA_{SH}/PVPON multilayer build up proceeds on the oligonucleotide-covered particle surface.[10]

To obtain stable capsules, the PMA_{SH} thiol groups were converted into disulfide linkages with the use of chloramine T,[11] the template particles were removed by dissolution with aqueous hydrofluoric acid/ammonium fluoride at pH 5,[12] and the capsules were washed and incubated at pH 7.2 for at least 24 h. Fluorescence analysis of the capsules (Figure 1) showed that in all three cases, the green fluorescence of the capsules was similar, including the capsules with TAMRA-$polyT_{15}C_{15}$. The red fluorescence of the capsules (curve 4) decreased and was similar to the level observed for the capsules obtained by using PMA_{SH} samples without the AF488 label (data not shown). These data provide evidence for the separation of TAMRA and AF488 dyes to a distance greater than the Förster radius and reflect separation of the oligonucleotide from the capsule wall into the interior of the capsule, that is, formation of the capsules with encapsulated free oligonucleotides.

Flow cytometry analysis of the capsules revealed that more than 90% of the capsules were filled with the DNA oligonucleotides (see the Supporting Information). The capsules are stabilized by disulfide linkages at physiological pH and retained the oligonucleotides over at least 72 h. As negligible loss of DNA was observed from the particle surface during multilayer assembly, each capsule contains up to 4.5×10^4 copies of the oligonucleotide. Compared with the 1-μm diameter of the template particles, the cross-linked PMA_{SH}/PVPON capsules at pH 7.2 are ≈1.5 μm in diameter, and the concentration of oligonucleotide chains corresponds to 40 μM (1.3 mM of phosphate groups).

Confocal laser scanning microscopy was used to visualize the oligonucleotide-filled capsules (Figure 2). The images

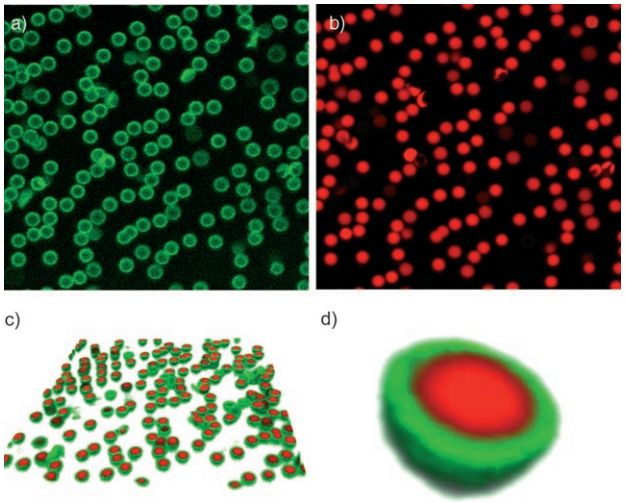

Figure 2. Confocal laser scanning microscopy images of 16-layer PMA_{SH}/PVPON capsules filled with $polyT_{15}C_{15}$ showing the fluorescence originating from the capsule walls owing to the PMA_{SH} labeled with AF488 (a) and the fluorescence of TAMRA-$polyT_{15}C_{15}$ (b), and 3D cross-section reconstruction images of the confocal data (c, d). The images (a–c) are 30×30 μm^2. The capsule in (d) is 1.5 μm.

provide proof of monodisperse capsules loaded with oligonucleotide sequences. The images show well-defined capsule walls (PMA_{SH} labeled with AF488, green, Figure 2 image a) and encapsulated DNA (TAMRA-$polyT_{15}C_{15}$, red, Figure 2, image b) distributed throughout the capsule interior. The charged PMA_{SH} capsule wall (pH 7.2) provides both steric hindrances to DNA diffusion[13] and also an energetic barrier for permeation of a negatively charged oligonucleotide through a negatively charged wall.[14]

Being stabilized solely through disulfide linkages, these capsules are deconstructed upon exposure to a thiol-disulfide exchange reagent, rapidly releasing the oligonucleotides into bulk solution (see the Supporting Information). Although in the current form these capsules exhibit burst-release characteristics, it should be possible to engineer the capsule properties to control the release of the cargo through rational design of the oligonucleotide length, capsule-wall thickness, and cross-linking density. We are currently investigating this to obtain release profiles to suit specific requirements.

In summary, we have developed a method to obtain monodisperse, degradable polyelectrolyte capsules filled with oligonucleotide sequences. The method permits essentially quantitative incorporation of the oligonucleotide into the capsules, which are stable for at least 72 h, and should allow facile control over capsule loading through variation of DNA to particle ratio. We also used this approach to encapsulate

 © 2006 Wiley-VCH Verlag GmbH & Co. KGaA, Weinheim

plasmid DNA by using 3-μm silica template particles with either PMA/PVPON or DNA oligonucleotides[15] as the capsule/membrane components. The plasmid DNA released from these capsules behaves like native DNA in hybridization assays and enzymatic reactions. Details of these studies will be presented in a future publication.

Experimental Section

Synthesis of the oligonucleotide-filled capsules. A suspension of the SiO_2^+ particles (0.25 wt%) was combined with a TAMRA-$T_{15}C_{15}$ solution and allowed to interact for 15 min, after which time the suspension was charged with PMA_{SH} to a final concentration of PMA_{SH} of 0.5 mg mL^{-1}. After an incubation time of 15 min, the particles were separated through centrifugation and washed three times with acetate buffer solution (10 mM; pH 4). The particles were resuspended in 250 μL of pH 4 buffer solution through vortexing (no sonication was used at any step of assembly) and combined with 250 μL of the adsorbing polymer solution. The solutions of PMA_{SH} used in the adsorption cycles (acetate buffer solution (1 mg mL^{-1} in 10 mM; pH 4)) were prepared from the 10 mg mL^{-1} stock solution of PMA_{SH} incubated with dithiothreitol (DTT; 100 mg mL^{-1}) in phosphate buffer solution (10 mM; pH 8) for at least 12 h. After completion of the multilayer build up, the particles were exposed to a 2 mM solution of chloramines T in 2-(*N*-morpholine)ethanesulfonic acid (MES) buffer solution (pH 6) for 1 min, followed by two washing cycles with MES buffer solution (pH 6).To form hollow capsules, the silica core was dissolved by treatment with HF/NH_4F solution (2:8 M; pH 5) at 20 °C for 5 min, followed by multiple centrifugation (4500 *g* for 10 min)/buffer solution washing cycles.[12] The washing cycles were repeated as necessary until the pH of the capsule suspension became identical to the pH of the washing buffer solution.

Received: July 13, 2006
Revised: August 22, 2006
Published online: October 31, 2006

Keywords: degradable capsules · DNA · drug delivery · layer-by-layer technique · oligonucleotides

[1] a) F. Caruso, R. A. Caruso, H. Möhwald, *Science* **1998**, *282*, 1111–1114; b) E. Donath, G. B. Sukhorukov, F. Caruso, S. A. Davis, H. Möhwald, *Angew. Chem.* **1998**, *110*, 2324–2327; *Angew. Chem. Int. Ed.* **1998**, *37*, 2202–2205.

[2] a) B. G. De Geest, R. E. Vandenbroucke, A. M. Guenther, G. B. Sukhorukov, W. E. Hennink, N. N. Sanders, J. Demeester, S. C. De Smedt, *Adv. Mater.* **2006**, *18*, 1005–1009; b) C. Picart, A. Schneider, O. Etienne, J. Mutterer, P. Schaaf, C. Egles, N. Jessel, J.-C. Voegel, *Adv. Funct. Mater.* **2005**, *15*, 1771–1780.

[3] Y. Lvov, A. A. Antipov, A. Mamedov, H. Möhwald. G. B. Sukhorukov, *Nano Letters* **2001**, *1*, 125–128.

[4] F. Caruso, D. Trau, H. Möhwald, R. Reneneberg, *Langmuir* **2000**, *16*, 1485–1488.

[5] A. J. Khodape, F. Caruso, *Biomacromolecules* **2002**, *3*, 1154–1162.

[6] D. G. Shchukin, A. A. Patel, G. B. Sukhorukov, Y. M. Lvov, *J. Am. Chem. Soc.* **2004**, *126*, 3374–3375.

[7] O. Kreft, R. Georgieva, H. Bäumler, M. Steup, B. Müller-Röber, G. B. Sukhorukov, H. Möhwald, *Macromol. Rapid Commun.* **2006**, *27*, 435–440.

[8] G. Lambert, E. Fattal, P. Couvreur, *Adv. Drug Delivery Rev.* **2001**, *47*, 99–112.

[9] A. N. Zelikin, J. F. Quinn, F. Caruso, *Biomacromolecules* **2006**, *7*, 27–30.

[10] An increase in TAMRA fluorescence was also observed while depositing PMA_{SH}/PVPON multilayers on SiO_2^+ particles with TAMRA-poly$T_{15}C_{15}$ by using PMA_{SH} without the AF488 dye. However, the magnitude of the fluorescence increase was much lower ($\approx$3 times) than that observed when the dye was present. Also, TAMRA fluorescence for the capsules remained greater than that for the SiO_2^+ particles with adsorbed oligonucleotide. These results show that the change in the local environment of TAMRA also plays an important role in the fluorescence observed.

[11] Chloramine T provides exclusive conversion of thiol groups into disulfide linkages, as opposed to hydrogen peroxide, utilized in our earlier research (reference [9]). See, a) Y. Shechter, Y. Burstein, A. Patchornik, *Biochemistry* **1975**, *14*, 4497–45–03; b) J. F. Finley, E. L. Wheeler, S. C. Witt, *J. Agric. Food Chem.* **1981**, *29*, 404–407.

[12] Y. Wang, F. Caruso, *Chem. Mater.* **2006**, *18*, 4089–4100. The amount of silica remaining in the capsules is typically lower than 1%, as assessed by FTIR and EDX measurements.

[13] A. P. R. Johnston, F. Caruso, *J. Am. Chem. Soc.* **2005**, *127*, 10014–10015.

[14] W. Tong, W. Dong, C. Gao, H. Mohwald, *J. Phys. Chem. B* **2005**, *109*, 13159–13165.

[15] A. P. R. Johnston, H. Mitomo, E. S. Read, F. Caruso, *Langmuir* **2006**, *22*, 3251–3258.

 © 2006 Wiley-VCH Verlag GmbH & Co. KGaA, Weinheim

Directed Evolution

DOI: 10.1002/anie.200602795

Iterative Saturation Mutagenesis on the Basis of B Factors as a Strategy for Increasing Protein Thermostability**

Manfred T. Reetz, José D. Carballeira, and Andreas Vogel*

Thermostability of proteins is a crucial issue when they are applied as catalysts in organic chemistry, polymer technology, and pollution cleanup, as well as components in detergents, as diagnostic tools (sensors), as bionanotechnological devices, and sometimes even as therapeutic drugs.[1] For this reason, considerable effort has been invested in the quest to enhance thermostability by such techniques as protein engineering,[1] posttranslational enzymatic or chemical modification,[1c,2] use of additives,[1c,3] and/or immobilization.[1c,4] Methods based on protein engineering include site-specific mutagenesis,[1a,c,d,5] which is often guided by the structural differences between mesophilic and thermophilic enzymes,[6] or by computational

[*] Prof. Dr. M. T. Reetz, Dr. J. D. Carballeira, Dr. A. Vogel
Max-Planck-Institut für Kohlenforschung
Kaiser-Wilhelm-Platz 1, 45470 Mülheim/Ruhr (Germany)
Fax: (+49) 208-306-2985
E-mail: reetz@mpi-muelheim.mpg.de

[**] We thank the Fonds der Chemischen Industrie and the German-Israeli Project Cooperation (DIP) for support.

© 2006 Wiley-VCH Verlag GmbH & Co. KGaA, Weinheim
InterScience

design.[7] Nevertheless, the difficulty in predicting the appropriate sites and the optimal amino acid substitution remains a challenge. Directed evolution,[8] a process comprising random gene mutagenesis, expression, and screening/selection is also appealing.[1b,c,e,9] Accordingly, the gene is targeted by random mutagenesis methods such as repeating cycles of error-prone PCR (epPCR) with formation of relatively large libraries of enzyme variants that have to be screened or selected for the desired but unfortunately rare variants.

We used a new approach to select the sites for amino acid exchanges coupled with an efficient evolutionary strategy, thereby eliminating the need to screen large libraries yet achieving pronounced increases in thermostability. Systematic structural studies regarding mesophilic and thermophilic enzymes have shown that the latter are characterized by higher degrees of rigidity resulting from the accumulation of a variety of different effects, many being rather subtle.[6] These include salt bridges, hydrogen bonds, and π–π interactions at crucial positions in the protein in addition to hydrophobic interactions and possible disulfide bridges, all of which help to prevent unfolding at various stages of denaturation.[1,5–7,9] Enhancing the thermostability of mesophilic enzymes should therefore be possible by increasing the rigidity at appropriate sites. The challenge is to achieve significant degrees of thermostabilization in an efficient manner without losing enzyme activity at room temperature. We anticipated that this goal can be reached in a practical and straightforward process. Firstly, the choice of the appropriate sites at which rigidity is to be increased is made on the basis of atomic displacement parameters obtained from X-ray data, namely the B factors (or B values).[10] They reflect smearing of atomic electron densities with respect to their equilibrium positions as a result of thermal motion and positional disorder.[10] Therefore, we target solely those amino acids in a protein that display the highest B factors, corresponding to the most pronounced degrees of thermal motion and thus flexibility. These sites, comprising one or more amino acids, are then chosen for saturation mutagenesis[8] with the formation of small focused libraries. The gene of the best hit is subsequently used as a template for a second round of saturation mutagenesis at one of the other selected sites and the process is continued by focusing on the remaining sites iteratively (one site may be considered more than once). Such a convergent process maximizes the possibility of additive and/or cooperative effects by combining sensitive amino acid sites (not specific mutations) in an iterative manner. This concept of "iterative saturation mutagenesis" is crucial for success. It is a novel evolutionary strategy that also forms the basis of iterative CASTing (CAST = combinatorial active-site saturation test) as a means to increase the enantioselectivity of enzymes.[11] Iterative saturation mutagenesis as was applied in this case provides variants that are statistically not readily accessible by the traditional random-mutagenesis methods that were used previously to evolve thermostability.[1b,c,e,9]

In a model study, the lipase from *Bacillus subtilis* (Lip A)[12] was chosen as the enzyme for enhancing thermostability. It is a mesophilic lipase composed of 181 amino acids, and it has been characterized by X-ray crystallography several times.[13] We chose the crystal structure from the most recent study, which contains a single independent molecule in the asymmetric unit.[13e,14] Only the resolved amino acids were considered, which means that in the particular case at hand, the nonresolved C and N termini were not addressed. The 10 amino acids that show the highest average B values[15] were then chosen as sites for randomization by using standard saturation mutagenesis[8] (Arg 33: average B factor = 50.9; Lys 69: 44.1; Gln 164: 40.7; Asp 34: 39.9; Lys 112: 39.6; Lys 35: 38.9; Met 134: 38.5; Tyr 139: 37.9; Ile 157: 37.4; Gly 13: 37.0). Eight libraries were then constructed, namely at sites A (Gly 13), B (Arg 33, Asp 34, Lys 35), C (Lys 69), D (Lys 112), E (Met 134), F (Tyr 139), G (Ile 157), and H (Gln 164) (see Figure 1).

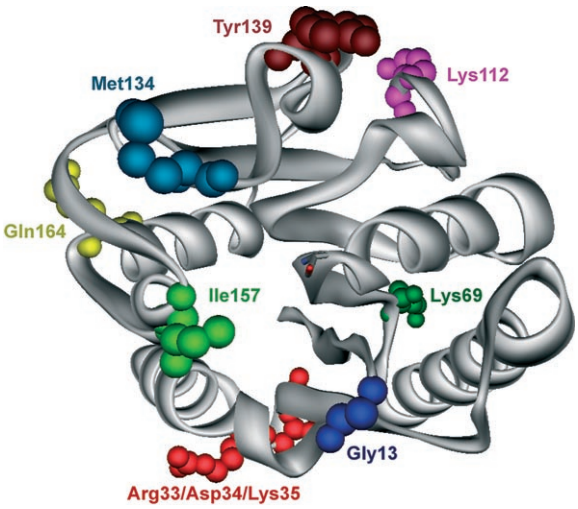

Figure 1. The sites in Lip A that were chosen for saturation mutagenesis. The picture shows a structural model based on the X-ray structure.[13] Library A (dark blue), library B (red), library C (dark green), library D (violet), library E (brown), library F (light blue), library G (light green), library H (yellow). Ser 77 is the catalytically active site.

The generation of the mutant libraries throughout this study was performed by using the QuikChange mutagenesis method from Stratagene.[16] Lip A was expressed in the supernatant of *E. coli* BL21(DE3) cell cultures by using a known expression system. Owing to the difficulties in performing high-throughput assays with triglycerides, which are the natural substrates, *p*-nitrophenyl caprylate was employed. Fast screening for improved thermostability in the initial eight libraries was performed in 96-well microtiter plates by heating the enzyme solutions (diluted supernatants) at 54 °C for 15 min with a PCR thermocycler. The reactions were monitored by a UV/Vis plate reader (405 nm). Under these test conditions, the wild-type (wt) enzyme displays a residual activity of only 9 % in the hydrolysis of *p*-nitrophenyl caprylate. Thermostability was assessed by measuring the residual activity subsequent to the exposure to high temperatures. In the literature, the so-called T_{50} value is often used to quantitatively characterize thermostability.[1,17] It is the temperature required to reduce the initial enzymatic activity by 50 % within a given period of time. T_{50} is near to or at the critical temperature of denaturation. To speed up screening, we applied a 15-min heat treatment, resulting in T_{50}^{15} values.

 © 2006 Wiley-VCH Verlag GmbH & Co. KGaA, Weinheim

The hits were then re-examined by applying heat treatment for one hour, resulting in T_{50}^{60} values. Exploratory experiments had shown that Lip A denatures irreversibly at high temperatures, and that $T_{50}^{15} = 50\,^{\circ}C$, whereas T_{50}^{60} was found to be 48 °C. In the case of libraries A, C, D, E, F, G, and H, each originating from a single amino acid site, saturation mutagenesis[8] was applied at the respective single positions and oversampling was performed to ensure > 95 % coverage (about 300 clones).[18] In doing so, we used NNK degeneracy (N: adenine/cytosine/guanine/thymine; K: guanine/thymine) to encode all 20 proteinogenic amino acids. In the case of library B, resulting from cassette mutagenesis that induces simultaneous randomization at positions 33, 34, and 35, a representative sample of only 3000 clones was examined, although about 100 000 clones would be required statistically for 95 % coverage. Variants showing an improved thermostability were grown again, reanalyzed three times, and then sequenced. In the first rounds of mutagenesis, improved variants were identified in libraries A, B, D, E, F, and G but none were found in libraries C and H (Figure 2). The most thermostable variant (IV) resulting from this first evolutionary step originates from library E (Met134Asp) and displays a T_{50}^{15} of 54.3 °C.

To increase thermostability further, two strategies appeared to be logical. One was to produce new variants simply by combining the mutations of the hits from the libraries A–G in various permutational ways. The second strategy, which we chose, involves a stepwise evolutionary approach based on iterative saturation mutagenesis[11] (Figure 2). First, the gene of the best hit, IV, was used as a template for performing saturation mutagenesis (NNK degeneracy) at position 157, the site defining library G in which the second best hit had been found in the first round of mutagenesis.[19] This gives the system the possibility to choose again between the 20 possible amino acids, but this time starting from a different gene. The outcome is mutation Ile 157 Met. Thus, in this case the result is identical to a variant that would have been obtained by combining the mutations of variants IV and VI. Saturation mutagenesis was then continued stepwise following the same criteria by "visiting" the other sites as shown in Figure 2. In the last two steps leading to variants IX, X, and XI, the mutations found were not those induced in the initial mutagenesis rounds. The largest stabilization effect was observed when variant IX, already with a respectable T_{50}^{15} of 62.8 °C, was subjected to cassette mutagenesis (NNK degeneracy) at positions 33, 34, and 35. This resulted in the identification of two hyperthermal variants X and XI (Figure 2) that showed no measurable decrease in activity at room temperature following heat treatment at 100 °C for 15 min. Owing to technical problems with the screening system at temperatures above 100 °C, further optimization by saturation mutagenesis at position 13 or by focusing on the nonresolved C and N termini was not attempted.

From this point on, we focused our attention on variants X and XI. Following purification of both variants, the respective residual activity curves, the T_{50}^{60} values (60-min heating time), the kinetic constants, as well as the substrate and selectivity profiles were determined. Figure 3 shows the residual activity curves of the wt and of variants X and XI, demonstrating the enormous differences in thermostability. The half-lives ($t_{1/2}$) at 55 °C were measured to be 905 and 980 min, respectively, whereas $t_{1/2}$ of the wt is < 2 min. The enhanced thermostability is also revealed by the T_{50}^{60} values of variants X and XI, which are 89 and 93 °C, respectively, compared with 48 °C for the wt. This means that ΔT_{50}^{60} values of 41 and 45 °C, respectively, have been achieved. We are not aware of other cases of such dramatic increases in thermostability.[20]

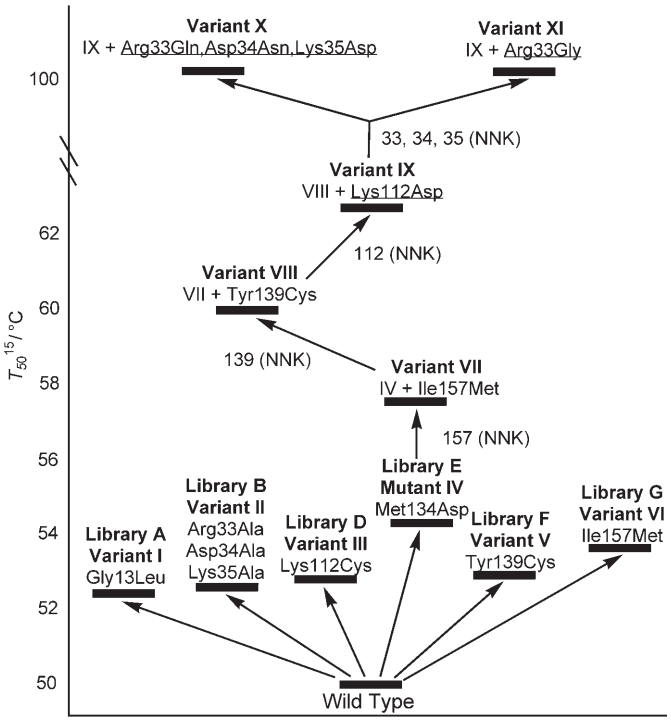

Figure 2. Thermostability diagram. Enzyme variants were characterized after preliminary screening by measuring T_{50}^{15}. The underlined amino acid exchanges indicate new mutational changes in the respective mutagenesis experiment; those that are not underlined appeared earlier in the evolutionary tree.

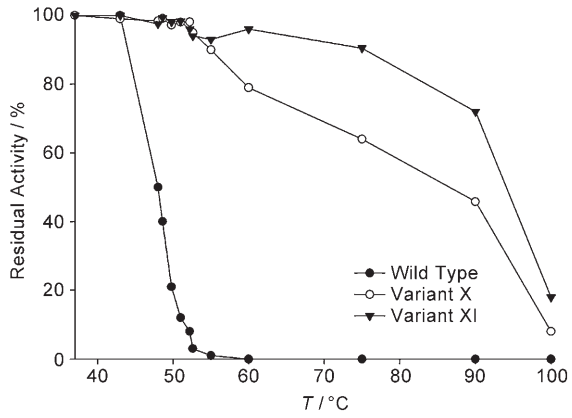

Figure 3. Thermostability of the purified wt and mutants X and XI of Lip A as displayed by the residual-activity curves. Activity in the hydrolysis of *p*-nitrophenyl caprylate was measured after the enzyme solutions were treated at various temperatures (37–100 °C) for 1 h.

© 2006 Wiley-VCH Verlag GmbH & Co. KGaA, Weinheim

To obtain more-detailed information regarding the crucial question of whether or not increased thermostability was evolved at the expense of activity,[1,6,7,9] further kinetic measurements were made by using *p*-nitrophenyl acetate (PNPA) as the substrate at 25 °C in potassium phosphate buffer solution (10 mM; pH 7.0). The values of K_m and k_{cat} of the wt and of the purified variants X and XI were derived from the corresponding Michaelis–Menten plots. The data show that no significant differences in catalytic parameters exist (wt: $K_m = 1.1$ mM; $k_{cat} = 6.5 \times 10^{-2}$ min^{-1}; $k_{cat}/K_m = 5.8 \times 10^{-2}$ mM^{-1} min^{-1}. Variant X: $K_m = 0.62$ mM; $k_{cat} = 5.8 \times 10^{-2}$ min^{-1}; $k_{cat}/K_m = 9.4 \times 10^{-2}$ mM^{-1} min^{-1}. variant XI: $K_m = 0.73$ mM; $k_{cat} = 6.3 \times 10^{-2}$ min^{-1}; $k_{cat}/K_m = 8.6 \times 10^{-2}$ mM^{-1} min^{-1}). Thus, the thermostability of the variants has been increased significantly without influencing enzyme activity. This conclusion was corroborated by measuring the activity and, when relevant, the enantioselectivity of the wt and variants X and XI as catalysts in the hydrolysis of 12 other *p*-nitrophenyl esters, some of which are chiral. Significant differences in the catalytic profile were not observed in any of the cases. For example, in the hydrolytic kinetic resolution of *p*-nitrophenyl-2-[4-(2-methylpropyl)phenyl]propanoate, the selectivity factor (E) in favor of the *R* enantiomer remains constant when going from the wt to the variants (wt: $E = 8.1$; variant X: $E = 8.2$; variant XI: $E = 8.5$).

The X-ray structure of Lip A exhibits a compact minimal α/β hydrolase fold with a six-stranded parallel β sheet flanked by five α helices, two of them on one side of the sheet and three on the other side.[13] The catalytic triad (Ser 77, Asp 133, and His 156), as well as the amino acids forming the oxyanion hole, reside in positions very similar to those of other lipases. A sound discussion regarding the source(s) of enhanced thermostability requires X-ray structural data of the variants coupled with a detailed theoretical analysis, which are not yet available. At this time we note that most of the mutations (positions 13, 33, 34, 35, 112, 134, and 157) lie in surface loops (Figure 4) where flexibility is expected to be highest. The respective amino acid exchanges help in stabilizing these loops and thus the protein through a variety of interactions.[1,6,9e] Solvent exposure of the randomized positions may also play a role. The power of our approach, from a practical point of view, has to do with the fact that these specific factors need not be assessed to obtain improved mutants.

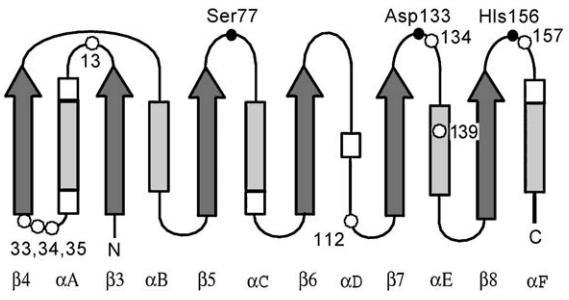

Figure 4. Secondary-structure topology of Lip A modified from the representation that was published earlier.[13] The nomenclature of the strands is taken from the canonical α/β hydrolase fold. All the positions that lead to thermostable variants are represented as white circles, the amino acids of the catalytic triad as black circles, and the termini of the protein as C and N. 3_{10} helical turns are represented as white boxes.

Clearly, a hyperthermophilic enzyme has been created, yet its catalytic profile is one of a mesophile. In some previous studies, enhanced thermostability also did not reduce activity, although the reported increases in thermostability were much smaller than in the present study.[1,9] Natural hyperthermophiles evolved not just to withstand extreme temperatures, but also to display optimal reaction rates under such conditions.[6] Excessively high activity at high temperatures would adversely effect the balance of metabolic transformations, which could be detrimental to the organism. This suggests that natural hyperthermophilic enzymes contain built-in structural features that slow down reaction rates, perhaps mainly in the interior of their globular structures. These are the regions that remain unaffected in our approach.[21] To engineer proteins for wide industrial applications, we suggest that after the improvement of thermostability by the present approach or through another method,[1,9] a second-step enhancement of substrate scope and/or enantioselectivity can be addressed (if needed) by applying such techniques as epPCR,[8] DNA shuffling,[8] or CASTing.[11,22] Indeed, this goes hand in hand with the recent conclusion that enhanced thermostability promotes the ease of evolvability.[23]

The strategy we have described constitutes a combination of rational design and directed evolution. In the present model study, less than 8000 clones were screened, yet it resulted in an impressive enhancement of thermostability without compromising the activity or enantioselectivity. The efficiency of the method is derived from the rapid build up of evolutionary pressure exerted by the iterative cycles of saturation mutagenesis at properly chosen sites in the enzyme. In contrast, repeating cycles of epPCR, previously used most often in the enhancement of thermostability,[1,9] would not be expected to result in the hyperthermophilic variants X and XI (from the present study) owing to statistical reasons. Our approach uses a physical parameter directly related to the known correlation between flexibility and stability. Nevertheless, it is currently not clear how general the method is because only one example has been reported so far.

Application of the strategy requires the availability of the X-ray structure of the wt. However, protocols for computing B factors[24] have emerged that can, in principle, be used in those cases in which crystallographic data is not available. Moreover, B factors correlate with the NMR relaxation data.[25] Finally, based on the same principle described herein, the targeted reduction in thermostability, which is desired for special applications,[26] should be possible by following a similar strategy, e.g., by focusing on sites with low B factors in nonregular structural units.

Experimental Section

Enzyme expression and screening system: Saturation mutagenesis libraries were generated by using the QuikChange mutagenesis strategy from (Stratagene, USA) by using NNK degenerate primers.[16]

 © 2006 Wiley-VCH Verlag GmbH & Co. KGaA, Weinheim

Culture conditions: *Bacillus subtilis* lipase A was expressed in the supernatant of *E. coli* BL21 (DE3; Novagen, Madison, USA) cell cultures by using the expression system based on the pET22 vector previously described.[13b] Supernatant expression avoids the use of whole cells, which lead to background reactions. The colonies were picked with a colony picker QPIX (Genetix, Boston, MA), and precultures were grown in deep-well plates by using 800 μL per well of lactose-free 505 media[11] (formula per liter: 20 mL of 50 × 505 solution (250 g L^{-1} glycerol, 25 g L^{-1} glucose, and distilled water), 50 mL of 20 × NPS solution (66 g L^{-1} $(NH_4)_2SO_4$, 136 g L^{-1} KH_2PO_4, and 142 g Na_2HPO_4), 2 mL of 1 M $MgSO_4$, and filled to a volume of 1 L with ZY media (10 g L^{-1} tryptone, 5 g L^{-1} yeast extract)). This preculture was used to inoculate, using a manual plate replicator, an expression culture with 900 μL per well of 5052 media[27] containing lactose as inducer (formula per liter: 20 mL of 50 × 5052 solution (100 g L^{-1} α-lactose, 250 g L^{-1} glycerol, 25 g L^{-1} glucose, and distilled water), 50 mL of 20 × NPS solution, 2 mL of 1 M MgSO4, and filled to a volume 1 L with ZY media).[27] In both media carbenicillin was used as antibiotic (100 μg mL^{-1}). The cultures were grown at 37 °C and 800 rpm for 24 h. The cultures were then centrifuged at 4000 rpm for 20 min.

Gene sequencing: Mutant genes were sequenced by using the standard T7-3T7 primer by Medigenomix (Martinsried, Germany).

Screening: The screening for thermostability was performed by using the supernatants in 96-well microtiter plates. *p*-Nitrophenyl caprylate was selected as the substrate for the preliminary screening. Stock solutions of the substrate (50 mM substrate in acetonitrile) were stored at −20 °C. The supernatants were diluted in double-distilled water in a 1:3 ratio (supernatant/water) to adjust the lipase activity, and 30 μL of this solution was tested against a solution of *p*-nitrophenyl caprylate in K_2HPO_4 (50 mM), Triton X-100 (0.1 %); pH 8 buffer solution (100 μL of 2.5 mM). The hydrolytic reaction was followed at 405 nm over 3 min by using a Spectramax Plus^{384} from Molecular Devices (Sunnyvale, USA). No significant background hydrolysis was observed when the supernatant was used under these working conditions.

Thermostability was assessed based on the residual activity subsequent to the exposure to high temperatures. 100 μL of diluted supernatants from the same deep-well plate was transferred to 200-μL PCR tube 96-well plates that were then heated for 15 min at a defined temperature; after cooling to 4 °C for 5 min (stop the heat shock), the samples were kept at room temperature for 15 min. A volume of 30 μL was transferred from each well to a microtiter plate, and the hydrolytic reaction **1**→**2** was repeated to compare the activity before and after the heat shock.

Exploratory experiments have shown that the lipase A from *Bacillus subtilis* denatures at high temperatures. The wt Lip A shows a T_{50}^{15} of 50 °C and a T_{50}^{60} of 48 °C.

According to these characteristics, a preliminary screening was developed to identify thermally stable variants from the designed libraries: heating the enzyme solutions at 54 °C for 15 min by using a PCR thermocycler. According to this test, the wt enzyme has an average residual activity of ≈10 % (average of 96 tests) in the hydrolysis of the *p*-nitrophenyl caprylate. Mutants showing more than 20 % retained activity (established as threshold for screening purposes) were considered as hits of the screening, and their thermostability was subsequently reproduced. The T_{50}^{15} was determined by measuring the activity after heating at different temperatures for 15 min. For this purpose, a gradient PCR thermocycler was used. The heat-shock temperature was then increased stepwise, according to the T_{50}^{15} of the variant selected as the template.

The kinetic constants of the purified mutants were calculated by using PNPA as the substrate. Initial rates of hydrolysis of PNPA at various concentrations were determined at 25 °C in potassium phosphate buffer (10 mM; pH 7.0). The values of K_m and k_{cat} of the purified variants were derived from the corresponding Michaelis–Menten plots.

The $t_{1/2}$ values of the mutants at 55 °C were determined by taking samples at different times and their hydrolytic activities then evaluated. The percentage of retained activity of each sample was then plotted against time. The half-life was determined from this plot as the time at which the activity is reduced to 50 % of the initial activity.

Enzyme purification: The enzyme variants were purified from the culture supernatant as previously reported[12a] and by means of a double ultrafiltration process by using Amicon Ultra Centrifugal filters of 10 NMWL (NMWL = nominal molecular weight limit) and 50 NMWL cut offs (Millipore, USA). The purity of the 19.4-kDa enzyme was confirmed by SDS-PAGE electrophoresis (10 % acrylamide).

Reaction conditions: To expression culture supernatant (100 μL), tris(hydroxymethyl)aminomethane hydrochloride (Tris-HCl) buffer solution (400 μL, 100 mM; pH 7.5) containing substrate (20 μL, 10 mg mL^{-1}) in acetonitrile were added. The reaction mixture was shaken at 800 rpm for 4 h at 30 °C. The solution was extracted with dichloromethane (500 μL). A second extraction step was performed by adding dichloromethane (500 μL) and HCl (20 μL, 10 %) to optimize acid extraction. The extracted organic phase was evaporated and redissolved in dichloromethane (100 μL) and analyzed by GC.

GC analysis: The chiral analyses of the kinetic resolution reactions of *p*-nitrophenyl-2-[4-(2-methylpropyl)phenyl]propanoate were performed by using a DiMePeBETA-Ivadex-1 chiral column (25 m, 0.25 mm, 0.15 μm) from IVA Analysentechnik, (Meerbusch, Germany). Conditions: Carrier (N_2) 1.4 mL min^{-1}. Temperature profile: 140 °C, 30 min, 10 °C min^{-1}, 200 °C for 90 min. Absolute configuration was determined by comparison with commercial enantiopure products.

Received: July 13, 2006
Revised: August 18, 2006
Published online: October 31, 2006

Keywords: biotransformation · directed evolution · enzymes · protein engineering · protein stability

[1] For reviews covering methods for increasing the thermostability of enzymes, see: a) T. Oshima, *Curr. Opin. Struct. Biol.* **1994**, *4*, 623–628; b) P. L. Wintrode, F. H. Arnold, *Adv. Protein Chem.* **2001**, *55*, 161–225; c) C. Ó'Fágáin, *Enzyme Microb. Technol.* **2003**, *33*, 137–149; d) V. G. H. Eijsink, A. Bjørk, S. Gåseidnes, R. Sirevåg, B. Synstad, B. van den Burg, G. Vriend, *J. Biotechnol.* **2004**, *113*, 105–120; e) V. G. H. Eijsink, S. Gåseidnes, T. V. Borchert, B. van den Burg, *Biomol. Eng.* **2005**, *22*, 21–30; f) N. S. Wingreen, H. Li, C. Tang, *Polymer* **2004**, *45*, 699–705; g) V. Renugopalakrishnan, R. Garduño-Juárez, G. Narasimhan, C. S. Verma, X. Wei, P. Li, *J. Nanosci. Nanotechnol.* **2005**, *5*, 1759–1767; h) A. S. Bommarius, J. M. Broering, *Biocatal. Biotransform.* **2005**, *23*, 125–139.

[2] a) C. Ó'Fágáin, *Biochim. Biophys. Acta* **1995**, *1252*, 1–14; b) T. Matsuura, K. Miyai, S. Trakulnaleamsai, T. Yomo, Y. Shima, S. Miki, K. Yamamoto, I. Urabe, *Nat. Biotechnol.* **1999**, *17*, 58–61; c) J.-H. Liu, C.-F. Tsai, J.-W. Liu, K.-J. Cheng, C.-L. Cheng, *Enzyme Microb. Technol.* **2001**, *28*, 582–589; d) M. Bakke, N. Kajiyama, *Appl. Biochem. Biotechnol.* **2004**, *112*, 123–131; e) R. J. Solá, K. Griebenow, *FEBS Lett.* **2006**, *580*, 1685–1690.

[3] a) R. Brugger, A. Kronenberger, A. Bischoff, D. Hug, M. Lehmann, A. P. G. M. van Loon, M. Wyss, *Biocatal. Biotransform.* **2001**, *19*, 505–516; b) C. Bieniarz, M. J. Cornwell, D. F. Young, *Bioconjugate Chem.* **1998**, *9*, 390–398; c) L. Gómez, H. L. Ramírez, R. Villalonga, *Biotechnol. Lett.* **2000**, *22*, 347–350; d) K. Khajeh, H. Naderi-Manesh, B. Ranjbar, A. Moosavi-Movahedi, M. Nemat-Gorgani, *Enzyme Microb. Technol.* **2001**,

 © 2006 Wiley-VCH Verlag GmbH & Co. KGaA, Weinheim

28, 543 – 549; e) S. K. Baier, D. J. McClements, *Food Res. Int.* **2003**, *36*, 1081 – 1087.

[4] "Immobilization of Enzymes and Cells": *Methods in Biotechnology*, *Vol. 22*, 3rd ed. (Ed.: J. M. Guisan), Humana, Totowa, **2006**.

[5] For typical examples, see: a) R. S. Stearman, A. D. Frankel, E. Freire, B. Liu, C. O. Pabo, *Biochemistry* **1988**, *27*, 7571 – 7574; b) B. van den Burg, G. Vriend, O. R. Veltman, G. Venema, V. G. H. Eijsink, *Proc. Natl. Acad. Sci. USA* **1998**, *95*, 2056 – 2060; c) L. Serrano, A. G. Day, A. R. Fersht, *J. Mol. Biol.* **1993**, *233*, 305 – 312; d) H. Kaneko, H. Minagawa, J. Shimada, *Biotechnol. Lett.* **2005**, *27*, 1777 – 1784; e) S. Nishikori, K. Shiraki, K. Yokota, N. Izumikawa, S. Fujiwara, H. Hashimoto, T. Imanaka, M. Takagi, *J. Biochem.* **2004**, *135*, 525 – 532; f) W.-C. Chiu, J.-Y. You, J.-S. Liu, S.-K. Hsu, W. H. Hsu, C.-H. Shih, J.-K. Hwang, W.-C. Wang, *J. Mol. Biol.* **2006**, *359*, 741 – 753; g) M. H. Hecht, J. M. Sturtevant, R. T. Sauer, *Proc. Natl. Acad. Sci. USA* **1984**, *81*, 5685 – 5689; h) M. Matsumura, S. Yasumura, S. Aiba, *Nature* **1986**, *323*, 356 – 358.

[6] a) B. W. Matthews, *Annu. Rev. Biochem.* **1993**, *62*, 139 – 160; b) R. Jaenicke, G. Böhm, *Curr. Opin. Struct. Biol.* **1998**, *8*, 738 – 748; c) C. Vieille, G. J. Zeikus, *Microbiol. Mol. Biol. Rev.* **2001**, *65*, 1 – 43; d) R. Sterner, W. Liebl, *Crit. Rev. Biochem. Mol. Biol.* **2001**, *36*, 39 – 106; e) A. Fersht, *Structure and Mechanism in Protein Science*, W. H. Freeman, New York, **1999**; f) T. Lazaridis, I. Lee, M. Karplus, *Protein Sci.* **1997**, *6*, 2589 – 2605; g) S. Kumar, R. Nussinov, *Cell. Mol. Life Sci.* **2001**, *58*, 1216 – 1233; h) M. Podar, A.-L. Reysenbach, *Curr. Opin. Biotechnol.* **2006**, *17*, 1 – 6; i) D. C. Demirjian, F. Morís-Varas, C. S. Cassidy, *Curr. Opin. Chem. Biol.* **2001**, *5*, 144 – 151; j) D. Rodriguez-Larrea, S. Minning, T. V. Borchert, J. M. Sanchez-Ruiz, *J. Mol. Biol.* **2006**, in press; k) H. Atomi, *Curr. Opin. Biotechnol.* **2005**, *9*, 166 – 173; l) G. Vogt, S. Woell, P. Argos, *J. Mol. Biol.* **1997**, *269*, 631 – 643; m) *Protein Folding Handbook*, (Eds.: J. Buchner, T. Kiefhaber), Wiley-VCH, Weinheim, **2005**.

[7] a) A. Korkegian, M. E. Black, D. Baker, B. L. Stoddard, *Science* **2005**, *308*, 857 – 860; b) S. M. Malakauskas, S. L. Mayo, *Nat. Struct. Biol.* **1998**, *5*, 470 – 475; c) D. T. Kamei, B. J. Lao, M. Speed Ricci, R. Deshpande, H. Xu, B. Tidor, D. A. Lauffenburger, *Biotechnol. Bioeng.* **2005**, *92*, 748 – 760; d) T. Wang, H. Zhu, X. Ma, Y. Ma, D. Wei, *Protein Pept. Lett.* **2006**, *13*, 177 – 183.

[8] a) *Methods and Molecular Biology*, *Vol. 230 (Directed Enzyme Evolution: Screening and Selection Methods)*, (Eds.: F. H. Arnold, G. Georgiou), Humana, Totowa, NJ, **2003**; b) S. V. Taylor, P. Kast, D. Hilvert, *Angew. Chem.* **2001**, *113*, 3408 – 3436; *Angew. Chem. Int. Ed.* **2001**, *40*, 3310 – 3335; c) K. A. Powell, S. W. Ramer, S. B. del Cardayré, W. P. C. Stemmer, M. B. Tobin, P. F. Longchamp, G. W. Huisman, *Angew. Chem.* **2001**, *113*, 4068 – 4080; *Angew. Chem. Int. Ed.* **2001**, *40*, 3948 – 3959; d) *Directed Molecular Evolution of Proteins (or How to Improve Enzymes for Biocatalysis)* (Eds.: S. Brakmann, K. Johnsson), Wiley-VCH, Weinheim, Germany, **2002**; e) S. Lutz, W. M. Patrick, *Curr. Opin. Biotechnol.* **2004**, *15*, 291 – 297.

[9] Typical examples: a) H. Liao, T. McKenzie, R. Hageman, *Proc. Natl. Acad. Sci. USA* **1986**, *83*, 576 – 580; b) H. Zhao, F. H. Arnold, *Protein Eng.* **1999**, *12*, 47 – 53; c) K. A. Gray, T. H. Richardson, K. Kretz, J. M. Short, F. Bartnek, R. Knowles, L. Kan, P. E. Swanson, D. E. Robertson, *Adv. Synth. Catal.* **2001**, *343*, 607 – 617; d) A. Martin, F. X. Schmid, V. Sieber in *Methods in Molecular Biology*, *Vol. 230 (Directed Enzyme Evolution: Screening and Selection Methods)* (Eds.: F. H. Arnold, D. Georgiou), Humana, Totowa, NJ, **2003**, pp. 57 – 70; e) P. Acharya, E. Rajakumara, R. Sankaranarayanan, N. M. Rao, *J. Mol. Biol.* **2004**, *341*, 1271 – 1281; f) S. Xu, J. Ju, H. Misono, K. Ohnishi, *Gene* **2006**, *368*, 126 – 137; g) P. Joyet, N. Declerck, C. Gaillardin, *Bio/Technology* **1992**, *10*, 1579 – 1583; h) Y. Makino, S. Negoro, I. Urabe, H. Okada, *J. Biol. Chem.* **1989**, *264*, 6381 – 6385; i) P. N. Bryan, M. L. Rollence, M. W. Pantoliano, J. Wood, B. C. Finzel, G. L. Gilliland, A. J. Howard, T. L. Poulos, *Proteins Struct. Funct. Genet.* **1986**, *1*, 326 – 334; j) C. Roodveldt, D. S. Tawfik, *Protein Eng. Des. Sel.* **2005**, *18*, 51 – 58; k) C. Yun, H. Matsuda, M. Kawamukai, *Biosci. Biotechnol. Biochem.* **2006**, *70*, 559 – 563; l) N. Amin, A. D. Liu, S. Ramer, W. Aehle, D. Meijer, M. Metin, S. Wong, P. Gualfetti, V. Schellenberger, *Protein Eng. Des. Sel.* **2004**, *17*, 787 – 793; m) J. Hoseki, T. Yano, Y. Koyama, S. Kuramitsu, H. Kagamiyama, *J. Biochem.* **1999**, *126*, 951 – 956; n) I. Masuda-Nishimura, T. Minamihara, Y. Koyama, *Biotechnol. Lett.* **1999**, *21*, 203 – 207; o) J. S. Pedersen, D. E. Otzen, P. Kristensen, *J. Mol. Biol.* **2002**, *323*, 115 – 123; p) N. Zhang, W.-C. Suen, W. Windsor, L. Xiao, V. Madison, A. Zaks, *Protein Eng.* **2003**, *16*, 599 – 605; q) S. Dao-pin, U. Sauer, H. Nicholson, B. W. Matthews, *Biochemistry* **1991**, *30*, 7142 – 7153; r) A. Nakamura, Y. Takakura, H. Kobayashi, T. Hoshino, *J. Biosci. Bioeng.* **2005**, *100*, 158 – 163; s) J. Hecky, K. M. Müller, *Biochemistry* **2005**, *44*, 12640 – 12654; t) J. Hoseki, A. Okamoto, N. Takada, A. Suenaga, N. Futatsugi, A. Konagaya, M. Taiji, T. Yano, S. Kuramitsu, H. Kagamiyama, *Biochemistry* **2003**, *42*, 14469 – 14475; u) R. A. Chica, N. Doucet, J. N. Pelletier, *Curr. Opin. Biotechnol.* **2005**, *16*, 378 – 384.

[10] a) P. A. Karplus, G. E. Schulz, *Naturwissenschaften* **1985**, *72*, 212 – 213; b) M. Vihinen, *Protein Eng.* **1987**, *1*, 477 – 480; c) S. Parthasarathy, M. R. N. Murthy, *Protein Eng.* **2000**, *13*, 9 – 13; d) Z. Yuan, J. Zhao, Z.-X. Wang, *Protein Eng.* **2003**, *16*, 109 – 114; e) P. Radivojac, Z. Obradovic, D. K. Smith, G. Zhu, S. Vucetic, C. J. Brown, J. D. Lawson, A. K. Dunker, *Protein Sci.* **2004**, *13*, 71 – 80; f) K. N. Trueblood, H.-B. Bürgi, H. Burzlaff, J. D. Dunitz, C. M. Gramaccioli, H. H. Schulz, U. Shmueli, S. C. Abrahams, *Acta Crystallogr. Sect. A* **1996**, *52*, 770 – 781.

[11] M. T. Reetz, L.-W. Wang, M. Bocola, *Angew. Chem.* **2006**, *118*, 1258 – 1263; *Angew. Chem. Int. Ed.* **2006**, *45*, 1236 – 1241; Erratum: M. T. Reetz, L.-W. Wang, M. Bocola, *Angew. Chem.* **2006**, *118*, 2556; *Angew. Chem. Int. Ed.* **2006**, *45*, 2494.

[12] a) V. Dartois, A. Baulard, K. Schanck, C. Colson, *Biochim. Biophys. Acta* **1992**, *1131*, 253 – 260; b) K.-E. Jaeger, B. W. Dijkstra, M. T. Reetz, *Annu. Rev. Microbiol.* **1999**, *53*, 315 – 351.

[13] a) G. van Pouderoyen, T. Eggert, K.-E. Jaeger, B. W. Dijkstra, *J. Mol. Biol.* **2001**, *309*, 215 – 226; b) S. A. Funke, A. Eipper, M. T. Reetz, N. Otte, W. Thiel, G. van Pouderoyen, *Biocatal. Biotransform.* **2003**, *21*, 67 – 73; c) E. Rajakumara, P. Acharya, S. Ahmad, V. M. Shanmugam, N. M. Rao, R. Sankaranarayanan, *Acta Crystallogr. Sect. D* **2004**, *60*, 160 – 162; d) M. J. Dröge, Y. L. Boersma, G. van Pouderoyen, T. E. Vrenken, C. J. Rüggeberg, M. T. Reetz, B. W. Dijkstra, W. J. Quax, *ChemBioChem* **2006**, *7*, 149 – 157; e) K. Kawasaki, H. Kondo, M. Suzuki, S. Ohgiya, S. Tsuda, *Acta Crystallogr. Sect. D* **2002**, *58*, 1168 – 1174.

[14] The choice of the sites for saturation mutagenesis are the same if the B factors of the other X-ray structures of Lip A are chosen or averaged.

[15] We used the average B factors of all atoms (except the H atoms) of a given amino acid in the protein. It is clear that this treatment may bias some amino acids such as lysine. However, this does not detract from the power of our approach. Refinement by correction factors according to the amino acid structure may improve the method in other cases.

[16] The widely used QuikChange protocol (QuikChange site-directed mutagenesis kit. Instruction Manual, **2003**, Stratagene, La Jolla, CA) is based on a number of previous publications. These and other developments have been reviewed in: a) C. N. Dominy, D. W. Andrews in *Methods in Molecular Biology*, *Vol. 235 (E. coli Plasmid Vectors)* (Eds.: N. Casali, A. Preston), Humana, Totowa, NJ, **2003**, 209 – 223; b) M. A. Vandeyar, M. P. Weiner, C. J. Hutton, C. A. Batt, *Gene* **1988**, *65*, 129 – 133; c) R. D. Kirsch, E. Joly, *Nucleic Acids Res.* **1998**, *26*, 1848 – 1850.

 © 2006 Wiley-VCH Verlag GmbH & Co. KGaA, Weinheim

[17] For examples of the use of T_{50} values or simply of data pertaining to residual activity after heat treatment at a given temperature, see: a) L. Sun, I. P. Petrounia, M. Yagasaki, G. Bandara, F. H. Arnold, *Protein Eng.* **2001**, *14*, 699–704; b) B. Morawski, S. Quan, F. H. Arnold, *Biotechnol. Bioeng.* **2001**, *76*, 99–107; c) J. Hao, A. Berry, *Protein Eng. Des. Sel.* **2004**, *17*, 689–697; d) N. Declerck, M. Machius, P. Joyet, G. Wiegand, R. Huber, C. Gaillardin, *Protein Eng.* **2003**, *16*, 287–293; e) S. Akanuma, A. Yamagishi, N. Tanaka, T. Oshima, *Protein Sci.* **1998**, *7*, 698–705; f) H. Zhao, F. H. Arnold, *Protein Eng.* **1999**, *12*, 47–53; g) B. Van den Burg, A. de Kreij, P. van der Veek, J. Mansfeld, G. Venema, *Biotechnol. Appl. Biochem.* **1999**, *30*, 35–40; h) K.-H. Oh, S.-H. Nam, H.-S. Kim, *Protein Eng.* **2002**, *15*, 689–695; i) M. G. Pikkemaat, A. B. M. Linssen, H. J. C. Berendsen, D. B. Janssen, *Protein Eng.* **2002**, *15*, 185–192; j) L.-J. Wang, X.-D. Kong, H.-Y. Zhang, X.-P. Wang, J. Zhang, *Biochem. Biophys. Res. Commun.* **2000**, *276*, 346–349; k) J. Mansfeld, G. Vriend, B. W. Dijkstra, O. R. Veltman, B. Van den Burg, G. Venema, R. Ulbrich-Hofmann, V. G. H. Eijsink, *J. Biol. Chem.* **1997**, *272*, 11152–11156; l) E. H. Muslin, S. E. Clark, C. A. Henson, *Protein Eng.* **2002**, *15*, 29–33; m) O. Turunen, M. Vuorio, F. Fenel, M. Leisola, *Protein Eng.* **2002**, *15*, 141–145; n) T. W. Johannes, R. D. Woodyer, H. Zhao, *Appl. Environ. Microbiol.* **2005**, *71*, 5728–5734; o) J.-H. Kim, G.-S. Choi, S.-B. Kim, W.-H. Kim, J.-Y. Lee, Y.-W. Ryu, G.-J. Kim, *J. Mol. Catal. B* **2004**, *27*, 169–175; p) D. E. Stephens, K. Rumbold, K. Permaul, B. A. Prior, S. Singh, *J. Biotechnol.* **2006**, DOI: 10.1016/j.jbiotec.2006.06.015.

[18] For the application of mathematical expressions useful in the construction, description, and evaluation of protein libraries, see: a) A. D. Bosley, M. Ostermeier, *Biomol. Eng.* **2005**, *22*, 57–61; b) M. A. Mena, P. S. Daugherty, *Protein Eng. Des. Sel.* **2005**, *18*, 559–561; c) A. E. Firth, W. M. Patrick, *Bioinformatics* **2005**, *21*, 3314–3315; d) W. M. Patrick, A. E. Firth, J. M. Blackburn, *Protein Eng.* **2003**, *16*, 451–457; e) see also reference [22b] regarding the CASTer program available free of charge.

[19] The order of choosing sites in the iterative process is not uniquely defined, and a different one can also be used. This aspect, as in iterative CASTing,[11] needs to be studied in future investigations.

[20] Direct comparisons of thermostabilization in various studies are sometimes difficult because different parameters have been used in the assessment of the observed effects.[1,9]

[21] If, in a given study, amino acid sites in the core of the enzyme turn out to have high B values, these can, but need not be, considered.

[22] a) M. T. Reetz, M. Bocola, J. D. Carballeira, D. Zha, A. Vogel, *Angew. Chem.* **2005**, *117*, 4264–4268; *Angew. Chem. Int. Ed.* **2005**, *44*, 4192–4196; b) M. T. Reetz, J. D. Carballeira, J. Peyralans, H. Höbenreich, A. Maichele, A. Vogel, *Chem. Eur. J.* **2006**, *12*, 6031–6038.

[23] J. D. Bloom, S. T. Labthavikul, C. R. Otey, F. H. Arnold, *Proc. Natl. Acad. Sci. USA* **2006**, *103*, 5869–5874.

[24] a) A. Schlessinger, G. Yachdav, B. Rost, *Bioinformatics* **2006**, *22*, 891–893; b) Y. Jin, R. L. Dunbrack, Jr., *Proteins Struct. Funct. Bioinf.* **2005**, *61 (Supp. 7)*, 167–175.

[25] a) A. Schlessinger, B. Rost, *Proteins Struct. Funct. Bioinf.* **2005**, *61*, 115–126; b) C. Wang, N. Karpowich, J. F. Hunt, M. Rance, A. G. Palmer, *J. Mol. Biol.* **2004**, *342*, 525–537.

[26] G. Feller, C. Gerday, *Nat. Rev. Microbiol.* **2003**, *1*, 200–208.

[27] F. W. Studier, *Protein Expression Purif.* **2005**, *41*, 207–234.

 © 2006 Wiley-VCH Verlag GmbH & Co. KGaA, Weinheim

Selective Adsorption

DOI: 10.1002/anie.200602278

How Hydration Drastically Improves Adsorption Selectivity for CO_2 over CH_4 in the Flexible Chromium Terephthalate MIL-53**

Philip L. Llewellyn, Sandrine Bourrelly, Christian Serre, Yaroslav Filinchuk, and Gérard Férey*

One of the technological problems that face society today is the environmentally friendly and economically feasible separation, recovery, and recovery/reuse of vapors and gases. Several examples are currently of interest: the selective recovery of solvents, the recovery of greenhouse gases, and the purification of hydrogen. Many processes include an adsorption step in which microporous adsorbents, such as activated carbon and zeolites, are used. Recently a new class of porous materials have found interest: these metal organic frameworks (MOFs)[1,2] or metal coordination polymers[3] are built up from inorganic subnetworks and organic complexing molecules (phosphonates, carboxylates, sulfonates). These subnetworks often contain divalent or trivalent cations connected by organic groups such as carboxylates. Such structures possess tunnels or cavities with pore sizes between 3 and 35 Å. Several of these organic–inorganic hybrid porous solids[4–11] have the interesting feature of being selectively flexible during the adsorption process by means of a breathing[12] or gate-opening process,[9] which depends on the nature of the adsorptive. Examples discovered by Ferey and coworkers include flexible porous carboxylates formed by chains of metallic centers (MIL-53, -69)[13,14] and with metal-center trimers (MIL-88A).[15] These solids have shown to "breath" with unprecedented increases in volume between 50 and 85% depending on the nature of the fluid. A consequence of this particular property is the possibility to develop novel selective separation and storage processes that could be less expensive than existing processes.

In many adsorption processes since the presence of water is detrimental, it is often removed using a precolumn. In the

[*] Dr. P. L. Llewellyn, S. Bourrelly
MADIREL
Université de Provence – CNRS (UMR 6121)
Centre de St Jérôme, 13397 Marseille Cedex 20 (France)
Fax: (+33) 4-9163-7111
E-mail: pllew@up.univ-mrs.fr

Dr. C. Serre, Prof. G. Férey
Institut Lavoisier (UMR CNRS 8637)
Université de Versailles Saint-Quentin-en-Yvelines
45 avenue des Etats-Unis, 78035 Versailles Cedex (France)

Dr. Y. Filinchuk
SNBL at ESRF
38043 Grenoble (France)

[**] The authors thank Alexandre Vimont for discussions concerning initial IR results. This work was supported by EU funding through the FP6-Specific Targeted Research Project "DeSANNS" (SES6-020133).

© 2006 Wiley-VCH Verlag GmbH & Co. KGaA, Weinheim

case of zeolites, this detrimental effect can be explained by the shielding of the specific cation sites by the water molecules.[16] In some cases, however, a small amount of water can be beneficial, for example, for the separation of xylenes over BaX[17] where the water frees up the barium cation making it more available to interact with the xylene molecules.

Prior studies have dealt with the interaction of water with MOF systems, for example, MIL-53 (chemical formula $M(OH)(O_2C\text{-}C_6H_4\text{-}CO_2)$).[18] The structure of MIL-53 is built up from infinite chains of corner-sharing $MO_4(OH)_2$ octahedra ($M = Cr^{3+}$, Al^{3+}, Fe^{3+}) interconnected by benzenedicarboxylate units.[13] This results in a 3D metal–organic framework containing 1D diamond-shaped channels with pores of free diameter close to 8.5 Å.

In the presence of water, the MIL-53 (Cr^{3+}, Al^{3+}) solids exhibit an original breathing phenomenon upon hydration–dehydration which involves ca. 5-Å atomic movements (Figure 1).[18] In the hydrated form (Figure 1, left) the pores

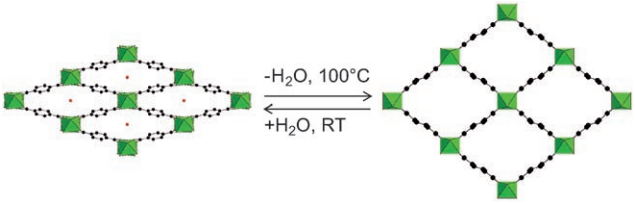

Figure 1. Hydration and dehydration process occurring in MIL-53(Cr, Al). Left: MIL-53LT (hydrated); right: MIL-53HT (dehydrated).

are slightly deformed owing to hydrogen-bond interactions between the hydrogen atoms of the water molecule and the oxygens of the carboxylate and the μ_2-hydroxo group. The water is rapidly removed upon heating to give a structure with the more open porosity (Figure 1, right).

The adsorption of carbon dioxide in these solids is also accompanied by unusual structural phenomena.[12] The dehydrated solid shows a marked two-step adsorption process, which has been interpreted as the initial closing of the structure before it reopens at higher pressures. This isotherm shape with carbon dioxide is in contrast to that with other molecules such as methane. Indeed, it is interesting to compare the adsorption of these greenhouse gases from basic principles. Whilst CO_2 has a significant quadrupole moment (-1.4×10^{-35} C m) that induces specific interactions with adsorbents (molecular orientation, hydrogen bonding…), CH_4 has no specific moment. It would thus seem that polar molecules have a distinct effect on the framework flexibility. With this in mind we studied the adsorption of carbon dioxide and methane on the hydrated form of MIL-53(Cr), in particular, in the presence of a second polar molecule (water). The thermodynamic and structural behavior of the hydrated form of the chromium form of MIL-53(Cr) was followed in adsorption and X-ray synchrotron measurements. The results indicate that the hydrated form is better suited than the dehydrated form for potential applications for the recovery of carbon dioxide from methane.

The gas adsorption isotherms (CO_2, CH_4) of the hydrated and dried MIL-53(Cr) solids are shown in Figure 2. First, the

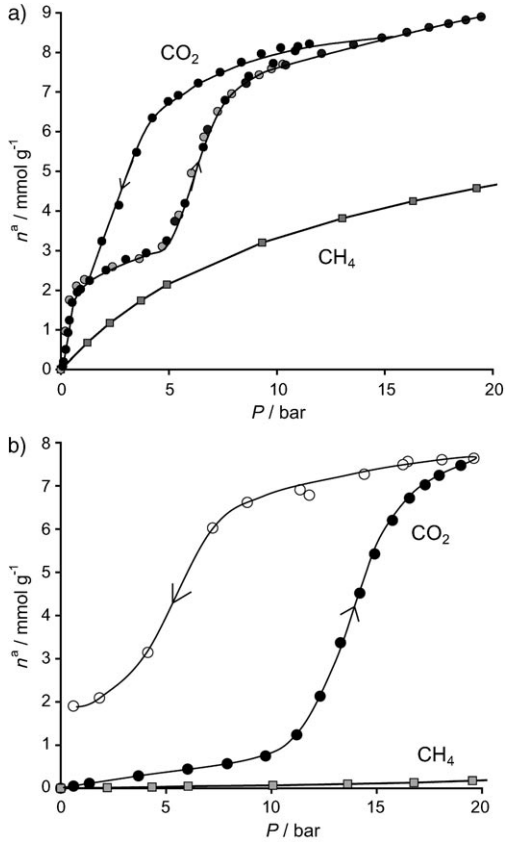

Figure 2. Comparison of the adsorption isotherms of carbon dioxide and methane at 304 K on a) dehydrated and b) hydrated forms of MIL-53(Cr). Grey- and black-filled circles represent two different experiments. n^a = amount adsorbed.

adsorption of carbon dioxide on the dehydrated MIL-53(Cr) sample occurs in a distinct two-step process with an initial plateau at around 3 mmol g^{-1} and a step in the 5–8-bar region of pressure with an uptake at the end of the step of around 8.5 mmol g^{-1}. Second, the adsorption of carbon dioxide on the hydrated sample shows very little uptake at pressures up to 10 bar, while a single and distinct uptake of ca. 7.7 mmol g^{-1} occurs in the 12–18-bar pressure range.

Previously, we suggested that a breathing process occurs for the adsorption of carbon dioxide[12] in dehydrated MIL-53(Cr). To observe the structural evolution of the hydrated sample MIL-53(Cr) under CO_2 atmosphere, we performed in situ X-ray diffraction experiments under various pressures of carbon dioxide using an adequate gas system and synchrotron radiation (Figure 3). Prior to gas introduction, the sample is hydrated and exists in the closed form, as reported previously.[18] This closed form is maintained for pressures up to 5 bar, although a small variation in cell parameters can be observed in this pressure region. In the region from 5 to 15 bar the open and closed structures coexist, while the amount of the former decreases as the proportion of the latter form increases. At 15 bar the open structure phase is almost pure. The cell parameters of this phase were determined by DicvolGV[19] and refined using Fullprof[20] as $a = 16.479(1)$, $b = 13.503(1)$, $c = 6.842(1)$ Å; $V = 1522.5$ Å^3 space group *Imcm* (no. 74). This is rather close to the cell parameters of

 © 2006 Wiley-VCH Verlag GmbH & Co. KGaA, Weinheim

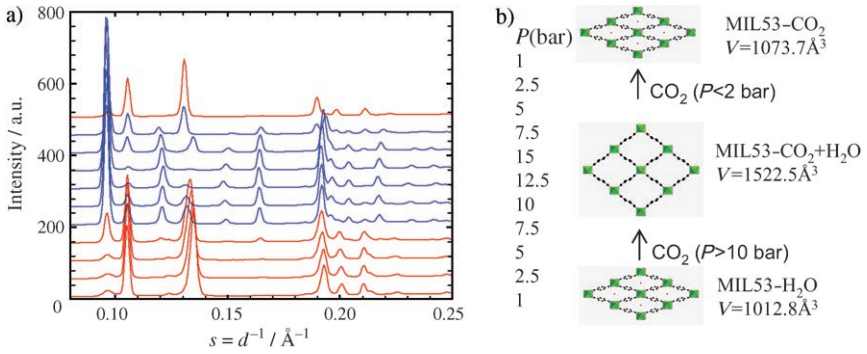

Figure 3. a) Evolution of X-ray diffraction patterns ($\lambda = 0.71118$ Å) with increasing pressure of carbon dioxide for the hydrated MIL-53(Cr) solid. b) Schematic view of the resulting breathing phenomenon for MIL-53(Cr).

the MIL-53_{HT} solid, that is, the "open" dehydrated phase: $a =$ 16.733(1), $b = 13.038(1)$, $c = 6.812(1)$ Å; $V = 1486.5$ Å^3, despite a slightly higher cell volume for the phase in the presence of CO_2 at 15 bar.

The closed structure allows the adsorption of only a small amount of carbon dioxide with around 0.8 mmol g^{-1} adsorbed before the step at 11 bar. This is in contrast with the dried sample, which has an uptake 2–3 mmol g^{-1} of CO_2 at 2 bar. Thus it would seem that the carbon dioxide is not able to enter this closed structure either because of steric hindrance or unfavorable interactions in the presence of water.

The adsorption of CO_2 above 11 bar leads to a total opening of the structure. Not only is the pressure associated with this step higher but also the pressure region of the adsorption step is much broader (11–18 bar) for the hydrated sample than for the dehydrated one (5–8 bar). The X-ray patterns suggest the coexistence of open and closed forms during this step and over a fairly large pressure domain. This may be a result of a particular particle size distribution where the smaller particles may undergo the opening process before the larger ones. A second explanation is the progressive diffusion of CO_2 into the core of the particle with increasing pressure. This process may occur over a large range of pressure as it may be accompanied by a displacement of the water. This point raises the question of the nature of the species adsorbed at high pressure (15 bar). Does CO_2 displace water, and is there a coexistence of the two species? Preliminary studies by IR spectroscopy suggest a replacement of the hydrogen-bonded water with CO_2 molecules.

The desorption isotherm obtained with the dried sample occurs in the 2–4-bar pressure region. This isotherm rejoins the adsorption branch at around 2 bar. The desorption isotherm obtained with the hydrated sample occurs below 6 bar. It is of interest that 1.9 mmol g^{-1} of gas is still adsorbed at the final point obtained here at 0.6 bar. This value is similar to that obtained with the dried sample and would suggest that CO_2 is present in majority in the pores and thus that the sample has more affinity for CO_2 than H_2O on desorption.

The adsorption of methane on dehydrated MIL-53(Cr) occurs with a gradual uptake for pressures up to 40 bar with an adsorbed amount close to 4.6 mmol g^{-1} at 20 bar. Adsorption of CH_4 on the hydrated samples shows almost no methane uptake (0.2 mmol g^{-1}) at 20 bar. This is probably a result of the repulsive effect of the free water present in the pores that block or induce highly unfavorable conditions for the introduction of the nonpolar methane molecules.

The important feature of these results is that the apparent selectivity is drastically increased for the hydrated sample; in other words, the relative amount of CO_2 adsorbed with respect to CH_4 is greater for the hydrated material. This is not the case for other carbon dioxide adsorbents such as zeolites where often the water blocks specific sites. It was shown previously that the present sample is stable to higher humidity, and thus a process in which a significant amount of water is present may not diminish the adsorption of carbon dioxide. Thus a preadsorber would not be required in a pressure-swing-adsorption-type process and process design could be simplified. Further work on the adsorption of carbon dioxide in the presence of increasing partial pressures of water is planned.

This work highlights the difference in adsorption behavior between a polar and nonpolar probe. In general, it will be important to examine other molecules of varying polarity. Nevertheless, these results are particularly interesting when one considers the recovery of carbon dioxide in mixed-gas streams or the use of such materials in sensor-type applications. As it would initially seem that the structural flexibility of these materials is related to the polar nature of the probe gas molecule, such results could pave the way for the use highly flexible MOFs for the separation of other mixtures of polar and nonpolar gases. Initially, it will be of interest to study the feasibility to recover CO_2 in natural-gas feeds in which the water content is significant.

Experimental Section

The adsorption of CO_2 and CH_4 was carried out at 304 K and up to 20 and 40 bar, respectively. The isotherms were obtained using an adsorption manometry device using a point-by-point introduction of gas to the sample. The CH_4 and CO_2 were obtained from Air Liquide (Alphagaz, France) and are of 99.9999 % purity. Each experiment was repeated several times, and each curve in the figures includes points from at least two experiments.

The in situ synchrotron powder diffraction experiments were carried out at the Swiss-Norwegian Beamlines at the European Synchrotron Radiation Facility. The data were collected on 0.7-mm quartz capillaries filled with the sample and attached to a gas manifold, using an MAR345 imaging plate at a sample-to-detector distance of 250 mm, $\lambda = 0.71110$ Å. The data were integrated using Fit2D program (Dr. A. Hammersley, ESRF) and a calibration measurement of a NIST LaB6 standard sample. CO_2 (Alphagaz, France, 99.9999 % purity) was introduced to each pressure point. The response of the system to the pressure increase was immediate, as evident from in situ powder diffraction. Equilibrium was assumed

 © 2006 Wiley-VCH Verlag GmbH & Co. KGaA, Weinheim

when two repeatedly measured diffraction patterns had become identical.

Received: June 7, 2006
Published online: October 20, 2006

Keywords: adsorption · carbon dioxide · microporous materials · organic–inorganic hybrid composites · X-ray diffraction

[1] G. Férey, C. Mellot-Draznieks, C. Serre, F. Millange, *Acc. Chem. Res.* **2005**, *38*, 217 – 225.
[2] O. M. Yaghi, M. O'Keeffe, N. W. Ockwig, H. K. Chae, M. Eddaoudi, J. Kim, *Nature* **2003**, *423*, 705 – 714.
[3] S. Kitagawa, R. Kitaura, S.-H. Noro, *Angew. Chem.* **2004**, *116*, 2388 – 2430; *Angew. Chem. Int. Ed.* **2004**, *43*, 2334 – 2375.
[4] A. J. Fletcher, E. J. Cussen, T. J. Prior, M. J. Rosseinsky, C. J. Kepert, K. M. Thomas, *J. Am. Chem. Soc.* **2001**, *123*, 10001 – 10011.
[5] K. Barthelet, J. Marrot, D. Riou, G. Férey, *Angew. Chem.* **2002**, *114*, 291—294; *Angew. Chem. Int. Ed.* **2002**, *41*, 281 – 284.
[6] R. Kitaura, K. Seki, G. Akiyama, S. Kitagawa, *Angew. Chem.* **2003**, *115*, 444—447; *Angew. Chem. Int. Ed.* **2003**, *42*, 428 – 431.
[7] D. Li, K. Kaneko, *Chem. Phys. Lett.* **2001**, *335*, 50 – 56.
[8] K. Seki, *Phys. Chem. Chem. Phys.* **2002**, *4*, 1968 – 1971.
[9] X. Zhao, B. Xiao, A. J. Fletcher, K. M. Thomas, D. Bradshaw, M. J. Rosseinsky, *Science* **2004**, *306*, 1012 – 1015.
[10] S. Takamizawa, T. Saito, T. Akatsuka, E. Nakata, *Inorg. Chem.* **2005**, *44*, 1421 – 1424.
[11] Y. Kubota, M. Takata, R. Matsuda, R. Kitaura, S. Kitagawa, T. C. Kobayashi, *Angew. Chem.* **2006**, *118*, 5054—5058; *Angew. Chem. Int. Ed.* **2006**, *45*, 4932 – 4936.
[12] S. Bourrelly, P. L. Llewellyn, C. Serre, F. Millange, T. Loiseau, G. Férey, *J. Am. Chem. Soc.* **2005**, *127*, 13519 – 13521.
[13] C. Serre, F. Millange, C. Thouvenot, M. Noguës, G. Marsolier, D. Louër, G. Férey, *J. Am. Chem. Soc.* **2002**, *124*, 13519 – 13526.
[14] T. Loiseau, C. Mellot-Draznieks, H. Muguerra, G. Férey, M. Haouas, F. Taulelle, *C. R. Chim.* **2005**, *8*, 765 – 772.
[15] a) C. Serre, F. Millange, S. Surblé, G. Férey, *Angew. Chem.* **2004**, *116*, 6445—6449; *Angew. Chem. Int. Ed.* **2004**, *43*, 6285 – 6289; b) C. Mellot-Draznieks, C. Serre, S. Surblé, N. Audebrand, G. Férey, *J. Am. Chem. Soc.* **2005**, *127*, 16273 – 16278.
[16] N. D. Hutson, S. C. Zajic, R. T. Yang, *Ind. Eng. Chem. Res.* **2000**, 39, 1775 – 1780.
[17] a) J.-C. Moiese, J.-P. Bellat, *J. Phys. Chem. B* **2005**, *109*, 17239 – 17244; b) C. Pichon, A. Methivier, M.-H. Simonot-Grange, C. Baerlocher, *J. Phys. Chem. B* **1999**, *103*, 10197 – 10203.
[18] T. Loiseau, C. Serre, C. Huguenard, G. Fink, F. Taulelle, M. Henry, T. Bataille, G. Férey, *Chem. Eur. J.* **2004**, *10*, 1373 – 1382.
[19] A. Boultif, D. J. Louër, *Appl. Crystallogr.* **1991**, *24*, 987 – 993.
[20] J. Rodriguez-Carvajal, Fullprof Suite, LLB Sacley & LCSIM Rennes, France, **2005**.

 © 2006 Wiley-VCH Verlag GmbH & Co. KGaA, Weinheim

Nanomedicine

DOI: 10.1002/anie.200602471

Designed Fabrication of Multifunctional Magnetic Gold Nanoshells and Their Application to Magnetic Resonance Imaging and Photothermal Therapy**

Jaeyun Kim, Sungjin Park, Ji Eun Lee, Seung Min Jin, Jung Hee Lee, In Su Lee, Ilseung Yang, Jun-Sung Kim, Seong Keun Kim, Myung-Haing Cho, and Taeghwan Hyeon**

Nanotechnology offers tremendous potential for future medical diagnosis and therapy. Various types of nanoparticles have been extensively studied for numerous biomedical applications.[1] Quantum dots modified with tumor-targeting ligands were used as in vivo cancer-targeting imaging agents.[2] Gold nanoparticles derivatized with oligonucleotides were used in an ultrasensitive biobarcode assay.[3]

[*] J. Kim,[$] J. E. Lee, Dr. I. S. Lee, Prof. Dr. T. Hyeon
National Creative Research Initiative Center for Oxide Nanocrystalline Materials and
School of Chemical and Biological Engineering
Seoul National University, Seoul 151-744 (Korea)
Fax: (+82) 2-886-8457
E-mail: thyeon@snu.ac.kr

S. Park,[$] J.-S. Kim, Prof. Dr. M.-H. Cho
Laboratory of Toxicology, College of Veterinary Medicine and BK21 Program for Veterinary Science
Seoul National University, Seoul 151-744 (Korea)
Fax: (+82) 2-873-1268
E-mail: mchotox@snu.ac.kr

Dr. S. M. Jin,[+] I. Yang, Prof. Dr. S. K. Kim
School of Chemistry
Seoul National University, Seoul 151-744 (Korea)

Prof. Dr. J. H. Lee
Department of Radiology, Samsung Medical Center
School of Medicine, Sungkyunkwan University
Seoul 137-200 (Korea)

[+] Present address:
Advanced Materials Division
Korea Research Institute of Chemical Technology
Daejeon 305-343 (Korea)

[$] These authors contributed equally to this work.

[**] T.H. acknowledges financial support by the Korean Ministry of Science and Technology through the National Creative Research Initiative Program of the Korea Science and Engineering Foundation (KOSEF). M.H.C. is supported by the NSI-NCRC program of KOSEF. S.K.K. is supported by a National Research Laboratory Grant and a Chemical Genomics Grant. J.H.L. is supported by the Centre for Biological Modulators of the 21st Century Frontier R&D Program.

Supporting information for this article (experimental details, demonstration of the rapid destruction of cancer cells by irradiation with a femtosecond-pulse laser, and the temporal distribution of the output power for a femtosecond-pulse laser versus that of a continuous-wave laser) is available on the WWW under http://www.angewandte.org or from the author.

WILEY InterScience DISCOVER SOMETHING GREAT
© 2006 Wiley-VCH Verlag GmbH & Co. KGaA, Weinheim

Molecular imaging using magnetic resonance imaging (MRI) is an emerging technology that can be used to image target tissues in vivo in a highly specific manner. Iron oxide nanoparticles, such as superparamagnetic iron oxide (SPIO) nanoparticles, have been extensively utilized as MRI contrast agents for molecular imaging.[4]

Recently, a great deal of attention has been paid to noninvasive photothermal therapy for the selective treatment of tumor cells. This type of therapy utilizes the large absorption cross section of nanomaterials in the near infrared (NIR) region. Owing to its weak absorption by tissues, NIR radiation is able to penetrate the skin without causing much damage to normal tissues and, thus, can be used to treat specific cells targeted by the nanomaterials. Several nanomaterials that strongly absorb NIR radiation, including gold nanoshells,[5] gold nanorods,[6] and single-walled carbon nanotubes,[7] were recently demonstrated to have potential therapeutic applications. The radiation that is absorbed by these nanomaterials is converted efficiently into heat, causing cell destruction on a picosecond time scale, as a result of electron–phonon and phonon–phonon processes.[5–8]

The clever combination of different nanoscale materials can lead to the development of multifunctional nanomedical platforms for simultaneous targeted delivery, fast diagnosis, and efficient therapy.[9] For example, Kopelman and coworkers reported multifunctional nanoparticles for the simultaneous targeted photodynamic therapy and in vivo MRI of a rat brain cancer;[9f] these polyacrylamide nanoparticles contained photosensitizers and MRI contrast agents, and their surfaces were coated with poly(ethylene glycol) (PEG) and molecular targeting groups. We herein propose that nanostructures with combined magnetic and optical properties can provide a novel nanomedical platform for diagnostic imaging, using the magnetic properties, and simultaneous treatment, using the optical properties. With this goal in mind, we fabricated magnetic gold nanoshells (Mag-GNS) consisting of gold nanoshells embedded with magnetic Fe_3O_4 nanoparticles, and conjugated them with a cancer-targeting agent. Cancer cells targeted by these Mag-GNS can be detected by a clinical MRI system and killed by NIR radiation. Femtosecond laser pulses are particularly useful in the selective, efficient, and rapid destruction of the targeted cancer cells.

The synthetic approach is represented in Figure 1a, and transmission electron microscope (TEM) images of the products obtained after each synthetic step are shown in Figure 1b–e. In this synthetic method, Fe_3O_4 (magnetite) nanoparticles and gold seed nanoparticles are assembled on amino-modified silica spheres;[10] gold shells are then grown around the silica spheres (see Supporting Information).[11] First, 100-nm silica spheres were synthesized using the Stöber method,[12] and the surfaces of the particles were modified with 3-aminopropyltrimethoxysilane (Figure 1b). Monodisperse 7-nm Fe_3O_4 nanoparticles stabilized with oleic acid were synthesized[13] and subsequently ligand-exchanged with 2-bromo-2-methylpropionic acid (BMPA).[14] The BMPA-stabilized Fe_3O_4 nanoparticles were then covalently attached to the amino-modified silica spheres through a direct nucleophilic substitution reaction between the bromo groups and the amino groups (Figure 1c).[15] Gold seed nanoparticles of 1–3 nm[16] were attached to the residual amino groups of the silica spheres (Figure 1d). Finally, a complete 15-nm-thick gold shell with embedded Fe_3O_4 nanoparticles was formed around the silica spheres, resulting in Mag-GNS (Figure 1e). Recently, similarly structured gold nanoshells embedded with magnetite nanoparticles were fabricated by Mirkin and coworkers.[17]

Figure 2a shows that the Mag-GNS are deep purple in color and disperse well in water. In the Vis/NIR spectrum of the Mag-GNS, an absorption band ranging from 700 nm to the NIR region is observed (Figure 2b). The field-dependent magnetization curve of the Mag-GNS at 300 K shows no hysteresis (Figure 2c), which is consistent with superpara-

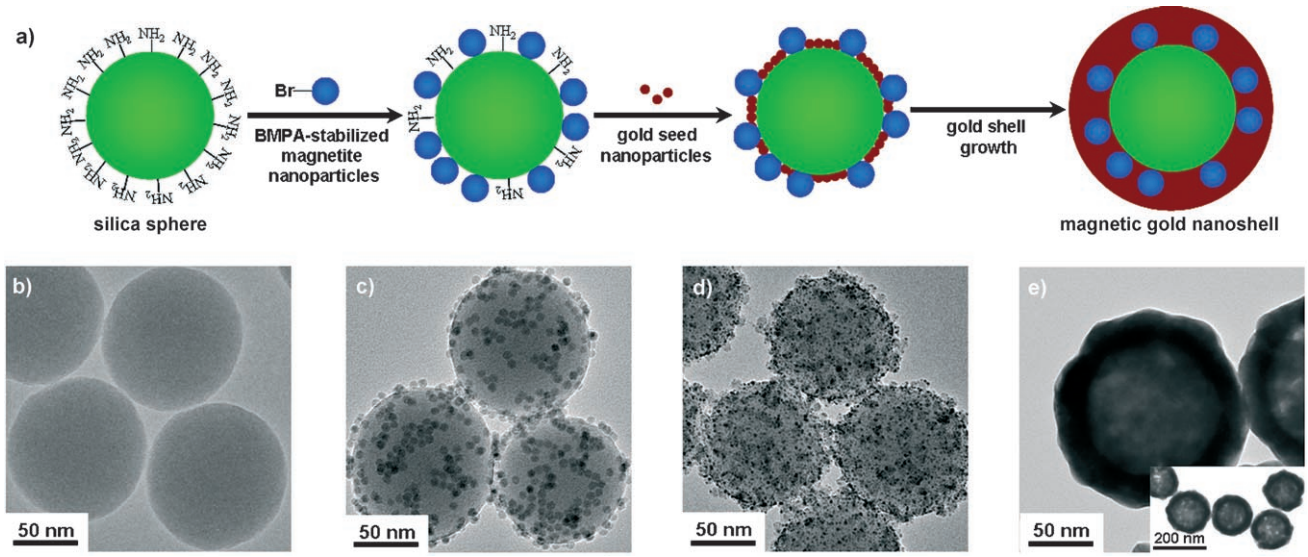

Figure 1. a) Synthesis of the magnetic gold nanoshells (Mag-GNS). TEM images of b) amino-modified silica spheres, c) silica spheres with Fe_3O_4 (magnetite) nanoparticles immobilized on their surfaces, d) silica spheres with Fe_3O_4 and gold nanoparticles immobilized on their surfaces, and e) the Mag-GNS.

 © 2006 Wiley-VCH Verlag GmbH & Co. KGaA, Weinheim

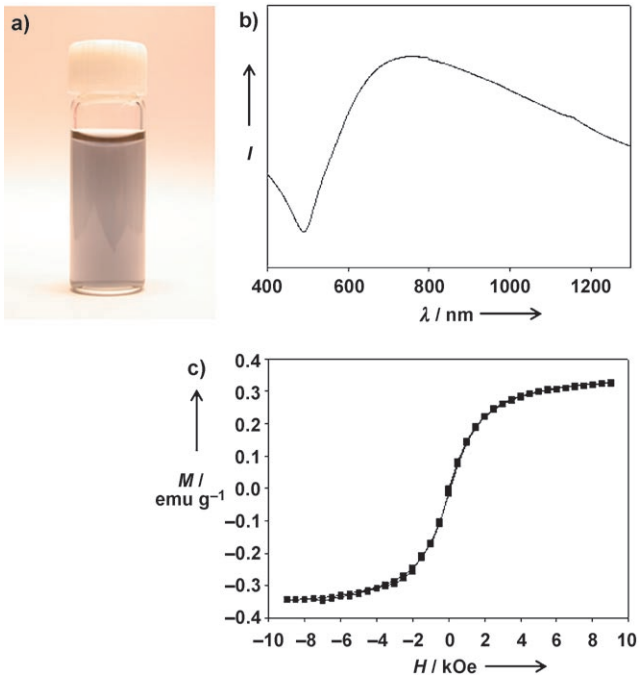

Figure 2. a) Photograph of the Mag-GNS dispersed in water. b) Vis/NIR spectrum of the Mag-GNS. c) Field dependence of the magnetization of the Mag-GNS at 300 K.

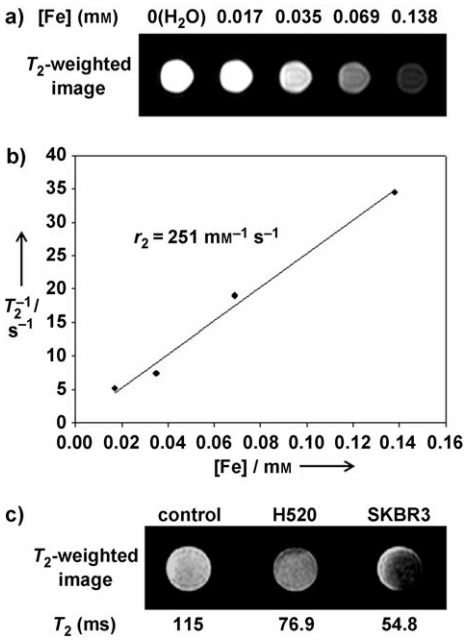

Figure 3. a) T_2-weighted MR images of the PEG-coated Mag-GNS at various concentrations in water. b) Plot of the spin–spin relaxation rate (T_2^{-1}) against iron concentration for the PEG-coated Mag-GNS, from which the specific relaxivity (r_2) is determined. c) T_2-weighted MR images of control SKBR3 cells, HER2/*neu*-negative H520 cells incubated with Mag-GNS-$Ab_{HER2/neu}$, and HER2/*neu*-positive SKBR3 cells incubated with Mag-GNS-$Ab_{HER2/neu}$; the corresponding T_2 relaxation times are indicated.

magnetic behavior arising from the embedded magnetite nanoparticles.

The Fe_3O_4 nanoparticles have a tendency to shorten the spin–spin relaxation times (T_2) of water, resulting in a decrease in the MRI signal intensity.[4] MR images of the PEG-coated Mag-GNS at various concentrations in water are shown in Figure 3a. As the concentration of the PEG-coated Mag-GNS increases, the signal intensity of the MR image decreases, owing to the presence of the embedded Fe_3O_4 nanoparticles. This behavior allows the Mag-GNS to be used as a T_2 contrast agent. The specific relaxivity, which is a measure of the change in the spin–spin relaxation rate (T_2^{-1}) per unit concentration, is $r_2 = 251\ mM^{-1}s^{-1}$ for the PEG-coated Mag-GNS (Figure 3b).

For targeted MRI and NIR photothermal therapy, we conjugated an antibody, anti-HER2/*neu* ($Ab_{HER2/neu}$), onto the surface of the Mag-GNS using a PEG linker (see Supporting Information), to prepare Mag-GNS that target the HER2/*neu* receptors of the breast cancer cells (Mag-GNS-$Ab_{HER2/neu}$). HER2/*neu*-positive SKBR3 breast cancer cells and HER2/*neu*-negative H520 lung cancer cells[18] were incubated with Mag-GNS-$Ab_{HER2/neu}$ for 2 h at 37 °C (see Supporting Information). T_2-weighted MR images were recorded for the SKBR3 and H520 cells treated with Mag-GNS-$Ab_{HER2/neu}$, as well as for untreated control SKBR3 cells, on a 3.0-T clinical MRI system (Figure 3c; see Supporting Information). The T_2-weighted MR image of the Mag-GNS-$Ab_{HER2/neu}$-treated SKBR3 cells was much darker than those of the Mag-GNS-$Ab_{HER2/neu}$-treated H520 cells and the control SKBR3 cells. The T_2 relaxation times of the Mag-GNS-$Ab_{HER2/neu}$-treated SKBR3 and H520 cells, and the control SKBR3 cells were 54.8, 76.9, and 115 ms, respectively. Thus, the Mag-GNS can be a contrast agent in targeted MRI for the detection of cancer cells.

Results of targeted NIR photothermal therapy against cancer cells using Mag-GNS-$Ab_{HER2/neu}$ are presented in Figure 4 (see Supporting Information). The Mag-GNS-$Ab_{HER2/neu}$-treated SKBR3 and H520 cells, and the control SKBR3 cells were exposed to a femtosecond-pulse laser with a wavelength of 800 nm and a beam diameter of 1 mm for 10 s. The power of the laser was varied from 20–80 mW in steps of 10 mW. After exposure to the NIR laser, the dead cells were stained blue by treating them with 0.4% trypan blue for 10 min. No destruction of the control SKBR3 cells was observed, even after exposure to a power of 80 mW (Figure 4a). The death of the Mag-GNS-$Ab_{HER2/neu}$-treated H520 cell began at 60 mW (Figure 4b). However, in the case of the Mag-GNS-$Ab_{HER2/neu}$-treated SKBR3 cells, cell death was observed even at a low power of 20 mW (Figure 4c). These results clearly demonstrate that the Mag-GNS-$Ab_{HER2/neu}$, which absorb NIR radiation, were more effectively targeted on the SKBR3 cells than on the H520 cells, because of a strong antigen–antibody interaction in the SKBR3 cells. At 20 mW, only the SKBR3 cells at the center of the laser beam were exposed to the high intensity of the femtosecond pulse, which has a Gaussian distribution, and thus destroyed. With increasing laser power, the area of the dead cells spread. The cells burst and died as a result of the local heating generated by the absorption of NIR radiation by the Mag-GNS-$Ab_{HER2/neu}$. The control SKBR3 cells, which stayed alive, exhibited normal morphology after exposure to a power of

 © 2006 Wiley-VCH Verlag GmbH & Co. KGaA, Weinheim

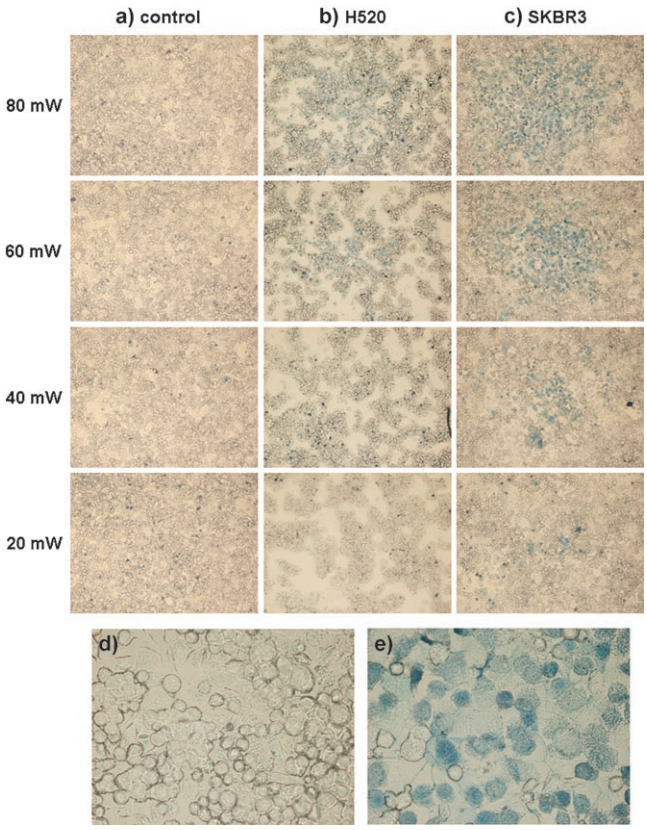

Figure 4. Optical microscope images of a) control SKBR3 cells, b) HER2/*neu*-negative H520 cells incubated with Mag-GNS-$Ab_{HER2/neu}$, and c) HER2/*neu*-positive SKBR3 cells incubated with Mag-GNS-$Ab_{HER2/neu}$ after irradiation for 10 s with a femtosecond-pulse laser (with a wavelength of 800 nm and a beam diameter of 1 mm) at various intensities and subsequent staining with trypan blue. High-magnification optical microscope images of d) control SKBR3 cells and e) SKBR3 cells incubated with Mag-GNS-$Ab_{HER2/neu}$ after irradiation at a power of 80 mW and subsequent staining.

80 mW (Figure 4d), whereas most of the Mag-GNS-$Ab_{HER2/neu}$-treated SKBR3 cells were burst, and the cytoplasm of the dead cells stained by trypan blue spread to the medium (Figure 4e).

The use of a femtosecond-pulse laser is crucial to this experiment.[19] Although the average power of a femtosecond-pulse laser may be comparable with that of a continuous-wave (CW) laser, its peak power greatly exceeds that of the CW laser.[20] The large amount of energy tightly packed in the femtosecond pulses imparts an enormous impact on the sample, both temporally and spatially.[21] Furthermore, the duration of a femtosecond pulse is much shorter than the characteristic time for relaxation through intermolecular energy transfer,[22] preventing the dissipation of the photon energy and, thus, resulting in very effective local heating by photo-excitation. These characteristics of the femtosecond pulse lead to a unique feature that could have an important implication for in vivo therapy: the photodegradation of the cancer cells is greatly accelerated, and thus, the required dose of radiation is correspondingly reduced. For example, irradiation for only 10 s is necessary for the destruction of the SKBR3 cells with a femtosecond-pulse laser, whereas 2–7 min is normally required with a CW laser at a similar or higher intensity.[5–7]

Recently, several multifunctional nanomedical platforms have been reported.[9] The probes encapsulated by biologically localized embedding (PEBBLEs) produced by the Kopelman group are particularly interesting, because different types of photosensitizers, imaging contrast agents, and targeting agents can be simultaneously incorporated into polymer or silica nanoparticles.[9f] Although the multifunctional nanomedical features of PEBBLEs are similar to those of our Mag-GNS, there are several key differences between these two nanomaterials. Firstly, the compositions are completely different. Our Mag-GNS consist of a silica nanosphere core surrounded by a gold nanoshell for photothermal therapy, with embedded magnetite nanoparticles for T_2 MRI contrast enhancement. In contrast, the PEBBLEs consist of polyacrylamide nanoparticles containing organic dyes for photodynamic therapy and gadolinium complexes for T_1 MRI contrast enhancement. Secondly, cancer cells are killed by the two nanomaterials through different mechanisms. In photothermal therapy using Mag-GNS, the NIR radiation absorbed by the gold nanoshells is converted efficiently into a sufficient amount of heat to kill cancer cells. In contrast, in photodynamic therapy using PEBBLEs,[9f] reactive oxygen species generated by laser irradiation of the photosensitizers kill the cancer cells. Thirdly, the Mag-GNS absorb NIR radiation, which is optimal for the treatment of deep tissues, because the absorption of NIR radiation in tissues is generally much less than that of visible light, and consequently tissue penetration is enhanced. Fourthly, irradiation of the cancer-targeting Mag-GNS-$Ab_{HER2/neu}$ using a femtosecond-pulse laser with an NIR wavelength makes it possible to kill cancer cells at a low power and in a short period of time. This very effective destruction of cancer cells through localized heating by photo-excitation results from the synergetic effects of the femtosecond laser pulse and the NIR irradiation.

In conclusion, multifunctional Mag-GNS consisting of gold nanoshells with embedded magnetic Fe_3O_4 nanoparticles were synthesized. Anti-HER2/*neu* was linked to the Mag-GNS for targeted MRI and NIR photothermal therapy of cancer cells. The embedded Fe_3O_4 nanoparticles resulted in high contrast in the MR images, and the gold nanoshells had an optical absorption cross section high enough for NIR photothermal therapy. Cancer cells targeted with the Mag-GNS-$Ab_{HER2/neu}$ in vitro were detectable by a commercial clinical MRI system, and were rapidly destroyed upon short exposure to femtosecond laser pulses with an NIR wavelength and a low power.

Received: June 20, 2006
Revised: August 21, 2006
Published online: October 30, 2006

Keywords: gold · magnetic resonance imaging · nanomedicine · nanostructures · photothermal therapy

 © 2006 Wiley-VCH Verlag GmbH & Co. KGaA, Weinheim

[1] a) C. M. Niemeyer, C. A. Mirkin, *Nanobiotechnology: Concepts, Applications and Perspectives*, Wiley-VCH, Weinheim, **2004**; b) U. Häfeli, W. Schütt, J. Teller, M. Zborowski, *Scientific and Clinical Applications of Magnetic Carriers*, Plenum, New York, **1997**; c) P. Alivisatos, *Nat. Biotechnol.* **2004**, *22*, 47; d) K. J. Klabunde, *Nanoscale Materials in Chemistry*, Wiley-Interscience, New York, **2001**; e) T. Hyeon, *Chem. Commun.* **2003**, 923; f) A. L. Rogach, D. V. Talapin, E. V. Shevchenko, A. Kornowski, M. Haase, H. Weller, *Adv. Funct. Mater.* **2002**, *12*, 653; g) A. P. Alivisatos, *Science* **1996**, *271*, 933; h) C. B. Murray, C. R. Kagan, M. G. Bawendi, *Annu. Rev. Mater. Sci.* **2000**, *30*, 545.

[2] a) M. Bruchez, Jr., M. Moronne, P. Gin, S. Weiss, A. P. Alivisatos, *Science* **1998**, *281*, 2013; b) W. C. W. Chan, S. Nie, *Science* **1998**, *281*, 2016; c) S. Kim, Y. T. Lim, E. G. Soltesz, A. M. De Grand, J. Lee, A. Nakayama, J. A. Parker, T. Mihaljevic, R. G. Laurence, D. M. Dor, L. H. Cohn, M. G. Bawendi, J. V. Frangioni, *Nat. Biotechnol.* **2004**, *22*, 93; d) I. L. Medintz, H. T. Uyeda, E. R. Goldman, H. Mattoussi, *Nat. Mater.* **2005**, *4*, 435; e) X. Gao, Y. Cui, R. M. Levenson, L. W. K. Chung, S. Nie, *Nat. Biotechnol.* **2004**, *22*, 969.

[3] a) T. A. Taton, C. A. Mirkin, R. L. Letsinger, *Science* **2000**, *289*, 1757; b) J.-M. Nam, C. S. Thaxton, C. A. Mirkin, *Science* **2003**, *301*, 1884; c) D. G. Georganopoulou, L. Chang, J.-M. Nam, C. S. Thaxton, E. J. Mufson, W. L. Klein, C. A. Mirkin, *Proc. Natl. Acad. Sci. USA* **2005**, *102*, 2273.

[4] a) J. W. M. Bulte, D. L. Kraitchman, *NMR Biomed.* **2004**, *17*, 484; b) L. Josephson, C.-H. Tung, A. Moore, R. Weissleder, *Bioconjugate Chem.* **1999**, *10*, 186; c) M. Zhao, D. A. Beauregard, L. Loizou, B. Davletov, K. M. Brindle, *Nat. Med.* **2001**, *7*, 1241; d) H. W. Kang, L. Josephson, A. Petrovsky, R. Weissleder, A. Bogdanov, Jr., *Bioconjugate Chem.* **2002**, *13*, 122; e) R. Weissleder, A. Moore, U. Mahmood, R. Bhorade, H. Benveniste, E. A. Chiocca, J. P. Basilion, *Nat. Med.* **2000**, *6*, 351; f) J. M. Perez, L. Josephson, T. O'Loughlin, D. Högemann, R. Weissleder, *Nat. Biotechnol.* **2002**, *20*, 816; g) J. W. M. Bulte, S.-C. Zhang, P. van Gelderen, V. Herynek, E. K. Jordan, I. D. Duncan, J. A. Frank, *Proc. Natl. Acad. Sci. USA* **1999**, *96*, 15256.

[5] a) C. Loo, A. Lowery, N. J. Halas, J. L. West, R. Drezek, *Nano Lett.* **2005**, *5*, 709; b) D. P. O'Neal, L. R. Hirsch, N. J. Halas, J. D. Payne, J. L. West, *Cancer Lett.* **2004**, *209*, 171; c) L. R. Hirsch, R. J. Stafford, J. A. Bankson, S. R. Sershen, B. Rivera, R. E. Price, J. D. Hazle, N. J. Halas, J. L. West, *Proc. Natl. Acad. Sci. USA* **2003**, *100*, 13549.

[6] X. Huang, I. H. El-Sayed, W. Qian, M. A. El-Sayed, *J. Am. Chem. Soc.* **2006**, *128*, 2115.

[7] N. W. S. Kam, M. O'Connell, J. A. Wisdom, H. Dai, *Proc. Natl. Acad. Sci. USA* **2005**, *102*, 11600.

[8] S. Link, M. A. El-Sayed, *Int. Rev. Phys. Chem.* **2000**, *19*, 409.

[9] a) L. Levy, Y. Sahoo, K.-S. Kim, E. J. Bergey, P. N. Prasad, *Chem. Mater.* **2002**, *14*, 3715; b) G. Zheng, J. Chen, H. Li, J. D. Glickson, *Proc. Natl. Acad. Sci. USA* **2005**, *102*, 17757; c) E. Garanger, D. Boturyn, Z. Jin, P. Dumy, M.-C. Favrot, J.-L. Coll, *Mol. Ther.* **2005**, *12*, 1168; d) I. J. Majoros, T. P. Thomas, C. B. Mehta, J. R. Baker, Jr., *J. Med. Chem.* **2005**, *48*, 5892; e) I. J. Majoros, A. Myc, T. Thomas, C. B. Mehta, J. R. Baker, Jr., *Biomacromolecules* **2006**, *7*, 572; f) R. Kopelman, Y.-E. L. Koo, M. Philbert, B. A. Moffat, G. R. Reddy, P. McConville, D. E. Hall, T. L. Chenevert, M. S. Bhojani, S. M. Buck, A. Rehemtulla, B. D. Ross, *J. Magn. Magn. Mater.* **2005**, *293*, 404; g) H. Xu, S. M. Buck, R. Kopelman, M. A. Philbert, M. Brasuel, B. D. Ross, A. Rehemtulla, *Isr. J. Chem.* **2004**, *44*, 317; h) F. Yan, H. Xu, J. Anker, R. Kopelman, B. Ross, A. Rehemtulla, R. Reddy, *J. Nanosci. Nanotechnol.* **2004**, *4*, 72; i) J. Kim, J. E. Lee, J. Lee, J. H. Yu, B. C. Kim, K. An, Y. Hwang, C.-H. Shin, J.-G. Park, J. Kim, T. Hyeon, *J. Am. Chem. Soc.* **2006**, *128*, 688.

[10] J. Kim, J. E. Lee, J. Lee, Y. Jang, S.-W. Kim, K. An, J. H. Yu, T. Hyeon, *Angew. Chem.* **2006**, *118*, 4907; *Angew. Chem. Int. Ed.* **2006**, *45*, 4789.

[11] a) S. J. Oldenburg, R. D. Averitt, S. L. Westcott, N. J. Halas, *Chem. Phys. Lett.* **1998**, *288*, 243; b) C. Graf, A. van Blaaderen, *Langmuir* **2002**, *18*, 524.

[12] W. Stöber, A. Fink, E. Bohn, *J. Colloid Interface Sci.* **1968**, *26*, 62.

[13] J. Park, K. An, Y. Hwang, J.-G. Park, H.-J. Noh, J.-Y. Kim, J.-H. Park, N.-M. Hwang, T. Hyeon, *Nat. Mater.* **2004**, *3*, 891.

[14] Y. Wang, X. Teng, J.-S. Wang, H. Yang, *Nano Lett.* **2003**, *3*, 789.

[15] a) K. Ha, Y.-J. Lee, H. J. Lee, K. B. Yoon, *Adv. Mater.* **2000**, *12*, 1114; b) S.-S. Bae, D. K. Lim, J.-I. Park, W.-R. Lee, J. Cheon, S. Kim, *J. Phys. Chem. B* **2004**, *108*, 2575.

[16] D. G. Duff, A. Baiker, P. P. Edwards, *Langmuir* **1993**, *9*, 2301.

[17] S. I. Stoeva, F. Huo, J.-S. Lee, C. A. Mirkin, *J. Am. Chem. Soc.* **2005**, *127*, 15362.

[18] P. A. Bunn, Jr., B. Helfrich, A. F. Soriano, W. A. Franklin, M. Varella-Garcia, F. R. Hirsch, A. Baron, C. Zeng, D. C. Chan, *Clin. Cancer Res.* **2001**, *7*, 3239.

[19] M. Sawa, K. Awazu, T. Takahashi, H. Sakaguchi, H. Horiike, M. Ohji, Y. Tano, *Br. J. Ophthalmol.* **2004**, *88*, 826.

[20] a) A. E. Siegman, *Lasers*, University Science Books, Sausalito, **1986**; b) O. Svelto, *Principles of Lasers*, Plenum, New York, **1998**.

[21] a) M. E. Fermann, A. Galvanauskas, G. Sucha, *Ultrafast Lasers: Technology and Application*, Marcel Dekker, New York, **2002**; b) W. Kaiser, *Ultrashort Laser Pulses: Generation and Application*, Springer, New York, **1993**.

[22] N. J. Turro, *Modern Molecular Photochemistry*, University Science Books, Sausalito, **1991**.

 © 2006 Wiley-VCH Verlag GmbH & Co. KGaA, Weinheim

Cluster Compounds

DOI: 10.1002/anie.200602203

Synthesis of Tellurido-Bridged $IrPt_2$, $IrPd_2$, and IrPtPd Clusters by Inserting Zero-Valent Pt and Pd Centers into Te–C Bonds**

*Takafumi Nakagawa, Hidetake Seino, Shoken Nagao, and Yasushi Mizobe**

Soluble transition-metal sulfido clusters have been investigated extensively because of their relevance to biological and industrial catalysts. In contrast, the chemistry of the analogues of tellurium, the heavier congener of sulfur, has been less-well developed.[1] This difference is presumably because, at least in

[*] T. Nakagawa, Dr. H. Seino, Dr. S. Nagao, Prof. Dr. Y. Mizobe
Institute of Industrial Science
The University of Tokyo
Komaba, Meguro-ku, Tokyo, 153-8505 (Japan)
Fax: (+81) 3-5452-6361
E-mail: ymizobe@iis.u-tokyo.ac.jp

[**] This work was supported by Grant-in-Aid for Scientific Research on Priority Areas (No. 14078206, "Reaction Control of Dynamic Complexes") from the Ministry of Education, Culture, Sports, Science and Technology, Japan, and by CREST of JST.

WILEY InterScience DISCOVER SOMETHING GREAT
© 2006 Wiley-VCH Verlag GmbH & Co. KGaA, Weinheim

part, good tellurido sources that can be used in organic media are scarce.[2]

In the last decade, studies in our group have focused on the pursuit of rational methods to construct metal sulfido and selenido cluster cores with desired structures and atom compositions.[3] In the course of these studies, we have demonstrated that newly prepared dinuclear μ-hydrosulfido and μ-hydroselenido complexes of the type [Cp*MCl(μ-EH)$_2$MCp*Cl] (M = Ru, Ir, Rh; E = S, Se; Cp* = η^5-C_5Me_5) can serve as versatile building blocks to synthesize a variety of homo- and heterometallic sulfido, selenido, and sulfido–selenido clusters.[3,4] However, preparation of the corresponding tellurido clusters is not yet feasible, as the hydrotellurido analogues of these μ-EH complexes are not accessible.

Formations of tellurido ligands from coordinated tellurolates have been observed for isolated or in situ-generated complexes of Cr,[5] Mo,[6] Re,[7] Pd,[8] Ag,[9] and Cu.[10] Furthermore, cleavage of the E–C bonds of organochalcogen compounds has also been demonstrated in a well-defined manner for the reactions with low-valent late transition metals,[11] which include the oxidative addition reactions of Ph_2Te with zero-valent Group 10 metal complexes.[12] On the basis of these findings, we have attempted the synthesis of mixed-metal tellurido clusters by a new route, which involves the initial preparation of an Ir tellurolato complex by using readily available RTeTeR compounds (in which R = aryl) as the Te source and subsequent transformation of this complex into the tellurido clusters through Te–C bond cleavage of the tellurolato ligands by using Group 10 noble metals.

Treatment of [Cp*Ir(CO)$_2$] with one equivalent of TolTeTeTol (Tol = *p*-$CH_3C_6H_4$) in benzene at room temperature afforded a bis(tellurolato) complex [Cp*Ir(CO)(TeTol)$_2$] (**1**) in high yield [Eq. (1)], which has been characterized by

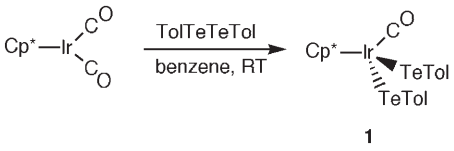

(1)

1

single-crystal X-ray analysis (Figure 1).[13] Complex **1** has an expected three-legged structure, for which the interatomic distances and angles are not unusual. Related thiolato and selenolato complexes [Cp*Ir(CO)(EPh)$_2$] (E = S, Se) are known, which were prepared from [Cp*Ir(CO)$_2$] and PhEEPh in THF by photo-irradiation. However, X-ray structures were not determined.[14]

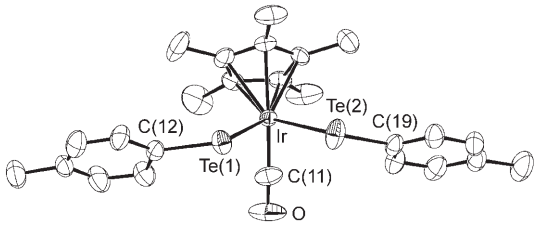

Figure 1. An ORTEP drawing of **1**. Hydrogen atoms are omitted for clarity (thermal ellipsoids shown at 30% probability). Selected bond lengths [Å] and angles [°]: Ir–Te(1) 2.6654(6), Ir–Te(2) 2.6579(8); Te(1)-Ir-Te(2) 79.46(2).

When **1** was treated with two equivalents of [Pt(PPh$_3$)$_3$] in THF at room temperature, the mixed-metal tellurido cluster [{Cp*Ir(CO)}(μ$_3$-Te)$_2${PtTol(PPh$_3$)}$_2$] (**2**) was obtained. The NMR spectra of the residue obtained from the reaction mixture after removal of solvent by evaporation showed the presence of the two isomers, **2a** and **2b** (Scheme 1). After

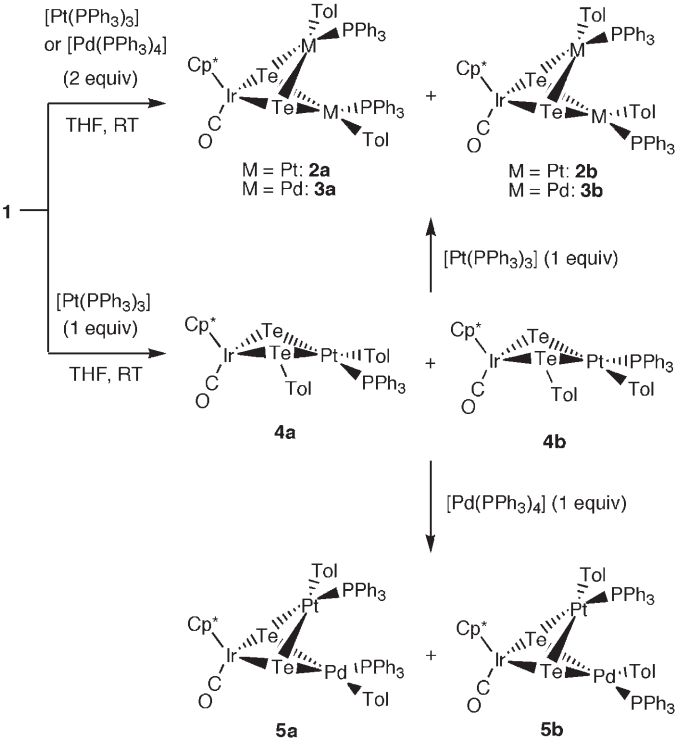

Scheme 1. Synthetic routes for mixed-metal tellurido clusters.

crystallization of the residue from a mixture of benzene and hexane, only the major isomer, **2a**, was isolated as single crystals and fully characterized by X-ray diffraction.[13] As shown in Figure 2, **2a** has a triangular IrPt$_2$ core with two capped tellurido ligands, for which, separations of Ir(1) from Pt(1) and Pt(2) by 3.8049(5)–3.8588(6) Å as well as Pt···Pt interatomic distances of 3.1539(6) and 3.2523(7) Å indicate the absence of any metal–metal bonding interactions. The Ir center has a three-legged geometry, while the geometry around two Pt atoms is square-planar. Two phosphine ligands are mutually *trans* with respect to the Pt–Pt vector, as are the two Tol ligands. The X-ray structure was not available for **2b**, but its NMR data are analogous to those of **2a** and suggest a structure with two mutually *cis*-phosphine ligands (shown in Scheme 1 for **2b**). Because of steric repulsion between the two phosphine ligands, **2b** is the less-favored isomer. Note that **2a** redissolved in C_6D_6 and converted readily into an equilibrium mixture of **2a** and **2b** at room temperature, the ratio of which was 4:1, thus indicating that the isomerization of **2a** into **2b** is fast for this IrPt$_2$ cluster.

Treatment of **1** with two equivalents of [Pd(PPh$_3$)$_4$] gave the Pd analogue of **2**, [{Cp*Ir(CO)}(μ$_3$-Te)$_2${PdTol(PPh$_3$)}$_2$]

 © 2006 Wiley-VCH Verlag GmbH & Co. KGaA, Weinheim

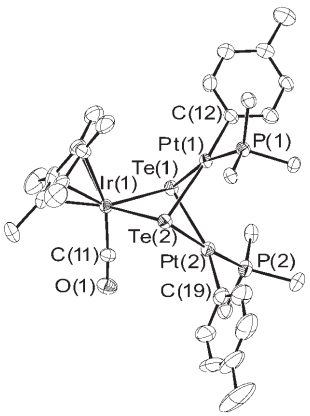

Figure 2. An ORTEP drawing of **2a**. Only one of the two independent molecules is shown (thermal ellipsoids shown at 30% probability). For clarity all the hydrogen atoms are omitted and only the carbon atom bound to P is shown for the phenyl groups of the PPh_3 units. Selected bond lengths [Å] and angles [°]: Ir–Te 2.6769(7)–2.6985(7), Pt–Te, 2.6347(8)–2.7052(7); Ir-Te-Pt, 89.82(2)–92.69(2), Pt-Te-Pt, 72.39(2)–75.23(2), Te-Ir-Te 75.26(2), 75.60(2), Te-Pt-Te, 75.86(2)–76.44(2). In isostructural **3a**: Ir···Pd 3.784(1)–3.837(1), Pd···Pd 3.185(2), 3.089(1), Ir-Te, 2.666(1)–2.689(1), Pd-Te, 2.605(1)–2.702(2), Ir-Te-Pd 89.49(4)–92.91(3), Pd-Te-Pd, 71.31(4)–74.12(4), Te-Ir-Te 75.68(3), 75.91(3), Te-Pd-Te, 76.60(4)–76.98(4).

(**3**), which is present as a mixture of **3a** and **3b** under the reaction conditions (Scheme 1). Workup of the product solution afforded only **3a** as single crystals and the X-ray analysis disclosed its structure to be analogous to that of **2a**.[13] When redissolved in C_6D_6, **3a** slowly converted into an equilibrium mixture of **3a** and **3b** to reach a molar ratio of 3:1. This isomerization of the $IrPd_2$ cluster is considerably slower than that of the $IrPt_2$ cluster, **2a**. As addition of 0.1 equivalents of PPh_3 to the solution of **3a** significantly decreases the rate of the formation of **3b**, this isomerization presumably proceeds through dissociation of PPh_3. The much-faster isomerization of **2a** than that of **3a** may be ascribable to the higher ability of PPh_3 to dissociate from a Pt center than from a Pd center.

The reaction of **1** with one equivalent of $[Pt(PPh_3)_3]$ in THF at room temperature resulted in the isolation of the intermediate in the conversion of **1** into **2**. Workup of the reaction mixture afforded the tellurido- and tellurolato-bridged dinuclear complex $[Cp^*Ir(CO)(\mu\text{-}Te)(\mu\text{-}TeTol)PtTol(PPh_3)]$ (**4**), which was isolated as a mixture of isomers, **4a** and **4b** (Scheme 1). For the major isomer, **4a**, the structure has been determined unambiguously by X-ray analysis of single crystals obtained after repeated crystallization of this mixture (Figure 3).[13] Two metal centers are connected by one μ-telluride and one μ-tellurolate, in which the tellurido and Tol ligands around Pt are mutually *cis*. Oxidative addition of a Pt^0 center across one Te–Tol bond in **1** and coordination of a Te atom of the other intact TeTol ligand to Pt affords **4a**. There are no bonding interactions between metal centers in **4a**. The Pt–Te(1) bond at 2.6563(7) Å is considerably longer than the Pt–Te(2) bond at 2.6013(7) Å presumably because of the strong *trans* influence exerted by the Tol ligand. Around the Ir center, the Ir-μ-tellurolato bond (Ir–Te(1) 2.6243(6) Å) is shorter than the Ir-μ-tellurido bond (Ir–Te(2) 2.6934(8) Å;

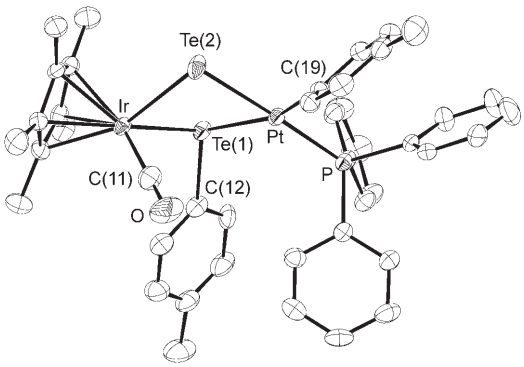

Figure 3. An ORTEP drawing of **4a**. Hydrogen atoms are omitted for clarity (thermal ellipsoids shown at 30% probability). Selected bond lengths [Å] and angles [°]: Ir···Pt 3.9198(5); Ir-Te(1)-Pt 95.98(2), Ir-Te(2)-Pt 95.50(2), Te-Ir-Te 76.38(2), Te-Pt-Te 77.42(2).

Figure 3). Unfortunately, an X-ray crystal structure was not obtainable for **4b**. However, spectroscopic data of **4b** are consistent with the structure shown in Scheme 1, in which only the geometry around Pt differs from that of **4a**. Complex **4a** dissolved in C_6D_6 and converted into a 2.2:1 mixture of **4a** and **4b** in equilibrium after 30 h at room temperature. A similar isomerization was reported for the reaction of $[Pt(PEt_3)_3]$ with *i*PrTePh, in which the initial product *cis*-$[PtPh(Te\textit{i}Pr)(PEt_3)_2]$ transformed smoothly into *trans*-$[PtPh(Te\textit{i}Pr)(PEt_3)_2]$.[11] Treatment of an equilibrium mixture of **4a** and **4b** with one equivalent of $[Pt(PPh_3)_3]$ afforded a mixture of **2a** and **2b**, which indicates that the complexes **4** are the intermediates in the reaction course of **1** to **2**.

It is noteworthy that from the reaction of **1** with $[Pd(PPh_3)_4]$, the telluride–tellurolato complex corresponding to **4** was not obtained. The reaction of equimolar **1** and $[Pd(PPh_3)_4]$ resulted in the formation of a mixture of the trinuclear tellurido cluster, **3**, and residual **1**, as indicated by the NMR spectra of the reaction mixture recorded soon after mixing.

It was also found that from the reaction of the Ir–Pt complex, **4**, with $[Pd(PPh_3)_4]$, another trinuclear cluster $[\{Cp^*Ir(CO)\}(\mu_3\text{-}Te)_2\{PtTol(PPh_3)\}\{PdTol(PPh_3)\}]$ (**5**) was available through the facile insertion of a Pd^0 center into the remaining Te–Tol bond in complex **4** (Scheme 1). The NMR spectra of the reaction mixture showed the presence of **5a**. After removal of the solvent by evaporation, crystallization of the residue from a mixture of THF and hexane afforded **5a** as single crystals. The NMR spectra of **5a** in C_6D_6 indicated its rapid transformation into an equilibrium mixture of **5a** and **5b** in a 3:1 molar ratio. The X-ray crystal structure of **5a** is depicted in Figure 4.[13] Cluster **5a** has the expected triangular core capped by two μ_3-tellurido ligands, in which the Pd atom occupies the vertex close to the CO ligand, presumably because the insertion of the Pd center into the Te–Tol bond occurs selectively at the sterically less-crowding side with respect to the $IrPtTe_2$ core in **4**, namely, from the direction opposite the Cp* ligand. Two PPh_3 ligands are mutually *trans* as observed for **2a** and **3a**, and similarly the structure of **5b** may be assigned as that with two PPh_3 ligands mutually *cis* around the Pt···Pd vector.

 © 2006 Wiley-VCH Verlag GmbH & Co. KGaA, Weinheim

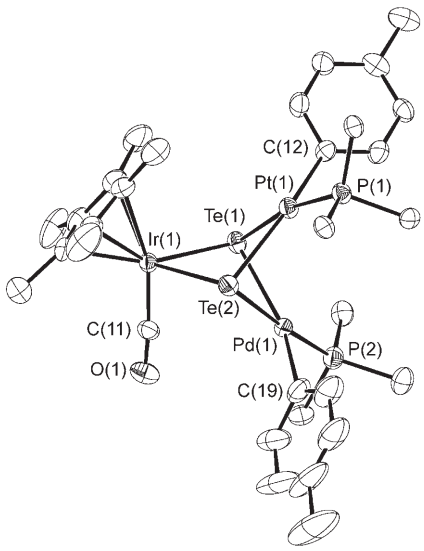

Figure 4. An ORTEP drawing of **5a**. Only one of the two independent molecules is shown (thermal ellipsoids shown at 30% probability). For clarity all the hydrogen atoms are omitted and only the carbon atom bound to P is shown for the phenyl groups of the PPh_3 units. Selected bond lengths [Å] and angles [°]: Ir···Pt, 3.8534(6), 3.8505(6), Ir···Pd 3.7821(8), 3.7879(7), Pt···Pd 3.2002(9), 3.1053(7), Ir-Te 2.6712(8)–2.6870(8), Pt-Te 2.6162(8)–2.6827(8), Pd-Te 2.6179(9)–2.718(1), Ir-Te-Pt 91.72(2)–93.52(2), Ir-Te-Pd 89.22(3)–91.47(3); Pt-Te-Pd, 71.39(2)–74.34(2), Te-Ir-Te 75.43(2), 75.85(2), Te-Pt-Te 76.44(2), 76.72(2), Te-Pd-Te 75.88(3), 76.55(2).

In conclusion, a versatile route for synthesizing mixed-metal tellurido clusters in solution has been developed, which involves the use of a readily available tellurolato complex as a metal–tellurido building block through Te–C bond scission with M^0 centers (M = Pt, Pd). Note that the reactions of **1** with Pt^{II} and Pd^{II} complexes $[MCl_2(cod)]$ (cod = cyclooctadiene) result in the formation of only the tellurolato-bridged dinuclear and trinuclear complexes $[Cp^*Ir(CO)(\mu\text{-}TeTol)_2MCl_2]$ (M = Pt, Pd) and $[\{Cp^*Ir(CO)(\mu\text{-}TeTol)_2\}_2Pt]$, which will be described elsewhere. Application of the method reported herein to the synthesis of a wide range of mixed-metal tellurido clusters is now in progress.

Experimental Section

All manipulations were carried out under an atmosphere of N_2 by using Schlenk techniques. Complexes $[Cp^*Ir(CO)_2]$,[15] $[Pt(PPh_3)_3]$,[16] $[Pd(PPh_3)_4]$,[17] and TolTeTeTol[18] were prepared by reported methods.

1: TolTeTeTol (230 mg, 0.526 mmol) was added to a solution of $[Cp^*Ir(CO)_2]$ (191 mg, 0.498 mmol) in benzene (10 mL) at room temperature. The reaction mixture was stirred for 3 h at room temperature and the resultant deep red solution was concentrated in vacuo. Addition of hexane afforded **1** as deep red crystals (315 mg, 79% yield). IR (KBr): $\tilde{\nu} = 1982\ cm^{-1}$, ν(CO); ^1H NMR (C_6D_6): $\delta =$ 1.55 (s, 15H, Cp*), 2.06 (s, 6H, Me in Tol), 6.75, 7.96 ppm (d, $J =$ 7.9 Hz, 4H each, C_6H_4); elemental analysis (%) calcd for $C_{25}H_{29}OIrTe_2$: C 37.87, H 3.69; found: C 37.51, H 3.53.

2: $[Pt(PPh_3)_3]$ (101 mg, 0.103 mmol) was added to a THF solution (5 mL) of **1** (41 mg, 0.051 mmol) and the mixture was stirred for 26 h at room temperature. The resultant red solution was evaporated to dryness in vacuo. The ^1H NMR spectrum of this residue indicated the presence of two products, **2a** and **2b**, in a molar ratio of 2:1. Crystallization of the residue from a mixture of benzene and hexane (1:10) afforded pure **2a**·0.25 C_6H_6 as red crystals (43 mg, 48% yield). Complex **2a** dissolved in C_6D_6 and converted into an equilibrium mixture of **2a** and **2b** in the ratio of 4:1. **2a**: IR (KBr): $\tilde{\nu} = 1979\ cm^{-1}$, ν(CO); ^1H NMR (C_6D_6): $\delta = 1.70$ (s, 15H, Cp*), 2.15, 2.21 (s, 3H each, Me in Tol), 6.73, 6.85, 7.53, 7.60 (d, $J = 7.6$ Hz, 2H each, C_6H_4), 7.0–7.1 (m, 18H, Ph), 7.8–8.0 ppm (m, 12H, Ph); $^{31}P\{^1H\}$ NMR (C_6D_6): $\delta = 7.1$ (d with ^{195}Pt satellites, $J_{P\text{-}P} = 5$ Hz, $J_{Pt\text{-}P} = 3790$ Hz), 7.4 ppm (d with ^{195}Pt satellites, $J_{P\text{-}P} = 5$ Hz, $J_{Pt\text{-}P} = 3700$ Hz); elemental analysis (%) calcd for $C_{62.5}H_{60.5}OIrP_2Pt_2Te_2$: C 43.46, H 3.53; found: C 43.65, H 3.52. Data assignable to **2b**: ^1H NMR (C_6D_6): $\delta = 1.71$ (s, 15H, Cp*), 2.14, 2.16 ppm (s, 3H each, Me in Tol); $^{31}P\{^1H\}$ NMR (C_6D_6): 6.6 (d with ^{195}Pt satellites, $J_{P\text{-}P} = 8$ Hz, $J_{Pt\text{-}P} = 3770$ Hz), 6.9 ppm (d with ^{195}Pt satellites, $J_{P\text{-}P} = 8$ Hz, $J_{Pt\text{-}P} = 3930$ Hz).

3: $[Pd(PPh_3)_4]$ (116 mg, 0.100 mmol) was added to a THF solution (5 mL) of **1** (40 mg, 0.050 mmol) and the resultant black solution was stirred at room temperature for 23 h. The NMR spectrum of the reaction mixture showed the presence of two isomeric products, **3a** and **3b**, in a 3:1 ratio. Hexane was added to the concentrated product solution and kept at −20 °C to yield black crystals of **3a**·0.25 C_6H_{14} (32 mg, 41% yield). When redissolved in C_6D_6, **3a** was converted very slowly into an equilibrium mixture of **3a** and **3b**. The rate constants for the conversion of **3a** into **3b** and its reverse reaction at 293 K were calculated to be $4.5 \times 10^{-5}\ s^{-1}$ and $13 \times 10^{-5}\ s^{-1}$, respectively, based on the ^1H NMR spectral change. IR (KBr): $\tilde{\nu} = 1971\ cm^{-1}$, ν(CO); elemental analysis (%) calcd for $C_{62.5}H_{62.5}OIrP_2Pd_2Te_2$: C 48.37; H 4.06; found: C 47.64, H 3.83. Data assignable to **3a**: ^1H NMR (C_6D_6): $\delta = 1.71$ (s, 15H, Cp*), 2.14, 2.23 (s, 3H each, Me in Tol), 6.73, 6.78, 7.40, 7.48 (d, $J = 8.0$ Hz, 2H each, C_6H_4), 7.0–7.1 (m, 18H, Ph), 7.8–8.0 ppm (m, 12H, Ph); $^{31}P\{^1H\}$ NMR (C_6D_6): $\delta = 14.7$ (d, $J =$ 7 Hz), 14.9 ppm (d, $J = 7$ Hz). Data assignable to **3b**: ^1H NMR (C_6D_6): $\delta = 1.75$ (s, 15H, Cp*), 2.13, 2.16 ppm (s, 3H each, Me in Tol); $^{31}P\{^1H\}$ NMR (C_6D_6): $\delta = 14.7$ (d, overlapping with the signal of **3a**), 15.5 ppm (d, $J = 8$ Hz).

4: A mixture of **1** (160 mg, 0.202 mmol) and $[Pt(PPh_3)_3]$ (200 mg, 0.204 mmol) in THF (5 mL) was stirred at room temperature for one day and the resultant dark green solution was evaporated to dryness in vacuo. The ^1H NMR spectra of the residue showed the presence of the products **4a** and **4b** in a molar ratio of 3:1. The residue was extracted with benzene and the addition of hexane to the concentrated extract afforded a 3:1 mixture of **4a** and **4b** as dark green crystals (177 mg, 70% combined yield). Single crystals of pure **4a** were obtained by repeated fractional crystallization from a mixture of benzene and hexane. **4a** was dissolved in C_6D_6 and allowed to stand for 30 h at room temperature; the resulting solution contained a mixture of **4a** and **4b** in equilibrium in a ratio of 2.2:1 as confirmed by ^1H NMR spectroscopy. IR (KBr): $\tilde{\nu} = 1991\ cm^{-1}$, ν(CO); elemental analysis (%) calcd for $C_{43}H_{44}OIrPPtTe_2$: C 41.31, H 3.55; found: C 41.06, H 3.69. Data assignable to **4a**: ^1H NMR (C_6D_6): $\delta = 1.63$ (s, 15H, Cp*), 1.97, 2.10 (s, 3H each, Me in Tol), 6.59, 7.19, 7.39, 7.71 ppm (d, $J = 8.0$ Hz, 2H each, C_6H_4); $^{31}P\{^1H\}$ NMR (C_6D_6): $\delta =$ 9.5 ppm (s with ^{195}Pt satellites, $J_{Pt\text{-}P} = 3910$ Hz). Data assignable to **4b**: ^1H NMR (C_6D_6): $\delta = 1.68$ (s, 15H, Cp*), 1.97, 2.12 ppm (s, 3H each, Me in Tol); $^{31}P\{^1H\}$ NMR (C_6D_6): $\delta = 20.4$ ppm (s with ^{195}Pt satellites, $J_{Pt\text{-}P} = 3900$ Hz).

5: $[Pd(PPh_3)_4]$ (58 mg, 0.050 mmol) was added to a THF solution (5 mL) of **4a** and **4b** (65 mg, 0.052 mmol) and this mixture was stirred for 5 h at room temperature. The NMR spectra of the reaction mixture showed the presence of **5a**. Addition of hexane to the concentrated product solution afforded **5a**·0.25 C_6H_{14} as red crystals (40 mg, 46% yield). When dissolved in C_6D_6, **5a** converted into an equilibrium mixture of **5a** and **5b** at room temperature, the ratio of which was 3:1. IR (KBr): $\tilde{\nu} = 1968\ cm^{-1}$, ν(CO); elemental analysis (%) calcd for $C_{62.5}H_{62.5}OIrP_2PdPtTe_2$: C 45.76, H 3.84; found: C 45.55, H 3.76. Data assignable to **5a**: ^1H NMR (C_6D_6): $\delta = 1.72$ (s, 15H, Cp*), 2.13, 2.21 (s, 3H each, Me in Tol), 6.72, 6.86, 7.38, 7.65 (d, $J =$

 © 2006 Wiley-VCH Verlag GmbH & Co. KGaA, Weinheim

7.6 Hz, 2H each, C_6H_4), 7.0–7.1 (m, 18H, Ph), 7.8–8.0 ppm (m, 12H, Ph); $^{31}P\{^1H\}$ NMR (C_6D_6): $\delta = 11.0$ (d with ^{195}Pt satellites, $J_{P\text{-}P} = 6$ Hz, $J_{Pt\text{-}P} = 3650$ Hz), 11.9 ppm (d, $J_{P\text{-}P} = 6$ Hz). Data assignable to **5b**: ^1H NMR (C_6D_6): $\delta = 1.69$ (s, 15H, Cp*), 2.15, 2.23 ppm (s, 3H each, Me in Tol); $^{31}P\{^1H\}$ NMR (C_6D_6): $\delta = 10.8$ (d, $J_{P\text{-}P} = 6$ Hz; ^{195}Pt satellites could not be resolved), 11.4 ppm (d, $J_{P\text{-}P} = 6$ Hz).

X-ray crystallography: Single crystals of **1**, **2a**·0.25 C_6H_6, **3a**·0.25 C_6H_{14}, **4a**, and **5a**·0.25 C_6H_{14} were sealed in glass capillaries under argon and mounted on a Rigaku Mercury-CCD diffractometer equipped with a graphite-monochromatized $Mo_{K\alpha}$ source. All diffraction studies were carried out at room temperature.

Structure solution and refinements were carried out by using the CrystalStructure program.[19] The positions of the non-hydrogen atoms were determined by Patterson methods (PATTY[20]) and subsequent Fourier synthesis (DIRDIF 99[21]). Non-hydrogen atoms were refined anisotropically by minimizing *wR*2 based on all data, for which full-matrix least-squares techniques are employed. All hydrogen atoms were placed at the calculated positions and included at the final stages of the refinements with fixed parameters.

Received: June 2, 2006
Revised: August 9, 2006
Published online: October 19, 2006

Keywords: cluster compounds · iridium · palladium · platinum · tellurium

[1] a) J. Wachter, *Eur. J. Inorg. Chem.* **2004**, 1367; b) D. Fenske, J. F. Corrigan, *Metal Clusters in Chemistry*, *Vol. 3* (Eds.: P. Braunstein, L. A. Oro, P. R. Raithby), Wiley-VCH, Weinheim, **1999**, chap. 4.2; c) I. Dance, K. Fisher, *Prog. Inorg. Chem.* **1994**, *41*, 637; d) L. C. Roof, J. W. Kolis, *Chem. Rev.* **1993**, *93*, 1037; e) M. A. Ansari, J. A. Ibers, *Coord. Chem. Rev.* **1990**, *100*, 223.

[2] Precedent tellurido clusters were obtained by using either the organotellurium reagents such as $R_3P{=}Te$ and $(Me_3Si)_2Te$ or the inorganic tellurium sources, for example, Te powder, Te_n^{2-} ($n = 2, 4$), NaTeH.[1]

[3] a) M. Hidai, Y. Mizobe, *Can. J. Chem.* **2005**, *83*, 358; b) M. Hidai, S. Kuwata, Y. Mizobe, *Acc. Chem. Res.* **2000**, *33*, 46.

[4] a) W.-Y. Yeh, H. Seino, T. Amitsuka, S. Ohba, M. Hidai, Y. Mizobe, *J. Organomet. Chem.* **2004**, *689*, 2338; b) H. Seino, T. Masumori, M. Hidai, Y. Mizobe, *Organometallics* **2003**, *22*, 3424; c) S. Nagao, H. Seino, M. Hidai, Y. Mizobe, *J. Organomet. Chem.* **2003**, *669*, 124, and references therein.

[5] L. Y. Goh, W. Chen, *J. Chem. Soc. Dalton Trans.* **1994**, 2697.

[6] Y.-C. Shi, *Polyhedron* **2004**, *23*, 1663.

[7] H. Egold, U. Flörke, *Z. Anorg. Allg. Chem.* **2001**, *627*, 2295.

[8] R. Oilunkaniemi, R. S. Laitinen, M. Ahlgren, *J. Organomet. Chem.* **2001**, *623*, 169.

[9] T. Langetepe, D. Fenske, *Z. Anorg. Allg. Chem.* **2001**, *627*, 820.

[10] a) J. F. Corrigan, D. Fenske, *Angew. Chem.* **1997**, *109*, 2070; *Angew. Chem. Int. Ed. Engl.* **1997**, *36*, 1981; b) D. Fenske, N. Zhu, *J. Cluster Sci.* **2000**, *11*, 135.

[11] For example: a) H. Kuniyasu, A. Ohtaka, T. Nakazono, M. Kinomoto, H. Kurosawa, *J. Am. Chem. Soc.* **2000**, *122*, 2375; b) H. Kuniyasu, T. Kato, M. Inoue, J. Terao, N. Kambe, *J. Organomet. Chem.* **2006**, *691*, 1873; c) R. Hua, H. Takeda, S. Onozawa, Y. Abe, M. Tanaka, *J. Am. Chem. Soc.* **2001**, *123*, 2899; d) L. A. Goj, M. Lail, K. A. Pittard, K. C. Riley, T. B. Gunnoe, J. L. Petersen, *Chem. Commun.* **2006**, 982, and references therein.

[12] L.-B. Han, N. Choi, M. Tanaka, *J. Am. Chem. Soc.* **1997**, *119*, 1795.

[13] X-ray data for **1**: $M_r = 792.92$, $0.20 \times 0.10 \times 0.10$ mm^3, monoclinic, space group $P2_1/n$, $a = 7.815(2)$, $b = 12.696(3)$, $c = 26.055(6)$ Å, $\beta = 95.889(1)°$, $V = 2571(1)$ Å^3, $Z = 4$, room temperature, $\rho_{calcd} = 2.048$ g cm^{-3}, $R1 = 0.0360$ (3428 data with $I > 2\sigma(I)$) and $wR2 = 0.0970$ (all 5887 unique data) for 291 variables, GOF = 1.031. **2a**·0.25 C_6H_6: $M_r = 1727.21$, $0.40 \times 0.20 \times 0.10$ mm^3, triclinic, space group $P\bar{1}$, $a = 14.987(3)$, $b = 18.459(4)$, $c = 22.293(5)$ Å, $\alpha = 97.113(3)$, $\beta = 102.993(3)$, $\gamma = 96.124(3)°$, $V = 5905(2)$ Å^3, $Z = 4$, room temperature, $\rho_{calcd} = 1.943$ g cm^{-3}, $R1 = 0.0380$ (17619 data with $I > 2\sigma(I)$) and $wR2 = 0.1290$ (all 26675 unique data) for 1351 variables, GOF = 1.019. **3a**·0.25 C_6H_{14}: $M_r = 1551.85$, $0.20 \times 0.10 \times 0.05$ mm^3, triclinic, space group $P\bar{1}$, $a = 14.966(6)$, $b = 18.422(6)$, $c = 22.259(9)$ Å, $\alpha = 97.023(5)$, $\beta = 103.306(6)$, $\gamma = 95.816(5)°$, $V = 5874(4)$ Å^3, $Z = 4$, room temperature, $\rho_{calcd} = 1.755$ g cm^{-3}, $R1 = 0.0660$ (10818 data with $I > 2\sigma(I)$) and $wR2 = 0.1930$ (all 25822 unique data) for 1395 variables, GOF = 1.008. **4a**: $M_r = 1250.30$, $0.50 \times 0.15 \times 0.02$ mm^3, monoclinic, space group $P2_1/a$, $a = 17.857(3)$, $b = 10.702(2)$, $c = 22.276(4)$ Å, $\beta = 104.8625(7)°$, $V = 4115(1)$ Å^3, $Z = 4$, room temperature, $\rho_{calcd} = 2.018$ g cm^{-3}, $R1 = 0.0410$ (6319 data with $I > 2\sigma(I)$) and $wR2 = 0.1300$ (all 9381 unique data) for 486 variables, GOF = 1.004. **5a**·0.25 C_6H_{14}: $M_r = 1640.54$, $0.30 \times 0.25 \times 0.15$ mm^3, triclinic, space group $P\bar{1}$, $a = 14.939(2)$, $b = 18.439(3)$, $c = 22.229(3)$ Å, $\alpha = 96.981(2)$, $\beta = 103.311(2)$, $\gamma = 95.562(2)°$, $V = 5865(2)$ Å^3, $Z = 4$, room temperature, $\rho_{calcd} = 1.858$ g cm^{-3}, $R1 = 0.0560$ (16567 data with $I > 2\sigma(I)$) and $wR2 = 0.1650$ (all 25735 unique data) for 1355 variables, GOF = 1.027. CCDC-616845–616849 (**1**, **2a**, **3a**, **4a**, and **5a**, respectively) contain the supplementary crystallographic data for this paper. These data can be obtained free of charge from The Cambridge Crystallographic Data Centre via www.ccdc.cam.ac.uk/data_request/cif.

[14] M. Herberhold, G.-X. Jin, A. L. Rheingold, *J. Organomet. Chem.* **1998**, *570*, 241.

[15] J. W. Kang, K. Moseley, P. M. Maitlis, *J. Am. Chem. Soc.* **1969**, *91*, 5970.

[16] R. Ugo, F. Cariati, G. La Monica, *Inorg. Synth.* **1968**, *11*, 105.

[17] D. R. Coulson, *Inorg. Synth.* **1972**, *13*, 121.

[18] W. S. Haller, K. J. Irgolic, *J. Organomet. Chem.* **1972**, *38*, 97.

[19] D. J. Watkin, C. K. Prout, J. R. Carruthers, P. W. Betteridge, CRYSTALS Issue 10, CrystalStructure 3.6.0: Crystal Structure Analysis Package, Rigaku and Rigaku/MSC, **2000–2004**, 9009 New Trails Dr., The Woodlands, TX 77381, USA.

[20] P. T. Beurskens, G. Admiraal, G. Beurskens, W. P. Bosman, S. Garcia-Granda, R. O. Gould, J. M. M. Smits, C. Smykall, PATTY, The DIRDIF program system; Technical Report of the Crystallography Laboratory: University of Nijmegen, Nijmegen, The Netherlands, **1992**.

[21] P. T. Beurskens, G. Admiraal, G. Beurskens, W. P. Bosman, R. de Gelder, R. Israel, J. M. M. Smits, DIRDIF99, The DIRDIF 99 Program System, Technical Report of the Crystallography Laboratory: University of Nijmegen, Nijmegen, The Netherlands, **1999**.

 © 2006 Wiley-VCH Verlag GmbH & Co. KGaA, Weinheim

Antibody–Stilbene Complexes

DOI: 10.1002/anie.200602720

The Effects of Antibodies on Stilbene Excited-State Energetics**

Feng Tian, Erik W. Debler, David P. Millar, Ashok A. Deniz, Ian A. Wilson, and Peter G. Schultz**

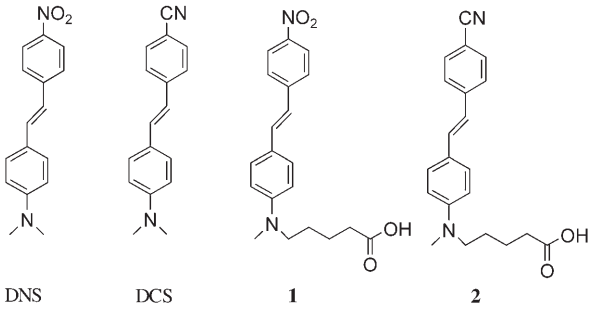

DNS DCS **1** **2**

Antibodies can be used to control the energetics and reactions of molecules in their ground states as well as in their electronically excited states.[1] For example, antibodies have been generated that catalyze the light-dependent cleavage of thymine dimers, and that modulate the excited-state behavior of *trans*-stilbene.[2,3] In particular, Lerner and co-workers generated a blue-fluorescent antibody, 19G2, which binds *trans*-stilbene to give a strongly fluorescent complex. Detailed structural and photophysical studies revealed that the antibody stabilizes the planar excited-state configuration through the formation of an exciplex between Trp^{H103} of the antibody and stilbene. To further explore the effects of the well-defined environments afforded by antibody binding sites on excited-state energy surfaces, we have generated antibodies to the donor–acceptor-substituted stilbene *trans*-4-*N*,*N*-dimethylamino-4′-cyanostilbene (DCS).

Unlike the widely accepted two-state model of photophysical unsubstituted *trans*-stilbene (Scheme 1), which consists of an initial emissive $^1t^*$ state and a subsequently populated nonemissive $^1p^*$ state (which is twisted by 90° about the C=C bond and undergoes internal conversion to give a mixture of *trans*- and *cis*-stilbene[4]), the photophysics of donor–acceptor-substituted stilbenes are more complicated.[5] A number of experimental and theoretical results have been interpreted in terms of an additional excited state, $^1a^*$, which corresponds to a relatively low-lying, twisted intramolecular charge-transfer (TICT) state in which the styryl-anilino C–C bond is rotated (Scheme 1).[6–8] Others have questioned the necessity of a TICT state and have suggested that the photophysics of substituted DCS analogues can be explained with a two-state model.[9–11]

Monoclonal antibodies (Mabs) provide a unique opportunity to study the photophysics of DCS in distinct steric and electronic enviroments without introducing any substituents. To this end, antibodies were generated against the DCS derivative **2**, as well as *trans*-4-*N*,*N*-dimethylamino-4′-nitrostilbene (DNS) derivative **1**, an analogue with a larger dipole moment (7.42 D)[13] which might more closely approximate

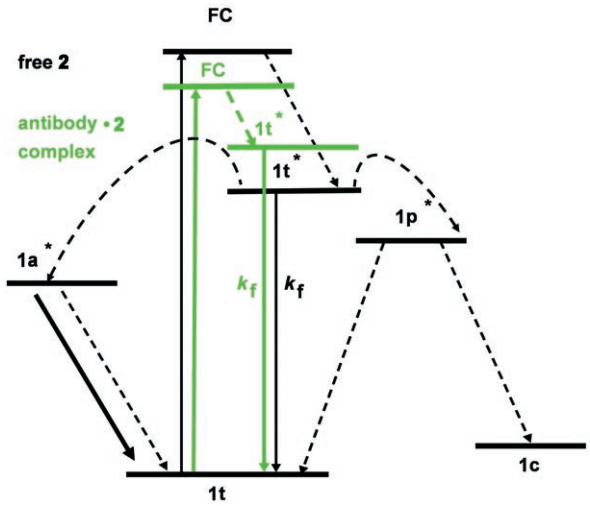

Scheme 1. Excited-state photochemistry of free **2** (black) and hypothesized primary pathway of the antibody–**2** complexes (green). Dashed lines: nonradiative transition; solid lines: radiative transitions. FC = Franck–Condon excited state.

the polar excited state of DCS. These antibody–stilbene complexes are highly fluorescent and emit blue to green light. Mabs 16E3, 17E3, and 17A4 elicited against hapten **2** and Mab 11G10 raised against the more polar hapten **1** were spectroscopically characterized (Table 1). The absorption

[*] E. W. Debler,[+] Prof. I. A. Wilson
Department of Molecular Biology
and The Skaggs Institute for Chemical Biology
The Scripps Research Institute
10550 North Torrey Pines Road, BCC206
La Jolla, CA 92037 (USA)
Fax: (+1) 858-784-2980
E-mail: wilson@scripps.edu

Dr. F. Tian,[+] Prof. P. G. Schultz
Department of Chemistry
and The Skaggs Institute for Chemical Biology
The Scripps Research Institute
10550 North Torrey Pines Road, SR202
La Jolla, CA 92037 (USA)
Fax: (+1) 858-784-9440
E-mail: Schultz@scripps.edu

Prof. D. P. Millar, Prof. A. A. Deniz
Department of Molecular Biology
The Scripps Research Institute
10550 North Torrey Pines Road, La Jolla, CA 92037 (USA)

[+] These authors contributed equally to this work.

[**] We thank Sharon Ferguson for expert assistance in Fab preparation and Dr. M. L. Tsao for his help in manuscript preparation. We acknowledge support from the NIH (grant GM56528 to P.G.S. and grant GM38273 to I.A.W.), The Skaggs Institute (predoctoral fellowship for E.W.D.), and the TSRI graduate program (Jairo H. Arévalo fellowship for E.W.D.).

Supporting information for this article is available on the WWW under http://www.angewandte.org or from the author.

 © 2006 Wiley-VCH Verlag GmbH & Co. KGaA, Weinheim

Table 1: Steady-state spectral data and affinities for haptens **1** and **2**, antibody–**2** complexes, and the 11G10–**1** complex.

Hapten and complex	λ_{abs} [nm]	λ_{em} [nm]	$\varepsilon_{max}\times10^{-3}$ [$M^{-1}cm^{-1}$]	Stokes shift [cm^{-1}]	Φ_f	K_d [nM]
1	430	[a]	7.30	[a]	0	[a]
11G10–**1**	532	684	9.45	4177	0.002	13
2	373	574	14.1	9388	0.16	[a]
11G10–**2**	424	515	23.0	4168	0.32	23
16E3–**2**	410	490	16.4	3982	0.60	30
17A4–**2**	412	505	14.4	4470	0.64	50
17E3–**2**	396	475	14.6	4200	0.57	75

[a] Not applicable.

spectra of free **2** and antibody–**2** complexes display no substructure (Figure 1). While free **2** absorbs with a λ_{max} of 373 nm, the absorption maxima of antibodies 16E3, 17E3, and

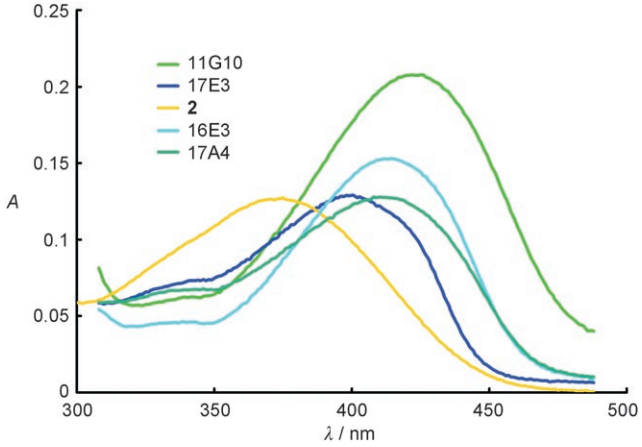

Figure 1. Steady-state absorption spectra of **2** (10 μM) and antibody–**2** complexes (10 μM) in phosphate-buffered saline (PBS) containing 5% DMF at room temperature.

17A4 complexed with **2** are red-shifted by 23–40 nm. When **2** is bound to antibody 11G10, the absorption maximum is red-shifted by 51 nm. This shift is consistent with the notion that 11G10, which was generated to the more polar DNS analogue **1**, is more complementary to the highly polar Franck–Condon (FC) excited state of DCS. The significant red-shifts of all antibody–stilbene complexes suggest that preorganized antibody combining sites are more effective in stabilizing the FC excited states of **1** and **2** than aqueous bulk solvent, which cannot reorganize to solvate the more polar excited state on the timescale of light absorption.

The steady-state fluorescence spectra of **2** and antibody–**2** complexes are also broad and devoid of any substructure. In contrast to the situation in bulk solution, in which the band widths at half-maximum increase with solvent polarity,[9] band widths at half-maximum for the antibody–**2** complexes are narrower than those of free **2**, suggesting that some rotatory conformations of **2** are constrained in the antibody combining sites. As expected for a stilbene molecule with an increased activation energy of rotation around the C=C bond in the excited state, the fluorescence quantum yields (Φ_f) of the antibody–**2** complexes are two to four times higher than that of free **2**; the rate constants for nonradiative decay, k_{nr}, obtained from time-resolved measurements decrease correspondingly (Table 2). All of the antibody–**2** complexes have large blue-shifts (59–99 nm) with respect to free **2** (Figure 2) and emit light of distinct colors ranging from blue for the 17E3–**2** complex (475 nm) to green for the 11G10–**2** complex (515 nm).

Table 2: Results of time-resolved fluorescence spectroscopy of **2** and antibody–**2** complexes.

Hapten and complex	τ_f [ns]	$\tau_r=\tau_f/\Phi_f$ [ns]	$k_r=1/\tau_r$ [ns^{-1}]	$k_{nr}=1/\tau_f-k_r$ [ns^{-1}]
2	1.01	6.3	0.16	0.83
11G10–**2**	2.68	8.4	0.12	0.25
16E3–**2**	2.78	4.6	0.22	0.14
17A4–**2**	2.88	4.5	0.22	0.13
17E3–**2**	2.53	4.4	0.23	0.17

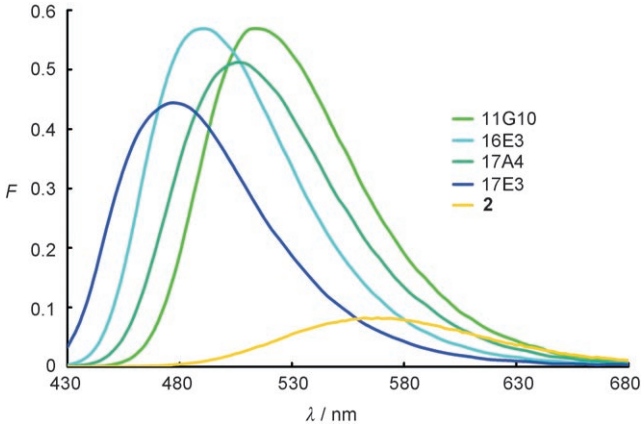

Figure 2. Steady-state fluorescence spectra of **2** (10 nM) and antibody–**2** complexes (10 nM) in PBS containing 5% DMF at room temperature. The λ_{abs} values listed in Table 1 were used as λ_{ex} for each corresponding spectrum.

The overall blue-shift in fluorescence of the antibody–**2** complexes relative to **2** in water can be ascribed to the preorganized nature of antibody combining sites. Bulk solvent has sufficient time to reorganize to preferentially stabilize the polar excited $^1t^*$ state of **2** relative to the less polar ground state prior to radiative decay. On the other hand, although the antibody binding site is more complementary to the polar excited state of DCS than to the ground state, it cannot reorganize to the same degree as bulk water, resulting in the large blue-shifts in fluorescence of the antibody–**2** complexes. Alternatively, if we assume that free **2** relaxes to an emissive low-lying TICT state ($^1a^*$), destabilization of the transition state by the antibody would lead to a switch to $^1t^*$ as the emissive state of the antibody–**2** complexes, which would equally well explain the blue-shift in fluorescence. The relative ordering of the antibodies with respect to the increasing emission maxima is the same ordering as for increasing absorption maxima (Table 1). This finding is consistent with a similar underlying mechanism for the two

 © 2006 Wiley-VCH Verlag GmbH & Co. KGaA, Weinheim

events, that is, stabilization of the FC excited state (absorption) and the emitting state (fluorescence) by the antibodies through electrostatic and van der Waals interactions.

To characterize the nature of an antibody–stilbene complex and its effect on the photophysics of DCS in atomic detail, we have determined the crystal structure of Fab 11G10 in complex with hapten **1** at 2.75-Å resolution (Figure 3, for details see the Supporting Information). The stilbene moiety is bound in a planar conformation. Rotation around the excited-state C=C bond as well as the styryl-anilino C–C bond are likely to be restricted by interactions between the ligand and antibody residues Phe^{L94}, Leu^{L89}, Leu^{L36}, Tyr^{H33}, Tyr^{H95}, and Val^{H93} (Figure 3c). The binding pocket possesses a relatively high percentage of polar residues in immediate vicinity to the ligand. The bottom of the cavity exhibits a positive electrostatic potential (Figure 3b) due to the positively charged guanidinium group of Arg^{L46} (Figure 3a,c). Towards the mouth of the cavity, the electrostatic potential becomes partially negative. Importantly, the charge distribution in the combining site together with the aromatic ring systems of Tyr^{H33}, Tyr^{H95}, and Phe^{L94} are well suited to stabilize charge separation in the excited state of DCS derivative **2**.

In summary, we have generated antibodies that bind donor–acceptor-substituted stilbenes to afford strong blue to green fluorescent complexes. Spectroscopic and structural data suggest a model in which the relatively rigid protein environment sterically increases the activation barriers connecting the planar $^1t^*$ to the twisted excited states $^1p^*$ (and possibly $^1a^*$) and modulates the energetics of the fluorescent $^1t^*$ state (Scheme 1). The antibodies appear to be more effective in stabilizing the polar FC excited state of **2** relative to the ground state, but less effective than bulk water in selectively stabilizing the light-emitting state. In practical terms, the relatively long excitation and emission wavelengths of the antibody–**2** complexes may make them useful for in vitro and in vivo applications as fluorescent biosensors.

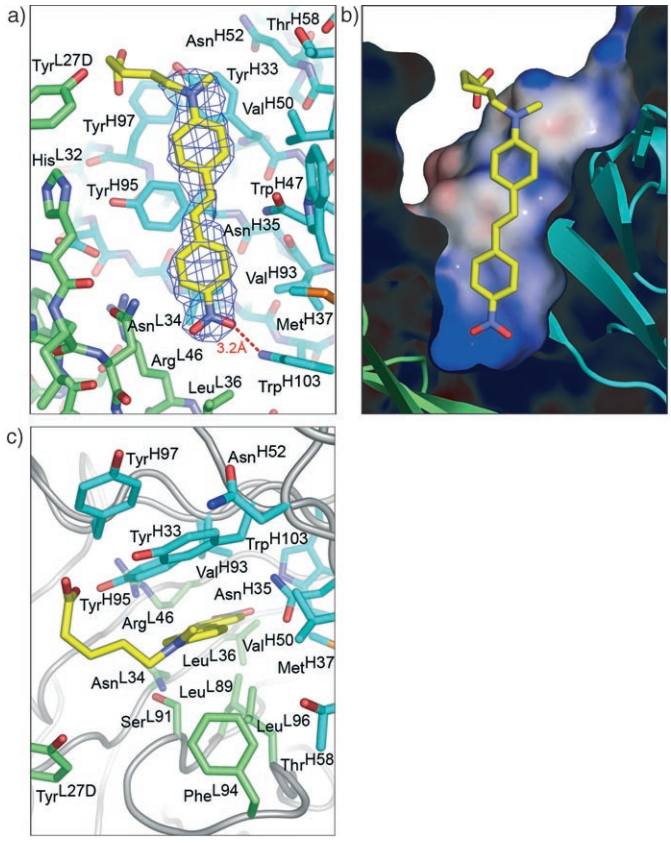

Figure 3. Antibody combining site of 11G10 in complex with hapten **1** with electron density contoured at 1.5 σ. a) A slice through the center of the antibody combining site is shown. The only hydrogen bond between **1** and 11G10 is illustrated as a red dashed line. b) Representation of the electrostatic surface; similar view to that in (a). c) View of the antibody binding pocket rotated horizontally by 90° to the view in (a).

Received: July 8, 2006
Revised: September 2, 2006
Published online: November 7, 2006

Keywords: antibodies · fluorescent probes · stilbene

[1] P. G. Schultz, R. A. Lerner, *Science* **1995**, *269*, 1835–1842.
[2] A. G. Cochran, R. Sugasawara, P. G. Schultz, *J. Am. Chem. Soc.* **1988**, *110*, 7888–7890.
[3] A. Simeonov, M. Matsushita, E. A. Juban, E. H. Z. Thompson, T. Z. Hoffman, A. E. Beuscher IV, M. J. Taylor, P. Wirsching, W. Rettig, J. K. McCusker, R. C. Stevens, D. P. Millar, P. G. Schultz, R. A. Lerner, K. D. Janda, *Science* **2000**, *290*, 307–313.
[4] J. Saltiel, O. C. Zafiriou, E. D. Megarity, A. A. Lamola, *J. Am. Chem. Soc.* **1968**, *90*, 4759–4760.
[5] Z. R. Grabowski, K. Rotkiewicz, W. Rettig, *Chem. Rev.* **2003**, *103*, 3899–4032.
[6] R. Lapouyade, K. Czeschka, W. Majenz, W. Rettig, E. Gilabert, C. Rulliere, *J. Phys. Chem.* **1992**, *96*, 9643–9650.
[7] W. Rettig, *Top. Curr. Chem.* **1994**, *169*, 253–299.
[8] D. Pines, E. Pines, W. Rettig, *J. Phys. Chem. A* **2003**, *107*, 236–242.
[9] J.-S. Yang, K.-L. Liau, C.-Y. Hwang, C.-M. Wang, *J. Phys. Chem. A* **2006**, *110*, 8003–8010.
[10] S. Arzhantsev, K. A. Zachariasse, M. Maroncelli, *J. Phys. Chem. A* **2006**, *110*, 3454–3470.
[11] S. A. Kovalenko, R. Schanz, T. A. Senyushkina, N. P. Ernsting, *Phys. Chem. Chem. Phys.* **2002**, *4*, 703–707.
[12] J.-S. Yang, K.-L. Liau, C.-M. Wang, C.-Y. Hwang, *J. Am. Chem. Soc.* **2004**, *126*, 12325–12335.
[13] K. B. Everard, L. Kumar, L. E. Sutton, *J. Chem. Soc.* **1951**, 2807–2815.

© 2006 Wiley-VCH Verlag GmbH & Co. KGaA, Weinheim

Protein Structures

DOI: 10.1002/anie.200602125

Protein Structure Similarity Clustering: Dynamic Treatment of PDB Structures Facilitates Clustering**

Bradley D. Charette, Richard G. MacDonald, Stefan Wetzel, David B. Berkowitz, and Herbert Waldmann**

Protein structure similarity clustering (PSSC)[1–3] is one of a number of potential guiding principles[4,5] that have been introduced to focus combinatorial-library design/protein targeting. PSSC clusters protein targets with similar ligand-binding cores in which little sequence or functional similarity is evident. Lead compounds for one member of the cluster then provide novel starting points in chemical space for ligand development for other members of the PSSC.

We describe herein a new clustering procedure that lends itself to ligand docking, molecular dynamics (MD), and the vector-alignment-search-tool (VAST)[6] algorithm. This MD-assisted approach offers an alternative to the serial structure retrieval/inspection steps used to generate the original protein structure similarity cluster, centered on Cdc25A.[2] Furthermore, in a particularly difficult de novo test, the mannose 6-phosphate/insulin-like growth factor II receptor (M6P/IGF2R), lends itself to clustering, with MD opening up connections to partners that the static crystal structure coordinates fail to find.

Ortholand and Ganesan[7] have described the disappointing early yield of clinical candidates from combinatorial chemistry/high-throughput screening as a "paradise lost" sentiment, probably attributable to unreasonable expectations and the need for maturation in approaches to combinatorial library design.[8] Both diversity-oriented synthesis (DOS) and biology-oriented synthesis (BIOS) have arisen in response to the this need. DOS utilizes more-complex, often fused polycyclic frameworks, richer in stereochemistry and frequently functionalizes them through annulation or coupling reactions.[9] Within BIOS,[10] biological relevance and prevalidation are employed as key arguments for the design of natural-product-derived/inspired[3,11] compound collections.

PSSC seeks to add value to such compound libraries by grouping targets into otherwise unrecognized clusters. In this way, a BIOS library, originally directed at enzymes of a specific functional or homology family, can be redirected at a PSSC partner protein and produce novel leads for this target. PSSC groups proteins based on a comparison of extracted "ligand-sensing cores", are independent of sequence or functional similarity. Importantly, core extraction is independent of domain or fold constraints and involves carving out a sphere around a key ligand or protein-based center in the binding pocket. This approach is complementary to a number of interesting, surface pattern recognition methods that compare binding pockets based upon exposed protein surface pseudocenters (CavBase,[12] SiteEngine[13]), triangles (pvSOAR),[14] cavities,[15] or residues (efSite,[16] PINTS[17]), and to the "all atom" approach exemplified by SitesBase.[18]

The PSSC approach begins in biological space and seeks to first identify a cluster of targets of pharmaceutical or bioorganic interest and then looks for an appropriate lead scaffold, drawing from binding data for one member of the cluster. The notion of a PSS cluster is related to the concept advanced by Sternberg and co-workers of "supersites", reflecting binding-site similarity in the absence of homology.[19] PSSC also resonates with interesting ideas put forth by Quinn and co-workers,[20] suggesting that structural motifs used to bind intermediates in enzymes along a biosynthetic pathway for a natural product might also be used to find (unrelated) target proteins for that same natural product.

The original identification of a PSS cluster[2] began from the single available X-ray crystal structure (1C25)[21] for the catalytic core of Cdc25A, a dual-specificity protein phosphatase (Figure 1). The Cdc isozymes may represent novel chemotherapeutic targets.[22] Initial structure similarity searches by using the combinatorial extension (CE)[23] and Dali-FSSP (families of structurally similar proteins)[24] algorithms connected Cdc25A with hydroxynitrile lyase (3YAS)[25] and methylene methanopterin dehydrogenase (1LU9),[26] respectively.

These initial cluster members indicated that the parent dual-specificity phosphatase could be related to proteins capable of promoting nucleophilic addition to carbonyl centers (perhaps presaging carboxyl esterase activity) and with nicotinamide-dependent dehydrogenase activity. Koch

[*] B. D. Charette, Prof. D. B. Berkowitz
Department of Chemistry
University of Nebraska
Lincoln, NE 68588 (USA)
Fax: (+1) 402-472-9402
E-mail: dbb@unlserve.unl.edu
S. Wetzel, Prof. H. Waldmann
Max-Planck-Institut für Molekulare Physiologie
Abteilung für Chemische Biologie
Otto-Hahn-Strasse 11, 44227 Dortmund (Germany)
and
Universität Dortmund
Fachbereich 3, Chemische Biologie
Fax: (+49) 231-133-2499
E-mail: herbert.waldmann@mpi-dortmund.mpg.de
Prof. R. G. MacDonald
Department of Biochemistry & Molecular Biology
University of Nebraska Medical Center
Omaha, NE 68198 (USA)

[**] This research was supported by the Max-Planck-Gesellschaft, the Deutsche Forschungsgemeinschaft, and the Fonds der Chemischen Industrie. D.B.B. thanks the Max-Planck-Gesellschaft (sabbatical stay), the American Heart Association (GIA 0650014Z), and NIH (CA 62034 and RR016544-01) for support. B.D.C. acknowledges a UCARE fellowship. R.G.M. acknowledges support from the NIH (CA 91885). We thank Dr. Ingrid R. Vetter for useful discussions. PDB = protein data bank.

Supporting information for this article is available on the WWW under http://www.angewandte.org or from the author.

 InterScience © 2006 Wiley-VCH Verlag GmbH & Co. KGaA, Weinheim

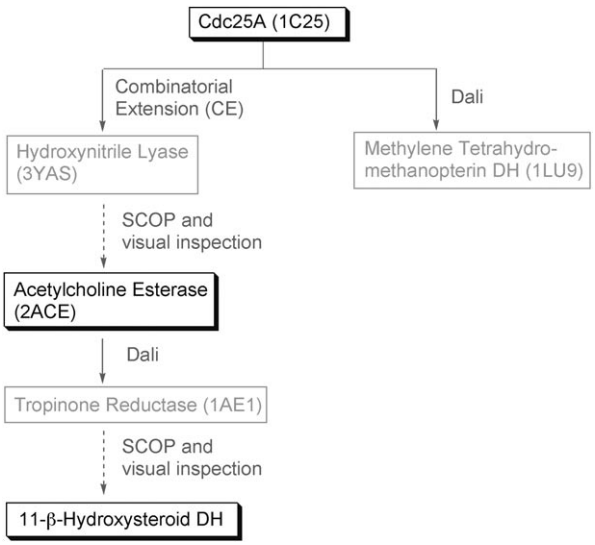

Figure 1. The pathway taken by Koch[2] to establish the original PSS cluster. Note the use of SCOP and intuition/manual inspection.

and co-workers next used SCOP (structural classification of proteins; scop@mrc-lmb.cam.ac.uk), a database from the MRC (The Medical Research Council, Cabridge, UK) that groups evolutionarily proteins based on conserved structural elements.[2,27] In this way, beginning from the 3YAS lead, structurally related proteins could be located, retrieved, DaliLite[4] or CE pairwise-aligned, and examined by visual inspection (Figure 1). This pathway led to acetylcholinesterase (AChE) as a PSS partner for Cdc25A (see Table 1).

A second iteration of this sequence was then carried out. This time, the Dali structural alignment identified tropinone reductase as an AChE partner. The idea that pyridine nucleotide-based dehydrogenases (DHs) might be in this PSSC had been foreshadowed by the initial 1LU9 hit. Indeed, manual inspection of the Rossmann fold superfamily, analogous to the earlier SCOP step, then led from tropinone reductase to 11β-hydroxysteroid dehydrogenase (11β-HSDH). Eventually, a 147-member library based on the sesterterpene Cdc25A inhibitor, dysidiolide,[28] also produced inhibitors for both AChE and 11β-HSDH (see the Supporting Information).[2]

Motivated by the success of this de novo application of PSSC to generate a target cluster that responds to a natural-product-inspired combinatorial library, we set out to examine the clustering protocol more closely. Namely, the initial formulation of this PSSC required two labor-intensive SCOP/superfamily searching steps (Figure 1). This meant the serial retrieval of a good number of PDB coordinate sets for cluster candidates and their evaluation for active-site structural homology with the catalytic core of Cdc25A. This was necessitated because available web-based structural comparison algorithms, including CE,[23] Dali,[24] and VAST,[6] all fail to find either AChE or 11β-HSDH as structural homologues when starting from 1C25, the only available structure for Cdc25A.

Given that such structure-comparison algorithms are usually limited to searching a static set of crystallographic coordinates in the PDB, we wondered whether introducing dynamics[29] would facilitate the structure-homology search. The notion is simply that the crystallographic snapshot of a protein that is deposited in the PDB is likely to be one of a number of conformations that an approaching ligand might encounter in solution. If one could begin from an array of conformations that Cdc25A likely samples in protein structure space, then a structural comparison might be able to identify PSSC partners that would not otherwise appear.

Toward this end, (−)-dysidiolide was initially docked with the 1C25 structure by using Autodock 3.0.[30] Then, a one-nanosecond MD simulation was carried out on the docked structure (Gromacs[31], Figure 2), collecting snapshots every picosecond. To analyze the variations in backbone conforma-

Table 1: MD simulation Cdc25 A with docked (−)-dysidiolide.

Time [ps][a]	Alignment length (AChE-1H22)[b]	RMSD [Å] (AChE-1H22)[b]	Alignment length (11β-HSDH-1XSE-A)[c]	RMSD [Å] (11β-HSDH-1XSE-A)[c]
0	88	6.0	85	4.2
100	90	6.3	90	4.5
200	90	5.9	81	3.6
300	70	3.4	81	3.5
400	95	5.7	80	3.6
500	86	3.7	96	4.8
600	86	4.0	88	4.3
700[d]	**91**	**4.3**	**90**	**3.9**
800	86	3.9	91	4.8
900	79	5.0	93	5.0
1000	83	4.5	92	5.4

[a] Representative conformers at 100-ps intervals in the MD simulation on the Cdc25A-dysidiolide docked structure. [b] Results of a DaliLite pairwise comparison with the 1H22 acetylcholinesterase crystal structure. [c] Results of a DaliLite pairwise comparison with the 11β-hydroxysteroid dehydrogenase structure 1XSE, molecule A in the unit cell. [d] Data in bold highlights the time region in which the simulation samples Cdc25A conformations that align especially well with these cluster partners.

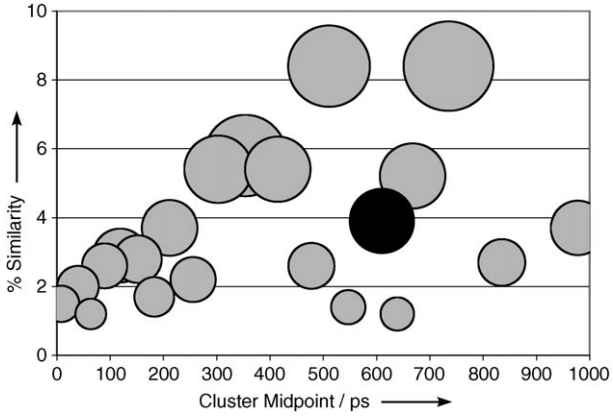

Figure 2. Cluster distribution of the 1000 conformers resulting from the MD simulation (Gromacs) on the dysidiolide-docked Cdc25A structure shown in Figure 3. All clusters with more than 10 members are shown as a function of the time of appearance of the midpoint conformer. Circle diameters are proportional to cluster size. The midpoint conformer of the black-shaded cluster is shown in Figure 3.

 © 2006 Wiley-VCH Verlag GmbH & Co. KGaA, Weinheim

tion with time, along the simulation, pairwise comparisons with the structures of AChE (1H22)[32] and of (11β-HSDH-1 (1XSE-A)[33] were performed at 100-ps intervals (see Table 1 for results). In particular, one notices that in the 600–700-ps regime, the conformations of Cdc25A being sampled apparently show greater structural homology with these two PSSC partner proteins.

The 1000 Cdc25A conformations sampled were clustered by using Gromos[31] (Figure 2). Of a total of 60 conformational clusters found, 26 have more than 10 members. The three most populated clusters only begin to appear near the midpoint, probably reflecting a large conformational change associated with "flap closure" dominating the initial part of the simulation. This motion is quite apparent from an animation of the MD simulation (see the Supporting Information) and can be inferred from a comparison of early and late snapshots (Figure 3).

The midpoint conformers of each of the top ten clusters were arbitrarily sampled for their ability to find members of the original PSS cluster (Figure 1). By using the VAST algorithm, all 10 midpoint conformers find hydroxynitrile lyase (HNL) and four find methylene tetrahydromethanopterin DH (MTHMP DH), which were the only two PSS partners that were initially identifiable from the static 1C25 structure. Pleasingly, however, a VAST search initiated from conformer 668 (midpoint of the cluster shaded black in Figure 2) finds all five members of the Cdc25A cluster. More specifically, this conformer hits a significant fraction of the available structures for these proteins in the PDB: HNL (22/23), MTHMP DH (2/2), tropinone reductase (3/6), AChE (14/66), and 11β-HSDH (1/6).

VAST finds good alignment of conformer 668 with 11β-HSDH-1(1XEA) in the following regions (residues 37–56, 63–66, 69–77, 91–98, 100–112, and 124–133). If one follows the average root mean square deviation (RMSD) for C_α atoms across these residues, relative to their position in the starting conformer, there is a sharp increase from approximately 0.7–1 Å in the time regime of 600–800 ps. Consistent with this, the conformer at 700 ps also finds four of the five cluster members (see the Supporting Information). A structural overlay of conformer 668 with AChE and 11β-HSDH-1 is presented in Figure 3 (bottom).

In light of the success of MD to open up new structural alignments with VAST, we next set our sights on a de novo test of the protocol. In this regard, a particularly difficult case was chosen; namely, the cation-independent, M6P-IGF2R (see Figure 4).[34] This large 300-kDa transmembrane receptor contains 15 homologous extracytoplasmic repeats. Domains 3 and 9 are known to have a high affinity for M6P. The receptor binds M6P-functionalized proteins and IGF-II independently (domain 11). In addition to serving a range of housekeeping functions associated primarily with channeling proteins to the lysosomes, the receptor is known to internalize circulating IGF-II and hence has been labeled a cancer-suppressor gene.[35] Internalization appears to be accelerated by M6P-type ligand binding,[36] increasing interest in high-affinity ligands for this site.[37]

Only three PDB entries are available for the M6P-sensing core of the receptor; namely of a domain 1–3 fragment, one unbound ligand (1Q25),[38] and two nearly identical structures with bound M6P (1SZ0 and 1SYO).[39] An initial VAST search of 1Q25 and 1SZ0 revealed few potential PSSC partners (three hits for each structure, see the Supporting Information). Therefore, MD simulations with 1000-ps intervals were performed on domains 1–3 of both the ligand-unbound (1Q25) and ligand-bound (1SZ0) structures. In the former

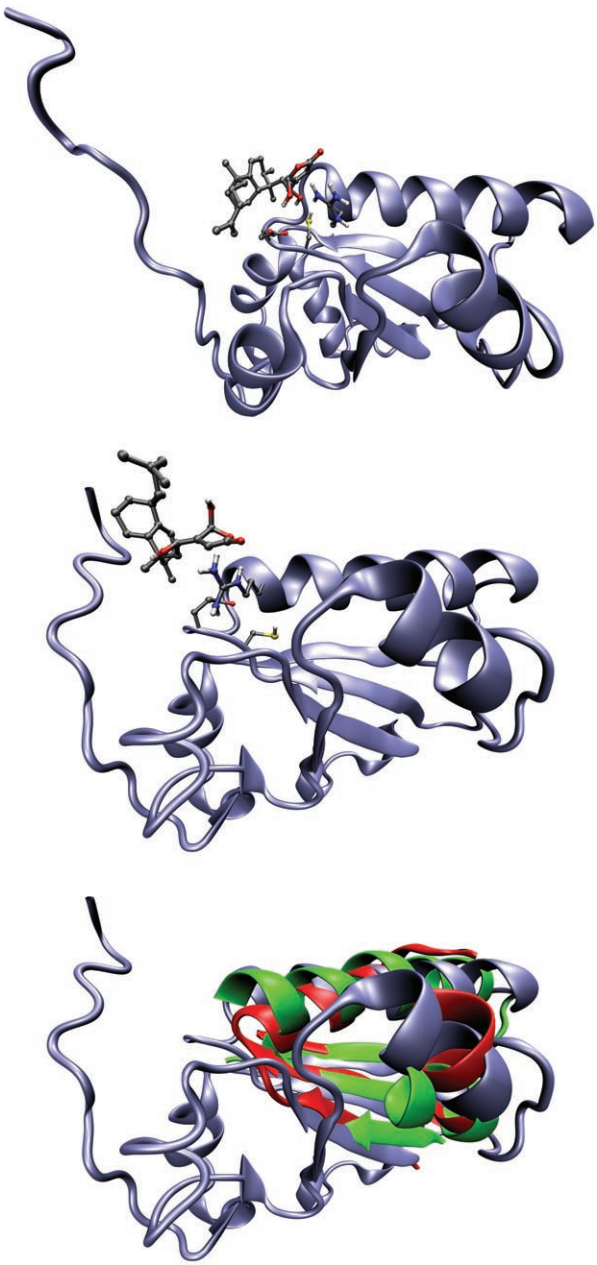

Figure 3. Top: Docked structure of Cdc25A (1C25) and dysidiolide. The highlighted residues are Cys430, Glu431, and Arg436. Middle: Conformer 668, the midpoint conformer of the black-shaded cluster shown in Figure 2 (see also Table 1 for evidence that MD samples particularly relevant conformational space for the Cdc25A/AChE/11HSD PSSC cluster in this time regime). Bottom: Structural overlay (DaliLite) of conformer 668 of Cdc25A following MD simulation (blue) with acetylcholinesterase (1H22, red) and 11β-HSD1 (1XSE, green). VAST finds this triplet only after the initial 1C25 coordinates are allowed to relax through MD.

 © 2006 Wiley-VCH Verlag GmbH & Co. KGaA, Weinheim

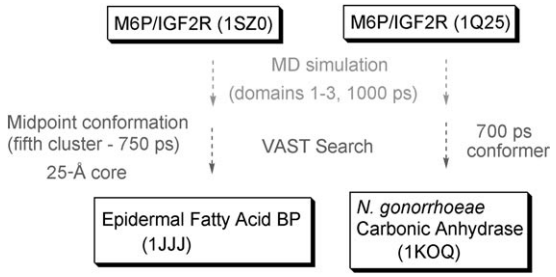

Figure 4. MD-assisted clustering procedure for the cation-indepedent mannose 6-phosphate/insulin-like growth factor II receptor. BP = binding protein.

case, conformers were arbitrarily sampled at 100-ps intervals and subjected directly to VAST searches. The 700-ps conformer identified the interesting carbonic anhydrase (CA) from *N. gonorrhoeae* (1KOQ)[40] as a potential cluster partner for this M6P receptor.

The ligand-bound conformers were clustered by domain 3, and VMD-extracted[41] 25-Å cores (centered on C5 of the M6P ligand) from midpoint conformers of the 10 most populated clusters were subjected to VAST searches. From the fifth cluster, a connection to epidermal fatty acid binding protein (E-FABP) emerged. E-FABP belongs to a family of lipid-binding proteins that are associated with fatty acid signaling, cell growth, and cell differentiation. E-FABP is known to be overexpressed in hyperproliferative skin diseases, such as psoriasis,[42] and also appears to be a cancer marker.[43] For these reasons, this target appears to be an excellent PSS cluster partner for the M6P-IGF2R. Neither *N. gonorrhoeae*, CA, nor E-FABP were identified by VAST searches without MD. An overlay of the ligand-bound receptor core (750-ps conformer) with E-FABP is presented in Figure 5.

In conclusion, we describe a new clustering procedure for PSSC that exploits MD and the VAST algorithm. This streamlined approach removes serial structure retrieval and visual alignment steps previously required for clustering (Cdc25A PSSC), and opens up new windows to structural neighbors not seen when dealing with fixed X-ray crystal structure coordinates (M6P/IGF2R PSSC). Our results suggest that, in general, by treating otherwise static PDB entries as an ensemble of conformers generated by MD, one can sample a broader, and potentially more relevant, swath of protein-structure space when searching for structural partners.

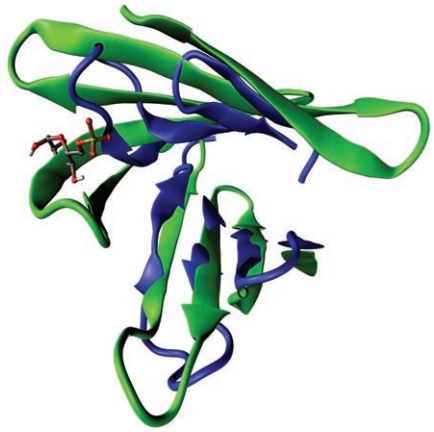

Figure 5. Overlay of the MD-relaxed (750 ps) M6P-IGF2R core (blue) with the human E-FABP (green). The 1SZ0-bound M6P ligand (position at 750 ps) is highlighted with a ball-and-stick model.

Received: May 27, 2006
Revised: August 25, 2006
Published online: October 31, 2006

Keywords: biological information · combinatorial chemistry · molecular dynamics · protein structures · target selection

[1] M. A. Koch, H. Waldmann, *Drug Discovery Today* **2005**, *10*, 471.
[2] M. A. Koch, L.-O. Wittenberg, S. Basu, D. A. Jeyaraj, E. Gourzoulidou, K. Reinecke, A. Odermatt, H. Waldmann, *Proc. Natl. Acad. Sci. USA* **2004**, *101*, 16721.
[3] R. Breinbauer, I. R. Vetter, H. Waldmann, *Angew. Chem.* **2002**, *114*, 3002; *Angew. Chem. Int. Ed.* **2002**, *41*, 2878.
[4] L. Holm, J. Park, *Bioinformatics* **2000**, *16*, 566.
[5] J. Fejzo, C. A. Lepre, J. W. Peng, G. W. Bemis, Ajay, M. A. Murcko, J. M. Moore, *Chem. Biol.* **1999**, *6*, 755.
[6] J.-F. Gibrat, T. Madej, S. H. Bryant, *Curr. Opin. Struct. Biol.* **1996**, *6*, 377.
[7] J.-Y. Ortholand, A. Ganesan, *Curr. Opin. Chem. Biol.* **2004**, *8*, 271.
[8] C. Lipinski, A. Hopkins, *Nature* **2004**, *432*, 855.
[9] a) D. S. Tan, *Nat. Chem. Biol.* **2005**, *1*, 74; b) M. D. Burke, E. M. Berger, S. L. Schreiber, *J. Am. Chem. Soc.* **2004**, *126*, 14095; c) M. D. Burke, S. L. Schreiber, *Angew. Chem.* **2004**, *116*, 48; *Angew. Chem. Int. Ed.* **2004**, *43*, 46.
[10] A. Noeren-Mueller, I. Reis-Correa, Jr., H. Prinz, C. Rosenbaum, K. Saxena, H. J. Schwalbe, D. Vestweber, G. Cagna, S. Schunk, O. Schwarz, H. Schiewe, H. Waldmann, *Proc. Natl. Acad. Sci. USA* **2006**, *103*, 10606.
[11] a) A. M. Boldi, *Curr. Opin. Chem. Biol.* **2004**, *8*, 281; b) D. J. Newman, G. M. Cragg, K. M. Snader, *J. Nat. Prod.* **2003**, *66*, 1022; c) M.-L. Lee, G. Schneider, *J. Comb. Chem.* **2001**, *3*, 284.
[12] a) G. Klebe, *Drug Discovery Today* **2006**, *11*, 580; b) N. Weskamp, D. Kuhn, E. Huellermeier, G. Klebe, *Bioinformatics* **2004**, *20*, 1522.
[13] A. Shulman-Peleg, R. Nussinov, H. J. Wolfson, *J. Mol. Biol.* **2004**, *339*, 607.
[14] T. A. Binkowski, L. Adamian, J. Liang, *J. Mol. Biol.* **2003**, *332*, 505.
[15] M. Stahl, C. Taroni, G. Schneider, F. Hoffmann, *Protein Eng.* **2000**, *13*, 83.
[16] K. Kinoshita, J. i. Furui, H. Nakamura, *J. Struct. Funct. Genomics* **2002**, *2*, 9.
[17] A. Stark, S. Sunyaev, R. B. Russell, *J. Mol. Biol.* **2003**, *326*, 1307.
[18] N. D. Gold, R. M. Jackson, *J. Mol. Biol.* **2006**, *355*, 1112.
[19] R. B. Russell, P. D. Sasieni, M. J. E. Sternberg, *J. Mol. Biol.* **1998**, *282*, 903.
[20] B. M. McArdle, M. R. Campitelli, R. J. Quinn, *J. Nat. Prod.* **2006**, *69*, 14.
[21] E. B. Fauman, J. P. Cogswell, B. Lovejoy, W. J. Rocque, W. Holmes, V. G. Montana, H. Piwnica-Worms, M. J. Rink, M. A. Saper, *Cell* **1998**, *93*, 617.
[22] M. A. Lyon, A. P. Ducruet, P. Wipf, J. S. Lazo, *Nat. Rev. Drug Discovery* **2002**, *1*, 961.
[23] a) I. N. Shindyalov, P. E. Bourne, *Nucleic Acids Res.* **2001**, *29*, 228; b) I. N. Shindyalov, P. E. Bourne, *Protein Eng.* **1998**, *11*, 739.
[24] L. Holm, C. Sander, *Nucleic Acids Res.* **1996**, *24*, 206.

 © 2006 Wiley-VCH Verlag GmbH & Co. KGaA, Weinheim

[25] J. Zuegg, K. Gruber, M. Gugganig, U. G. Wagner, C. Kratky, *Protein Sci.* **1999**, *8*, 1990.
[26] U. Ermler, C. H. Hagemeier, A. Roth, U. Demmer, W. Grabarse, E. Warkentin, J. A. Vorholt, *Structure* **2002**, *10*, 1127.
[27] a) A. Andreeva, D. Howorth, S. E. Brenner, T. J. P. Hubbard, C. Chothia, A. G. Murzin, *Nucleic Acids Res.* **2004**, *32*, D226; b) L. Lo Conte, S. E. Brenner, T. J. P. Hubbard, C. Chothia, A. G. Murzin, *Nucleic Acids Res.* **2002**, *30*, 264; c) A. G. Murzin, S. E. Brenner, T. Hubbard, C. Chothia, *J. Mol. Biol.* **1995**, *247*, 536.
[28] S. P. Gunasekera, P. J. McCarthy, M. Kelly-Borges, E. Lobkovsky, J. Clardy, *J. Am. Chem. Soc.* **1996**, *118*, 8759.
[29] a) W. Sherman, T. Day, M. P. Jacobson, R. A. Friesner, R. Farid, *J. Med. Chem.* **2006**, *49*, 534; b) C. A. Sotriffer, O. Kraemer, G. Klebe, *Proteins Struct. Funct. Bioinf.* **2004**, *56*, 52.
[30] D. S. Goodsell, A. J. Olson, *Proteins Struct. Funct. Genet.* **1990**, *8*, 195.
[31] X. Daura, K. Gademann, B. Jaun, D. Seebach, W. F. VanGunsteren, A. E. Mark, *Angew. Chem.* **1999**, *111*, 249; *Angew. Chem. Int. Ed.* **1999**, *38*, 236.
[32] D. M. Wong, H. M. Greenblatt, H. Dvir, P. R. Carlier, Y.-F. Han, Y.-P. Pang, I. Silman, J. L. Sussman, *J. Am. Chem. Soc.* **2003**, *125*, 363.
[33] D. Ogg, B. Elleby, C. Norstroem, K. Stefansson, L. Abrahmsen, U. Oppermann, S. Svensson, *J. Biol. Chem.* **2005**, *280*, 3789.
[34] a) A. B. Hassan, *Am. J. Pathol.* **2003**, *162*, 3; b) J. C. Byrd, J. H. Y. Park, B. S. Schaffer, F. Garmroudi, R. G. MacDonald, *J. Biol. Chem.* **2000**, *275*, 18647; c) R. G. MacDonald, S. R. Pfeffer, L. Coussens, M. A. Tepper, C. M. Brocklebank, J. E. Mole, J. K. Anderson, E. Chen, M. P. Czech, A. Ullrich, *Science* **1988**, *239*, 1134.
[35] a) J. Li, G. G. Sahagian, *Oncogene* **2004**, *23*, 9359; b) D. B. O'Gorman, J. Weiss, A. Hettiaratchi, S. M. Firth, C. D. Scott, *Endocrinology* **2002**, *143*, 4287; c) G. R. Hankins, A. T. De Souza, R. C. Bentley, M. R. Patel, J. R. Marks, J. D. Iglehart, R. L. Jirtle, *Oncogene* **1996**, *12*, 2003.
[36] S. J. York, L. S. Arneson, W. T. Gregory, N. M. Dahms, S. Kornfeld, *J. Biol. Chem.* **1999**, *274*, 1164.
[37] D. B. Berkowitz, G. Maiti, B. D. Charette, C. D. Dreis, R. G. MacDonald, *Org. Lett.* **2004**, *6*, 4921.
[38] L. J. Olson, R. D. Yammani, N. M. Dahms, J.-J. P. Kim, *EMBO J.* **2004**, *23*, 2019.
[39] L. J. Olson, N. M. Dahms, J.-J. P. Kim, *J. Biol. Chem.* **2004**, *279*, 34000.
[40] S. Huang, Y. Xue, E. Sauer-Eriksson, L. Chirica, S. Lindskog, B.-H. Jonsson, *J. Mol. Biol.* **1998**, *283*, 301.
[41] W. Humphrey, A. Dalke, K. Schulten, *J. Mol. Graphics* **1996**, *14*, 33.
[42] G. Siegenthaler, R. Hotz, D. Chatellard-Gruaz, S. Jaconi, J. H. Saurat, *Biochem. Biophys. Res. Commun.* **1993**, *190*, 482.
[43] a) L. H. Gutierrez-Gonzalez, C. Ludwig, C. Hohoff, M. Rademacher, T. Hanhoff, H. Ruterjans, F. Spener, C. Lucke, *Biochem. J.* **2002**, *364*, 725; b) P. Sinha, G. Hutter, E. Kottgen, M. Dietel, D. Schadendorf, H. Lage, *Electrophoresis* **1999**, *20*, 2952.

 © 2006 Wiley-VCH Verlag GmbH & Co. KGaA, Weinheim

Solid-State Metal Hydrides

DOI: 10.1002/anie.200603651

Isolated $[Ni_2H_7]^{7-}$ and $[Ni_4H_{12}]^{12-}$ Ions in $La_2MgNi_2H_8$**

*Jean-Noël Chotard, Yaroslav Filinchuk, Bernard Revaz, and Klaus Yvon**

Solid-state metal hydrides provide a safe and efficient way of storing hydrogen. Those useful for applications in the energy sector, such as proton-exchange membrane (PEM) fuel cells, are mainly derived from stable intermetallic compounds and alloys. These hydrides are usually metallic and nonstoichiometric, and are called "interstitial" because hydrogen atoms occupy interstices in the metal-atom network. "Complex" metal hydrides form a distinctly different class of materials. Their name is derived from the presence of discrete metal–hydrogen complexes (where the metal is a p- or d-block element) in the structures, for example, the iron-based $[FeH_6]^{4-}$ ions in Mg_2FeH_6 or the aluminum-based $[AlH_4]^-$ ions in $NaAlH_4$. These hydrides are not derived from stable intermetallic compounds and are usually stoichiometric and nonmetallic.

Among the hydrides based on d-block elements, the first member and textbook example is K_2ReH_9. This compound was reported in 1964 and was found to contain tricapped trigonal-prismatic $[ReH_9]^{2-}$ complex anions. In the 1980s, many other complex transition-metal hydrides were discovered, such as the members of the series $Mg_2FeH_6/Mg_2CoH_5/Mg_2NiH_4$, which contain octahedral $[FeH_6]^{4-}$, square-pyramidal $[CoH_5]^{4-}$, or tetrahedral $[NiH_4]^{4-}$ 18-electron complex anions, respectively. Since then, the number of such hydrides has continuously increased, and it now totals over 80 compounds containing some 30 different transition-metal hydride complexes.[1]

Almost all of the known solid-state transition-metal hydride complexes are mononuclear and have terminal

[*] J.-N. Chotard, Dr. Y. Filinchuk,[+] Prof. Dr. K. Yvon
Laboratoire de Cristallographie
Université de Genève
Quai Ernest Ansermet 24, 1211 Genève 4 (Switzerland)
Fax: (+41) 223–796–108
E-mail: klaus.yvon@cryst.unige.ch

Dr. B. Revaz
Département de Physique de la Matière Condensée
Université de Genève
Quai Ernest Ansermet 24, 1211 Genève 4 (Switzerland)

[+] Current address:
Swiss–Norwegian Beam Lines at ESRF, BP 220
38043 Grenoble (France)

[**] This work was supported by the Swiss National Science Foundation and the Swiss Federal Office of Energy. We thank Dr. Nick Clayton (Siemens, Oxon) for the electrical-resistance measurements and Jean-Luc Lorenzoni (Geneva) for technical help.

Supporting information for this article is available on the WWW under http://www.angewandte.org or from the author.

WILEY InterScience DISCOVER SOMETHING GREAT
© 2006 Wiley-VCH Verlag GmbH & Co. KGaA, Weinheim

hydride ligands. Polynuclear hydride complexes with bridging hydride ligands are less common, but are of considerable interest because of possible links to interstitial hydrides. An example involving a 5d metal is the dinuclear $[Pt_2H_9]^{5-}$ complex anion in $Li_5Pt_2H_9$, which contains a linear Pt–H–Pt bond.[2] No examples of polynuclear solid-state complexes involving 3d metals have yet been reported. Likewise, hydride structures containing more than one type of transition-metal complex are very rare. The only known cases are $Mg_6T_2H_{11}$ (T = Co,[3] Ir[4]), which contain partially disordered square-pyramidal $[TH_5]^{4-}$ and saddle-like $[TH_4]^{5-}$ complex anions.

Herein, we report the discovery of the first polynuclear solid-state hydride complexes of a 3d metal, nickel. The only previously known solid-state nickel hydride complex is the mononuclear tetrahedral 18-electron $[NiH_4]^{4-}$ anion, which occurs in Mg_2NiH_4, $MMgNiH_4$ (M = Ca, Sr, Eu, Yb), and the recently reported $LaMg_2NiH_7$.[5] The compound described herein, $La_2MgNi_2H_8$, belongs to the same system, and contains a fully ordered arrangement of isolated dinuclear $[Ni_2H_7]^{7-}$ and tetranuclear $[Ni_4H_{12}]^{12-}$ complexes. Furthermore, its formation is associated with a hydrogen-induced metal–insulator transition, which is a relatively rare phenomenon in transition-metal–hydrogen systems.

The new compound $La_2MgNi_2H_8$ can be obtained readily by hydrogenation of the intermetallic compound La_2MgNi_2,[6] which crystallizes in the tetragonal Mo_2FeB_2 structure type. Hydrogenation in an autoclave at a temperature of 100 °C and a pressure of 30 bar over 24 h yields single-phase samples in a fairly reproducible manner. The analogous deuteride forms under the same conditions. For 10 samples, no significant variation of the cell parameters or hydrogen content was observed. Thus, the hydride can be considered as an essentially stoichiometric compound. The mass increase during hydrogenation corresponds to a hydrogen content of approximately eight hydrogen atoms per formula unit, that is, to a composition of $La_2MgNi_2H_8$. The corresponding weight and volume efficiencies for hydrogen storage are 1.89 wt% and 97 g L^{-1}. During hydrogenation, the host structure undergoes a monoclinic distortion and a lattice expansion of $\Delta V/V \approx 20\%$.[7] Attempts to desorb the hydride ligands under technically accessible conditions were unsuccessful. The application of a vacuum (ca. 1×10^{-3} bar) while heating at 300 °C over 24 h led to a partial segregation into the binary hydride LaH_3 and a secondary phase. Thus, $La_2MgNi_2H_8$ should be considered as a nonreversible hydride, with respect to the conditions typical of possible applications in the energy sector.

The structure of $La_2MgNi_2H_8$ was determined from synchrotron X-ray and neutron diffraction data collected for powder samples of the deuteride. In $La_2MgNi_2D_8$, the arrangement of the metal atoms is very similar to that in hydrogen-free La_2MgNi_2, the maximum atomic shifts being approximately 0.65 Å. The deuterium atoms fall into two classes, depending on whether or not they are bonded to nickel atoms. As shown in Figure 1, those bonded to nickel atoms (D11–D14, D21–D24, D31, D32, D41–43) form two sorts of polynuclear nickel–deuterium complexes (**I**, **II**). All of the nickel atoms are surrounded by terminal (D11, D14, D21, D22, D24, D31, D32, D41–D43) and bridging (D12, D13, D23) deuteride ligands in approximately tetrahedral configurations.

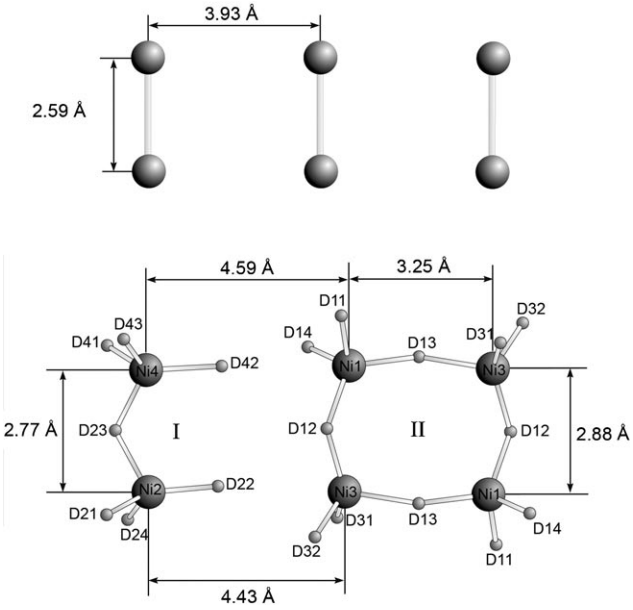

Figure 1. Arrangement of the $[Ni_2D_7]^{7-}$ (**I**) and $[Ni_4D_{12}]^{12-}$ (**II**) complex anions in the structure of $La_2MgNi_2D_8$ (bottom), and comparison with the arrangement of the nickel atoms in La_2MgNi_2 (top).

The dinuclear $[Ni_2D_7]^{7-}$ complex **I** consists of a pair of nickel-centered (Ni2, Ni4) tetrahedra, which share a corner (D23). The tetranuclear $[Ni_4D_{12}]^{12-}$ complex **II** consists of four nickel-centered (2 Ni1, 2 Ni3) tetrahedra, which each share two corners (D12, D13). Given that the Ni–D distances within the complexes (**I**: Ni–D 1.52–1.71 Å, **II**: Ni–D 1.50–1.70 Å) are much shorter than those between the complexes (Ni3–D22 2.86 Å, Ni1–D42 2.88 Å), the complexes are well-isolated from one another. The D-Ni-D bond angles deviate from the ideal tetrahedral angle of 109° (terminal: D-Ni-D 92–129°, bridging: Ni1-D13-Ni3 157°, Ni1-D12-Ni3 127°, Ni2-D23-Ni4 125°). In particular, the Ni2–D23–Ni4 bridge in **I** is significantly opened, but much less so than the linear Pt–H–Pt bridge found in the dinuclear $[Pt_2H_9]^{5-}$ complex of $Li_5Pt_2H_9$.[2]

The stereochemical activity of the deuteride ligands is not only apparent from the bond angles, but also from the changes in the Ni–Ni distances that are induced by deuteration. While the nickel atoms in the deuterium-free compound are arranged in equidistant pairs (intrapair: Ni–Ni 2.59 Å, interpair: Ni–Ni 3.93 Å; Figure 1, top), those in the deuteride are rearranged, such that the distances between the nickel pairs in **II** (Ni1–Ni3 3.25 Å) are considerably shortened (Figure 1, bottom), owing to the presence of bridging deuteride ligands (D13). On the other hand, the Ni–Ni distances between the pairs in **I** and **II** are much longer (Ni2–Ni3 4.43 Å, Ni1–Ni4 4.59 Å), owing to the absence of bridging deuteride ligands. The distances within the nickel pairs are lengthened in both complexes (**I**: Ni2–Ni4 2.77 Å, **II**: Ni1–Ni3 2.88 Å), owing to the presence of the bridging ligands D23 and D12. Finally, the Ni–D distances involving the terminal deuterium atoms are slightly shorter on average

 © 2006 Wiley-VCH Verlag GmbH & Co. KGaA, Weinheim

(Ni–D 1.58 Å) than those involving the bridging deuterium atoms (Ni–D 1.61 Å), and compare well with those in the mononuclear $[NiD_4]^{4-}$ complexes of other complex metal hydrides, such as $LaMg_2NiD_7$ (Ni–D 1.58 Å), Mg_2NiD_4 (Ni–D 1.54 Å) and $CaMgNiD_4$ (Ni–D 1.60 Å). The three remaining deuterium atoms in the structure are not bonded to nickel atoms and have octahedral La_4Mg_2 or tetrahedral La_2Mg_2 coordination environments.

When considered together, the structural features suggest a bonding description in terms of La^{3+} and Mg^{2+} cations, and $[Ni_2H_7]^{7-}$, $[Ni_4H_{12}]^{12-}$, and H^- anions. The corresponding limiting ionic formula is $4\,La_2MgNi_2H_8 = 8\,La^{3+} + 4\,Mg^{2+} + [Ni_4H_{12}]^{12-} + 2\,[Ni_2H_7]^{7-} + 6\,H^-$. In this picture, the electronic requirements of the nickel atoms in each complex anion (**I**: 34 electrons, **II**: 64 electrons) can be rationalized in terms of the 18-electron rule by attributing two-centre two-electron (2c-2e) bonds to the terminal hydrogen atoms, and three-center two-electron (3c-2e) bonds to the bridging hydrogen atoms. This model implies that the nickel atoms are essentially zero-valent and have sp^3-hybridized valence orbitals; that is, the nickel d bands are filled, and the compound is possibly diamagnetic and insulating.

While the intermetallic compound La_2MgNi_2 has a very low electrical resistance, consistent with metallic behavior, the hydride is clearly semiconducting. However, owing to the inability to compact the powder samples sufficiently, a reliable value for the band gap could not be obtained. Magnetic measurements revealed that $La_2MgNi_2H_8$ is slightly ferromagnetic, rather than diamagnetic as expected. Samples of both the intermetallic compound and the hydride exhibited a small hysteresis, and the saturation moment of the hydride (ca. 0.096 emu g^{-1} at 2 K) was approximately twice as large as that of the hydrogen-free compound (ca. 0.044 emu at 2 K). This behavior is probably due to traces of ferromagnetic nickel that were not detected by X-ray diffraction (La_2MgNi_2: ca. 0.25 wt%, $La_2MgNi_2H_8$: ca. 0.77 wt%; as estimated from the saturation magnetization). Additional nickel may have been formed at the grain boundaries during hydrogenation. This so-called "surface segregation" effect has been observed in related metal–hydrogen systems, such as $LaNi_5$–H,[8] and presumably masks the expected diamagnetism of $La_2MgNi_2H_8$.

In conclusion, we have reported the first case of a solid-state metal hydride containing polynuclear hydride complexes of a 3d metal. In contrast to the known nickel-based metal hydrides, which contain exclusively mononuclear tetrahedral $[NiH_4]^{4-}$ complexes with terminal hydride ligands, $La_2MgNi_2H_8$ contains (fully ordered) dinuclear $[Ni_2H_7]^{7-}$ and tetranuclear $[Ni_4H_{12}]^{12-}$ complexes with both terminal and bridging hydride ligands. The geometries of the complexes are unique for complex metal hydrides, and remotely resemble those of the $[Si_2O_7]^{6-}$ and $[Si_4O_{12}]^{8-}$ anions in soro- and ring silicates, respectively.

The nonmetallic character of $La_2MgNi_2H_8$ presumably results from the condensation of valence electrons into metal–hydrogen bonds in $[Ni_2H_7]^{7-}$ and $[Ni_4H_{12}]^{12-}$ anions having closed-shell electron configurations (18 electrons per nickel atom). This is the fourth example of a hydrogenation-induced metal–nonmetal transition in a transition-metal–hydrogen system. In all four cases, metallic compounds (Mg_2Ni, Mg_3Ir, $LaMg_2Ni$, and La_2MgNi_2) transform into nonmetallic hydrides (brownish-red Mg_2NiH_4, red $Mg_6Ir_2H_{11}$, dark gray $LaMg_2NiH_7$, and $La_2MgNi_2H_8$) containing transition-metal hydride complexes. Such transitions are of both fundamental and technological interest. They shed new light on metal–hydrogen interactions at the frontier between covalently bonded and metallic systems.

While the hydrogen-atom positions and hydrogen contents of covalently bonded systems can be rationalized in terms of covalent bonds (for example, 2c-2e) with directional character (for example, sp^3) and in terms of closed-shell electron configurations (for example, 18 electrons), those in metallic systems cannot. Hydrogen in metallic systems is generally considered as a stereochemically inert species that occupies the available interstices in the metal-atom framework on purely geometric grounds; hence, such systems are called "interstitial" hydrides. While such a description allows the prediction of some possible hydrogen sites, it generally does not allow the rationalization of all possible hydrogen sites and, thus, hydrogen contents. Clearly, directional bonding around the transition metals, charge transfer, and valence-electron counts must be considered as well. Furthermore, systems at the border between metallic and insulating are of interest for practical applications, such as optical mirrors (for example, Mg_2Co–H[9] and other systems[10]) and hydrogen detectors. These applications require, however, systems that are reversible at practical temperatures. Thus, a future challenge is the investigation of additional transition-metal–hydrogen systems, in particular those likely to contain polynuclear and/or heteronuclear complex anions that are fully reversible. The prospects of finding such complexes are good, since the possible element combinations are numerous and have not yet been fully explored.

Experimental Section

Synthesis: Samples of nominal composition La_2MgNi_2 were synthesized by sintering arc-melted LaNi with elemental magnesium in sealed tantalum tubes. The tubes were placed in a resistance furnace and annealed under vacuum for 2 h at 400 °C, then for 2 h at 600 °C, and finally for 3 h at 680 °C. The resulting samples were single-phase, according to powder X-ray diffraction. Samples of $La_2MgNi_2H_8$ and $La_2MgNi_2D_8$ were prepared by activating a powder sample of La_2MgNi_2 under vacuum at 100 °C for 14 h and then heating it with 30 bar of hydrogen or deuterium gas for 24 h at 100 °C in an autoclave.

Powder synchrotron X-ray diffraction: A sample of $La_2MgNi_2D_8$ was studied at one of the Swiss–Norwegian Beam Lines (BM01) at the ESRF (Grenoble, France). The powder sample was filled into a glass capillary (0.4-mm diameter) and was measured in Debye–Scherrer geometry: $\lambda = 0.37504$ Å, $2\theta = 2.2$–$32.4°$, step size $= 0.004°$. The powder pattern was indexed (DICVOL04[11]) in a monoclinic cell, and the systematic absences were consistent with the centrosymmetric space group $P2_1/c$. The structure refinement was carried out with FULLPROF, starting with atomic coordinates found by FOX[12] (four lanthanum, four nickel, and two magnesium sites, all on 4*a* equipoint (Wyckoff) positions).

Powder neutron diffraction: Data were collected for a powder sample of $La_2MgNi_2D_8$ (ca. 6 g) on the HRPT diffractometer at the SINQ of the PSI (Villigen, Switzerland) in high-intensity mode: $\lambda = 1.8857$ Å, $2\theta = 5$–$164°$, step size $= 0.1°$, data collection time ≈ 12 h. The deuterium atoms were found using FOX.[12] Sixteen deuterium-

 © 2006 Wiley-VCH Verlag GmbH & Co. KGaA, Weinheim

atom sites were located on 4*a* equipoint (Wyckoff) positions in space group $P2_1/c$, consistent with the composition $La_2MgNi_2D_8$, and were subsequently refined by the Rietveld method.

Electrical resistance: Electrical-resistance measurements were made on a pressed-powder pellet of $La_2MgNi_2H_8$ ($10\times4\times1$ mm^3) using the four-contact technique. Voltage and current leads were attached using silver paint. The pellet was mounted on an electrically insulated support and then attached to the cold finger of a cryocooler. Data were recorded upon cooling from room temperature to 10 K in steps of 5 K with applied direct currents of 1×10^{-4}–1×10^{-8} A during three consecutive runs.

Magnetism: The magnetic properties of La_2MgNi_2 and $La_2MgNi_2H_8$ were studied on a MPMS SQUID magnetometer. Magnetization curves were measured for pressed-powder samples (ca. 200 mg) at 2, 10, and 50 K. The maximum applied field was 5.5 T. To avoid ferromagnetic contamination, samples were prepared from very pure starting elements (nickel powder and magnesium pieces, 99.999 %, Sigma-Aldrich; lanthanum pieces containing 5.22 ppm iron, 0.56 ppm nickel, and 0.09 ppm cobalt, Ames Laboratory). From the stated purities, the total amount of iron and other metal impurities was estimated to be less than 27 ppm.

Further experimental details, diffraction patterns, crystallographic data, interatomic distances, electrical-resistance data, and magnetic data are given in the Supporting Information.

Received: September 6, 2006
Published online: November 7, 2006

Keywords: electrical properties · hydride ligands · hydrides · neutron diffraction · nickel

[1] For a recent review: K. Yvon, G. Renaudin in *Encyclopedia of Inorganic Chemistry*, 2nd ed. (Ed.: R. B. King), Wiley, New York, **2005**, pp. 1814–1846.
[2] W. Bronger, L. à Brassard, *Angew. Chem.* **1995**, *107*, 984; *Angew. Chem. Int. Ed. Engl.* **1995**, *34*, 898.
[3] R. Černý, F. Bonhomme, K. Yvon, P. Fischer, P. Zolliker, D. E. Cox, A. Hewat, *J. Alloys Compd.* **1992**, *187*, 233.
[4] R. Černý, J. M. Joubert, H. Kohlmann, K. Yvon, *J. Alloys Compd.* **2002**, *340*, 180.
[5] K. Yvon, G. Renaudin, C. M. Wei, M. Y. Chou, *Phys. Rev. Lett.* **2005**, *94*, 066403.
[6] R.-D. Hoffmann, A. Fugmann, U. C. Rodewald, R. Pöttgen, *Z. Anorg. Allg. Chem.* **2000**, *626*, 1733.
[7] $\vec{a}_{mono}=\vec{a}_{tetra}+2\,\vec{c}_{tetra}$; $\vec{b}_{mono}=\vec{b}_{tetra}$; $\vec{c}_{mono}=\vec{a}_{tetra}+2\,\vec{c}_{tetra}$; La_2MgNi_2: $a_{tetra}=7.656(1)$, $c_{tetra}=3.9250(8)$ Å, $V_{tetra}=230.10(7)$ Å^3; $La_2MgNi_2D_8$: $a_{mono}=11.84482(1)$, $b_{mono}=7.821099(8)$, $c_{mono}=11.96310(1)$ Å, $\beta=92.780(1)°$, $V_{mono}=1106.96(2)$ Å^3.
[8] L. Schlapbach, *J. Phys. F* **1980**, *10*, 2477.
[9] T. J. Richardson, J. L. Slack, B. Farangis, M. D. Rubin, *Appl. Phys. Lett.* **2002**, *80*, 1349, and references therein.
[10] R. Griessen, *Europhys. News* **2001**, *32*, 41.
[11] A. Boultif, D. Louër, *J. Appl. Crystallogr.* **2004**, *37*, 724.
[12] V. Favre-Nicolin, R. Černý, *J. Appl. Crystallogr.* **2002**, *35*, 734; see also: http://objcryst.sourceforge.net.

 © 2006 Wiley-VCH Verlag GmbH & Co. KGaA, Weinheim

Nanostructures

DOI: 10.1002/anie.200602228

SiO_2/Ta_2O_5 Core–Shell Nanowires and Nanotubes**

Yu-Lun Chueh, Li-Jen Chou, and Zhong Lin Wang*

One-dimensional nanostructures such as nanowires, nanobelts, and nanotubes have attracted much attention as a result of their unique properties, which can be applied in the fabrication of biomedical sensors, optoelectronic devices, field-effect transistors, and field-emission devices, for example.[1] In particular, one-dimensional nanostructures of metal oxides such as ZnO,[2] SnO_2,[3] α-Fe_2O_3,[4] WO_3,[5] and Ta_2O_5,[6] so-called functional materials, have been widely studied. The synthesis of these functional metal oxide nanostructures are investigated widely through physical and chemical reactions, including vapor–liquid–solid (VLS),[7] solution–liquid–solid (SLS),[8] vapor–solid (VS),[9] and other template-based approaches.[10]

Ta_2O_5 is a fascinating functional material that has been used in applications such as dynamic random access memory (DRAM) devices, antireflection coating layers, gas sensors, photocatalysts, and capacitors owing to its high dielectric constant, high refractive index, chemical stability, and high-temperature piezoelectric properties.[6a,11] However, the synthesis of Ta_2O_5 nanostructures (e.g. nanowires or nanotubes) has had little success as a result of its high melting point. On the other hand, silica (SiO_2) nanowires are well developed for electronic and optoelectronic applications.[12] Various methods of synthesizing SiO_2 nanowires include pulsed laser ablation,[12a] directed growth from a silica substrate or silica nanoparticles in a reductive atmosphere,[13] direct growth from a Si substrate with catalyst,[14] carbon-assisted and carbothermal reduction of silicon dioxide or metal oxides,[15] and the sol–gel method.[16] All of these approaches are direct, simple, and high-yielding, which are important factors for commercial applications.

[*] Y.-L. Chueh, Prof. L.-J. Chou
Department of Materials Science and Engineering
National Tsing Hua University
Hsinchu, Taiwan 300 (ROC)
Fax: (+886) 3-572-2366
E-mail: ljchou@mx.nthu.edu.tw
Y.-L. Chueh, Prof. Z. L. Wang
School of Materials Science and Engineering
Georgia Institute of Technology
Atlanta, Georgia 30332-0245 (USA)

[**] This research was supported by the National Science Council (grant no. NSC 94-2215-E-007-019), the Ministry of Education (grant no. 93-E-FA04-1-4), the Thousand Horse Program (no. 095-2917-1-007-014), the NSF, the NASA Vehicle System Program, the Department of Defense Research and Engineering (DDR&E), and the Defense Advanced Research Project Agency (N66001-040-1-18903).

Supporting information for this article is available on the WWW under http://www.angewandte.org or from the author.

© 2006 Wiley-VCH Verlag GmbH & Co. KGaA, Weinheim

Herein, we present a technique for the fabrication of SiO_2/Ta_2O_5 core–shell nanotubes, Ta_2O_5 nanotubes, and Ta_2O_5 nanowires by using SiO_2 nanowires as template. The structures were prepared by annealing SiO_2 nanowires in an atmosphere of Ta at 950 °C at a pressure of 1×10^{-6} Torr. The diameter of the SiO_2 core in the SiO_2/Ta_2O_5 core–shell structure was readily controlled, and the silica template could be removed from the core–shell structures by using dilute HF solution to leave Ta_2O_5 nanotubes. Furthermore, Ta_2O_5 nanowires could be synthesized by increasing the reduction (annealing) time so that all of the SiO_2 in the core–shell structure was reduced by Ta vapors. The subsequent characterization of the core–shell structures as well as the Ta_2O_5 nanotubes and nanowires was carried out by cathodoluminescence (CL) and field-emission measurements.

The scanning electron microscopy (SEM) image of SiO_2 nanowires, prepared by annealing a 2-nm-thick layer of Au on a Si wafer under N_2 atmosphere at 1150 °C for 2 h, is shown in Figure 1 a. The diameter of these SiO_2 nanowires is almost uniform, and the length is up to several hundred micrometers. The corresponding transmission electron microscopy (TEM) image indicates that most of the SiO_2 nanowires have a smooth morphology, with a diameter of 100–150 nm (Figure 1 b). The diffraction pattern (upper inset in Figure 1 b) displays a highly diffusive ring, indicating that the silica nanowires are amorphous. The atomic concentration of Si and O for these synthesized nanowires is about 34 % and 66 %, respectively, and a ratio of 1:2 Si/O was inferred from quantitative TEM/EDS (energy-dispersive spectrometry) measurements (lower inset in Figure 1 b). After annealing the nanowires at 950 °C for 12 h and subjecting them to a reductive Ta atmosphere, the morphology of the resultant SiO_2/Ta_2O_5 structures was similar (Figure 1 c). The corresponding magnified SEM image (upper inset in Figure 1 c) clearly shows the wirelike features. The phase and structure of these nanowires was characterized by X-ray diffraction (XRD; Figure 1 d) and revealed the Ta_2O_5 phase to have an orthorhombic structure (*C*2*mm* space group) and lattice constants of $a = 0.618$, $b = 0.366$, and $c = 0.388$ nm, respectively (ICSD-43498).[17] Note that the $TaSi_2$ phase found in the XRD spectrum originates from a silicide reaction between the Si substrate and Ta vapors during the reduction procedure.

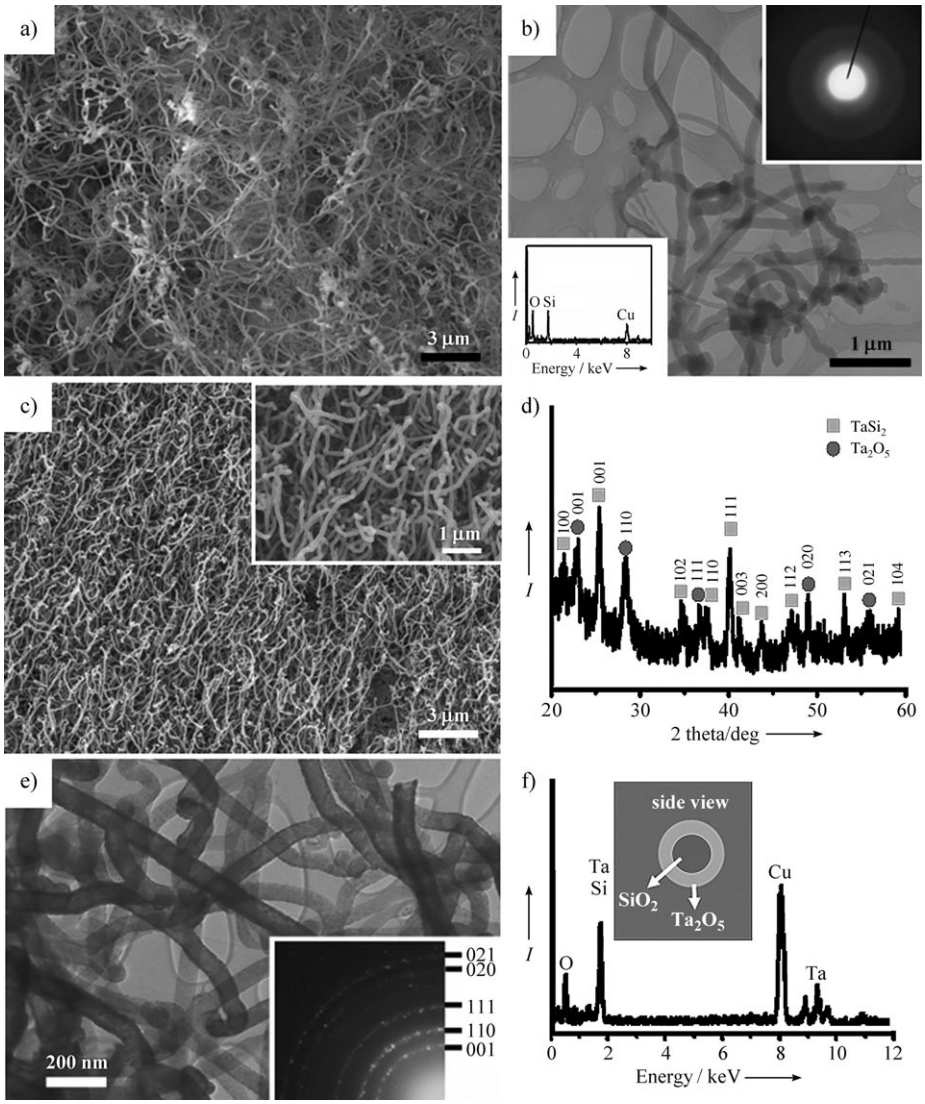

Figure 1. a) Top-view SEM image and b) corresponding TEM image of SiO_2 nanowires. The upper inset in (b) shows an electron diffraction pattern from a nanowire, while the lower inset shows the EDS spectrum. c) Top-view SEM image of SiO_2/Ta_2O_5 core–shell nanostructures formed by annealing SiO_2 nanowires under a Ta atmosphere at 950 °C for 12 h. The inset in (c) shows the magnified SEM image. d) XRD spectrum corresponding to the sample in (c). e) TEM image of SiO_2/Ta_2O_5 core–shell nanostructures. The inset in (e) shows the diffraction pattern. f) EDS spectrum recorded on the Ta_2O_5 shell of a SiO_2/Ta_2O_5 nanostructure and schematic of the configuration of the core–shell nanostructure.

TEM analysis was essential to examine the detailed microstructures of these nanowires (Figure 1 e). The different contrast between the inside and the outside of these nanowires provides significant evidence of a core–shell structure. The lower inset in Figure 1 e shows the diffraction pattern and plane indices recorded from a SiO_2/Ta_2O_5 core–shell structure. The pattern is consistent with the results of XRD studies, indicating the polycrystalline characteristic of the SiO_2/Ta_2O_5 core–shell structure (see the Supporting Information). Diffusive white contrast was also observed confirming that SiO_2

 © 2006 Wiley-VCH Verlag GmbH & Co. KGaA, Weinheim

nanowires were surrounded by a Ta_2O_5 shell. Note that SiO_2 or Si is incorporated inside the Ta_2O_5 shell during the reduction process, but the main phase remains that of Ta_2O_5 as determined by both the XRD and diffraction patterns (Figure 1d and e, respectively). TEM/EDS measurements of the shell of a SiO_2/Ta_2O_5 structure revealed that it consists of 20% Ta, 71% O, and 9% Si. Upon examining in detail many SiO_2/Ta_2O_5 core–shell structures, the maximum concentration of Si in these Ta_2O_5 shells was found to be no more than 15%.

The morphology of the core–shell structure was tunable, depending on the original shape of the SiO_2 nanowire. If the SiO_2 nanowire had a spiral morphology, the SiO_2/Ta_2O_5 core–shell structure formed after the reduction process also revealed a spiral morphology. An example of the spiral morphology of a SiO_2/Ta_2O_5 core–shell structure is highlighted in Figure 2a (see also the Supporting Information), while the corresponding TEM image is shown in Figure 2b. The phase was confirmed to be that of Ta_2O_5 by the diffraction pattern (see inset in Figure 2b). The thickness of the Ta_2O_5 layer outside the SiO_2 nanowires could be tuned by controlling the annealing (reduction) time (see Supporting Information). The thickness of the Ta_2O_5 shell increased as the reduction time was increased at a constant temperature of 950°C or simply if the temperature was increased.

How do the Ta atoms reduce the SiO_2 to form the SiO_2/Ta_2O_5 core–shell structure? Figure 2c shows the heat of formation ($-\Delta H_f$ [kcal atom^{-1}]) per oxygen atom for various transition-metal oxides and SiO_2.[18] Note that the heats of formation for transition-metal oxides such as HfO_2, TiO_2, and Ta_2O_5 are lower than that of SiO_2, which results in the reduction of SiO_2 at high annealing temperatures. On the other hand, the reduction of SiO_2 is prohibited if the heat of formation of transition-metal oxides such as MnO_3 is higher than that of SiO_2. Figure 2d shows plots of the thickness of the Ta_2O_5 shell of the SiO_2/Ta_2O_5 core–shell structure as a function of the reduction time at 950°C. The relationship between the thickness of the Ta_2O_5 shell and the reduction time is nonlinear, revealing that the reduction mechanism is under diffusion control, that is, $X^2 = Dt$ (X, D, and t denote the oxide thickness, parabolic reduction rate constant, and reduction time, respectively).[19] The reduction rate constant, D, was evaluated as about 2×10^{-16} cm^{2}s^{-1} by plotting the thickness of the oxide shell as a function of the square root of the reduction time (see inset in Figure 2d). The thermal kinetic motion of Ta ions during the reduction process involves their diffusion through SiO_2 and reduction of the SiO_2 layer. The diffusion-limited mechanism indicates that the diffusion through the SiO_2 layer is rather slow, resulting in easier control over the reduction process. The measured rate constant represents the rate constant of diffusion. Also, the Si signal detected in EDS studies in various Ta_2O_5 shells indicates that the Si atoms from SiO_2 reduced by Ta vapors are involved in the Ta_2O_5 sublattice or excluded from the grain boundary.

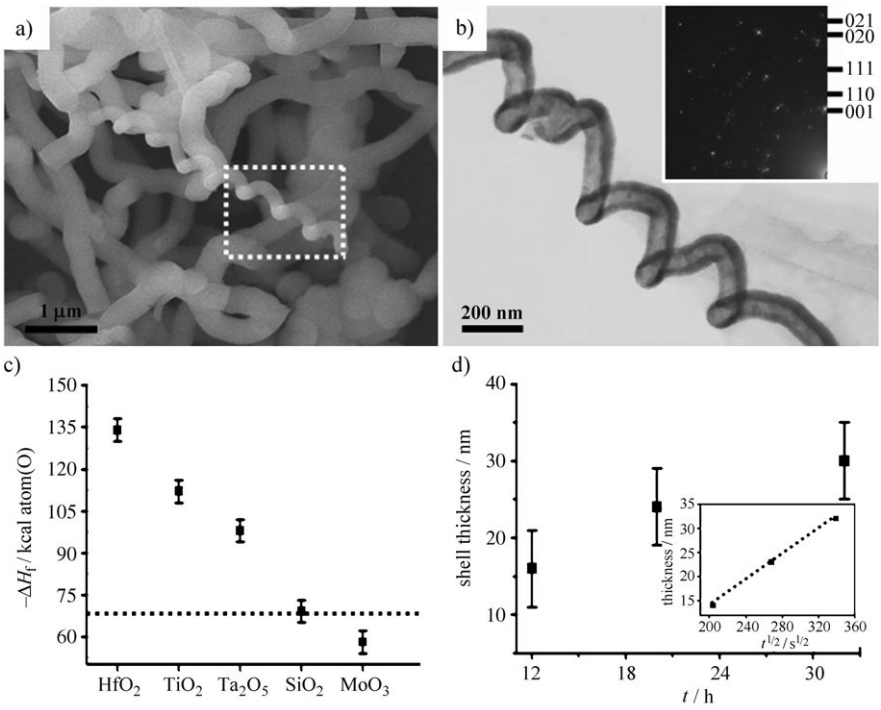

Figure 2. a) SEM image of a spiral SiO_2/Ta_2O_5 core–shell nanostructure obtained by annealing SiO_2 nanowires in a Ta atmosphere at 950°C for 12 h. b) TEM image corresponding to the dashed rectangular area in (a). The inset shows the corresponding electron diffraction pattern. c) Heats of formation ($-\Delta H_f$) for different metal oxides (the dashed line is shown to compare other metal oxides with SiO_2). d) Variation in the thickness of the Ta_2O_5 shell as a function of reduction (annealing) time. The inset shows the linear relationship between the square root of reduction time and the shell thickness.

After dipping the core–shell structures in a diluted solution of HF to remove the SiO_2 inside the SiO_2/Ta_2O_5 core–shell structure, the morphology was unchanged. The inner SiO_2 nanowires could be removed to leave Ta_2O_5 nanotubes intact (see Figure 3a and Supporting Information). The residual $TaSi_2$ formed by the reduction procedure could be completely etched by HF solution. The XRD results for the nanotubes showed no peaks for $TaSi_2$ and indicate that the amorphous SiO_2 region was eliminated (see Supporting Information).[18]

Ta_2O_5 nanowires could also be prepared by increasing the reduction time of the silica nanowires. For example, after annealing SiO_2 nanowires with a diameter of less than 60 nm in a reductive Ta atmosphere at 950°C for 32 h, then Ta_2O_5 nanowires with lengths of over several hundred micrometers were formed instead of the SiO_2/Ta_2O_5 core–shell structure (Figure 3b). The TEM image of a Ta_2O_5 nanowire with a diameter of 100 nm is shown in Figure 3c and indicates the polycrystalline feature of the structure. From the quantitative EDS measurements, it can be seen that the concentration of Si is about 3–14%. Although

 © 2006 Wiley-VCH Verlag GmbH & Co. KGaA, Weinheim

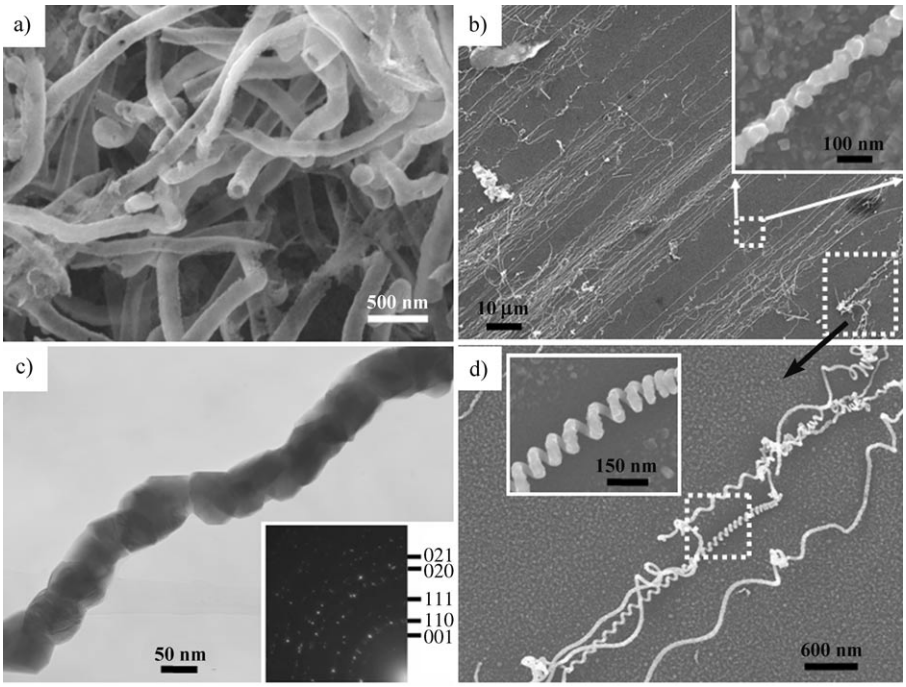

Figure 3. a) Top-view SEM image of Ta_2O_5 nanotubes prepared by dipping a sample of SiO_2/Ta_2O_5 core–shell nanostructures in diluted HF solution to remove the SiO_2 nanowire core. b) Top-view SEM image of Ta_2O_5 nanowires. The inset shows the magnified SEM image recorded from the dashed rectangle area indicated by arrows. c) Typical TEM image of a Ta_2O_5 nanowire. The inset shows the corresponding electron diffraction pattern. d) SEM image showing the spiral morphology of Ta_2O_5 nanowires taken from the larger dashed rectangular area in (b). The inset shows the magnified SEM image.

the concentration of Si inside the Ta_2O_5 nanowires is fairly high, the main phase remains that of Ta_2O_5, as confirmed by the diffraction pattern shown in the lower inset in Figure 3c. The morphology of the Ta_2O_5 nanowires could be modified according to the original morphology of the SiO_2 nanowire template (lower right inset of Figure 3b shows the spiral morphology of Ta_2O_5 nanowires). The magnified SEM image of the spiral morphology of the Ta_2O_5 nanowires as well as a magnification of this spiral structure are clearly seen in Figure 3d. The polycrystalline feature is suggested to arise as a result of two possible factors: 1) the segregation of Si during the reduction process through the grain boundary of Ta_2O_5 nanowires and 2) anisotropic reduction along the SiO_2 nanowires. Moreover, dislocations can be found inside the grain of Ta_2O_5 which may be caused by the location of Si atoms in the substitutional or interstitial sites in the sublattice of Ta_2O_5 (see Supporting Information).

Figure 4a shows the SEM image of a Ta_2O_5 nanotube after dipping it into a dilute solution of HF for 5 h. The CL spectra record from two areas of the sample labeled as A and B are shown in the insets of Figure 4a. Two peaks from the area labeled as A were detected, whereas no peak was found from the area B. The CL image under excitation at 15 kV was also measured (Figure 4b). Figure 4c shows the CL spectrum from the Ta_2O_5 nanotube sample (area A) after Gaussian fitting and reveals two clear peaks at 563 nm (2.2 eV) and 301 nm (4.1 eV), as well as a broad peak in the range of 2–5 eV. The band gap of Ta_2O_5 is about 4.1–4.2 eV, which results in some radiative recombination emission caused by oxygen deficiency.[20] The peak at 563 nm (2.2 eV) is attributed to the oxygen vacancies inside the Ta_2O_5 shell. The broad band at 2–5 eV may be derived from a combination of two peaks at 460 and 355 nm which originate from the residual SiO_2 inside the Ta_2O_5 nanotube or from the initial Si substrate. The peak at 301 nm (4.1 eV, violet region) in the CL spectrum originates from the d-band transition between the e_g and t_{2g} states, induced by

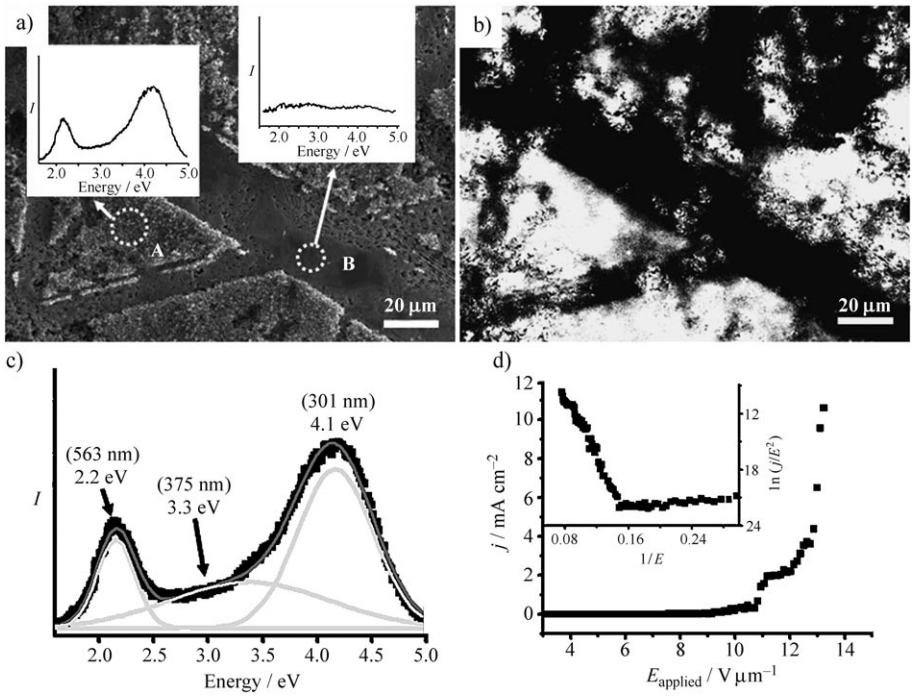

Figure 4. a) SEM image of a Ta_2O_5 nanotube after dipping it into diluted HF solution; the insets show CL spectra recorded from two areas labeled A and B. b) CL image of the sample in (a) excited at 15 kV. c) CL spectrum recorded from a Ta_2O_5 nanotube (black line) after Gaussian curve fitting (pale gray line; deconvoluted spectra are shown in dark gray). d) Field-emission properties of a Ta_2O_5 nanotube obtained from dipping a SiO_2/Ta_2O_5 core–shell structure into diluted HF solution (j = current density). The inset shows the corresponding $\ln(j/E^2)$ versus $1/E$ plot (see text for details).

 © 2006 Wiley-VCH Verlag GmbH & Co. KGaA, Weinheim

ligand-field splitting (see Supporting Information).[21] A similar phenomenon is found in other materials, such as α-Fe_2O_3 nanoparticles.[22] The violet peak derived from the oxygen deficiency transition inside the Ta_2O_5 is also the factor for the CL peak at 301 nm. Violet light is of interest in fundamental research and for applications in full-color displays. Here, by controlling the thickness of the SiO_2 core inside the SiO_2/Ta_2O_5 core–shell structure, which in turn defines the CL wavelength, the nanotubes may be used in optical transportation phenomena, such as light propagation.

The current density as a function of the applied electric field for the Ta_2O_5 nanotube sample at a fixed distance of 100 μm between the anode and the surface of the nanotube is shown in Figure 4d. Two parameters, the turn-on field and the threshold field, are defined as the applied voltage (E) needed to produce a current density of 0.01 and 10 mA cm^{-2}, respectively, for which respective values of 8 and 13 V μm^{-1} were determined. The inset in Figure 4d shows a plot of $\ln(j/E^2)$ versus $1/E$. The linear relationship is consistent with the so-called Fowler–Nordheim plot (F-N plot; Figure 4d) and indicates that the field-emission behavior obeys the F-N rule, that is, electrons tunnel through the potential barrier from the conduction band to the vacuum state.[23] Although these values are somewhat higher than for other oxide materials, such as ZnO,[24] SnO_2,[2b] and $W_{18}O_{49}$,[25] the core–shell structures here still show great promise in display applications owing to their straightforward and high-yielding production and the ease with which they can be integrated in silicon-based industries.

In summary, SiO_2/Ta_2O_5 core–shell structures were synthesized by annealing SiO_2 nanowires under a reductive atmosphere of Ta at 950 °C. The morphology of the nanostructures was tunable depending on the morphology of the original SiO_2 nanowires, and the diameter of the SiO_2 nanowire inside the SiO_2/Ta_2O_5 core–shell structure could also be modified. Furthermore, Ta_2O_5 nanotubes could be prepared by removal of the template from the core—shell structures and Ta_2O_5 nanowires could be prepared directly by increasing the reduction time. The electrical and optical properties reported herein indicate that the SiO_2/Ta_2O_5 core–shell structures, Ta_2O_5 nanotubes, and Ta_2O_5 nanowires may have many interesting applications in nanotechnology.

Experimental Section

Single-crystal Si(001) wafers (resistivity: 1–30 Ω cm) were cleaned using standard cleaning procedures and then dipped in diluted HF solution (1:50 HF/H_2O) for 30 s before being loaded into the deposition system ($P > 5 \times 10^{-6}$ Torr). A 2-nm-thick layer of Au was deposited on the Si substrate at a pressure of 5×10^{-6} Torr with a deposition rate of 0.01 nm s^{-1}. Subsequently, as-deposited samples were annealed in a horizontal furnace at 1150 °C for 2 h under an atmosphere of N_2 to grow the SiO_2 nanowires. The high-density SiO_2 nanowire samples were transferred into a Ta-filament heating chamber for annealing ($P > 1 \times 10^{-6}$ Torr) at 950 °C for 12–32 h to produce SiO_2/Ta_2O_5 core–shell nanowire structures; Ta atoms were constantly vaporized from the supplementary source in this chamber (see Supporting Information). Ta_2O_5 nanotubes could be formed by dipping the core–shell structures into dilute HF solution (1:50 HF/H_2O) to remove the inner SiO_2 nanowires.

Grazing incidence X-ray diffractometry (GIXRD) with a fixed incident angle at 0.5° was carried out to identify the phases of the nanostructures. The surface morphology was examined by a field-emission scanning electron microscope (JSM-6500F) operated at 15 kV. To prepare the TEM specimen, all samples were sonicated in ethanol and then dispersed on a copper grid supported by a holey carbon film. A field-emission transmission electron microscope (JEM-3000F) operated at 300 kV, with a point-to-point resolution of 0.17 nm and equipped with an energy-dispersion spectrometer, an electron energy loss spectrometer, as well as a high-angle annular dark field detector, was used to characterize the microstructures and chemical compositions. Electron field-emission behavior was measured in a vacuum of 1×10^{-7} Torr by using a spherical stainless-steel probe (1-mm diameter) as the anode. The lowest emission current was recorded on the level of nA. The measurement distance between the anode and the emitting surface was fixed at 100 μm. The CL spectrum was measured in the scanning electron microscope with an electron probe microanalyzer (Shimadzu EPMA-1500). CL spectra were accumulated in single-shot mode within a short time of 1 s. In general, the CL excitation was performed with a beam current of about 100 nA in television scanning mode of 2.9×10^{-5} cm^2.

Received: June 3, 2006
Published online: October 20, 2006

Keywords: nanostructures · reduction · silicon · tantalum · template synthesis

[1] a) C. Yu, Q. Hao, S. Saha, L. Shi, X. Kong, Z. L. Wang, *Appl. Phys. Lett.* **2005**, *86*, 063101; b) C. S. Lao, J. Liu, P. X. Gao, L. Zhang, D. Davidovic, R. Tummala, Z. L. Wang, *Nano Lett.* **2006**, *6*, 263; c) A. B. Greytak, C. J. Barrelet, Y. Li, C. M. Lieber, *Appl. Phys. Lett.* **2005**, *87*, 151103; d) Y. L. Chueh, L. J. Chou, C. M. Hsu, S. C. Kung, *J. Phys. Chem. B* **2005**, *109*, 21831; e) Z. L. Wang, *Adv. Mater.* **2003**, *15*, 432; f) M. S. Arnold, P. Avouris, Z. W. Pan, Z. L. Wang, *J. Phys. Chem. B* **2004**, *108*, 659.

[2] a) Z. W. Pan, Z. R. Dai, Z. L. Wang, *Science* **2001**, *291*, 1947; b) P. X. Gao, Y. Ding, W. J. Mai, W. L. Hughes, C. S. Lao, Z. L. Wang, *Science* **2005**, *309*, 1700.

[3] J. H. He, T. H. Wu, C. L. Hsin, K. M. Li, L. J. Chen, Y. L. Chueh, L. J. Chou, Z. L. Wang, *Small* **2006**, *2*, 116.

[4] M. Cao, T. Liu, S. Gao, G. Sun, X. Wu, C. Hu, Z. L. Wang, *Angew. Chem.* **2005**, *117*, 4269; *Angew. Chem. Int. Ed.* **2005**, *44*, 4197.

[5] J. Zhou, Y. Ding, S. Z. Deng, L. Gong, N. S. Xu, Z. L. Wang, *Adv. Mater.* **2005**, *17*, 2107.

[6] a) Y. Zhu, F. Yu, Y. Man, Q. Tian, Y. He, N. Wu, *J. Solid State Chem.* **2005**, *178*, 224; b) H. Schulz, L. Mädler, S. E. Pratsinis, P. Burtscher, N. Moszner, *Adv. Mater.* **2005**, *17*, 830; c) A. Arranz, V. Pérez-Dieste, C. Palacio, *Phys. Rev. B* **2002**, *66*, 675420.

[7] A. M. Morales, C. M. Lieber, *Science* **1998**, *279*, 208.

[8] T. J. Trentler, K. M. Hickman, S. C. Geol, A. M. Viano, P. C. Gibbons, W. E. Buhro, *Science* **1995**, *270*, 1791.

[9] P. D. Yang, C. M. Lieber, *J. Mater. Res.* **1997**, *12*, 2981.

[10] Y. Wu, J. Xiang, C. Yang, W. Li, C. M. Lieber, *Nature* **2004**, *430*, 61.

[11] a) J. Y. Zhang, L. J. Bie, I. W. Boyd, *J. Appl. Phys.* **1998**, 37, L27; b) R. T. Webb, *Ten Years of TWT Progress Electron Power* **1985**, *2*, 120; c) S. Ezhilvalavan, T. Y. Tseng, *J. Mater. Sci. Mater. Electron.* **1999**, *10*, 9.

[12] a) D. P. Yu, Q. L. Hang, Y. Ding, H. Z. Zhang, Z. G. Bai, J. J. Wang, Y. H. Zou, W. Qian, G. C. Xiang, S. Q. Feng, *Appl. Phys. Lett.* **1998**, *73*, 3076; b) J. H. He, T. H. Wu, C. L. Hsin, L. J. Chen, Z. L. Wang, *Electrochem. Solid State Lett.* **2005**, *8*, G254.

[13] K. H. Lee, S. W. Lee, R. R. Vanfleet, W. Sigmund, *Chem. Phys. Lett.* **2003**, *376*, 498.

[14] Z. W. Pan, Z. R. Dai, C. Ma, Z. L. Wang, *J. Am. Chem. Soc.* **2002**, *124*, 1817.

 © 2006 Wiley-VCH Verlag GmbH & Co. KGaA, Weinheim

[15] S. H. Li, X. F. Zhu, Y. P. Zhao, *J. Phys. Chem. B* **2005**, *108*, 17032.
[16] M. Zhang, E. Ciocan, Y. Bando, K. Wada, L. L. Cheng, P. Pirouz, *Appl. Phys. Lett.* **2002**, *80*, 491.
[17] Further details of the crystal structure investigation may be obtained from the Fachinformationszentrum Karlsruhe, 76344 Eggenstein-Leopoldshafen, Germany (fax: (+49) 7247-808-666; e-mail: crysdata@fiz-karlsruhe.de, http://www.fiz-informationsdienste.de/en/DB/icsd/depot_anforderung.html) on quoting the deposition number ICSD-43498.
[18] S. P. Murarka, *J. Vac. Sci. Technol.* **1980**, *17*, 775.
[19] S. P. Murarka, *Silicides For VULS Application*, Academic Press, New York, **1983**, p. 107.
[20] a) W. H. Knausenberger, R. N. Tauber, *J. Electrochem. Soc.* **1973**, *120*, 927; b) A. G. Revesz, J. J. Reynolds, J. F. Allison, *J. Electrochem. Soc.* **1976**, *123*, 889; c) J. Jasapara, A. V. V. Nampoothir, W. Rudolph, *Phys. Rev. B* **2001**, *63*, 045117.
[21] F. M. F. de Groot, G. Grioni, J. C. Fuggle, *Phys. Rev. B* **1989**, *40*, 5715.
[22] H. Fei, X. Ai, M. Gao, Y. Yang, T. Zhang, J. Shen, *J. Lumin.* **1996**, *66–67*, 345.
[23] a) Y. L. Chueh, L. J. Chou, S. L. Cheng, J. H. He, W. W. Wu, L. J. Chen, *Appl. Phys. Lett.* **2005**, *86*, 133112; b) Y. L. Chueh, L. J. Chou, S. L. Cheng, C. J. Tasi, *Appl. Phys. Lett.* **2005**, *87*, 223113.
[24] C. J. Lee, T. J. Lee, S. C. Lyu, Y. Zhang, H. Ruh, H. J. Lee, *Appl. Phys. Lett.* **2002**, *81*, 5048.
[25] J. Zhou, L. Gong, S. Z. Deng, J. Chen, J. C. She, N. S. Xu, R. Yang, Z. L. Wang, *Appl. Phys. Lett.* **2005**, *87*, 223108.

 © 2006 Wiley-VCH Verlag GmbH & Co. KGaA, Weinheim

Ionic Liquids

DOI: 10.1002/anie.200602756

Surface Enrichment and Depletion Effects of Ions Dissolved in an Ionic Liquid: An X-ray Photoelectron Spectroscopy Study

Florian Maier, J. Michael Gottfried, Jürgen Rossa, Dirk Gerhard, Peter Steffen Schulz, Wilhelm Schwieger, Peter Wasserscheid, and Hans-Peter Steinrück*

Ionic liquids (ILs)—salts with melting points below 100 °C—have found increasing scientific interest over the past decade.[1,2] Attracted by their structural diversity and their unique physicochemical properties (for example, negligible volatility,[3] unusual solvation and miscibility properties,[4] and electroconductivity[5]), many research groups have studied applications of these materials in catalysis,[6] electrochemistry,[5] analytics,[7] and as "engineering fluids" (for example, separation technologies[8]). Several industrial applications have been reported recently.[9]

While the "bulk" properties of common ILs have been studied to some extent, very little is known about their surface and interfacial properties.[10–12] However, the latter are pivotal for multiphasic reactions with ILs, such as catalytic reactions involving gaseous reactants in contact with bulk ILs or IL films supported on surfaces (a concept known as supported ionic liquid phase (SILP) catalysis.[13–15])

As a result of the very low vapor pressure of ILs, X-ray photoelectron spectroscopy (XPS)—well-established but usually limited to ultrahigh vacuum (UHV) conditions—can be used to access IL surfaces on a molecular level. XPS is an ideal tool in surface science because of the small mean free path of photoelectrons.[16] Recently, the IL 1-ethyl-3-methylimidazolium ethyl sulfate ([EMIM][$EtOSO_3$]) was studied for the first time by Licence et al. using XPS.[17] They assigned the core-level signals of the atoms of the IL to different chemical environments and also observed signals of a dissolved Pd complex.

In our case, the salt $[Pt(NH_3)_4]Cl_2$ dissolved in [EMIM]-[$EtOSO_3$] was chosen because of our interest in ligand-exchange phenomena in ILs. Moreover, Pt salts are interesting as precursors for catalytic applications, for example, in Pt-catalyzed olefin hydroformylation.[18] In particular, we were able to distinguish the concentration and chemical nature of ions and dissolved species in the top surface layer of the ionic solution from those in the layers beneath by selective detection of photoelectrons emitted under different angles ϑ to the surface normal. The probe depth, from which 90 % of the XPS intensities originate, varies with $\cos\vartheta$ and decreases from about 3 nm for $\vartheta = 0°$ (normal emission) to about 1 nm for $\vartheta = 70°$ (grazing emission).[19] In the latter case, XPS probes less than the first two molecular layers. Consequently, an increase in core-level intensity with increasing detection angle, and thus with increasing surface sensitivity, indicates enrichment of this element in the first layer.

An X-ray photoelectron (XP) spectrum of the pure IL is shown in Figure 1 (dashed curve). Besides IL-related signals (O 1s, C 1s, N 1s, S 2s, and S 2p; see inset of Figure 1), no other elements could be detected, thus proving that the surface was free from contaminants. (Note that the Si impurities observed by Licence et al.[17] were avoided by using pure ILs from our own laboratories. See Supporting Information for synthesis details.) Taking the sensitivity factors for the individual core levels[20] into account, these intensities agree with the expected ratios S/O/C/N = 1:4:8:2, thus confirming surface cleanliness. The XP spectra taken at 0° and 70° were virtually identical, which indicates homogeneous distribution of IL cations and anions, and randomly oriented molecules in the near-surface region of the pure IL (while orientation effects were observed for 1-butyl-3-methylimidazolium IL surfaces[21]).

In contrast, we observed strong angle-dependent intensity variations on the solution of the Pt salt in the IL, as revealed

[*] Dr. F. Maier, Dr. J. M. Gottfried, J. Rossa, Prof. Dr. H.-P. Steinrück
Lehrstuhl Physikalische Chemie II
Universität Erlangen
Egerlandstrasse 3, 91058 Erlangen (Germany)
Fax: (+49) 9131-852-8867
E-mail: florian.maier@chemie.uni-erlangen.de
Homepage: http://www.chemie.uni-erlangen.de/steinrueck
D. Gerhard, Dr. P. S. Schulz, Prof. Dr. W. Schwieger,
Prof. Dr. P. Wasserscheid
Lehrstuhl Chemische Reaktionstechnik
Universität Erlangen
Egerlandstrasse 3, 91058 Erlangen (Germany)

Supporting information for this article is available on the WWW under http://www.angewandte.org or from the author.

InterScience
© 2006 Wiley-VCH Verlag GmbH & Co. KGaA, Weinheim

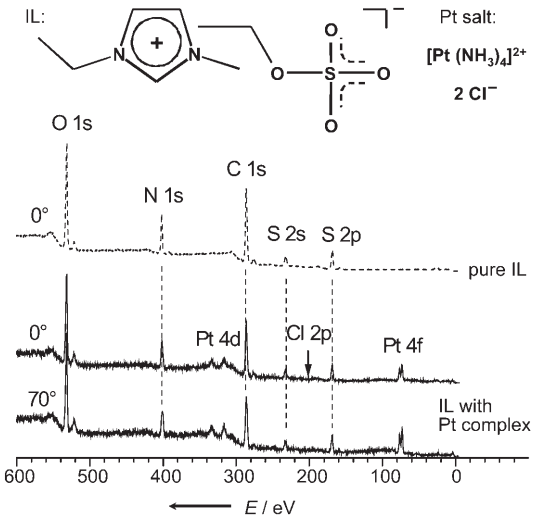

Figure 1. Survey XP spectra of pure [EMIM][$EtOSO_3$] and a solution of $[Pt(NH_3)_4]Cl_2$ in the IL, taken at different emission angles; E = binding energy. Top: pure [EMIM][$EtOSO_3$] at 0°; middle and bottom: solution of $[Pt(NH_3)_4]Cl_2$ in [EMIM][$EtOSO_3$] at 0° (more bulk-sensitive) and 70° (more surface-sensitive).

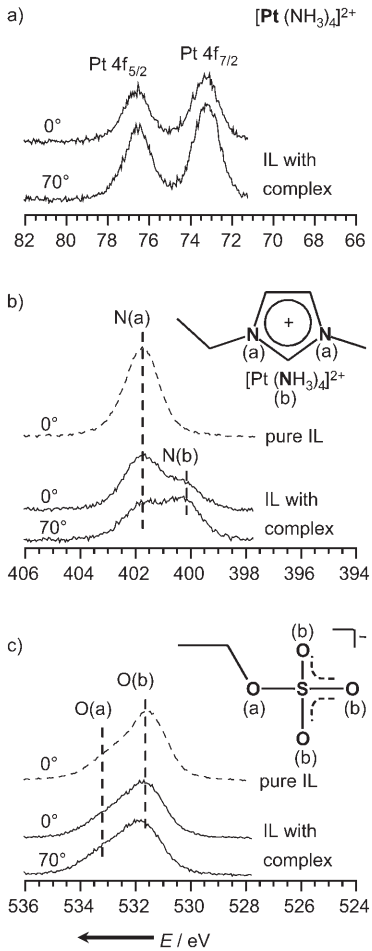

Figure 2. XP spectra of the Pt 4f (a), N 1s (b), and O 1s (c) regions of a solution of $[Pt(NH_3)_4]Cl_2$ in [EMIM][$EtOSO_3$]. All spectra were normalized to the same photon flux of the X-ray source and shifted. The spectra were taken at emission angles of 0° and 70°; spectra of the pure IL are added for comparison (-----).

by the O 1s, N 1s, and Pt 4f regions. Most striking is the increase of the Pt 4f signals (Figure 2a) at higher surface sensitivity, which indicates an increased density of Pt in the surface layer.

This finding is supported by the N 1s signals (Figure 2b). For the pure IL, the two nearly equivalent imidazolium nitrogen atoms (N(a)) lead to a single peak at 401.8 eV. In the case of the solution, the NH_3 ligands (N(b)) of the Pt complex contribute a second signal at 400.3 eV. The intensity related to N(a) decreases whereas that for N(b) increases with increasing surface sensitivity. Hence, our data provide unambiguous proof of a surface enrichment of species b and, thus, of the Pt complex at the expense of species a and, thus, of the IL cation. As the atomic ratio N(b)/Pt is close to 4:1, the expected ratio for $[Pt(NH_3)_4]^{2+}$, we conclude that the Pt complex is stable in the IL under the conditions of our experiment. This conclusion is confirmed by the Pt $4f_{7/2}$ binding energy of 73.2 eV, which is close to that of solid $Pt[NH_3]_4Cl_2$ (73.4 eV[22]).

To estimate the enrichment factor for the Pt complex, we make use of the fact that the N 1s spectrum taken at 70° predominantly probes the topmost molecular layer. With this argument, the atomic ratio N(a)/N(b) = 1:1.1 shows that the ratio of IL cations to complex Pt cations is about 2:1 in the surface, which is at least three times more than expected from the bulk concentration.

Surprisingly, no chloride-related signals were observed (for example, Cl 2p, expected at around 200 eV; see arrow in Figure 1), which proves that the near-surface region is depleted of chloride within our XPS detection limit for Cl of about 0.03 at%. In contrast to the described exchange of the imidazolium ions for the $[Pt(NH_3)_4]^{2+}$ ions in the surface layer, distribution of the IL anion is apparently homogeneous and not influenced by the Pt complex. The O 1s signals in Figure 2 (with a shoulder that reflects the two different O atoms in the IL anion) as well as the sulfur signals are not affected by the detection geometry, neither for the pure IL nor for the solution.

The key to understanding the contrary behavior of the two ions, $[Pt(NH_3)_4]^{2+}$ and Cl^-, is provided by previous theoretical and experimental studies of surfaces in aqueous and other solutions (see Refs. [23–25], and references therein). These studies show that the surface concentration of solvated ions at aqueous surfaces depends on their polarizabilities and is higher for large and more polarizable ions.[24,25] This finding could explain qualitatively why the large $[Pt(NH_3)_4]^{2+}$ ion is enriched at the surface, while the less polarizable Cl^- ion is depleted. A similar effect was previously proposed by Law et al.[11] for pure ILs where small anions like Cl^- and Br^- were not observed at the surface. Whether specific interactions between the ions of the IL and that of the Pt salt in our case are also involved (such as the surfactant effects known for detergents) will be a subject for future studies.

In conclusion, we have shown for the first time that soft Pt complex ions can be enriched in the top layer of an IL surface. Chloride, as the counterion of the Pt complex, is virtually absent from the surface, whereas the IL anion density is not

 © 2006 Wiley-VCH Verlag GmbH & Co. KGaA, Weinheim

affected. Fundamentally, the presented methodology of surface-sensitive XPS in combination with a nonvolatile liquid may have substantial impact on the understanding of liquid surfaces in general. Practically, our finding that soft transition-metal ions can enrich in the top layer of an IL may give an important starting point to interpreting the kinetic data of transition-metal-catalyzed gas-phase reactions with ILs or supported ILs in a better and more realistic way. In addition, our findings give important hints for appropriate concepts to modify and design the surface properties (for example, surface tension) of ILs. From our results we would expect that the addition of small amounts of salts comprising soft ions should have a very strong effect on the surface properties of an IL.

Experimental Section

$[Pt(NH_3)_4]Cl_2$ (15 mg, 0.045 mmol) and [EMIM][$EtOSO_3$] (0.3 mL, 1.6 mmol) were shaken for 12 h under an argon atmosphere, which resulted in a turbid solution with some residual precipitate. A portion of this solution (0.02 mL) was deposited on a planar Au support ($10 \times 10 \times 0.1$ mm^3) and introduced into a UHV system. After pumping for 10 h, the background pressure of 5×10^{-10} mbar hardly exceeded the base pressure in the system, which confirmed the very low vapor pressure of the IL and the absence of volatile impurities. XPS was performed with an ESCALAB 200 system with an $Al_{K\alpha}$ source ($h\nu =$ 1486.6 eV) and overall energy resolution of 0.9 eV. The Au $4f_{7/2}$ signal (binding energy $E_B = 83.55$ eV) was used as a reference for the reported binding energies. No charging was observed, which corroborated the sufficient conductivity of the IL film. Note that the absolute intensities of the signals related to the Pt complex slowly increased during the experiment by a factor of 2.4 to a maximum level, which was stable for several hours. We attribute this increase to dissolution of residual undissolved salt still present in the turbid solution, possibly induced by warming of the solution by the X-ray source, which also emits infrared radiation. However, all spectra showed the described enrichment and depletion effects, irrespective of absolute signal intensities and duration of the experiment. The displayed XP spectra were repeatedly and reproducibly recorded over a period of more than 6 h when no intensity variations with time were observed. To check for beam damage effects, ^1H NMR spectra of the IL and the solution were taken before and after the XPS experiments (detection limit for proton-containing impurities ≈ 1 mol%). These spectra did not reveal any changes induced by the experiment. All signals could be exclusively assigned to the expected components.

Received: July 11, 2006
Revised: September 11, 2006
Published online: October 24, 2006

Keywords: biphasic catalysis · ion exchange · ionic liquids · photoelectron spectroscopy · surface analysis

[1] *Ionic Liquids in Synthesis* (Eds.: P. Wasserscheid, T. Welton), Wiley-VCH, Weinheim, **2003**.
[2] J. Dupont, P. A. Z. Suarez, *Phys. Chem. Chem. Phys.* **2006**, *8*, 2441 – 2452.
[3] a) M. J. Earle, J. Esperanca, M. A. Gilea, J. N. C. Lopes, L. P. N. Rebelo, J. W. Magee, K. R. Seddon, J. A. Widegren, *Nature* **2006**, *439*, 831 – 834; b) P. Wasserscheid, *Nature* **2006**, *439*, 797.
[4] R. P. Swatloski, R. D. Rogers, J. D. Hlobrey, WO 03/029329, **2003**.
[5] F. Endres, S. Z. El Abedin, *Phys. Chem. Chem. Phys.* **2006**, *8*, 2101 – 2116.
[6] T. Welton, *Coord. Chem. Rev.* **2004**, *248*, 2459 – 2477.
[7] J. L. Anderson, D. W. Armstrong, G. T. Wei, *Anal. Chem.* **2006**, *78*, 2892 – 2902.
[8] C. Jork, C. Kristen, D. Pieraccini, A. Stark, C. Chiappe, Y. A. Beste, W. Arlt, *J. Chem. Thermodyn.* **2005**, *37*, 537 – 558.
[9] M. Maase in *Multiphase Homogeneous Catalysis* (Eds.: B. Cornils, W. A. Herrmann, I. T. Horvath, W. Leitner, S. Mecking, H. Olivier-Bourbigou, D. Vogt), Wiley-VCH, Weinheim, **2005**, pp. 560 – 566.
[10] T. J. Gannon, G. Law, P. R. Watson, A. J. Carmichael, K. R. Seddon, *Langmuir* **1999**, *15*, 8429 – 8434.
[11] G. Law, P. R. Watson, A. J. Carmichael, K. R. Seddon, B. Seddon, *Phys. Chem. Chem. Phys.* **2001**, *3*, 2879 – 2885.
[12] C. Hardacre, *Annu. Rev. Mater. Res.* **2005**, *35*, 29 – 49.
[13] A. Riisager, R. Fehrmann, M. Haumann, B. S. K. Gorle, P. Wasserscheid, *Ind. Eng. Chem. Res.* **2005**, *44*, 9853 – 9859.
[14] A. Riisager, R. Fehrmann, S. Flicker, R. van Hal, M. Haumann, P. Wasserscheid, *Angew. Chem.* **2005**, *117*, 826 – 830; *Angew. Chem. Int. Ed.* **2005**, *44*, 815 – 819.
[15] A. Riisager, B. Jorgensen, P. Wasserscheid, R. Fehrmann, *Chem. Commun.* **2006**, 994 – 996.
[16] M. P. Seah, W. A. Dench, *Surf. Interface Anal.* **1979**, *1*, 2 – 11.
[17] E. F. Smith, I. J. Villar Garcia, D. Briggs, P. Licence, *Chem. Commun.* **2005**, 5633 – 5635.
[18] C. F. Weber, R. Puchta, N. J. R. van Eikema Hommes, P. Wasserscheid, R. van Eldik, *Angew. Chem.* **2005**, *117*, 6187 – 6192; *Angew. Chem. Int. Ed.* **2005**, *44*, 6033 – 6038.
[19] A. Jablonski, C. J. Powell, *J. Vac. Sci. Technol. A* **2003**, *21*, 274 – 283.
[20] C. D. Wagner, L. E. Davis, M. V. Zeller, J. A. Taylor, R. M. Raymond, L. H. Gale, *Surf. Interface Anal.* **1981**, *3*, 211 – 225.
[21] R. M. Lynden-Bell, M. Del Popolo, *Phys. Chem. Chem. Phys.* **2006**, *8*, 949 – 954.
[22] Y. V. Salyn, V. I. Nefedov, A. G. Makarov, G. N. Kuznetsova, *Zh. Neorg. Khim.* **1978**, *23*, 829.
[23] P. Jungwirth, D. J. Tobias, *J. Phys. Chem. B* **2002**, *106*, 6361 – 6373.
[24] G. Andersson, T. Krebs, H. Morgner, *Phys. Chem. Chem. Phys.* **2005**, *7*, 2948 – 2954.
[25] B. Winter, R. Weber, I. V. Hertel, M. Faubel, L. Vrbka, P. Jungwirth, *Chem. Phys. Lett.* **2005**, *410*, 222 – 227.

 © 2006 Wiley-VCH Verlag GmbH & Co. KGaA, Weinheim

N-Oxide Arylation

DOI: 10.1002/anie.200602773

Palladium-Catalyzed Cross-Coupling Reactions of Diazine *N*-Oxides with Aryl Chlorides, Bromides, and Iodides**

*Jean-Philippe Leclerc and Keith Fagnou**

The use of palladium-catalyzed cross-coupling reactions in biaryl synthesis[1] is linked to, and limited by, the synthetic and commercial availability of organometallic reagents such as aryl boronic acids. Not only are most of these compounds expensive, important classes of aryl organometallic are very challenging prepare and/or use in cross-coupling reactions, including electron-deficient nitrogen heterocycles. The importance of these building blocks in medicinal chemistry and materials sciences[2] has prompted continued methodological efforts, and two very recent reports highlight the importance of this goal.[3,4] Absent from these and the predominance of reports are some of the most problematic organometallic reagents—azines bearing the metal adjacent to a nitrogen atom. The problem is even more severe with diazines (Scheme 1). These organometallic compounds are unstable, can rarely be isolated, and commonly decompose under cross-coupling reaction conditions. While some are commercially available, the price reflects both their value and the challenge associated with their preparation.[5]

Recently, the potential of direct arylation as an efficient alternative to standard cross-couplings is becoming recognized,[6] and we have been studying the use of *N*-oxides as replacements for unstable/unreactive organometallics.[7] In the context of this strategy, diazine *N*-oxides are more challenging than simple pyridine *N*-oxides since they possess a free nitrogen atom that could bind and poison the catalyst.[8] They are also more π-electron-deficient and less nucleophilic than pyridine *N*-oxides.

Herein we describe the establishment of reaction conditions that enable the use of readily available,[9] bench-stable[10] diazine *N*-oxides as cheap, high-yielding reagents in palladium-catalyzed cross-coupling reactions (Scheme 1). To overcome catalyst poisoning associated with some *N*-oxide substrates, a benefical effect of copper(I) salts was uncovered,

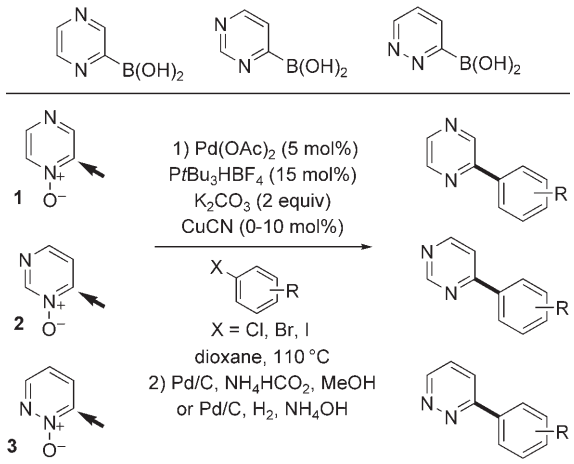

Scheme 1. Direct arylation in aryl diazine synthesis. Pyrazine, pyrimidine, and pyridazine boronic acids are unstable, difficult to prepare, and unsuited for cross-coupling reactions. Their *N*-oxides are readily prepared, bench-stable replacements for the organometallic reagent in biaryl synthesis.

and we demonstrate that the *N*-oxide functionality can be removed easily after cross-coupling or transformed into a wide range of other functional groups. These new reactions can be performed with aryl iodides, bromides, and chlorides and include the first examples of *N*-oxide arylation with equimolar ratios of the two coupling partners. Furthermore, the relative reactivities and regioselectivities point to C–H acidity as a critical factor in reactivity, encouraging consideration of this property in the design of other novel direct arylation processes.

Initial reaction screens with *N*-oxides **1**–**3** under previously described conditions led to disappointing results. Noting that the *N*-oxides were only sparingly soluble in toluene, we reinvestigated the reaction conditions. We found that changing the solvent from toluene to dioxane provides superior conversions with *N*-oxides **1** and **3**, giving the cross-coupled products **4** and **5** in yields of 75% and 72%, respectively (Table 1, entries 1 and 2). These two substrates are actually more reactive than pyridine *N*-oxide, as demonstrated by a competition experiment between **1** and pyridine *N*-oxide, which resulted in exclusive arylation of **1** (Table 1, entry 4). In contrast to the excellent results obtained with **1** and **3**, the reaction of pyrimidine *N*-oxide (**2**) proceeds in very low yield (Table 1, entry 3).

Further investigations revealed that the poor outcomes associated with **2** do not result from low reactivity alone. For example, the addition of pyrimidine *N*-oxide (**2**) to a reaction with pyrazine *N*-oxide (**1**) results in the exclusive formation of **4** but in a significantly lower yield (9%) than when the reaction was performed in the absence of **2** (75% yield; Table 1, entries 5 and 1). The reason for catalyst inhibition with **2** and not with **1** or **3** is a focus of ongoing study.[11,12] We note that neither pyridine *N*-oxide nor pyridine poison the reaction of **1** (Table 1, entries 4 and 6), indicating that these deleterious effects are specific to pyrimidine *N*-oxide.[12]

To overcome catalyst inhibition, a variety of additives were investigated including phosphines, halides, and metals.

[*] J.-P. Leclerc, Prof. Dr. K. Fagnou
Center for Catalysis Research and Innovation
Department of Chemistry, University of Ottawa
10 Marie Curie, Ottawa, ON K1N 6N5 (Canada)
Fax: (+1) 613-562-5170
E-mail: keith.fagnou@science.uottawa.ca

[**] We thank NSERC, CFI, OIT the University of Ottawa, the Ontario government (PREA, K.F.), and the Research Corporation (Cottrell Scholar Award, K.F.) for support of this work. Additional research support was provided by Boehringer Ingelheim (Laval) and Merck Frosst Canada. We thank Dr. Greg Hughes (Merck Frosst) for obtaining and providing differential scanning calorimetry data.

Supporting information for this article is available on the WWW under http://www.angewandte.org or from the author.

 © 2006 Wiley-VCH Verlag GmbH & Co. KGaA, Weinheim

Table 1: Cross-coupling reactions of *N*-oxides **1**–**3** with aryl bromides.[a]

Entry	*N*-Oxide	Aryl bromide	Additive	Product	Yield [%][b]
1	**1**	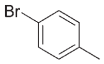	none	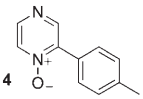 **4**	75
2	**3**	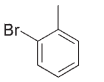	none	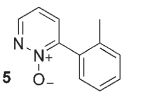 **5**	72
3	**2**	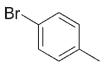	none	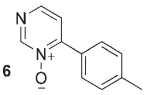 **6**	17
4	**1**	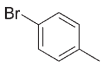		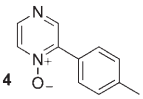 **4**	70
5	**1**	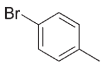	**2**	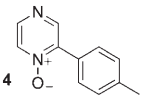 **4**	9
6	**1**	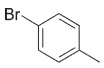		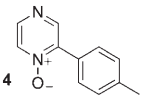 **4**	69
7	**2**	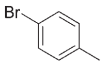	CuCN (10 mol%)	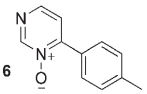 **6**	61[c]
8			CuBr (10 mol%)		54[c]

[a] Reaction conditions: The *N*-oxide (2 equiv), aryl halide, $Pd(OAc)_2$ (5 mol%), $PtBu_3$–HBF_4 (15 mol%), K_2CO_3 (2 equiv), and the additive (if indicated, 2 equiv) were added to a round-bottomed flask. Dioxane was added, and the reaction mixture was heated to 110°C. [b] Yield of isolated product. [c] 3 equivalents of **2** employed.

From these efforts, copper(I) salts such as CuCl, CuBr, and CuCN emerged as promising leads. CuCN and CuBr were selected for further optimization, and we found that when 10 mol% CuCN or CuBr was added under the new arylation conditions, biaryl **6** was obtained in 61 and 54% yield, respectively, as one regioisomer (Table 1, entries 7 and 8).[13] The yields observed with CuCN as the additive were typically higher than those with CuBr.

The scope of these transformations with respect to the aryl halide was evaluated with pyrazine *N*-oxide (**1**) (Table 2). High- yielding arylations are possible not only with aryl bromides but also with aryl iodides (Table 2, entries 17 and 18) and even with aryl chlorides (entries 13–16). With aryl iodides, Ag_2CO_3 must be employed as an additive. A variety of substituents are tolerated on the aryl halide including electron-donating (Table 2, entries 3, 6, and 7) and electron-withdrawing groups (entries 4, 8–10 and 16). More sterically encumbered aryl halides may also be employed (Table 2, entries 2, 5, 9, 10, 13, and 14). If an excess of aryl halide is used relative to the pyrazine *N*-oxide, the product of double direct arylation can be obtained in 50% yield (Table 2, entry 11).

The scope of diazine *N*-oxide substrates was also evaluated (Table 3). Quinoxaline *N*-oxide (**7**) is an excellent substrate in these reactions, and an equimolar ratio of the *N*-oxide and aryl halide could be used for the first time (Table 3, entries 1–7). More sterically encumbered alkyl-substituted pyrazine *N*-oxides may also be coupled in synthetically useful yields (Table 3, entries 8–11). Different aryl halides were also examined in reactions with both pyridazine *N*-oxide (**3**) (Table 3, entries 12–15) and pyridimine *N*- oxide (**2**) (Table 3, entries 16–22). With **2**, 10 mol% CuCN or CuBr must be added to the reaction to achieve cross-coupling. In each case useful yields of the cross-coupled product are obtained.

If desired, the direct-arylation products can be easily deoxygenated (Table 4). Treatment of pyrazine *N*-oxides with ammonium formate and palladium/carbon in methanol at room temperature gives the corresponding free base in excellent yields (Table 4, entries 1–5, method A). This protocol is incompatible with pyridazine *N*-oxides, however (Table 4, entry 6). An extensive survey of methods for the reduction of *N*-oxides led to the discovery that high yields can be obtained with catalytic Pd/C in ammonium hydroxide under a hydrogen atmosphere (Table 4, entries 7–9, method B). Products from the direct arylation of pyrimidine *N*-oxide may also be deoxygenated by this second protocol in high yield (Table 4, entry 10).

N-Oxides are key intermediates in many processes that introduce functionality adjacent to the nitrogen atom. For example, for the pyrazine derivative shown in Scheme 2, a new carbon–oxygen bond adjacent to the nitrogen atom may be formed by reaction with acetic anhydride and heating to give **8**.[14] A second direct arylation can add a second aromatic group as in the formation of **9**. Alternatively, the *N*-oxide may be converted to chloropyrazine **10** by reaction with $POCl_3$[15] and subsequently used in a wide range of palladium catalyzed-cross coupling reactions. To illustrate this possibility, a Buchwald–Hartwig amination was performed, giving **11** in 70% yield.[16] Chloride **10** may also be treated with alkoxides

 © 2006 Wiley-VCH Verlag GmbH & Co. KGaA, Weinheim

Table 2: Scope of the direct arylation of pyrazine *N*-oxide (**1**).[a]

Entry	**1** [equiv]	ArX	Product	Yield [%][b]
1	2		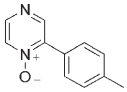	75
2	2		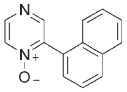	89
3	2	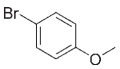	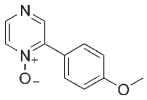	82
4	2	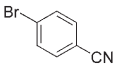	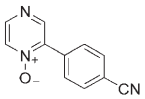	53
5	2		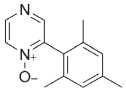	70
6	2	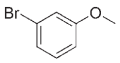	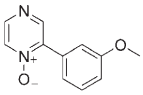	72
7	3			84
8	2	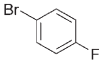	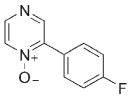	70
9	2	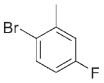	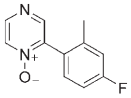	50
10	4			96
11	0.3	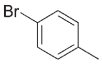	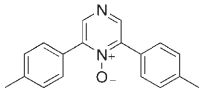	50
12	3	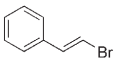	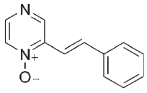	40
13	2		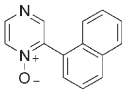	60
14	3			68
15	2		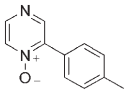	75
16	2	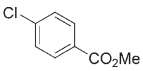	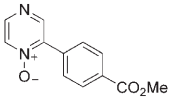	82
17	2		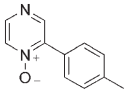	17
18	2[c]			77

[a] Reaction conditions: **1**, aryl halide, $Pd(OAc)_2$ (5 mol%), $PtBu_3$–HBF_4 (15 mol%), and K_2CO_3 (2 equiv) were added to a round-bottomed flask. Dioxane was added, and the reaction mixture was heated to 110°C. [b] Yield of isolated product. [c] Ag_2CO_3 (0.5 equiv) added.

to give compounds such as **12** in good yield. The diazine *N*-oxide ring may also be reduced to give arylpiperazine **13** in 68% yield by treatment with Pt_2O and H_2.

The relative reactivities of diazine *N*-oxides **1**–**3** as well as the regioselectivity of the reaction with **2** provide insight into the reaction mechanism. In competition studies[17] **1** is approximately twice as reactive as **3**. While significant catalyst inhibition is observed in competition experiments of **1** with **2**, exclusive reaction of **1** is observed. In each case, the reaction is completely selective for reaction at the carbon adjacent to the N–O functionality.[18] Furthermore, with pyrimidine *N*-oxide (**2**), direct arylation occurs exclusively at the position *para* to the free nitrogen atom.[18] All of these outcomes parallel the relative acidities of the different C–H bonds of the *N*-oxide substrates.[19] We observed a similar dependence on pK_a in reactions with perfluoroarenes which were deter-

 © 2006 Wiley-VCH Verlag GmbH & Co. KGaA, Weinheim

Table 3: Scope of the direct arylation of diazine *N*-oxides.[a]

Entry	*N*-Oxide	*N*-Oxide [equiv]	Aryl halide	Product	Yield [%][b]
1	**7**	1	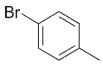	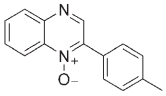	68
2	**7**	1		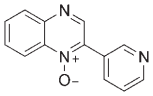	50
3		2			80
4	**7**	1	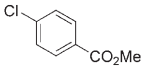	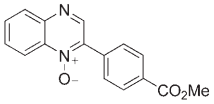	84
5	**7**	1	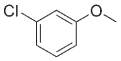	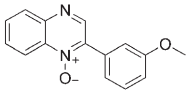	57
6	**7**	1	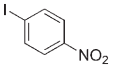	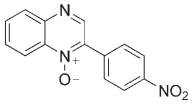	70[c]
7	**7**	1		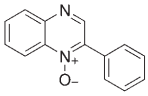	84[c]
8		2	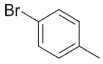	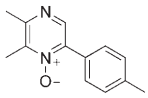	48
9		3			56
10		2	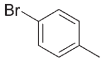	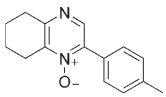	52
11		3			56
12		2		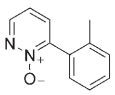	76
13	**3**	2	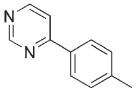	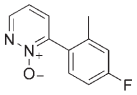	74
14	**3**	2		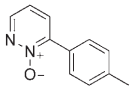	73
15	**3**	2		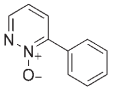	92[c,d]
16		3 (CuCN[e])	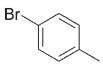	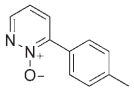	61
17		3 (CuBr[e])			54
18	**2**	3 (CuCN[e])	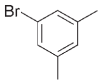	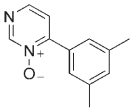	55
19	**2**	3 (CuCN[e])	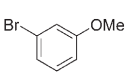	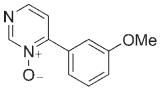	62
20	**2**	3 (CuBr[e])			45
21	**2**	3 (CuCN[e])	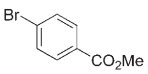	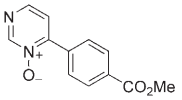	50
22	**2**	3 (CuBr[e])			41

[a] Reaction conditions: Diazine *N*-oxide, aryl halide, $Pd(OAc)_2$ (5 mol%), $P\mathit{t}Bu_3$–HBF_4 (15 mol%), and K_2CO_3 (2 equiv) were added to a round-bottomed flask. followed by the addition of dioxane and heating to 110°C. Dioxane was added, and the reaction mixture was heated to 110°C. [b] Yield of isolated product. [c] Ag_2CO_3 (0.5 equiv) added. [d] Performed on a 1-g scale. [e] 10 mol% Cu salt as additive.

 © 2006 Wiley-VCH Verlag GmbH & Co. KGaA, Weinheim

Table 4: Deoxygenation of the direct-arylation products.

Entry	*N*-Oxide	Method[a]	Product	Yield [%][b]
1	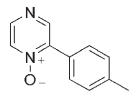	A	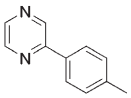	86
2	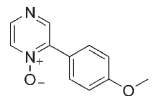	A	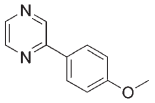	82
3	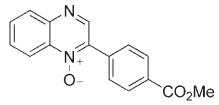	A	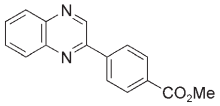	98
4	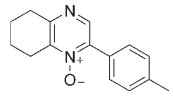	A	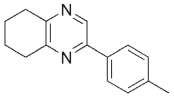	84
5	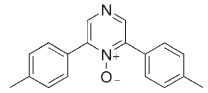	A	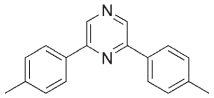	76
6	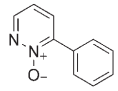	A	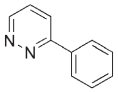	0[c]
7		B		87
8	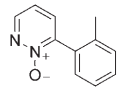	B	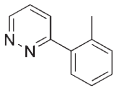	70
9	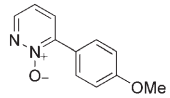	B	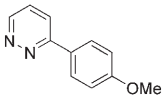	70
10	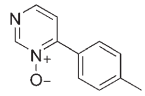	B	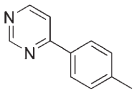	81

[a] Reaction conditions: Method A: Pd/C (10 mol%), NH_4HCO_2, MeOH; Method B: Pd/C, H_2, NH_4OH. [b] Yield of isolated product. [c] Decomposition.

mined to occur by a concerted palladation–deprotonation pathway.[20] A similar reaction mechanism may be operable here and is under investigation.

In conclusion, diazine *N*-oxides are convenient, inexpensive, and readily available replacements for problematic diazine organometallic substates in palladium-catalyzed cross-coupling reactions. In some cases the necessary reactivity could be achieved by the addition of copper salts, and the products can be easily converted into a wide range of substituted nitrogen heterocycles by taking advantage of the *N*-oxide functionality. This chemistry should be of considerable use in the synthesis of these medicinally important compounds.

Experimental Section

Caution: Some aromatic *N*-oxides can undergo thermally induced exothermic decomposition at elevated temperatures.[21] The diazine *N*-oxide starting materials and representative examples of direct arylation products were analyzed by differential scanning calorimetry up to 250 °C. In no instance was there indication of exothermic decomposition.[22] Regardless, we recommend that controlled heating be employed and calorimetry data be obtained if the reactions are to be conducted on large scale.

To a dried flask was added the diazine *N*-oxide (1.0–3.0 equiv), K_2CO_3 (2.0 equiv), $Pd(OAc)_2$ (5 mol%), and $HP(tBu)_3BF_4$ (15 mol%). If the aryl halide is a solid, it was added at this point (1.0 equiv). The flask and its contents were then purged under nitrogen for 10 min. If the aryl halide is a liquid, it was added by syringe after purging, and then degassed dioxane was added (to produce a reaction concentration of 0.3 M). The reaction mixture was then heated at 110 °C for 8–16 h (overnight), after which the

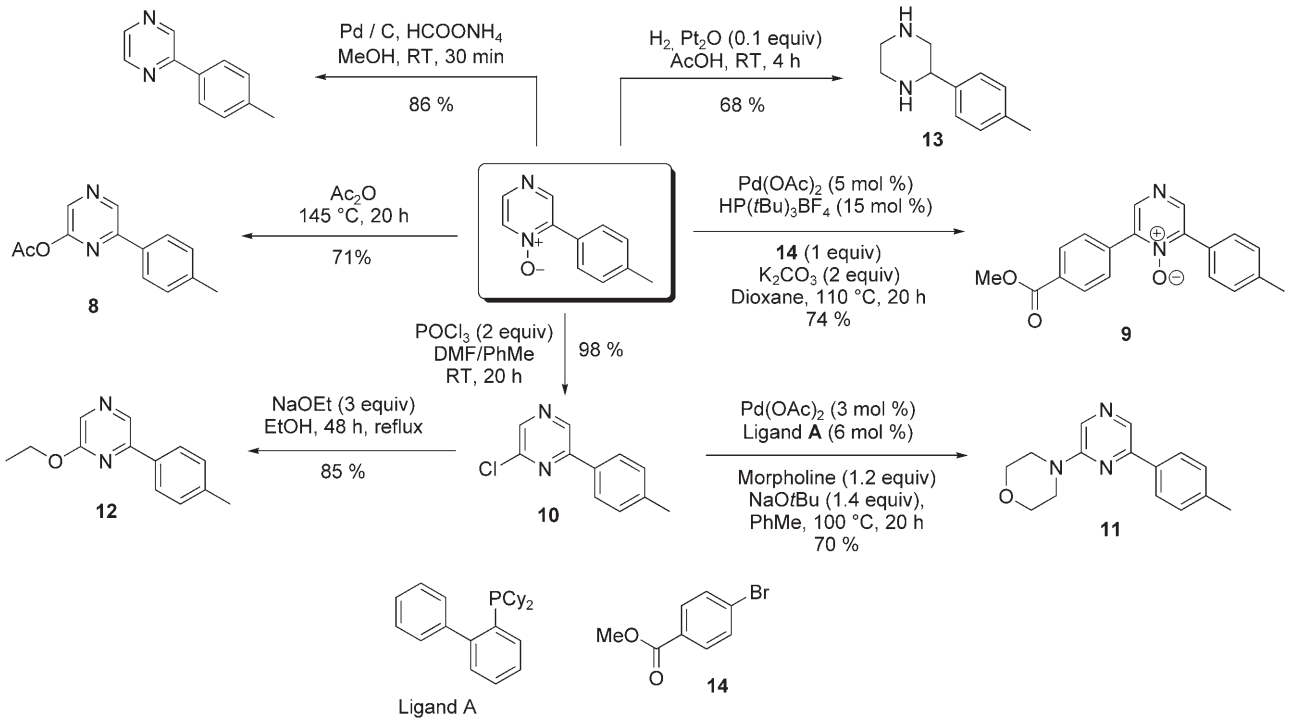

Scheme 2. Further reactions of a pyrazine derivative for the preparation of substituted nitrogen heterocycles.

 © 2006 Wiley-VCH Verlag GmbH & Co. KGaA, Weinheim

volatiles were removed under reduced pressure and the residue was purified by silica gel column chromatography.

Received: July 12, 2006
Published online: October 24, 2006

Keywords: arylation · biaryls · nitrogen heterocycles · *N*-oxides · palladium

[1] For reviews on this topic, see: a) *Metal-Catalyzed Cross-Coupling Reactions* (Eds.: F. Diederich, P. J. Stang), Wiley-VCH, New York, **1998**; b) J. Hassan, M. Sévignon, C. Gozzi, E. Shulz, M. Lemaire, *Chem. Rev.* **2002**, *102*, 1359; c) O. Beudoin, *Eur. J. Org. Chem.* **2005**, 4223.

[2] A. F. Pozharski, A. T. Soldartenko, A. Katritsky, *Heterocycles in Life and Society*, Wiley, New York, **1997**.

[3] N. Kudo, M. Perseghini, G. C. Fu, *Angew. Chem.* **2006**, *118*, 1304; *Angew. Chem. Int. Ed.* **2006**, *45*, 1282.

[4] K. L. Billingsley, K. W. Anderson, S. L. Buchwald, *Angew. Chem.* **2006**, *118*, 3564; *Angew. Chem. Int. Ed.* **2006**, *45*, 3484.

[5] For example, a number of pinacol boronic esters of the type illustrated in Scheme 1 are commercially available from Combiphos Catalysts, Inc. for approximately 1000 USD per gram (http://www.combiphos.com).

[6] For recent reviews, see: a) F. Kakiuchi, S. Murai, *Acc. Chem. Res.* **2002**, *35*, 826; b) V. Ritleng, C. Sirlin, M. Pfeffer, *Chem. Rev.* **2002**, *102*, 1731; c) M. Miura, M. Nomura, *Top. Curr. Chem.* **2002**, *219*, 211; d) F. Kakiuchi, N. Chatani, *Adv. Synth. Catal.* **2003**, *345*, 1077; e) L.-C. Campeau, K. Fagnou, *Chem. Commun.* **2005**, 1253.

[7] L. C. Campeau, S. Rousseaux, K. Fagnou, *J. Am. Chem. Soc.* **2005**, *127*, 18020.

[8] During preliminary studies with pyridine *N*-oxides, we found that pyridine was an effective poison for the palladium catalyst, completely inhibiting direct arylation. L. C. Campeau, K. Fagnou, unpublished results. See also Table 1, entry 6 herein.

[9] High-yielding oxidation of the corresponding free diazine could be achieved by reaction with *m*CPBA.

[10] The *N*-oxides used in this study are bench stable and show no signs of decomposition after storage in vials at room temperature for several months.

[11] It is noteworthy that resonance contributions for **2** induce properties different from those of **1** and **3**. For example, distribution of the positive charge within the ring places a positive charge on the free nitrogen of **1** and **3** but not **2**. This may result in a diminished capacity to bind to palladium and explain the experimental observations. On the other hand, mesomeric resonance forms where electrons are pushed from the oxyanion into the ring put negative charges on the free nitrogen of **1** and **3** but not **2**. This should produce a trend opposite to that predicted above and to that obtained experimentally.

[12] Other poisoning studies, in which the positions adjacent to the *N*-oxide functional group of pyrimidine *N*-oxide were blocked with aryl groups, also resulted in catalyst inhibition. This indicates that an interaction with either of these positions is not responsible for the poor reaction of **2**. See the Supporting Information for details.

[13] Use of CuCN may result in the in situ formation of a more nucleophilic heteroarylcopper species or reversibly bind the free nitrogen atom.

[14] Adapted from T. Choshi, Y. Matsuya, M. Okita, K. Inada, E. Sugino, S. Hibino, *Tetrahedron Lett.* **1998**, *39*, 2341.

[15] P. J. M. van Galen, et al., *J. Med. Chem.* **1991**, *34*, 1202.

[16] J. P. Wolfe, H. Tomori, J. P. Sadighi, J. Yin, S. L. Buchwald, *J. Org. Chem.* **2005**, *70*, 1158.

[17] See the Supporting Information for details.

[18] Arylation regioselectivity was proven by X-ray crystal analysis for pyridazine *N*-oxide and pyrimidine *N*-oxide. Regioselectivity for pyriazine *N*-oxide was proven by treatment with $POCl_3$ to give a known compound. See the Supporting Information for details.

[19] a) S. A. Kreuger, W. W. Paudler, *J. Org. Chem.* **1972**, *37*, 4188; b) W. W. Paudler, S. A. Humphrey, *J. Org. Chem.* **1970**, *35*, 3467.

[20] M. Lafrance, C. N. Rowley, T. K. Woo, K. Fagnou, *J. Am. Chem. Soc.* **2006**, *128*, 8754.

[21] Examples of exothermic onset temperatures (T_o): Pyridine *N*-oxide: 288 °C; 2,6-lutidine *N*-oxide: 288 °C; nicotinic acid *N*-oxide: 302 °C; γ-picoline *N*-oxide: 285 °C; picolinic acid *N*-oxide: 307 °C; from: T. Ando, Y. Fujimoto, S. Morisaki, *J. Hazard. Mater.* **1991**, *28*, 251.

[22] See the Supporting Information for details.

 © 2006 Wiley-VCH Verlag GmbH & Co. KGaA, Weinheim

Thiopeptide Antibiotics

DOI: 10.1002/anie.200602798

Total Synthesis of Antibiotics GE2270A and GE2270T**

K. C. Nicolaou, Bin Zou, Dattatraya H. Dethe, Dong Bo Li, and David Y.-K. Chen**

Among the thiopeptide antibiotics, GE2270A (**1**) and GE2270T (**2**, Scheme 1) occupy a commanding position, not only because of their novel molecular architectures but also as a result of their potent activities against Gram positive bacteria.[1] These thiazolyl peptide antibiotics isolated from *Planobispora rosea* ATCC53773 exert their selective anti-

[*] Prof. Dr. K. C. Nicolaou, Dr. B. Zou, Dr. D. H. Dethe, Dr. D. B. Li, Dr. D. Y.-K. Chen
Chemical Synthesis Laboratory@Biopolis
Institute of Chemical and Engineering Sciences (ICES)
Agency for Science, Technology, and Research (A*STAR)
11 Biopolis Way, The Helios Block, Nos. 03–08
Singapore 138667 (Singapore)
E-mail: david_chen@ices.a-star.edu.sg
Prof. Dr. K. C. Nicolaou
Department of Chemistry and
The Skaggs Institute for Chemical Biology,
The Scripps Research Institute,
10550 North Torrey Pines Road, La Jolla, CA 92037 (USA)
and
Department of Chemistry and Biochemistry,
University of California, San Diego,
9500 Gilman Drive, La Jolla, CA 92093 (USA)
E-mail: kcn@scripps.edu

[**] We thank Dr. J. Lim (Institute of Bioengineering and Nanotechnology, A*STAR) for assistance in obtaining the ^{13}C NMR spectra of GE2270A (**1**) and GE2270T (**2**), and D. Tan (ICES) for assistance with high resolution mass spectrometry (HRMS). Financial support for this work was provided by A*STAR, Singapore.

Supporting information for this article is available on the WWW under http://www.angewandte.org or from the author.

WILEY InterScience DISCOVER SOMETHING GREAT
© 2006 Wiley-VCH Verlag GmbH & Co. KGaA, Weinheim

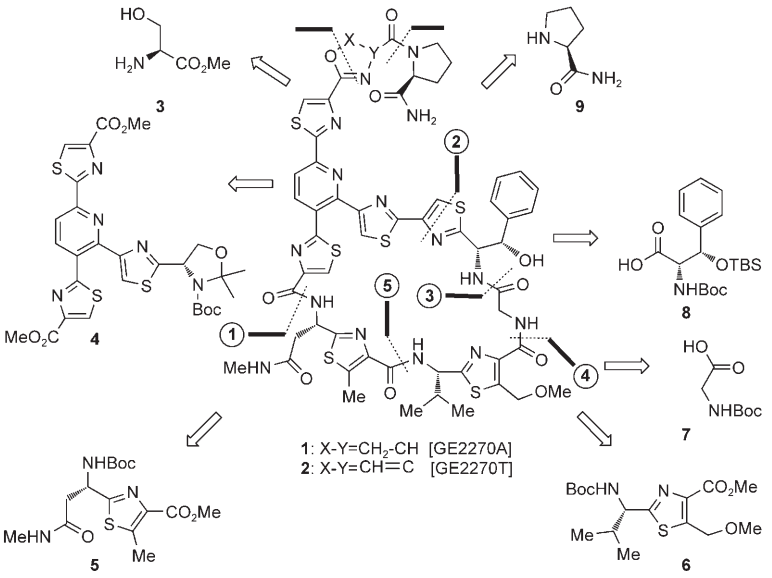

Scheme 1. Retrosynthetic analysis of antibiotics GE2270A (**1**) and GE2270T (**2**) leading to key fragments **3**–**9**. Boc = *tert*-butyloxycarbonyl, TBS = *tert*-butyldimethylsilyl.

bacterial properties through inhibition of the bacterial elongation factor Tu, but not the eukaryote elongation factor-1 alpha.[2] The complete structure of GE2270A (**1**) has been fully established through the notable efforts of Tavecchia and co-workers,[3] and of Heckmann and Bach.[4] Furthermore, synthetic studies toward the GE2270 factors were also reported by the research groups of Bach[4,5] and Shin.[6] Herein, we report the total synthesis of GE2270A (**1**) and GE2270T (**2**) through a convergent strategy that features a hetero-Diels–Alder/dimerization process[7] to construct the trithiazolyl pyridine core of the molecule.

Inspection of the structures of GE2270A (**1**) and GE2270T (**2**) reveals, in addition to the 29-membered macrocycle, the presence of one pyridine, one phenyl, one proline, and six thiazole rings, as well as one oxazoline system in the case of **1**, or one oxazole moiety in the case of **2**. A convergent strategy towards **2** that would provide the oxazoline intermediate en route should additionally provide access to **1**, and therefore was preferred. Furthermore, the introduction of the proline-containing tail in the final stages of the synthesis would allow a convenient entry into a range of designed analogues of these naturally occurring antibiotics for structure–activity-relationship (SAR) studies.[2b] Scheme 1 shows the seven key building blocks **3**–**9** required for such a strategy, as derived from the indicated retrosynthetic analysis. The assembly of **3**–**9** into the final structures **1** and **2** would demand the construction of the remaining three rings, namely one thiazole, one oxazoline- or oxazole-ring system, and the macrocycle. The latter ring could, in principle, be conveniently closed at any of the five indicated sites through amide bond formation (①–⑤, Scheme 1).

Scheme 2 summarizes the construction of the pyridine core **4**, which is the central scaffold equipped with suitable functionalities for extension in three directions as required for the target molecules. Thus, the thiazole derivative **10**, which had been previously synthesized,[7a] was converted into its methyl ester **11** (84% yield) by simple ester exchange.[8] Removal of the Boc-acetonide protecting group from methyl ester thiazole derivative **11** with TFA provided the amino thiol **12**. Engagement of **12** with aldehyde **13** (prepared by adaptation of a literature procedure)[7a] proceeded smoothly in the presence of $KHCO_3$ to afford thiazolidine **14** (82% yield for the two steps), an intermediate that served admirably as a precursor to heterodiene **15** (Ag_2CO_3, DBU, pyridine, $BnNH_2$).[7a] The latter species **15** proved quite fleeting and furnished under the reaction conditions, and after hydrolysis, the intended [4+2]-cycloaddition/dimerization product, the amino dehydropiperidine fragment **16** in 60% yield as a 1:1 mixture of *trans* diastereoisomers.[7a] Finally, heating a solution of **16** with DBU in EtOAc to reflux gave the desired trisubstituted pyridine core **4** in 50% yield through aromatization, which involved expulsion of ammonia and dehydrogenation.

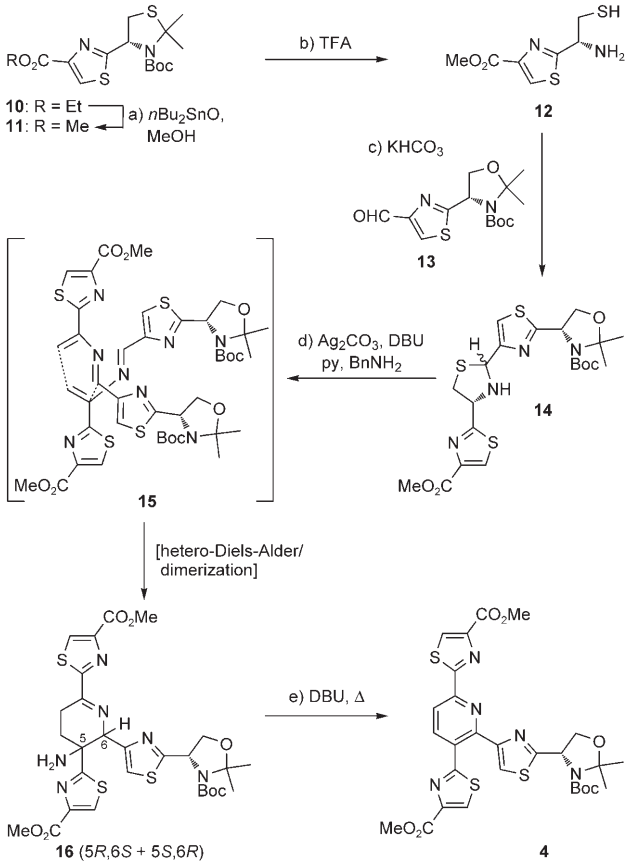

Scheme 2. Synthesis of trithiazole-substituted pyridine **4**. Reagents and conditions: a) nBu_2SnO, MeOH, reflux, 6 h, 84%; b) TFA/CH_2Cl_2 (1:1), 25 °C, 4 h; then MeOH/H_2O (1:1), 25 °C, concentration in vacuo; c) **12**·TFA (1.0 equiv), **13** (1.0 equiv), $KHCO_3$ (3.0 equiv), MeOH/H_2O (1:1), 25 °C, 16 h, 82% for the two steps; d) Ag_2CO_3 (1.1 equiv), $BnNH_2$ (1.0 equiv), DBU (0.25 equiv), py, −15 °C, 1 h; then H_2O/EtOAc (1:1), 1 h, 60%; e) DBU (5.0 equiv), EtOAc, reflux, 5 h, 50%. DBU = 1,8-diazabicyclo[5.4.0]undec-7-ene, py = pyridine, TFA = trifluoroacetic acid.

 © 2006 Wiley-VCH Verlag GmbH & Co. KGaA, Weinheim

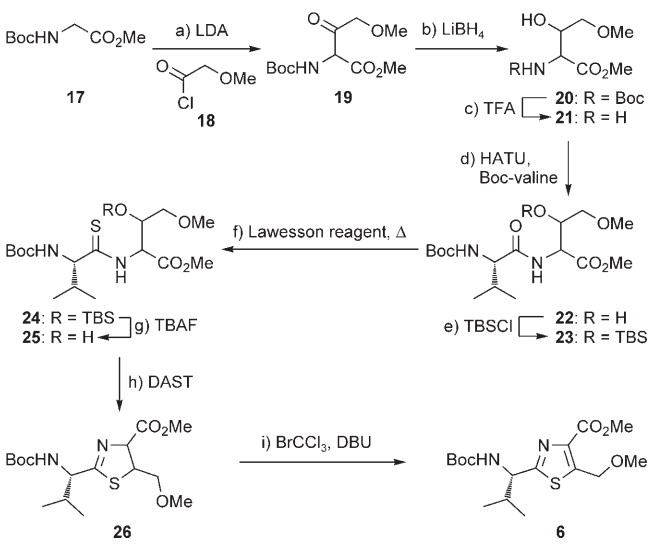

Scheme 3. Synthesis of trisubstituted thiazole **6**. Reagents and conditions: a) LDA (2.5 equiv), methoxyacetyl chloride (1.2 equiv), THF, −78 to 25 °C, 16 h, 59%; b) $LiBH_4$ (1.0 equiv), THF/CH_2Cl_2/MeOH (4:2:1), −78 °C, 5 min; c) TFA/CH_2Cl_2 (1:4), 0 °C, 1 h; d) Boc-valine (1.1 equiv), HATU (1.5 equiv), iPr_2NEt (3.0 equiv), CH_2Cl_2, 25 °C, 3 h, 71% for the three steps; e) TBSCl (1.1 equiv), imidazole (1.5 equiv), DMF, 20 °C, 16 h, 77%; f) Lawesson reagent (1.5 equiv), THF, reflux, 16 h, 66%; g) TBAF (1.1 equiv), THF, 5 h, 93%; h) DAST (1.5 equiv), CH_2Cl_2, −78 °C, 1 h; i) $BrCCl_3$ (1.1 equiv), DBU (2.2 equiv), CH_2Cl_2, 0 °C, 1 h, 84% for the two steps. DAST = *N*,*N*′-diethylaminosulfur trifluoride, HATU = *O*-(7-azabenzotriazol-1-yl)-1,1,3,3-tetramethyluronium hexafluorophosphate, LDA = lithium diisopropylamide, TBAF = tetrabutylammonium fluoride.

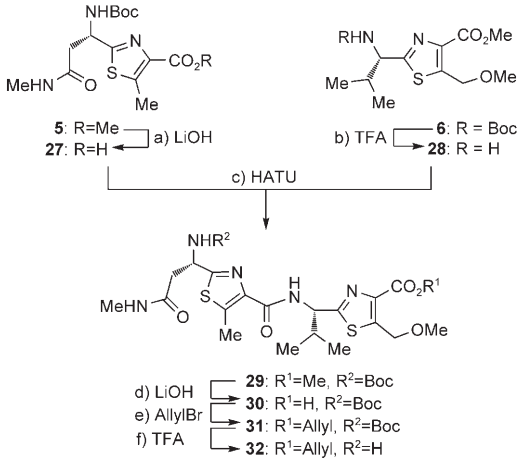

Scheme 4. Synthesis of bisthiazole subunits **30** and **32**. Reagents and conditions: a) LiOH (3.5 equiv), MeOH, 25 °C, 16 h; b) TFA/CH_2Cl_2 (1:4), 25 °C, 1 h; c) HATU (1.1 equiv), iPr_2NEt (2.0 equiv), CH_2Cl_2, 25 °C, 3 h, 80% for the two steps from **5**; d) LiOH (3.5 equiv), MeOH, 25 °C, 16 h; e) $KHCO_3$ (3.0 equiv), allyl bromide (2.0 equiv), DMF, 25 °C, 3 h, 70% for the two steps; f) TFA/CH_2Cl_2 (1:4), 25 °C, 1 h, 90%.

Scheme 3 summarizes the synthesis of the thiazole derivative **6** from the Boc-glycine methyl ester **17**. Thus, C-acylation of **17** with methoxyacetyl chloride (**18**) as facilitated by LDA at −78 °C produced the Boc derivative **19** (59% yield). Sequential exposure of **19** to $LiBH_4$ and TFA reduced the ketone moiety and liberated the amine, which provided amino alcohol **21** via intermediate **20**. Reaction of **21** with Boc-valine in the presence of HATU and iPr_2NEt afforded the hydroxy dipeptide **22** in 71% yield over the three steps. Protection of the hydroxy group of **22** as a TBS ether furnished derivative **23** (77% yield). Exposure of **23** to Lawesson reagent in refluxing THF led to thioamide **24** in 66% yield. Removal of the TBS group gave **25** (93% yield) and subsequent treatment first with DAST,[9] and then with $BrCCl_3$ and DBU,[10] furnished the thiazole intermediate **6**, through the intermediacy of compound **26**, in 84% overall yield for the two steps.

With all seven required fragments **3**–**9** now available, their assembly into the target molecules **1** and **2** became our next task. From all the possible strategies, we chose first to pursue the one involving macrocycle construction by forming amide bond ① (Scheme 1). To this end, the carboxylic acid **27** (generated by saponification of methyl ester **5**,[11] Scheme 4) was coupled with amine **28** (generated by removal of the Boc group from **6**) under the influence of HATU and iPr_2NEt to afford peptide **29** in 80% overall yield from **5**

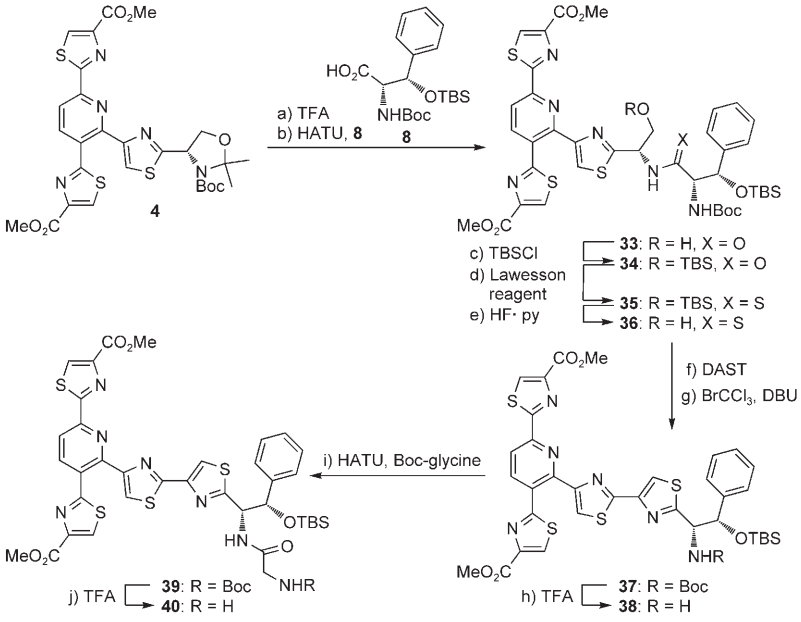

Scheme 5. Synthesis of tetrathiazole **40**. Reagents and conditions: a) TFA/H_2O (3:1), 25 °C, 1 h; b) **8** (1.1 equiv), HATU (1.2 equiv), iPr_2NEt (3.0 equiv), CH_2Cl_2, 25 °C, 3 h, 85% for the two steps from **4**; c) TBSCl (2.0 equiv), imidazole (3.0 equiv), DMF, 25 °C, 16 h, 82%; d) Lawesson reagent (1.5 equiv), benzene, reflux, 16 h, 80%; e) HF·py (10 equiv), pyridine/THF (1:8), 25 °C, 2 h, 92%; f) DAST (1.5 equiv), CH_2Cl_2, −78 °C, 1 h; g) $BrCCl_3$ (1.5 equiv), DBU (3.0 equiv), CH_2Cl_2, 0 °C, 1 h, 69% for the two steps from **36**; h) TFA/CH_2Cl_2 (1:4), 25 °C, 1 h; i) Boc-glycine (1.1 equiv), HATU (1.2 equiv), iPr_2NEt (3.0 equiv), CH_2Cl_2, 25 °C, 24 h, 90% for the two steps; j) TFA/CH_2Cl_2 (1:4), 25 °C, 1 h.

 © 2006 Wiley-VCH Verlag GmbH & Co. KGaA, Weinheim

(Scheme 4). Basic hydrolysis of the methyl ester of compound **29** then led to carboxylic acid **30**. Next to be targeted was the hexacyclic system **40**, whose construction from the pyridine core structure **4** is summarized in Scheme 5. Thus, **4** was exposed to acidic conditions (TFA/H_2O) which led to the collapse of the Boc-acetonide protecting group, thereby generating the corresponding amino alcohol. This amino alcohol was then coupled with the carboxylic acid derivative **8** (prepared through a modification of a literature procedure)[12] in the presence of HATU and iPr$_2$NEt to afford the hydroxy dipeptide **33** in 85% yield over the two steps. In preparation for the construction of the fourth thiazole system required in the growing fragment, compound **33** was sequentially converted into the TBS-ether derivative **34** (TBSC1, 82% yield), thioamide **35** (Lawesson reagent, 80% yield), and hydroxy thioamide **36** (HF·py, 92% yield). Conversion of **36** into tetrathiazole **37** was carried out by sequential exposure to DAST[9] and $BrCCl_3$/DBU[10] in 69% overall yield. The Boc group was then cleaved off this intermediate (TFA/CH_2Cl_2), which allowed its elongation to the glycine derivative **40** through a sequence that involved liberation of the amine to afford **38** (TFA), coupling with the Boc-glycine (HATU/iPr$_2$NEt) to give **39** (90% overall yield) and cleavage of the newly introduced Boc group (TFA).

The resulting amine **40** was coupled with the dithiazole-containing carboxylic acid **30** (Scheme 6) through the action of HATU and iPr$_2$NEt to afford peptide **41** (66% overall yield from **39**), which was further elaborated to the macrocycle **46** as indicated in Scheme 6. Thus, treatment of diester **41** with 1.0 equiv of Me_3SnOH[13] resulted in the formation of the two monoacids **42** and **43** in 40% combined yield and in around a 1:1 ratio (90% based on recovered starting material). Chromatographic separation of the two regioisomers gave the pure carboxylic acids **42** and **43**, each of which was separately subjected to Boc removal (TFA) and macrocyclization conditions. While the amino acid **45** derived from the less polar isomer **43** ($R_f = 0.58$, silica gel, EtOAc/MeOH 1:1) underwent smooth ring closure (verified by LC-MS analysis) to furnish macrocycle **46**, the regioisomeric amino acid **44**, derived from the more polar isomer **42** ($R_f = 0.47$, silica gel, EtOAc/MeOH 1:1), failed to cyclize. In light of these observations, subsequent cyclizations were carried out with the mixture of amino acids **44** and **45** (FDPP/iPr$_2$NEt, CH_2Cl_2/DMF 4:1, 0.0003 M), a practice that proved more convenient and efficient, and which led to the isolation of macrocycle **46** in 20% overall yield from **42**/**43**.

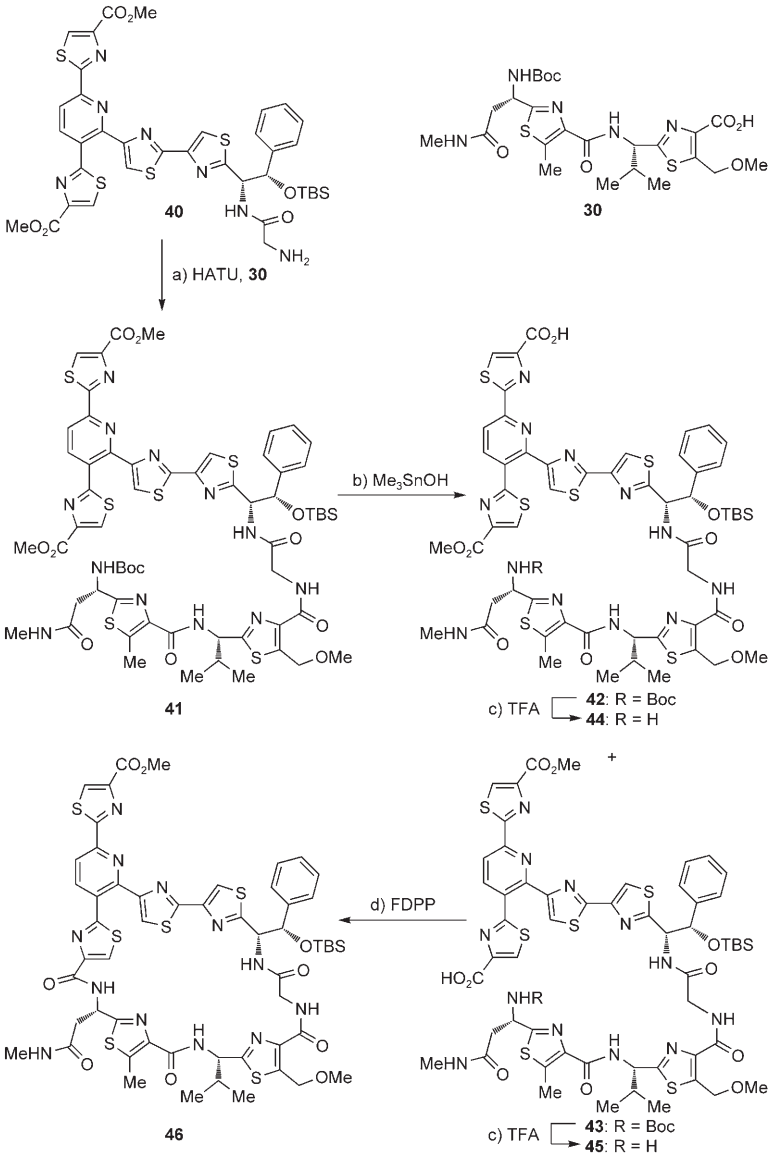

Scheme 6. Construction of macrocycle **46** (ring closure ①, Scheme 1). Reagents and conditions: a) **30** (1.1 equiv), HATU (1.5 equiv), iPr$_2$NEt (3.0 equiv), CH_2Cl_2, 25 °C, 24 h, 66% for the two steps from **39**; b) Me_3SnOH (1.0 equiv), 1,2-dichloroethane, 60 °C, 16 h, **42**: 20% and **43**: 20% (90% based on recovered starting material); c) TFA/CH_2Cl_2 (1:4), 25 °C, 1 h; d) FDPP (5.0 equiv), DMF/CH_2Cl_2 (1:4), 0.0003 M, 24 h, 20% for the two steps. FDPP = pentafluorophenyl diphenylphosphinate.

The identical macrocycle **46** was obtained through a modified route in which the macrocycle was formed by ring closure ④ (see Scheme 1) as shown in Scheme 7. Thus, compound **39** was hydrolyzed with Me_3SnOH[13] to afford a mixture of inseparable monocarboxylic acids **47** and **48** (ca. 1:1 ratio, 45% along with 50% recovered starting material). Acids **47** and **48** were then coupled with amine **32**, which was obtained from **30** by allylation ($KHCO_3$/allyl bromide, 70% from **29** via intermediate **31**) and TFA-induced removal of the Boc group (90%, Scheme 4), in the presence of HATU and

 © 2006 Wiley-VCH Verlag GmbH & Co. KGaA, Weinheim

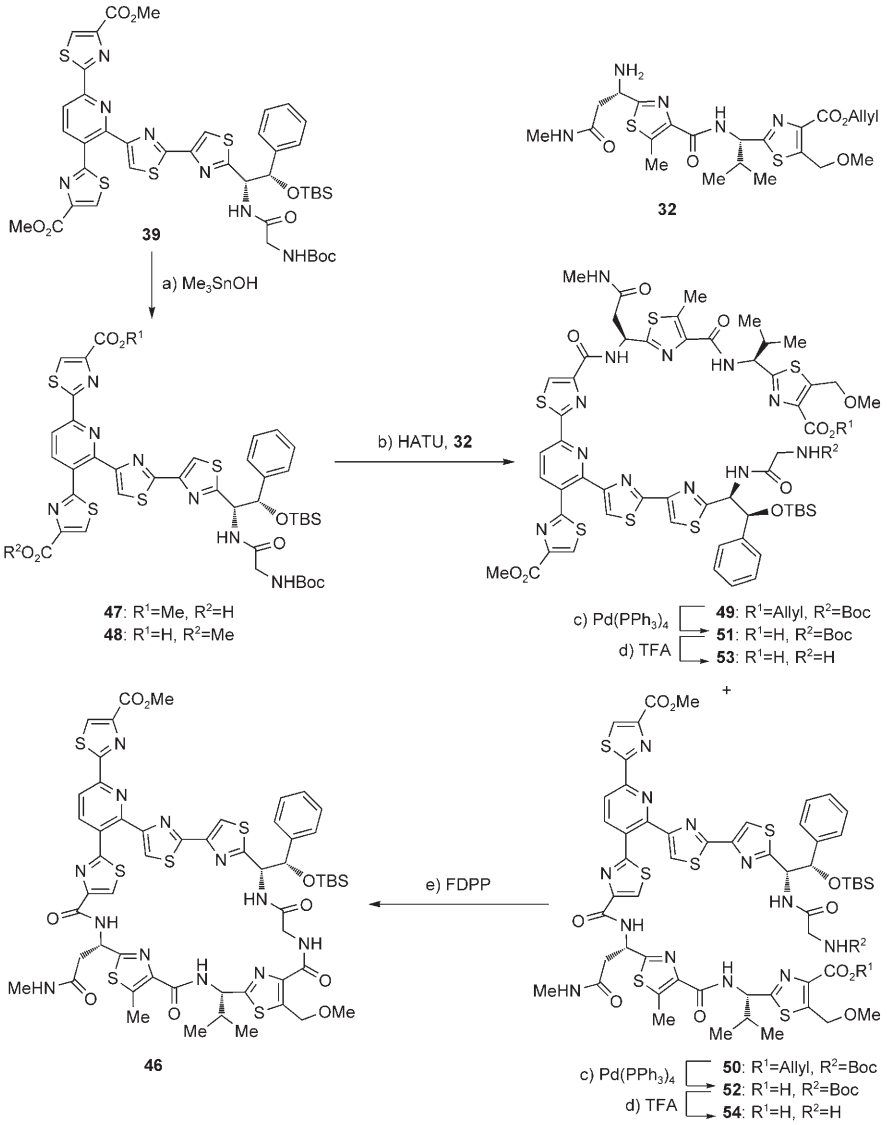

Scheme 7. Alternative construction of macrocycle **46** (ring closure ④, Scheme 1). Reagents and conditions: a) Me_3SnOH (1.0 equiv), 1,2-dichloroethane, 60 °C, 20 h, **47**/**48** (ca. 1:1 ratio) 45% (90% based on 50% recovered starting material); b) **32** (1.1 equiv), HATU (1.5 equiv), iPr_2NEt (3.0 equiv), CH_2Cl_2, 25 °C, 16 h, 70%; c) $[Pd(PPh_3)_4]$ (20 mol%), NMA (2.0 equiv), THF, 25 °C, 1 h; d) TFA/CH_2Cl_2 (1:4), 25 °C, 1 h; e) FDPP (5.0 equiv), iPr_2NEt (10 equiv), CH_2Cl_2/DMF (1:4, 0.30 mM), 25 °C, 24 h, 30% for the three steps. NMA = *N*-methylaniline.

iPr_2NEt, to afford the coupling products **49** and **50**. The mixture of **49**/**50** was converted into cyclization precursors **53** and **54** by deallylation with $[Pd(PPh_3)_4]$ and Boc removal (TFA). Exposure of the mixture of **53** and **54** to the macrolactamization conditions (FDPP/iPr_2NEt, CH_2Cl_2/DMF 4:1, 0.0003 M) again furnished only one macrocycle **46** (30% overall yield from **49**/**50** for the three steps), which was proven from chromatographic and spectroscopic data to be identical to the one obtained from **43** or **42**/**43**, as described earlier (Scheme 6). Again, the formation of a single regioisomer **46** in this cyclization reaction points to a unique structural feature of these systems. The structural identity of the formed macrocycle and the precise reasons for its preference in these reactions were not known at this stage. While the tentatively assigned structure **46** was later proven by its eventual conversion to the natural products **1** and **2** (described below), the rationale for its formation in preference to its regioisomer remains to be elucidated.

Macrolactamizations were also performed at sites ③ and ⑤ (see Scheme 1) using amino acid precursors prepared by modifications of the chemistry described above.[14] Interestingly, while ring closure at site ⑤ proceeded smoothly and again furnished the same macrocycle **46** (15% overall yield for the last three steps involving deprotection of the amino acid and formation of the peptide bond) as from the ring closures at ① and ④, macrolactamization at site ③ was not feasible because of the reluctance of fragments longer than glycine to couple with the amino group of that site.

The final stages of the total synthesis of GE2270A (**1**) are shown in Scheme 8. Thus, the methyl ester of advanced

 © 2006 Wiley-VCH Verlag GmbH & Co. KGaA, Weinheim

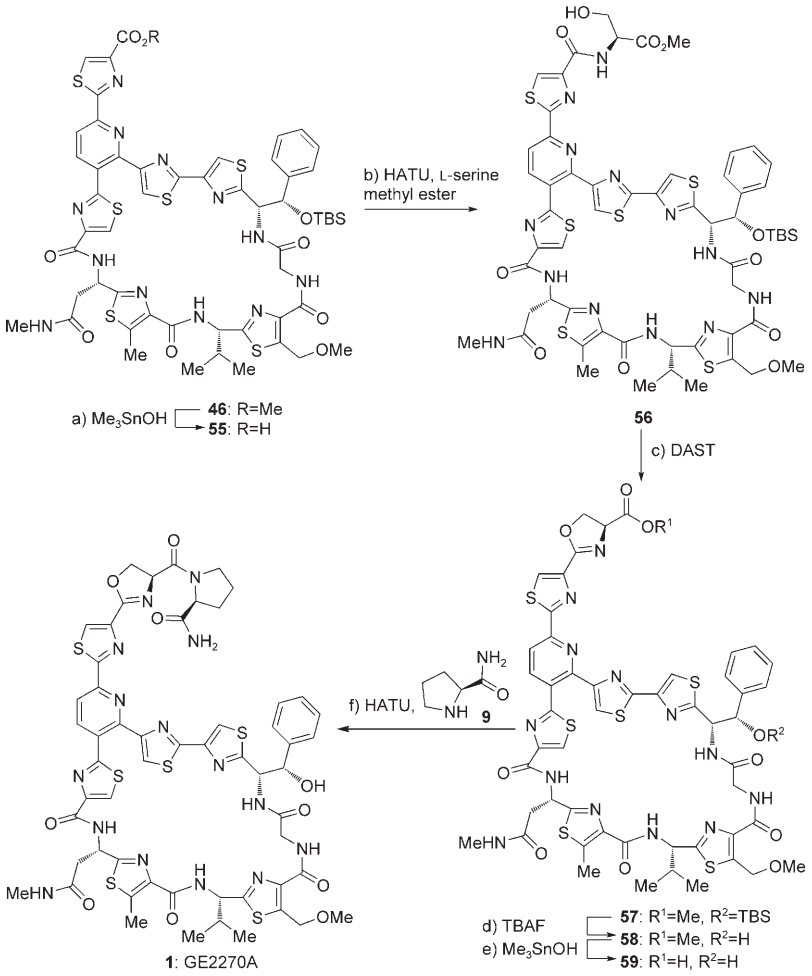

Scheme 8. Completion of the total synthesis of GE2270A (**1**). Reagents and conditions: a) Me_3SnOH (10 equiv), 1,2-dichloroethane, 80 °C, 5 h; b) L-serine methyl ester (1.1 equiv), HATU (1.5 equiv), iPr_2NEt (3.0 equiv), CH_2Cl_2, 25 °C, 16 h, 55% for the two steps; c) DAST (1.5 equiv), CH_2Cl_2, −25 °C, 1 h, 85%; d) TBAF (1.2 equiv), THF, 25 °C, 80%; e) Me_3SnOH (10 equiv), 1,2-dichloroethane, 80 °C, 1 h; f) L-proline amide (1.1 equiv), HATU (1.2 equiv), iPr_2NEt (2.0 equiv), CH_2Cl_2, 25 °C, 3 h, 60% for the two steps.

macrocycle **46** was hydrolyzed with Me_3SnOH,[13,15] affording carboxylic acid **55**. The convergent strategy for the introduction of the required dipeptide fragment (L-serine-L-prolin-amide) was unsuccessful. A stepwise approach was adopted whereby attachment of the L-serine moiety was carried out first, thereby yielding hydroxy methyl ester **56** in 55% overall yield for the two steps. Generation of the desired oxazoline moiety was then carried out by exposing hydroxy amide **56** to DAST[9] in CH_2Cl_2 at −25 °C to furnish ester silyl ether **57** in 85% yield. Sequential treatment of the latter compound with TBAF followed by Me_3SnOH[13,15] led, through the intermediacy of hydroxy methyl ester **58** (80% yield), to hydroxy carboxylic acid **59**, which was set for the final coupling. Indeed, reaction of **59** with L-proline amide **9** in the presence of HATU and iPr_2NEt furnished GE2270A (**1**) in 60% overall yield from **58**. Synthetic **1** exhibited identical physical properties (in ^1H and ^{13}C NMR spectra, and MS) to those reported[1c] for the naturally occurring substance. Although no specific optical rotation has been reported for GE2270A (**1**), we assumed that **1** and its congeners were derived in nature from natural amino acids, as previously suggested by degradation studies.[3]

Advanced intermediate oxazoline **58** encountered along the way to **1** was also converted into GE2270T (**2**) as shown in Scheme 9. Thus, exposure of oxazoline **58** to the action of $BrCCl_3$ and DBU[10] gave oxazole methyl ester **60**. Hydrolysis of **60** to give carboxylic acid **61** was smoothly accomplished by Me_3SnOH.[13,15] Finally, coupling of **61** with L-proline amide **9**, facilitated by HATU and iPr_2NEt as described above, furnished GE2270T (**2**) in 40% overall yield from **58** (three steps). The physical properties of synthetic **2** were in accordance with its assigned structure and the literature data.[1c]

The chemistry described herein demonstrates the applicability of the [4+2]-cycloaddition/dimerization cascade involving heterodienes[7] in complex molecule construction, and the exquisite regioselective preferences of the ring-closing reactions in thiopeptide-like substrates. Furthermore, the high convergency associated with this route renders this strategy particularly suited for analogue synthesis and SAR

 © 2006 Wiley-VCH Verlag GmbH & Co. KGaA, Weinheim

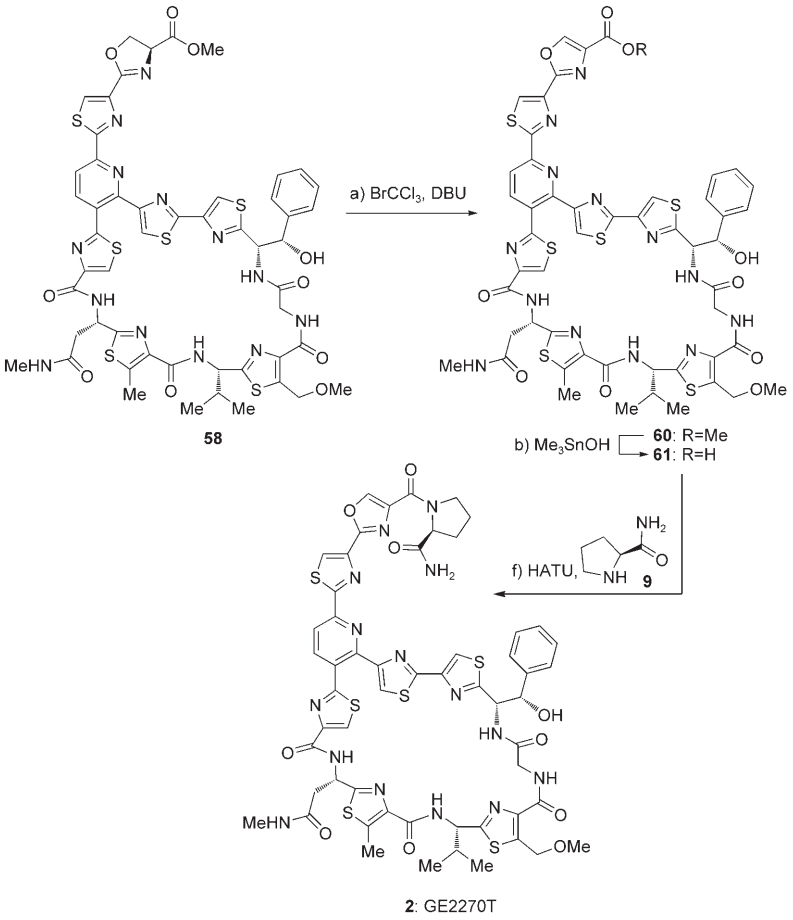

Scheme 9. Completion of the total synthesis of GE2270T (**2**). Reagents and conditions: a) $BrCCl_3$ (1.5 equiv), DBU (3.0 equiv), CH_2Cl_2, 0 to 25 °C, 16 h; b) Me_3SnOH (10 equiv), 1,2-dichloroethane, 80 °C, 6 h; c) L-proline amide (1.1 equiv), HATU (1.2 equiv), iPr_2NEt (1.5 equiv), CH_2Cl_2, 25 °C, 5 h, 40% for the three steps.

studies, especially at the proline–oxazole tail end[2b] of the molecule, with an advanced intermediate serving as a common precursor to a wide variety of designed molecules as potential new antibacterial agents.

Received: July 13, 2006
Published online: October 24, 2006

Keywords: antibiotics · hetero-Diels–Alder reaction · macrocycles · natural products · total synthesis

[1] a) E. Selva, G. Beretta, N. Montanini, G. S. Saddler, L. Gastaldo, P. Ferrari, R. Lorenzetti, P. Landini, F. Ripamonti, B. P. Goldstein, M. Berti, L. Montanaro, M. Denaro, *J. Antibiot.* **1991**, *44*, 693–701; b) J. Kettenring, L. Colombo, P. Ferrari, P. Tavecchia, M. Nebuloni, K. Vekey, G. G. Gallo, E. Selva, *J. Antibiot.* **1991**, *44*, 702–715; c) E. Selva, P. Ferrari, M. Kurz, P. Tavecchia, L. Colombo, S. Stella, E. Restelli, B. P. Goldstein, F. Ripamonti, M. Denaro, *J. Antibiot.* **1995**, *48*, 1039–1042.

[2] a) S. E. Heffron, F. Jurnak, *Biochemistry* **2000**, *39*, 37–45; b) J. Clough, S. Chen, E. M. Gordon, C. Hackbarth, S. Lam, J. Trias, R. J. White, G. Candiani, S. Donadio, G. Romanò, R. Ciabatti, J. W. Jacobs, *Bioorg. Med. Chem. Lett.* **2003**, *13*, 3409–3414.

[3] P. Tavecchia, P. Gentili, M. Kurz, C. Sottani, R. Bonfichi, E. Selva, S. Lociuro, E. Restelli, R. Ciabatti, *Tetrahedron* **1995**, *51*, 4867–4890.

[4] G. Heckmann, T. Bach, *Angew. Chem.* **2005**, *117*, 1223–1226; *Angew. Chem. Int. Ed.* **2005**, *44*, 1199–1201.

[5] O. Delgado, G. Heckmann, H. M. Müller, T. Bach, *J. Org. Chem.* **2006**, *71*, 4599–4608.

[6] a) K. Okumura, T. Suzuki, C. Shin, *Heterocycles* **2000**, *54*, 765–770; b) T. Suzuki, A. Nagasaki, K. Okumura, C. Shin, *Heterocycles* **2001**, *55*, 835–840; c) K. Okumura, H. Saito, C. Shin, K. Umemura, J. Yoshimura, *Bull. Chem. Soc. Jpn.* **1998**, *71*, 1863–1870.

[7] a) K. C. Nicolaou, M. Nevalainen, B. S. Safina, M. Zak, S. Bulat, *Angew. Chem.* **2002**, *114*, 2021–2025; *Angew. Chem. Int. Ed.* **2002**, *41*, 1941–1945; b) K. C. Nicolaou, B. S. Safina, M. Zak, A. A. Estrada, S. H. Lee, *Angew. Chem.* **2004**, *116*, 5197–5202; *Angew. Chem. Int. Ed.* **2004**, *43*, 5087–5092; c) K. C. Nicolaou, B. S. Safina, M. Zak, S. H. Lee, M. Nevalainen, M. Bella, A. A. Estrada, C. Funke, F. J. Zecri, S. Bulat, *J. Am. Chem. Soc.* **2005**, *127*, 11159–11175.

[8] P. Baumhof, R. Mazitschek, A. Giannis, *Angew. Chem.* **2001**, *113*, 3784–3786; *Angew. Chem. Int. Ed.* **2001**, *40*, 3672–3674.

[9] A. J. Phillips, Y. Uto, P. Wipf, M. J. Reno, D. R. Williams, *Org. Lett.* **2000**, *2*, 1165–1168.

[10] D. R. Williams, S. Patnaik, M. P. Clark, *J. Org. Chem.* **2001**, *66*, 8463–8469.

[11] L. Somogyi, G. Haberhauer, J. Rebek, *Tetrahedron* **2001**, *57*, 1699–1708.

[12] a) D. B. Hansen, M. M. Joullié, *Tetrahedron: Asymmetry* **2005**, *16*, 3963–3969; b) D. B. Hansen, X. Wan, P. J. Carroll, M. M. Joullié, *J. Org. Chem.* **2005**, *70*, 3120–3126; c) E. Freund, F. Vitali, A. Linden, J. A. Robinson, *Helv. Chim. Acta* **2000**, *83*, 2572–2579.

[13] K. C. Nicolaou, A. A. Estrada, M. Zak, S. H. Lee, B. S. Safina, *Angew. Chem.* **2005**, *117*, 1402–1406; *Angew. Chem. Int. Ed.* **2005**, *44*, 1378–1382.

[14] Details of these experiments will be described in the full account of this work.

[15] K. C. Nicolaou, M. Zak, B. S. Safina, A. A. Estrada, S. H. Lee, M. Nevalainen, *J. Am. Chem. Soc.* **2005**, *127*, 11176–11183.

 © 2006 Wiley-VCH Verlag GmbH & Co. KGaA, Weinheim

Multicomponent Reactions

DOI: 10.1002/anie.200602836

A Ring-Expansion Methodology Involving Multicomponent Reactions: Highly Efficient Access to Polysubstituted Furan-Fused 1,4-Thiazepine Derivatives**

Cheng Ma, Hanfeng Ding, Yiping Zhang, and Ming Bian*

1,4-Thiazepine fragments are present in a wide range of natural and synthetic biologically active agents.[1] Among these, analogues of 1,4-thiazepines fused with aryl and heteroaryl groups represent an important class of compounds with interesting pharmacological properties,[2] such as antiarrhythmic, antispasmodic, angiogenic, and central nervous system activity, and are therefore promising synthetic targets for exploring novel physiologically active agents.[3]

Ring transformations of heterocyclic compounds are an important area of chemistry from both theoretical and practical viewpoints.[4] Such processes may provide interesting synthetic routes to derivatives that can only be obtained with great difficulty or not at all by other procedures. We previously developed a facile method for the preparation of 3-aminofuran compounds[7] based on the nucleophilicity of N-heterocarbenes (NHCs) derived from thiazolium salts **1**.[5,6] These aminofuran compounds could not be formed according to other established protocols.[8] It was proposed that the formation of the aromatic furan through ring opening of the spirocycle intermediate **2** provides the driving force to complete the tandem reaction (Scheme 1).

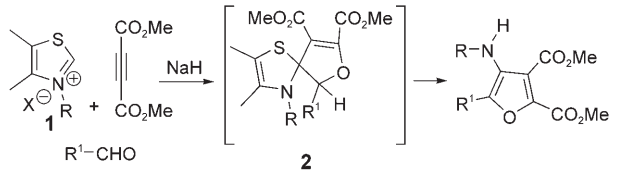

Scheme 1. Thiazolium-mediated multicomponent reaction for the synthesis of 3-aminofuran derivatives.

Although ketenes react efficiently with some nucleophiles, their reaction with carbenes has received only scant attention.[9] Moreover, to the best of our knowledge, carbene-triggered multicomponent reactions from ketenes have not been disclosed thus far. As a part of our research into NHCs[7] and ketene chemistry,[10] we report herein a conceptually novel three-component synthesis of unique polysubstituted furan-fused 1,4-thiazepines from thiazolium salts, 1,1-disubstituted ketenes, and activated alkynes.[11]

We began our investigations by looking into the reaction of 3-ethyl-4,5-dimethylthiazolium bromide (**1a**), 1,1-diphenylketene (**3a**), and dimethylacetylenedicarboxylate (DMAD) in the presence of NaH (Scheme 2). To our surprise, a three-component adduct **4** was isolated and the structure was unambiguously confirmed by single-crystal X-ray diffraction.[12] Interestingly, contrary to our previous results from the synthesis of 3-aminofurans, the yield of **4** was improved from 56% to 78% using iPr$_2$NEt as the base instead of sodium hydride.

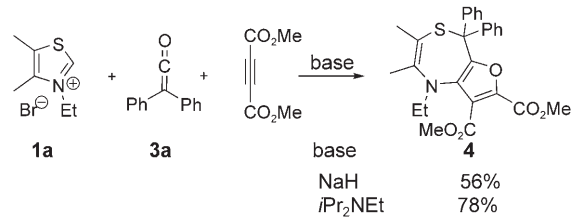

Scheme 2. Three-component reaction of thiazolium salt **1a**, diphenylketene (**3a**), and DMAD.

The cyclization of ketenes have attracted enormous attention from organic chemists since their first preparation in 1905.[13,14] In this context, ketenes typically add to substrates across one of their cumulated double bonds to construct cyclic compounds.[15] Very recently, we found that aryl methyl ketenes acted as one-carbon components to form five-membered rings on reaction with 1-methylimidazole and DMAD.[10b] In contrast, notably both of the double bonds (C=C and C=O) in 1,1-diphenylketene were used in the assembly of the highly substituted bicyclic compound **4** in this reaction.

As ketenes are rarely isolable species and usually are generated as transient intermediates, (for example, by the action of diisopropylethylamine (Hunig's base) on acyl halides) the replacement of ketenes by their precursors (which were transformed to ketenes in situ) should be of greater synthetic interest. Thus we were pleased to find that the reaction of **1a**, diphenylacetyl chloride (**3b**), and DMAD with iPr$_2$NEt (2.25 equiv) as the base proceeded smoothly and gave **4** in almost the same yield as in the reaction using **3a** (Scheme 3).

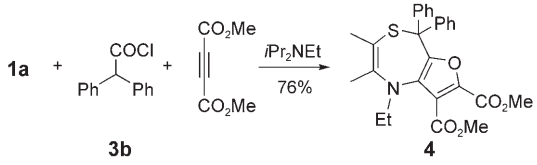

Scheme 3. Three-component reaction of thiazolium salt **1a**, diphenylacetyl chloride (**3b**), and DMAD.

[*] Prof. C. Ma, H. Ding, Y. Zhang, M. Bian
Department of Chemistry, Zhejiang University
20 Yugu Road, Hangzhou 310027 (P.R. China)
Fax: (+86) 571-8795-3375
E-mail: mcorg@zju.edu.cn

[**] Financial support from the National Natural Science Foundation of China is gratefully acknowledged.

Supporting information for this article is available on the WWW under http://www.angewandte.org or from the author.

© 2006 Wiley-VCH Verlag GmbH & Co. KGaA, Weinheim

We investigated the effect of the reaction conditions by using **1a**, α-methylphenylacetyl chloride (**5a**), and DMAD as the model system (Table 1). An initial screen of the solvents demonstrated that CH_2Cl_2 is the solvent of choice (entries 1 and 2, Table 1). It was shown that the reaction temperature played a significant role in this transformation. The best yield was obtained when the reaction was conducted by adding a mixture of **5a** and DMAD dropwiseto the solution of **1a** and iPr$_2$NEt in CH_2Cl_2 at −78 °C, and then stirring the reaction mixture at room temperature for an additional four hours (entry 2, Table 1). Only a trace amount of product was obtained when the reaction temperature was maintained below 0 °C (entry 3, Table 1). Moreover, iPr$_2$NEt proved to be the optimum base among those we examined, and the yield decreased dramatically when another base such as NEt_3[16] or DBU was used (entries 8 and 9, Table 1).

Table 1: Reaction of thiazolium salt **1a**, acetyl chloride **5a**, and DMAD under differing conditions.[a]

Entry	Base	Solvent	T [°C]	t [h][b]	Yield [%][c]
1	iPr$_2$NEt	CH_2Cl_2	−20 to 25	8	64
2	iPr$_2$NEt	CH_2Cl_2	−78 to 25	4	83
3	iPr$_2$NEt	CH_2Cl_2	−78 to 0	3	<5
4	iPr$_2$NEt	THF	−78 to 25	8	<5
5	iPr$_2$NEt	toluene	−25 to 25	8	0
6	iPr$_2$NEt	CH_3CN	−40 to 25	8	45
7	iPr$_2$NEt	DME	−65 to 25	9	0
8	NEt_3	CH_2Cl_2	−78 to 25	7	25
9	DBU	CH_2Cl_2	−78 to 25	8	0

[a] General conditions: **1a** (1 mmol), **5a** (1 mmol), DMAD (1.5 mmol), and base (2.25 mmol). [b] Reaction time for consuming all of the starting materials. [c] Yields of isolated products. DBU = 1,8-diazabicyclo-[5.4.0]undec-7-ene, DME = 1,2-dimethoxyethane.

As shown in Table 2, the reaction was found to be applicable to a variety of α-alkyl aryl acetyl chlorides **5**, to give furan-fused 1,4-thiazepines **6a–i** in good to excellent yields, regardless of whether the aromatic group of the acetyl chloride was bulky (entries 4, 7, and 8, Table 2), electron rich (entries 2–4), or electron poor (entries 5–9). However, the acetyl chlorides with an electron-rich aromatic group performed better than their electron-poor counterparts; for example, α-methyl 4-nitrophenylacetyl chloride afforded the product **6j** in only 28% yield (entry 10, Table 2). Moreover, a larger alkyl group on the acetyl chloride **5** was shown to have some positive effects on the reaction, with a shorter reaction time observed for **5k** (entry 11, Table 2) possibly because of the increased bulk assisting the ring-expansion step.[17]

Table 2: Reaction of thiazolium salt **1a**, α-alkyl arylacetyl chlorides **5**, and DMAD for the synthesis of furan-fused 1,4-thiazepines **6a–k**.

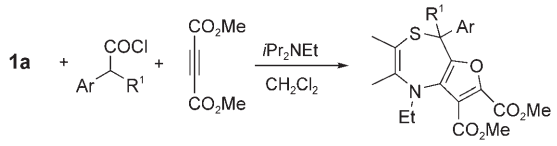

5 **6**

Entry	R^1	Ar	**5**	t [h][a]	Yield of **6** [%][b]
1	Me	Ph	**5a**	4	**6a**, 83
2	Me	4-MeOC$_6$H$_4$	**5b**	5.5	**6b**, 85
3	Me	4-MeC$_6$H$_4$	**5c**	7	**6c**, 84
4	Me	1-naphthyl	**5d**	9.5	**6d**, 59
5	Me	4-ClC$_6$H$_4$	**5e**	8	**6e**, 74
6	Me	4-BrC$_6$H$_4$	**5f**	7	**6f**, 72
7	Me	2-ClC$_6$H$_4$	**5g**	3.5	**6g**, 81
8	Me	2-BrC$_6$H$_4$	**5h**	4.5	**6h**, 77
9	Me	3-ClC$_6$H$_4$	**5i**	7	**6i**, 83
10	Me	4-NO$_2$C$_6$H$_4$	**5j**	17	**6j**, 28
11	Et	Ph	**5k**	2.5	**6k**, 91

[a] Reaction time for consumption of all of the starting materials. [b] Yields of isolated products.

Furthermore, the reactions of 1,1-dialkyl acetyl chlorides **7a–d** with the thiazolium salt **1a** and DMAD were also investigated (Table 3). Under the same experimental conditions, the furo[2,3-c]thiazepines **8** were formed in good yields. In the case of the cyclic carboxylic chlorides **7c** and **7d**, the tricyclic products **8c** and **8d** were easily and efficiently formed from simple substrates.

Table 3: Formation of product **8a–d** by the reaction of thiazolium salt **1a**, 1,1-dialkyl acetyl chloride **7a–d**, and DMAD.

Entry	Acetyl chloride **7**		t [h][a]	Product **8**, yield[b]	
1		**7a**	7	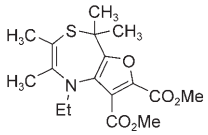	**8a**, 84%
2		**7b**	7	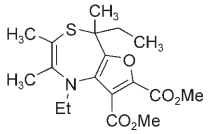	**8b**, 88%
3	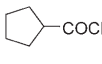	**7c**	6	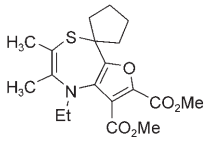	**8c**, 81%
4	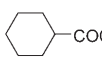	**7d**	7	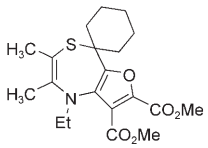	**8d**, 85%

[a] Reaction time for consumption of all of the starting materials. [b] Yields of isolated products.

Next, we examined the reactions of the thiazolium salts **1b–g** from the commercially available thiazoles substituted in the 4- and 4,5-positions (Table 4). As a result, a range of furo[2,3-c]thiazepines **6l–6s** with various substituents were obtained in one step by simply mixing thiazolium salts, 1,1-disubstituted acetyl chlorides, and DMAD.

Finally, the scope of activated alkynes was studied. When diethylacetylenedicarboxylate was used as the alkyne component, the anticipated products **9a–c** were afforded from the corresponding substrates under the optimum conditions we had used for the reactions using DMAD (Scheme 4). To further increase the molecular diversity of this process, the possibility of using 4-oxo-2-alkynoates as the alkyne compo-

 © 2006 Wiley-VCH Verlag GmbH & Co. KGaA, Weinheim

Table 4: Formation of product **6** by the reaction of thiazolium salts **1b–g**, acetyl chloride **5**, and DMAD.

Entry	Tiazolium salt **1**	Acetyl chloride **5**	*t* [h][a]	Yield of **6**[b]
1	**1b**	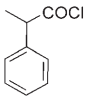 **5a**	5.5	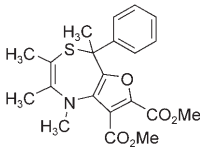 **6l**, 78%
2	**1b**	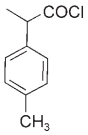 **5c**	5	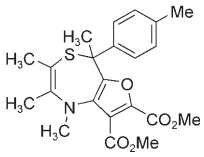 **6m**, 80%
3	**1b**	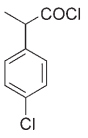 **5e**	7	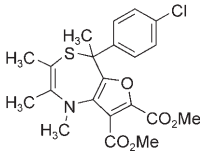 **6n**, 74%
4	**1c**	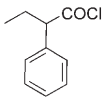 **5k**	6	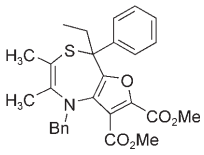 **6o**, 84%
5	**1d**	**5c**	7	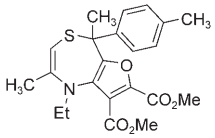 **6p**, 78%
6	**1e**	**5k**	4.5	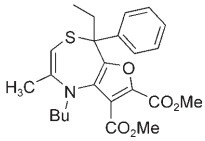 **6q**, 86%
7	**1f**	**5k**	3	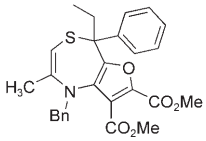 **6r**, 81%
8	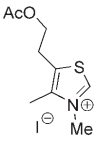 **1g**	**5k**	7	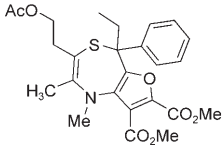 **6s**, 71%

[a] Reaction time for consumption of all of the starting materials. [b] Yields of isolated products.

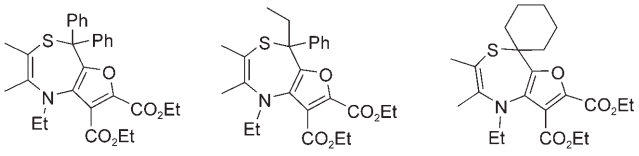

9a, 78% **9b**, 83% **9c**, 81%

Scheme 4. Products from diethylacetylenedicarboxylate and corresponding substrates.

nent was explored (Scheme 5). The preliminary results revealed that, when treated with sodium hydride, both aryl- and *tert*-butyl-substituted alkynes **10a–d** performed well in these reactions and furnished 1,4-thiazepines **11a–d** exclusively.[18] However, *i*Pr$_2$NEt proved to be unsuitable for this transformation with only trace amounts of the products detected.[19]

The mechanism of this novel domino reaction has not been unequivocally established, but one reasonable possibility is outlined in Scheme 6. Thus, the thiazol-2-ylidene **A**, first generated in situ from a thiazolium salt, would react with the 1,1-disubstituted ketene to afford the zwitterion **B**. Presumably, for steric reasons, the latter would undergo an oxa-Michael addition to the activated alkyne, followed by intramolecular annulation to furnish the spirocycle intermediate **C**. Finally, the ring expansion of **C** would occur, thus providing the furothiazepine **D** through a [1,3] sigmatropic sulfur shift.[20]

In conclusion, we have developed a novel and very efficient ring-expansion process for the synthesis of furan-fused 1,4-thiazepine derivatives from thiazole-carbene-triggered multicomponent reactions, which involve activated alkynes and 1,1-disubstituted ketenes generated in situ. This process generates compounds with a high level of complexity from simple and readily accessible starting materials. Furthermore, the operational simplicity and good chemical yields, combined atom-economic aspects and a small number of steps, make this new synthetic strategy highly attractive and promising for the formation of 1,4-thiazepine compounds with potential synthetic and biological uses.

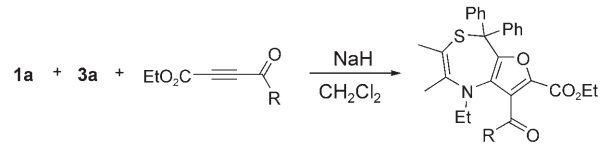

10
10a: R = Ph
10b: R = 4-MePh
10c: R = 4-BrPh
10d: R = *t*Bu

11
11a, 81%
11b, 83%
11c, 87%
11d, 85%

Scheme 5. Three-component reaction of thiazolium salt **1a**, diphenylketene (**3a**), and 4-oxo-2-alkynoates **10a–d**.

 © 2006 Wiley-VCH Verlag GmbH & Co. KGaA, Weinheim

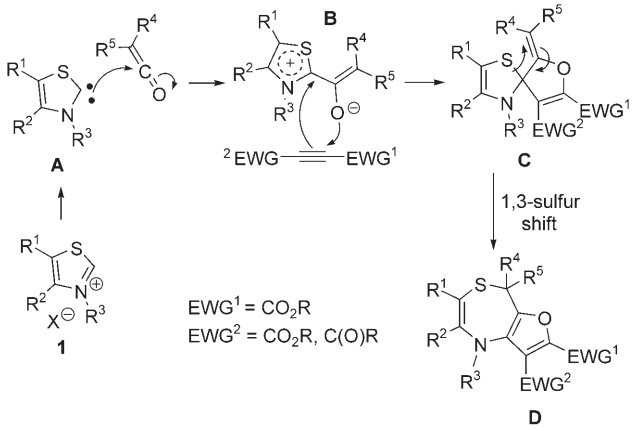

Scheme 6. Proposed mechanism for the formation of furan-fused 1,4-thiazepine derivatives **D**. EWG = electron-withdrawing group.

Experimental Section

Representative procedure (Table 2, entry 1): *i*Pr_2NEt (290 mg, 2.25 mmol) was added to a solution of thiazolium salt **1a** (222 mg, 1.0 mmol) in anhydrous CH_2Cl_2 (3 mL) at −78 °C. After 10–15 min, a solution of α-methyl *p*-methylphenylacetyl chloride (183 mg, 1.0 mmol) and DMAD (213 mg, 1.5 mmol) in CH_2Cl_2 (2 mL) was added dropwise over 10 min and the reaction mixture was stirred at this temperature for 30 min. The reaction temperature was then raised slowly to RT over 4 h. On completion of the reaction, the solvent was removed under vacuum, the residue was quickly passed through a short pad of neutral Al_2O_3 (hexane/diethyl ether 5:1), and the product thus obtained was recrystallized from hexane to afford **6a** (345 mg, 83 % yield) as a colorless solid: m.p. 124–126 °C; IR (film): $\tilde{\nu}$ = 3005, 2970, 1718, 1710, 1437, 1419, 1345, 1296, 828, 767 cm^{-1}; ^{1}H NMR (500 MHz, [D_6]DMSO, tetramethylsilane): δ = 7.32 (t, J = 7.5 Hz, 2H), 7.25 (t, J = 7.0 Hz, 1H), 7.11 (d, J = 7.5 Hz, 2H), 3.91 (s, 3H), 3.75 (s, 3H), 3.35–3.22 (m, 2H), 1.98 (s, 3H), 1.88 (s, 3H), 1.48 (s, 3H), 1.05 ppm (t, J = 7.0 Hz, 3H); ^{13}C NMR (125 MHz, [D_6]DMSO, tetramethylsilane): δ = 164.5, 157.8, 150.8, 147.2, 144.2, 136.5, 130.9, 128.6, 127.6, 126.7, 122.2, 118.4, 53.5, 52.7, 49.8, 44.3, 27.1, 22.8, 17.0, 14.7 ppm; HRMS (ESI): calcd for $C_{22}H_{25}NO_5SNa$: $[M+Na]^+$ 438.1346, found 438.1325.

Received: July 17, 2006
Published online: October 20, 2006

Keywords: carbenes · cyclization · ketenes · multicomponent reactions · ring expansion

[1] a) J. W. Skiles, J. T. Suh, B. E. Williams, P. R. Menard, J. N. Barton, B. Love, H. Jones, E. S. Neiss, A. Schwab, W. S. Mann, *J. Med. Chem.* **1986**, *29*, 784–796; b) H. Umemiya, H. Fukasawa, M. Ebisawa, L. Eyrolles, E. Kawachi, G. Eisenmann, H. Gronemeyer, Y. Hashimoto, K. Shudo, H. Kagechika, *J. Med. Chem.* **1997**, *40*, 4222–4234; c) A. M. Venkatesan, Y. Gu, O. Dos Santos, T. Abe, A. Agarwal, Y. Yang, P. J. Petersen, W. J. Weiss, T. S. Mansour, M. Nukaga, A. M. Hujer, R. A. Bonomo, J. R. Knox, *J. Med. Chem.* **2004**, *47*, 6556–6568.

[2] a) R. Malli, M. Frieden, M. Trenker, W. F. Graier, *J. Biol. Chem.* **2005**, *280*, 12114–12122; b) N. Neamati, J. A. Turpin, H. E. Winslow, J. L. Christensen, K. Williamson, A. Orr, W. G. Rice, Y. Pommier, A. Garofalo, A. Brizzi, G. Campiani, *J. Med. Chem.* **1999**, *42*, 3334–3341; c) H. Maruenda, F. Johnson, *J. Med. Chem.* **1995**, *38*, 2145–2151.

[3] a) A. Crescenza, M. Botta, F. Corelli, A. Santini, A. Tafi, *J. Org. Chem.* **1999**, *64*, 3019–3025; b) A. P. Ilyn, M. V. Loseva, V. Y. Vvedensky, E. B. Putsykina, S. E. Tkachenko, D. V. Kravchenko, A. V. Khvat, M. Y. Krasavin, A. V. Ivachtchenko, *J. Org. Chem.* **2006**, *71*, 2811–2819; c) B. J. Margolis, J. J. Swidorski, B. N. Rogers, *J. Org. Chem.* **2003**, *68*, 644–647.

[4] For reviews of ring transformations of heterocyclic compounds, see: a) N. Vivona, S. Buscemi, V. Frenna, G. Gusmano, *Adv. Heterocycl. Chem.* **1993**, *56*, 49–154; b) G. Hajós, Z. Riedl, G. Kollenz, *Eur. J. Org. Chem.* **2001**, 3405–3414.

[5] a) R. Breslow, *J. Am. Chem. Soc.* **1958**, *80*, 3719–3726; b) R. Breslow, C. Schmuck, *Tetrahedron Lett.* **1996**, *37*, 8241–8242.

[6] For recent reviews of the reactions of NHCs, see: a) Y. Cheng, O. Meth-Cohn, *Chem. Rev.* **2004**, *104*, 2507–2530; b) V. Nair, S. Bindu, V. Sreekumar, *Angew. Chem.* **2004**, *116*, 5240–5245; *Angew. Chem. Int. Ed.* **2004**, *43*, 5130–5135; c) V. Nair, C. Rajesh, A. U. Vinod, S. Bindu, A. R. Sreekanth, J. S. Mathen, L. Balagopal, *Acc. Chem. Res.* **2003**, *36*, 899–907.

[7] a) C. Ma, Y. Yang, *Org. Lett.* **2005**, *7*, 1343–1345; b) C. Ma, H. Ding, G. Wu, Y. Yang, *J. Org. Chem.* **2005**, *70*, 8919–8923.

[8] a) V. Nair, A. U. Vinod, *Chem. Commun.* **2000**, 1019–1020; b) V. Nair, V. Sreekumar, S. Bindu, E. Suresh, *Org. Lett.* **2005**, *7*, 2297–2230.

[9] For the reaction of ketenes with carbenes, see: a) J. H. Rigby, Z. Wang, *Org. Lett.* **2003**, *5*, 263–264; b) R. W. Hoffmann, W. , Lilienblum, B. Dittrich, *Chem. Ber.* **1974**, *107*, 3395–3341; c) J. D. Colomvakos, I. Egle, J. Ma, D. L. Pole, T. T. Tidwell, J. Warkentin, *J. Org. Chem.* **1996**, *61*, 9522–9527.

[10] a) H. Ding, C. Ma, Y. Yang, Y. Wang, *Org. Lett.* **2005**, *7*, 2125–2127; b) C. Ma, H. Ding, Y. Wang, *Org. Lett.* **2006**, *8*, 3133–3136.

[11] For an overview of multicomponent reactions, see: a) *Multicomponent Reactions* (Eds.: J. Zhu, H. Bienaymé), Wiley-VCH, Weinheim, 2005. For recent reviews, see: b) D. J. Ramón, M. Yus, *Angew. Chem.* **2005**, *117*, 1628–1661; *Angew. Chem. Int. Ed.* **2005**, *44*, 1602–1634; c) C. Simon, T. Constantieux, J. Rodriguez, *Eur. J. Org. Chem.* **2004**, 4957–4980; d) R. V. A. Orru, M. de Greef, *Synthesis* **2003**, 1471; e) J. Zhu, *Eur. J. Org. Chem.* **2003**, 1133–1144; f) H, Bienaymé, C. Hulme, G. Oddon, P. Schmitt, *Chem. Eur. J.* **2000**, *6*, 3321–3329; g) A. Dömling, I. Ugi, *Angew. Chem.* **2000**, *112*, 3300–3344; *Angew. Chem. Int. Ed.* **2000**, *39*, 3168–3210.

[12] CCDC-614678 contains the supplementary crystallographic data for this paper. See Ref. [18].

[13] H. Staudinger, *Ber. Dtsch. Chem. Ges.* **1905**, *38*, 1735–1739.

[14] a) For a monograph, see: T. T. Tidwell, *Ketenes*, Wiley, New York, **1995**; for reviews, see: b) T. T. Tidwell, *Eur. J. Org. Chem.* **2006**, 563–576; c) J. Hyatt, R. W. Raynolds, *Org. React.* **1994**, *45*, 159–646; d) B. B. Snider, *Chem. Rev.* **1988**, *88*, 793–811.

[15] For the cycloaddition of ketene through the C=O bond, see: a) D. C. England, C. G. Krespan, *J. Am. Chem. Soc.* **1965**, *87*, 4019–4020; b) T. DoMinh, O. P. Strautz, *J. Am. Chem. Soc.* **1970**, *92*, 1766–1768; c) S. Yamabe, T. Dai, T. Minato, T. Machiguchi, T. Hasegawa, *J. Am. Chem. Soc.* **1996**, *118*, 6518–6519; d) T. Machiguchi, J. Okamoto, Y. Morita, T. Hasegawa, S. Yamabe, T. Minato, *J. Am. Chem. Soc.* **2006**, *128*, 44–45.

[16] Using NEt_3 as the base, dimethyl-(*E*)-2-diethylaminobutenoate was formed in 61 % yield accompanied by product **6a**.

[17] Unidentified products were obtained when monosubstituted ketenes were used in the reaction.

[18] The structure of **11a** was confirmed by X-ray crystallography. CCDC-619544 contains the supplementary crystallographic data for this paper. These data can be obtained free of charge from The Cambridge Crystallographic Data Centre via www.ccdc.cam.ac.uk/data_request/cif.

 © 2006 Wiley-VCH Verlag GmbH & Co. KGaA, Weinheim

[19] On comparison with the blank experiment without a thiazolium salt, the main un-isolable side product was derived from the reaction of ketene and alkyne in the presence of iPr$_2$NEt.
[20] For rearrangements in the thizaole system, see: a) P. J. Abbott, R. M. Acheson, U. Eisner, D. J. Watkin, J. R. Carruthers, *J. Chem. Soc. Chem. Commun.* **1975**, 155 – 158; b) K. T. Potts, D. R. Choudhury, T. R. Westby, *J. Org. Chem.* **1976**, *41*, 187 – 191.

 © 2006 Wiley-VCH Verlag GmbH & Co. KGaA, Weinheim

Conjugated Polymers

DOI: 10.1002/anie.200602863

Soluble Poly(*p*-phenylenevinylene)s through Ring-Opening Metathesis Polymerization**

*Chin-Yang Yu and Michael L. Turner**

Soluble semiconducting polymers are attractive synthetic targets as they can be deposited from solution using low-cost processing routes to fabricate organic electronic devices such as light-emitting diodes, photovoltaics, and field-effect transistors.[1] One of the most widely studied systems are the poly(*p*-phenylenevinylene)s (PPVs), first reported by Burroughes et al. to show electroluminescence in polymeric light-emitting diodes.[2] The parent unsubstituted PPV is insoluble, and substituents are appended to the phenylene groups to produce soluble PPVs. A number of synthetic routes to these polymers has been described,[3] but all of these routes lead to polydispersities consistent with termination processes and consequently these are not living polymerizations.

Ring-opening metathesis polymerization (ROMP) offers the opportunity for precise control of the conjugated-polymer molecular weight, low polydispersities, and the preparation of block copolymers. This method has been applied to the synthesis of polyacetylene by Feast et al.[4] and has been exploited in the synthesis of PPV polymers and copolymers.[5,6] Initial reports focused on the preparation of precursors that can be converted into insoluble PPV homopolymer. ROMP of [2.2]paracyclophane-1,9-diene gives PPV directly as an insoluble yellow fluorescent powder. Soluble copolymers of PPV have been prepared by ROMP with cyclopentene, cyclooctene, and cycloocta-1,5-diene comonomers. However, incorporation of more than 5% of PPV units gives insoluble polymers.[6] Herein we report the first polymerization of substituted [2.2]paracyclophanedienes using ruthenium-based metathesis catalysts to give monodisperse, soluble phenylenevinylene homopolymers.

The ROMP of the tetra-alkoxy-substituted [2.2]paracyclophanediene derivative **1**, dissolved in THF, was initiated by addition of a THF solution of the second-generation Grubbs catalyst **2** (Scheme 1).[7] The reaction mixture was heated at reflux and then quenched by addition of ethyl vinyl ether. The resulting polymers **3** were purified by filtering through silica gel and isolated by evaporation of the solvent. Polymers with a range of molecular weights were prepared by varying the monomer-to-catalyst ratio. An extended reaction time (36 h) was necessary to achieve complete conversion of monomer, indicating a slow rate of polymerization.[5b,8]

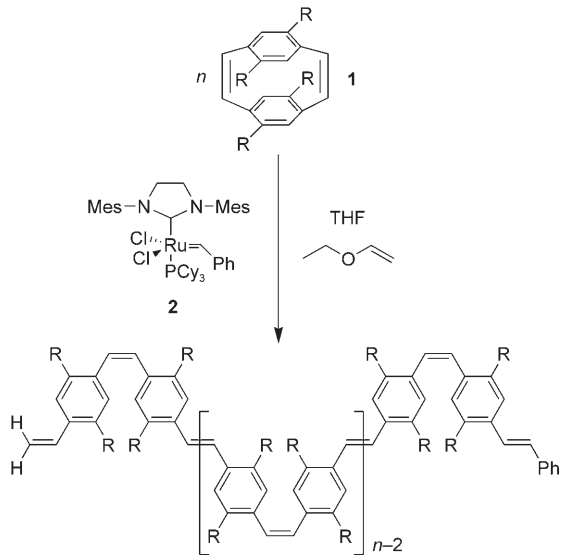

Scheme 1. ROMP of cyclophanediene **1** to give monodisperse, soluble PPVs **3**. R = OC_8H_{17}.

The molecular weights of the polymers were determined by gel permeation chromatography (GPC) in THF solution. The number-average molecular weight (M_n) increased monotonically with the initial monomer-to-catalyst ratio (Figure 1) with a correlation coefficient of 0.999, and the polydispersities were all close to 1.2. The apparent discrepancy between the expected and the observed molecular weights (Figure 1) is due to the difference in the hydrodynamic radii of PPV and polystyrene.[9] From the linear relationship between the monomer-to-catalyst ratio and the degree of polymerization, the low polydispersities, and the complete consumption of monomer, we conclude that chain transfer, back-biting, or termination are absent and the polymerizations could be regarded as living.[10,11]

The living nature of this polymerization was confirmed by an experiment in which a second charge of monomer was added to the polymerization reaction. The initial reaction gave a polymer with $M_n = 7428$ (expected $M_n = 7264$) and a polydispersity of 1.20. A second addition of one third amount of monomer increased M_n to 9554 (expected $M_n = 9412$;

[*] C.-Y. Yu, Prof. M. L. Turner
Organic Materials Innovation Centre
School of Chemistry, University of Manchester
Oxford Road, Manchester M13 9PL (UK)
Fax: (+44) 161-275-4273
E-mail: michael.turner@manchester.ac.uk

[**] Financial support from the UK DTI and the University of Manchester is gratefully acknowledged.

Supporting information for this article is available on the WWW under http://www.angewandte.org or from the author.

© 2006 Wiley-VCH Verlag GmbH & Co. KGaA, Weinheim

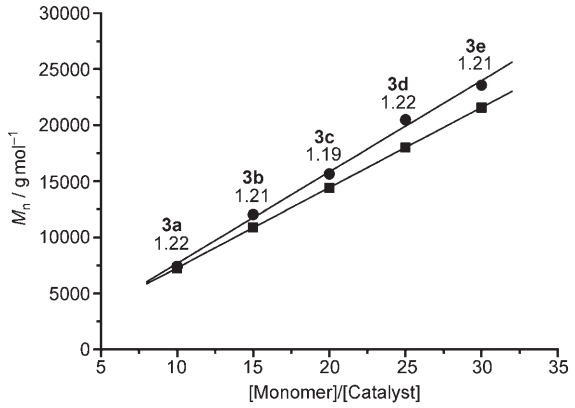

Figure 1. Dependence of the molecular weight (M_n) of polymer **3** on the ratio **1**/**2**. The polydispersities are given for expected $n = 10$, 15, 20, 25, 30. ●: GPC with refractive index (RI) detection; ■: calculated.

polymer **3 f**) with no change in the polydispersity (Figure 2), consistent with a living polymerization and demonstrating the potential of this chemistry to prepare conjugated block copolymers.

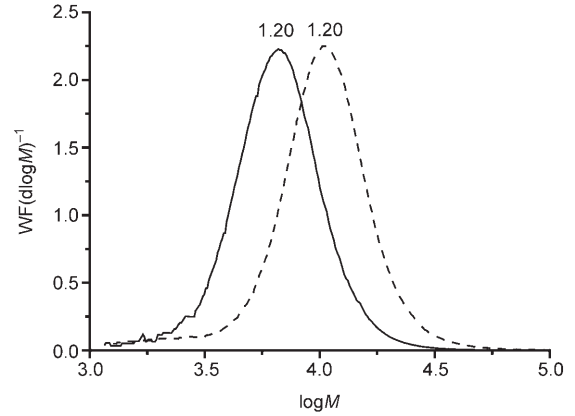

Figure 2. Molecular weight (M) distribution and polymer dispersities for stepwise synthesis of a polymer from $n = 10$ (solid line) to $n = 13$ (dashed line), using calculated Mark–Houwink parameters.

The MALDI-TOF mass spectrum of polymer **3 a**, isolated by a single filtration through silica gel followed by washing with methanol, shows a series of peaks separated by an interval of 716 mass units, corresponding to the molecular weight of the monomer (Figure 3). This series is consistent with PPVs capped with vinyl and phenyl end groups, as expected, and is accompanied by peaks associated with the addition of one sodium ion per polymer chain. There was no evidence for the defect structures commonly seen for other synthetic routes.[3]

The ^{1}H NMR spectrum of **3** showed the high level of control achieved in this polymerization (Figure 4). Relief of significant ring strain within monomer **1** is achieved by opening of only one vinylene linkage and it is expected that polymer **3** has a backbone of regularly alternating *cis* and *trans* vinylene linkages. Peaks at $\delta = 3.96$ and 3.50 ppm can be assigned to the methylene groups attached to oxygen atoms

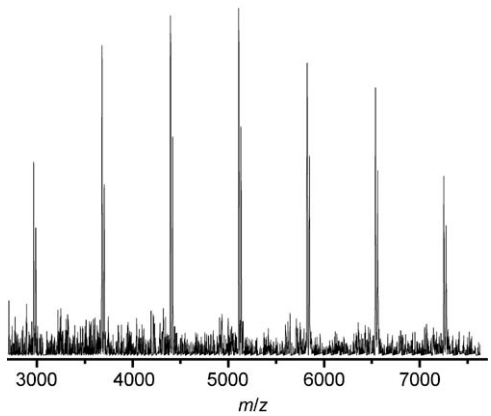

Figure 3. MALDI-TOF mass spectrum of polymer **3 a** (expected: $n = 10$).

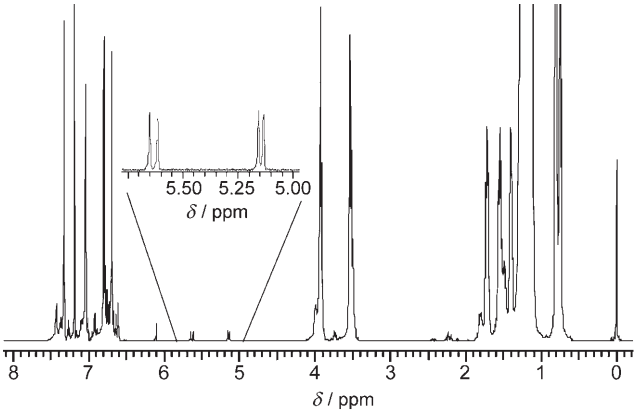

Figure 4. ^{1}H NMR spectrum of **3 f** in $CDCl_3$ solution. The inset shows an expansion of the signals associated with the vinyl end groups.

for the *trans* and *cis* vinylene links of the polymer backbone, respectively.[12,13] Integration of these signals gave the expected 1:1 ratio. The precise control of the polymer microstructure was confirmed by the simplicity of the NMR signals associated with the aromatic and vinylene groups (i.e., the peaks between $\delta = 6.60$ and 7.50 ppm). The signals at $\delta =$ 6.66 and 6.83 ppm are associated with the aromatic and *cis* vinylene units, respectively; whereas those at $\delta = 7.35$ and 7.10 ppm are assigned to hydrogen atoms of the *trans* vinylene and associated aromatic groups. Again the integration of these signals is consistent with a 1:1 ratio of *cis*/*trans* linkages.

Further evidence for the structure of **3** was the presence of C–H out-of-plane deformation vibrations for the *cis* and *trans* vinylene links, at 850 and 965 cm^{-1}, respectively, in the FTIR spectra (see Supporting Information). Absolute values for the degree of polymerization were determined by integration of the signals for the vinyl end groups observed at $\delta = 5.15$ and 5.64 ppm against those for the methylene groups attached to oxygen atoms. In all cases the values obtained are consistent with the expected number of repeat units, derived from the monomer-to-catalyst ratio (Table 1).

It has been previously reported that the physical properties of PPVs are strongly dependent on the configuration of the vinylene units.[14–16] Son et al. demonstrated that PPVs

 © 2006 Wiley-VCH Verlag GmbH & Co. KGaA, Weinheim

Table 1: Molecular weight, UV/Vis, and photoluminescence (PL) data for **3a–f**.

3, *n*	M_n[a]	M_n[b]	PDI[b]	M_n[c]	λ_{max}^{Abs} [nm][d]	λ_{max}^{PL} [nm][d]
3a, 10	7264	7428	1.22	7207	482	556
3b, 15	10844	12025	1.21	10570	491	556
3c, 20	14424	15644	1.19	15235	496	557
3d, 25	18004	20492	1.22	17745	497	556
3e, 30	21584	23584	1.21	[e]	502	557
3f, 13	9412	9554	1.20	9548	490	556

[a] Expected M_n (including end groups). [b] Determined by GPC with RI detection. [c] Determined by ^{1}H NMR spectroscopy. [d] In CH_2Cl_2. [e] Intensity of the signals for vinyl end groups comparable to spectral noise.

having a moderate ratio of *cis* and *trans* vinylene units exhibited higher electroluminescence efficiencies than the all-*trans* analogues.[12,14,15] UV/Vis spectroscopy (Figure 5) shows

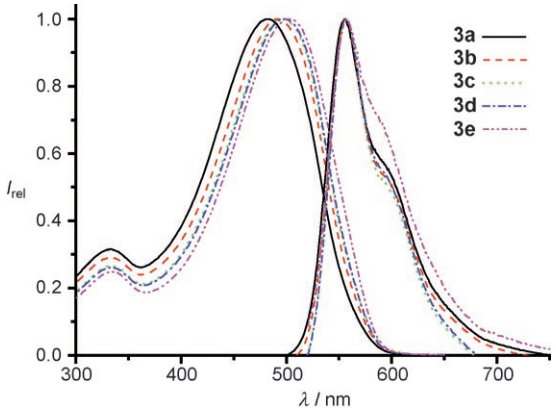

Figure 5. UV (left) and PL (right) spectra of **3a–e**.

that the wavelength of the absorption maximum for **3** increases with the polymer chain length and hence the conjugation length increases. The photoluminescence spectra recorded for **3** (Figure 5) are identical as emission occurs from the most conjugated segment of the polymer, regardless of the chain length.

In summary, soluble PPV homopolymers of well-defined molecular weight with an alternating *cis-trans* microstructure can be prepared by ROMP. The living character of this polymerization has been demonstrated by controlled chain extension on addition of additional monomer. This approach has tremendous potential in the preparation of well-defined PPV block copolymers, and the synthesis of these materials is the focus of ongoing investigation.

Experimental Section

All experiments were performed under a nitrogen atmosphere in a Radleys GreenHouse or by using standard Schlenk techniques. All reagents were used as received from commercial suppliers without further purification. THF was distilled over sodium/benzophenone ketyl under dry nitrogen. Monomer **1** was prepared by a modification of established procedures.[17]

Synthesis of **3a–f**: In a nitrogen-filled Radleys GreenHouse, monomer **1** (50.1 mg, 0.07 mmol) was charged into five separate tubes and dissolved in 1.2, 0.8, 0.6, 0.48, and 0.4 mL of dry THF. Catalyst **2** (23 mg) was dissolved in 2 mL of dry THF and stirred for at least 10 min to fully dissolve. Aliquots of the catalyst solution (517, 345, 258, 207, and 172 μL) were added into the monomer solutions, and the GreenHouse was heated at 68 °C for 36 h. The reaction mixtures were cooled to room temperature, and excess ethyl vinyl ether (2 mL) was added to quench the reaction. After stirring for a further 4 h at room temperature the reaction mixtures were concentrated under vacuum. The products were redissolved in chloroform and filtered through a short plug of silica to remove the catalyst. The solvent was removed under reduced pressure, and the resulting solid was exhaustively washed with methanol. The polymers obtained were dried under vacuum at 40 °C for 24 h. Yields ranged from 93 to 98 %.

Received: July 18, 2006
Published online: October 24, 2006

Keywords: cyclophanes · metathesis · poly(*p*-phenylenevinylene)s · ring-opening polymerization · soluble polymers

[1] "Molecular Materials in Electronic and Optoelectronic Devices" (Eds.: J. R. Sheats, P. F. Barbara): *Acc. Chem. Res.* **1999**, *32*, 191–276.
[2] J. H. Burroughes, D. D. C. Bradley, A. R. Brown, N. R. Mark, K. Mackay, R. H. Friend, P. L. Burns, A. B. Holmes, *Nature* **1990**, *347*, 539–541.
[3] A. Kraft, A. C. Grimsdale, A. B. Holmes, *Angew. Chem.* **1998**, *110*, 416–443; *Angew. Chem. Int. Ed.* **1998**, *37*, 402–428.
[4] a) J. H. Edwards, W. J. Feast, *Polymer* **1980**, *21*, 595–596; b) J. H. Edwards, W. J. Feast, D. C. Bott, *Polymer* **1984**, *25*, 395–398; c) W. J. Feast, J. N. Winter, *J. Chem. Soc. Chem. Commun.* **1985**, 202–203.
[5] a) V. P. Conticello, D. L. Gin, R. H. Grubbs, *J. Am. Chem. Soc.* **1992**, *114*, 9708–9710; b) M. W. Wagaman, R. H. Grubbs, *Macromolecules* **1997**, *30*, 3978–3985.
[6] a) E. Thorn-Csányi, H. D. Höhnk, *J. Mol. Catal.* **1992**, *76*, 101–105; b) E. Thorn-Csányi, K. P. Pleug, *Macromol. Chem.* **1993**, *194*, 2287–2294; c) E. Thorn-Csányi, P. Kraxner, J. Hammer, *J. Mol. Catal.* **1994**, *90*, 15–20.
[7] a) C. W. Bielawski, R. H. Grubbs, *Angew. Chem.* **2000**, *112*, 3025–3028; *Angew. Chem. Int. Ed.* **2000**, *39*, 2903–2906; b) J. A. Love, M. S. Sanford, M. W. Day, R. H. Grubbs, *J. Am. Chem. Soc.* **2003**, *125*, 10103–10109.
[8] E. Thorn-Csányi, P. Kraxner, A. Strachota, *Macromol. Rapid Commun.* **1998**, *19*, 223–228.
[9] a) P. M. Cotts, T. M. Swager, Q. Zhou, *Macromolecules* **1996**, *29*, 7323–7328; b) U. Stalmach, B. de Boer, A. D. Post, P. F. van Hutten, G. Hadziioannou, *Angew. Chem.* **2001**, *113*, 442–444; *Angew. Chem. Int. Ed.* **2001**, *40*, 428–430.
[10] K. J. Ivin, J. C. Mol, *Olefin Metathesis and Metathesis Polymerization*, Academic Press, San Diego, CA, **1997**, pp. 6–19, 41–43, 233.
[11] K. Matyjaszewski, *Macromolecules* **1993**, *26*, 1787–1788.
[12] L. Liao, Y. Pang, L. Ding, F. E. Karasz, *Macromolecules* **2001**, *34*, 6756–6760.
[13] a) S. Jacobs, W. Eevers, G. Verreyt, H. J. Geise, A. De Groot, R. Dommisse, *Synth. Met.* **1993**, *61*, 189–193; b) H. Becker, H.

 © 2006 Wiley-VCH Verlag GmbH & Co. KGaA, Weinheim

Spreitzer, K. Ibrom, W. Kreuder, *Macromolecules* **1999**, *32*, 4925 – 4932.
[14] S. Son, A. Dodabalapur, A. J. Lovinger, M. E. Glavin, *Science* **1995**, *269*, 376 – 378.
[15] H. Katayama, M. Nagao, T. Nishimura, Y. Matsui, Y. Fukuse, M. Wakioka, F. Ozawa, *Macromolecules* **2006**, *39*, 2039 – 2048.
[16] W. Holzer, A. Penzkofer, S. H. Gong, A. Bleyer, D. D. C. Bradley, *Adv. Mater.* **1996**, *8*, 974 – 978.
[17] a) V. Boekelheide, P. H. Anderson, T. A. Hylton, *J. Am. Chem. Soc.* **1974**, *96*, 1558 – 1564; b) R. H. Mitchell, T. Otsubo, V. Boekelheide, *Tetrahedron Lett.* **1975**, *16*, 219 – 222; c) S. E. Potter, I. O. Sutherland, *J. Chem. Soc. Chem. Commun.* **1973**, 520 – 521.

 © 2006 Wiley-VCH Verlag GmbH & Co. KGaA, Weinheim

Organic Light-Emitting Diodes

DOI: 10.1002/anie.200602906

Multifunctional Iridium Complexes Based on Carbazole Modules as Highly Efficient Electrophosphors**

Wai-Yeung Wong, Cheuk-Lam Ho, Zhi-Qiang Gao, Bao-Xiu Mi, Chin-Hsin Chen, Kok-Wai Cheah, and Zhenyang Lin*

Since the seminal work on organic green-light-emitting diodes using *fac*-[Ir(ppy)$_3$] (Hppy = 2-phenylpyridine),[1] intensive research effort has been directed towards the development of efficient phosphorescent materials for potential use in full-color flat-panel-display technology.[2] Although the emission efficiency and the color of Ir-based organic light-emitting diodes (OLEDs) can be tuned by structural modifications of the ligand chromophores,[3] the performance of the device is greatly influenced by the charge balance between the electrons and holes from opposite electrodes. It is highly desirable that the designed phosphor shows improved charge-balancing features and permits a complete transfer of energy between the host and the dopant in the device. Interestingly, small-molecule Ir^{III} complexes derived from hole-transporting (HT) carbazole units have not been reported to date. Many carbazole derivatives are known to transport predominantly positive charge carriers in organic systems. For example, poly(9-vinylcarbazole) (PVK) is often described as being a unipolar hole transporter whereas 4,4′-*N*,*N*′-dicarbazolebiphenyl (CBP) is recognized to have a more bipolar transport character.[4] Typically, purely organic carbazole-based compounds are high-mobility HT materials with a tunable and high triplet energy level, and they are widely used as the host materials for electrophosphors emitting different colors.[5] The integration of HT carbazole modules and emissive Ir complexes seems to be a wise choice for vacuum-evaporated OLED materials with multicomponent molecules, which are essential for more efficient charge transport in the electroluminescence process.[6] We report here two robust Ir^{III} triplet emitters of green light that are based on the rigid 2-[3-(*N*-arylcarbazolyl)]pyridine system and possess the dual functions of light emission and hole transportation, and also show improved charge-transporting properties and morphological stability.

The green-light-emitting multifunctional metal chelates **1** and **2** can be synthesized in moderate to good yields by a one-step cyclometalation of L^1 and L^2 with [Ir(acac)$_3$] (acac = acetylacetone) in refluxing glycerol (Figure 1a).[3f] Purification of the mixture by preparative thin-layer chromatography (TLC) on silica gel furnished homoleptic *fac*-[Ir(X-Cz-py)$_3$] (X = H, **1**; X = F, **2**; Cz = carbazolyl, py = pyridyl) as air-stable yellow powders in high purity. Their 1D ^{1}H NMR spectra are consistent with a facial geometry around the Ir center, which was also confirmed by a single-crystal X-ray analysis of **1** (Figure 1b).[7] Both **1** and **2** show excellent thermal stability, with their onset decomposition temperatures (T_d) greater than 420 °C, as revealed by thermogravimetric analysis (TGA, Table 1), and with **1** being thermally much more stable than **2** and *fac*-[Ir(ppy)$_3$] (423 °C). Furthermore, both of them can be vacuum-evaporated without decomposition and show good film-forming qualities.

The nature of the X group on the carbazole ring does not have a great influence on the absorption and photoluminescence (PL) spectra of **1** and **2** (Table 1). The first two bands appear to be ligand-based transitions that closely resemble the spectra of the free ligands (λ_{abs}: ca. 252 and 297 nm). Somewhat weaker bands are observed at lower energies in the visible region which correspond to electronic excitations to the allowed and spin-forbidden metal-to-ligand charge-transfer states (^{1}MLCT and ^{3}MLCT, respectively). These assignments were supported by DFT calculations on **1**, which show that the highest occupied molecular orbitals (HOMOs) are derived from the out-of-phase combinations of the Ir "t_{2g}" set of d orbitals and the π orbitals of the three Ir-bonded phenyl rings of the three N−C bidenate ligands. In each of the first three HOMOs, the Ir(d) orbitals make an approximate 20% contribution, with the N(amine) p_π orbitals also contributing to the HOMOs. The lowest unoccupied molecular orbitals (LUMOs) are the π* orbitals of the three pyridine rings. Both

[*] Dr. W.-Y. Wong, C.-L. Ho
Department of Chemistry
Hong Kong Baptist University
Waterloo Road, Kowloon Tong, Hong Kong (P.R. China)
Fax: (+852) 3411-7348
E-mail: rwywong@hkbu.edu.hk
Dr. Z.-Q. Gao, Dr. B.-X. Mi, Prof. C.-H. Chen, Prof. K.-W. Cheah
Centre for Advanced Luminescence Materials
Hong Kong Baptist University
Waterloo Road, Kowloon Tong, Hong Kong (P.R. China)
Dr. Z. Lin
Department of Chemistry
The Hong Kong University of Science and Technology
Clearwater Bay, Hong Kong (P.R. China)

[**] This work was supported by a CERG Grant from the Hong Kong Research Grants Council (HKBU 2022/03P) and a Faculty Research Grant from the Hong Kong Baptist University (FRG/04-05/II-59).

Supporting information for this article is available on the WWW under http://www.angewandte.org or from the author.

InterScience
© 2006 Wiley-VCH Verlag GmbH & Co. KGaA, Weinheim

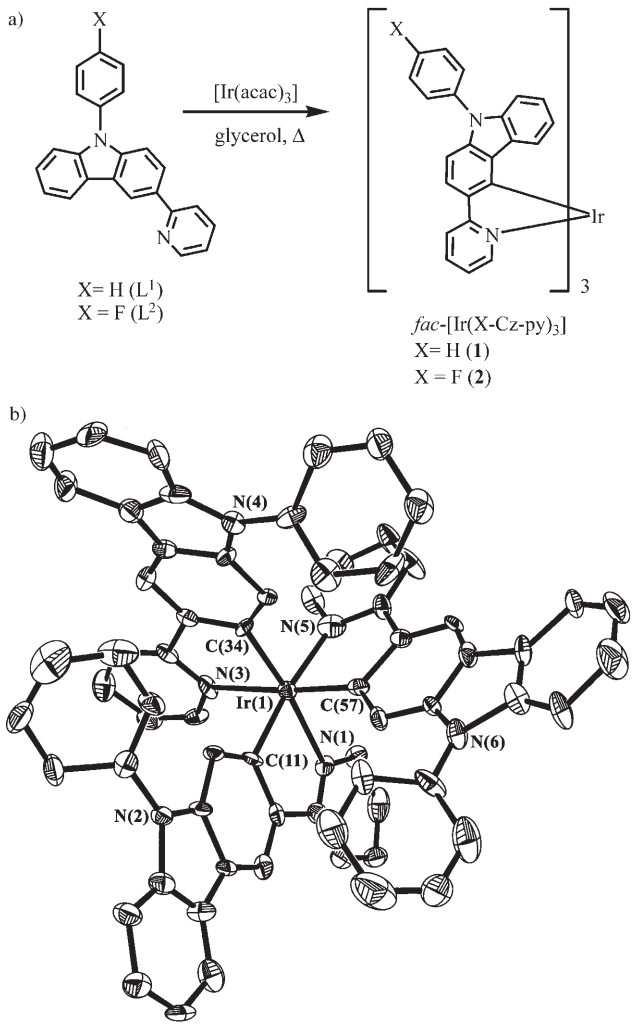

Figure 1. a) Synthesis of **1** and **2**; b) ORTEP plot of **1**, with the hydrogen atoms omitted for clarity.

Table 1: Photophysical, electrochemical, and thermal data for **1** and **2**.

	Absorption[a]	Emission		$E_{1/2}^{ox}$ [V][d]	$E_{1/2}^{red}$ [V][e]	HOMO [eV]	LUMO [eV]	T_d [°C][f]
	λ_{abs} [nm]	λ_{em} [nm][b]	τ_P [μs][c]					
1	291 sh (4.69), 316 (4.69), 398 sh (0.20)	515 (0.43)	0.46	0.07	−2.56	−4.87	−2.24	477
2	281 sh (4.89), 315 (4.85), 400 sh (0.16)	514 (0.33)	0.54	0.13	−2.49	−4.93	−2.31	421

[a] In degassed CH_2Cl_2 at 293 K; logε values are shown in parentheses; sh = shoulder. [b] Φ_P values are shown in parentheses versus *fac*-[Ir(ppy)$_3$] ($\Phi_P = 0.40$), $\lambda_{ex} = 380$ nm. [c] Triplet lifetimes at 293 K. [d] 0.1 M $[Bu_4N]PF_6$ in CH_2Cl_2, versus the ferrocene/ferrocinium (Fc/Fc^+) couple. [e] 0.1 M $[Bu_4N]PF_6$ in THF, versus Fc/Fc^+ couple. [f] At a heating rate of 20 °C min^{-1} under N_2.

complexes emit strong phosphorescence (λ_{em} ca. 514 nm, Stokes shifts ca. 200 nm) at room temperature in CH_2Cl_2. The triplet energy levels (T_1: ca. 2.41 eV) of the two complexes are very similar and also similar to that of *fac*-[Ir(ppy)$_3$] (2.43 eV).[1a] The phosphorescence quantum yields Φ_P in CH_2Cl_2 of these triplet emitters of green light are approximately 0.33–0.43 relative to a *fac*-[Ir(ppy)$_3$] standard ($\Phi_P = 0.40$).[8] The triplet lifetimes τ_P are very short at 0.46–0.54 μs for **1** and **2** in the solid state. Accordingly, the triplet radiative lifetimes (τ_r) deduced from $\tau_r = \tau_P/\Phi_P$ are 1.07–1.64 μs, which are shorter than that of *fac*-[Ir(ppy)$_3$] (ca. 4.75 μs)[3f] and other Ir^{III} complexes.[3]

Cyclic voltammetric studies show that both **1** and **2** undergo a reversible one-electron oxidation of the Ir–carbazolyl ring system ($E_{1/2}^{ox}$ 0.07, **1**; 0.13 V, **2**). The attachment of electron-withdrawing F substituents in **2** causes the oxidation to occur at a more anodic potential, which would have a major impact on the device properties (see below). Both **1** and **2** were oxidized at less-positive potentials than *fac*-[Ir(ppy)$_3$], thus indicating a greater propensity for **1** and **2** to lose an electron.[3k,5b] Cathodic sweeps in THF reveal an irreversible wave at −2.49 to −2.56 V. There is subtle changes in the HOMO and LUMO levels arising from the presence of different X groups in **1** and **2**, and we were able to tune the HOMO level without influencing the triplet energy of these Ir phosphors. The HOMO levels are significantly elevated (−4.87, **1**; −4.93 eV, **2**) relative to those of *fac*-[Ir(ppy)$_3$] (−5.50 eV).[3k,5b] This finding indicates that they have a lower ionization potential (IP) than *fac*-[Ir(ppy)$_3$], thus leading to a better HT ability in **1** and **2** which favors the transport of holes. The LUMO levels of **1** and **2** are comparable to that of the widely used electron-transporting/hole-blocking 2-(4-biphenylyl)-5-(4-*tert*-butylphenyl)-1,3,4-oxadiazole (−2.4 eV). Our complexes show T_1 levels well below the level of those of the CBP host (2.56 eV) which prevents reverse energy transfer from the guest back to the host, and confines triplet excitons to the guest molecules.

The optoelectronic properties of both Ir^{III} complexes were characterized, and efficient OLEDs **I** and **II** were fabricated using **1** and **2**, respectively, as phosphorescent dopant emitters in a four-layer structure of ITO/NPB (40 nm)/6% **1** or **2** in CBP (20 nm)/BCP (8 nm)/Alq_3 (20 nm)/Mg:Ag (200 nm) (ITO = indium tin oxide, NPB = 4,4′-bis[*N*-(1-naphthyl)-*N*-phenylamino]biphenyl, BCP = 2,9-dimethyl-4,7-diphenyl-1,10-phenanthroline, Alq_3 = tris(8-hydroxyquinoline)). CBP acts as the host material for the electrophosphor and NPB as a hole-transport layer. A thin hole-blocking barrier layer of BCP inserted between the CBP and the electron-transporting Alq_3 was necessary to confine excitons within the luminescent zone and hence maintain high efficiencies. The electroluminescence (EL) spectra consist only of a green phosphor emission without any residual emission from the host and/or adjacent layers, even at high drive currents—an indication of complete energy and/or charge transfer from the host exciton to the phosphor upon electrical excitation. The EL spectra and Commission Internationale de L'Eclairage (CIE) coordinates

 © 2006 Wiley-VCH Verlag GmbH & Co. KGaA, Weinheim

for the devices exhibited no significant change on variation of the current and operating bias voltages from 5 V to 12 V (Figure 2a), and both of the devices **I** and **II** show a sharp EL peak at 508 nm. The turn-on voltages (defined as the bias at a

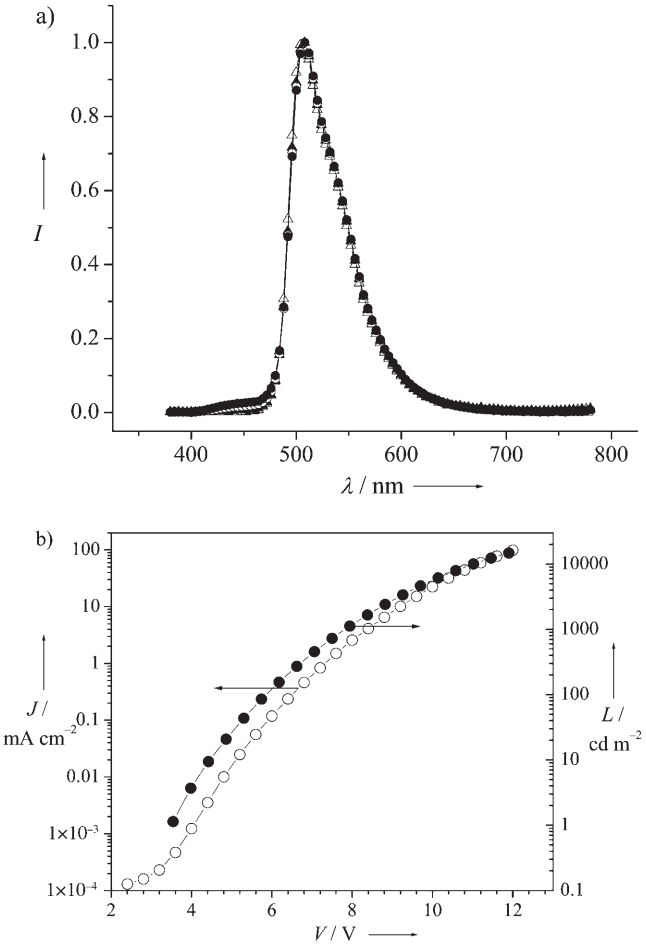

Figure 2. a) The EL spectra of device **I** at 5 (△), 8 (▲), 10 (○), and 12 V (●) and b) current–voltage–luminance (*J-V-L*) characteristics for device **I**.

brightness of 1 cd m^{-2}) are 4.4 and 4.8 V for devices **I** and **II**, respectively, with the CIE color coordinates being (0.24, 0.63) and (0.27, 0.60), which correspond to the bright green region of the chromaticity diagram. There is a close resemblance between the EL and PL spectra in each case.

Phosphors **1** and **2** show outstanding EL performance, presumably because of the short τ_P value and good hole-transporting properties of carbazole, which may help diminish the quenching of the triplet exciton. Figure 2b shows the current density–voltage–luminance (*J-V-L*) curve of device **I**. Complex **1** was shown to be a more efficient electrophosphor than **2**, which suggests that the F substituents are rather unimportant here in relieving intermolecular interactions in the Ir complex, as is commonly the case in [Ir(C–N)$_3$]-type compounds with simpler ligands.[3k,l] Moreover, since **2** has a T_1 lifetime comparable to that of **1**, its poor EL performance may be attributed to its lower Φ_P value relative to that of **1**. The difference in the efficiency for **1** and **2** are also a consequence of the lower $E^{ox}_{1/2}$ value of **1**. As the HOMO of **1** is positioned higher in energy than that of **2** (relative to the CBP level of 6.3 eV), the efficiency of recombination by sequential charge trapping is increased in **1**. The performance parameters of device **I** (maximum external quantum efficiency (η_{ext}): 11.6% photons/electron, luminance efficiency (η_L): 38 cd A^{-1}, power efficiency (η_P): 24 Lm W^{-1}) clearly outweigh those of a prototypical green-light-emitting device of ITO/NPB/*fac*-[Ir(ppy)$_3$]:CBP/BCP/Alq$_3$/Mg:Ag (maximum η_{ext}: 7.5%, η_L: 26 cd A^{-1}, η_P: 19 Lm W^{-1}) in a device of similar structure, and this represents a tremendous improvement of about 55% in the η_{ext} value.[1a] The maximum luminance of device **I** is 14730 cd m^{-2} at 12 V, with the full width at half maximum (fwhm) only 56 nm at 8 V. With **2** as the dopant, device **II** has a maximum brightness of 19360 cd m^{-2} and a luminance efficiency of approximately 22 cd A^{-1}, which corresponds to a η_{ext} value of 6.7% and a η_P value of approximately 13 Lm W^{-1}. We can surmise that it is probably the carbazolyl moiety that brings about a more balanced electron and hole recombination in the host matrix of CBP, and/or that the rigid carbazole spacers play a crucial role in alleviating the self-quenching of the [Ir(X-Cz-py)$_3$] luminophores, and consequently increase the emission efficiency. Typical efficiency roll-off at higher currents, attributable to a combination of triplet–triplet annihilation and field-induced quenching effects, is also observed here, but at the reference luminance of 100 cd m^{-2} (6.5 V) the efficiencies remain high at 10.6%, 35 cd A^{-1}, and 17 Lm W^{-1} for device **I**. These values correspond to a loss of only 8% from the maximum η_{ext} value. Likewise, a loss of 7% was noted in the η_{ext} value for device **II**. Although the performance of these devices has yet to be optimized, it is our intention to highlight the potential merits of this prominent class of carbazole-based Ir phosphors in high-efficiency OLED applications.

In summary, we have reported some triplet-harvesting carbazolyl-substituted multicomponent iridium complexes, and this approach can offer advantages in terms of lowering the first IP, facilitating hole transport, and enhancing EL efficiencies relative to the prototypical *fac*-[Ir(ppy)$_3$]. Given the ease of synthesis and performance advantages inherent to these carbazole-based phosphors, extension of the system to other emission colors warrants further examination.

Received: July 20, 2006
Published online: October 24, 2006

Keywords: carbazoles · iridium · optical properties · phosphorescence · structure elucidation

[1] a) M. A. Baldo, S. Lamansky, P. E. Burrows, M. E. Thompson, S. R. Forrest, *Appl. Phys. Lett.* **1999**, *75*, 4; b) M. A. Baldo, M. E. Thompson, S. R. Forrest, *Nature* **2000**, *403*, 750.

[2] a) X. Gong, M. R. Robinson, J. C. Ostrowki, D. Moses, G. C. Bazan, A. J. Heeger, *Adv. Mater.* **2002**, *14*, 581; b) A. Köhler, J. S. Wilson, R. H. Friend, *Adv. Mater.* **2002**, *14*, 701; c) J. G. C. Veinot, T. J. Marks, *Acc. Chem. Res.* **2005**, *38*, 632; d) S. R. Forrest, *Org. Electron.* **2003**, *4*, 45.

[3] a) E. Holder, B. M. W. Langeveld, U. S. Schubert, *Adv. Mater.* **2005**, *17*, 1109; b) C.-L. Li, Y.-J. Su, Y.-T. Tao, P.-T. Chou, C.-H.

 © 2006 Wiley-VCH Verlag GmbH & Co. KGaA, Weinheim

Chien, C.-C. Cheng, R.-S. Liu, *Adv. Funct. Mater.* **2005**, *15*, 387; c) D. K. Rayabarapu, B. M. J. S. Paulose, J.-P. Duan, C.-H. Cheng, *Adv. Mater.* **2005**, *17*, 349; d) Y.-H. Song, S.-J. Yeh, C.-T. Chen, Y. Chi, C.-S. Liu, J.-K. Yu, Y.-H. Hu, P.-T. Chou, S.-M. Peng, G.-H. Lee, *Adv. Funct. Mater.* **2004**, *14*, 1221; e) T. D. Anthopoulos, M. J. Frampton, E. B. Namdas, P. L. Burn, I. D. W. Samuel, *Adv. Mater.* **2004**, *16*, 557; f) A. B. Tamayo, B. D. Alleyne, P. I. Djurovich, S. Lamansky, I. Tsyba, N. N. Ho, R. Bau, M. E. Thompson, *J. Am. Chem. Soc.* **2003**, *125*, 7377; g) Y.-J. Su, H.-L. Huang, C.-L. Li, C.-H. Chien, Y.-T. Tao, P.-T. Chou, S. Datta, R.-S. Liu, *Adv. Mater.* **2003**, *15*, 884; h) W.-S. Huang, J.-T. Lin, C.-H. Chien, Y.-T. Tao, S.-S. Sun, Y.-S. Wen, *Chem. Mater.* **2004**, *16*, 2480; i) P. Coppo, E. A. Plummer, L. De Cola, *Chem. Commun.* **2004**, 1774; j) J. Ding, J. Gao, Y. Cheng, Z. Xie, L. Wang, D. Ma, X. Jing, F. Wang, *Adv. Funct. Mater.* **2006**, *16*, 575; k) S. Jung, Y. Kang, H.-S. Kim, Y.-H. Kim, C.-L. Lee, J.-J. Kim, S.-K. Lee, S.-K. Kwon, *Eur. J. Inorg. Chem.* **2004**, 3415; l) V. V. Grushin, N. Herron, D. D. LeCloux, W. J. Marshall, V. A. Petrov, Y. Wang, *Chem. Commun.* **2001**, 1494.

[4] a) D. M. Pai, J. F. Yanus, M. Stolka, *J. Phys. Chem.* **1984**, *88*, 4714; b) H. Kanai, S. Ichinosawa, Y. Sato, *Synth. Met.* **1997**, *91*, 195.

[5] a) S.-J. Yeh, M.-F. Wu, C.-T. Chen, Y.-H. Song, Y. Chi, M.-H. Ho, S.-F. Hsu, C. H. Chen, *Adv. Mater.* **2005**, *17*, 285; b) K. Brunner, A. van Dijken, H. Börner, J. J. A. M. Bastiaansen, N. M. M. Kiggen, B. M. W. Langeveld, *J. Am. Chem. Soc.* **2004**, *126*, 6035; c) M.-H. Tsai, H.-W. Lin, H.-C. Su, T.-H. Ke, C.-C. Wu, F.-C. Fang, Y.-L. Liao, K.-T. Wong, C.-I. Wu, *Adv. Mater.* **2006**, *18*, 1216; d) K. R. Justin Thomas, J. T. Lin, Y.-T. Tao, C.-W. Ko, *J. Am. Chem. Soc.* **2001**, *123*, 9404; e) P. Strohriegl, J. V. Grazulevicius, *Adv. Mater.* **2003**, *15*, 445.

[6] a) N. J. Lundin, A. G. Blackman, K. C. Gordon, D. L. Officer, *Angew. Chem.* **2006**, *118*, 2644; *Angew. Chem. Int. Ed.* **2006**, *45*, 2583; b) M. H. Chisholm, A. J. Epstein, J. C. Gallucci, F. Feil, W. Pirkle, *Angew. Chem.* **2005**, *117*, 6695; *Angew. Chem. Int. Ed.* **2005**, *44*, 6537; c) A. Kraft, A. C. Grimsdale, A. B. Holmes, *Angew. Chem.* **1998**, *110*, 416; *Angew. Chem. Int. Ed.* **1998**, *37*, 402; d) C. D. Entwistle, T. B. Marder, *Angew. Chem.* **2002**, *114*, 3051; *Angew. Chem. Int. Ed.* **2002**, *41*, 2927.

[7] CCDC-607186 contains the supplementary crystallographic data for this paper. These data can be obtained free of charge from The Cambridge Crystallographic Data Centre via www.ccdc.cam.ac.uk/data_request/cif.

[8] K. A. King, P. J. Spellane, R.-J. Watts, *J. Am. Chem. Soc.* **1985**, *107*, 1431.

 © 2006 Wiley-VCH Verlag GmbH & Co. KGaA, Weinheim

Heterocycle Synthesis

DOI: 10.1002/anie.200602996

Synthesis of Nitrogen Heterocycles by the Ring Opening of Pyridinium Salts**

*Aaron M. Kearney and Christopher D. Vanderwal**

The ring-opening reaction of pyridinium salts dates back over a century to the pioneering work of Zincke and König.[1] Activation of pyridines as their pyridinium salts renders the heterocycle electrophilic at the 2- and 4-positions and enables a diverse range of productive chemistry, with or without ring opening.[2] Treatment of appropriately activated pyridinium salts, such as **1** (Scheme 1), with primary amines leads to the

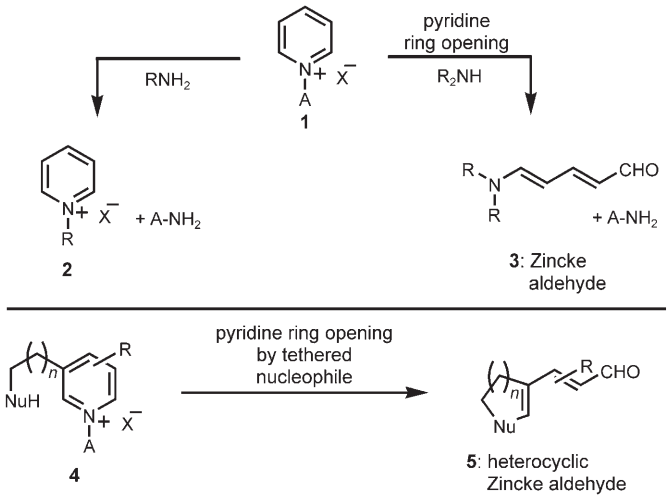

Scheme 1. Proposed use of tethered nucleophiles to induce pyridinium ring opening leading to substituted heterocycles. A = generic activating group.

formation of new pyridinium salts (**2**), whereas the use of secondary amines cleanly affords the products of ring opening.[3,4] Both the ring-opening process and the product 5-amino-2,4-pentadienals (**3**),[4a] now known as Zincke alde-

[*] A. M. Kearney, Prof. C. D. Vanderwal
Department of Chemistry
University of California-Irvine
1102 Natural Sciences II, Irvine, CA 92697-2025 (USA)
Fax: (+1) 949-824-2210
E-mail: cdv@uci.edu

[**] We would like to thank the School of Physical Sciences of the University of California, Irvine, for generous startup funding. Acknowledgment is made to the donors of the American Chemical Society Petroleum Research Fund for partial support of this research through a Type G Starter Grant. New faculty awards from Amgen and Eli Lilly are also gratefully acknowledged. We also thank Joel Silverston for experimental assistance.

Supporting information for this article is available on the WWW under http://www.angewandte.org or from the author.

 © 2006 Wiley-VCH Verlag GmbH & Co. KGaA, Weinheim

hydes, appear ideally suited for manifold applications in synthesis; to date, however, this potential has remained largely unrealized.[5]

We anticipated that the ring opening of activated pyridines by nucleophiles tethered at pyridine C3 would generate a range of useful heterocycles bearing a versatile propenal side chain at C3 of the newly formed ring (**4**→**5**, Scheme 1). By rendering the initial step of this process intramolecular, we hoped to extend the range of nucleophiles beyond simple secondary amines. Thus, the appropriate selection of tether and nucleophile would provide access to a variety of different heterocycles. Our initial progress toward this goal, which entails a nonobvious route to nitrogen heterocycles from pyridines, is the subject of this communication.

The indole nucleus is ubiquitous in natural products and medicinal chemistry. As a result, numerous different approaches to this ring system exist, each offering different levels of practicality for varying applications;[6] indeed, new methods are continually being developed.[7] We expected that a convergent biaryl coupling/pyridine ring opening sequence would provide access to a family of indole derivatives of significant utility, while concurrently providing proof of principle for our general heterocycle synthesis.

A series of pyridinyl-aniline precursors of type **6** (Scheme 2) were synthesized efficiently by Suzuki biaryl couplings.[8] A variety of activating agents were screened,[9] and inexpensive cyanogen bromide emerged as the reagent of choice for indole formation (**6**→**7**). Thus, treatment of a variety of pyridinyl anilines with cyanogen bromide in warm ethanol rapidly afforded the desired indoles (**7**) after hydrolysis of the presumed *N*-cyanoimine intermediate (Table 1). A plausible mechanism to account for the formation of these products is provided in Scheme 2.[10]

To date, this indolization procedure has proven to be general; Table 1 lists every substrate of type **6** that we have subjected to these conditions. A variety of substituents of varying electronic nature are tolerated, and good to excellent yields are observed in nearly every case. The sole outlier is entry 2 of Table 1, wherein the formation of a stable imine condensation product of the aniline and the indole product **7b** occurs under standard conditions, thus preventing completion of the reaction. This problem was easily circumvented by using more dilute reaction conditions, which served to minimize this undesired bimolecular condensation.

Table 1: Formation of substituted indoles from pyridinyl anilines.

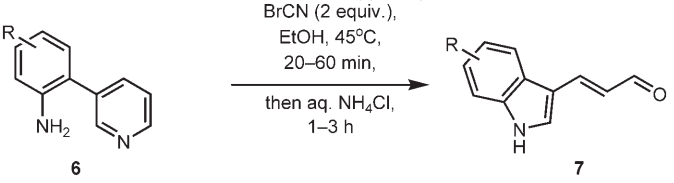

6 7

Entry	Product	Yield [%]	Entry	Product	Yield [%]
1	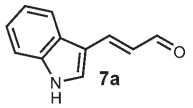 **7a**	78[a]	5	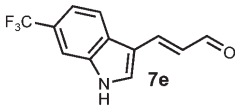 **7e**	78
2	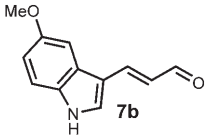 **7b**	73[b]	6	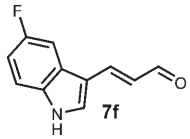 **7f**	65
3	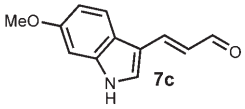 **7c**	80	7	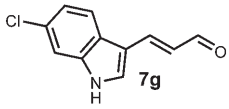 **7g**	74
4	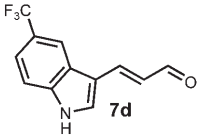 **7d**	63	8	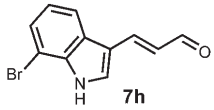 **7h**	80

[a] In a single 110-mmol experiment, a 60% yield was obtained, affording over 10 g of **7a**. [b] Performed at 0.8 mM; the typical procedure is performed at 0.10 M.

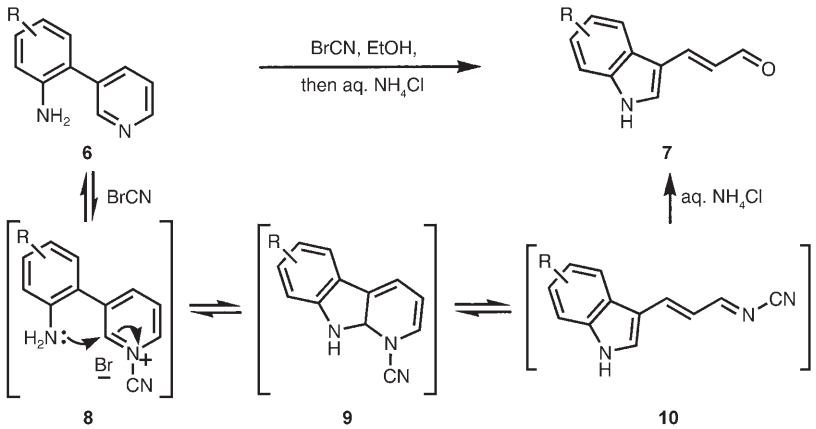

Scheme 2. Presumed reaction course for the conversion of pyridinyl anilines into indoles.

The strength of this strategy lies in its ability to deliver benzene-ring-substituted indoles with the propenal side chain at C3. The location of such a versatile handle at this position distinguishes this method of indole construction; one could imagine a myriad of uses for the enal function. Very useful [4+2] cycloaddition reactivity of either the enal (as dienophile) or the aminopentadienal (as diene) is anticipated for these and related products. In addition, recent work of MacMillan and co-workers suggests that a number of useful enantioselective transformations might be performed on the unsaturated aldehyde moiety of these indole products.[11,12]

Although the results in Table 1 clearly demonstrate versatility with respect to substitution on the carbocyclic ring of the indole, we anticipated that the use of functionalized pyridines would enable the introduction of substituents on the enal side chain. The preliminary experiment shown in [Eq. (1)] supports this idea as the 4-methylpyridine derivative **11** is converted into **12** in a yield comparable to those obtained with unsubstituted pyridines. In addition,

 © 2006 Wiley-VCH Verlag GmbH & Co. KGaA, Weinheim

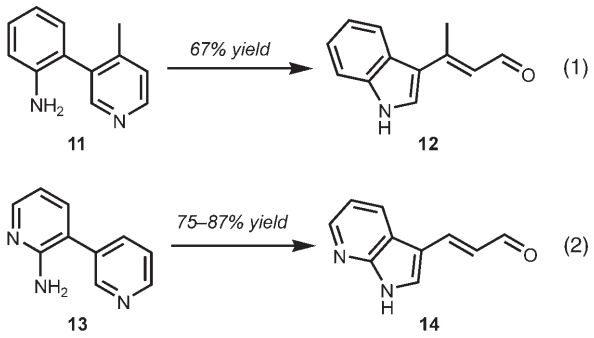

this reaction works especially well in the formation of a 7-azaindole (**14**, [Eq. (2)]) starting from the interesting bipyridine **13**. Given the importance of azaindoles in medicinal chemistry,[13] this is a significant result.

Initial efforts to expand this reactivity to pyridines bearing non-aniline nucleophiles, such as 3-(2-ethylamino)-pyridine (**15**), led, as anticipated, to exclusive *N*-cyanation of the primary amine. We considered the balance of nucleophilicity associated with anilines of type **6** and expected that, by depressing the nucleophilicity of the tethered amine in substrates such as **15**, our strategy might be amenable to the synthesis of other nitrogen heterocycles. With the *N*-benzoyl amide of 3-(2-ethylamino)-pyridine (**16**), no productive reactivity was observed upon exposure to the optimal conditions for indole formation. However, generation of the *N*-arylated pyridinium salt **17**, and subsequent treatment of this activated pyridine with excess dimethylamine with warming in an open flask, led to *N*-benzoyl dihydropyrrole **18** in 57% yield over two steps (Scheme 3). This transformation may proceed through an initial pyridinium ring opening by dimethylamine to form **19**, followed by cyclization of the amide onto the conjugated iminium ion to afford **20** with release of volatile dimethylamine; this iminium ion is hydrolyzed upon workup to afford **18**. Other mechanisms have not been ruled out.

The use of the century-old pyridinium-ring-opening reaction with tethered nucleophiles has led to a convergent two-step synthesis of a series of indole-3-propenals. Preliminary experiments with tethered amides have indicated that, with the correct choice of experimental parameters, variation of nucleophile/tether combinations is also tolerated. Therefore, this reaction of pyridinium salts represents not simply a new indole synthesis, but rather the first step towards a potentially general protocol for heterocycle synthesis. We envision extension to oxygen- and sulfur-containing heterocycles, and carbocycles, as well as applications in natural-product synthesis and medicinal chemistry.

Experimental Section

General procedure for cyanogen bromide mediated pyridine ring opening: (*E*)-3-(1*H*-Indol-3-yl)-propenal (**7a**): To a 100-mL round-bottom flask equipped with a magnetic stir bar was added 2-pyridin-3-ylphenylamine (1.05 g, 6.2 mmol) and absolute ethanol (55.0 mL). The light-yellow solution was warmed to 40 °C before the addition of cyanogen bromide (1.31 g, 12.4 mmol) as a solution in EtOH (5 mL). After 20 min 10% aqueous ammonium chloride (20.0 mL) was added to the dark-red solution, which was allowed to stir at 40 °C for 3 h. The crude reaction mixture was concentrated in vacuo, and the residue was taken up in EtOAc, washed with saturated $NaHCO_3$, concentrated in vacuo, preloaded onto silica gel, and purified by flash chromatography (40% → 60% EtOAc/hexanes) to afford pure **7a** as a orange solid (695 mg, 70%): m.p. 108–110 °C (EtOAc); ^{1}H NMR (500 MHz, CD_3OD, 298 K): $\delta = 9.53$ (d, $J = 8.1$ Hz, 1H), 8.71 (d, $J = 15.7$ Hz, 1H), 7.89 (d, $J = 7.1$ Hz, 1H), 7.83 (s, 1H), 7.49 (d, $J = 7.2$ Hz, 1H), 7.30–7.23 (m, 2H), 6.75 (dd, $J = 8.1$, 15.7 Hz, 1H); ^{13}C NMR (125 MHz, CD_3OD, 298 K): $\delta = 196.8$, 150.9, 139.6, 133.9, 126.7, 124.4, 124.1, 122.9, 121.2, 114.6, 113.5; IR (KBr) 3252, 2238, 1651, 1609 cm^{-1}; TLC $R_f = 0.80$ (100% EtOAc); LRMS (ESI) *m*/*z* (relative intensity): 172 (100); HRMS (CI) *m*/*z* calcd for $C_{11}H_{10}NO$ $[M+H]^+$, 172.0762, found 172.0760.

Received: July 25, 2006
Published online: October 30, 2006

Keywords: biaryls · cyclization · indoles · nitrogen heterocycles · pyridinium salts

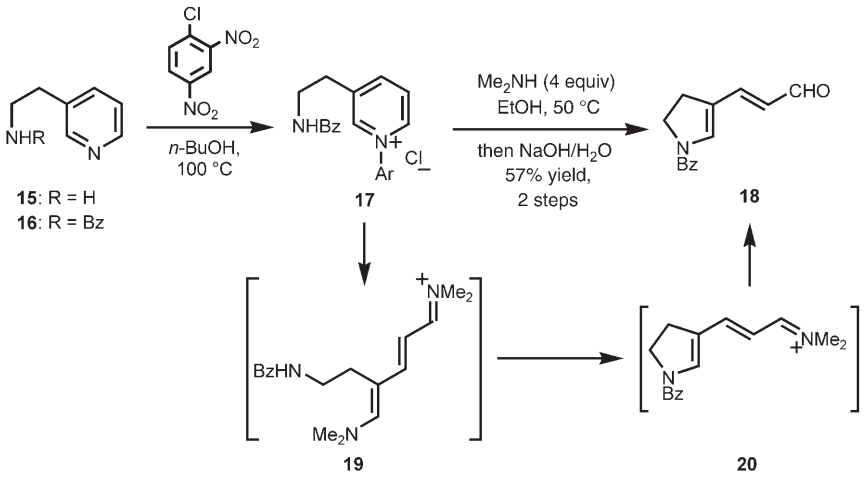

Scheme 3. The synthesis of *N*-protected dihydropyrrole **18** exemplifies alternative pyridine activation strategy for weak nucleophiles. Ar = 2,4-dinitrophenyl, Bz = benzoyl.

[1] a) T. Zincke, *Justus Liebigs Ann. Chem.* **1903**, *330*, 361–374; b) T. Zincke, *Justus Liebigs Ann. Chem.* **1904**, *333*, 296–345; c) T. Zincke, W. Wurker, *Justus Liebigs Ann. Chem.* **1905**, *338*, 107–141; d) W. König, *J. Prakt. Chem.* **1904**, *69*, 105–137.

[2] For selected examples of reactions that occur without ring opening, see the following leading references: a) D. L. Comins, J. J. Sahn, *Org. Lett.* **2005**, *7*, 5227–5228; b) E. J. Corey, Y. Tian, *Org. Lett.* **2005**, *7*, 5535–5537; c) T. Focken, A. B. Charette, *Org. Lett.* **2006**, *8*, 2985–2988.

[3] Please see the Supporting Information for plausible mechanisms for these transformations.

[4] For reviews, please see: a) J. Becher, *Synthesis* **1980**, 589–613; b) W.-C.

 © 2006 Wiley-VCH Verlag GmbH & Co. KGaA, Weinheim

Cheng, M. J. Kurth, *Org. Prep. Proced. Int.* **2002**, *34*, 587 – 608; c) C. M. Rojas in *Name Reactions in Heterocyclic Chemistry* (Ed.: J. J. Li), Wiley, Hoboken, **2005**, pp. 355 – 374. Also, see J. Becher, L. Finsen, I. Winckelmann, *Tetrahedron* **1981**, *37*, 2375 – 2378.

[5] a) For applications of these compounds in the dye industry, see: A. Mishra, R. K. Behera, P. K. Behera, B. K. Mishra, G. B. Behera, *Chem. Rev.* **2000**, *100*, 1973 – 2011; b) For a two-step azulene synthesis featuring 5-amino-2,4-pentadienals, see: K. Hafner, K.-D. Asmus, *Justus Liebigs Ann. Chem.* **1964**, *671*, 31 – 40; c) For one application in natural product synthesis, see: K. Jakubowicz, K. B. Abdeljelil, M. Herdemann, M.-T. Martin, A. Gateau-Olesker, A. A. Mourabit, C. Marazano, B. C. Das, *J. Org. Chem.* **1999**, *64*, 7381 – 7387.

[6] For a comprehensive review of methods for indole synthesis, see: J. A. Joule, *Sci. Synth.* **2001**, *10*, 361 – 652.

[7] Selected recent indole syntheses: a) T. J. Greshock, R. L. Funk, *J. Am. Chem. Soc.* **2006**, *128*, 4946 – 4947; b) D. F. Taber, W. Tian, *J. Am. Chem. Soc.* **2006**, *128*, 1058 – 1059, and references therein.

[8] For a review, see: A. Suzuki in *Modern Arene Chemistry* (Ed.: D. Astruc), Wiley-VCH, Weinheim, **2002**, pp. 53 – 106. Please see the Supporting Information for experimental details.

[9] Typical activating agents include 2,4-dinitrochlorobenzene, cyanogen halides, and sulfur trioxide. See references [1] and [4a].

[10] The conversion of **9** into **10** could conceivably occur through an electrocyclic pathway or a simple ionic mechanism; either would be followed by simple alkene geometrical isomerizations.

[11] Y. Huang, A. M. Walji, C. H. Larsen, D. W. C. MacMillan, *J. Am. Chem. Soc.* **2005**, *127*, 15051 – 15053, and references therein. Although we suspect that the reactivity of products of type **7** will almost certainly be different from regular α,β-unsaturated aldehydes owing to the conjugation of the indole nitrogen, the incorporation of an electron-withdrawing *N*-protecting group might result in reasonable reactivity in iminium-based asymmetric organocatalysis. For a relevant example, please see reference [12].

[12] An indole-3-propenal was used in an asymmetric organocatalytic Diels–Alder reaction in a synthesis of hapalindole Q: A. C. Kinsman, M. A. Kerr, *J. Am. Chem. Soc.* **2003**, *125*, 14120 – 14125.

[13] For a few select examples, see: Neurological therapy: a) N. R. Curtis, J. J. Kulagowski, P. D. Leeson, M. P. Ridgill, F. Emms, S. B. Freedman, S. Patel, S. Patel, *Bioorg. Med. Chem. Lett.* **1999**, *9*, 585 – 588; b) G. A. Showell, F. Emms, R. Marwood, D. O'Connor, S. Patel, P. D. Leeson, *Bioorg. Med. Chem.* **1998**, *6*, 1 – 8; Antiviral therapy: c) T. Wang, Z. Zhang, O. B. Wallace, M. Deshpande, H. Fang, Z. Yang, L. M. Zadjura, D. L. Tweedie, S. Huang, F. Zhao, S. Ranadive, B. S. Robinson, Y.-F. Gong, K. Ricarrdi, T. P. Spicer, C. Deminie, R. Rose, H.-G. H. Wang, W. S. Blair, P.-Y. Shi, P.-f. Lin, R. J. Colonno, N. A. Meanwell, *J. Med. Chem.* **2003**, *46*, 4236 – 4239.

 © 2006 Wiley-VCH Verlag GmbH & Co. KGaA, Weinheim

Photocatalysis

DOI: 10.1002/anie.200602473

Noble-Metal/Cr_2O_3 Core/Shell Nanoparticles as a Cocatalyst for Photocatalytic Overall Water Splitting**

*Kazuhiko Maeda, Kentaro Teramura, Daling Lu, Nobuo Saito, Yasunobu Inoue, and Kazunari Domen**

Catalytic overall water splitting (OWS) in the presence of a semiconductor photocatalyst has been studied extensively as a potential method to supply clean and renewable hydrogen. Although a number of metal oxides have been reported to be active photocatalysts for this reaction, most only function under UV irradiation owing to the large band-gap energy of the materials (>3 eV).[1] To utilize solar energy to drive this reaction, it is therefore necessary to develop a visible-light-responsive photocatalyst, and numerous attempts have been made in recent years to produce such a material.[2–4] We have reported that certain oxynitrides, such as TaON,[3a] $LaTiO_2N$,[3b] and the $(Ga_{1-x}Zn_x)(N_{1-x}O_x)$ solid solution,[4] are promising stable photocatalysts for OWS under visible-light irradiation. Although these oxynitrides exhibit high photocatalytic activity for water oxidation in the presence of an appropriate electron acceptor,[3,4d] their activity for water reduction is approximately one order of magnitude lower than that for water oxidation. An effective modification method to promote the water reduction is therefore required to improve the overall efficiency of these oxynitrides.

Noble metals or transition-metal oxides are often employed as a cocatalyst to facilitate water reduction. Such cocatalysts are typically applied as nanoparticles (NPs) to the catalyst surface by impregnation or in situ photodeposition. In the impregnation method, active species are dispersed randomly on the photocatalyst surface and an activation

[*] K. Maeda, Dr. K. Teramura, Prof. Dr. K. Domen
Department of Chemical System Engineering
School of Engineering
The University of Tokyo
7-3-1 Hongo, Bunkyo-ku, Tokyo, 113-8656 (Japan)
Fax: (+81) 3-5841-8838
E-mail: domen@chemsys.t.u-tokyo.ac.jp
Dr. D. Lu, Prof. Dr. K. Domen
Solution-Oriented Research for Science and Technology (SORST)
Programs of the Japan Science and Technology Corporation (JST)
4-1-8 Honcho, Kawaguchi-shi, Saitama 332-0012 (Japan)
Dr. N. Saito, Prof. Dr. Y. Inoue
Department of Chemistry
Nagaoka University of Technology
1603-1 Kamitomioka, Nagaoka, Niigata 940-2188 (Japan)

[**] This work was supported by the SORST program of the Japan Science and Technology (JST) Agency and the 21st Century Center of Excellence (COE) program of the Ministry of Education, Culture, Sports, Science, and Technology of Japan.

Supporting Information for this article is available on the WWW under http://www.angewandte.org or from the author.

WILEY InterScience DISCOVER SOMETHING GREAT
© 2006 Wiley-VCH Verlag GmbH & Co. KGaA, Weinheim

treatment, such as reduction or oxidation, is necessary to obtain high activity.[1,4] This approach appears to be somewhat unsuitable for oxynitrides as they are less thermally stable than the corresponding metal oxides.[5] In contrast, in situ photodeposition allows the cocatalysts to be loaded selectively at reaction sites without the need for an activation treatment.[6] However, most of the cocatalysts suitable for introduction by this method are noble metals (e.g., Rh, Pd, and Pt), which act as a catalyst not only for water reduction but also for water formation from H_2 and O_2, an undesirable backward reaction.[1b] Although Kudo et al. have reported that La-doped $NaTaO_3$ ($NaTaO_3$:La) photodeposited with IrO_2 has a higher photocatalytic activity for OWS than $NaTaO_3$:La alone, it has been confirmed that the loaded IrO_2 functions as a promoter of water oxidation.[1h] A new modification method that realizes a water-reducing cocatalyst without the need for an activation treatment is therefore desirable. Herein, a new strategy for the production of a water-reduction catalyst is proposed. In this approach, cocatalyst NPs consisting of a noble-metal core and Cr_2O_3 shell are prepared for use with the $(Ga_{1-x}Zn_x)(N_{1-x}O_x)$ solid solution,[4] and this catalytic system is demonstrated to be effective for visible-light-driven OWS.

Noble-metal/Cr_2O_3 (core/shell) NPs were prepared by an in situ photodeposition method[6] from a noble-metal complex salt (e.g., $Na_3RhCl_6{\cdot}2H_2O$) and K_2CrO_4 as precursors. Noble-metal NPs were first photodeposited on $(Ga_{1-x}Zn_x)(N_{1-x}O_x)$ ($x = 0.12$; represented as GaN:ZnO hereafter), which was prepared by a reported method.[4a,b] Figure 1a shows a high-resolution (HR) TEM image of a catalyst loaded with 1 wt% Rh. The primary particle size of the introduced Rh NPs is 2–3 nm, although some of them aggregate to form larger secondary particles. The Rh-loaded sample (0.3 g) was then dispersed in an aqueous K_2CrO_4 solution (0.234 mM). After evacuation, the solution was exposed to visible-light irradiation ($\lambda > 400$ nm) for 4 h to reduce K_2CrO_4 to Cr_2O_3.[7] The final product was washed thoroughly with distilled water and dried overnight at 343 K. The HR-TEM images of this sample are shown in Figure 1b, which shows that the Rh NPs have been coated with a shell layer about 2 nm thick to form a core/shell nanostructure. Although some of them form large agglomerates, the shell thickness is almost constant (ca. 2 nm) regardless of the size of the Rh particle. Examining over 50 particles irradiated with visible light in an aqueous K_2CrO_4 solution showed that all the particles had a core/shell structure. It was confirmed by X-ray absorption fine-structure spectroscopy (XAFS) and X-ray photoelectron spectroscopy (XPS) that the core and the shell consist of metallic Rh and Cr_2O_3, respectively.

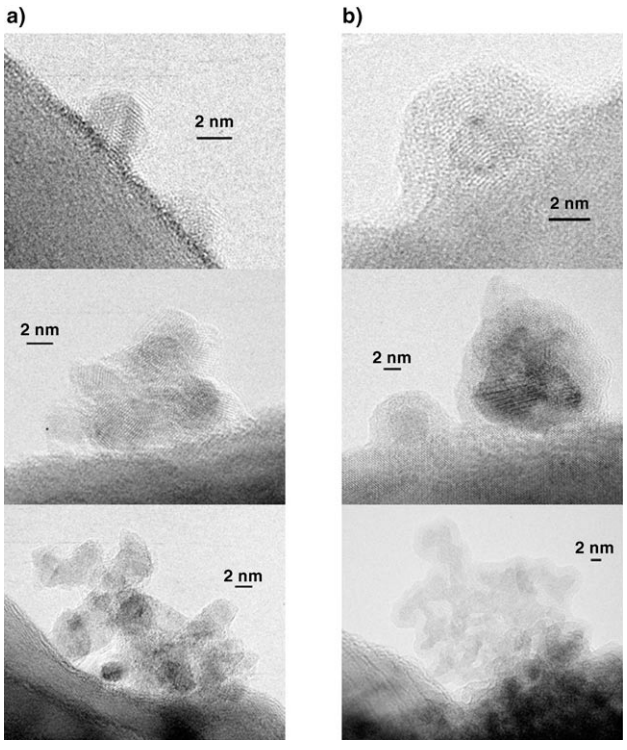

Figure 1. HR-TEM images of Rh-loaded $(Ga_{1-x}Zn_x)(N_{1-x}O_x)$ before (a) and after (b) photodeposition of the Cr shell.

After shell formation, the particle size distribution (Figure 2b; based on the HR-TEM observations) is shifted to larger size compared with that before shell formation (Figure 2a), which suggests an increase in particle size. The

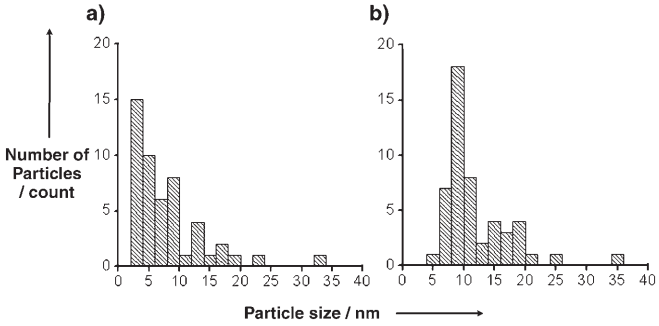

Figure 2. Particle size distribution histograms of Rh-loaded $(Ga_{1-x}Zn_x)$-$(N_{1-x}O_x)$ before (a) and after (b) photodeposition of the Cr shell.

average sizes of 50 different particles of Rh and Rh/Cr_2O_3 were calculated to be about 7.6 and 11.8 nm, respectively. The difference in these average sizes (4.2 nm) is close to twice the Cr_2O_3 shell thickness (ca. 2 nm) surrounding the Rh NPs. This result supports the idea that a Cr_2O_3 shell about 2-nm thick covers all of the Rh NPs, as indicated by the TEM images (Figure 1b).

Rh-loaded GaN:ZnO exhibits little photocatalytic activity for OWS even after extended periods of irradiation, probably because of rapid water formation on the Rh NPs.[1b] However, GaN:ZnO loaded with the Rh/Cr_2O_3 core/shell cocatalyst gives stoichiometric H_2 and O_2 evolution from pure water. A typical time course of OWS on Rh/Cr_2O_3-loaded GaN:ZnO under visible-light irradiation ($\lambda > 400$ nm) is shown in Figure 3a.[8] Both H_2 and O_2 evolve steadily and stoichiometrically as the reaction proceeds, thereby indicating migration of the electrons photogenerated[9] in the GaN:ZnO to the surface of the Cr_2O_3 shell to reduce H^+ to H_2. Addition of the Rh-loaded catalyst to the reactant suspension containing the Rh/Cr_2O_3-loaded catalyst resulted in a marked decrease in the rates of both H_2 and O_2 evolution (Figure 3b). It is thus clear that water formation from H_2 and

 © 2006 Wiley-VCH Verlag GmbH & Co. KGaA, Weinheim

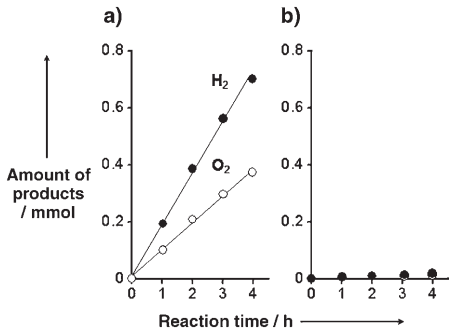

Figure 3. Time courses of OWS using Rh/Cr_2O_3-loaded $(Ga_{1-x}Zn_x)(N_{1-x}O_x)$ under visible-light irradiation ($\lambda > 400$ nm). a) 0.15 g of catalyst, b) mixture of 0.15 g of catalyst with 0.15 g of a sample loaded with Rh-NPs. Reactions were performed in pure water (370 mL) with illumination from a high-pressure mercury lamp (450 W) through an aqueous 2 M $NaNO_2$ solution filter.

O_2 on unmodified Rh NPs is significant in the OWS reaction and that the suppression of water formation is therefore essential to achieve efficient evolution of H_2 and O_2 in this system.

The use of other noble metals, such as Ir and Pt, as a core with the Cr_2O_3 shell in the same manner achieves similar results to those observed for Rh (see Supporting Information, Table S1). This modification method could be applicable to other photocatalysts for OWS, such as $SrTiO_3$ and $NaTaO_3$.

A schematic illustration of the reaction mechanism of OWS on Rh/Cr_2O_3-loaded GaN:ZnO is shown in Figure 4. As demonstrated above, H_2 evolution occurs on the Cr_2O_3-coated Rh NPs, whereas the impregnation of GaN:ZnO with Cr_2O_3 NPs alone (3–10 nm) does not promote OWS.[4d] This behavior indicates that Cr_2O_3 on GaN:ZnO cannot induce the migration of photogenerated electrons from the bulk to the catalyst surface but instead provides sites at which adsorbed protons (H^+) are reduced to H atoms by photogenerated electrons to form H_2 molecules. H_2 evolution also occurs on Rh NPs loaded on GaN:ZnO in the absence of O_2,[4e] thus indicating that the electrons photogenerated in the GaN:ZnO bulk by visible-light absorption can indeed migrate to the

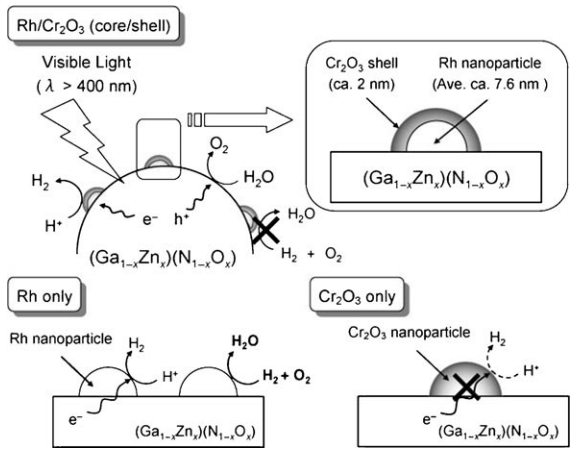

Figure 4. A schematic reaction mechanism of OWS on Rh/Cr_2O_3-loaded $(Ga_{1-x}Zn_x)(N_{1-x}O_x)$ and the corresponding processes on supported Rh NPs and Cr_2O_3 NPs. See text for details.

Rh NPs and cause H_2 evolution. However, in the presence of O_2, this H_2 reacts immediately with O_2 on the Rh NPs to form H_2O as mentioned above. Nosaka et al. have reported that noble metals dispersed on TiO_2 can generate an electronic field between the noble metal and the TiO_2, thereby promoting electron transfer from the TiO_2 to the noble metal.[10] A similar promotion effect on the electron transfer from GaN:ZnO to Rh NPs is therefore expected to occur in the present case. Accordingly, in the Rh/Cr_2O_3/GaN:ZnO system, the Rh NPs forming the core are considered to play the role of inducing the migration of photogenerated electrons from the GaN:ZnO bulk and the Cr_2O_3 shell provides an H_2 evolution site at the external surface while preventing water formation from H_2 and O_2 on Rh. Thus, the sandwich structure of Rh/Cr_2O_3/GaN:ZnO is indispensable for achieving OWS. In photocatalytic OWS, cocatalysts such as NiO_x,[1a,c,d,g] RuO_2,[1e,f,4a–c] and $Rh_{2-y}Cr_yO_3$,[4d,e] play at least two roles simultaneously, namely extraction of photogenerated electrons or holes from the photocatalyst bulk and reduction of H^+ to H_2 or oxidation of H_2O to O_2 on the cocatalyst surface. In contrast, these two roles are successfully separated in the present core/shell cocatalyst, which is of interest in considering the role of cocatalysts loaded on a photocatalyst.

Another core/shell cocatalyst, namely Ni/NiO core/shell NPs, for photocatalytic OWS has been reported by some of us and applied to many heterogeneous photocatalytic systems.[1a,c,d,g] Compared with Ni/NiO, the present core/shell cocatalyst has several advantages, including the possibility of selectively introducing active species for OWS at the reduction sites of the photocatalyst, the possibility of using various noble metals as the core for extraction of photogenerated electrons from the bulk, and elimination of the need for activation treatment by oxidation or reduction. Although the performance of the present Rh/Cr_2O_3-loaded GaN:ZnO catalyst is lower than that reported for the $Rh_{2-y}Cr_yO_3$-loaded catalyst,[4d,e] the present modification method offers a new strategy to create a water-reducing cocatalyst for photocatalytic OWS. This method may also be useful for reducing Cr^{6+} ion pollution in industrial waste water[7] through the use of solar energy as well as hydrogen production by OWS. This possibility is currently under investigation.

Received: June 20, 2006
Revised: September 1, 2006
Published online: October 27, 2006

Keywords: heterogeneous catalysis · hydrogen · nanostructures · photolysis · semiconductors

[1] a) K. Domen, S. Naito, M. Soma, T. Onishi, K. Tamaru, *J. Chem. Soc. Chem. Commun.* **1980**, 543–544; b) K. Yamaguti, S. Sato, *J. Chem. Soc. Faraday Trans. 1* **1985**, *81*, 1237–1246; c) K. Domen, A. Kudo, T. Onishi, N. Kosugi, H. Kuroda, *J. Phys. Chem.* **1986**, *90*, 292–295; d) K. Domen, A. Kudo, T. Onishi, *J. Catal.* **1986**, *102*, 92–98; e) Y. Inoue, T. Kubokawa, K. Sato, *J. Phys. Chem.* **1991**, *95*, 4059–4063; f) J. Sato, N. Saito, H. Nishiyama, Y. Inoue, *J. Phys. Chem. B* **2001**, *105*, 6061–6063; g) H. Kato, A. Kudo, *Catal. Today* **2003**, *78*, 561–569; h) A. Iwase, H. Kato, A. Kudo, *Chem. Lett.* **2005**, *34*, 946–947.

 © 2006 Wiley-VCH Verlag GmbH & Co. KGaA, Weinheim

[2] a) A. Kudo, H. Kato, I. Tsuji, *Chem. Lett.* **2004**, *33*, 1534 – 1539; b) H. G. Kim, P. H. Borse, W. Choi, J. S. Lee, *Angew. Chem.* **2005**, *117*, 4585 – 4589; *Angew. Chem. Int. Ed.* **2005**, *44*, 4585 – 4589; c) R. Abe, K. Sayama, H. Sugihara, *J. Phys. Chem. B* **2005**, *109*, 16052 – 16061; d) P. G. Hoertz, T. E. Mallouk, *Inorg. Chem.* **2005**, *44*, 6828 – 6840.

[3] a) G. Hitoki, T. Takata, J. N. Kondo, M. Hara, H. Kobayashi, K. Domen, *Chem. Commun.* **2002**, 1698 – 1699; b) A. Kasahara, K. Nukumizu, G. Hitoki, T. Takata, J. N. Kondo, M. Hara, H. Kobayashi, K. Domen, *J. Phys. Chem. A* **2002**, *106*, 6750 – 6753.

[4] a) K. Maeda, T. Takata, M. Hara, N. Saito, Y. Inoue, H. Kobayashi, K. Domen, *J. Am. Chem. Soc.* **2005**, *127*, 8286 – 8287; b) K. Maeda, K. Teramura, T. Takata, M. Hara, N. Saito, K. Toda, Y. Inoue, H. Kobayashi, K. Domen, *J. Phys. Chem. B* **2005**, *109*, 20504 – 20510; c) K. Teramura, K. Maeda, T. Saito, T. Takata, N. Saito, Y. Inoue, K. Domen, *J. Phys. Chem. B* **2005**, *109*, 21915 – 21921; d) K. Maeda, K. Teramura, D. Lu, T. Takata, N. Saito, Y. Inoue, K. Domen, *Nature* **2006**, *440*, 295; e) K. Maeda, K. Teramura, H. Masuda, T. Takata, N. Saito, Y. Inoue, K. Domen, *J. Phys. Chem. B* **2006**, *110*, 13107 – 13112.

[5] L. L. Gendre, R. Marchand, Y. Laurent, *J. Eur. Ceram. Soc.* **1997**, *17*, 1813 – 1818.

[6] B. Kraeutler, A. J. Bard, *J. Am. Chem. Soc.* **1978**, *100*, 4317 – 4318.

[7] B. Sun, E. P. Reddy, P. G. Smirniotis, *Environ. Sci. Technol.* **2005**, *39*, 6251 – 6259.

[8] The reaction was carried out as reported elsewhere; see reference [4].

[9] Herein we define photogenerated electrons as electrons generated in the conduction bands of GaN:ZnO by visible-light absorption.

[10] Y. Nosaka, K. Norimatsu, H. Miyama, *Chem. Phys. Lett.* **1984**, *106*, 128 – 131.

 © 2006 Wiley-VCH Verlag GmbH & Co. KGaA, Weinheim

Nonnatural Base Pairs

DOI: 10.1002/anie.200602579

Stability and Polymerase Recognition of Pyridine Nucleobase Analogues: Role of Minor-Groove H-Bond Acceptors**

*Yoonkyung Kim, Aaron M. Leconte, Yoshiyuki Hari, and Floyd E. Romesberg**

The information potential of a genome is limited by the four-letter, two-base-pair genetic alphabet. Significant efforts have been directed towards developing a third, unnatural base pair, which would expand the genetic alphabet and lay the foundations of an expanded genetic code. Studies from the Benner and Kool groups have elegantly demonstrated that the interbase hydrogen bonds (H-bonds) may be rearranged,[1] or removed altogether,[2] without complete loss of stability or polymerase recognition; this information has inspired design strategies based on the use of predominantly hydrophobic nucleobase analogues.[3]

While base-pair stability and efficient replication are required for any unnatural base-pair candidate, predominantly hydrophobic analogues are consistently limited by extension, that is, efficient primer elongation after synthesis of the unnatural base pair at a primer terminus.[3a,c] One possible explanation for inefficient extension is that, while properly positioned H-bonds are not required to mediate interbase recognition, they are required at the primer terminus to appropriately engage the polymerase for efficient DNA synthesis.[4,5] We have previously optimized nucleobase analogues by the inclusion of natural-nucleobase-like carbonyl groups in a position β to an *N*-glycosidic linkage.[6] However, this natural-like H-bond acceptor also reintroduces interbase H-bonds and facilitates mispairing. By contrast, H-bond acceptors at the α position of C-nucleosides should be less recognized by the natural nucleobases but may still be able to engage the polymerase appropriately for DNA synthesis.

Here, we report the synthesis and analysis of three pyridyl nucleotide analogues that are designed to explore the effect of positioning a nitrogen atom in the minor groove (**2Py**), the interbase interface (**3Py**), or the major groove (**4Py**) (Scheme 1). We focus on the evaluation of the corresponding self pairs (that is, pairs formed between two identical analogues). Each nucleoside was synthesized, converted into the corresponding phosphoramidite, and incorporated into DNA as described in the Supporting Information.

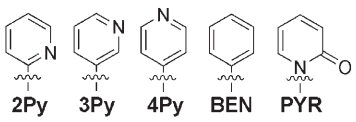

Scheme 1. Unnatural nucleobases. **BEN**[3c,7b] and **PYR**[6] have been previously reported and are included for comparison (see the text).

To explore the effect of aza substitution on thermal stability and selectivity, the melting temperatures (T_m) of duplexes containing the unnatural base pairs or mispairs were determined (Table 1). The **2Py** self pair was the most stable ($T_m = 52.2\,°C$), followed by the **3Py** and **4Py** self pairs ($T_m =$ 50.2 and 48.1 °C, respectively). Thus, the introduction of a single nitrogen substituent can alter self-pair stability by more than 4 °C. This is in contrast to the much smaller variations associated with fluoro, bromo, cyano, or methyl derivatization, which were each less than 2 °C.[3b,7] For all but **2Py**, the self pairs are significantly less stable than the parental, unsubstituted **BEN** self pair ($T_m = 52.8\,°C$; Scheme 1). We also examined the stability of heteropairs formed between the pyridyl nucleotides; heteropairs containing **2Py** were again

[*] Y. Kim, A. M. Leconte, Y. Hari, Prof. Dr. F. E. Romesberg
Department of Chemistry
The Scripps Research Institute
10550 North Torrey Pines Road, La Jolla, CA 92037 (USA)
Fax: (+1) 858-784-7472
E-mail: floyd@scripps.edu

[**] We acknowledge the National Institutes of Health (GM60005 to F.E.R.) and the Uehara Memorial Foundation (Y.H.) for financial support.

Supporting information for this article is available on the WWW under http://www.angewandte.org or from the author.

 © 2006 Wiley-VCH Verlag GmbH & Co. KGaA, Weinheim

Table 1: Denaturation temperatures for duplex DNA containing **2Py**, **3Py**, and **4Py**.[a]

5′-dGCGTAC**X**CATGCG
3′-dCGCATG**Y**GTACGC

X	Y	T_m [°C]	X	Y	T_m [°C]	X	Y	T_m [°C]
2Py	**2Py**	52.2	**3Py**	**2Py**	51.1	**4Py**	**2Py**	50.1
2Py	**3Py**	51.1	**3Py**	**3Py**	50.2	**4Py**	**3Py**	49.6
2Py	**4Py**	49.6	**3Py**	**4Py**	49.1	**4Py**	**4Py**	48.1
2Py	A	50.2	**3Py**	A	50.2	**4Py**	A	49.1
2Py	C	44.2	**3Py**	C	44.7	**4Py**	C	45.1
2Py	G	49.2	**3Py**	G	52.7	**4Py**	G	49.6
2Py	T	47.7	**3Py**	T	49.2	**4Py**	T	50.1

[a] Determined in 10 mM 1,4-piperazinediethanesulfonic acid (PIPES), 10 mM $MgCl_2$, and 100 mM NaCl (pH 7). The error in the T_m values is ±0.1 °C

the most stable, although they were not as stable as the **2Py** self pair (Table 1).

The stability of the pyridyl base pairs probably results from a compromise between stabilizing hydrophobic forces, due to transfer of the hydrophobic analogues into the less polar duplex interior, and destabilizing desolvation effects. Forced desolvation will destabilize base-pair formation as the pyridyl analogues are expected to be more favorably solvated in single-stranded DNA.[8] Forced desolvation also explains the relative stability of the pairs involving **2Py**, as only its nitrogen atom will be oriented into the duplex minor groove where stabilizing H-bonds with water molecules from the spine of solvation[9] can offset the cost of desolvation.

Interestingly, as described above, **2Py** formed more stable unnatural base pairs than **3Py** and **4Py**; however, it did not form more stable mispairs (Table 1). Thus, the **2Py** self pair is thermally selective by 2.0–8.0 °C. This compares favorably to the thermal selectivity observed among natural base pairs.[10] The thermal selectivity of the **3Py** and **4Py** self pairs is limited by stable mispairing with dG or dT, respectively. In each case, the stability of the mispair may result from H-bonding (Scheme 2).[9b,11] While only speculative, these arguments

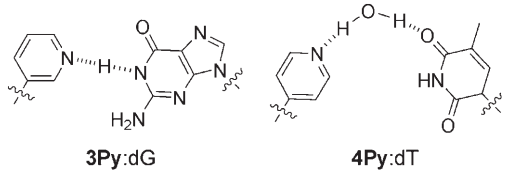

Scheme 2. H-bonding interactions that may underlie the relative stability of the **3Py**:dG and **4Py**:dT mispairs.

are consistent with the idea that desolvation is important for both mispair and unnatural base-pair stability, as H-bonds within the duplex environment would again compensate for the H-bonds with water that are lost upon duplex formation. Regardless of the interpretation, it appears that the minor-groove H-bond acceptor at the α position of **2Py** is not appropriately positioned to interact with the H-bond donors of the natural nucleobases.

The ability of the exonuclease-deficient Klenow fragment of *Escherichia coli* DNA polymerase I (Kf) to extend each self pair was examined by using single-nucleotide-incorporation steady-state kinetics (Table 2). As reported previously, extension of the fully carbocyclic **BEN** self pair, by incorporation of deoxycytidine triphosphate (dCTP) opposite deoxyguanosine (dG) in the template, occurs with a second-order rate constant of $1.6\times10^3\,\text{M}^{-1}\,\text{min}^{-1}$.[3c] The **3Py** and **4Py** self pairs are extended with rates that are too low to detect ($k_{cat}/K_M < 10^3\,\text{M}^{-1}\,\text{min}^{-1}$). However, the **2Py** self pair is extended by Kf with a k_{cat}/K_M value of $3.4\times10^4\,\text{M}^{-1}\,\text{min}^{-1}$, at least 34-fold more efficiently than the other pyridyl analogues. Thus, as with base-pair stability, aza substitution has a large effect

Table 2: Correct extension of unnatural self pairs.[a]

5′-dTAATACGACTCACTATAGGGAGA**X**
3′-dATTATGCTGAGTGATATCCCTCT**X**GCTAGGTTACGGCAGGATCGC
↓dCTP
5′-dTAATACGACTCACTATAGGGAGA**X**C
3′-dATTATGCTGAGTGATATCCCTCT**X**GCTAGGTTACGGCAGGATCGC

Unnatural self pair	k_{cat}[b] [min^{-1}]	K_M[b] [μM]	k_{cat}/K_M[b] [M^{-1} min^{-1}]
2Py	2.1 ± 0.8	61 ± 17	3.4×10^4
3Py	n.d.[c]	n.d.[c]	$<1.0\times10^3$
4Py	n.d.[c]	n.d.[c]	$<1.0\times10^3$

[a] See the Supporting Information for experimental details. [b] k_{cat} = rate of catalysis, K_M = Michaelis constant. [c] n.d. = not determined. Rates were too slow for the determination of k_{cat} and K_M independently.

on self-pair extension, with substitution at the *ortho* position substantially increasing the rate of extension and substitution at the *meta* or *para* positions decreasing the rate of extension. The fidelity of **2Py** self-pair extension was also high; the rates of self-pair extension by deoxyguanosine triphosphate (dGTP), deoxyadenosine triphosphate (dATP), or deoxythymidine triphosphate (dTTP) insertion opposite dG were all too low to detect ($k_{cat}/K_M < 10^3\,\text{M}^{-1}\,\text{min}^{-1}$).

The efficiency and fidelity of **2Py** self-pair extension suggests that the *ortho*-pyridyl nitrogen atom is positioned in the developing minor groove and productively engages the polymerase. Interestingly, extension of the **2Py** self pair is only about twofold less efficient than the pyridone scaffold (**PYR**, Scheme 1; extended at $8.2\times10^4\,\text{M}^{-1}\,\text{min}^{-1}$).[6] This small difference is somewhat surprising when it is considered that the minor-groove H-bond acceptor of **2Py** is located at the α position relative to the glycosidic bond, whereas the H-bond acceptor of **PYR** is located at a position β to the glycosidic bond, which is more analogous to the natural nucleobases (Scheme 3).

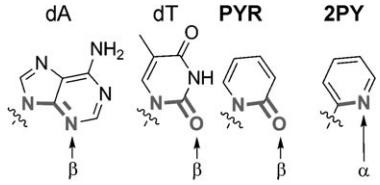

Scheme 3. Minor-groove H-bond acceptors within natural and unnatural scaffolds.

 © 2006 Wiley-VCH Verlag GmbH & Co. KGaA, Weinheim

Based on the efficiency and fidelity of **2Py** self-pair extension, we synthesized the corresponding nucleoside triphosphate (see the Supporting Information) and examined the efficiency of Kf-mediated self-pair synthesis (Table 3).

Table 3: Triphosphate insertion opposite pyridyl analogues in the template.[a]

5′-dTAATACGACTCACTATAGGGAGA
3′-dATTATGCTGAGTGATATCCCTCT**X**GCTAGGTTACGGCAGGATCGC
↓dYTP
5′-dTAATACGACTCACTATAGGGAGA**Y**
3′-dATTATGCTGAGTGATATCCCTCT**X**GCTAGGTTACGGCAGGATCGC

X	Y	k_{cat} [min^{-1}]	K_M [μM]	k_{cat}/K_M [$M^{-1}min^{-1}$]
2Py	**2Py**	0.92 ± 0.16	149 ± 12	6.2×10^3
	A	3.6 ± 1.2	18 ± 2	2.0×10^5
	C	0.16 ± 0.02	98 ± 30	3.2×10^3
	G	0.8 ± 0.3	41 ± 9	2.0×10^4
	T	0.16 ± 0.06	39 ± 9	4.1×10^3
3Py	A	6.8 ± 0.9	25 ± 0.5	2.7×10^5
	C	n.d.[b]	n.d.[b]	$< 1.0 \times 10^3$
	G	11 ± 3	58 ± 13	1.9×10^5
	T	0.54 ± 0.05	83 ± 15	6.5×10^3
4Py	A	11 ± 3	20 ± 6	5.5×10^5
	C	n.d.[b]	n.d.[b]	$< 1.0 \times 10^3$
	G	n.d.[b]	n.d.[b]	$< 1.0 \times 10^3$
	T	1.6 ± 0.3	49 ± 16	3.3×10^4

[a] See the Supporting Information for experimental details. [b] Rates were too slow for the determination of k_{cat} and K_M independently.

The self pair is synthesized with a second-order rate constant of $6.2 \times 10^3\,M^{-1}min^{-1}$. While this synthesis is less efficient than that of self pairs comprised of nucleobase analogues with a large, extended aromatic surface area[3a] or more highly substituted phenyl rings,[3b,c] it is actually high compared to other minimally substituted scaffolds. For example, the **BEN** and **PYR** self pairs are both synthesized at rates less than $10^3\,M^{-1}min^{-1}$.[3c,6]

We also examined the rates at which each natural triphosphate is inserted opposite each pyridyl analogue (Table 3). As with most small hydrophobic analogues, dATP was the most efficiently incorporated deoxynucleoside triphosphate (dNTP) opposite the pyridyl analogues. The rate of dATP insertion showed little dependence on aza substitution and ranged from only 2×10^5–$5.5 \times 10^5\,M^{-1}min^{-1}$. The magnitude and template independence of the rate of dATP insertion suggests that it results from nonspecific hydrophobic interactions. dGTP was the next most efficiently inserted natural triphosphate opposite **2Py** and **3Py**, but its insertion was not detectable opposite **4Py**. The rates are at least roughly correlated with the expected ability of the pyridine moiety to H-bond with guanosine (Scheme 2). The absolute rate at which the **2Py**:dG, **PYR**:dG ($1.2 \times 10^4\,M^{-1}min^{-1}$), and **BEN**:dG ($1.6 \times 10^3\,M^{-1}min^{-1}$) mispairs are formed suggests that while the *ortho* nitrogen atom does not form stable H-bonds with dG in duplex DNA, it facilitates dGTP insertion, although less efficiently than the *meta* nitrogen substituent of **3Py**. dTTP misincorporation opposite **2Py** and **3Py** proceeded with rates of $\approx 5 \times 10^3\,M^{-1}min^{-1}$; however, its insertion was an order of magnitude more efficient opposite **4Py**. Perhaps the same factors that stabilize the **4Py**:dT mispair also contribute to its efficient synthesis. dCTP was not efficiently inserted opposite any of the pyridyl analogues. Overall, the rates at which **2Py** directs the synthesis of mispairs are similar to those of **BEN**,[3c] a result suggesting that the minor-groove H-bond acceptor has only a minor effect on mispair synthesis.

The data demonstrate that the phenyl-ring nucleobase scaffold may be optimized for both base-pair stability and replication by derivatization with an *ortho* nitrogen atom. This H-bond acceptor, which is at the α position relative to the glycosidic linkage, appears to be well positioned to mediate critical minor-groove interactions with water molecules of solvation or with polymerase-based H-bond donors. In contrast to H-bond acceptors introduced at the β position,[6] this H-bond acceptor does not stabilize mispairs in duplex DNA. While the *ortho* nitrogen atom does appear to somewhat facilitate dGTP mispair synthesis, the mispair is synthesized only inefficiently and, in fact, not significantly faster than mispairs among the natural nucleotides.[12] More problematic is the insertion of dATP opposite **2Py**, which is probably mediated by hydrophobic interactions. However, dATP insertion opposite **2Py** is less efficient than with other scaffolds that have already been successfully optimized by derivatization.[7,3b,c] Combination of these modifications with *ortho* aza substitution may result in the simultaneous optimization of interbase interactions and nucleobase–polymerase interactions and it should result in unnatural base pairs that are both more stable and efficiently replicated.

Received: June 28, 2006

Keywords: DNA replication · hydrophobic effects · nucleobases · polymerases · pyridines

[1] J. L. Piccirilli, T. Krauch, S. E. Moroney, S. A. Benner, *Nature* **1990**, *343*, 33–37.
[2] S. Moran, R. X.-F. Ren, S. Rumney IV, E. T. Kool, *J. Am. Chem. Soc.* **1997**, *119*, 2056–2057.
[3] a) D. L. McMinn, A. K. Ogawa, Y. Wu, J. Liu, P. G. Schultz, F. E. Romesberg, *J. Am. Chem. Soc.* **1999**, *121*, 11585–11586; b) A. A. Henry, A. G. Olsen, S. Matsuda, C. Yu, B. H. Geierstanger, F. E. Romesberg, *J. Am. Chem. Soc.* **2004**, *126*, 6923–6931; c) S. Matsuda, A. A. Henry, F. E. Romesberg, *J. Am. Chem. Soc.* **2006**, *128*, 6369–6375; d) T. Mitsui, A. Kitamura, M. Kimoto, T. To, A. Sato, I. Hirao, S. Yokoyama, *J. Am. Chem. Soc.* **2003**, *125*, 5298–5307; e) K. Kinkaid, J. Beckman, A. Zivkovic, R. L. Halcomb, J. W. Engels, R. D. Kuchta, *Nucleic Acids Res.* **2005**, *33*, 2620–2628.
[4] Y. Li, G. Waksman, *Protein Sci.* **2001**, *10*, 1225–1233.
[5] A. S. Meyer, M. Blandolino, T. E. Spratt, *J. Biol. Chem.* **2004**, *279*, 33043–33046.
[6] A. M. Leconte, S. Matsuda, G. T. Hwang, F. E. Romesberg, *Angew. Chem.* **2006**, *118*, 4432–4435; *Angew. Chem. Int. Ed.* **2006**, *45*, 4326–4329.
[7] a) G. T. Hwang, F. E. Romesberg, *Nucleic Acids Res.* **2006**, *34*, 2037–2045; b) S. Matsuda, F. E. Romesberg, *J. Am. Chem. Soc.* **2004**, *126*, 14419–14427.
[8] a) I. Papai, G. Jansco, *J. Phys. Chem. A* **2000**, *104*, 2132–2137; b) L. Partay, P. Jedlovszky, G. Jansco, *J. Phys. Chem. B* **2005**, *109*, 8097–8102.
[9] a) A. N. Lane, T. C. Jenkins, T. A. Frenkiel, *Biochim. Biophys. Acta* **1997**, *1350*, 205–220; b) F. Eisenhaber, V. G. Tumanyan, F. Eisenmenger, W. Gunia, *Biopolymers* **1989**, *28*, 741–761; c) F.-Y.

 © 2006 Wiley-VCH Verlag GmbH & Co. KGaA, Weinheim

Dupradeau, D. A. Case, C. Yu, R. Jimenez, F. E. Romesberg, *J. Am. Chem. Soc.* **2005**, *127*, 15612 – 15617.
[10] M. Berger, A. K. Ogawa, D. L. McMinn, Y. Wu, P. G. Schultz, F. E. Romesberg, *Angew. Chem.* **2000**, *112*, 3069 – 3071; *Angew. Chem. Int. Ed.* **2000**, *39*, 2940 – 2942.
[11] a) Y. X. Wang, S. Huang, D. E. Draper, *Nucleic Acids Res.* **1996**, *24*, 2666 – 2672; b) L. Zendlov, P. Hobza, M. Kabel, *ChemPhysChem* **2006**, *7*, 439 – 447.
[12] K. A. Eckert, T. A. Kunkel, *J. Biol. Chem.* **1993**, *268*, 13462 – 13471.

 © 2006 Wiley-VCH Verlag GmbH & Co. KGaA, Weinheim

Polymer Brushes

DOI: 10.1002/anie.200602508

Reversibly Cross-Linked Surface-Grafted Polymer Brushes**

David M. Loveless, Nehal I. Abu-Lail, Marian Kaholek, Stefan Zauscher, and Stephen L. Craig**

Surface-grafted polymer brushes impart chemical functionality to surfaces and interfaces, and control properties such as colloidal stability, adhesion, wettability, and friction.[1,2] The ability to introduce and modulate cross-links within surface-grafted polymer brushes is expected to influence their mechanical and chemical stability, permeability, and swelling characteristics.[3] Here we report that reversibly cross-linked polymer brushes provide a previously untapped resource for modulating the mechanical properties of surfaces. Bimetallic pincer-Pd^{II} complexes (Figure 1) provide reversible, exogenous cross-linking of end-grafted poly(4-vinylpyridine) (PVP) brushes. Atomic force microscopy (AFM) experiments show that structurally similar cross-linkers with different kinetic reactivities have different effects on the lateral mechanical properties of the brush layer. Surprisingly, not only the magnitude but also the direction of the change in lateral force upon cross-linking depends on the dissociation kinetics of the cross-linkers, which therefore provide a molecular handle by which to control the mechanical properties of surface-grafted polymer brushes.

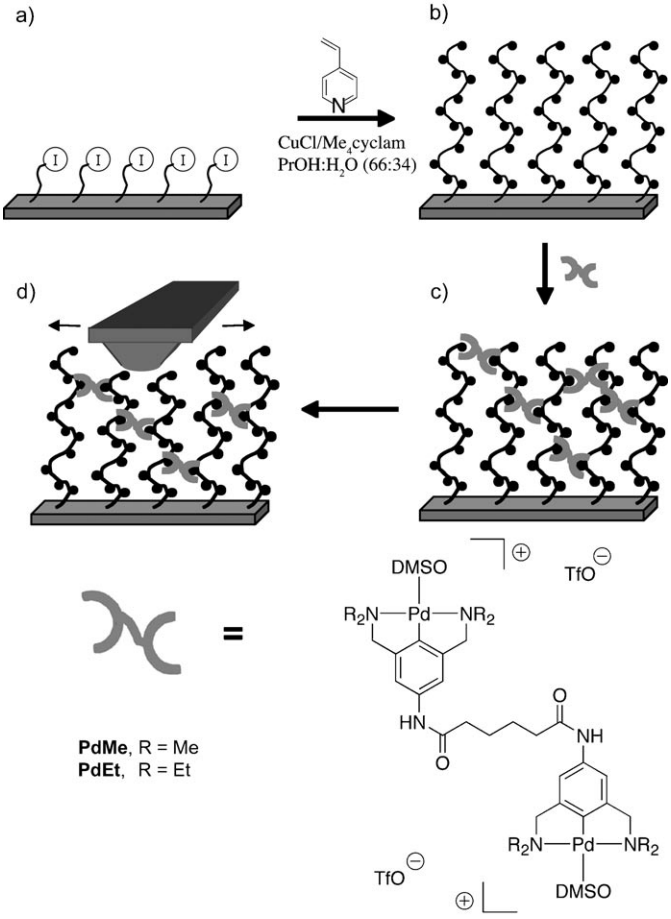

Figure 1. Schematic description of the synthesis of cross-linked brushes and characterization. On a monolayer of mercaptoundecyl bromoisobutyrate on gold (a), (4-vinylpyridine) is polymerized to generate a surface-grafted polymer brush (b). Addition of the cross-linker **PdMe** or **PdEt** in DMSO yields a reversibly cross-linked polymer brush (c), whose lateral mechanics are probed by dragging an AFM tip across the surface (d). The figure is not to scale and does not imply a specific loading or distribution of the cross-links.

Reversibly cross-linkable polymer brushes were synthesized by atom-transfer radical polymerization (ATRP)[4] from an ω-mercaptoundecyl bromoisobutyrate initiator anchored to a gold surface (Figure 1). A low concentration[4,5] (0.020 mM) of the Cu^{I} catalyst was used to decrease the steady-state concentration of radicals and to minimize bimolecular termination reactions. Under these conditions, PVP brushes with a dry thickness of 33.5 nm (50 nm in DMSO) could be polymerized in two hours. Brush heights were inferred from cross-sectional profiles obtained by AFM imaging.[6]

The PVP brush substrate was divided in half, and the PVP brush was then cross-linked by the addition of DMSO solutions that contained the bis(Pd^{II}-pincer) compounds

[*] Dr. N. I. Abu-Lail, Dr. M. Kaholek, Prof. S. Zauscher
Department of Mechanical Engineering and Materials Science
Center for Biologically Inspired Materials and Material Systems
144 Hudson Hall, Duke University
Durham, NC 27708 (USA)
Fax: (+1) 919-660-5409
E-mail: zauscher@duke.edu
D. M. Loveless, Prof. S. L. Craig
Department of Chemistry
Center for Biologically Inspired Materials and Material Systems
P.M. Gross Chemical Laboratory, Duke University
Durham, NC 27708-0346 (USA)
Fax: (+1) 919-660-1605
E-mail: stephen.craig@duke.edu

[**] This work was supported by the NSF (0503907) and by the NIH (EB-001037). D.M.L. acknowledges an NSF IGERT Fellowship (DGE-0221632) and Burroughs Wellcome Fellowship (Duke Department of Chemistry). S.Z. acknowledges an NSF CAREER award (NSF DMR-0239769). D.M.L. and N.I.A. contributed equally to this work.
Supporting information for this article is available on the WWW under http://www.angewandte.org or from the author.

InterScience
© 2006 Wiley-VCH Verlag GmbH & Co. KGaA, Weinheim

PdMe or **PdEt** (Figure 1), which reversibly coordinate to PVP. The compound abbreviations reflect the alkyl substituents on the amino groups of the Pd^{II}-pincer complexes. The steric bulk of these substituents has a minimal effect on the thermodynamics of pyridine (Pyr) coordination (K_{eq}(**PdMe**–Pyr) = 33 M^{-1}, K_{eq}(**PdEt**–Pyr) = 29 M^{-1}),[7] and so the uptake of **PdMe** and **PdEt** from equimolar solutions into the identical PVP brushes should be effectively equivalent, producing samples with comparable structure (number and placement of cross-links). A high concentration of the pincer complex (≈9 mM) was used initially to ensure significant cross-linking (≈30% of Pyr is bound to Pd^{II}, if K_{eq} is unchanged in the brush). The mechanical response of the cross-links, however, is determined by the ligand dissociation rates, k_{off}, and the bulk of the alkyl group has a dramatic influence on those rates (k_{off}(**PdMe**–Pyr) ≈ 1100 s^{-1}, k_{off}(**PdEt**–Pyr) = 17 s^{-1}).[7] The difference in the rates thus provides a probe of "mechanochemistry" that is reminiscent of the kinetic isotope effect in reaction chemistry.[8]

To study the effect of cross-linking on brush mechanics, we measured the lateral force exerted onto an AFM cantilever as the cantilever tip was dragged across the brush surface (scan size 1 μm, frequency 20 Hz). The lateral force, which is phenomenologically similar to friction, was measured as a function of the applied normal force for a range of solution conditions. Figure 2 shows the relationship between lateral force and normal force for six samples. The slope of the linear regression through each data set reports the dependence of lateral force on normal force (hereafter, the coefficient of lateral resistance, or C_{lat}).[9] The addition of cross-linker causes a dramatic change in lateral force. When the faster **PdMe** cross-linker is added, both the absolute lateral force values and C_{lat} drop to ≈30% of those of the noncross-linked PVP control (Figure 2a). That this change is due to **PdMe**–PVP coordination is verified by the addition of 100 mM dimethylaminopyridine (DMAP) inhibitor, which competes for the **PdMe** and restores the lateral forces to their original values. The slower cross-linker **PdEt** also changes the mechanics, but in this case the absolute lateral force values and C_{lat} increase by more than twofold (Figure 2b). As with **PdMe**, the effect of cross-linking can be chemically reversed to close to that of the noncross-linked state by the addition of DMAP inhibitor.

Although the quantitative study of the mechanical properties of thin polymer brushes poses still a significant technical challenge, lateral force measurements by AFM provide a sensitive, qualitative measure of changes in the surface mechanical properties of polymer thin films. To facilitate interpretation, the PVP brushes were fabricated and treated in parallel, and AFM conditions were kept constant for all samples. Furthermore, the two cross-linkers are structurally similar, and the thermodynamics of the cross-linking equilibria are effectively equal. C_{lat} values are relatively independent of variations between samples (0.18 ± 0.05) for noncross-linked PVP brushes of different heights (40–130 nm) and roughnesses (2.5–6 nm rms over 1 μm^2) in DMSO. The changes induced by cross-linking fall well outside of this experimental uncertainty. The magnitude of the lateral forces should depend also on the scan rate, and it

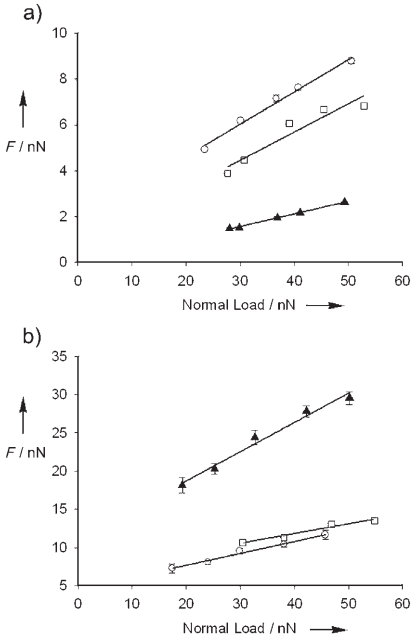

Figure 2. a) Lateral force as a function of applied normal load, measured between a silicon nitride cantilever and PVP brushes in DMSO (○), 10 mg **PdMe** + 1 mL DMSO (▲), and 10 mg **PdMe** + 1 mL of 0.1 M DMAP (□) (C_{lat} equals 0.14, 0.05, and 0.12 for the three solution conditions, respectively). b) Lateral force as a function of applied normal load, measured between a silicon nitride cantilever and PVP brushes in DMSO (○), 10 mg **PdEt** + 1 mL DMSO (▲), and 10 mg **PdEt** + 1 mL 0.1 M DMAP (□) (C_{lat} equals 0.16, 0.38, and 0.13 for the three solution conditions, respectively). The slope of each solid regression line through the data is C_{lat}. Error bars represent the standard error of the mean. Note the different scale for the *y* axis in (a) and (b).

is possible that the differences in the measured lateral forces might disappear altogether under certain experimental conditions. To test the effect of scan rate, we measured lateral force on our brush surfaces over a lateral scan rate range from 2 to 40 μm s^{-1}. Within this range, the rate dependencies in the measured lateral forces are small compared to the differences measured between the **PdMe** and **PdEt** samples. This demonstrates that the different mechanics are not limited to an isolated set of experimental conditions (see the Supporting Information).

Cross-linking could affect the measured lateral forces by changing the presentation of "dangling polymer ends", heterogeneity, and roughness of the surface.[11,12] The structural effects should be in principle, and are in practice, indistinguishable for the two cross-linkers. The surfaces have minimal roughness (2–5 nm over 1 μm^2) that varies little with or without cross-linker (Table 1). Normal force measurements show that the decay length of the steric repulsion provided by the brush surfaces of cross-linked brushes is significantly less than that for the noncross-linked brushes (data not shown). Importantly, however, the extent of the steric repulsion is independent of cross-linker type. The divergent effects of the two cross-linkers on lateral force thus suggest that the kinetics of the interaction, in addition to structural effects of the cross-linkers in the brush, make important contributions to brush mechanics.

 © 2006 Wiley-VCH Verlag GmbH & Co. KGaA, Weinheim

Table 1: A summary of the PVP brush heights and roughnesses measured on two samples fabricated in parallel, each in DMSO and then with 9 mM cross-linker. Initiator density in the monolayer is ca. 5 nm^{-2} (complete monolayer).

Solution	Height [nm][a]	Roughness [nm][b]
in DMSO	48.6 ± 4.4	5.1 ± 1.8
+ 9 mM **PdMe**	53.5 ± 2.3	4.0 ± 0.2
in DMSO	54.7 ± 3.9	2.2 ± 0.1
+ 9 mM **PdEt**	65.6 ± 4.7	2.8 ± 0.2

[a] Estimated from dry height of 33.5 nm, assuming an active initiator density of ≈0.6 nm^{-2}.[18] [b] Measured on an area of 1 × 1 μm^2.

Kinetics contributions could originate from adhesion and adhesion hysteresis, and from molecular relaxations in the brush.[10–12] Non-zero intercepts in the C_{lat} regression lines suggest a contribution to the lateral force from adhesion,[13] and the intercept is greater for **PdEt**–PVP than for **PdMe**–PVP. The greater adhesion in **PdEt**–PVP that is implied by the intercepts is also observed directly; under identical experimental conditions for both surfaces, the force at which the AFM tip dissociates from the PVP–**PdEt** surface is greater than that observed for the PVP–**PdMe** surface (see the Supporting Information). In addition, the differences in C_{lat} could arise from cross-links that bear lateral shear stress exerted by the AFM tip, in that the kinetic stability of the cross-links influences the magnitude of their resistance. Such behavior is observed in bulk PVP–**PdMe** and PVP–**PdEt**[7,8] and the rupture of single molecules.[14]

The data thus suggest that cross-links reduce the lateral forces by limiting dangling-end contacts and/or penetration of the tip into the brush surface, but they increase the lateral force through mechanical resistance which depends on cross-link dissociation kinetics. The molecular origin of friction on "soft/wet" surfaces in general is an important and open area of research.[15] The use of well-defined kinetic probes, in combination with more sophisticated AFM techniques (e.g., microrheology[16]), offers potential for further mechanistic insight, for example, through frequency scaling.[7]

Polymer brush layers with controlled and stimuli-responsive properties are of significant current interest,[17] with potential applications in biomedical surface engineering and nanofabrication.[1] The modulation of cross-linking interactions is shown here to be one method by which to exert control. The cross-linking is reversed here by chemical competition, but responsiveness to other stimuli, such as temperature, could be engineered. Both the magnitude of the cross-linking effect and the importance of the cross-linking kinetics must depend on the specific context, including among other factors grafting density, polymer molecular weight, the number and distribution of cross-links, and solvent quality. Ongoing work in our laboratories is addressing these relationships.

Received: June 22, 2006
Revised: August 28, 2006
Published online: October 25, 2006

Keywords: cross-linking · polymers · supramolecular polymers · surface chemistry

[1] a) J. Rühe in *Polymer Brushes: Synthesis, Characterization, Applications* (Eds.: R. C. Advincula, W. J. Brittain, K. C. Caster, J. Rühe), Wiley-VCH, Weinheim, **2004**, pp. 1–32; b) K. C. Caster in *Polymer Brushes: Synthesis, Characterization, Applications* (Eds.: R. C. Advincula, W. J. Brittain, K. C. Caster, J. Rühe), Wiley-VCH, Weinheim, **2004**, pp. 331–352.
[2] G. J. Fleer, M. A. Cohen Stuart, J. M. H. M. Scheutjens, T. Cosgrove, B. Vincent, *Polymers at Interfaces*, Chapman and Hall, London, **1993**.
[3] a) W. Hyang, G. L. Baker, M. L. Bruening, *Angew. Chem.* **2005**, *117*, 1558–1560; *Angew. Chem. Int. Ed.* **2001**, *40*, 1510–1512; b) S. Edmondson, W. T. S. Huck, *Adv. Mater.* **2004**, *16*, 1327–1331; c) L. Ionov, M. Stamm, S. Minko, F. Hoffmann, T. Wolff, *Macromol. Symp.* **2004**, *210*, 229–235; d) M. Ulbricht, H. Yang, *Chem. Mater.* **2005**, *17*, 2622–2631; e) T. A. von Werne, D. S. Germack, E. C. Hagberg, V. V. Sheares, C. J. Hawker, K. R. Carter, *J. Am. Chem. Soc.* **2003**, *125*, 3831–3838.
[4] J. Xia, K. W. Zhang, K. Matyjaszewski, *Macromolecules* **1999**, *32*, 3531–3533.
[5] J. B. Kim, W. X. Huang, M. D. Miller, G. L. Baker, M. L. Bruening, *J. Polym. Sci. Part A* **2003**, *41*, 386–394.
[6] M. Kaholek, W. K. Lee, S. J. Ahn, H. W. Ma, K. C. Caster, B. LaMattina, S. Zauscher, *Chem. Mater.* **2004**, *16*, 3688–3696.
[7] W. C. Yount, D. M. Loveless, S. L. Craig, *J. Am. Chem. Soc.* **2005**, *127*, 14488–14496.
[8] W. C. Yount, D. M. Loveless, S. L. Craig, *Angew. Chem.* **2005**, *117*, 2806–2808; *Angew. Chem. Int. Ed.* **2005**, *44*, 2746–2748.
[9] The regression lines need not be linear (see reference [10]), and C_{lat} is used here only phenomenologically.
[10] S. Sills, R. M. Overney, *Phys. Rev. Lett.* **2003**, *91*, 95501.
[11] N. Chen, N. Maeda, M. Tirrell, J. Israelachvili, *Macromolecules* **2005**, *38*, 3491–3503.
[12] R. Szoszkiewicz, B. Bhushan, B. D. Huey, A. J. Kulik, G. Gremaud, *J. Chem. Phys.* **2005**, *122*, 144708(6).
[13] C. LaTorre, B. Bhusan, *Ultramicroscopy* **2006**, *106*, 720–734.
[14] F. Kersey, W. C. Yount, S. L. Craig, *J. Am. Chem. Soc.* **2006**, *128*, 3886–3887.
[15] J. P. Gong, *Soft Matter* **2006**, *2*, 544–552.
[16] J. Alcaraz, L. Buscemi, M. Puig-de-Morales, J. Colchero, A. Baro, D. Navajas, *Langmuir* **2002**, *18*, 716–721.
[17] a) M. C. LeMieux, S. Minko, D. Usov, H. Shulha, M. Stamm, V. V. Tsukruk, *Polym. Mater. Sci. Eng.* **2004**, *90*, 372–373; b) M. Kaholek, W.-K. Lee, B. LaMattina, K. C. Caster, S. Zauscher, *Polym. Mater. Sci. Eng.* **2004**, *90*, 226–227; c) A. M. Granville, S. G. Boyes, B. Akgun, M. D. Foster, W. J. Brittain, *Macromolecules* **2004**, *37*, 2790–2796; d) M. Kaholek, W.-K. Lee, B. LaMattina, K. C. Caster, S. Zauscher, *Nano Lett.* **2004**, *4*, 373–376; e) J. N. Kizhakkedathu, R. Norris-Jones, D. E. Brooks, *Macromolecules* **2004**, *37*, 734–743; f) M. Motornov, S. Minko, K.-J. Eichhorn, M. Nitschke, F. Simon, M. Stamm, *Langmuir* **2003**, *19*, 8077–8085; g) S. Minko, M. Stamm, E. Goreshnik, D. Usov, A. Sidorenko, *Polym. Mater. Sci. Eng.* **2000**, *83*, 533–534; h) S. Moya, O. Azzaroni, T. Farhan, V. L. Osborne, W. T. S. Huck, *Angew. Chem.* **2005**, *117*, 4654–4657; *Angew. Chem. Int. Ed.* **2005**, *44*, 4578–4581.
[18] D. M. Jones, A. A. Brown, W. T. S. Huck, *Langmuir* **2002**, *18*, 9394–9395.

 © 2006 Wiley-VCH Verlag GmbH & Co. KGaA, Weinheim

Peptide Nucleic Acids

DOI: 10.1002/anie.200603391

Chemodosimeter for Cu^{II} Detection Based on Cyclic Peptide Nucleic Acids**

*János Kovács, Thomas Rödler, and Andriy Mokhir**

DNA and RNA binders (for example, short oligonucleotides or their analogues), whose binding ability is triggered by chemical compounds[1] or physical factors,[2] can be used in the control of gene expression and potentially in analysis. The preparation of such specialized binders includes modification of their backbone, bases, or termini with protecting groups. In the protected state the oligonucleotides do not bind to nucleic acids, while in the presence of a trigger the protecting groups are either removed or modified, thus restoring their binding ability.

Cyclization could be a generally applicable alternative to the existing methods. This statement is based on the following considerations. Oligonucleotides bind complementary nucleic acids to form rigid, rodlike duplexes.[3] Bending of these structures is energetically unfavorable but it occurs in exceptional cases, when certain base sequences are repeated in phase with the DNA helical repeat, for example, poly-A tracts. Therefore, short cyclic oligonucleotides would be expected to have low or no affinity to complementary nucleic acids. Surprisingly, this is not generally the case. For example, cyclic oligonucleotides with specific sequences bind linear nucleic acids in a sequence-specific fashion to form non-canonical base tetrads within four-stranded structures, such as G:C:G:C and G:C:A:T.[4] As a result of this interaction the linear nucleic acids are bent and adopt a looplike conformation. The four-stranded structure is also formed in a solution of cyclic TGCTCGCT[5] and is found in a dimer of HIV-1 RNAs (kissing-loop dimer).[6]

Kool et al. have demonstrated unambiguously that even 12-base cyclic DNAs bind complementary nucleic acids to form duplexes, which are recognized by polymerases. In this case, partial rather than full-length duplexes are formed.[7] The conclusions of Kool and co-workers have been indirectly corroborated by the data of Levy and Ellington,[8] who demonstrated that cyclic DNA–RNA hybrids can be cleaved at a specific site by a DNAzyme. Catalytic activity of the DNAzyme is possible only if the cyclic hybrid binds to the linear single-stranded (ss) DNA part of the DNAzyme. A single report has been published to date, in which it was claimed that cyclization of 20–300-base-long DNAs leads to the loss of their affinity toward the complementary RNAs.[9] Unfortunately, no experimental evidence of this claim has been provided.

Herein, we demonstrate for the first time that cyclization of nucleic acid binders through optimized linkers leads to a complete loss of their binding ability. We used peptide nucleic acids (PNAs) for this optimization, because a) chemical modification of PNAs is straightforward[10] and b) our group has extensive experience in PNA chemistry.[1d,11] PNAs are synthetic analogues of DNAs. Linear PNAs bind complementary nucleic acids with high affinity and specificity.[10] Cyclic PNAs have been prepared before by classical organic synthesis, and were tested as binders of loops in hairpin regions of HIV-1 RNA.[12] No studies of binding of cyclic PNAs to linear nucleic acids have been reported to date.

We also demonstrate a possible application of the optimized cyclic PNAs. In particular, we show that a cyclic PNA, which has a covalent bond sensitive to Cu^{II} ions, can be used as a chemodosimeter for the sensitive and selective detection of Cu^{II}. Cleavage of this cyclic PNA with formation of the linear PNA is dependent on the Cu^{II} concentration (Figure 1). The linear PNA can be detected as a result of its ability to open molecular beacons, which leads to a dramatic increase of the fluorescence intensity. The fluorescence of the majority of reagents for Cu^{II} detection is quenched in the presence of Cu^{II}.[13] Examples of a Cu^{II}-induced increase in fluorescence intensity are rare.[14]

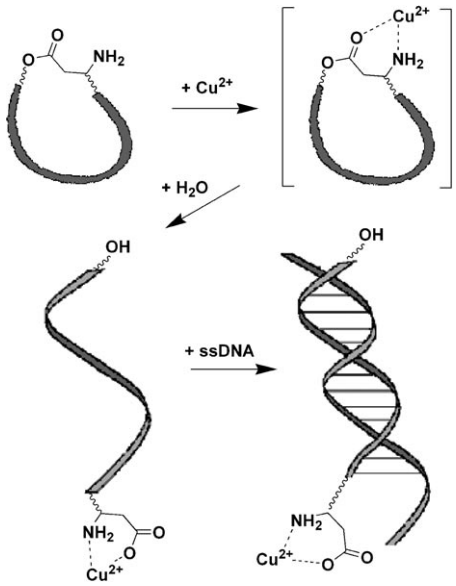

Figure 1. Principle of a chemodosimeter for Cu^{II} detection based on cyclic PNA.

First, we prepared the cyclic PNA **cPNA1** (Scheme 1), which has a 21-atom-long linker between the termini.[15] The β-amino acid ester fragment in this linker can coordinate Cu^{II} through the amino group and the oxygen atom of the carbonyl group to form a stable, six-atom chelating cycle.[16] The

[*] Dr. J. Kovács, T. Rödler, Dr. A. Mokhir
Anorganisch-Chemisches Institut
Ruprecht-Karls-Universität Heidelberg
Im Neuenheimer Feld 270, 69120 Heidelberg (Germany)
Fax: (+49) 6221-548-439
E-mail: andriy.mokhir@urz.uni-heidelberg.de

[**] This work was funded by the Deutsche Forschungsgemeinschaft (Emmy-Noether Program) and partially by Gemeinnützige Hertie-Stiftung and AvH (postdoctoral fellowship to J.K.)

Supporting information for this article is available on the WWW under http://www.angewandte.org or from the author.

© 2006 Wiley-VCH Verlag GmbH & Co. KGaA, Weinheim

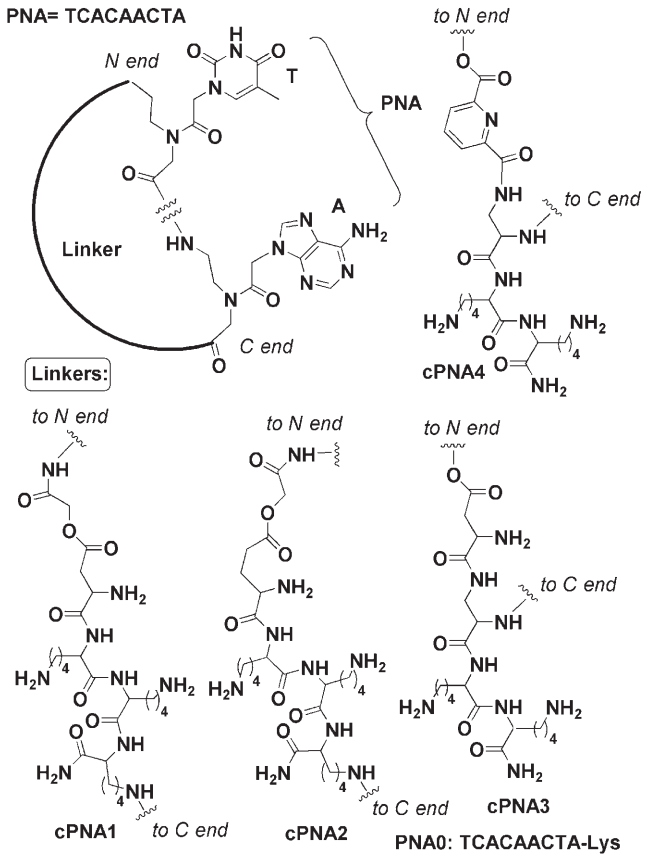

Scheme 1. Structures of PNAs studied.

coordination polarizes the carbonyl group, which facilitates ester hydrolysis. **cPNA1** (1 μM) is fully hydrolyzed 60 min after addition of Cu^{II} (10 equiv). In the absence of the metal ion, **cPNA1** is hydrolyzed much more slowly.[15] To confirm that hydrolysis of **cPNA1** occurs as a result of direct coordination of Cu^{II} to the ester, we prepared an analogue of **cPNA1** (**cPNA2**) containing one additional methylene group between the ester and the metal-anchoring amino group. This minor modification was expected to strongly affect the coordination ability of the ester, as seven-atom chelating cycles are much less stable than the corresponding six-atom chelating cycles. We found that **cPNA2** is not hydrolyzed in the presence of Cu^{II}. Its ester group can be cleaved under harsher conditions, for example, upon incubation with aqueous ammonia (20%).[15]

Binding of **cPNA1** to the complementary DNA was tested using molecular beacon probes **MB1** and **MB2** modified at their termini with Tamra and Dabcyl dyes.[17] The probes differ from each other in their stem length: **MB2** (Tamra-CCTTTAGTTGTGAAAGG-Dabcyl) has one base pair more. Comparable effects have been observed for both compounds. The fluorescence intensity of **MB1** is increased 16-fold after addition of unmodified PNA (1 equiv).[15] Surprisingly, addition of **cPNA1** (1 equiv) to the beacon also leads to a substantial increase in the fluorescence (14-fold).[15] This finding indicates that the DNA affinities of **cPNA1** and **PNA0** are comparable. Analysis of molecular models of **cPNA1**/DNA shows that the linker of **cPNA1** does not destabilize the duplex providing that it has the structure close to A-DNA. Cyclic PNAs with shorter linkers (less than 10 atoms) could not be accommodated within the duplex structure. To test the results of the modeling we prepared **cPNA3** with a nine-atom linker between its termini. The affinity of this compound toward the molecular beacon is significantly weaker than that of **cPNA1**, but is not negligible. The fluorescence of the beacon is increased eightfold after addition of **cPNA3** (1 equiv).[15] This result may indicate the formation of short duplexes of **cPNA3** with the DNA[7] or noncanonical four-stranded structures.[4–6]

To further weaken binding of cyclic PNAs to the complementary DNA, we substituted the aspartic acid residue for a more rigid picolinic acid residue. Analogously to amino acid esters, hydrolysis of picolinic acid esters is catalyzed by Cu^{II}.[18] The fluorescence of an equimolar mixture of **MB2** and **cPNA4** is practically the same as that of the beacon alone (Figure 2), which indicates that **cPNA4** does not bind the DNA under these conditions. This finding is corroborated by gel electrophoresis experiments under native conditions (Figure 3).

To determine the stability constants of PNA/**MB1** we conducted titrations of **MB1** with the PNAs: $\log K = 8.3 \pm 0.2$

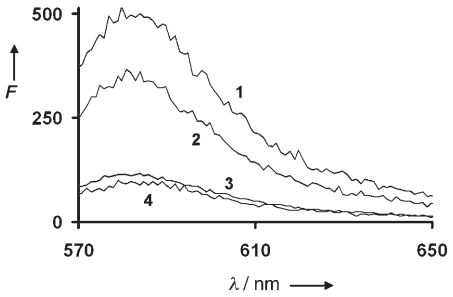

Figure 2. Effect of PNAs (1 equiv) on the fluorescence (*F*) of the molecular beacon **MB2** (100 nM). MOPS, 10 mM; NaCl, 3 mM; EDTA, 2 μM; pH 7. 1) **PNA0** treated with Cu^{II} (10 equiv) for 30 min at 40°C; 2) **cPNA4** treated with Cu^{II} (1 equiv) for 30 min at 40°C; 3) **cPNA4**, no Cu^{II}; 4) no PNA. MOPS = 3-(*N*-morpholino)propanesulfonic acid, EDTA = ethylenediaminetetraacetic acid.

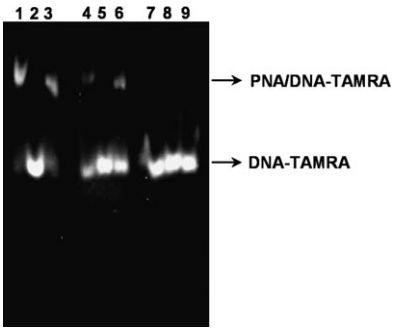

Figure 3. Gel electrophoresis experiment (native conditions). Each sample contained MOPS (10 mM), NaCl (50 mM), and labeled linear DNA: 5′-Tamra TAG TTG TGA (1.7 μM). Lane 1: **PNA0** (3.4 μM); lane 2: **cPNA4** (3.4 μM); lane 3: **cPNA4** (3.4 μM) treated with Cu^{II} (10 equiv) at 40°C for 30 min; lane 4: **PNA0** (1.7 μM); lane 5: **cPNA4** (1.7 μM); lane 6: **cPNA4** (1.7 μM) treated with Cu^{II} (10 equiv) at 40°C for 30 min; lanes 7–9: without PNA.

 © 2006 Wiley-VCH Verlag GmbH & Co. KGaA, Weinheim

(**PNA0**/**MB1**), 8.0 ± 0.1 (**cPNA1**/**MB1**), 7.2 ± 0.1 (**cPNA3**/**MB1**).[15] The stability of the **cPNA4**/**MB1** duplex is so low that conditions of PNA binding saturation could not be achieved at reasonable concentrations of the PNA, and its stability constant could not be determined. Hydrolysis of **cPNA1**, **cPNA3**, and **cPNA4** at pH 7 does not take place in the presence of metal ions other than Cu^{II}, namely Zn^{II}, Ni^{II}, $Fe^{II/III}$, Co^{II}, Mn^{II}, Zr^{IV}, Ce^{III}, Ln^{III}, Eu^{III}, or Pr^{III}. Ratios of catalyzed to background hydrolysis rates are decreased in the following order: **cPNA4** (286:1), **cPNA3** (118:1), and **cPNA1** (25:1). As a result of the low affinity of the β-amino acid ester (**cPNA1**, **cPNA3**) for Cu^{II}, a 10 equivalent excess of the metal ion is required for its hydrolysis. In contrast, the metal binding affinity of the picolinic acid ester (**cPNA4**) is high enough to bind the metal ion at lower concentrations. In particular, hydrolysis of **cPNA4** in the presence of only 0.3 equivalents of Cu^{II} is still about five times faster than its background hydrolysis.[15] The absolute amount of Cu^{II} used in the latter experiment was 300 fmol. The Cu^{II} sensitivity can be further increased by incorporation of stronger Cu^{II}-binding ligands within the cyclic PNA (data not shown).

After hydrolysis, **cPNA4** becomes an excellent binder of DNA as well as RNA.[15] In particular, a substantial increase in **MB2** fluorescence after addition of the hydrolyzed PNA (Figure 2) is observed. Linear **PNA0** induces a comparable increase in the fluorescence of **MB2**. Similar effects have been found with **MB1**, which contains a shorter stem region. Both linear PNA and hydrolyzed **cPNA4** form stable duplexes with the linear complementary DNA and RNA under the conditions used for gel electrophoresis experiments (Figure 3).

In summary, we have demonstrated that the binding affinity of cyclic PNAs to nucleic acids can be reduced by variation of the linker between their termini. The Cu^{II} ion acts as an efficient trigger of binding of cyclic PNAs to nucleic acids. This effect can be used for the detection of as little as 300 fmol of Cu^{II}. Our method relies on the modification of the termini rather than the nucleobases or backbone of the probes. Preparation of the cyclic PNAs is fully based on solid-phase synthesis and commercially available starting materials (see Supporting Information). This allows quick tuning of the properties of the cPNAs, which is an important advantage. Specific ester groups can be selectively cleaved by stimuli other than Cu^{II}. For example, Zn^{II}, imidazole derivatives, and UV light all trigger hydrolysis of nitrophenyl esters. These stimuli can potentially be used for activation of the cyclic PNAs in the cell, providing that their substrates are introduced within a linker less than ten atoms long in the cyclic PNA.

Received: August 18, 2006
Published online: October 24, 2006

Keywords: analytical methods · copper · fluorescence · nucleic acids · peptide nucleic acids

[1] a) E. W. Gerner, F. L. Meyskens, *Nat. Rev. Cancer* **2004**, *4*, 781 – 792; b) C. J. Frederickson, *Int. Rev. Neurobiol.* **1989**, *31*, 145 – 238; c) P. D. Zalewski, X. Jian, L. L. Soon, W. G. Breed, R. F. Seamark, S. F. Lincoln, A. D. Ward, F. Z. Sun, *Reprod. Fertil. Dev.* **1996**, *8*, 1097 – 1105; d) A. Mokhir, R. Krämer, H. Wolf, *J. Am. Chem. Soc.* **2004**, *126*, 6208 – 6209.

[2] a) W. T. Monroe, F. R. Haselton in *Dynamic Studies in Biology: Phototriggers, Photoswitches, and Caged Biomolecules* (Eds.: M. Goeldner, R. Givens), Wiley-VCH, Weinheim, **2005**, pp. 513 – 531; b) H. Ando, T. Furuta, R. Y. Tsien, H. Okamoto, *Nat. Genet.* **2001**, *28*, 317 – 325; c) W. T. Monroe, M. M. McQuain, M. S. Chang, J. S. Alexander, *J. Biol. Chem.* **1999**, *274*, 20895 – 20900; d) S. G. Chaulk, A. M. MacMillan, *Nucleic Acids Res.* **1998**, *26*, 3173 – 3178; e) L. Kröck, A. Heckel, *Angew. Chem.* **2005**, *117*, 475 – 477; *Angew. Chem. Int. Ed.* **2005**, *44*, 471 – 473; f) M. Liu, H. Asanuma, M. Komiyama, *J. Am. Chem. Soc.* **2006**, *128*, 1009 – 1015; g) W. He, P. Conrad, B. Belisle, A. Zhang, L. Pastor, Q. Nguyen, G. McMaster, R. Chavli, Genospectra, Inc.: http://www.genospectra.com, application note: *Initiation of Gene Silencing After Batch Transfection Using Light-Controllable siRNA (csiRNA)*.

[3] V. A. Bloomfield, D. M. Crothers, I. Tinoco, Jr., *Nucleic Acids: Structures, Properties, and Functions*, University Science Books, Sausalito, CA, **1999**, p. 794.

[4] N. Escaja, I. Gomez-Pinto, J. Viladoms, M. Rico, E. Pedroso, C. Gonzalez, *Chem. Eur. J.* **2006**, *12*, 4035 – 4042.

[5] N. Escaja, J. L. Gelpi, M. Orozco, M. Rico, E. Pedroso, C. Gonzalez, *J. Am. Chem. Soc.* **2003**, *125*, 5654 – 5662.

[6] A. Mujeeb, J. L. Clever, T. M. Billeci, T. L. James, T. G. Parslow, *Nat. Struct. Biol.* **1998**, *5*, 432 – 436.

[7] M. Frieden, E. Pedroso, E. T. Kool, *Angew. Chem.* **1999**, *111*, 3870 – 3874; *Angew. Chem. Int. Ed.* **1999**, *38*, 3654 – 3657.

[8] M. Levy, A. D. Ellington, *Proc. Natl. Acad. Sci. USA* **2003**, *100*, 6416 – 6421.

[9] H. Shiono, H. Kodama, M. Kojima, US patent 5919917, **1999**.

[10] P. E. Nielsen, M. Egholm in *Peptide Nucleic Acids: Protocols and Applications* (Eds.: P. E. Nielsen, M. Egholm), Horizon Scientific Press, Wymondham, UK, **1999**, pp. 1 – 19.

[11] a) I. Boll, E. Jentzsch, R. Krämer, A. Mokhir, *Chem. Commun.* **2006**, 3447 – 3449; b) I. Boll, L. Kovbasyuk, R. Krämer, A. Mokhir, *Bioorg. Med. Chem. Lett.* **2006**, *16*, 2781 – 2785; c) I. Boll, R. Krämer, J. Brunner, A. Mokhir, *J. Am. Chem. Soc.* **2005**, *127*, 7849 – 7856; d) I. Boll, R. Krämer, A. Mokhir, *Bioorg. Med. Chem. Lett.* **2005**, *15*, 505 – 509; e) A. Mokhir, R. Krämer, Y. Z. Voloshin, O. A. Varzatskii, *Bioorg. Med. Chem. Lett.* **2004**, *14*, 2927 – 2930.

[12] a) G. Depecker, N. Patino, C. Di Giorgio, R. Terreux, D. Cabrol-Bass, C. Bailly, A.-M. Aubertin, R. Condom, *Org. Biomol. Chem.* **2004**, *2*, 74 – 79; b) G. Upert, M. Mehiri, M.-L. Goddard, A. Di Giorgio, R. Benhida, R. Condom, N. Patino, *Tetrahedron Lett.* **2005**, *46*, 4081 – 4085.

[13] For selected reviews, see: a) P. Jiang, Z. Guo, *Coord. Chem. Rev.* **2004**, *248*, 205 – 229; b) F. Pina, M. A. Bernardo, E. García-España, *Eur. J. Inorg. Chem.* **2000**, 2143 – 2157; c) L. Fabbrizzi, M. Licchelli, P. Pallavicini, L. Parodi, A. Taglietti, *Perspect. Supramol. Chem.* **1999**, *5*, 93 – 134; d) R. Krämer, *Angew. Chem.* **1998**, *110*, 804 – 806; *Angew. Chem. Int. Ed.* **1998**, *37*, 772 – 773; e) A. P. de Silva, H. Q. N. Gunaratne, T. Gunnlaugsson, A. J. M. Huxley, C. P. McCoy, J. T. Rademacher, T. E. Rice, *Chem. Rev.* **1997**, *97*, 1515 – 1566; f) L. Fabbrizzi, M. Licchelli, P. Pallavicini, A. Perotti, A. Taglietti, D. Sacchi, *Chem. Eur. J.* **1996**, *2*, 75 – 82.

[14] a) Y. Xiang, A. Tong, P. Jin, Y. Ju, *Org. Lett.* **2006**, *8*, 2863 – 2866; b) R. Kierat, R. Krämer, *Bioorg. Med. Chem. Lett.* **2005**, *15*, 4824 – 4827; c) V. Dujols, F. Ford, A. W. Czarnik, *J. Am. Chem. Soc.* **1997**, *119*, 7386 – 7387.

[15] See Supporting Information.

[16] H. Kroll, *J. Am. Chem. Soc.* **1952**, *74*, 2036 – 2039.

[17] S. Tyagi, F. R. Kramer, *Nat. Biotechnol.* **2003**, *21*, 303 – 308.

[18] P. Scrimin, P. Tecilla, U. Tonellato, *J. Org. Chem.* **1994**, *59*, 18 – 24.

 © 2006 Wiley-VCH Verlag GmbH & Co. KGaA, Weinheim

Polymerization

DOI: 10.1002/anie.200603178

Highly Heteroselective Ring-Opening Polymerization of *rac*-Lactide Initiated by Bis(phenolato)scandium Complexes**

*Haiyan Ma, Thomas P. Spaniol, and Jun Okuda**

Currently there is considerable interest in the controlled ring-opening polymerization (ROP) of lactides (LAs) by well-defined metal initiators because of the biodegradable and biocompatible nature of polylactides (PLAs) and their potentially wide-ranging commercial applications.[1,2] Particularly interesting is that some discrete metal complexes initiate the ROP of *rac*-LA or *meso*-LA in a stereoselective manner,[3–9] and thus PLAs with a variety of architectures ranging from isotactic,[3d–i] syndiotactic,[5] to heterotactic[6–8] can be obtained. Enantiomerically pure or racemic aluminum complexes with chiral salen-type ligands (salen = *N*,*N*′-bis(salicylidene)ethylenediamine) were reported to polymerize *rac*-LA to form isotactic or stereoblock/stereogradient PLA,[3a–g] and to polymerize *meso*-LA to form syndiotactic PLA through enantiomorphic site control.[5a] Achiral aluminum–salen or salan complexes (salan = *N*,*N*′-bis(*ortho*-hydroxybenzyl)ethylenediamine) produce isotactic or heterotactic PLA from *rac*-LA through a chain-end control mechanism.[3h,i,6] Magnesium,[7b,d] zinc,[7c,d] calcium,[7d,e] and yttrium[8] complexes are highly active for ROP of *rac*-LA, in some cases showing significant preference for heterotactic dyad enchainment. Despite considerable efforts devoted to initiator design,[3–10] factors governing stereocontrol during the ROP of lactides are still not well understood. Herein we report that a series of scandium complexes with 1,ω-dithiaalkanediyl-bridged bisphenolato (OSSO)-type ligands (Table 1) show high heterotactic selectivity during the ROP of *rac*-LA. This selectivity involves a new type of dynamic monomer recognition based on the fluxionality of the ancillary ligand. Group 3 complexes with such ligands have previously been found to be active initiators for ROP of L-LA,[11a,b] and a slight heterotactic preference during the ROP of *rac*-LA has been noted for the corresponding aluminum complexes.[11c]

Table 1: Scandium complexes **1**–**7**.

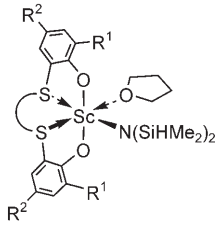

1–5, 7

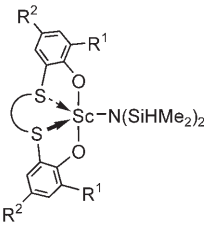

5a, 6

Bridge	-∩-	R^1	R^2	OSSO	Complex
C_2	-$(CH_2)_2$-	*t*Bu	Me	etbmp	**1**
	-$(CH_2)_2$-	cumyl	cumyl	etccp	**2**
		*t*Bu	Me	cytbmp	**3**
C_3	-$(CH_2)_3$-	*t*Bu	Me	ptbmp	**4**
C_4		*t*Bu	Me	xytbmp	**5**, **5a**
		1-ada[a]	Me	xytamp	**6**
		*t*Bu	Me	cmtbmp	**7**

[a] ada = adamantyl.

As was reported for scandium complexes **1** and **4**,[11a] the derivatives **2**, **3**, and **5**–**7** (Table 1) were readily synthesized by using the amine elimination reaction of $[Sc\{N(SiHMe_2)_2\}_3(thf)]$ with the corresponding bridged bisphenol in toluene at 50–60 °C. Chiral bisphenols cytbmpH_2 and cmtbmpH_2 were used as racemates. With the sterically bulkier bisphenols xytbmpH_2 and xytampH_2, complexes **5a** and **6** were isolated free of the thf ligand. Complexes **2** and **3** with a C_2 bridge show C_1 symmetry in solution (^{1}H NMR, C_6D_6), whereas the other scandium complexes with longer bridges show C_2 or C_s symmetry as a result of fluxional behavior, similar to findings previously observed.[11a] The monomeric nature of both complexes, which include a distorted octahedral geometry around the scandium center, was confirmed by single-crystal X-ray crystallographic analysis of **5** and **7** (see the Supporting Information).

As shown in Table 2, the scandium complexes **1**–**7** with bisphenolato ligands were moderately active for the polymerization of *rac*-LA at ambient temperature in THF. Complexes **1**–**7** displayed almost the same level of activity.

The microstructural analysis[7b,12] of PLAs formed from *rac*-LA with complexes **1**–**7** revealed that the structure of the complex exerts a significant influence on the tacticity of the growing polymer chain (Table 2). All the scandium complexes showed substantial heterotactic selectivity, with a maximum P_r value of 0.96 observed for complex **4**. The heterotactic selectivity of scandium complexes **1**–**4** improved as the size of the bisphenolato ligand increased. As recently pointed out by Carpentier and co-workers,[8b] bulky and conformationally flexible *ortho* substituents enhanced the heteroselectivity. However, the influence of the bridge turned out to be most significant. For example, the introduction of one additional

[*] Prof. Dr. H. Ma, Dr. T. P. Spaniol, Prof. Dr. J. Okuda
Institut für Anorganische Chemie
RWTH Aachen
Landoltweg 1, 52056 Aachen (Germany)
Fax: (+49) 241–809–2288
E-mail: jun.okuda@ac.rwth-aachen.de
Prof. Dr. H. Ma
Laboratory of Organometallic Chemistry
Institute of Applied Chemistry
East China University of Science and Technology
PO Box 310, 130 Meilong Road, 200237 Shanghai (P.R. China)

[**] We thank the Deutsche Forschungsgemeinschaft and the Fonds der Chemischen Industrie for financial support.

Supporting information for this article is available on the WWW under http://www.angewandte.org or from the author.

InterScience
© 2006 Wiley-VCH Verlag GmbH & Co. KGaA, Weinheim

Table 2: ROP of *rac*-lactide initiated by complexes **1–7**.[a]

Cat.	$[i\text{PrOH}]_0/[\text{Sc}]_0$	t [h]	Conv.[c] [%]	M_{calcd}[d] ($\times10^4$)	M_n[e] ($\times10^4$)	M_w/M_n[e]	P_r[f]
1	–	9	82	3.55	17.8	1.89	0.78
2	–	8	85	3.68	25.9	1.66	0.80
3	–	9	79	3.42	23.8	1.88	0.82
4	–	8	81	3.50	12.6	1.85	0.95
5	–	21	89	3.85	14.3	1.88	0.94
6	–	8	84	3.63	9.30	1.84	0.93
7	–	5	75	3.25	28.5	1.60	0.94
4	1:1	8	63	2.72	5.38	1.55	0.96
4	2:1	8	59	1.28	1.88	1.15	0.94
4	3:1	8	40	0.58	1.09	1.12	0.90
4	3:1	96	93	1.34	1.83	1.06	0.86
5	1:1	5	71	3.07	4.73	1.29	0.94
5	1:1[b]	72	83	3.59	4.42	1.12	0.67

[a] $[\text{LA}]_0/[\text{Sc}]_0 = 300$, $[\text{Sc}] = 2.9$ mmol L^{-1}, THF, 25 °C. [b] In toluene. [c] Determined by ^{1}H NMR spectroscopy. [d] $M_{calcd} = (300\times\%\text{conv.}\times144.13)/m$, where $m = 1$ (without alcohol) and $m = [i\text{PrOH}]_0/[\text{Sc}]_0$ (with alcohol). [e] Determined by GPC. [f] The probability of forming a new *r* dyad, determined by homonuclear decoupled ^{1}H NMR spectroscopy.

carbon atom into the bridge resulted in a surge of heterotacticity, with the P_r value increasing from 0.78 for complex **1** to 0.95 for complex **4**; whereas the variation of the *ortho* substituent from *tert*-butyl to 1-methyl-1-phenylethyl (cumyl) led to only a slight improvement ($P_r = 0.80$). The chirality of the ligand skeleton in complexes **3** and **7** did not influence the tacticity, which suggests an absence of enantiomorphic site control during the ROP of *rac*-LA by these scandium complexes.

The addition of excess alcohol to similar initiators was previously found to result in the living polymerization of L-LA.[11b] When *rac*-LA was polymerized with **4** or **5** in the presence of 2-propanol in THF, the number-average molecular weights and the molecular-weight distributions of the resulting PLAs decreased significantly, thereby indicating a more-controlled polymerization. Changing the initiating group from silyl amido to isopropoxide had no influence on the heterotacticity of the PLAs.[8b] The heterotactic selectivity of complexes **4** and **5** was maintained, with P_r values as high as 0.96, which decreased slightly when more than one equivalent of 2-propanol was added. Longer polymerization times also caused some loss of the stereoselectivity because of transesterification reactions.[11b] The use of toluene as the solvent led to a dramatic decrease in the heterotacticity from 0.96 to 0.67, thus indicating that the use of THF as the solvent is crucial for the high heterotactic selectivity; a similar effect has been reported for the well-defined Zn, Ca, and Y systems.[7c,d,8b]

To understand the origin of the high heteroselectivity, complex **5** was treated with (*R*)-*tert*-butyl lactate to give complex **8** as a single diastereomer (Scheme 1), which possesses a dimeric structure in the solid state according to results of an X-ray diffraction study (Figure 1).[13] ^{1}H NMR spectroscopic analysis (C_6D_6) of the crude mixture from the reaction of **5** with (*R*)-*tert*-butyl lactate showed that complex **8** with a Λ,Λ configuration was detected as almost the only product (ca. 95%).[14b] As depicted in Figure 1, the linear

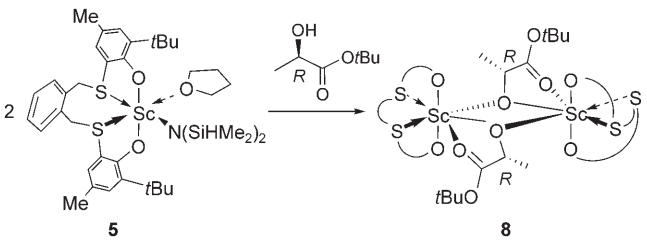

Scheme 1. Synthesis of the dimeric complex **8** with a Λ,Λ configuration.

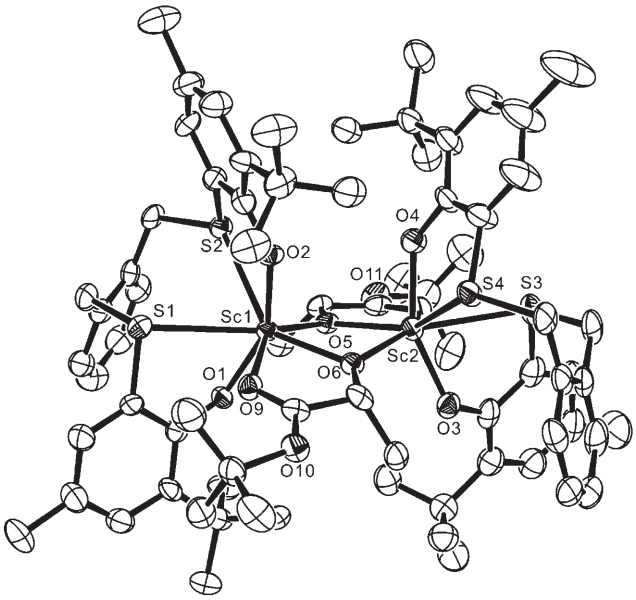

Figure 1. Molecular structure of **8** (with hydrogen atoms omitted) at the 50% probability level. Selected bond lengths [Å] and angles [°]: Sc1–O1 2.019(4), Sc1–O2 1.983(4), Sc1–O5 2.098(4), Sc1–O6 2.129(4), Sc1–O9 2.254(4), Sc1–S1 2.930(2), Sc1–S2 2.9501(19), Sc2–O3 2.039(5), Sc2–O4 2.006(5), Sc2–O5 2.126(4), Sc2–S3 2.862(2), Sc2–S4 2.931(2); O1-Sc1-O2 151.06(19), S1-Sc1-S2 76.01(5), O1-Sc1-S1 69.35(13), O2-Sc1-S2 65.74(12), S1-Sc1-O5 146.66(12), S2-Sc1-O5 79.59(12), O5-Sc1-O6 72.03(16), O5-Sc1-O9 140.74(16), O3-Sc2-O4 153.2(2), S3-Sc2-S4 76.34(6).

OSSO-type ligands wrap around both scandium centers in **8** with a Λ configuration.[14a] It is evident that for each scandium center, the "upper" *tert*-butyl group of the bisphenolato ligand is located above the Sc-O-C-C-O chelate ring, whereas the α-methyl group of the (*R*)-*tert*-butyl lactate points to the "lower" side. The "lower" *tert*-butyl group is turned away from this methyl group, with a short contact of 2.62 Å between them still being observed. Complex **8** shows a dimeric structure with C_2 symmetry in solution according to its ^{1}H NMR spectra (C_6D_6, [D_8]THF). The addition of [D_8]THF to a solution of C_6D_6 did not lead to any change in the chemical shifts. Although a monomeric species cannot be excluded from the ^{1}H NMR spectroscopic data, by taking the solid structure into account, the dimeric structure of complex **8** is most likely retained in solution. The two subunits of a single bisphenolato ligand are chemically inequivalent: four doublets are displayed for the SCH_2 protons of a single ligand up to 95 °C (^{1}H NMR, [D_8]toluene), thus indicating a rigid

 © 2006 Wiley-VCH Verlag GmbH & Co. KGaA, Weinheim

conformation of the ligand around each metal center. From the fluxional behavior of complex **5** in solution, it is therefore reasonable to assume that the *R* configuration of the lactate ester has selectively induced the *Λ* conformation of the OSSO ligand in complex **8** because of steric repulsion. Taking into account the similarity of the lactate ester and a ring-opened lactide monomer, the same effect can be assumed to be operative during the polymerization of *rac*-LA.

When complex **8**, generated in situ in [D_8]THF, was used for the ROP of *rac*-LA, a highly heterotactic PLA was obtained ($P_r = 0.93$). The M_n value was significantly larger than the theoretical value, probably because the cleavage process of the dimer by the lactide monomer was slow, as has been previously reported.[11b] Based on this evidence, we propose the mechanism shown in Scheme 2 for the stereocontrol during ROP of *rac*-LA by complex **8**. First, dimeric **8** is cleaved in the presence of excess lactide. The close contact between the "lower" *tert*-butyl and the α-methyl groups of the (*R*)-*tert*-butyl lactate in **8** blocks the coordination face below the Sc-O-C-C-O chelate ring.

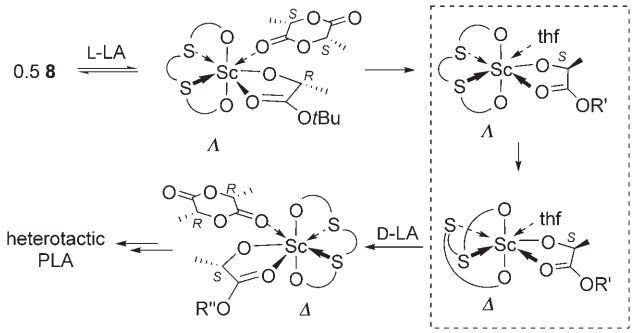

Scheme 2. Proposed mechanism for the stereocontrol in heteroselective ROP of *rac*-LA by complex **8**.

A recent computational study of the β-diketiminatomagnesium initiator[10a] indicated that a stable transition state features a weak interaction between the O_{acyl} atom of the approaching monomer and the coordinated $C_{carbonyl}$ atom of ring-opened LA, as well as a stronger interaction between the metal–alkoxy oxygen atom and the $C_{carbonyl}$ atom of the approaching monomer. Thus, these interactions, together with the steric repulsion between the "upper" *tert*-butyl group and the incoming lactide molecule, would favor the coordination of L-LA (*S*,*S* chirality, Scheme 2). After ring opening, the steric repulsion between the "upper" *tert*-butyl group and α-methyl group of the (*S*)-lactate would become pronounced. To minimize this effect, the "upper" *tert*-butyl would move away and the change in the configuration of the ligand from *Λ* to *Δ* may be triggered. The resulting species would thus favor the coordination of D-LA (*R*,*R* chirality), eventually resulting in heterotactic PLA. Thus, a dynamic monomer-recognition process involving interconversion of the ligand configuration from *Λ* into *Δ* would lead to high heterotactic selectivity.[15]

This assumption is further supported by the fact that the P_r value exhibited by complex **4** was much higher than that of complex **1**. From our previous study,[11a] scandium silylamido complexes with longer bridges (of three or four carbon atoms) show high fluxionality in solution, while complexes with a C_2 bridge are rigid. Apparently the transformation between the *Λ* and *Δ* configurations of the ligand in complex **4**, in which there is a more flexible C_3 bridge, allows ready adaptation to the incoming lactide configuration (L-LA → (*S*)-lactate → *Δ* configuration → D-LA → (*R*)-lactate → *Λ* configuration).[16] This stereoregulating mechanism is somewhat different from what is commonly known as chain-end control and will be investigated in more detail in the future.

Experimental Section

Synthesis of [{(xytbmp)Sc(μ-(*R*)-(+)-OCHMeCOO*t*Bu)}$_2$] (**8**): (*R*)-(+)-*tert*-Butyl lactate (59.1 mg, 0.404 mmol) was added slowly to a solution of complex **5** (300 mg, 0.404 mmol) in toluene (15 mL) at room temperature. The colorless solution was stirred for 16 h. Then, the volatiles were evaporated under vacuum to give a white powder, which was further dried under vacuum for 2 h. The colorless solid was dissolved in pentane (30 mL) and filtered; the clear solution was then concentrated to about 10 mL at elevated temperatures. After cooling the solution to room temperature and then to −30 °C, colorless crystals were formed (173 mg, 63 %). ^{1}H NMR (C_6D_6, 500 MHz): $\delta =$ 7.34 (d, $^4J = 2.0$ Hz, 1 H, 5-H), 7.12 (d, $^4J = 2.0$ Hz, 1 H, 5′-H), 6.95 (d, $^4J = 2.0$ Hz, 1 H, 3-H), 6.89 (d, $^4J = 2.0$ Hz, 1 H, 3′-H), 6.86 (td, $^3J =$ 7.5 Hz, $^4J = 1.5$ Hz, 1 H, Ar-H), 6.78 (dd, $^3J = 7.5$ Hz, $^4J = 1.5$ Hz, 1 H, Ar-H), 6.68 (td, $^3J = 7.5$ Hz, $^4J = 1.5$ Hz, 1 H, Ar-H), 6.06 (d, $^3J =$ 7.5 Hz, 1 H, Ar-H), 5.86 (q, $^3J = 7.0$ Hz, 1 H, OC*H*(CH_3)), 3.94 (d, $^2J = 12.5$ Hz, 1 H, SCH_2), 3.83 (d, $^2J = 12.5$ Hz, 1 H, SCH_2), 3.46 (d, $^2J = 13.0$ Hz, 1 H, SCH_2), 3.34 (d, $^2J = 13.0$ Hz, 1 H, SCH_2), 2.34 (s, 3 H, 4-CH_3), 2.29 (s, 3 H, 4′-CH_3), 1.50 (s, 9 H, 6-C(CH_3)$_3$), 1.35 (s, 9 H, 6′-C(CH_3)$_3$), 1.33 (d, $^3J = 7.0$ Hz, 3 H, OCH(CH_3)), 0.93 ppm (s, 9 H, OC(CH_3)$_3$); ^{13}C{^{1}H} (C_6D_6, 125 MHz): $\delta = 185.4$ (C=O), 166.8 (C1), 160.7 (C1′), 137.9 (C6), 136.9 (C6′), 135.7 (Ar-C), 135.4 (Ar-C), 133.3 (C3), 131.0 (C3′), 128.7 (C5), 127.4 (C5′), 127.1 (Ar-C), 126.7 (Ar-C), 126.2 (Ar-C), 124.7 (Ar-C), 124.4 (C4), 124.1 (C2), 122.5 (C2′), 86.9 (O*C*(CH_3)$_3$), 75.1 (O*C*H(CH_3)), 40.9 (SCH_2), 39.1 (SCH_2), 35.3 (SCH_2), 34.8 (SCH_2), 34.4 (6-*C*(CH_3)$_3$) 30.5 (6-C(*C*H_3)$_3$), 30.3 (6′-C(*C*H_3)$_3$), 29.7 (6′-*C*(CH_3)$_3$) , 27.4 (OCH(*C*H_3)), 22.69 (OC(*C*H_3)$_3$), 21.4 (4-CH_3), 20.9 ppm (4′-CH_3). Elemental analysis calcd for $C_{74}H_{98}O_{10}S_4Sc_2 \cdot 0.66(C_5H_{12})$: C 65.75, H 7.56, S 9.08; found: C 65.70, H 7.41, S 9.40.

Typical polymerization procedure: A solution of the initiator (0.5 mL, 2.9 mM) from a stock solution in THF was injected sequentially to a series of 6 mL vials loaded with *rac*-lactide (0.125 g, 0.87 mmol) and THF (0.5 mL) in a glovebox. After specified time intervals, each vial was taken out of the glovebox, aliquots were drawn and quickly quenched with *n*-pentane, with the bulk polymerization mixture quenched at the same time by adding an excess amount of *n*-pentane. All the volatiles in the aliquots were removed and the monomer conversions of the residues were determined by comparing the integrations of the methine or methyl resonances of the monomer and polymer in the ^{1}H NMR spectra ($CDCl_3$, 200 MHz). The precipitates collected from the bulk mixture were dried in air, dissolved in dichloromethane, and sequentially precipitated into methanol. The obtained polymer was further dried in a vacuum oven at 60 °C for 16 h for gel-permeation chromatography (GPC) and ^{1}H,^{13}C homonuclear decoupled ^{1}H NMR analyses. In the cases where 2-propanol was used, the initiator solution in THF or toluene was treated first with a solution of 2-propanol in the same solvent for 10 min, and then injected into the solution of *rac*-lactide. Otherwise the procedures were the same.

Received: August 4, 2006
Revised: September 8, 2006
Published online: October 26, 2006

 © 2006 Wiley-VCH Verlag GmbH & Co. KGaA, Weinheim

Keywords: lactides · ligand effects · polymerization · scandium · stereoselectivity

[1] a) O. D. Cabaret, B.-M. Vaca, D. Bourissou, *Chem. Rev.* **2004**, *104*, 6147 – 6176; b) R. E. Drumright, P. R. Gruber, D. E. Henton, *Adv. Mater.* **2000**, *12*, 1841 – 1846; c) C. K. Ha, J. A. Gardella, Jr., *Chem. Rev.* **2005**, *106*, 4205 – 4232.

[2] a) B. J. O'Keefe, M. A. Hillmyer, W. B. Tolman, *J. Chem. Soc. Dalton Trans.* **2001**, 2215 – 2224; b) K. Nakano, N. Kosaka, T. Hiyama, K. Nozaki, *Dalton Trans.* **2003**, 4039 – 4050; c) M. H. Chisholm, Z. Zhou, *J. Mater. Chem.* **2004**, *14*, 3081 – 3092.

[3] a) N. Spassky, M. Wisnieski, C. Pluta, A. Le Borgne, *Macromol. Chem. Phys.* **1996**, *197*, 2627 – 2637; b) T. M. Ovitt, G. W. Coates, *J. Polym. Sci. A: Polym. Chem.* **2000**, *38*, 4686 – 4692; c) K. Majerska, A. Duda, *J. Am. Chem. Soc.* **2004**, *126*, 1026 – 1027; d) C. P. Radano, G. L. Baker, M. R. Smith III, *J. Am. Chem. Soc.* **2000**, *122*, 1552 – 1553; e) Z. Zhong, P. J. Dijkstra, J. Feijen, *Angew. Chem.* **2002**, *114*, 4692 – 4695; f) Z. Zhong, P. J. Dijkstra, J. Feijen, *J. Am. Chem. Soc.* **2003**, *125*, 11291 – 11298; g) M. H. Chisholm, N. J. Patmore, Z. Zhou, *Chem. Commun.* **2005**, 127 – 129; h) N. Nomura, R. Ishii, M. Akakura, K. Aoi, *J. Am. Chem. Soc.* **2002**, *124*, 5938 – 5939; i) Z. Tang, X. Chen, X. Pang, Y. Yang, X. Zhang, X. Jing, *Biomacromolecules* **2004**, *5*, 965 – 970.

[4] X. Wang, K. Liao, D. Quan, Q. Wu, *Macromolecules* **2005**, *38*, 4611 – 4617.

[5] a) T. M. Ovitt, G. W. Coates, *J. Am. Chem. Soc.* **1999**, *121*, 4072 – 4073; b) M. H. Chisholm, N. W. Eilerts, J. C. Huffman, S. S. Iyer, M. Pacold, K. Phomphrai, *J. Am. Chem. Soc.* **2000**, *122*, 11845 – 11854.

[6] P. Hormnirun, E. L. Marshall, V. C. Gibson, A. J. P. White, D. J. Williams, *J. Am. Chem. Soc.* **2004**, *126*, 2688 – 2689.

[7] a) M. Cheng, A. B. Attygalle, E. B. Lobkovsky, G. W. Coates, *J. Am. Chem. Soc.* **1999**, *121*, 11583 – 11584; b) B. M. Chamberlain, M. Cheng, D. R. Moore, T. M. Ovitt, E. B. Lobkovsky, G. W. Coates, *J. Am. Chem. Soc.* **2001**, *123*, 3229 – 3238; c) M. H. Chisholm, J. C. Gallucci, K. Phomphrai, *Inorg. Chem.* **2005**, *44*, 8004 – 8010; d) M. H. Chisholm, J. C. Gallucci; K. Phomphrai, *Inorg. Chem.* **2004**, *43*, 6717 – 6725; e) M. H. Chisholm, J. Gallucci, K. Phomphrai, *Chem. Commun.* **2003**, 48 – 49.

[8] a) C.-X. Cai, A. Amgoune, C. W. Lehmann, J.-F. Carpentier, *Chem. Commun.* **2004**, 330 – 331; b) A. Amgoune, C. M. Thomas, T. Roisnel, J.-F. Carpentier, *Chem. Eur. J.* **2006**, *12*, 169 – 179; c) F. Bonnet, A. R. Cowley, P. Mountford, *Inorg. Chem.* **2005**, *44*, 9046 – 9055.

[9] a) Y. Kim, G. K. Jnaneshwara, J. G. Verkade, *Inorg. Chem.* **2003**, *42*, 1437 – 1447; b) S. K. Russel, C. L. Gamble, K. J. Gibbins, K. C. S. Juhl, W. S. Mitchell III, A. J. Tumas, G. E. Hofmeister, *Macromolecules* **2005**, *38*, 10336 – 10340.

[10] E. L. Marshall, V. C. Gibson, H. S. Rzepa, *J. Am. Chem. Soc.* **2005**, *127*, 6048 – 6051.

[11] a) H. Ma, T. P. Spaniol, J. Okuda, *Dalton Trans.* **2003**, 4770 – 4780; b) H. Ma, J. Okuda, *Macromolecules* **2005**, *38*, 2665 – 2673; c) H. Ma, G. Melillo, L. Oliva, T. P. Spaniol, U. Englert, J. Okuda, *Dalton Trans.* **2005**, 721 – 727.

[12] a) M. H. Chisholm, S. S. Iyer, M. E. Matison, D. G. McCollum, M. Pagel, *Chem. Commun.* **1997**, 1999 – 2000; b) K. A. M. Thakur, R. T. Kean, E. S. Hall, *Anal. Chem.* **1997**, *69*, 4303 – 4309; c) K. A. M. Thakur, R. T. Kean, M. T. Zell, B. E. Padden, E. J. Munson, *Chem. Commun.* **1998**, 1913 – 1914.

[13] Data for the X-ray crystal structure of **8**: $C_{74}H_{98}O_{10}S_4Sc_2 \cdot 3(C_6H_{14})$, $M_r = 1624.20$, $T = 110$ K, crystal size $0.6 \times 0.5 \times 0.4$ mm^3, trigonal, $P3_221$ (no. 154), $a = 27.6572(11)$, $b = 27.6572(11)$, $c = 28.7044(16)$, $\alpha = \beta = 90°$, $\gamma = 120°$, $Z = 6$, $U = 19015.0(15)$ Å^3, $\rho_{calcd} = 0.851$ g cm^{-1}, $\mu = 0.212$ mm^{-1}, 98698 collected, 25100 unique ($R_{int} = 0.1025$), final $R_1 = 0.1005$, wR_2 [$I > 2\sigma(I)$] = 0.2612, residual electron density extremes were 1.328 and -0.653 e Å^{-3}. CCDC-616875 contains the supplementary crystallographic data for this paper. These data can be obtained free of charge from The Cambridge Crystallographic Data Centre via www.ccdc.cam.ac.uk/data_request/cif.

[14] a) The product from the analogous reaction of **4** and (*R*)-(+)-*tert*-butyl lactate also contains a dimeric structure with both scandium centers in a Λ configuration (see the Supporting Information); b) three diastereomers, (*R*,*R*,Λ,Λ), (*R*,*R*,Δ,Λ), and (*R*,*R*,Δ,Δ) are conceivable which should display distinct resonances in the ^{1}H NMR spectrum as a result of the rigidity of the structure.

[15] A similar interconversion between the Λ and Δ configurations of the ligand in the corresponding titanium complexes has been suggested to be responsible for the syndiotactic selectivity during styrene polymerization; see: a) C. Capacchione, A. Proto, H. Ebeling, R. Mülhaupt, K. Möller, T. P. Spaniol, J. Okuda, *J. Am. Chem. Soc.* **2003**, *125*, 4964 – 4965; b) C. Capacchione, R. Manivannan, M. Barone, K. Beckerle, R. Centore, L. Oliva, A. Proto, A. Tuzi, T. P. Spaniol, J. Okuda, *Organometallics* **2005**, *24*, 2971 – 2982. Site isomerization between monomer insertions as a consequence of the polymer chain end was proposed for the syndioselective propylene polymerization with bis(salicylaldiminato)titanium (FI-) catalysts; see: c) J. Tian, G. W. Coates, *Angew. Chem.* **2000**, *112*, 3772 – 3775; *Angew. Chem. Int. Ed.* **2000**, *39*, 3626 – 3629; d) M. Mitani, R. Furuyama, J. Mohri, J. Saito, S. Ishii, H. Terao, T. Nakano, H. Tanaka, T. Fujita, *J. Am. Chem. Soc.* **2003**, *125*, 4293 – 4304; e) H. Makio, T. Fujita, *Bull. Chem. Soc. Jpn.* **2005**, *78*, 52 – 66.

[16] The influence of the C_3 bridge compared with the C_2 bridge was also observed for aluminum complexes with salen-type ligand,[3h] where high isotactic selectivity was obtained for complexes with a C_3 bridge.

 © 2006 Wiley-VCH Verlag GmbH & Co. KGaA, Weinheim

NMR Spectroscopy

DOI: 10.1002/anie.200603036

Acquisition Regime for High-Resolution Heteronuclear 2D NMR Spectra

*Igor Baskyr, Torsten Brand, Matthias Findeisen, and Stefan Berger**

Two-dimensional NMR techniques are normally based on the detection of a set of one-dimensional spectra using a pulse sequence with an incremented delay within the evolution time.[1] These delays provide the second or indirect dimension and are incremented so that the set of time increments allows the sampling of all frequencies in the indirect dimension. The

[*] I. Baskyr, T. Brand, Dr. M. Findeisen, Prof. Dr. S. Berger
Institut für Analytische Chemie
Universität Leipzig
Linnéstrasse 3, 04103 Leipzig (Germany)
Fax: (+49) 341-973-6115
E-mail: stberger@rz.uni-leipzig.de

Supporting information for this article is available on the WWW under http://www.angewandte.org or from the author.

© 2006 Wiley-VCH Verlag GmbH & Co. KGaA, Weinheim

number of time increments and thus the resolution in the indirect dimension are always limited. The acquisition of heteronuclear 2D NMR spectra is time consuming, while their resolution is very poor when using the full spectral width in the indirect dimension. Compared with the resolution of a routine 1D ^{13}C NMR spectrum, for example, this can be regarded as insufficient.

The ^{1}H,^{13}C HSQC and HMBC techniques are currently the most important routine methods that provide information about one- and multibond connectivities.[2] The problem of increasing the resolution in the indirect dimension without increasing the experiment time of a two-dimensional experiment is therefore of great importance. Significant solutions to this problem seem to belong to the realm of data handling using appropriate mathematical tools.[3] Covariance-based approaches[4,5] have been proposed for some homonuclear techniques which produce symmetric spectra. The methods suitable for high-resolution heteronuclear NMR spectroscopy,[3,6,7] such as Hadamard or filter diagonalization concepts, normally use different kinds of prior information about the chemical shifts in the indirect dimension and/or the number and shape of the peaks. An approach recently proposed by Jeannerat et al.[8,9] seems to be very promising within this context. It uses spectral aliasing as a means of reconstructing the full spectrum, when only a narrow band of the latter is physically acquired.

Unfortunately this method in its published form is also limited to the case when all frequencies of the ^{13}C NMR spectrum are known beforehand. It then becomes possible to optimize the conditions for acquiring the aliased 2D spectrum. This is, however, not possible when working with an unknown substance, since there might be insufficient material available to acquire a ^{13}C NMR spectrum with a significant signal-to-noise ratio in an acceptable time. Herein, we discuss a more general use of an aliasing technique to obtain HSQC- and HMBC-like spectra with high resolution in the ^{13}C dimension but with no prior information on the ^{13}C chemical shifts.

By aliasing one considers the appearance of artefact signals in the spectrum sampled with a too-narrow spectral width. Whereas this is suppressed on recent NMR spectrometers by filter techniques in the direct dimension, we will use this here in the indirect dimension. If a signal with the apparent chemical shift δ_{apparent} is found within a too-narrow spectral width SW in the indirect dimension, the genuine value of the chemical shift δ_{genuine} can be expressed as Equation (1), where k can be any arbitrary natural number.

$$\delta_{\text{genuine}} = \delta_{\text{apparent}} \pm k \times \text{SW} \quad (1)$$

Jeannerat et al. have proposed using the aliased spectra recorded in the indirect (^{13}C) dimension under optimized conditions, thus allowing k to be determined unambiguously. The use of spectral widths of, for example, 1 ppm instead of the 150–250 ppm needed to span the whole carbon spectrum allows the resolution to be improved dramatically.

Instead of using a priori information about ^{13}C chemical shifts, we propose here to acquire spectra with different SW values, for example, two—SW_1 and SW_2. At first, we assume a single chemical shift in the ^{13}C NMR spectrum corresponding to a given signal in the ^{1}H direction as it is valid for HSQC. If the condition shown in Equation (2) is fulfilled for all possible k_1 and k_2 values within the full genuine spectral width SW_{full}, it becomes possible to unambiguously find the δ_{genuine} value in Equation (1) from the two δ_{apparent} values.

$$k_1 \times \text{SW}_1 \neq k_2 \times \text{SW}_2 \quad (2)$$

Such SW_i values that satisfy both Equation (2) and the intention to minimize the spectral width, and thus improve the resolution, can be chosen as follows. If one considers the SW_{full} value, given in ppm, and a desired resolution R, given in ppm per point, one can define the number of resolution points $Z = \text{SW}_{\text{full}}/R$, for example, $Z = 150$ ppm/0.2 ppm per point = 750 points.

The numbers of the chosen points Z_1 and Z_2 that fulfil the condition $k_1 Z_1 \neq k_2 Z_2$ must be larger than $Z^{1/2}$, since the product $Z_i \times Z_j$ should be larger than Z to provide unequivocal aliasing. The easiest way to ensure the absence of common multiples less than Z is to choose Z_i and Z_j as prime numbers. In our example, these can be the numbers 29 and 31. For HSQC or HMQC type spectra, where each proton signal is only connected to one ^{13}C frequency, two different Z_i values are sufficient and this provides an elegant option of obtaining HSQC spectra in very high resolution, as is required in the field of residual dipolar couplings.[10]

The situation is more complex for HMBC spectra, since each proton signal may be connected to several ^{13}C frequencies. The number of HMBC spectra to be recorded in the indirect dimension with different spectral widths should be equal to $N+1$, where N is the maximum number of expected correlations between one proton and the carbon atoms. The same principle should be used when an aliased HSQC spectrum exhibits additional peaks for a single proton frequency because of a strong overlap of protons. From our experience, $N = 6$ is sufficient in most HMBC spectra. For the case $\text{SW}_{\text{full}} = 200$–$230$ ppm and a desired resolution of 0.2 ppm, one can choose the prime numbers 37, 41, 43, 47, 53, 59, and 61. In our method these numbers directly serve as time domain (TD) points. Multiplication with the desired resolution R (0.2 ppm per point) yields the spectral widths SW_i of 7.4, 8.2, 8.6, 9.4, 10.6, 11.8, and 12.2 ppm. Thus, the seven HMBC spectra are recorded with a total number of 341 time increments.

The spectra were reconstructed using a Matlab routine, which is available from the authors. It works as follows: Within each of the $N+1$ spectra, for each proton frequency, only the N most intensive maxima are considered as significant. The significant signal magnitudes are regarded as corresponding to all possible values of the hypothetical δ_{genuine} value found by Equation (1) for all values of k. So each spectrum is "unfolded" from its SW_i to the SW_{full}. The geometric means of the magnitudes taken in the same points of the $N+1$ "unfolded" spectra produce the final reconstructed spectrum and remove artifacts. The final spectrum exhibits peaks in the points where the maxima in different individual "unfolded" spectra coincide. Zero-filling to 128 points in the ^{13}C dimension resulted in different digital

 © 2006 Wiley-VCH Verlag GmbH & Co. KGaA, Weinheim

resolution, which was subsequently corrected by the spline interpolation within our routine.

The reconstructed spectra were reimported into the Bruker Topspin software and further processing was performed there. Figure 1a shows some expansions of the reconstructed HSQC spectrum of strychnine (**1**) which

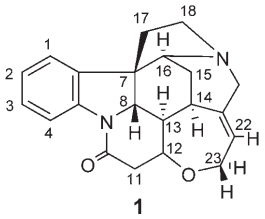

1

correspond to the two pairs of the most closely resonating ^{13}C atoms, and Figure 1b shows the same expansions of the HSQC spectrum acquired within the same total experimental

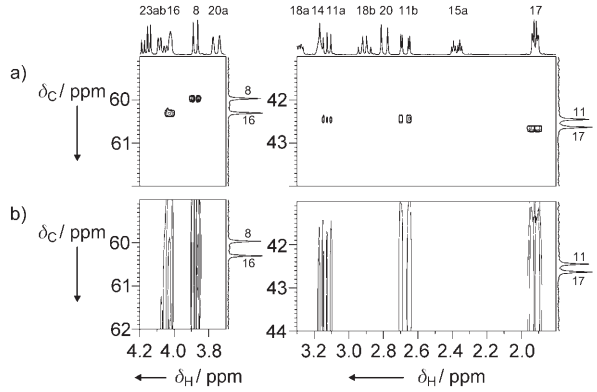

Figure 1. Expansions of the HSQC spectrum of strychnine (**1**) for the regions $\delta_C = 41$–44 ppm and $\delta_C = 59$–62 ppm: a) Spectrum reconstructed from two recordings with SW = 5.8 ppm (TD = 29) and SW = 6.2 ppm (TD = 31) and interpolated to a digital resolution of 0.05 ppm per point; b) the conventional magnitude-mode HSQC recorded with TD = 60 within the full ^{13}C spectral width of 150 ppm. The corresponding regions of the ^{1}H and ^{13}C spectra are shown along the axes.

time for the full spectrum without aliasing. The same regions of the reconstructed long-range HSQC (HMBC-like) spectrum versus the conventional long-range HSQC spectrum acquired within the same time (TD = 341) are shown in Figure 2a and b, respectively.

When any of the HMBC standard pulse sequences is used, the modulation by proton–proton spin coupling in the indirect dimension becomes clearly visible at this resolution. A variant of long-range HSQC[11–13] should be used instead. One developed from the approach of Ref. [11] (see the Supporting Information) has provided HMBC-like, but distortionless spectra. The magnitude-mode variants of the pulse sequences

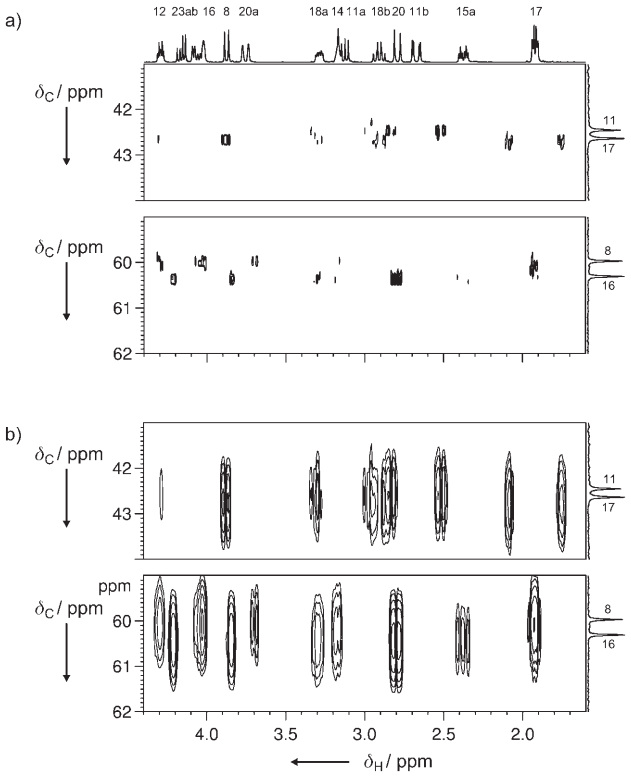

Figure 2. Expansions of the long-range HSQC spectrum of strychnine (**1**) for the regions $\delta_C = 41$–44 ppm and $\delta_C = 59$–62 ppm: a) Spectrum reconstructed from seven long-range HSQC spectra recorded with different SW and TD values (see text) corresponding to a resolution of 0.2 ppm per point and interpolated to 0.1 ppm per point; b) The conventional magnitude-mode long-range HSQC spectrum recorded over the same time. The corresponding regions of the ^{1}H and ^{13}C spectra are shown along the axes.

were used throughout since our post-processing does not retain the phase information.

The reconstructed spectra exhibit all the peaks of the HSQC and HMBC spectra of strychnine. The digital resolution achieved through spline interpolation actually comprised 5 Hz per point for the HSQC spectrum and 10 Hz per point for the long-range HSQC spectrum, and allowed the closest ^{13}C resonances to be distinguished. The sensitivity is reduced because of the very high splittings, according to the principle of "exclusive correlation spectroscopy" (E. COSY),[14] which is visible only in high resolution. For a comparison with the conventional spectrum and a discussion of the relative signal to noise ratios see the Supporting Information.

In conclusion, we have demonstrated here a new acquisition technique[15] for 2D NMR spectra that provides a significantly better resolution within the same given experimental time. Further developments will aim to fully reconstruct 1D ^{13}C NMR spectra by using this approach.

Experimental Section

The spectra of a 3% (w/v) solution of strychnine in $CDCl_3$ were acquired on a Bruker Avance DRX400 spectrometer fitted with a

 © 2006 Wiley-VCH Verlag GmbH & Co. KGaA, Weinheim

5 mm inverse probe head. For the pulse sequence used and spectrometer details see the Supporting Information.

Received: July 27, 2006
Published online: October 30, 2006

Keywords: analytical methods · NMR spectroscopy · pulse sequences · structure elucidation

[1] S. Berger, S. Braun, *200 and More NMR Experiments*, Wiley-VCH, Weinheim, **2004**, chap. 10.
[2] B. L. Marquez, W. H. Gerwick, R. T. Williamson, *Magn. Reson. Chem.* **2001**, *39*, 499 – 530.
[3] R. Freeman, E. Kupce, *J. Biomol. NMR* **2003**, *27*, 101 – 113.
[4] N. Trbovic, S. Smirnov, F. Zhang, R. Brüschweiler, *J. Magn. Reson.* **2004**, *171*, 277 – 283.
[5] B.-W. Hu, P. Zhou, I. Noda, G.-Z. Zhao, *Anal. Chem.* **2005**, *77*, 7534 – 7538.
[6] J. Chen, A. A. De Angelis, V. A. Mandelshtam, A. J. Shaka, *J. Magn. Reson.* **2003**, *162*, 74 – 89.
[7] D. Rovnyak, D. P. Frueh, M. Sastry, Z.-Y. J. Sun, A. S. Stern, J. C. Hoch, G. Wagner, *J. Magn. Reson.* **2004**, *170*, 15 – 21.
[8] D. Jeannerat, *Magn. Reson. Chem.* **2003**, *41*, 3 – 17.
[9] D. Jeannerat, D. Ronan, Y. Baudry, A. Pinto, J. P. Sauliner, S. Matile, *Helv. Chim. Acta* **2004**, *87*, 2190 – 2207.
[10] K. Fehér, S. Berger, K. E. Kövér, *J. Magn. Reson.* **2003**, *163*, 340 – 346.
[11] R. Marek, L. Kralik, V. Sklenar, *Tetrahedron Lett.* **1997**, *38*, 665 – 668.
[12] R. T. Williamson, B. L. Marquez, W. H. Gerwick, K. E. Köver, *Magn. Reson. Chem.* **2000**, *38*, 265 – 273.
[13] H. Koskela, I. Kilpeläinen, S. Heikkinen, *J. Magn. Reson.* **2003**, *164*, 228 – 232.
[14] C. Griesinger, O. W. Sørensen, R. R. Ernst, *J. Am. Chem. Soc.* **1985**, *107*, 6394 – 6396.
[15] Note added in proof: For HSQC, a related approach was recently published: A. J. Dunn, P. J. Sidebottom, *Magn. Reson. Chem.* **2005**, *43*, 124 – 131.

 © 2006 Wiley-VCH Verlag GmbH & Co. KGaA, Weinheim

Shape-Controlled Nanoparticles

DOI: 10.1002/anie.200603068

Morphological Control of Catalytically Active Platinum Nanocrystals**

*Hyunjoo Lee, Susan E. Habas, Sasha Kweskin, Derek Butcher, Gabor A. Somorjai, and Peidong Yang**

Colloidal metallic nanocrystals have been explored for catalytic applications, including fine chemicals synthesis,[1] fuel-cell technology,[2] hydrogen production,[3] and gas sensing.[4] The catalytic activity of a metallic catalyst depends strongly on its surface properties. For instance, hexagonal (111) Pt surfaces are 3–7-times more active than cubic (100) surfaces for aromatization reactions.[5] The reactivity and selectivity of nanoparticles can therefore be tuned by controlling the morphology because the exposed surfaces of the particles have distinct crystallographic planes depending on the shape.

A variety of Pt nanostructures, including polyhedra,[6] wires,[7] tubes,[8] dendritic structures,[9] and multipods[10] have been synthesized by regulating growth at specific surfaces or by templating methods. Amphiphilic polymers or surfactants typically stabilize high-energy surfaces of nanoparticles. However, chemical reactions can only occur effectively on catalytically "clean" nanoparticles when the reactants adsorb more strongly to the particle surface than the surface-stabilizing agents do.[11] When the interaction between the stabilizing agent and metal surface is too strong, the catalytic activity is greatly reduced. For instance, the carbonyl group of polyvinylpyrrolidone (PVP) or polyacrylate, which are the most widely used surface-regulating polymers in shaped-nanoparticle synthesis, interacts strongly with the platinum surface[12] and thus blocks a significant number of active sites. On the other hand, alkylammonium ions have been widely used in synthesizing Au nanoparticles,[13] and their interactions with Pt surfaces are considerably weaker than that of the carbonyl group. Therefore, this class of molecules could serve as ideal surface-stabilizing agents that can regulate the shape of nanoparticles while preserving catalytically active sites.

[*] H. Lee, S. E. Habas, S. Kweskin, D. Butcher, Prof. G. A. Somorjai, Prof. P. Yang
Department of Chemistry
University of California, Berkeley
Materials Science Division
Lawrence Berkeley National Laboratory
Berkeley, CA 94720 (USA)
Fax: (+1) 510-642-7301
E-mail: p_yang@uclink.berkeley.edu

[**] This work was supported by the Director, Office of Science, Office of Basic Energy Sciences, Chemical Sciences, Materials Sciences and Engineering Division of the U.S. Department of Energy under contract No. DE-AC02-05CH11231. We thank the National Center for Electron Microscopy for the use of their facilities.

Supporting Information for this article is available on the WWW under http://www.angewandte.org or from the author.

InterScience
© 2006 Wiley-VCH Verlag GmbH & Co. KGaA, Weinheim

Interestingly, shape-control of platinum nanoparticles using alkylammonium ions has not been reported.

The addition of foreign metal ions is very effective for controlling morphology. Xia and co-workers, for example, have obtained multipods and nanowires by altering the reduction kinetics with Fe ions.[7a,14] We have also reported recently that highly uniform Pt cubes, cuboctahedra, and octahedra can be prepared by adding Ag ions prior to the reduction of the Pt precursor.[6c] The catalytic activity of these particles, however, is greatly reduced by the presence of Ag. As the amount of Ag is increased from the cubic to the octahedral samples, the reaction rate for ethylene hydrogenation decreases accordingly.[15] Therefore, shape-control of uniform Pt nanoparticles without the aid of foreign metal ions is highly desirable for catalytic applications.

Herein, we report the preparation of cuboctahedra, cubes, and porous Pt nanoparticles by varying the reduction method, as illustrated in Scheme 1. Near-monodisperse nanoparticles

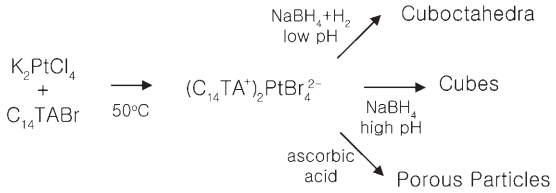

Scheme 1. Reduction of a metal–surfactant complex can be kinetically controlled to produce cuboctahedra, cubes, and porous particles.

are obtained in which tetradecyltrimethylammonium bromide ($C_{14}TABr$) is bound to the Pt surfaces. Potassium tetrachloroplatinate (K_2PtCl_4) forms a precipitate upon mixing with $C_{14}TABr$ in aqueous solution. After heating at 50 °C, the solution becomes clear pale yellow and then turns dark brown after reduction. The UV/Vis spectra show that after mixing with the surfactant the characteristic absorption of K_2PtCl_4 at 216 nm disappears and a new band appears at 271 nm (Supporting Information, Figure S1). It has been reported that $[PdCl_4]^{2-}$ ions interact with $C_{14}TABr$ to form the stoichiometric metal–surfactant complex $(C_{14}TA)_2PdBr_4$.[16] Likewise, the complex of $(C_{14}TA)_2PtBr_4$ is considered to be the real precursor during the reduction process.

To optimize the conditions for nanoparticle preparation various concentrations and ratios of K_2PtCl_4 and $C_{14}TABr$ were explored. Particle formation was observed over a broad range of reagent concentrations (20–200 mM $C_{14}TABr$ and 0.5–5 mM K_2PtCl_4) and ratios ($C_{14}TABr/K_2PtCl_4 = 25$–$400$). Generally, the size of the nanoparticles was found to increase as the concentration of the reagents and ratio of K_2PtCl_4 to $C_{14}TABr$ increased. Shape evolution of the nanoparticles from dendritic structures to faceted nanoparticles, such as cubes, was observed when sodium borohydride ($NaBH_4$) was used as the reducing agent. On the other hand, porous particles of various sizes dominated when the reducing agent was ascorbic acid. The reactant composition and the amount of reducing agent were finely tuned to 1) achieve a uniform distribution of size and shape, and 2) prepare particles of differing morphology within the same size range.

Figure 1 shows TEM and high-resolution (HR) TEM images of Pt nanoparticles with different morphologies.

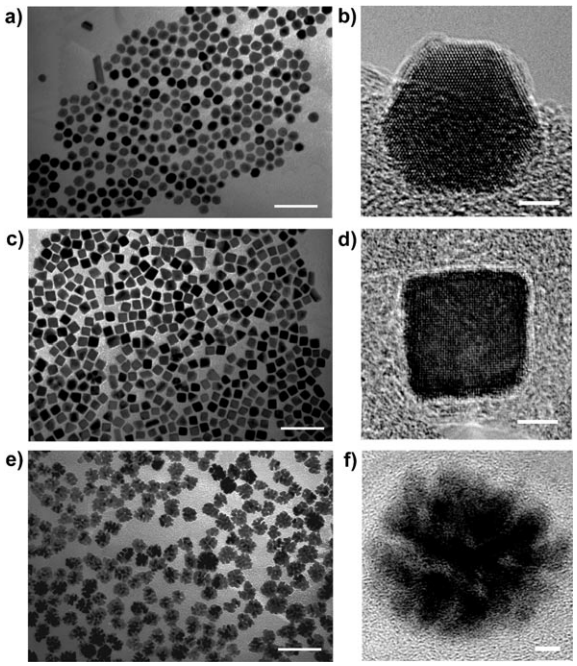

Figure 1. TEM images of a) cuboctahedra, c) cubes, and e) porous particles. HRTEM images of b) a cuboctahedron along the [111] zone axis, d) a cube along the [100] zone axis, and f) a porous particle. The scale bar is 50 nm in the TEM images and 3 nm in the HRTEM images.

Cuboctahedral particles (91 % cuboctahedra, 9 % spheres or irregular particles) with an average size of (12.6 ± 1.8) nm (vertex-to-vertex) were prepared from a solution of 150 mM $C_{14}TABr$ and 1.5 mM K_2PtCl_4 reduced with 7.5 mM $NaBH_4$ in a mild H_2 flow. Figure 1b provides a representative HRTEM image of a Pt cuboctahedron along the [111] zone axis. Threefold symmetry from the (111) surface on the top of the particle can clearly be seen. Cubic particles (73 % cubes, 5 % tetrahedra, 22 % irregular particles) with an average size of (13.4 ± 1.8) nm (diagonal) were prepared from a 100 mM $C_{14}TABr$ and 1 mM K_2PtCl_4 solution reduced with 30 mM $NaBH_4$. The excess $NaBH_4$ reacts vigorously with water to produce a large amount of H_2. The resulting pressure inside the reaction vessel was released by inserting a needle into the septum covering the reactor. The HRTEM image of a Pt cube along the [100] zone axis is shown in Figure 1 d (Figure S2 a of the Supporting Information provides an electron diffraction pattern for a single Pt cube along the [100] zone axis). Porous particles (100 % yield) were obtained from a solution containing 50 mM $C_{14}TABr$ and 2 mM K_2PtCl_4 reduced with 6 mM ascorbic acid. The average size was estimated as (19.3 ± 3.1) nm by measuring the longest axis. The HRTEM image of the porous particle in Figure 1 f clearly shows its porous nature. The BET surface area was determined to be 25 $m^2 g^{-1}$

 © 2006 Wiley-VCH Verlag GmbH & Co. KGaA, Weinheim

based on nitrogen gas absorption and desorption isotherm measurements. Interestingly, a single porous particle exhibits an electron diffraction pattern characteristic of a single crystalline particle (Supporting Information, Figure S2b).

For the same concentrations of C_{14}TABr and K_2PtCl_4, the amount of $NaBH_4$ used for reduction has a significant impact on the resulting particle morphology. This effect is illustrated in Figure 2. Dendritic particles were obtained for 7.5 mM $NaBH_4$, cuboctahedra for 30 mM $NaBH_4$, and cubes for 45 mM $NaBH_4$. Higher concentrations of $NaBH_4$ gave particles with irregular shapes. Notably, the particle size does not differ significantly for 30, 45, and 60 mM $NaBH_4$ (Figures 2b, c and d). If the addition of $NaBH_4$ causes instantaneous nucleation, as reported,[13b] the final particle size should be smaller for larger amounts of $NaBH_4$ owing to the increased number of initial nucleates. Also, the color of the solution generally turned dark brown a couple of hours after the addition of $NaBH_4$, thus disproving the immediate nucleation. These observations suggest that the H_2 produced by reaction of $NaBH_4$ with water might be truly responsible for the final morphology of the Pt nanoparticles rather than $NaBH_4$. It has also been reported that hydrogen-based reduction proceeds by slow nucleation and fast autocatalytic surface growth, thereby enabling the preparation of nearly monodisperse metal (Ir) nanoclusters.[17] A control experiment in the absence of H_2 was conducted by removing the septum from the reaction vessel to allow the H_2 to escape. Rather than the faceted nanoparticles obtained in the presence of H_2, the majority of the product precipitated as bulk Pt. TEM analysis of the gray supernatant solution showed aggregated particulates. It is noteworthy that the cuboctahedral Pt nanoparticles shown in Figure 1a were prepared similarly to the particles shown in Figure 2a but passing additional H_2 through the reactor.

The production of H_2 by $NaBH_4$ is greatly accelerated by an increase in temperature.[18] In contrast to the majority of other syntheses, which proceed at room temperature, the reactions described herein are performed at 50 °C. On the other hand, in the absence of $NaBH_4$ when only an H_2 flow was used to reduce a solution of 150 mM C_{14}TABr and 1.5 mM K_2PtCl_4, nanoparticles with various shapes and sizes were obtained (Supporting Information, Figure S3). The production of H_2 in situ throughout the solution by $NaBH_4$ seems to be critical for the synthesis of uniform Pt nanoparticles.

During the reaction of $NaBH_4$ with water, the pH value increases as a result of the formation of the strongly basic metaborate ion.[18] In fact, the pH value increases to 9.41, 9.63, 9.77, and 9.97 after the reduction of solutions containing 7.5, 20, 30, and 40 mM $NaBH_4$, respectively (Figure 2). This pH change is believed to cause the distinct morphologies reported herein. When only H_2 was used as the reductant (Supporting Information, Figure S3), the pH value decreased to 2.51. To mimic the change in pH value observed with the addition of $NaBH_4$, NaOH was added to a reaction under the conditions described for cuboctahedral growth. Starting from the cuboctahedral shape shown in Figure 3a, more cubic particles appear as NaOH is added, as shown in Figure 3b (0.01 mM NaOH) and Figure 3c (1 mM NaOH). For 3 mM NaOH, only aggregated particulates were obtained. When an excess of NaOH is added (pH ≈ 12), no reduction occurs even after 24 h. Cubic nanoparticles could also be prepared by adding NaOH when the reactant solution was reduced only with H_2 gas (Supporting Information, Figure S4). A higher pH value was found to decrease the reduction rate, with slower reduction enabling selective growth on the (100) surfaces to produce cubic nanoparticles.

The catalytic activity was tested for ethylene hydrogenation on two-dimensional nanoparticle arrays prepared by the Langmuir–Blodgett technique. The activity of the Pt nano-

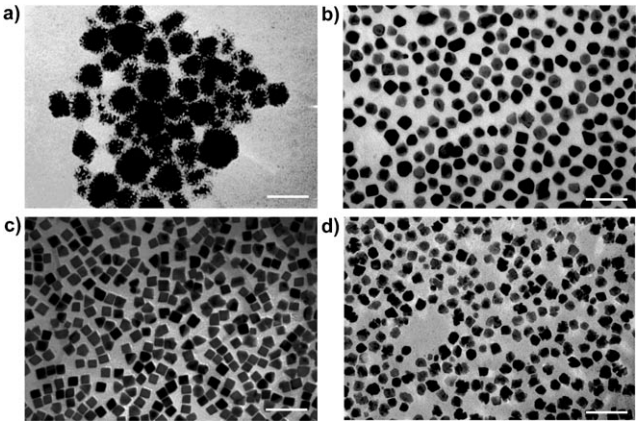

Figure 2. TEM images of Pt nanoparticles obtained by adding a) 7.5, b) 30, c) 45, and d) 60 mM $NaBH_4$ to a clear aqueous solution of 150 mM C_{14}TABr and 1.5 mM K_2PtCl_4. Shape evolution was clearly observed from dendritic nanostructures (a) to hexagonal (b), cubic (c), and irregular particles (d). The scale bar is 50 nm.

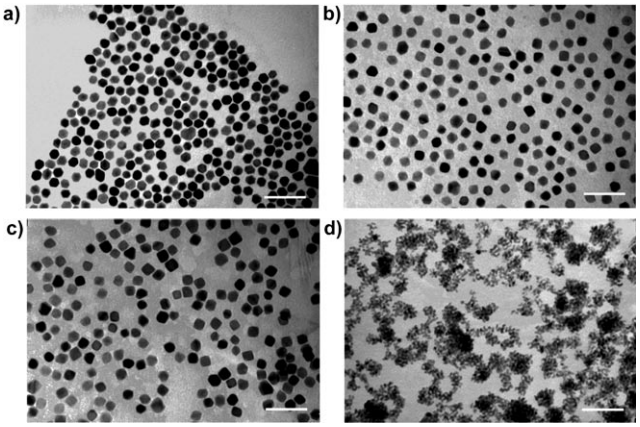

Figure 3. TEM images of Pt nanoparticles showing the effect of additional NaOH. The nanoparticles in a) were obtained from an aqueous solution with a composition of 150 mM C_{14}TABr, 1.5 mM K_2PtCl_4, and 7.5 mM $NaBH_4$ under mild H_2 flow. Addition of b) 0.01, c) 1, and d) 3 mM NaOH to a solution with the same composition as (a). More cubic nanoparticles were observed when NaOH was added, while an excess of NaOH produced only aggregated particulates. The scale bar is 50 nm.

 © 2006 Wiley-VCH Verlag GmbH & Co. KGaA, Weinheim

particles synthesized in this work was compared with Pt nanoparticles prepared as reported previously.[6c] Cubes with an average size of 9.4 nm (diagonal) and cuboctahedra with an average size of 9.1 nm (vertex-to-vertex) were prepared using a polymeric capping agent (PVP) and Ag (1.1 and 11 mol%, respectively).[6c] The C_{14}TABr-capped Pt nanoparticles have much higher catalytic activity than PVP-capped Pt nanoparticles (Figure 4). At 373 K, the C_{14}TABr-capped

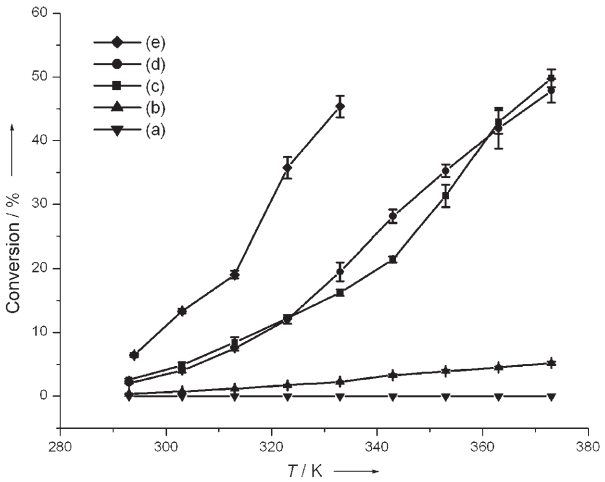

Figure 4. Comparison of catalytic activity for ethylene hydrogenation when using a) (▼) PVP-capped Pt cuboctahedra with 11 mol% Ag (9.1 nm, vertex-to-vertex), b) (▲) PVP-capped Pt cubes with 1.1 mol% Ag (9.4 nm, diagonal), c) (■) C_{14}TABr-capped Pt cubes (13.4 nm, diagonal), d) (●) C_{14}TABr-capped Pt cuboctahedra (12.6 nm, vertex-to-vertex), and e) (◆) C_{14}TABr-capped Pt porous particles (19.3 nm, longest axis). No treatment was performed to remove the capping agents.

cubes are about 10-times more active than the PVP-capped cubes. PVP-capped cuboctahedra prepared with 11 mol% Ag show no catalytic activity under these reaction conditions. The C_{14}TABr-capped porous nanoparticles have the highest activity for ethylene hydrogenation owing to their having a much larger surface area than the cubes or cuboctahedra.[19] The effect of different shapes on catalytic activity will be investigated in a future study.

In summary, cubic, cuboctahedral, and porous Pt nanoparticles have been prepared using tetradecyltrimethylammonium bromide as a surface-stabilizing reagent. The morphology was controlled by adjusting the reduction method. H_2 production in situ from $NaBH_4$ has enabled the synthesis of uniform nanoparticles. By changing the pH value, which contributes to controlling the reduction rate, shape evolution from cuboctahedra to cubes was observed. These nanoparticles, which are electrostatically capped with alkylammonium ions and shape-controlled without the aid of foreign metal ions, show superior catalytic activity to nanoparticles prepared with a polymeric stabilizing reagent and silver.

Experimental Section

In a typical synthesis, aqueous solutions of K_2PtCl_4 (Alfa Aesar, 99.9%) and C_{14}TABr (Aldrich, 99%) were mixed in a 20-mL vial at room temperature. The mixture was heated at 50°C for about 5 min until the solution became clear. The vial was capped with a rubber septum immediately after adding ice-cold $NaBH_4$ (Strem Chemicals, 98%) and the H_2 gas pressure inside the vial was released through a needle in the septum for 10 min. The needle was then removed and the solution was kept at 50°C for 6 h. When L-ascorbic acid (Aldrich, 99 + %) was used as the reducing agent the solution was kept at 70°C. The total volume of the solution was maintained at 10 mL. When necessary, H_2 gas was passed through the solution slowly for 5 min and then pressurized for 1 min without an exit needle. The product was centrifuged at 3000 rpm for 30 min. The supernatant solution was separated and centrifuged again at 12000 rpm for 10 min. The precipitate was collected and re-dispersed in 5 mL of deionized water by sonication.

UV/Vis absorption spectra were recorded with an Agilent 8453 UV/Vis system. TEM and HRTEM images were obtained with a Jeol 200CX microscope and a Philips CM200 microscope, respectively, operating at 200 kV, at the National Center for Electron Microscopy at the Lawrence Berkeley National Laboratory. The surface area was measured with a Quantachrome Autosorb-1 analyzer at 77 K using nitrogen as the adsorption gas. Before the measurement, degassing was conducted at 150°C for 48 h to remove possible moisture. The pH value was measured with a Mettler Toledo MP220 pH meter.

A special cell was constructed for ethylene hydrogenation studies under continuous gas-flow conditions. A silicon wafer with Pt nanoparticles deposited by the Langmuir–Blodgett (LB) technique was compressed against a rubber O-ring (16 mm I.D.) by tightening a Teflon block by two set screws. The reaction cell was connected to a stainless-steel gas manifold, which was equipped with mass flow controllers (MFC, Porter Instrument Company). The flow rate of C_2H_4 (AirGas, CP grade), H_2 (Praxair, UHP, 99.999%), and He (Praxair, UHP, 99.999%) was 1.0, 13.9, and 83.0 mL min^{-1}, respectively. The flow reactor was sampled periodically by gas chromatography (GC). The coverage of Pt nanoparticles on the substrate was examined and the conversion of ethylene into ethane was corrected by considering the different coverage for direct comparison of the LB samples.

Received: July 28, 2006
Published online: November 7, 2006

Keywords: heterogeneous catalysis · morphology control · nanostructures · platinum · surfactants

[1] a) F. Porta, M. Rossi, *J. Mol. Catal. A* **2003**, *204–205*, 553; b) H. Bonnemann, W. Brijoux, A. S. Tilling, K. Siepen, *Top. Catal.* **1997**, *4*, 217; c) N. Toshima, Y. Shiraishi, T. Teranishi, M. Miyake, T. Tominaga, H. Watanabe, W. Brijoux, H. Bonnemann, G. Schmid, *Appl. Organomet. Chem.* **2001**, *15*, 178.
[2] a) J. Prabhuram, X. Wang, C. L. Hui, I.-M. Hsing, *J. Phys. Chem. B* **2003**, *107*, 11057; b) Z. Chen, X. Qiu, B. Lu, S. Zhang, W. Zhu, L. Chen, *Electrochem. Commun.* **2005**, *7*, 593.
[3] L. Sun, D. V. Ca, J. A. Cox, *J. Solid State Electrochem.* **2005**, *9*, 816.
[4] A. Kolmakov, D. O. Klenov, Y. Lilach, S. Stemmer, M. Moskovits, *Nano Lett.* **2005**, *5*, 667.
[5] S. M. Davis, F. Zaera, G. A. Somorjai, *J. Catal.* **1984**, *85*, 206.
[6] a) T. S. Ahmadi, Z. L. Wang, A. Henglein, M. A. El-Sayed, *Chem. Mater.* **1996**, *8*, 1161; b) J. M. Petroski, A. L. Wang, T. C. Green, M. A. El-Sayed, *J. Phys. Chem. B* **1998**, *102*, 3316; c) H. Song, F. Kim, S. Connor, G. A. Somorjai, P. Yang, *J. Phys. Chem. B* **2005**, *109*, 188; d) T. Teranishi, R. Kurita, M. Miyake, *J. Inorg. Organomet. Polym.* **2000**, *10*, 145; e) A. Miyazaki, Y. Nakano, *Langmuir* **2000**, *16*, 7109; f) B. Veisz, L. Toth, D. Teschner, Z.

 © 2006 Wiley-VCH Verlag GmbH & Co. KGaA, Weinheim

Paal, N. Gyorffy, U. Wild, R. Schlögl, *J. Mol. Catal. A* **2005**, *238*, 56.
[7] a) J. Chen, T. Herricks, M. Geissler, Y. Xia, *J. Am. Chem. Soc.* **2004**, *126*, 10854; b) X. Fu, Y. Wang, N. Wu, L. Gui, Y. Tang, *J. Mater. Chem.* **2003**, *13*, 1192.
[8] a) T. Kijima, T. Yoshimura, M. Uota, T. Ikeda, D. Fujikawa, S. Mouri, S. Uoyama, *Angew. Chem.* **2004**, *116*, 230; *Angew. Chem. Int. Ed.* **2004**, *43*, 228; b) B. Mayers, X. Jiang, D. Sunderland, B. Cattle, Y. Xia, *J. Am. Chem. Soc.* **2003**, *125*, 13364.
[9] a) Y. Song, Y. Yang, C. J. Medforth, E. Pereira, A. K. Singh, H. Xu, Y. Jiang, C. J. Brinker, F. van Swol, J. A. Shelnutt, *J. Am. Chem. Soc.* **2004**, *126*, 635; b) X. Zhong, Y. Feng, I. Lieberwirth, W. Knoll, *Chem. Mater.* **2006**, *18*, 2468; c) X. Teng, X. Liang, S. Maksimuk, H. Yang, *Small* **2006**, *2*, 249.
[10] X. Teng, H. Yang, *Nano Lett.* **2005**, *5*, 885.
[11] R. Narayanan, M. A. El-Sayed, *J. Phys. Chem. B* **2005**, *109*, 12663.
[12] Y. Borodko, S. E. Habas, M. Koebel, P. Yang, H. Frei, G. A. Somorjai, *J. Phys. Chem. B* **2006**, in press.
[13] a) J. Gao, C. M. Bender, C. J. Murphy, *Langmuir* **2003**, *19*, 9065; b) T. K. Sau, C. J. Murphy, *J. Am. Chem. Soc.* **2004**, *126*, 8648; c) F. Kim, J. H. Song, P. Yang, *J. Am. Chem. Soc.* **2002**, *124*, 14316; d) J. Perez-Juste, L. M. Liz-Marzan, S. Carnie, D. Y. C. Chan, P. Mulvaney, *Adv. Funct. Mater.* **2004**, *14*, 571.
[14] J. Chen, T. Herricks, Y. Xia, *Angew. Chem.* **2005**, *117*, 2645; *Angew. Chem. Int. Ed.* **2005**, *44*, 2589.
[15] R. M. Rioux, H. Song, M. Grass, S. Habas, K. Niesz, J. D. Hoefelmeyer, P. Yang, G. A. Somorjai, *Top. Catal.* **2006**, in press.
[16] B. Veisz, Z. Kiraly, *Langmuir* **2003**, *19*, 4817.
[17] M. A. Watzky, R. G. Finke, *J. Am. Chem. Soc.* **1997**, *119*, 10382.
[18] H. I. Schlesinger, H. C. Brown, A. E. Finholt, J. R. Gilbreath, H. R. Hoekstra, E. K. Hyde, *J. Am. Chem. Soc.* **1953**, *75*, 215.
[19] The porous nanoparticles showed little change in conversion at temperatures higher than 333 K, probably because of mass-transfer limitations at the given flow rate. The mass-transfer rate of C_2H_4 to the Pt surface is slower than the reaction rate of C_2H_4 on a Pt surface at high temperature, so the overall conversion is governed by the mass-transfer rate rather than by Pt catalyst activation. In fact, the conversion can be increased significantly by changing the flow rate. Catalyst deactivation was not observed.

 © 2006 Wiley-VCH Verlag GmbH & Co. KGaA, Weinheim

Singlet Diradicals

DOI: 10.1002/anie.200603287

An Extremely Long-Lived Singlet 4,4-Dimethoxy-3,5-diphenylpyrazolidine-3,5-diyl Derivative: A Notable Nitrogen-Atom Effect on Intra- and Intermolecular Reactivity**

Manabu Abe, Emi Kubo, Koichi Nozaki, Takashi Matsuo, and Takashi Hayashi*

Dedicated to Professor Waldemar Adam on the occasion of his 70th birthday and to Professor Masatomo Nojima on the occasion of his 65th birthday

The central focus in chemistry is the formation and cleavage of bonds, which can be either heterolytic or homolytic. Singlet diradicals are key intermediates in homolytic processes. In general, these reactive intermediates are quite short-lived and have no chance to react intermolecularly.[1] Recent studies directed toward stabilizing singlet diradicals have provided opportunities to examine the chemistry of such electronically and structurally unique molecules. Thus, the singlet diradicals **1**,[2] **2**,[3] and **3**[4] were isolated as examples of kinetically stabilized four-membered ring systems. Inagaki and co-workers computationally predicted an isolable singlet diradical **4**.[5,6] Borden and co-workers reported on the singlet ground

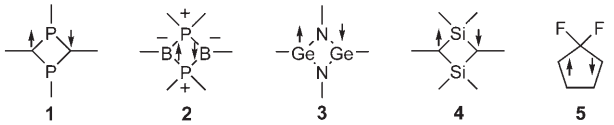

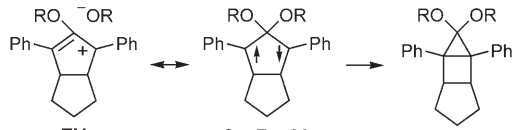

[*] Prof. Dr. M. Abe, E. Kubo, T. Matsuo, T. Hayashi
Department of Applied Chemistry, Graduate School of Engineering
Osaka University (HANDAI)
2-1 Yamadaoka, Suita, Osaka 565-0871 (Japan)
Fax: (+81) 6-6879-7930
E-mail: abe@chem.eng.osaka-u.ac.jp
Prof. Dr. K. Nozaki
Department of Chemistry, Graduate School of Science
Osaka University (HANDAI)
1-16 Machikaneyama, Toyonaka, Osaka 560-0043 (Japan)

[**] This work was supported in part by the Ministry of Education, Science, Sports, and Culture, Japan (Grant-in-Aid for Scientific Research (B), No. 17350019), the Mitsubishi Chemical Corporation Fund, and the Tokuyama Scientific Fund. We thank the Analytical Center of Faculty of Engineering, Osaka University.

Supporting information for this article is available on the WWW under http://www.angewandte.org or from the author.

InterScience
© 2006 Wiley-VCH Verlag GmbH & Co. KGaA, Weinheim

state of 2,2-difluorocyclopentane-1,3-diyls **5**.[7] We previously studied the long-lived singlet 2,2-dialkoxy-1,3-diphenylcyclopentane-1,3-diyls **6** ($\tau_{\mathbf{6a}} = 320$ ns and $\tau_{\mathbf{6b}} = 880$ ns in benzene at 293 K), which are, to date, the longest lived five-membered singlet diradicals; they react intramolecularly to afford the ring-closure compounds **CP1** in quantitative yield.[8] In the hyperconjugative resonance structure **ZI1**, the geminal alkoxy groups are thought to stabilize the lowest energy singlet state.[8e]

In the present study, we designed the nitrogen-substituted diradical **7**, since the hyperconjugative resonance structure **ZI2** of the lowest energy singlet state of diradical **7** should be further stabilized by the electron-donating nitrogen atom as reflected by the resonance structure **ZI3**. Actually, 4,4-dimethoxy-1,2-dimethylpyrazolidine-3,5-diyl **7** (R = Me) was predicted to be a singlet ground-state molecule, and the singlet–triplet energy gap ($\Delta E_{ST} = E_S - E_T = -14.4$ kcal mol^{-1}) was calculated to be significantly larger than that of 2,2-dimethoxycyclopentane-1,3-diyl (**8**; $\Delta E_{ST} = -6.1$ kcal mol^{-1})[8d] at the UB3LYP/6-31G(d) level of theory.[9] Furthermore, we found, based on computation, that the energy difference between the ring-closure compound **CP3** and the singlet state of **7**, $\Delta E = E_7 - E_{\mathbf{CP3}} = -4.0$ kcal mol^{-1}, is significantly smaller than that between 5,5-dimethoxybicyclo[2.1.0]pentane **CP2** and the singlet 2,2-dimethoxycyclopentane-1,3-diyl (**8**, $\Delta E' = E_8 - E_{\mathbf{CP2}} = +22.1$ kcal mol^{-1}). Thus, the computational results clearly indicate that the singlet state of diradical **7** (R = Me) is energetically more stable than the ring-closure compound **CP3** (R = Me).

Here we report on the generation of the extremely long-lived singlet 4,4-dimethoxy-3,5-diphenyl-pyrazolidine-3,5-diyl derivative **9a**, which displays a lifetime of up to ca. 10 ms and inter- and intramolecular reactivity.[10] For the generation of diradical **9a**, we carried out the photodenitrogenation of the azoalkane **AZa** ($\lambda_{max} = 416$ nm, $\varepsilon = 585$ in toluene; Scheme 1). The azoalkane **AZa** was prepared from the cycloaddition of the corresponding isopyrazole with 4-phenyl-1,2,4-triazoline-3,5-dione (PTAD) as depicted in Scheme 1. First, the steady-state photolysis ($\lambda_{exc} = 360$–440 nm) of the azoalkane **AZa** was performed in toluene at room temperature in order to study the intramolecular reactivity. The clean denitrogenation was observed to afford the product of 1,2-oxygen migration **10a** (70% isolated yield). No evidence for the formation of the ring-closure product **11a** was found in the photolysate of **AZa** in [D_8]toluene. The result clearly indicates that 1,2-oxygen migration is an energetically more favored process than ring closure. A model ring-closure compound **11b** was calculated to be higher in energy than a model singlet-diradical **9b** and a model 1,2-migration product **10b** by 2.8 kcal mol^{-1} and 27.2 kcal mol^{-1}, respectively, at the B3LYP/6-31G(d) level of theory.

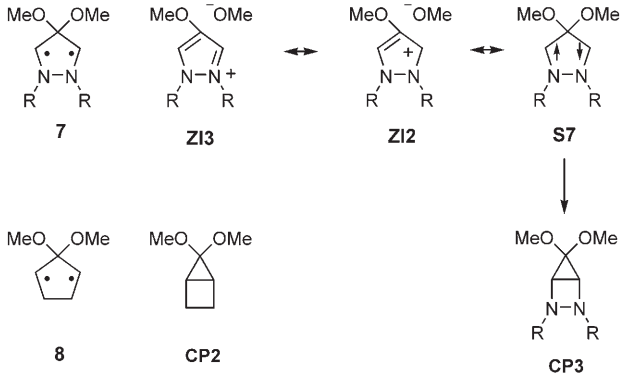

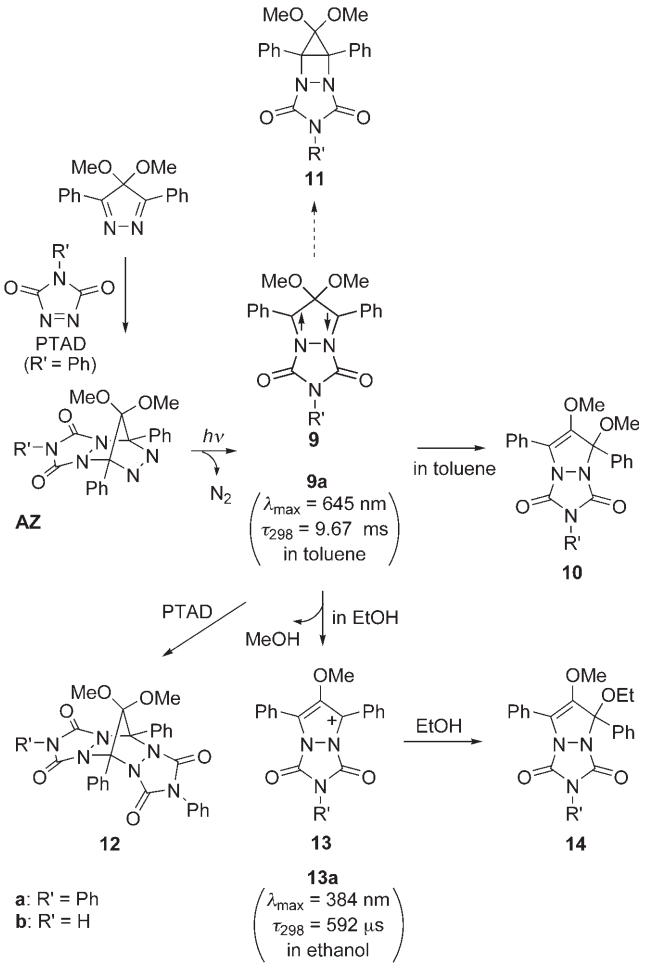

Scheme 1. Preparation of azoalkane **AZ**, the photochemical generation of singlet diradical **9**, and its intra- and intramolecular reactions.

The transient absorption spectra and decay trace of the intermediate in the denitrogenation of **AZa** were measured in degassed toluene by means of laser-flash photolysis ($\lambda_{exc} =$ 355 nm) at 298 K. A strong absorption was observed in the visible region ($\lambda_{max} = 645$ nm, Figure 1 a), which decayed with clean first-order kinetics ($\tau_{298} = 9.67 \pm 0.07$ ms, Figure 1 b). A similar absorption band ($\lambda_{max} = 630$ nm) was observed in the photolysis ($\lambda_{exc} = 380$–440 nm) of **AZa** in a 2-methyltetrahydrofuran (MTHF) matrix at 77 K (Figure 1 c), which was persistent up to ca. 120 K. The transient species was assigned to the singlet diradical **9a**, based on the following evidence: 1) The absorption maximum at around 650 nm is similar to the absorption band of singlet diradical **6** (around 600 nm); 2) The species absorbing at 630 nm was EPR-silent in a MTHF matrix at 77 K; 3) The singlet state of a model

 © 2006 Wiley-VCH Verlag GmbH & Co. KGaA, Weinheim

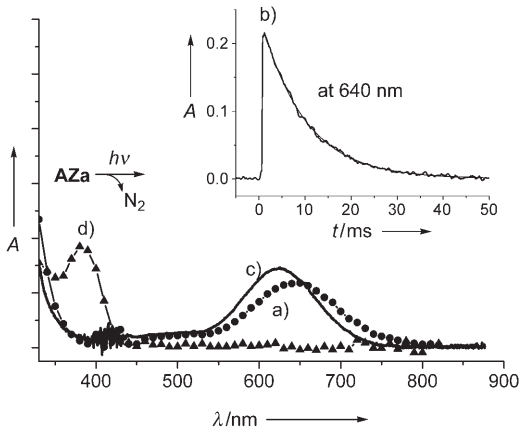

Figure 1. a) Transient absorption spectrum for the singlet diradical **9a** obtained after 5 ms of laser-flash photolysis of azoalkane **AZa** ($\lambda_{exc}=355$ nm) at 298 K in degassed toluene. b) Transient decay trace of **9a** ($\lambda_{obs}=640$ nm) generated by the photolysis of **AZa** at 298 K. c) Absorption spectrum of **9a** obtained after the photolysis ($\lambda_{exc}=360$–440 nm) of **AZa** in a MTHF matrix at 77 K. d) Transient absorption spectrum for the allylic cation **13a** obtained after 8 μs of laser flash photolysis of **AZa** at 298 K in degassed ethanol.

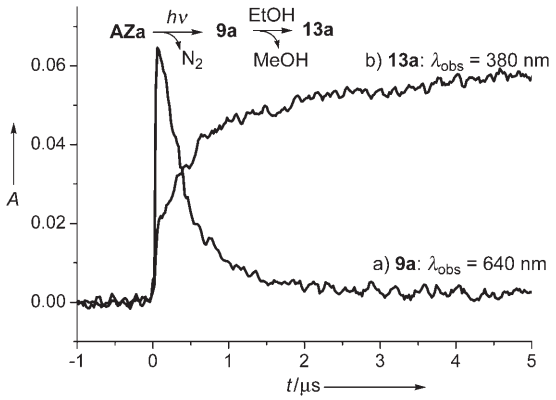

Figure 2. a) Transient decay trace for the singlet diradical **9a** ($\lambda_{obs}=640$ nm) generated by laser flash photolysis of **AZa** in ethanol, b) the concomitant growth of the allylic cation **13a** ($\lambda_{obs}=380$ nm).

diradical **9b** (R′ = H) was calculated to be lower in energy than the triplet state with a significant singlet–triplet energy gap, $\Delta E_{ST}=-3.9$ kcal mol^{-1}; $S^2=0.77$ at the UB3LYP/6-31G(d) level of theory; 4) The calculation of the absorption maximum for the singlet state of **9b** ($\lambda_{calcd}=710$ nm; $f=0.14$ at the TD-UB3LYP/6-31G(d) level of theory) is in good agreement with the experimental absorption maximum.[11–12] The vertical excitation energy corresponds to the HOMO (ψ_S)→LUMO (ψ_A) electronic excitation; 5) The lifetime of the transient absorbing at 645 nm was not significantly affected by the presence of molecular oxygen; 6) The disappearance of the persistent species at 77 K was observed when PTAD was added while the sample warmed from 77 K to 120 K, at which temperature the species absorbing at ca. 630 nm is thermally stable. After careful analysis of the products formed on quenching, the PTAD adduct **12a** was isolated in 42% yield (Scheme 1).

To obtain further information on the reactivity of the extremely long-lived singlet diradical **9a**, the photodenitrogenation of **AZa** was performed in protic solvent. In toluene, the singlet diradical **9a** ($\lambda_{max}=645$ nm) was the only detectable species. In ethanol, however, the decay of the transient absorbing at 645 nm ($\tau_{298}=431\pm3$ ns) was accompanied by concomitant increasing absorption at 380 nm (Figure 1d and Figure 2). The ethanol adduct **14a** (45% yield) was obtained from the steady-state photolysis of **AZa** in ethanol at room temperature. The oxygen-migration product **10a** was intact in ethanol. Thus, the transient absorbing at ca. 380 nm is assigned to the allylic cation **13a**, $\tau_{298}=607\pm18$ μs, which can be formed from the singlet diradical **9a** (Scheme 1).[13] The observed absorption maximum for **13a** was in good agreement with the computational calculation for the model allylic cation **13b** (R′ = H; $\lambda_{calcd}=427$ nm, $f=0.49$) at the TD-RB3LYP/6-31G(d) level of theory.

In summary, in this combined theoretical and experimental study, we found a notable effect of a nitrogen atom on the lifetime of singlet 2,2-dimethoxycyclopentane-1,3-diyls, and their intra- and intermolecular reactivity. Computationally, the nitrogen-containing singlet diradicals **7** and **9** were calculated to be lower in energy than the corresponding ring-closure compounds **CP3** and **11**. The introduction of nitrogen atoms in the five-membered ring system effectively increased the lifetime of the singlet 2,2-dimethoxypropane-1,3-diyl to the millisecond time scale. The extremely long-lived singlet 1,3-diradical was found to react intermolecularly with PTAD to afford the cycloaddition product. A 1,2-oxygen migration reaction was revealed for intramolecular reactivity. These remarkable findings should stimulate future computations and experiments on the novel reactivity of extremely long-lived singlet diradicals, especially intermolecular reactions of singlet diradicals.

Received: August 11, 2006
Published online: October 24, 2006

Keywords: photolysis · quantum chemical calculations · reactive intermediates · singlet diradicals

[1] S. DeFeyter, E. W.-G. Diau, A. H. Zewail, *Angew. Chem.* **2000**, *112*, 266–269; *Angew. Chem. Int. Ed.* **2000**, *39*, 260–263.
[2] a) E. Niecke, A. Fuchs, F. Baumeister, M. Nieger, W. W. Schoeller, *Angew. Chem.* **1995**, *107*, 640–642; *Angew. Chem. Int. Ed. Engl.* **1995**, *34*, 555–557; b) H. Sugiyama, S. Ito, M. Yoshifuji, *Angew. Chem.* **2003**, *115*, 3932–3934; *Angew. Chem. Int. Ed.* **2003**, *42*, 3802–3804; c) M. Sebastian, M. Nieger, D. Szieberth, L. Nyulászi, E. Niecke, *Angew. Chem.* **2004**, *116*, 647–651; *Angew. Chem. Int. Ed.* **2004**, *43*, 637–641.
[3] a) D. Scheschkewitz, H. Amii, H. Gornitzka, W. W. Schoeller, D. Bourissou, G. Bertrand, *Science* **2002**, *295*, 1880–1881; b) M. Seierstad, C. R. Kinsinger, C. J. Cramer, *Angew. Chem.* **2002**, *114*, 4050–4052; *Angew. Chem. Int. Ed.* **2002**, *41*, 3894–3896; c) H. Amii, L. Vranicar, H. Gornitzka, D. Bourissou, G. Bertrand, *J. Am. Chem. Soc.* **2004**, *126*, 1344–1345; d) D. Scheschkewitz, H. Amii, H. Gornitzka, W. W. Schoeller, D. Bourissou, G. Bertrand, *Angew. Chem.* **2004**, *116*, 595–597; *Angew. Chem. Int. Ed.* **2004**, *43*, 585–587; e) A. Rodriguez, F. S. Tham, W. W. Schoeller, G. Bertrand, *Angew. Chem.* **2004**, *116*, 4988–4991; *Angew. Chem. Int. Ed.* **2004**, *43*, 4876–4880.

 © 2006 Wiley-VCH Verlag GmbH & Co. KGaA, Weinheim

[4] C. Cui, M. Brynda, M. M. Olmstead, P. P. Power, *J. Am. Chem. Soc.* **2004**, *126*, 6510 – 6511.
[5] J. Ma, Y. Ding, K. Hattori, S. Inagaki, *J. Org. Chem.* **2004**, *69*, 4245 – 4255.
[6] For the silicon-atom effect in five-membered ring systems, see: M. Abe, C. Ishihara, A. Takegami, *J. Org. Chem.* **2004**, *69*, 7250 – 7255.
[7] a) J. D. Xu, D. A. Hrovat, W. T. Borden, *J. Am. Chem. Soc.* **1994**, *116*, 5425 – 5427; b) W. Adam, W. T. Borden, C. Burda, H. Foster, T. Heidenfelder, M. Jeubes, D. A. Hrovat, F. Kita, S. B. Lewis, D. Scheutzow, J. Wirz, *J. Am. Chem. Soc.* **1998**, *120*, 593 – 594; c) W. T. Borden, *Chem. Commun.* **1998**, 1919 – 1925.
[8] a) M. Abe, W. Adam, T. Heidenfelder, W. M. Nau, X. Zhang, *J. Am. Chem. Soc.* **2000**, *122*, 2019 – 2026; b) M. Abe, W. Adam, M. Hara, M. Hattori, T. Majima, M. Nojima, K. Tachibana, S. Tojo, *J. Am. Chem. Soc.* **2002**, *124*, 6540 – 6541; c) M. Abe, C. Ishihara, S. Kawanami, A. Masuyama, *J. Am. Chem. Soc.* **2005**, *127*, 10 – 11; d) M. Abe, W. Adam, W. T. Borden, M. Hattori, D. A. Hrovat, M. Nojima, K. Nozaki, J. Wirz, *J. Am. Chem. Soc.* **2004**, *126*, 574 – 582; e) M. Abe, M. Hattori, A. Takegami, A. Masuyama, T. Hayashi, S. Seki, S. Tagawa, *J. Am. Chem. Soc.* **2006**, *128*, 8008 – 8014.
[9] Gaussian 03 (Revision C.02): M. J. Frisch et al., see Supporting Information.
[10] A triplet ground state of 4,4-dimethyl-3,5-diphenyl-pyrazolidine-3,5-diyl derivative was reported; see: a) D. R. Arnold, A. B. Evnin, P. H. Kasai, *J. Am. Chem. Soc.* **1969**, *91*, 784 – 785; b) A. B. Evnin, D. R. Arnold, L. A. Karnischky, E. Strom, *J. Am. Chem. Soc.* **1970**, *92*, 6218 – 6231.
[11] The observable absorption maximum for the triplet state was calculated to be 366 nm ($f = 0.03$) at the same level of theory.
[12] a) A. D. Becke, *J. Chem. Phys.* **1993**, *98*, 5648 – 5652; b) C. Lee, W. Yang, R. G. Parr, *Phys. Rev. B* **1988**, *37*, 785 – 789; c) J. B. Foresman, M. Head-Gordon, J. A. Pople, M. J. Frisch, *J. Phys. Chem.* **1992**, *96*, 135 – 149; d) R. E. Stratmann, G. E. Scuseria, M. J. Frisch, *J. Chem. Phys.* **1998**, *109*, 8218; e) R. Bauernschmitt, R. Ahlrichs, *Chem. Phys. Lett.* **1996**, *256*, 454; f) M. E. Casida, C. Jamorski, K. C. Casida, D. R. Salahub, *J. Chem. Phys.* **1998**, *108*, 4439.
[13] The generation of allylic cations from the singlet diradicals **6** was also observed in protic solvents; see References [8a,e].

 © 2006 Wiley-VCH Verlag GmbH & Co. KGaA, Weinheim

Organocatalysis

DOI: 10.1002/anie.200603199

Cooperative Coexistence: Effective Interplay of Two Brønsted Acids in the Asymmetric Synthesis of Isoquinuclidines**

Magnus Rueping and Cengiz Azap*

The application of Brønsted acids in chemical syntheses continues to rise. As well as inorganic Brønsted acids, more and more achiral and chiral organic Brønsted acids are being applied.[1] The main function of Brønsted acids is the activation of the electrophile or nucleophile. On the one hand, the transfer of a proton from the Brønsted acid to the electrophile can lead to a lowering of the energy of the LUMO, which results in activation of the electrophile and enables it to react with a nucleophile. On the other hand, the addition of Brønsted acids can lead to activation of a nucleophile, as demonstrated by the acid-catalyzed keto–enol tautomerism. In most cases only catalytic amounts of Brønsted acid are required for complete product formation. Recently, chiral Brønsted acids (*BH) enabled enantioselective transformations with aldimines and ketimines for the first time [Eq. (1)].[2–4] In the first step of these reactions a proton

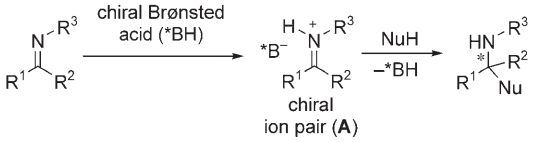

(1)

is transferred from the Brønsted acid to the substrate to form a chiral ion pair that contains an iminium ion, which subsequently reacts with a nucleophile to form the corresponding amine and the regenerated Brønsted acid. We recently used this concept of chiral ion pair catalysis to develop highly enantioselective reactions, such as transfer hydrogenations[3] and hydrocyanations.[4]

Herein we report the development of a new, double Brønsted acid catalyzed reaction in which both the electrophile and the nucleophile are activated and which provides a straightforward and effective route to isoquinuclidines in remarkably high enantioselectivities. Isoquinuclidines (**5**, azabicyclo[2.2.2]octanes) have N-bicyclic structures, which are the structural element of numerous naturally occurring alkaloids with interesting biological properties.[5] Furthermore, these products can be readily converted into the biologically active pipecolic acids.[6] A retrosynthetic analysis shows that these isoquinuclidines (**5**) can be prepared from imines (**3**) and cyclohexenone (**4**) [Eq. (2)].[7]

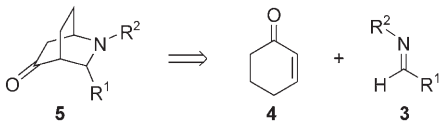

(2)

On the basis of our previous work we assumed that an asymmetric Brønsted acid catalyzed reaction should enable the formation of these valuable products. Our concept, based on the direct reaction between **3** and **4**, provides the simultaneous, double Brønsted acid catalyzed activation of an electrophile (by a chiral Brønsted acid *BH, **1**) and a nucleophile (by an achiral Brønsted acid BH, **2**), whereby both activation processes behave cooperatively (Scheme 1). The fundamental requirement for a successful reaction process must be that the achiral Brønsted acid BH **2** is *not* able to activate the imine **3**.

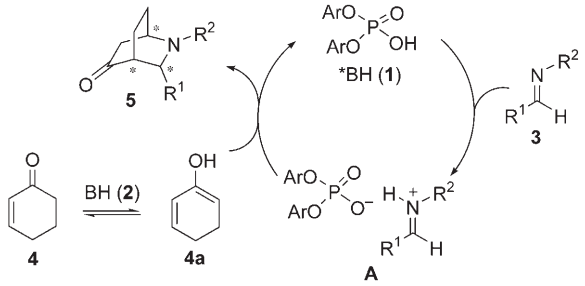

Scheme 1. Cooperative Brønsted acid catalyzed synthesis of isoquinuclidines.

In previous work by ourselves and others it was shown that binol phosphates (**1**, binol = 2,2′-dihydroxy-1,1′-binaphthyl) are excellent Brønsted acid catalysts for chiral ion pair catalysis.[2–4] Hence, we initially decided to use binol phosphates as catalysts for the activation of the imine electrophile and to investigate the use of suitable proton sources/Brønsted acids (**2**) for the parallel step, namely, the shift of the keto–enol equilibrium. As the equilibrium favors the enone **4** and only a low concentration of reactive dienol **4a** is present, we examined the reactivity of a broad range of Brønsted acids **2**.[8] Their pK_a values needed to be greater than those of the binol phosphates **1** to suppress any interference of the two activation processes and thus activation of the imine by the achiral **2**, which would result in reduced enantioselectivity. Hence, the initial reactions were conducted using binol phosphate **1a** and various protonated pyridine derivatives, alcohols, and acids (Table 1).[9] The pyridinium salts afforded the product **5a** with the lowest enantioselectivities (Table 1, entries 1–4). The best enantiomeric ratios were

[*] Prof. Dr. M. Rueping, Dr. C. Azap
Degussa Endowed Professorship
Institute of Organic Chemistry and Chemical Biology
Johann Wolfgang Goethe-University Frankfurt am Main
Max-von-Laue-Strasse 7, 60438 Frankfurt am Main (Germany)
Fax: (+49) 69-798-29248
E-mail: M.rueping@chemie.uni-frankfurt.de

[**] The authors acknowledge Degussa AG for generous support.
Supporting information for this article is available on the WWW under http://www.angewandte.org or from the author.

InterScience
© 2006 Wiley-VCH Verlag GmbH & Co. KGaA, Weinheim

Table 1: Brønsted acids **2** for the asymmetric synthesis of isoquinuclidines.

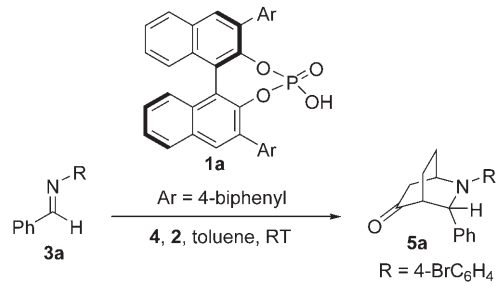

Entry[a]	2	mol%	e.r.[b]
1		20	80:20
2		20	81:19
3		100	76:24
4	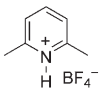	20	85:15
5		20	90:10
6	HCO_2H	20	91:9
7	CH_3CO_2H	20	93:7
8		100	90:10
9	$(CF_3)_2CHOH$	20	91:9

[a] Reaction conditions: imine **3a**, 5 mol% **1a**, enone **4** (8 equiv), **2** (0.1 M solution in toluene; 4 h). [b] Determined by HPLC analysis on a chiral column (Chiralcel OD-H).

observed with carbonic acids, phenol, and 1,1,1,3,3,3-hexafluoropropanol, which gave **5a** with up to 93:7 e.r. (Table 1, entries 5–9). Of the two carbonic acids, the best selectivity was observed with the less acidic acetic acid. The low enantiomeric ratio of the pyridinium derivatives give cause to believe that the conjugated acids arising from the equilibrium of the pyridinium salts activate the aldimine and thereby unwanted interference of the catalysis process takes place.

To optimize the reaction further, binol phosphate catalysts, different imine protecting groups, the solvent, the temperature, the catalyst loading, and the enone concentration were varied.[10] The best reactivities and selectivities were observed with 10 mol% of the binol phosphate **1a** or **1b** and 20 mol% acetic acid in toluene at room temperature. Under these optimized conditions, various aldimines were applied in the double Brønsted acid catalyzed enantioselective synthesis of isoquinuclidines (Table 2). In general, aromatic as well as heteroaromatic substituted isoquinuclidines with electron-withdrawing and electron-donating substituents could be isolated in good yields and with high enantiomeric ratios, with *exo*/*endo* ratios between 1:3 and 1:9. Comparison of the binol phosphates **1a** and **1b** reveals that better results are obtained with the more sterically shielding 2-napthyl-substituted catalyst, which is in agreement with our earlier findings (Table 2).[3–4] The relative and absolute configurations of the products were obtained by X-ray crystal structure analysis.[11] The *endo* product exhibits an *S* configuration at the C-3 atom of the bicycle, whereas the bridgehead atoms C-1 and C-4 are *R* configured (Figure 1).

We assume that the reaction mechanism of isoquinuclidine synthesis comprises two part reactions, whereby subsequent Mannich and aza-Michael reactions are the key steps (Scheme 2).[12]

In the first step, analogous to ion-pair catalysis,[3–4] proton transfer from the chiral Brønsted acid **1** to the imine occurs and the chiral ion pair **A** is formed which is now activated to react with the nucleophile. The dienol **4a**, functioning as a nucleophile, is formed from cyclohexenone **4** in the presence of the second achiral Bronsted acid **2** (acetic acid) through a shift of the keto–enol equilibrium.[13] The subsequent Mannich reaction provides the adduct **B**, an exceptionally reactive Michael acceptor, which leads directly to the corresponding isoquinuclidine **5** as well as the regenerated chiral binol phosphate **1**.

In summary, we report herein the double Brønsted acid catalyzed enantioselective synthesis of various aromatic and heteroaromatic substituted isoquinuclidines. A special feature of this Mannich–aza-Michael reaction is the effective interplay of an achiral and a chiral Brønsted acid, which cooperatively activate the enone and aldimine to enable an asymmetric reaction process, thereby forming three new stereocenters. A fundamental requirement for the successful development of such a process is the fine-tuning of both

Table 2: Scope of the enantioselective Brønsted acid catalyzed synthesis of isoquinuclidines.

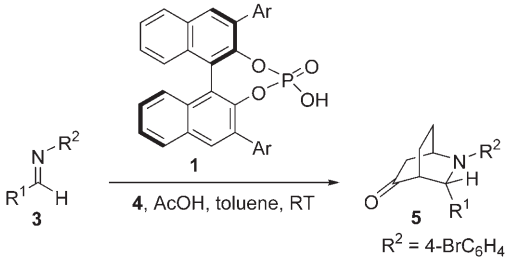

		1a: Ar = 4-biphenyl			1b: Ar = 2-naphthyl		
Product[a]	R^1	*exo*/*endo*[b]	Yield [%]	e.r.[c]	*exo*/*endo*[b]	Yield [%]	e.r.[b]
5a	Ph	1:4	62	92:8[d]	1:4	71	93:7
5b	4-$CF_3C_6H_4$	1:4	51	93:7[d]	1:3	74	92:8
5c	2-thienyl	1:4	63	93:7	1:4	70	94:6
5d	4-ClC_6H_4	1:4	57	93:7	1:4	73	94:6
5e	9-pyrene	1:5	65	94:6	1:4	67	93:7
5f	2,3-$(OMe)_2C_6H_3$	1:9	76	93:7	1:8	84	93:7
5g	4-biph[e]	1:4	64	90:10	1:4	54	92:8
5h	2-FC_6H_4	1:4	60	92:8	1:4	74	94:6
5i	3-ClC_6H_4	1:4	60	92:8	1:4	62	91:9
5j	3,4,5-$(OMe)_3C_6H_2$	1:5	70	88:12	1:4	71	92:8

[a] Reaction conditions: imine **3**, 10 mol% **1**, enone **4** (8 equiv), 20 mol% AcOH, 0.15 M solution in toluene at RT. [b] Determined by ^{1}H NMR spectroscopy. [c] Determined by HPLC analysis on a chiral column (Chiralcel OD-H). [d] >99:1 e.r. after one recrystallization. [e] biph = biphenyl.

© 2006 Wiley-VCH Verlag GmbH & Co. KGaA, Weinheim

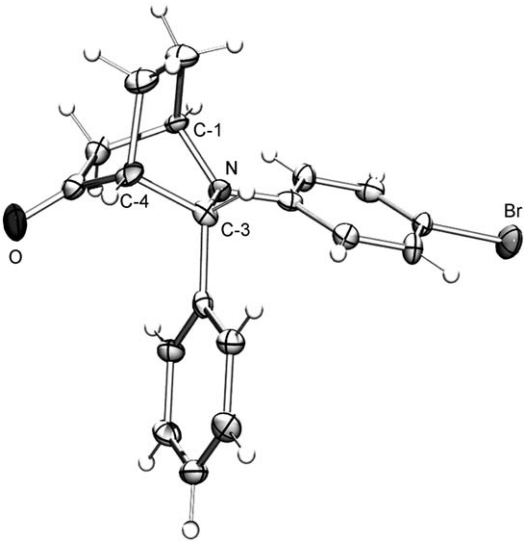

Figure 1. Molecular structure of **5a**.

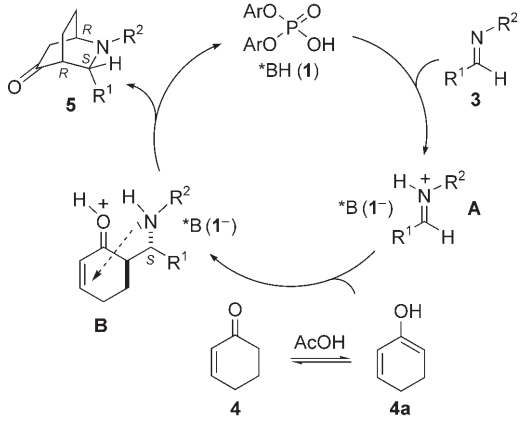

Scheme 2. Postulated catalytic cycle of the Brønsted acid catalyzed Mannich–aza-Michael reaction.

Brønsted acid catalysts. Further experiments will be directed to the development new catalyst systems as well as similar Brønsted acid assisted enantioselective Brønsted acid catalyzed reactions.

Received: August 7, 2006
Published online: November 2, 2006

Keywords: asymmetric synthesis · ion pairs · isoquinuclidines · Mannich bases · Michael addition

[1] Reviews: a) P. R. Schreiner, *Chem. Soc. Rev.* **2003**, *32*, 289; b) P. M. Pihko, *Angew. Chem.* **2004**, *116*, 2110; *Angew. Chem. Int. Ed.* **2004**, *43*, 2062; c) C. Bolm, T. Rantanen, I. Schiffers, L. Zani, *Angew. Chem.* **2005**, *117*, 1788; *Angew. Chem. Int. Ed.* **2005**, *44*, 1758; d) H. Yamamoto, K. Futatsugi, *Angew. Chem.* **2005**, *117*, 1958; *Angew. Chem. Int. Ed.* **2005**, *44*, 1924; e) M. S. Taylor, E. N. Jacobsen, *Angew. Chem.* **2006**, *118*, 1550; *Angew. Chem. Int. Ed.* **2006**, *45*, 1520; f) T. Akiyama, J. Itoh, K. Fuchibe, *Adv. Synth. Catal.* **2006**, *348*, 999.

[2] a) T. Akiyama, J. Itoh, K. Yokota, K. Fuchibe, *Angew. Chem.* **2004**, *116*, 1592; *Angew. Chem. Int. Ed.* **2004**, *43*, 1566; b) D. Uraguchi, M. Terada, *J. Am. Chem. Soc.* **2004**, *126*, 5356; c) D. Uraguchi, K. Sorimachi, M. Terada, *J. Am. Chem. Soc.* **2004**, *126*, 11804; d) T. Akiyama, H. Morita, J. Itoh, K. Fuchibe, *Org. Lett.* **2005**, *7*, 2583; e) T. Akiyama, Y. Saitoh, H. Morita, K. Fuchibe, *Adv. Synth. Catal.* **2005**, *347*, 1523; f) G. B. Rowland, H. Zhang, E. B. Rowland, S. Chennamadhavuni, Y. Wang, J. C. Antilla, *J. Am. Chem. Soc.* **2005**, *127*, 15696; g) M. Terada, K. Sorimachi, D. Uraguchi, *Synlett* **2006**, 13; h) S. Hofmann, A. M. Seayad, B. List, *Angew. Chem.* **2005**, *117*, 7590; *Angew. Chem. Int. Ed.* **2005**, *44*, 7424; i) T. Akiyama, Y. Tamura, J. Itoh, H. Morita, K. Fuchibe, *Synlett* **2006**, 141; j) R. I. Storer, D. E. Carrera, Y. Ni, D. W. C. MacMillan, *J. Am. Chem. Soc.* **2006**, *128*, 84; k) J. Seayad, A. M. Seayad, B. List, *J. Am. Chem. Soc.* **2006**, *128*, 1087; l) M. Terada, K. Machioka, K. Sorimachi, *Angew. Chem.* **2006**, *118*, 2312; *Angew. Chem. Int. Ed.* **2006**, *45*, 2254; m) S. Mayer, B. List, *Angew. Chem.* **2006**, *118*, 4299; *Angew. Chem. Int. Ed.* **2006**, *45*, 4193; n) J. Itoh, K. Fuchibe, T. Akiyama, *Angew. Chem.* **2006**, *118*, 4914; *Angew. Chem. Int. Ed.* **2006**, *45*, 4796; o) D. Nakashima, H. Yamamoto, *J. Am. Chem. Soc.* **2006**, *128*, 9626; p) A. Hasegawa, Y. Naganawa, M. Fushimi, K. Ishihara, H. Yamamoto, *Org. Lett.* **2006**, *8*, 3175.

[3] a) M. Rueping, C. Azap, E. Sugiono, T. Theissmann, *Synlett* **2005**, 2367; b) M. Rueping, E. Sugiono, C. Azap, T. Theissmann, M. Bolte, *Org. Lett.* **2005**, *7*, 3781; c) M. Rueping, A. P. Antonchick, T. Theissmann, *Synlett* **2006**, 1071; d) M. Rueping, A. P. Antonchick, T. Theissmann, *Angew. Chem.* **2006**, *118*, 3765; *Angew. Chem. Int. Ed.* **2006**, *45*, 3683; e) M. Rueping, A. P. Antonchick, T. Theissmann, *Angew. Chem.* **2006**, *118*, 6903; *Angew. Chem. Int. Ed.* **2006**, *45*, 6751.

[4] M. Rueping, E. Sugiono, C. Azap, *Angew. Chem.* **2006**, *118*, 2679; *Angew. Chem. Int. Ed.* **2006**, *45*, 2617.

[5] R. J. Sundberg, S. Q. Smith in *The Alkaloids*, *Vol. 59* (Ed.: G. A. Cordell), Academic Press, **2002**, p. 261.

[6] a) G. R. Krow, C. A. Johnson, J. P. Guare, D. Kubrak, K. J. Henz, D. A. Shaw, S. W. Szczepanski, J. T. Carey, *J. Org. Chem.* **1982**, *47*, 5239; b) A. B. Holmes, J. Thompson, A. J. G. Baxter, J. Dixon, *J. Chem. Soc. Chem. Commun.* **1985**. 37; c) G. R. Krow, S. W. Szczepanski, J. Y. Kim, N. Liu, A. Sheikh, Y. Xiao, J. Yuan, *J. Org. Chem.* **1999**, *64*, 1254.

[7] Isoquinuclidines have been obtained as products in Lewis acid catalyzed reactions and as a by-product in the Lewis base catalyzed Baylis–Hillman reaction of cyclohexenone with aldimines: a) G. Babu, P. T. Perumal, *Tetrahedron* **1998**, *54*, 1627; b) M. Shi, Y.-M. Xu, *Chem. Commun.* **2001**, 1876. Recently, a direct aza-Diels–Alder reaction by covalent aminocatalysis was reported: H. Sunden, I. Ibrahem, L. Eriksson, A. Cordova, *Angew. Chem.* **2005**, *117*, 4955; *Angew. Chem. Int. Ed.* **2005**, *44*, 4877.

[8] A small shift of the keto–enol equilibrium is sufficient for a reaction, as the formed dienol will be extracted directly from the equilibrium. Other cyclic enones such as cyclopentenone showed no reactivity under these conditions.

[9] A large number of chiral Brønsted acids were tested. Table 1 shows only the general trend of reactivity.

[10] The use of other binol phosphates, other chlorinated and aromatic solvents, aliphatic aldimines, as well as the variation of catalyst loading and enone concentration resulted in inferior enantioselectivities.

[11] The X-ray crystal structure of the *exo* product is shown in the Supporting Information.

[12] Examples of such a stepwise addition–cyclization mechanism have been reported earlier for the reaction of silylenol ethers with aldimines: a) T. N. Birkinshaw, A. B. Tabor, A. B. Holmes,

 © 2006 Wiley-VCH Verlag GmbH & Co. KGaA, Weinheim

P. R. Raithby, *J. Chem. Soc. Chem. Commun.* **1988**, 1601; b) S. Kobayashi, H. Ishitani, S. Nagayama, *Synthesis* **1995**, 1195; S. Hermitage, J. A. K. Howard, D. Jay, R. G. Pritchard, M. R. Probert, A. Whiting, *Org. Biomol. Chem.* **2004**, *2*, 2451.

[13] The rate-determining step of the reaction is presumably the dienol formation, as no considerable conversion was observed without the addition of Brønsted acid **2.**

 © 2006 Wiley-VCH Verlag GmbH & Co. KGaA, Weinheim

Natural Products

DOI: 10.1002/anie.200602840

Photochemical Origin of the Immunosuppressive SNF4435C/D and Formation of Orinocin through "Polyene Splicing"**

Markus Müller, Björn Kusebauch, Guangxin Liang, Christopher M. Beaudry, Dirk Trauner, and Christian Hertweck**

Polyketides comprise a large group of structurally diverse secondary metabolites, many of which are endowed with medicinally relevant biological activities.[1] Irrespective of their diverse carbon frameworks they all arise from repetitive Claisen condensations of activated acetate or propionate building blocks in analogy to the biosynthesis of fatty acids.[2] Depending on the degree of β-keto procession, polyphenols, polyenes, or highly reduced polyketides are produced. It is known that polyketide-derived polyene systems, in particular those equipped with strong chromophores, easily undergo light-induced photoisomerization. This reaction can initiate fascinating rearrangement cascades, which may result in a plethora of reorganized carbon skeletons.[3,4]

Spectinabilin (neoaureothin, **1**)[5,6] and aureothin (**2**) represent unusual nitroaryl-substituted polyene metabolites produced by *Streptomyces thioluteus* and *Streptomyces spectabilis*, respectively. Biosynthetic studies at the chemical, biochemical, and genetic levels revealed that these cytotoxic metabolites are assembled from nitrobenzoate,[7–11] malonate, and methylmalonate[12] by modular polyketide synthases[13,14] followed by tailoring reactions (Scheme 1).[15,16] Apparently the diene moiety of aureothin is assembled from two propionate units, while four propionates give rise to the tetraene system of **1**. The discovery of the intriguing constitutional isomers of **1**, the immunosuppressant SNF4435C (**3a**) and SNF4435D (**3b**),[17–19] from *S. spectabilis* (Scheme 2)

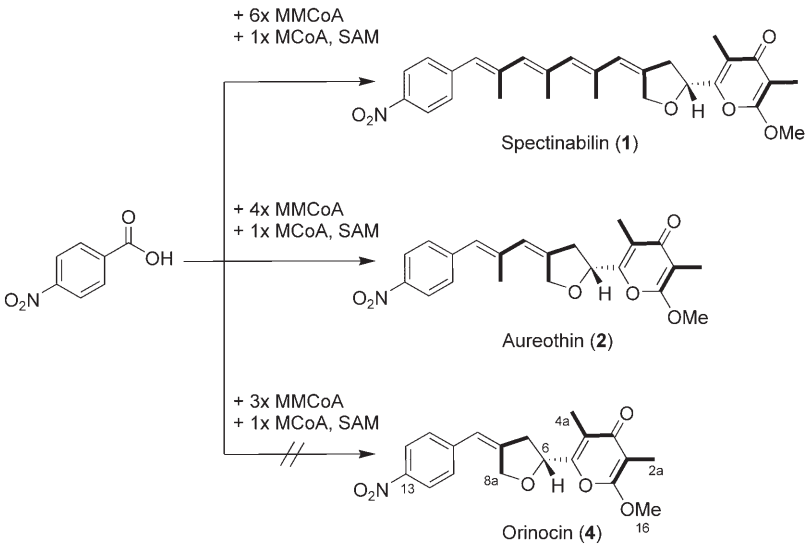

Scheme 1. Structures of nitroaryl-substituted pyrone metabolites from *Streptomyces* sp. CoA = coenzyme A, M = malonyl, MM = methylmalonyl, SAM = *S*-adenosylmethionine.

propelled substantial synthetic efforts.[20–26] Based on biosynthetic considerations and biomimetic models it has been suggested that the rare bicyclo[4.2.0]octadienes are formed from an isomer of the tetraene **1** through an 8π–6π electrocyclization cascade (Scheme 2).[20,21,25,26] However, the origin of the putative biogenetic precursor, an *E*,*Z*,*Z*,*Z*-tetraene intermediate, has remained unclear to date.

We thus reinvestigated the metabolic profile of *S. orinoci*, a producer of spectinabilin, under various growth conditions. Using synthetic **3a** as a reference, we noted that the diastereoisomeric bicyclo[4.2.0]octadienes are formed only when the culture is exposed to daylight (0.1–0.3 mg L^{-1}; see the Supporting Information). When fermentation and workup were conducted in the dark, no formation of **3a**/**b** could be observed. This result immediately implied that the spectinabilin isomer is not formed enzymatically but is a result of a photoinduced *E*/*Z* isomerization. We were able to confirm this observation in vitro by exposing pure spectinabilin isolated from *S. orinoci* to daylight and artificial light at room temperature. In the HPLC profile of aliquots taken from the mixture the occurrence of various isomers is clearly

[*] M. Müller, B. Kusebauch, Prof. Dr. C. Hertweck
Department of Biomolecular Chemistry
Leibniz-Institute for Natural Product Research and Infection Biology, HKI
Beutenbergstrasse 11a, 07745 Jena (Germany)
Fax: (+49) 3641-656-705
E-mail: christian.hertweck@hki-jena.de
G. Liang, C. M. Beaudry, Prof. Dr. D. Trauner
Department of Chemistry
University of California, Berkeley
Berkeley, CA 94720-1460 (USA)
Fax: (+1) 501-643-9480
E-mail: trauner@berkeley.edu

[**] This project was generously funded by the DFG Priority Programme SPP1152 "Evolution of Metabolic Diversity" (HE3468/2 for C.H.) and supported by the National Institutes of Health grant R01 GM067636 (to D.T.).

Supporting information for this article is available on the WWW under http://www.angewandte.org or from the author.

 © 2006 Wiley-VCH Verlag GmbH & Co. KGaA, Weinheim

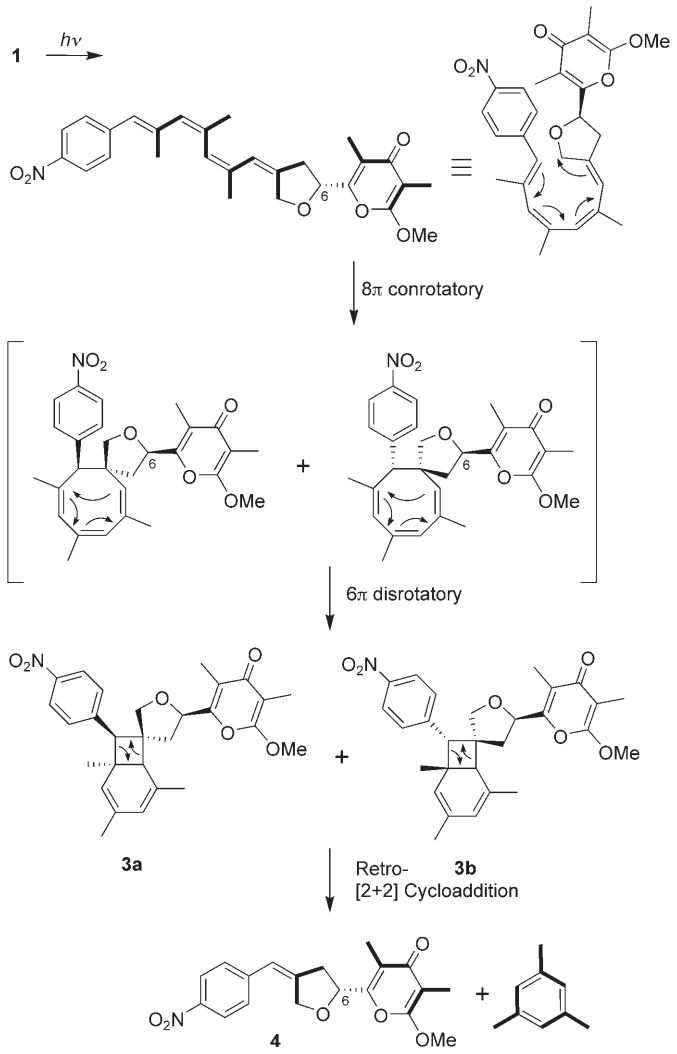

Scheme 2. Photoinduced electrocyclic rearrangement cascade from **1** to **4** via **3**.

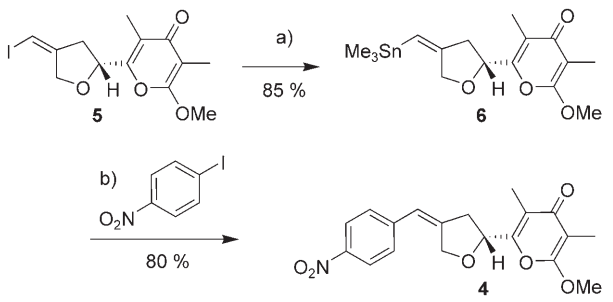

Scheme 3. De novo synthesis of orinocin. a) 10 mol% $[Pd(PPh_3)_4]$, $Me_3Sn{-}SnMe_3$, THF, 80 °C; b) 25 mol% $[Pd_2(dba)_3]$, THF, 50 °C. dba = *trans*,*trans*-dibenzylideneacetone.

detectable with subsequent formation of **3a/b** (see the Supporting Information).

These results demonstrate unequivocally that **3a** and **3b** are indeed derivatives of spectinabilin and result from a nonenzymatic, photoinduced isomerization–electrocyclization sequence (see Scheme 2). Nonetheless, we were surprised to find that this fascinating 8π–6π electrocyclic rearrangement is not the end of this intriguing reaction cascade.

In the course of our studies we noted by HPLC-MS monitoring that minute amounts (0.3 mg mL^{-1}) of another nitroaryl-substituted metabolite (**4**) with *m*/*z* 357 are formed. Surprisingly, this novel compound, named orinocin, occurred mainly in fractions containing **3a** and **3b**. The structure of **4** was fully established by 1D- and 2D-NMR spectroscopy, including NOESY experiments, and proved to be a truncated homologue of **1** and **2**.[27] In addition to spectroscopic methods, the structure of **4** was unequivocally confirmed by a synthetic reference. Our total synthesis of racemic orinocin started from the vinyl iodide building block **5** (Scheme 3), which was previously developed for our synthesis of aureothin and related polyketides.[28] Iodine–tin exchange, followed by Stille coupling with *p*-iodonitrobenzene afforded pure (±)-**4** (see the Experimental Section).

The structure of orinocin suggests a biogenesis analogous to that of **1** and **2**. In contrast to its higher homologues, which result from five and seven Claisen condensations, respectively, orinocin biosynthesis would correspond to only four rounds of elongation. However, the simultaneous occurrence of **4** and **3** prompted us to consider also an alternative route that would involve the fragmentation of the bicyclo-[4.2.0]octadienes. This hypothesis was proven by investigating pure natural and synthetic **3** under fermentation conditions (daylight, 28 °C).

As evident from the HPLC-MS profile (Figure 1), **4** is directly derived from **3a**. The retro-[2+2]cycloaddition-type fragmentation of **3** would lead to the concomitant production of a side product composed of three propionate units, mesitylene. The formation of this rather unusual "polyketide" was in fact detected by GC-MS. In the GC profiles of both the methanolic solution of **3a** and a mesitylene reference peaks with identical retention time and *m*/*z* 121 and the characteristic fragmentation were observed. Consequently, mesitylene is liberated directly from **3**. It should be noted that this reaction is also photoinduced and was not observed in the dark. This finding is in full agreement with the Woodward–Hoffmann rules, according to which thermal retro-[2+2] cycloaddition would be symmetry forbidden.[29] The reaction cascade with alternating photochemical and thermal pericyclic steps is somewhat reminiscent of vitamin D biosynthesis.[3] However, the present reaction cascade, which leads to a chain-contracted polyketide backbone as a result of the excision of internal ketide units from a polyene precursor, represents the first report of a process which we have termed "polyene splicing".

In summary, we have demonstrated that the formation of **3a** and **3b** from **1** by a 8π–6π electrocyclic rearrangement cascade[30] is initiated by a photoinduced isomerization in vivo and in vitro. This direct evidence also supports the reassignment of the configuration at C6 of **3a** and **3b**, which has been made on the basis of biosynthetic considerations[31] and synthetic studies.[23,24] Furthermore we have isolated and identified **4** as a new member of the aureothin/spectinabilin family from *S. orinoci* and confirmed its structure by total synthesis. The most surprising finding is that this novel metabolite is not the immediate product of a polyketide

 © 2006 Wiley-VCH Verlag GmbH & Co. KGaA, Weinheim

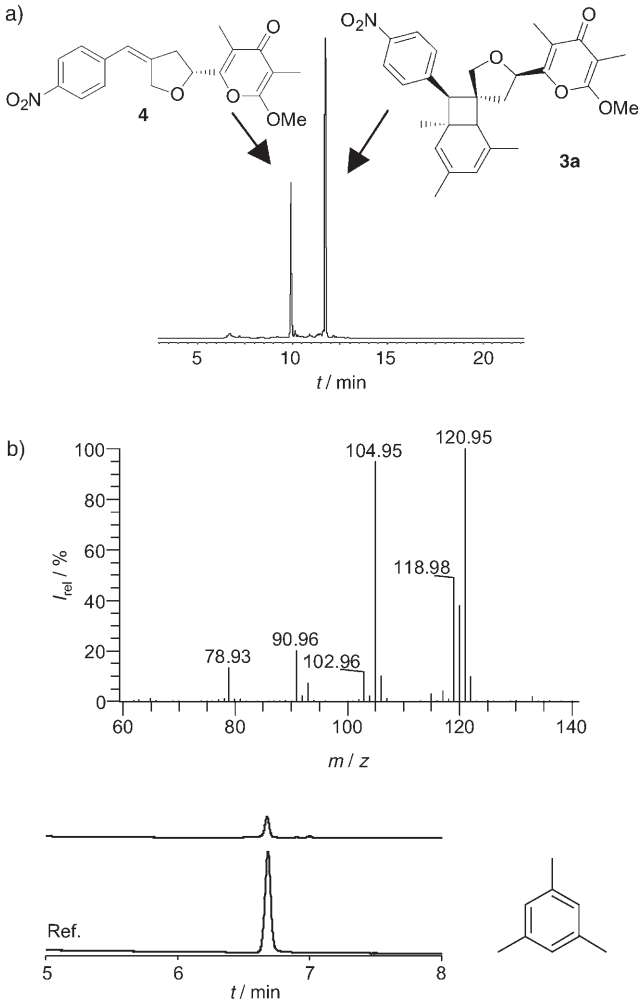

Figure 1. Monitoring the formation of orinocin (**4**) and mesitylene from **3**. a) HPLC profile; b) top, middle: GC-MS detection of mesitylene formation from SNF4435C (**3a**), bottom: mesitylene reference; m/z 121 corresponds to $[M+H]^+$, which arises at this high fragmentation energy.

synthase but is derived from **1** by excision of three propionate units. LC- and GC-MS analyses revealed that **4** originates from **3** by a [2+2] cycloreversion with concomitant formation of mesitylene. The entire sequence, which was termed "polyene splicing", is unprecedented for natural products and represents an important example for the generation of structural diversity through nonenzymatic downstream processes. Finally, we have devised a biosynthetic route to mesitylene, which has not yet been described as a natural product. Our results reveal that it is clearly composed of three propionate units—and thus represents a polyketide.

Experimental Section

Fermentation of *S. orinoci*: Cultures of *S. orinoci* (21 × 0.5 L, each supplemented with 2.5 g adsorber resin XAD4) were fermented for 5 d in analogy to the protocol reported.[15] One flask (reference) was wrapped in aluminum foil and incubated with strict exclusion of light.

Isolation of **1** and **4**: Harvested mycelium and resin were exhaustively extracted with ethanol. The crude product was purified by open-column chromatography on silica using ethyl acetate/hexanes (v/v = 1:1) and by preparative HPLC on a Kromasil C18 column (250 × 20 mm) using MeOH/H_2O (v/v = 70:30) as the eluent at a flow rate of 20 mL min^{-1}. Yield: 450 mg of **1**. Compound **4** was obtained from repeated preparative reversed-phase HPLC using C18 Kromasil and acetonitrile/water 40:60 and 60% MeOH as eluents. Yield: 3.2 mg.

MS (ESI+): 736.9 ([2M+Na$^+$], 380 [M+Na$^+$], 358.2 (100, M+H$^+$); ^{1}H NMR (500 MHz, $CDCl_3$) see Table 1; ^{13}C NMR (125 MHz, $CDCl_3$): δ = 6.9 (CH_3, C2a), 9.5 (CH_3, C4a), 38.4 (CH_2, C7), 55.2 (CH_3, C16), 70.3 (CH_2, C8a), 73.5 (CH, C6), 100.2 (C, C2), 120.2 (CH, C9), 120.3 (C, C4), 124.1 (CH, C12, C14), 128.3 (CH, C11, C15), 143.0 (C, C8), 145.2 (CH, C10), 146.4 (C, C13), 154.4 (C, C5), 162.1 (C, C1), 180.5 ppm (C, C3); IR (ATR, solid): $\tilde{\nu}$ = 2924, 1665, 1594, 1342 cm^{-1}; UV (MeOH): λ = 215, 315 nm; HRMS (EI) calcd. for $C_{19}H_{20}NO_6$ [M+H$^+$]: 358.1291; found: 358.1318.

Table 1: ^{1}H NMR data (δ [ppm]) of isolated and synthetic **4**.

	Isolated **4** (J in Hz)	Synthetic **4** (J in Hz)
C12, C14	8.21 (d, 8.8, 2H)	8.23 (d, 8.8, 2H)
C11, C15	7.25 (d, 8.8, 2H)	7.26 (d, 8.8, 2H)
C9	6.59 (m, 2.2, 1H)	6.61 (m, 2.2, 1H)
C6	5.21 (dd, 7.2, 6.5, 1H)	5.23 (dd, 7.3, 6.4, 1H)
C8a	4.86 (d, 14.3, 1H)	4.88 (d, 14.5, 1H)
C8a	4.76 (d, 14.3, 1H)	4.78 (d, 14.4, 1H)
C16	3.81 (s, 3H)	3.83 (s, 3H)
C7	3.17 (br dd, 16.3, 7.6, 1H)	3.20 (m, 1H)
C7	3.05 (br dd, 16.5, 6.1, 1H)	3.07 (m, 1H)
C4a	2.03 (s, 3H)	2.04 (s, 3H)
C2a	1.83 (s, 3H)	1.84 (s, 3H)

Monitoring formation of **4** and mesitylene from **3**: Compound **4** was detected by HPLC–MS using an Agilent 1100 Series HPLC System coupled to an LC/MSD Trap and additional UV detection with a DAD (254 nm). A Zorbax Eclipse XDB C18 column (5 µ, 150 × 4.6 mm) was used as the stationary phase. Eluent: MeOH/H_2O 0–10 min: 20:80 to 100:0; 10–20 min: 100:0. Mesitylene was detected by GC–MS using a TRACE GC ULTRA (Thermo) equipped with a BPX 50 (SGE, 30 m × 0.25 mm ID) capillary column coupled in parallel to a CTC Analytics FID detector and a POLARIS Q (Thermo) quadrupole mass detector. GC parameters: injection in the splitless mode, He carrier gas, constant flow rate 1.0 mL min^{-1}, T = 40 °C (0.0–1.0 min), 40–280 °C (1.0–17.0 min, 15.0 °C min^{-1}), 280 °C (17.0–18.0 min). MS parameters: CI, methane reactant gas, flow rate 0.7 mL min^{-1}, ion source 200 °C.

Synthesis of **4**: Please see the Supporting Information.

Received: July 17, 2006
Published online: October 25, 2006

Keywords: electrocyclic reactions · natural products · polyenes · polyketides · streptomyces

[1] D. O'Hagan, *The Polyketide Metabolites*, Ellis Horwood, Chichester, **1991**.
[2] J. Staunton, K. J. Weissman, *Nat. Prod. Rep.* **2001**, *18*, 380.
[3] C. M. Beaudry, J. P. Malerich, D. Trauner, *Chem. Rev.* **2005**, *105*, 4757.
[4] A. K. Miller, D. Trauner, *Synlett* **2006**, *14*, 229.
[5] G. Cassinelli, A. Grein, P. Orezzi, P. Pennella, A. Sanfilippo, *Arch. Microbiol.* **1967**, *55*, 358.

 © 2006 Wiley-VCH Verlag GmbH & Co. KGaA, Weinheim

[6] K. Kakinuma, C. A. Hanson, K. L. Rinehart, *Tetrahedron* **1976**, *32*, 217.
[7] J. He, C. Hertweck, *J. Am. Chem. Soc.* **2004**, *126*, 3694.
[8] R. Winkler, C. Hertweck, *Angew. Chem.* **2005**, *117*, 4152; *Angew. Chem. Int. Ed.* **2005**, *44*, 4083.
[9] M. Ziehl, J. He, H.-M. Dahse, C. Hertweck, *Angew. Chem.* **2005**, *117*, 4443; *Angew. Chem. Int. Ed.* **2005**, *44*, 1202.
[10] R. Cardillo, C. Fuganti, D. Ghiringhelli, D. Giangrasso, P. Grasselli, *Tetrahedron Lett.* **1972**, 4875.
[11] R. Cardillo, C. Fuganti, D. Ghiringhelli, D. Giangrasso, P. Grasselli, A. Santopietro-Amisano, *Tetrahedron* **1974**, *30*, 459.
[12] M. Yamazaki, Y. Maebayashi, H. Katoh, J.-I. Ohishi, Y. Koyama, *Chem. Pharm. Bull.* **1975**, *23*, 569.
[13] J. He, C. Hertweck, *Chem. Biol.* **2003**, *10*, 1225.
[14] J. He, C. Hertweck, *ChemBioChem* **2005**, *6*, 908.
[15] J. He, M. Müller, C. Hertweck, *J. Am. Chem. Soc.* **2004**, *126*, 16742.
[16] M. Müller, J. He, C. Hertweck, *ChemBioChem* **2006**, *7*, 37.
[17] K. Takahashi, E. Tsuda, K. Kurosawa, *J. Antibiot.* **2001**, *54*, 548.
[18] K. Kurosawa, K. Takahashi, E. Tsuda, *J. Antibiot.* **2001**, *54*, 541.
[19] K. Kurosawa, K. Takahashi, N. Fujise, Y. Yamashita, N. Washida, E. Tsuda, *J. Antibiot.* **2002**, *55*, 71.
[20] C. M. Beaudry, D. Trauner, *Org. Lett.* **2002**, *4*, 2221.
[21] J. E. Moses, J. E. Baldwin, R. Marquez, R. M. Adlington, A. R. Cowley, *Org. Lett.* **2002**, *4*, 3731.
[22] J. E. Moses, J. E. Baldwin, S. Bruckner, S. J. Eade, R. M. Adlington, *Org. Biomol. Chem.* **2003**, *1*, 3670.
[23] K. A. Parker, Y. H. Lim, *J. Am. Chem. Soc.* **2004**, *126*, 15968.
[24] C. M. Beaudry, D. Trauner, *Org. Lett.* **2005**, *7*, 4475.
[25] M. F. Jacobsen, J. E. Moses, R. M. Adlington, J. E. Baldwin, *Tetrahedron* **2006**, *62*, 1675.
[26] M. F. Jacobsen, J. E. Moses, R. M. Adlington, J. E. Baldwin, *Org. Lett.* **2005**, *7*, 2473.
[27] Compound **4** easily isomerizes, yielding a 1:1 mixture of *E* and *Z* isomers.
[28] G. Liang, I. B. Seiple, D. Trauner, *Org. Lett.* **2005**, *7*, 2837.
[29] R. B. Woodward, R. Hoffmann, *Angew. Chem.* **1969**, *81*, 797.
[30] For pioneering work on 8π–6π electrocyclization cascades, see: a) R. Huisgen, A. Dahmen, H. Huber, *J. Am. Chem. Soc.* **1967**, *89*, 7130; b) W. M. Bandaranayake, J. E. Banfield, S. St. C. Black, G. D. Fallon, B. M. Gatehouse, *J. Chem. Soc. Chem. Commun.* **1980**, 162; c) K. C. Nicolaou, N. A. Petasis, J. Uenishi, R. Zipkin, *J. Am. Chem. Soc.* **1982**, *104*, 555.
[31] K. A. Parker, Y. H. Lim, *Org. Lett.* **2004**, *6*, 161.

 © 2006 Wiley-VCH Verlag GmbH & Co. KGaA, Weinheim

Amination

DOI: 10.1002/anie.200603089

General Preparation of Primary, Secondary, and Tertiary Aryl Amines by the Oxidative Coupling of Polyfunctional Aryl and Heteroaryl Amidocuprates**

*Vicente del Amo, Srinivas Reddy Dubbaka, Arkady Krasovskiy, and Paul Knochel**

Aromatic and heterocyclic amines are important target molecules in organic synthesis because of their potential applications as biologically active compounds and as precursors for polymers or materials.[1] Besides several electrophilic amination methods,[2] the palladium-catalyzed amination of aromatic halides and related electrophiles have become a widely used method for the preparation of aryl amines.[3] However, this latter reaction has some limitations, such as long reaction times for sterically hindered systems[4] and the necessity to carefully choose the appropriate phosphine or carbene ligand to obtain optimum yields. Also, the preparation of triaryl amines can usually not be performed by this method.[5] Furthermore, some functional groups such as iodides (and bromides) are not compatible with this Pd-catalyzed amination procedure.

Recently, we reported a new transition-metal-free oxidative coupling procedure for organomagnesium and organozinc reagents using diphenoquinone or chloranil (**1**) as the oxidative agents.[6] Inspired by the pioneering work of Yamamoto and Marouka,[7] Ricci and co-workers,[8] Lipshutz et al.,[9] and others,[10] who described the oxidative coupling of amidocuprates or organo(cyano)cuprates using oxygen or 1,3-dinitrobenzene derivatives as oxidants, we have now examined the oxidative amination reaction of various polyfunctional amidocuprates and developed an experimental procedure that allows the preparation of primary, secondary, as well as tertiary aromatic and heterocyclic amines.

In preliminary experiments, we treated PhMgCl·LiCl[11a] with various copper salts of the type CuX·*n* LiCl.[12,13] This was followed by the addition of Et_2NLi (3 equiv) and one of three representative quinones (1.2 equiv): 3,3′,5,5′-tetra-*tert*-butyldiphenoquinone,[6] 2,3-dichloro-5,6-dicyano-1,4-benzoqui-

[*] Dr. V. del Amo, Dr. S. R. Dubbaka, Dr. A. Krasovskiy, Prof. Dr. P. Knochel
Ludwig-Maximilians-Universität München
Department Chemie und Biochemie
Butenandtstrasse 5–13, Haus F, 81377 München (Germany)
Fax: (+49) 892-1807-7680
E-mail: paul.knochel@cup.uni-muenchen.de

[**] We thank the Fonds der Chemischen Industrie and Merck Research Laboratories (MSD) for financial support. V.d.A. and S.R.D. thank the Alexander von Humboldt Foundation for fellowships. We also thank Chemetall GmbH (Frankfurt) and BASF AG (Ludwigshafen) for the generous gift of chemicals.

Supporting information for this article is available on the WWW under http://www.angewandte.org or from the author.

WILEY InterScience DISCOVER SOMETHING GREAT
© 2006 Wiley-VCH Verlag GmbH & Co. KGaA, Weinheim

none (DDQ), and 2,3,5,6-tetrachloro-1,4-benzoquinone (**1**, chloranil), with addition at −78 °C and then 12 h at −40 °C. The combination of **1** with CuCl·2 LiCl gave the best results and allowed the isolation of $PhNEt_2$ in 84 % yield.[13]

We have extended and adapted this procedure to the preparation of various primary, secondary, and tertiary amines. Thus, for the synthesis of primary amines, the diester **2a** was magnesiated with TMPMgCl·LiCl[14] (1.1 equiv, 0 °C, 1 h) which led to the aryl magnesium derivative **3a**[15] (TMP = 2,2,6,6-tetramethylpiperidyl). This was treated with CuCl·2 LiCl[12,13] (1.2 equiv) at −50 °C followed by the addition of bis[2-(*N*,*N*-dimethylamino)ethyl]ether (1.2 equiv)[16] and lithium hexamethyldisilazide (LiHMDS (2 equiv); −50 °C, 90 min) to afford the amidocuprate **5a**. Treatment of **5a** with **1** (1.2 equiv, −78 to −50 °C, 12 h) led to the *N*,*N*-bis(trimethylsilyl)amine derivative **6a** in 76 % yield. A facile desilylation was achieved with TBAF (2.5 equiv, 25 °C, 10 min) to give the aryl amine **7a** in 94 % yield (Scheme 1). This method has been used to prepare various primary amines (**7b–f**) bearing electron-withdrawing substituents such as a nitrile, an ester, or a nitro group (entries 1, 2, and 5, Table 1) or electron-donating substituents such as a methoxy or an iodide (entries 3 and 4, Table 1). In all these cases, the Grignard reagents were prepared by an I/Mg or Br/Mg exchange reaction.[11] Highly functionalized aryl magnesium reagents such as **3g**, which can be conveniently obtained by deprotonation with TMPMgCl·LiCl,[14,15] can be aminated (entry 6 (78 %), Table 1). This procedure can also be used with heterocyclic Grignard reagents such as the pyridine derivative **3h**, the benzothiophene **3i**, and benzothiazole **3j** (see entries 7–9, Table 1). The resulting primary amines of type **7** are obtained in 69–80 % yield, after cleavage of the corresponding *N*,*N*-

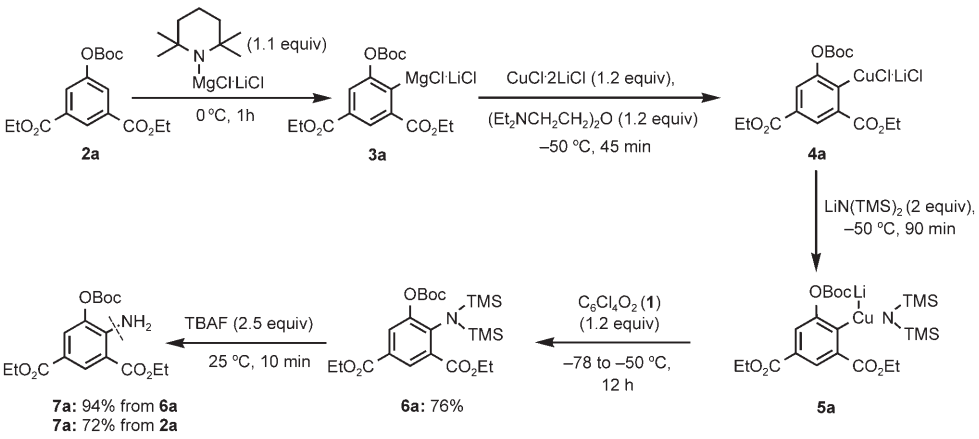

Scheme 1. Preparation of primary amines through an oxidative amination with a magnesiated polyfunctional aryl derivative such as **3a** and LiHMDS using **1**. Boc = *tert*-butoxycarbonyl, TBAF = tetrabutylammonium fluoride, TMS = trimethylsilyl.

Table 1: Synthesis of amines by the oxidative coupling of aryl and heteroaryl amidocuprates.

Entry	Grignard reagent	Lithium amide	Product	Yield [%][a]
	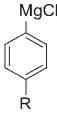	LiHMDS	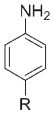	
1	**3b**: R = CN		**7b**: R = CN	86[b]
2	**3c**: R = CO_2Et		**7c**: R = CO_2Et	84[b]
3	**3d**: R = OMe		**7d**: R = OMe	88[b]
4	**3e**: R = I		**7e**: R = I	60[b]
	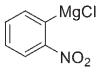	LiHMDS	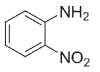	
5	**3f**		**7f**	61[c]
	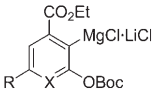	LiHMDS	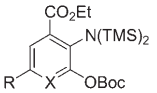	
6	**3g**: X = CH, R = OBoc		**6b**: X = CH, R = OBoc	78[d]
7	**3h**: X = N, R = OBoc		**6c**: X = N, R = OBoc	72[d]
	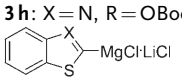	LiHMDS	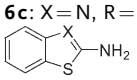	
8	**3i**: X = CH		**7g**: X = CH	69[d]
9	**3j**: X = N		**7h**: X = N	80[d]
		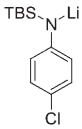	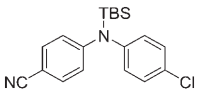	
10	**3b**	**10b**	**12b**	65[b]
	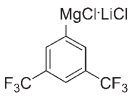		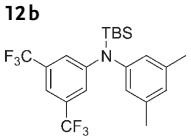	
11	**3k**	**10c**	**12c**	70[b]
	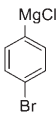	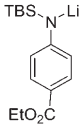	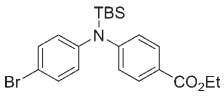	
12	**3l**	**10d**	**12d**	70[b]

© 2006 Wiley-VCH Verlag GmbH & Co. KGaA, Weinheim

Table 1: (Continued)

Entry	Grignard reagent	Lithium amide	Product	Yield [%][a]
13	**3m**	**10e**	**12e**	60[d]
14	**3o**: R = H	**14b**	**16b**: R = H	63[b]
15	**3d**	**14b**	**16c**: R = OMe	58[b]
16	**3p**	**14c**	**16d**	57[b]
17	**3e**	**14d**	**16e**	66[b]

[a] Yield of analytically pure product. [b] The aryl magnesium reagent was formed through an I/Mg exchange reaction with *i*PrMgCl·LiCl. [c] The aryl magnesium reagent was prepared through an I/Mg exchange reaction with PhMgCl. [d] The aryl magnesium reagent was prepared through deprotonation using TMPMgCl·LiCl (1.1 equiv).

bis(trimethylsilyl) group with TBAF (2.5 equiv, 25 °C, 10 min).

Secondary amines can also be prepared from an aniline derivative such as **8a** (Scheme 2). Its in situ protection with a TBS group can be achieved by lithiation with MeLi (1.1 equiv, −50 °C, 10 min) followed by the addition of TBSCl (1.2 equiv, −50 to 25 °C, 0.5 h) to give the *N*-silylaniline **9a**. Further treatment with MeLi (1.1 equiv, −50 °C, 10 min) provides the lithium amide **10a** which was treated with the aryl copper species **4d** for 2 h at −50 °C. This copper reagent was prepared from 4-iodoanisole (**2d**) by an I/Mg exchange with *i*PrMgCl·LiCl (1.1 equiv, 25 °C, 20 min), followed by the addition of CuCl·2 LiCl (1.1 equiv, −50 °C, 30 min) in the presence of $(i\text{Pr})_2$NH (1.1 equiv). The resulting lithium amidocuprate **11a** was treated with **1** (1.2 equiv, −78 to −50 °C, 12 h) to provide the silyl-protected diaryl amine **12a** in 72 % yield (Scheme 2).

This reaction proved to be quite general and a number of functionalized Grignard reagents such as **3b** and **3k**,**l** bearing a cyano, trifluoromethyl, or bromine substituent undergo a smooth oxidative amination with lithiated *N*-TBS-anilines (**10b–d**) bearing various functional groups such as a chloride, an ester, or a methoxy group. The resulting TBS-protected secondary amines **12b–d** are obtained in 65–70 % overall yield (entries 10–12, Table 1). The TBS-protected secondary amine **12c** (entry 11, Table 1) was readily desilylated with TBAF (1.1 equiv, 25 °C, 10 min).[17] Interestingly, the heterocyclic copper derivative prepared from 3,5-dibromo-2-pyridylmagnesium chloride (**3m**) reacts equally as well with lithiated 4-methoxyaniline (**10e**) to provide the corresponding 2-aminopyridine derivative **12e** in 60 % yield (entry 13, Table 1).

Finally, the preparation of polyfunctional triaryl amines can be performed using the same approach. Thus, the lithiation of the secondary amine **13a** with lithium diisopropylamide (LDA; 1.05 equiv, −40 °C, 1 h) in the presence of an additional equivalent of $(i\text{Pr})_2$NH provides the lithium amide **14a** which reacted with the copper reagent **4n** to afford the lithium amidocuprate **15a**. This copper reagent **4n** was prepared by an I/Mg exchange on 1,3-diiodobenzene (**2n**) with *i*PrMgCl·LiCl (1.1 equiv, 0 °C, 15 min) to give the Grignard reagent **3n**, followed by a transmetalation with CuCl·2 LiCl (1.1 equiv, −40 °C, 30 min). The resulting lithium amidocuprate **15a** was treated with **1** (1.2 equiv, −78 to −40 °C, 12 h) to provide the triaryl amine **16a** in 71 % yield (Scheme 3).[13] This sequence can be performed with several aryl magnesium reagents (**3d**, **3e**,

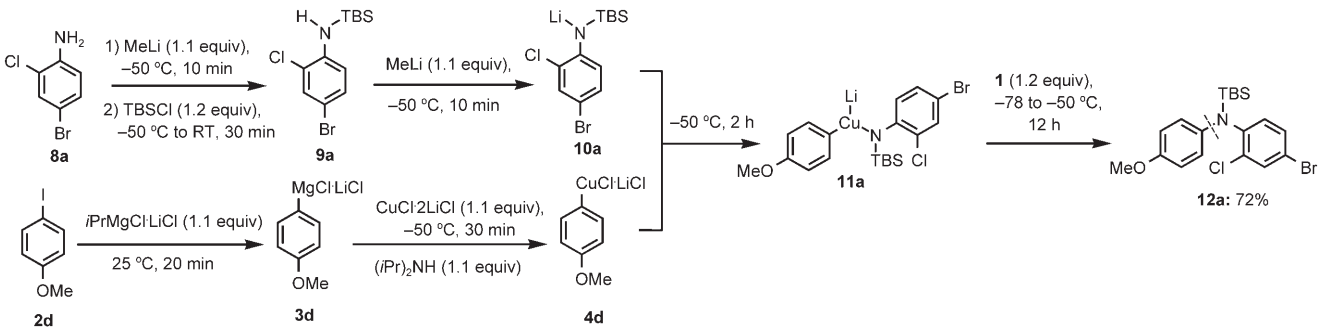

Scheme 2. Preparation of TBS-protected secondary amines through an oxidative amination with a functionalized aryl magnesium reagent (**3d**) and a lithium amide (**10a**) using **1**. TBS = *tert*-butyldimethylsilyl.

 © 2006 Wiley-VCH Verlag GmbH & Co. KGaA, Weinheim

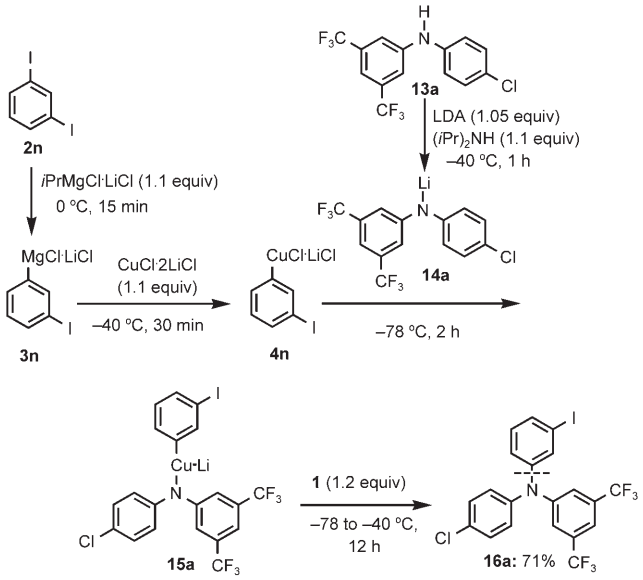

Scheme 3. Preparation of a tertiary amine through an oxidative amination with a magnesiated aryl derivative (**3n**) and a functionalized lithium amide (**14a**) using **1**.

3o, and **3p**) bearing various functional groups such as a methoxy, an iodide, and an amide group, as well as with various lithium amides bearing functional groups such as a bromide, a nitrile, and an ester group (**14b–d**) to afford the tertiary amines **16b–e** in 57–66% yield (entries 14–17, Table 1).

Remarkably, this amination reaction can be extended to the preparation of very sterically hindered amines using either sterically hindered copper reagents such as **4q** and **4g** with the lithium amide **17** or a sterically hindered lithium amide such as **18** by the oxidative coupling of the lithium amidocuprates **19a**,**b** and **20**. The expected tertiary amines (**21a**,**b** and **22**) are obtained in 61–70% yield (Scheme 4).

In summary, we have developed a new general amination procedure using readily available lithium amidocuprates. The scope of the method is quite broad and is not hampered by steric hindrance. It is a useful complement to the Pd-catalyzed amination reactions. Further applications are currently being investigated.

Experimental Section

Typical procedure (synthesis of **7a**; see Scheme 1): A dry and argon-flushed Schlenk flask, equipped with a magnetic stirring bar and a septum, was charged with a solution of **2a** (338 mg, 1.0 mmol) in dry THF (3 mL). After cooling the mixture to 0°C, TMPMgCl·LiCl (0.92 mL, 1.20 M in THF, 1.1 mmol) was added dropwise and stirred for 1 h to afford the corresponding Grignard reagent **3a**. This organomagnesium reagent was added dropwise to a solution of CuCl·2 LiCl (1.2 mL, 1.0 M in THF, 1.2 mmol) and bis[2-(*N*,*N*-dimethylamino)ethyl]ether (192 mg, 1.2 mmol) at −50°C under argon, and the mixture was stirred for 45 min. LiHMDS (2.0 mL, 1.0 M in THF, 2.0 mmol) was added dropwise to the resulting aryl cuprate (**5a**), and the mixture was further stirred for 90 min at −50°C. The reaction mixture was cooled to −78°C, then a solution of **1** (295 mg, 1.2 mmol) in dry THF (7 mL) was added slowly over a period of 45 min. The reaction mixture was then allowed to reach −50°C and stirred for 12 h. Et_2O (10 mL) was poured into the crude reaction mixture and the reaction mixture then filtered through celite and the residue washed with Et_2O (ca. 100 mL). The organic phase was washed with 2 × 10 mL portions of aqueous NH_4OH (2.0 M) and extracted with Et_2O. The combined organic layers were dried ($MgSO_4$), filtered, and concentrated under reduced pressure. This crude material was dissolved in Et_2O (3 mL) before TBAF (2 mL, 1.0 M in THF, 2 mmol) was added in one portion. The mixture was stirred at room temperature for 10 min, poured into EtOAc (10 mL), and washed with water (3 × 10 mL). The combined organic extracts were dried ($MgSO_4$), filtered, and concentrated in vacuum. Purification by flash chromatography (pentane/Et_2O; 4:1) yielded the aromatic amine **7a** (254 mg, 72%) as a white crystalline solid (m.p. 86.7–88.1°C).

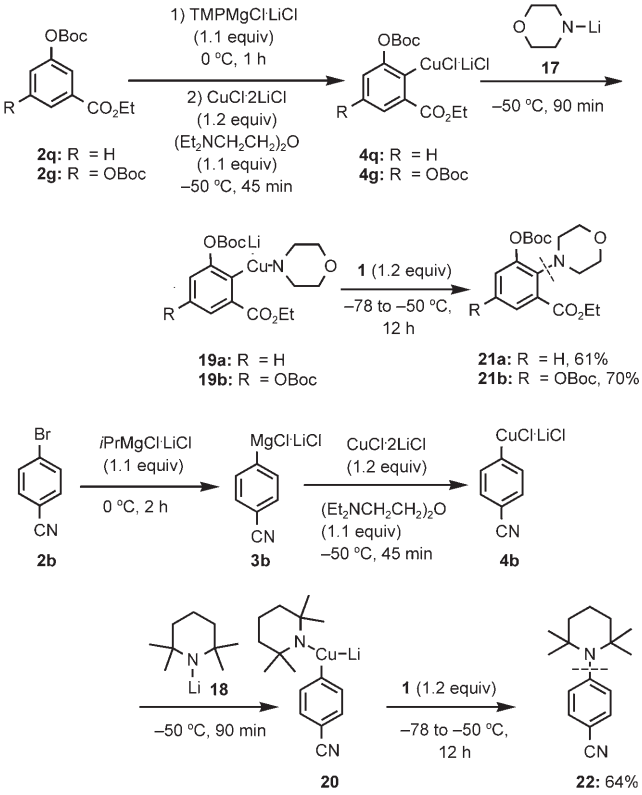

Scheme 4. Preparation of sterically hindered tertiary amines through an oxidative amination with sterically hindered copper reagents (**4q** and **4g**) or lithium amide (**18**) with **1**.

Received: July 31, 2006
Published online: October 31, 2006

Keywords: amination · amines · C–N bond formation · cuprates · Grignard reagents

[1] a) A. Zapf, M. Beller, *Top. Catal.* **2002**, *19*, 101; b) J. G. de Vries, *Can. J. Chem.* **2001**, *79*, 1086, and references therein; c) applications in the preparation of biologically active compounds: M. Prashad, *Top. Organomet. Chem.* **2004**, *6*, 181; d) applications in polymer synthesis: C. Desmarets, B. Champagne, A. Walcarius, C. Bellouard, R. Omar-Amrani, A. Ahajji, Y. Fort, R. Schneider, *J. Org. Chem.* **2006**, *71*, 1351; e) applications as materials: P. Bordat, R. Brown, *Chem. Phys. Lett.* **2000**, *331*, 439; f) applica-

 © 2006 Wiley-VCH Verlag GmbH & Co. KGaA, Weinheim

tions in electrical devices: S. Miao, C. G. Bangcuyo, M. D. Smith, U. H. F. Bunz, *Angew. Chem.* **2006**, *118*, 667; *Angew. Chem. Int. Ed.* **2006**, *45*, 661; g) applications in liquid crystals: R. S. Wright, T. K. Vinod, *Tetrahedron Lett.* **2003**, *44*, 7129; h) photophysical applications: Z. Liu, X. Zhang, R. C. Larock, *J. Am. Chem. Soc.* **2005**, *127*, 15716.

[2] I. Sapountzis, P. Knochel, *Angew. Chem.* **2004**, *116*, 915; *Angew. Chem. Int. Ed.* **2004**, *43*, 897.

[3] For selected reviews, see: a) J. F. Hartwig, *Angew. Chem.* **1998**, *110*, 2154; *Angew. Chem. Int. Ed.* **1998**, *37*, 2046; b) J. F. Hartwig, *Acc. Chem. Res.* **1998**, *31*, 852; c) J. F. Hartwig, *Pure Appl. Chem.* **1999**, *67*, 805; d) B. H. Yang, S. L. Buchwald, *J. Organomet. Chem.* **1999**, *576*, 125; e) J. P. Wolfe, S. L. Buchwald, *Angew. Chem.* **1999**, *111*, 2570; *Angew. Chem. Int. Ed.* **1999**, *38*, 2413; f) J. P. Wolfe, S. Wagaw, J.-F. Marcoux, S. L. Buchwald, *Acc. Chem. Res.* **1998**, *31*, 805; g) A. R. Muci, S. L. Buchwald, *Top. Curr. Chem.* **2002**, *219*, 131; h) H.-U. Blaser, A. Indolese, F. Naud, U. Nettekoven, A. Schnyder, *Adv. Synth. Catal.* **2004**, *346*, 1583; i) B. Schlummer, U. Scholz, *Adv. Synth. Catal.* **2004**, *346*, 1599; j) J. F. Hartwig, *Synlett* **2006**, 1283.

[4] The reaction between *ortho*-substituted aryl halides and LiHMDS generally fails to form C–N bonds because of the steric hindrance of the two bulky silyl groups; for a discussion, see: a) S. Lee, M. Jørgensen, J. F. Hartwig, *Org. Lett.* **2001**, *3*, 2729; b) X. Huang, S. L. Buchwald, *Org. Lett.* **2001**, *3*, 3417.

[5] For the synthesis of unfunctionalized triaryl amines, see: a) S. Thayumanavan, S. Barlow, S. R. Marder, *Chem. Mater.* **1997**, *9*, 3231; b) T. Yamamoto, M. Nishiyama, Y. Koie, *Tetrahedron Lett.* **1998**, *39*, 2367; c) J. Louie, J. F. Hartwig, *J. Am. Chem. Soc.* **1997**, *119*, 11695; d) M. Watanabe, T. Yamamoto, M. Nishiyama, *Chem. Commun.* **2000**, 133; e) M. C. Harris, O. Geis, S. L. Buchwald, *J. Org. Chem.* **1999**, *64*, 6019; f) G. N. Tew, M. U. Pralle, S. I. Stupp, *Angew. Chem.* **2000**, *112*, 527; *Angew. Chem. Int. Ed.* **2000**, *39*, 517; g) T. Braig, D. C. Muller, M. Gross, K. Meerholz, O. Nuyken, *Macromol. Rapid Commun.* **2000**, *21*, 583; h) M. Thelakkhat, J. Hagen, D. Haarer, H. -W. Schmidt, *Synth. Met.* **1999**, *102*, 1125; i) M. C. Harris, S. L. Buchwald, *J. Org. Chem.* **2000**, *65*, 5327, and references therein.

[6] A. Krasovskiy, A. Tishkov, V. del Amo, H. Mayr, P. Knochel, *Angew. Chem.* **2006**, *118*, 5132; *Angew. Chem. Int. Ed.* **2006**, *45*, 5010.

[7] H. Yamamoto, K. Maruoka, *J. Org. Chem.* **1980**, *45*, 2739.

[8] a) A. Casarini, P. Dembech, D. Lazzari, E. Marini, G. Reginato, A. Ricci, G. Seconi, *J. Org. Chem.* **1993**, *58*, 5620; b) A. Alberti, F. Canè, P. Dembech, D. Lazzari, A. Ricci, G. Seconi, *J. Org. Chem.* **1996**, *61*, 1677; c) F. Canè, D. Brancaleoni, P. Dembech, A. Ricci, G. Seconi, *Synthesis* **1997**, 545; d) P. Bernardi, P. Dembech, G. Fabbri, A. Ricci, G. Seconi, *J. Org. Chem.* **1999**, *64*, 641.

[9] a) B. H. Lipshutz, K. Siegmann, E. Garcia, *Tetrahedron* **1992**, *48*, 2579; b) B. H. Lipshutz, K. Siegmann, E. Garcia, F. Kayser, *J. Am. Chem. Soc.* **1993**, *115*, 9276, and references therein.

[10] Homocoupling of organocuprates: a) D. S. Surry, X. Su, D. J. Fox, V. Franckevicius, S. J. F. Macdonald, D. A. Spring, *Angew. Chem.* **2005**, *117*, 1904; *Angew. Chem. Int. Ed.* **2005**, *44*, 1870; b) Y. Miyake, M. Wu, M. J. Rahman, Y. Kuwatani, M. Iyoda, *J. Org. Chem.* **2006**, *71*, 6110; c) for a review on the oxidation of organocuprates, see: D. S. Surry, D. A. Spring, *Chem. Soc. Rev.* **2006**, *35*, 218.

[11] a) Br/Mg exchange: A. Krasovskiy, P. Knochel, *Angew. Chem.* **2004**, *116*, 3396; *Angew. Chem. Int. Ed.* **2004**, *43*, 3333; b) A. Krasovskiy, B. Straub, P. Knochel, *Angew. Chem.* **2006**, *118*, 165; *Angew. Chem. Int. Ed.* **2006**, *45*, 159; c) I/Mg exchange of *o*-nitroaryl iodides: I. Sapountzis, P. Knochel, *Angew. Chem.* **2002**, *114*, 1680; *Angew. Chem. Int. Ed.* **2002**, *41*, 1610; d) A. E. Jensen, W. Dohle, I. Sapountzis, D. M. Lindsay, V. A. Vu, P. Knochel, *Synthesis* **2002**, 565.

[12] P. Knochel, M. C. P. Yeh, S. C. Berk, J. Talbert, *J. Org. Chem.* **1988**, *53*, 2390.

[13] See the Supporting Information.

[14] A. Krasovskiy, V. Krasovskaya, P. Knochel, *Angew. Chem.* **2006**, *118*, 3024; *Angew. Chem. Int. Ed.* **2006**, *45*, 2958.

[15] W. Lin, O. Baron, P. Knochel, *Org. Lett.* **2006**, submitted.

[16] This additive improves the yield of the amination reaction; for other uses, see: X.-J. Wang, X. Sun, L. Zhang, Y. Xu, D. Krishnamurthy, C. H. Senanayake, *Org. Lett.* **2006**, *8*, 305.

[17] The corresponding secondary amine was obtained in 96% yield upon deprotection.

 © 2006 Wiley-VCH Verlag GmbH & Co. KGaA, Weinheim

Combinatorial Biosynthesis

DOI: 10.1002/anie.200603176

On the Acceptor Substrate of C-Glycosyltransferase UrdGT2: Three Prejadomycin C-Glycosides from an Engineered Mutant of *Streptomyces globisporus* 1912 Δ*lndE*(*urdGT2*)**

Irfan Baig, Madan Kharel, Anton Kobylyanskyy, Lili Zhu, Yuriy Rebets, Bohdan Ostash, Andriy Luzhetskyy, Andreas Bechthold, Victor A. Fedorenko, and Jürgen Rohr**

The landomycins **1**–**4** produced by *Streptomyces cyanogenus* S-136 and *S. globisporus* 1912 are angucycline antibiotics with a strong activity against various cancer cell lines, in particular

[*] A. Kobylyanskyy,[+] Dr. Y. Rebets, Dr. B. Ostash, Prof. Dr. V. A. Fedorenko
L'viv National University
Department of Genetic and Biotechnology
Grushevskyy St. 4, 79005 L'viv (Ukraine)
E-mail: v_fedorenko@franko.lviv.ua
Dr. I. Baig,[+] Dr. M. Kharel,[+] Dr. L. Zhu,[+] Prof. Dr. J. Rohr
University of Kentucky
Department of Pharmaceutical Sciences, College of Pharmacy
725 Rose Street, Lexington, KY 40536-0082 (USA)
Fax: (+1) 859-257-7564
E-mail: jrohr2@email.uky.edu
Dr. A. Luzhetskyy, Prof. Dr. A. Bechthold
Albert-Ludwigs-Universität Freiburg
Pharmazeutische Biologie
Stefan-Meier-Strasse 19, 79104 Freiburg (Germany)
E-mail: andreas.bechthold@pharmazie.uni-freiburg.de
[+] These four authors contributed equally to this work.

[**] This work was supported financially by the U.S. National Institutes of Health (NIH grant CA 102102 to J.R.) and by the DAAD (DAAD fellowship A/05/28943 to Y.R.). The University of Kentucky core facilities for NMR spectroscopy and mass spectrometry are acknowledged for the use of their instruments and their service, respectively.

Supporting information for this article is available on the WWW under http://www.angewandte.org or from the author.

WILEY InterScience DISCOVER SOMETHING GREAT
© 2006 Wiley-VCH Verlag GmbH & Co. KGaA, Weinheim

against prostate cancer cell lines.[1–6] The landomycins are closely related to the urdamycins (e.g., urdamycin A (**5**)).[7–9]

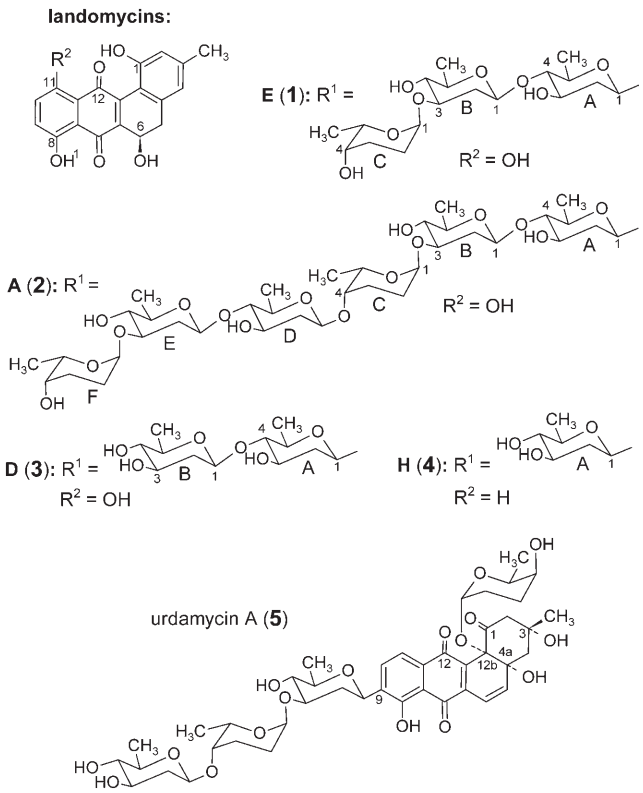

Both possess a polyketide-derived angucyclinone core and sugar moieties consisting of D-olivose and L-rhodinose building blocks. Major structural differences were found in the assembly of the sugar moieties and in the oxygenation pattern of the polyketide core moiety.[1,4,5,10–12]

The availability of the biosynthetic gene clusters of urdamycins and landomycins[7,13–17] made it possible to track down the genes encoding the biosynthetic enzymes responsible for the unique structural features of the two types of compounds, which are also responsible for the significant variations in the biological activities of these related anticancer drugs.[18] The overall structural and biosynthetic similarity between these two closely related sets of antibiotics allowed several successful combinatorial, biosynthetic gene-combination experiments, leading to new hybrid molecules.[5,6,15,19–24]

The most striking structural difference is that the trisaccharide chain found in the urdamycins is C-glycosidically linked at C9, while the oligosaccharide chains found in the different landomycins are O-glycosidically linked at the 8-position. The enzymes responsible for the first glycosyl transfer step for these chains, the glycosyl transferases (GT) UrdGT2 and LanGT2/LndGT2, are closely related. LndGT2 shows 53% amino acid identity (68% similarity) with UrdGT2. However, the acceptor substrates of these related GTs appear quite different, not only because one is a C-GT and the other an O-GT, but also with regard to the timing of the first GT step within the urdamycin and landomycin biosyntheses. In landomycin biosynthesis, all but one oxygenation step in the aglycon formation appear to occur prior to the first GT step,[5] while for the urdamycin biosynthesis the sequence of biosynthetic events (oxygen attachment at 12- and 12b-positions by UrdE and UrdM, respectively, before or after the C-glycosylation step) remained the subject of debate, and the nature of the acceptor substrate of the important C-glycosyltransferase UrdGT2 was still ambiguous.[8,11]

Here we describe our attempts to further investigate UrdGT2, to identify its acceptor substrate, and to possibly generate C-glycosidic landomycin derivatives through heterologous expression of the corresponding gene *urdGT2*. Our work has showed that the C-glycosylation in the urdamycin biosynthesis occurs prior to the two aglycon oxygenations through oxygenases UrdE and UrdM, and that the early intermediate UWM6 serves as the acceptor substrate for UrdGT2.

Regarding the oxygenases of the landomycin biosynthesis, it was found that oxygenase Lan/LndZ5 is responsible for the 11-hydroxylation,[5] and Lan/LndM2 for the 6-hydroxylation,[12] while Lan/LndE most likely catalyzes the 12-oxygenation (quinone formation), which was assumed to be the first oxygenation step in the landomycin biosynthesis. All oxygenations steps except the 11-hydroxylation occur before Lan/LndGT2 attaches the first sugar moiety. Thus we first wanted to confirm these conclusions regarding the oxygenation sequence in landomycin biosynthesis by inactivation of *lndE*, leading to the early block mutant *S. globisporus* Δ*lndE*. This mutant of the landomycin E producer accumulates prejadomycin (2,3-dehydro-UWM6; **6**), an early intermediate

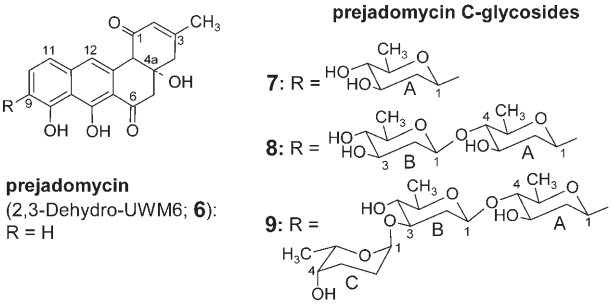

of various angucyclines and angucycline-derived compounds that was first discovered in the context of the jadomycin biosynthesis; more recently it was was also found in blocked mutants of the gilvocarcin V and the oviedomycin producers. The *S. globisporus* Δ*lndE* was obtained by directed disruption of the *lndE* gene within the chromosome of *S. globisporus* Smu622 by insertion of the hygromycin resistance cassette. The accumulation of **6** clearly supports the conclusion that LndE is the first acting oxygenase of the landomycin pathway. Moreover, the mutant *S. globisporus* Δ*lndE* appeared to be an ideal host for a heterologous expression of *urdGT2*, the gene encoding C-GT in urdamycin biosynthesis, since it provided prejadomycin (**6**), a compound almost identical to UWM6 (**10**), which was recently discussed as a possible acceptor substrate of UrdGT2,[19] as well as NDP-activated D-

 © 2006 Wiley-VCH Verlag GmbH & Co. KGaA, Weinheim

olivose, its sugar donor substrate. Moreover, the construction of an *S. globisporus* Δ*lndE* (*urdGT2*) mutant not only promised to provide information about the acceptor substrate of UrdGT2 but also would allow us to further test the promiscuity of the other *lnd/lan* glycosyltransferases, two of which (LndGT1 and LndGT4) were present in the construct along with their required NDP-activated sugar donor substrates. Finding GTs that can elongate a sugar moiety into di-, tri-, or longer saccharide chains regardless of where and how the first sugar is attached, is important for future saccharide constructs by combinatorial biosynthesis. While one such experiment was already successfully completed with LanGT1, which is closely related to LndGT1,[19] LndGT4/LanGT4 were never tested on unnatural acceptor substrates.

The *S. globisporus* Δ*lndE* (*urdGT2*) recombinant strain was constructed by introduction of plasmid pUWLurdGT2 harboring the *urdGT2* gene, which was controlled by the P*ermE* promoter through intergeneric conjugation into the Δ*lndE* mutant. The presence of the plasmid was proven by physical isolation, transfer into *E. coli* XL1-blue MRF, restriction enzyme mapping, Southern blotting with *urdGT2* amplified from the urdamycin producer *S. fradiae* Tü2717, and sequencing of the PCR product obtained from the plasmid with suitable primers for *urdGT2*. The resulting construct *S. globisporus* Δ*lndE* (*urdGT2*) was cultivated in 4 L of a soya-glucose medium, and the accumulated natural products were isolated. Three novel compounds could be isolated and their structures were elucidated using NMR spectroscopy and mass spectrometry. The mass and UV spectra revealed immediately the chromophore of the polyketide moiety to be prejadomycin.[25–27] Typical for this chromophore are the absorption maxima at $\lambda = 405$ nm and 266 nm. Furthermore, the mass spectra data reveal also the presence of three, two, and one deoxysugar moiety, respectively, because of characteristic fragmentations ($[M-115] = M-$rhodinose for the monosaccharide, $[M-115-130] = M-$rhodinose−olivose for the disaccharide, and $[M-115-130-130] = M-$rhodinose−olivose−olivose for the trisaccharide). Comparison of the NMR data with those of prejadomycin and the known landomycins[5] indicated the structures to be 9-*C*-β-D-olivosylprejadomycin (**7**, 3 mg), 9-*C*-β-D-olivosyl-1,4-β-D-olivosylprejadomycin (**8**, 9 mg), and 9-*C*-α-L-rhodinosyl-1,3-β-D-olivosyl-1,4-β-D-olivosylprejadomycin (**9**, 4.5 mg). The conformation and connectivity of the sugar units (to each other and to the polyketide core) was confirmed from 2D NMR experiments (NOESY and CIGAR-HMBC).[28,29] For instance, the anomeric 1A-H of the C-glycosidically linked D-olivose unit shows NOE couplings with 10-H, 2A-H_e, 3A-H, and 5A-H; and $^3J_{C,H}$ couplings can be observed in the CIGAR-HMBC between 1A-H and C8, C10 and C3A along with a weaker $^2J_{C,H}$ coupling with C9 (see the Supporting Information). This clearly determines this sugar to be in the $^4C_1$ conformation typical for D-sugars, attached directly at C9, and, based on the large coupling constant between 1A-H and 2A-H_a of $^3J_{H,H} = 10$ Hz, containing a β-glycosidic linkage.

In summary, the heterologous expression of gene *urdGT2* into the *lndE*-minus mutant of the landomycin E producer *S. globisporus* 1912 yielded three novel prejadomycin analogues that differ in their C-glycosidically bound moieties attached at C9. The sugar residue and oligosaccharide moieties are the same as those previously found in landomycins H (**4**), D (**3**), and E (**1**), but they are attached C-glycosidically at C9 instead of O-glycosidically at C8-O, a position shift that was expected from using UrdGT2. The glycosyl transfer step occurred on an early angucyclinone intermediate, prejadomycin (**6**), also called 2,3-dehydro-UWM6, which was found to be an intermediate of several pathways. The heterologously expressed C-glycosyl transferase UrdGT2 from the urdamycin biosynthetic pathway, but not its natural competitor, the O-GT LndGT2, which was also present, was able to glycosylate compound **6**, thereby redirecting the attachment of the landomycin sugar chain towards the C9-position. The GTs responsible for the elongation to the landomycin E trisaccharide, LndGT4 and LndGT1, could attach their sugars although the aglycon was structurally quite different and the first sugar unit was C-attached and at different position. Our results strongly suggest that UrdGT2 naturally acts on UWM6 (**10**, Scheme 1) as its acceptor substrate, which differs from prejadomycin (**6**) only by its 3-OH group. Thus the ambiguity is resolved regarding the previously not clearly identified acceptor substrate for UrdGT2, and also the C-GT step in urdamycin biosynthesis is indicated to most likely occur *prior to* the two aglycon oxygenation steps catalyzed by UrdE and UrdM (see Scheme 1).[8,19]

To find out whether prejadomycin (**6**) is an early intermediate of the landomycin pathway or an early intermediate of a shunt pathway branching from the landomycin pathway (Scheme 1), we performed a crossfeeding experiment, in which prejadomycin (**6**, obtained from *Streptomyces globisporus* Δ*lndE*) was fed to an early block mutant of the landomycin biosynthetic pathway (the *lndF* mutant F133).[12] In this mutant the PKS-associated fourth ring cyclase gene *lndF* was inactivated, and consequently it cannot produce any useful polyketides. But the mutant expresses all downstream enzymes necessary for the completion of landomycin E biosynthesis when it is fed with an intermediate containing a completely cyclized polyketide intermediate. Strain *S. globisporus* F133 was cultivated for 24 h, and prejadomycin (**6**) was fed in a single portion (2 mg). HPLC-MS monitoring (every 12 h) showed that significant amounts of landomycin E were produced. This clearly proves that prejadomycin (**6**) is also an intermediate of the landomycin pathway but cannot be glycosylated by LndGT2, since this enzyme acts strictly on a later intermediate, in which two of three oxygenation events have already occurred. Thus, the urdamycin and landomycin pathways differ significantly with regard to their first glycosylation step. For the landomycin biosynthesis, earlier evidence was found that the first glycosylation step, the O-glycosylation at 8-O with D-olivose catalyzed by LndGT2, occurred prior to the 11-hydroxylation, catalyzed by LndZ4/Z5, but after the oxygen atoms had been introduced into both the 12- and 6-positions by LndE and LndM2, respectively.[5] In particular, it was recently shown that the non-glycosylated angucyclinones tetrangomycin (**11**) and rabelomycin (**12**) can be further converted into landomycin E (**1**) by the *lndF* mutant F133, and thus **11** and **12** are biosynthetic intermedi-

 © 2006 Wiley-VCH Verlag GmbH & Co. KGaA, Weinheim

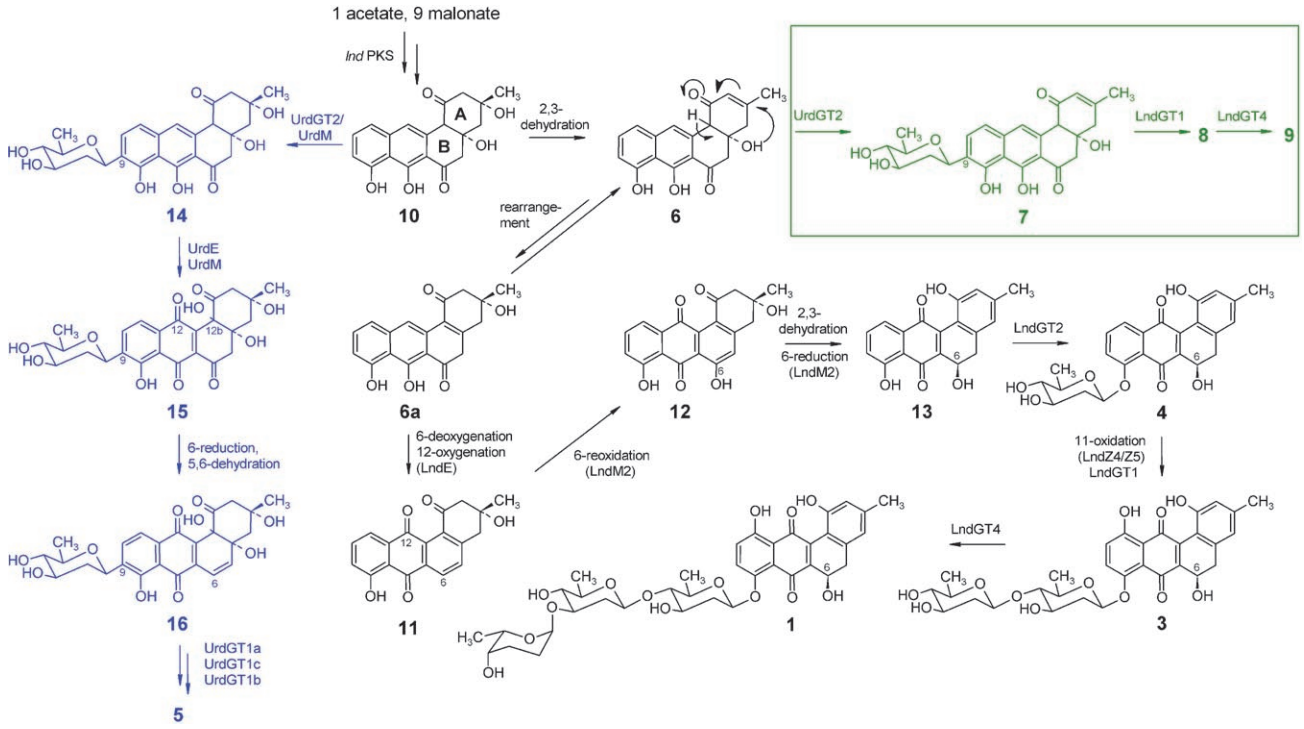

Scheme 1. Biosynthetic pathways for landomycin (black) and urdamycin (blue) and the hybrid pathway to the C-glycosylated prejadomycins **7**–**9** (green). The early urdamycin biosynthetic pathway (blue) proceeds via the hypothetical intermediates **14** and **15**.

ates.[12] The results described here confirm this description of a—compared to the urdamycin pathway—later first glycosylation step. The fact that none of the new prejadomycin C-glycosides including monoglycoside **7** could be further modified by the oxygenases that exist in *S. globisporus* Δ*lndE* (*urdGT2*), for example, by LndM2 and LndZ4/Z5, shows that these oxygenases require non-glycosylated substrates. The finding that a compound without 3-OH group, namely **6**, serves as an earlier intermediate than two compounds with 3-OH groups, namely **11** and **12**, seems contradictive. However, in studies with the overexpressed oxygenase JadH, an enzyme responsible for the 12-oxygenation in the jadomycin pathway,[25,26] prejadomycin (**6**) was in part directly converted into rabelomycin (**12**), which could be explained only by a rearrangement initiated by a Michael addition of the 4a-OH group at the 3-position.[31] Such a rearrangement was also observed by Hutchinson et al. but not explained.[30] Scheme 1 shows this rearrangement and illustrates the most probable sequences of the urdamycin and landomycin pathways. It also includes the "hybrid" pathway to the new prejadomycin C-glycosides that was initiated by the heterologously expressed UrdGT2.

Received: August 4, 2006
Published online: October 24, 2006

Keywords: biosynthesis · combinatorial biosynthesis · glycosides · landomycins · polyketides

[1] S. Weber, C. Zolke, J. Rohr, J. M. Beale, *J. Org. Chem.* **1994**, *59*, 4211.
[2] R. T. Crow, B. Rosenbaum, R. Smith III, Y. Guo, K. S. Ramos, G. A. Sulikowski, *Bioorg. Med. Chem. Lett.* **1999**, *9*, 1663.
[3] H. Depenbrock, S. Bornschlegl, R. Peter, J. Rohr, P. Schmid, P. Schweighart, T. Block, J. Rastetter, A. R. Hanauske, *Ann. Hematol.* **1996**, *73(Suppl. II)*, A80/316.
[4] S.-E. Wohlert, A. Bechthold, C. Beninga, T. Henkel, M. Holzenkämpfer, A. Kirschning, C. Oelkers, M. Ries, S. Weber, U. Weissbach, L. Westrich, J. Rohr in *Bioorganic Chemistry* (Eds.: U. Diederichsen, T. K. Lindhorst, B. Westermann, L. A. Wessjohann), Wiley-VCH, Weinheim, **1999**, p. 305.
[5] B. Ostash, U. Rix, L. L. Remsing Rix, T. Liu, F. Lombo, A. Luzhetskyy, O. Gromyko, W. C. , A. F. Braña, C. Méndez, J. A. Salas, V. Fedorenko, J. Rohr, *Chem. Biol.* **2004**, *11*, 547.
[6] A. Luzhetskyy, M. Fedoryshyn, C. Durr, T. Taguchi, V. Novikov, A. Bechthold, *Chem. Biol.* **2005**, *12*, 725.
[7] A. Trefzer, D. Hoffmeister, E. Künzel, S. Stockert, G. Weitnauer, L. Westrich, U. Rix, J. Fuchser, K. U. Bindseil, J. Rohr, A. Bechthold, *Chem. Biol.* **2000**, *7*, 133.
[8] E. Künzel, B. Faust, C. Oelkers, U. Weissbach, D. W. Bearden, G. Weitnauer, L. Westrich, A. Bechthold, J. Rohr, *J. Am. Chem. Soc.* **1999**, *121*, 11058.
[9] J. Rohr, J. M. Beale, H. G. Floss, *J. Antibiot.* **1989**, *42*, 1151.
[10] G. Udvarnoki, T. Henkel, R. Machinek, J. Rohr, *J. Org. Chem.* **1992**, *57*, 1274.
[11] U. Rix, L. L. Remsing, D. Hoffmeister, A. Bechthold, J. Rohr, *ChemBioChem* **2003**, *4*, 109.
[12] L. Zhu, B. Ostash, U. Rix, M. Nur-e-Alam, A. Mayers, A. Luzhetskyy, C. Méndez, J. A. Salas, A. Bechthold, V. Fedorenko, J. Rohr, *J. Org. Chem.* **2005**, *70*, 631.
[13] H. Decker, S. Haag, *J. Bacteriol.* **1995**, *177*, 6126.
[14] D. Hoffmeister, K. Ichinose, A. Bechthold, *Chem. Biol.* **2001**, *8*, 557.

 © 2006 Wiley-VCH Verlag GmbH & Co. KGaA, Weinheim

[15] D. Hoffmeister, K. Ichinose, S. Domann, B. Faust, A. Trefzer, G. Dräger, A. Kirschning, C. Fischer, E. Künzel, D. W. Bearden, J. Rohr, A. Bechthold, *Chem. Biol.* **2000**, *7*, 821.
[16] L. Westrich, S. Domann, B. Faust, D. Bedford, D. A. Hopwood, A. Bechthold, *FEMS Microbiol. Lett.* **1999**, *170*, 381.
[17] Y. Rebets, B. Ostash, A. Luzhetskyy, D. Hoffmeister, A. F. Braña, C. Méndez, J. A. Salas, A. Bechthold, V. Fedorenko, *FEMS Microbiol. Lett.* **2003**, *222*, 149.
[18] K. Krohn, J. Rohr, *Top. Curr. Chem.* **1997**, *188*, 127.
[19] A. Trefzer, G. Blanco, L. L. Remsing, E. Künzel, U. Rix, A. F. Braña, C. Méndez, J. Rohr, A. Bechthold, J. A. Salas, *J. Am. Chem. Soc.* **2002**, *124*, 6056.
[20] A. Luzhetskyy, A. Vente, A. Bechthold, *Mol. BioSyst.* **2005**, 117.
[21] A. Trefzer, C. Fischer, S. Stockert, L. Westrich, E. Künzel, U. Girreser, J. Rohr, A. Bechthold, *Chem. Biol.* **2001**, *8*, 1239.
[22] A. Luzhetskyy, T. Liu, M. Fedoryshyn, B. Ostash, V. Fedorenko, J. Rohr, A. Bechthold, *ChemBioChem* **2004**, *5*, 1567.
[23] A. Luzhetskyy, L. Zhu, M. Gibson, M. Fedoryshyn, C. Durr, C. Hofmann, D. Hoffmeister, B. Ostash, C. Mattingly, V. Adams, V. Fedorenko, J. Rohr, A. Bechthold, *ChemBioChem* **2005**, *6*, 675.
[24] D. Hoffmeister, B. Wilkinson, G. Foster, P. J. Sidebottom, K. Ichinose, A. Bechthold, *Chem. Biol.* **2002**, *9*, 287.
[25] U. Rix, C. Wang, Y. Chen, F. M. Lipata, L. L. Remsing Rix, L. M. Greenwell, L. C. Vining, K. Yang, J. Rohr, *ChemBioChem* **2005**, *6*, 838.
[26] Y. H. Chen, C. C. Wang, L. Greenwell, U. Rix, D. Hoffmeister, L. C. Vining, J. Rohr, K. Q. Yang, *J. Biol. Chem.* **2005**, *280*, 22508.
[27] T. Liu, C. Fischer, C. Beninga, J. Rohr, *J. Am. Chem. Soc.* **2004**, *126*, 12262.
[28] V. V. Krishnamurthy, D. J. Russell, C. E. Hadden, G. E. Martin, *J. Magn. Reson.* **2000**, *146*, 232.
[29] W. F. Reynolds, R. G. Enriquez, *J. Nat. Prod.* **2002**, *65*, 221.
[30] K. Kulowski, E. Wendt-Pienkowski, L. Han, K. Q. Yang, L. C. Vining, C. R. Hutchinson, *J. Am. Chem. Soc.* **1999**, *121*, 1786.
[31] M. K. Kharel, C. Wang, J. Rohr, unpublished results.

 © 2006 Wiley-VCH Verlag GmbH & Co. KGaA, Weinheim

Host–Guest Systems

DOI: 10.1002/anie.200602892

Unprecedented Insight into Diffusion by Monitoring the Concentration of Guest Molecules in Nanoporous Host Materials**

Jörg Kärger, Pavel Kortunov, Sergey Vasenkov, Lars Heinke, Dhananjai B. Shah, Rainer A. Rakoczy, Yvonne Traa, and Jens Weitkamp**

Nanoporous materials[1] may be visualized as sponges with holes of molecular dimensions. They are a key to novel and environmentally friendly technologies for the isolation of value-added products through heterogeneous catalysis and mass separation.[2–4] They also offer potential for gas sensors and opto-electronic devices.[5–7] Recent progress in synthesis methods has led to an explosion in the number of structure types[8] and, thus, to a broad spectrum of nanoporous materials.

To understand the functionality of these host materials, knowledge of the distribution of adsorbed guest molecules and its temporal evolution are necessary. A number of techniques, broadly classified as either macroscopic or microscopic, are available for characterizing diffusion in porous materials. However, conventional techniques, such as uptake and release experiments,[9,10] are not capable of providing information on the temporal evolution of internal concentration profiles. These techniques measure changes in macroscopic properties, from which information about the intrinsic processes must be deduced on the basis of numerous model assumptions.[11]

Nor is the required information about internal concentration profiles accessible by microscopic techniques such as quasi-elastic neutron scattering[10,12] and pulsed field gradient (PFG) NMR spectroscopy,[10,13] since these methods measure

[*] Prof. Dr. J. Kärger, Dr. P. Kortunov, L. Heinke
Fakultät für Physik und Geowissenschaften
Universität Leipzig
Linnéstrasse 5, 04103 Leipzig (Germany)
Fax: (+49) 341-97-32-549
Homepage: http://www.grenzflaechenphysik.de

Prof. Dr. S. Vasenkov
Department of Chemical Engineering
University of Florida, P.O. Box 116005
Gainesville, FL 32611-6005 (USA)

Prof. Dr. D. B. Shah
Department of Chemical & Biomedical Engineering
Cleveland State University, 2121 Euclid Avenue
Cleveland, OH 44115 (USA)

Dr. R. A. Rakoczy, Dr. Y. Traa, Prof. Dr. J. Weitkamp
Institute of Chemical Technology
Universität Stuttgart
70550 Stuttgart (Germany)
Fax: (+49) 711-685-64065
E-mail: jens.weitkamp@itc.uni-stuttgart.de

[**] We gratefully acknowledge financial support from the Deutsche Forschungsgemeinschaft.

 WILEY InterScience DISCOVER SOMETHING GREAT

© 2006 Wiley-VCH Verlag GmbH & Co. KGaA, Weinheim

only the average molecular displacements in the sample. NMR imaging techniques (such as MR tomography),[13] which have become indispensable in medical diagnosis, are still far from the necessary spatial (down to micrometers) and temporal (down to seconds) resolution.

From this point of view, the introduction of interference microscopy to zeolite science has been a breakthrough.[14,15] The technique is based on the principle that the optical density of zeolite crystallites (or other transparent media) depends on the amount and nature of the guest molecules. As a consequence, the phase shift between two light beams, one passing through the crystal and the other through the surrounding atmosphere, is a measure of the average guest concentration along the direction of the light beam through the crystal. The mean concentration (that is, the total amount of molecules in the beam direction) can be deduced by analyzing the interference pattern of the two beams. The experimental method is illustrated in Figure 1.

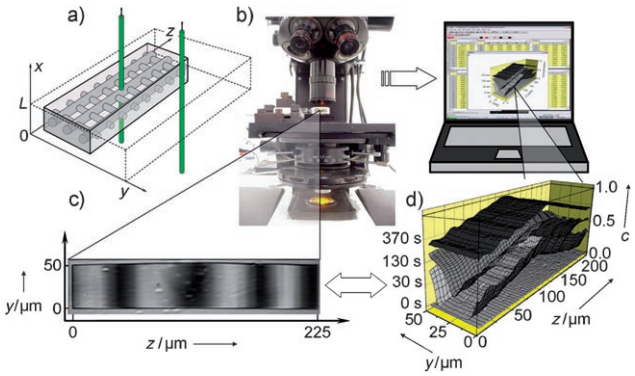

Figure 1. Interference microscopy. a) Two light beams, one passing through the crystal and the other through the surrounding atmosphere ($L \approx 10$ μm). b) The interference microscope. c) Interference pattern arising from the two beams passing through media with different optical properties. d) Concentration profiles at different times, calculated from interference patterns.

The introduction of interference microscopy to zeolite science and technology has far-reaching consequences, since it allows the in situ detection of the spatial evolution of the concentration distribution in solid host systems. As a result, for the first time, experimentally measured concentration profiles can be directly compared with the predictions of the classical Fick's equations. According to Fick's first law [Eq. (1)], the particle flux j is proportional to the gradient of the particle concentration c. In general, the proportionality factor, the (transport) diffusivity D, is a function of particle concentration. To predict the evolution of the concentration distribution $c(x,t)$, Equation (1) is combined with the law of conservation of matter [Eq. (2)], yielding Fick's second law [Eq. (3)].

$$j = -D\frac{\partial c}{\partial x} \tag{1}$$

$$\frac{\partial c}{\partial t} = -\frac{\partial j}{\partial x} \tag{2}$$

$$\frac{\partial c}{\partial t} = \frac{\partial}{\partial x}\left(D(c(x))\frac{\partial c}{\partial x}\right) = \frac{\partial D}{\partial c}\left(\frac{\partial c}{\partial x}\right)^2 + D(c(x))\frac{\partial^2 c}{\partial x^2} \tag{3}$$

For simplicity, Equations (1) to (3) have been written for the special case of a one-dimensional concentration profile. Concentration gradients cannot be determined along the direction of observation by using interference microscopy, owing to its measuring principle. The situation described by Equation (3) (with x as a coordinate along an axis perpendicular to the light beam and, therefore, to the observation direction) correctly represents our experimental conditions, as is demonstrated below.

We performed adsorption and desorption experiments with methanol on a ferrierite zeolite, the structure of which is depicted in Figure 2a, and determined the concentration

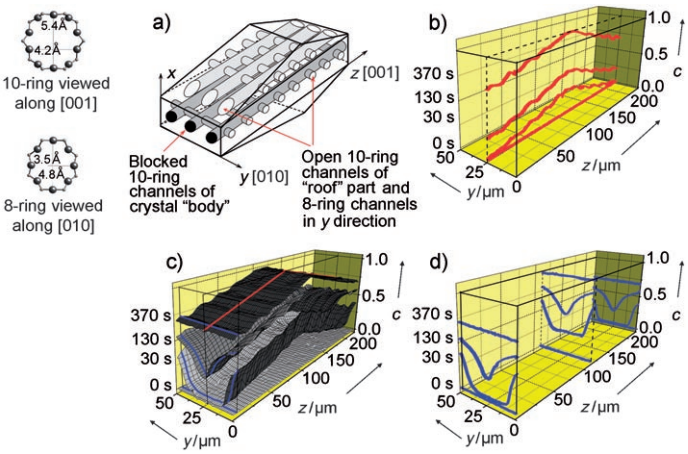

Figure 2. Temporal evolution of concentration profiles of methanol in a ferrierite crystal for a pressure step from 0 to 80 mbar. a) Shape and pore structure of the ferrierite crystal. b) Concentration profiles in the z direction at $y = 25$ μm. c) Two-dimensional concentration profiles in the y and z directions. d) Concentration profiles in the y direction at the center of the crystal ($z = 120$ μm) and at two locations near the edges. A relative concentration of 1.0 corresponds to the equilibrium concentration of methanol in ferrierite at 80 mbar.

profiles of methanol in the crystal interior. The ferrierite crystal was activated under high vacuum at a temperature of 673 K for 4 h. To ensure the complete removal of organic residues, the sample was heated in an oxygen atmosphere at 973 K for 4 h prior to the activation. The observed adsorption profiles, which are presented in Figure 2b–d, yield two astonishing results:

a) Almost immediately after the onset of adsorption, a concentration profile associated with the rooflike part of the crystal is established. During desorption, this part of the profile disappears equally rapidly.
b) Concentration gradients, which indicate the direction of mass transfer into the crystal during adsorption and out of the crystal during desorption, are observed exclusively in the y direction for the central part of the crystal.

Both of these results can be unambiguously attributed to the particular features of the channels that run along the z direction of the ferrierite crystal. These channels are surrounded by 10-rings (formed by 10 silicon and 10 oxygen atoms). As the channels that run along the y direction of the

 © 2006 Wiley-VCH Verlag GmbH & Co. KGaA, Weinheim

ferrierite crystal are composed of smaller 8-rings, intracrystalline mass transfer is expected to proceed much faster in the z direction. Thus, the rooflike part of the crystal is occupied by guest molecules immediately after the onset of adsorption and is emptied immediately after the onset of desorption (result (a)). The occurrence of such high-speed transport processes in channels of molecular dimensions has been reported several times.[16]

Another interesting feature of the concentration profiles is that in the central parallelepiped part of the crystal, there are no concentration gradients (and hence no fluxes) in the z direction. Apparently, the channels along the z direction are blocked in this part of the crystal, whereas they are wide open in the rooflike part of the crystal, which is defined by inclined faces. The formation of similar pore or channel blockages is a relatively common structural feature of nanoporous materials.[5] As a consequence of this blockage, any mass transfer in the central (and by far the largest) part of the crystal can only occur in the y direction, along the 8-ring channels, as indicated by the concentration gradients (result (b)). This particular pattern of pore blocking in ferrierite leads to the situation that mass transfer in the main part of the crystal occurs only in the y direction, even though the molecular mobility (diffusivity) is much larger in the z direction because of the larger pore size. Electron microscopy studies of intracrystalline guest concentrations have found analogous patterns of guest distribution in ferrierite.[17]

An extensive set of internal concentration profiles have been measured as a function of time. The concentration profiles for a pressure step from 0 to 5 mbar at different times during the adsorption of methanol in a ferrierite crystal are shown in Figure 3. The concentration profiles obtained in this manner are much more informative than similar profiles that have previously been obtained for diffusion in solids[18,19] and fluids.[20] Moreover, interference microscopy is nondestructive and is an ideal method for in situ measurements.

We can now use the temporal evolution of the concentration profiles to determine diffusivities through the microscopic application of Fick's laws. The knowledge of the concentration profiles at different times allows us to calculate the rate of change of concentration with time ($\frac{\partial c}{\partial t}$) at any coordinate y, as well as the first and second spatial derivatives of the concentration ($\frac{\partial c}{\partial y}$ and $\frac{\partial^2 c}{\partial y^2}$) at any y and t. The diffusivities were determined from the profiles in two steps. In the first step, diffusivities were calculated at the center of the concentration profiles, because at this position all of the profiles are flat (with slopes of zero). Hence, Equation (3) has only two terms, and D can be calculated from the knowledge of $\frac{\partial c}{\partial t}$ and $\frac{\partial^2 c}{\partial y^2}$. The result provides an initial estimate of the variation of the diffusivity with concentration. In the second step, this information is used in conjunction with the shapes of the profiles at other locations to obtain better estimates of the diffusivities and their dependence on concentration. This type of analysis opens up a completely new avenue for the microscopic determination of diffusivities. Since local diffusivity is a direct indicator of structural peculiarities, important structural information that was previously obscured is now available.

Several features of the experimental technique and analysis require further explanation. The concentration profiles shown in Figure 3 were determined from the two-dimensional data sets in Figure 2c, and these were determined from the primary interference patterns (Figure 1c) by taking the weighted averages over adjacent data points. As a consequence of this necessary smoothing procedure, minor structural defects, such as occur in highly structured materials,[5] may be masked. In particular, mass transfer in the x direction, which is not possible in the ideal structure of ferrierite (Figure 2a), but which may occur due to structural defects, may be hidden. Moreover, in the analysis according to Fick's second law, a complete homogeneity of the crystal is assumed; that is, the diffusivity $D(c,x)$ is assumed to be solely a function of concentration $D(c)$, which is the same throughout the crystal. Because of all these considerations, perfect agreement between theory and experiment is not likely.

Figure 4 provides an overview of the diffusivities determined from the various uptake and release experiments. The intracrystalline diffusivity is a strong function of concentration and varies by nearly two orders of magnitude. In Figure 4, as in all other Figures, the concentration is expressed as a

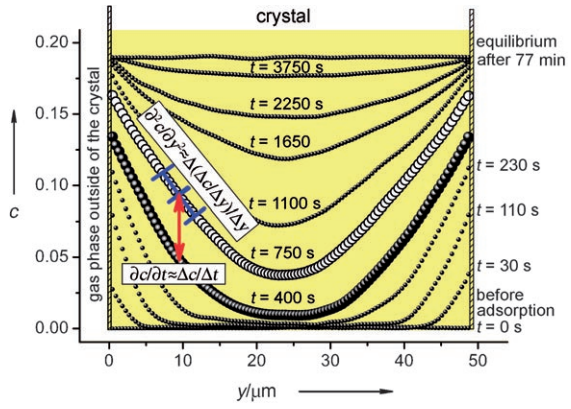

Figure 3. Temporal evolution of concentration profiles of methanol in the y direction in the ferrierite crystal (near the edge, at $z = 2$ μm) for a pressure step from 0 to 5 mbar. The method of evaluating the terms $\frac{\partial^2 c}{\partial y^2}$ and $\frac{\partial c}{\partial t}$ is also indicated.

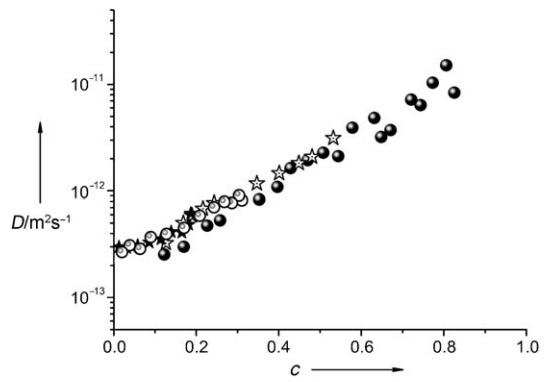

Figure 4. Diffusivities evaluated as a function of concentration for different pressure steps: desorption from 5 to 0 mbar (filled stars), desorption from 10 to 0 mbar (open spheres), adsorption from 0 to 20 mbar (open stars), and desorption from 40 to 0 mbar (filled spheres).

 © 2006 Wiley-VCH Verlag GmbH & Co. KGaA, Weinheim

fraction of the equilibrium concentration of methanol adsorbed by ferrierite at 80 mbar, which is estimated from our work and published data[21] to be $0.163\,cm^3\,g^{-1} \approx 4\,mmol\,g^{-1} \approx 8.5$ molecules/unit cell. All experiments consisted of consecutive cycles of adsorption and desorption on the same single crystal,[22] a technique which is unprecedented.

We have verified the calculated values of diffusivity by comparing the experimental concentration profiles (Figure 3) with those calculated from the numerical solution of Fick's second law using the estimated $D(c)$ values (Figure 4). The excellent agreement between the two sets of profiles for both adsorption and desorption validates the method of analysis.

Thus, the information obtained on the temporal evolution of the internal concentration profiles leads to fully self-consistent results for the relevant transport parameters, namely, the concentration dependence of the intracrystalline diffusivity. In view of the increasing number and variety of nanoporous materials, the application spectrum of this new method for the investigation of diffusion and internal pore structure is essentially unlimited.

The practical relevance of this finding is illustrated by considering adsorption and desorption under the conventional conditions of uptake and release experiments. The information available from uptake experiments (transient sorption curves) can also be obtained by integrating the concentration profiles corresponding to the central part of the crystal. The transient sorption curves determined in this manner agree well with theoretical predictions based on the microscopically determined ("differential") diffusivities. However, there is no way to determine the differential diffusivities from the sorption curves. With the microscopic diffusion measurements reported herein, precisely these quantities can now be determined, offering new prospects for diffusion measurements on nanoporous materials.

Received: July 19, 2006
Published online: October 24, 2006

Keywords: host–guest systems · interference microscopy · micropore diffusion · nanoporous materials · zeolites

[1] F. Schüth, K. S. W. Sing, J. Weitkamp, *Handbook of Porous Solids*, Wiley-VCH, Weinheim, **2002**.
[2] S. M. Kuznicki, V. A. Bell, S. Nair, H. W. Hillhouse, R. M. Jacubinas, C. M. Braunbarth, B. H. Toby, M. Tsapatsis, *Nature* **2001**, *412*, 720.
[3] Z. Lai, G. Bonilla, I. Diaz, J. G. Nery, K. Sujaoti, M. A. Amat, E. Kokkoli, O. Terasaki, R. W. Thompson, M. Tsapatsis, D. G. Vlachos, *Science* **2003**, *300*, 456.
[4] M. E. Davis, *Science* **2003**, *300*, 438.
[5] F. Laeri, F. Schüth, U. Simon, M. Wark, *Host–Guest Systems Based on Nanoporous Crystals*, Wiley-VCH, Weinheim, **2003**.
[6] M. E. Davis, *Nature* **2002**, *417*, 813.
[7] M. Tsapatsis, *AIChE J.* **2002**, *48*, 654.
[8] M. Sumper, E. Brunner, *Adv. Funct. Mater.* **2006**, *16*, 17.
[9] N. Y. Chen, T. F. Degnan, C. M. Smith, *Molecular Transport and Reaction in Zeolites*, VCH, New York, **1994**.
[10] J. Kärger, D. M. Ruthven, *Diffusion in Zeolites and Other Microporous Solids*, Wiley, New York, **1992**.
[11] J. Kärger, S. Vasenkov, *Microporous Mesoporous Mater.* **2005**, 85, 195.
[12] H. Jobic, *Curr. Opin. Solid State Mater. Sci.* **2002**, 6, 415.
[13] P. T. Callaghan, *Principles of NMR Microscopy*, Clarendon Press, Oxford, **1991**.
[14] E. Lehmann, S. Vasenkov, J. Kärger, G. Zadrozna, J. Komatowski, Ö. Weiss, F. Schüth, *J. Phys. Chem. B* **2003**, *107*, 4685.
[15] J. Kärger, R. Valiullin, S. Vasenkov, *New J. Phys.* **2005**, *7*, 15.
[16] S. Jakobtorweihen, M. G. Verbeek, C. P. Lowe, F. J. Keil, B. Smit, *Phys. Rev. Lett.* **2005**, *95*, 044501.
[17] S. van Donk, J. H. Bitter, A. Verberckmoes, M. Versluijs-Helder, A. Broersma, K. P. de Jong, *Angew. Chem.* **2005**, *117*, 1384; *Angew. Chem. Int. Ed.* **2005**, *44*, 1360.
[18] M. E. Glicksman, *Diffusion in Solids*, Wiley, New York, **1999**.
[19] H. Mehrer in *Diffusion in Condensed Matter: Methods, Materials, Models* (Eds: P. Heitjans, J. Kärger), Springer, Berlin, **2005**, p. 3.
[20] H. J. V. Tyrrell, R. K. Harris, *Diffusion in Liquids*, Butterworth, London, **1984**.
[21] Y. Long, M. Ma, Y. Sun, H. Jiang, *J. Inclusion Phenom. Macrocyclic Chem.* **2000**, *37*, 103.
[22] P. Kortunov, "Rate Controlling Processes of Diffusion in Nanoporous Materials", Dissertation, Universität Leipzig (Germany), **2005**.

 © 2006 Wiley-VCH Verlag GmbH & Co. KGaA, Weinheim

Cover Picture

Ulrich Klar,* Bernd Buchmann, Wolfgang Schwede, Werner Skuballa, Jens Hoffmann, and Rosemarie B. Lichtner

Nature is a brilliant architect for the design of compounds with interesting biological functions. Epothilone B (top), a metabolite of myxobacteria (fruiting body in background), served as the lead structure for the development of an anticancer drug candidate. Optimization efforts led to ZK-EPO (bottom) as a candidate for clinical development. ZK-EPO has an improved therapeutic window and is not recognized by multidrug-resistance efflux pumps. Its total synthesis starting from simple compounds (blue) is described by U. Klar et al. on page 7942 ff.

Anion Coordination
Crystallographic data are used to categorize the coordination modes of anions with amide-based ligands according to coordination number and geometry. This classification is explained by K. Bowman-James and co-workers in the Minireview on page 7882 ff.

Gold Catalysis
Gold is equally effective as a heterogeneous and a homogeneous catalyst. An account of the chemistry of gold catalysis, with particular emphasis on redox reactions and nucleophilic additions, is found in the Review by A. S. K. Hashmi and G. J. Hutchings on page 7896 ff.

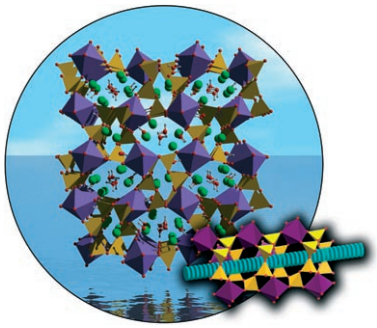

Chiral Microporous Materials
In their Communication on page 7938 ff., J. Rocha et al. describe the discrimination of enantiomeric domains in microporous lanthanide silicates with unpolarized light and in the absence of external fields. This phenomenon could be important in the interaction of light with condensed matter.

Contents

VIP *The following Communications have been judged by at least two referees to be "very important papers" and will be published online at www.angewandte.org soon:*

*E. Terreno, C. Cabella, C. Carrera, D. D. Castelli, R. Mazzon, S. Rollet, J. Stancanello, M. Visigalli, S. Aime**
From "Spherical" to "Osmotically Shrinked" Paramagnetic Liposomes: An Improved Generation of LIPOCEST MRI Agents with Highly Shifted Water Protons

*W. H. Bernskoetter, E. Lobovsky, P. J. Chirik**
Nitrogen–Carbon Bond Formation from N_2 and CO_2 Promoted by a Hafnocene Dinitrogen Complex Leads to the Liberation of a Substituted Hydrazine

J. A. Teprovich, Jr., E. Prasad, R. A. Flowers II**
Solvation-Controlled Luminescence of Sm^{II} Complexes

*Y. Xiong, J. M. McLellan, Y. Yin, Y. Xia**
Synthesis of Palladium Icosahedrons with a Twinned Structure by Blocking Oxidative Etching with Citric Acid or Citrate Ion

*X. Liu, L. Shi, W. Niu, H. Li, G. Xu**
Environmentally Friendly and Highly Sensitive Ruthenium(II) Tris(2,2'-bipyridyl) Electrochemiluminescent System Using 2-(Dibutylamino)ethanol as Co-reactant

*L.-M. Yan, A. Velkova, M. Tatarek-Nossol, E. Andreetto, A. Kapurniotu**
Designed IAPP Mimic Blocks Aβ Cytotoxic Self-Assembly: Cross-Suppression of Amyloid Toxicity of Aβ and IAPP Suggests a Molecular Link between Alzheimer's Disease and Type 2 Diabetes

News

Polymer Chemistry: J. M. J. Fréchet awarded ——— **7872**

Catalysis: H.-J. Freund honored ——— **7872**

Carbohydrate Chemistry: Prize to P. Sinaÿ ——— **7872**

Books

Soft Matter — Gerhard Gompper, Michael Schick — *reviewed by M. Ballauff* ——— **7874**

Introduction to Microfluidics — Patrick Tabeling — *reviewed by K. Jacobs* ——— **7875**

Highlights

Organocatalysis

C. Palomo,* A. Mielgo ——— **7876 – 7880**

Diarylprolinol Ethers: Expanding the Potential of Enamine/Iminium-Ion Catalysis

Organocatalysts based on diarylprolinol ethers mediate a broad range of reactions involving enamine or iminium-ion activation or a combination of both. The reactions are characterized by efficient steric control of the approach of the respective electrophile/nucleophile to the enamine/iminium-ion counterpart, thus complementing reactions involving hydrogen-bond donors as directing key elements.

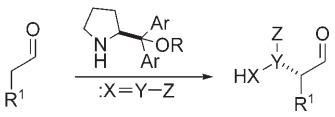

WILEY InterScience DISCOVER SOMETHING GREAT
© 2006 Wiley-VCH Verlag GmbH & Co. KGaA, Weinheim

Minireviews

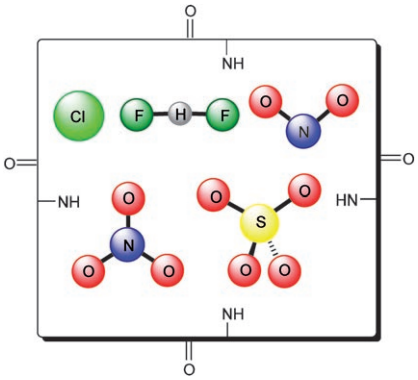

Coordinating anions: The coordination chemistry of anions with amide-based ligands is described on the basis of crystallographic data for simple anions of five different shapes: spherical, linear, V-shaped, trigonal planar, and tetrahedral. Binding data are also provided where available. The examples are arranged according to coordination number and geometry, and correlations are made to transition-metal coordination complexes.

Anion Coordination

S. O. Kang, R. A. Begum, K. Bowman-James* ——— **7882 – 7894**

Amide-Based Ligands for Anion Coordination

Reviews

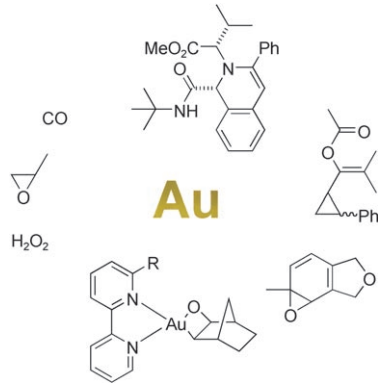

Gold fever: Gold, long considered an immutable nonreactive metal, can in fact display remarkable catalytic activity as both a homogeneous and a heterogeneous catalyst when present as soluble complexes of gold(I), gold(III), or highly dispersed nanocrystals (see examples of the range of compounds that can be formed).

Gold Catalysis

A. S. K. Hashmi,* G. J. Hutchings* ——— **7896 – 7936**

Gold Catalysis

Communications

Chiral microporous lanthanide silicates $Na_3[(Y,Ln)Si_3O_9]\cdot 3H_2O$ (**1**; Ln = Eu, Tb, Er, Ce) have enantiomeric domains that can be discriminated by means of Eu^{3+} photoluminescence spectroscopy. In the framework of **1** (see picture), $(Si_3O_9)_\infty$ spiral chains interconnect the $\{(Y,Ln)O_6\}$ octahedra, and channels along [100] contain Na^+ ions and water molecules. Color code: $\{(Y,Ln)O_6\}$ yellow; $\{SiO_4\}$ green; O red; Na purple; H white.

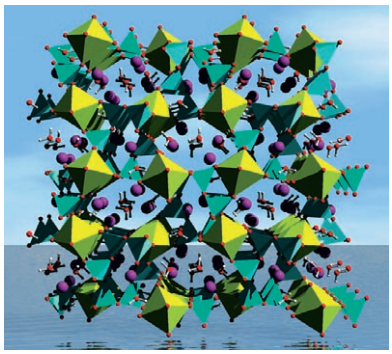

Lanthanide Silicates

D. Ananias, F. A. Almeida Paz, L. D. Carlos, C. F. G. C. Geraldes, J. Rocha* ——— **7938 – 7942**

Optical Detection of Solid-State Chiral Structures with Unpolarized Light and in the Absence of External Fields

For the USA and Canada:
ANGEWANDTE CHEMIE International Edition (ISSN 1433-7851) is published weekly by Wiley-VCH PO Box 191161, D 69451 Weinheim, Germany. Air freight and mailing in the USA by Publications Expediting Inc. 200 Meacham Ave., Elmont, NY 11003. Periodicals postage paid at Jamaica NY 11431. US POSTMASTER: send address changes to *Angewandte Chemie*, Wiley-VCH, 111 River Street, Hoboken, NJ 07030. Annual subscription price for institutions: US$ 5685/5168 (valid for print and electronic / print or electronic delivery); for individuals who are personal members of a national chemical society prices are available on request. Postage and handling charges included. All prices are subject to local VAT/sales tax.

© 2006 Wiley-VCH Verlag GmbH & Co. KGaA, Weinheim

The best in chemistry –

for more than a hundred years

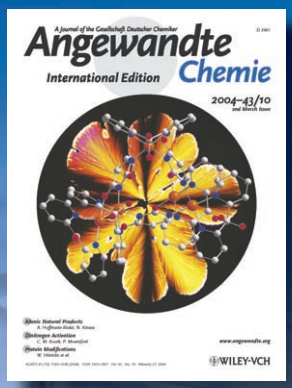

A Journal of the Gesellschaft Deutscher Chemiker

Angewandte
International Edition **Chemie**

www.angewandte.org

1888: ***The beginning of a success story***

Constant Innovations

1962: First issue of the International Edition
1976: Graphical abstracts
1979: Cover pictures
1988: Centenary of Angewandte
1989: Routine use of color
1991: New section: Highlights
1992: Computerized editorial tracking system
1995: Internet service for readers
1998: Regular press service; full-text online
2000: New section: Essays; EarlyView: Communications available online ahead of the printed version
2001: New section: Minireviews
2002: Online submission of manuscripts
2003: Weekly publication; new section: News; new layout
2004: Backfiles (1962-1997); ManuscriptXpress: Online system for authors and referees

Angewandte's advisors...

Seiji Shinkai
Kyushu University, Fukuoka

*» **Angewandte Chemie** is my favorite journal and I am honored to serve on its International Advisory Board. The research essence of an article can be understood rapidly because text and illustrations are finely harmonized. Furthermore, the high quality contents, which have a strong impact, are published very quickly. «*

Angewandte Chemie International Edition *is a journal of the German Chemical Society (GDCh)*

GDCh

WILEY InterScience® DISCOVER SOMETHING GREAT

WILEY-VCH

1190140_4_gu

Going to trial: From about 350 active epothilone analogues synthesized by a highly convergent synthesis, one (ZK-EPO, see picture) has been chosen for clinical development on the basis of its outstanding preclinical data. This compound exhibits higher activity and efficacy than taxanes (e.g. paclitaxel) and second-generation epothilones, a fast and efficient cellular uptake, no recognition by efflux mechanisms, and an improved therapeutic window.

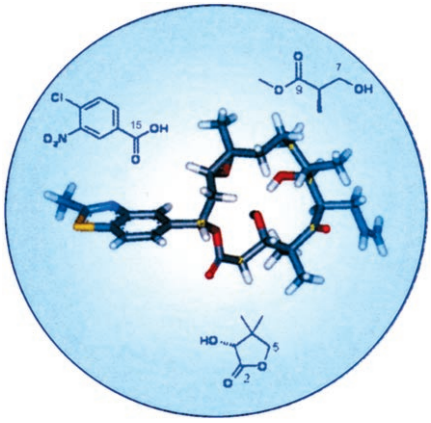

Natural Products

U. Klar,* B. Buchmann, W. Schwede, W. Skuballa, J. Hoffmann, R. B. Lichtner ——— **7942 – 7948**

Total Synthesis and Antitumor Activity of ZK-EPO: The First Fully Synthetic Epothilone in Clinical Development

A wheel surprise: Reaction of resorcinol and 1,5-pentanedial in ethanol at 80 °C for 48 h in the presence of HCl surprisingly afforded a soluble cyclic oligomer in high yield (83 %) under thermodynamic control. Single-crystal X-ray analysis revealed a waterwheel-like structure with a large hydrophobic hole through the center (see picture). A carboxylic ester derivative of the compound was shown to be highly selective for Rb^+ ions.

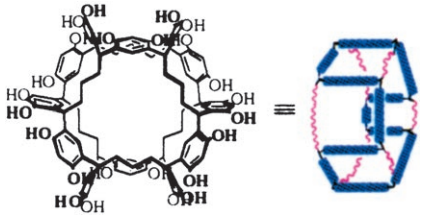

Macrocycle Synthesis

H. Kudo, R. Hayashi, K. Mitani, T. Yokozawa, N. C. Kasuga, T. Nishikubo* ——— **7948 – 7952**

Molecular Waterwheel (Noria) from a Simple Condensation of Resorcinol and an Alkanedial

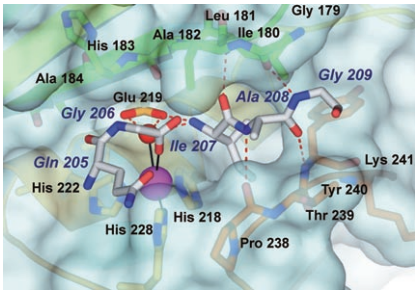

The series of events that occur in the catalytic cycle of matrix metalloproteinases were modeled on the basis of X-ray crystal structures of the active, uninhibited enzymes and of the same enzymes following the hydrolysis of a peptide substrate. After the peptide bond has been broken, both peptide fragments remain bound to the protein initially (see structure of the active-site cavity of the enzyme MMP-12 immediately after substrate hydrolysis).

Enzyme Mechanisms

I. Bertini,* V. Calderone, M. Fragai, C. Luchinat, M. Maletta, K. J. Yeo ——— **7952 – 7955**

Snapshots of the Reaction Mechanism of Matrix Metalloproteinases

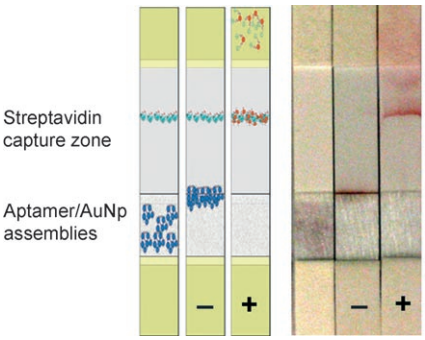

A quick plunge: By using lateral flow devices as a platform to separate aptamer-assembled nanoparticle (NP) aggregates, highly sensitive and selective colorimetric sensors were constructed that mimic litmus paper tests. Detection of cocaine in serum was also realized.

Sensors

J. Liu, D. Mazumdar, Y. Lu* ——— **7955 – 7959**

A Simple and Sensitive "Dipstick" Test in Serum Based on Lateral Flow Separation of Aptamer-Linked Nanostructures

© 2006 Wiley-VCH Verlag GmbH & Co. KGaA, Weinheim

Contents

Protein Analysis

E. Oh, D. Lee, Y. P. Kim, S. Y. Cha, D. B. Oh, H. A. Kang, J. Kim, H. S. Kim* ——— **7959 – 7963**

Nanoparticle-Based Energy Transfer for Rapid and Simple Detection of Protein Glycosylation

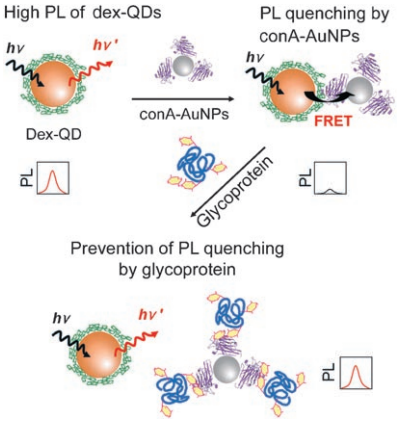

Photoluminescence quenching of dextran-conjugated quantum dots (dex-QDs) by gold nanoparticles conjugated with concanavalin A (conA-AuNPs) can be prevented by adding a glycoprotein, which inhibits the association of dex-QDs with conA-AuNPs (see scheme). This phenomenon can be used as an analytical tool for the detection of protein glycosylation. PL = photoluminescence.

Host–Guest Systems

J. Wang, D. Wang,* N. S. Sobal, M. Giersig, M. Jiang, H. Möhwald ——— **7963 – 7966**

Stepwise Directing of Nanocrystals to Self-Assemble at Water/Oil Interfaces

Included in the meeting: The specific inclusion of adamantane by cyclodextrins is used to direct nanocrystals to self-assemble into macroscopic monolayers at the water/oil interface. The use of functionalized cyclodextrins allows stepwise interfacial self-assembly of different nanocrystals into macroscopic heterogeneous multilayers (see picture).

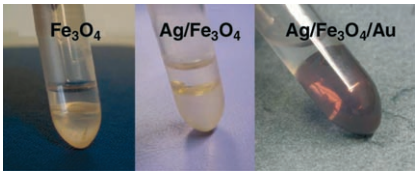

Crystal Design

M. Wenger, J. Bernstein* ——— **7966 – 7969**

Designing a Cocrystal of γ-Amino Butyric Acid

It takes two: The possibility of developing a strategy for the controlled preparation of cocrystals (see picture) with a predesigned structure is demonstrated. It relies on recognizing and utilizing a specific hydrogen-bond pattern, defined in graph-set notation ($R_4^2(8)$), as a supramolecular synthon for the systematic generation of individual four-molecule clusters.

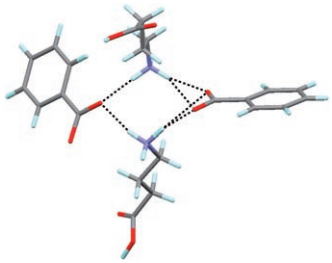

Ozonides

H. Nuss, M. Jansen* ——— **7969 – 7972**

$Cs_5([12]crown\text{-}4)_2(O_3)_5$: A Supramolecular Compound Containing the Confined Ozonide Partial Structure $^1_\infty\{Cs_8(O_3)_{10}\}^{2-}$

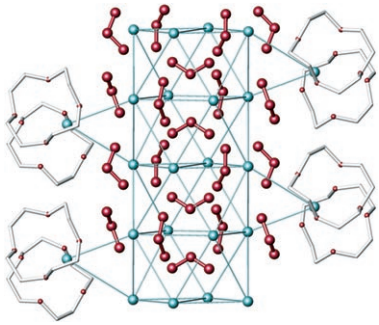

Rod-shaped: The supramolecular ozonide $Cs_5([12]crown\text{-}4)_2(O_3)_5$ contains a distorted tetragonal packing of $^1_\infty\{Cs_8(O_3)_{10}\}^{2-}$ rods separated by $[Cs([12]crown\text{-}4)_2]^+$ units (see picture; Cs blue, C gray, O red). This packing arrangement leads to the shortest intermolecular O···O distance yet observed between adjacent ozonide ions in the solid state.

© 2006 Wiley-VCH Verlag GmbH & Co. KGaA, Weinheim

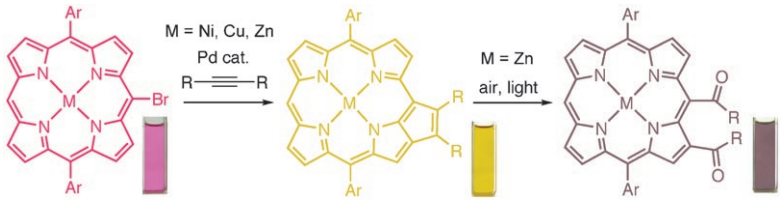

Going round the outside: The palladium-catalyzed coupling of meso-bromoporphyrins with a variety of internal alkynes efficiently provides peripherally cyclopentadiene-fused porphyrins. This modification has a significant impact on the electronic system of the porphyrin rings (see scheme), which results in non-porphyrin-like absorption spectra and narrower HOMO–LUMO gaps. Oxidation of the outer C=C bond is facilitated by the induced strain.

Porphyrinoids

A. K. Sahoo, S. Mori, H. Shinokubo,* A. Osuka* ——— 7972 – 7975

Facile Peripheral Functionalization of Porphyrins by Pd-Catalyzed [3+2] Annulation with Alkynes

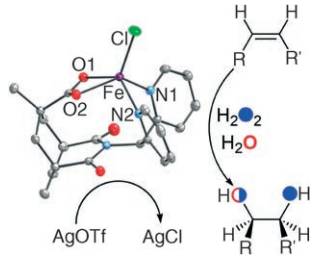

An attractive model: The iron complex shown on the left models the 2-His-1-carboxylate active sites of Rieske dioxygenases both in terms of structure and function. ^{18}O-labeling studies of olefin dihydroxylation support the involvement of a high-valent iron-oxo species.

Enzyme Models

P. D. Oldenburg, C.-Y. Ke, A. A. Tipton, A. A. Shteinman, L. Que, Jr.* 7975 – 7978

A Structural and Functional Model for Dioxygenases with a 2-His-1-carboxylate Triad

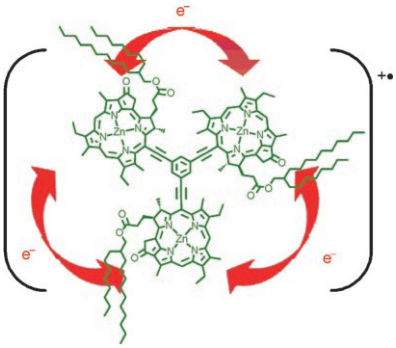

Share and share alike: Chlorophylls are appended to rigid linkers with threefold symmetry. The efficiency of both energy and charge transfer between the chlorophylls is controlled by the structure of the central linker. Direct chlorophyll–ethynyl linkage facilitates charge sharing between all three chlorophylls on the EPR/ENDOR timescale (10^7 Hz). ENDOR = electron nuclear double resonance.

Electron Transfer

R. F. Kelley, M. J. Tauber, M. R. Wasielewski* ——— 7979 – 7982

Linker-Controlled Energy and Charge Transfer within Chlorophyll Trefoils

Whole scheme of things: The kinetics and efficiency of photoinduced hole transport across DNA A tracts with 1–7 base pairs have been determined from femtosecond transient absorption spectroscopic data. These values are strongly distance dependent over the first four base pairs, but are relatively insensitive to distance at longer distances. These kinetic results (□, ■) parallel the DNA-strand-cleavage results of Giese et al. (○, ●).

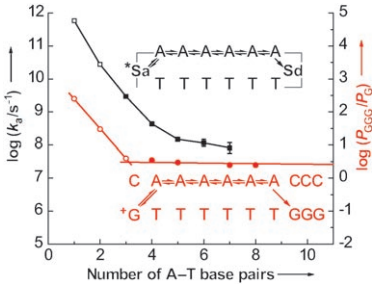

Electron Transfer

F. D. Lewis,* H. Zhu, P. Daublain, B. Cohen, M. R. Wasielewski* ——— 7982 – 7985

Hole Mobility in DNA A Tracts

© 2006 Wiley-VCH Verlag GmbH & Co. KGaA, Weinheim

Contents

Enantiomeric Enrichment

M. Klussmann,* A. J. P. White, A. Armstrong, D. G. Blackmond* _____ 7985 – 7989

Rationalization and Prediction of Solution Enantiomeric Excess in Ternary Phase Systems

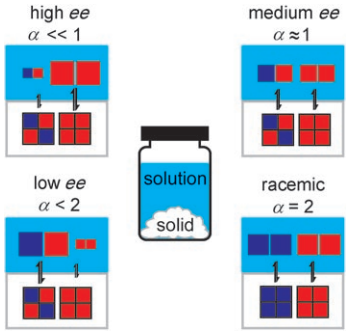

Solubility and enantiomeric excess: A general model based on simple solubility concepts rationalizes the value of the *ee* at the eutectic for a wide range of chiral substances including amino acids and common chiral ligands. A novel crystal structure in which one $CHCl_3$ molecule is incorporated in a highly insoluble ($\alpha = 0.002$) proline racemate explains the strong asymmetric amplification observed in the proline/$CHCl_3$ system.

Asymmetric Catalysis

M. Klussmann, S. P. Mathew, H. Iwamura, D. H. Wells, Jr., A. Armstrong, D. G. Blackmond* _____ 7989 – 7992

Kinetic Rationalization of Nonlinear Effects in Asymmetric Catalysis Based on Phase Behavior

A model of proline as a "kinetic conglomerate" can rationalize both the nonlinear effect in proline-catalyzed aldol reactions observed in early studies and the linearity observed more recently, in a manner that remains compatible with the currently accepted one-proline reaction mechanism. Care must be taken to distinguish between equilibrium and kinetic effects in heterogeneous systems—and to separate these physical influences from nonlinear effects of a true chemical origin.

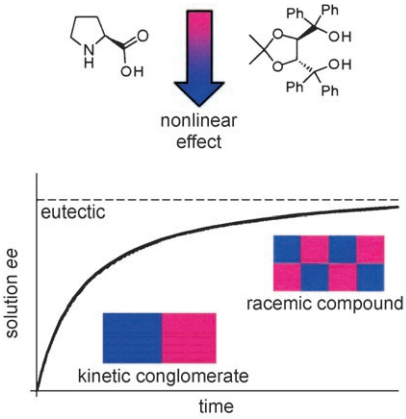

Asymmetric Catalysis

R. Matsubara, S. Kobayashi* 7993 – 7995

Catalytic Asymmetric Amination of Enecarbamates

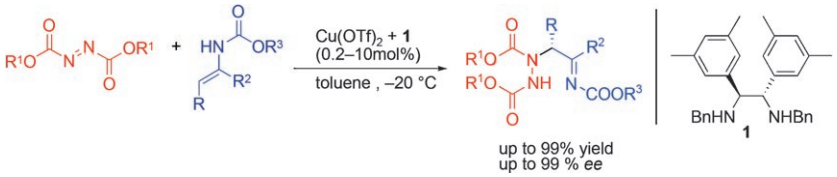

A little catalyst goes a long way: The title reaction was attained using a chiral Cu^{II}-diamine complex as catalyst. Azodicarboxylates react with various enecarbamates derived from aromatic and aliphatic ketones and aldehydes to provide acylimines in good yields with high enantioselectivity. The catalyst loading necessary for high enantioselectivity was generally low, with 0.2 mol% catalyst sufficient in some cases.

Laser Switching of Ring Currents

M. Kanno, H. Kono, Y. Fujimura* _____ 7995 – 7998

Control of π-Electron Rotation in Chiral Aromatic Molecules by Nonhelical Laser Pulses

Turning on the ring current: π Electrons in a chiral aromatic molecule, such as dichloro(3,6)pyrazinophanes (see scheme), can be rotated along the aromatic ring by linearly polarized laser pulses. Selective generation of an (approximate) angular momentum eigenstate consisting of optically allowed, quasi-degenerate π-electronic excited states is responsible for the rotation. The direction of the photoinduced ring current is controllable in each enantiomer.

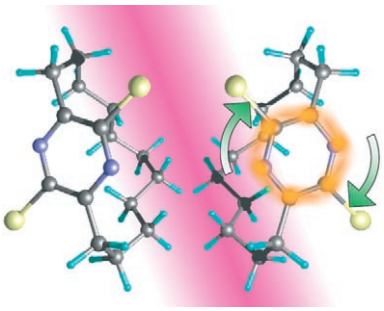

© 2006 Wiley-VCH Verlag GmbH & Co. KGaA, Weinheim

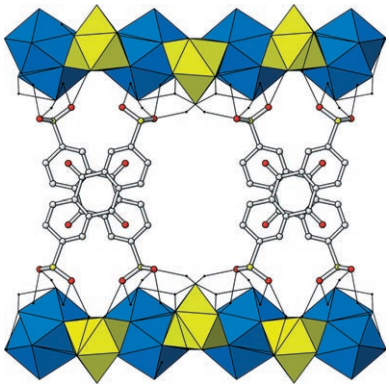

The combined advantages of layered double-hydroxide catalysts and rare-earth compounds are found in the layered rare-earth hydroxides $[R_4(OH)_{10}(H_2O)_4]_nA_n$ (R = Y, Dy, Ho, Yb; A = organic anion). These crystalline materials (see structure) comprise rigid organic anions (balls and sticks) intercalated between inorganic layers (polyhedra). They are selective heterogeneous catalysts for hydrodesulfurization and sulfide oxidation.

Layered Compounds

F. Gándara, J. Perles, N. Snejko, M. Iglesias, B. Gómez-Lor, E. Gutiérrez-Puebla,* M. A. Monge* _____ **7998 – 8001**

Layered Rare-Earth Hydroxides: A Class of Pillared Crystalline Compounds for Intercalation Chemistry

Pouring in: The picture shows an STEM image of 7-nm Au-InAs metal–semiconductor hybrid nanoparticles where a gold core (yellow) is surrounded by an amorphous InAs shell (pink). These nanoparticles form by diffusion of Au into InAs particles.

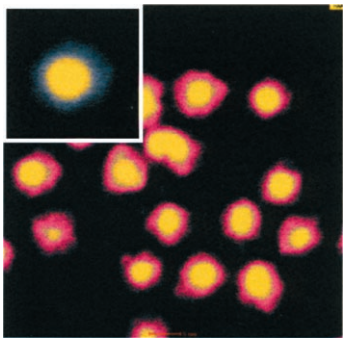

Core–Shell Nanoparticles

T. Mokari, A. Aharoni, I. Popov, U. Banin* _____ **8001 – 8005**

Diffusion of Gold into InAs Nanocrystals

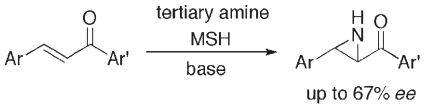

Without protection: α-Keto aziridines have been formed in a novel amine-promoted direct aziridination of chalcones using an aminimide generated in situ from a tertiary amine and *O*-mesitylenesulfonylhydroxylamine (MSH) in the presence of base (see scheme). The aziridination proceeds well using a catalytic amount of the tertiary amine. Furthermore, nonracemic aziridines are obtained using a chiral amine.

Small Ring Systems

Y.-M. Shen, M.-X. Zhao, J. Xu, Y. Shi* _____ **8005 – 8008**

An Amine-Promoted Aziridination of Chalcones

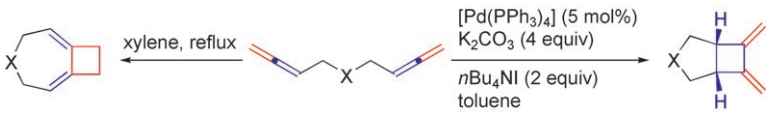

Come on allenes: [2+2] Cycloadditions of 1,5-bisallenyl compounds were realized in controllable head-to-head and tail-to-tail manners, resulting in the formation of [3.2.0] and [5.2.0] bicyclic compounds, respectively (see scheme). The bicyclic compounds include double bonds suitable for further elaboration and thus these reactions may be powerful tools in organic synthesis.

Cyclobutanes

X. Jiang, X. Cheng, S. Ma* _ **8009 – 8013**

Controllable [2+2] Cycloadditions of 1,5-Bisallenyl-Substituted Compounds

© 2006 Wiley-VCH Verlag GmbH & Co. KGaA, Weinheim

Contents

Zeolites

Á. Cantín, A. Corma,* M. J. Díaz-Cabañas, J. L. Jordá, M. Moliner, F. Rey ——— **8013 – 8015**

Synthesis and Characterization of the All-Silica Pure Polymorph C and an Enriched Polymorph B Intergrowth of Zeolite Beta

Previously elusive, the all-silica pure polymorph C of zeolite beta and a material enriched with polymorph B (see picture) are prepared by high-throughput (HT) synthesis in the presence of a cationic organic structure-directing agent (SDA). The presence of K^+ ions is essential for the formation of these materials; furthermore, a high ratio of OH^- ions to silicon atoms favors the crystallization of polymorph C.

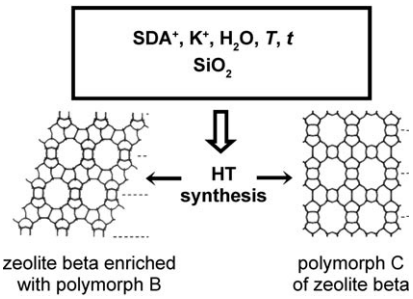

Biotransformations

R. Winkler, M. E. A. Richter, U. Knüpfer, D. Merten, C. Hertweck* ——— **8016 – 8018**

Regio- and Chemoselective Enzymatic N-Oxygenation In Vivo, In Vitro, and in Flow

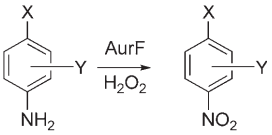

X = COOH, SO_3H, CH_2COOH
Y = CH_3, OH, NH_2

Action by the para: Evaluation of the nitro-group-forming N-oxygenase AurF in vivo, in vitro, and immobilized as a fusion protein with simply H_2O_2 as oxidant (peroxide shunt) reveals *para*-regioselective oxygenation of aromatic amines (see scheme). This effect includes the selective oxygenation of diamino compounds.

Natural Products Synthesis

C. H. Kim, H. J. An, W. K. Shin, W. Yu, S. K. Woo, S. K. Jung, E. Lee* ——— **8019 – 8021**

Total Synthesis of (−)-Amphidinolide E

The unique structural features of the cytotoxic marine macrolide (−)-amphidinolide E make it an intriguing synthetic target. Its total synthesis has now been completed by employing a radical cyclization of a β-alkoxy acrylate to form the oxolane ring, a Kocienski–Julia olefination to create the *E* C=C bond, and a lactonization reaction to close the macrocyclic ring.

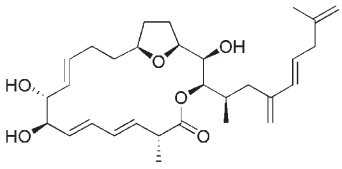

Amphidinolide E

DNA Detection

B.-A. Du, Z.-P. Li,* C.-H. Liu **8022 – 8025**

One-Step Homogeneous Detection of DNA Hybridization with Gold Nanoparticle Probes by Using a Linear Light-Scattering Technique

Matchmaker, matchmaker: A gold-nanoparticle-based light-scattering assay has been developed for sensitive detection of DNA hybridization. The assay relies on the enhancement of light scattering that originates from the aggregation of oligonucleotide-functionalized gold nanoparticles directed by the target DNA. The assay also exhibits a high degree of discrimination between perfectly matched target DNA and targets with single base-pair mismatches.

© 2006 Wiley-VCH Verlag GmbH & Co. KGaA, Weinheim

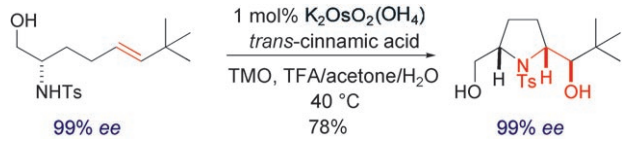

A new pathway for oxidative cyclization: N-protected α-amino alcohols with distal alkene units cyclize with complete stereoselectivity and stereospecificity to *cis*-pyrrolidines, dependent on the substitution pattern of the starting material. In addition to providing nitrogen- and oxygen-containing heterocycles in good to excellent yields, the catalyst loadings can be reduced to just 0.2 mol% osmium. TMO = Me_3NO, TFA = trifluoroacetic acid, Ts = toluene-4-sulfonyl.

Synthetic Methods

T. J. Donohoe,* G. H. Churchill, K. M. P. Wheelhouse (née Gosby), P. A. Glossop ——— **8025 – 8028**

Stereoselective Synthesis of Pyrrolidines: Catalytic Oxidative Cyclizations Mediated by Osmium

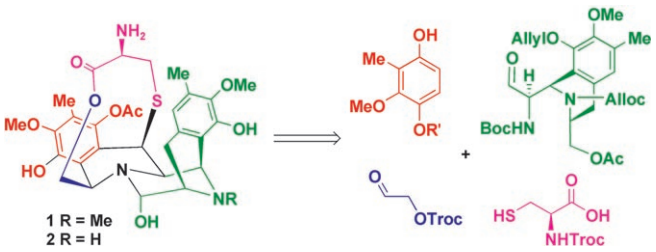

The limited availability of bioactive natural products for pharmaceutical studies and drug development is a problem that can be solved, in principle, by total synthesis. The potent antitumor marine natural products ecteinascidin 597 (**1**) and ecteinascidin 583 (**2**) have now been synthesized from readily accessible starting materials in a highly convergent and stereoselective fashion (see scheme).

Natural Products Synthesis

J. Chen, X. Chen, M. Willot, J. Zhu* ——— **8028 – 8032**

Asymmetric Total Syntheses of Ecteinascidin 597 and Ecteinascidin 583

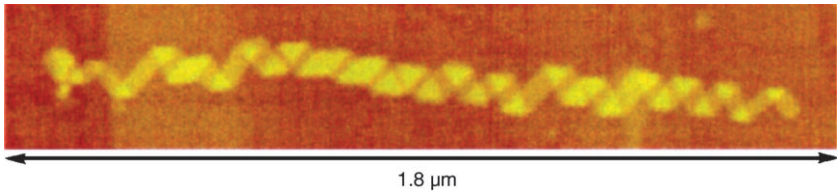

Stir it up! Comparison of the evolution with time of J-aggregates of the title porphyrin in stagnant and vortex-stirred solutions showed that chiral-sign selection is due to the action of hydrodynamic gradients (shear flows) on particle folding. Brownian dynamics (stagnant solution) result in irregularly folded mesophases, whereas hydrodynamic gradients (vortex stirring) lead to long-order folding and formation of helical ribbons (see picture).

Porphyrin Aggregation

C. Escudero, J. Crusats,* I. Díez-Pérez, Z. El-Hachemi, J. M. Ribó* ——— **8032 – 8035**

Folding and Hydrodynamic Forces in J-Aggregates of 5-Phenyl-10,15,20-tris-(4-sulfophenyl)porphyrin

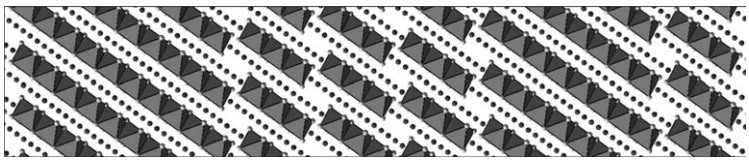

A discovery in the electron microscope: New rare earth clusters with variable sizes containing one to ten condensed octahedra of rare earth metals were found. These cluster compounds exhibit a surprising parallelism with the structural chemistry of reduced oxomolybdates.

Cluster Compounds

L. Kienle, H. Mattausch, A. Simon* ——— **8036 – 8038**

Searched For and Found: Analogies between Reduced Oxomolybdates and Cluster Compounds of Rare Earth Metals

© 2006 Wiley-VCH Verlag GmbH & Co. KGaA, Weinheim

Contents

Low-Valent Carbon

R. Tonner, F. Öxler, B. Neumüller,* W. Petz,* G. Frenking* ____ **8038 – 8042**

Carbodiphosphoranes: The Chemistry of Divalent Carbon(0)

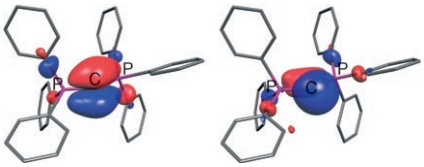

A combined experimental/theoretical study gives strong evidence that carbodiphosphoranes are divalent carbon(0) compounds. The calculations show that carbodiphosphoranes have two lone pairs of electrons (see picture), which give rise to unusual properties as confirmed by experiment. The synthesis of a triply charged molecules in which two protonated carbodiphosphoranes serve as donor ligands to an Ag^+ center supports the bonding model.

Nanowires and Nanotubes

L. Zhao, M. Yosef, E. Pippel, H. Hofmeister, M. Steinhart, U. Gösele, S. Schlecht* ____ **8042 – 8045**

"Four Birds with One Stone": Synthesis of Nanostructures of ZnTe, Te, $ZnAl_2O_4$, and Te/$ZnAl_2O_4$ from a Single-Source Precursor

Four shape-defined anisotropic nanostructures: Single-crystalline nanowires of ZnTe and elemental tellurium, core–shell structures of the type Te/$ZnAl_2O_4$ (see picture), and nanotubes of zinc spinel $ZnAl_2O_4$ could selectively be produced from [Zn(TePh)$_2$(tmeda)] (tmeda = *N*,*N*,*N*′,*N*′-tetramethylethylenediamine) as a single-source precursor. Porous alumina templates with a pore diameter of 25 nm were used both as shape-defining molds and chemical reactants.

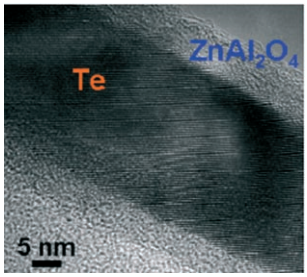

Functionalized Polymers

S. Hilf, E. Berger-Nicoletti, R. H. Grubbs, A. F. M. Kilbinger* ____ **8045 – 8048**

Monofunctional Metathesis Polymers via Sacrificial Diblock Copolymers

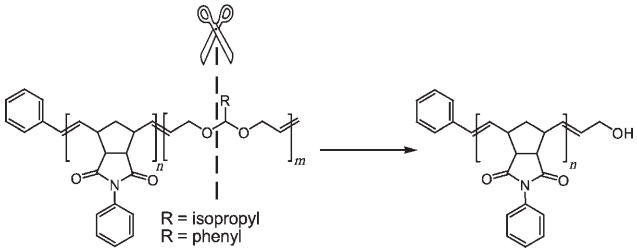

A small price to pay: The second block of a diblock copolymer is "sacrificed" in order to leave behind a monofunctionalized metathesis polymer with a hydroxy end group. By incorporation of a dioxepine unit into the copolymer, a breaking point is created between the block to be end-functionalized and the block to be sacrificed.

Catalytic Diboration

H. Braunschweig,* T. Kupfer, M. Lutz, K. Radacki, F. Seeler, R. Sigritz ____ **8048 – 8051**

Metal-Mediated Diboration of Alkynes with [2]Borametalloarenophanes under Stoichiometric, Homogeneous, and Heterogeneous Conditions

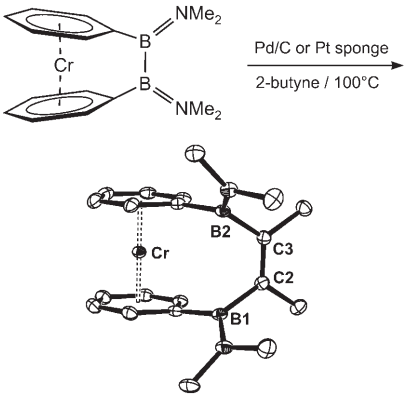

***ansa*-[2]Borabis(benzene)chromophane** and *ansa*-[2]boraferroarenophane were treated with alkynes in the presence of catalytic amounts of platinum or palladium/charcoal (see example) to afford the corresponding *ansa*-bis(boryl)alkenes in excellent yields and without detectable side products. The use of Pt and Pd are the first examples of diboration reactions of alkynes to be conducted under heterogeneous conditions.

© 2006 Wiley-VCH Verlag GmbH & Co. KGaA, Weinheim

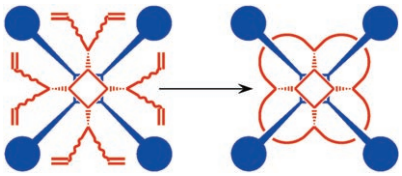

Capsular heterodimers are formed exclusively from a tetra(tosylurea)calix[4]arene (blue) and tetrakis(3,5-dibutenyloxyphenylurea)- or tetrakis(dipentenyloxyphenylurea)calix[4]arenes (red). Metathesis between the prearranged alkenyl groups and subsequent hydrogenation leads to mechanically interlocked capsules which can neither dissociate nor release the included guest(s) owing to their fourfold [2]rotaxane structure.

Rotaxanes

O. Molokanova, M. O. Vysotsky,* Y. Cao, I. Thondorf, V. Böhmer* ____ **8051 – 8055**

Fourfold [2]Rotaxanes of Calix[4]arenes by Ring Closure

The core of the matter: Reactions of $Ag(PhCO_2)$ with $(Me_2N)C_6H_4(SSiMe_3)$ and $E(SiMe_3)_2$ (E = S, Se) lead to three clusters with new silver chalcogenide cores. For example, the core of $[Ag_{88}Se_{12}(SC_6H_4NMe_2)_{63}(PPh_3)_6]$ (see picture) consists of bent hexagonal layers of selenium and sulfur atoms (yellow), with interstitial silver atoms (blue). The inorganic cores of the clusters are surrounded by organic shells.

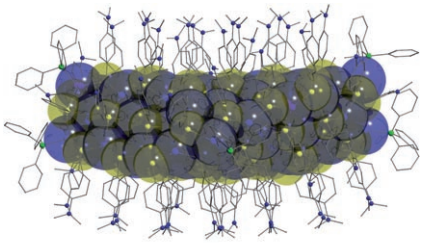

$[Ag_{88}Se_{12}(SC_6H_4NMe_2)_{63}(PPh_3)_6]$

Cluster Compounds

S. Chitsaz, D. Fenske, O. Fuhr* ____ **8055 – 8059**

Silver Chalcogenide Clusters with Dimethylanilinomercapto Ligands: Syntheses and Crystal Structures of $[Ag_{65}S_{13}(SC_6H_4NMe_2)_{39}(dppm)_5]$, $[Ag_{76}Se_{13}(SC_6H_4NMe_2)_{50}(PPh_3)_{6.5}]$, and $[Ag_{88}Se_{12}(SC_6H_4NMe_2)_{63}(PPh_3)_6]$

The self-activated silyl-assisted polyonio-substitution (SASAPOS) protocol allows the synthesis of the first representatives of 1,2-bisonio-1,2-bis(dialkylamino)-ethenes (see picture; DMAP = 4-dimethylaminopyridine). Depending on the onio substituent L, one of two types of structures with different stereoelectronic configurations is adopted.

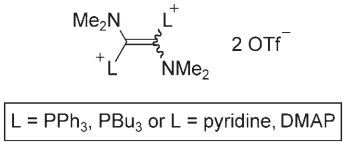

Alkenes

R. Weiss,* S. M. Huber, F. W. Heinemann, P. Audebert, F. G. Pühlhofer **8059 – 8062**

Structure, Stereoelectronics, and Synthetic Potential of 1,2-Bisonio-1,2-bis(dialkylamino)ethenes

Supporting information is available on the WWW (see article for access details).

A video clip is available as Supporting Information on the WWW (see article for access details).

Looking for outstanding employees?

Do you need another expert for your excellent team?
... Chemists, PhD Students, Managers, Professors, Sales Representatives...

Place an advert in the printed version and have it made available online for 1 month, free of charge!

Angewandte Chemie International Edition
Advertising Sales Department: Marion Schulz
Phone: 0 62 01 - 60 65 65
Fax: 0 62 01 - 60 65 50
E-Mail: MSchulz@wiley-vch.de

Service

Keywords ____ *8066*

Authors ____ *8067*

Angewandte's Sister Journals ____ *8063 – 8065*

Vacancies ____ *7881*

Preview ____ *8069*

© 2006 Wiley-VCH Verlag GmbH & Co. KGaA, Weinheim

Corrigenda

Intramolecular C–H Activation by an Open-Shell Cobalt(III) Imido Complex

D. T. Shay, G. P. A. Yap, L. N. Zakharov, A. L. Rheingold, K. H. Theopold*

1508–1510

Angew. Chem. Int. Ed. **2005**, *44*

DOI 10.1002/anie.200462529

In this Communication, the imido complex [Tp^{tBu,Me}Co=NAd] (**1**) was incorrectly characterized as a paramagnetic compound with a spin ground state of $S=1$. Further investigation has now revealed that this compound, like all other known Co(III) imido complexes, has a spin ground state of $S=0$ and is diamagnetic at low temperatures. However, at $T>280$ K, **1** undergoes a spin crossover to a thermally accessible open-shell state. All the experimental observations reported in the original Communication remain unchanged, but their interpretation is more complicated than originally realized.

Configurationally Stable Molecular Propellers: First Resolution of Residual Enantiomers

T. Benincori, G. Celentano, T. Pilati, A. Ponti, S. Rizzo, F. Sannicolò*

6193–6196

Angew. Chem. **2006**, *45*

DOI 10.1002/anie.200601869

Since publication of their Communication, it has been brought to the authors' attention that the resolution of a carbon-centered propeller was previously reported (Reference [1]). The authors apologize for this oversight and would like to amend the title of their Communication to read as "Configurationally Stable Molecular Propellers: The Resolution of Phosphorus-Centered Residual Enantiomers".

[1] C. Foces-Foces, F. H. Cano, M. Martínez-Ripoll, R. Faure, C. Roussel, R. M. Claramunt, C. López, D. Sanz, J. Elguero, *Tetrahedron: Asymmetry* **1990**, *1*, 65.

RSS Feed

Journal content prior to publication in an issue can be found online on our **Early View** page at www.angewandte.org. Stay updated on the latest journal content by registering for our **free e-mail alerts** at http://interscience.wiley.com/alerts.

Keep up with the latest research with our **RSS feed**, which provides the titles, authors, and the Digital Object Identifiers (DOIs) of Early View articles, including links to the full texts. RSS ("Really Simple Syndication") is an XML-based format for sharing and distributing web content. To receive the RSS feed, just click on the orange feed icon at www.angewandte.org, and visit http://interscience.wiley.com/rss for more information.

For more information on Chemistry—An Asian Journal see www.chemasianj.org

 © 2006 Wiley-VCH Verlag GmbH & Co. KGaA, Weinheim

Awarded...

Arthur C. Cope Award to J. M. J. Fréchet

One of the most prestigious prizes of the American Chemical Society (ACS), the Arthur C. Cope Award, will be awarded to Jean M. J. Fréchet (University of California at Berkeley, USA) in 2007. Fréchet studied chemistry and chemical engineering at the Institut de Chimie et Physique Industrielle (Institute of Industrial Chemistry and Physics; now CPE), Lyon, France, and completed his PhD in organic and polymer chemistry at the State University of New York. He joined the University of Ottawa (Canada) in 1973 and remained there until 1987, when he moved to Cornell University (Ithaca, NY). He has held a professorship at the University of California at Berkeley as well as a position as senior scientist at the Lawrence Berkeley National Laboratory since 1997. His research interests lie in the area of nanoscience and nanotechnology and are directed toward the design, synthesis, and applications of functional macromolecules. Current topics include new synthetic approaches to macromolecules with controlled architecture, including dendrimers. The ACS recognizes Fréchet for the breadth and quality of his work in areas such as molecular machines, light-harvesting and energy conversion, lithography, catalysis, separation processes, and drug delivery.

J. M. J. Fréchet

Fréchet recently reported on one-pot reaction cascades using star-shaped polymers with core-confined catalysts in *Angewandte Chemie*,[1a] and discussed the dendrimer effect in homogeneous catalysis in a review in *Advanced Synthesis & Catalysis*.[1b] He is a member of the advisory boards for both of these journals.

Gabor A. Somorjai Award to Hajo Freund

Hans-Joachim Freund (Fritz-Haber-Institut der Max-Planck-Gesellschaft, Berlin) will receive the Gabor A. Somorjai Award for Creative Research in Catalysis from the ACS in 2007. The prize is sponsored by the Gabor A. and Judith K. Somorjai Endowment Fund and recognizes outstanding theoretical, experimental, or developmental research resulting in the advancement of understanding or application of catalysis. Residents of the USA are normally given preference. The research interests of Freund's group are focused on the chemistry and physics of solid surfaces, including the structure and dynamics of oxide surfaces. His group is also interested in model systems for heterogeneous catalysis as well as in nanostructures and clusters. He recently described the size-dependent oxidation mechanism of supported Pd nanoparticles[2b] and the synthesis and structure of ultrathin aluminosilicate films in *Angewandte Chemie*.[2b]

H. Freund

Freund studied at the Universität zu Köln (Germany) and went on to obtain his PhD there in 1978 under the guidance of G. Hohlneicher. At the same time, he worked as a high school teacher at the Gymnasium Solingen. In 1979, he joined the University of Pennsylvania and Xerox Corporation (USA) as a postdoctoral researcher. He returned to Cologne in 1981 to complete his habilitation (1983). He then joined the Universität Erlangen and remained there until 1987, when he accepted a position at the Ruhr-Universität Bochum. He has been a director at the Fritz Haber Institute since 1996.

Photo: M. Jacoby, C&EN

Claude S. Hudson Award to P. Sinaÿ

The Claude S. Hudson Award in Carbohydrate Chemistry will be awarded to Pierre Sinaÿ (Ecole Normale Supérieure, Paris, France) in 2007. Sinaÿ's research activities are focused on oligosaccharides and glycoconjugates, cyclodextrins, and glycosidase inhibitors. He recently discussed the influence of ceramide on carbohydrate–carbohydrate recognition in *Angewandte Chemie*[3a] and described a new method for the synthesis of fluorinated *exo*-glycals and their time-dependent inhibition of UDP-galactopyranose mutase in *Chemistry – A European Journal*.[3b]

Sinaÿ completed his engineering degree at the Ecole Nationale Supérieure des Industries Chimiques (National College for Chemical Industries), Nancy, France, and completed his PhD in 1966 at the University of Nancy under the guidance of S. David. He subsequently joined the group of R. W. Jeanloz at Harvard University, Massachusetts General Hospital in Boston (USA) as a research fellow. He returned to France in 1968 and joined the CNRS in Orsay (Paris). A year later, he accepted an associate professorship at the University of Orléans, where he was later appointed Professor of Biochemistry (1972). In 1986, he joined the University of Paris and the Ecole Normale Supérieure (Paris) as Professor of Organic Chemistry. He was named a corresponding member of the French Academy of Science in 1996 and became a full member in 2003. Sinaÿ is an editorial board member for *Chemistry – A European Journal*.

P. Sinaÿ

WILEY InterScience DISCOVER SOMETHING GREAT
© 2006 Wiley-VCH Verlag GmbH & Co. KGaA, Weinheim

Chemistry Calendar 2007

This beautiful 2007 calendar with the best chemistry covers from our journals in 2006 will be distributed along with print issues. For your personal or extra copies, write to angewandte@wiley-vch.de while stocks last.

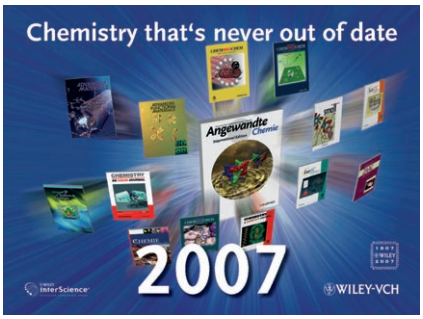

[1] a) B. Helms, S. J. Guillaudeu, Y. Xie, M. McMurdo, C. J. Hawker, J. M. J. Fréchet, *Angew. Chem.* **2005**, *117*, 6542; *Angew. Chem. Int. Ed.* **2005**, *44*, 6384; b) B. Helms, J. M. J. Fréchet, *Adv. Synth. Catal.* **2006**, *348*, 1125.

[2] a) T. Schalow, B. Brandt, D. E. Starr, M. Laurin, S. K. Shaikhutdinov, S. Schauermann, J. Libuda, H.-J. Freund, *Angew. Chem.* **2006**, *118*, 3775; *Angew. Chem. Int. Ed.* **2006**, *45*, 3693; b) D. Stacchiola, S. Kaya, J. Weissenrieder, H. Kuhlenbeck, S. Shaikhutdinov, H.-J. Freund, M. Sierka, T. Kumanova Todorova, J. Sauer, *Angew. Chem.* **2006**, *118*, 7798; *Angew. Chem. Int. Ed.* **2006**, *45*, 7636.

[3] a) C. Gourier, F. Pincet, E. Perez, Y. Zhang, Z. Zhu, J.-M. Mallet, P. Sinaÿ, *Angew. Chem.* **2005**, *117*, 1711; *Angew. Chem. Int. Ed.* **2005**, *44*, 1683; b) A. Caravano, H. Dohi, P. Sinaÿ, S. P. Vincent, *Chem. Eur. J.* **2006**, *12*, 3114.

DOI: 10.1002/anie.200604577

© 2006 Wiley-VCH Verlag GmbH & Co. KGaA, Weinheim

Organocatalysis

DOI: 10.1002/anie.200602943

Diarylprolinol Ethers: Expanding the Potential of Enamine/Iminium-Ion Catalysis**

Claudio Palomo and Antonia Mielgo*

Keywords:
domino reactions · enamines · iminium ions · organocatalysis

Catalytic asymmetric synthesis is providing chemists with new and powerful tools for the efficient synthesis of complex molecules.[1] Although for many years asymmetric catalysis has been linked to the use of chiral transition-metal complexes,[2] recently, processes catalyzed by metal-free species—organocatalytic methods—have emerged as a complementary tool.[3] While chiral Brønsted acids[4] and bifunctional chiral Brønsted acid/Brønsted base catalysts[5] have been employed, the asymmetric catalysis of carbonyl transformations via iminium ion[6] and enamine intermediates[7] using chiral amines has grown most remarkably. One of the main goals for chemists is to devise a general organocatalyst suitable for a broad range of transformations; in many cases this requires tedious screening of a large number of catalysts because only a few stand out for their broad utility.[8] Relevant examples are MacMillan's imidazolidinones[6] and the amino acid proline (**1**), which have often been described as fairly general and efficient amine-based catalysts (see Figure 2).

Indeed, enamine catalysis using **1** has been applied to both intermolecular and intramolecular nucleophilic addition reactions with a variety of electrophiles.[7] In addition to carbonyl compounds (C=O),[9] these include imines (C=N) in Mannich reactions,[10] azodicarboxylates (N=N),[11] nitrosobenzene (O=N),[12] and Michael acceptors.[13] In these processes the configuration of the final adducts is generally controlled by a hydrogen-bond interaction between the acidic proton of proline and the incoming electrophile (**A** in Figure 1). Thus,

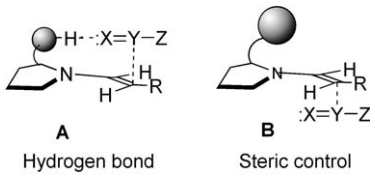

Figure 1. Pictogram showing how the complementary pyrrolidine catalysts function: model **A**: L-proline, through a hydrogen bond; model **B**: diarylprolinol ethers, through steric control.

this interaction, whilst activating the electrophile, guides its approach from the upper face of the enamine. A similar pattern is also followed by protonated amine-based catalysts[14] and, in general, by catalysts bearing a hydrogen-bond donor at the α position of the pyrrolidine nitrogen.[7d,e,15]

Recently, other pyrrolidine derivatives, diarylprolinol ethers, have emerged as potentially general enamine organocatalysts. Most significantly, with these catalysts the configuration of the final adduct is controlled by the steric hindrance of the substituent α to the pyrrolidine nitrogen (**B** in Figure 1). This forces the approach of the electrophile to the lower face of the enamine, thus affording products of opposite configuration compared to those obtained with L-proline as catalyst.

Although (*S*)-2,2-diphenylprolinol (**2a**; Figure 2) may promote reactions with a good level of stereocontrol, the

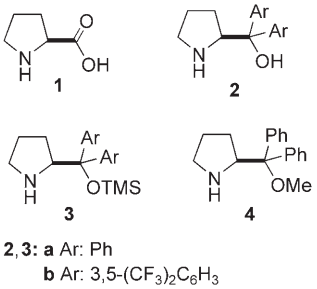

Figure 2. Developed organocatalysts.

processes are characterized by low catalyst turnover. This fact has been mainly ascribed to the formation of the relatively stable and unreactive hemiaminal species, which removes a significant amount of the catalyst from the catalytic cycle. To sidestep hemiaminal formation, trimethylsilyl (TMS) ethers **3** and methyl ether **4** have been developed.

Diarylprolinol silyl ethers **3** have been applied successfully to the α-functionalization of aldehydes, and a large variety of transformations such as C–X (X = F, Br, S) bond formation, α-aminations, and Mannich reactions have been reported (Scheme 1).[7d,e,16] The reactions all proceed in good to high yields and with excellent enantioselectivities. Remarkably significant is the Mannich reaction with glyoxylate imines, which turned out to be highly *anti* diastereoselective.[16] It is worth noting that only two other papers by Barbas et al. and Maruoka et al. have presented (3*R*,5*R*)-5-methylpyrrolidine-3-carboxylic acid[17] and an axially chiral aminosulfona-

[*] Prof. Dr. C. Palomo, Dr. A. Mielgo
Departamento de Química Orgánica I
Facultad de Química
Universidad del País Vasco
Apdo. 1072, 20080 San Sebastián (Spain)
Fax: (+34) 943-015-270
E-mail: claudio.palomo@ehu.es

[**] This work was supported financially by The University of the Basque Country (UPV/EHU) and Ministerio de Educación y Ciencia (MEC, Spain).

InterScience
© 2006 Wiley-VCH Verlag GmbH & Co. KGaA, Weinheim

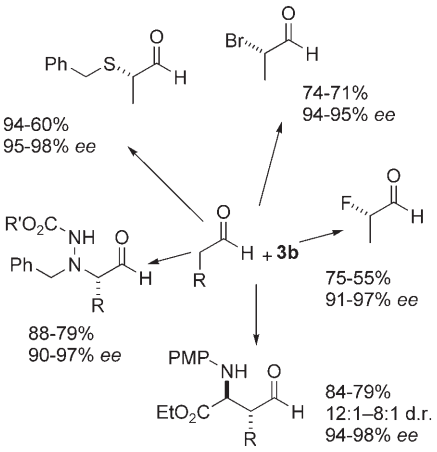

Scheme 1. α-Functionalization of aldehydes catalyzed by **3b**. PMP = *p*-methoxyphenyl.

mide,[18] respectively, as catalysts for promoting the *anti* Mannich reaction with high diastereo- and enantioselectivities. These results complement those reported with L-proline where high *syn* diastereoselectivities are observed.[10] In the same context, Gellman and Chi have recently described the α-aminomethylation of aldehydes through a catalytic asymmetric Mannich reaction involving a formaldehyde-derived iminium electrophile and by using **3a** as organocatalyst together with AcOH and LiCl[19] (Scheme 2). The expected adducts are reduced in situ to afford the γ-aminoalcohols in good yields and excellent enantioselectivities.

Diarylprolinol silyl ethers have also been investigated as organocatalysts for the epoxidation of α,β-unsaturated aldehydes. Jørgensen et al. have demonstrated that catalyst **3b** is efficient in promoting this reaction in the presence of hydrogen peroxide as oxidant (Scheme 3).[20] In this case the reaction occurs through the iminium ion intermediate **C**; the steric bulk of the α substituent also forces the approach of the hydrogen peroxide to the opposite face. Further nucleophilic attack of the resulting enamine carbon atom at the electrophilic peroxygen atom, followed by hydrolysis of the iminium intermediate results in epoxide formation. Other oxidants can also be employed in these reactions. For example, Lattanzi has reported the epoxidation of α,β-enones with *tert*-butyl hydroperoxide and catalyst **2a** to yield the corresponding epoxides although with moderate enantioselectivities.[21]

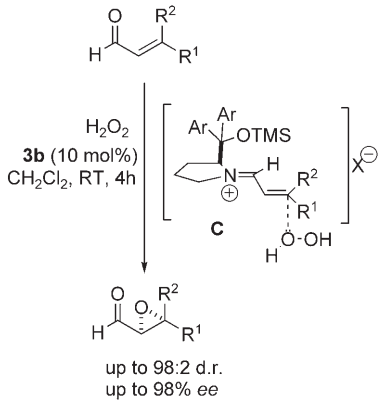

Scheme 3. Epoxidation of α,β-unsaturated aldehydes catalyzed by **3b**.

Asymmetric conjugate additions for C–C bond formation are another important challenge in organic synthesis. The enantioselective version of this process[22] has also been explored with diarylprolinol ether derivatives by both enamine and iminium-ion strategies. A recent example is the conjugate addition of malonates to α,β-unsaturated aldehydes[23] catalyzed by **3b** (Scheme 4) providing the addition products by iminium-ion activation in good yields and excellent enantioselectivities. Likewise, Hayashi et al.[24] have documented the Michael addition of aldehydes to nitroalkenes catalyzed by **3a** (Scheme 5). In this case an enamine pathway is followed, which is more effective with nitrostyrenes, while with β-alkyl-substituted nitroalkenes moderate yields are obtained. In a related context, Gellman and co-workers[25] showed the utility of diphenylprolinol methyl ether **4** in the conjugate addition of aldehydes to vinyl ketones (Scheme 6). Optimum results were achieved when the reactions were carried out in the presence of a catechol derivative as a cocatalyst, which apparently electrophilically activates the

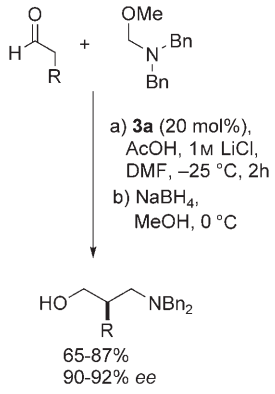

Scheme 2. Enantioselective aminomethylation of aldehydes catalyzed by **3a**. Bn = benzyl.

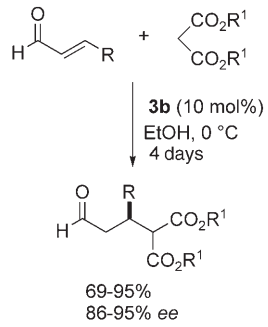

Scheme 4. Conjugate addition of malonates to α,β-unsaturated aldehydes catalyzed by **3b**.

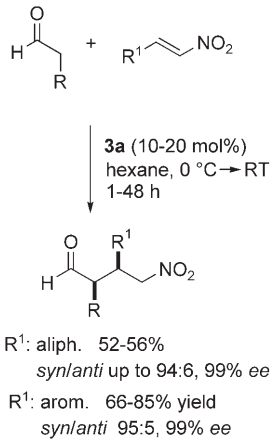

Scheme 5. Conjugate addition of aldehydes to nitroalkenes catalyzed by **3a**.

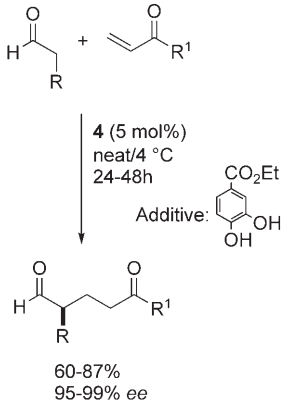

Scheme 6. Conjugate addition of aldehydes to vinyl ketones catalyzed by **4**.

© 2006 Wiley-VCH Verlag GmbH & Co. KGaA, Weinheim

enone by hydrogen-bond donation to the carbonyl oxygen.

Catalytic and stereoselective domino or cascade reactions are tools of particular interest as they can be used for the one-pot synthesis of complex organic molecules with multiple stereogenic centers.[26] In particular, secondary amines, capable of both enamine and iminium-ion catalysis, are good candidates for the design of this type of process.[7c,27] Four important contributions on this subject which use diarylprolinol silyl ethers as catalysts have recently appeared. The first, by Jørgensen et al.,[28] presents the pioneering multicomponent domino conjugate thiol addition/electrophilic amination reaction that gives access, after in situ reduction and cyclization of the resulting adducts, to highly functionalized oxazolidinones in good yields and with over 99% *ee* (Scheme 7). This example combines first iminium-ion activation to promote the conjugate addition of thiols to α,β-unsaturated aldehydes, and then enamine activation to effect the amination reaction. The second report, from the same research group, describes the one-pot Michael addition/aldol/S_N2 reaction of α,β-unsaturated aldehydes and γ-chloro-β-ketoesters (Scheme 8) in the presence of NaOAc followed by further treatment with K_2CO_3. Iminium-ion and enamine activations are successively combined to afford epoxycyclohexanone derivatives with up to four stereocenters in very good diastereo- and enantiomeric ratios.[29] The third contribution in this area, by Wang et al.,[30] describes the organocatalytic asymmetric Michael addition/aldol dehydration reaction of α,β-unsaturated aldehydes and 2-mercaptobenzaldehydes in the presence of benzoic acid through iminium-ion/enamine activation; the corresponding adducts are obtained in excellent yields and enantioselectivities (Scheme 9). The fourth report, by Enders and co-workers, is an elegant example of the control of four stereocenters in a triple cascade organocatalytic reaction of a linear aldehyde, a nitroalkene, and an α,β-unsaturated aldehyde with catalyst **3a** to afford tetrasubstituted cyclohexene carbaldehydes with high diastereoselectivity and essentially complete enantiocontrol[31] (Scheme 10). In contrast to Jørgensen's and Wang's work, the catalytic cycle here starts with enamine activation of the linear aldehyde **D** (Figure 3), which then selectively adds to the nitroalkene **E** in a Michael reaction, in analogy to the mechanism proposed by Hayashi et al. (see Scheme 5). The subsequent hydrolysis liberates the catalyst, which is now able to form the iminium ion of the α,β-unsaturated aldehyde **F** to accomplish the conjugate addition with nitroalkane **5**.[32] In the subsequent third step, an enamine activation of the resulting enamine intermediate **6** leads to an intramolecular aldol condensation via **7**. Hydrolysis completes the catalytic cycle and releases the tetrasubstituted cyclohexene carbaldehyde **8**. It is noteworthy that in all four cascade processes described by Jørgensen, Wang, and Enders, one of the steps is a conjugate addition reaction.[33]

In conclusion, diarylprolinol ethers have greatly contributed to increase the power of aminocatalysis in asymmetric C–C and C–X bond-forming reactions. The efficiency of these catalysts is based on the principle of "steric control approach", and they have assisted in the understanding of the mechanisms of reactant activation and reaction stereoselectivity. Nevertheless, aminocatalysis is still in the first stages of development, and new powerful enantioselective transformations, including multicomponent/domino reactions, are waiting to be

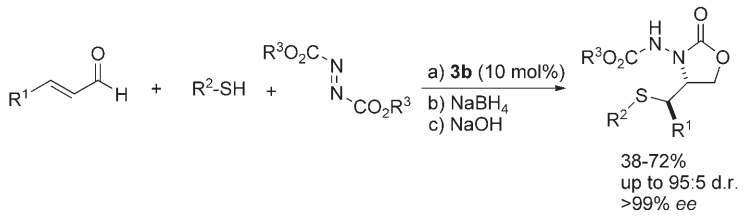

Scheme 7. Domino addition/amination reaction of α,β-unsaturated aldehydes catalyzed by **3b**.

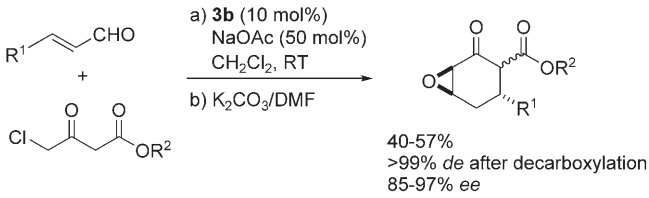

Scheme 8. One-pot Michael addition/aldol/S_N2 reaction of α,β-unsaturated aldehydes and γ-chloro-β-ketoesters catalyzed by **3b**.

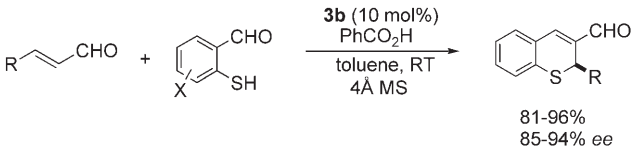

Scheme 9. Cascade Michael addition/aldol dehydratation reactions of α,β-unsaturated aldehydes and 2-mercaptobenzaldehydes catalyzed by **3b**.

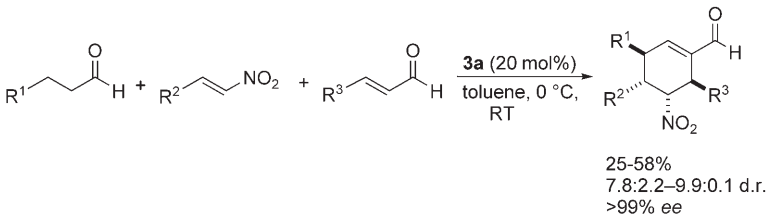

Scheme 10. Three-component multistep reaction cascade catalyzed by **3a**.

 © 2006 Wiley-VCH Verlag GmbH & Co. KGaA, Weinheim

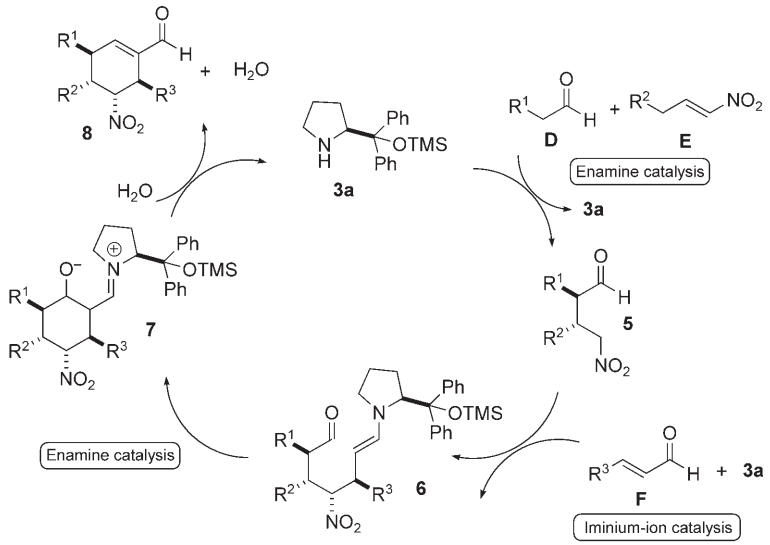

Figure 3. Proposed catalytic cycle of a triple cascade reaction affording substituted cyclohexenes.

discovered.[34] Yet, catalyst recovery has to be solved and catalyst loading has to be reduced.

[1] For a review on the art and science of total synthesis, see: K. C. Nicolaou, D. Vourloumis, N. Winssinger, P. S. Baran, *Angew. Chem.* **2000**, *112*, 46–126; *Angew. Chem. Int. Ed.* **2000**, *39*, 44–122.

[2] For leading references, see: a) *Comprehensive Asymmetric Catalysis* (Eds.: E. N. Jacobsen, A. Pfaltz, H. Yamamoto), Springer, Heidelberg, **1999**; b) *Asymmetric Catalysis in Organic Synthesis* (Ed.: R. Noyori), Wiley, New York, **1994**; c) *Catalytic Asymmetric Synthesis* (Ed.: I. Ojima), Wiley, New York, **2000**; d) *Transition Metals for Organic Synthesis*, 2nd ed. (Eds.: M. Beller, C. Bolm), Wiley-VCH, Weinheim, **2004**; e) H. Gröger, J. Wilken, *Angew. Chem.* **2001**, *113*, 545–548; *Angew. Chem. Int. Ed.* **2001**, *40*, 529–532; f) See also the special issue *Acc. Chem. Res.* **2000**, *33*, 323–440.

[3] For general reviews on organocatalysis, see: a) P. I. Dalko, L. Moisan, *Angew. Chem.* **2001**, *113*, 3840; *Angew. Chem. Int. Ed.* **2001**, *40*, 3726; b) E. R. Jarvo, S. J. Miller, *Tetrahedron* **2002**, *58*, 2481; c) P. I. Dalko, L. Moisan, *Angew. Chem.* **2004**, *116*, 5248; *Angew. Chem. Int. Ed.* **2004**, *43*, 5138; d) J. Seayad, B. List, *Org. Biomol. Chem.* **2005**, *3*, 719; e) A. Berkessel, H. Gröger, *Asymmetric Organocatalysis: From Biomimetic Concepts to Applications in Asymmetric Synthesis*, Wiley-VCH, **2005**; See also special issues on organocatalysis: f) *Acc. Chem. Res.* **2004**, *37*; g) *Adv. Synth. Cat.* **2004**, *346*.

[4] For recent reviews, see: a) P. R. Schreiner, *Chem. Soc. Rev.* **2003**, *32*, 289–296; b) P. M. Pihko, *Angew. Chem.* **2004**, *116*, 2110–2113; *Angew. Chem. Int. Ed.* **2004**, *43*, 2062–2064; c) T. Akiyama, J. Itoh, K. Fuchibe, *Adv. Synth. Catal.* **2006**, *348*, 999–1010; d) S. J. Connon, *Angew. Chem.* **2006**, *118*, 4013–4016; *Angew. Chem. Int. Ed.* **2006**, *45*, 3909–3912.

[5] For recent reviews, see: a) P. M. Pihko, *Lett. Org. Chem.* **2005**, *2*, 398–403; b) Y. Takemoto, *Org. Biomol. Chem.* **2005**, *3*, 4299–4306; c) M. S. Taylor, E. N. Jacobsen, *Angew. Chem.* **2006**, *118*, 1550–1573; *Angew. Chem. Int. Ed.* **2006**, *45*, 1520–1543; d) S. J. Connon, *Chem. Eur. J.* **2006**, *12*, 5418–5427.

[6] G. Lelais, D. W. C. MacMillan, *Aldrichimica Acta* **2006**, *39*, 79–87.

[7] For reviews, see: a) B. List, *Tetrahedron* **2002**, *58*, 5573–5590; b) B. List, *Acc. Chem. Res.* **2004**, *37*, 548–557; c) B. List, *Chem. Commun.* **2006**, 819–824; d) M. Marigo, K. A. Jørgensen, *Chem. Commun.* **2006**, 2001–2011; e) G. Guillena, D. J. Ramón, *Tetrahedron: Asymmetry* **2006**, *17*, 1465–1492.

[8] T. P. Yoon, E. N. Jacobsen, *Science* **2003**, *299*, 1691–1693.

[9] a) B. List, A. Lerner, C. F. Barbas III, *J. Am. Chem. Soc.* **2000**, *122*, 2395–2396; b) K. Sakthivel, W. Notz, T. Bui, C. F. Barbas III, *J. Am. Chem. Soc.* **2001**, *123*, 5260–5267; c) A. B. Northrup, I. K. Mangion, F. Hettche, D. W. C. MacMillan, *Angew. Chem.* **2004**, *116*, 2204–2206; *Angew. Chem. Int. Ed.* **2004**, *43*, 2152–2154.

[10] Reviews: a) M. M. B. Marques, *Angew. Chem.* **2006**, *118*, 356–360; *Angew. Chem. Int. Ed.* **2006**, *45*, 348–352; b) A. Córdova, *Acc. Chem. Res.* **2004**, *37*, 102–112.

[11] Review: a) R. O. Duthaler, *Angew. Chem.* **2003**, *115*, 1005–1008; *Angew. Chem. Int. Ed.* **2003**, *42*, 975–978; For a review on electrophilic α-amination of carbonyl compounds, see: b) C. Greck, B. Drouillat, C. Thomassigny, *Eur. J. Org. Chem.* **2004**, 1377–1385.

[12] Reviews: a) P. Merino, T. Tejero, *Angew. Chem.* **2004**, *116*, 3055–3058; *Angew. Chem. Int. Ed.* **2004**, *43*, 2995–2997; b) H. Yamamoto, N. Nomiyama, *Chem. Commun.* **2005**, 3514–3525.

[13] a) B. List, P. Pojarliev, H. J. Martin, *Org. Lett.* **2001**, *3*, 2423–2425; b) D. Enders, A. Seki, *Synlett* **2002**, 26–28; c) P. Kotrusz, S. Toma, H.-G. Schmalz, A. Adler, *Eur. J. Org. Chem.* **2004**, 1577–1583.

[14] C. Bolm, T. Rantanen, I. Schiffers, L. Zani, *Angew. Chem.* **2005**, *117*, 1788–1793; *Angew. Chem. Int. Ed.* **2005**, *44*, 1758–1763.

[15] Some apparent exceptions are the conjugate additions of carbonyl compounds to nitroalkenes catalyzed by protonated amine catalysts and related compounds. For some examples, see: a) J. Wang, H. Li, B. Lou, L. Zu, H. Guo, W. Wang, *Chem. Eur. J.* **2006**, *12*, 4321–4332; b) T. Ishi, S. Fujioka, Y. Sekiguchi, H. Kotsuki, *J. Am. Chem. Soc.* **2004**, *126*, 9558–9559; c) N. Mase, R. Thayumanavan, F. Tanaka, C. F. Barbas III, *Org. Lett.* **2004**, *6*, 2527–2530. See also Ref. [13].

[16] a) J. Frazén, M. Marigo, D. Fielenbach, T. C. Wabnitz, A. Kjaersgard, K. A. Jørgensen, *J. Am. Chem. Soc.* **2005**, *127*, 18296–18304; b) I. Ibrahem, A. Córdova, *Chem. Commun.* **2006**, 1760–1762.

[17] S. Mitsumori, H. Zhang, P. H.-Y. Cheong, K. N. Houk, F. Tanaka, C. F. Barbas III, *J. Am. Chem. Soc.* **2006**, *128*, 1040–1041.

[18] T. Kano, Y. Yamaguchi, O. Tokuda, K. Maruoka, *J. Am. Chem. Soc.* **2005**, *127*, 16408–16409.

[19] Y. Chi, S. H. Gellman, *J. Am. Chem. Soc.* **2006**, *128*, 6804–6805.

[20] a) M. Marigo, J. Franzén, T. B. Poulsen, W. Zhuang, K. A. Jørgensen, *J. Am. Chem. Soc.* **2005**, *127*, 6964–6965; b) W. Zhuang, M. Marigo, K. A. Jørgensen, *Org. Biomol. Chem.* **2005**, *3*, 3883–3885; see also: c) H. Sundén, I. Ibrahem, A. Córdova, *Tetrahedron Lett.* **2006**, *47*, 99–103.

[21] A. Lattanzi, *Adv. Synth. Catal.* **2006**, *348*, 339–346.

[22] M. P. Sibi, S. Manyem, *Tetrahedron* **2000**, *56*, 8033–8062.

[23] S. Brandau, A. Landa, J. Franzén, M. Marigo, K. A. Jørgensen, *Angew. Chem.* **2006**, *118*, 4411–4415; *Angew. Chem. Int. Ed.* **2006**, *45*, 4305–4309.

 © 2006 Wiley-VCH Verlag GmbH & Co. KGaA, Weinheim

[24] Y. Hayashi, H. Gotoh, T. Hayasi, M. Shoji, *Angew. Chem.* **2005**, *117*, 4284 – 4287; *Angew. Chem. Int. Ed.* **2005**, *44*, 4212 – 4215. For a recent application of a recyclable fluorous diphenyl prolinol silyl ether in the same reaction, see: L. Zu, H. Li, J. Wang, X. Yu, W. Wang, *Tetrahedron Lett.* **2006**, *47*, 5131 – 5134.
[25] Y. Chi, S. H. Gellmann, *Org. Lett.* **2005**, *7*, 4253 – 4256.
[26] For some reviews, see: a) L. F. Tietze, *Chem. Rev.* **1996**, *96*, 115 – 136; b) J.-C. Wasilke, S. J. Obreg, R. T. Baker, G. C. Bazan, *Chem. Rev.* **2005**, *105*, 1001 – 1020; c) D. J. Ramón, M. Yus, *Angew. Chem.* **2005**, *117*, 1628 – 1661; *Angew. Chem. Int. Ed.* **2005**, *44*, 1602 – 1634.
[27] a) J. W. Yang, M. T. Hechavarria Fonseca, B. List, *J. Am. Chem. Soc.* **2005**, *127*, 15036 – 15037; b) Y. Huang, A. M. Walji, C. H. Larsen, D. W. C. MacMillan, *J. Am. Chem. Soc.* **2005**, *127*, 15051 – 15053; c) D. B. Ramachary, C. F. Barbas III, *Chem. Eur. J.* **2004**, *10*, 5323 – 5331.
[28] M. Marigo, T. Schulte, J. Franzén, K. A. Jørgensen, *J. Am. Chem. Soc.* **2005**, *127*, 15710 – 15711.
[29] M. Marigo, S. Bertelsen, A. Landa, K. A. Jørgensen, *J. Am. Chem. Soc.* **2006**, *128*, 5475 – 5479.
[30] W. Wang, H. Li, J. Wang, L. Zu, *J. Am. Chem. Soc.* **2006**, *128*, 10354 – 10355.
[31] D. Enders, M. R. M. Hüttl, C. Grondal, G. Raabe, *Nature* **2006**, *441*, 861 – 863.
[32] For an iminium-ion strategy for the conjugate addition of nitroalkanes, see: A. Prieto, N. Halland, K. A. Jørgensen, *Org. Lett.* **2005**, *7*, 3897 – 3900.
[33] For catalytic asymmetric tandem transformations triggered by conjugate additions, see: H. C. Guo, J. A. Ma, *Angew. Chem.* **2006**, *118*, 362 – 375; *Angew. Chem. Int. Ed.* **2006**, *45*, 354 – 366.
[34] Additional papers published after completion of this account: a) For an asymmetric γ-amination of aldehydes catalyzed by **3b**, see: S. Bertelsen, M. Marigo, S. Brandes, P. Diner, K. A. Jørgensen, *J. Am. Chem. Soc.* **2006**, *128*, 12973 – 12980. b) For a tandem oxa-Michael addition/aldol reaction of salicyl aldehydes with α,β-unsaturated aldehydes promoted by **3a**, see: T. Govender, L. Hojabri, F. M. Moghaddam, P. I. Arvidsson, *Tetrahedron: Asymmetry* **2006**, *17*, 1763 – 1767. c) For a direct asymmetric reductive Mannich-type reaction of α,β-unsaturated aldehydes catalyzed by **3a**, see: G.-L. Zhao, A. Córdova, *Tetrahedron Lett.* **2006**, *47*, 7417 – 7421. d) For **3a**-based recyclable dendritic catalysts for the Michael addition of various unmodified aldehydes with nitrostyrenes, see: Y. Li, X.-Y. Liu, G. Zhao, *Tetrahedron: Asymmetry*, **2006**, *17*, 2034 – 2039.

 © 2006 Wiley-VCH Verlag GmbH & Co. KGaA, Weinheim

DOI: 10.1002/anie.200602006

Anion Coordination

Amide-Based Ligands for Anion Coordination

*Sung Ok Kang, Rowshan Ara Begum, and Kristin Bowman-James**

Keywords:
amides · anions · coordination modes · hydrogen bonds · receptors · supramolecular chemistry

Dedicated to Professor Jean-Marie Lehn

Anion recognition is an active area of research in supramolecular chemistry. The rapidly increasing amount of structural data now allows anion coordination chemistry to be formalized in terms of coordination numbers and geometries based on hydrogen-bonding interactions between the host (ligand) and the guest (anion). This Minireview targets just one class of anion receptors, namely, amide-based ligands. The structural data for a series of five anion shapes are compiled according to coordination number, and distinct commonalities are observed within a given anion topology. The results also indicate a number of similarities between the coordination of anions and transition-metal ions.

1. Introduction

Anions represent an elusive species in terms of the design and synthesis of truly selective binding agents or, in supramolecular terms, hosts or receptors for them. Nonetheless the field has expanded rapidly in the last two decades, and a myriad of receptors have been designed to target specific anions.[1–4] As the field has evolved, so have the classes of receptors, which include a number of different hydrogen-bond-donor groups.

As structural knowledge for host–guest complexes involving anions has accumulated, preferences have been observed for specific anions with respect to the number of hydrogen bonds and coordination geometries.[4] This Minireview describes crystallographic results for simple inorganic ions of five different shapes: spherical, linear, V-shaped, trigonal planar, and tetrahedral. Binding data are also provided where available. The focus is on simple amide receptors as opposed to receptors appended to scaffolds such as transition-metal complexes or to organic templates such as calixarenes or other host compounds, and the coverage is limited generally to more recent findings, although a few classic ammonium and natural hosts are also highlighted. Each of the sections is subdivided into coordination numbers.

[*] Dr. S. O. Kang, Dr. R. A. Begum, Prof. K. Bowman-James
University of Kansas
1251 Wescoe Hall Drive, Lawrence, KS 66045 (USA)
Fax: (+1) 785-864-5396
E-mail: kbjames@ku.edu

2. Spherical Anions

Halides are the simplest anions in terms of shape and are thus the closest analogue of metal ions. In general, they prefer a four-coordinate, tetrahedral geometry, which is understandable in terms of the four lone pairs in an sp^3-hybridized electronic shell. Indeed, the most common coordination numbers are two, three, and four. However, other coordination numbers up to nine can be cited. Clearly the higher coordination numbers cannot be attributed to specific lone-pair interactions of the anion with the nearby hydrogen atoms of the host. Rather, they are often structurally imposed by virtue of the placement of the hydrogen-bonding units within the host framework. Interestingly, a number of commonalities can be seen for coordination preferences within the halide group when this approach is used. Table 1 lists a series of halide complexes along with their coordination numbers, geometries, and, where available, binding constants *K*.

Halides play major roles both in the environment and in biology. In the biochemical world, for example, ion channels have been of considerable interest; the 2003 Nobel Prize in Chemistry was awarded to MacKinnon for his work on ion channels and to Agre for his work on water channels.[5] Indeed, chloride ion channels are widespread in both prokaryotic and eukaryotic cells in nature, and, although their functions are not totally established, they are known to play a critical role in certain diseases such as cystic fibrosis.[6] The crystal structures of two chloride ion channels from *S. typhimurium* and *E. coli*, reported by MacKinnon and coworkers in 2002 (Scheme 1), have provided much-needed insight into the mechanisms of ion selectivity in ion channels.[7] Both of the structures contain essentially the same ion pores, and chloride is held by four hydrogen bonds, two from main-chain amide groups (Phe 357 and Ile 3356) and two from side-chain hydroxyl groups (Ser 107 and Tyr 445).

WILEY InterScience DISCOVER SOMETHING GREAT

© 2006 Wiley-VCH Verlag GmbH & Co. KGaA, Weinheim

Table 1: Coordination numbers (C.N.), geometries, and association constants (K [M^{-1}])[a] for halide complexes with **ClC** and **1**–**22**.

Complex	C.N.	Geometry	K (Solvent)	Ref.
ClC·Cl^-	4	pseudotetrahedral	n.r.[b]	[7]
H_2**1**$^{2+}$·Cl^-	2	linear	4 (H_2O)	[8]
2·Br^-	2	V-shaped	7100 (CD_2Cl_2)	[10]
3·2 I^-	2	V-shaped	160 ([D_6]DMSO)	[11]
4·Na^+·Cl^-	2	V-shaped	50 ([D_6]DMSO)	[13]
4·K^+·Cl^-	2	V-shaped	460 ([D_6]DMSO)	[13]
5·Cl^-	3	tine-shaped	3.8 (0.5% H_2O/[D_6]DMSO) 590 (CH_3CN)[c]	[17]
6·2 Cl^-	3	tine-shaped	n.r.[b]	[18]
(H**7**$^+$·Cl^-)$_2$	3	Y-shaped	n.r.[b]	[20]
8·2 Cl^-·H_2O	3	Y-shaped	40 (25% CD_2Cl_2/CD_3CN)	[22]
[**9**-H]$^-$·Cl^-	4	pseudo square planar	n.r.[b]	[25]
(**10**·F^-)$_2$	4	pseudo square planar	n.r. [b]	[26]
11·Cl^-	4	pyramidal	1930 ([D_6]DMSO)	[28]
12·Cl^-·2 H_2O	4	tetrahedral	18 ([D_6]DMSO)	[28]
13·2 Cl^-·2 H_2O	4	square planar	n.r.[b]	[29]
H_2**14**·2 Cl^-·H_2O	4	tetrahedral	180 ([D_6]DMSO)	[24]
15·2 Cl^-·2 H_2O	4	tetrahedral	3100 ([D_6]DMSO)	[24]
16·Cl^-·H_2O	5	square pyramidal	45 ([D_6]DMSO)	[28]
17·F^-·H_2O	5	square pyramidal	830 ([D_6]DMSO)	[30]
17·Cl^-·H_2O	5	square pyramidal	65 ([D_6]DMSO)	[30]
18·Cl^-	5	pentagonal planar	2148 ([D_6]DMSO) 555 (5% H_2O/[D_6]DMSO)	[32]
19$_2$·I^-	6	trigonal prism	$K_{11}=30$, $K_{21}=7670$[d] (50% D_2O/CD_3OD)[e]	[35]
20·Cl^-	6	hexagonal planar	n.r.[b]	[36]
21·F^-	6	trigonal prism	$>10^5$ ([D_6]DMSO)	[37]
21·Cl^-	6	uncertain	3000 ([D_6]DMSO)	[37]
22·F^-	9	tricapped trigonal prism	32000 ([D_6]DMSO)	[38]

[a] Determined by NMR titration using $n$$Bu_4N^+$ as counterion if not otherwise indicated (errors in $K<$ 15%). [b] n.r. not reported. [c] Determined by UV/Vis spectrophotometric titration. [d] 2:1 L:A complex ($LA+L \rightleftharpoons L_2A$). [e] NaI used for binding study (errors in $K<40$%).

The first synthetic halide receptors are normally considered to be the chloride inclusion complexes of the bicyclic katapinands **1** reported by Park and Simmons.[8] Although the halide inclusion phenomenon was reported in 1968 on the basis of NMR data, structural confirmation came only in 1975, when the structure of the chloride complex with diprotonated 1,11-diazabicyclo[9,9,9]nonacosane (H_2**1**$^{2+}$·Cl^-; Scheme 1) was reported.[9]

2.1. Coordination Number 2

The coordination numbers for most examples of hydrogen-bond coordination of anions begin at two. The bromide complex **2**·Br^- was characterized by X-ray crystallography, which showed that the bromide is hydrogen bonded in a two-coordinate V-shaped geometry with a *syn*,*syn* coordination mode and the two amide hydrogen atoms at distances of 2.39 and 2.68 Å from the bromide.[10] The amide groups are out of the phenyl plane, possibly as a result of the large size of the bromide ion.

The pyridine nitrogen atom in macrocycle **3** serves to preorganize the two adjacent amide groups for chelation, as illustrated by the two-coordinate V-shaped iodide complex. The amide N···I distances in this complex are 3.67 and 3.68 Å; these distances are nearly identical, which indicates that the fit of the iodide is relatively unstrained.[11]

Smith and co-workers extensively studied dual-host ditopic receptors (for example, receptor **4**) for both anions and cations, including halides and alkali-metal ions.[12–15] The cavity situation in these receptors often leads to a coordination number of two for halides, and the geometry is usually V-shaped. The additional electrostatic binding component provided by an adjacent cation also assists in stabilizing the complex. When Li^+ is the counterion, there is also room for water to reside in the cavity and to participate in hydrogen bonding with the anion.[14] Likewise, when ammonium is the counterion, it forms additional hydrogen bonds to the anion.[15]

Sung Ok Kang was born in Gwangju, Korea. She studied chemistry at Chonnam National University and completed her PhD there in supramolecular chemistry with Professor Kye Chun Nam in 2002. She has been a postdoctoral fellow with Professor Kristin Bowman-James at the University of Kansas since 2002. Her research focuses on developing anion receptors for the selective binding of anions.

Kristin Bowman-James was born in Philadelphia, Pennsylvania. She received her bachelor and PhD degrees from Temple University, held a postdoctoral appointment at The Ohio State University with Professor Daryle H. Busch, and has been at The University of Kansas since 1975, where she served for six years as Chair of the Department of Chemistry and is currently Professor of Chemistry. She is project director of the Kansas NSF Experimental Program To Stimulate Competitive Research (EPSCoR). Her research interests include biomimetic and supramolecular chemistry, and the synthesis of selective ion receptors.

© 2006 Wiley-VCH Verlag GmbH & Co. KGaA, Weinheim

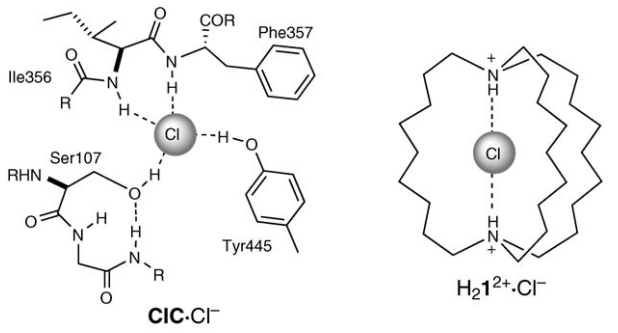

Scheme 1. Structure of the chloride site in the chloride ion channel (**ClC**·Cl⁻)[7] and the classic example of halide encapsulation in a katapinand, $H_2\mathbf{1}^{2+}$·Cl.[8,9]

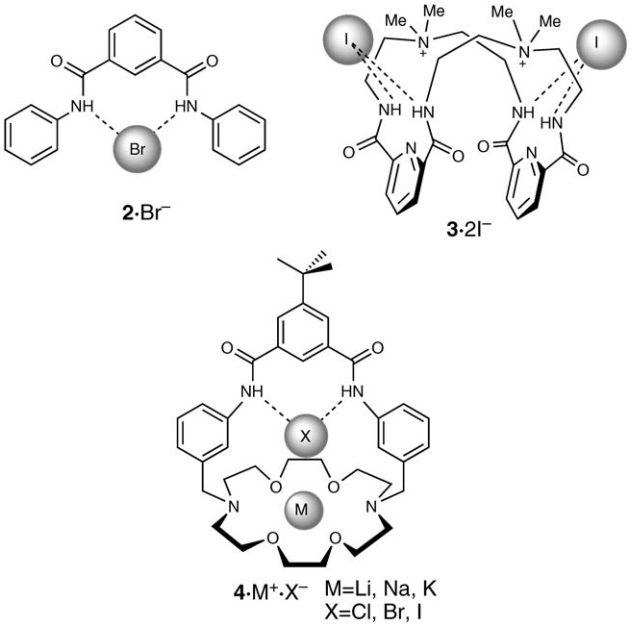

2.2. Coordination Number 3

Coordination number three is often observed with pincer type chelating ligands that contain three available hydrogen-bond-donor groups. Diamidopyrroles are excellent pincer ligands for three-point hydrogen bonding, and Gale et al. were the first to report the use of this framework for anion binding.[16] For example, in the diamidopyrrole receptor **5** reported later by Zieliński and Jurczak, the chloride ion is bound to the ligand by three hydrogen bonds to the amide and pyrrole hydrogen atoms (**5**·Cl⁻).[17] If this were a transition

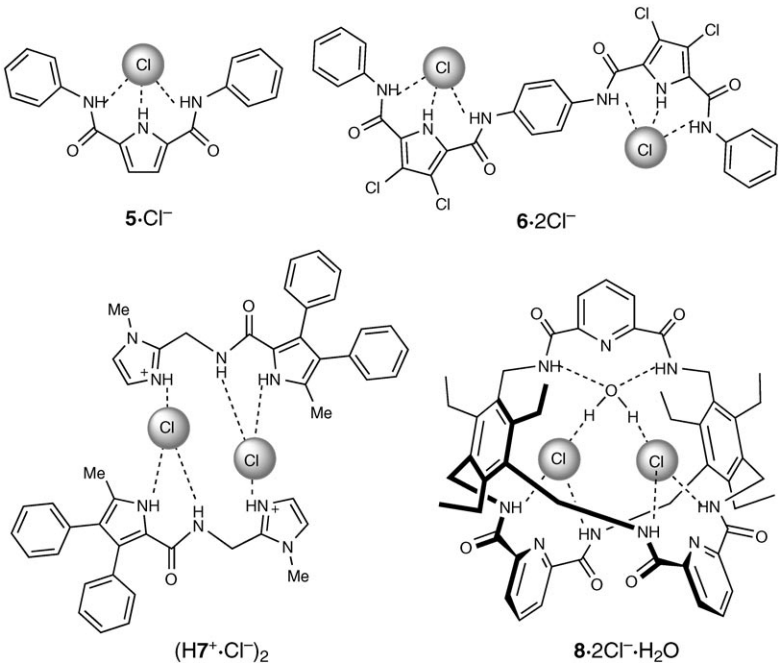

metal complex, the position of the metal ion would probably be in line with the two amides, and the geometry would be described as T-shaped. However, because of the geometrical placement of the hydrogen bonds imposed by the rigid ligand framework, the geometry of the anion complex approximates that of the splayed tines of a fork. The pyrrole N···Cl distance is fairly short (3.07 Å), whereas the two amide distances are 3.33 and 3.39 Å. The authors attributed the differences in bond lengths to a slightly imperfect fit of the chloride ion in the pincer cavity. This host framework resembles the isophthalamide-based amide receptor **2**.[10]

The related ditopic ligand **6**, a dichloro analogue of **5** that was synthesized to enhance the hydrogen-bonding capabilities, readily holds two chloride ions in the two separate binding sites. In the solid state, each Cl^- ion is bound by three NH groups: two amide groups (N···Cl = 3.27 and 3.28 Å) and a pyrrole donor (N···Cl = 3.07 Å).[18] Crystallization in the presence of $n\mathrm{Bu_4N^+F^-}$, however, results in deprotonation of the pyrrole owing to the highly basic nature of F^- in acetonitrile, which results in polymeric chains.[19]

A related potentially tridentate ligand, the mixed imidazolium/pyrrole **7**, was synthesized as a model for the prodigiosins.[20] Prodigiosins are natural products that contain three pyrrole units and can transport HCl across lipid membranes.[21] Studies indicate that **7** can induce the release of chloride across bilayer membranes. Transport is dependent on pH, being most efficient for pH gradients that range from acidic inside the vesicles (pH 4.0) to neutral outside (pH 6.7). The crystal structure indicates a dimeric complex with hydrogen bonding from the pyrrole (N···Cl = 3.24 Å) and amide (N···Cl = 3.29 Å) groups of one host to the chloride ion,

Rowshan Ara Begum completed her MS in chemistry at the University of Dhaka, Bangladesh, and her PhD in organometallic chemistry in Japan (2002) at Nara Women's University. She has held postdoctoral appointments with Professor Paul R. Sharp at the University of Missouri-Columbia (2002–2004), with Kristin Bowman-James at The University of Kansas (2004–2006), and is currently a research associate at York University in Toronto with Professor A. B. P. Lever.

© 2006 Wiley-VCH Verlag GmbH & Co. KGaA, Weinheim

and from the imidazolium NH group (N···Cl = 3.01 Å) on an adjacent dimer. In this manner, two chloride ions reside in a semichannel formed by the two hosts, with polar/ionic interactions within the channel and the lipophilic CH groups lining the outside.

Another three-coordinate halide is found in the chloride complex of the trigonally symmetric amide-based cyclophane **8**.[22] Two chloride ions are held by hydrogen bonding with amide hydrogen atoms of two of the three pyridine spacers. The water molecule is held by the amide groups of the third spacer, and bridges the two chloride ions. The chloride–water–chloride chain can be considered an anion analogue of transition-metal cascade complexes, which have a metal–anion–metal bridge or cascade,[3] and is seen in other polyammonium anion complexes[23] as well as another polyamide receptor (**14**), as described in Section 2.3.[24]

2.3. Coordination Number 4

Probably the most common coordination number for halides is four. The chloride complex of the acyclic pyrrole-based ligand **9** shows a rather unanticipated four-coordinate geometry, with hydrogen bonds from the two amide hydrogen atoms and two hydrogen atoms on the appended dinitrophenyl rings. Although pincer-like coordination with the pyrrole hydrogen atom might have been anticipated, exposure of the ligand to fluoride led to deprotonation of the pyrrole NH group. A similar reaction was also observed for **6**, as described above.[19] Gale suggests that a three-step complexation process occurs in anion binding: 1) The initial equivalent of fluoride added is coordinated, and a downfield shift of the CH protons on the aromatic ring is observed in the NMR spectrum; 2) With the second equivalent of fluoride, the pyrrole NH group is deprotonated, and bifluoride (FHF^-) is formed; 3) The third equivalent of fluoride is then coordinated. In the absence of the pyrrole hydrogen atom, this third fluoride ion avails itself of the phenyl CH groups in addition to the amide groups for hydrogen bonding. The crystal structure of the chloride complex, isolated serendipitously from a solution of the ligand and excess fluoride, confirmed the loss of the NH hydrogen and the hydrogen-bonding interactions with the phenyl CH groups.[25]

The acyclic thiophene-based amide ligand **10** forms a dimeric complex with flouride $[(\mathbf{10}\cdot F^-)_2]$,[26] in contrast to the monomeric complex of **5**, which has a similar framework with the exception of an available pyrrole hydrogen.[17] Two hydrogen bonds in $(\mathbf{10}\cdot F^-)_2$ form from the amide hydrogen atoms and two more from the two CH groups of the thiophene. The N···F distances are 2.59 and 2.62 Å, whereas the C···F distances are considerably longer at 3.05 and 3.13 Å, which leads one to speculate as to whether this complex should be considered to be a linear two-coordinate hydrogen-bonded complex. A similar binding preference was also observed by Zieliński and Jurczak in a pyrrole analogue with thioamide rather than amide hydrogen-bond donors.[17] In a recent computational investigation into the importance of CH···X hydrogen-bonding interactions, Bryantsev and Hay reported that arenes can form CH···X hydrogen bonds with strengths greater than 50% of those for commonly occurring OH and NH bonds, and concluded that these interactions could also play a major role in stabilizing host–guest complexes.[27]

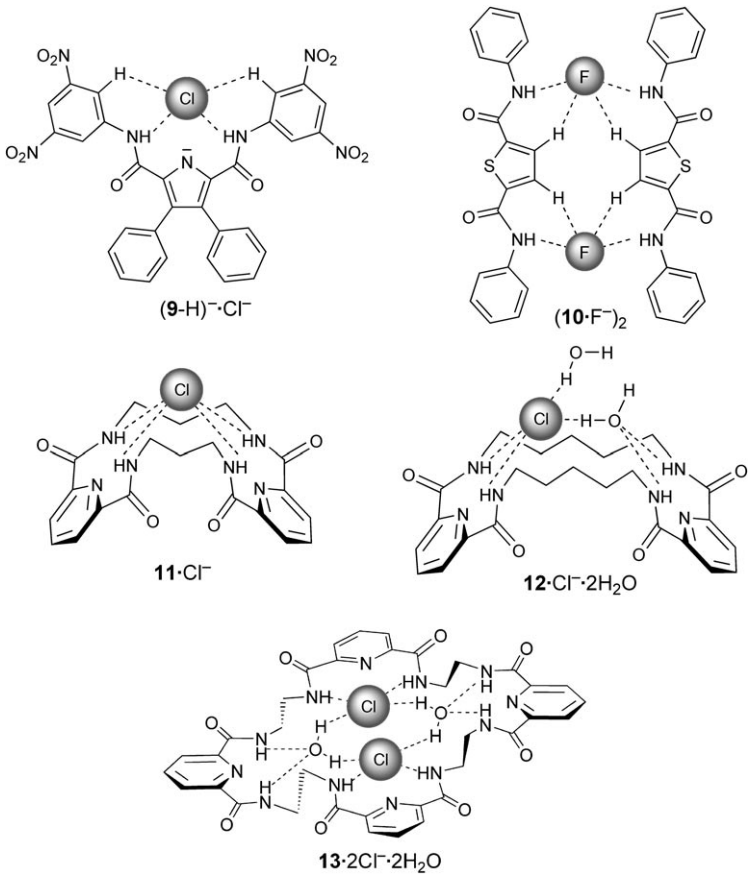

Anion complexes of a number of tetraamide macrocyclic hosts were found to have four-coordinate geometries. For example, the 20-membered ring **11** binds one chloride ion. For most efficient binding, the ligand bends and the chloride ion sits on top of the ligand above the mean plane of the four amide nitrogen atoms,[28] hydrogen-bonded to the four host amide NH groups (N···Cl = 3.24, 3.32, 3.33, and 3.34 Å). The coordination mode is pyramidal and similar to what is sometimes found for transition-metal complexes with macrocyclic ligands that are too small to incorporate the metal ion.

The somewhat larger macrocycle **12** also binds chloride, together with a water molecule slightly above the macrocyclic cavity.[28] Two of the coordination sites for the chloride ion are provided by the amide NH groups (N···Cl = 3.22 and 3.41 Å), a third from the neighboring water molecule (O···Cl = 3.24 Å), and a fourth from a water molecule from an adjacent macrocycle (O···Cl = 3.21 Å), which gives what could be described as a distorted tetrahedral geometry.

© 2006 Wiley-VCH Verlag GmbH & Co. KGaA, Weinheim

An expanded version of Jurczak's tetraamide-based macrocycles is the 36-membered-ring lactam **13** that results from a [4+4] condensation of the methyl ester of pyridine-2,6-dicarboxylate and ethylenediamine.[29] The macrocyclic framework has a steplike geometry, in which two opposing 2,6-pyridinedicarbamoyl groups are essentially coplanar and one of the remaining units is above and one is below that plane. Crystallographic results for the large macrocycle revealed four guests: two chloride ions bridged by two water molecules, all within the macrocyclic cavity (**13**·2 Cl^-·2 H_2O). Each chloride ion forms four hydrogen bonds, two with the amide groups, N···Cl = 3.33 and 3.37 Å, and two with different water molecules, O···Cl = 3.27 and 3.31 Å. Likewise, the water molecules form two rather long hydrogen bonds with the amide groups (N···O = 3.31 and 3.39 Å) in addition to hydrogen bonds to the two chloride ions, thus resulting in four coordination for both chloride ions and water molecules. The result is pseudo-square-planar coordination around each chloride ion.

The pyridine-based bicyclic receptor **14** and its methylated quaternary-amine form **15** were reported by our group.[24] In the chloride complex H_2**14**$^{2+}$·2 Cl^-·H_2O, the bridgehead amines are protonated and two of the amide loops fold in one direction while the other loop points in the opposite direction. Two chloride ions are held within the cryptand and are bridged by a water molecule. The partnership between chloride ion and water molecule seems to be prevalent in a number of these host–guest complexes (e.g., chloride complexes of **8**,[22] **12**,[28] and **13**[29]) and has also been observed for ammonium receptors.[23] One hydrogen bond is observed from the chloride ion to the bridgehead amine nitrogen (N···Cl = 3.17 Å), two others to the amide nitrogen atoms (N···Cl = 3.23 and 3.56 Å), and a fourth to the bridging water molecule (O···Cl = 3.15 Å). The result is a pseudotetrahedral coordination for each chloride ion.

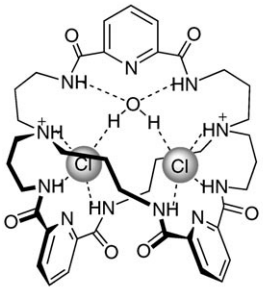

H_2**14**$^{2+}$·2 Cl^-·H_2O

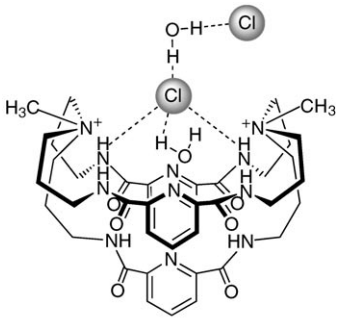

15·2 Cl^-·2 H_2O

The quaternary-amine cryptand **15** also binds chloride (**15**·2 Cl^-·2 H_2O).[24] In this case, all three amide loops of the ligand fold in the same direction, thus forming a bowl-like shape. Rather than being encapsulated, one chloride ion sits at the top of the bowl and is centered between the two charged amines. A second chloride ion is located off to one side of the macrocycle and is linked by water molecules to the first chloride ion. The chloride ion directly above the host is bound to two of the amide hydrogen atoms of **15** (N···Cl = 3.34 Å), with two additional linkages to the waters "floating" on top of the host to result in a pseudotetrahedral geometry.

2.4. Coordination Number 5

The common geometries of five-coordinate transition-metal complexes are square pyramidal and trigonal bipyramidal. Five-coordinate halide complexes are frequently found for simple tetraamide hosts, both acyclic and macrocyclic.

The acyclic host in **16**·Cl^-·H_2O is deformed slightly from planarity, and the two planar 2,6-pyridinedicarbamoyl groups are canted with respect to each other.[28] The chloride ion acts as a template and forms four hydrogen bonds to the amide hydrogen atoms; the N···Cl distances range from 3.25 to 3.31 Å. There is an additional hydrogen bond to a water molecule on one side of the macrocycle with a relatively short O···Cl distance of 3.18 Å. The resulting coordination geometry is pseudo square pyramidal. A tetrabutylammonium cation on the other side of the ligand is also nearby with a C···Cl contact of 3.67 Å. Although this contact is longer than the other hydrogen bonds, one could also reasonably argue for a pseudooctahedral geometry for this complex, as the authors did.

The 18-membered-ring macrocycle **17** forms both fluoride and chloride complexes (**17**·X^-·H_2O). Although the 18-membered ring might be considered an ideal size for the relatively small ion, the four amide groups undergo a slight tetrahedral distortion to accommodate the fluoride ion. With the fifth hydrogen bond to a water molecule, the resulting geometry is pseudo square pyramidal.[30] The N···F distances range from 2.74 to 2.88 Å, and the water molecule is poised above the fluoride ion at 2.54 Å. A similar geometry is found in the chloride structure, but the larger chloride ion sits 1.9 Å above the mean plane that passes through the four amide nitrogen atoms. Also, the binding of the anion is not symmetrical: two of the four amide hydrogen bonds are considerably shorter (N···Cl = 3.21 Å) than the other two

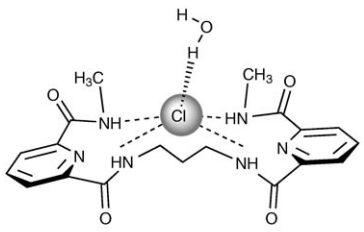

16·Cl^-·H_2O

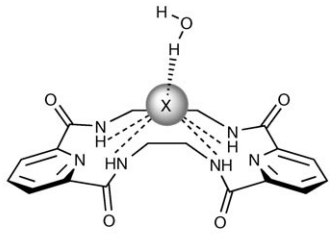

17·X^-·H_2O
X = F, Cl

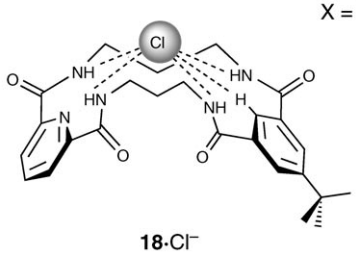

18·Cl^-

© 2006 Wiley-VCH Verlag GmbH & Co. KGaA, Weinheim

(N···Cl = 3.42 and 3.52 Å). Three of the distances to a neighboring tetraphenyl phosphonium countercation are also within van der Waals radii and possibly indicative of hydrogen bonding (C···Cl = 3.76–3.84 Å), which could make this complex formally eight-coordinate. Thus, assigning a coordination number is not always straightforward. The thioamide analogue of the **17** showed similar chloride binding.[31]

The hybrid tetraamide receptor **18** contains both 2,6-diamidopyridine and 1,3-diamidobenzene groups and also binds one chloride ion. The solid-state structure of the chloride complex (**18**·Cl^-) shows the chloride ion held through five hydrogen bonds inside the cavity of the macrocycle.[32] The NH groups form four hydrogen bonds and the aromatic CH group forms the fifth bond with the chloride ion. The isophthalamide tilts up slightly, so that the CH hydrogen binds from slightly over the macrocyclic ring (C···Cl = 3.56 Å). The distance between the chloride ion and amide nitrogen atoms is slightly shorter on the pyridine side (N···Cl = 3.27 Å) than on the isophthalamide side (N···Cl = 3.34 Å). The authors attribute this effect to the more rigid geometric constraints imposed by the hydrogen bonding of the amides with the pyridine lone pair as opposed to the more flexible "outspread" arms of the isophthalamide.

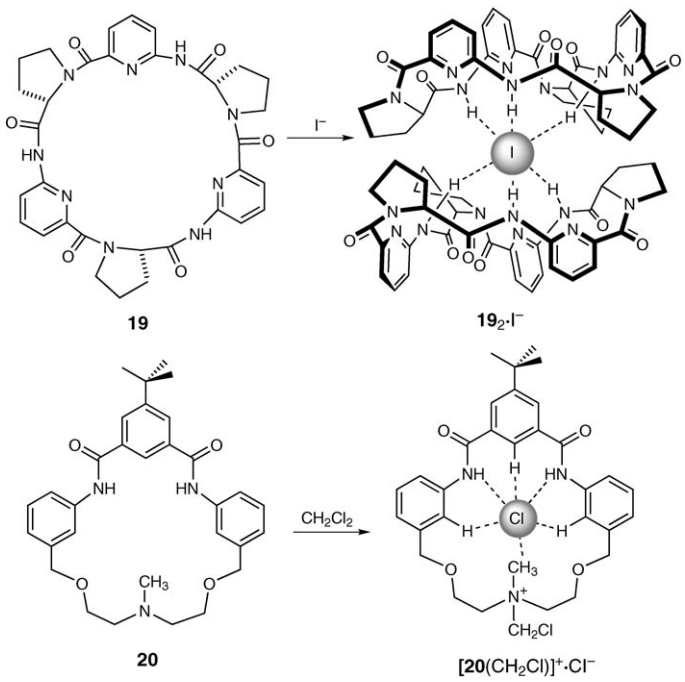

2.5. Coordination Number 6

Coordination number six is quite common in transition-metal complexes, in which the prevalent geometry is octahedral, and perfect trigonal prismatic geometry is rarer. Often there is some distortion in the L-M-L dihedral angles, as viewed down the threefold axis, from 0° (perfect trigonal-prismatic geometry) to 60° (perfect octahedral geometry), so that the actual geometry is somewhat in between the two. Such an effect is called a trigonal twist, and is especially noted for triscatecholate transition-metal complexes of amide-based cryptands.[33] Six-coordinate halide complexes also appear to be relatively common.

The cyclic hexapeptide **19**, which contains three amide groups, was found to bind halides even in aqueous solution.[34] The crystal structure of the iodide complex revealed a 2:1 complex **19**$_2$·I^- in which the iodide ion is sandwiched between the two cyclopeptides. There are two crystallographically independent iodide complexes in the unit cell, both of which have virtually identical structures, indicating that a sandwich complex is the preferred coordination mode in this environment. The two cyclopeptides in both complexes are almost perfectly aligned with each other, so that there is only minor deviation from trigonal-prismatic geometry. The iodide ion is associated with the six amide hydrogen atoms, which point into the cavity, with I···N distances ranging from 3.65 to 3.94 Å. Electrospray ionization mass spectra indicate that the stability of the halide complexes of **19** increases with increasing size: $Cl^- < Br^- < I^-$.[34,35]

Smith and co-workers recently reported an example of solvent fixation by the potentially ditopic receptor **20**. The crystal structure of the complex isolated from CH_2Cl_2 revealed that the CH_2Cl_2 had undergone nucleophilic attack by the amine lone pair with the released chloride ion being bound within the cavity to yield [**20**(CH_2Cl)]$^+$·Cl^-.[36] The Cl^- ion is hydrogen bonded to two amide hydrogen atoms (N···Cl = 3.29 and 3.32 Å), three *m*-xylyl CH groups (C···Cl = 3.36, 3.64 and 3.74 Å), and a methyl CH group (C···Cl = 3.26 Å); the resulting arrangement of coordination sites is hexagonal planar.

The bicyclic receptor **21** reported by our group was found to be selective for fluoride. All six NH groups are within

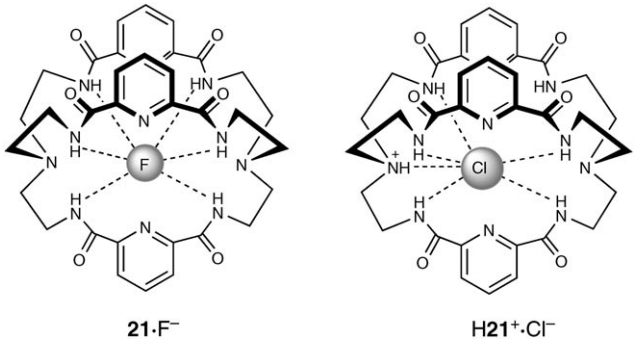

hydrogen-bonding distances (N···F = 2.84–2.89 Å) of the encapsulated fluoride ion.[37] The distance between the two bridgehead amines is 7.39 Å. The coordination geometry of the fluoride ion is approximately midway between trigonal prismatic and octahedral; the trigonal twist angle is 37°. A septet is observed in the ^{19}F NMR spectrum of the complex in [D_6]DMSO for the coupling of the $I = {}^1/_2$ fluoride nucleus with the six amide hydrogen atoms, which indicates that encapsulation prevails even in solution. Deuterium exchange between the [D_6]DMSO and the cryptand amide hydrogen atoms is also observed in solution, facilitated by the strongly basic nature of the fluoride ion in DMSO. This exchange phenom-

© 2006 Wiley-VCH Verlag GmbH & Co. KGaA, Weinheim

enon leads to a change in the pattern of multiplets in the ^{19}F NMR spectrum over time from the septet to a singlet, the latter indicative of complete amide deuteration.[38]

The bridgehead amines in **21** may be protonated upon complexation. The crystal structure of **21** with chloride indicates a monoprotonated complex $H\mathbf{21}^{+}\cdot Cl^{-}$. In fact, **21** acts as a scavenger for any HCl present in solution in chloroform; there is evidence for the formation of both 1:1 ($H\mathbf{21}^{+}\cdot Cl^{-}$) and 1:2 ($H_2\mathbf{21}^{2+}\cdot 2\,Cl^{-}$) complexes.[37] In the crystal structure of the chloride complex $H\mathbf{21}^{+}\cdot Cl^{-}$, a single chloride sits at one side of the cryptand with hydrogen bonds to five amide hydrogen atoms and a protonated bridgehead amine. The distance between the two bridgehead amines is 7.07 Å, which is shorter than that in $\mathbf{21}\cdot F^{-}$.[37] The hydrogen bonds to the amide groups (N···Cl) range from 3.33 to 3.60 Å, and the distance to the bridgehead amine nitrogen atom is 3.20 Å.

2.6. Coordination Numbers 7 and 8

These coordination numbers are relatively high for halides. Thus, we found no structurally characterized examples of anion complexes with amide-based receptors. One possible exception is the complex $\mathbf{17}\cdot Cl^{-}$, which is potentially eight-coordinate if the rather long CH···Cl bonds from the tetraphenyl phosphonium counterion are counted. However, we chose instead to consider that complex as an example of a pentacoordination.[30] However, coordination numbers seven and eight can be found in ligands with other hydrogen-bond-donor groups, for example, in the bromide complex of a macrobicyclic azaphane[39] and the chloride complex of a calix[4]bipyrrole,[40] respectively.

2.7. Coordination Number 9

What may be the highest coordination number found for the halides with amide-based receptors is observed with the *m*-xylyl analogue **22** of the pyridine-containing cryptand **21**.[38] The crystal structure of the fluoride complex indicates nine coordination: six bonds to the amide hydrogen atoms and an additional three interactions with the *m*-xylyl CH groups. The N···F and C···F distances both average 3.05 Å and vary from 3.04 to 3.08 Å for C···F and from 2.94 to 3.11 for N···F. The ^{19}F NMR spectra support the existence of all nine hydrogen bonds. Deuterium exchange in [D_6]DMSO again occurs, as was seen for **21** with fluoride, but in this case the final coupling pattern is a quartet, which is indicative of coupling of the $I = {}^{1}/_{2}$ fluoride ion with the three remaining nonexchangeable *m*-xylyl CH groups.

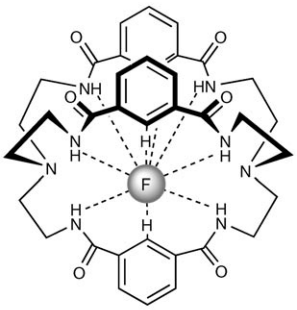

$\mathbf{22}\cdot F^{-}$

3. Linear Anions

Examples of linear anions include azide, thiocyanate, cyanide, and bifluoride. However, to our knowledge, only one example of a crystallographically characterized linear anion complex with an amide host has been reported to date.[41] The first inclusion complex of a linear anion was observed by Lehn for azide in an octaazacryptand.[42] Although it was envisioned that bifluoride should also bind in these "linear" azacryptand receptors, a selective receptor for bifluoride was only recently reported, along with a crystal structure.[41]

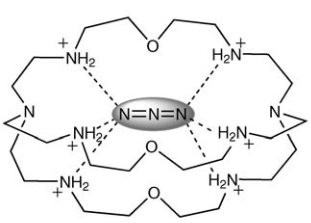

$H_6\mathbf{23}^{6+}\cdot N_3^{-}$

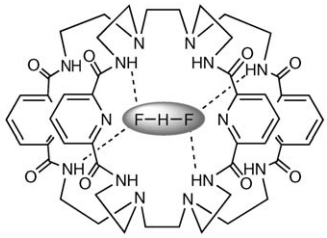

$\mathbf{24}\cdot HF_2^{-}$

In the crystal structure of azide complex of **23**, the seminal example of a linear anion complex, all six of the secondary amine groups are protonated and are hydrogen bonded to the linear N_3^{-} ion in a C_3-trigonal-prismatic symmetry pattern. The azide terminal N···N distance is very short (2.32 Å) and the hydrogen-bond distances from the azide terminus to the secondary amines are 2.94 Å.[42]

The isolation and structural characterization of the encapsulated azide complex led researchers to seek the sequestering of another linear anion, namely bifluoride (FHF^{-}), within a receptor cavity. Although this goal has not been achieved to date for bicyclic hosts, we recently reported the tricyclic amide-based receptor **24**, which binds bifluoride.[41] The structurally characterized FHF^{-} complex of the tricycle **24** contains a linear FHF^{-} ion bridging the two macrocyclic caps of the cylindrical tricycle. Although **24** contains eight amide groups as potential hydrogen-bonding sites, only four are utilized, which results in a tetrahedral four-coordinate geometry based on the topology of the four bound NH groups around the anion. The other four amide hydrogen atoms are involved in three-atom hydrogen-bonding networks between the amide hydrogen atoms, and the pyridine and tertiary amine nitrogen lone pairs. The F···F distance in **24** is 2.47 Å. Binding studies revealed selective binding for FHF^{-} over other anions with binding constants $K = 5500$ and $> 10^5$ in [D_6]DMSO and $CDCl_3$, respectively (Table 2).

© 2006 Wiley-VCH Verlag GmbH & Co. KGaA, Weinheim

Table 2: Coordination numbers (C.N.), geometries, and association constants (K [M^{-1}])[a] of **23** and **24** with linear anions.

Complex	C.N.	Geometry	K (Solvent)	Ref.
H_6**23**$^{6+}\cdot N_3^-$	6	trigonal prism	40000 (H_2O, pH 5)[b]	[42]
24$\cdot HF_2^-$	4	tetrahedral	5500 ([D_6]DMSO)	[41]
			$>10^5$ ($CDCl_3$)[c]	

[a] Determined by NMR titration (errors in $K<15\%$). [b] NaN_3 used for binding study. [c] $n$$Bu_4N$(FHF) used for binding study.

4. V-Shaped Anions

For the purposes of this Minireview, we assign the geometry of carboxylate anions as V-shaped by virtue of their two binding sites. Thus, in addition to truly V-shaped anions such as nitrite, simple carboxylates such as acetate and benzoate will also be considered in this section.

4.1. Coordination Number 1

As described above, dual-host receptors such as **4**, consisting of crown ethers covalently attached to amide-containing straps, bind halides along with their associated cation. This mode of binding also works with other anion shapes, for example, nitrite. However, in the relatively rare example of a crystal structure of a nitrite complex (**4**$\cdot Na^+\cdot NO_2^-$), it would appear that the main driving force for binding is chelation of the two nitrite oxygen atoms with the Na^+ counterion. One of the nitrite oxygen atoms is associated with one of the amides (N···O = 2.90 Å), and the distance between the nitrite nitrogen atom and the other amide nitrogen atom is 3.33 Å.[43] In view of this rather long distance, the nitrite ion may appropriately be considered singly coordinated.

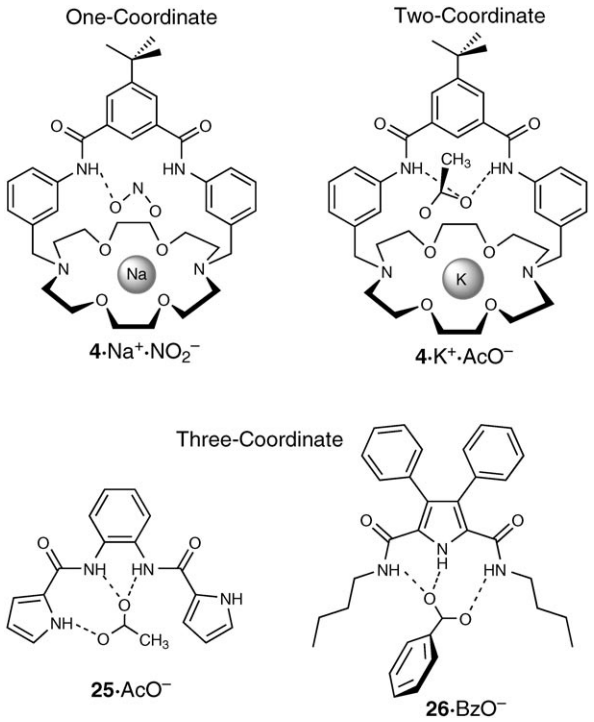

4.2. Coordination Number 2

The acetate complex of **4** is an example of a two-coordinate receptor in which the anion is also chelated by its counterion (K^+), and the acetate ion lies somewhat outside the cavity. Again, only one of the oxygen atoms is hydrogen bonded to the amide portion of the receptor, but in this case to both amides (N···O distances of 2.93 and 3.01 Å),[43] which makes this a two-coordinate V-shaped geometry.

4.3. Coordination Number 3

Cheng and co-workers were the first to report **25** as an anion receptor.[44] Shortly thereafter, Gale and co-workers reported the crystal structures of the acetate complex of **25**[45] and the benzoate complex of **26**.[46] Both complexes exhibit three hydrogen-bonding interactions between the anions and the amide and pyrrole hydrogen atoms. In the acetate structure with **25**, the two hydrogen bonds to the amides (N···O) are 2.73 and 2.75 Å, and the hydrogen bond to the pyrrole NH group is slightly longer (N···O = 2.78 Å). The other pyrrole ring is oriented *exo* to the anion-binding site and links to an amide oxygen atom of an adjacent complex. These geometries are a bit more difficult to assign, but if one just considers directionality, perhaps these geometries most closely approximate the tine-like binding seen for some of the three-coordinate halide complexes.

Host **26** shows a very high selectivity for benzoate in CD_3CN ($K = 2500$, Table 3).[46] In the crystal structure, one of the benzoate oxygen atoms is bound by two hydrogen bonds (one to the pyrrole and one to the amide), and the other is bound by just one hydrogen bond to the other amide. N···O distances range from 2.77 to 2.84 Å, and one of the amides is tilted out of the plane of the pyrrole ring and other amide.

Table 3: Coordination numbers (C.N.), geometries, and association constants (K [M^{-1}])[a] of ligands **4**, **8**, **17**, **25**, and **26** with V-shaped anions.

Complex	C.N.	Geometry	K (Solvent)	Ref.
4$\cdot Na^+\cdot NO_2^-$	1	linear	n.r.[b]	[43]
4$\cdot K^+\cdot AcO^-$	2	V-shaped	n.r.[b]	[43]
25$\cdot AcO^-$	3	tine-shaped	251 ([D_6]DMSO)	[45]
26$\cdot BzO^-$	3	tine-shaped	2500 (CD_3CN)	[46]
8$\cdot AcO^-$	4	pyramidal/square planar	770 (25% CD_2Cl_2/CD_3CN)	[22]
17$\cdot AcO^-\cdot H_2O$	5	square pyramidal	2640 ([D_6]DMSO)	[30]
$\mathbf{17}_2\cdot AcO^-$	8	tilted square prism	2640 ([D_6]DMSO)	[30]

[a] Determined by NMR titration using $n$$Bu_4N^+$ as counterion (errors in $K<15\%$). [b] n.r. not reported.

4.4. Coordination Number 4

The trigonally symmetric amide-based cyclophane **8** was originally designed to be selective for anions with C_3 symmetry. As expected, this receptor is selective for the trigonal-planar nitrate ion and for acetate with binding constants $K = 300$ and 770, respectively in 25% CD_2Cl_2/CD_3CN.[22] The crystal structure of the acetate complex

© 2006 Wiley-VCH Verlag GmbH & Co. KGaA, Weinheim

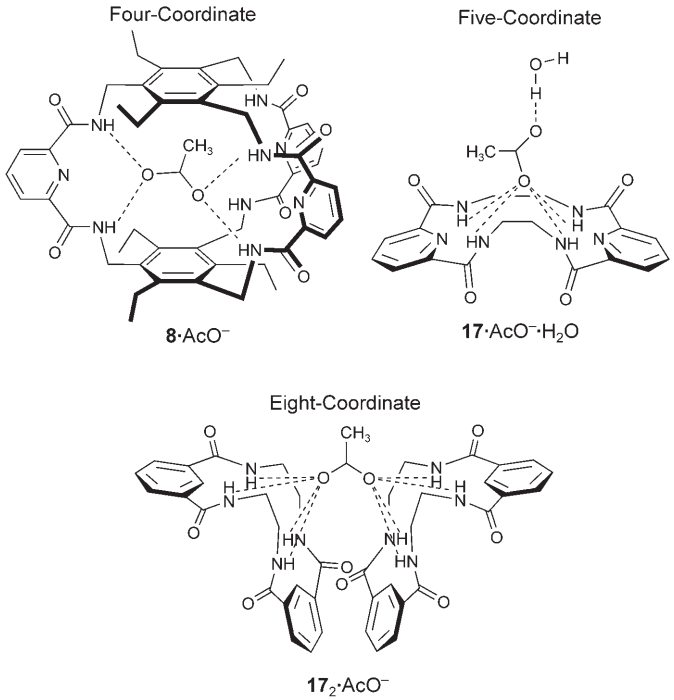

revealed four hydrogen-bonding interactions (two hydrogen bonds from each oxygen atom to amides of the pyridine-2,6-diamide spacers) and a pyramidal or possibly square-planar-like coordination geometry.

4.5. Coordination Number 5

Crystal structures of the acetate complexes of tetraamide macrocycle **17** revealed both 1:1 and 2:1 ligand:anion stoichiometries with five- and eight-coordinate geometries, respectively. In the 1:1 complex, grown from tetramethylammonium acetate, one of the acetate oxygen atoms is involved in four hydrogen-bonding interactions with all four amide hydrogen atoms with N···O distances ranging from 2.89 to 3.03 Å. The remaining acetate oxygen atom is hydrogen bonded to an axial water molecule at an O···O distance of 2.70 Å. The result is a square-pyramidal structure similar to those seen for this ligand with halides (see Section 2.4).[30]

4.6. Coordination Number 8

In contrast, when crystals are grown from tetrabutylammonium acetate a sandwichlike structure with **17** is observed. In this case, each acetate oxygen atom is hydrogen bonded to all four amide hydrogen atoms of the adjacent macrocycle (N···O = 2.99–3.06 Å).[30] The result is octacoordination and a pseudo (tilted) square prismatic geometry.

5. Trigonal-Planar Anions

One of the classic examples of host–guest binding of a trigonal-planar anion is the nitrate complex of the tren-based amine cryptand system **27**. Two nitrate ions are encapsulated

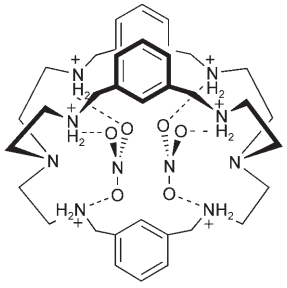

in **27** in an eclipsed conformation with distances $N_{nitrate}\cdots N_{nitrate} = 3.34$ Å and $N_{nitrate}\cdots N_{bridgehead} = 3.07$ and 3.09 Å[47] (only slightly less than the sum of the van der Waals radii: 3.10 Å).[48] The distance between the bridgehead amines is 9.48 Å. All six secondary amine groups in **27** are protonated, and each set of trigonally symmetric amines shows bifurcated hydrogen-bonding contacts with two of the nitrate oxygen atoms, one at a shorter distance (N···O ≈ 2.9 Å) and the other at a slightly longer distance (N···O ≈ 3.0 Å). (In the drawing only one hydrogen bond per nitrate oxygen atom is shown for clarity.) Once again the geometrical complementarity of the host, one of the important factors in a host–guest complex, clearly plays a role in the binding of the trigonal-planar nitrate. More recently, Hay et al. used crystallographic data and electronic structure calculations to determine geometrical preferences for hydrogen bonding of nitrate with host molecules,[49] and showed that a six-coordinate geometry, as observed for **27**, is optimum.

5.1. Coordination Number 2

Macrocycle **28**, which possesses oxamido and amine units, is capable of binding anions or metal ions. The crystal structure of the dinitrate complex revealed interesting structural similarities to the dinitrate complex of **27**. In $H_4\mathbf{28}^{4+}\cdot 2NO_3^-$, the macrocycle is tetraprotonated and shows only two hydrogen-bonding interactions for each nitrate ion. As with **27**, the two nitrate ions bind in an eclipsed conformation at an $N_{nitrate}\cdots N_{nitrate}$ distance of 3.5 Å and are each about 4 Å from the oxamido caps.[50]

The dual-host receptor **4**, described earlier for encapsulation of halides, acetate, and nitrite, also binds nitrate. Several crystal structures have been obtained with nitrate and three different cations (Li^+, Na^+, and K^+). For both Na^+ and K^+, two of the nitrate oxygen atoms chelate the cation, and the third is hydrogen bonded to the amide part of the ligand. The third oxygen in the Na^+ complex sits at rather lengthy distances (3.14 and 3.24 Å) from the two amide nitrogen atoms. With the larger K^+ ion, the nitrate sits further outside

© 2006 Wiley-VCH Verlag GmbH & Co. KGaA, Weinheim

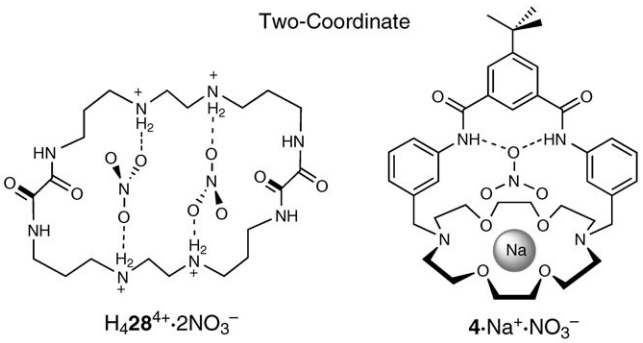

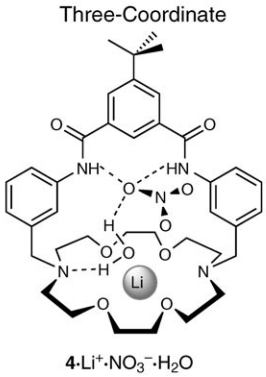

the cavity and is situated asymmetrically with respect to the two amide hydrogen atoms in a disordered structure, which makes one of the two potential hydrogen-bonding interactions virtually nonexistent (N···O = 2.90 and 3.84 Å).[43] Hence, it might more appropriately be considered an example of monocoordination in terms of hydrogen bonds.

5.2. Coordination Number 3

With the smaller Li^+ complex of **4**, however, there is room for an additional guest, in this case water, and, rather than chelating the Li^+, the nitrate is associated with the cation through a water bridge. The nitrate ion in this structure is almost coplanar with the crown ether and only one of its oxygen atoms points inside the cavity to hydrogen bond with the two amide hydrogen atoms (N···O distances of 3.07 and 3.03 Å). In somewhat unusual binding, the hydrogen bond from the bridging water molecule appears to be directed, not to one of the remaining lone pairs of the nitrate oxygen atom, but rather to the π cloud of that oxygen atom.[43]

Carbonate is also a trigonal-planar anion. Carbonate structures with amide-based ligands have not been reported to our knowledge. However, there are a number of carbonate structures with other types of hosts, for example, naphthalimide,[51] urea,[52] and calixpyrrole receptors.[53]

Table 4: Coordination numbers (C.N.), geometries, and association constants (K [M^{-1}])[a] of **4**, **27**, and **28** with nitrate.

Complex	C.N.	Geometry	K (Solvent)	Ref.
H_6**27**$^{6+}$·2 NO_3^-	3	trigonal planar	K_{11} = 1050 (H_2O), K_{12} = 240 (H_2O)[b]	[47]
H_4**28**$^{4+}$·2 NO_3^-	2	V-shaped	n.r.[c]	[50]
4·Na^+·NO_3^-	2	V-shaped	n.r.[c]	[43]
4·Li^+·NO_3^-·H_2O	3	T-shaped	n.r.[c]	[43]

[a] Association constants were determined by potentiometric titrations. [b] 1:2 L:A complex (LA + L⇌L_2A). [c] n.r. not reported.

Table 4 summarizes the coordination parameters for host–guest compounds with trigonal-planar anions.

6. Tetrahedral anions

Phosphate and sulfate are key anions in biological systems, and the phosphate-binding (**PBP**) and sulfate-binding (**SBP**) proteins provide classic examples of selective receptors for these tetrahedral anions. These two proteins are capable of highly selective binding of sulfate and monohydrogen phosphate (K values approximately 10^6; Table 5). The crystal structures of both proteins reveal multiple and strong hydrogen bonding through a mixture of functional groups, including amides as well as pyrrole (tryptophan), carboxylate, and guanidinium (arginine) groups. Twelve hydrogen bonds in total hold the monohydrogen phosphate in place in the **PBP** and a mere seven hydrogen bonds hold the sulfate in the

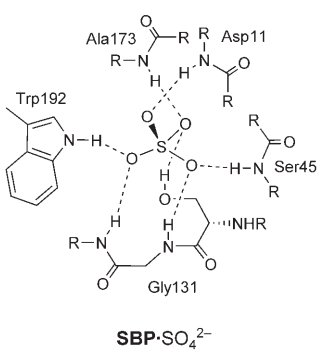

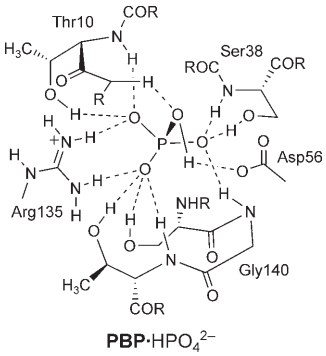

Table 5: Coordination numbers (C.N.), geometries, and association constants (K [M^{-1}])[a] of **SBP**, **PBP**, **14**, **21**, and **29–31** with sulfate.

Complex	C.N.	Geometry	K (Solvent)	Ref.
SBP·SO_4^{2-}	7	monocapped trigonal prism	ca. 10^6 (H_2O, pH 5–8.1)	[55]
PBP·HPO_4^{2-}	12	uncertain	10^6 (H_2O, pH 8.3)	[54]
H_2**29**$^{2+}$·SO_4^{2-}·H_2O	6	pseudooctahedral	108000 (CH_3CN)[b]	[57]
H_2**14**$^{2+}$·SO_4^{2-}·3 H_2O	7	monocapped trigonal prism	2700 ([D_6]DMSO)	[24]
30$_2$·SO_4^{2-}	8	pseudo square prism	794 ([D_6]DMSO) 31600 ($CDCl_3$)	[58]
H_2**21**$^{2+}$·SO_4^{2-}	8	bicapped trigonal prism	68 ([D_6]DMSO) 91200 ($CDCl_3$)	[59]
H_2**31**$^{2+}$·SO_4^{2-}	8	uncertain	n.r.[c]	[60]

[a] Determined by NMR titration using $n$$Bu_4N^+$ as counterion (errors in K < 15%). [b] Determined by UV/Vis spectrophotometric titration. [c] n.r. not reported.

© 2006 Wiley-VCH Verlag GmbH & Co. KGaA, Weinheim

SBP.[54,55] Following these crystallographic reports by Quiocho and co-workers of the anion-bound complexes of phosphate- and sulfate-binding proteins, researchers have sought to design selective receptors with high affinities for oxoanions by mimicking these natural hosts.

Five structures of amide-based receptors for sulfate, which range in coordination number from six to eight, serve to illustrate sulfate-binding patterns. Three of the five structures are eight-coordinate. Hay and co-workers postulated a maximum coordination preference of 12 for sulfate,[49] but dodecacoordination was found only recently in a trifurcated urea-based host.[56] Since that host did not contain amide groups, it will not be discussed here.

6.1. Coordination Number 6

The lowest coordination number for tetrahedral anions (six) was observed in the hybrid amide/pyrrole mixed cyclic receptor **29**.[57] A neutral complex was isolated in which both

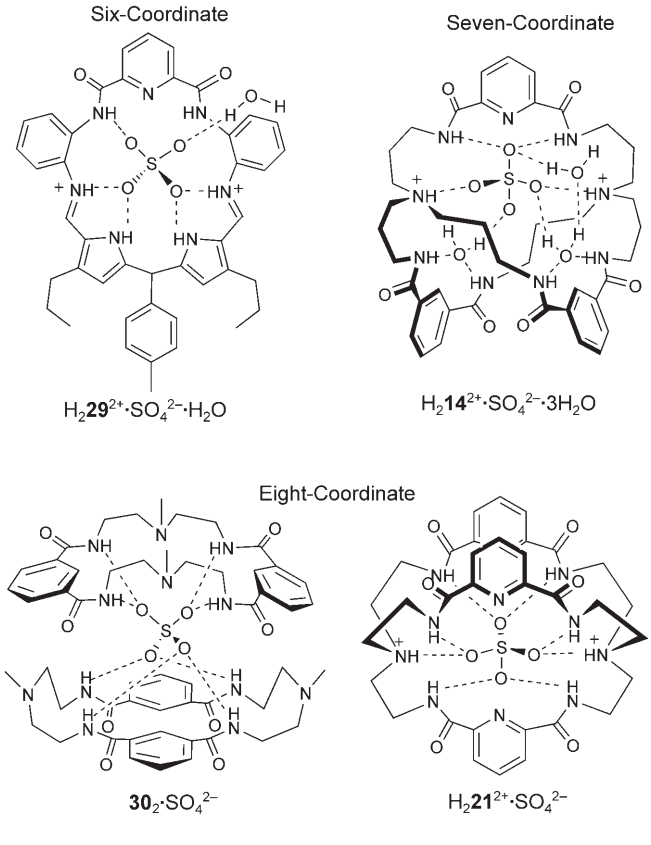

of the imine nitrogen atoms are protonated. Sulfate is held slightly above the ring, and two of the sulfate oxygen atoms are each hydrogen bonded to both a pyrrole (N···O = 2.79 and 2.75 Å) and a protonated imine (N···O = 2.71 and 2.72 Å). One of the other oxygen atoms is hydrogen bonded to one of the amide hydrogen atoms. The remaining sulfate oxygen atom is hydrogen bonded to a nearby water molecule. The structure could be considered pseudooctahedral on the basis of the placement of the hydrogen-bond donors.

6.2. Coordination Number 7

A seven-coordinate complex was observed for **14**, which is large enough to hold multiple guests.[24] In this case, a sulfate ion and two water molecules are held within the cavity; the sulfate ion acts as a bridge between the two bound water molecules. This is the reverse of what is seen for **8** and **14** with chloride, in which a water molecule bridges two chloride ions (xSections 2.2 and 2.3, respectively). Sulfate is bound inside the cavity by seven hydrogen bonds: two to amide hydrogen atoms of one of the three loops (N···O = 2.94 and 2.88 Å), two to the protonated amines (N···O = 2.69 and 2.79 Å), two to the bound water molecules (O···O = 2.78 and 2.79 Å), and one to a water outside the cavity (O···O = 2.84 Å).

6.3. Coordination Number 8

The simple tetraamide macrocycle **30** was found to be selective for tetrahedral oxo acids.[58] The crystal structure of **30** with sulfate revealed a sandwich complex with a dinegatively charged sulfate ion held between two macrocycles. Each of the sulfate oxygen atoms is held by two amide bonds at N···O distances ranging from 2.86 to 2.98 Å. The two macrocycles are rotated by 90° with respect to each other, which results in a similar coordination mode and accommodates the S_4 symmetry axis of the sulfate ion. The resulting coordination geometry, in which a total of eight amide hydrogen atoms bind to the sulfate ion, is pseudo square prismatic.

An eight-coordinate complex is also observed for the sulfate complex with the bicyclic amido cryptand **21**. All six amide hydrogen atoms and two additional hydrogen atoms on the protonated bridgehead amines are utilized for hydrogen bonding. The geometry of the neutral complex is best described as a distorted bicapped trigonal prism with amide N···O distances ranging from 2.74 to 2.97 Å and slightly shorter amine distances (both N···O distances are 2.66 Å).[59]

Another hybrid receptor, the sulfate complex H_2**31**$^{2+}$·SO_4^{2-}, which is a [3+3] condensation product of bipyrrole and pyridinediamide, was isolated during the crystallization of the [2+2] condensate with sulfate.[60] The isolation of the higher-order analogue indicates that the anion plays an important role as a template in promoting the formation of the higher-order condensate. In the crystal structure of the sulfate complex, the huge macrocycle is diprotonated and twisted to accommodate the sulfate. There are eight hydrogen bonds to the sulfate ion: six from the three bipyrroles and two from the protonated imines. Although there was some disorder in the sulfate ion, interestingly, the amides do not participate in hydrogen bonding.

7. Summary and Outlook

Now that the structural data for amide-based anion receptors has reached a critical mass, trends for coordination number and geometries are emerging that parallel those in transition-metal coordination. As anticipated, halides, with

© 2006 Wiley-VCH Verlag GmbH & Co. KGaA, Weinheim

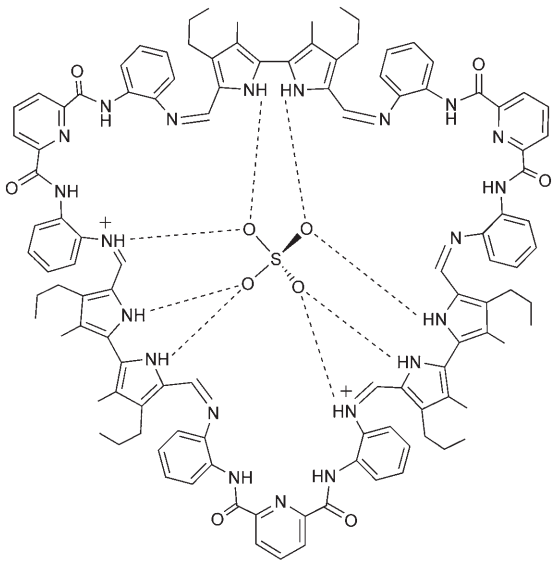

H_2**31**$^{2+}$·SO_4^{2-}

their sp^3-hybridized lone pairs, often form complexes with tetrahedral, four-coordinate geometries. However, with pincer hosts, they can also form three-coordinate complexes as a result of the three chelating coordination sites. Higher coordination numbers are also observed. For example, square-pyramidal pentacoordination can occur for transition-metal coordination complexes, especially with macrocyclic ligands, which tend to form the square plane around the macrocycle, leaving one or two open axial coordination sites. In halide coordination, the same phenomenon is observed. Halides can form simple square-planar or pyramidal-like geometries with macrocycles (e.g., **11**·Cl^-), or pseudo-square-pyramidal coordination as seen for **16**·Cl^-·H_2O and **17**·Cl^-·H_2O. However, when appropriate binding sites are in place, halides can form even higher coordination numbers, as high as nine.

Coordination geometries for the other topologies also have some commonalities within a given shape. For example, V-shaped ions can form anywhere from one- to five-coordinate complexes, whereas one would expect for simple carboxylates that four coordinate—two bonds to each oxygen atom—would be the norm. Although this is the case for **8** with acetate, carboxylate oxygen atoms may in fact acquire as many as four hydrogen bonds each, as seen for the monomeric and dimeric complexes of **17** with acetate. Although trigonal-planar geometries might be anticipated for nitrate, as seen for H_6**27**$^{6+}$·$2NO_3^-$, in other structures not all of the nitrate oxygen atoms are held by hydrogen bonds. Sulfate clearly prefers the higher coordination numbers, which range from six to eight in the amide-based receptors described herein (and, as noted in Section 6, potentially twelve for other hosts).

Another key feature of the anion coordination complexes described above is the frequent presence of one or more molecules of water in the coordination sphere. This feature is, in fact, another similarity between anion and transition-metal coordination chemistry, especially when water fills a vacant coordination site. This phenomenon is seen for hosts **8** and **12**–**17** with chloride, the monomeric **17** with acetate, **4** with $LiNO_3$, and **14** and **29** with sulfate.

Although it would be appealing to be able to correlate anion affinities with coordination number in these complexes, this is clearly not possible, as even a cursory glance at the binding constants included in Tables 1–5 reveals. Binding affinities will be influenced by many factors including ligand size, flexibility, dimensionality (e.g., acyclic, monocyclic, bicyclic, etc.), and the positioning of hydrogen-bond-donor groups. External factors such as solvation and desolvation effects for the ligand and the anion, as well as the identity of the solvent itself, play critical roles in the determining anion affinities.

Anion coordination chemistry is finally achieving the recognition and respect that it deserves, and the outlook for this incredibly exciting field has never been better. Over the last forty years tremendous advances have been made in understanding the basic driving forces that are operative in anion binding and the relation of these forces to observed selectivity patterns. As a result, the field abounds with elegantly designed and targeted receptors for a variety of anions of all shapes and sizes. This thought is shared by Nobel Laureate Jean-Marie Lehn: *"In harmony with the important role played by anionic species both in chemistry and in biology, anion coordination chemistry has become an established new domain of a generalized coordination chemistry."*[1]

We thank the National Science Foundation (CHE-0316623) and the Environmental Management Science Program of the US Department of Energy (DE-FG02-04ER63745) for support of our work reported herein.

Received: May 19, 2006
Published online: October 30, 2006

[1] *Supramolecular Chemistry of Anions* (Eds.: A. Bianchi, K. Bowman-James, E. García-España), Wiley-VCH, New York, **1997**.
[2] a) F. P. Schmidtchen, M. Berger, *Chem. Rev.* **1997**, *97*, 1600–1646; b) P. D. Beer, P. A. Gale, *Angew. Chem.* **2001**, *113*, 502–532; *Angew. Chem. Int. Ed.* **2001**, *40*, 486–516; c) P. A. Gale, *Coord. Chem. Rev.* **2003**, *240*, 191–221; d) J. M. Llinares, D. Powell, K. Bowman-James, *Coord. Chem. Rev.* **2003**, *240*, 57–75; e) C. R. Bondy, S. J. Loeb, *Coord. Chem. Rev.* **2003**, *240*, 77–99; f) J. L. Sessler, S. Camiolo, P. A. Gale, *Coord. Chem. Rev.* **2003**, *240*, 17–55; g) S. Kubik, C. Reyheller, S. Stüwe, *J. Inclusion Phenom. Macrocyclic Chem.* **2005**, *52*, 137–187; h) P. D. Beer, S. R. Bayly, *Top. Curr. Chem.* **2005**, *255*, 125–162; i) R. J. T. Houk, S. L. Tobey, E. V. Anslyn, *Top. Curr. Chem.* **2005**, *255*, 199–229.
[3] V. Amendola, L. Fabbrizzi, C. Mangano, P. Pallavicini, A. Poggi, A. Taglietti, *Coord. Chem. Rev.* **2001**, *219–221*, 821–837.
[4] K. Bowman-James, *Acc. Chem. Res.* **2005**, *38*, 671–678.
[5] a) R. MacKinnon, *Angew. Chem.* **2004**, *116*, 4363–4376; *Angew. Chem. Int. Ed.* **2004**, *43*, 4265–4277; b) P. Agre, *Angew. Chem.* **2004**, *116*, 4377–4390; *Angew. Chem. Int. Ed.* **2004**, *43*, 4278–4290.
[6] F. M. Ashcroft, *Ion Channels and Disease*, Academic Press, San Diego, **2000**.
[7] R. Dutzler, E. B. Campbell, M. Cadene, B. T. Chait, R. MacKinnon, *Nature* **2002**, *415*, 287–294.

 © 2006 Wiley-VCH Verlag GmbH & Co. KGaA, Weinheim

[8] C. H. Park, H. E. Simmons, *J. Am. Chem. Soc.* **1968**, *90*, 2431 – 2432.
[9] R. A. Bell, G. G. Christoph, F. R. Fronczek, R. E. Marsh, *Science* **1975**, *190*, 151 – 152.
[10] K. Kavallieratos, S. R. de Gala, D. J. Austin, R. H. Crabtree, *J. Am. Chem. Soc.* **1997**, *119*, 2325 – 2326.
[11] M. A. Hossain, S. O. Kang, D. Powell, K. Bowman-James, *Inorg. Chem.* **2003**, *42*, 1397 – 1399.
[12] a) M. J. Deetz, M. Shang, B. D. Smith, *J. Am. Chem. Soc.* **2000**, *122*, 6201 – 6207; b) J. M. Mahoney, G. U. Nawaratna, A. M. Beatty, P. J. Duggan, B. D. Smith, *Inorg. Chem.* **2004**, *43*, 5902 – 5907.
[13] J. M. Mahoney, A. M. Beatty, B. D. Smith, *J. Am. Chem. Soc.* **2001**, *123*, 5847 – 5848.
[14] J. M. Mahoney, A. M. Beatty, B. D. Smith, *Inorg. Chem.* **2004**, *43*, 7617 – 7621.
[15] J. M. Mahoney, J. P. Davis, A. M. Beatty, B. D. Smith, *J. Org. Chem.* **2003**, *68*, 9819 – 9820.
[16] a) P. A. Gale, S. Camiolo, G. J. Tizzard, C. P. Chapman, M. E. Light, S. J. Coles, M. B. Hursthouse, *J. Org. Chem.* **2001**, *66*, 7849 – 7853; b) P. A. Gale, S. Camiolo, C. P. Chapman, M. E. Light, M. B. Hursthouse, *Tetrahedron Lett.* **2001**, *42*, 5095 – 5097.
[17] T. Zieliński, J. Jurczak, *Tetrahedron* **2005**, *61*, 4081 – 4089.
[18] M. E. Light, P. A. Gale, K. Navakhun, *Acta Crystallogr. Sect. E* **2005**, *61*, o1300 – o1301.
[19] P. A. Gale, K. Navakhun, S. Camiolo, M. E. Light, M. B. Hursthouse, *J. Am. Chem. Soc.* **2002**, *124*, 11228 – 11229.
[20] P. A. Gale, *Chem. Commun.* **2005**, 3761 – 3772.
[21] A. Fürstner, *Angew. Chem.* **2003**, *115*, 3706 – 3728; *Angew. Chem. Int. Ed.* **2003**, *42*, 3582 – 3603.
[22] A. P. Bisson, V. M. Lynch, M.-K. C. Monahan, E. V. Anslyn, *Angew. Chem.* **1997**, *109*, 2435 – 2437; *Angew. Chem. Int. Ed. Engl.* **1997**, *36*, 2340 – 2342.
[23] a) M. A. Hossain, J. M. Llinares, S. Mason, P. Morehouse, D. Powell, K. Bowman-James, *Angew. Chem.* **2002**, *114*, 2441 – 2444; *Angew. Chem. Int. Ed.* **2002**, *41*, 2335 – 2338; b) M. A. Hossain, P. Morehouse, D. Powell, K. Bowman-James, *Inorg. Chem.* **2005**, *44*, 2143 – 2149.
[24] S. O. Kang, D. Powell, K. Bowman-James, *J. Am. Chem. Soc.* **2005**, *127*, 13478 – 13479.
[25] S. Camiolo, P. A. Gale, M. B. Hursthouse, M. E. Light, *Org. Biomol. Chem.* **2003**, *1*, 741 – 744.
[26] S. J. Coles, P. A. Gale, M. B. Hursthouse, M. E. Light, C. N. Warriner, *Supramol. Chem.* **2004**, *16*, 469 – 486.
[27] V. S. Bryantsev, B. P. Hay, *J. Am. Chem. Soc.* **2005**, *127*, 8282 – 8283.
[28] M. J. Chmielewski, J. Jurczak, *Chem. Eur. J.* **2005**, *11*, 6080 – 6094.
[29] A. Szumna, J. Jurczak, *Helv. Chim. Acta*, **2001**, *84*, 3760 – 3765.
[30] A. Szumna, J. Jurczak, *Eur. J. Org. Chem.* **2001**, 4031 – 4039.
[31] Y. Inoue, T. Kanbara, T. Yamamoto, *Tetrahedron Lett.* **2003**, *44*, 5167 – 5169.
[32] M. J. Chmielewski, J. Jurczak, *Tetrahedron Lett.* **2005**, *46*, 3085 – 3088.
[33] T. B. Karpishin, T. D. P. Stack, K. N. Raymond, *J. Am. Chem. Soc.* **1993**, *115*, 182 – 192.
[34] S. Kubik, R. Goddard, R. Kirchner, D. Nolting, J. Seidel, *Angew. Chem.* **2001**, *113*, 2722 – 2725; *Angew. Chem. Int. Ed.* **2001**, *40*, 2648 – 2651.
[35] S. Kubik, R. Kirchner, D. Nolting, J. Seidel, *J. Am. Chem. Soc.* **2002**, *124*, 12752 – 12760.
[36] J. J. Lee, K. J. Stanger, B. C. Noll, C. Gonzalez, M. Marquez, B. D. Smith, *J. Am. Chem. Soc.* **2005**, *127*, 4184 – 4185.
[37] S. O. Kang, J. M. Llinares, D. Powell, D. VanderVelde, K. Bowman-James, *J. Am. Chem. Soc.* **2003**, *125*, 10152 – 10153.
[38] S. O. Kang, D. VanderVelde, D. Powell, K. Bowman-James, *J. Am. Chem. Soc.* **2004**, *126*, 12272 – 12273.
[39] C. A. Ilioudis, D. A. Tocher, J. W. Steed, *J. Am. Chem. Soc.* **2004**, *126*, 12395 – 12402.
[40] J. L. Sessler, D. An, W.-S Cho, V. Lynch, M. Marquez, *Chem. Commun.* **2005**, 540 – 542.
[41] S. O. Kang, D. Powell, V. W. Day, K. Bowman-James, *Angew. Chem.* **2006**,*118*, 1955 – 1959; *Angew. Chem. Int. Ed.* **2006**, *45*, 1921 – 1925.
[42] J.-M. Lehn, E. Sonveaux, A. K. Willard, *J. Am. Chem. Soc.* **1978**, *100*, 4914 – 4916.
[43] J. M. Mahoney, K. A. Stucker, J. Jiang, I. Carmichael, N. R. Brinkmann, A. M. Beatty, B. C. Noll, B. D. Smith, *J. Am. Chem. Soc.* **2005**, *127*, 2922 – 2928.
[44] Z. Yin, Z. Li, A. Yu, J. He, J. -P. Cheng, *Tetrahedron Lett.* **2004**, *45*, 6803 – 6806.
[45] S. J. Brooks, P. A. Gale, M. E. Light, *Chem. Commun.* **2005**, 4696 – 4698.
[46] a) S. Camiolo, P. A. Gale, M. B. Hursthouse, M. E. Light, *Tetrahedron Lett.* **2002**, *43*, 6995 – 6996; b) P. A. Gale, S. Camiolo, C. P. Chapman, M. E. Light, M. B. Hursthouse, *Tetrahedron Lett.* **2001**, *42*, 5095 – 5097.
[47] S. Mason, T. Clifford, L. Seib, K. Kuczera, K. Bowman-James, *J. Am. Chem. Soc.* **1998**, *120*, 8899 – 8900.
[48] N. W. Alcock, *Bonding and Structure*, Ellis Horwood Limited, New York, **1990**.
[49] B. P. Hay, M. Gutowski, D. A. Dixon, J. Garza, R. Vargas, B. A. Moyer, *J. Am. Chem. Soc.* **2004**, *126*, 7925 – 7934.
[50] L. Cronin, P. A. McGregor, S. Parsons, S. Teat, R. O. Gould, V. A. White, N. J. Long, N. Robertson, *Inorg. Chem.* **2004**, *43*, 8023 – 8029.
[51] T. Gunnlaugsson, P. E. Kruger, P. Jensen, F. M. Pfeffer, G. M. Hussey, *Tetrahedron Lett.* **2003**, *44*, 8909 – 8913.
[52] M. Boiocchi, L. D. Boca, D. E. Gómez, L. Fabbrizzi, M. Licchelli, E. Monzani, *J. Am. Chem. Soc.* **2004**, *126*, 16507 – 16514.
[53] R. Custelcean, L. H. Delmau, B. A. Moyer, J. L. Sessler, W.-S. Cho, D. Gross, G. W. Bates, S. J. Brooks, M. E. Light, P. A. Gale, *Angew. Chem.* **2005**, *117*, 2593 – 2598; *Angew. Chem. Int. Ed.* **2005**, *44*, 2537 – 2542.
[54] H. Luecke, F. A. Quiocho, *Nature* **1990**, *347*, 402 – 406.
[55] a) J. W. Pflugrath, F. A. Quiocho, *Nature* **1985**, *314*, 257 – 260; b) B. L. Jacobson, F. A. Quiocho, *J. Mol. Biol.* **1988**, *204*, 783 – 787.
[56] R. Custelcean, B. A. Moyer, B. P. Hay, *Chem. Commun.* **2005**, 5971 – 5973.
[57] J. L. Sessler, E. Katayev, G. D. Pantos, P. Scherbakov, M. D. Reshetova, V. N. Khrustalev, V. M. Lynch, Y. A. Ustynyuk, *J. Am. Chem. Soc.* **2005**, *127*, 11442 – 11446.
[58] M. A. Hossain, J. M. Llinares, D. Powell, and K. Bowman-James, *Inorg. Chem.* **2001**, *40*, 2936 – 2937.
[59] S. O. Kang, M. A. Hossain, D. Powell, K. Bowman-James, *Chem. Commun.* **2005**, 328 – 330.
[60] E. A. Katayev, G. D. Pantos, M. D. Reshetova, V. N. Khrustalev, V. M. Lynch, Y. A. Ustynyuk, J. L. Sessler, *Angew. Chem.* **2005**, *117*, 7552 – 7556; *Angew. Chem. Int. Ed.* **2005**, *44*, 7386 – 7390.

© 2006 Wiley-VCH Verlag GmbH & Co. KGaA, Weinheim

A. S. K. Hashmi and G. J. Hutchings

DOI: 10.1002/anie.200602454

Gold Catalysis

Gold Catalysis**

A. Stephen K. Hashmi and Graham J. Hutchings**

Keywords:
gold · heterogeneous catalysis · homogeneous catalysis · promoters · supports

© 2006 Wiley-VCH Verlag GmbH & Co. KGaA, Weinheim

Catalysis by gold has rapidly become a hot topic in chemistry, with a new discovery being made almost every week. Gold is equally effective as a heterogeneous or a homogeneous catalyst and in this Review we attempt to marry these two facets to demonstrate this new found and general efficacy of gold. The latest discoveries are placed within a historical context, but the main thrust is to highlight the new catalytic possibilities that gold-catalyzed reactions currently offer the synthetic chemist, in particular in redox reactions and nucleophilic additions to π systems. Indeed gold has proved to be an effective catalyst for many reactions for which a catalyst had not been previously identified, and many new discoveries are still expected.

From the Contents

1. Introduction 7897
2. Hydrogenation 7898
3. Reactions Involving Carbon Monoxide 7903
4. Selective Oxidation 7912
5. Nucleophilic Additions to π Systems 7916
6. Conclusion and Future Perspectives 7929

1. Introduction

Gold has a rich coordination and organometallic chemistry,[1] but was considered to be catalytically inactive for a long time.[2] However, early and scattered reports on the use of gold as a catalyst existed, but none of these showed it to be superior to other catalysts.[3] This changed in 1973 when Bond et al.[4] reported the hydrogenation of olefins over supported gold catalysts. More than a decade later, Haruta and Hutchings simultaneously[5] and independently prognosticated gold to be an extraordinary good catalyst and subsequently demonstrated it experimentally: Haruta et al. investigated the low-temperature oxidation of CO[6] and Hutchings the hydrochlorination of ethyne to vinyl chloride,[7] both heterogeneous reactions. For the first time these studies showed gold to be the best catalyst for these reactions, in stark contrast to the previous reports on the poor activity of gold.

At about the same time a unique milestone in homogeneous asymmetric catalysis was established, when Ito et al. reported the first example of a catalytic asymmetric aldol reaction. They applied a gold(I) catalyst and an enantiomerically pure ferrocene diphosphane ligand for the addition of a carbon nucleophile to a carbonyl group.[8] The next important step in homogeneous catalysis was the addition of nucleophiles to alkynes, conceptually based on Hutchings heterogeneous hydrochlorination of acetylene. This approach was first investigated for alcohols, water, and amines by Fukuda and Utimoto,[9] almost another ten years later Teles et al.[10] showed that cationic gold(I) species gave excellent turnover numbers (TONs) and turnover frequencies (TOFs) for the addition of alcohols to alkynes. Haruta et al. demonstrated that high selectivity in the heterogeneous oxidation of propene to propene oxide, one of the top targets in industrial chemistry, could be achieved with gold on titania.[11] The positional-selective oxidation of different alcohols and even carbohydrates with molecular oxygen, as developed by Prati and Rossi, represents another milestone in the story of gold catalysis.[12]

A next crucial step for homogeneous catalysis followed in 2000 when Hashmi et al. extended the nucleophilic additions from alkynes to olefins for both the intramolecular additions of alcohols and the intermolecular addition of arenes.[13] Subsequent studies by Yang and He investigated intermolecular reactions of alkenes with O nucleophiles[14] and provided evidence that the reactions with electron-rich arenes proceeded by an initial activation of an aryl-C–H bond.[15] The other development initiated in 2000 by Hashmi et al. was the gold-catalyzed isomerization of ω-alkynylfurans,[16] which possess an enyne substructure, to phenols. Echavarren and co-workers[17] later finally demonstrated the involvement in this reaction of gold–carbene species, one of the newest facets of gold catalysis. In 2002 Hutchings and co-workers[18] showed gold to be effective under inherently safe conditions for the direct synthesis of hydrogen peroxide, one of the most challenging selectivity problems in oxidation chemistry. Figure 1 shows the impact since 1900 of the innovations mentioned above on the publication output in this field, which in the meantime has become a highly dynamic hot spot in catalysis research and resulted in the European Union research training network AURICAT.

This Review is organized by chemical transformation, so both homogeneous and heterogeneous examples for the same reaction will be discussed in the same section.

[*] Prof. Dr. A. S. K. Hashmi
Institut für Organische Chemie
Universität Stuttgart
Pfaffenwaldring 55, 70569 Stuttgart (Germany)
Fax: (+49) 711-685-64321
E-mail: hashmi@hashmi.de
Prof. Dr. G. J. Hutchings
School of Chemistry
Cardiff University
Main Building, Park Place, Cardiff (UK), CF10 3AT
Fax: (+44) 2920874075
E-mail: hutch@cf.ac.uk

[**] We thank Umicore, the World Gold Council, and the European Union for their support (AURICAT EU-RTN, HPRN-CT-2002-00174).

© 2006 Wiley-VCH Verlag GmbH & Co. KGaA, Weinheim

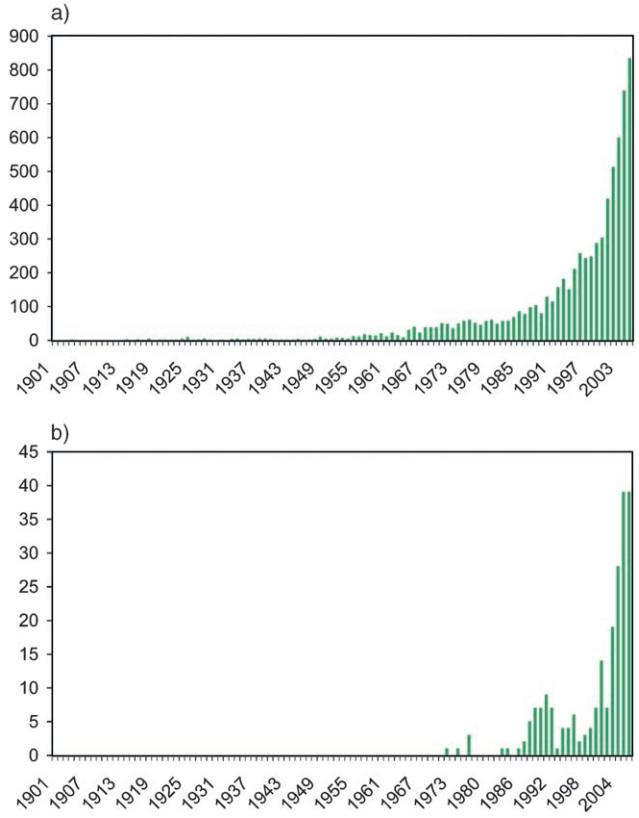

Figure 1. Publications on gold catalysis. a) Number of publications on "gold catalysis" from 1900 to May 2006. b) Number of publications on "homogeneous gold catalysis" only, showing how heterogeneous catalysis is still dominating, but in May 2006 the total number for 2005 had already been reached.

2. Hydrogenation

Gold-catalyzed hydrogenation is not only the oldest of the reactions to be discussed in this Review, it also has the distinct advantage that the metal catalysis is not competing with an uncatalyzed background reaction, which is the case for many oxidation reactions. For this reason this topic will be discussed first.

2.1. Alkenes

Probably the first example of a gold-catalyzed reaction of an alkene involving hydrogen was published as early as 1906 by Bone and Wheeler,[19] who studied the uptake of hydrogen by gold in the presence of O_2 at 600 °C.[20] At that time the only directly observable parameter was the pressure in the apparatus, thus the possibilities in the interpretation of the results was quite limited. Nevertheless, it was found that the rate of reaction is mainly dependent on the pressure of hydrogen and that oxygen had a slight retarding effect, thereby providing possible evidence for the interaction of hydrogen with the catalyst being the rate-limiting step. Indeed later work confirmed that finding.[21] In 1950 Couper and Eley[22] demonstrated that gold surfaces could convert *para*-hydrogen into *ortho*-hydrogen. A number of studies also showed that both gold foil[23,24] and supported gold catalysts[25–28] were active for exchange reactions above 200 °C. These early studies demonstrated clearly that gold surfaces can activate hydrogen.

The starting point for alkene hydrogenation was the reaction of cyclohexene (**1**), which simultaneously served as a hydrogen donor and as the substrate for hydrogenation. In 1963 Erkelens, Kemball, and Galwey[29] reported that gold films at 196–342 °C catalyze this reaction to deliver both the hydrogenation product cyclohexane (**2**) and the dehydrogenation product benzene (**3**). In 1966 Chambers and Boudart observed the same reactivity for gold powder at 203–285 °C [Eq. (1)].[46] As expected on the basis of thermodynamic

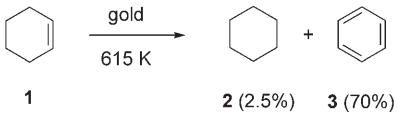

(1)

grounds, the amount of benzene increased with increasing temperature and decreasing hydrogen pressure. The energy of activation for the hydrogenation was significantly higher than the one for dehydrogenation, thus the dehydrogenation product **3** dominated.

In 1966 Wood and co-workers investigated the gas-phase hydrogenation of 1-butene and cyclohexene at 110 °C with highly dispersed gold on a support material.[30] Reaction rates were first order in alkene pressure and second order in

A. Stephen K. Hashmi studied chemistry at the LMU Munich where he obtained his Diploma and PhD with Prof. G. Szeimies in the field of strained organic compounds. He then carried out postdoctorate research with Prof. B. M. Trost at Stanford University. After his Habilitation with Prof. J. Mulzer in Berlin, Frankfurt, and Vienna, he was awarded a Heisenberg fellowship in 1998 for a project on gold-catalyzed reactions for organic synthesis—still a major focus of his research group. After positions at the universities of Tasmania and Marburg, in 2001 he became Professor for Organic Chemistry at Stuttgart University.

Graham Hutchings has been Research Professor at the School of Chemistry, Cardiff University since 2006, having previously been Head of School since 1997. He has worked in the field of gold catalysis since 1982, and has worked in the field of heterogeneous catalysis since 1975, initially in industry at ICI Petrochemicals Division and AECI Ltd. In 1984, he was appointed to the academic staff at the University of Witwatersrand, where he is currently a visiting Professor. In 1987, he returned to the UK to help establish the Leverhulme Centre for Innovative Catalysis at Liverpool University, before moving to Cardiff in 1997.

 © 2006 Wiley-VCH Verlag GmbH & Co. KGaA, Weinheim

chemisorbed hydrogen (the latter being supplied through a palladium–silver alloy membrane under the gold layer). In 1971 more reactive alkynes were investigated:[31] 2-butyne at temperatures between 335 °C and 355 °C showed an induction period in which (*Z*)-2-butene was formed, after which (*E*)-2-butene and finally *n*-butane were also obtained; 1-butene was observed only in traces. At higher temperatures C–C bond cleavage to methane, ethane, ethylene, propylene, and propyne was also detected. The skeletal isomerization of neopentane at 427–477 °C on gold powder described by Boudart and Ptak is closely related, since C–C bond cleavage also takes place in an isomerization.[32] In the same context, one could discuss the increased formation of pentane from butane on Pt/Au alloys as the Au content of the alloy increased (up to 31 % with 52 % Au at 408 °C).[33]

A milestone paper by Bond et al. followed in 1973[4] in which they showed that an efficient hydrogenation is possible at only 100–217 °C with gold on silica, γ-alumina, or boehmite (with as little as 0.01 wt % gold on the SiO_2 support, for example, in the hydrogenation of **4** to **5**) [Eq. (2)]. They

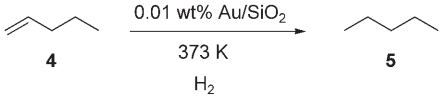

(2)

investigated 1,3-butadiene (**6**) and 2-butyne (**10**) as substrates and observed a chemoselective monohydrogenation, with no diastereoselectivity in the case of 1,3-butadiene ($E/Z = 1{:}1$) but a good diastereoselectivity ($E/Z = 1{:}8$) in the case of 2-butyne (Scheme 1).

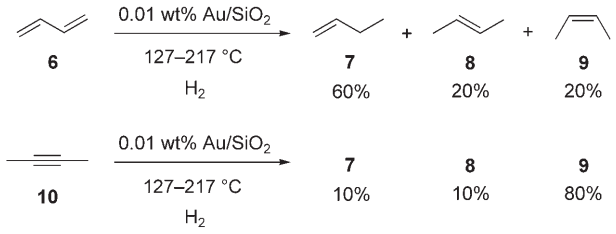

Scheme 1. Selective reduction of 1,3-dienes and alkynes.

$Au/\gamma\text{-}Al_2O_3$ catalysts containing less than 5 % Au[27] were inactive for the hydrogenation of 1-pentene. However, very different results were obtained using Au/SiO_2 catalysts: with a massive excess of hydrogen, low concentrations of Au supported on SiO_2 were active for the hydrogenation of 1-pentene, with the maximum activity observed at 0.04 wt % Au. This observation indicates that hydrogenation reactions could be sensitive to both Au particle size and the nature of the support, as has been observed with oxidation reactions (see Section 3.1). The hydrogenation of ethene with 5 % Au/SiO_2 is first order in hydrogen, the order of reaction for ethene is 0.4.[27] Interesting results were obtained with deuterium and propene on Au/SiO_2:[34] D_2 reacts much slower than H_2, thus suggesting that the breaking of a H–H bond is the rate-determining step.

In 2004 Guzman and Gates investigated the hydrogenation of ethene with mononuclear gold complexes on MgO powder at atmospheric pressure and 80 °C. EXAFS and XANES data provided evidence for Au^{III} as the active species, while IR spectroscopy showed ethylgold species to be the reactive intemediate. The reaction order in hydrogen was 0.5.[35]

Table 1 compiles a summary of the few alkene and alkyne substrates that have been investigated in heterogeneous gold-catalyzed hydrogenation to date. The hydrogenation of

Table 1: Alkenes and alkynes investigated in gold-catalyzed hydrogenation.

N[a]	Substrate	Ref.
C_2	ethene	[35, 36]
	ethyne	[4, 37, 38]
C_3	propene	[28, 34, 39]
	propyne	[40, 41]
C_4	1-butene	[30b, c]
	1,3-butadiene	[4, 42, 43, 44]
	2-butyne	[4]
C_5	1-pentene	[27]
C_6	cyclohexene	[29, 30a, c, 45, 46]
	2-hexyne	[47]
	benzene	[48]
C_7	toluene	[49]
C_8	styrene	[50]
	phenylacetylene	[51]
C_{10}	naphthalene	[49, 52]

[a] Number of carbon atoms.

benzene, a reaction with the remarkably high activation energy of 209 kJ mol^{-1}, was investigated as early as 1966.[48] Kinetic data for the electrocatalytic reduction of ethylene on gold was measured by Bryne and Kuhn. They determined the kinetic isotope effect for hydrogen versus deuterium evolvement on gold to be 4 and that for ethane hydrogenation versus deuteration to be 1.5.[53]

Despite all these efforts, it is impossible to correlate the results (if one ignores all the speculations and assumptions) because of the different supports, catalyst precursors, substrates, temperatures, and pressures used. No clear mechanistic picture of these relatively simple hydrogenation exists today[54,55]—a major difference to homogeneous gold-catalyzed hydrogenations (see Section 2.3), where after a much shorter time a quite good mechanistic insight was achieved. The chemoselectivity observed in the hydrogenation of alkynes and α,β-unsaturated carbonyl compounds (see Section 2.2) justifies future investigation.

© 2006 Wiley-VCH Verlag GmbH & Co. KGaA, Weinheim

Additional information might be gained from dehydrogenation, which in some cases can be connected with hydrogenation by the principle of microscopic reversibility (and the first step of dehydrogenation is intrinsically connected to isomerization). Early experiments had shown that gold in the form of foil, wire, powder, and sponge as well as Au/SiO_2 and Au/Al_2O_3 are capable of decomposing (dehydrogenate) formic acid to hydrogen and CO_2 at temperatures between 100 and 250 °C.[56] Activation energies are typically around 60 kJ mol^{-1}.

In 1969 Inami et al. described the isomerization of 1-butene to 2-butene to be catalyzed by gold at 300–400 °C.[30b] Amazingly a dehydrogenative cyclization of *n*-pentane to cyclopentadiene and cyclopentene with a gold film at 377–427 °C was described by Kane and Clarke in 1980.[57,58] A study by Parravano concerned the hydrogen-transfer reaction between cyclohexane and benzene over different supported gold catalysts at −73 to −23 °C.[59] These experiments are closely related to the formation of cyclohexane and benezene in the hydrogenation of cyclohexene described above.[29,46] Sachtler et al. reported that one monolayer of gold on platinum enhanced the rate for cyclohexene dehydrogenation at 100 °C by a factor of five.[60]

The formation of butene from 1-butyne over metallic gold films without any added hydrogen was reported by Gault.[61] Chemically related is the reaction of silanes, for which an H/D exchange[62] and the addition to 1-octene[63] was also observed. However, all these results do not help to gain better insight into the mechanism of hydrogenation.

2.2. Hydrogenation of α,β-Unsaturated Aldehydes

Supported gold catalysts can show very high selectivity for the hydrogenation of α,β-unsaturated aldehydes **11** (Scheme 2), and much of this work has recently been reviewed by Claus.[54]

Bailie et al.[64,65] were the first to demonstrate that Au/ZrO_2 and Au/ZnO catalysts are highly selective for the formation of crotyl alcohol (**12**, $R^2 = H$, $R^1, R^3 = Me$) through the hydrogenation of crotonaldehyde, and selectivities up to 81 % at conversions of 5–10 % could be observed, that is, these supported gold catalysts preferentially hydrogenated the C=O bond rather than the C=C bond. They also showed that the addition of small amounts of thiophene promoted this selective hydrogenation. This is one of the few examples of promotion in a gold catalyst and it can be anticipated that this will become a useful research approach for the design of improved catalysts. The observation of a promotional effect of thiophene is analogous to that observed for Cu[66–68] and Ag[69] catalysts. The selectivity for crotyl alcohol was only enhanced by thiophene with relatively small particles (ca. 2 nm diameter); at larger particle sizes the promotional effect decreased. However, the selectivity for crotyl alcohol increased as the Au particle size increased. This effect was demonstrated by the calcination of 5 wt % Au/ZnO between 250–400 °C, and the crotyl alcohol selectivity increased dramatically (Figure 2).

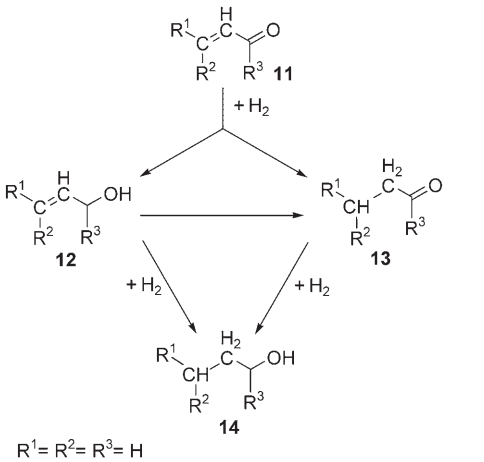

Scheme 2. Reduction of α,β-unsaturated carbonyl compounds.

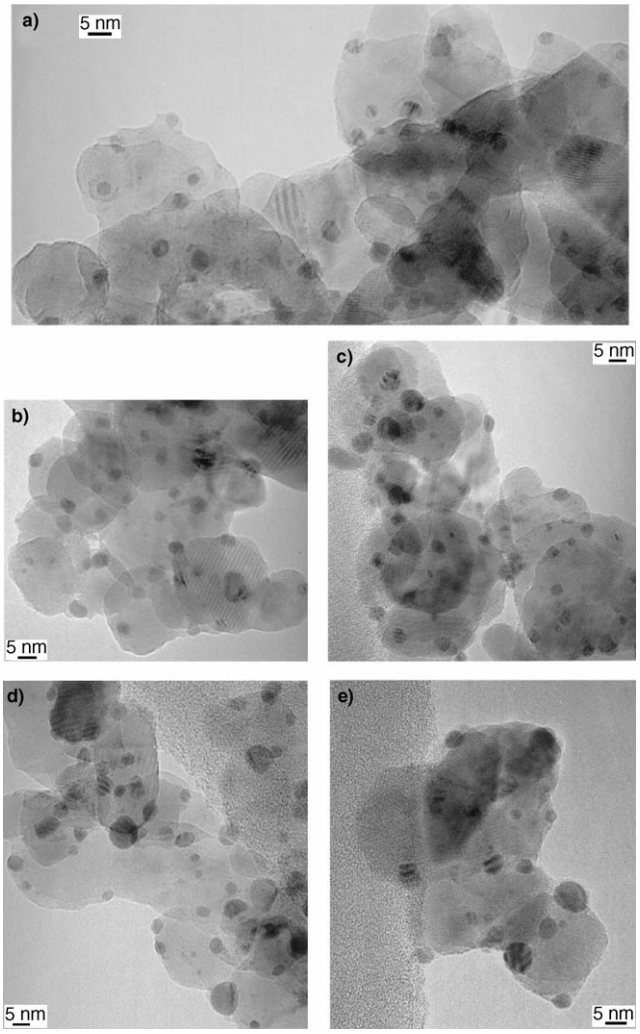

Figure 2. Transmission electron microscopy (TEM) images of fresh calcined Au/ZnO catalysts (5 wt %). a) Unreduced material; the others were reduced at b) 250, c) 300, d) 350, and e) 400 °C and show the increase in Au particle size. The selectivity for for the hydrogenation of crotonaldehyde to crotyl alcohol at 250 °C is b) 54 %, c) 64 %, d) 64 %, and e) 81 % (Ref. [69]).

 © 2006 Wiley-VCH Verlag GmbH & Co. KGaA, Weinheim

The hydrogenation of acrolein (**11**, $R^1,R^2,R^3 = H$) has subsequently been extensively studied by Claus and co-workers[70–76] using Au/SiO_2, Au/ZrO_2, Au/TiO_2, Au/ZnO, and Au-In/ZnO. Since then, supported gold catalysts have been applied to more complex hydrogenations, including citral,[77] benzal acetone,[78,79] and pent-3-en-2-one.[80] The studies by Claus and co-workers on the hydrogenation of acrolein were comprehensive and concentrated on designing catalysts comprising gold nanoparticles (ca. 5 nm diameter). They found that the support influences the morphology of the gold nanoparticle: more-rounded particles were present on TiO_2, while highly faceted particles were present on ZnO (Figure 3).

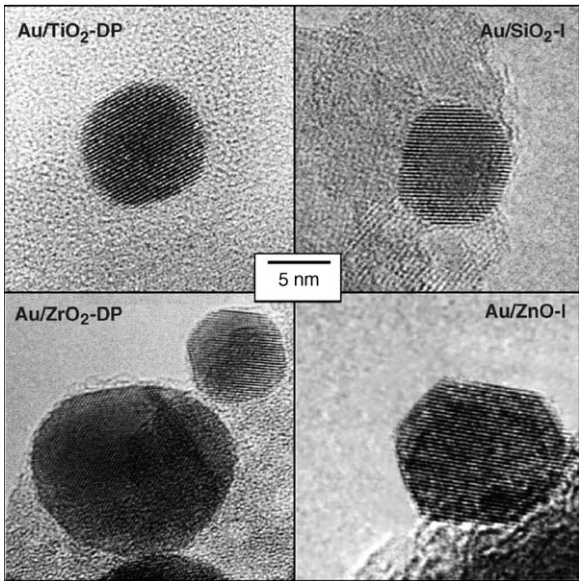

Figure 3. Representative gold particles on different supports (DP: deposition–precipitation method, I: impregnation method; see Section 3.1.2; Ref. [80]).

The higher activity observed with the Au/TiO_2 catalysts was associated with the more-rounded morphology of the particles accompanied by a higher relative amount of low-coordinate surface sites.[74] In an interesting development of this approach, Claus and co-workers have shown that the bimetallic Au-In/ZnO catalyst gives enhanced selectivity for C=O hydrogenation in acrolein. This is an important example demonstrating that the selectivity of supported gold catalysts can be finely tuned by the addition of a second metal. Detailed transmission electron microscopy studies have shown that the indium decorates the gold faces on the nanoparticle, and this is considered to be the origin of the enhanced selectivity (Figure 4). In this way it is analogous to the selectivity effects induced on Pt catalysts by the addition of Bi, which is known to decorate specific sites,[80] and the effects observed by Bailie et al.[64,65] on addition of thiophene to small gold nanocrystals may have a similar origin.

Very recently, Corma and Serna demonstrated the regio-selective selective reduction of a nitro group in the presence of other reducible functions using gold nanoparticles sup-

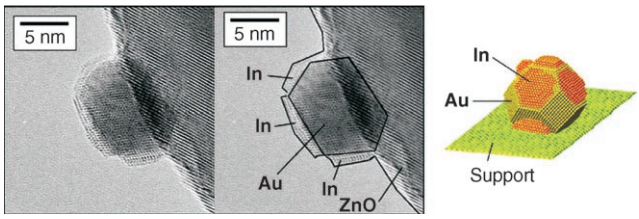

Figure 4. HRTEM image of Au-In/ZnO (left) and the surface model (right). Indium preferentially decorates the outer faces of the gold particles while the edges remain uncovered (Ref. [55]).

ported on TiO_2 or Fe_2O_3.[81] Thus, they developed a new route for the synthesis of the industrially important cyclohexanone oxime from 1-nitro-1-cyclohexene.

2.3. Homogeneous Hydrogenation, Mechanistic Understanding

The first mention of a homogeneous hydrogenation goes back to Muller,[82] who in a publication in the *Gold Bulletin*[83] in 1974 stated that $HAuCl_4/Sb(SC_6F_5)_3$ hydrogenates ethene to ethane in ethanol at 0 °C at 1 atm of hydrogen, but details were not provided. Almost 30 years later, Arcadi and co-workers[84] developed a gold-catalyzed synthesis of pyridines (details are given in Section 5); the final step of this reaction is the dehydrogenation of the initially formed dihydropyridine intermediate **17** to the pyridine **18** (Scheme 3). Such a

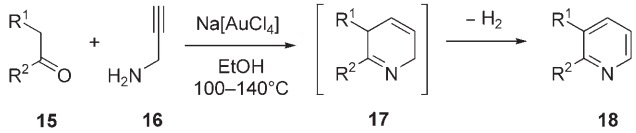

Scheme 3. Dehydrogenation step in the pyridine by synthesis Arcadi and co-workers.

dehydrogenation could be connected with hydrogenation by the principle of microscopic reversibility. However, the fate of the hydrogen liberated was not investigated—two equivalents of alkyne **16** were used in these reactions and thus it is possible that a transfer hydrogenation directly delivers the hydrogen to the alkyne **16**.

Very recently Corma and co-workers reported the enantioselective hydrogenation of alkenes and imines by gold(I)-Me-duphos complexes (Me-duphos = 2′,5′,2″,5″tetramethyl-substituted 1,2-bis(phospholanyl)benzene).[85] The reactions proceeded at 4 bar H_2 pressure and room temperature with 0.1 mol % of catalyst. The results are shown in Table 2. With the exception of substrate **19**, the gold catalyst reaches the activity of the platinum and iridium catalysts. With **21** and especially with **22** the *ee* values clearly exceed the values obtained with the other two classical hydrogenation catalysis metals Pt and Ir. Corma and co-workers[86] could show on the basis of calculations for non-asymmetric hydrogenation using semi-salen-type ligands (Scheme 4) that a heterolytic mode of hydrogen activation and not a homolytic mode in the sense of, for example, an oxidative addition is the probable pathway.

 © 2006 Wiley-VCH Verlag GmbH & Co. KGaA, Weinheim

Table 2: Turnover frequencies and enantiomeric excess for the Me-duphos-gold(I)-catalyzed hydrogenation.

Metal → / Substrate ↓	Au TOF	Au *ee*	Pt TOF	Pt *ee*	Ir TOF	Ir *ee*
EtO_2C, EtO_2C **19**	3942	20	10188	3	8088	1
EtO_2C, EtO_2C, Ph **20**	906	80	926	90	1110	26
EtO_2C, EtO_2C, 2-Naphthyl **21**	214	75	250	15	325	68
Ph, Ph **22**	1005	75	1365	15	1118	15

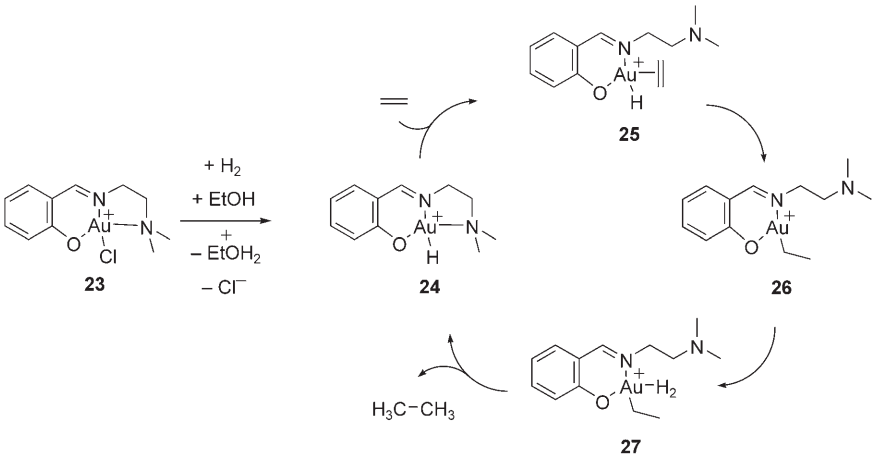

Scheme 4. Mechanism of the gold-catalyzed homogeneous hydrogenation.

The oxidation state of the gold remains unchanged in such a pathway.

The first step is the heterolysis of hydrogen, which attaches a hydride ligand to the gold (**23**→**24**) and the solvent takes up a proton. The alkene then substitutes the amine ligand (**25**)[87] and inserts into the Au–H bond (**26**). The next hydrogen molecule then coordinates (**27**), which sets free the ethane and reforms **24** by heterolysis. The rate-limiting step is, very similar to the heterogenous hydrogenations, the activation of the hydrogen, here in the step from **23** to **24**. This was confirmed experimentally by the observation of an induction period. However, none of the species **24**–**27** could be observed.

The most unusual species would be the gold–monohydride complex **25**. Recent studies have proven the existence of gold hydride anions,[88,89] but in general gold hydrides are a rare species and difficult to access; gold, for example, shows no tendency to undergo a β-hydrogen elimination. A direct experimental example of that was provided by Baker et al. in 1995: efforts to diborylate styrene **29** with a rhodium catalyst mainly delivered unsaturated, monoborylated species **31** and **32** by β-hydrogen elimination; a gold catalyst formed in situ from [(PEt_3)AuCl] and 1,2-dicyclohexylphosphanylethane only delivers the desired diborylated product **30** [Eq. (3)].[90] Baker et al. also described the gold-catalyzed hydroboration of imines. The reaction catalyzed by phosphanegold(I) chloride complex was more than 40 times faster than the uncatalyzed reaction.[91]

Hexaalkyldistannanes are useful reagents for organic synthesis, but they are quite expensive.[92] Hosomi and co-workers reported the formation of hexabutyldistannane **34** from the relatively cheap tributylstannane **33** in 1999 by an *intermolecular* dehydrogenative dimerization resulting in the formation of a tin–tin bond [Eq. (4)].[93] In 2000, Hosomi and co-workers reported the successful hydrosilylation of ketones and imines with $PhMe_2SiH$ and 3 mol% of the [AuCl(PPh_3)]/PBu_3 catalyst.[94] After workup, the primary alcohols or the secondary amines could be isolated. This methodology parallels the hydroboration of imines reported above,[91] and it is chemoselective since it allows a differentiation between aldehydes and ketones, the latter not being reduced.

Ito et al. recently discovered the dehydrogenative silylation of alcohols with $HSiEt_3$ and the gold–xantphos complex **36**.[95] The chemoselectivity is nicely demonstrated by substrate **35**: the product **37** still contains the α,β-unsaturated enone subunit which is not reduced [Eq. (5)]. Other functional groups such as alkenes, alkynes, alkyl halides, tertiary alcohols, aldehydes, ketones, and carbamates are tolerated. The reaction mechanism for these reactions was proposed to involve a gold monohydride

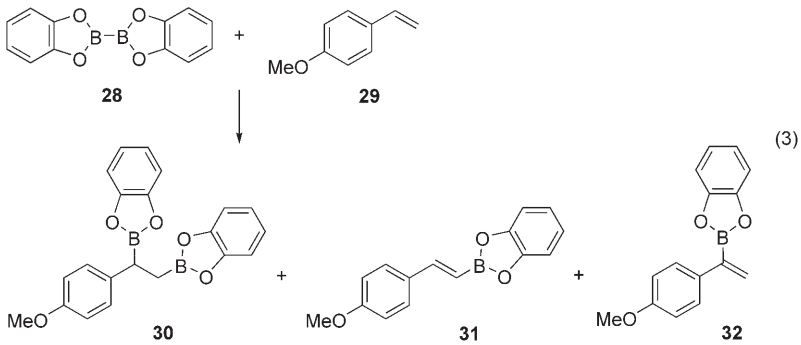

(3)

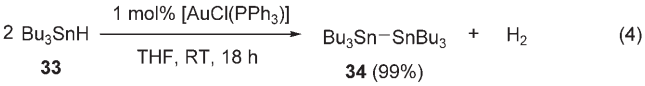

(4)

 © 2006 Wiley-VCH Verlag GmbH & Co. KGaA, Weinheim

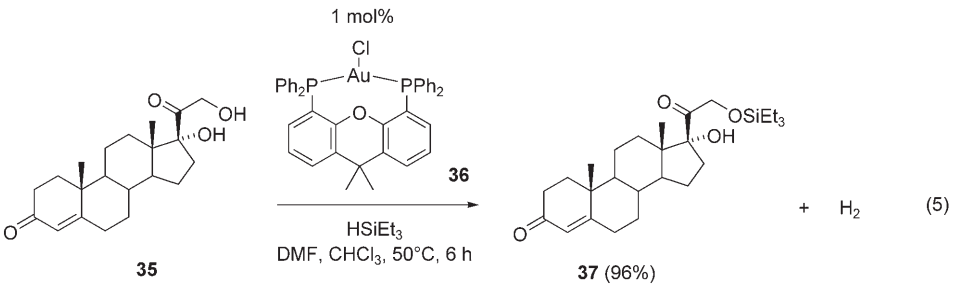

(5)

species, analogous to the suggestion by Corma et al. for hydrogenation.[86]

Relatively few publications have appeared in this area to date, but it is impressive to see how much mechanistic insight has already been achieved. There is, without doubt, much potential for further methodical and synthetic studies.

3. Reactions Involving Carbon Monoxide

3.1. Carbon Monoxide Oxidation

3.1.1. Historical Perspective

In the 1980s Haruta et al. recognized that supported gold nanocrystals can be highly effective catalysts for the oxidation of CO at very low temperatures (Figure 5) and, in particular, at temperatures significantly below 0 °C.[6,96] This is a surprisingly high activity and is not replicated by other metals. In this early work it was found that α-Fe_2O_3 was an excellent support and Haruta et al. recognized that the method of preparation was crucial for a high catalyst activity.

Initially it was considered that the high activity resulted from a new type of composite oxide catalyst, however, after detailed electron microscopy studies it was found that the very active catalysts comprised small gold nanoparticles approximately 2–4 nm in diameter. It is now widely recognized that this discovery of the remarkable catalytic activity in the low-temperature oxidation of CO spurred the fantastic growth in studies related to heterogeneous gold catalysis. However, many questions remain concerning the relatively simple reaction of CO oxidation, for example, what is the reaction mechanism and what is the nature of the active site?

Furthermore, many research groups prepare catalysts in different ways, testing them under different conditions, and each appears to have a preferred methodology for preparing highly active catalysts, with many groups claiming to have high-activity catalysts. This immense amount of research activity is, in many cases, helping to confuse the central issues rather than provide clarification. Although the field of oxidation catalysis by gold resembles this state of scientific frenzy, it is clear that heterogeneous gold catalysts do have a unique catalytic activity for oxidation reactions.

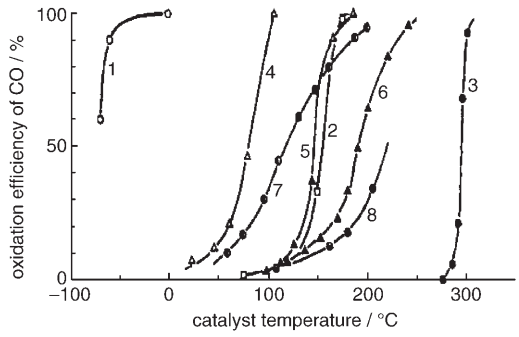

Figure 5. CO conversion over various catalysts as a function of temperature. 1) Au/α-Fe_2O_3 (Au/Fe = 1/19, co-precipitation, 400 °C), 2) 0.5 wt% Pd/γ-Al_2O_3 (impregnation, 300 °C), 3) fine Au powder, 4) Co_3O_4 (carbonate, 400 °C), 5) NiO (hydrate, 200 °C), 6) α-Fe_2O_3 (hydrate, 400 °C), 7) 5 wt% Au/α-Fe_2O_3 (impregnation, 200 °C), and 8) 5 wt% Au/γ-Al_2O_3 (impregnation, 200 °C)).

In their initial work, Haruta et al. showed that α-Fe_2O_3 was active, and subsequently also showed that Au/TiO_2 was equally effective.[96] Since then many supports have been found to be effective. Most recently, Lahr and Ceyer[97] have extended the temperature range at which activity for CO oxidation is observed to as low as −203 °C by using an Au/Ni(111) surface, thus questioning the potential role of the oxide supports.

3.1.2. Preparation of Active Catalysts

Considerable emphasis has been placed on catalyst preparation, in particular the nature of the support, and most investigators agree that high-activity catalysts can be observed with α-Fe_2O_3,[98–105] and TiO_2,[106–114] and recently with CeO_2[115,116] as supports.

Most detailed studies have concentrated on TiO_2. It is well established that the method of preparation is crucial in controlling the activity of the catalyst.[111] In general, impregnation (a method in which an active component is added to support by stirring the support with a solution of the metal salt) of titania tends to produce large particles (> 10 nm) that are inactive for CO oxidation. Hence, Haruta et al. devised the method of deposition precipitation (DP) in which a preformed support is stirred in a solution of a gold compound and the pH value is varied by the addition of a base (NaOH or urea, which leads to NH_4^+ on heating) and small gold nanocrystals are deposited on the surface of the support. Recently, this has been studied in great detail for Au/TiO_2 catalysts,[111] and Haruta et al. synthesized a large batch of this catalyst by using this method as one of the World Gold Council's standard gold catalysts, and this has been made available to the academic community.

The preparation of Au/TiO_2 catalysts by the DP method has been recently studied in detail by Moreau et al.[109] They note that the method involves the close control of many experimental variables, namely:

1) the concentration of the $HAuCl_4$ solution,
2) the ratio of its volume and concentration to the mass of the support,

© 2006 Wiley-VCH Verlag GmbH & Co. KGaA, Weinheim

3) the type of TiO_2 (Degussa P-25 is the most commonly chosen),
4) the base chosen to neutralize the $HAuCl_4$ solution,
5) the temperature,
6) the pH value, both at the time the TiO_2 is added and in the subsequent reaction,
7) the time and the temperature allowed for the deposition to occur,
8) the method of filtration, washing, and drying,
9) the conditions for calcination if performed,
10) the apparent sensitivity of the precursor to light.

It is therefore clear that these preparation methods can produce a wide range of materials, particularly as different research groups tend to use a wide range of combinations of these variables. Moreau et al.[109] expected that a critical factor in this preparation procedure was the nature of the gold species in solution at the time the support is introduced, so it is important to know how their concentrations vary with the pH value. This has been reasonably well studied for gold compounds[117–119] and the hydrolysis of $AuCl_4^-$ proceeds through a complex set of equilibria as the pH value of the solution rises (Scheme 5).

$$[AuCl_4]^- + H_2O \rightleftharpoons [AuCl_3(H_2O)] + Cl^-$$
$$[AuCl_3(H_2O)] \rightleftharpoons [AuCl_3(OH)]^- + H^+$$
$$[AuCl_3(OH)]^- + H_2O \rightleftharpoons [AuCl_2(H_2O)(OH)] + H^+ + Cl^-$$
$$[AuCl_2(H_2O)(OH)] \rightleftharpoons [AuCl_2(OH)_2]^- + H^+$$
$$[AuCl_2(OH)_2]^- + H_2O \rightleftharpoons [AuCl(OH)_3]^- + H^+ + Cl^-$$
$$[AuCl(OH)_3]^- + H_2O \rightleftharpoons [Au(OH)_4]^- + H^+ + Cl^-$$

Scheme 5. Hydrolysis of $[AuCl]^-$ with increasing pH value.

The adsorption of these species onto the TiO_2 surface will also depend on the pH value and the isoelectric point.[120] Moreau et al.[109,121] studied in great detail the effect of the pH value on the preparation of Au/TiO_2 catalysts. It is clear from the equilibria shown in Scheme 5 that the pH value will vary as the hydrolysis reaction proceeds. This variation was also studied and the final pH value was considered to be important for obtaining an active catalyst for CO oxidation. Active catalysts could be obtained if the final pH value was closely controlled—pH 8.5–9—regardless of the starting pH value used for the preparation (Figure 6). At low pH values the surface of the TiO_2 is positively charged and the species in solution anionic, hence an electrostatic mechanism can explain the deposition of Au. However, the uptake is rapid, large particles form and the catalysts have low catalytic activity. As the pH value is increased the amount of gold deposited on the support decreases but the activity increases. Moreau et al. noted that above pH 8 the adsorbed gold complex is substantially chlorine-free which leads to a catalyst containing little chlorine (which is an effective poison for CO oxidation) and consisting of small particles, hence the catalysts display high activity.[109] This study is instructive as it provides insight into the key parameters that need to be controlled during the preparation of an active supported gold catalyst.

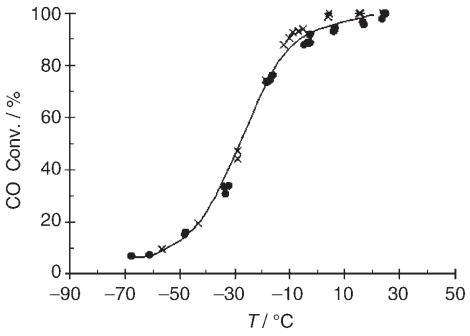

Figure 6. CO conversion as a function of the temperature for uncalcined catalysts; standard test conditions: (×) 0.47% Au/TiO_2 ($pH_{initial} = 4$ and $pH_{final} = 9$) and (●) 0.55% Au/TiO_2 ($pH_{initial} = 11$ and $pH_{final} = 8.5$).

There continues to be significant interest in the design of supported gold catalysts for the oxidation of CO at low temperature. For example, the specific form of TiO_2 used is important[122] and there has been significant recent interest in the use of mesoporous ordered structures, for example, MCM and SBA structures,[123–127] as well as nanoparticles of SiO_2-Al_2O_3.[128] Corma and co-workers demonstrated that very active catalysts can be prepared by using microcrystalline supports.[115,129] These catalysts have been found to be an order of magnitude more active than comparable catalysts prepared using a non-nanocrystalline support for CO oxidation (Figure 7)[129–131] and are also exceptionally active for coupling reactions.[132]

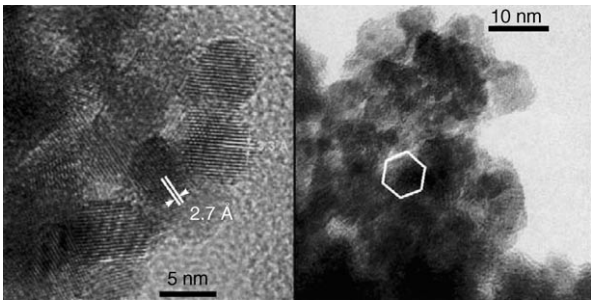

Figure 7. HRTEM of Au/CeO_2. On the left image, the white lines correspond to the (202)-Ce_6O_{11} (3.3 A) and the (200)-CeO_2 (2.7 A) lattice spacing. On the right image, a hexagonal faceted (111) Au crystal is circled.

Promotion of supported Au catalysts has, to date, been a subject that has received almost no attention. However, Solsona et al. have reported that the catalytic activity of Au/TiO_2 can be significantly enhanced by the addition of NO_3^- ions.[133] The effect requires very low levels of NO_3^- ions (Figure 8) and was observed with catalysts doped with sodium and potassium nitrate. Catalysts were prepared by the impregnation of the nitrate solution by the incipient wetness method and the catalysts were dried carefully to ensure that the nitrate was not decomposed. The effect may

 © 2006 Wiley-VCH Verlag GmbH & Co. KGaA, Weinheim

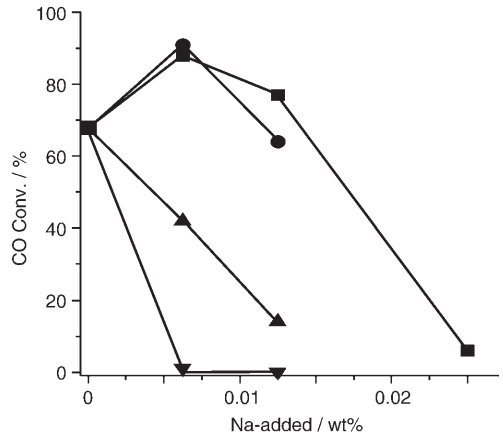

Figure 8. Influence of the alkali-metal dopant (Na or K) on the activity for the CO oxidation. Alkali-metal source: sodium nitrate (■), potassium nitrate (●), sodium citrate (▲), sodium acetate (▼). Reaction conditions: 25 °C, CO/air (mol ratio 0.5:99.5), flow rate 50 mL min^{-1}, catalyst (15 mg); time on line 500 min.

relate to the variable catalyst performance that has been reported in many studies.

3.1.3. *Nature of the Active Site*

As noted in Section 3.1.2, active catalysts are prepared by precipitation, and many of the active catalysts are typically found to comprise small gold crystallites, 2–4 nm in diameter, supported on an oxide. There has been much debate concerning the nature of the active site of these catalysts and, in 2000 Bond and Thompson proposed a model where Au atoms at the interface between the Au particle and the oxide are the active oxidation centers.[134] Figure 9 shows cuboctahedral gold nanoparticles supported on ZnO which acts as a very active CO oxidation catalyst. The periphery of the particle bound on the support is clearly visible and it is these peripheral atoms that have been the focus of much of the mechanistic debate. However, it remains unclear whether Au^{3+} or Au^0 is the active form of gold; Bond and Thompson have suggested that these peripheral atoms could be cationic gold and it is these atoms that are responsible for the activation of dioxygen in the catalytic process.[134] Kung et al. later also used this as the basis for their mechanistic discussion.[135] However, it should be noted that this is an area of intense study at present, but although there has been much research using model systems, a definitive study has not been published concerning the relative roles of Au^0 and Au^{n+} in the catalytic oxidation of CO.

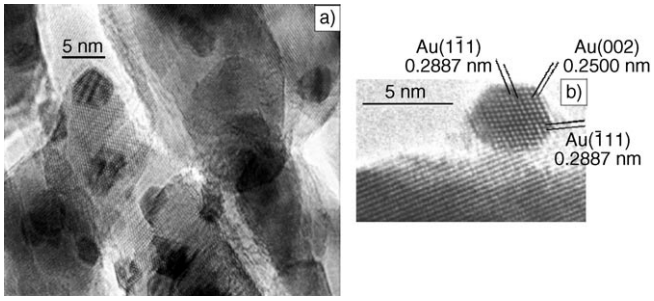

Figure 9. TEM images for oxide-supported Au catalysts. a) Au/α-Fe_2O_3 calcined at 100 °C showing the presence of cuboctahedral gold particles with diameters of 2–5 nm; b) Au/ZnO calcined at 400 °C showing a cuboctahedral gold particle of diameter 5 nm and the interface with the support.

Goodman and co-workers used, for example, a combination of scanning tunneling microscopy (STM) and spectroscopy to consider whether the unusual reactivity could be due to quantum size effects of the very small gold particles.[136] Indeed the catalyst activity correlated with the transition of the electronic state of gold. As noted by Haruta[137] this observation is questionable as far as CO oxidation is concerned, since the transition of the electronic state of the gold was determined for one specific gold cluster of a defined diameter by using STM under very controlled conditions, whereas the catalysis was determined using an entire Au/TiO_2 sample with a range of gold cluster diameters for which the mean diameter correlated with the electronic transition observed by STM. Subsequently, Boyen et al. concluded that Au particles containing 55 atoms and 1.4 nm in diameter are extraordinarily stable, and these Au_{55} particles could be the active site for CO oxidation.[138] Lopez and Nørskov showed by using DFT calculations that the activation of CO was the energetically favored reaction path on Au particles with 10 atoms.[139] However, others have focused on the role of Au^{3+}.

Davies, in particular, noted that trying to explain the enhanced reactivity of small gold nanocrystals on the basis of size alone neglects the importance of the underlying support.[140] However, it must be noted that nonsupported gold nanocrystals can be active for oxidation reactions.[141] The interface between the small gold particles and the support together with the availability of defect sites at this interface are probably the important features of the active centers, and this re-emphasises the key part of the mechanism proposed by Bond and Thompson. However, it must be stressed that the model of the active site proposed by Bond and Thompson[134] or Kung et al.[135] has yet to be verified experimentally, but this has been addressed by Haruta.[128,137] Haruta and co-workers have reassessed the mechanism of CO oxidation on the basis of the models developed by Bond and Thompson as well as by Kung et al., that is, that the CO is activated by adsorption onto Au^0 on the surface of the gold nanoparticles and that dioxygen is activated by the atoms at the boundary between the support and the gold nanocrystals. The atoms at the boundary are proposed by Haruta and co-workers to be cationic in nature, possibly $Au(OH)_3$ or Au(OH) formed by the presence of water vapor that is essential for the observed high activity catalysts.[142]

A recent model study by Chen and Goodman has tried to address the role played by these peripheral atoms by designing well-ordered monolayers and bilayers of gold atoms that completely cover the TiO_2 support, thus not containing any of these peripheral sites.[143] They found that the bilayers were more active than the monolayers (Figure 10a), thus indicating that the catalysis can proceed on the extended gold surface created. Choudhary and Goodman have shown that the

© 2006 Wiley-VCH Verlag GmbH & Co. KGaA, Weinheim

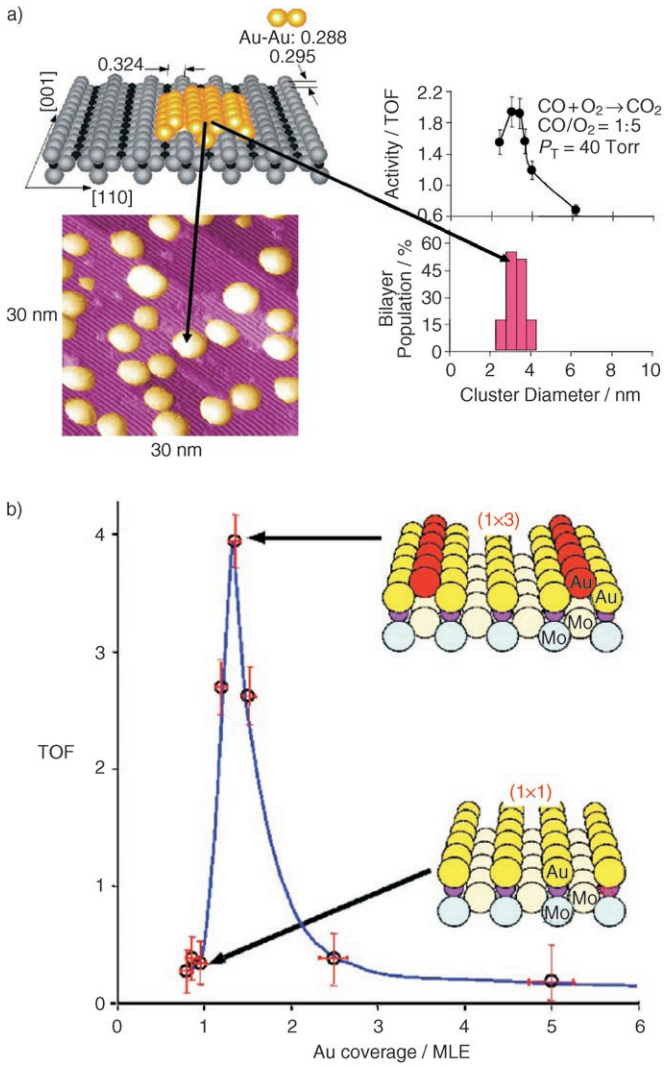

Figure 10. a) TEM image (bottom left) and schematic representation (upper left) of Au bilayer clusters on TiO_2(110), whose population are dominant (lower right) for the most active Au/TiO_2 catalyst for CO oxidation (upper right). The activity (at 77 °C) is expressed as turnover frequency (TOF) in units of s^{-1}. b) CO oxidation activity as a function of Au coverage on Mo(112)–(8×2)-TiO_x. $CO/O_2 = 2:1$; total pressure = 5 Torr. Schematic models for the (1×1)- and (1×3)-Au/TiOx surfaces are shown in the insets; the Au structure was determined by low-energy electron diffraction (LEED).[30] Au coverage is defined as: 1 monolayer equivalent (MLE) = 1.4×10^{15} atoms cm^{-2}.

particles present in an active Au/TiO_2 catalyst closely resemble the model systems used in the previous study (Figure 10b).[143,144] Most recently, Chen and Goodman have concluded that the atoms at the periphery in both model and real catalysts are metallic in nature.[145] However, in these studies no technique was used that could distinguish between cationic or metallic gold, and consequently the influence of the TiO_2 support on the electronic state of the gold cannot be ruled out. Indeed the electronic nature of very small gold particles can be expected to be significantly influenced by the nature of the support, especially the availability of defect sites.

Other investigators have used X-ray photoelectron spectroscopy and Mössbauer spectroscopy to observe cationic forms of gold. Hutchings and co-workers proposed that Au^{3+} in Au/Fe_2O_3 was an important component of very active catalysts for the oxidation of CO.[98,99] In 2003, Flytzani-Stephanopoulos and co-workers demonstrated that the cationic form of gold was an important factor in obtaining a high activity catalyst based on Au for the water gas shift by deposition onto nanocrystalline 10% La-doped CeO_2 (ca. 5 nm) by the DP method.[146] The catalysts were subsequently leached with 2% NaCN to remove 90% of the gold, and—importantly—no Au clusters or metallic particles remained. The catalytic activity was not only retained, it was significantly enhanced, which is a remarkable experimental observation. CO oxidation can be viewed as an elementary reaction in the water gas shift reaction and so the observations by Flytzani-Stephanopoulos and co-workers may be of general significance; however, these NaCN-treated systems have yet to be subjected to the full range of characterization techniques.

A very recent study by Okazaki, Haruta, and co-workers has sought to shed more light on the electronic nature of small gold nanocrystals supported on TiO_2[147] by utilizing electron holography, STM, and first principle calculations. They found that the electronic structure of the gold nanocrystals is highly dependent on their size and the stoichiometry of the TiO_2 surface. They investigated very small particles (2 nm; Figure 11) as well as relatively large particles to determine the mean inner potential theoretically, and showed that the experimental and theoretical values were in reasonable

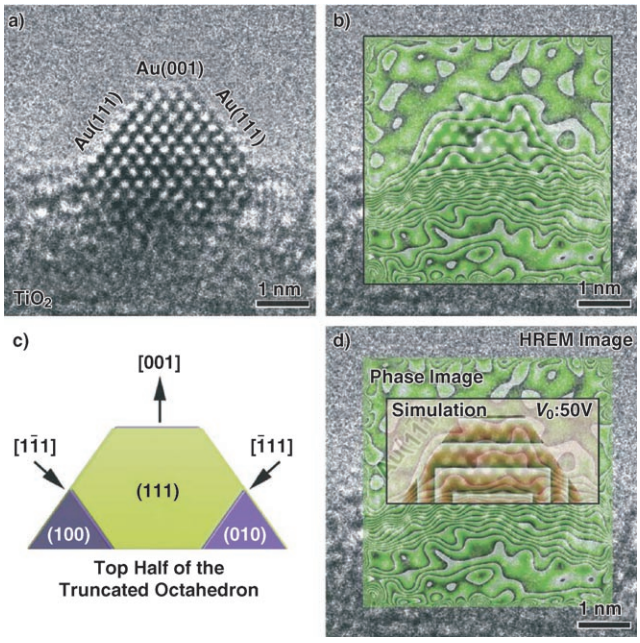

Figure 11. a) High-resolution electron microscopy (HREM) image and b) phase image reconstructed from the hologram of an Au particle on a TiO_2 support. The diameter of the gold particle is under 2 nm. The phase image is amplified 30-fold and superimposed on the HREM image. c) Schematic 3D model, whose shape is the top half of the truncated octahedron. d) Simulated phase image of the model with a superimposed reconstructed phase image.

© 2006 Wiley-VCH Verlag GmbH & Co. KGaA, Weinheim

agreement for particles of approximately 5 nm in diameter. However the potential increased with decreasing particle size and increased dramatically below about 2 nm. The authors note that this tendency for the potential of the gold nanocrystals to increase correlates well with the catalytic behavior of these particles for CO oxidation. It should be noted that Lopez et al.[148] have also indicated that very small particles are active.

Okazaki et al. concluded that the oxygen-rich surface of TiO_2 is important in the consideration of real Au/TiO_2 catalysts prepared by the DP method and calcined in air as the final preparative step.[147] They concluded that electron transfer and orbital hybridization at the interface may be the source of the catalytic activity. However, these elegant studies show that one cannot assume that the gold atoms retain their metallic nature when they are contained in very small nanostructures.

One of the intriguing features of the oxidation of CO over supported gold catalysts is the sensitivity of this reaction to water: While high partial pressures of water tend to poison the reaction through competitive adsorption, the reaction does not proceed at all unless certain threshold levels of H_2O are present. This has been most notably demonstrated in the detailed studies of Haruta[137] for Au/TiO_2 catalysts, but has also been observed with other supports, particularly Al_2O_3.[149] Costello et al. studied the deuterium isotope effect of added water over $Au/\gamma\text{-}Al_2O_3$ together with the reduction of hydrogen and concluded that their observations are consistent with the model of the active site consisting of an ensemble of metallic Au atoms and a cationic $Au^{\delta+}$ center that is associated with a hydroxy group.[149] Studies by Kung et al.[135] confirm this observation in the case of Au/Al_2O_3 catalysts.

Daniells et al. have also confirmed the importance of water for Au/Fe_2O_3, and concluded that the deactivation they observed in their studies could be attributed to a loss of hydroxy groups and reduction of Au^{3+} centers to metallic gold.[150] They suggested that the role of the hydroxy group was to promote the decomposition of a surface carbonate species. The importance of hydroxy groups for the observation of high activity has been recently shown with Au/CeO_2 prepared by DP methods.[151] Certainly, the experimental evidence obtained using real catalysts in flow reactors would suggest a role for a hydroxy function in the mechanism; however, this could be associated with the support rather than the gold nanoparticle. In view of this, many researchers have used spectroscopic techniques to attempt to unravel the role of cationic and metallic gold.

Fan et al. have used X-ray photoelectron spectroscopy (XPS) to study Au/TiO_2 prepared by using a suspension spray method.[152] They concluded that the deconvolution of the uncalcined material suggests that gold is present in both cationic and metallic forms, and the latter predominates when the material is prepared at a higher temperature; this finding coincides with higher activity. The initial reaction rate for CO oxidation correlates with the temperature of the spray reaction and with the amount of metallic gold determined by XPS. On this basis they propose that metallic gold is the active site in this system. However, it must be noted that the use of a single spectroscopic technique that is used ex situ can be misleading. Furthermore, XPS of gold nanoparticles is affected markedly by final state effects, and the binding energy of the Au^0 is highly size-dependent for small nanoparticles.[153] For this reason, current research uses a battery of complementary techniques and, in particular, the use of in situ methods is gaining ground. In this respect, the studies by Gates and co-workers using in situ X-ray absorption spectroscopy (XAS)[35,36,154] have shown that cationic gold is active in Au/MgO and Au/zeolite catalysts where the materials are prepared from mononuclear gold complexes. The catalysts were prepared from $[Au(CH_3)_2(acac)]$ (acac = acetylacetonate) and characterized in situ by using XAS and IR spectroscopy in the presence of the reacting gases under flow conditions. X-ray absorption near edge structure (XANES) data coupled with ν(CO) data showed that the Au^{3+} initially present was reduced to Au^+ and the catalyst also lost its activity. Under these flow conditions there was no evidence for the presence of metallic gold and the authors concluded that their in situ study presented clear evidence that cationic gold was essential for CO oxidation activity in these systems. In contrast, Schwartz et al.[155] carried out an XAS study on Au/TiO_2 catalysts prepared from mesoporous TiO_2, and concluded that oxidized gold was not necessary for high activity. Similar results have also been reported for Au/TiO_2 by Yang et al.,[156] in which they used a combination of in situ XAS and FTIR spectroscopy complemented by XPS, microcalorimetry, and TEM characterization.

In contrast to these in situ studies, combined model and theoretical studies[157,158] continue to focus on fundamental aspects such as charge transfer from oxide defects (for example, F-center defects on MgO (100) surfaces) and the adsorption and activation of reactant molecules. At present there appears to be little effort being made to bridge the gap between these two approaches. Okazaki et al. have carried out a fundamental DFT investigation on the Au/TiO_2 catalyst by studying the adsorption of gold on three TiO_2 (110) surfaces.[159] They found that the surface conditions (for example, defects) strongly affect the absorption energy and the electronic structure of the Au adlayer. The authors note that this can be closely related to the catalytic activity of these catalysts. As noted previously, Okazaki et al. pioneered the use of electron holography together with STM,[147] and in these studies showed that the electronic structure of the Au is highly dependent on the particle size, and this makes it much more difficult to correlate model studies on well-defined surface structure with real catalysts used in flow reactors. This is an area where further studies are urgently needed. Indeed, the observations on the electronic nature of very small nanoparticles is highly relevant to the recent model studies by Chen and Goodman (Figure 10),[143] since clearly these effects must also be present in the well-defined model structures if they are reasonable models of the active catalysts.

The use of Mössbauer effect spectroscopy is particularly incisive for supported Au catalysts since Au^0, Au^+, and Au^{3+} can be distinguished and the method can be used in situ. Au/Fe_2O_3 catalysts have been studied in detail by using this technique. Studies by Hutchings and co-workers showed that the most active catalysts for this system are those prepared

 © 2006 Wiley-VCH Verlag GmbH & Co. KGaA, Weinheim

without calcination and with Au^{3+} (Figure 12) within the experimental limits of detection (ca. 2%),[98,159] a feature that has been observed in a number of studies.[105,160–163] Studies of

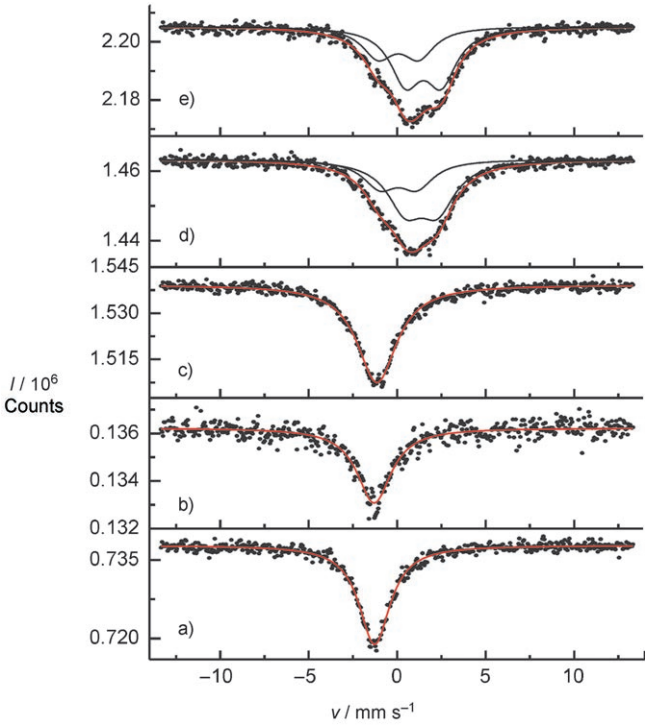

Figure 12. Mössbauer effect spectroscopy of Au/Fe_2O_3 catalysts a) dried at 25 °C, Au^{3+}, CO conversion 100%; b) dried at 100 °C, Au^{3+}, CO conversion 100%; c) calcined at 400 °C, Au^0, CO conversion 91%; d) calcined at 400 °C followed by 550 °C, Au^0, CO conversion 31%; e) calcined at 60 °C, Au^0, CO conversion 0%. Reaction conditions: 0.5% CO in air, 24000 h^{-1}, catalyst (50 mg), 25 °C.

the active Au/Fe_2O_3 catalysts following exposure to CO confirmed that the gold remained present as Au^{3+}.[164] A recent publication by Hutchings et al. using Mössbauer spectroscopy in combination with a range of complementary spectroscopies has provided further evidence for the role of Au^{3+} in Au/Fe_2O_3 catalysts.[165] Boyd et al. carried out detailed Mössbauer spectroscopic investigations of Au/TiO_2, Au/Fe_2O_3, and Au-HY zeolites (HY refers to the protonated form of a zeolite from the Faujasit structure type), in which the Au was introduced by ion exchange of $[Au(en)_2]^{3+}$ (en = ethylenediamine) and concluded that Au^+ was active in these catalysts and an initial reduction period was required to produce Au^+ from Au^{3+}.[166] Furthermore, they investigated the effect of treating Au/TiO_2 catalysts with CN^- under oxidising conditions and showed that the specific activity of the Au increases with decreasing gold content. They concluded that these results demonstrated the role of an oxidized gold species (namely, Au^+) in the CO oxidation reaction, but the combined role of an oxidized gold species with Au^0 could not be ruled out.

The nature of the support appears to be crucial for the stabilization of cationic gold species, as can be expected from the pioneering studies by Okazaki et al.[147,159] For example, Calla and Davis[167] showed by using XAS that Au^{3+}, formed by treatment of Au/Al_2O_3 with CN^-, was not stabilized on the alumina. However, detailed studies by Corma and co-workers[115,129–132,168] show that Au^{3+} is stabilized on rare-earth oxides, for example, CeO_2 and Y_2O_3, and that the catalytic activity for CO oxidation correlates directly with the concentration of Au^{3+}. Fierro-Gonzalez et al.[169,170] have shown that cationic gold can also be stabilized on zeolite Y and La_2O_3 in the case of catalysts prepared using mononuclear gold complexes $[Au(CH_3)_2(C_5H_7O_2)]$. Okumura et al. have also studied by using a combination of quick EXAFS and IR spectroscopy the effect of heating on the stability of Au^{3+} prepared on zeolites by the DP method.[171] These materials were remarkably sensitive to the treatment conditions, thus confirming the complexity of trying to evaluate the nature of the species in active catalysts. They noted that on heating, the particle growth proceeded via the formation of Au-55 clusters. Pestryakov et al.[172] have shown that cationic gold species can also be prepared using mordenite as a support.

There are many emerging reports concerning cationic gold as having a pivotal role in the CO oxidation mechanism. It is clear that all researchers agree that the catalyst activity of supported gold catalysts increases as the mean particle size decreases. The most compelling data for this have been published in 2004 by Lopez et al.[148] As the particle diameter decreases, the proportion of gold atoms in contact with the support increases and the electronic nature of these atoms will be influenced by the support, as demonstrated by Okazaki et al.[147,159] This effect becomes highly significant for particle diameters less than 2 nm, which coincides with a dramatic enhancement in activity. In addition, there is further compelling evidence for the involvement of surface hydroxy groups in the reaction mechanism, and again this suggests an essential role for cationic gold in the active site, as was originally proposed by Bond and Thompson[134] (Figure 13).

It is clear that the debate over the active center of the gold-catalyzed oxidation of CO will continue for the immediate future. There are two reasons for finding an answer to this key question: The first is scientific curiosity—put very simply it would be preferable to know the answers to the mechanistic questions—and second the oxidation of CO is seen as a crucial aspect of using methanol or hydrocarbons as

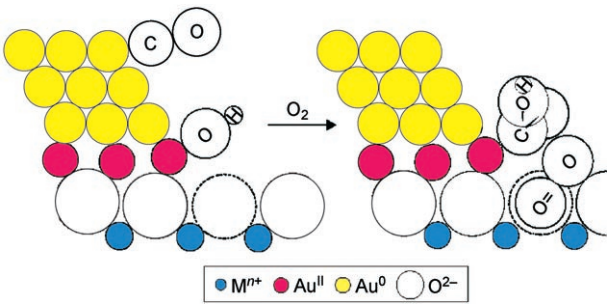

Figure 13. Proposed model for the active site of a supported gold catalyst incorporating the essential features of cationic gold at the interface of the gold nanoparticle with the support, surface vacancies, and the involvement of a hydroxy group. Much of the current experimental evidence is in agreement with this proposal.

© 2006 Wiley-VCH Verlag GmbH & Co. KGaA, Weinheim

fuels in fuel cells. Traces of CO are present in the feedstock for fuel cells and this must be removed as they poison the electrodes, and gold catalysts may provide a mechanism for removing these trace amounts; this is addressed in the next section.

3.2. Water Gas Shift Reaction

Since supported Au catalysts have been shown to exhibit excellent catalytic activity for the oxidation of CO, it is not unexpected that they have been used for the water gas shift reaction [Eq. (6)]. This reaction is crucial for the production

$$CO + H_2O \longrightarrow CO_2 + H_2 \quad (6)$$

of hydrogen on an industrial scale,[173] and for many catalysts the oxidation of CO is considered as one component of the water gas shift reaction which can act as an intermediate and react with an adsorbed oxygen atom O(a) (Scheme 6).

$$H_2O \longrightarrow O(a) + H_2$$
$$CO + O(a) \longrightarrow CO_2$$

Scheme 6. Steps in the water gas shift reaction.

Recent interest in small-scale fuel cells, such as the polymer electrolyte fuel cell (PEFC), has spurred a great deal of interest in the design of new catalysts for the water gas shift reaction, particularly those that are active at low temperatures (< 250 °C). The conventional low-temperature catalysts for the water gas shift reaction are based on Cu, and these are not well suited to the application in PEFC systems because they become poisoned on exposure to air during the operating conditions. In this respect a supported Au catalyst has a clear advantage over a Cu-based system.

Water gas shift activity of Au catalysts at low-temperature was first reported by Andreeva and co-workers for Au/Fe_2O_3 catalysts.[174–180] Subsequently, Venugopal et al. studied Au/Fe_2O_3 catalysts[181] and showed that the addition of Ru to this catalyst, that is, to give a bimetallic $Au\text{-}Ru/Fe_2O_3$ catalyst,[182] significantly enhances the performance, and they showed that hydroxyapatite was also a useful support for Au catalysts.[183] Hua et al. have shown that the addition of metal oxides to Au/Fe_2O_3 can enhance the performance in the water gas shift reaction.[184]

Daniells et al. investigated Au/Fe_2O_3 catalysts under water gas shift conditions and have shown that although traces of water enhance the rate of CO oxidation at ambient temperature, much higher temperatures are required when higher concentrations of water are used.[150] They found that at the higher temperatures any cationic gold was reduced to metallic gold. Haruta and co-workers have reported that Au/TiO_2 catalysts are also active,[185] and Idakiev et al. have also shown that mesoporous TiO_2 can be an effective support.[186]

Most recent interest has focused on the use of CeO_2 as a support after Fu et al.[187] reported this catalyst was more active than Au/TiO_2. Au/CeO_2 has now attracted many studies.[188–193] It is interesting to note that Au/Fe_2O_3, Au/TiO_2, and Au/CeO_2 have all been shown to be highly effective catalysts for the oxidation of CO at ambient and low temperatures. Kim and Thompson have shown that while many Au/CeO_2 catalysts are significantly more active than commercial Cu catalysts, they are prone to deactivation, which is caused by carbonates and/or formates blocking the active sites.[194]

Fu et al.[146] showed that the catalytic activity of the Au/CeO_2 catalyst was significantly enhanced by treatment with CN^- ions. This treatment removed most of the gold from the catalyst, and it was proposed that cationic gold resulting from the CN^- treatment was the active species present in these active catalysts. Indeed, DFT calculations have been used to demonstrate that the presence of empty localized nonbonding f states in CeO_2 permit the oxidation of Au, thus enabling subsequent CO adsorption.[195] The active site for the water gas shift reaction was considered to be Au clusters of 4–6 atoms associated with an O vacancy on the CeO_2 surface. However, these calculations are probably more closely related to CO oxidation at ambient temperature, since gold cations are known to be thermally unstable at the elevated temperatures required for the water gas shift reaction. Haruta and co-workers made a detailed study of the structure of Au/CeO_2 catalysts by using annular dark field scanning transmission microscopy (ADF-STEM).[116] They observed that the Au nanoparticles had a diameter of about 3 nm (Figure 14). By using transient experiments with CO and H_2O pulsing into H_2 and He it was deduced that the water gas shift reaction was catalyzed at the interface of the small Au particles and a reduced CeO_2 surface.

Tibiletti et al. used a combined experimental (EXAFS, XANES) and theoretical approach to study Au/CeO_2 catalysts for the water gas shift reaction, and they observed that although the fresh noncalcined catalysts comprised highly dispersed gold cations, even at temperatures as low as 100 °C the experimental data was only consistent with these gold species being reduced to metallic gold.[196] However, they observed that 15 % of the gold could be re-oxidized by exposure to air at 150 °C and they concluded that this was due to the close interaction of these gold atoms with the support. The DFT calculations suggested a model in which gold was present in a partially oxidized form at a Ce^{4+} vacancy. They indicated that the small amounts of these oxidized species are below the detection limit of the XANES method, which only showed the presence of metallic gold under the water gas shift reaction conditions.

3.3. CO Oxidation at Low Temperature

The high activity of supported gold catalysts for the oxidation of CO at ambient temperature should be of interest for respiratory protection. For many decades the catalyst of

 © 2006 Wiley-VCH Verlag GmbH & Co. KGaA, Weinheim

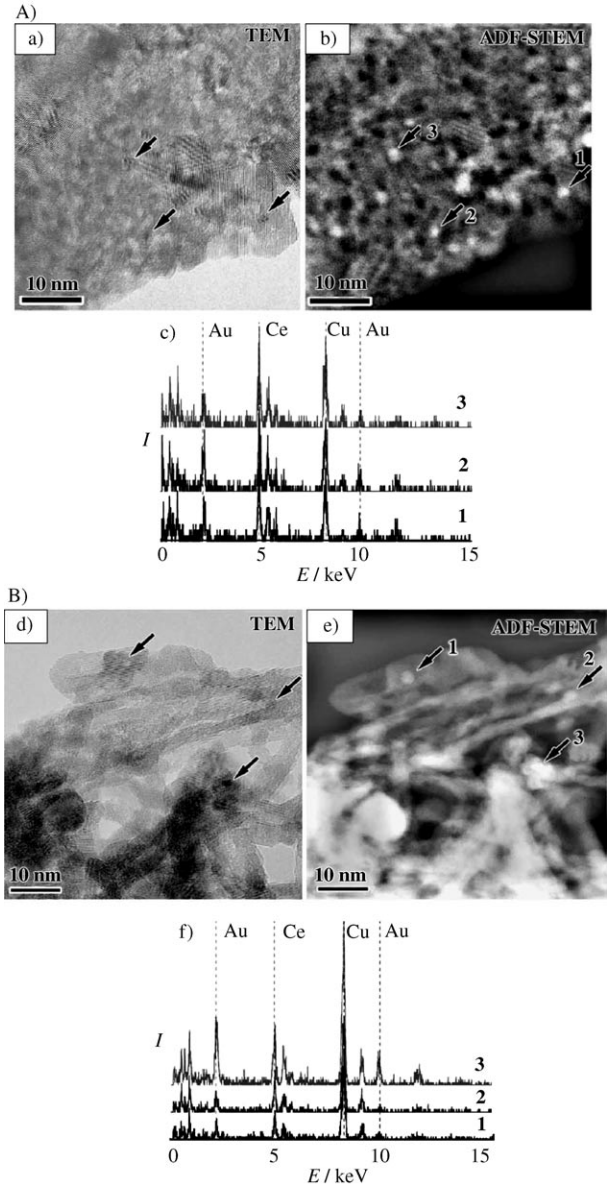

Figure 14. a) TEM and b) ADF-STEM images of an Au/CeO_2 (A) catalyst taken at an original magnification of 300000; and c) energy-dispersive spectroscopy (EDS) spectrum obtained from each particle indicated in the ADF-STEM image; d) TEM and e) ADF-STEM images of an Au/CeO_2 (B) catalyst taken at an original magnification of 400000, f) EDS spectra obtained from each particle indicated in the ADF-STEM image.

choice in respirators for the removal of CO in toxic environments has been hopcalite, which is a copper manganese oxide. Supported gold catalysts have yet to become established in this application. However, one particular application for which supported gold catalysts may find a niche market is in fuel cells[197–202] and in particular in polymer electrolyte fuel cells (PEFC), which are used in electric vehicles and operate at about 80–100 °C. Gold catalysts may also have potential for the production of hydrogen by steam reforming of methanol.[203] PEFCs operate by the oxidation of hydrogen produced from methanol by steam reforming and water gas shift reactions. Residual CO can poison the Pt anode at the low operating temperature, and hence trace amounts of CO have to be removed from the H_2 in the presence of water to ensure long cell lifetimes. Although conceptually simple, the oxidation of CO in the presence of excess moist H_2, without oxidizing the hydrogen, is a particularly difficult reaction which is now attracting considerable research effort. An alternative strategy would be to design PEFCs that can tolerate the residual CO, but to date this has also proved to be unsuccessful, so both approaches are currently being actively pursued.

Considerable effort has been applied to the design of suitable catalysts for the competitive oxidation of CO in the presence of H_2. The most commonly used partial oxidation catalysts (alumina-supported Pt, Ru, and Rh) are unsuitable as they require temperatures in the range of 150 to 200 °C to be effective,[204–206] and even then significant conversion of H_2 is observed. Catalysts based on mixed oxides of copper are active in the appropriate temperature range, but supported gold catalysts display superior activity. Kandoi et al. have calculated the activation barriers for CO oxidation to be 0.18 eV on Au(111), 0.82 eV on Cu(111), and 0.96 eV on Pt(111), whereas the barriers for the formation of OH, the first step in the oxidation of H, was 0.90, 1.28, and 0.83 eV, respectively.[207] A microkinetic model based on these DFT results indicates that the trends in the relative activities of Au, Cu, and Pt for the preferential oxidation of CO over H_2 are due to differences in the rate constants of these competitive reactions as well as the surface coverage of CO and H. Hence, this DFT study provides an insight into the origin of the selectivity displayed by supported gold catalysts in the preferential oxidation of CO in the presence of H_2.

Haruta and co-workers first demonstrated that supported Au nanoparticles could be active at much lower temperatures, but again H_2 was oxidized together with CO at temperatures greater than 70 °C.[208,209] Kahlich et al. studied Au/Fe_2O_3 catalysts calcined at 400 °C, but found that significant H_2 oxidation occurred at 80 °C.[100] Qiao and Deng showed that noncalcined Au/Fe_2O_3 catalysts, dried only at 120 °C, were very selective for CO oxidation in the presence of H_2 at 25 °C, but the selectivity was lost at higher temperatures.[101] To date, some of the best results for this demanding reaction have been reported by Grigorova et al. for an Au/CeO_2 catalyst promoted with SnO_2, but even this catalyst gives significant (ca. 5 %) H_2 conversion at temperatures greater than 70 °C, with CO conversions of about 40–60 %.[210] Schumacher et al. have shown that H_2 competes with CO for adsorption on Au/TiO_2 by raising the reaction order for CO significantly.[211] Calla and Davis have shown that the addition of H_2O decreases the reaction order of CO on Au/Al_2O_3.[212]

Pansare et al. have shown that the particle size of the gold is an important factor, with high dispersion catalysts giving the highest activity, as would have been expected from the extensive studies on CO oxidation carried out with these catalysts.[213] Recently, Corma and co-workers reported a nanocrystalline CeO_2-supported gold catalyst that gave appreciable selectivity at 60 °C with a dry CO/H_2 mixture.[130] Jain et al.[214] have also shown the high activity of Au/CeO_2 catalysts, and Lomello-Tafin et al.[215] have shown that Au/ZrO_2 also displays high activity for the preferential oxidation

 © 2006 Wiley-VCH Verlag GmbH & Co. KGaA, Weinheim

of CO. However, a recent study by Rossignol et al. has shown that the support effects observed for the oxidation of CO alone decrease in the presence of added H_2, and that Au/Al_2O_3, Au/TiO_2, and Au/ZrO_2 all show similar activity.[216]

Unfortunately, all these studies used dry reactants and consequently are not applicable to the humid conditions prevailing in fuel cells, which in addition also contain significant quantities of CO_2. Schubert et al. have shown that a calcined Au/Fe_2O_3 can operate under realistic fuel-cell conditions in which CO_2 and H_2O are present, and reasonable selectivity has been achieved.[217]

The successful operation of a catalyst in a fuel cell in which H_2 is generated from reforming hydrocarbons or methanol needs to achieve high CO conversion in the presence of excess CO_2 as well as excess H_2 and H_2O. Hence for successful operation as a selective CO oxidation catalyst in a reformer-PEFC system, the catalyst must operate at about 80 °C in a complex feed comprising CO, O_2, H_2, CO_2, H_2O, and N_2, and be capable of reducing the CO concentration from about 1 % to below 50 ppm—this is equivalent to a CO conversion of at least 99.5 %. Furthermore, this conversion must be achieved without the addition of excess O_2, and the competitive oxidation of H_2 must be minimized. This selectivity is defined as the percentage of the oxygen feed that is consumed in the oxidation of CO; for commercial operation a selectivity of 50 % is acceptable, since at this selectivity a minimal quantity of H_2 is oxidized to water. Taken together, this represents a demanding target and until recently this has not been achieved.

Avgouropolous et al. came very close to achieving the target: their system worked at 100 °C and used an Au/Fe_2O_3 catalyst calcined at 400 °C, but required excess O_2 and low levels of CO_2.[102] This catalyst has been used in many studies to date. Furthermore, it is apparent that the CO conversion decreased markedly at higher reaction temperatures (Figure 15) which is considered to be due to the reverse water gas shift reaction becoming an important factor, and which would lead to the formation of CO from CO_2 [Eq. (7)].

$$CO_2 + H_2 \longrightarrow CO + H_2O \qquad (7)$$

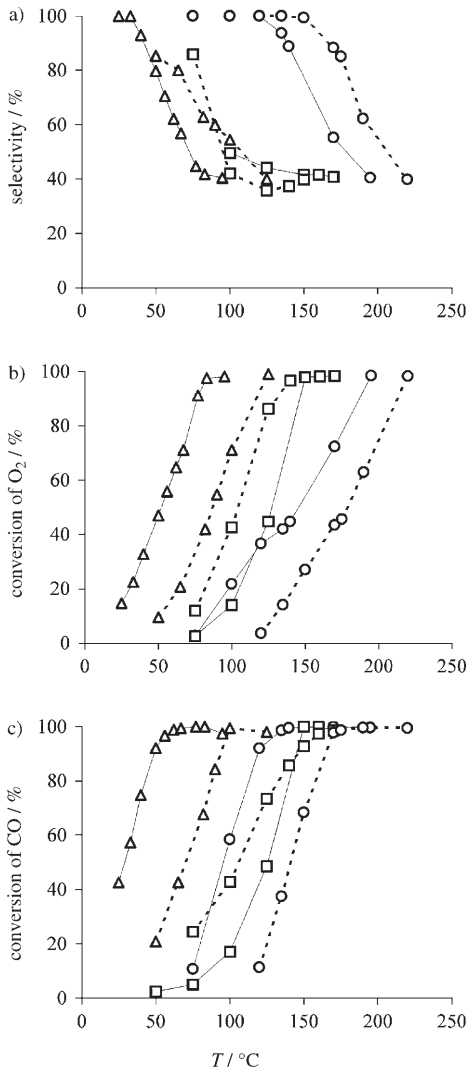

Figure 15. Variation of the CO and O_2 conversion and of the selectivity with the reaction temperature for the selective oxidation of CO, at $W/F = 0.144\ g\,s\,cm^{-3}$ (W/F = weight of catalyst/flow rate of reactant gases) over the Au/Fe_2O_3 (△), $CuO\text{-}CeO_2$, (○), and Pt/Al_2O_3 (□) catalysts in the presence of 15 vol % CO_2 (solid lines) and in the presence of both 15 vol % CO_2 and 10 vol % H_2O in the reactant feed (•••••).

Subsequently, Hutchings and co-workers have shown that an Au/Fe_2O_3 catalyst prepared using a two-stage calcination at 400 °C and 550 °C leads to a catalyst that, for the first time, can achieve this demanding target (Figure 16).[104,105] The two-stage calcination removes the catalytic sites that are responsible for the reverse water gas shift reaction. These sites can be either cationic gold or very small gold nanoparticles. As described in Section 3.2, supported Au catalysts are very effective for the forward water gas shift reaction, and hence they can be expected to be catalysts for the reverse reaction. Of course, Au catalysts tend to become active for the water gas shift reaction at temperatures well in excess of those employed in PEFCs, but it should be noted that only a relatively insignificant reverse water gas shift activity is required to ensure that the demanding catalytic target for CO conversion is not met. Hence, the most important factor in the

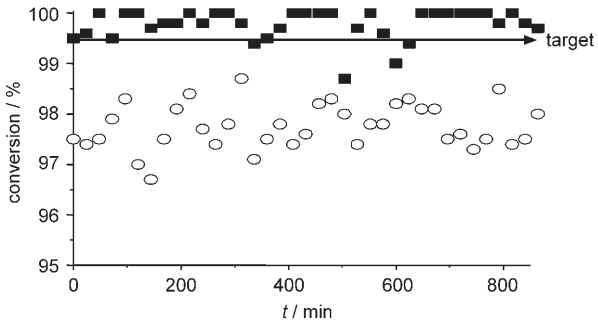

Figure 16. Variation of CO (■) and O_2 (○) conversion with time on line for a 5 % Au/Fe_2O_3 catalyst calcined in air at 400 + 550 °C. Reaction conditions: 80 °C, 0.9 % CO, 0.9 % O_2, 50 % H_2, 22 % CO_2, 4.7 % H_2O in N_2; 100 mg of catalyst were used with a total flow rate of 20 mL min^{-1}, GHSV = 12000 h^{-1} (GHSV = gas hourly space volume).

© 2006 Wiley-VCH Verlag GmbH & Co. KGaA, Weinheim

design of a successful catalyst for this application is the need to control the activity of the catalyst for the reverse water gas shift reaction whilst retaining the activity for CO oxidation. Under the conditions used in the competitive experiments shown in Figure 16 the equilibrium concentration of CO expected from the reverse water gas shift reaction can be several hundred ppm, yet the target level is less than 50 ppm. Armed with this knowledge we can now anticipate that Au catalysts will be designed with much higher activity for the preferential oxidation of CO for application in PEFCs.

4. Selective Oxidation

Supported gold catalysts have been found to be particularly effective for the epoxidation of alkenes and the oxidation of alcohols; in addition, there are some studies that indicate that C–H activation may be feasible with supported gold catalysts. Supported gold catalysts when alloyed with Pd are particularly effective as catalysts for the direct formation of hydrogen peroxide from the reaction of H_2 and O_2, which is acknowledged to be one of the most difficult and demanding selective oxidation processes. The recent developments in this emerging field of catalysis by gold are summarized in the following sections.

4.1. Epoxidation

Most research has focused on the oxidation of propene to propene oxide, as the latter is used as a commodity chemical in the manufacture of polyurethane and polyols. Although the epoxidation of ethene with dioxygen is a commercial process that operates with selectivities in excess of 90% when using a supported Ag catalyst,[218] the oxidation of propene has proved to be much more problematic and typically selectivities lower than 10% are observed with many catalysts. However, very recently Lambert and co-workers have shown that supported catalysts can give selectivities of about 50% at 0.25% conversion,[219] but the selectivity declines rapidly with increasing conversion.

Haruta and co-workers were the first to demonstrate the potential of supported gold catalysts for the epoxidation of propene with dioxygen in the presence of H_2 as a sacrificial reductant. H_2 permits the activation of O_2 at relatively low temperatures, thereby permitting the selective oxidation of propene to occur.[5,220,221] Haruta and co-workers found that Au/TiO_2 prepared using the DP method was selective for the epoxidation of propene and that the catalysis was associated with an intimate contact between hemispherical gold nanocrystals (2–5 nm in diameter) and the TiO_2 support (Figure 17), as revealed by high-angle ADF-STEM. Initial selectivities were low but promising, and improvements were made by using different titanium-containing supports such as TS-1, Ti-zeolite β, Ti-MCM-41, and Ti-MCM-48.[140,141,222–239]

All these studies confirm that Au/TiO_x catalysts are very effective for this epoxidation when H_2 is used as a sacrificial reactant. Many of the early studies concentrated on the use of TS-1 as a support as it is known that this material is selective

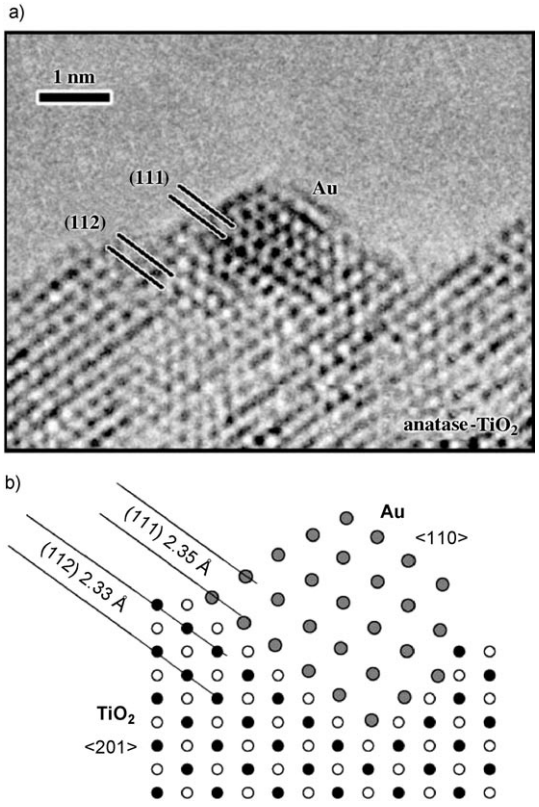

Figure 17. a) TEM images of the Au/TiO_2 contact interface and b) its schematic representation (Ref. [228]).

for the epoxidation of propene with H_2O_2.[222] Haruta and co-workers found the Au/TS-1 catalysts produced more propanal than propene oxide.[223] In contrast, Moulijn and co-workers clearly showed that Au/TS-1 catalysts could be very selective for the formation of propene oxide, and that the catalysts were stable under the chosen reaction conditions.[224] Recent mechanistic studies by Moulijn and co-workers have shown that a bidentate propoxy species is formed as an intermediate,[225] and more recent studies by Delgass and co-workers have confirmed these findings.[226,229] The gold loading in particular requires careful tuning[228] to obtain high selectivities and activities.[229] After normalizing for the gold content, yields of 350 $g\,h^{-1}$ propene oxide per gram of gold are achievable at 200 °C for a 0.01 wt% Au/TS-1 catalyst with an Si/Ti ratio of 500:1. The active species in these catalysts are considered to be gold species with diameters much smaller than 2 nm.

Haruta and co-workers have shown that the use of mesoporous titanoslicates as the support[142] gives reasonably efficient H_2 consumption as well as high yields of propene oxide (93 $g\,h^{-1}\,kg_{cat.}^{-1}$ at 160 °C) and propene oxide selectivities of > 90% at propene conversions of about 7% and a hydrogen efficiency of 40%.[230] Although these catalysts showed relatively short lifetimes, they could be reactivated and these catalysts are of commercial potential.

Very recently, trimethylamine was identified as a gas-phase promoter for the epoxidation of propene with supported gold catalysts.[231] This is an important observation,

 © 2006 Wiley-VCH Verlag GmbH & Co. KGaA, Weinheim

since the epoxidation of ethene is greatly enhanced by a complex mixture of gas-phase promoters.

The need for sacrificial H_2 for the epoxidation of alkenes with supported gold catalysts has been shown not to be essential in a recent study by Hughes et al.,[232] in which it was shown that using catalytic amounts of peroxides could initiate the oxidation of alkenes with O_2. A range of substrates were used to show the effect and very high selectivities of the epoxides were observed with cyclohexene, styrene, *cis*-stilbene, and cyclooctene. The selectivity was shown to be highly dependent on the solvent and the best results were achieved with substituted benzenes. These catalysts were also effective in the absence of solvent (Table 3), which coupled with the mild reaction temperatures certainly addresses the credentials for a new "green" technology. The yields of epoxides obtained under these solvent-free conditions were similar to those obtained for supported gold catalysts using sacrificial H_2.[142,230]

Table 3: Oxidation of *cis*-cyclooctene with molecular oxygen in the absence of a solvent.[a][232]

Catalyst	TBHP	Conv.	Selectivity [%]				
	[g]	[%]			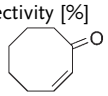	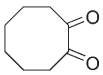	Σ_{sel} C_8
1% Au/graphite	0.12	7.9	81.2	9.3	4.1	0.5	95.1
1% Au/graphite	0.02	7.1	79.2	6.8	3.0	0.5	89.5
1% Au/graphite	0.002	1.3	82.6	7.4	2.1	0.6	92.7
no catalyst	0.008	2.0	trace	0.0	0.0	0.0	–
graphite	0.008	2.3	trace	0.0	0.0	0.0	–

[a] Reaction conditions: 0.12 g catalyst, *cis*-cyclooctene (10 mL, 0.066 mol), 80 °C, 24 h, in a stirred autoclave with 3 bar O_2. TBHP = *tert*-butylhydroperoxide.

These studies were extended by Carrettin et al. to show that Au supported on graphite can oxidize glycerol to glycerate with 100% selectivity by using dioxygen as the oxidant under relatively mild conditions, with yields approaching 60%.[237–239] The selectivity was found to be very dependent upon the glycerol/NaOH ratio. In general, exceptionally high selectivities to glyceric acid could be observed with high concentrations of NaOH. However, decreasing the concentration of glycerol, and increasing the mass of the catalyst and the concentration of oxygen, led to the formation of tartronic acid through consecutive oxidation of glyceric acid. Interestingly, this product is stable in the presence of these catalysts. It is apparent that, with careful control of the reaction conditions, 100% selectivity to glyceric acid could be obtained with 1 wt% Au/C. Under comparable conditions, supported Pd/C and Pt/C always gave other C_3 and C_2 products in addition to glyceric acid and, in particular, also gave some C_1 by-products. Subsequent studies by Porta and Prati have shown further aspects of this complex oxidation.[252] Basheer et al. have shown that a simple capillary reactor can be used for the selective oxidation of glucose, thus showing that oxidations in a flow reactor are feasible using a supported gold catalyst.[253]

In many catalytic studies the support–catalyst interaction is a crucial factor controlling reactivity. Interestingly, Rossi and co-workers have shown that "naked" gold colloidal particles can be very effective catalysts for the oxidation of glucose to gluconic acid.[141] The initial rates for these nonsupported particles were identical to the rates observed with Au/C catalysts operated under the same conditions, hence confirm-

4.2. Oxidation of Alcohols and Aldehydes

The oxidation of alcohols and polyols to chemical intermediates represents a demanding target. Supported platinum and palladium nanoparticles are generally acknowledged as effective catalysts for the oxidation of polyols, for example, in carbohydrate chemistry for the oxidation of glucose to gluconic acid and the oxidation of glycerol to glyceric acid. However, these catalysts, although well established have disadvantages, namely they exhibit poor selectivity with complex substrates. Rossi, Prati, and co-workers[12,240–252] have shown in their seminal studies that supported gold nanoparticles can be very effective catalysts for the oxidation of alcohols, including diols. The presence of base was found to be essential for activity—it is considered to be essential for the first hydrogen abstraction—and this is a significant difference from Pd and Pt catalysts, which are effective in acidic as well as basic conditions. The catalysts were based on Au/C systems and they were observed to be effective for a range of substrates (Figure 18). The catalysts were shown to be effective with gas-phase reactants and in this case no base addition was required.[233] These studies have been extended to the oxidation of sugars, and similar high catalytic efficiency for the oxidation of glucose and sorbitol has been observed.[234,235] In recent studies the synergistic effect of the addition of Pd or Pt to the Au/C catalysts for the selective oxidation of D-sorbitol to gluconic and gulonic acids were reported.[236]

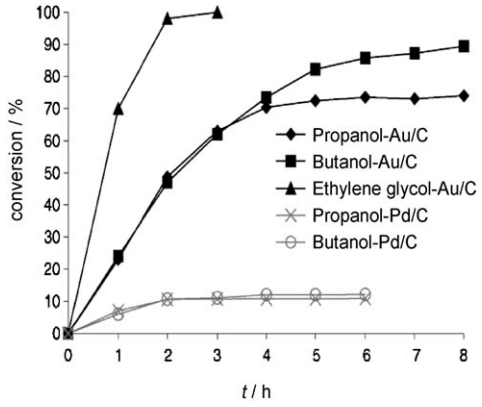

Figure 18. Oxidation of alcohols. Reaction conditions: [alcohol] = 0.35 M; alcohol/M = 1000:1 (mol/mol); NaOH = 1 equiv; $p(O_2)$ = 3 atm; T = 343 K (Ref. [271]).

© 2006 Wiley-VCH Verlag GmbH & Co. KGaA, Weinheim

ing that the support is of limited importance in the origin of the catalyst activity in these oxidation reactions. The support–catalyst interaction is, however, essential for the observation of a stable catalyst system. Subsequently Mertens et al. have also shown that colloidal gold can catalyze the oxidation of 1,2-diols.[254,255] Recently, Tsunoyama et al. have shown that benzyl alcohol can be oxidized using oxygen in aqueous media with gold nanoclusters stabilized on polymers.[256]

One of the most significant advances in the field of alcohol oxidation has come from Corma and co-workers:[257,258] they showed that an Au/CeO_2 catalyst is active for the selective oxidation of alcohols to aldehydes and ketones as well as the oxidation of aldehydes to acids under relatively mild conditions, without the addition of a solvent, and using O_2 as the oxidant without the requirement for the addition of NaOH. The results, in terms of activity and selectivity, were shown to be comparable to or higher than the highest activities previously reported with supported Pd catalysts.[259] The catalytic activity was ascribed to the Au/CeO_2 catalyst stabilizing a reactive peroxy intermediate from O_2. Subsequently, Enache et al. showed that alloying Pd with the Au in supported Au/TiO_2 catalysts enhanced the activity for alcohols in solvent-free conditions by a factor of over 25.[260] Primary alcohols and diols can be readily oxidized with these reactive catalysts, thus further extending the scope of selective oxidation reactions that are possible with gold catalysts.

More recently attention has been given to the mechanism of the oxidation of alcohols using gold catalysts, mainly for homogenous systems. The best molecular model for oxidation with oxygen in the presence of supported gold catalysts was developed by Rossi et al.[235] Since the oxidation of an aldehyde to a carboxylic acid proceeds through an aldehyde hydrate, it is conceivable that the oxidation of an alcohol proceeds in an analogous manner. On the basis of a thorough kinetic analysis[235] of the oxidation of glucose to gluconic acid,[141] which, for example, has an activation energy of $(47 \pm 1.7)\ kJ\,mol^{-1}$ (quite similar to the value of $(49.6 \pm 4.4)\ kJ\,mol^{-1}$ observed for the enzyme hyderase) and with the reaction being first order in oxygen, the authors suggest a fast adsorption of the glucose on the gold; the rate-determining step would then be the oxidation of the glucose by oxygen dissolved in the liquid (aqueous) phase. Hydrogen peroxide could be detected, but it decomposed quickly under the reaction conditions. These glucose oxidations can reach an initial TOF of $50\,120\ h^{-1}$.

In a subsequent investigation Rossi et al. showed that these oxidations do not proceed by a radical pathway but delivers gluconate and hydrogen peroxide by a two-electron mechanism.[261] The hydrogen peroxide decomposes because of the basic medium before it reaches a concentration at which it would efficiently compete with oxygen as the oxidant. Scheme 7 shows the mechanism for that oxidation reaction.

In aqueous medium the two cyclic diastereomers of glucose (β-D-glucose, as depicted in **38**) and the acyclic aldehyde form are in equilibrium. Nucleophilic addition of hydroxide will form **40**, which is adsorbed onto the catalyst **41**. Oxygen then reacts with **40** to form the peroxy complex **42**, and the hydrogen atom of the coordinated aldehyde hydrate

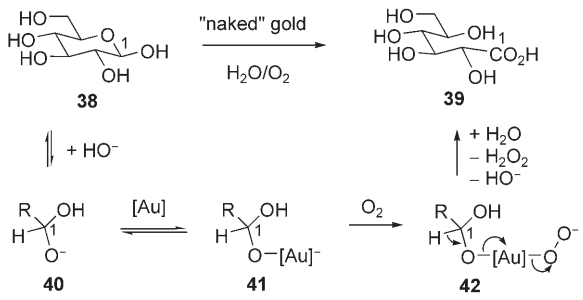

Scheme 7. Mechanistic model by Rossi et al. for glucose oxidation.

is eliminated as a proton. The product gluconic acid (**39**) then leaves the catalyst and hydrogen peroxide is also released.

While gold colloids with a mean particle diameter of 3.6 nm (Rossi's "naked" gold particles)[141] lie on the border between heterogeneous and homogeneous catalysis, Shi and co-workers[262] recently described the selective oxidation of alcohols to aldehydes or ketones using complexes of gold soluble in toluene. This reaction also works in air; for example with benzyl alcohol (**43**) and the catalyst **44** (which is formed in situ from AuCl and an anionic ligand), a 100% conversion and a 99% selectivity towards the product benzaldehyde (**45**, Scheme 8) was detected by gas chromatography.

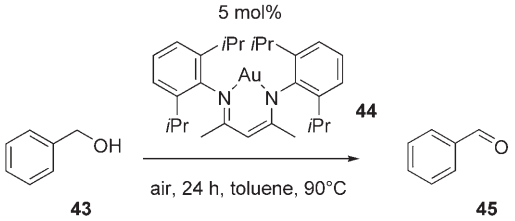

Scheme 8. Homogeneous gold-catalyzed oxidation of alcohols by Shi and co-workers.

These reactions allow an oxidation by molecular oxygen, sometimes even by air, and thus are a beautiful example of "green" chemistry.

4.3. C–H Bond Activation

The activation of C–H bonds in alkanes is of immense commercial significance. As supported nanocrystaline gold catalysts have been shown to be effective for the selective oxidation of alkenes and alcohols, it is not surprising that attention is now being given to the oxidation of C–H bonds. In this respect, attention has so far been focused on the activation of cyclohexene under mild conditions. One of the most important alkane activation processes currently operated industrially is the oxidation of cyclohexane to cyclohexanol and cyclohexanone, which has been acknowledged to be a reaction that continues to be a significant challenge.[263] The aerobic oxidation of cyclohexane is central to the production of nylon-6 and nylon-6,6, the worldwide production of which exceeds 10^6 tonnes per annum. Commercially

 © 2006 Wiley-VCH Verlag GmbH & Co. KGaA, Weinheim

the process is operated at 150–160 °C with cobalt naphthenate as an initiator for the radical oxidation process which gives 70–85 % selectivity at 4 % conversion. Operation at high conversions leads to total oxidation, and consequently this large-scale commercial process has been designed to operate at low conversion. There is clearly scope to produce a more efficient process, but given the current focus on "green" chemistry the main goal is to design a system that gives 100 % specificity. Ratnasamy and co-workers have shown that μ_3-oxo-bridged Co/Mn cluster complexes are very selective as homogeneous catalysts,[264] but it is generally recognized that a heterogeneous catalyst is preferred. Nowotny et al. have investigated the immobilization of cobalt complexes, but leaching occurs under the reaction conditions used.[265] Thomas and co-workers have shown that aluminophosphates substituted with Mn^{III}, Co^{III}, and Fe^{III} ions gave very high selectivities when operated at 130 °C.[266] It is against the background of these recent initiatives that potential gold-based systems need to be assessed.

The use of gold catalysis for this application was initiated by Zhao et al., who have shown that gold can activate cyclohexane at 150 °C.[267,268] Selectivities of about 90 % can be achieved with the Au/ZSM-5 catalyst and more than 90 % with a Au/MCM-41 catalyst, although an initial induction period was apparent with these catalysts. It was also shown that these gold catalysts can be reused, but the activity gradually declines and the selectivity shifts from cyclohexanone to cyclohexanol. These studies show that supported gold catalysts are indeed active for the activation of C–H bonds and that high selectivities can be achieved, but the temperature used for these studies was 140–160 °C.

A recent study by Xu et al. has investigated the potential oxidation of cyclohexane at temperatures well below 100 °C by using oxygen as oxidant and a gold catalyst, since, at this temperature higher selectivities might be expected.[269] In this study Au/C catalysts were compared with supported Pt and Pd catalysts. The Au/C catalysts were identical to those found to be highly effective for the epoxidation of alkenes.[226] In this study, a reaction inhibitor was also investigated (1,4-difluorobenzene). The selectivity for cylohexanone and cyclohexanol was very high at low conversion, but this declined rapidly with enhanced conversion and longer reaction times. However, the gold catalysts were found to give identical performance to the Pt and Pd catalysts, and in general the selectivity observed depended on the cyclohexene conversion (Figure 19).

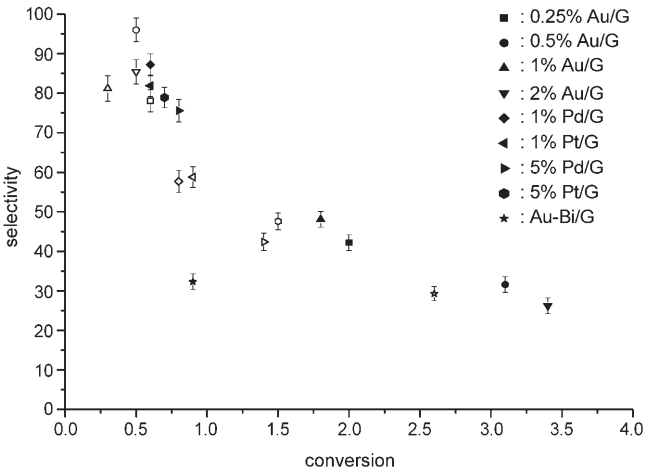

Figure 19. Relationship between cyclohexane conversion and the total selectivity for cyclohexanol and cyclohexanone; data were collected after 9 h reaction time. Solid symbols represent the reaction without the inhibitor 1,4-difluorobenzene, open symbols represent the reaction in the presence of the inhibitor.

4.4. Direct Synthesis of Hydrogen Peroxide

Hydrogen peroxide is a noted "green" oxidant that has widespread applications in many large-scale processes such as for bleaching and as a disinfectant. Such uses account for the majority of the H_2O_2 manufactured. Its use in the fine-chemical industry accounts for a much lower fraction of its consumption, for example, epoxidized oils, catechol, hydroquinone, peracetic acid, and caprolactone, and tends to require only small amounts of hydrogen peroxide. At present, hydrogen peroxide is produced by the sequential hydrogenation and oxidation of an alkyl anthraquinone.[270] However, there are problems associated with the anthraquinone route, including the cost of the quinone solvent system and the requirement for the periodic replacement of anthraquinone because of hydrogenation. In addition, the process is only economically viable on a relatively large scale ($4–6 \times 10^4$ tonnes per year), and this necessitates the transportation and storage of concentrated solutions of hydrogen peroxide when required for use in the fine chemicals industry, since only relatively small amounts are required at any one time. Hence, the development of a new, highly efficient, and smaller-scale manufacturing process for H_2O_2 is of significant commercial interest.

The identification of a direct route for the synthesis of hydrogen peroxide from the reaction of dioxygen and hydrogen would be highly beneficial, since this presents the tantalizing possibility of small-scale synthesis where required. At present, no commercial process exists for the direct process, even though there has been considerable research effort on this topic for over 90 years,[271–275] however, until recently the topic attracted only limited interest from the academic community. Up until 2002 the catalysts used in these investigations were based on Pd. Since it is important to try to achieve the highest rate of product formation, most of these earlier studies used H_2/O_2 mixtures in the explosive region, and solutions of over 35 wt % hydrogen peroxide have been made by reacting H_2/O_2 over Pd catalysts at elevated pressures.[276] However, the commercial operation of such a process in the explosive region is extremely dangerous, and more recently studies have concentrated on carrying out the reaction with dilute H_2/O_2 mixtures well away from the explosive regime.[18,276]

Hutchings and co-workers were the first to show that Au/Al_2O_3 catalysts were effective for the direct reaction. However, the key discovery was the observation that the direct synthesis of H_2O_2 was significantly enhanced by using Au/Pd alloys supported on alumina, and these catalysts resulted in

© 2006 Wiley-VCH Verlag GmbH & Co. KGaA, Weinheim

significant improvements in the rate of hydrogen peroxide formation compared with that with the Pd or Au only catalysts.[18,276] However, in common with pure Pd catalysts, these Al_2O_3-supported Au/Pd alloys gave low selectivity based on H_2, and in these initial studies selectivities of about only 14% were observed. Selectivity is the key problem with this reaction since the conditions that are required to produce hydrogen peroxide also promote 1) its decomposition to oxygen and water, 2) its hydrogenation to water, or 3) the direct nonselective formation of water (Scheme 9). In this respect the direct oxidation of hydrogen represents one of the most challenging targets concerning the control of reaction selectivity for a heterogeneously catalyzed reaction.

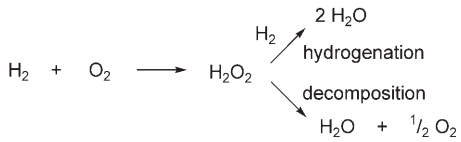

Scheme 9. Reaction scheme for the synthesis of hydrogen peroxide.

Subsequently, Haruta and co-workers[227] and Ishihara et al.[278] have shown that Au/SiO_2 and $Au\text{-}Pd/SiO_2$ catalysts are also effective for this reaction at only 10°C. Representative data are given in Figure 20. The authors concluded that the enhanced activity observed by the addition of Pd to Au was due to the enhanced activation of hydrogen, but if too much Pd was added the decomposition activity of the hydrogen peroxide was also enhanced and so the rate declined.

In recent studies, Hutchings and co-workers have shown that the selectivity for H_2 utilization can be significantly enhanced when Fe_2O_3 and TiO_2 are used as supports.[279,280]

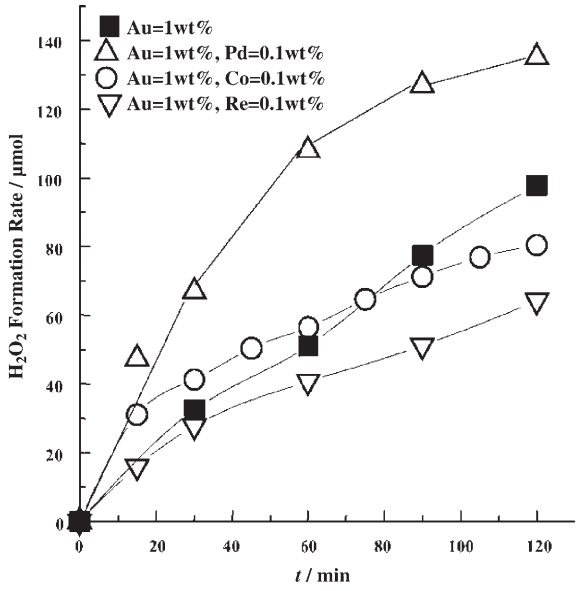

Figure 20. Effects of additives on the amount of H_2O_2 formed in the direct oxidation of H_2 on a Au/SiO_2 catalyst. (283 K, $H_2/O_2 = 1{:}6$, $W/F = 4$ g catalyst h mol^{-1}).

Indeed, at short reaction times the selectivity can be greater than 95% (Table 4) for the reaction of dilute H_2/O_2 mixtures (1:1, 5 vol%) diluted with CO_2 (95 vol%). Very high rates of reaction were observed with noncalcined $Au\text{-}Pd/TiO_2$ catalysts (Table 5), but these catalysts were unstable, losing both Au and Pd during the reaction, and they could not be successfully reused. However, if the catalysts are calcined at 400°C prior to use then very stable reusable catalysts are obtained. Detailed structural investigation of these active stable catalysts using XPS and TEM showed that the catalysts have a core–shell structure with a gold-rich core and a palladium-rich shell. It was concluded that the Au was acting as an electronic promotor for the Pd-rich surface of the Au-Pd nanocrystals (Figure 21).

Table 4: The influence of reaction time on the conversion of H_2 and selectivity to hydrogen peroxide synthesis.[a]

t [min]	Productivity[b]	H_2 conv. [%]	H_2O_2 selectivity [%]	H_2O_2 yield [%]
5	114	8	93	7.6
30	66	44	60	26.4
120	17	93	29	27.6

[a] 2.5% Au, 2.5% Pd/TiO_2 catalyst (20 mg) calcined at 400°C. [b] Productivity in mol H_2O_2 h^{-1} $kg_{cat.}^{-1}$.

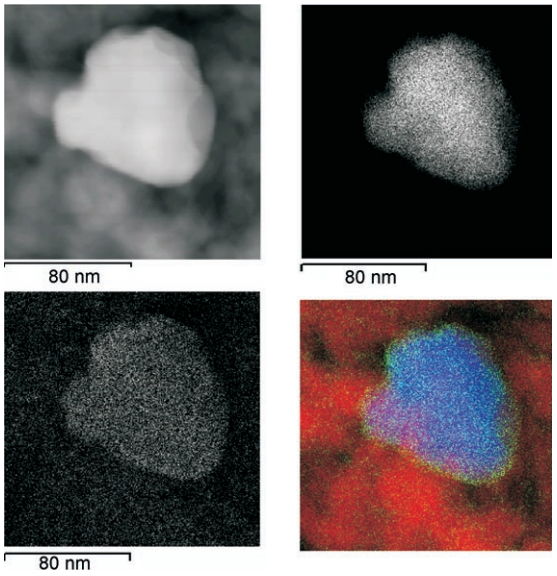

Figure 21. STEM-ADF image of a catalyst of 2.5 wt% Au and 2.5 wt% Pd on TiO_2 calcined at 400°C, showing a large alloy particle (a); Au M_2 STEM-XEDS map (b), Pd L_1 STEM-XEDS map (c); the STEM color map shows that the Pd signal appears to originate from a larger area than that of the Au signal: blue Au, green Pd and red Ti.

5. Nucleophilic Additions to π Systems

The coordination of cumulated, conjugated, or isolated C–C triple bonds to gold complexes very efficiently activates them for the attack of a nucleophile. Furthermore, C–O

 © 2006 Wiley-VCH Verlag GmbH & Co. KGaA, Weinheim

Table 5: The effect of catalyst calcination and/or reduction treatment on H_2O_2 synthesis.[a]

Catalyst	Pretreatment	Productivity[b]	H_2O_2 [wt%]	H_2 conversion [%]	H_2O_2 selectivity [%]
2.5% Pd/TiO_2	air, 25 °C	90	0.180	38	48
5% Pd/TiO_2	air, 25 °C	173	0.346	86	40
2.5% Au, 2.5% Pd/TiO_2	air, 25 °C	202	0.404	46	89
5% Pd/TiO_2	air, 200 °C, 3 h	99	0.198	42	47
2.5% Au, 2.5% Pd/TiO_2	air, 200 °C, 3 h	124	0.248	34	73
2.5% Pd/TiO_2	air, 400 °C, 3 h	24	0.048	19	25
5% Pd/TiO_2	air, 400 °C, 3 h	31	0.062	29	21
2.5% Au, 2.5% Pd/TiO_2	air, 400 °C, 3 h	64	0.128	21	61
2.5% Au, 2.5% Pd/TiO_2	air, 400 °C, 3 h + H_2 500 °C	32	0.064	n.d.	n.d.

[a] Reaction time 30 min; mass of catalyst 10 mg; n.d.: not determined. [b] Productivity in mol H_2O_2 h^{-1} $kg_{cat.}^{-1}$.

double bonds in carbonyl groups can also be activated for the addition of a nucleophile. Most of the reactions by far use alkynes as the substrates,[281] alkenes have become increasingly popular only recently, while allenes are still seldom used. Most mechanisms are at least supported by labeling experiments or other experimental evidence; one important aspect is the absence of paramagnetic species, and consequently the reactions can be conveniently monitored by NMR spectroscopy. Nevertheless, for most of the intermediates shown below, there exists no direct experimental proof; they are depicted to help the reader visualize the substrate/product relationship and to show similarities between the reactions. While the structures of the precatalysts are known, in most cases it is unclear what the active species looks like—hence a generalized gold complex fragment "[Au]" is used in the reactions of this section to symbolize the unknown active species. For reasons of electroneutrality, occasionally the "[Au]" carries a negative charge; if the corresponding gold complex fragment is cationic, the complex would overall be uncharged. Most of the reactions tolerate both oxygen and acidic protons; thus, neither air nor humidity need to be excluded, which is a very important aspect for this application. In most cases the gold catalysts are significantly more active than related complexes of other transition metals which catalyze the same reaction (if such complexes exist). Only a few citations of references of this section have been published before 2001, which demonstrates the exponential growth of this area.[282]

5.1. Simple Unconjugated Nucleophiles

In this section the simplest case of nucleophilic addition to a C–C multiple bond in an organic substrate **46** is described. First, the gold catalyst interacts with the π system of the substrate to form the intermediate **47**, and then the nucleophile attacks (Scheme 10). There is much evidence that the nucleophile and gold diastereoselectively add in an *anti* manner to deliver **48**. In the case of norbornenes, however, a case of a *syn* addition was reported.[282] In the last step of the reaction the organogold intermediate **48** sets free the addition product **49** and the gold catalyst by protodemetallation.

5.1.1. Reactions of Alkynes

The first experiments in this field were reported as early as 1976 by Thomas and co-workers.[283] They investigated the reaction of different alkynes (such as **50**) with tetrachloroauric acid in aqueous methanol and observed the corresponding ketones (Markovnikov regioselectivity of the addition; such as **51**)

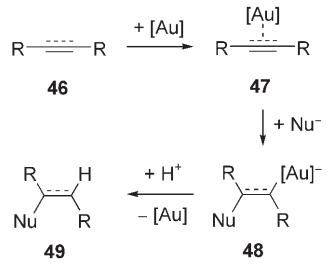

Scheme 10. Activation of C–C multiple bonds as the most important reactivity principle in homogeneous gold catalysis.

as the major products [Eq. (8)], accompanied by small amounts (less than 5%) of the corresponding methyl vinyl ethers (such as **52**) and vinyl chlorides (such as **53**). In fact this is a key paper in the field, as it reported types of products

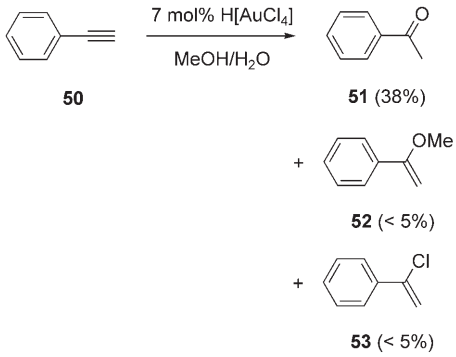

(8)

which later became very important in gold catalysis. Unfortunately the authors did not recognize the potential of their investigation: they did not continue this research and they call the reaction with $H[AuCl_4]$ a "gold(III) oxidation"—although the reaction with, for example, ethynylbenzene (**50**) reached almost six turnovers ("570% yield"), and thus it was clear that gold is a catalyst and not a stoichiometric oxidant.

© 2006 Wiley-VCH Verlag GmbH & Co. KGaA, Weinheim

Hutchings in 1985 recognized that the efficiency in catalyzing the hydrochlorination of ethyne (**54**) to vinyl chloride (**55**) [Eq. (9)], a very important industrial process,

(9)

correlates with the standard reduction potential of the supported metal cation.[7,284] This was the origin of the finding that gold(III) is the most active catalyst for that process.

The intramolecular addition of amines was first described in 1987 by Utimoto and co-workers,[285] who investigated the hydroamination reaction of alkynes. Initially an enamine is formed, but the thermodynamically more stable imine tautomer is observed as the final product. Utimoto and co-workers used sodium tetrachloroaurate as the catalyst and needed relatively high catalyst loadings of 5 mol%. A typical example would be the conversion of **56** into **57** [Eq. (10),

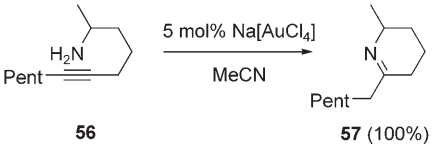

(10)

Pent = pentyl]. Later, Müller et al. found that a quantitative conversion of related substrates with an initial TOF of 212 h^{-1} could be achieved with only 1 mol% of the cationic $[AuCl(triphos)](NO_3)_2$ catalyst (triphos = 1,1,1-tris(diphenylphosphanylmethyl)ethane).[286]

In their initial work Fukuda and Utimoto[9,287] had also observed that alcohols and water can serve as nucleophiles in the gold-catalyzed reactions of alkynes if $Na[AuCl_4]$ is used as the catalyst; a later example for that was reported by Arcadi et al.[288] In 1998 Teles et al.[10] reported that very high activities (TON up to 10^5, TOF up to 5400 h^{-1}) could be obtained for the addition of alcohols to alkynes by using cationic gold(I)–phosphane complexes. This type of cationic complexes is still the most used type of homogenous gold catalyst; the $[Au(PPh)_3P^+X^-]$ system was applied, in particular, by many of the authors cited in this section. The use of CO as coligand allowed Hayashi and co-workers to even improve the activity of the catalysts developed by Teles et al.; a TOF of 15600 s^{-1} was accessible with the CO coligand.[289]

The addition of alcohols to alkynes has become a benchmark test for new catalysts. Gold(I) complexes of heterocyclic carbenes by Raubenheimer and co-workers,[290] organometallic gold complexes by Laguna and co-workers,[291] N-heterocyclic carbenes by Herrmann and co-workers,[292] and phosphane complexes with carboxylate and sulfonate counterions by Schmidbaur and co-workers[293] have been studied. A nucleophilic addition to the C–C triple bond in the presence of alkynylphosphane–gold complexes was also reported by Laguna and co-workers,[294] but there is no evidence for the participation of the gold as a catalyst; similar to the classic Reppe vinylation, alcoholate was the nucleophile.

Many different examples of intramolecular versions of the alcohol addition have been reported. Hashmi et al. first demonstrated that (*Z*)-3-ethynylallyl alcohols **58** can efficiently cyclize to furans **60** via intermediate **59**, which then tautomerizes to the thermodynamically more stable heteroaromatic furan [Eq. (11)].[13] Liu et al. used that method and extended it to the diastereoselective synthesis of alkylidenedihydrofurans **59** (for the case of R^5 not being H, which cannot tautomerize).[295]

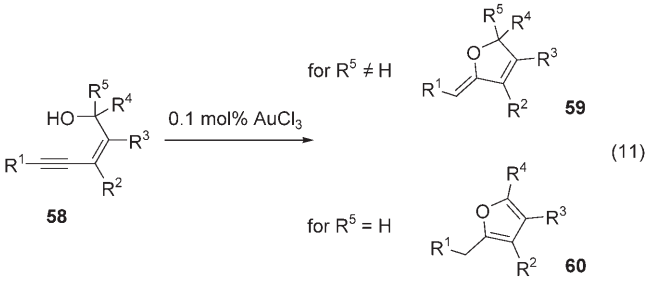

(11)

With two alcohol groups suitably positioned, as in **61**, interesting bicyclic ketals **62** were obtained by Genêt and co-workers [Eq. (12)].[296] This example nicely illustrates that under these reactions the styrene-like olefin in the other side chain, which is equidistant from the hydroxy groups, does not compete with the alkyne.

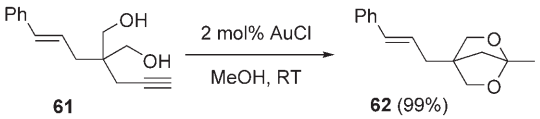

(12)

A combination of a cyclization to an enol ether followed by a subsequent Prins-type cyclization, which generated bicyclic compounds **64** containing an eight-membered ring from open-chained **63** [Eq. (13)], was reported by Barluenga

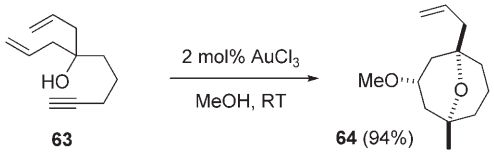

(13)

et al.[297] Other recent examples of the gold-catalyzed addition of alcohols to alkynes were reported by Jung and Floreancig[298] (for the addition of water, see Wessig and Teubner[299]).

In a combination of mass spectrometric and theoretical studies Schwarz and co-workers[300] observed that the reaction does not proceed in the gas phase, thus suggesting that solvent-assisted hydrogen migration might be crucial for the reactions.

 © 2006 Wiley-VCH Verlag GmbH & Co. KGaA, Weinheim

The intermolecular reaction with anilines also gives very good results; Tanaka and co-workers were able to isolate the corresponding amines in up to 98% yield by using only 0.2 mol% of a gold(I) catalyst.[301] Products analogous to **60** were synthesized by Dyker et al. The starting materials **65** were assembled by a Ugi four-component reaction and the cyclization delivered the products of both an 5-*exo*-dig cyclization (**66**) and a 6-*endo*-dig cyclization (**67**), the latter route delivering only the diastereomer shown [Eq. (14)].[302]

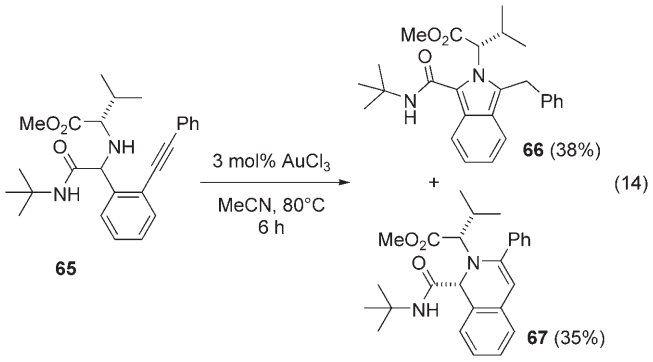

(14)

The intramolecular addition of carboxylic acids delivers lactones. Genêt and co-workers[303] observed good yields in the AuCl-catalyzed conversions. Even in the presence of a styrene side chain, such as in **68**, no competition of the activated alkene with the alkyne (both the same distance from the nucleophilic group) was observed, and **69** was the only product formed [Eq. (15)].

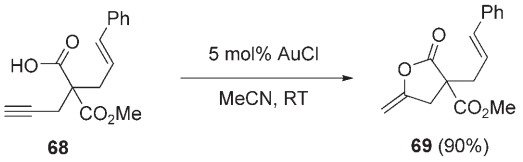

(15)

Instead of a free acid, *tert*-butyl esters can also be used. Kang and Shin[304] have shown this for carbonates of homopropargylic alcohols, where the free acid would not be stable but the *tert*-butyl carbonates are. $AuCl_3$ and gold(I) catalysts are active for these reactions, which ultimately lead to β-hydroxy ketones.

Reetz and Sommer explored the intermolecular hydroarylation of alkynes such as phenylacetylene, for which a combination of $AuCl_3$ and $AgSbF_6$ were optimal, and ethyl propiolate, for which gold(I) catalysts gave the best results.[305] Shi and He were able to obtain high yields under solvent-free conditions.[306] A related investigation also covered different heterocycles and gold(III) catalysts.[307] Intramolecular, gold(I)-catalyzed versions have also been reported by Nevado and Echavarren.[308] The formation of eight-membered rings is possible when indoles are used as the intramolecular partner. These rings are formed by a 7-*endo-dig* cyclization followed by a ring expansion (1,2-shift) and not by a direct 8-*endo-dig* cyclization.[309]

β-Ketoesters can also serve as nucleophiles. Toste and co-workers reported both the 5-*exo-dig* and the 5-*endo-dig* cyclization,[310] including a palladium-catalyzed enantioselective version of this reaction.

5.1.2. Reactions of Allenes

Allenes are the most difficult substrates in addition reactions. Chemoselectivity, diastereoselectivity, regioselectivity, and positional selectivity are an issue here.[311]

After Hashmi et al. had demonstrated that nucleophilic attacks at carbonyl oxygen atoms next to allenes are successful (see Section 5.2), Hoffmann-Röder et al. showed that the cycloisomerization of allenyl carbinols such as **70** to 2,5-dihydrofurans **71** proceeds with good diastereoselectivity [Eq. (16), TBS = *tert*-butyldimethylsilyl].[312] While these reactions also took place in the presence of acidic catalysts, only $AuCl_3$ gave good yields of the desired heterocycles in the case of acid-labile substrates.

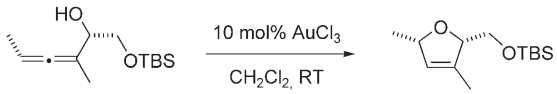

(16)

Hashmi et al. obtained evidence for an in situ reduction of the $AuCl_3$.[313] With disubstituted allenylcarbinols of type **72**, the products of an oxidative dimerization **73** were obtained in the absence of other oxidants and in amounts correlating with the amount of $AuCl_3$ [Eq. (17)].

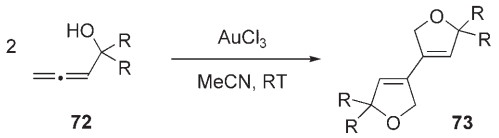

(17)

Different related amines can also be cyclized. While the use of free amino groups lead to reaction times of several days, with sulfonamides as well as acetyl or Boc protecting groups result in a fast conversion (but with the latter two the diastereoselectivity was low).[314] Ohno, Tanaka, et al. have recently shown that the sulfonamides readily cyclize with potassium carbonate in DMF in the absence of any transition-metal catalyst.[315] Lee et al. have applied the gold-catalyzed methodology to the synthesis of bicyclic β-lactams.[316] Nishina and Yamamoto have shown that the intermolecular $AuBr_3$-catalyzed addition of anilines to chiral allenes such as **74** proceeds with a high axial to central chirality transfer and a high regioselectivity [Eq. (18)].[317]

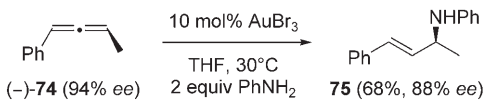

(18)

© 2006 Wiley-VCH Verlag GmbH & Co. KGaA, Weinheim

In a very impressive investigation Morita and Krause have demonstrated that even allenyl thiocarbinols can be cyclized to 2,5-dihydrothiophenes.[318] The best results were obtained with AuCl in CH_2Cl_2. Thus, **76** delivers **77** in excellent diastereoselectivity [Eq. (19)].

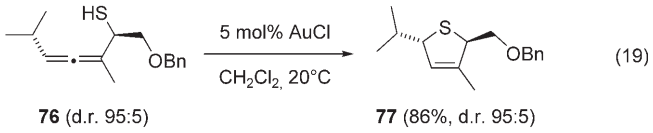

76 (d.r. 95:5) **77** (86%, d.r. 95:5) (19)

5.1.3. Reactions of Alkenes

Pioneering experiments using stoichiometric amounts of gold were carried out as early as 1976 by Thomas and co-workers.[319] In this case gold was, unlike the experiments described by Thomas and co-workers in the introduction to Section 5.1.1., truly an oxidant. Nevertheless, the products justified the assumption of an initial nucleophilic attack on a gold(III)-coordinated olefin.

Twenty-four years later Hashmi et al. described the first intramolecular addition of a hydroxy group to an activated alkene **79** to form spirocycle **80** (Scheme 11).[13] The hydro-

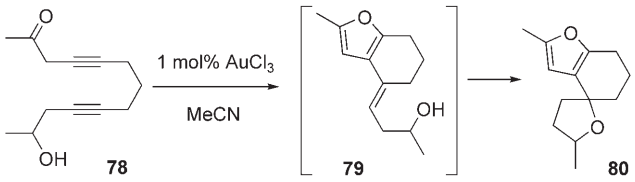

78 **79** **80**

Scheme 11. First example for a gold-catalyzed addition of an alcohol to an alkene.

arylation of α,β-unsaturated alkenes **82** by furans **81** was reported in the same publication (Scheme 12). Here two pathways were conceivable: Either the activation of the alkene and a Friedel–Crafts-like electrophilic substitution (**84**; here the electron-rich arene would serve as a nucleophile) or a direct auration of the furan (**83**; such aurations have been observed in pioneering stoichiometric reactions by Kharasch and Beck[320] as well as Fuchita et al.[321]) followed by a 1,4-addition to the enone. In both cases the same intermediate **85** is formed and transformed into the product **86** by a proto-deauration; unsaturated products and reduction of the gold catalyst by a β-hydrogen elimination were observed. Other electron-rich arenes were also shown to react.[322]

Such organogold compounds of furans have recently been described by Schmidbaur and co-workers.[323] The concept of the direct auration of electron-rich arenes was confirmed by Shi and He[15] when they investigated the gold(III)-catalyzed reaction of sulfonated primary alcohols with donor-substituted benezenes (a related investigation describes the intramolecular reactions of arenes with epoxides).[324] Pyrroles are so nucleophilic that the reactions are difficult to control—a

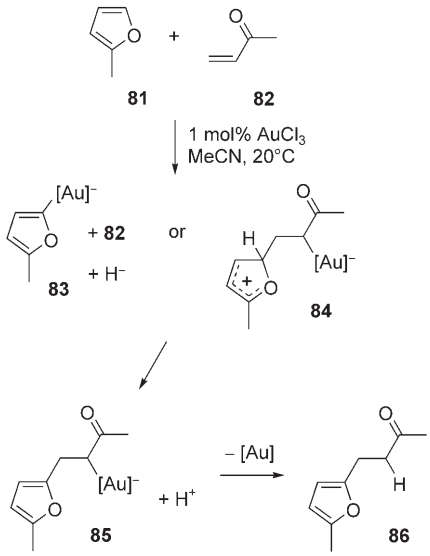

Scheme 12. Two possible intermediates, **83** and **84**, in the gold-catalyzed hydroarylation of furans.

twofold addition often dominates in an unselective reaction; indoles on the other hand give a highly selective monohydroarylation.[325–327] The same is true for 7-azaindoles,[327] and benzofurans have also been investigated.[307] Kobayashi et al.[328] discovered that $AuCl_3$ is the most active catalyst for the aza-Michael reaction of enones with carbamates.

In a very important paper, Yang and He reported that even the intermolecular addition of weak nucleophiles such as phenols and carboxylates to unactivated terminal alkenes is catalyzed by 5 mol% of [AuCl(PPh_3)]/AgOTf in toluene at 85 °C.[14] Li and co-workers[329] extended this principle to 1,3-dienes **87**, and found an interesting annulation of phenols **88** to give **91** (Scheme 13). A mixture of both diastereomers of the product is formed, it is unknown whether the C–C bond, as shown in **89**, or the C–O bond, as shown in **90**, is formed first.

Cinellu et al.[330] were able to isolate the first and so far only organometallic analogoue of an intermediate of a gold-catalyzed reaction in the reaction of bis(μ-oxo)–gold(III) complexes **92** with norbornene **93**, in this specific case the gold-catalyzed addition of water to an alkene (Scheme 14). The auraoxetane **95** could be separated from the olefin complex **94** and unambigously characterized by an X-ray crystal-structure analysis. In a stoichiometric reaction it ultimatively delivers the epoxide **96**.

Gold catalysts have only recently became successful in the hydroamination of alkenes. He et al. described the intermolecular addition of sulfonamides to unactivated alkenes with 5 mol% of [AuCl(PPh_3)]/AgOTf in toluene at 85 °C,[331] and the intermolecular hydroamination of 1,3-dienes with 5 mol% [Au(OTf)(PPh_3)] in 1,2-dichloroethane (DCE) at room temperature,[332] again with sulfonamides but also with the synthetically much more useful carbobenzoxy (Cbz) protecting group. The latter reaction regioselectively leads to the protected allyl amines **98**, and only a slight excess (1.2 equiv) of diene **87** was necessary for a selective mono-

 © 2006 Wiley-VCH Verlag GmbH & Co. KGaA, Weinheim

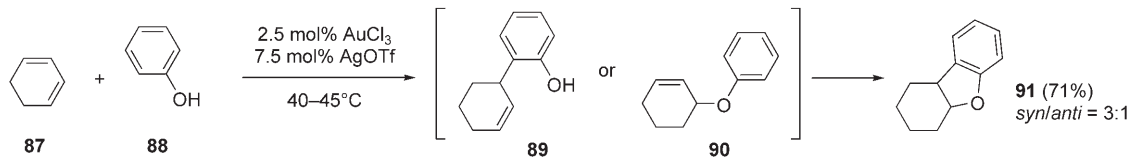

Scheme 13. Annulation with 1,3-dienes and phenols by Li and co-workers.

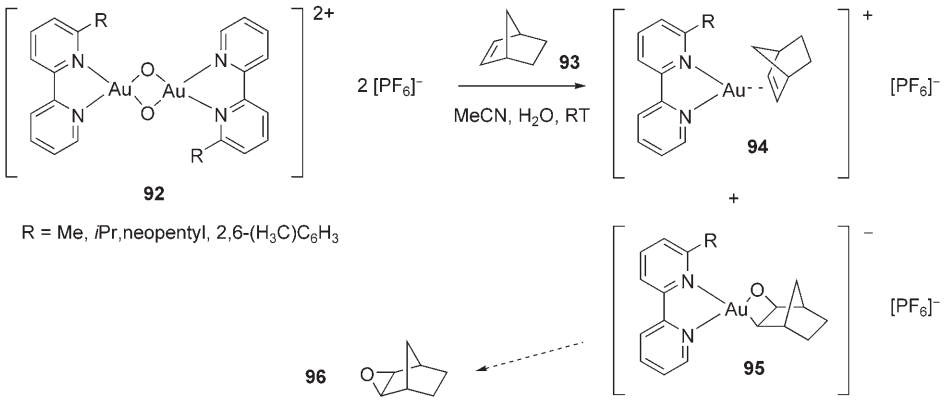

Scheme 14. First organometallic analogue of an intermediate in gold-catalyzed reactions by Cinellu et al.

Che and co-workers have investigated gold(III)–porphyrin complexes for the cycloisomerization of allenyl ketones to furans at 60 °C in the presence of triflouroacetic acid, and could reach a TON of 8300.[335] These complexes are also active for the hydroamination and hydration of phenylacetylene. Their overall activity raises the question about the mode of coordination to the alkyne—a normal square-planar tetradentate coodination of the porphyrin would not leave a free coordination site for the substrate.

addition [Eq. (20)]. Simultaneously, Han and Widenhoefer[333a] reported the intramolecular hydroamination of isolated alkenes, again with CBz-protected amino groups, at

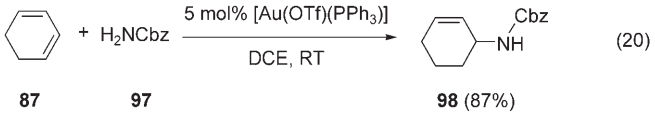

(20)

60–100 °C in dioxane; 5 mol % of a gold(I)–phosphane complex were used. A recent publication shows that quite similar results can be obtained for the addition of amines and alcohols to alkenes by using triflic acid.[333b]

1,3-Dicarbonyl compounds can be added in a C–C coupling reaction to activated alkenes with styrene groups, norbornene, and enol ethers.[334]

5.2. Conjugated Nucleophiles

The first reaction of this type, the cycloisomerization of allenyl ketones **99**, was reported by Hashmi et al.[13] Here the carbonyl oxygen atom serves as an intramolecular nucleophile, which delivers the Wheland-type intermediate **100**. The product **101** is formed through aromatization to **102** by proton loss and subsequent proto-deauration (Scheme 15). The furan rings can react with the allenyl ketone a second time through the **81** to **86** transformation described in Section 5.1.3. Propargyl ketones also deliver the furan derivatives; most probably the gold catalyst initially catalyzes the tautomerization to the allenyl ketones.

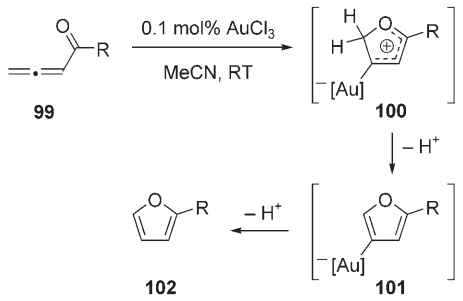

Scheme 15. Cycloisomerization of allenyl ketones.

Gevorgyan and co-workers observed two different constitutional isomers of the furans, **107** and **108**, when using bromoallenyl ketone **102** (Scheme 16).[336] Depending on the oxidation state, either one or the other isomer dominated, which was interpreted by an enhanced oxophilic behavior of gold(III) in the sense of intermediates **103** and **105**, while gold(I) is more carbophilic (intermediates **104** and **106**).

Closely related to these reactions of allenyl ketones are the reactions of *tert*-butyl allenoates. The initial cyclization step is the same, a nucleophilic attack by a carbonyl group, but then the *tert*-butyl group is eliminated and a butenolide is formed.[337]

Experiments by Larock and co-workers[338] indicate that the reaction of 2-alkynyl-2-alken-1-ones **109** with $AuCl_3$ (Scheme 17) seems to follow a similar mechanism as suggested by Hashmi et al. for the allenyl ketones **99**.[13] The alkyne coordinates to the catalyst (**110**) and then the carbonyl oxygen atom attacks as an intramolecular nucleophile, thus

 © 2006 Wiley-VCH Verlag GmbH & Co. KGaA, Weinheim

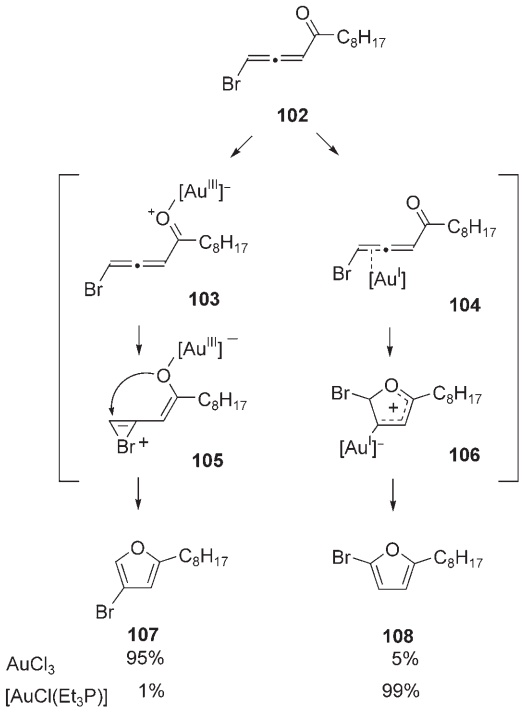

Scheme 16. Influence of the oxidation state of the gold catalyst on the chemoselectivity of the allenyl ketone cycloisomerization.

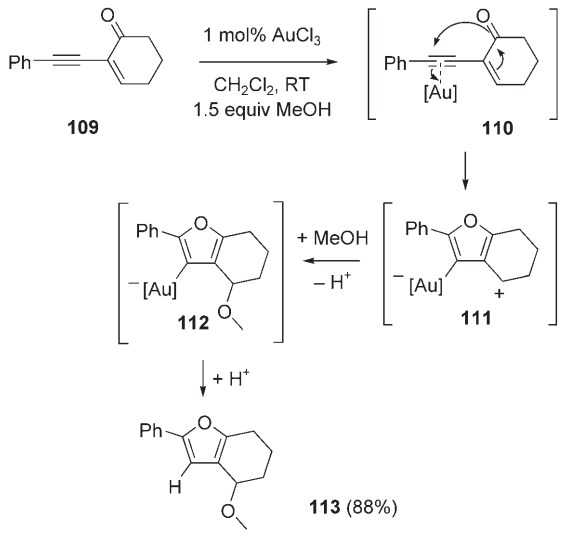

Scheme 17. Furans from 2-alkynyl-2-alken-ones **109**.

leading directly to the furylic cation **111**. The latter then adds methanol in an intermolecular reaction, thus delivering **113** as the final product. Other alcohols, electon-rich arene, and 1,3-dicarbonyl compounds can also be used as external nucleophiles.

Yamamoto and co-workers investigated the reactions of *ortho*-alkynylbenzaldehydes **114** in DCE (Scheme 18).[339] A related nucleophilic attack of the carbonyl oxygen atom initially leads to the pyrylium intermediates **115**, which readily undergo an intermolecular [4+2] cycloaddition with alkynes to give intermediate **116**, a ring opening then delivers

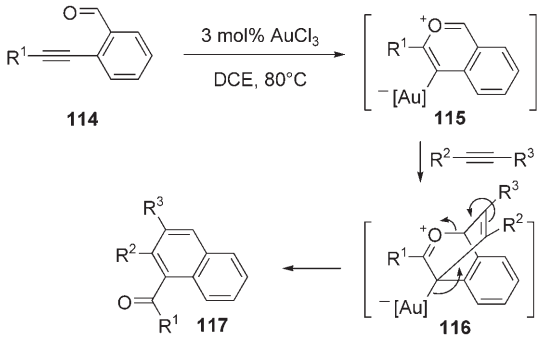

Scheme 18. Synthesis of acylnaphthalines **117** Yamamoto and co-workers R^1 = Alkyl, R^2, R^3 = alkyl, aryl, trimethylsilyl, CO_2Et..

117. This mechanism was supported by a calculation by Straub,[340] who also found that both AuCl and $AuCl_3$ have similar overall barriers for this process. Yamamoto and co-workers also reported that $AuBr_3$ is a more active catalyst for this conversion.[341]

Dyker et al. were able to extend that method to electron-rich alkenes;[342] for example, the annulated **120** was obtained in excellent regio- and diastereoselectivity from benzofuran (**118**) and **119** in the presence of water [Eq. (21)]. Yamamoto et al.[343] were also able to use enols as interceptors for the pyrylium ions.

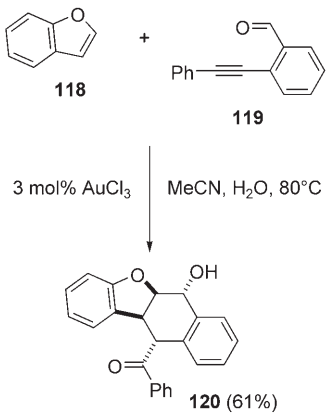

(21)

For the total synthesis of heliophenanthrone, Dyker and Hildebrandt started from a diyne substrate and used an intramolecular alkyne as the cycloaddition partner for the pyrylium ion.[344] A similar strategy was reported by Yamamoto and co-workers for the total synthesis of (+)-ochromycinone and (+)-rubiginone B_2.[345] They also investigated the effect of tethering a second alkynyl group at the carbonyl group, and the corresponding ketones were found to react as expected.[346] Subsequently, Oh and co-workers described an alternative pathway:[347] starting from substrate **121**, a 1,3-dipolar cycloaddition of the pyrylium intermediate **122** delivered the seven-membered cyclic ketone **125** (Scheme 19). The use of $AuBr_3$ as the most efficient catalyst for the synthesis of products of type **125** as well as the geminal disubstitution in the malonate seemed to be crucial for this pathway—without the geminal disubstitution only the usual

© 2006 Wiley-VCH Verlag GmbH & Co. KGaA, Weinheim

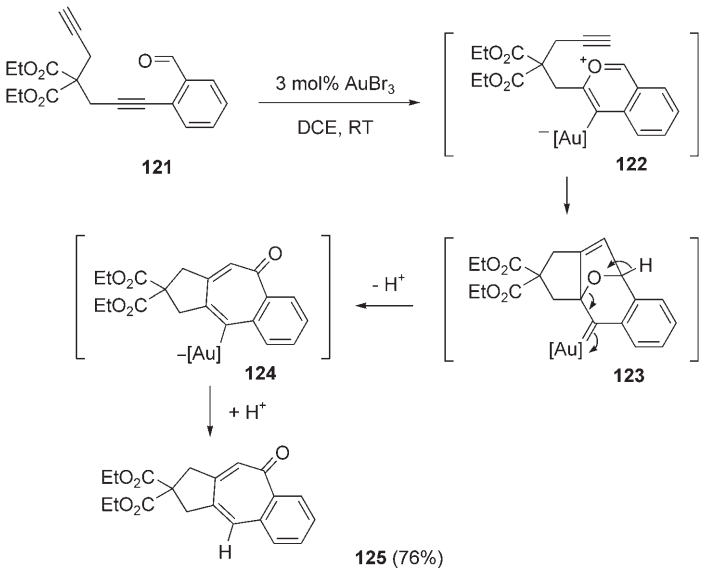

Scheme 19. Intramolecular trapping of the pyrylium intermediate.

naphthaline products were observed. In both the pathways proposed by Yamamoto et al. and Oh et al., the second alkyne unit can be replaced by an alkene.[346,347]

Oh and co-workers then used allenes such as in **126** as intramolecular alkene partners for the pyrylium intermediates [Eq. (22)],[348] which turned out to be a very efficient access to polycyclic frameworks of type **127**. The pyrylium salts can also be directly proto-deaurated, this concept was used by Porco and co-workers in the synthesis of azaphilones.[349]

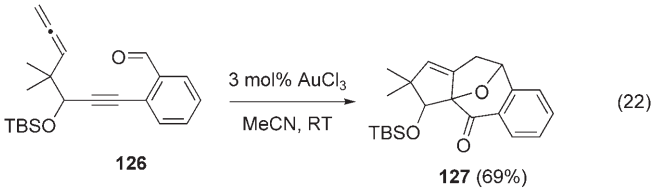

(22)

Nucleophiles in an *ortho* position to an alkynyl group on an arene such as in **128** readily cyclized to the corresponding five-membered heterocycles **131** by an 5-*endo-dig* cyclization (Scheme 20). The first example for that was provided by Hashmi et al. for X = O with $AuCl_3$ in acetonitrile at room temperature;[350] subsequent studies by Arcadi et al. demonstrated that for X = NH an efficient cyclization is possible with $Na[AuCl_4]\cdot H_2O$ in ethanol under similar conditions.[351] The reaction can be combined with a coupling of α,β-unsaturated ketones.[352] Other components can be included in the products: Kamijo and Yamamoto investigated the reaction of 2-(alkynyl)phenylisocyanates with alcohols.[353]

The latest observation in this field was reported by Iwasawa and co-workers:[354] Imines of 2-alkynylanilines **132** cyclize to the azomethine ylide intermediate **133**, which after a 1,3-dipolar cycloaddition with an alkene (to **134**) and subsequent 1,2-migration of a substituent delivers the mitosene skeleton **135** (Scheme 21).

Dankwardt showed that enol ether and enamine substrates of type **136** and **138** (Scheme 22) cyclize in an 6-*endo-dig* manner to deliver arenes **137** and **139**.[355] Not only do electron-rich heteroarenes, such as **138**, react readily, donor-substituted phenyl rings also do.[356] Halogen substituents on the alkyne suffer an interesting 1,2-migration with AuCl as the catalyst, thus providing evidence for the participation of vinylidene species.[357]

5.3. Ring Enlargements

The first example of a gold-catalyzed ring enlargement was provided by Hashmi and Sinha.[358] Alkynyl epoxides such as **140**, themselves easily available by a Sonogashira coupling and an epoxidation, delivered furans **144** with interesting substitution patterns (Scheme 23). The nucleophilic addition of the epoxide

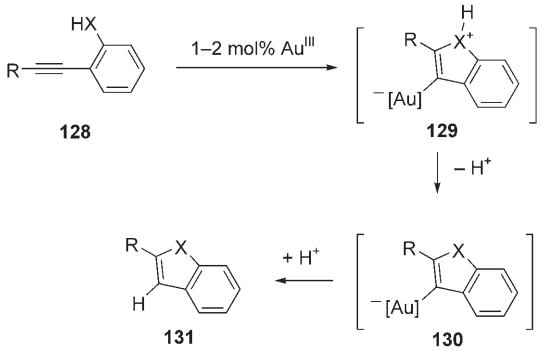

Scheme 20. Cyclization of *o*-alkynyl phenols or anilines.

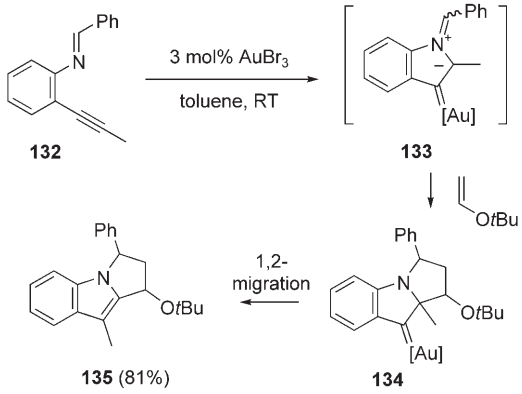

Scheme 21. In situ generation of 1,3-dipoles.

oxygen atom in the alkyne complex **141**, to give intermediate **142**, is faster than the nucleophilic addition of the hydroxy group. Again, Wheland-type intermediates and a proto-deauration are involved.

Toste and co-workers reported the ring expansion of 1-ethynylcyclopropanols and -cyclobutanols; a typical example

 © 2006 Wiley-VCH Verlag GmbH & Co. KGaA, Weinheim

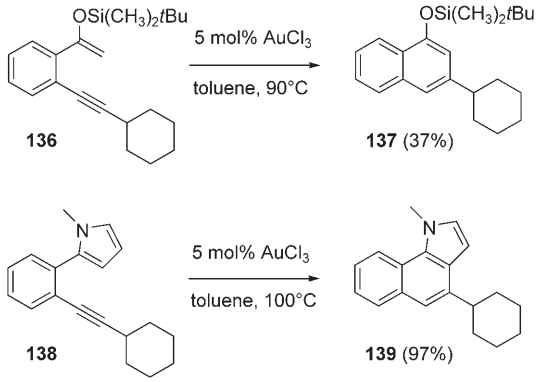

Scheme 22. Dankwardt's route to naphthalenes.

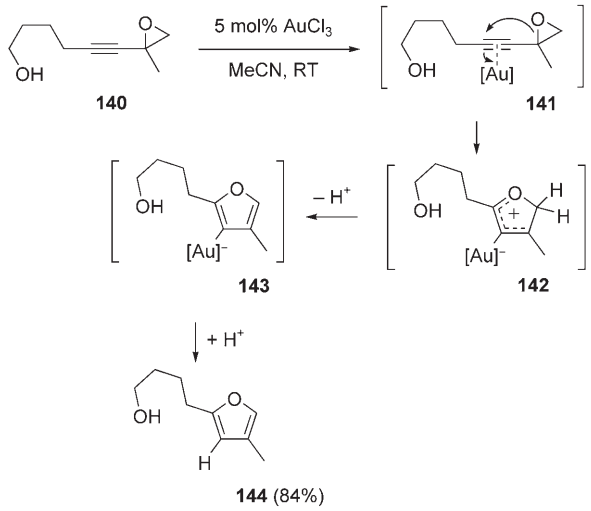

Scheme 23. Furan derivatives from alkynylepoxides.

is the conversion of **145** into **148** (Scheme 24).[359] Here the strained ring in **145** forms a bond to the proximal carbon atom of the alkyne and not to the distal one. The proton of the

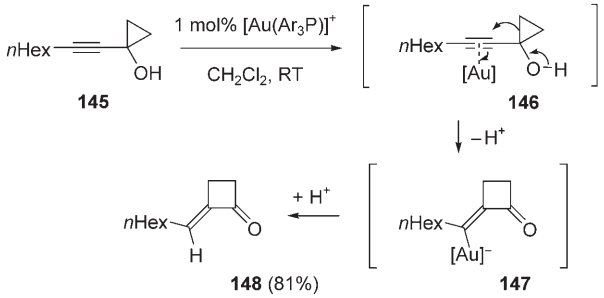

Scheme 24. Alkylidenecyclobutanones from 1-alkynylcyclopropanols.

hydroxy group is eliminated instead of the proton on the arenium intermediate **142**.

5.4. Ambidentate Nucleophilic Groups in Propargylic Position

This is a quite important case, but also more complex than the previous ones, since the reaction can proceed by different pathways. The initial point of interaction between the gold catalyst and the generalized substrate **149** is again the C–C triple bond. Compound **150** then has two possibilities (Scheme 25): a) attack of the nucleophilic group Y in a

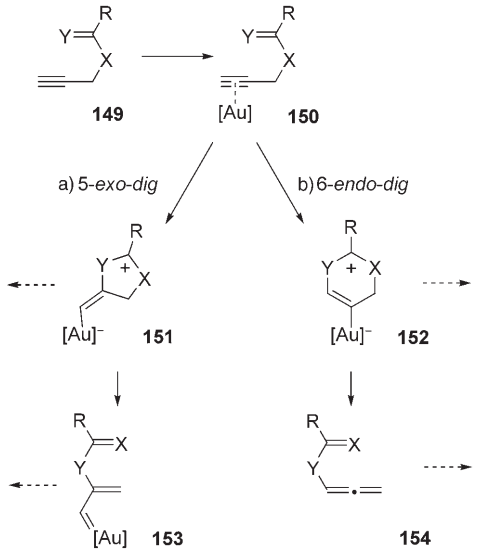

Scheme 25. Reaction patterns for gold-catalyzed reactions of ambidentate groups in the propargylic position.

5-*exo-dig* mode (as will be shown later, for X = NH the intermediate **151** can directly lead to stable products); alternatively **151** rearranges to vinyl carbenoids **153**, which then, for example cyclopropanate an alkene; b) attack of the nucleophilic group Y in an 6-*endo-dig* mode; this stepwise [3,3] rearrangement then leads to allenes **154**, which subsequently react with the gold catalyst once more to deliver other products.

5.4.1. Reactions via Vinyl Carbenoids

This reaction mode was first observed for gold-catalyzed reactions by Miki et al.[360] The vinyl carbenoids generated from substrates **155** were intercepted with styrene and two diastereomers of the product **156** were formed (Scheme 26).

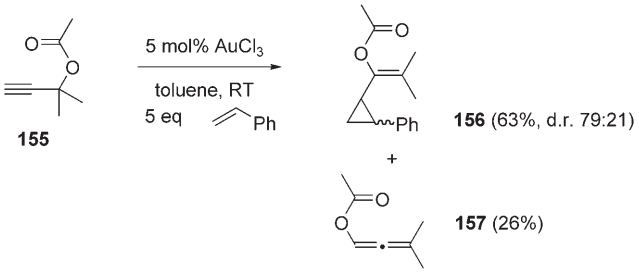

Scheme 26. Trapping of the vinyl carbenoid intermediate.

 © 2006 Wiley-VCH Verlag GmbH & Co. KGaA, Weinheim

In addition, isomerization to the allenyl ester **157** was observed. The gold-catalyzed reactions were very fast compared to those with other transition-metal catalysts. Recently, an enantioselective version of this reaction using gold(I) complexes of chiral phosphanes was reported by Toste and co-workers.[361]

Fürstner and Hannen used that approach for the preparation of carene terpenoids [Eq. (23)] by trapping the vinyl carbenes intramolecularly with an olefin at a suitable distance

(23)

(**158** to **159**).[362] The diastereoselectivity was excellent and different from that found in the study by Miki et al., where only "marginal amounts" of the isomeric allenyl acetate were detectable in the crude reaction mixture. A bicyclo-[3.1.0]hexane was also accesible by this approach,[363] and the face selectivity with chiral substrates for the synthesis of (−)-cubebol was studied.[364]

Toste and co-workers applied this concept to allylic propargylic esters.[365] Better results were obtained by using a gold(I) catalyst and pivaloates; a typical example is the transformation of **160** to **165** (Scheme 27). This reaction, the Rautenstrauch rearrangement, first delivers the enol ester **164** which then hydrolyses in situ to the ketone **165**. A chirality-transfer was also possible when chiral centers were present at the propargylic–allylic position. A computational study of that chirality transfer indicated that the helicity of the intermediate pentadienyl cation **162**, a carbenoid-like species, conserves the chiral information in the intermediate.[366]

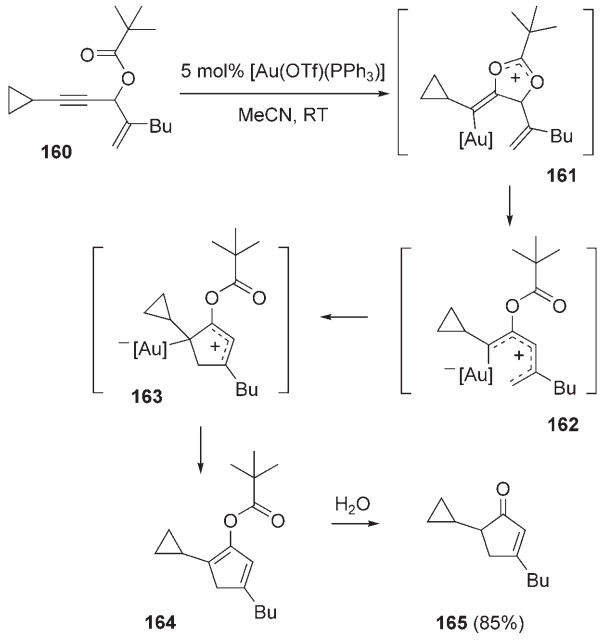

Scheme 27. Path to cyclopentenones by Toste and co-workers.

5.4.2. *Reactions via Allenyl esters*

Zhang and Wang reported a tandem 3,3-rearrangement/[2+2] cycloaddition[367] and a tandem 3,3-rearrangement/Nazarov cyclization.[368] A substrate such as **166** leads in the usual manner to the allenyl ester **167**, and then the electrophilic gold(I) catalyst delivers the pentadienyl cation **168**, which ultimately yields cyclopentenone **169** (Scheme 28).

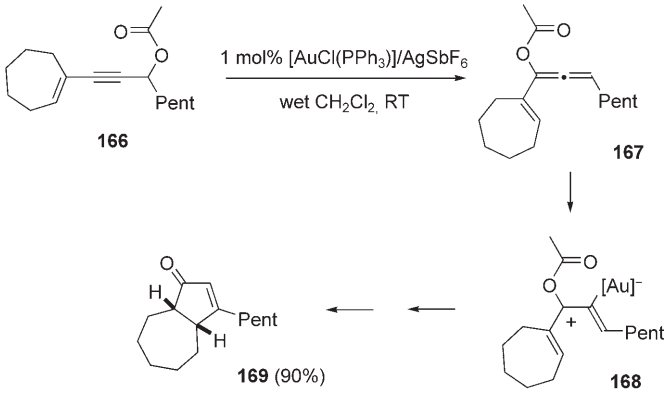

Scheme 28. Path to cyclopentenones by Zhang and Wang.

Propargyl vinyl ethers can also undergo a 3,3-rearrangement to the allene, with a high diastereoselectivity and an efficient chirality transfer reported.[369] Kirsch and co-workers[370] used similar propargyl-Claisen rearrangements and subsequent normal nucleophilic ring closures for the synthesis of highly substituted furan rings; in combination with amines the synthesis gave highly substituted pyrrole rings.[371]

5.4.2. *Reactions via Vinylgold Species*

A vinylgold species is involved in both the 5-*exo-dig* and the 5-*endo-dig* pathways. When there is an NH group in the propargylic position, a proton can be eliminated at the stage of the vinylgold species and the gold catalyst is released by proto-demetalation. Thus, after the first step these reactions divert to other pathways and do not deliver vinyl carbenoids or allenes. The first example of this kind was reported by Lok et al.:[372] 2-(*N*-propargylamino)benzoxazoles such as **170** delivered the dihydropyrimidine **171** [Eq. (24)].

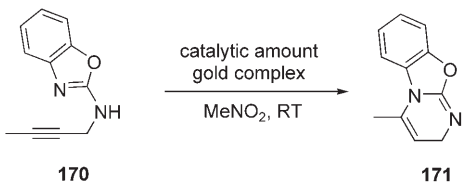

(24)

In 2004 Uemura and co-workers[373] and Hashmi et al.[374] independently investigated the cycloisomerization of *N*-propargylcarboxamides, which proceeds by an 5-*exo-dig*

© 2006 Wiley-VCH Verlag GmbH & Co. KGaA, Weinheim

cyclization. Uemura and co-workers followed an elegant concept: carboxamides and propargyl alcohols were coupled with 2.5 mol% of a ruthenium catalyst to give the *N*-propargylcarboxamides, and then 20 mol% of $AuCl_3$ was used for the cycloisomerization in DCE at 80°C, which delivered the oxazoles under the reaction conditions. Hashmi et al. started from the *N*-propargylcarboxamides **172** and used only 5 mol% of $AuCl_3$ in either MeCN or CH_2Cl_2 at 20–50°C. They could obtain very good yields of the oxazoles **175**. Furthermore, under the mild reaction conditions used the methyleneoxazolines **174** could be obtained in up to 95% yield (Scheme 29). This detection of the organic intermediate, accessible for the first time thanks to the mild conditions of

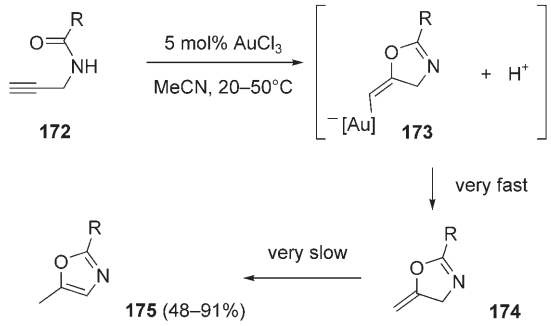

Scheme 29. First preparative route to alkylideneoxazolines. R = alkyl, vinyl, aryl, heteroaryl.

gold catalysis, allowed a direct study of the diastereoselectivity of the individual steps. The results obtained by isotope labeling indicate that the first step is an *anti* oxyauration, while the second step is a proto-deauration with retention of the relative arrangement of the substituents. This methodology was already used by Merck as a step in the synthesis of a pharmaceutically active substance.[375]

Gagosz and Buzas succeeded in the cyclization of propargyl *tert*-butyl carbonates.[376] As described for the studies of Shin,[304] the *tert*-butyl group instead of a proton is eliminated (then gives isobutene and a proton) and cyclic carbonates are obtained. An example showing the selectivity is the reaction of the dialkyne **176**, which cleanly gives **179** (Scheme 30). A shift of the carbonate group by one carbon

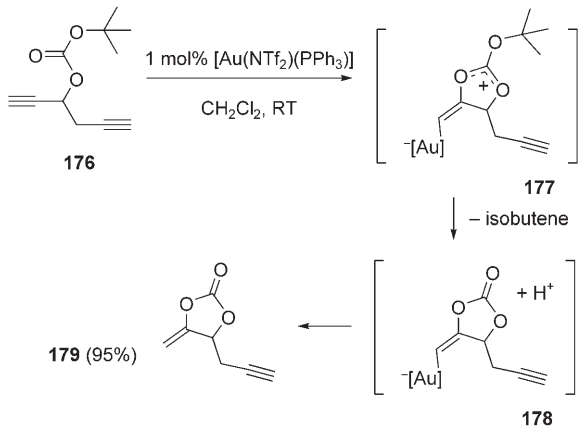

Scheme 30. The *tert*-butyl group in carbonates as a leaving group.

atom was observed with certain substituents, for example, electron-rich groups on the alkyne.

5.5. Enyne Cyclization

The cycloisomerization of enynes has a long history in transition-metal catalysis, but gold catalysts were able to add some new perspectives for these substrates. The starting point was the reaction of furan with a terminal alkyne unit such as in **180**, which with 2 mol% of $AuCl_3$ gave the highly substitued phenol **181**, as reported by Hashmi et al.[16] [Eq. (25) enyne substructure shown in bold]. The gold-catalyzed reaction was highly selective and no side products that might provide some insight into the mechanism were detected. Only an intramolecular migration of the oxygen atom could be proven by isotope labeling.

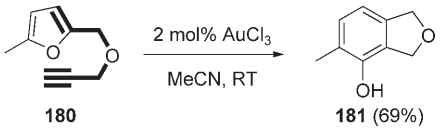

(25)

One year later Echavarren and co-workers reported that platinum(II) also catalyzes this conversion, but is less selective.[377] The side products observed in combination with a computational investigation led to the concept of an intial formation of an cyclopropyl carbene intermediate **182** (Scheme 31). In the case of a furan as the reaction partner of

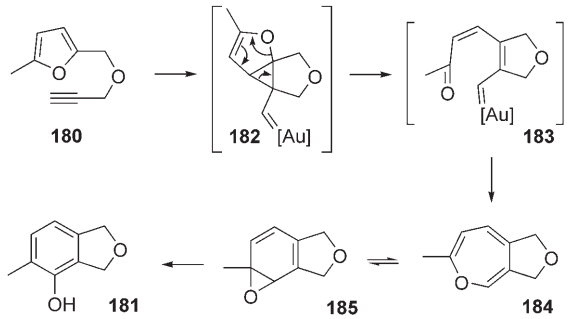

Scheme 31. First example of a gold-catalyzed reaction of a 1,6-enyne substructure.

the alkyne, a ring opening then delivers **183**. The vinyl carbene intermediate then reacts with the carbonyl group to deliver the oxepin/arene oxide tautomer pair (**184**/**185**). Further ring opening of the arene oxide finally leads to the phenol **181**.

Hashmi et al.[378] later demonstrated that the arene oxides are the intermediates of the reaction, the arene oxide could be accumulated to more than 80% in the reaction mixture by chosing an N,O ligand on the gold center. Full spectroscopic analysis as well as an interception of the intermediates by a Diels–Alder reaction were possible. Synthetically, this reaction has proven to be very successful for the synthesis of benzofurans,[350] biaryls,[379] the synthesis of jungianol and *epi*-

 © 2006 Wiley-VCH Verlag GmbH & Co. KGaA, Weinheim

jungianol,[380] and a simplyfied formal synthesis of jungianol by a domino hydroarylation/cycloisomerization.[381]

The use of N,O ligands also allowed an efficient ring closure with four atoms in the tether, thus tetrahydroisoquinolines were an interesting target.[382] Although, for example, an acceptor substituent on the furan ring is not tolerated,[383] mesityl and adamantyl substituents presented no problems in the reaction.[384] Corma, Hashmi, and co-workers[385] have also use a heterogenized gold catalyst, gold nanoparticles on nanocrystalline cerium oxide, for such gold-catalyzed syntheses of phenol. Finally, with a new gold(I) catalyst Hashmi et al.[386] succeeded for the very first time in the formation of such a gold carbenoid intermediate from *intermolecular* reactions: the reaction of **186** and **187** delivers **188** along with the hydroarylation product **189** [Eq. (26), Mes = mesityl].

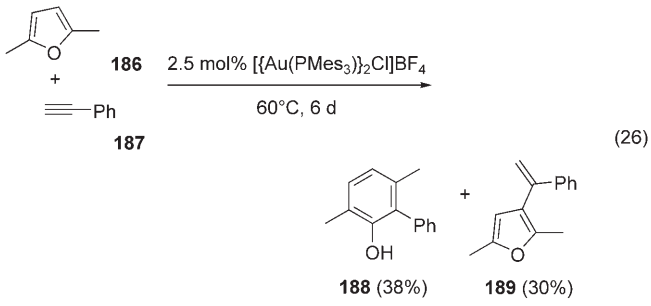

(26)

Echavarren and co-workers thoroughly investigated the behavior of "normal" 1,6-enynes without a furan ring in gold-catalyzed reactions. After initial problems using $AuCl_3$,[17,377] very promising results were obtained in methanol with substrates which still contained the enol ether substructure of a furan ring.[387] For example, **193** was obtained in very good yield from **190** (Scheme 32).

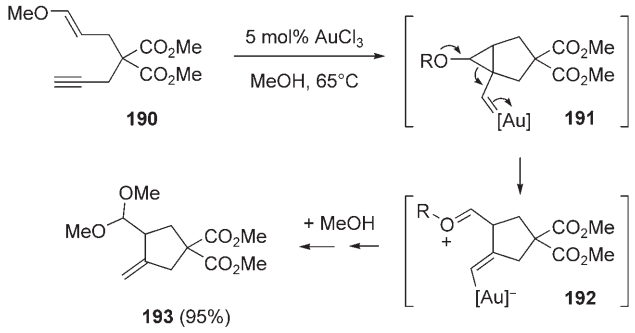

Scheme 32. Reaction of 1,6-enynes in the presence of alcohols as nucleophiles by Echavarren and co-workers.

The use of triarylphosphinegold(I) complexes has turned out to be extremely successful.[388] Products of the enyne metathesis could be obtained in high selectivity (for example, **194** to **195**) [Eq. (27)]. Other products were methylenecyclohexenes; a second olefin unit offered intramolecularly could

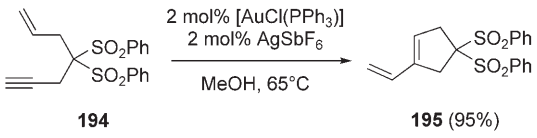

(27)

be cyclopropanated by the gold carbenoid intermediate (gold carbenoid species generated from ethyl diazoacetate and a gold(I) complex also cyclopropanated olefins).[389] Bicyclic products could be obtained with an additional double bond on the alkyne;[390] chiral complexes were investigated for enantioselective reactions.[391] Gagosz and co-workers investigated additional pathways these gold carbenoids can follow[392] as well as a series of interesting phosphane–gold(I) bis(trifluoromethansulfonyl)imidate catalysts.[393] Kashyap and Hotha have used diastereoselective reactions for the synthesis of α-glucosides.[394]

A cycloisomerization of siloxy enynes to cyclohexadienes[395] and a double cyclization with a nucleophilic group attached to the enyne structure was reported by Zhang and Kozmin.[396] Shortening the tether to 1,5-enynes delivered interesting bicyclo[3.1.0]hexenes, for example, **197** [Eq. (28)][397]

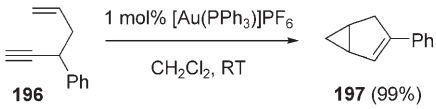

(28)

5.6. Electrophilic Activation of Carbonyl Groups

The catalytic asymmetric aldol reaction of aldehydes **198** with isocyanoacetates **199** (Cy = cyclohexyl) was a milestone not only for gold catalysis, but for asymmetric catalysis in general. Ito et al. used gold(I) complexes of chiral ferrocene ligands L* for the synthesis of enantiomerically pure oxazolines **200** [Eq. (29)].[8] The *trans* diastereomer of **200** is the major product, the hydrolysis of which delivers the interesting *syn*-β-hydroxy-α-amino acids. The postulated transition state **201** would nicely explain the stereoselectivty.[398] The amino group in the side arm of the ligand (shown in bold)

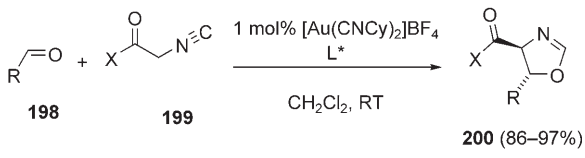

(29)

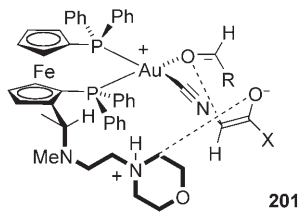

© 2006 Wiley-VCH Verlag GmbH & Co. KGaA, Weinheim

deprotonates the isocyanoacetate which is coordinated to the gold center (and thus acidified). An ion-pair bonding[399] keeps the isocyanoacetate at that coordination site of the gold complex, whereupon the carbonyl oxygen atom of the aldehyde then coordinates to the other site, thus directing the facial selectivity of the deprotonated isocanoacetate. Overall, the carbonyl group and the nucleophile are activated by the gold catalyst. The facial selectivity at the aldehyde is determined by minimal interaction of the group R. The absolute configuration is determined by the planar and central chirality of the ferrocene ligand (for the cooperativity of these stereochemical units, see Ref. [400]). After the inital aldol addition, the substrate immediately cyclizes to the oxazoline. Conformational studies on the ferrocenyl ligands by 2D NMR spectroscopy were conducted by Togni et al.[401] The many notable achievements concerning this reaction have been reviewed.[402]

Arcadi et al. described the condensation of 1,3-dicarbonyl compounds such as **203** with amines, alcohols, and even thiol **202** under mild conditions with Na[$AuCl_4$] [Eq. (30)].[403] This

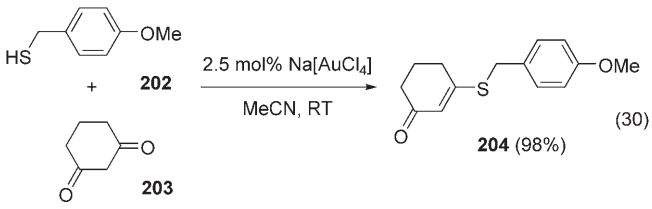

(30)

made the in situ formation of enamines of type **207** and their cycloisomerization to pyrroles possible, for example **208** (Scheme 33).[404,405] The Friedländer quinoline synthesis can also be catalyzed by Na[$AuCl_4$],[406] as can the Pictet–Spengler reaction[407] and the three-component Mannich reaction.[408]

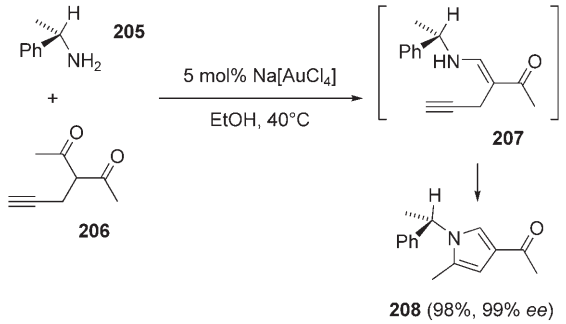

Scheme 33. Chiral pyrroles by the condensation of 1,3-dicarbonyl compounds and chiral amines.

Other nucleophilic groups that can add are indoles (**209**) [Eq. (31)]. These can either be used directly or be prepared in situ from 2-alkynylanilines (see Section 5.2). The usual addition/elimination steps lead to products **211**.[409]

Nair et al. reported that related α,β-unsaturated aldehydes such as **203** react with indoles or furans (**212**) to form 1:3 addition products such as **214** [Eq. (32)].[410] Aldehydes condense in a 1:2 ratio.[411]

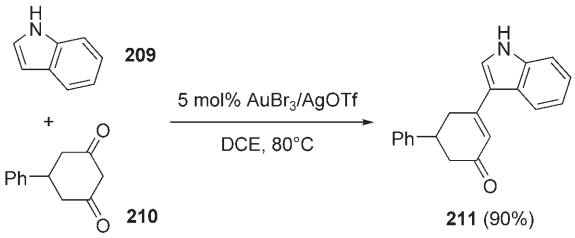

(31)

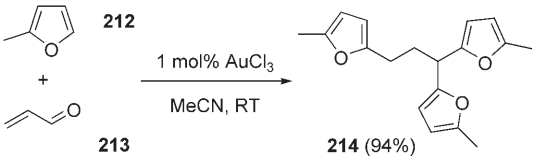

(32)

However, Hashmi et al.[412] were able to show that this reaction is neither restricted to the more reactive aldehydes—ketones such as acetone react as well—nor is it specific to gold as a catalyst: Mercury(II), thallium(III), and even a simple Bronsted acid with a nonnucleophilic counterion, such as 4-toluenesulfonic acid, are equally active. Furthermore, the twofold reaction with a carbonyl group first forms a benzylic alcohol which then eliminates to the benzyl cation, which can act as an electrophile and react with the second electron-rich arene. Kinetic studies revealed that this benzylic electron-rich alcohol cannot be detected under the reaction conditions. This means that the first step, the reaction of the carbonyl compound with the arene, is rate-limiting. In light of these results, the gold-catalyzed reactions of benzylic propargylic alcohols[413] or benzylic acetates[414] have to be interpreted with care. It is highly possible that simple acid, formed from water and the gold(III) salt, is the catalyst.

A different subfield of nucleophilic addition to carbonyl compounds is the gold-catalyzed activation of the nucleophile. Komiya et al.[415] reported the use of triphenylphosphanegold alkoxides for the Knoevenagel reaction under mild conditions. The three-component coupling of an aldehyde, an alkyne, and an amine, first reported by Wei and Li,[416] is another example in which the gold catalyst activates the nucleophile. The reaction can be conducted in water, and even the allyl groups in **215** are tolerated [Eq. (33)].

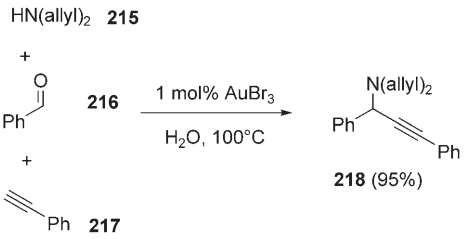

(33)

The methodology has been extended to acyl iminium ions as electrophiles[417] and the addition of electron-rich arenes to *N*-tosylimines.[418] Gold(III)–salen complexes have been used

 © 2006 Wiley-VCH Verlag GmbH & Co. KGaA, Weinheim

as catalysts, and the use of chiral amines as substrates gave excellent diastereoselectivities.[419]

5.7. CO as a Nucleophile

Xu et al. reported that the reaction of terminal olefins **219** with an Au^I catalyst, sulfuric acid, and only one atmosphere of CO delivers tertiary carboxylic acids **223** (Scheme 34).[420] It is

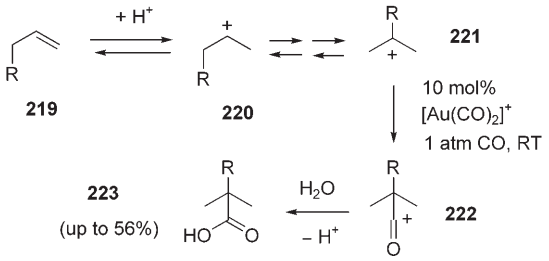

Scheme 34. Gold-catalyZed low-pressure variation of the Koch–Haaf reaction Xu et al.

assumed that the sulfuric acid first protonates the olefin, then the secondary carbeniumion **220** isomerizes to the tertiary carbenium ion **221** by a Wagner–Meerwein rearrangement. Finally, the carbon monoxide is transferred to this carbenium ion, the resulting acyl cation **222** is then attacked by water, and a proton is lost. Overall, this transformation is a low-pressure equivalent of the Koch–Haaf reaction,[421] which normally needs up to 100 atm of CO.

6. Conclusion and Future Perspectives

From the extensive literature presented it is clear that gold offers many opportunities in catalysis, both in solution as Au^I and Au^{III} complexes or at solid/gas and solid/liquid/gas interfaces when Au is present in nanocrystalline form. However, it is also clear that this has only recently been recognized. Gold is no longer the "Cinderella" of the periodic table—for many years the preconception that gold was a noble immutable element has hindered progress in this field of chemistry. This is surprising, since the early reports of catalysis by gold were significant. However, it took many years before this significance was truly recognized; gold catalysis is now considered a scientific hotspot, with tens of papers appearing weekly.

We have set out the topics in this Review in the sequence that they have appeared in the literature. The oldest reaction type is hydrogenation, and it is clear that there is potential for the selective monohydrogenation of alkynes and selective monohydrogenation of α,β-unsaturated carbonyl compounds to allylic alcohols. However, the mechanisms of the heterogeneous reactions are not yet well understood, whereas the mechanisms have been well explored in the case of the homogeneous reactions and even enantioselective reactions are possible. The realization that gold was effective for reactions under mild conditions, particularly CO oxidation—which is possible at subambient temperatures—has made a lasting impression on this field. Supported gold catalysts are exceptionally active for this reaction, and potential applications in fuel cells continues to spur this interest. However, our understanding of the mechanism of this relatively simple reaction and the nature of the active sites remains obscure at present, and detailed mechanistic studies have yet to appear.

In contrast, an area in which gold can play a significant role in the development of new "green" technologies is receiving much less attention at present, namely selective oxidation, particularly using molecular oxygen. Here the applicability of gold to new reactions is being unraveled and the role of bimetallic catalysts, particularly Au/Pd alloys is becoming apparent for the direct oxidation of H_2 to hydrogen peroxide and the oxidation of alcohols to aldehydes. Many new examples have been discovered in the past four years in the area the nucleophlic additions, but alkyne reactions are still dominant. However, the reactions of allenes and alkenes are now being investigated, and these are revealing a rich chemistry. There are already some applications in synthesis, and domino and asymmetric reactions probably have the highest potential for future major contributions in this field. Gold catalysis is therefore a fast growing field with new reactions being discovered and explored. In the near future we anticipate that this new chemistry will find industrial application.

Addendum (October 30, 2006)

The trend expected from Figure 1 continued. For example, in the few months that have passed between submission of the manuscript and receipt of the proofs, over 60 new publications have appeared on homogeneous catalysis. The majority of these describe reactions discussed above, and the sheer number of these publications does not allow a discussion of all in such an addendum. Only a few new developments are mentioned here.

Liu et al. has managed to combine the cyclization of (*Z*)-enynols **58** [compare Eq. (11)] with an in situ oxidative cleavage by molecular oxygen, which afforded the furanones **224** [Eq. (34)].[422]

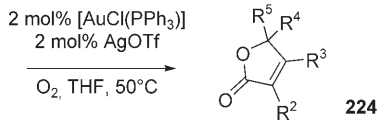

(34)

The reaction of 1,7-diaryl-1,6-diynes to give interesting annelated systems of five- and six-membered ring systems through a [3 + 2]-cycloaddition-type reaction was reported by Liu and co-workers.[423]

A new and interesting approach to the steroid framework was developed by Hildebrandt and Dyker.[424] This approach is based on the type of reaction described in Scheme 18.

Shi et al. used methylenecyclopropanes **225** and sulfonamides for the preparation of pyrrolidine derivatives **227** (Scheme 35).[425]

 © 2006 Wiley-VCH Verlag GmbH & Co. KGaA, Weinheim

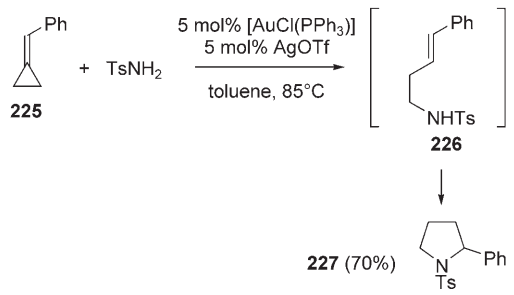

Scheme 35.

Finally, a procedure for the regioselective gold-catalyzed hydration of terminal alkynes was published by Tanaka and co-workers.[426]

Received: June 19, 2006

[1] a) B. Armer, H. Schmidbaur, *Angew. Chem.* **1970**, *82*, 120–133; *Angew. Chem. Int. Ed. Engl.* **1970**, *9*, 101–113; H. Schmidbaur, *Angew. Chem.* **1976**, *88*, 830–843; *Angew. Chem. Int. Ed. Engl.* **1976**, *15*, 728–740; H. Schmidbaur, A. Schier in *Science of Synthesis*, *Vol. 3* (Ed.: I. A. O'Neil), Thieme, Stuttgart, **2004**, pp. 691–761; b) M. C. Gimeno, A. Laguna in *Comprehensive Coordination Chemistry II*, *Vol. 5* (Eds.: E. C. Constable, J. R. Dilworth), Elsevier, Oxford, **2004**, pp. 911–1145; c) A. Burini, A. A. Mohamed, J. P. Fackler, *Comments Inorg. Chem.* **2003**, *24*, 253–280.

[2] "Catalytically dead" was used in the literature. For a discussion, see: H. Schmidbaur, *Naturwiss. Rundsch.* **1995**, *48*, 443–451.

[3] For an inclusion of these early examples, see: a) G. C. Bond, *Gold Bull.* **1972**, *5*, 11–13; b) A. S. K. Hashmi, *Gold Bull.* **2004**, *37*, 51–65.

[4] G. C. Bond, P. A. Sermon, G. Webb, D. A. Buchanan, P. B. Wells, *J. Chem. Soc. Chem. Commun.* **1973**, 444–445.

[5] a) M. Haruta, *Nature* **2005**, *437*, 1098–1099; b) G. J. Hutchings, *Catal. Today* **2005**, *100*, 55–61.

[6] M. Haruta, T. Kobayashi, H. Sano, N. Yamada, *Chem. Lett.* **1987**, *16*, 405–408.

[7] G. J. Hutchings, *J. Catal.* **1985**, *96*, 292–295.

[8] Y. Ito, M. Sawamura, T. Hayashi, *J. Am. Chem. Soc.* **1986**, *108*, 6405–6406.

[9] Y. Fukuda, K. Utimoto, *J. Org. Chem.* **1991**, *56*, 3729–3731.

[10] J. H. Teles, S. Brode, M. Chabanas, *Angew. Chem.* **1998**, *110*, 1475–1478; *Angew. Chem. Int. Ed.* **1998**, *37*, 1415–1418.

[11] M. Haruta, A. Ueda, R. M. Torres Sanchez, K. Tanaka, *Prp. Pet. Div. ACS Symp.*, New Orleans, **1996**; T. Hayashi, K. Tanaka, M. Haruta, *Prp. Pet. Div. ACS Symp.*, New Orleans, **1996**.

[12] L. Prati, M. Rossi, *J. Catal.* **1998**, *176*, 552–560.

[13] A. S. K. Hashmi, L. Schwarz, J.-H. Choi, T. M. Frost, *Angew. Chem.* **2000**, *112*, 2382–2385; *Angew. Chem. Int. Ed.* **2000**, *39*, 2285–2288.

[14] C.-G. Yang, C. He, *J. Am. Chem. Soc.* **2005**, *127*, 6966–6967.

[15] Z. Shi, C. He, *J. Am. Chem. Soc.* **2004**, *126*, 13596–13597.

[16] A. S. K. Hashmi, T. M. Frost, J. W. Bats, *J. Am. Chem. Soc.* **2000**, *122*, 11553–11554.

[17] B. Martin-Matute, C. Nevado, D. J. Cardenas, A. M. Echavarren, *J. Am. Chem. Soc.* **2003**, *125*, 5757–5766.

[18] P. Landon, P. J. Collier, A. J. Papworth, C. J. Kiely, G. J. Hutchings, *Chem. Commun.* **2002**, 2058–2059.

[19] W. A. Bone, R. V. Wheeler, *Philos. Trans. R. Soc. London Ser. A* **1906**, *206*, 1–67; gold is discussed specifically on pages 45–50.

[20] In the publication P. A. Sermon, *Gold Bull.* **1976**, *9*, 129–131 it is even cited that Michael Faraday in 1834 reported that gold efficiently catalyzes the reaction between hydrogen and oxygen at ambient temperature: M. Faraday, *Experimental Researches in Electricity*, J. M. Dent, London, **1914**, p. 94.

[21] a) B. M. W. Trapnell, *Proc. R. Soc. London Ser. A* **1953**, *218*, 566–577; b) J. Pritchard, F. C. Tompkins, *Trans. Farad. Soc.* **1960**, *56*, 540–550; c) J. Pritchard, *Trans. Farad. Soc.* **1963**, *59*, 437–452; d) D. J. C. Yates, *J. Colloid Interface Sci.* **1969**, *29*, 194–204; e) A. G. Sault, R. J. Madix, C. T. Campbell, *Surf. Sci.* **1986**, *169*, 347–356; f) G. A. Attard, D. A. King, *Surf. Sci.* **1989**, *223*, 1–12; g) D. M. Cox, R. Brickman, K. Creegan, A. Kaldor, *Z. Phys. D* **1991**, *19*, 353–355; h) S. D. Lin, M. A. Vannice, *Catal. Lett.* **1991**, *10*, 47–61; i) L. Stobinski, R. Dus, *Czech. J. Phys.* **1993**, *43*, 1035–1040; j) L. Stobinski, R. Dus, *Surf. Sci.* **1993**, *298*, 101–106; k) L. Stobinski, R. Dus, *Vacuum* **1994**, *45*, 299–301.

[22] A. Couper, D. D. Eley, *Discuss. Faraday Soc.* **1950**, *8*, 172–184; A. Couper, D. D. Eley, M. J. Hulatt, D. R. Rossington, *Bull. Soc. Chim. Belg.* **1958**, *67*, 343–357; for a related investigation, see: S. J. Holden, D. R. Rossington, *J. Phys. Chem.* **1964**, *68*, 1061–1067.

[23] R. J. Mikovsky, M. Boudart, H. S. Taylor, *J. Am. Chem. Soc.* **1954**, *76*, 3814–3819.

[24] H. Wise, K. M. Sancier, *J. Catal.* **1963**, *2*, 149–151.

[25] G. Cocco, S. Enzo, G. Fagherazzi, L. Schiffini, I. W. Bassi, G. Vlaic, S. Galvagno, G. Parravano, *J. Phys. Chem.* **1979**, *83*, 2527–2538.

[26] G. C. Bond, P. A. Sermon, *Gold Bull.* **1973**, *6*, 102–105.

[27] P. A. Sermon, G. C. Bond, P. B. Wells, *J. Chem. Soc. Faraday Trans. 1* **1979**, *75*, 385–394.

[28] A. Saito, M. Tanimoto, *J. Chem. Soc. Chem. Commun.* **1988**, 832–833.

[29] J. Erkelens, C. Kemball, A. K. Galway, *Trans. Faraday Soc.* **1963**, *59*, 1181–1191.

[30] a) B. J. Wood, H. Wise, *J. Catal.* **1966**, *5*, 135–145; b) S. H. Inami, B. J. Wood, H. Wise, *J. Catal.* **1969**, *13*, 397–403; c) R. S. Yolles, B. J. Wood, H. Wise, *J. Catal.* **1971**, *21*, 66–69.

[31] H. G. Rushford, D. A. Whan, *Trans. Faraday Soc.* **1971**, *67*, 3577–3584.

[32] M. Boudart, L. D. Ptak, *J. Catal.* **1970**, *16*, 90–96.

[33] R. P. Dessing, V. Ponec, W. M. H. Sachtler, *J. Chem. Soc. Chem. Commun.* **1972**, 880–881.

[34] A. Saito, M. Tanimoto, *J. Chem. Soc. Faraday Trans. 1* **1988**, *84*, 4115–4124.

[35] J. Guzman, B. C. Gates, *J. Catal.* **2004**, *226*, 111–119.

[36] J. Guzman, B. C. Gates, *Angew. Chem.* **2003**, *115*, 714–717; *Angew. Chem. Int. Ed.* **2003**, *42*, 690–693.

[37] J. Jia, K. Haraki, J. N. Kondo, K. Domen, K. Tamaru, *J. Phys. Chem. B* **2000**, *104*, 11153–11156.

[38] T. V. Choudhary, C. Sivadinarayana, A. Dantye, D. Kumar, W. D. Goodman, *Catal. Lett.* **2003**, *86*, 1–8.

[39] J. Chou, N. R. Franklin, S.-H. Baeck, T. F. Jaramillo, E. W. McFarland, *Catal. Lett.* **2004**, *95*, 107–111.

[40] M. Shibata, N. Kawata, T. Masumoto, H. Kimura, Japan-France Seminar on Catalysis with Metal Compounds, Tokyo, **1987**, pp. 98–100.

[41] J. A. Lopez-Sanchez, D. Lennon, *Appl. Catal. A* **2005**, *291*, 230–237.

[42] D. A. Buchanan, G. Webb, *J. Chem. Soc. Faraday Trans. 1* **1978**, *70*, 134–144.

[43] S. Schimpf, M. Lucas, P. Claus, Proceedings of DGMK-Conference "Creating Value from Light Olefins—Production and Conversion", October 10–12, Hamburg, Germany, **2001**, pp. 97–102.

[44] M. Okumura, T. Akita, M. Haruta, *Catal. Today* **2002**, *74*, 265–269.

 © 2006 Wiley-VCH Verlag GmbH & Co. KGaA, Weinheim

[45] P. Mukherjee, C. R. Patra, A. Gosh, R. Kumar, M. Sastri, *Chem. Mater.* **2002**, *14*, 1678 – 1684.
[46] R. P. Chambers, M. Boudart, *J. Catal.* **1966**, *5*, 517 – 528.
[47] G. Schmid, H. West, J.-O. Malm, J.-O. Bovin, C. Grenthe, *Chem. Eur. J.* **1996**, *2*, 1099 – 1103.
[48] D. A. Cadenhead, N. G. Masse, *J. Phys. Chem.* **1966**, *70*, 3558 – 3566.
[49] A. M. Venezia, V. La Parola, B. Pawelec, J. L. G. Fierro, *Appl. Catal. A* **2004**, *264*, 43 – 51.
[50] P. Mukherjee, C. R. Patra, R. Kumar, M. Sastry, *PhysChemComm* **2001**, *4*, 24 – 25.
[51] D. V. Sokol'skii, A. Ualikhanova, *Russ. J. Phys. Chem.* **1982**, *56*, 633.
[52] B. Pawelec, A. M. Venezia, V. La Parola, S. Thomas, J. L. G. Fierro, *Appl. Catal. A* **2005**, *283*, 165 – 175.
[53] M. Bryne, A. T. Kuhn, *J. Chem. Soc. Faraday Trans.* **1972**, 1898 – 1907.
[54] P. Claus, *Appl. Catal. A* **2005**, *291*, 222 – 229.
[55] In a review (G. C. Bond, D. T. Thompson, *Catal. Rev. Sci. Eng.* **1999**, *41*, 319 – 388) it is mentioned on page 366 that in 1993 a theoreticl calculation explained why "gold is inactive in catalytic hydrogenation": R. L. Augustine, K. M. Lahanas, F. Cole in *Proceeding of 10th International Congress on Catalysis, Vol. B* (Eds.: L. Guzci, F. Solymosi, P. Tetenyi), Elsevier, Amsterdam, **1993**, p. 1567.
[56] a) C. H. D. Clark, B. Toplet, *J. Phys. Chem.* **1928**, *32*, 121 – 126; b) D. D. Eley, P. Luetic, *Trans. Farad. Soc.* **1957**, *53*, 1483 – 1487; c) W. M. H. Sachtler, N. H. deBoer, *J. Phys. Chem.* **1960**, *64*, 1579 – 1580; d) G. C. Bond, *Catalysis by Metals*, Academic Press, London, **1962**.
[57] A. F. Kane, J. K. A. Clarke, *J. Chem. Soc. Faraday Trans. 1* **1980**, *76*, 1640 – 1651.
[58] For a related study with Pt/Au alloys, see: J. R. H van Schaik, R. P. Dessing, V. Ponec, *J. Catal.* **1975**, *38*, 273 – 282.
[59] a) G. Parravano, *J. Catal.* **1970**, *18*, 320 – 328; b) S. Galvagno, G. Parravano, *J. Catal.* **1979**, *57*, 272 – 286.
[60] J. W. A. Sachtler, M. A. van Hove, J. P. Bibérian, G. A. Somorjai, *Phys. Rev. Lett.* **1980**, *45*, 1601 – 1603.
[61] Y. Gault, *J. Chem. Soc. Chem. Commun.* **1973**, 478 – 479.
[62] D. I. Bradshaw, R. B. Moyes, P. B. Wells, *J. Chem. Soc. Chem. Commun.* **1975**, 137 – 138.
[63] G. Schmid, H. West, H. Mehles, A. Lehnert, *Inorg. Chem.* **1997**, *36*, 891 – 895.
[64] J. E. Bailie, G. J. Hutchings, *Chem. Commun.* **1999**, 2151 – 2152.
[65] J. E. Bailie, H. A. Abdullah, J. A. Anderson, C. H. Rochester, N. V. Richardson, N. Hodge, J.-G. Zhang, A. Burrows, C. J. Kiely, G. J. Hutchings, *Phys. Chem. Chem. Phys.* **2001**, *3*, 4113 – 4121.
[66] G. J. Hutchings, F. King, I. P. Okoye, M. B. Padley, C. H. Rochester, *J. Catal.* **1994**, *148*, 453 – 463.
[67] G. J. Hutchings, F. King, I. P. Okoye, M. B. Padley, C. H. Rochester, *J. Catal.* **1994**, *148*, 464 – 469.
[68] M. B. Padley, C. H. Rochester, G. J. Hutchings, F. King, *J. Catal.* **1994**, *148*, 438 – 452.
[69] J. E. Bailie, G. J. Hutchings, *Catal. Commun.* **2001**, *2*, 291 – 294.
[70] P. Claus, A. Brueckner, C. Mohr, H. Hofmeister, *J. Am. Chem. Soc.* **2000**, *122*, 11430 – 11439.
[71] C. Mohr, H. Hofmeister, M. Lucas, P. Claus, *Chem. Ing. Tech.* **1999**, *71*, 869 – 873.
[72] C. Mohr, H. Hofmeister, M. Lucas, P. Claus, *Chem. Eng. Technol.* **2000**, *23*, 324 – 328.
[73] S. Schimpf, M. Lucas, C. Mohr, U. Rodemerck, A. Bruckner, J. Radnik, H. Hofmeister, P. Claus, *Catal. Today* **2002**, *72*, 63 – 78.
[74] C. Mohr, H. Hofmeister, P. Claus, *J. Catal.* **2003**, *213*, 86 – 94.
[75] C. Mohr, H. Hofmeister, J. Radnik, P. Claus, *J. Am. Chem. Soc.* **2003**, *125*, 1905 – 1911.
[76] J. Radnik, C. Mohr, P. Claus, *Phys. Chem. Chem. Phys.* **2003**, *5*, 172 – 177.
[77] C. Milone, M. L. Tropeano, G. Gulino, G. Neri, R. Ingoglia, S. Galvagno, *Chem. Commun.* **2002**, 868 – 869.
[78] C. Milone, R. Ingoglia, M. L. Tropeano, G. Neri, S. Galvagno, *Chem. Commun.* **2003**, 868 – 869.
[79] C. Milone, R. Ingoglia, A. Pistone, G. Neri, F. Frusteri, S. Galvagno, *J. Catal.* **2004**, *222*, 348 – 356.
[80] P. Fordham, M. Besson, P. Gallezot, *Stud. Surf. Sci. Catal.* **1997**, *108*, 429 – 436.
[81] A. Corma, P. Serna, *Science* **2006**, *313*, 332 – 334.
[82] M. C. Muller, *Gold Bull.* **1974**, *7*, 39 – 40.
[83] For most chemists *Gold Bulletin* looks like an exotic, difficult to access journal which is not available in most libraries. However, all papers from this highly specialized journal are availabe on the internet free of charge: http://www.goldbulletin.org/.
[84] G. Abbiati, A. Arcadi, G. Bianchi, S. Di Giuseppe, F. Marinelli, E. Rossi, *J. Org. Chem.* **2003**, *68*, 6959 – 6966.
[85] C. González-Arellano, A. Corma, M. Iglesias, F. Sánchez, *Chem. Commun.* **2005**, 3451 – 3453.
[86] A. Comas-Vives, C. González-Arellano, A. Corma, M. Iglesias, F. Sánchez, G. Ujaque, *J. Am. Chem. Soc.* **2006**, *128*, 4756 – 4765.
[87] For the investigation of ring openings in related C-O chelates, see: G. Marangoni, B. Pitteri, G. Annibale, M. Bortoluzzi, *Eur. J. Inorg. Chem.* **2006**, 765 – 771.
[88] X. Wang, L. Andrews, *Angew. Chem.* **2003**, *115*, 5359 – 5364; *Angew. Chem. Int. Ed.* **2003**, *42*, 5201 – 5206.
[89] M.-J. Crawford, T. M. Klapötke, *Angew. Chem.* **2002**, *114*, 2373 – 2375; *Angew. Chem. Int. Ed.* **2002**, *41*, 2269 – 2271.
[90] R. T. Baker, P. Nguyen, T. B. Marder, S. A. Westcott, *Angew. Chem.* **1995**, *107*, 1451 – 1452; *Angew. Chem. Int. Ed. Engl.* **1995**, *34*, 1336 – 1338.
[91] R. T. Baker, J. C. Calabrese, S. A. Westcott, *J. Organomet. Chem.* **1995**, *498*, 109 – 117.
[92] T. N. Mitchell in *Encyclopedia of Reagents for Organic Synthesis, Vol. 4* (Ed.: L. A. Paquette), Wiley, Chichester, **1995**, pp. 2664 – 2666.
[93] H. Ito, T. Yajima, J.-i. Tateiwa, A. Hosomi, *Tetrahedron Lett.* **1999**, *40*, 7807 – 7810.
[94] H. Ito, T. Yajima, J.-i. Tateiwa, A. Hosomi, *Chem. Commun.* **2000**, 981 – 982.
[95] H. Ito, K. Takagi, T. Miyahara, M. Sawamura, *Org. Lett.* **2005**, *7*, 3001 – 3004.
[96] M. Haruta, N. Yamada, T. Kobayashi, S. Iijima, *J. Catal.* **1989**, *115*, 301 – 309.
[97] D. L. Lahr, S. T. Ceyer, *J. Am. Chem. Soc.* **2006**, *128*, 1800 – 1801.
[98] R. M. Finch, N. A. Hodge, G. J. Hutchings, A. Meagher, Q. A. Pankhurst, M. R. H. Siddiqui, F. E. Wagner, R. Whyman, *Phys. Chem. Chem. Phys.* **1999**, *1*, 485 – 489.
[99] S. Golunski, R. Rajaram, N. Hodge, G. J. Hutchings, C. J. Kiely, *Catal. Today* **2002**, *72*, 107 – 113.
[100] M. J. Kahlich, H. A. Gasteiger, R. J. Behm, *J. Catal.* **1999**, *182*, 430 – 440.
[101] B. Qiao, Y. Deng, *Chem. Commun.* **2003**, 2192 – 2193.
[102] G. Avgouropoulos, T. Ioannides, C. Papadopoulou, J. Batista, S. Hocevar, H. K. Matralis, *Catal. Today* **2002**, *75*, 157 – 167.
[103] G. Avgouropoulos, T. Ioannides, H. K. Matralis, J. Batista, S. Hocevar, *Catal. Lett.* **2001**, *73*, 33 – 40.
[104] P. Landon, J. Ferguson, B. E. Solsona, T. Garcia, A. F. Carley, A. A. Herzing, C. J. Kiely, S. E. Golunski, G. J. Hutchings, *Chem. Commun.* **2005**, 3385 – 3387.
[105] P. Landon, J. Ferguson, B. E. Solsona, T. Garcia, S. Al-Sayari, A. F. Carley, A. A. Herzing, C. J. Kiely, M. Makkee, J. A. Moulijn, A. Overweg, S. E. Golunski, G. J. Hutchings, *J. Mater. Chem.* **2006**, *16*, 199 – 208.

 © 2006 Wiley-VCH Verlag GmbH & Co. KGaA, Weinheim

[106] M. Haruta, *Catal. Surv. Jpn.* **1997**, *1*, 61 – 73.
[107] M. Haruta, *Osaka Kogyo Gijutsu Kenkyusho Hokoku* **1999**, *393*, 69 – 71.
[108] M. Haruta, H. Kageyama, N. Kamijo, T. Kobayashi, F. Delannay, *Stud. Surf. Sci. Catal.* **1989**, *44*, 33 – 42.
[109] F. Moreau, G. C. Bond, A. O. Taylor, *J. Catal.* **2005**, *231*, 105 – 114.
[110] R. Zanella, S. Giorgio, C. R. Henry, C. Louis, *J. Phys. Chem. B* **2002**, *106*, 7634 – 7642.
[111] R. Zanella, L. Delannoy, C. Louis, *Appl. Catal. A* **2005**, *291*, 62 – 72.
[112] R. Zanella, C. Louis, *Catal. Today* **2005**, *107–108*, 768 – 777.
[113] W.-C. Li, M. Comotti, F. Schueth, *J. Catal.* **2006**, *237*, 190 – 196.
[114] M. Comotti, W.-C. Li, B. Spliethoff, F. Schueth, *J. Am. Chem. Soc.* **2006**, *128*, 917 – 924.
[115] J. Guzman, S. Carrettin, A. Corma, *J. Am. Chem. Soc.* **2005**, *127*, 3286 – 3287.
[116] H. Sakurai, T. Akita, S. Tsubota, M. Kiuchi, M. Haruta, *Appl. Catal. A* **2005**, *291*, 179 – 187.
[117] C. F. Baes, Jr., R. E. Mesmer, *The Hydrolysis of Cations*, Wiley, New York, **1976**.
[118] H. G. Raubenheimer, *Gold: Progress in Chemistry, Biochemistry and Technology*, Wiley, Chichester, **1999**.
[119] R. J. H. Grisel, P. J. Kooyman, B. E. Nieuwenhuys, *J. Catal.* **2000**, *191*, 430 – 437.
[120] "Basic Principles in Applied Catalysis": in Springer Ser. Chem. Phys. (Ed.: M. Baerns), **2004**, p. 75.
[121] F. Moreau, G. C. Bond, *Appl. Catal. A* **2006**, *302*, 110 – 117.
[122] W. Yan, B. Chen, S. M. Mahurin, V. Schwartz, D. R. Mullins, A. R. Lupini, S. J. Pennycook, S. Dai, S. H. Overbury, *J. Phys. Chem. B* **2005**, *109*, 10676 – 10685.
[123] Z. Konya, V. F. Puntes, I. Kiricsi, J. Zhu, J. W. Ager III, M. K. Ko, H. Frei, P. Alivisatos, G. A. Somorjai, *Chem. Mater.* **2003**, *15*, 1242 – 1248.
[124] C.-M. Yang, M. Kalwei, F. Schuth, K.-j. Chao, *Appl. Catal. A* **2003**, *254*, 289 – 296.
[125] K.-J. Chao, M.-H. Cheng, Y.-F. Ho, P.-H. Liu, *Catal. Today* **2004**, *97*, 49 – 53.
[126] W. Yan, B. Chen, S. M. Mahurin, S. Dai, S. H. Overbury, *Chem. Commun.* **2004**, 1918 – 1919.
[127] C. Aprile, A. Abad, H. Garcia, A. Corma, *J. Mater. Chem.* **2005**, *15*, 4408 – 4413.
[128] M. Haruta, *J. New Mater. Electrochem. Syst.* **2004**, *7*, 163 – 172.
[129] J. Guzman, S. Carrettin, J. C. Fierro-Gonzalez, Y. Hao, B. C. Gates, A. Corma, *Angew. Chem.* **2005**, *117*, 4856 – 4859; *Angew. Chem. Int. Ed.* **2005**, *44*, 4778 – 4781.
[130] S. Carrettin, P. Concepción, A. Corma, J. M. Lopez Nieto, V. F. Puntes, *Angew. Chem.* **2004**, *116*, 2282 – 2285; *Angew. Chem. Int. Ed.* **2004**, *43*, 2538 – 2540.
[131] J. Guzman, A. Corma, *Chem. Commun.* **2005**, 743 – 745.
[132] S. Carrettin, A. Corma, M. Iglesias, F. Sanchez, *Appl. Catal. A* **2005**, *291*, 247 – 252.
[133] B. Solsona, M. Conte, Y. Cong, A. Carley, G. Hutchings, *Chem. Commun.* **2005**, 2351 – 2353.
[134] G. C. Bond, D. T. Thompson, *Gold Bull.* **2000**, *33*, 41 – 52.
[135] H. H. Kung, M. C. Kung, C. K. Costello, *J. Catal.* **2003**, *216*, 425 – 432.
[136] M. Valden, X. Lai, D. W. Goodman, *Science* **1998**, *281*, 1647 – 1650.
[137] M. Haruta, *Gold Bull.* **2004**, *37*, 27 – 36.
[138] H. G. Boyen, G. Kaestle, F. Weigl, B. Koslowski, C. Dietrich, P. Ziemann, J. P. Spatz, S. Riethmueller, C. Hartmann, M. Moeller, G. Schmid, M. G. Garnier, P. Oelhafen, *Science* **2002**, *297*, 1533 – 1536.
[139] N. Lopez, J. K. Norskov, *J. Am. Chem. Soc.* **2002**, *124*, 11262 – 11263.
[140] R. J. Davis, *Science* **2003**, *301*, 926 – 927.
[141] M. Comotti, C. Della Pina, R. Matarrese, M. Rossi, *Angew. Chem.* **2004**, *116*, 5936 – 5939; *Angew. Chem. Int. Ed.* **2004**, *43*, 5812 – 5815.
[142] A. K. Sinha, S. Seelan, S. Tsubota, M. Haruta, *Angew. Chem.* **2004**, *116*, 1572 – 1574; *Angew. Chem. Int. Ed.* **2004**, *43*, 1546 – 1548.
[143] M. S. Chen, D. W. Goodman, *Science* **2004**, *306*, 252 – 255.
[144] T. V. Choudhary, D. W. Goodman, *Appl. Catal. A* **2005**, *291*, 32 – 36.
[145] M. S. Chen, D. W. Goodman, *Catal. Today* **2006**, *111*, 22 – 33.
[146] Q. Fu, H. Saltsburg, M. Flytzani-Stephanopoulos, *Science* **2003**, *301*, 935 – 938.
[147] K. Okazaki, S. Ichikawa, Y. Maeda, M. Haruta, M. Kohyama, *Appl. Catal. A* **2005**, *291*, 45 – 54.
[148] N. Lopez, T. V. W. Janssens, B. S. Clausen, Y. Xu, M. Mavrikakis, T. Bligaard, J. K. Norskov, *J. Catal.* **2004**, *223*, 232 – 235.
[149] C. K. Costello, J. H. Yang, H. Y. Law, Y. Wang, J. N. Lin, L. D. Marks, M. C. Kung, H. H. Kung, *Appl. Catal. A* **2003**, *243*, 15 – 24.
[150] S. T. Daniells, M. Makkee, J. A. Moulijn, *Catal. Lett.* **2005**, *100*, 39 – 47.
[151] M. Jia, Y. Shen, C. Li, Z. Bao, S. Sheng, *Catal. Lett.* **2005**, *99*, 235 – 239.
[152] L. Fan, N. Ichikuni, S. Shimazu, T. Uematsu, *Appl. Catal. A* **2003**, *246*, 87 – 95.
[153] M. G. Mason, *Phys. Rev. B* **1983**, 27, 748 – 762.
[154] J. C. Fierro-Gonzalez, B. C. Gates, *J. Phys. Chem. B* **2004**, *108*, 16999 – 17002.
[155] V. Schwartz, D. R. Mullins, W. Yan, B. Chen, S. Dai, S. H. Overbury, *J. Phys. Chem. B* **2004**, *108*, 15782 – 15790.
[156] J. H. Yang, J. D. Henao, M. C. Raphulu, Y. Wang, T. Caputo, A. J. Groszek, M. C. Kung, M. S. Scurrell, J. T. Miller, H. H. Kung, *J. Phys. Chem. B* **2005**, *109*, 10319 – 10326.
[157] U. Heiz, E. L. Bullock, *J. Mater. Chem.* **2004**, *14*, 564 – 577.
[158] C. Lemire, R. Meyer, S. Shaikhutdinov, H.-J. Freund, *Angew. Chem.* **2004**, *116*, 121 – 124; *Angew. Chem. Int. Ed.* **2004**, *43*, 118 – 121.
[159] K. Okazaki, Y. Morikawa, S. Tanaka, K. Tanaka, M. Kohyama, *Phys. Rev. B* **2004**, *69*, 235404.
[160] K.-C. Wu, Y.-L. Tung, Y.-L. Chen, Y.-W. Chen, *Appl. Catal. B* **2004**, *53*, 111 – 116.
[161] M. Khoudiakov, M. C. Gupta, S. Deevi, *Appl. Catal. A* **2005**, *291*, 151 – 161.
[162] H.-Y. Lin, Y.-W. Chen, *Ind. Eng. Chem. Res.* **2005**, *44*, 4569 – 4576.
[163] C.-T. Wang, S.-H. Ro, *J. Non-Cryst. Solids* **2006**, *352*, 35 – 43.
[164] S. T. Daniells, A. R. Overweg, M. Makkee, J. A. Moulijn, *J. Catal.* **2005**, *230*, 52 – 65.
[165] G. J. Hutchings, M. S. Hall, A. F. Carley, P. Landon, B. E. Solsona, C. J. Kiely, A. Herzing, M. Makkee, J. A. Moulijn, A. Overweg, J. Carlos Fierro-Gonzalez, J. Guzman, B. C. Gates, *J. Catal.* **2006**, *242*, 71 – 81.
[166] D. Boyd, S. Golunski, G. R. Hearne, T. Magadzu, K. Mallick, M. C. Raphulu, A. Venugopal, M. S. Scurrell, *Appl. Catal. A* **2005**, *292*, 76 – 81.
[167] J. T. Calla, R. J. Davis, *Catal. Lett.* **2005**, *99*, 21 – 26.
[168] P. Concepción, S. Carrettin, A. Corma, *Appl. Catal. A* **2006**, *307*, 42 – 45.
[169] J. C. Fierro-Gonzalez, B. G. Anderson, K. Ramesh, C. P. Vinod, J. W. Niemantsverdriet, B. C. Gates, *Catal. Lett.* **2005**, *101*, 265 – 274.
[170] J. C. Fierro-Gonzalez, V. A. Bhirud, B. C. Gates, *Chem. Commun.* **2005**, 5275 – 5277.
[171] K. Okumura, K. Yoshino, K. Kato, M. Niwa, *J. Phys. Chem. B* **2005**, *109*, 12380 – 12386.

 © 2006 Wiley-VCH Verlag GmbH & Co. KGaA, Weinheim

[172] A. Pestryakov, I. Tuzovskaya, E. Smolentseva, N. Bogdanchikova, F. C. Jentoft, A. Knop-Gericke, *Int. J. Mod. Phys. B* **2005**, *19*, 2321 – 2326.
[173] C. Rhodes, G. J. Hutchings, A. M. Ward, *Catal. Today* **1995**, *23*, 43 – 58.
[174] D. Andreeva, V. Idakiev, T. Tabakova, A. Andreev, *J. Catal.* **1996**, *158*, 354 – 355.
[175] D. Andreeva, V. Idakiev, T. Tabakova, A. Andreev, R. Giovanoli, *Appl. Catal. A* **1996**, *134*, 275 – 283.
[176] D. Andreeva, T. Tabakova, V. Idakiev, P. Christov, R. Giovanoli, *Appl. Catal. A* **1998**, *169*, 9 – 14.
[177] F. Boccuzzi, A. Chiorino, M. Manzoli, D. Andreeva, T. Tabakova, *J. Catal.* **1999**, *188*, 176 – 185.
[178] T. Tabakova, V. Idakiev, D. Andreeva, I. Mitov, *Appl. Catal. A* **2000**, *202*, 91 – 97.
[179] F. Boccuzzi, A. Chiorino, M. Manzoli, D. Andreeva, T. Tabakova, L. Ilieva, V. Iadakiev, *Catal. Today* **2002**, *75*, 169 – 175.
[180] D. Andreeva, *Gold Bull.* **2002**, *35*, 82 – 88.
[181] A. Venugopal, M. S. Scurrell, *Appl. Catal. A* **2004**, *258*, 241 – 249.
[182] A. Venugopal, J. Aluha, D. Mogano, M. S. Scurrell, *Appl. Catal. A* **2003**, *245*, 149 – 158.
[183] A. Venugopal, M. S. Scurrell, *Appl. Catal. A* **2003**, *245*, 137 – 147.
[184] J. Hua, Q. Zheng, Y. Zheng, K. Wei, X. Lin, *Catal. Lett.* **2005**, *102*, 99 – 108.
[185] H. Sakurai, A. Ueda, T. Kobayashi, M. Haruta, *Chem. Commun.* **1997**, 271 – 272.
[186] V. Idakiev, T. Tabakova, Z. Y. Yuan, B. L. Su, *Appl. Catal. A* **2004**, *270*, 135 – 141.
[187] Q. Fu, A. Weber, M. Flytzani-Stephanopoulos, *Catal. Lett.* **2001**, *77*, 87 – 95.
[188] H. Sakurai, S. Tsubota, M. Haruta, *Shokubai* **2002**, *44*, 416 – 418.
[189] D. Andreeva, V. Idakiev, T. Tabakova, L. Ilieva, P. Falaras, A. Bourlinos, A. Travlos, *Catal. Today* **2002**, *72*, 51 – 57.
[190] Q. Fu, S. Kudriavtseva, H. Saltsburg, M. Flytzani-Stephanopoulos, *Chem. Eng. J.* **2003**, *93*, 41 – 53.
[191] T. Tabakova, F. Boccuzzi, M. Manzoli, D. Andreeva, *Appl. Catal. A* **2003**, *252*, 385 – 397.
[192] T. Tabakova, F. Boccuzzi, M. Manzoli, J. W. Sobczak, V. Idakiev, D. Andreeva, *Appl. Catal. B* **2004**, *49*, 73 – 81.
[193] D. Andreeva, I. Ivanov, L. Ilieva, M. V. Abrashev, *Appl. Catal. A* **2006**, *302*, 127 – 132.
[194] C. H. Kim, L. T. Thompson, *J. Catal.* **2005**, *230*, 66 – 74.
[195] Z.-P. Liu, S. J. Jenkins, D. A. King, *Phys. Rev. Lett.* **2005**, *94*, 196102.
[196] D. Tibiletti, A. Amieiro-Fonseca, R. Burch, Y. Chen, J. M. Fisher, A. Goguet, C. Hardacre, P. Hu, D. Thompsett, *J. Phys. Chem. B* **2005**, *109*, 22553 – 22559.
[197] D. Cameron, R. Holliday, D. Thompson, *J. Power Sources* **2003**, *118*, 298 – 303.
[198] M. M. Maye, J. Luo, L. Han, N. N. Kariuki, C.-J. Zhong, *Gold Bull.* **2003**, *36*, 75 – 83.
[199] J. Zhang, Y. Wang, B. Chen, C. Li, D. Wu, X. Wang, *Energy Convers. Manage.* **2003**, *44*, 1805 – 1815.
[200] A. Luengnaruemitchai, S. Osuwan, E. Gulari, *Int. J. Hydrogen Energy* **2004**, *29*, 429 – 435.
[201] G. Panzera, V. Modafferi, S. Candamano, A. Donato, F. Frusteri, P. L. Antonucci, *J. Power Sources* **2004**, *135*, 177 – 183.
[202] T. Tabakova, V. Idakiev, K. Tenchev, F. Boccuzzi, M. Manzoli, A. Chiorino, *Appl. Catal. B* **2006**, *63*, 94 – 103.
[203] M. Bowker, L. Millard, J. Greaves, D. James, J. Soares, *Gold Bull.* **2004**, *37*, 170 – 173.
[204] M. J. Kahlich, H. A. Gasteiger, R. J. Behm, *J. Catal.* **1997**, *171*, 93 – 105.
[205] S. Ozkara, A. E. Aksoylu, *Appl. Catal. A* **2003**, *251*, 75 – 83.
[206] P. V. Snytnikov, V. A. Sobyanin, V. D. Belyaev, P. G. Tsyrulnikov, N. B. Shitova, D. A. Shlyapin, *Appl. Catal. A* **2003**, *239*, 149 – 156.
[207] S. Kandoi, A. A. Gokhale, L. C. Grabow, J. A. Dumesic, M. Mavrikakis, *Cata. Lett.* **2004**, *93*, 93 – 100.
[208] R. M. T. Sanchez, A. Ueda, K. Tanaka, M. Haruta, *J. Catal.* **1997**, *168*, 125 – 127.
[209] M. Okumura, S. Nakamura, S. Tsubota, T. Nakamura, M. Azuma, M. Haruta, *Catal. Lett.* **1998**, *51*, 53 – 58.
[210] B. Grigorova, J. Mellor, A. Palazov, F. Greyling, (Anglo American Research Laboratories (Proprietary) Limited, S. Afr.), WO 2000/059631, **2000**, p. 14.
[211] B. Schumacher, Y. Denkwitz, V. Plzak, M. Kinne, R. J. Behm, *J. Catal.* **2004**, *224*, 449 – 462.
[212] J. T. Calla, R. J. Davis, *Ind. Eng. Chem. Res.* **2005**, *44*, 5403 – 5410.
[213] S. S. Pansare, A. Sirijaruphan, J. G. Goodwin, *J. Catal.* **2005**, *234*, 151 – 160.
[214] A. Jain, X. Zhao, S. Kjergaard, S. M. Stagg-Williams, *Catal. Lett.* **2005**, *104*, 191 – 197.
[215] M. Lomello-Tafin, A. A. Chaou, F. Morfin, V. Caps, J.-L. Rousset, *Chem. Commun.* **2005**, 388 – 390.
[216] C. Rossignol, S. Arrii, F. Morfin, L. Piccolo, V. Caps, J.-L. Rousset, *J. Catal.* **2005**, *230*, 476 – 483.
[217] M. M. Schubert, A. Venugopal, M. J. Kahlich, V. Plzak, R. J. Behm, *J. Catal.* **2004**, *222*, 32 – 40.
[218] G. Boxhoorn (Shell Internationale Research Maatschappij B.V., Netherlands), EP 255975, **1988**, p. 8.
[219] O. P. H. Vaughan, G. Kyriakou, N. Macleod, M. Tikhov, R. M. Lambert, *J. Catal.* **2005**, *236*, 401 – 404.
[220] T. Hayashi, K. Tanaka, M. Haruta, *J. Catal.* **1998**, *178*, 566 – 575.
[221] M. Haruta, M. Date, *Appl. Catal. A* **2001**, *222*, 427 – 437.
[222] T. A. Nijhuis, T. Visser, B. M. Weckhuysen, *J. Phys. Chem. B* **2005**, *109*, 19309 – 19319.
[223] B. S. Uphade, S. Tsubota, T. Hayashi, M. Haruta, *Chem. Lett.* **1998**, 1277 – 1278.
[224] T. A. Nijhuis, B. J. Huizinga, M. Makkee, J. A. Moulijn, *Ind. Eng. Chem. Res.* **1999**, *38*, 884 – 891.
[225] T. A. Nijhuis, T. Q. Gardner, B. M. Weckhuysen, *J. Catal.* **2005**, *236*, 153 – 163.
[226] N. Yap, R. P. Andres, W. N. Delgass, *J. Catal.* **2004**, *226*, 156 – 170.
[227] A. Zwijnenburg, M. Makkee, J. A. Moulijn, *Appl. Catal. A* **2004**, *270*, 49 – 56.
[228] C. Qi, T. Akita, M. Okumura, K. Kuraoka, M. Haruta, *Appl. Catal. A* **2003**, *253*, 75 – 89.
[229] B. Taylor, J. Lauterbach, W. N. Delgass, *Appl. Catal. A* **2005**, *291*, 188 – 198.
[230] A. K. Sinha, S. Seelan, M. Okumura, T. Akita, S. Tsubota, M. Haruta, *J. Phys. Chem. B* **2005**, *109*, 3956 – 3965.
[231] B. Chowdhury, J. J. Bravo-Suarez, M. Date, S. Tsubota, M. Haruta, *Angew. Chem.* **2006**, *118*, 426 – 429; *Angew. Chem. Int. Ed.* **2006**, *45*, 412 – 415.
[232] M. D. Hughes, Y.-J. Xu, P. Jenkins, P. McMorn, P. Landon, D. I. Enache, A. F. Carley, G. A. Attard, G. J. Hutchings, F. King, E. H. Stitt, P. Johnston, K. Griffin, C. J. Kiely, *Nature* **2005**, *437*, 1132 – 1135.
[233] S. Biella, M. Rossi, *Chem. Commun.* **2003**, 378 – 380.
[234] M. Comotti, C. Della Pina, R. Matarrese, M. Rossi, A. Siani, *Appl. Catal. A* **2005**, *291*, 204 – 209.
[235] P. Beltrame, M. Comotti, C. Della Pina, M. Rossi, *Appl. Catal. A* **2006**, *297*, 1 – 7.
[236] N. Dimitratos, F. Porta, L. Prati, A. Villa, *Catal. Lett.* **2005**, *99*, 181 – 185.
[237] S. Carrettin, P. McMorn, P. Johnston, K. Griffin, G. J. Hutchings, *Chem. Commun.* **2002**, 696 – 698.

 © 2006 Wiley-VCH Verlag GmbH & Co. KGaA, Weinheim

[238] S. Carrettin, P. McMorn, P. Johnston, K. Griffin, C. J. Kiely, G. A. Attard, G. J. Hutchings, *Top. Catal.* **2004**, *27*, 131 – 136.
[239] S. Carrettin, P. McMorn, P. Johnston, K. Griffin, C. J. Kiely, G. J. Hutchings, *Phys. Chem. Chem. Phys.* **2003**, *5*, 1329 – 1336.
[240] L. Prati, M. Rossi, *Stud. Surf. Sci. Catal.* **1997**, *110*, 509 – 516.
[241] L. Prati, G. Martra, *Gold Bull.* **1999**, *32*, 96 – 101.
[242] S. Coluccia, G. Martra, F. Porta, L. Prati, M. Rossi, *Catal. Today* **2000**, *61*, 165 – 172.
[243] L. Prati, F. Porta, S. Biella, M. Rossi, *Catal. Lett.* **2003**, *90*, 23 – 29.
[244] F. Porta, L. Prati, M. Rossi, G. Scari, *J. Catal.* **2002**, *211*, 464 – 469.
[245] C. Bianchi, F. Porta, L. Prati, M. Rossi, *Top. Catal.* **2000**, *13*, 231 – 236.
[246] C. Bianchi, S. Biella, A. Gervasini, L. Prati, M. Rossi, *Catal. Lett.* **2003**, *85*, 91 – 96.
[247] S. Biella, L. Prati, M. Rossi, *J. Mol. Catal. A* **2003**, *197*, 207 – 212.
[248] S. Biella, L. Prati, M. Rossi, *Inorg. Chim. Acta* **2003**, *349*, 253 – 257.
[249] S. Biella, L. Prati, M. Rossi, *J. Catal.* **2002**, *206*, 242 – 247.
[250] S. Biella, G. L. Castiglioni, C. Fumagalli, L. Prati, M. Rossi, *Catal. Today* **2002**, *72*, 43 – 49.
[251] L. Prati, F. Porta, *Appl. Catal. A* **2005**, *291*, 199 – 203.
[252] F. Porta, L. Prati, *J. Catal.* **2004**, *224*, 397 – 403.
[253] C. Basheer, S. Swaminathan, H. K. Lee, S. Valiyaveettil, *Chem. Commun.* **2005**, 409 – 410.
[254] P. G. N. Mertens, M. Bulut, L. E. M. Gevers, I. F. J. Vankelecom, P. A. Jacobs, D. E. De Vos, *Catal. Lett.* **2005**, *102*, 57 – 61.
[255] P. G. N. Mertens, I. F. J. Vankelecom, P. A. Jacobs, D. E. De Vos, *Gold Bull.* **2005**, *38*, 157 – 162.
[256] H. Tsunoyama, H. Sakurai, Y. Negishi, T. Tsukuda, *J. Am. Chem. Soc.* **2005**, *127*, 9374 – 9375.
[257] A. Abad, P. Concepción, A. Corma, H. García, *Angew. Chem.* **2005**, *117*, 4134 – 4137; *Angew. Chem. Int. Ed.* **2005**, *44*, 4066 – 4069.
[258] A. Corma, M. E. Domine, *Chem. Commun.* **2005**, 4042 – 4045.
[259] K. Mori, T. Hara, T. Mizugaki, K. Ebitani, K. Kaneda, *J. Am. Chem. Soc.* **2004**, *126*, 10657 – 10666.
[260] D. I. Enache, J. K. Edwards, P. Landon, B. Solsona-Espriu, A. F. Carley, A. A. Herzing, M. Watanabe, C. J. Kiely, D. W. Knight, G. J. Hutchings, *Science* **2006**, *311*, 362 – 365.
[261] M. Comotti, C. Della Pina, E. Falletta, M. Rossi, *Adv. Synth. Catal.* **2006**, *348*, 313 – 316.
[262] B. Guan, D. Xing, G. Cai, X. Wan, N. Yu, Z. Fang, L. Yang, Z. Shi, *J. Am. Chem. Soc.* **2005**, *127*, 18004 – 18005.
[263] C. L. Hill, I. A. Weinstock, *Nature* **1997**, *388*, 332 – 333.
[264] S. A. Chavan, D. Srinivas, P. Ratnasamy, *J. Catal.* **2002**, *212*, 39 – 45.
[265] M. Nowotny, L. N. Pedersen, U. Hanefeld, T. Maschmeyer, *Chem. Eur. J.* **2002**, *8*, 3724 – 3731.
[266] R. Raja, G. Sankar, J. M. Thomas, *J. Am. Chem. Soc.* **1999**, *121*, 11926 – 11927.
[267] R. Zhao, D. Ji, G. Lu, G. Qian, L. Yan, X. Wang, J. Suo, *Chem. Commun.* **2004**, 904 – 905.
[268] G. Lue, R. Zhao, G. Qian, Y. Qi, X. Wang, J. Suo, *Catal. Lett.* **2004**, *97*, 115 – 118.
[269] Y.-J. Xu, P. Landon, D. Enache, A. F. Carley, M. W. Roberts, G. J. Hutchings, *Catal. Lett.* **2005**, *101*, 175 – 179.
[270] H. T. Hess, I. Kroschwitz, M. Howe-Grant, *Kirk-Othmer Encyclopedia of Chemical Engineering*, *Vol. 13*, Wiley, New York, **1995**, p. 961.
[271] H. Henkel, W. Weber, US 1108752, **1914**.
[272] G. A. Cook, (Carbide & Carbon Chemicals Corp.), US 2368640, **1945**.
[273] M. Nystrom, J. Wanngard, W. Herrmann (Akzo Nobel N. V., Netherlands; Eka Chemicals AB), WO 99/32399, **1999**, p. 17.
[274] J. Van Weynbergh, J. P. Schoebrechts, J. C. Colery, (Interox International S. A., Belgium), WO 92/15520, **1992**, p. 19.
[275] B. Zhou, L.-K. Lee (Hydrocarbon Technologies, Inc., USA), US 6168775, **2001**, p. 11.
[276] P. Landon, P. J. Collier, A. F. Carley, D. Chadwick, A. J. Papworth, A. Burrows, C. J. Kiely, G. J. Hutchings, *Phys. Chem. Chem. Phys.* **2003**, *5*, 1917 – 1923.
[277] M. Okumura, Y. Kitagawa, K. Yamagcuhi, T. Akita, S. Tsubota, M. Haruta, *Chem. Lett.* **2003**, *32*, 822 – 823.
[278] T. Ishihara, Y. Ohura, S. Yoshida, Y. Hata, H. Nishiguchi, Y. Takita, *Appl. Catal. A* **2005**, *291*, 215 – 221.
[279] J. K. Edwards, B. E. Solsona, P. Landon, A. F. Carley, A. Herzing, C. J. Kiely, G. J. Hutchings, *J. Catal.* **2005**, *236*, 69 – 79.
[280] J. K. Edwards, B. Solsona, P. Landon, A. F. Carley, A. Herzing, M. Watanabe, C. J. Kiely, G. J. Hutchings, *J. Mater. Chem.* **2005**, *15*, 4595 – 4600.
[281] A. S. K. Hashmi, *Gold Bull.* **2003**, *36*, 3 – 9.
[282] a) A. S. K. Hashmi, *Angew. Chem.* **2005**, *117*, 7150 – 7154; *Angew. Chem. Int. Ed.* **2005**, *44*, 6990 – 6993; b) S. Ma, S. Yu, Z. Gu, *Angew. Chem.* **2006**, *118*, 206 – 209; *Angew. Chem. Int. Ed.* **2006**, *45*, 200 – 203.
[283] R. O. C. Norman, W. J. E. Parr, C. B. Thomas, *J. Chem. Soc. Perkin Trans. 1* **1976**, 1983 – 1987.
[284] a) G. J. Hutchings, *Gold Bull.* **1996**, *29*, 123 – 130; b) G. J. Hutchings, *Catal. Today* **2002**, *72*, 11 – 17; c) G. J. Hutchings, *Spec. Chem. Mag.* **2003**, *23*, 12 – 14.
[285] a) Y. Fukuda, K. Utimoto, H. Nozaki, *Heterocycles* **1987**, *25*, 297 – 300; b) Y. Fukuda, K. Utimoto, *Synthesis* **1991**, 975 – 978.
[286] a) T. E. Müller, *Tetrahedron Lett.* **1998**, *39*, 5961 – 5962; b) T. E. Müller, M. Grosche, E. Herdtweck, A.-K. Pleier, E. Walter, Y.-K. Yan, *Organometallics* **2000**, *19*, 170 – 183.
[287] Y. Fukuda, K. Utimoto, *Bull. Chem. Soc. Jpn.* **1991**, *64*, 2013 – 2015.
[288] A. Arcadi, G. Cerichelli, M. Chiarini, S. Di Giuseppe, F. Marinelli, *Tetrahedron Lett.* **2000**, *41*, 9195 – 9198.
[289] E. Mizushima, K. Sato, T. Hayashi, M. Tanaka, *Angew. Chem.* **2002**, *114*, 4745 – 4747; *Angew. Chem. Int. Ed.* **2002**, *41*, 4563 – 4565.
[290] M. Detlefs, H. G. Raubenheimer, M. W. Esterhuysen, *Catal. Today* **2002**, *72*, 29 – 41.
[291] R. Casado, M. Contel, M. Laguna, P. Romero, S. Sanz, *J. Am. Chem. Soc.* **2003**, *125*, 11925 – 11935.
[292] S. K. Schneider, W. A. Herrmann, E. Herdtweck, *Z. Anorg. Allg. Chem.* **2003**, *629*, 2363 – 2370.
[293] P. Roembke, H. Schmidbaur, S. Cronje, H. Raubenheimer, *J. Mol. Catal. A* **2004**, *212*, 35 – 42.
[294] M. Bardají, A. Laguna, P. G. Jones, *Organometallics* **2001**, *20*, 3906 – 3912.
[295] Y. Liu, F. Song, Z. Song, M. Liu, B. Yan, *Org. Lett.* **2005**, *7*, 5409 – 5412.
[296] S. Antoniotti, E. Genin, V. Michelet, J.-P. Genêt, *J. Am. Chem. Soc.* **2005**, *127*, 9976 – 9977.
[297] J. Barluenga, A. Diéguez, A. Fernández, F. Rodríguez, F. J. Fananás, *Angew. Chem.* **2006**, *118*, 1 – 4; *Angew. Chem. Int. Ed.* **2006**, *45*, 2091 – 2093.
[298] H. H. Jung, P. E. Floreancig, *Org. Lett.* **2006**, *8*, 1949 – 1951.
[299] P. Wessig, J. Teubner, *Synlett* **2006**, 1543 – 1546.
[300] J. Roithová, J. Hrusák, D. Schröder, H. Schwarz, *Inorg. Chim. Acta* **2005**, *358*, 4287 – 4292.
[301] E. Mizushima, T. Hayashi, M. Tanaka, *Org. Lett.* **2003**, *5*, 3349 – 3352.
[302] D. Kadzimirsz, D. Hildebrandt, K. Merz, G. Dyker, *Chem. Commun.* **2006**, 661 – 662.
[303] E. Genin, P. Y. Tullec, S. Antoniotti, C. Brancour, J.-P. Genêt, V. Michelet, *J. Am. Chem. Soc.* **2006**, *128*, 3112 – 3113.
[304] a) S. Shin, *Bull. Korean Chem. Soc.* **2005**, *26*, 1925 – 1926; b) J.-E. Kang, S. Shin, *Synlett* **2006**, 717 – 720.

 © 2006 Wiley-VCH Verlag GmbH & Co. KGaA, Weinheim

[305] M. T. Reetz, K. Sommer, *Eur. J. Org. Chem.* **2003**, *68*, 3485 – 3496.
[306] Z. Shi, C. He, *J. Org. Chem.* **2004**, *69*, 3669 – 3671.
[307] Z. Li, Z. Shi, C. He, *J. Organomet. Chem.* **2005**, *690*, 5049 – 5054.
[308] a) C. Nevado, A. M. Echavarren, *Chem. Eur. J.* **2005**, *11*, 3155 – 3164; for recent intermolecular examples, see: b) A. S. K. Hashmi, M. C. Blanco, *Eur. J. Org. Chem.* **2006**, 4340 – 4342.
[309] C. Ferrer, A. M. Echavarren, *Angew. Chem.* **2006**, *118*, 1123 – 1127; *Angew. Chem. Int. Ed.* **2006**, *45*, 1105 – 1109.
[310] a) J. J. Kennedy-Smith, S. T. Staben, F. D. Toste, *J. Am. Chem. Soc.* **2004**, *126*, 4526 – 4527; b) S. T. Staben, J. J. Kennedy-Smith, F. D. Toste, *Angew. Chem.* **2004**, *116*, 5464 – 5466; *Angew. Chem. Int. Ed.* **2004**, *43*, 5350 – 5352; c) B. K. Corkey, F. D. Toste, *J. Am. Chem. Soc.* **2005**, *127*, 17168 – 17169.
[311] A. S. K. Hashmi, *Angew. Chem.* **2000**, *112*, 3737 – 3740; *Angew. Chem. Int. Ed.* **2000**, *39*, 3590 – 3593.
[312] a) A. Hoffmann-Röder, N. Krause, *Org. Lett.* **2001**, *3*, 2537 – 2538; b) N. Krause, A. Hoffmann-Röder, J. Cansius, *Synthesis* **2002**, 1759 – 1774.
[313] A. S. K. Hashmi, M. C. Blanco, D. Fischer, J. W. Bats, *Eur. J. Org. Chem.* **2006**, 1387 – 1389.
[314] N. Morita, N. Krause, *Org. Lett.* **2004**, *6*, 4121 – 4123.
[315] H. Ohno, Y. Kadoh, N. Fujii, T. Tanaka, *Org. Lett.* **2006**, *8*, 947 – 950.
[316] P. H. Lee, H. Kim, K. Lee, M. Kim, K. Noh, H. Kim, D. Seomoon, *Angew. Chem.* **2005**, *117*, 1874 – 1877; *Angew. Chem. Int. Ed.* **2005**, *44*, 1840 – 1843.
[317] N. Nishina, Y. Yamamoto, *Angew. Chem.* **2006**, *118*, 3392 – 3395; *Angew. Chem. Int. Ed.* **2006**, *45*, 3314 – 3317.
[318] N. Morita, N. Krause, *Angew. Chem.* **2006**, *118*, 1930 – 1933; *Angew. Chem. Int. Ed.* **2006**, *45*, 1897 – 1899.
[319] R. O. C. Norman, W. J. E. Parr, C. B. Thomas, *J. Chem. Soc. Perkin Trans. 1* **1976**, 811 – 817.
[320] M. S. Kharash, T. M. Beck, *J. Am. Chem. Soc.* **1934**, *56*, 2057 – 2060.
[321] a) Y. Fuchita, H. Ieda, M. Yasutake, *J. Chem. Soc. Dalton Trans.* **2000**, 271 – 274; b) Y. Fuchita, Y. Utsunomiya, M. Yasutake, *J. Chem. Soc. Dalton Trans.* **2001**, 2330 – 2334.
[322] G. Dyker, E. Muth, A. S. K. Hashmi, L. Ding, *Adv. Synth. Catal.* **2003**, *345*, 1247 – 1252.
[323] K. A. Porter, A. Schier, H. Schmidbaur, *Organometallics* **2003**, *22*, 4922 – 4927.
[324] Z. Shi, C. He, *J. Am. Chem. Soc.* **2004**, *126*, 5964 – 5965.
[325] A. S. K. Hashmi, R. Salathé, T. M. Frost, L. Schwarz, J.-H. Choi, *Appl. Catal. A* **2005**, *291*, 238 – 246.
[326] A. Arcadi, G. Bianchi, M. Chiarini, G. D'Anniballe, F. Marinelli, *Synlett* **2004**, 944 – 950.
[327] M. Alfonsi, A. Arcadi, G. Bianchi, F. Marinelli, A. Nardini, *Eur. J. Org. Chem.* **2006**, *71*, 2393 – 2402.
[328] S. Kobayashi, K. Kakumoto, M. Sugiura, *Org. Lett.* **2002**, *4*, 1319 – 1322.
[329] R.-V. Nguyen, X. Yao, C.-J. Li, *Org. Lett.* **2006**, *8*, 2397 – 2399.
[330] M. A. Cinellu, G. Minghetti, F. Cocco, S. Stoccoro, A. Zucca, *Angew. Chem.* **2005**, *117*, 7052 – 7055; *Angew. Chem. Int. Ed.* **2005**, *44*, 6892 – 6895.
[331] J. Zhang, C.-G. Yang, C. He, *J. Am. Chem. Soc.* **2006**, *128*, 1798 – 1799.
[332] C. Brouwer, C. He, *Angew. Chem.* **2006**, *118*, 1776 – 1779; *Angew. Chem. Int. Ed.* **2006**, *45*, 1744 – 1747.
[333] a) X. Han, R. A. Widenhoefer, *Angew. Chem.* **2006**, *118*, 1779 – 1781; *Angew. Chem. Int. Ed.* **2006**, *45*, 1747 – 1749; b) D. C. Rosenfeld, S. Shekhar, A. Takemiya, M. Utsunomiya, J. F. Hartwig, *Org. Lett.* **2006**, *8*, 4179 – 4182.
[334] a) X. Yao, C.-J. Li, *J. Am. Chem. Soc.* **2004**, *126*, 6884 – 6885; b) R.-V. Nguyen, X.-Q. Yao, D. S. Bohle, C.-J. Li, *Org. Lett.* **2005**, *7*, 673 – 675; c) for coodination modes of 1,3-dicarbonyl compounds to gold, see: M. A. Cinellu, G. Minghetti, M. V. Pinna, S. Stoccoro, A. Zucca, M. Manassero, *J. Chem. Soc. Dalton Trans.* **1999**, 2823 – 2831.
[335] C.-Y. Zhou, P. W. H. Chan, C.-M. Che, *Org. Lett.* **2006**, *8*, 325 – 328.
[336] A. W. Sromek, M. Rubina, V. Gevorgyan, *J. Am. Chem. Soc.* **2005**, *127*, 10500 – 10501.
[337] J.-E. Kang, E.-S. Lee, S.-I. Park, S. Shin, *Tetrahedron Lett.* **2005**, *46*, 7431 – 7433.
[338] a) T. Yao, X. Zhang, R. C. Larock, *J. Am. Chem. Soc.* **2004**, *126*, 11164 – 11165; b) T. Yao, X. Zhang, R. C. Larock, *J. Org. Chem.* **2005**, *70*, 7679 – 7685.
[339] N. Asao, K. Takahashi, S. Lee, T. Kasahara, Y. Yamamoto, *J. Am. Chem. Soc.* **2002**, *124*, 12650 – 12651.
[340] B. Straub, *Chem. Commun.* **2004**, 1726 – 1728.
[341] N. Asao, T. Nogami, S. Lee, Y. Yamamoto, *J. Am. Chem. Soc.* **2003**, *125*, 10921 – 10925.
[342] G. Dyker, D. Hildebrandt, J. Liu, K. Merz, *Angew. Chem.* **2003**, *115*, 4536 – 4538; *Angew. Chem. Int. Ed.* **2003**, *42*, 4399 – 4402.
[343] N. Asao, H. Aikawa, Y. Yamamoto, *J. Am. Chem. Soc.* **2004**, *126*, 7458 – 7459.
[344] G. Dyker, D. Hildebrandt, *J. Org. Chem.* **2005**, *70*, 6093 – 6096.
[345] K. Sato, N. Asao, Y. Yamamoto, *J. Org. Chem.* **2005**, *70*, 8977 – 8981.
[346] N. Asao, K. Sato, Meggenbateer, Y. Yamamoto, *J. Org. Chem.* **2005**, *70*, 3682 – 3685.
[347] N. Kim, Y. Kim, W. Park, D. Sung, A. K. Gupta, C. H. Oh, *Org. Lett.* **2005**, *7*, 5289 – 5291.
[348] A. K. Gupta, C. Y. Rhim, C. H. Oh, R. S. Mane, S.-H. Han, *Green Chem.* **2006**, *8*, 25 – 28.
[349] J. Zhu, A. R. Germain, J. A. Porco, *Angew. Chem.* **2004**, *116*, 1259 – 1263; *Angew. Chem. Int. Ed.* **2004**, *43*, 1239 – 1243.
[350] A. S. K. Hashmi, T. M. Frost, J. W. Bats, *Org. Lett.* **2001**, *3*, 3769 – 3771.
[351] A. Arcadi, G. Bianchi, F. Marinelli, *Synthesis* **2004**, 610 – 618.
[352] M. Alfonsi, A. Arcadi, M. Aschi, G. Bianchi, F. Marinelli, *J. Org. Chem.* **2005**, *70*, 2265 – 2273.
[353] S. Kamijo, Y. Yamamoto, *J. Org. Chem.* **2003**, *68*, 4764 – 4771.
[354] H. Kusama, Y. Miyashita, J. Takaya, N. Iwasawa, *Org. Lett.* **2006**, *8*, 289 – 292.
[355] J. W. Dankwardt, *Tetrahedron Lett.* **2001**, *42*, 5809 – 5812.
[356] A. Fürstner, V. Mamane, *J. Org. Chem.* **2002**, *67*, 6264 – 6267.
[357] V. Mamane, P. Hannen, A. Fürstner, *Chem. Eur. J.* **2004**, *10*, 4556 – 4575.
[358] A. S. K. Hashmi, P. Sinha, *Adv. Synth. Catal.* **2004**, *346*, 432 – 438.
[359] J. P. Markham, S. T. Staben, F. D. Toste, *J. Am. Chem. Soc.* **2005**, *127*, 9708 – 9709.
[360] a) K. Miki, K. Ohe, S. Uemura, *Tetrahedron Lett.* **2003**, *44*, 2019 – 2022; b) K. Miki, K. Ohe, S. Uemura, *J. Org. Chem.* **2003**, *68*, 8505 – 8513.
[361] M. J. Johansson, D. J. Gorin, S. T. Staben, F. D. Toste, *J. Am. Chem. Soc.* **2005**, *127*, 18002 – 18003.
[362] a) A. Fürstner, P. Hannen, *Chem. Commun.* **2004**, 2546 – 2547; b) A. Fürstner, P. Hannen, *Chem. Eur. J.* **2006**, *12*, 3006 – 3019.
[363] V. Mamane, T. Gress, H. Krause, A. Fürstner, *J. Am. Chem. Soc.* **2004**, *126*, 8654 – 8655.
[364] C. Fehr, J. Galindo, *Angew. Chem.* **2006**, *118*, 2967 – 2970; *Angew. Chem. Int. Ed.* **2006**, *45*, 2901 – 2904.
[365] X. Shi, D. J. Gorin, F. D. Toste, *J. Am. Chem. Soc.* **2005**, *127*, 5802 – 5803.
[366] O. N. Faza, C. S. López, R. Álvarez, A. R. de Lera, *J. Am. Chem. Soc.* **2006**, *128*, 2434 – 2437.
[367] L. Zhang, *J. Am. Chem. Soc.* **2005**, *127*, 16804 – 16805.
[368] L. Zhang, S. Wang, *J. Am. Chem. Soc.* **2006**, *128*, 1442 – 1443.
[369] B. D. Sherry, F. D. Toste, *J. Am. Chem. Soc.* **2004**, *126*, 15978 – 15979.

 © 2006 Wiley-VCH Verlag GmbH & Co. KGaA, Weinheim

[370] M. H. Suhre, M. Reif, S. F. Kirsch, *Org. Lett.* **2005**, *7*, 3925 – 3927.
[371] J. T. Binder, S. F. Kirsch, *Org. Lett.* **2006**, *8*, 2151 – 2153.
[372] a) R. Lok, R. E. Leone, A. J. Williams, *J. Org. Chem.* **1996**, *61*, 3289 – 3297; b) R. Lok, A. J. Williams, US 5,576,432, **1996**; CAN 126:59961.
[373] M. D. Milton, Y. Inada, Y. Nishibayashi, S. Uemura, *Chem. Commun.* **2004**, 2712 – 2713.
[374] a) A. S. K. Hashmi, J. P. Weyrauch, W. Frey, J. W. Bats, *Org. Lett.* **2004**, *6*, 4391 – 4394; for the use of gold(I) catalysts and examples with the isomeric imidates, see: b) A. S. K. Hashmi, M. Rudolph, S. Schymura, J. Visus, W. Frey, *Eur. J. Org. Chem.* **2006**, 4905 – 4909.
[375] D. Dorsch, L. T. Burgdorf, R. Gericke, N. Beier, W. Mederski, PCT Int. Appl. WO 2005123688A2, **2005**; CAN 144:69837.
[376] A. Buzas, F. Gagosz, *Org. Lett.* **2006**, *8*, 515 – 518.
[377] a) B. Martín-Matute, D. J. Cardenas, A. M. Echavarren, *Angew. Chem.* **2001**, *113*, 4890 – 4893; *Angew. Chem. Int. Ed.* **2001**, *40*, 4754 – 4757; b) M. Méndez, M. P. Munoz, C. Nevade, D. J. Cárdenas, A. M. Echavarren, *J. Am. Chem. Soc.* **2001**, *123*, 10511 – 10520.
[378] A. S. K. Hashmi, M. Rudolph, J. P. Weyrauch, M. Wölfle, W. Frey, J. W. Bats, *Angew. Chem.* **2005**, *117*, 2858 – 2861; *Angew. Chem. Int. Ed.* **2005**, *44*, 2798 – 2801.
[379] A. S. K. Hashmi, T. M. Frost, J. W. Bats, *Catal. Today* **2001**, *72*, 19 – 27.
[380] a) A. S. K. Hashmi, L. Ding, J. W. Bats, P. Fischer, W. Frey, *Chem. Eur. J.* **2003**, *9*, 4339 – 4345; the assignment obtained from this investigation was used for a comparison with calculated NMR spectra: G. V. J. da Silva, Á. C. Neto, *Tetrahedron* **2005**, *61*, 7763 – 7767.
[381] A. S. K. Hashmi, L. Grundl, *Tetrahedron* **2005**, *61*, 6231 – 6236.
[382] a) A. S. K. Hashmi, J. P. Weyrauch, M. Rudolph, E. Kurpejovic, *Angew. Chem.* **2004**, *116*, 6707 – 6709; *Angew. Chem. Int. Ed.* **2004**, *43*, 6545 – 6547; b) A. S. K. Hashmi, P. Haufe, C. Schmid, A. Rivas Nass, W. Frey, *Chem. Eur. J.* **2006**, *12*, 5376 – 5382.
[383] A. S. K. Hashmi, J. P. Weyrauch, E. Kurpejovic, T. M. Frost, B. Miehlich, W. Frey, J. W. Bats, *Chem. Eur. J.* **2006**, *12*, 5806 – 5814.
[384] A. S. K. Hashmi, R. Salathé, W. Frey, *Chem. Eur. J.* **2006**, *12*, 6991 – 6996.
[385] S. Carrettin, M. C. Blanco, A. Corma, A. S. K. Hashmi, *Adv. Synth. Catal.* **2006**, *348*, 1283 – 1288.
[386] A. S. K. Hashmi, M. C. Blanco, E. Kurpejović, W. Frey, J. W. Bats, *Adv. Synth. Catal.* **2006**, *348*, 709 – 713.
[387] C. Nevado, D. J. Cárdenas, A. M. Echavarren, *Chem. Eur. J.* **2003**, *9*, 2627 – 2635.
[388] C. Nieto-Oberhuber, M. P. Muñoz, E. Buñuel, C. Nevado, D. J. Cárdenas, A. M. Echavarren, *Angew. Chem.* **2004**, *116*, 2456 – 2460; *Angew. Chem. Int. Ed.* **2004**, *43*, 2402 – 2406.
[389] M. R. Fructos, T. R. Belderrain, P. de Frémont, N. M. Scott, S. P. Nolan, M. M. Díaz-Requejo, P. J. Pérez, *Angew. Chem.* **2005**, *117*, 5418 – 5422; *Angew. Chem. Int. Ed.* **2005**, *44*, 5284 – 5288.
[390] C. Nieto-Oberhuber, S. López, A. M. Echavarren, *J. Am. Chem. Soc.* **2005**, *127*, 6178 – 6179.
[391] M. P. Muñoz, J. Adrio, J. C. Carretero, A. M. Echavarren, *Organometallics* **2005**, *24*, 1293 – 1300.
[392] F. Gagosz, *Org. Lett.* **2005**, *7*, 4129 – 4132.
[393] N. Mezailles, L. Ricard, F. Gagosz, *Org. Lett.* **2005**, *7*, 4133 – 4136.
[394] S. Kashyap, S. Hotha, *Tetrahedron Lett.* **2006**, *47*, 2012 – 2023.
[395] L. Zhang, S. A. Kozmin, *J. Am. Chem. Soc.* **2004**, *126*, 11806 – 11807.
[396] L. Zhang, S. A. Kozmin, *J. Am. Chem. Soc.* **2005**, *127*, 6962 – 6963.
[397] M. R. Luzung, J. P. Markham, F. D. Toste, *J. Am. Chem. Soc.* **2004**, *126*, 10858 – 10859.
[398] M. Sawamura, Y. Nakayama, T. Kato, Y. Ito, *J. Org. Chem.* **1995**, *60*, 1727 – 1732.
[399] M. Sawamura, Y. Ito, *Chem. Rev.* **1992**, *92*, 857 – 871.
[400] a) S. D. Pastor, A. Togni, *Helv. Chim. Acta* **1991**, *74*, 905 – 933; b) A. Togni, S. D. Pastor, *J. Org. Chem.* **1990**, *55*, 1649 – 1664.
[401] A. Togin, R. E. Blumer, P. S. Pregosin, *Helv. Chim. Acta* **1991**, *74*, 1533 – 1543.
[402] M. Sawamura, Y. Ito in *Catalytic Asymmetric Synthesis*, 2nd ed. (Ed. I. Ojima), Wiley-VCH, Weinheim, **2000**, pp. 493 – 512.
[403] A. Arcadi, G. Bianchi, S. Di Giuseppe, F. Marinelli, *Green Chem.* **2003**, *5*, 64 – 67.
[404] A. Arcadi, S. Di Giuseppe, F. Marinelli, E. Rossi, *Adv. Synth. Catal.* **2001**, *343*, 443 – 446.
[405] A. Arcadi, S. Di Giuseppe, F. Marinelli, E. Rossi, *Tetrahedron: Asymmetry* **2001**, *12*, 2715 – 2720.
[406] A. Arcadi, M. Chiarini, S. Di Giuseppe, F. Marinelli, *Synlett* **2003**, 203 – 206.
[407] S. W. Yuon, *J. Org. Chem.* **2006**, *71*, 2521 – 2523.
[408] L.-W. Xu, C.-G. Xia, L. Li, *J. Org. Chem.* **2004**, *69*, 8482 – 8484.
[409] A. Arcadi, M. Alfonsi, G. Bianchi, G. D'Anniballe, F. Marinelli, *Adv. Synth. Catal.* **2006**, *348*, 331 – 338.
[410] V. Nair, N. Vidya, K. G. Abhilash, *Tetrahedron Lett.* **2006**, *47*, 2871 – 2873.
[411] V. Nair, K. G. Abhilash, N. Vidya, *Org. Lett.* **2005**, *7*, 5857 – 5859.
[412] A. S. K. Hashmi, L. Schwarz, P. Rubenbauer, M. C. Blanco, *Adv. Synth. Catal.* **2006**, *348*, 705 – 708.
[413] J. Liu, E. Muth, U. Flörke, G. Henkel, K. Merz, J. Sauvageau, E. Schwake, G. Dyker, *Adv. Synth. Catal.* **2006**, *348*, 456 – 462.
[414] K. Mertins, I. Iovel, J. Kischel, A. Zapf, M. Beller, *Adv. Synth. Catal.* **2006**, *348*, 691 – 695.
[415] S. Komiya, T. Sone, Y. Usui, M. Hirano, A. Fukuoka, *Gold Bull.* **1996**, *29*, 131 – 136.
[416] C. Wei, C.-J. Li, *J. Am. Chem. Soc.* **2003**, *125*, 9584 – 9585.
[417] C. Wei, C.-J. Li, *Lett. Org. Chem.* **2005**, *2*, 410 – 414.
[418] Y. Luo, C.-J. Li, *Chem. Commun.* **2004**, 1930 – 1931.
[419] V. K, -Y. Lo, Y. Liu, M.-K. Wong, C.-M. Che, *Org. Lett.* **2006**, *8*, 1529 – 1532.
[420] a) Q. Xu, Y. Imamura, M. Fujiwara, Y. Souma, *J. Org. Chem.* **1997**, *62*, 1594 – 1598; b) Q. Xu, Y. Souma, US 6,011,171, **2000**; CAN 132:49750.
[421] H. Koch, W. Haaf, *Angew. Chem.* **1958**, *70*, 311 – 311.
[422] Y. Liu, F. Song, S. Guo, *J. Am. Chem. Soc.* **2006**, *128*, 11332 – 11333.
[423] J.-J. Lian, P.-C. Chen, Y.-P. Lin, H.-C. Ting, R.-S. Liu, *J. Am. Chem. Soc.* **2006**, *128*, 11372 – 11373.
[424] D. Hildebrandt, G. Dyker, *J. Org. Chem.* **2006**, *71*, 6728 – 6733.
[425] M. Shi, L.-P. Liu, J. Tang, *Org. Lett.* **2006**, *8*, 4043 – 4046.
[426] E. Mizushima, D.-M. Cui, D. Chandra, D. Nath, T. Hayashi, M. Tanaka, *Org. Synth.* **2006**, *83*, 55 – 60.

 © 2006 Wiley-VCH Verlag GmbH & Co. KGaA, Weinheim

Lanthanide Silicates

DOI: 10.1002/anie.200602849

Optical Detection of Solid-State Chiral Structures with Unpolarized Light and in the Absence of External Fields**

*Duarte Ananias, Filipe A. Almeida Paz, Luís D. Carlos, Carlos F. G. C. Geraldes, and João Rocha**

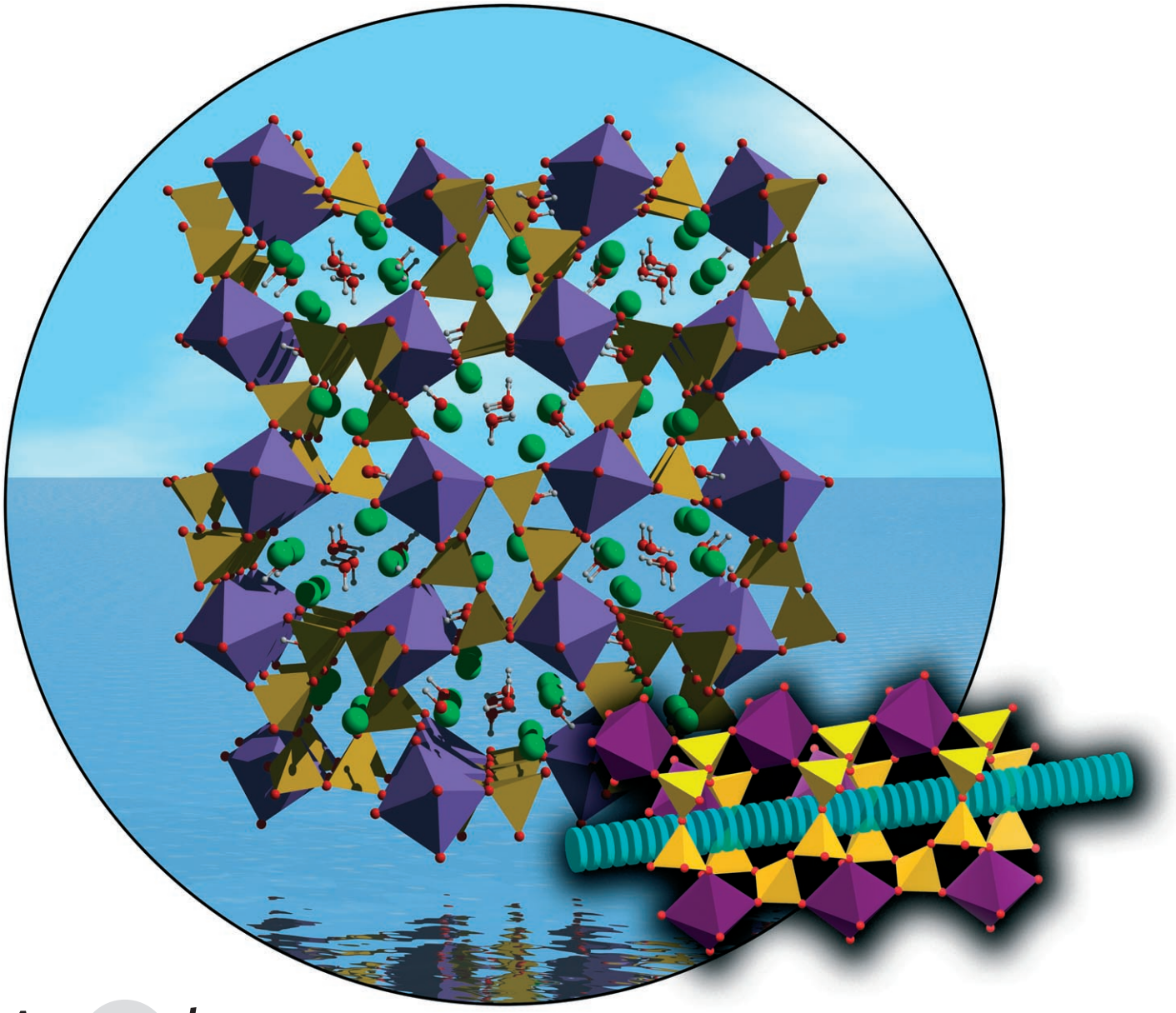

InterScience

© 2006 Wiley-VCH Verlag GmbH & Co. KGaA, Weinheim

Zeolites are microporous aluminosilicate materials of considerable industrial importance because they are excellent molecular sieves, ion exchangers, and heterogeneous catalysts. With the advent of the nanotechnology era, and increasing interest in the use of molecular sieves for device applications, novel zeolite-type materials containing stoichiometric amounts of lanthanide (Ln) metals that exhibit photoluminescence and magnetic properties have been investigated.[1–3] Herein we report the remarkable framework of $Na_3[(Y,Ln)Si_3O_9]\cdot 3H_2O$ (Ln = Eu, Tb, Er, Ce), an unprecedented chiral, photoluminescent, and microporous Ln–silicate system. Only two zeolite-type silicates exhibit chiral polymorphism, namely zeolite beta and ETS-10, but neither of these materials is photoluminescent.[4,5] The crystal structure of $Na_3[(Y,Ln)Si_3O_9]\cdot 3H_2O$ materials displays $(Si_3O_9)_\infty$ chiral spirals interconnected by $\{(Y,Ln)O_6\}$ octahedra, and it exhibits a statistical excess of one enantiomer over the other. For the first time, we show that Eu^{3+} photoluminescence spectroscopy with excitation by unpolarized light in the absence of an external magnetic field is able to identify, and possibly quantify, enantiomeric domains in chiral frameworks. This enantioselectivity phenomenon may be of importance in the context of fundamental interactions between light and condensed matter.

Although conventional zeolites are built up of tetrahedral $\{SiO_4\}$ and $\{AlO_4\}$ units, microporous silicates whose frameworks contain transition-metal heteropolyhedra have been known since the early 1990s.[1–3] The most prominent member of this family is titanosilicate ETS-10, which contains $\{TiO_6\}$ and $\{SiO_4\}$ units.[5] The constituent elements of heteropolyhedral silicates have been recently extended to lanthanides, and thus properties such as photoluminescence and magnetism have been explored. However, so far only a handful of microporous (stoichiometric) lanthanide silicates are known.[2]

Previously, chirality involving lanthanide complexes has been sensed by magnetochiral dichroism (MChD)[6,7] and circular dichroism (CD) methods, such as Ln-centered absorption, ligand absorption, and Ln-centered circularly polarized luminescence (CPL).[8,9] Whereas CPL measures the difference in emission intensity between left and right circularly polarized light, MChD evaluates the difference in luminescence intensity in the directions parallel and antiparallel to an externally applied magnetic field using unpolarized light (e.g., from a Hg-discharge lamp). Enantiodiscrimination typically uses the magnetic dipole-allowed $Eu(^5D_0\rightarrow{}^7F_1)$, $Tb(^5D_4\rightarrow{}^7F_5)$, and $Yb(^5F_{5/2}\rightarrow{}^2F_{7/2})$ transitions in CPL experiments, whereas in MChD the $^5D_0\rightarrow{}^7F_{1,2}$ transitions are employed.[6–9]

The solids described herein were obtained as byproducts in the hydrothermal synthesis of dense $Na_3[LnSi_3O_9]$ phosphors.[10–12] Crystals suitable for single-crystal X-ray diffraction were prepared for small-pore materials $Na_3[(Y_{0.9}Tb_{0.04}Eu_{0.025}Ce_{0.035})Si_3O_9]\cdot 3H_2O$ (**1a**) and $Na_3[(Y_{0.995}Er_{0.005})Si_3O_9]\cdot 3H_2O$ (**1b**). Isostructural $Na_3[(Y_{0.7}Eu_{0.3})Si_3O_9]\cdot 3H_2O$ (**1c**) and $Na_3[(Y_{0.70}Tb_{0.30})Si_3O_9]\cdot 3H_2O$ (**1d**) were also synthesized as powders and used in the photoluminescence studies. These solids are chiral orthorhombic phases exhibiting a statistical enantiomeric excess (see the Supporting Information). A second type of smaller, monoclinic, centrosymmetric crystals which often cocrystallize with **1**, namely, $H_{0.5}Na_{2.5}[(Y_{0.995}Er_{0.005})Si_3O_9]\cdot 3H_2O$ (**2**), were manually harvested and analyzed on a rotating-anode diffractometer.

The structure of dense $Na_3[LnSi_3O_9]$ is constructed from complex double spiral chains $(Si_{24}O_{72})_\infty$ with a period of 15.14 Å, which connect isolated $\{LnO_6\}$ octahedra.[10] The chiral (**1**) and centrosymmetric (**2**) materials share a common type of $(Si_3O_9)_\infty$ chain (Figure 1b and Supporting Information) running along the [100] direction (period of one *a*-axis length, ca. 6.97 Å). Although the $(Si_{24}O_{72})_\infty$ and $(Si_3O_9)_\infty$ chains are different they are both built up of triortho groups Si_3O_{10}, and the latter chain readily transforms into the former on calcining solids **1** and **2** at 800 °C. We speculate that the Si_3O_{10} group is the structural motif that first forms in the gel and templates the synthesis of the three phases. The silicon oxide chains not only connect individual $\{LnO_6\}$ octahedra but they also isolate them, at minimal Ln···Ln distances of about 6.32 and 5.88 Å in **1** and **2**, respectively (Figure 1 and Supporting Information1). Such separation of the optically active centers is important because it effectively avoids self-quenching.

Although the $(Si_3O_9)_\infty$ structural motif is similar for both **1** and **2**, the way it is linked to the metal centers is different. Consider the first coordination sphere of the $\{(Y,Ln)O_6\}$ distorted octahedra (see the Supporting Information): whereas in **1** chelation of the metal center by three Si_2O_7 moieties ultimately leads to a chiral structure, in **2** one of the chelate rings is broken. As a result, the small-pore structure of the former contains one-dimensional mixed 8-ring channels along the [100] direction, which have a cross section of about 2.0×4.0 Å (Figure 1a) and host Na^+ ions and hydrogen-bonded water molecules, whereas the comparatively dense framework of the latter has 6-ring tunnels housing Na^+ and H^+ ions and water molecules (see the Supporting Information).

[*] Dr. D. Ananias, Dr. F. A. Almeida Paz, Prof. J. Rocha
Departamento de Química
CICECO
Universidade de Aveiro
3810-193 Aveiro (Portugal)
Fax: (+351) 234-370-730
E-mail: rocha@dq.ua.pt
Prof. L. D. Carlos
Departamento de Física
CICECO
Universidade de Aveiro
3810-193 Aveiro (Portugal)
Dr. D. Ananias, Prof. C. F. G. C. Geraldes
Departamento de Bioquímica
Universidade de Coimbra
3001-401 Coimbra (Portugal)

[**] We thank the Portuguese Foundation for Science and Technology (FCT), POCTI, and FEDER, FAME NoE for financial support of this work.

Supporting information for this article is available on the WWW under http://www.angewandte.org or from the author.

 © 2006 Wiley-VCH Verlag GmbH & Co. KGaA, Weinheim

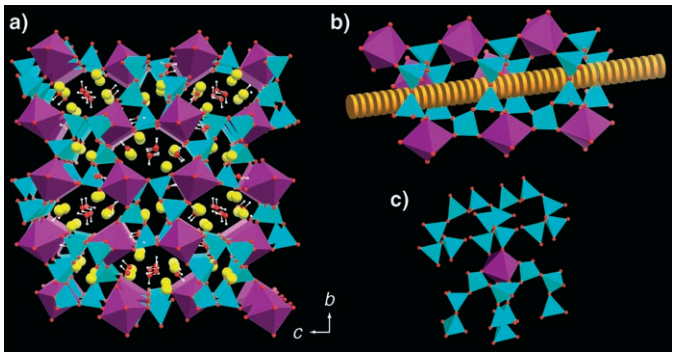

Figure 1. a) Perspective view along the [100] direction of the crystal packing of **1a** and **1b**. b) Portion of the anionic frameworks showing one $(Si_3O_9)_\infty$ spiral chain interconnecting individual $\{(Y,Ln)O_6\}$ octahedra (Ln = Tb^{3+}, Ce^{3+}, Eu^{3+}, or Er^{3+}). c) Idealized representation of a $\{(Y,Ln)O_6\}$ octahedron connected to two $(Si_3O_9)_\infty$ spirals with opposite handedness. Color code: purple $\{(Y,Ln)O_6\}$; blue $\{SiO_4\}$; red O^{2-}; yellow Na^+; white H.

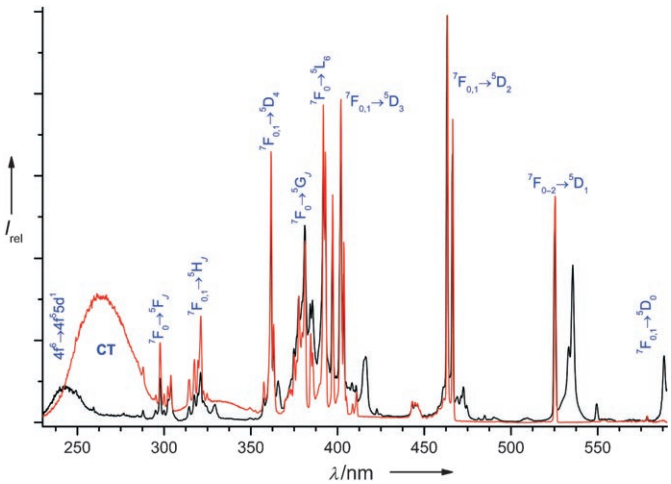

Figure 2. Excitation spectra of **1c** recorded at room temperature (black line) and 10 K (red line). Emission was monitored at 607.2 nm.

Excitation and emission spectra of **1d** were recorded at room temperature and 10 K (Supporting Information). In the excitation spectra, the sharp lines between 280 and 500 nm are assigned to $^7F_6 \rightarrow ^5D_{4-0}$, $^5L_{10}$, $^5G_{6-3}$, $^5H_{7-4}$, and $^5F_{5,4}$ intraconfigurational forbidden $4f^8 \rightarrow 4f^8$ transitions of Tb^{3+}. The broad band between 250 and 280 nm is ascribed to the spin-forbidden (high-spin, HS) interconfigurational $4f^8 \rightarrow 4f^75d^1$ transition of Tb^{3+} (see reference [13] and references therein). This type of spin-forbidden fd band may be observed for (heavy) Ln^{3+} ions with more than seven 4f electrons at an energy lower than that of spin-allowed (low-spin, LS) fd transitions. The broad band at about 236 nm is assigned to the spin-allowed (LS) interconfigurational fd transition of Tb^{3+}. The emission spectra of **1d**, excited at 265 nm, show a series of sharp lines between 475 and 700 nm, assigned to the $^5D_4 \rightarrow ^7F_J$ ($J = 6$–1) transitions of Tb^{3+} (see the Supporting Information). The same emission is obtained with excitation at the intra-$^5D_3$ (377 nm) line.

The excitation spectra of **1c** recorded at room temperature and 10 K (Figure 2) display a series of sharp lines assigned to the $^7F_{0-2} \rightarrow ^5D_{4-0}$, $^5L_6$, $^5G_{2-6}$, $^5H_{3-7}$, and $^5F_{1-5}$ Eu^{3+} intra-$4f^6$ transitions. The faint broad band ($4f^6 \rightarrow 4f^55d^1$) at high energy is probably the beginning of the spin-allowed, interconfigurational fd Eu^{3+} transition band, which normally appears at higher energy than the equivalent Tb^{3+} band. At 10 K the spectrum exhibits an additional broad band that peaks at 264.5 nm and is attributed to ligand-to-Eu^{3+} charge transfer (CT). The energy (4.69 eV) and full-width at half-maximum (0.58 eV) of the CT band are in the range of values reported for many structures containing Eu^{3+}.[14]

The sharp lines of the emission spectra (Figure 3) are assigned to transitions between the first excited nondegenerate $^5D_0$ state and the $^7F_{0-4}$ levels of the fundamental Eu^{3+} septet. Local-field splitting of the $^7F_{1,2}$ levels into three and five Stark components (inset in Figure 3, green line) supports the presence of a single low-symmetry Eu^{3+} environment, as indicated by the crystal structure. Surprisingly, when the sample is excited at the CT band (265 nm) the number of $^7F_{1,2}$ Stark components doubles (inset in Figure 3, magenta line).

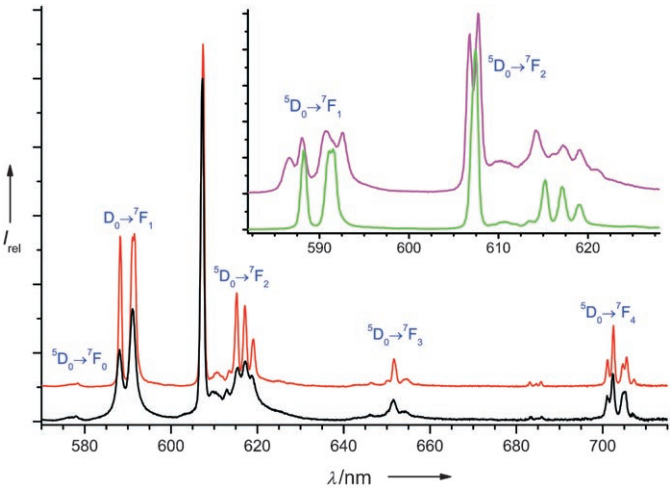

Figure 3. Emission spectra of **1c** recorded at room temperature (black line) and 10 K (red line). Excitation was performed at 525.4 nm. The inset shows an expansion of the Eu^{3+} $^5D_0 \rightarrow ^7F_{1,2}$ transitions, collected at 10 K and excited at 526 nm for the $^5D_1$ level of Eu^{3+} (green line) and at 265 nm for the CT band (magenta line).

We note that this is only observed between 10 and about 120 K, the temperature range in which the CT band is also detected (despite the fact that the X-ray data, collected at 100 K, call for the presence of a single Eu^{3+} site).

Because the $^5D_0 \rightarrow ^7F_0$ line is very faint, we did not draw any conclusions from its evolution when the excitation wavelength was varied from the CT to the intra-4f lines. The relative intensities of the two main $^5D_0 \rightarrow ^7F_2$ Stark components depend on the particular sample studied (see the Supporting Information). This observation constitutes first (though not unequivocal) evidence for the presence of two enantiomers in **1c**. Moreover, the enantioselective detection of Eu^{3+}-containing molecular compounds by CPL and MChD has been found to be much more sensitive in the magnetic dipole-allowed $^5D_0 \rightarrow ^7F_1$ transition than in the induced electric-dipole $^5D_0 \rightarrow ^7F_2$ transition.[6,8,9] In **1c** we observe maximum splittings of the $^5D_0 \rightarrow ^7F_1$ transition of 172 and

 © 2006 Wiley-VCH Verlag GmbH & Co. KGaA, Weinheim

95 cm^{-1}, respectively for excitation at the CT band and intra-$4f^6$ lines (inset in Figure 3). For the $^5D_0 \rightarrow {}^7F_2$ transition the maximum splittings are 373 and 310 cm^{-1}, respectively, for the same excitations. Thus, the maximum splitting difference is significantly larger for the $^5D_0 \rightarrow {}^7F_1$ transition (77 cm^{-1}, compared with 63 cm^{-1} for the other transitions).

Measurements of $^5D_0$ lifetimes for $Na_3[(Y_{1-a}Eu_a)Si_3O_9]\cdot 3H_2O$ ($a = 0.2$, 0.3; see the Supporting Information) clearly support this conclusion. In all measurements, the $^5D_0$ decay curves are well fitted by a single exponential (Supporting Information). At 10 K the two samples display a similar lifetime ((1.59 ± 0.01) ms) for excitation in the $^5D_1$ level (526 nm) and detection in the strongest $^7F_2$ Stark component (608.5 nm). However, excitation in the CT band leads to different lifetimes. Whereas the sample with $a = 0.2$ has the same lifetime for the two main $^7F_2$ Stark components at 607.8 and 609.1 nm ((1.48 ± 0.01) ms), that with $a = 0.3$ displays different lifetimes of (1.39 ± 0.01) and (1.54 ± 0.01) ms for detection at these wavelengths, respectively.

We now try to rationalize the unusual detection of enantiomeric domains by photoluminescence spectroscopy with excitation by unpolarized light and in the absence of an external applied magnetic field. Consider Figure 1c: Structurally, the Y^{3+}/Eu^{3+} ions link in different ways to two adjacent $(Si_3O_9)_\infty$ spiral chains which, for the sake of argument, we assume to be enantiomeric. Each Y^{3+}/Eu^{3+} octahedron shares four corners with a spiral of a given handedness, and two corners with a spiral of opposite handedness.

When the material is excited on the CT band, expansion of the Eu^{3+}–O bonds of the two adjacent enantiomeric spirals gives rise to two discernible Eu^{3+} local environments. Indeed, a CT transition involves considerable reorganization of the charge density distribution around the Eu^{3+} ion, which is accompanied by expansion of the Eu^{3+}–O bonds in the excited state.[15] The above-mentioned decrease in the $^5D_0$ lifetime for CT excitation (Supporting Information) lends support to this Eu^{3+}–O expansion. Moreover, as the two main $^5D_0 \rightarrow {}^7F_2$ transitions of the sample with $a = 0.2$ exhibit similar intensities and lifetimes, this material does not contain a significant enantiomeric excess. In contrast, the emission spectrum of the sample with $a = 0.3$ suggests a small enantiomeric excess, slight difference in intensity of the two lines, and distinct lifetimes (see the Supporting Information). Further work is in progress to fully understand the intriguing phenomenon of domain enantioselectivity in microporous framework silicates by photoluminescence spectroscopy.

In conclusion, to the best of our knowledge, discrimination between enantiomeric domains has so far only been achieved by using CPL or MChD.[6–9] Our results raise the exciting possibility that Eu^{3+} photoluminescence spectroscopy may, at least in certain cases, be used to detect, and possibly quantify, enantiomeric domains in chiral frameworks.

Experimental Section

The syntheses of rare-earth-metal silicates were carried out in teflon-lined autoclaves under static hydrothermal conditions in ovens preheated to 150–230 °C. All lanthanide salts were of 99.9 % purity. In all the syntheses, autoclaves were removed and quenched in cold water after an appropriate time. The obtained microcrystalline powders were filtered, washed at room temperature with distilled water, and dried at 100 °C.

Typical synthesis of single crystals of **1a**: An alkaline solution was made by mixing sodium silicate solution (6.83 g, 27 wt % SiO_2, 8 wt % Na_2O, Merck), H_2O (10.07 g), and NaOH (6.59 g, Panreak). A mixture of $YCl_3\cdot 6H_2O$ (1.05 g, Aldrich), $TbCl_3\cdot 6H_2O$ (0.058 g, Aldrich), $EuCl_3\cdot 6H_2O$ (0.035 g, Aldrich), and $CeCl_3\cdot 7H_2O$ (0.050 g, Aldrich) in H_2O (10.0 g) was added to this solution, and the solution was stirred thoroughly. The gel, with composition $2.97\,Na_2O{:}1.00\,SiO_2{:}0.057\,Y_2O_3{:}0.0021\,Tb_2O_3{:}0.0014\,Eu_2O_3{:}0.0014\,Ce_2O_3{:}36.3\,H_2O$, was heated in autoclaves (volume 37 cm^3) for 8 d at 230 °C. The resulting sample also contained single crystals of **2** and dense $Na_3[(Y_{0.9}Tb_{0.04}Eu_{0.025}Ce_{0.035})Si_3O_9]$ (Supporting Information).[10–12]

Typical synthesis of single crystals of **2**: An alkaline solution was made by mixing sodium silicate solution (7.91 g, 27 wt % SiO_2, 8 wt % Na_2O, Merck), H_2O (12.20 g), and NaOH (7.72 g, Panreak). A mixture of $YCl_3\cdot 6H_2O$ (1.293 g, Aldrich) and $ErCl_3\cdot 6H_2O$ (0.008 g, Aldrich) in H_2O (10.0 g) was added to this solution and the solution was stirred thoroughly. The gel, with composition $3.00\,Na_2O{:}1.00\,SiO_2{:}0.060\,Y_2O_3{:}0.0003\,Er_2O_3{:}34.7\,H_2O$, was heated in autoclaves (volume 42 cm^3) for 5 d at 230 °C. The resulting sample also contains small amounts of **1b** and dense $Na_3[(Y_{0.995}Er_{0.005})Si_3O_9]$.[10–12] Ultrasonication of a water suspension of the material disperses the crystals of **2**. Unlike the dense material[10–12] and **1b** crystals, crystals of **2** remain in the aqueous phase and are easily isolated.

Pure samples of **1c** and **1d** were prepared from a similar initial gel by introducing the desired Y^{3+} and Eu^{3+} or Tb^{3+} contents and heating for 13 d at 150 °C (see the Supporting Information).

The chemical composition of the samples was ascertained by energy-dispersive X-ray spectroscopy. Thermogravimetry confirmed that materials **1** and **2** contain three water molecules per formula unit.

Further details on the crystal structure investigations may be obtained from the Fachinformationszentrum Karlsruhe, 76344 Eggenstein-Leopoldshafen, Germany (fax: (+49) 7247-808-666; e-mail: crysdata@fiz-karlsruhe.de), on quoting the depository numbers CSD-415853 (**1a**), -415852 (**1b**), and -415852 (**2**). See also the Supporting Information.

Crystal data for **1a**: $H_{24}Ce_{0.14}Eu_{0.10}Na_{12}O_{48}Si_{12}Tb_{0.16}Y_{3.60}$, $M = 1785.47$, orthorhombic, space group $P2_12_12_1$, $Z = 1$, $a = 6.9724(14)$, $b = 11.687(2)$, $c = 13.404(3)$ Å, $V = 1092.2(4)$ Å^3, $\mu(Mo_{K\alpha}) = 5.864$ mm^{-1}, $\rho_{calcd} = 2.715$ $g\,cm^{-3}$. Of a total of 10557 reflections collected, 2408 were independent ($R_{int} = 0.0525$). Crystal size $0.08 \times 0.07 \times 0.04$ mm. Final $R1 = 0.0288$ [$I > 2\sigma(I)$] and $wR2 = 0.0650$ (all data).

Crystal data for **1b**: $H_{24}Er_{0.02}Na_{12}O_{48}Si_{12}Y_{3.98}$, $M = 1762.36$, orthorhombic, space group $P2_12_12_1$, $Z = 1$, $a = 6.9610(14)$, $b = 11.669(2)$, $c = 13.375(3)$ Å, $V = 1086.4(4)$ Å^3, $\mu(Mo_{K\alpha}) = 5.892$ mm^{-1}, $\rho_{calcd} = 2.694$ $g\,cm^{-3}$. Of a total of 9102 reflections collected, 2226 were independent ($R_{int} = 0.0453$). Crystal size $0.10 \times 0.09 \times 0.06$ mm. Final $R1 = 0.0268$ [$I > 2\sigma(I)$] and $wR2 = 0.0566$ (all data).

Crystal data for **2**: $H_{26}Er_{0.02}Na_{10}O_{48}Si_{12}Y_{3.98}$, $M = 1718.40$, monoclinic, space group $P2_1/n$, $Z = 1$, $a = 9.073(4)$, $b = 8.823(4)$, $c = 12.963(5)$ Å, $\beta = 107.68(2)°$, $V = 988.8(7)$ Å^3, $\mu(Mo_{K\alpha}) = 13.675$ mm^{-1}, $\rho_{calcd} = 2.886$ $g\,cm^{-3}$. Of a total of 2571 reflections collected, 990 were independent ($R_{int} = 0.1025$). Crystal size $0.05 \times 0.05 \times 0.01$ mm^3. Final $R1 = 0.0882$ [$I > 2\sigma(I)$] and $wR2 = 0.2095$ (all data).

Photoluminescence measurements were performed on a Fluorolog-3 Model FL3-2T with double excitation spectrometer (Triax 320), fitted with a 1200-grooves mm^{-1} grating blazed at 330 nm, and a single emission spectrometer (Triax 320), fitted with a 1200-grooves mm^{-1} grating blazed at 500 nm, coupled to an R928P photomultiplier. The excitation source was a 450-W xenon lamp. Excitation

 © 2006 Wiley-VCH Verlag GmbH & Co. KGaA, Weinheim

spectra were corrected from 240 to 600 nm for the spectral distribution of the lamp intensity by using a photodiode reference detector. Emission and excitation spectra, recorded between 10 K and room temperature in 20–30-K steps by using a closed-cycle He cryostat, were also corrected for the spectral response of the monochromators and the detector by using typical correction spectra provided by the manufacturer. Time-resolved measurements were carried out with a 1934D3 phosphorimeter coupled to the Fluorolog-3 and a Xe–Hg flash lamp (6 μs/pulse half width and tail of 20–30 μs) was used as excitation source.

Received: July 17, 2006
Revised: September 11, 2006
Published online: October 19, 2006

Keywords: hydrothermal synthesis · lanthanides · luminescence · microporous materials · silicates

[1] J. Rocha, M. W. Anderson, *Eur. J. Inorg. Chem.* **2000**, 801 – 818.
[2] J. Rocha, Z. Lin, *Reviews in Mineralogy and Geochemistry, Vol. 57* (Eds.: G. Ferraris, S. Merlino), Mineralogical Society of America, Geochemical Society, **2005**, chap. 6, pp. 173 – 201.
[3] M. Tsapatsis, *AIChE J.* **2002**, *48*, 654 – 660.
[4] J. M. Newsham, M. M. J. Treacy, W. T. Koetsier, C. B. De Gruyter, *Proc. R. Soc. London Ser. A* **1988**, *420*, 375 – 405.
[5] M. W. Anderson, O. Terasaki, T. Ohsuna, A. Philippou, S. P. Mackay, A. Ferreira, J. Rocha, S. Lidin, *Nature* **1994**, *367*, 347 – 351.
[6] G. L. J. A. Rikken, E. Raupach, *Nature* **1997**, *390*, 493 – 494.
[7] F. S. Richardson, J. P. Riehl, *Chem. Rev.* **1977**, *77*, 773 – 792.
[8] J. P. Riehl, F. S. Richardson, *Chem. Rev.* **1986**, *86*, 1 – 16.
[9] J.-C. G. Bünzli, C. Piguet, *Chem. Soc. Rev.* **2005**, *34*, 1048 – 1077.
[10] D. Ananias, J. P. Rainho, A. Ferreira, M. Lopes, C. M. Morais, J. Rocha, L. D. Carlos, *Chem. Mater.* **2002**, *14*, 1767 – 1772.
[11] D. Ananias, A. Ferreira, L. D. Carlos, J. Rocha, *Adv. Mater.* **2003**, *15*, 980 – 985.
[12] D. Ananias, L. D. Carlos, J. Rocha, *Opt. Mater.* **2006**, *28*, 582 – 586.
[13] D. Ananias, M. Kostova, F. A. A. Paz, A. Ferreira, L. D. Carlos, J. Klinowski, J. Rocha, *J. Am. Chem. Soc.* **2004**, *126*, 10410 – 10417.
[14] P. Dorenbos, *J. Phys. Condens. Matter* **2003**, *15*, 8417 – 8434.
[15] L. van Pieterson, M. Heeroma, E. de Heer, A. Meijerink, *J. Lumin.* **2000**, *31*, 177 – 193.

 © 2006 Wiley-VCH Verlag GmbH & Co. KGaA, Weinheim

Natural Products

DOI: 10.1002/anie.200602785

Total Synthesis and Antitumor Activity of ZK-EPO: The First Fully Synthetic Epothilone in Clinical Development**

Ulrich Klar, Bernd Buchmann, Wolfgang Schwede, Werner Skuballa, Jens Hoffmann, and Rosemarie B. Lichtner*

The clinical success of paclitaxel (PT) in the treatment of ovarian and breast cancer strongly contributed to the assessment that tubulin is one of the best clinically validated targets in tumor therapy. However, one disadvantage with PT and other taxane analogues is their recognition by cellular efflux mechanisms, such as the p-glycoprotein (p-gp), which contribute to a loss of activity in cells overexpressing the multidrug-resistance (MDR) phenotype.

In 1995 Bollag et al.[1] reported that the natural product class of epothilones mimics the biological activity of PT with respect to its action on the tubulin system. Thus, the cell cycle is arrested in the G2/M phase and the cells are driven into mitotic catastrophe and/or apoptosis. In contrast to PT, epothilones possess the potential to overcome MDR in vitro and, most importantly, in vivo.[2–5] These findings stimulated intensive research activities in chemistry, pharmacology, and medicine.

Epothilones were first discovered by Reichenbach, Höfle, and co-workers who characterized the compounds they had isolated from the myxobacterial strain *Sorangium cellulosum*.[6,7] They also described their cytotoxic potential in a patent application filed in 1991.[8]

The first total syntheses of epothilone A were reported in 1996/1997 by the research groups of Danishefsky, Nicolaou, and Schinzer.[9–11] Since we had no access to the more potent compound epothilone B, from the start of our project we focused on total synthesis to evaluate the potential of this compound class. During our own investigations, the total syntheses of epothilones B and D were reported.[12–15] Epo-

[*] Dr. U. Klar, Dr. B. Buchmann, Dr. W. Schwede, Prof. W. Skuballa, Dr. J. Hoffmann, Dr. R. B. Lichtner
Schering AG, Research Center Europe
Müllerstrasse 178, 13342 Berlin (Germany)
Fax: (+49) 30-468-92635
E-mail: ulrich.klar@schering.de
Homepage: http://www.schering.de

[**] We thank Siegfried Bäsler, Stefan Barm, Angela Bieseke, Klaus Burmeister, Klaus Cornelius, Gisbert Depke, Ralf Günther, Wolfgang Halfbrodt, Frank Halwass, Karola Henschel, Hiltraud Hillmann, Klaus-Dieter Joachim, Frank Kuczynski, Hue-Quan Lao, Günter Michl, Gerhard Neumann, Christian Pingel, Ingrid Pissarczyk, Peter Pretsch, Bodo Röhr, Oliver Schenk, Michael Schirner, Jürgen Skupsch, Marion Slopianka, Daniela Wrobel, and Henk Zimmermann for their excellent scientific and technical assistance.

Supporting information for this article is available on the WWW under http://www.angewandte.org or from the author.

 InterScience © 2006 Wiley-VCH Verlag GmbH & Co. KGaA, Weinheim

thilone B proved to be highly active in proliferation assays, but also highly toxic in animal models. On the basis of these results we started a lead optimization program, with the primary goal being to maintain the high activity of the natural compound while improving the therapeutic window.

A highly convergent total synthesis enabled us to introduce structural modifications at nearly every position of the macrolactone. We found that epothilone D and most of its analogues had a significantly reduced activity compared with epothilone B. Even though they are not good substrates for p-gp, a delayed cellular uptake and an easy cellular release was observed, which strengthened our focus on compounds of the epothilone B type.[16]

To increase the chemical as well as the enzymatic stability we replaced the lactone by a lactam moiety, and were surprised to discover that the compounds were then well recognized by MDR mechanisms thus resulting in a taxane-like profile. Several other structural modifications have since been identified that also change the compound profile in this unwanted direction. During extensive studies on structure/property—as well as structure/activity—relationships we learned that it is possible to further improve the activity of the natural compounds in multi-drug resistant cell lines and to reduce the toxicity in vivo without reducing the antitumor efficacy. The side chain at C15[17] and the residue at C6 were identified as key positions for tuning tolerability and efficacy.[18,19] From about 350 active[20] epothilone analogues synthesized in our laboratories, we have chosen ZK-EPO (**20**) on the basis of its outstanding preclinical properties for clinical development. This compound combines high activity and efficacy, a fast and efficient cellular uptake, no recognition by efflux mechanisms, and an improved therapeutic window.

Scheme 1 shows the four epothilones currently undergoing advanced clinical development.[21,22] The natural compounds epothilones B and D are produced by biosynthesis and the lactam BMS 247550 by partial synthesis starting from epothilone B. We now disclose the chemical structure of ZK-EPO (**20**) as well as the synthetic route developed in our research.

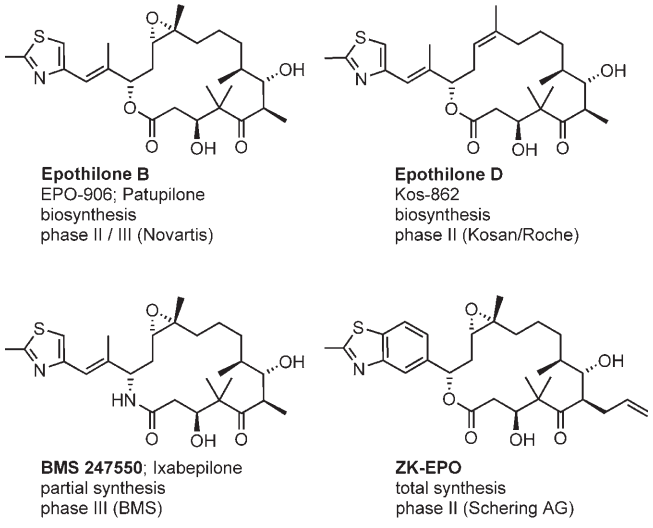

Scheme 1. Epothilones in advanced clinical trials, their names, production method, and development status.

We applied a highly convergent strategy based on our lead-optimization program that offered good flexibility for introducing structural modifications at nearly every position of the 16-membered-ring skeleton. This strategy is reflected in our synthetic route to ZK-EPO (Scheme 2) where we applied a Wittig reaction to connect C12 and C13, an aldol reaction[10,11] to establish stereocenters C6 and C7, and finally a Yamaguchi cyclization for macrolactonization.[12]

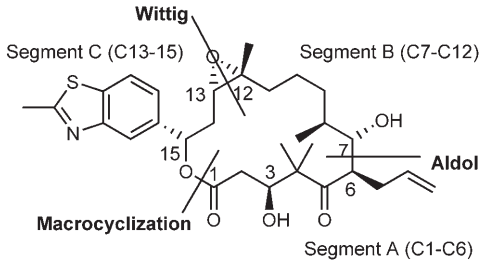

Scheme 2. Strategic bond formation in the construction of ZK-EPO.

Segment A is constructed from a chiral pool synthesis starting with (−)-pantolactone (Scheme 3).[23] Even though 11 steps were required, this synthesis allows the preparation of C6-modified building blocks in large quantities.

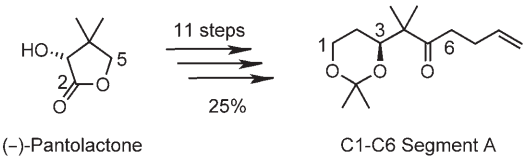

Scheme 3. Synthesis of the C1–C6 segment (segment A) from (−)-pantolactone.

Besides the possibility for structural modifications, segment B represents a central strategic synthon. By using an appropriate protecting-group strategy the segments can be connected either by the sequence C + B→CB + A→CBA or by the sequence A + B→AB + C→ABC. This flexibility was achieved during the synthesis of potential drug compounds through an 11-step synthesis that allowed us to incorporate the most valuable building blocks A or C last.[19]

After selecting ZK-EPO as the candidate for development, and favoring the connection sequence C + B→CB + A→CBA, the synthesis of segment B can be shortened considerably (Scheme 4).

The readily available chiral starting material **1** (Roche ester) is first protected as a tetrahydropyranyl ether. After reduction of the ester moiety, the resulting primary alcohol is derivatized to tosylate **2**. Coupling of **2** with 2-methyl-1-butenyl-4-magnesium bromide (**4**) in the presence of a catalytic amount of Li_2CuCl_4[24,25] leads to **5**. Bishydroxylation of the double bond followed by oxidative degradation provides methyl ketone **6** in an overall yield of 47% starting from **1**.

 © 2006 Wiley-VCH Verlag GmbH & Co. KGaA, Weinheim

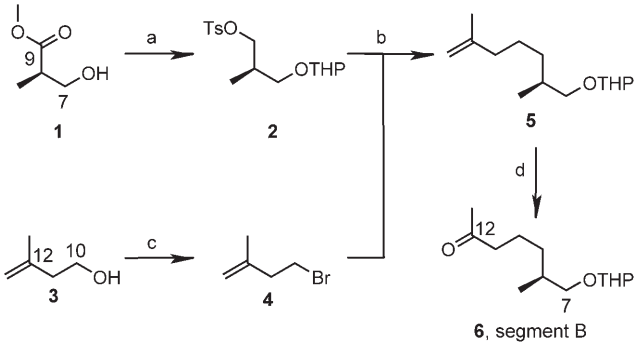

Scheme 4. Stringent synthetic route to the C7–C12 segment (segment B). Reagents and conditions: a) 1. DHP, pTsOH, CH_2Cl_2; 2. LAH, diethyl ether, RT, 87%; 3. TsCl, pyridine, RT, 97%; b) Mg/Li_2CuCl_4 (cat.), THF, −70°C to RT, 75%; c) NBS, PPh_3, CH_2Cl_2, RT, 51%; d) OsO_4, $NaIO_4$, H_2O, THF, RT, 74%. THP = tetrahydropyranyl, DHP = dihydropyran, pTsOH = toluene-4-sulfonic acid, LAH = lithium aluminum hydride, Ts = toluene-4-sulfonyl, NBS = *N*-bromosuccinimide.

Benzothiazole **8** is obtained from benzoic acid **7** in a one-pot reaction (Scheme 5). Aldehyde **9** is prepared by a reduction–oxidation sequence and then submitted to an Evans aldol addition of 3-acetyl-(4*S*,5*R*)-4-methyl-5-phenyl-2-oxazolidinone (**10**) to establish the stereogenic center at C15. The excess of chiral auxiliary can be considerably reduced by the presence of zinc chloride to give a 8:2 mixture of diastereoisomers from which pure **11** is isolated directly by crystallization.[26] The relative stereochemistry was determined by X-ray analysis of **11**, thereby confirming the correct absolute configuration at C15.

The most efficient way to recover the chiral auxiliary was transesterification to **12** and subsequent reduction to the corresponding alcohol, which is then transformed to crystalline phosphonium salt **13** (segment C). The overall yield starting from **7** is 16%.

Segments B (**6**) and C (**13**) are connected by a Wittig reaction to afford a nearly 1:1 mixture of *E*/*Z* isomers.[12] After removal of the tetrahydropyranyl ether the isomers can be separated by chromatography to yield stereochemically pure (*Z*)-**14** and (*E*)-**14** (Scheme 6). The configuration of the double bond was assigned unambiguously by NOE experiments. (*E*)-**14** can be isomerized by irradiation with light with a wavelength greater than 280 nm to give a 6:4 mixture of (*E*)-**14** and (*Z*)-**14** in a total yield of over 90%. Finally, alcohol (*Z*)-**14** is oxidized to aldehyde **15** (segment BC). The total yield is 36% (photochemical recycling not included).

Aldehyde **15** was treated with segment A in an aldol reaction to yield **16** with good selectivity, along with minor amounts of its 6,7 diastereoisomer that is removed by chromatography (Scheme 7). The addition of zinc chloride significantly improves the diastereoselectivity, which normally decreases with increasing size of residues at C6. The remaining transformations to the target molecule are well established in the total synthesis of epothilones.[27–29] Removal of the ketal group in **16** followed by persilylation generates tetrasilyl ether **17**. The primary silyl ether is removed under mild acidic conditions followed by a two-step oxidation sequence which establishes carboxylic acid **18**. Next, the benzylic alcohol is released and the crude hydroxy acid subjected to Yamaguchi cyclization conditions to generate the 16-membered macrolactone. The remaining protecting groups are removed to yield epothilone D analogue **19**. The addition of hexafluorosilicic acid significantly

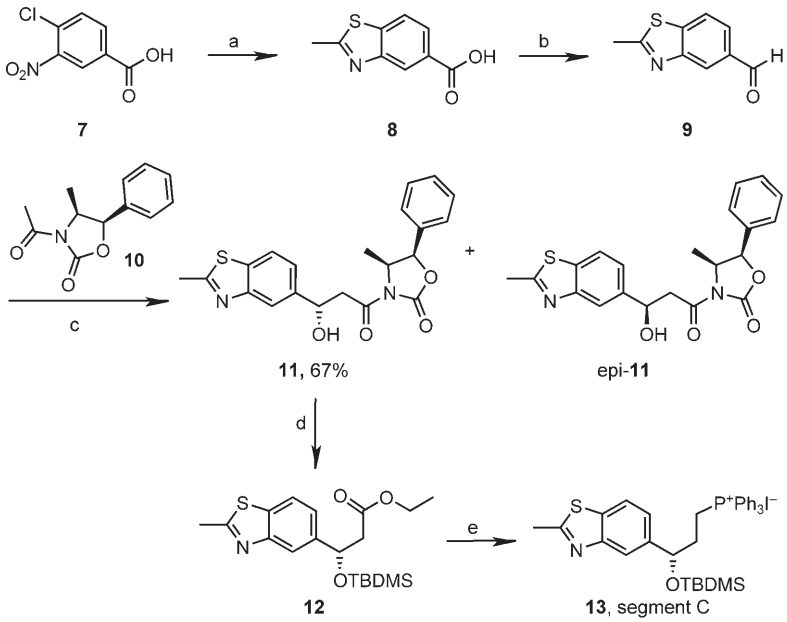

Scheme 5. Synthesis of the C13–C15 segment (segment C). Reagents and conditions: a) Na_2S, Ac_2O, HOAc, reflux, 71%; b) 1. LAH, THF, RT to reflux, 71%; 2. SO_3·pyridine, Et_3N, CH_2Cl_2/DMSO, RT, 95%; c) *n*BuLi, $ZnCl_2$, THF, −70°C; d) 1. TBDMSCl, imidazole, DMF, RT, 91%; 2. $Ti(OEt)_4$, EtOH, reflux, 91%; e) 1. DIBAH, toluene, CH_2Cl_2, −40°C, crude; 2. I_2, PPh_3, CH_2Cl_2, RT, 92%; 3. PPh_3, toluene, 100°C, 87%. TBDMS = *tert*-butyldimethylsilyl, DIBAH = diisobutylaluminum hydride.

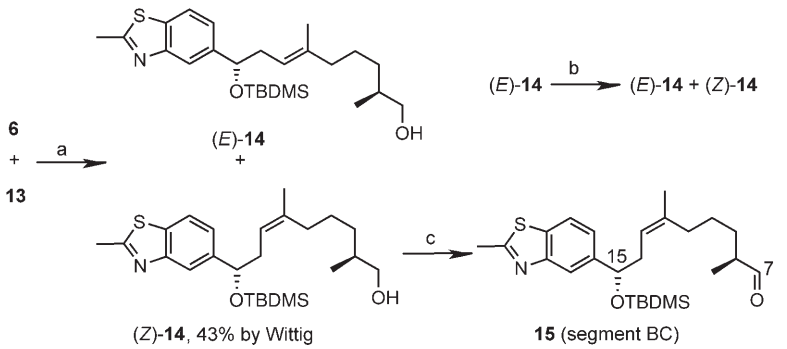

Scheme 6. Synthesis of C7–C15 segment (segment BC). Reagents and conditions: a) 1. NaHMDS, THF, 0°C to RT, 83%; 2. pTsOH (cat.), EtOH, RT, 86%; b) *hν*, toluene/acetone, RT, 92%; c) Swern oxidation, crude. HMDS = 1,1,1,3,3,3-hexamethyldisilazane.

 © 2006 Wiley-VCH Verlag GmbH & Co. KGaA, Weinheim

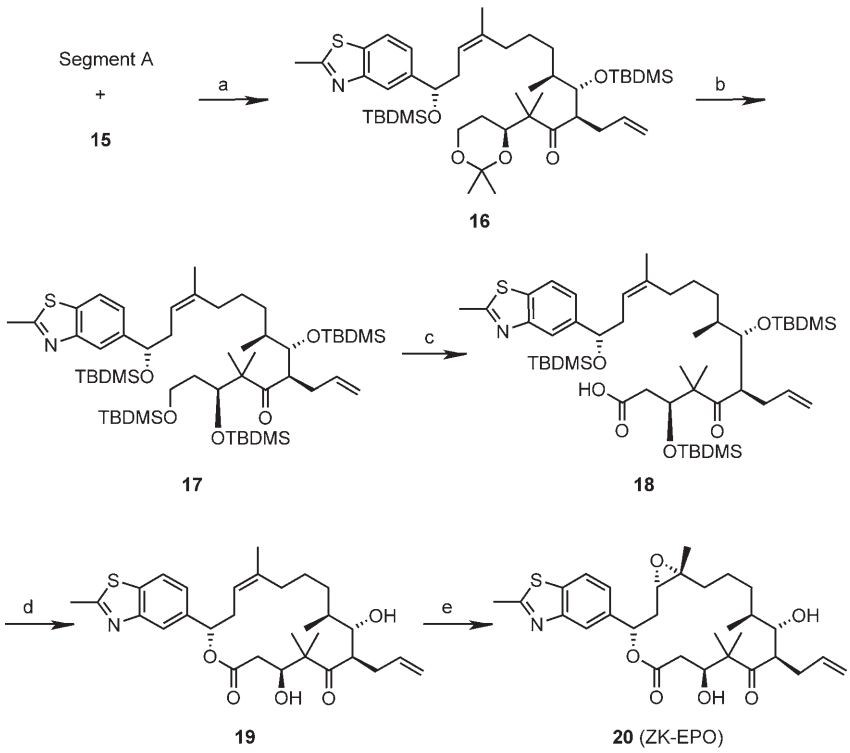

Scheme 7. Synthesis of the C1–C15 segment (segment ABC) and completion of the synthesis of ZK-EPO (**20**). Reagents and conditions: a) LDA, $ZnCl_2$, THF, −70 °C; 64 %; b) 1. pTsOH (cat.), EtOH, RT, 97 %; 2. TBDMSOTf, 2,6-lutidine, CH_2Cl_2, −70 °C to 0 °C, 96 %; c) 1. CSA, CH_2Cl_2, MeOH, RT, 80 %; 2. Swern oxidation, crude; 3. $NaOCl_2$, NaH_2PO_4, 2-methyl-2-butene, THF, H_2O, *t*BuOH, 0 °C to 15 °C, 85 %; d) 1. TBAF, THF, RT, crude; 2. Yamaguchi cyclization, 60 %; 3. HF·pyridine, hexafluorosilicic acid, THF, RT, 87 %; e) DMDO, acetone, CH_2Cl_2, −78 °C, 71 % + 10 % β-epoxide. LDA = lithium diisopropylamide, Tf = trifluoromethanesulfonyl, CSA = camphorsulfonic acid, TBAF = tetrabutylammonium fluoride, DMDO = 3,3-dimethyldioxirane.

facilitates the cleavage of both silyl ethers in terms of reaction time, yield, and insensitivity to the quality of different batches of HF·pyridine. Epoxidation of the double bond affords the α-epoxide ZK-EPO (**20**) with high stereoselectivity and in 15 % overall yield along with minor amounts of the biologically less active β-epoxide.

The longest linear sequence (C→CB→ZK-EPO) involves 22 steps and occurs in an overal yield of 0.9 %. With this synthetic route we succeeded in producing 36 g of compound, which was sufficient to perform nearly all the preclinical investigations.

The relative and absolute configuration of ZK-EPO was confirmed by X-ray analysis (Figure 1, left). It is interesting to note that the observed conformation differs considerably from that of epothilone B (Figure 1, right):[30] in ZK-EPO, both hydroxy groups as well as the epoxide are oriented towards the center of the macrocyle. A similar conformation was postulated for 14(*S*)-methyl-epothilone B, as deduced from its corresponding 14(*R*)-methyl-epothilone D analogue—the latter showing significantly reduced antiproliferative activity relative to its 14(*S*) epimer which adopts a conformation similar to epothilone B.[31] These investigations suggest that the conformation of ZK-EPO in the crystal lattice might not be the conformation adopted at the common taxane/epothilone tubulin binding site.

A panel of 20 different human tumor cell lines was exposed to different concentrations of ZK-EPO and compared with PT (Figure 2, top), doxorubicin (adriamycin ADM), cisplatin (CDDP), and camptothecin (CPT, Figure 2, bottom). The degree of growth inhibition was measured three days after initiation of drug treatment. The activity of each compound is given as a concentration that inhibits cell proliferation by 50 % (IC_{50} values). Cell lines marked in red show significant resistances to standard cytotoxic drugs. ZK-EPO proved to be highly active in all of these proliferating human tumor cell lines, irrespective of their MDR phenotype, and showed a mean IC_{50} value below 1 nM.

To determine whether ZK-EPO also influences nonproliferating nontumor cells, ZK-EPO was tested on proliferating or confluent (nonproliferating) human immortal keratinocyte HaCat cells and the results compared with those with PT.[32] The growth of proliferating HaCat cells was potently inhibited by PT and ZK-EPO while only minor effects were observed on confluent cells. This observation indicates a very low toxic potential on normal, nondividing cells.

Even modest structural modifications may have considerable effects on the recognition through MDR-related pathways; this is illustrated by comparing the antiproliferative activity in the sensitive MDR(−) human breast cancer cell line MCF-7 (PT-sensitive) with the multidrug-resistant MDR(+) cancer cell line NCI/ADR (PT-insensitive; Figure 3). Epothilone B is highly active towards the

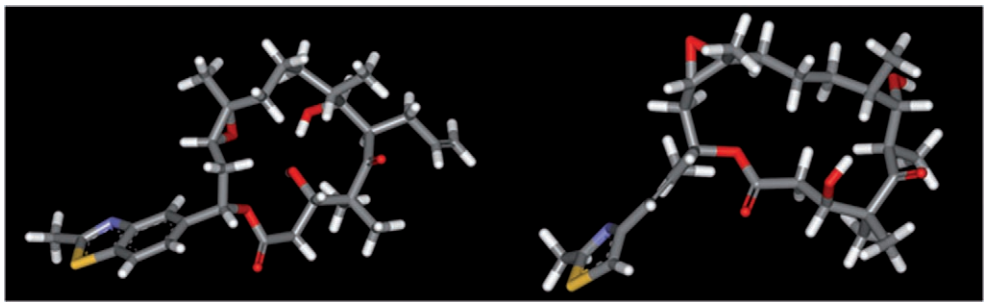

Figure 1. The absolute and relative configuration of ZK-EPO (**20**; left) and comparison with the conformation of epothilone B (right).

© 2006 Wiley-VCH Verlag GmbH & Co. KGaA, Weinheim

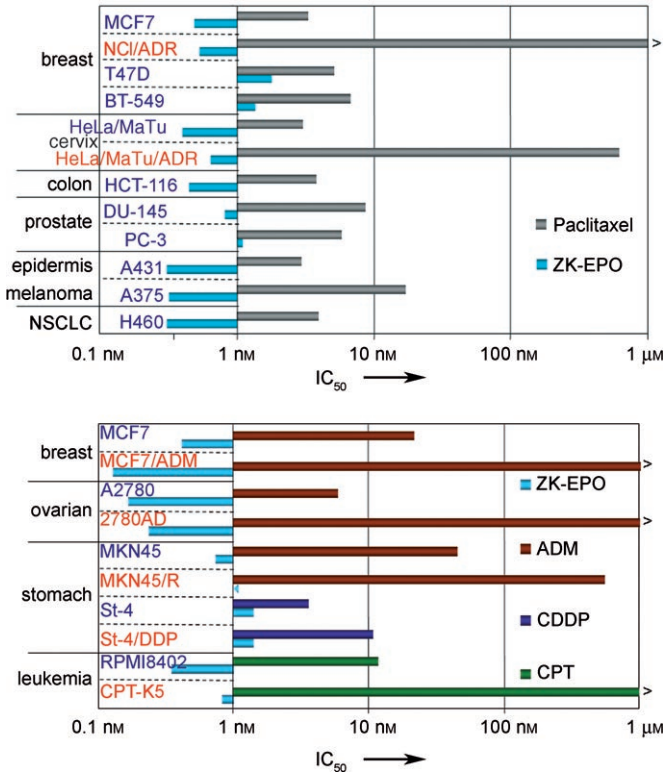

Figure 2. ZK-EPO efficiently inhibits cell proliferation of different human tumor types in vitro.

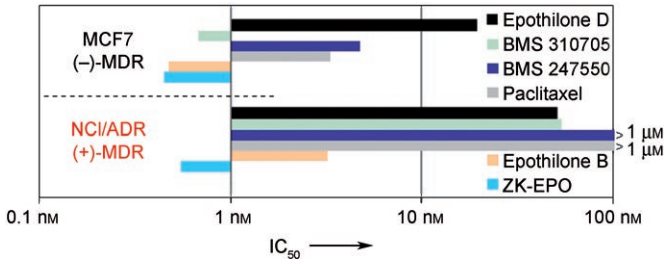

Figure 3. ZK-EPO maintains its high antiproliferative activity even in tumor cell lines overexpressing the MDR phenotype.

MDR(−) cell line and also displays considerable activity towards the MDR(+) cell line, although the activity is reduced about tenfold. If the lactone is replaced by a lactam moiety (for example, in BMS247550[33,34]), the activity at the MDR(−) cell line is significantly reduced and is nearly lost with the MDR(+) cell line, thus resulting in a PT-like profile. Replacement of the methyl group on the thiazole ring in the side chain of epothilone B by an aminomethylene group (for example, as in BMS310705[35]) generates a compound that shows nearly the same activity towards the MDR(−) cell line as epothilone B, but the activity towards the MDR(+) cell line is reduced about 100-fold. The natural product epothilone D possesses comparable activity in both cell lines, but with a significantly reduced overall activity.[36] ZK-EPO, however, maintains its high activity also towards the MDR(+) cell line. This finding is an indication that, in contrast to other epothilones or PT, ZK-EPO is not exported by the p-gp.

In the next experiment we tested whether ZK-EPO or epothilone B are still recognized by efflux mechanisms. The action of verapamil on drug accumulation in cells is often used to show that the efflux is mediated by the MDR1 p-gp. Thus, 10 μM verapamil was added together with paclitaxel, epothilone B, or ZK-EPO to NCI/ADR cells and the cellular growth estimated after three days of exposure. As expected, verapamil renders NCI/ADR cells responsive to growth inhibition by 100 nM PT. Furthermore, verapamil decreases the IC_{50} value for growth inhibition by epothilone B from 2.4 to 0.3 nM, but does not further enhance the potent antiproliferative effects of ZK-EPO on p-gp that overexpress NCI/ADR cells.[32] These data further indicate that ZK-EPO is not recognized by cellular efflux pumps such as p-gp.

The following examples demonstrate that the activity seen in vitro also translate into in vivo models. Human cervix cancer cells (HeLa/MaTu) from large cervix tumors were xenotransplanted into nude mice. The growth of these HeLa/MaTu cervix tumors could be efficiently inhibited by treatment with PT (12 $mg\,kg^{-1}$ once daily for 5 consecutive days; data not shown). A single treatment with ZK-EPO resulted in an almost complete inhibition of tumor growth whereas the untreated control showed rapid growth (Figure 4, top). Treatment with ZK-EPO resulted in a dose-dependent inhibition of the tumor growth. Response was seen at all doses after one initial treatment. Further tumor growth was completely inhibited at a dose of 8 $mg\,kg^{-1}$. At the highest dose level (8 $mg\,kg^{-1}$, application at days 6 and 25) the compound was well tolerated, as demonstrated by a modest reduction in body weight (about 5%) and a time to recover of less than seven days (Figure 4, bottom).

In the multidrug-resistant HeLa/MaTu/ADR cervix cancer model PT did not show an antitumor effect, while treatment with ZK-EPO resulted in an almost complete inhibition of tumor growth, whereas the untreated control showed rapid growth (Figure 5, left). A single application of 6 $mg\,kg^{-1}$ of ZK-EPO resulted in a complete regression in 50% of these highly resistant tumors. A second dose was not given in this experiment to determine the time to progression. Severe toxic side effects were not observed with these treatment schedules.

The models discussed are selected from tumor indications suitable for chemotherapy and include breast, ovarian, small cell lung, non-small cell lung, prostate, and colorectal cancers. ZK-EPO shows high efficacy in all these tumor types, including both MDR-negative and MDR-positive tumors.[37]

In addition, ZK-EPO displays high efficacy in tumor types normally not sensitive to chemotherapy. Among these tumor types are pancreatic, cholangio, renal cell, and hepatocellular cancers, melanoma, and brain tumors. An example of a melanoma cancer model demonstrating the high efficacy of ZK-EPO is depicted in Figure 5 (right).

Our preclinical data indicate that ZK-EPO exhibits a more potent antitumor activity than taxanes (for example, paclitaxel) and second-generation epothilones such as ixabepilone (BMS247550). ZK-EPO eludes the cellular efflux pumps normally responsible for MDR and has activity against both taxane-resistant and taxane-sensitive tumor models. ZK-EPO uptake may be unaffected by MDR-pump activity, thus

 © 2006 Wiley-VCH Verlag GmbH & Co. KGaA, Weinheim

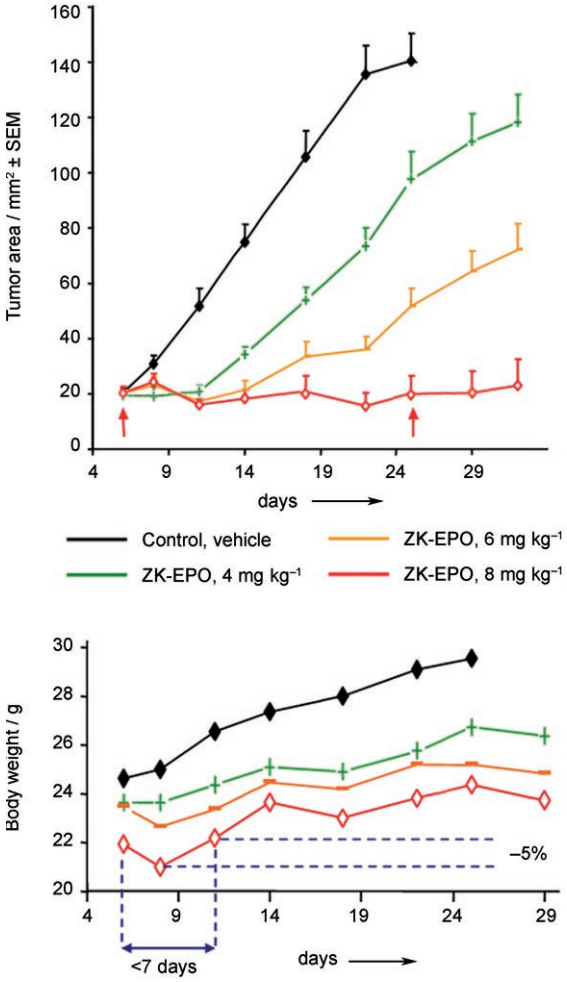

Figure 4. Therapeutic effect of ZK-EPO in nude mice bearing human cervix xenografts HeLa/MATU after intravenous injection. Changes in tumor area over time are shown (top). Evaluation of body weight as a parameter for drug-related toxicity during treatment with ZK-EPO. During the treatment period the body weight is measured twice weekly. The change in body weight over time is shown (bottom). The red arrows indicate when ZK-EPO was administered.

suggesting efficient maintenance within tumor cells. Therefore, ZK-EPO may be clinically effective as a first-line therapy that delays or prevents MDR-based resistance.

Following successful phase I clinical trials,[38] the potential of ZK-EPO in the treatment of different human tumors is now beeing evaluated in an extensive phase II clinical trials program.

Received: July 13, 2006
Published online: September 27, 2006

Keywords: clinical development · epothilones · natural products · total synthesis

[1] D. M. Bollag, P. A. McQueeney, J. Zhu, O. Hensens, L. Koupal, J. Liesch, M. Goetz, E. Lazarides, C. M. Woods, *Cancer Res.* **1995**, *55*, 2325.
[2] T.-C. Chou, X.-G. Zhang, A. Balog, D.-S. Su, D. Meng, K. Savin, J. R. Bertino, S. J. Danishefsky, *Proc. Natl. Acad. Sci. USA* **1998**, *95*, 9642.
[3] T.-C. Chou, X.-G. Zhang, C. R. Harris, S. D. Kuduk, A. Balog, K. Savin, J. R. Bertino, S. J. Danishefsky, *Proc. Natl. Acad. Sci. USA* **1998**, *95*, 15798.
[4] L. Sepp-Lorenzino, A. Balog, D.-S. Su, D. Meng, N. Timaul, H. I. Scher, S. J. , Danishefsky, N. Rosen, *Prostate Cancer Prostatic Dis.* **1999**, *2*, 41.
[5] R. Christina, C. R. Harris, S. J. Danishefsky, *J. Org. Chem.* **1999**, *64*, 8434.
[6] K. Gerth, N. Bedorf, G. Höfle, H. Irschik, H. Reichenbach, *J. Antibiot.* **1996**, *49*, 560.
[7] G. Höfle, N. Bedorf, H. Steinmetz, D. Schomburg, K. Gerth, H. Reichenbach, *Angew. Chem.* **1996**, *108*, 1671; *Angew. Chem. Int. Ed. Engl.* **1996**, *35*, 1567.
[8] G. Hoefle, N. Bedorf, K. Gerth, H. Reichenbach (GBF), DE 4138042 C2, **1993**.
[9] A. Balog, D. Meng, T. Kamenecka, P. Bertinato, D.-S. Su, E. J. Sorensen, S. J. Danishefsky, *Angew. Chem.* **1996**, *108*, 2976; *Angew. Chem. Int. Ed. Engl.* **1996**, *35*, 2801.
[10] K. C. Nicolaou, Y. He, D. Vourloumis, H. Vallberg, Z. Yang, *Angew. Chem.* **1997**, *109*, 170; *Angew. Chem. Int. Ed. Engl.* **1997**, *36*, 166.

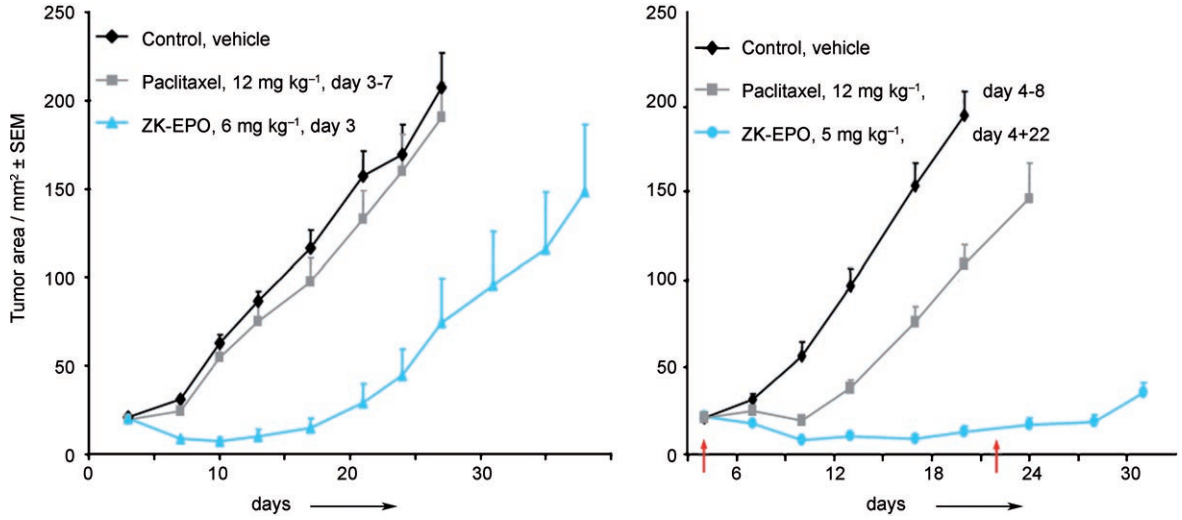

Figure 5. Tumor-inhibiting effect of ZK-EPO and PT in the human multidrug-resistant HeLa/MaTu/ADR cervix tumor (left) and A-375 melanoma (right) xenograft models in nude mice after intravenous injection. The red arrows indicate when ZK-EPO was administered.

 © 2006 Wiley-VCH Verlag GmbH & Co. KGaA, Weinheim

[11] D. Schinzer, A. Limberg, A. Bauer, O. M. Böhm, M. Cordes, *Angew. Chem.* **1997**, *109*, 543; *Angew. Chem. Int. Ed. Engl.* **1997**, *36*, 523.
[12] K. C. Nicolaou, S. Ninkovic, F. Sarabia, D. Vourloumis, Y. He, H. Vallberg, M. R. V. Finlay, Z. Yang, *J. Am. Chem. Soc.* **1997**, *119*, 7974.
[13] D. Meng, P. Bertinato, A. Balog, D.-S. Su, T. Kamenecka, E. J. Sorensen, S. J. Danishefsky, *J. Am. Chem. Soc.* **1997**, *119*, 10073.
[14] D. Schinzer, A. Bauer, J. Schieber, *Chem. Eur. J.* **1999**, *5*, 2492.
[15] E. J. Sorensen, S. J. Danishefsky, Y.-H. Zheng, T.-C. Chou, L. He, S. B. Horwitz, *J. Am. Chem. Soc.* **1997**, *119*, 2733.
[16] R. B. Lichtner, A. Rotgeri, T. Bunte, B. Buchmann, J. Hoffmann, W. Schwede, W. Skuballa, U. Klar, *Proc. Natl. Acad. Sci. USA* **2001**, *98*, 11743.
[17] In parallel, colleagues from Novartis had also replaced the side chain at C15 with bicyclic heteroaromatic groups: K.-H. Altmann, G. Bold, G. Caravatti, A. Flörsheimer, V. Guagnano, M. Wartmann, *Bioorg. Med. Chem. Lett.* **2000**, *10*, 2765.
[18] Since the IUPAC nomenclature of epothilone D is completely different from epothilone B we prefer to use the numbering depicted in Scheme 2 throughout the following discussions.
[19] "Synthesis and biological activity of epothilones": U. Klar, W. Skuballa, B. Buchmann, W. Schwede, T. Bunte, J. Hoffmann, R. B. Lichtner in *Anticancer Agents. Frontiers in Cancer Chemotherapy* (Eds.: I. Ojima, G. D. Vite, K.-H. Altmann), Oxford University Press, New York, **2001**, pp. 131–147.
[20] Compounds that inhibit the proliferation of tumor cells by 50% at concentrations below 100 nM are defined as active.
[21] Three other epothilones have been investigated in early clinical studies (phase I): Kos-1584 (Kosan/Roche), ABJ879 (Novartis), BMS310705 (BMS).
[22] J. M. G. Larkin, S. B. Kaye, *Expert Opin. Invest. Drugs* **2006**, *15*, 691–702.
[23] U. Klar, B. Röhr, F. Kuczynski, W. Schwede, M. Berger, W. Skuballa, B. Buchmann, *Synthesis* **2005**, 301.
[24] J. Wu, K. Mori, *Agric. Biol. Chem.* **1991**, *55*, 2667.
[25] G. Fouquet, M. Schlosser, *Angew. Chem.* **1974**, *86*, 50; *Angew. Chem. Int. Ed. Engl.* **1974**, *13*, 82.
[26] Only stereochemically homogeneous material obtained from the direct crystallization was used in the calculation. Additional product can be obtained from the mother liquor.
[27] E. Watkins, A. G. Chittiboyina, J.-C. Jung, M. A. Avery, *Curr. Pharm. Des.* **2005**, *11*, 1615.
[28] K.-H. Altmann, *Org. Biomol. Chem.* **2004**, *2*, 2137.
[29] R. Zhang, Z. Liu, *Curr. Org. Chem.* **2004**, *8*, 267.
[30] G. Höfle, N. Bedorf, H. Steinmetz, D. Schomburg, K. Gerth, H. Reichenbach, *Angew. Chem.* **1996**, *108*, 1671; *Angew. Chem. Int. Ed. Engl.* **1996**, *35*, 1567.
[31] R. E. Taylor, Y. Chen, A. Beatty, D. C. Myles, Y. Zhou, *J. Am. Chem. Soc.* **2003**, *125*, 26.
[32] See supporting information.
[33] F. Y. F. Lee, R. Borzilleri, C. R. Fairchild, S.-H. Kim, B. H. Long, C. Reventos-Suarez, G. D. Vite, W. C. Rose, R. A. Kramer, *Clin. Cancer Res.* **2001**, *7*, 1429.
[34] R. M. Borzilleri, X. Zheng, R. J. Schmidt, J. A. Johnson, S.-H. Kim, J. D. DiMarco, C. R. Fairchild, J. Z. Gougoutas, F. Y. Lee, B. H. Long, G. D. Vite, *J. Am. Chem. Soc.* **2000**, *122*, 8890.
[35] R. M. Borzilleri G. D. Vite, *Drugs Future* **2002**, *27*, 1149.
[36] K.-H. Altmann, M. Wartmann, T. O'Reilly, *Biochim. Biophys. Acta* **2000**, *1470*, M79.
[37] J. Hoffmann, B. Buchmann, W. Schwede, W. Skuballa, R.B. Lichtner, G. Siemeister, S. Hammer, K. Mittelstaedt, S. Winsel, J. Eschenbrenner, C. Demarche, U. Klar, unpublished results.
[38] The first clinical data for ZK-EPO were presented at the 41st Annual Meeting of the American Society of Clinical Oncology (ASCO) in spring 2005.

 © 2006 Wiley-VCH Verlag GmbH & Co. KGaA, Weinheim

Macrocycle Synthesis

DOI: 10.1002/anie.200603013

Molecular Waterwheel (Noria) from a Simple Condensation of Resorcinol and an Alkanedial**

*Hiroto Kudo, Rieko Hayashi, Kouji Mitani, Tsutomu Yokozawa, Noriko C. Kasuga, and Tadatomi Nishikubo**

The condensation reaction of phenols with aldehydes to afford bakelite was developed by Baekland in 1907,[1] and since then many papers and patents dealing with the synthesis and applications of phenolic resins have been reported.[2] About 40 years after the first report, it was found that oligomers could be similarly synthesized by reactions of phenols with formaldehydes.[3] Early structural studies[4] were brought to a successful conclusion more than 30 years later, when Erdtman, Gutsche, and their co-workers proved the oligomers to be large cyclic compounds by means of single-crystal X-ray analyses, and named them calixarenes.[5] Many applications of calixarenes have been reported in the field of host–guest chemistry.[6] Although the synthetic strategies for calixarenes have not basically changed since 1940, Gutsche et al. recently showed that dynamic covalent chemistry (DCC) systems could afford these compounds in high yield.[7] Furthermore, macromolecular capsule compounds, cavitands, and carcerands have been derived from calixarenes.[8]

Herein, we present the condensation reaction of resorcinol, as a difunctional compound, with 1,5-pentanedial $[(CH_2)_n(CHO)_2]$ $(n=3)$, as a tetrafunctional compound, by using a similar approach to that employed for the synthesis of calixarenes to give a unique double-cyclic ladder-type oligomer with a central hole which resembles a waterwheel in structure (Scheme 1).

The reaction of resorcinol (2.2 g, 20 mmol) and 1,5-pentanedial (0.50 g, 5 mmol) was carried out in ethanol (4.5 mL) at 80 °C in the presence of concentrated HCl

[*] Dr. H. Kudo, R. Hayashi, K. Mitani, Dr. T. Yokozawa, Dr. T. Nishikubo
Department of Material and Life Chemistry
Faculty of Engineering
Kanagawa University
3-27-1, Rokkakubashi, Kanagawa-ku, Yokohama, 221-8686 (Japan)
Fax: (+81) 45-413-9770
E-mail: nishikubot@kanagawa-u.ac.jp
Dr. N. C. Kasuga
Department of Chemistry
Faculty of Science
Kanagawa University
Tsuchiya, Hiratsuka, Kanagawa, 259-1293 (Japan)

[**] Support of this work by a Grant-in-Aid for Scientific Research, in Japan (no. 18681015) from the ministry of Education, Culture, Sports, Science, and Technology is gratefully acknowledged. Noria is Latin for waterwheel.

Supporting information for this article is available on the WWW under http://www.angewandte.org or from the author.

WILEY InterScience DISCOVER SOMETHING GREAT
© 2006 Wiley-VCH Verlag GmbH & Co. KGaA, Weinheim

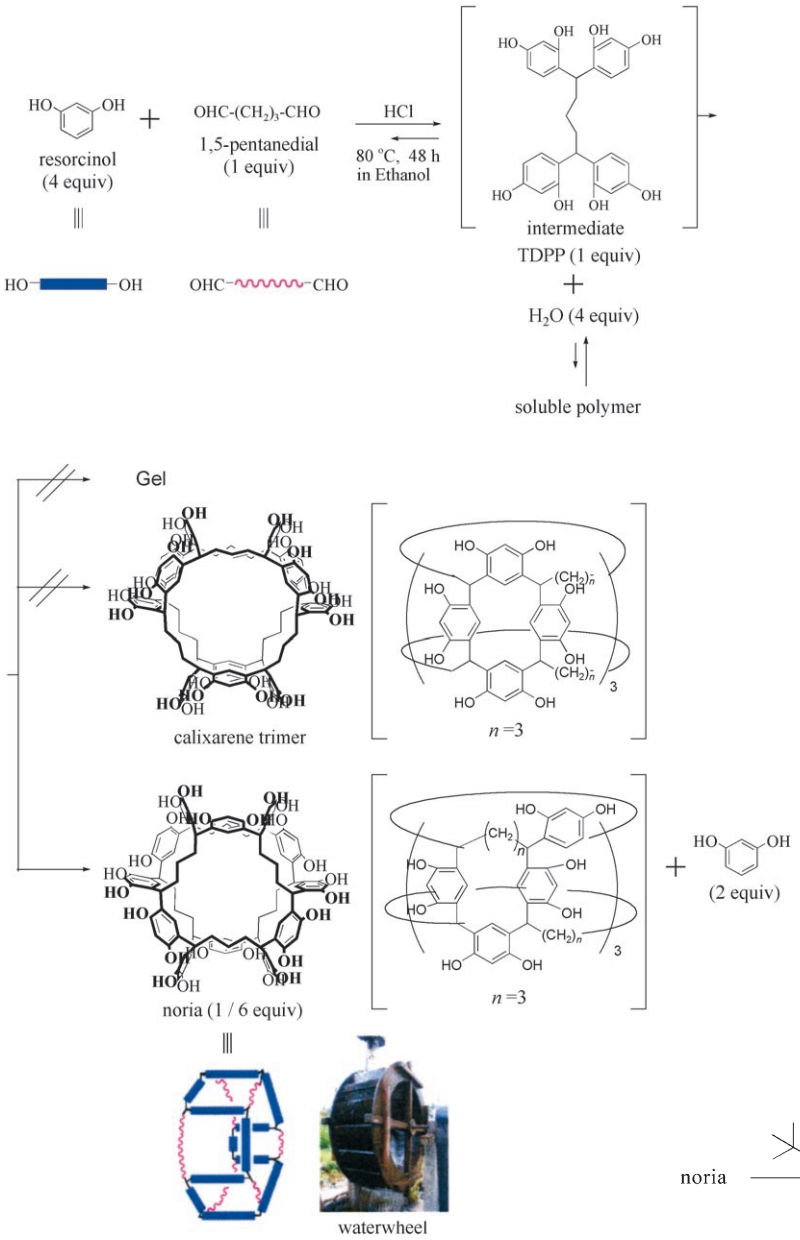

Scheme 1. The reaction of resorcinol with 1,5-pentanedial.

(3.0 mL). The initially homogenous reaction mixture afforded an insoluble product after 48 h. The reaction mixture was poured into methanol, and the precipitated product was washed with diethyl ether several times, then dried in vacuo at 60 °C for 12 h. The product (0.94 g) was soluble in aprotic, highly polar solvents, such as dimethylformamide (DMF), dimethylsulfoxide (DMSO), dimethylacetamide (DMAC), and 1-methyl-2-pyrrolidinone (NMP). The ^{1}H NMR spectrum showed that the product contained aromatic, methine, and methylene protons. The ratio of the units derived from resorcinol and 1,5-pentanedial was calculated to be 2:1 from the ratios of the signal integrals in the ^{1}H NMR spectrum. Furthermore, the MALDI-TOF mass spectrum of this product after doping with Na^+ ions showed parent ion signals at *m*/*z* 1705.86 and 1727.63, which correspond to the mass of a cyclic oligomer obtained by the condensation of two equivalents of resorcinol with one equivalent of 1,5-pentanedial, as shown in Scheme 1. It should be noted that only a soluble, large cyclic molecule was obtained, and there was no gel formation under the optimized conditions. On the basis of these data, we speculated that the product consisted of a calixarene-like trimer, as shown in Scheme 1.

We next determined the structure of this cyclic oligomer by single-crystal X-ray analysis. To increase the solubility, all the hydroxy groups were converted into *tert*-butoxycarbonyloxy groups by reaction with di-*tert*-butyl dicarbonate (Scheme 2).

A single platelike crystal of this derivative was obtained by recrystallization from chloroform/hexane. Surprisingly, the X-ray analysis showed that this derivative is not a calixarene trimer, but a double-cyclic ladder oligomer, in which each ring consists of alternating resorcinol and methylene units, and the two rings are connected through six resorcinol units (Figure 1).[9] It has 24 hydroxy groups, 6 cavities in the side, and a large hydrophobic hole through the center of the molecule, thus resembling a waterwheel in appearance (Scheme 1). We named it noria, which means waterwheel in Latin. It is noteworthy that such a complicated three-dimensional molecule was synthesized in one pot in high yield (83 %).

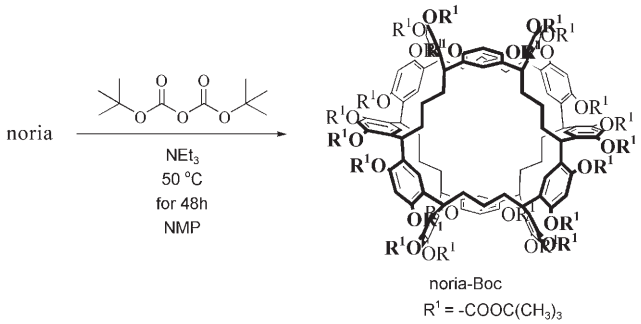

Scheme 2. The reaction of noria and di-*tert*-butyl dicarbonate.

The reaction conditions for the synthesis of the waterwheel-like product were examined by using various feed molar ratios of resorcinol and 1,5-pentanedial at temperatures between 0 and 80 °C. The amount of gel product decreased with increasing reaction temperature. The reaction at 0 °C for 24 h at a resorcinol/1,5-pentanedial feed ratio of 2/1 afforded the gel product in quantitative yield, while at 25, 40, and 60 °C the yields of gel decreased to 70, 52, and 12 %, respectively. At 80 °C, no gel was obtained and only noria was obtained in 7 % yield. No other product, such as polymer or oligomer, was produced, and starting materials were recovered under these reaction conditions.

 © 2006 Wiley-VCH Verlag GmbH & Co. KGaA, Weinheim

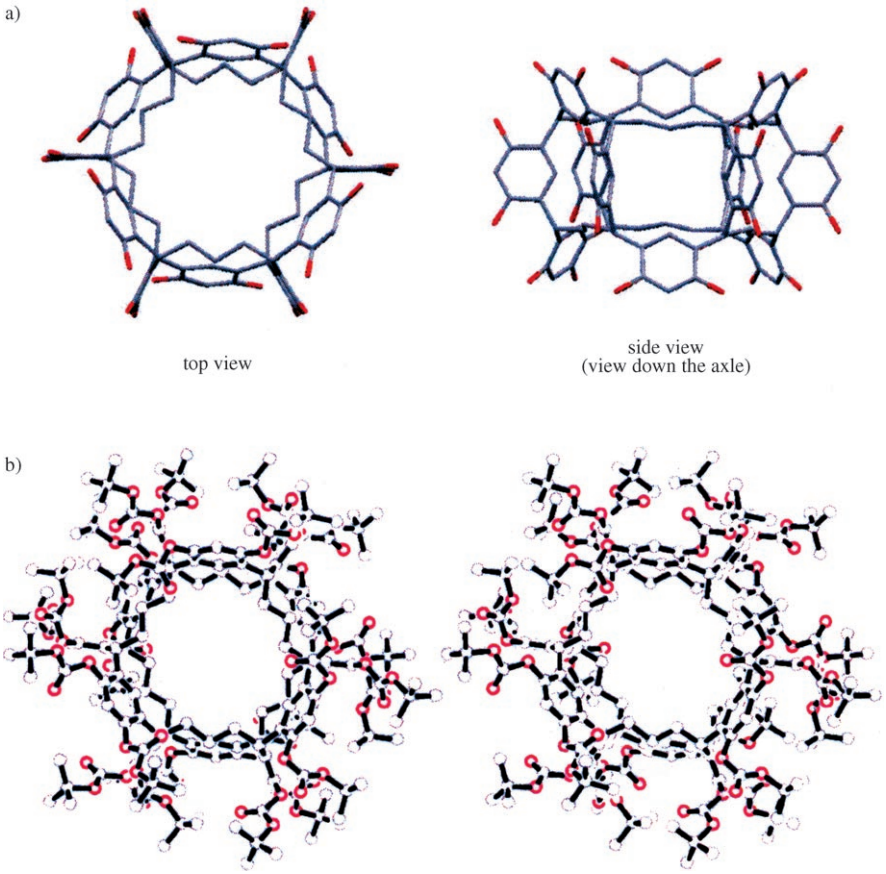

Figure 1. a) Top view and side view of synthetic noria. b) Stereoview of noria-Boc in the crystal. Boc = *tert*-butoxycarbonyl.

Resorcinol/1,5-pentanedial feed ratios of 2.6/1, 5/1, 6.8/1, and 10/1 at 80 °C afforded noria in yields of 56, 81, 76, and 68 %, respectively. Finally, we found that the use of a 4/1 ratio of resorcinol/1,5-pentanedial at 80 °C for 48 h afforded the highest yield of noria (83 %), with no gel formation.

To examine the mechanism of the reaction leading to noria, we examined the size-exclusion chromatography (SEC) profiles of the obtained products over time (Figure 2). After 5 minutes, peaks of polymer and oligomer were observed with retention times of 28 and 24 minutes, respectively. A decrease in the molecular weight of the polymer and an increase in the amount of noria were subsequently observed as the reaction time was increased. The retention time of the oligomer remained at 24 minutes for all the reaction times. This reaction behavior indicates that noria was constructed by a reversible reaction between polymer, oligomer, resorcinol, and 1,5-pentanedial. The oligomer with the retention time of 24 minutes appeared to be the key compound leading to noria.

This product was separated by column chromatography on silica gel, and was determined to be 1,1,5,5-tetra(2,4-dihydroxyphenyl)pentane (TDPP), which would have been formed by the condensation reaction of four equivalents of resorcinol with 1,5-pentanedial.

When TDPP was heated at 80 °C for 48 h in ethanol containing concentrated HCl noria was obtained in quantitative yield, accompanied by the formation of resorcinol. These results suggest that TDPP was formed by a reversible reaction between polymer, resorcinol, and 1,5-pentanedial, followed by the elimination reaction of resorcinol with TDPP in the presence of HCl as a catalyst to produce 1/6 equivalent of noria under complete thermodynamic control. That is, the condensation reaction for the synthesis of noria is related to the DCC system.[10] These reactions were accompanied by the formation of four equivalents of H_2O and two equivalents of resorcinol. This finding is consistent with the observation that noria was obtained in the highest yield at a resorcinol/1,5-pentanedial molar ratio of 4/1.

The structure of noria is similar to those of cavitands and carcerands, which are cyclic oligomers obtained from calixarenes through multiple synthetic steps. Therefore, noria, with its large central cavity, is expected to be useful as a new functional material in the field of host–guest chemistry. Several calixarene derivatives containing additional carboxylic ester moieties, such as a *para-tert*-butylcalix[8]arene derivative (BCA-COOEt) and a calix[4]resorcinarene derivative (CRA-COOEt), have been synthesized and their properties examined in solvent extraction experiments.[11] We therefore synthesized a noria derivative (noria-COOEt) containing carboxylic ester moieties by the reaction of noria with ethyl bromoacetate in the presence of potassium carbonate in NMP (Scheme 3).

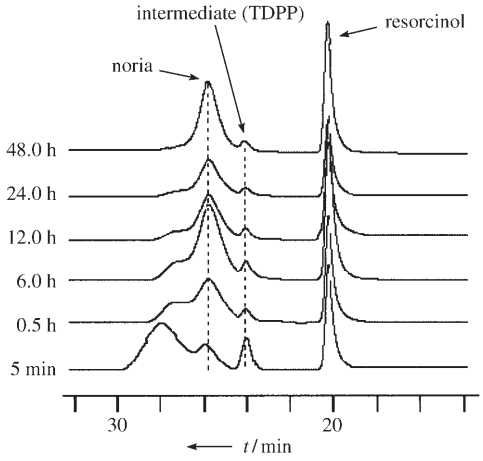

Figure 2. SEC profiles of the products obtained by the reaction of resorcinol (20 mmol) and 1,5-pentanedial (5 mmol) in the presence of conc. HCl (3 mL) in ethanol (4 × 5 mL) at 80 °C.

Its application in the liquid–liquid extraction of alkali metal cations were examined using picrate salts in water and dichloromethane. The results are summarized, together with those for BCA-COOEt and CRA-COOEt, in Table 1.[12]

The remarkable selectivity of BCA-COOEt suggests that the six oxygen atoms of pendant carbonyl groups of BCA-

 © 2006 Wiley-VCH Verlag GmbH & Co. KGaA, Weinheim

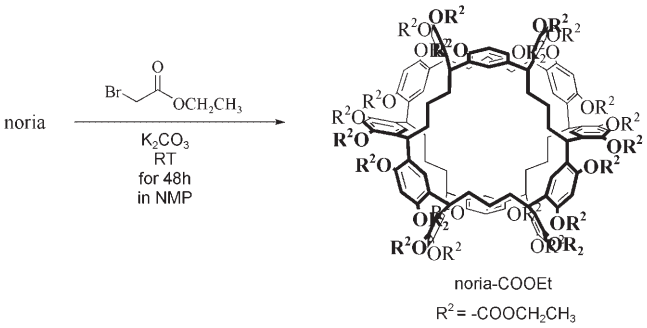

Scheme 3. The reaction of noria and ethyl bromoacetate.

Table 1: Extraction of picrate salts with calixarene derivatives (BCA-COOEt, CRA-COOEt) and noria derivative (noria-COOEt).[a]

Ligand	Na^+ 2.04 Å[b]	K^+ 2.76 Å[b]	Rb^+ 2.98 Å[b]	Cs^+ 3.40 Å[b]
CRA[4]-COOEt	< 1	< 1	< 1	< 1
BCA[8]-COOEt	4.5	21.5	16.8	15.6
noria-COOEt	< 1	< 1	23.8	4.7

[a] Percentage cation extraction from an aqueous neutral alkali solution (2.5×10^{-4} mol dm^{-3}) into dichloromethane by the host (CRA[4]-COOEt, BCA[8]-COOEt, noria-COOEt; 2.5×10^{-4} mol dm^{-3}) at 25 °C. [b] Ionic diameter; see Reference [13].

COOEt can enclose metal ions within a sphere because of the rigid structure of the molecule. However, CRA-COOEt showed no significant ability to extract the metal ions, presumably because of its flexible structure. Noria-COOEt showed excellent selectivity for Rb^+ ions: the Rb^+ ion may be enclosed within the central hole of the molecule through interaction with the six oxygen atoms of the carbonyl groups.

In summary, we have synthesized in high yield a unique double-cyclic oligomer with ladderlike links between the two rings that resembles a waterwheel. This approach represents a new application of DCC. Single-crystal X-ray analysis of a derivative of this molecule, termed noria, confirmed it had a double-cyclic ladderlike structure with 24 hydroxy groups, 6 cavities in the side, and a large hydrophobic central hole. This molecule showed high selectivity for the complexation of a Rb^+ ion, which was presumably enclosed in the central hole in the molecule. We are currently examining the synthesis of other cyclic oligomers by using α,ω-dialdehydes.

Experimental Section

Synthesis of noria: A mixture of resorcinol (20 mmol) and 1,5-pentanedial (4.0 mmol) in ethanol was stirred at 80 °C for 48 h in the presence of conc. HCl (3.0 mL), then poured into a large amount of methanol to precipitate a white solid. The solid was washed with diethyl ether several times and dried in vacuo at 60 °C for 12 h. Yield 83 % (0.94 g). IR (film): $\tilde{\nu}=3406$ (νO–H), 2931 (νC–H), 1621, 1505, and 1436 cm^{-1} (νC=C aromatic). ^{1}H NMR (600 MHz, [D$_6$]DMSO, tetramethylsilane): $\delta=0.86$–2.35 (m, 36H, -$CH_2CH_2CH_2$-), 3.98–4.22 (m, 12H, > CH-), 6.09–7.42 (m, 24H, Ar-H), 8.65–9.56 ppm (m, 24H, OH); MALDI-TOF-MS: m/z $[M+H]^+$ calcd for ($C_{102}H_{96}O_{24}$+H): 1705.63, found: 1705.86; MALDI-TOF-MS: m/z $[M+Na]^+$ calcd for ($C_{102}H_{968}O_{24}$+Na): 1727.86, found: 1727.63.

Liquid–liquid extraction of alkali-metal cations: A mixture of solution (4.0 mL) of the noria-COOEt (2.5×10^{-4} mol dm^{-3}) in dichloromethane and an aqueous solution (4.0 mL) of a metal picrate (2.5×10^{-4} mol dm^{-3}) was stirred at 25 °C for 24 h and then allowed to stand for 1 h. The aqueous phase was examined by UV/Vis spectroscopy. The extraction ratio was calculated from the decrease in the intensity of the peak at $\lambda_{max}=355$ nm.

The experimental procedures, ^{1}H, ^{13}C NMR, and IR spectroscopic analysis, MS data, and elemental analysis data of the noria derivative (noria-BOC, noria-COOEt), TDPP, and metal picrates are described in the Supportng Information.

Received: July 26, 2006
Published online: November 9, 2006

Keywords: condensation reaction · dynamic covalent chemistry · inclusion compounds · macrocycles · resorcinol

[1] L. H. Baekland, *J. Ind. Eng. Chem.* **1911**, *3*, 932.
[2] For example; C. C. Lin, *Ind. Eng. Chem. Res.* **2002**, *41*, 1986.
[3] a) J. B. Niederl, H. J. Vogel, *J. Am. Chem. Soc.* **1940**, *62*, 2512; b) A. Zinke, E. Ziegler, *Ber. Dtsch. Chem. Ges. B* **1941**, *74*, 1729.
[4] a) A. Zinke, R. Kretz, E. Legewie, K. Hossinger, *Monatsh. Chem.* **1952**, *83*, 1213; b) J. W. Cornforth, H. P. D'Arcy, G. A. Nicholls, R. J. W. Rees, J. Stock, *Br. J. Pharmacol.* **1955**, *10*, 73; c) B. T. Hayes, R. F. Hunter, *Chem. Ind.* **1956**, 193; d) B. T. Hayes, R. F. Hunter, *J. Appl. Chem.* **1958**, *8*, 743.
[5] a) H. Ertdman, S. Hogberg, S. Abrahamsson, B. Nilsson, *Tetrahedron Lett.* **1968**, 1679; b) C. D. Gutsche, B. Dhawan, K. H. No, R. Muthukrishnan, *J. Am. Chem. Soc.* **1981**, *103*, 3782; c) C. D. Gutsche, *Calixarenes*, *Monographs in Supramolecular Chemistry*, *Vol. 1* (Ed.: J. F. Stoddart), Royal Society of Chemistry, Cambridge, **1989**.
[6] For example: C. D. Gutsche, *Calixarenes*, Royal Society of Chemistry, Cambridge, **1989**.
[7] C. D. Gutsche, D. E. Johnston, Jr., D. R. Stewart, *J. Org. Chem.* **1999**, *64*, 3747.
[8] a) D. J. Cram, *Science* **1983**, *219*, 1177; b) for example: A. Jasat, J. Sherman, *Chem. Rev.* **1999**, *99*, 931; c) for example: P. Timmerman, W. Verboom, N. Reinhoudt, *Tetrahedron* **1996**, *52*, 2663; d) for example: R. Hooley, S. Biros, J. Rebek, *Angew. Chem.* **2006**, *45*, 3597; *Angew. Chem. Int. Ed.* **2006**, *45*, 3517.
[9] X-ray data for the noria derivative (noria-Boc·$CHCl_3$·H_2O·C_6H_{14}) ($C_{229}H_{305}O_{73}Cl_3$, $M_r=4332.23$): $0.35\times0.20\times0.05$ mm, colorless plate, space group $P\bar{1}$(no. 2), $a=17.4163(8)$, $b=19.589(1)$, $c=20.0063(9)$ Å, $\alpha=107.992(3)$, $\beta=106.857(3)$, $\gamma=94.700(3)$°, $V=6101.6(6)$ Å^3, $Z=1$, $\rho_{calcd}=1.18$ mg m^{-3}, $F(000)=2312$, radiation: $Cu_{K\alpha}=1.5418$ Å, $T=93$ K, reflections collected/unique 100073/21803 ($R_{int}=0.0065$). Coordinates and anisotropic thermal parameters of non-hydrogen atoms except solvated molecules were refined. Hydrogen atoms were positioned geometrically. $R_1=0.1097$, $wR_2=0.3067$, GOF = 1.049. CCDC-279300 contains the supplementary crystallographic data for this paper. These data can be obtained free of charge from The Cambridge Crystallographic Data Centre via www.ccdc.cam.ac.uk/data_request/cif. Elemental analysis data for (noria−Boc+$CHCl_3$+hexane) calcd for $C_{229}H_{303}O_{72}Cl_3$: C 63.70, H 7.02; found: C 63.96, H 7.14.
[10] Reviews: a) S. J. Rowan, S. J. Cantrill, G. R. L. Cousin, J. K. M. Sanders, J. F. Stoddart, *Angew. Chem.* **2002**, *114*, 938; *Angew. Chem. Int. Ed.* **2002**, *41*, 898; Erratum: S. J. Rowan, S. J. Cantrill, G. R. L. Cousin, J. K. M. Sanders, J. F. Stoddart, *Angew. Chem.* **2002**, *114*, 1528; *Angew. Chem. Int. Ed.* **2002**, *41*, 1460; b) O. Ramstrom, T. Bunyapaiboonsri, S. Lohmann, J.-M. Lehn, *Biochim. Biophys. Acta* **2002**, *1572*, 178.

 © 2006 Wiley-VCH Verlag GmbH & Co. KGaA, Weinheim

[11] a) S. K. Chang, I. Cho, *J. Chem. Soc. Perkin Trans. 1* **1986**, 211; b) P. M. Marcos, S. Felix, J. R. Asceno, M. A. P. Segurado, J. L. C. Pereira, P. K. Parsa, V. H. Bruder, F. Arnaud-Neu, *New J. Chem.* **2004**, *28*, 748.
[12] The *para-tert*-butylcalix[8]arene derivative (BCA-COOEt) and calix[4]resorcinarene derivative (CRA-COOEt) were synthesized by the reactions of *para-tert*-butylcalix[8]arene (BCA) and calixresorcin[4]arene (CRA), respectively, with ethyl bromoacetate using K_2CO_3 in NMP.
[13] P. M. Marcos, J. R. Asceno, M. A. P. Segurado, J. L. C. Periera, *J. Phys. Org. Chem.* **1999**, *12*, 695.

 © 2006 Wiley-VCH Verlag GmbH & Co. KGaA, Weinheim

Enzyme Mechanisms

DOI: 10.1002/anie.200603100

Snapshots of the Reaction Mechanism of Matrix Metalloproteinases**

Ivano Bertini, Vito Calderone, Marco Fragai, Claudio Luchinat, Massimiliano Maletta, and Kwon Joo Yeo*

Matrix metalloproteinases (MMPs) are a family of proteins involved in tissue remodeling and cell signaling.[1–3] As such, they are validated drug targets.[4,5] MMPs are endopeptidases with zinc at the active site of a catalytic domain.[6]

The enzymology of peptidases has been a popular area of research since the investigation of carboxypeptidase A (CPA)[7–11] and thermolysin (TLN)[12–15] in the 1980s. Both proteins are rich in charged and ionizable groups, such as Glu, Arg, and His, in the active site. A role for these residues in catalysis was proposed. In contrast, MMPs are simple proteins with only one Glu residue in the active site besides the three His residues coordinated to the catalytic zinc ion. In the most widely accepted mechanism, which is similar to that proposed for CPA and TLN, this Glu residue assists in the nucleophilic attack at the relevant peptide carbonyl group of the substrate by a zinc-coordinated water molecule.[16] The interest in MMPs has grown again because of the need for inhibitors that are as specific as possible for each of the 23 human proteins.[17–22]

We have now solved a series of X-ray crystal structures under a variety of conditions in an attempt to obtain models of the various steps of the reaction mechanism of MMPs. The protein tends to digest itself, so crystallization is always carried out in the presence of an inhibitor. By experimenting with various crystals under crystal-washing conditions we could solve the structure of the uninhibited form of MMP-12 at a resolution of 1.2 Å (Figure 1a; see also the Supporting Information) and that of MMP-8 at a resolution of 1.7 Å (see the Supporting Information). These are the first X-ray crystal structures of the uninhibited, active form of MMP. In MMP-12, the active site contains three water molecules coordinated to zinc, one of which is hydrogen bonded to Glu219, in an almost regular octahedral geometry. In the case of MMP-8, only the water molecule that is hydrogen bonded to Glu219 has full occupancy, whereas the other two water molecules have occupancies of only about 20%. Despite the lower resolution of the MMP-8 structure, the electron densities of the latter water molecules are clearly appreciable (see the Supporting Information). If these two water molecules are neglected, the resulting geometry is a flattened tetrahedron, with ample room for the binding of an exogenous ligand.

We then attempted to soak the 204–209 peptide fragment of type I/III of the alpha-1 collagen chain, *ProGlnGlyIle-AlaGly*, which is known to be cleaved at the *Gly–Ile* bond, into the active MMP-12 and MMP-8 crystals. No peptide-bound form could be identified, as a result of rapid hydrolysis. Even with the mutation Glu219Ala, which had been reported to lower the enzymatic activity of MMP-7 by three orders of magnitude,[23] the substrate underwent hydrolysis. On the other hand, well-resolved X-ray crystallographic structures that show a hydrolysis product inside the active site could be obtained for both MMP-12 (resolution: 1.1 Å; Figure 1d) and MMP-8 (resolution: 1.5 Å; see the Supporting Information), and for the former even a structure with both hydrolysis products was obtained (resolution: 1.8 Å; Figure 1c). We then modeled the substrate in the form of a tetrahedral *gem*-diol intermediate (in analogy to the structure of a pseudosubstrate described in the literature[24]) by taking the uninhibited form of MMP-12 and that with two peptides in the active site as the starting points (Figure 1b). Figure 1a–d show a plausible series of events in the catalytic cycle of MMPs, as discussed below. A four-snapshot movie of the steps illustrated in Figure 1a–d can be downloaded as Supporting Information for this article.

The cycle starts with the uninhibited MMP-12 enzyme (Figure 1a). Figure 1b shows that one of the two oxygen atoms of the *gem*-diol that results from substrate binding

[*] Prof. I. Bertini, V. Calderone, M. Fragai, C. Luchinat, M. Maletta, K. J. Yeo
Magnetic Resonance Center (CERM)
University of Florence
Via L. Sacconi 6, 50019 Sesto Fiorentino (Italy)
Fax: (+39) 055-457-4271
E-mail: ivanobertini@cerm.unifi.it
Prof. I. Bertini, M. Maletta
Department of Chemistry
University of Florence
Via della Lastruccia 3, 50019 Sesto Fiorentino (Italy)
M. Fragai, C. Luchinat
Department of Agricultural Biotechnology
University of Florence
Via Maragliano 75–77, 50144 Florence (Italy)

[**] We thank Dr. Andrea Giachetti for help with computational analysis. This research was supported by the EC (projects: LSHG-CT-2004-512077 and "Structural Proteomics in Europe" Grant QLG2-CT-2002-00988), the MIUR (PRIN 2005, Prot. N. 2005039878, Prot. N. 4455, and RBAU013NSB), and Ente Cassa di Risparmio di Firenze (Innovative Strategies for Drug Design). We acknowledge the support and assistance of the ESRF (Grenoble) and DESY (Hamburg) synchrotron radiation facilities for the data collection.

Supporting information for this article is available on the WWW under http://www.angewandte.org or from the author.

InterScience
© 2006 Wiley-VCH Verlag GmbH & Co. KGaA, Weinheim

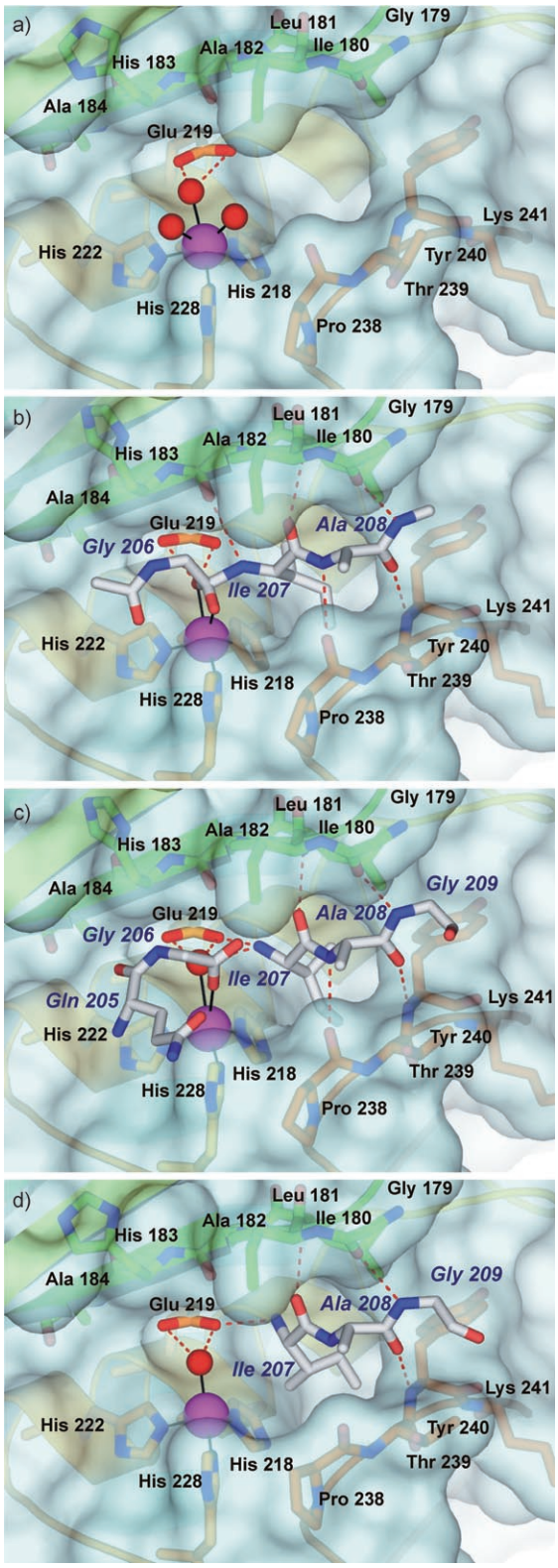

Figure 1. a) Active, uninhibited form of MMP-12. b) A plausible *gem*-diol intermediate[24] of MMP-12 modeled by using the structures of the uninhibited (a) and two-peptide (c) forms as templates. c) Two-peptide intermediate observed upon soaking the active uninhibited MMP-12 crystals with the collagen fragment *ProGlnGlyIleAlaGly*. d) *IleAlaGly* adduct of MMP-12.

indeed sits in the position previously occupied by the catalytically relevant water molecule and is also hydrogen bonded to Glu 219, whereas the other occupies a coordination site between the positions of the other two more external water molecules in Figure 1 a. The peptide NH group of the scissile bond is hydrogen bonded to the carbonyl oxygen atom of Ala 182, and the side chain of *Ile 207* partially enters the S_1' cavity, whereas the rest of the body of the peptide is stabilized by four hydrogen-bonding interactions with the backbone of the protein. The latter interactions involve the carbonyl oxygen atom of *Ile 207* and the nitrogen atom of Leu 181, the nitrogen atom of *Ala 208* and the carbonyl oxygen atom of Pro 238, the carbonyl oxygen atom of *Ala 208* and the nitrogen atom of Tyr 240, and the nitrogen atom of *Gly 209* and the carbonyl oxygen atom of Gly 179. As the modeling did not provide a convincing conformation for the Pro and Gln residues of the peptide, they are omitted from Figure 1 b.

After peptide-bond cleavage, both hydrolysis fragments, *ProGlnGly* and *IleAlaGly*, sit in the active-site cavity, as shown in Figure 1 c. The peptide *ProGlnGly*, for which a clear electron density is observed only for the whole *Gly 206* residue and part of *Gln 205*, is apparently not involved in any significant stabilizing interaction with the protein backbone. The carboxylate end of *Gly 206* binds the zinc ion in an *anti*-monodentate fashion. A water molecule is also semicoordinated to zinc (Zn–O distance: 2.8 Å) and hydrogen bonded to the catalytically relevant Glu 219 residue; it acts as a "spacer" between Glu 219 and the coordinated carboxylate end of *Gly 206*. The zinc ion is thus five-coordinated in this intermediate. The semicoordinated water molecule occupies a position similar to that of the catalytically relevant water molecule observed in the free uninhibited enzyme. The full *IleAlaGly* fragment can be detected clearly. Its orientation in the active site is such that the side chain of *Ile 207* partially enters the S_1' cavity, whereas the rest of the body of the peptide is stabilized by four hydrogen-bonding interactions with the backbone of the protein. The hydrogen-bonding distances are 2.91 Å between the carbonyl oxygen atom of *Ile 207* and the nitrogen atom of Leu 181, 3.16 Å between the nitrogen atom of *Ala 208* and the carbonyl oxygen atom of Pro 238, 2.81 Å between the carbonyl oxygen atom of *Ala 208* and the nitrogen atom of Tyr240, and 2.71 Å between the nitrogen atom of *Gly 209* and the carbonyl oxygen atom of Gly 179. The N-terminal nitrogen atom of the *IleAlaGly* fragment is involved in two strong hydrogen-bonding interactions with the water molecule coordinated to the zinc atom (2.69 Å) and with one oxygen atom of Glu 219 (2.24 Å), whereas there are no hydrogen-bonding interactions of this nitrogen atom with the protein backbone. It is difficult to ascertain whether the N-terminal nitrogen atom is part of a neutral NH_2 group or a positive NH_3^+ group. Overall, the active-site crevice is slightly more open than in the active uninhibited enzyme, in contrast to what was observed for thermolysin and astacin.[25,26]

The *ProGlnGly* fragment, which is coordinated to zinc through the carboxylate group of the C-terminal *Gly 206* residue, is the first to leave the cavity, whereas the *IleAlaGly* fragment remains in the cavity (Figure 1 d; see also the Supporting Information). The zinc ion appears in this case to

 © 2006 Wiley-VCH Verlag GmbH & Co. KGaA, Weinheim

be tetracoordinated, with a more strongly bound water molecule (2.28 Å), which is in turn hydrogen-bonded to Glu219. The interaction between this water molecule and Glu219 is still very strong; they are separated by a distance of 2.60 Å. This water molecule occupies roughly the same position as in the free uninhibited enzyme, but the other two coordinated water molecules are not present, so that the zinc ion has a flattened tetrahedral coordination sphere. Given the high resolution of the structure, the existence of other immobilized water molecules in the zinc coordination sphere can be safely ruled out (see the Supporting Information). The bond lengths around the zinc ion (see the Supporting Information) are also consistent with a lower coordination number of the zinc center. The amino terminus of the *IleAlaGly* fragment moves away from the zinc center and loses the strong hydrogen-bonding interaction with the zinc-coordinated water molecule, whereas the interaction with one of the oxygen atoms of Glu219 (2.74 Å) is retained. The side chain of *Ile207* alters its position and increases its interactions with the S_1' cavity. The rest of the body of the peptide is stabilized by three of the four hydrogen-bonding interactions with the backbone of the protein that were observed when two peptides occupied the active site (carbonyl oxygen atom of *Ile207* with the nitrogen atom of Leu181, 2.77 Å; carbonyl oxygen atom of *Ala208* with the nitrogen atom of Tyr240, 2.74 Å; nitrogen atom of *Gly209* with the carbonyl oxygen atom of Gly179, 3.03 Å). However, the interaction between the nitrogen atom of *Ala208* and the carbonyl oxygen atom of Pro238 no longer exists, and this carbonyl bond is itself reoriented by almost 90° away from the center of the active crevice, as observed in several inhibitor adducts with hydrophobic groups in the S_1' cavity.[27] Overall, the active-site crevice is more open with respect to the previous snapshot (Figure 1c). The observation of a similar adduct with MMP-8[*] (see the Supporting Information) and in a self-interacting form of MMP-12[28] confirms the generality of our findings.

Based on the details of the structures shown in Figure 1a–d and in the corresponding movie, a consistent sequence of events emerges:

1) The uninhibited enzyme has a coordinated water molecule whose position is determined by a strong hydrogen bond with Glu219. The position of this water molecule suggests that the Zn-H_2O-Glu219 moiety has lost at least one proton, as has already been proposed for CPA and TLN. During catalysis the water hydrogen atom in the hydrogen bond to the carboxylate group of Glu219 may actually move to Glu219 as a proton; the coordinated water molecule is thus transformed into a hydroxide ion and its nucleophilicity increased.[29] The active-site crevice is in a "closed" form; that is, it is somewhat narrower than when observed in the presence of the hydrolysis products or inhibitors.
2) The incoming substrate binds zinc with the carbonyl group of *Gly206* (replacing the additional labile water molecules when present), and establishes a number of stabilizing interactions with the protein through its C-terminal section (*IleAlaGly*). It is thought that the N-terminal section may not be involved in relevant interactions with the protein on the basis of the bent conformation observed for the Gln side chain in the product (Figure 1c). The strongly coordinated water molecule (hydroxide ion) performs a nucleophilic attack on the *Gly206* carbonyl group to give the *gem*-diol intermediate modeled in Figure 1b.
3) After the peptide bond has been broken, both peptide fragments remain bound to the protein initially. However, the *ProGlnGly* fragment is only held in place by monodentate coordination of the *Gly206* carboxylate group to the zinc center, whereas the *IleAlaGly* fragment is strongly bound to the protein (Figure 1c). An incoming water molecule loosely binds zinc and separates the bound carboxylate group from the Glu219 residue. The formation of this five-coordinate intermediate facilitates the detachment of the *ProGlnGly* fragment through an associative ligand-exchange mechanism.
4) The remaining protein-bound fragment *IleAlaGly* (Figure 1d) undergoes a relatively small but significant rearrangement in the active-site cavity. The driving force for this rearrangement could rest in the possibly strained pose of this fragment in the two-peptide adduct as a result of several interactions that still exist between the two fragments; these interactions are mediated by the zinc-coordinated water molecule and the Glu219 residue. After the release of the *ProGlnGly* fragment, the increased repulsion between the positively charged zinc ion and the incipient NH_3^+ moiety cause the Ile side chain to enter deeper into the S_1' cavity and optimize its hydrophobic interactions with the cavity. The change in the position of the Ile side chain occurs at the expense of the interaction between the nitrogen atom of *Ala208* and the carbonyl oxygen atom of Pro238; this interaction is lost as a result of the opening up of the cavity. The release of the *IleAlaGly* fragment would from this point follow the same pathway as that of any S_1'-directed inhibitor.

This model may also provide some clues on the pH dependence of the catalytic activity of MMPs. The k_{cat}/K_M profile is bell-shaped, as it is for CPA and TLN, with pK_a values of 4.3 and 9.6. In the absence of any other ionizable groups in the active-site cavity, the simplest interpretation would be that the two pK_a values apply to the successive deprotonations of the coordinated water–Glu219 system. However, mutations in which Glu219 is replaced by a nonionizable residue decrease but do not abolish activity, and, more importantly, the bell-shaped activity profile is maintained.[23] For example, the Glu219Ala mutation in MMP-7 reduces the activity to 0.1%, shifts the first pK_a value to 5.4 (an increase of 1.1 pH units), and does not change the second pK_a value appreciably.[23] In this mutant, the only ionizable residue is the coordinated water molecule, which itself can not account for two pK_a values. One possibility is that one of the

[*] In the MMP-8 adduct the orientation of the *IleAlaGly* fragment is more similar to that observed in the two-peptide adduct of MMP-12, and two water molecules are coordinated to zinc; these water molecules occupy similar positions to those of the two *gem*-diol oxygen atoms in the modeled structure in Figure 1b.

 © 2006 Wiley-VCH Verlag GmbH & Co. KGaA, Weinheim

two pK_a values is product-linked. Our mechanism might suggest that the high pK_a value of 9.6 corresponds to the deprotonation of the *IleAlaGly* product. A neutral NH_2 amino terminus could stabilize the *IleAlaGly* adduct, thereby preventing the clearance of the active site for the next enzymatic reaction.

Experimental Section

The catalytic domains of MMP-12 (Gly106–Gly263, F171D mutant) and MMP-8 (Asn85–Gly242) were expressed and purified as reported previously.[30] Crystal growing, data collection, and structure refinement are described in the Supporting Information. The following structures have been deposited to the PDB: Uninhibited MMP-12; the adduct of MMP-12 with two peptides; the adduct of MMP-12 with one peptide; uninhibited MMP-8; the adduct of MMP-8 with one peptide. The PDB file of the model of the MMP-12–*gem*-diol adduct is available as Supporting Information.

Received: July 31, 2006
Published online: November 10, 2006

Keywords: enzyme catalysis · metalloproteins · peptides · reaction mechanisms · X-ray diffraction

[1] S. D. Shapiro, *Curr. Opin. Cell Biol.* **1998**, *10*, 602–608.
[2] A. Boire, L. Covic, A. Agarwal, S. Jacques, S. Sherifi, A. Kuliopulos, *Cell* **2005**, *120*, 303–313.
[3] P. Koolwijk, N. Sidenius, E. Peters, C. F. Sier, R. Hanemaaijer, F. Blasi, V. W. van Hinsbergh, *Blood* **2001**, *97*, 3123–3131.
[4] M. Whittaker, C. D. Floyd, P. Brown, A. J. Gearing, *Chem. Rev.* **1999**, *99*, 2735–2776.
[5] J. W. Skiles, N. C. Gonnella, A. Y. Jeng, *Curr. Med. Chem.* **2004**, *11*, 2911–2977.
[6] N. Borkakoti, *Prog. Biophys. Mol. Biol.* **1998**, *70*, 73–94.
[7] K. S. Larsen, D. S. Auld, *Biochemistry* **1989**, *28*, 9620–9625.
[8] W. L. Mock, J.-T. Tsay, *J. Biol. Chem.* **1988**, *263*, 8635–8641.
[9] D. W. Christianson, J. D. Lipscomb, *Acc. Chem. Res.* **1989**, *22*, 62–69.
[10] D. W. Christianson, W. N. Lipscomb, *J. Am. Chem. Soc.* **1987**, *109*, 5536–5538.
[11] B. L. Vallee, D. S. Auld, *Proc. Natl. Acad. Sci. USA* **1990**, *87*, 220–224.
[12] D. G. Hangauer, A. F. Monzingo, B. W. Matthews, *Biochemistry* **1984**, *23*, 5730–5741.
[13] B. W. Matthews, *Acc. Chem. Res.* **1988**, *21*, 333–340.
[14] D. R. Holland, A. C. Hausrath, D. Juers, B. W. Matthews, *Protein Sci.* **1995**, *4*, 1955–1965.
[15] D. H. Juers, J. Kim, B. W. Matthews, S. M. Sieburth, *Biochemistry* **2005**, *44*, 16524–16528.
[16] B. Lovejoy, A. M. Hassell, M. A. Luther, D. Weigl, S. R. Jordan, *Biochemistry* **1994**, *33*, 8207–8217.
[17] L. M. Coussens, B. Fingleton, L. M. Matrisian, *Science* **2002**, *295*, 2387–2392.
[18] N. Borkakoti, *Biochem. Soc. Trans.* **2004**, *32*, 17–20.
[19] V. Lukacova, Y. F. Zhang, M. Mackov, P. Baricic, S. Raha, J. A. Calvo, S. Balaz, *J. Biol. Chem.* **2004**, *279*, 14194–14200.
[20] C. Andreini, L. Banci, I. Bertini, C. Luchinat, A. Rosato, *J. Proteome Res.* **2004**, *3*, 21–31.
[21] J. F. Fisher, S. Mobashery, *Cancer Metastasis Rev.* **2006**, *25*, 115–136.
[22] C. M. Overall, O. Kleifeld, *Br. J. Cancer* **2006**, *94*, 941–946.
[23] J. Cha, D. S. Auld, *Biochemistry* **1997**, *36*, 16019–16024.
[24] A. L. Gall, M. Ruff, R. Kannan, P. Cuniasse, A. Yiotakis, V. Dive, M. C. Rio, P. Basset, D. Moras, *J. Mol. Biol.* **2001**, *307* 577–586.
[25] F. Grams, V. Dive, A. Yiotakis, I. Yiallouros, S. Vassiliou, R. Zwilling, W. Bode, W. Stocker, *Nat. Struct. Biol.* **1996**, *3*, 671–675.
[26] W. N. Lipscomb, N. Strater, *Chem. Rev.* **1996**, *96*, 2375–2433.
[27] H. Brandstetter, F. Grams, D. Glitz, A. Lang, R. Huber, W. Bode, H. W. Krell, R. A. Engh, *J. Biol. Chem.* **2001**, *276*, 17405–17412.
[28] I. Bertini, V. Calderone, M. Fragai, C. Luchinat, S. Mangani, B. Terni, *Angew. Chem.* **2003**, *115*, 2777–2780; *Angew. Chem. Int. Ed.* **2003**, *42*, 2673–2676.
[29] I. Bertini, C. Luchinat, M. Rosi, A. Sgamellotti, F. Tarantelli, *Inorg. Chem.* **1990**, *29*, 1460–1463.
[30] I. Bertini, V. Calderone, M. Cosenza, M. Fragai, Y.-M. Lee, C. Luchinat, S. Mangani, B. Terni, P. Turano, *Proc. Natl. Acad. Sci. USA* **2005**, *102*, 5334–5339.

 © 2006 Wiley-VCH Verlag GmbH & Co. KGaA, Weinheim

Sensors

DOI: 10.1002/anie.200603106

A Simple and Sensitive "Dipstick" Test in Serum Based on Lateral Flow Separation of Aptamer-Linked Nanostructures**

*Juewen Liu, Debapriya Mazumdar, and Yi Lu**

Aptamers are single-stranded nucleic acids that can be selected from a large random library to bind a number of molecules with high affinity and specificity. Therefore, they are considered to be the nucleic acid version of antibodies.[1,2] Since its first discovery in the early 1990s,[3,4] the use of aptamers for sensing and diagnostic applications has been extensively explored.[5–11] Many detection methods developed for antibodies have been successfully adapted to aptamer-based detections.[11–15] In many cases, aptamers show similar or even better performance when compared with antibodies in the laboratory.[12–14] However, practical applications of aptamer-based sensing and diagnostics, such as home and

[*] Dr. J. Liu, D. Mazumdar, Prof. Y. Lu
Department of Chemistry
Beckman Institute for Advanced Science and Technology
University of Illinois at Urbana-Champaign
Urbana, IL 61801 (USA)
Fax: (+1) 217-333-2685
E-mail: yi-lu@uiuc.edu
Homepage: http://www.scs.uiuc.edu/chem/lu.htm

[**] This material is based upon work supported by the US Department of Energy (DE-FG02-01ER63179), the National Science Foundation through a Science and Technology Center of Advanced Materials for Purification of Water with Systems (WaterCAMPWS; CTS-0120978) and a Nanoscale Science and Engineering Center (NSEC; DMR-0117792) program, and by the US Army Research Laboratory and the US Army Research Office (DAAD19-03-1-0227).

Supporting information for this article is available on the WWW under http://www.angewandte.org or from the author.

© 2006 Wiley-VCH Verlag GmbH & Co. KGaA, Weinheim

clinical tests, are still lagging behind antibody-based tests because aptamer-based sensors are not as yet user-friendly for average users who have limited training in chemical or biological laboratories.

Recent reports of colorimetric sensors based on signaling aptamers are a positive step towards improving user-friendliness as detection results can be observed with the naked eye without the need for sophisticated instruments.[16–20] For example, by using DNA aptamers to assemble DNA-functionalized gold nanoparticles, we have constructed colorimetric sensors with instantaneous color response for a wide range of analytes, such as adenosine, cocaine, K^+, and their combinations.[20,21] However, two disadvantages have prevented their practical applications in homes and in the field. The first disadvantage, common to all aptamer-based sensing methods reported so far, is that detection still requires professional laboratory-type operations, such as precise transfer of solutions, making it less useful for people who do not have a scientific background. Second, the sensors have low sensitivity for instrument-free observation. For example, to observe a distinct color change with the naked eye, a concentration of 0.5 mM or higher of adenosine was needed for the adenosine sensor, which was approximately 50-times higher than the K_d value ($\approx 10\ \mu M$) of this aptamer.[22] The low sensitivity is attributable to the multiplex connecting nature of the nanoparticle aggregates that gives a strong purple background. At low adenosine concentrations, only a small fraction of nanoparticles dissociate from the aggregates and change to a red color, which is likely to be masked by the strong purple background.

One of the most useful methods to convert antibody-based assays to user-friendly test kits is the lateral-flow technology, and a well-known example is the commercially available pregnancy test kit. Despite the wide applications in antibody assays, nucleic acid based lateral flow devices were only demonstrated for DNA detection.[23] To overcome the two limitations of aptamer-based sensors in the solution phase, we report herein, aptamer-based lateral flow devices that can be used as simple "dipsticks" or a litmus-test type of assay.[24] We show that these devices are not only simpler to operate, but also more sensitive than solution-based tests owing to the integration of binding, separation, and detection on a simple test-paper-like platform with no background interference.

We first chose the adenosine aptamer to build a model system to study aptamer-based lateral flow devices. Adenosine-responsive nanoparticle aggregates containing two kinds of DNA-functionalized gold nanoparticles (particles 1 and 2 in Figure 1a) and an aptamer DNA were prepared. Detailed DNA sequences, modifications, and linkages are shown in Figure 1b. Two kinds of thiol-modified DNA were used to functionalize particle 2: biotinylated and non-biotinylated. The biotin modifications (★) allowed the nanoparticles to be captured by streptavidin. The optimal ratio between the two DNA molecules was determined to be 1:1 because using 100% biotinylated DNA led to low yield of nanoparticle aggregates (<20%), whereas 10% led to inadequate streptavidin capture (data not shown). As the association rates of the two DNA molecules to gold nanoparticles were unknown,

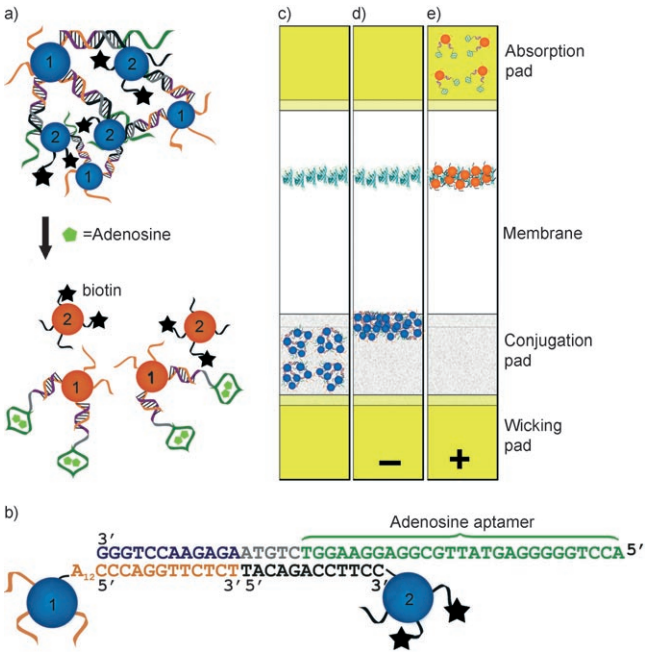

Figure 1. Aptamer/nanoparticle-based lateral flow device. a) Adenosine-induced disassembly of nanoparticle aggregates into red-colored dispersed nanoparticles. Biotin is denoted as black stars (★). b) DNA sequences and linkages in nanoparticle aggregates. Lateral flow devices loaded with the aggregates (on the conjugation pad) and streptavidin (on the membrane in cyan color) before use (c) and in a negative (d) or a positive (e) test.

the ratio of the two DNA molecules on particle 2 was only estimated to be 1:1.

The lateral flow devices consisted of four overlapping pads placed on a backing (Figure 1c,d,e). The four pads were as follows (from top to bottom): absorption pad (15 mm), HiFlow Plus membrane (25 mm), glass fiber conjugation pad (13 mm), and wicking pad (15 mm). The aptamer-linked nanoparticle aggregates were spotted on the conjugation pad, and streptavidin was applied on the membrane as a thin line (Figure 1c). The whole device was then dried overnight at room temperature before use. We hypothesize that nanoparticle aggregates are too large to migrate along the membrane, whereas dispersed nanoparticles can. If the wicking pad of the device is dipped into a solution, the solution will move up along the device and rehydrate the aggregates. In the absence of adenosine, the rehydrated aggregates will migrate to the bottom of the membrane where they stop because of their large size (Figure 1d). In the presence of adenosine, the nanoparticles would be disassembled owing to binding of adenosine by the aptamer (Figure 1a).[9,20] The dispersed nanoparticles can then migrate along the membrane and be captured by streptavidin to form a red line (Figure 1e).

To successfully carry out the detection, the first challenge is to preserve the aptamer activity and the connections between nanoparticles in the dry state. Each aggregate contains hundreds to thousands of DNA-linked nanoparticles. Direct drying in buffer solution could damage the aggregates. Sucrose is a commonly used additive to keep DNA in its

 © 2006 Wiley-VCH Verlag GmbH & Co. KGaA, Weinheim

native state, and the effect of sucrose on drying was first studied. Five conditions with varying sucrose concentrations were tested (Figure 2a). At each sucrose concentration, three devices were used with the first one being an unused device, the second one being a negative test (without adenosine), and the third one being a positive test (with 0.5 mM adenosine). Direct drying (no sucrose) deactivated the aggregates, and no red band was observed in the presence of adenosine (Figure 2a, 0% sucrose). Interestingly, inclusion of 2% sucrose helped preserve the aggregates and a slight red band was observed on the membrane. With 8% sucrose, an intense red band was observed in the positive test, whereas no band was observed in the negative test. Instead, a dark band at the boundary between the conjugation pad and the membrane was observed. This observation supported our hypothesis that the aggregates cannot migrate along the membrane. The presence of aggregates on the boundary provides a useful control. If no such line is observed for a negative sample, the test is invalid, indicating poor rehydration or flow of the device. A further increase in the sucrose concentration up to 30% also showed intense red bands for positive tests, but slight bands in the negative tests could also be observed. Therefore, 8% sucrose was chosen for further experiments.

Under optimized drying conditions, sensitivity and selectivity of the devices were tested. The devices were dipped into buffer solutions containing various nucleoside species at different concentrations (Figure 2b). No red band was observed in the absence of adenosine. With increasing adenosine concentrations, more intense red bands were observed, and the detection limit was ca. 20 μM. For the other ribonucleosides, no red bands were observed with 1 mM cytidine or uridine, suggesting that the high selectivity of the aptamer was maintained. Guanosine was not tested because of its poor solubility at room temperature. Because the detections are solely based on intensity of the same color instead of color change, such sensors can provide qualitative or semiquantitative results. In fact, for most lateral flow based detections, such as the pregnancy test, only a yes or no answer is needed.

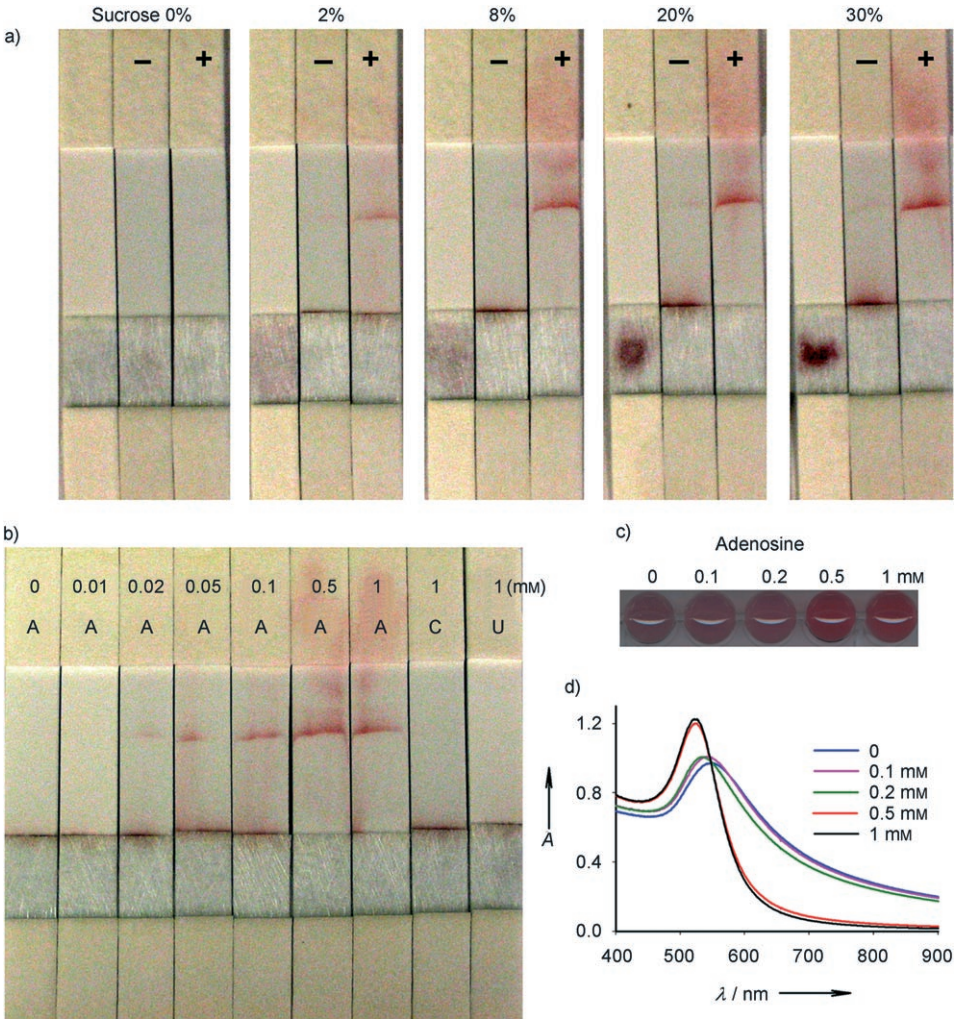

Figure 2. Lateral flow based detection of adenosine. a) The effect of sucrose concentration during drying. b) Test of the adenosine sensing lateral flow device with varying concentrations of nucleosides. A = adenosine, C = cytidine, U = uridine. c) Scanned image of adenosine-dependent color change of the aptamer-linked aggregates in solution phase. d) UV/Vis spectra of the samples in (c).

A solution-phase reaction was also carried out for comparison. To insure a fair comparison, the same batch of aggregates was used for both flow-based and solution-phase reactions under optimized conditions. As can be observed in Figure 2c, 0.5 mM adenosine was needed to observe a red color. The extinction spectra of the solution-phase samples were also recorded on a spectrophotometer (Figure 2d), and a small shift was observable with only 0.1 mM adenosine. This difference, however, cannot be distinguished by the naked eye. Compared with solution-phase results, the flow device had at least 10-fold higher sensitivity if the naked eye was used as a detector. Further improvement of sensitivity could be realized by color-enhancing methods (e.g., gold nanoparticles can be used as a catalyst to grow metallic silver to drastically improve the sensitivity for visual detection.[25])

To demonstrate the generality of the method described herein, we further prepared nanoparticle aggregates linked by a cocaine aptamer,[16,20,26] as shown in Figure 3a. The aggregates were loaded in lateral flow devices, and the device

 © 2006 Wiley-VCH Verlag GmbH & Co. KGaA, Weinheim

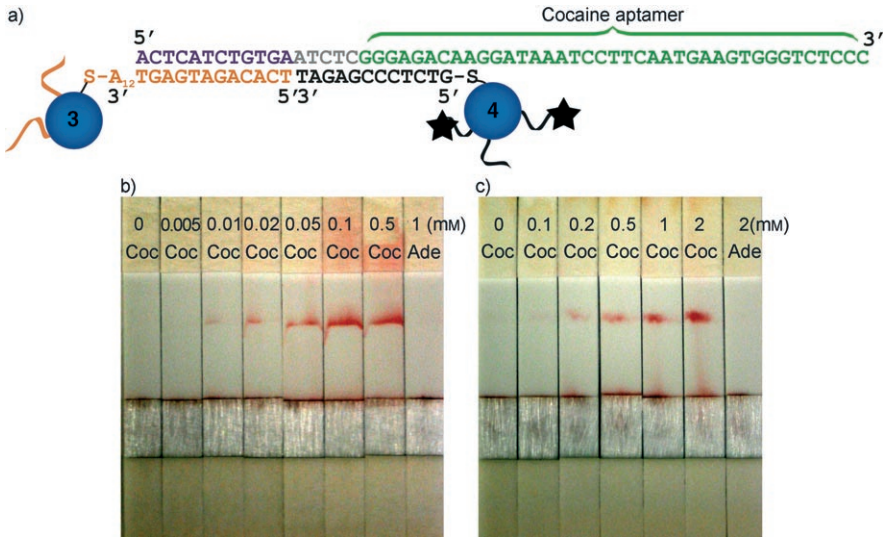

Figure 3. Lateral flow based detection of cocaine. a) DNA sequences and linkages in cocaine aptamer-linked nanoparticle aggregates. Test of the cocaine-sensing lateral flow device with varying concentrations of cocaine in buffer solution (b) and in undiluted human blood serum (c). Coc = cocaine, Ade = adenosine.

responses to varying concentration of cocaine were tested (Figure 3b). The intensity of the red bands increased with increasing cocaine concentration, and the detection limit was ca. 10 μM. As a negative control, the device did not show a red line with 1 mM adenosine (the last strip in Figure 3b).

Finally, we investigated the possibility of using such devices to detect analytes in human blood serum. Cocaine was spiked into untreated serum, and 10 μL of the serum samples were added directly to the conjugation pads to rehydrate and react with the nanoparticle aggregates. After 20 seconds, the wicking pad part of the device was dipped into a running buffer solution. As can be seen in Figure 3c, a distinct red line can be observed when the serum contained 0.2 mM cocaine and the color intensity increased with increasing cocaine concentration; adenosine failed to produce a red line. These results demonstrate that the device is compatible with biological samples, making applications in medical diagnostics possible. The sensitivity in serum was about 20-fold lower compared with that in buffer solution, which was mainly attributed to the difference in buffer-solution conditions and possible cocaine degradation in serum. The serum sample was directly used without any dilution or desalting and, as a result, the ionic strength appeared to be higher than the optimal conditions for the sensor, which leaves us with room for further optimization to increase sensitivity.

In summary, we have immobilized both adenosine and cocaine aptamer-linked nanoparticle aggregates onto a lateral flow device, resulting in a simpler and more excitingly, a more sensitive "dipstick" test than the corresponding test in solution. Significantly, the device can perform in complex sample matrix such as in human blood serum. A novel aspect of the lateral flow device described herein is that it takes advantage of the physical size difference of nanoparticles in various assembly states, and the fact that aggregated nanostructures do not move along the membrane, which provide a critical control for the performance of the device. As aptamers for a broad range of molecules have been obtained,[1,2] this lateral flow method should be general enough so that it can be adapted to develop dipstick tests for any analyte that is compatible with the nanoparticle/aptamer-based assay.

Experimental Section

Materials: All DNA samples were purchased from Integrated DNA Technologies Inc. Nucleosides, cocaine, avidin from egg white, and human blood serum were purchased from Aldrich. Streptavidin was purchased from Promega. Gold nanoparticles were prepared following literature procedures.[27]

Device preparation: The Millipore Hi-Flow Plus Assembly Kit (Millipore Corporation, Bedford, MA) was used. The kit contains a Hi-Flow Plus Cellulose Ester Membrane with a nominal capillary flow time of 90 seconds/4 cm, an absorption pad, a wicking, and a glass fiber conjugation pad. The device assembly was shown in Figure 1c (see also the Supporting Information). Nanoparticle preparation, functionalization, and assembly have been described in detail previously.[20,28] Note that particles 2 and 4 (Figure 1a,b and Figure 3a) were functionalized with two kinds of thiol-modified DNA with an equal molar ratio. One DNA contained a biotin moiety at one end, whereas the other did not contain a biotin. For functionalization, 1.5 μM of each DNA was added to the nanoparticles. Particles 1 or 3 were functionalized with only a thiol-modified DNA. After forming nanoparticle aggregates, the aggregates were separated from dispersed nanoparticles and free DNA by centrifugation. To allow a fast disassembly of nanoparticle aggregates, very brief centrifugation was used to avoid formation of very large aggregates and the supernatant was removed by a pipette. The purified nanoparticle aggregates were dispersed in designated buffer solutions (in most experiments: 8% sucrose, 200 mM NaCl, 25 mM Tris acetate; pH 8.2) and agitated vigorously with a pipette. The color of the aggregates should be dark purple. Nanoparticle aggregates (6 μL) were spotted on each conjugation pad, and 10 mg mL^{-1} streptavidin (2 μL) was applied on the membrane by a 2 μL pipet to form a line. The loaded strips were stored in a drawer overnight before use. To detect cocaine in serum, 100 mg mL^{-1} egg white avidin (3 μL) was applied on the membrane for each device.

Detection: For adenosine detection, varying concentrations of nucleosides were dissolved in a buffer solution containing 100 mM NaCl, 25 mM Tris acetate, pH 8.2. For cocaine detection in buffer solution, the NaCl concentration was 50 mM. The wicking pad part of each device was dipped into the solutions for ca. 20 seconds when the conjugation pad was fully hydrated and the liquid started to migrate on the membrane. Then the device was placed horizontally on a plastic surface for the flow to continue. For cocaine detection in serum, 10 μL of serum was added on the conjugation pad. After 20 seconds, the wicking pad was placed in a running buffer solution containing 100 mM NaCl, 25 mM Tris acetate, pH 8.2 to allow flow to happen. A digital camera was used to take pictures of the devices after ca. 5 minutes. For solution-phase reactions, the same aggregates were dispersed in 200 mM NaCl, 25 mM Tris acetate, pH 8.2. Varying concentration of adenosine was added and the color of each solution was acquired by a scanner and quantified by a UV/Vis spectrometer (Hewlett-Packard 8453).

Received: August 1, 2006
Revised: September 19, 2006
Published online: November 9, 2006

 © 2006 Wiley-VCH Verlag GmbH & Co. KGaA, Weinheim

Keywords: aptamers · cocaine · lateral flow · sensors · trace analysis

[1] D. S. Wilson, J. W. Szostak, *Annu. Rev. Biochem.* **1999**, *68*, 611.
[2] S. D. Jayasena, *Clin. Chem.* **1999**, *45*, 1628.
[3] A. D. Ellington, J. W. Szostak, *Nature* **1990**, *346*, 818.
[4] C. Tuerk, L. Gold, *Science* **1990**, *249*, 505.
[5] R. R. Breaker, *Curr. Opin. Chem. Biol.* **1997**, *1*, 26.
[6] M. Famulok, *Curr. Opin. Struct. Biol.* **1999**, *9*, 324.
[7] S. E. Osborne, I. Matsumura, A. D. Ellington, *Curr. Opin. Chem. Biol.* **1997**, *1*, 5.
[8] J. S. Hartig, S. H. Najafi-Shoushtari, I. Gruene, A. Yan, A. D. Ellington, M. Famulok, *Nat. Biotechnol.* **2002**, *20*, 717.
[9] R. Nutiu, Y. Li, *J. Am. Chem. Soc.* **2003**, *125*, 4771.
[10] R. Nutiu, Y. Li, *Chem. Eur. J.* **2004**, *10*, 1868.
[11] N. K. Navani, Y. Li, *Curr. Opin. Chem. Biol.* **2006**, *10*, 272.
[12] D. W. Drolet, L. Moon-McDermott, T. S. Romig, *Nat. Biotechnol.* **1996**, *14*, 1021.
[13] Y. Wang, J. Killian, K. Hamasaki, R. R. Rando, *Biochemistry* **1996**, *35*, 12338.
[14] M. Liss, B. Petersen, H. Wolf, E. Prohaska, *Anal. Chem.* **2002**, *74*, 4488.
[15] M. D. Schlensog, T. M. A. Gronewold, M. Tewes, M. Famulok, E. Quandt, *Sens. Actuators B* **2004**, *101*, 308.
[16] M. N. Stojanovic, D. W. Landry, *J. Am. Chem. Soc.* **2002**, *124*, 9678.
[17] H.-A. Ho, M. Leclerc, *J. Am. Chem. Soc.* **2004**, *126*, 1384.
[18] V. Pavlov, Y. Xiao, B. Shlyahovsky, I. Willner, *J. Am. Chem. Soc.* **2004**, *126*, 11768.
[19] C.-C. Huang, Y.-F. Huang, Z. Cao, W. Tan, H.-T. Chang, *Anal. Chem.* **2005**, *77*, 5735.
[20] J. Liu, Y. Lu, *Angew. Chem.* **2006**, *45*, 96; *Angew. Chem. Int. Ed.* **2006**, *45*, 90.
[21] J. Liu, Y. Lu, *Adv. Mater.* **2006**, *18*, 1667.
[22] D. E. Huizenga, J. W. Szostak, *Biochemistry* **1995**, *34*, 656.
[23] K. Glynou, P. C. Ioannou, T. K. Christopoulos, V. Syriopoulou, *Anal. Chem.* **2003**, *75*, 4155.
[24] M. Famulok, G. Mayer, *Nature* **2006**, *439*, 666.
[25] T. A. Taton, C. A. Mirkin, R. L. Letsinger, *Science* **2000**, *289*, 1757.
[26] M. N. Stojanovic, P. de Prada, D. W. Landry, *J. Am. Chem. Soc.* **2000**, *122*, 11547.
[27] J. J. Storhoff, R. Elghanian, R. C. Mucic, C. A. Mirkin, R. L. Letsinger, *J. Am. Chem. Soc.* **1998**, *120*, 1959.
[28] J. Liu, Y. Lu, *Nat. Protocols* **2006**, *1*, 246.

 © 2006 Wiley-VCH Verlag GmbH & Co. KGaA, Weinheim

Protein Analysis

DOI: 10.1002/anie.200601948

Nanoparticle-Based Energy Transfer for Rapid and Simple Detection of Protein Glycosylation**

*Eunkeu Oh, Dohoon Lee, Young-Pil Kim, Seung Youp Cha, Doo-Beyong Oh, Hyun Ah Kang, Jungbae Kim, and Hak-Sung Kim**

Glycosylation is one of the most important posttranslational modifications of proteins. The specific oligosaccharide structure or moiety at each glycosylation site plays an essential role in determining the properties of the glycoprotein, including in vivo biological activity, solubility, protease resistance, immunogenicity, signal transduction, and pharmacokinetics.[1–4] The development of protein therapeutics requires stringent control of the glycosylation type and the degree of glycosylation in the target protein. These properties can be controlled by modulating the operating parameters, such as the glycan-processing enzymes, culture conditions, and host strains, in the production of the target protein.[5] In this regard, the structural or quantitative analysis of oligosaccharides is of great importance in terms of both practical and fundamental aspects. However, most conventional analytical methods are based on mass spectrometry and chromatography, which require complex and laborious sample preparation, such as deglycosylation.[1]

Approaches based on nanoparticles (NPs) have drawn much attention as more efficient methods for the detection of biomolecules because of their size-dependent physical and chemical characteristics.[6–15] Recently, the signal quenching

[*] Dr. E. Oh,[+] Dr. D. Lee, Y. P. Kim, Prof. H. S. Kim
Department of Biological Sciences
Korea Advanced Institute of Science and Technology
Daejeon, 305-701 (Korea)
Fax: (+82) 42-869-2610
E-mail: hskim76@kaist.ac.kr

S. Y. Cha, Dr. D. B. Oh, Dr. H. A. Kang
Protein Therapeutics Center
Korea Research Institute of Bioscience and Biotechnology
Daejeon, 305-600 (Korea)

Dr. J. Kim
Pacific Northwest National Laboratory
902 Battelle Boulevard, P.O. Box 999, Richland, WA 99352 (USA)

[+] Current address:
Samsung SDI Co., 428-5 Gongse-dong, Giheung-gu
Yongin-si, Gyeongggi-do, 446-577 (Korea)

[**] We acknowledge financial support by the Nano/Bio Science & Technology Program (M1053609000205N3609-00210) and the Nano Science & Technology Program (M10503000218-05M0300-21810) of MOST, the Korea Health 21C R&D Project (0405-MN01-0604-0007) of MHW, and the Next-Generation New-Technology Development Program of MOCIE. We also thank H. C. Yoon of Ajou University and KBSI for technical assistance with BioLC and TEM analyses.

Supporting information for this article is available on the WWW under http://www.angewandte.org or from the author.

© 2006 Wiley-VCH Verlag GmbH & Co. KGaA, Weinheim

due to the energy transfer between a quantum dot (QD) and a gold nanoparticle (AuNP) in close proximity was investigated for use in biosensing, owing to its speed, simplicity, and even sensitivity.[14,15] Several mechanisms have been proposed to explain this quenching phenomenon and investigated rigorously, such as fluorescence resonance energy transfer (FRET)[13,14] and surface energy transfer (SET).[11] Herein, we describe an approach for the rapid and simple detection of protein glycosylation based on the energy transfer between lectin-conjugated AuNPs and carbohydrate-conjugated QDs (Figure 1). We also demonstrate the potential of our system in the high-throughput analysis of glycosylation degree, which is critical for the development of protein therapeutics.

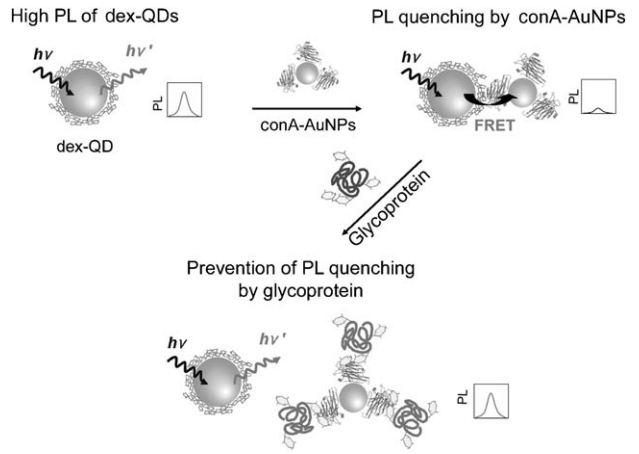

Figure 1. NP-based energy transfer for the detection of protein glycosylation. Top left: free dex-QDs; top right: dex-QDs and conA-AuNPs; bottom: the addition of a glycoprotein prevents PL quenching of dex-QDs by inhibiting the association between dex-QDs and conA-AuNPs, and thus restores the degree of PL of the dex-QDs to that of free dex-QDs.

For the construction of an NP-based detection system, AuNPs were conjugated with concanavalin A (conA), which is a lectin with preferred binding affinity to manno- and glucooligosaccharides (see the Supporting Information),[16] and QDs were conjugated with dextran, which is a polymeric form of glucose. We examined the binding of conA-conjugated AuNPs (conA-AuNPs) to dextran-conjugated QDs (dex-QDs) by measuring the emission spectrum of the dex-QDs. The photoluminescence (PL) quenching of dex-QDs at 605 nm increased as more conA-AuNPs were added. The apparent binding constant (K_a) of $6.7 \times 10^7\,\text{M}^{-1}$ between conA-AuNPs and dex-QDs calculated from this result (see the Supporting Information) is similar to the previously reported value of $1.1 \times 10^7\,\text{M}^{-1}$,[17] which confirms that the PL quenching of dex-QDs occurs specifically by conA-AuNPs. We also checked whether the PL quenching can be prevented by a protein that inhibits the interaction between conA-AuNPs and dex-QDs. The PL intensity of the dex-QDs was quenched by about 70% in the presence of conA-AuNPs (Figure 2). Upon the addition of free conA, the PL recovered to almost the same level of that of free dex-QDs, thus indicating that the free conA added inhibited the binding of conA-AuNPs to dex-QDs. These results suggested that this system could be used for the study of protein glycosylation as depicted in Figure 1.

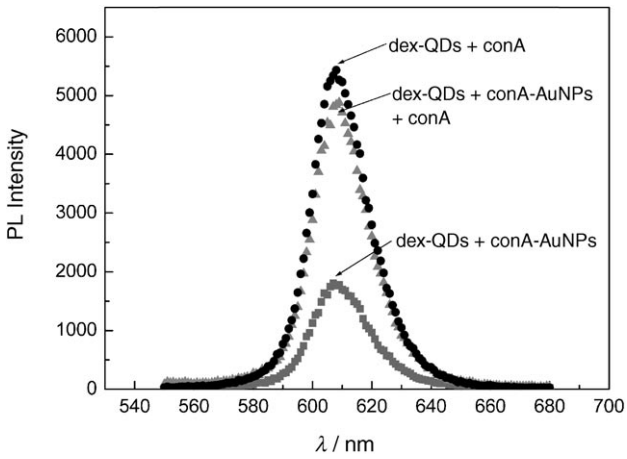

Figure 2. Inhibition assay with dex-QDs and conA-AuNPs. PL of free dex-QDs: ●; PL quenching of dex-QDs by conA-AuNPs: ■; PL quenching was inhibited by the addition of conA (5 μM): ▲.

To demonstrate the validity of this concept, we tested whether the system can distinguish the presence of a glycan moiety on intact proteins. As proposed above, the detection of a glycoprotein relies on a change in the efficiency of energy transfer between conA-AuNPs and dex-QDs; the glycan moiety on the glycoprotein caused this change by inhibition. Avidin and its deglycosylated counterpart neutravidin (Pierce, Rockford, USA) were employed as model proteins. Each subunit of avidin has one potential glycosylation site and about four mannose residues.[18] The PL intensity of the dex-QDs was measured after the addition of each protein. In the case of avidin, the PL intensity at 605 nm, PL_A, increased as the avidin concentration increased up to 100 μM. In contrast, the PL intensity of neutravidin, PL_N, displayed no concentration dependency (data not shown). This result indicates that avidin, which has a glycan moiety, acts as a competitive inhibitor of the binding of dex-QDs to the conA of conA-AuNPs, but neutravidin does not. The PL difference between avidin and neutravidin was normalized against the maximum PL difference at excess protein concentration. As a result, the normalized PL difference, $(PL_A - PL_N)/(PL_A - PL_N)_{max}$, increased with a logarithmic increase in protein concentration (Figure 3). By fitting the data to the four-parameter logistic equation (see the Supporting Information), the IC_{50} value (the protein concentration at which the normalized PL difference is half its maximal value) of avidin was estimated to be 8.5 μM. In another test with bovine serum albumin (BSA) and its chemically neoglycosylated form 22-MB (BSA–α-D-mannopyranosylphenyl isothiocyanate with 22 mannose units per molecule of BSA) a similar trend was observed (Figure 3). However, the IC_{50} value of 22-MB was thus estimated to be 120 nM, two orders of magnitude lower than that of avidin. This result indicates that 22-MB has many more mannose residues and a higher inhibition efficiency than avidin.

This system we had developed was applied to the analysis of proteins with varying degrees of glycosylation. For this purpose, mannose residues were conjugated chemically to the

 © 2006 Wiley-VCH Verlag GmbH & Co. KGaA, Weinheim

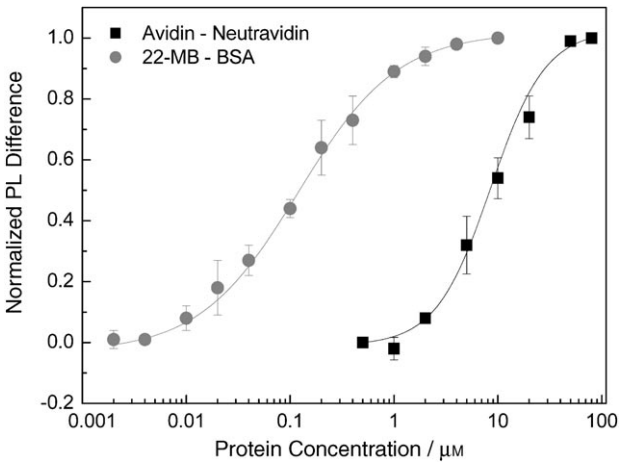

Figure 3. Detection of the glycan moiety of different glycoproteins. Normalized PL differences for avidin–neutravidin (■), $(PL_A-PL_N)/(PL_A-PL_N)_{max}$, and for 22-MB–BSA (●), $(PL_{22\text{-}MB}-PL_{BSA})/(PL_{22\text{-}MB}-PL_{BSA})_{max}$. The solid lines were obtained by fitting the four-parameter logistic equation to the data. Scale bars correspond to the standard deviation in triplicate experiments. In both curves, R^2 values are larger than 0.99.

BSA in different molar ratios. The mannose moiety of α-D-mannopyranosylphenyl isothiocyanate (MPI) was coupled with the lysine residue of the BSA through a covalent bond. The resulting differently mannosylated BSA molecules (Man-BSAs) were analyzed to quantify the number of conjugated mannose units per BSA molecule by using BioLC chromatography (see the Supporting Information). After the addition of each Man-BSA to the assay solution containing dex-QDs and conA-AuNPs we measured PL. The emission spectrum of the dex-QDs changed with an increasing number of mannose moieties on the BSA (Figure 4a), and the normalized PL difference between Man-BSAs and the native BSA at 605 nm, $(PL_{Man\text{-}BSA}-PL_{BSA})/(PL_{Man\text{-}BSA}-PL_{BSA})_{max}$, was enhanced as the occupancy number of the mannosylation sites increased (Figure 4b). These results illustrate that this system can be used effectively for the analysis of the degree of glycosylation of proteins.

In an attempt to expand the utility of our detection system, we tested glycoproteins with different glycan profiles. First, three kinds of recombinant glucose oxidases (rGOxs) with different lengths of high-mannose-type glycans were produced from the yeast strains *Saccharomyces cerevisiae* (*S. cerevisiae*), *Hansenula polymorpha* (*H. polymorpha*), and the glycosylation-defective mutant strain *Hpalg3*Δ of *H. polymorpha*. The GOx from *Aspergillus niger* (*A. niger*) was also tested as the authentic glycoprotein. The HPLC profile analysis of N-linked oligosaccharides clearly revealed that the GOx of each host strain has a distinct glycan profile, that is, a different distribution of mannose chains attached to the GOx (Figure 5a and the Supporting Information). As shown in Figure 5b, the responsive PL intensity of the assay with dex-QDs and conA-AuNPs varied distinctly with respect to the degree of mannosylation of the GOx. The hypermannosylated GOx from *S. cerevisiae* exhibited the highest PL intensity, which indicates that this GOx inhibited the PL quenching by conA-AuNPs most effectively. As expected, the

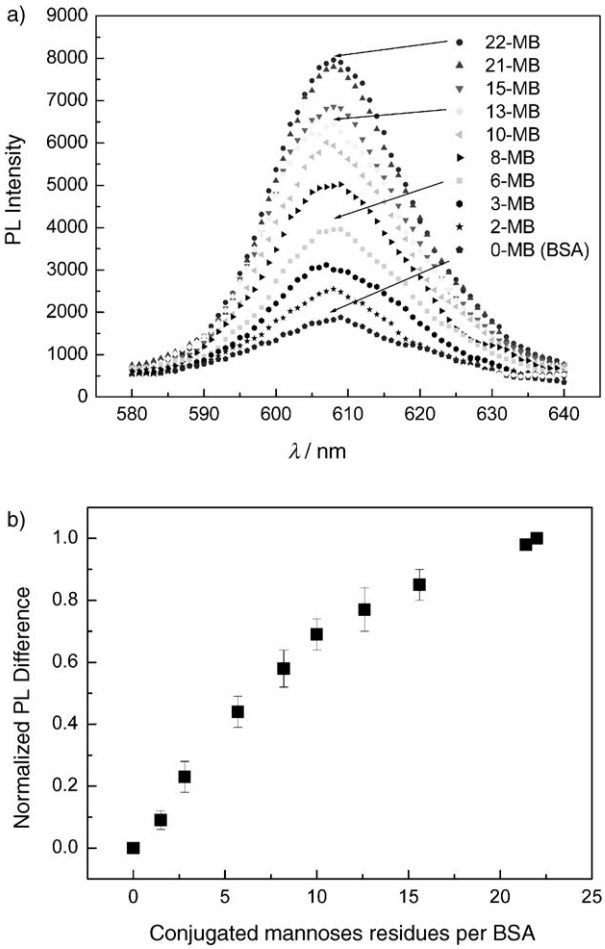

Figure 4. Changes in PL quenching of dex-QDs in the presence of diversely mannosylated BSA. a) Change in the emission spectra of dex-QDs caused by various Man-BSAs. The number in front of -MB indicates the number of conjugated mannose residues per BSA molecule. b) Normalized PL differences between Man-BSAs and native BSA, $(PL_{Man\text{-}BSA}-PL_{BSA})/(PL_{Man\text{-}BSA}-PL_{BSA})_{max}$. Scale bars indicate the standard deviation in quadruplicate experiments. The Man-BSA concentration was 1 μM, at which the inhibition effect by 22-MB was sufficient but smaller than that at saturation (see the Supporting Information).

hypomannosylated GOx from *Hpalg3*Δ gave rise to the lowest PL intensity. On the basis of these observations, it is evident that the PL intensity correlates well with the length of branched mannose chains on the proteins. Thus, these results clearly demonstrate the utility of our detection system.

To examine the possibility of high-throughput analysis of the degree of glycosylation, we conducted parallel detection of Man-BSAs by using a miniwell plate. The protein amount and the total volume of each assay were 556 ng and 5 μL, respectively. The PL intensity from the well plate was measured with a luminescent image analyzer (Figure 6), and the normalized PL difference increased with an increasing number of occupied mannosylation sites (see the Supporting Information). This is a similar trend to that observed for the PL described in Figure 4b.

We have demonstrated that NP-based energy transfer can be used effectively for the detection of glycan moieties and

 © 2006 Wiley-VCH Verlag GmbH & Co. KGaA, Weinheim

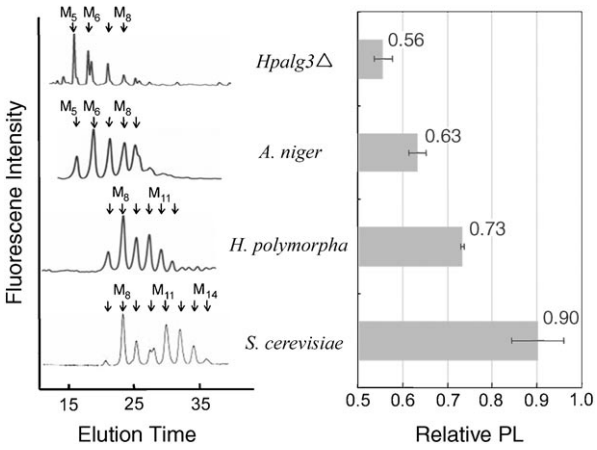

Figure 5. Detection of GOxs with varied glycan profiles. a) Glycan profiles of N-linked oligosaccharides released from GOxs were analyzed by HPLC. The length distribution of the mannose chains was assigned by comparison of the elution time with those of the reference oligosaccharides $Man_nGlcNAc_2$-PA (M_n; $n = 5, 6, 8, 11, 14$), which are indicated by arrows. The GOx produced from *Hpalg3*Δ contained the shortest chains with a distribution of mainly five to seven mannose residues. GOx produced by wild-type *S. cerevisiae* exhibited the longest chains (ranging from 8 to 14 residues). GOxs from wild-type *H. polymorpha* and *A. niger* were found to be mainly composed of 8–11 and 6–9 residues, respectively. b) Relative PL intensity of dex-QDs in the presence of the GOx. The assay was conducted by using apo-GOxs to eliminate the signal interference from flavin adenine dinucleotide coenzyme. GOx concentration: 75 nM.

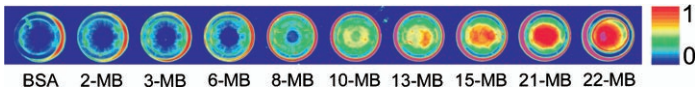

Figure 6. Pseudocolor image created by a luminescent image analyzer of a miniwell plate containing Man-BSAs and the assay solution. The number in front of -MB indicates the number of conjugated mannose residues per BSA molecule. A warmer color indicates a higher intensity at 605 nm.

the degree of glycosylation of proteins. This rapid and simple approach provides a reliable assay of protein glycosylation without tedious traditional deglycosylation and labeling steps. Only tiny amounts of glycoprotein and NPs are required for the completion of an assay because of high PL intensity and negligible bleaching of QDs. Furthermore, the dynamic range and sensitivity of this system can be modulated or extended readily by controlling the size, surface properties, and quantity of the NPs, as well as the number of conjugated molecules on the NPs. This system involving NP-based energy transfer could be implemented for multiplexed detection by using combinations of different lectins and QDs, and could contribute to a high-throughput analytical method for the development of glycoprotein and carbohydrate therapeutics. We also expect to be able to determine the complex glycan profile of a glycoprotein by employing a variety of lectins.

Experimental Section

Production of rGOxs: GOx from *A. niger* has eight potential sites for N-linked glycosylation.[19] rGOxs from other hosts were prepared by previously reported methods (Supporting Information).[20,21]

Synthesis of conA-AuNPs: AuNPs of 3.2 nm in size were synthesized and conjugated with conA (type IV from *Canavalia ensiformis*, Sigma) by direct adsorption (see the Supporting Information).[22] The number of conjugated conA molecules per AuNP was estimated to be three or four by considering the size of the AuNPs, each of which contains approximately 1000 Au atoms.[23]

Synthesis of dex-QDs: Amine-functionalized QDs (rod shaped; diameter ≈5 nm, length 10–15 nm, Quantum Dot Corporation) with an emission peak at 605 nm were conjugated to dextran activated with 1,1′-carbonyldiimidazole (see the Supporting Information).[24]

Synthesis of neoglycoprotein: MPI was used for the conjugation of mannose to BSA according to the reported method (see the Supporting Information).[25]

Preparation of apo-Gox: Apo-GOx was prepared by using ammonium sulfate as described elsewhere (see the Supporting Information).[26]

Detection of PL: The emission spectrum and PL intensity at 605 nm of dex-QDs were measured after excitation at 440 nm by a PL spectrometer (SLM-AMINCO). The assay solution was composed of conA-AuNPs (2.5 nM), dex-QDs (200 pM), Ca^{2+} (1.3 mM), Mn^{2+} (1 mM), and Mg^{2+} (1 mM) in doubly distilled water (200 μL).

Parallel analysis in miniwell plates: The CCD image of a miniwell plate containing dex-QDs was created and analyzed by a luminescent image analyzer (LAS-3000, Fujifilm, Japan, excitation at 460 nm, emission at 605 nm). The assay solution was composed of conA-AuNPs (4.17 nM), dex-QDs (333 pM), Man-BSA (1.67 μM, 556 ng), Ca^{2+} (1.3 mM), Mn^{2+} (1 mM), and Mg^{2+} (1 mM) in doubly distilled water (5 μL).

Received: May 17, 2006
Revised: July 14, 2006
Published online: November 2, 2006

Keywords: carbohydrates · energy transfer · glycoproteins · gold nanoparticles · quantum dots

[1] Y. Mechref, M. V. Novotny, *Chem. Rev.* **2002**, *102*, 321–369.
[2] A. Kobata, *Eur. J. Biochem.* **1992**, *209*, 483–501.
[3] A. Varki, *Glycobiology* **1993**, *3*, 97–130.
[4] M. Takeuchi, N. Inoue, T. W. Strickland, M. Kubota, M. Wada, R. Shimizu, S. Hoshi, H. Koizumi, S. Takasaki, A. Kobata, *Proc. Natl. Acad. Sci. USA* **1989**, *86*, 7819–7822.
[5] T. U. Gerngross, *Nat. Biotechnol.* **2004**, *22*, 1409–1414.
[6] P. Alivisatos, *Nat. Biotechnol.* **2004**, *22*, 47–52.
[7] C.-C. You, M. De, V. M. Rotello, *Curr. Opin. Chem. Biol.* **2005**, *9*, 639–646.
[8] P. P. Cheng, D. Silvester, G. Wang, G. Kalyuzhny, A. Douglas, R. W. Murray, *J. Phys. Chem. B* **2006**, *110*, 4637–4644.
[9] A. R. Clapp, I. L. Medintz, H. Tetsuo Uyeda, B. R. Fisher, E. R. Goldman, M. G. Bawendi, H. Mattoussi, *J. Am. Chem. Soc.* **2006**, *128*, 18212–18221.
[10] J. Lee, A. O. Govorov, N. A. Kotov, *Nano Lett.* **2005**, *5*, 2063–2069.
[11] C. S. Yun, A. Javier, T. Jennings, M. Fisher, S. Hira, S. Peterson, B. Hopkins, N. O. Reich, G. F. Strouse, *J. Am. Chem. Soc.* **2005**, *127*, 3115–3119.
[12] D. M. Willard, T. Mutschler, M. Yu, J. Jung, A. Van Orden, *Anal. Bioanal. Chem.* **2006**, *384*, 564–571.
[13] R. Wargnier, A. V. Baranov, V. G. Maslov, V. Stsiapura, M. Artemyev, M. Pluot, A. Sukhanova, I. Nabiev, *Nano Lett.* **2004**, *4*, 451–457.
[14] Z. Gueroui, A. Libchaber, *Phys. Rev. Lett.* **2004**, *93*, 166108.
[15] E. Oh, M. Y. Hong, D. Lee, S. H. Nam, H. C. Yoon, H. S. Kim, *J. Am. Chem. Soc.* **2005**, *127*, 3270–3271.
[16] D. Loganathan, S. E. Osborne, G. D. Glick, I. J. Goldstein, *Arch. Biochem. Biophys.* **1992**, *299*, 268–274.

 © 2006 Wiley-VCH Verlag GmbH & Co. KGaA, Weinheim

[17] G. Blagoi, N. Rosenzweig, Z. Rosenzweig, *Anal. Chem.* **2005**, *77*, 393 – 399.
[18] R. C. Bruch, H. B. White, *Biochemistry* **1982**, *21*, 5334 – 5341.
[19] K. R. Frederick, J. Tung, R. S. Emerick, F. R. Masiarz, S. H. Chamberlain, A. Vasavada, S. Rosenberg, S. Chakraborty, L. M. Schopfer, V. Massey, *J. Biol Chem.* **1990**, *265*, 3793 – 3802.
[20] M. W. Kim, S. K. Rhee, J. Y. Kim, Y. Shimma, Y. Chiba, Y. Jigami, H. A. Kang, *Glycobiology* **2004**, *14*, 243 – 251.
[21] M. W. Kim, E. J. Kim, J. Y. Kim, J. S. Park, D. B. Oh, Y. Shimma, Y. Chiba, Y. Jigami, S. K. Rhee, H. A. Kang, *J. Biol. Chem.* **2006**, *281*, 6261 – 6272.
[22] K. C. Grabar, K. J. Allison, B. E. Baker, R. M. Bright, K. R. Brown, R. G. Freeman, A. P. Fox, C. D Keating, M. D. Musick, M. J. Natan, *Langmuir* **1996**, *12*, 2353 – 2361.
[23] M. C. Danial, D. Astruc, *Chem. Rev.* **2004**, *104*, 293 – 346.
[24] G. T. Hermanson, *Bioconjugate Techniques*, Academic Press, San Diego, **1996**.
[25] K. S. Raja, Q. Wang, M. G. Finn, *ChemBioChem* **2003**, *4*, 1348 – 1351.
[26] S. Chinnayelka, M. J. McShane, *Biomacromolecules* **2004**, *5*, 1657 – 1661.

 © 2006 Wiley-VCH Verlag GmbH & Co. KGaA, Weinheim

Host–Guest Systems

DOI: 10.1002/anie.200602395

Stepwise Directing of Nanocrystals to Self-Assemble at Water/Oil Interfaces**

Jing Wang, Dayang Wang, Nelli S. Sobal, Michael Giersig, Ming Jiang, and Helmuth Möhwald*

The self-assembly of inorganic nanocrystals (NCs) into hierarchical structures on all length scales is pivotal for nanotechnology.[1] In this context, water/oil interfaces have gained increasing attention because their fluidity may heal defects and their rich phase separation behavior may diversify the structural complexity. The study of the attachment of micrometer-sized particles at the interface has a century-long history.[2] Nonetheless, the controlled interfacial self-assembly of NCs has been successfully realized only recently.[3–5] The appropriate surface hydrophobicity of NCs is crucial for NCs to self-assemble at the interface because of their fairly small interfacial attachment energy. This is usually realized by the proper design of the capping ligands on the NCs.[3,4] Herein, we demonstrate an alternative approach to render NCs interfacially active by entrapping their hydrophobic functional groups within the hydrophobic interior cavities of cyclodextrins (CDs). Furthermore, the functional groups on the hydrophilic exterior walls of CDs allow different NCs to be differentially directed from either the aqueous or organic phase to the interface, thus realizing stepwise interfacial self-assembly to form macroscopic heterogeneous multilayers of NCs over areas on the order of square centimeters.

CDs are characterised by having a hydrophilic exterior surface and a hydrophobic interior cavity that may include entirely or partially hydrophobic molecules through non-covalent interactions.[6] This inclusion shows a strong size selectivity. α-CDs can efficiently trap long alkyl chains, and this was used to realize the phase transfer of NCs from an organic to an aqueous phase[7] and vice versa.[8] In contrast, β-CDs have cavities of around 7.0 Å in size, which selectively trap large molecular cages such as adamantane (7 Å in diameter).[9] The specific inclusion of CDs and adamantane was used to grow multilayers of Au NCs on planar substrates layer by layer.[10]

In the present study hydrophobic 6-nm-diameter $CoPt_3$ NCs capped with 1-adamantylcarboxylic acid (ACA) and hexadecylamine (HDA) were prepared as explained elsewhere.[11] The simultaneous presence of HDA and ACA is essential for the colloidal stability of the $CoPt_3$ NCs; their partial removal leads to agglomeration of the NCs.[11] Hence one cannot render $CoPt_3$ NCs interfacially active through ligand exchange. In our study, solutions of $CoPt_3$ NCs in toluene were brought into contact with water, in which β-CDs or their derivatives were dissolved. Since the hydrophobic cavities of β-CDs or their derivatives selectively entrap the ACA group rather than the HDA,[6b,9b,c] their hydrophilic exterior walls convert the hydrophobic ACA domains on the $CoPt_3$ NCs into hydrophilic ones. The coexistence of hydrophobic HDAs and hydrophilic β-CDs or their derivatives may render the $CoPt_3$ NCs active at the interface, thus driving the NCs to self-assemble into a close-packed monolayer (Figure 1).

2-Hydroxypropyl-β-cyclodextrins (HPCDs) were used as models to demonstrate our concept because of their excellent water solubility.[12] An aqueous solution of the HPCDs (10 mM) was added to a solution of the $CoPt_3$ NCs in toluene (0.1 mg mL^{-1}). After gently shaking the mixture, a yellow thin film formed at the water/toluene interface (Figure 2a). In contrast, no such thin film formed in the absence of the HPCDs (see the Supporting Information). The UV/Vis spectra of the bulk phases showed little detectable absorption, thereby indicating that all the $CoPt_3$ NCs were located at the interface. This result also suggests that no phase transfer occurred. Transmission electron microscopy (TEM) imaging of these thin films, transferred from the interface, revealed a

[*] J. Wang, Dr. D. Wang, Prof. H. Möhwald
Max-Planck-Institut für Kolloide und Grenzflächen
14424 Potsdam (Germany)
Fax: (+49) 331-567-9253
E-mail: dayang.wang@mpikg-golm.mpg.de
J. Wang, Prof. M. Jiang
Department of Macromolecular Science
Fudan University
200433, Shanghai (P.R. China)
Dr. N. S. Sobal, Prof. M. Giersig
Center of Advanced European Studies and Research (CAESAR)
53175 Bonn (Germany)

[**] H. Zhang is acknowledged for help with the preparation of the CdTe nanocrystals. G. Zhang, J. Hartmann, O. Niemeyer, and T. Walther (CAESAR) are acknowledged for assistance with the AFM, TEM/EDX, and NMR measurements, as well as EDX mapping. We thank the Max-Planck-Gesellschaft for financial support.

Supporting information for this article is available on the WWW under http://www.angewandte.org or from the author.

 © 2006 Wiley-VCH Verlag GmbH & Co. KGaA, Weinheim

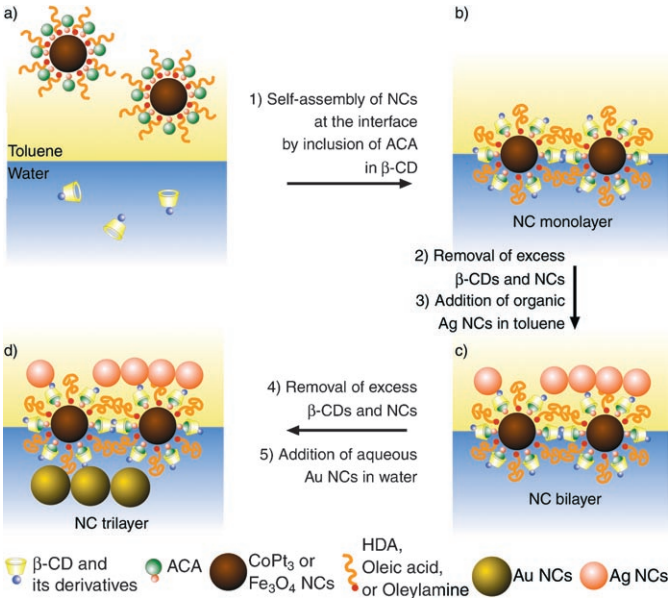

Figure 1. Schematic illustration of the self-assembly of ACA-stabilized NCs at the water/oil interface by the inclusion of ACA-capped NCs from an oil phase into CDs dissolved in water (a and b) and of the consecutive self-assembly with other hydrophilic and hydrophobic NCs into bilayers (c) or trilayers (d) based on the interaction of functional groups, such as NH_2 or SH, linked to CDs.

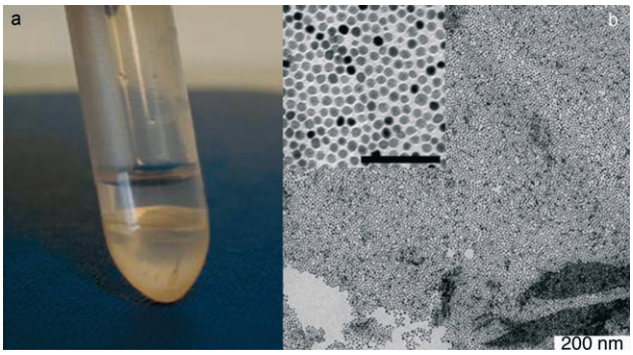

Figure 2. a) Photograph of the thin film of 6-nm-diameter $CoPt_3$ nanocrystals self-assembled at the water/toluene interface. b) TEM image of a thin film of the $CoPt_3$ nanocrystals transferred from the interface. The inset shows a high-magnification TEM image, the scale bar is 50 nm. HPCD is used for trapping the $CoPt_3$ nanocrystals at the interface.

monolayer of randomly close-packed NCs over a large area (Figure 2b).

We prepared 6-nm- and 17-nm-diameter Fe_3O_4 NCs stabilized with oleic acid and oleylamine in toluene by the oxidation of iron(III) acetylacetonate.[13] The initial capping groups of the Fe_3O_4 NCs were quantitatively replaced with ACA by ligand exchange. Incubating the Fe_3O_4 NCs in solutions of ACA in toluene at concentrations of 2, 10, and 20 $mg\,mL^{-1}$ for two days resulted in the number of ACA groups per NC being 62, 128, and 199, as determined by ^1H NMR spectroscopy (see the Supporting Information). Note that the maximal number of ACA groups per NC is calculated as 264. The inclusion of ACA by HPCD led to the interfacial self-assembly of the Fe_3O_4 NCs (Figure 3a,b). We envisioned that the reduction in the absorbance of the Fe_3O_4 NCs in the toluene phase should be proportional to the number of NCs attached at the water/toluene interface.

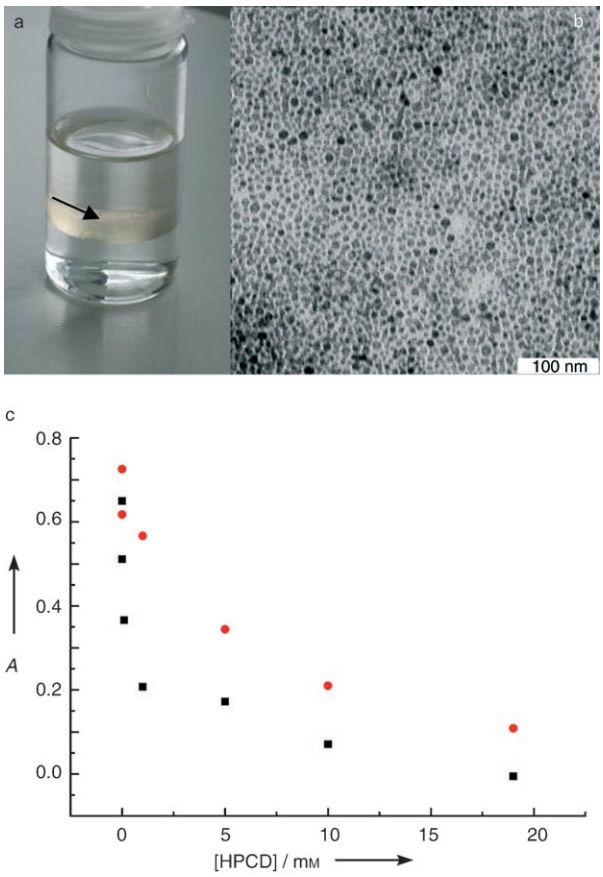

Figure 3. a) Photograph of a film derived from the self-assembly of 6-nm-diameter Fe_3O_4 NCs at the water/toluene interface and b) TEM image of the resulting thin film. The aqueous phase is 10 mM HPCD solution. The number of ACA groups per NC is 128. The water/toluene interface is highlighted by an arrow. c) Profile of the reduction in the absorption intensity of 6-nm-diameter Fe_3O_4 NCs in the toluene phase at 500 nm versus the concentration of HPCD in water. After mixing 1 mL toluene, containing 0.3 mg Fe_3O_4 NCs, with 1 mL of an aqueous solution of HPCD by shaking for 5 min, 0.8 mL organic aliquots were taken for UV/Vis absorption measurements. The numbers of ACA groups per NC are 128 (circle) and 199 (square).

Accordingly, we quasi-quantitatively evaluated the interfacial attachment of the Fe_3O_4 NCs at the interface between the toluene solution and the HPCD aqueous solution at different concentrations (see the Supporting Information). Figure 3c shows that the number of HPCDs required for the entire interfacial attachment of Fe_3O_4 NCs increases with the number of ACA groups functionalizing the NCs. This underlines that the interfacial self-assembly of the Fe_3O_4 NCs predominantly relies on the inclusion of ACA by HPCD.

Native β-CDs usually have a rather poor solubility in water because of intramolecular hydrogen-bonding interactions.[14] In the current study, the interfacial self-assembly of NCs was realized by using a rather dilute aqueous solution of

 © 2006 Wiley-VCH Verlag GmbH & Co. KGaA, Weinheim

β-CD (1 mM). We found that incubation at high temperature favored the formation of monolayers of NCs at the water/toluene interface: heating may weaken the intra- and intermolecular hydrogen bonding between the β-CD and the inclusion of ACA[15] (see the Supporting Information). In comparison to HPCD, β-CDs enhanced the stability of the emulsions. By staining with aqueous solutions of CdTe NCs, we found that the emulsions obtained were of the oil-in-water type (see the Supporting Information).

After the ACA functional groups on the $CoPt_3$ or Fe_3O_4 NCs had been inserted within the hydrophobic cavities of the β-CDs, the hydrophilic exterior walls of the latter were envisioned not only to result in the NCs becoming hydrophilic but also to provide flexibility for the further modification and conjugation with other materials. This encouraged us to utilize β-CDs with functional groups on the exterior walls to absorb different nanosized objects onto macroscopic monolayers of close-packed $CoPt_3$ or Fe_3O_4 NCs. Thus, heterogeneous multilayers composed of different NCs may be generated, which should be of great importance for microelectronics applications.[16] β-CDs functionalized with one SH or NH_2 group on the exterior walls, namely, mono{6-deoxy-6-[(mercaptohexamethylene)thio]}-β-cyclodextrin (SH-β-CDs)[17] and 6-monodeoxy-6-monoamino-β-cyclodextrin (NH_2-β-CDs) were recruited as new functional groups to direct different NCs to consecutively self-assemble at the water/oil interface (Figure 1). Similar to HPCDs, the NH_2-β-CDs and SH-β-CDs were able to direct ACA-capped NCs ($CoPt_3$ and Fe_3O_4) to self-assemble into randomly close-packing monolayers through the inclusion of ACA into the CD (see the Supporting Information). After the aqueous solution of SH-β-CDs was replaced by pure water, hydrophobic 6-nm-diameter Ag NCs stabilized with oleic acid were introduced into the toluene phase. The strong interaction between the SH groups on the β-CDs and the Ag NCs led to the interfacial attachment of the Ag NCs on the monolayers of the 6-nm-diameter Fe_3O_4 NCs (Figure 4a), accompanied by the appearance of a stronger metallic luster to the film and the disappearance of the dark-yellow color in the toluene phase (Figure 3a). TEM imaging demonstrated the formation of bilayers of close-packed NCs, but it was hard to distinguish the chemical nature of these two NCs because of their similar size and electron contrast (see the Supporting Information). Similarly, bilayers composed of 6-nm-diameter $CoPt_3$ and 12-nm-diameter Au NCs were formed at the interface by absorbing citrate-stabilized Au NCs from the aqueous phase using NH_2 groups attached to β-CDs (see the Supporting Information).

The resulting Ag/Fe_3O_4 NC bilayers are envisaged to have a hydrophobic surface in contact with the toluene, because of the free oleic acid capping the Ag NCs, and a slightly hydrophilic lower surface in contact with the water, as a result of free SH-β-CDs capping the Fe_3O_4 NCs. The free SH groups on the Fe_3O_4 NCs may be employed to attach other hydrophilic NCs from the aqueous phase (Figure 1). In the current study, 12-nm-diameter citrate-stabilized Au NCs were introduced into the aqueous phase. Figure 4b shows that after gentle shaking, the Ag/Fe_3O_4 NC bilayer films located at the interface appear purple when viewed in the transmittance mode and golden in the reflectance mode, thus suggesting the interfacial attachment of 12-nm-diameter Au NCs. TEM imaging of broken areas of the resulting thin films revealed a trilayer structure (see the Supporting Information). The existence of different NCs was demonstrated by energy-dispersive X-ray spectroscopy (EDX) and EDX mapping (see the Supporting Information). The thickness of the trilayers was nearly 25–30 nm, which is consistent with the formation of an Ag/Fe_3O_4/Au NC trilayer (see the Supporting Information). Note that both the bilayers and trilayers remain magnetic because of the existence of magnetic NCs (see the Supporting Information).

In summary, we have demonstrated that the use of the specific inclusion of adamantane by CD can direct hydrophobic ACA-capped NCs to self-assemble into macroscopic randomly close-packing monolayers at water/oil interfaces. By introducing functional groups, such as NH_2 or SH, onto the exterior surfaces of CDs, we succeeded in directing different hydrophobic and hydrophilic NCs to self-assemble in a stepwise manner at the water/oil interface, thereby generating macroscopic heterogeneous multilayers. This result demonstrates the unique amphoteric character of the water/oil interface—being able to conjugate both hydrophilic and hydrophobic NCs from water and oil phases. Since the success of our approach relies on the molecular structure of CDs, it should pave a versatile and efficient way to the stepwise self-assembly of NCs with different chemical natures and surface wettability into macroscopic lamellar superlattices of NCs based on well-established host–guest chemistry. The trilayer films of Ag/Fe_3O_4/Au NCs, which is a magnetic NC monolayer sandwiched between two metallic NC ones, should hold immense promise in technical applications, such as magnetic information storage and processing.

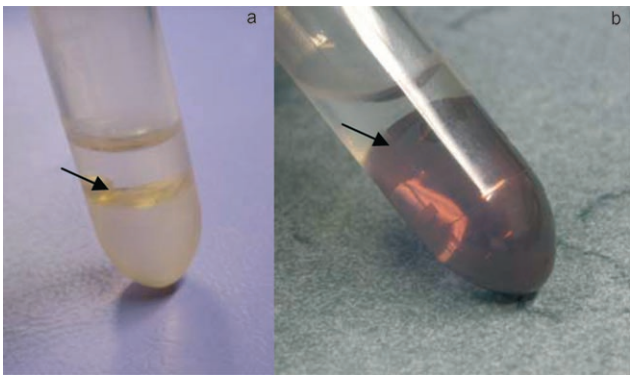

Figure 4. Photographs of the thin film obtained by consecutive self-assembly at the water/toluene interface to form bilayers of 6-nm-diameter Fe_3O_4 and 6-nm-diameter Ag NCs (a) and trilayers of 6-nm-diameter Fe_3O_4, 6 nm-diameter Ag, and 12-nm-diameter Au NCs (b). SH-β-CD is used for interfacial self-assembly. The water/toluene interface is highlighted by an arrow.

Experimental Section

Aqueous solutions (0.2 mL) of β-CD or its derivatives were brought into contact with solutions of NCs in toluene (0.2 mL). The gentle shaking led to a thin film being formed at the interface and the

 © 2006 Wiley-VCH Verlag GmbH & Co. KGaA, Weinheim

toluene phase turning colorles. SH-β-CDs or NH_2-β-CDs were used to form heterogeneous multilayers of NCs at the water/toluene interface. After monolayers of NCs were formed at the interface, excess CDs and magnetic NCs were removed by replacing the aqueous and organic phases by water and toluene, respectively. Hydrophobic Ag or hydrophilic Au NCs were then introduced into the toluene or water phase, respectively. A gentle shaking led to bilayers of metallic and magnetic NCs at the interface. After removing the excess metallic NCs, the addition of new metallic NCs in another phase yielded metallic/magnetic/metallic trilayer films at the interface.

UV/Vis absorption spectra were recorded on a Cary 50 UV/Vis spectrophotometer. TEM images were obtained on a Zeiss EM 912 Omega microscope. EDX and EDX mapping were conducted on a Philips XL30 and a LEO 922 A electron microscope.

Received: June 14, 2006
Revised: September 7, 2006
Published online: October 30, 2006

Keywords: host–guest systems · interfaces · multilayers · nanostructures · self-assembly

[1] a) A. P. Alivisatos, *Science* **1996**, *271*, 933 – 937; b) C. Collier, T. Vossmeyer, J. Heath, *Annu. Rev. Phys. Chem.* **1998**, *49*, 371 – 404; c) H. Weller, *Philos. Trans. R. Soc. London Ser. A* **2003**, *361*, 229 – 240.
[2] a) B. Binks, *Curr. Opin. Colloid Interface Sci.* **2002**, *7*, 21 – 41; b) R. Aveyard, B. Binks, J. Clint, *Adv. Colloid Interface Sci.* **2003**, *100*, 503 – 546.
[3] a) Y. Lin, H. Skaff, T. Emrick, A. Dinsmore, T. Russell, *Science* **2003**, *299*, 226 – 229; b) Y. Lin, H. Skaff, A. Boker, A. Dinsmore, T. Emrick, T. Russell, *J. Am. Chem. Soc.* **2003**, *125*, 12690 – 12691; c) J. Russell, Y. Lin, A. Boker, L. Su, P. Carl, H. Zettl, J. He, K. Sill, R. Tangirala, T. Emrick, K. Littrell, P. Thiyagarajan, D. Cookson, A. Fery, Q. Wang, T. Russell, *Angew. Chem.* **2005**, *117*, 2472 – 2478; *Angew. Chem. Int. Ed.* **2005**, *44*, 2420 – 2426; d) E. Glogowski, J. He, T. Russell, T. Emrick, *Chem. Commun.* **2005**, 4050 – 4052.
[4] a) D. Wang, H. Duan, H. Möhwald, *Soft Matter* **2005**, *1*, 412 – 416; b) H. Duan, D. A. Wang, D. Kurth, H. Möhwald, *Angew. Chem.* **2004**, *116*, 5757 – 5760; *Angew. Chem. Int. Ed.* **2004**, *43*, 5639 – 5642; c) H. Duan, D. Wang, N. Sobal, M. Giersig, D. Kurth, H. Möhwald, *Nano Lett.* **2005**, *5*, 949 – 952; d) F. Reincke, W. Kegel, H. Zhang, M. Nolte, D. Wang, D. Vanmaekelbergh, H. Möhwald, *Phys. Chem. Chem. Phys.* **2006**, *8*, 3828 – 3835.
[5] F. Reincke, S. Hickey, W. Kegel, D. Vanmaekelbergh, *Angew. Chem.* **2004**, *116*, 464 – 468; *Angew. Chem. Int. Ed.* **2004**, *43*, 458 – 462.
[6] a) J. Szejtli, *Chem. Rev.* **1998**, *98*, 1743 – 1753; b) M. Rekharsky, Y. Inoue, *Chem. Rev.* **1998**, *98*, 1875 – 1917.
[7] Y. Wang, J. Wong, X. Teng, X. Lin, H. Yang, *Nano Lett.* **2003**, *3*, 1555 – 1559.
[8] N. Lala, S. Lalbegi, S. Adyanthaya, M. Sastry, *Langmuir* **2001**, *17*, 3766 – 3768.
[9] a) R. Fort, P. von R. Schleyer, *Chem. Rev.* **1964**, *64*, 277 – 300; b) W. Cromwell, K. Bystrom, M. Eftink, *J. Phy.Chem.* **1985**, *89*, 326 – 332; c) M. Eftink, M. Andy, K. Bystrom, H. Perlmutter, D. Kristol, *J. Am. Chem. Soc.* **1989**, *111*, 6765 – 6772.
[10] O. Crespo-Biel, B. Dordi, D. Reinhoudt, J. Huskens, *J. Am. Chem. Soc.* **2005**, *127*, 7594 – 7600.
[11] a) E. Shevchenko, D. Talapin, A. Rogach, A. Kornowski, M. Haase, H. Weller, *J. Am. Chem. Soc.* **2002**, *124*, 11480 – 11485; b) X. Teng, H. Yang, *Nano Lett.* **2005**, *5*, 885 – 891.
[12] S. Gould, R. Scott, *Food Chem. Toxicol.* **2005**, *43*, 1451 – 1459.
[13] S. Sun, H. Zeng, D. Robinson, S. Raoux, P. Rice, S. Wang, G. Li, *J. Am. Chem. Soc.* **2004**, *126*, 273 – 279.
[14] a) K. Connors, *Chem. Rev.* **1997**, *97*, 1325 – 1357; b) A. Coleman, I. Nicolis, N. Keller, J. P. Dalbiez, *J. Inclusion Phenom. Mol. Recognit. Chem.* **1992**, *13*, 139 – 143; c) A. Buvari-Barcza, L. Barcza, *J. Inclusion Phenom. Macrocyclic Chem.* **2000**, *36*, 355 – 370.
[15] R. Auzely-Velty, M. Rinaudo, *Macromolecules* **2002**, *35*, 7955 – 7962.
[16] a) M. Islam, Y. Xia, M. Steigerwald, M. Yin, Z. Liu, S. O'Brien, R. Levicky, I. Herman, *Nano Lett.* **2003**, *3*, 1603 – 1606; b) M. Brust, C. Kiely, *Colloids Surf. A* **2002**, *202*, 175 – 186.
[17] G. Nelles, M. Weisser, R. Back, P. Wohlfart, G. Wenz, S. MittlerNeher, *J. Am. Chem. Soc.* **1996**, *118*, 5039 – 5046.

 © 2006 Wiley-VCH Verlag GmbH & Co. KGaA, Weinheim

Crystal Design

DOI: 10.1002/anie.200603241

Designing a Cocrystal of γ-Amino Butyric Acid**

*Mazal Wenger and Joel Bernstein**

Organic salts are generally the preferred crystal form of active pharmaceutical ingredients because of their higher solubilities and/or increased degree of crystallinity. The potential number of suitable organic salts is limited to the counterions specified by the food and drug association (FDA) as GRAS (generally regarded as safe). A recently suggested alternative to the common inorganic salts is the preparation of cocrystals[1] or organic salts, some of which have been shown to improve therapeutic utility while reducing side effects.[2–4]

Candidates for cocrystal formation with a particular structural motif for achieving desired physical properties[5,6] are chosen on the basis of their ability to utilize known intermolecular interactions in forming those crystals. Because hydrogen bonds are among the strongest and most preferentially directional intermolecular interactions, they have been the leading candidates for the interactions to be utilized in forming cocrystals,[7–10] although other interactions have also been suggested.[11a,b]

Particular preference in the development of the strategy for cocrystal formation utilizing hydrogen bonds has traditionally been based on the tendency of carboxylic acids and amides[12,13] to form the homo- or heterointermolecular synthons[14–16] described in Etter's graph-set notation[17,18] as

[*] M. Wenger, Prof. J. Bernstein
Department of Chemistry
Ben Gurion University of the Negev
P.O. Box 635, Beer Sheva (Israel)
Fax: (+972) 647-7641
E-mail: yoel@bgumail.bgu.ac.il

[**] This work is supported by a U.S.-Israel Binational Science Foundation Grant (no. 2004118). We are grateful to Dr. Dmitry Mogilyanski and Shoshana Lach for the XRPD measurements on the powders obtained by traditional methods (Figure 3) and for technical assistance.

WILEY InterScience DISCOVER SOMETHING GREAT
© 2006 Wiley-VCH Verlag GmbH & Co. KGaA, Weinheim

an $R_2^2(8)$ ring (which interprets as a ring (R) motif containing eight atoms with two hydrogen-bond donors (subscript) and two hydrogen-bond acceptors (superscript); Scheme 1). However, other hydrogen-bonding motifs such as $R_1^2(4)$ (Scheme 1), have also been investigated.[19,20] Herein we demonstrate the potential for utilizing another, as yet little recognized and not yet utilized, hydrogen-bonded synthon $R_4^2(8)$ (Scheme 1).

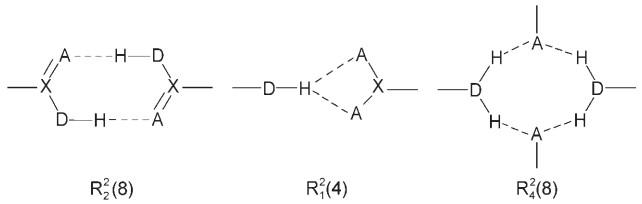

Scheme 1. The $R_2^2(8)$, $R_1^2(4)$, and $R_4^2(8)$ synthons. Some possible acceptors (A) and donors (D) for the $R_4^2(8)$ synthon: A: =O, =S, −F, −Cl, −Br, −I, F^-, Cl^-, Br^-, I^-, C≡N, C≡O; D: $=CH_2$, $-NH_2$, $-OH_2$, $-CRH_2$, $-N^+RH_2$, $^+OH_3$.

A survey of the Cambridge Structural Database (CSD version 1.8, 2006) has identified over 12000 instances of this synthon, virtually all of which involve four individual and nonconnected (but not necessarily chemically different) moieties in the solid state. Many of these cases involve two chemically different moieties, often resulting in a pattern that is crystallographically centrosymmetric or pseudocentrosymmetric. Perhaps the most remarkable feature about this synthon in terms of cocrystal formation is that it potentially involves the intermolecular recognition and supramolecular synthesis of four different molecules.

In the CSD, there are 918 hits for structures utilizing the $R_4^2(8)$ synthon (Scheme 1) in which the donor is the amino group (NH_2) and the acceptor is the carbonyl group (C=O). These are broken down into specific functional groups like (C=O)O^-, N(C=O), N(C=O)N, (C=O)OH, C(C=O)C, C(C=O)H, -NH_3^+, C−NH_2, NH_4^+, and N−NH_2. This survey clearly indicates that the highest incidence of participation in the $R_4^2(8)$ synthon is for carboxylate acceptors and ammonium cation donors.

In our cocrystallization attempts to achieve this synthon, we chose to use amino acids, starting with γ-amino butyric acid (GABA). As the CSD search indicated a preference for the ionized species -NH_3^+ and COO^- in the formation of the desired $R_4^2(8)$, we attempted crystallization in the pH range for which the amino group of GABA will be in the form of -NH_3^+ and the carboxylic group of the oxalic acid and benzoic acid will be in the form of -CO_2^-. The molar fractions[21] for the ionized species in different pH ranges can be calculated from the pK_a values of the acid and base. Figure 1 represents the calculated molar fraction for GABA and oxalic acid. For GABA, pK_a = 10.43, pK_b = 9.77, and the isoelectric point is pI = 7.33. For oxalic acid, pK_{a1} = 1.23 and pK_{a2} = 4.19. It is clear from Figure 1 that the crystallization for a 1:1 GABA/oxalic acid cocrystal should be carried out in the pH range 0–4.19 and crystallization for 2:1 cocrystal ratio should be carried out in the pH range 4.19–10.43. Our initial experiments were carried out at pH 5.

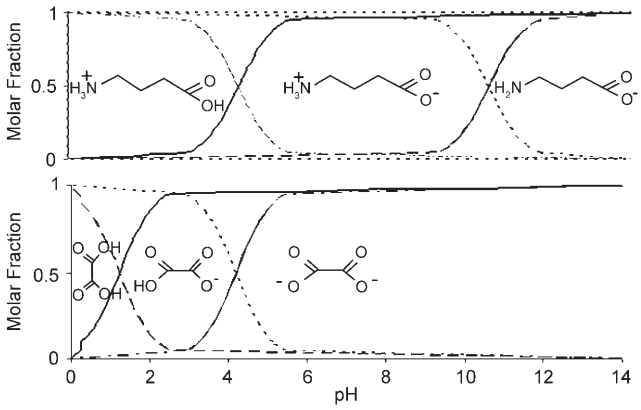

Figure 1. Solution speciation of GABA (top) and oxalic acid (bottom) showing the relative amounts of protonated and unprotonated species at each pH value.

The same calculations and molar fraction diagrams were prepared for the crystallization of GABA and benzoic acid. The pK_a value for benzoic acid is 4.19, which is the same as GABA. The crystallization attempts were carried out at three different pH values: 4, 6, and 12. At pH 4, the two species of benzoic acid and the two species of first dissociation of GABA are in equilibrium (see the Supporting Information). Experiments on oxalic acid and GABA yielded a 1:2 cocrystal of GABA/oxalic acid. As expected from Figure 1, GABA is protonated and the oxalic acid is a dianion. Charge neutrality therefore requires a 1:2 ratio of GABA and oxalic acid.

The crystal structure shown in Figure 2 clearly reveals three of the four hydrogen bonds required to complete the

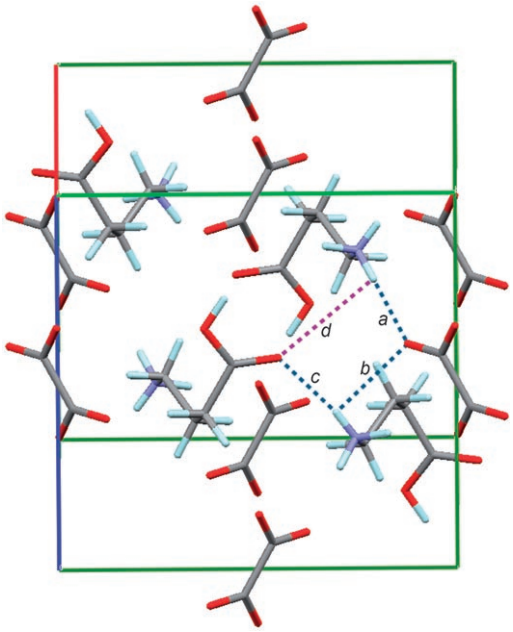

Figure 2. Unit cell of the 2:1 cocrystal of GABA/oxalic acid with hydrogen bonds (in blue) indicating the incipient formation of the $R_4^2(8)$ synthon. The pink line indicates the questionable hydrogen bond. The D···A distances are a = 1.913, b = 2.517, c = 2.063, and d = 3.242 Å. Other hydrogen bonds have been omitted for clarity. C gray, H light blue, N violet, O red.

© 2006 Wiley-VCH Verlag GmbH & Co. KGaA, Weinheim

$R_4^2(8)$ synthon. The donor–acceptor (D···A) distances, a = 1.913 Å, b = 2.517 Å, and c = 2.063 Å, are in the range of normal hydrogen bonds. The distance d (3.242 Å) is considerably long for an N–H···O hydrogen bond, but the incipient pattern of the synthon $R_4^2(8)$ still appears to be utilized in this structure.

Additional crystallizations were carried out at pH 0, 3, and 12. The results of X-ray powder diffraction (XRPD) studies, when compared with those of the starting materials (Figure 3 A), indicate the presence of new crystalline phases

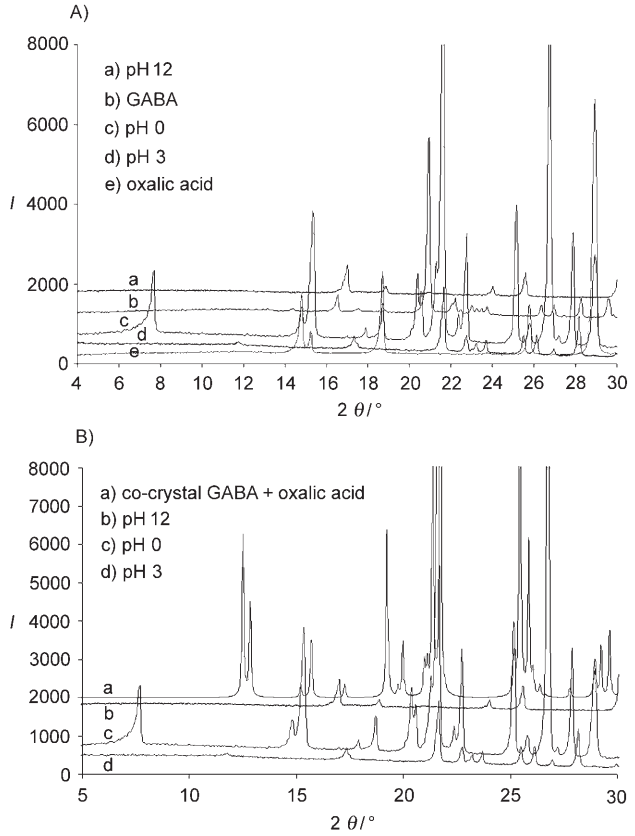

Figure 3. A) Comparison of the XRPD analyses from products of cocrystallization experiments at pH 0, 3, and 12 with the starting materials GABA and oxalic acid. B) Comparison of the XRPD analyses from products of cocrystallizations experiments at pH 0, 3, and 12 with the calculated XRPD from the single-crystal structure of the cocrystals of GABA and oxalic acid cocrystallized at pH 5.

(polymorph, hydrate, or differing stoichiometry) of the resulting powders. However, crystals suitable for structure analysis have not yet been obtained. These new phases can result from the different species coexisting at each pH value. From the crystal structure obtained at pH 5 (Figure 2), the acceptor that participates in the hydrogen bonds that are labeled *a*–*d* is the carboxylate group of GABA. This species can exist only above pH 4 (Figure 1). This fact can account for the different phases at the pH values of 0 and 3. One possibility for the appearance of a different phase obtained at pH 12 is that the donor for all the hydrogen bonds that participates in the hydrogen bonding is the amino group of GABA, which is protonated below pH 10 (see Figure 1); above this pH value (e.g. pH 12), the amino group will not be protonated and will likely participate in different hydrogen-bonding patterns.

A cocrystal of 1:1 benzoic acid/GABA was obtained from aqueous solution at pH 4. The small colorless crystals appeared a few minutes after adding water to a mixture of the solids. In the structure, the GABA is protonated and the benzoic acid is in the anionic form. Charge neutrality therefore requires a 1:1 ratio of GABA and benzoic acid. Figure 4 clearly reveals that the crystal structure utilizes two instances of the $R_4^2(8)$ synthon with hydrogen bonds *a* and *b* common to the two synthons.

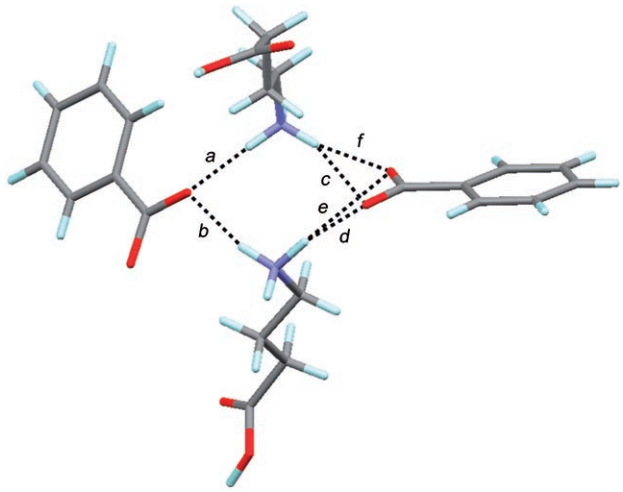

Figure 4. $R_4^2(8)$ synthons utilized in the structure of the cocrystal of 1:1 benzoic acid/GABA. The D···A distances in the first $R_4^2(8)$ synthon are a = 1.892, b = 1.909, c = 2.866, d = 1.799, e = 2.982, and f = 1.909 Å. Other hydrogen bonds have been omitted for clarity.

We have described a strategy to design cocrystals based on the $R_4^2(8)$ synthon by using pH as a controlling tool. Two cocrystals were obtained with the active pharmaceutical ingredient GABA, namely $(GABA)_2$ oxalate and GABA benzoate. The identification of other robust and versatile synthons can be utilized as an aid in the selection of potential cocrystal formers. Note that in the course of this work, we have also isolated and obtained the crystal structure of two previously unreported hydrates of oxalic acid, a dimorphic sesquihydrate. These will be reported in due course.

Experimental Section

Oxalic acid and GABA were weighed into a vial in a 1:1 stoichiometric ratio (likewise benzoic acid and GABA), water was added to dissolve the mixture, and then the pH was adjusted to pH 0, 3, 5, or 12 with NaOH or HCl solutions as needed.

X-ray crystal structural analysis for the cocrystal of oxalic acid/GABA: Data were collected at 297 K by using a Bruker SMART 6000 CCD diffractometer with $Mo_{K\alpha}$ radiation (λ = 0.71073 Å) M_r = 98.76, monoclinic space group $R2_1/c$, a = 7.4566(9), b = 10.2685(13), c = 9.7924(12) Å, β = 108.478(3)°, V = 711.13(15) Å^3, Z = 4, ρ_{calcd} = 1.384 g cm^{-3}, $\mu(Mo_{K\alpha})$ = 0.120 mm^{-1}, $F(000)$ = 316, θ_{min} = 2.9°, θ_{max} = 28.3°, R = 0.056, wR = 0.1374 observed data (with $I > 2\sigma I$) = 1646,

 © 2006 Wiley-VCH Verlag GmbH & Co. KGaA, Weinheim

total = 7832, unique = 1762, R(int) = 0.0293, Goof = 1.117 for 131 parameters.

X-ray crystal structural analysis for the cocrystal of benzoic acid/GABA: Data were collected at 297 K by using a Bruker SMART 6000 CCD diffractometer with $Mo_{K\alpha}$ radiation ($\lambda = 0.71073$ Å) M_r = 225.4, monoclinic space group $P2_1/n$, $a = 13.424(3)$ Å, $b = 6.212(1)$ Å, $c = 13.999(3)$ Å, $\beta = 101.748(4)°$, $V = 1142.8(4)$ Å^3, $Z = 4$, ρ_{calcd} = 1.309 gcm^{-3}, $\mu(Mo_{K\alpha}) = 0.100$ mm^{-1}, $F(000) = 480$, $\theta_{min} = 1.9°$, θ_{max} = 28.3°, $R = 0.046$, $wR = 0.1128$ observed data (with $I > 2\sigma I$) = 1663, total = 7108, unique = 2710 R(int) = 0.034, Goof = 1.011 for 205 parameters.

Received: August 9, 2006
Revised: September 9, 2006
Published online: November 9, 2006

Keywords: cocrystals · crystal engineering · hydrogen bonds · pH control · synthons

[1] a) J. J. Remenar, S. L. Morissette, M. L. Peterson, B. Moulton, J. M. MacPhee, H. Guzmán, Ö. Almarsson, *J. Am. Chem. Soc.* **2003**, *125*, 8456 – 8457; b) Ö. Almersson, M. J. Zaworotko, *Chem. Commun.* **2004**, 1889 – 1896.
[2] M. L. Brader, M. Sukumar, A. H. Pekar, D. S. McClellan, R. E. Chance, D. B. Flora, A. L. Cox, L. Irwin, S. R. Myers, *Nat. Biotechnol.* **2002**, *20*, 800 – 804.
[3] S. R. Ray, J. B. Bonanno, K. R. Rajashankar, M. G. Pinho, G. He, M. De Lencastere, A. Tomasz, S. K. Burley, *Structure* **2002**, *10*, 1499 – 1508.
[4] S. S. C. Koch et al., *J. Med. Chem.* **2002**, *45*, 4961 – 4974.
[5] L. R. MacGillivray, J. L Reid, J. A. Ripmeester, *J. Am. Chem. Soc.* **2000**, *122*, 7817 – 7818.
[6] M. C. Etter, G. M. Frankenbach, *Chem. Mater.* **1989**, *1*, 10 – 12.
[7] R.-F. Liao, J. W. Lauher, F. W. Fowler, *Tetrahedron* **1996**, *52*, 3143 – 3162.
[8] N. Shan, A. D. Bond, W. Jones, *Cryst. Eng.* **2002**, *5*, 9 – 24.
[9] T.-J. M. Luo, G. T. R. Palmore, *Cryst. Growth Des.* **2002**, *2*, 337 – 350.
[10] S. Mathew, G. Paul, K. Shivasankar, A. Choudhury, C. N. R. Rao, *J. Mol. Struct.* **2002**, *641*, 263 – 279.
[11] a) B. K. Saha, A. Nangia, M. Jaskolski, *CrystEngComm* **2005**, *7*, 355 – 358; b) C. B. Aakeroy, D. J. Salmon, *CrystEngComm* **2005**, *7*, 439 – 448.
[12] L. Leiserowitz, *Acta Crystallogr Sect. B* **1976**, *32*, 775.
[13] M. C. Etter, *Isr. J. Chem.* **1985**, *25*, 312 – 319.
[14] C. K. Huang, L. Leiserowitz, G. M. J. Schmidt, *J. Chem. Soc.* **1973**, *2*, 503 – 508.
[15] C. Tamura, N. Sakurai, S Sato, *Bull. Chem. Soc. Jpn.* **1971**, *44*, 1473 – 1479.
[16] C. Tamura, S. Sato, T. Tata, *Bull. Chem. Soc. Jpn.* **1973**, *46*, 2388 – 2394.
[17] M. C. Etter, *Acc. Chem. Res.* **1990**, *23*, 120 – 126.
[18] J. Bernstein, R. E. Davis, L. Shimoni, N.-L. Chang, *Angew. Chem.* **1995**, *107*, 1687 – 1706; *Angew. Chem. Int. Ed. Engl.* **1995**, *34*, 1555 – 1573.
[19] M. C. Etter, Z. Urbanczyk-Lipkowska, M. Zia-Ebrahimi, T. W. Panunto, *J. Am. Chem. Soc.* **1990**, *112*, 8415 – 8426.
[20] H. Dadon, J. Bernstein, *Inorg. Chem.* **1997**, *36*, 2898 – 2900.
[21] H. P. Jones, R. J. Davey, B. G. Cox, *J. Phys. Chem. B* **2005**, *109*, 5273 – 5278.

 © 2006 Wiley-VCH Verlag GmbH & Co. KGaA, Weinheim

Ozonides

DOI: 10.1002/anie.200603734

$Cs_5([12]crown\text{-}4)_2(O_3)_5$: A Supramolecular Compound Containing the Confined Ozonide Partial Structure $^1_\infty\{Cs_8(O_3)_{10}\}^{2-}$**

*Hanne Nuss and Martin Jansen**

Over the past twenty years, the chemistry of ionic ozonides has advanced significantly.[1] As an outcome of these efforts, the ozonides of the alkali metals Na–Cs are now accessible in high purities and in gram amounts.[2] This availability has allowed their full structural and basic physical characterization.[3–6] Even more importantly, the alkali-metal ozonides can now be employed as starting materials for the synthesis of ionic ozonides with a broad variety of other (complex) cations by metathesis[7] or ion-exchange reactions in liquid ammonia.[8–10] Whereas liquid ammonia is the only suitable solvent for the alkali-metal ozonides, yielding highly concentrated solutions with long-term stability below 243 K, the ozonides of voluminous organic cations readily dissolve in common solvents, such as tetrahydrofuran (THF), dimethyl sulfoxide (DMSO), dimethylformamide (DMF), or CH_2Cl_2. Ozonide solutions in CH_2Cl_2 are particularly stable and can be stored for weeks at 200 K without any indication of degradation. The availability of such solutions is a crucial requirement for subsequent chemistry involving the ozonide ion (O_3^-) in coordination or main-group molecular chemistry.

One of the most fascinating perspectives of ozonide chemistry is the potential dimerization of the radical ion. In analogy to the known equilibria of isoelectronic species (Scheme 1), two different mechanisms of dimerization, mediated through either the terminal (as for S_3^-) or the central (as for NF_2 and SO_2^-) atoms of the ozonide ion are conceivable. Although no indication of a monomer–dimer equilibrium has been detected in solution, a confinement and reduction in the

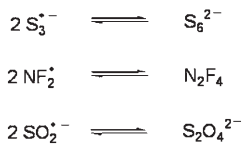

Scheme 1. Dimerization equilibria of species isoelectronic to O_3^-.

[*] Dipl.-Chem. H. Nuss, Prof. Dr. M. Jansen
Max Planck Institute for Solid State Research
Heisenbergstrasse 1, 70569 Stuttgart (Germany)
Fax: (+49) 711-689-1502
E-mail: m.jansen@fkf.mpg.de

[**] The authors thank Ms. A. Müller for help with the sample preparation, Mrs. E. Brücher for the SQUID magnetometry, Dr. R. Kremer for discussions about the magnetic measurements, and Mr. W. König for the IR spectroscopy.

Supporting information for this article is available on the WWW under http://www.angewandte.org or from the author.

© 2006 Wiley-VCH Verlag GmbH & Co. KGaA, Weinheim

dimensionality of the ozonide partial structure in the solid state might force the ozonide ions to approach one another. Such a reduction in dimensionality could possibly be achieved by employing one of the concepts of crystal engineering, the use of a combination of polar and nonpolar constituents, which tend to occupy separate volumes in the crystal.[11–13]

For cesium ozonide, this goal has been reached through the addition of the crown ether [12]crown-4, which does not match the size of the Cs^+ ion and, thus, coordinates weakly to one side of the ion.[19,20] Indeed, the crystal structure[21] of the transparent, deep red product $Cs_5([12]crown\text{-}4)_2(O_3)_5$ exhibits a one-dimensional host–guest arrangement. As illustrated in Figure 1, the crystal structure can be understood as a distorted tetragonal packing of $^1_\infty\{Cs_8(O_3)_{10}\}^{2-}$ rods, which run along the [100] direction and are separated by $[Cs([12]crown\text{-}4)_2]^+$ units.

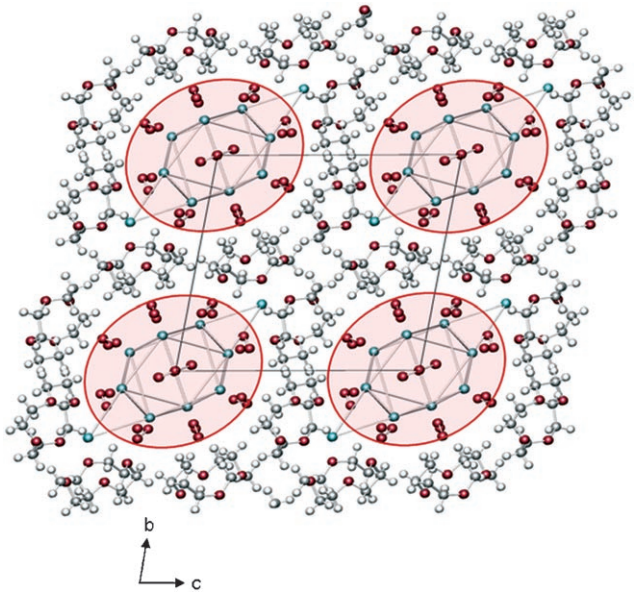

Figure 1. View of the structure of $Cs_5([12]crown\text{-}4)_2(O_3)_5$, showing the distorted tetragonal packing of $^1_\infty\{Cs_8(O_3)_{10}\}^{2-}$ rods, which are outlined by red circles. The lines connecting the Cs atoms are to aid visualization. Cs blue, C gray, H white, O red.

The rods have a diameter of approximately 1 nm and exhibit symmetry corresponding to rod group $p\bar{1}$ (no. 2).[22] They consist of stacks of tetragonal antiprisms of Cs^+ ions (with an average Cs···Cs distance of 456 pm), which are each centered by one ozonide ion and surrounded by four other crystallographically independent ozonide ions (Figure 2). The eight-fold coordination environment of the central ozonide ion is reminiscent of the situation in α-CsO_3 and β-CsO_3; however, in these CsCl-type structures, the ozonide ions are surrounded by Cs^+ ions in a cubic arrangement.[2e,f] The bond lengths and angles of the ozonide ions lie within the expected ranges. Those outside of the antiprisms are more distorted than the central ozonide ions, which have nearly perfect C_{2v} symmetry.

Furthermore, the structural restrictions imposed by this packing arrangement lead to the shortest intermolecular O···O distance yet observed between ozonide ions in the solid

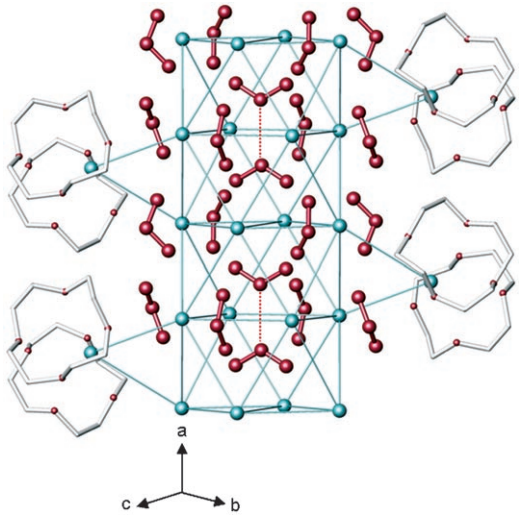

Figure 2. Side view of a $^1_\infty\{Cs_8(O_3)_{10}\}^{2-}$ rod and surrounding $[Cs([12]crown\text{-}4)_2]^+$ units. The short intermolecular distance (275.3(8) pm) between the central atoms of adjacent O_3^- ions is indicated by a red dotted line. The lines connecting the Cs atoms are to aid visualization. Geometry of the O_3^- ions: mean O–O distance 131(4) pm, O-O-O angles 115.5(4)–121.7(4)°. Cs blue, C gray, O red; H atoms are omitted for clarity.

state. The distance between the central oxygen atoms of two adjacent ozonide ions within the stacks of antiprisms is 275.3(8) pm (indicated by the red dotted lines in Figure 2). Previous investigations on alkali-metal ozonides showed that the arrangement of adjacent ozonide ions is mainly determined by dipole–dipole interactions between the negatively polarized terminal atoms and the positively polarized central atoms.[2] This interaction mode does not occur in the structure of $Cs_5([12]crown\text{-}4)_2(O_3)_5$. Apart from the rather short intermolecular distance described above, the next closest contacts of 347–368 pm occur between the terminal oxygen atoms of adjacent ozonide anions outside of the stacks of antiprisms. We ascribe these features to the structural confinement of the $^1_\infty\{Cs_8(O_3)_{10}\}^{2-}$ substructure by the nonpolar shell of $[Cs([12]crown\text{-}4)_2]^+$ units.

The Cs^+ ions of the $[Cs([12]crown\text{-}4)_2]^+$ units are coordinated by two crown ether molecules in a sandwich-like arrangement. The mean distance between the oxygen-atom planes of the crown ether molecules and the coordinated Cs^+ ions is 252 pm, and the tilt angle (the angle between the normals of these planes) is 135°. The IR spectrum of $Cs_5([12]crown\text{-}4)_2(O_3)_5$ demonstrates that the interaction between the Cs^+ ions and the [12]crown-4 molecules is weak: the five characteristic stretching modes of free [12]crown-4 in the fingerprint region, which have been shown to be sensitive to M^+–O interactions, are not shifted.[23,24]

The 19-valence-electron anion O_3^- exhibits the rarely encountered p-electron magnetism, which arises from the one unpaired electron. Ionic ozonides usually display Curie–Weiss paramagnetism, with a tendency towards antiferromagnetic ordering, depending on the intermolecular O···O distance and the type of interaction between the ozonide ions (terminal–terminal, terminal–central, or central–central). The mean

 © 2006 Wiley-VCH Verlag GmbH & Co. KGaA, Weinheim

magnetic moment is normally close to the spin-only value of 1.73 μ_B.[25] A significant interaction between the unpaired electrons, imposed by the short distance between the oxygen atoms, would lead to spin compensation and, thus, to a magnetic moment that is lower than the spin-only value. To determine whether such a scenario takes place, we investigated the magnetic properties of $Cs_5([12]crown\text{-}4)_2(O_3)_5$ by means of measurements on a superconducting quantum interference device (SQUID) magnetometer. The magnetic susceptibility χ of $Cs_5([12]crown\text{-}4)_2(O_3)_5$ in an applied field of 1 T is plotted against temperature T in Figure 3. The magnetic

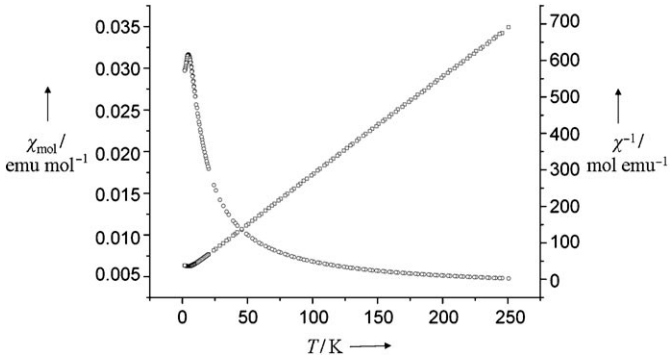

Figure 3. Temperature dependence of the magnetic susceptibility of $Cs_5([12]crown\text{-}4)_2(O_3)_5$ (○) and its inverse (□) in an applied field of 1 T (see Supporting Information for data at 0.1 and 7 T).

behavior above approximately 20 K can be described by the Curie–Weiss law $\chi = C/(T-\theta)+\chi_0$, with a temperature-independent contribution of $\chi_0 = 1.08(4)\times10^{-3}$ emu mol^{-1}. The calculated magnetic moment of 1.72 μ_B is close to the spin-only value of 1.73 μ_B expected for a single unpaired electron. Antiferromagnetic ordering occurs below the Néel temperature of $T_N = 4.5$ K (the Weiss parameter is $\theta = -5.1(4)$ K). Apparently, the O···O distance between the ozonide ions is too long to allow a measurable interaction between the unpaired electrons. However, further experiments, in particular, by means of electron paramagnetic resonance (EPR) spectroscopy, seem worthwhile, since the SQUID magnetometer detects only mean values of magnetization, from which the contributions of the interactions between the ozonide ions inside and outside of the stacks of antiprisms cannot be distinguished.

By applying the tools of crystal engineering to ionic ozonides, we were able to synthesize the first supramolecular ozonide with a one-dimensional host–guest structure. Structural confinement in this compound leads to a remarkably short intermolecular O···O distance between the ozonide ions. Although no evidence of an electronic interaction between the ions has yet been found, this supramolecular approach appears to be promising for the dimerization of ozonide ions.

Experimental Section

Attention: Ionic ozonides tend to decompose explosively. They should always be handled with care and should only be produced in small amounts.

All experiments were carried out under argon using modified Schlenk techniques or a glovebox (M. Braun; H_2O and O_2 less than 0.1 ppm). Ammonia (3.8, Westfalen AG) was stored as a potassium–ammonia solution at 195 K prior to use. [12]crown-4 (97%, Acros Organics) was used as received. CsO_3 was synthesized according to a literature procedure.[2c]

An H-shaped reaction vessel with a glass frit (porosity 3) was charged with [12]crown-4 (15.6 mg, 8.84×10^{-5} mol) and cooled to approximately 200 K using ethanol/dry ice. CsO_3 (40.0 mg, 2.21×10^{-4} mol) was added, and the reaction vessel was then filled with ammonia (ca. 10 mL) through condensation. The deep red reaction mixture was brought to the boiling point several times, until the crown ether dissolved completely. After 1 h, the deep red solution was filtered and reduced to half its volume. After 5 d at 200 K, red needles were isolated from the solution. For the single-crystal structure determination, the extremely sensitive crystals were handled according to the procedure described by Stalke and Kottke.[26]

Magnetic susceptibilities were determined with a MPMS7 Quantum Design SQUID magnetometer in applied fields of 0.1, 1, and 7 T over the temperature range 2–250 K. Powder samples were sealed under cooling into Suprasil quartz tubes filled with helium gas enabling fast thermal equilibration. Data were corrected for the magnetization of the empty tubes and for the diamagnetic contributions of the samples, using the increment method of Pascal and Pascal and of Gallais and Labarre.[27,28] A Honda–Owen correction was made to account for the contributions of small amounts of ferromagnetic impurities.[29,30]

Received: September 12, 2006
Published online: November 9, 2006

Keywords: cesium · crown compounds · host–guest systems · ozonides · supramolecular chemistry

[1] a) W. Hesse, M. Jansen, W. Schnick, *Prog. Solid State Chem.* **1989**, *19*, 47; b) "Ionische Ozonide": M. Jansen in *20 Jahre Wilhelm-Klemm-Stiftung* (Eds.: Kuratorium der Klemm-Stiftung), Shaker, Aachen, **2006**, pp. 84–124.
[2] a) W. Klein, K. Armbruster, M. Jansen, *Chem. Commun.* **1998**, 707; b) W. Schnick, M. Jansen, *Rev. Chim. Miner.* **1987**, *24*, 446; c) W. Schnick, M. Jansen, *Angew. Chem.* **1985**, *97*, 48; *Angew. Chem. Int. Ed. Engl.* **1985**, *24*, 54; d) W. Schnick, M. Jansen, *Z. Anorg. Allg. Chem.* **1986**, *532*, 37; e) M. Jansen, W. Hesse, *Z. Anorg. Allg. Chem.* **1988**, *560*, 47; f) M. Jansen, W. Assenmacher, *Z. Kristallogr.* **1991**, *194*, 315.
[3] G. Steffen, W. Hesse, M. Jansen, D. Reinen, *Inorg. Chem.* **1991**, *30*, 1923.
[4] W. Assenmacher, M. Jansen, *Z. Anorg. Allg. Chem.* **1998**, *624*, 661.
[5] T. Kellersohn, N. Korber, M. Jansen, *J. Am. Chem. Soc.* **1993**, *115*, 11254.
[6] W. Koch, G. Frenking, G. Steffen, D. Reinen, M. Jansen, W. Assenmacher, *J. Chem. Phys.* **1993**, *99*, 1271.
[7] W. Hesse, M. Jansen, *Inorg. Chem.* **1991**, *30*, 4380.
[8] N. Korber, M. Jansen, *Chem. Ber.* **1992**, *125*, 1383.
[9] W. Klein, M. Jansen, *Z. Anorg. Allg. Chem.* **2000**, *626*, 947.
[10] H. Seyeda, K. Armbruster, M. Jansen, *Chem. Ber.* **1996**. *129*, 997.
[11] A. Müller, H. Reuter, S. Dillinger, *Angew. Chem.* **1995**, *107*, 2505; *Angew. Chem. Int. Ed. Engl.* **1995**, *34*, 2328.
[12] M. C. T. Fyfe, J. F. Stoddart, *Acc. Chem. Res.* **1997**, *30*, 393.
[13] Similar approaches have been successfully employed in the supramolecular chemistry of silver halides, molybdenum compounds, and Zintl phases, for example.[14–18]
[14] L. A. Mundi, R. C. Haushalter, *J. Am. Chem. Soc.* **1991**, *113*, 6340.

 © 2006 Wiley-VCH Verlag GmbH & Co. KGaA, Weinheim

[15] L.-J. Chen, X. He, C.-K. Xia, Q.-Z. Zhang, J.-T. Chen, W.-B. Yang, C.-Z. Lu, *Cryst. Growth Des.* **2006**, *6*, 2076.

[16] H.-H. Li, Z.-R. Chen, J.-Q. Li, C.-C. Huang, Y.-F. Zhang, G.-X. Jia, *Eur. J. Inorg. Chem.* **2006**, 2447, and references therein.

[17] R. C. Burns, J. D. Corbett, *Inorg. Chem.* **1985**, *24*, 1489.

[18] T. F. Fässler, R. Hoffmann, *Angew. Chem.* **1999**, *111*, 526; *Angew. Chem. Int. Ed.* **1999**, *38*, 543.

[19] J. W. Steed, *Coord. Chem. Rev.* **2001**, *215*, 171.

[20] N. S. Poonia, A. V. Bajaj, *Chem. Rev.* **1979**, *79*, 389.

[21] Crystal data for $Cs_5([12]crown\text{-}4)_2(O_3)_5$: $C_{16}H_{32}O_{23}Cs_5$ $M_r = 1256.94\ g\,mol^{-1}$, triclinic, space group $P\bar{1}$ (no. 2), $a = 775.43(3)$, $b = 1445.10(5)$, $c = 1590.71(6)$ pm, $\alpha = 100.235(1)$, $\beta = 95.558(1)$, $\gamma = 98.599(1)°$, $V = 1720.4(1) \times 10^6\ pm^3$, $\rho_{calcd} = 2.431\ g\,cm^{-1}$, $Z = 2$, $\mu(Mo_{K\alpha}) = 5.33\ mm^{-1}$, $F(000) = 1174$, $\lambda = 71.073$ pm, Bruker AXS Smart APEX diffractometer, graphite monochromator, $T = 100$ K, ω scan, 10015 measured reflections, 8711 independent reflections, $2\theta_{max} = 60.0°$, 525 refined parameters, semi-empirical absorption correction with SADABS,[31] structure solution and refinement with SHELXTL,[32] $R_1 = 0.0406$, $wR_2 = 0.1035$ ($F_0 > 4\sigma(F_0)$), $R_1 = 0.0473$, $wR_2 = 0.1102$ (all data), residual electron density $3.99/-2.11 \times 10^{-6}\ e\,pm^{-3}$. CCDC 620501 contains the supplementary crystallographic data for this paper. These data can be obtained free of charge from The Cambridge Crystallographic Data Centre via www.ccdc.cam.ac.uk/data_request/cif.

[22] *International Tables for Crystallography*, *Vol. E: Subperiodic Groups*, *1st ed.* (Eds.: V. Kopský, D. B. Litvin), Kluwer, Dordrecht, **2002**.

[23] T. Akutagawa, T. Hasegawa, T. Nakamura, S. Takeda, T. Inabe, K. Sugiura, Y. Sakata, A. E. Underhill, *Inorg. Chem.* **2000**, *39*, 2645.

[24] A. A. El-Azhary, A. A. Al-Kahtani, *J. Phys. Chem. A* **2005**, *109*, 4505.

[25] H. Lueken, M. Deussen, M. Jansen, W. Hesse, W. Schnick, *Z. Anorg. Allg. Chem.* **1987**, *553*, 179.

[26] T. Kottke, D. Stalke, *J. Appl. Crystallogr.* **1993**, *26*, 615; D. Stalke, *Chem. Soc. Rev.* **1998**, *27*, 171.

[27] H. Lueken, *Magnetochemie*, Teubner, Stuttgart, **1999**.

[28] R. R. Gupta in *Landolt–Börnstein: Numerical Data and Functional Relationships in Science and Technology*, *New Series*, *Vol. 16* (Eds.: K.-H. Hellwege, A. M. Hellwege), Springer, Berlin, **1986**, pp. 1–10.

[29] K. Honda, *Ann. Phys.* **1910**, *32*, 1027.

[30] M. Owen, *Ann. Phys.* **1910**, *37*, 657.

[31] G. M. Sheldrick, SADABS Version 2.0, program for absorption correction, Bruker AXS, Madison (USA), **2001**.

[32] G. M. Sheldrick, SHELXTL Version 6.12, program suite for the solution and refinement of crystal structures, Bruker AXS, Madison (USA), **2000**.

 © 2006 Wiley-VCH Verlag GmbH & Co. KGaA, Weinheim

Porphyrinoids

DOI: 10.1002/anie.200603580

Facile Peripheral Functionalization of Porphyrins by Pd-Catalyzed [3+2] Annulation with Alkynes**

Akhila K. Sahoo, Shigeki Mori, Hiroshi Shinokubo, and Atsuhiro Osuka**

The electronic nature of a porphyrin ring is susceptible to modifications through the introduction of fused π-conjugated segments at the periphery.[1] This feature has been employed as a strategy for the creation of a variety of conjugated porphyrin systems that exhibit unique optical and electrochemical properties and which are expected to have applications in various types of functional materials. However, the introduction of such fused π systems on porphyrins often requires laborious multistep synthesis and suffers from frustratingly low yields. It is clear that novel and direct transformations of porphyrins are needed for further development of this area.[2]

A few transition-metal-catalyzed cross-coupling reactions, such as the Sonogashira and Suzuki–Miyaura reactions, have been successfully applied to porphyrins.[3] However, application of modern transition-metal-catalyzed reactions to porphyrin synthesis is still limited. We envisaged that a carbon–carbon bond-forming reaction of meso-bromoporphyrins with alkynes by carbopalladation[4] would be useful in generating a new molecular entity. We report herein an efficient way to incorporate a fused cyclopentadiene moiety into porphyrins such that the porphyrin π system is significantly perturbed. The wide scope of this procedure offers us rapid access to a diverse range of functionalized porphyrins. In addition, this cross-annulative coupling reaction allows a modular approach to a fascinating π system, namely, 7,8-dehydropurpurin.[5–7]

A mixture of 5-bromo-10,20-bis(3,5-di-*tert*-butylphenyl)-porphyrinnickel(II) (**1**; M = Ni) and diphenylacetylene (1.2 equiv) in 1,4-dioxane was heated at reflux in the presence of a catalytic amount of $Pd(OAc)_2/Ph_3P$ and K_2CO_3. We found

[*] Dr. A. K. Sahoo, S. Mori, Prof. Dr. H. Shinokubo, Prof. Dr. A. Osuka
Department of Chemistry
Graduate School of Science
Kyoto University
PRESTO & CREST
Japan Science and Technology Agency (JST)
International Innovation Center (IIC)
Kyoto University
Sakyo-ku, Kyoto 606-8502 (Japan)
Fax: (+81) 75-753-3970
E-mail: hshino@kuchem.kyoto-u.ac.jp
osuka@kuchem.kyoto-u.ac.jp

[**] This work was partly supported by a Grant-in-Aid for Scientific Research (no. 18685013) from MEXT. H.S. acknowledges the Asahi Glass Foundation for financial support.

Supporting information for this article is available on the WWW under http://www.angewandte.org or from the author.

© 2006 Wiley-VCH Verlag GmbH & Co. KGaA, Weinheim

that dehydropurpurin **2a** (M = Ni, R = Ph) was formed in 10% yield along with the debrominated porphyrin (Scheme 1). The parent mass ion peak of **2a** (M = Ni) was observed at *m*/*z* 918.4136 (calcd for $[C_{62}H_{60}N_4Ni]^+ = 918.4166$ $[M]^+$) in its high-resolution electrospray-ionization time-of-flight (HRESI-TOF) mass spectrum. ^{1}H NMR and H-H COSY spectra of **2a** (M = Ni) showed the presence of seven pyrrolic β protons: six doublets and one singlet ($\delta = 7.36$ ppm) appear, and the singlet can be assigned as H^1 (see the Supporting Information). After extensive optimization, the catalyst system comprising $[Pd_2(dba)_3]$/tris(*o*-tolyl)phosphine and dicyclohexylmethylamine in toluene delivered **2a** (M = Ni) in 78% yield. The reaction proceeded cleanly without by-products, other than the debrominated porphyrin, and none of the simple addition product without cyclization was detected in the reaction mixture.

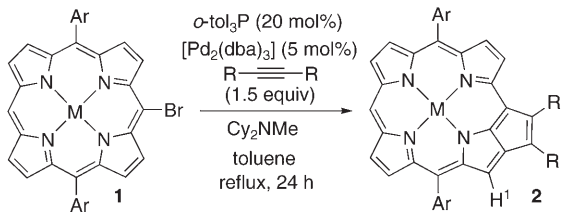

Scheme 1. Pd-catalyzed [3+2] annulation of porphyrin with alkynes. Cy = cyclohexyl, dba = *trans*,*trans*-dibenzylideneacetone, tol = tolyl.

Table 1: Pd-catalyzed [3+2] annulation of porphyrin with alkynes.[a]

Entry	R	M	Product	Yield (%)
1	Ph	Ni	**2a** (M = Ni)	78
2	4-CF_3(C_6H_4)	Ni	**2b** (M = Ni)	81
3	4-MeO(C_6H_4)	Ni	**2c** (M = Ni)	78
4	2-thienyl	Ni	**2d** (M = Ni)	82
5	*n*Pr	Ni	**2e** (M = Ni)	85
6	Ph	Cu	**2a** (M = Cu)	87
7	*n*Pr	Cu	**2e** (M = Cu)	86
8	Ph	Zn	**2a** (M = Zn)	79
9	4-CF_3(C_6H_4)	Zn	**2b** (M = Zn)	78
10[b]	4-MeO(C_6H_4)	Zn	**2f** (M = Zn)	69

[a] Reaction conditions: $[Pd_2(dba)_3]$ (1.5 μmmol), *o*-tol$_3$P (6.0 μmmol), meso-bromoporphyrin (30 μmmol), alkyne (45 μmmol), Cy_2NMe (0.15 mmol), toluene (1.5 mL), reflux, and 16–24 h. Ar = 3,5-di-*tert*-butylphenyl. [b] Ar = 3,5-dioctyloxyphenyl.

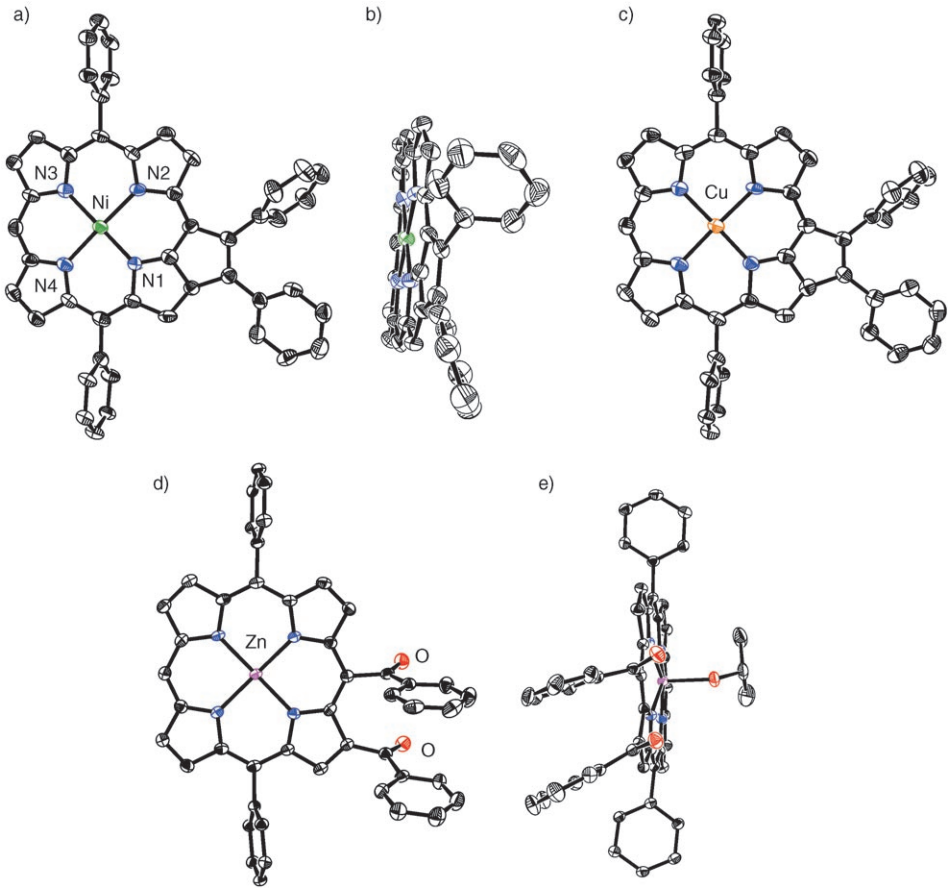

Figure 1. X-ray structures of **2a** (M = Ni and Cu) and **3**·*i*PrOH. a) Top view and b) side view of **2a** (M = Ni), and c) top view of **2a** (M = Cu); d) top view and e) side view of **3**. The thermal ellipsoids are at the 50% probability level. Hydrogen atoms and *tert*-butyl groups are omitted for clarity.

The annulation reaction with various alkynes is summarized in Table 1. This process was found to have a wide scope in regard to the metal ions at the center of the porphyrin ring and the alkynyl substituents. The reaction provided the desired products in good to excellent yields with aromatic and aliphatic alkynes. Zinc and copper porphyrins **1** (M = Zn and Cu) also underwent this annulation reaction with excellent yields.

X-ray crystallographic analyses unambiguously elucidated the structures of **2a** (M = Ni or Cu), and showed the presence of a fused five-membered ring (Figure 1).[8] The porphyrin framework of the nickel derivative is almost flat but slightly ruffled with small deviations (< 0.2 Å) from the mean plane. Annulation with a diphenylethene moiety results in contraction of the inner cavity, which leads to a better fit of the small nickel(II) ion. The Ni–N1 bond (1.904 Å) is shorter than the other Ni–N bonds (1.942–2.002 Å). Interestingly, one of the phenyl groups on the diphenylethene moiety is nearly perpendicular (72.8°) to the cyclopentadiene ring, but the other one is nearly coplanar (32.0°), which may permit its effective conjugation with the porphyrinic π network. The C–C double bond is relatively long at 1.374 Å, which indicates that this bond participates in the aromatic conjugated system. The copper derivative exhibits a similar structure.

© 2006 Wiley-VCH Verlag GmbH & Co. KGaA, Weinheim

Scheme 2 shows a plausible catalytic cycle. Oxidative addition of Pd^0 to the C–Br bond of **1** triggers the formation of porphyrinylpalladium **A**. Subsequent carbopalladation of **A** at the C–C triple bond provides alkenylpalladium species

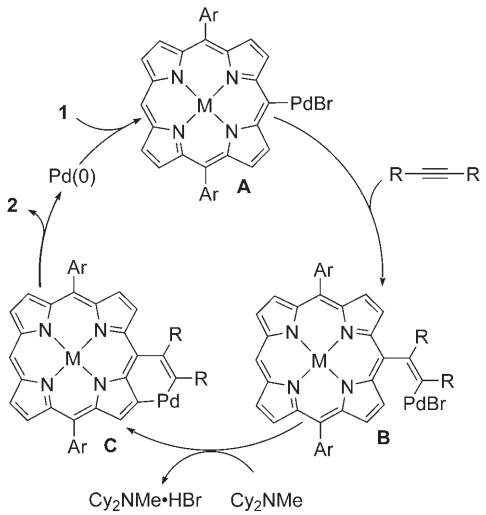

Scheme 2. A plausible mechanism for the Pd-catalyzed [3+2] anulation.

B, which is then converted into palladacycle **C** by intramolecular activation of the C–H bond. Reductive elimination eventually furnishes cyclized porphyrin **2** and regenerates the Pd^0 species. An intramolecular Heck-type reaction (carbopalladation–elimination sequence) of **B** is another possible pathway, but this involves unfavorable anti-β-hydride elimination.

The UV/Vis absorption spectra of **2a** (M = Ni and Cu) and **2e** (M = Ni; Figure 2a) exhibit substantially different shapes from those of typical porphyrins. Split Soret bands indicate the electronic structure has been significantly altered. In fact, DFT calculations elucidate significant development of frontier orbitals in the five-membered ring along with a much smaller gap between the highest occupied molecular orbital (HOMO) and the lowest unoccupied molecular orbital (LUMO; see the Supporting Information). Cyclic voltammetry studies showed a small separation between the first oxidation and the first reduction potential ($\Delta E = 1.66$ V) for **2a** (M = Ni) relative to that of 5,15-bis(3,5-di-*tert*-butylphenyl)porphyrinnickel(II) ($\Delta E = 2.29$ V). Incorporation of π orbitals from the C–C double bond resulted in a breaking of the symmetry of the porphyrin π system and expansion of the porphyrinic π network, as evident from the absorption spectra, which differ significantly from the typical spectra of porphyrins. Characteristically, the absorption spectra reach into the near infrared region.

During the measurement of the absorption spectra we encountered an interesting phenomenon with **2a** (M = Zn). The absorption spectrum of **2a** (M = Zn) in $CHCl_3$ was completely different from that of the typical porphyrin-like shape after exposure of the solution to air under room light for 3 h (Figure 2b). This process was found to be quantitative conversion of **2a** (M = Zn) into meso,β-dibenzoylporphyrin **3**

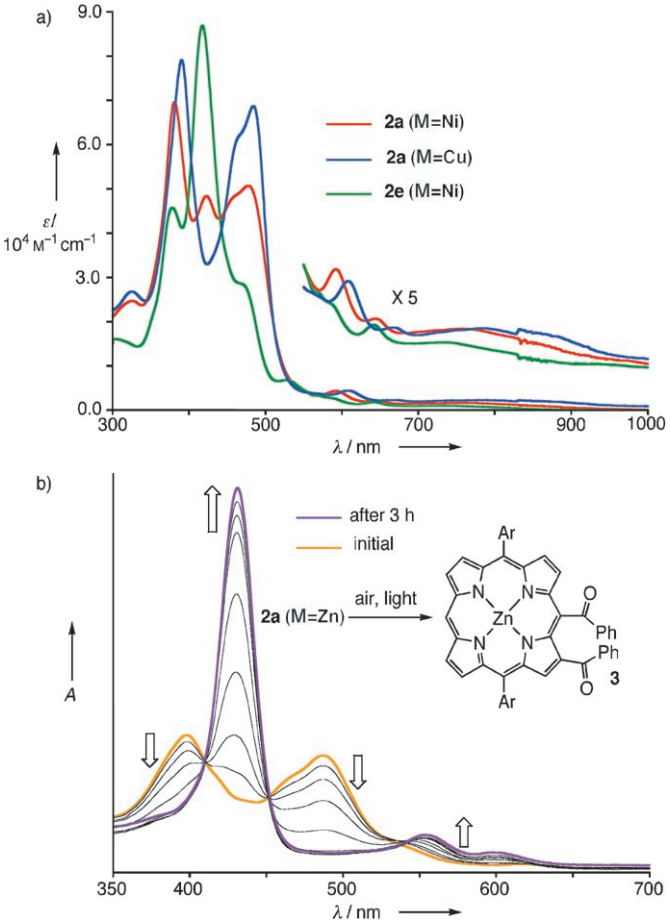

Figure 2. a) UV/Vis absorption spectra of **2a** (M = Ni and Cu), and **2e** (M = Ni) in $CHCl_3$. b) Change in the UV/Vis absorption spectra of **2a** (M = Zn) in $CHCl_3$ under ambient conditions.

by oxidation of the outer C–C double bond. The assignment of **3** was based on HRESI-TOF mass and ^{13}C NMR spectra, the latter of which indicated the presence of two carbonyl groups in **3**. Final elucidation of the structure was accomplished by X-ray crystallographic analysis of crystals of **3** grown by vapor diffusion of isopropyl alcohol into a chloroform solution (Figure 1de).[9] The porphyrin framework of **3** is perfectly flat, without any distortion. The two benzoyl groups are positioned close to each other and this accounts for the temperature-dependent ^1H NMR spectra of **3** (see the Supporting Information). The strain induced by a bicyclo[3.3.0]octane skeleton would increase the reactivity of **2** toward oxidation. Contrasting photochemical stabilities of **2a** (M = Ni and Cu) suggested the involvement of singlet oxygen in this conversion.

In conclusion, the palladium-catalyzed coupling reaction of meso-bromoporphyrins with a variety of internal alkynes efficiently provides peripherally cyclopentadiene-fused porphyrins by a rational one-step synthetic protocol. Incorporation of the C–C double bond alters both the electronic and chemical properties of porphyrins. This efficient and direct functionalization indicates the prospect of using transition-metal-catalyzed reactions in porphyrin chemistry. Investigations on the application of this strategy to multiporphyrinic

 © 2006 Wiley-VCH Verlag GmbH & Co. KGaA, Weinheim

compounds and elucidation of the mechanism of oxidative cleavage of **2a** (M = Zn) are currently in progress.

Received: September 1, 2006
Published online: November 9, 2006

Keywords: alkynes · fused-ring systems · oxidation · palladium · porphyrinoids

[1] a) M. G. H. Vicente, K. M. Smith, *J. Porphyrins Phthalocyanines* **2004**, *8*, 26; b) H. S. Gill, M. Harmjanz, J. Santamaria, I. Finger, M. J. Scott, *Angew. Chem.* **2004**, *116*, 491; *Angew. Chem. Int. Ed.* **2004**, *43*, 485; c) S. Richeter, C. Jeandon, J. P. Gisselbrecht, R. Ruppert, H. J. Callot, *J. Am. Chem. Soc.* **2002**, *124*, 6168; d) D. M. Shen, C. Liu, Q. Y. Chen, *Chem. Commun.* **2005**, 4982; e) S. Fox, R. W. Boyle, *Chem. Commun.* **2004**, 1322; f) K. Kurotobi, K. S. Kim, S. B. Noh, D. Kim, A. Osuka, *Angew. Chem.* **2006**, *118*, 4048; *Angew. Chem. Int. Ed.* **2006**, *45*, 3944; g) O. Yamane, K. Sugiura, H. Miyasaka, K. Nakamura, T. Fujimoto, K. Nakamura, T. Kaneda, Y. Sakata, M. Yamashita, *Chem. Lett.* **2004**, *33*, 40; h) H. J. Callot, E. Schaeffer, R. Cromer, F. Metz, *Tetrahedron* **1990**, *46*, 5253; i) A. Tsuda, A. Osuka, *Science* **2001**, *293*, 79.

[2] For a review on recent examples of novel transformations of porphyrins, see: M. O. Senge, J. Richter, *J. Porphyrins Phthalocyanines* **2004**, *8*, 934.

[3] For reviews, see: a) W. M. Sharman, J. E. Van Lier, *J. Porphyrins Phthalocyanines* **2000**, *4*, 441; b) J. Setsune, *J. Porphyrins Phthalocyanines* **2004**, *8*, 93.

[4] For annulation reactions with alkynes induced by carbopalladation, see: a) G. Wu, A. Rheingold, S. J. Geib, R. F. Heck, *Organometallics* **1987**, *6*, 1941; b) R. Grigg, P. Kennewell, A. Teasdale, V. Sridharan, *Tetrahedron Lett.* **1993**, *34*, 153; c) R. C. Larock, M. J. Doty, Q. Tian, J. M. Zenner, *J. Org. Chem.* **1997**, *62*, 7536.

[5] a) A. Nakano, N. Aratani, H. Furuta, A. Osuka, *Chem. Commun.* **2001**, 1920; b) C. Bauder, R. Ocampo, H. J. Callot, *Tetrahedron* **1992**, *48*, 5135; c) H. Klement, M. Helfrich, U. Oster, S. Schoch, W. Rüdiger, *Eur. J. Biochem.* **1999**, *265*, 862.

[6] Purpurins are a class of porphyrins which have potential application in artificial photosynthesis and photodynamic therapy.

[7] The synthesis of porphyrins with fused five-membered exocyclic rings is also challenging and extensively studied. For leading references, see: a) J. K. Laha, C. Muthiah M. Taniguchi, J. S. Lindsey, *J. Org. Chem.* **2006**, *71*, 7049; b) B. Zhang, T. D. Lash, *Tetrahedron Lett.* **2003**, *44*, 7253; c) K. M. Smith, K. C. Langry, O. M. Minnetian, *J. Org. Chem.* **1984**, *49*, 4602.

[8] Crystal data of **2a** (M = Ni): $C_{68}H_{64}Cl_2N_4Ni$, $M_r = 1066.84$, monoclinic, space group *Cc* (no. 9), $a = 35.997(12)$, $b = 5.8843(15)$, $c = 26.293(8)$ Å, $\beta = 96.469(12)°$, $V = 5534(3)$ Å^3, $Z = 4$, $\rho_{calcd} = 1.280$ g cm^{-3}, $T = 90(2)$ K, 10185 measured reflections, 7628 unique reflections, $R = 0.0971$, $R_w = 0.2832$ (all data), GOF = 1.041 ($I > 2.0\sigma(I)$). Crystal data of **2a** (M = Cu): $C_{68}H_{64}Cl_2N_4Cu$, $M_r = 1071.67$, monoclinic, space group *Cc* (no. 9), $a = 35.996(13)$, $b = 5.847(2)$, $c = 26.325(9)$ Å, $\beta = 96.380(13)°$, $V = 5506(3)$ Å^3, $Z = 4$, $\rho_{calcd} = 1.293$ g cm^{-3}, $T = 123.1$ K, 11657 measured reflections, 8262 unique reflections, $R = 0.0774$, $R_w = 0.2285$ (all data), GOF = 1.056 ($I > 2.0\sigma(I)$). CCDC-619420 (**2a** (M = Ni)), CCDC-619421 (**2a** (M = Cu)), and CCDC-619419 (**3**) contain the supplementary crystallographic data for this paper. These data can be obtained free of charge from The Cambridge Crystallographic Data Centre via www.ccdc.cam.ac.uk/data_request/cif.

[9] Crystal data of **3**: $C_{71}H_{84}O_5N_4Zn$, $M_r = 1138.85$, triclinic, space group $P\bar{1}$ (no. 2), $a = 11.688(3)$, $b = 15.783(4)$, $c = 19.429(6)$ Å, $\alpha = 112.513(10)$, $\beta = 95.172(11)$, $\gamma = 104.909(8)°$, $V = 3127.3(14)$ Å^3, $Z = 2$, $\rho_{calcd} = 1.209$ g cm^{-3}, $T = 123(2)$ K, 30667 measured reflections, 14114 unique reflections, $R = 0.0601$, $R_w = 0.1708$ (all data), GOF = 1.033 ($I > 2.0\sigma(I)$).

 © 2006 Wiley-VCH Verlag GmbH & Co. KGaA, Weinheim

Enzyme Models

DOI: 10.1002/anie.200603486

A Structural and Functional Model for Dioxygenases with a 2-His-1-carboxylate Triad**

*Paul D. Oldenburg, Chun-Yen Ke, A. Alex Tipton, Albert A. Shteinman, and Lawrence Que, Jr.**

Nature has evolved many oxygen-activating enzymes that catalyze a variety of metabolically important oxidations.[1] In the subset containing mononuclear non-heme iron active sites, the 2-His-1-carboxylate facial triad has emerged as a common coordinative motif in which two His residues and either an Asp or Glu residue occupy one face of the iron octahedron.[2] The remaining coordination sites can then be utilized for binding and activating the substrate and/or O_2. Although the available crystallographic data for enzymes with this motif shows the carboxylate ligand to be monodentate in most cases, bidentate carboxylate binding has been demonstrated for naphthalene dioxygenase (NDO)[3] and nitrobenzene dioxygenase (NBDO)[4] in their substrate-bound forms. NDO and NBDO are classified as Rieske dioxygenases, enzymes that initiate the biodegradation of aromatic molecules in soil bacteria by carrying out a novel *cis*-dihydroxylation of the aromatic ring.[5] Based on crystallographic data of their ESO_2 adducts, O_2 activation is thought to proceed through a side-on bound dioxygen moiety that delivers two oxygen atoms stereospecifically to the aromatic substrate.[3,5c] Thus, two *cis*-oriented labile sites on the iron center are important for dioxygen activation.

The recent emergence of the 2-His-1-carboxylate facial triad as a recurring motif for many non-heme iron enzymes[2d] has spurred efforts to obtain synthetic models for this class of enzymes. Some success has been achieved in obtaining structural models by using N,N,O ligand sets (Scheme 1);[6] however, only one of these, **3**, serves as a functional model and its O ligand is not a carboxylate, but an amide carbonyl

[*] P. D. Oldenburg, Dr. C.-Y. Ke, Dr. A. A. Tipton, Prof. Dr. L. Que, Jr.
Department of Chemisty and Center for Metals in Biocatalysis
University of Minnesota
207 Pleasant Street SE, Minneapolis, MN 55455 (USA)
Fax: (+1) 612-624-7029
E-mail: que@chem.umn.edu
Prof. Dr. A. A. Shteinman
Institute of Problems of Chemical Physics
Russian Academy of Sciences
Chernogolovka, Moscow Region 142432 (Russia)

[**] This work was supported by the U.S. Department of Energy (DOE DE-FG02-03ER15455) and the U.S. Civilian Research and Development Foundation (CRDF RC1-2058). We would like to acknowledge Dr. Maren Pink and Dr. Victor G. Young, Jr. and the X-Ray Crystallographic Laboratory of the University of Minnesota for solving the structure of complex **1**-Cl.

Supporting information (including characterization data) for this article is available on the WWW under http://www.angewandte.org or from the author.

© 2006 Wiley-VCH Verlag GmbH & Co. KGaA, Weinheim

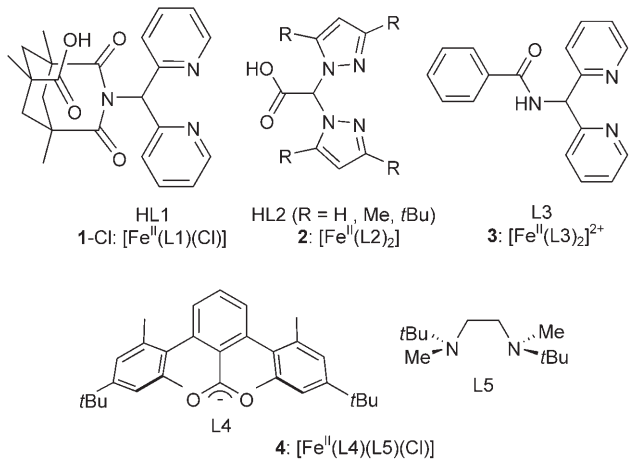

Scheme 1. The structures of HL1 and other ligands used to model 2-His-1-carboxylate non-heme iron enzymes (see Ref. [6]).

instead.[6c] Herein, we report the synthesis of a new polydentate ligand HL1 (Scheme 1) that provides two pyridines and one bidentate carboxylate. Iron(II) complexes of this ligand activate H_2O_2 to carry out olefin epoxidation and *cis*-dihydroxylation, thereby serving as both structural and functional models for the active site of the Rieske dioxygenases.

The ligand 3-(dipyridin-2-yl-methyl)-1,5,7-trimethyl-2,4-dioxo-3-azabicyclo[3.3.1]nonane-7-carboxylic acid (HL1, Scheme 1) was synthesized from the reaction of Kemp's acid chloroanhydride[7] with di(2-pyridyl)methylamine[8] by using 4-dimethylaminopyridine (DMAP) as a catalyst. Combination of deprotonated HL1 and $Fe^{II}Cl_2$ in CH_3CN afforded the complex $[Fe^{II}(L1)Cl]$ (**1**-Cl), which was purified by recrystallization from CH_3OH/Et_2O. Single crystals of **1**-Cl that were suitable for crystallographic analysis were obtained from CH_3CN at −20 °C.[9]

The crystal structure of **1**-Cl (Figure 1) reveals a square-pyramidal ($\tau = 0.03$) iron center with an apical chloride ligand and the tetradentate L1 occupying the basal plane with metal–ligand distances that are typical of a high-spin iron(II) center.[6] The dioxoazabicyclic moiety, which serves as the framework to tether the pyridines and the bidentate carboxylate, wraps underneath the iron center and prevents the coordination of another ligand *trans* to the chloride. This ligand conformation appears energetically stable with the cyclohexyl ring in the chair conformation and the three methyl groups situated equatorially. This conformation positions the carboxylate to bind in a bidentate fashion to the iron center.

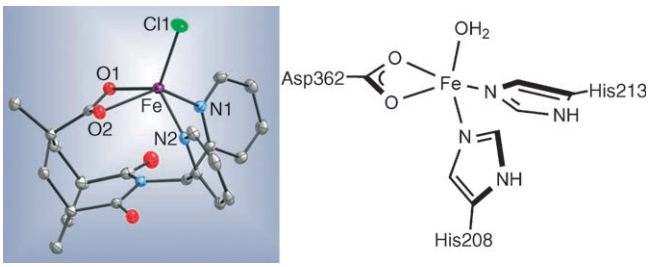

Figure 1. The ORTEP plot for $[Fe^{II}(L1)(Cl)]$ (**1**-Cl) showing 50% probability ellipsoids (left) and the mono-iron site of the substrate-bound form of naphthalene 1,2-dioxygenase (right, PDB 1O7G). Hydrogen atoms and noncoordinated solvent molecules have been omitted for clarity. Selected bond lengths are listed in Table 1.

Complex **1**-Cl differs in some respects from other iron(II) complexes that model the 2-His-1-carboxylate triad (**2**–**4**, Table 1).[6] Complexes **2**[6a,b] and **3**[6c] feature facial N,N,O ligand sets in which the carboxylate (or carboxamide) moiety is bound in a monodentate fashion, with Fe–O bond lengths (2.00–2.08 Å) that are shorter than for the bidentate carboxylate in **1**-Cl (2.15 Å). Furthermore, these are isolated as six-coordinate ML_2 complexes. On the other hand, **1**-Cl and **4**[6d] are both five-coordinate complexes with N_2O_2Cl ligand sets and resemble the iron centers found in the substrate-bound complexes of two Rieske dioxygenases (Figure 1 and Table 1). The metal–ligand distances found for **1**-Cl, however, more closely approximate those in the enzymes, particularly the more symmetric binding of the bidentate carboxylate. The main difference between **1**-Cl and the enzyme complexes lies in the arrangement of the ligands. For **1**-Cl, the chloride is the apical ligand, but for the enzymes, the water ligand that corresponds to the chloride occupies a nonapical position. Nevertheless, in either arrangement, there appears to be sufficient coordination flexibility to allow coordination of a bidentate oxidant in place of the chloride or water.

Table 1: Bond lengths [Å] and τ values observed for the iron centers in **1**–**4** and the substrate-bound forms of NDO and NBDO.

	1-Cl	**2** and **3**	**4**	NDO[a]	NBDO[b]
Fe-N1[c]	2.124(2)	2.15–2.35	2.226	2.0	2.1
Fe-N2[c]	2.137(2)	2.15–2.35	2.221	2.1	2.2
Fe-O1	2.145(1)	2.00–2.08	2.058	2.4	2.3
Fe-O2	2.150(1)	–	2.360	2.3	2.4
Fe-Cl/OH_2	2.250(1)		2.258	2.1	2.2
τ	0.03		0.49	0.51	0.20

[a] PDB 1O7G. [b] PDB 2BMQ. [c] For NDO, N1 = His 213 and N2 = His 208; for NBDO, N1 = His 211 and N2 = His 206.

To investigate whether **1**-Cl may serve also as a functional model of Rieske dioxygenases, reactions with H_2O_2 as the oxidant were carried out in the presence of olefin substrates. The results listed in Table 2 reveal that **1**-Cl can activate H_2O_2 to epoxidize electron-rich olefins. Epoxidation occurred with some loss of configuration for *cis*-2-heptene, with 47% retention of configuration (% RC; see also the footnote in Table 2) for *cis*-epoxide formation. However, only about a 30% yield of epoxide was obtained relative to iron complex.

The oxidation of electron-poor olefins, such as acrylate and fumarate, by **1**-Cl/H_2O_2 was even less effective, with only trace amounts of product observed in the reactions; instead, these oxidations afforded diols, the *cis*-diol in the case of fumarate. Our previous studies of other bio-inspired non-heme iron oxidation catalysts have demonstrated a requirement for *cis*-labile sites on the metal center to effect *cis*-

 © 2006 Wiley-VCH Verlag GmbH & Co. KGaA, Weinheim

Table 2: Epoxidation (E) and *cis*-dihydroxylation (D) of olefins promoted by **1**-Cl and **1**-OTf with H_2O_2 oxidant.[a]

	1-Cl		**1**-OTf	
Substrate	E	D	E	D
cis-2-heptene	0.32(4) [47]	< 0.05	0.37(1) [51]	0.47(5) [96]
1-octene	0.26(6)	< 0.05	0.11(1)	0.67(2)
tert-butyl acrylate	< 0.05	0.08(1)		0.58(4)
dimethyl fumarate	< 0.05	< 0.05 [99]		0.42(4) [99]

[a] Reaction conditions: H_2O_2 (10 equiv per iron) was added by a syringe pump over a 25-min period to a solution of **1**-X (0.7 mM) and substrate (0.35 M) in CH_3CN under argon. Product yields were analyzed following 120 min of additional stirring. Yields are expressed as μmol product per μmol iron complex with standard deviation values shown in parentheses. Numbers in square brackets represent %RC values; $\%RC = 100 \times (A-B)/(A+B)$, where *A* is the yield of *cis*-diol or epoxide with retention of configuration and *B* is the yield of epimer.

dihydroxylation.[10] Thus, the small yields of diol may be due to partial loss of the chloride ligand during the reaction.

To test this hypothesis, pale yellow **1**-Cl was treated with a single equivalent of AgOTf (OTf = trifluoromethanesulfonate) in CH_3CN to precipitate AgCl and form a greenish-brown complex formulated as [Fe^{II}(L1)OTf] (**1**-OTf). Reaction of **1**-OTf with H_2O_2 in the presence of olefin substrates yielded epoxide and *cis*-diol products (Table 2). With 1-octene, the epoxide-to-diol ratio dramatically changed from > 50:1 for **1**-Cl in favor of epoxide to 1:6 for **1**-OTf in favor of diol; even electron-poor olefins could be oxidized to diols in comparable yield. Dihydroxylation occurs in a highly stereoselective fashion, with the diols from *cis*-2-heptene and dimethyl fumarate with %RC values of 96% and 99%, respectively. Like **1**-Cl, **1**-OTf affords less than one turnover of product, suggesting that the active oxidant cannot be regenerated, even in the presence of more H_2O_2 (see the Supporting Information). In support, the mass spectra of reaction solutions at the end of the reaction show evidence only for the free ligand, indicating the decomposition of the complex during the course of the reaction (see the Supporting Information).

^{18}O-labeling experiments have proven instructive in deducing mechanisms by establishing the source of the oxygen atoms incorporated into the products.[6c,10,11] For **1**-Cl, the required addition of 200 equivalents of H_2O (present in the 10 wt% $H_2{}^{18}O_2$ solution) significantly inhibited epoxide formation. As a result, labeling experiments were carried out with a 1:3 mixture of $H_2{}^{18}O_2/H_2{}^{16}O_2$ to decrease the amount of added water (75 equiv H_2O). A 20% incorporation of ^{18}O was observed for the *cis*-2-heptene oxide product (80% normalized), whereas the corresponding experiment with 75 equivalents of added $H_2{}^{18}O$ afforded only 3% label incorporation (Table 3). Thus, the *cis*-epoxide oxygen atom is derived mainly from H_2O_2. On the other hand, no label incorporation from either $H_2{}^{18}O$ or $H_2{}^{18}O_2$ was observed for the minor *trans*-epoxide product, suggesting that this product derives from autoxidation.

For **1**-OTf, ^{18}O-labeling studies of the epoxidation of *cis*-2-heptene showed nearly identical results as those for **1**-Cl. On the other hand, dihydroxylation of *cis*-2-heptene and 1-octene yielded diols with 85% and 81% double label incorporation, respectively. Furthermore with 50:50 $H_2{}^{16}O_2/H_2{}^{18}O_2$, the two diol oxygens incorporated were derived from one molecule of H_2O_2, demonstrating that **1**-OTf serves as an exemplary dioxygenase model. Interestingly, the complementary $H_2{}^{18}O$ labeling experiment revealed 7–8% singly labeled *cis*-diol products.

The reactivities of **1**-Cl and **1**-OTf suggest the formation of distinct oxidants for epoxidation and dihydroxylation (Scheme 2). Given the comparable epoxide yields and ^{18}O-labeling results, both **1**-Cl/H_2O_2 and **1**-OTf/H_2O_2 likely produce a common oxidant that epoxidizes *cis*-2-heptene by oxygen-atom transfer from bound H_2O_2. A plausible epoxidizing agent, the η^2-OOH species shown in Scheme 2 is analogous to that observed for the ESO_2 adduct of NDO and is proposed for non-water-assisted epoxidation by Fe(bpmen) (bpmen = *N*,*N*′-dimethyl-*N*,*N*′-bis(2-pyridylmethyl)-1,2-diaminoethane).[12] More importantly, a dihydroxylating agent must be generated that incorporates both oxygen atoms of H_2O_2 into the *cis*-diol product and is capable of some label exchange with H_2O. We propose that this oxidant is formed upon dissociation of X (much more favored for OTf than for Cl) that promotes the isomerization of the Fe-η^2-OOH unit to a higher-valent iron-oxo/hydroxo species. Binding of H_2O to the iron center during oxidation provides a mechanism for label exchange, like that shown previously for **3**.[6c] We note that NDO also exhibits label exchange with solvent water in the dihydroxylation of naphthalene by H_2O_2 (Table 3),[13] implicating involvement of

Table 3: Results of ^{18}O-labeling experiments.[a]

	Substrate	Product(s)	$H_2{}^{18}O_2$[b]	$H_2{}^{18}O$[b]
1-Cl	*cis*-2-heptene	*cis*-oxide	20/80	97/3
		trans-oxide	100/0	100/0
1-OTf	*cis*-2-heptene	*cis*-oxide	23/77	99/1
		trans-oxide	98/2	100/0
		cis-diol	1/14/85	93/7
	1-octene	*cis*-diol	1/18/81	92/8
NDO[c]	naphthalene	*cis*-dihydrodiol	1/10/89	96/3

[a] For reaction conditions, see footnote [a] of Table 2. [b] Values are reported as the percentage of 0/1 O label that is incorporated into epoxide products and 0/1/2 O labels incorporated into diol products. [c] Results reported in Ref. [13].

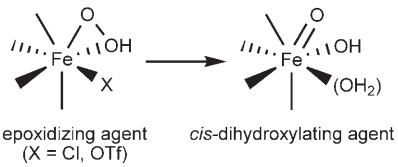

Scheme 2. Proposed active oxidants derived from **1**-X with H_2O_2.

 © 2006 Wiley-VCH Verlag GmbH & Co. KGaA, Weinheim

an analogous dihydroxylating agent in the enzyme mechanism.

We have thus designed a ligand that gives rise to iron complexes that approximate the 2-His-1-carboxylate environment of the Rieske dioxygenases. Even though less than one turnover of olefin oxidation is achieved, the activation of H_2O_2 by the triflate complex leads to the *cis*-dihydroxylation of double bonds. Label incorporation from $H_2{}^{18}O$ implicates a high-valent iron-oxo species as the oxidant for this novel reaction.

Experimental Section

HL1: A mixture of Kemp's acid chloroanhydride[7] (970 mg, 3.75 mmol), di-(2-pyridyl)methylamine[8] (842.8 mg, 2.86 mmol), and DMAP (4-dimethylaminopyridine, 37 mg) in freshly distilled pyridine (12 mL) was heated under argon to 90 °C and stirred for 2 days. Upon cooling to room temperature, the solvent was removed in vacuo, leaving a dark solid. Water (10 mL) was added to this solid, and the product was extracted into ethyl acetate (3×25 mL). This crude yellow product obtained from the extraction was purified with chromatography on a silica gel column with an ethyl acetate/methanol gradient to obtain a white solid (1.35 g, 89% yield), which was characterized by ^{1}H and ^{13}C NMR spectroscopy (see the Supporting Information). Minor impurities included monoacylated and acyclic diacylated products. ESIMS (CH_3CN): m/z 408 ($[HL1+H]^+$).

1-Cl: A solution of HL1 (168.9 mg, 0.44 mmol) and Et_3N (41.9 mg, 0.44 mmol) in CH_3CN (2 mL) was added dropwise to a stirred solution of $FeCl_2$ (52.6 mg, 0.44 mmol) in CH_3CN (2 mL) in an anaerobic glove box. Overnight stirring at room temperature afforded a yellow solid, which was recrystallized from MeOH/Et_2O (112 mg, 51% yield). Further recrystallization in CH_3CN at −20 °C resulted in the overnight formation of yellow blocks suitable for X-ray crystallographic studies. UV/Vis (CH_3CN), λ_{max} (ε [$M^{-1}cm^{-1}$]): 264 (5800), 310 (1600), 450 nm onset. ESIMS (CH_3OH): m/z 869 ($[Fe(L1)_2+H]^+$), 498 ($[Fe(L1)(Cl)+H]^+$), 462 ($[Fe(L1)]^+$), 408 ($[HL1+H]^+$). Elemental analysis (%) calcd for $C_{23}H_{24}ClFeN_3O_4$: C 55.50, H 4.86, N 8.44, Cl 7.12; found: C 55.68, H 5.14, N 8.76, Cl 6.87.

1-OTf: Ag(OTf) (67.8 mg, 0.264 mmol) in CH_3CN (1.5 mL) was added to a yellow suspension of **1**-Cl (131.2 mg, 0.264 mmol) in CH_3CN (2.5 mL) in an anaerobic glove box. After stirring at room temperature overnight, the reaction suspension was concentrated to produce a brown-green dark solid. UV/Vis (CH_3CN), λ_{max} (ε [$M^{-1}cm^{-1}$]): 260 (9100), 356 nm (sh, 3000). ESIMS (CH_3OH; see Figure S4 in the Supporting Information): m/z 869 ($[Fe(L1)_2+H]^+$), 612 ($[Fe(L1)(OTf)+H]^+$), 462 ($[Fe(L1)]^+$), 408 ($[HL1+H]^+$).

Received: August 25, 2006
Revised: October 2, 2006
Published online: November 10, 2006

Keywords: dihydroxylation · dioxygenases · enzyme models · epoxidation · oxidation

[1] *Biological Inorganic Chemistry* (Eds.: I. Bertini, H. B. Gray, E. I. Stiefel, J. S. Valentine), University Science Books, Sausalito, **2006**.
[2] a) M. Costas, M. P. Mehn, M. P. Jensen, L. Que, Jr., *Chem. Rev.* **2004**, *104*, 939; b) M. M. Abu-Omar, A. Loaiza, N. Hontzeas, *Chem. Rev.* **2005**, *105*, 2227; c) K. D. Koehntop, J. P. Emerson, L. Que, Jr., *J. Biol. Inorg. Chem.* **2005**, *10*, 87.
[3] A. Karlsson, J. V. Parales, R. E. Parales, D. T. Gibson, H. Eklund, S. Ramaswamy, *Science* **2003**, *299*, 1039.
[4] R. Friemann, M. M. Ivkovic-Jensen, D. J. Lessner, C.-L. Yu, D. T. Gibson, R. E. Parales, H. Eklund, S. Ramaswamy, *J. Mol. Biol.* **2005**, *348*, 1139.
[5] a) D. T. Gibson, V. Subramanian, in *Microbial Degradation of Organic Compounds* (Ed.: D. T. Gibson), Marcel Dekker, New York, **1984**, p. 181; b) L. P. Wackett, *Enzyme Microb. Technol.* **2002**, *31*, 577; c) D. J. Ferraro, L. Gakhar, S. Ramaswamy, *Biochem. Biophys. Res. Commun.* **2005**, *338*, 175.
[6] a) A. Beck, B. Weibert, N. Burzlaff, *Eur. J. Inorg. Chem.* **2001**, 521; b) A. Beck, A. Barth, E. Hubner, N. Burzlaff, *Inorg. Chem.* **2003**, *42*, 7182; c) P. D. Oldenburg, A. A. Shteinman, L. Que, Jr., *J. Am. Chem. Soc.* **2005**, *127*, 15672; d) S. J. Friese, B. E. Kucera, L. Que, Jr., W. B. Tolman, *Inorg. Chem.* **2006**, **45**, 8003.
[7] D. S. Kemp, K. S. Petrakis, *J. Org. Chem.* **1981**, *46*, 5140.
[8] M. Renz, C. Hemmert, B. Meunier, *Eur. J. Org. Chem.* **1998**, 1271.
[9] Single-crystal structure and refinement data for **1**-Cl: $C_{23}H_{24}ClFeN_3O_4$, $M_w = 497.75$, monoclinic, space group $P2_1/n$, $a = 10.8970(6)$, $b = 13.3325(7)$, $c = 15.0564(8)$ Å, $\alpha = 90.000(1)$, $\beta = 95.9000(1)$, $\gamma = 90.000(1)°$, $V = 2175.9(2)$ Å^3, $Z = 4$, $\rho_{calcd} = 1.519$ Mg m^{-3}, $Mo_{K\alpha}$ radiation ($\lambda = 0.71073$ Å, $\mu = 0.852$ mm^{-1}), $T = 173(2)$ K. A total of 4946 ($R_{int} = 0.0388$) independent reflections with $2\theta < 27.49°$ were collected. The resulting parameters were refined to converge at $R_1 = 0.0379$ ($I > 2\theta$) for 292 parameters on 4946 independent reflections ($wR_2 = 0.0926$). Max./min. residual electron density 0.501/−0.281 e Å^{-3}; GOF = 1.006. Further experimental details are provided in the Supporting Information. CCDC-613027 contains the supplementary crystallographic data for this paper. These data can be obtained free of charge from The Cambridge Crystallographic Data Centre via www.ccdc.cam.ac.uk/data_request/cif.
[10] a) K. Chen, M. Costas, J. Kim, A. K. Tipton, L. Que, Jr., *J. Am. Chem. Soc.* **2002**, *124*, 3026; b) K. Chen, M. Costas, L. Que, Jr., *Dalton Trans.* **2002**, 672.
[11] a) K. Chen, L. Que, Jr., *Angew. Chem.* **1999**, *111*, 2365; *Angew. Chem. Int. Ed.* **1999**, *38*, 2227; b) K. Chen, L. Que, Jr., *J. Am. Chem. Soc.* **2001**, *123*, 6327; c) M. Klopstra, G. Roelfes, R. Hage, R. M. Kellogg, B. L. Feringa, *Eur. J. Inorg. Chem.* **2004**, 846.
[12] D. Quiñonero, K. Morokuma, D. G. Musaev, R. Mas-Ballesté, L. Que, Jr., *J. Am. Chem. Soc.* **2005**, *127*, 6548.
[13] M. D. Wolfe, J. D. Lipscomb, *J. Biol. Chem.* **2003**, *278*, 829.

 © 2006 Wiley-VCH Verlag GmbH & Co. KGaA, Weinheim

Electron Transfer

DOI: 10.1002/anie.200603046

Linker-Controlled Energy and Charge Transfer within Chlorophyll Trefoils**

*Richard F. Kelley, Michael J. Tauber, and Michael R. Wasielewski**

Dedicated to Professor Klaus Möbius on the occasion of his 70th birthday

Photosynthetic organisms frequently use chemically identical chlorophylls (Chls) as donors and acceptors of both energy and charge. The specific tasks that these Chls carry out are differentiated largely by their interactions with other Chls, nearby redox cofactors, and the surrounding protein.[1–3] To mimic this versatility in artificial photosynthetic systems, we have prepared Chl trefoil arrays **1** and **3**, in which both energy and charge transfer are controlled by the structure of the rigid linker between three identical Chls. These molecules use the 20-position of Chl as the point of attachment to the linkers,[4] thereby leaving the central metals and the 13^1 carbonyl groups available for self-assembly of these building blocks into larger structures for light harvesting as well as charge separation and transport.[5–10]

Molecules **1**–**3** were synthesized in 10–20% overall yields (see the Supporting Information), and **4** was reported previously.[4] The 20-ethynylchlorophyll linkages were made by using a copper-free Sonogashira reaction[11] in DMF/Et_3N at room temperature, whereas the 20-phenylchlorophyll linkages were made by using Suzuki coupling. The UV/Vis spectra of **1**–**4** in THF (Figure 1) show that both the Soret and Q bands of trefoil **1** and its monomeric reference **2** are red-shifted by approximately 10 nm relative to those of the corresponding molecules **3** and **4**. This is because of the small increase in π conjugation afforded by direct attachment of the ethynyl group to the Chl. Excitation of **1** and **2** in THF with 665-nm, 120-fs laser pulses yields transient absorption spectra of their respective lowest excited singlet states ^{1*}**1** (Figure 2a) and ^{1*}**2** (see the Supporting Information). The spectra are nearly identical, yet the decay of ^{1*}**2** is monoexponential with

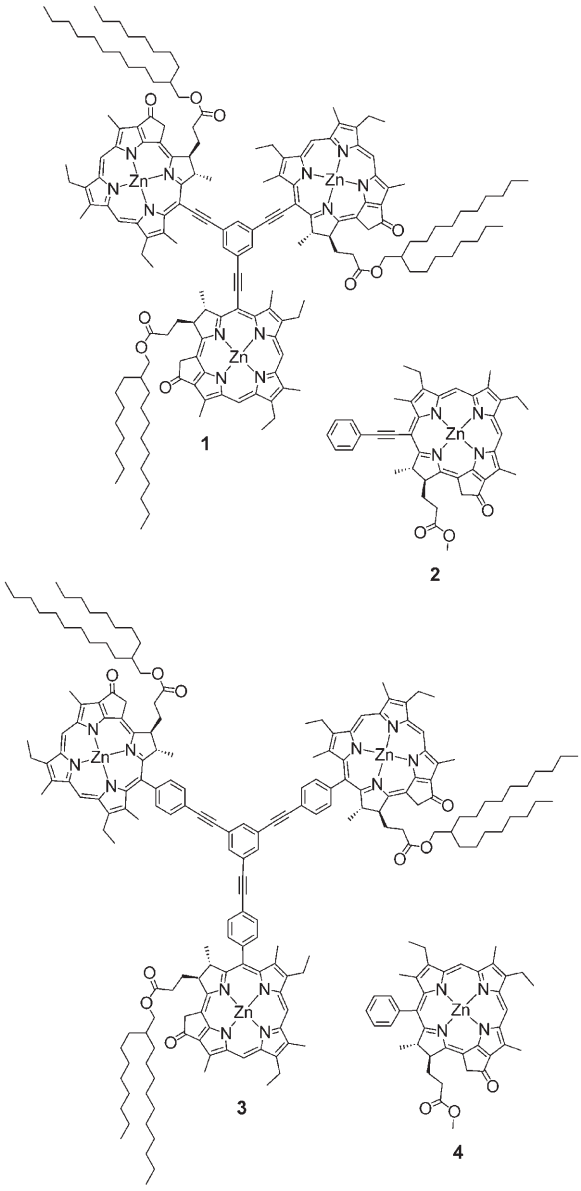

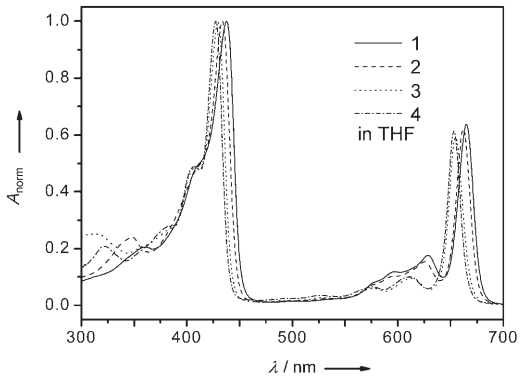

Figure 1. Ground-state electronic absorption spectra of **1**–**4**. A_{norm} = normalized absorbance.

[*] R. F. Kelley, Dr. M. J. Tauber, Prof. M. R. Wasielewski
Department of Chemistry and
International Institute for Nanotechnology
Northwestern University
Evanston, IL 60208-3113 (USA)
Fax: (+1) 847-467-1425
E-mail: m-wasielewski@northwestern.edu

[**] This work was supported by the Division of Chemical Sciences, Office of Basic Energy Sciences, Department of Energy (grant no. DE-FG02-99ER14999). We thank Qixi Mi and Randall H. Goldsmith for valuable discussions and Dr. Jenny Lockard (NU) and Dr. Ralph Weber (Bruker-Biospin, Inc.) for assistance with time-resolved fluorescence and ENDOR experiments, respectively. M.J.T. acknowledges the donors of the American Chemical Society Petroleum Research Fund for partial support of this research. The Bruker E-580 spectrometer was purchased with partial support from the NSF (grant no. CHE-0131048).

Supporting information for this article is available on the WWW under http://www.angewandte.org or from the author.

© 2006 Wiley-VCH Verlag GmbH & Co. KGaA, Weinheim

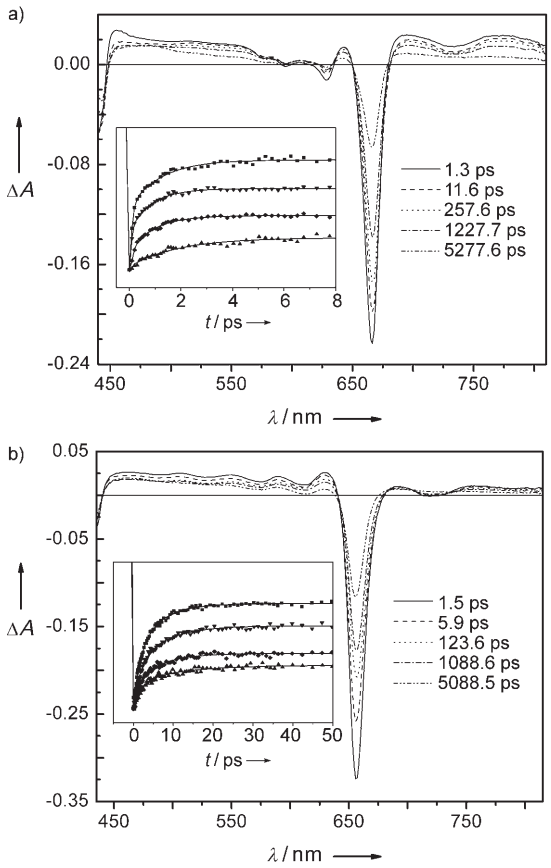

Figure 2. Transient absorption spectra for **1** and **3** in THF. a) Spectra of **1** following excitation with 665-nm, 120-fs laser pulses. Inset: power-dependent transient absorption kinetics of **1** monitored at 658 nm using 1.00 μJ (■), 0.66 μJ (▼), 0.33 μJ (◆), and 0.11 μJ (▲) per pulse. Nonlinear least-squares fits to the kinetic data are also shown. b) Spectra of **3** following excitation with 655-nm, 120-fs laser pulses. Inset: power-dependent transient absorption kinetics of **3** monitored at 658 nm using 1.00 μJ (■), 0.33 μJ (▼), 0.11 μJ (◆), and 0.06 μJ (▲) per 655-nm excitation pulse.

a lifetime of $\tau = 4.1$ ns, whereas that of ^{1*}**1** is biexponential with $\tau = (0.9 \pm 0.1)$ ps and 4.1 ns. Excitation of **3** and **4** with 655-nm, 120-fs laser pulses yields transient absorption spectra of ^{1*}**3** (Figure 2b) and ^{1*}**4** (see Reference [4]). Again, the spectra are nearly identical and the decay of ^{1*}**4** is monoexponential with $\tau = 4.0$ ns, whereas the decay of ^{1*}**3** is biexponential with $\tau = (3.0 \pm 0.1)$ ps and 4.0 ns. The components with $\tau \approx 4$ ns in the transient absorption decay kinetics of ^{1*}**1**–^{1*}**4** match their fluorescence lifetimes in THF measured by using an apparatus with an instrument response time of 20 ps (data not shown). The amplitudes of the 0.9 and 3.0 ps components in the decay of ^{1*}**1** and ^{1*}**3**, respectively, are laser-power dependent and indicative of singlet–singlet annihilation (see insets to Figure 2a and b, respectively). Assuming annihilation is the result of random exciton transfer between adjacent chromophores, the time constant for exciton hopping (energy transfer) within the trefoil, τ_h, can be derived from the annihilation lifetime, τ_a, by using the formula developed for cyclic arrays of N chromophores:[12] $\tau_a = \tau_h/(8\sin^2(\pi/2N))$. By using this model, $N = 3$, and the measured values of τ_a, $\tau_h = (1.8 \pm 0.1)$ ps and (6.0 ± 0.1) ps for **1** and **3**, respectively. To verify this approach for analysis of the exciton hopping rates in the trefoils, we prepared a derivative of **3** with only one Zn Chl and two free-base pheophorbides (Pheo), **3–1Zn**. As the lowest excited singlet state of Pheo is slightly lower in energy than that of the Zn Chl, selective excitation of the Zn Chl with 645-nm, 120-fs laser pulses results in a singlet–singlet energy-transfer rate to Pheo of $((14 \pm 1)\ \text{ps})^{-1}$. This rate is only about a factor of two slower than that obtained for **3** by using the annihilation rate. Although we do not expect the energy-transfer rates for **3–1Zn** and **3** to be the same because they are not chemically identical, this result shows that energy transfer within these structurally related chlorophyll trefoil molecules is much faster than that observed for analogous porphyrin systems, which are discussed below, and that the annihilation analysis is reasonable.

The experimental data show that the Chl–Chl energy-transfer rate within **1** is only three-times faster than in **3**. Energy transfer within covalently linked chromophore arrays can occur by the through-space Förster mechanism and the through-bond Dexter mechanism.[13] Calculated Förster energy-transfer rates for **1** ($(3\ \text{ps})^{-1}$) and **3** ($(31\ \text{ps})^{-1}$) predict a 10:1 (**1**/**3**) ratio for the rate (see the Supporting Information). These calculations primarily reflect the significant change in the Chl–Chl distances, r, between **1** (15.1 Å) and **3** (21.5 Å) owing to the $1/r^6$ dependence of the dipole–dipole interaction. The values are only approximate owing to the size of the Chl macrocycles and the resultant length of their transition dipoles relative to the distances between them. Energy-transfer rates have been measured for analogous phenyl–ethynyl–phenyl and phenyl–ethynyl linked porphyrin and oxochlorin dyads.[14,15] In that work, placing an additional phenyl in the linkage results in a 10-fold slowing of the energy-transfer rate. The energy-transfer rates for the oxochlorin dyads with both linkages agree with the predictions of Förster calculations, whereas the rates for the corresponding porphyrin dyads support a substantially faster through-bond contribution. The similarity of the energy-transfer rates between **1** and **3** suggests that a through-bond or Dexter-type energy-transfer mechanism may be an important contributor in both trefoils. Efficient through-bond energy transfer within threefold-symmetric porphyrin arrays with a 1,3,5-triphenylbenzene linker has also been reported.[16] Although the porphyrin electron density at the site of the linker attachment is larger than that for **1** and **3** owing to the difference between the porphyrin (a_{2u})[17] and Chl (a_2)[18] highest occupied molecular orbitals (HOMOs), the energy-transfer rates for **1** and **3** are 150- and 45-times faster, respectively, than those of the porphyrin trefoils. This results from relatively poor orbital overlap between the porphyrin π systems owing to the large dihedral angles between the porphyrins and the phenyls attached to them as well as between these same phenyls and the benzene core.[16] The differences in energy-transfer rates displayed among all these examples highlight the importance of through-bond electronic coupling between chromophores in organized covalent arrays.[19,20]

Charge transport within the Chl trefoils was studied by generating their radical cations, which were characterized by

 © 2006 Wiley-VCH Verlag GmbH & Co. KGaA, Weinheim

using electron nuclear double resonance (ENDOR) spectroscopy. Solutions of **1**–**4** ($2–5\times10^{-4}$ M) in a mixture of CH_2Cl_2/THF (9:1)[18] were generated by the addition of a solution of I_2 and $AgClO_4$ dissolved in acetonitrile. The oxidation of **1** and **3** was carried out to approximately 30 % completion to produce the singly oxidized species. The extent of the oxidation was monitored by using UV/Vis spectroscopy (e.g. see the spectra for $\mathbf{1}^{+\bullet}$ and $\mathbf{2}^{+\bullet}$ and the Supporting Information). Oxidized samples were loaded into quartz tubes and sealed under vacuum after successive freeze–pump–thaw cycles. Electron paramagnetic resonance (EPR) and ENDOR[21] spectra were acquired at 290 K and 140 K by using a Bruker E-580 spectrometer fitted with an EN801 resonator, and a RF power amplifier (ENI A-500). A spline fit baseline correction was applied to the spectra. The EPR spectra of $\mathbf{1}^{+\bullet}$–$\mathbf{4}^{+\bullet}$ are inhomogeneously broadened into single unresolved lines owing to the large number of electron–nuclear hyperfine interactions within each molecule. In such cases, the number of sites over which the radical ion hops or is delocalized can be estimated from EPR line-width changes.[6,22,23] For example, charge hopping within a linear multiporphyrin array was studied recently by using this method.[24] The peak-to-peak Gaussian line widths of $\mathbf{2}^{+\bullet}$–$\mathbf{4}^{+\bullet}$ are all 0.73 mT, whereas that of $\mathbf{1}^{+\bullet}$ is only 0.45 mT (see the Supporting Information). The line-width ratio of $\mathbf{2}^{+\bullet}/\mathbf{1}^{+\bullet}$ is 1.6, which is very close to the value predicted for charge sharing over three sites by using the treatment of Norris et al.[22]

Alternatively, ENDOR spectroscopy has been shown to provide a substantial improvement in spectral resolution of the hyperfine splittings of tetrapyrrole macrocycle radical cations.[18,21,25–28] The proton ENDOR spectra of $\mathbf{2}^{+\bullet}$–$\mathbf{4}^{+\bullet}$ at 290 K each exhibit four line pairs with average isotropic hyperfine splittings of 7.6, 6.5, 3.3, and 0.4 MHz (see Figure 3 and the Supporting Information). The similarity between the spectra of $\mathbf{2}^{+\bullet}$ and $\mathbf{4}^{+\bullet}$ indicates that the attachment of an ethynyl linker directly to the Chl macrocycle only slightly affects the spin (charge) distribution in $\mathbf{2}^{+\bullet}$. Earlier work has shown that the presence of the phenyl in $\mathbf{4}^{+\bullet}$ does not change the spin distribution within the Chl macrocycle.[4] The similar hyperfine splittings for $\mathbf{3}^{+\bullet}$ and $\mathbf{4}^{+\bullet}$ confirm that the radical cation is localized on a single Chl within trefoil $\mathbf{3}^{+\bullet}$. In contrast, the proton ENDOR spectrum of $\mathbf{1}^{+\bullet}$ at 290 K exhibits four line pairs with hyperfine splittings that correspond to those of $\mathbf{2}^{+\bullet}$, but are reduced by a factor of three. This indicates that, on the ENDOR timescale ($>10^7$ Hz), the unpaired electron is shared between all three Chls in the assembly. The weak additional lines at 12.2 and 16.8 MHz (4.6 MHz hyperfine splitting) observed in the spectrum of $\mathbf{1}^{+\bullet}$ at 290 K may be due to the 17- and 18-position protons on the reduced rings within a minor conformer of $\mathbf{1}^{+\bullet}$. These lines disappear when the temperature is lowered to 250 K (see the Supporting Information). ENDOR spectra of $\mathbf{1}^{+\bullet}$–$\mathbf{4}^{+\bullet}$ were also obtained in frozen solution at 140 K and show that the hyperfine splittings for $\mathbf{1}^{+\bullet}$–$\mathbf{4}^{+\bullet}$ are essentially identical (Figure 3). The observed localization of the radical cation in $\mathbf{1}^{+\bullet}$ in frozen solution is most likely due to the inability of the counter anion to move between the Chls sufficiently fast to accommodate hopping of the positive charge on the ENDOR timescale.

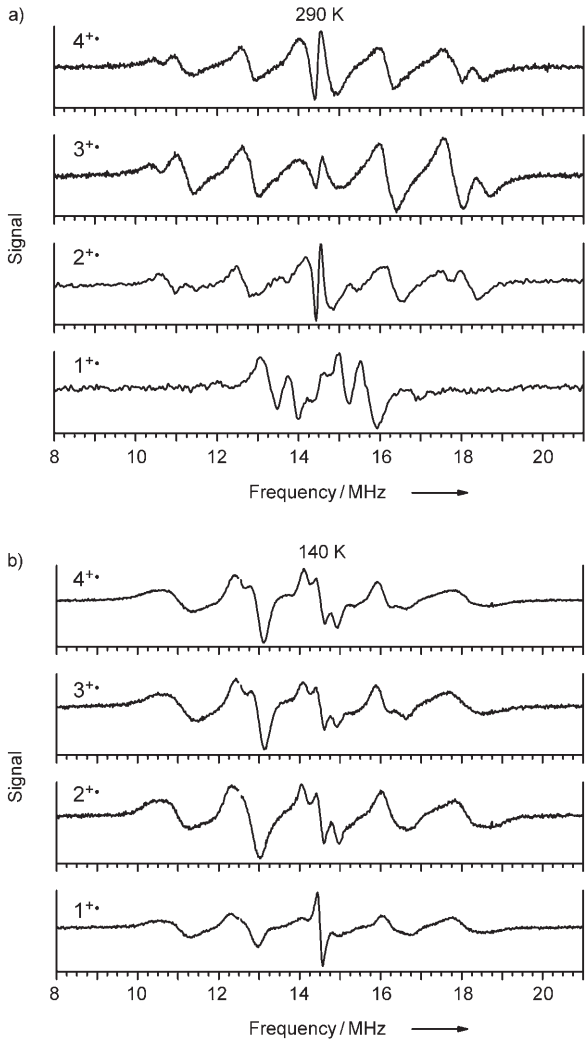

Figure 3. Proton ENDOR spectra in CH_2Cl_2/THF (9:1). Radiofrequency (RF) power was 400 W with a frequency modulation depth of 50 kHz. Microwave power was 100 mW at 290 K (a) and 20 mW at 140 K (b).

Charge sharing in $\mathbf{1}^{+\bullet}$ most likely results from an increase in through-bond electronic coupling between its Chls relative to those in $\mathbf{3}^{+\bullet}$. Overlap of the π orbital of the ethynyl group with that of the Chl HOMO is greater in $\mathbf{1}^{+\bullet}$ relative to that of the 20-phenyl group in $\mathbf{3}^{+\bullet}$ because of the relatively large dihedral angle between the π systems of the Chl and the phenyl.[4] Thus, attaching an ethynyl group to the 20-position of Chl provides both a means of generating rigid chromophore arrays and increasing the electronic interaction between the Chls. These qualities will be exploited to generate new building blocks for the self-assembly of artificial photosynthetic systems.

Received: July 27, 2006
Revised: September 22, 2006
Published online: November 3, 2006

Keywords: electron transfer · femtochemistry · photochemistry · photosynthesis

 © 2006 Wiley-VCH Verlag GmbH & Co. KGaA, Weinheim

[1] J. J. Katz, L. L. Shipman, T. M. Cotton, T. R. Janson in *The Porphyrins*, *Vol. V* (Ed.: D. Dolphin), Academic Press, New York, **1978**, p. 401.
[2] J. Deisenhofer, O. Epp, K. Miki, R. Huber, H. Michel, *J. Mol. Biol.* **1984**, *180*, 385.
[3] K. N. Ferreira, T. M. Iverson, K. Maghlaoui, J. Barber, S. Iwata, *Science* **2004**, *303*, 1831.
[4] R. F. Kelley, M. J. Tauber, M. R. Wasielewski, *J. Am. Chem. Soc.* **2006**, *128*, 4779.
[5] D. L. Worcester, T. J. Michalski, J. J. Katz, *Proc. Natl. Acad. Sci. USA* **1986**, *83*, 3791.
[6] M. K. Bowman, T. J. Michalski, R. L. Tyson, D. L. Worcester, J. J. Katz, *Proc. Natl. Acad. Sci. USA* **1988**, *85*, 1498.
[7] H. Tamiaki, M. Amakawa, A. R. Holzwarth, K. Schaffner, *Photosynth. Res.* **2002**, *71*, 59.
[8] V. I. Prokhorenko, A. R. Holzwarth, M. G. Mueller, K. Schaffner, T. Miyatake, H. Tamiaki, *J. Phys. Chem. B* **2002**, *106*, 5761.
[9] C. Roeger, M. G. Mueller, M. Lysetska, Y. Miloslavina, A. R. Holzwarth, F. Würthner, *J. Am. Chem. Soc.* **2006**, *128*, 6542.
[10] V. Huber, M. Katterle, M. Lysetska, F. Würthner, *Angew. Chem.* **2005**, *117*, 3208; *Angew. Chem. Int. Ed.* **2005**, *44*, 3147.
[11] R. W. Wagner, T. E. Johnson, F. Li, J. S. Lindsey, *J. Org. Chem.* **1995**, *60*, 5266.
[12] G. Trinkunas, *J. Lumin.* **2003**, *102–103*, 532.
[13] J. R. Lakowicz, *Principles of Fluorescence Spectroscopy*, Kluwer, Dordrecht, **1999**.
[14] E. Hindin, C. Kirmaier, J. R. Diers, K.-Y. Tomizaki, M. Taniguchi, J. S. Lindsey, D. F. Bocian, D. Holten, *J. Phys. Chem. B* **2004**, *108*, 8190.
[15] M. Taniguchi, D. Ra, C. Kirmaier, E. Hindin, J. K. Schwartz, J. R. Diers, R. S. Knox, D. F. Bocian, J. S. Lindsey, D. Holten, *J. Am. Chem. Soc.* **2003**, *125*, 13461.
[16] H. S. Cho, H. Rhee, J. K. Song, C.-K. Min, M. Takase, N. Aratani, S. Cho, A. Osuka, T. Joo, D. Kim, *J. Am. Chem. Soc.* **2003**, *125*, 5849.
[17] M. Gouterman in *The Porphyrins*, *Vol. III* (Ed.: D. Dolphin, Academic Press, New York, **1978**, pp. 1.
[18] H. Käss, W. Lubitz, G. Hartwig, H. Scheer, D. Noy, A. Scherz, *Spectrochim. Acta Part A* **1998**, *54*, 1141.
[19] K. Kilsa, J. Kajanus, J. Martensson, B. Albinsson, *J. Phys. Chem. B* **1999**, *103*, 7329.
[20] N. Aratani, A. Osuka, H. S. Cho, D. Kim, *J. Photochem. Photobiol. C* **2002**, *3*, 25.
[21] K. Möbius, M. Plato, W. Lubitz, *Phys. Rep.* **1982**, *87*, 171.
[22] J. R. Norris, R. A. Uphaus, H. L. Crespi, J. J. Katz, *Proc. Natl. Acad. Sci. USA* **1971**, *68*, 625.
[23] N. Srivatsan, S. Weber, D. Kolbasov, J. R. Norris, *J. Phys. Chem. B* **2003**, *107*, 2127.
[24] K. Susumu, P. R. Frail, P. J. Angiolillo, M. J. Therien, *J. Am. Chem. Soc.* **2006**, *128*, 8380.
[25] J. R. Norris, M. E. Druyan, J. J. Katz, *J. Am. Chem. Soc.* **1973**, *95*, 1680.
[26] G. Feher, A. J. Hoff, R. A. Isaacson, L. C. Ackerson, *Ann. N. Y. Acad. Sci.* **1975**, *244*, 239.
[27] M. Huber, F. Lendzian, W. Lubitz, E. Tränkle, K. Möbius, M. R. Wasielewski, *Chem. Phys. Lett.* **1986**, *132*, 467.
[28] M. Huber, H. Kurreck, B. Von Maltzan, M. Plato, K. Möbius, *J. Chem. Soc. Faraday Trans.* **1990**, *86*, 1087.

 © 2006 Wiley-VCH Verlag GmbH & Co. KGaA, Weinheim

Electron Transfer

DOI: 10.1002/anie.200603455

Hole Mobility in DNA A Tracts**

Frederick D. Lewis, Huihe Zhu, Pierre Daublain, Boiko Cohen, and Michael R. Wasielewski**

A unique feature of electron transfer in duplex DNA is the ability of positive charge (holes) to migrate over long distances in poly(dA)–poly(dT) base pair domains,[1,2] known as A tracts.[3] "A hopping" has been observed in numerous studies of oxidative strand cleavage at GG and GGG sites.[4–6] Giese et al. reported that the relative efficiency of hole transport from an isolated oxidized G to a GGG hole trap separated by a variable number of A–T base pairs (bp) displayed a highly distinctive distance dependence.[7] The relative efficiency of hole transport was observed to be highly distance dependent at short distances (1–3 bp) but weakly distance dependent at longer distances (4–16 bp). This change was attributed to a change in mechanism from tunneling at short distances to multistep hole hopping at longer distances. Giese's report prompted numerous theoretical analyses[8–12] as well as experimental efforts to determine the rate constants for hole transport through A hopping.[13–15]

We report herein the kinetics and efficiency of photoinduced hole transport across A tracts consisting of 1–7 bp in DNA hairpin conjugates, as determined by femtosecond transient absorption spectroscopy measurements. The values for these parameters are strongly distance dependent over the first 4 bp, but are relatively insensitive to distance from 5–7 bp. Hole arrival times roughly parallel the relative strand-cleavage efficiencies reported by Giese et al.[7] Competition of hole trapping with charge return of the hole while in the A tract results in low quantum yields for hole trapping in the longer base-pair domains.

We have previously investigated the dynamics of charge separation in DNA-hairpin conjugates with a stilbenedicarboxamide (**Sa**) capping group and a stilbenediether (**Sd**) hairpin linker separated by 1–4 A–T base pairs (Scheme 1).[16,17] Selective excitation of the **Sa** capping group at 350–355 nm permits observation of the decay of

[*] Prof. F. D. Lewis, H. Zhu, P. Daublain, B. Cohen, Prof. M. R. Wasielewski
Department of Chemistry
Northwestern University
Evanston, IL 60208-3113 (USA)
Fax: (+1) 847-467-2184
E-mail: fdl@northwestern.edu
m-wasielewski@northwestern.edu

[**] This research is supported by the Division of Chemical Sciences, Office of Basic Energy Sciences, U.S. Department of Energy under grants DE-FG02-96ER14604 (F.D.L.), and DE-FG02-99ER14999 (MRW). We thank T. Fiebig and Y. A. Berlin for helpful discussions.

Supporting information for this article including transient absorption spectra for conjugates **3**, **4**, **6**, and **7** is available on the WWW under http://www.angewandte.org or from the author.

© 2006 Wiley-VCH Verlag GmbH & Co. KGaA, Weinheim

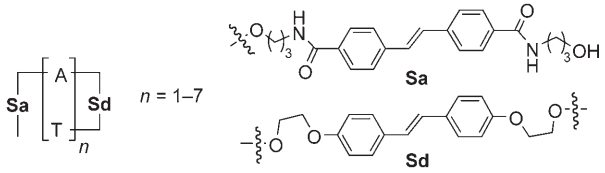

Scheme 1. Condensed structures for the hairpins **1**–**7**, **Sa**, and **Sd**.

^{1}**Sa*** (both fluorescence and stimulated emission with a 385-nm band maximum), and the formation of **Sa**$^{-\bullet}$ (575-nm band maximum) and **Sd**$^{+\bullet}$ (525-nm band maximum). Hole arrival times for **1**–**4** were estimated from the rise in the band ratio at 525/575 nm.[17] In the cases of **1** and **2**, decay of **Sa*** and formation of **Sd**$^{+\bullet}$ occur simultaneously, leading to the conclusion that charge separation occurs through a single-step tunneling process. In the cases of **3** and **4**, the hole arrival times are slower than the fast component of **Sa*** decay ($\approx$40 ps) attributed to hole injection, in accord with a hole-hopping mechanism for charge separation. Hole arrival times for **5**–**7** were too long for measurement by femtosecond transient spectroscopy (2-ns time window) and too short for measurement by nanosecond transient spectroscopy ($\approx$20-ns time resolution).[17]

We have now determined the hole arrival times for conjugates **3**–**7** from the rise of the 525/575-nm band ratio obtained from transient absorption spectra recorded with a time window of 0–6 ns. Transient spectra obtained at several delay times are shown in Figure 1 for **5** and in the Supporting

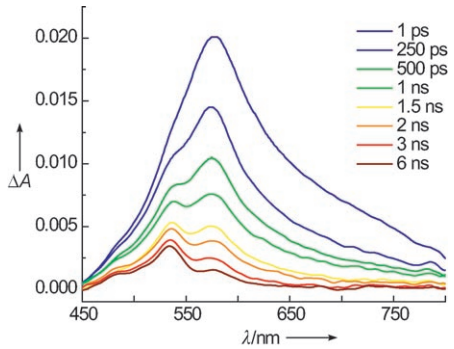

Figure 1. Transient absorption spectra of **5** at delay times of 1 ps (ΔA/2.5) to 6.0 ns following fs laser excitation at 350 nm.

Information for the other hairpins. Plots of the time-dependent 525/575-nm single wavelength intensity ratios for **1**–**7** are shown in Figure 2. The curved lines for **3**–**5** are fit to first-order kinetics by using data obtained following the initial rise in the 525/575-nm intensity ratio ($\approx$100 ps), which occurs upon hole injection.[17] The rate constants for hole arrival (k_a) and hole arrival times ($\tau_a = k_a^{-1}$) obtained from these fits are reported in Table 1. The straight lines for **6** and **7** are the initial slopes for the rise in the 525/575-nm ratio (0.2–2.0 ns).[18] Comparison of these slopes with that for **5** provides values of k_a and τ_a for **6** and **7**. The values of $\tau_a = 7$–12 ns for **5**–**7** are consistent with earlier estimates, which were based on the failure to observe hole arrival on longer time scales.[13–15,17]

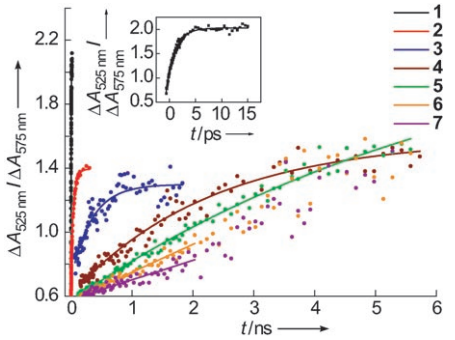

Figure 2. Time-dependent 525/575-nm band intensity ratios for **1**–**7** (data for **1** and **2** from reference [17]). The curved lines for **3**–**5** are single exponential fits to the data obtained following the initial fast rise attributed to hole injection ($\approx$100 ps). The straight lines for **6** and **7** are linear fits to the 0.2–2.0-ns data.

Table 1: Quantum yields of hole trapping, hole arrival rate constants, and hole arrival times for charge transfer in **Sa/Sd** hairpins.

hairpin	Φ_t[a]	$k_a \times 10^{-9}$ [s^{-1}][b]	τ_a [ns][c]
1	1.0 ± 0.1	580[d]	0.0017[d]
2	1.0 ± 0.1	27[d]	0.036[d]
3	0.6 ± 0.1	2.9 ± 0.3 (3.4[d])	0.34
4	0.3 ± 0.1	0.43 ± 0.03	2.3
5	0.3 ± 0.1	0.15 ± 0.02	6.7
6	0.2 ± 0.1	0.12 ± 0.03	8.3
7	0.2 ± 0.1	0.08 ± 0.03	12

[a] Estimated quantum yields and errors for hole trapping (see text). [b] Rate constants for hole arrival and errors obtained from single exponential fits to the data for **1**–**5** and initial rates for **6** and **7** in Figure 2. [c] Hole arrival time $\tau_a = k_a^{-1}$. [d] Data from reference [17].

A plot of the distance dependence of the hole arrival rate constants for **1**–**7** is shown in Figure 3 along with Giese's plot for relative hole-transport efficiencies from G to GGG.[7] The parallel between our kinetic data and Giese's data for strand cleavage data may be fortuitous as hole injection is most likely to be the rate-determining step in Giese's study,[7] whereas hole transport is the rate-determining step for conjugates **3**–**7**.

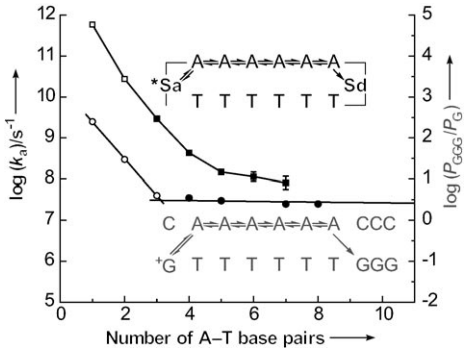

Figure 3. Rate constants for hole arrival in hairpins **1**–**7** (data from Table 1) and relative efficiencies of strand cleavage at G versus GGG (data from reference [7]). Open symbols for tunneling and filled symbols for hopping mechanisms. Our kinetic results (□, ■) parallel the DNA-strand-cleavage results of Giese et al. (○, ●).Error bars for **3**–**5** are smaller than the symbols.

 © 2006 Wiley-VCH Verlag GmbH & Co. KGaA, Weinheim

Quantum yields (Φ_t) for hole trapping by **Sd** can be estimated from a comparison of the integrated area of the transient spectra at approximately 1.0 ps and after the 525/575-nm band ratio approaches its maximum value. A value of $\Phi_t \approx 1.0$ for **1** and **2** is assumed on the basis of their fast hole arrival times and absence of significant **Sa** fluorescence.[17] The values of Φ_t reported in Table 1 decrease rapidly for 2–4 bp and more gradually for 5–7 bp. The values of Φ_t for **4**–**7** are larger than those reported by Takada et al. for A-tract hole transport between a different donor–acceptor pair.[14,15]

The photoinduced charge-separation process for **3**–**7** can be described in terms of hole transport through either a localized hole-hopping model,[8] as shown in Scheme 2 for **3**,

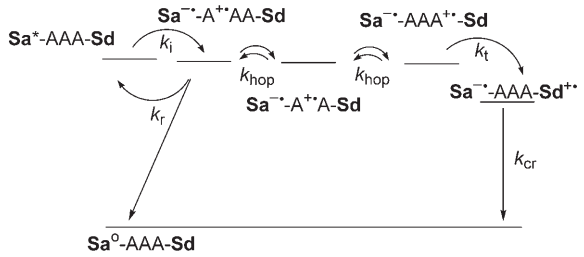

Scheme 2. Simplified kinetic scheme for hole injection (k_i), hole hopping (k_{hop}), hole trapping (k_t), $\mathbf{Sa}^{-\bullet}/\mathbf{A}^{+\bullet}$ charge recombination (k_r), and $\mathbf{Sa}^{-\bullet}/\mathbf{Sd}^{+\bullet}$ charge recombination (k_{cr}) in hairpin **3**.

or through a delocalized hole model, as shown in Scheme 3 for **7**. In both models, hole injection (k_i) and hole trapping (k_t) are assumed to be faster than hole transport,[17] and hole

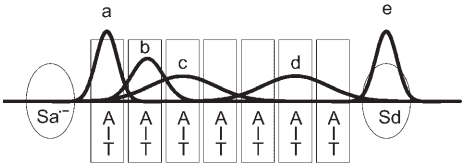

Scheme 3. Conceptualized hole transport in hairpin **7**: a) the $\mathbf{Sa}^{-\bullet}/\mathbf{A}^{+\bullet}$ contact radical ion pair, b) and c) hole delocalization, d) hole migration, and e) hole trapping on **Sd**.

transport is the rate-determining step for the hole arrival process. Hole trapping results in the formation of relatively long-lived $\mathbf{Sa}^{-\bullet}/\mathbf{Sd}^{+\bullet}$ charge-separated states, which decay through charge recombination (k_{cr}). Charge recombination of $\mathbf{Sa}^{-\bullet}/\mathbf{Sd}^{+\bullet}$ is slower than hole arrival for **3**–**7**[17] and thus does not significantly affect the efficiency of hole trapping (Φ_t). Recombination of the hole in the A tract with $\mathbf{Sa}^{-\bullet}$ (k_r) does compete with hole trapping and results in formation of both the ground and excited states of **Sa**.[17] The low values of Φ_t for **4**–**7** are attributed to the competition of hole arrival with $\mathbf{Sa}^{-\bullet}/\mathbf{A}^{+\bullet}$ charge recombination (Scheme 2). In the case of **6** and **7**, the value of $\Phi_t = 0.2$ indicates that $k_r \approx 4k_a$. As the length of the A tract increases, hole arrival times at **Sd** become slower and less efficient. Beyond 3 bp, values of Φ_t become essentially constant. Some charge return may still occur at these distances, however, the change in the value of Φ_t would be too small to measure.

The similar values of τ_a for **5**–**7** suggests that hole transport becomes weakly distance dependent at long distances. The differences in τ_a values for **5**–**7** provide an incremental value of approximately 2 ns per bp for a hole-hopping mechanism (Scheme 2), which may become shorter at even longer distances as the hole moves further away from $\mathbf{Sa}^{-\bullet}$. This value is slower than the value of 50 ps per bp, which was estimated by Takada et al.[14] An estimated hopping rate of approximately $10^9\ s^{-1}$ can be used to calculate a value of $4 \times 10^{-5}\ cm^2\,V^{-1}\,s^{-1}$ for A-tract hole mobility, μ, from the relation $\mu = (e/kT)w\delta^2$, where e is the charge, w the hopping rate, and δ the distance between base pairs (3.4 Å).[19] This value is distinctly smaller than values of μ for discotic liquid crystals of planar aromatics such as triphenylene, which has a value of $\mu \approx 0.1\ cm^2\,V^{-1}\,s^{-1}$.[20,21] This value is also smaller than the values calculated for hypothetical poly(dG)–poly(dC) oligomers, even when corrected for static disorder.[22]

The hole-transport model shown in Scheme 3 is based upon several theoretical models that have been developed to explain Giese's results.[7] Berlin et al. have described A-tract hole migration as a motion in the tight-binding band.[9] Conwell has advanced a polaron model in which the hole is delocalized over 3–5 adenine molecules,[12,23] and an ion-gated polaron-like hole-transport model has been proposed by Schuster, Landman, and co-workers.[24] Renger and Marcus proposed a delocalized state model in which the splitting between bridge states increases as the bridge becomes longer.[11] The Conwell and Renger–Marcus models are consistent with our observation of a more-pronounced decrease in the hole-transport rate for **3**–**5** than is present at longer distances, at which point transport of the delocalized hole becomes necessary. Both static and dynamic disorders are expected to reduce A-tract hole mobility.[11,22] Basko and Conwell have considered the effects of solvent and counterions on hole mobility in DNA.[25] Their value of $\tau = 0.65$ ns calculated through Debye–Hückel screening by counterions is consistent with our estimate of the effective hole-transport rate per base pair.

In summary, we have determined the hole arrival times and efficiencies for a family of DNA conjugates with donor and acceptor stilbenes at the ends of A tracts consisting of 1–7 base pairs. The hole arrival times provide an estimated value for the A-tract hole mobility that is significantly lower than the values for columnar π-stacked discotic materials.[21] The low hole mobilities plausibly result from a combination of weak coupling, static and dynamic disorder, and solvent and ion gating. Although our estimated value for the hole mobility is lower than previous estimates, it is still significantly faster than strand cleavage at G-containing sites.[4] The relatively low hole mobility and rapid charge return in our system result in low hole-trapping efficiencies in longer A tracts.

Received: August 24, 2006
Published online: October 30, 2006

Keywords: DNA conjugates · electron transfer · hole hopping · hole injection · hole trapping

 © 2006 Wiley-VCH Verlag GmbH & Co. KGaA, Weinheim

[1] *Long-Range Charge Transfer in DNA, I and II*, *Vol. 236*, *237* (Ed.: G. B. Schuster), Springer, Heidelberg, **2004**.
[2] H. A. Wagenknecht, *Charge Transfer in DNA*, Wiley-VCH, Weinheim, **2005**.
[3] J. G. Nadeau, D. M. Crothers, *Proc. Natl. Acad. Sci. USA* **1989**, *86*, 2622 – 2626.
[4] B. Giese, A. Biland, *Chem. Commun.* **2002**, 667 – 672.
[5] G. B. Schuster, *Acc. Chem. Res.* **2000**, *33*, 253 – 260.
[6] T. T. Williams, D. T. Odom, J. K. Barton, *J. Am. Chem. Soc.* **2000**, *122*, 9048 – 9049.
[7] B. Giese, J. Amaudrut, A.-K. Köhler, M. Spormann, S. Wessely, *Nature* **2001**, *412*, 318 – 320.
[8] J. Jortner, M. Bixon, A. A. Voityuk, N. Rösch, *J. Phys. Chem. A* **2002**, *106*, 7599 – 7606.
[9] Y. A. Berlin, A. L. Burin, M. A. Ratner, *Chem. Phys.* **2002**, *275*, 61 – 74.
[10] M. Bixon, J. Jortner, *Chem. Phys.* **2002**, *281*, 393 – 408.
[11] T. Renger, R. A. Marcus, *J. Phys. Chem. A* **2003**, *107*, 8404 – 8419.
[12] E. M. Conwell, *Proc. Natl. Acad. Sci. USA* **2005**, *102*, 8795 – 8799.
[13] J. Yoo, S. Delaney, E. D. A. Stemp, J. K. Barton, *J. Am. Chem. Soc.* **2003**, *125*, 6640 – 6641.
[14] T. Takada, K. Kawai, X. Cai, A. Sugimoto, M. Fujitsuka, T. Majima, *J. Am. Chem. Soc.* **2004**, *126*, 1125 – 1129.
[15] T. Takada, K. Kawai, M. Fujitsuka, T. Majima, *J. Am. Chem. Soc.* **2006**, *128*, 11012 – 11013.
[16] F. D. Lewis, Y. Wu, L. Zhang, X. Zuo, R. T. Hayes, M. R. Wasielewski, *J. Am. Chem. Soc.* **2004**, *126*, 8206 – 8215.
[17] F. D. Lewis, H. Zhu, P. Daublain, T. Fiebig, M. Raytchev, Q. Wang, V. Shafirovich, *J. Am. Chem. Soc.* **2006**, *128*, 791 – 800.
[18] For a discussion of initial-rate kinetics, see: E. V. Anslyn, D. A. Dougherty, *Modern Physical Organic Chemistry*, University Science Books, Sausalito, CA, **2004**.
[19] M. Pope, C. E. Swenberg, *Electronic Processes in Organic Crystals and Polymers*, Oxford University Press, Oxford, **1999**.
[20] A. M. van de Craats, J. M. Warman, M. P. de Haas, D. Adam, J. Simmerer, D. Haarer, P. Schuhmacher, *Adv. Mater.* **1996**, *8*, 823 – 826.
[21] A. M. van de Craats, J. M. Warman, *Adv. Mater.* **2001**, *13*, 130 – 133.
[22] F. C. Grozema, L. D. A. Siebbeles, Y. A. Berlin, M. A. Ratner, *ChemPhysChem* **2002**, *3*, 536 – 539.
[23] E. M. Conwell, S. V. Rakhmanova, *Proc. Natl. Acad. Sci. USA* **2000**, *97*, 4556 – 4560.
[24] R. N. Barnett, C. L. Cleveland, A. Joy, U. Landman, G. B. Schuster, *Science* **2001**, *294*, 567 – 571.
[25] D. M. Basko, E. M. Conwell, *Phys. Rev. Lett.* **2002**, *88*, 98102.

 © 2006 Wiley-VCH Verlag GmbH & Co. KGaA, Weinheim

Enantiomeric Enrichment

DOI: 10.1002/anie.200602520

Rationalization and Prediction of Solution Enantiomeric Excess in Ternary Phase Systems**

Martin Klussmann, Andrew J. P. White, Alan Armstrong, and Donna G. Blackmond**

In memory of Hendrik Willem Bakhuis Roozeboom (1854–1907)

The evolution of homochirality from a prebiotic environment has intrigued scientists for more than a century. Theoretical models[1,2] have suggested how an initial small imbalance in enantiomeric excess (*ee*) could be amplified by autocatalytic processes. Proof of concept of such "far-from-equilibrium" models was realized in the case of the Soai autocatalytic reaction,[3] but the reaction itself is unlikely to have been viable in a prebiotic environment. Most recently, we introduced a fundamentally different model for the origin of homochirality based on the equilibrium phase behavior of proteinogenic amino acids.[4] At the eutectic point, where saturated solution and two different solid phases coexist in equilibrium,[5–7] the solution composition of a chiral substance is fixed at a given temperature, regardless of its overall *ee* value. This leads to strong asymmetric amplification of solution *ee* values for amino acids exhibiting a high eutectic *ee* value; for example, we showed that serine at overall 1% *ee* exhibits a virtually enantiopure solution at more than 99% *ee*. However, the eutectic composition for any particular chiral compound is not known a priori, and it would appear that high enantiopurity in solution is achievable for only a select few chiral compounds by this approach.

Here we present a model based on simple solubility concepts that rationalizes and predicts the eutectic composition of chiral compounds in terms of the relative solubilities of racemic versus enantiopure mixtures. In addition, we explore the role of solvent in dictating the solution *ee* value under equilibrium conditions. We reveal a case where the eutectic *ee* value of an amino acid is significantly enhanced by incorporation of a small achiral molecule in the structure of the racemic D:L cocrystals. This implies that it may in fact be possible to produce enantiopure solutions for chiral com-

[*] Dr. M. Klussmann, Dr. A. J. P. White, Prof. A. Armstrong, Prof. D. G. Blackmond
Department of Chemistry
Imperial College
London SW7 2AZ (UK)
Fax: (+44) 20-759-45804
E-mail: klusi@imperial.ac.uk
d.blackmond@imperial.ac.uk

[**] We are grateful for generous support from the EPSRC and Astra Zeneca. We thank Richard Sweeney for X-ray powder diffraction analysis.

Supporting information for this article is available on the WWW under http://www.angewandte.org or from the author.

© 2006 Wiley-VCH Verlag GmbH & Co. KGaA, Weinheim

pounds of lower eutectic values, a concept that may have implications for prebiotic chemistry.

The concentration at the eutectic was first described for conglomerates (compounds that form separate crystals of the two enantiomers) by "Meyerhoffer's double solubility rule",[8] and is now commonly expressed using the solubility ratio α [Eq. (1)], with [*rac*] and [ep] representing the solubility of

$$\alpha = \frac{[rac]}{[ep]} \tag{1}$$

racemic and enantiopure mixtures, respectively. Ideal conglomerates exhibit an α value of 2, and their eutectic composition is identical with the racemate.[9]

The magnitude of the solubility ratio (α) and the eutectic composition for substances that form racemic compounds (compounds in which the enantiomers cocrystallise in 1:1 ratio in the elementary cell) is less straightforward. In our earlier studies of the ternary phase behavior of amino acids,[4] we noticed that the concentration of the excess enantiomer at the eutectic closely corresponds to the solubility of the pure enantiomer, whereas the concentration of the minor enantiomer at the eutectic is generally lower than in the case of the pure racemic compound. With these observations in mind, and assuming ideal behavior, for example, no association/dissociation or other interaction between enantiomers in solution, we derived relationships that describe the composition of a chiral compound X at the eutectic. In the following, the excess enantiomer of X is arbitrarily assigned as (+), the minor one as (−). Our derivation is based on the concept of a constant solubility product (SP) of enantiomers in solution for mixed enantiomer cases.[10] The solubility product may be written either for the racemic system or for any scalemic system of enantiomers, and these descriptions may be equated [Eq. (2)].

$$SP = [(+)]_{rac}\,[(-)]_{rac} = [(+)]_{eut}\,[(-)]_{eut} \tag{2}$$

The enantiomers $(+)_{rac}$ and $(-)_{rac}$ are present in equal concentrations in the racemic system [Eq. (3)]. On the basis

$$[(+)]_{rac} = [(-)]_{rac} = \frac{[rac]}{2} \tag{3}$$

of the experimental observations mentioned above, the concentration of the excess enantiomer at the eutectic, $[(+)]_{eut}$, is assumed to be equal to [ep], the solubility of the enantiopure substance [Eq. (4)].

$$[(+)]_{eut} = [ep] \tag{4}$$

Using these relationships, the solubility product (SP) from Equation (2) may be rewritten as in Equation (5), from which

$$SP = \frac{[rac]^2}{4} = [ep]\,[(-)]_{eut} \tag{5}$$

we may derive a relationship for $[(-)]_{eut}$ in terms of racemic and enantiopure solubilities [Eq. (6)].

$$[(-)]_{eut} = \frac{[rac]^2}{4\,[ep]} \tag{6}$$

The total solution concentration of compound X, $[X]_{eut}$, can then be expressed by combining Equations (1), (4), and (6) to give Equation (7). Equally, the eutectic *ee* value is described by a simple expression based solely on the solubility ratio (α) [Eq. (8)].

$$[X]_{eut} = [(+)]_{eut} + [(-)]_{eut} = [ep]\left(1 + \frac{\alpha^2}{4}\right) \tag{7}$$

$$ee_{eut} = \frac{[(+)]_{eut} - [(-)]_{eut}}{[(+)]_{eut} - [(-)]_{eut}}\,100\,\% = \frac{1 - \frac{\alpha^2}{4}}{1 + \frac{\alpha^2}{4}}\,100\,\% \tag{8}$$

These relationships hold true for $\alpha \leq 2$, because otherwise the assumption of Equation (4) would no longer be valid. As for the special case of $\alpha = 2$, the calculated ee_{eut} value is 0 % and thereby the "double solubility rule" for ideal conglomerates is also accommodated by this model.[11]

To examine the predictive capability of Equations (7) and (8), we measured the eutectic compositions of a variety of amino acids along with their solubilities of racemate and enantiopure substance in solvents to determine α values for each case (Table 1). Figure 1 shows a plot of eutectic *ee* values versus the solubility ratio (α) for both our own experimental data as well as for a compilation of published data[12] in comparison with the prediction made by Equation (8).

Figure 1 shows very good agreement between experimental and theoretical eutectic *ee* values from our own experimental data. In addition, our solubility data of amino acids in water generally agrees well with reported values, where available.[13,14] The data we compiled from the literature for other chiral compounds also follow the trend of the model for ee_{eut} values, but in some cases deviation is observed in the region of higher α values. Two notably interesting cases are mandelic acid[12d] and benzylidene camphor[12c] (highlighted with a dotted and dashed box, respectively, in Figure 1), for which α and eutectic *ee* values have been reported as a function of temperature. Clearly, a different model than the one presented in this work must be invoked to account for a eutectic *ee* value that does not change with changing α value, and indeed for any behavior resulting in $\alpha > 2$. A possible explanation for this could be temperature-dependent association/dissociation or agglomeration phenomena that would not be accounted for in our model. However, in the cases where we have studied temperature effects on eutectic *ee* values for amino acids, we found that the values for α change with temperature and the eutectic *ee* changes in accordance with the model of Equation (8) (methionine: entries 5 and 6 in Table 1, + in Figure 1; valine: entries 13 and 14 in Table 1, × in Figure 1).

The eutectic *ee* values found for amino acids span the whole range from 0 to almost 100 % *ee*. Intriguingly, serine exhibits a eutectic *ee* value of over 99 % *ee*, while threonine, which differs in structure by one methyl group (to create a second stereogenic center), is known to be a conglomerate with 0 % *ee* at the eutectic.[5]

 © 2006 Wiley-VCH Verlag GmbH & Co. KGaA, Weinheim

Table 1: Solubility ratio (α) and eutectic *ee* values of selected amino acids and chiral ligands **1**–**4**.[a]

Entry	Compound	Symbol[b]	Solvent	[rac][a]	[ep][a]	α[c]	$[X]_{eut}$[a]	calcd $[X]_{eut}$[d]	ee_{eut}[a] [%]	calcd ee_{eut}[e] [%]
1	alanine	◆	water	34.11	33.39	1.021	n.d.	42.10	60.4[f]	58.6
2	histidine	◆	water	1.78	4.66	0.383	4.79	4.83	93.7[f]	92.9
3	isoleucine	◆	water	5.38	4.66	1.155	6.15	6.21	51.8	50.0
4	leucine	◆	water	1.36	3.19	0.426	3.31	3.33	87.9[f]	91.3
5	methionine	+	water	3.88	7.33	0.529	7.72	7.85	85.3[f]	86.9
6[g]	methionine	+	water	8.26	11.02	0.750	12.10	12.57	78.8	75.3
7	phenylalanine	◆	water	1.56	2.97	0.525	3.22	3.18	83.2[f]	87.1
8	proline	◆	DMSO	1.33	1.15	1.155	1.73	1.53	49.6[f]	50.0
9	proline	◆	$CHCl_3$	0.001	0.51	0.002	0.36	0.51	99.2	100.0
10	proline	◆	$CHCl_3$/MeOH[h]	1.21	31.49	0.038	36.07	31.50	96.4	99.9
11	proline	◆	$CHCl_3$/MeOH[i]	7.92	63.84	0.124	67.90	64.08	93.6	99.2
12	serine	◆	water	8.64	63.74	0.130	64.81	64.03	>99.0[f]	99.1
13	valine	×	water	11.27	9.15	1.231	n.d.	12.62	46.7[f]	45.1
14[g]	valine	×	water	16.52	12.49	1.323	16.95	17.95	36.8	39.1
15	binol (**1**)	▲	toluene	2.29	5.66	0.405	5.95	5.89	91.0	92.1
16	binap (**2**)	●	toluene	0.29	5.95	0.048	5.91	5.95	99.9	99.9
17	taddol (**3**)	■	toluene	0.25	28.63	0.009	28.89	28.63	99.8	100.0
18	salen (**4**)	▼	hexane	7.03	3.42	2.057	6.97	7.03	0.0	−2.8

[a] Data measured at 25 °C unless noted otherwise. Concentrations in 10^{-3} molar fraction. [b] See Figure 1. [c] According to Equation (1). [d] According to Equation (7). [e] According to Equation (8). [f] From Ref. [4]. [g] At 60 °C. [h] 1.0 M MeOH. [i] 2.0 M MeOH. n.d. = not determined.

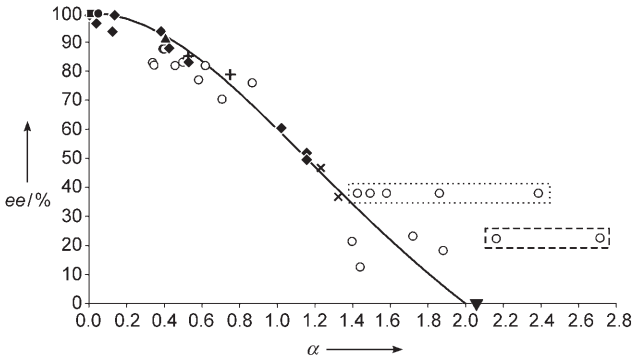

Figure 1. Experimental eutectic *ee* values for chiral compounds as a function of the solubility ratio α. Black line: Equation (8); black symbols (◆, ■, ●, ▲, ▼, +, ×): this work (see Table 1); ○: literature data (see Supporting Information); dotted and dashed boxes: data measured at different temperatures (see text for details).

Figure 1 shows that the predictive capability of our simple model of Equation (8) extends beyond amino acids for a number of common chiral ligands (Table 1, entries 15–18: binol (**1**), binap (**2**), taddol (**3**), and salen (**4**); see Supporting Information for structures). This has implications for studies of nonlinear effects in asymmetric catalysis involving these ligands. If catalyst preparation and reaction procedures are not carried out under homogeneous conditions, the *ee* value of the species present during catalytic turnover may be influenced by solid–liquid phase behavior.

The case of proline deserves special comment. Proline was found to exhibit very different eutectic *ee* values in different solvents: 50% *ee* in DMSO compared to 99% *ee* in $CHCl_3$, spanning a 500-fold difference in α values. Recently, Hayashi et al. reported a similar enhancement in solution *ee* values for proline in $CHCl_3$/CH_3CH_2OH, which they rationalized in terms of preferential precipitation of D:L cocrystals.[15,16] However, the D:L structure they presented was obtained through crystallization from ethanol, in which the eutectic *ee* value is significantly lower than it is in $CHCl_3$ ($\approx$54% *ee*, see Supporting Information), and is similar to a D:L structure reported previously crystallized from methanol.[17] The role of $CHCl_3$ in enhancing solution *ee* values is difficult to rationalize from these results.

Enantiopure proline crystallized from $CHCl_3$ gives a powder X-ray pattern identical to that published[18] for anhydrous proline crystallized from ethanol (see Supporting Information). We found, however, that the solid racemate crystallized from proline in $CHCl_3$/CH_3OH exhibits a novel structure differing from all those previously published for the proline racemate.[17,19] Figure 2 shows that cocrystals of a 1:1 D:L compound are formed, incorporating one molecule of $CHCl_3$ per pair of proline molecules (see Supporting Information). The proline molecules exist in zwitterionic form in an extensive hydrogen-bonding network that includes the proton from chloroform. The structure contains two independent molecules of proline in the asymmetric unit, one with the carboxylate unit in a pseudo-equatorial position with respect to the pyrrolidine ring, and the other in a pseudo-axial position. These proline molecules are linked to each other and neighboring symmetry-related molecules in the racemic crystal by a series of N–H···O hydrogen-bonding interactions that extend to form a two-proline-thick corrugated two-dimensional sheet (Figure 3). The chloroform molecule, and its symmetry-related counterparts, are located on the top and bottom faces of this sheet and are held in place by a C–H···O hydrogen bond to one of the carboxylate oxygen atoms of the pseudo-axial proline molecule. The 2D sheet is particularly notable in that the axial and equatorial proline units are comprised of opposite enantiomers, and these conformations switch in the adjacent centrosymmetrically related sheets.

As predicted by our model, the reduced solubility of this novel racemate compared to enantiopure proline causes a significant enhancement of the eutectic *ee* value of the system in $CHCl_3$, thus providing a virtually enantiopure solution. The

 © 2006 Wiley-VCH Verlag GmbH & Co. KGaA, Weinheim

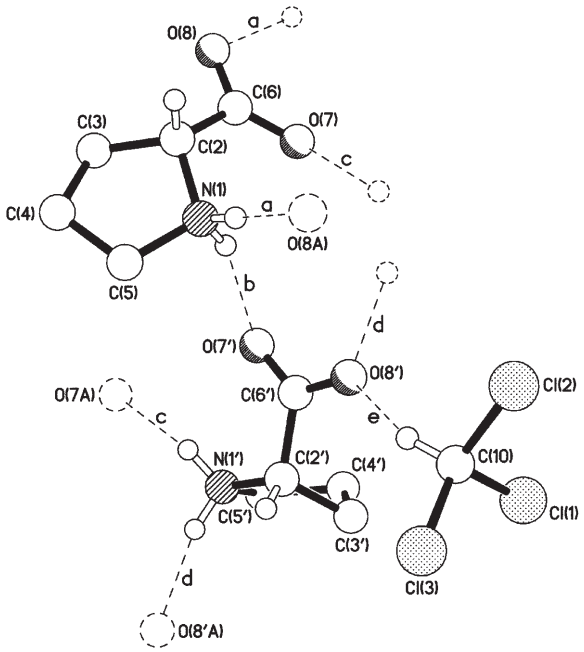

Figure 2. The asymmetric unit of DL-proline/chloroform showing the hydrogen-bonding interactions between the two independent proline molecules and the included chloroform solvent molecule (ellipsoids shown at 50% probability). The hydrogen-bonding geometries (X···O [Å], H···O [Å], X–H···O [°]) are a) 2.708(2), 1.81, 178; b) 2.826(3), 2.01, 150; c) 2.809(2), 2.00, 148; d) 2.761(2), 1.88, 165; e) 3.098(3), 2.22, 152.

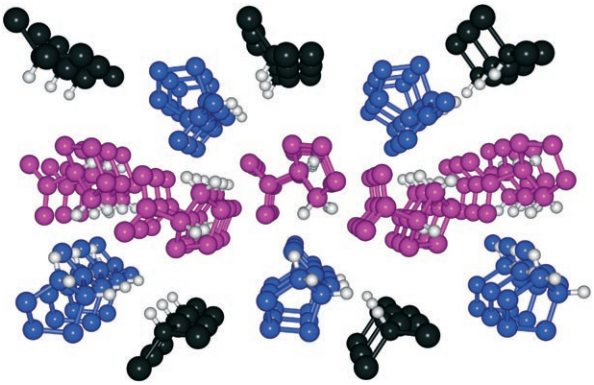

Figure 3. Structure of racemic proline crystallized from a $CHCl_3$/CH_3OH mixture, with one $CHCl_3$ molecule (black) incorporated per pair of proline molecules. The blue proline molecules correspond to one enantiomer, while the magenta proline molecules correspond to the opposite enantiomer. These conformations switch in adjacent sheets.

extensive hydrogen-bonding network within the structure of the DL-proline/chloroform cocrystals may help to explain the significant decrease in the solubility of DL-proline in chloroform compared to racemates crystallized from DMSO, CH_3CH_2OH, or water. Hayashi et al. have also suggested that the greater stability of D:L cocrystals helps to rationalize the amplification of solution *ee* values for proline, but their study did not uncover the role of $CHCl_3$ in promoting this stability.[15,20]

The case of proline also addresses the question of whether a single binary phase diagram of enantiomers may be used to predict ternary phase behavior. It has been shown in some cases that the enantiomeric composition at the eutectic in the ternary phase diagram is closely related to that in the binary phase diagram.[12c–e,21] However, a similar number of examples are known which show that this is not always a reliable basis for the direct prediction of ternary phase behavior; while binary phase diagrams necessarily provide a eutectic only at the melting temperature, the eutectics of ternary phase diagrams can be temperature-dependent.[12a–c] Clearly a single binary phase diagram could not have predicted the solvent-dependent ternary phase behavior that we observed with proline, while our model based on the solubility ratio (α) does. With the solvent composition of the eutectic, the enantiopure and racemic case thus known, the key points of a ternary phase diagram are already delineated (see Supporting Information for phase diagrams of most compounds in Table 1).

In summary, we have developed a model based on simple solubility concepts that successfully rationalizes and predicts solution *ee* values for chiral compounds in solid–solution equilibrium. In addition, our finding that the enantiomeric excess of an amino acid in solution may be significantly enhanced by incorporation of a small, achiral molecule into its solid racemate suggests a general and facile route to homochirality that may have prebiotic relevance. Such enantiomerically enriched solutions may provide asymmetric catalysts or synthetic building blocks for construction of the complex molecules required for recognition, replication, and ultimately for the chemical basis of life.

Received: June 22, 2006
Revised: August 8, 2006
Published online: September 20, 2006

Keywords: amino acids · chirality · enantioselectivity · phase diagrams · solvent effects

[1] F. C. Frank, *Biochim. Biophys. Acta* **1953**, *11*, 459.
[2] M. Calvin, *Molecular Evolution*, Oxford University Press, Oxford, **1969**.
[3] K. Soai, T. Shibata, H. Morioka, K. Choji, *Nature* **1995**, *378*, 767–768.
[4] M. Klussmann, H. Iwamura, S. P. Mathew, D. H. Wells, Jr., U. Pandya, A. Armstrong, D. G. Blackmond, *Nature* **2006**, *441*, 621–623.
[5] J. Jacques, A. Collet, S. H. Wilen, *Enantiomers, Racemates and Resolution*, Krieger Publishing Company, Florida, **1991** (earlier edition: Wiley, New York, **1981**).
[6] W. L. Eliel, S. H. Wilen, L. N. Mander, *Stereochemistry of Organic Compounds*, Wiley-Interscience, New York, **1994**.
[7] Although the eutectic was originally defined in terms of binary system phase behavior, here we adopt the usage of the textbooks (Refs. [5,6]) for ternary systems of enantiomers and solvent. In addition, Refs. [12a–e] and [21] use this definition. The eutectic point in these ternary systems is also known as an "isothermal invariant point"; see: S. Glasstone, *Textbook of Physical Chemistry*, 2nd ed., MacMillan, London, **1948**, p. 804.
[8] W. Meyerhoffer, *Ber. Dtsch. Chem. Ges.* **1904**, *37*, 2604–2610.
[9] A more detailed discussion is described in Ref. [5].

 © 2006 Wiley-VCH Verlag GmbH & Co. KGaA, Weinheim

[10] A discussion of solubility product in the context of enantiomeric enrichment was given in: H. J. Morowitz, *J. Theor. Biol.* **1969**, *25*, 495.
[11] The eutectic composition is defined for substances that form conglomerates and racemic compounds, but not for the rare cases of compounds that form pseudoracemates or anomalous racemates; see Ref. [5]. The cases of substances that crystallize as pseudoracemates or anomalous racemates will not be described with this model.
[12] a) J. Worlitschek, M. Bosco, M. Huber, V. Gramlich, M. Mazzotti, *Helv. Chim. Acta* **2004**, *87*, 279–291; b) Y. Wang, R. LoBrutto, R. W. Wenslow, I. Santos, *Org. Process Res. Dev.* **2005**, *9*, 670–676; c) J. Jacques, J. Gabard, *Bull. Soc. Chim. Fr.* **1972**, 342–350; d) H. Lorenz, D. Sapoundjiev, A. Seidel-Morgenstern, *J. Chem. Eng. Data* **2002**, *47*, 1280–1284; e) Y. H. Lu, C. B. Ching, *Chirality* **2004**, *16*, 541–548; f) B. K. Singh, O. N. Perti, *Proc. Indian Acad. Sci. Sect. A* **1945**, *22*, 170–176.
[13] a) J. P. Amend, H. C. Helgeson, *Pure Appl. Chem.* **1997**, *69*, 935–942; b) J. P. Greenstein, M. Winitz, *Chemistry of the Amino Acids*, *Vols. 1–3*, Wiley, New York, **1961**; c) J. Huang, L. Yu, *J. Am. Chem. Soc.* **2006**, *128*, 1873–1878.
[14] In the case of isoleucine, differing data have been reported but our data fit very well with those in Ref. [13c].
[15] Y. Hayashi, M. Matsuzawa, J. Yamaguchi, S. Yonehara, Y. Matsumoto, M. Shoji, D. Hashizume, H. Koshino, *Angew. Chem.* **2006**, *118*, 4709–4713; *Angew. Chem. Int. Ed.* **2006**, *45*, 4593–4597.
[16] Ref. [15] appeared while this manuscript was under review.
[17] S. Myung, M. Pink, M.-H. Baik, D. E. Clemmer, *Acta Crystallogr. Sect. C* **2005**, *61*, 506–508.
[18] R. L. Kayushina, B. K. Vainshtein, *Sov. Phys. Crystallogr. Rep.* **1966**, *10*, 698–706.
[19] S. Padmanabhan, S. Suresh, M. Vijayan, *Acta Crystallogr. Sect. C* **1995**, *51*, 2098–2100.
[20] The authors of Ref. [15] suggested that enrichment of an enantiomer in solution from a solid of low *ee* value involves dissolution and crystallization mechanisms that are "completely different to that of any other known resolution"; in fact, such solution enrichment commonly occurs in all cases of chiral compounds where the overall composition of enantiomers is below the eutectic *ee* value. Ref. [5] (pp. 192–193) notes that this is a very important feature of enantiomer mixtures that form racemic compounds.
[21] Y. Liu, X. Wang, J.-K. Wang, C. B. Ching, *Chirality* **2006**, *18*, 259–264.

 © 2006 Wiley-VCH Verlag GmbH & Co. KGaA, Weinheim

Asymmetric Catalysis

DOI: 10.1002/anie.200602521

Kinetic Rationalization of Nonlinear Effects in Asymmetric Catalysis Based on Phase Behavior**

*Martin Klussmann, Suju P. Mathew, Hiroshi Iwamura, David H. Wells, Jr., Alan Armstrong, and Donna G. Blackmond**

The rapidly expanding field of organocatalysis has received considerable attention[1–4] since the earliest reports of the proline-mediated intramolecular aldol reaction.[5,6] Observation of a weak negative nonlinear effect in this reaction led Kagan and co-workers to include this example in their earliest reports on developing mathematical models for nonlinear effects of catalyst enantiomeric excess (*ee*) on product enantioselectivity in asymmetric catalysis.[7] The two-proline mechanism that was offered to explain the nonlinear effect has since been discounted, however, by experimental studies[8–10] that revealed linearity between proline and product enantiomeric excess values in both inter- and intramolecular aldol reactions, supported by theoretical studies.[10] The prevailing model for proline-catalyzed aldol and related reactions involves the reaction of one proline molecule with a donor molecule to form an enamine, followed by attack on an electrophile;[11,12] nonlinear effects would appear to be incompatible with this model. Nevertheless, the original observation of a nonlinear effect remains unreconciled, and instances of nonlinear behavior in proline-mediated reactions have persisted.[13–16]

Our reports in 2004 of nonlinear effects in proline-mediated α-aminoxylation[14] and α-amination[15] reactions rekindled interest in exploring such behavior in amino acid catalysis. We recently showed that these effects are not related to the catalytic reaction mechanism, as we had previously suggested, but instead to the ternary phase behavior of proline in solvent.[17] This finding was extended to include other amino acids and has implications for the evolution of biological homochirality. However, the nonlinear

[*] Dr. M. Klussmann, Dr. S. P. Mathew, Dr. H. Iwamura,[+] Dr. D. H. Wells, Jr.,[++] Prof. A. Armstrong, Prof. D. G. Blackmond
Department of Chemistry
Imperial College
London SW7 2AZ (UK)
Fax: (+44) 20-7594-5804
E-mail: d.blackmond@imperial.ac.uk

[+] Present address:
Mitsubishi Pharma
Kamisu, Ibaraki 314-0255 (Japan)

[++] Present address:
Department of Chemistry
University of Calgary (Canada)

[**] We are grateful for generous support from the EPSRC, AstraZeneca, and Mitsubishi Pharma.

Supporting information for this article is available on the WWW under http://www.angewandte.org or from the author.

© 2006 Wiley-VCH Verlag GmbH & Co. KGaA, Weinheim

trends originally reported by Kagan and co-workers[7] remain unexplainable by the equilibrium model developed in that work.

We report here how the concept of a "kinetic conglomerate" phase can rationalize the findings of Kagan and co-workers[7] in a manner that remains compatible with the currently accepted one-proline reaction mechanism and reconciles reports of both linearity and nonlinearity in this system. Implications of this behavior for the interpretation of nonlinear effects in general are shown to extend beyond amino acid catalysis and are demonstrated for the particular case of a tetraaryl-1,3-dioxolane-4,5-dimethanol (taddol) ligand system.

Although the solid–solution phase behavior of racemic and enantiopure compounds was studied more than a century ago[18] and is well understood,[19] scalemic mixtures of amino acids have received less attention. Of the twenty proteinogenic amino acids, only threonine and asparagine crystallize as "conglomerates" or separate enantiomeric solid phases. All of the others, including proline, cocrystallize in a 1:1 ratio of the enantiomers, known as a "racemic compound".[19] For a scalemic system at equilibrium, the solution composition at the eutectic point is fixed and is necessarily 0% *ee* for amino acids that form conglomerates; for racemic compounds, however, the eutectic *ee* can have a value anywhere between 0–100% *ee* and is not known a priori. We reported the first measurements of eutectic *ee* values for proteinogenic amino acids that form racemic compounds.[17] Most recently, we have developed a model to predict the eutectic *ee* of a chiral substance based on simple solubility concepts.[20]

In these earlier studies, we reported that the eutectic for proline in dimethyl sulfoxide (DMSO) at 25°C is approximately 50% *ee*. Under solid–solution equilibrium, this eutectic value dictates the enantiomeric excess of the solution for all values of scalemic proline *ee* employed, which in turn dictates the product *ee* that may be achieved in solution-phase reactions catalyzed by scalemic proline. This fact rationalized our unusual observation of a constant product *ee* value in aldol reactions over a wide range of total proline *ee* values, manifested as a positive nonlinear effect at overall proline *ee* values below the eutectic *ee*, and as a negative nonlinear effect at proline *ee* values above the eutectic *ee*. However, it is clear that such an equilibrium model cannot explain the fact that negative nonlinear effects were reported by Kagan and co-workers at *all* proline *ee* values.[7]

We turned instead to consideration of the phase behavior of proline under the non-equilibrium conditions that ensue during catalyst dissolution. In studies of nonlinear behavior where, typically, the desired proportions of the two pure enantiomers are physically mixed with the other components of the reaction mixture, it might be expected that the enatiomeric excess of the solution would initially represent a linear combination of the two separate enantiomers as the catalyst begins to dissolve, ultimately to establish either equilibrium solid–solution phase behavior or a homogeneous system. Figure 1 shows that in fact the solution *ee* value for scalemic proline is close to zero immediately following addition of the enantiomers in any proportion. The solution *ee* value rises from near zero over time to stabilize at the value

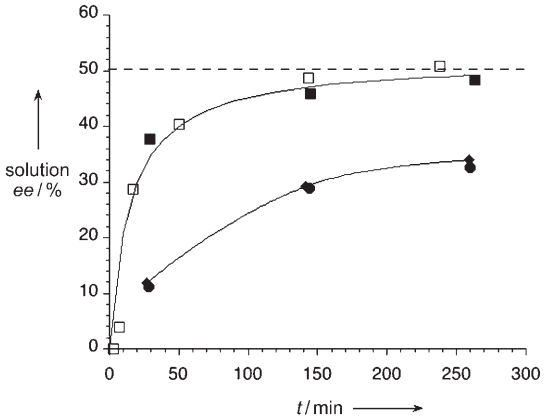

Figure 1. Solution *ee* values as a function of time for physical mixtures of pure D- and pure L-proline in DMSO at 25°C at different overall proline *ee* values. Total proline concentration: 12 mg mL^{-1}, unless noted otherwise. Filled squares (■): 20% *ee*; open squares (□): 19% *ee*, 40 mg mL^{-1}; filled circles (●): 40% *ee*; filled diamonds (◆): 60% *ee*. The dashed line represents the eutectic *ee* value for proline in DMSO.

of its eutectic composition under solid–solution equilibrium, regardless of whether the initial proportions of the enantiomers is lower or higher than the eutectic value. We also found that the addition of water results in a faster equilibration. Interestingly, the solution concentration of proline for the cases shown in Figure 1 is *higher* during this transient initial period—in fact, exceeding its equilibrium concentration by as much as 40%—and decreases over time concomitant with the rise in solution *ee* (see Supporting Information).

These unexpected observations may be rationalized by considering that the solid L- and solid D-proline mixture is more similar to a conglomerate than to a racemic compound when first mixed in solvent at the outset of the experiment; thus it exhibits the phase behavior known for this type of solid before equilibrating to the true racemic compound that proline forms at equilibrium.[21] The low solution *ee* value at the outset is observed because the D and L crystals are separately in equilibrium with the solution phase as in a conglomerate, which exhibits 0% *ee* at the eutectic. The anomalously high proline solution concentration observed during the transient period occurs because conglomerates exhibit a higher solubility at the eutectic relative to the enantiopure phase than do racemic compounds.[19,20] These considerations indicate that solid–solution equilibration of the pure enantiomers as shown in Equations (1) and (2) is rapid and occurs before a significant fraction of the solid DL racemate has formed [Eq. (3)].[22]

$$\text{L(solid)} \rightleftharpoons \text{L(liquid)} \quad (1)$$

$$\text{D(solid)} \rightleftharpoons \text{D(liquid)} \quad (2)$$

$$\text{L(liquid)} + \text{D(liquid)} \rightleftharpoons \text{DL(solid)} \quad (3)$$

Ultimately, at equilibrium, the scalemic system will consist of a solution phase at its eutectic composition and two separate solid phases, the racemic DL(solid) and the enantio-

 © 2006 Wiley-VCH Verlag GmbH & Co. KGaA, Weinheim

pure solid of the enantiomer in excess (L in this case). The minor enantiomer (D in this case) will no longer retain its own enantiopure solid phase—and the process in Equation (2) will no longer occur—at equilibrium. Thus, we propose that our observations may be attributed to the transition between a transient "kinetic conglomerate" phase and the true racemic compound that proline forms at equilibrium.

The concept of a kinetic conglomerate phase may have a significant impact in studies of nonlinear effects in asymmetric catalysis. The data in Figure 1 suggest that if proline dissolution occurs simultaneously with turnover in an asymmetric reaction, the product *ee* may be lower than expected based on total proline *ee*. This suggestion is confirmed in Figure 2, which shows product *ee* versus proline *ee* for the

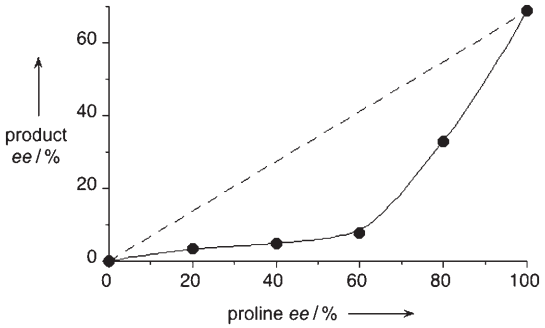

Figure 2. Product *ee* values versus overall proline *ee* for the aldol reaction of Scheme 1 carried out in DMSO at 25 °C using 40 mg proline per mL of DMSO. Reaction time: 30–45 min; conversion was greater than 98 % in all cases. The dashed line represents the expected linear relationship.

aldol reaction shown in Scheme 1 initiated by adding a mixture of separate solid D- and L-proline to a solution containing solvent and reactants, instead of premixing the

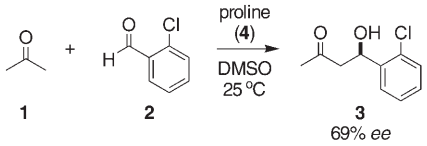

Scheme 1. Proline-mediated aldol reaction.

proline in solvent prior to addition of the substrate.[23] These results provide the first explanation of the origin of the negative nonlinear effect observed by Kagan and co-workers[7] in intramolecular aldol reactions.[24] The sensitivity of the solution *ee* to factors such as mixing times and water content help to rationalize observed differences in reactions carried out under seemingly identical conditions.

The implications of the phase behavior reported here are not limited to amino acid catalyst systems but have significance in general for understanding nonlinear effects in other asymmetric catalyst systems. Probing of nonlinear effects has become a common tool in mechanistic studies in all areas of asymmetric catalysis. The observation of nonlinear behavior is in many cases assumed to be diagnostic of the presence of more than one chiral ligand in the transition state, and explanations such as Kagan's ML_n models are typically invoked.[7,25] However, such interpretations could be misleading if the observed nonlinearity is due to physical phase behavior as we have described. Our work shows that temporal evolution of catalyst *ee* in solution may occur in any case where full solubility of chiral catalysts, ligands, or auxiliaries has not been established either prior to reaction or prior to formation of the active catalyst, even in instances where homogeneous conditions are ultimately achieved.

The quantitative phase behavior of most commonly employed chiral ligands remains virtually unexplored, although nonlinear effects have been reported in a number of cases that may be related to factors influenced by solid–solution phase behavior, such as the concentration and preparation of the catalyst as well as reaction protocols.[25–30] This work shows that both the sign and the magnitude of the observed nonlinear effect may depend on the kinetics of catalyst dissolution. As an example, we studied both the equilibrium phase behavior and the dissolution kinetics of taddol derivative **5**; nonlinear behavior has been reported in a variety of asymmetric reactions using this class of compounds.[25–27] We found that **5** forms a true racemic compound exhibiting an extremely high eutectic *ee* value of over 99 % *ee* under solid–solution equilibrium.[20] Figure 3 reveals that taddol exhibits the behavior of a kinetic conglomerate phase as it dissolves; for a 40 % *ee* taddol mixture, solution *ee* values spanning the entire range from nearly racemic to nearly enantiopure are obtained over time.

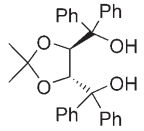

5

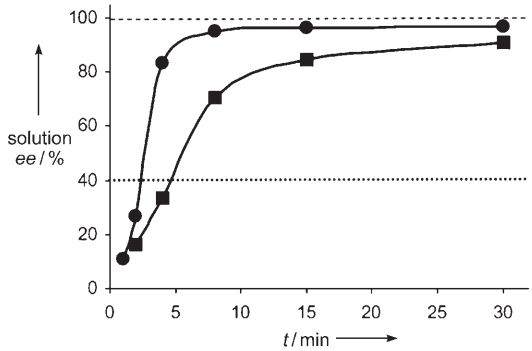

Figure 3. Solution *ee* values versus time for dissolution of taddol **5** in hexane (1.76 wt %) at 21 °C (●) and 0 °C (■). Overall *ee* for taddol: 40 % (••••); eutectic *ee* for taddol: 99 % (----).

This result suggests that a wide range of possibilities for both positive and negative nonlinear effects on product *ee* may result in asymmetric reactions using **5** in cases where dissolution occurs concomitant with reaction or with preparation of active catalyst species. Indeed, the experimental protocol in many taddol-mediated reactions involves initiation by mixing catalyst and reaction components at temperatures as low as −78 °C; the time dependence of solution *ee*

 © 2006 Wiley-VCH Verlag GmbH & Co. KGaA, Weinheim

values may be expected to be more significant at lower temperature. The reaction often proceeds non-isothermally as the vial is allowed to warm to ambient temperature. Such conditions may be conducive to simultaneous catalyst dissolution and catalytic turnover, giving the potential for nonlinear effects due to transient phase behavior.

In summary, this report demonstrates that reactions using enantioimpure catalysts must be probed carefully in order to elucidate the origin of an observed nonlinear effect. Most importantly, nonlinear effects of a true chemical origin such as that described by Kagan's ML_n models must be distinguished from those caused by physical phase behavior. Nonlinear effects observed in mixed-phase systems must be further characterized according to whether the effects originate from equilibrium or kinetic behavior. These concepts apply not only to the amino acid systems we originally studied but also to other asymmetric catalysts and ligands that are used to prepare asymmetric catalysts. Further studies are underway to identify and quantify nonlinear effects in asymmetric catalysis that may be traced to physical phase behavior.

Received: June 22, 2006
Revised: August 10, 2006
Published online: October 24, 2006

Keywords: amino acids · asymmetric catalysis · chirality · nonlinear effects · phase transitions

[1] J. Seayad, B. List, *Org. Biomol. Chem.* **2005**, *3*, 719.
[2] B. List, *Acc. Chem. Res.* **2004**, *37*, 548.
[3] W. Notz, F. Tanaka, C. F. Barbas III, *Acc. Chem. Res.* **2004**, *37*, 580.
[4] P. I. Dalko, L. Moisan, *Angew. Chem.* **2004**, *116*, 5248; *Angew. Chem. Int. Ed.* **2004**, *43*, 5138.
[5] Z. G. Hajos, D. R. Parrish, *J. Org. Chem.* **1974**, *39*, 1615.
[6] U. Eder, G. Sauer, R. Wiechert, *Angew. Chem.* **1971**, *83*, 492; *Angew. Chem. Int. Ed. Engl.* **1971**, *10*, 496.
[7] C. Puchot, O. Samuel, E. Dunach, S. Zhao, C. Agami, H. B. Kagan, *J. Am. Chem. Soc.* **1986**, *108*, 2353.
[8] K. Sakthivel, W. Notz, T. Bui, C. F. Barbas III, *J. Am. Chem. Soc.* **2001**, *123*, 5260.
[9] B. List, *Synlett* **2001**, *11*, 1675.
[10] L. Hoang, S. Bahmanyar, K. N. Houk, B. List, *J. Am. Chem. Soc.* **2003**, *125*, 16.
[11] F. R. Clemente, K. N. Houk, *Angew. Chem.* **2004**, *116*, 5890; *Angew. Chem. Int. Ed.* **2004**, *43*, 5766.
[12] S. Bahmanyar, K. N. Houk, H. J. Martin, B. List, *J. Am. Chem. Soc.* **2003**, *125*, 2475.
[13] S. Hanessian, V. Pham, *Org. Lett.* **2000**, *2*, 2975.
[14] S. P. Mathew, H. Iwamura, D. G. Blackmond, *Angew. Chem.* **2004**, *116*, 3379; *Angew. Chem. Int. Ed.* **2004**, *43*, 3317.
[15] H. Iwamura, S. P. Mathew, D. G. Blackmond, *J. Am. Chem. Soc.* **2004**, *126*, 11770.
[16] A. Córdova, M. Engqvist, I. Ibrahem, J. Casas, H. Sundén, *Chem. Commun.* **2005**, 2047.
[17] M. Klussmann, H. Iwamura, S. P. Mathew, D. H. Wells, Jr., U. Pandya, A. Armstrong, D. G. Blackmond, *Nature* **2006**, *441*, 621.
[18] H. W. B. Roozeboom, *Z. Phys. Chem. Stoechiom. Verwandtschaftsl.* **1899**, *28*, 494.
[19] J. Jacques, A. Collet, S. H. Wilen, *Enantiomers, Racemates and Resolution*, Krieger Publishing Company, Florida, **1991**.
[20] M. Klussmann, A. P. White, A. Armstrong, D. G. Blackmond, *Angew. Chem.*, DOI: 10.1002/ange.200602520; *Angew. Chem. Int. Ed.*, DOI: 10.1002/anie.200602520.
[21] It was suggested by a referee that different particle sizes of D- and L-proline could give different solubilization rates and thus account for the results of Figure 1. However, this explanation cannot account for near-racemic initial solution *ee* values obtained from experiments using mixtures of solid D- and L-proline at both high and low *ee* values. In addition, the finding that the proline solution concentration during this transient period is higher than its equilibrium value cannot be explained by a particle size effect.
[22] Formation of a racemic compound can proceed in the solid phase but is accelerated by solvent; see: F. Toda, K. Tanaka, H. Miyamoto, H. Koshima, I. Miyahara, K. Hirotsu, *J. Chem. Soc. Perkin Trans.* 2 **1997**, 9, 1877.
[23] The studies by Kagan and co-workers (Ref. [7]) and List (Ref. [10]) were both carried out by mixing L- and D-proline as in the present work. However, studies of nonlinear effects are often carried out by mixing the racemic compound with the appropriate amount of the enantiopure compound. In such a case, with the DL compound preformed, the system might be expected to equilibrate at its eutectic point more rapidly.
[24] The stronger negativity of the nonlinear effect observed in Figure 2 compared to the weakly negative nonlinear effect reported by Kagan and co-workers[7] may be attributed to the faster kinetics of the aldol reaction of Scheme 1 compared to the intramolecular version studied by Kagan, which means that a greater fraction of the reaction turnover occurred under non-equilibrated conditions in the present study.
[25] C. Girard, H. B. Kagan, *Angew. Chem.* **1998**, *110*, 3088; *Angew. Chem. Int. Ed.* **1998**, *37*, 2922. A second important type of model involving "reservoir effects" invokes off-cycle dimer formation with only one chiral ligand present in the transition state; see: M. Kitamura, S. Suga, H. Oka, R. Noyori, *J. Am. Chem. Soc.* **1998**, *120*, 9800.
[26] N. Iwasawa, Y. Hayashi, H. Sakurai, K. Narasaka, *Chem. Lett.* **1989**, 1581.
[27] A. Cuenca, M. Medio-Simón, G. A. Guilar, D. Weibel, A. K. Beck, D. Seebach, *Helv. Chim. Acta* **2000**, *83*, 3153.
[28] T. O. Luukas, D. R. Fenwick, H. B. Kagan, *C. R. Chim.* **2002**, *5*, 487.
[29] M. De Rosa, M. R. Acocella, R. Villano, A. Soriente, A. Scettri, *Tetrahedron Lett.* **2003**, *44*, 6087.
[30] P. Melchiorre, K. A. Jørgensen, *J. Org. Chem.* **2003**, *68*, 4151.

 © 2006 Wiley-VCH Verlag GmbH & Co. KGaA, Weinheim

Asymmetric Catalysis

DOI: 10.1002/anie.200603776

Catalytic Asymmetric Amination of Enecarbamates**

*Ryosuke Matsubara and Shū Kobayashi**

Asymmetric electrophilic amination reactions have recently received much attention.[1] In particular, the asymmetric amination of carbonyl compounds has been developed to obtain biologically important α-amino acids and their derivatives. A number of compounds, such as sulfonyl azides,[2] 1-chloro-1-nitroso reagents,[3] and nitroso benzenes,[4] are known to act as electrophilic nitrogen sources, but perhaps the most prominent are azodicarboxylates. A catalytic asymmetric α-amination of carbonyl compounds using azodicarboxylates was pioneered by Evans and Nelson, who used a chiral magnesium bis(sulfonamide) complex as a catalyst.[5] Subsequently, Evans's group[6] and our group[7] reported the catalytic asymmetric amination using silicon enolates. List and Jørgensen and co-workers reported asymmetric proline-catalyzed amination of linear aldehydes using azodicarboxylates,[8] and furthermore Jørgensen and co-workers examined the direct use of ketones in proline-catalyzed amination of azodicarboxylates.[9] Direct α-amination of 2-ketoesters and β-ketoesters in the presence of a chiral bisoxazoline-Cu^{II} complex[10] and direct organocatalytic amination of α-substituted α-cyanoacetates[11] are also alternative methods for the synthesis of enantioenriched α-amino carbonyl compounds. Whereas those methods gave excellent enantioselectivities (in general over 90% *ee*), relatively high catalyst loadings (in almost all cases, not less than 5 mol%) were necessary to obtain high enantioselectivies and substrates are limited in many reactions.[12] Herein, we report the first catalytic asymmetric amination of enecarbamates catalyzed by a chiral diamine-Cu^{II} complex using azodicarboxylates. Yields and enantioselectivities are generally high for various kinds of enecarbamates derived from aromatic and aliphatic ketones, and aldehydes, and lower levels of catalyst loadings have been attained (in some cases, 0.2 mol% of the catalyst was sufficient). We also describe the facile synthesis of optically active *trans*-1,2-diamine compounds by using this method.

We first investigated the amination of propiophenone-derived enecarbamate **2a** (Table 1).[13] When $AgClO_4$-binap

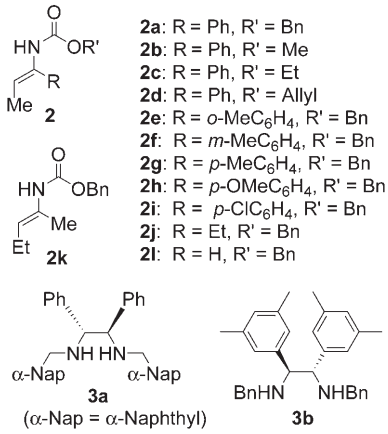

Table 1: Optimization of reaction conditions.[a]

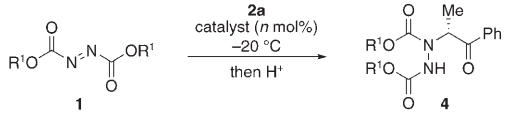

Entry	R^1	Catalyst	*n* [mol%]	**2a**	Solvent	*t* [h]	Yield [%]	*ee* [%]
1[b]	Bn	$AgClO_4$ + (*S*)-binap	10	*Z*	THF	72	77	36
2[b]	Bn	$Zn(OTf)_2$ + **3a**	10	*Z*	CH_2Cl_2	144	51	32[c]
3[b]	Bn	$Cu(OTf)_2$ + **3a**	10	*Z*	CH_2Cl_2	30	96	66[c]
4[b]	Bn	$Cu(OTf)_2$ + **3a**	10	*E*	CH_2Cl_2	1.5	98	70[c]
5[d]	Bn	$Cu(OTf)_2$ + **3b**	10	*E*	toluene	6	99	85
6[d]	Bn	$Cu(BF_4)_2 \cdot x H_2O$ + **3b**	10	*E*	toluene	7	100	87
7[d]	*i*Pr	$Cu(BF_4)_2 \cdot x H_2O$ + **3b**	10	*E*	toluene	4	100	93
8[d]	*i*Pr	$Cu(BF_4)_2 \cdot x H_2O$ + **3b**	1	*E*	toluene	52	34	88
9	*i*Pr	$Cu(BF_4)_2 \cdot x H_2O$ + **3b**	1	*E*	toluene	36	97	89
10	*i*Pr	$Cu(OTf)_2$ + **3b**	1	*E*	toluene	6	94	95

[a] Reactions conducted with 1.1 equivalents of **1** relative to **2** in the indicated solvent (0.067 M in substrate). Bn = benzyl, OTf = trifluoromethanesulfonate. [b] 0 °C. [c] Opposite enantiomer. [d] 3-Å molecular sieves (M.S.; 100 mg mmol^{-1}) were added.

complex, which gave high enantioselectivity in the reaction of azodicarboxylate with silicon enolates,[7] was used as a catalyst, the ketone product **4** was obtained after hydrolysis with low enantioselectivity (Table 1, entry 1). While the catalytic activity of $Zn(OTf)_2$-diamine **3a** was also found to be low (Table 1, entry 2),[14] $Cu(OTf)_2$-**3a** complex[15] gave higher enantioselectivity (entry 3). Moreover, it was found that changing the enecarbamate geometry from *Z* to *E* resulted in a dramatic improvement of the reactivity (Table 1, entry 4), and that the use of diisopropyl azodicarboxylate in toluene improved enantioselectivity significantly (entries 5–7).[16] The yield was decreased when the catalyst loading was reduced to 1 mol% (Table 1, entry 8), but was improved

[*] R. Matsubara, Prof. Dr. S. Kobayashi
Graduate School of Pharmaceutical Sciences
University of Tokyo
HFRE Division, ERATO
Japan Science Technology Agency (JST)
Hongo, Bunkyo-ku, Tokyo 113-0033 (Japan)
Fax: (+81) 3-5684-0634
E-mail: skobayas@mol.f.u-tokyo.ac.jp

[**] This work was partially supported by a Grant-in-Aid for Scientific Research from the Japan Society for the Promotion of Sciences (JSPS). We thank Nissan Chemical Co. Ltd. for providing us with ligand **3b**.

Supporting information for this article is available on the WWW under http://www.angewandte.org or from the author.

© 2006 Wiley-VCH Verlag GmbH & Co. KGaA, Weinheim

when the reaction was conducted in the absence of 3-Å M.S. (entry 9). Finally, the best result was obtained when $Cu(OTf)_2$ was used as the metal source (Table 1, entry 10). The absolute configuration of the product was determined to be *R* by comparison with literature data by HPLC analysis.

The scope of the catalytic asymmetric amination of enecarbamates was then surveyed under the optimized reaction conditions (Table 2). A wide range of azodicarboxylates and enecarbamates derived from aromatic ketones bearing substituents with various electronic and steric properties, aliphatic ketones, and aldehydes were found to react with azodicarboxylates efficiently to afford the desired products in good yields with high enantioselectivities. The initially formed acylimines **5(A)** were readily converted into ketone products **5(B)** after hydrolysis or 1,2-diamine derivatives **5(C)** after highly stereoselective reduction (see footnote of Table 2). It is of particular note that the amination reaction of enecarbamates followed by $NaBH_4$ reduction can be conducted on a gram scale. The reaction of 3 g enecarbamate (*E*)-**2a** with diisopropyl azodicarboxylate was catalyzed with 0.6 mol% of the catalyst $Cu(OTf)_2$ (24 mg of $Cu(OTf)_2$ as used), followed by reduction with $NaBH_4$ to provide 4.9 g of the 1,2-diamino compound (92% yield; *syn*/*anti* = < 5 : > 95; 96% *ee* for *anti*).

trans-1,2-Diamine derivatives, which are seen in many biologically important compounds as well as in useful chiral ligand skeletons,[18] can be obtained using this new methodology. The product **6a** was efficiently converted into the free amine **7**, whose structure was unambiguously determined by X-ray crystallographic analysis. Deprotection of the carbamate moieties followed by N–N bond cleavage using Raney Ni and benzoylation afforded *trans*-1,2-diamine derivative **8** in high yield (Scheme 1).

Table 2: Catalytic asymmetric α-amination of enecarbamates.[a]

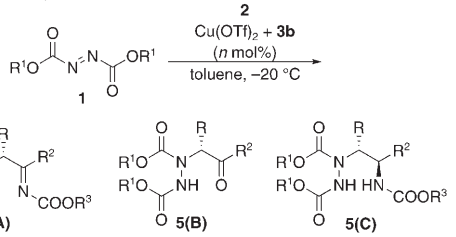

Entry	R^1	2	*n* [mol%]	*t* [h]	Yield [%]	*ee* [%]	Product[b]
1[c]	*i*Pr	**2a**	0.2	22	84	98	**C**
2	*i*Pr	**2b**	1	25	90	92	**B**
3	*i*Pr	**2c**	1	24	87	84	**B**
4	*i*Pr	**2d**	1	24	62	83	**B**
5	Me	**2a**	3	24	83	82	**B**
6	Et	**2a**	3	24	91	84	**B**
7[d]	Bn	**2a**	10	6	99	85	**B**
8	*i*Pr	**2e**	5	20	84	96	**A**
9	*i*Pr	**2f**	1	24	93	97	**B**
10	*i*Pr	**2g**	5	10	90	94	**B**
11[c]	*i*Pr	**2h**	3	6	81	90	**C**
12[c]	*i*Pr	**2i**	0.2	24	79	96	**C**
13[e]	*i*Pr	**2j**	2	6	82[f]	82	**C**
14[g]	*i*Pr	**2k**	5	4	70	86	**C**
15[e]	*i*Pr	**2l**	5	26	82	67[h]	**C**

[a] Reactions conducted with 1.1 equivalents of **1** relative to **2** in toluene (0.067 M in substrate). [b] **A**: Acylimine (no treatment); **B**: ketone by hydrolysis; **C**: 1,2-diamino derivative by reduction (*syn*/*anti* = < 5 : > 95). [c] −10 °C. [d] 3-Å M.S. were added (100 mg mmol^{-1}). [e] Ligand **3a** was used instead of **3b**. [f] *syn*/*anti* = 28:72. [g] 3-Å M.S. were added (50 mg mmol^{-1}). [h] See reference [17].

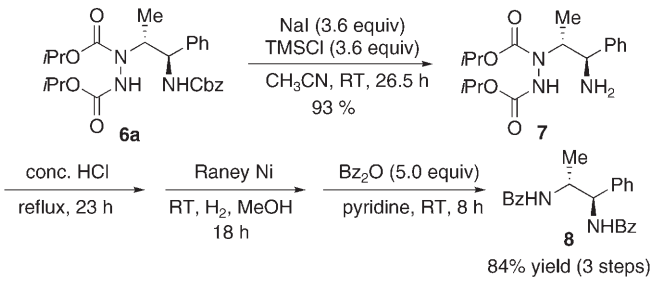

Scheme 1. Synthesis of *trans*-1,2-diamine derivatives **7** and **8**. Cbz = carbobenzyloxy, TMS = trimethylsilyl, Bz = benzoyl.

On the basis of the absolute configuration and the fact that both *E*- and *Z*-enecarbamates gave the same absolute configuration (Table 1, entries 3 and 4),[19] we propose an acyclic concerted transition-state model (Figure 1).[20] We assume that a diamine ligand and azodicarboxylate coordinate to the copper in bidentate fashion, and that the copper adopts a slightly distorted square-planar geometry.[15c] The *Re* face of the azodicarboxylate is shielded by the neighboring benzyl group of the diamine ligand, and an enecarbamate attacks from the *Si* face predominantly (see the Supporting Information). As for the facial selectivity of the enecarbamate, TS-1 and TS-2 in which the enecarbamate reacts with azodicarboxylate through an *antiperiplanar* transition state are reasonable to minimize steric repulsions between the enecarbamate and the copper catalyst or the carbamate group of the azodicarboxylate. TS-1, which gives the *R*-configured product, is more plausible because of the critical steric repulsion between the substituent of the enecarbamate and the copper catalyst in TS-2.

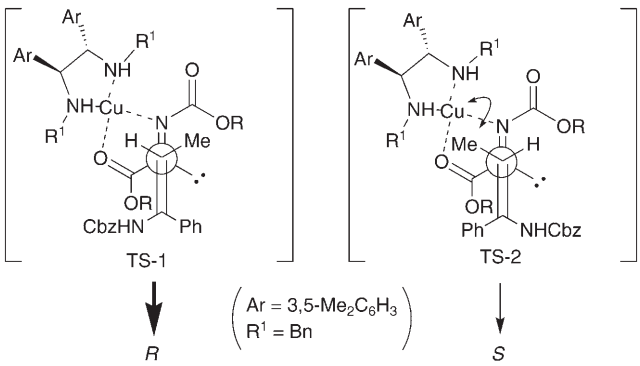

Figure 1. Proposed transition-state model.

In conclusion, we have developed the first catalytic asymmetric amination of enecarbamates using a $Cu(OTf)_2$-diamine complex as catalyst. Yields and enantioselectivities are high in most cases, and catalyst loadings are generally low. This new reaction provides not only α-amino carbonyl

 © 2006 Wiley-VCH Verlag GmbH & Co. KGaA, Weinheim

compounds but also α-amino acylimines, which can be readily converted into 1,2-diamine derivatives stereoselectively. We have also shown that this amination reaction can be conducted on a gram scale. Moreover, a transition-state model to explain the absolute configuration observed in this amination reaction of enecarbamates is proposed. Further investigations to apply this new protocol to the synthesis of biologically important compounds are in progress.

Received: September 14, 2006
Published online: November 10, 2006

Keywords: amination · asymmetric catalysis · azodicarboxylates · copper · enecarbamates

[1] a) C. Greck, B. Drouillat, C. Thomassigny, *Eur. J. Org. Chem.* **2004**, *7*, 1377; b) E. Erdik, *Tetrahedron* **2004**, *60*, 8747; c) J.-P. Genet, C. Greck, D. Lavergne, *Modern Amination Methods* (Ed.: A. Ricci), Wiley-VCH, Weinheim, **2000**, chap. 3.
[2] D. A. Evans, T. C. Britton, J. A. Ellman, R. L. Dorow, *J. Am. Chem. Soc.* **1990**, *112*, 4011.
[3] W. Oppolzer, O. Tamura, *Tetrahedron Lett.* **1990**, *31*, 991.
[4] N. Momiyama, H. Yamamoto, *J. Am. Chem. Soc.* **2003**, *125*, 6038, and references therein.
[5] D. A. Evans, S. G. Nelson, *J. Am. Chem. Soc.* **1997**, *119*, 6452.
[6] D. A. Evans, D. S. Johnson, *Org. Lett.* **1999**, *1*, 595.
[7] Y. Yamashita, H. Ishitani, S. Kobayashi, *Can. J. Chem.* **2000**, *78*, 666.
[8] a) B. List, *J. Am. Chem. Soc.* **2002**, *124*, 5656; b) A. Bøgevig, K. Juhl, N. Kumaragurubaran, W. Zhuang, K. A. Jørgensen, *Angew. Chem.* **2002**, *114*, 1868; *Angew. Chem. Int. Ed.* **2002**, *41*, 1790; see also, c) C. Thomassigny, D. Prim, C. Greck, *Tetrahedron Lett.* **2006**, *47*, 1117.
[9] N. Kumaragurubaran, K. Juhl, W. Zhuang, A. Bøgevig, K. A. Jørgensen, *J. Am. Chem. Soc.* **2002**, *124*, 6254.
[10] a) K. Juhl, K. A. Jørgensen, *J. Am. Chem. Soc.* **2002**, *124*, 2420; b) M. Marigo, K. Juhl, K. A. Jørgensen, *Angew. Chem.* **2003**, *115*, 1405; *Angew. Chem. Int. Ed.* **2003**, *42*, 1367.
[11] a) S. Saaby, M. Bella, K. A. Jørgensen, *J. Am. Chem. Soc.* **2004**, *126*, 8120; b) X. Liu, H. Li, L. Deng, *Org. Lett.* **2005**, *7*, 167.
[12] Catalyst loadings were not less than 1 mol% in all cases except those reported in references [10b] and [11a].
[13] Compound **2a** can be synthesized from benzonitrile in one step: Y. H. Suen, A. Horeau, H. B. Kagan, *Bull. Soc. Chim. Fr.* **1965**, *5*, 1454.
[14] T. Hamada, K. Manabe, S. Kobayashi, *J. Am. Chem. Soc.* **2004**, *126*, 7768.
[15] This complex was successfully employed as a catalyst for nucleophilic additions to acylimines. a) S. Kobayashi, H. Kiyohara, Y. Nakamura, R. Matsubara, *J. Am. Chem. Soc.* **2004**, *126*, 6558; b) R. Matsubara, Y. Nakamura, S. Kobayashi, *Angew. Chem.* **2004**, *116*, 1711; *Angew. Chem. Int. Ed.* **2004**, *43*, 1679; c) S. Kobayashi, R. Matsubara, Y. Nakamura, H. Kitagawa, M. Sugiura, *J. Am. Chem. Soc.* **2003**, *125*, 2507.
[16] After screening various ligands, such as diamines bearing 1,2-diphenylethylenediamine and 1,2-dicyclohexane diamine backbones, ligand **3b** was found to be the best.
[17] When aldehyde-derived enecarbamate **2l** was used, the initially formed product after Cu-catalyzed reaction was not acylimine but a cyclic product, which was reduced by using triethylsilyl hydride and trimethylsilyl triflate instead of $NaBH_4$. See the Supporting Information for details.
[18] S. R. S. S. Kotti, C. Timmons, G. Li, *Chem. Biol. Drug Des.* **2006**, *67*, 101, and references therein.
[19] Contrary to this result, in reference [6] the sense of asymmetric induction is dependent on the geometry of the silicon enolates.
[20] a) R. Matsubara, N. Kawai, S. Kobayashi, *Angew. Chem.* **2006**, *118*, 3898; *Angew. Chem. Int. Ed.* **2006**, *45*, 3814; b) R. Matsubara, P. Vital, Y. Nakamura, H. Kiyohara, S. Kobayashi, *Tetrahedron* **2004**, *60*, 9769; c) R. Matsubara, Y. Nakamura, S. Kobayashi, *Angew. Chem.* **2004**, *116*, 3320; *Angew. Chem. Int. Ed.* **2004**, *43*, 3258.

 © 2006 Wiley-VCH Verlag GmbH & Co. KGaA, Weinheim

Laser Switching of Ring Currents

DOI: 10.1002/anie.200602479

Control of π-Electron Rotation in Chiral Aromatic Molecules by Nonhelical Laser Pulses**

*Manabu Kanno, Hirohiko Kono, and Yuichi Fujimura**

The control of electron dynamics in molecules or molecular assemblies by irradiation is a fascinating research field.[1,2] Control of the photocurrents of molecular devices in the ultrashort time regime is essential for nanotechnology. However, fundamental issues remain to be clarified for the manipulation of electron motions, especially in large molecules such as those having aromatic rings. Aromatic molecules are characterized by delocalized π electrons that can in principle be controlled using UV/Vis light. One of the issues is how to control their rotation direction (ring current) using ultrashort UV/Vis laser pulses. It is unclear whether π electrons can be rotated along an aromatic ring by a nonhelical, linearly polarized laser pulse, though π-electron rotation can be performed using a circularly polarized laser pulse.[3] In the latter case, the rotation direction is predetermined by the applied pulse. If π-electron rotation is induced by a linearly polarized laser pulse, the rotation direction should be intrinsic to the molecule of interest because a nonhelical photon has no angular momentum. Therefore, its electron dynamics should reflect the asymmetry of the molecule itself.

We show here that the polarization direction of a linearly polarized laser pulse determines the initial direction of π-electron rotation in a chiral aromatic molecule. We then propose a pump–dump control method for determining

[*] M. Kanno, Prof. H. Kono, Prof. Y. Fujimura
Department of Chemistry
Graduate School of Science, Tohoku University
Sendai 980-8578 (Japan)
Fax: (+81) 22-795-7715
E-mail: fujimurayuichi@mail.tains.tohoku.ac.jp

[**] M.K. is grateful to Dr. K. Hoki, Dr. Y. Teranishi, and Prof. T. Kato for fruitful discussions and acknowledges financial support from a JSPS Research Fellowship for Young Scientists (No. 18·5252). This work was partly supported by a JSPS Research Grant (No. 17350004).

Supporting information for this article is available on the WWW under http://www.angewandte.org or from the author.

© 2006 Wiley-VCH Verlag GmbH & Co. KGaA, Weinheim

unidirectional rotation of π electrons in a chiral aromatic molecule.

A chiral aromatic molecule with a six-membered ring, 2,5-dichloro[*n*](3,6)pyrazinophane (DCP; *n* specifies the length of the ethylene bridge $(CH_2)_n$), was chosen (Figure 1). DCP

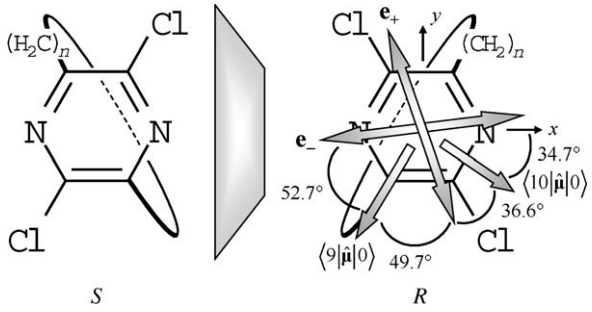

Figure 1. *S* and *R* enantiomers of DCP. The directions of transition dipole moments $\langle 9|\hat{\boldsymbol{\mu}}|0\rangle$ and $\langle 10|\hat{\boldsymbol{\mu}}|0\rangle$ of an *R* enantiomer are shown as well as those of photon polarization vectors $\mathbf{e}_\pm$ defined as $\langle 9|\hat{\boldsymbol{\mu}}|0\rangle\,\mathbf{e}_\pm = \pm\langle 10|\hat{\boldsymbol{\mu}}|0\rangle\,\mathbf{e}_\pm$. The magnitudes of $\langle 9|\hat{\boldsymbol{\mu}}|0\rangle$ and $\langle 10|\hat{\boldsymbol{\mu}}|0\rangle$ are 2.02 ea_0 and 1.63 ea_0, respectively.

has quasi-degenerate π-electronic excited states. We use a coherent superposition of the quasi-degenerate states for controlling temporal behavior of an electron wave packet. The length of the ethylene bridge $(CH_2)_n$ is restricted ($n \lesssim 10$) to avoid conversion between enantiomers through free rotation of the aromatic ring. We assume that the molecule is fixed to a surface by the ethylene bridge. Since the period of π-electron rotation is shorter by one order than the vibration periods of nuclei, the nuclei in the molecule are treated as being fixed.

The Hamiltonian of an aromatic molecule interacting with a classical laser field $\boldsymbol{\varepsilon}(t)$ is expressed in the dipole approximation as Equation (1), where $\hat{H}_\pi$ is the effective π-electronic Hamiltonian and $\hat{\boldsymbol{\mu}}$ is the electric dipole moment operator.

$$\hat{H}(t) = \hat{H}_\pi - \hat{\boldsymbol{\mu}}\,\boldsymbol{\varepsilon}(t) \tag{1}$$

For $\hat{H}_\pi$ we use the semiempirical Pariser—Parr–Pople (PPP) model, which has been demonstrated to reproduce various optical properties of π-conjugated systems with a proper choice of parameters.[4,5] The effect of the nonaromatic ethylene bridge is ignored in the PPP model. Then, DCP is regarded as being of C_{2h} symmetry and having eight p_z orbitals and 10 π electrons in this description of π-electron dynamics. Parameters for one-electron energies and Coulomb repulsions are set as employed for linear polyenes,[5] and the energetic properties of Cl and N atoms are introduced as originally formulated by Streitwieser.[6] The aromatic ring forms a planar structure, and we simply assume that the C–C and C–N bond lengths are 1.40 Å, the C–Cl bond length is 1.80 Å, and $\sphericalangle$(N-C-Cl) = 120°.

The time-dependent Schrödinger equation (TDSE) [Eq. (2)] can be solved by expanding $|\Psi(t)\rangle$ in terms of 136 singlet eigenstates of $\hat{H}_\pi$ obtained at the level of singly and doubly excited configuration interaction (SDCI), that is, $|\Psi(t)\rangle = \sum_{k=0}^{135} c_k(t) e^{-iE_k t/\hbar}|k\rangle$, where $|0\rangle = |1^1A_g\rangle$ is the ground state.[7] By inserting the expanded form of $|\Psi(t)\rangle$ into the TDSE [Eq. (2)], we derive the coupled equations of motion for the expansion coefficients $\{c_k(t)\}$.

$$i\hbar\frac{\partial}{\partial t}|\Psi(t)\rangle = \hat{H}(t)|\Psi(t)\rangle \tag{2}$$

In this model, π-electron rotation can be quantified by the momentum expectation value $p(t) \equiv \langle\Psi(t)|\hat{p}|\Psi(t)\rangle$, where $\hat{p}$ is defined using the momentum of complex molecular orbitals for a circular path along an aromatic ring.[7] Here, in a circular motion of a particle, angular velocity of the particle is equivalent to its velocity divided by the radius of the circle. Thus, we also define the rotational angle of π electrons, $\theta(t)$, in Equation (3), where b is the radius of the ring. The expectation values $p(t)$ and $\theta(t)$ are used as measures of π-electron rotation.

$$\theta(t) \equiv \frac{1}{m_e b}\int_0^t \mathrm{d}\tau\, p(\tau) \tag{3}$$

DCP has quasi-degenerate π-electronic excited states $|9\rangle = |5^1B_u\rangle$ and $|10\rangle = |6^1B_u\rangle$ with the energy gap $2\Delta E \equiv E_{10} - E_9 = 0.105$ eV ($E_9 - E_0 = 7.66$ eV). The transition dipole moments $\langle 9|\hat{\boldsymbol{\mu}}|0\rangle$ and $\langle 10|\hat{\boldsymbol{\mu}}|0\rangle$ of an *R* enantiomer of DCP are illustrated in Figure 1, and those of an *S* enantiomer are their mirror images. Linear combinations of $|9\rangle$ and $|10\rangle$ give the approximate eigenstates of the angular momentum operator $\ell = b\hat{p}$, denoted as $|+\rangle$ and $|-\rangle$, where $\langle\pm|\ell|\pm\rangle = \pm 0.862\hbar$: For an *R* enantiomer this is described by Equation (4), and for an *S* enantiomer, the sign $\pm$ on the right-hand side of Equation (4) is replaced by $\mp$. π Electrons with positive (negative) angular momentum travel counterclockwise (clockwise) around the ring in Figure 1.

$$|\pm\rangle = 2^{-1/2}(|9\rangle \pm i|10\rangle) \tag{4}$$

We now design a linearly polarized laser pulse $\boldsymbol{\varepsilon}(t)$ to generate predominantly either $|+\rangle$ or $|-\rangle$. First, the central frequency ω of $\boldsymbol{\varepsilon}(t)$ is determined as $\omega = (E_9 + \Delta E - E_0)/\hbar$. Next, the polarization direction of $\boldsymbol{\varepsilon}(t)$ is determined by its alignment relative to $\langle 9|\hat{\boldsymbol{\mu}}|0\rangle$ and $\langle 10|\hat{\boldsymbol{\mu}}|0\rangle$. This is obtained from a three-level model analysis in the short-pulse limit: $|9\rangle$ and $|10\rangle$ are independently coupled to $|0\rangle$ by a linearly polarized laser pulse with a Dirac-delta-function-like envelope. The polarization unit vector of the pulse is chosen in two ways, $\mathbf{e}_+$ or $\mathbf{e}_-$ defined as $\langle 9|\hat{\boldsymbol{\mu}}|0\rangle\,\mathbf{e}_\pm = \pm\langle 10|\hat{\boldsymbol{\mu}}|0\rangle\,\mathbf{e}_\pm$ for each enantiomer. The directions of $\mathbf{e}_\pm$ for an *R* enantiomer are illustrated in Figure 1. At the moment of irradiation ($t = t_i$), the pulse with $\mathbf{e}_+$ ($\mathbf{e}_-$) produces an in-phase superposition $|9\rangle + |10\rangle$ (out-of-phase superposition $|9\rangle - |10\rangle$) in $|\Psi(t_i)\rangle$. At $t > t_i$, the electron wave packet propagates freely. Hence, $|9\rangle \pm |10\rangle$ in $|\Psi(t_i)\rangle$ temporally evolves as $|9\rangle \pm e^{-i\phi(t)}|10\rangle$ except for the global phase factor, where $\phi(t) = 2\Delta E(t - t_i)/\hbar$.[7] $e^{-i\phi(t)}$ changes as $+1 \to -i \to -1 \to +i \to +1 \to \cdots$ with the progression of $t - t_i$, $0 \to T/4 \to T/2 \to 3T/4 \to T \to \cdots$, where $T \equiv \pi\hbar/\Delta E$. This indicates that, in the first quarter period of T after

 © 2006 Wiley-VCH Verlag GmbH & Co. KGaA, Weinheim

excitation, $|\mp\rangle$ is created in an *R* enantiomer, while $|\pm\rangle$ is created in an *S* enantiomer. The polarization direction determines the initial direction of π-electron rotation. Afterwards, the rotation direction switches between clockwise and counterclockwise with the period *T*. If a molecule is highly symmetric, e.g., benzene, $e^{-i\phi(t)}$ takes an infinite time to reach $-i$ since $\Delta E = 0$. That is, lowering the molecular symmetry is essential for the selective generation of either $|+\rangle$ or $|-\rangle$ by a linearly polarized laser pulse. Finally, the peak intensity *f* and the pulse duration t_d of $\boldsymbol{\varepsilon}(t)$ are determined so that the pulse area is equal to π, following the idea of the so-called π pulse.[8]

To demonstrate this, a numerical simulation within 136-state expansion was carried out for an *R* enantiomer with a linearly polarized laser pulse $\boldsymbol{\varepsilon}(t)$ designed to initially create $|-\rangle$. The polarization vector of the pulse is $\mathbf{e}_+$. Figure 2a shows the temporal behavior in $\boldsymbol{\varepsilon}(t)$. In Figure 2b, the solid, dotted, and dashed-dotted lines denote the temporal behavior in the populations of $|0\rangle$, $|+\rangle$, and $|-\rangle$, respectively. The values for $p(t)$ and $\theta(t)$ are plotted in Figure 2c and d, respectively. If the pulse duration t_d is less than the oscillation period *T*, $|9\rangle + |10\rangle$ is mainly produced around the pulse peak, that is, $t_i = t_d/2 = 13.3$ fs. At $t > 13.3$ fs, a significant amount of the population is transferred to $|9\rangle - i|10\rangle$, that is, $|-\rangle$ (Figure 2b), and accordingly π electrons start to rotate clockwise (see Figure 1 and Figure 2c). The total population of π electrons in $|+\rangle$ and $|-\rangle$ reaches 0.908 when the laser pulse ceases at $t = 26.6$ fs. From the energy–time uncertainty relation, the final value of the total population is maximum at the pulse duration $t_d = 26.6$ fs: A smaller bandwidth of a longer pulse does not cover the energy gap $2\Delta E$ sufficiently, and, on the other hand, a broader bandwidth of a shorter pulse populates other excited states. At $t > 26.6$ fs, the population of 0.908 is exchanged between $|+\rangle$ and $|-\rangle$ as expected. $p(t)$ and $\theta(t)$ thus oscillate with the period of $T = 39.5$ fs, and π electrons are estimated to circulate around the ring more than nine times within this period (Figure 2d).

The three-level model analysis in a short-pulse limit also provides a clue to a simple control method for determining unidirectional rotation of π electrons: The population created in $|-\rangle$ can be dumped to $|0\rangle$ by applying a dump pulse with $\mathbf{e}_-$ just after the population has completely shifted to $|9\rangle - |10\rangle$. Figure 3 shows the results of a pump–dump control simulation of an *R* enantiomer, which were obtained within 136-state expansion. Around the peak of the dump pulse at $t = 29.1$ fs, the populations of $|+\rangle$ and $|-\rangle$ are nearly equal; in other words, an out-of-phase superposition $|9\rangle - |10\rangle$ is created (Figure 3b). At $t > 29.1$ fs, most of the population is dumped to $|0\rangle$; the rest is brought to higher excited states. Consequently, the value of $p(t)$ is almost zero, and reverse rotation is successfully prevented (Figure 3c and d). A pair of pump and dump pulses realizes unidirectional rotation of π electrons. Moreover, repetition of the unidirectional rotation can be achieved by a sequence of pulse pairs.

π-Electron rotation in an *S* enantiomer can be controlled in the same way. By reversing the polarization directions of

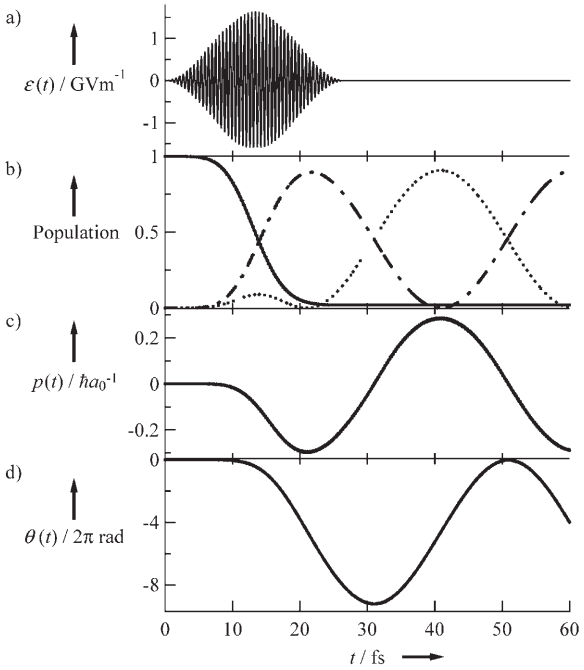

Figure 2. a) The linearly polarized laser pulse to initially create $|-\rangle$ of an *R* enantiomer, $\boldsymbol{\varepsilon}(t) = \mathbf{e}_+ f \sin^2(\pi t/t_d)\cos(\omega t)$ for $0 < t < t_d$ and otherwise $\boldsymbol{\varepsilon}(t) = 0$. Here, $\omega = 7.72$ eV/ħ, $f = 1.63$ GVm^{-1}, and $t_d = 26.6$ fs. b) Temporal behavior in the populations of $|0\rangle$ (solid line), $|+\rangle$ (dotted line), and $|-\rangle$ (dashed-dotted line). c) Expectation value of momentum $p(t)$. d) Expectation value of rotational angle $\theta(t)$.

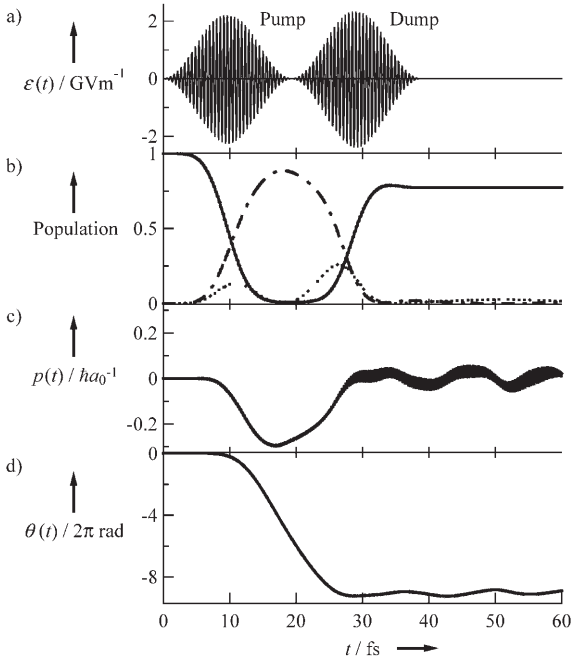

Figure 3. a) Pump and dump pulses for clockwise rotation of π-electrons in an *R* enantiomer. The polarization vectors of the pump and dump pulses are $\mathbf{e}_+$ and $\mathbf{e}_-$, respectively. For the pump pulse, $\omega = 7.72$ eV/ħ, $f = 2.24$ GVm^{-1}, $t_d = 19.4$ fs; for the dump pulse, $\omega = 7.72$ eV/ħ, $f = 2.37$ GVm^{-1}, $t_d = 19.4$ fs. The delay time between the pulses is 19.4 fs. b) Temporal behavior in the populations of $|0\rangle$ (solid line), $|+\rangle$ (dotted line), and $|-\rangle$ (dashed-dotted line). c) Expectation value of momentum $p(t)$. d) Expectation value of rotational angle $\theta(t)$.

 © 2006 Wiley-VCH Verlag GmbH & Co. KGaA, Weinheim

the pump and dump pulses for an *R* enantiomer with respect to a reflection plane, π electrons in an *S* enantiomer are rotated counterclockwise in Figure 1.

π-Electron rotation controlled by linearly polarized laser pulses may be detected experimentally using attosecond time-resolved photoelectron spectroscopy. Electron dynamics in molecules or ions are now analyzed using photoelectron-imaging techniques in an attosecond time regime.[9,10] The results of a theoretical study on π-electron rotation in photoelectron spectra of chiral aromatic molecules will be reported elsewhere.

In conclusion, we have presented the theoretical foundations of switching on and off photocurrents in chiral systems. By means of quantum mechanical simulation within a semi-empirical molecular orbital theory, we have shown that π electrons can be rotated along the ring of a chiral aromatic molecule using a single-color linearly polarized laser pulse. π-Electron rotation originates from creation of an (approximate) angular momentum eigenstate consisting of optically allowed, quasi-degenerate π-electronic excited states. Lowering the molecular symmetry is crucial for the selective generation of one of the approximate eigenstates. The rotation direction depends on the polarization direction of the applied pulse. Unidirectional rotation of π electrons can be performed by pump and dump pulses whose polarization directions are properly chosen. By adjusting the alignments of *S* and *R* enantiomers relative to the polarization directions, it is possible to produce photoinduced ring currents in opposite directions or a photoinduced ring current in only one of the enantiomers. Optical control of π-electron motions in a large, three-dimensional system, such as fullerene derivatives, is one of the challenging targets for further applications.

Received: June 28, 2006
Revised: August 2, 2006
Published online: November 3, 2006

Keywords: chirality · electron dynamics · laser chemistry · ring currents

[1] P. Krause, T. Klamroth, P. Saalfrank, *J. Chem. Phys.* **2005**, *123*, 074105.
[2] M. F. Kling, C. Siedschlag, A. J. Verhoef, J. I. Khan, M. Schultze, T. Uphues, Y. Ni, M. Uiberacker, M. Drescher, F. Krausz, M. J. J. Vrakking, *Science* **2006**, *312*, 246.
[3] I. Barth, J. Manz, *Angew. Chem.* **2006**, *118*, 3028; *Angew. Chem. Int. Ed.* **2006**, *45*, 2962; I. Barth, J. Manz, Y. Shigeta, K. Yagi, *J. Am. Chem. Soc.* **2006**, *128*, 7043.
[4] S. Abe, J. Yu, W. P. Su, *Phys. Rev. B* **1992**, *45*, 8264; V. A. Shakin, S. Abe, *Phys. Rev. B* **1994**, *50*, 4306.
[5] M. Chandross, Y. Shimoi, S. Mazumdar, *Phys. Rev. B* **1999**, *59*, 4822; M. Suzuki, S. Mukamel, *J. Chem. Phys.* **2003**, *119*, 4722.
[6] A. Streitwieser, Jr., *Molecular Orbital Theory for Organic Chemists*, Wiley, New York, **1961**, p. 117.
[7] See Supporting Information for this communication.
[8] B. W. Shore, *The Theory of Coherent Atomic Excitation*, *Vol. 1*, Wiley, New York, **1990**, p. 304.
[9] J. Itatani, J. Levesque, D. Zeidler, H. Niikura, H. Pépin, J. C. Kieffer, P. B. Corkum, D. M. Villeneuve, *Nature* **2004**, *432*, 867.
[10] G. L. Yudin, A. D. Bandrauk, P. B. Corkum, *Phys. Rev. Lett.* **2006**, *96*, 063002.

 © 2006 Wiley-VCH Verlag GmbH & Co. KGaA, Weinheim

Layered Compounds

DOI: 10.1002/anie.200602502

Layered Rare-Earth Hydroxides: A Class of Pillared Crystalline Compounds for Intercalation Chemistry**

Felipe Gándara, Josefina Perles, Natalia Snejko, Marta Iglesias, Berta Gómez-Lor, Enrique Gutiérrez-Puebla, and M. Ángeles Monge**

The well-known layered double hydroxides (LDHs) and their thermal-treatment products, which are used as adsorbents, drug-delivery vehicles, polymer stabilizers, and catalysts,[1–7] are generally based on brucite-like materials doped with d-block elements, although studies on a Li^+–Al^{3+} LDH[8] and on ionic europium and gadolinium complexes intercalated in pillared LDHs have recently been reported.[9] Compounds of the type presented herein, which are formed by pure cationic rare-earth hydroxide layers, have not yet been reported; they represent a new generation of pillared materials, in which the properties of intercalation materials are combined with those of rare-earth elements. $[R_4(OH)_{10}(H_2O)_4]_nA_n$ (R = rare-earth ions, A = intercalated organic anions, 2,6-naphthalenedisulfonate (NDS^{2-}) and 2,6-anthraquinonedisulfonate ($AQDS^{2-}$)) is the first family of layered rare-earth hydroxides (LRHs). In these LRHs, the positive charge of the inorganic layer is created only by trivalent rare-earth hydroxocations, which arises from the high and variable coordinative capability of the rare-earth centers and to the tendency of the hydroxide ion to form μ_n connections in structures that contain these rare-earth centers. Rigid organic anions are intercalated to neutralize the positive charge. Apart from their potential as ion exchangers, these new materials contain a great number of active metal centers with the capability of varying the coordination number in catalytic processes, which confers to them great possibilities in the field of green chemistry. In fact, the performed tests in hydrodesulfurization (HDS), sulfide oxidation, and redox reactions reveal these new LRHs to be high-quality heterogeneous catalysts. Other interesting physical properties emerging from both the f–f interactions and those of intercalated organic anions are also to be expected.

[*] F. Gándara, J. Perles, Dr. N. Snejko, Dr. M. Iglesias, Dr. B. Gómez-Lor, Prof. Dr. E. Gutiérrez-Puebla, Prof. Dr. M. A. Monge
Instituto de Ciencia de Materiales de Madrid
Cantoblanco, 20849-Madrid (Spain)
Fax: (+34) 91-3720623
E-mail: amonge@icmm.csic.es

[**] F.G. and J.P. acknowledge their FPI fellowship from Spanish Ministry for Education and Science (MEC) co-funded by Fondo Social Europeo. This work was supported by the Spanish MCYT projects MAT 2004-02001, CTQ2004-02865/BQU, and CAM-CSIC 200580M133).

Supporting information for this article is available on the WWW under http://www.angewandte.org or from the author.

WILEY InterScience DISCOVER SOMETHING GREAT
© 2006 Wiley-VCH Verlag GmbH & Co. KGaA, Weinheim

The compounds were synthesized under hydrothermal conditions. Single crystals suitable for X-ray diffraction studies were obtained only for the YbAQDS and YNDS compounds. Powder diffraction patterns show that the DyAQDS, HoAQDS, and YbAQDS compounds have the same structure (Figure 1), whereas in the diffraction pattern of YNDS, a shift of the first peak (020) shows that the corresponding structure has a shorter basal spacing.

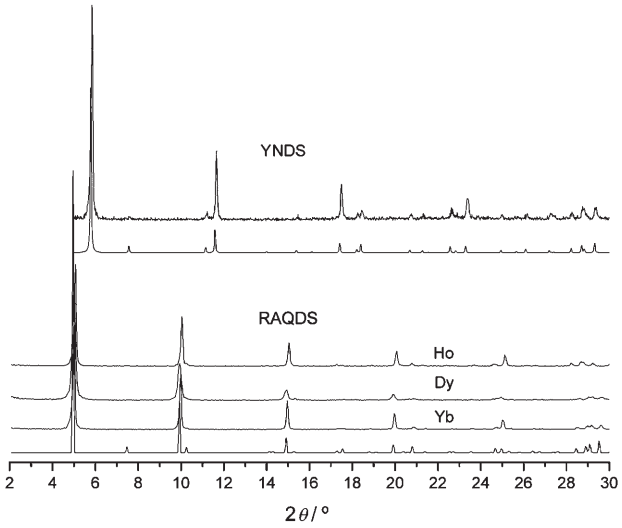

Figure 1. Experimental (upper) and calculated (lower) powder X-ray diffraction patterns. Top: YNDS; bottom: HoAQDS, DyAQDS, and YbAQDS. The first peak is (020).

YbAQDS and YNDS crystallize in the orthorhombic system (see Experimental Section). The structures consist of $[R_4(OH)_{10}(H_2O)_4]^{2+}{}_n$ cationic layers formed by eight- and nine-coordinated rare-earth atoms, which are linked through μ_3-hydroxy groups. In addition to the coordination from the OH groups, each rare-earth atom is coordinated by one water molecule to give two different coordination polyhedra: one is a dodecahedron, the other is a monocapped square antiprism. Polyhedra of the same type are placed in alternating rows parallel to the [001] direction to form the layers parallel to the *ac* plane. These hydroxide layers are separated by *b*/2 (17.826 Å for YbAQDS and 15.263 Å for YNDS), and their positive charge is compensated by organic anions, which are localized between the layers with the sulfonate groups directed toward the cationic layers. In previous work, values of the basal spacing in LDHs with intercalated $AQDS^{2-}$[10] and NDS^{2-}[11] were reported on the basis of powder X-ray diffraction measurements, which predicted a tilted orientation of the organic molecules into the interlayer space. In these new LRH compounds, the titling angles formed between the S–S axes of the organic anions and the normal of the respective hydroxide layers are 30.86° and 37.80° for the $AQDS^{2-}$ and NDS^{2-} compounds. These anions are situated parallel to the *ab* plane in an alternating configuration, and separated by 3.5 Å (*c*/2) and 12.5 Å (*a*) along the [001] and [100] directions, respectively (Figure 2). This arrangement gives rise to π–π stacking interactions among the $AQDS^{2-}$

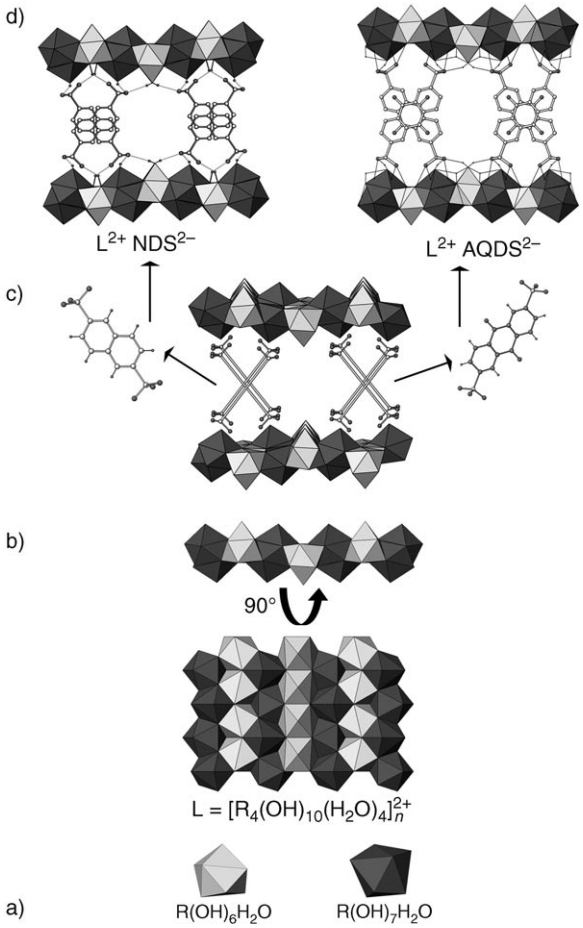

Figure 2. a) Rare-earth polyhedra; b) a layer of polyhedra (top and side view); c) organic ions (sticks represent the S–S axes) intercalated between two layers; d) structures of $[R_4(OH)_{10}(H_2O)_4]^{2+}{}_n$ with NDS^{2-} (left) and $AQDS^{2-}$ (right).

central rings, and O–π stacking interactions among one oxygen atom from each quinone moiety and lateral aromatic rings. In the YNDS compound only C–π stacking interactions are possible. In the 3D lanthanide polymeric framework (LnPF) reported previously Ln(1,5)NDS,[12] the NDS^{2-} ligands are $\eta^2\mu^2,\eta^2\mu^2$ and $\eta^3\mu^3,\eta^3\mu^3$ coordinatively bonded to the metal atoms. In contrast, in the LRHs the organic anions are hydrogen-bonded to the rare-earth hydroxide cationic layers (Table 1). Apart from the more convenient configuration of the (2,6)NDS^{2-} isomer, the LRH structure seems to be kinetically favored by small rare-earth ions. However, ongoing screenings of the synthesis conditions do not rule out the possibility of obtaining LRH materials for the first half of the rare-earth series. A proper choice of synthesis conditions—molar composition, temperature, and dilution—seems to be decisive in obtaining either an LRH or an LnPF metal-oxide framework (MOF) as a pure phase. Zigzag channels of approximately 10×10 Å or 8×8 Å in the $AQDS^{2-}$ and NDS^{2-} compounds, respectively, run along the *a* direction. In the LDH materials, the interlayer region is substantially disordered.[13] However, the interlayer galleries of the LRHs are well-ordered, thus supplying a high control of the basal spacing from the as-synthesized products, which has a value of

 © 2006 Wiley-VCH Verlag GmbH & Co. KGaA, Weinheim

Table 1: Bond lengths [Å] and angles [°] of hydrogen bonds in YNDS and YbAQDS (in italics).[a]

D–H···A	*d*(D–H)	*d*(H···A)	*d*(D···A)	∢(D-H-A)
O_{W1}–H···O (×2)	0.82	2.04	2.81	156
	0.85	*1.94*	*2.77*	*167*
O_{W2}–H···O (×2)				
	0.85	*2.12*	*2.85*	*144*
O_H–H···O (×2)	0.98	2.00	2.939	163
	1.12	*2.32*	*3.023*	*119*
O_H–H···O	0.98	2.14	3.032	151
	0.92	*2.60*	*3.097*	*115*

[a] The hydrogen bonds are between oxygen atoms from the ligand sulfonate ions and water molecules (O_W) or hydroxy groups (O_H) around the rare-earth ions in the inorganic layers. D = donor, A = acceptor.

b/2. From a crystallographic point of view, a direct relation exists between the brucite-derived hexagonal lattice of the LDHs and that of the new LRHs. Given that in the latter there are two independent well-ordered R atoms because of their asymmetric coordination environments, the ideal hexagonal superlattice would have an a' parameter twice that of the mineral (that is, $a' = 2a$). As the interatomic distances among R atoms are not uniform, this hexagonal superlattice has a distortion that gives rise to a larger orthorhombic cell. The lattice vectors of the LRH unit cell can be deduced from those of the LDH cell by applying the transformation matrix $(2\,{-}2\,0,\ 0\,0\,{-}1,\ 2\,2\,0)$, as shown in Figure 3.

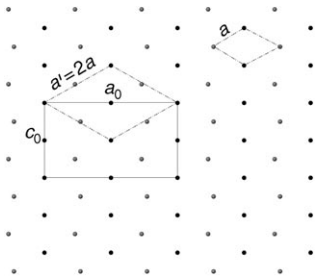

Figure 3. Crystallographic transformation from the ideal brucite-type structure to the new orthorhombic LRH structure. See text for details.

Thermogravimetric analysis and simultaneous differential thermal analysis (TGA–DTA) in an N_2 atmosphere ($50\,mL\,min^{-1}$) and thermodiffraction X-ray experiments (vacuum) show that the NDS^{2-} compounds are stable up to 600 °C and the $AQDS^{2-}$ compounds up to 500 °C. The IR spectra of these compounds show a broad band near $3500\,cm^{-1}$, with several maxima corresponding to the ν(M–OH) frequencies of the coordinated hydroxy groups and water molecules. The broadening of this band is due to the hydrogen bonding between these coordinated oxygen atoms and the sulfonate groups. The uncoordinated SO_3 group gives rise to unsplit bands in the region 1000–$1100\,cm^{-1}$, which are consistent with the retention of C_{3v} symmetry.

Rare-earth metals are increasingly being used as catalysts in various organic transformations. These new materials offer the possibility of combining the catalytic properties of rare-earth atoms with the advantages of a solid catalyst. The capability of the new LRH materials as heterogeneous catalysts has been tested on key processes in green chemistry. 1) In the hydrodesulfurization (HDS) of thiophene, YbAQDS shows a conversion of 50 % in 26 h to yield hydrogen sulfide and butane (both components are easily separable) under 7 bar of H_2 at only 70 °C. It is worth pointing out that these results are obtained under much milder conditions than those usually used (high H_2 pressure (30–60 bar) at 350–400 °C[14,15]). 2) As an alternative to hydrodesulfurization reactions, the removal of refractory sulfur-containing compounds can be accomplished by oxidation. This catalyst effects the oxidation of various alkyl phenyl sulfides. Sulfides were selectively mono-oxygenated to the corresponding sulfoxides (100 %) in 30 min by using H_2O_2 as oxidant. The YbAQDS catalyst has a remarkably high turnover frequency (TOF) of $2000\,h^{-1}$,[12] which is due to the small quantity of catalyst (0.1 %) needed and the fast conversion of the substrate. The results here are better, both in activity and in selectivity, than those previously obtained with a rare-earth succinate polymeric framework.[16] 3) The catalytic activity for the competitive epoxidation of 3,7-dimethylocta-1,6-dien-3-ol (linalool) using an excess of hydrogen peroxide was also tested. Linalool was oxidized to pyranoid and furanoid ethers (ratio 1:1) with > 80 % conversion over 24 h by using YNDS as a bifunctional redox–acid catalyst. The catalyst activity is comparable with that of both LnPF-1[12] and microporous bifunctional titanium aluminosilicate.[17] The sulfoxidation reaction proceeds through the corresponding peroxo species, as happens in the hydrolysis of phosphodiesters[18] and RNA[19] when these are catalyzed by peroxide rare-earth complexes formed in rare-earth/H_2O_2 mixtures.

To verify that the observed process is a heterogeneous catalysis, the reactions were carried out under standard conditions. After about 30 % conversion, the solid was removed by filtration whereupon the reactions stopped completely. The solid was then used again without any loss of performance. A powder X-ray diffraction pattern of the recovered catalysts showed no change in the structure of the catalyst.

In conclusion, LRHs have an ordered and tunable porous structure and combine advantages of LDH catalysts with the chemical and physical properties of rare-earth compounds. Although the full range of properties of these compounds have yet to be elucidated,[20–23] their discovery should be of general interest.

Experimental Section

Synthesis and characterization: All reagents were purchased at high purity (AR) grade from Aldrich and used without further purification. $R(NO_3)_3{\cdot}6H_2O$ (R = Yb, Dy, Ho, Y) was used as the source of rare-earth cations; the sulfonic acids were used in their disodium salt forms. In a typical synthesis procedure, the initial mixture with molar composition $R^{3+}/A^{2-}/H_2O = 4{:}1{:}4400$ was adjusted to pH 6.5 with Et_3N ($Et_3N/R^{3+} = 2.5$). The mixture was stirred for about 20 min and sealed in a 46 mL teflon-lined stainless-steel bomb. The bomb was kept at 180 °C under autogenous pressure for 18 h. After the reaction mixture was cooled to room temperature, the product was removed by filtration and washed with deionized water and acetone. A grayish

 © 2006 Wiley-VCH Verlag GmbH & Co. KGaA, Weinheim

white (Dy and Yb) or pink (Ho) powder was obtained for the $AQDS^{2-}$ compounds, and a pale yellow powder for YNDS.

The IR spectra from KBr pellets were recorded in the range 4000–400 cm^{-1} on a Perkin–Elmer spectrometer. TGA–DTA were performed with a SEIKO TG/DTA 320 apparatus between 25 and 700 °C in N_2 (flow rate of 50 mL min^{-1}) at a heating rate of 5 K min^{-1}.

X-ray structural analyses: Data for single crystals of the YbAQDS and YNDS compounds were collected on a Bruker SMART CCD diffractometer equipped with a normal focus, 2.4 kW sealed-tube X-ray source ($Mo_{K\alpha}$ radiation = 0.71073 Å). Data were collected over a hemisphere of the reciprocal space by a combination of three sets of exposures. Each exposure of 20 s covered 0.3° in ω. Unit-cell dimensions were determined by a least-squares fit of 60 reflections with $I > 2\sigma(I)$. The compounds crystallize in the orthorhombic system, space group *Ibam*, with $a = 12.5401(6)$, $b = 35.652(2)$, and $c = 7.0347(4)$ Å for YbAQDS, and $a = 12.639(1)$, $b = 30.525(2)$, and $c = 7.1348(6)$ Å for YNDS. The structures were solved by direct methods. The final cycles of refinement were carried out by full-matrix least-squares analyses with anisotropic thermal parameters for all non-hydrogen atoms. The hydrogen atoms of the hydroxy groups and water molecules were located in difference Fourier maps. Calculations were carried out by using the SMART program for data collection and data reduction, and SHELXTL. CCDC-604276 (YNDS) and CCDC-604277 (YbAQDS) contain the supplementary crystallographic data for this paper. These data can be obtained free of charge from The Cambridge Crystallographic Data Centre via www.ccdc.cam.ac.uk/data_request/cif.

The compounds reported herein are covered under the patent: F. Gándara, J. Perles, N. Snejko, M. Iglesias, B. Gómez-Lor, E. Gutiérrez-Puebla, M. A. Monge (ICMM, CSIC), ES200601422, **2006**.

Received: June 21, 2006
Revised: September 11, 2006
Published online: November 10, 2006

Keywords: heterogeneous catalysis · hydrogen bonds · intercalations · layered compounds · rare earths

[1] a) G. R. Williams, T. G. Dunbar, A. J. Beer, A. M. Fogg, D. O'Hare, *J. Mater. Chem.* **2006**, *16*, 1222; b) G. R. Williams, T. G. Dunbar, A. J. Beer, A. M. Fogg, D. O'Hare, *J. Mater. Chem.* **2006**, *16*, 123.
[2] H. Cai, A. C. Hillier, K. R. Franklin, C. C. Nunn, M. D. Ward, *Science* **1994**, *266*, 1551.
[3] B. Sels, D. De Vos, M. Buntinx, F. Pierard, A. Kirsch-De Mesmaeker, P. Jacobs, *Nature* **1999**, *400*, 855.
[4] B. F. Sels, D. E. De Vos, P. A. Jacobs, *Catal. Rev.* **2001**, *43*, 443.
[5] *Handbook of layered Materials*, Dekker, New York, **2004**.
[6] V. Rives, *Layered Double Hydroxides: Present and Future*, Nova Science Publishers, New York, **2001**.
[7] M. J. Climent, A. Corma, S. Iborra, J. Primo, *J. Catal.* **1995**, *151*, 60.
[8] M. B. J. Roeffaers, B. F. Sels, H. Uji-i, F. C. De Schryver, P. A. Jacobs, D. E. De Vos, J. Hofkens, *Nature* **2006**, *439*, 572.
[9] S. Gago, M. Pillinger, R. A. S. Ferreira, L. D. Carlos, T. M. Santos, I. S. Goncalves, *Chem. Mater.* **2005**, *17*, 5803.
[10] a) E. Kanezaki, S. Sugiyama, Y. Ishikawa, *J. Mater. Chem.* **1995**, *5*, 1969; b) W. K. Kuk, Y. D. Huh, *J. Mater. Chem.* **1997**, *7*, 1933.
[11] L. Raki, J. J. Beaudoin, L. Mitchell, *Cem. Concr. Res.* **2004**, *34*, 1717.
[12] N. Snejko, C. Cascales, B. Gomez-Lor, E. Gutiérrez-Puebla, M. Iglesias, C. Ruiz-Valero, M. A. Monge, *Chem. Commun.* **2002**, 1366.
[13] G. S. Thomas, P. V. Kamath, *J. Chem. Sci.* **2006**, *118*, 127.
[14] K. R. Sharma, E. S. Olson in *Processing and Utilization of High-Sulfur Coals IV* (P. R. Dugan, D. R. Quigley, Y. A. Attia), Elsevier Science, Amsterdam, **1991**, p. 377.
[15] T. Chapus, F. Morel (Institut Français du Pétrol), US 2002195375, **2002**.
[16] J. Perles, M. Iglesias, C. Ruiz-Valero, N. Snejko, *J. Mater. Chem.* **2004**, *14*, 2683.
[17] A. Corma, M. Iglesias, F. Sánchez, *J. Chem. Soc. Chem. Commun.* **1995**, 1635.
[18] Y. Mejia-Radillo, A. K. Yatsimirsky, *Inorg. Chim. Acta* **2002**, *328*, 241, and references therein.
[19] J. Kamitani, J. Sumaoka, H. Asanuma, M. Komiyama, *J. Chem. Soc. Perkin Trans. 2* **1998**, 523.
[20] R. M. Jones, T. S. Bergstedt, D. W. McBranch, D. G. Whitten, *J. Am. Chem. Soc.* **2001**, *123*, 6726.
[21] N. D. Hutson, S. A. Speakman, E. A. Payzant, *Chem. Mater.* **2004**, *16*, 4135.
[22] A. I. Khan, D. O'Hare, *J. Mater. Chem.* **2002**, *12*, 3191.
[23] A. I. Khan, L. X. Lei, A. J. Norquist, D. O'Hare, *Chem. Commun.* **2001**, 2342.

 © 2006 Wiley-VCH Verlag GmbH & Co. KGaA, Weinheim

Core–Shell Nanoparticles

DOI: 10.1002/anie.200602559

Diffusion of Gold into InAs Nanocrystals**

*Taleb Mokari, Assaf Aharoni, Inna Popov, and Uri Banin**

Multicomponent nanoparticles are at the forefront of research into nanomaterials.[1–5] The combination of a metal and a semiconductor in the same nanoparticle is of particular interest as the metal can provide an anchor point for electrical and chemical connections to the functional semiconductor part. This possibility was demonstrated recently by the growth of gold tips on the apexes of CdSe nanorods to form nano-dumbbells,[6] where at a high Au-to-rod concentration a transition from two- to one-sided growth occurs.[7] Au was also recently grown on lead chalcogenide nanoparticles, leading to segregated portions of the metal and semiconductor.[8] Au has been found to undergo surface diffusion between neighboring wires at moderate temperatures on Si nanowires grown by a vapor–liquid–solid method with Au as catalyst.[9,10] Herein we

[*] T. Mokari, A. Aharoni, Dr. I. Popov, Prof. U. Banin
Department of Physical Chemistry and
Center for Nanoscience and Nanotechnology
The Hebrew University of Jerusalem
Jerusalem 91904 (Israel)
Fax: (+972) 2-658-4148
E-mail: banin@chem.ch.huji.ac.il

[**] We thank Professor Ulrich Gösele for helpful discussions. This research was supported in part by the EU-FP6 program under project SA-NANO, and by the US–Israel bi-national science foundation (BSF). T.M. thanks the Ministry of Science, Israel, for an Eshkol Fellowship.

© 2006 Wiley-VCH Verlag GmbH & Co. KGaA, Weinheim

report a completely different behavior in the room-temperature reaction of Au with InAs nanoparticles. In this case, Au diffuses into the InAs particles to give a Au core coated by an amorphous shell.

The diffusion of metals into semiconductors has been studied extensively for bulk materials[11,12] because this process has significant relevance for the processing of integrated electronic circuits. Indeed, solid-state diffusion, which is typically carried out at high temperatures, is used extensively in their fabrication. Low-temperature reactions and diffusion have been detected for various metal–semiconductor pairs such as Au-Si and Au with binary semiconductors. Hiraki, for example, has found that low-temperature reaction and diffusion of the metals generally occurs when the semiconductor band-gap energy (E_g) is lower than about 2.5 eV and the dielectric constant $\varepsilon > 8$.[13] The diffusion properties of the specific metal also determine the possibility of room-temperature diffusion into the semiconductor. Metals that show such room-temperature diffusion are classified as "fast" diffusers,[14] and diffusion coefficient of these metals is larger than the self-diffusion coefficient.

Fast diffusion in semiconductors covers a wide range of different mechanisms. Among these, the interstitial-substitutional mechanisms are of interest here. The most important mechanisms that have been studied and proposed for fast diffusers (impurities) incorporated in semiconductors are:[15] 1) host interstitial mediated diffusion, also known as the "kick-out" mechanism,[16] in which atoms move rather rapidly by a direct interstitial mechanism until they eventually displace a lattice atom, and 2) the "Frank–Turnbull" mechanism,[16,17] which initiates at a vacancy in the host. In this case the impurity atom does not dislodge the lattice atom but becomes trapped in a vacancy, thereby becoming almost immobile. These mechanisms occur in numerous systems, including metals in III–V semiconductors (that is, where III is an element from Group III of the periodic table and V is an element from Group V), diffusion of elements into silicon and germanium, and probably also in II–VI compounds.

Diffusion into nanoparticles was recently used to form hollow particles by taking advantage of the "Kirkendall effect",[18] in which pores form because of the difference in diffusion rates between two components in a diffusion couple.[19] Room-temperature diffusion is also involved in ion-exchange reactions that lead to the transformation of nanoparticle composition, for example, from CdSe to Ag_2Se.[20] These recent examples show the richness of the possible routes for performing chemistry in nanoparticles and herein we provide another example concerning the diffusion of gold into InAs nanocrystals at room temperature.

The diffusion coefficient can be expressed in an Arrhenius form [Equation (1)] where D_0 is the pre-exponential factor and E_a is the activation energy.

$$D = D_0 \, e^{(-E_a/RT)} \tag{1}$$

Typically, these values are measured at high temperature[21] and therefore room-temperature values can be obtained only by extrapolation. An estimate for the typical diffusion distance with time is given by the root-mean-square (RMS) distance (X), which is given by Equation (2).

$$X = \sqrt{2\,D\,T} \tag{2}$$

The reaction of Au with InAs nanoparticles is similar to our earlier synthesis of Au-CdSe nano-dumbbells.[6] It was carried out at room temperature by adding an $AuCl_3$ solution to InAs dots dissolved in toluene. The gold solution contains the gold salt, didodecyldimethylammonium bromide (DDAB, to bring the Au salt into the organic solution), and dodecylamine (DDA), which stabilizes the dots and serves as a reducing agent (see Experimental Section for details). Figure 1 shows TEM images of InAs dots after reaction

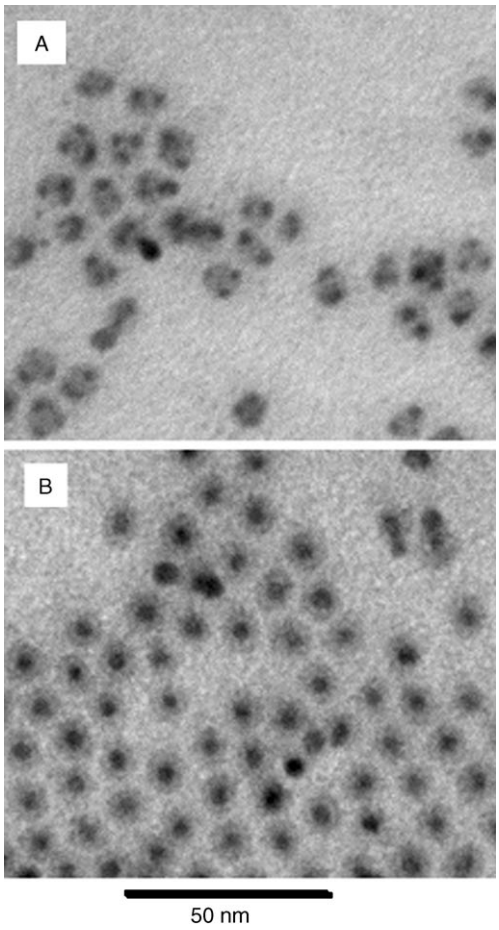

Figure 1. TEM images of InAs nanocrystals after treatment with gold in toluene solution as a function of increasing gold concentration: A) after adding 2.75×10^{-6} mol of gold; B) after adding 5.5×10^{-6} mol of gold. Reaction time: 2 min.

with Au. At a low concentration of Au (Figure 1 A), Au patches are formed on the InAs surface, as can be seen by the dark spots. Upon doubling the Au concentration a completely different behavior is seen: the Au diffuses to the center of the nanoparticle and is coated with a shell with much lower contrast in the TEM image. This behavior is in contrast to that observed for the reaction of Au with CdSe nanoparticles, where gold grows in patches on the surface (or on the apexes

 © 2006 Wiley-VCH Verlag GmbH & Co. KGaA, Weinheim

of rods), and at high concentrations transforms into one patch (or one side for rods) through a ripening process.

Optical and structural characterization of the Au-InAs system was carried out by various methods. Figure 2A presents the absorption spectra of the original InAs dots (7-nm diameter) before and after their reaction with gold; note that the excitonic peak of the InAs dots has been washed out. Figure 2B shows the powder X-ray diffraction (XRD) pattern acquired from the original 7-nm InAs dots before the Au growth (Figure 2B, top), which agrees with the zincblende structure of bulk crystalline InAs (peak positions are represented by the upper stick-spectrum). The XRD pattern of the Au-InAs composite (Figure 2B, bottom) is also shown. In this pattern, we can identify three peaks attributed to Au, with the (111) peak being especially strong. The fourth, broad diffraction peak (marked by an arrow) can be attributed to the (222) planes of zincblende-type In_2O_3 (see the stick pattern at the bottom of Figure 2B). Thus, no evidence of the presence of crystalline InAs appears in the XRD pattern of the Au-InAs nanocomposite. By comparing the diffraction results for InAs nanodots and the Au-InAs nanocomposite we can therefore conclude that the latter material is less ordered.

The energy-dispersive X-ray spectrum of the Au-InAs nanocomposite is shown in Figure 2C. In addition to the In and the As from the original core, a Au peak appears for the Au-InAs system. Quantification of this spectrum resulted in an In/As/Au ratio of 0.89:0.83:1.

The Au-InAs nanocomposite was also studied by high-resolution TEM (HRTEM) measurements (Figure 3). These gave a lattice spacing in the dark core of 2.35 Å, which agrees with the (111) lattice spacing of Au. This Au lattice was identified in the center of many particles. Studying the shell proved difficult owing to the low contrast, which differs significantly from the core. However, by focusing on the shell of the composite particles we were able to find evidence for an average lattice spacing of 2.95 Å (10 particles), which may indicate the presence of (111) planes of In_2O_3, as shown in Figure 3B.

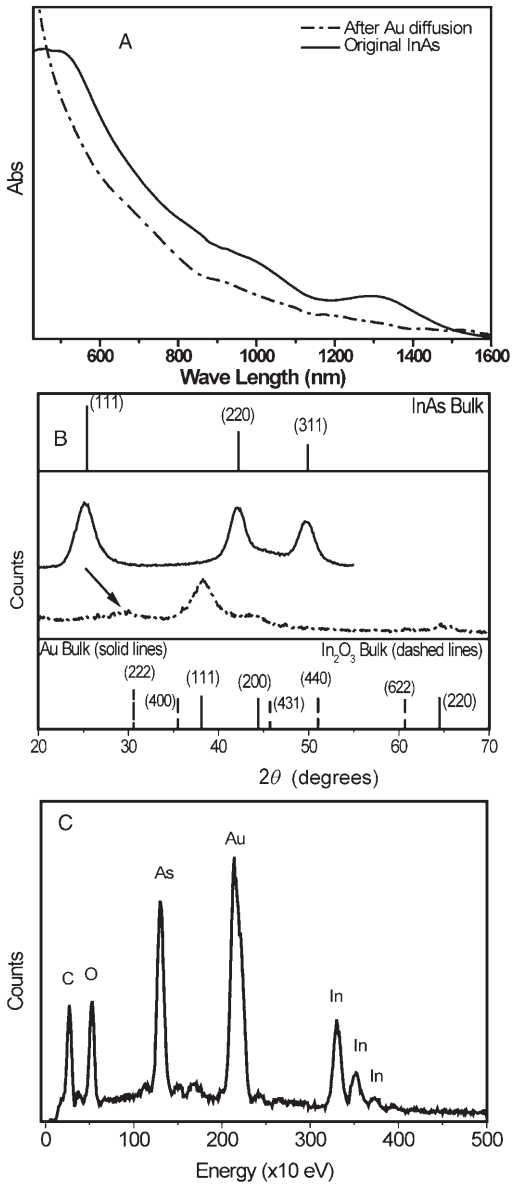

Figure 2. Optical and structural characterization of the Au-InAs nanocomposite: A) absorption spectra of 7-nm InAs dots before (solid line) and after reaction with Au (dashed line); B) powder XRD patterns of InAs (top) and Au-InAs (bottom) and the stick-patterns of bulk InAs (top), gold, and In_2O_3; arrow indicates peak assigned to the (222) planes of zincblende-type In_2O_3; C) EDS spectrum of the Au-InAs nanocomposite.

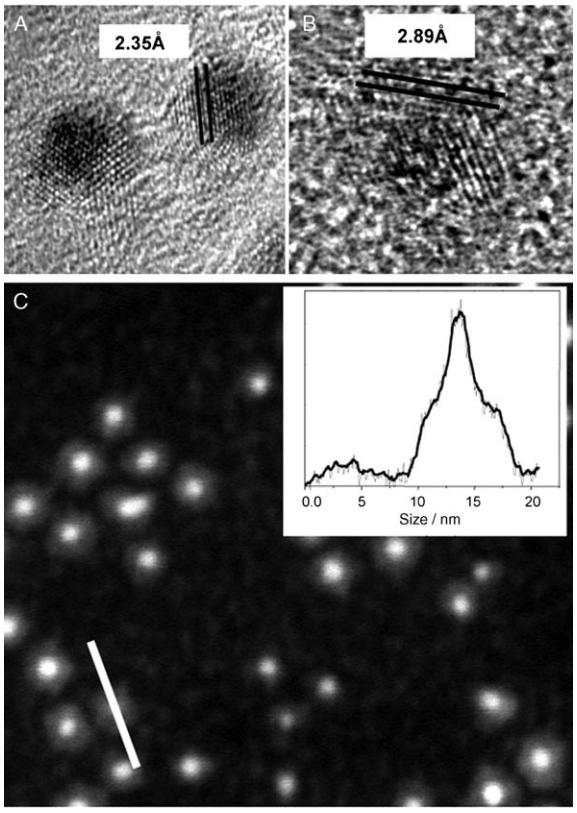

Figure 3. Structural characterization of Au-InAs particles: A) HRTEM image of two particles; the measured lattice spacing in the core is 2.35 Å; B) HRTEM image of the particle taken by focusing on the shell; the measured lattice spacing is 2.89 Å. C) STEM-HAADF image of *Z*-contrast observed in several particles. The intensity distribution across a single particle (white line) is presented in the inset.

© 2006 Wiley-VCH Verlag GmbH & Co. KGaA, Weinheim

To further study the structure of the Au-InAs nanocomposite, we used the scanning transmission electron microscopy (STEM) technique with a high angular annular dark-field detector (HAADF). The integrated intensity of the signal is proportional to the average atomic number of the sampled elements (Z-contrast imaging). Figure 3C shows an STEM-HAADF image of the nanocomposite. A significant contrast difference between the core and the shell, where the bright core indicates the presence of the heavier Au component, can be seen for the particles. This feature can also be seen in the inset, which shows a cross-section of a single particle taken along the marked line. A main peak is observed with two weaker shoulders corresponding to the shell.

The role of solid-state diffusion in the creation of the Au-InAs particles was emphasized by performing a reaction in the solid state. Thus, after adding 1×10^{-6} mol of Au solution to the InAs solution (similar to the solution experiment), an aliquot was taken and deposited on the TEM grid. The results show a typical behavior for this specific concentration with gold patches on the surface (Figure 4A). The same grid was stored and examined again 48 h later, thereby allowing for further reaction to proceed. The TEM image in Figure 4B clearly shows that the gold has diffused inside to yield a result very similar to that obtained in solution for a high Au concentration.

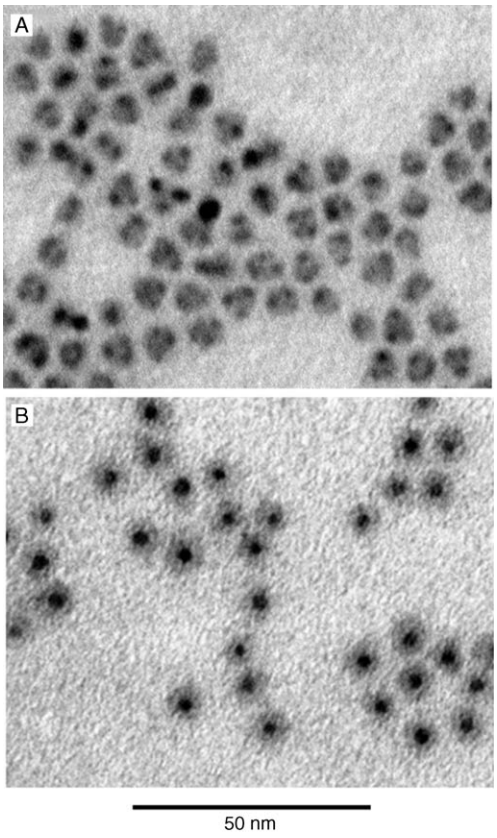

Figure 4. TEM images of gold diffused inside InAs nanocrystals as a function of time. 1×10^{-6} mol of gold was added and an aliquot was deposited on the TEM grid and characterized after 2 h (A) and 48 h (B). The reaction time in solution was 2 min.

This latter experiment resembles classical diffusion studies in bulk materials, where metal films are deposited on a substrate and heated up and the diffusion is monitored by measuring the metal concentration profile inside the bulk material, although in the bulk these experiments are performed at very high temperature.[11,15]

Our observations clearly show that Au diffuses into the InAs dots. During this diffusion, the InAs loses its crystalline order and becomes an amorphous shell (under inert conditions), while In is converted into In_2O_3 in the oxidizing environment. To examine the feasibility of such room-temperature diffusion, we used Equation (1) to estimate the diffusion coefficient (D) for Au in InAs at room temperature. A value of about $3 \times 10^{-14}\,m^2 s^{-1}$ was obtained. From Equation (2) we calculated approximately that the RMS diffusion distance, X, will be around 1000 nm in 24 h. This diffusion behavior differs significantly from that observed in CdSe dots, where Au forms patches on the surface that ripen to one patch at high Au concentration. We could not determine D values for Au in CdSe, but for the similar system of Au in CdS, D at room temperature is much smaller, approximately $1 \times 10^{-29}\,m^2 s^{-1}$, and correspondingly X over 24 h is negligible (approximately 2×10^{-5} nm). Much smaller values were also calculated for the CdTe system. The main difference is the much lower activation energy in the Au-InAs case (0.65 eV versus 1.8 eV for Au in CdS and 2 eV for Au in CdTe).[21] The diffusion of Au into InAs also agrees with the criteria for room-temperature diffusion of fast diffusers as the InAs dots have an energy gap of 1.1 eV and the dielectric constant is high (14.2 for InAs).

The detailed diffusion behavior in this case can be attributed to an interstitial-substitution mechanism.[16,17] This diffusion process is indeed a typical solid-state reaction and can also take place on the grid in the absence of solvent. The gold atoms hop from the surface into the nanoparticles through the interstitial sites of the InAs nanocrystal and simultaneously substitute atoms of the InAs lattice. Free In and As atoms simultaneously diffuse out and may be readily oxidized in the absence of an inert atmosphere. Migrating interstitial gold atoms distort the atomic lattice of the hosting InAs nanocrystal because these atoms are still relatively large for interstitial positions, even for the 6.058-Å unit cell of InAs. Therefore, the mass substitution of In atoms at high Au concentrations results in the formation of an amorphous shell.

The diffusion process does not lead to a homogeneous distribution of Au across the particle. Rather, Au is concentrated in the center of the nanoparticles. This arrangement is probably due to the preferred strong interaction between the Au atoms. The original InAs nanocrystals with a size of 7 nm should be composed of roughly 20 atomic planes of the (111) type (d-spacing of 3.498 Å), which means that only 10 interatomic jumps are required for a migrating gold atom to get to a core position within the InAs particle. On the other hand, the gold content in the Au-InAs nanocomposite reaches a level of 30% atomic concentration, which apparently determines the minimum-energy geometry of the composite as a dense, compact gold core (19 $g\,cm^{-3}$; about 2 nm in size) surrounded by an amorphous InAs shell instead of an amorphous particle containing a mixture of Au, In, and As atoms with a density

 © 2006 Wiley-VCH Verlag GmbH & Co. KGaA, Weinheim

close to 5.7 $g\,cm^{-3}$, as for the InAs crystal, and a size larger than that of the original InAs nanodots.

To summarize, the diffusion of gold into InAs semiconductor nanocrystals has been reported. The diffusion of Au occurs either in solution or in a solid-state reaction. In the first stage gold patches grow on the nanocrystal surface, and a further increase in the gold concentration, or waiting for 24 h, leads to gold diffusion into the nanocrystals. This behavior differs from the CdSe case, where Au grows on the surface and ripens to form one gold patch in high concentration. As a result of the Au diffusion, the InAs is converted into an amorphous InAs or oxidized shell. This process points to a new strategy for metal doping in semiconductor nanoparticles.[22]

Experimental Section

The InAs nanocrystals were prepared as reported elsewhere.[23,24]

In a typical reaction, a gold solution was prepared from $AuCl_3$ (2.5 mg, 0.008 mmol), DDAB (20 mg, 0.04 mmol), and DDA (35 mg, 0.185 mmol) in toluene (4 mL) and sonicated for 5 min at room temperature. The solution changed color from dark orange to light yellow. InAs quantum dots (0.8 mg, 2.35×10^{-10} mol of dots) were dissolved in toluene (5 mL) in a three-necked flask under argon and the gold solution was added dropwise at room temperature. During the addition, the color gradually changed to dark brown. Separation of the Au-InAs product from the growth solution was performed by adding of methanol (1 mL), which leads to precipitation, and centrifuging for 5 min.

TEM images were obtained with a FEI Tecnai 12 microscope or a FEI Tecnai F20G^2 microscope operating at 200 kV. Energy-dispersive X-ray spectroscopy (EDS) was carried out with a 5-kV acceleration voltage on an HR SEM FEI Sirion equipped with an EDAX EDS detector. Powder XRD patterns were measured with a Philips PW 1830/40 X-ray diffractometer with $Cu_{K\alpha}$ radiation. Absorption measurements were taken with a Jasco UV-VIS-NIR spectrophotometer.

Received: June 27, 2006
Revised: August 29, 2006
Published online: November 2, 2006

Keywords: core–shell nanoparticles · gold · materials science · solid-phase synthesis

[1] D. J. Milliron, S. M. Hughes, Y. Cui, L. Manna, J. Li, L. W. Wang, A. P. Alivisatos, *Nature* **2004**, *430*, 190 – 195.
[2] S. Kudera, L. Carbone, M. F. Casula, R. Cingolani, A. Falqui, E. Snoeck, W. J. Parak, L. Manna, *Nano Lett.* **2005**, *5*, 445 – 449.
[3] D. V. Talapin, R. Koeppe, S. Gotzinger, A. Kornowski, J. M. Lupton, A. L. Rogach, O. Benson, J. Feldmann, H. Weller, *Nano Lett.* **2003**, *3*, 1677 – 1681.
[4] T. Teranishi Y. Inoue, M. Nakaya, Y. Oumi, T. Sano, *J. Am. Chem. Soc.* **2004**, *126*, 9914 – 9915.
[5] H. Yu, M. Chen, P. M. Rice, S. X. Wang, R. L. White, S. Sun, *Nano Lett.* **2005**. *5*, 379 – 382.
[6] T. Mokari, E. Rothenberg, I. Popov, R. Costi, U. Banin, *Science* **2004**, *304*, 1787 – 1791.
[7] T. Mokari, C. G. Sztrum, A. Salant, E. Rabani, U. Banin, *Nat. Mater.* **2005**, *4*, 855 – 862.
[8] W. Shi, H. Zeng, Y. Sahoo, T. Y. Ohulchanskyy, Y. Ding, Z. L. Wang, M. Swihart, P. N. Prasad, *Nano Lett.* **2006**, *6*, 875 – 881.
[9] J. B. Hannon, S. Kodambaka, F. M. Ross, R. M. Tromp, *Nature* **2006**, *440*, 69 – 71.
[10] U. Gösele, *Nature* **2006**, *440*, 34 – 35.
[11] A. F. W. Willoughby, *Rep. Prog. Phys.* **1978**, *41*, 1665 – 1705.
[12] U. Gösele, *Annu. Rev. Mater. Sci.* **1988**, *18*, 257 – 282.
[13] A. Hiraki, *Surf. Sci. Rep.* **1984**, *3*, 357 – 412.
[14] A. Seeger, K. P. Chik, *Phys. Status Solidi B* **1968**, *29*, 455 – 542.
[15] D. Mathiot, *Phys. Rev. B* **1992**, *45*, 13345 – 13355.
[16] U. Gösele, W. Frank, A. Seeger, *Appl. Phys.* **1980**, *23*, 361 – 368.
[17] F. C. Frank, D. Turnbull, *Phys. Rev.* **1956**, *104*, 617 – 618.
[18] A. D. Smigelskas, E. O. Kirkendall, *Trans. AIME* **1947**, *171*, 130 – 142.
[19] Y. Yin, R. M. Rioux, C. K. Erdonmez, S. Hughes, G. A. Somorjai, A. P. Alivisatos, *Science* **2004**, *304*, 711 – 714.
[20] D. H. Son, S. M. Hughes, Y. Yin, A. P. Alivisatos, *Science* **2004**, *306*, 1009 – 1012.
[21] M. B. Dutt, B. L. Sharma in *Diffusion in Semiconductors and Non-Metallic Solids* (Ed.: D. L. Beke), Springer, Berlin, **1998**, pp. 1 – 3.
[22] S. C. Erwin, L. Zu, M. I. Haftel, A. L. Efros, T. A. Kennedy, D. J. Norris, *Nature* **2005**, *436*, 91 – 94.
[23] A. A. Guzelian, U. Banin, A. V. Kadavanich, X. Peng, A. P. Alivisatos, *Appl. Phys. Lett.* **1996**, *69*, 1432 – 1434.
[24] A. Aharoni, T. Mokari, I. Popov, U. Banin, *J. Am. Chem. Soc.* **2006**, *128*, 257 – 264.

 © 2006 Wiley-VCH Verlag GmbH & Co. KGaA, Weinheim

Small Ring Systems

DOI: 10.1002/anie.200602586

An Amine-Promoted Aziridination of Chalcones**

*Yu-Mei Shen, Mei-Xin Zhao, Jiaxi Xu, and Yian Shi**

Aziridines are versatile building blocks that can undergo various synthetically useful transformations and are also an important part of many biologically active molecules.[1] Great efforts and progress have been made in the development of various aziridination methods.[1–15] As part of our general interest in the area of small-ring synthesis from olefins, we have been investigating new methods to prepare aziridines, particularly those without protecting groups on the nitrogen atom, such as the aziridination of electron-deficient olefins with aminimide **1** (Scheme 1).

[*] Y.-M. Shen, M.-X. Zhao, J. Xu, Prof. Dr. Y. Shi
Department of Chemistry
Colorado State University
Fort Collins, CO 80523 (USA)
Fax: (+1) 970-491-1801
E-mail: yian@lamar.colostate.edu

[**] We are grateful to the generous financial support from the Monfort Foundation (Colorado State University).

Supporting information for this article (aziridination procedures, characterization including an X-ray crystallographic analysis, and the determination of the *ee* values) is available on the WWW under http://www.angewandte.org or from the author.

© 2006 Wiley-VCH Verlag GmbH & Co. KGaA, Weinheim
WILEY InterScience DISCOVER SOMETHING GREAT

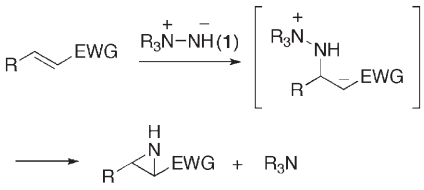

Scheme 1. Aziridination of electron-deficient olefins with aminimide **1**. EWG = electron-withdrawing group.

In 1980, Ikeda et al. reported that the aminimide **2** (prepared from 1,1-dimethylhydrazine and propylene oxide) can directly iminate chalcones to form aziridines.[16] Since

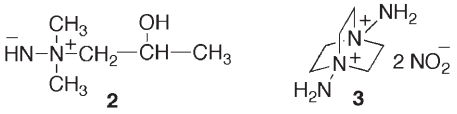

then, little has been reported on this reaction. Initial studies by our research group have shown that this aziridination could be extended to other aminimides. For example, the aminimide derived from hydrazinium nitrate **3** (prepared from 1,4-diazabicyclo[2.2.2]octane (DABCO) and hydroxylamine-*O*-sulfonic acid in the presence of barium oxide and barium nitrate)[17] can effectively aziridinate chalcones.[18] To further develop this aziridination reaction, we wanted to investigate whether this system could be developed into a catalytic and eventually an asymmetric process to form nonracemic α-keto aziridines, and herein report our preliminary results.

Our studies started with the investigation of a one-pot process which involved the in situ generation of a hydrazinium salt, deprotonation of the hydrazinium to form an aminimide, and subsequent aziridination (Scheme 2). It has

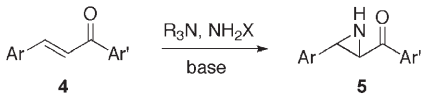

Scheme 2. Aziridination of chalcones **4** with aminimide formed in situ.

been shown that *O*-mesitylenesulfonylhydroxylamine (MSH) can readily aminate various tertiary amines to give the corresponding hydrazinium salts in high yield.[19,20] The aziridination was then examined by treating MSH and tertiary amines with base and chalcone **4**. Treating MSH (2.0 equiv) with DABCO (1.0 equiv), KOH (3.0 equiv), and **4** (Ar = Ar′ = Ph, 1.0 equiv) in CH_3CN at room temperature and stirring the reaction mixture for four hours gave the aziridine product **5** in 73% yield. A higher yield (85%) was obtained on using *N*-methylmorpholine (NMM; Table 1, entry 1a). As shown in Table 1 (entries 2a–8a), other chalcones can be efficiently aziridinated in a short time with good yield.

Encouraged by the feasibility of this one-pot reaction, we next pursued the possibility of making the process catalytic. When NMM was reduced to 0.1 equivalents, the aziridine **5** was obtained in 52% yield (Table 1, entry 1b). A slightly

Table 1: Stoichiometric[a] and catalytic[b] aziridination of chalcones.

Entry	Substrate	Equiv. of amine	Yield [%][c]
1a	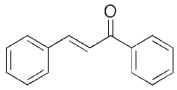	1.0	85
1b		0.1	52[d]
1c		0.1	65
1d		0.2	80
2a	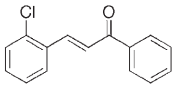	1.0	80
2b		0.2	60
3a	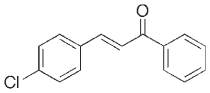	1.0	82
3b		0.2	59
4a	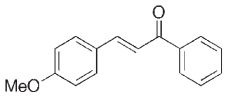	1.0	49
4b		0.2	65
5a	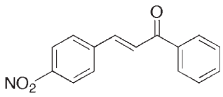	1.0	56
5b		0.2	21
6a	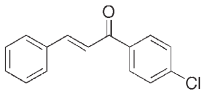	1.0	64
6b		0.2	39
7a	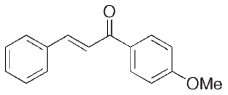	1.0	78
7b		0.2	67
8a	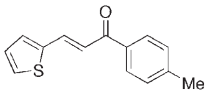	1.0	54
8b		0.2	42

[a] All reactions were carried out with substrate (0.5 mmol), NMM (0.5 mmol), MSH (1.0 mmol), and KOH (1.5 mmol) in CH_3CN (1.5 mL) at room temperature for 4 h (for entry 5a, 3 h; for entry 8a, 5 h). [b] All reactions were carried out with substrate (0.5 mmol), NMM (0.05–0.10 mmol), MSH (1.0 mmol), and $CsOH·H_2O$ (3.0 mmol) in CH_3CN/CH_2Cl_2 (2:1, 2.5 mL) at 0°C to room temperature for 7 h unless otherwise noted. [c] Yield of isolated product. [d] KOH was used as the base and CH_3CN was used as the solvent.

higher yield was obtained by replacing KOH with $CsOH·H_2O$ (Table 1, entry 1c). This catalytic process was further illustrated by the aziridination of a number of substrates (Table 1, entries 2b–8b). In some cases, the yields achieved were similar to those obtained with a stoichiometric amount of tertiary amine. However, in other cases (Table 1, entries 5b and 6b), the yields dropped significantly.

While a detailed understanding of the reaction mechanism awaits further study, a plausible catalytic cycle is shown in Scheme 3.[21] The tertiary amine NMM reacts with MSH to form the hydrazinium salt **6**, which then reacts with $CsOH·H_2O$ to give the aminimide **7**. The aminimide **7** then undergoes conjugate addition to the chalcone **4** followed by cyclization to form the aziridine **5** and regenerate the tertiary amine. No aziridination was observed in the absence of NMM or $CsOH·H_2O$, thereby indicating that a tertiary amine and base are required for the reaction, which is consistent with the proposed mechanism.

The feasibility of the aziridination using a catalytic amount of the tertiary amine and MSH in the presence of

 © 2006 Wiley-VCH Verlag GmbH & Co. KGaA, Weinheim

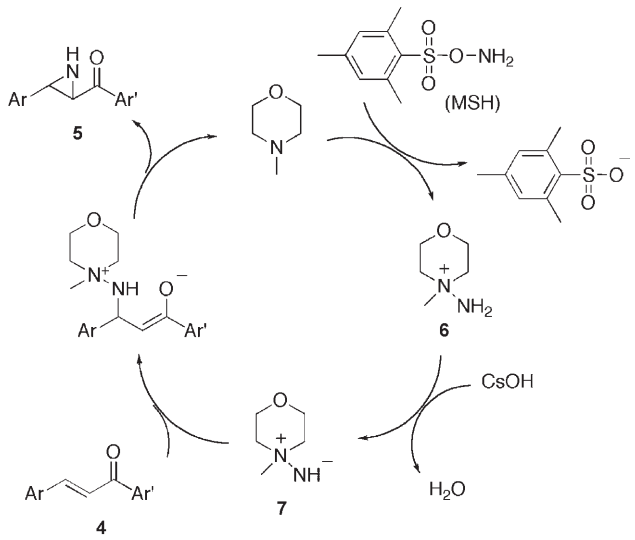

Scheme 3. A proposed catalytic cycle for the aziridination.

$CsOH{\cdot}H_2O$ prompted us to investigate whether a chiral tertiary amine could induce any enantioselectivity for the aziridination. Treating chalcone **4** with 30 mol% (+)-Tröger's base, MSH, and $CsOH{\cdot}H_2O$ afforded the aziridine in 81% yield and 55% *ee* (Scheme 4; Table 2, entry 3).[22] A slightly higher enantioselectivity was obtained with 4′-chlorochalcone (Table 2, entries 5 and 6), and the *ee* value could be improved to 98% upon recrystallization (Table 2, entry 7). These results illustrate that a catalytic asymmetric aziridination process occurs.

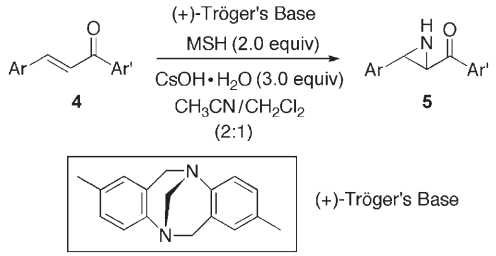

Scheme 4. Asymmetric aziridination of **4** using Tröger's base.

Table 2: Asymmetric aziridination of chalcones.[a]

Entry	Substrate	Equiv. of (+)-Tröger's base	Yield [%][b]	*ee* [%][c]
1	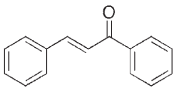	1.0	90	55[d]
2		0.6	85	55
3		0.3	81	55
4	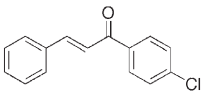	1.0	93	62
5		0.6	62	62
6		0.3	50	62
7		0.6[e]	66	67 (98[f])

[a] All reactions were carried out at 0°C with substrate (0.1 mmol), (+)-Tröger's base (0.03–0.1 mmol), MSH (0.2 mmol), and $CsOH{\cdot}H_2O$ (0.3 mmol) in CH_3CN/CH_2Cl_2 (2:1, 1.5 mL) for 7 h (entries 1–3) or 5 h (entries 4–6). [b] Yield of isolated product. [c] The enantioselectivity was determined by HPLC on a chiral stationary phase (chiracel OD). [d] The absolute configuration was determined by comparing the rotation of a known compound and is 2*R*,3*S* (see Ref. [9c]). [e] At −20°C for 24 h. [f] After recrystallization.

In summary, we have found that the aminimide generated in situ from tertiary amine and MSH in the presence of a base is an effective NH-transfer reagent for the aziridination of chalcones. The amine promoter in this aziridination process can be used in a catalytic amount, and a reasonable level of enantioselectivity can be obtained when the chiral tertiary amine, Tröger's base, is used. More effective tertiary amine catalysts and also an expansion of the substrate scope are currently being pursued.

Experimental Section

Representative procedure asymmetric aziridination (Table 2, entry 7): MSH (22.0 mg, 0.10 mmol) and $CsOH{\cdot}H_2O$ (25.0 mg, 0.15 mmol) were added to a solution of (+)-Tröger's base (15.0 mg, 0.06 mmol) and 4′-chlorochalcone (24.0 mg, 0.10 mmol) in CH_3CN/CH_2Cl_2 (1.5 mL, 2:1, v/v) at −20°C. After stirring the reaction mixture for 1 h, further MSH (11.0 mg, 0.05 mmol) and $CsOH{\cdot}H_2O$ (12.5 mg, 0.075 mmol) were added. After another 1 h, additional MSH (11.0 mg, 0.05 mmol) and $CsOH{\cdot}H_2O$ (12.5 mg, 0.075 mmol) were added. The reaction was stirred for a further 22 h at −20°C (total reaction time of 24 h), then diluted with EtOAc (10 mL), filtered, and the filter cake washed with EtOAc (2 × 5 mL). The filtrate was subsequently concentrated and purified by flash chromatography (the silica gel was buffered with 1% Et_3N in hexanes, hexanes/EtOAc = 10:1) to give the aziridine as a pale yellow solid (17.0 mg, 66% yield, 67% *ee*).

Received: June 29, 2006
Revised: September 23, 2006
Published online: November 6, 2006

Keywords: asymmetric catalysis · aziridines · chalcones · nitrogen heterocycles · small ring systems

[1] For leading reviews on the synthesis and application of aziridines, see: a) D. Tanner, *Angew. Chem.* **1994**, *106*, 625; *Angew. Chem. Int. Ed. Engl.* **1994**, *33*, 599; b) J. Du Bois, C. S. Tomooka, J. Hong, E. M. Carreira, *Acc. Chem. Res.* **1997**, *30*, 364; c) A.-H. Li, L.-X. Dai, V. K. Aggarwal, *Chem. Rev.* **1997**, *97*, 2341; d) H. M. I. Osborn, J. Sweeney, *Tetrahedron: Asymmetry* **1997**, *8*, 1693; e) T. Ibuka, *Chem. Soc. Rev.* **1998**, *27*, 145; f) E. N. Jacobsen in *Comprehensive Asymmetric Catalysis* (Eds.: E. N. Jacobsen, A. Pfaltz, H. Yamamoto), Springer, Berlin, **1999**, chap. 17; g) R. S. Atkinson, *Tetrahedron* **1999**, *55*, 1519; h) W. McCoull, F. A. Davis, *Synthesis* **2000**, 1347; i) J. B. Sweeney, *Chem. Soc. Rev.* **2002**, *31*, 247; j) M. D. Redlich, M. F. Mayer, M. M. Hossain, *Aldrichimica Acta* **2003**, *36*, 3; k) P. Müller, C. Fruit, *Chem. Rev.* **2003**, *103*, 2905; l) X. E. Hu, *Tetrahedron* **2004**, *60*, 2701; m) Y. Tang, S. Ye, X.-L. Sun, *Synlett* **2005**, 2720; n) T. Katsuki, *Chem. Lett.* **2005**, *34*, 1304; o) I. D. G. Watson, L. Yu, A. K. Yudin, *Acc. Chem. Res.* **2006**, *39*, 194.

[2] For leading references on the bromine- and iodine-catalyzed aziridination of olefins, see: a) J. U. Jeong, B. Tao, I. Sagasser, H. Henniges, K. B. Sharpless, *J. Am. Chem. Soc.* **1998**, *120*, 6844; b) T. Ando, D. Kano, S. Minakata, I. Ryu, M. Komatsu, *Tetrahedron* **1998**, *54*, 13485.

[3] For leading references on the asymmetric aza-Darzens-type aziridination, see: a) F. A. Davis, P. Zhou, G. V. Reddy, *J. Org. Chem.* **1994**, *59*, 3243; b) A. B. McLaren, J. B. Sweeney, *Org.*

 © 2006 Wiley-VCH Verlag GmbH & Co. KGaA, Weinheim

Lett. **1999**, *1*, 1339; c) S. Hanessian, L.-D. Cantin, *Tetrahedron Lett.* **2000**, *41*, 787; d) T. Satoh, Y. Fukuda, *Tetrahedron* **2003**, *59*, 9803; e) F. Ferreira, M. Audouin, F. Chemla, *Chem. Eur. J.* **2005**, *11*, 5269.

[4] For leading references on the aziridination of imines with ylides, see: a) A.-H. Li, L.-X. Dai, X.-L. Hou, *Chem. Commun.* **1996**, 491; b) V. K. Aggarwal, A. Thompson, R. V. H. Jones, M. C. H. Standen, *J. Org. Chem.* **1996**, *61*, 8368; c) A.-H. Li, Y.-G. Zhou, L.-X. Dai, X.-L. Hou, L.-J. Xia, L. Lin, *Angew. Chem.* **1997**, *109*, 1375; *Angew. Chem. Int. Ed. Engl.* **1997**, *36*, 1317; d) V. K. Aggarwal, E. Alonso, G. Fang, M. Ferrara, G. Hynd, M. Porcelloni, *Angew. Chem.* **2001**, *113*, 1482; *Angew. Chem. Int. Ed.* **2001**, *40*, 1433.

[5] For leading references on the aziridination of imines with diazo compounds, see: a) R. Bartnik, G. Mloston, *Synthesis* **1983**, 924; b) K. B. Hansen, N. S. Finney, E. N. Jacobsen, *Angew. Chem.* **1995**, *107*, 750; *Angew. Chem. Int. Ed. Engl.* **1995**, *34*, 676; c) J. C. Antilla, W. D. Wulff, *J. Am. Chem. Soc.* **1999**, *121*, 5099; d) K. Juhl, R. G. Hazell, K. A. Jørgensen, *J. Chem. Soc. Perkin Trans. 1* **1999**, 2293; e) V. K. Aggarwal, M. Ferrara, *Org. Lett.* **2000**, *2*, 4107.

[6] For leading references on the metal-catalyzed aziridination of olefins, see: for racemic systems: a) H. Kwart, A. A. Khan, *J. Am. Chem. Soc.* **1967**, *89*, 1951; b) J. T. Groves, T. Takahashi, *J. Am. Chem. Soc.* **1983**, *105*, 2073; c) D. Mansuy, J.-P. Mahy, A. Dureault, G. Bedi, P. Battioni, *J. Chem. Soc. Chem. Commun.* **1984**, 1161; d) D. A. Evans, M. M. Faul, M. T. Bilodeau, *J. Org. Chem.* **1991**, *56*, 6744; e) D. A. Evans, M. M. Faul, M. T. Bilodeau, *J. Am. Chem. Soc.* **1994**, *116*, 2742; f) J. Du Bois, J. Hong, E. M. Carreira, M. W. Day, *J. Am. Chem. Soc.* **1996**, *118*, 915; g) S.-M. Au, J.-S. Huang, W.-Y. Yu, W.-H. Fung, C.-M. Che, *J. Am. Chem. Soc.* **1999**, *121*, 9120; h) P. Brandt, M. J. Södergren, P. G. Andersson, P.-O. Norrby, *J. Am. Chem. Soc.* **2000**, *122*, 8013; i) P. Dauban, L. Sanière, A. Tarrade, R. H. Dodd, *J. Am. Chem. Soc.* **2001**, *123*, 7707; j) A. Padwa, T. Stengel, *Org. Lett.* **2002**, *4*, 2137; k) K. Guthikonda, J. Du Bois, *J. Am. Chem. Soc.* **2002**, *124*, 13672; l) Y. Cui, C. He, *J. Am. Chem. Soc.* **2003**, *125*, 16202; m) W.-L. Man, W. W. Y. Lam, S.-M. Yiu, T.-C. Lau, S.-M. Peng, *J. Am. Chem. Soc.* **2004**, *126*, 15336; n) A. J. Catino, J. M. Nichols, R. E. Forslund, M. P. Doyle, *Org. Lett.* **2005**, *7*, 2787; o) H. Lebel, K. Huard, S. Lectard, *J. Am. Chem. Soc.* **2005**, *127*, 14198. for asymmetric systems: p) D. A. Evans, K. A. Woerpel, M. M. Hinman, M. M. Faul, *J. Am. Chem. Soc.* **1991**, *113*, 726; q) R. E. Lowenthal, S. Masamune, *Tetrahedron Lett.* **1991**, *32*, 7373; r) Z. Li, K. R. Conser, E. N. Jacobsen, *J. Am. Chem. Soc.* **1993**, *115*, 5326; s) D. A. Evans, M. M. Faul, M. T. Bilodeau, B. A. Anderson, D. M. Barnes, *J. Am. Chem. Soc.* **1993**, *115*, 5328; t) Z. Li, R. W. Quan, E. N. Jacobsen, *J. Am. Chem. Soc.* **1995**, *117*, 5889; u) S. Minakata, T. Ando, M. Nishimura, I. Ryu, M. Komatsu, *Angew. Chem.* **1998**, *110*, 3596; *Angew. Chem. Int. Ed.* **1998**, *37*, 3392; v) C. J. Sanders, K. M. Gillespie, D. Bell, P. Scott, *J. Am. Chem. Soc.* **2000**, *122*, 7132; w) H. Kawabata, K. Omura, T. Katsuki, *Tetrahedron Lett.* **2006**, *47*, 1571.

[7] For recent leading references on nitrogen transfer to olefins using *N*-acetoxyamino compounds, see: a) R. S. Atkinson, R. D. Draycott, D. J. Hirst, M. J. Parratt, T. M. Raynham, *Tetrahedron Lett.* **2002**, *43*, 2083; b) T. Siu, A. K. Yudin, *J. Am. Chem. Soc.* **2002**, *124*, 530; c) K.-S. Yang, K. Chen, *Org. Lett.* **2002**, *4*, 1107; d) J. Li, P. W. H. Chan, C.-M. Che, *Org. Lett.* **2005**, *7*, 5801.

[8] For leading references on the addition of primary amines to 2-halo-substituted α,β-unsaturated carbonyl compounds, see: a) O. Ploux, M. Caruso, G. Chassaing, A. Marquet, *J. Org. Chem.* **1988**, *53*, 3154; b) P. Garner, O. Dogan, S. Pillai, *Tetrahedron Lett.* **1994**, *35*, 1653; c) G. Cardillo, L. Gentilucci, C. Tomasini, M. P. V. Castejon-Bordas, *Tetrahedron: Asymmetry* **1996**, *7*, 755; d) M. T. Barros, C. D. Maycock, M. R. Ventura, *Tetrahedron Lett.* **2002**, *43*, 4329; e) A. Mekonnen, R. Carlson, *Tetrahedron* **2006**, *62*, 852.

[9] For leading references using $RONH_2$, see: a) I. Coldham, A. J. Collis, R. J. Mould, R. E. Rathmell, *Tetrahedron Lett.* **1995**, *36*, 3557; b) G. Cardillo, S. Casolari, L. Gentilucci, C. Tomasini, *Angew. Chem.* **1996**, *108*, 1939; *Angew. Chem. Int. Ed. Engl.* **1996**, *35*, 1848; c) X. L. Jin, H. Sugihara, K. Daikai, H. Tateishi, Y. Z. Jin, H. Furuno, J. Inanaga, *Tetrahedron* **2002**, *58*, 8321; d) N. Yamagiwa, S. Matsunaga, M. Shibasaki, *J. Am. Chem. Soc.* **2003**, *125*, 16178.

[10] For leading references using $NsONHCO_2R$, see: a) S. Fioravanti, L. Pellacani, S. Stabile, P. A. Tardella, R. Ballini, *Tetrahedron* **1998**, *54*, 6269; b) S. Fioravanti, A. Morreale, L. Pellacani, P. A. Tardella, *J. Org. Chem.* **2002**, *67*, 4972; c) D. Colantoni, S. Fioravanti, L. Pellacani, P. A. Tardella, *Org. Lett.* **2004**, *6*, 197.

[11] For leading references on asymmetric aziridination using $R^1R^2S{=}NH$, see: a) T. Yoshimura, T. Akasaka, N. Furukawa, S. Oae, *Heterocycles* **1977**, *7*, 287; b) N. Furukawa, T. Yoshimura, M. Ohtsu, T. Akasaka, S. Oae, *Tetrahedron* **1980**, *36*, 73.

[12] For leading references using diaziridine, see: a) K. Hori, H. Sugihara, Y. N. Ito, T. Katsuki, *Tetrahedron Lett.* **1999**, *40*, 5207; b) H. Ishihara, Y. N. Ito, T. Katsuki, *Chem. Lett.* **2001**, 984; c) H. Ishihara, K. Hori, H. Sugihara, Y. N. Ito, T. Katsuki, *Helv. Chim. Acta* **2002**, *85*, 4272.

[13] For a recent leading reference on the aziridination by addition of azides to olefins, see: J. M. Mahoney, C. R. Smith, J. N. Johnston, *J. Am. Chem. Soc.* **2005**, *127*, 1354.

[14] For aziridination of olefins with $HN(OCH_3)_2/BF_3$ or trimethylsilyltriflate, see: a) V. F. Rudchenko, S. M. Ignatov, R. G. Kostyanovsky, *J. Chem. Soc. Chem. Commun.* **1990**, 261; b) E. Vedejs, H. Sano, *Tetrahedron Lett.* **1992**, *33*, 3261.

[15] For aziridination of olefins with MSH, see: a) J. C. Bottaro, *J. Chem. Soc. Chem. Commun.* **1980**, 560; b) P. Métra, J. Hamelin, *J. Chem. Soc. Chem. Commun.* **1980**, 1038.

[16] I. Ikeda, Y. Machii, M. Okahara, *Synthesis* **1980**, 650.

[17] G. A. Olah, M. B. Sassaman, M. Zuanic, C. B. Rao, G. K. S. Prakash, *J. Org. Chem.* **1992**, *57*, 1585.

[18] a) J. Xu, P. Jiao, *J. Chem. Soc. Perkin Trans. 1* **2002**, 1491; Erratum: b) J. Xu, P. Jiao, *J. Chem. Soc. Perkin Trans. 1* **2002**, 2561.

[19] For leading references on amination of tertiary amines with MSH, see: a) Y. Tamura, J. Minamikawa, Y. Kita, J. H. Kim, M. Ikeda, *Tetrahedron* **1973**, *29*, 1063; b) Y. Tamura, J. Minamikawa, M. Ikeda, *Synthesis* **1977**, 1.

[20] For the preparation of MSH, see: a) C. R. Johnson, R. A. Kirchhoff, H. G. Corkins, *J. Org. Chem.* **1974**, *39*, 2458; b) Y. Tamura, J. Minamikawa, K. Sumoto, S. Fujii, M. Ikeda, *J. Org. Chem.* **1973**, *38*, 1239.

[21] For an amine-catalyzed asymmetric cyclopropanation, see: C. D. Papageorgiou, M. A. Cubillo de Dios, S. V. Ley, M. J. Gaunt, *Angew. Chem.* **2004**, *116*, 4741; *Angew. Chem. Int. Ed.* **2004**, *43*, 4641.

[22] About 93% of the chiral Tröger's base could be recovered after the reaction, and the recovered chiral amine provided similar reactivity and enantioselectivity for the aziridination.

 © 2006 Wiley-VCH Verlag GmbH & Co. KGaA, Weinheim

Cyclobutanes

DOI: 10.1002/anie.200602847

Controllable [2+2] Cycloadditions of 1,5-Bisallenyl-Substituted Compounds**

*Xuefeng Jiang, Xin Cheng, and Shengming Ma**

Cyclobutanes[1] are key structural units frequently found in biologically important compounds[2] and may be easily formed from the [2+2] cycloaddition of two C=C bonds. The [2+2] cycloaddition reaction using an allene as one or both of the partners has attracted much attention[3] because there is at least one extra carbon–carbon double bond ready for further elaboration. Reactions of allenenes **1** activated thermally[4] and photochemically[5] have been reported to afford distal adducts[4] **2** and proximal adducts[5] **3**, respectively, as a result of the regioselectivity of the reactions (Scheme 1). [2+2] Cycloadditions of allenynes **4** have been realized by heating,[4d] or from the catalytic action of transition-metal complexes.[6] However, to the best of our knowledge, reports of [2+2] cycloaddition reactions between two allenes are limited.[7,8] In this reaction the control of regioselectivity (head-to-head, tail-to-tail, head-to-tail) would be a formidable challenge[3b] (Scheme 1). Herein we report our recent observations of regiocontrollable [2+2] cycloadditions of 1,5-bisallenyl-substituted compounds.

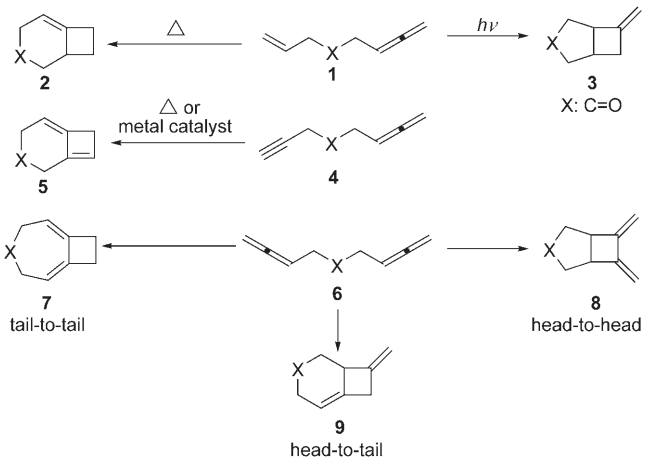

Scheme 1. Intramolecular [2+2] cycloadditions of allenenes, allenynes, and bisallenes.

During our study of the cyclization of bisallenes,[9] we observed a facile regioselective [2+2] cycloaddition reaction of 1,5-bisallenyl compound **6**, which solely afforded the bicyclo[5.2.0] products **7** in moderate to good yields on heating in the absence of the *trans*-[RhCl(CO)(PPh_3)$_2$] complex, thereby differing from the formation of head-to-head products as reported by Skattebøl and Solomon.[7a] This thermal [2+2] cycloaddition reaction of bisallenes is very sensitive to the concentrations of the reagents in the reaction system. After screening the reaction conditions, we found that the best yields of bicyclo[5.2.0] products were obtained from reactions that were heated to reflux with a 0.04 M solution of the substrate in xylene. Bisallenes substituted at the allene moiety gave better results, possibly because the diradical intermediates would be stabilized by these substituents.[4a,b] Furthermore, it was observed that yields were much improved with a bulkier X group (Table 1). This result can be explained by the fact that a bulky X group may bring the two allene functionalities closer. The general structures of **7** were confirmed from the X-ray crystal structure of **7e** (Figure 1).[10]

Conversely, unsaturated carbon–carbon bonds may undergo cyclometalation with many transition metals,[11] such as Rh, Ru, Pd, Ir, Pt, Fe, Co, and Ni. As a result of the ring strain in four-membered cycles, the reductive elimination of metallacyclopentanes and metallacyclopentenes is the key step in affording the four-membered carbocyclic ring.[7h,i] It is noteworthy that the reductive elimination of metallacyclopentanes and metallacyclopentenes has been observed in a limited number of catalytic reactions.[12] After some screening of reaction conditions, we found that the reaction catalyzed by [$Pd(PPh_3)_4$]/K_2CO_3/$n$$Bu_4NI$ provides an exclusive pathway to the bicyclo[3.2.0] product **8a** from 1,5-bisallenyl compound **6a**. In the course of optimizing the Pd^0-catalyzed [2+2] cycloaddition of bisallenes, we noted the following: 1) no reaction was observed in the absence of K_2CO_3 and $n$$Bu_4NI$ (entry 1, Table 2); 2) on adding only four equivalents of K_2CO_3, the reaction afforded trace amounts of bicyclo[3.2.0] product **8a** as determined by ^{1}H NMR analysis of the crude reaction mixture (entry 2, Table 2); and 3) the reaction failed on using $n$$Bu_4NI$ alone (entry 3, Table 2). After much experimentation, we determined the optimal conditions (entry 4, Table 2). The I^{-1} species in $n$$Bu_4NI$ may act as a ligand facilitating the reductive elimination process.[13] The structure and stereochemistry of **8a** was confirmed by X-ray crystal-structure analysis (Figure 2).[14]

With these optimized conditions in hand, the generality of the Pd^0-catalyzed [2+2] cycloaddition of 1,5-bisallenyl compounds was explored (Table 3). However, compounds **6e**–**6k** with substituents on the proximal side did not give the expected bicyclo[3.2.0] products **8e**–**k** probably because of steric reasons. The formation of other regioisomers was not observed. Polymerization of the starting material may be partially responsible for the relatively low yields.

Furthermore, when X is the chiral L-valine ester, compound **8m** was formed in greater than 99% *ee* (Table 3), which indicates that the reaction proceeded without racemization of the α-amino acid ester. We attempted many

[*] X. Jiang, X. Cheng, Prof. Dr. S. Ma
State Key Laboratory of Organometallic Chemistry
Shanghai Institute of Organic Chemistry
Chinese Academy of Sciences
354 Fenglin Lu, Shanghai 200032 (P.R. China)
Fax: (+86) 21-6416-7510
E-mail: masm@mail.sioc.ac.cn

[**] Financial support from the National Natural Science Foundation of China (20121202, 20423001, and 20332060) and the Shanghai Municipal Committee of Science and Technology are greatly appreciated. We thank Z. Liang in our research group for reproducing the reactions of **6j** in Table 1 and **6c** in Table 3.

Supporting information for this article is available on the WWW under http://www.angewandte.org or from the author.

 © 2006 Wiley-VCH Verlag GmbH & Co. KGaA, Weinheim

Table 1: Thermal [2+2] cycloaddition of 1,5-bisallenyl compounds.[a]

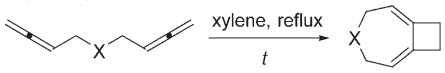

6 7

Bisallene	*t* [h]	Bicyclo[5.2.0]	Yield[b] [%]	Bisallene	*t* [h]	Bicyclo[5.2.0]	Yield[b] [%]
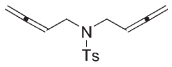 **6a**	24	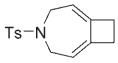 **7a**	43	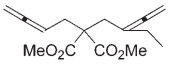 **6g**	10	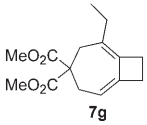 **7g**	56
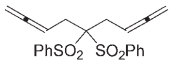 **6b**	3	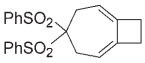 **7b**	61	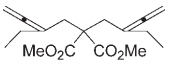 **6h**	24	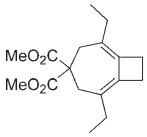 **7h**	70
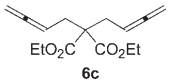 **6c**	46	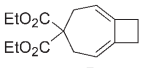 **7c**	38	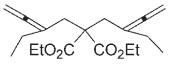 **6i**	6	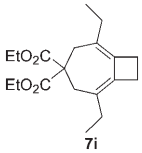 **7i**	69
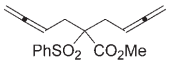 **6d**	8	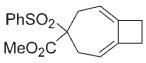 **7d**	61	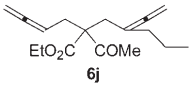 **6j**	5	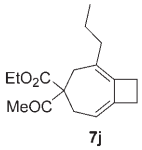 **7j**	70
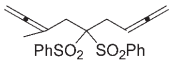 **6e**	1.5	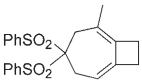 **7e**	69	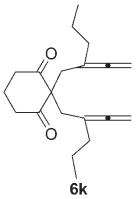 **6k**	0.5	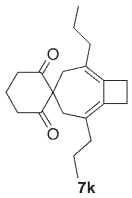 **7k**	78
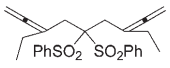 **6f**	1	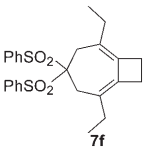 **7f**	74				

[a] Reactions were carried out in xylene (0.04 M), heated to reflux. [b] Yield of isolated products. Ts = toluene-4-sulfonic acid.

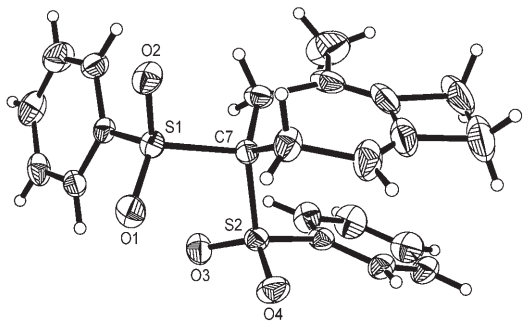

Figure 1. ORTEP representation of **7e** with thermal ellipsoids at the 30% probability level.

reactions to determine the absolute structure of **8m**, and it was found that the methyl ester analogue of **8m** (that is, **8n**)

Table 2: Pd^0-catalyzed [2+2] cycloaddition of 1,5-bisallenyl compounds under different conditions.

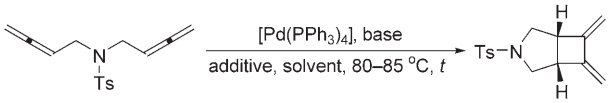

6a **8a**

Entry	$[Pd(PPh_3)_4]$ [mol%]	Base	Additive	Solvent	*t* [h]	Yield of **8a**[a] [%]
1	10	–[b]	–[b]	toluene	8	n.r.
2	10	K_2CO_3 (4 equiv)	–[b]	xylene	4	trace
3	10	–[b]	nBu_4NI (2 equiv)	xylene	10	n.r.
4	**5**	**K_2CO_3 (4 equiv)**	**nBu_4NI (2 equiv)**	**toluene**	**4**	**59**

[a] Yield of isolated product. [b] Without additive. n.r. = no reaction.

 © 2006 Wiley-VCH Verlag GmbH & Co. KGaA, Weinheim

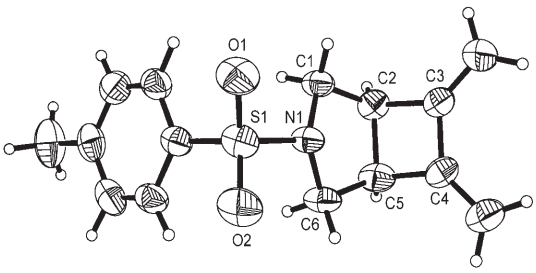

Figure 2. ORTEP representation of **8a** with thermal ellipsoids at the 30% probability level.

Table 3: Pd^0-catalyzed [2+2] cycloaddition of 1,5-bisallenyl compounds.

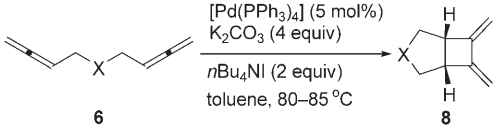

Bisallene	*t* [h]	Bicyclo[3.2.0]	Yield[a] [%]
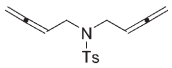 **6a**	4	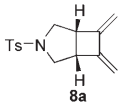 **8a**	59
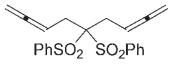 **6b**	4	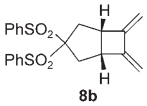 **8b**	62
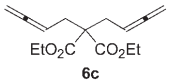 **6c**	19	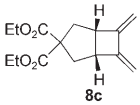 **8c**	45
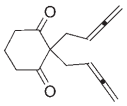 **6l**	8	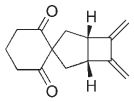 **8l**	54
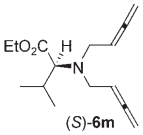 (*S*)-**6m**	5[b]	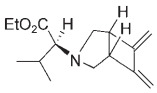 **8m** (>99% ee)	66

[a] Yield of isolated products. [b] 10 mol% of $[Pd(PPh_3)_4]$ was used.

could react with *N*-phenylmaleimide to afford a solid tetracyclic compound **9na** (Scheme 2). The X-ray crystal structure of **9na**[15] led to the assignment of the absolute structures of **8m**, **8n**, and **9na** (Figure 3).

A plausible working model for the highly diastereoselective Pd^0-catalyzed [2+2] cycloaddition of 1,5-bisallenyl compound (*S*)-**6m** is depicted in Scheme 3. The coordination between the Pd atom and the lone pair of electrons of the N atom in the intermediate **10**, along with the requirement of the Pd atom to be distant from the bulkier CO_2Et group, leads to the exclusive formation of **8m**. The inversion of the nitrogen center may be very difficult in this case because of the presence of the bicyclic skeleton.

In summary, we have realized two different [2+2] cycloaddition pathways of 1,5-bisallenyl compounds that result in the formation of two types of bicyclic products **7** and **8** with a single four-membered ring. As a result of the challenge often

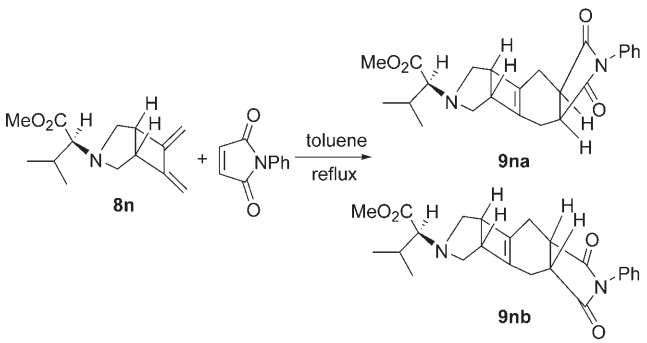

100 % yield, **9na**/**9nb** 100:3
(determined by 300 MHz ^{1}H NMR analysis)

Scheme 2. Diels–Alder reaction of **8n** with *N*-phenylmaleimide.

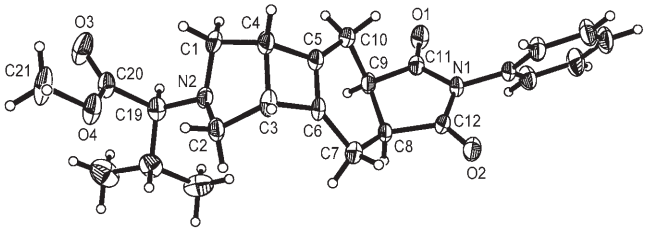

Figure 3. ORTEP representation of **9na** with thermal ellipsoids at the 30% probability level.

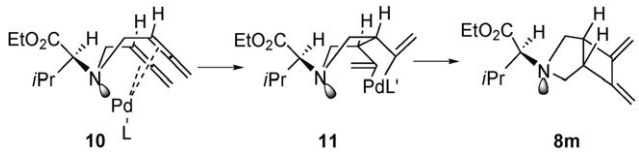

Scheme 3. Proposed working model for the highly diastereoselective formation of **8m**.

encountered in the synthesis of four-membered rings and their biological importance, these reactions may be powerful tools in organic synthesis and medicinal chemistry. Further studies, including the determination of the mechanism of thermal [2+2] cycloadditions of 1,5-bisallenyl compounds and the role of K_2CO_3 and nBu_4NI on the reductive elimination, are being pursued.

Experimental Section

General procedure I: A solution of bisallene **6a** (145 mg, 0.53 mmol) in dry xylene (12 mL) was heated at reflux under Ar for 24 h. After the reaction was complete by TLC (petroleum ether/ethyl acetate 5:1), rotary evaporation followed by flash chromatography on silica gel (petroleum ether/diethyl ether 20:1) afforded 62 mg (43%) of the product **7a**: liquid; ^{1}H NMR (300 MHz, $CDCl_3$): $\delta = 7.68$ (d, $J =$ 8.1 Hz, 2H), 7.21 (d, $J = 8.1$ Hz, 2H), 5.22 (s, 2H), 4.12 (d, $J =$ 2.7 Hz, 4H), 2.39 (s, 3H), 2.28 ppm (s, 4H); ^{13}C NMR (75.4 MHz, $CDCl_3$): $\delta = 143.2$, 142.7, 137.9, 128.8, 127.7, 119.6, 50.7, 26.0, 21.4 ppm; MS (ESI): *m*/*z* (%) 274 ($[M-H]^+$, 100), 275 (M^+, 45), 277 ($[M+Na-H]^+$, 40); IR (neat): $\tilde{\nu} = 2926$, 1710, 1674, 1598, 1495, 1448, 1338, 1161 cm^{-1}; HR-MS (ESI) calcd for $C_{15}H_{16}NO_2S$: $[M-H]^+$ 274.0896; found 274.0890.

 © 2006 Wiley-VCH Verlag GmbH & Co. KGaA, Weinheim

General procedure II: K_2CO_3 (281 mg, 2.04 mmol, 4 equiv) and nBu$_4$NI (369 mg, 1 mmol, 2 equiv)were added to a stirred solution of bisallene **6a** (140 mg, 0.51 mmol) and [Pd(PPh$_3$)$_4$] (27 mg, 0.023 mmol, 5 mol%) in dry toluene (5 mL). The reaction mixture was heated at 80–85 °C for 4 h. After the reaction was complete by TLC (petroleum ether/ethyl acetate 5:1), rotary evaporation followed by flash chromatography on silica gel (petroleum ether/diethyl ether 20:1) afforded 82 mg (59%) of the product **8a**: solid; m.p. 77–79 °C (petroleum ether, ethyl acetate); ^{1}H NMR (300 MHz, $CDCl_3$): $\delta =$ 7.68 (d, $J = 8.1$ Hz, 2H), 7.31 (d, $J = 8.1$ Hz, 2H), 5.21 (s, 2H), 4.79 (s, 2H), 3.62 (d, $J = 9.9$ Hz, 2H), 3.30 (d, $J = 4.5$ Hz, 2H), 2.72 (dd, $J =$ 9.9, 4.5 Hz, 2H), 2.42 ppm (s, 3H); ^{13}C NMR (75.4 MHz, $CDCl_3$): $\delta =$ 149.0, 143.5, 132.1, 129.4, 128.0, 105.5, 53.3, 44.6, 21.5 ppm; MS (EI): m/z (%) 275 ([M]$^+$, 4.41); 91 (100); IR (neat): 2923, 2851, 1459, 1344, 1167 cm^{-1}.

Diels–Alder reaction of [3.2.0]bicyclic compounds with *N*-phenylmaleimide: A solution of **8n** (13 mg, 0.055 mmol) and *N*-phenylmaleimide (19 mg, 0.11 mmol, 2 equiv) in dry toluene (2 mL) was heated at reflux under Ar for 8 h to afford 24 mg (100%) of the product **9n** (**9na**/**9nb** 100:3, determined by ^{1}H NMR analysis); $[\alpha]_D^{20} =$ −20.6 ($c = 1.00$ in $CHCl_3$): solid; m.p. 123–124 °C (petroleum ether/ethyl ether); ^{1}H NMR (300 MHz, $CDCl_3$): $\delta = 7.50$–7.41 (m, 2H), 7.41–7.32 (m, 1H), 7.28 (d, $J = 7.8$ Hz, 2H), 3.67 (s, 3H), 3.30–3.22 (m, 2H), 3.22–3.10 (m, 2H), 2.95 (d, $J = 10.5$ Hz, 1H), 2.80–2.68 (m, 2H), 2.58–2.30 (m, 4H), 2.18–2.04 (m, 2H), 2.10–1.85 (m, 1H), 0.91 (d, $J =$ 6.9 Hz, 3H), 0.87 ppm (d, $J = 6.9$ Hz, 3H); the following data are discernible for the minor isomer **9nb**: $\delta = 3.65$ (s), 0.79 (d, $J = 6.6$ Hz), 0.76 ppm (d, $J = 6.6$ Hz); ^{13}C NMR (75.4 MHz, $CDCl_3$): $\delta =$ 178.88, 178.85, 172.5, 138.4, 132.0, 129.1, 128.4, 126.3, 70.0, 50.5, 50.3, 46.6, 46.0, 44.3, 37.8, 37.7, 28.0, 20.7, 20.5, 19.6, 19.2 ppm; MS (ESI): m/z (%) 409 ([M+H]$^+$, 100), 441 ([M+Na]$^+$, 30); IR (neat): $\tilde{\nu} =$ 2924, 2854, 1714, 1500, 1457, 1379, 1171, 1150 cm^{-1}; HR-MS (MALDI/2,5-dihydroxybenzoic acid matrix) calcd for $C_{24}H_{29}N_2O_4$ [M+H]$^+$: 409.2122; found: 409.2129.

Received: July 17, 2006
Revised: September 9, 2006
Published online: November 3, 2006

Keywords: bicyclic compounds · bisallenes · cycloaddition · cyclobutanes · palladium

[1] a) J. E. Baldwin in *Comprehensive Organic Synthesis*, *Vol. 5* (Eds.: B. M. Trost, I. Fleming), Pergamon, Oxford, **1991**, pp. 63–84; b) M. T. Crimmins in *Comprehensive Organic Synthesis*, *Vol. 5* (Eds.: B. M. Trost, I. Fleming), Pergamon, Oxford, **1991**, pp. 123–150; c) Z. J. Rappoport, J. F. Liebman, *The Chemistry of Cyclobutanes*, Wiley, **2005**; d) *Advances in Cycloaddition*, *Vols. 1–6*, JAI Press, Greenwich (CT), **1988–1999**; e) N. E. Schore, *Chem. Rev.* **1988**, *88*, 1081; f) M. Lautens, W. Klute, W. Tam, *Chem. Rev.* **1996**, *96*, 59.

[2] a) S. Beckman, H. Geiger in *Methoden der Organischen Chemie (Houben–Weyl)*, *Vol. 4* (Ed.: E. Müller), Thieme, Stuttgart, **1971**, pp. 449–478; b) R. M. Ortuno, A. G. Moglioni, G. Y. Moltrasio, *Curr. Org. Chem.* **2005**, *9*, 237.

[3] For reviews of the [2+2] cycloaddition of allenes, see: a) D. J. Pasto, *Tetrahedron* **1984**, *40*, 2805; b) M. Murakami, T. Matsuda in *Modern Allene Chemistry*; *Vol. 2* (Eds.: N. Krause, A. S. K. Hashmi), Wiley-VCH, Weinheim, **2004**, 727–815; c) S. Ma, *Chem. Rev.* **2005**, *105*, 2829.

[4] a) A. Padwa, M. A. Filipkowski, M. Meske, S. H. Watterson, Z. Ni, *J. Am. Chem. Soc.* **1993**, *115*, 3776; b) A. Padwa, M. Meske, S. S. Murphree, S. H. Watterson, Z. Ni, *J. Am. Chem. Soc.* **1995**, *117*, 7071; c) B. Alcaide, P. Almendros, C. Aragoncillo, *Org. Lett.* **2003**, *5*, 3795; d) H. Ohno, T. Mizutani, Y. Kadoh, K. Miyamura, T. Tanaka, *Angew. Chem.* **2005**, *117*, 5243; *Angew. Chem. Int. Ed.* **2005**, *44*, 5113.

[5] a) D. Becker, Z. Harel, D. Birnbaum, *J. Chem. Soc. Chem. Commun.* **1975**, *377*; D. Becker, Z. Harel, M. Nagler, A. Gillon, *J. Org. Chem.* **1982**, *47*, 3297; D. Becker, N. H. Y. Sahali, *Tetrahedron Lett.* **1989**, *30*, 4429; b) W. G. Dauben, V. P. Rocco, G. Shapiro, *J. Org. Chem.* **1985**, *50*, 3155; c) E. M. Carreira, C. A. Hastings, M. S. Shepard, L. A. Yerkey, *J. Am. Chem. Soc.* **1994**, *116*, 6622; M. S. Shepard, E. M. Carreira, *J. Am. Chem. Soc.* **1997**, *119*, 2597.

[6] a) Q. Shen, G. B. Hammond, *J. Am. Chem. Soc.* **2002**, *124*, 6534; b) K. M. Brummond, D. Chen, *Org. Lett.* **2005**, *7*, 3473; c) C. H. Oh, A. K. Gupta, D. I. Park, N. Kim, *Chem. Commun.* **2005**, 5670; for theoretical studies of these reactions, see: B. Engels, M. Hanrath, *J. Am. Chem. Soc.* **1998**, *120*, 6356; P. G. Wenthold, M. A. Lipton, *J. Am. Chem. Soc.* **2000**, *122*, 9265; P. W. Musch, B. Engels, *J. Am. Chem. Soc.* **2001**, *123*, 5557.

[7] a) L. Skattebøl, S. Solomon, *J. Am. Chem. Soc.* **1965**, *87*, 4506; b) K. M. Nicholas, *J. Am. Chem. Soc.* **1975**, *97*, 3255; c) P. J. Garratt, S. B. Neoh, *J. Org. Chem.* **1979**, *44*, 2667; d) F. Toda, K. Tdnaka, I. Sano, T. Isozaki, *Angew. Chem.* **1994**, *106*, 1856; *Angew. Chem. Int. Ed. Engl.* **1994**, *33*, 1757; e) T. Shimizu, K. Sakamaki, N. Kamigata, *Tetrahedron Lett.* **1997**, *38*, 8529; f) T. Shimizu, K. Sakamaki, D. Miyasaka, N. Kamigata, *J. Org. Chem.* **2000**, *65*, 1721; g) S. Saito, K. Hirayama, C. Kabuto, Y. Yamamoto, *J. Am. Chem. Soc.* **2000**, *122*, 10776; for the Pd-catalyzed formation of four-membered products from an intramolecular coupling reaction starting from bisallenes and Bu$_3$SnH or Bu$_3$SnMBu$_3$ (M = Sn or Ge), see: h) S.-K. Kang, T.-G. Baik, A. N. Kulak, Y.-H. Ha, Y. Lim, J. Park, *J. Am. Chem. Soc.* **2000**, *122*, 11529; i) Y.-T. Hong, S.-K. Yoon, S.-K. Kang, C.-M. Yu, *Eur. J. Org. Chem.* **2004**, 4628.

[8] For benzoannulation of 1,4-bisallenes, see: P. Aubert, B. Princet, J. Pornet, *Synth. Commun.* **1997**, *27*, 2615; S. Kitagaki, Y. Okumura, C. Mukai, *Tetrahedron Lett.* **2006**, *47*, 1849.

[9] S. Ma, P. Lu, L. Lu, H. Hou, J. Wei, Q. He, Z. Gu, X. Jiang, X. Jin, *Angew. Chem.* **2005**, *117*, 5409; *Angew. Chem. Int. Ed.* **2005**, *44*, 5275.

[10] Crystal data for compound **7e**: $C_{22}H_{22}O_4S_2$, $M_r = 414.52$, monoclinic, space group $P2(1)/c$, $a = 13.4605(12)$, $b = 9.1336(8)$, $c =$ 16.4267(15) Å, $\alpha = 90$, $\beta = 93.632(2)$, $\gamma = 90°$, $V = 2015.5(3)$ Å^3, $T = 293(2)$ K, $Z = 4$, final R indices [$I > 2\sigma(I)$], $R1 = 0.0525$, $wR2 = 0.1323$, R indices (all data), $R1 = 0.0726$, $wR2 = 0.1402$, , reflections collected/unique: 11518/4362 ($R_{int} = 0.0572$).

[11] a) J. Tsuji, *Transition Metal Reagents and Catalysts*, Wiley, Chichester, **2000**; b) *Handbook of Organopalladium Chemistry for Organic Synthesis* (Ed.: E. Negishi), Wiley-Interscience, **2002**; J. Tsuji, *Palladium Reagents and Catalysts*, Wiley, Chichester, **2004**; *Palladium in Organic Synthesis* (Ed.: J. Tsuji), Springer, **2005**; c) *Modern Rhodium-Catalyzed Organic Reactions* (Ed.: P. A. Evans), Wiley-VCH, Weinheim, **2005**; d) *Ruthenium in Organic Synthesis* (Ed.: S.-I. Murahashi), Wiley-VCH, Weinheim, **2004**; e) *Modern Organonickel Chemistry* (Ed.: Y. Tamaru), Wiley-VCH, Weinheim, **2004**; f) C. Aubert, O. Buisine, M. Malacria, *Chem. Rev.* **2002**, *102*, 813; g) Ir: T. Shibata, T. Fujimoto, K. Yokota, K. Takagi, *J. Am. Chem. Soc.* **2004**, *126*, 8382.

[12] a) M. Lautens, W. Klute, W. Tam, *Chem. Rev.* **1996**, *96*, 49; N. E. Schore, *Chem. Rev.* **1988**, *88*, 1081; b) S. Ohtsuka, K. Mori, F. Imaizumi *J. Am. Chem. Soc.* **1965**, *85*, 3017; c) S. Ohtsuka, K. Mori, T. Suminoe, F. Imaizumi, *Eur. Polym. J. Chem.* **1967**, *3*, 73; d) S. Ohtsuka, A. Nakamura, K. Tani, S. Ueda, *Tetrahedron Lett.* **1969**, *10*, 297; e) F. W. Hoover, R. V. Lindsey, Jr. *J. Org. Chem.* **1969**, *34*, 3051; f) R. J. De Pasquale, *J. Organomet. Chem.* **1971**, *32*, 381; g) S. Ohtsuka, K. Tani, T. Yamagata, *J. Chem. Soc. Dalton Trans.* **1973**, 2491; h) D. J. Pasto, N.-Z. Huang, C. W. Eigenbrot, *J. Am. Chem. Soc.* **1985**, *107*, 3160; i) D. J. Pasto, N.-Z.

 © 2006 Wiley-VCH Verlag GmbH & Co. KGaA, Weinheim

Huang, C. W. Eigenbrot, *Organometallics* **1985**, *4*, 1386; j) K. Takagi, I. Tomita, T. Endo, *Macromolecules* **1998**, *31*, 6741, and references therein; k) G. Ingrosso, M. Iqbal, R. Rossi, L. Porri, *Chim. Ind.* **1973**, *55*, 540; l) M. Iyoda, S. Tanaka, M. Nose, M. Oda, *J. Chem. Soc. Chem. Commun.* **1983**, 1058; M. Iyoda, S. Tanaka, H. Otani, M. Nose, M. Oda, *J. Am. Chem. Soc.* **1988**, *110*, 8494; M. Iyoda, Y. Kuwatani, M. Oda, *J. Am. Chem. Soc.* **1989**, *111*, 3761; m) K. C. Chao, D. K. Rayabarapu, C.-C. Wang, C.-H. Cheng, *J. Org. Chem.* **2001**, *66*, 8804.

[13] A. Togni, L. M. Venanzi, *Angew. Chem.* **1994**, *106*, 517; *Angew. Chem. Int. Ed. Engl.* **1994**, *33*, 497; .

[14] Crystal data for compound **8a**: $C_{15}H_{17}NO_2S$, $M_r = 275.36$, monoclinic, space group $P2(1)/n$, $a = 8.2755(12)$, $b = 10.8834(17)$, $c = 16.437(2)$ Å, $\alpha = 90$, $\beta = 101.394(3)$, $\gamma = 90°$, $V = 1451.3(4)$ Å^3, $T = 293(2)$ K, $Z = 4$, final R indices $[I > 2\sigma(I)]$, $R1 = 0.0455$, $wR2 = 0.0731$, R indices (all data), $R1 = 0.1847$, $wR2 = 0.0991$, reflections collected/unique: 8406/3162 (Rint = 0.0989).

[15] Crystal data for compound **9na**: $C_{24}H_{28}N_2O_4$, $M_r = 408.48$, monoclinic, space group $P2(1)$, $a = 10.7399$ (18), $b = 5.7808$ (9), $c = 17.346(3)$ Å, $\alpha = 90$, $\beta = 97.128(3)$, $\gamma = 90°$, $V = 1068.6(3)$ Å^3, $T = 293$ (2) K, $Z = 2$, final R indices $[I > 2\sigma(I)]$, $R1 = 0.0543$, $wR2 = 0.1196$, R indices (all data), $R1 = 0.0675$, $wR2 = 0.1245$, reflections collected/unique: 6334/2563 (R(int) = 0.1458). CCDC-291779 (**7e**), CCDC-291780 (**8a**), CCDC-60887 (**9na**) contains the supplementary crystallographic data for this paper. These data can be obtained free of charge from the Cambridge Crystallographic Data Centre via www.ccdc.cam.ac.uk/data_request/cif.

 © 2006 Wiley-VCH Verlag GmbH & Co. KGaA, Weinheim

Zeolites

DOI: 10.1002/anie.200603027

Synthesis and Characterization of the All-Silica Pure Polymorph C and an Enriched Polymorph B Intergrowth of Zeolite Beta**

Ángel Cantín, Avelino Corma, María J. Díaz-Cabañas, Jose L. Jordá, Manuel Moliner, and Fernando Rey*

Zeolite beta was first reported by Mobil Oil in 1967 and was the first example of a tridirectional large-pore zeolite with low aluminum content.[1] This work initiated further research in the synthesis of zeolitic structures with large and extralarge pores.[2–6] The structure of zeolite beta was only determined in 1988 by Treacy and Newsam,[7] as an intergrowth of two closely related polymorphs, named polymorphs A and B, which are present in a ratio of 60:40. A third polymorph (named polymorph C) was also proposed, which, in contrast to polymorphs A and B, contains double 4-ring (D4R) cages as secondary building units and a 3D intersecting channel system formed by straight 12-ring pores (see Supporting Information). This hypothetical material remained elusive until recently when Conradsson et al. and our group reported the synthesis of pure polymorph C of zeolite beta (International Zeolite Association (IZA) code: BEC) as the pure germanate (FOS-5)[8] and as a silicogermanate (ITQ-17).[9] Later, pure silica with the polymorph C structure was detected by high-resolution TEM as an overgrowth on zeolite beta.[10] However, the X-ray diffraction pattern of this material, named ITQ-14, was similar to that of pure silica zeolite beta, as polymorph C appears as a minor impurity in the beta intergrowth.[11]

The preparation of siliceous and silicoaluminate analogues of pure polymorph C of zeolite beta will open new possibilities for applications.[12] It will also allow us to rationalize differences in stability between this polymorph and zeolite beta.[13]

We show herein that it is possible to obtain the all-silica, pure polymorph C of zeolite beta by using the cation 4,4-dimethyl-4-azoniatricyclo[5.2.2.$0^{2,6}$]undec-8-ene as a structure-directing agent (SDA) and that the presence of K^+ ions and relatively high ratios of OH^- ions to silicon atoms greatly favor the crystallization of the pure silica polymorph C structure. Furthermore, depending on the synthesis conditions, this SDA allows the production of a material that corresponds to a new intergrowth of zeolite beta, which is enriched in polymorph B.

In a first set of synthesis experiments, it was found that the crystallized product consisted of zeolite beta with 20% polymorph C. Attempts to increase the yield of polymorph C in this mixture gave variable results depending on the batch of the SDA used for the synthesis; some reactions gave pure polymorph C. Careful analyses of all the experiments undertaken showed that K^+ ions were present in the synthesis gel, and that the synthesis gel containing the most K^+ ions yielded the material with the highest proportion of polymorph C. The K^+ ions were not deliberately introduced, but originated from the $KHCO_3$ used to deprotonate the secondary amine during its quaternization by ICH_3 (see Supporting Information). At this point, careful recrystallization of the SDA was performed, and in all subsequent cases, the absence of K^+ ions was specifically verified.

A systematic study of the SDA:K^+ ratio was performed by adding controlled amounts of K^+ ions to the syntheses. The parameters screened by high-throughput (HT) synthesis were the ratios of SDA:Si, K^+:Si, H_2O:Si, OH^-:Si, and F^- (from NH_4F):Si, temperature, and time of crystallization.[14] The phases identified by powder X-ray diffraction are given in Figure 1. Pure polymorph C was obtained when K^+ ions were present in the synthesis gel and crystallization was carried out at relatively high ratios of OH^-:Si. It is noticeable that polymorph C always formed with an impurity, which was

[*] Dr. Á. Cantín, Prof. A. Corma, Dr. M. J. Díaz-Cabañas, Dr. J. L. Jordá, M. Moliner, Dr. F. Rey
Instituto de Tecnología Química (CSIC-UPV)
Universidad Politécnica de Valencia
Avda. de los Naranjos s/n. 46022-Valencia (Spain)
Fax: (+34) 96-387-7809
E-mail: acorma@itq.upv.es

[**] J.L.J. thanks the Spanish MEC for a Juan de la Cierva contract, and M.M. CSIC for an I3P grant. The authors thank the Spanish CICYT for financial support (MAT2003-07945-C02-01 and MAT2003-07769-C02-01).

Supporting information for this article is available on the WWW under http://www.angewandte.org or from the author.

 © 2006 Wiley-VCH Verlag GmbH & Co. KGaA, Weinheim

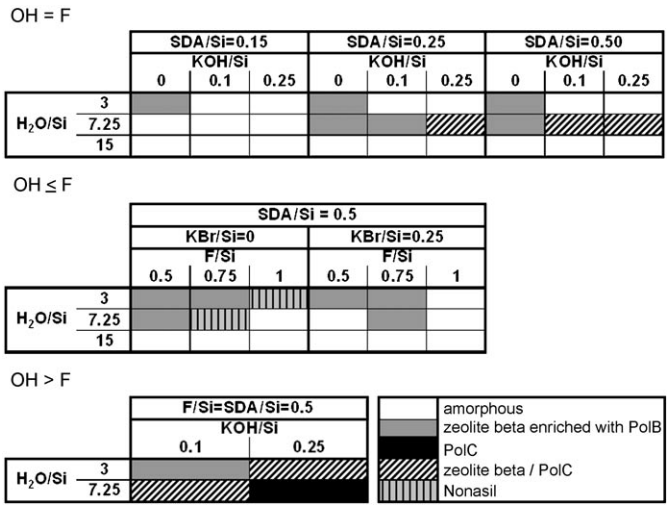

Figure 1. Phase diagram obtained by means of HT synthesis. The crystallization conditions for this set of data were 175 °C and 14 d. PolB/C = polymorph B/C. The SDA was introduced in the hydroxide form. $[OH^-] = [SDA] + [KOH]$.

identified as K_2SiF_6 by X-ray diffraction and ^{19}F magic-angle spinning (MAS) NMR spectroscopy. The impurity was easily removed by washing the product with boiling water for 15 min, and the remaining solid was the all-silica form of pure polymorph C of zeolite beta.

Rietveld analysis of the X-ray diffraction pattern (Figure 2)[15] unambiguously confirms that the all-silica polymorph C of zeolite beta was synthesized. The tetragonal unit cell ($P4_2/mmc$) of $a = 12.6241$ and $c = 13.1255$ Å is consistent with that for the germanium-containing material ITQ-17,[9] but the superlattice reported for FOS-5 is not observed.[8] This point is confirmed by the ^{29}Si MAS NMR spectrum of the calcined sample, which shows three very narrow resonances at

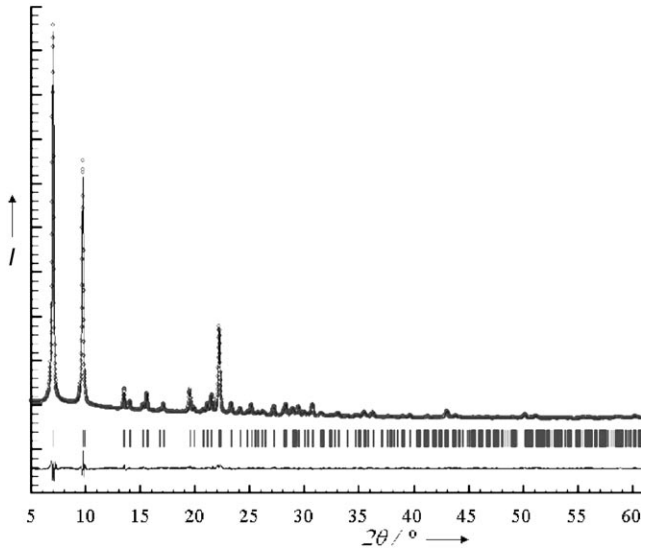

Figure 2. Observed (circles) and calculated (line) powder X-ray diffraction patterns of polymorph C of zeolite beta (top), and a difference profile (bottom). The short bars below the patterns give the positions of the Bragg reflections.

−110, −112, and −116 ppm that correspond to the three crystallographic positions described for ITQ-17 and not to the nine sites expected for FOS-5. Moreover, the ^{19}F MAS NMR spectrum of the as-synthesized material shows a single signal at −38.3 ppm (see Supporting Information). This resonance is assigned to the presence of F^- ions encaged within D4R units,[17] which are uniquely present in the C polymorph of those described for the beta family.

When the syntheses were carried out in absence of K^+ ions or at lower ratios of OH^-:Si, a new material that closely resembles zeolite beta was obtained. This new zeolite is a form of zeolite beta enriched with polymorph B. Simulation of the diffraction patterns of zeolite beta with different ratios of polymorphs A:B, using the program DIFFaX,[18] indicates that the material is formed by an intergrowth ratio (A:B) of 35:65, instead the 60:40 ratio present in zeolite beta (see Supporting Information). During the growth of polymorph B-enriched zeolite beta, some polymorph C was frequently detected under all the synthesis conditions studied. Indeed, a kinetic study shows that the first phase observed is the polymorph B-enriched zeolite, which evolves towards the polymorph C structure.

This observation has been further confirmed by carrying out an experiment in which polymorph B-enriched zeolite was used as the silica source for the synthesis. The initial zeolite transformed into polymorph C, which indicates that polymorph C is thermodynamically more stable than polymorph B of zeolite beta under these conditions. Therefore, the main conclusions arising from the HT syntheses are: 1) The all-silica polymorph C of zeolite beta can be synthesized as a pure phase. 2) A new zeolite closely related to zeolite beta, but enriched in polymorph B has been synthesized. 3) The presence of K^+ ions and high OH^-:Si ratios in the synthesis gel strongly favors the crystallization of the pure-silica polymorph C of zeolite beta.

The role of K^+ ions in the crystallization media was investigated on the basis of two different hypotheses. In the first hypothesis, K^+ ions are incorporated into the final polymorph C because of the relatively small size of the K^+ ion with respect to the organic SDA. Thus, more positive charges are incorporated with a corresponding increase in the number of F^- counterions. A higher number of F^- ions should favor the structure with the most D4R units,[19] which is polymorph C. This hypothesis was easily tested by analyzing the amount of K^+ ions incorporated into polymorph C. The results showed that K^+ ions are found in the pure polymorph C only at trace levels, and therefore, this hypothesis was rejected as an explanation of the role of K^+ ions in the crystallization of the polymorph C structure.

In the second hypothesis, we considered that owing to the formation of K_2SiF_6, which was detected in conjunction with polymorph C of zeolite beta, the concentration of F^- ions during crystallization is strongly reduced with respect to those of syntheses performed in the absence of K^+ ions. In principle, this effect should stop or at least strongly decrease the crystallization rate of the zeolite, as a large fraction of the mobilizing agent (F^- ion) is removed from the synthesis media. However, we also found that the synthesis of polymorph C requires high ratios of OH^-:Si (Figure 1),

 © 2006 Wiley-VCH Verlag GmbH & Co. KGaA, Weinheim

which suggests that the initial mobilizing agent of the silica is the OH^- ion rather than the F^- ion.

Consequently, a picture of the crystallization of polymorph C of zeolite beta could be as follows. In the first stage, fluorosilicate species formed from the amorphous silica evolve towards the polymorph B-enriched zeolite. The zeolite then accommodates F^- ions in high concentration in the $[4^15^4]$ cages, as it contains 12 of such units per 64 SiO_2 groups. These anions provide the possibility of compensating the occluded organic cations and also introduce flexibility in establishing the pairs of charge-compensated organic-cation/F^--anion pairs within the structure. At this stage of the process, no K_2SiF_6 was detected in our experiments. The transformation of the polymorph B-enriched zeolite beta into polymorph C of zeolite beta is accompanied by the formation of K_2SiF_6 (note that a small quantity of this salt implies a large consumption of F^- ions from the synthesis gel). This observation suggests that polymorph C grows in media that are defective in ions with respect to the synthesis gel, but crystallizes in a fluoride-buffered medium produced by the presence of K_2SiF_6. If this is the case, shifting the equilibrium constant of SiF_6^{2-} should not produce polymorph C of zeolite beta. This hypothesis was supported by experiments in which Na^+ ions were added instead of K^+ ions. Na_2SiF_6 is much less soluble than K_2SiF_6, and therefore, no polymorph C was formed.

In conclusion, we have shown that it is now possible to synthesize the all-silica pure polymorph C of zeolite beta. A new beta-type material enriched with polymorph B has also been synthesized, and this material evolves to form polymorph C with time. Polymorph C has been obtained by using an organic SDA in the presence of K^+ ions. A hypothesis has been put forward to explain the role of the K^+ ions. We propose that OH^- ions are the silica-mobilizing agents and that a small but continuous supply of F^- ions allows the synthesis of the all-silica polymorph C of zeolite beta.

Experimental Section

The steps involved in the synthesis of the SDA are presented as Supporting Information. The general gel composition was SiO_2:*x* SDA:*y* KOH:*z* NH_4F:*w* H_2O, and the synthesis parameters studied were the values of *x*, *y*, *z*, and *w*. The synthesis gel was prepared by mixing the silica source with alkaline solutions of the SDA and KOH. When the mixture was homogeneous, a solution of aqueous NH_4F was added to give a thick gel. This gel was transferred to teflon-lined stainless-steel autoclaves, which were heated at different crystallization temperatures for different periods of time. The solids were recovered by filtration, extensively washed with boiling water, and dried at 373 K overnight.

A typical synthesis of the all-silica polymorph C of zeolite beta is given in the Supporting Information.

Received: July 27, 2006
Published online: October 30, 2006

Keywords: crystal growth · porous materials · silicates · sol–gel processes · zeolites

[1] R. L. Wadlinger, G. T. Kerr, E. J. Rosinski, US Pat. No 3308069, **1967**, Mobil Oil Corporation.
[2] L. A. Villaescusa, P. A. Barret, M. A. Camblor, *Angew. Chem.* **1999**, *111*, 2164–2167; *Angew. Chem. Int. Ed.* **1999**, *38*, 1997–2000.
[3] A. Corma, M. J. Diaz-Cabañas, J. Martinez-Triguero, F. Rey, J. Rius, *Nature* **2002**, *418*, 514–517.
[4] A. Corma, M. J. Diaz-Cabañas, F. Rey, S. Nicolopoulus, K. Boulahya, *Chem. Commun.* **2004**, 1356–1357.
[5] J. L. Paillaud, B. Harbuzaru, J. Patarin, N. Bats. *Science* **2004**, *304*, 990–992.
[6] D. L. Dorset, G. J. Kennedy, K. G. Strohmaier, M. J. Diaz-Cabañas, F. Rey, A. Corma, *J. Am. Chem. Soc.* **2006**, *128*, 8862–8867.
[7] M. M. J. Treacy, J. M. Newsam, *Nature* **1988**, *332*, 249–251.
[8] T. Conradsson, M. S. Dadachov, X. D. Zou, *Microporous Mesoporous Mater.* **2000**, *41*, 183–191.
[9] A. Corma, M. T. Navarro, F. Rey, J. Rius, S. Valencia, *Angew. Chem.* **2001**, *113*, 2337–2340; *Angew. Chem. Int. Ed.* **2001**, *40*, 2277–2280.
[10] Z. Liu, T. Ohsuna, O. Terasaki, M. A. Camblor, M. J. Diaz-Cabañas, K. Hiraga, *J. Am. Chem. Soc.* **2001**, *123*, 5370–5371.
[11] M. A. Camblor, P. A. Barret, M. J. Díaz-Cabañas, L. A. Villaescusa, M. Puche, T. Boix, E. Perez, H. Koller, *Microporous Mesoporous Mater.* **2001**, *48*, 11–22.
[12] M. E. Davis, *Nature* **2002**, *417*, 813–821.
[13] O. Li, A. Navrotsky, F. Rey, A. Corma, *Microporous Mesoporous Mater.* **2003**, *59*, 177–183.
[14] A. Corma, M. J. Diaz-Cabañas, M. Moliner, C. Martinez, *J. Catal.* **2006**, *241*, 312–318.
[15] Crystal data: SiO_2, tetragonal, $P4_2/mmc$, $a = 12.6241(5)$, $c = 13.1255(6)$ Å, $V = 2091.79(16)$ Å^3, $Z = 32$. The intensity data were collected on an X'Pert Philips diffractometer using $Cu_{K\alpha1,2}$ radiation ($\lambda_1 = 1.5406$, $\lambda_2 = 1.5444$ Å) at 303 K in a Bragg–Brentano geometry (tube voltage and intensity: 45 kV and 40 mA; divergence slit: fixed (1/16); scan range (2θ): 3–75°; step size (2θ): 0.017°, time per step: 600 s). The structure was refined using the Rietveld method with the FullProf program.[16] $R_{wp} = 0.09$, $R_{exp} = 0.05$, $\chi^2 = 3.24$, $R_B = 0.04$, $R_F = 0.06$. Further details of the crystal-structure investigation may be obtained from the Fachinformationszentrum Karlsruhe, 76344 Eggenstein-Leopoldshafen, Germany (fax: (+49) 7247-808-666; e-mail: crysdata@fiz-karlsruhe.de) on quoting the deposition number CSD-416768.
[16] J. Rodriguez-Carvajal, FullProf, version 3.30, Laboratoire Léon Brillouin (LLB), **2005**.
[17] P. Caullet, J. L. Guth, J. Hazm, J. M. Lamblin, *Eur. J. Solid State Inorg. Chem.* **1991**, *28*, 359.
[18] M. M. J. Treacy, M. W. Deem, J. M. Newsam, DIFFaX: A computer program for calculating diffraction from faulted crystals, **1997**.
[19] P. Caullet, J.-L. Paillaud, A. Simon-Masseron, M. Soulard, J. Patarin, *C. R. Chim.* **2005**, *8*, 245–266.

 © 2006 Wiley-VCH Verlag GmbH & Co. KGaA, Weinheim

Biotransformations

DOI: 10.1002/anie.200603060

Regio- and Chemoselective Enzymatic N-Oxygenation In Vivo, In Vitro, and in Flow**

*Robert Winkler, Martin E. A. Richter, Uwe Knüpfer, Dirk Merten, and Christian Hertweck**

The use of oxygenases in biotransformations can expand vastly the repertoire of synthetic methods.[1] A hallmark of these enzymes is their exquisite specificity and their application under environmentally friendly and technically safe conditions.[2–4] However, the use of these biocatalysts may be restricted by the need for cofactor recycling,[5] which can be circumvented by whole-cell biotransformations.[1] The most notable success of oxygenases has come with the oxygenation of nonactivated carbon or the regioselective oxidation of polyhydroxy compounds.[1]

Considering the breadth of biotransformations available, it is remarkable that enzymes catalyzing the selective oxidation of amino groups are only little explored. To date, only two genuine nitro-group-forming N-oxygenases have been identified. Aminopyrrolnitrin N-oxygenase (PrnD) is involved in pyrrolnitrin biosynthesis in *Pseudomonas fluorescens*, and belongs to the Rieske-type oxygenases.[6] In contrast, *para*-aminobenzoate N-oxygenase (AurF) from *Streptomyces thioluteus* represents an unparalleled enzyme that does not show any sequence similarity to known oxygenases.[7] This unusual biocatalyst transforms *para*-aminobenzoic acid (PABA) into *para*-nitrobenzoic acid (PNBA), the rare aureothin polyketide synthase starter unit (Scheme 1).[7,8] Recent in vivo studies coupled to an "at-line" liquid chromatographic (LC) analysis revealed that the oxygenation reaction occurs stepwise via hydroxylamine and, most probably, nitroso intermediates.[9,10]

With the intention of exploring the synthetic potential of AurF, we have addressed the scope of this unique oxygenase, and its chemo- and regioselectivity, and have established an in vitro N-oxygenation method that circumvents the need for cumbersome cofactor regeneration. We first carried out a comparative study in a validated whole-cell approach using the geometrical isomers of aminobenzoate. While AurF readily transforms PABA into PNBA, neither of the two

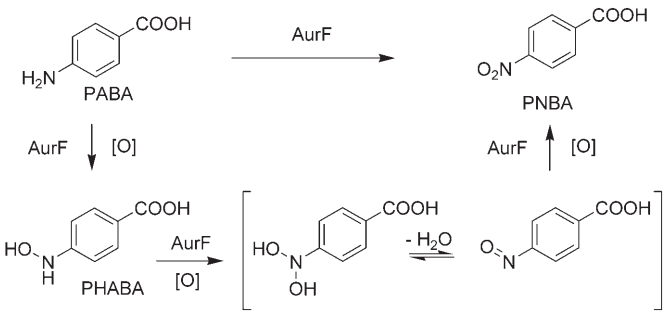

Scheme 1. Proposed mechanism of N-oxygenation by AurF. PHABA = *para*-(hydroxyamino)benzoic acid.

isomers, *ortho*- and *meta*-aminobenzoic acid, was oxygenated (Scheme 2, entries B and C; Figure 1). This result clearly

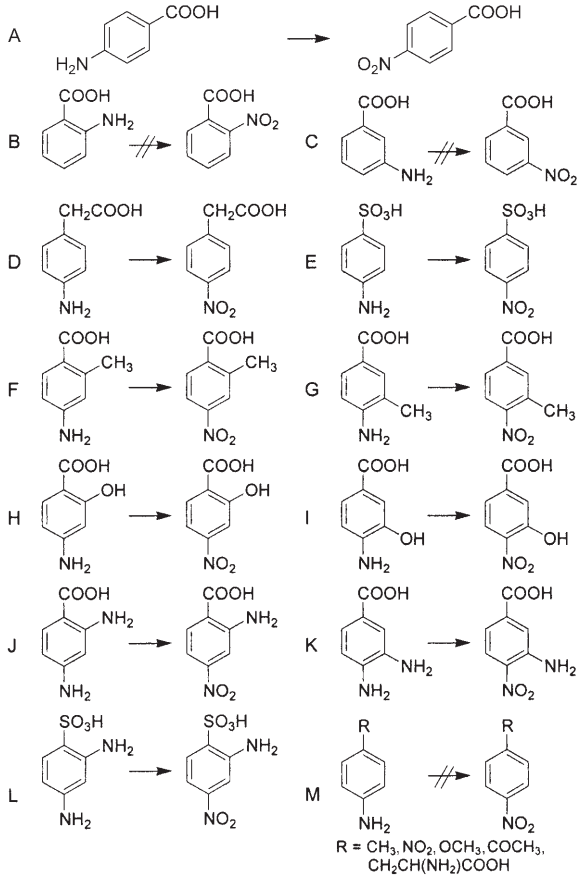

Scheme 2. Substrate specificity of AurF.

indicates a high *para* regioselectivity of AurF. Most PABA analogues substituted at the carboxy moiety with various substituents, such as methoxy (*para*-anisidine), acetyl (*para*-aminoacetophenone), alaninyl (*para*-amino-L-phenylalanine), and methyl (*para*-toluidine), are not transformed (Scheme 2, entry M). However, AurF also accepts *para*-aminophenyl acetic acid and *para*-aminophenyl sulfonic acid as substrates and converts them into *para*-nitrophenyl acetic acid and *para*-nitrophenyl sulfonic acid, respectively (Scheme 2, entries D and E). Hence, it can be concluded

[*] R. Winkler, M. E. A. Richter, U. Knüpfer, Prof. Dr. C. Hertweck
Abteilung Biomolekulare Chemie
Leibniz-Institut für Naturstoff-Forschung und Infektionsbiologie, HKI
Beutenbergstrasse 11a, 07745 Jena (Germany)
Fax: (+49) 3641-656-705
E-mail: Christian.Hertweck@hki-jena.de
Dr. D. Merten, Prof. Dr. C. Hertweck
Friedrich-Schiller-Universität Jena
07745 Jena (Germany)

[**] This project has been generously funded by the DFG.

Supporting information for this article is available on the WWW under http://www.angewandte.org or from the author.

InterScience
© 2006 Wiley-VCH Verlag GmbH & Co. KGaA, Weinheim

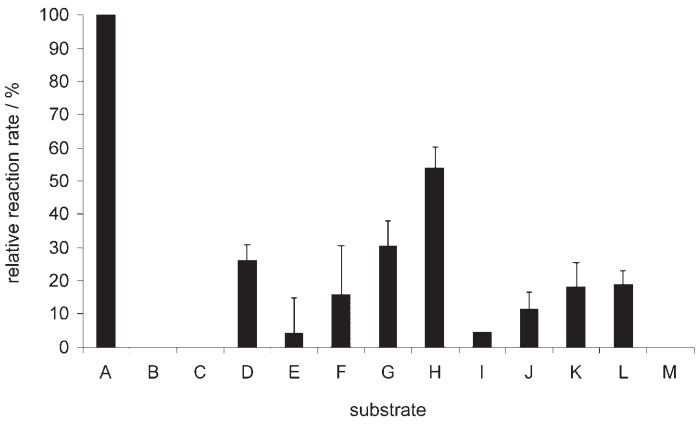

Figure 1. Relative reaction rates (with reference to PABA (substrate A)).

that the enzyme allows only some degree of variation at the carboxy group. Comparing these probes, it is notable that all converted substrates bear an acidic group adjacent to the aromatic ring. This fact strongly suggests that the presence of an acidic residue is important for substrate binding.[11]

To investigate the impact of additional ring substitutions, substrates with extra methyl and hydroxy groups in either the *ortho* or *meta* position to the carboxy group were administered. All the tested monosubstituted PABA derivatives resulted in the corresponding nitro product (Scheme 2, entries F–I)). Acceptance of both methyl and hydroxy substituents on either the *ortho* or *meta* position is amazing, as the first accounts for a $+I$ effect and the latter for a $-I$ effect. Apparently some variation of the electrochemical state of the substrate seems to be tolerated. The substrate-binding site allows for a certain range of flexibility, which was already indicated by the successful transformation of *para*-aminophenyl acetic acid.

The absent oxygenation of 3-amino-4-methylbenzoic acid and 3-amino-5-methylbenzoic acid (not shown) further supports the strict regioselectivity of AurF in regard to the amino group, whilst the failure in oxidizing 4-amino-2,3,5,6-tetrafluorobenzoic acid (not shown) could be a result of exaggerated electron withdrawal from the ring system, or may be caused by space constraints at the active site.

To exploit the limited substrate tolerance in conjunction with the strict *para* specificity, the diamino surrogates 2,4-diaminobenzoic acid, 3,4-diaminobenzoic acid, and 2,4-diaminobenzenesulfonic acid were probed. Strikingly, all transformations resulted exclusively in products with a nitro group at the *para* position and unaltered amino groups at the *meta* and *ortho* positions (Scheme 2, entries J–L). Such strict site-directed N-oxygenations are unprecedented and have not been achieved by standard synthetic protocols.

To establish a convenient in vitro N-oxygenation method for this unique biocatalyst, various attempts to yield pure enzyme were undertaken. Initial trials to overexpress native or 6×His-tagged protein in *S. lividans* or *Escherichia coli* failed. However, soluble MalE–AurF fusion protein was produced at high levels in *E. coli*, and in vivo tests proved the catalytic activity of the chimeric enzyme. Large amounts of the enzyme were produced by high-cell-density cultivation (HCDC) in minimal salt medium. Enrichment of acetate was prevented by controlled feeding of glucose,[12] which yielded a final wet cell mass of 133 g L^{-1}. Protein expression was induced by addition of isopropyl-β-D-thiogalactopyranoside (IPTG; 1 mM) and performed at 26 °C to support correct protein folding by chaperones.[13] One-step affinity purification of clarified disintegrates from a 20-g cell pellet on a 17-mL amylose column yielded over 100 mg of fusion protein with more than 90 % purity (SDS-PAGE) per batch.

Interestingly, UV/Vis and fluorescence spectroscopy gave no hint of flavin, heme, or other typical oxygenase cofactors. However, inductively coupled plasma optical emission spectrometry (ICP-OES) investigations showed significant contents of iron and manganese in the purified protein. This finding was confirmed by colorimetric assays for iron and manganese and comparison with the culture media, which also revealed that manganese is enriched by a factor of about 20 in relation to iron. Such a high selectivity of the protein for manganese provides strong evidence that AurF employs manganese as an oxygen-activating cofactor.

It is astonishing that the addition of H_2O_2 to MalE–AurF preparations restored the enzymatic activity in vitro without the need for other supplements. This is in strong contrast to the N-oxygenase PrnD, which requires proteolytic cleavage of the fusion enzyme and additional coenzymes for in vitro activity.[14] Presumably, the reaction mechanism employed by AurF is similar to that of heme or iron-dependent oxygenases, which allow bypassing of the native enzyme regeneration by H_2O_2 via a so-called "peroxide shunt".[15]

The strict *para* selectivity of AurF can be rationalized by a simplified model (Figure 2). The substrate is most likely

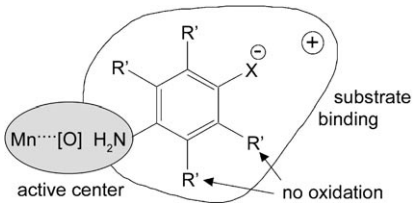

Figure 2. Model for regioselective N-oxygenation by AurF; R′ = H, NH_2; X = COO, CH_2COO, SO_3.

tethered by ion interactions to a positively charged protein residue, which allows the *para*-substituted amino group to enter the reactive hot spot, probably a Mn–oxo species. In stark contrast to AurF, haloperoxidases, which are not genuine N-oxygenases, catalyze nitro group formation in a nonspecific way through the formation of reactive peroxo species in the absence of halide ions.[16–18]

Apart from its remarkable selectivity, AurF has another advantage over other systems. Most conveniently, the loaded amylose column with immobilized enzyme can be used directly as an N-oxygenator "in flow". This is simply achieved by addition of substrate and H_2O_2 to the loading buffer. In a pilot experiment, a single pass of PABA and H_2O_2 immediately resulted in 27 % conversion to PNBA. To challenge the

 © 2006 Wiley-VCH Verlag GmbH & Co. KGaA, Weinheim

method, a mixture of 2-, 3-, and 4-aminobenzoic acids was circulated about 140 times. LC analyses demonstrated that a steady state is reached at 47% conversion to PNBA, and that only 4-aminobenzoic acid is oxidized, while the regioisomers remain unchanged (Figure 3).

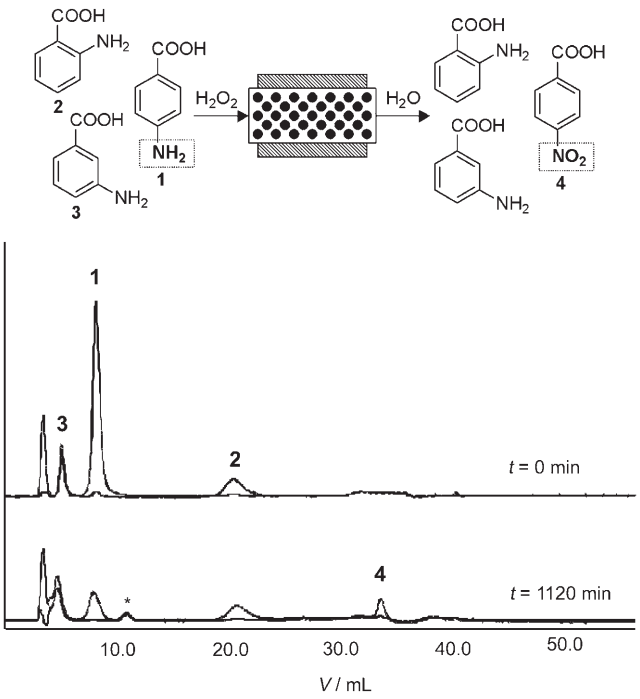

Figure 3. Top: Continuous regio- and chemoselective N-oxygenation on a fixed bed (column with thermostat) with immobilized MalE–AurF enzyme (spheres). Bottom: Chromatographic profiles of selective biotransformation; the asterisk indicates an unknown side product from PABA. The peak of **4** is significantly reduced in relation to that of **1** as a result of lower absorption of the nitro compound at 280 nm.

The possibility of using an immobilized enzyme, supplied with only H_2O_2, for the selective biotransformation of aromatic amines is notable, because it allows for a number of applications, such as the design of continuous flow processes, which are increasingly relevant to the future of chemoenzymatic syntheses. The urgent need for such novel techniques is a contemporary challenge in organic syntheses.[19] Possible uses of enzymatic N-oxygenation are "green" regio- and chemoselective modification of valuable fine chemicals,[20] or the separation and extraction of aromatic amines by previous oxidation, as well as in analytical applications.

In summary, various substrates have been probed for N-oxygenation by AurF, which revealed a strict regio- and chemoselectivity for an aromatic amino group *para* to an acidic group. A number of modifications on the carboxy group (carboxymethyl, sulfonate) and additional ring substituents (CH_3, OH, NH_2) are tolerated by AurF, although reaction rates are reduced compared to those of PABA (Figure 1). The most remarkable result is the selective oxygenation of diamino compounds. The excellent *para* specificity can be rationalized on the basis of an active-site model.

Preparative amounts of an active MalE–AurF fusion protein were manufactured and the enzyme was proven functional in vitro by addition of H_2O_2 (peroxide shunt). The chimeric enzyme could be immobilized and successfully applied in a fixed-bed tube reactor for regioselective amine transformation. To our knowledge, this is the first report of an enzymatic process for the chemo- and regioselective oxygenation of aromatic amines to nitro compounds, which could not be emulated in a single step using current synthetic protocols. Future studies of AurF will include elucidation of the structure of the enzyme and protein engineering techniques, with the goal of increasing reaction rates and altering the scope of accepted substrates.

Received: July 28, 2006
Published online: November 2, 2006

Keywords: amines · biotransformations · enzymes · oxygenation · regioselectivity

[1] K. Faber, *Biotransformations in Organic Chemistry: A Textbook*, Springer, Heidelberg, **2004**.
[2] Z. Li, J. B. van Beilen, W. A. Duetz, A. Schmid, A. de Raadt, H. Griengl, B. Withold, *Curr. Opin. Chem. Biol.* **2002**, *6*, 136.
[3] R. D. Schmid, V. Urlacher, *Curr. Opin. Biotechnol.* **2002**, *13*, 557.
[4] A. Straathof, S. Panke, A. Schmid, *Curr. Opin. Biotechnol.* **2002**, *13*, 548.
[5] S. Fetzner, *Appl. Microbiol. Biotechnol.* **2002**, *60*, 243.
[6] S. Kirner, P. E. Hammer, D. S. Hill, A. Altmann, I. Fischer, L. J. Weislo, M. Lanahan, K.-H. van Pee, J. M. Ligon, *J. Bacteriol.* **1998**, *180*, 1939.
[7] J. He, C. Hertweck, *Chem. Biol.* **2003**, *10*, 1225.
[8] M. Ziehl, J. He, H.-M. Dahse, C. Hertweck, *Angew. Chem.* **2005**, *117*, 1226; *Angew. Chem. Int. Ed.* **2005**, *44*, 1202.
[9] R. Winkler, C. Hertweck, *Angew. Chem.* **2005**, *117*, 4152; *Angew. Chem. Int. Ed.* **2005**, *44*, 4083.
[10] This finding has been confirmed for PrnD; D. J. Lee, H. Zhao, *Angew. Chem.* **2006**, *118*, 638; *Angew. Chem. Int. Ed.* **2006**, *45*, 622.
[11] Previously reported results obtained with a *S. thioluteus* strain (S. Kawai, K. Kobayashi, T. Oshima, F. Egami, *Arch. Biochem. Biophys.* **1965**, *112*, 537) could not be reproduced.
[12] U. Horn, W. Strittmatter, A. Krebber, U. Knüpfer, M. Kujau, R. Wenderoth, K. Müller, S. Matzku, A. Plückthun, D. Riesenberg, *Appl. Microbiol. Biotechnol.* **1996**, *46*, 524.
[13] M. Ferrer, T. Chernikova, M. Yakimov, P. Golyshin, K. Timmis, *Nat. Biotechnol.* **2003**, *21*, 1266.
[14] J. Lee, M. Simurdiak, H. Zhao, *J. Biol. Chem.* **2005**, *280*, 36719.
[15] M. Sono, M. P. Roach, E. D. Coulter, J. H. Dawson, *Chem. Rev.* **1996**, *96*, 2841.
[16] N. Itoh, N. Morinaga, T. Kouzai, *Biochem. Mol. Biol. Int.* **1993**, *29*, 785.
[17] M. D. Corbett, B. R. Chipko, A. O. Batchelor, *Biochem. J.* **1980**, *187*, 893.
[18] S. Kirner, K.-H. van Pee, *Angew. Chem.* **1994**, *106*, 346; *Angew. Chem. Int. Ed. Engl.* **1994**, *33*, 352.
[19] G. Jas, A. Kirschning, *Chem. Eur. J.* **2003**, *9*, 5708.
[20] A. Bruggink, A. Straathof, L. van der Wielen, *Adv. Biochem. Eng. Biotechnol.* **2003**, *80*, 69.

 © 2006 Wiley-VCH Verlag GmbH & Co. KGaA, Weinheim

Natural Products Synthesis

DOI: 10.1002/anie.200603363

Total Synthesis of (−)-Amphidinolide E**

*Chan Hyuk Kim, Hyo Jung An, Won Kyo Shin, Wei Yu, Sang Kook Woo, Soon Kyu Jung, and Eun Lee**

Amphidinolide E (**1**) is a unique 18-membered macrolide isolated from the Y-5′ strain of the dinoflagellate *Amphidinium* sp.[1] It exhibits cytotoxic activity against L1210 (IC_{50} = 2.0 μg mL^{-1}) and L5178Y (IC_{50} = 4.8 μg mL^{-1}) murine leukemia cells in vitro. Owing to its unique structural features and limited availability, amphidinolide E (**1**) has been the target of intense synthetic studies.[2] We report herein the results of our recent efforts towards the total synthesis of **1**.

According to our retrosynthetic analysis, **1** could be synthesized by lactonization of the *seco* acid **A**, which we intended to prepare by the Julia coupling of fragments **B** and **C**. In this way, potential problems arising from the intrinsic lability at C2 of **1** would only be faced at the end of the synthetic sequence. We also decided to introduce the triene side chain relatively early in the synthesis, thus forestalling difficulties which might arise from manipulations of the unstable macrolide intermediates. Fragment **B** may be obtained from the known tartrate acetonide precursors, and fragment **C** may be prepared from fragment **D**. Fragment **D** may in turn be obtained by radical cyclization of the β-alkoxy acrylate derivative **E**, which should be accessible from fragment **F** (Scheme 1).

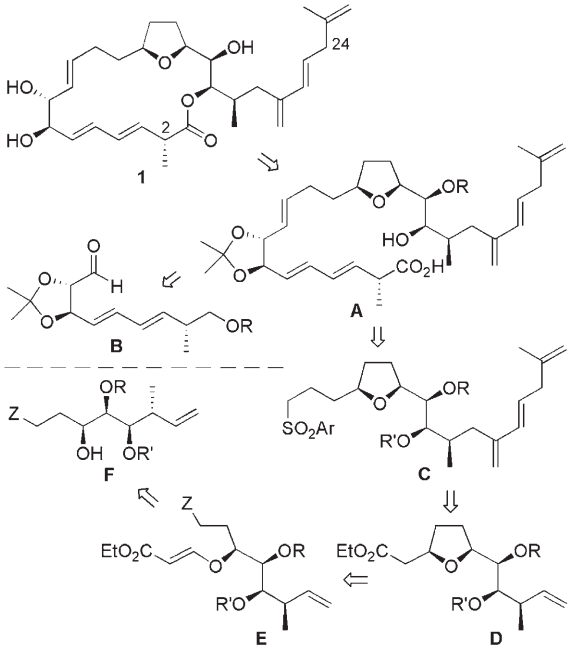

Scheme 1. Retrosynthetic analysis of **1**.

For the synthesis of fragment **B**, methyl (*S*)-3-hydroxy-2-methylpropanoate (**2**; commercially available) was converted into the corresponding TBDPS ether, from which vinyl boronic acid **3** was obtained through reduction, oxidation, Corey–Fuchs homologation,[3] and hydroboration–hydrolysis.[4] Suzuki coupling[5] of **3** with the known vinyl iodide **4**[6] proceeded smoothly, and the resulting diene was transformed into aldehyde **5** by removal of the TBS protecting group and oxidation (Scheme 2).

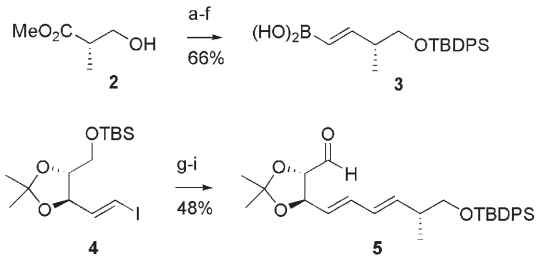

Scheme 2. Preparation of fragment **B**: a) TBDPSCl, imidazole, CH_2Cl_2, 0 °C→RT; b) $LiBH_4$, Et_2O; c) SO_3·pyridine, Et_3N, DMSO/CH_2Cl_2 (1:1), 0 °C→RT; d) CBr_4, Ph_3P, Zn, CH_2Cl_2, 0 °C→RT; e) *n*BuLi, THF, −78 °C; f) $BHBr_2$·SMe_2, CH_2Cl_2, 0 °C→RT; H_2O/Et_2O (1:3), 0 °C→RT; g) **3**, $[Pd(PPh_3)_4]$, TlOEt, THF/H_2O (4:1); h) PPTS, EtOH; i) SO_3·pyridine, Et_3N, DMSO/CH_2Cl_2 (1:1), 0 °C→RT. DMSO = dimethyl sulfoxide, PPTS = pyridinium *p*-toluenesulfonate, TBDPS = *tert*-butyldiphenylsilyl, TBS = *tert*-butyldimethylsilyl.

The known diol **6**[7] served as the starting material in the synthesis of fragment **C**. DDQ oxidation of **6** provided the corresponding PMP cyclic acetal, which was converted into aldehyde **7** by MOM protection of the remaining hydroxy group and reduction with DIBAL. Roush crotylation[8] of **7** by treatment with boronate **8** provided a product mixture that contained mainly the desired homoallylic alcohol **9** (d.r. 16:1). TIPS protection of **9** and oxidative deprotection of the acetal with CAN produced diol **10**. Selective tosylation of the primary hydroxy group in **10**, treatment with ethyl propiolate, and substitution of the tosylate group with iodide led to the β-alkoxy acrylate **11**. Radical cyclization[9] of **11** proceeded smoothly in the presence of tris(trimethylsilyl)silane and triethylborane, and the oxolane product **12** was obtained in high yield (Scheme 3).

Hydroboration–oxidation of alkene **12** produced the corresponding primary alcohol, which was converted into the corresponding aldehyde. At this point, a variety of methods were tested to find an effective way to build up the

[*] C. H. Kim, H. J. An, W. K. Shin, W. Yu, S. K. Woo, S. K. Jung, Prof. E. Lee
Department of Chemistry
College of Natural Sciences
Seoul National University
Seoul 151-747 (Korea)
Fax: (+82) 2-889-1568
E-mail: eunlee@snu.ac.kr

[**] This work was supported by a grant from MarineBio21, Ministry of Maritime Affairs and Fisheries, Korea and a grant from the Center for Bioactive Molecular Hybrids (Yonsei University and KOSEF). BK21 graduate fellowship grants to C. H. Kim, H. J. An, W. Yu, and S. K. Jung and Seoul Science Fellowship grants to C. H. Kim are gratefully acknowledged.

Supporting information for this article is available on the WWW under http://www.angewandte.org or from the author.

 © 2006 Wiley-VCH Verlag GmbH & Co. KGaA, Weinheim

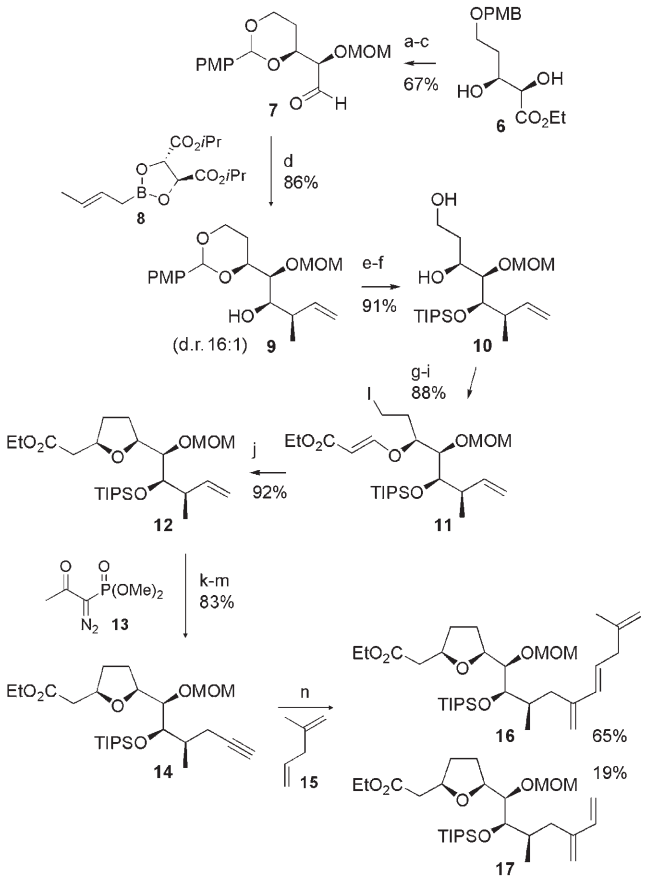

Scheme 3. Preparation of fragment **C**: a) DDQ, 3-Å MS, CH_2Cl_2, 0 °C; b) MOMCl, DIPEA, DMAP, CH_2Cl_2, reflux; c) DIBAL, CH_2Cl_2, −78 °C; d) **8**, 4-Å MS, toluene, −78 °C; e) TIPSOTf, collidine, CH_2Cl_2; f) CAN, $MeCN/H_2O$ (9:1), 0 °C; g) TsCl, Et_3N, CH_2Cl_2, 0 °C; h) $CHCCO_2Et$, NMM, CH_2Cl_2; i) NaI, acetone, reflux; j) $(TMS)_3SiH$, Et_3B, toluene, −20 °C; k) $(Sia)_2BH$, THF, 0 °C; $NaBO_3 \cdot 4H_2O$, H_2O; l) Dess–Martin periodinane, pyridine, CH_2Cl_2, 0 °C→RT; m) **13**, Cs_2CO_3, EtOH, 0 °C→RT; n) CH_2CH_2, $[(H_2IMes_2)RuCl_2(P(c\text{-}Hex)_3)]$, CH_2Cl_2; **15**, sealed tube, 40 °C. CAN = ceric ammonium nitrate, DIBAL = diisobutylaluminum hydride, DIPEA = *N*,*N*-diisopropylethylamine, DDQ = 2,3-dichloro-5,6-dicyano-1,4-benzoquinone, DMAP = 4-dimethylaminopyridine, Mes = mesityl, MOM = methoxymethyl, NMM = *N*-methylmorpholine, PMB = *p*-methoxybenzyl, PMP = *p*-methoxyphenyl, Sia = siamyl, TIPS = triisopropylsilyl, Tf = trifluoromethanesulfonyl, TMS = trimethylsilyl, Ts = *p*-toluenesulfonyl.

side chain. For example, a Nozaki–Hiyama–Kishi reaction[10] of the aldehyde with 1-iodo-4-methyl-1,4-pentadiene[11] proceeded efficiently to yield a mixture of allylic alcohols, which was eventually converted into the desired triene **16** by oxidation and Wittig olefination. Alternatively, the alkyne **14** was obtained from the aldehyde by treatment with diazophosphonate **13**.[12] Alkyne **14** was first treated with ethylene in the presence of the second-generation Grubbs catalyst,[13] and the crude product was treated with 2-methyl-1,4-pentadiene (**15**; commercially available). In this way, the desired triene **16** was obtained in 65% yield accompanied by diene **17** in 19% yield. Subjection of the isolated sample of diene **17** to the same reaction conditions provided an additional amount of triene **16** (10%).

DIBAL reduction of **16** produced the corresponding aldehyde, which was transformed into the homologous aldehyde by Wittig methoxymethylidenation and hydrolysis. Further reduction with $NaBH_4$, Mitsunobu-type substitution of the primary hydroxy group with thiol **18**, and selective oxidation led to sulfone **19**. Conditions for the Kocienski–Julia reaction[14] between sulfone **19** and aldehyde **5** were then investigated; the best result was obtained when the lithio derivative of sulfone **19** prepared in THF was treated with aldehyde **5** in DMF/DMPU (3:1) at −78 °C. In this way, a product mixture in which the major isomer was the desired *E* alkene **20** was obtained in 74% yield (*E*/*Z* 10:1). The selective removal of the TBDPS group in **20** was possible under alkaline conditions, but the oxidative conversion of the primary hydroxy group into a carboxylic acid group proved painfully difficult; for example, Dess–Martin oxidation resulted in a scrambling of the NMR spectroscopic signals from the side-chain region. Eventually, it was found that treatment of the primary alcohol with IBX[15] provided the corresponding aldehyde cleanly. The aldehyde was then converted into the hydroxy carboxylic acid **21** by oxidation with sodium chlorite and removal of the TIPS protecting group (Scheme 4).

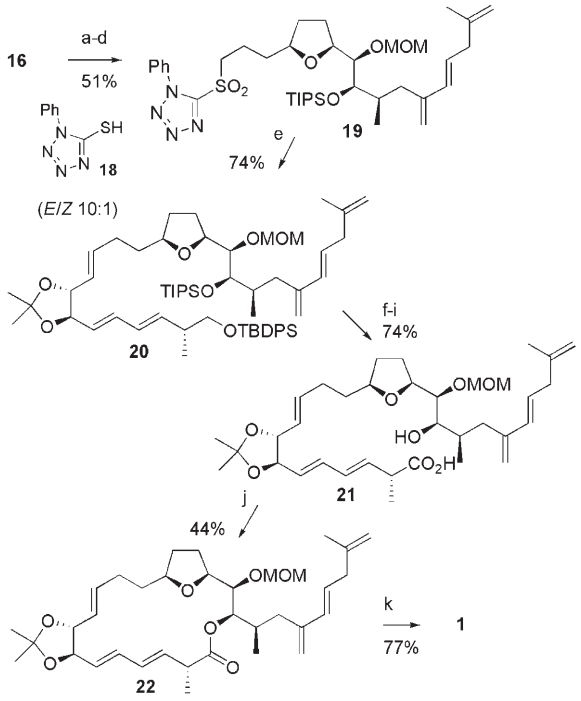

Scheme 4. Synthesis of amphidinolide E (**1**): a) DIBAL, THF, −78 °C; b) $(Ph_3P^+CH_2OMe)Cl^-$, *t*BuOK, THF, 0 °C→RT; $Hg(OAc)_2$, THF/H_2O (10:1), 0 °C; c) $NaBH_4$, MeOH; d) **18**, PPh_3, DIAD, THF; H_2O_2, $(NH_4)_6[Mo_7O_{24}] \cdot 4H_2O$, EtOH; e) LiHMDS, THF, −78→−40 °C; **5**, DMF/DMPU (3:1), −78 °C→RT; f) 15% NaOH/DMPU (1:10); g) IBX, DMSO/THF (1:1); h) $NaClO_2$, NaH_2PO_4, *t*BuOH/2-methyl-2-butene/H_2O (1:1:1); i) TBAF, THF; j) EtOCCH, $[\{RuCl_2(p\text{-cymene})\}_2]$, toluene, 0 °C→RT; CSA, RT→50 °C; k) 4 N HCl, MeOH. CSA = camphorsulfonic acid, DIAD = diisopropylazodicarboxylate, DMF = *N*,*N*-dimethylformamide, DMPU = 1,3-dimethyl-3,4,5,6-tetrahydro-2(1*H*)-pyrimidinone, HMDS = hexamethyldisilazide, IBX = 2-iodoxybenzoic acid, TBAF = tetrabutylammonium fluoride.

 © 2006 Wiley-VCH Verlag GmbH & Co. KGaA, Weinheim

For the lactonization of **21**, the protocol of Kita et al.[16] gave the best result; thus, macrolide **22** was produced in 44% yield. It was not possible to obtain **22** in reasonable yield under Yamaguchi lactonization conditions. Finally, removal of the MOM protecting group and cleavage of the acetonide under acidic conditions produced amphidinolide E (**1**) in 77% yield.[17]

In summary, a radical cyclization reaction of a β-alkoxy acrylate was employed for the stereoselective construction of the oxolane unit in our synthesis of amphidinolide E (**1**). The general fragility of **1**, particularly at C2 and C24, necessitated careful analysis and the judicious choice of reaction conditions for the successful culmination of the total synthesis.

Experimental Section

Macrolide **22**: Ethoxyacetylene (40% in hexanes, 0.030 mL, 0.13 mmol) was added to a solution of the *seco* acid **21** (52.6 mg, 0.0873 mmol) and $[\{RuCl_2(p\text{-cymene})\}_2]$ (1.0 mg, 0.0016 mmol) in toluene (8 mL) at 0 °C. The resulting mixture was warmed to room temperature and stirred for a further 30 min. The dark red solution was then filtered through a pad of silica gel, and the silica gel was washed with dry Et_2O (50 mL) under a nitrogen atmosphere. The filtrate was concentrated under reduced pressure. The crude ethoxyvinyl ester was dissolved in toluene (3 mL) and added to a solution of CSA (2.0 mg, 0.0087 mmol) in toluene (14 mL). The reaction mixture was heated to 50 °C and stirred at this temperature for 2 h, then filtered through a pad of silica gel and concentrated. The residue was purified by flash column chromatography (hexanes/EtOAc, 10:1) to afford lactone **22** (22.5 mg, 44%).

$R_f = 0.45$ (hexanes/EtOAc, 4:1); ^{1}H NMR (500 MHz, $CDCl_3$): $\delta =$ 6.30 (dd, $J = 14.9$, 10.8 Hz, 1H), 6.19 (dd, $J = 14.9$, 10.8 Hz, 1H), 6.04 (d, $J = 15.7$ Hz, 1H), 5.68–5.76 (m, 2H), 5.55 (dd, $J = 14.7$, 9.3 Hz, 2H), 5.31 (ddd, $J = 15.2$, 8.6, 1.5 Hz, 1H), 5.12 (d, $J = 7.1$ Hz, 1H), 4.98 (s, 1H), 4.87 (s, 1H), 4.73 (s, 1H), 4.70 (s, 1H), 4.67 (d, $J = 6.8$ Hz, 1H), 4.64 (dd, $J = 10.3$, 1.2 Hz, 1H), 4.02 (t, $J = 8.5$ Hz, 1H), 3.98 (t, $J = 8.5$ Hz, 1H), 3.72 (dd, $J = 8.9$, 1.3 Hz, 1H), 3.52 (td, $J = 9.3$, 6.4 Hz, 1H), 3.36 (s, 3H), 3.24–3.32 (m, 2H), 2.77 (d, $J = 7.1$ Hz, 2H), 2.30–2.39 (m, 3H), 1.86–1.98 (m, 2H), 1.82 (dd, $J = 14.3$, 11.9 Hz, 1H), 1.71 (s, 3H), 1.62–1.70 (m, 1H), 1.46–1.54 (m, 2H), 1.43 (s, 3H), 1.43 (s, 3H), 1.26–1.32 (m, 1H), 1.24 (d, $J = 6.6$ Hz, 3H), 1.11–1.19 (m, 1H), 0.91 ppm (d, $J = 6.6$ Hz, 3H); ^{13}C NMR (75 MHz, $CDCl_3$): $\delta = 174.5$, 144.5, 144.1, 138.5, 135.8, 135.4, 133.3, 131.3, 127.9, 127.7, 125.4, 115.7, 110.8, 109.0, 97.2, 83.0, 82.3, 80.7, 79.2, 78.0, 77.7, 77.2, 56.3, 44.0, 41.3, 35.8, 32.1, 31.6, 28.8, 27.7, 27.1, 27.1, 22.5, 17.1, 14.7 ppm. IR (neat): $\tilde{\nu}_{max} = 3443$, 3063, 3078, 2981, 2929, 1732, 1653, 1604, 1454, 1377, 1238, 1171, 1090, 1030, 991, 885, 758, 580 cm^{-1}; MALDI-TOF MS: m/z 607 $[M+Na]^+$; HRMS (FAB): m/z calcd for $C_{35}H_{52}O_7Na$ $[M+Na]^+$: 607.3611, found: 607.3627; $[\alpha]_D^{25} = -178.7$ ($c = 0.46$, $CHCl_3$).

Received: August 17, 2006
Published online: November 9, 2006

Keywords: anticancer agents · macrolides · marine natural products · radical cyclization · total synthesis

[1] a) J. Kobayashi, M. Ishibashi, T. Murayama, M. Takamatsu, M. Iwamura, Y. Ohizumi, T. Sasaki, *J. Org. Chem.* **1990**, *55*, 3421 – 3423; b) T. Kubota, M. Tsuda, J. Kobayashi, *J. Org. Chem.* **2002**, *67*, 1651 – 1656.

[2] For reports on the partial synthesis of **1**, see: a) M. K. Gurjar, S. Mohapatra, U. D. Phalgune, V. G. Puranik, D. K. Mohapatra, *Tetrahedron Lett.* **2004**, *45*, 7899 – 7902; b) C. L. Heitzman, W. T. Lambert, E. Mertz, J. B. Shotwell, J. M. Tinsley, P. Va, W. R. Roush, *Org. Lett.* **2005**, *7*, 2405 – 2408; c) J. A. Marshall, G. Schaaf, A. Nolting, *Org. Lett.* **2005**, *7*, 5331 – 5333.

[3] E. J. Corey, P. L. Fuchs, *Tetrahedron Lett.* **1972**, *13*, 3769 – 3772.

[4] H. C. Brown, N. G. Bhat, V. Somayaji, *Organometallics* **1983**, *2*, 1311 – 1316.

[5] a) N. Miyaura, A. Suzuki, *Chem. Rev.* **1995**, *95*, 2457 – 2483; b) S. A. Frank, H. Chen, R. K. Kunz, M. J. Schnaderbeck, W. R. Roush, *Org. Lett.* **2000**, *2*, 2691 – 2694.

[6] L. O. Haustedt, S. B. Panicker, M. Kleinert, I. V. Hartung, U. Eggert, B Niess, H. M. R. Hoffmann, *Tetrahedron* **2003**, *59*, 6967 – 6977.

[7] J. Uenishi, M. Ohmi, K. Matsui, M. Iwano, *Tetrahedron* **2005**, *61*, 1971 – 1979.

[8] W. R. Roush, K. Ando, D. B. Powers, A. D. Palkowitz, R. L. Halterma, *J. Am. Chem. Soc.* **1990**, *112*, 6339 – 6348.

[9] For examples of the radical cyclization of β-alkoxy acrylates and β-alkoxy methacrylates, see: a) E. J. Kang, E. J. Cho, M. K. Ji, Y. E. Lee, D. M. Shin, S. Y. Choi, Y. K. Chung, J.-S. Kim, H.-J. Kim, S.-G. Lee, M. S. Lah, E. Lee, *J. Org. Chem.* **2005**, *70*, 6321 – 6329; b) H. Y. Song, J. M. Joo, J. W. Kang, D.-S. Kim, C.-K. Jung, H. S. Kwak, J. H. Park, E. Lee, C. Y. Hong, S. Jeong, K. Jeon, J. H. Park, *J. Org. Chem.* **2003**, *68*, 8080 – 8087; c) E. J. Jeong, E. J. Kang, L. T. Sung, S. K. Hong, E. Lee, *J. Am. Chem. Soc.* **2002**, *124*, 14655 – 14662; d) E. Lee, S. J. Choi, H. Kim, H. O. Han, Y. K. Kim, S. J. Min, S. H. Son, S. M. Lim, W. S. Jang, *Angew. Chem.* **2002**, *114*, 184 – 186; *Angew. Chem. Int. Ed.* **2002**, *41*, 176 – 178.

[10] Y. Okude, S. Hirano, T. Hiyama, H. Nozaki, *J. Am. Chem. Soc.* **1977**, *99*, 3179 – 3181.

[11] Prepared by the hydrozirconation–iodination of 2-methylpent-1-en-4-yne.

[12] a) S. Ohira, *Synth. Commun.* **1989**, *19*, 561 – 564; b) S. Müller, B. Liepold, G. J. Roth, H. J. Bestmann, *Synlett* **1996**, 521 – 522.

[13] a) H. Y. Lee, B. G. Kim, M. L. Snapper, *Org. Lett.* **2003**, *5*, 1855 – 1858; b) T. W. Funk, J. Efskind, R. H. Grubbs, *Org. Lett.* **2005**, *7*, 187 – 190.

[14] a) P. R. Blackemore, W. J. Cole, P. J. Kocienski, A. Morley, *Synlett* **1998**, 26 – 28; b) P. Liu, E. N. Jacobsen, *J. Am. Chem. Soc.* **2001**, *123*, 10772 – 10773.

[15] M. Frigerio, M. Santagostino, S. Sputore, *J. Org. Chem.* **1999**, *64*, 4537 – 4538.

[16] a) Y. Kita, H. Maeda, K. Omori, T. Okuno, Y. Tamura, *J. Chem. Soc. Perkin Trans. 1* **1993**, 2999 – 3005; b) B. M. Trost, J. D. Chisholm, *Org. Lett.* **2002**, *4*, 3743 – 3745.

[17] $[\alpha]_D^{30} = -131.1$ ($c = 0.21$, $CHCl_3$); the specific rotation of the natural sample was not reported.[1]

 © 2006 Wiley-VCH Verlag GmbH & Co. KGaA, Weinheim

DNA Detection

DOI: 10.1002/anie.200603331

One-Step Homogeneous Detection of DNA Hybridization with Gold Nanoparticle Probes by Using a Linear Light-Scattering Technique**

Bao-An Du, Zheng-Ping Li, and Cheng-Hui Liu*

As the human genome project has uncovered the full sequence of human genomes and post-genome technologies have been rapidly developed, detection of specific DNA sequences has become increasingly important in the diagnosis of hereditary diseases, detection of infectious agents, discovery of gene-targeted drugs, and a variety of biomedical studies. Many detection systems make use of solid-phase sandwich DNA hybridization methods that contain oligonucleotide probes covalently linked to reporter groups.[1] These assays have several merits, such as high specificity, low background, and high throughput. However, they also have a fundamental weakness in that they usually need a long dwell time owing to several cycles of consecutive hybridization and washing steps. In addition, the requirement of washing steps to remove the unhybridized probes precludes the use of real-time hybridization studies and the local detection of specific nucleic acids in living cells. As a way to circumvent the limitations, several schemes have been put forward for detecting specific nucleic acids in homogeneous solution,[2] such as fluorescence polarization,[3,4] fluorescence resonance energy transfer,[5–8] TaqMan,[9,10] molecular beacons,[11,12] and light-up probes.[13,14] Among these assays, molecular beacons have been widely used for detection of DNA hybridization in homogeneous solutions[2] and gene expression in living cells[15,16] owing to their high specificity and high sensitivity (0.3-nM detection limit).[17] However, they suffer from a difficult synthesis, are susceptible to photobleaching, and are expensive to employ.

In recent years, great attention has been focused on the use of metal nanoparticle labels on oligonucleotide probes to overcome the problems associated with fluorescent labels. Mirkin and co-workers first developed an entirely new colorimetric detection scheme for DNA hybridization in a homogeneous solution based on aggregation of oligonucleotide-functionalized gold nanoparticles that are directed by the target DNA and the distance-dependent optical properties of gold nanoparticles.[18,19] However, the main limitation of these approaches is their low sensitivity, which is still not as good as the best results from fluorophore-based assays.[20] To improve the sensitivity, many detection techniques, such as the scanometric method,[21] surface plasmon resonance (SPR),[22] laser diffraction,[23] colorimetric scatter on glass waveguide,[24] surface-enhanced Raman spectroscopy,[25] and array-based electrical detection,[26] have been developed. These approaches can push the detection limits of target DNA to picomolar, and even femtomolar values. However, all these assays need to detect gold nanoparticles on a solid phase and inevitably need a sophisticated process and expensive instruments.

Herein, we report a highly sensitive light-scattering assay for DNA hybridization in a homogeneous solution by using gold nanoparticles as the labels of oligonucleotide probes. The assay relies on the observation of greatly enhanced light scattering that originated from the aggregation of oligonucleotide-functionalized gold nanoparticles directed by the target DNA. Notably, a gold-nanoparticle-based hyper-Rayleigh scattering (nonlinear light scattering) has recently been explored for the detection of DNA hybridization in which 10 nM target DNA can be detectable.[27] However, here, the light scattering can be easily measured by using a common spectrofluorimeter equipped with a 150-W high pressure Xenon lamp.[28] Hence it should be considered as linear light scattering because the nonlinear light scattering can only be observed with laser excitation. With the proposed light-scattering assay, target DNA with a concentration as low as 0.1 pM can be detected and no washing steps are needed. The sensitivity increases by at least four orders of magnitude greater over that of the gold-nanoparticle-based colorimetric method[18] and the hyper-Rayleigh scattering assay.[27] Moreover, the light-scattering assay exhibits a high degree of discrimination between perfectly matched target DNA and targets with single base-pair mismatches.

As shown in Figure 1, the target DNA is a 30-base fragment of human p53 gene (exon 8). Probe 1 and probe 2, made of 15 bases, are complementary to part of the target DNA. By functionalizing the gold nanoparticles with either 3′ or 5′ termini of the thiol-capped oligouncleotide probes, the gold nanoparticles would align in a tail-to-tail (a), tail-to-head (b), or head-to-head (c) fashion onto the target DNA. Owing to many oligonucleotide probes immobilized on the surface of one nanoparticle, the hybridization in each alignment fashion can result in the formation of extended polymeric network aggregates.[18]

Figure 2 shows that the light-scattering intensity of the gold nanoparticles modified with probe 1 and probe 2 is very weak in the absence of target DNA. The light scattering would be only Rayleigh scattering because the diameter of the gold nanoparticles ($\approx$13 nm) is smaller than 1/20 of the incident wavelengths in the range of 260–700 nm.[29] A weak resonance Rayleigh scattering (RSS) peak can be observed at 545 nm, which is near the maximum absorbance wavelength (520 nm) of the gold nanoparticles. The light-scattering intensities of the gold nanoparticles can be greatly enhanced by the addition of complementary target DNA in the

[*] B.-A. Du, Prof. Dr. Z.-P. Li, C.-H. Liu
College of Chemistry and Environment Science
Hebei University
Baoding 071002, Hebei Province (P.R. China)
Fax: (+86) 312-507-9525
E-mail: lzpbd@mail.hbu.edu.cn

[**] The authors would like to thank Prof. H. J. Wang for helpful discussion of light-scattering theory. The project is supported by NSFC (No. 20375011), Program for New Century Excellent Talents in the University (NCET-05-0258), and the National Science Foundation of Hebei (B2006000967).

Supporting information for this article is available on the WWW under http://www.angewandte.org or from the author.

InterScience
© 2006 Wiley-VCH Verlag GmbH & Co. KGaA, Weinheim

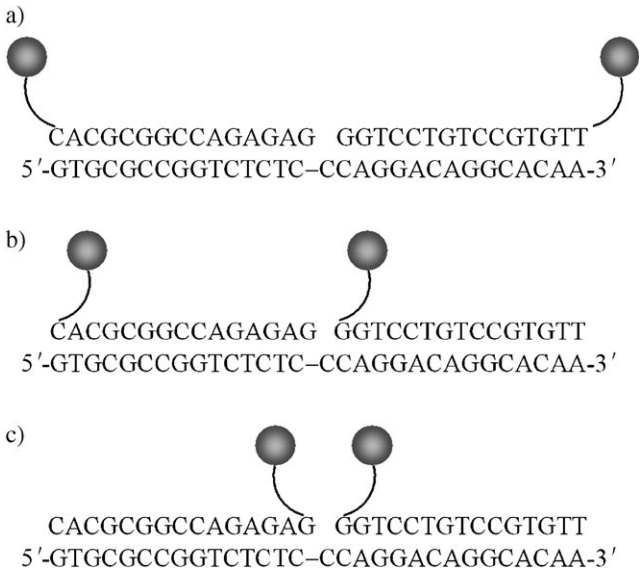

Figure 1. The three fashions of gold nanoparticles modified respectively with probe 1 and probe 2 at the 3′ or 5′ terminus aligning onto a target DNA. a) tail to tail, b) tail to head, c) head to head.

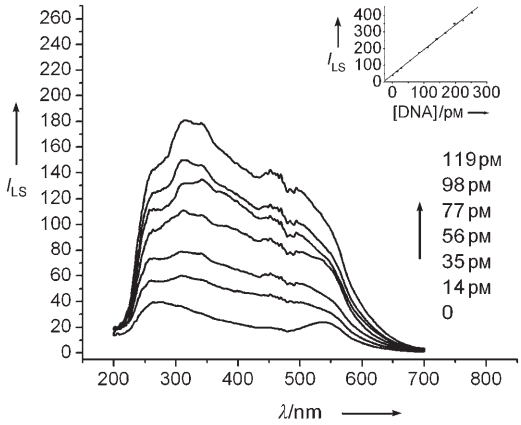

Figure 2. The light-scattering spectra of gold nanoparticles modified respectively with probe 1 and probe 2 in the absence and in the presence of the complementary DNA target at different concentrations. The inset shows the calibration curve of the target-DNA concentration versus the intensity of the light scattering (I_{LS}). The gold nanoparticles are align in the tail-to-tail fashion onto the target DNA. The DNA hybridization is performed in phosphate buffer solution (10 mM; pH 7.0) containing NaCl (0.7 M), and the hybridization time is 5 min at room temperature.

wavelength range of 250–650 nm. Interestingly, however, the RRS peak disappears, which is likely because the size of the aggregates induced by the DNA hybridization exceeds the range to produce RRS.[30] It can also be seen from Figure 2 that the enhanced light-scattering intensities linearly increase and the light-scattering spectra maintain almost the same pattern as the concentration of the target DNA increases. This means that the light scattering of gold nanoparticle aggregates formed in solution has no obvious wavelength selectivity. However, on the glass surface, different-sized gold nanoparticles can scatter light at different wavelengths.[31] Furthermore, the color of scattered light of the gold nanoparticles modified with oligonucleotide probes is different from that of the aggregates of the gold nanoparticles that are directed by the hybridization between the probes and the complementary target DNA.[24] Therefore, the great enhancement of light scattering induced by DNA hybridization in solution cannot be simply explained by the increased size of the formed aggregates of gold nanoparticles because the aggregates have a polymeric network structure and are still water soluble in the solution.

In the polymeric network structure of the gold nanoparticle aggregates, the gold nanoparticles are interlocked by multiple short duplex segments[18] in which the gold nanoparticle concentration would be much greater than that of the surrounding solution. Namely, the aggregation of the gold nanoparticles directed by DNA hybridization can lead to the great concentration fluctuation of the gold nanoparticles in the solution, which can consequently induce the great enhancement of light scattering according to Einstein's fluctuation theory for light scattering. Therefore, light scattering is a very sensitive and powerful technique for the detection of aggregation and self-assembly of nanoparticles in a solution.

The quantitative assessment of the proposed light-scattering assay for DNA hybridization is based on monitoring the dependence of the light-scattering intensity at 315 nm on the target-DNA concentration. As shown in the inset of Figure 2, the corresponding calibration plot of light-scattering intensity versus the target-DNA concentration is linear over the range of 0.7–119 pM. The correlation equation is $I_{LS} = 44.6 + 1.49c$ (where I_{LS} = the intensity of light scattering and c = the target-DNA concentration in pM) with a correlation coefficient of $r = 0.9980$. A series of 11 repetitive measurements of target DNA (0.7 pM) were used to evaluate the precision, and the relative standard deviation (RDS) was determined to be 2.6%. The corresponding detection limit (3σ, $n = 11$) was estimated to be 0.1 pM.

A variety of factors can affect the aggregation of the gold nanoparticles in the DNA hybridization system.[32] For a given system, salt concentration and the gold nanoparticle position on the oligonucleolide probes (either 3′ or 5′ terminus), that is, the alignment fashions of the gold nanoparticles on the DNA hybrids, are critical. Our experimental results show that the light-scattering intensity that resulted from the DNA hybridization almost linearly increases with an increase in the salt concentration, from 0.25 M to 0.7 M, and then levels off. This result is consistent with the conclusion that electrostatic interactions (repulsion between gold nanoparticles) are the dominant factors that affect stability of the DNA hybrids.[32] Owing to a screening effect of the salt, high salt concentration can minimize the electrostatic repulsion resulting in to more hybridization events taking place. On the other hand, the tail-to-tail arrangement is more favorable to the aggregates directed by the DNA hybridization among the three alignment fashions because the tail-to-tail fashion results in the longest interparticle distance, which then exhibits the smallest particle-to-particle repulsion. Therefore, the salt concentration of 0.7 M and the tail-to-tail fashion are employed for the proposed light-scattering assay for DNA hybridization.

 © 2006 Wiley-VCH Verlag GmbH & Co. KGaA, Weinheim

The specificity of the proposed light-scattering assay is evaluated by detecting the light-scattering intensities arising from a complementary target, one-base-mismatched DNA strand, in which the point mutation of C to T corresponds to the single-nucleotide polymorphism (SNP) of Arg283His in the human p53 gene (exon 8) and a three-base-mismatched DNA strand. All of DNA molecules tested in the experiment are at a concentration of 66 pM.

Figure 3 shows that a well-defined light-scattering response is observed for the complementary target DNA, whereas the three-base-mismatched DNA strand yields a

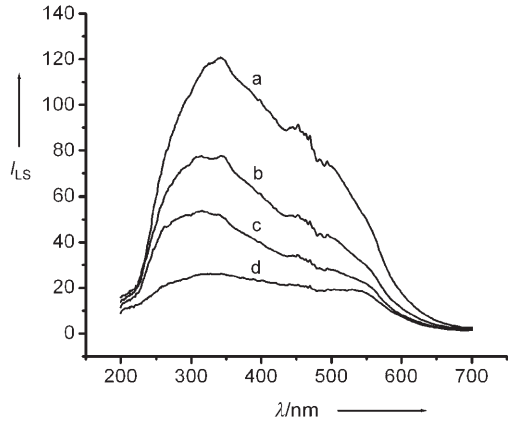

Figure 3. The light-scattering spectra of the gold nanoparticle probes in the presence of perfectly complementary DNA (a), one-base-mismatched DNA strands (b), three-base-mismatched DNA strands (c) at a concentration of 66 pM, and in the absence of the DNA target (d). The pH of the solutions are adjusted to be 7.0 by phosphate buffer solution (10 mM) containing NaCl (0.7 M). The hybridization time is 5 min at room temperature.

weaker light-scattering signal. It was also found that the light-scattering intensity of the one-base-mismatched DNA strand is much smaller (only 55%) than that of the perfectly complementary target. Therefore, with the proposed light-scattering assay, the single-base-mismatched DNA strands can be directly discriminated from the perfectly complementary targets without stringently controlling the temperature, indicating the high specificity of the assay. Controlling the temperature would be expected to differentiate the single-base mutation from the perfectly complementary targets and to apply to SNP analysis.

In summary, we have demonstrated a new gold-nanoparticle-based light-scattering strategy for detecting sequence-specific DNA in homogeneous solution. The sensitivity of the light-scattering assay compares favorably with the previously reported homogeneous detection methods for DNA hybridization, and the assay can be accomplished with one-step operation by using a common spectrofluorimeter. The light-scattering assay also exhibits such high specificity that a one-base difference in DNA targets can be directly discriminated without controlling the temperature. More importantly, it has been demonstrated that the light-scattering technique is a simple and sensitive tool for detecting the aggregation of nanoparticles in homogeneous solution. The nanoparticles functionalized by appropriate biomolecules can provide a variety of specific recognition and bioaffinity interactions which can result in the nanoparticle aggregation.[33] Therefore, the proposed light-scattering method would be expected to be extended for immunoassays, drug discovery based on the interactions between drugs and DNA (or protein) targets, etc. On the other hand, the homogeneous assay should be suited for monitoring the synthesis of specific nucleic acids in real time. If the gold nanoparticles functionalized with oligonucleotide probes are introduced into living cells, the light-scattering assay can probably open new avenues for the analysis of gene expression in living cells by using fluorescence microscopy with appropriate designs.

Experimental Section

Tetrachloroauric acid ($HAuCl_4 \cdot 4H_2O$) was obtained from Sinopharm Group Chemical Reagent Co. (Shanghai, China). All of the oligonucleotides used in this paper were purchased from TaKaRa Biotechnology (Dalian, P.R. China) Co., Ltd. The sequences are as follows:

probe 1:	5′-(SH-C_6)-(T)10-TTG TGC CTG TCC TGG-3′
	5′-TTG TGC CTG TCC TGG-$(T)_{10}$-(C_3-SH)-3′
probe 2:	5′-GAG AGA CCG GCG CAC-$(T)_{10}$-(C_3-SH)-3′
	5′-(SH-C_6)-(T)10 -GAG AGA CCG GCG CAC-3′
complementary target strand:	5′-GTG CGC CGG TCT CTC CCA GGA CAG GCA CAA-3′
one-base-mismatched strand:	5′-GTG CGT CGG TCT CTC CCA GGA CAG GCA CAA-3′
three-base-mismatched strand:	5′-GTG CGT CGG TTT CTC TCA GGA CAG GCA CAA-3′

Twice-distilled deionized water was used throughout. NaH_2PO_4, NaOH, and NaCl (Third Chemical Reagent Factory of Tianjin, Tianjin, China) were of analytical reagent grade and used to prepare the buffer solution.

A F-4500 spectrofluorimeter (Hitachi, Japan) was used to measure the light-scattering spectra and light-scattering intensities. A WH-861 vortex mixer (Huangjin Instrumental Co., Jiangsu, China) was used to blend the solutions. The TEM images of the colloidal gold were acquired on a JEM-1200EX II transmission electron microscope (JEOL, Japan).

Gold nanoparticles were prepared by the reduction of $HAuCl_4$ by trisodium citrate (Tianjin Beichen Chemical Reagent Co., Tianjin, China) according to the literature,[34] and the TEM image demonstrated a average diameter of 13 nm. Colloidal gold-labeled oligonucleotides were synthesized by derivatizing the gold-nanoparticle solution with 3′- and 5′-alkanethiol-capped oligonucleotides according to the previous report, but with some modifications (see the Supporting Information).[35]

In a typical experiment for DNA detection, a homogeneous three-component sandwich assay is used in the hybridization reaction. Briefly, under ambient temperatures, a solution of the gold nanoparticles functionalized with probe 1 (1 mL) and a solution of the gold nanoparticles functionalized with probe 2 (1 mL) in phosphate buffer solution (10 mM; pH 7.0) containing NaCl (0.3 M) were added to a dry 5-mL test tube. The NaCl concentration in the solution was then adjusted to 0.7 M. Afterward, a series of dilutions of target DNA dissolved in phosphate buffer solution (10 mM; pH 7.0) were pipetted into the test tubes by using microsyringes. The mixtures were blended by the WH-861 vortex mixer and heated at 70 °C for 5 min. After the mixtures were cooled to room temperature, another 5 min was needed to complete the hybridization. The light-scattering spectra were then recorded by synchronously scanning the excitation and

 © 2006 Wiley-VCH Verlag GmbH & Co. KGaA, Weinheim

emission monochromators from 200 nm to 700 nm (namely, $\Delta\lambda = 0$) by using the F-4500 spectrofluorimeter.

Received: August 16, 2006
Revised: September 20, 2006
Published online: November 8, 2006

Keywords: base-pair mismatches · DNA recognition · gold nanoparticles · light scattering · nucleotides

[1] *Gene Probes 1* (Eds.: B. D. Hames, S. J. Higgins), IRL, New York, **1995**.
[2] S. A. E. Marras, S. Tyagi, F. R. Kramer, *Clin. Chim. Acta* **2006**, *363*, 48 – 60.
[3] X. Chen, L. Levine, P. Y. Kwok, *Genome Res.* **1999**, *9*, 492 – 498.
[4] S. Latif, I. Bauer-Sarsdina, K. Ranade, K. J. Livak, P. Y. Kwok, *Genome Res.* **2001**, *11*, 436 – 440.
[5] R. A. Cardullo, S. Agrawal, C. Flores, P. C. Zamecnik, D. E. Wolf, *Proc. Natl. Acad. Sci. USA* **1988**, *85*, 8790 – 8794.
[6] X. Chen, P. Y. Kwok, *Nucleic Acids Res.* **1997**, *25*, 347 – 353.
[7] E. Lopez-Crapez, H. Bazin, E. Andre, J. Noletti, J. Grenier, G. Mathis, *Nucleic Acids Res.* **2001**, *29*, e70.
[8] M. Xiao, P. Y. Kwok, *Genome Res.* **2003**, *13*, 932 – 939.
[9] P. M. Holland, R. D. Abramson, R. Watson, D. H. Gelfand, Proc. *Natl. Acad. Sci. USA* **1991**, *88*, 7276 – 7280.
[10] D. Whitecombe, J. Rownie, H. L. Gillard, D. McKechnie, J. Theaker, C. R. Newton, S. Little, *Clin. Chem.* **1998**, *44*, 918 – 923.
[11] S. Tyagi, F. R. Kramer, *Nat. Biotechnol.* **1996**, *14*, 303 – 308.
[12] S. Tyagi, D. P. Bratu, F. R. Kramer, *Nat. Biotechnol.* **1998**, *16*, 49 – 53.
[13] N. Svanvik, G. Westman, D. Wang, M. Kubista, *Anal. Biochem.* **2000**, *281*, 26 – 35.
[14] E. Privat, T. Melvin, U. Asseline, P. Vigny, *Photochem. Photobiol.* **2001**, *74*, 532 – 541.
[15] D. P. Bratu, B. J. Cha, M. M. Mhlanga, F. R. Kramer, S. Tyagi, *Proc. Natl. Acad. Sci. USA* **2003**, *100*, 13308 – 13313.
[16] D. L. Sokol, X. Zhang, P. Lu, A. M. Grewirtz, *Proc. Natl. Acad. Sci. USA* **1998**, *95*, 11538 – 11543.
[17] X. Liu, W. Farmerie, S. Schuster, W. Tan, *Anal. Biochem.* **2000**, *283*, 56 – 63.
[18] R. Elghanian, J. J. Storhoff, R. C. Mucic, R. L. Letsinger, C. A. Mirkin, *Science* **1997**, *277*, 1078 – 1081.
[19] R. A. Reynolds, C. A. Mirkin, R. L. Letsinger, *J. Am. Chem. Soc.* **2000**, *122*, 3795 – 3796.
[20] N. L. Rosi, C. A. Mirkin, *Chem. Rev.* **2005**, *105*, 1547 – 1562.
[21] T. A. Taton, C. A. Mirkin, R. L. Letsinger, *Science* **2000**, *289*, 1757 – 1760.
[22] L. He, M. D. Musick, S. R. Nicewarner, F. G. Salinas, S. J. Benkovic, M. J. Natan, C. D. Keating, *J. Am. Chem. Soc.* **2000**, *122*, 9071 – 9077.
[23] C. R. Bailey, J. M. Nam, C. A. Mirkin, J. T. Hupp, *J. Am. Chem. Soc.* **2003**, *125*, 13541 – 13547.
[24] J. J. Storhoff, A. D. Lucas, V. Garimella, Y. P. Bao, U. R. Muller, *Nat. Biotechnol.* **2004**, *22*, 883 – 887.
[25] Y. W. Cao, R. Jin, T. A. Taton, C. A. Mirkin, *Science* **2002**, *297*, 1536 – 1540.
[26] S. J. Park, T. A. Taton, C. A. Mirkin, *Science* **2002**, *295*, 1503 – 1506.
[27] P. C. Ray, *Angew. Chem.***2006**, *118*, 1169 – 1172; *Angew. Chem. Int. Ed.* **2006**, *45*, 1151 – 1154.
[28] R. F. Pasternack, C. Bustamante, P. J. Collings, A. Giannetto, E. J. Gibbs, *J. Am. Chem. Soc.* **1993**, *115*, 5393 – 5399.
[29] G. A. Miller, *J. Phys. Chem.* **1978**, *82*, 616 – 618.
[30] R. F. Pasternack, P. J. Collings, *Science* **1995**, *269*, 935 – 939.
[31] T. A. Taton, G. Lu, C. A. Mirkin, *J. Am. Chem. Soc.* **2001**, *123*, 5164 – 5165.
[32] R. Jin, G. Wu, Z. Li, C. A. Mirkin, G. C. Schatz, *J. Am. Chem. Soc.* **2003**, *125*, 1643 – 1654.
[33] E. Katz, I. Willner, *Angew. Chem.* **2004**, *116*, 6166 – 6235; *Angew. Chem. Int. Ed.* **2004**, *43*, 6042 – 6018.
[34] K. C. Grabar, R. G. Freeman, M. B. Hommer, M. J. Natan, *Anal. Chem.* **1995**, *67*, 735 – 743.
[35] K. Sato, K. Hosokawa, M. Maeda, *J. Am. Chem. Soc.* **2003**, *125*, 8102 – 8103.

 © 2006 Wiley-VCH Verlag GmbH & Co. KGaA, Weinheim

Synthetic Methods

DOI: 10.1002/anie.200603240

Stereoselective Synthesis of Pyrrolidines: Catalytic Oxidative Cyclizations Mediated by Osmium**

Timothy J. Donohoe, Gwydion H. Churchill, Katherine M. P. Wheelhouse (née Gosby), and Paul A. Glossop*

Since its discovery by Klein and Rojahn in 1965, the oxidative cyclization of 1,5-dienes to give 2,5-disubstituted tetrahydrofurans has received a considerable amount of attention with a number of metal oxo species now capable of accomplishing this transformation.[1] We have recently developed the use of catalytic OsO_4 under acidic conditions to give *cis*-tetrahydrofurans (THFs) in high yields.[2] Attempts to induce asymmetric induction in this reaction with the addition of chiral amine ligands failed, presumably owing to the low pH of the reaction. However, we subsequently reported that vicinal diols derived from 1,5-dienes undergo cyclization in a regio- and stereoselective manner to give *cis*-THFs under conditions comparable to diene cyclization (Scheme 1).[3] We have evidence to suggest that Os complexes to the diol (chelation is essential) before perfoming an intramolecular, and stereo-

[*] Prof. T. J. Donohoe, Dr. G. H. Churchill, K. M. P. Wheelhouse (née Gosby)
Department of Chemistry
University of Oxford
Chemistry Research Laboratory
Mansfield Road, Oxford OX1 3TA (UK)
Fax: (+44) 1865-275-708
E-mail: timothy.donohoe@chem.ox.ac.uk
Homepage:
http://www.chem.ox.ac.uk/researchguide/tjdonohoe.html
P. A. Glossop
Pfizer Global R&D
Pfizer Limited
Ramsgate Road, Sandwich, Kent CT13 9NJ (UK)

[**] We thank the EPSRC and Pfizer for supporting this project. Merck, AstraZeneca, Pfizer, and Novartis are thanked for unrestricted funding.

Supporting information for this article is available on the WWW under http://www.angewandte.org or from the author.

© 2006 Wiley-VCH Verlag GmbH & Co. KGaA, Weinheim

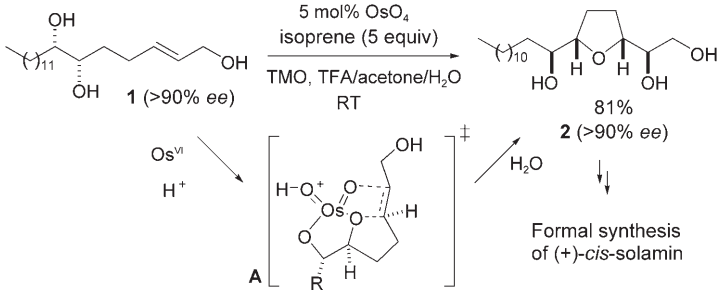

Scheme 1. Stereoselective oxidative cyclization of diols. TMO = Me_3NO; TFA = trifluoroacetic acid.

specific, oxidation of the pendant alkene (**A**). Furthermore, there is no loss of stereochemical integrity during the cyclization, and enantiopure diols give enantiopure THFs; this methodology was then applied to a formal synthesis of (+)-*cis*-solamin.[3]

The results shown above extend the possibility to take this reaction in a fundamentally new direction and allow the formation of *nitrogen* heterocycles via oxidative cyclization of amino alcohols. Although the oxidative cyclization of 1,5-dienes has not been modified to form pyrrolidines, we chose to examine the cyclization of vicinal amino alcohols as our starting point.[4] Our rationale was that in synthesizing enantiopure amino alcohols separately, we would be able to obtain enantiopure pyrrolidines by oxidative cyclization. If successful, we would uncover a new catalytic reaction capable of making important heterocycles in a stereoselective fashion.[5]

Substrates **3**, **5**, **7**, **9** were readily prepared and subjected to the oxidation conditions;[6] pleasingly, *cis*-pyrrolidines **4**, **6**, **8**, **10** were formed in 80–90% yield (Scheme 2). The reaction is stereoselective, giving *cis*-pyrrolidines in all cases, and stereospecific (see oxidation of **7**, **9**). Moreover, the *syn* addition of nitrogen and oxygen atoms across the distal alkene was proven rigorously.[7]

The cyclization of the sterically bulky alkene **9** to give **10** is also notable for its high yield. Catalyst loadings were successfully reduced to 1 mol% osmium (**4**, **8**, and **10**) and even as low as 0.2 mol% for **3**, giving compound **4** in 68% yield. Furthermore, we have applied these conditions to the cyclization of enantiopure starting materials (**7**, **9**)[6] without loss of enantiomeric purity during the reaction. Note that *trans*-cinnamic acid is added to these oxidations as a sacrificial alkene[3] and was found to be optimal for these transformations (see below).

The information detailed above reveals that the range of potentially chelating substrates that can undergo oxidative cyclization is large. We were intrigued by the possibility of subjecting other chelating derivatives to this procedure, to give differently substituted THFs.

Therefore, enantiopure hydroxy amide **11** was subjected to oxidative conditions and cyclized in high yield to give the amido THF **12** (Scheme 3).[8] This result

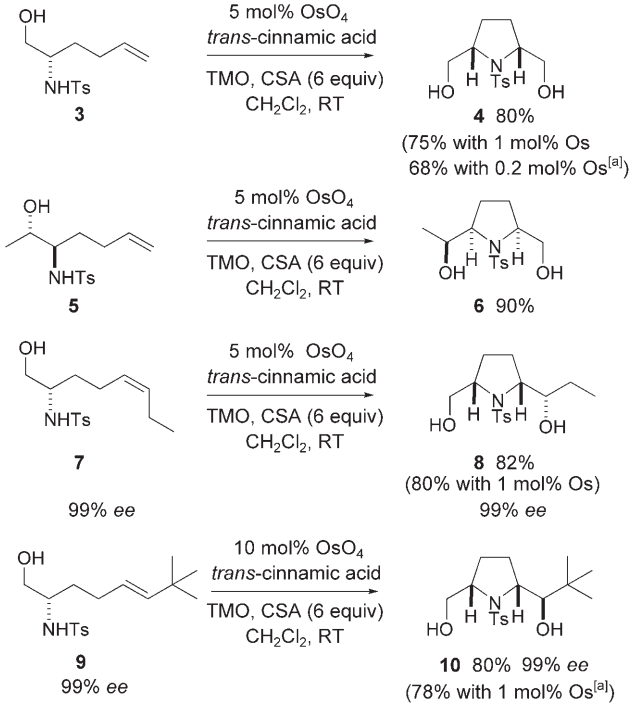

Scheme 2. Oxidative cyclization to form pyrrolidines. [a] Reactions carried out at 40 °C. Ts = toluene-4-sulfonyl; CSA = camphorsulfonic acid.

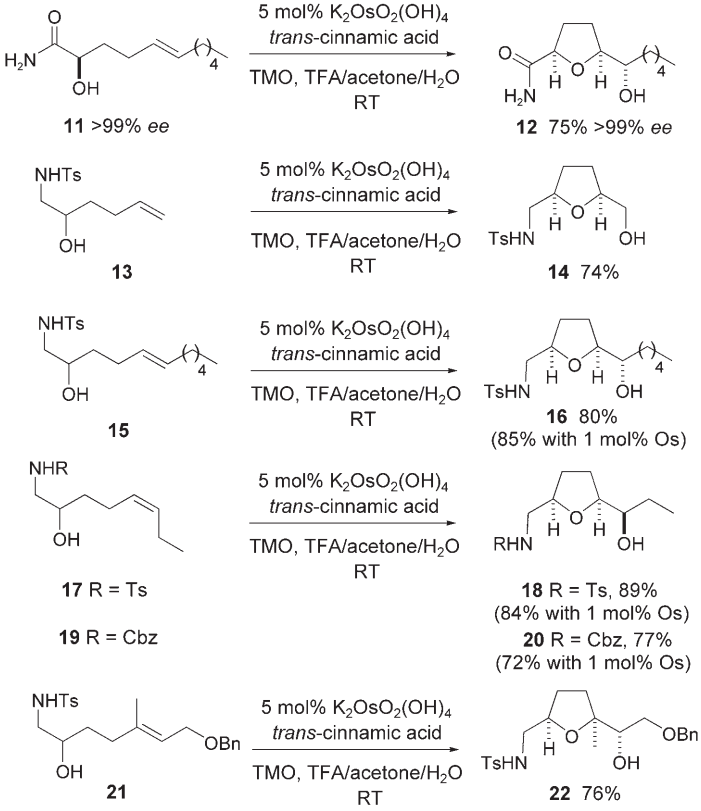

Scheme 3. Alternative chelating functionality for cyclization. Cbz = benzyloxycarbonyl; Bn = benzyl.

 © 2006 Wiley-VCH Verlag GmbH & Co. KGaA, Weinheim

demonstrates the generality possible in the initiating functionality. Next, the amino alcohol substrates shown were subjected to oxidative cyclization to give *cis*-THFs in good to excellent yields. The stereospecific *syn* addition is exemplified by the stereochemistry of the products **16** and **18**.[7] The *N*-Ts group was found to be optimal for these cyclizations, although carbamates do cyclize, albeit in lower yields (see **19**).

We investigated the mechanism of cyclization by preparing the competition substrate **23** (Scheme 4), which bears the 1,2-hydroxysulfonamide functionality and two distal terminal alkenes. Oxidative cyclization of **23** should form an osmium chelate (see **B**),[4] and then cyclization will reveal a preference for formation of either N- or O-heterocycles. We also wished

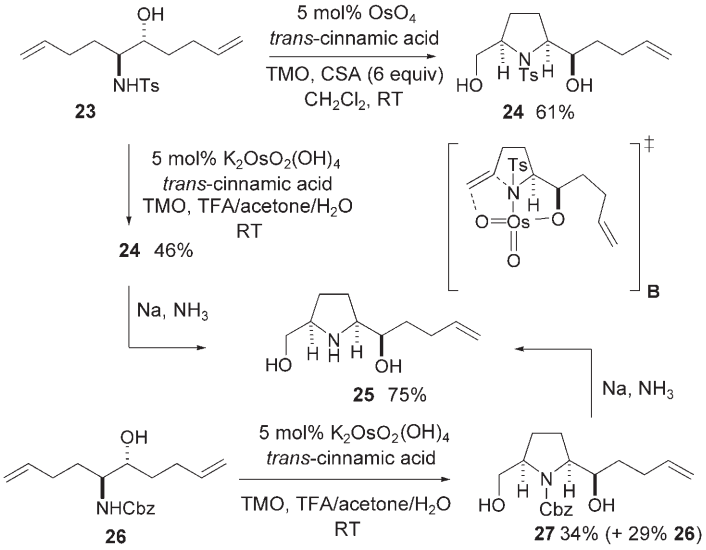

Scheme 4. Mechanistic probes for pyrrolidine formation.

to examine the role of solvent on any competitive cyclization, and in this regard it is worth noting that formation of oxygen and nitrogen heterocycles works best in different solvents (compare Scheme 2 and Scheme 3).

When **23** was subjected to the OsO_4/CSA conditions, the *cis*-pyrrolidine **24** was formed in 61% yield. The structure of **24** was proven by X-ray crystallography and none of the corresponding THF was observed during this reaction. It was then anticipated that use of the $K_2OsO_2(OH)_4$/TFA conditions (that is, those which have proved optimal for the synthesis of THFs; see Scheme 3) would provide the THF congener of **24**. These conditions also returned the pyrrolidine **24**, but in a lower yield (46%). The carbamate derivative **26** proved completely inert to OsO_4/CSA conditions, but gave a low yield of the *cis*-pyrrolidine **27** when subjected to $K_2OsO_2(OH)_4$/TFA cyclization. These reactions serve to underline the overriding preference for cyclization to nitrogen-containing heterocycles over those containing oxygen, and provide further evidence for the enhanced participation of Os–N bonds over Os–O bonds whenever there is a choice.[9] The removal of N-protecting groups with Na in liquid NH_3 then established the formation of pyrrolidine **25** from both substrates **24** and **27**.

Examination of the reaction of **23** revealed interesting information about the nature of the catalyst involved in chelation and cyclization (Table 1). In entry 1 it is seen that stoichiometric Os^{VI} is capable of chelating and then cyclizing

Table 1: Reaction of **23** to give **24**.

Entry	Conditions	Yield of **24**
1	1 equiv $K_2OsO_2(OH)_4$, CSA, CH_2Cl_2	63%
2	1 equiv OsO_4, CSA, CH_2Cl_2	<20%[a]
3	cat. OsO_4, CSA, TMO, CH_2Cl_2	<5%
4	cat. OsO_4, CSA, *trans*-cinnamic acid, TMO, CH_2Cl_2	61%

[a] Products derived from dihydroxylation of **23** were observed.

($Os^{VI} \rightarrow Os^{IV}$).[10] Moreover, entry 2 reveals that Os^{VIII} preferentially dihydroxylates an alkene rather than cyclizes a diol onto it.[11] We suspect that the small amount of **24** formed here comes from dihydroxylation and subsequent ligand exchange on Os^{VI} and cyclization. Thus, the role of the sacrificial alkene becomes clear; it must be dihydroxylated in preference to the alkene in the substrate. In so doing it prevents unwanted diol by-products and forms Os^{VI}, which is a more competent catalyst (compare entries 3 and 4, Table 1). *trans*-Cinnamic acid is ideal because the diol formed from dihydroxylation is polar and easily separable from the cyclized products.

To conclude, we have shown that N-protected 1,2-amino alcohols are excellent substrates for catalytic oxidative cyclization. The synthesis of pyrrolidines and THFs is both stereoselective and stereospecific, high-yielding, and governed by the position of the heteroatoms in the starting material. Enantiopure starting materials are readily accessible and give enantiopure products after cyclization.

Received: August 9, 2006
Published online: November 3, 2006

Keywords: catalysis · cyclization · nitrogen heterocycles · osmium · pyrrolidines

[1] Mn: a) E. Klein, W. Rojahn, *Tetrahedron* **1965**, *21*, 2353–2358; b) J. E. Baldwin, M. J. Crossley, E. -M. M. Lehtonen, *J. Chem. Soc. Chem. Commun.* **1979**, 918–920; c) D. M. Walba, M. D. Wand, M. C. Wilkes, *J. Am. Chem. Soc.* **1979**, *101*, 4396–4397; d) R. C. D. Brown, J. F. Keily, *Angew. Chem.* **2001**, *113*, 4628–4630; *Angew. Chem. Int. Ed.* **2001**, *40*, 4496–4498; e) R. C. D. Brown, C. J. Bataille, R. M. Hughes, A. Kenney, T. J. Luker, *J. Org. Chem.* **2002**, *67*, 8079–8085; Ru: f) P. H. J. Carlsen, T. Katsuki, V. S. Martin, K. B. Sharpless, *J. Org. Chem.* **1981**, *46*, 3936–3938; g) L. Albarella, D. Musumeci, D. Sica, *Eur. J. Org. Chem.* **2001**, 997–1003; h) V. Piccialli, N. Cavallo, *Tetrahedron Lett.* **2001**, *42*, 4695–4699; i) S. Roth, S. Göhler, H. Cheng, C. B. W. Stark, *Eur. J. Org. Chem.* **2005**, 4109–4118.

[2] Os: a) M. de Champdoré, M. Lasalvia, V. Piccialli, *Tetrahedron Lett.* **1998**, *39*, 9781–9784; b) T. J. Donohoe, S. Butterworth, *Angew. Chem.* **2003**, *115*, 978–981; *Angew. Chem. Int. Ed.* **2003**, *42*, 948–951; c) T. J. Donohoe, S. Butterworth, *Angew. Chem.*

 © 2006 Wiley-VCH Verlag GmbH & Co. KGaA, Weinheim

2005, *117*, 4844 – 4846; *Angew. Chem. Int. Ed.* **2005**, *44*, 4766 – 4768.
[3] D. M. Walba, G. S. Stoudt, *Tetrahedron Lett.* **1982**, *23*, 727 – 730; see also reference [2c].
[4] There is good evidence to suggest that NTs amino alcohols are ligands for osmium: M. A. Andersson, R. Epple, V. V. Fokin, K. B. Sharpless, *Angew. Chem.* **2002**, *114*, 490 – 493; *Angew. Chem. Int. Ed.* **2002**, *41*, 472 – 475.
[5] For examples of pyrrolidine synthesis using catalysis, see: a) B. M. Trost, A. B. Pinkerton, D. Kremzow, *J. Am. Chem. Soc.* **2000**, *122*, 12 007 – 12 008; b) C. V. Galliford, M. A. Beenen, S. T. Nguyen, K. A. Scheidt, *Org. Lett.* **2003**, *5*, 3487 – 3490; c) Q. Yang, J. E. Ney, J. P. Wolfe, *Org. Lett.* **2005**, *7*, 2575 – 2578; d) C. Welter, A. Dahnz, B. Brunner, S. Streiff, P. Dübon, G. Helmchen, *Org. Lett.* **2005**, *7*, 1239 – 1242; e) F. A. Davis, H. Xu, Y. Wu, J. Zhang, *Org. Lett.* **2006**, *8*, 2273 – 2276.
[6] The enantiopure amino alcohols reported here were made by a convenient route that involved: 1) reaction of OTr glycidol with an allyl Grignard reagent, 2) Mitsunobu inversion with BocNHTs, and then 3) deprotection. OTr = *O*-trityl, Boc = *tert*-butoxycarbonyl.
[7] The structures of **6**, **8**, **10**, **16**, **18**, **22**, and **24** were proven unambiguously by X-ray crystallography.
[8] Although the yields are sensitive to the solvent used and the pH, they are not influenced unduly by the source of osmium.
[9] This preference was first noted by Sharpless and co-workers: D. W. Patrick, L. K. Truesdale, S. A. Biller, K. B. Sharpless, *J. Org. Chem.* **1978**, *43*, 2628 – 2638.
[10] Os^{VI} is prone to disproportionation under acidic conditions. Control experiments have shown that this is relatively slow under the experimental conditions reported here; see: P. Dupau, R. Epple, A. A. Thomas, V. V. Fokin, K. B. Sharpless, *Adv. Synth. Catal.* **2002**, *344*, 421 – 433.
[11] J. R. Ragazzo, E. J. Behrman, *Bioinorg. Chem.* **1976**, *5*, 343 – 352; while the studies here indicate that Os^{VI} is desirable for formation of a chelate, we have unpublished results which show that both Os^{VI} and Os^{VIII} osmate esters can cyclize under acidic conditions.

 © 2006 Wiley-VCH Verlag GmbH & Co. KGaA, Weinheim

Natural Products Synthesis

DOI: 10.1002/anie.200603179

Asymmetric Total Syntheses of Ecteinascidin 597 and Ecteinascidin 583**

*Jinchun Chen, Xiaochuan Chen, Matthieu Willot, and Jieping Zhu**

Dedicated to Professor Yulin Li on the occasion of his retirement

The ecteinascidins, a family of tetrahydroisoquinoline alkaloids isolated from the Caribbean tunicate *Ecteinascidia turbinata*,[1] display a wide range of antitumor and antimicrobial activities.[2] One member of this family, ecteinascidin 743 (Et 743, **1**; Scheme 1), is currently in late phase II/III clinical trials against ovarian, endometrium, and breast cancer, and several other types of sarcoma. The restricted natural availability of the ecteinascidins (1 g of Et 743 from 1 ton of tunicate) in conjunction with their potent antiproliferative activities and complex molecular architecture has made them attractive synthetic targets.[3] Since the landmark synthesis of Et 743 by Corey and co-workers in 1996,[4] Fukuyama and co-workers[5] and our research group[6] have also completed total syntheses of this molecule, and Danishefsky and co-workers[7] very recently reported a formal total synthesis of Et 743. A semisynthesis of Et 743 from cyanosafracin B was developed by Cuevas, Manzanares, and co-workers at PharmaMar,[8] and further synthetic approaches have been reported by a number of research groups.[9–14]

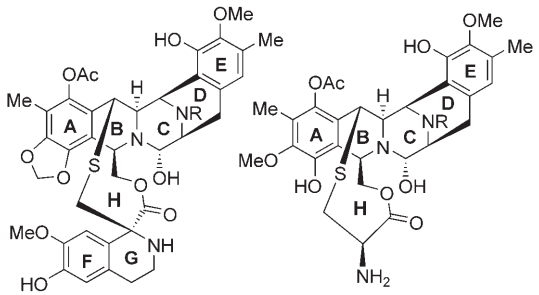

1 R = Me, Et 743
2 R = H, Et 729

3 R = Me, Et 597
4 R = H, Et 583

Scheme 1. Structure of representative ecteinascidins.

[*] Dr. J. Chen, X. Chen, M. Willot, Dr. J. Zhu
Institut de Chimie des Substances Naturelles
CNRS, 91198 Gif-sur-Yvette Cedex (France)
Fax: (+33) 1-69077247
E-mail: zhu@icsn.cnrs-gif.fr

[**] Financial support from the CNRS and the Institut de Chimie des Substances Naturelles are gratefully acknowledged.

Supporting information for this article (experimental procedures, product characterization, and copies of ^{1}H and ^{13}C NMR spectra of synthetic Et 597 (**3**) and Et 583 (**4**)) is available on the WWW under http://www.angewandte.org or from the author.

© 2006 Wiley-VCH Verlag GmbH & Co. KGaA, Weinheim

Ecteinascidins 597 (Et 597, **3**) and 583 (Et 583, **4**; Scheme 1) are putative biosynthetic precursors of other ecteinascidins.[1d,15] Although the cytotoxicity of Et 597 (**3**), which lacks the third tetrahydroisoquinoline unit, is generally 2.5–10 times less potent than that of Et 743 against P 388, A 549, HT 29, and CV-1 cell lines, its antiproliferative activity is even greater than that of taxol and camptothecin.[1d] In continuation of our research towards the development of an efficient synthetic route to this family of marine natural products and on the structure–activity relationships (SARs) of these compounds, we became interested in the synthesis of Et 597 (**3**) and Et 583 (**4**). In a different approach to our previous strategy,[6] we envisaged that we could take advantage of the presence of two free hydroxy groups in ring A of **3** and **4**, as illustrated in Scheme 2. We planned to construct the

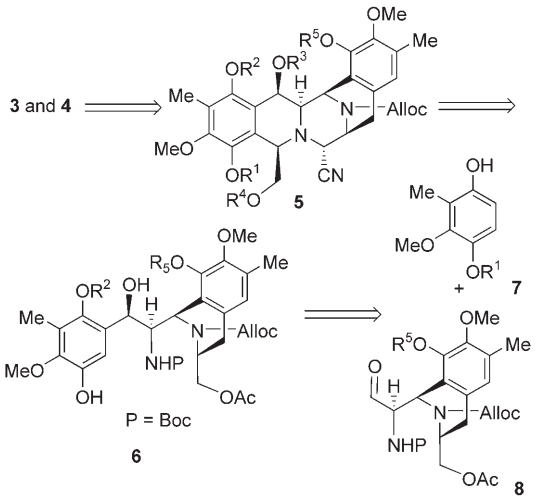

Scheme 2. Retrosynthetic analysis of Et 597 (**3**) and Et 583 (**4**). Alloc = allyloxycarbonyl, Boc = *tert*-butoxycarbonyl.

highly oxygenated A–B ring system by starting from phenol **7** and tetrahydroisoqinoline **8** and carrying out a sequence of phenolic aldol condensations followed by a Pictet–Spengler reaction. An intramolecular Strecker reaction would then afford the entire A–B–C–D–E pentacycle, whereupon the closure of the 10-membered lactone by formation of the carbon–sulfur bond would lead to the natural products.

The synthesis of the aromatic segment **7** is summarized in Scheme 3. 3-Methoxy-4-hydroxybenzaldehyde (**9**) was converted into **10** through a well-established three-step sequence. Interestingly, *ortho* lithiation of **10** followed by the addition of methyl iodide[16] gave a compound in which both the aromatic ring and the TBS protecting group had been methylated. Under optimized conditions (3 equivalents of *n*BuLi, 4 equivalents of MeI), the dual-methylation product **11** was isolated in 92 % yield. The MOM group could be removed without touching the silyl ether by treatment with TMSBr to provide phenol **7** in excellent yield.[17]

Our synthetic route to the pentacyclic compound **18** is depicted in Scheme 4. The synthesis of the tetrahydroisoquinoline **12** featured a highly diastereoselective Pictet–Spengler condensation of the (*S*)-Garner aldehyde with (*S*)-3-hydroxy-4-methoxy-5-methylphenylalanol.[6,18] The selective

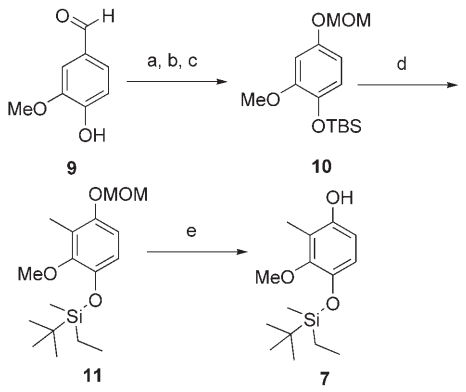

Scheme 3. Synthesis of the A-ring unit **7**: a) TBSCl, imidazole, DMF, RT, 98 %; b) mCPBA, $CHCl_3$, 45 °C; then Na_2CO_3, MeOH, RT, 85 %; c) MOMCl, DIPEA, CH_2Cl_2, 0 °C → reflux, 96 %; d) *n*BuLi, THF, −10 °C; then MeI, −78 °C → RT, 92 %; e) TMSBr, CH_2Cl_2, −20 → 0 °C, 90 %. TBS = *tert*-butyldimethylsilyl, mCPBA = *m*-chloroperbenzoic acid, MOM = methoxymethyl, DIPEA = *N*,*N*-diisopropylethylamine, DMF = *N*,*N*-dimethylformamide.

hydrolysis of the oxazolidine moiety in **12** was more difficult than expected. Eventually, reaction conditions that were previously developed for the cleavage of acetonides ($CeCl_3 \cdot 7H_2O$, oxalic acid, acetonitrile, room temperature) afforded alcohol **13** in 91 % yield.[19] Swern oxidation[20] of the primary alcohol furnished the corresponding aminoaldehyde **8**, which without purification underwent the stereoselective phenolic aldol condensation with the magnesium phenolate of **7**[21,22] to provide the *syn* aminoalcohol **14** in 74 % yield. The *anti* aminoalcohol was neither isolated nor detected. The existence of rotamers made NMR spectroscopic analysis of **14** difficult, and it was hard to determine if this product was a mixture of two diastereomers with respect to the stereogenic silicon center.[23] Nevertheless, the question of diastereomers was of no consequence, as the silyl protecting group was due to be removed in the next step. Compound **14** was transformed into aminoalcohol **15** in excellent overall yield by a three-step sequence: 1) protection of the phenol and secondary alcohol as the corresponding methoxymethyl ethers, 2) simultaneous removal of the *N*-Boc and *O*-silyl protecting groups according to the procedure of Sakaitani and Ohfune,[24] and 3) hydrolysis of the acetate. The Pictet–Spengler reaction[25] of **15** and $TrocOCH_2CHO$ (**16**; prepared in two steps from ethyleneglycol)[26] was the key step of our synthesis. To our pleasure, the desired transformation proceeded efficiently in dichloromethane in the presence of acetic acid and 3-Å molecular sieves to provide **17** as a single diastereomer in 90 % yield. Swern oxidation of the aminoalcohol **17** followed by a zinc chloride catalyzed intramolecular Strecker reaction provided aminonitrile **18** as a single stereoisomer to complete the highly efficient construction of the pentacyclic ring system.

The relative configuration of compound **17** was determined upon its conversion into **19**. The characteristic NOEs observed between H1/H3, H3/H4, and H11/H13 (ecteinascidin numbering) indicated that the configuration of **19**, and hence that of **17**, is 1*R*, 3*R*, 4*R*, 11*R*, 13*S*. The configuration at C21 was determined to be *R* by detailed NMR spectroscopic

 © 2006 Wiley-VCH Verlag GmbH & Co. KGaA, Weinheim

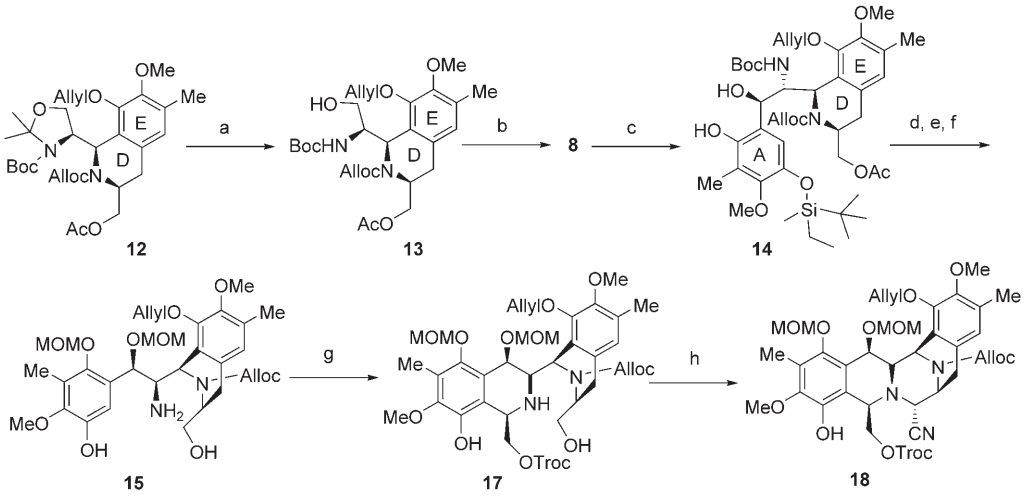

Scheme 4. Synthesis of the pentacyclic compound **18**: a) $CeCl_3 \cdot 7H_2O$, oxalic acid, acetonitrile, RT, 91%; b) oxalyl chloride, DMSO, CH_2Cl_2, −60°C, then Et_3N; c) MeMgCl, THF, **7**; then **8**, CH_2Cl_2, RT, 74%; d) MOMCl, DIPEA, $CHCl_3$, 0°C→reflux, 88%; e) TBSOTf, 2,6-lutidine, CH_2Cl_2, −78°C→RT; then KF, MeOH, RT, 86%; f) K_2CO_3, MeOH, RT, 94%; g) AcOH, $TrocOCH_2CHO$ (**16**), 3-Å MS, CH_2Cl_2, RT, 90%; h) oxalyl chloride, DMSO, CH_2Cl_2, −60°C; then TMSCN, $ZnCl_2$, CH_2Cl_2, RT, 87%. DMSO = dimethyl sulfoxide, Tf = trifluoromethanesulfonyl, TMS = trimethylsilyl, Troc = 2,2,2-trichloroethoxycarbonyl.

studies of the *N*-de-Alloc derivative **20** (NOEs observed for H21/H22 and H14/H21; Scheme 5).

The high diastereoselectivity observed in the condensation of **15** and **16** could be explained by assuming that the iminium intermediate had a *trans* configuration and that the substituents at C3 and C4 were both pseudoequatorial (**A**, Scheme 5).[27] However, at the present stage an alternative sequence involving a phenolic aldol condensation and β elimination to give the orthoquinone methide intermediate **B** (Scheme 5) followed by intramolecular Michael addition of the tethered amine can not be eliminated as a possibility.[28] It is nevertheless interesting to note that the presence of the free

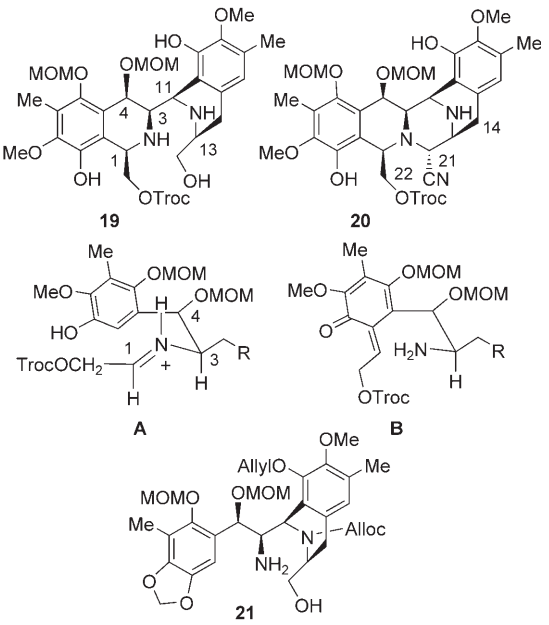

Scheme 5. Structures for the discussion of configuration and possible reaction pathways.

phenol group in ring A is essential to the success of the reaction; the condensation of amine **21** with 2-benzyloxyacetaldehyde (or ethyl glyoxylate) failed to provide the desired tetrahydroisoquinoline.

The total synthesis of Et 597 (**3**) and Et 583 (**4**) was completed as shown in Scheme 6. Unmasking of the Troc-protected primary alcohol under reductive conditions followed by chemoselective allylation of the phenol group provided compound **22**, which was coupled with (*R*)-*N*-Troc-*S*-4,4′,4″-trimethoxytritylcysteine to afford the corresponding ester **23** in excellent yield. The cyclization of **23** was examined under a variety of reaction conditions; the acid (*p*-toluenesulfonic acid, TFA, $MeSO_3H$, TMSBr), the solvent (CH_2Cl_2, toluene, 2,2,2-trifluoroethanol, MeCN), and the temperature were varied, and the reaction was carried out in the presence or absence of molecular sieves. Unfortunately, no combination provided the desired 10-membered lactone **25**. The attempted cyclization of phenol **28** also met with failure. We then decided to separate the S-deprotection and cyclization steps. Removal of the *S*-4,4′,4″-trimethoxytrityl group from **23** with Et_3SiH/TFA afforded the stable thiol **24** in 88% yield after flash column chromatography.[29] Gratifyingly, the treatment of thiol **24** with TMSBr afforded the bridged macrocycle **25**, after the phenol had been masked as the corresponding acetate, in 60% yield.[30] In this simple experiment, a complex reaction sequence involving *O*-MOM deprotection, 1,4-elimination to give the orthoquinone methide,[31] and macrocyclization through an intramolecular Michael addition occurred in a highly ordered manner to bring about the key C–S bond formation.

Simultaneous removal of the *N*-Alloc and *O*-allyl functionalities as described by Guibé and co-workers[32] provided amine **26** in 85% yield. A sequence of reductive N methylation, removal of the *N*-Troc group (zinc/AcOH), and conversion of the aminonitrile functionality into a hemiaminal ($AgNO_3$ in a mixture of acetonitrile and water) afforded

 © 2006 Wiley-VCH Verlag GmbH & Co. KGaA, Weinheim

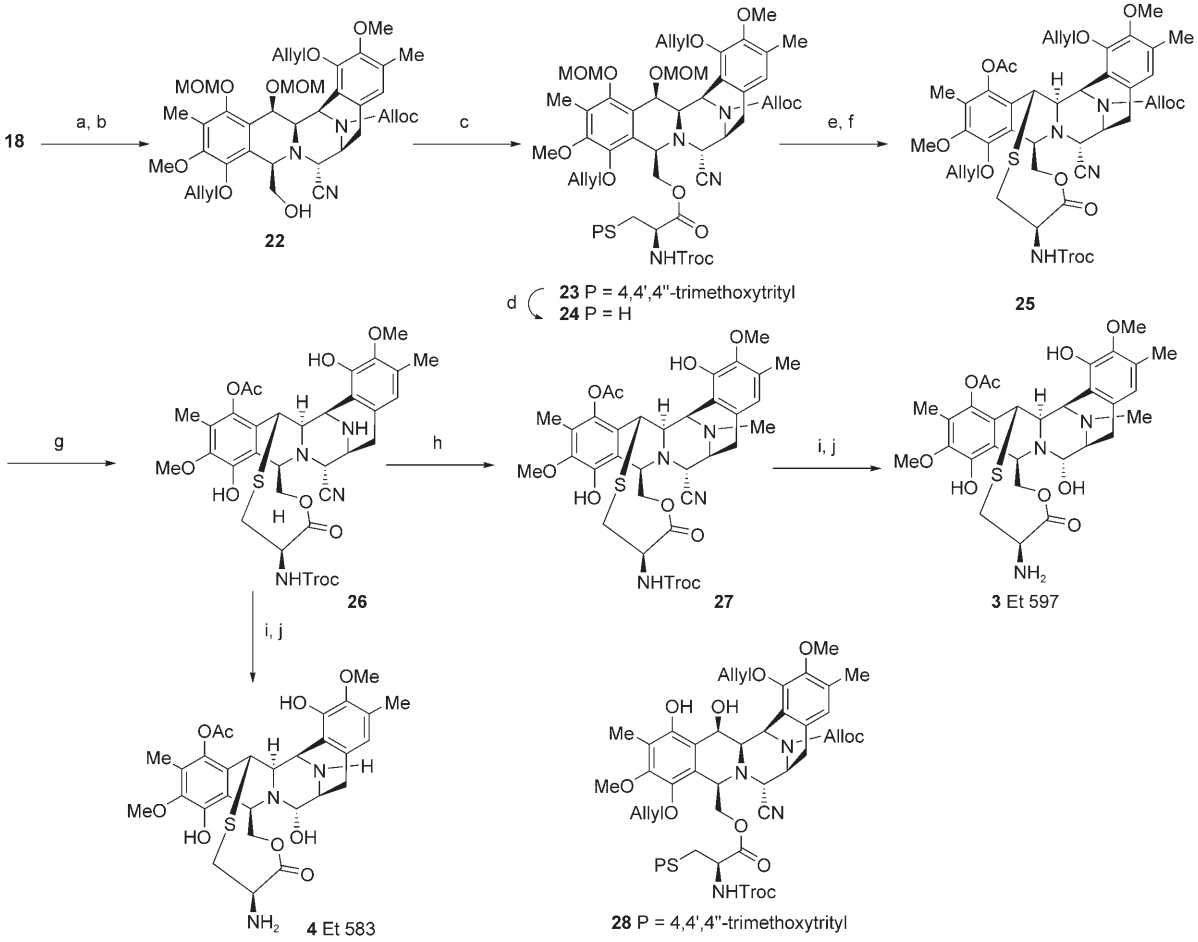

Scheme 6. Synthesis of Et 597 (**3**) and Et 583 (**4**): a) Zn, AcOH, Et_2O, RT, 90%; b) allyl bromide, K_2CO_3, acetonitrile, RT, 94%; c) EDCI, DMAP, (*R*)-*N*-Troc-*S*-4,4′,4″-trimethoxytritylcysteine, CH_2Cl_2, RT, 93%; d) Et_3SiH, TFA, CH_2Cl_2, RT, 87%; e) TMSBr, CH_2Cl_2, −20°C→10°C; f) Ac_2O, pyridine, DMAP, CH_2Cl_2, RT, 60%; g) $[Pd(PPh_3)_4]$, nBu_3SnH, AcOH, CH_2Cl_2, RT, 85%; h) CH_2O, $NaBH_3CN$, AcOH, MeCN/MeOH, RT, 95%; i) Zn, AcOH, Et_2O, RT, 89% for Et 597, 86% for Et 583; j) $AgNO_3$, MeCN/H_2O, RT, 92% for **3**, 88% for **4**. DMAP = 4-dimethylaminopyridine, TFA = trifluoroacetic acid, EDCI = 1-(3-dimethylaminopropyl)-3-ethylcarbodiimide hydrochloride.

ecteinascidin 597 (**3**) in excellent overall yield. Similarly, amine **26** was converted into ecteinascidin 583 (**4**) in a two-step sequence. Synthetic Et 597 (**3**) and Et 583 (**4**) exhibited physical, spectroscopic, and spectrometric characteristics (^1H, ^{13}C NMR, IR, $[\alpha]_D$, and HRMS) identical to those reported for the natural products.

In summary, convergent total syntheses of Et 597 (**3**) and Et 583 (**4**) have been completed for the first time from readily accessible starting materials. Notable features of our approach include: 1) a stereoselective aldol reaction for the coupling of the A-ring moiety **7** with the D–E unit **8**, 2) a highly stereoselective Pictet–Spengler reaction for the construction of the B ring, and 3) TMSBr-promoted macrocyclization of the thiol **24** to give the 1,4-bridged 10-membered ring. This straightforward synthesis does not require sophisticated reaction conditions and should potentially be amenable to large-scale production. We are currently exploiting this strategy for the synthesis of ecteinascidin analogues for detailed SAR studies.[33]

Received: August 4, 2006
Published online: November 13, 2006

Keywords: alkaloids · antitumor agents · asymmetric synthesis · marine natural products · Pictet–Spengler reaction

[1] a) A. E. Wright, D. A. Forleo, G. P. Gunawardana, S. P. Gunasekera, F. E. Koehn, O. J. McConnell, *J. Org. Chem.* **1990**, *55*, 4508–4512; b) K. L. Rinehart, T. G. Holt, N. L. Fregeau, J. G. Stroh, P. A. Keifer, F. Sun, L. H. Li, D. G. Martin, *J. Org. Chem.* **1990**, *55*, 4512–4515; c) R. Sakai, K. L. Rinehart, Y. Guan, A. H. J. Wang, *Proc. Natl. Acad. Sci. USA* **1992**, *89*, 11456–11460; d) R. Sakai, E. A. Jares-Erijman, I. Manzanares, M. V. S. Elipe, K. L. Rinehart, *J. Am. Chem. Soc.* **1996**, *118*, 9017–9023; e) K. Suwanborirux, K. Charupant, S. Amnuoypol, S. Pummangura, A. Kubo, N. Saito, *J. Nat. Prod.* **2002**,*65*, 935–937.

[2] K. L. Rinehart, *Med. Drug. Rev.* **2000**, 1–27.

[3] J. D. Scott, R. M. Williams, *Chem. Rev.* **2002**, *102*, 1669–1730.

[4] a) E. J. Corey, D. Y. Gin, R. S. Kania, *J. Am. Chem. Soc.* **1996**, *118*, 9202–9203; b) E. J. Martinez, E. J. Corey, *Org. Lett.* **2000**, *2*, 993–996.

[5] a) A. Endo, A. Yanagisawa, M. Abe, S. Tohma, T. Kan, T. Fukuyama, *J. Am. Chem. Soc.* **2002**, *124*, 6552–6554; b) A. Endo, T. Kann, T. Fukuyama, *Synlett* **1999**, 1103–1105.

 © 2006 Wiley-VCH Verlag GmbH & Co. KGaA, Weinheim

[6] J. Chen, X. Chen, M. Bois-Choussy, J. Zhu, *J. Am. Chem. Soc.* **2006**, *128*, 87 – 89.

[7] a) S. Zheng, C. Chan, T. Furuuchi, B. J. D. Wright, B. Zhou, J. Guo, S. J. Danishefsky, *Angew. Chem.* **2006**, *118*, 1786 – 1791; *Angew. Chem. Int. Ed.* **2006**, *45*, 1754 – 1759; b) C. Chan, S. Zheng, B. Zhou, J. Guo, R. H. Heid, B. J. D. Wright, S. J. Danishefsky, *Angew. Chem.* **2006**, *118*, 1781 – 1786; *Angew. Chem. Int. Ed.* **2006**, *45*, 1749 – 1754; c) B. Zhou, S. Edmondson, S. J. Danishefsky, *Tetrahedron Lett.* **2000**, *41*, 2039 – 2042; d) B. Zhou, J. Guo, S. J. Danishefsky, *Tetrahedron Lett.* **2000**, *41*, 2043 – 2046; e) B. Zhou, J. Guo, S. J. Danishefsky, *Org. Lett.* **2002**, *4*, 43 – 46.

[8] a) C. Cuevas, M. Pérez, M. J. Martin, J. L. Chicharro, C. Fernández-Rivas, M. Flores, A. Francesch, P. Gallego, M. Zarzuelo, F. De La Calle, J. Gracía, C. Polanco, I. Rodriguez, I. Manzanares, *Org. Lett.* **2000**, *2*, 2545 – 2548; b) R. Menchaca, V. Martínez, A. Rodríguez, N. Rodríguez, M. Flores, P. Gallego, I. Manzanares, C. Cuevas, *J. Org. Chem.* **2003**, *68*, 8859 – 8866.

[9] a) N. Saito, K. Tashiro, Y. Maru, K. Yamaguchi, A. Kubo, *J. Chem. Soc. Perkin Trans. 1* **1997**, 53 – 69; b) N. Saito, H. Kamayachi, M. Tachi, A. Kubo, *Heterocycles* **1999**, *51*, 9 – 12; c) N. Saito, M. Tachi, R. Seki, H. Kamayachi, A. Kubo, *Chem. Pharm. Bull.* **2000**, *48*, 1549 – 1557.

[10] a) B. Herberich, M. Kinugawa, A. Vazquez, R. M. Williams, *Tetrahedron Lett.* **2001**, *42*, 543 – 546; b) W. Jin, R. M. Williams, *Tetrahedron Lett.* **2003**, *44*, 4635 – 4639; c) W. Jin, S. Metobo, R. M. Williams, *Org. Lett.* **2003**, *5*, 2095 – 2098; d) D. Fishlock, R. M. Williams, *Org. Lett.* **2006**, *8*, 3299 – 3301.

[11] P. Magnus, K. S. Matthews, V. Lynch, *Org. Lett.* **2003**, *5*, 2181 – 2184.

[12] Y.-F. Tang, Z.-Z. Liu, S.-Z. Chen, *Tetrahedron Lett.* **2003**, *44*, 7091 – 7094.

[13] S. Aubry, S. Pellet-Rostaing, B. Fenet, M. Lemaire, *Tetrahedron Lett.* **2006**, *47*, 1319 – 1323.

[14] P. A. Ceballos, M. Péres, C. Cuevas, A. Francesch, I. Manzanares, A. M. Echavarren, *Eur. J. Org. Chem.* **2006**, 1926 – 1933.

[15] R. G. Kerr, N. F. Miranda, *J. Nat. Prod.* **1995**, *58*, 1616 – 1621.

[16] M. R. Winkle, R. C. Ronald, *J. Org. Chem.* **1982**, *47*, 2101 – 2108.

[17] S. Hanessian, D. Delorme, Y. Dufresne, *Tetrahedron Lett.* **1984**, *25*, 2515 – 2518.

[18] M. De Paolis, X. Chen, J. Zhu, *Synlett* **2004**, 729 – 731.

[19] X. Xiao, D. Bai, *Synlett* **2001**, 535 – 537.

[20] A. J. Mancuso, D. S. Brownfain, D. Swern, *J. Org. Chem.* **1979**, *44*, 4148 – 4150.

[21] G. Casiraghi, M. Cornia, G. Rassu, *J. Org. Chem.* **1988**, *53*, 4919 – 4922.

[22] a) M. De Paolis, A. Chiaroni, J. Zhu, *Chem. Commun.* **2003**, 2896 – 2897; b) X. Chen, J. Chen, M. De Paolis, J. Zhu, *J. Org. Chem.* **2005**, *70*, 4397 – 4408.

[23] For a recent review, see: S. Rendler, M. Oestreich, *Synthesis* **2005**, 1727 – 1747.

[24] a) M. Sakaitani, Y. Ohfune, *J. Org. Chem.* **1990**, *55*, 870 – 876; b) A. J. Zhang, D. H. Russel, J. Zhu, K. Burgess, *Tetrahedron Lett.* **1998**, *39*, 7439 – 7442.

[25] E. D. Cox, J. M. Cook, *Chem. Rev.* **1995**, *95*, 1797 – 1842.

[26] $TrocOCH_2CHO$ (**16**) was prepared in two steps from ethyleneglycol: 1) TrocCl (1 equiv), pyridine (1.1 equiv), ethyleneglycol (10 equiv), CH_2Cl_2, 86%; 2) Dess–Martin periodinane (1.1 equiv), CH_2Cl_2, 80%. Compound **16** has a high tendency to undergo trimerization and should be used immediately after preparation.

[27] For a 1,3-*cis*-selective Pictet–Spengler reaction, see: a) G. Massiot, T. Mulamba, *J. Chem. Soc. Chem. Commun.* **1983**, 1147 – 1149; b) P. D. Bailey, S. P. Hollinshead, N. R. McLay, K. Morgan, S. J. Palmer, S. N. Prince, C. D. Reynolds, S. D. Wood, *J. Chem. Soc. Perkin Trans. 1* **1993**, 431 – 439; c) A. G. Myers, D. W. Kung, B. Zhong, M. Movassaghi, S. Kwon, *J. Am. Chem. Soc.* **1999**, *121*, 8401 – 8402; d) A. G. Myers, D. W. Kung, *J. Am. Chem. Soc.* **1999**, *121*, 10828 – 10829.

[28] One of the referees proposed that we isolate the orthoquinone methide intermediate by using N-protected starting materials to probe the reaction sequence. We are investigating in detail the mechanism of this reaction.

[29] V. T. Ravikumar, A. H. Krotz, D. L. Cole, *Tetrahedron Lett.* **1995**, *36*, 6587 – 6590.

[30] M. De Paolis, J. Blankenstein, M. Bois-Choussy, J. Zhu, *Org. Lett.* **2002**, *4*, 1235 – 1238.

[31] For a recent comprehensive review, see: R. W. Van De Water, T. R. R. Pettus, *Tetrahedron* **2002**, *58*, 5367 – 5405.

[32] a) F. Guibé, Y. Saint M'Leux, *Tetrahedron Lett.* **1981**, *22*, 3591 – 3594; b) P. Four, F. Guibé, *Tetrahedron Lett.* **1982**, *23*, 1825 – 1828; c) for a review, see: F. Guibé, *Tetrahedron* **1998**, *54*, 2967 – 3042.

[33] Owing to the restricted availability of this family of natural products, there are very few reports in the literature that deal with SARs of these compounds, despite their medical importance; see: E. J. Martinez, T. Owa, S. L. Schreiber, E. J. Corey, *Proc. Natl. Acad. Sci. USA* **1999**, *96*, 3496 – 3501.

 © 2006 Wiley-VCH Verlag GmbH & Co. KGaA, Weinheim

Porphyrin Aggregation

DOI: 10.1002/anie.200603182

Folding and Hydrodynamic Forces in J-Aggregates of 5-Phenyl-10,15,20-tris-(4-sulfophenyl)porphyrin**

Carlos Escudero, Joaquim Crusats, Ismael Díez-Pérez, Zoubir El-Hachemi, and Josep M. Ribó**

Amphiphilic anionic porphyrins self-assemble to J-aggregates with spontaneous breaking of mirror symmetry.[1] In the case of **2** (Scheme 1) it has been statistically shown that a stirring vortex can select the resulting chirality sign.[1b–c] Although a similar result has been described in another system,[2] the

[*] C. Escudero, Dr. J. Crusats, Dr. Z. El-Hachemi, Prof. Dr. J. M. Ribó
Departament de Química Orgànica
Universitat de Barcelona
c. Martí i Franquès 1, 08028 Barcelona, Catalonia (Spain)
Fax: (+34) 933-397-878
E-mail: j.crusats@ub.edu
jmribo@ub.edu

I. Díez-Pérez
Departament de Química Física
Universitat de Barcelona
Martí i Franquès 1, 08028 Barcelona, Catalonia (Spain)

[**] This work was supported by the Ministerio de Educación y Ciencia (MAT2003-00430, AYA2006-95648-01) and belongs to the COST Action D27 (WG 0004/2). J.C. acknowledges financial support from the MEC Ramón y Cajal program. We thank Prof. F. Cunill and Dr. J. Llorens for their kind advice on the stirring hydrodynamics.

Supporting information for this article is available on the WWW under http://www.angewandte.org or from the author.

WILEY InterScience DISCOVER SOMETHING GREAT
© 2006 Wiley-VCH Verlag GmbH & Co. KGaA, Weinheim

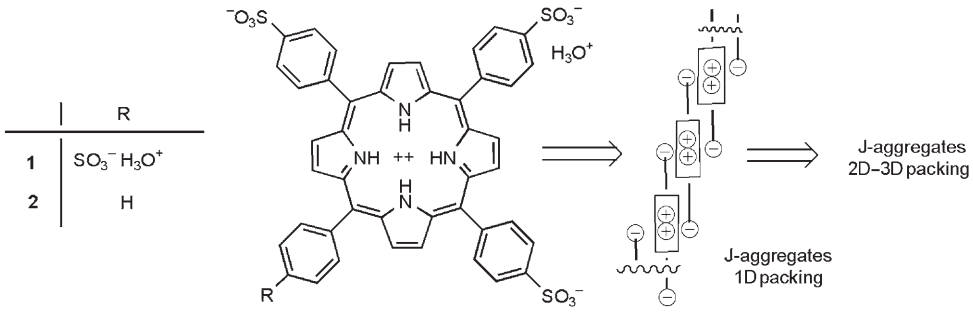

Scheme 1. Constitutional formulas of **1**, **2**, and their 1D J-aggregate structures.

origin and cause of such a singular effect is not yet understood. Here we report on new experimental results that show how the title J-aggregates undergo spontaneous folding that can be driven to helical folded tapes by hydrodynamic forces. Thereby, selection of the chirality sign, as detected by circular dichroism (CD), would be an effect of the mechanical forces of chiral hydrodynamic gradients on the formation of mesophases by way of structural transmission of chirality.

The aggregation of diprotonated 4-sulfonato-substituted *meso*-tetraphenylporphyrins is a well-studied topic.[3] All J-aggregates of this homologous series show very similar UV/Vis spectra[3f] corresponding to a basic one-dimensional (1D) structure of zwitterions stabilized by intermolecular electrostatic bonding and hydrophobic interactions (Scheme 1). However, the shape of the resulting colloidal particles depends on the *meso*-substitution pattern of the porphyrin.[1c] We have worked with pure water solutions of the free sulfonic acid forms of **1** and **2**,[3n] so that the porphyrin has only protons as counterions (absence of ion-pairing effects) in a medium of low ionic strength. Therefore, porphyrin aggregation depends only on its own concentration, which determines both the pH value of the solution (protonation of the porphyrin ring) and self-assembly to J-aggregates. Freshly prepared solutions of these porphyrins (ca. 1 mM or 0.1 mM) show fast initial J-aggregation of the monomeric zwitterions (detected by the characteristic absorption band at ca. 490 nm). Then, aggregation steadily increases in the course of weeks, in agreement with a hierarchical self-assembly process. This dramatic difference in the time evolution of the initial particles of J-aggregates compared to acidified solutions of the sodium salts of the porphyrins[1,3] has allowed us to follow the shape evolution of the mesophases during the aggregation process by tapping-mode atomic force microscopy (AFM).

In the case of **2**, freshly prepared solutions show straight tapes with constant height (3.2 ± 0.1 nm), widths of 35–60 nm, and lengths of 200–400 nm. In concentrated solutions, these initial tapes of **2** mostly adhered one to another. In some of the particles the borders and the corners show a thickness of only 1.5 nm, which points to a double-layer structure for the particle (Figure 1). A thickness of 1.5–1.6 nm agrees with that of a molecule tilted 45° (total length ca. 2.2 nm, i.e., 1.95 nm for the porphyrin molecule plus the water layers necessary to solvate the protons acting as counterions of the anionic sulfonato groups). This bilayer structure (Scheme 2) implies a hydrophobic central region. Stagnant solutions show increasing aggregation with time (UV/Vis) that corresponds to an increase in number and length of the deposited particles, which have similar width and the same thickness as the initial particles. However, after one day, the straight tapes begin to fold. This folding is accelerated by temperature (solutions in the refrigerator show folding much later than samples at room temperature). Stirring the solution also accelerates aggrega-

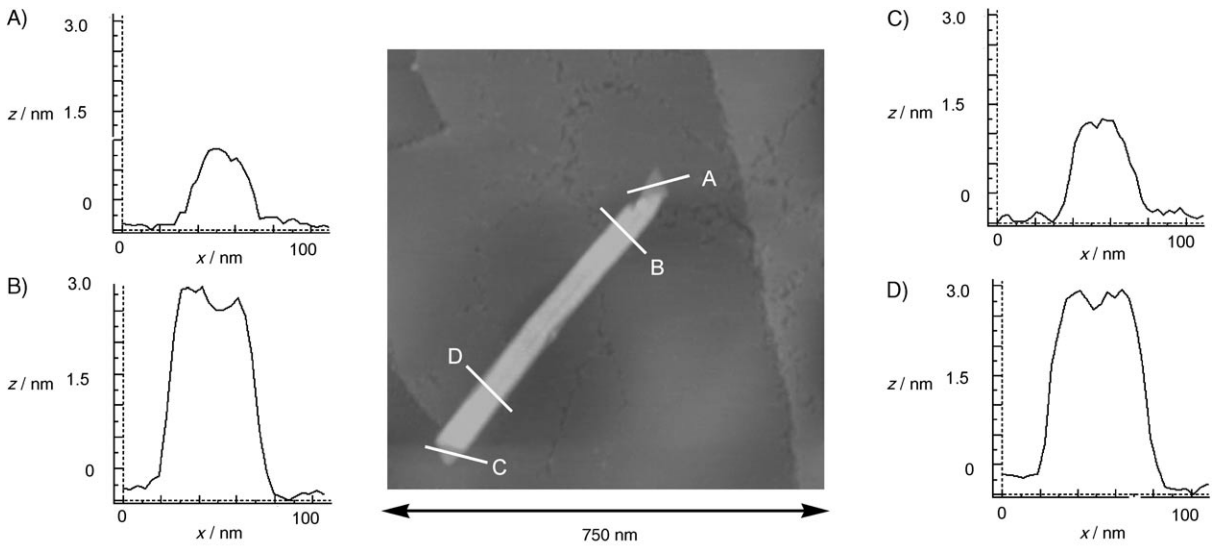

Figure 1. AFM topography image of a J-aggregate of **2**. 1.3 mM freshly prepared solution deposited on highly oriented pyrolytic graphite (HOPG; see Supporting Information). The indentation effect, manifested by differences in step height, highlights the bilayer nature of the particles. A–D) Height profiles of the indicated segments of the topography image.

 © 2006 Wiley-VCH Verlag GmbH & Co. KGaA, Weinheim

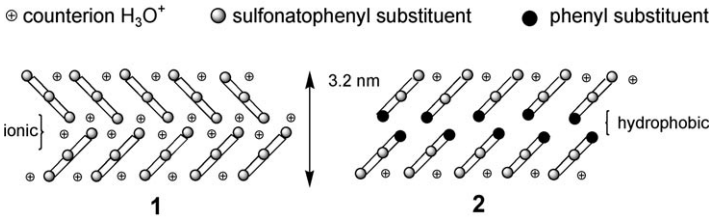

Scheme 2. Bilayer of **1** and **2** mesophases. The J-aggregation axis (Scheme 1) goes from back to front and forms an angle of about 70° to the paper plane. The present data do not allow one to infer whether the two monolayers are parallel or oblique.

tion: Freshly prepared solutions after 6 h of uniform magnetic stirring in a small tube (Supporting Information) show a degree of aggregation similar to those found in one-day-old stagnant solutions. However, the folding behavior in stagnant solutions differs dramatically from that of vortex-stirred solutions (Figure 2). In the latter, a very large proportion of

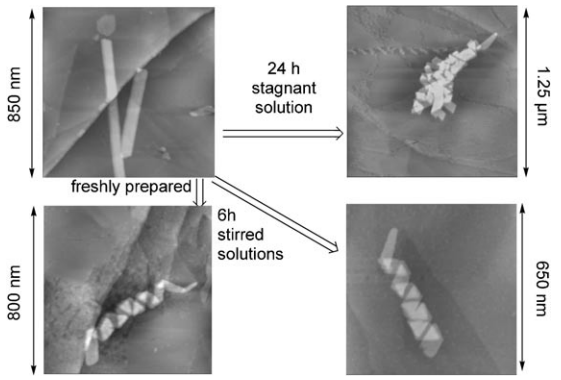

Figure 2. AFM topography images of particles of **2** (1.3 mM, deposited on HOPG) showing the onset of folding in stagnant and stirred solutions. After 6 h the stagnant solutions did not show folding. Stirring for 6 h results mostly in nonadhering long-order folded ribbons. In stagnant solutions, folding appears later and yields irregularly folded ribbons mostly adhering in bundles.

the tapes displays long-range folding order (helical ribbons), while irregular folding and bundles of tapes are rarely detected. The absence of bundles must be attributed to the effect of squeezing flows (see below), which would avoid aggregation between tapes. Furthermore, the stirred solutions show good correlation between the chirality sign of their CD spectra and the direction of stirring (Supporting Information).[4] Note that in previous studies on acidified solutions of the sodium salts,[1b–d] such a relationship could only be obtained by rotary evaporation of very dilute solutions of porphyrin, and that here the slow aggregation rates allow us to perform such experiments at constant porphyrin concentration.

Freshly prepared solutions of **1** (1.0–1.6 mM) initially show straight tapes similar to those of **2** (35–60 nm wide, 300–800 nm long, and 3.2 ± 0.2 nm in height: Supporting Information),[5] but they do not evolve to folded particles. Stagnant solutions show increased J-aggregation after one week, which according to AFM corresponds to an increase in the number of particles and in their length (micrometer size order), but with similar width and the same thickness as the initial particles. After two months, the particles can be longer than 10 μm, but no folding can be observed. Stirring increases the rate of aggregation but, in contrast to **2**, it does not lead to folding. However, the final particles in strongly stirred solutions show a narrow distribution of lengths (≤ 2 μm), which points to a mechanical breaking of the long whiskers by hydrodynamic shear forces or by impact with the stirring bar.

A recent theoretical model[6] that treats the transition from straight tubes to helices in solution as an entropically driven process can be applied to the folding observed here. In this model, the straight tube interacts with spherical particles in solution, so that folding decreases the volume available for the interaction and a free-energy gain is thus generated by the release of particles to the bulk of the solution. The entropy gain depends on the number of depleted spherical particles, their size, the dimensions of the tape, and the curvature of folding. In our case, the folding is possible for J-aggregates of **2** (hydrophobic interaction between the two layers) but not for those of **1** (ionic structure between the two layers; Scheme 2). The latter compound has only one possible planar arrangement between the two monolayers, and therefore only breaking of the tapes is possible. However, in the case of **2** the hydrophobically bonded monolayers show a plethora of structural states differing only slightly in enthalpy. In this respect, it is significant that folding only occurs when the width becomes greater than about 28 nm (Figure 3). This

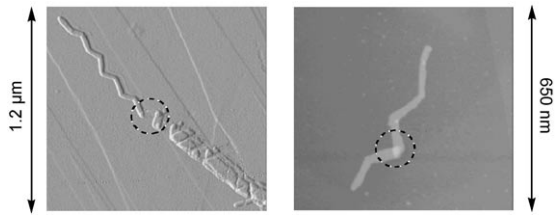

Figure 3. AFM topography (right) and amplitude (left) images of J-aggregate particles of **2** obtained by stirring. Folding (circled) only appears above a critical width (ca. 28 nm). Below this width only a zigzag shape was detected (stirred solutions).

implies that the depletion interaction occurs with rather large particles and excludes a pure hydrophobic effect as the origin of folding. These particles must be small-sized J-aggregates, oligomers, and the already relatively large monomeric porphyrin (ca. 2.5 nm^3). Since the tapes of J-aggregates and the interacting particles are both electrically charged species, the interactions between them are those acting in colloidal systems.

The role of stirring in the folding of the tapes of **2** points to the influence of hydrodynamic effects on the folding kinetics. A liquid plays a crucial role in selecting and achieving equilibrium structures in soft-matter components: It allows transition states to be reached and thereby modifies kinetic pathways.[7] The role of water in protein folding is a paradigm for this. In this respect, Brownian dynamics act as a thermal bath that provides the necessary activation energy to cross transition states. This would explain the folding in our

 © 2006 Wiley-VCH Verlag GmbH & Co. KGaA, Weinheim

stagnant solutions. Conversely, the long-order folding in vortex-stirred solutions must be the signature of hydrodynamic interactions with laminar flow (turbulent flow would have a similar effect to that of Brownian dynamics). However, a rough estimation of the Reynolds number *Re* of our experimental setup indicated that the system is not stirring in a low-*Re* regime, that is, a turbulent vortex is implied. Nevertheless, it is well known that laminar flow at the wall of the container cannot be suppressed. Thus, the long-order effect on folding is expected to have its origin in the laminar flow at the wall of the container, that is, in the return flow from the bottom to the top of the tube. Note that the helical sign of the vortex created by a stirring bar from the top to the bottom (e.g., P) changes its sign (i.e., M) in the fluid returning to the surface (same sense of circular rotation but inverse direction of progress). The fact that the previously reported selection of chirality sign in rotary evaporation experiments[1b,c] was opposite to that reported here under magnetic stirring agrees with the argument that the chirality-inducing flow is that originating at the walls: In the rotary evaporator flask the significant flow is the progress of the fluid from the top to the bottom of the flask in the last stages of the evaporation process. However, a laminar flow alone cannot explain the chiral-selection effect, because at low stirring speeds, that is, smaller *Re*, chiral selection disappears (Supporting Information). In consequence, the important point is the presence of sufficiently large hydrodynamic gradients in the boundary layer of the laminar flow created at the wall surface.

Enantiomorphic objects in a circular flow exhibit enantiotropic trajectories, as has been shown both experimentally (hemihedric crystals, 30 years ago!)[8] and theoretically (helices).[9] In our case, the resulting trajectories for enantiomorphic helices must be diastereotropic, because the shear flow is already chiral. All this suggests an evolutionary selection of one of the two helix senses, that is, particles with a given helical sense can follow the trajectory of the laminar flow while the others will be ejected towards the chaotic flow regions where "recycling" to the monomer via small oligomeric species will be more pronounced. Note that a such mechanism is only possible for chiral-shaped objects that can be classified into two homochiral classes (e.g., helices).[10]

The present results are an experimental example of how shear flows[7] can select among different pathways in a hierarchical self-assembly, and therefore between supramolecular polymorphs. This is of interest not only in the field of biopolymers, but also in supramolecular chemistry, for example, in the self-assembly of porphyrinoids mimicking natural systems.[11] In fact, previous experimental results on the influence of gravity on the mesophase structures obtained by self-assembly[12] also have their origin in hydrodynamic effects.

Received: August 4, 2006
Revised: September 1, 2006
Published online: November 13, 2006

Keywords: aggregation · chirality · foldamers · helical structures · porphyrinoids

[1] a) O. Ohno, Y. Kaizu, H. Kobayashi, *J. Chem. Phys.* **1993**, *99*, 4128–4139; b) J. M. Ribó, J. Crusats, F. Sagues, J. M. Claret, R. Rubires, *Science* **2001**, *292*, 2063–2066; c) R. Rubires, J.-A. Farrera, J. M. Ribó, *Chem. Eur. J.* **2001**, *7*, 436–446; d) J. Crusats, J. Claret, I. Diéz-Pérez, Z. El-Hachemi, H. García-Ortega, R. Rubires, F. Sagues, J. M. Ribó, *Chem. Commun.* **2003**, 1588–1589.

[2] T. Yamaguchi, T. Kimura, H. Matsuda, T. Aida, *Angew. Chem.* **2004**, *116*, 6510–6515; *Angew. Chem. Int. Ed.* **2004**, *43*, 6350–6355.

[3] a) R. F. Pasternack, P. R. Huber, P. Boyd, G. Engasser, L. Francesconi, E. Gibbs, P. Fasella, G. C. Venturo, L. de C. Hinds, *J. Am. Chem. Soc.* **1972**, *94*, 4511–4517; b) T. P. G. Sutter, R. Rahimi, P. Hambright, J. C. Bommer, M. Kumar, P. Neta, *J. Chem. Soc. Faraday Trans.* **1993**, *89*, 495–502; c) J. M. Ribó, J. Crusats, J.-A. Farrera, M. L. Valero, *J. Chem. Soc. Chem. Commun.* **1994**, 681–682; d) D. L. Akins, H.-R. Zhu, C. Guo, *J. Phys. Chem.* **1994**, *98*, 3612–3618; e) N. C. Maiti, M. Ravikanth, S. Mazumdar, N. Periasamy, *J. Phys. Chem.* **1995**, *99*, 17192–17197; f) R. Rubires, J. Crusats, Z. El-Hachemi, T. Jaramillo, M. López, E. Valls, J. A. Farrera, J. M. Ribó, *New J. Chem.* **1999**, *23*, 189–198; g) N. Micali, F. Mallamace, A. Romeo, R. Purrello, L. Monsu Scolaro, *J. Phys. Chem. B* **2000**, *104*, 5897–5904; h) N. Micali, A. Romeo, R. Lauceri, R. Purrello, F. Mallamace, L. Monsu Scolaro, *J. Phys. Chem. B* **2000**, *104*, 9416–9420; i) M. A. Castriciano, A. Romeo, V. Villari, N. Micali, L. Monsu Scolaro, *J. Phys. Chem. B* **2003**, *107*, 8765–8771; j) L. Zhang, J. Yuan, M. Liu, *J. Phys. Chem. B* **2003**, *107*, 12768–12773; k) R. Lauceri, M. De Napoli, A. Mammama, S. Nardi, A. Romeo, R. Purello, *Synth. Met.* **2004**, *147*, 49–55; l) S. Jiang, M. Liu, *J. Phys. Chem. B* **2004**, *108*, 2880–2884; m) M. A. Castriciano, A. Romeo, V. Villari, N. Micali, L. Monsu Scolaro, *J. Phys. Chem. B* **2004**, *108*, 9054–9059; n) C. Escudero, Z. El-Hachemi, J. Crusats, J. M. Ribó, *J. Porphyrins Phthalocyanines* **2006**, *9*, 852–863; o) N. Micali, V. Villari, M. A. Castriciano, A. Romeo, L. Monsu Scolaro, *J. Phys. Chem. B* **2006**, *110*, 8289–8295.

[4] Statistical AFM counting of the folding signs of the deposited particles is not possible due to the microscale of the AFM technique. The sign of the enantiomeric excess was indirectly detected by CD spectroscopy.

[5] Previous reports[1d] on the J-aggregates obtained from the sodium salts show similar types of particles, but with different and nonconstant thickness (3 and 15 nm, with steps of 1.5 nm). This points to a bilayer structure for the J-aggregates obtained here and to a multilayered structure in the case of acidified solutions of the sodium salts, due to different ionic strengths and ion-pairing effects.

[6] Y. Snir, R. D. Kamien, *Science* **2005**, *307*, 1067.

[7] a) N. Kikuchi, A. Gent, J. M. Yeomans, *Eur. Phys. J. E* **2002**, *9*, 63–66; b) H. Tanaka, *J. Phys. Condens. Matter* **2005**, *17*, S2795–S2803.

[8] D. W. Howard, E. N. Lightfoot, J. O. Hirschfelder, *AIChE J.* **1976**, *22*, 794–798.

[9] M. Makino, M. Doi, *Phys. Fluids* **2005**, *17*, 103605.

[10] E. Ruch, *Angew. Chem.* **1977**, *89*, 67–75; *Angew. Chem. Int. Ed. Eng.* **1977**, *16*, 65–72.

[11] T. S. Balaban, *Acc. Chem. Res.* **2005**, *38*, 612–623.

[12] C. Papaseit, N. Pochon, J. Tabony, *Proc. Natl. Acad. Sci. USA* **2000**, *97*, 8364–8368.

 © 2006 Wiley-VCH Verlag GmbH & Co. KGaA, Weinheim

Cluster Compounds

DOI: 10.1002/anie.200603169

Searched For and Found: Analogies between Reduced Oxomolybdates and Cluster Compounds of Rare Earth Metals**

*Lorenz Kienle, Hansjürgen Mattausch, and Arndt Simon**

The concept of cluster condensation[1] has proved valuable as an ordering scheme for structures of metal-rich compounds, and it has frequently opened new areas.[2] Reduced oxomolybdates illustrate the value of the concept particularly well. In their structures discrete cluster anions $[Mo_{4n+2}O_{6n+4}]^{(n+3)-}$ occur which are formed from $n\{Mo_6O_{12}\}$ clusters linked through opposite edges of the Mo_6 octahedra. So far, monomeric and oligomeric entities with $n = 1$–6[3] are known as well as the polymeric Mo_4O_6 chain with $n = \infty$.[4] Oligomeric clusters occur in crystal structures which are composed of a single type of cluster only, as well as of different types of clusters in ordered[5] or disordered arrays.[6]

With rare earth metals (Ln), compounds containing discrete $[Ln_6ZX_{12}]$[7] and $[Ln_{10}(Z)_2X_{18}]$[8] clusters (X = halide) have been known for a long time. These compounds correspond to the initial members ($n = 1$ and 2, respectively) of the molybdenum cluster series. Owing to the electron deficiency of the rare earth metals, additional endohedral atoms or groups of atoms (Z) are incorporated in the cluster centers which (over)compensate for the lack of metal–metal bonding by strong Ln–Z bonding.[2a,9] The polymeric chain Ln_4ZX_6 was also found repeatedly.[10] Recently, we characterized $Ln_{14}(C_2)_3I_{20}$ (Ln = La, Ce) as the first representatives for $n = 3$.[11] The details of preparation of the ordered phases are quite critical. Minute deviations from the optimized reaction temperatures[12] lead to heterogeneous products which exhibit characteristic disorder phenomena in the crystals. The disorder is seen in single-crystal X-ray analyses, and its nature becomes clear from investigations of the real structure in the electron microscope.

The heterogeneous character of a sample of $La_{14}(C_2)_3I_{20}$ prepared at 900 °C shows up in the X-ray as well as the electron diffraction pattern of a selected single crystal. The observed reflections in the latter are shown and interpreted (Figure 1) in terms of coherently intergrown domains of $La_{14}(C_2)_3I_{20}$ and $La_{10}(C_2)_2I_{18}$ clusters that are arranged layerwise. Real structures of this type[13] have not been detected before in cluster phases of rare earth metals; however, they

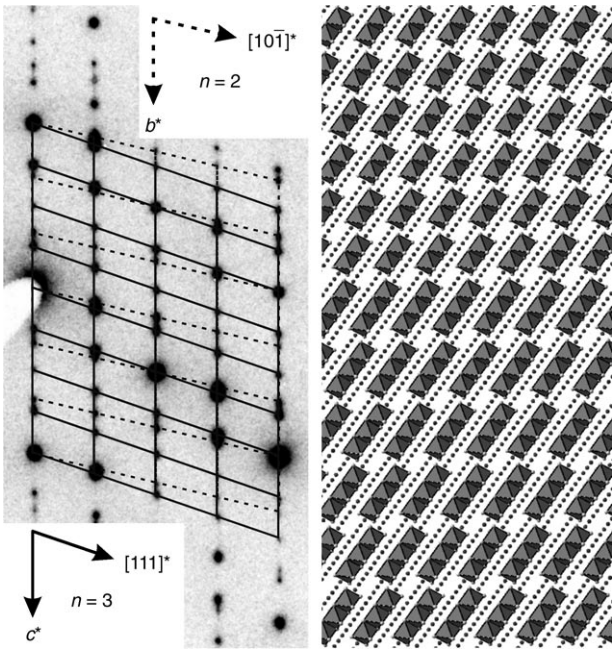

Figure 1. Left: Electron diffraction pattern, zone axis [$\bar{1}$10] referring to $n = 3$; right: scheme of an intergrowth of $La_{14}(C_2)_3I_{20}$ ($n = 3$) and $La_{10}(C_2)_2I_{15}$ ($n = 2$).

are reminiscent of a similar intergrowth with oxomolybdates, for which larger clusters ($n > 3$) also frequently occur.[6]

A systematic search for such larger clusters with rare earth metals finally was successful through concentration on crystals which attracted attention owing to diffuse streaks in their electron diffraction patterns. In Figure 2 simulated contrasts of a model structure are shown which is composed of cluster layers with $n = 2$, 3, and 4. There is a clear correlation between the respective length of the cluster and the corresponding contrasts at varying focus values. The different unit cells for each layer are evident. In the Scherzer focus[14] the distances between the elongated light spots (parallelogram corners) are a measure of the cluster length. Figure 3 presents the experimentally observed contrasts in a disordered sample of mean composition $Ce_{14}(C_2)_3I_{20}$. These contrasts can be associated with well-defined cluster sizes. Whereas Figure 3a reproduces layered domains of clusters with $n = 1$, 2, and 3 which are well-known, though observed for the first time in compounds of cerium, Figure 3b contains the images of significantly larger clusters ($n = 8$, 10). Extended investigations of numerous crystals verify the existence of an entire spectrum of clusters with $n > 3$.

The results described above establish surprising similarities in the structural chemistry of reduced oxomolybdates and that of carbide halides of rare earth metals. However, significant differences also exist. On the one hand, the cluster sizes that are observed with the compounds of rare earth metals exceed those of oxomolybdates, which does not seem to be a principal difference but rather hints at experimental deficiencies to be investigated further. On the other hand, there is an essential difference. In the oxomolybdates the clusters are anions and have to be interconnected in a definite way to provide space for the cations, for example, in

[*] Dr. L. Kienle, Dr. H. Mattausch, Prof. Dr. A. Simon
Max-Planck-Institut für Festkörperforschung
Heisenbergstr. 1, 70569 Stuttgart (Germany)
Fax: (+49) 711-689-1642
E-mail: A.Simon@fkf.mpg.de

[**] Thanks are due to Viola Duppel for electron microscopic investigations and to Roland Eger for numerous sample preparations.

InterScience
© 2006 Wiley-VCH Verlag GmbH & Co. KGaA, Weinheim

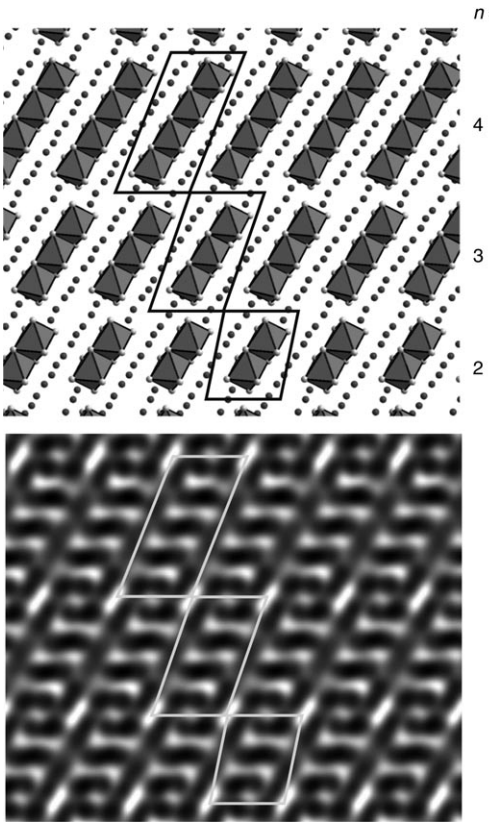

Figure 2. Structure model with $n = 2$, 3, and 4; top: projection, zone axis [$\bar{1}10$] referring to $n = 3$; bottom: simulated micrograph ($\Delta f = -55$ nm, thickness: 3.5 nm).

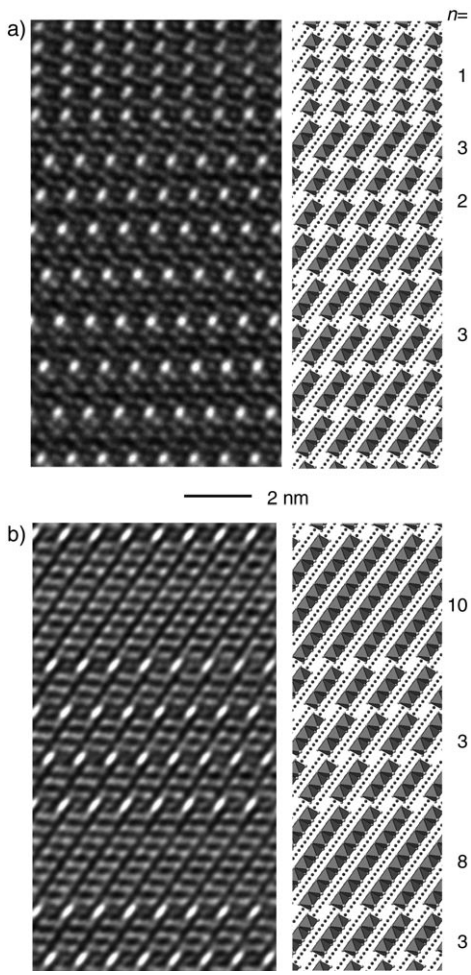

Figure 3. High-resolution micrograph and structure schemes for intergrowth of layers with a) $n = 1$, 2, 3 and b) $n = 3$ and $n = 8$, 10 (zone axis: [$\bar{1}10$] referring to $n = 3$).

$In_{n+1}Mo_{4n+2}O_{6n+4}$.[3–5] In contrast, the carbide halide clusters are neutral entities, allowing for variable patterns of interconnection and resulting in three homologous series ($Ln_{4n+2}Z_nX_{6n+4}$[15,10], $Ln_{4n+2}Z_nX_{6n+6}$,[8] and $Ln_{4n+2}Z_nX_{5n+5}$[15]), which are characterized by different kinds of bridging through X atoms.[11] Representatives of all these series are known particularly for $n = 2$ and as final members with $n = \infty$. With these findings, a wide-open field of systematic preparations lies ahead.

Experimental Section

Heavily disordered real crystals of $La_{14}(C_2)_3I_{20}$ are obtained by weighing La/LaI_3/C in a ratio of 11:10:9 and annealing at 900 °C (12 days).

Strongly disordered crystals of $Ce_{14}(C_2)_3I_{20}$ are obtained by weighting Ce/CeI_3/C in a ratio of 9:10:3 (900 °C, 21 days) with $Ce_5C_2I_9$ and $Ce_6C_2I_{10}$ as by-products.[11]

Electron microscopy: HRTEM investigations were performed with a Philips CM30 ST electron microscope (300 kV, LaB_6 cathode). Crystals of the moisture-sensitive compounds were ground under dry argon and transferred to the microscope by using a self-constructed tool (P. O. Jeitschko, A. Simon, R. Ramlau, H. Mattausch, *Eur. Microsc. Anal.* **1997**, *2*, 21). For SAED investigations, a diaphragm limited the electron diffraction to a selected circular area (diameter 100 nm). All high-resolution micrographs were filtered after Fourier transformation by applying a suitable mask (software: Digital Micrograph 3.6.1, Gatan). The EMS program package (P. A. Stadelmann, *Ultramicroscopy* **1987**, *21*, 131) served for the simulation of high-resolution micrographs (multislice procedure $C_s = 1.15$ mm, $\Delta = 7$ nm, $\alpha = 1.2$ mrad).

X-ray diffraction: Powders of the reaction products were analyzed by X-ray diffraction ($Cu_{K\alpha 1}$, $\lambda = 1.54056$ Å, internal standard Si with $a = 5.43035$ Å, Fujifilm BAS-5000 image-plate system) by means of a modified Guinier technique (A. Simon, *J. Appl. Crystallogr.* **1970**, *3*, 11) to characterize the phases under investigation. Precession photographs were recorded for checking the quality of single crystals.

Received: August 4, 2006
Published online: October 30, 2006

Keywords: cerium · cluster compounds · electron microscopy · lanthanum · rare earths

[1] A. Simon, *Angew. Chem.* **1981**, *93*, 23; *Angew. Chem. Int. Ed. Engl.* **1981**, *20*, 1; A. Simon, *Angew. Chem.* **1988**, *100*, 163; *Angew. Chem. Int. Ed. Engl.* **1988**, *27*, 159.

[2] a) A. Simon, H. Mattausch, G. J. Miller, W. Bauhofer, R. K. Kremer in *Handbook on the Physics and Chemistry of Rare Earths*, *Vol. 15* (Eds.: K. A. Gschneidner, L. Eyring), Elsevier Science, Amsterdam, **1991**, p. 191; b) J. D. Corbett, *J. Chem. Soc. Dalton Trans.* **1996**, 575; c) G. Meyer, *Chem. Rev.* **1998**, *98*, 3295;

 © 2006 Wiley-VCH Verlag GmbH & Co. KGaA, Weinheim

d) A. Simon, H. Mattausch, M. Ryazanov, R. K. Kremer, *Z. Anorg. Allg. Chem.* **2006**, *632*, 919.
[3] a) $n=1$: S. J. Hibble, A. K. Cheetham, A. R. L. Bogle, H. R. Wakerley, D. E. Cox, *J. Am. Chem. Soc.* **1988**, *110*, 3295; b) $n=2$: R. Dronskowski, A. Simon, *Angew. Chem.* **1989**, *101*, 775; *Angew. Chem. Int. Ed. Engl.* **1989**, *28*, 758; c) $n=3$: G. L. Schimek, D. E. Nagaki, R. E. McCarley, *Inorg. Chem.* **1994**, *33*, 1259; d) $n=4$: E. Fais, H. Borrmann, H. Mattausch, A. Simon, *Z. Anorg. Allg. Chem.* **1995**, *621*, 1178; e) $n=5$: R. Dronskowski, H. Mattausch, A. Simon, *Z. Anorg. Allg. Chem.* **1993**, *619*, 1397.
[4] C. C. Torardi, R. E. McCarley, *J. Am. Chem. Soc.* **1979**, *101*, 3963.
[5] H. Mattausch, A. Simon, E.-M. Peters, *Inorg. Chem.* **1986**, *25*, 3428.
[6] a) A. Simon, W. Mertin, H. Mattausch, R. Gruehn, *Angew. Chem.* **1986**, *98*, 831; *Angew. Chem. Int. Ed. Engl.* **1986**, *25*, 845; b) R. Ramlau, *J. Solid State Chem.* **1997**, *130*, 290.
[7] T. Hughbanks, J. D. Corbett, *Inorg. Chem.* **1989**, *28*, 631.
[8] E. Warkentin, R. Masse, A. Simon, *Z. Anorg. Allg. Chem.* **1982**, *491*, 323.
[9] S. Satpathy, O. K. Andersen, *Inorg. Chem.* **1985**, *24*, 2604.
[10] a) For Sc_4Cl_6C: S.-J. Hwu, J. D. Corbett, *J. Solid State Chem.* **1986**, *64*, 331; b) for Gd_4SiBr_6: H. Mattausch, A. Simon, *Z. Kristallogr. New Cryst. Struct.* **2005**, *220*, 1.
[11] H. Mattausch, A. Simon, L. Kienle, C. Hoch, C. Zheng, R. Kremer, *Z. Anorg. Allg. Chem.* **2006**, *632*, 1661.
[12] Ordered crystals were only obtained in long-term-annealed samples ($T=930\,^{\circ}C$).
[13] A. Magneli, *Microsc. Microanal. Microstruct.* **1990**, *5*/6, 299.
[14] O. Scherzer, *J. Appl. Phys.* **1949**, *20*, 20.
[15] H. Mattausch, E. Warkentin, O. Oeckler, A. Simon, *Z. Anorg. Allg. Chem.* **2000**, *626*, 2117.

 © 2006 Wiley-VCH Verlag GmbH & Co. KGaA, Weinheim

Low-Valent Carbon

DOI: 10.1002/anie.200602552

Carbodiphosphoranes: The Chemistry of Divalent Carbon(0)

Ralf Tonner, Florian Öxler, Bernhard Neumüller, Wolfgang Petz,* and Gernot Frenking**

The synthetic chemistry of carbon is mostly concerned with tetravalent carbon(IV) compounds in which all four valence electrons are used for chemical bonding. The divalent carbon(II) chemistry of carbene compounds played only a minor role until 1991 when Arduengo et al.[1] introduced imidazolin-2-ylidenes (N-heterocyclic carbenes, NHCs) as synthetically useful stable molecules. It was later realized that stable carbenes had already been isolated in 1985 by Bertrand and co-workers,[2] but it took several years before phosphanylcarbenes were recognized as C^{II} compounds. The chemistry of carbenes, which have one σ-type lone-pair orbital, has enormously flourished, and the scope of divalent carbon(II) chemistry has been significantly extended since the successful isolation of the first stable carbenes.[3] In a recent communication Baceiredo and co-workers[4a] reported the first syntheses of five-membered cyclic carbodiphosphoranes that are stable at room temperature,[4b] and these were described as further examples of divalent carbon compounds.

Herein, we present theoretical and experimental evidence suggesting that carbodiphosphoranes (CDPs), unlike carbenes, are divalent carbon(0) compounds in which the valence electrons of carbon remain as two lone pairs of electrons which are not engaged in chemical bonding in the free molecules (Scheme 1). CDPs have a divalent carbon atom

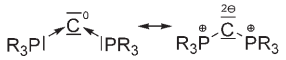

Scheme 1. Bonding situation in carbodiphosphoranes in terms of donor–acceptor interactions (left) yielding the Lewis structure (right).

like carbenes, but the carbon–phosphorous bonds in $(R_3P)_2C$ come from P→C donor–acceptor interactions rather than electron-sharing C−R bonds in carbenes R_2C. The chemistry of the former compounds exhibits novel features which distinguish them from carbenes.

The first CDP, $(Ph_3P)_2C$ (**1e**), was synthesized already in 1961 by Ramirez et al., who discussed several resonance forms for describing the carbon–phosphorous bonding situation.[5] The chemistry of CDPs was studied experimentally in the following years by several groups, and numerous compounds containing the CDP moieties were isolated.[6] The bonding in CDP compounds has in a few cases been described in terms of two electron pairs[7] at the central carbon atom, but the general description of the bonding situation in carbodiphosphoranes either uses the notation $R_3P{=}C{=}PR_3$ or it is compared with carbenes.[4,6]

Figure 1 shows the two highest-lying MOs of **1e**. The shape of the orbitals suggests that the HOMO and HOMO−1 should be interpreted as lone-pair MOs of π and σ symmetry, but not as bonding orbitals. This interpretation is supported

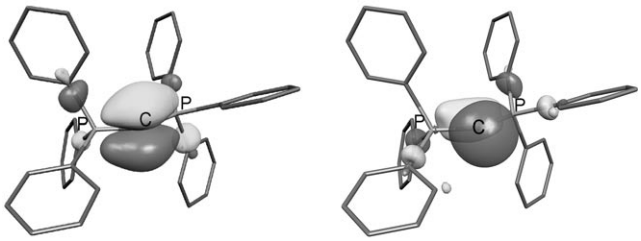

Figure 1. HOMO (left) and HOMO−1 (right) of $C(PPh_3)_2$ (**1e**). The picture shows the Kohn–Sham orbitals taken from BP86/SVP calculations.

[*] R. Tonner, F. Öxler, Prof. Dr. B. Neumüller, Prof. Dr. W. Petz, Prof. Dr. G. Frenking
Fachbereich Chemie
Philipps-Universität Marburg
Hans-Meerwein-Strasse, 35032 Marburg (Germany)
Fax: (+49) 6421-282-5566
E-mail: neumuell@chemie.uni-marburg.de
petz@staff.uni-marburg.de
frenking@chemie.uni-marburg.de

Supporting information for this article is available on the WWW under http://www.angewandte.org or from the author.

InterScience
© 2006 Wiley-VCH Verlag GmbH & Co. KGaA, Weinheim

by a natural bond orbital (NBO) analysis of **1e**. Inspection of the occupied natural orbitals reveals that there are two lone-pair orbitals at the central carbon atom and two P–C1 σ-bonding orbitals, but no lone-pair orbitals at phosphorous. The latter MOs indicate that the bonding between the phosphane groups and the central carbon atom comes from donor–acceptor interactions between the phosphorous lone-pair orbitals and empty valence orbitals on carbon. The atomic partial charge at the central carbon atom calculated by the NBO method has a large negative value ($-1.43e$), which agrees with the bonding scheme. The four valence electrons of carbon make up two lone-pair orbitals which have only small coefficients at the P atoms and α-C atoms of the phenyl groups, thus indicating weak back-donation of the lone-pair MOs into the antibonding P–C^{Ph} orbitals. The latter interaction, which is also called negative hyperconjugation,[8] is characteristic for the bonding in ylides.[9]

Is the theoretical finding about the bonding situation in **1e** supported by its chemical properties? Table 1 gives the calculated[10] first and second proton affinities (PAs) for acyclic CDPs $(R_3P)_2C$ (**1a–h**) and for some P-heterocyclic CDPs **2a–m** together with the PA values for NHCs **3a**, **3b**, and proton sponge **4** as reference molecules (Scheme 2). The syntheses and X-ray structures of **2f** and **2g** were reported in the paper by Baceiredo et al.[4a] The calculations predict that all CDPs have a very large PA. Depending on the substituent, the PA of the CDPs may become clearly larger than the PA of previously investigated NHCs **3**[11] and proton sponge **4**.[12] Even the second PA of **1a–h** is still rather high. The theoretical result is supported by experimental observations. The salt compound $[(PPh_3)_2CH_2][FeCl_4]_2$ containing the dication $[\mathbf{1e}(H)_2]^{2+}$ has been prepared, and X-ray structure analyses were reported by two groups.[13] Table 2 gives the most important experimental and theoretical bond lengths and angles in **1e**, $[\mathbf{1e}H]^+$, and $[\mathbf{1e}(H)_2]^{2+}$.

The experimental P-C-P angle in $[\mathbf{1e}(H)_2]^{2+}$ (123.4(2)°) is more acute than the related angle in singly protonated $[\mathbf{1e}H]^+$ (130.4(3)°).[14] The calculated P-C-P angles for **1e** (135.0°) and for $[\mathbf{1e}H]^+$ (132.4°) are only slightly larger than the experimental data. The theoretical value for $[\mathbf{1e}(H)_2]^{2+}$ (131.0°) indicates further closing of the P-C-P angle, but not as much as given by the experimental value. The calculations indicate that the smaller P-C-P angle in the dication could be a result of intermolecular forces. In the series **1e**, $[\mathbf{1e}H]^+$, $[\mathbf{1e}(H)_2]^{2+}$, the experimental average P–C1 bond lengths increase from 163.5(5) to 169.9(3) to 181.6(4) pm, respectively, which is in good agreement with the calculated data (Table 2). The lengthening of the P–C bond from the neutral compound to the dication can be explained with the loss of

Table 1: Calculated (RI-MP2/TZVPP//RI-BP86/SVP) first and second proton affinities (PAs) in kcal mol^{-1}. For the structural formulas, see Scheme 2.

			1st PA	2nd PA
	Carbodiphosphoranes			
	R			
1a	F		209.3	70.6
1b	Cl		227.9	116.4
1c	H		255.7	114.4
1d	Me		278.4	156.2
1e	Ph		280.0	185.6
1f	NH_2		280.0	153.5
1g	NMe_2		279.9	174.9
1h			287.6	188.9
	P-heterocyclic CDPs			
	R^1	R^2		
2a	N-H	H	251.5	110.5
2b	N-H	Me	270.8	143.3
2c	N-H	NH_2	271.4	138.1
2d	N-H	NMe_2	275.3	157.8
2e	N-Me	NMe_2	277.6	160.3
2f	N-Ph	$NiPr_2$	284.2	188.3
2g	N-Ph	$NiPr_2$, $iPr_2N(CH_2)_2NiPr_2$	284.5	179.0
2h	C-H	H	261.8	119.1
2i	C-H	Me	278.2	149.7
2k	C-H	NH_2	277.5	144.6
2l	C-H	NMe_2	280.0	162.6
2m	C-H	$NiPr_2$	287.3	190.5
	Reference molecules			
3a			273.4	104.8
$C(NMe_2)_2$ (**3b**)			271.7	13.8
4			253.1	–

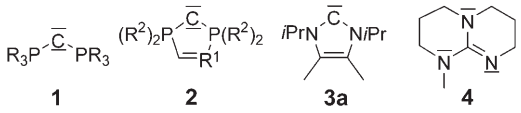

Scheme 2. Carbodiphosphoranes (**1**); P-heterocyclic carbodiphosphoranes (**2**); NHCs (**3**); proton sponge (**4**).

Table 2: Experimental and calculated bond lengths [pm] and angles [°] and atomic partial charge of the central carbon atom q(C) at the BP86/TZVPP2//RI-BP86/SVP level.

Variable	$(Ph_3P)_2C$ **1e** Exptl[a] (*calcd*)	$[(Ph_3P)_2CH]^+$ $[\mathbf{1e}H]^+$ Exptl[b] (*calcd*)	$[(Ph_3P)_2CH_2]^{2+}$ $[\mathbf{1e}(H)_2]^{2+}$ Exptl[c] (*calcd*)	$[\{(Ph_3P)_2CH\}_2Ag]^{3+}$ $[(\mathbf{1e}H)_2Ag]^{3+}$ Exptl[d] (*calcd*)
d(P-C1)	163.5(5) (*166.2*)	169.9(3) (*173.5*)	180.1(4)–181.6(4) (*186.9*)	177.0(7) (*182.8*, *183.0*)
d(C1-H)	–	86(4) (*110.0*)	97(4) (*110.0*)	81(7) (*111.2*)
d(P-C^{Ph})	183.1(5) (*185.9–186.8*)	179.4(2)–181.7(2) (*183.7–184.1*)	178.3(4)–180.1(4) (*181.2–182.0*)	178.3(6)–181.6(6) (*182.2–182.5*)
∢(P-C1-P)	131.7(3) (*135.0*)	130.4(3) (*132.4*)	123.4(2) (*131.0*)	119.9(4) (*120.9*)
q(C)	*−1.43*	*−1.33*	*−1.07*	*−1.34*

[a] Reference [5b]. [b] Reference [14]. [c] Reference [13a]. [d] This work.

 © 2006 Wiley-VCH Verlag GmbH & Co. KGaA, Weinheim

charge donation from the carbon lone-pair orbitals into the P–C^{Ph} vacant antibonding orbitals. Table 2 shows that the P–C^{Ph} bond lengths decrease in the series **1e**, $[\mathbf{1e}H]^+$, $[\mathbf{1e}(H)_2]^{2+}$. Note that the carbene carbon atom retains its negative partial charge in the cation $[\mathbf{1e}H]^+$ ($-1.33\,e$) and even in the dication $[\mathbf{1e}(H)_2]^{2+}$ ($-1.07\,e$).

Using theoretical methods, we explored whether **1e** might be capable of binding two Lewis acids that are bulkier than H^+. To this end we calculated complexes of $(R_3P)_2C$ where R = H, Me, Ph (**1c–e**) with two ligands BH_3, BCl_3, and $AlCl_3$. Table 3 shows that **1c** and **1d** should bind two Lewis acids of each kind while **1e** binds only two BH_3 molecules. This result can be explained with steric repulsion of the bulky PPh_3 groups. We carried out experiments aiming at the synthesis of complexes of **1e** with two Lewis acids. Reaction of **1e** with diborane gave only the complex with one BH_3 ligand.[15]

Table 3: Calculated (RI-MP2/TZVPP//RI-BP86/SVP) bond dissociation energies D_o^{298} [kcal mol^{-1}] of CDP complexes with various Lewis acids (LA).

		R_3P, R_3P C–LA → R_3P, R_3P C + LA			R_3P, R_3P C(LA)(LA) → R_3P, R_3P C–LA + LA		
	R	BH_3	BCl_3	$AlCl_3$	BH_3	BCl_3	$AlCl_3$
1c	H	29.3	33.9	44.0	25.5	14.8	23.1
1d	Me	34.0	36.4	51.0	28.4	9.6	27.0
1e	Ph	27.5	35.9	50.9	15.8	−32.7	−3.9

However, we succeeded in the synthesis of another dicoordinated CDP complex in which the HOMO and the HOMO−1 of **1e** are engaged in the bonding to two ligands. When $AgBF_4$ is treated with readily available $[(PPh_3)_2CH][BF_4]$, the complex $[\{(PPh_3)_2CH\}_2Ag][BF_4]_3$ (**5**), which contains the trication $[(\mathbf{1e}H)_2Ag]^{3+}$, can be isolated in good yield.[16] The crystals of **5**, which include five CH_2Cl_2 solvent molecules in the unit cell, were obtained from CH_2Cl_2/*n*-pentane solution. The unit cell contains two crystallographically independent salt units. The molecular structure of one unit is shown in Figure 2.[17] The trication is centrosymmetric with the silver atom at the inversion center. The $[BF_4]^-$ counterions are disordered; one of them could be refined in two positions. There are no remarkable contacts between the trication and the anions or the solvent molecules. All CH_2Cl_2 molecules are more or less disordered, and three of the five molecules were refined in split positions. Owing to the centrosymmetry of the cation, the C-Ag-C angle is exactly linear. The Ag–C bond length (220.9(7) pm) is one of the longest known silver–carbon bond lengths, which normally range between 200 and 220 pm. The Ag–C bond length in a related biscarbene complex that contains an NHC-type ligand is about 207 pm,[18] and that in $[Ag(CO)_2]^+$ is 214 pm.[19] The C1 atom in **5** is in an approximately tetrahedral environment. The P–C1 bond lengths in **5** (177.0(7) pm) are about 8 pm longer than in the free cation, but shorter than in the dication of $[(PPh_3)_2CH_2][FeCl_4]_2$. The calculated geometry of $[(\mathbf{1e}H)_2Ag]^{3+}$ is in very good agreement with experimental data (Table 2). The bonding situation in **5** is highly unusual—two protonated CDP cations serve as electron donors (!) to the Ag^+ center to yield a stable trication. The NBO analysis suggests that the carbon donor atoms in $[(\mathbf{1e}H)_2Ag]^{3+}$ still have *negative* partial charges of $-1.34\,e$. The related complexes $[(PPh_3)_2CHAuX][CF_3SO_3]$ (X = Cl, C_6H_5) have been isolated, and the structures were characterized by X-ray analysis by Laguna and co-workers.[20] The latter compounds contain a singly charged cation in which the CDP serves as a four-electron donor.

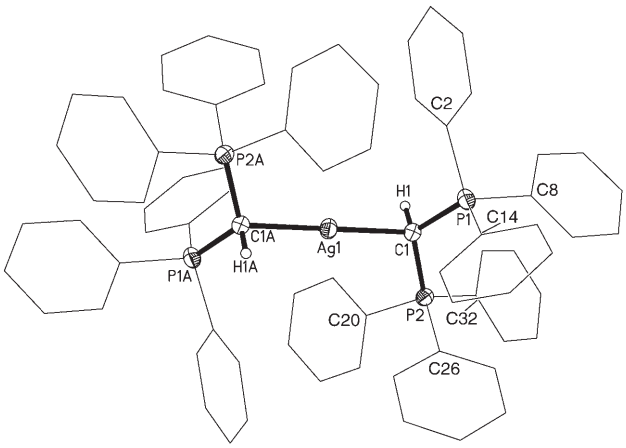

Figure 2. X-ray crystal structure of $[(\mathbf{1e}H)_2Ag]^{3+}$, the trication of **5**. The hydrogen atoms on the phenyl rings are omitted for clarity. The atoms are represented by Gaussian ellipsoids set at 40% probability. Selected bond lengths [pm] and angles [°]: Ag1-C1 220.9(6), P1-C1 177.0(7), P1-C2 180.8(8), P1-C8 180.6(6), P1-C14 179.6(7), P2-C1 177.9(7), P2-C20 178.3(7), P2-C26 179.3(7), P2-C32 180.6(6), C1-H1 81(7); C1-Ag1-C1a 180.00(0), C1-P1-C2 108.2(4), C1-P1-C8 113.2(4), C1-P1-C14 113.1(4), C1-P2-C20 108.8(4), C1-P2-C26 111.6(4), C1-P2-C32 113.9(3), Ag1-C1-P1 113.4(4), Ag1-C1-P2 111.0(4), P1-C1-P2 119.9(4), Ag1-C1-H1 97.(6), P1-C1-H1 103.(6), P2-C1-H1 110.(6).

As a further probe for the ability of CDP to serve as a four-electron donor, we calculated[10] the geometry and bond-dissociation energy (BDE) of the complex $[(PH_3)_2C(AuCl)_2]$ (**6**) and compared it with the carbene complex [(Im)C-$(AuCl)_2$] (**7**) [(Im)C = 1,3-dihydroimidazol-2-ylidene]. The BDE of one AuCl ligand in **6** ($D_e = 72.3$ kcal mol^{-1}) is much higher than in **7** ($D_e = 51.1$ kcal mol^{-1}). Nevertheless, the latter value should be large enough to synthesize **7** in a condensed phase. We analyzed the bonding situation in **6** and **7** with the atoms-in-molecule (AIM) method.[21] Figure 3 shows the Laplacian distribution of the two molecules possessing C_{2v} symmetry in the $C(AuCl)_2$ plane.

The contour-line diagrams exhibit significant differences between the two compounds. The carbon donor atom of $[(PH_3)_2C(AuCl)_2]$ has two areas of charge concentration ($\nabla^2\rho(r) < 0$, solid lines) pointing in the direction of the AuCl ligands (Figure 3a) while the carbene carbon atom of [(Im)C-$(AuCl)_2$] has only one broadly distributed charge concentration (Figure 3b). The latter compound has an Au–Au bond path and a ring critical point while the former compound does not. According to the AIM results there is a gold–gold bond (aurophilic interaction[22]) in the carbene complex but not in the CDP complex. The related complex $[(PPh_3)_2C(AuCl)_2]$ ($[\mathbf{1e}(AuCl)_2]$) has recently been synthesized by Vicente et al.[23] The experimental Au–C bond lengths in $[\mathbf{1e}(AuCl)_2]$

 © 2006 Wiley-VCH Verlag GmbH & Co. KGaA, Weinheim

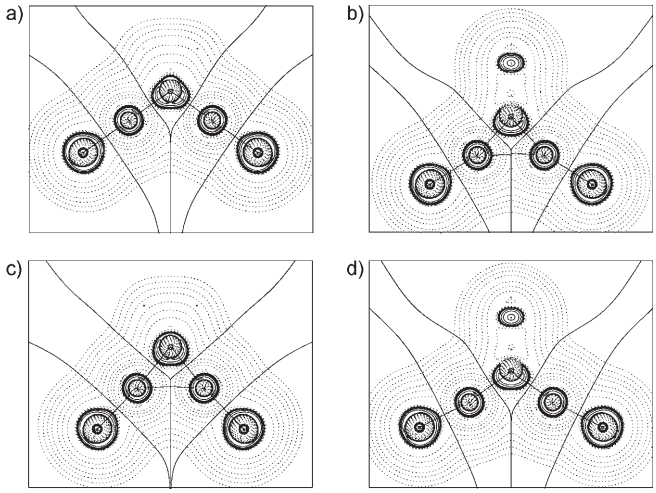

Figure 3. Contour-line diagrams $\nabla^2\rho(r)$ of the CDP and carbene complexes: a) $[(PH_3)_2C(AuCl)_2]$, optimized geometry; b) $[(Im)C(AuCl)_2]$, optimized geometry; c) $[(PH_3)_2C(AuCl)_2]$, calculated with the shorter Au–Au distance of the carbene complex (275.0 pm); d) $[(Im)C(AuCl)_2]$, calculated with the longer Au–Au distance of the CDP complex (342.3 pm). Solid lines indicate areas of charge concentration ($\nabla^2\rho(r) < 0$) while dashed lines show areas of charge depletion ($\nabla^2\rho(r) > 0$). The thick solid lines connecting the atomic nuclei are the bond paths. The thick solid lines separating the atomic basins indicate the zero-flux surfaces crossing the molecular plane.

(207.8 and 207.4 pm) are in good agreement with the calculated value for $[(PH_3)_2C(AuCl)_2]$ (208.8 pm), but the theoretical Au–Au distance (342.3 pm) is significantly longer than the experimental data (314.3 pm). The shorter Au–Au bond revealed by the X-ray structure might be caused by solid-state effects. A geometry optimization of **6**, whereby the Au–Au distance was frozen at the experimental value, gave a structure which was only slightly higher in energy (ca. 1 kcal mol^{-1}) than the energy-minimum form. The topological analysis of the electronic structure with the AIM method yielded the same pattern as with the fully optimized structure, that is, there is no Au–Au bond path. The calculated Au–Au distance in $[(Im)C(AuCl)_2]$ is much shorter (275.0 pm) than in $[(PH_3)_2C(AuCl)_2]$. We optimized the geometry of the carbene complex $[(Im)C(AuCl)_2]$ with the longer Au–Au distance from the CDP complex that was kept frozen. We also optimized the geometry of $[(PH_3)_2C(AuCl)_2]$ with the shorter gold–gold distance of the carbene complex. Figure 3c shows that the latter species now has an Au–Au bond path, but the carbon donor atom retains two distinctive areas of charge concentration in the direction of the gold–carbon bonds. The Laplacian of $[(Im)C(AuCl)_2]$, calculated with the longer Au–Au distance (Figure 3d), has no Au–Au bond path anymore, but there is still only one broad area of charge concentration whose maximum points toward the midpoint of the Au–Au distance.

In summary, our joint theoretical and experimental study provides evidence that carbodiphosphoranes are carbon(0) compounds which have two electron lone pairs at the central carbon atom. This situation yields an extremely high proton affinity. The latter can be utilized for synthesizing compounds that exhibit unusual features, such as dication $[(Ph_3P)_2CH_2]^{2+}$ and trication $[\{(Ph_3P)_2CH\}_2Ag]^{3+}$. We think that there might be still more surprising structures and reactivities waiting to be explored for CDP compounds and related species of the general formula L_2E with donor–acceptor bonds L→E. For example, substitution of the PR_3 ligands in CDP by CO leads to phosphaketene ylides $(R_3P)C(CO)$ and carbon suboxide C_3O_2. The former compound with R = phenyl has a P-C-P angle of 145.5°[24] Experimental studies have been mainly interpreted and guided by sketching the bonding situation as $R_3P{=}C{=}C{=}O$.[6b] The chemistry of carbon suboxide, which has a quasilinear equilibrium geometry with a shallow bending potential,[25] has so far been focused on the reactivity of the double bonds O=C=C=C=O.[26] It thus appears worthwhile to study the reactivity of the compounds considering a bonding situation with a central carbon(0) atom.

Received: June 26, 2006
Published online: October 31, 2006

Keywords: bonding analysis · carbodiphosphoranes · carbon · cations · donor–acceptor systems

[1] A. J. Arduengo III, R. L. Harlow, M. Kline, *J. Am. Chem. Soc.* **1991**, *113*, 2801.
[2] a) A. Baceiredo, G. Bertrand, G. Sicard, *J. Am. Chem. Soc.* **1985**, *107*, 4781; b) A. Igau, H. Grützmacher, A. Baceiredo, G. Bertrand, *J. Am. Chem. Soc.* **1988**, *110*, 6463; c) A. Igau, A. Baceiredo, G. Trinquier, G. Bertrand, *Angew. Chem.* **1989**, *101*, 617; *Angew. Chem. Int. Ed. Engl.* **1989**, *28*, 621.
[3] a) W. Kirmse, *Angew. Chem.* **2004**, *116*, 1799; *Angew. Chem. Int. Ed.* **2004**, *43*, 1767; b) *Carbene Chemistry* (Ed.: G. Bertrand), Marcel Dekker, New York, **2002**.
[4] a) S. Marrot, T. Kato, H. Gornitzka, A. Baceiredo, *Angew. Chem.* **2006**, *118*, 2660; *Angew. Chem. Int. Ed.* **2006**, *45*, 2598; b) the first cyclic CDP was reported in: U. Schubert, C. Kappenstein, B. Milewski-Mahrla, H. Schmidbaur, *Chem. Ber.* **1981**, *114*, 3070.
[5] a) F. Ramirez, N. B. Desai, B. Hansen, N. McKelvie, *J. Am. Chem. Soc.* **1961**, *83*, 3539; b) G. E. Hardy, J. I. Zink, W. C. Kaska, J. C. Baldwin, *J. Am. Chem. Soc.* **1978**, *100*, 8002.
[6] Recent reviews: a) N. D. Jones, R. G. Cavell, *J. Organomet. Chem.* **2005**, *690*, 5485; b) O. I. Kolodiazhnyi, *Phosphorous Ylides: Chemistry and Application in Organic Synthesis*, Wiley-VCH, Weinheim, **1999**; c) O. I. Kolodiazhnyi, *Tetrahedron* **1996**, *52*, 1855; d) *Ylides and Imines of Phosphorus* (Ed.: A. W. Johnson), Wiley, New York, **1993**.
[7] a) W. C. Kaska, D. K. Mitchell, R. F. Reichelderfer, *J. Organomet. Chem.* **1973**, *47*, 391; b) W. C. Kaska, K. A. O. Starzewski, *Ylides and Imines of Phosphorus* (Ed.: A. W. Johnson), Wiley, New York, **1993**, p. 485.
[8] a) P. von R. Schleyer, A. J. Kos, *Tetrahedron* **1983**, *39*, 1141; b) H. Grützmacher, C. M. Marchand, *Coord. Chem. Rev.* **1997**, *163*, 287.
[9] D. G. Gilheany, *Chem. Rev.* **1994**, *94*, 1339.
[10] Geometry optimizations without symmetry constraints were carried out using the Gaussian 03 optimizer[27] together with TurboMole 5.7.1[28] energies and gradients at the BP86[29]/SVP[30] level of theory. For the phenyl rings of the PPh_3 groups, except for the α-C atom, a minimal basis set was used (benzene BS). Stationary points were characterized as minima by calculating the Hessian matrix analytically at this level. Thermodynamic corrections were taken from these calculations. The standard state for all thermodynamic data was $T = 298.15$ K and $p =$

 © 2006 Wiley-VCH Verlag GmbH & Co. KGaA, Weinheim

1 atm. Improved energies have been derived with the MP2 method by applying the frozen-core approximation for non-valence-shell electrons using the def2-TZVPP[31] basis set. For both methods the resolution-of-identity method was applied.[32] For **6** and **7** the geometries where optimized at the MP2/SVP level because the aurophilic interactions may not be reliably described using DFT. Quasirelativistic ECPs were used for the calculations of Ag and Au.[33] The full set of calculated geometries and energies is given in the Supporting Information.

[11] A. M. Magill, K. J. Cavell, B. F. Yates, *J. Am. Chem. Soc.* **2004**, *126*, 8717.

[12] B. Kovacevic, Z. B. Maksic, *Org. Lett.* **2001**, *3*, 1523.

[13] a) J. D. Walker, R. Poli, *Polyhedron* **1989**, *8*, 1293; b) W. P. Jensen, H. Gehrke, D. R. Jones, I.-H. Suh, R. A. Jacobson, *Z. Kristallogr.* **1996**, *211*, 829.

[14] a) W. Petz, C. Kutschera, S. Tschan, F. Weller, B. Neumüller, *Z. Anorg. Allg. Chem.* **2003**, *629*, 1235 – 1244; b) W. Petz, F. Weller, *Z. Kristallogr.* **1997**, *212*, 157; c) A. Schmidtpeter, F. Zwaschka, W. S. Sheldrick, *Chem. Ber.* **1985**, *118*, 1078; d) P. J. Carroll, D. D. Titus, *J. Chem. Soc. Dalton Trans.* **1977**, 824.

[15] F. Öxler, Diploma thesis, Marburg, **2006**.

[16] A 1:2 mixture of $AgBF_4$ and $[(Ph_3P)_2CH][BF_4]$ was stirred in CH_2Cl_2 solution for 2 h. The clear colorless solution was layered with *n*-pentane. Crystals separated in about 80 % yield and could be identified by X-ray analysis as the salt-like complex $[\{(PPh_3)_2CH\}_2Ag][BF_4]_3 \cdot 5\,CH_2Cl_2$ (**5**·5 CH_2Cl_2).[17] ^{31}P NMR (CH_2Cl_2): $\delta = 23.6$ ppm.

[17] Crystallographic data for **5**·5 CH_2Cl_2: $C_{79}H_{72}AgB_3Cl_{10}F_{12}P_4$, $M_r = 1868.15$, colorless blocks, $0.41 \times 0.31 \times 0.26$ mm^3, triclinic, space group $P\bar{1}$ (Nr. 2), $a = 1304.4(1)$, $b = 1338.4(2)$, $c = 2641.1(3)$ pm, $\alpha = 94.20(1)$, $\beta = 103.78(2)$, $\gamma = 109.91(1)°$, $V = 4149.8(2)$ pm$^3 \times 10^6$, $Z = 2$, $\rho_{calcd} = 1.495$ g cm^{-3}, $\mu(Mo_{K\alpha}) = 7.1$ cm^{-1}, $T = 193$ K, $R_1(F) = 0.0611$ (reflections, $F_o > 4\sigma(F_o) = 6092$), parameter = 530, $wR_2 = 0.1528$ for all data. CCDC-612361 (**5**·5 CH_2Cl_2) contains the supplementary crystallographic data for this paper. These data can be obtained free of charge from The Cambridge Crystallographic Data Centre via www.ccdc.cam.ac.uk/data_request/cif.

[18] A. J. Arduengo, III, H. V. R. Dias, J. C. Calabrese, F. Davidson, *Organometallics* **1993**, *12*, 3405.

[19] P. K. Hurlburt, J. J. Rack, S. F. Dec, O. P. Anderson, S. H. Strauss, *Inorg. Chem.* **1993**, *32*, 373.

[20] I. Romeo, M. Bardají, M. C. Gimeno, M. Laguna, *Polyhedron* **2000**, *19*, 1837.

[21] R. F. W. Bader, *Atoms in Molecules: A Quantum Theory*, Oxford University Press, Oxford, **1990**.

[22] H. Schmidbaur, *Chem. Soc. Rev.* **1995**, *24*, 391.

[23] J. Vicente, A. R. Singhal, P. G. Jones, *Organometallics* **2002**, *21*, 5887.

[24] J. J. Daly, P. Wheatley, *J. Chem. Soc. A* **1966**, 1703.

[25] J. Koput, *Chem. Phys. Lett.* **2000**, *320*, 237.

[26] T. Kappe, E. Ziegler, *Angew. Chem.* **1974**, *86*, 529; *Angew. Chem. Int. Ed. Engl.* **1974**, *13*, 491.

[27] Gaussian 03 (Revision D.01): M. J. Frisch et al., see the Supporting Information.

[28] R. Ahlrichs, M. Baer, M. Haeser, H. Horn, C. Koelmel, *Chem. Phys. Lett.* **1989**, *162*, 165.

[29] A. D. Becke, *Phys. Rev. A* **1988**, *38*, 3098; J. P. Perdew, *Phys. Rev. B* **1986**, *33*, 8822.

[30] A. Schaefer, H. Horn, R. Ahlrichs, *J. Chem. Phys.* **1992**, *97*, 2571.

[31] F. Weigend, R. Ahlrichs, *Phys. Chem. Chem. Phys.* **2005**, *7*, 3297.

[32] K. Eichkorn, O. Treutler, H. Ohm, M. Häser, R. Ahlrichs, *Chem. Phys. Lett.* **1995**, *242*, 652.

[33] D. Andrae, U. Häussermann, M. Dolg, H. Stoll, H. Preuss, *Theor. Chim. Acta* **1990**, *77*, 123.

 © 2006 Wiley-VCH Verlag GmbH & Co. KGaA, Weinheim

Nanowires and Nanotubes

DOI: 10.1002/anie.200602093

"Four Birds with One Stone": Synthesis of Nanostructures of ZnTe, Te, $ZnAl_2O_4$, and Te/$ZnAl_2O_4$ from a Single-Source Precursor**

*Lili Zhao, Maekele Yosef, Eckhard Pippel, Herbert Hofmeister, Martin Steinhart, Ulrich Gösele, and Sabine Schlecht**

One-dimensional nanostructures have received much attention owing to their distinct properties and potential applications in nanoscale electronics and optoelectronics.[1] The use of porous templates containing aligned nanochannels[2,3] is a versatile method to fabricate arrays of aligned nanowires, predominantly by electrochemical[4] and chemical deposition.[5] However, it still remains a challenge to extend the range of functional target materials that can be formed as nanowires with low defect density and high aspect ratios. Recently, template-assisted thermolysis of single-source precursors inside nanopores and macropores has been exploited to form nanowires, nanotubes, and microtubes.[6,7] Regarding suitable types of single-source precursors, arylchalcogenolates of Group 12 and 14 metals were found to be a versatile class of compounds with similar molecular architecture and thermal properties, which have been employed to generate II/VI and IV/VI compound semiconductors.[7,8]

Herein, we show that arylchalcogenolates and self-ordered porous alumina templates[9,10] represent a construction kit for the synthesis of single-crystalline nanowires of different types of target materials with varying morphology. Dependent on the conditions applied, $[Zn(TePh)_2(tmeda)]$[11] (tmeda = *N*,*N*,*N*′,*N*′-tetramethylethylenediamine) yields single-crystalline nanowires of zinc telluride (ZnTe), core/shell structures composed of tellurium/zinc spinel (Te/$ZnAl_2O_4$), pure tellurium nanowires, or nanotubes of zinc spinel ($ZnAl_2O_4$).

[*] Dr. M. Yosef, Prof. Dr. S. Schlecht
Freie Universität Berlin
Institut für Chemie und Biochemie
Fabeckstrasse 34–36, 14195 Berlin (Germany)
Fax: (+49) 30-838-53310
E-mail: schlecht@chemie.fu-berlin.de
Homepage: http://userpage.chemie.fu-berlin.de/~aacadmin/aac/ag_schlecht.htm
L. Zhao, Dr. E. Pippel, Dr. H. Hofmeister, Dr. M. Steinhart, Prof. Dr. U. Gösele
Max-Planck-Institut für Mikrostrukturphysik Halle
Weinberg 2, 06120 Halle (Germany)

[**] The authors would like to thank the Deutsche Forschungsgemeinschaft for funding as part of the priority program SPP 1165 "Nanowires and Nanotubes" (SCHL 529/2-2 and STE 1127/2-2) and K. Schwirn, S. Grimm, and K. Sklarek for template preparations.

Supporting information for this article is available on the WWW under http://www.angewandte.org or from the author.

WILEY InterScience DISCOVER SOMETHING GREAT
© 2006 Wiley-VCH Verlag GmbH & Co. KGaA, Weinheim

ZnTe is one of the most important II/VI-type compound semiconductors, a class of materials that is of considerable interest for potential applications in the fields of sensor technology[12] and light-emitting diodes.[13] Trigonal elemental tellurium crystallizes in a noncentrosymmetric space group and shows several interesting properties, for instance, photoconductivity,[14a] thermoelectricity,[14b] and piezoelectricity.[14c] The zinc spinel $ZnAl_2O_4$ is widely used as a catalyst for cracking, dehydration, hydrogenation, and dehydrogenation.[15] For core–shell nanostructures such as the tellurium wires with a zinc spinel shell described here, applications as photoconducting cables with a transparent, insulating, and chemically robust shell can well be imagined.

In a general synthetic procedure for the preparation of the nanostructures, a solution of $[Zn(TePh)_2(tmeda)]$[11] (5 wt% in chloroform) was added dropwise onto ordered porous alumina with a pore diameter of 25 nm under ambient conditions. After the solvent had evaporated, the templates with the precursor inside the pores were heated to 280 °C and kept at this temperature for two hours. Then, the samples were heated to 500 °C, annealed at this temperature for 24 or 48 hours, and slowly cooled to room temperature.

When samples wetted in this manner were annealed in vacuum for 48 hours at 500 °C, ZnTe nanowires were obtained, which could be released by etching the templates with aqueous KOH. Figure 1a shows a representative transmission electron microscopy (TEM) image of a ZnTe nanowire with a diameter, D, of 25 nm corresponding to the diameter of the template pores and an aspect ratio (length/diameter) of about 120. Figure 1b shows a detail at higher magnification. The selected area electron diffraction (SAED) pattern (Figure 1a, inset) of a segment of the ZnTe nanowire evidences the single-crystalline nature as it contains only indexed Bragg reflections. The high-resolution (HR) TEM image of a ZnTe nanowire (Figure 1c) shows the (111) lattice planes ($d = 3.48$ Å) of cubic ZnTe (space group $F\bar{4}3m$).[16] We assume that the formation of the ZnTe nanowires occurs according to the well-known degradation mechanism of $[Zn(TePh)_2(tmeda)]$.[11a]

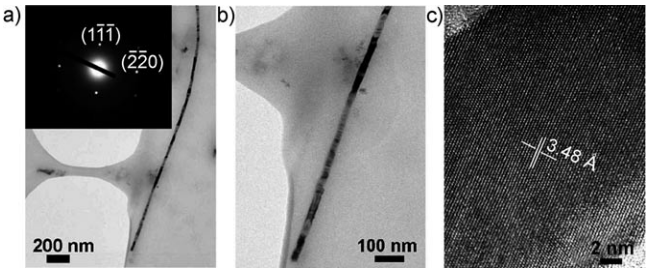

Figure 1. a) TEM image and SAED pattern (inset, zone axis [1$\bar{1}$2]) of a single-crystalline ZnTe nanowire. b) Bottom part of the wire at higher magnification. c) HRTEM image of a ZnTe nanowire showing (111) lattice planes ($d = 3.48$ Å).

When the wetted samples were not annealed in vacuum, but in air for 24 hours at 500 °C, single-crystalline tellurium nanowires ($D = 25$ nm) surrounded by a polycrystalline $ZnAl_2O_4$ shell of thickness 8 nm were obtained. The core/shell structure of these Te/$ZnAl_2O_4$ nanowires is evident in Figure 2. The Te/$ZnAl_2O_4$ nanowires have an aspect ratio of about 200. The core/shell structure has a diameter of about

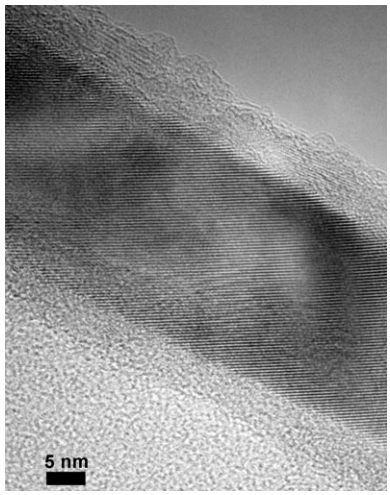

Figure 2. HRTEM image of a Te/$ZnAl_2O_4$ core/shell structure. The lattice fringes of the tellurium core correspond to the (101) planes ($d = 3.1$ Å).

40 nm, which is larger than that of the template pores. This larger diameter indicates that the pore walls act as chemical reactants in the formation of the core/shell wires. The single-crystalline tellurium core can be seen in the HRTEM image (Figure 2). The distance between the lattice planes of the tellurium core was found to be 3.1 Å, which corresponds to the d value of the (101) lattice planes.

The chemical composition of released core/shell nanowires was analyzed by energy-dispersive X-ray spectroscopy (EDX; Figure 3). Exclusively strong tellurium peaks and a weak oxygen peak are found in the spectrum measured on a wire segment where the $ZnAl_2O_4$ shell had peeled off (the copper peak originates from the TEM grid onto which the wires had been deposited; Figure 3a). This observation indicates that the core consists of pure tellurium, possibly covered by a thin oxide layer. A segment consisting only of the $ZnAl_2O_4$ shell was selected for a second EDX scan (Figure 3b). The signals of aluminum, zinc, and oxygen can be seen in the spectrum, whereas no tellurium could be detected. The Zn/Al/O ratio of 1:1.9:3.7 deduced from the EDX spectrum is in accordance with the composition of $ZnAl_2O_4$. A third EDX spectrum was measured on an intact core/shell segment (Figure 3c). Here, the peaks of zinc, aluminum, oxygen, and tellurium can be seen. All EDX spectra indicate that the nanowires consist of a $ZnAl_2O_4$ shell with a tellurium core.

We suggest the following mechanism for the formation of the Te/$ZnAl_2O_4$ core/shell nanowires. After thermolysis of $[Zn(TePh)_2(tmeda)]$, the telluride in the initially formed ZnTe is oxidized, thereby resulting in the formation of ZnO and elemental tellurium within the pores. Freshly formed, active ZnO reacts with the alumina template, as previously

 © 2006 Wiley-VCH Verlag GmbH & Co. KGaA, Weinheim

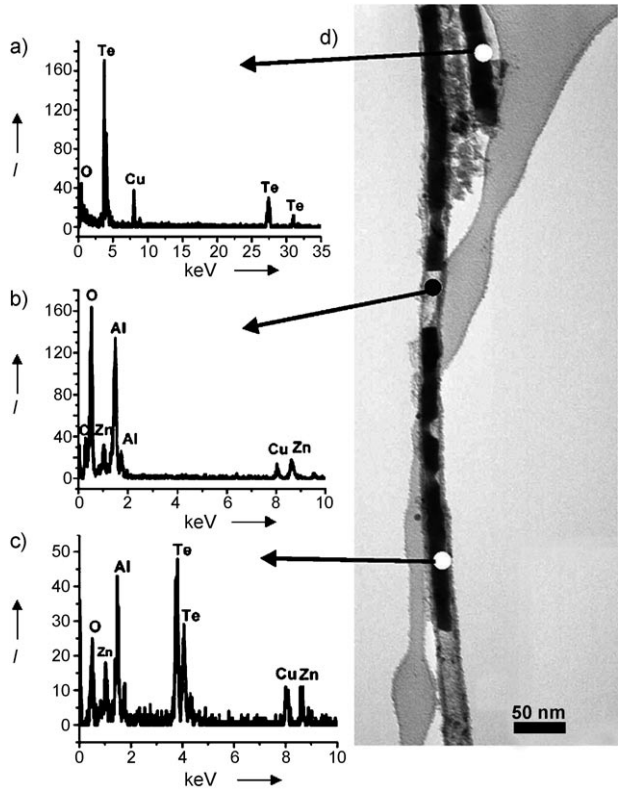

Figure 3. Chemical composition analysis of $Te/ZnAl_2O_4$ nanowires by EDX spectroscopy. a) EDX point spectrum of a pure tellurium nanowire measured at the location indicated in (d). b) EDX point spectrum of a pure $ZnAl_2O_4$ shell measured at the location indicated in (d). c) EDX point spectrum of a $Te/ZnAl_2O_4$ core/shell structure measured at the location indicated in (d). d) TEM image of the investigated nanowire segments.

reported by Wang and Wu,[17] to form the polycrystalline $ZnAl_2O_4$ shell. The formation of the compact and single-crystalline tellurium core is greatly facilitated by the fact that elemental tellurium, with a melting point of 452 °C,[18] is formed in its liquid state at the annealing temperature of 500 °C. A slow cooling process following the annealing step leads to the formation of single-crystalline tellurium structures inside the spinel shell.

Sonification of the core/shell structures resulted in the removal of the $ZnAl_2O_4$ crystallites, and the liberated single-crystalline tellurium nanowires can be obtained (Figure 4). The SAED patterns of these samples (Figure 4, inset) show only Bragg reflections that can be assigned to trigonal tellurium (space group $P3_121$).[19] This finding gives evidence for the single-crystalline nature of the tellurium wires and the lack of relevant structural disorder in these products.

Not only could the core without the shell be obtained, but also the shell without the core could be isolated by etching of the tellurium core with aqueous KOH at 90 °C for four hours. A TEM image of the isolated shells is seen in Figure 5a. The corresponding SAED pattern (Figure 5b) contains ring patterns corresponding to the (220), (311), (400), (511), and (440) reflections of $ZnAl_2O_4$ (spinel, space group $Fd3m$),[20] thus indicating that the shell consists of polycrystalline $ZnAl_2O_4$.

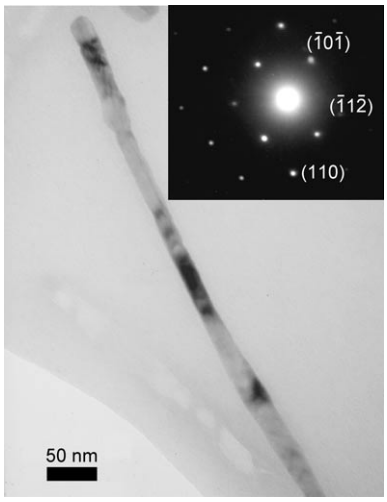

Figure 4. Released single-crystalline tellurium nanowire ($D = 25$ nm) and its indexed SAED pattern (inset, zone axis [1̄13]).

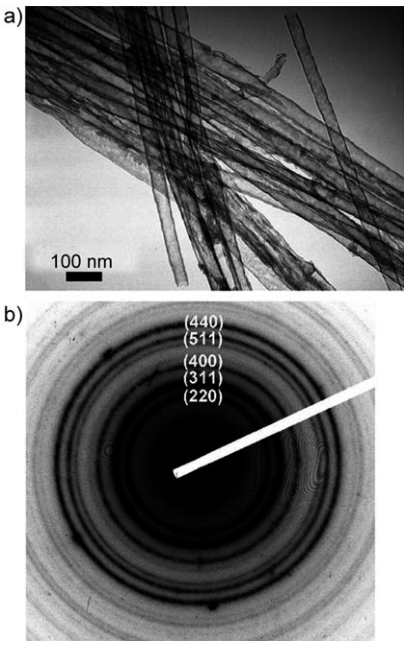

Figure 5. a) TEM image of $ZnAl_2O_4$ nanotubes and b) SAED pattern showing their polycrystallinity.

To investigate whether or not $ZnAl_2O_4$ nanotubes also form in the absence of tellurium, we infiltrated alumina templates with a dilute solution of $ZnCl_2$ (5 wt %) in THF and applied the same protocol as in case of the thermolysis of $[Zn(TePh)_2(tmeda)]$. However, no $ZnAl_2O_4$ nanotubes were obtained, thus indicating that the slower formation of ZnO from the tellurolate precursor and the ZnTe intermediate is crucial.

In conclusion, we have shown that proper variation of the conditions under which the template-assisted thermolysis of $[Zn(TePh)_2(tmeda)]$ is performed yields single-crystalline nanowires of ZnTe or of a tellurium core in a $ZnAl_2O_4$ shell. Interestingly, nanotubes of $ZnAl_2O_4$ and isolated nano-

 © 2006 Wiley-VCH Verlag GmbH & Co. KGaA, Weinheim

wires of tellurium can be prepared after selective removal of either the core or the shell.

Received: May 25, 2006
Revised: August 2, 2006
Published online: October 31, 2006

Keywords: nanostructures · spinels · tellurium · template synthesis · zinc

[1] a) Y. Xia, P. Yang, Y. Sun, Y. Wu, B. Mayers, B. Gates, Y. Yin, F. Kim, H. Yan, *Adv. Mater.* **2003**, *15*, 353; b) J. T. Hu, T. W. Odom, C. M. Lieber, *Acc. Chem. Res.* **1999**, *32*, 435; c) R. Tenne, M. Homyonfer, Y. Feldman, *Chem. Mater.* **1998**, *10*, 3225.
[2] C. R. Martin, *Science* **1994**, *266*, 1961.
[3] a) M. Steinhart, J. H. Wendorff, A. Greiner, R. B. Wehrspohn, K. Nielsch, J. Schilling, U. Gösele, *Science* **2002**, *296*, 1997; b) M. Steinhart, Z. Jia, A. Schaper, R. B. Wehrspohn, U. Gösele, J. H. Wendorff, *Adv. Mater.* **2003**, *15*, 706.
[4] C. J. Brumlik, C. R. Martin, *J. Am. Chem. Soc.* **1991**, *113*, 3174.
[5] V. P. Menon, C. R. Martin, *Anal. Chem.* **1995**, *67*, 1920.
[6] L. Zhao, M. Steinhart, M. Yosef, S. K. Lee, T. Geppert, E. Pippel, R. Scholz, U. Gösele, S. Schlecht, *Chem. Mater.* **2005**, *17*, 3.
[7] L. Zhao, M. Yosef, M. Steinhart, P. Göring, H. Hofmeister, U. Gösele, S. Schlecht, *Angew. Chem.* **2006**, *118*, 317; *Angew. Chem. Int. Ed.* **2006**, *45*, 311.
[8] a) J. Brennan, T. Siegrist, P. J. Carroll, S. M. Stuczynski, P. Reynders, L. E. Brus, M. L. Steigerwald, *Chem. Mater.* **1990**, *2*, 403; b) J. Arnold, *Prog. Inorg. Chem.* **1995**, *43*, 353.
[9] H. Masuda, K. Fukuda, *Science* **1995**, *268*, 1466.
[10] H. Masuda, F. Hasegawa, S. Ono, *J. Electrochem. Soc.* **1997**, *144*, L127.
[11] a) Y. Jun, C. S. Choi, J. Cheon, *Chem. Commun.* **2001**, 101; b) H. Pfistner, D. Fenske, *Z. Anorg. Allg. Chem.* **2001**, 627, 575.
[12] a) M.-C. Jeong, B.-Y. Oh, O.-H. Nam, T. Kim, J.-M. Myoung, *Nanotechnology* **2006**, *17*, 526; b) P. Feng, Q. Wan, T. H. Wang, *Appl. Phys. Lett.* **2005**, *87*, 213111.
[13] a) A. V. Nurmikko, R. L. Gunshor, *Solid State Phys.* **1995**, *49*, 205; b) S.-B. Che, I. Nomura, T. Takada, A. Kikuchi, K. Shimomura, K. Kishino, *Jpn. J. Appl. Phys. Part 1* **2001**, *40*, 6747.
[14] a) V. A. Vis, *J. Appl. Phys.* **1964**, *35*, 360; b) Y. I. Dutchak, I. P. Klyus, V. Y. Prokhorenko, *Phys. Stat. Solidi* **1969**, *31*, 25; c) G. Quentin, J. M. Thuillier, *Solid State Commun.* **1964**, *2*, 115.
[15] a) T. El-Nabarawy, A. A. Attia, M. N. Alaya, *Mater. Lett.* **1995**, *24*, 319; b) B. S. Girgis, A. M. Youssef, M. N. Alaya, *Surf. Technol.* **1980**, *10*, 105.
[16] JCPDS card no. 15-746.
[17] Y. Wang, K. Wu, *J. Am. Chem. Soc.* **2005**, *127*, 9687.
[18] *CRC Handbook of Chemistry and Physics*, 48th ed., The Chemical Rubber Company, Cleveland, USA, **1967**, p. B-241.
[19] JCPDS card no. 5-669.
[20] *CRC Handbook of Chemistry and Physics*, 48th ed., The Chemical Rubber Company, Cleveland, USA, **1967**, p. B-230.

 © 2006 Wiley-VCH Verlag GmbH & Co. KGaA, Weinheim

Functionalized Polymers

DOI: 10.1002/anie.200602323

Monofunctional Metathesis Polymers via Sacrificial Diblock Copolymers**

*Stefan Hilf, Elena Berger-Nicoletti, Robert H. Grubbs, and Andreas F. M. Kilbinger**

Ring-opening olefin metathesis polymerization (ROMP) is a powerful tool for the synthesis of highly functionalized polymers.[1] The first well-defined ROMP catalyst systems based on titanium,[2] molybdenum, and tungsten[3] exhibited relatively low tolerance toward functional groups. This low tolerance could be exploited in the end-functionalization of metathesis polymers. The high oxophilicity of the metal centers made end functionalization possible by addition of aldehydes to the polymerization mixture.[4] Late-transition-metal catalysts based on ruthenium[5] do not allow for olefin metathesis functionalization with aldehydes. Nonetheless, several pathways have been described in the literature for the end functionalization of ruthenium-catalyzed metathesis polymers.

The most common method of terminating a ruthenium carbene at the chain end of a polymer is achieved by adding ethyl vinyl ether.[6] A methylene group is transferred onto the polymer while cleaving the catalyst off the polymer chain end at the same time. It could be shown that the cleaved-off Fischer-type carbene can undergo further olefin metathesis reactions under certain conditions.[7] For most polymer synthetic applications, however, this species can be regarded as inactive. In the presence of vinyl sulfides it could be shown that such "Fischer carbenes" react as chain-transfer agents to yield monofunctional polymers.[8] The polymers that were prepared in this way show broad polydispersity indices (PDI between 1.3 and 3).

Substituted methyl vinyl ethers have also been used for the termination of living metathesis polymers.[9] In this way, a variety of functional groups could be transferred to the polymer chain end. Gibson and co-workers reported an end-capping reaction whereby the polymerization reaction mixture was exposed to an oxygen atmosphere, which resulted in

[*] S. Hilf, Dr. E. Berger-Nicoletti, Dr. A. F. M. Kilbinger
Institut für Organische Chemie
Johannes Gutenberg-Universität Mainz
Duesbergweg 10–14, 55099 Mainz (Germany)
Fax: (+49) 6131-39-26138
E-mail: akilbing@uni-mainz.de
Prof. Dr. R. H. Grubbs
Arnold and Mabel Beckman Laboratories of Chemical Synthesis
Division of Chemistry and Chemical Engineering
California Institute of Technology, Pasadena, CA 91125 (USA)
E-mail: rhg@caltech.edu

[**] A.F.M.K. thanks the Fonds der Chemischen Industrie (FCI) for financial support and Dr. Oren Scherman for helpful discussions.

Supporting information for this article is available on the WWW under http://www.angewandte.org or from the author.

© 2006 Wiley-VCH Verlag GmbH & Co. KGaA, Weinheim

an aldehyde end group after a reaction time of 24 hours.[10] A further method describes the stoichiometric addition of one equivalent of functional monomer to the catalyst, thereby turning the catalyst into a monofunctional initiator.[11]

The end-functionalization reactions described above suffer from several drawbacks. They typically take several hours to complete, during which the metathesis-active catalytic species can undergo further polymerization or secondary metathesis reactions. These end-capping methods can therefore not be employed in the presence of residual monomer without significant broadening of the molecular weight distribution. Even in the absence of residual monomer, long reaction times for the termination reaction can lead to molecular weight broadening as a result of chain-transfer reactions to the polymer (back-biting), a fact that is exploited in the equilibration of telechelics.[12] True monofunctionality is also not guaranteed rigorously by some of the above examples. It is important to stress that the presence of exactly one functional group at the chain end is essential for many applications, such as the synthesis of block copolymers, the synthesis of conjugates with biomacromolecules like proteins, polysaccharides, or polynucleotides, or the functionalization of surfaces and nanoparticles. Today, many of these applications employ monofunctional polymers that are prepared by anionic polymerization.

Herein, we describe the monofunctionalization of the chain end of ruthenium-catalyzed metathesis polymers, which can be carried out in the presence of residual monomer, yields narrow molecular weight distributions, and allows the presence of functional groups in the monomer structure. To prove our synthetic concept, we chose *exo*-*N*-phenylnorbornene-2,3-dicarboximide (PNI) as the monomer as it can be polymerized in a living fashion.[13] PNI was initiated with catalyst **1** (Scheme 1) and polymerized to only 60% conversion. Polymerization to low monomer conversion allowed us to evaluate the influence of residual monomer on the polydispersity of the monofunctional polymer. An analytical sample was taken and quenched with ethyl vinyl ether. Next, a large excess of dioxepine monomer **4a** or **4b** was introduced into the reaction mixture, thereby resulting in the formation of a diblock copolymer, which was quenched with excess ethyl vinyl ether.

Figure 1 shows gel permeation chromatography (GPC) traces of the first block **3a** and diblock **6a**, which clearly show that the living chain end of **3** was an effective initiator for the second monomer **4a**. As the first monomer had only been consumed to about 60%, the second block was most likely a statistical mixture of monomers **2** and **4a**. Polymerization of **2** to higher conversions (60–90%) before addition of the second monomer was also successful. Molecular weight control of the first polymer block is therefore possible by either varying the reaction time before adding the second monomer or by varying the monomer/catalyst ratio. After isolation and purification, the block copolymer was dissolved in a mixture of methanol/dichloromethane/HCl to cleave the acetal groups of the second block.[14] As can be seen in Scheme 1, cleavage of the acetal groups decomposes the second polymer block (to form **7**) but leaves half a monomer unit of **4a** attached to the first block at a C–C double bond.

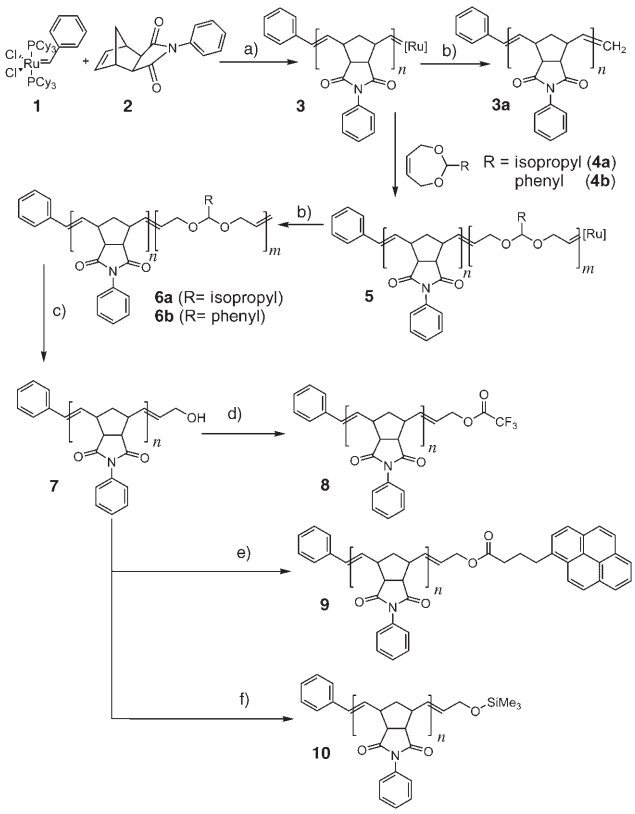

Scheme 1. Synthesis and cleavage of the block copolymers. a) PPh_3, dichloromethane, room temperature; b) ethyl vinyl ether; c) 6 N HCl, methanol, dichloromethane; d) trifluoroacetic anhydride; e) pyrenebutyroyl chloride; f) trimethylsilyl chloride.

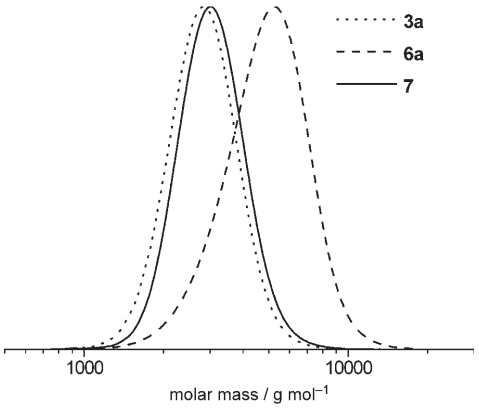

Figure 1. GPC traces (THF, calibration with polystyrene) of the first polymer block of monomer **2** (polymer **3a**, dotted line), the diblock copolymer of monomers **2** and **4a** (polymer **6a**, dashed line), and monofunctional polymer **7** (solid line).

GPC analysis revealed that the molecular weight of the first block (**3a**, Figure 1) and monofunctional polymer (**7**, Figure 1) are almost identical. Moreover, the polydispersity indices for polymers **3a** and **7** (Figure 1) are identical and very narrow (PDI = 1.1). The presence of residual monomer **2,** which can lead to severe molecular weight broadening in many of the previously reported end-capping procedures, was

 © 2006 Wiley-VCH Verlag GmbH & Co. KGaA, Weinheim

shown not to have any effect on the polydispersity of the monofunctional polymer.

The same experiment was carried out with the dioxepine monomer **4b**. The GPC trace of diblock copolymer **6b** was also shifted towards higher molecular weights in comparison with that of **3a**, thus indicating good reinitiation from the first to the second block (see the Supporting Information). The monofunctional polymer **7** that was prepared by acidic cleavage of the polyacetal block of **4b** shows a virtually identical molecular weight and polydispersity index (PDI = 1.1) as the first block. It is important to stress at this point that the propagation rate of the dioxepine monomer is of no importance for successful end functionalization of the first polymer block. As the second polymer block is eventually "sacrificed", only the reinitiation of the first polymer block to the first unit of the dioxepine monomer is crucial. This incorporation of the first unit of the dioxepine monomer represents a breaking point, the junction between the end-functionalized and sacrificed polymer block.

To obtain proof for the presence of a hydroxy functionality at the polymer chain end, polymer **7** (from **6a**) was treated with pyrenebutyroyl chloride to give the corresponding ester **9**. A GPC experiment with UV detection at $\lambda = 340$ nm (characteristic for pyrenebutyric acid derivatives) showed a signal for the pyrene-functionalized polymer **9** while hydroxyl-functionalized polymer **7** shows no absorption at this wavelength (see the Supporting Information). This finding shows that the pyrene group was covalently attached to the polymer chain. The ^{1}H NMR spectrum of polymer **7** reveals a singlet at $\delta = 4.14$ ppm, which was attributed to the methylene group adjacent to the hydroxy functionality (Figure 2 bottom). Addition of trifluoroacetic anhydride to the NMR tube resulted in a shift of the peak to $\delta = 4.82$ ppm, which is in agreement with the described assignment (Figure 2 top). Furthermore, the olefinic protons H^1 and H^2 of the styrene-like initiator group can be observed in the ^{1}H NMR spectrum of **7** at $\delta = 6.33$ and 6.60 ppm. Comparing the integrals of the olefinic protons H^1 and H^2 with the integral from H^4 reveals that end functionalization in excess of 97%

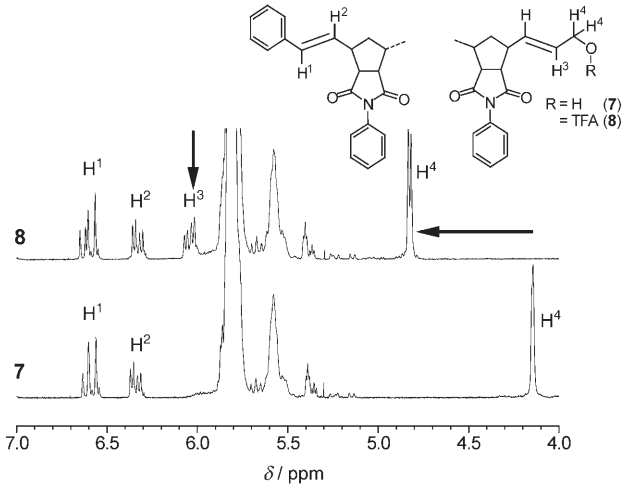

Figure 2. ^{1}H NMR spectroscopic end-group analysis of polymers **8** (top) and **7** (bottom). The structures show the two end groups of the polymer chain.

had occurred. In the ^{1}H NMR spectrum of the trifluoroacetate-functionalized polymer **8** (Figure 2 top), the terminal olefinic protons (H^3, $\delta = 6.04$ ppm) are separated from other olefinic peaks in the spectrum and can also be used for end-group analysis. Reaction of polymer **7** with trimethylsilyl chloride gave the trimethylsilyl-functionalized polymer **10**. The ^{1}H NMR spectrum revealed the methyl end groups at $\delta = 0.17$ ppm (see the Supporting Information).

Polymers **3a** and **7** were analyzed by MALDI-TOF mass spectrometry (**7** from **6a**, see Figure 3; **7** from **6b**, see the Supporting Information). The mass distribution of polymer **7**

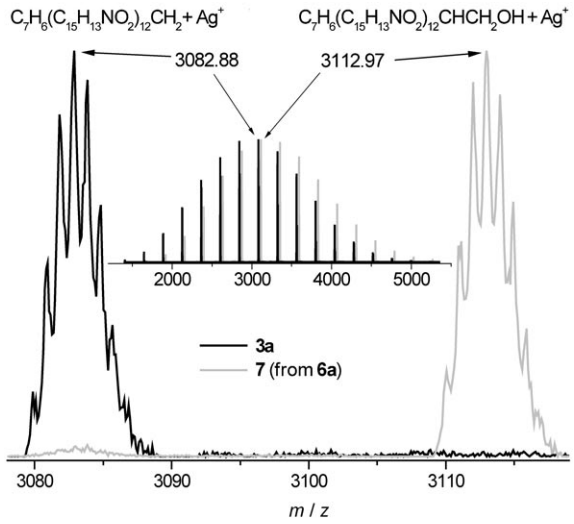

Figure 3. MALDI-TOF mass spectra of **3a** and **7** (from **6a**) showing isotopically resolved mass peaks; inset: complete mass distribution.

is shifted by m/z 30.09 compared to that of polymer **3** (the exact mass of CH_2O is 30.01 g mol^{-1}). This difference corresponds to the mass difference between the ethyl vinyl ether end-capped polymer **3a** and the hydroxy-functionalized polymer **7**. The mass distribution for polymer **7** provides no evidence for a second monomer distribution from residual dioxepine monomer. However, a very small mass distribution owing to unfunctionalized polymer **3** (which is structurally identical to **3a**) can be seen in the mass spectrum of **7** (Figure 3). The functionalization of **7** with trimethylsilyl chloride to give the silyl-protected alcohol was also successful and was confirmed by MALDI-TOF mass spectrometry (see the Supporting Information).

In conclusion, we have presented a route to monofunctionalized olefin metathesis polymers. This route allows the preparation of narrowly distributed polymers with commercially available ruthenium catalysts. Monomeric *exo-N*-phenyl-norbornene-2,3-dicarboximide was polymerized to the desired molecular weight and subsequently turned into a diblock copolymer by adding a cyclic olefinic acetal as a second monomer. The second polymer block was decomposed under acidic conditions, thereby leaving exactly one hydroxyl group at the end of the initial polymer block. We believe that this route to monofunctional ring-opening metathesis polymers presents a viable and less laborious alternative to carbanionic polymerization. Such polymers with

 © 2006 Wiley-VCH Verlag GmbH & Co. KGaA, Weinheim

monofunctionalized end groups and narrow polydispersity will allow numerous new applications in fields that previously relied on monofunctionalized polymers from carbanionic polymerization.

Experimental Section

General procedure for the synthesis of block copolymers: Triphenylphosphine (6.3 equiv) and **2** were sealed in a Schlenk flask, which was evacuated and charged with nitrogen twice. Dichloromethane (ca. 10 mL per gram of monomer) was then added by cannula transfer. Polymerization was initiated by quickly adding a solution of the appropriate amount of catalyst **1** in dichloromethane (ca. 1 mL per 100 mg of **1**) by syringe to the stirred solution. Reaction times were dependent on the desired molecular weight of the polymer (7 h for 3000 g mol^{-1}, 13 h for 5000 g mol^{-1}, 24 h for 10000 g mol^{-1}, all at room temperature). Upon completion of the reaction time, the cyclic olefinic acetal was added to the mixture (1 mL of **4a** or **4b** per gram of polymer) and allowed to react for another 10 h. The reaction was quenched with ethyl vinyl ether (1 mL). The product was precipitated into methanol, dissolved in chloroform, and reprecipitated into methanol. The block copolymer was dried to yield 70–80% of a brown solid.

General procedure for cleaving of the second block: HCl (6 M, 4 mL) and methanol (2 mL) were added to a solution of the block copolymer (1 g) in dichloromethane (10 mL). The mixture was stirred for 12 h at room temperature and subsequently precipitated into methanol. The solid was recovered, dissolved in chloroform, and reprecipitated into methanol. The polymer was dried under vacuum to give a white solid (850 mg, ca. 80%, depending on the block ratio).

Detailed experimental procedures are described in the Supporting Information.

Received: June 9, 2006
Revised: August 29, 2006
Published online: October 31, 2006

Keywords: block copolymers · dioxepine · metathesis · polymer chemistry · ring-opening polymerization

[1] U. Frenzel, O. Nuyken, *J. Polym. Sci. Part A* **2002**, *40*, 2895; C. Slugovc, *Macromol. Rapid Commun.* **2004**, *25*, 1283.
[2] L. R. Gilliom, R. H. Grubbs, *J. Am. Chem. Soc.* **1986**, *108*, 733.
[3] M. B. O'Donoghue, R. R. Schrock, A. M. LaPointe, W. M. Davis, *Organometallics* **1996**, *15*, 1334; J. S. Murdzek, R. R. Schrock, *Macromolecules* **1987**, *20*, 2640; R. R. Schrock, J. S. Murdzek, G. C. Bazan, J. Robbins, M. DiMare, M. O'Regan, *J. Am. Chem. Soc.* **1990**, *112*, 3875.
[4] K. A. Brown-Wensley, S. L. Buchwald, L. Cannizzo, L. Clawson, S. Ho, D. Meinhardt, J. R. Stille, D. Straus, R. H. Grubbs, *Pure Appl. Chem.* **1983**, *55*, 1733; D. Albagli, G. C. Bazan, R. R. Schrock, M. S. Wrighton, *J. Phys. Chem.* **1993**, *97*, 10211; D. Albagle, G. C. Bazan, R. R. Schrock, M. S. Wrighton, *J. Am. Chem. Soc.* **1993**, *115*, 7328; K. Nomura, S. Takahashi, Y. Imanishi, *Macromolecules* **2001**, *34*, 4712.
[5] S. T. Nguyen, L. K. Johnson, R. H. Grubbs, *J. Am. Chem. Soc.* **1992**, *114*, 3974; S. T. Nguyen, R. H. Grubbs, *J. Am. Chem. Soc.* **1993**, *115*, 9858; P. Schwab, R. H. Grubbs, J. W. Ziller, *J. Am. Chem. Soc.* **1996**, *118*, 100; A. K. Chatterjee, J. P. Morgan, M. Scholl, R. H. Grubbs, *J. Am. Chem. Soc.* **2000**, *122* ,3783; M. Scholl, S. Ding, C. W. Lee, R. H. Grubbs, *Org. Lett.* **1999**, *1*, 953; J. Huang, E. D. Stevens, S. P. Nolan, J. L. Peterson, *J. Am. Chem. Soc.* **1999**, *121*, 2674; T. Weskamp, F. J. Kohl, W. Hieringer, D. Gleich, W. A. Herrmann, *Angew. Chem.* **1999**, *111*, 2573; *Angew. Chem. Int. Ed.* **1999**, *38*, 2416; W. A. Herrmann, *Angew. Chem.* **2002**, *114*, 1342; *Angew. Chem. Int. Ed.* **2002**, *41*, 1290.
[6] H. D. Maynard, R. H. Grubbs, *Macromolecules* **1999**, *32*, 6917; M. Weck, B. Mohr, B. R. Maughon, R. H. Grubbs, *Macromolecules* **1997**, *30*, 6430.
[7] H. Katayama, H. Urushima, F. Ozawa, *Chem. Lett.* **1999**, 269; H. Katayama, H. Urushima, T. Nishioka, C. Wada, M. Nagao, F. Ozawa, *Angew. Chem.* **2000**, *112*, 4687; *Angew. Chem. Int. Ed.* **2000**, *39*, 4513; P. A. van der Schaaf, R. Kolly, H.-J. Kirner, F. Rime, A. Mühlebach, A. Hafner, *J. Organomet. Chem.* **2000**, *606*, 65; J. Louie, R. H. Grubbs, *Organometallics* **2002**, *21*, 2153.
[8] H. Katayama, H. Urushima, F. Ozawa, *J. Organomet. Chem.* **2000**, *606*, 16.
[9] R. M. Owen, J. E. Gestwicki, T. Young, L. L. Kiessling, *Org. Lett.* **2002**, *4*, 2293; J. E. Gestwicki, C. W. Cairo, D. A. Mann, R. M. Owen, L. L. Kiessling, *Anal. Biochem.* **2002**, *305*, 149; E. J. Gordon, J. E. Gestwicki, L. E. Strong, L. K. Kiessling, *Chem. Biol.* **2000**, *7*, 9; B. Chen, H. F. Sleiman, *Macromolecules* **2005**, *38*, 1084.
[10] S. C. G. Biagini, R. G. Davie, V. C. Gibson, M. R. Giles, E. L. Marshall, M. North, *Polymer* **2001**, *42*, 6669.
[11] K. S. Roberts, N. S. Sampson, *Org. Lett.* **2004**, *6*, 3253.
[12] T. Morita, B. R. Maughon, C. W. Bielawski, R. H. Grubbs, *Macromolecules* **2000**, *33*, 6621.
[13] C. W. Bielawski, R. H. Grubbs, *Macromolecules* **2001**, *34*, 8838.
[14] C. Fraser, M. A. Hillmyer, E. Gutierrez, R. H. Grubbs, *Macromolecules* **1995**, *28*, 7256.

 © 2006 Wiley-VCH Verlag GmbH & Co. KGaA, Weinheim

Catalytic Diboration

DOI: 10.1002/anie.200603130

Metal-Mediated Diboration of Alkynes with [2]Borametalloarenophanes under Stoichiometric, Homogeneous, and Heterogeneous Conditions**

Holger Braunschweig, Thomas Kupfer, Matthias Lutz, Krzysztof Radacki, Fabian Seeler, and Rainer Sigritz*

Dedicated to Professor Manfred Christl on the occasion of his 65th birthday

Boron compounds are among the most useful reagents for the functionalization of unsaturated organic substrates,[1] and many borylated organic species thus obtained have become of

[*] Prof. H. Braunschweig, T. Kupfer, Dr. M. Lutz, Dr. K. Radacki, F. Seeler, R. Sigritz
Institut für Anorganische Chemie
Bayerische Julius-Maximilians-Universität Würzburg
Am Hubland, 97074 Würzburg (Germany)
Fax: (+49) 931-888-4623
E-mail: h.braunschweig@mail.uni-wuerzburg.de

[**] This work was supported by the DFG. T.K. thanks the FCI for a Ph.D. stipend. We are grateful to the BASF AG for a generous donation of chemicals.

Supporting information for this article is available on the WWW under http://www.angewandte.org or from the author.

© 2006 Wiley-VCH Verlag GmbH & Co. KGaA, Weinheim

major importance for various applications, for example, in organic synthesis or materials science.[2] Over the past 15 years a broad variety of transition-metal-catalyzed protocols have been developed for the preparation of specific organoboranes,[3] and detailed knowledge on boryl and bis(boryl) complexes, which commonly occur as key intermediates in such homogeneously catalyzed transformations,[4] has helped to establish them as standard procedures. While hydroboration is probably the best-known of these reactions, the metal-mediated diboration, first reported in 1993,[5] is likewise a versatile synthetic method facilitating the addition of a diborane(4) to organic substrates such as alkynes, alkenes, dienes, or α,β-unsaturated ketones.[3f,g] The mechanism for this homogeneous catalysis is well-understood and involves the oxidative addition of a diborane(4) to a low-valent metal center, most commonly Pt^0, with formation of a *cis*-bis(boryl) species.[4–6]

Detailed knowledge about catalytically active species allows for the development of "tailor-made" catalysts with specific highly selective properties, which is generally recognized as the major advantage of homogeneous catalysis.[7] Nevertheless, the proportion of heterogeneous protocols in industrially applied catalytic processes still amounts to about 80%, since heterogeneous catalysis facilitates the separation of catalyst and products and, in addition, the handling and lifetime of heterogeneous catalysts are usually advantageous.[8]

In the course of our recent studies on [2]borametalloarenophanes,[9] we observed a pronounced reactivity of the bridging B–B bond toward the oxidative addition to Pt^0 centers. We anticipated that the moderately strained, however thermally stable [2]borametalloarenophanes could serve as facile diborane(4) precursors for the diboration of alkynes. Herein, we report on the metal-mediated insertion of alkynes into the B–B bridge of Cr- and Fe-based [2]borametalloarenophanes. This diboration was achieved under homogeneous and heterogeneous conditions and represents, to the best of our knowledge, the first instance of a heterogeneously catalyzed diboration of an unsaturated organic substrate.

The readily accessible [2]borametalloarenophanes **1** and **2** were prepared according to known procedures[9c,10] and treated with stoichiometric amounts of $[Pt(PEt_3)_3]$ to yield the [3]boraplatinacomplexes **3** and **4** (Scheme 1).

The oxidative addition of the boron–boron bond to the Pt center leads to the expected[9a] significant low-field shift of the ^{11}B NMR resonances (**3**: $\delta = 61.6$ ppm; **4**: $\delta = 62.2$ ppm) compared to those of the starting materials (**1**: $\delta = 44.4$ ppm; **2**: $\delta = 46.3$ ppm), and to the appearance of broad ^{31}P NMR resonances (**3**: $\delta = 11.35$ ppm; **4**: $\delta = 11.50$ ppm), which are flanked by characteristic ^{195}Pt satellites ($J_{P,Pt} = 1127.6$ Hz (**3**), $J_{P,Pt} = 1154.6$ Hz (**4**)) with peak widths at half height of about 50 Hz.

Single-crystal diffraction studies of **3** and **4** were conducted (Figure 1)[11] and reveal structural parameters which resemble those of previously reported related complexes. The incorporation of the $\{Pt(PEt_3)_2\}$ fragment into the B–B bond leads to a significant release of the intramolecular strain, as illustrated by the tilt angles $\alpha = 5.0°$ (**3**) and 4.2° (**4**) with respect to the parent sandwich complexes (**1**: $\alpha = 12.8°$; **2**: $\alpha =$ 10.1°),[9c] thus allowing the carbocyclic ligands in **3** and **4** to adopt an almost parallel arrangement. The Pt centers display distorted square-planar environments, and pertinent bond lengths and angles lie within previously reported ranges (**3**: Pt1–B1 2.116(3), Pt1–B2 2.109(3), Pt1–P1 2.3402(7), Pt1–P2 2.3322(7) Å; B1-Pt1-B2 75.42(11), P1-Pt1-P2 100.75(3)°; **4**: Pt1–B1 2.109(7), Pt1–B2 2.108(8), Pt1–P1 2.3319(17), Pt1–P2 2.3445(16) Å; B1-Pt1-B2 76.1(3), P1-Pt1-P2 97.48(7)°).[4a,9a,12,13]

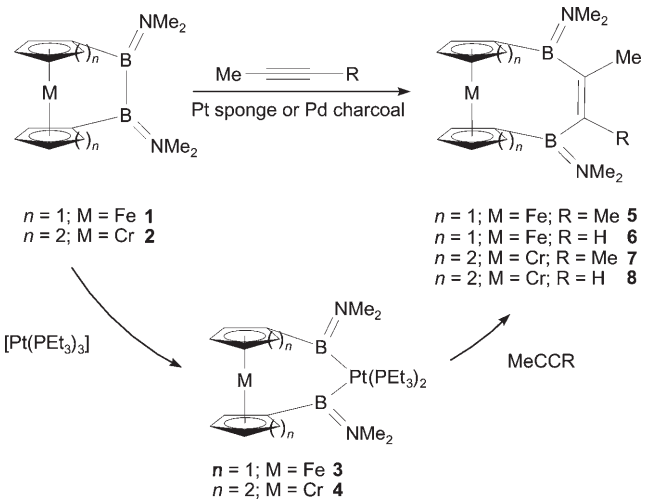

Scheme 1. Oxidative cleavage of the boron–boron bond and formation of *ansa*-bis(boryl)alkenes.

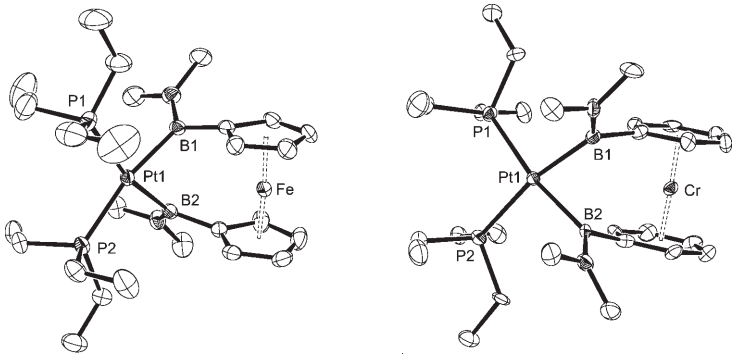

Figure 1. Structures of **3** (left) and **4** (right) in the solid state. Thermal ellipsoids are shown at 50% probability.

To confirm the anticipated propensity of [2]borametalloarenophanes to undergo Pt-mediated insertion of alkynes into the B–B bond, the isolated species **3** and **4** were treated with a 10-fold excess of propyne or 2-butyne to yield after extraction and crystallization from hexanes the corresponding novel *ansa*-bis(boryl)alkenes **5**–**8**. In solution, the ^1H NMR spectra display characteristic resonances for the Me (**5**, **7**) and H substituents (**6**, **8**) of the bridging -C(Me)=C(R)-moiety (**5**: $\delta = 1.91$ ppm (6H); **7**: $\delta = 1.96$ ppm (6H); **6**: $\delta = 2.14$ (3H), 6.44 ppm (1H); **8**: $\delta = 2.18$ (3H), 6.48 ppm (1H)). The incorporation of the unsymmetrical propyne molecule furnishes four resonances for the aminomethyl groups in **6** and **8** in the ^1H NMR spectra (**6**: $\delta = 2.61$, 2.65, 2.68, 2.69 ppm; **8**: $\delta = 2.66$, 2.67, 2.70, 2.74 ppm) while the detection of only two

 © 2006 Wiley-VCH Verlag GmbH & Co. KGaA, Weinheim

corresponding resonances in **5** and **7** (**5**: $\delta = 2.63, 2.68$ ppm; **7**: $\delta = 2.65$, 2.74 ppm) suggests C_2 symmetry in solution for the latter compounds. The ^{11}B NMR resonances for **5** ($\delta = 40.6$ ppm), **6** ($\delta = 40.5$ ppm), **7** ($\delta = 43.3$ ppm), and **8** ($\delta = 41.8$, 43.1 ppm) resemble those of the starting compounds **1** ($\delta =$ 44.4 ppm) and **2** ($\delta = 46.3$ ppm). While both **6** and **8** comprise two chemically nonequivalent boron nuclei, the expected two distinct resonances were only resolved in the case of the latter.[14] Owing to the quadrupolar momentum of the neighboring boron nuclei, the ^{13}C NMR signals of the olefinic bridge are broadened, but can be unequivocally determined in the two-dimensional long-range ^{13}C,^{1}H NMR spectra (**5**: $\delta = 143.8$ ppm; **7**: 144.3 ppm; **6**: 139.3, 156.0 ppm; **8**: 139.1, 155.6 ppm).

Furthermore, a single-crystal X-ray diffraction study of **7** was conducted (Figure 2).[11] The methyl groups of the bis(boryl)alkene subunit adopt a mutual *cis* arrangement,

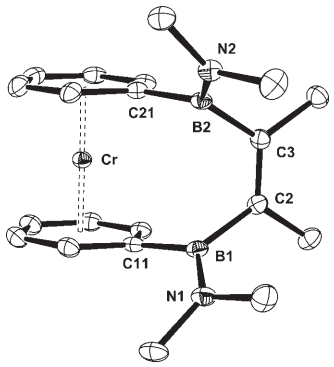

Figure 2. Structure of **7** in the solid state. Thermal ellipsoids are shown at 50% probability.

with torsion angles B1-C2-C3-B2 = −2.13°, C11-B1-C2-C3 = 78.12°, and C21-B2-C3-C2 = −72.94°. Further notable metric parameters include the B–C bond lengths (1.587(2), 1.581(2) Å) and the C–C bond length (1.351(2) Å), which lie in the expected range for B–C single and C–C double bonds.[12d,15] In contrast to the modest strain that is still present in **3** and **4**, the incorporation of the B–C=C–B moiety allows for an almost parallel alignment of the carbocyclic ligands in **7**, as indicated by the tilt angle $\alpha = 2.03(9)°$.

In subsequent experiments, the [2]borametalloarenophanes **1** and **2** were treated with propyne and 2-butyne, respectively, in the presence of catalytic amounts of [Pt(PEt$_3$)$_3$] or a finely dispersed Group 10 metal (Table 1). In a typical experiment, a sealable tube was charged with the *ansa* complex, a 10-fold excess of the alkyne, and 5 mol% of [Pt(PEt$_3$)$_3$] or 6 mol% of the freshly prepared platinum sponge, and was heated to 80 °C or 100 °C. The progress of the reaction was monitored by multinuclear NMR spectroscopy,

Table 1: Comparison of the reaction conditions upon formation of the *ansa*-bis(boryl)alkenes **5**–**8**.

	Stoichiometric[a]		Catalytic[b]					
Catalyst			[Pt(PEt$_3$)$_3$]		Pt		Pd	
ansa compound	**3**	**4**	**1**	**2**	**1**	**2**	**1**	**2**
mol% cat.[c]			5	5	6	6	6	6
mmol propyne	1.7	1.7	1.7	1.7	1.7	1.7	1.7	1.7
mmol 2-butyne	1.7	1.7	1.7	1.7	1.7	1.7	1.7	1.7
T [°C][c]	–[d]	–[d]	80	80	100	100	100	100
t [days] (CH_3CCH)	–[d]	–[d]	1	1	5	4	6	8
t [days] (CH_3CCCH_3)	–[d]	–[d]	2	2	8	7	14	16
yield[e] [%](CH_3CCH)	52	57	68	83	95	92	91	93
yield[e] [%](CH_3CCCH_3)	58	51	75	80	89	87	90	93

[a] For the stoichiometric experiments, 0.17 mmol of the corresponding [3]boraplatinacomplex was used. [b] For the catalytic experiments, 0.17 mmol of the corresponding *ansa* compound was employed. [c] Conditions given for propyne and 2-butyne. [d] Reactions occurred spontaneously. [e] Yields of isolated product after work up.

and the data confirmed a gradual consumption of the starting materials and the formation of the aforementioned products **5**–**8**. It should be noted that the NMR data indicated the absence of any soluble side or degradation products. Reaction times depended on the conditions (homogeneous or heterogeneous) and the organic substrate, and were found to be in the range of one to two days in the case of [Pt(PEt$_3$)$_3$], and four to eight days in the case of Pt metal. After work up and recrystallization from pentanes, the pure products **5**–**8** were isolated in very good yields of up to 95%.

Corresponding experiments were conducted with commercially available Pd/charcoal under otherwise analogous conditions. While reactions were found to take 6–16 days, and hence, somewhat longer than in the case of Pt, the products were isolated in very high yields, and their formation was, according to multinuclear NMR spectroscopy, not accompanied by the formation of soluble side products. It should be noted that control experiments were carried out, which proved that the [2]boraarenophanes **1** and **2** underwent no reaction with propyne and 2-butyne under analogous conditions in the absence of platinum and palladium.

In conclusion, we provide in this article our results on the heterogeneous diboration of alkynes employing finely dispersed palladium or platinum. Relative to its lighter congener, platinum exhibits superior reactivity in the heterogeneous borylation of propyne and 2-butyne.

Experimental Section

All experimental details are contained in the Supporting Information.

Received: August 2, 2006
Published online: November 8, 2006

Keywords: boron · diboration · heterogeneous catalysis · palladium · platinum

[1] Reviews: a) D. E. Kaufmann, D. S. Matteson, *Science of Synthesis, Boron Compounds*, Thieme, Stuttgart, **2005**; b) H. C. Brown, *Angew. Chem.* **1980**, *92*, 675–683.
[2] a) A. Suzuki, N. Miyaura, *Chem. Rev.* **1995**, *95*, 2457–2483; b) F. Jäkle *J. Inorg. Organomet. Polym. Mater.* **2005**, *15*, 293–307;

 © 2006 Wiley-VCH Verlag GmbH & Co. KGaA, Weinheim

c) D. Entwistle, T. B. Marder, *Angew. Chem.* **2002**, *114*, 3051 – 3056; *Angew. Chem. Int. Ed.* **2002**, *41*, 2927 – 2931; d) H. Braunschweig, D. Rais, *Angew. Chem.* **2005**, *117*, 8036 – 8038; *Angew. Chem. Int. Ed.* **2005**, *44*, 7826 – 7828.

[3] a) A.-M. Carroll, T. P. O'Sullivan, P. J. Guiry, *Adv. Synth. Catal.* **2005**, *347*, 609 – 631; b) H. C. Brown, B. Singaram, Acc. *Chem. Res.* **1988**, *21*, 287 – 293; c) K. Burgess, M. J. Ohlmeyer, *Chem. Rev.* **1991**, *91*, 1179 – 1191; d) I. Beletskaya, A. Pelter, *Tetrahedron* **1997**, *53*, 4957 – 5026; e) H. Wadepohl, *Angew. Chem.* **1997**, *109*, 2547 – 2550; *Angew. Chem. Int. Ed. Engl.* **1997**, *36*, 2441 – 2444; f) T. B. Marder, N. C. Norman, *Top. Catal.* **1998**, *5*, 63 – 73; g) T. Ishiyama, N. Miyaura, *J. Organomet. Chem.* **2000**, *611*, 392 – 402; h) T. Ishiyama, N. Miyaura, *Chem. Rec.* **2004**, *4*, 271 – 280; i) L.-B. Han, M. Tanaka, *Chem. Commun.* **1999**, 395 – 402.

[4] a) G. J. Irvine, M. J. G. Lesley, T. B. Marder, N. C. Norman, C. R. Rice, E. G. Robins, W. R. Roper, G. R. Whittell, L. J. Wright, *Chem. Rev.* **1998**, *98*, 2685 – 2722; b) H. Braunschweig, M. Colling, *Coord. Chem. Rev.* **2001**, *223*, 1 – 51.

[5] T. Ishiyama, N. Matsuda, N. Miyaura, A. Suzuki, *J. Am. Chem. Soc.* **1993**, *115*, 11 018 – 11 019.

[6] T. Ishiyama, N. Matsuda, M. Murata, F. Ozawa, A. Suzuki, N. Miyaura, *Organometallics* **1996**, *15*, 713 – 720.

[7] a) J. M. Thomas, R. Raja, D. W. Lewis, *Angew. Chem.* **2005**, *117*, 6614 – 6641; *Angew. Chem. Int. Ed.* **2005**, *44*, 6456 – 6482; b) K. C. Gupta, H. K. Abdulkadir, S. Chand, *J. Appl. Polym. Sci.* **2003**, *90*, 1398 – 1411; c) J. M. Thomas, W. J. Thomas, *Principles and Practice of Heterogeneous Catalysis*, VCH, Weinheim, **1997**; d) M. Röper, *Chem. Unserer Zeit* **2006**, *40*, 126 – 135; e) F. Schüth, *Chem. Unserer Zeit* **2006**, *40*, 92 – 103.

[8] *Catalysis from A to Z—A Concise Encyclopedia* (Eds.: B. Cornils, W. A. Herrmann, R. Schlögl, C.-H. Wong), Wiley-VCH, Weinheim, **2000**, and references cited therein.

[9] a) H. Braunschweig, M. Lutz, K. Radacki, *Angew. Chem.* **2005**, *117*, 5792 – 5796; *Angew. Chem. Int. Ed.* **2005**, *44*, 5647 – 5651; b) H. Braunschweig, M. Groß, M. Kraft, M. O. Kristen, D. Leusser, *J. Am. Chem. Soc.* **2005**, *127*, 3282 – 3283; c) H. Braunschweig, M. Homberger, C. Hu, X. Zheng, E. Gullo, C. Clentsmith, M. Lutz, *Organometallics* **2004**, *23*, 1968 – 1970.

[10] M. Herberhold, U. Doerfler, B. Wrackmeyer, *J. Organomet. Chem.* **1997**, *530*, 117 – 120.

[11] Experimental details of all X-ray crystal structure determinations are deposited in the Supporting Information. CCDC-616570 (**3**), CCDC-616569 (**4**), and CCDC-616568 (**7**) contain the supplementary crystallographic data for this paper. These data can be obtained free of charge from The Cambridge Crystallographic Data Centre via www.ccdc.cam.ac.uk/data_request/cif.

[12] a) N. Lu, N. C. Norman, A. G. Orpen, M. J. Quayle, P. L. Timms, G. R. Whittell, *J. Chem. Soc. Dalton Trans.* **2000**, 4032 – 4037; b) D. Curtis, M. J. G. Lesley, N. C. Norman, A. G. Orpen, J. Starbuck, *J. Chem. Soc. Dalton Trans.* **1999**, 1687 – 1694; c) C. N. Iverson, M. R. Smith, *J. Am. Chem. Soc.* **1995**, *117*, 4403 – 4404; d) G. Lesley, P. Nguyen, N. J. Taylor, T. B. Marder, A. J. Scott, W. Clegg, N. C. Norman, *Organometallics* **1996**, *15*, 5137 – 5154.

[13] a) T. Ishiyama, N. Matsuda, N. Miyaura, A. Suzuki, *J. Am. Chem. Soc.* **1993**, *115*, 11 018 – 11 019; b) T. Ishiyama, N. Matsuda, M. Murata, F. Ozawa, A. Suzuki, N. Miyaura, *Organometallics* **1996**, *15*, 713 – 720; c) C. N. Iverson, M. R. Smith, *Organometallics* **1996**, *15*, 5155 – 5165; d) R. L. Thomas, F. E. S. Souza, T. B. Marder, *J. Chem. Soc. Dalton Trans.* **2001**, 1650 – 1656.

[14] Two separated signals could only be detected at 161 MHz. At lower field strengths the compounds displayed one broad resonance in the ^{11}B NMR spectra (**8**: $\delta = 43.6$ ppm).

[15] a) N. Metzler, H. Nöth, M. Thomann, *Organometallics* **1993**, *12*, 2423 – 2425; b) G. Desurmont, R. Klein, S. Uhlenbrock, E. Laloë, L. Deloux, D. M. Giolando, Y. W. Kim, S. Pereira, M. Srebnik, *Organometallics* **1996**, *15*, 3323 – 3328.

 © 2006 Wiley-VCH Verlag GmbH & Co. KGaA, Weinheim

Rotaxanes

DOI: 10.1002/anie.200602166

Fourfold [2]Rotaxanes of Calix[4]arenes by Ring Closure**

Olena Molokanova, Myroslav O. Vysotsky, Yudong Cao, Iris Thondorf, and Volker Böhmer**

The synthesis of topologically interesting molecules[1] such as (multiple) catenanes or rotaxanes is not only an intellectual challenge. Mechanically connected assemblies of these types, in which the molecular substructures (interlocking rings or wheels and axles) have a certain mobility with respect to each other, have been frequently proposed as "molecular machines".[2] Various potential applications ranging from two-stage[3] and multi-stage "molecular switches"[4] to nanomechanical devices[5] and information storage[6] have been discussed. Various examples for topologically complex molecules are known also from nature.[7,8]

Recently, we showed[9–12] that the preorganization of two molecules into homo- and heterodimers of tetraureacalix[4]arenes **1** (Figure 1 a) can be used for the selective covalent connection of reactive groups that are attached to them, for example by metathesis reaction[13] of alkenyl groups.[14]

The exclusive formation of heterodimers in a 1:1 mixture of tetra(aryl urea)- (**1**) and tetra(tosylurea)calix[4]arenes (**2**) has long been known.[15] Metathesis between alkenyl groups in heterodimers of **1a** or **1b** with **2** as template furnished di- and tetraloop derivatives **3** and **4** in high yields.[9] For steric reasons **3** and **4** do not form homodimers, which would require an unfavorable overlap of the loops. Consequently they form heterodimers with **1** (or **2**), since this is the only way to get all urea groups "saturated" by hydrogen bonds. This process could be used to synthesize multiple catenanes in excellent yields by metathesis and subsequent hydrogenation.[10,11] On the other hand, heterodimers of **4** with **1c** were easily converted to fourfold [2]rotaxanes by introduction of bulky stoppers by Diels–Alder cycloaddition of a tetraalkoxy anthracene residue,[12] a reaction often dubbed "stoppering".

[*] O. Molokanova, Dr. M. O. Vysotsky, Dr. Y. Cao, Dr. V. Böhmer
Abteilung für Lehramtskandidaten der Chemie
Fachbereich Chemie, Pharmazie und Geowissenschaften
Johannes Gutenberg-Universität Mainz
Duesbergweg 10–14, 55099 Mainz (Germany)
Fax: (+49) 6131-39-25419
E-mail: vysotsky@mail.uni-mainz.de
vboehmer@mail.uni-mainz.de

Priv.-Doz. Dr. I. Thondorf
Institut für Biochemie
Fachbereich Biochemie/Biotechnologie
Martin-Luther-Universität Halle-Wittenberg
Kurt-Mothes-Strasse 3, 06099 Halle (Germany)

[**] This work was supported by the Deutsche Forschungsgemeinschaft (Bo 523/14).

Supporting information for this article is available on the WWW under http://www.angewandte.org or from the author.

© 2006 Wiley-VCH Verlag GmbH & Co. KGaA, Weinheim

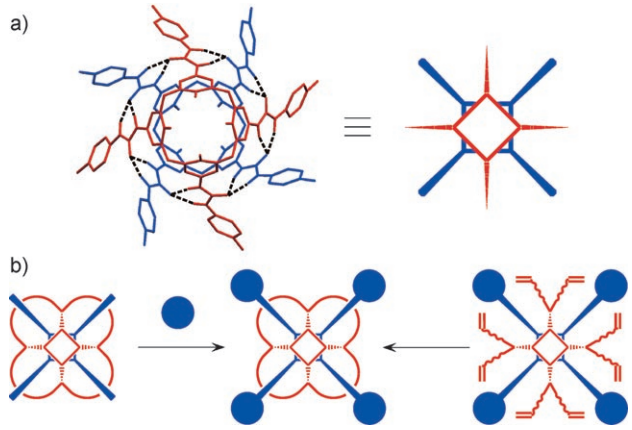

Figure 1. a) Hydrogen-bonded dimer of tetraureacalix[4]arenes as seen from one narrow rim and its schematic representation. b) Schematic representation of the synthesis of fourfold [2]rotaxanes by the attachment of bulky stoppers ("stoppering") or by fourfold ring closure ("clipping").

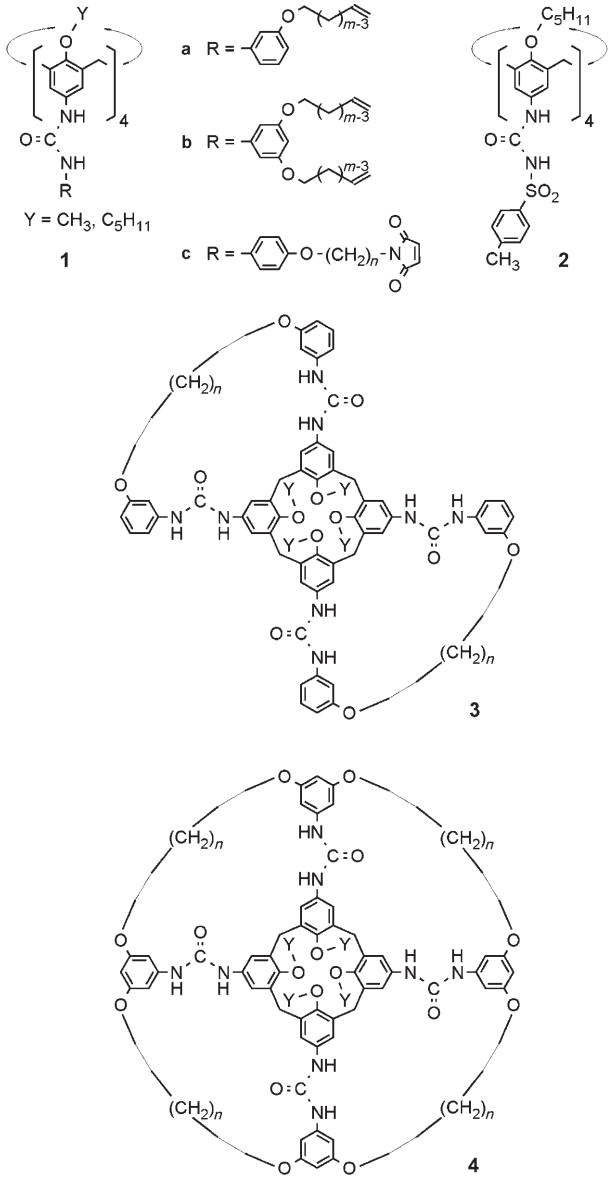

As shown schematically in Figure 1 b, there should also be the possibility to obtain such fourfold [2]rotaxanes by a "clipping" (ring closure) procedure. We describe herein the first examples, which we discovered serendipitously.

Usually the tetraloop compound **4** (formed after metathesis and hydrogenation of the double bonds) is detached from the template **2** under hydrogen-bond-breaking conditions, for example, in THF as solvent, and can be isolated and purified by column chromatography. However, for reactions carried out with the dialkenyl compounds **1b** ($m = 4, 5$) this detachment was not possible. In these cases chromatographic purification furnished in remarkably high yields (55–88%) a product that was still a dimer containing a guest, as proved by ^{1}H NMR spectroscopy and mass spectrometry. Obviously the expected tetraloop compounds **4** with six and eight methylene groups ($n = 2m-2 = 6, 8$) in the connecting ether chains cannot slip from the tosylurea arms, and we obtained the rotaxanes **5a–d** (Figure 2). A potential reason may be found in the tetrahedral arrangement of the substituents at the sulfur atom (N-S-C angle ca. 109°; compare Figure 3).

Although we obtained several single crystals of rotaxanes **5a–d**, their structures could not be solved. Structural information was provided by molecular dynamics (MD) simulations[16] of **5b** and **5d**. The time-averaged conformation of **5b**

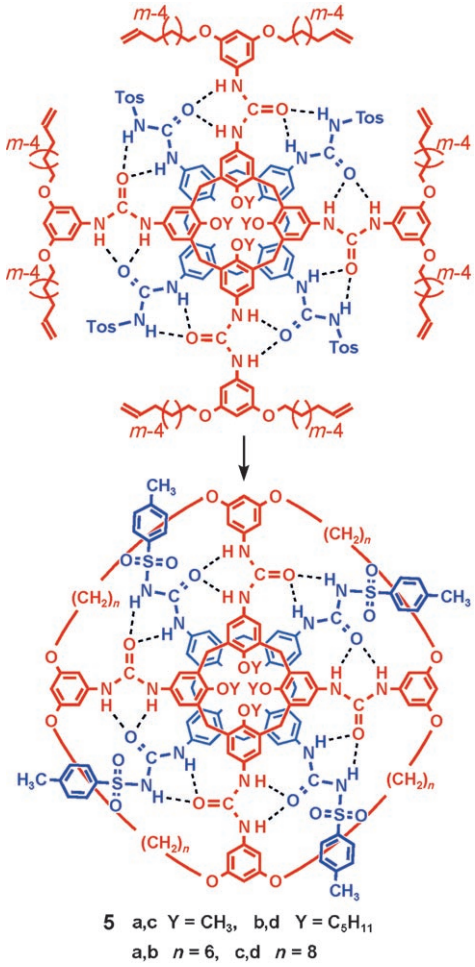

Figure 2. Synthesis of fourfold [2]rotaxanes **5** by metathesis and subsequent hydrogenation. (OY partly omitted for clarity).

 © 2006 Wiley-VCH Verlag GmbH & Co. KGaA, Weinheim

(Figure 3) demonstrates that the aliphatic chains -$(CH_2)_n$- connecting the aryl residues of **4** are "hooked" on the tosyl groups of **2**, which by their volume alone are not too big to slip through the loops (as demonstrated by tolyl and other aryl

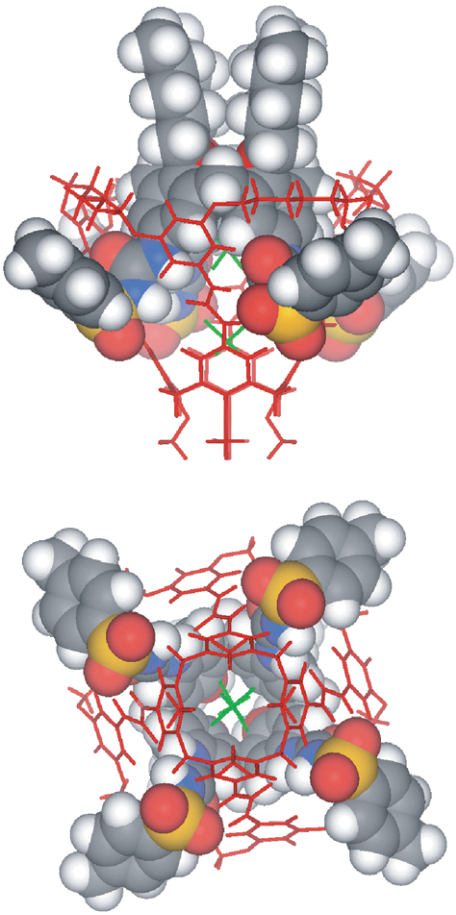

Figure 3. Molecular shape of rotaxane **5b** obtained by MD simulation of an assembly of **4** (red, stick presentation) and **2** (space-filling model; C gray, H white, S orange, O red, N blue) including two dichloromethane guest molecules (green); top: side view; bottom: view from the narrow rim of **4**.

residues). In contrast to the capsules composed of two molecules of **1**, in **5b** and **5d** additional intermolecular hydrogen bonds can be formed between the urea protons of **4** and the sulfonyl oxygen atoms of **2**. These hydrogen bonds are stronger as judged from the N–H···O separations and angles than the usual ones involving the urea carbonyl group. The different hydrogen-bonding pattern causes an enlargement of the capsule by about 30–35 % (260–270 Å^3) as compared to the capsules **1**·**1** and enables the inclusion of more than one guest molecule (see below). The interaction energies of the two calixarenes are nearly equal in both cases (**5b**: $\Delta E = -227.7 \pm 4.8$ kcal mol^{-1}; **5d**: $\Delta E = -229.4 \pm 5.2$ kcal mol^{-1}), thus indicating that the two molecules forming the fourfold rotaxane are more or less "unstrained".

Interestingly, the rotaxanes **5c**,**d** with loops of eight methylene groups contain ethyl acetate as a guest (as shown by MALDI-TOF MS), although the metathesis reaction was carried out in dichloromethane. Obviously, the initial guest was exchanged during the chromatographic work up, which was carried out using mixtures of ethyl acetate and hexane as eluant. The inclusion of ethyl acetate can be seen also in the ^{1}H NMR spectrum in [D_8]THF. For **5d** it is exchanged against the solvent in a clear first-order reaction ($\tau_{1/2} = 32$ min) while the capsule itself proves (relatively) stable under these conditions owing to the fourfold [2]rotaxane structure (see below).[17]

For rotaxanes **5a**,**b** ($n = 6$) a guest exchange is obviously not possible under similar conditions, and the ^{1}H NMR spectra in [D_8]THF do not change with time.[18] Compound **5a** contains *two* molecules of dichloromethane per capsule, as shown by the respective peak in the MS. This is the first example for the inclusion of two guest molecules in the cavity of a tetraurea dimer.[19] For **5b** an additional peak with lower intensity corresponds to a species with one encapsulated CH_2Cl_2 molecule. The presence of two rotaxane complexes is clearly shown by the ^{1}H NMR spectrum in C_6D_6. Integration of suitable signals revealed a ratio of [**5b**@2 CH_2Cl_2]/[**5b**@ CH_2Cl_2] = 3:1.

As usual for dimeric capsules of tetraureacalix[4]arenes[20] (and common for cages with aromatic walls[21]) the ^{1}H NMR signals for the included guest are shifted upfield because of the shielding by the π-electron systems. In the present case we are able to report such $\Delta\delta$ values for the rotaxanes **5** in THF, a solvent in which (hetero)dimeric capsules such as **4**·**2** do not exist. For the encapsulated CH_2Cl_2 molecule in **5b** one singlet is observed for the 1:1 complex ($\Delta\delta = -3.23$ ppm) as well as for the 1:2 complex ($\Delta\delta = -3.30$ ppm). Obviously the filling with two molecules causes a "closer" contact to the aromatic walls, but still both encapsulated molecules are "freely" rotating. For the incorporated ethyl acetate molecule in **5d** three values are found: $\Delta\delta = -4.54$ ($C(O)CH_3$), $\Delta\delta = -3.47$ (CH_2CH_3), and $\Delta\delta = -2.13$ ppm. This suggests that the CH_2 groups mainly occupy an "equatorial" position (oriented towards the urea belt),[20] while the acetyl methyl groups of the incorporated ethyl acetate molecules are mainly oriented towards the aromatic rings/π electrons. Time-averaged, the CH_2CH_3 protons assume an intermediate position.

The rotaxanes were usually isolated only after hydrogenation to avoid complications by *cis*/*trans* isomers, but it is also worth having a look at the original reaction product of the metathesis reaction. In the case of **5d′** (precursor of **5d**) six singlets (of different intensity) for the $C(O)CH_3$ group of the incorporated ethyl acetate molecule are observed (^{1}H NMR in CD_2Cl_2), which would correspond to the six isomers **5d′** expected by all possible combinations of *cis*/*trans* double bonds. Although not strictly proved, this does not seem unreasonable. For the nonhydrogenated rotaxane **5b′** (a 3:1 mixture of two complexes; see above) the major set of signals corresponds to a C_4-symmetric species, consistent with the formation of only one isomer with four identical double bonds (presumably in *trans* configuration). This would mean that the small loop size determines the stereochemistry of the double bonds formed.

The slippage of stopper groups in rotaxanes, and hence the stability of a rotaxane, can be solvent-dependent.[22] Dramatic differences in the stability of **5a**,**b** versus **5c**,**d** were found with other hydrogen-bond-breaking solvents. Dissolving **5a** or **5b**

 © 2006 Wiley-VCH Verlag GmbH & Co. KGaA, Weinheim

in [D_5]pyridine or [D_6]DMSO does not affect their rotaxane structure. No change occurs in the ^{1}H NMR spectrum of **5b** in [D_5]pyridine over three weeks at 25 °C, while **5a** loses one of the two incorporated CH_2Cl_2 molecules with an estimated half-life of 12 days, thus indicating that the capsule with methoxy groups is slightly more flexible. For **5c**,**d**, on the other hand, only two sets of signals corresponding to the "monomeric" **4** and to **2** were observed immediately after dissolution.[23] Although pyridine and DMSO are more powerful hydrogen-bond acceptors than THF, an overall change of the conformation and/or flexibility of the whole assembly owing to different solvation may be responsible for the rapid dissociation.

In conclusion, we have shown that fourfold [2]rotaxanes can be prepared by fourfold ring closure (metathesis) using the preorganization available in heterodimers of octaalkenyl-substituted tetraureacalix[4]arenes **1b** with tetra(tosylurea)-calix[4]arenes **2**. In contrast to (schematically) identical fourfold [2]rotaxanes obtained by "slipping and stoppering"[12] the novel pathway allows for shorter axles and smaller rings (wheels). Thus, not only the whole assembly is stable in solvents which break hydrogen bonds, but also the guest exchange can be completely suppressed. Fourfold [2]rotaxanes **5a**,**b** may be regarded as mechanically interlocked equivalents to (hemi)carcerands. Among various possible applications, this opens up an easy way to have incorporated guests also in polar, protic solvents where they could be liberated on demand.

Experimental Section

5a: Compounds **2** (0.294 g, 0.190 mmol) and **1b** (0.200 g, 0.127 mmol) were dissolved in dichloromethane (400 mL) and stirred for 48 h (to ensure complete formation of the heterodimer) at room temperature. Nitrogen was bubbled through the solution for 30 min, then a solution of Grubbs' catalyst (0.042 g, 0.051 mol) in dichloromethane (5 mL) was added, and the nitrogen stream was continued for 30 min. After 48 h in the dark, the solution was evaporated, and the residue was dissolved again in dichloromethane (5 mL). The catalyst was removed by column chromatography (silica gel, ethyl acetate/hexane 2:1). The product was dissolved in toluene (20 mL), PtO_2 (0.052 g) was added, and the suspension was stirred under hydrogen (1 atm) for 24 h. After evaporation the residue was dissolved again in dichloromethane (5 mL) and purified by column chromatography (ethyl acetate/hexane 1:3) to remove the last traces of the catalysts. Yield: 0.321 g (79 %), characterized as the complex with dichloromethane.

^{1}H NMR (400 MHz, [D_6]benzene, 295 K): $\delta = 11.25$ (s, 4H, NH), 8.89 (s, 4H, NH), 8.35 (d, $^4J(H,H) = 2.4$ Hz, 4H, CH_{calix}), 8.27 (s, 4H, NH), 8.15 (d, $^3J(H,H) = 8.5$ Hz, 8H, CH_{tolyl}), 7.84 (s, 4H, NH), 7.69 (d, $^4J(H,H) = 2.4$ Hz, 4H, CH_{calix}), 7.60 (brt, 4H, CH), 7.16 (d, overlap with the solvent signal, 4H, CH_{calix}), 7.07 (brt, 4H, CH), 6.88 (d, $^3J(H,H) = 8.5$ Hz, 8H, CH_{tolyl}), 6.28 (brt, 4H, CH), 5.25 (d, $^4J(H,H) = 2.4$ Hz, 4H, CH_{calix}), 4.46 (d, $^2J(H,H) = 11.7$ Hz, 4H, $ArCH_2Ar$), 4.26 (d, $^2J(H,H) = 11.6$ Hz, 4H, $ArCH_2Ar$), 4.23 (m, 4H, OCH_2), 4.00 (dt, $^2J(H,H) = 12.1$ Hz, $^3J(H,H) = 5.1$ Hz, 4H, OCH_2 (loop)), 3.76 (d, $^2J(H,H) = 12.5$ Hz, 4H, $ArCH_2Ar$), 3.73 (s and m, 20H, OCH_3, OCH_2), 3.44 (brm, 4H, CH_2 (loop)), 3.04 (brm, 4H, CH_2 (loop)), 2.84 (d, $^2J(H,H) = 11.7$ Hz, 4H, $ArCH_2Ar$), 2.61 (s, 4H, encapsulated CH_2Cl_2), 2.33 (brm, 4H, CH_2 (loop)), 1.96 (s and m, 20H, $ArCH_3$, CH_2), 1.51 (brm, 4H, CH_2 (loop)), 1.36 (quin, $^3J(H,H) = 7.0$ Hz, 8H, CH_2), 1.28 (m, 8H, CH_2), 0.94 (t, $^3J(H,H) = 7.0$ Hz, 12H, CH_3), 0.80 (brm, 16H, CH_2 (loop)), 0.59 (brm, 4H, CH_2 (loop)), 0.13 ppm (brm, 4H, CH_2 (loop)).

MALDI-TOF: m/z calcd: 3305.39 $[M+Ag+2(CH_2Cl_2)]^+$; found: 3305.03.

Received: May 31, 2006
Revised: July 20, 2006
Published online: October 25, 2006

Keywords: calixarenes · hydrogen bonding · metathesis · molecular capsules · rotaxanes

[1] *Molecular Catenanes, Rotaxanes and Knots* (Eds.: J.-P. Sauvage, C. Dietrich-Buchecker), Wiley-VCH, Weinheim, **1999**.
[2] a) V. Balzani, M. Gómez-López, J. F. Stoddart, *Acc. Chem. Res.* **1998**, *31*, 405 – 414; b) J.-P. Collin, C. Dietrich-Buchecker, P. Gaviña, M. C. Jimenez-Molero, J.-P. Sauvage, *Acc. Chem. Res.* **2001**, *34*, 477 – 487; c) C. A. Schalley, K. Beizai, F. Vögtle, *Acc. Chem. Res.* **2001**, *34*, 465 – 476.
[3] J. W. Choi. A. H. Flood, D. W. Steuerman, S. Nygaard, A. B. Braunschweig, N. N. P. Moonen, B. W. Laursen, Y. Luo, E. DeIonno, A. J. Peters, J. O. Jeppesen, K. Xu, J. F. Stoddart, J. R. Heath, *Chem. Eur. J.* **2006**, *12*, 261 – 279.
[4] D. A. Leigh, J. K. Y. Wong, F. Dehez, F. Zerbetto, *Nature* **2003**, *424*, 174 – 179.
[5] a) N. C. Seeman, *Trends Biochem. Sci.* **2005**, *30*, 119 – 125; b) T. J. Huang, B. Brough, C.-M. Ho, Y. Liu, A. H. Flood, P. A. Bonvallet, H.-R. Tseng, J. F. Stoddart, M. Baller, S. Magonov, *Appl. Phys. Lett.* **2004**, *85*, 5391 – 5393; c) J. D. Badjić, V. Balzani, A. Credi, S. Silvi, J. F. Stoddart, *Science* **2004**, *303*, 1845 – 1849.
[6] a) C. P. Collier, E. W. Wong, M. Belohradsky, F. M. Raymo, J. F. Stoddart, P. J. Kuekes, R. S. Williams, J. R. Heath, *Science* **1999**, *285*, 391 – 394; b) C. P. Collier, G. Mattersteig, E. W. Wong, Y. Luo, K. Beverly, J. Sampaio, F. M. Raymo, J. F. Stoddart, J. R. Heath, *Science* **2000**, *289*, 1172 – 1175.
[7] a) D. A. Koster, V. Croquette, C. Dekker, S. Shuman, N. H. Dekker, *Nature* **2005**, *434*, 671 – 674; b) A. Bergerat, B. de Massy, D. Gadelle, P. C. Varoutas, A. Nicolas, P. Forterre, *Nature* **1997**, *386*, 414 – 417.
[8] W. R. Wikoff, L. Lijas, R. L. Duda, H. Tsuruta, R. W. Hendrix, J. E. Johnson, *Science* **2000**, *289*, 2129 – 2133.
[9] A. Bogdan, M. O. Vysotsky, L. Wang, V. Böhmer, *Chem. Commun.* **2004**, 1268 – 1269.
[10] M. O. Vysotsky, A. Bogdan, T. Ikai, Y. Okamoto, V. Böhmer, *Chem. Eur. J.* **2004**, *10*, 3324 – 3330.
[11] L. Wang, M. O. Vysotsky, A. Bogdan, M. Bolte, V. Böhmer, *Science* **2004**, *304*, 1312 – 1314.
[12] C. Gaeta, M. O. Vysotsky, A. Bogdan, V. Böhmer, *J. Am. Chem. Soc.* **2005**, *127*, 13136 – 13137.
[13] T. M. Trnka, R. H. Grubbs, *Acc. Chem. Res.* **2001**, *34*, 18 – 23.
[14] Examples for metathesis in supramolecular systems: a) B. Mohr, M. Weck, J.-P. Sauvage, R. H. Grubbs, *Angew. Chem.* **1997**, *109*, 1365 – 1367; *Angew. Chem. Int. Ed. Engl.* **1997**, *36*, 1308 – 1310; b) D. A. Leigh, P. J. Lusby, S. J. Teat, A. J. Wilson, J. K. Y. Wong, *Angew. Chem.* **2001**, *113*, 1586 – 1591; *Angew. Chem. Int. Ed.* **2001**, *40*, 1538 – 1543; c) T. D. Clark, K. Kobayashi, M. R. Ghadiri, *Chem. Eur. J.* **1999**, *5*, 782 – 792; d) M. S. Wendland, S. C. Zimmerman, *J. Am. Chem. Soc.* **1999**, *121*, 1389 – 1390; e) S. C. Zimmerman, M. S. Wendland, N. A. Rakow, I. Zharov, K. S. Suslick, *Nature* **2002**, *418*, 399 – 403; f) X.-Z. Zhu, C.-F. Chen, *J. Am. Chem. Soc.* **2005**, *127*, 13158 – 13159.
[15] a) R. K. Castellano, B. H. Kim, J. Rebek, Jr., *J. Am. Chem. Soc.* **1997**, *119*, 12671 – 12672; b) R. K. Castellano, J. Rebek, Jr., *J. Am. Chem. Soc.* **1998**, *120*, 3657 – 3663.
[16] MD simulations of **5a** and **5c** with two molecules of dichloromethane were performed with the compounds in a rectangular box of chloroform molecules. For details, see reference [20].

 © 2006 Wiley-VCH Verlag GmbH & Co. KGaA, Weinheim

[17] Dissociation in THF occurs with an estimated half-life of 10–20 days.
[18] About 20% of the initial guest is exchanged in boiling ethyl acetate after 60 h.
[19] For the inclusion of several guests into larger hydrogen-bonded molecular capsules, see: a) S. K. Körner, F. C. Tucci, D. M. Rudkevich, J. Rebek, Jr., *Chem. Eur. J.* **2000**, *6*, 187–195; b) A. Scarso, A. Shivanyuk, J. Rebek, Jr., *J. Am. Chem. Soc.* **2003**, *125*, 13981–13983; c) L. Avram, Y. Cohen, *Org. Lett.* **2006**, *8*, 219–222.
[20] F. Broda, M. O. Vysotsky, V. Böhmer, I. Thondorf, *Org. Biomol. Chem.* **2006**, *4*, 2424–2432, and references therein.
[21] a) J. A. Bryant, M. T. Blanda, M. Vincenti, D. J. Cram, *J. Am. Chem. Soc.* **1991**, *113*, 2167–2172; b) C. Naumann, S. Place, J. C. Sherman, *J. Am. Chem. Soc.* **2002**, *124*, 16–17; c) D. Ajami, T. Iwasawa, J. Rebek, Jr., *Proc. Natl. Acad. USA* **2006**, *103*, 8934–8936.
[22] a) P. R. Ashton, M. Bělohradský, D. Philp, J. F. Stoddart, *J. Chem. Soc. Chem. Commun.* **1993**, 1269–1274; b) M. Asakawa, P. R. Ashton, R. Ballardini, V. Balzani, M. Bělohradský, M. T. Gandolfi, O. Kocian, L. Prodi, F. M. Raymo, J. F. Stoddart, M. Venturi, *J. Am. Chem. Soc.* **1997**, *119*, 302–310.
[23] Interestingly, a dimeric capsule formed by a bulky tetra(trityl-urea)calix[4]arene with tetramethylammonium as guest is easily "destroyed" in THF, while it is very stable in [D_6]DMSO; see: M. O. Vysotsky, I. Thondorf, V. Böhmer, *Chem. Commun.* **2001**, 1890–1891.

 © 2006 Wiley-VCH Verlag GmbH & Co. KGaA, Weinheim

Cluster Compounds

DOI: 10.1002/anie.200602709

Silver Chalcogenide Clusters with Dimethylanilinomercapto Ligands: Syntheses and Crystal Structures of $[Ag_{65}S_{13}(SC_6H_4NMe_2)_{39}(dppm)_5]$, $[Ag_{76}Se_{13}(SC_6H_4NMe_2)_{50}(PPh_3)_{6.5}]$, and $[Ag_{88}Se_{12}(SC_6H_4NMe_2)_{63}(PPh_3)_6]$**

*Soheila Chitsaz, Dieter Fenske, and Olaf Fuhr**

Dedicated to Professor Michael Binnewies on the occasion of his 60th birthday

Although many large inorganic clusters have been synthesized, the targeted preparation of such compounds remains a challenge. Particularly impressive cluster complexes include $Na_{48}[H_xMo_{368}O_{1032}(H_2O)_{240}(SO_4)_{48}]\cdot n\,H_2O$ ($x \approx 16$; $n \approx 1000$),[1] $[Pd_{145}(CO)_x(PEt_3)_{30}]$ ($x \approx 60$),[2] and $[Ga_{84}\{N(SiMe_3)_2\}_{20}Li_6Br_2(thf)_{20}]$ (thf = tetrahydrofuran).[3]

The conditions for the growth of such complex compounds, some of which have dimensions of several nanometers, are largely unknown. For some time, we have tried to understand the conditions for the formation of metal chalcogenide clusters.[4] Although many such compounds are known, no conclusions about the influence of the reaction conditions and ligands on cluster growth can yet be made.

Metal-rich silver chalcogenide clusters can be obtained through the reaction of silver salts with silylated derivatives of sulfur, selenium, or tellurium in the presence of stabilizing tertiary phosphines. One example is the formation of $[Ag_{188}S_{94}(PnPr_3)_{20}]$ from the reaction of $Ag(CF_3CO_2)$ with $PnPr_3$ and $S(SiMe_3)_2$; $[Ag_{262}S_{100}(StBu)_{62}(dppb)]$ can be synthesized through the reaction of $Ag(PhCO_2)$ with 1,4-bis(diphenylphosphanyl)butane (dppb) and a mixture of $S(SiMe_3)_2$ and $S(tBu)SiMe_3$.[5] Recently, we reported the preparation of $[Ag_{344}S_{124}(StBu)_{96}]$ through the reaction of $Ag(PhCO_2)$ with $S(tBu)SiMe_3$ and $S(SiMe_3)_2$ in the presence of 1,4-bis(diphenylphosphanylmethyl)benzene.[6] In these compounds, a gradual transformation from "molecular" clusters with no structural relationship to binary silver chalcogenides to ligand-protected silver chalcogenide particles with unusual silver chalcogenide substructures is observed.

The variation in the physical properties of the clusters with size is also remarkable. Small silver clusters (with less than ca. 100 silver atoms) are yellow to red in color, whereas clusters containing more silver atoms are black. This observation demonstrates that the separation between the highest occupied molecular orbital (HOMO) and the lowest unoccupied molecular orbital (LUMO) is size-dependent. Another feature of these compounds is an increasing disorder of the silver and chalcogenide ions with cluster size; in this respect, the behavior of the molecules is similar to that of the binary Ag_2E phases (E = S, Se, Te).[7–10]

We have now attempted to prepare further examples of ligand-protected clusters and have focused on varying the ligand shell, in particular. For the first time, we have used 4-(*N*,*N*-dimethylanilino)mercaptotrimethylsilane ($(Me_2N)C_6H_4(SSiMe_3)$) as the sulfur agent. We hoped that the dimethylanilino groups would improve the solubility of the clusters in organic solvents, allowing more extensive characterization in solution. Furthermore, the use of this ligand led to clusters with new molecular structures.

The reaction of a solution of silver benzoate and bis(diphenylphosphanyl)methane (dppm) in THF with a mixture of $(Me_2N)C_6H_4(SSiMe_3)$ and $S(SiMe_3)_2$ at low temperature yielded a yellow solution, which became darker in color upon slow warming to room temperature. By layering the solution with diethyl ether, yellow crystals of cluster **1** were obtained [Eq. (1)].

$$Ag(PhCO_2) + dppm + S(SiMe_3)_2 + (Me_2N)C_6H_4(SSiMe_3) \rightarrow [Ag_{65}S_{13}(SC_6H_4NMe_2)_{39}(dppm)_5]\ (\mathbf{1}) \quad (1)$$

[*] Dr. S. Chitsaz, Prof. Dr. D. Fenske, Dr. O. Fuhr
Institut für Nanotechnologie
Forschungszentrum Karlsruhe
Postfach 3640, 76021 Karlsruhe (Germany)
Fax: (+49) 7247-826368
E-mail: olaf.fuhr@int.fzk.de
and
Institut für Anorganische Chemie der Universität Karlsruhe
Engesserstrasse 15, Geb. 30.45, 76131 Karlsruhe (Germany)

[**] This work was supported by the Deutsche Forschungsgemeinschaft (DFG; Centre for Functional Nanostructures (CFN)), the Deutsch-Israelische Projektkooperation (DIP), and the Fonds der Chemischen Industrie. dppm = bis(diphenylphosphanyl)methane.

 © 2006 Wiley-VCH Verlag GmbH & Co. KGaA, Weinheim

In an analogous reaction with triphenylphosphine and $Se(SiMe_3)_2$ instead of dppm and $S(SiMe_3)_2$, two different clusters crystallized from the reaction solution, depending on the work-up conditions. Upon layering with diethyl ether, crystals of **2** were isolated over a short time period; without the addition of diethyl ether, cluster **3** precipitated after a few weeks [Eq. (2)].

$$\begin{aligned} Ag(PhCO_2)+PPh_3 + Se(SiMe_3)_2 + (Me_2N)C_6H_4(SSiMe_3) \rightarrow \\ [Ag_{76}Se_{13}(SC_6H_4NMe_2)_{50}(PPh_3)_{6.5}]\ (\mathbf{2}) \\ +[Ag_{88}Se_{12}(SC_6H_4NMe_2)_{63}(PPh_3)_6]\ (\mathbf{3}) \end{aligned} \quad (2)$$

Considerable problems were associated with the X-ray crystal-structure analysis of these compounds. On one hand, such large clusters tend to have disordered silver and chalcogenide ions. On the other hand, the crystals contained a large amount of disordered noncoordinating solvent, which was associated with very diffuse electron density in the areas between the cluster molecules.[11–13] The ordered cluster molecules can be pictured as "swimming" in a sea of disordered solvent. We found no evidence of the incorporation of diethyl ether in the voids of **1** and **2**; during thermal decomposition, only THF was detected in both cases. The given compositions of the compounds are based on the results of the single-crystal X-ray analysis and agree with the elemental analysis, within standard deviations, if it is assumed that the crystals release all of the incorporated solvent during drying under high vacuum at 100 °C. All of the clusters are uncharged; neither the X-ray structure analyses nor mass spectroscopic investigations gave any indication of counterions.

Clusters **1**–**3** are built up in a shell-like manner. In the inner silver chalcogenide cores, the silver ions have linear, trigonal planar, or tetrahedral coordination geometries. The cores are surrounded by organic shells consisting of phosphine ligands coordinated to silver ions and dimethylanilino groups bonded to sulfur atoms. Compounds **2** and **3** can be described as core–shell particles with silver selenide cores surrounded by silver sulfide shells. We recently reported similar copper chalcogenide clusters, for example, $[Cu_{36}Se_8(SPh)_{20}(PPh_3)_8]$ and $[Cu_{72}Se_{14}(SPh)_{36}(CH_3CO_2)_8(PPh_3)_6]$.[14]

Compound **1** (Figure 1, top) crystallizes in the orthorhombic space group *Iba*2 with eight formula units per cell. The inner part of the cluster contains 13 sulfur atoms (S40–S52) that do not bear any organic substituents and, therefore, have a charge of −2. This S_{13} core (orange in Figure 1, top) can be described as part of a double hexagonal close-packed (ABAC) lattice, with three sulfur atoms (S40–S42) representing an A layer, six sulfur atoms (S43–S48) a B layer, three sulfur atoms (S49–S51) another A layer, and atom S52 a C layer. The core is surrounded by a shell of 39 sulfur atoms (yellow in Figure 1, top), each of which is bonded to a dimethylanilino group and has a charge of −1. However, these sulfur atoms are not arranged in close-packed layers. For charge balance, 65 silver ions are incorporated into the sulfur substructure. In the X-ray structure analysis, 60 of these ions were unambiguously located; the five remaining silver ions are disordered over 10 positions (Ag61–Ag70). The metal ions in the β-modification of Ag_2S are also severely disordered, resulting in a significant ionic conductivity.[10] The inorganic part of cluster **1** consisting of silver and sulfide ions has a diameter of approximately 1.7 nm; if the organic shell of dimethylanilino groups and dppm ligands is also taken into account, the total particle size is approximately 2.8 nm. In the crystal lattice, the nearly spherical clusters are arranged in a distorted face-centered cubic packing. A free volume of 25000 Å^3 per unit cell is calculated, which is filled by approximately 250 disordered THF molecules.[11]

Compound **2** (Figure 1, bottom) crystallizes in the triclinic space group $P\bar{1}$ with two formula units per cell. Close examination reveals that **2** is a mixture of two different cluster compounds, one with the composition $[Ag_{76}Se_{13}(SC_6H_4NMe_2)_{50}(PPh_3)_7]$ and the other with the composition $[Ag_{76}Se_{13}(SC_6H_4NMe_2)_{50}(PPh_3)_6]$. The structures

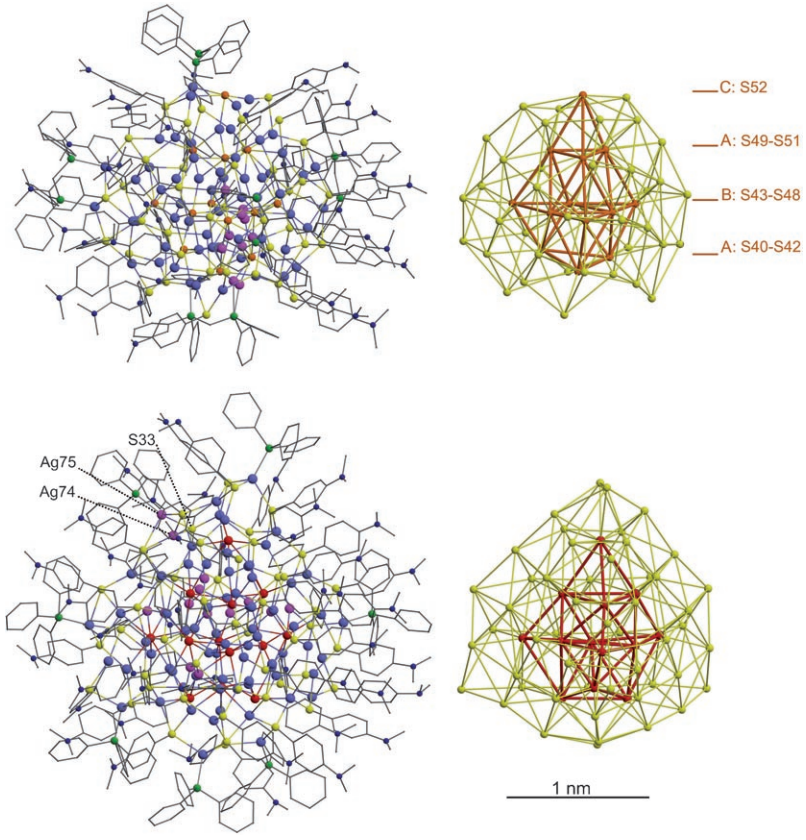

Figure 1. Structures of clusters **1** (top) and **2** (bottom): the molecular structures (left) and the chalcogen substructures (right). Ag blue (disordered Ag violet), Se red, S^{2-} orange, SR yellow, P green, N small dark blue, C gray. The lines connecting the chalcogen atoms in the substructures are for visualization and do not represent bonds. The ABAC layers of the double hexagonal close-packed S^{2-} core of **1** are indicated (left).

 © 2006 Wiley-VCH Verlag GmbH & Co. KGaA, Weinheim

of both clusters are identical, with the exception that the dimethylanilino group bonded to S33 has a different orientation in each. Thus, in the first cluster, Ag75 bears a PPh_3 ligand, but in the second cluster this silver atom occupies position Ag74, which bears no PPh_3 ligand, in the inner part of the cluster. As a result, **2** has 6.5 PPh_3 ligands on average. Apparently, this small difference does not influence the arrangement of the two clusters in the crystal lattice. No indications of an ordered superstructure were observed; evidently, **2** is a cocrystal of two very similar clusters, which are randomly arranged in the lattice.

The core of **2** consists of 13 selenium atoms (red in Figure 1, bottom), which are arranged in the same way as the S^{2-} ions in **1**. In **2**, the core is completely surrounded by the 50 sulfur atoms of the $SC_6H_4NMe_2$ groups. The selenide core of **2** has a diameter of nearly 1.1 nm; if the sulfide shell is also considered, the inorganic part of the cluster has a size of 1.9 nm. With the organic shell, **2** has a particle size of approximately 3.1 nm. In the crystal lattice, the clusters are arranged in a distorted body-centered cubic packing. The free volume of 11500 Å^3 per unit cell is filled with approximately 115 THF molecules, which could not be localized (as in **1**).

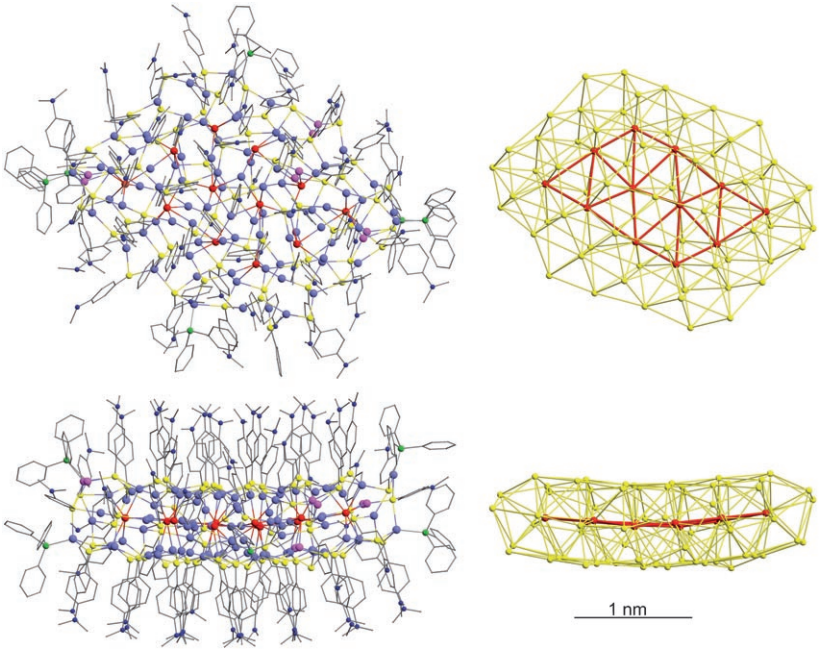

Figure 2. Structure of cluster **3**: the molecular structure (left) and the chalcogen substructure (right) in two perpendicular projections (top and bottom). Ag blue (disordered Ag violet), Se red, S yellow, P green, N small dark blue, C gray. The lines connecting the chalcogen atoms in the substructures are for visualization and do not represent bonds.

Compound **3** (Figure 2) crystallizes in the tetragonal space group $P4_2/n$ with eight formula units per cell. In contrast to the nearly spherical clusters **1** and **2**, cluster **3**, which contains 88 silver atoms, has a layered structure. The 12 selenium atoms of the core (red in Figure 2) form a 3×4 hexagonal layer, which however, is not planar, but slightly bent. The core is completely surrounded by a shell consisting of 63 sulfur atoms; the atoms above and below the selenium layer are also arranged in a hexagonal pattern. The resulting charge for the chalcogenide substructure is −87. According to the X-ray structure analysis, there are 88 silver atoms in cluster **3**, one more than is necessary for charge balance. Of these, 82 silver atoms occupy holes in the chalcogenide core and have linear, trigonal planar, or tetrahedral coordination geometries. Only the six silver atoms bearing phosphine ligands are located outside of the sulfur shell; one is coordinated by two sulfur atoms and one phosphorous atom in a trigonal planar geometry, and the other five are bonded to three sulfur atoms and one phosphorous atom. In **3**, some silver atoms are again disordered. As no counterions were detected, one of the 88 silver atoms must be formally uncharged. However, no such atom could be identified on the basis of its coordination environment; rather, it is assumed that the +87 charge is equally distributed over the 88 silver atoms. This phenomenon is typical for the modifications of silver sulfide, which exhibit a certain phase width ($Ag_{2+x}S$).[10] The platelike silver chalcogenide core of **3** has dimensions of $0.5 \times 1.8 \times 2.2$ nm^3. With its organic shell, the size of the whole cluster **3** is $2.0 \times 3.0 \times 3.3$ nm^3. In the crystal lattice, there is a free volume of 53500 Å^3 per unit cell, which is filled by approximately 535 THF molecules.

In all three compounds, the silver–chalcogen bonds fall within the expected ranges (**1**: Ag–S^{2-}: 2.06(1)–2.96(1) Å, Ag–SR: 2.32(1)–2.914(8) Å; **2**: Ag–Se: 2.489(3)–3.088(3) Å, Ag–S: 2.285(7)–2.924(6) Å; **3**: Ag–Se: 2.480(3)–2.984(3) Å, Ag–S: 2.26(1)–2.964(6) Å). In Figure 3, the statistics of the distances of each cluster are presented as histograms. It is difficult to define sharp upper limits for the silver–chalcogen

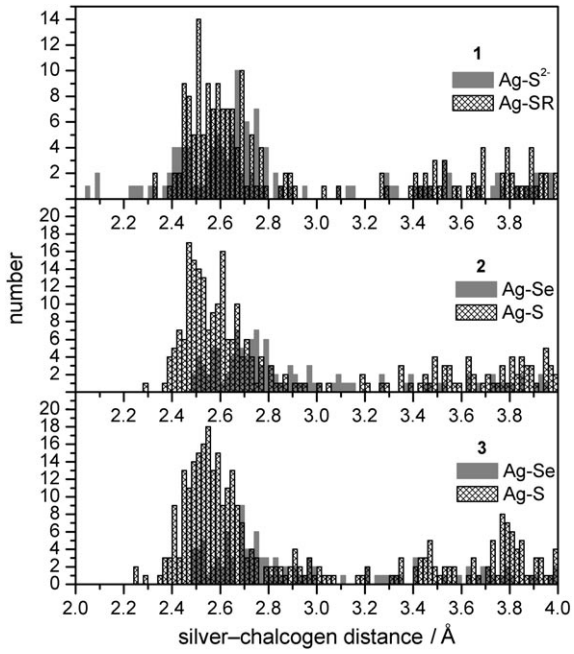

Figure 3. Histograms of the silver–chalcogen distances in **1** (top), **2** (middle), and **3** (bottom).

 © 2006 Wiley-VCH Verlag GmbH & Co. KGaA, Weinheim

bonds. All three clusters contain linearly coordinated silver atoms that are shifted from their ideal positions because of interactions with a third, more remote chalcogen atom; similarly, many three-coordinate silver atoms are shifted out of the plane formed by their three neighbors because of interactions with a fourth, more remote atom. In general, the silver–chalcogen distances correlate with the coordination number, being relatively short for linear coordination environments and longer in tetrahedral environments. In compound **1**, the Ag–S bonds involving the S^{2-} ions in the cluster core are shorter than those involving the sulfur atoms of the $SC_6H_4NMe_2$ groups. As expected, the Ag–Se bonds in **2** and **3** are, on average, approximately 0.15 Å longer than the Ag–S bonds.

We are currently investigating reactions similar to those described herein in a systematic manner. Depending on the reaction conditions, we have already isolated medium-sized (for example, $[Ag_{33}Se_7(SC_6H_4NMe_2)_{18}(dppm)_6]$) and very large clusters. These compounds seem to have particularly interesting photophysical properties, which will be discussed in forthcoming reports.

Experimental Section

All reactions were carried out under a purified nitrogen atmosphere. THF and diethyl ether were dried over sodium/benzophenone, and *n*-hexane over $LiAlH_4$. $E(SiMe_3)_2$ (E = S, Se) were prepared by standard methods.[15]

$(Me_2N)C_6H_4(SSiMe_3)$: 4-bromo-*N*,*N*-dimethylaniline (50 g, 0.25 mol) was treated with magnesium (6.1 g, 0.25 mol) in THF (120 mL) to give the Grignard compound. This solution was added dropwise at −60 °C to a suspension of sulfur (8 g, 0.25 mol) in THF (40 mL). After the mixture warmed to room temperature and the sulfur dissolved completely, Me_3SiCl (35 mL, 0.275 mol) was added dropwise. Subsequently, the reaction mixture was heated under reflux for 2 h. After cooling, toluene (50 mL) was added to completely precipitate the magnesium halides. The precipitate was separated by filtration and washed with toluene. The volume of the filtrate was reduced to a few milliliters and mixed with *n*-hexane (50 mL) to give the crude product as a yellow precipitate. The product was isolated as a colorless solid by sublimation (yield: 35.4 g, 63 %). ^{1}H NMR (300 MHz, C_6D_6, 25 °C, TMS): $\delta = 7.58$ (d, 2H), 6.54 (d, 2H), 2.53 (s, 6H), 0.37 ppm (s, 9H).

1: Silver benzoate (0.28 g, 1.24 mmol) and dppm (0.24 g, 0.64 mmol) were dissolved in THF (40 mL), and then treated with $(Me_2N)C_6H_4(SSiMe_3)$ (0.28 g, 1.24 mmol) and $S(SiMe_3)_2$ (0.035 mL, 0.25 mmol) at −60 °C. As the solution slowly warmed to room temperature, the color became darker. After reducing the volume by half, the solution was layered with diethyl ether. Within one week, **1** crystallized as yellow blocks (yield: 115 mg, 40 %). Elemental analysis (%) calcd for $C_{437}H_{500}Ag_{65}N_{39}P_{10}S_{52}$ (15287.1): C 34.33, H 3.30, N 3.57, S 10.91; found: C 35.04, H 3.21, N 3.52, S 10.58.

2: Silver benzoate (0.23 g, 1.02 mmol) and triphenylphosphine (0.26 g, 1.02 mmol) were dissolved in THF (40 mL), and then treated with $(Me_2N)C_6H_4(SSiMe_3)$ (0.23 g, 1.02 mmol) and $Se(SiMe_3)_2$ (0.035 mL, 0.156 mmol) at −60 °C. As the solution warmed to room temperature over 2 h, the color changed from red to black. A precipitate formed and was separated by filtration. The volume of the filtrate was reduced by half, and the solution was then layered with diethyl ether. Within one week, **2** crystallized as black needles (yield: 75 mg, 35 %). Elemental analysis (%) calcd for $C_{517}H_{597.5}Ag_{76}N_{50}P_{6.5}S_{50}Se_{13}$ (18540.8): C 33.49, H 3.25, N 3.78, S 8.65; found: C 32.30, H 3.25, N 3.75, S 9.02.

3: Silver benzoate (0.51 g, 2.22 mmol) and triphenylphosphine (0.58 g, 2.22 mmol) were dissolved in THF (30 mL), and then treated with $(Me_2N)C_6H_4(SSiMe_3)$ (0.58 g, 2.22 mmol) and $Se(SiMe_3)_2$ (0.08 mL, 0.37 mmol) at −60 °C. As the reaction mixture warmed to room temperature over 2 h, the color changed from red to black. A precipitate formed and was separated by filtration. The volume of the filtrate was reduced by half. Within 3 or 4 weeks, **3** crystallized as black plates (yield: 195 mg, 30 %). Elemental analysis (%) calcd for $C_{612}H_{720}Ag_{88}N_{63}P_6S_{63}Se_{12}$ (21604.1): C 34.02, H 3.36, N 4.08, S 9.35; found: C 34.36, H 3.38, N 4.12, S 9.59.

Received: July 7, 2006
Revised: August 2, 2006
Published online: November 6, 2006

Keywords: cluster compounds · selenium · silver · structure elucidation · sulfur

[1] A. Müller, E. Beckmann, H. Bögge, M. Schmidtmann, A. Dress, *Angew. Chem.* **2002**, *114*, 1210–1215; *Angew. Chem. Int. Ed.* **2002**, *41*, 1161–1167.
[2] N. T. Tran, D. R. Powell, L. F. Dahl, *Angew. Chem.* **2000**, *112*, 4287–4291; *Angew. Chem. Int. Ed.* **2000**, *39*, 4121–4125.
[3] A. Schnepf, H. Schnöckel, *Angew. Chem.* **2001**, *113*, 733–737; *Angew. Chem. Int. Ed.* **2001**, *40*, 711–715.
[4] S. Dehnen, A. Eichhöfer, D. Fenske, *Eur. J. Inorg. Chem.* **2002**, 269–275.
[5] a) X. J. Wang, T. Langetepe, C. Persau, B. S. Kang, G. S. Sheldrick, D. Fenske, *Angew. Chem.* **2002**, *114*, 3972–3977; *Angew. Chem. Int. Ed.* **2002**, *41*, 3818–3822; b) D. Fenske, C. Persau, S. Dehnen, C. E. Anson, *Angew. Chem.* **2004**, *116*, 309–313; *Angew. Chem. Int. Ed.* **2004**, *43*, 305–309.
[6] D. Fenske, C. E. Anson, A. Eichhöfer, O. Fuhr, A. Ingendoh, C. Persau, C. Richert, *Angew. Chem.* **2005**, *117*, 5376–5381; *Angew. Chem. Int. Ed.* **2005**, *44*, 5242–5246.
[7] a) G. A. Wiggers, *Am. Mineral.* **1971**, *56*, 1882–1888; b) Z. G. Pinsker, C. Chiang Ling, R. M. Imamov, E. L. Lapidus, *Sov. Phys. Crystallogr. (Engl. Transl.)* **1965**, *7*, 225–233.
[8] a) F. C. Kracek, *Trans. Am. Geophys. Union* **1946**, 27, 364–374; b) S. Djurle, *Acta Chem. Scand.* **1958**, *12*, 1427–1436; c) P. Rahlfs, *Z. Phys. Chem. Abt. B* **1936**, *31*, 157–194; d) E. Rickert, *Z. Phys. Chem. (Muenchen Ger.)* **1960**, *24*, 418–421; e) A. Böttcher, G. Haase, H. Treupel, *Z. Angew. Phys.* **1955**, *7*, 478–487; f) P. Junod, *Helv. Phys. Acta* **1959**, *32*, 567–600.
[9] A. J. Früh, *Z. Kristallogr.* **1958**, *110*, 136–144.
[10] H. Schmatzried, *Prog. Solid State Chem.* **1980**, *13*, 119–157, and references therein.
[11] X-ray structure analyses: Stoe IPDS II, $Mo_{K\alpha}$ radiation (**1** and **2**) or 0.9-Å synchrotron radiation (**3**), numerical absorption correction, solution and refinement with SHELXD and SHELX-97.[12] All of the carbon and nitrogen atoms of the $C_6H_4NMe_2$ groups and the phosphine ligands were located in difference Fourier maps. In the final refinement, most of the phenyl rings were treated as rigid groups. The silver, selenium, sulfur, and phosphorus atoms were refined anisotropically, and the carbon and nitrogen atoms isotropically. Some of the silver atoms were disordered over different positions with partial occupancies; some of the ligands were also disordered. The cocrystallized solvent molecules (THF) could not be satisfactorily localized. Therefore, after all of the cluster atoms were refined, the free volumes in each of the unit cells were calculated using the program PLATON, and the SQUEEZE function was used to determine the contribution of the disordered solvent to the structure factors.[13] The modified F_o^2 were used in the final refinement cycles. By assuming that a THF molecule has a volume of 100 Å^3, the number of solvent molecules in the calculated free volume was estimated. These values are in good agreement (within a few percent) with the observed weight loss

 © 2006 Wiley-VCH Verlag GmbH & Co. KGaA, Weinheim

of the crystals in vacuum. **1**: $C_{437}H_{500}Ag_{65}N_{39}P_{10}S_{52}\cdot n\,C_4H_8O$ ($n\sim 30$), $T=100$ K, orthorhombic, space group *Iba*2 (no. 45), $Z=8$, $a=46.00(1)$, $b=69.30(1)$, $c=35.121(7)$ Å, $V=111\,957$ Å^3, $\mu(Mo_{K\alpha})=2.48$ mm^{-1}, $2\theta_{max}=46°$, 235 943 data measured, 74 585 independent, 39 508 with $I>2\sigma(I)$, $R_{int}=0.166$, $R_\sigma=0.166$, 2386 parameters, $R_1(I>2\sigma(I))=0.082$, R_1(without SQUEEZE) = 0.108, R_1(all data) = 0.147, $wR_2=0.166$, GOF = 0.962, Flack parameter = −0.01, max. residual electron density = 1.159 e Å^{-3}. **2**: $C_{517}H_{597.5}Ag_{76}N_{50}P_{6.5}S_{50}Se_{13}\cdot n\,C_4H_8O$ ($n\sim 55$), $T=100$ K, triclinic, space group $P\bar{1}$ (no. 2), $Z=2$, $a=32.046(6)$, $b=34.165(7)$, $c=34.248(7)$ Å, $\alpha=91.52(3)$, $\beta=90.70(3)$, $\gamma=100.79(3)°$, $V=36\,815$ Å^3, $\mu(Mo_{K\alpha})=2.81$ mm^{-1}, $2\theta_{max}=48°$, 206 416 data measured, 104 800 independent, 38 765 with $I>2\sigma(I)$, $R_{int}=0.071$, $R_\sigma=0.116$, 3584 parameters, $R_1(I>2\sigma(I))=0.080$, R_1(without SQUEEZE) = 0.110, R_1(all data) = 0.154, $wR_2=0.189$, GOF = 0.834, max. residual electron density = 1.022 e Å^{-3}. **3**: $C_{612}H_{720}Ag_{88}N_{63}P_6S_{63}Se_{12}\cdot n\,C_4H_8O$ ($n\sim 65$), $T=100$ K, tetragonal, space group $P4_2/n$ (no. 86), $Z=8$, $a=55.340(8)$ Å, $c=56.79(1)$ Å, $V=173\,917$ Å^3, $\mu=2.63$ mm^{-1}, $2\theta_{max}=54°$, 326 261 data measured, 88 404 independent, 57 609 with $I>2\sigma(I)$, $R_{int}=0.098$, $R_\sigma=0.075$, 3186 parameters, $R_1(I>2\sigma(I))=0.097$, R_1(without SQUEEZE) = 0.122, R_1(all data) = 0.139, $wR_2=0.217$, GOF = 0.992, max. residual electron density = 1.022 e Å^{-3}. CCDC-613233 (**1**), CCDC-613234 (**2**), and CCDC-613235 (**3**) contain the supplementary crystallographic data for this paper. These data can be obtained free of charge from The Cambridge Crystallographic Data Centre via www.ccdc.cam.ac.uk/data_request/cif.

[12] G. M. Sheldrick, SHELX-97, Program for the Solution and Refinement of Crystal Structures, Universität Göttingen, **1997**.

[13] A. L. Spek, *J. Appl. Crystallogr.* **2003**, *36*, 7–13; P. van der Sluis, A. L. Spek, *Acta Crystallogr. Sect. A* **1990**, *46*, 194–201.

[14] O. Fuhr, L. Fernandez-Recio, D. Fenske, *Eur. J. Inorg. Chem.* **2005**, 2306–2314.

[15] H. Schmidt, H. Ruf, *Z. Anorg. Allg. Chem.* **1963**, *321*, 270–273.

 © 2006 Wiley-VCH Verlag GmbH & Co. KGaA, Weinheim

Alkenes

DOI: 10.1002/anie.200602693

Structure, Stereoelectronics, and Synthetic Potential of 1,2-Bisonio-1,2-bis(dialkylamino)-ethenes**

Robert Weiss, Stefan M. Huber, Frank W. Heinemann, Pierre Audebert, and Frank G. Pühlhofer*

During an early stage in the development of the self-activated silyl-assisted polyonio-substitution (SASAPOS) protocol,[1] we synthesized highly electrophilic oniodimethyliminium systems such as **4** (Scheme 1) for the first time and examined their behavior towards nucleophilic substrates.[2] In deprotonation experiments on **4a**, we neither detected the desired phosphonio-substituted carbene **5a**, nor its dimer **3a**. Recently, however, Bertrand and co-workers generated the corresponding diisopropyl-substituted carbene **5a** (with R = *i*Pr) by a largely analogous procedure and characterized the kinetically stable compound.[3] Remarkably, the carbene did not dimerize into the corresponding ethene derivative **3a**. The alkenes **3**, which have been inaccessible to date, are of considerable interest, owing to their new indigoid chromophore, as well as their potential a^1/a^2 or d^1/d^2 reactivity.[4] Herein, we report the syntheses and some characteristic properties of the first representatives of this class of compounds.

As early as 1981, Böhme and Sutoyo reported the synthesis of 1,2-dichloro-1,2-bis(dimethylamino)ethene (**2**; Scheme 1) by treating dimethylformamide (DMF; **1**) with oxalyl chloride and Huenig's base ($NEt_i Pr_2$).[5] Compound **2** was isolated in very low yields (ca. 10 %[6]) as an *E*/*Z*-isomer mixture, in the form of a colorless, extremely hydrolysis-sensitive solid. The analogous tetraisopropyl compound was synthesized by Bertrand and co-workers by an alternative route.[7]

When compound **2**, prepared by a slightly modified synthesis route, is treated in situ with neutral nucleophiles L and trimethylsilyl trifluoromethanesulfonate (TMSOTf),

[*] Prof. Dr. R. Weiss, Dipl.-Chem. S. M. Huber, Dr. F. G. Pühlhofer
Institut für Organische Chemie
Henkestrasse 42, 91054 Erlangen (Germany)
Fax: (+49) 9131-8529132
E-mail: weiss@chemie.uni-erlangen.de
Dr. F. W. Heinemann
Institut für Anorganische Chemie
Egerlandstrasse 1, 91058 Erlangen (Germany)
Prof. Dr. P. Audebert
PPSM (CNRS UMR 8531)
Ecole Normale Supérieure de Cachan
61, avenue de Président Wilson
94235 Cachan Cedex (France)

[**] S.M.H. thanks the Studienstiftung des Deutschen Volkes for a doctoral scholarship.

Supporting information for this article is available on the WWW under http://www.angewandte.org or from the author.

© 2006 Wiley-VCH Verlag GmbH & Co. KGaA, Weinheim

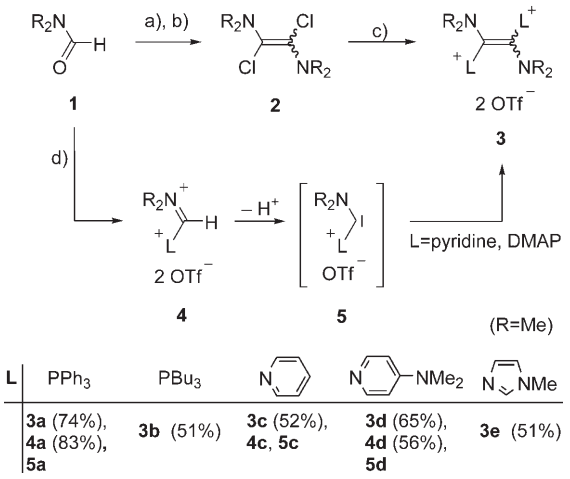

Scheme 1. Synthesis of **3**; a) $C_2O_2Cl_2$, toluene, RT, 1 h; b) Huenig's base ($NEtiPr_2$), −5 °C for 1 h, RT for 2 h; c) 2 L, 2 TMSOTf, toluene/CH_2Cl_2; d) $C_2O_2Cl_2$, CH_2Cl_2, 1 h; 2 L, 2 TMSOTf; yields of **3** are based on DMF. R = Me, TMSOTf = trimethylsilyl trifluoromethanesulfonate, DMAP = 4-dimethylaminopyridine.

according to the SASAPOS protocol,[1] the corresponding bisonio-substituted bis(dimethylamino)ethenes **3** are obtained in good yields (Scheme 1).[8] However, all efforts to prepare the formal dimer of the carbene synthesized by Bertrand and co-workers (**5** with R = *i*Pr) from diisopropylformamide by an analogous route failed, probably because of steric reasons.

In contrast to the phosphonio-substituted dimethyliminium compound **4a**, the pyridinio- and 4-dimethylaminopyridinio ($dmap^+$)-substituted compounds **4c** and **4d** can be converted to the corresponding dimers **3c** and **3d** by deprotonation (Scheme 1).[9] This dimerization is probably initiated by the reaction of the intermediately generated (and unknown) carbene salts **5c**/**5d** with their immediate precursors **4c**/**4d**.[10] Thus, another independent synthetic route to ethenes **3c** and **3d** is available. The substitution pattern of two vicinal donor functions and two vicinal onio substituents present in alkenes **3** was previously unknown and has distinct electronic consequences, as discussed below.

The deeply red salt **3c** is obtained as a 1:1 *E*/*Z*-isomer mixture, according to ^{1}H NMR spectroscopy. Starting from the 1:8 *E*/*Z*-isomer mixture of the deeply yellow salt **3d** obtained from the synthesis, the main *Z* isomer could be isolated in pure form by recrystallization from hot water, and its structure was determined by single-crystal X-ray diffraction. When the *Z* isomer was treated with catalytic amounts of DMAP, the thermodynamic *E*/*Z*-isomer ratio of 1:8 was again obtained.

The phosphonio-substituted compounds **3a** and **3b** are isolated as colorless or pale yellow solids, respectively, which are air-stable for several hours; however, **3a** undergoes rapid hydrolysis in solution. The ^{31}P NMR spectrum of **3b**, which is stable towards hydrolysis in solution, demonstrates that the compound exists as a single isomer; an X-ray structure analysis reveals that the isomer has an *E* configuration (see below).

The molecular structures of **3d** and **3b**, and density functional theory (DFT) calculations on model compounds[11] demonstrate that two fundamentally different stereoelectronic donor/acceptor (D/A) interaction patterns are realized in these alkenes, with distinct consequences on their structure and reactivity. The D/A interaction pattern in **3d** (and **3c**) corresponds to that of a classic push–pull system of the indigo type. Analysis of both the structure (Figure 1a)[12,13] and the

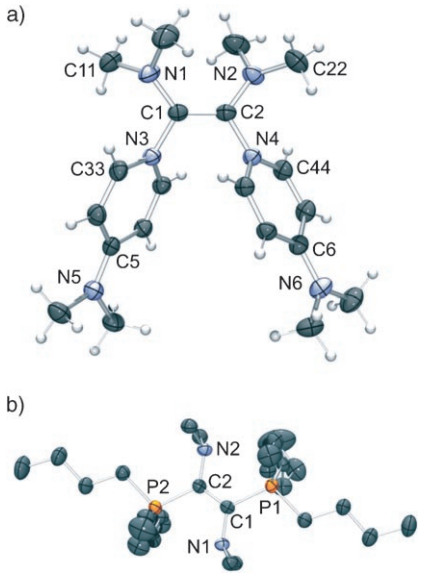

Figure 1. a) Molecular structure of **3d**;[13] anions omitted for clarity; thermal ellipsoids set at 50% probability. Selected bond lengths [Å] and angles [°]: C1–C2 1.352, C1–N1 1.376, C1–N3 1.454, C5–N5 1.350; C11-N1-C1-N3 52.5, C33-N3-C1-N1 47.1, N1-C1-C2-N4 155.9; sum of angles at N1 359.1. b) Molecular structure of **3b**;[15] anions and hydrogen atoms omitted for clarity; thermal ellipsoids set at 50% probability. Selected bond lengths [Å] and angles [°]: C1–C2 1.345, C1–N1 1.412, C1–P1 1.867; N2-C2-C1 118.9, P2-C2-C1 117.4, N2-C2-C1-N1 176.5; sum of angles at N2 345.2.

model calculations[11] reveals that a charge transfer from the 2p donor functions on the nitrogen centers into the π* acceptor functions, which are predominantly localized on the pyridinio groups, occurs. The electrostatically more strongly activating pyridinio substituent causes the UV transition of **3c** to occur at a lower wavelength (by ca. 80 nm) than that of the DMAP derivative **3d**.

The planar dimethylamino groups and the relatively short $N–C_{alkene}$ bonds of **3d** stand out as stereoelectronic indicators for these mesomeric interactions. For steric reasons, the planes of the four substituents are rotated conrotatorily from the alkene plane by approximately 45°, which does not substantially diminish the energetically favorable push–pull resonance. The charge transfer already present in the ground state leads (among other consequences) to stronger bonds between the pyridinio substituents and the central olefinic unit, making the substitution of the onio groups by external nucleophiles (for example, water; see above) much more difficult. As expected for an indigoid system, the n→π* charge transfer increases considerably in the color-generating

 © 2006 Wiley-VCH Verlag GmbH & Co. KGaA, Weinheim

HOMO–LUMO UV/Vis transition, according to our model calculations.[11]

In contrast, the structures of the 1,2-bisphosphonio-substituted representatives **3a** and **3b** are significantly affected by anomeric n→σ* charge-transfer interactions between the nitrogen lone pairs and the C_{alkene}–P σ* orbitals of the geminally orientated phosphonio substituents, according to our model calculations and the structure of **3b** (Figure 1b).[15] Characteristic stereoelectronic indicators for this type of interaction are observed. The lone pairs of the pyramidalized nitrogen donor functions are oriented antiperiplanar relative to the C_{alkene}–P bonds and are, thus, orthogonal to the central π system. In addition, the C_{alkene}–P bonds are relatively long,[14] as a result of the population of the C_{alkene}–P σ* orbital through charge transfer. Because the lone pairs on the nitrogen atoms do not interact with the central π system, **3a** and **3b** do not show an intense UV/Vis transition.[11] Another remarkable consequence of this stereoelectronic configuration is the inertness of **3b** towards electrophiles such as elemental bromine and trifluoromethanesulfonic acid.

As a result of the anomeric interactions, the phosphonio substituents in **3a** and **3b** can be displaced by several neutral and anionic nucleophiles under thermodynamic control. For example, **3a** reacts with DMAP at room temperature to selectively form the "mixed" bisonio compound **6** within a few hours (Scheme 2). Compound **6** could be isolated and completely characterized. The subsequent substitution of the second PPh_3 substituent by DMAP requires thermal activation.

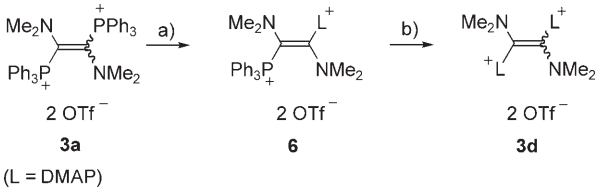

Scheme 2. Substitution of PPh_3 in **3a** by DMAP; a) DMAP, CH_2Cl_2, RT, 1 d, 95%; b) DMAP, CH_3CN, reflux, 8 h.

The molecular structure of **6** reveals that, in this case, both mesomeric and anomeric interactions occur. A planar dimethylamino group with a short N–C_{alkene} bond length (1.359 Å) on the dmap$^+$-substituted part of the alkene is accompanied by a pyramidalized dimethylamino group with a comparatively long N–C_{alkene} bond length (1.434 Å) on the phosphonio-substituted part. All other characteristic features of the two types of structures (**3d** and **3b**) are also present.

This and further reactions demonstrate that **3a** and comparable bisonio systems show latent a^1/a^2 reactivity. Thus, **3a** can be regarded as a synthetic equivalent of the ethene bisiminium synthon **7** and consequently of the C_2O_2 synthon **8** (Scheme 3),[16] which is not stable under normal reaction conditions.

The latent 1,2-bis-electrophilic reactivity of **3a**, in combination with its simple preparation and convenient handling, offers new synthetic possibilities. In this context, we will soon report the direct synthesis of the first representatives of 4,5-bis(dialkylamino)-substituted imidazolium compounds, as well as their structure and reactivity.[17]

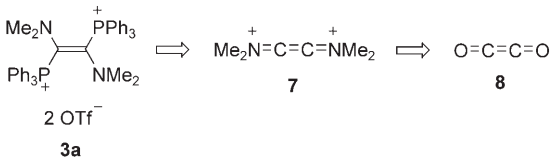

Scheme 3. Compound **3a** as a synthetic equivalent of the synthon C_2O_2.

Experimental Section

3a: A solution of DMF (6 mmol, 0.439 g) in toluene (20 mL) was treated with $C_2O_2Cl_2$ (6 mmol, 0.761 g) at 0 °C and then stirred for 1 h at room temperature. Subsequently, a solution of Huenig's base (6 mmol, 0.775 g) in toluene (10 mL) was added slowly dropwise, again at −5 °C. The resulting bright yellow suspension was stirred at 0 °C for 1 h and then at room temperature for 2 h. After collecting the protonated base by filtration, the yellow mother liquor was treated with CH_2Cl_2 (30 mL) and PPh_3 (12 mmol, 3.14 g) and stirred for 15 h at room temperature. After the addition of TMSOTf (12 mmol, 2.67 g) and diethyl ether (30 mL), a yellow precipitate was obtained, which was collected by filtration, washed twice with Et_2O (10 mL), and dried in high vacuum. For further experimental details, see the Supporting Information

Received: July 6, 2006
Published online: November 7, 2006

Keywords: ab initio calculations · alkenes · carbenes · dyes/pigments · heterocycles

[1] See the Supporting Information; R. Weiss, S. M. Huber, F. G. Pühlhofer, *Eur. J. Org. Chem.* **2005**, 3530–3535; R. Weiss, S. Engel, *Angew. Chem.* **1992**, *104*, 239–240; *Angew. Chem. Int. Ed. Engl.* **1992**, *31*, 216–217; F. Pühlhofer, R. Weiss, *Eur. J. Org. Chem.* **2004**, 1002–1007; R. Weiss, N. J. Salomon, G. E. Miess, R. Roth, *Angew. Chem.* **1986**, *98*, 925–926; *Angew. Chem. Int. Ed. Engl.* **1986**, *25*, 917–919; R. Weiss, J. Seubert, F. Hampel, *Angew. Chem.* **1994**, *106*, 2038–2039; *Angew. Chem. Int. Ed. Engl.* **1994**, *33*, 1952–1953; R. Weiss, B. Pomrehn, F. Hampel, W. Bauer, *Angew. Chem.* **1995**, *107*, 1446–1448; *Angew. Chem. Int. Ed. Engl.* **1995**, *34*, 1319–1321; R. Weiss, R. May, B. Pomrehn, *Angew. Chem.* **1996**, *108*, 1319–1321; *Angew. Chem. Int. Ed. Engl.* **1996**, *35*, 1232–1234; R. Weiss, F. Pühlhofer, F. Hampel, *Z. Naturforsch. B* **2001**, *56*, 1209–1216; R. Weiss, F. Pühlhofer, *Z. Naturforsch. B* **2001**, *56*, 1360–1368; R. Weiss, F. Pühlhofer, N. Jux, K. Merz, *Angew. Chem.* **2002**, *114*, 3969–3971; *Angew. Chem. Int. Ed.* **2002**, *41*, 3815–3817.
[2] R. Roth, Dissertation, Universität Erlangen-Nürnberg, **1989**; M. Rechinger, Dissertation, Universität Erlangen-Nürnberg, **1995**; R. Weiss, R. Roth, *Synthesis* **1987**, 870–872; R. Weiss, R. Roth, *J. Chem. Soc. Chem. Commun.* **1987**, 317–318.
[3] S. Conejero, Y. Canac, F. S. Tham, G. Bertrand, *Angew. Chem.* **2004**, *116*, 4181–4185; *Angew. Chem. Int. Ed.* **2004**, *43*, 4089–4093.
[4] D. Seebach, *Angew. Chem.* **1979**, *91*, 259–278; *Angew. Chem. Int. Ed. Engl.* **1979**, *18*, 239–258.
[5] H. Böhme, P. Sutoyo, *Tetrahedron Lett.* **1981**, *22*, 1671–1674.
[6] P. Sutoyo, Dissertation, Universtität Marburg, **1981**.

 © 2006 Wiley-VCH Verlag GmbH & Co. KGaA, Weinheim

[7] M. Otto, S. Conejero, Y. Canac, V. D. Romanenko, V. Rudzevitch, G. Bertrand, *J. Am. Chem. Soc.* **2004**, *126*, 1016 – 1017.
[8] In the case of L = DMAP, the corresponding chloride salt of **3d** could be obtained in the absence of TMSOTf.
[9] In the case of **4c**, pyridine itself functions as the base. In the case of **4d**, Huenig's base was added. In the case of **4c**, the protonated base could not be separated. According to ^{1}H NMR spectroscopy, **4d** is formed in almost quantitative yield. **4c** was detected by mass spectrometry.
[10] R. W. Alder, L. Chaker, F. P. V. Paolini, *Chem. Commun.* **2004**, 2172 – 2173.
[11] See the Supporting Information.
[12] A similar molecular structure was also determined by X-ray diffraction for the chloride salt of **3d**.
[13] Structure determination and crystallographic data for **3d**: Crystals were obtained by slow diffusion of diethyl ether into a solution of **3d** in acetonitrile. $C_{22}H_{36}F_6N_6O_8S_2$, M_r = 690.69 g mol^{-1}, monoclinic, space group $P2_1/c$, a = 17.8116(5), b = 11.2095(4), c = 17.3480(5) Å, β = 114.381(2)°, V = 3154.80(17) Å^3, Z = 4, ρ_{calcd} = 1.454 g cm^{-3}, T = 173(2) K, μ = 0.257 mm^{-1}, $F(000)$ = 1440, $4.42 < 2\theta < 54.96°$, $\lambda(Mo_{K\alpha})$ = 0.71073 Å, crystal size 0.20 × 0.15 × 0.15 mm^3. Intensity data were collected with a Nonius KappaCCD diffractometer. 13595 reflections, 7230 independent (R_{int} = 0.0334), empirical absorption correction (Scalepack), structure solution using direct methods (SHELXS-97), structure refinement on F^2 using full-matrix least-squares procedures (SHELXL-97), R_1 = 0.0596 ($I > 2\sigma(I)$), wR_2 = 0.1868 (all data), GOF = 1.127, max./min. residual electron density = 0.836/−0.566 e Å^{-3}.
[14] For comparison, in 1,2-bis(tributylphosphonio)ethene diacetate, the C_{alkene}–P bond length is 1.789 Å; E. Vedejs, S. T. Diver, *J. Am. Chem. Soc.* **1993**, *115*, 3358 – 3359.
[15] Structure determination and crystallographic data for **3b**: Crystals were obtained by slow diffusion of diethyl ether into a solution of **3b** in acetonitrile. $C_{32}H_{66}F_6N_2O_6P_2S_2$, M_r = 814.93 g mol^{-1}, triclinic, space group $P\bar{1}$, a = 9.4769(2), b = 20.5009(5), c = 22.3180(5) Å, α = 91.699(1), β = 93.805(1), γ = 96.354(2)°, V = 4296.92(17) Å^3, Z = 4, ρ_{calcd} = 1.260 g cm^{-3}, T = 173(2) K, μ = 0.264 mm^{-1}, $F(000)$ = 1744, $2.66 < 2\theta < 50.04°$, $\lambda(Mo_{K\alpha})$ = 0.71073 Å, crystal size 0.25 × 0.25 × 0.25 mm^3. Intensity data were collected with a Nonius KappaCCD diffractometer. 27399 reflections, 14928 independent (R_{int} = 0.0357), empirical absorption correction (Scalepack), structure solution using direct methods (SHELXS-97), structure refinement on F^2 using full-matrix least-squares procedures (SHELXL-97), R_1 = 0.0516 ($I > 2\sigma(I)$), wR_2 = 0.1623 (all data), GOF = 1.025, max./min. residual electron density = 0.741/−0.473 e Å^{-3}. CCDC-613189 (**3d**) and CCDC-613190 (**3b**) contain the supplementary crystallographic data for this paper. These data can be obtained free of charge from The Cambridge Crystallographic Data Centre via www.ccdc.cam.ac.uk/data_request/cif.
[16] L. M. Nxumalo, E. K. Ngidi, T. A. Ford, *J. Mol. Struct.* **2006**, *786*, 168 – 174, and references therein.
[17] R. Weiss, S. M. Huber, unpublished results.

 © 2006 Wiley-VCH Verlag GmbH & Co. KGaA, Weinheim

Cover Picture

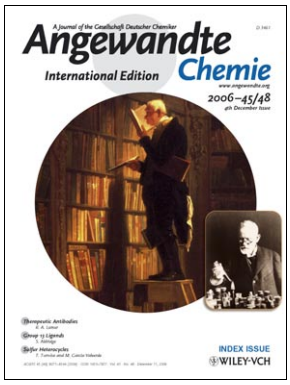

Richard A. Lerner*

In Paul Ehrlich's era selecting an antibody for a specific target was a physical process, involving live animals. R. A. Lerner shows in his Review on page 8106 ff. how combinatorial libraries are the incarnation of Ehrlich's (see inset in the cover picture showing "Der Bücherwurm" by Carl Spitzweg) "magic bullet", proposed more than 100 years ago, and nowadays hundreds of millions of different antibodies can be provided in a couple of hundred microliters of solution in a test tube.

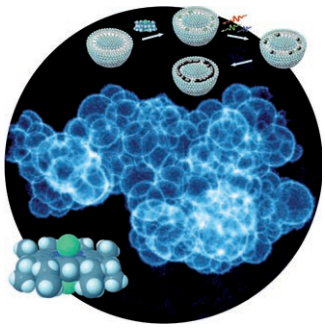

Hollow Nanostructures
Dendritic platinum nanosheets grow and link together within a liposomal bilayer to form spherical hollow nanocages. J. A. Shelnutt and co-workers describe this method in their Communication on page 8126 ff.

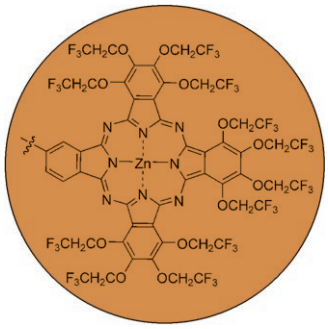

Fluorinated Phthalocyanines
The unique photosensitivity of monomeric trifluoroethoxy-substituted zinc phthalocyanines conjugated with deoxyribonucleosides is described in the Communication by N. Shibata, T. Toru, and co-workers on page 8163 ff.

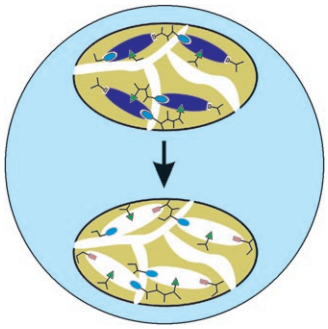

Molecular Recognition
G.-T. Li and co-workers describe in their Communication on page 8145 ff. a combined molecular imprinting and colloidal crystal approach to prepare ordered 3D macroporous photonic polymer films for specific enantiomer recognition.

Contents

VIP *The following Communications have been judged by at least two referees to be "very important papers" and will be published online at www.angewandte.org soon:*

*M. L. Maddess, M. N. Tackett, H. Watanabe, P. E. Brennan, C. D. Spilling, J. S. Scott, D. P. Osborn, S. V. Ley**
Total Synthesis of Rapamycin

*J. H. Lee, F. D. Toste**
Gold(I)-Catalyzed Synthesis of Functionalized Cyclopentadienes

*E. Terreno, C. Cabella, C. Carrera, D. D. Castelli, R. Mazzon, S. Rollet, J. Stancanello, M. Visigalli, S. Aime**
From "Spherical" to "Osmotically Shrinked" Paramagnetic Liposomes: An Improved Generation of LIPOCEST MRI Agents with Highly Shifted Water Protons

*W. H. Bernskoetter, E. Lobovsky, P. J. Chirik**
Nitrogen–Carbon Bond Formation from N_2 and CO_2 Promoted by a Hafnocene Dinitrogen Complex Leads to the Liberation of a Substituted Hydrazine

J. A. Teprovich, Jr., E. Prasad, R. A. Flowers, II**
Solvation-Controlled Luminescence of Sm^{II} Complexes

*Y. Xiong, J. M. McLellan, Y. Yin, Y. Xia**
Synthesis of Palladium Icosahedrons with a Twinned Structure by Blocking Oxidative Etching with Citric Acid or Citrate Ion

Obituary

Guy Ourisson (1926–2006) — *M. Rohmer* — **8088**

Books

The Jahn–Teller Effect — Isaac B. Bersuker — *reviewed by B. Tsukerblat* — **8089**

Highlights

Sulfur Heterocycles

T. Torroba,*
M. García-Valverde — **8092 – 8096**

Rigid Annulated Carbon–Sulfur Structures

Open or closed? The first heterocyclic circulene, octathio[8]circulene, was recently synthesized through a highly efficient sulfurization and pyrolysis sequence (see picture; S yellow, C gray). This macrocyclic compound as well as chiral, helical oligothiophenes are rigid structures that open fascinating possibilities for applications in molecular electronics.

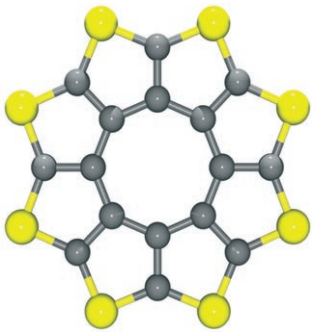

Group 13 Ligands

S. Aldridge* — **8097 – 8099**

Platinum Complexes Featuring Terminally Bound Ga^+ and In^+ Ions

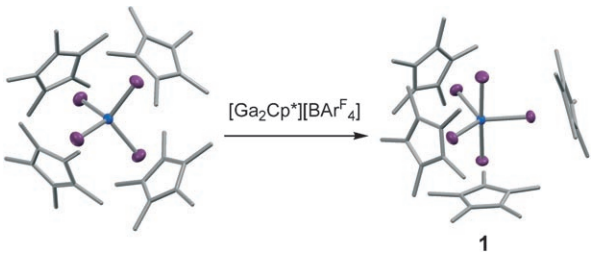

1

Alone at the apex: The first metal complexes with Ga^+ or In^+ cations as terminally bound ligands have recently been synthesized. Structural and computational studies suggest a Lewis acid/base Pt–Ga interaction for $[GaPt(GaCp^*)_4]^+$ (**1**; Pt blue, Ga violet, C gray; $Ar^F = C_6H_3(CF_3)_2$-3,5). The Group 13 cation therefore functions as an acceptor ligand, with significant components of both σ and π symmetry contributing to the Pt–Ga linkage.

© 2006 Wiley-VCH Verlag GmbH & Co. KGaA, Weinheim

Correspondence

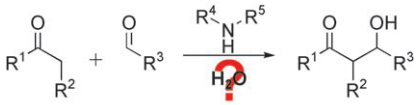

Reactions *with*, *in*, or *on* water? Despite claims to the contrary, few examples of truly aqueous organocatalysis have been reported. Close examination of the data from recent reports reveals that these reactions likely occur in concentrated organic phases.

Organocatalysis

A. P. Brogan, T. J. Dickerson,*
K. D. Janda* ——— **8100 – 8102**

Enamine-Based Aldol Organocatalysis in Water: Are They Really "All Wet"?

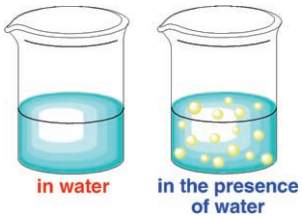

What expression best conveys the recent examples of "aqueous" organocatalyzed aldol reactions? It is suggested that a reaction occurs "in water" if the participating reactants are dissolved homogeneously in water (or buffer), or "in the presence of water" if it proceeds in a concentrated organic phase with water present as a second phase that influences the reaction in the former.

Organocatalysis

Y. Hayashi* ——— **8103 – 8104**

In Water or in the Presence of Water?

Reviews

Diplomatic immunity: Therapeutic antibodies are, arguably, the most important class of new drugs for the treatment of a wide range of illnesses. Combinatorial antibody libraries gives access to antibodies for whatever antigen is desired, with a diversity that exceeds that of the natural repertoire. The methods developed to accomplish this seemingly formidable task now allow construction of antibodies in a test tube to any antigen (see picture).

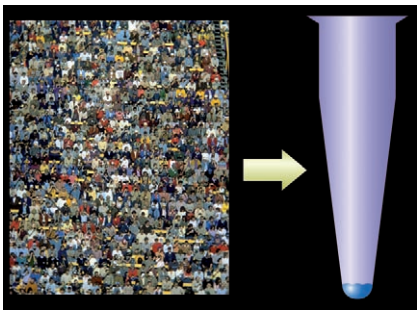

Therapeutic Antibodies

R. A. Lerner* ——— **8106 – 8125**

Manufacturing Immunity to Disease in a Test Tube: The Magic Bullet Realized

Communications

Sphere we go: Unilamellar liposomes containing porphyrin photocatalysts are used to generate novel spherical platinum nanocages. The porous hollow nanospheres are formed by many small joined dendritic platinum nanosheets grown within the confines of the liposomal bilayer. They have 2-nm thick shells and can have outer diameters up to 200 nm, (see TEM image) making them suitable for catalytic and other applications.

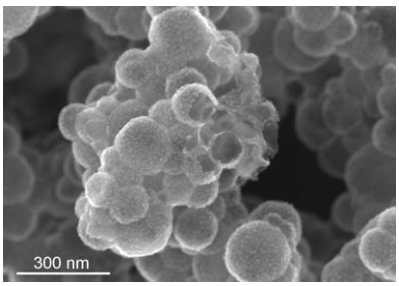

Hollow Nanostructures

Y. Song, R. M. Garcia, R. M. Dorin, H. Wang, Y. Qiu, J. A. Shelnutt* ——— **8126 – 8130**

Synthesis of Platinum Nanocages by Using Liposomes Containing Photocatalyst Molecules

For the USA and Canada:
ANGEWANDTE CHEMIE International Edition (ISSN 1433-7851) is published weekly by Wiley-VCH PO Box 191161, D 69451 Weinheim, Germany. Air freight and mailing in the USA by Publications Expediting Inc. 200 Meacham Ave., Elmont, NY 11003. Periodicals postage paid at Jamaica NY 11431. US POSTMASTER: send address changes to *Angewandte Chemie*, Wiley-VCH, 111 River Street, Hoboken, NJ 07030. Annual subscription price for institutions: US$ 5685/5168 (valid for print and electronic / print or electronic delivery); for individuals who are personal members of a national chemical society prices are available on request. Postage and handling charges included. All prices are subject to local VAT/sales tax.

© 2006 Wiley-VCH Verlag GmbH & Co. KGaA, Weinheim

The best in chemistry –

for more than a hundred years

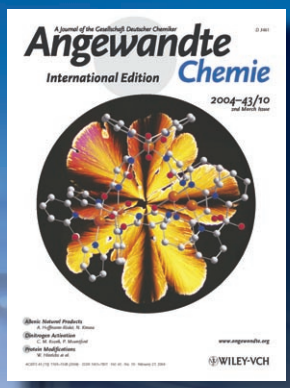

A Journal of the Gesellschaft Deutscher Chemiker

Angewandte
International Edition **Chemie**

www.angewandte.org

1888: ***The beginning of a success story***

Constant Innovations

1962: *First issue of the International Edition*
1976: *Graphical abstracts*
1979: *Cover pictures*
1988: *Centenary of Angewandte*
1989: *Routine use of color*
1991: *New section: Highlights*
1992: *Computerized editorial tracking system*
1995: *Internet service for readers*
1998: *Regular press service; full-text online*
2000: *New section: Essays; EarlyView: Communications available online ahead of the printed version*
2001: *New section: Minireviews*
2002: *Online submission of manuscripts*
2003: *Weekly publication; new section: News; new layout*
2004: *Backfiles (1962-1997); ManuscriptXpress: Online system for authors and referees*

Angewandte's advisors...

Ulrich Stilz
Aventis, Frankfurt/Main

» With its interdisciplinary and international orientation ***Angewandte Chemie*** *has set the benchmark for publishing innovative results. The editorial team is acknowledged for the success of this renowned journal, that provides scientists with a unique forum, in which to discuss their discoveries.«*

Angewandte Chemie International Edition *is a journal of the German Chemical Society (GDCh)*

GDCh

WILEY InterScience® DISCOVER SOMETHING GREAT

WILEY-VCH

1198/404_gu

Weight of the world: Masses of whole viruses with sizes in the range of 80–300 nm were determined for the first time by using a miniature cylindrical ion trap equipped with a transparent end-cap electrode. Three viruses (vaccinia virus, grouper iridovirus, and recombinant human adenovirus) have been successfully examined, suggesting a broad and promising application of this new technology to viral systems.

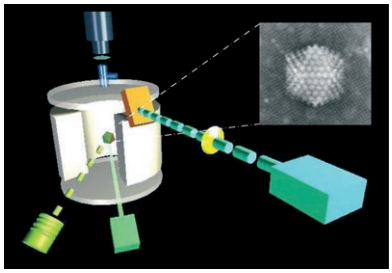

Mass Determination

Z. X. Nie, Y.-K. Tzeng, H.-C. Chang,* C.-C. Chiu, C.-Y. Chang, C.-M. Chang, M.-H. Tao ——— **8131 – 8134**

Microscopy-Based Mass Measurement of a Single Whole Virus in a Cylindrical Ion Trap

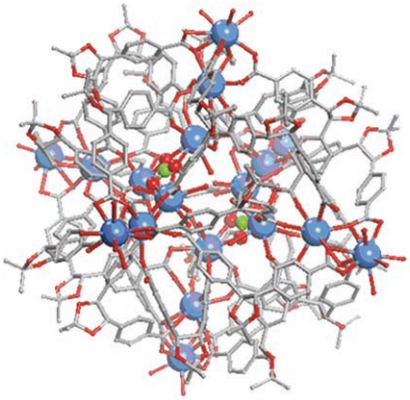

(*S*)-lanthanitin

A chiral supramolecule, obtained by self-assembly of 24 chiral ditopic carboxylate ligands, 18 La ions, and two carbonate anions, has been dubbed lanthanitin because of its structural resemblance to ferritin. The picture shows the molecular structure of one enantiomer of lanthanitin. Color code: La blue, carbonate C green, C gray, O red; H omitted.

Chiral Nanoballs

K. S. Jeong, Y. S. Kim, Y. J. Kim, E. Lee, J. H. Yoon, W. H. Park, Y. W. Park, S.-J. Jeon, Z. H. Kim, J. Kim, N. Jeong* ——— **8134 – 8138**

Lanthanitin: A Chiral Nanoball Encapsulating 18 Lanthanum Ions by Ferritin-Like Assembly

There and back: Through the formation of colloidally stable suspensions of dextran-coated single-walled nanotubes (SWNTs), it was possible to fabricate an affinity sensor based on SWNT photoluminescence. Aggregation could be controlled through introduction of a glucose-binding protein and glucose, which results in a reversible glucose sensor.

Biosensors

P. W. Barone, M. S. Strano* **8138 – 8141**

Reversible Control of Carbon Nanotube Aggregation for a Glucose Affinity Sensor

© 2006 Wiley-VCH Verlag GmbH & Co. KGaA, Weinheim

Contents

Protein Engineering

W. Kim, K. I. Hardcastle, V. P. Conticello* ——— **8141 – 8145**

Fluoroproline Flip-Flop: Regiochemical Reversal of a Stereoelectronic Effect on Peptide and Protein Structures

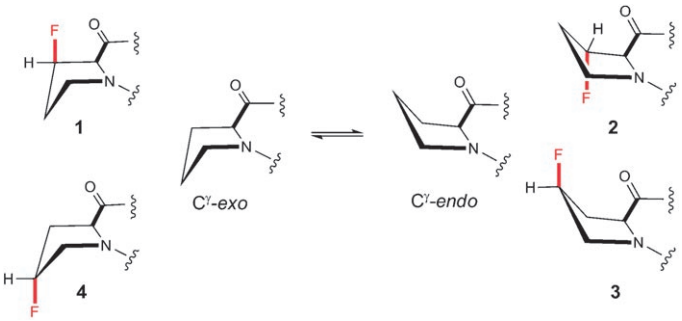

Pucker up! Structural analysis of the epimeric *N*-acetyl-(2*R*,3*R*)- and *N*-acetyl-(2*R*,3*S*)-3-fluoroproline methyl esters (**1** and **2**; see scheme) reveals opposing ring puckers that invert the conformational preferences of the corresponding 4-fluoroproline derivatives **3** and **4**. Substitution of these fluoroprolines into proteins provides a method for controlling local conformation through stereoelectronic and steric effects.

Molecular Recognition

X-B. Hu, Q. An, G-T. Li,* S-Y. Tao, J. Liu ——— **8145 – 8148**

Imprinted Photonic Polymers for Chiral Recognition

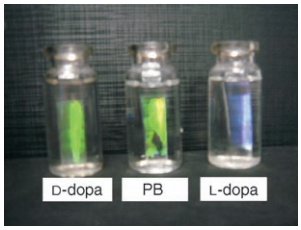

A general protocol to prepare self-reporting photonic polymer films for specific enantiomer recognition is described. The combined molecular imprinting and colloidal crystal approach produces films with interconnected macroporous arrays and cavities that are complementary to the analyte. Binding of the analyte can be directly detected by the change in optical diffraction of the periodic macroporous array (see picture; PB = phosphate buffer).

Antitumor Agents

V. Bagalkot, O. C. Farokhzad,* R. Langer, S. Jon* ——— **8149 – 8152**

An Aptamer–Doxorubicin Physical Conjugate as a Novel Targeted Drug-Delivery Platform

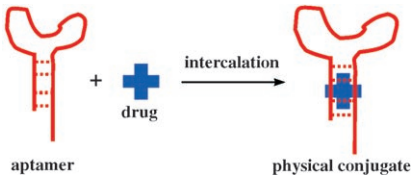

Trojan aptamer: A novel strategy for targeted drug delivery to cancer cells was developed through the formation of a physical conjugate (see scheme) between doxorubicin (Dox) and the A10 RNA aptamer that binds to the prostate-specific membrane antigen (PSMA). The aptamer–Dox conjugate could efficiently bind to PSMA-expressing cells, thereby resulting in its uptake and the intracellular release of Dox.

Anticancer Agents

H.-K. Liu, S. J. Berners-Price, F. Wang, J. A. Parkinson, J. Xu, J. Bella, P. J. Sadler* ——— **8153 – 8156**

Diversity in Guanine-Selective DNA Binding Modes for an Organometallic Ruthenium Arene Complex

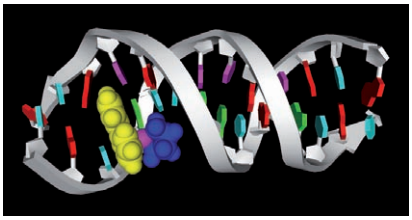

Seek and hide! An organometallic ruthenium arene anticancer complex with ruthenium (pink ball) chelated by ethylenediamine (blue) is selective for guanine bases on DNA and can bury the non-coordinated phenyl ring of its arene ligand (yellow) between bases in the double helix.

© 2006 Wiley-VCH Verlag GmbH & Co. KGaA, Weinheim

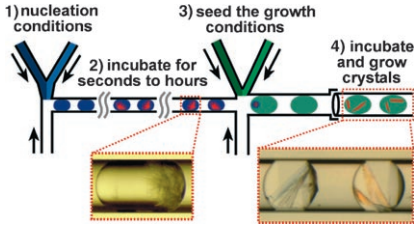

Sowing seeds: The growth of well-ordered protein crystals requires control of the two key stages of crystallization, namely, nucleation and growth. However, the ideal conditions for these two stages are often different. A microfluidic system (see picture) was used to perform time-controlled crystal seeding in nL volumes. Single crystals of the protein Oligoendopeptidase F were obtained and used to determine its X-ray crystal structure.

Microfluidics

C. J. Gerdts, V. Tereshko, M. K. Yadav, I. Dementieva, F. Collart, A. Joachimiak, R. C. Stevens, P. Kuhn, A. Kossiakoff, R. F. Ismagilov* ——— **8156 – 8160**

Time-Controlled Microfluidic Seeding in nL-Volume Droplets To Separate Nucleation and Growth Stages of Protein Crystallization

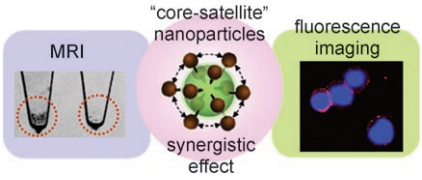

Working together: A "core–satellite" hybrid nanoparticle probe provides highly improved fluorescence and magnetic resonance (MR) imaging capabilities through synergistic enhancement of its respective components. These hybrid nanoprobes can be used for dual-modal fluorescence and MR imaging of neuroblastoma with expressed polysialic acids.

Nanoparticle Probes

J.-H. Lee, Y.-w. Jun, S.-I. Yeon, J.-S. Shin,* J. Cheon* ——— **8160 – 8162**

Dual-Mode Nanoparticle Probes for High-Performance Magnetic Resonance and Fluorescence Imaging of Neuroblastoma

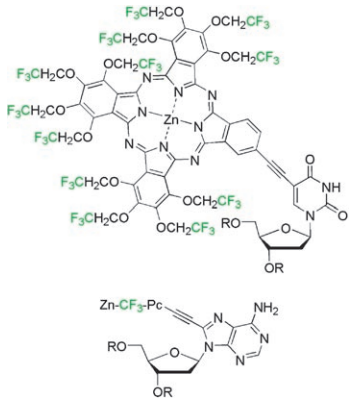

The single life: The UV/Vis spectra together with the strong fluorescence emission of trifluoroethoxy-substituted zinc phthalocyanines conjugated with deoxyribonucleosides (see picture) suggest that these compounds prefer monomeric forms over aggregation. Their unique photosensitivity can be controlled by the addition of base or by the solvent used.

Fluorinated Phthalocyanines

M. R. Reddy, N. Shibata,* Y. Kondo, S. Nakamura, T. Toru* ——— **8163 – 8166**

Design, Synthesis, and Spectroscopic Investigation of Zinc Dodecakis(trifluoroethoxy)phthalocyanines Conjugated with Deoxyribonucleosides

NMR dipolar couplings can be measured for weakly aligned proteins and are sensitive probes of their structure and dynamics. The combination of fixed geometry and ^{1}H–^{1}H couplings alone from two alignment media provides access to ultrahigh-resolution structures. The apparent precision, as measured by independent cross-validation and structure comparison, is comparable to that available from high-resolution X-ray crystallography.

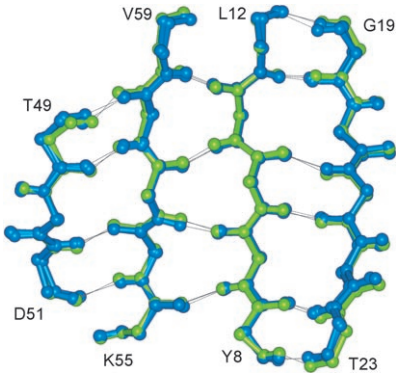

Protein Structure Determination

G. Bouvignies, S. Meier, S. Grzesiek,* M. Blackledge* ——— **8166 – 8169**

Ultrahigh-Resolution Backbone Structure of Perdeuterated Protein GB1 Using Residual Dipolar Couplings from Two Alignment Media

© 2006 Wiley-VCH Verlag GmbH & Co. KGaA, Weinheim

Contents

Helical Peptides

M. Lundqvist, P. Nygren, B.-H. Jonsson,* K. Broo* ——— **8169 – 8173**

Induction of Structure and Function in a Designed Peptide upon Adsorption on a Silica Nanoparticle

Small change: Nanoparticles can induce a functional helix from an unstructured peptide (see picture). The ability to generate stable, well-defined structures on surfaces opens up the possibility of creating nanosystems with a variety of functionalities, which is demonstrated by the introduction of a catalytic site for ester hydrolysis.

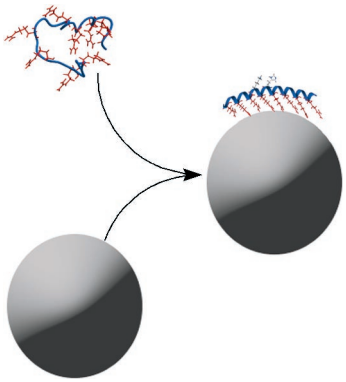

Helical Structures

K. Okoshi,* S.-I. Sakurai, S. Ohsawa, J. Kumaki, E. Yashima* ——— **8173 – 8176**

Control of Main-Chain Stiffness of a Helical Poly(phenylacetylene) by Switching On and Off the Intramolecular Hydrogen Bonding through Macromolecular Helicity Inversion

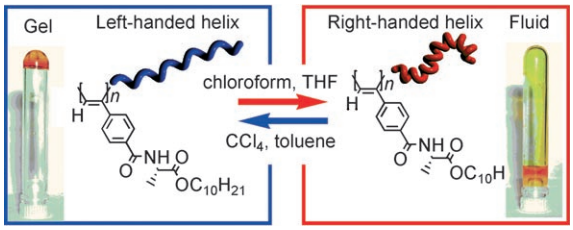

A hard twist: A helical poly(phenylacetylene) with L- or D-alanine pendants with a long alkyl chain showed an unprecedented change in the main-chain stiffness accompanied by inversion of the helical sense of the polymer, resulting from the "on and off" fashion of the intramolecular hydrogen-bonding networks in polar and nonpolar solvents.

Fullerenes

A. Rodríguez-Fortea,* J. M. Campanera, C. M. Cardona, L. Echegoyen, J. M. Poblet* ——— **8176 – 8180**

Dancing on a Fullerene Surface: Isomerization of $Y_3N@(N$-Ethylpyrrolidino-$C_{80})$ from the 6,6 to the 5,6 Regioisomer

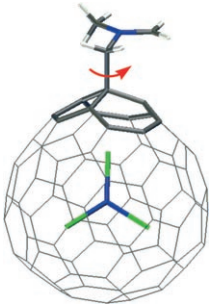

Dancing partners: Density functional calculations have been used to unravel the different reactivity of endohedral metallofullerenes $M_3N@C_{80}$ (M = Sc or Y) with respect to 1,3-dipolar *N*-ethylazomethine cycloaddition. The mechanism for the isomerization of $Y_3N@(N$-ethylpyrrolidino-$C_{80})$ from the 6,6 to the 5,6 regioisomer during thermalization of the kinetically favored product is proposed to involve a "dancing" of the pyrrolidine on the fullerene surface.

C–H Activation

B. Marciniec,* B. Dudziec, I. Kownacki ——— **8180 – 8184**

A New Catalytic Route for the Activation of sp-Hybridized Carbon–Hydrogen Bonds

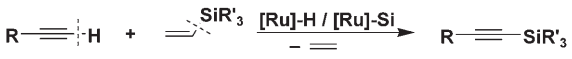

R = alkyl, cycloalkyl, trialkylsilyl
R' = alkyl, aryl, alkoxyl

Vinyl-substituted silicon compounds react selectively with terminal alkynes in the presence of complexes containing [Ru]—H and [Ru]—Si bonds to form functionalized silylethynes (see picture). This reaction opens up a new catalytic route for the preparation of a class of potent organosilicon reagents for organic synthesis.

© 2006 Wiley-VCH Verlag GmbH & Co. KGaA, Weinheim

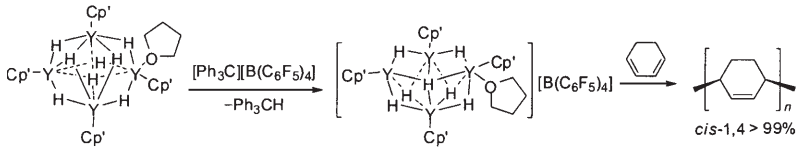

Rare activity from rare earths: Cationic rare-earth hydrides show regio- and stereoselectivity for the polymerization of 1,3-cyclohexadiene (CHD) to afford soluble crystalline *cis*-1,4-linked poly(CHD) that was previously unavailable. These cationic clusters are made by treating the corresponding neutral complexes with a borate activator (see scheme; Cp′: $C_5Me_4SiMe_3$).

Polymerization

X. Li, J. Baldamus, M. Nishiura, O. Tardif, Z. Hou* ——— **8184 – 8188**

Cationic Rare-Earth Polyhydrido Complexes: Synthesis, Structure, and Catalytic Activity for the *cis*-1,4-Selective Polymerization of 1,3-Cyclohexadiene

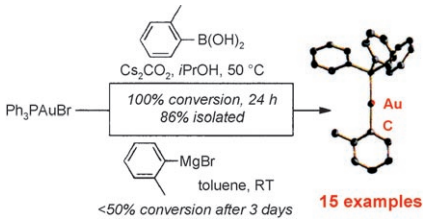

Gilded organometallics: Carbon–gold bond formation occurs selectively and in high yields upon reaction of gold(I) bromides with arylboronic acids in the presence of Cs_2CO_3. The reaction is broadly tolerant of sensitive functionalities. The resulting aryl gold(I) compounds are stable to air and water.

C–Au Bond Formation

D. V. Partyka, M. Zeller, A. D. Hunter, T. G. Gray* ——— **8188 – 8191**

Relativistic Functional Groups: Aryl Carbon–Gold Bond Formation by Selective Transmetalation of Boronic Acids

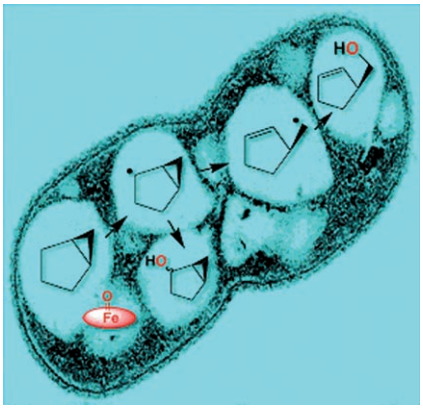

On home ground: The reaction mechanisms of bacterial alkane-oxidizing cytochrome P450s were determined in their native environment using a novel diagnostic substrate probe, bicyclohexane, in whole cells and cell-free extracts (see picture). Purified P450cam also oxidizes bicyclohexane. Clear evidence for a substrate-based radical with a lifetime of 75–250 ps was obtained.

Cytochrome P450

R. N. Austin,* D. Deng, Y. Jiang, K. Luddy, J. B. van Beilen, P. R. Ortiz de Montellano, J. T. Groves* ——— **8192 – 8194**

The Diagnostic Substrate Bicyclohexane Reveals a Radical Mechanism for Bacterial Cytochrome P450 in Whole Cells

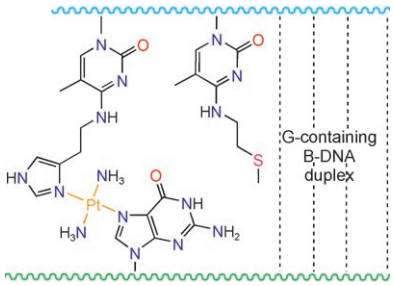

Stabilizing strands: Selectively cross-linked duplexes can be obtained either by hybridization-promoted rearrangement of platinated oligonucleotides or by annealing thioether- and imidazole-modified oligonucleotides and their complementary chains in the presence of transplatin (see structure).

Duplex Cross-Links

B. Algueró, J. López de la Osa, C. González, E. Pedroso, V. Marchán,* A. Grandas* ——— **8194 – 8197**

Selective Platination of Modified Oligonucleotides and Duplex Cross-Links

© 2006 Wiley-VCH Verlag GmbH & Co. KGaA, Weinheim

Contents

Electrochemistry

Q. Wang, S. M. Zakeeruddin, D. Wang, I. Exnar, M. Grätzel* ——— **8197 – 8200**

Redox Targeting of Insulating Electrode Materials: A New Approach to High-Energy-Density Batteries

A compact energy-storage system based on redox targeting is proposed, by which insulating $LiFePO_4$ particles can be reversibly charged and discharged by redox shuttle molecules (**S**; see scheme) even in the absence of conducting additives. The energy density of such batteries is expected to be greatly improved.

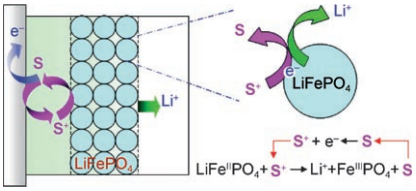

Synthetic Methods

Z. Ikeda, T. Hirayama, S. Matsubara* ——— **8200 – 8203**

Chemo- and Regioselective Preparation and Reaction of a Kinetic Zinc Enolate Formed from a Thiol Ester and Bis(iodozincio)methane

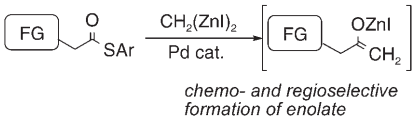

chemo- and regioselective formation of enolate

Reactive functionalized enolates that are otherwise difficult to obtain can be prepared in a simple procedure by the treatment of a thiol ester with bis(iodozincio)methane in the presence of a palladium catalyst (see scheme). The terminal zinc enolates thus formed are kinetically controlled and react with a variety of electrophiles, such as aldehydes, ketones, and acyl cyanides. FG = functional group.

Hypervalent Iodine Compounds

M. Ochiai,* T. Sueda, K. Miyamoto, P. Kiprof, V. V. Zhdankin ——— **8203 – 8206**

trans Influences on Hypervalent Bonding of Aryl λ^3-Iodanes: Their Stabilities and Isodesmic Reactions of Benziodoxolones and Benziodazolones

Large and small or twice moderate: Both combinations of *trans* influences of the substituents favor the formation of highly stable aryl λ^3-iodanes ArILL′ (examples: PhI(OH)OTs and $PhI(OAc)_2$). *trans* influences also seem to explain why iodosylbenzene adopts an oxo-bridged zigzag polymer structure in contrast to $PhI(OH)_2$, which is monomeric.

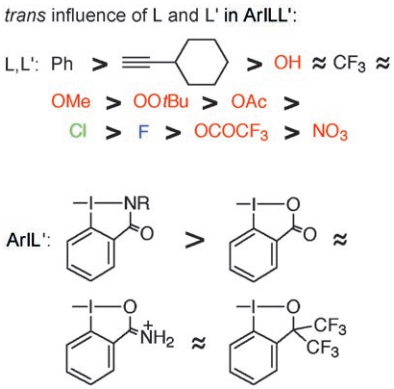

Foldamers

G. V. M. Sharma,* V. Subash, K. Narsimulu, A. R. Sankar, A. C. Kunwar* ——— **8207 – 8210**

De Novo Design and Synthesis of Helix–Turn–Helix Structure from Short and Robust Mixed Helices Derived from C-Linked Carbo-β-Amino Acids

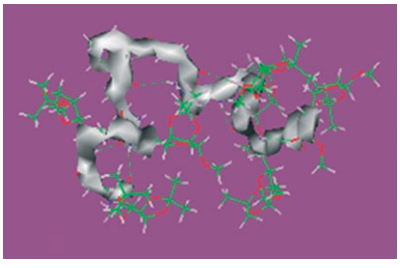

In a twist: Tethering of short peptides with robust 10/12-mixed helices, derived from C-linked carbo-β-amino acids, to the turn-inducing motif, β-hGly-D-Pro-Gly-β-hGly, permitted a de novo design of the helix–turn–helix motif in the foldamer domain.

© 2006 Wiley-VCH Verlag GmbH & Co. KGaA, Weinheim

To join the groove: Equipping basic-region bZIP peptides with a noncovalent heterodimerizing unit allows their major-groove DNA-binding capability to be triggered upon addition of appropriate external ligands that bind into adjacent minor-groove sites. The resulting noncovalent hybrids bind relatively long DNA sites with good affinity and very high specificity.

DNA-Binding Peptides

J. B. Blanco, V. I. Dodero, M. E. Vázquez, M. Mosquera, L. Castedo, J. L. Mascareñas* ——— **8210 – 8214**

Sequence-Specific DNA Binding by Noncovalent Peptide–Tripyrrole Conjugates

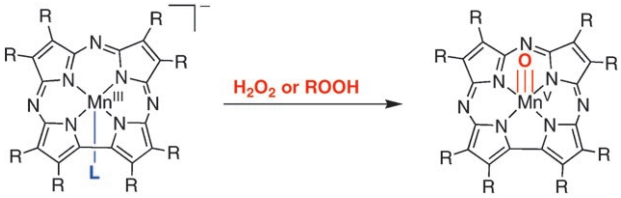

Upside-down push: Reaction of an Mn^{III} corrolazine complex with H_2O_2 or ROOH leads to O–O-bond cleavage to give an $Mn^{V}{\equiv}O$ complex (see scheme). Dramatic and unexpected axial-ligand (or "push") effects are observed, namely, the more electron-poor the axial ligand L, the faster and more heterolytic the cleavage.

Ligand Effects

D. E. Lansky, A. A. Narducci Sarjeant, D. P. Goldberg* ——— **8214 – 8217**

Inverse Axial-Ligand Effects in the Activation of H_2O_2 and ROOH by an Mn^{III} Corrolazine

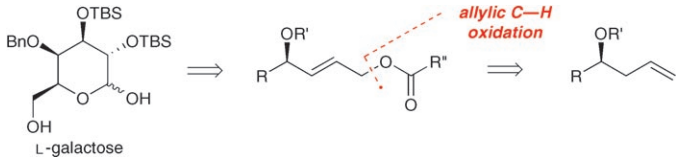

Carbohydrates from hydrocarbons: A hydrocarbon oxidation strategy for the synthesis of chiral polyols is validated by the enantioselective, de novo synthesis of differentially protected L-galactose (see scheme, TBS = *tert*-butyldimethylsilyl, Bn = benzyl). Key to this strategy is the selective C–H oxidation method for transforming protected chiral allylic alcohols into (*E*)-2-butene-1,4-diol derivatives.

C–H Oxidation

D. J. Covell, N. A. Vermeulen, N. A. Labenz, M. C. White* **8217 – 8220**

Polyol Synthesis through Hydrocarbon Oxidation: De Novo Synthesis of L-Galactose

Not the ferryl oxidant? The oxidation of thiafatty acids by $P450_{BM3}$ (CYP102A1) was shown to be consistent with oxidation by the ferric hydroperoxy species (Cpd 0) rather than the expected ferryl species (Cpd 1). This is the first indication that sulfur oxidation in a wildtype P450 occurs via the hydroperoxy species.

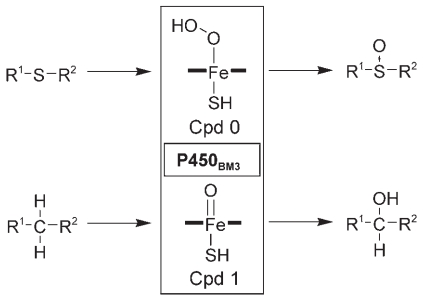

Enzyme Catalysis

M. J. Cryle, J. J. De Voss* — **8221 – 8223**

Is the Ferric Hydroperoxy Species Responsible for Sulfur Oxidation in Cytochrome P450s?

© 2006 Wiley-VCH Verlag GmbH & Co. KGaA, Weinheim

Contents

Supported Catalysts

P. M. Arnal, M. Comotti, F. Schüth* ——— 8224 – 8227

High-Temperature-Stable Catalysts by Hollow Sphere Encapsulation

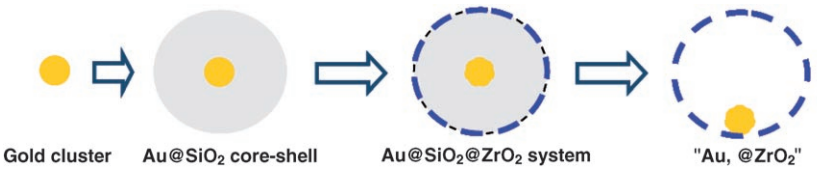

Stable companions: Hollow zirconia shells that each contain one gold nanoparticle (see picture) are stable to sintering and can be used as heterogeneous catalysts in reactions such as the oxidation of CO in air. The performance of Au, @ZrO_2 is unaffected by calcination at 800 °C.

Hydrogen Storage

M. Latroche,* S. Surblé, C. Serre, C. Mellot-Draznieks, P. L. Llewellyn, J.-H. Lee, J.-S. Chang, S. H. Jhung, G. Férey ——— 8227 – 8231

Hydrogen Storage in the Giant-Pore Metal–Organic Frameworks MIL-100 and MIL-101

Large hydrogen-storage capacity at liquid-nitrogen temperature is exhibited by the metal–organic framework MIL-101. In the zeotype architecture of this porous solid (see picture) each intersection of the cages is occupied by a supertetrahedron formed by trimers of chromium octahedra assembled with benzene-1,4-dicarboxylate ligands.

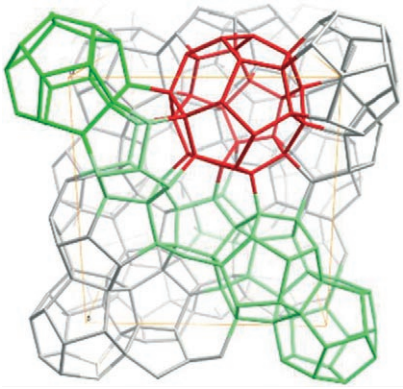

C–H Bond Activation

R. Martinez, R. Chevalier, S. Darses,* J.-P. Genet* ——— 8232 – 8235

A Versatile Ruthenium Catalyst for C–C Bond Formation by C–H Bond Activation

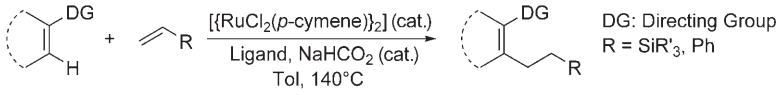

Easily modified: the electronic and steric properties of a ruthenium catalyst highly active for C–H bond activation (see scheme) can be modified by fine-tuning the ligand. This makes this catalytic system very versatile as it allows functionalization of a variety of substrates. The catalyst is generated in situ from a stable and easily available ruthenium(II) source.

Heterogeneous Catalysis

B. H. Lipshutz,* B. R. Taft ——— 8235 – 8238

Heterogeneous Copper-in-Charcoal-Catalyzed Click Chemistry

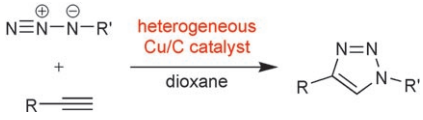

Click here for Cu/C: Copper-in-charcoal (Cu/C) is an active catalyst for effecting click reactions between organic azides and 1-alkynes. Rates of cycloaddition are increased dramatically when carried out in the presence of Et_3N or using microwave assistance. There is no sensitivity to air or moisture, and the catalyst can be recycled several times without loss of activity or selectivity for the 1,4-adduct.

© 2006 Wiley-VCH Verlag GmbH & Co. KGaA, Weinheim

Working under pressure: BiB_3O_6 is a well-known material with nonlinear optical properties. The use of high-pressure/high-temperature conditions led to the synthesis of a new non-centrosymmetric bismuth triborate (δ-BiB_3O_6). The picture shows a six-membered ring in the crystal structure of δ-BiB_3O_6 (orange spheres: Bi, blue spheres: O, red spheres: B).

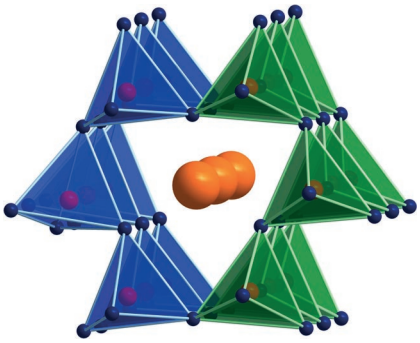

Bismuth Triborate

J. S. Knyrim, P. Becker, D. Johrendt, H. Huppertz* ——— **8239 – 8241**

A New Non-Centrosymmetric Modification of BiB_3O_6

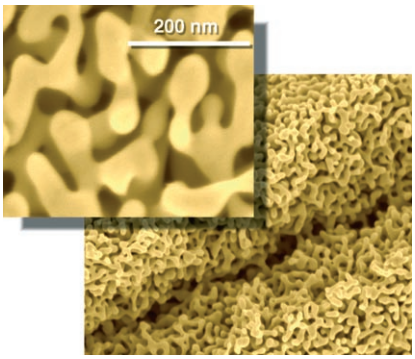

No support: Unsupported nanoporous gold foams with a spongelike morphology (see images) are formed through the selective leaching of silver from a gold–silver alloy. These gold foams are highly active catalysts for CO oxidation at ambient pressures and temperatures down to −20 °C, and have potential applications as membrane catalysts.

Gold Catalysis

V. Zielasek, B. Jürgens, C. Schulz, J. Biener, M. M. Biener, A. V. Hamza, M. Bäumer* ——— **8241 – 8244**

Gold Catalysts: Nanoporous Gold Foams

Two of a kind: $[Fe_2(StBu)_6]^{2-}$ shows a new form of isomerism. Besides the isomer of classical structure **1a** (red Fe, yellow S) there is also a variant (**1b**) in which the central Fe_2S_2 rhomb is inverted and the Fe–S bonds are distinctly shorter. **1b** can be regarded as a transition state during the inversion of the bridging sulfur atoms of **1a** that is stabilized by significant π interactions.

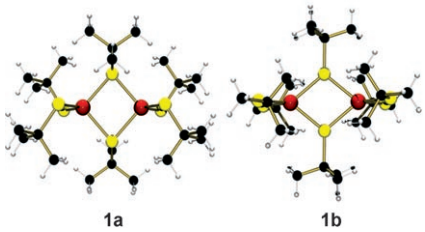

Bond-Stretch Isomers

B. Hammann, C. Chen, U. Flörke, R. Hauptmann, E. Bill, S. Sinnecker, G. Henkel* ——— **8245 – 8249**

α- and β-$[Fe_2(\mu\text{-}StBu)_2(StBu)_4]^{2-}$: Coexistence of Two Bond-Stretch Isomers of a Classical Bitetrahedral Metal Chalcogenolate Compound

Supporting information is available on the WWW (see article for access details).

A video clip is available as Supporting Information on the WWW (see article for access details).

WILEY InterScience® DISCOVER SOMETHING GREAT

"**Hot Papers**" are chosen by the Editors for their importance in a rapidly evolving field of high current interest. A preview with the graphical abstracts of these articles can be found on the *Angewandte Chemie* homepage in Wiley InterScience at www.angewandte.org.

All articles in *Angewandte Chemie* are published online several weeks ahead of print. They are found under the "**EarlyView**" link on the journal's homepage in Wiley InterScience.

Service

Keywords ——— *8254*

Authors ——— *8255*

Angewandte's Sister Journals ——— *8251 – 8253*

Preview ——— *8343*

© 2006 Wiley-VCH Verlag GmbH & Co. KGaA, Weinheim

Corrigenda

Preparation, Adsorption Properties, and Catalytic Activity of 3D Porous Metal–Organic Frameworks Composed of Cubic Building Blocks and Alkali-Metal Ions

R.-Q. Zou, H. Sakurai, Q. Xu* ——— **2542–2546**

Angew. Chem. Int. Ed. **2006**, *45*

DOI 10.1002/anie.200503923

The authors have recognized some errors in their Communication since its publication. In the Experimental Section, the flow rate of the reactant gas should read as 100 mL min^{-1} (third paragraph) and TCD-GS should be corrected to FID-GC (fourth paragraph). Additionally, the data shown in Figures 2 and 3 for the reaction rates, R_{QMS} and R_{GC}, over catalyst **2** should be halved. The authors apologize for the oversight.

Macrocyclization by Ring-Closing Metathesis in the Total Synthesis of Natural Products: Reaction Conditions and Limitations

A. Gradillas, J. Pérez-Castells* ——— **6086–6101**

Angew. Chem. Int. Ed. **2006**, *45*

DOI 10.1002/anie.200600641

The authors wish to cite two additional papers in their discussion of the synthesis of salicylihalamides. The reports by De Brabander and co-workers and Fürstner et al. are of particular interest as they include studies on the conditions for ring-closing metathesis reactions for the control of *Z*/*E* stereochemistry of the double bond formed. Reference [25] should therefore read as follows:

[25] For recent syntheses of salicylihalamides, see: C. Herb, A. Bayer, M. E. Maier, *Chem. Eur. J.* **2004**, *10*, 5649 – 5660. For impressive studies on RCM reaction conditions in the synthesis of these products, see: a) Y. Wu, L. Esser, J. K. De Brabander, *Angew. Chem.* **2000**, *112*, 4478 – 4480; *Angew. Chem. Int. Ed.* **2000**, *39*, 4308 – 4310; b) A. Fürstner, T. Dierkes, O. R. Thiel, G. Blanda, *Chem. Eur. J.* **2001**, *7*, 5286 – 5298.

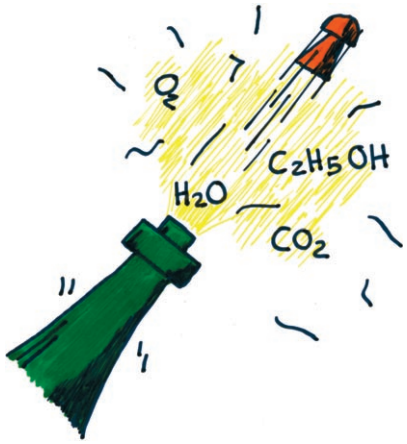

The editorial staff and the publishers thank all readers, authors, referees, and advertisers for their interest and support over the past year and wish them all a happy new year.

 © 2006 Wiley-VCH Verlag GmbH & Co. KGaA, Weinheim

Sulfur Heterocycles

DOI: 10.1002/anie.200603461

Rigid Annulated Carbon–Sulfur Structures**

Tomás Torroba and María García-Valverde*

Keywords:
annulenes · helical structures · macrocycles · polythiophenes · sulfur heterocycles

Polythiophenes constitute a largely studied class of compounds because of their interesting properties as highly ordered conducting polymers[1] for thin-film organic electronic devices (light-emitting diodes,[2] field-effect transistors,[3] organic photovoltaics for solar cells,[4] and electrochromic windows[5]) and as soluble polyelectrolytes for polynucleotide or polypeptide sensing.[6] This research area is rapidly expanding, attracting scientists from different disciplines in the search for organic electronics and their development. Particular attention has been paid to oligothiophenes, both as a result of their stability and ease of synthetic modification, for the preparation of active electronic materials[7] and self-assembled nanoscopic structures for controlled bottom-up fabrication of electronic devices.[8]

One key advantage of the oligomer approach to conjugated materials is their defined structure, which allows correlation of properties to chain and conjugation length. In addition, oligomers can provide more flexibility than monomers in the formation of the thin films needed for most devices. As the variation in the three-dimensional folding of oligothiophenes is of particular importance for the electronic properties of the subsequent material, several approaches to control the self-organizing process into highly stereoregular arrangements have been attempted. In this way, several hybrid materials that contain oligothiophene cores and dendrimeric appendages have been prepared to enhance the solubility and therefore improve the preparation of new nanocomposite materials.[9] In contrast, dendrimer **1**, composed only of thiophene units, was recently described by Advincula and co-workers (Figure 1).[10] Through self-organization of

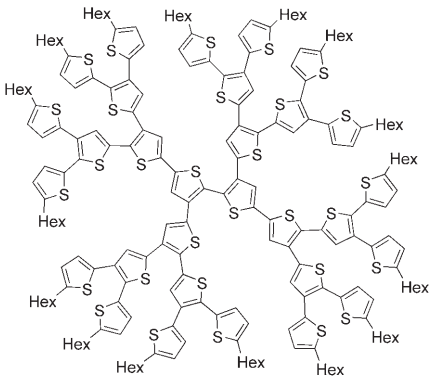

1

Figure 1. Dendrimer **1**.[8b]

the thiophene dendrimer, globular aggregates on mica surfaces and nanowires on graphite surfaces were obtained, showing that the molecular shape, size, and the presence of noncovalent intermolecular interactions control the formation of nanostructures of **1** on surfaces.

A recent approach to the design of improved oligothiophenes is the combination of the stability of the thiophene ring with the planarity of rigid or self-rigidifying groups.[11] Systems such as **2**, reported by Roncali and co-workers, retain the desirable properties of oligothiophenes, while limiting deviations from planarity that disrupt conjugation and affect the band gap in the solid state (Figure 2).[11c]

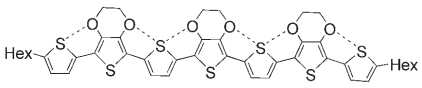

2

Figure 2. Intramolecular interactions in oligothiophene **2**.[11c]

Another innovative approach was recently reported by Bäuerle and coworkers through which a new family of oligothiophenes, namely, the cyclic oligothiophenes, were obtained. Macrocyclic cyclo[*n*]thiophenes ($n = 8$, 12, 16, and 18) and fully conjugated oligothiophenediacetylenes, with dibutyl substituents on alternate thiophene units, were synthesized. These novel molecules and their physical properties were discussed in several papers by the same group.[12] Thus, reaction of *cis*-[Pt(dppp)Cl_2] and terthiophenediyne **3** in the presence of CuI and NEt_3 gave **4** (91%), which following reductive elimination with iodine afforded the strained cyclodimeric terthiophenediyne **5** (54%), which in turn was transformed into cyclo[8]thiophene **6** (19%) by treatment with disodium sulfide (Scheme 1).[12a]

By a similar procedure, ter- and quinquethiophenediynes **3** and **7**, respectively, were coupled in the presence of $CuCl_2$/pyridine to give macrocyclic oligothiophenediacetylenes **8** (up to 12% yield), further reaction of which with Na_2S yielded cyclo[*n*]thiophenes **9** ($n = 12$; 23%), **10** ($n = 16$; 27%), and **11** ($n = 18$; 7%; Scheme 2).[12b–c] Remarkably, heterocycle **11** contains an inner cavity composed of 54 chain members with a diameter of 2 nm.

[*] Prof. T. Torroba, Dr. M. García-Valverde
Department of Chemistry
University of Burgos
09001 Burgos (Spain)
Fax: (+34) 947-258087
E-mail: ttorroba@ubu.es

[**] Financial support from the Dirección General de Investigación of Spain (CTQ2006-15456-C04-04/BQU) is gratefully acknowledged.

InterScience

© 2006 Wiley-VCH Verlag GmbH & Co. KGaA, Weinheim

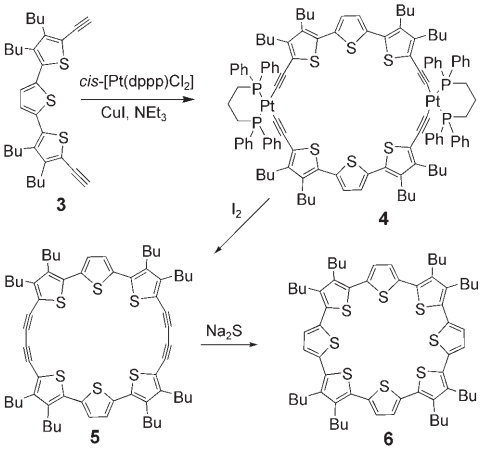

Scheme 1. Synthesis of octabutylcyclo[8]thiophene **6**.[11a] dppp = 1,3-bis(diphenylphosphanyl)propane.

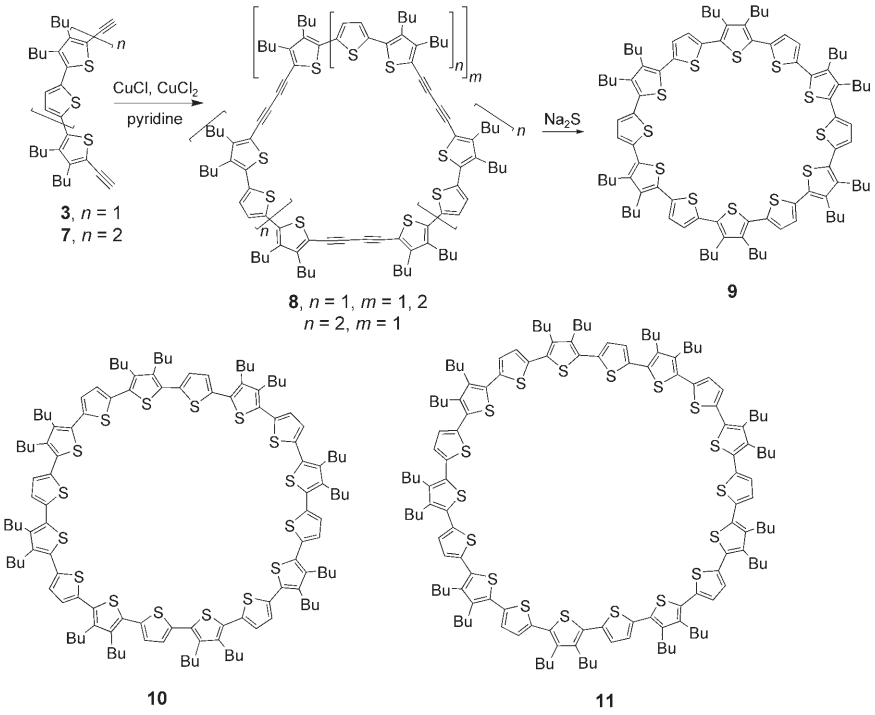

Scheme 2. Synthesis of cyclo[12]-, cyclo[16]-, and cyclo[18]thiophene (**9**–**11**, respectively).[12c]

The molecular arrangement in the solid state of some of these molecules has been studied by scanning tunneling microscopy, which reveals well-ordered hexagonal nanoarrays.[12d–e] Larger rings, such as cyclo[30]thiophene in the *anti* conformation, have been predicted as stable polythiophene models.[13] However, deviation from planarity through torsion about single bonds decreases conjugation in all of these α-oligothiophenes. Such effects do not arise in fully fused conjugated oligomers that have a rigid structure; stability is vastly improved and π-stacked molecular packing facilitates charge transport. Fully fused α-oligothiophenes, or oligothienoacenes, are studied as an emerging class of conjugated materials that combine the rigid planarity and extended conjugation of acenes with the chemical stability of oligothiophenes. Their rigid π-conjugated frameworks, which are free of conformational disorder, lead to unique electronic properties. They are also of considerable interest as models for the hypothetical thienoacene $(C_2S)_n$ polymer.

The synthesis of a disilylated pentathienoacene through an intramolecular triple cyclization of a bis(*o*-bromothienyl)diacetylene followed by sulfur extrusion was recently reported by Yamaguchi and co-workers.[14] Pentathienoacene itself was prepared by Matzger and coworkers using a different, but very efficient, synthesis of oligothienoacenes that was also used for the synthesis of heptathienoacene **15**.[15b] Pd-catalyzed coupling of $Bu_3SnSSnBu_3$ and dithieno[3,2-*b*;2′,3′-*d*]thiophene **13**, itself obtained in 54% yield from **12**, gave **14** (75%; Scheme 3). Subsequent oxidative ring closure of **14** led to **15** (68%), protodesilylation of which with trifluoroacetic acid proceeded in near-quantitative yield to give the parent heptathienoacene. The effects of ring fusion on the solid-state properties of fused α-oligothiophenes were also studied.[15a]

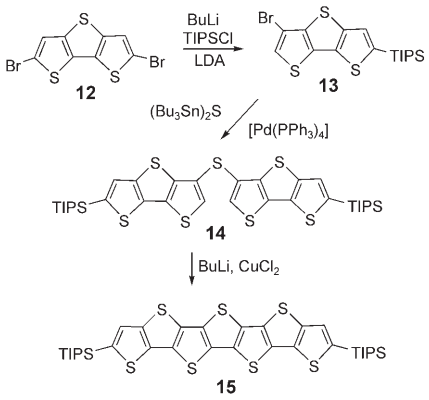

Scheme 3. Synthesis of heptathienoacene **15**.[15b] TIPS = triisopropylsilyl, LDA = lithium diisopropylamide.

In contrast to fused α-oligothiophenes, which are planar, quasi-linear, conjugated π systems, thiophene-based annelation of linear β-oligothiophenes gives rise to helical carbon–sulfur $(C_2S)_n$ oligomers for large values of *n* which reveal moderate curvature characteristic of helicenes.[16] Such aesthetically pleasing structures are also associated with cross-conjugated π systems for carbon–carbon frameworks, however, in the β-oligothiophenes all sulfur atoms are positioned at the molecular periphery, thereby facilitating multiple short

 © 2006 Wiley-VCH Verlag GmbH & Co. KGaA, Weinheim

intermolecular S···S contacts, which increase the effective dimensionality of the electronic structure and lead to enhanced transport properties. An innovative breakthrough in this area was reported by Rajca and co-workers with the successive asymmetric synthesis and resolution of helically annelated chiral β-heptathiophene **18** and β-undecathiophene **24** (Scheme 4).[17]

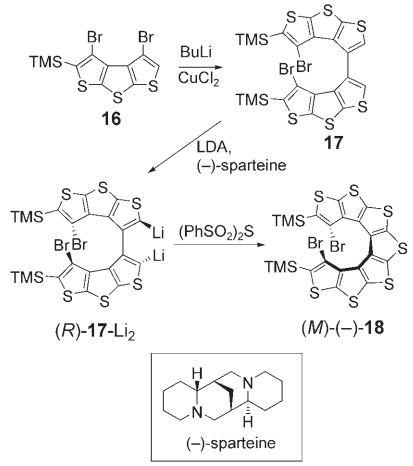

Scheme 4. Synthesis of nonracemic carbon–sulfur [7]helicene **18**.[17b] TMS = trimethylsilyl.

Nonracemic β-heptathiophene **18** was obtained by Li/Br exchange on dithienothiophene **16** (obtained from 3,4-dibromothiophene), followed by oxidation of the intermediate aryl lithium to provide bis(dithienothiophene) **17** (60%). Treatment of **17** with LDA and (−)-sparteine afforded the axially chiral α,α′-dilithiated **17**-Li_2, which underwent reaction with bis(phenylsulfonyl)sulfide to give [7]helicene (−)-**18** (37% yield, 47% *ee*; Scheme 4).

As the sparteine-mediated synthesis gave only a relatively low *ee* of (−)-**18**, a resolution-based approach to the [7]helicene was developed by the same authors, employing the menthol-derivatized chiral chlorosiloxane, (−)-menthoxyPh_2SiCl (Scheme 5). Starting with racemic **18**, both TMS groups were removed using TFA, then LDA-mediated dilithiation at both α-positions was quenched with (−)-menthoxyPh_2SiCl. The diastereomeric mixture of disiloxanes was then separated by chromatography. Removal of the siloxanes using TFA gave [7]helicenes (−)-**19** and (+)-**19** (R = H; Scheme 5).[17b] An enantiomerically pure phenylene-thiophene[7]-helicene was also reported by Rajca and co-workers.[17c]

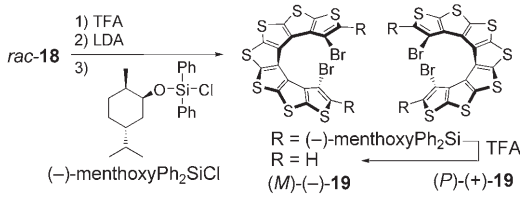

Scheme 5. Resolution of carbon–sulfur [7]helicene **19**.[17b] TFA = trifluoroacetic acid.

Cross-conjugated [*n*]helicenes with large *n* values are materials with extraordinary chiral properties and transparency in the optical region, as Rajca and co-workers established following a landmark asymmetric synthesis of the helical α-undecathiophene **24**. The synthetic approaches to **24** were based upon either mono- or trisannelation, using (−)-sparteine-mediated asymmetric induction (Scheme 6).[17a] In the mono-annelation approach, Pd-mediated reductive C–C homocoupling of [5]helicene **20** led to decathiophene **21** (70%). Treatment of **21** with LDA in the presence of (−)-sparteine followed by addition of $(PhSO_2)_2S$ gave [11]helicene (−)-**24** (59%, 19% *ee*). In the second approach, Pd-mediated reductive C–C homocoupling of tetrathiophene **22** afforded octathiophene **23** (74%), which was treated with LDA/(−)-sparteine and subsequently quenched with $(PhSO_2)_2S$ to give the tris-annelation product (+)-**24** (3%, 17% *ee*).[17d] Therefore, the mono- and tris-annelation pathways afforded [11]helicene **24** with opposite configurations.

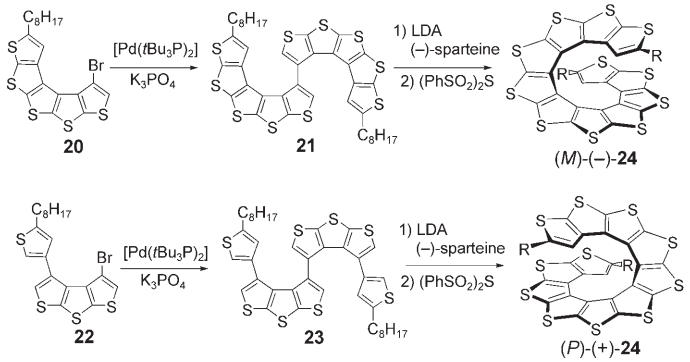

Scheme 6. Synthesis of carbon–sulfur [11]helicene **24** (R = C_8H_{17}).[17a]

In a new design, such helical structures have been ring-closed to give macrocycles, thus forming highly symmetric molecules with unusual electronic properties. These polythiacirculenes consist of annelated thiophenic rings with the formula $(C_2S)_n$ for any number of rings (*n*) and represent another form of carbon sulfide. In the most recent report in this area, Nenajdenko and coworkers calculated the minimum strain energy for flat *n* = 8 and *n* = 9 thiophene circulenes and reported a short and effective synthesis of the first heterocyclic circulene, octathio[8]circulene (**27**; Scheme 7).[18] Thus, treatment of **25** (obtained from 3,4-dibromothiophene) with LDA and sulfur resulted in com-

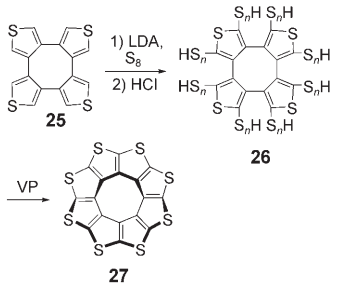

Scheme 7. Synthesis of octathio[8]circulene (**27**).[18a] VP = vacuum pyrolysis.

 © 2006 Wiley-VCH Verlag GmbH & Co. KGaA, Weinheim

plete sulfurization of free thiophene sites and efficient formation of an intermediate polythiolate, which was converted into polythiol **26** by acidification. Subsequent vacuum pyrolysis of the crude polythiol afforded the target circulene **27** (80% from **25**; Scheme 7).[18] For comparison, the unknown [8]circulene ($C_{32}H_{16}$) was predicted as a ruffled nonplanar aromatic structure, and only large hollow annulenes are predicted to be planar stable compounds.[19] The structures of **18**, **24**, and **27** have all been confirmed by X-ray diffraction studies as carbon–sulfur rigid macrostructures with sulfur atoms located at the peripheries (Figure 3).[17–18]

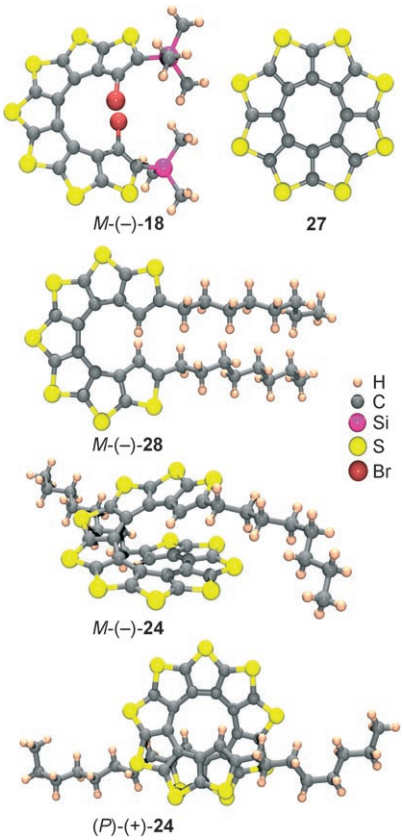

Figure 3. X-ray crystal structures of helicenes **18** and **24**, circulene **27**, and a dialkyl [7]helicene **28**.[17–18]

The synthetic methodology of such unusual structures should now be applicable to new heterocyclic strained hydrocarbons to create novel materials with diverse electronic properties. The only limit is imagination. Very recently, the first chiral Möbius [16]annulene hydrocarbons were described, which has opened a debate about their aromaticity.[20] It is probably the moment to introduce some sulfur (thiophenes) in the Möbius annulenes area to discover new organic electronic materials.

Published online: November 17, 2006

[1] a) M. Jeffries-EL, G. Sauvé, R. D. McCullough, *Adv. Mater.* **2004**, *16*, 1017–1019; b) H. Meng, D. F. Perepichka, F. Wudl, *Angew. Chem.* **2003**, *115*, 682–685; *Angew. Chem. Int. Ed.* **2003**, *42*, 658–661; c) E. Mena-Osteritz, A. Meyer, B. M. W. Langeveld-Voss, R. A. J. Janssen, E. W. Meijer, P. Bäuerle, *Angew. Chem.* **2000**, *112*, 2791–2796; *Angew. Chem. Int. Ed.* **2000**, *39*, 2679–2684; d) G. Zotti, S. Zecchin, G. Schiavon, B. Vercelli, A. Berlin, W. Porzio, *Chem. Mater.* **2004**, *16*, 2091–2100.

[2] a) I. F. Perepichka, D. F. Perepichka, H. Meng, F. Wudl, *Adv. Mater.* **2005**, *17*, 2281–2305; b) F. Zhang, M. Svensson, M. R. Andersson, M. Maggini, S. Bucella, E. Menna, O. Inganäs, *Adv. Mater.* **2001**, *13*, 1871–1874.

[3] a) N. Sakai, G. K. Prasad, Y. Ebina, K. Takada, T. Sasaki, *Chem. Mater.* **2006**, *18*, 3596–3598; b) B. S. Ong, Y. Wu, P. Liu, S. Gardner, *Adv. Mater.* **2005**, *17*, 1141–1144.

[4] J. Hou, Z. Tan, Y. Yan, Y. He, C. Yang, Y. Li, *J. Am. Chem. Soc.* **2006**, *128*, 4911–4916.

[5] a) G. Sonmez, F. Wudl, *J. Mater. Chem.* **2005**, *15*, 20–22; b) H. W. Heuer, R. Wehrmann, S. Kirchmeyer, *Adv. Funct. Mater.* **2002**, *12*, 89–94.

[6] a) G. Barbarella, M. Melucci, G. Sotgiu, *Adv. Mater.* **2005**, *17*, 1581–1593; b) B. Liu, G. C. Bazan, *Chem. Mater.* **2004**, *16*, 4467–4476.

[7] Organic field-effect transistors: a) G. Zotti, S. Zecchin, B. Vercelli, M. Pasini, S. Destri, F. Bertini, A. Berlin, *Chem. Mater.* **2006**, *18*, 3151–3161; b) J. Roncali, *Chem. Soc. Rev.* **2005**, *34*, 483–495; c) E. Amir, S. Rozen, *Angew. Chem.* **2005**, *117*, 7540–7544; *Angew. Chem. Int. Ed.* **2005**, *44*, 7374–7378; d) Y. Sun, Y. Liu, D. Zhu, *J. Mater. Chem.* **2005**, *15*, 53–65. Electroluminescent diodes: W. Porzio, S. Destri, U. Giovanella, S. V. Meille, G. Raos, R. Consonni, G. Zotti, *Chem. Mater.* **2005**, *17*, 242–249. Photoresponsive devices: W. Huang, G. Masuda, S. Maeda, H. Tanaka, T. Ogawa, *Chem. Eur. J.* **2006**, *12*, 607–619.

[8] a) S. Westenhoff, A. Abrusci, W. J. Feast, O. Henze, A. F. M. Kilbinger, A. P. H. J. Schenning, C. Silva, *Adv. Mater.* **2006**, *18*, 1281–1285; b) O. Henze, W. J. Feast, F. Gardebien, P. Jonkheijm, R. Lazzaroni, P. Leclère, E. W. Meijer, A. P. H. J. Schenning, *J. Am. Chem. Soc.* **2006**, *128*, 5923–5929; c) A. Herland, P. Björk, K. P. R. Nilson, J. D. M. Olsson, P. Åsberg, P. Konradsson, P. Hammarström, O. Inganäs, *Adv. Mater.* **2005**, *17*, 1466–1471; d) P. Leclère, M. Surin, P. Viville, R. Lazzaroni, A. F. M. Kilbinger, O. Henze, W. J. Feast, M. Cavallini, F. Biscarini, A. P. H. J. Schenning, E. W. Meijer, *Chem. Mater.* **2004**, *16*, 4452–4466 (review).

[9] a) S. Deng, J. Locklin, D. Patton, A. Baba, R. C. Advincula, *J. Am. Chem. Soc.* **2005**, *127*, 1744–1751; b) D. Patton, J. Locklin, M. Meredith, Y. Xin, R. Advincula, *Chem. Mater.* **2004**, *16*, 5063–5070; c) P. Furuta, J. M. J. Fréchet, *J. Am. Chem. Soc.* **2003**, *125*, 13173–13181; d) J. Alvarez, L. Sun, R. M. Crooks, *Chem. Mater.* **2002**, *14*, 3995–4001; e) J. J. Apperloo, R. A. J. Janssen, P. R. L. Malenfant, L. Groenendaal, J. M. J. Fréchet, *J. Am. Chem. Soc.* **2000**, *122*, 7042–7051.

[10] a) C. Xia, X. Fan, J. Locklin, R. C. Advincula, A. Gies, W. Nonidez, *J. Am. Chem. Soc.* **2004**, *126*, 8735–8743; b) C. Xia, X. Fan, J. Locklin, R. C. Advincula, *Org. Lett.* **2002**, *4*, 2067–2070. A hybrid dendrimer: c) W. J. Mitchell, N. Kopidakis, G. Rumbles, D. S. Ginley, S. E. Shaheen, *J. Mater. Chem.* **2005**, *15*, 4518–4528.

[11] a) K. R. Radke, K. Ogawa, S. C. Rasmussen, *Org. Lett.* **2005**, *7*, 5253–5256; b) D. J. Crouch, P. J. Skabara, M. Heeney, I. McCulloch, S. J. Colesc, M. B. Hursthouse, *Chem. Commun.* **2005**, 1465–1467; c) M. Turbiez, P. Frère, M. Allain, C. Videlot, J. Ackermann, J. Roncali, *Chem. Eur. J.* **2005**, *11*, 3742–3752.

[12] a) G. Fuhrmann, T. Debaerdemaeker, P. Bäuerle, *Chem. Commun.* **2003**, 948–949; b) G. Fuhrmann, J. Krömer, P. Bäuerle, *Synth. Met.* **2001**, *119*, 125–126; c) J. Krömer, I. Rios-Carreras, G. Fuhrmann, C. Musch, M. Wunderlin, T. Debaerdemaeker, E. Mena-Osteriz, P. Bäuerle, *Angew. Chem.* **2000**, *112*, 3623–3628; *Angew. Chem. Int. Ed.* **2000**, *39*, 3481–3486. Self-assembly: d) E. Mena-Osteriz, *Adv. Mater.* **2002**, *14*, 609–616; e) E. Mena-Osteriz, P. Bäuerle, *Adv. Mater.* **2001**, *13*, 243–246.

[13] S. S. Zade, M. Bendikov, *J. Org. Chem.* **2006**, *71*, 2972–2981.

[14] a) T. Okamoto, K. Kudoh, A. Wakamiya, S. Yamaguchi, *Org. Lett.* **2005**, *7*, 5301–5304; b) K. Kudoh, T. Okamoto, S. Yamaguchi, *Organometallics* **2006**, *25*, 2374–2377.

[15] a) X. Zhang, J. P. Johnson, J. W. Kampf, A. J. Matzger, *Chem. Mater.* **2006**, *18*, 3470–3476; b) X. Zhang, A. P. Côté,

© 2006 Wiley-VCH Verlag GmbH & Co. KGaA, Weinheim

A. J. Matzger, *J. Am. Chem. Soc.* **2005**, *127*, 10502 – 10503. Previous synthesis reviewed: c) T. Ozturk, E. Ertas, O. Mert, *Tetrahedron* **2005**, *61*, 11055 – 11077.

[16] A. Urbano, *Angew. Chem.* **2003**, *115*, 4116 – 4119; *Angew. Chem. Int. Ed.* **2003**, *42*, 3986 – 3989 (highlight).

[17] a) M. Miyasaka, A. Rajca, M. Pink, S. Rajca, *J. Am. Chem. Soc.* **2005**, *127*, 13806 – 13807; b) A. Rajca, M. Miyasaka, M. Pink, H. Wang, S. Rajca, *J. Am. Chem. Soc.* **2004**, *126*, 15211 – 15222; c) M. Miyasaka, A. Rajca, M. Pink, S. Rajca, *Chem. Eur. J.* **2004**, *10*, 6531 – 6539; d) A. Rajca, H. Wang, M. Pink, S. Rajca, *Angew. Chem.* **2000**, *112*, 4655 – 4657; *Angew. Chem. Int. Ed.* **2000**, *39*, 4481 – 4483. Calculations on large rings: e) M. Miyasaka, A. Rajca, *J. Org. Chem.* **2006**, *71*, 3264 – 3266.

[18] a) K. Yu. Chernichenko, V. V. Sumerin, R. V. Shpanchenko, E. S. Balenkova, V. G. Nenajdenko, *Angew. Chem.*, DOI: 10.1002/ange.200602190; *Angew. Chem. Int. Ed.*, DOI: 10.1002/anie.200602190. Half-circulene synthesis: b) V. G. Nenajdenko, V. V. Sumerin, K. Yu. Chernichenko, E. S. Balenkova, *Org. Lett.* **2004**, *6*, 3437 – 3439.

[19] a) R. Salcedo, L. E. Sansores, A. Picazo, L. Sansón, *J. Mol. Struct. (Theochem)* **2004**, *678*, 211 – 215; b) B. Hajgat, M. S. Deleuze, K. Ohno, *Chem. Eur. J.* **2006**, *12*, 5757 – 5769.

[20] a) D. Ajami, K. Hess, F. Köhler, C. Näther, O. Oeckler, A. Simon, C. Yamamoto, Y. Okamoto, R. Herges, *Chem. Eur. J.* **2006**, *12*, 5434 – 5445; b) D. Ajami, O. Oeckler, A. Simon, R. Herges, *Nature* **2003**, *426*, 819 – 821. Aromaticity calculations: c) C. Castro, Z. Chen, C. S. Wannere, H. Jiao, W. L. Karney, M. Mauksch, R. Puchta, N. J. R. van Eikema Hommes, P. von R. Schleyer, *J. Am. Chem. Soc.* **2005**, *127*, 2425 – 2432.

 © 2006 Wiley-VCH Verlag GmbH & Co. KGaA, Weinheim

Group 13 Ligands

DOI: 10.1002/anie.200603643

Platinum Complexes Featuring Terminally Bound Ga^+ and In^+ Ions

*Simon Aldridge**

Keywords:
cations · gallium · indium · Lewis acids · subvalent ligands

The coordination chemistry of low-valent Group 13 ligand systems represents a synthetically challenging and highly topical area of modern main-group chemistry that has experienced considerable progress in recent years.[1] In part, this stems from a desire to elucidate fundamental patterns of electronic structure/bonding and reactivity, and to compare such properties with the textbook organometallic ligand systems of Group 14 (for example, carbonyls, carbenes, vinylidenes).[2] For the heavier Group 13 elements, synthetic routes to diyl ligands (of the type RE:) and related base-stabilized systems have been developed recently, and their main-group and transition-metal coordination chemistries have been investigated.[1,3–7] Thus, the fundamental σ-donor and π-acceptor properties of these ligands have been debated (Figure 1), in some cases arousing no small amount of controversy.[8–10] Such properties are strongly dependent on the nature of the diyl substituent R; thus, Cp*Ga is known to be a very good σ-donor ligand but to function as a weak π acceptor towards transition-metal centers owing to strongly competing π donation from the Cp* fragment.[1,10] Alkyl substituents offer less competition in this regard, and hence a greater π component to the M–E bond is found in metal complexes containing, for example, the {$(Me_3Si)_3C$}Ga ligand.[8] Extrapolating this argument to its logical conclusion, it might be expected that "naked" gallium/indium cations featuring no pendant diyl substituent would display very strong π-acceptor properties. However, although transition-metal complexes featuring such "naked" Group 13 atoms that adopt *bridging* modes of coordination between two or more metal centers have previously been reported (Scheme 1)[11–14] and although the essentially noncovalent interaction of Tl^+ with noble metal centers is well-precedented,[15] terminally bound Ga^+ or In^+ ligands were unknown until a very recent report by Frenking, Fischer, and co-workers.[16]

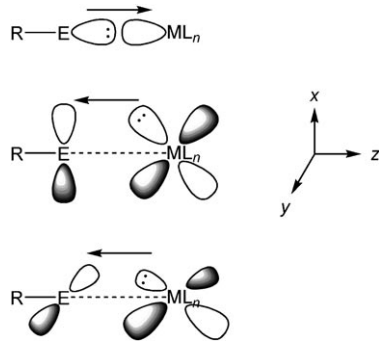

Figure 1. σ-Donor and π-acceptor orbital interactions of a Group 13 diyl ligand (RE:) with a transition-metal center.

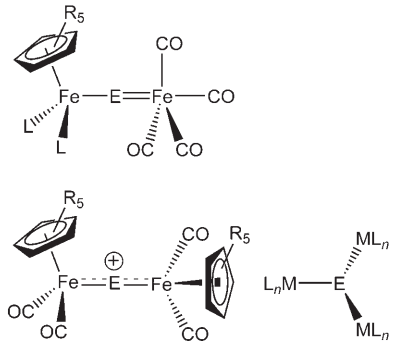

Scheme 1. Previously reported classes of transition-metal complexes featuring "naked" Group 13 atoms as bridging ligands.

The key to the synthetic route adopted by these authors (Scheme 2) is the availability of soluble sources of Ga^I and In^I ions featuring weakly coordinating counterions. A number of Ga^+ and In^+ reagents of this type have been reported in recent years by the groups of Cowley, MacDonald, and Fischer,[17–19] and by exploiting the reactivity of one of these, $[Ga_2Cp^*]^+[BAr^F_4]^-$ ($Ar^F = C_6H_3(CF_3)_2$-3,5),[19] towards the electron-rich d^{10} platinum(0) complex $[Pt(GaCp^*)_4]$ (**1**),[20] the novel species $[GaPt(GaCp^*)_4]^+[BAr^F_4]^-$ (**3**) has been synthesized.[16] In a similar vein, reaction of **1** with the Brønsted acid $[H(OEt_2)_2]^+$-$[BAr^F_4]^-$ gives $[HPt(GaCp^*)_4]^+[BAr^F_4]^-$ (**4**) together with the dinuclear species $[(Cp^*Ga)_4Pt(\mu\text{-}Ga)Pt(GaCp^*)_3H]^{2+}$-$[BAr^F_4]^-_2$ (**5**), which contains a bridging Ga^+ ligand between two platinum centers. Related chemistry exploiting the novel In^I source $In^+[BAr^F_4]^-$ has been used to generate $[InPt(PPh_3)_3]^+[BAr^F_4]^-$ (**6**) from $[Pt(PPh_3)_4]$ (**2**) with concomitant loss of one phosphine ligand. The structures of **3** and **6** in the solid state have been determined crystallographically and are significant in representing the first structurally characterized transition-metal complexes containing "naked" Ga^+ or In^+ cations as terminally bound ligands.

The structure of the $[GaPt(GaCp^*)_4]^+$ cation in **3** consists of an

[*] Dr. S. Aldridge[+]
Centre for Fundamental and Applied Main Group Chemistry
School of Chemistry
Cardiff University
Main Building, Park Place
Cardiff, CF10 3AT (UK)
Fax: (+44) 2920-874-030
E-mail: AldridgeS@cardiff.ac.uk

[+] Address as of January 01, 2007:
Inorganic Chemistry, University of Oxford
South Parks Road, Oxford, OX1 3QR (UK)

© 2006 Wiley-VCH Verlag GmbH & Co. KGaA, Weinheim

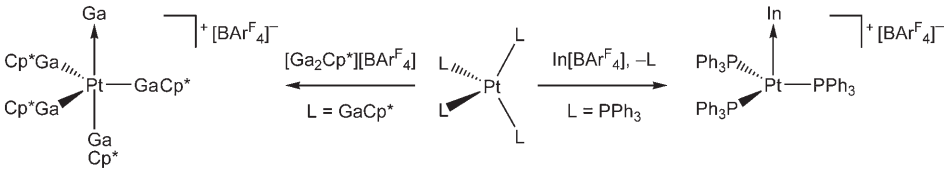

3 **1**: L = GaCp* **2**: L = PPh_3 **6**

Scheme 2. Syntheses of complexes **3** and **6** featuring the first examples of Ga^+ and In^+ acting as a terminally bound ligand to a transition-metal center ($Ar^F = C_6H_3(CF_3)_2$-3,5).

approximately trigonal-bipyramidal coordination geometry at the platinum center with the Ga^+ ligand occupying one of the apical coordination sites. In a similar fashion, $[InPt(PPh_3)_3]^+$ features a trigonal-pyramidal geometry, in which the In^+ ligand occupies the apical site, with the corresponding *trans* position left vacant, presumably for steric reasons. The Pt–Ga bonds associated with the equatorial GaCp* ligands in **3** (mean Pt–Ga bond length 2.352 Å) are lengthened only marginally relative to the corresponding linkages in the tetracoordinate homoleptic precursor **1** (2.335 Å).[16,20] As expected for a trigonal-bipyramidal system, the Pt–Ga bond to the axial GaCp* ligand is markedly longer (2.444(1) Å). Interestingly, and despite the clearly reduced steric demands of the Ga^+ ligand (relative to those of GaCp*), the Pt–Ga bond associated with the "naked" Ga^+ ligand is even longer still (2.459(1) Å).

The nature of the bonding between the Ga^+ or In^+ ligand and the platinum center is one of the key questions investigated in this study. At a basic level, the authors favor an overall bonding description for **3** featuring a Lewis acid/base interaction between the 18-electron closed-shell $\{PtL_4\}$ system (acting as the Lewis base) and the soft Lewis acid Ga^+. A more in-depth analysis has been carried out using a DFT-derived energy decomposition analysis to quantify the various components (Pauli-repulsive; electrostatic- and orbital-attractive) to the instantaneous interaction energy between $\{Pt(GaCp)_4\}$ and Ga^+ fragments in the model complex $[GaPt(GaCp)_4]$ (**3′**). This analysis not only implies that the orbital (covalent) contribution to the Pt–Ga interaction is of key importance (representing 57% of the overall interaction energy), but that components of both σ and π symmetry are significant (representing 61 and 39%, respectively, of the orbital term). For the related system $[InPt(PMe_3)_3]$ (**6′**), utilized as a model for triphenylphosphine complex **6**, the relative importance of π-symmetry interactions is calculated to be even greater (48%), albeit with the orbital term being of relatively lower significance (only 47% of the overall interaction energy). These conclusions are further supported by Mulliken orbital population analyses, which reveal significant population of both p(σ) (that is, p_z) and p(π) (that is, p_x and p_y) orbitals at gallium/indium. Thus, for **3′** the calculated populations of the p(σ) and p(π) orbitals at gallium are 0.58 and 0.30, respectively, while for **6′** the corresponding values (for indium) are 0.45 and 0.38.

Furthermore, orbital population analyses also give an indication as to whether the Ga^+/In^+ ligand acts as a net electron donor or acceptor. For both model systems **3′** and **6′**, the total occupation of the σ orbitals (valence s and p_z) at the Group 13 element is calculated to be significantly greater than 2 (2.49 and 2.28, respectively). This, taken together with the small calculated partial positive charge at the gallium/indium ligand (for example, +0.21 at gallium in **3′**) and the significantly higher positive charge at the platinum center, suggests that the E^+ ligands (E = Ga or In) function as net electron acceptors (that is, as Z-type ligands).[21] The electronic origins of the differing ligand properties of "naked" Ga^+ relative to other Ga^I donors can thus be elucidated. In contrast to the strongly directional lone pair at the gallium atom in diyl and related ligand systems, the electron pair at the Ga^+ ligand in **3′** is described as being almost entirely of s character. Ga^+ is thus a poor σ donor in such complexes. The lack of a gallium-bound substituent with π-donor orbitals further means that in contrast to Cp*Ga, for example, Ga^+ is a good π acceptor.

To conclude, the first examples of transition-metal complexes containing Ga^+ or In^+ cations as terminally bound ligands feature the "naked" Group 13 fragment acting as a pure acceptor (or Z-type) ligand. Thus, such systems can be described as metal analogues of H^+ (which shows similar reactivity towards **1**), and have much in common with the tethered boratrane systems pioneered by Hill et al.,[22] with the caveat that the Ga^+/In^+ ligand acts as an acceptor through interactions of both σ and π symmetry. The contrast with other E^I ligand systems, such as the strong σ-donor diyl family (RE:), represents the ultimate extension of how the nature of the substituent drives the ligating properties of the Group 13 donor. Given the more widespread availability of soluble cationic E^I reagents that have been revealed in the recent literature, significant novel chemistry and new bonding environments are sure to result from further studies in this area.

Published online: November 10, 2006

[1] For recent reviews, see, for example: a) R. A. Fischer, J. Weiß, *Angew. Chem.* **1999**, *111*, 302–3022; *Angew. Chem. Int. Ed.* **1999**, *38*, 2830–2850; b) G. Linti, H. Schnöckel, *Coord. Chem. Rev.* **2000**, *206–207*, 285–319; c) A. H. Cowley, *Chem. Commun.* **2004**, 2369–2375; d) C. Gemel, T. Steinke, M. Cokoja, A. Kempter, R. A. Fischer, *Eur. J. Inorg. Chem.* **2004**, 4161–4176; e) S. Aldridge, D. L. Coombs, *Coord. Chem. Rev.* **2004**, *248*, 535–559; f) R. J. Baker, C. Jones, *Coord. Chem. Rev.* **2005**, *249*, 1857–1869; g) H. Braunschweig, D. Rais, C. Kollann, *Angew. Chem.* **2006**, *118*, 5380–5400; *Angew. Chem. Int. Ed.* **2006**, *45*, 5254–5274.

 © 2006 Wiley-VCH Verlag GmbH & Co. KGaA, Weinheim

[2] See, for example: W. A. Nugent, J. M. Mayer, *Metal Ligand Multiple Bonds*, Wiley Interscience, New York, **1988**.
[3] a) C. Dohmeier, C. Robl, M. Tacke, H. Schnöckel, *Angew. Chem.* **1991**, *103*, 594 – 595; *Angew. Chem. Int. Ed. Engl.* **1991**, *30*, 564 – 565; b) D. Loos, E. Baum, A. Ecker, H. Schnöckel, A. J. Downs, *Angew. Chem.* **1997**, *109*, 894 – 896; *Angew. Chem. Int. Ed. Engl.* **1997**, *36*, 860 – 862; c) P. Jutzi, B. Neumann, G. Reumann, H. G. Stammler, *Organometallics* **1998**, *17*, 1305 – 1314; d) O. T. Beachley, R. Blom, M. R. Churchill, K. Faegri, Jr., J. C. Fettinger, J. C. Pazik, L. Victoriano, *Organometallics* **1989**, *8*, 346 – 356.
[4] a) R. J. Wright, A. D. Phillips, S. Hino, P. P. Power, *J. Am. Chem. Soc.* **2005**, *127*, 4794 – 4799; b) N. J. Hardman, R. J. Wright, A. D. Phillips, P. P. Power, *J. Am. Chem. Soc.* **2003**, *125*, 2667 – 2679; c) S. T. Haubrich, P. P. Power, *J. Am. Chem. Soc.* **1998**, *120*, 2202 – 2203; d) R. J. Wright, A. D. Phillips, P. P. Power, *J. Am. Chem. Soc.* **2003**, *125*, 10784 – 10785.
[5] a) W. Uhl, W. Hiller, M. Layh, W. Schwarz, *Angew. Chem.* **1992**, *104*, 1378 – 1380; *Angew. Chem. Int. Ed. Engl.* **1992**, *31*, 1364 – 1366; b) R. D. Schluter, A. H. Cowley, D. Atwood, R. A. Jones, J. A. Atwood, *J. Coord. Chem.* **1993**, *30*, 25 – 28; c) W. Uhl, R. Graupner, M. Layh, U. Schütz, *J. Organomet. Chem.* **1995**, *493*, C1 – C5.
[6] a) C. Cui, H. W. Roesky, H.-G. Schmidt, M. Noltemeyer, H. Hao, F. Cimpoescu, *Angew. Chem.* **2000**, *112*, 4444 – 4446; *Angew. Chem. Int. Ed.* **2000**, *39*, 4274 – 4276; b) N. J. Hardman, B. E. Eichler, P. P. Power, *Chem. Commun.* **2000**, 1991 – 1992; c) M. S. Hill, P. B. Hitchcock, R. Pongtavornpinyo, *Dalton Trans.* **2005**, 273 – 277; d) Y. Cheng, P. B. Hitchcock, M. F. Lappert, M. Zhou, *Chem. Commun.* **2005**, 752 – 754.
[7] C. Jones, P. C. Junk, J. A. Platts, A. Stasch, *J. Am. Chem. Soc.* **2006**, *128*, 2206 – 2207.
[8] W. Uhl, M. Benter, S. Melle, W. Saak, G. Frenking, J. Uddin, *Organometallics* **1999**, *18*, 3778 – 3880.
[9] a) J. Su, X.-W. Li, R. C. Crittendon, C. F. Campana, G. H. Robinson, *Organometallics* **1997**, *16*, 4511 – 4513; b) F. A. Cotton, X. Feng, *Organometallics* **1998**, *17*, 128 – 130.
[10] For selected quantum chemical studies, see: a) C. L. B. MacDonald, A. H. Cowley, *J. Am. Chem. Soc.* **1999**, *121*, 12113 – 12126; b) G. Frenking, N. Fröhlich, *Chem. Rev.* **2000**, *100*, 717 – 774; c) J. Uddin, G. Frenking, *J. Am. Chem. Soc.* **2001**, *123*, 1683 – 1693.
[11] N. A. Compton, R. J. Errington, N. C. Norman, *Adv. Organomet. Chem.* **1990**, *31*, 91 – 182.
[12] K. Ueno, T. Watanabe, H. Tobita, H. Ogino, *Organometallics* **2003**, *22*, 4375 – 4377.
[13] a) N. R. Bunn, S. Aldridge, D. L. Coombs, A. Rossin, D. J. Willock, C. Jones, L.-L. Ooi, *Chem. Commun.* **2004**, 1732 – 1733; b) N. R. Bunn, S. Aldridge, D. L. Kays, N. D. Coombs, A. Rossin, D. J. Willock, C. Jones, L.-L. Ooi, *Organometallics* **2005**, *24*, 5891 – 5900.
[14] a) H. Braunschweig, K. Radacki, D. Scheschkewitz, G. R. Whittell, *Angew. Chem.* **2005**, *117*, 1685 – 1688; *Angew. Chem. Int. Ed.* **2005**, *44*, 1659 – 1660; b) H. Braunschweig, G. R. Whittell, *Chem. Eur. J.* **2005**, *11*, 6128 – 6133; c) H. Braunschweig, K. Radacki, D. Rais, F. Seeler, *Angew. Chem.* **2006**, *118*, 1087 – 1090; *Angew. Chem. Int. Ed.* **2006**, *45*, 1066 – 1069.
[15] See, for example: J. R. Stork, M. M. Olmstead, A. L. Balch, *J. Am. Chem. Soc.* **2005**, *127*, 6512 – 6513.
[16] B. Buchin, C. Gemel, T. Cadenbach, I. Fernández, G. Frenking, R. A. Fischer, *Angew. Chem.* **2006**, *118*, 5331 – 5334; *Angew. Chem. Int. Ed.* **2006**, *45*, 5207 – 5210.
[17] a) A. H. Cowley, C. L. B. MacDonald, J. S. Silverman, J. D. Gorden, A. Voight, *Chem. Commun.* **2001**, 175 – 176; b) J. N. Jones, C. L. B. MacDonald, J. D. Gorden, A. H. Cowley, *J. Organomet. Chem.*, **2003**, *666*, 3 – 5; c) A. H. Cowley, *Chem. Commun.* **2004**, 2369 – 2375.
[18] C. L. B. MacDonald, A. M. Corrente, C. G. Andrews, A. Taylor, B. D. Ellis, *Chem. Commun.* **2004**, 250 – 251.
[19] a) B. Buchin, C. Gemel, T. Cadenbach, R. Schmid, R. A. Fischer, *Angew. Chem.* **2006**, *118*, 1091 – 1093; *Angew. Chem. Int. Ed.* **2006**, *45*, 1074 – 1076; b) B. Buchin, C. Gemel, T. Cadenbach, R. Schmid, R. A. Fischer, *Angew. Chem.* **2006**, *118*, 1703; *Angew. Chem. Int. Ed.* **2006**, *45*, 1674.
[20] C. Gemel, T. Steinke, D. Weiss, M. Cokoja, M. Winter, R. A. Fischer, *Organometallics* **2003**, *22*, 2705 – 2710.
[21] a) M. L. H. Green, *J. Organomet. Chem.* **1995**, *500*, 127 – 148; b) G. Parkin, *Organometallics* **2006**, *25*, 4744 – 4747; c) A. F. Hill, *Organometallics* **2006**, *25*, 4741 – 4743.
[22] A. F. Hill, G. R. Owen, A. J. P. White, D. J. Williams, *Angew. Chem.* **1999**, *111*, 2920 – 2923; *Angew. Chem. Int. Ed.* **1999**, *38*, 2759 – 2761.

 © 2006 Wiley-VCH Verlag GmbH & Co. KGaA, Weinheim

Organocatalysis

DOI: 10.1002/anie.200601392

Enamine-Based Aldol Organocatalysis in Water: Are They Really "All Wet"?**

Andrew P. Brogan, Tobin J. Dickerson, and Kim D. Janda**

Keywords:
aldol reaction · asymmetric catalysis · green chemistry · organocatalysis

Organocatalysis is a burgeoning field of organic synthesis that employs substoichiometric amounts of an organic compound to accelerate a reaction.[1,2] Recent advances in organocatalysis include a wide range of reactions and often enable asymmetric induction in organic solvents. In particular, the aldol reaction is a key C–C bond-forming reaction that has tremendous synthetic utility and is often the platform of choice to examine new organocatalysts. Nature has perfected the stereospecific aldol reaction by using aldolase enzymes. While these enzymes have synthetic utility, they are limited by the lack of large-scale compatibility and typically do not have broad substrate recognition.

There are several examples of small-molecule (MW<600)-organocatalyzed aldol reactions that are capable of asymmetric induction in organic solvents.[1,2] However, from a green chemistry perspective, the use of water instead of organic solvent is preferred to decrease environmental contamination. Therefore, given the synthetic utility of the asymmetric aldol reaction, there is growing interest in the identification of organocatalysts that are capable of efficiently performing this reaction in water. In this context, we note that the first de novo tailored aqueous organocatalysts with high enantioselectivities were catalytic antibodies.[3–5] The importance and utility of these biomacromolecular catalysts cannot be understated, however, alternative small-molecule-organocatalyzed reactions in water with sufficient asymmetric induction would have immense synthetic utility.

Two recent studies, one by Hayashi et al.[6] (catalysts **1**–**4**) and the other by Barbas and co-workers[7] (catalysts **5**–**6**), described asymmetric small-molecule amine catalysts that were proposed to utilize enamine intermediates in water (Figure 1). Reports of small-molecule enamine-based aldol catalysis in water are not limited to these publications and have been scattered throughout the literature over the last several years.[8–12] Furthermore, others have raised the possibility of "prebiotic" relevance; however, to date only organic solvents have been utilized, thus diminishing the strength of this argument.[9,13,14] At first glance, these developments would be significant advances in organocatalysis and green chemistry. However, the reactions are not performed under truly aqueous conditions. While each of these reports depict enamine-catalyzed aldol reactions in varying degrees of an aqueous environment, we focus here on the recent findings of Hayashi and Barbas as representative examples, as these studies directly state their reactions are performed in water. In the spirit of constructive dialogue, we draw attention to particular aspects of developing small-molecule-organocatalyzed asymmetric aldol reactions in water.

It is well established that aldol reactions can be catalyzed by a general base, and small-molecule aqueous catalysts were published as early as 1909.[15] However, to promote enantioselectivity by an enamine-based mechanism in

[*] Dr. A. P. Brogan, Prof. Dr. T. J. Dickerson, Prof. Dr. K. D. Janda
Departments of Chemistry and Immunology
Skaggs Institute for Chemical Biology, and Worm Institute of Research & Medicine (WIRM)
The Scripps Research Institute
10550 N. Torrey Pines Road, La Jolla, CA 92037 (USA)
Fax: (+1) 858-784-2595
E-mail: tobin@scripps.edu
kdjanda@scripps.edu

[**] Comments to several reports on enamine-based organocatalysis of aldol reactions in water (Refs. [6–12]). We thank Prof. Dale L. Boger for helpful discussions during the preparation of this manuscript.

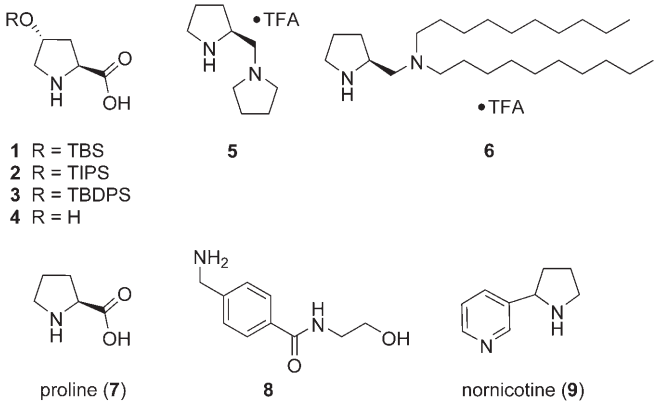

Figure 1. Structures of amine catalysts used in organocatalytic aldol reactions. TBS = *tert*-butyldimethylsilyl; TIPS = triisopropylsilyl; TBDPS = *tert*-butyldiphenylsilyl; TFA = trifluoroacetic acid.

InterScience
© 2006 Wiley-VCH Verlag GmbH & Co. KGaA, Weinheim

water, general-base catalysis must be minimized. Therefore, buffered conditions are a prerequisite. To our knowledge, the only research groups to have demonstrated small-molecule enamine-based aldol reactions under buffered aqueous conditions are those of Reymond,[16,17] Joyce,[18] and our own.[19] Specifically, Reymond and Chen found that proline (**7**), benzylic amine **8**, and a variety of amino acids can function as catalysts under buffered aqueous conditions, while Joyce and Oberhuber described aldol catalysis on a DNA template using a variety of small-molecule amines, including lysine and putrecine. We reported that nornicotine (**9**), a nicotine metabolite and minor component of tobacco smoke, catalyzes aldol reactions under buffered aqueous conditions (pH 7–8).[19] Modest asymmetric induction was observed by using enantiopure nornicotine (20% *ee*), while no asymmetric induction was reported by Reymond[16,17] or Joyce.[18]

Enamine formation in water is counterintuitive (Figure 2). However, the nornicotine–acetone enamine can be

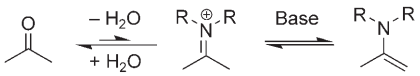

Figure 2. Enamine formation in water.

observed in D_2O by ^1H NMR spectroscopy.[20] In fact, no organic solvent was necessary for enamine formation with nornicotine, although small amounts of DMSO (5%) were used to dissolve the reactants.[19–25] Kinetic analysis verified the presence of least one water molecule at or before the rate-determining step of this reaction,[20] and density functional calculations proposed a two-step model that utilizes a water molecule in each high-energy transition state (Figure 3).[23] With the exception of our own work and that of Reymond[16,17] and Joyce,[18] there is no direct evidence in other reports that enamine catalysis occurs in water.

A fundamental phenomenon overlooked by some researchers is that when a basic compound is placed in non-buffered water, the pH value of the solution will increase. Catalysts **1**–**9** have a primary or secondary amine necessary for enamine-based catalysis and each of

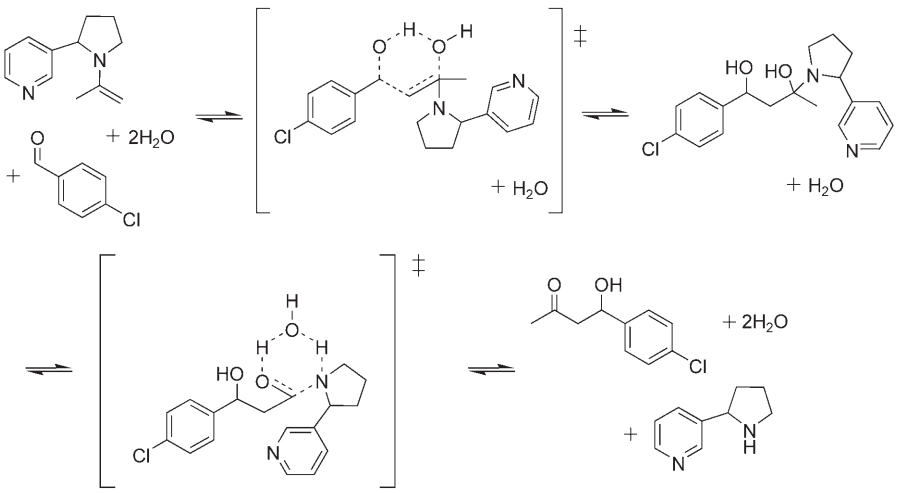

Figure 3. Proposed mechanism for nornicotine-catalyzed aqueous aldol reaction based on density functional calculations and kinetic isotope effect studies.

these amines has $pK_a \approx 11$. If catalysts **5** or **6** are placed in non-buffered water, the pH value of the solution will increase and catalysis of the aldol reaction will in turn be dominated by a general-base mechanism.[26] For example, a typical procedure using catalyst **6**[7] involved 50 μmol of catalyst in 1.0 mL of water (50 mM solution of catalyst). Assuming a pK_a value of 11 for **6**, simple calculations lead to a pH value of 11.8 for the reaction mixture. Catalysis observed for **5** in non-buffered water is also attributable to general-base catalysis. Consequently, it was not until TFA or other strong acids were added that high diastereo- and enantioselectivities were observed, characteristic of an enamine mechanism. Catalysts **1**–**4** include a carboxylic acid in addition to the amine and, therefore, are likely zwitterionic in water. However, Hayashi et al. used approximately the same amount of catalyst (60 μmol) as Barbas and co-workers reported in their study, although in much less water (0.32 mL); in fact, there is less water than either of the reactants (0.6 mL of benzaldehyde and 3.1 mL of cyclohexanone).[6] Given that there is a tenfold excess of cyclohexanone over water, cyclohexanone should be regarded as the solvent or the reaction should be deemed neat with 9% water. With this amount of water, the reaction should not be considered aqueous. Furthermore, from a green chemistry perspective the cyclohexanone waste is essentially organic solvent waste unless the cyclohexanone is easily recycled; therefore, the reaction appears to have little green chemistry benefit.

We would argue that catalysis in any of these reports is not really occurring in water. The solubility of catalysts **1**–**3** and **6** in water at concentrations of 50 mM is expected to be minimal given the large hydrophobic groups that each contain. Furthermore, when compared with the common cationic detergent C_{16}TAB, which has a critical micellar concentration of 1 mM, these amphilic catalysts are likely to form micelles at the concentrations reported. Contrary to the title of the study by Hayashi et al., a few drops of water does not constitute that the reaction is performed in water (see above).[6] Indeed, it is stated that the reaction mixture is biphasic in the discussion. The report by Barbas and co-workers makes note of the limited solubility of catalyst **6** and accurately portrays catalysis, describing the reaction mixture as an emulsion.[7] Yet, these reactions are not truly in water as opposed to being isolated from water.

Conditions for catalyst **6** to provide enantiomeric enrichment requires a stoichometric amount of TFA relative to catalyst **6**. However, the reaction then takes approximately five times longer to reach completion.[7] The increased reaction rate and lack of enantiomeric enrichment without the addition of acid suggests that catalysis in the absence of TFA is dominated by a general-base mechanism. As the addition of a stoichiometric amount of TFA (or any acid) favors the formation of micelles by

 © 2006 Wiley-VCH Verlag GmbH & Co. KGaA, Weinheim

increasing the amphiphilic character of the catalysts, the enantiomeric enrichment observed with the addition of TFA occurs from catalysis in what is accurately described as a "concentrated organic phase", whereby the hydrophobicity of catalyst **6** is concluded to sequester the enamine intermediate and concomitant transition state(s) away from water.[7] The reaction is not really in water and is likely occurring in a micelle, resulting in the exclusion of water and generating a formally biphasic reaction mixture.

These results can be compared to the pioneering study by Breslow and Rideout in which the rate of a Diels–Alder reaction was increased by performing the reaction in water.[27] In that case, hydrophobic molecules are forced into close contact,[28] in contrast to recent amine-catalyzed aldol reactions in which the reactants are excluded from water by the amphiphilic catalyst. Perhaps a more accurate term for these organocatalyzed reactions in concentrated organic phases or micelles would be the "on water" concept recently introduced by Sharpless et al.[29] Nonetheless, the study by Hayashi et al. is not carried out in water and the study by Barbas and co-workers is carried out with an emulsion. Thus, a more accurate description should be used to delineate these systems from truly aqueous systems.

The latest reports of enamine-based aldol reactions in water have prompted us to highlight some aspects in this active topic of research. We do not wish to diminish the significance of the enantiomeric enrichment observed in the reports by Barbas and co-workers and by Hayashi et al., nor do we wish to argue against catalysis occurring in concentrated or isolated organic environments. However, there is a clear distinction between what is described in this work and others where enamine-based catalysis is actually occurring in a buffered milieu.[16–24] Finally, no small-molecule (MW < 600) catalysts have provided synthetically relevant enantioselectivity in aqueous buffered solution—a hallmark of catalytic antibodies and biologically derived catalysts such as enzymes. We recognize the reports of "minimal aldolases",[30–32] yet these polypeptides cannot be considered small molecules. Thus, a clear challenge remains: Can small-molecule catalysts be developed to catalyze reactions in buffered solution with suitable asymmetric induction?

Received: April 8, 2006
Published online: September 25, 2006

[1] P. I. Dalko, L. Moisan, *Angew. Chem.* **2004**, *116*, 5248–5286; *Angew. Chem. Int. Ed.* **2004**, *43*, 5138–5175.
[2] A. Berkessel, H. Gröger, *Asymmetric Organocatalysis*, Wiley-VCH, Weinheim, **2005**.
[3] A. Tramontano, K. D. Janda, R. A. Lerner, *Proc. Natl. Acad. Sci. USA* **1986**, *83*, 6736–6740.
[4] A. Tramontano, K. D. Janda, R. A. Lerner, *Science* **1986**, *234*, 1566–1570.
[5] S. J. Pollack, J. W. Jacobs, P. G. Schultz, *Science* **1986**, *234*, 1570–1573.
[6] Y. Hayashi, T. Sumiya, J. Takahashi, H. Gotoh, T. Urushima, M. Shoji, *Angew. Chem.* **2006**, *118*, 972–975; *Angew. Chem. Int. Ed.* **2006**, *45*, 958–961.
[7] N. Mase, Y. Nakai, N. Ohara, H. Yoda, K. Takabe, F. Tanaka, C. F. Barbas III, *J. Am. Chem. Soc.* **2006**, *128*, 734–735.
[8] Y. Y. Peng, Q. P. Ding, Z. Li, P. G. Wang, J. P. Cheng, *Tetrahedron Lett.* **2003**, *44*, 3871–3875.
[9] A. Cordova, W. Notz, C. F. Barbas III, *Chem. Commun.* **2002**, 3024–3025.
[10] P. Dziedzic, W. Zou, J. Hafren, A. Cordova, *Org. Biomol. Chem.* **2006**, *4*, 38–40.
[11] H. Torii, M. Nakadai, K. Ishihara, S. Saito, H. Yamamoto, *Angew. Chem.* **2004**, *116*, 2017–2020; *Angew. Chem. Int. Ed.* **2004**, *43*, 1983–1986.
[12] Y. S. Wu, Y. Chen, D. S. Deng, J. Cai, *Synlett* **2005**, 1627–1629.
[13] A. Cordova, I. Ibrahem, J. Casas, H. Sunden, M. Engqvist, E. Reyes, *Chem. Eur. J.* **2005**, *11*, 4772–4784.
[14] A. Cordova, H. Sunden, M. Engqvist, I. Ibrahem, J. Casas, *J. Am. Chem. Soc.* **2004**, *126*, 8914–8915.
[15] H. D. Dakin, *J. Biol. Chem.* **1909**, *7*, 49–55.
[16] J. L. Reymond, Y. Chen, *J. Org. Chem.* **1995**, *60*, 6970–6979.
[17] J. L. Reymond, Y. Chen, *Tetrahedron Lett.* **1995**, *36*, 2575–2578.
[18] M. Oberhuber, G. F. Joyce, *Angew. Chem.* **2005**, *117*, 7752–7755; *Angew. Chem. Int. Ed.* **2005**, *44*, 7580–7583.
[19] T. J. Dickerson, K. D. Janda, *J. Am. Chem. Soc.* **2002**, *124*, 3220–3221.
[20] C. J. Rogers, T. J. Dickerson, K. D. Janda, *Tetrahedron* **2006**, *62*, 352–356.
[21] T. J. Dickerson, K. D. Janda, *Proc. Natl. Acad. Sci. USA* **2002**, *99*, 15084–15088.
[22] T. J. Dickerson, K. D. Janda, *Proc. Natl. Acad. Sci. USA* **2003**, *100*, 8182–8187.
[23] T. J. Dickerson, T. Lovell, M. M. Meijler, L. Noodleman, K. D. Janda, *J. Org. Chem.* **2004**, *69*, 6603–6609.
[24] C. J. Rogers, T. J. Dickerson, A. P. Brogan, K. D. Janda, *J. Org. Chem.* **2005**, *70*, 3705–3708.
[25] A. P. Brogan, T. J. Dickerson, G. E. Boldt, K. D. Janda, *Proc. Natl. Acad. Sci. USA* **2005**, *102*, 10433–10438.
[26] X. Zhang, K. N. Houk, *J. Org. Chem.* **2005**, *70*, 9712–9716.
[27] D. C. Rideout, R. Breslow, *J. Am. Chem. Soc.* **1980**, *102*, 7816–7817.
[28] Computational studies have shown that hydrogen bonding of water molecules to the substrate can play a greater role than the hydrophobic effect in the observed catalysis. See: J. Chandrasekhar, S. Shariffskul, W. L. Jorgensen, *J. Phys. Chem. B* **2002**, *106*, 8078–8085.
[29] S. Narayan, J. Muldoon, M. G. Finn, V. V. Fokin, H. C. Kolb, K. B. Sharpless, *Angew. Chem.* **2005**, *117*, 3339–3343; *Angew. Chem. Int. Ed.* **2005**, *44*, 3275–3279.
[30] F. Tanaka, R. Fuller, C. F. Barbas III, *Biochemistry* **2005**, *44*, 7583–7592.
[31] F. Tanaka, C. F. Barbas III, *J. Am. Chem. Soc.* **2002**, *124*, 3510–3511.
[32] F. Tanaka, C. F. Barbas III, *Chem. Commun.* **2001**, 769–770.

 © 2006 Wiley-VCH Verlag GmbH & Co. KGaA, Weinheim

Organocatalysis

DOI: 10.1002/anie.200603378

In Water or in the Presence of Water?**

*Yujiro Hayashi**

Keywords:
aldol reaction · asymmetric catalysis · organocatalysis · water

Water exhibits special properties as compared to commonly employed organic solvents. For instance, Breslow and co-workers reported acceleration of the Diels–Alder reaction "in water" with the reaction performed at very high dilution to dissolve the reactants,[1] while Sharpless and co-workers described "on water" conditions under which substantial rate acceleration was observed when the organic reactants were insoluble in the aqueous phase.[2] Regardless of whether the reactants are soluble or not in water, reactions using this solvent have attracted great attention from a synthetic point of view because water is environmentally friendly and safe, and the problems of pollution that arise with organic solvents can be avoided.[3]

The aldol reaction is a synthetically important carbon–carbon bond-forming reaction.[4] Enzymes and antibodies can catalyze the asymmetric aldol reaction using water as a medium[4,5] when some reaction proceeds in a hydrophobic pocket. There are several examples of the asymmetric aldol reaction "in the presence of water"; for example, the Mukaiyama aldol reaction is catalyzed by a combined chiral Lewis acid/surfactant catalyst "in the presence of water" (up to 69% *ee*).[6] Zn/proline also promotes the aldol reaction in aqueous media with moderate enantioselectivity (up to 56% *ee*).[7] In this case, a mixture of acetone and water was used, with the acetone acting not only as nucleophile but also as co-solvent.

After the seminal discovery of the proline-mediated, asymmetric aldol reaction by List, Lerner, and Barbas[8] which proceeds in a polar organic solvent, many papers concerning similar asymmetric aldol reactions have appeared. Some reactions have been performed under aqueous conditions,[9,10] with the presence of water reported to increase the reactivity and stereoselectivity.[9] At the time we started our research on the aldol reaction "in the presence of water", to the best of our knowledge there had been no reports of a highly enantioselective, catalytic aldol reaction proceeding "in the presence of water" without using any organic solvent.

At the end of 2005, Barbas and co-workers[11] and our own group[12] both independently reported the asymmetric aldol reaction "in the presence of water". We recently published another paper concerning this topic.[13] Our first report described an aldehyde–ketone aldol reaction catalyzed by siloxyproline (Scheme 1),[12,14] and the second report concerned an aldehyde–aldehyde reaction catalyzed by a combined proline/surfactant organocatalyst (Scheme 2).[13] Both reactions proceed in the presence of a large excess of water to afford the aldol products with excellent diastereo- and enantioselectivities. In the system using the siloxyproline catalyst, water appears to play a special role as a decrease in diastereomer ratio and enantioselectivity was observed under solvent-free conditions or in organic solvents. Thus, the reaction does not simply occur in a "concentrated organic phase" as suggested by Janda and co-workers.[15]

In the main discussion of both papers, we used the phrase "in the presence of water" and described clearly that both reactions proceed in an organic phase, as a biphasic system in the first report[12] and as an emulsion in the second.[13] One of the important and novel points observed with these reactions, in my opinion, is that highly enantioselective reactions proceed even "in the presence of a large excess amount of water".[13,14] This is a first asymmetric aldol reaction with excellent enantioselectivity in the presence of a large amount of water.

There have been several reports on the asymmetric aldol reaction using water as the only medium, one in which the reactants are not soluble. These reactions are described differently in the various papers, sometimes as "in water" and sometimes as "aqueous".

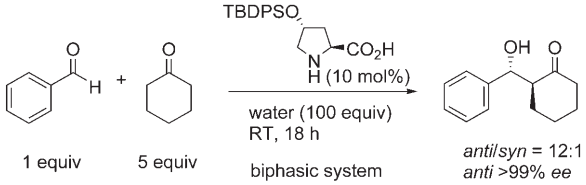

Scheme 1. Aldehyde–ketone aldol reaction (TBDPS = *tert*-butyldiphenylsilyl).

[*] Prof. Dr. Y. Hayashi
Department of Industrial Chemistry
Faculty of Engineering
Tokyo University of Science
Kagurazaka, Shinjuku-ku
Tokyo 162-8601 (Japan)
Fax: (+81) 3-5261-4631
E-mail: hayashi@ci.kagu.tus.ac.jp
Homepage: http://www.ci.kagu.tus.ac.jp/lab/org-chem1/

[**] Response to Correspondence by Janda and co-workers (see preceding article). The author thanks the referee for helpful suggestions. The work carried out on this subject was partially supported by the Toray Science Foundation and a Grant-in-Aid for Scientific Research on Priority Areas 16073219 from MEXT.

© 2006 Wiley-VCH Verlag GmbH & Co. KGaA, Weinheim

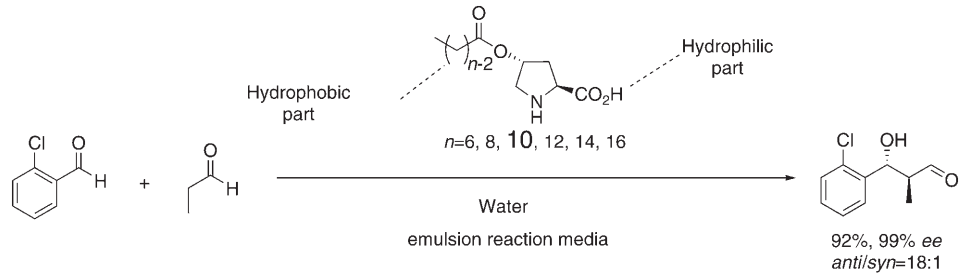

Scheme 2. Aldehyde–aldehyde aldol reaction in an emulsion.

What is a suitable term to describe the present reactions? Previously it had seemed to me that "aqueous" might not be suitable because it does not necessarily mean a reaction in which water is the only medium, but also includes the combined use of water and organic solvent. Nor would "on water" be suitable because these reactions are not necessarily accelerated "in the presence of water" in the way Sharpless has described.[2] Janda and co-workers have now proposed the term "concentrated organic phases".[15] This may often be appropriate, but I feel it does not adequately represent the effect of water or the difference seen between conditions with water present and solvent-free conditions, as we observed in the reaction reported in the earlier of our two papers.[12] What expression best conveys the effect of water in this reaction? We propose to use the terminology "in the presence of water".

As there is confusion over the terminology "in water", it is necessary at this point to clarify the terms "in water" and "in the presence of water". We propose to define "a reaction in water" as one in which the reactants participating in the reaction are dissolved homogeneously in water (or buffer, for pH control), whereas "a reaction in the presence of water" should be used for a reaction that proceeds in a concentrated organic phase with water being present as a second phase that influences the reaction in the organic phase. Sharpless' reactions "on water" are covered by the more general term "in the presence of water".[2]

Although the development of a small organic molecule that catalyzes the enantioselective, direct aldol reaction "in water"—and not just "in the presence of water"—with suitable asymmetric induction has been a longstanding challenge,[15] we have recently developed such a small-molecule catalyst. These exciting results will be reported in due course.[16]

Published online: November 14, 2006

[1] a) D. C. Rideout, R. Breslow, *J. Am. Chem. Soc.* **1980**, *102*, 7816; b) R. Breslow, *Acc. Chem. Res.* **1991**, *24*, 159.

[2] S. Narayan, J. Muldoon, M. G. Finn, V. V. Fokin, H. C. Kolb, K. B. Sharpless, *Angew. Chem.* **2005**, *117*, 3339; *Angew. Chem. Int. Ed.* **2005**, *44*, 3275.

[3] a) *Organic Synthesis in Water* (Ed.: P. A. Grieco), Blackie A & P, London, **1998**; b) U. M. Lindstrom, *Chem. Rev.* **2002**, *102*, 2751; c) C.-J. Li, *Chem. Rev.* **2005**, *105*, 3095.

[4] *Modern Aldol Reactions Vols. 1, 2* (Ed.: R. Mahrwald), Wiley-VCH, Weinheim, **2004**.

[5] T. D. Machajewski, C.-H. Wong, *Angew. Chem.* **2000**, *112*, 1406; *Angew. Chem. Int. Ed.* **2000**, *39*, 1352.

[6] S. Kobayashi, Y. Mori, S. Nagayama, K. Manabe, *Green Chem.* **1999**, *1*, 175.

[7] a) T. Darbre, M. Machuqueiro, *Chem. Commun.* **2003**, 1090; b) R. Fernandez-Lopez, J. Kofoed, M. Machuqueiro, T. Darbre, *Eur. J. Org. Chem.* **2005**, 5268.

[8] a) B. List, R. A. Lerner, C. F. Barbas III, *J. Am. Chem. Soc.* **2000**, *122*, 2395. For a review, see: b) A. Berkessel, H. Groger, *Asymmetric Organocatalysis*, Wiley-VCH, Weinheim, **2005**; c) P. I. Dalko, L. Moisan, *Angew. Chem.* **2004**, *116*, 5248; *Angew. Chem. Int. Ed.* **2004**, *43*, 5138.

[9] For organocatalyst-mediated asymmetric aldol reactions in aqueous solvent, see: a) H. Torii, M. Nakadai, K. Ishihara, S. Saito, H. Yamamoto, *Angew. Chem.* **2004**, *116*, 2017; *Angew. Chem. Int. Ed.* **2004**, *43*, 1983; b) A. I. Nyberg, A. Usano, P. M. Pihko, *Synlett* **2004**, 1891; c) Z. Tang, Z.-H. Yang, L.-F. Cun, L.-Z. Gong, A.-Q. Mi, Y.-Z. Jiang, *Org. Lett.* **2004**, *6*, 2285; d) J. Casas, H. Sunden, A. Cordova, *Tetrahedron Lett.* **2004**, *45*, 6117; e) D. E. Ward, V. Jheengut, *Tetrahedron Lett.* **2004**, *45*, 8347; f) I. Ibrahem, A. Cordova, *Tetrahedron Lett.* **2005**, *46*, 3363; g) M. Amedjkouh, *Tetrahedron: Asymmetry* **2005**, *16*, 1411; h) A. Cordova, W. Zou, I. Ibrahem, E. Reyes, M. Engqvist, W.-W. Liao, *Chem. Commun.* **2005**, 3586; i) Y.-S. Wu, Y. Chen, D.-S. Deng, J. Cai, *Synlett* **2005**, 1627; j) P. Dziedzic, W. Zou, J. Hafren, A. Cordova, *Org. Biomol. Chem.* **2006**, *4*, 38; k) P. M. Pihko, K. M. Laurikainen, A. Usano, A. I. Nyberg, J. A. Kaavi, *Tetrahedron* **2006**, *62*, 317.

[10] a) J.-L. Reymond, Y. Chen, *J. Org. Chem.* **1995**, *60*, 6970; b) A. Cordova, W. Notz, C. F. Barbas III, *Chem. Commun.* **2002**, 3024; c) T. J. Dickerson, K. D. Janda, *J. Am. Chem. Soc.* **2002**, *124*, 3220; d) Y.-Y. Peng, Q.-P. Ding, Z. Li, P. G. Wang, J.-P. Cheng, *Tetrahedron Lett.* **2003**, *44*, 3871; e) Y.-S. Wu, W.-Y. Shao, C.-Q. Zheng, Z.-L. Huang, J. Cai, Q.-Y. Deng, *Helv. Chim. Acta* **2004**, *87*, 1377; f) T. J. Dickerson, T. Lovell, M. M. Meijler, L. Noodleman, K. D. Janda, *J. Org. Chem.* **2004**, *69*, 6603; g) S. S. Chimni, D. Mahajan, V. V. S. Babu, *Tetrahedron Lett.* **2005**, *46*, 5617; h) C. J. Rogers, T. J. Dickerson, A. P. Brogan, K. D. Janda, *J. Org. Chem.* **2005**, *70*, 3705; i) S. S. Chimni, D. Mahajan, *Tetrahedron* **2005**, *61*, 5019; j) C. J. Rogers, T. J. Dickerson, K. D. Janda, *Tetrahedron* **2006**, *62*, 352.

[11] N. Mase, Y. Nakai, N. Ohara, H. Yoda, K. Takabe, F. Tanaka, C. F. Barbas III, *J. Am. Chem. Soc.* **2006**, *128*, 734.

[12] Y. Hayashi, T. Sumiya, J. Takahashi, H. Gotoh, T. Urushima, M. Shoji, *Angew. Chem.* **2006**, *118*, 972; *Angew. Chem. Int. Ed.* **2006**, *45*, 958.

[13] Y. Hayashi, S. Aratake, T. Okano, J. Takahashi, T. Sumiya, M. Shoji, *Angew. Chem.* **2006**, *118*, 5653; *Angew. Chem. Int. Ed.* **2006**, *45*, 5527.

[14] S. Aratake, T. Itoh, T. Okano, T. Sumiya, M. Shoji, Y. Hayashi, unpublished results.

[15] A. P. Brogan, T. J. Dickerson, K. D. Janda, *Angew. Chem.*, **2006**, *118*, 8278; *Angew. Chem. Int. Ed.*, **2006**, *45*, 8100.

[16] S. Aratake, T. Itoh, T. Okano, T. Usui, M. Shoji, Y. Hayashi, unpublished results.

 © 2006 Wiley-VCH Verlag GmbH & Co. KGaA, Weinheim

DOI: 10.1002/anie.200603381

Therapeutic Antibodies

Manufacturing Immunity to Disease in a Test Tube: The Magic Bullet Realized

*Richard A. Lerner**

Keywords:
antibodies · combinatorial chemistry · drug design · gene technology · immunochemistry

Dedicated to Manfred Eigen

© 2006 Wiley-VCH Verlag GmbH & Co. KGaA, Weinheim

Although it took over one hundred years, Ehrlich's concept of the magic bullet is now a reality. Today, therapeutic antibodies are, arguably, the most important class of new drugs for the treatment of illnesses ranging from Alzheimer's disease to cancer. The emergence of therapeutic antibodies had to wait for advances in immunochemistry that allowed construction of antibodies in vitro. The centerpiece of the new technology is the combinatorial antibody library, which essentially allows one to synthesize an artificial immune system with a diversity that exceeds that of the natural repertoire. The construction of such libraries was perceived to be difficult because, if the natural immune system was to be used as the starting material, construction of the libraries would entail protocols that are the opposite of usual cloning. In gene cloning one starts with complexity and reduces it to a singularity. In the generation of diversity by construction of combinatorial antibody libraries, one starts with a collection of clones, randomly expands their complexity, and then returns them to recoverable singularities. The methods developed to accomplish this seemingly formidable task now allow construction of antibodies in a test tube to any antigen. These synthetic antibodies may be qualitatively and quantitatively superior to those of nature.

From the Contents

1. Introduction	8107
2. Then and Now	8107
3. Solving the Diversity Problem with Combinatorial Antibody Libraries	8109
4. Requirements of an Artificial Immune System	8110
5. Comparison of the Natural Immune System to Combinatorial Antibody Libraries	8111
6. The Frequency Problem	8111
7. Linking Recognition and Replication	8112
8. A Solution to the Tolerance Problem Results from the Unnatural Pairs	8114
9. Summary of the Main Features of Combinatorial Antibody Libraries	8114
10. Synthetic Antibodies, Nonimmunogenic Antigens, and the Meaning of Jackpot and Chemical Consensus	8114
11. Obtaining Useful Diversity Exceeding the Natural Repertoire by Chain Shuffling	8116
12. Access of Very Rare Antibody Specifities for Therapy	8117
13. The Missing Piece Solved: Mutation Strategies	8120
14. The Embarrassment of Riches Problem	8122
15. Letting Phenotype Declare Itself	8123
16. The Future	8123

1. Introduction

Like chemistry itself, immunochemistry has evolved into a precise science. However, unlike mainstream chemistry, which progressed smoothly and logically through its conceptual and practical triumphs, immunochemistry has moved in fits and starts.[1,2] It has taken over one hundred years for the concept of the "magic bullet" to be realized. This Review will illustrate the current status of immunochemistry, with particular emphasis on the generation of therapeutic antibodies. However, rather than providing a chronological listing of the many therapeutic antibodies used in clinical practice today, the focus will be on the major concepts that currently drive the field. When nuances are stripped away, one realizes that the main challenge to immunochemistry was to achieve a solution to the diversity problem. As chemists, we can define this solution as the synthesis in vitro of an antibody repertoire with diversity equal to or greater than that of the natural systems of animals. The construction of combinatorial antibody libraries that led to a chemical solution to the diversity problem is described. Once that problem was solved, synthetic fully human therapeutic antibodies emerged and entered clinical practice

2. Then and Now

Figure 1 illustrates how the state of knowledge about the nature of antibodies has evolved over more than one hundred years, from Ehrlich's concepts of side chains to the crystal structure of an antibody molecule.[3,4] Perhaps the most

[*] Prof. R. A. Lerner
Department of Chemistry, The Scripps Research Institute and The Skaggs Institute of Chemical Biology
10550 North Torrey Pines Road, La Jolla, CA 92037 (USA)
Fax: (+1) 858-784-9899
E-mail: rlerner@scripps.edu

© 2006 Wiley-VCH Verlag GmbH & Co. KGaA, Weinheim

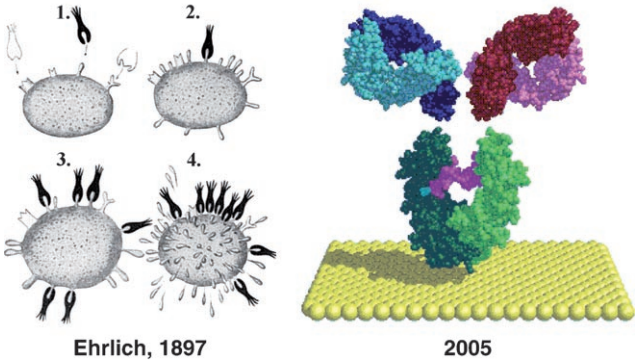

Figure 1. Ehrlich's side-chain theory (left) compared to the crystal structure of an antibody molecule (right). The antibody molecule shows the heavy and light chains as well as a disulfide bridge. Also indicated is the nature of the packing interaction of the heavy and light chains. The site of the antigen recognition is at the tips of the molecule where the heavy and light chains interact.

remarkable feature of this comparison is that there is not very much difference. Note how closely Ehrilch's concept of the "structure" of the antibody molecule agrees with the determination of the actual structure carried out by methods that couldn't even be conceived a hundred years earlier. As noted by Silverstein,[1] Ehrlich already anticipated a diversity system in which each antibody had different specificities, as indicated by their different shapes in his drawing (Figure 1). Studies into the structure and chemistry of antibodies is today a robust field, and largely beyond the scope of this Review. All that needs to be pointed out is that in a given repertoire, each antibody is different from the next.

An individual antibody has six protein loops or complementarity determining regions (CDRs) that are so named because they are the regions that bind to an antigen or, said in another way, are complementary to it. An antibody molecule is nature's most sophisticated combinatorial device in that each member of a collection approximates in space six different CDRs on two protein chains (heavy and light), thus achieving a three-dimensional combinatorial matrix that occupies approximately 700 A^2 of binding surface and 3000 A^3 of volume, with an unlimited number of shapes. When reduced to its chemical essence, an antibody molecule can be said to be a combinatorial display system for peptide loops.

In addition to his remarkable intuition about the nature of antibodies, Ehrlich was equally prophetic when he made his proclamation about the Zauberkugel or "magic bullet". In the Hal B. Wallis Warner Brothers movie entitled "Dr. Ehrlich's Magic Bullet", produced in 1940, Paul Ehrlich (Edward G. Robinson) is "heard" telling the finance minister that "*it will be possible one day to manufacture immunity to disease in a test tube more little magic bullets to shoot into the blood stream and destroy invading microbes*" (Figure 2). Again, from the point of view that nothing really changes, the finance minister responds by remarking that he can't go to a budget committee with that! For a more complete and fascinating account of this history, the reader is referred to Bernard Witkop's authorative article.[5] However, in spite of Ehrlich's remarkable insights it took over one hundred years for the concept of the magic bullet to be realized.

Figure 2. Scene from Hal Wallis' movie. Edward G. Robinson (left) plays Paul Ehrlich.

The modern incarnation of Ehrlich's test tube full of "magic bullets" is the combinatorial antibody library, where 10^{11} different antibodies can be contained in a few hundred microliters of solution. Antibodies from such libraries have found a wide range of uses in the laboratory and medical practice. Despite this extensive delay between concept and utility, therapeutic antibodies are now widely used in clinical practice and, arguably, are the most robust component of today's pharmaceutical pipeline. Today there are 18 antibodies in clinical use for the treatment of diseases ranging from cancer to rheumatoid arthritis. These antibodies generate tens of billions of dollars in annual sales and there are over 370 new antibodies against more than 70 different target antigens currently in clinical trials.[6] However, the number of antibodies in clinical use does not give a complete picture of the therapeutic revolution because several antibodies have multiple indications. For example, humira, an antibody against tumor necrosis factor (TNF), has been approved for treatment of both rheumatoid arthritis and psoriasis, and has shown very promising results in Crohn's disease. Therapeutic

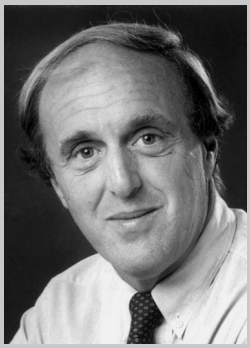

Richard A. Lerner graduated from Northwestern University and obtained an MD at Stanford Medical School in 1964. He then carried out postdoctoral training in experimental pathology at Scripps Clinic and Research Foundation. He currently holds the Cecil H. and Ida M. Green Chair in Chemistry at The Scripps Research Institute. He has received many awards and has been elected to the Royal Swedish Acadamy of Sciences and the United States National Academy of Sciences. He is best known for his work in immunochemistry especially in the area of catalytic antibodies and combinatorial antibody libraries.

 © 2006 Wiley-VCH Verlag GmbH & Co. KGaA, Weinheim

antibody programs are in place in almost every major pharmaceutical company and about 55% of new drug applications are for antibodies.

Given this history, the most often asked question about antibodies is: What happened to allow the emergence of antibody therapeutics? The primary answer is that advances in immunochemistry allowed a chemical solution to the diversity problem. As will be seen, the chemical solution was necessary for a variety of reasons:

1) the true potential of the antibody repertoire could be tapped;
2) the tolerance problem could be circumvented;
3) antibodies could be formatted so as to render them suitable for therapeutic use.

The diversity problem can be most easily grasped when it is formulated in terms of an opportunity rather than a problem. In each individual there are about 1.0×10^8 different antibodies, and prior to the developments described below only a very small percentage of them could be harvested by the biological process of constructing hybridomas[7] Thus, as spectacular as the hybridoma technology is, it can only yield a few of the approximately 1.0×10^8 antibodies in a mouse and did not solve the tolerance problem. Also, hybridomas did not allow for chemical changes to be made to the antibody molecule.

Research into a chemical solution to the diversity problem took as its challenge the task of harvesting, in functional form, the entire antibody repertoire of an individual. Although Ehrlich could not have known about the size of the immune diversity system, the goal of the modern immunochemists was, in fact, the same as his prophetic dream of having thousands of magic bullets in a test tube. Only the modern goal was to have hundreds of billions rather than thousands.

As the technology matured, alternatives to the harvesting of repertoires from animals or humans emerged, and nowadays one or several of the six CDRs of antibodies can often be made synthetically, thereby offering almost unlimited diversity. The combinatorial antibody libraries contain larger numbers of distinct chemical entities (10^{11}) than synthetic chemical libraries of organic compounds (10^6) or natural product libraries (10^4–10^5). Combinatorial antibody libraries start with a diversity that can be three orders of magnitude larger than the natural repertoire of man. The members of these antibody libraries have binding constants for their target (antigen) that are on the order of 10^9–$10^{14}\,\text{M}^{-1}$, which corresponds to several orders of magnitude tighter binding than most small molecules for their target. The combinatorial libraries of antibodies often contain numerous different antibodies with similar affinity for the target, thus representing multiple solutions to the problem of binding to an antigen. The fact that one can obtain multiple solutions to the problem of selective binding underscores the extraordinary power that combinatorial antibody libraries bring to the diversity problem.

While the now thirty-year-old hybridoma technology[7] could, in principle, have recognized antigens of therapeutic interest, the fact that the antibodies were from mice rendered them largely unsuitable for therapy because they are foreign to humans and would be removed by the patients own immune system. An early solution to this problem was devised by Winter and co-workers, whereby mouse antibodies were "humanized" by replacing all the regions except the CDRs with corresponding human antibody sequences.[8,9] The essence of the reasoning was that because the variable regions of antibodies are all different, there is no such thing as a CDR that belongs to any species, in contrast to the constant regions of the molecule that are species specific.

These concepts of Winter and co-workers opened the way to the construction of many therapeutic antibodies.[8,9] However, while one could render a given antibody suitable for therapeutic use, the diversity problem had not been surmounted. Even if one assumes that it would someday be possible to abandon experimental animals altogether in favor of harvesting human hybridomas, the diversity problem remains because one immediately encounters the tolerance problem, which, arguably, was the largest obstacle to fully human therapeutic antibodies. The phenomenon of tolerance is a central point of immunological theory, but a detailed discussion of it is beyond the scope of this Review. Immunological tolerance simply means that the production of antibodies to self is forbidden. This constitutes a major problem for therapeutic human antibodies because, except for infectious agents, the target for such antibodies is something that is conserved among individuals and, therefore, is self.

3. Solving the Diversity Problem with Combinatorial Antibody Libraries

The solution to the problems of diversity and tolerance came when combinatorial antibody libraries were achieved.[10–28] Before defining exactly what a combinatorial antibody library is, one can simply state that it is a device to synthesize unlimited antibody diversity. One can begin by asking about the nature of the driving force that led to the preparation of antibody libraries. Such libraries emerged at a time when research and drug development were uncovering ever more antigenic space. This, in turn, dictated the need for the development of large numbers of antibodies so that for any antigen one can choose from a large variety of chemical solutions to recognition and binding. As the antigenic space expanded, so did the need for more stringency in binding so as to take best advantage of the new knowledge about the growing number of novel antigenic targets. In the not very distant past the goal of immunochemistry was simply to make an antibody that somehow bound to a protein.

Emboldened by new technologies and the knowledge they brought, scientists wanted to dictate the region of the protein where binding occurred, what affinities were appropriate, and even how to provide specificity for rare protein conformations that, for example, distinguished active from inactive states of receptors. A special need was in the area of catalytic antibodies where the mechanism of binding is critical to the success of a catalyst. For example, in an aldolase catalytic antibody one needs to select for a concert of appropriately spaced amino acids including a lysine with a highly shifted pK_a value, which is a rare event. This occurrence is even rarer

© 2006 Wiley-VCH Verlag GmbH & Co. KGaA, Weinheim

when it must approximate the nascent enamine nucleophile to the acceptor carbonyl functionality with acceptable stereoelectronic parameters.[29–34] Then, one may want to repeat the process to harvest a second antibody with the same concert of amino acids differently placed so as to achieve the antipodal reaction. As for binding to rare protein conformations, these are low-probability events that require one to sort through very large numbers of antibodies to find those with a concert of amino acid side chain reactivities that are suitable for catalysis. As will be seen, combinatorial antibody libraries have features that fulfill all these needs.

Most importantly, the combinatorial antibody library allows the creation of an artificial immune system with unlimited diversity. Although many of the consequences of these large numbers will be returned to shortly, let me simply now state that one of their most important features is that they allow for the discovery of binding "jackpots" as well as consensus sequences. A "jackpot" is when in a binding assay the same antibody is recovered multiple times; while a "consensus" is a shared amino acid sequence somewhere within the CDRs of different antibodies. Often a whole binding region of 4–8 amino acids in a CDR is found repeatedly among several different members of the antibody library, thereby demonstrating selection and functional convergence. The events necessary to reach a "jackpot" or consensus occur in the same library, and even in the very same test tube. This same phenomenon is seen when optimizing members of chemical libraries for binding to a common drug target. Different research groups starting with different leads often end up with compounds that have already been synthesized by others. Finally, the combinatorial antibody technology allows antibodies to be handled in a similar way as small molecules in that they can easily be recovered, modified, and produced on a large scale.

4. Requirements of an Artificial Immune System

If the antibody component of the natural immune system is to be mimicked, the artificial system must possess four main features:

1. It must be clonal.
2. It must consist of large numbers of antibodies, equal to or exceeding the complexity of the natural antibody repertoire.
3. Recognition and replication must be linked.
4. It must have a robust mutation strategy to optimize affinity.

To better understand what these features mean and the requirements for their implementation, it is useful to compare the corresponding features of the natural immune system. The key feature of the natural immune system is its clonal nature Figure 3. The clonality of the system means that each cell produces only one type of antibody, so that a repertoire of 1.0×10^8 antibodies requires that they must be provided in a corresponding number of different cells. The B cell is the packaging element that associates a unique pair of heavy and light chains. Antibody specificity is expressed on the cellular

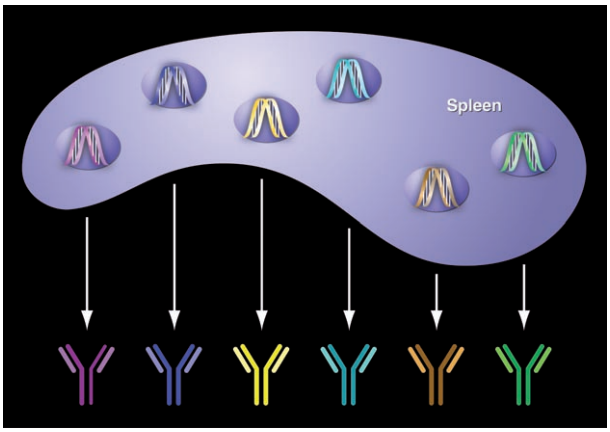

Figure 3. Schematic representation showing the organization of six splenic B cells out of the one hundred million cells, each of which contain a different antibody. Each cell packages a unique heavy- and light-chain combination.

surface, so that when a surface antibody recognizes an antigen the cell displaying an antibody is triggered to divide. Thus, the small numbers of cells that recognize the antigen replicate, while those that do not remain dormant. When the system responds to a challenge, such as a viral infection, the cells capable of responding with an antibody of sufficient affinity ($K_d < 10^{-6}$ M) replicate so that ultimately there are many copies of cells that now each produce either that antibody or a variant that has been improved by mutation. There are many details of this process that are not covered here. However, the key organizational feature of the natural immune system is that it is contained in cellular packages such that each cell contains one heavy and one light chain in combination, and this pairing remains inviolate throughout the course of an immune response

Another very important feature of this clonal expansion system is that it operates with repeated mutation and selection. The need for a biological device that incorporates diversification and selection stems from the fact that the solution to the binding-energy problem must evolve from a starting population of relatively small numbers, and do it quickly if the organism is to survive an infectious assault. The selected cells also start to produce soluble antibody that retains the overall specificity of the original cell-surface antibody, but which may have improved affinity because cellular replication is accompanied by mutation. A key feature of the system is that it is driven by the antigen while producing an ever more efficient product antibody that removes that same antigen. Such a machine that depends on an inducer for replication while simultaneously making a mutable product that lowers the concentration of the inducer will, on thermodynamic grounds, drive toward a higher affinity for the inducer. It is often erroneously stated that the immunological repertoire in a germ line contains antibody to this or that specific antigen. In fact, because of the property of mutation and selection, it is better to think of the system as containing antibodies to no special antigen at the beginning of a cascade, but with the ability to produce antibodies to

 © 2006 Wiley-VCH Verlag GmbH & Co. KGaA, Weinheim

everything at its end.[*] At some early time point in antigen presentation very large numbers obviate the need for mutation and selection, but it is as yet unclear where the crossover point towards fewer antibodies with increased binding energy might occur.

5. Comparison of the Natural Immune System to Combinatorial Antibody Libraries

It is important for what follows to segregate the chemical potential of the immune system from its cellular packaging because the former lends itself to a chemical solution, whereas the later is a physiological device that has evolved in the complex milieu of the whole organism. Thus, one must synthesize diversity and display it in a device that incorporates the principles of the natural immune system, although not necessarily duplicating those elements pertaining to whole animal systems. This way of thinking about creating and selecting antibodies changes a biological problem into one that is largely chemical.

Initially, there were two main problems that one needed to face if the operating principles of the antibody component of the immune system were to be mimicked and perhaps improved. The entire repertoire of heavy and light chains needed to be replicated and the system had to have a packaging feature so that antigen recognition and antibody replication could be linked. The need for the entire repertoire is clear because one did not want to build a system with less diversity than the natural system. If anything, the artificial system should exceed the diversity of the natural one because many constraints are removed when the self/nonself distinction is no longer relevant. The need to link recognition and replication may not be clear to those less familiar with antibody work. It stems from the fact that one must sort through hundreds of millions of individual antibodies to find those with the highest binding energy. Once a high binding affinity antibody is found, the easiest way to recover it nowadays is to use molecular biological methods to harvest the gene(s) that encoded the protein rather than the protein itself. As for the cells of the natural immune system, this reduces the situation to a packaging issue such that each package must contain one heavy and one light chain and the packages must replicate without violating clonality. At this point, it has probably occurred to the reader that if the *entire* system were to be cloned in the ordinary way, it would involve the impossible task of a hundred million cloning events. The solution to this problem lies in the nature of the combinatorial antibody library.

[*] I would be remiss if I failed to point out there is some immunological theory that the antibody repertoire evolved as a response to the challenges that infection posed to the survival of jawed vertebrates starting about 450 million years ago. As such, the repertoire would be biased toward infectious agents, many of which are now extinct. This does not substantially change the landscape, and simply means that a starting clone must show cross-reactivity between today's antigen and an infectious agent that appeared in the evolutionary landscape of the past.

The contrast between the natural antibody system and combinatorial antibody libraries is illustrated in Figure 4. The essence of artificial combinatorial libraries is that the "quantum packing" of the naturally expressed antibody genes is violated by breaking the packages of the heavy and light chains of antibodies, and instead combining the two chains at random. Conceptually, this is the exact opposite of the usual cloning exercise in that one starts with clonality and disrupts it in favor of increased complexity, instead of starting with complexity and reducing it to clonality. When this problem first surfaced, two main conceptual issues immediately arose. The first was that one needed to harvest the entire repertoire of both heavy and light chains. The second was that recognition and replication needed to be linked at some point in the system if there was to be a return to clonality.

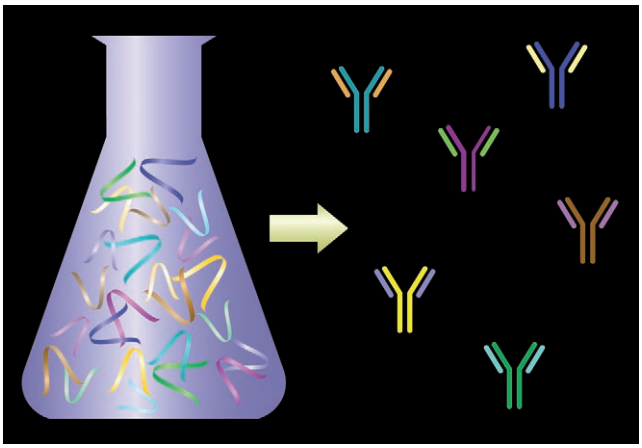

Figure 4. Schematic representation illustrating the key principle that combinatorial antibody libraries are made from a random assortment of antibody heavy and light chains in which the original cellular packaging of the original pairs is disrupted (compare with Figure 3).

6. The Frequency Problem

In the jargon of the time, the need to clone the entire immune repertoire became known as the "frequency problem". The discussion focused on the notion that regardless of the method used, it was mandatory to recover the original pairings. Given that there are about 1.0×10^8 unique pairs of heavy and light chains in an individual, when combined at random this is a combinatorial complexity of 1.0×10^{16}, of which only one out of 1.0×10^8 are the original pair of heavy and light chains. Although possible at the time, searching through 1.0×10^8 clones to find the one original pair was heroic and to search through 1.0×10^{16} clones would not be possible even today. So, what was the point of creating the potential for random combination if after all the trouble one could only get one original antibody?

The solution to the frequency problem came from the realization that the system is degenerate at two levels. At the biochemical level, any heavy and any light chain can pair with each other. The combinatorial diversity is more of a one-way

© 2006 Wiley-VCH Verlag GmbH & Co. KGaA, Weinheim

street in that, in terms of binding energy, many light chains can complement a given heavy chain. The opposite is also true, but the focus has been on complementation of heavy chains because, for genetic reasons, most of the antigen-recognizing diversity is provided by the heavy chain. Also, from the many crystal structures of antibody–antigen complexes, we know that, in many cases, the heavy chains dominate the binding interactions. In fact, as it turns out, nature also used this degeneracy principle. A more refined look at the antibody genes of an individual shows that there are about 55000 possible heavy-chain genes and only about 3000 possible light-chain genes that together encode the chain pairs of different antibodies. This skewing in favor of heavy-chain diversity has one minor and one major consequence for the construction of antibody libraries. The minor consequence is that it reduces the size of the combinatorial matrix that is required if one only wishes to duplicate the natural repertoire. The major consequence is that there is much room to increase light-chain diversity to match that of the heavy chains. However, as will be seen later, unnatural light chains may be far much more than neutral with respect to binding energy.

Setting aside the more arcane details of complementarily, it is the intrinsic degeneracy of the system that enables the success of combinatorial antibody libraries. Put another way, the antibody to everything and the antibody to nothing aspect of the system is preserved. It is simply a matter of binding energies and numbers, where the number of possible solutions to binding increases as a function of the individual attempts.

7. Linking Recognition and Replication

Once it was realized that the chemical solution to the diversity problem required disruption of the co-packaging of the original antibody chain pairs, attention turned to where in the process clonality should be reestablished by repackaging so that each new pair could be treated as a single entity. In principle one could deal with the proteins, but it was evident that one needed a genetic solution because we are much better equipped to recover a few copies of a gene than to recover a few copies of its corresponding protein. Such a genetic solution required two levels of linkage. First, the genes for the heavy and light chains needed to be linked to each other, and then they had to be linked to the proteins they encoded in a manner that allowed the package to be recovered and replicated. The requirement for replication is simply the need to amplify binding events that may be very rare.

With this set of requirements, viruses immediately come to mind.[13,14] In particular, one could envision the construction of a system in which there are a large number of replicating particles in which genes that encode the individual antibody pairs are on the inside and the corresponding proteins are on the outside. Either the proteins could be expressed in viral plaques or could actually be physically linked to the surface of the virion. In this way the entire packaging element could be selected on the basis of its ability to bind to the antigen and then replicated. This was the incarnation of Ehrlich's "magic bullet", in that hundreds of millions of different antibodies could be provided in a test tube containing only a couple of hundred microliters of solution. Moreover, any antibody of interest, even if it were a single molecule, could be replicated. For therapeutic antibodies, the exciting concept was that one could bottle the entire diversity system of an individual in a test tube. Moreover, if the unnatural pairs are considered, the diversity could be thousands of times greater than that which existed in the individual. In regards to the current state of the art, it is worth noting that commercial antibody companies, such as Cambridge Antibody Technologies, have combinatorial antibody libraries in phage that contain more than 100 billion distinct antibodies.[35]

Several solutions for the construction of the package that links replication and replication have emerged (Figure 5), but in each the central concept is that antibodies of a single specificity are expressed by the replicating package and the genes that encode the antibody chains are on the inside.[13,14,36–68] The antibody genes are arranged so that

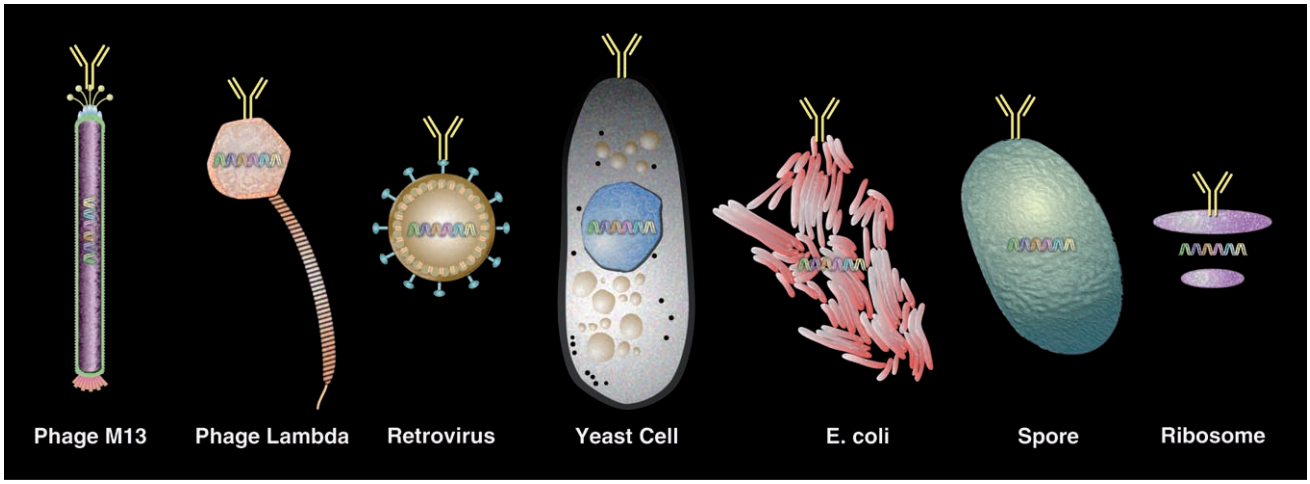

Figure 5. A variety of systems that have been used to link the replication and recognition of antibody genes and their encoded proteins so that members of the combinatorial antibody library can be selected and replicated.

 © 2006 Wiley-VCH Verlag GmbH & Co. KGaA, Weinheim

they replicate in tandem with the genes that encode the elements of the package. One such popular device is illustrated in Figure 6, where the antibody is expressed on the surface of the filamentous phage M13 and the genes that encode it are contained in the interior of the viral particle. The M13 virus is a micrometer-long rod that has four proteins on one end of the rod that are encoded by gene 3 of the virus.[69,70] The trick is to develop a genetic construction that inserts itself into the virus maturation process such that the antibody expression is linked to one (or rarely two) of the four gene 3 encoded proteins, while the gene that encoded the antibody is packaged inside the virus.

The various methods to accomplish this seemingly formidable task can be found in the original references.[13,14] However, there is an interesting chemical point that is worth noting here. One main task of the system is to cause the two antibody chains to pair up. This is easily accomplished when both chains are directed to the periplasmic space of *E. coli*. for assembly. The volume of the periplasmic space is less than 1.0×10^{-15} liters, which contains only a few hundred molecules, but at micromolar concentration, which greatly exceeds the nanomolar formation constant of chain pairing. Furthermore, yield is not relevant in the usual sense applied to chemical synthesis because the reaction products replicate.

Visualization of the system can be seen in Figure 7 where a combinatorial antibody library was constructed against the

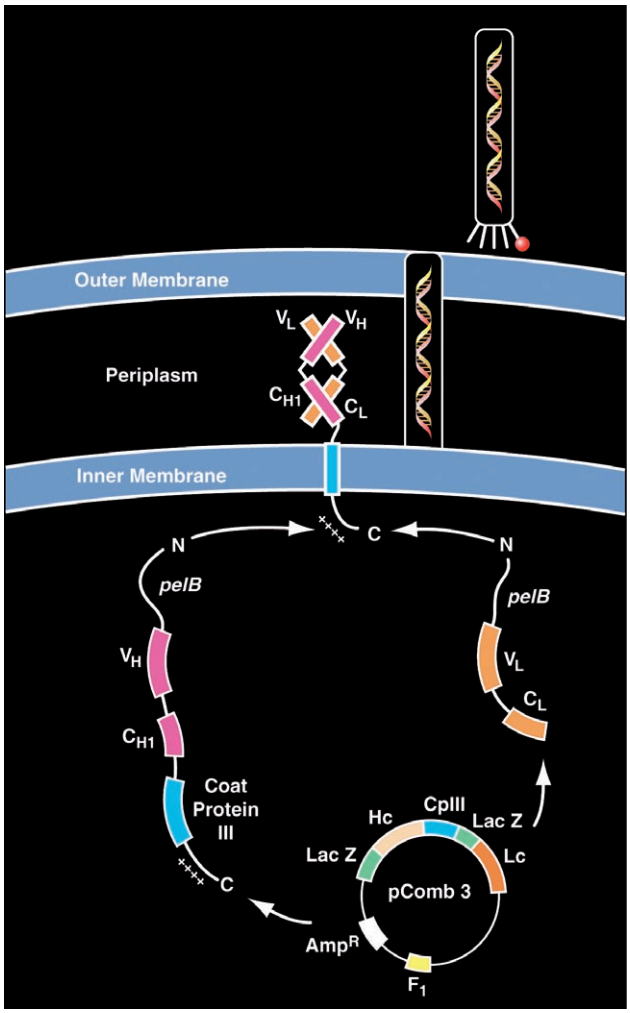

Figure 6. A system for expressing antibody heavy and light genes in phage M13. The pComb 3 phagemid vector can accommodate the light-chain (V_L and C_L) and heavy-chain genes (V_H and C_{H1}). The heavy-chain gene construct also encodes the viral gene 3 protein. In practice the antibody heavy- and light-chain gene products are directed to the periplasmic space by the pelB leader sequence where they assemble and become attached to the gene 3 protein of the phage during virus maturation and assembly. In a sense, the virus is tricked into incorporating the antibody molecule because it is attached to its own gene 3 protein (red dot upper right). As "helper" virus is used, there are two types of gene 3 protein present in the cell: native gene 3 protein that is required for infection and gene 3 protein with an antibody molecule affixed. The ratio of these proteins on the phage surface is determined by competition during viral assembly and maturation, but only phage bearing antibodies are selectable on the antigen during a process called "panning". Finally, the gene that encoded the heavy- and light-chain proteins is packaged inside the virus. In the presence of "helper" virus, the phage F1 intergenic region in the vector allows the single-stranded phagemid to be packaged inside the virus. The net effect is that one has a phage particle with an antibody on the outside (red dot upper right) and the gene that encoded it on the inside.

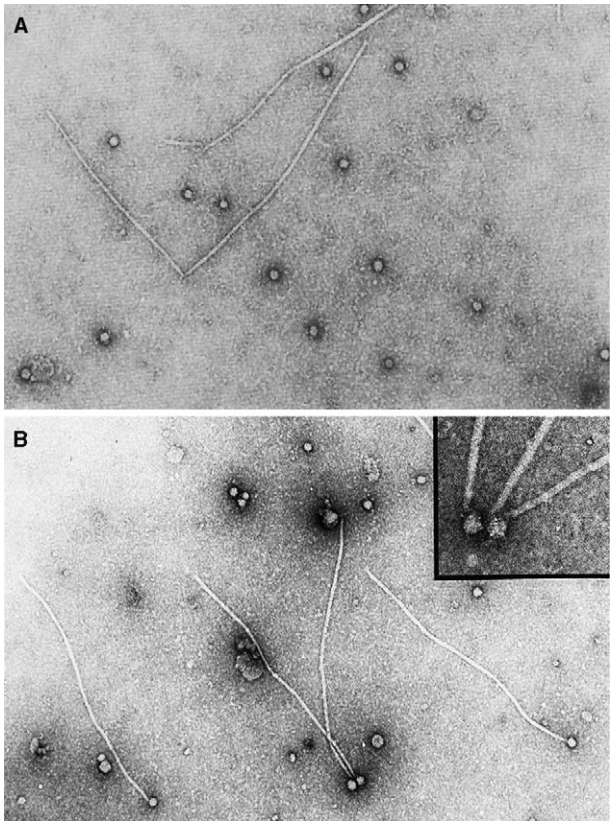

Figure 7. Electron microscopy image of HBsAg particles and filamentous phage. Fresh phage were prepared from the pre-pan stage (A) or third pan stage (B) of the JM_K library and incubated with HBsAG particles for 30 min. These complexes were added to rabbit anti-HBsAg antibody attached to a grid and then were washed, fixed, and negatively stained. The grids were viewed with a Hitachi electron microscope. Note that in the upper panel (control) none of the phage rods are attached at their ends to hepatitis B particles (small spheres) whereas in the lower panel all phage (antibody-containing) are attached to the the hepatitis B virions.[71] Copyright National Academy of Sciences.

 © 2006 Wiley-VCH Verlag GmbH & Co. KGaA, Weinheim

hepatitis B virus. As both the phage and the hepatitis virus are of sufficient size to be visualized by electron microscopy, the ultrastructure of their relationship can be observed.[71] Note that every phage particle (rod) is attached to the hepatitis B virus (spherical particle), and that the only point of attachment is on the end of the phage where the antibody is expressed on the gene 3 protein. Although there is usually one binding event, the inset shows an example of two phage rods attached to a common hepatitis virus particle. This can occur because the hepatitis virus coat is constructed out of many copies of a single protein (the antigen). As the gene 3 protein also is required for phage attachment to *E. coli*, during infection not all four gene 3 proteins can be derivatized by the antibody, or the phage will not be infectious. Thus, any phage with four antibodies can not be selected, even if it binds to the antigen. Although it is not known with certainty, there are likely to be steric considerations that usually restrict the gene 3 constructs to single copy expression of antibodies. While it is not considered here, an alternative is to express multiple copies of the antibody along the length of the phage rod by attaching the chains to the gene 8 protein, whose 2700 copies make up the helical surface of the one-micrometer-long phage rod.[69,70] Although this approach has found some applications, its drawback is that, in contrast to the gene 3 protein site, the large copy number of antibodies attached to the gene 8 proteins allows selection of weakly binding antibodies that may not be effective as single molecules, but are selected as an entire surface that is covered by them.

8. A Solution to the Tolerance Problem Results from the Unnatural Pairs

One of the most important factors of the combinatorial antibody libraries is that they offer a solution to the tolerance problem posed in vivo. As with other aspects of immunochemistry discussed here, the problem of immunological tolerance is a subject of much discussion and investigation, and is beyond the scope of this Review. For our purposes, it can simply be stated that immunological tolerance means that one can not make an antibody to self. Thus, the biological generation of human antibodies to human proteins is forbidden. This is a problem for therapeutic antibodies because, except for infectious diseases, most therapeutic antibodies are directed to a target that is self. Usually one wants to remove a pathogenic compound from the body, such as a molecule toxic to the joints in the case of rheumatoid arthritis or a cancer cell that has a unique cell-surface epitope. However, because the biological phenomenon of tolerance operates at the cellular level, which by definition involves the natural heavy- and light-chain pairs, it need not extend to the unnatural pairs. In other words, tolerance is not involved when the solution to antigen binding is purely chemical. Thus, as can be seen in Figure 8, the 10 unique heavy and 10 unique light chains from 10 different antibodies shown in the example yield a combinatorial library of 100 antibodies, of which 90 are composed of the unnatural pairs. If this library were human, the therapeutic antibodies might well be selected from this pool of unnatural pairs.

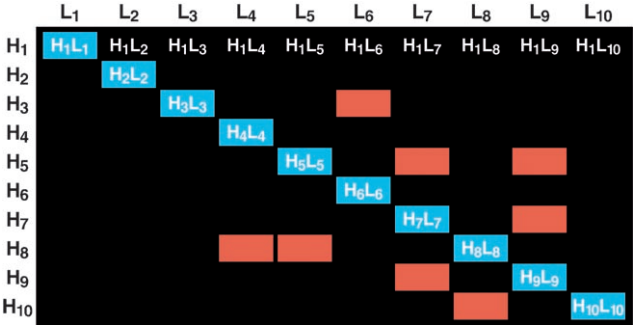

Figure 8. A theoretical library made from 10 antibodies in which the heavy and light chains are separated then recombined. Only 10 of the 100 recombinants are the original pairs (blue diagonal), while 90 are non-original pairs.

9. Summary of the Main Features of Combinatorial Antibody Libraries

Before turning to experimental examples that illustrate some of the main conceptual features of combinatorial antibody libraries, it is worth summarizing those features here.

1. Immunization is not required.
2. The libraries are not subject to tolerance.
3. The libraries are not limited to natural specificities because of the opportunity for creating novel heavy–light chain pairs.
4. Antibodies can be harvested from humans as clonal entities.
5. Any antibody ever made by the organism can be harvested, regardless of whether if it is currently being produced.
6. One has access to very rare specificities.
7. Antigens need not be immunogenic in vivo, for example, crystals and metal ions.
8. The libraries allow the analysis of a "jackpot" and determination of chemical consensus.
9. Combinatorial antibody libraries offer a platform from which one can improve upon antibody affinity.

10. Synthetic Antibodies, Nonimmunogenic Antigens, and the Meaning of "Jackpot" and Chemical Consensus

When one generates combinatorial antibody libraries, the experimenter has two choices as to the source of the antibody genes. They can be harvested from an animal (immunized or nonimmunized) or the oligonucleotides encoding the six CDRs can simply be synthesized. As an example, consider a study of the ability of a totally synthetic antibody library to bind to metal ions and crystals of inorganic molecules.[72] These are some of the simplest possible targets. In this case the genes encoding the antibody CDRs were synthetic and totally randomized (Figure 9). The binding energy was achieved by the approximation in three-dimensional space of the six synthetic CDRs to achieve a coordination complex.

 © 2006 Wiley-VCH Verlag GmbH & Co. KGaA, Weinheim

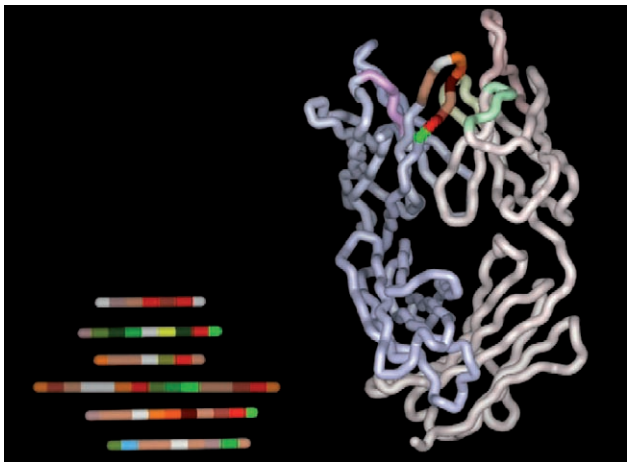

Figure 9. A representation of the six synthetic antibody CDRS (lower left) in the context of their location in the antibody molecule. The antibody-combining site cavity (top) and the six CDR loops that form the three-dimensional combinatorial matrix are more easily appreciated than in the space-filling format of Figure 1.

The library under consideration is of modest diversity, with only 1.0×10^8 unique members. Antibody clones were selected for their ability to bind to copper, cerium, zinc, iron, or lead ions or to magnetite crystals. Needless to say none of these antigens are immunogenic in that, unlike proteins and small-molecule haptens, they are incapable of inducing antibodies when injected into animals. Indeed, magnetite crystals cannot even be injected as such. Prior to selection, the metal ions were bound to chelating sepharose gel, and antibody-containing phage that bound to the metal ions were selected. In the case of magnetite crystals, advantage was taken of the magnetic nature of the crystals to separate binding from nonbinding phage. After exposing the crystals to the phage library, a simple magnet was used to separate the crystals and their bound phage containing binding antibodies from bulk solution.[72]

The sequences of the CDRs of several different antibodies selected for metal-ion binding are shown in Figure 10. Note that for each metal ion all the sequences are different. Thus, in the absence of chemical knowledge, there is no direct suggestion of the best way to achieve binding to the metal ions. However, once one applies knowledge of coordination chemistry, the mechanism of antibody–metal binding becomes apparent. For example, many of the sequences that were selected for Cu^{2+} and Zn^{2+} binding are rich in histidine, consistent with the known role of nitrogenous ligands in coordination complexes with these metal cations. Indeed, metalloenzymes utilize multiple imidazole rings in their active sites to coordinate copper and zinc ions. An analysis of the other sequences will reveal much to those interested in metal-ion coordination at protein–enzyme active sites. However, we can simply say that the large number of antibodies selected revealed a large number of chemical solutions to the metal-coordination problem, although no clear consensus was apparent. Nevertheless, one begins to see already the importance of obtaining a large number of solutions to a binding problem. Comparative analysis of multiple antibodies that are capable of binding to the same target illuminates details that can not be seen when only a few events are studied.

Cu^{2+}	Ce^{3+}	Pb^{2+}
GRVHHHSLDV	GQVMZELGDA	GNLRRKTSDI
SWKHHAHWDV	GLTEZQLQDG	GESDSKREDG
GSWDHRGCDG	GYSYSVSPDA	GGPSLAVGDW
GHHMYGGWDH	GRLGLVMTDE	GPLQHTYPDY
GHWGRHSLDT	STWPGRQRLGZALSDS	GWKVTAEDSTEGLFDL
GHILHHQLDL	GYELSWGVDZQEWWDI	GTRVWRVCQWNHEEDG
SSQRLMLGDN	GPVRGLDZSKGVRYDN	GEWWCSFAMCPARWDF
SHHGHHYLNH	GLSZHIVSETQSSGDL	GDTIFGVTMGYYAMDV
GKLMMSWCRDTEGCDH	GLESLKVLGVZLGGDL	
GDTHRGHLRHHLPHDW	GNMILGGPGCWSSADI	
GWGLWMKPFVWRAWDM	GCWNVZRLVVYHPPDG	Fe^{3+}
	GFEVTCSWFGHWGRDS	SASMRSAIGLWRTMDY
Zn^{2+}		GDREIFHMZWPLRVDV
SHTHALPLDF		SZNPQQVCGVRCGZDK
GRVHHHSLDV		GNRLSSGHLLKQGZDG
GQSSGGDTDD		GGSDWZIGACCREDDL
GQWTPRGDDF		GMVSMMGQSRPTQCDC
GRCCPSSCDE		GVIKWIRRWVRTARDV
GPAKHRHRHVGQMHDS		GWFWRLLPTPRAPSDV

Figure 10. Amino acid sequences of HCDR3 regions selected for binding various metal ions. Z represents an amber stop codon, which, in the supE strain used for expression, is translated as Q. [72]

When one studies antibodies that were selected for binding to magnetite crystals (iron oxide, Fe_2O_3) one sees a qualitative yet important difference in the selected antibody sequences (Figure 11). There are eight protein sequences in which two different sequences are each repeated three times. This is the "jackpot" that library workers look for because in a library of 10^8 different members there is little chance that the same sequences would appear repeatedly at random, the "jackpot" means that within the sequences one has a chemical solution to binding. It is important to realize that in a true "jackpot" the degeneracy of the genetic code allows different nucleotides to encode the same protein sequence, so that the genes for each antibody sequence may actually be different. Consequently, the selection at the protein level is for different members of the library rather than for duplicates. However, in very large libraries the selection of duplicates can give important information regarding binding preferences.

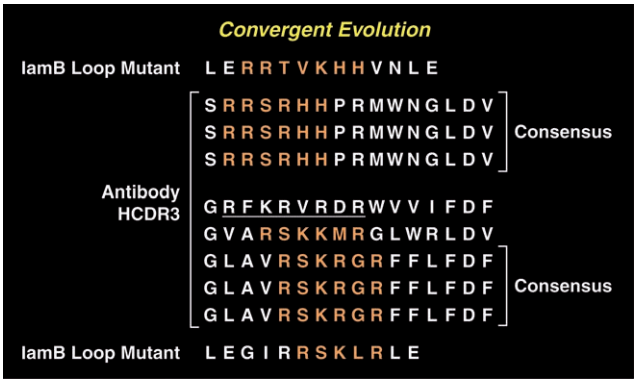

Figure 11. Comparison of amino acid sequences of the HCDR3 regions selected for binding to magnetite with lamB mutants, which were selected in a similar manner. Boxed regions highlight the similarities between the clones. The underlined region of the third clone highlights an unusual basic region.[72] Copyright National Academy of Sciences.

As powerful as a "jackpot" is, one does not yet know which of the amino acid residues are most important and which are degenerate. This information can be obtained by

 © 2006 Wiley-VCH Verlag GmbH & Co. KGaA, Weinheim

determining a "consensus" sequence based on antibodies that bind the target but are not a member of any selected "jackpot". We see such a sequence in Figure 11 where it can be observed that the RSK motif of one "jackpot" (lower set of sequences) is preserved, while the rest of the sequence is different. Thus, on the basis of selection from a large number of antibodies, analysis of the "jackpot" and consensus informs us that the RSK motif is an important element in the binding energy. In this analysis there is one antibody that does not share homology with either "jackpot", and all that one can say is that, similar to the members of the "jackpot", it is rich in basic amino acid residues that appear at the exact same position as those in one of the "jackpot sequences". Thus, its value in determining how binding energy is achieved is only realized when it is considered in context with other members of the "jackpot" ensemble, again illustrating the power of obtaining and analyzing large numbers of chemical solutions for antibody–antigen binding.

In nature the process of Darwinian evolution proceeds by mutation and selective amplification so as to provide an advantageous solution to a physiological problem. In enzyme evolution, for example, the selection might result in an improved catalytic rate (k_{cat}) or optimization for selectivity of binding of a given substrate (K_D). Often there is a preferred answer to the problem, and multiple systems are found to converge on a common answer through what is termed convergent evolution. The analysis of a selected antibody library is similar in that we look for convergence in the solution to a binding problem. So far in this discussion mutation and selection have not been considered because at some level the use of very large numbers can obviate this need. The question is whether the advantage of having large numbers in the first place can compete with the power of repeated mutation and selection that allows refinement of particular solutions. The answer to this important question depends on how many independent solutions one can start with versus the amount of time required for mutation and selection to generate an improved solution. One expects that the answer will be very system-dependent. However, it is known that one can see convergence among systems in the laboratory when the different libraries contain large numbers of potential solutions. One question that can be asked is whether there is convergence between antibodies and other nonimmune proteins when they are each selected to bind to the same antigen. The amino acid sequences used by the nonimmune proteins to achieve binding are often similar to those found in antibodies. A case in point is binding to magnetite. A separate group of researchers selected for *E. coli*.variants that would bind to magnetite by using random sequences inserted into the phage lambda receptor protein (LamB), which is on the surface of the bacterium.[65,66,73] They selected two sequences that are highly homologous to those found in the antibody "jackpots" isolated from approximately 10^6 random sequences (Figure 11). This is a dramatic example of convergent evolution in that the overall protein fold of the antibodies and LamB are doubtless different, yet very similar sequences were selected in both contexts. In summary, access to large numbers of antibodies allows the assessment of chemical solutions to a binding problem. The important features are "jackpot", consensus, and convergent evolution. As will be seen, the important point is that although these features were originally revealed for the simplest of antigens, they apply similarly when important therapeutic antibodies are considered.

11. Obtaining Useful Diversity Exceeding the Natural Repertoire by Chain Shuffling

We have already discussed how combinatorial libraries can be used to harvest antibodies that circumvent the tolerance problem, which is important because most therapeutic antibodies are intrinsically directed against self. Given what is now known, one would expect that the protocols for construction and screening antibody libraries would be more or less fixed. However, the means by which the therapeutic antibody humira was selected is somewhat unusual and illustrates several concepts. Humira is an antibody against tumor necrosis factor alpha (TNF), a strong inflammatory lymphokine, which when present in high concentration causes much of the injury associated with psoriasis and rheumatoid arthritis. Thus, removal of this self-antigen would be expected to have therapeutic value and, indeed, such antibodies constitute an important therapeutic class of drugs that are used worldwide. Humira was developed by Cambridge Antibody Technologies (now owned by Astra–Zeneca). In essence they started with a mouse antibody to TNF as a template for the selection of a human antibody. Their procedure is illustrated in Figure 12. The central idea was to use a known mouse monoclonal antibody against TNF as a template. Libraries of human light and heavy chains were used to select those that would complement the heavy and light chains, respectively, of the mouse antibody. These

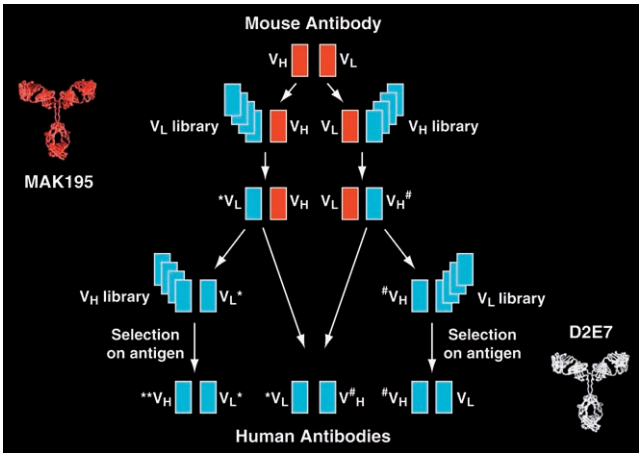

Figure 12. Method used to generate humira (D2E7). The antibody molecule in red (upper left) is the mouse monoclonal antibody MAK195, while the antibody in white (lower right) is the therapeutic antibody D2E7. The blue boxes indicate human antibody chains and the red boxes indicate mouse antibody chains. The MAK195 mouse monoclonal antibody was used as a template to select complementary human heavy and light chains in what was largely a template-guided shuffling exercise. The Figure is courtesy of Sir Gregory Winter.

 © 2006 Wiley-VCH Verlag GmbH & Co. KGaA, Weinheim

preselected human chains were then recombined into what is now a fully human antibody.

To a first approximation, the protocol that led to humira restricted the number of antibody chains that could be considered in the final library because every member was required to have already demonstrated competence in a complementation analysis. However, given the power of modern screens to access large libraries, the template step may not be necessary because all combinations, including those that might be selected by complementation, are already present in the large starting library. Nowadays diversity is not an issue, and the problem is mainly one of access to members of the library. Nevertheless, the elegant method used to select the important fully human therapeutic antibody humira illustrates the principle of chain shuffling, which has it roots in the chain-degeneracy principle discussed earlier.[24,74,75] Also, the use of non-original pairs to generate human antibodies to self is underscored. I like to refer to this as "my great grandfathers axe problem" because it reflects the great tradition that compels one to preserve historical roots. When contemplating a historical site, one might observe that this is the building where one's ancestor had worked 800 years ago even though the inside was replaced 400 years ago and the outside was replaced in the last century. Or one can say that this is my great grandfather's axe, although my grandfather replaced the blade and my father replaced the handle.

12. Access of Very Rare Antibody Specifities for Therapy

Figure 13 represents, in schematic fashion, a feature of antibody libraries that allows access to any antibody an individual or population of individuals has ever produced, regardless of whether the antibody is currently being produced by these individuals. In essence, the entire immunological history of an individual or population is now contained in a few hundred microliters of solution. This concept is termed the "fossil record" of an immunological history.[76] For most of its modern incarnation, immunochemistry was limited in its access to the repertoire of antibodies currently being produced by an individual. The goal of these activities was largely diagnostic, where one wanted to obtain information about an infection or active autoimmunity. Thus, if an individual had an increasing antibody titer to a virus, this was evidence of a recent infection. Likewise, antibodies to self, such as the presence of anti-DNA antibodies, gave evidence of an autoimmune disease. However, once the infection had subsided, evidence of its presence often retreated into the memory of the immune system.

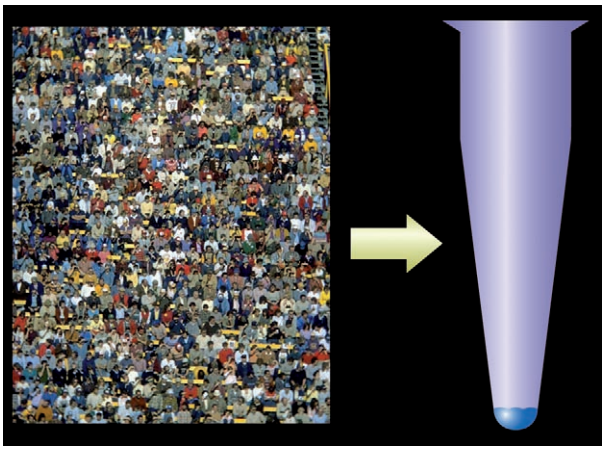

Figure 13. A visual underscoring that the method of combinatorial libraries allows one to "bottle" the antibody repertoire of an individual or population of individuals in only a few hundred microliters. Since one obtains the genes and expressed proteins for any antibody ever made, the library is termed the "fossil record" of an individual's immunological history. Since the record was obtained from the genes, incorporation into the record is not conditioned on current production of the antibody.

Immunological memory simply means that the lymphocyte clones that proliferated during an immune response are not totally eliminated, and are stored as memory cells to be activated should the assault reoccur. This phenomenon underlies the concept of vaccination, which depends not so much on maintaining the presence of circulating antibodies, but rather on giving the immune system a head start. Once there is the memory of an antigen (vaccine), the immune system can mount a so-called secondary response that is much faster than a primary response because there is a ready pool of highly evolved and selected lymphocytes that can quickly re-emerge. These memory cells do not produce much antibody for export; their production is largely limited to their plasma membrane, where it functions as an antigen receptor. However, because antibody libraries operate at the gene level one can recover the genetic record of an individual's immunological history regardless of the rarity of a particular antibody in the storage compartment.

There is one additional concept to be considered before giving an experimental example of how the "fossil record" was used to access rare antibody specificities. This is the concept of immunological surveillance that pertains to the notion that malignant cellular transformations occur regularly, but most often they are recognized by the immune system as foreign, and the transformed cells are destroyed before they can take hold as a malignancy. The existence of this phenomenon has been difficult to prove because, as just discussed, we could not expect much evidence to remain at the antibody protein level for such a process once the transformed cell has been eliminated. To use combinatorial antibody libraries to test these ideas, an antibody library was constructed from 20 cancer patients with a variety of malignancies.[77] This library was challenged to see if it would yield antibodies specific for metastatic cells. The screening method is illustrated in Figures 14 and 15. Cells from a human breast cancer were selected for those that metastasize and those that do not. Then antibodies from the library were selected for those that only bound to the cells that metastasize. The presence in the library of such antibodies turned out to be very rare and only three out of 1.0×10^8 clones had such a property. Further analysis of these antibodies showed them to have remarkable features that went beyond the fact that they were rare.[77] The first clue to their uniqueness was that they required divalent cations to

© 2006 Wiley-VCH Verlag GmbH & Co. KGaA, Weinheim

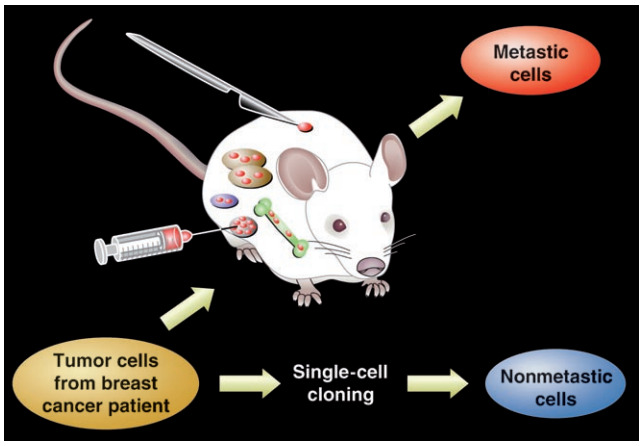

Figure 14. Method used to select for breast cancer cells with metastatic and nonmetastatic phenotypes. Human breast cancer cells were passed through mice to select cell clones that either always or never metastasize. These human cells were harvested from the mammary fat pad and various other mouse organs. They were cloned to obtain permanent lines with either the metastatic or nonmetastatic phenotype.

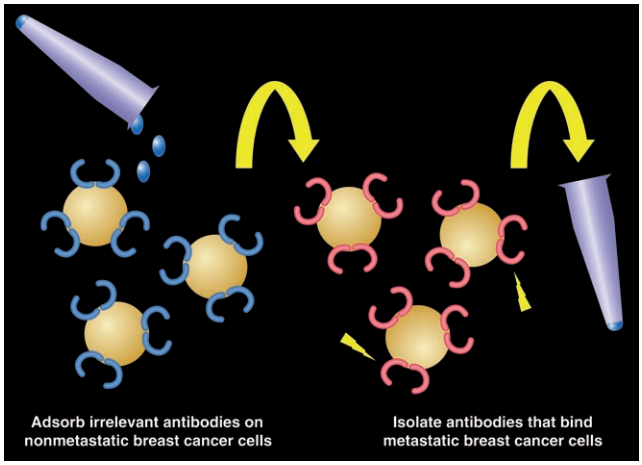

Figure 15. Method used to select antibodies that bound only to a metastatic cell. Combinatorial antibody libraries in phage from 20 cancer patients with breast cancer were first selected on nonmetastatic cells to remove antibodies that were just directed to nonmetastatic cancer cells. Phage remaining after the initial screen were then selected for those that selectively bind to metastatic breast cancer cells.

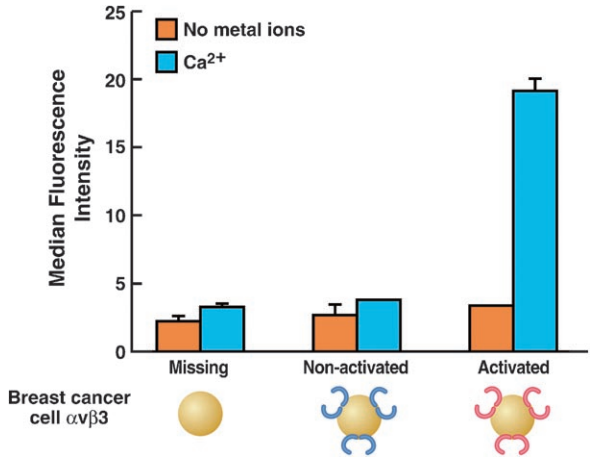

Figure 16. Combinatorial antibodies that selectively bound metastatic human breast cancer cells required three conditions to bind: 1) The cells had to have the integrin αvβ3 on their surface, 2) the integrin had to be activated, and 3) divalent cations had to be present. A fluorescence method was used to detect the antibodies binding to the cell surface of cells.

bind to the cells (Figure 16). This was reminiscent of a similar requirement when integrin molecules bind to their activated receptors. With this clue in hand, it was not long until it was revealed that the antigenic target for these rare antibodies was, in fact, an integrin molecule. More interestingly, the selected antibodies not only bound to the integrn αvβ3, but were further restricted to the activated form of the integrin molecule Figure 16). Indeed, metatastic cells are known to have the activated form of this integrin, in which activation is likely accompanied by a conformational change in the protein. The final surprise came when these antibodies were sequenced and shown to contain the argenine-glycine-aspartic acid (RGD) amino acid motif which forms the centerpiece in the binding of all natural ligands to integrins (Figure 17). This RGD sequence in the antibody was required for recognition of the metatastic tumor cells by their integrins (Figure 17) because binding was lost when it was mutated to RGE. Thus, as seen earlier for simple antibodies to magnetite, there is a remarkable convergence of sequences used by both rare human antibodies and natural ligands in their binding to the integrin αvβ3. However, what do these antibodies do? In subsequent studies the antibodies were shown both to block cells from metastasizing to the lungs of mice and reduce existing metastasis (Figures 18 and 19). The mechanism by which these antibodies function was revealed by cellular studies, in which it was shown that after binding, these antibodies—together with their surface antigen—are internalized, and likely induce cell death by an apoptotic mechanism (Figure 20). It is important to note that when the key RGD sequence was mutated to RGE the biological effects of these antibodies disappeared, thus verifying the importance of precise convergence. These antibodies are now being pursued for clinical trials in cancer, where it is hoped to take advantage of the fact that they are human and that they are directed to a rare specific antigen on cancer cells.

Given the rare and interesting specificity of these selected anti-integrin antibodies, it is interesting to step back and consider them more conceptually. Natural evolution has selected the interaction between the integrin and the RGD motif of the ligand for recognition in a process that evolved over millions of years. The surprise is that antibodies evolved the same recognition motif, likely in a cancer-induced immune response, in the time frame of weeks. This is remarkable because an antibody could have chosen to bind any region of the integrin antigen, but it chose the RGD in the same way as the natural recognition interaction. Furthermore, once the RGD site was chosen, the antibody could have recognized it in any number of ways, but chose RGD. The reason this can happen is because the immune response is a

 © 2006 Wiley-VCH Verlag GmbH & Co. KGaA, Weinheim

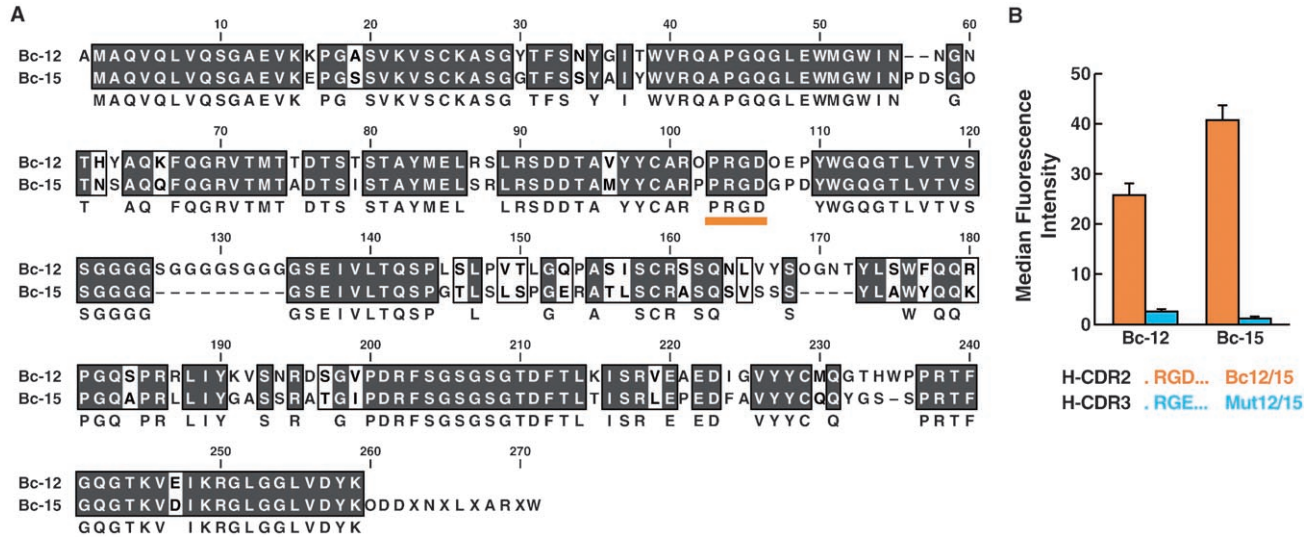

Figure 17. Translation of scFv DNA sequence analyses of antibodies selective for metastatic breast cancer cells. Consensus sequence of Bc-12 and Bc-15 (specific for activated αvβ3), compared with Bc-20 (reactive with non-activated αvβ3). Flow cytometric analysis (right) with BMS human breast cancer cells indicates loss of binding in mutants of Bc-12 and Bc-15 containing RGE instead of RGD in CDR-H3 (Mut-12 and Mut-15). The Mut-15 signal is equivalent to a negative control.[77] Copyright National Academy of Sciences.

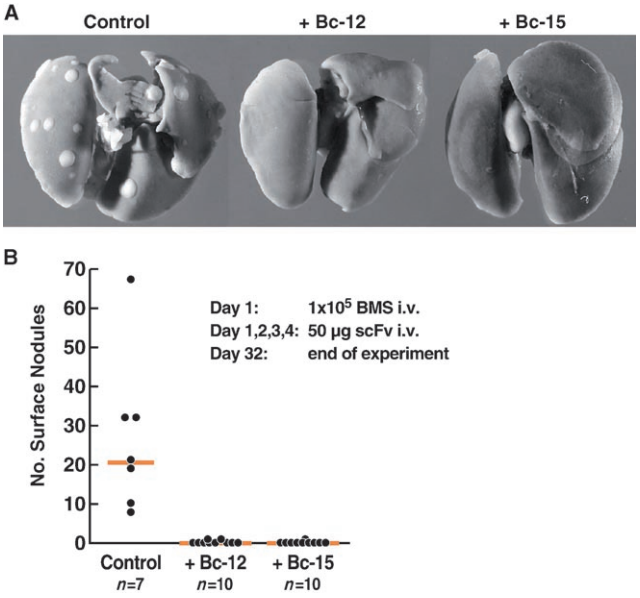

Figure 18. Effect of Bc-12 and Bc-15 on lung colonization by human breast cancer cells. A) Lungs of female mice with severe combined immunodeficiency 32 days after intravenous injection with 1×10^5 BMS cells. The mice were treated with either 50 µg of Bc-12 or Bc-15 (intravenous) on days 1, 2, 3, and 4. Controls received phosphate-buffered saline (PBS). B) Number of lung-surface metastases for each animal. The horizontal line indicates the median number of metastases per group. ScFv-treated mice, had significantly fewer metastases ($P<0.001$ by the Kruskal–Wallis test).[77] Copyright National Academy of Sciences.

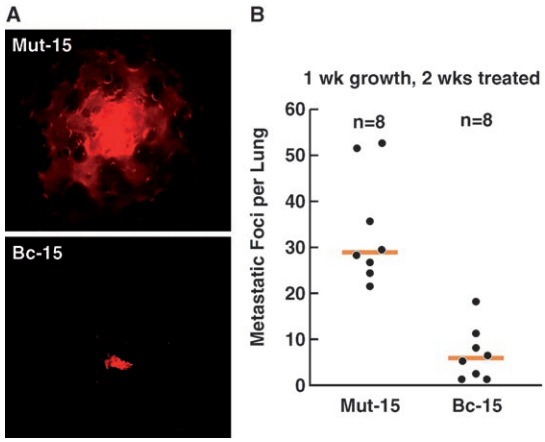

Figure 19. Effect of Bc-15 treatment on established breast cancer metastasis in the lungs. A) Female mice with severe combined immunodeficiency were injected intraveneously with 5×10^5 DsRed2-tagged MDA-MB-435 breast cancer cells expressing constitutively activated integrin $\alpha v\beta3_{D723R}$. Mice were treated on days 7, 9, 11, 14, 16, and 18 by intravenous injections of either scFvBc-15 or its RGE mutant Mut-15 (40 µg per does). Metastatic foci were enumerated by fluorescence microscopy on day 19. The images show the typical tumor foci within the lung tissue in Mut-15-treated (upper) or Bc-15-treated (lower) mice. B) Number of metastatic foci within the lung tissue of each animal. The horizontal line shows the median number of metastases per group. Bc-15-treated mice had significantly fewer metastases than Mut-15-treated mice ($P<0.001$ by the two sided Mann–Whitney U test).[77] Copyright National Academy of Sciences.

binding-energy machine that will drive toward the highest possible binding energy and, thus, one expects this process to converge on the same optimal protein–protein interaction solutions that natural selection has evolved. This idea is, of course, conditioned on the notion that there are a restricted number of optimal solutions to a given binding-energy problem. Further evidence for this will be given in the next section.

Another area in which the ability to access the "fossil record" has yielded important results and potential therapeutic antibodies is in infectious disease. This is an arena where the combinatorial antibody technology has proved

 © 2006 Wiley-VCH Verlag GmbH & Co. KGaA, Weinheim

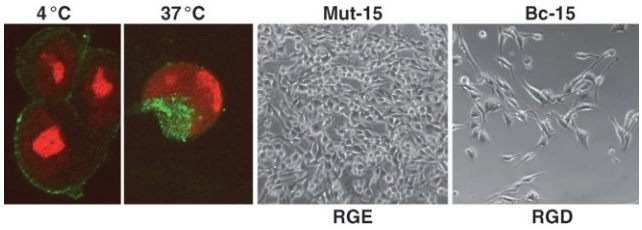

Figure 20. Studies on the mechanism of cell injury by antibodies to activated αvβ3. Patient-derived ligand-mimetic scFvs against activated αvβ3 are internalized and affect the survival of breast cancer cells. Antibody scFv Bc-15 is internalized by breast cancer cells isolated from patient blood: confocal images of BMS cells incubated for 4 h with FITC-Bc-15 at 4 °C (binding) versus 37 °C (allowing internalization). The internalized antibody also kills the cells by an apoptotic mechanism. Note the mutant antibody that contains RGE instead of RGD does not kill the cells.[77] Copyright National Academy of Sciences.

itself to be particularly robust.[78–104] In infections, antibody records from a set of individuals can give evidence about the nature of the evolutionary contest between viruses and antibodies, something that Burton et al. have termed the "clash of evolutionary titans".[101] It is instructive to note from their work how often a single research group can return to a comprehensive library to "check out" different human antibodies with interesting specifities.

13. The Missing Piece Solved: Mutation Strategies

If one were to ask some scientists what is missing if the power of the natural immune system were to be duplicated, they would respond that it requires selection and not simply screening. The natural system derives its power from the evolutionary process of mutation and selection, while combinatorial antibody libraries rely on the screening of large numbers. A central question for the field is whether a chemical approach to binding energy that uses very large numbers of potential solutions can duplicate or even exceed that of the more random evolutionary process of nature. In essence the question is: Can chemistry equal the power of the biological process of mutation and selection? There are many reasons to suspect that this may be true because, in spite of its power, the natural immune system has constraints that are not present in chemical approaches. These include a rather limited number for its starting combinatorial library, uneven generation of diversity amongst the CDRs, and a relatively short time constant for the process. Furthermore, even though the mutatation rate for antibody genes during immune induction is about 1.0×10^6-fold higher than the spontaneous rate, it is only 10^{-5} to 10^{-3} per base pair per generation.[105,106] Most importantly, there is this "good enough" aspect to the immune system in that it terminates when the selected antibodies are of sufficient binding energy and concentration to remove the antigenic inducer that is driving the antibody evolution. Thus, the natural immune system is geared toward sufficient rather than optimal affinity. The chemist, however, has many advantages.

1. In chemistry the experimenter works with diversity that is only limited by accessibility, and can choose the end point of the experiment.
2. Chemical intuition is brought to bear as opposed to the unguided process of nature.
3. The size of modern antibody libraries means that the chemist can start with a larger pool of starting materials. When coupled with chemical insight, manipulation of this starting pool may yield a better product than that obtained by random mutation and selection when evolution is constrained to a real-time process.
4. There are many more algorithms available to the chemist when working incrementally to combine different parts of the molecule.
5. The CDRs have evolved to be highly changeable protein loops with few restrictions forbidden in terms of sequence, well beyond those that might be represented in a natural repertoire.

The central idea is that once one has a combinatorial antibody library, then a strictly chemical approach to mutagenesis is possible.

There have been many experiments that illustrate how the affinities of antibodies from combinatorial libraries can be improved.[107–109] In general, these methods employ chain shuffling and/or site-specific mutagenesis to mutate a limited number of positions in the antibody molecule. A more recent experiment of particular interest was conceived by Crea and co-workers to test whether a combinatorial chemical approach to improvement in the binding energy (affinity maturation) could match or exceed that of nature.[110] The test object was the antibody humira, which is a difficult case because it had already been highly optimized (K_d 1 nM), and was already good enough to be employed in a therapeutic setting. There will always be an interest in constraints on the size of the combinatorial library because one can easily imagine potential variants that greatly exceed what can be realized. For example if there are 60 positions in the six CDR loops (humira has 57) and all combinations of the 20 naturally occurring amino acids were tested, this would yield an unmanageably large library of greater than 10^{78} members. The trick is to not waste diversity by only allowing changes that chemical intuition dictates might have the best chance to improve binding.

The overall strategy used by Crea et al., in what is a highly iterative process, is shown in Figure 21.[110] The first step in the process is called "look through" mutagenesis. Here, a set of nine amino acids, selected for their chemical properties in that they represent the major side-chain functionalities, is used to generate a set of positional mutants at every position in all six CDRs of an antibody (Figure 21). Libraries with single mutations in each CDR (6 libraries), single mutations in two CDRs (15 libraries), and libraries with single mutations in three CDRs (20 libraries) were constructed and screened for improved binding. By using this approach with only nine amino acids, the most diverse triple mutant library was constrained to a manageable 1.4×10^6 members. In terms of binding, there were 14 positions in which mutation was not allowed. Thirty eight mutations in 21 positions were identified

 © 2006 Wiley-VCH Verlag GmbH & Co. KGaA, Weinheim

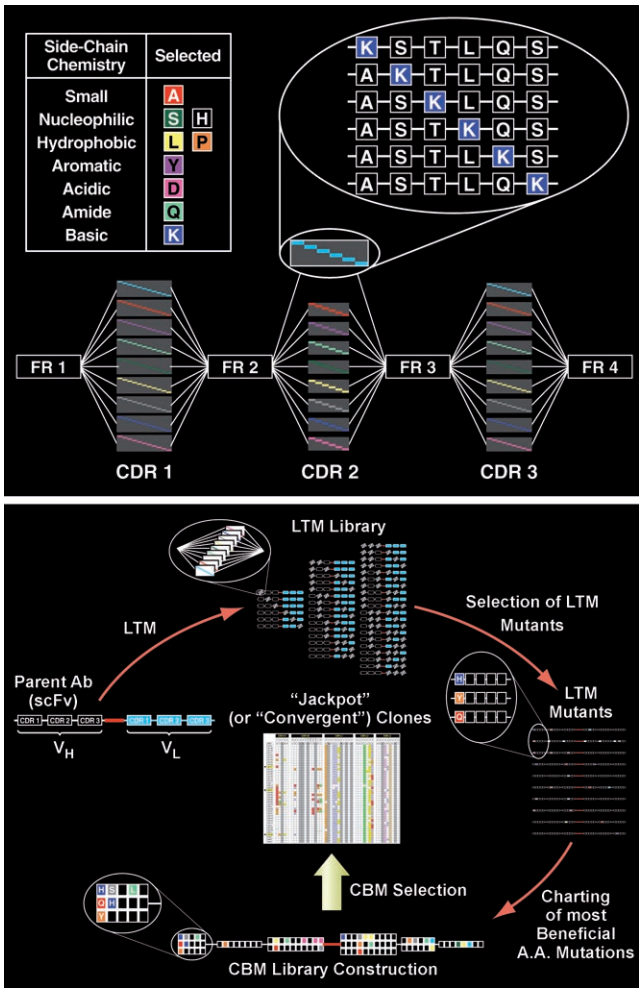

Figure 21. General scheme for antibody mutagenesis using the "look through" and "combinatorial" (CBM) antibody mutagenesis. Top: Triple LTM example. Nine amino acids, representative of the 20 natural amino acids, were selected for the LTM process based on their side-chain chemical functionalities (inset left). Discrete CDR oligonucleotides are synthesized to produce a mutagenized CDR with one target amino acid mutation at each CDR position (inset right). In the triple CDR library, all combinations of CDR1, CDR2, and CDR3 oligonucleotides are combined to produce libraries with three simultaneously mutagenized CDRs.[110] Bottom: Once the beneficial LTM mutants are selected, those mutations that appear in multiple clones are encoded by degenerate oligonucleotides which are combined in the CBM process to select the most beneficial mutants. Copyright National Academy of Sciences.

as changes that improved antibody affinity (Table 1). These beneficial mutations were combinatorialy combined separately for the heavy chains (diversity of 2.0×10^5) and light chains (diversity of 6.0×10^5). After initial selection, the heavy- and light-chain libraries were combined and selected. This yielded 58 mutants with improved binding energy, which in some cases approached three orders of magnitude better (to $K_D = 10^{-12}$, Table 1). When sequence analysis was carried out on the selected clones, only minimal convergence was seen for the heavy chains (Figure 22). However, a remarkable convergence was observed for the 14 light-chain positions that were mutated (Figure 22). For example, in CDRL1 there is a

Table 1: Affinities of improved humira clones. D2E7 is the starting clone whose affinity is improved about three orders of magnitude.

scFv	k_{on} [$\times10^6$ M^{-1} x^{-1}]	k_{off} [$\times10^{-5}$ x^{-1}]	K_D [pM]	Relative improvement in K_D
D2E7	1.12	107	955 ± 17	
A1	11.1	2.086	1.88 ± 0.05	500
cb2-44	5.8	0.637	1.10 ± 0.08	870
cb1-3	7.1	0.770	1.08 ± 0.02	870
cb2-6	4.0	0.0454	1.1 ± 0.3	870

strict requirement for His 24, Lys 27, and Arg 28, as well as a conservative Ile 29 to Leu 29 change. Many other convergent sequences can be seen, but the uniform requirement for a Pro 94 substitution adjacent to an unmutated Pro 95 residue is particularly noteworthy in that it suggests a requirement for conformational change in this region. Here we see another important aspect of combinatorial libraries for proteins. While one might have guessed that an Asp 92 group in CDR-L3 might be useful, no methodology exists to predict that it had to be in combination with comutation of an adjacent proline to presumably effect a conformational change that allows the Asp carboxalate group to be positioned correctly. This underscores the fact that, for proteins, a combinatorial matrix needs to be played out in three-dimensional space, thereby greatly complicating the problem.

These results raise two very interesting issues. The first concerns the question of why did the power of this process exceed that of natural evolution in terms of binding-energy maturation? Secondly, why was there such remarkable convergence of sequences in the light chains? The efficiency of the process it likely to be the result of the fact that the in vitro iterative process uses a genetic algorithm that is not allowed in nature. In nature, recombination occurs before mutation and selection, and further recombination does not occur—thereby eliminating any possibility for synergy between the two processes. The in vitro process allows observation of beneficial mutations followed by a "combinatorial backcross", thereby allowing synergistic gains and elimination of nonproductive combinations. The fact that the light-chain improvements exceeded those of the heavy chain supports the concept that in nature there is more heavy-chain than light-chain diversity. Thus, there is more room for light-chain than heavy-chain improvement because heavy-chain diversity is already the product of relatively large numbers coupled to a moderately successful natural genetic algorithm. Thus, synthetic antibody libraries that start with larger numbers than the natural repertoire and use an algorithm that allows for both V_H and V_L optimization by a concerted process of recombination and mutation might be more powerful than the genetic algorithm of nature.[110]

The antibody affinity was improved such that the K_D values are in the picomolar range, which may approach the binding-energy limit for this antigen. It is likely that convergence is seen because this binding energy approaches the limit for this protein–protein system. As the binding energy increases, the number of chemical solutions to the problem decreases. This is especially true at the limit where

 © 2006 Wiley-VCH Verlag GmbH & Co. KGaA, Weinheim

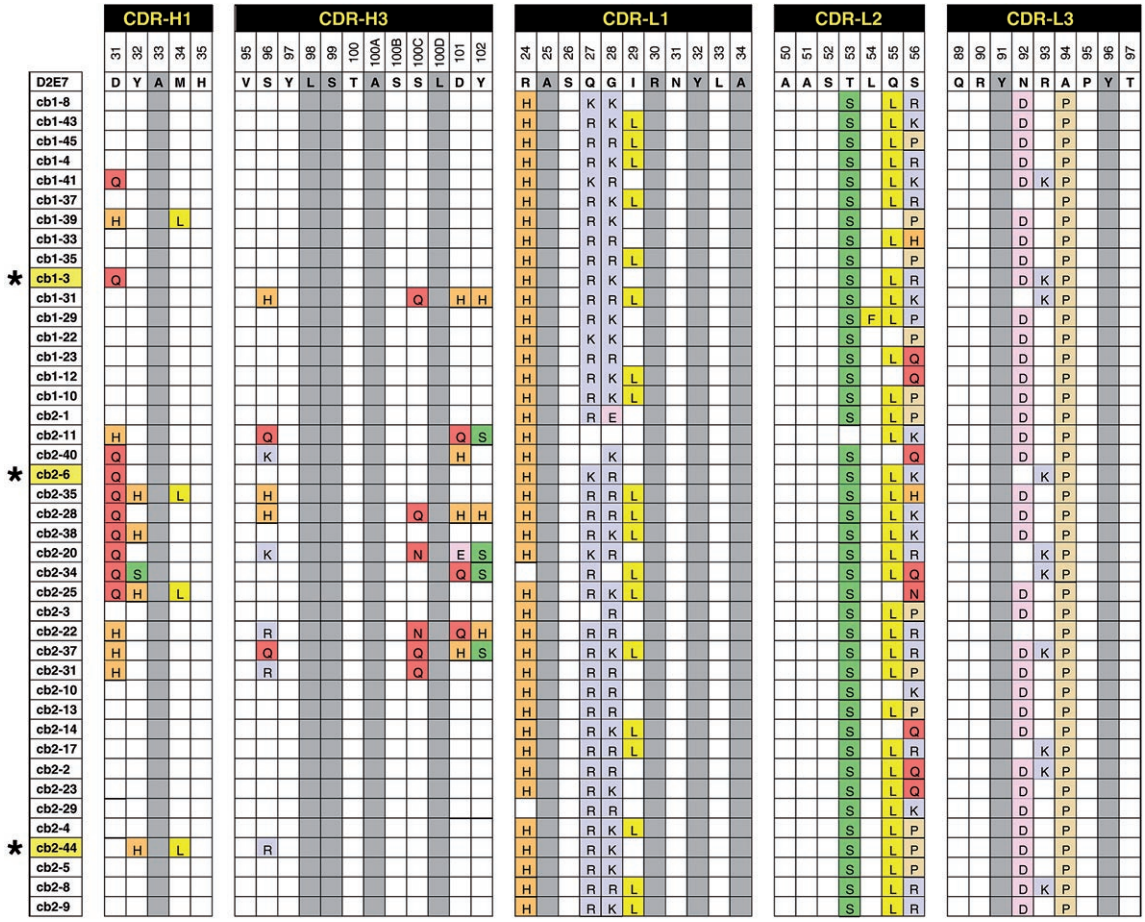

Figure 22. Sequence of CBM clones displaying higher affinity for TNF-α.[110] Copyright National Academy of Sciences.

there is one best solution and near the limit where there are only a few nearly optimal solutions. Said another way, convergence indicates that the limit is being approached. One caveat to these assumptions is the possibility that local minima on the free-energy surface may have trapped the search prior to its reaching an optimal solution for binding energy.

Finally, to give a chemical perspective, it is interesting to compare the selection and optimization strategies for chemical and combinatorial antibody libraries to improve affinity and selectivity. A large chemical library may have up to one million members from which a "hit" may be selected. Typically the "hit" may have a micromolar K_D value, which can be improved by medicinal chemistry to yield an optimized drug with nanomolar affinity for the target. By contrast, the size of synthetic combinatorial antibody libraries is in the 10^8–10^{11} range, from which binders with K_D values of approximately 10^{-8} are easily selected. From there, binding can be improved by mutagenesis and/or chain shuffling to yield optimized therapeutic antibodies with K_D values in the picomolar range. Again, we see the tremendous power that resides in the vast numbers.

14. The Embarrassment of Riches Problem

In methodology, power not used is power squandered. Prior to the advent of combinatorial antibody libraries, one often had access from hybridoma technology to a limited number of antibodies for a given target, and one simply made do with what one had. Thus, the choice of using an antibody either as a reagent or therapeutic was comparatively simple. However, in library work one often has thousands of antibodies that bind to a given target and the choice of which to pursue becomes formidable. The problem is further complicated by the fact that the configuration of the antibody molecules in the most powerful selection formats does not lend itself to biochemical assessment of the protein. In practical terms, the problem centers on how can one express thousands of different antibodies in sufficient quantities so as to determine which is most efficient for a given task. Sometimes binding energy is only the first cut, and antibodies with equal binding energy will behave quite differently in a biochemical assay or therapeutic application such as virus neutralization. Although, there is as yet not a complete solution to the problem, there are many promising advances in packaging and expression.[22] The most interesting new direction is in the library of libraries approach, in which the

 © 2006 Wiley-VCH Verlag GmbH & Co. KGaA, Weinheim

genes selected for in a binding assay are directly ported into an expression system in such a way as to preserve clonality and/or shuffle the chains. These systems have the advantage that milligram quantities of each antibody are made in small volumes, such as microtiter formats. However, because no two antibodies are the same, it will always be the case that expression levels can vary; however if there is enough of each antibody for an assay, the absolute quantities do not matter. Such systems are likely to allow the full potential of large libraries to be realized.

15. Letting Phenotype Declare Itself

When one works with powerful diversity-generating systems such as combinatorial antibody libraries, there is a temptation to try and improve their efficiency by dictating certain constraints. One way would be to use chemical intuition, as was seen in the affinity maturation experiments described above. However, in that case the goal was largely a matter of restricting the library size to that which could be managed by the display system. It is quite a different matter when one attempts to dictate and/or improve chemical choices by, for example, favoring guanidinium residues over primary amines because they pair better with carboxylate groups or forcing periodic bends in the protein loops by insertion of proline residues. Since, we don't yet know all the rules, it is generally found that it is better to make the numbers as large as possible and let the system teach you rather than you teach the system. The main reason for this is because, in the absence of full knowledge, the main power of these systems stems from their randomness and much less on design. Thus, to the extent that design constrains the random search algorithm, it may do more harm than good. For example, if one dictates a proline residue, how can it be known whether it bends an adjacent carboxylate group toward or away from a neighboring guanidinium residue. To be sure, there will come a day when random systems are augmented by the incorporation of design features such that the combination is a net positive. However, that time is not yet here and, for the moment, it is generally best to let phenotype declare itself. This is especially true for antibody–antigen systems where each system is different from the next.

16. The Future

Through combinatorial antibody libraries one has access to antibodies for whatever antigen one wants. The therapeutic challenge now shifts to what one wants. We can expect therapeutic antibodies to extend to diseases and involve target antigens where immunological intervention was unimaginable only a short time ago. This is, in part, because our knowledge of the molecular basis of disease is expanding rapidly and because many new pathogenic antigens are being defined. The therapeutic climate that surrounds antibodies is also important. As more and more antibodies become approved by the FDA and other regulatory agencies, the scientific community becomes more emboldened to try interesting approaches. For example, while some could easily envision their role in cancer therapies or in infection, few would have imagined that therapeutic antibodies could be used in macular degeneration, Alzheimer's disease, and even obesity. Could one imagine that antibodies will be used to perturb the equilibrium between molecules in the blood and their deposition in arterial walls such that antibodies could slow the progression or even reduce atherosclerotic plaques? These examples, real and imagined, illustrate the way that the community is currently thinking.

Antibodies are good at removing antigens, and it is important to decide what should be removed or lowered to achieve a particular therapeutic effect. Yet, even with its many successes and with doubtless more to come, this way of thinking is very limiting and is likely only at the beginning. The next wave of antibody therapeutics may involve a class of reagents termed "mechanistic antibodies" because they have agonist or antagonistic activities. There is already one such antibody in clinical trials for treatment of steroid-refractory graft versus host disease.[110] This antibody (visilizumab) is a well-studied anti-CD3 antibody that induces apoptosis only in activated T cells.[111] We can expect mechanistic antibodies to be used experimentally in animals to activate selectively cellular components of the immune system to study their participation in autoimmunity and cancer. For example, if the consequence of antibody activation of a cell type results in arthritis, much would be revealed about the pathogenesis of this disease. Additionally, therapy might be targeted to that cell type or the regulatory and/or effector molecules it produces.

Finally, the antigenic space that is currently being explored is largely limited to targets that are extracellular, either because they are secreted and/or are on the cell surface. In the future, we expect that the addressable antigenic space will greatly expand to include intracellular targets, perhaps using cell-penetrating peptides to transport antibodies into interior cellular compartments.[112]

In the safety-conscious world of therapeutic development, antibodies with their exquisite selectivity and specificity and their natural amino acid composition are attractive therapeutic tools. They are being developed by ever increasing numbers of large pharmaceutical companies who are following in the wake of the success of the biotechnology companies working with therapeutic antibodies. Big and small pharmaceutical companies are likely to produce many more novel therapeutics by selecting antibodies from large combinatorial libraries.[113]

I would like to thank my many co-workers who contributed to the development of combinatorial antibody libraries, especially, Carlos Barbas, Dennis Burton, and Kim Janda. I also thank Tamas Bartfai, Jerry Joyce, and Greg Winter for many suggestions about this manuscript and Lenore Horowitz for preparation of the frontispiece picture. Any remaining errors and/or misconceptions are, however, mine.

Received: August 18, 2006
Published online: November 22, 2006

 © 2006 Wiley-VCH Verlag GmbH & Co. KGaA, Weinheim

[1] A. Silverstein, *Nat. Immunol.* **2003**, *4*, 425 – 428.
[2] S. Arrhenius, *Immunochemistry*, MacMillan New York, **1907**.
[3] P. Ehrlich, *Klin. Jahrb.* **1897**, *6*, 299 – 333.
[4] P. Ehrlich, *Proc. R. Soc. London Ser. B* **1900**, *66*, 424 – 448.B.
[5] B. Witkop, *Proc. Am. Philos. Soc.* **1999**, *143*, 540 – 557.
[6] Antibodies in Oncology: Drug Pipeline update, **2006**, Bio-Seeker Group AB.
[7] G. Kohler, C. Milstein, *Nature* **1975**, *256*, 495 – 497.
[8] L. Riechmann, M. Clark, H. Waldmann, G. Winter, *Nature* **1988**, *332*, 323 – 327.
[9] P. Jones, P. H. Dear, J. Foote, M. S. Neuberger, G. Winter, *Nature* **1986**, *321*, 522 – 525.
[10] L. Sastry, M. Alting-Mees, W. D. Huse, J. M. Short, J. A. Sorge, B. N. Hay, K. D. Janda, S. J. Benkovic, R. A. Lerner, *Proc. Natl. Acad. Sci. USA* **1989**, *86*, 5728 – 5732.
[11] R. Orlandi, D. H. Gussow, P. T. Jones, G. Winter, *Proc. Natl. Acad. Sci. USA* **1989**, *86*, 3833 – 3837.
[12] W. D. Huse, L. Sastry, S. A. Iverson, A. S. Kang, M. Alting-Mees, D. R. Burton, S. J. Benkovic, R. A. Lerner, *Science* **1989**, *246*, 1275 – 1281.
[13] J. McCafferty, A. D. Griffiths, G. Winter, D. J. Chiswell, *Nature* **1990**, *348*, 552 – 554.
[14] C. F. Barbas, A. S. Kang, R. A. Lerner, S. J. Benkovic, *Proc. Natl. Acad. Sci. USA* **1991**, *88*, 7978 – 7982.
[15] H. R. Hoogenboom, A. D. Griffiths, K. S. Johnson, D. J. Chiswell, P. Hudson, G. Winter, *Nucleic Acids Res.* **1991**, *19*, 4133 – 4137.
[16] H. R. Hoogenboom, G. Winter, *J. Mol. Biol.* **1992**, *227*, 381 – 388.
[17] J. D. Marks, H. R. Hoogenboom, T. P. Bonnert, J. McCafferty, A. D. Griffiths, G. Winter, *J. Mol. Biol.* **1991**, *222*, 581 – 597.
[18] A. S. Kang, C. F. Barbas, K. D. Janda, S. J. Benkovic, R. A. Lerner, *Proc. Natl. Acad. Sci. USA* **1991**, *88*, 4363 – 4366.
[19] C. F. Barbas, J. D. Bain, D. M. Hoekstra, R. A. Lerner, *Proc. Natl. Acad. Sci. USA* **1992**, *89*, 4457 – 4461.
[20] C. Gao, S. Mao, G. Kaufmann, P. Wirsching, R. A. Lerner, K. D. Janda, *Proc. Natl. Acad. Sci. USA* **2002**, *99*, 12612 – 12616.
[21] R. A. Lerner, A. S. Kang, J. D. Bain, D. R. Burton, C. F. Barbas, *Science* **1992**, *258*, 1313 – 1314.
[22] D. R. Burton, C. F. Barbas, *Adv. Immunol.* **1994**, *57*, 191 – 280.
[23] A. Bradbury, L. Persic, T. Werge, A. Cattaneo, *Bio/Technology* **1993**, *11*, 1565 – 1569.
[24] J. D. Marks, A. D. Griffiths, M. Malmqvist, T. Clackson, J. M. Bye, G. Winter, *Bio/Technology* **1992**, *10*, 779 – 783.
[25] C. F. Barbas, D. R. Burton, J. K. Scott, G. J. Silverman, *Phage Display: A Laboratory Manual*, CSH Laboratory Press, **2001**.
[26] J. Marx, *Science* **1989**, *246*, 1250 – 1251.
[27] A. D. Griffiths, M. Malmqvist, J. D. Marks, J. M. Bye, M. J. Embleton, J. McCafferty, M. Baier, K. P. Holliger, B. D. Gorick, N. C. Hughes-Jones, H. R. Hoogenboom, G. Winter, *EMBO J.* **1993**, *12*, 725 – 734.
[28] R. A. Lerner, C. F. Barbas, K. D. Janda, *Harvey Lect.* **1998**, *92*, 1 – 40.
[29] J. Wagner, R. A. Lerner, C. F. Barbas, *Science* **1995**, *270*, 1797 – 1800.
[30] G. Zhong, T. Hoffmann, R. A. Lerner, S. Danishefsky, C. F. Barbas, *J. Am. Chem. Soc.* **1997**, *119*, 8131 – 8132.
[31] C. F. Barbas, A. Heine, G. Zhong, T. Hoffmann, S. Gramatikova, R. Björnestedt, B. List, J. Anderson, E. A. Stura, I. A. Wilson, R. A. Lerner, *Science* **1997**, *278*, 2085 – 2092.
[32] M. G. Finn, R. A. Lerner, C. F. Barbas, *J. Am. Chem. Soc.* **1998**, *120*, 2963 – 2964.
[33] B. List, C. F. Barbas, R. A. Lerner, *Proc. Natl. Acad. Sci. USA* **1998**, *95*, 15351 – 15355.
[34] G. Zhong, D. Shabat, B. List, J. Anderson, S. C. Sinha, R. A. Lerner, C. F. Barbas, *Angew. Chem.* **1998**, *110*, 2609 – 2612; *Angew. Chem. Int. Ed.* **1998**, *37*, 2481 – 2484.
[35] See: http://www.cambridgeantibody.com.
[36] G. P. Smith, *Science* **1985**, *228*, 1315 – 1317.
[37] J. F. Smothers, S. Henikoff, P. Carter, *Science* **2002**, *298*, 621 – 622.
[38] D. W. Colby, B. A. Kellogg, C. P. Graff, Y. A. Yeung, J. S. Swers, K. D. Wittrup, *Methods Enzymol.* **2004**, *388*, 348 – 358.
[39] D. W. Colby, P. Garg, T. Holden, G. Chao, J. M. Webster, A. Messer, V. M. Ingram, K. D. Wittrup, *J. Mol. Biol.* **2004**, *342*, 901 – 912.
[40] W. Ernst, R. Grabherr, D. Wegner, N. Borth, A. Grassauer, H. Katinger, *Nucleic Acids Res.* **1998**, *26*, 1718 – 1723.
[41] M. C. Kieke, B. K. Cho, E. T. Boder, D. M. Kranz, K. D. Wittrup, *Protein Eng.* **1997**, *10*, 1303 – 1310.
[42] S. A. Richman, S. J. Healan, K. S. Weber, D. L. Donermeyer, M. L. Dossett, P. D. Greenberg, P. M. Allen, D. M. Kranz, *Protein Eng. Des. Sel.* **2006**, *19*, 255 – 264.
[43] E. T. Boder, K. D. Wittrup, *Nat. Biotechnol.* **1997**, *15*, 553 – 557.
[44] M. J. Feldhaus, R. W. Siegel, L. K. Opresko, J. R. Coleman, J. M. Weaver Feldhaus, Y. A. Yeung, J. R. Cochran, P. Heinzelman, D. Colby, J. Swers, C. Graff, H. S. Wiley, K. D. Wittrup, *Nat. Biotechnol.* **2003**, *21*, 163 – 170.
[45] E. T. Boder, K. D. Wittrup, *Biotechnol. Prog.* **1998**, *14*, 55 – 62.
[46] J. Hanes, C. Schaffitzel, A. Knappik, A. Plückthun, *Nat. Biotechnol.* **2000**, *18*, 1287 – 1292.
[47] E. T. Boder, K. D. Wittrup, *Methods Enzymol.* **2000**, *328*, 430 – 444.
[48] J. A. Francisco, R. Campbell, B. L. Iverson, G. Georgiou, *Proc. Natl. Acad. Sci. USA* **1993**, *90*, 10444 – 10448.
[49] Y. Boublik, P. Di Bonito, I. M. Jones, *Biotechnology* **1995**, *13*, 1079 – 1084.
[50] E. T. Boder, K. S. Midelfort, K. D. Wittrup, *Proc. Natl. Acad. Sci. USA* **2000**, *97*, 10701 – 10705.
[51] H. R. Hoogenboom, *Nat. Biotechnol.* **2005**, *23*, 1105 – 1116.
[52] X. X. Wang, E. V. Shusta, *J. Immunol. Methods* **2005**, *304*, 30 – 42.
[53] M. N. Hall, T. J. Silhavy, *Annu. Rev. Genet.* **1981**, *15*, 91 – 142.
[54] M. Agterberg, H. Adriaanse, J. Tommassen, *Gene* **1987**, *59*, 145 – 150.
[55] R. Freudl, S. MacIntyre, M. Degen, U. Henning, *J. Mol. Biol.* **1986**, *188*, 491 – 494.
[56] I. M. Taylor, J. L. Harrison, K. N. Timmis, C. D. O'Connor, *Mol. Microbiol.* **1990**, *4*, 1259 – 1268.
[57] P. Fuchs, F. Breitling, S. Dübel, T. Seehaus, M. Little, *Bio/Technology* **1991**, 1369 – 1372.
[58] T. Klauser, J. Pholner, T. F. Meyer, *EMBO J.* **1990**, *9*, 1991 – 1999.
[59] J. A. Francisco, C. F. Earhart, G. Georgiou, *Proc. Natl. Acad. Sci. USA* **1992**, *89*, 2713 – 2717.
[60] J. A. Francisco, C. Stathopoulos, R. A. J. Warren, D. G. Kilburn, G. Georgiou, *Bio/Technology* **1993**, *11*, 491 – 495.
[61] L. Hedegaard, P. Klemm, *Gene* **1989**, *85*, 115 – 124.
[62] G. Kuwajima, J.-I. Asaka, T. Fujiwara, T. Fujiwara, K. Nakano, E. Kondoh, *Bio/Technology* **1988**, *6*, 1080 – 1083.
[63] S. M. Newton, C. O. Jacob, B. A. Stocker, *Science* **1989**, *244*, 70 – 72.
[64] A. Charbit, A. Molla, W. Saurin, M. Hofnung, *Gene* **1988**, *70*, 181 – 189.
[65] L. Steidler, E. Remaut, W. Fiers, *Mol. Gen. Genet.* **1993**, *236*, 187 – 192.
[66] J. C. Boulain, A. Charbit, M. Hofnung, *Mol. Gen. Genet.* **1986**, *205*, 339 – 348.
[67] A. Plückthun, A. Skerra, *Methods Enzymol.* **1989**, *178*, 497 – 515.
[68] J. W. Kehoe, B. K. Kay, *Chem. Rev.* **2005**, *105*, 4056 – 4072.

 © 2006 Wiley-VCH Verlag GmbH & Co. KGaA, Weinheim

[69] D. A. Marvin, L. C. Welsh, M. F. Symmons, W. R. P. Scott, S. K. Straus, *J. Mol. Biol.* **2006**, *355*, 294 – 309.
[70] K. A. Williams, M. Glibowicka, Z. Li, H. Li, A. R. Khan, Y. M. Y. Chen, J. Wang, D. A. Marvin, C. M. Deber, *J. Mol. Biol.* **1995**, *252*, 6 – 14.
[71] S. L. Zebedee, C. F. Barbas, Y.-L. Hom, R. H. Caothien, R. Graff, J. DeGraw, J. Pyati, R. La Polla, D. R. Burton, R. A. Lerner, G. B. Thornton, *Proc. Natl. Acad. Sci. USA* **1992**, *89*, 3175 – 3179.
[72] C. F. Barbas, J. S. Rosenblum, R. A. Lerner, *Proc. Natl. Acad. Sci. USA* **1993**, *90*, 6385 – 6389.
[73] S. Brown, *Proc. Natl. Acad. Sci. USA* **1992**, *89*, 8651 – 8655.
[74] T. A. Collet, P. Roben, R. O'Kennedy, C. F. Barbas, D. R. Burton, R. A. Lerner, *Proc. Natl. Acad. Sci. USA* **1992**, *89*, 10026 – 10030.
[75] A. S. Kang, T. M. Jones, D. R. Burton, *Proc. Natl. Acad. Sci. USA* **1991**, *88*, 11120 – 11123.
[76] R. A. Lerner, C. F. Barbas, A. S. Kang, D. R. Burton, *Proc. Natl. Acad. Sci. USA* **1991**, *88*, 9705 – 9706.
[77] B. Felding-Habermann, R. A. Lerner, A. Lillo, S. Zhuang, M. R. Weber, S. Arrues, C. Gao, S. Mao, A. Saven, K. D. Janda, *Proc. Natl. Acad. Sci. USA* **2004**, *101*, 17210 – 17215.
[78] D. R. Burton, C. F. Barbas, M. A. A. Persson, S. Koenig, R. M. Chanock, R. A. Lerner, *Proc. Natl. Acad. Sci. USA* **1991**, *88*, 10134 – 10137.
[79] C. F. Barbas, E. Björling, F. Chiodi, N. Dunlop, D. Cababa, T. M. Jones, S. L. Zebedee, M. A. A. Persson, P. L. Nara, E. Norrby, D. R. Burton, *Proc. Natl. Acad. Sci. USA* **1992**, *89*, 9339 – 9343.
[80] C. F. Barbas, J. E. Crowe, Jr., D. Cababa, T. M. Jones, S. L. Zebedee, B. R. Murphy, R. M. Chanock, D. R. Burton, *Proc. Natl. Acad. Sci. USA* **1992**, *89*, 10164 – 10168.
[81] C. F. Barbas, T. A. Collett, W. Amberg, P. Rogen, J. M. Binley, D. Hoekstra, D. Cababa, T. M. Jones, R. A. Williamson, G. R. Pilkington, N. L. Haigwood, A. C. Satterthwait, I. Sanz, D. R. Burton, *J. Mol. Biol.* **1993**, *230*, 812 – 823.
[82] R. A. Williamson, R. Burioni, P. Sanna, L. Partridge, C. F. Barbas, D. R. Burton, *Proc. Natl. Acad. Sci. USA* **1993**, *90*, 4141 – 4145.
[83] J. E. Crowe Jr., B. R. Murphy, R. M. Chanock, R. A. Williamson, C. F. Barbas, D. R. Burton, *Proc. Natl. Acad. Sci. USA* **1994**, *91*, 1386 – 1390.
[84] C. F. Barbas, D. Hu, N. Dunlop, L. Sawyer, D. Cababa, R. M. Hendry, P. L. Nara, D. R. Burton, *Proc. Natl. Acad. Sci. USA* **1994**, *91*, 3809 – 3813.
[85] E. Bender, G. R. Pilkington, D. R. Burton, *Hum. Antibodies Hybridomas* **1994**, *5*, 3 – 8.
[86] P. Roben, J. P. Moore, M. Thali, J. Sodroski, C. F. Barbas, D. R. Burton, *J. Virol.* **1994**, *68*, 4821 – 4828.
[87] D. R. Burton, J. Pyati, R. Koduri, S. J. Sharp, G. B. Thornton, P. W. H. I. Parren, L. S. W. Sawyer, R. M. Hendry, N. Dunlop, P. L. Nara, M. Lamacchi, E. Garratty, E. R. Stiehm, Y. J. Bryson, Y. Cao, J. P. Moore, D. D. Ho, C. F. Barbas, *Science* **1994**, *266*, 1024 – 1027.
[88] I. Moreno de Alborán, C. Martinéz-Alonso, C. F. Barbas, D. R. Burton, H. J. Ditzel, *Immunotechnology* **1995**, *1*, 21 – 28.
[89] R. A. Williamson, D. Peretz, N. Smorodinsky, R. Bastidas, T. Blochberger, A. Serban, S. DeArmond, S. B. Prusiner, D. R. Burton, *Proc. Natl. Acad. Sci. USA* **1996**, *93*, 7279 – 7282.
[90] J. M. Binley, H. J. Ditzel, C. F. Barbas, N. Sullivan, J. Sodroski, P. W. H. I. Parren, D. R. Burton, *AIDS Res. Hum. Retroviruses* **1996**, *12*, 911 – 924.
[91] H. J. Ditzel, K. Itoh, D. R. Burton, *J. Immunol.* **1996**, *157*, 739 – 749.
[92] P. W. H. I. Parren, P. Fisicaro, H. J. Ditzel, W.-P. Yang, C. F. Barbas, D. R. Burton, *J. Virol.* **1996**, *70*, 9046 – 9050.
[93] R. A. Williamson, D. Peretz, C. Pinilla, H. Ball, R. B. Bastidas, R. Rozenshteyn, R. A. Houghten, S. B. Prusiner, D. R. Burton, *J. Virol.* **1998**, *72*, 9413 – 9418.
[94] T. Maruyama, P. W. H. I. Parren, A. Sanchez, I. Rensink, L. L. Rodriguez, A. S. Khan, C. J. Peters, D. R. Burton, *J. Infect. Dis.* **1999**, *179*, S235 – 9.
[95] M. P. Burgoon, R. A. Williamson, G. P. Owens, O. Ghausi, R. B. Bastidas, D. R. Burton, D. H. Gilden, *J. Neuroimmunol.* **1999**, *94*, 204 – 211.
[96] C. D. C. Nicacio, A. Williamson, P. W. H. I. Parren, A. Lundkvist, D. R. Burton, E. Bjorling, *J. Virol.* **2002**, *76*, 251 – 258.
[97] D. R. Burton, *Trends Biotechnol.* **1991**, *9*, 169 – 175.
[98] D. R. Burton, C. F. Barbas, *Chem. Immunol.* **1993**, *56*, 112 – 126.
[99] D. R. Burton, *Acc. Chem. Res.* **1993**, *26*, 405 – 411.
[100] D. R. Burton, C. F. Barbas, *Adv. Immunol.* **1994**, *57*, 191 – 280.
[101] D. R. Burton, R. L. Stanfield, I. A. Wilson, *Proc. Natl. Acad. Sci. USA* **2005**, *102*, 14943 – 14948.
[102] S. M. Kipriyanov, *Expert Opin. Ther. Pat.* **2004**, *14*, 135 – 140.
[103] L. Kausmally, K. Waalen, I. Lobersli, E. Hvattum, G. Berntsen, T. E. Michaelsen, O. H. Brekke, *J. Gen. Virol.* **2004**, *85*, 3493 – 3500.
[104] J. Sui, W. Li, A. Murakami, A. Tamin, L. J. Matthers, S. K. Wong, M. J. Moore, A. St. Clair Tallarico, M. Olurinde, H. Choe, L. J. Anderson, W. J. Bellini, M. Farzan, W. A. Marasco, *Proc. Natl. Acad. Sci. USA* **2004**, *101*, 2536 – 2541.
[105] Z. Li, C. J. Woo, M. D. Iglesias-Ussel, D. Ronai, M. D. Scharff, *Genes Dev.* **2004**, *18*, 1 – 11.
[106] K. Rajewsky, I. Forster, A. Cumano, *Science* **1987**, *238*, 1088 – 1094.
[107] H. Gram, L.-A. Marconi, C. F. Barbas, T. A. Collet, R. A. Lerner, A. S. Kang, *Proc. Natl. Acad. Sci. USA* **1992**, *89*, 3576 – 3580.
[108] R. E. Hawkins, S. J. Russell, G. Winter, *J. Mol. Biol.* **1992**, *226*, 889 – 896.
[109] W.-P. Yang, K. Green, S. Pinz-Sweeney, A. T. Briones, D. R. Burton, C. F. Barbas, *J. Mol. Biol.* **1995**, *254*, 392 – 403.
[110] A. Rajpal, N. Beyaz, L. Haber, G. Cappuccilli, H. Yee, R. R. Bhatt, T. Takeuchi, R. A. Lerner, R. Crea, *Proc. Natl. Acad. Sci. USA* **2005**, *102*, 8466 – 8471.
[111] P. A. Carpenter, F. R. Appelbaum, L. Corey, H. J. Deeg, K. Doney, T. Gooley, J. Krueger, P. Martin, S. Pavlovic, J. Sanders, J. Slattery, D. Levitt, R. Storb, A. Woolfrey, C. Anasetti, *Blood J.* **2002**, *99*, 2712 – 2719.
[112] U. Langel, *Handbook of Cell Penetrating Peptides*, CRC, Boca Raton, **2002**.
[113] *Adv. Drug Delivery Rev.* **2006**, *58*, 631 – 766.

 © 2006 Wiley-VCH Verlag GmbH & Co. KGaA, Weinheim

Hollow Nanostructures

DOI: 10.1002/anie.200602403

Synthesis of Platinum Nanocages by Using Liposomes Containing Photocatalyst Molecules**

*Yujiang Song, Robert M. Garcia, Rachel M. Dorin, Haorong Wang, Yan Qiu, and John A. Shelnutt**

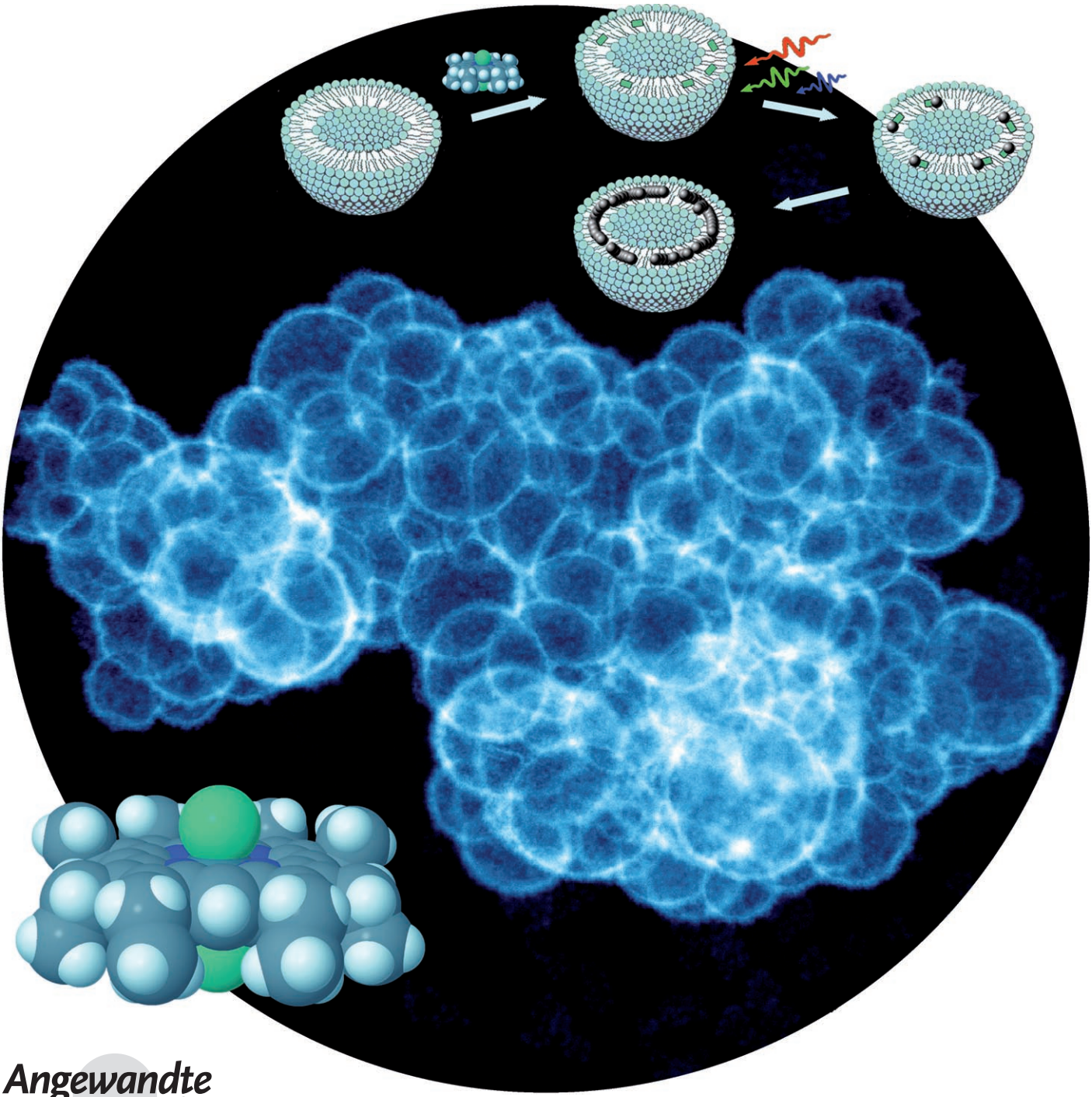

WILEY InterScience DISCOVER SOMETHING GREAT

© 2006 Wiley-VCH Verlag GmbH & Co. KGaA, Weinheim

Hollow nanospheres are of interest because of their tunable structural features, including shell thickness, interior cavity size, and chemical compositions. In particular, metallic hollow nanospheres have drawn much attention because of their high surface area, low density, material economy, cost reduction, and in some cases surface permeability compared with solid nanospheres. These unique properties lead to a diverse range of reported biomedical,[1,2] catalytic,[3] and optical[4] applications.

The synthesis of metallic hollow nanospheres is limited mainly to two approaches. One is the deposition of metal onto solid nanospheres of silica,[5–7] latex,[8,9] metal,[4,10–13] and other materials,[14–16] with subsequent removal of the templating core, typically by replacement reactions[10–13,17] or corrosion.[4,18,19] The other approach is the co-assembly[20–22] of metallic nanoparticles with organic molecules into hollow nanospheres. A disadvantage of these approaches is that the hollow nanospheres are mainly composed of discrete nanoparticles, making them relatively unstable and apparently precluding the possibility of making hollow nanospheres larger than 100 nm in diameter with thin 2–3-nm shells.

Herein, we report a new method for making hollow metallic nanospheres using templating liposomes containing photocatalyst molecules. Platinum is used to demonstrate this concept in light of its catalytic activity in many applications.[23,24] This synthetic approach gives novel porous platinum nanocages with 2-nm shell thickness and diameters up to 200 nm. These cages are assembled from joined dendritic nanosheets instead of individual nanoparticles. Synthetic control over their structure was achieved by simply varying the concentration of platinum complex. The dendritic character of the constituent nanosheets makes the hollow spheres highly porous.

Scheme 1 shows the proposed synthesis method that leads to the hollow platinum nanocages. The unilamellar liposomes containing hydrophobic Sn^{IV} octaethylporphyrin (SnOEP) in the liposomal bilayer (Scheme 1B) were prepared by a process of solvent evaporation, hydration, and extrusion.[25] The UV/Vis spectrum of SnOEP in the liposomal bilayer (see Supporting Information Figure S1) shows that the porphyrin molecules are monodisperse. Photocatalytic reduction of Pt complex produces metal seed particles upon irradiation of the liposomes containing the SnOEP with white light; the Pt nanoparticles, which are seeds for the dendritic Pt nanosheets, are rapidly generated according to the simplified Equations (1)–(3) where ascorbic acid (AA) is used as the electron donor (ED) and Pt^{2+} is from aged aqueous platinum salt (K_2PtCl_4).

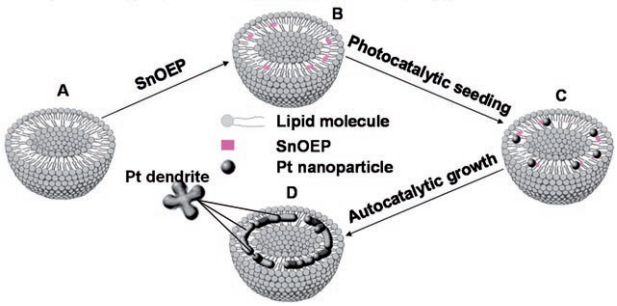

Scheme 1. Diagram of steps in the synthesis of spherical platinum nanocages. A) cross-section view of a liposome (cholesterol molecules are left out for simplicity); B) a liposome containing SnOEP molecules within its bilayer; C) a liposome with Pt seed particles grown photocatalytically in the vicinity of SnOEP molecules; D) a liposome with joined Pt dendritic nanosheets after autocatalytic growth of the original seeds.

$$\mathrm{SnOEP} + h\nu \rightarrow \mathrm{SnOEP}^* \quad (1)$$

$$\mathrm{SnOEP}^* + \mathrm{ED} \rightarrow [\mathrm{SnOEP}]^{-\cdot} + \mathrm{ED}_{ox} \quad (2)$$

$$2\,[\mathrm{SnOEP}]^{-\cdot} + \mathrm{Pt}^{2+} \rightarrow 2\,\mathrm{SnOEP} + \mathrm{Pt}^0 \quad (3)$$

AA and a prevalent hydrolyzed form of the Pt salt ($Pt(H_2O)_2Cl_2$) are both uncharged at pH 3, and thus electron transport between the SnOEP inside the bilayer and these compounds is likely. Presumably the Pt seed particles grow in the vicinity of SnOEP molecules as indicated in Scheme 1C; we have previously presented evidence that the Pt seeds reside within the liposomal bilayer.[25] When the seed particles reach a certain size they become catalytic and begin to grow by catalytic oxidation of ascorbic acid and reduction of Pt complex at their surfaces,[25–27] forming dendritic nanosheets as indicated in Scheme 1D (also see Figure 1c,d). The dendritic growth continues until the Pt complex is exhausted, thus the size of the Pt dendrites is determined by the total Pt complex available and the number of seeds produced.

The key to making the nanocages is to incorporate a large number of SnOEP molecules into each liposome to ensure that the neighboring nascent seed particles are close enough for the dendrites to grow together when the appropriate amount of platinum complex is provided. In this way, many small circular dendritic sheets grow until they link with neighboring nanosheets to form the rigid platinum structures.

[*] Dr. Y. Song, R. M. Garcia, R. M. Dorin, Dr. H. Wang, Y. Qiu, Prof. J. A. Shelnutt
Advanced Materials Laboratory
Sandia National Laboratories
Albuquerque, NM 87106 (USA)
Fax: (+1) 505-272-7077
E-mail: jasheln@unm.edu
Homepage: http://jasheln.unm.edu/
R. M. Garcia, R. M. Dorin, Dr. H. Wang, Y. Qiu
Departments of Chemistry
Biology and Chemical & Nuclear Engineering
The University of New Mexico
Albuquerque, NM 87106 (USA)
Prof. J. A. Shelnutt
Department of Chemistry
University of Georgia
Athens, Georgia 30602-2556 (USA)

[**] Sandia is multiprogram laboratory operated by Sandia Corporation, a Lockheed Martin Company, for the United States Department of Energy's National Nuclear Security Administration under Contract DEAC04-94AL85000.

Supporting information for this article is available on the WWW under http://www.angewandte.org or from the author.

 © 2006 Wiley-VCH Verlag GmbH & Co. KGaA, Weinheim

The network of joined nanosheets replicate the spherical shapes of the templating liposomes (Scheme 1 D; see also Figure 1 a,b) even after the surfactant has been washed away. We have reported on a series of nanoscale Pt dendrites in the form of discrete flat sheets and large convoluted continuous sheets using liposomal aggregates with and without SnOEP as templates.[25,27] For these platinum nanomaterials, a low concentration of SnOEP (or no SnOEP) gives a small number of widely separated seed particles. Depending on the amount of Pt, these conditions result in discrete large circular nanosheets or foam-like materials in which large continuous convoluted dendritic Pt sheets spread over the interfaces of multiple aggregated liposomes.

A reaction system containing aged platinum complex (1 mM), SnOEP (7.9 μM), and 170-nm average-diameter liposomes composed of 1 mM total lipid concentration, when irradiated, gives the hollow Pt nanocages. The average number of SnOEP molecules in a liposome of 160 nm diameter is calculated to be approximately 2400, based on the average cross-sectional areas of 0.39 nm^2 for cholesterol[28] and 0.65 nm^2 for 1,2-dioctadecanoyl-*sn*-glycero-3-phosphocholine (DSPC)[29] and the known concentrations of SnOEP (7.9 μM), DSPC (0.5 mM), and cholesterol (0.5 mM). After irradiation of the reaction mixture with white light for 30 min, a black precipitate forms at the bottom of the reaction vessel leaving a colorless and transparent supernatant, which indicates that the reduction is complete (see Experimental Section and Supporting Information).

Figure 1 a,b shows transmission electron microscope (TEM) images of the nanostructures formed under the above conditions. Hollow nanospheres with diameters in the range from 60 to 200 nm, consistent with the size distribution of the templating liposomes, are observed (see Supporting Information Figure S2). Energy-dispersive X-ray spectroscopy (EDX) confirms that the nanospheres are composed of platinum (Supporting Information Figure S3). The selected-area electron diffraction (SAED) pattern shows that they are polycrystalline (Supporting Information Figure S4). Under these conditions, the coverage of Pt on the liposomes is incomplete, but sufficient to render intact porous spheres (Figure 1 a,b). The yield of the hollow nanospheres is estimated to be 70% based on Pt content in the TEM images. The remaining Pt is in the form of discrete dendritic nanosheets (Figure 1 c) with an average diameter of (12.9 ± 2.3) nm and a thickness of 2 nm as determined previously for the dendritic sheets templated on liposomes.[25] The small Pt dendrites may come partly from liposomes that get relatively small numbers of SnOEP molecules or that receive less light exposure. They may also originate from dendrites that simply fail to link to neighboring dendrites and become dislodged when the surfactant is washed away in preparing the TEM grid. The loose dendrites might also come from broken nanocages, although few large pieces of the nanocages are seen in the TEM images.

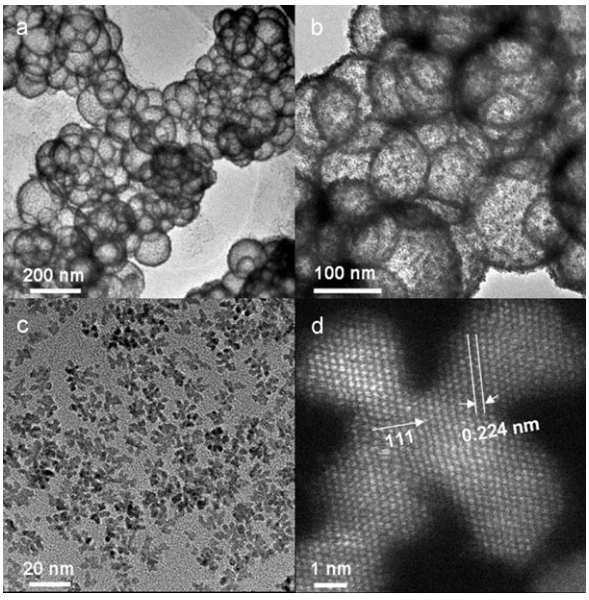

Figure 1. a), b) TEM images of hollow platinum nanocages at different magnifications. c) TEM and d) HAADF scanning TEM image of dendritic nanosheets, which join together upon liposomes to form hollow cages. The [111] direction in the crystal and the spacing of the ⟨111⟩ planes (0.224 nm) is indicated in (d).

Figure 1 d shows a high-angle annular dark-field (HAADF) scanning TEM image of a small Pt dendritic nanosheet. The entire dendrite is one single crystal of platinum as are the others that we have examined. These dendritic nanosheets may grow much larger (> 150 nm) while retaining their single-crystalline nature.[25,27]

Note that the shell thickness appears to be 5 to 10 nm in TEM images (Figure 1 b), while the individual nanosheets are 2 nm thick. The apparent thickness of the shell is mostly due to the tilting of dendrites from their exact edge-on geometry as they curve around the spheres, but some piercing of the outer surface of the bilayer by globular dendrites[25,27] and the low contrast of the images may also contribute to the apparent thickness.

The hollow nanocages agglomerate together to form superstructures, showing some foam-like distortion at the interfaces from the ideal spherical structures. The agglomeration is probably caused by the continuous variation of the solution conditions while the reaction is running, which causes aggregation of liposomes.[30]

Scanning electron microscope (SEM) images of the spherical nanocages are shown in Figure 2 a,b, revealing the hollow interior of several broken cages (Figure 2 a). It appears that some of the interiors of the nanospheres may be interconnected through large openings between adjacent cages (Figure 2 b), providing porosity at a larger scale. The shell thickness of approximately 2 nm, expected from the thickness of the Pt nanosheets,[25,27] is verified by measuring the edges of the broken cages (Supporting Information Figure S5). The high-contrast HAADF scanning TEM[31,32] images confirms the 2-nm thick walls when measured by the width of the bright line formed by the edge of the sphere in Figure 2 c,d. Considering that the outer diameter of the liposomes is up to 200 nm, the ratio of outer diameter and shell thickness is as large as 100:1.

The scanning TEM image of broken cages in Supporting Information Figure S6 more clearly show that the cages are

 © 2006 Wiley-VCH Verlag GmbH & Co. KGaA, Weinheim

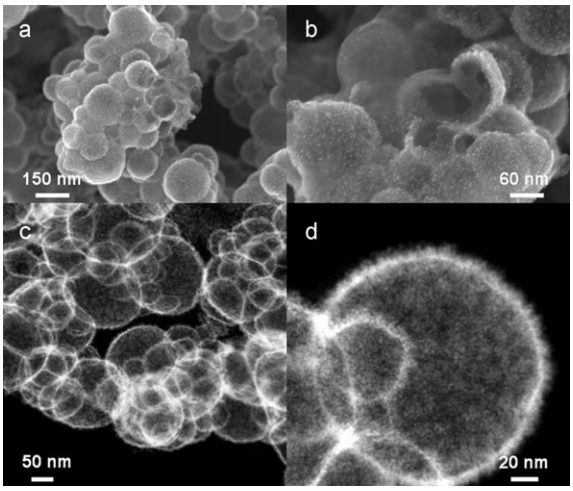

Figure 2. Hollow platinum nanocages: a), b) SEM images at different magnifications; c) and d) HAADF scanning TEM images at different magnifications.

composed of interconnected small dendritic nanosheets. The arms of the nanosheets forming the cages are also barely discernable in Figure 2d. The strong connectivity of dendrites that have grown together in the cages might be expected to provide higher structural stability than for spheres composed of discrete nanoparticles, and indeed the cages do survive under ambient conditions for at least a year, mild sonication, and cleaning by using water, ethanol, and chloroform.

As demonstrated in Figure 3, simply varying the concentration of the Pt complex while holding the SnOEP concentration and light intensity constant controls the structure obtained in the reaction. At low concentrations of Pt complex (0.25 mM), nanoparticles were found in circular groups of the same sizes as the liposomes (Figure 3a), indicating that there was insufficient Pt for growth of even small dendrites. This result is consistent with the suggested formation of Pt seed particles (Scheme 1c). At high concentrations of Pt complex (5 mM), platinum nanocages obtained still have an inner shell thickness of 2 nm, but a furry exterior (Figure 3b) and larger diameter dendritic sheets were observed (Supporting Information Figure S7). Many of the nanosheets show evidence of globular dendrite growth (Supporting Information Figure S7), but most of the dendritic sheets do not show thickening in good agreement with the proposed confined growth within the liposomal bilayers.[25] At the higher concentration of Pt complex (10 mM), the liposomes apparently can not effectively confine the growth of the dendrites and we observe considerable additional globular dendritic growth out from the outer surfaces, especially at interfaces between liposomes (Figure 3c,d).

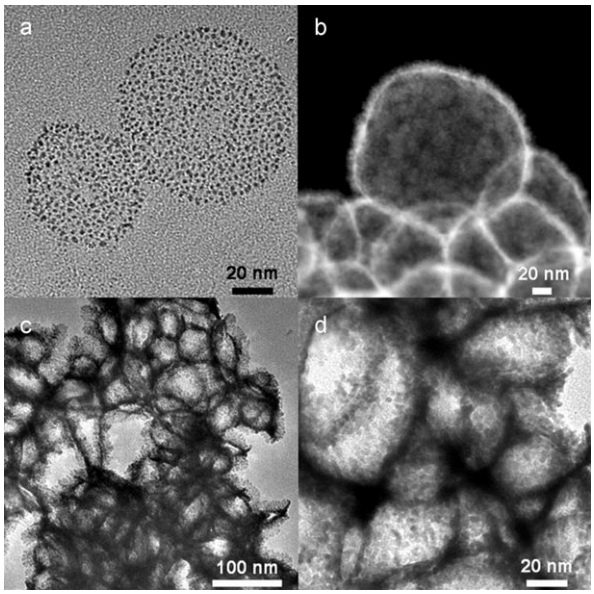

Figure 3. TEM images of platinum nanostructures obtained at various concentration of platinum complex: a) 0.25 mM; b) 5 mM; c) and d) 10 mM. (b) is a dark-field image.

If there is a one-to-one correspondence between a porphyrin molecule and the seed (and thus Pt dendrite) that it produces and, in addition, if the seed particle remains at the location of the porphyrin molecule, then the Pt nanoparticles could be grown and used as nanotags to reveal the location of the Sn-porphyrin in the membrane. The techniques used in this case to produce nanospheres might also be generalized to porphyrin-labeled molecules (e.g., lipids, drug molecules, proteins, or other biological structures) for growing nanometer-sized tags, which can be imaged using electron microscopy to give a high resolution picture of the spatial distribution of the porphyrin-labeled species.

The nanocages offer the opportunity to determine the number of Pt seed particles produced per porphyrin molecule. Since the number of porphyrins per liposome can be calculated, the seed:porphyrin ratio can be determined in two ways—either by counting the number of seed particles in a liposome of known size (e.g., a circle of seeds in Figure 3a) or by determining the average size of the dendrites required for them to link together with others to preserve the spherical structure (estimated by determining the average size from a field of nanosheets as in Figure 1c). Explicitly, the number of porphyrin molecules in the 80-nm diameter liposome of Figure 3a is calculated to be 600, and therefore the 80-nm liposome should ideally contain 600 Pt nanoparticles. Counting the particles using a conservative estimate of the spot density in the image that represents a particle leads to approximately 400 particles; an estimate using a more liberal low-density limit gives about 2000 particles. We find then that the observed number of seeds is within the range of the number of porphyrin molecules in the liposome, and thus the seed:porphyrin ratio obtained by this method is near 1:1 within the large uncertainty in counting introduced by the level of electron density that is deemed to represent a particle.

Another estimate of the seed:porphyrin ratio is given by the average diameter of dendrites required for them to link together to form the nanocages. For the concentrations of lipid and porphyrin used herein, the average liposomal surface area associated with each porphyrin molecule is 33 nm^2. Thus, the average distance between neighboring porphyrin molecules (for idealized hexagonal packing) is

 © 2006 Wiley-VCH Verlag GmbH & Co. KGaA, Weinheim

6.2 nm. Therefore, we expect the average diameter of the dendrites to be at least 7 nm for them to join well enough to form a connection. This value is close to the observed average diameter of the dendrites that form the nanocages shown in Figure 1 ((12.3 ± 2.3) nm), again indicating close to one dendrite (or seed) per porphyrin.

The metal nanocages described herein may be suitable for many applications (e.g., as catalysts and electrocatalysts) for which platinum is required to be in an open, low-density, high surface area form. Additional synthetic control over the nanocages can be realized by variation of parameters, such as light exposure, porphyrin concentration, and the size of the templating liposomes. Further, nanocages composed of other metals and alloys can be made.

Experimental Section

SnOEP-containing unilamellar liposomes with a composition of 1:1 DSPC:cholesterol mole ratio were prepared by an extrusion procedure similar to that described previously.[25] In the synthesis, 1 mL of the liposomes ([DSPC] = 0.5 mM, [cholesterol] = 0.5 mM, [AA] = 150 mM, [SnOEP] = 7.9 μM) was mixed with 1 mL of the aged Pt salt solutions (0.5, 2, 10, 20 mM) in a glass vial. The Pt nanocages were produced in the reactions using 2 and 10 mM Pt complex solutions. TEM (200 keV JEOL 2010), HRTEM, HAADF STEM (200 keV JEOL 2010F), EDX, SAED, and SEM (30 keV S-5200) images of the nanostructures were obtained. Additional experimental details are provided in the Supporting Information.

Received: June 15, 2006
Revised: August 18, 2006
Published online: October 25, 2006

Keywords: liposomes · nanostructures · platinum · porphyrinoids · templating

[1] L. R. Hirsch, J. B. Jackson, A. Lee, N. J. Halas, J. West, *Anal. Chem.* **2003**, *75*, 2377 – 2381.
[2] L. R. Hirsch, R. J. Stafford, J. A. Bankson, S. R. Sershen, B. Rivera, R. E. Price, J. D. Hazle, N. J. Halas, J. L. West, *Proc. Natl. Acad. Sci. USA* **2003**, *100*, 13549 – 13554.
[3] S. W. Kim, M. Kim, W. Y. Lee, T. Hyeon, *J. Am. Chem. Soc.* **2002**, *124*, 7642 – 7643.
[4] Y. J. Xiong, B. Wiley, J. Y. Chen, Z. Y. Li, Y. D. Yin, Y. N. Xia, *Angew. Chem.* **2005**, *117*, 8127 – 8131; *Angew. Chem. Int. Ed.* **2005**, *44*, 7913 – 7917; .
[5] P. Jiang, J. F. Bertone, V. L. Colvin, *Science* **2001**, *291*, 453 – 457.
[6] E. Prodan, C. Radloff, N. J. Halas, P. Nordlander, *Science* **2003**, *302*, 419 – 422.
[7] L. H. Lu, R. Capek, A. Kornowski, N. Gaponik, A. Eychmuller, *Angew. Chem.* **2005**, *117*, 6151 – 6155; *Angew. Chem. Int. Ed.* **2005**, *44*, 5997 – 6001; .
[8] M. L. Breen, A. D. Dinsmore, R. H. Pink, S. B. Qadri, B. R. Ratna, *Langmuir* **2001**, *17*, 903 – 907.
[9] Z. J. Liang, A. Susha, F. Caruso, *Chem. Mater.* **2003**, *15*, 3176 – 3183.
[10] Y. Vasquez, A. K. Sra, R. E. Schaak, *J. Am. Chem. Soc.* **2005**, *127*, 12504 – 12505.
[11] Y. G. Sun, Y. N. Xia, *Science* **2002**, *298*, 2176 – 2719.
[12] H. P. Liang, H. M. Zhang, J. S. Hu, Y. G. Guo, L. J. Wan, C. L. Bai, *Angew. Chem.* **2004**, *116*, 1566 – 1569; *Angew. Chem. Int. Ed.* **2004**, *43*, 1540 – 1543; .
[13] J. Y. Chen, B. Wiley, J. McLellan, Y. J. Xiong, Z. Y. Li, Y. N. Xia, *Nano Lett.* **2005**, *5*, 2058 – 2062.
[14] X. Y. Gao, J. S. Zhang, L. Zhang, *Adv. Mater.* **2002**, *14*, 290 – 293.
[15] Y. J. Song, S. R. Challa, C. J. Medforth, Y. Qiu, R. K. Watt, D. Pena, J. E. Miller, F. van Swol, J. A. Shelnutt, *Chem. Commun.* **2004**, 1044 – 1045.
[16] D. B. Zhang, L. M. Qi, J. M. Ma, H. M. Cheng, *Adv. Mater.* **2002**, *14*, 1499 – 1502.
[17] P. R. Selvakannan, M. Sastry, *Chem. Commun.* **2005**, 1684 – 1686.
[18] Y. J. Xiong, J. M. McLellan, J. Y. Chen, Y. D. Yin, Z. Y. Li, Y. N. Xia, *J. Am. Chem. Soc.* **2005**, *127*, 17118 – 17127.
[19] Y. J. Xiong, J. Y. Chen, B. Wiley, Y. N. Xia, *J. Am. Chem. Soc.* **2005**, *127*, 7332 – 7333.
[20] M. S. Wong, J. N. Cha, K. S. Choi, T. J. Deming, G. D. Stucky, *Nano Lett.* **2002**, *2*, 583 – 587.
[21] V. S. Murthy, J. N. Cha, G. D. Stucky, M. S. Wong, *J. Am. Chem. Soc.* **2004**, *126*, 5292 – 5299.
[22] J. N. Cha, H. Birkedal, L. E. Euliss, M. H. Bartl, M. S. Wong, T. J. Deming, G. D. Stucky, *J. Am. Chem. Soc.* **2003**, *125*, 8285 – 8289.
[23] D. R. Rolison, *Science* **2003**, *299*, 1698 – 1701.
[24] E. Antolini, *Mater. Chem. Phys.* **2003**, *78*, 563 – 573.
[25] Y. J. Song, W. A. Steen, D. Pena, Y. B. Jiang, C. J. Medforth, Q. S. Huo, J. L. Pincus, Y. Qiu, D. Y. Sasaki, J. E. Miller, J. A. Shelnutt, *Chem. Mater.* **2006**, *18*, 2335 – 2346.
[26] Y. J. Song, Y. B. Jiang, H. R. Wang, D. A. Pena, Y. Qiu, J. E. Miller, J. A. Shelnutt, *Nanotechnology* **2006**, *17*, 1300 – 1308.
[27] Y. J. Song, Y. Yang, C. J. Medforth, E. Pereira, A. K. Singh, H. F. Xu, Y. B. Jiang, C. J. Brinker, F. van Swol, J. A. Shelnutt, *J. Am. Chem. Soc.* **2004**, *126*, 635 – 645.
[28] R. Villegas, F. V. Barnola, *J. Gen. Physiol.* **1972**, *59*, 33 – 46.
[29] P. Balgavy, M. Dubnickova, N. Kucerka, M. A. Kiselev, S. P. Yaradaikin, D. Uhrikova, *Biochim. Biophys. Acta* **2001**, *1512*, 40 – 52.
[30] J. H. Collier, P. B. Messersmith, *Annu. Rev. Mater. Res.* **2001**, *31*, 237 – 263.
[31] A. V. Crewe, *Chem. Scr.* **1979**, *14*, 17 – 20.
[32] Z. L. Wang, *Adv. Mater.* **2003**, *15*, 1497 – 1514.

 © 2006 Wiley-VCH Verlag GmbH & Co. KGaA, Weinheim

Mass Determination

DOI: 10.1002/anie.200603839

Microscopy-Based Mass Measurement of a Single Whole Virus in a Cylindrical Ion Trap**

Zongxiu Nie, Yan-Kai Tzeng, Huan-Cheng Chang, Chi-Chien Chiu, Chi-Yao Chang, Chia-Ming Chang, and Mi-Hua Tao*

Measuring the mass of a single whole virus is a technological challenge in the field of mass spectrometry.[1] The measurement is also important because knowing the masses of individual virus particles and the mass variability of each population is essential for the development of concepts about the structure and nature of these genetically diverse agents. Recent studies show that viruses are the most abundant biological entities in the world's oceans and are second to prokaryotes in terms of biomass on the planet.[2] It is thus timely and of interest to develop mass spectrometry of whole viruses to expand our understanding of the simplest "life forms".

With the development of soft ionization techniques such as electrospray ionization (ESI)[3] and laser-induced acoustic desorption (LIAD),[4] it has become possible to measure both masses[5–7] and sizes[8–10] of intact viruses (and viral capsids) in the gas phase with high accuracy. One of the most successful methods developed to date is charge detection mass spectrometry, which measures masses of the individual viral ions generated by ESI with a charge-sensitive detector.[6] Thousands of virus particles can be analyzed in a reasonably short period of time ($\approx$30 min). However, the typical error involved in the measurement was $\pm$15% as derived from the image current detection as well as the time of flight of the viral ions through the charge-sensitive tube. To achieve higher mass resolution and measurement accuracy, we have previously proposed an alternative scheme to determine the absolute mass of a single virus particle in a quadrupole ion trap (QIT) by using a scattered light detection method.[11] The technique, reminiscent of Millikan oil drop experiments, has permitted mass measurement of a single *E. coli* whole cell with an accuracy better than 1%.[7,12]

Although a QIT provides an ideal environment for long-term interrogation of a single trapped ion, the hyperbolic shape of the electrodes makes collection of scattered laser light difficult. For example, when the light was collected through a small hole drilled in one of the end-cap electrodes, virus particles with a size of less than 300 nm could not be readily detected.[7] In contrast to the QIT, a cylindrical ion trap (CIT) has a much simpler geometry although the equation of motion of the trapped ion is complex and cannot be solved analytically.[13] Cooks and co-workers[14] recently demonstrated that after geometry optimization to minimize higher-order field contributions, the CIT can achieve a performance comparable to that of a standard QIT with hyperbolic electrodes. It holds the advantage that one of its end-cap electrodes can be replaced by a flat, electrically conductive glass plate that enables collection of more than 10% of the light radiating from the trapped particle. Furthermore, the dimension of this trap can be varied at the user's convenience without complicated machine operations. Such a technological advancement allows integration of the transparent CIT with a variety of highly sensitive optical methods, such as the interferometric technique,[15] to detect particles of approximately 10 nm in diameter. Herein, we present a demonstration of this approach by using a CIT equipped with transparent end-cap electrodes to determine the absolute mass of a single whole virus in the gas phase.

Three viruses were examined in this study: recombinant human adenovirus type 5 (Ad5), grouper iridovirus (GIV), and vaccinia virus (VV). Their sizes range from 80 to 300 nm with the corresponding masses varying by two orders of magnitude. Figure 1a shows a schematic diagram of the experimental setup. Similar to our previous work,[7] LIAD was used as the ion source to generate multiply charged viral ions. Three major modifications have been made to improve the performance as well as detection sensitivity of the apparatus designed for investigation of monomeric virus particles: 1) a miniature transparent CIT was employed as the mass analyzer, 2) a small AC voltage (10 V) was applied between two end-cap electrodes to select ions with smaller mass-to-charge ratios (m/z), and 3) a fast Fourier transform (FFT) method was adopted to determine the oscillation frequencies of the trapped particle from its modulated scattered light signal (Figure 1b).[16] To calibrate this home-built mass spectrometer, we used the NIST polystyrene size standard SRM 1963, which has a nominal diameter of

[*] Dr. Z. X. Nie, Y.-K. Tzeng, Dr. H.-C. Chang
Institute of Atomic and Molecular Sciences
Academia Sinica
Taipei 106 (Taiwan)
Fax: (+886) 2-2362-0200
E-mail: hcchang@po.iams.sinica.edu.tw
Y.-K. Tzeng, Dr. H.-C. Chang
Department of Chemistry
National Taiwan Normal University
Taipei 106 (Taiwan)
Dr. Z. X. Nie
Department of Physics, Wuhan University
Wuhan 430072 (P.R. China)
Dr. C.-C. Chiu, Dr. C.-Y. Chang
Institute of Cellular and Organismic Biology
Academia Sinica
Taipei 115 (Taiwan)
C.-M. Chang, Dr. M.-H. Tao
Institute of Biomedical Sciences, Academia Sinica
Taipei 115 (Taiwan)
C.-M. Chang
Graduate Institute of Life Sciences
National Defense Medical Center
Taipei 114 (Taiwan)

[**] This work was supported by grants from Academia Sinica and the National Science Council (grant no. NSC 93-3112-B-001-012-Y) of Taiwan, R.O.C. We thank C.-S. Chung for preparation of the vaccinia virus and F. P. Cui for technical assistance.

Supporting information for this article is available on the WWW under http://www.angewandte.org or from the author.

 © 2006 Wiley-VCH Verlag GmbH & Co. KGaA, Weinheim

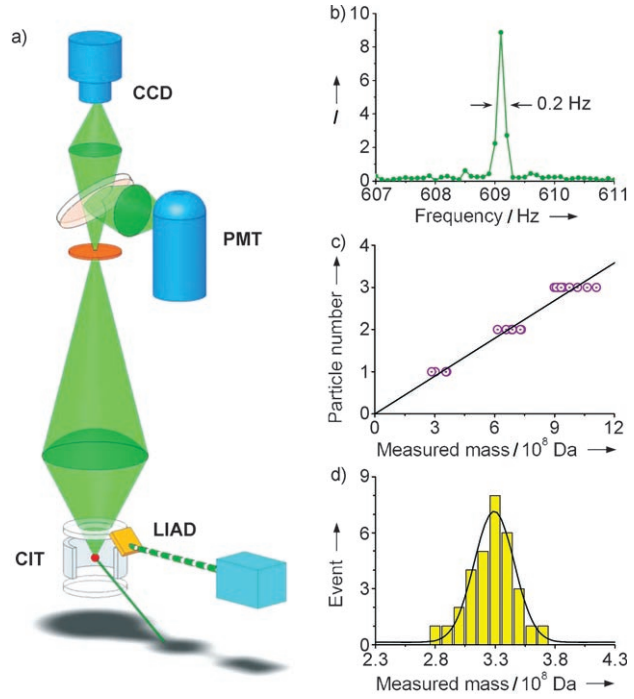

Figure 1. a) Schematic of the experimental setup consisting of a CIT made of a stainless steel barrel and two flat indium tin oxide (ITO)-coated glass plates. The scattered laser light was collected with a long working distance objective (numerical aperture of 0.42) arranged in a confocal configuration. One-half of the collected light was directed toward an electron-multiplier charge-coupling device (CCD) for trajectory imaging to ensure trapping of a single particle.[7,12] The other half was detected by a photomultiplier tube (PMT) for frequency spectrum analysis.[16] b) Typical frequency spectrum obtained by FFT of the time-domain signal acquired by PMT for 10 s. c) Plot of measured masses versus assigned particle numbers for the polystyrene size standard, SRM 1963. d) Mass distribution of the monomeric 100-nm polystyrene spheres.

100 nm.[17] Figure 1c shows the result of the mass measurement for this sample. In accord with previous observations,[7,12] both monomeric and cluster particles were detected. From 40 independent measurements (Figure 1d), we obtained a number-average mass of $3.32 \pm 0.12 \times 10^8$ Da or a mean size of 100.0 ± 1.2 nm calculated from the density of $1.055\ g\,cm^{-3}$ for the polystyrene spheres.[18] This measured size is in excellent agreement with the diameter of 99.7 ± 1.7 nm certified by NIST.

Vaccinia viruses (VVs) are large, brick-shaped particles with dimensions of approximately $360 \times 270 \times 250\ nm^3$.[19] They have a linear double-stranded DNA genome of 192 kbp in length and can potentially express more than 200 proteins.[20] An application of the microscopy-based CIT technique to this virus yielded a mean mass of 3.26×10^9 Da, which corresponds to the dry mass of the whole VV particle. Note that this measured mass is identical to our previous measurement that used a QIT as the mass analyzer for the same virus within experimental errors.[7] The major improvement made here is that we can detect monomeric VV particles quite easily with this new setup owing to the approximately 10^3-fold increase in detection sensitivity. Applying the same technique to smaller viruses such as GIV, we obtained a mean mass of 4.48×10^8 Da, accompanied with a mass variation of $\pm 0.26 \times 10^8$ Da. The result was obtained by measuring more than 40 monomeric and cluster particles (Figure 2a), requiring approximately 10 min for each successful measurement. As the accuracy of the mass measurement for each particle is better than 1%, the observed mass variation should represent the intrinsic mass distribution of these virus particles or, more likely, is a combined result of this mass distribution, degradation of the virions upon desorption/ionization, incomplete dehydration, and formation of adducts.

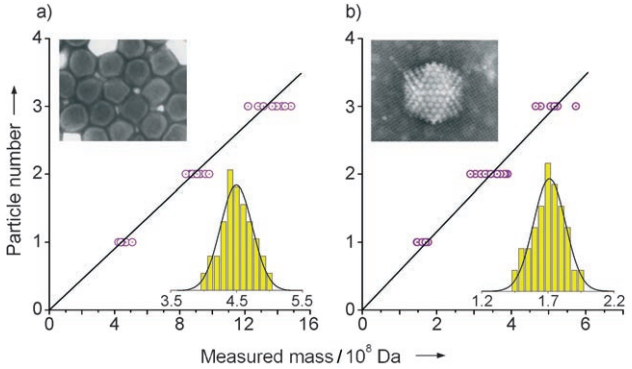

Figure 2. Plots of measured masses versus particle numbers for a) grouper iridoviruses and b) recombinant human adenoviruses. Upper insets: electron micrographs of negatively stained iridoviruses (≈170 nm in diameter)[21a] and adenoviruses (≈80 nm in diameter).[24] Lower insets: mass distributions of the respective viruses. The typical trapping parameters ($\Omega/2\pi$ and V_{ac}) used in each measurement were 5 kHz and 1000 V (a) and 7 kHz and 1000 V (b). Comparison of the mass and size of these two viruses suggests that about 70% of the total weight of the iridovirus in its native form is contributed by water.

The grouper iridovirus studied herein is an icosahedral virus with a diameter of about 170 nm.[21a] The virus is composed of a proteinaceous capsid, a lipid membrane, and a central deoxyribonucleoprotein core holding a single linear molecule of double-stranded DNA. The genome contains approximately 140 kbp (49% G + C in content)[21b] and has a calculated mass of 9.1×10^7 Da. Compared with our measured mass of 4.48×10^8 Da for the whole virus, it suggests that the iridoviruses extracted from diseased yellow groupers contain 20% nucleic acids by weight. Such a dry mass measurement also allows estimation of the number of copies of major capsid proteins in GIV. According to sequence analysis of the GIV gene, the capsid protein consists of 463 amino acids with a predicted mass of 50272 Da.[21c] Although the exact surface structure of this virus particle is not yet known, the major capsid protein was determined to account for about 40% of the total virion protein mass. Based upon this mass ratio, the genome mass, and assuming a lipid content of approximately 10% by weight,[22] we estimate that the capsid of GIV comprises about 2500 copies of the proteins self-assembled to form an icosahedral cage.

Human adenovirus Ad5 is the smallest and simplest virus examined in this study. The virus (≈80 nm in diameter) is non-enveloped, icosahedral, and has a double-stranded DNA of 36 kbp and 55% G + C in content.[23] The capsid of this

 © 2006 Wiley-VCH Verlag GmbH & Co. KGaA, Weinheim

virus is built of 252 capsomers, of which 240 are hexavalent and 12 (situated at the apices) are pentavalent.[24] The total mass estimated for the adenovirus is in the range of 1.5–1.8 × 10^8 Da.[25] Figure 2b shows the result of our measurements for 40 recombinant Ad5 particles. We obtained a number-average mass of 1.72×10^8 Da, which falls nicely into the calculated mass range. The observed mass variation is $\pm 0.13 \times 10^8$ Da, or $\pm 7\%$, which translates to a size distribution of about 2% for spheroidal particles like adenoviruses. One may compare this size distribution directly with the distribution measured by Thomas et al.,[9] who used charge-reduced ESI ion mobility spectrometry to characterize the supermolecular structure of human pathogen adenovirus in the gas phase. They determined a modal diameter of 79.1 nm with a size distribution (full width at half maximum) of 72–88 nm. Our measured size distribution is about fivefold narrower than their measurement and expected to be further reduced after refinement of the experimental conditions.

Light scattering is an attractive technique for detection of nanoscale particles because of its non-destructive nature, high sensitivity, and the potential for real-time analysis.[15] Compared with conventional techniques such as quantitative electron microscopy and sedimentation field-flow fractionation that have been used to measure the dry mass of the vaccinia virus[26] and chlorovirus,[27] respectively, the ion-trap method as presently illustrated can clearly provide more direct and precise mass information. Furthermore, the design of this CIT mass spectrometer is simpler and its size can be reduced to that of an optical fluorescence microscope. However, an inherent disadvantage of the light scattering technique is that the observed light intensity (I) decreases very rapidly with the particle diameter (d) as $I \propto d^6$. This sets a lower detection limit of $d \approx 50$ nm for monomeric virus particles by using the present setup. An ultimate approach to overcome this size limitation is to measure the electromagnetic field amplitude (instead of the intensity) of the scattered light interferometrically, which gives a d^3 dependence and has been shown to be capable of detecting a single 15-nm polystyrene sphere in water.[15] An integration of this method with the CIT is expected to extend the present detection limit to the 20 nm region, where the experimentally determined masses can be compared directly with their calculated values for model virus particles such as MS2 bacteriophage[5] and rice yellow mottle virus.[6]

To conclude, we have illustrated a technique capable of determining the absolute mass of a single whole virus with a size as small as 80 nm. The typical mass-to-charge ratio determined for these medium-sized virus particles was in the range of 1×10^7, which overlaps closely with the highest m/z region covered by cryodetection time-of-flight mass spectrometry as recently demonstrated for single megadalton protein ions.[28] This microscopy-based technique is complementary to such existing commercial instruments and can be applied to mass measurement of nanoscale particles in general.

Experimental Section

Recombinant human adenoviruses were prepared by cotransfection of 293 cells with appropriate plasmids (pJM17 and pAdvPGK) and isolated according to the procedures described in reference [29]. Iridoviruses were isolated from spleen tissues of diseased yellow groupers (*Epinephelus awoara*), propagated in grouper kidney cells, and purified with ultracentrifugation in CsCl gradients.[21a] Wild-type vaccinia viruses were prepared as intracellular mature virus stocks in BSC40 cells and isolated and purified as described in reference [30]. All these virus particles, after additional purification by dialysis, were resuspended in filtered (0.2 μm pore size filter) deionized water at a concentration of about 1×10^9 particles mL^{-1} before use. To prepare the sample for LIAD,[7] an aliquot (10 μL) of the virus suspension was deposited on a bare Si wafer and dried in a dust-free desiccator. After loading into the vacuum chamber for further dehydration, intact viral ions were vaporized from the Si substrate and introduced into the CIT by laser-induced acoustic desorption. The miniature CIT has a dimension of $r_0 = z_0 = 5.0$ nm, where r_0 is the radius of the ring electrode and z_0 is half the separation between the two end-cap electrodes. Further experimental details about the mass determination of these viruses by using the CIT can be found in reference [7] and also in the Supporting Information.

Received: September 19, 2006

Keywords: ion trap · mass determination · mass spectrometry · microscopy · viruses

[1] a) G. Siuzdak, B. Bothner, M. Yeager, C. Brugidou, C. M. Fauquet, K. Hoey, C. M. Chang, *Chem. Biol.* **1996**, *3*, 45–48; b) B. Bothner, G. Siuzdak, *ChemBioChem* **2004**, *5*, 258–260.
[2] C. A. Suttle, *Nature* **2005**, *437*, 356–361.
[3] S. F. Wong, C. K. Meng, J. B. Fenn, *J. Phys. Chem.* **1988**, *92*, 546–550.
[4] V. V. Golovlev, S. L. Allman, W. R. Garrett, N. I. Taranenko, C. H. Chen, *Int. J. Mass Spectrom. Ion Processes* **1997**, *169*, 69–78.
[5] M. A. Tito, K. Tars, K. Valegard, J. Hajdu, C. V. Robinson, *J. Am. Chem. Soc.* **2000**, *122*, 3550–3551.
[6] S. D. Fuerstenau, W. H. Benner, J. J. Thomas, C. Brugidou, B. Bothner, G. Siuzdak, *Angew. Chem.* **2001**, *113*, 559–562; *Angew. Chem. Int. Ed.* **2001**, *40*, 542–544; Corrigendum: S. D. Fuerstenau, W. H. Benner, J. J. Thomas, C. Brugidou, B. Bothner, G. Siuzdak, *Angew. Chem.* **2001**, *113*, 1011; *Angew. Chem. Int. Ed.* **2001**, *40*, 982.
[7] W.-P. Peng, Y.-C. Yang, M.-W. Kang, Y.-K. Tzeng, Z. X. Nie, H.-C. Chang, W. Chang, C.-H. Chen, *Angew. Chem.* **2006**, *45*, 1451–1454; *Angew. Chem. Int. Ed.* **2006**, *45*, 1423–1426.
[8] G. Bacher, W. W. Szymanski, S. L. Kaufman, P. Zollner, D. Blaas, G. Allmaier, *J. Mass Spectrom.* **2001**, *36*, 1038–1052.
[9] J. J. Thomas, B. Bothner, J. Traina, W. H. Benner, G. Siuzdak, *Spectroscopy* **2004**, *18*, 31–36.
[10] C. J. Hogan, E. M. Kettleson, B. Ramaswami, D.-R. Chen, P. Biswas, *Anal. Chem.* **2006**, *78*, 844–852.
[11] W.-P. Peng, Y. Cai, H.-C. Chang, *Mass Spectrom. Rev.* **2004**, *23*, 443–465.
[12] W.-P. Peng, Y.-C. Yang, M.-W. Kang, Y. T. Lee, H.-C. Chang, *J. Am. Chem. Soc.* **2004**, *126*, 11766–11767.
[13] R. E. March, J. F. J. Todd, *Quadrupole Ion Trap Mass Spectrometry*, 2nd ed., Wiley, New York, **2005**, chap. 6, and references therein.
[14] a) J. M. Wells, E. R. Badman, R. G. Cooks, *Anal. Chem.* **1998**, *70*, 438–444; b) E. R. Badman, J. M. Wells, H. A. Bui, R. G. Cooks, *Anal. Chem.* **1998**, *70*, 3545–3547.
[15] F. V. Ignatovich, L. Novotny, *Phys. Rev. Lett.* **2006**, *96*, 013901.
[16] S. Schlemmer, J. Illemann, S. Wellert, D. Gerlich, *J. Appl. Phys.* **2001**, *90*, 5410–5418.
[17] Certificate of analysis for NIST Standard Reference Material 1963.
[18] H. Kahler, B. J. Lloyd, Jr., *Science* **1951**, *114*, 34–35.

 © 2006 Wiley-VCH Verlag GmbH & Co. KGaA, Weinheim

[19] M. Cyrklaff, C. Risco, J. J. Fernandez, M. V. Jimenez, M. Esteban, W. Baumeister, J. L. Carrascosa, *Proc. Natl. Acad. Sci. USA* **2005**, *102*, 2772 – 2777.
[20] S. J. Goebel, G. P. Johnson, M. E. Perkus, S. W. Davis, J. P. Winslow, E. Paoletti, *Virology* **1990**, *179*, 247 – 266.
[21] a) Y.-S. Lai, S. Murali, H.-Y. Ju, M.-F. Wu, I.-C. Guo, S.-C. Chen, K. Fang, C.-Y. Chang, *J. Fish Dis.* **2000**, *23*, 379 – 388; b) C.-T. Tsai, J.-W. Ting, M.-H. Wu, M.-F. Wu, I.-C. Guo, C.-Y. Chang, *J. Virol.* **2005**, 79, 2010 – 2023; c) S. Murali, M.-F. Wu, I.-C. Guo, S.-C. Chen, H.-W. Yang, C.-Y. Chang, *J. Fish Dis.* **2002**, *25*, 91 – 100.
[22] http://www.ncbi.nlm.nih.gov/ICTVdb/ICTVdB/00.036.htm.
[23] J. Chroboczek, F. Bieber, B. Jacrot, *Virology* **1992**, *186*, 280 – 285.
[24] R. C. Valentine, H. G. Pereira, *J. Mol. Biol.* **1965**, *13*, 13 – 20.
[25] http://www.ncbi.nlm.nih.gov/ICTVdb/ICTVdB/01000000.htm.
[26] G. F. Bahr, W. D. Foster, D. Peters, E. H. Zeitler, *Biophys. J.* **1980**, *29*, 305 – 314.
[27] C. R. Yonker, K. D. Caldwell, J. C. Giddings, J. L. Van Etten, *J. Virol. Methods* **1985**, *11*, 145 – 160.
[28] R. J. Wenzel, U. Matter, L. Schultheis, R. Zenobi, *Anal. Chem.* **2005**, *77*, 4329 – 4337.
[29] A. J. Bett, W. Haddara, L. Prevec, F. L. Graham, *Proc. Natl. Acad. Sci. USA* **1994**, *91*, 8802 – 8806.
[30] C. S. Chung, J. C. Hsiao, Y. S. Chang, W. Chang, *J. Virol.* **1998**, *72*, 1577 – 1585.

 © 2006 Wiley-VCH Verlag GmbH & Co. KGaA, Weinheim

Chiral Nanoballs

DOI: 10.1002/anie.200603622

Lanthanitin: A Chiral Nanoball Encapsulating 18 Lanthanum Ions by Ferritin-Like Assembly**

*Kyung Seok Jeong, Young Shin Kim, Yun Ju Kim, Eunsung Lee, Ji Hye Yoon, Won Hwa Park, Young Woo Park, Seung-Joon Jeon, Zee Hwan Kim, Jaheon Kim, and Nakcheol Jeong**

In self-assembly through metal–organic coordination chemistry, strong interaction between metal ions and polydentate ligands is the primary driving force. Contrary to processes involving weak intermolecular forces, the much stronger interactions between metal ions and polydentate organic ligands make the contribution of weak interactions less significant.[1,2] Thus, the number of factors to be considered in the process is substantially decreased, and the outcome is often predictable. Many efforts were successfully directed to obtaining geometrically intriguing supramolecules such as molecular polygons,[3] highly symmetrical cage molecules,[4] and metal–organic frameworks[5] by rational design of metal–ligand motifs. However, precise prediction of the outcome is still not always possible, and there is more to be explored, especially for the f-block elements because of their versatile coordination numbers.[6] Potential applications of self-assembled lanthanide-containing nanoparticles in catalytic reactions, optoelectronics, and magnetic materials have attracted much interest.[7] Despite intensive studies, enantiopure lanthanide coordination compounds still represent a formidable challenge.[8]

We herein report a unique chiral lanthanum-containing supramolecule, dubbed lanthanitin because it forms by ferritin-like assembly.[9] In addition, its incorporation into a chiral double helix in crystals in an unprecedented manner constitutes a new class of crystal packing other than that of the helicates.[10] Chiral ligands (*S*,*S*)-**1**H_2 and (*R*,*R*)-**1**H_2 (acid forms of **1**) used in this study were both synthesized from 4,4′-dibromostilbene in optically pure form by taking advantage of Sharpless asymmetric dihydroxylation (Scheme 1).[11] Chirality is introduced on the ethylene bridge. The ditopic carboxyl groups on *para* positions of the aromatic rings will serve to bridge various metal ions. Tying up the two hydroxyl groups with a 1,1′-dimethylmethylene group eliminated the flexibility of the molecule. Thus, the molecule has a fixed conformation and a dihedral angle between the two benzoic acid groups of about 80°.

Colorless antiprismatic crystals of (*S*)-lanthanitin suitable for X-ray diffraction were grown from a mixture of (*S*,*S*)-**1**H_2 and $LaCl_3 \cdot 6H_2O$ in *N*,*N*′-diethylformamide (DEF) solution at 60 °C over two weeks (Figure 1a). X-ray crystallographic studies revealed that the crystal belongs to the enantiomorphous space group $P4_122$. The asymmetric unit containing a trigonal arrangement of nine La^{III} ions and 12 (*S*,*S*)-**1** linking ligands forms a supramolecular hemisphere. When the crystallographic twofold symmetry is applied to the asymmetric unit, two hemispheres fuse to form a spherical molecule with a diameter of 3.0 nm.

Twenty four ligands encompass the metal ions in a unit having the formula $[La_{18}\{(S,S)\text{-}\mathbf{1}\}_{24}(CO_3)_2(H_2O)_{32}]^{2+}$ (Figure 1b). In the core of the molecule, two carbonate anions (Figure 2) each bind three lanthanum ions. The presence of the carbonate core as a seed is critical for the formation of crystals, even though the origin of carbonate is not clear. It may come from atmospheric carbon dioxide. This unusual kind of nucleation was reported previously only in two cases, one of which includes a Gd^{III} complex.[12]

One of the most notable structural features of (*S*)-lanthanitin is that the 18 La^{III} ions form an octahedral arrangement with six sets of three lanthanide ions. The three La^{III} ions in each set are arranged linearly with average interatomic distances of 4.145 Å. These sets are, if we consider

[*] K. S. Jeong, Y. S. Kim, Y. J. Kim, W. H. Park, Y. W. Park, Prof. S.-J. Jeon, Prof. Z. H. Kim, Prof. N. Jeong
Department of Chemistry
Korea University
Seoul 136-701 (Korea)
Fax: (+82) 2-3290-3121
E-mail: njeong@korea.ac.kr
E. Lee, J. H. Yoon, Prof. J. Kim
Department of Chemistry and CAMDRC
Soongsil University
Seoul 156-743 (Korea)

[**] N.J. thanks KOSEF (grant No. R02-2002-000-00128-0 of the Basic Research Program), CMDS and Korea University for their financial support. K.S.J., Y.S.K, and Y.J.K are grateful to BK21 program. J.K. thanks the Korea Research Foundation for the grant (KRF 2003-070-C00029).

Supporting information for this article is available on the WWW under http://www.angewandte.org or from the author.

InterScience
© 2006 Wiley-VCH Verlag GmbH & Co. KGaA, Weinheim

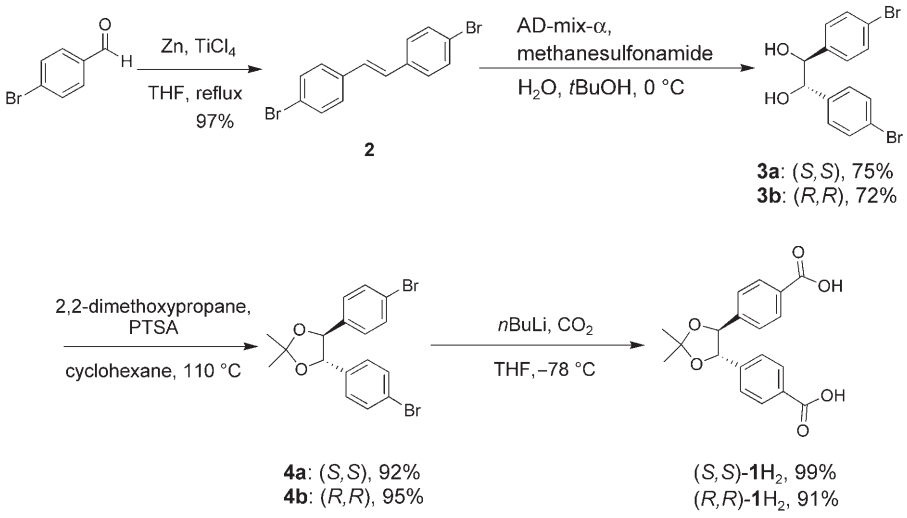

Scheme 1. Preparation of ligands (*S*,*S*)-**1**H$_2$ and (*R*,*R*)-**1**H$_2$. See the Supporting Information. PTSA = *para*-toluenesulfonic acid.

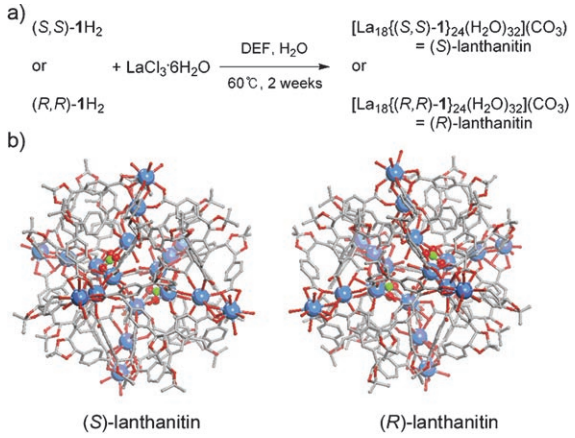

Figure 1. a) Preparation of lanthanitin enantiomers. b) Molecular structures of lanthanitins with octahedral arrangement of 18 La ions as large blue balls and the central carbonate carbon atoms as small green balls. Hydrogen atoms are omitted for clarity. Color code: C gray, O red.

the asymmetric unit, {La(1),La(4),La(7)}, {La(2),La(5),La(8)}, and {La(3),La(6),La(9)} which together form a pyramidal shape with a small triangle {La(1),La(2),La(3)} linked by a carbonate anion at the apex (Figure 2b). The interplanar distance among the sets is 1.90 Å. The outer lanthanum ions {La(7),La(8),La(9)} and their twofold symmetry pairs define a slightly distorted octahedron with an average edge length of 17.624 Å (16.818–18.794 Å).

The average diagonal distance between La vertices is 24.886 Å. Most La^{III} ions in the hemisphere have a coordination number of eight, except for La(8) and La(9), which are ten-coordinate (Figure 3). All three central lanthanum ions located on the first sphere, {La(1), La(2), and La(3)}, are coordinated by three kinds of ligands: two oxygen atoms of CO_3^{2-}, four oxygen atoms from carboxylate in bis-monodentate fashion, and two water molecules. The water molecules are engaged in hydrogen bonds with adjacent water molecules. All six water molecules are bound to three La^{III} ions in the core of the molecule and their symmetry-related partners form hydrogen bonds among themselves and leave no void space. The La^{III} ions on the second sphere, {La(4), La(5), and La(6)}, have eight oxygen atoms as ligands, all of which are from carboxylates. The coordination between La^{III} and carboxylate exhibits three different modes: monodentate, bis-monodentate, and chelating, μ-O tridentate, except for one carboxylate group (Figure 3). For the La^{III} ions on the third sphere, additional water molecules are required to complete the respective coordination numbers besides oxygen atoms from carboxylates in bis-monodentate and bidentate chelating modes.

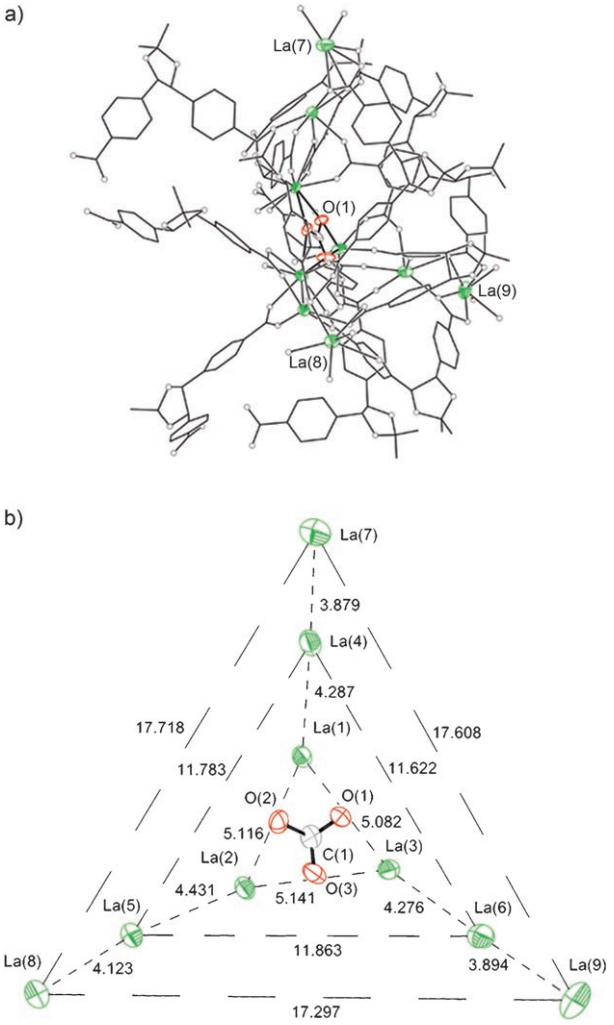

Figure 2. a) ORTEP drawing of the crystallographic asymmetric unit of (*S*)-lanthanitin, which is a half of the whole assembly as a result of crystallographic twofold symmetry. b) The arrangement of the nine La^{III} ions in the asymmetric unit around the central carbonate ion with interatomic distances in Å.

 © 2006 Wiley-VCH Verlag GmbH & Co. KGaA, Weinheim

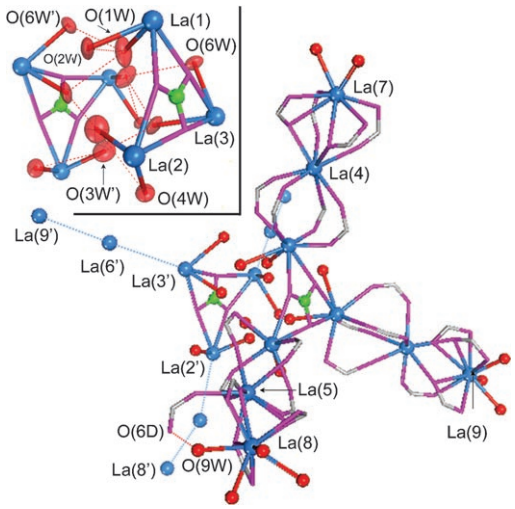

Figure 3. Coordination environment of the La^{III} atoms (blue) with partial atomic numbering scheme is shown with only carboxylate moieties (gray and pink), carbonate ions (green and pink), and coordinating water molecules (red) for simplicity. The primed numbers denote twofold-symmetry-related atoms. The 12 coordinating water molecules attached to the central 6 La atoms, O(1W)–O(6W) and O(1W′)–O(6W′) are drawn with thermal ellipsoids in the inset. Possible hydrogen bonds are indicated as dotted red lines. One of the carboxylate oxygen atoms, O(6D), is not bound to an La atom and instead forms a hydrogen bond with O(9W).

To grasp the framework structure, the molecule can be disassembled schematically into six $La_3[(S,S)\text{-}\mathbf{1}]_4$ units which are related with each other by pseudo-octahedral symmetry (Figure 4a). Each unit is interconnected with another four

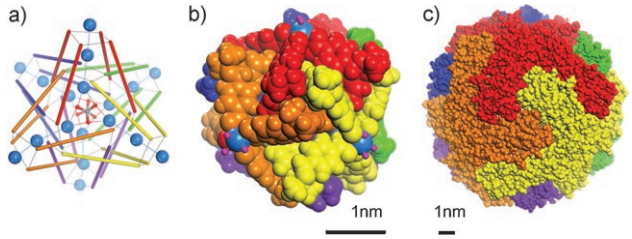

Figure 4. a) Schematic representation of lanthanitin which shows that six sets of $La_3(\mathbf{1})_4$ moieties come together around the central carbonate ions to form the whole molecule. The 24 ligands are grouped into six sets, drawn with different colors. b) Space-filling model of lanthanitin. Colors match those of (a). c) Structure of bacterioferritin (PDB code: 1BFR). Twenty four subunits are grouped as six sets for comparison with the arrangement of ligands in lanthanitin.

equatorial units by four organic ligands to form a completely integrated assembly. This assembly pattern endows lanthanitin with a close structural resemblance to ferritin.[9] The arrangement of the organic linkers in lanthanitin is the same as that of the protein subunits in ferritin (Figure 4b and c).

Neglecting the minor distortions around the La^{III} coordination sphere, the lanthanum ions are aligned along three pseudomolecular fourfold rotational axes that pass through the molecule. In addition, three pseudo-threefold axes penetrate a set of trigonal-antiprismatic triangles, and six pseudo-twofold axes penetrate six sets of edges. The symmetry of the molecule is close to point group *O* or crystallographic 432, because there is no inversion center due to the chirality. Such an analogy to the well-known 432 molecular symmetry of ferritin is rarely seen in synthetic supramolecules.

Interestingly, (*S*)-lanthanitin molecules form a right-handed double helix with pitch length of 80.460 Å and radius of 13.829 Å around the helical axis at (0.5,0.5,*z*) (Figure 5a). (*S*)-Lanthanitin units contact each other through 1,1′-dimethylmethylene (DMM) groups. Two DMM groups form a chiral cavity in which the two methyl groups of the DMM moieties of neighboring balls are incorporated (Figure 5b and c). The hydrogen atoms on the stereogenic carbon atoms are in good van der Waals contacts with the neighboring DMM groups.

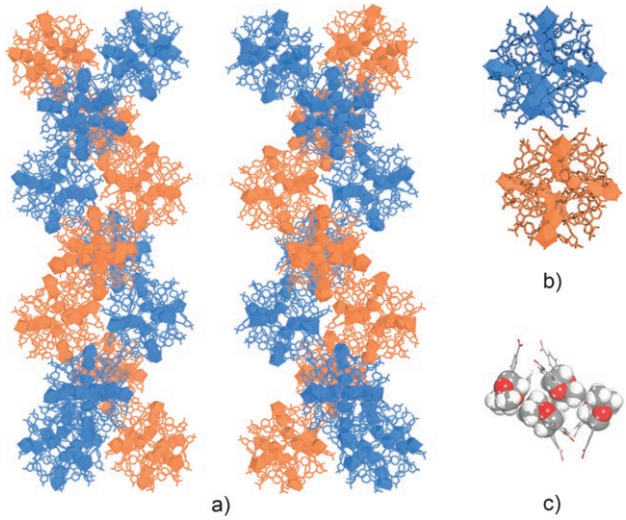

Figure 5. a) Double helices formed by the lanthanitins with 1.5 helical turns. The two single helices are distinguished by blue and light brown colors. (*S*)-Lanthanitin (left) forms a right-handed double helix, and (*R*)-lanthanitin a left-handed one (right). b) Two lanthanitin molecules in contact showing the boundary region. c) Two ligands from each lanthanitin unit participate in the contact; the acetonide moieties including the DMM groups of the ligands are drawn as space-filling models.

(*R*)-Lanthanitin, the chiral counterpart of (*S*)-lanthanitin, was prepared by employing $(R,R)\text{-}\mathbf{1}H_2$ in place of $(S,S)\text{-}\mathbf{1}H_2$. As we expected, (*R*)-lanthanitin belongs to space group $P4_322$, which forms an enantiomorphous pair with $P4_122$ of (*S*)-lanthanitin. Furthermore, (*R*)-lanthanitin also forms a double helix in the crystal lattice, with opposite handedness (Figure 5a). As confirmed by solid-state circular dichroism (CD), the chirality derived from the ligands is preserved in the crystals (Figure 6). Both (*S*)- and (*R*)-lanthanitin crystals in KBr pellet give mirror-symmetrical CD spectra with opposite signs, that is, each crystal has only one sense of helical structure. In addition, although there is an example of self-assembly of spherical colloids into single helical chains by capillary forces,[13] it is very unusual that supramolecular double helices are formed by discrete entities through

 © 2006 Wiley-VCH Verlag GmbH & Co. KGaA, Weinheim

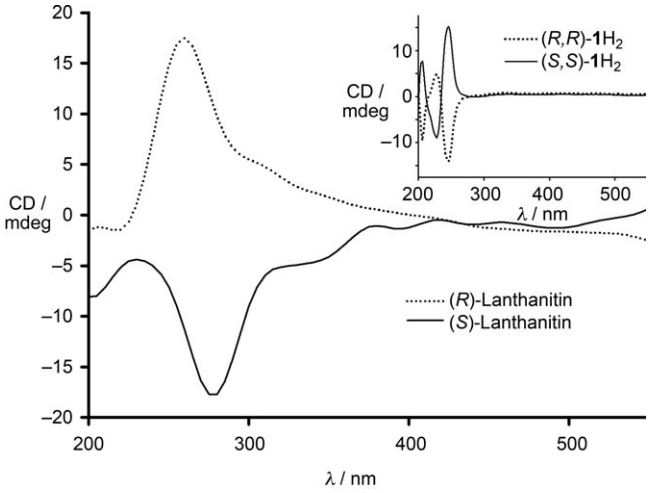

Figure 6. CD data obtained from a transparent disk with a radius of 5 mm made from a mixture of crystalline lanthanitin (3 mg) and KBr (100 mg). The inset shows the CD spectra of the ligands in methanol.

nondirectional van der Waals interactions. Usually most artificial helices or double helices, denoted as helicates, have been guided by relatively strong interactions such as hydrogen bonds or coordination bonds.[14]

In conclusion, we have obtained novel supramolecules containing lanthanum ions: (*S*) and (*R*)-lanthanitin, in which many ligands work together to bind numerous metal ions and form a spherical supramolecule with unique structural resemblance to ferritin. Furthermore, the chiral supramolecules resulting from the use of enantiomerically pure ligands form double helices in the crystal with a single handedness. Various combinations of lanthanides and chiral ligands could provide supramolecule lanthanide nanoparticles with potential optoelectronic, magnetic, and catalytic applications. Their solution properties and applications will be subjects of future study.

Experimental Section

Synthesis of (*S*)- and (*R*)-lanthanitin: Ligands (*S*,*S*)-**1**H_2 and (*R*,*R*)-**1**H_2 were prepared according to the methods described in the Supporting Information. A mixture of $LaCl_3{\cdot}6H_2O$ (0.010 g, 0.10 mmol) and (*S*,*S*)-**1**H_2 or (*R*,*R*)-**1**H_2 (0.010 g, 0.10 mmol) in DEF (3 mL) and H_2O (3 mL) was heated at 60 °C for two weeks. Colorless prismatic crystals were obtained in 30% yield. The crystals were sparingly soluble in water before sonication, and insoluble in common organic solvents. Elemental analysis (%) calcd for (*S*)-lanthanitin $[La_{18}(CO_3)_2(C_{19}H_{16}O_6)_{24}(H_2O)_{32}]CO_3{\cdot}20.5H_2O{\cdot}1.5$ DEF: C 46.90, H 4.27, N 0.18; found: C 46.90, H 4.11, N 0.15.

X-ray structural analysis of (*S*)-lanthanitin: Prismatic colorless crystal, $0.50\times0.30\times0.30$ mm^3, $C_{466.5}H_{505.5}N_{1.5}O_{207}La_{18}$, $M=11945.6$, tetragonal, space group $P4_122$ (No. 91), $T=243(2)$ K, $a=27.5037(10)$, $c=80.460(3)$ Å, $V=60864(4)$ Å^3, $Z=4$, $\rho_{calcd}=1.304$ g m^{-3}, $\mu(Mo_{K\alpha})=1.312$ mm^{-1}. A crystal was attached to a glass capillary, which was positioned in a $N_{2(g)}$ stream at 243(2) K after mounting on a Bruker SMART CCD diffractometer equipped with a normal-focus and graphite-monochromated Mo-target X-ray tube ($\lambda=0.71073$ Å). A total of 1315 frames were collected, and integrated with the SAINT software package with a narrow-frame algorithm. An absorption correction was applied by using SADABS. The structure was solved by direct methods and subsequent difference Fourier syntheses and refined with the SHELXTL software package. A total of 211188 reflections were collected in the range $1.05\le\theta\le20.84°$, of which 32002 were independent and 22331 were observed ($I>2\sigma(I)$). All stages of weighted full-matrix least-squares refinement were conducted on F_o^2 data and converged to give $R1=0.0835$ ($I>2\sigma(I)$), $wR2=0.2268$ (all data), and GOF = 1.029. Most non-hydrogen atoms were refined anisotropically, except for six atoms with nonpositive-definite problems. Hydrogen atoms were generated with the ideal geometry. The absolute configuration was confirmed by the Flack *x* parameter of 0.060(19).

X-ray structural analysis of (*R*)-lanthanitin: prismatic colorless crystal, $0.35\times0.30\times0.25$ mm^3, $C_{466.5}H_{505.5}N_{1.5}O_{207}La_{18}$, $M=11945.6$, tetragonal, space group $P4_322$ (No. 95), $T=130(2)$ K, $a=27.2922(6)$, $c=79.728(3)$ Å, $V=59386(4)$ Å^3, $Z=4$, $\rho_{calcd}=1.336$ g m^{-3}, $\mu(Mo_{K\alpha})=1.345$ mm^{-1}. Final refinement converged to $R1=0.0921$ ($I>2\sigma(I)$), $wR2=0.2341$ (all data), GOF = 1.076, and a Flack parameter of $x=0.13(3)$. CCDC 619112 ((*S*)-lanthanitin) and 619113 ((*R*)-lanthanitin) contain the supplementary crystallographic data for this paper. These data can be obtained free of charge from The Cambridge Crystallographic Data Centre via www.ccdc.cam.ac.uk/data_request/cif.

UV/Vis absorption spectra of various solutions were measured between 800 and 200 nm with a Jasco UVIDEC 650 spectrophotometer. CD spectra were recorded on a Jasco J-810 spectropolarimeter. DRCD spectra were obtained by inserting a diffuse-reflectance sphere in the optical path of the instrument. This J-810 was specifically modified to allow simultaneous detection of LD (linear dichroism) as a simple way to verify potential artifacts.

Received: September 5, 2006
Published online: November 17, 2006

Keywords: carboxylate ligands · helical structures · lanthanum · nanostructures · self-assembly

[1] B. Moulton, M. J. Zaworotko, *Chem. Rev.* **2001**, *101*, 1629.
[2] D. Caulder, K. N. Raymond, *Acc. Chem. Res.* **1999**, *32*, 975.
[3] a) L. R. MacGillivray, J. L. Atwood, *Angew. Chem.* **1999**, *111*, 1080; *Angew. Chem. Int. Ed.* **1999**, *38*, 1018; b) B. Olenyuk, J. A. Whiteford, A. Fechtenkötter, P. J. Stang, *Nature* **1999**, *398*, 796; c) P. J. Stang, B. Olenyuk, *Acc. Chem. Res.* **1997**, *30*, 502; d) H. Jiang, W. Lin, *J. Am. Chem. Soc.* **2003**, *125*, 8084.
[4] a) N. Takeda, K. Umemoto, K. Yamaguchi, M. Fujita, *Nature* **1999**, *398*, 794; b) S. R. Seidel, P. J. Stang, *Acc. Chem. Res.* **2002**, *35*, 972.
[5] a) O. M. Yaghi, M. O'Keeffe, N. W. Ockwig, H. K. Chae, M. Eddaoudi, J. Kim, *Nature* **2003**, *423*, 705; b) S. Kitagawa, R. Kitaura, S. Noro, *Angew. Chem.* **2004**, *116*, 2388; *Angew. Chem. Int. Ed.* **2004**, *43*, 2334.
[6] a) Y. Zhou, M. Hong, X. Wu, *Chem. Commun.* **2006**, 135; b) Z. Zheng, *Chem. Commun.* **2001**, 2521.
[7] a) K. Mikami, M. Terada, H. Matsuzawa, *Angew. Chem.* **2002**, *114*, 3704; *Angew. Chem. Int. Ed.* **2002**, *41*, 3554; b) M. Ziegler, A. von Zelewsky, *Coord. Chem. Rev.* **1998**, *177*, 257; c) S. P. Fricker, *Chem. Soc. Rev.*, **2006**, *35*, 524; d) M. Bottrill, L. Kwok, N. J. Long, *Chem. Soc. Rev.* **2006**, *35*, 557; e) D. Gatteschi, R. Sessoli, *Angew. Chem.* **2003**, *115*, 278; *Angew. Chem. Int. Ed.* **2003**, *42*, 268.
[8] With carboxylate ligands: a) O. Mamula, M. Lama, S. G. Telfer, A. Nakamura, R. Kuroda, H. Stoeckli-Evans, R. Scopelitti, *Angew. Chem.* **2005**, *117*, 2583; *Angew. Chem. Int. Ed.* **2005**, *44*, 2527. With bipyridine ligands: b) O. Mamula, A. von Zelewsky, G. Bernardinelli, *Angew. Chem.* **1998**, *110*, 302; *Angew. Chem. Int. Ed.* **1998**, *37*, 289; c) O. Mamula, T. Bark, A. von Zelewsky, G. Bernardinelli, *Angew. Chem.* **1999**, *111*, 3129; *Angew. Chem.*

 © 2006 Wiley-VCH Verlag GmbH & Co. KGaA, Weinheim

Int. Ed. **1999**, *38*, 2945; d) O. Mamula, A. von Zelewsky, *Coord. Chem. Rev.* **2003**, *242*, 87; e) L.-E. Perret-Aebi, A. von Zelewsky, C. Dietrich-Buchecker, J.-P. Sauvage, *Angew. Chem.* **2004**, *116*, 4582; *Angew. Chem. Int. Ed.* **2004**, *43*, 4482.
[9] X. Liu, E. C. Theil, *Acc. Chem. Res.* **2005**, *38*, 167.
[10] a) M. Albrecht, *Chem. Rev.* **2001**, *101*, 3457; b) C. Piguet, G. Bernardinelli, G. Hopfgartner, *Chem. Rev.* **1997**, *97*, 2005.
[11] H. C. Kolb, M. S. Van Nieuwenhze, K. B. Sharpless, *Chem. Rev.* **1994**, *94*, 2483.
[12] a) C. A. Chang, L. C. Francesconi, M. F. Malley, K. Kumar, J. Z. Gougoutas, M. F. Tweedle, D. W. Lee, L. J. Wilson, *Inorg. Chem.* **1993**, *32*, 3501; b) X. Liang, J. A. Parkinson, S. Parsons, M. Weishäupl, P. J. Sadler, *Inorg. Chem.* **2002**, *41*, 4539.
[13] Y. Yin, Y. Xia, *J. Am. Chem. Soc.* **2003**, *125*, 2048.
[14] a) G. W. Orr, L. J. Barbour, J. L. Atwood, *Science* **1999**, *285*, 1049; b) H. Engelkamp, S. Middelbeek, R. J. M. Nolte, *Science* **1999**, *284*, 785.

 © 2006 Wiley-VCH Verlag GmbH & Co. KGaA, Weinheim

Biosensors

DOI: 10.1002/anie.200603138

Reversible Control of Carbon Nanotube Aggregation for a Glucose Affinity Sensor**

*Paul W. Barone and Michael S. Strano**

Single-walled carbon nanotubes (SWNT) have garnered much interest as sensing elements[1–6] owing to their quasi-one-dimensional electronic structure, which renders them sensitive to surface adsorption events.[7,8] The majority of studies have been based on SWNT field effect transistors;[4–6,9–11] however, recently we demonstrated that SWNT near-infrared (NIR) photoluminescence (PL) can be used in the selective detection of small molecules[1,2] and nucleic acids.[3] Although most conventional fluorophores fluoresce in the visible range where tissue and biological media emit a strong autofluorescent background[12] and are strongly absorbing[13,14] and scattering, SWNT-PL occurs in the NIR[15] where these complications are minimized. Additionally, SWNT remain photostable, unlike other NIR fluorophores.[16] A central challenge in the development of SWNT fluorescence sensors is designing a sensing scheme that retains the nanotube optical properties. Covalent functionalization of the nanotube disrupts the electronic structure and SWNT-PL;[17,18] thus, only noncovalent methods can be used. Herein we describe the design and function of the first SWNT based affinity sensor for glucose. Previously, nanotubes have been utilized in electronic biosensors[11] and glucose detection.[9,10]

A nanotube sensor was fabricated following the reaction path outlined in Scheme 1. Equilibrium binding between proteins and a target analyte has been used in a number of biosensors.[19–26] Generally, the sensors operate by taking advantage of the competitive binding between a target analyte and analogue for a protein binding site. The resulting signal change is from fluorescence resonance energy transfer between the analogue and a fluorophore-labeled protein. For our system, the SWNT fluorophores are initially suspended in aqueous solution with a phenoxy-derivatized dextran, a polysaccharide that functions as a glucose analogue. The addition of 8–15 μM Concanavalin A (ConA), a plant lectin with four saccharide binding sites at pH 7.4, induces aggregation of the dextran–nanotube complexes and a decrease in SWNT-PL. The introduction of 3–11 mM glucose causes aggregate dissolution and PL recovery owing to competitive binding between the glucose and dextran for ConA binding sites.

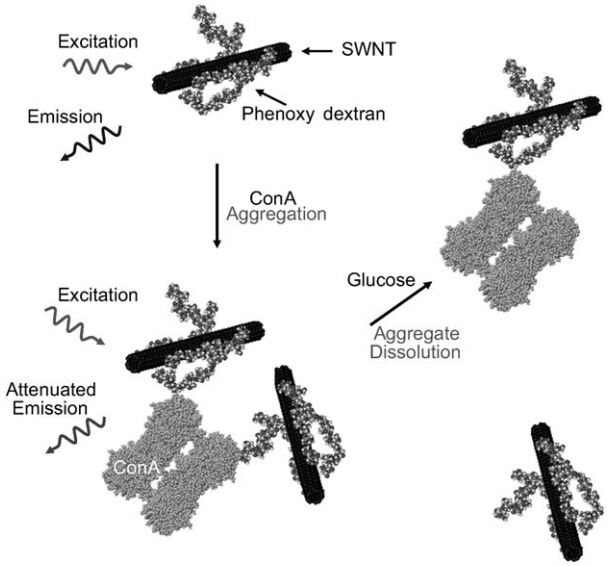

Scheme 1. Representation of SWNT affinity sensor operation.

Modification of the dextran with hydrophobic moieties is necessary to observe stable nanotube suspension. Dialysis of 1 wt% dextran (64–76 kDa, unmodified) and a sodium cholate suspended SWNT mixture against 10 mM phosphate-buffered saline (PBS) removes the cholate[1,3] but results in SWNT aggregation and PL quenching.[15] Hydrophobic dextran derivatives (**3**) were synthesized and used to functionalize the nanotubes (**4**, Scheme 2). The phenoxy content (wt%) in compound **3** affects the nanotube dispersability and optical properties. Figure 1a shows the PL spectra of **4** synthesized with a phenoxy content of **3** ranging from 3.5 to 8.3 wt%. The normalized PL intensity increases with

[*] P. W. Barone, Dr. M. S. Strano
Department of Chemical and Biomolecular Engineering
University of Illinois Urbana – Champaign
Urbana, IL 61801 (USA)
Fax: (+1) 217-333-5052
E-mail: strano@uiuc.edu

[**] This work was supported by the National Science Foundation (grant CTS-0330350). The authors would like to thank E. Mock for help with DLS measurements.

Supporting information for this article is available on the WWW under http://www.angewandte.org or from the author.

InterScience
© 2006 Wiley-VCH Verlag GmbH & Co. KGaA, Weinheim

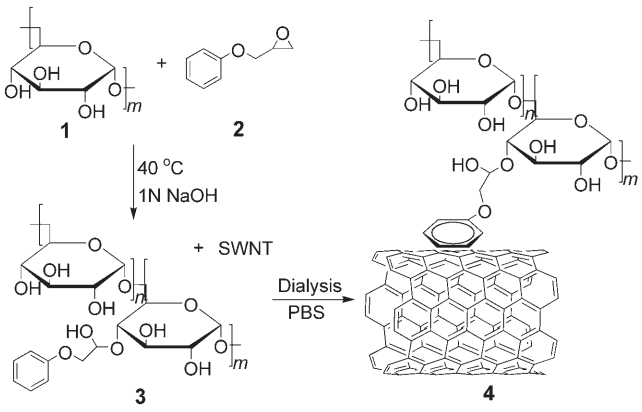

Scheme 2. Reaction of dextran (**1**) with 1,2-epoxy-3-phenoxypropane (**2**) to make hydrophobic dextran derivatives (**3**) that are used to noncovalently functionalize SWNT making a dextran–SWNT complex (**4**).

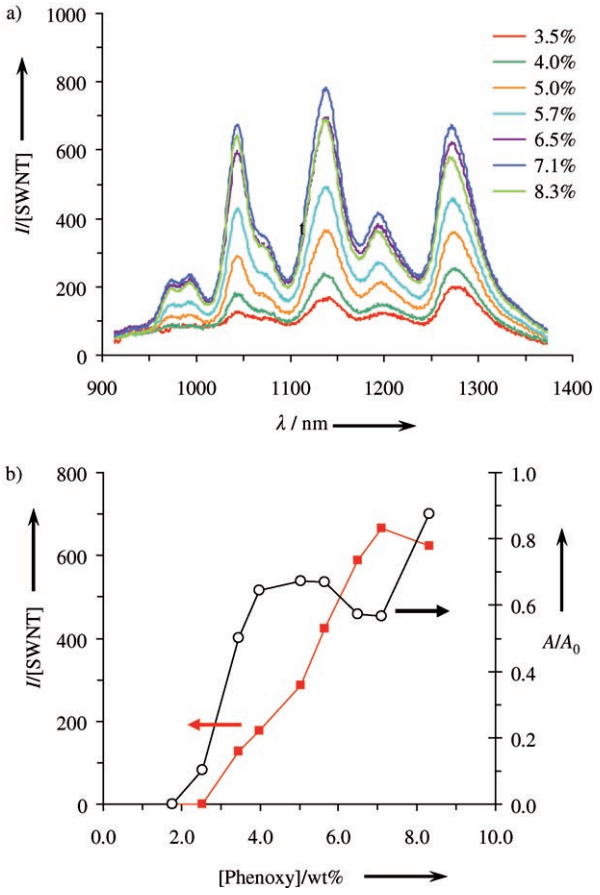

Figure 1. Effect of the amount of phenoxy (wt%) in (**3**) on SWNT suspension and colloidal stability. a) PL spectra normalized to nanotube concentration for complex **4** for varying phenoxy content (wt%) in **3**. b) The relationship between nanotube PL and nanotube concentration (I/[SWNT]; squares) and the ratio of suspended SWNT concentration to initial SWNT concentration (measured by absorption, A/A_0) before dextran adsorption (circles) versus phenoxy content (wt%) in **3**.

phenoxy content of **3** (Figure 1b), with the fraction of nanotubes in solution remaining constant above a phenoxy content of 3.5 wt%. Examination of SWNT photoabsorption (see Supporting Information) shows that nanotube absorption transitions are broadened and red-shifted as the phenoxy content decreases. This is due to either an increase in the number of small bundles or to the localization of water near the surface of the nanotube.[27] For all sensing experiments, **4** synthesized with a phenoxy content of 8.5 wt% was used.

Nanotube PL decreases with increasing ConA concentration concomitant with aggregate formation. The transient PL intensity of an aliquot of **4** during additions of 1.8 μM ConA followed by 3.7 mM additions of glucose is shown in Figure 2a. The first three ConA additions caused no PL

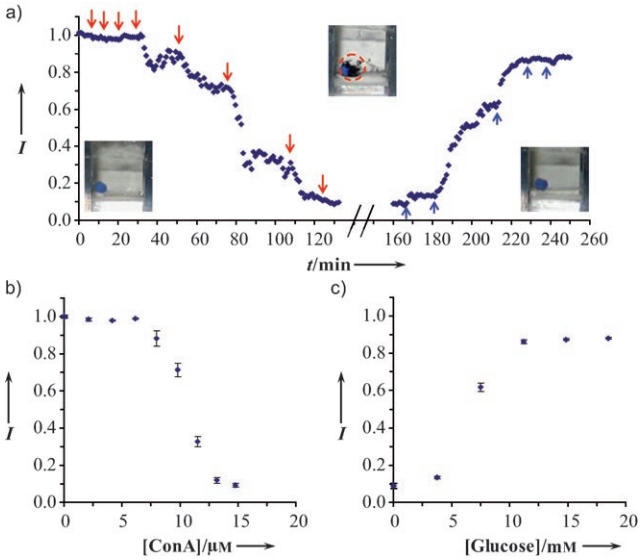

Figure 2. Response of **4** to ConA and glucose. a) Nanotube PL intensity versus time for 1.8 μM additions of ConA (red arrows) and 3.7 mM additions of glucose (blue arrows). Insets show pictures of the aggregation state of the solution initially (left), after 14.7 mM ConA (middle), and upon subsequent addition of 18 mM glucose (right). The steady-state nanotube PL intensity is plotted versus ConA concentration (b) and glucose concentration (c).

response and small aggregates began to become visible, whereas subsequent additions showed a decrease in SWNT-PL. The PL response times ranged from 12 to 20 minutes to reach steady state. The insets of Figure 2a show pictures before ConA addition (left), with no visible aggregation, and after the addition of 14.7 μM ConA (middle), when aggregation was evident. Subsequent additions of glucose result in dissolution of the aggregates (right) and recovery of SWNT-PL (Figure 2a), with the recovery response times ranging from 3 to 28 min to reach steady state. The steady-state PL response versus ConA concentration and glucose concentration is given in Figure 2b,c. We expect there is a portion of **3** free in solution and not adsorbed to the nanotubes. This source of unbound **3** competes for binding with ConA, and thus delays the onset of critical aggregation, when measurable decrease in SWNT-PL occurs. Removal of free phenoxy-derivatized dextran (**3**) causes the SWNT-PL to decrease at lower ConA concentrations. The steady-state PL recovery versus glucose concentration in Figure 2b shows the largest

 © 2006 Wiley-VCH Verlag GmbH & Co. KGaA, Weinheim

increase, between 3.8 and 11 mM glucose. A commercially viable glucose sensor will be responsive to glucose concentrations between 2 and 30 mM.[28] The response range is ConA concentration dependent and can be tuned based on ConA concentration.[29] We note that additions of glycerol, a hydrogen-bond-breaking agent, cause no response in the Dextran–SWNT–ConA aggregate, indicating specificity of the system to glucose.

Dynamic light scattering suggests that **4** remains unchanged following aggregate dissolution. Scattering measurements were carried out on **4** before aggregation and after aggregate dissolution. Calculated diffusion coefficients for **4** are 6.96 $\mu m^2 s^{-1}$ and 5.74 $\mu m^2 s^{-1}$ before ConA addition and after aggregate dissolution, respectively. Comparison of diffusion coefficients for **4** before aggregation and after recovery with glucose shows the two values to be within 1 $\mu m^2 s^{-1}$, suggesting that **4** is not permanently altered during the aggregation/disaggregation process. The fact that the diffusion coefficient is slightly lower after recovery is not unexpected as ConA is still in the solution, of which some fraction is likely bound to **4**.

Removal of glucose, through dialysis, results in reformation of aggregates. Glucose was removed from the recovered sample using dialysis. Aggregates were visibly formed, although not as dense as those shown in Figure 2a. Additions of glucose resulted in aggregate dissolution; however, the sensor did not respond to subsequent cycles of glucose removal and addition. We speculate that ConA becomes denatured during the process resulting in a limited lifetime of the sensor, but that is beyond the scope of this Communication and protein stability will be addressed in a future study.

In conclusion, we have shown that it is possible to fabricate an affinity sensor based on SWNT-PL. We formed colloidally stable suspensions of dextran-coated SWNT by first covalently adding phenyl groups to dextran. Addition of ConA induces nanotube aggregation and decreases SWNT-PL, whereas subsequent additions of glucose break apart the aggregates, resulting in a restoration of SWNT-PL. These results demonstrate the first solution-phase nanotube affinity sensor. The methodology outlined herein is generic and can conceivably be extended to other analytes of interest.

Experimental Section

Materials: Single-walled carbon nanotubes were obtained from the Rice University research reactor (Run 107). ConA, BSA, 64–76 kD MW dextran, 1,2-epoxy-3-phenoxypropane, and glucose were obtained from Sigma Aldrich (St. Louis). Hydrophobic dextran derivatives were synthesized similar to previously published methods.[30] Phenoxy content was determined by absorption at 269 nm[31] in a Shimadzu UV-PC 3101 UV/Vis/NIR spectrophotometer. SWNTs were initially dispersed in an aqueous 2 wt % sodium cholate solution using previously published methods,[1,15] and hydrophobic dextran was adsorbed to the nanotube surface through dialysis.[1,3] All collected samples were centrifuged (16000 × g) for 30 min to remove unsuspended nanotubes.

Detection: Nanotube aggregation and PL monitoring were performed in a well-stirred cuvette. The solution was illuminated with the dispersed beam of a 632.8 nm HeNe laser. SWNT-PL was collected at 90° with a Princeton Array Spectrometer. Initially, 10 mg mL^{-1} BSA (50 μL) in PBS was added to prevent ConA adsorption to the walls of the cuvette.

Dynamic light scattering: A goniometer (Brookhaven Instruments BI-200 SM) with a 514 nm laser (Lexel Argon-Ion Model 95) was used with the detector at a 90° angle from the light source to the sample.

Received: August 2, 2006
Revised: October 2, 2006
Published online: November 13, 2006

Keywords: aggregation · biosensors · carbon nanotubes · glucose · nanomaterials

[1] P. W. Barone, S. Baik, D. A. Heller, M. S. Strano, *Nat. Mater.* **2005**, *4*, 86.
[2] D. A. Heller, E. S. Jeng, T. K. Yeung, B. M. Martinez, A. E. Moll, J. B. Gastala, M. S. Strano, *Science* **2006**, *311*, 508.
[3] E. S. Jeng, A. E. Moll, A. C. Roy, J. B. Gastala, M. S. Strano, *Nano Lett.* **2006**, *6*, 371.
[4] A. Guiseppi-Elie, C. H. Lei, R. H. Baughman, *Nanotechnology* **2002**, *13*, 559.
[5] R. J. Chen, S. Bangsaruntip, K. A. Drouvalakis, N. W. S. Kam, M. Shim, Y. M. Li, W. Kim, P. J. Utz, H. J. Dai, *Proc. Natl. Acad. Sci. USA* **2003**, *100*, 4984.
[6] J. Wang, M. Musameh, Y. H. Lin, *J. Am. Chem. Soc.* **2003**, *125*, 2408.
[7] R. Saito, M. S. Dresselhaus, G. Dresselhaus, *Physical Properties of Carbon Nanotubes*, Imperial College, London, **1998**.
[8] T. Durkop, S. A. Getty, E. Cobas, M. S. Fuhrer, *Nano Lett.* **2004**, *4*, 35.
[9] K. Besteman, J. O. Lee, F. G. M. Wiertz, H. A. Heering, C. Dekker, *Nano Lett.* **2003**, *3*, 727.
[10] Y. H. Lin, F. Lu, Y. Tu, Z. F. Ren, *Nano Lett.* **2004**, *4*, 191.
[11] J. Wang, *Electroanalysis* **2005**, *17*, 7.
[12] R. Weissleder, V. Ntziachristos, *Nat. Med.* **2003**, *9*, 123.
[13] W. Cui, L. E. Ostrander, B. Y. Lee, *IEEE Trans. Biomed. Eng.* **1990**, *37*, 632.
[14] S. Wray, M. Cope, D. T. Delpy, J. S. Wyatt, E. O. R. Reynolds, *Biochim. Biophys. Acta* **1988**, *933*, 184.
[15] M. J. O'Connell, S. M. Bachilo, C. B. Huffman, V. C. Moore, M. S. Strano, E. H. Haroz, K. L. Rialon, P. J. Boul, W. H. Noon, C. Kittrell, J. P. Ma, R. H. Hauge, R. B. Weisman, R. E. Smalley, *Science* **2002**, *297*, 593.
[16] D. A. Heller, S. Baik, T. E. Eurell, M. S. Strano, *Adv. Mater.* **2005**, *17*, 2793.
[17] M. S. Strano, C. A. Dyke, M. L. Usrey, P. W. Barone, M. J. Allen, H. W. Shan, C. Kittrell, R. H. Hauge, J. M. Tour, R. E. Smalley, *Science* **2003**, *301*, 1519.
[18] M. L. Usrey, E. S. Lippmann, M. S. Strano, *J. Am. Chem. Soc.* **2005**, *127*, 16129.
[19] L. J. McCartney, J. C. Pickup, O. J. Rolinski, D. J. S. Birch, *Anal. Biochem.* **2001**, *292*, 216.
[20] O. J. Rolinski, D. J. S. Birch, L. J. McCartney, J. C. Pickup, *J. Photochem. Photobiol. B* **2000**, *54*, 26.
[21] Y. Wickramasinghe, Y. Yang, S. A. Spencer, *J. Fluoresc.* **2004**, *14*, 513.
[22] R. Ballerstadt, A. Polak, A. Beuhler, J. Frye, *Biosens. Bioelectron.* **2004**, *19*, 905.
[23] J. S. Schultz, S. Mansouri, I. J. Goldstein, *Diabetes Care* **1982**, *5*, 245.
[24] R. Ballerstadt, J. S. Schultz, *Anal. Chim. Acta* **1997**, *345*, 203.
[25] H. R. Clark, T. A. Barbari, G. Rao, *Biotechnol. Prog.* **1999**, *15*, 259.
[26] B. G. Knecht, A. Strasser, R. Dietrich, E. Martlbauer, R. Niessner, M. G. Weller, *Anal. Chem.* **2004**, *76*, 646.

 © 2006 Wiley-VCH Verlag GmbH & Co. KGaA, Weinheim

[27] M. S. Strano, C. B. Huffman, V. C. Moore, M. J. O'Connell, E. H. Haroz, J. Hubbard, M. Miller, K. Rialon, C. Kittrell, S. Ramesh, R. H. Hauge, R. E. Smalley, *J. Phys. Chem. B* **2003**, *107*, 6979.
[28] R. Ballerstadt, J. S. Schultz, *Anal. Chem.* **2000**, *72*, 4185.
[29] P. W. Barone, R. S. Parker, M. S. Strano, *Anal. Chem.* **2005**, *77*, 7556.
[30] C. Fournier, M. Leonard, I. Lecoqleonard, E. Dellacherie, *Langmuir* **1995**, *11*, 2344.
[31] C. Fournier, M. Leonard, E. Dellacherie, M. Chikhi, H. Hommel, A. P. Legrand, *J. Colloid Interface Sci.* **1998**, *198*, 27.

 © 2006 Wiley-VCH Verlag GmbH & Co. KGaA, Weinheim

Protein Engineering

DOI: 10.1002/anie.200603227

Fluoroproline Flip-Flop: Regiochemical Reversal of a Stereoelectronic Effect on Peptide and Protein Structures**

*Wookhyun Kim, Kenneth I. Hardcastle, and Vincent P. Conticello**

The de novo design of protein structure relies on the ability to uniquely define a polypeptide chain conformation through introduction of specific stabilizing interactions into the amino acid sequence, which act cooperatively to overcome the loss of conformational entropy associated with the protein folding process. Within this concept, the stereoelectronic effect has recently emerged as a means to restrict the local chain conformation of polypeptide sequences and to modulate the thermodynamic stability of secondary and supersecondary structural elements.[1–5]

Substituted proline residues are particularly susceptible to the influence of stereoelectronic effects that alter the conformational energetics of the pyrrolidine ring. Introduction of an electronegative substituent (X = N, O, F) at the C3 or C4 position of the pyrrolidine ring establishes a vicinal N-C-C-X arrangement between the prolyl amide group and the electronegative atom.[6,7] A preference for a *gauche* stereochemical relationship is observed between the two substituents as a result of hyperconjugative delocalization, in which the magnitude of the effect depends on the electronegativity of the substituent. These stereoelectronic interactions strongly influence the equilibrium conformational population of the pyrrolidine ring-pucker isomers, such that epimeric pairs of substituted proline derivatives have opposite ring-pucker preferences and often display antagonistic effects on protein stability that depend on structural context.[1,8,9] Most comparative analyses have employed the (4*S*)- and (4*R*)-fluoroproline epimeric pair, in which strong conformational preferences are observed for the C^{γ}-*endo* and C^{γ}-*exo* puckers, respectively. Herein, we report a structural comparison between the (3*S*)- and (3*R*)-fluoroproline epimers, in which the altered regiochemistry results in a reversal of conformational preferences compared to the corresponding 4-fluoroproline epimers, which has structural implications for protein design and engineering.

To evaluate the effect of 3-fluoro substitution on pyrrolidine ring conformation, the epimeric proline derivatives **1** and **2** were synthesized and their structures were determined by single-crystal X-ray diffraction analysis (Figure 1). Prior structural investigations of substituted *N*-acetylproline methyl ester derivatives[6,10] have established that these compounds provide reliable structural models to assess the conformational preferences of the pyrrolidine ring. The structural data indicated that both **1** and **2** crystallized with a *trans* configuration of the prolyl–peptide bond; however, significant differences were observed between **1** and **2** with respect to the conformation of the substituted pyrrolidine ring. The values of the N-C^{α}-C^{β}-F torsion angles for **1** and **2** were 90.7 and −87.4°, respectively, which indicated a *gauche* arrangement of the vicinal fluorine and amide substituents, as expected for the strong fluorine–amide stereoelectronic

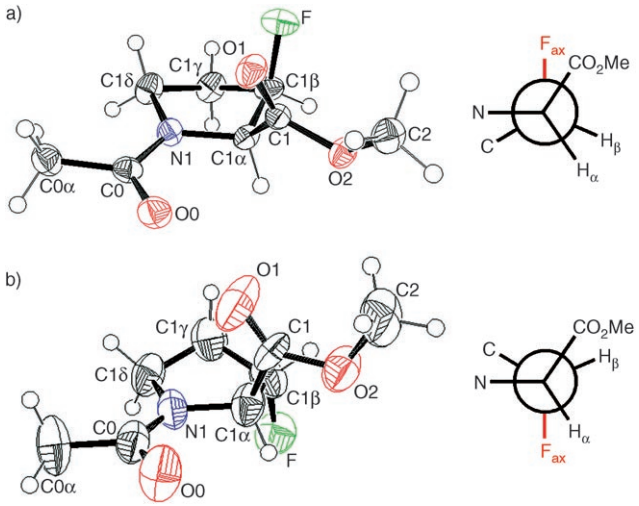

Figure 1. Crystallographically determined structures of a) *N*-acetyl-(2*R*,3*R*)-3-fluoroproline methyl ester (**1**) and b) *N*-acetyl-(2*R*,3*S*)-3-fluoroproline methyl ester (**2**) in conjunction with the Newman projections along the C^{α}–C^{β} bond vector, which depict the *gauche* relation between the amide and fluorine substituents.

[*] W. Kim, Dr. K. I. Hardcastle, Prof. V. P. Conticello
Department of Chemistry
Emory University
1515 Dickey Drive, Atlanta, GA 30322 (USA)
Fax: (+1) 404-727-6586
E-mail: vcontic@emory.edu

[**] We acknowledge the financial support of the Herman Frasch Foundation (418-97HF), the NIH (5R01L071136-04), and the NSF (EEC-9731643). The CD spectropolarimeter, differential scanning calorimeter, and X-ray diffractometer were obtained with the assistance of NSF and NIH grants.

Supporting information for this article is available on the WWW under http://www.angewandte.org or from the author.

© 2006 Wiley-VCH Verlag GmbH & Co. KGaA, Weinheim

interaction.[11] As observed for the 4-fluoroproline epimeric pair, the *gauche* interaction enforced opposing pyrrolidine ring puckers between **1** and **2**. The conformation of **1** corresponded to a C^{β}-*endo*/C^{γ}-*exo* arrangement (displacements from C^{δ}-N-C^{α} mean plane: C^{β}, 0.112 Å; C^{γ}, 0.460 Å), whereas that of **2** corresponded to a C^{β}-*exo*/C^{γ}-*endo* arrangement (displacements from C^{δ}-N-C^{α} mean plane: C^{β}, 0.308 Å; C^{γ}, 0.230 Å). The relatively small displacement of C^{β} for **1** may result from steric hindrance as a result of close contacts between the fluorine atom and the carbon (C1) and oxygen (O1) atoms of the carbonyl group of the methyl ester, in which the nonbonding distances ($d_{F\cdots C} = 2.67$ and $d_{F\cdots O} = 2.94$ Å) were less than the sum of the corresponding van der Waals radii (3.17 and 2.99 Å, respectively).

Hodges et al. have reported computational analyses of the conformational energetics of **1** and **2**,[7] which indicate that the preferred ring pucker in each case corresponded to that observed in the respective crystal structure. However, the thermodynamic preference of **2** for the C^{γ}-*endo* isomer (estimated 97% population) was significantly greater than that of **1** for the C^{γ}-*exo* isomer (estimated 69% population). The steric congestion surrounding the C^{β} atom observed in the crystal structure of **1** may account for the weaker conformational preference in the latter case. The persistence of the C^{γ}-*endo* conformation of **2** in solution may be inferred from the very small value of $^{3}J_{H\alpha H\beta}$ (≤ 1 Hz) in the ^{1}H NMR spectrum in D_2O, which is consistent with the corresponding value of 0.79 Hz that was calculated from the Karplus equation for the observed H^{α}-C^{α}-C^{β}-H^{β} dihedral angle of −92.6° in the crystal structure of **2**.

The availability of crystallographic and computational data permits a comparison of the structural and thermodynamic parameters of the 3-fluoroproline (3-FPro) derivatives with the corresponding 4-FPro regioisomers (Table 1). Notably, the ring-pucker conformational preferences were reversed between *N*-Ac-FPro-OMe species that had similar *syn* (**1** and **3**) or *anti* (**2** and **4**) orientations of the fluoro substituent with respect to the fixed L-configuration of C^{α}. Thus, an *anti* orientation of the fluoro group resulted in a predominant C^{γ}-*endo* pucker for the 3-fluoroproline derivative **2** and a predominant C^{γ}-*exo* pucker for the 4-fluoroproline derivative **4**, whereas the opposite was true for the respective *syn*-oriented fluoroproline epimers **1** and **3** (Table 1).

Table 1: Thermodynamic data and main-chain torsion angles for the *N*-acetylfluoroproline methyl ester derivatives.

Ac-FPro-OMe	$K_{trans/cis}$[a]	$\Delta E_{exo/endo}$ [kcal mol^{-1}][b]	ϕ [°][c]	ψ [°][c]
(3*R*)-**1** (*syn*,*exo*)	8.9	−0.48	−56.4	151.5
(3*S*)-**2** (*anti*,*endo*)	4.3	2.13	−71.2	158.4
(4*S*)-**3** (*syn*,*endo*)	2.5	0.61	−76.4	172.0
(4*R*)-**4** (*anti*,*exo*)	6.7	−0.85	−55.1	140.5

[a] The values of the equilibrium constants $K_{trans/cis}$ were calculated from integration of the well-resolved H^{α} peaks in the ^{1}H NMR spectra of **1** and **2** in D_2O solution at 25 °C. [b] Energy values were obtained from DFT calculations with B3YLP at 6-311 + G(2d,p).[6,7] [c] Dihedral angles were determined from the crystal structures of **1**, **2**, and **4** and from DFT calculations for **3**.[6,7]

Prior analyses of proteins within the structural database,[12] as well as small-molecule proline analogues,[6–8] suggested that the pyrrolidine ring pucker strongly influenced the main-chain torsion angles ϕ and ψ that define the peptide backbone conformation. Moreover, the main-chain dihedral angles appeared to be correlated with the pyrrolidine ring pucker. Thus, the C^{γ}-*exo* pucker of **4** displayed a less negative value of the angle ϕ and a smaller value of the angle ψ than did the C^{γ}-*endo* pucker of **3** (Table 1). A similar, although less pronounced, difference was observed between the corresponding torsional angles for **1** and **2**. The observed values of ϕ and ψ for the C^{γ}-*exo* ring pucker were rationalized on the basis of an energetic stabilization associated with a nonbonded $n\rightarrow\pi^*$ interaction between the p-type lone pair of the amide oxygen atom and the antibonding orbital of the ester carbonyl group.[6a] Raines et al. have postulated that the close contact between the O0 and C1 atoms ($\delta_{BD} = 2.76$ Å) and the relatively large value of the O0···C1=O1 angle (98°) that were observed in the crystal structure of **4** resembled the Bürgi–Dunitz (BD) trajectory[13] for approach of a nucleophile to a carbonyl group.[1a,b,6a] Similarly, a close contact (2.81 Å) was observed between O0 and C1 in the crystal structure of **1**, albeit with a more acute value of the O0···C1=O1 angle (91°) than that observed in the crystal structure of **4**. These data imply the presence of an $n\rightarrow\pi^*$ interaction in the C^{γ}-*exo* conformation of **1** and **4**, although the apparently stronger interaction in the latter case reduces the corresponding values of the ϕ and ψ dihedral angles to a greater extent than for **1**. Notably, the nonbonded contacts observed between O0 and C1 for the energetically preferred C^{γ}-*endo* conformations of **2** and **3** ($\delta_{BD} = 3.08$ and 3.23 Å, respectively) were beyond the range in which a significant energetic stabilization could be reasonably expected.

The origin of the observed differences in ϕ and ψ between **1** and **4** could conceivably arise from the anticipated steric repulsion between the *syn*-oriented fluorine atom and the carbonyl group of the methyl ester. This repulsive interaction presumably distorts the C^{γ}-*exo* conformation of **1** from that observed in the crystal structure of **4**. A similar repulsive interaction was invoked to rationalize the variance of the ϕ and ψ torsions that was observed in a computational analysis of the conformational energetics of **3**.[6a] In the latter case, a 1,3-diaxial steric interaction between the *syn*-oriented fluoro and carbomethoxy substituents significantly distorts values of the ϕ and ψ torsions of the C^{γ}-*endo* ring pucker in comparison to the corresponding conformations for the unsubstituted *N*-acetylproline methyl ester or the *anti*-substituted derivatives **2** and **4**. These results suggest that lone pair/lone pair repulsion between the *syn*-oriented fluorine atom and the carbonyl oxygen atom (O0) of the ester can significantly alter the peptide torsions of the *syn*-substituted fluoroproline derivatives **1** and **3**. Thus, two potentially conflicting structural considerations can modulate the conformational energetics of fluoroproline derivatives: the stereoelectronic *gauche* effect and the steric repulsion between *syn*-oriented substituents. The interplay between these two factors may determine the

 © 2006 Wiley-VCH Verlag GmbH & Co. KGaA, Weinheim

energetic effect of fluoroproline substitution into polypeptide sequences.

The subtle differences in conformational properties between the C$^{\gamma}$-*exo* and C$^{\gamma}$-*endo* ring puckers suggested that fluoroproline substitution may be employed as a mechanism to interrogate local structural effects that arise from the presence of proline residues in polypeptide sequences.[1–5,7,14] We recently demonstrated that stereoelectronic effects that result from 4-fluoroproline substitution altered the thermodynamics of self-assembly of an elastin-mimetic polypeptide.[9] The differences in macromolecular properties between the elastin derivatives were interpreted on the basis of differential stabilization of the β-turn structures[15–20] that develop in the VPGVG structural repeats above the phase transition (Scheme 1). The greater stability of the (4*R*)-

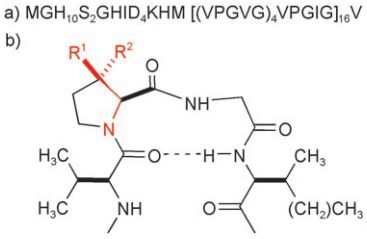

Scheme 1. a) Amino acid sequence of the elastin-mimetic model polypeptide. b) Structural representation of the β-turn unit of the elastin pentapeptide repeat. The bond vectors that geometrically define the stereoelectronic fluorine–amide *gauche* interactions within the substituted proline residues are highlighted in red for elastin-1 ($R^1 = F$; $R^2 = H$) and elastin-2 ($R^1 = H$; $R^2 = F$).

fluoroproline-substituted elastin (elastin-4) was attributed to the close correspondence between the observed values of the angles ϕ and ψ for the preferred C$^{\gamma}$-*exo* pucker of **4** and the range of ϕ and ψ angles associated with proline residues in the $(i+1)$ position of a type II β-turn conformation (ideal β_{II} ϕ, ψ: −60°, 120°).[21] In contrast, the deviation of the angles ϕ and ψ for the preferred C$^{\gamma}$-*endo* conformation of **3** from those of the type II β-turn conformation caused a destabilization of the corresponding elastin derivative (elastin-3). DFT calculations on model turn segments provided evidence for a relative destabilization of the type II β-turn structure in relation to the type I β-turn structure in the latter situation, which was supported by the conformational analysis of the corresponding elastin-mimetic polypeptides.[9]

To assess the effect of 3-fluoroproline substitution in a well-defined polypeptide model system, the elastin-mimetic proteins elastin-1 and elastin-2 were synthesized for comparison to the 4-fluoroproline derivatives elastin-3 and elastin-4 (Scheme 1). On the basis of the observed regiochemical reversal of ring-pucker preferences for **1** and **2** in relation to **3** and **4**, we expected that elastin-1 and elastin-2 would display opposite tendencies in conformational and thermodynamic behavior compared to the corresponding 4-fluoroproline derivatives.

The elastin-mimetic polypeptides elastin-1 and elastin-2 were prepared through the biosynthetic approach that we reported earlier for elastin-3 and elastin-4.[22] The purified proteins were obtained in comparable yield to the 4-fluoroproline elastin derivatives. MALDI-TOF mass spectrometry of the elastin-1 and elastin-2 indicated virtually complete substitution of proline with the respective analogue. The ^{1}H–^{1}H NOESY NMR spectra of elastin-1 and elastin-2 revealed that the *trans* configuration of the prolyl–peptide bond was the dominant one in aqueous solution. In addition, the values of the coupling constants, $^3J_{H\alpha H\beta}$ and $^3J_{H\alpha F\beta}$, for the substituted proline residues in the elastin-mimetic polypeptides were similar to the corresponding values for **1** and **2**, which indicated that the ring-pucker preferences of the analogues were conserved within the respective polypeptides.

Circular dichroism (CD) studies of elastin-mimetic polypeptides have established that a conformational rearrangement occurs as the temperature increases through the transition point, which corresponds to a conversion of the local secondary structure of the pentapeptide repeats from a random coil conformation to a more ordered type II β-turn conformation. This conformational transition can be detected in the CD spectra of elastin-1 as a function of temperature, in that the random coil signature (negative ellipticity near 196 nm) is gradually replaced with the type II β-turn signature (positive ellipticity near 208 nm) as the temperature is increased through the transition point (Figure 2).[15,18,23] In contrast, the CD temperature manifold for elastin-2 displays a different spectroscopic profile in which a strong negative ellipticity (minimum at 223 nm) develops above the transition temperature. This spectroscopic feature is not consistent with the formation of a type II β-turn conformation, but more closely resembles the CD spectrum of a type I β-turn structure.[24] Thus, the CD spectroscopic data indicate a formal reversal of turn preferences for the 3-fluoroproline-substituted elastin sequences with respect to those previously observed for the 4-fluoroproline derivatives. The C$^{\gamma}$-*exo* pucker of (4*R*)-fluoroproline significantly stabilized the type II β-turn conformation for elastin-4, whereas the C$^{\gamma}$-*endo* pucker of (4*S*)-fluoroproline in elastin-3 appreciably destabilized the type II β-turn conformation relative to alternative turn structures.[9] The CD spectroscopic data for both sets of fluoroproline-substituted elastin derivatives suggest that the C$^{\gamma}$-*exo* pucker is more compatible with a type II β-turn structure, and, conversely, the C$^{\gamma}$-*endo* pucker is less compatible with a type II β-turn structure to the point that the alternative type I β-turn conformation becomes energetically competitive, if not dominant, for the ordered state of the polypeptide.

In addition, the *syn* versus *anti* stereochemistry of the proline analogue may strongly influence the thermodynamic parameters associated with the elastin assembly. The CD thermal transition curves indicated that the disappearance of the low-temperature random coil conformation adheres to a quasi-two-state transition for both elastin-1 and elastin-2 (Figure 2c).[23] The mathematical fits of these thermal transitions provided estimates for the respective transition temperatures (T_t) of 30.1 and 10.9 °C. Differential scanning calorimetry (DSC) measurements provided T_t values of 35.9 and 13.6 °C for elastin-1 and elastin-2, respectively, which correlate well with those determined from the CD temperature profiles. These T_t values[25] provide an indication of the

 © 2006 Wiley-VCH Verlag GmbH & Co. KGaA, Weinheim

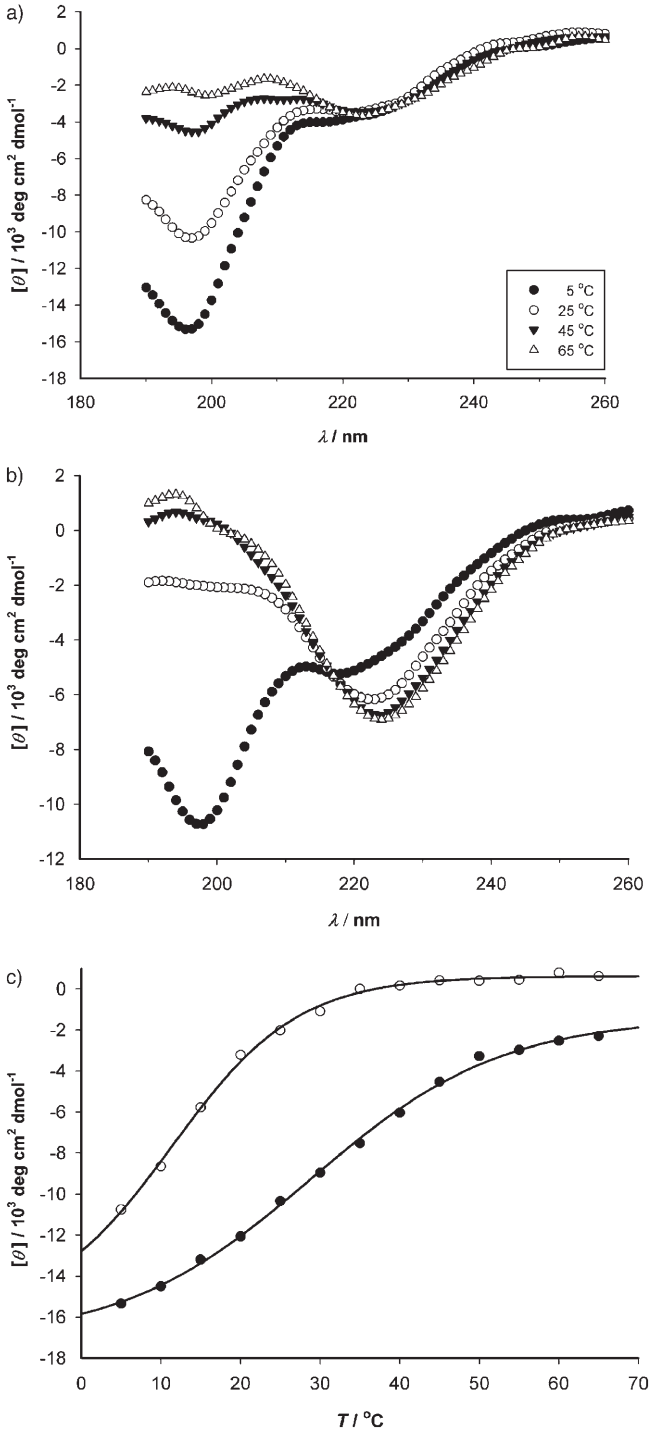

Figure 2. a, b) Temperature-dependent CD spectroscopic manifolds for elastin-1 and elastin-2, respectively. c) Thermal transition curves for the disappearance of the random coil CD signal $[\theta]_{198}$ for elastin-1 (●) and elastin-2 (○).

facility with which the elastin assembly occurs, which, as a disorder-to-order conformational transition, depends on the thermodynamic stabilization of the turn structures in relation to the random coil conformation. The DSC data indicate that the self-assembled state of elastin-2 is stabilized with respect to that of elastin-1 by approximately 22 °C. Similarly, a stabilization of 20 °C was observed for the ordered state of elastin-4 versus that of elastin-3.[9] In both cases, incorporation of the *syn*-fluoroproline derivative significantly raises the transition temperature for self-assembly of the elastin-mimetic polypeptide with respect to that of the corresponding *anti*-fluoroproline derivative. These data strongly suggest that the steric repulsion that develops within the *syn*-oriented fluoroproline derivatives can adversely influence the energetics of elastin assembly, and, more generally, of local turn-folding events compared to the *anti*-fluoroproline derivatives. Moreover, manifestation of this effect is independent of the intrinsic ring-pucker preference of the proline derivative and the observed turn type of the elastin analogue.

In conclusion, we have demonstrated that the conformational energetics of a polypeptide can be altered through a combination of stereoelectronic and steric effects that arise from the presence of substituted proline residues at structurally critical positions. In the specific case under consideration, the assembly of a series of elastin-mimetic polypeptides could be interpreted in terms of the influence of the preferred fluoroproline ring pucker on the conformational energetics of the local β-turn structures. This "proline editing"[26] strategy—based on a set of four related fluoroproline derivatives[1–5,7,9]—may represent a general approach to interrogating the structural and functional role of specific proline residues within a polypeptide sequence, through comparison of the differential effect of fluoroproline substitution on the thermodynamics of folding and assembly among the resulting group of structural variants.

Received: August 8, 2006
Published online: November 16, 2006

Keywords: amino acids · bioorganic chemistry · peptides · protein engineering · stereoelectronic effect

[1] a) J. A. Hodges, R. T. Raines, *J. Am. Chem. Soc.* **2003**, *125*, 9262–9263; b) L. E. Bretscher, C. L. Jenkins, K. M. Taylor, M. L. DeRider, R. T. Raines, *J. Am. Chem. Soc.* **2001**, *123*, 777–778; c) S. K. Holmgren, L. E. Bretscher, K. M. Taylor, R. T. Raines, *Chem. Biol.* **1999**, *6*, 63–70; d) S. K. Holmgren, K. M. Taylor, L. E. Bretscher, R. T. Raines, *Nature* **1998**, *392*, 666–667.
[2] a) D. Barth, A. G. Milbradt, C. Renner, L. Moroder, *ChemBioChem* **2004**, *5*, 79–86; b) D. Barth, H. M. Musiol, M. Schutt, S. Fiori, A. G. Milbradt, C. Renner, L. Moroder, *Chem. Eur. J.* **2003**, *9*, 3692–3702.
[3] A. V. Persikov, J. A. Ramshaw, A. Kirkpatrick, B. Brodsky, *J. Am. Chem. Soc.* **2003**, *125*, 11500–11501.
[4] M. Doi, Y. Nishi, S. Uchiyama, Y. Nishiuchi, T. Nakazawa, T. Ohkubo, Y Kobayashi, *J. Am. Chem. Soc.* **2003**, *125*, 9922–9923.
[5] a) M. Umashankara, I. R. Babu, K. N. Ganesh, *Chem. Commun.* **2003**, 2606–2607; b) I. R. Babu, K. N. Ganesh, *J. Am. Chem. Soc.* **2001**, *123*, 2079–2080.
[6] a) M. L. DeRider, S. J. Wilkens, M. J. Waddell, L. E. Bretscher, L. F. Weinhold, R. T. Raines, J. L. Markley, *J. Am. Chem. Soc.* **2002**, *124*, 2497–2505; b) E. S. Eberhardt, N. Panasik, Jr., R. T. Raines, *J. Am. Chem. Soc.* **1996**, *118*, 12261–12266; c) N. Panasik, Jr., E. S. Eberhardt, A. S. Edison, D. R. Powell, R. T. Raines, *Int. J. Pept. Protein Res.* **1994**, *44*, 262–269.
[7] J. A. Hodges, R. T. Raines, *J. Am. Chem. Soc.* **2005**, *127*, 15923–15932.

 © 2006 Wiley-VCH Verlag GmbH & Co. KGaA, Weinheim

[8] C. Renner, S. Alefelder, J. H. Bae, N. Budisa, R. Huber, L. Moroder, *Angew. Chem.* **2001**, *113*, 949 – 951; *Angew. Chem. Int. Ed.* **2001**, *40*, 923 – 925.
[9] W. Kim, R. A. McMillan, J. P. Snyder, V. P. Conticello, *J. Am. Chem. Soc.* **2005**, *127*, 18121 – 18132.
[10] C. L. Jenkins, L. E. Bretscher, I. A. Guzei, R. T. Raines, *J. Am. Chem. Soc.* **2003**, *125*, 6422 – 6427.
[11] a) D. O'Hagan, C. Bilton, J. A. K. Howard, L. Knight, D. J. Tozer, *J. Chem. Soc. Perkin Trans. 2* **2000**, 605 – 607; b) C. R. S. Briggs, D. O'Hagan, J. A. K. Howard, D. S. Yufit, *J. Fluorine Chem.* **2003**, *119*, 9 – 13.
[12] L. Vitagliano, R. Berisio, L. Mazzarella, A. Zagari, *Biopolymers* **2001**, *58*, 459 – 464.
[13] a) H. B. Bürgi, J. Dunitz, E. Shefter, *Acta Crystallogr. Sect. B* **1974**, *30*, 1517 – 1527; b) H. B. Bürgi, J. M. Lehn, G. Wipff, *J. Am. Chem. Soc.* **1974**, *96*, 1965 – 1966; c) H. B. Bürgi, J. D. Dunitz, J. M. Lehn, G. Wipff, *Tetrahedron* **1974**, *30*, 1563 – 1572; d) H. B. Bürgi, J. D. Dunitz, E. Shefter, *J. Am. Chem. Soc.* **1973**, *95*, 5065 – 5067.
[14] J. C. Horng, R. T. Raines, *Protein Sci.* **2006**, *15*, 74 – 83.
[15] D. W. Urry, R. G. Shaw, K. U. Prasad, *Biochem. Biophys. Res. Commun.* **1985**, *130*, 50 – 57.
[16] G. J. Thomas, Jr., B. Prescott, D. W. Urry, *Biopolymers* **1987**, *26*, 921 – 934.
[17] D. W. Urry, N. R. Krishna, D. H. Huang, T. L. Trapane, K. U. Prasad, *Biopolymers* **1989**, *28*, 819 – 833.
[18] H. Reiersen, A. R. Clarke, A. R. Rees, *J. Mol. Biol.* **1998**, *283*, 255 – 264.
[19] B. Li, D. O. Alonso, V. Daggett, *J. Mol. Biol.* **2001**, *305*, 581 – 592.
[20] X. L. Yao, M. Hong, *J. Am. Chem. Soc.* **2004**, *126*, 4199 – 4210.
[21] C. M. Wilmot, J. M. Thornton, *J. Mol. Biol.* **1988**, *203*, 221 – 232.
[22] W. Kim, A. George, M. Evans, V. P. Conticello, *ChemBioChem* **2004**, *5*, 928 – 936.
[23] T. Yamaoka, T. Tamura, Y. Seto, T. Tada, S. Kunugi, D. A. Tirrell, *Biomacromolecules* **2003**, *4*, 1680 – 1685.
[24] a) A. Perczel, M. Hollosi, P. Sandor, G. D. Fasman, *Int. J. Pept. Protein Res.* **1993**, *41*, 223 – 236; b) A. Perczel, E. Kollat, M. Hollosi, G. D. Fasman, *Biopolymers* **1993**, *33*, 665 – 685.
[25] a) D. W. Urry, C.-H. Luan, T. M. Parker, D. C. Gowda, K. U. Prasad, M. C. Reid, A. Safavy, *J. Am. Chem. Soc.* **1991**, *113*, 4346 – 4347; b) D. W. Urry, D. C. Gowda, T. M. Parker, C.-H. Luan, *Biopolymers* **1992**, *32*, 1243 – 1250.
[26] K. M. Thomas, D. Naduthambi, G. Tririya, N. J. Zondlo, *Org. Lett.* **2005**, *7*, 2397 – 2400.

 © 2006 Wiley-VCH Verlag GmbH & Co. KGaA, Weinheim

Molecular Recognition

DOI: 10.1002/anie.200601849

Imprinted Photonic Polymers for Chiral Recognition**

Xiaobin Hu, Qi An, Guangtao Li, Shengyang Tao, and Jian Liu*

Molecular imprinting is a well-established and facile technique to synthesize molecularly imprinted polymers (MIPs) with specific molecular-recognition sites for a large variety of applications, such as chromatographic separations, membranes, catalysis, biosensors, and artificial antibodies.[1–12] Molecular recognition and separation is generally based on bulk polymers, which have the disadvantages of long diffusion paths and the absence of accessible cavities for the analyte in the bulk, thus resulting in low specific capacities and long response times. Recently, the groups of Mosbach and Sellergren overcame these drawbacks of bulk MIPs by using hierarchical imprinting of template molecules on the surface of a porous silica support.[6–10] However, for assays with traditional MIPs, the analyte must contain a chromophore or fluorophore or be electroactive to generate a readable optical or electronic signal. Otherwise, the analyte must be modified or tagged. Thus, it is attractive to prepare label-free sensitive films[11–12] that give a readable signal upon binding guest molecules to detect and quantify the target analyte directly.

Colloidal crystals have been widely used as templates to create porous films with highly ordered 3D inverse opal structures.[13–15] The periodic variety of the refractive index of these porous films gives rise to interesting optical properties.[16–18] Particularly, if the films are made from hydrogel polymers, they may swell or contract in aqueous solution upon environmental changes, which leads to spectral shifts in the Bragg diffraction wavelength. Thus, they can be used as self-reporting sensors to measure various environmental changes, such as pH and temperature.[19–23] In this respect, Asher's group developed several hydrogel photonic films to sense Pb^{2+}, glucose, and creatinine.[19–20] Braun's group also synthesized hydrogel films of inverse opal structure that displayed a tunable optical response sensitive to pH value and glucose.[22–23] It was conceivable that, if two promising concepts (molecular imprinting and photonic crystals) were

[*] Dr. X-B. Hu, Q. An, Prof. Dr. G-T. Li, S-Y. Tao, J. Liu
Key Lab of Organic Photoelectronic and Molecular Engineering
Department of Chemistry
Tsinghua University
Beijing 100084 (P.R. China)
Fax: (+86) 10-6279-2905
E-mail: lgt@mail.tsinghua.edu.cn

[**] The work was supported by the National Science Foundation of China (20473044, 20533050).

Supporting information for this article is available on the WWW under http://www.angewandte.org or from the author.

© 2006 Wiley-VCH Verlag GmbH & Co. KGaA, Weinheim

combined, a novel self-reporting sensing film could be constructed that exhibits high sensitivity and selectivity.

Herein, we adopt colloidal silica crystals as a template in collaboration with molecular-imprinting techniques to prepare highly ordered 3D macroporous hydrogel films that display highly selective and specific chiral molecular recognition properties. These films generate a readable optical signal directly (self-reporting) upon binding a target analyte without the need for labeling. Scheme 1 outlines the preparation of the inverse opal hydrogel films imprinted with chiral molecules. Monodisperse silica particles were fabricated by the Stöber method,[24] and a colloidal array template with highly ordered 3D structure was generated on a glass substrate by vertical deposition[25] of the silica spheres in ethanol (Figure 1 A). The size of monodisperse silica particles can be tuned in the range of 150 to 400 nm by changing the fabrication conditions. In the present work, monodisperse silica spheres with a diameter of 186 nm were used to form close-packed face-centered-cubic (fcc) photonic crystal films with a thickness of about 2 μm as a template (see the Supporting Information). Methacrylic acid (MAA) was used as functional monomer, and L-3,4-dihydroxyphenyalanine (L-dopa), a chiral electroactive analyte, was chosen as the template molecule in the molecular-imprinting process. Prior to its infiltration into the crystalline voids of the silica, MAA was mixed with L-dopa in a mixture of water and ethanol for sufficient intermolecular interaction to form a stable complex. Appropriate amounts of ethylene glycol dimethylacrylate (EGDMA) as cross-linker and 2,2′-azobisisobutyronitrile (AIBN) as initiator were added, and the mixture of precursors in the interstitial voids of the colloidal crystal template was photopolymerized in an ice bath. The silica nanoparticles were removed with 1% hydrofluoric acid, and L-dopa was eluted with 0.1M acetic acid. The film was rinsed with deionized water to obtain a macroporous L-dopa-imprinted hydrogel film (MIP film; Figure 1 B). These films with a thickness of about 2 μm (see the Supporting Information) not only have well-defined 3D ordered macroporous structure and large internal surface area, but also have a number of cavities left by the imprinted molecules, with complementary shape and binding sites[1–3] to L-dopa. Moreover, the macropores of these films are interconnected, which is favorable for the transport of molecules and significantly enhances the sensing response by shortening the diffusion path of analyte during the binding process.

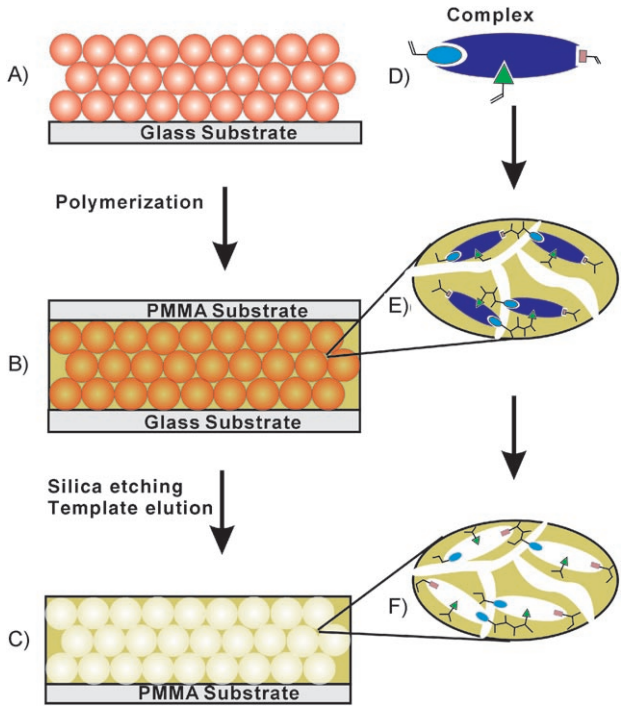

Scheme 1. Protocol for the preparation of photonic MIP films: A) SiO_2 colloidal crystals on glass substrate; B) infiltration of complex solution into colloidal template followed by photopolymerizition; C) photonic MIP film after the removal of SiO_2 nanoparticles and dopa template molecules; D) complex of monomer and template molecule; E) imprinted molecules within the polymer matrix; F) imprinted cavities with complementary shape and binding sites to the template molecule.

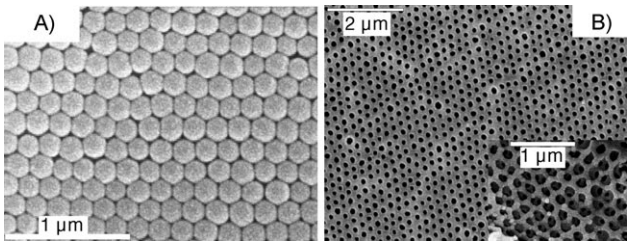

Figure 1. A) SEM image of colloidal crystal formed with SiO_2 spheres of diameter 186 nm. B) Top-view SEM image of the fabricated photonic MIP film. Inset: Magnified cross-section SEM image of MIP film showing the interconnection between the macropores of the fabricated MIP film.

L-Dopa is an amino acid that is able to reversibly form a stable complex with MAA by noncovalent interactions (e.g., electrostatic, hydrogen bonding, van der Waals).[5] These intermolecular interactions between L-dopa and MAA can be detected by fluorescence spectroscopy. Figure 2 A shows the fluorescent emission spectra of L-dopa in deionized water as well as in an MIP film. As a control experiment, the spectrum of a non-imprinted polymer film (non-MIP) prepared under the same conditions is also shown. A red shift of the emission peak from 320 to 331 nm is evident for L-dopa molecules

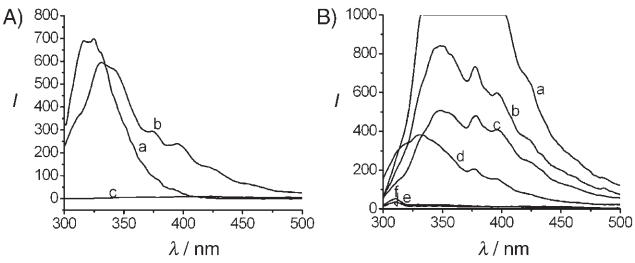

Figure 2. A) Fluorescence spectra of 1 mM L-dopa in deionized water (a), MIP film with entrapped L-dopa (b), and non-MIP film (c) on a PMMA substrate. B) Fluorescence spectra of MIP films exposed to L-dopa solutions of different concentrations.

 © 2006 Wiley-VCH Verlag GmbH & Co. KGaA, Weinheim

trapped in the MIP film, but no emission is observed for the non-imprinted film. This result indicates that L-dopa was entrapped in the MIP matrix and has strong interaction with the polymer matrix, which leads to the shift of its emission peak. The imprinting of L-dopa in the polymer films was also confirmed by fluorescence spectroscopy. After the etching and eluting processes, the blank polymer films obtained were immersed into aqueous solutions of pure L-dopa or D-dopa at various concentrations. After thorough rinsing with deionized water to remove nonspecifically adsorbed analyte, the polymer films were checked by fluorescence spectroscopy for selective chiral adsorption. As expected, fluorescence was observed for the films exposed to L-dopa solution (Figure 2B). For the sake of comparison, the fluorescent spectra of the relative concentrations of pure L-dopa in solution are given in the Supporting Information. In agreement with the results in Figure 2A, there is a red shift of the emission peak when L-dopa molecule is rebound to the MIP film. Moreover, it was found that the extent of the red shift is dependent on the concentration of L-dopa in the solution (Figure 2B). When the concentration of L-dopa was 0.01 mM, a maximum red shift (28 nm) of the emission peak was observed. In contrast, no emission was observed for MIP films immersed in aqueous solutions of D-dopa at various concentrations. These results clearly indicate that the prepared MIP film has distinctive chiral selectivity for dopa. The imprinted cavities in polymer film with complementary shape and binding sites only to L-dopa are responsible for the observed chiral recognition. Also, the formation of polymer domains with lower dielectric constants possibly favors such interactions.

The chiral recognition of the prepared MIP films was also studied by UV/Vis spectroscopy by exposing these blank MIP films to a series of solutions of pure enantiomer of dopa at different concentrations. The MIP films were incubated in pure L-dopa or D-dopa in phosphate buffer solution (0.1M phosphate buffer) for 2 minutes, and their UV/Vis spectra were measured (Figure 3). The optical absorbance of the macroporous MIP film is very sensitive to the rebinding of L-dopa molecule, and the absorption peak shifts gradually to shorter wavelength (blue shift) with increase in the concentration of L-dopa (Figure 3A). The absorbance peak of an MIP film soaked in 10 mM L-dopa is blue shifted by 66 nm relative to that of the blank MIP film in 0.1M phosphate buffer. In contrast, the absorption peak remains almost unshifted for MIP films exposed to various concentrations of D-dopa (Figure 3B). Clearly, owing to its complementary shape with the binding sites, only L-dopa rather than D-dopa can occupy the imprinted cavities within the MIP films. Furthermore, as the isoelectric point of dopa is 5.52 at 25 °C,[26] the dopa molecules exist mainly in zwitterionic form in neutral buffer solution. The binding of L-dopa to MIP films is more effective through electrostatic interactions, which results in contraction of the hydrogel and a consequent blue shift of absorption peak of the MIP film. Notably, this enantioselective detection is highly sensitive, as evident from the detection of 0.01 μM dopa solutions (Figure 3A). Also, as a result of the interconnected macroporous structure, the prepared MIP films exhibit very fast response times, and the binding process can be completed within 20 s (see the

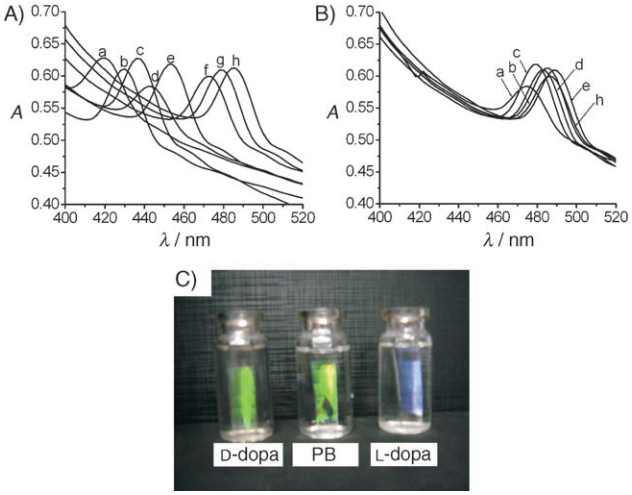

Figure 3. UV/Vis spectra of blank MIP films exposed to L-dopa (A) and D-dopa (B) in phosphate buffer at different concentrations: 10 mM (a); 1 mM (b); 0.1 mM (c); 0.01 mM (d); 1 μM (e); 0.1 μM (f); 0.01 μM (g), and deionized water (h). C) Three blank MIP films exposed to 0.1 M phosphate buffer (PB), 10 mM D-dopa, and 10 mM L-dopa in phosphate buffer.

Supporting Information). More importantly, the chiral recognition process can be easily and rapidly visualized by the naked eye (Figure 3C). Moreover, the binding behavior of L-dopa is affected by the pH value of the buffer solution. The rebinding efficiency decreases with decreasing pH value (see the Supporting Information). The neutral buffer solution provides an effective environment for the molecular recognition of the MIP film. The preparation of the MIP film as well as the characterization of its chiral recognition behavior was repeated several times, and good reproducibility was observed.

Consistent with the results described above, electrochemical methods further confirmed the chiral recognition behavior of the prepared MIP films. The experimental details as well as the results are presented in the Supporting Information.

The prepared MIP hydrogel films were evaluated under acidic and basic conditions. In particular, besides the chiral recognition function, these ordered macroporous hydrogel films can swell or contract upon changes of certain external conditions, such as pH value, temperature, ionic strength, and added electrolyte.[19,22] Figure 4 shows that upon changing the solution from 0.1M HCl to 0.1M NaOH, the absorption peak of the film is red shifted, which is in agreement results reported by Lee and Braun.[22] The reason for this shift is the presence of carboxyl groups with the macroporous network which can be deprotonated when OH^- ions diffuse from the bulk solution into the gel phase. As a result, the osmotic pressure within the gel is increased owing to the increased Donnan potential inside the polyelectrolyte network; this pressure increase drives the hydrogel swelling.

In summary, to the best of our knowledge, this is the first report of a general protocol for the synthesis of an ordered 3D macroporous MIP film with a self-reporting chiral recognition function by using both colloidal crystals and molecular-

 © 2006 Wiley-VCH Verlag GmbH & Co. KGaA, Weinheim

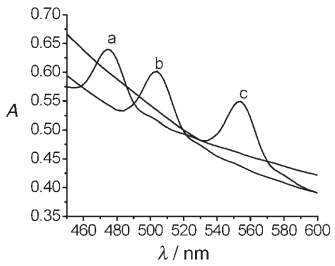

Figure 4. Normal incidence transmission UV/Vis spectra of the prepared MIP film exposed to 0.1 M HCl (a), deionized water (b), and 0.1 M NaOH (c).

imprinting techniques. The current method emphasizes the use of a readable optical signal caused by structural changes upon binding of the analyte. The result shows that this special MIP film has many advantages in specific recognition, such as quick response time, high sensitivity, and high selectivity. The described concept not only provides a potential alternative to create optical diffraction-based chemical or biological sensors, but also extends the applications of MIP films in other areas such as drug separation, clinical assays, and catalysis.

Experimental Section

Monodispersed silica particles were synthesized by the Stöber method. Colloidal SiO_2 crystals were fabricated by vertical deposition on glass slides. These preparations are described in the Supporting Information. MAA (4 mL, 47.16 mmol, Acros), EGDMA (2 mL, 10.59 mmol, Acros), and L-dopa (0.02 g, 10.14 mmol, Sigma) were mixed in a mixture of anhydrous ethanol (3 mL) and deionized water (1 mL). AIBN (ca. 0.01 g, 6.1 mmol, Acros) was added, the mixture was bubbled with nitrogen for 10 minutes, and the resulting homogeneous monomer mixture was infiltrated into the colloidal silica crystals. Once the colloidal crystals became transparent, excess precursors were removed by covering a clean PMMA slide (1.5 mm thick), and the remaining mixture was photopolymerized in an ice bath under a UV light at 365 nm (16 W) for 2 h. The sandwich structure was immersed in 1 % HF solution for 2 h to separate double slides and completely etch the silica colloids. The formed polymer was washed with 0.1M acetic acid for 2 h and then rinsed thoroughly with deionized water until no L-dopa was detected by fluorescence at 320 nm in the eluent, thus indicating full removal of L-dopa from the imprinted films. For preparation of free-standing films, a glass slide was used instead of the PMMA slide as the cover.

The fluorescence spectra of pure L-dopa in deionized water and L-dopa entrapped in the MIP film were obtained with a Perkin–Elmer LS55 spectrometer. The blank MIP films obtained by complete removal of the L-dopa template were used for the rebinding process. An excitation wavelength of 282 nm was used for the fluorescence measurements, and the slit width was 8 nm. All optical responses the of MIP films supported on PMMA were performed on an UV/Vis spectrometer (Perkin–Elmer Lambda 35). Phosphate buffer (0.1M, pH 7.6) was prepared from NaH_2PO_4 and Na_2HPO_4 (Beijing Chemicals), and various D- and L-dopa solutions were prepared at various concentrations in the phosphate buffer. In all cases, prior to detection, the MIP films were washed with 0.1M acetic acid followed by deionized water until no dopa was detected. After each UV/Vis measurement, the film was rinsed with deionized water and phosphate buffer. The sequence of measurements was performed from low to high concentration to eliminate contamination.

Received: May 11, 2006
Revised: September 4, 2006
Published online: November 14, 2006

Keywords: colloids · macroporous materials · molecular recognition · polymers

[1] K. Haupt, K. Mosbach, *Chem. Rev.* **2000**, *100*, 2495 – 2504.
[2] B. Sellergren, *Angew. Chem.* **2000**, *112*, 1071 – 1078; *Angew. Chem. Int. Ed.* **2000**, *39*, 1031 – 1037.
[3] G. Wulff, *Chem. Rev.* **2002**, *102*, 1 – 27.
[4] R. A. Potyrailo, *Angew. Chem.* **2006**, *118*, 718 – 738; *Angew. Chem. Int. Ed.* **2006**, *45*, 702 – 723.
[5] T. Takeuchi, T. Mukawa, H. Shinmon, *Chem. Rec.* **2005**, *5*, 263 – 275.
[6] E. Yilmaz, K. Haupt, K. Mosbach, *Angew. Chem.* **2000**, *112*, 2178 – 2181; *Angew. Chem. Int. Ed.* **2000**, *39*, 2115 – 2118.
[7] K. Lettau, A. Warsinke, A. Laschewsky, K, Mosbach, E. Yilmaz, F. W. Scheller, *Chem. Mater.* **2004**, *16*, 2745 – 2749.
[8] M. M. Titirici, A. J. Hall, B. Sellergren, *Chem. Mater.* **2003**, *15*, 822 – 824.
[9] M. M. Titirici, B. Sellergren, *Chem. Mater.* **2006**, *18*, 1773 – 1779.
[10] M. M. Titirici, A. J. Hall, B. Sellergren, *Chem. Mater.* **2002**, *14*, 21 – 23.
[11] J. Matsui, K. Akamatsu, S. Nishiguchi, D. Miyoshi, H. Nawafune, K. Tamaki, N. Sugimoto, *Anal. Chem.* **2004**, *76*, 1310 – 1315.
[12] P. Manesiotis, A. J. Hall, M. Emgenbroich, M. Quaglia, E. D. Lorenzi, B. Sellergren, *Chem. Commun.* **2004**, *20*, 2278 – 2279.
[13] O. D. Velev, E. W. Kaler, *Adv. Mater.* **2000**, *12*, 531 – 534.
[14] Y. Xia, *Adv. Mater.* **2001**, *13*, 369.
[15] C. Lopez, *Adv. Mater.* **2003**, *15*, 1679 – 1703.
[16] Z. Z. Gu, R. Horie, S. Kubo, Y. Yamada, A. Fujishima, O. Sato, *Angew. Chem.* **2002**, *114*, 1201 – 1204; *Angew. Chem. Int. Ed.* **2002**, *41*, 1153 – 1156.
[17] P. Jiang, *Angew. Chem.* **2004**, *116*, 1554 – 1557; *Angew. Chem. Int. Ed.* **2004**, *43*, 5625 – 5628.
[18] T. Sen, G. J. T. Tiddy, J. L. Casci, M. W. Anderson, *Angew. Chem.* **2003**, *115*, 4797 – 4801; *Angew. Chem. Int. Ed.* **2003**, *42*, 4649 – 4653.
[19] J. H. Holtz, S. A. Asher, *Nature* **1997**, *389*, 829 – 832.
[20] A. C. Sharma, T. Jana, R. Kesavamoorthy, L. Shi, M. A. Virji, D. N. Finegold, S. A. Asher, *J. Am. Chem. Soc.* **2004**, *126*, 2971 – 2977.
[21] A. C. Aresnault, T. J. Clark, G. V. Freymann, L. Cademartiri, R. Sapienza, J. Bertolotti, E. Vekris, S. Wong, V. Kitaev, I. Manners, R. Z. Wang, S. John, D. Wiersma, G. A. Ozin, *Nat. Mater.* **2006**, *5*, 179 – 184.
[22] Y. J. Lee, P. V. Braun, *Adv. Mater.* **2003**, *15*, 563 – 566.
[23] Y. J. Lee, S. A. Pruzinsky, P. V. Braun, *Langmuir* **2004**, *20*, 3096 – 3106.
[24] W. Stöber, A. Fink, *J. Colloid Interface Sci.* **1968**, *26*, 62 – 69.
[25] P. Jiang, J. F. Bertone, K. S. Hwang, V. L. Colvin, *Chem. Mater.* **1999**, *11*, 2132.
[26] T. M. Pekol, N. Poopisut, J. A. Cox, *Talanta* **1994**, *41*, 663 – 668.

 © 2006 Wiley-VCH Verlag GmbH & Co. KGaA, Weinheim

Antitumor Agents

DOI: 10.1002/anie.200602251

An Aptamer–Doxorubicin Physical Conjugate as a Novel Targeted Drug-Delivery Platform**

Vaishali Bagalkot, Omid C. Farokhzad, Robert Langer, and Sangyong Jon**

The active targeting of drugs in a cell-, tissue-, or disease-specific manner represents a potentially powerful technology with widespread applications in medicine, including the treatment of cancers. In a typical approach, a drug and a ligand are complementarily functionalized to allow for covalent or noncovalent (for example, biotin–streptavidin) conjugation for targeted delivery. The resulting chemical modifications of the drugs and/or the ligands may adversely affect the safety and efficacy profile of the drugs and the binding characteristics of the ligands, thereby resulting in less efficacious drug–ligand conjugates. It would be desirable to develop simple but effective targeted drug-delivery strategies that do not require chemical modification of the drug or the ligands.

Recently our group and other investigators have used nucleic acid ligands or aptamers for therapeutic and diagnostic targeted-delivery applications.[1–6] Aptamers are structured single-stranded DNA or RNA molecules that can specifically bind to small molecules,[7] peptides and proteins,[8] and oligosaccharides[9] with high affinity and specificity.

Here we report a novel strategy for the targeted delivery of doxorubicin (Dox) to cancer cells through the formation of an aptamer–Dox physical conjugate. Dox is a well-known anticancer drug which has shown efficacy against a range of neoplasms, including acute lymphoblastic and myeloblastic leukemias, malignant lymphomas, soft tissue and bone sarcomas, and breast, ovarian, prostate, bladder, gastric, and bronchogenic carcinomas. This widely used oncology drug is also associated with dose-dependent cardiotoxicities, including dilated cardiomyopathy and congestive heart failure, which make the development of targeted Dox-delivery systems of particular importance.[10] Dox is known to intercalate within the DNA strand due to the presence of flat aromatic rings in this molecule. Other closely associated drugs, such as donarubicin, have also been shown to be intercalated into a double helix of DNA.[11] Since aptamers are known to form tertiary conformations with short double-stranded regions through intramolecular base pairing,[12] we hypothesized that doxorubicin may intercalate into these double-stranded regions and form a physical complex with the aptamers through noncovalent intercalation, a process requiring no modification of the drug or the aptamer (Figure 1). We postulated that the resulting aptamer–Dox

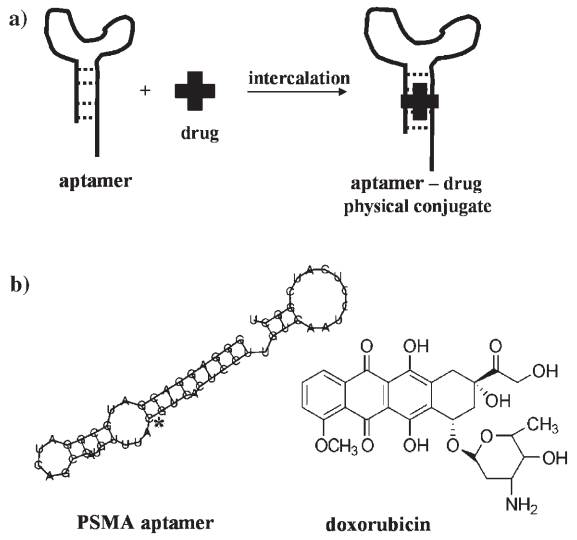

Figure 1. a) Physical-conjugate formation between an aptamer and a model drug. b) 2D structure of the A10 PSMA aptamer as predicted by M fold program and the chemical structure of doxorubicin.

physical conjugate may be used for the targeted delivery of Dox by taking advantage of the aptamer's binding specificity to its target antigen. In this study, we have examined the feasibility of this concept by using the A10 2′-fluoropyrimidine RNA aptamer[13] that binds to the prostate-specific membrane antigen (PSMA) with high affinity and specificity.

The two-dimensional structure of the A10 PSMA[13] aptamer used herein was predicted by the M fold program.[14] It is well known that the anthracycline class of drugs, including Dox, have fluorescence properties that become quenched after intercalation into DNA.[15,16] To examine whether such intercalation also occurs within the RNA aptamer, we carried out binding studies between the A10 PSMA aptamer and Dox. Fluorescence spectroscopy was used to examine the binding of doxorubicin to the A10 PSMA aptamer. Sequential decreases in the native fluorescence spectrum of Dox were observed when a fixed concentration of

[*] V. Bagalkot, Prof. Dr. S. Jon
Department of Life Science
Gwangju Institute of Science and Technology
1 Oryoung-dong, Buk-gu, Gwangju 500712 (South Korea)
Fax: (+82) 62-970-2504
E-mail: syjon@gist.ac.kr
V. Bagalkot, Prof. Dr. O. C. Farokhzad
Department of Anaesthesiology
Brigham and Women's Hospital and Harvard Medical School
75 Francis Street, Boston, MA 02115 (USA)
Fax: (+1) 617-730-2801
E-mail: ofarokhzad@partners.org
Prof. Dr. R. Langer
Department of Chemical Engineering
Massachusetts Institute of Technology
E25-342, 45 Carleton Street, Cambridge, MA 02139 (USA)

[**] This work was supported by Korea Science and Technology Foundation grant R01-2006-000-10818-0 (S.J. and V.B.) and USA National Institutes of Health grants CA119349 (R.L., O.F., and V.B.) and EB003647 (O.F.). We also thank Prof. C. S. Park for helpful discussions. This work is dedicated to the families of patients with cancer.

Supporting information for this article is available on the WWW under http://www.angewandte.org or from the author.

 © 2006 Wiley-VCH Verlag GmbH & Co. KGaA, Weinheim

Dox was incubated with an increasing molar ratio of the A10 PSMA aptamer, results consistent with the intercalation of Dox within the A10 PSMA aptamer (Figure 2). Dox is known to preferentially bind to double-stranded 5′-GC-3′ or 5′-CG-3′

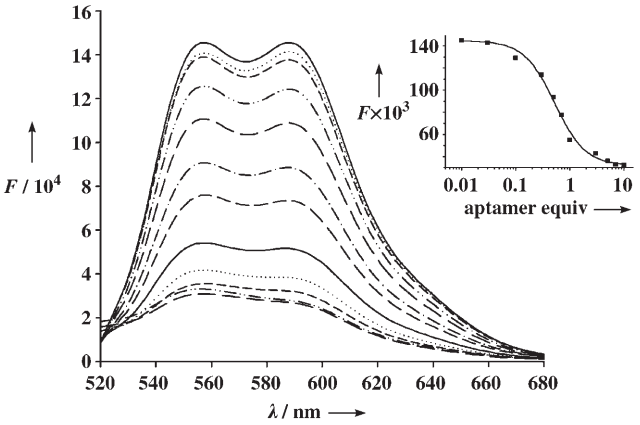

Figure 2. Fluorescence spectra of doxorubicin solution (1.5 μM) with increasing molar ratios of the aptamer (from top to bottom: 0, 0.01, 0.03, 0.1, 0.3, 0.5, 1, 3, 5, 7, and 10 equiv). Inset: A Hill plot for the aptamer titration (K_d = 0.6 μM; 0.52 equiv of the aptamer).

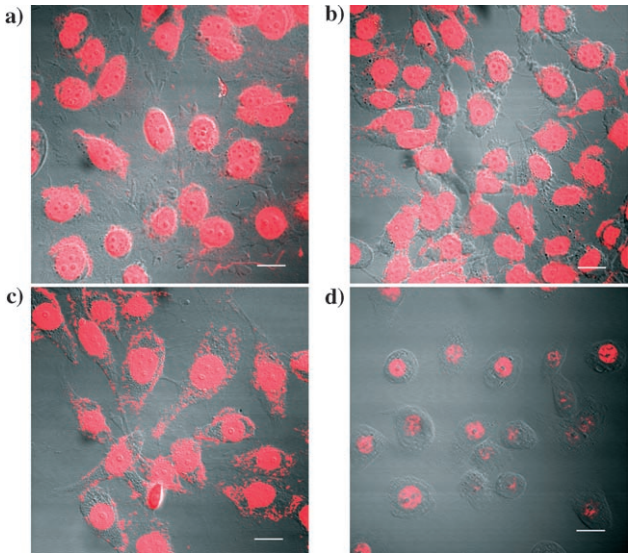

Figure 3. Confocal laser scanning microscopy images (superimposed images of fluorescence and transmittance) of LNCaP (a and c) and PC3 (b and d) cells after treatments of 1.5 μM free doxorubicin (a and b) and of 1.5 μM aptamer–Dox physical conjugate (c and d) for 2 h. Scale bars: 20 μm.

sequences,[17,18] and evaluation of the predicted A10 aptamer secondary structure reveals one possible site for Dox intercalation, as marked by an asterisk in Figure 1b. The incubation of Dox with the A10 aptamer results in maximal quenching of the Dox fluorescence at approximately 1:1.2 molar equivalence of Dox to aptamer, a result suggesting that Dox makes a physical conjugate with the A10 aptamer by intercalating into its predicted CG sequence (Figure 2). The inset of Figure 2 shows a Hill plot of fluorescence quenching as a function of increasing aptamer concentration. The dissociation constant (K_d = 600 nM) of the aptamer–Dox physical conjugate was derived from this figure and suggests a spontaneously formed stable physical conjugate. The stability of the aptamer–Dox conjugate was further confirmed by high-pressure liquid chromatography (HPLC) where the conjugate peak appeared at a different elution time from those of the native aptamer and Dox (data not shown). A study of the release of Dox from the aptamer–Dox physical conjugate over time was conducted by using a dialysis tube (see Figure S1 in the Supporting Information). Upon dialysis, more than 80% Dox release was observed in 6 h with zero-order kinetics, which suggests that the Dox molecule is released from the conjugate beyond the concentration of its dissociation constant by simple diffusion.

To evaluate the feasibility of the aptamer–Dox physical conjugate as a targeted drug-delivery platform, we performed in vitro binding and uptake studies with the LNCaP prostate epithelial cells which express the target PSMA protein on their plasma membrane. We used the PC3 prostate epithelial cells which do not express any detectable level of the PSMA protein as a negative control (Figure 3). Our confocal laser scanning microscopy data demonstrate that while free Dox readily diffuses through the plasma membrane of LNCaP and PC3 cells with equal efficiency (Figure 3a and b), there is a remarkable specificity in the uptake of the aptamer–Dox conjugate by LNCaP but not PC3 cells (Figure 3c and d), as marked by strong nuclear fluorescence that is consistent with the intercalation of Dox within the genomic DNA.

The mechanisms of uptake of the aptamer–Dox physical conjugate and the free Dox by LNCaP cells appear distinct.[19] Unlike free Dox, which exclusively stains the nuclei, the aptamer–Dox conjugate demonstrates both nuclear and cytosolic staining, with the latter predominately in the form of punctuate granules that are consistent with compartmentalization of the Dox within endosomes (Figure 3c). This pattern of cytosolic staining is consistent with receptor-mediated endocytic uptake of the aptamer–Dox physical conjugate, which results after binding of the conjugate to the PSMA protein on the LNCaP plasma membrane. The aptamer–Dox physical conjugate failed to produce any cytosolic staining of the PC3 cells, a result consistent with the lack of PSMA protein expression in these cells (Figure 3d). The weak fluorescence staining of the PC3 nuclei after incubating with the aptamer–Dox conjugate is likely attributable to a small amount of free Dox that may be present in the media bathing the cells. Indeed, the LNCaP- and PC3-binding data suggest that the majority of Dox remains in the form of a complex with the aptamer, thereby demonstrating the stability of the aptamer–Dox physical conjugate over time in the culture media. Furthermore, the data demonstrate the ability of an aptamer to retain its binding characteristics while the Dox is intercalated within it, so allowing the targeted delivery of Dox to the cells that express the aptamer target. We next compared the binding characteristics of an equimolar concentration of the aptamer–Dox physical conjugate to the free aptamer in LNCaP-binding assays.[20] By using quantitative PCR amplification of the LNCaP-bound aptamers, about 84% of the binding ability

 © 2006 Wiley-VCH Verlag GmbH & Co. KGaA, Weinheim

of the A10 aptamer was shown to be retained by the aptamer–Dox physical conjugate (see Figure S2 in the Supporting Information). This result also demonstrates the ability of an aptamer to retain its binding characteristics while the Dox is intercalated within it, thereby allowing the targeted delivery of Dox to the cells that express the aptamer target.

The targeting specificity of the aptamer–Dox physical conjugate was next quantified by flow cytometry experiments (Figure 4). The data demonstrate near-identical staining of LNCaP and PC3 cells after treatment of these cells with free Dox (Figure 4a and b). However, when LNCaP and PC3 cells were incubated with the aptamer–Dox physical conjugate, there was a significant enhancement in the fluorescence signal from LNCaP cells as compared to that from PC3 cells (FL2 log intensity for LNCaP was 123 ± 4.66 versus 35 ± 1.79 for PC3; mean $\pm$ standard error (SE), number of samples (N) = 4), which validates the targeting specificity of the aptamer–Dox physical conjugate (Figure 4c). Taken together, our microscopy and flow cytometry data demonstrate the proof of concept for the feasibility of the aptamer–Dox physical conjugate to serve as a novel drug-delivery platform for a variety of applications in oncology.

We next examined whether the targeted delivery of the aptamer–Dox physical conjugate to LNCaP cells results in enhanced cellular cytotoxicity[21] compared to that in PC3 control cells. We first demonstrated in escalating-dose studies that the cytotoxicity of free Dox to LNCaP and PC3 cells is equipotent (data not shown). At a dose where the cytotoxicity of free Dox had reached a plateau near its maximum, we compared the cytotoxic efficacy of free Dox (5 μM) to that of the aptamer–Dox physical conjugate (5 μM), as well as that of free aptamer without Dox, on LNCaP and PC3 cells by MTT assay. The data demonstrate that while the cytotoxicity of free Dox is equipotent against LNCaP and PC3 cells, the cytotoxicity of the aptamer–Dox conjugate is significantly enhanced against the targeted LNCaP cells as compared to the nontargeted PC3 cells (cellular viability: $52.8\% \pm 1.73$ LNCaP versus $75.2\% \pm 1.19$ PC3; mean $\pm$ SE, $N = 5$; probability value (p) < 0.005; Figure 5). Interestingly, the data demonstrate a near-equipotent cytotoxicity of the aptamer–Dox physical conjugate to the LNCaP cells as compared to that of free Dox. The free aptamer without Dox had no inherent cytotoxicity to LNCaP or PC3 cells (Figure 5). Our data suggest that, after endocytic uptake, the aptamer–Dox physical conjugate releases the Dox molecules inside the LNCaP cells, possibly due to the aptamer–Dox dissociation constant favoring the release of Dox because of the relatively negligible concentrations of Dox inside the cells. Alternatively, the release of Dox from the aptamer–Dox physical conjugate may occur through gradual degradation of the aptamer by endonucleases in the lysosomes after cellular uptake. We postulate that a combination of these factors may contribute to the observed findings. In contrast to the dramatic cytotoxic effects of the aptamer–Dox complex to the LNCaP cells, the cytotoxicity of this physical-conjugate system to PC3 cells was significantly less pronounced, a result consistent with the lack of PSMA expression in PC3 cells.

In conclusion, by exploiting the ability of anthracycline drugs to intercalate between bases of polynucleotides, a novel

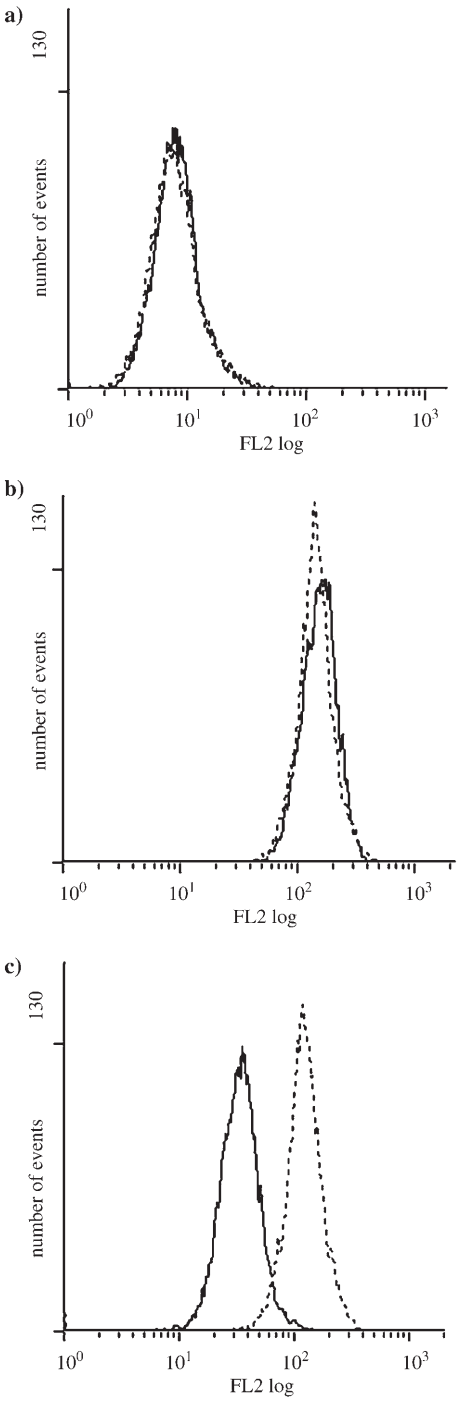

Figure 4. Flow cytometry histogram profiles of LNCaP (dotted line) and PC3 (solid line) cells obtained after treatments with a) nothing, b) 1.5 μM free doxorubicin, and c) 1.5 μM aptamer–Dox physical conjugate. FL2 log = fluorescence intensity of FL2 sensor (band pass filter, 575 nm).

physical conjugate was made between the anticancer drug Dox and the A10 RNA aptamer that binds to the PSMA protein on the surface of prostate cancer cells. The stability and efficacy of this conjugate to serve as a novel drug-delivery platform was further demonstrated in vitro. Our data suggest that the aptamer–Dox physical conjugate is stable in the cell-culture medium and could differentially and with high

 © 2006 Wiley-VCH Verlag GmbH & Co. KGaA, Weinheim

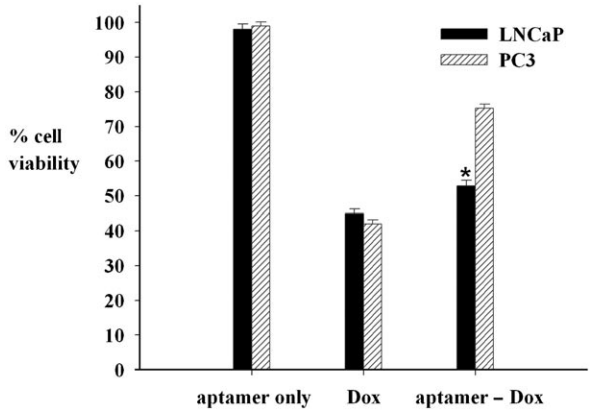

Figure 5. Growth-inhibition assay (MTT) results for prostrate cancer cell lines LNCaP and PC3 after 2 h of incubation with free doxorubicin (5 μM) and the physical conjugate (5 μM) and 24 h of subsequent incubation. * indicates the LNCaP result that is significantly different from that with PC3 cells ($p < 0.005$, $N = 5$).

efficiency target the PSMA-expressing LNCaP cells. The specificity of the system was further demonstrated by the lack of targeting of the PSMA-negative PC3 cells. We expect that the small size of the aptamer–Dox physical-conjugate system ($\approx$18 kD) as compared to that of similar antibody-based immunoconjugates ($\approx$150 kD) may facilitate the rapid vascular extravasation and intratumoral penetration of the former, thereby making it a therapeutically effective drug-delivery system for in vivo applications.[22] The much larger nanoparticle drug-delivery systems compensate for their size disadvantage through their capacity to release a large payload of drug in a controlled manner, a property that makes each ligand–target biorecognition a potentially relevant therapeutic event. Each of these systems may contribute in a unique way to our arsenal of cancer-therapy options in the future.[23] Furthermore, these systems may be combined such that a targeted nanoparticle–aptamer bioconjugate system may deliver distinct drugs through encapsulation within the nanoparticles and through intercalation within the aptamers, with the result of a temporally distinct release of two or more drugs for combination chemotherapy.[1–3] We anticipate that the aforementioned aptamer–drug platform technology based on the intercalation of anthracyclines within the bases of aptamers may be utilized in distinct ways to develop novel targeted therapeutic modalities for more effective cancer chemotherapy. In the next phase of our studies, we will be evaluating the in vivo efficacy of the aptamer–Dox physical conjugate in animal models of cancer.

Received: June 6, 2006
Revised: September 18, 2006
Published online: November 13, 2006

Keywords: antitumor agents · aptamers · conjugation · drug delivery · targeted therapy

[1] O. C. Farokhzad, J. Cheng, B. A. Teply, I. Sherifi, S. Jon, P. W. Kantoff, J. P. Richie, R. Langer, *Proc. Natl. Acad. Sci. USA* **2006**, *103*, 6315.
[2] O. C. Farokhzad, S. Jon, A. Khademhosseini, T. N. Tran, D. A. Lavan, R. Langer, *Cancer Res.* **2004**, *64*, 7668.
[3] O. C. Farokhzad, J. M. Karp, R. Langer, *Expert Opin. Drug Delivery* **2006**, *3*, 311.
[4] B. J. Hicke, A. W. Stephens, T. Gould, Y. F. Chang, C. K. Lynott, J. Heil, S. Borkowski, C. S. Hilger, G. Cook, S. Warren, P. G. Schmidt, *J. Nucl. Med.* **2006**, *47*, 668.
[5] C. Pestourie, B. Tavitian, F. Duconge, *Biochimie* **2005**, *87*, 921.
[6] a) T. C. Chu, J. W. Marks, III, L. A. Lavery, S. Faulkner, M. G. Rosenblum, A. D. Ellington, M. Levy, *Cancer Res.* **2006**, *66*, 5989; b) J. O. McNamara, 2nd, E. R. Andrechek, Y. Wang, K. D. Viles, R. E. Rempel, E. Gilboa, B. A. Sullenger, P. H. Giangrande, *Nat. Biotechnol.* **2006**, *24*, 1005.
[7] J. Flinders, S. C. DeFina, D. M. Brackett, C. Baugh, C. Wilson, T. Dieckmann, *ChemBioChem* **2004**, *5*, 62.
[8] D. J. Patel, A. K. Suri, F. Jiang, L. Jiang, P. Fan, R. A. Kumar, S. Nonin, *J. Mol. Biol.* **1997**, *272*, 645.
[9] S. Jeong, T. Eom, S. Kim, S. Lee, J. Yu, *Biochem. Biophys. Res. Commun.* **2001**, *281*, 237.
[10] G. Minotti, P. Menna, E. Salvatorelli, G. Cairo, L. Gianni, *Pharmacol. Rev.* **2004**, *56*, 185.
[11] P. Fan, A. K. Suri, R. Fiala, D. Live, D. J. Patel, *J. Mol. Biol.* **1996**, *258*, 480.
[12] D. Sussman, J. C. Nix, C. Wilson, *Nat. Struct. Biol.* **2000**, *7*, 53.
[13] S. E. Lupold, B. J. Hicke, Y. Lin, D. S. Coffey, *Cancer Res.* **2002**, *62*, 4029.
[14] M. Zuker, *Nucleic Acids Res.* **2003**, *31*, 3406.
[15] H. T. Haj, M. Salerno, W. Priebe, H. Kozlowski, A. Garnier-Suillerot, *Chem. Biol. Interact.* **2003**, *145*, 349..
[16] L. Valentini, V. Nicolella, E. Vannini, M. Menozzi, S. Penco, F. Arcamone, *Farmaco [Sci]* **1985**, *40*, 377.
[17] J. B. Chaires, J. E. Herrera, M. J. Waring, *Biochemistry* **1990**, *29*, 6145.
[18] C. A. Frederick, L. D. Williams, G. Ughetto, G. A. van der Marel, J. H. van Boom, A. Rich, A. H. Wang, *Biochemistry* **1990**, *29*, 2538.
[19] H. S. Yoo, K. H. Lee, J. E. Oh, T. G. Park, *J. Controlled Release* **2000**, *68*, 419.
[20] T. C. Chu, F. Shieh, L. A. Lavery, M. Levy, R. Richards-Kortum, B. A. Korgel, A. D. Ellington, *Biosens. Bioelectron.* **2006**, *21*, 1859.
[21] S. Akaishi, M. Kobari, K. Takeda, S. Matsuno, *Tohoku J. Exp. Med.* **1995**, *175*, 29.
[22] A. M. Wu, P. D. Senter, *Nat. Biotechnol.* **2005**, *23*, 1137.
[23] S. S. Feng, *Expert Rev. Med. Devices* **2004**, *1*, 115.

 © 2006 Wiley-VCH Verlag GmbH & Co. KGaA, Weinheim

Anticancer Agents

DOI: 10.1002/anie.200602873

Diversity in Guanine-Selective DNA Binding Modes for an Organometallic Ruthenium Arene Complex**

*Hong-Ke Liu, Susan J. Berners-Price, Fuyi Wang, John A. Parkinson, Jingjing Xu, Juraj Bella, and Peter J. Sadler**

Ruthenium(II) arene complexes of the type $[(\eta^6\text{-arene})Ru(en)Cl]^+$ (arene = e.g. *p*-cymene or biphenyl; en = ethylenediamine) can exhibit anticancer activity in vitro and in vivo.[1] They are pseudooctahedral, half-sandwich, "piano-stool" complexes with one reactive coordination site (the Ru–Cl bond). Analysis of the distribution of ruthenium in cancer cells in culture[2] shows that the level of DNA ruthenation is similar to that of platination by the anticancer drug cisplatin. The binding of cisplatin to DNA gives rise to DNA bending, followed by protein recognition and induction of apoptosis.[3] Ruthenium arene complexes are not cross-resistant with cisplatin.[1] This may indicate that structural distortions induced in DNA by ruthenium arenes differ significantly from those induced by cisplatin. Calculations[4] on adducts of Ru^{II} arene complexes with DNA have suggested that this is the case, but experimental evidence is needed. The extent of DNA ruthenation and the nature of the structural distortions in DNA appear to correlate with cytotoxic potency,[5] and also influence protein recognition.[6] The studies reported herein reveal novel and varied modes of interaction of $[(\eta^6\text{-biphenyl})Ru(en)Cl]^+$ (**1**) with duplex DNA.

We chose duplex **III** for study because an NMR analysis has previously been carried out and the kinking induced by GG platination of strand **I** by cisplatin has been characterized.[7]

$A_1\ T_2\ A_3\ C_4\ A_5\ T_6\ G_7\ G_8\ T_9\ A_{10}C_{11}A_{12}T_{13}A_{14}$ **I**

$T_{28}A_{27}T_{26}G_{25}T_{24}A_{23}C_{22}C_{21}A_{20}T_{19}G_{18}T_{17}A_{16}T_{15}$ **II**

I + **II** = duplex **III**

Initially, attempts were made to prepare single strands **I** or **II** that were monoruthenated so that site-specifically ruthenated duplexes could be obtained by addition of the (nonruthenated) complementary strand.[8] Reaction of **1** with the GG strand **I** in a 1:1 molar ratio for 48 h at 310 K gave rise to two monoruthenated products, as separated and identified by HPLC–ESIMS (Figure 1a and Supporting Information).

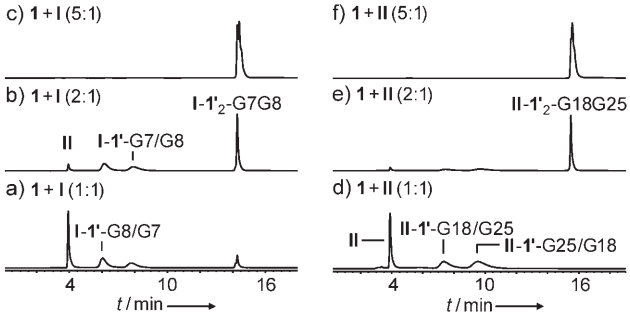

Figure 1. HPLC chromatograms for reaction of $[(\eta^6\text{-biphenyl})Ru(en)Cl]PF_6$ (**1**-PF_6) with 0.1 mM single-stranded DNA d(ATACATGGTACATA) (**I**) or d(TATGTACCATGTAT) (**II**) in 100 mM $NaClO_4$ at **1**/**I** (or **II**) molar ratios of 1:1, 2:1, and 5:1. At a **1**/**I** or **1**/**II** molar ratio of 5:1, the diruthenated adduct is the only product. **1′** ($\{(\eta^6\text{-biphenyl})Ru(en)\}^{2+}$) is bound to GN7. Specific assignments of monoruthenation sites to G7 or G8, and G18 or G25 were not made and hence the four adducts are labeled G7/G8, G8/G7, G18/G25, and G25/G18.

When the molar ratio of **1**:**I** was increased to 2:1 and 5:1, the diruthenated single strand predominated. These data are consistent with selective ruthenation of guanine bases (i.e. G7 and G8) as expected on the basis of competitive mononucleotide reactions.[9] Similarly, reactions of **1** with strand **II** gave rise to new HPLC peaks assignable to ruthenation of G18 and G25 (Figure 1d–f and Supporting Information).

For NMR studies, we annealed strand **I** with monoruthenated strand **II**. The fraction corresponding to monoruthenated **II**-**1′**-G18/G25 (Figure 1d) was collected by semipreparative HPLC. This fraction gave a single HPLC peak when it was rechromatographed, which suggests that it was stable. It was annealed with the complementary (nonruthenated) strand **I** by heating to 353 K for 2 min followed by slow cooling to 288 K over 3 h.

We expected that the sample of ruthenated duplex **III** prepared in this way would be ruthenated with $\{(\eta^6\text{-biphenyl})Ru(en)\}^{2+}$ (**1′**) at a single site on strand **II**. However, subsequent analysis of the 2D NOESY NMR data showed

[*] Dr. H.-K. Liu, Dr. F. Wang, J. Xu, J. Bella, Prof. Dr. P. J. Sadler
School of Chemistry
The University of Edinburgh
King's Buildings
West Mains Road, Edinburgh EH9 3JJ (UK)
Fax: (+44) 131-650-6452
E-mail: P.J.Sadler@ed.ac.uk
Dr. H.-K. Liu
School of Chemistry and Environmental Science
Nanjing Normal University
Nanjing 210046 (P.R. China)
Prof. Dr. S. J. Berners-Price
School of Biomedical
Biomolecular & Chemical Sciences
The University of Western Australia
35 Stirling Highway, Crawley WA 6009 (Australia)
Dr. J. A. Parkinson
WestChem
Department of Pure and Applied Chemistry
Thomas Graham Building
University of Strathclyde
295 Cathedral Street, Glasgow G1 1XL (UK)

[**] We thank the Wellcome Trust (Travelling Fellowship for H.L. and facilities in the Edinburgh Protein Interaction Centre), the University of Western Australia (Study Leave Grant for S.J.B.-P.), ORS (studentship for J.X.), RC-UK (Rasor), and Oncosense Ltd for support, and colleagues in EC COST Action D20 for stimulating discussions.

Supporting information for this article is available on the WWW under http://www.angewandte.org or from the author.

 © 2006 Wiley-VCH Verlag GmbH & Co. KGaA, Weinheim

that all four of the guanine residues were ruthenated at N7, and at one of the sites (G18), two different conformers were identified. These adducts are labeled **III-1′**-G7, **III-1′**-G8, **III-1′**-G25, **III-1′**-G18i, and **III-1′**-G18n.

A near-complete assignment of the NOESY NMR spectrum of **III-1′** was achieved for the mixture of five adducts, although the complexity precluded full structural determinations. Assignment was possible because of the known selectivity of **1** for guanines, the localization of structural perturbations to residues close to the ruthenated guanine residue, and the lack of precursor duplex **III** in the HPLC purified sample. Thus, sequential assignments along each strand always led to cross-peaks that were largely identical to those of the nonruthenated duplex. Despite extensive overlap of NOE cross-peaks, little ambiguity in the assignments of individual resonances was found, and cross-validation of signal assignments from related connectivities was possible. The ^{1}H NMR chemical shifts of the ^{1}H resonances associated with these five adducts are listed in the Supporting Information, and the induced chemical-shift changes are plotted in Figure 2 and the Supporting Information. Structural perturbations induced by ruthenation are clearly localized to within a few (± 2) base pairs of the ruthenation site in all cases.

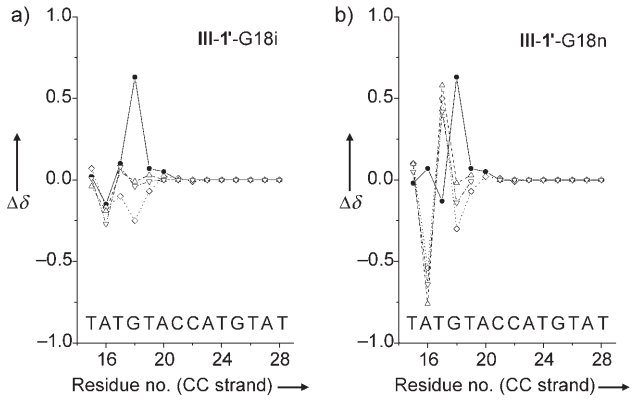

Figure 2. ^{1}H NMR chemical-shift changes ($\Delta\delta = \delta$(**III-1′**)$-\delta$(**III**)) induced by ruthenation of duplex **III** for resonances of the -CC- strand of a) the **III-1′**-G18i adduct and b) the **III-1′**-G18n adduct. Key: ● aromatic (H6/H8) protons; ◇ H1′, △ H2′, ▽ H2″ sugar protons.

In the absence of DNA, the amino protons in **1** point towards (NH_u, $\delta = 6.19$ ppm) or away (NH_d $\delta = 4.14$ ppm) from the coordinated arene (Scheme 1).[10] On binding to DNA the two amino groups become nonequivalent. A total of ten different pairs of NH_u and NH_d resonances would therefore be anticipated for the mixture of five different ruthenated adducts. Five distinct NH_u–NH_d cross-peaks were identifiable in the 2D NOESY NMR spectrum at 298 K (see the Supporting Information), thus suggesting that some NH resonances have similar chemical shifts or are not observed for other reasons. The downfield shifts of NH resonances in the adducts are consistent with the presence of H-bonding to

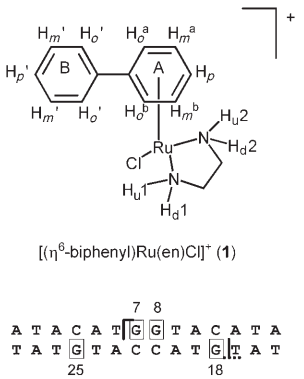

Scheme 1. Atom labeling for complex **1** (top) and sites of ruthenation and intercalation on duplex **III** (bottom).

the C6 carbonyl of the coordinated guanine residue.[10] Although it was not possible to assign all of the en amino proton resonances, structural information was obtained in specific cases from the observation and interpretation of intramolecular NOEs (see the Supporting Information).

One distinct environment for the noncoordinated phenyl ring B was readily identified from the characteristic pattern of intramolecular NOEs (Supporting Information) and strong shielding of the $H_{o'}$, $H_{m'}$, and $H_{p'}$ protons ($\Delta\delta \approx -1$ ppm). The NOEs and chemical-shift changes are consistent with intercalation of the arene ring B between DNA bases.[11] In the 2D NOESY spectrum at 298 K, only one set of resonances was observed for each of the pairs of *ortho* ($H_{o'}$) and *meta* ($H_{m'}$) protons, but at 283 K the observation of two slightly different chemical shifts for the $H_{o'}$ cross-peaks provided evidence for slowing of the rotation of the noncoordinated arene in this (intercalated) environment. The assignment of intramolecular NOEs between DNA H1′ and arene protons of **1′** revealed that these protons have identical chemical shifts in two of the monoruthenated adducts (**III-1′**-G18i and **III-1′**-G7), which therefore have intercalated arenes in very similar environments.

In three cases, the NMR data were sufficient to allow models to be constructed for the ruthenated adducts on the basis of both observed NOEs and the significant perturbations in chemical shifts of DNA protons with respect to **III** (the nonruthenated duplex). The two adducts ruthenated at G18 are assignable to conformations in which the noncoordinated phenyl ring is either intercalated between G18 and T17 (**III-1′**-G18i; Scheme 1) or nonintercalated (**III-1′**-G18n). The adducts show significant differences in chemical-shift changes for the bases in the sequence T15–G18 (see the Supporting Information and Figure 2). In particular, the A16n and T17n bases of **III-1′**-G18n are significantly distorted, whereas A16i and T17i appear far less perturbed in **III-1′**-G18i.

For **III-1′**-G18i, NOEs between A12 H2 on the complementary strand and the noncoordinated phenyl ring protons, and the strong shielding of the protons of this arene ring ($\Delta\delta \approx -1$ ppm, see the Supporting Information), in particular, indicate that arene ring B is intercalated between G18 and T17 (Figure 3 a). The slight shielding of the T17i CH_3 protons and deshielding of the T17i H2′ and H2″ protons (Supporting

 © 2006 Wiley-VCH Verlag GmbH & Co. KGaA, Weinheim

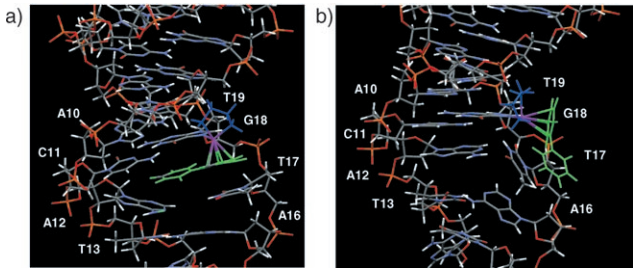

Figure 3. Molecular models of two conformers of duplex **III** ruthenated at N7 of G18 with **1′**. a) **III-1′**-G18i showing the intercalation of the arene between G18 and T17. b) **III-1′**-G18n in which the arene is nonintercalated but stacked on a tilted T17. Color code: en blue, biphenyl green.

Information) are consistent with stacking of the Ru-coordinated arene ring A over the T17i aromatic ring and edge-on juxtaposition to the T17i sugar ring.

In contrast, the NOESY and chemical-shift data suggest that the pendant arene in **III-1′**-G18n lies on the surface of the major groove (Figure 3b), thus forcing the T17n base to stack underneath it by tilting, accompanied by a tilt of the A16n base. Such a model explains why the H1′ resonances of A16n and T17n are significantly altered with respect to **III** and **III-1′**-G18i and shows how nonintercalation can induce dramatic changes in DNA structure. In the **III-1′**-G18i and **III-1′**-G18n models, the T19 bases are in identical environments, consistent with the NMR data (Supporting Information).

The intramolecular NOEs and strong shielding of the protons of the noncoordinated phenyl ring for the G7 adduct suggest that this ring is intercalated between G7 and T6. The T6 residue appears to be strongly perturbed: no NOESY cross-peaks to either G7 or A5 could be identified and the T6 H2′/H2″ protons appear to be strongly deshielded (see the Supporting Information).

These studies reveal unique modes of binding of the anticancer complex **1** to duplex DNA. The monofunctional fragment $\{(\eta^6\text{-biphenyl})Ru(en)\}^{2+}$ is highly specific for G N7, but mobile at elevated temperature at which migration between guanine residues is facile.[12] In contrast, such migration of Pt^{II} am(m)ines is rare. This behavior suggests that organometallic Ru^{II} arene complexes can be readily removed from DNA, which may be beneficial for reversing DNA damage in cells. The specificity of $\{(\eta^6\text{-biphenyl})Ru(en)\}^{2+}$ for guanine is aided by strong H-bonding between an NH of en and C6 carbonyl of G, and by π–π stacking involving the noncoordinated phenyl ring of the biphenyl ligand and DNA bases. Such stacking can occur through intercalation between DNA bases (G and T bases in the adducts **III-1′**-G7 and **III-1′**-G18i), or with a partially extruded T base, as in **III-1′**-G18n. Arene–base stacking may play a role in determining the rates of reactions of Ru^{II} arene en complexes with DNA, as appears to be the case for mononucleotides.[9] Other examples of metal complexes containing DNA-intercalating ligands include Ru^{II}, Rh^{III}, and di-Rh^{II} complexes with phenanthroline derivatives,[13] and Pt^{II} complexes with directly bonded or pendant acridine arms.[14] It is well known that DNA structures are relatively flexible. Some intercalators can rotate within intercalation sites.[15] Our data suggest that ruthenium arene intercalation is dynamic: equilibria can exist between intercalated (**III-1′**-G18i) and nonintercalated (**III-1′**-G18n) conformers. The present studies provide a structural basis for understanding how the nature of the arene in $[(\eta^6\text{-arene})Ru(en)Cl]^+$ complexes can exert a significant effect on cytotoxicity,[1] on excision repair of DNA lesions,[6] and on DNA destabilization,[16] and provide a basis for future work on sequence-dependent effects of DNA duplex ruthenation.

Experimental Section

Ruthenated DNA: For ruthenation of single strands, microliter aliquots of **1**-PF_6 (10.0 mM) were added to a solution of **I** (17 μL, 1.80 mM), $NaClO_4$ (15 μL, 2.0 M), and H_2O (265 μL), to give 1:1, 2:1, or 5:1 molar ratios of **1**/**I**, and the mixtures were incubated for 48 h at 310 K in the dark. Similarly, aliquots of **1** were added to **II** (14 μL, 2.13 mM), $NaClO_4$ (15 μL, 2.0 M), and H_2O (268 μL). The ruthenations were monitored by 1D ^1H NMR spectroscopy, the mixtures separated by HPLC, and the peaks characterized by HPLC–ESIMS.

A similar 1:1 reaction mixture of **1** + **II** (on a 10-mL scale) was separated on a semipreparative C8 ACE-5 column. The fraction eluting at 7.4 min (monoruthenated single-strand fraction **II-1′**-G18/G25, Figure 1d) was collected, freeze-dried, and desalted on a NAP-10 column (Pharmacia Biotech). The sample was then freeze-dried, dissolved in deionized water (200 μL), and analyzed by HPLC and UV/Vis spectroscopy. Finally, $NaClO_4$ (12.5 μL, 2.0 M), D_2O (50 μL), **I** (140 μL, 1.80 mM), and H_2O (101 μL) were added to a solution of **II-1′**-G18/G25 (196 μL, 1.29 mM) together with dioxane as an internal ^1H NMR reference. The final concentration of the monoruthenated duplex **III-1′** was 0.51 mM. The resulting DNA solution was annealed by heating briefly from 288 to 353 K for 2 min and cooling slowly to 288 K over 3.5 h. 2D NOESY ^1H NMR spectra were then recorded at 298 and 283 K.

Modeling studies: A structure for duplex d(ATACATGGTACATA)·d(TATGTACCATGTAT) calculated on the basis of NMR data[7] was used to model ruthenated DNA with the biopolymer module of Sybyl (version 6.3, Tripos Inc.). Coordinates from the X-ray crystal structures of **1**-PF_6 (CCDC-170362) allowed accurate incorporation of the Ru complex into the model DNA–Ru construct.

Details of materials used, HPLC, HPLC–ESIMS, NMR, modeling studies, and pH measurements are given in the Supporting Information.

Received: July 18, 2006
Revised: September 7, 2006
Published online: November 22, 2006

Keywords: anticancer agents · bioinorganic chemistry · DNA · NMR spectroscopy · ruthenium

[1] Y.-K. Yan, M. Melchart, A. Habtemariam, P. J. Sadler, *Chem. Commun.* **2005**, 4764–4776, and references therein.
[2] F. Wang, B. Zeitlin, P. J. Sadler, D. I. Jodrell, unpublished results.
[3] D. Wang, S. J. Lippard, *Nat. Rev. Drug Discovery* **2005**, *4*, 307–320.
[4] M. C. Colombo, C. Gossens, I. Tavernelli, U. Röthlisberger in *Modelling Molecular Structure and Reactivity in Biological Systems* (Eds.: K. J. Naidoo, M. Hann, J. Gao, M. Field, J. Brady), RSC, Cambridge, **2006**, in press, and references therein.

 © 2006 Wiley-VCH Verlag GmbH & Co. KGaA, Weinheim

[5] F. Wang, A. Habtemariam, E. P. L. van der Geer, R. Fernández, M. Melchart, R. J. Deeth, R. Aird, S. Guichard, F. P. A. Fabbiani, P. Lozano-Casal, I. D. H. Oswald, D. I. Jodrell, S. Parsons, P. J. Sadler, *Proc. Natl. Acad. Sci. USA* **2005**, *102*, 18269 – 18274.
[6] O. Novakova, J. Kasparkova, V. Bursova, C. Hofr, M. Vojtiskova, H. Chen, P. J. Sadler, V. Brabec, *Chem. Biol.* **2005**, *12*, 121 – 129.
[7] J. A. Parkinson, Y. Chen, P. del S. Murdoch, Z. Guo, S. J. Berners-Price, T. A. Brown, P. J. Sadler, *Chem. Eur. J.* **2000**, *6*, 3636 – 3644.
[8] HPLC showed that all four G residues in **III** are readily ruthenated at 310 K; see the Supporting Information.
[9] H. Chen, J. A. Parkinson, R. E. Morris, P. J. Sadler, *J. Am. Chem. Soc.* **2003**, *125*, 173 – 186.
[10] H. Chen, J. A. Parkinson, S. Parsons, R. A. Coxall, R. O. Gould, P. J. Sadler, *J. Am. Chem. Soc.* **2002**, *124*, 3064 – 3082.
[11] Recently we studied ruthenation of the 6 mer d$(CGGCCG)_2$: H. Liu, F. Wang, J. A. Parkinson, J. Bella, P. J. Sadler, *Chem. Eur. J.* **2006**, *12*, 6151 – 6165. The NMR data suggested that arene intercalation can occur, but were not sufficient to allow models of the interactions to be constructed.
[12] HPLC studies of similar adducts of the related complex $[(\eta^6\text{-}p\text{-cymene})Ru(en)Cl]^+$ with duplex **III** show that such migration is very slow at ambient temperature.
[13] a) K. E. Erkkila, D. T. Odom, J. K. Barton, *Chem. Rev.* **1999**, *99*, 2777 – 2795; b) L. M. Wilhelmsson, F. Westerlund, P. Lincoln, B. Norden, *J. Am. Chem. Soc.* **2002**, *124*, 12092 – 12093; c) A. Greguric, I. D. Greguric, T. W. Hambley, J. R. Aldrich-Wright, J. G. Collins, *J. Chem. Soc. Dalton Trans.* **2002**, 849 – 855.
[14] a) B. E. Bowler, S. J. Lippard, *Biochemistry* **1986**, *25*, 3031 – 3038; b) W. I. Sundquist, D. P. Bancroft, S. J. Lippard, *J. Am. Chem. Soc.* **1990**, *112*, 1590 – 1596; c) E. Ceci, R. Cini, A. Karaulov, M. B. Hursthouse, L. Maresca, G. Natile, *J. Chem. Soc. Dalton Trans.* 1993, 2491 – 2497; d) J. R. Choudhury, U. Bierbach, *Nucleic Acids Res.* **2005**, *33*, 5622 – 5632.
[15] J. Gallego, *Nucleic Acids Res.* **2004**, *32*, 3607 – 3614.
[16] O. Novakova, H. Chen, O. Vrana, A. Rodger, P. J. Sadler, V. Brabec, *Biochemistry* **2003**, *42*, 11544 – 11554.

 © 2006 Wiley-VCH Verlag GmbH & Co. KGaA, Weinheim

Microfluidics

DOI: 10.1002/anie.200602946

Time-Controlled Microfluidic Seeding in nL-Volume Droplets To Separate Nucleation and Growth Stages of Protein Crystallization**

*Cory J. Gerdts, Valentina Tereshko, Maneesh K. Yadav, Irina Dementieva, Frank Collart, Andrzej Joachimiak, Raymond C. Stevens, Peter Kuhn, Anthony Kossiakoff, and Rustem F. Ismagilov**

This paper describes a method of time-controlled seeding to separate the stages of nucleation and growth in protein crystallization using a microfluidic device. We quantified microfluidic seeding using a model protein, developed a

[*] C. J. Gerdts, Prof. R. F. Ismagilov
Department of Chemistry and Institute for Biophysical Dynamics
University of Chicago
5735 S. Ellis Avenue Chicago, IL 60615 (USA)
Fax: (+1) 773-702-0805
E-mail: r-ismagilov@uchicago.edu
Homepage: http://ismagilovlab.uchicago.edu/

Dr. V. Tereshko, Prof. A. Kossiakoff
Department of Biochemistry & Molecular Biology
University of Chicago, Chicago, IL (USA)

M. K. Yadav, Prof. R. C. Stevens
Department of Molecular Biology, The Scripps Research Institute
La Jolla, CA (USA)

Prof. P. Kuhn
Department of Cellular Biology, The Scripps Research Institute
La Jolla, CA (USA)

Dr. I. Dementieva
Department of Pediatrics, Institute for Molecular Pediatric Sciences
Pritzker School of Medicine, University of Chicago
Chicago, IL (USA)

Dr. F. Collart, Dr. A. Joachimiak
Midwest Center for Structural Genomics
Argonne National Laboratory, Argonne, IL (USA)

[**] This work was supported by NIH Protein Structure Initiative Specialized Centers Grant GM074961 (ATCG3D) and the NIH (R01 EB001903). Use of the Advanced Photon Source was supported by the US Department of Energy (contract no. W-31–109-Eng-38). Use of the BioCARS Sector 14 was supported by the NIH National Center for Research Resources (grant number RR07707). GM/CA-CAT has been funded in whole or in part by the National Cancer Institute (Y1-CO-1020) and the National Institute of General Medical Sciences (Y1-GM-1104). Funding for functional and structural proteomics of SARS CoV-related proteins is provided through NIH-NIAID contract HHSN266200400058C. We thank Ruslan Sanishvili (GM/CA Cat station 23ID-D staff support) for technical assistance; Scott Lovell and Lance Stewart (deCODE Biostructures) for helpful assistance and discussions; Shu Moy (Midwest Center for Structural Genomics) for cloning work on Oligoendopeptidase F; Vanitha Subramanian (The Scripps Research Institute) for cloning, expression, and purification of SARS nucleocapsid N-terminal domain; and L. Spencer Roach (University of Chicago) for help with thaumatin X-ray diffraction comparisons.

Supporting information for this article is available on the WWW under http://www.angewandte.org or from the author.

WILEY InterScience DISCOVER SOMETHING GREAT
© 2006 Wiley-VCH Verlag GmbH & Co. KGaA, Weinheim

strategy to produce diffraction-quality crystals of proteins recalcitrant to traditional methods, and solved de novo the X-ray crystal structure of Oligoendopeptidase F. Proteins are crystallized to determine their three-dimensional structures, to understand protein function, and aid in drug design, but crystallization can be an unpredictable and stochastic process.[1–4] Microfluidics is emerging as a tool to perform crystallization trials faster, cheaper, in smaller volumes, and with a higher level of control.[5–9] The two general stages of protein crystallization—crystal nucleation and crystal growth—generally have differing optimal conditions.[10–12] Ideally, the protein forms crystal nuclei at a supersaturation where ordered growth is possible (Figure 1a). However, for

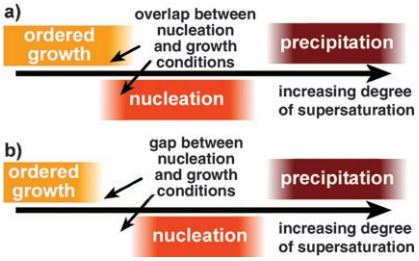

Figure 1. The nucleation and growth of protein crystals may not occur under the same conditions. a) For some proteins, there is an overlap between the supersaturation regions for nucleation and ordered growth, corresponding to the optimal crystallization condition. b) For other proteins, there is a supersaturation gap between nucleation and ordered growth such that both cannot occur at the same supersaturation.

some proteins a supersaturation gap exists, where there is no overlap between nucleation and growth conditions (Figure 1b). In the case of a supersaturation gap, solutions at low supersaturation that promote the ordered growth of crystals may not induce nucleation. Conversely, solutions at high supersaturation that promote nucleation may lead to growth of clustered crystals or microcrystals. Supersaturation gaps may be bridged by decreasing concentration from high to low supersaturation, but in traditional vapor diffusion, supersaturation increases during the trial. Other techniques, such as free-interface diffusion,[1,8,13] decrease supersaturation during the trial and may bridge the supersaturation gap.

Bridging the supersaturation gap by inducing nucleation has been attempted by addition of minerals,[14] synthetically designed nucleants,[15] altering supersaturation,[1,8,13] varying temperature,[16] and crystal seeding.[10,17,18] Seeding eliminates the need for nucleation and growth to occur in the same solution and separates the two stages of protein crystallization in trials that use microliter volumes and larger.[14,15,19–21] However, seeding using small (nL) volumes can be more difficult or not possible at all, because seeds are too small to be seen[22,23] or are too delicate to be handled.[17] To overcome these challenges, we have developed a plug-based microfluidic system to perform seeding and bridge the supersaturation gap in nL volumes. In this system, nucleation and growth stages of protein crystallization are separated and controlled independently to allow the growth of single protein crystals.

The system uses soft lithography microfluidics[24] to form plugs[5] of controlled size and composition surrounded by a fluorocarbon carrier fluid in glass microcapillaries.[25] To separate the nucleation and growth stages, a microfluidic device was designed to control multiple reactions in sequence and in time (Figure 2a).[26] In the nucleation stage, highly

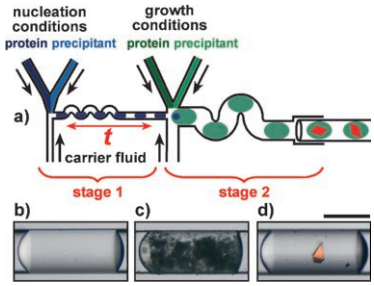

Figure 2. a) The process of microfluidic seeding. In stage 1 of the device, solutions at concentrations that promote nucleation are combined. After a delay ($t = 3$–15 s, depending on the flow rate), seed crystals formed in stage 1 are merged into stage 2 of the device, where solutions that promote crystal growth are combined. b–d) Microphotographs of typical plugs containing thaumatin: b) at low supersaturation (growth conditions) no nucleation occurs and no crystals form; c) at high supersaturation (nucleation conditions) precipitation occurs; d) a single thaumatin crystal was nucleated in stage 1 and grown in stage 2. Scale bar: 200 μm.

concentrated solutions of protein and precipitants were combined to form plugs of a highly supersaturated mixture conducive to the formation of seed crystals (functional cores/centers that lead to the formation of a protein crystal when added to a supersaturated crystallization solution). Seeds must contain protein but may be too small to be seen and may be liquid,[12,16] amorphous, or microcrystalline. The generation of seeds may take as little as a few seconds or as long as several days, depending on the protein. By controlling flow rates and channel length used for the nucleation stage, time control of seconds, minutes, hours, or even days[6,26] is achievable.

To illustrate the microfluidic seeding method, seed crystals of thaumatin protein were generated in the nucleation stage in 3–15 seconds by fixing the length of the channel and varying the flow rates of the solutions. After 3–15 seconds, plugs containing seeds were merged into the growth stage, where protein and precipitants were combined to form plugs at lower supersaturation, conducive to ordered crystal growth. Plugs from the growth stage were flowed into a glass microcapillary, where plugs were incubated and observed. When these two stages are combined, this system displays time control[5,26] on two time scales: in seconds when generating seeds,[26] and in hours to days when incubating plugs.[25] When growth conditions were used alone, no crystals grew (Figure 2b). When nucleation conditions were used alone, precipitation resulted (Figure 2c). When nucleation conditions were combined with growth conditions under time control, single crystals grew (Figure 2d).

We used the model protein thaumatin to test the hypothesis that the number of crystals formed can be

 © 2006 Wiley-VCH Verlag GmbH & Co. KGaA, Weinheim

controlled by varying the nucleation time. Tests performed at two levels of supersaturation in the growth stage confirmed that longer nucleation times lead to more seeds and, therefore, more crystals (Figure 3). Crystals grown without seeding

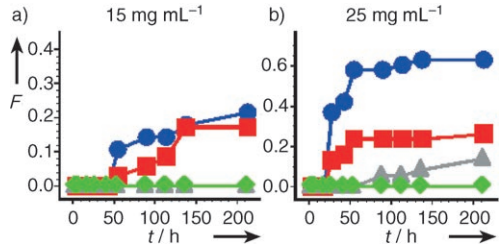

Figure 3. Fraction (F) of plugs with crystals versus incubation time for different nucleation times (t_{nuc}). a) At a protein concentration of 15 mg mL^{-1} in the growth stage, seeded plugs yielded crystals whereas unseeded plugs did not yield crystals. b) At a protein concentration of 25 mg mL^{-1} in the growth stage, seeded plugs yielded more crystals in a shorter period of time than unseeded plugs. ◆ control 1 (no seeding), ● t_{nuc} = 9 s, ■ t_{nuc} = 5 s, ▲ control 2 (no seeding).

were compared by X-ray diffraction with crystals grown with seeding.[25,27,28] To ensure that no variables were introduced by handling or cryoprotecting, crystals were analyzed inside the capillary (in situ) by obtaining ten-frame sets of diffraction data over a 10-degree rotation range and comparing the average signal-to-noise ratios of the detected reflections in the corresponding resolution shells (see the Supporting Information). Relative to the controls, crystals grew more rapidly and in higher yield with microfluidic seeding and were of the same quality.

To validate this method with challenging structurally uncharacterized targets, we crystallized SARS nucleocapsid N-terminal domain ("SARS protein") and Oligoendopeptidase F from *Bacillus stearothermophilus*. At high supersaturation, plugs containing solutions of "SARS protein" consistently gave microcrystalline clusters similar to those seen in standard vapor-diffusion methods (Figure 4, left), but no single crystals were observed. The formation of microcrystalline clusters is consistent with either multiple independent nucleation events or defects during growth, which are typically observed at high supersaturation.[1] At low supersaturation, nucleation did not occur, and no crystals grew, thus suggesting a supersaturation gap (Figure 1b). Separation of the nucleation and growth stages was achieved in four steps (Figure 4): i) Plugs were formed under nucleation conditions. ii) The flow was stopped to grow clusters of microcrystals over several days. iii) The clusters of microcrystals were dispersed throughout the plug under flow. Each plug of crystals was used to seed multiple plugs. iv) Plugs at low supersaturation (growth conditions) containing the microcrystalline seeds were flowed into a glass capillary for incubation. This method produced single "SARS protein" crystals (Figure 4, right). Preliminary data showed diffraction to a resolution of 3.5 Å.

As a second example, we investigated Oligoendopeptidase F, a member of the metallopeptidase family M3 that performs proteolytic cleavage of proteins at Leu-Gly. This protein was selected as a target by several structural genomics

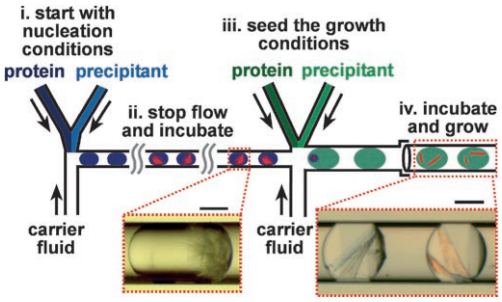

Figure 4. Separating the stages of nucleation and growth in the crystallization of "SARS protein" yields single crystals. i) Protein and precipitant solutions of high concentration are combined to form plugs. ii) The flow is stopped, and the plugs are incubated to generate seed crystals (left microphotograph: a typical "SARS protein" crystal grown in solutions of high supersaturation in which excess nucleation leads to clustered microcrystals). iii) Protein and precipitant solutions of lower concentration are combined to form plugs containing solutions at a lower degree of supersaturation that lead to crystal growth. Each plug containing seed crystals seeds multiple growth plugs. iv) Growth plugs that contain seed crystals are flowed into a glass capillary and incubated (right microphotograph: two typical plugs of low supersaturation that have been seeded with "SARS protein" microcrystals). Scale bars: 100 μm.

centers (http://sg.pdb.org). Although there has been some success in expression, purification, and crystallization of this protein, no crystal structure has been published. The putative protein sequence from *Bacillus stearothermophilus* was selected by the Midwest Center for Structural Genomics (MCSG, http://www.mcsg.anl.gov) in 2003, and the purified protein was kept frozen at −80 °C after the first run of the crystallization trials. In traditional vapor-diffusion trials (see the Supporting Information), clustered crystals (Figure 5b) of Oligoendopeptidase F grew from a microcrystalline precipitation (Figure 5a) but were unsuitable for X-ray analysis. We used microfluidics to take "seeds" from the precipitate and flow them into "growth" crystallization solutions at lower supersaturation. The key to the success of this approach was the very high dilution of the seeding mixture—approximately

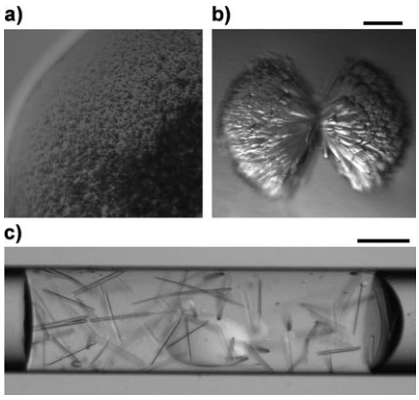

Figure 5. Crystallization of Oligoendopeptidase F. a) Microphotograph of the precipitation that results from a traditional vapor-diffusion trial. b) Microphotograph of a typical crystal grown at high degree of supersaturation whereby excess nucleation led to clustered crystals. c) Microphotograph of single crystals in a typical plug seeded by microfluidic methods. Scale bars: 100 μm.

 © 2006 Wiley-VCH Verlag GmbH & Co. KGaA, Weinheim

one nL of seeds was used to seed each "growth" plug (20–100 nL). As a result of microfluidic seeding, single needlelike crystals grew, which were used for two subsequent rounds of seeding to wash the crystals and allow them to grow larger (Figure 5c).[18]

Microfluidic seeding significantly increased the rate of success in obtaining single crystals of Oligoendopeptidase F suitable for X-ray analysis. Each microfluidic seeding experiment (ca. 1 μL of protein total) resulted in dozens of single crystals (ca. 50 plugs, most containing single crystals). The crystal structure (Figure 6) of Oligoendopeptidase F was solved by the single-wavelength anomalous diffraction (SAD) technique at a resolution of 3.3 Å by using one crystal grown in a microfluidic capillary (see the Supporting Information). To expand the refinement resolution to 3.1 Å (PDB code: 2H1J), we merged two data sets collected from two different crystals grown in a microfluidic capillary.

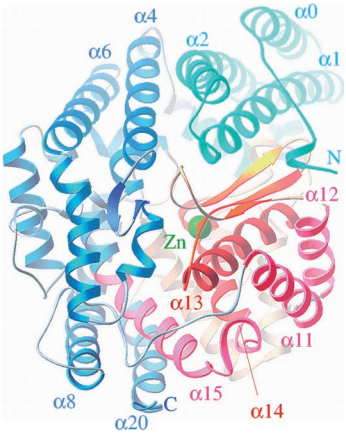

Figure 6. Ribbon structure of Oligoendopeptidase F. The protein has neurolysin topology with a mainly α-helical scaffold. The central groove divides the protein into two "subdomains" (shown in cyan and red). One Zn^{2+} ion (shown as a small, green sphere) is bound at the active site. The helix α13 contains the HEXXH zinc-binding motif with its two zinc-coordinating histidine residues (His356 and His360). Additional coordination is provided by Glu384 on helix α14. The α-helix numbering from the PDB 1O86 structure[29] was used.

To confirm that crystals grown by microfluidic seeding are isomorphous to ones grown by the traditional hanging-drop vapor-diffusion method, approximately one hundred hanging-drop vapor-diffusion trials were set up with similar crystallization conditions (ca. 100 μL of protein total). We were fortunate that one trial—a control experiment set up during the microfluidic trials—produced clustered crystals of suitable thickness for a piece to be extracted manually from the cluster for X-ray analysis. The cluster was transferred to cryoprotectant, and a single crystal was separated from the cluster by using crystal manipulation tools. The structure was determined independently from the microfluidic crystal at a resolution of 3.0 Å (PDB code: 2H1N). Crystals grown by both microfluidic and hanging-drop techniques are isomorphous and belong to space group $P3_121$ with cell dimensions $a = b = 119.5$ Å, $c = 250$ Å. The crystals contained two protein molecules (564 amino acids, 14 Se-Met residues per molecule) in the asymmetric unit with a solvent content of approximately 70%. Data collection, phasing, and refinement statistics are compared in the Supporting Information.

By using time-controlled microfluidic seeding, we have separated and achieved direct control over the nucleation and growth stages of protein crystallization. This system presents a solution to the potential conflict between nucleation (requiring high supersaturation) and ordered growth (requiring low supersaturation) and enables three advances that are difficult to achieve with traditional technologies: i) control of the nucleation time with subsecond precision; ii) the seeding of nL volumes; and iii) the use of a single plug to seed dozens of growth plugs by injecting less than one nL of seeding solution into each growth plug. Seeding with a small part of a single plug containing many seed crystals is important both to obtain a few single crystals in each growth plug and to use a single sample containing microcrystalline seed crystals to optimize growth conditions. We have not yet explored the potential of cross-seeding proteins, as was proposed for similar proteins of different species, protein–DNA, or protein–ligand complexes that have already been crystallized in their apo form,[1] though this work could be valuable. We conclude that microfluidic seeding may be used to achieve crystallization of some proteins that currently fail to crystallize and may be used to increase the success rate of future crystallization trials.

Received: July 22, 2006
Revised: September 12, 2006
Published online: November 13, 2006

Keywords: crystal growth · microfluidics · nucleation · protein structures

[1] A. McPherson, *Crystallization of Biological Macromolecules*, *Vol. 1*, 1st ed., Cold Spring Harbor Laboratory Press, Cold Spring Harbor, New York, **1999**.
[2] A. McPherson, *Methods* **2004**, *34*, 254.
[3] R. C. Stevens, *Curr. Opin. Struct. Biol.* **2000**, *10*, 558.
[4] N. E. Chayen, *Curr. Opin. Struct. Biol.* **2004**, *14*, 577.
[5] H. Song, J. D. Tice, R. F. Ismagilov, *Angew. Chem.* **2003**, *115*, 792; *Angew. Chem. Int. Ed.* **2003**, *42*, 768.
[6] H. Song, R. F. Ismagilov, *J. Am. Chem. Soc.* **2003**, *125*, 14613.
[7] B. Zheng, L. S. Roach, R. F. Ismagilov, *J. Am. Chem. Soc.* **2003**, *125*, 11170.
[8] C. L. Hansen, S. Classen, J. M. Berger, S. R. Quake, *J. Am. Chem. Soc.* **2006**, *128*, 3142.
[9] C. L. Hansen, E. Skordalakes, J. M. Berger, S. R. Quake, *Proc. Natl. Acad. Sci. USA* **2002**, *99*, 16531.
[10] T. Bergfors, *J. Struct. Biol.* **2003**, *142*, 66.
[11] D. M. Blow, N. E. Chayen, L. F. Lloyd, E. Saridakis, *Protein Sci.* **1994**, *3*, 1638.
[12] O. Galkin, P. G. Vekilov, *J. Am. Chem. Soc.* **2000**, *122*, 156.
[13] F. R. Salemme, *Arch. Biochem. Biophys.* **1972**, *151*, 533.
[14] A. McPherson, P. Shlichta, *Science* **1988**, *239*, 385.
[15] N. E. Chayen, E. Saridakis, R. P. Sear, *Proc. Natl. Acad. Sci. USA* **2006**, *103*, 597.
[16] O. Galkin, P. G. Vekilov, *J. Phys. Chem. B* **1999**, *103*, 10965.
[17] N. E. Chayen, *Prog. Biophys. Mol. Biol.* **2005**, *88*, 329.
[18] C. Thaller, L. H. Weaver, G. Eichele, E. Wilson, R. Karlsson, J. N. Jansonius, *J. Mol. Biol.* **1981**, *147*, 465.

 © 2006 Wiley-VCH Verlag GmbH & Co. KGaA, Weinheim

[19] Y. Iimura, I. Yoshizaki, L. Rong, S. Adachi, S. Yoda, H. Komatsu, *J. Cryst. Growth* **2005**, *275*, 554.
[20] J. R. Luft, G. T. DeTitta, *Acta Crystallogr. Sect. D* **1999**, *55*, 988.
[21] D. Y. Zhu, Y. Q. Zhu, Y. Xiang, D. C. Wang, *Acta Crystallogr. Sect. D* **2005**, *61*, 772.
[22] E. Saridakis, N. E. Chayen, *Protein Sci.* **2000**, *9*, 755.
[23] E. Saridakis, K. Dierks, A. Moreno, M. W. M. Dieckmann, N. E. Chayen, *Acta Crystallogr. Sect. D* **2002**, *58*, 1597.
[24] G. M. Whitesides, E. Ostuni, S. Takayama, X. Y. Jiang, D. E. Ingber, *Annu. Rev. Biomed. Eng.* **2001**, *3*, 335.
[25] B. Zheng, J. D. Tice, L. S. Roach, R. F. Ismagilov, *Angew. Chem.* **2004**, *116*, 2562; *Angew. Chem. Int. Ed.* **2004**, *43*, 2508.
[26] C. J. Gerdts, D. E. Sharoyan, R. F. Ismagilov, *J. Am. Chem. Soc.* **2004**, *126*, 6327.
[27] A. McPherson, *J. Appl. Crystallogr.* **2000**, *33*, 397.
[28] M. K. Yadav, C. J. Gerdts, R. Sanishvili, W. W. Smith, L. S. Roach, R. F. Ismagilov, P. Kuhn, R. C. Stevens, *J. Appl. Crystallogr.* **2005**, *38*, 900.
[29] M. Comellas-Bigier, R. Lang, W. Bode, K. Maskos, *J. Mol. Biol.* **2005**, *349*, 99.

 © 2006 Wiley-VCH Verlag GmbH & Co. KGaA, Weinheim

Nanoparticle Probes

DOI: 10.1002/anie.200603052

Dual-Mode Nanoparticle Probes for High-Performance Magnetic Resonance and Fluorescence Imaging of Neuroblastoma**

Jae-Hyun Lee, Young-wook Jun, Soo-In Yeon, Jeon-Soo Shin, and Jinwoo Cheon**

Inorganic nanoparticles are emerging as potential probes in next-generation biomedical applications.[1] Their enhanced properties arising from nanoscale effects and their comparable size to biofunctional molecules have allowed for ultrasensitive detection of biomolecular targets.[1–3] Of the various nanoparticles, quantum dots and fluorescent-dye-doped silica nanoparticles are representative examples of optical nanoprobe systems.[2] Dye-doped silica nanoparticles have several advantages for optical imaging: 1) high photostability arising from the stabilization of dye molecules in a protective silica matrix,[2a] 2) amplification of the fluorescent signal owing to high dye-incorporation capabilities of silica nanoparticles,[2b,c] and 3) the silica is known to be relatively biocompatible and less toxic.[2d]

On the other hand, magnetic nanoparticles exhibit a unique magnetic-resonance (MR) contrast enhancement effect that enables noninvasive MR imaging of cell trafficking, gene expression, and cancer.[3] However, retrieving detailed biological information on a subcellular level is difficult owing to limited resolution and low sensitivity of the MRI technique. Until now, most previous studies that utilized optical and/or magnetic nanoparticle probes have been focused on monofunctional probes, except for a few primitive dual probes such as the single magnetic nanoparticle that was directly linked to organic dyes.[4]

Our strategy for the development of the next generation of nanoprobes has been to fuse multiple fluorescent dyes and multiple magnetic nanoparticles into a single nanoprobe that provides superior fluorescence and MR imaging capabilities through the synergistic enhancement of its respective components. Specifically, we have fabricated new "core–satellite" structured dual functional nanoparticles comprised of a dye-doped silica "core" and multiple "satellites" of magnetic nanoparticles. We further demonstrate their utilization as simultaneous optical and MR imaging of neuroblastoma cells expressing polysialic acids (PSAs). Detection of PSA is important as it is not only an important carbohydrate associated with neural pathways, such as synaptic plasticity, learning and memory, and cell-to-cell interaction,[5] but it is also a marker of neuroblastoma, lung carcinoma, and Wilms' tumors.[6]

Rhodamine-dye-doped silica ($DySiO_2$) nanoparticles with surface amine groups were synthesized by a modified literature method.[2e] The obtained nanoparticles have a homogeneous size of 30 nm (Figure 1b). High-quality water-soluble iron oxide (Fe_3O_4, abbreviated as WSIO) nanoparticles were synthesized following a method previously reported by us.[7] The WSIO nanoparticles are 9 nm in diameter with high monodispersity ($\sigma \approx 5\%$) and coated with 2,3-dimercaptosuccinic acid (DMSA; Figure 1c).

Our core–satellite nanoparticles were fabricated through the conjugation of these $DySiO_2$ nanoparticles with WSIO by using sulfosuccinimidyl-(4-*N*-maleimidomethyl)cyclohexane-1-carboxylate (sulfo-SMCC, Pierce) cross-linkers (Figure 1a). First, the amine groups of the $DySiO_2$ nanoparticle were modified with maleimide groups by reacting them with sulfo-SMCC cross-linkers. The reactions between the maleimide groups of the silica nanoparticle and the thiol groups of WSIO nanoparticles subsequently yielded hybrid nanoparticles ($(DySiO_2–(Fe_3O_4)_n$, $n = 10 \pm 2$) of a dye-doped silica core and iron oxide satellites.

[*] S.-I. Yeon, Prof. J.-S. Shin
Department of Microbiology
College of Medicine
Yonsei University
Seoul 120-752 (Korea)
E-mail: jsshin6203@yumc.yonsei.ac.kr
J.-H. Lee, Dr. Y.-w. Jun, Prof. J. Cheon
Department of Chemistry
Yonsei University
Seoul 120-749 (Korea)
Fax: (+82) 2-364-7050
E-mail: jcheon@yonsei.ac.kr

[**] We thank Dr. H. S. Kwon and J.-M. Oh for TEM analyses (KBSI-Chuncheon), and Prof. J.-S. Suh, Prof. Y.-M. Huh (Yonsei), Dr. O. H. Han, and S. H. Kim for MRI (KBSI-Daegu). This work was supported in part by the National Research Laboratory (M10600000255), R&D Program for Cancer Control of Ministry of Health & Welfare (0320250-2), NCRC (R15-2004-024-00000-0), NCI Center for Nanotechnology Excellence, IT Leading R&D Support Project, AOARD-AFOSR, 2nd stage BK21 for Medical Science and Chemistry, and Korea Health 21 R&D Project of Ministry of Health & Welfare (A050260).

Supporting information for this article is available on the WWW under http://www.angewandte.org or from the author.

WILEY InterScience DISCOVER SOMETHING GREAT
© 2006 Wiley-VCH Verlag GmbH & Co. KGaA, Weinheim

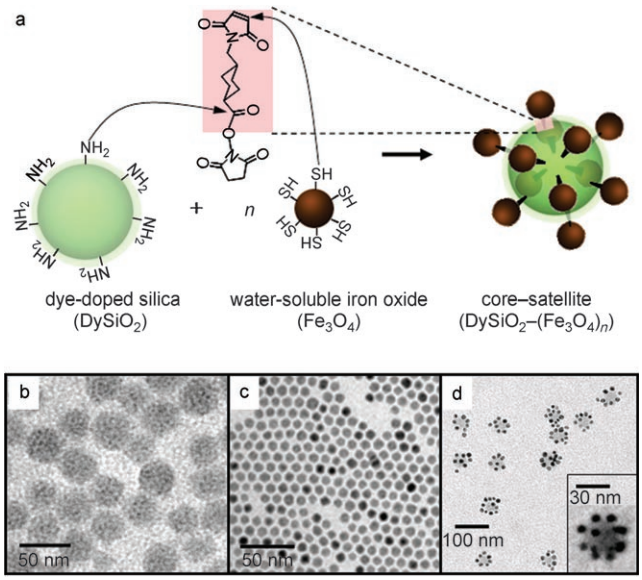

Figure 1. a) Schematic diagram for the synthesis of core–satellite $DySiO_2$–$(Fe_3O_4)_n$ nanoparticles. b–d) TEM images of b) rhodamine-doped silica ($DySiO_2$), c) iron oxide (Fe_3O_4), and d) core–satellite $DySiO_2$–$(Fe_3O_4)_n$ nanoparticles.

Figure 1d shows a transmission electron microscopy (TEM) image of obtained $DySiO_2$–$(Fe_3O_4)_n$ nanoparticles. The hybrid nanoparticles are composed of a silica core linked by roughly 10 WSIO nanoparticle satellites. Both nanoparticle components retained their initial sizes, and the overall size of the hybrid nanoparticles is approximately 45 nm. Hybrid nanoparticles are stable in aqueous media and phosphate buffer solution.

We first examined the MR contrast effect of $DySiO_2$–$(Fe_3O_4)_n$ nanoparticles in comparison with that of free WSIO nanoparticles with the same iron concentration. In the spin–spin relaxation time (T2) weighted spin echo MRI at 9.4 T, the free WSIO nanoparticles show weak MR contrast with a T2 relaxivity coefficient ($r2$) of 116 $mM^{-1}s^{-1}$ (Figure 2a,c). In contrast, the $DySiO_2$–$(Fe_3O_4)_n$ nanoparticles provide a remarkably dark MR contrast of an approximate 3.4-fold increased T2 relaxivity coefficient of 397 $mM^{-1}s^{-1}$ (Figure 2a,b). Such a significant improvement in the MR signal arises from the synergistic magnetism of multiple Fe_3O_4 satellites surrounding a core silica nanoparticle.[8] Furthermore, our $DySiO_2$–$(Fe_3O_4)_n$ nanoparticles exhibit enhanced fluorescence behavior at $\lambda \approx 580$ nm of rhodamine dye molecules with approximately 1.7-times more intense emission, compared with that of directly conjugated rhodamine-Fe_3O_4 nanoparticles (see the Supporting Information).[2a]

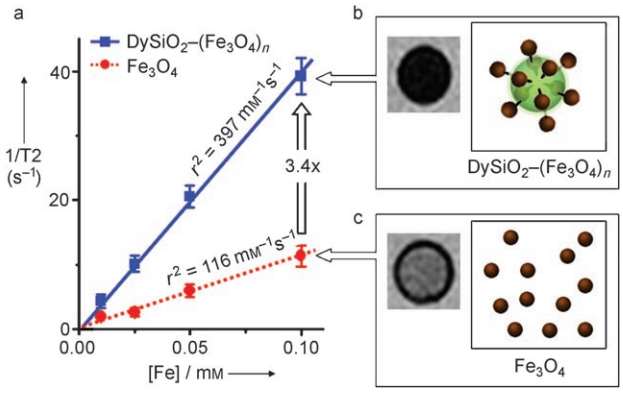

Figure 2. Synergistic MR enhancement effect of $DySiO_2$–$(Fe_3O_4)_n$. T2 relaxivity coefficients ($r2$; a) and T2-weighted MR images (b,c) of $DySiO_2$–$(Fe_3O_4)_n$ nanoparticles (b) and free Fe_3O_4 nanoparticles (c). A 3.4-fold increase in $r2$ is observed for $DySiO_2$–$(Fe_3O_4)_n$ nanoparticles.

As a case study for their utilization in dual-mode imaging of neuroblastoma model cells expressing PSAs, we conjugated $DySiO_2$–$(Fe_3O_4)_n$ hybrid nanoparticles with HmenB1 antibodies through sulfo-SMCC conjugation. HmenB1 antibody has been known to specifically target cells with PSAs.[9] The nanoparticle–HmenB1 conjugates were then tested on two different cell lines: target CHP-134 cells with overexpression of PSA and control HEK293T cells without PSA expression. In the T2*-weighted gradient echo images at 9.4 T, a high MR contrast effect is seen for the nanoparticle–HmenB1 conjugate treated CHP-134 cells (Figure 3a),

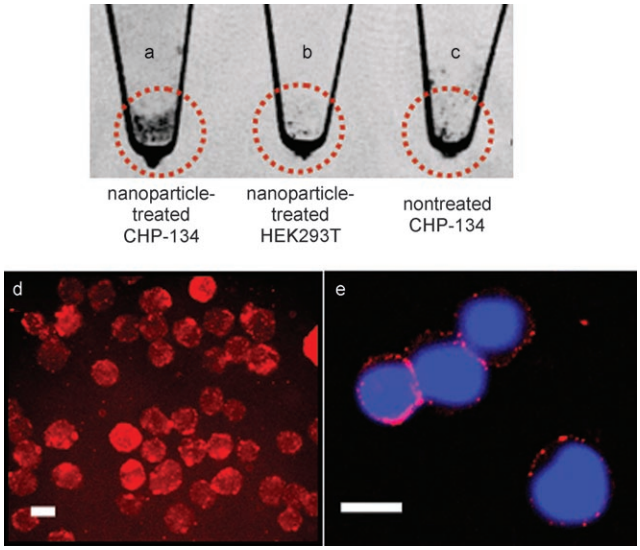

Figure 3. Dual-mode detection of PSAs. T2*-weighted MR images of CHP-134 cells treated with the $DySiO_2$–$(Fe_3O_4)_n$–HmenB1 conjugate (a), HEK293T cells treated with the $DySiO_2$–$(Fe_3O_4)_n$–HmenB1 conjugate (b), and nontreated CHP-134 cells (c). d) Fluorescence and e) confocal microscopy images of the same sample used in (a). Cell nuclei were stained a blue color with DAPI for confocal imaging. Scale bars: 10 μm.

whereas no MR contrast is observed from the nanoparticle–HmenB1 conjugate treated HEK293T cells (Figure 3b) and nontreated CHP-134 cells (Figure 3c). Fluorescence imaging of these cells shows consistent results. Strong red fluorescence is observed from the $DySiO_2$–$(Fe_3O_4)_n$ nanoparticle–HmenB1 conjugate treated CHP-134 cells (Figure 3d), whereas no fluorescence activity is observed from the control HEK293T cells. Confocal microscope imaging provides spatial distribution of PSA expressions in which red fluorescence is only detected in the membrane regions of the CHP-134 cells

 © 2006 Wiley-VCH Verlag GmbH & Co. KGaA, Weinheim

(Figure 3e). PSAs are expressed on the neural cell adhesion molecules (NCAMs) of the cell membrane, which is consistent with our observation.[5] As it is not possible to have such detailed cellular information from the MRI results, it is noteworthy that dual-mode imaging is clearly advantageous to obtain both macroscopic and detailed subcellular information of biological events.

In summary, we have demonstrated the realization of high performance "core–satellite" structured nanoparticles with a synergistic MR contrast enhancement effect and good fluorescent properties. Subsequently, such nanoparticles were confirmed as excellent dual-imaging probes for the detection of PSAs expressed on various cell lines. The concept of multifunctional core–satellite hybrid nanoparticles can serve as a platform technology for the next-generation probes in the detection and imaging of biological targets.

Experimental Section

Synthesis of $DySiO_2$–$(Fe_3O_4)_n$ nanoparticles: Dye-doped silica ($DySiO_2$) and 9-nm water-soluble iron oxide (Fe_3O_4, WSIO) nanoparticles were synthesized by a literature method.[2e,4a] Our hybrid nanoparticles were fabricated through conjugation of these dye-doped silica nanoparticles with WSIO by using sulfo-SMCC (Pierce) cross-linkers. In a typical experiment, $DySiO_2$ nanoparticles were dissolved in 10 mM phosphate buffer solution (0.1 mL) with a final concentration of 5 mg mL^{-1}. The nanoparticle surface amine was modified with a maleimide group by adding sulfo-SMCC cross-linker molecules (30 μg). After 30 min, excess cross-linkers were removed by passing them through a desalting column and a 10 mg mL^{-1} WSIO nanoparticle solution (50 μL) was added to the maleimide-modified silica nanoparticle solution. Unreacted WSIO nanoparticles were removed by passing them through Sephacryl S-300 column (Amersham Biosciences). The formation of $DySiO_2$–$(Fe_3O_4)_n$ nanoparticles was confirmed by gel electrophoretic analysis. A new band with delayed migration appears in both optical and fluorescence images when compared to those of WSIO and $DySiO_2$ nanoparticles (see the Supporting Information).

Iron oxide concentration determination: The iron oxide nanoparticle concentration was determined by repetitive measurement ($n = 4$) of Fe ion concentration through inductively coupled plasma atomic emission spectroscopy (ICP-AES) measurement after dissolving the nanoparticles in 1M sulfuric acid solution. The standard deviation is about 0.5%.

Conjugation of $DySiO_2$–$(Fe_3O_4)_n$ nanoparticles with HmenB1 antibody: HmenB1 antibody (2 mg) was dissolved in 10 mM phosphate buffer solution (0.1 mL; pH 7.2) and sulfo-SMCC (30 μg) was added to the above solution. After 15 min, the maleimide-activated HmenB1 antibody was purified by applying the reaction mixture to a Sephadex G-25 (Aldrich) desalting column. Collected fractions ($\approx$200 μL) containing maleimide-activated HmenB1 antibody were immediately mixed with a 2 mg Fe/mL $DySiO_2$–$(Fe_3O_4)_n$ solution (100 μL) and reacted for 8 h at 4 °C. $DySiO_2$–$(Fe_3O_4)_n$–HmenB1 conjugates were purified through gel filtration with a Sephacryl S-400 column.

MR imaging procedure: MR imaging was performed with a 9.4 T MRI instrument with a micro-47 surface coil (Bruker Analytische GmbH, DSX 400 MHz). For T2*-weighted MR gradient echo imaging, the following parameters were adopted: point resolution of 117×117 μm^2, section thickness of 0.4 mm, TR = 500 ms, TE = 5 ms, number of acquisitions = 4, flip angle = 30°.

Received: July 28, 2006
Published online: November 14, 2006

Keywords: colloids · diagnostic agents · hybrid materials · nanotechnology · NMR imaging

[1] a) A. P. Alivisatos, *Nat. Biotechnol.* **2004**, *22*, 47–52; b) R. Elgahanian, J. J. Storfoff, R. C. Mucic, R. L. Lestinger, C. A. Mirkin, *Science* **1997**, *277*, 1078–1081; c) X. Michalet, F. F. Pinaud, L. A, Bentolila, J. M. Tsay, S. Doose, J. J. Li, G. Sundaresan, A. M. Wu, S. S. Gambhir, S. Weiss, *Science* **2005**, *307*, 538–544.

[2] a) H. Ow, D. R. Larson, M. Srivastava, B. A. Baird, W. W. Webb, U. Wiesner, *Nano Lett.* **2005**, *5*, 113–117; b) X. Zhao, R. Tapec-Dytioco, W. Tan, *J. Am. Chem. Soc.* **2003**, *125*, 11474–11475; c) X. Zhao, L. R. Hilliard, S. J. Menchery, Y. Wang, R. P. Bagwe, S. Jin, W. Tan, *Proc. Natl. Acad. Sci. USA* **2004**, *101*, 15027–15032; d) T. J. Brunner, P. Wick, P. Manser, P. Spohn, R. N. Grass, L. K. Limbach, A. Bruinink, W. J. Stark, *Environ. Sci. Technol.* **2006**, *40*, 4374–4381; e) D. J. Bharali, I. Klejbor, E. K. Stachowiak, P. Dutta, I. Roy, N. Kaur, E. J. Bergey, P. N. Prasad, M. K. Stachowiak, *Proc. Natl. Acad. Sci. USA* **2005**, *102*, 11539–11544.

[3] a) L. Josephson, C. H. Tung, A. Moore, R. Weissleder, *Bioconjugate Chem.* **1999**, *10*, 186–191; b) M. Zhao, D. A. Beauregard, L. Loizou, B. Davletov, K. M. Brindle, *Nat. Med.* **2001**, *7*, 1241–1244; c) D. Artemov, N. Mori, B. Okollie, A. M. Bhujwalla, *Magn. Reson. Med.* **2003**, *49*, 403–408; d) R. Weissleder, A. Moore, U. Mahmood, R. Bhorade, H. Benveniste, E. A. Chiocca, J. P. Basilion, *Nat. Med.* **2000**, *6*, 351–355.

[4] a) O. Veiseh, C. Sun, J. Gunn, N. Kohler, P. Gabikian, D. Lee, N. Bhattarai, R. Ellenbogen, R. Sze, A. Lallahan, J. Olson, M. Zhang, *Nano Lett.* **2005**, *5*, 1003–1008; b) M. F. Kircher, U. Mahmood, R. S. King, R. Weissleder, L. Joshephson, *Cancer Res.* **2003**, *63*, 8122–8125; c) E. A. Schellenberger, D. Sosnovik, R. Weissleder, L. Josephson, *Bioconjugate Chem.* **2004**, *15*, 1062–1067.

[5] a) R. Probstmeier, A. Bilz, J. Schneider-Schaulies, *J. Neurosci. Res.* **1994**, *37*, 324–335; b) U. Rutishauser, M. Watanabe, J. Silver, F. A. Troy, E. R. Vimr, *J. Cell Biol.* **1985**, *101*, 1842–1849; c) M. Fukuda, *Cancer Res.* **1996**, *56*, 2237–2244; d) U. Rutishauser, *J. Cell. Biochem.* **1998**, *70*, 304–312.

[6] a) R. Seidenfaden, A. Krauter, F. Schertzinger, R. Gerardy-Schahn, H. Hildebrandt, *Mol. Cell. Biol.* **2003**, *23*, 5908–5918; b) D. Figarella-Branger, P. Durbec, G. N. Rougon, *Cancer Res.* **1990**, *50*, 6364–6370; c) L. Daniel, P. Durbec, E. Gautherot, E. Rouvier, G. Rougon, D. Figarella-Branger, *Oncogene* **2001**, *20*, 997–1004.

[7] a) Y. Jun, Y.-M. Huh, J.-s. Choi, J.-H. Lee, H.-T. Song, S. J. Kim, S. Yoon, K.-S. Kim, J.-S. Shin, J.-S. Suh, J. Cheon, *J. Am. Chem. Soc.* **2005**, *127*, 5732–5733; b) Y.-M. Huh, Y. Jun, H. T. Song, S. Kim, J.-s. Choi, J.-H. Lee, S. Yoon, K.-S. Kim, J.-S. Shin, J.-S. Suh, J. Cheon, *J. Am. Chem. Soc.* **2005**, *127*, 12387–12391.

[8] a) J. M. Perez, L. Josephson, T. O'Loughlin, D. Hogemann, R. Weissleder, *Nat. Biotechnol.* **2002**, *20*, 816–820; b) J.-F. Berret, N. Schonbeck, F. Gazeau, D. El Kharrat, O. Sandre, A. Vacher, M. Airiau, *J. Am. Chem. Soc.* **2006**, *128*, 1755–1761.

[9] J.-S. Shin, J. S. Lin, P. W. Anderson, R. A. Insel, M. H. Nahm, *Infect. Immun.* **2001**, *69*, 3335–3342.

 © 2006 Wiley-VCH Verlag GmbH & Co. KGaA, Weinheim

Fluorinated Phthalocyanines

DOI: 10.1002/anie.200603590

Design, Synthesis, and Spectroscopic Investigation of Zinc Dodecakis(trifluoroethoxy)-phthalocyanines Conjugated with Deoxyribonucleosides**

Mamidi Ramesh Reddy, Norio Shibata, Yuki Kondo, Shuichi Nakamura, and Takeshi Toru**

The design and synthesis of an efficient drug carrier that facilitates drug delivery has become a major challenge in drug development, especially for cancer treatment.[1] Among the novel carriers, such as liposome aerosol and fullerene, designed to interact with the tumor cell at specific sites,[2] we are interested in the dyes porphyrins and phthalocyanines.[3] Both are under intensive study in the modern photodynamic therapy (PDT) for cancer.[4] It is well known that these dyes accumulate in the tumor cells and cause localized cellular damage on excitation by visible light; as a result, they act as efficient drug carriers and photoinitiated cancer drugs. A particularly attractive target for such a purpose is phthalocyanines.[5] Although the main absorption of porphyrins is around 400 nm, phthalocyanines display an intense absorption at 600–700 nm. This is particularly favorable because the dyes should be effectively activated by available red light at 630 nm in PDT. Another benefit of phthalocyanines is that the lipophilicity, hydrophilicity, and self-aggregation properties can be biased by altering the substituents on the periphery of the phthalocyanine core. As part of our ongoing research programs directed to the development of a new methodology leading to functionalized phthalocyanines[6] and the synthesis of fluorine-containing biologically active compounds,[7] we describe herein the design, synthesis, and spectroscopic investigations of fluorine-containing phthalocyanine–deoxyribonucleoside conjugates **1** and **2** towards PDT agents. The twelve peripheral trifluoroethoxy substitutions in the phthalocyanine side chains improve the properties of phthalocyanines as phototherapeutic agents such that they have no aggregation properties, higher lipophilicity, a strong absorption band at long wavelength, and acceptable photosensitivity. The nucleoside appendage at one of the benzene units of **1** and **2** would play a key role in binding at the DNA recognition site, which assists radical-induced selective cleavage of the DNA strand in the tumor cell under irradiation.

The structures of the target conjugates, zinc dodecakis-(trifluoroethoxy)phthalocyanines/ethynyluridine (Zn-CF_3-Pc-U, **1**) and zinc dodecakis(trifluoroethoxy)phthalocyanines/ethynyladenosine (Zn-CF_3-Pc-Ad, **2**), are shown in Scheme 1. In addition to the highly specific reasons to make

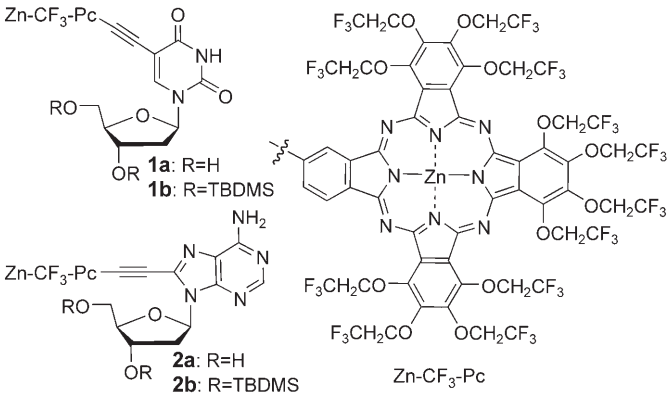

Scheme 1. Structures of zinc dodecakis(trifluoroethoxy)-phthalocyanines conjugated with deoxyribonucleosides **1** and **2**. TBDMS = *tert*-butyldimethylsilyl.

use of trifluoromethylated functional groups in medicinal chemistry,[8] the fluorinated conjugates would be promising reporter molecules in vivo based on an ^{19}F NMR technique. Although unique properties of per(trifluoroethoxy)phthalocyanines have been revealed,[9] no example of per(trifluoroethoxy)phthalocyanines conjugated with biomolecules has been reported. We therefore considered the introduction of a nucleoside to per(trifluoroethoxy)phthalocyanines. The nucleoside moieties should enhance water solubility and potentially improve the sensitivity towards tumor cells. As tumor cells generally divide faster than normal cells, they require more of the nucleosides. Therefore, the nucleosides conjugated with phthalocyanines would be good substrates for nucleoside transporter proteins responsible for the uptake of natural nucleosides,[10] and they could likely be taken into tumor cells. A deoxyribonucleoside unit is connected with the phthalocyanine ring by an ethynyl linker because 1) ethynylpurine and pyrimidine nucleosides, in particular those tethering the ethynyl moiety to the C8 position in purine nucleosides and the C6 position in pyrimidine nucleosides, are of great interest in view of their potential biological activities,[11] and 2) an ethynyl rigid-rod system would represent a useful way to strengthen the fluorophore properties of phthalocyanines.[12] Moreover, the short spacer length between a nucleoside and a phthalocyanine may be favorable due to the site-selective scission in a DNA strand. Several examples of phthalocyanines conjugated with biomolecules including nucleobases have been reported.[13] Many examples of porphyrin–nucleoside conjugates are also known.[14] However, the phthalocyanines directly conjugated with nucleic acids were rare until we started this chemistry one year ago.[15] It should be pointed out that, in 2006, Sessler et al. reported

[*] M. R. Reddy, Prof. N. Shibata, Y. Kondo, Dr. S. Nakamura, Prof. T. Toru
Department of Applied Chemistry, Graduate School of Engineering
Nagoya Institute of Technology
Gokiso, Showa-ku, Nagoya 466-8555 (Japan)
Fax: (+) 81-52-735-5442
E-mail: nozshiba@nitech.ac.jp
toru@nitech.ac.jp

[**] Support was provided by JSPS KAKENHI (17350047, 17590087, and 16655035). N.S. thanks Fuji Photo Film Co., Ltd. for an Award in Synthetic Organic Chemistry (Japan).

Supporting information for this article is available on the WWW under http://www.angewandte.org or from the author.

© 2006 Wiley-VCH Verlag GmbH & Co. KGaA, Weinheim

the synthesis of a cytidine-tethered non-fluorinated phthalocyanine under a different concept.[16] This report prompted us to disclose our studies concerning this class of compounds.

The synthesis of Zn-CF_3-Pc-U **1** was accomplished by the use of two palladium-catalyzed Sonogashira cross-couplings of iodides and terminal alkynes as key reactions (Scheme 2).

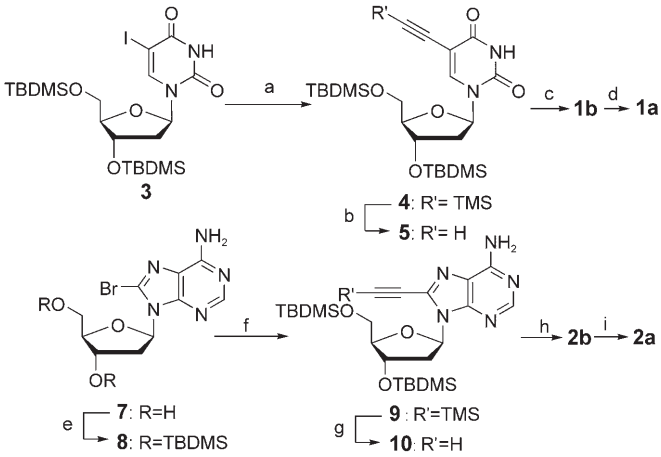

Scheme 2. a) Trimethylsilylacetylene, [Pd(PPh$_3$)$_2$Cl$_2$], CuI, Et$_3$N, THF, RT, 24 h, 94%; b) K_2CO_3, MeOH, RT, 0.5 h, 82%; c) Zinc 23-iodo-1,2,3,4,8,9,10,11,15,16,17,18-dodecakis(2,2,2-trifluoroethoxy)phthalocyaninate (**6**), [Pd(PPh$_3$)$_2$Cl$_2$], CuI, Et$_3$N, THF, RT, 36 h, 66%; d) TBAF, THF, 0°C–RT, 0.5 h, 48%; e) TBDMSCl, imidazole, DMF, RT, 24 h, 90%; f) Trimethylsilylacetylene, [Pd(PPh$_3$)$_2$Cl$_2$], CuI, Et$_3$N, THF, RT, 24 h, 85%; g) K_2CO_3, MeOH, RT, 0.5 h, 70%; h) **6**, [Pd(PPh$_3$)$_2$Cl$_2$], CuI, Et$_3$N, THF, RT, 36 h, 52%; i) TBAF, THF, 0°C–RT, 0.5 h, 64%. TBAF = tetrabutylammonium fluoride.

2′-Deoxy-3′,5′-bis(*O-tert*-butyldimethylsilyl)-5-iodouridine (**3**)[17] was first coupled with trimethylsilylacetylene under Sonogashira cross-coupling conditions ([Pd(PPh$_3$)$_2$Cl$_2$], CuI, Et$_3$N in THF) to furnish trisilylated 2′-deoxy-5-ethynyluridine **4** in 94% yield. The trimethylsilyl group on **4** was removed by using K_2CO_3 in MeOH to give 2′-deoxy-3′,5′-bis(*O-tert*-butyldimethylsilyl)-5-ethynyluridine (**5**) in 82% yield. The second Sonogashira coupling reaction was performed between zinc 23-iodo-1,2,3,4,8,9,10,11,15,16,17,18-dodecakis(2,2,2-trifluoroethoxy)phthalocyaninate (**6**)[9b] with terminal acetylene **5** to give TBDMS-protected Zn-CF_3-Pc-U **1b** in 66% yield. Finally, deprotection of all TBDMS groups on **1b** by using TBAF in THF gave Zn-CF_3-Pc-U **1a** in 48% yield as a blue solid.

The phthalocyanine–deoxyadenosine conjugate Zn-CF_3-Pc-Ad **2** was synthesized in a manner similar to that described for the synthesis of Zn-CF_3-Pc-U **1**. TBDMS protection of two hydroxy groups of 2′-deoxy-8-bromoadenosine **7**[18] was done with 2 equivalents of TBDMSCl in *N*,*N*-dimethylformamide (DMF) in the presence of imidazole to give 2′-deoxy-3′,5′-bis(*O-tert*-butyldimethylsilyl)-8-bromoadenosine **8**. This was coupled with trimethylsilylacetylene under Sonogashira coupling conditions to furnish TMS-protected 2′-deoxy-3′,5′-bis(*O-tert*-butyldimethylsilyl)-8-ethynyladenosine **9** in 85% yield, which was then deprotected in the presence of K_2CO_3 in MeOH to give 2′-deoxy-8-ethynyladenosine **10** in 70% yield. The second-round Sonogashira coupling between **10** and the unsymmetrical phthalocyanine **6** gave TBDMS-protected Zn-CF_3-Pc-Ad **2b**, which was then treated with TBAF in THF to give Zn-CF_3-Pc-Ad **2a** in good yield (Scheme 2).

The conjugates **1** and **2** were analyzed by ^{1}H and ^{19}F NMR spectroscopy, UV/Vis spectroscopy, and MALDI-TOF mass spectrometry (see the Supporting Information), clearly proving the expected structures. They have appreciable solubility in both polar and less-polar organic solvents presumably due to the unique character of twelve trifluoroethoxy substituents on the phthalocyanine macrocycle. It should be noted that both the ^{1}H and ^{19}F NMR spectra ([D$_6$]acetone) of the conjugates **1** and **2** showed extremely resolved, easily assignable signals in accordance with the proposed structures independent of the protective groups (see the Supporting Information). The high resolution in these spectra is indicative of a low degree of aggregation in the solution state. The results are noted because a structurally similar compound reported by Sessler et al. has a high tendency to self-aggregate as judged by UV/Vis spectroscopy.[16] It is quite obvious that the strong repulsion effect of the twelve peripheral trifluoroethoxy groups effectively reduces the chance of self-aggregation.

The UV/Vis spectra of the conjugates in a variety of solvents (acetone, dioxane, 20% CH_2Cl_2/toluene for **1b** and **2b**, acetone, dioxane, and DMF for **1a** and **2a**) with a concentration range of 1×10^{-5} M to 1×10^{-6} M suggest similar conclusions. All the conjugates are present mainly as monomers irrespective of the solvent and characterized by the sharp absorption bands in the B-band region (365 nm) and Q-band region (700 nm). As expected from the previous studies of per(trifluoroethoxy)phthalocyanines,[9] the conjugates display strong absorption bands appearing at longer wavelengths. Figure 1 shows the selected example of absorption

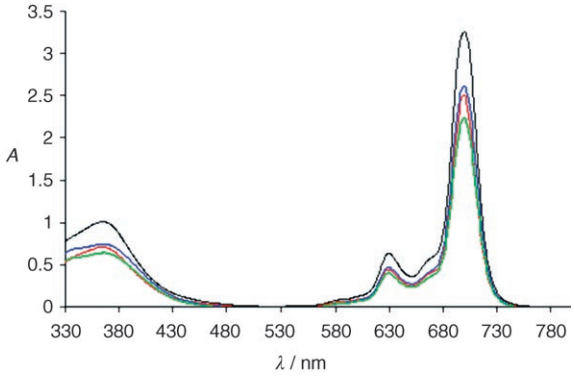

Figure 1. UV/Vis absorption spectra of **1a** (black), **1b** (red), **2a** (green), and **2b** (blue) in acetone (1×10^{-5} M).

spectra of the conjugates in acetone at 1×10^{-5} M, and similar behavior was also found in a variety of solvents at different concentrations (see the Supporting Information). Strong Q- and B-band absorptions at 700 (6.43), 700 (6.41), 700 (6.40), 700 (6.38) and 361 (5.93), 363 (5.90), 362 (5.91), 364 (5.90) for **1a**, **1b**, **2a** and **2b** are observed, respectively. Despite the unsymmetrical structure of **1** and **2**, the Q bands do not split at all, which is different from the observation by Sessler et al.

 © 2006 Wiley-VCH Verlag GmbH & Co. KGaA, Weinheim

concerning the alkylated-phthalocyanine–cytidine hybrid.[16] A weak broad blue-shifted absorption centered at 639 nm indicates a cofacial aggregation of phthalocyanines. The strong fluorescence emission at 726 nm (quantum yield (Φ_f) = 0.43 for **1b** and 0.44 for **2b**) in toluene with 1% pyridine also suggests that these compounds are relatively free from aggregation.[19]

We should point out that the conjugate **1** is acceptably stable, but it is sensitive to strong light in CH_2Cl_2. After fluorescence spectroscopy had been recorded in CH_2Cl_2 at 680 nm (see the Supporting Information), conjugates **1b** and **2b** show completely different UV/Vis spectra (see Figure 2,

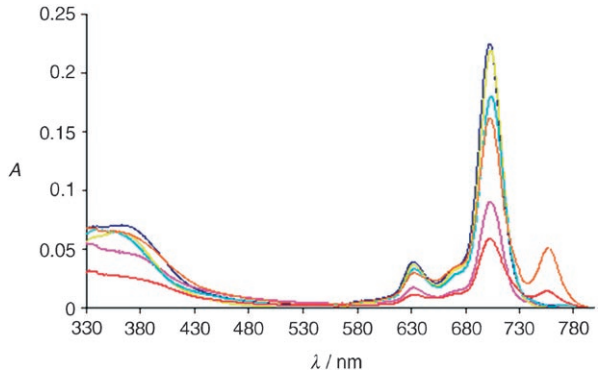

Figure 2. UV/Vis absorption spectra of **1b** in CH_2Cl_2 (blue, 1×10^{-6} M), **1b** in CH_2Cl_2 after fluorescence (orange, 1×10^{-6} M), **1b** in CH_2Cl_2 with pyridine after fluorescence (yellow, 1×10^{-6} M), **2b** in CH_2Cl_2 (pink, 1×10^{-6} M), **2b** in CH_2Cl_2 after fluorescence (red, 1×10^{-6} M), and **2b** in CH_2Cl_2 with pyridine after fluorescence (turquoise, 1×10^{-6} M).

blue versus orange lines and pink versus red lines). This can also be observed as a change in the solution color from green to yellowish green. These observations suggest that the conjugates quickly decompose through photocatalytic generation of highly reactive radicals and/or carbenes from CH_2Cl_2.[20] The decomposition was effectively suppressed by a drop of pyridine (yellow and turquoise lines), presumably through an axial coordination of pyridine with the zinc. To ascertain the sensitivity of **1b** and **2b**, time-dependent fluoresence spectra were recorded both in CH_2Cl_2 and dioxane (Figure 3). Immediate decreases in the fluorescence

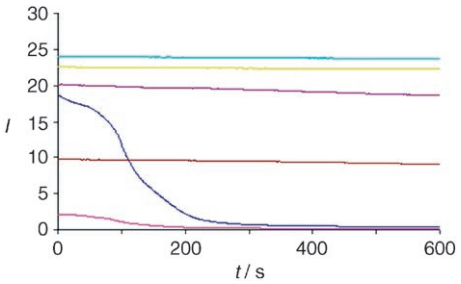

Figure 3. Time-dependent fluorescence spectra of **1b** at 708 nm in CH_2Cl_2 (blue, 1×10^{-6} M), **1b** in dioxane (yellow, 1×10^{-6} M), **1b** in CH_2Cl_2 with pyridine (violet, 1×10^{-6} M), **2b** in CH_2Cl_2 (pink, 1×10^{-6} M), **2b** in dioxane (turquoise, 1×10^{-6} M), and **2b** in CH_2Cl_2 with pyridine (brown, 1×10^{-6} M).

intensity of **1b** and **2b** within 200 s were monitored by fluorescence spectroscopy in CH_2Cl_2 (blue and pink lines). As expected, the decreases of fluorescence were inhibited in the presence of pyridine (violet and brown lines). No decomposition of **1b** and **2b** was observed in dioxane (yellow and turquoise lines). The results presented herein demonstrate that the peripheral twelve trifluoroethoxy groups of phthalocyanines clearly play an important role concerning the photosensitivity in solution state. The strong electron-withdrawing effect of the fluorine atoms enhances the stability of the phthalocyanine conjugates by lowering the energies of the highest occupied molecular orbitals (HOMOs). On the other hand, the sensitivity towards oxidation might be increased by the positive mesomeric effect of the peripheral trifluoroethoxy chains. A balance between an electron-withdrawing fluorine effect, trifluoroethoxy mesomeric effects, solvent effects, and the intrinsic lability of unsymmetrical phthalocyanines can be the main reason for the overall photosensitivity of the conjugates.

In conclusion, the design and synthesis of novel trifluoroethoxy-substituted zinc phthalocyanines conjugated with deoxyribonucleosides, Zn-CF_3-Pc-U **1a**,**b** and Zn-CF_3-Pc-Ad **2a**,**b** have been described through twofold Sonogashira alkynylation protocols in good yields. The effect of twelve peripheral trifluoroethoxy groups in the phthalocyanine core is quite obvious. In contrast with the peripheral *tert*-butylated cytidine–phthalocyanine hybrid,[16] our trifluoromethylated-phthalocyanine hybrids **1** and **2** prefer monomeric forms instead of aggregation, and they show a unique photosensitivity that can be controlled by the addition of base or the solvent used. Although interesting effects of perfluoroalkyl groups at the periphery of phthalocyanines have already been disclosed,[21] this result corresponds to one more possible application of fluorine's unique powers in phthalocyanine chemistry. This strategy will be highly useful in the development of phototherapeutic drugs,[22] especially in further combination with drug-delivery systems. Investigations of whether the conjugates are sufficient and efficient in site-selective cleavage of DNA strand under irradiation will be conducted in due course.

Received: September 2, 2006
Published online: November 10, 2006

Keywords: aggregation · DNA · fluorinated substituents · phthalocyanines · synthetic methods

[1] R. Haag, F. Kratz, *Angew. Chem.* **2006**, *118*, 1218; *Angew. Chem. Int. Ed.* **2006**, *45*, 1198.
[2] a) T. Y. Zakharian, A. Seryshev, B. Sitharaman, B. E. Gilbert, V. Knight, L. J. Wilson, *J. Am. Chem. Soc.* **2005**, *127*, 12508; b) N. V. Koshkina, J. C. Waldrep, V. Knight, *Curr. Cancer Drug Targets* **2003**, *3*, 251; c) N. V. Koshkina, J. C. Waldrep, L. E. Roberts, E. Golunski, S. Melton, V. Knight, *Clin. Cancer Res.* **2001**, *7*, 3258.
[3] a) J. G. Moser, *J. Porphyrins Phthalocyanines* **2000**, *4*, 129; b) W. M. Sharman, C. M. Allen, J. E. van Lier, *Drug Discovery Today* **1999**, *4*, 507; c) H. Ali, J. E. van Lier, *Chem. Rev.* **1999**, *99*, 2379.
[4] I. J. Macdonald, T. J. Dougherty, *J. Porphyrins Phthalocyanines* **2001**, *5*, 105.

 © 2006 Wiley-VCH Verlag GmbH & Co. KGaA, Weinheim

[5] C. M. Allen, W. M. Sharman, J. E. van Lier, *J. Porphyrins Phthalocyanines* **2001**, *5*, 161.

[6] a) H. Uchida, M. Mitsui, P. Y. Reddy, S. Nakamura, T. Toru, *ARKIVOC* **2005**, 17; b) H. Uchida, H. Yoshiyama, P. Y. Reddy, S. Nakamura, T. Toru, *Bull. Chem. Soc. Jpn.* **2004**, *77*, 1401; c) H. Uchida, H. Yoshiyama, P. Y. Reddy, S. Nakamura, T. Toru, *Synlett* **2003**, 2083; d) H. Uchida, P. Y. Reddy, S. Nakamura, T. Toru, *J. Org. Chem.* **2003**, *68*, 8736; e) H. Uchida, T. Shimizu, P. Y. Reddy, S. Nakamura, T. Toru, *Synthesis* **2003**, 1236.

[7] a) T. Fukuzumi, N. Shibata, M. Sugiura, H. Yasui, S. Nakamura, T. Toru, *Angew. Chem.* **2006**, *118*, 5095; *Angew. Chem. Int. Ed.* **2006**, *45*, 4973; b) N. Shibata, J. Kohno, K. Takai, T. Ishimaru, S. Nakamura, T. Toru, S. Kanemasa, *Angew. Chem.* **2005**, *117*, 4276; *Angew. Chem. Int. Ed.* **2005**, *44*, 4204; c) N. Shibata, T. Ishimaru, T. Nagai, J. Kohno, T. Toru, *Synlett* **2004**, 1703; d) N. Shibata, T. Ishimaru, M. Nakamura, T. Toru, *Synlett* **2004**, 2509; e) N. Shibata, T. Tarui, Y. Doi, K. L. Kirk, *Angew. Chem.* **2001**, *113*, 4593; *Angew. Chem. Int. Ed.* **2001**, *40*, 4461; f) N. Shibata, E. Suzuki, Y. Takeuchi, *J. Am. Chem. Soc.* **2000**, *122*, 10728; g) N. Shibata, E. Suzuki, T. Asahi, M. Shiro, *J. Am. Chem. Soc.* **2001**, *123*, 7001; h) N. Shibata, T. Ishimaru, E. Suzuki, K. L. Kirk, *J. Org. Chem.* **2003**, *68*, 2494.

[8] *Organofluorine Compounds in Medicinal Chemistry and Biomedical Applications* (Eds.: R. Filler, Y. Kobayashi, L. M. Yagupolskii), Elsevier, Amsterdam, **1993**.

[9] a) H. Weitman, S. Schatz, H. E. Gottlieb, N. Kobayashi, B. Ehrenberg, *Photochem. Photobiol.* **2001**, *73*, 473; b) M. Tian, T. Wada, H. Sasabe, *J. Heterocycl. Chem.* **2000**, *37*, 1193; c) M. Tian, T. Wada, H. Sasabe, *J. Heterocycl. Chem.* **1997**, *34*, 171; d) W. Eberhardt, M. Hanack, *Synthesis* **1997**, 95.

[10] a) J. R. Mackey, S. A. Baldwin, J. D. Young, C. E. Cass, *Drug Resist. Updates* **1998**, *1*, 310; b) D. A. Griffith, S. M. Jarvis, *Biochim. Biophys. Acta* **1996**, *1286*, 153.

[11] a) D. Rai, M. Johar, T. Manning, B. Agrawal, D. Y. Kunimoto, R. Kumar, *J. Med. Chem.* **2005**, *48*, 7012; b) M. E. Perlman, K. A. Watanabe, R. F. Schinazi, J. J. Fox, *J. Med. Chem.* **1985**, *28*, 741.

[12] a) K. Nakatani, T. Yoshida, I. Saito, *J. Am. Chem. Soc.* **2002**, *124*, 2118; b) M. V. Skorobogatyi, A. A. Pchelintseva, A. L. Petrunina, I. A. Stepanova, V. L. Andronova, G. A. Galegov, A. D. Malakhov, V. A. Korshun, *Tetrahedron* **2006**, *62*, 1279.

[13] a) P. P. S. Lee, P.-C. Lo, E. Y. M. Chan, W.-P. Fong, W.-H. Ko, D. K. P. Ng, *Tetrahedron Lett.* **2005**, *46*, 1551; b) X.-Y. Li, D. K. P. Ng, *Tetrahedron Lett.* **2001**, *42*, 305; c) U. Drechsler, M. Pfaff, M. Hanack, *Eur. J. Org. Chem.* **1999**, 3441; d) P. Maillard, J. L. Guerquin-Kern, M. Momenteau, S. Gaspard, *J. Am. Chem. Soc.* **1989**, *111*, 9125.

[14] a) J. L. Sessler, J. Jayawickramarajah, G. Andreas, T. Torres, D. M. Guldi, S. Maldonado, K. J. Stevenson, *Chem. Commun.* **2005**, 1892; b) I. Bouamaied, E. Stulz, *Synlett* **2004**, *9*, 1579; c) V. Malinovski, L. Tumir, I. Piantanida, M. Zinic, H.-J. Schneider, *Eur. J. Org. Chem.* **2002**, 3785; d) M. Sirish, B. G. Maiya, *J. Porphyrins Phthalocyanines* **1998**, *2*, 327; e) M. Cornia, S. Binacchi, T. D. Soldato, F. Zanardi, G. Casiraghi, *J. Org. Chem.* **1995**, *60*, 4964; f) A. Berman, E. S. Izreali, H. Levanon, B. Wang, J. L. Sessler, *J. Am. Chem. Soc.* **1995**, *117*, 8252; g) J. L. Sessler, B. Wang, A. Harriman, *J. Am. Chem. Soc.* **1995**, *117*, 704; h) X. Jiang, R. K. Pandey, K. M. Smith, *Tetrahedron Lett.* **1995**, *36*, 365; i) N. Ono, M. Bougauchi, K. Maruyama, *Tetrahedron Lett.* **1992**, *33*, 1629.

[15] M. R. Reddy, Y. Kondo, S. Nakamura, N. Shibata, T. Toru, 36th Annual Meeting of Union of Chemistry-Related Societies in Chubu Area, Japan, September 23 and 24, **2005**, 2H24.

[16] J. L. Sessler, J. Jayawickramarajah, A. Gouloumis, G. D. Pantos, T. Torres, D. M. Guldi, *Tetrahedron* **2006**, *62*, 2123.

[17] H. Sugiyama, S. Matsuda, K. Kino, Z. Qiu-Mei, S. Yonei, I. Saito, *Tetrahedron Lett.* **1996**, *37*, 9067.

[18] R. G. Eason, D. M. Burkhardt, S. J. Philips, D. P. Smith, S. S. David, *Nucleic Acids Res.* **1996**, *24*, 890.

[19] The zinc phthalocyanine was used as reference ($\Phi_f = 0.30$ in 1 % pyridine in toluene). See P. S. Vincett, E. M. Voigt, K. E. Rieckhoff, *J. Chem. Phys.* **1971**, *55*, 4131.

[20] X. À. Micó, S. I. Vagin, L. R. Subramanian, T. Ziegler, M. Hanack, *Eur. J. Org. Chem.* **2005**, 4328.

[21] a) R. Minnes, H. Weitman, H.-J. Lee, S. M. Gorun, B. Ehrenberg, *Photochem. Photobiol.* **2006**, *82*, 593; b) S. P. Keizer, J. Mack, B. A. Bench, S. M. Gorun, M. J. Stillman, *J. Am. Chem. Soc.* **2003**, *125*, 7067; c) H.-J. Lee, W. W. Brennessel, J. A. Lessing, W. W. Brucker, V. G. Young, Jr., S. M. Gorun, *Chem. Commun.* **2003**, 1576; d) B. A. Bench, A. Beveridge, W. M. Sharman, G. J. Diebold, J. E. van Lier, S. M. Gorun, *Angew. Chem.* **2002**, *114*, 773; *Angew. Chem. Int. Ed.* **2002**, *41*, 748; e) B. A. Bench, W. W. Brennessel, H.-J. Lee, S. M. Gorun, *Angew. Chem.* **2002**, *114*, 776; *Angew. Chem. Int. Ed.* **2002**, *41*, 750.

[22] The conjugates are not sufficiently soluble in water; however, they are soluble in DMF, acetone, dioxane, and alcohols. Therefore, mixed aqueous solution systems such as DMF/water would be helpful for biological application of the conjugates.

 © 2006 Wiley-VCH Verlag GmbH & Co. KGaA, Weinheim

Protein Structure Determination

DOI: 10.1002/anie.200603627

Ultrahigh-Resolution Backbone Structure of Perdeuterated Protein GB1 Using Residual Dipolar Couplings from Two Alignment Media**

Guillaume Bouvignies, Sebastian Meier, Stephan Grzesiek, and Martin Blackledge**

NMR spectroscopy has evolved into a routine tool for the resolution of three-dimensional protein structures in solution,[1] relying almost exclusively on the measurement of a large number of interproton dipole–dipole nuclear Over-

[*] Dr. S. Meier,[+] Prof. S. Grzesiek
Biozentrum, Universität Basel
Klingelbergstrasse 70
4056 Basel (Switzerland)
Fax: (+41) 61-267-2100
E-mail: stephan.grzesiek@unibas.ch
G. Bouvignies,[+] Dr. M. Blackledge
Institute de Biologie Structurale Jean-Pierre Ebel
CNRS-CEA-UJF UMR 5075
41 rue Jules Horowitz, 38027 Grenoble Cedex (France)
Fax: (+33) 4-3878-9554
E-mail: martin.blackledge@ibs.fr
[+] These authors contributed equally to this work.

[**] G.B. receives a grant from the CEA. This work was supported by the EU through EU-NMR JRA3 and by the French Research Ministry through ANR NT05-4_42781 and SNF grant 31-61'757.00 to S.G.
Supporting information for this article is available on the WWW under http://www.angewandte.org or from the author.

WILEY InterScience DISCOVER SOMETHING GREAT
© 2006 Wiley-VCH Verlag GmbH & Co. KGaA, Weinheim

hauser effects (NOE).[2] Despite this success, NOEs are notoriously difficult to quantify in terms of precise interatomic distances, with clear consequences on the limits of attainable structural resolution. This imprecision arises in part from the existence of numerous leakage mechanisms capable of contributing significantly to the measured interaction.[3]

Residual dipolar couplings (RDCs), measurable under weak alignment conditions,[4] have shown remarkable promise, predominantly for complementing NOE-based structure elucidation, but also for ab initio fold determination.[5,6] In contrast to NOEs, interpretation of RDCs in terms of structure and dynamics is susceptible to relatively few sources of error and therefore should provide access to more precise structural definition.[7,8] Although RDCs have been routinely measured between covalently bound spins of fixed internuclear distance, long-range RDCs also provide potentially very powerful structural information.[9,10] It has been shown that measurement of ^{1}H–^{1}H RDCs can be made to high levels of precision in highly deuterated proteins, where dipolar truncation effects are avoided. The aim of this study is to determine, de novo, the backbone structure of perdeuterated protein GB1 in solution to the highest possible precision using only RDCs and residual $^{13}C'$ NMR chemical shifts (RCSs) measured in two different alignment media.

We have applied the meccano approach[6] to determine the structure of GB1, using a modified version of the algorithm that allows for local molecular flexibility and incorporates long-range RDCs. In the structure calculation, 55 and 54 ^{15}N–$^{1}H^{N}$ couplings, 53 and 47 $^{13}C'^{(i-1)}$–$^{1}H^{N}$, 55 and 54 $^{13}C'$–$^{13}C^{\alpha}$, 37 and 35 $^{13}C^{\alpha}$–$^{1}H^{N}$, 22 and 15 $^{13}C^{\alpha(i-1)}$–$^{1}H^{N(i)}$, 55 and 55 $^{15}N^{(i)}$–$^{13}C'^{(i-1)}$, 50 and 50 $^{13}C^{\alpha}$–$^{13}C^{\beta}$, and 54 and 0 RCSs from protein G aligned in Pf1 bacteriophage[11] and a lyotropic medium,[12] respectively, were used in the structure calculation. Critically, 75 and 52 $^{1}H^{N}$–$^{1}H^{N}$ RDCs were also used.[10]

The initial step in the meccano protocol requires evaluation of the alignment induced by the two liquid-crystalline media, with no knowledge of the protein structure. This entails determination of the components (D_a, D_r, θ, φ, ψ) of both tensors (where D_a and D_r correspond to the axial and rhombic components, respectively), the orientation of each peptide plane, and a parameter accounting for dynamic fluctuation of each plane (using one-dimensional Gaussian axial fluctuation[13] or a common scaling factor for each coupling).[14] The alignment tensor was also determined using a static description. In this case, a component of the motion can be expected to be absorbed into the smaller effective eigenvalues (D_a^{av} and D_r^{av}).[15,16]

Following structure-free determination of the components of the two alignment tensors, the algorithm constructs the protein backbone by sequential positioning of peptide planes and intervening tetrahedral junctions.[14] To allow for experimental outliers, a robust maximum-likelihood estimator was used in place of a classical χ^2 function.[17] Use of fixed-geometry RDCs alone to construct the backbone is termed protocol I. Plane orientation is accompanied by optimiszation of a motional amplitude; again the most appropriate is selected from the dynamic modes described above. In the absence of a simple description of the dynamics of $^{13}C^{\alpha}$–$^{13}C^{\beta}$ vectors because of reorientation of adjacent peptide planes, motion was incorporated by expressing these RDCs relative to the dynamically averaged tensor D_a^{av} and D_r^{av}.

Protocol II uses the same couplings as protocol I, but in addition introduces $^{1}H^{N}$–$^{1}H^{N}$ RDCs between the current peptide plane and those that are already constructed.[14] As the sign of these RDCs is not known, the absolute value is used. Following construction of the chain, the total target function is minimized simultaneously using a standard χ^2 function with a simple repulsive interaction based on the van der Waals radii of the backbone atoms. Motion of $^{1}H^{N}$–$^{1}H^{N}$ vectors was incorporated by using the dynamically averaged tensor D_a^{av} and D_r^{av}. If significant dynamics were apparent from the effective order parameter S^2 of either or both of the participating $^{1}H^{N}$ sites, an additional scaling of $^{1}H^{N}$–$^{1}H^{N}$ couplings was effective.[14]

Protocol I successfully determines the overall fold of the protein using this approach, with a backbone root-mean-square deviation (rmsd), compared to the two closest homologue crystal structures, namely protein GB1 (code 1pga[18]) and protein GB3 (1igd[19]), of 1.3 and 1.4 Å, respectively, for all amino acids (Figure 1, left). Although

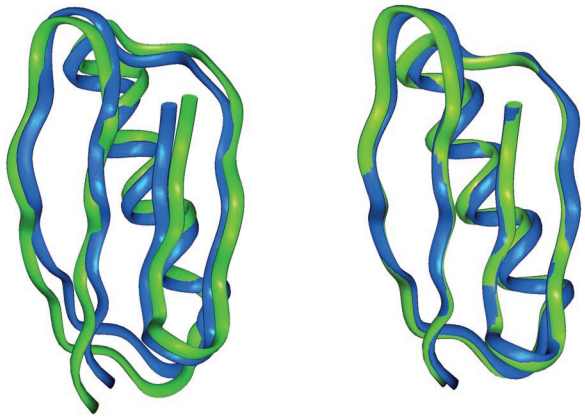

Figure 1. Comparison of the meccano structures (green) calculated without (left) and with (right) ^{1}H–^{1}H RDCs and the X-ray crystal structure of 1pga (blue). All (C′, C^{α}, N) atoms were used for the superposition of coordinates (left: 1.32 Å, right: 0.55 Å). The sequence of 1pga differs from the studied molecule as follows: Q7T, A11I.

the resolution of 1pga is lower than that of 1igd (2.1 Å compared with 1.1 Å) these two structures are very similar, with an rmsd between all backbone atoms of 0.38 Å. The sequence of the protein studied here differs from 1pga and 1igd by two and six amino acids, respectively. The apparent resolution of the meccano structure is in line with previous applications of the protocol using fixed-geometry restraints.[6,20] The main differences between the crystal and meccano structures are due to small translational shifts, for example, between β-sheets, that are expected when only local orientational information is used to determine the fold.

Addition of the $^{1}H^{N}$–$^{1}H^{N}$ couplings (protocol II) drastically improves the structure (Figure 1, right) giving a full backbone rmsd of 0.55 Å compared to 1pga and 0.65 Å compared to 1igd. Removal of five amino acids (14–18) in the first loop region from the comparison reduces the rmsd values

 © 2006 Wiley-VCH Verlag GmbH & Co. KGaA, Weinheim

to 0.41 Å and 0.46 Å for the two crystallographic structures, respectively. The remarkable similarity in the central β-sheet region of the three proteins is shown in Figure 2, where the backbone atoms of 18 amino acids superimpose to a

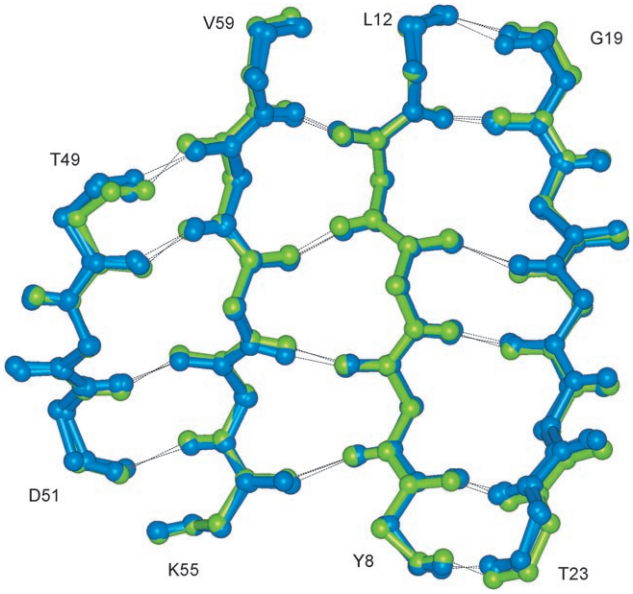

Figure 2. Comparison of the meccano structure calculated with ^{1}H–^{1}H RDCs (green) and the crystal structures 1pga and 1igd (both blue). Only the β-strand region is shown. Backbone (C′, C^{α}, N) atoms (8–12, 19–23, 48–51, 55–59) were used for coordinate superposition (0.24 Å compared to 1pga; 0.25 Å compared to 1igd). Hydrogen bonds are shown as dotted lines between donor and acceptor atoms.

resolution of 0.24 Å and 0.25 Å compared to the crystal structures (different by 0.22 Å rmsd). Not surprisingly the structural quality is high with respect to the population of the most-favored regions of the Ramachandran plot (91% compared to 93% for 1igd and 87% for 1pga). The quality of the protocol II meccano structure is further assessed as described below.

Three types of RDC ($^{13}C'^{(i)}$–$^{1}H^{N(i)}$, $^{1}H^{N(i)}$–$^{13}C^{\beta(i)}$, and trans-hydrogen-bond $^{13}C'$–$^{1}H^{N}$) from both alignment media were left out of the structure calculation and used for cross-validation. These vectors are not colinear with the peptide plane and are therefore not defined by other measured RDCs, but rather provide fully independent assessment of both local and long-range structure. The sign of these RDCs is unknown, so absolute values were calculated from the structure. The close reproduction of these RDCs underlines the high resolution of the meccano structure.[14] Notably, reproduction of all 130 RDCs (rmsd = 0.45 Hz) is slightly better than that found with the crystal structures for 1igd (0.48 Hz) and 1pga (0.50 Hz) and very close to experimental error (0.4 Hz).

We have compared the hydrogen-bonding network present in the meccano structure with that present in the two crystal structures (Figure 3). The comparison shows striking similarities throughout the protein. Hydrogen bonds that are found to be weaker in the crystal structures, (d(NH–O) > 2.0 Å), are weak in the meccano structure, and consistently stronger interactions are also reproduced. Orientations of

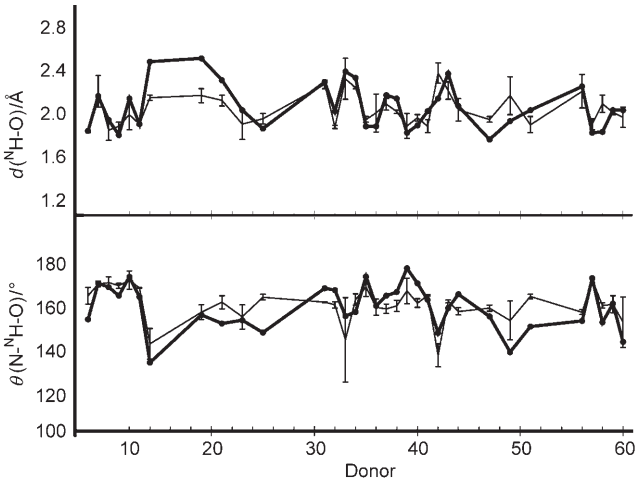

Figure 3. Comparison of hydrogen-bond geometries in the ^{1}H–^{1}H meccano (thick lines) and crystal structures 1pga and 1igd (thin lines). Top: Distance (d) between proton and acceptor. Bottom: N-^{H}N-O angle (θ). The mean geometry of crystal structures is shown as the center of the error bar; extremities are the values for the two structures.

hydrogen-bonding partners are very similar, with consistently eccentric hydrogen-bond angles (θ(N-^{N}H-O) < 160°) found at the same sites in all three structures.

Although protein G is a compact protein with relatively little flexibility, the dynamic parameter extracted from protocol I allows the conformation to successfully find the fold, whereas a static version, in which only the orientation of the plane is optimized, fails. The effective order parameter extracted from the calculation shows similar features to those determined in a recent study of protein G backbone dynamics using data from seven alignment media[20] (Figure 4), although Gly46 does not show the increased dynamics determined previously. When extracted from only two alignment media this term may be expected to contain contributions from experimental and structural noise in addition to conformational disorder, and we suggest that this parameter be interpreted in a similar way to the crystallographic B factor.

It appears then that fixed-geometry and ^{1}H–^{1}H RDCs, in combination with standard peptide-chain geometry, can

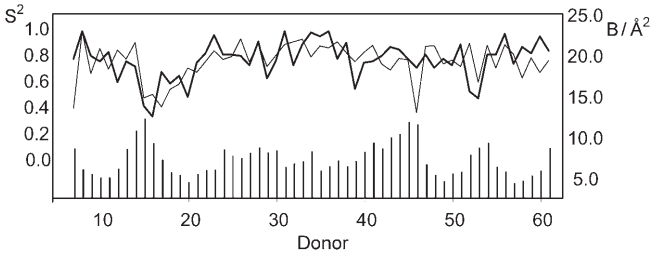

Figure 4. Dynamic amplitude parameter (S^2) recalculated from 1D Gaussian axial fluctuation (GAF) motional amplitudes or axial motional model. The effective order parameter for the NH bond (thick line) is compared to the order parameter derived from 3D GAF analysis of data from seven alignment media (thin line), and the B factor for 1igd (bars).

 © 2006 Wiley-VCH Verlag GmbH & Co. KGaA, Weinheim

afford a level of structural precision rarely found from studies of proteins in solution. The accuracy of RDCs alone is sufficient to determine backbone structure; no force-field terms besides simple steric repulsion, and no side chains beyond C^{β}, were considered in the algorithm. Despite standardization of protein alignment techniques, this level of precision remains largely unexploited, possibly because RDCs are often combined with less accurate structural constraints such as NOE. We note that our attempts to refine the X-ray crystal structures using RDC-driven restrained molecular dynamic simulations with the same data resulted in apparently lower quality structures and poorer reproduction of hydrogen-bonding geometries (not shown).

In conclusion, this study clearly demonstrates the power of combining local orientational definition from fixed-geometry RDCs, with long-range structural information from ^{1}H–^{1}H RDCs, to determine protein structure. Use of these constraints alone provides access to ultrahigh-resolution structures of a precision that is apparently comparable to that available from high-resolution X-ray crystallography as measured by independent cross-validation and structure comparison. We are convinced that this level of precision will have a significant impact on the understanding of more subtle aspects of biomolecular structure and dynamics in solution.

Received: September 5, 2006
Published online: November 22, 2006

Keywords: NMR spectroscopy · protein dynamics · protein structures · residual dipolar couplings

[1] K. Wüthrich, *NMR of Proteins and Nucleic Acids*, Wiley, New York, **1986**.
[2] G. M. Clore, A. M. Gronenborn, *Nat. Struct. Biol.* **1997**, *4*, 849–853.
[3] D. Neuhaus, M. P. Williamson, *The Nuclear Overhauser Effect*, Wiley, New York, **2000**.
[4] N. Tjandra, A. Bax, *Science* **1997**, *278*, 1111–1116.
[5] F. Delaglio, G. Kontaxis, A. Bax, *J. Am. Chem. Soc.* **2000**, *122*, 2142–2143.
[6] J.-C. Hus, D. Marion, M. Blackledge, *J. Am. Chem. Soc.* **2001**, *123*, 1541–1542.
[7] J. H. Prestegard, H. M. Al-Hashimi, J. R. Tolman, *Q. Rev. Biophys.* **2000**, *33*, 371–424.
[8] M. Blackledge, *Prog. Nucl. Magn. Reson. Spectrosc.* **2005**, *46*, 23–61.
[9] J. J. Chou, A. Bax, *J. Am. Chem. Soc.* **2001**, *123*, 3844–3845.
[10] S. Meier, D. Häussinger, P. Jensen, M. Rogowski, S. Grzesiek, *J. Am. Chem. Soc.* **2003**, *125*, 44–45.
[11] M. R. Hansen, L. Müller, A. Pardi, *Nat. Struct. Biol.* **1998**, *5*, 1065–1074.
[12] M. Rückert, G. Otting, *J. Am. Chem. Soc.* **2000**, *122*, 7793–7797.
[13] R. Brüschweiler, P. E. Wright, *J. Am. Chem. Soc.* **1994**, *116*, 8426-8427.
[14] See Supporting Information.
[15] P. Bernado, M. Blackledge, *J. Am. Chem. Soc.* **2004**, *126*, 4907–4920.
[16] G. Bouvignies, P. Bernado, M. Blackledge, *J. Magn. Reson.* **2005**, *173*, 328–338.
[17] P. W. Holland, R. E. Welsch, *Comm. Stat A* **1977**, *6*, 813–827.
[18] T. Gallagher, P. Alexander, P. Bryan, G. L. Gilliland, *Biochemistry* **1994**, *33*, 4721–4729.
[19] J. P. Derrick, D. B. Wigley, *J. Mol. Biol.* **1994**, *243*, 906–918.
[20] S. Béraud, B. Bersch, B. Brutscher, P. Gans, F. Barras, M. Blackledge, *J. Am. Chem. Soc.* **2002**, *124*, 13709–13715.
[21] G. Bouvignies, P. Bernado, S. Meier, K. Cho, S. Grzesiek, R. Brüschweiler, M. Blackledge, *Proc. Natl. Acad. Sci. USA* **2005**, *102*, 13885–13890.

 © 2006 Wiley-VCH Verlag GmbH & Co. KGaA, Weinheim

Helical Peptides

DOI: 10.1002/anie.200600965

Induction of Structure and Function in a Designed Peptide upon Adsorption on a Silica Nanoparticle**

Martin Lundqvist, Patrik Nygren, Bengt-Harald Jonsson, and Klas Broo**

The ability to regulate biological processes at the molecular level is often achieved by controlling the function of proteins. Efficient use of proteins and peptides in industrial processes and diagnostic tools also requires means to induce and maintain their functional conformations. Interestingly, the current discussion[1] on the origin of life has highlighted the fact that reactions such as vesicle creation[2] and peptide formation[3,4] are promoted by clay particles. Also in this context, it is interesting to investigate whether silica (which is a main constituent of most clay surfaces) could have a role in inducing functional conformations of peptides. Herein, we present a novel approach in which adsorption on silica nanoparticles is used to induce a well-defined structure in a designed peptide. The ability to generate stable structures on surfaces opens up the possibility of creating closely regulated

[*] Dr. M. Lundqvist,[+] P. Nygren,[+] Prof. B.-H. Jonsson
Division of Molecular Biotechnology, IFM
Linköping University
58183 Linköping (Sweden)
Fax: (+46) 1312-2587
E-mail: nalle@ifm.liu.se

Dr. K. Broo
Division of Applied Optics, IFM
Linköping University
58183 Linköping (Sweden)
Fax: (+46) 705-121-674
E-mail: klabr@amm.gu.se

Dr. K. Broo
Department of Occupational and Environmental Medicine
Sahlgrenska Academy at Göteborg University
Göteborg (Sweden)

[+] These authors contributed equally to this work.

[**] The silica particles were kindly provided by EKA Chemicals, Stenungsund, Sweden. This work was supported by a grant from the Swedish National Science Research Council to B.-H.J. (K5104-5999) and by a grant from the Knut and Alice Wallenberg Foundation to K.B.

 © 2006 Wiley-VCH Verlag GmbH & Co. KGaA, Weinheim

systems with a variety of potential functionalities, which we demonstrate by introduction of a catalytic site.

The introduction of functionality into designed peptides was achieved earlier by Benner and co-workers,[5] who constructed an efficient oxaloacetate decarboxylase, and by Ghadiri and co-workers,[6,7] who constructed a self-replicating peptide and an efficient catalytic synthetic peptide ligase. Chmielewski and co-workers designed a replicating peptide system in which the reactivity is under the control of pH or salt.[8,9] DNA recognition modules, such as the basic region leucine zipper, are unfolded in solution but adopt a stable, ordered conformation upon interaction with DNA.[10–12] DeGrado and co-workers[13] analyzed the leucine zipper proteins, and found fundamental principles for the design of peptides that adopt a helical structure upon interaction with recognition sites in DNA. One important factor for induction of a helical structure is charge–charge interaction between basic residues and negative charges (phosphate groups) on DNA. Thus, it should be possible to induce a helical structure in a designed peptide that contains a motif of basic residues by providing a surface with appropriately spaced negative charges.

From these considerations, we designed a peptide (peptide **1**; Figure 1) that would be unstructured in solution but "forced" to adopt a well-defined helical structure upon adsorption onto silica nanoparticles. The design of peptide **1** was further developed in peptide **2** to include precisely placed amino acids, intended to form a catalytic site[14] upon folding of the helix. To ensure that the induction of structure by interaction with silica nanoparticles will have switchlike properties, it is essential to incorporate a combination of positive and negative design elements; that is, the design

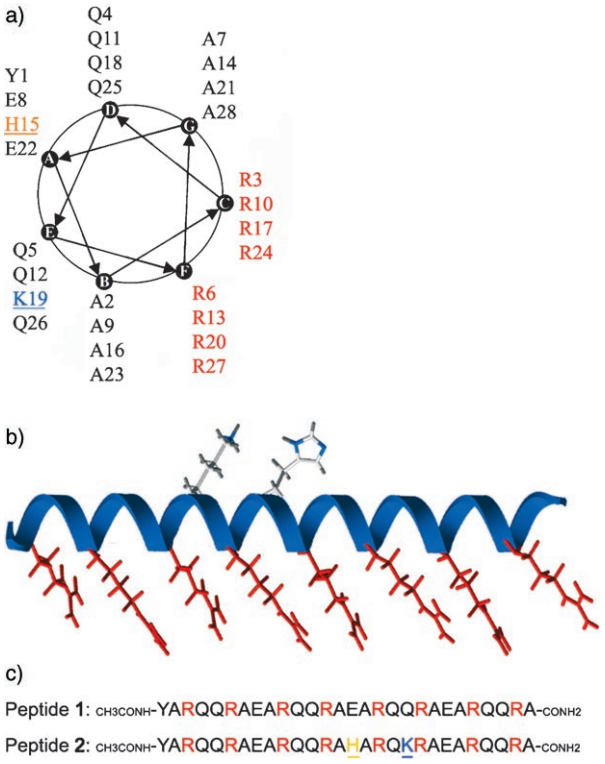

Figure 1. Peptide **2** displayed as a) a helical wheel and b) a helix viewed from the side showing the side chains of Arg and the catalytic His–Lys pair. c) The amino acid sequences of the two peptides.

should strongly favor the formation of helical structure upon binding to the nanoparticles and strongly disfavor an ordered structure in solution. For this reason, we decided to use electrostatic interactions as the structure-determining factor. Herein, we focus on the interactions between a silica nanoparticle and a peptide (peptide **2**) with two rows of positively charged side chains and residues that can form a reactive site (Figure 1).

Silica nanoparticles were chosen as the solid material for two main reasons: their high negative surface charge density and their size, which allows structural investigations of the peptide/nanoparticle complex in solution with standard spectroscopic techniques[15,16] and analytical ultracentrifugation.[17] Arginine residues were incorporated in the design rather than lysine because of their guanidinium group, which has a delocalized positive charge, high pK_a value, and low reactivity. The arginine residues were positioned so that two neighboring rows (Figure 1) would give rise to a large interaction area when a helix was formed upon contact with the negatively charged nanoparticle surface. The positive charge density of the helix interaction surface is of the same magnitude as the negative charge density of the silica nanoparticles at the ion concentration used in this study.[18] The majority of the remaining amino acids in the peptide were selected for their high helix-forming propensities.[19] The requirement for the peptide to be unstructured in solution was also considered in the design. The introduction of arginine side chains in rows C and F should efficiently prevent helix formation in solution, because the electrostatic repulsion between them tends to elongate the peptide. His 15 and Lys 19 (Figure 1) were also included, to introduce a reactive site for ester hydrolysis upon induction of the helical structure.[14]

Sedimentation equilibrium experiments were conducted to determine the aggregation state of the free peptide in solution and its binding to the nanoparticles. The data in Figure 2 b show that a mixture of peptide **2** and particles sediments between 2500 and 8000 rpm, that is, all peptide molecules bind to the particles. The nanoparticles used in this study have a particle weight of ≈425 kDa and sediment completely at 8000 rpm as previously shown.[17] In the absence of particles the peptide does not sediment at these rotor speeds, that is, the peptide does not form large aggregates in solution (Figure 2 a), and experiments at higher rotor speeds indicated that the peptide behaves as a monomer in solution (data not shown). Similar results were observed for peptide **1** (data not shown).

To determine the extent of formation of the secondary structure, samples of free peptide and peptide bound to the nanoparticles were analyzed by far-UV CD. The small diameter (9 nm) of the silica nanoparticles allows UV light to penetrate the sample without scattering, and therefore conventional light spectroscopy can be used to characterize these systems.[20–22] As illustrated in Figure 3 a, the CD signals indicate that the free peptide in solution has no defined secondary structure, irrespective of the pH used in this study (pH 7.9–9.8). Calculations carried out with ContinLL[23] indicate ≈9% α helix for free peptide **1** and ≈8% α helix for free peptide **2**. However, addition of nanoparticles to the

 © 2006 Wiley-VCH Verlag GmbH & Co. KGaA, Weinheim

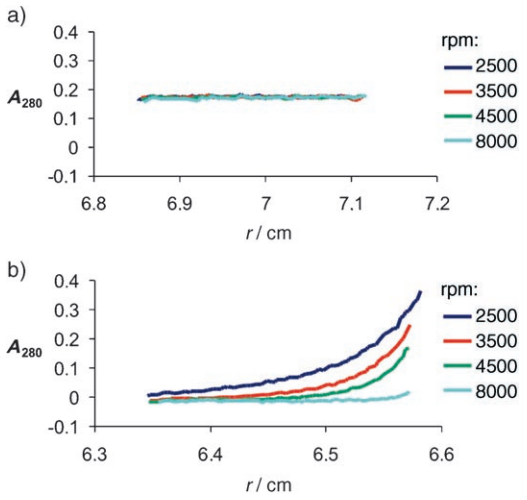

Figure 2. Sedimentation equilibrium analysis of peptide **2** by ultracentrifugation monitored at A_{280} a) without and b) with 9-nm silica particles at pH 9 and 22 °C. The colors represent different rotor speeds (rpm).

solution gave rise to a CD spectrum that is typical for the helical conformation; that is, the nanoparticles induced formation of a helical structure upon interaction with the peptide. Figure 3a also shows that the deletion of the His–Lys pair results in an increase of adopted α helix upon binding of the peptide to the nanoparticle, and the calculations indicate that peptide **1** has 39 % α helix compared with 29 % for peptide **2**. There is a clear correlation between the amount of induced secondary structure in the peptide and the pH of the solution, as demonstrated for peptide **2** in Figure 3b. The calculated amount of α helix is 25, 29, and 35 % at pH 7.9, 9.0, and 9.8, respectively. The nanoparticles induce more secondary structure at higher pH values, probably because the density of negative charges on the surface is increased by raising the pH.[18] The results of melting experiments (Figure 3c) clearly suggest that the helical structure content decreases gradually (noncooperatively) upon increasing the temperature from 25 to 85 °C. The data also reveal that the temperature-dependent structural change is fully reversible, that is, when the sample is cooled to 25 °C the original amount of helix is observed in the sample (Figure 3c, inset).

Peptide **2** includes a His–Lys pair that forms a catalytic unit for ester hydrolysis, provided that peptide **2** becomes helical. Thus, strong proof of a successful design would be a significant rate enhancement of ester hydrolysis in samples containing both peptide **2** and nanoparticles. Experiments in which peptide **2** or the nanoparticles were dissolved in buffer showed no detectable rate enhancement over the background reaction in buffer alone. Notably, samples containing the peptide **2**/nanoparticle complex showed a dramatically higher catalytic efficiency (Figure 4). A control experiment with the peptide **1**/nanoparticle complex showed no rate enhancement over the background reaction in buffer alone. Thus, the enhancement of catalysis requires both the His–Lys pair and the formation of structure upon binding to the nanoparticles.

The design of the catalytic His–Lys site was inspired by the study of Lundh et al.,[14] in which the imidazole moiety of a

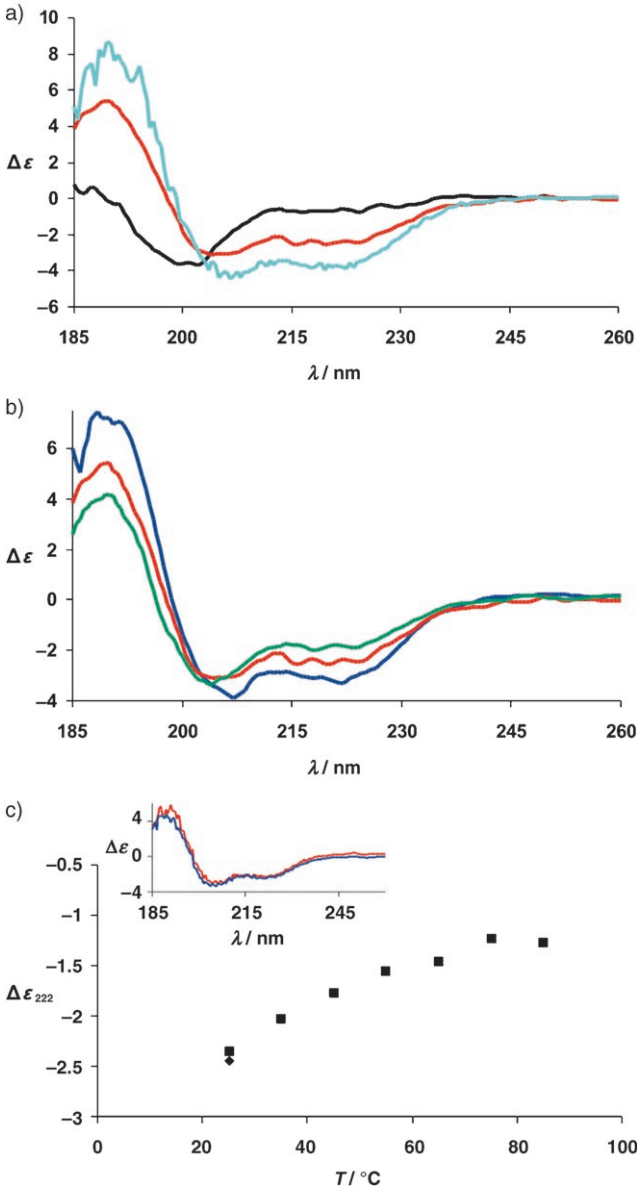

Figure 3. a) CD data for peptides **1** and **2** at pH 9.0 and 22 °C. Black = peptide **2** in solution, blue = peptide **1** with 9-nm silica particles, and red = peptide **2** with 9-nm silica particles. b) CD data for peptide **2** at pH 7.9 (green), 9.0 (red), and 9.8 (blue) with 9-nm silica particles. c) Melting of peptide **2** adsorbed on 9-nm particles (■). The (◆) represents the observed CD value after the sample was cooled to 25 °C. The inset shows the CD spectrum of the sample at 25 °C before heating (red) and after heating to 85 °C and subsequent cooling (blue).

His residue acts as a nucleophile and the positive charge of a nearby ornithine (Orn) residue may stabilize the transition state of the reaction. A comparison of second-order rate constants shows that the peptide **2**/nanoparticle complex ($k_2 = 0.25\ \mathrm{mM^{-1}\,min^{-1}}$) is 54 times more efficient in catalysis than peptide **2** ($k_2 = 0.0046\ \mathrm{mM^{-1}\,min^{-1}}$) alone. Clearly, the nanoparticles can be used as an efficient switch to turn on catalysis. Notably, catalysis with the peptide **2**/nanoparticle complex is 40 times more efficient than the catalysis reported for the peptide that was designed by Lundh et al., and 410 times more efficient than catalysis by imidazole.

 © 2006 Wiley-VCH Verlag GmbH & Co. KGaA, Weinheim

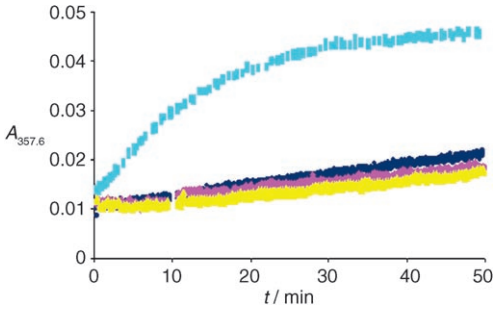

Figure 4. Ester bond hydrolysis by: the peptide **2**/nanoparticle complex (turquoise); peptide **2** (pink); nanoparticles (yellow); and buffer (dark blue). The reaction product *m*-nitrophenol was monitored at $A_{357.6}$.

It is difficult to distinguish between the alternatives that either all peptide molecules adopt a partial helical structure or an equilibrium situation occurs, in which a fraction of peptides is completely helical while another fraction is without helical conformation. The latter alternative would indicate that the temperature dependence of the catalytic activity is directly correlated to the temperature-dependent change in CD signal shown in Figure 3c. However, measurements of ester hydrolysis show that the peptide **2**/nanoparticle complex is catalytically active at 12 °C ($k_2 = 0.17$ mM^{-1} min^{-1}) and 22 °C ($k_2 = 0.25$ mM^{-1} min^{-1}), while there is no observable increase over the background buffer catalysis at 32 and 52 °C. Apparently, the helical conformation at the catalytic site is critically affected in the 22–32 °C temperature range. Thus, the peptides on the silica surface probably all adopt a partial helical conformation, which gradually melts at higher temperatures. Notably, the original esterase activity is completely restored (98 %) after heating to 80 °C and subsequent cooling to 22 °C, which further shows that the catalytic activity is well-correlated to the formation of a helix, that is, the system can be regulated by temperature.

The results of the experiments collectively show that the designed peptides adsorb efficiently and bind strongly to silica nanoparticles, and that they adopt a defined helical structure upon binding. Moreover, the design strategy also successfully incorporated the planned functional properties, as the observed catalysis of ester hydrolysis shows that the formation of a helix leads to a catalytic unit that is oriented away from the surface of the nanoparticles so that catalysis can proceed unhindered.

The described method has potential use in the creation of novel recognition elements and catalysts that can be switched on by the introduction of nanoparticles. By adjusting the design it might also be possible to construct a two-state system that would allow the activity to be switched on and off by small changes in temperature. The ability to create surfaces with well-defined properties (such as reactive groups arranged at predetermined distances on the nanometer scale) would have several important applications in areas such as biocatalysis, biosensing, and nanotechnology. Moreover, it is well-known that interaction with inorganic surfaces tends to induce conformational and functional changes in proteins.[15–17,21,23] Interestingly, it has recently been shown that these rearrangements do not occur at random, but instead bring positively charged side chains closer to the silica surface.[23,24] These observations, together with the results of the present study, point toward the possibility that peptides with a high fraction of positively charged amino acid residues have a high probability of forming well-defined structures on clay. As the amino acid content in peptides can be highly diverse, the adsorption on clay offers rich possibilities that side chains are brought together into functional (catalytic) units. In fact, the possibility for diversity is much larger on peptides than on RNA, which has been suggested to form functional structures on clay.[25] Hence, the results add a new twist to the hypothesis that inorganic clays had an important role in the prebiotic chemistry that led to the origin of life.

Experimental Section

CD spectra were recorded as described by Lundqvist et al.[17] The samples consisted of peptide (≈0.1 mM) with 9-nm silica particles added to give a peptide/nanoparticle ratio of 1:0.25. The helical content was calculated by use of the program ContinLL.[26] Ultracentrifugation experiments were performed and analyzed as described by Lundqvist et al.[17] The samples were the same as those used in the CD analysis. The kinetics of esterase activity were measured at pH 8.2 in Tris buffer (20 mM), with 4-sulfamoyl(benzoylamino)acetic acid 3-nitrophenyl ester (0.04 mM) as substrate. The reaction was monitored at the isosbestic point for *m*-nitrophenol of 357.6 nm. The peptide concentration was 0.1 mM and the concentration of silica nanoparticles was approximately 0.05 mM. Under these conditions, the rate with buffer solution alone was indistinguishable from those measured on samples with nanoparticles or on samples with free peptide in solution. To determine the (very low) rate enhancement from free peptide in solution, experiments with 2 mM peptide were performed under otherwise identical conditions. Catalysis by 10 and 50 mM imidazole was also measured. Second-order rate constants k_2 were calculated after subtraction of the background rate in buffer alone. The peptides were synthesized by standard 9-fluorenylmethoxycarbonyl (fmoc) protection group chemistry.

Received: March 11, 2006
Revised: September 21, 2006

Keywords: amino acids · catalysis · helical structures · nanoparticles · peptides

[1] M. J. Russell, *Science* **2003**, *302*, 580.
[2] M. M. Hanczyc, S. M. Fujikawa, J. W. Szostak, *Science* **2003**, *302*, 618.
[3] C. Huber, G. Wachtershauser, *Science* **1998**, *281*, 670.
[4] C. Huber, W. Eisenreich, S. Hecht, G. Wachtershauser, *Science* **2003**, *301*, 938.
[5] K. Johnsson, R. K. Allemann, H. Widmer, S. A. Benner, *Nature* **1993**, *365*, 530.
[6] K. Severin, D. H. Lee, A. J. Kennan, M. R. Ghadiri, *Nature* **1997**, *389*, 706.
[7] D. H. Lee, J. R. Granja, J. A. Martinez, K. Severin, M. R. Ghadiri, *Nature* **1996**, *382*, 525.
[8] S. Yao, I. Ghosh, R. Zutshi, J. Chmielewski, *Angew. Chem.* **1998**, *37*, 478; *Angew. Chem. Int. Ed.* **1998**, *37*, 478.
[9] S. Yao, I. Ghosh, R. Zutshi, J. Chmielewski, *Nature* **1998**, *396*, 447.
[10] L. Patel, C. Abate, T. Curran, *Nature* **1990**, *347*, 572.
[11] R. V. Talanian, C. J. McKnight, P. S. Kim, *Science* **1990**, *249*, 769.
[12] M. A. Weiss, T. Ellenberger, C. R. Wobbe, J. P. Lee, S. C. Harrison, K. Struhl, *Nature* **1990**, *347*, 575.

 © 2006 Wiley-VCH Verlag GmbH & Co. KGaA, Weinheim

[13] K. T. O'Neil, R. H. Hoess, W. F. DeGrado, *Science* **1990**, *249*, 774.
[14] A. C. Lundh, K. Broo, L. Baltzer, *J. Chem. Soc. Perkin Trans. 2* **1997**, 209.
[15] P. Billsten, P. O. Freskgård, U. Carlsson, B. H. Jonsson, H. Elwing, *FEBS Lett.* **1997**, *402*, 67.
[16] M. Karlsson, L. G. Mårtensson, B. H. Jonsson, U. Carlsson, *Langmuir* **2000**, *16*, 8470.
[17] M. Lundqvist, I. Sethson, B. H. Jonsson, *Langmuir* **2004**, *20*, 10639.
[18] J. Sonnefeld, *J. Colloid Interface Sci.* **1996**, *183*, 597.
[19] S. J. Anthony-Cahill, P. A. Benfield, R. Fairman, Z. R. Wasserman, S. L. Brenner, W. F. Stafford, C. Altenbach, W. L. Hubbell, W. F. DeGrado, *Science* **1992**, *255*, 979.
[20] A. Kondo, S. Oku, K. Higashitani, *J. Colloid Interface Sci.* **1991**, *143*, 214.
[21] W. Norde, J. P. Favier, *Colloids Surf.* **1992**, *64*, 87.
[22] S. R. Clark, P. Billsten, H. Elwing, *Colloids Surf. B* **1994**, *2*, 457.
[23] M. Karlsson, U. Carlsson, *Biophys. J.* **2005**, *88*, 3536.
[24] M. Lundqvist, C. Andresen, S. Christensson, S. Johansson, M. Karlsson, K. Broo, B. H. Jonsson, *Langmuir* **2005**, *21*, 11903.
[25] J. P. Ferris, G. Ertem, *J. Am. Chem. Soc.* **1993**, *115*, 12270.
[26] G. Deléage, C. Geourjon, *Comput. Appl. Biosci.* **1993**, *9*, 197.

 © 2006 Wiley-VCH Verlag GmbH & Co. KGaA, Weinheim

Helical Structures

DOI: 10.1002/anie.200603663

Control of Main-Chain Stiffness of a Helical Poly(phenylacetylene) by Switching On and Off the Intramolecular Hydrogen Bonding through Macromolecular Helicity Inversion**

Kento Okoshi, Shin-ichiro Sakurai, Sousuke Ohsawa, Jiro Kumaki, and Eiji Yashima**

Rodlike helical polymers with an excess of one-handedness arising from an optically active component incorporated into the main chain or at the pendants often show chiral liquid-crystalline (LC) phases in concentrated solutions or in a melt.[1] Since the 1980s, such LC helical polymers have been extensively studied with much interest. Typical biological macromolecules, such as DNA,[2] polysaccharides,[3] and polypeptides,[4] which adopt an ordered structure such as a helical structure, with a controlled helix sense stabilized by intra- and/or intermolecular hydrogen-bonding networks, also exhibit chiral LC phases resulting from the rigid-rod characteristics of the polymer main chains. Intramolecular hydrogen bonding has been used to construct synthetic helical polymers, such as polyisocyanopeptides,[5] and amino acid bound polyacetylenes.[6] The former helical polymers showed a clear cholesteric LC phase.

Recently, we reported the first helical poly(phenylacetylene)s bearing L- or D-alanine pendants with a long alkyl chain (poly-L-**1** and poly-D-**1**, respectively) that showed cholesteric LC phases in organic solvents owing to their main-chain stiffness assisted by intramolecular hydrogen bonds; their persistence lengths were determined to be approximately 40 nm in chloroform,[7] whereas the previously prepared monosubstituted polyacetylenes appear to be too flexible to exhibit LC phases.[6a–c,8] We also found inversion of the helicity of poly-L-**1** and poly-D-**1** in response to the solvent polarity; the Cotton effect signs corresponding to the helix sense of poly-**1** in benzene were inverted to the opposite signs in polar solvents such as THF and chloroform.[9] Furthermore, the macromolecular helicity inversion process could be directly visualized by atomic force microscopy (AFM), which revealed their diastereomeric helical conformations and enabled the determination of the helical sense.[9,10]

We now show a dramatic change in the main-chain stiffness of poly-L-**1**[11] accompanied with inversion of the helical sense of the polymer (Figure 1), resulting from the "on and off" fashion of the intramolecular hydrogen-bonding networks in polar and nonpolar solvents as revealed by the changes in their circular dichroism (CD) and IR spectra, persistence lengths, and rheological properties.

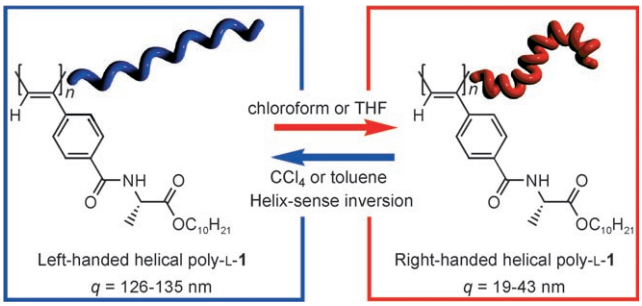

Figure 1. Illustration of the helix-sense inversion of poly-L-**1** regulated by solvents with different polarities, leading to diastereomeric helical poly-L-**1**s with extremely different main-chain stiffnesses. The helical senses of the diastereomeric poly-L-**1**s were determined by AFM.[9]

Figure 2a shows the CD spectra of poly-L-**1** in polar and nonpolar solvents. Poly-L-**1** exhibited split-type intense induced circular dichroisms (ICDs) in the conjugated polyene chromophore region. The ICD patterns measured in nonpolar

[*] Dr. K. Okoshi, Dr. S.-I. Sakurai, Dr. J. Kumaki, Prof. E. Yashima
Yashima Super-structured Helix Project
Exploratory Research for Advanced Technology (ERATO)
Japan Science and Technology Agency (JST)
101 Creation Core Nagoya
Shimoshidami, Moriyama-ku, Nagoya 463-0003 (Japan)
Fax: (+81) 52-739-2083
E-mail: kokoshi@yp-jst.jp
yashima@apchem.nagoya-u.ac.jp
S. Ohsawa, Prof. E. Yashima
Department of Molecular Design and Engineering
Graduate School of Engineering
Nagoya University
Chikusa-ku, Nagoya 464-8603 (Japan)
Fax: (+81) 52-789-3185
Homepage: http://helix.mol.nagoya-u.ac.jp/

[**] We are deeply grateful to Professor T. Sato (Osaka University) for his fruitful discussions.

Supporting information for this article is available on the WWW under http://www.angewandte.org or from the author.

© 2006 Wiley-VCH Verlag GmbH & Co. KGaA, Weinheim

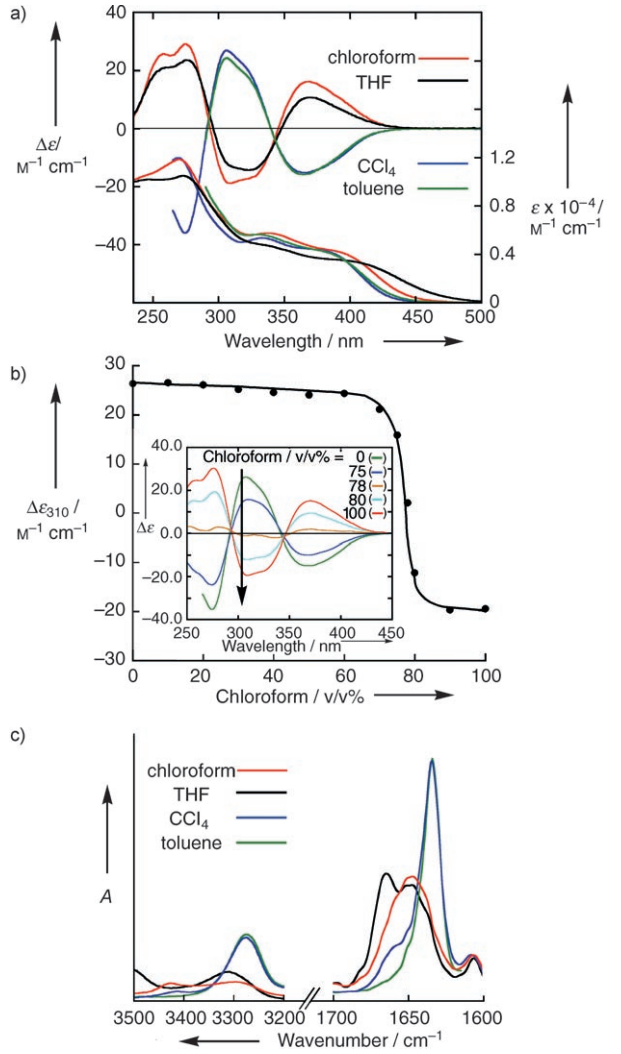

Figure 2. a) CD and absorption spectra of poly-L-**1** taken in CCl_4 at 25 °C (blue line), toluene at 0 °C (green line), chloroform at 25 °C (red line), and THF at 0 °C (black line) in dilute solution (0.2 mg mL^{-1}) in a 1.0-mm quartz cell. b) Changes in the CD intensity (second Cotton effect) of poly-L-**1** (0.2 mg mL^{-1}) in chloroform 25 °C. Inset: effect of the different chloroform concentrations. c) FTIR spectra of poly-L-**1** (5 mg mL^{-1}) taken in CCl_4 (blue line), toluene (green line), chloroform (red line), and THF (black line) at ambient temperatures.

solvents such as CCl_4, toluene, and benzene are almost mirror images of those in polar solvents, such as chloroform and THF, indicating inversion of the helicity of poly-L-**1** induced by solvent polarity as reported previously.[9] The changes in the ICD patterns were accompanied by a slight red shift in the absorption spectra in polar solvents probably owing to the difference in their diastereomeric right- and left-handed helical conformations.[12] As expected, the preferred helical sense of poly-L-**1** can be controlled by the composition of the polar and nonpolar solvents. Figure 2b shows the changes in the second Cotton intensity of poly-L-**1** at approximately 310 nm in $CCl_4/CHCl_3$ mixtures at 25 °C. In sharp contrast to the previously reported solvent-induced helicity inversion in synthetic helical polymers,[6c,13] the ICD intensity suddenly changed and the sign became inverted from the positive to negative direction, yielding almost mirror images in the presence of about 80 vol % chloroform.

The IR spectra of poly-L-**1** were then measured in the polar and nonpolar solvents showing opposite Cotton effect signs to investigate the origin of the helicity inversion (Figure 2c). Poly-L-**1** showed sharp amide NH and carbonyl stretching (amide I) bands at approximately 3275 and 1635 cm^{-1}, respectively, in nonpolar solvents such as CCl_4 and toluene, whereas in the polar chloroform and THF, the NH and amide I bands significantly shifted to higher wavenumbers accompanied by significant band broadening and/or splitting (see the Supporting Information). These band positions imply that poly-L-**1** forms an intramolecular hydrogen-bonding network through the neighboring amide groups in nonpolar solvents, whereas in polar solvents, such hydrogen bonding is weakened or switched off,[14] resulting in the formation of a different helical conformation, in this particular case, the opposite helical conformation, thus showing inversion of the Cotton effect signs.

We anticipated that such solvent-induced on–off switching of the intramolecular hydrogen-bonding networks in the pendant amide residues of poly-L-**1** might lead to a significant change not only in the main-chain stiffness, resulting in a change in the persistence length (q), but also in the rheological property of the polymer fluids. The q values of poly-L-**1** in polar and nonpolar solvents were then estimated on the basis of the wormlike chain model. This model can be described as an analytical function of the molecular weight (M_w) and the radius of gyration (S) if the q values and the molar mass per unit contour length (M_L), which eventually leads to the monomer unit height (h), are given.[15] In this way, the dependence of the molecular weight on the radius of gyration of poly-L-**1** in polar and nonpolar solvents was explored by using a size-exclusion chromatography (SEC) system equipped with multiangle light scattering (MALS) and refractive-index detectors in a series (Figure 3a). This series is a powerful method to evaluate the q value of polymers in a facile way in conjunction with the wormlike chain model.[16] The solid curves in the plots were calculated by using the parameters determined from the fits of the unperturbed wormlike chain model over the entire M_w studied range, and are represented by the theoretical values of $\langle S^2 \rangle^{0.5}$.

The calculated h values of poly-L-**1** in polar and nonpolar solvents almost coincide with the reported value (0.22 nm) of poly(4-carboxyphenylacetylene) (PCPA),[8] indicating that poly-L-**1** appears to take a similar helical conformation irrespective of the solvent polarity.[7] The calculated q values of poly-L-**1** in nonpolar CCl_4 and toluene are 134.5 and 126.3 nm, respectively; these values are the highest among all synthetic helical polymers reported so far, including the polyisocyanates, polyisocyanides, and polysilanes,[17] and are even stiffer than double-helical DNA (< 60 nm).[20] In sharp contrast, poly-L-**1** showed a dramatic decrease in its persistence length to 42.9 and 19.2 nm in the polar solvents chloroform[7] and THF, respectively, leading to a rather semirigid polymer. These results clearly demonstrate that the main-chain stiffness of poly-L-**1** can be readily controlled by the on–off switching of the intramolecular hydrogen-bonding networks of the pendant amide groups as generated

 © 2006 Wiley-VCH Verlag GmbH & Co. KGaA, Weinheim

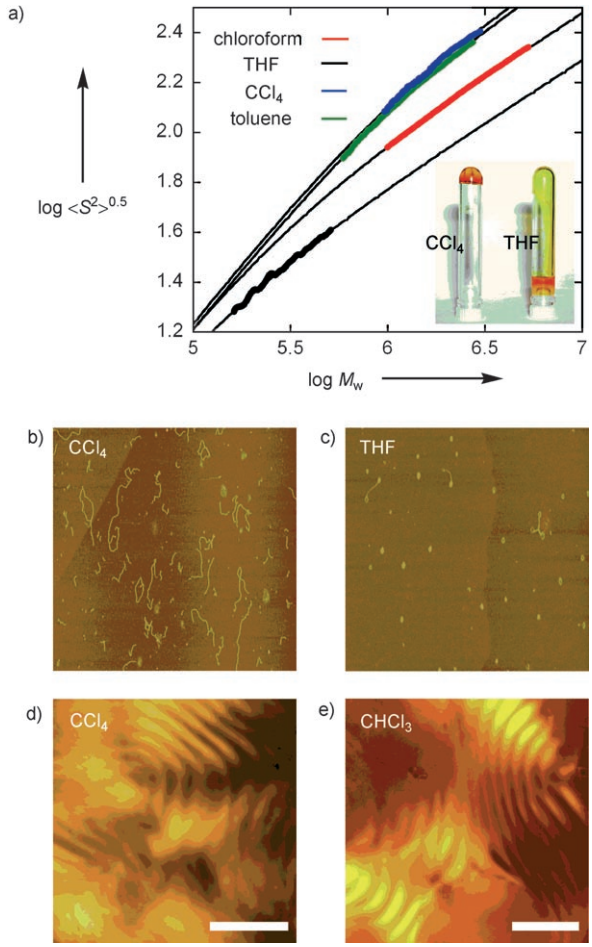

Figure 3. a) Double-logarithmic plots of the radius of gyration versus the molecular weight of poly-L-**1** in CCl_4 (blue points), toluene (green points), chloroform (red points), and THF (black points) obtained by SEC-MALS measurements at 25 °C. Solid curves (black lines) were obtained on the basis of the wormlike chain theory and fit well with the experimental data. The evaluated parameters are as follows: In CCl_4, $q = 134.5$ nm, $M_L = 1613.0$ nm^{-1}, $h = 0.22$ nm; in toluene, $q = 126.3$ nm, $M_L = 1699.6$ nm^{-1}, $h = 0.21$ nm; in chloroform, $q = 42.9$ nm, $M_L = 1537.7$ nm^{-1}, $h = 0.23$ nm; in THF, $q = 19.2$ nm, $M_L = 1663.8$ nm^{-1}, $h = 0.21$ nm. The inset shows the visible difference in poly-L-**1** ($M_w = 166.2 \times 10^4$ and $M_w/M_n = 2.12$) in CCl_4 and THF, taken at ambient temperature (10 mg/100 μL). b, c) AFM height images (5.0×5.0 μm^2) of poly-L-**1** cast from a dilute solution in CCl_4 (b) and THF (c) on mica modified with trimethoxypropylsilane. d, e) Polarized optical micrographs of poly-L-**1** in 15 wt% CCl_4 (d) and chloroform (e) solutions in glass capillary tubes taken at ambient temperature (20–25 °C). Scale bars: 50 μm.

by solvent polarity, which also induces inversion of the helicity of poly-L-**1** simultaneously.[21]

Additional strong evidence of the change in the main-chain stiffness of the polymer depending on the solvent polarity was obtained from AFM measurements. Figure 3b and c show typical AFM images of isolated poly-L-**1** chains on mica modified with trimethoxypropylsilane prepared by spin-casting a dilute solution of poly-L-**1** in CCl_4 and THF (0.2 mg mL^{-1}), respectively. Individual poly-L-**1** chains with an extended structure can be directly visualized on the mica prepared from a nonpolar CCl_4 solution, indicating the stiff main-chain conformation. On the contrary, the polymer cast from polar THF appears highly tangled on the AFM images as a result of the flexible main-chain conformation.

As expected, the on–off switching of intramolecular hydrogen bonds brought about a change in the rheological property of poly-L-**1**, which can be visibly observed as a viscosity change in solution (Figure 3a, inset). A solution of poly-L-**1** in polar THF (10% w/v) is highly viscous but still fluid, whereas in nonpolar CCl_4, the solution became a viscous liquid and subsequently gelled. These visible changes are in good agreement with the difference in their persistence lengths in each solvent assisted by the on–off switching of the intramolecular hydrogen bonds.

Another interesting and unique feature of rigid rodlike helical polymers is the formation of chiral LC phases. Combined with a specific property of inversion of the helicity of poly-L-**1** regulated by solvent polarity, cholesteric LC phases of poly-L-**1** with an opposite twist sense to each other can be produced by using nonpolar and polar solvents (Figure 3d and e). We then estimated the q values of poly-L-**1** in different solvents by measuring their isotropic–cholesteric LC phase boundary concentrations (see the Supporting Information).[22] The q values calculated by the theory of Khokhlov and Semenov[22a,b] in CCl_4, toluene, chloroform, and THF were 175.3, 163.9, 70.5, and 33.5 nm, respectively; these values are in rough agreement with those estimated by the SEC-MALS measurement.

In conclusion, we have demonstrated that the macromolecular helicity and main-chain stiffness of poly-L-**1** can be controlled simultaneously by solvent polarity, resulting from the "on and off" fashion of the intramolecular hydrogen-bonding networks, which further results in a change in the rheological property of the polymer solutions. Changing the solvent polarity also allows one to control the mesoscopic cholesteric states of the opposite twist sense derived from inversion of the macromolecular helicity of the polymer chain. The present results will provide a novel approach for the rational design of chiral materials with inversion of the macromolecular helicity-based rheology switching.

Received: September 7, 2006
Published online: November 16, 2006

Keywords: helical structures · helix inversion · hydrogen bonds · liquid crystals · poly(phenylacetylene)s

[1] a) T. Sato, Y. Sato, Y. Umemura, A. Teramoto, Y. Nagamura, J. Wagner, D. Weng, Y. Okamoto, K. Hatada, M. M. Green, *Macromolecules* **1993**, *26*, 4551–4559; b) K. Okoshi, H. Kamee, G. Suzaki, M. Fujiki, J. Watanabe, *Macromolecules* **2002**, *35*, 4556–4559; c) J. Kim, B. M. Novak, A. J. Waddon, *Macromolecules* **2004**, *37*, 8286–8292.

[2] a) T. E. Strzelecka, M. W. Davidson, R. L. Rill, *Nature* **1988**, *331*, 457–460; b) F. Livolant, A. M. Levelut, J. Doucet, J. P. Benoit, *Nature* **1989**, *339*, 724–726.

[3] a) S. Fortin, G. Charlet, *Macromolecules* **1989**, *22*, 2286–2292; b) S. Inatomi, Y. Jinbo, T. Sato, A. Teramoto, *Macromolecules* **1992**, *25*, 5013–5019.

[4] a) C. Robinson, J. C. Ward, *Nature* **1957**, *180*, 1183–1184; b) Y. Tsujita, I. Yamanaka, A. Takizawa, *Polym. J.* **1979**, *11*, 749–754;

 © 2006 Wiley-VCH Verlag GmbH & Co. KGaA, Weinheim

c) S. M. Yu, V. P. Conticello, G. Zhang, C. Kayser, M. J. Fournier, T. L. Mason, D. A. Tirrel, *Nature* **1997**, *389*, 167 – 170.
[5] a) J. J. L. M. Cornelissen, J. J. M. Donners, R. de Gelder, W. S. Graswinckel, G. A. Metselaar, A. E. Rowan, N. A. J. M. Sommerdijk, R. J. M. Nolte, *Science* **2001**, *293*, 676 – 680; b) P. Samorí, C. Ecker, I. Gösell, P. A. J. de Witte, J. J. L. M. Cornelissen, G. A. Metselaar, M. B. J. Otten, A. E. Rowan, R. J. M. Nolte, J. P. Rabe, *Macromolecules* **2002**, *35*, 5290 – 5294.
[6] a) R. Nomura, J. Tabei, T. Masuda, *J. Am. Chem. Soc.* **2001**, *123*, 8430 – 8431; b) R. Nomura, J. Tabei, S. Nishiura, T. Masuda, *Macromolecules* **2003**, *36*, 561 – 564; c) J. W. Y. Lam, B. Z. Tang, *Acc. Chem. Res.* **2005**, *38*, 745 – 754. For intramolecular hydrogen-bond-stabilized helix formation of foldamers, see: d) B. Gong, *Chem. Eur. J.* **2001**, *7*, 4336 – 4342; e) J. M. Cary, J. S. Moore, *Org. Lett.* **2002**, *4*, 4663 – 4666; f) J. J. van Gorp, J. A. J. M. Vikemans, E. W. Meijer, *Chem. Commun.* **2004**, 60 – 61; g) I. Huc, *Eur. J. Org. Chem.* **2004**, 17 – 29.
[7] K. Okoshi, K. Sakajiri, J. Kumaki, E. Yashima, *Macromolecules* **2005**, *38*, 4061 – 4064.
[8] Y. Ashida, T. Sato, K. Morino, K. Maeda, Y. Okamoto, E. Yashima, *Macromolecules* **2003**, *36*, 3345 – 3350.
[9] S.-i. Sakurai, K. Okoshi, J. Kumaki, E. Yashima, *J. Am. Chem. Soc.* **2006**, *128*, 5650 – 5651.
[10] S.-i. Sakurai, K. Okoshi, J. Kumaki, E. Yashima, *Angew. Chem.* **2006**, *118*, 1267 – 1270; *Angew. Chem. Int. Ed.* **2006**, *45*, 1245 – 1248.
[11] Poly-L-**1** was prepared by the polymerization of the corresponding optically pure monomer with a rhodium catalyst in THF according to a previously reported method.[7] The weight-average molecular weight (M_w) and its distribution (M_w/M_n; M_n = number-average molecular weight) are 166.2×10^4 and 2.12, respectively, as estimated by SEC.
[12] A similar solvent-regulated inversion of the macromolecular helicity has also been observed in other helical polyacetylenes, polyisocyanates, and polysilanes.[6c,13]
[13] a) M. Fujiki, J. R. Koe, M. Motonaga, H. Nakashima, K. Terao, A. Teramoto, *J. Am. Chem. Soc.* **2001**, *123*, 6253 – 6261; b) H. Nakako, R. Nomura, T. Masuda, *Macromolecules* **2001**, *34*, 1496 – 1502; c) K. K. L. Cheuk, J. W. Y. Lam, J. Chen, L. M. Lai, B. Z. Tang, *Macromolecules* **2003**, *36*, 9752 – 9762; d) K. Maeda, H. Mochizuki, M. Watanabe, E. Yashima, *J. Am. Chem. Soc.* **2006**, *128*, 7639 – 7650.
[14] No indication of hydrogen bonding was observed for the monomer L-**1** in solution independent of the solvent polarity (see the Supporting Information).
[15] The persistence length q, a parameter of this model, is a useful measure to evaluate the stiffness of rodlike polymers, but only a limited number of q values have been determined for helical polymers. See Refs. [6b] and [7].
[16] a) H. Yamakawa, M. Fujii, *Macromolecules* **1974**, *7*, 128 – 135; b) H. Yamakawa, T. Yoshizaki, *Macromolecules* **1980**, *13*, 633 – 643.
[17] The reported high q values for synthetic helical polymers are 20–40 nm for poly(*n*-hexyl isocyanate),[18] 76 nm for polyisocyanopeptides,[5b] and 103 nm for poly((*R*)-3,7-dimethyloctyl-(*S*)-3-methylpentylsilylene).[19]
[18] H. Gu, Y. Nakamura, T. Sato, A. Teramoto, M. M. Green, C. Andreola, *Polymer* **1999**, *40*, 849 – 856.
[19] a) A. Teramoto, K. Terao, Y. Terao, N. Nakamura, T. Sato, M. Fujiki, *J. Am. Chem. Soc.* **2001**, *123*, 12303 – 12310; b) T. Sato, K. Terao, A. Teramoto, M. Fujiki, *Polymer* **2003**, *44*, 5477 – 5495.
[20] T. Sato, A. Teramoto, *Adv. Polym. Sci.* **1996**, *126*, 85 – 116.
[21] Such a change in the main-chain stiffness of poly-L-**1** is as drastic as the coil–to–helix transition of polypeptides in which the persistence length remarkably increases from a few nm to a hundred nm.[20] However, importantly, poly-L-**1** undergoes the helix-to-helix transition during the change in the main-chain stiffness.
[22] a) A. R. Khokhlov, A. N. Semenov, *Phys. A* **1981**, *108*, 546 – 556; b) A. R. Khokhlov, A. N. Semenov, *Phys. A* **1982**, *112*, 605 – 614; c) K. Nagai, K. Sakajiri, K. Maeda, K. Okoshi, T. Sato, E. Yashima, *Macromolecules* **2006**, *39*, 5371 – 5380.

 © 2006 Wiley-VCH Verlag GmbH & Co. KGaA, Weinheim

Fullerenes

DOI: 10.1002/anie.200604052

Dancing on a Fullerene Surface: Isomerization of $Y_3N@(N$-Ethylpyrrolidino-$C_{80})$ from the 6,6 to the 5,6 Regioisomer**

Antonio Rodríguez-Fortea, Josep M. Campanera, Claudia M. Cardona, Luis Echegoyen, and Josep M. Poblet**

The prototype of the family of trimetallic nitride template (TNT) endohedral fullerenes $Sc_3N@C_{80}$ was first synthesized in 1999.[1] In these fullerenes the least stable icosahedral (I_h) isomer of C_{80} is stabilized by a formal six-electron transfer from the TNT moiety to the carbon cage.[2,3] Since the $M_3N@C_{80}$ species can be isolated in a quite remarkably high yield, the design of $M_3N@C_{80}$ derivatives has considerable potential in material science and biochemistry. Several reports of the functionalization of endohedral metallofullerenes with isolated and well-characterized adducts exist.[4–17] Among these, the pyrrolidinofullerene derivatives of $Sc_3N@C_{80}$ and $Y_3N@C_{80}$ show unexpected chemical and electrochemical properties.[18] Cycloaddition reactions on

[*] Dr. A. Rodríguez-Fortea, Prof. Dr. J. M. Poblet
Departament de Química Física i Inorgànica
Universitat Rovira i Virgili
c/Marcel·lí Domingo, s/n
Campus Sescelades, 43007 Tarragona (Spain)
Fax: (+34) 977-559-563
E-mail: antonio.rodriguezf@urv.cat
josepmaria.poblet@urv.cat

Dr. J. M. Campanera
Department of Chemistry
University of Sussex
Brighton, BN1 9QJ (UK)

Dr. C. M. Cardona, Prof. Dr. L. Echegoyen
Department of Chemistry
Clemson University
219 Hunter Laboratories, Clemson, SC 29634-0973 (USA)

[**] This work was supported by the Spanish Ministry of Science and Technology (Project no. CTQ2005-06909-C02-01/BQU and the Ramón y Cajal Program (ARF)) and by the DURSI of the Generalitat de Catalunya (2005SGR-00104). Part of the computer resources (CPMD calculations) were provided by the Barcelona Supercomputer Center (BSC).

Supporting information for this article is available on the WWW under http://www.angewandte.org or from the author.

InterScience
© 2006 Wiley-VCH Verlag GmbH & Co. KGaA, Weinheim

$Sc_3N@C_{80}$ usually take place regioselectively at a 5,6 ring junction (corannulene-type site) on the I_h C_{80} isomer. A Diels–Alder derivative and two 1,3-dipolar cycloadducts of *N*-ethyl- and *N*-methylazomethine ylide which give rise to the *N*-ethyl- and *N*-methylpyrrolidinofullerene, respectively, are examples of such a regioselectivity.[6,9,11,13] However, Dorn and co-workers have recently obtained a mixture of the 5,6 and 6,6 regioisomers in the synthesis of the *N*-tritylpyrrolidinofullerene adduct.[19] Interestingly, similar cycloaddition reactions on the I_h $Y_3N@C_{80}$ derivative occur exclusively at a 6,6 ring junction (pyrene-type site).[8] Isomerization of the 6,6 regioisomer of $Y_3N@$(*N*-ethylpyrrolidino-C_{80}) to produce exclusively the 5,6 regioisomer after thermalization has been reported by Echegoyen and co-workers.[18] Figure 1 illustrates

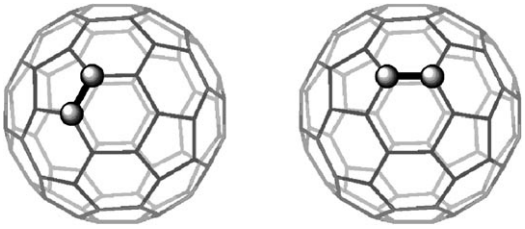

Figure 1. Two possible sites of addition to the I_h C_{80} cage: on the left, a 5,6 ring junction (a corannulene-type site), and on the right, a 6,6 ring junction (a pyrene-type site).

the two possible sites of addition to the I_h C_{80} fullerene cage, the double bonds between a five- and a six-membered ring and between two six-membered rings. Hence, reactivity of TNT endohedral metallofullerenes toward exohedral chemical functionalizaton is affected and controlled by the nature of the endohedral metal cluster. In the case of the 1,3-dipolar *N*-ethylazomethine cycloaddition on $Y_3N@C_{80}$, the experimental results suggest that the reaction gives rise to the kinetic product. The 5,6 regioisomer would be the most stable minimum energy form because it is the unique isomer found after thermalization. Thus, the transition state (TS) to obtain the 6,6 isomer should be lower in energy than the TS that yields the 5,6 isomer. Herein, we report on the thermodynamic stability of reactants, intermediates, and products of the 1,3-dipolar *N*-ethylazomethine cycloaddition on $M_3N@C_{80}$ (M = Sc, Y), as well as on the different reactivity observed in experiments with the scandium- and yttrium-based compounds.

Theoretical calculations indicated that the TNT unit may easily rotate inside the cage in underivatized $Sc_3N@C_{80}$, a finding that is in good agreement with ^{13}C NMR spectroscopic analyis.[2] We have observed that the TNT unit may also rotate inside the fullerene cage in $Y_3N@C_{80}$ because several orientational isomers show energy differences of less than 3 kcal mol^{-1}. For the two different pyrrolidinofullerene regioisomers, we performed a conformational search for the position of the TNT with respect to the C–C bond of the cage where the pyrrolidine was formed. A representation of the isomers considered in the search is found in Figure 2. Reaction energies are fairly exothermic for all the isomers (Table 1), regardless of the type of metal cluster, Y_3N or Sc_3N.

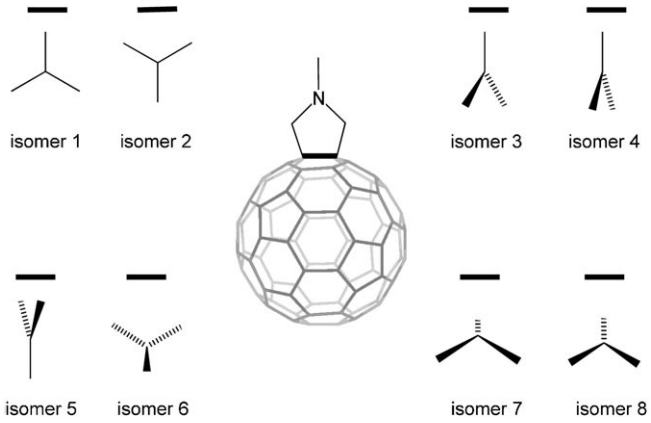

Figure 2. Representation of the relative position of the TNT unit with respect to the C–C bond of the fullerene where the adduct is formed for the different isomers that have been computed in this work.

Table 1: Reaction energies for the different product isomers of the 1,3-dipolar cycloaddition of *N*-ethylazomethine to $M_3N@C_{80}$ (M = Sc, Y).[a]

	$Y_3N@$pyrrolidino-C_{80}		$Sc_3N@$pyrrolidino-C_{80}	
Isomer	5,6 [kcal mol^{-1}]	6,6 [kcal mol^{-1}]	5,6 [kcal mol^{-1}]	6,6 [kcal mol^{-1}]
1	−33.6	−33.6	−26.5	−19.8
2	−33.2	−22.7	−36.1	−24.6
3	−35.6	−33.7	−26.3	−21.5
4	−34.0	−31.5	−24.2	−19.8
5	−20.8	−22.9	−24.7	−25.0
6	−35.2	−22.5	−37.0	−24.6
7	−23.7	−18.3	−25.5	−18.5
8	−22.3	−22.5	−24.6	−21.6

[a] The reaction energies for the cycloaddition to the bonds between a five- and a six-membered ring and between two six-membered rings of C_{80} are −50.2 and −35.5 kcal mol^{-1}, respectively.

From Table 1, it is evident that the rotation of the TNT unit inside the functionalized fullerene is more hindered than in the underivatized $M_3N@C_{80}$ counterparts. Moreover, the TNT unit rotates more easily in the 5,6 regioisomer than in the 6,6 one. Recently, Yamada et al. also suggested on the basis of computed electrostatic potential maps of $La_2@C_{80}$-$(CH_2)_2NH$ that the La_2 unit is fixed in the 6,6 isomer, but it can move randomly in the 5,6 isomer.[17]

The relative stability of the 5,6 regioisomer with respect to the 6,6 regioisomer in pyrrolidino-C_{80} (14.7 kcal mol^{-1}) is reduced when the fullerene cage encapsulates the TNT unit. For M = Sc, the stability of the two regioisomers is similar only for a few orientations of the TNT unit that lay at high energies (isomers **5** and **8**). For M = Y, however, there are several orientational isomers with low energy for which the energy difference between the two regioisomers is small. For the Y-based metallofullerene, the lowest energy 5,6 isomer **3** is only 1.9 kcal mol^{-1} more stable than the most stable 6,6 structure, whereas for the Sc-based metallofullerene the corresponding difference is 12 kcal mol^{-1}. Therefore, the relative stability of the 5,6 versus 6,6 coordination is decreased when Sc is changed for Y. A larger charge transfer to the cage and a larger size of the TNT derivative (Y > Sc) appear to stabilize the 6,6 regioisomer with respect to the 5,6 regioisomer.

 © 2006 Wiley-VCH Verlag GmbH & Co. KGaA, Weinheim

The two global minima **3** and **6** for the 5,6 adduct of Y_3N@pyrrolidino-C_{80} are almost degenerate, with an energy difference of only 0.4 kcal mol^{-1}. The X-ray structure,[10] which shows some disorder in the position of the Y atoms inside the cage, is almost identical to the structure computed for isomer **6** (see the Supporting Information). The most stable isomers for the 6,6 adduct, have one Y atom oriented toward the substituted C–C bond.

We have also looked for the transition states so as to unravel the mechanism of the 1,3-dipolar cycloaddition to TNT endohedral fullerenes and to shed light on the different behavior of Sc- and Y-based compounds. Figure 3 displays the energy profiles for the stepwise addition of *N*-methylazomethine (our computational model) to $M_3N@C_{80}$. When M = Y, the electronic barrier for the addition to a bond between two six-membered rings ($TS_{1,66}$) is 0.4 kcal mol^{-1}, a value that is much smaller than the barrier of 3.9 kcal mol^{-1} found for the addition to a bond between a five and a six-membered ring ($TS_{1,56}$). The intermediate that gives rise to the 6,6 adduct (I_{66}) is around 5 kcal mol^{-1} more stable than the intermediate that originates the 5,6 adduct (I_{56}). We have also located the TS that connects I_{66} with the 6,6 adduct ($TS_{2,66}$). It lies 0.8 kcal mol^{-1} higher in energy than I_{66}, so it is also an almost barrierless step. Although transition states that connect I_{56} to the 5,6 adduct have not been located ($TS_{2,56}$), we assume that these processes are almost barrierless as well. Therefore, present DFT calculations confirm that the formation of the 6,6 adduct from the reaction between $Y_3N@C_{80}$ and *N*-ethylazomethine is under kinetic control.[20] For M = Sc (Figure 3b), transition states for 5,6 and 6,6 additions show similar energies, with $TS_{1,56}$ being slightly favored. As the experiment shows only the presence of the 5,6 adduct, we infer from our energy profile that the process is thermodynamically controlled.

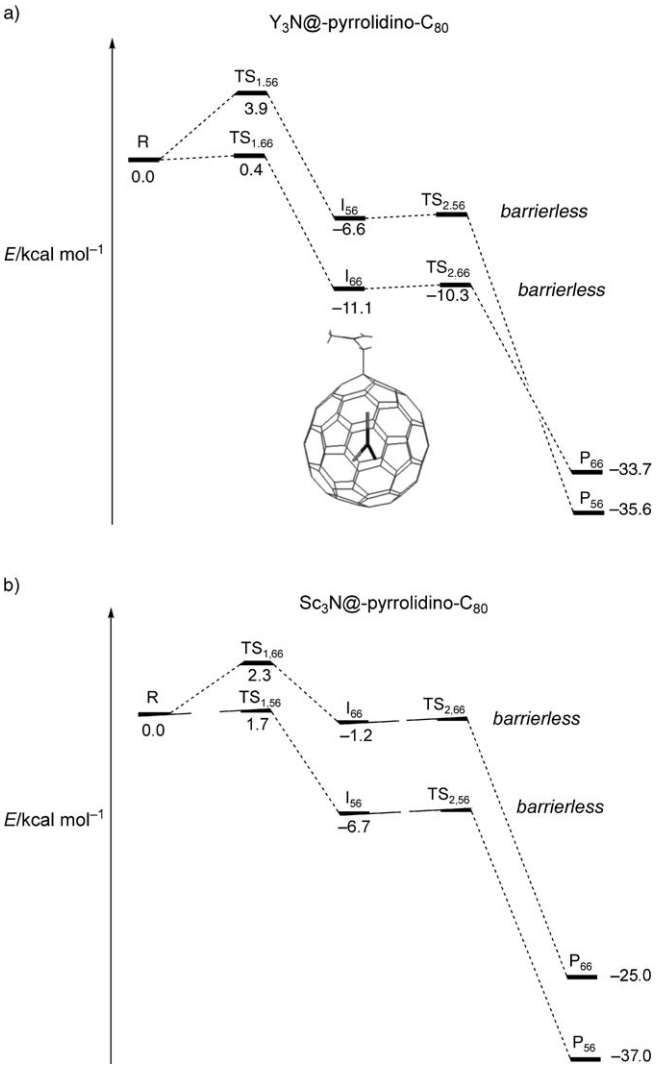

Figure 3. Energy profile of the most relevant stationary points for the *N*-methylazomethine addition to the endohedral metallofullerene a) $Y_3N@C_{80}$ and b) $Sc_3N@C_{80}$.

We finally addressed the 6,6-to-5,6 isomerization observed in experiments after thermalization of the kinetically favored product. A pirouette-kind of mechanism has been proposed by the research groups of both Echegoyen and Dorn.[18,19] Furthermore, Echegoyen and co-workers have shown this transformation directly by NMR spectroscopy, starting with the pure 6,6 regioisomer, which transformed quantitatively to the 5,6 isomeric form. Based on this experimental evidence and on the computed energy profile for the stepwise cycloaddition (Figure 3a), we put forward the mechanism depicted in Figure 4. The 6,6 adduct (P_{66}) is converted into a 5,6 intermediate (I'_{56}) through a TS (TS_{66to56}) with an energy similar to I'_{56}. The formation of I_{66} through TS_{66} is energetically favored, but no isomerization process is then possible. Rotation around the remaining C1–C3 bond is needed to obtain a 5,6 adduct. Either clockwise or anticlockwise rotations will involve situations in which the C2-C1-C3-N dihedral angle is zero or near to zero (namely, eclipsed bonds). Our estimation for the energy of such an "eclipsed TS" is 1.8 kcal mol^{-1}.[21] This value is smaller than the energy of $TS_{1,56}$, so the isomerization mechanism is more favored than the mechanism involving retrocycloaddition–cycloaddition to the bond between a five-and a six-membered ring (3.9 kcal mol^{-1}). Therefore, during thermalization, pyrrolidine "dances" on the fullerene surface when the "couple" inside is Y_3N, but no isomerization is observed once the most stable regioisomer is formed, as occurs for $Sc_3N@C_{80}$.

The somewhat different exohedral reactivity and stability of the resulting adducts of $M_3N@C_{80}$ fullerenes (M = Sc, Y) seems to be related to the size of the TNT unit and the amount of charge transfer to the cage. The larger the size of TNT and the charge transfer (Y > Sc) the more stable are the 6,6 regioisomers with respect to 5,6 regioisomers. Preliminary results for M = La that show orientational isomers for which the 6,6 adduct is more stable than the 5,6 adduct also point to this direction.

Methods Section

The calculations were carried out by using DFT methodology with the ADF 2004 program.[22,23] The exchange-correlation funtionals of Becke[24] and Perdew[25] were used. Relativistic corrections were included by means of the ZORA formalism. Triple-ζ polarization basis sets were employed to describe the valence electrons of the C, N,

 © 2006 Wiley-VCH Verlag GmbH & Co. KGaA, Weinheim

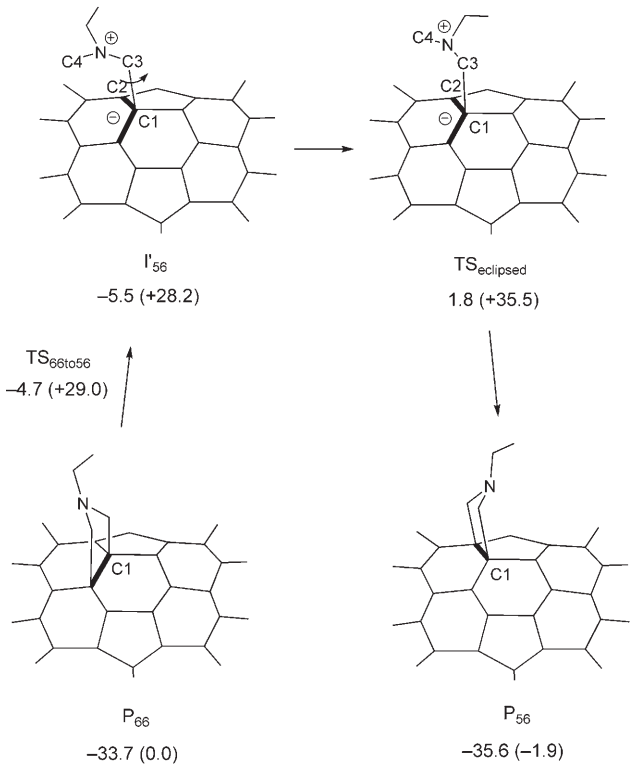

Figure 4. Proposed mechanism for the isomerization of the 6,6 regioisomer of Y_3N@pyrrolidino-C_{80} to the 5,6 regioisomer. Relative energies with respect to reactants in kcal mol^{-1} are displayed (relative to that of P_{66} in parenthesis). In the $TS_{eclipsed}$, the C–C bond between the five- and the six-membered ring and the C–N bond of the pyrrolidine are in an eclipsed conformation. The negative charge in I'_{56} and $TS_{eclipsed}$ is mainly delocalized over the three C atoms bonded to C1. Pyrrolidine "dances" on the fullerene surface when the "couple" inside is Y_3N.

Sc, and Y atoms. All the computed stationary points have closed-shell electronic structure. To locate the transition states, we made use of the metadynamics method associated with Car–Parrinello molecular dynamics,[26] as implemented in the CPMD program.[27] From the snapshots in the transition regions of the metadynamics trajectory we performed a conventional TS search with pseudo Newton–Raphson methods computing numerically the initial Hessian matrix and updating it progressively with the Broyden–Fletcher–Goldfarb–Shanno (BFGS) algorithm. The approximate final Hessian matrix, with a unique negative eigenvalue, is employed as the initial Hessian matrix in the TS search made with the ADF 2004 code. The stationary points with an approximate Hessian matrix with a unique negative eigenvalue are what we call TS thorough this study. The structures of the most representative stationary points are found in the Supporting Information.

Received: October 2, 2006

Keywords: density functional calculations · fullerenes · host–guest systems · isomerization · surface chemistry

[1] S. Stevenson, G. Rice, T. Glass, K. Harich, F. Cromer, M. R. Jordan, J. Craft, E. Hadju, R. Bible, M. M. Olmstead, K. Maitra, A. J. Fisher, A. L. Balch, H. C. Dorn, *Nature* **1999**, *401*, 55–57.

[2] J. M. Campanera, C. Bo, M. M. Olmstead, A. L. Balch, J. M. Poblet, *J. Phys. Chem. A* **2002**, *106*, 12356–12364.

[3] J. M. Campanera, C. Bo, J. M. Poblet, *Angew. Chem.* **2005**, *117*, 7396–7399; *Angew. Chem. Int. Ed.* **2005**, *44*, 7230–7233.

[4] T. Akasaka, T. Kato, K. Kobayashi, S. Nagase, K. Yamamoto, H. Funasaka, T. Takahashi, *Nature* **1995**, *374*, 600–601.

[5] T. Akasaka, S. Nagase, K. Kobayashi, T. Suzuki, T. Kato, K. Kikuchi, Y. Achiba, K. Yamamoto, H. Funasaka, T. Takahashi, *Angew. Chem.* **1995**, *107*, 2303–2304; *Angew. Chem. Int. Ed. Engl.* **1995**, *34*, 2139–2141.

[6] T. Cai, Z. X. Ge, E. B. Iezzi, T. E. Glass, K. Harich, H. W. Gibson, H. C. Dorn, *Chem. Commun.* **2005**, 3594–3596.

[7] B. P. Cao, T. Wakahara, Y. Maeda, A. H. Han, T. Akasaka, T. Kato, K. Kobayashi, S. Nagase, *Chem. Eur. J.* **2004**, *10*, 716–720.

[8] C. M. Cardona, A. Kitaygorodskiy, L. Echegoyen, *J. Am. Chem. Soc.* **2005**, *127*, 10448–10453.

[9] C. M. Cardona, A. Kitaygorodskiy, A. Ortiz, M. A. Herranz, L. Echegoyen, *J. Org. Chem.* **2005**, *70*, 5092–5097.

[10] L. Echegoyen, C. J. Chancellor, C. M. Cardona, B. Elliott, J. Rivera, M. M. Olmstead, A. L. Balch, *Chem. Commun.* **2006**, 2653–2655.

[11] E. B. Iezzi, J. C. Duchamp, K. Harich, T. E. Glass, H. M. Lee, M. M. Olmstead, A. L. Balch, H. C. Dorn, *J. Am. Chem. Soc.* **2002**, *124*, 524–525.

[12] K. Kobayashi, S. Nagase, Y. Maeda, T. Wakahara, T. Akasaka, *Chem. Phys. Lett.* **2003**, *374*, 562–566.

[13] H. M. Lee, M. M. Olmstead, E. Iezzi, J. C. Duchamp, H. C. Dorn, A. L. Balch, *J. Am. Chem. Soc.* **2002**, *124*, 3494–3495.

[14] Y. Maeda, Y. Matsunaga, T. Wakahara, S. Takahashi, T. Tsuchiya, M. O. Ishitsuka, T. Hasegawa, T. Akasaka, M. T. H. Liu, K. Kokura, E. Horn, K. Yoza, T. Kato, S. Okubo, K. Kobayashi, S. Nagase, K. Yamamoto, *J. Am. Chem. Soc.* **2004**, *126*, 6858–6859.

[15] Y. Maeda, J. Miyashita, T. Hasegawa, T. Wakahara, T. Tsuchiya, T. Nakahodo, T. Akasaka, N. Mizorogi, K. Kobayashi, S. Nagase, T. Kato, N. Ban, H. Nakajima, Y. Watanabe, *J. Am. Chem. Soc.* **2005**, *127*, 12190–12191.

[16] M. Yamada, T. Nakahodo, T. Wakahara, T. Tsuchiya, Y. Maeda, T. Akasaka, M. Kako, K. Yoza, E. Horn, N. Mizorogi, K. Kobayashi, S. Nagase, *J. Am. Chem. Soc.* **2005**, *127*, 14570–14571.

[17] M. Yamada, T. Wakahara, T. Nakahodo, T. Tsuchiya, Y. Maeda, T. Akasaka, K. Yoza, E. Horn, N. Mizorogi, S. Nagase, *J. Am. Chem. Soc.* **2006**, *128*, 1402–1403.

[18] a) Reported for the first time by L. Echegoyen in the 207th Electrochemical Society Meeting, May 15–May 20, Quebec City, Canada, **2005**. b) C. M. Cardona, B. Elliott, L. Echegoyen, *J. Am. Chem. Soc.* **2006**, *128*, 6480–6485.

[19] T. Cai, C. Slebodnick, L. Xu, K. Harich, T. E. Glass, C. Chancellor, J. C. Fettinger, M. M. Olmstead, A. L. Balch, H. W. Gibson, H. C. Dorn, *J. Am. Chem. Soc.* **2006**, *128*, 6486–6492.

[20] We located a concerted TS that connects reactants and products directly. The concerted reaction is found to be very asynchronous: the two C···C distances in the TS are very different. The barriers are also very small: that for the 6:5 adduct is even slightly smaller than $TS_{1,56}$ (3.1 versus 3.9 kcal mol^{-1}). We have also computed the triplet state of I_{66} and have found it to be much destabilized (22 kcal mol^{-1} higher than the closed-shell singlet). Hence, we infer that a radical mechanism is not likely.

[21] To estimate the energy of $TS_{eclipsed}$, we have constructed a reaction path in which the C4···C2 distance was changed from 3.95 (the value for I'_{56}) to 2.05 Å. The highest energy of that path (+1.8 kcal mol^{-1}) is our best estimation of $E(TS_{eclipsed})$ (see the Supporting Information). The energy of TS_{66to56} (−4.7 kcal mol^{-1}) has been roughly estimated by adding 0.8 kcal mol^{-1},

 © 2006 Wiley-VCH Verlag GmbH & Co. KGaA, Weinheim

our estimation for the barrier of the second step of the reaction I_{66} to P_{66}, to $E(I'_{56})$.
[22] ADF 2004.01, Department of Theoretical Chemistry, Vrije Universiteit, Amsterdam.
[23] G. T. te Velde, F. M. Bickelhaupt, E. J. Baerends, C. F. Guerra, S. J. A. Van Gisbergen, J. G. Snijders, T. Ziegler, *J. Comput. Chem.* **2001**, *22*, 931 – 967.
[24] A. D. Becke, *Phys. Rev. A* **1988**, *38*, 3098 – 3100.
[25] J. P. Perdew, *Phys. Rev. B* **1986**, *33*, 8822 – 8824.
[26] M. Iannuzzi, A. Laio, M. Parrinello, *Phys. Rev. Lett.* **2003**, *90*, 238302.
[27] CPMD v3.9, Copyright IBM Corp. 1990 – 2001, Copyright MPI für Festkörperforschung Stuttgart 1997 – 2001.

 © 2006 Wiley-VCH Verlag GmbH & Co. KGaA, Weinheim

C–H Activation

DOI: 10.1002/anie.200603582

A New Catalytic Route for the Activation of sp-Hybridized Carbon–Hydrogen Bonds**

Bogdan Marciniec, Beata Dudziec, and Ireneusz Kownacki*

In the last two decades we have developed a new type of transition-metal (TM)-catalyzed reaction of vinyl-substituted organosilicon compounds with olefins, known as a silylative coupling (SC, or *trans*-silylation; Scheme 1), that is complementary to metathesis. This reaction occurs by cleavage of the =C–H bond of an olefin and the =C–Si bond of a vinylsilane, in contrast to cross-metathesis, which uses the same substrates and also gives the same products (except the *gem*-isomer), by cleavage of the C=C bond. Various TM complexes (i.e. Ru, Rh, Ir, and Co) containing an M–H and M–Si bond initially, or one generated in situ, catalyze this process.[1,2])

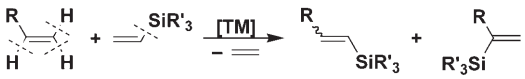

R = alkyl, phenyl, OR, SiR_3, 2-pyrrolidinone, carbazole
R'= alkyl, aryl, alkoxy

Scheme 1. Silylative coupling of olefins with vinylsilanes.

The mechanism for SC catalyzed by ruthenium complexes elucidated by Wakatsuki[3] and by us[4] involves insertion of a vinylsilane into the M–H bond and β-Si transfer to the metal, with elimination of ethylene, to generate M–Si species, then insertion of the alkene into the M–Si bond and β-H transfer to the metal, with elimination of a substituted vinylsilane as product, and regeneration of the catalyst.

The SC process under optimum conditions has become an excellent synthetic tool for the regio- and stereoselective synthesis of functionalized vinylsilicon compounds such as (*E*)-*N*-(silyl)vinylcarbazole,[5a] amides,[5b] 1-silyl-1-(boryl)-ethenes,[5c] functionalized cyclosiloxanes, cyclosilazanes,[5d] and silsesquioxanes[5e] as well as macromolecular organosilicon compounds containing (*E*)-1,2-bis(silyl)fragments.[6] These compounds can be used as synthetic reagents for organic synthesis and as materials precursors and are difficult to prepare by other TM-catalyzed reactions such as cross-metathesis. The *trans*-silylation reaction has recently been extended to other metalloids such as boron[7] and germanium.[8]

The catalytic addition of the =C–H bond in aromatic ketones, esters, and amines to vinylsilanes has been reported by Murai et al. to yield compounds of the type $ArCH_2CH_2SiR_3$.[9a,b] These authors have also reported a $[Ru_3(CO)_{12}]$-catalyzed coupling (silylation) of 3-acetylthiophene with trimethylvinylsilane that gives 3-acetyl-2-(trimethylsilyl)thiophene (64%, toluene, 20 h, 115 °C),[9c] and Park et al. have reported a rhodium-catalyzed silylation of benzyl alcohol with trimethylvinylsilane that yields a siloxy derivative (93%, toluene, 2 h, 200 °C).[9d] Ethylene was produced in both reactions as a secondary product. In view of all the results cited above it is worth emphasizing that the vinylsilicon compounds function as a silylating agent and a hydrogen acceptor.

Herein we present a new catalytic reaction that involves a coupling of terminal alkynes with vinylsilanes of the general formula $H_2C{=}CHSiR_3$ (where SiR_3 is $SiMe_2Ph$, $Si(OEt)_3$, $SiMe(OSiMe_3)_2$, and $SiMe_2(OSiMe_3)$ as well as divinyltetramethyldisiloxane and divinyltetramethyldisilazane), which, by analogy, can be considered a silylative coupling of alkynes and which proceeds in the presence of complexes containing [Ru]–H and/or [Ru]–Si bonds, such as $[RuHCl(CO)(PCy_3)_2]$ (**I**, Cy = cyclohexyl), $[RuHCl(CO)(iPr_3)_2]$ (**II**), $[RuH(CO)(MeCN)_2(PCy_3)_2][BF_4]$ (**III**), $[Ru(SiMe_3)Cl(CO)(PPh_3)_2]$ (**IV**),[10] and $[RuHCl(CO)(PPh_3)_3]$ (**V**), and leads to the evolution of ethylene and formation of the silyl-substituted derivatives (Scheme 2). Interestingly, the hexacoordinate complex **V** appears to be inactive in this reaction.

Substituted alkynylsilanes are commonly used as alkynylating agents in the synthesis of organic and natural prod-

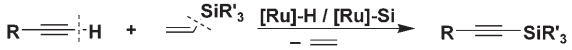

R = alkyl, cycloalkyl, trialkylsilyl
R' = alkyl, aryl, alkoxyl

Scheme 2. Coupling of terminal alkynes with vinylsilanes.

[*] Prof. Dr. B. Marciniec, B. Dudziec, Dr. I. Kownacki
Department of Organometallic Chemistry
Faculty of Chemistry, Adam Mickiewicz University
Grunwaldzka 6, 60-780 Poznan (Poland)
Fax: (+48) 618-291-508
E-mail: Bogdan.Marciniec@amu.edu.pl

[**] Financial support from the Ministry of Science and Higher Education (Poland) (grants 3T09A 145 26 and PBZ-KBN 118/T09/17) is gratefully acknowledged.

Supporting Information for this article is available on the WWW under http://www.angewandte.org or from the author.

WILEY InterScience DISCOVER SOMETHING GREAT
© 2006 Wiley-VCH Verlag GmbH & Co. KGaA, Weinheim

ucts[11] as well as precursors of optoelectronic materials.[12] They can be prepared by classical stoichiometric routes from organometallic reagents and, more recently, by metal-complex-catalyzed silylation of terminal alkynes with aminosilanes[13a] and chlorosilanes,[13b] dehydrogenative silylation with hydrosilanes,[13c] or other transformations of silyl-substituted alkynes.[13d] These reactions have been reviewed recently.[14]

The use of ruthenium catalysts **I**–**IV** for silylative cross-coupling of the selected alkynes, that is, alkyl, cycloalkyl, and silyl ethynes, gives, under the optimum conditions, the respective alkynylsilane, alkynylvinyltetramethyldisiloxane, and alkynylvinyltetramethyldisilazane as the main or exclusive product (see Tables 1 and 2), in some cases accompanied by the products of homo-coupling of the vinylsilicon compounds used in excess. The turnover frequency (TOF) parameters are of the order of 16–27 h^{-1} (Table 1).

All the products were detected by GC and GC-MS methods and identified by ^{1}H, ^{13}C, and ^{29}Si NMR spectroscopy. The reaction was examined in the presence of catalysts **I**–**V** in an open system in toluene, or without solvent, under a gentle stream of argon, although when volatile 3,3-dimethyl-1-butyne was used the reaction was conducted in a closed system. The equimolar reaction of vinylsilanes with alkynes yields some enynes as a result of the dimerization of alkynes, therefore an excess of vinylsilane (two- to fivefold) is necessary to prevent the formation of these enynes. Silylation of 1-ethynyl-1-(trimethylsiloxy)cyclohexane with divinylsiloxane and divinylsilazane, even with a 6- or 10-fold excess of vinylsilicon compound, yields exclusively the monoalkynylvinyldisiloxane and -disilazane with high yield and selectivity (Table 2), accompanied by the homocoupling product of the vinylsilicon substrates. It is noteworthy that, under the conditions examined, the silylation of phenylacetylene with vinylsilane does not occur (only traces).

To explain the mechanism of this new alkyne transformation a series of experiments involving the equimolar reactions of $[Ru(SiMe_3)Cl(CO)(PPh_3)_2]$ (**IV**) with phenylacetylene and silylacetylene were carried out to yield the respective main insertion products (identified by ^{1}H NMR spectroscopy and GC-MS) according to Scheme 3. The spectra taken at various temperatures between −20 and +30 °C unexpectedly show an important difference in the reaction of **IV** with the given acetylenes. Thus, while the reaction with phenylacetylene occurs immediately, even at −20 °C, to form the vinylenephenylruthenium complex **VI** and no [Ru]–H is detected (see Figure 1), the same process with silylacetylene at low temperatures allows the formation of a [Ru]–H complex to be detected, as confirmed by the appearance of a doublet of triplets at $\delta = -6.63$ ppm ($J_{H,P} = 105.2$, $J_{H,P} = 24.3$ Hz), which at room temperature yields the vinylenesilylruthenium analogue **VII** (see Figure 2).

The [Ru]–H complex is apparently produced in both experiments at elevated temperatures (similar to the insertion of olefins into a Ru–Si bond[3,4]). This complex is active (in the absence of vinylsilane) for the hydrogenation of acetylenes as well as for transformations of ruthenium complexes into

Table 1: Silylative coupling of terminal alkynes with vinylsilanes.

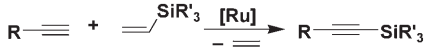

R	R'_3	Cat. (Temp. [°C])	Cat./alkyne/vinylsilane	Conversion [%] (TOF [h^{-1}])	Yield [%]
*t*Bu[a]	Me_2Ph	**I** (100)	10^{-2}:1:5[b]	100	100
		I (110)	10^{-2}:1:3.15[c]	93 (21)	88[d]
		II (100)	10^{-2}:1:2[c]	93	90[e]
$SiEt_3$		**I** (120)	10^{-2}:1:2[c]	100 (27)	94[d]
$SiEt_3$		**I** (100)	10^{-2}:1:4[b]	43	43
$SiEt_3$		**I** (120)	5×10^{-3}:1:2[c]	63	63
$SiEt_3$		**IV** (120)	10^{-2}:1:2[c]	35	35
$SiEt_3$		**IV** (120)	2×10^{-2}:1:5[f]	67	67[e]
Si(*t*Bu)Me_2		**I** (120)	10^{-2}:1:2.3[f]	70	70[d]
*t*Bu[a]	$(OEt)_3$	**I** (100)	10^{-2}:1:10[g]	92	92
		I (110)	10^{-2}:1:4[c]	100 (16)	92[d]
		III (120)	10^{-2}:1:5[h]	100	100
		II (110)	10^{-2}:1:4[b]	50	50
$SiEt_3$	**I** (120)	10^{-2}:1:3.5[c]	90	74[d,e]	
	$Me(OSiMe_3)_2$	**I** (120)	10^{-2}:1:4[c]	100	91[d,e]
	$Me_2(OSiMe_3)$	**I** (120)	10^{-2}:1:4[c]	100	90[d,e]

[a] Closed reaction vessel. [b] CH_2Cl_2 (0.5 M), closed reaction vessel. [c] Toluene (0.5 M). [d] Yield of isolated product. [e] Accompanied by traces of vinyl-substituted silane homo-coupling product. Initial TOF measured after 0.5 h of reaction and expressed in moles of alkyne per mole of Ru per hour. Reaction time: 24 h. Yields were determined by GC analysis. [f] Toluene (0.6 M). [g] Toluene (0.35 M). [h] Without solvent.

Table 2: Silylative coupling of terminal alkynes with divinyldisiloxane and -disilazane.

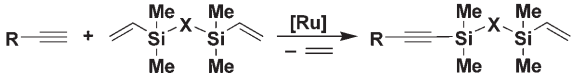

R	X	Cat./alkyne/divinylsilicon compound	Conversion [%]	Yield [%]
$SiEt_3$	O	2×10^{-2}:1:10[a]	100	100[b]
	O	10^{-2}:1:2[c]	52	52[d]
	NH	10^{-2}:1:2[c]	45	45[d]
	NH	10^{-2}:1:6[c]	64	64[b]
	NH	2×10^{-2}:1:10[a]	68	68[b]
	O	10^{-2}:1:5[e]	95	95[b]
	O	2×10^{-2}:1:10[a]	100	100[b]
	O	10^{-2}:1:2[c]	94	94[d]
	NH	10^{-2}:1:6[c]	97	97[d]
	NH	2×10^{-2}:1:10[a]	100	87[d,f]

[a] Toluene (0.3 M). [b] Accompanied by divinylsilicon compound homo-coupling products. [c] Toluene (0.6 M). [d] Accompanied by traces of divinylsilicon compound homo-coupling products. [e] Toluene (0.5 M). [f] Yield of isolated product. Reaction time: 24 h. Yields were determined by GC analysis. Cat.: $[RuHCl(CO)(PCy_3)_2]$ (**I**); temperature: 120 °C.

 © 2006 Wiley-VCH Verlag GmbH & Co. KGaA, Weinheim

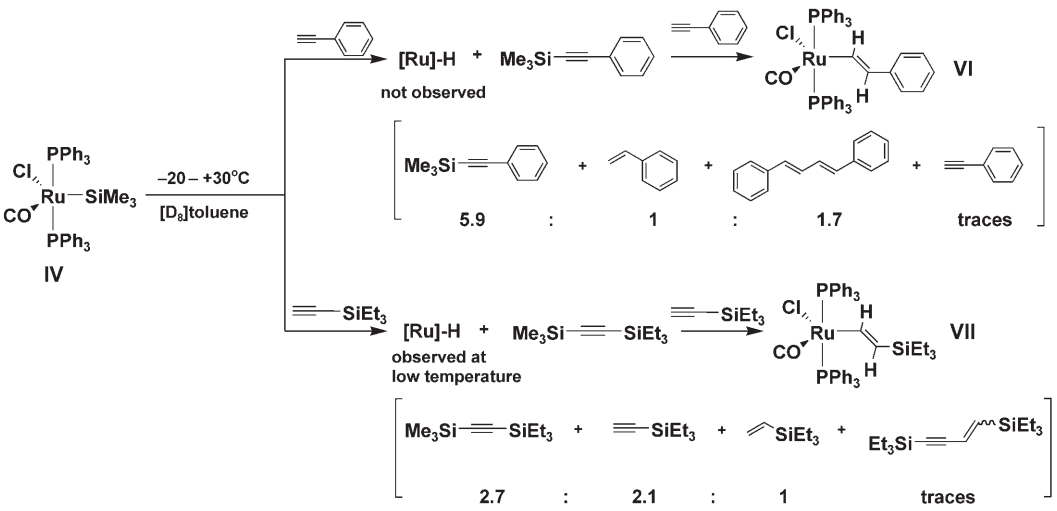

Scheme 3. Equimolar reactions of **IV** with acetylenes.

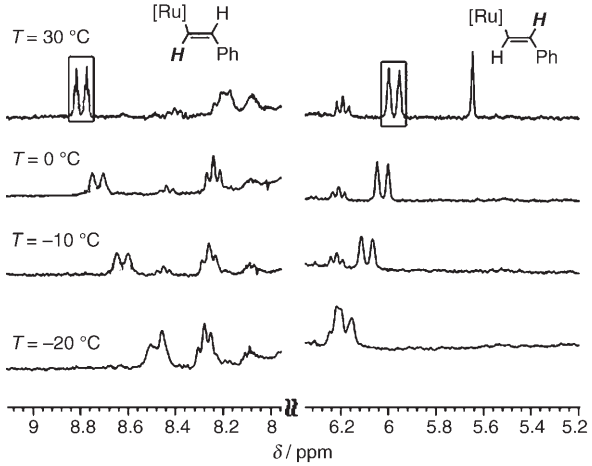

Figure 1. Temperature dependence of the ^{1}H NMR spectra of the reaction of **IV** with phenylacetylene. The boxed signals correspond to those of the vinyl hydrogen atoms shown in italics.

clusters. Acetylene dimerization and co-dimerization with styrene is also observed as a result of the well-known catalysis of these reactions by ruthenium complexes.[15]

In separate experiments, we monitored the equimolar reaction of the hexacoordinate complex **V** with silylacetylene and phenylacetylene at room temperature. These reactions lead to the formation of vinylene complexes **VI** and **VII**, both of which were isolated. The evidence for their vinyleneruthenium structure comes from the ^{1}H NMR spectra of the isolated complexes, in which two doublets of triplets for the vinylene signals appear at $\delta = 8.93$ ($J_{H,H} = 13.3$, $J_{H,P} = 2.3$ Hz) and 6.09 ppm ($J_{H,H} = 13.2$, $J_{H,P} = 2.0$ Hz; phenylvinylene) and $\delta = 8.84$ ($J_{H,H} = 13.0$, $J_{H,P} = 1.7$ Hz) and 5.70 ppm ($J_{H,H} = 13.0$, $J_{H,P} = 2.1$ Hz; triethylsilylvinylene). The NMR spectroscopic data for both isolated vinylene complexes are identical to those reported in references [16,17]. The above experiments provide evidence that the insertion of acetylene into the Ru–Si bond occurs in a similar manner to the insertion of alkenes.[3,4b] Under stoichiometric conditions (i.e. in the absence of vinylsilicon compounds) the [Ru]–H complex formed reacts with acetylenes to give dimers and hydrogenated products as well as vinyleneruthenium complexes,

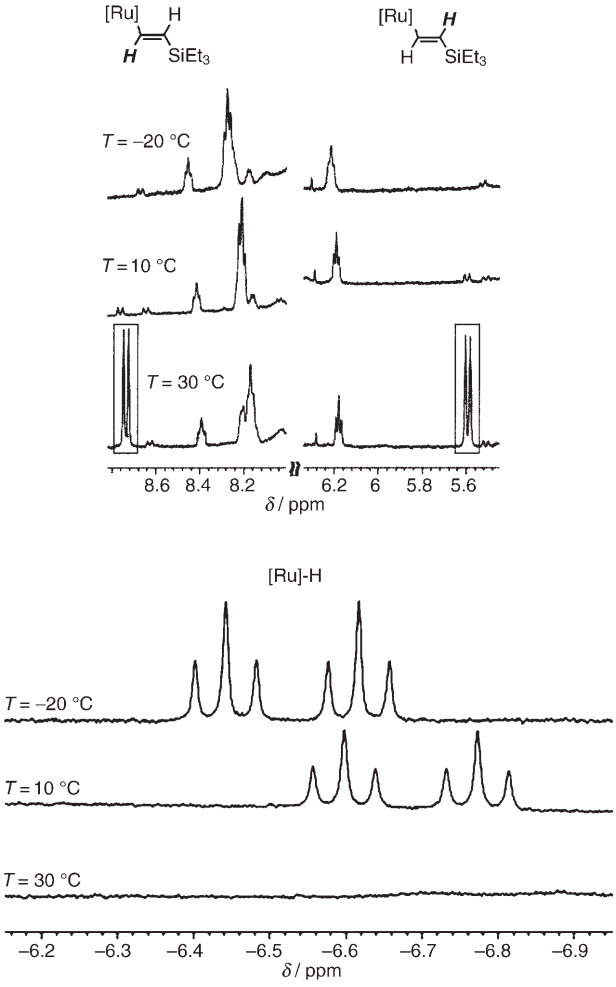

Figure 2. Temperature dependence of the ^{1}H NMR spectra of the reaction of **IV** with $HC \equiv CSiEt_3$. The boxed signals correspond to those of the vinyl hydrogen atoms shown in italics.

 © 2006 Wiley-VCH Verlag GmbH & Co. KGaA, Weinheim

whereas under the conditions of catalysis (80–120 °C) vinylsilane, particularly if added in excess, reacts preferentially with the ruthenium hydride complex according to a well-documented process to yield a [Ru]–Si complex (see, for example, references [3,4]) and ethylene (see Scheme 4),

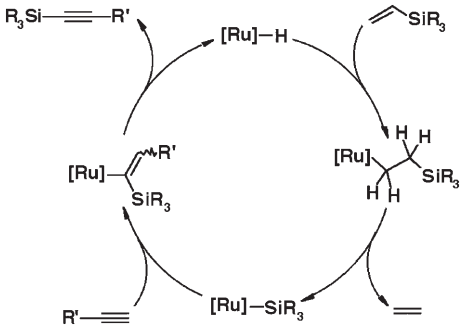

Scheme 4. Mechanism of the silylative coupling of alkynes with vinylsilicon compounds.

which explains the catalytic activity of the [Ru]–H/[Ru]–Si systems in the SC of alkynes. However, in the case of phenylacetylene, the ^{1}H NMR spectra of the equimolar experiments indicate that its reaction with the [Ru]–H complex to form the vinylene complex occurs much faster than with the [Ru]–Si moiety and therefore we do not observe the silylation of phenylacetylene under the conditions studied.

The results of the above experiments allow us to propose a mechanism for the reaction of vinylsilicon compounds with substituted acetylenes. The SC of alkynes with vinylsilane involves insertion of the alkyne into the [Ru]–Si bond with subsequent β-H elimination to give silyl-substituted ethyne and the well-known insertion of a vinylsilicon compound into the [Ru]–H bond, and subsequent β-Si elimination of ethylene. Dissociation of a phosphane (observed by GC-MS) from the pentacoordinate [Ru] complexes **I**–**IV** and the inactivity of the hexacoordinate [Ru] species **V** under these reaction conditions suggest that only four-coordinate ruthenium complexes are active catalysts for this process (Scheme 4). This general mechanism is demonstrated by the stoichiometric study of the insertion of a vinylsilicon compound into the ruthenium hydride bond and the above-described insertion of acetylene into the [Ru]–Si bond.

In conclusion, we have shown that the general reaction reported herein opens up a new catalytic route for the activation of ≡C–H bonds and, in combination with the well-known activation of =C–Si bonds, is an efficient method for the selective synthesis of a variety of molecular compounds with an acetylene functionality. The silylalkynyl derivatives synthesized in this manner could play a very important role as organometallic reagents in organic synthesis.[11a]

Experimental Section

General procedure: All experiments were performed under dry and oxygen-free argon using standard Schlenk techniques for the organometallic synthesis.

See Supporting Information for full experimental procedures and the ^{1}H, ^{13}C, and ^{29}Si NMR spectra, the GC-MS traces, and the elemental analysis data of the products.

Received: September 1, 2006

Keywords: alkynes · C–H activation · homogeneous catalysis · ruthenium · silanes

[1] a) B. Marciniec, C. Pietraszuk in *Handbook On Metathesis* (Ed.: R. H. Grubbs), Wiley, Weinheim, **2003**, ch. 2.13, and references therein; b) B. Marciniec, C. Pietraszuk, *Curr. Org. Chem.* **2003**, *7*, 691–735, and references therein.

[2] B. Marciniec, *Coord. Chem. Rev.* **2005**, *249*, 2374–2390, and references therein.

[3] Y. Wakatsuki, H. Yamazaki, M. Nakano, Y. Yamamoto, *J. Chem. Soc., Chem. Commun.* **1991**, 703–704.

[4] a) B. Marciniec, C. Pietraszuk, *Organometallics* **1997**, *16*, 4320–4326; b) B. Marciniec, C. Pietraszuk, *J. Chem. Soc., Chem. Commun.* **1995**, 2003–2004.

[5] a) B. Marciniec, M. Majchrzak, W. Prukała, M. Kubicki, D. Chadyniak, *J. Org. Chem.* **2005**, *70*, 8550–8555; b) B. Marciniec, D. Chadyniak, S. Krompiec, *Tetrahedron Lett.* **2004**, *45*, 4065–4068; c) M. Jankowska, B. Marciniec, C. Pietraszuk, J. Cytarska, M. Zaidlewicz, *Tetrahedron Lett.* **2004**, *45*, 6615–6618; d) Y. Itami, B. Marciniec, M. Kubicki, *Organometallics* **2003**, *22*, 3717–3722; e) Y. Itami, B. Marciniec, M. Kubicki, *Chem. Eur. J.* **2004**, *10*, 1239–1248.

[6] a) B. Marciniec, E. Małecka, *Macromol. Rapid Commun.* **1999**, *20*, 475–479; b) M. Majchrzak, Y. Itami, B. Marciniec, P. Pawluć, *Tetrahedron Lett.* **2000**, *41*, 10303–10307; c) B. Marciniec, E. Małecka, M. Ścibiorek, *Macromolecules* **2003**, *36*, 5545–5550; d) M. Majchrzak, B. Marciniec, Y. Itami, *Adv. Synth. Catal.* **2005**, *347*, 1285–1294.

[7] B. Marciniec, M. Jankowska, C. Pietraszuk, *Chem. Commun.* **2005**, 663–665.

[8] B. Marciniec, H. Ławicka, M. Majchrzak, M. Kubicki, I. Kownacki, *Chem. Eur. J.* **2006**, *12*, 244–250.

[9] a) F. Kakiuchi, N. Chatani in *Topics in Organometallic Chemistry, Vol. 11, Ruthenium Catalysts and Fine Chemistry* (Eds.: C. Bruneau, P. H. Dixneuf), Springer, Berlin, **2004**, pp. 45–79, and references therein; b) S. Murai, F. Kakiuchi, S. Sekine, Y. Tanaka, A. Kamatani, M. Sonoda, N. Chatani, *Nature* **1993**, *366*, 529–531; c) F. Kakiuchi, M. Matsumoto, M. Sonoda, T. Fukuyama, N. Chatani, S. Murai, N. Furukawa, Y. Seki, *Chem. Lett.* **2000**, *29*, 750–751; d) J. W. Park, H. J. Chang, C. H. Jun, *Synlett* **2006**, 771–775.

[10] B. Marciniec, B. Dudziec, K. Szubert, Polish Patent P-380422, **2006**.

[11] a) T. W. Greene, P. G. M. Wuts, *Protective Groups in Organic Synthesis*, Wiley, New York, **1999**; b) J. E. Casida, *J. Agric. Food Chem.* **1991**, *39*, 1335–1341; c) J. C. Anderson, R. H. Munday, *J. Org. Chem.* **2004**, *69*, 8971–8974.

[12] G. Brizius, U. H. F. Bunz, *Org. Lett.* **2002**, *4*, 2829–2831.

[13] a) A. A. Anreev, V. V. Konshin, N. V. Komarov, M. Rubin, C. Brouwer, V. Gevorgyan, *Org. Lett.* **2004**, *6*, 421–424; b) L.-M. Yang, L.-F. Huang, T.-Y. Luh, *Org. Lett.* **2004**, *6*, 1461–1463; c) R. Shimizu, T. Fuchikami, *Tetrahedron Lett.* **2000**, *41*, 907–910; d) A. Fürstner, C. Mathes, *Org. Lett.* **2001**, *3*, 221–223.

[14] M. D. Fletcher in *Comprehensive Organic Functional Group Transformations, Vol. 2* (Eds.: A. R. Katritzky, R. J. K. Taylor), Elsevier, Oxford, **2005**, pp. 1181–1189, and references therein.

[15] a) C. Bruneau in *Topics in Organometallic Chemistry Vol. 11* (Eds.: C. Bruneau, P. H. Dixneuf), Springer, Berlin, **2004**, pp. 138–141, and references therein; b) C. Slugovc, K. Mereiter, E. Zobetz, R. Schmidt, K. Kirchner, *Organometallics* **1996**, *15*,

 © 2006 Wiley-VCH Verlag GmbH & Co. KGaA, Weinheim

5275 – 5277; c) C. Bianchini, M. Peruzzini, F. Zanobini, P. Frediani, A. Albinati, *J. Am. Chem. Soc.* **1991**, *113*, 5453 – 5454; d) C. Bianchini, P. Frediani, D. Masi, M. Peruzzini, F. Zanobini, *Organometallics* **1994**, *13*, 4616 – 4632; e) C. S. Yi, N. Liu, *Organometallics* **1996**, *15*, 3968 – 3971; f) Y. Wakatsuki, H. Yamazaki, N. Kumegawa, T. Satoh, J. Y. Satoh, *J. Am. Chem. Soc.* **1991**, *113*, 9604 – 9610; g) Y. Wakatsuki, H. Yamazaki, N. Kumegawa, P. S. Johar, *Bull. Chem. Soc. Jpn.* **1993**, *66*, 987 – 989.

[16] M. R. Torres, A. Vegas, A. Santos, *J. Organomet. Chem.* **1986**, *309*, 169 – 177.

[17] S. M. Maddock, C. E. F. Rickard, W. P. Roper, L. J. Wright, *Organometallics* **1996**, *15*, 1793 – 1803.

 © 2006 Wiley-VCH Verlag GmbH & Co. KGaA, Weinheim

Polymerization

DOI: 10.1002/anie.200603450

Cationic Rare-Earth Polyhydrido Complexes: Synthesis, Structure, and Catalytic Activity for the *cis*-1,4-Selective Polymerization of 1,3-Cyclohexadiene**

*Xiaofang Li, Jens Baldamus, Masayoshi Nishiura, Olivier Tardif, and Zhaomin Hou**

Metal hydrides are fundamental components in a wide range of stoichiometric and catalytic reactions. Their importance in modern inorganic and organic chemistry cannot be overemphasized. Rare-earth (Group 3 and lanthanide) hydrides are among the most active metal–hydride complexes. Together with their alkyl analogues, metal–hydride complexes of the rare-earth metals have occupied an especially important position in the development of the organometallic chemistry of the rare-earth elements. Generally, cationic complexes differ in their structure and reactivity from their neutral analogues. However, although a large number of metal–hydride complexes of the rare-earth metals have been synthesized and structurally characterized,[1] cationic complexes of this type have not been reported previously.

[*] Dr. X. Li, J. Baldamus, Dr. M. Nishiura, Dr. O. Tardif, Prof. Dr. Z. Hou
Organometallic Chemistry Laboratory
RIKEN (The Institute of Physical and Chemical Research)
Hirosawa 2-1, Wako, Saitama 351-0198 (Japan)
and
PRESTO
Japan Science and Technology Agency (JST) (Japan)
Fax: (+81) 48-462-4665
E-mail: houz@riken.jp

[**] This work was partly supported by Grant-in-Aid for Scientific Research from the Ministry of Education, Culture, Sports, Science, and Technology of Japan.

Supporting information for this article is available on the WWW under http://www.angewandte.org or from the author.

We recently reported the synthesis and hydrogenation reactions of a new class of polynuclear rare-earth polyhydrido complexes exemplified by $[Y_4(C_5Me_4SiMe_3)_4H_8(thf)_n]$ (**1a**: $n=0$, **1b**: $n=1$, **1c**: $n=2$).[2,3] In view of the unique reactivity of these hydride clusters[2b–e,g] and the excellent olefin-polymerization activity of the related cationic rare-earth–alkyl complexes,[4,5] we became interested in the cationic hydrido species generated from these rare-earth–hydride clusters.

Herein, we report the synthesis, structural characterization, and olefin-polymerization catalysis of the cationic hydride complexes obtained from **1a–c** (Scheme 1) and related rare-earth–hydride clusters. These cationic polyhydrido complexes not only are the first cationic rare-earth–hydride complexes but also show excellent regio- and stereoselectivity for the polymerization of 1,3-cyclohexadiene (CHD), which afforded, for the first time, soluble crystalline *cis*-1,4-linked poly(CHD) (1,4 selectivity: 100%; *cis* selectivity: 99%). For comparison, the reaction of the neutral hydride cluster, **1b**, with CHD is also described. This reaction leads to the formation of a structurally well-defined CHD insertion product instead of the polymerization of CHD. Various metal catalysts and initiators were reported previously for the polymerization of CHD, but most yielded a mixture of 1,4- and 1,2-poly(CHD)[6–10] or insoluble polymers,[10,11] and none was reported to produce pure soluble crystalline *cis*-1,4-linked poly(CHD).

Reaction of the thf-free octahydrido yttrium cluster **1a**[2b,f] with one equivalent of $[Ph_3C][B(C_6F_5)_4]$ in chlorobenzene or toluene at 25°C gave the cationic heptahydrido complex **2a** and Ph_3CH (Scheme 1). In contrast to the neutral complex **1a**, which shows a good solubility in most organic solvents, the cationic complex **2a** was only slightly soluble in benzene and toluene, and almost insoluble in hexane. Recrystallization of **2a** from chlorobenzene/hexane afforded colorless single

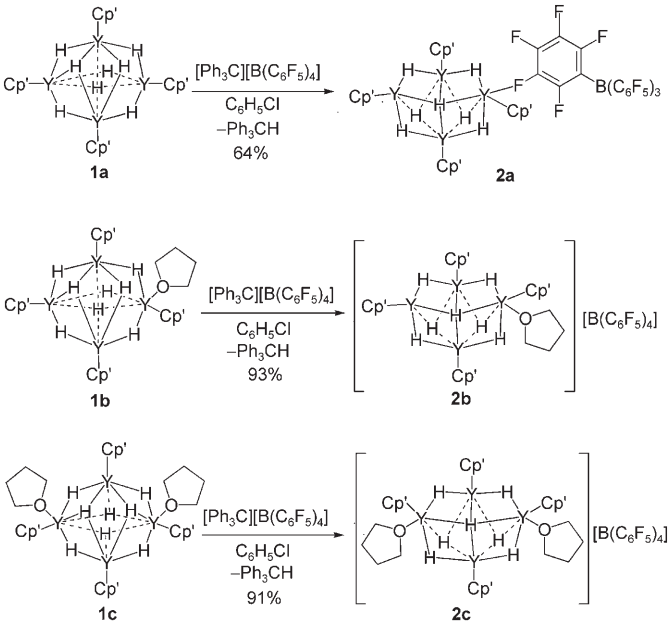

Scheme 1. Synthesis of cationic yttrium–hydride clusters. Cp′: $C_5Me_4SiMe_3$.

InterScience
© 2006 Wiley-VCH Verlag GmbH & Co. KGaA, Weinheim

crystals suitable for an X-ray diffraction study. X-ray analysis revealed that **2a** has a distorted tetrahedral Y_4 frame, which is bound by seven hydride ligands, one in μ_4, two in μ_3, and four in μ_2 bonding modes (Figure 1 and Table 1). The Y–(μ_4-H) bonds in **2a** with lengths from 2.23(6) Å (Y1–H1) to 2.43(6) Å (Y3–H1) and an average value of 2.36(6) Å are significantly longer than those in **1a** (average 2.17(2) Å),[2f] as a result of more distortion of the Y_4 frame in **2a** than in **1a** from a normal tetrahedron. The lengths of the Y–(μ_3-H) and Y–(μ_2-H) bonds in **2a** are, however, similar to those in **1a** (Table 1). A direct bonding interaction between the $[(C_5Me_4SiMe_3)_4Y_4H_7]^+$ ion and the $[B(C_6F_5)_4]^-$ ion through a Y–F bond (Y1–F4: 2.405(4) Å) was also found in **2a**.[12]

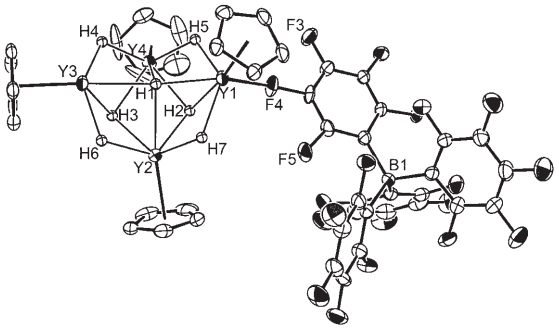

Figure 1. ORTEP drawing of **2a** with 30% thermal ellipsoids. The Me_3Si and Me groups in $C_5Me_4SiMe_3$ are omitted for clarity.

Table 1: Summary of selected bond lengths (Å) of neutral and cationic yttrium–hydride clusters.[13] Cp′: $C_5Me_4SiMe_3$.

	1a[2f]	**1b**[2a,b]	**1c**[2a,3b]	**2a**	**2c**	**3**
Cp′–Y_{avg}	2.599(3)	2.624(4)	2.669(3)	2.583(10)	2.614(5)	2.626(4)
Y–(μ_4-H)$_{avg}$	2.17(2)	2.20(4)	–	2.36(6)	2.45(3)	2.29(3)
Y–(μ_3-H)$_{avg}$	2.39(2)	2.27(3)	2.24(3)	2.28(6)	2.23(3)	2.26(3)
Y–(μ_2-H)$_{avg}$	2.17(3)	2.16(3)	2.12(3)	2.08(6)	2.07(2)	2.10(3)
Y–O_{avg}	–	2.403(3)	2.407(2)	–	2.304(3)	–
Y1–F4	–	–	–	2.405(4)	–	–

The ^{1}H NMR spectrum of **2a** in C_6D_5Cl at room temperature showed a broad singlet at 4.62 ppm for the seven hydride ligands and one set of signals for the four $C_5Me_4SiMe_3$ ligands (see the Supporting Information). Similarly, the four C_6F_5 groups in the borate ion $[B(C_6F_5)_4]^-$ also showed one set of ^{19}F NMR signals. These results suggest that **2a** is highly fluxional in solution, probably because of the rapid dissociation and coordination of $[B(C_6F_5)_4]^-$ ions or solvent molecules. This fluxionality was not fixed even at −40 °C in C_6D_5Cl, which was shown by the ^{1}H and ^{19}F NMR spectra.

A similar reaction of the mono-thf complex, **1b**,[2a,b] with $[Ph_3C][B(C_6F_5)_4]$ in chlorobenzene afforded analogously complex **2b** (Scheme 1). In contrast to the observation made for **2a**, the four $C_5Me_4SiMe_3$ groups in **2b** gave four sets of signals and the seven hydride ligands showed a broad singlet (1 μ_4-H) at 1.45 ppm, a pair of quartets (2 μ_3-H) at 3.24 ($J_{Y,H}$ = 21.0 Hz) and 3.53 ppm ($J_{Y,H}$ = 25.2 Hz), and a pair of triplets (4 μ_2-H) at 4.98 ($J_{Y,H}$ = 37.5 Hz) and 5.40 ppm ($J_{Y,H}$ = 36.9 Hz) in the corresponding ^{1}H NMR spectrum in C_6D_5Cl at room temperature, which suggests that the unsymmetrical $\{Y_4H_7(thf)\}$ core in **2b** is rigid. The four C_6F_5 groups in the borate unit, however, showed one set of ^{19}F NMR signals, which indicates that the $[B(C_6F_5)_4]^-$ ion of **2b** does not have a strong (or direct bonding) interaction with the cation. Attempts to obtain a single crystal of the mono-thf complex **2b** were not successful: Recrystallization of **2b** from THF yielded colorless single crystals of the bis-thf adduct **2c**. Alternatively, **2c** could be made by reaction of the bis-thf neutral complex **1c**[2a,3b] with $[Ph_3C][B(C_6F_5)_4]$ or by reaction of **1b** with $[Ph_3C][B(C_6F_5)_4]$ in THF (Scheme 1).

An X-ray analysis established that **2c** has a butterfly-like $\{Y_4\}$ core bound by one μ_4-, two μ_3-, and four μ_2-hydride ligands (Figure 2), which contrasts with the structure of the neutral precursor **1c**. This complex adopts a tetrahedral $\{Y_4H_8\}$ core structure with four μ_3- and four μ_2-hydride ligands.[14] The interatomic distance between Y1 and Y2 in **2c** (5.2879(6) Å) is much longer than the other Y···Y interatomic distances (3.4947(6)–3.5539(5) Å), and also much longer than the Y···Y separations found in **1c** (3.3287(5)–3.9220(4) Å).[14] In accordance with the butterfly arrangement of the four Y atoms in **2c**, the Y1–H1 and Y2–H1 bonds are much longer than the Y3–H1 and Y4–H1 bonds (2.68(3) and 2.61(3) versus 2.31(3) Å and 2.21(3) Å), while the Y–(μ_3-H) and Y–(μ_2-H) bond lengths in **2c** are comparable with those in **1c** (Table 1). Because of the greater electron deficiency of the cationic metal centers in **2c**, the Y–Cp′ bonds in **2c** are significantly shorter than those in **1c**, as are the Y–O(thf) separations (Table 1). No direct bonding interaction between the $[(C_5Me_4SiMe_3)_4Y_4H_7(thf)_2]^+$ ion and the $[B(C_6F_5)_4]^-$ ion was observed.

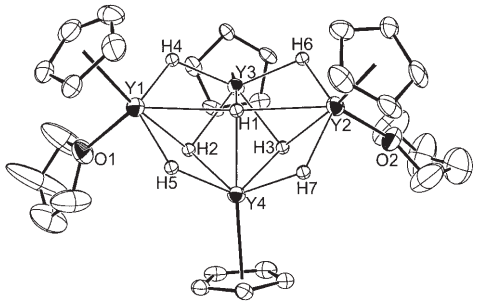

Figure 2. ORTEP drawing of **2c** with 30% thermal ellipsoids. The Me_3Si and Me groups in $C_5Me_4SiMe_3$, hydrogen atoms in THF, and the $[B(C_6F_5)_4]^-$ ion are omitted for clarity.

The $\{Y_4H_7(thf)_2\}$ core in **2c** showed a similarly high rigidity in solution as that in **2b**. Signals corresponding to μ_4-H, μ_3-H, and μ_2-H ligands could be distinguished at 2.83 ppm (br s), 3.14 ppm (br m), and 5.41 ppm (dd, $J_{Y,H}$ = 39.6, 36.8 Hz), respectively, in the room-temperature NMR spectrum of **2b** in C_6D_5Cl. The four $C_5Me_4SiMe_3$ groups showed two sets of ^{1}H NMR signals, while the four C_6F_5 groups in the

 © 2006 Wiley-VCH Verlag GmbH & Co. KGaA, Weinheim

borate unit gave one set of ^{19}F NMR signals. These results are consistent with the crystal structure of **2c**.

To the best of our knowledge, complexes **2a–c** are the first examples of cationic rare-earth–hydride complexes. The thf-free cationic complex **2a** and its mono-thf adduct **2b** showed very high activity for the polymerization of ethylene (ca. 10^3 kg of polyethylene per mol of Y, h, and atm) and syndiospecific polymerization of styrene (ca. 10 kg of polystyrene per mol of Y and h, *rrrr* > 99 %).[15] More remarkably, these cationic complexes showed excellent regio- and stereoselectivity for the polymerization of CHD, which afforded almost pure *cis*-1,4-poly(CHD) (1,4 selectivity: 100 %; *cis* selectivity: 99 %; see the Supporting Information for details). The bis-thf adduct **2c** did not show polymerization activity under the same conditions. Use of an isolated cationic hydrido complex such as **2a** or **2b** is not required for the polymerization of CHD. The cationic species generated in situ by the reaction of **1a** or **1b** with one equivalent of $[Ph_3C][B(C_6F_5)_4]$ also showed similar or higher activity (Table 2, entry 3). As an activator, $[PhMe_2NH][B(C_6F_5)_4]$ (**B**) was also effective, whereas $B(C_6F_5)_3$ (**C**) showed much lower activity under the same conditions (Table 2, entries 4 and 5). In addition to Y, analogous rare-earth metal clusters, such as those of Gd, Dy, Ho, Er, Tm, and Lu,[17] were also effective catalysts for the *cis*-1,4-selective polymerization of CHD under similar conditions (Table 2). Moreover, a significant influence of the ionic radius of the rare-earth metal centers on the catalytic activity was observed, that is, an increase of the ionic radius led to an almost linear increase in the catalytic activity among the metals examined (Figure 3). In contrast, the polymerization initiated by the trityl cation, $[Ph_3C][B(C_6F_5)_4]$ (**A**), alone showed very poor regio- and stereoselectivity and yielded poly(CHD) with mixed 1,2- and 1,4-*cis*/*trans* microstructures (Table 2, entry 1).[18] The activators **B** and **C** alone showed no activity for CHD polymerization under the same conditions.

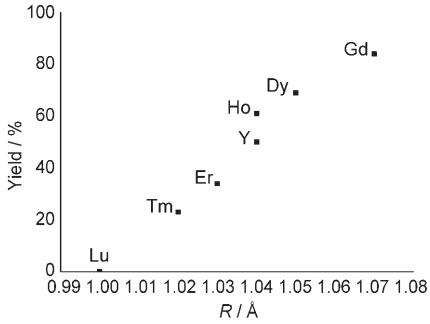

Figure 3. Plot of activity in the CHD polymerization versus the ionic radius, *R*, of the cationic rare-earth polyhydrido complexes.

Table 2: Regio- and stereoselective polymerization of CHD by cationic rare-earth polyhydrido complexes.[a]

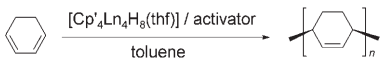

Entry	Ln	*R*[b] [Å]	A[c]	*T* [°C]	Polymer yield		1,4-Poly(CHD) isomers[d]			M_n[e] [×10³]	M_w/M_n[e]	T_m[f] [°C]
					[g]	[%]	*trans*	*cis*	*tac*			
1[g]	–	–	**A**	25	0.80	100	43[h]	57	–	1.9	2.17	–
2	Y	1.04	–	25	–	–	–	–	–	–	–	–
3	Y	1.04	**A**	25	0.40	50	1	99	73	6.1	2.23	253
4	Y	1.04	**B**	25	0.34	42	3	97	75	6.3	2.18	254
5	Y	1.04	**C**	25	0.07	9	5	95	–	4.2	2.00	236
6[i]	Gd	1.07	**A**	0	0.12	15	< 1	> 99	85	3.6	1.78	249
7	Gd	1.07	**A**	25	0.67	84	6	94	72	3.5	1.84	247
8	Gd	1.07	**A**	50	0.51	64	25	75	–	2.0	1.93	248
9	Dy	1.05	**A**	25	0.55	69	1	99	74	4.5	2.10	251
10	Ho	1.04	**A**	25	0.49	61	1	99	76	7.8	1.85	247
11	Er	1.03	**A**	25	0.27	34	1	99	72	6.8	1.89	250
12	Tm	1.02	**A**	25	0.18	23	1	99	70	2.9	1.72	226
13	Lu	1.00	**A**	25	trace	–	–	–	–	–	–	–

[a] Conditions: $[(C_5Me_4SiMe_3)_4Ln_4H_8(thf)]$: 40 μmol, activator: 40 μmol, CHD: 10 mmol, $V = 2$ mL (toluene), $t = 15$ h, unless otherwise noted. [b] Ionic radius of Ln^{3+} for CN = 6; see reference [16]. [c] Activator: **A** = $[Ph_3C][B(C_6F_5)_4]$, **B** = $[PhMe_2NH][B(C_6F_5)_4]$, **C** = $B(C_6F_5)_3$. [d] Determined by ^1H and ^{13}C NMR spectroscopy. Tacticity (*tac*, either isotactic or syndiotactic) was determined by integrating the ratio of the ^{13}C NMR signals at 39.42 and 39.64 ppm for the *cis*-1,4-polymer, but was not unequivocally identified. [e] Determined by gel permeation chromatography (GPC) in *o*-dichlorobenzene at 140 °C with polystyrene standard. M_n: number-average molecular weight of the polymer, M_w: weight-average molecular weight. [f] Melting temperature of the polymer; measured by differential scanning calorimetry (DSC). [g] $t = 1$ min. [h] 1,4-Structure: 75 %. [i] $t = 35$ h.

For comparison, the reaction of the neutral polyhydrido complex **1b** with CHD was also examined. It gave selectively the single CHD insertion product, **3**, in a quantitative yield (Scheme 2). The overall structure of the Y_4 frame in **3** is similar to that of **1b**. The resultant cyclohexenyl ligand adopts an allylic form, which bridges two Y atoms through the two terminal carbon atoms of the allyl moiety, each bonding to one metal center in an η^1 fashion (Figure 4). As with those of **2a** and **2c**, the $\{Y_4H_7\}$ core in **3** also has one μ_4-H, two μ_3-H, and four μ_2-H ligands. The ^1H NMR signals for the μ_4-H and the two μ_3-H ligands of **3** in C_6D_6 at room temperature appear at 2.50 ppm (br s) and 3.91 ppm (br m), respectively, while those for the four μ_2-H ligands give two triplets at 5.15 (t, $J_{Y,H} = 35.7$ Hz) and 5.40 ppm (t, $J_{Y,H} = 35.7$ Hz),

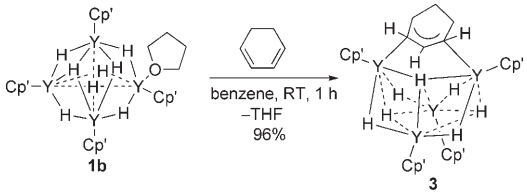

Scheme 2. Reaction of **1b** with 1,3-cyclohexadiene.

 © 2006 Wiley-VCH Verlag GmbH & Co. KGaA, Weinheim

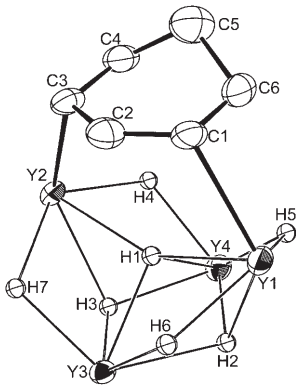

Figure 4. ORTEP drawing of **3** with thermal ellipsoids set at 30% probability. The $C_5Me_4SiMe_3$ ligands and hydrogen atoms in the CHD unit are omitted for clarity. Selected bond lengths [Å] and angles [°]: Y1–C1 2.550(3), Y2–C3 2.568(3), C1–C2 1.357(5), C1–C6 1.476(6), C2–C3 1.401(5), C3–C4 1.524(6), C4–C5 1.484(5), C5–C6 1.552(5); C2-C1-C6 115.4(3), C1-C2-C3 128.4(4), C2-C3-C4 115.8(3), C2-C1-Y1 114.6(2), C2-C3-Y2 114.7(2).

respectively. These results are consistent with the crystal structure of **3** and show that the $\{Y_4H_7(C_6H_9)\}$ core of **3** is rigid.[19] No reaction was observed between **3** and CHD at room temperature in $[D_8]$toluene. However, on treatment with one equivalent of $[Ph_3C][B(C_6F_5)_4]$, **3** became active for the *cis*-1,4-polymerization of CHD.[20]

In summary, by treating neutral rare-earth–hydride clusters such as **1a–c** with one equivalent of a borate compound such as $[Ph_3C][B(C_6F_5)_4]$, we have isolated and structurally characterized the corresponding cationic polyhydrido complexes such as **2a,c**. In contrast to the neutral hydride cluster **1b**, which yielded a single Y–H addition product, **3**, on treatment with CHD, the cationic hydride clusters (either isolated or generated in situ) act as excellent catalysts for the regio- and stereoselective *cis*-1,4-polymerization of CHD. Studies on the reactions of cationic rare-earth–hydride clusters with other unsaturated substrates, the activation of small molecules, and the polymerization/copolymerization of CHD by related cationic rare-earth–alkyl complexes are in progress.

Received: August 23, 2006
Revised: September 25, 2006
Published online: November 14, 2006

Keywords: cations · cluster compounds · hydride ligands · polymerization · rare earths

[1] Selected reviews: a) Z. Hou, *Bull. Chem. Soc. Jpn.* **2003**, *76*, 2253–2266; b) J. Okuda, *Dalton Trans.* **2003**, 2367–2378; c) S. Arndt, J. Okuda, *Chem. Rev.* **2002**, *102*, 1953–1976; d) G. A. Molander, J. A. C. Romero, *Chem. Rev.* **2002**, *102*, 2161–2185; e) R. Anwander in *Applied Homogeneous Catalysis with Organometallic Compounds*, *Vol. 2* (Eds.: B. Cornils, W. A. Herrmann), VCH, Weinheim, **1996**, pp. 866–892; f) Z. Hou, Y. Wakatsuki in *Science of Synthesis*, *Vol. 2* (Eds.: T. Imamoto, R. Noyori), Thieme, Stuttgart, **2002**, pp. 849–942; g) A. J. Hoskin, D. W. Stephan, *Coord. Chem. Rev.* **2002**, *233–234*, 107–129; h) M. Ephritikhine, *Chem. Rev.* **1997**, *97*, 2193–2242; i) H. Schumann, J. A. Meese-Marktscheffel, L. Esser, *Chem. Rev.* **1995**, *95*, 865–986; j) F. T. Edelmann in *Comprehensive Organometallic Chemistry II*, *Vol. 4* (Eds.: E. W. Abel, F. G. A. Stone, G. Wilkinson, M. F. Lappert), Pergamon, Oxford, **1995**, pp. 11–192; k) C. J. Schaverien, *Adv. Organomet. Chem.* **1994**, *36*, 283–362.

[2] a) O. Tardif, M. Nishiura, Z. Hou, *Organometallics* **2003**, *22*, 1171–1173; b) D. Cui, O. Tardif, Z. Hou, *J. Am. Chem. Soc.* **2004**, *126*, 1312–1313; c) O. Tardif, D. Hashizume, Z. Hou, *J. Am. Chem. Soc.* **2004**, *126*, 8080–8081; d) D. Cui, M. Nishiura, Z. Hou, *Angew. Chem.* **2005**, *117*, 981–984; *Angew. Chem. Int. Ed.* **2005**, *44*, 959–962; e) D. Cui, M. Nishiura, Z. Hou, *Macromolecules* **2005**, *38*, 4089–4095; f) Y. Luo, J. Baldamus, O. Tardif, Z. Hou, *Organometallics* **2005**, *24*, 4362–4366; g) T. Shima, Z. Hou, *J. Am. Chem. Soc.* **2006**, *128*, 8124–8125.

[3] For the formation and structure of **1c**, see also: a) K. C. Hultzsch, T. P. Spaniol, J. Okuda, *Angew. Chem.* **1999**, *111*, 163–165; *Angew. Chem. Int. Ed.* **1999**, *38*, 227–230; b) K. C. Hultzsch, P. Voth, T. P. Spaniol, J. Okuda, *Z. Anorg. Allg. Chem.* **2003**, *629*, 1272–1276.

[4] Selected reviews on cationic rare-earth–alkyl complexes: a) P. M. Zeimentz, S. Arndt, B. R. Elvidge, J. Okuda, *Chem. Rev.* **2006**, *106*, 2404–2433; b) Z. Hou, Y. Luo, X. Li, *J. Organomet. Chem.* **2006**, *691*, 3114–3121; c) S. Arndt, J. Okuda, *Adv. Synth. Catal.* **2005**, *347*, 339–354; d) J. Gromada, J. F. Carpentier, A. Mortreux, *Coord. Chem. Rev.* **2004**, *248*, 397–410; e) W. E. Piers, D. J. H. Emslie, *Coord. Chem. Rev.* **2002**, *233–234*, 131–135; f) Z. Hou, Y. Wakatsuki, *Coord. Chem. Rev.* **2002**, *231*, 1–22.

[5] a) Y. Luo, J. Baldamus, Z. Hou, *J. Am. Chem. Soc.* **2004**, *126*, 13910–13911; b) X. Li, Z. Hou, *Macromolecules* **2005**, *38*, 6767–6769; c) X. Li, J. Baldamus, Z. Hou, *Angew. Chem.* **2005**, *117*, 984–987; *Angew. Chem. Int. Ed.* **2005**, *44*, 962–964; d) L. Zhang, Y. Luo, Z. Hou, *J. Am. Chem. Soc.* **2005**, *127*, 14562–14563.

[6] For examples of CHD polymerization by radical initiators, see: a) G. Lefebvre, F. Dawans, *J. Polym. Sci. Part A* **1964**, *2*, 3277–3295; b) H. Stücklen, H. Thayer, P. Willis, *J. Am. Chem. Soc.* **1940**, *62*, 1717–1719.

[7] For examples of CHD polymerization by anionic initiators, see: a) H. Lussi, J. Braman, *Helv. Chim. Acta* **1967**, *50*, 1233–1243; b) L. A. Mango, R. W. Lenz, *Polym. Prepr. Am. Chem. Soc. Polym. Chem. Div.* **1971**, *12*, 402–409; c) Z. Sharaby, J. Jagur-Grodzinski, M. Martan, D. Vofsi, *J. Polym. Sci. Polym. Chem. Ed.* **1982**, *20*, 901–915; d) B. François, X. F. Zhong, *Makromol. Chem.* **1990**, *191*, 2743–2753; e) P. E. Cassidy, C. S. Marvel, S. Ray, *J. Polym. Sci. Part A* **1965**, *3*, 1553–1565; f) I. Natori, S. Inoue, *Macromolecules* **1998**, *31*, 4687–4694; g) K. L. Hong, J. W. Mays, *Macromolecules* **2001**, *34*, 782–786; h) D. T. Wiliamson, J. F. Elman, P. H. Masison, A. J. Pasquale, T. E. Long, *Macromolecules* **2001**, *34*, 2108–2114; i) R. P. Quirk, F. You, C. Wesdemiotis, M. A. Arnould, *Macromolecules* **2004**, *37*, 1234–1242.

[8] For examples of CHD polymerization by cationic initiators, see: a) D. A. Frey, M. Hasegawa, C. S. Marvel, *J. Polym. Sci. Part A* **1963**, *1*, 2057–2065; b) G. Lefebvre, F. Dawans, *J. Polym. Sci. Part A* **1964**, *2*, 3277–3295.

[9] For examples of CHD polymerization by Ziegler–Natta catalysts, see: a) C. S. Marvel, G. E. Hartzell, *J. Am. Chem. Soc.* **1959**, *81*, 448–452; b) A. H. K. Yousufzi, V. End, T. Otsu, *J. Polym. Sci. Polym. Chem. Ed.* **1975**, *13*, 1601–1605.

[10] For examples of CHD polymerization by homogeneous titanium catalysts, see: D. E. Heiser, J. Okuda, S. Gambarotta, R. Mülhaupt, *Macromol. Chem. Phys.* **2005**, *206*, 195–202.

 © 2006 Wiley-VCH Verlag GmbH & Co. KGaA, Weinheim

[11] For examples of CHD polymerization by nickel catalysts, see: a) D. L. Gin, V. P. Conticello, R. H. Grubbs, *J. Am. Chem. Soc.* **1994**, *116*, 10507 – 10519; b) M. Nakano, Q. Yao, A. Usuki, S. Tanimura, T. Matsuoka, *Chem. Commun.* **2000**, 2207 – 2208; c) R. Po, R. Santi, A. M. Romano, *J. Polym. Sci. Part A* **2000**, *38*, 3004 – 3009; d) P. Longo, C. Freda, O. R. Ballesteros, F. Grisi, *Macromol. Chem. Phys.* **2001**, *202*, 409 – 412.

[12] Interactions between rare-earth metals and fluorine were observed previously in analogous base-free tetrakis(pentaflurophenyl)borate complexes; see: a) M. W. Bouwkamp, P. H. M. Budzelaar, J. Gercama, I. D. H. Morales, J. de Wolf, A. Meetsma, S. I. Troyanov, J. H. Teuben, B. Hessen, *J. Am. Chem. Soc.* **2005**, *127*, 14310 – 14319; b) S. Kaita, Z. Hou, M. Nishiura, Y. Doi, J. Kurazumi, A. C. Horiuchi, Y. Wakatsuki, *Macromol. Rapid Commun.* **2003**, *24*, 179 – 184; c) P. G. Hayes, W. E. Piers, R. McDonald, *J. Am. Chem. Soc.* **2002**, *124*, 2132 – 2133; d) X. Song, M. Thornton-Pett, M. Bochmann, *Organometallics* **1998**, *17*, 1004 – 1006.

[13] CCDC-617797 (**1c**), CCDC-617794 (**2a**), CCDC-617795 (**2c**), and CCDC-617796 (**3**) contain the supplementary crystallographic data for this paper. These data can be obtained free of charge from The Cambridge Crystallographic Data Centre via www.ccdc.cam.ac.uk/data_request/cif.

[14] See the Supporting Information for details. See also references [2a] and [3b].

[15] The reaction of the neutral hydride cluster **1b** with styrene was reported previously and gave a simple Y–H insertion product: reference [2b].

[16] R. D. Shannon, *Acta Crystallogr. Sect. A* **1976**, *32*, 751 – 767.

[17] The Lu complex was reported previously; see reference [2a]. Other rare-earth–hydride clusters were prepared analogously to **1b**. The Dy and Gd complexes were also structurally characterized by X-ray analyses, which showed a tetranuclear structure similar to that of **1b**. More details will be reported elsewhere.

[18] Z. Sharaby, M. Martan, J. Jagur-Grodzinski, *Macromolecules* **1982**, *15*, 1167 – 1173.

[19] The $\{Y_4H_7(C_6H_9)\}$ core in **3** can be viewed as having a quasi "mirror" symmetry, with Y1, Y3, H1, C2, and C5 being placed in the mirror plane.

[20] In the absence of CHD, **2a** was obtained when **3** was treated with one equivalent of $[Ph_3C][B(C_6F_5)_4]$.

 © 2006 Wiley-VCH Verlag GmbH & Co. KGaA, Weinheim

C–Au Bond Formation

DOI: 10.1002/anie.200603350

Relativistic Functional Groups: Aryl Carbon–Gold Bond Formation by Selective Transmetalation of Boronic Acids**

*David V. Partyka, Matthias Zeller, Allen D. Hunter, and Thomas G. Gray**

The rational design of triplet-state sensitizers for the photodynamic therapy of cancers[1–3] and other diseases[4] remains an obdurate challenge. A prominent strategy[5–7] is the modification of existing photosensitizers with bromine ($Z = 35$) or iodine ($Z = 53$); the resulting heavy-atom effects potentiate the generation of therapeutic $^1\Delta_g$ O_2. The (phosphane)gold(I) fragment is σ-isolobal with the proton. Terminal substitution of aromatic organic molecules with gold ($Z = 79$) has clear desirability for developing phototherapy mediators. What is missing are mild means of carbon–gold bond formation in the presence of sensitive functional groups. We describe here a selective protocol that installs gold(I)–carbon bonds along the peripheries of organic molecules. Reducible, polar moieties are tolerated, including nitro groups, aldehydes, ketones, and esters. The organometallic compounds described here withstand air and water indefinitely. The ability to modify organic fluorophores with gold raises immediate opportunities in metallopharmaceuticals design.[8–10] Finally, the new protocol affords organogold(I) compounds more rapidly and in higher yield than by traditional methods[11] of arylating gold.

In the palladium-catalyzed Suzuki–Miyaura cross-coupling,[12,13] carbon–carbon bond formation is believed to follow transmetalation from boron to palladium. The reaction often requires an auxiliary base, which is thought to quaternize boron and promote transmetalation.[14] Related precedents include observations by the groups of Schmidbaur[15] and Fackler[16] of phenyl-group transfer from BPh_4^- to gold(I) in aqueous and non-aqueous media.

[*] Dr. D. V. Partyka, Prof. Dr. T. G. Gray
Department of Chemistry
Case Western Reserve University
Cleveland, OH 44106 (USA)
Fax: (+1) 216-368-3006
E-mail: tgray@case.edu
Dr. M. Zeller, Prof. Dr. A. D. Hunter
Department of Chemistry
Youngstown State University
Youngstown, OH 44555 (USA)

[**] We thank Case Western Reserve University and the donors of the Petroleum Research Fund, administered by the American Chemical Society (grant 42312-G3 to T.G.G.) for support. The diffractometer was funded by NSF grant 0087210, the Ohio Board of Regents grant CAP-491, and Youngstown State University.

Supporting information for this article is available on the WWW under http://www.angewandte.org or from the author.

WILEY InterScience DISCOVER SOMETHING GREAT
© 2006 Wiley-VCH Verlag GmbH & Co. KGaA, Weinheim

Transmetalation of (triphenylphosphane)gold(I) bromide with *o*-tolylboronic acid in isopropyl alcohol in the presence of cesium carbonate causes disappearance over 24 h of the ^{31}P NMR resonance at $\delta =$ 35.2 ppm, with concomitant growth of a singlet at $\delta = 44.4$ ppm attributable to **1** (Scheme 1). No other products were discernible by ^{31}P NMR spectroscopy. For comparison, an independent synthesis of **1** from Ph_3PAuBr and (*o*-tol)MgBr in toluene achieved less than 50% conversion after 3 days. Similar reactions proceed for a range of arylboronic acids, all in moderate to excellent yields. Gold(I) bromide complexes of triaryl, trialkyl, and mixed alkyl-aryl phosphanes transmetalate effectively. The reaction tolerates steric bulk and accommodates *o*-biphenyl, *o*-tolyl, and mesityl substituents, affording gold aryls in 61% (**4**), 79% (**5**), and 65% (**6**) yields upon isolation (Table 1). Transmetalation also proceeds for substrates bearing electron-withdrawing groups (**7**, **9**, and **10**). The protocol is not limited to substituted phenylboronic acids as witnessed by transmetalation of ferrocenyl and 2-thienyl boronic acids (**11** and **12**). Control experiments found no reaction in the absence of base. The new organogold(I) compounds are stable to air, water, and laboratory lighting over periods of months.

Products were characterized by multinuclear NMR spectroscopy and elemental analysis. Figure 1 depicts crystal structures of representative organogold(I) species.[17,18] In complex **11** an expected two-coordination about gold is found. The P-Au-$C_{\sigma\text{-aryl}}$ angle is 173.74(10)°; the gold–carbon bond length is 2.040(3) Å; and the gold–phosphorus separation is 2.2970(9) Å. No intermolecular contacts between gold atoms are observed.

Complexes of sterically imposing phosphane ligands transmetalate efficiently. Dia-

Table 1: Arylgold(I) products, reaction conditions, and isolated yields.

Gold(I) precursor	Arylboronic acid	Boronic acid [equiv]	*t* [h]	Product		Yield [%][a]
Ph_3PAuBr	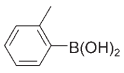	1.8	24	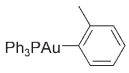	**1**	86
Ph_3PAuBr	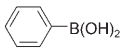	1.9	24	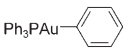	**2**	59
Cy_3PAuBr	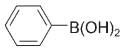	1.9	24	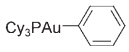	**3**	89
Cy_3PAuBr	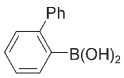	1.8	24	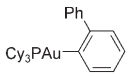	**4**	61
Cy_3PAuBr	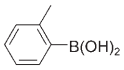	1.9	24	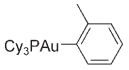	**5**	79
Cy_3PAuBr	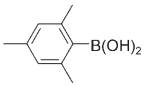	2.6	48	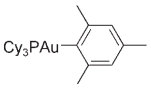	**6**	65
Cy_3PAuBr	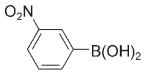	2.5	36	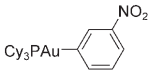	**7**	94
Cy_3PAuBr	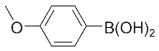	2.5	30	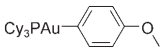	**8**	85
Cy_3PAuBr	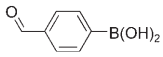	2.0	36	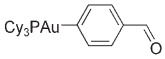	**9**	90
Cy_3PAuBr[b]	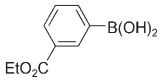	2.2	36	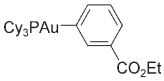	**10**	80
Cy_3PAuBr	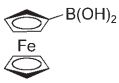	2.3	48	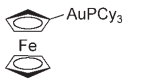	**11**	85
Cy_3PAuBr	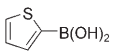	1.8	24	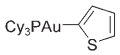	**12**	86
Cy_3PAuBr	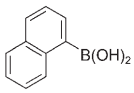	1.9	24	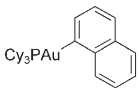	**13**	86
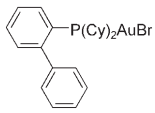	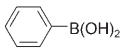	2.0	30	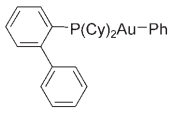	**14**	84
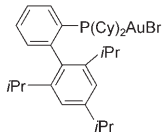	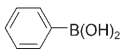	2.3	30	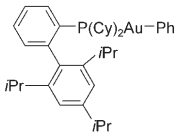	**15**	74

[a] Isolated material of ≥95% purity. [b] Reaction run in ethanol. Cy = cyclohexyl.

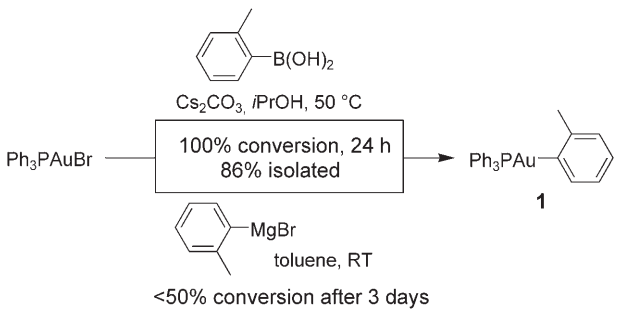

Scheme 1. Syntheses of **1** from boronic acid and Grignard reagent precursors.

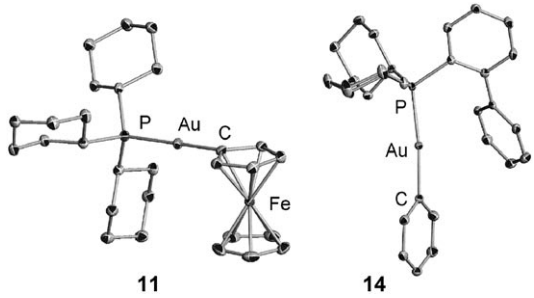

Figure 1. Crystal structures of **11** and **14** (50% probability ellipsoids shown).

© 2006 Wiley-VCH Verlag GmbH & Co. KGaA, Weinheim

lkylbiarylphosphanes[19,20] undergo widespread use in palladium-catalyzed reactions; they are increasingly applied in gold(I) catalysis.[21] Transmetalation of biarylphosphane complexes with phenylboronic acid proceeded smoothly and in high yields; reaction times are comparable to those of other entries in Table 1. The crystal structure of **14** is shown in Figure 1. Close approaches occur between gold and two carbon atoms of the pendant aryl ring (non-phosphorus-bound) of each biarylphosphane: 3.3063(18) Å (Au–C_{ipso}) and 3.2469 (19) Å (Au–C_{ortho}). The P-Au-$C_{\sigma\text{-aryl}}$ bond angle is a modestly nonlinear 174.18(6)°.

The new organogold(I) compounds do not significantly absorb visible light except for ferrocenyl complex **11** (orange) and **13** (pale yellow). Complex **13** is luminescent in THF solution upon excitation with UV light. A conflated absorption and emission spectrum of **13** is shown in Figure 2.

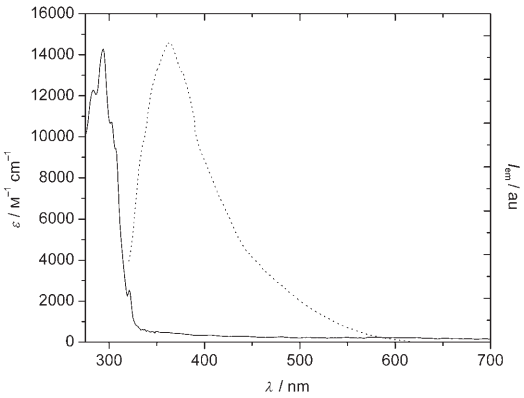

Figure 2. Room-temperature absorption (——) and emission (-----) spectra of **13** in THF (10^{-8} M, λ_{ex} = 310 nm).

Absorption extends from ca. 340 nm to the solvent limit of THF. Vibronic structure is apparent in the absorption at 293 nm, with an average spacing of 1050 cm^{-1} (9.57 nm). Room-temperature emission of **13** extends from ca. 350–600 nm. The absorption cutoff of **13**, but not the emission maximum, is red-shifted relative to that of the parent hydrocarbon.[22] Upon increasing the sample concentration to 10^{-6} M, emission features appear between 480–560 nm that have no counterpart in the fluorescence (Supporting Information). We attribute these emissions to oligomeric gold species. Time-dependent characterization of new arylgold(I) complexes is in progress.

Static and time-dependent density functional theory (DFT) calculations were conducted on Me_3PAu(1-naphthyl), **13′**[23,24] (see the Supporting Information for full details). Implicit THF solvation was included with the polarizable continuum model of Tomasi and co-workers.[25–27] The calculated (observed) Au–C bond length is 2.066 (2.030(4)) Å, the Au–P distance is 2.367 (2.3008(10)) Å, and the P-Au-C angle is 178.9 (176.52(12))°. A Kohn–Sham orbital energy diagram of **13′** appears in the Supporting Information (Figure S2). Images of selected orbitals are inset. The energy gap between the highest occupied and lowest unoccupied Kohn–Sham orbitals (HOMO and LUMO, respectively) is calculated to be 3.290 eV, and the LUMO←HOMO transition is optically allowed. Both orbitals have predominant naphthyl character. A fragment orbital calculation finds the LUMO of **13′** to be 87.5% derived from the LUMO of the naphthyl monoanion, and the HOMO is 93.2% composed of naphthyl anion HOMO−1. The HOMO−1 of **13′** is the primary C–Au σ-bonding combination. This orbital carries a 42.4% contribution from the a_1 LUMO of Me_3PAu^+, which is an sd hybrid orbital of σ symmetry.[28] The lower energy of the gold-heavy HOMO−1 (of **13′**), 0.63 eV below the HOMO, effectively precludes luminescence deactivation by electron transfer from Au^I. A Dapprich–Frenking charge decomposition analysis[29,30] finds a net charge donation of 0.33e from the naphthyl ligand to the (phosphane)gold fragment. The Au–C Wiberg bond order[31] in the Löwdin basis is 0.970; that of the Au–P bond is 0.984.

Time-dependent DFT calculation[32] of the low-lying singlet excited states of **13′** indicates an allowed excitation at 324.3 nm of mixed parentage, deriving mainly from a LUMO←HOMO transition with an admixed LUMO+1←HOMO excitation; both are π*←π transitions. The calculated oscillator strength is $f = 0.209$. Weaker absorption transitions are calculated at 258 and 254 nm, with $f = 0.0201$ and 0.0489, respectively. No other singlet–singlet transitions of significant oscillator strength were calculated in the absorption window of THF. The lowest-energy triplet state (computed for the singlet geometry) is calculated at 452.1 nm.

To summarize, a general protocol for creating gold(I) carbon bonds is presented. The reaction entails transmetalation from boronic acids to (phosphane)gold(I) bromides in the presence of base. Significant steric encumbrance is supported, both in the phosphane and the transmetalating aryl group. The gold(I) products are robust compounds that are stable in air and water for prolonged periods. Terminal (phosphane)gold(I) functionality is compatible with luminescence of the aromatic parent compound. The ability to tether gold(I) fragments to organic skeletons invites syntheses of more potent photodynamic therapy mediators that operate at reduced dosages. Gold(I) compounds that can be prepared by the new method hold added potential as rheumatoid arthritis prodrugs. Lipophilicity and cell permeability are adjustable in principle through the ancillary phosphane. Transmetalation from boronic acids proffers gold compounds bearing Grignard- and organolithium-incompatible functional groups. Further investigations of this process and applications to photoactive organic species are ongoing.

Experimental Section

13: Cs_2CO_3 (98 mg, 0.30 mmol) and 1-naphthylboronic acid (53 mg, 0.31 mmol) were suspended in isopropyl alcohol (5 mL). Cy_3PAuBr (88 mg, 0.16 mmol) was added to the suspension, and the mixture was stirred at 50 °C for 24 h. After cooling, the solvent was evaporated in vacuo, the residue was extracted into benzene, the solution was filtered through celite, and the filtrate was concentrated by rotary evaporation. The residue was triturated with pentane, and the pentane was removed by rotary evaporation. The pale yellow solid was washed with pentane, dried, and extracted into benzene. Then the solution was filtered through celite and concentrated to saturation. Vapor diffusion of pentane caused separation of a colorless crystalline mass, which was washed with cold methanol and pentane, dried, and

 © 2006 Wiley-VCH Verlag GmbH & Co. KGaA, Weinheim

collected. Yield: 82 mg (86%). ^{1}H NMR (C_6D_6): $\delta = 9.10$ (d, 1H, 1-naphthyl), 8.21 (td, 1H, 1-naphthyl), 7.89 (d, 1H, 1-naphthyl), 7.77 (d, 1H, 1-naphthyl), 7.65–7.58 (m, 2H, 1-naphthyl), 7.41–7.36 (m, 1H, 1-naphthyl), 1.95–0.94 ppm (m, 33H, C_6H_{11}); ^{31}P NMR (C_6D_6): $\delta =$ 58.0 ppm; UV/Vis (THF, 10^{-6} M): λ (ε) = 283 (11800), 293 (13500), 302 (10000), 321 nm (2300 $cm^{-1}M^{-1}$); emission (THF, 10^{-8} M, $\lambda_{ex} =$ 310 nm): $\lambda = 363$ nm; emission (THF, 10^{-6} M, $\lambda_{ex} = 310$ nm): $\lambda = 363$, 483, 494 (sh), 520, 560 nm. Elemental analysis (%) calcd for $C_{28}H_{40}AuP$: C 55.63, H 6.67; found: C 55.60, H 6.83.

Received: August 16, 2006
Revised: September 22, 2006
Published online: November 17, 2006

Keywords: boron · gold · phosphane ligands · photodynamic therapy · transmetalation

[1] N. L. Oleinick, R. L. Morris, I. Belichenko, *Photochem. Photobiol. Sci.* **2002**, *1*, 1–21.
[2] D. E. J. G. J. Dolmans, D. Fukumura, R. K. Jain, *Nat. Rev. Cancer* **2003**, *3*, 380–387.
[3] P. N. Prasad, *Introduction to Biophotonics*, Wiley-Interscience, New York, **2003**, pp. 433–463.
[4] C. Y. Hooper, R. H. Guymer, *Clin. Exp. Ophthamol.* **2003**, *31*, 376–391.
[5] T. Yogo, Y. Urano, Y. Ishitsuka, F. Maniwa, T. Nagano, *J. Am. Chem. Soc.* **2005**, *127*, 12162–12163.
[6] A. Gorman, J. Killoran, C. O'Shea, T. Kenna, W. M. Gallagher, D. F. O'Shea, *J. Am. Chem. Soc.* **2004**, *126*, 10619–10631.
[7] M. C. DeRosa, R. J. Crutchley, *Coord. Chem. Rev.* **2002**, *233–234*, 351–371.
[8] C. F. Shaw III, *Chem. Rev.* **1999**, *99*, 2589–2600.
[9] S. Y. Ho, E. R. T. Tiekink in *Metallotherapeutic Drugs & Metal-Based Diagnostic Agents: The Use of Metals in Medicine* (Eds.: M. Gielen, E. R. T. Tiekink), Wiley, New York, **2005**, pp. 507–528.
[10] P. J. Barnard, L. E. Wedlock, M. V. Baker, S. J. Berners-Price, D. A. Joyce, B. W. Skelton, J. H. Steer, *Angew. Chem.* **2006**, *118*, 6112–6116; *Angew. Chem. Int. Ed.* **2006**, *45*, 5966–5970.
[11] a) E. J. Fernández, A. Laguna, M. E. Olmos, *Adv. Organomet. Chem.* **2005**, *52*, 77–142; b) "Organogold Compounds": H. Schmidbaur in *Gmelin Handbuch der Anorganischen Chemie*, 8th ed. (Ed.: A. Slawisch), Springer, Berlin, **1980**; c) "Organogold Chemistry": H. Schmidbaur, A. Grohmann, M. E. Olmos in *Gold: Progress in Chemistry, Biochemistry and Technology* (Ed.: H. Schmidbaur), Wiley, Chichester, **1999**; d) H. Schmidbaur, A. Schier, *Sci. Synth.* **2004**, *3*, 691–761.
[12] N. Miyaura, A. Suzuki, *Chem. Rev.* **1995**, *95*, 2457–2483.
[13] A. F. Littke, G. C. Fu, *Angew. Chem.* **2002**, *114*, 4350–4386; *Angew. Chem. Int. Ed.* **2002**, *41*, 4176–4211; .
[14] K. Matos, J. A. Soderquist, *J. Org. Chem.* **1998**, *63*, 461–470.
[15] A. Sladek, S. Hofreiter, M. Paul, H. Schmidbaur, *J. Organomet. Chem.* **1995**, *501*, 47–51.
[16] J. M. Forward, J. P. Fackler, Jr., R. J. Staples, *Organometallics* **1995**, *14*, 4194–4198.
[17] CCDC 616180 and 616190 contain the supplementary crystallographic data for this paper. These data can be obtained free of charge from The Cambridge Crystallographic Data Centre via www.ccdc.cam.ac.uk/data_request/cif.
[18] Full structural characterization of new gold compounds will be reported in a forthcoming full paper.
[19] J. P. Wolfe, H. Tomori, J. P. Sadighi, J. Yin, S. L. Buchwald, *J. Org. Chem.* **2000**, *65*, 1158–1174.
[20] T. E. Barder, S. D. Walker, J. R. Martinelli, S. L. Buchwald, *J. Am. Chem. Soc.* **2005**, *127*, 4685–4696.
[21] Selected recent reports of Au in catalysis: a) S. López, E. Herrero-Gómez, P. Pérez-Galán, C. Nieto-Oberhuber, A. M. Echavarren, *Angew. Chem.* **2006**, *118*, 6175–6178; *Angew. Chem. Int. Ed.* **2006**, *45*, 6029–6032; ; b) S. T. Staben, J. J. Kennedy-Smith, D. Huang, B. K. Corkey, R. L. LaLonde, F. D. Toste, *Angew. Chem.* **2006**, *118*, 6137–6140; *Angew. Chem. Int. Ed.* **2006**, *45*, 5991–5994; ; c) A. Corma, P. Serna, *Science* **2006**, *313*, 332–334; d) Z. Zhang, C. Liu, R. E. Kinder, X. Han, H. Qian, R. A. Widenhoefer, *J. Am. Chem. Soc.* **2006**, *128*, 9066–9073; e) J. Zhao, C. O. Hughes, F. D. Toste, *J. Am. Chem. Soc.* **2006**, *128*, 7436–7437; f) M. R. Fructos, P. de Frémont, S. P. Nolan, M. M. Díaz-Requejo, P. J. Pérez, *Organometallics* **2006**, *25*, 2237–2241; g) J. Zhang, C.-G. Yang, C. He, *J. Am. Chem. Soc.* **2006**, *128*, 1798–1799; h) C. Nieto-Oberhuber, M. P. Muñoz, S. López, E. Jiménez-Núñez, C. Nevado, E. Herrero-Gómez, M. Raducan, A. M. Echavarren, *Chem. Eur. J.* **2006**, *12*, 1677–1693; i) C. Nieto-Oberhuber, S. López, M. P. Muñoz, E. Jiménez-Núñez, E. Buñuel, D. J. Cárdenas, A. M. Echavarren, *Chem. Eur. J.* **2006**, *12*, 1694–1702; j) C. Ferrer, A. M. Echavarren, *Angew. Chem.* **2006**, *118*, 1123–1127; *Angew. Chem. Int. Ed.* **2006**, *45*, 1105–1109; ; k) F. Gagosz, *Org. Lett.* **2005**, *7*, 4129–4132; l) P. Roembke, H. Schmidbaur, S. Cronje, H. Raubenheimer, *J. Mol. Catal. A* **2004**, *212*, 35–42; m) L. Zhang, S. A. Kozmin, *J. Am. Chem. Soc.* **2004**, *126*, 11806–11807; n) M. T. Reetz, K. Sommer, *Eur. J. Org. Chem.* **2003**, 3485–3496.
[22] S. L. Murov, I. Carmichael, G. L. Hug, *Handbook of Photochemistry*, 2nd ed., Dekker, New York, **1993**.
[23] For reviews of quantum chemical calculations of gold-containing systems, see: a) P. Pyykkö, *Angew. Chem.* **2004**, *116*, 4512–4557; *Angew. Chem. Int. Ed.* **2004**, *43*, 4412–4456; b) P. Pyykkö, *Inorg. Chim. Acta* **2005**, *358*, 4113–4130.
[24] Gaussian 03 (Revision D.01): M. J. Frisch et al., see the Supporting Information.
[25] S. Miertus, E. Scrocco, J. Tomasi, *Chem. Phys.* **1981**, *55*, 117–129.
[26] M. Cossi, G. Scalmani, N. Rega, V. Barone, *J. Chem. Phys.* **2002**, *117*, 43–54.
[27] J. Tomasi, B. Mennucci, R. Cammi, *Chem. Rev.* **2005**, *105*, 2999–3093.
[28] D. S. Laitar, P. Müller, T. G. Gray, J. P. Sadighi, *Organometallics* **2005**, *24*, 4503–4505.
[29] S. Dapprich, G. Frenking, *J. Phys. Chem.* **1995**, *99*, 9352–9362.
[30] For applications of CDA to Group 11 organometallics, see: a) X. Hu, I. Castro-Rodriguez, K. Olsen, K. Meyer, *Organometallics* **2004**, *23*, 755–764; b) D. Nemcsok, K. Wichmann, G. Frenking, *Organometallics* **2004**, *23*, 3640–3646.
[31] K. B. Wiberg, *Tetrahedron* **1968**, *24*, 1083–1096.
[32] M. A. L. Marques, E. K. U. Gross, *Annu. Rev. Phys. Chem.* **2004**, *55*, 427–455.

 © 2006 Wiley-VCH Verlag GmbH & Co. KGaA, Weinheim

Cytochrome P450

DOI: 10.1002/anie.200603282

The Diagnostic Substrate Bicyclohexane Reveals a Radical Mechanism for Bacterial Cytochrome P450 in Whole Cells**

Rachel N. Austin, Dayi Deng, Yongying Jiang, Kate Luddy, Jan B. van Beilen, Paul R. Ortiz de Montellano, and John T. Groves**

Few enzymatic transformations have attracted more attention than the processes by which cytochrome P450 (CYP) activates molecular oxygen to catalyze the hydroxylation of the inert C–H bonds of alkanes.[1–3] This reaction cycle elicits great interest due to the fundamental intellectual challenges posed by the mechanistic chemistry, the elusiveness of the reactive intermediates involved, and the significance of the transformations to human health, global carbon cycling, and "green" chemical processing. The consensus "oxygen rebound" mechanism for aliphatic hydroxylation by cytochrome P450, which involves a stepwise process and a short-lived substrate radical, rests on a body of experimental observations of substrate rearrangements. This scenario is supported by comparisons to model studies,[4] experiments with diagnostic substrates,[5–8] and theoretical approaches.[9–12] The recent recognition that informative mechanistic information can be obtained from whole-cell assays[5,13–15] offers a means to characterize enzymes of interest that have not yet been isolated and purified. Here we report results for the hydroxylation of the novel diagnostic substrate probe, bicyclo[3.1.0]hexane, with cell-free extracts and whole cells containing CYP153A1, a bacterial P450 hydroxylase found in *Acinetobacter* sp. strain EB104,[16] and CYP153A6 from a *Mycobacterium* sp. strain HXN-1500.[17] The results are compared to those obtained from isolated, purified P450cam (CYP101). Bicyclohexane has provided unusually clear evidence for substrate-based radical intermediates that persists in the enzyme active site for 75–250 ps with all three CYPs studied.

Substrates that display mechanistically diagnostic molecular rearrangements have been useful in characterizing enzymatic oxygen-transfer reactions.[2,3] Cyclopropylcarbinyl rearrangements have been particularly revealing, in that radical and cation intermediates have been shown to rearrange by different pathways. Further, the rates of the radical rearrangement have been used to clock the lifetime of intermediate radicals. Still, various interpretations have been offered for the array of products obtained for a given diagnostic substrate, such as norcarane,[8,18] and the apparent lack of correlation between intrinsic radical rearrangement rates and the degree of rearrangement observed for some cases.[19] Possible complicating factors are the participation of multiple reactive species (Fe=O and Fe–OOH[20]), divergent behaviors of different Fe=O spin states (the two-state hypothesis[9]), and dynamical properties intrinsic to the recombination of reactive species in an active site cage.[21] Also likely are potential shortcomings in the substrates themselves and technical difficulties in the analyses. Given these challenges, we have examined a new diagnostic substrate which benefits from particular chemical characteristics that simplify the product analysis and the subsequent mechanistic interpretation.

Bicyclo[3.1.0]hexane is a diagnostic substrate similar to norcarane but whose hydroxylated products chromatograph with exceptional resolution. Like norcarane, bicyclohexane generates distinct products for a substrate-based radical (3-hydroxymethyl-cyclopentene, **2**) and a substrate-based cation (cyclohex-2-en-1-ol, **3**), a property that permits informative mechanistic conclusions to be drawn. An overview of possible reaction routes for bicyclohexane is provided in Figure 1 (see the Supporting Information for additional details).

As bicyclohexane has not been used before to characterize an enzyme reaction mechanism, the ring-opening rate for the 2-bicyclohexyl radical was determined. Barton PTOC (pyridine-2-thioenoxycarbonyl) esters for both the 2-bicyclohexyl and 2-norcaranyl cases were prepared, and the photo-

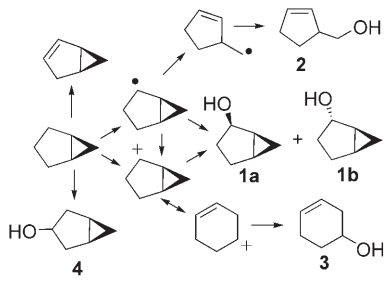

Figure 1. Overview of bicyclohex-2-yl rearrangement chemistry.

[*] Prof. J. T. Groves, D. Deng
Department of Chemistry, Princeton University
Princeton, NJ 08544 (USA)
Fax: (+1) 609-258-0348
E-mail: jtgroves@princeton.edu
Prof. R. N. Austin, K. Luddy
Department of Chemistry, Bates College
Lewiston, ME 04240 (USA)
Fax: (+1) 207-786-8336
E-mail: raustin@bates.edu
Dr. Y. Jiang, Prof. P. R. Ortiz de Montellano
Department of Pharmaceutical Chemistry
University of California at San Francisco
San Francisco, CA 94143-0446 (USA)
Dr. J. B. van Beilen
Institut für Biotechnologie
ETH Zürich
8093 Zürich (Switzerland)

[**] We thank Dr. Enrico Funhoff for advice with the cell-free extract methodology, Charlotte Lehmann for technical assistance, and FMC Corp. (Princeton, NJ) for access to GC-MS instrumentation. We thank the NSF for funding (CHE-0221978 to R.N.A. and J.T.G. through the Environmental Molecular Sciences Institute CEBIC at Princeton University; CHE-0116233 to R.N.A.), the Camille and Henry Dreyfus Foundation (R.N.A.), and the NIH (GM072506 to R.N.A., and GM036298 to J.T.G.).

Supporting information for this article is available on the WWW under http://www.angewandte.org or from the author.

InterScience
© 2006 Wiley-VCH Verlag GmbH & Co. KGaA, Weinheim

lytically generated radicals were trapped with thiophenol.[22] The Barton ester of 2-bicyclohexyl carboxylic acid afforded 25% 3-methyl-cyclopent-1-ene, 73% bicyclohexane, and 1.9% cyclohexene, while that of 2-norcaranyl carboxylic acid yielded 70% 3-methylcyclohex-1-ene, 0.5% cycloheptene, and 30% norcarane. Accordingly, the rearrangement rate for the 2-bicyclohexyl radical was determined to be $2.9 \times 10^7\ s^{-1}$ by comparison to the known rearrangement rate for the 2-norcaranyl radical ($2 \times 10^8\ s^{-1}$).[8] This result is consistent with products of the reaction of 2-bicyclohexyl chloride with tin hydride and experiments with bicyclohexane through the photochemically induced radical chain decomposition of *tert*-butyl hypochlorite.[8,23]

Two bacterial cytochrome P450s, CYP153A1 and CYP153A6, were cloned into an expression vector for co-expression with ferredoxin and ferredoxin reductase and inserted into *Pseudomonas putida* GPo12, a strain lacking other alkane-degrading hydroxylases.[24] Bicyclohexane was oxidized by these enzymes either in whole-cell assays[5,15] or in cell-free extract experiments.[16] Cytochrome P450cam (CYP101) was purified and used for substrate oxygenation as previously described.[8,25]

Bicyclohexane proved to be a good P450 substrate, with over 50% conversion. Product distributions for the three P450 systems were remarkably similar, with *endo*- and *exo*-2-bicyclohexanol, **1a** and **1b**, as the major products. The radical rearrangement product 3-hydroxymethylcyclopentene (**2**) was detected in all cases. This mechanistically significant product has a distinct mass spectrum and was chromatographically well separated from the other bicyclohexane-derived product peaks, facilitating its identification and quantification. Also contributing to the simplicity of the assay was the apparent lack of secondary oxidation products.[25] Small amounts of the cationic rearrangement product cyclohex-1-en-2-ol (**3**) were also detected in the P450cam samples (0.5%) and in one cell-free extract containing CYP153A6 (0.02%). 3-Bicyclohexanol (**4**) and 2-bicyclohexanone (**5**) were also detected. GC-MS data for the reaction mixture are shown in Figure 2, and the product distributions are reported in Table 1.

The product ratios observed are consistent with a stepwise radical process for these hydroxylation reactions, with a rebound rate for the [Fe^{IV}–OH + ·R] radical pair in the range of $10^{10}\ s^{-1}$. Thus, the whole-cell and cell-free extracts give evidence for a substrate-based radical generated by these bacterial P450s that persists for tens of picoseconds for bicyclohexane. These are very similar values to those reported by us for other cyclopropylcarbinyl substrates, norcarane,[8] bicyclopentane,[5] and thujone.[25,26]

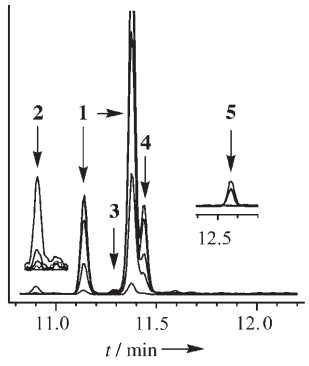

Figure 2. Ion chromatogram of CYP153A6 whole-cell oxidation of bicyclo[3.1.0]hexane for *m/e* 96, 80, 79, 67, and 54.

Table 1: Product distribution based on total bicyclohexane products, for CYP systems examined.

System	Product distribution [%]					Radical
	1a+**1b**	**2**[a]	**3**[b]	**4**	**5**	lifetime [ps]
CYP153A1 whole cell	95.4	0.3	nd	nd	4.3	107
CYP153A1 cell free	99.5	0.3	nd	0.4	nd	104
CYP153A6 whole cell	92.9	0.2	0.02	4.4	2.5	75
CYP153A6 cell free	97.8	0.2	nd	2.0	nd	74
P450cam	92.2	0.7	0.5	6.3	1.4	252

[a] All entries represent the average of two of more experiments. [b] In one experiment from P450cam the cationic peak appeared to co-elute with a compound unrelated to the substrate. An upper limit on the amount of cyclohexenol was estimated in that case. nd = not detected.

By contrast, when *trans*-2-phenylmethylcyclopropane, with a rearrangement rate of $1.8 \times 10^{11}\ s^{-1}$,[27] was used as a substrate probe with CYP153A1 and CYP153A6 in the whole-cell and cell-free assays, the lifetime of the substrate-based radical was found to be 0.3–0.4 ps. A substrate-based radical lifetime of 1.4 ps for *trans*-phenylmethylcyclopropane and P450cam has been reported by Newcomb and co-workers,[27] while Woggon and Sbaragli used this substrate probe with a biomimetic P450 metalloporphyrin and observed a substrate-based radical lifetime of 0.63 ps.[28] These very similar results with an isolated P450, whole-cell and cell-free extracts containing CYP153, as well as a model O=Fe porphyrin/iodosylbenzene system argue that similar processes are being probed in each case. Thus, the 10- to 50-fold lower amounts of rearrangement with the *trans*-phenylmethylcyclopropane probe derive from intrinsic properties of the ferryl heme reaction with this substrate as we have discussed.[2,21]

Several conclusions regarding the mechanism of substrate oxygenation by bacterial P450s can be drawn from this work. Bicyclo[3.1.0]hexane is a useful and robust probe molecule that confirms the presence of a short-lived radical intermediate in the CYP reaction cycle. This information was obtained with a much simplified, and arguably more lifelike, whole-cell assay approach, thus presenting opportunities for more facile surveys of the emerging class of alkane-oxidizing bacterial P450s[29–32] that do not require isolation of the proteins of interest. Further, the radical lifetime criterion of simple hydrocarbon probes could be used to characterize unknown hydroxylases in novel cell cultures.

Experimental Section

For whole-cell experiments, cells were grown to an optical density (OD) of 1 (600 nm) in MSB (mineral salts based) medium with octane as the sole carbon source as we have previously described.[15] In the "growing cell" approach, diagnostic substrate was simply provided in lieu of octane and cells were allowed to grow for another 2–3 h. The samples were centrifuged at $8000 \times g$, and the supernatant was extracted with ethyl acetate, dried, and concentrated. In the "resting cell" approach, cells were centrifuged at OD = 1 and resuspended in

 © 2006 Wiley-VCH Verlag GmbH & Co. KGaA, Weinheim

50 mM phosphate buffer (pH 7.2). The substrate was then provided, and the cells were incubated for 2—3 h. The workup was the same as described above. Both protocols yielded comparable results.

For cell-free extract experiments, growing cells were centrifuged at $8000 \times g$, and the cell pellet was resuspended in 50 mM potassium phosphate buffer (pH 7.4) with 5% glycerol, 1 mM DTT (dithiothreitol), and 200 μM PMSF (phenylmethylsulfonyl fluoride) at a concentration of 20 g cell dry weight per liter (100 g cell wet weight/L). The cells were sonicated on ice water and then centrifuged at $100000 \times g$ for 20 min. 2 mL of substrate and DTT (1 mM) were added to 1 mL of decanted supernate, and the mixture was stirred for 2 min. NADH (12.5 mM) was added, and the reaction was shaken in a 37°C incubator for 2 h. The reaction was quenched with the addition of 1 mL CH_2Cl_2, and the mixture was then vortexed and centrifuged. The CH_2Cl_2 layer was removed and dried with anhydrous sodium sulfate.

Received: August 10, 2006
Published online: November 14, 2006

Keywords: alkanes · cytochromes · oxidation · radical ions · reaction mechanisms

[1] J. T. Groves, *Proc. Natl. Acad. Sci. USA* **2003**, *100*, 3569 – 3574.
[2] J. T. Groves in *Cytochrome P450: Structure, Mechanism, and Biochemistry*, 3rd ed. (Ed.: P. R. Ortiz de Montellano), Klewer Academic/Plenum, New York, **2005**, pp. 1 – 44.
[3] P. R. Ortiz de Montellano, J. J. De Voss in *Cytochrome P450 Structure, Mechanism, and Biochemistry*, 3rd ed. (Ed.: P. R. Ortiz de Montellano), Klewer Academic/Plenum, New York, **2005**, pp. 183 – 245.
[4] J. T. Groves, D. V. Adhyam, *J. Am. Chem. Soc.* **1984**, *106*, 2177 – 2181.
[5] P. R. Ortiz de Montellano, R. A. Stearns, *J. Am. Chem. Soc.* **1987**, *109*, 3415 – 3420.
[6] V. W. Bowry, K. U. Ingold, *J. Am. Chem. Soc.* **1991**, *113*, 5699 – 5707.
[7] T. S. Dowers, D. A. Rock, D. A. Rock, J. P. Jones, *J. Am. Chem. Soc.* **2004**, *126*, 8868 – 8869.
[8] K. Auclair, Z. B. Hu, D. M. Little, P. R. Ortiz de Montellano, J. T. Groves, *J. Am. Chem. Soc.* **2002**, *124*, 6020 – 6027.
[9] S. Shaik, D. Kumar, S. P. de Visser, A. Altun, W. Thiel, *Chem. Rev.* **2005**, *105*, 2279 – 2328.
[10] T. Kamachi, K. Yoshizawa, *J. Am. Chem. Soc.* **2003**, *125*, 4652 – 4661.
[11] A. Altun, V. Guallar, R. A. Friesner, S. Shaik, W. Thiel, *J. Am. Chem. Soc.* **2006**, *128*, 3924 – 3925.
[12] V. Guallar, B. F. Gherman, S. J. Lippard, R. A. Friesner, *Curr. Opin. Chem. Biol.* **2002**, *6*, 236 – 242.
[13] L. A. Moe, Z. B. Hu, D. Y. Deng, R. N. Austin, J. T. Groves, B. G. Fox, *Biochemistry* **2004**, *43*, 15688 – 15701.
[14] R. N. Austin, H.-K. Chang, G. J. Zylstra, J. T. Groves, *J. Am. Chem. Soc.* **2000**, *122*, 11747 – 11748.
[15] E. Bertrand, R. Sakai, E. Rozhkova-Novosad, L. Moe, B. G. Fox, J. T. Groves, R. N. Austin, *J. Inorg. Biochem.* **2005**, *99*, 1998 – 2006.
[16] J. B. van Beilen, E. G. Funhoff, *Curr. Opin. Biotechnol.* **2005**, *16*, 308 – 314.
[17] J. B. van Beilen, E. G. Funhoff, A. van Loon, A. Just, L. Kaysser, M. Bouza, R. Holtackers, M. Röthlisberger, Z. Li, B. Witholt, *Appl. Environ. Microbiol.* **2006**, *72*, 59 – 65.
[18] M. Newcomb, R. N. Shen, Y. Lu, M. J. Coon, P. F. Hollenberg, D. A. Kopp, S. J. Lippard, *J. Am. Chem. Soc.* **2002**, *124*, 6879 – 6886.
[19] M. Newcomb, P. H. Toy, *Acc. Chem. Res.* **2000**, *33*, 449 – 455.
[20] R. E. P. Chandrasena, K. P. Vatsis, M. J. Coon, P. F. Hollenberg, M. Newcomb, *J. Am. Chem. Soc.* **2004**, *126*, 115 – 126.
[21] J. T. Groves, *J. Inorg. Biochem.* **2006**, *100*, 434 – 447.
[22] M. Newcomb, A. G. Glenn, *J. Am. Chem. Soc.* **1989**, *111*, 275 – 277.
[23] J. M. Tanko, J. F. Blackert, *J. Chem. Soc. Perkin Trans. 2* **1996**, 1775 – 1779.
[24] J. B. van Beilen, R. Holtackers, D. Lüscher, U. Bauer, B. Witholt, W. A. Duetz, *Appl. Environ. Microbiol.* **2005**, *71*, 1737 – 1744.
[25] Y. Y. Jiang, X. He, P. R. Ortiz de Montellano, *Biochemistry* **2006**, *45*, 533 – 542.
[26] X. He, P. R. Ortiz de Montellano, *J. Biol. Chem.* **2004**, *279*, 39479 – 39484.
[27] P. H. Toy, M. Newcomb, M. J. Coon, A. D. N. Vaz, *J. Am. Chem. Soc.* **1998**, *120*, 9718 – 9719.
[28] L. Sbaragli, W. D. Woggon, *Synthesis* **2005**, 1538 – 1542.
[29] M. Sekine, et al., *Environ. Microbiol.* **2006**, *8*, 334 – 346.
[30] P. Meinhold, M. W. Peters, A. Hartwick, A. R. Hernandez, F. H. Arnold, *Adv. Synth. Catal.* **2006**, *348*, 763 – 772.
[31] O. Lentz, A. Feenstra, T. Habicher, B. Hauer, R. D. Schmid, V. B. Urlacher, *ChemBioChem* **2006**, *7*, 345 – 350.
[32] S. G. Bell, N. Hoskins, F. Xu, D. Caprotti, Z. H. Rao, L. L. Wong, *Biochem. Biophys. Res. Commun.* **2006**, *342*, 191 – 196.

 © 2006 Wiley-VCH Verlag GmbH & Co. KGaA, Weinheim

Duplex Cross-Links

DOI: 10.1002/anie.200603128

Selective Platination of Modified Oligonucleotides and Duplex Cross-Links**

Berta Algueró, Jaime López de la Osa, Carlos González, Enrique Pedroso, Vicente Marchán, and Anna Grandas**

Since synthetic oligonucleotides complementary to mRNA sequences were shown to inhibit Rous sarcoma virus replication,[1] oligonucleotide chemists have synthesized all types of analogues to render oligonucleotides suitable as antisense agents. In this context, platinated oligonucleotides have been

[*] Dr. B. Algueró, Prof. E. Pedroso, Dr. V. Marchán, Prof. A. Grandas
Departament de Química Orgànica
Facultat de Química
Universitat de Barcelona
Martí i Franquès 1–11, 08028 Barcelona (Spain)
Fax: (+34) 93-339-7878
E-mail: vmarchan@ub.edu
anna.grandas@ub.edu
J. López de la Osa, Dr. C. González
Instituto de Química Física Rocasolano, CSIC
Serrano 119, 28006 Madrid (Spain)

[**] This work was supported by funds from the Ministerio de Educación y Ciencia (grant no. CTQ2004-8275) and the Generalitat de Catalunya (grant no. 2005SGR-693 and Centre de Referència de Biotecnologia).

Supporting information for this article is available on the WWW under http://www.angewandte.org or from the author.

WILEY InterScience DISCOVER SOMETHING GREAT
© 2006 Wiley-VCH Verlag GmbH & Co. KGaA, Weinheim

evaluated as potential drugs that may promote the formation of interchain cross-links and strengthen hybridization with the target RNA.

Duplexes with platinum cross-links have been obtained by annealing oligonucleotide strands either to platinated oligonucleotides with one labile bond[2] or to chains with *trans*-$Pt(NH_3)_2$–GNG adducts (N = any nucleoside).[3] Biological assays have proven that GNG-platinated oligoribonucleotides are able to modulate gene expression.[4] Alternatively, by taking advantage of the high affinity of phosphorothioate groups for platinum(II) complexes,[5] oligonucleotides containing a single phosphorothioate modification have been cross-linked to other oligonucleotide chains or to proteins.[6] Nevertheless, the scope of applications of platinated oligonucleotides has been limited because the preference of platinum for guanine rather than the other nucleobases restricts the position and number of guanines in the chain designed to first react with the metal.[2,3]

We have found that end-modified oligonucleotides with thioether and imidazole groups appended to 5-methylcytosines in neighboring positions (Scheme 1, X^S and X^I denote both the nucleobase and the nucleoside) react with transplatin to give chelates in which the platinum coordinates to the thioether and imidazole groups even in chains containing various guanines.[7] Hence, we have exploited such modified oligonucleotides to prepare duplexes with *trans*-$Pt(NH_3)_2$ cross-links without sequence restriction, either by using preplatinated oligonucleotides or by mixing all the components in a one-pot reaction. The results of this study are reported here.

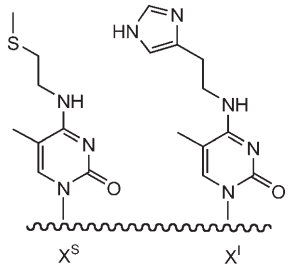

Scheme 1. Structures of the modified nucleobases containing the thioether and imidazole groups.

Platinated oligonucleotides $\mathbf{X^IX^S}$ACGTTGAG (**3**) and $\mathbf{X^SX^I}$ACGTTGAG (**4**; the coordination positions are highlighted in bold) were obtained by the reaction of transplatin with the corresponding modified oligonucleotides, X^IX^SACGTTGAG (**1**) and X^SX^IACGTTGAG (**2**).[7] Then, **3** (or **4**) was annealed to an equimolar amount of the complementary chain $^{5'}$dCTCAACGTGTTTG (**5**), and ligand-exchange substitution afforded exclusively the interchain-cross-linked product **6** (or **7**; Figure 1 A).

The formation of **6** or **7** in the reaction mixture was detected both by anion exchange HPLC and polyacrylamide gel electrophoresis (PAGE; see the Supporting Information).

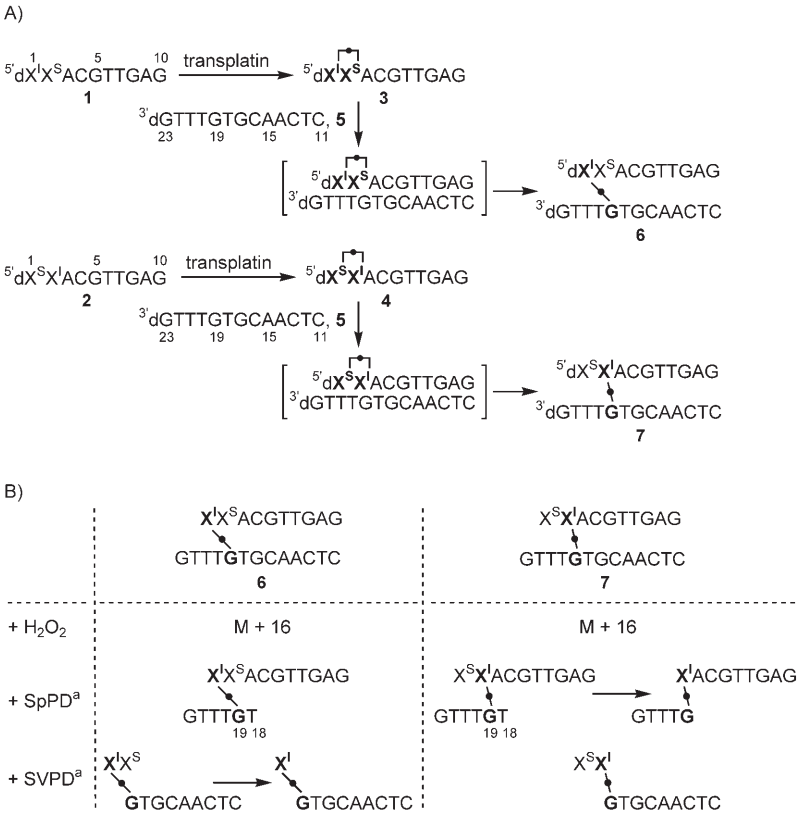

Figure 1. A) Reaction of the platinated oligonucleotides **3** and **4** with **5**. B) Characterization of the adducts formed. [a]SpPD = calf spleen phosphodiesterase (5′-exonuclease); SVPD = snake venom phosphodiesterase (3′-exonuclease).

Yet the presence of **3** and **4** could only be assessed by anion exchange HPLC, a result showing that the N–Pt–S adducts are not stable in the electrophoresis analysis conditions.

Cross-linked duplexes **6** and **7** were isolated by anion exchange HPLC, and their structures were inferred from MALDI-TOF mass spectrometry analysis before (see the Supporting Information) and after chemical and enzymatic reactions (Figure 1 B).[8] The isolated products contained two chains and the *trans*-$Pt(NH_3)_2$ moiety, and their oxidation by H_2O_2 (indicated by m/z ratios that were 16 units higher, the result of thioether to sulfoxide conversion) indicated that X^S was not linked to the metal. Platinum coordination to X^I of chain **1** and G19 of chain **5** (base numbers are shown in Figure 1 A) was surmised from the results of the digestions with the two exonucleases. The enzymatic elimination (3′-exonuclease) of X^S, placed next to platinated X^I, was slower than that of the other nucleosides. It was also found that digestion of chain **5** with the 5′-exonuclease did not stop at the platinated nucleobase but at the previous one. In the case of **7**, T18 was removed after longer digestion times, thereby confirming coordination to G19. In the case of **6**, coordination to G19 could be presumed from the well-known platinum preference for guanine rather than thymine and it was definitely established by NMR spectroscopy (see below).

The possibility of obtaining (*trans*-$Pt(NH_3)_2$)-cross-linked duplexes without previous platination of one of the two strands was then explored. One-pot cross-linking experiments were carried out by mixing equimolar amounts of the

 © 2006 Wiley-VCH Verlag GmbH & Co. KGaA, Weinheim

modified oligonucleotide (**1** or **2**), the complementary chain **5**, and transplatin in duplex-forming conditions. In both cases, the same cross-linked duplexes as in the previous experiments (**6** and **7**) were formed (Figure 2).

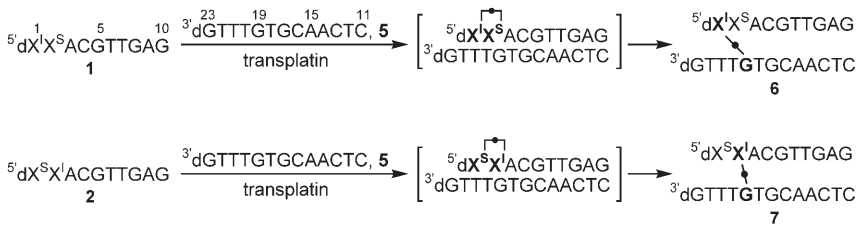

Figure 2. Synthesis of the cross-linked duplexes in a one-pot reaction.

Anion exchange HPLC monitoring of the evolution of the reactions allowed chelates **3** and **4** to be detected, which indicates that platination of the modified strand in the duplex precedes the rearrangement that yields the cross-link; this probably accounts for the slower formation of the cross-linked duplexes in these one-pot reactions.

To get further insight into the platination sites in **6** and the possible distortions produced by the cross-link in the structure of the duplex, the reaction between **1**, **5**, and transplatin was repeated on a larger scale, and an NMR spectroscopy study of compound **6** was carried out (the duplex formed by **1** and **5** was used as a control). Most of the ^{1}H signals could be assigned by following standard procedures (see the Supporting Information). Significant chemical-shift differences between the two duplexes were observed in the protons of residues X^I, X^S, A3, and C4, as well as in T18, G19, and T20. The largest difference was observed in the signal for H8 of G19, which was downfield shifted by 0.7 ppm in **6** (see the Supporting Information). This was a clear indication of platination at position *N*7 of this guanine. Other residues, including the remaining guanines, were mainly unaffected. Interprotonic distances derived from NOE cross-peaks indicated that the duplex was not much distorted by the cross-link.

In many of the residues close to the cross-link, two sets of signals were observed (see the Supporting Information). This effect was not the consequence of a chemical-exchange process, since no signal coalescence was observed upon a rise in temperature. The NMR spectra were consistent with the formation of two isomers, which result from platinum coordination to either of the two nitrogen atoms of the imidazole ring.[8]

UV-monitored thermal-denaturation experiments showed that the metal linkage between the two strands was highly stabilizing. The melting temperature (T_m) of the control duplex (**1** + **5**) was 32 °C, while that of **6** was 72 °C ($\Delta T_m = 40$ °C). Duplex stabilization has also been found in other *trans*-Pt(NH_3)$_2$ cross-linked chains,[9] but not to such an extent. The higher stability of **6** as compared with other cross-linked duplexes may be because the metal is not directly linked to the *N*4 atom of the cytosine; this probably decreases the distortion created by the platinum cross-link.

To assess the effect of the presence and position of guanine residues in the overhang of the complementary chain, different oligonucleotides (**8**–**10**) were synthesized and treated with **1** and transplatin in duplex-forming conditions (Figure 3). Isolation and characterization of the cross-linked duplexes showed that, in all cases, the *trans*-Pt(NH_3)$_2$ unit was linked to X^I and the guanine facing X^S in the complementary strand. This result proves that the regioselectivity of the rearrangement is very high and shows that, even when there are two guanines close to each other (as in chain **10**), the platinum prefers to migrate to the guanine opposite X^S rather than to its neighbor. This finding also agrees with the fact that formation of cross-linked duplex **7**, which involved platinum migration from X^S to the guanine opposite X^I, was slower than formation of cross-linked duplex **6** regardless of the synthetic procedure.

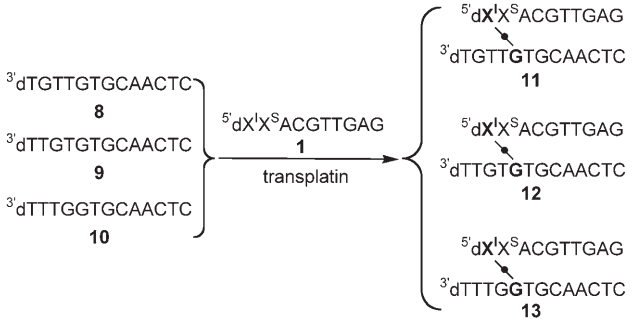

Figure 3. Results of the reactions of transplatin with **1** and complementary strands with different sequences.

Finally, transplatin was treated with **1** and three strands of different length that were noncomplementary to **1** ($^{5'}$dGATCTAAAAGACTTT, $^{5'}$dCGGATATACCG, and $^{5'}$dACCATTCGTAGC). Chelate **3** was the only platinated product found in the reaction mixtures. Hence, hybridization is required for platinum migration, and non-complementary strands do not become cross-linked.

In summary, the reaction between transplatin and oligonucleotides with thioether and imidazole groups appended to neighboring nucleobases afforded thioether–Pt–imidazole chelates that, upon hybridization with a complementary strand, underwent a rearrangement process that yielded duplexes with X^I–guanine *trans*-Pt(NH_3)$_2$ cross-links. The cross-link did not interfere with base-pairing and greatly stabilized the duplex.

Exactly the same cross-linked products were obtained by mixing equimolar amounts of transplatin and the two oligonucleotide chains in duplex-forming conditions, a result proving that previous isolation of the platinated modified oligonucleotide is not necessary. However, the thioether–Pt–imidazole chelates were always detected in these one-pot reaction mixtures, which suggests that their formation preceded that of the cross-linked duplexes. The fact that no other chelates were detected confirms our previous finding that the high affinity of sulfur for the metal drives the formation of the intrachain thioether–Pt–imidazole adducts[7] and prevents other oligonucleotide sequences from being platinated, even if they contain various guanine residues.

 © 2006 Wiley-VCH Verlag GmbH & Co. KGaA, Weinheim

The ligand-exchange substitution process was found to be highly regioselective, as platinum migration from the thioether to the guanine opposite X^S was preferred over migration to the guanine opposite X^I, and the former was more rapid than the latter. Cross-linking processes were rather slow, but, based on findings previously reported by Leng and coworkers,[3b] the replacement of 2′-deoxyoligonucleotides by oligoribonucleotides is expected to increase the rate of the rearrangement that yields the cross-linked duplex.

Finally, it is important to point out that cross-linking is the result of an annealing-promoted rearrangement. In other words, the cross-linking process is also sequence selective, since it only takes place if the two chains are complementary.

To the best of our knowledge, the goal of targeting and cross-linking complementary oligonucleotides without sequence restriction has been achieved here for the first time. Work is in progress to examine the potential therapeutic use of thioether- and imidazole-modified oligonucleotides.

Experimental Section

Cross-linking reaction between platinated oligonucleotides **3** or **4** and the complementary chain **5**: Modified oligonucleotide **1** (or **2**; optical density units at 260 nm (OD_{260} units) = 3.0) was treated with transplatin (3.2 μL of a 10 mM aqueous solution) in perchlorate buffer (3.16 mL; final oligonucleotide concentration = 10 μM) for 24 h at room temperature. Platinated oligonucleotides were isolated by reversed-phase HPLC.[7] **3** (or **4**; OD_{260} units = 0.45) and an equimolar amount of **5** was dissolved in phosphate buffer (0.47 mL). The mixture (duplex concentration = 10 μM; pH 6.8–6.9) was stirred at 16 °C for 12 days, and the target duplex **6** (or **7**) was isolated by anion exchange HPLC.

One-pot cross-linking reactions: Modified oligonucleotide **1** (or **2**; OD_{260} units = 1.0) and either the complementary (**5**, **8**, **9**, or **10**) or non-complementary chain (1 equiv) were dissolved in phosphate buffer (1.05 mL). The solution was heated to 90 °C and allowed to cool down slowly (overnight) to room temperature to favor duplex formation. After addition of transplatin (1 equiv; 1.1 μL of a 10 mM aqueous solution), the mixture (final duplex concentration = 10 μM; pH 6.8–6.9) was stirred in a bath at 16 °C for 12–19 days. The progress of the reaction was monitored by MALDI-TOF MS, anion exchange HPLC, and PAGE (20% acrylamide, 7 M urea). The cross-linked duplex was isolated by anion exchange HPLC and desalted by elution through a Sep-Pak column.

Spectroscopic studies: Thermal denaturation and NMR experiments were carried out in phosphate buffer, with 2 and 200 μM solutions of duplex, respectively (see the Supporting Information for additional details).

Received: August 2, 2006
Published online: November 16, 2006

Keywords: cross-links · imidazoles · oligonucleotides · platinum · thioethers

[1] P. C. Zamecnik, M. L. Stephenson, *Proc. Natl. Acad. Sci. USA* **1978**, *75*, 280–284.

[2] a) V. V. Vlassov, V. V. Gorn, E. M. Ivanova, S. A. Kazakov, S. V. Mamaev, *FEBS Lett.* **1983**, *162*, 286–289; b) C. A. Lepre, L. Chassot, C. E. Costello, S. J. Lippard, *Biochemistry* **1990**, *29*, 811–823; c) V. Brabec, M. Leng, *Proc. Natl. Acad. Sci. USA* **1993**, *90*, 5345–5349; d) M. B. L. Janik, B. Lippert, *J. Biol. Inorg. Chem.* **1999**, *4*, 645–653; e) M. Escaffre, J.-C. Chottard, S. Bombard, *Nucleic Acids Res.* **2002**, *30*, 5222–5228.

[3] a) R. Dalbiès, D. Payet, M. Leng, *Proc. Natl. Acad. Sci. USA* **1994**, *91*, 8147–8151; b) R. Dalbiès, M. Boudvillain, M. Leng, *Nucleic Acids Res.* **1995**, *23*, 949–953; c) M.-J. Giraud-Panis, M. Leng, *Pharmacol. Ther.* **2000**, *85*, 175–181; d) B. Andersen, E. Bernal-Méndez, M. Leng, E. Sletten, *Eur. J. Inorg. Chem.* **2000**, 1201–1210.

[4] a) M. Boudvillain, M. Guérin, R. Dalbiès, T. Saison-Behmoaras, M. Leng, *Biochemistry* **1997**, *36*, 2925–2931; b) K. Aupeix-Schleidler, S. Chabas, L. Bidou, J.-P. Rousset, M. Leng, J.-J. Toulmé, *Nucleic Acids Res.* **2000**, *29*, 438–445.

[5] K. G. Strothkamp, S. J. Lippard, *Proc. Natl. Acad. Sci. USA* **1976**, *73*, 2536–2540.

[6] a) B. C. F. Chu, L. E. Orgel, *Nucleic Acids Res.* **1990**, *18*, 5163–5171; b) B. C. F. Chu, L. E. Orgel, *Nucleic Acids Res.* **1992**, *20*, 2497–2502.

[7] B. Algueró, E. Pedroso, V. Marchán, A. Grandas, unpublished results.

[8] a) V. Marchán, V. Moreno, E. Pedroso, A. Grandas, *Chem. Eur. J.* **2001**, *7*, 808–815; b) V. Marchán, E. Pedroso, A. Grandas, *Chem. Eur. J.* **2004**, *10*, 5369–5375. See references cited therein for literature concerning S versus N coordination.

[9] a) C. Hofr, V. Brabec, *J. Biol. Chem.* **2001**, *276*, 9655–9661; b) C. Hofr, V. Brabec, *Biopolymers* **2005**, *77*, 222–229.

 © 2006 Wiley-VCH Verlag GmbH & Co. KGaA, Weinheim

Electrochemistry

DOI: 10.1002/anie.200602891

Redox Targeting of Insulating Electrode Materials: A New Approach to High-Energy-Density Batteries**

*Qing Wang, Shaik M. Zakeeruddin, Deyu Wang, Ivan Exnar, and Michael Grätzel**

Electrochemical devices are currently under intense investigation for sustainable and environmentally benign electric-energy production and storage. The surge of portable

[*] Dr. Q. Wang,[+] Dr. S. M. Zakeeruddin, Dr. D. Wang, Prof. M. Grätzel
Laboratoire de photonique et interfaces
Ecole Polytechnique Fédérale de Lausanne
1015 Lausanne (Switzerland)
Fax: (+41) 216-936-100
E-mail: michael.graetzel@epfl.ch
Homepage: http://isic2.epfl.ch/page58671.html
Dr. I. Exnar
HPL SA
1015 Lausanne (Switzerland)
[+] Current address:
National Renewable Energy Laboratory (USA)

[**] We acknowledge financial support of this work by a CTI project (contract No. 7136.3 EPRP-IW). We thank Dr. H. Li at the Institute of Physics, Chinese Academy of Sciences, for the kind help of making the carbon-free $LiFePO_4$ sample.

Supporting information for this article is available on the WWW under http://www.angewandte.org or from the author.

© 2006 Wiley-VCH Verlag GmbH & Co. KGaA, Weinheim

consumer electronics has galvanized research on portable high-capacity power sources. Improvement of the energy density in electrochemical power sources ranging from conventional lead–acid batteries through to Ni–Cd, Ni–MH, and the state-of-the-art lithium-ion batteries has been a key issue for the past several decades.[1,2] The electroactive materials must be electrochemically addressable for their capacity to be explored fully. However, owing to a lack of electronic conductivity of the electrode material, a large amount of conducting additive, such as carbon black, has to incorporated into the electrode sheet to form a continuous conducting network for electron percolation.[3,4] Consequently, the energy density of the battery is greatly decreased by the presence of a large volume of inactive conducting agent.

Molecular wiring of poorly conducting battery materials promises to reduce the need for carbon addition.[5] In this case, the charges are transported from the current collector through a molecular layer adsorbed at the surface of the lithium-intercalating particles. As the molecular relay is chosen such that its Nernst potential matches the Fermi level of the substrate, interfacial charge transfer coupled to lithium release or insertion takes place, thus resulting in charging or discharging of the electrode material. Although intriguing, molecular wiring can have stability problems because of the possibility of desorption of the redox mediator from the insertion material during the charge and discharge cycle. Furthermore, the current output is limited by the rate of cross-surface charge percolation and interfacial charge transfer.

Herein we introduce redox targeting by freely diffusing relay molecules to address insulating or poorly conducting lithium-insertion materials. To our knowledge this approach has not been described previously. Figure 1 illustrates the

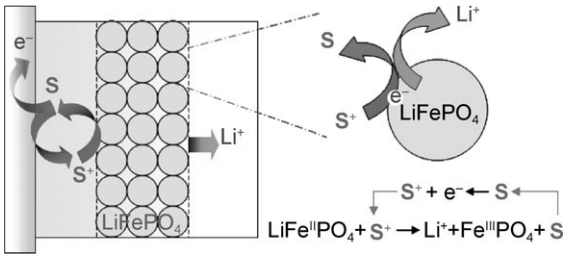

Figure 1. The principle of redox targeting of an insulating electrode material such as $LiFePO_4$ by a freely diffusing molecular shuttle **S**.

principle of the method by using as an example $LiFePO_4$, a large-band-gap semiconductor that is widely employed as positive-electrode material in lithium-ion batteries.[2,6] The molecular redox shuttle (**S**) is dissolved in the electrolyte of the cathodic compartment of the cell. During charging **S** is oxidized at the current collector to $\mathbf{S}^+$, which delivers the charge to the $LiFePO_4$ particles by bulk diffusion. Because the standard redox potential of $\mathbf{S}^+$ matches closely the Fermi level of $LiFePO_4$, $\mathbf{S}^+$ will be reduced back to **S** by hole injection in the $LiFePO_4$ particles, thus resulting in the oxidation of Fe^{II} to Fe^{III} and the release of lithium ions [Eq. (1)].

$$\mathbf{S}^+ + LiFePO_4 \rightarrow \mathbf{S} + Li^+ + FePO_4 \quad (1)$$

By contrast, during the discharging process, $\mathbf{S}^+$ is reduced at the current collector to **S**, which in turn delivers electrons to $FePO_4$ [the reverse of Eq. (1)]. The advantage of using a freely diffusing redox shuttle over molecular wiring is that it allows charge transport to proceed at a much faster rate, thus enhancing greatly the power output of the battery.

In principle, any reversible redox couple whose standard Nernst potential closely matches the Fermi level of the battery material is suitable for the redox-targeting process. The present study employs osmium polypyridyl complexes as mediators. The Os^{II}/Os^{III} redox couple is stable and reversible, and electron exchange proceeds very rapidly (near the diffusion-limited rate) by an outer-sphere mechanism associated with a low reorganization energy. By changing the properties of the ligands, the redox potential can be readily tuned. Osmium complexes have been widely employed in electrochemical devices, such as sensors and bio-fuel cells,[7–9] as well as dye-sensitized solar cells and optoelectronic systems.[10–12]

The Os complexes $[Os(mbpy)_3]Cl_2$ (**1**) and $[Os(mobpy)_3]Cl_2$ (**2**) were used here for redox targeting of the

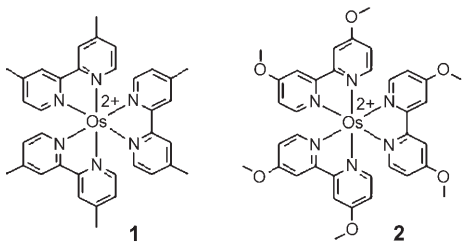

$LiFePO_4$ insertion material (mbpy = 4,4′-dimethyl-2,2′-bipyridine; mobpy = 4,4′-dimethoxy-2,2′-bipyridine). Figure 2 shows the cyclic voltammogram of a mixture of these two complexes measured with FTO (F-doped SnO_2) coated conducting glass as the working electrode. Two reversible one-electron waves are observed; the formal potentials

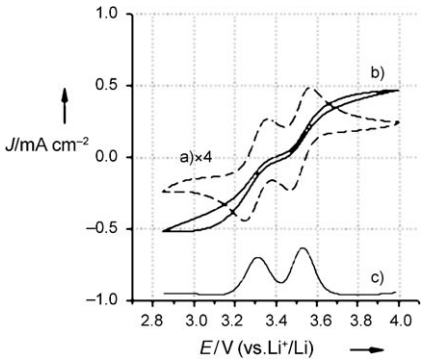

Figure 2. a,b) Cyclic voltammograms of a mixture of 4 mM $[Os(mbpy)_3]^{2+}/[Os(mobpy)_3]^{2+}$ in 1 M $LiPF_6$/EC + EMC (1:1) electrolyte with FTO glass (a, dashed line) and carbon-free $LiFePO_4$ coated on FTO glass (b, solid line) electrodes. The current scale of (a) has been magnified by 4. The scan rate is 0.1 Vs^{-1}. c) Square-wave voltammogram obtained with the FTO electrode.

 © 2006 Wiley-VCH Verlag GmbH & Co. KGaA, Weinheim

determined from square-wave voltammetry are 3.53 and 3.32 V (vs. Li^+/Li) for **1** and **2**, respectively. The peak current is proportional to the square root of the scan rate (see the Supporting Information), which indicates the occurrence of a semi-infinite diffusion-controlled redox process.[13] The diffusion coefficients were calculated to be approximately $1.5 \times 10^{-7}\ cm^2 s^{-1}$ for both complexes in the 1 M $LiPF_6$/EC + EMC (1:1, w/w) electrolyte (EC = ethylene carbonate; EMC = ethyl methyl carbonate). The redox potential for the two couples straddle the Fermi level of the $LiFePO_4$ cathode material, which is about 3.45 V (vs. Li^+/Li). Hence, on thermodynamic grounds, $LiFePO_4$ can be oxidized to $FePO_4$ by $[Os(mbpy)_3]^{3+}$ and the later reduced back by $[Os(mobpy)_3]^{2+}$.

Unambiguous evidence for these redox processes is presented by the voltammogram in Figure 2b, for which the working electrode was a film of carbon-free $LiFePO_4$ deposited on the FTO glass. In the absence of the redox relays, this electrode fails to exhibit any electrochemical response in the investigated potential range because of the insulating character of the $LiFePO_4$ material. Strikingly, the addition of the two redox mediators produces two well-defined current plateaus for the oxidation and reduction processes. This result stands in marked contrast to the behavior with the bare FTO glass electrode, in which case the anodic and cathodic currents pass through peaks as a result of the growth of the diffusion layer. The appearance of the catalytic waves indicates that the two redox couples are recycled by charge injection in the battery material; $[Os(mbpy)_3]^{2+}$ is regenerated from $[Os(mbpy)_3]^{3+}$ by hole injection into the $LiFePO_4$ layer and $[Os(mobpy)_3]^{3+}$ from $[Os(mobpy)_3]^{2+}$ by electron injection into the $FePO_4$ layer during the charging and discharging, respectively. As a consequence, the current is not limited by the diffusion of the molecules and is around four times higher than that obtained with the FTO electrode alone. Furthermore, it was found that the plateau currents are almost independent of the scan rates (see the Supporting Information), which suggests finite-length diffusion behavior of the molecules confined in the pores of the electrode sheet.[14]

Following these encouraging results, a three-compartment electrochemical cell (shown in the Supporting Information) was used to charge and discharge the insulating $LiFePO_4$ material. Each compartment of the cell was separated by a glass frit. A small quantity of the dark-brown electrolyte containing the two Os complexes was injected into the working-electrode compartment, and the other two compartments were filled with normal electrolyte. There was no appreciable leakage of the redox mediators across the frit during the experiments, which lasted for a few hours. Figure 3 depicts the voltage profiles of the electrodes during a galvanostatic charge and discharge cycle. Extended voltage plateaus were observed during the charge and discharge processes, which indicates that lithium extraction and insertion are sustained by the two redox relays. By contrast, no extended plateaus appear when bare FTO glass is used as a working electrode, because the $[Os(mbpy)_3]^{2+}$ and $[Os(mobpy)_3]^{3+}$ mediators are depleted by the oxidation and reduction processes, respectively. These results confirm that

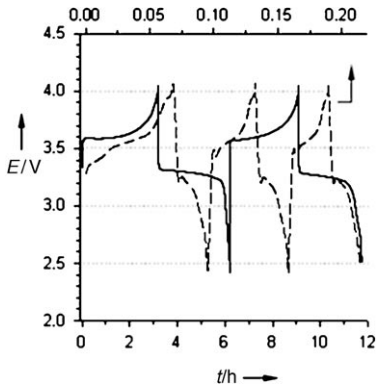

Figure 3. Voltage profiles of FTO (dashed line, top time axis) and carbon-free $LiFePO_4$/FTO (solid line, bottom time axis) electrodes obtained with a three-compartment electrochemical cell during galvanostatic charge/discharge processes. The electrolyte in the working-electrode compartment is 1 M $LiPF_6$/EC + EMC (1:1) containing 32 mM $[Os(mbpy)_3]^{2+}/[Os(mobpy)_3]^{2+}$ with a volume of 30 μL. The electrolytes in the other two compartments are 1 M $LiPF_6$/EC + EMC (1:1). The constant current is 0.05 $mA\,cm^{-2}$.

insulating $LiFePO_4$ materials can be charged and discharged by using redox targeting by freely diffusing molecular relays even in the absence of conducting additives.

As well as by using two redox couples whose standard Nernst potentials straddle the Fermi level of the battery material, the redox targeting can also be effected by a single molecule. One example is 10-methylphenothiazine (MPTZ), whose standard potential is only slightly higher than that of $LiFePO_4$.[15] With an FTO electrode, the voltammogram (see the Supporting Information) shows the normal redox waves of MPTZ, the peak currents of which are limited by the semi-infinite diffusion MPTZ in electrolyte. By contrast, with the $LiFePO_4$ electrode, the typical feature of a catalytic wave is again observed; the current plateaus show sustained oxidation and reduction processes resulting from molecular redox targeting. Thus, in the presence of MPTZ in the electrolyte, reversible lithium extraction/insertion involving the insulating $LiFePO_4$ is possible.

It should be noted that in conventional batteries, the active electrode materials are in electronic contact with the current collector. The electrode materials are normally prepared with conducting additives to form an electrode sheet that is attached to a metal support. A novel configuration of a compact energy-storage system based on redox targeting may be conceived, as shown in Figure 4. The active electrode materials could be stored in separate tanks and electrochemically addressed by the redox relay surrounding them. These molecular redox shuttles establish the electronic communication between the local electrode material and the current collector. As no conducting additives are needed, the energy density is expected to be greatly improved. Moreover, with such configuration, the battery can be recharged by simply replacing the tanks with charged electrode materials, thus avoiding long charging times.

In summary, a novel concept to address battery materials electrochemically by using redox targeting has been introduced and demonstrated with $LiFePO_4$ as an example. By

 © 2006 Wiley-VCH Verlag GmbH & Co. KGaA, Weinheim

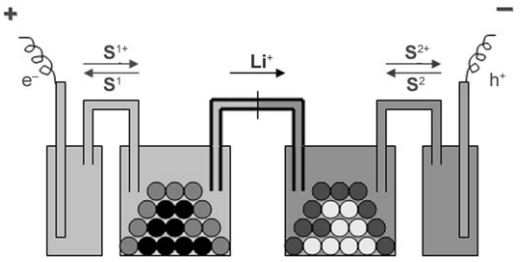

Figure 4. Configuration of a compact electric-energy-storage system. The active electrode materials are stored in tanks separated from the current collectors. The charges are transported between current collectors and active materials by the diffusion of molecular redox relays in the electrolyte.

using appropriate molecular shuttles, these concepts could be applied to other electrode materials, such as $LiCoO_2$, $LiMnPO_4$, $Li_4Ti_5O_{12}$, or even electrode materials for secondary batteries that do not employ lithium-insertion materials. In comparison with molecular wiring, larger power output can be expected for the targeting process. However, the challenge in this case is that a special separator has to be used to prevent the redox shuttle molecules from contacting the counter electrode, which leads to self-discharge. We propose that a solid Li^+ conductor, such as lithium phosphorus oxynitride (LiPON),[16] $70Li_2S{\cdot}30P_2S_5$,[17,18] and ceramic nanofiltration membranes[19] could be used for this purpose. Although such practical issues still need to be addressed, applications are feasible and offer opportunities for using insulating electrode materials in high-energy-storage systems.

Experimental Section

The syntheses of $[Os(mbpy)_3]Cl_2$ and $[Os(mobpy)_3]Cl_2$ can be found in reference [8]. 10-Methylphenothiazine was purchased from Acros and used as received. These molecules were dissolved at different concentrations in an electrolyte of 1 M $LiPF_6$/ EC + EMC mixture (1:1, w/w).

$LiFePO_4$ powder was synthesized by a solid-state reaction.[20] The electrode was prepared by mixing the $LiFePO_4$ powder with 8 wt.% PVDF and stirring with *N*-methyl-2-pyrrolidone (NMP). The resulting homogeneous slurry was then doctor bladed onto FTO conducting glass. The films were dried in an oven at 100 °C overnight, then cut into smaller pieces. The typical thickness of the film was 5–7 μm.

Voltammetric and galvanostatic measurements employed a PC-controlled AutoLab PSTA30 electrochemical workstation (Eco Chimie) with counter and reference electrodes of lithium foil. The electrolyte was 1 M $LiPF_6$/EC + EMC (1:1, w/w).

Received: July 19, 2006
Published online: November 16, 2006

Keywords: electrochemistry · energy storage · lithium-ion batteries · redox chemistry

[1] M. Winter, R. J. Brodd, *Chem. Rev.* **2004**, *104*, 4245 – 4269.
[2] J. M. Tarascon, M. Armand, *Nature* **2001**, *414*, 359 – 367.
[3] L. Aymard, C. Lenain, L. Courvoisier, F. Salver-Disma, J. M. Tarascon, *J. Electrochem. Soc.* **1999**, *146*, 2015 – 2023.
[4] J. K. Hong, J. H. Lee, S. M. Oh, *J. Power Sources* **2002**, *111*, 90 – 96.
[5] Q. Wang, N. Evans, S. M. Zakeeruddin, I. Exnar, M. Grätzel, *J. Am. Chem. Soc.* **2006**, submitted.
[6] A. K. Padhi, K. S. Nanjundaswamy, J. B. Goodenough, *J. Electrochem. Soc.* **1997**, *144*, 1188 – 1194.
[7] A. Heller, *J. Phys. Chem.* **1992**, *96*, 3579 – 3587.
[8] S. M. Zakeeruddin, D. M. Fraser, M. K. Nazeeruddin, M. Grätzel, *J. Electroanal. Chem.* **1992**, *337*, 253 – 283.
[9] F. Mao, N. Mano, A. Heller, *J. Am. Chem. Soc.* **2003**, *125*, 4951 – 4957.
[10] R. Argazzi, G. Larramona, C. Contado, C. A. Bignozzi, *J. Photochem. Photobiol. A* **2004**, *164*, 15 – 21.
[11] D. Kuciauskas, M. S. Freund, H. B. Gray, J. R. Winkler, N. S. Lewis, *J. Phys. Chem. B* **2001**, *105*, 392 – 403.
[12] G. Sauve, M. E. Cass, S. J. Doig, I. Lauermann, K. Pomykal, N. S. Lewis, *J. Phys. Chem. B* **2000**, *104*, 3488 – 3491.
[13] A. J. Bard, L. R. Faulkner, *Electrochemical Methods: Fundamentals and Applications*, 2nd ed., Wiley, **2000**.
[14] E. V. Milsom, H. R. Perrott, L. M. Peter, F. Marken, *Langmuir* **2005**, *21*, 9482 – 9487.
[15] C. Buhrmester, L. Moshurchak, R. C. L. Wang, J. R. Dahn, *J. Electrochem. Soc.* **2006**, *153*, A288 – A294.
[16] S. D. Jones, J. R. Akridge, F. K. Shokoohi, *Solid State Ionics* **1994**, *69*, 357 – 368.
[17] A. Hayashi, S. Hama, H. Morimoto, M. Tatsumisago, T. Minami, *J. Am. Ceram. Soc.* **2001**, *84*, 477 – 479.
[18] R. Mercier, J. P. Malugani, B. Fahys, G. Robert, *Solid State Ionics* **1981**, *5*, 663 – 666.
[19] S. Benfer, U. Popp, H. Richter, C. Siewert, G. Tomandl, *Sep. Purif. Technol.* **2001**, *22–3*, 231 – 237.
[20] D. Y. Wang, L. Hong, Z. X. Wang, X. D. Wu, Y. C. Sun, X. J. Huang, L. Q. Chen, *J. Solid State Chem.* **2004**, *177*, 4582 – 4587.

 © 2006 Wiley-VCH Verlag GmbH & Co. KGaA, Weinheim

Synthetic Methods

DOI: 10.1002/anie.200602950

Chemo- and Regioselective Preparation and Reaction of a Kinetic Zinc Enolate Formed from a Thiol Ester and Bis(iodozincio)methane**

*Zenichi Ikeda, Takaharu Hirayama, and Seijiro Matsubara**

Bis(iodozincio)methane (**1**), which has a methylene carbon atom with two nucleophilic sites, has been used for a variety of molecular transformations in which C–C bond formation is repeated at the same carbon atom.[1,2] In other words, it functions as a zinciomethylation reagent. Such zinciomethy-

[*] Z. Ikeda, T. Hirayama, Prof. Dr. S. Matsubara
Department of Material Chemistry
Graduate School of Engineering, Kyoto University
Kyoutodaigaku-Katsura, Nishikyo, Kyoto 615-8501 (Japan)
Fax: (+81) 75-383-2461
E-mail: matsubar@orgrxn.mbox.media.kyoto-u.ac.jp

[**] This work was supported financially by the Japanese Ministry of Education, Science, Sports, and Culture and by the Chugai Pharmaceutical Co., Ltd.

WILEY InterScience DISCOVER SOMETHING GREAT
© 2006 Wiley-VCH Verlag GmbH & Co. KGaA, Weinheim

lation of acylating reagents should afford the kinetic enolates of ketones. Many functional groups should be tolerated during the transformation because of the modest reactivity of organozinc compounds.[3] However, in previous studies some combinations of acylating reagents and **1**, regardless of their stoichiometric relationship, resulted in the formation of symmetrical 1,3-diketones through a double acylation of **1**. For example, the treatment of benzoyl chloride with **1** in any ratio in the presence of a palladium catalyst gave 1,3-diphenylpropane-1,3-dione.[4a] The treatment of an acyl cyanide with **1** gave a similar result.[4b] These highly reactive acylating reagents react preferentially with the α-zincioketone intermediate over bis(iodozincio)methane (**1**). A mild and chemoselective transformation reported by Fukuyama and co-workers in which thiol esters are converted into ketones with alkyl zinc reagents in the presence of a palladium catalyst[5–7] suggested to us that a thiol ester may react with bis(iodozincio)methane (**1**)[2c] in the presence of a palladium catalyst to give an α-zincioketone, that is, an enolate[8] that would not readily undergo palladium-catalyzed coupling with the thiol ester. The transformation should be chemoselective because of the modest reactivity of **1**. Furthermore, the terminal enolate formed initially would not isomerize to the corresponding thermodynamic enolate under these reaction conditions (Scheme 1).

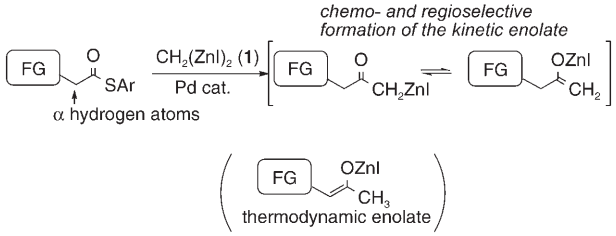

Scheme 1. Preparation of a kinetic zinc enolate by zinciomethylation of a thiol ester. FG = functional group.

Arene thiol esters[9] of 5-hexenoic acid, **2**, were mixed with bis(iodozincio)methane (**1**) in the presence of a palladium(0) catalyst, which was prepared in situ from $[Pd_2(dba)_3]$ (dba = *trans*,*trans*-dibenzylideneacetone) and triphenylphosphane, and treated subsequently with benzaldehyde (Scheme 2).

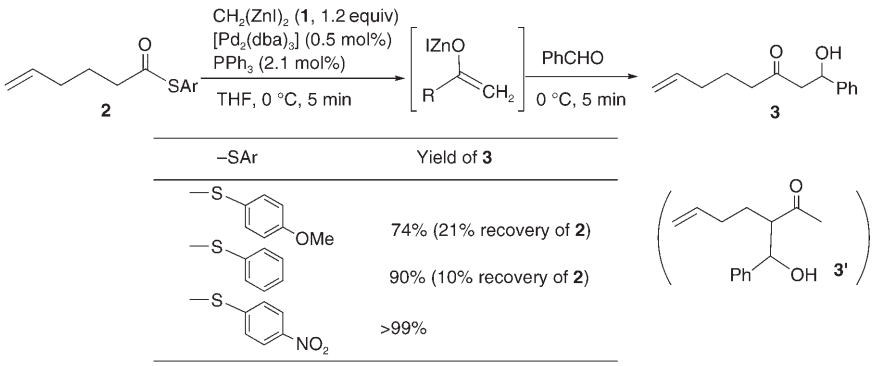

–SAr	Yield of **3**
–S–C6H4–*p*-OMe	74% (21% recovery of **2**)
–S–C6H5	90% (10% recovery of **2**)
–S–C6H4–*p*-NO2	>99%

Scheme 2. Preparation of the kinetic zinc enolate from thiol esters **2** and reaction with benzaldehyde.

Tuning of the electron density of the aromatic ring of the thiol improved the yield. The aldol product **3** was obtained quantitatively when 4-nitrobenzenethiol was used to form the thiol ester. The only other possible aldol product **3′**, which may result if the enolate formed initially isomerizes to the thermodynamic enolate, was not observed. The use of ethanethiol ester as a substrate[5] resulted in the recovery of the starting material.

Various types of electrophiles can be added to the prepared kinetic enolate as reactants, as shown in Scheme 3. Treatment with acyl cyanides gave 1,3-diketones. Conjugate addition was not observed in the reaction of (*E*)-MeCH=CHCOPh with the kinetic enolate formed from **2′**.

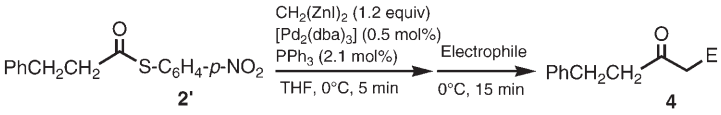

Electrophile	E in **4**	Yield of **4** [%]
PhCOCN	PhCO–	89
MeCOCN	MeCO–	70
PhCHO	PhCH(OH)–	>99
EtCHO	EtCH(OH)–	>99
PhCOMe	PhCMe(OH)–	86
cyclohexanone	1-hydroxycyclohexyl–	99
(*E*)-MeCH=CHCOPh	(*E*)-MeCH=CHCPh(OH)–	62

Scheme 3. Reaction of the kinetic enolate prepared from thiol ester **2′** with various electrophiles.

Functional-group tolerance in the formation of the kinetic enolate was examined (Scheme 4). Terminal alkyne (in **5d**), primary bromide (in **5e**), silyl ether (in **5i**), and ester (in **5j**) functionalities remained intact during the reaction. Neither a bromophenyl (in **5f**) nor a sulfide (in **5g**) group interfered with the formation of the kinetic enolate, although these functional groups often interact with palladium(0) catalysts.

The chemo- and regioselective preparation of the kinetic enolate in the presence of a keto group was an attractive goal.[10] Unfortunately, the treatment of a thiol ester containing a keto group with bis(iodozincio)methane (**1**) in the presence of a palladium catalyst gave a polymeric compound formed by an intermolecular reaction of the keto group with the enolate. The addition of the electrophile to the reaction mixture prior to the formation of the enolate, however, prevented this self-condensation. Mixtures of a thiol ester with a keto group, **7**, and benzoyl cyanide were treated with the dizinc reagent **1** in the presence of a palladium catalyst (Scheme 5). The desired triketones were formed in excellent yields. The initially formed kinetic enolate reacted with the electrophile without being transposed to the other methyl ketone in the same molecule, as shown by the reactions of **7d** and **7e**.

 © 2006 Wiley-VCH Verlag GmbH & Co. KGaA, Weinheim

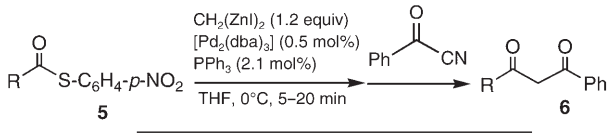

R		Yield of **6** [%]
$PhCH_2CH_2$–	**5a**	89
Ph–	**5b**	80
$CH_2=CH(CH_2)_3$–	**5c**	96
$HC\equiv C(CH_2)_6$–	**5d**	87
$BrCH_2(CH_2)_6$–	**5e**	93
p-BrC_6H_4–	**5f**	80
$PhCH_2SCH_2$–	**5g**[a]	83
$PhO(CH_2)_{10}$–	**5h**	85
t$BuMe_2SiO(CH_2)$–	**5i**	84
$EtO_2C(CH_2)_6$–	**5j**	93

Scheme 4. Chemoselectivity in the formation of the kinetic enolate. [a] $[Pd_2(dba)_3]$ (1.0 mol%) and PPh_3 (4.2 mol%) were used.

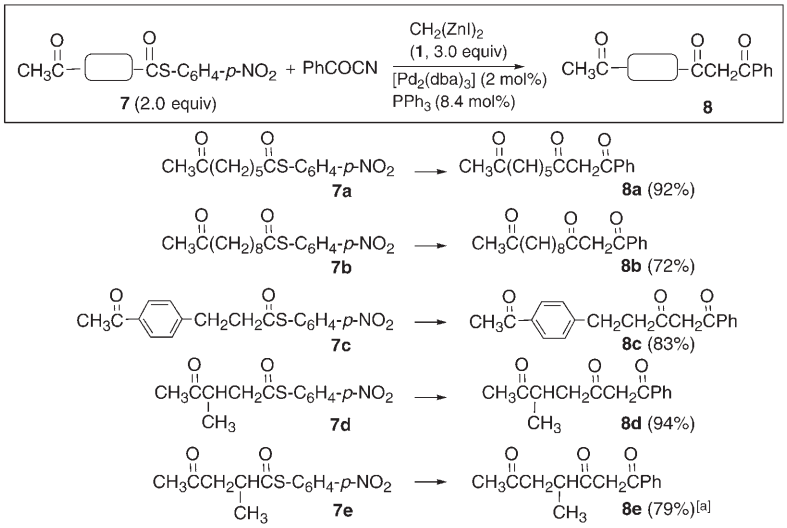

Scheme 5. Preparation of triketones **8** by the treatment of benzoyl cyanide with enolates that contain a keto group. [a] P(2-furyl)$_3$ was used instead of PPh_3.

The formation from the thiol esters and reaction of the enolates proceeded chemo- and regioselectively.

No loss of enantiomeric purity was observed in the transformation of the enantiomerically pure thiol ester **9** into the diketone **10**.[11] The thiol ester **9** was prepared readily from L-proline. The chiral 1,3-diketone is a potentially useful compound for organic synthesis (Scheme 6).

Thus, these results allow us to propose a novel method for the preparation of a kinetic zinc enolate from a thiol ester and bis(iodozincio)methane. The modest reactivity of the zinc reagent makes the transformation chemo- and regioselective. The method is simple, but provides access to reactive functionalized enolates which are otherwise hard to obtain.

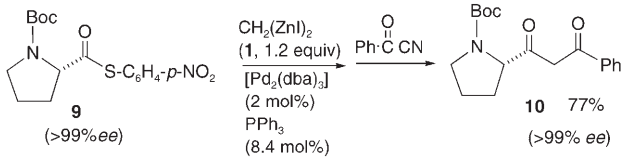

Scheme 6. Conversion of thiol ester **9**, prepared from enantiomerically pure L-proline, into the enantiomerically pure 1,3-diketone **10**.[11] Boc = *tert*-butoxycarbonyl.

Experimental Section

Typical Procedure: Triphenylphosphane (0.02 mmol, 5.5 mg) was added to a solution of $[Pd_2(dba)_3]$ (0.005 mmol, 4.6 mg) in THF (0.8 mL) at 25 °C. The mixture was stirred for 10 min, then cooled to 0 °C, whereupon the *p*-nitrobenzenethiol ester of 5-hexenoic acid (1.0 mmol, 0.25 g) was added as a solution in THF (1.0 mL), followed by bis(iodozincio)methane (**1**) in THF (0.45 M, 1.2 mmol, 2.7 mL). The resulting mixture was stirred for 5 min at 0 °C. A solution of benzaldehyde (1.5 mmol, 0.16 g) in THF (1.0 mL) was then added, and the reaction mixture was stirred for a further 5 min at 0 °C. A saturated aqueous solution of ammonium chloride (1.0 mL) was added, and the mixture was extracted with diethyl ether. The combined organic layers were washed with saturated, aqueous $NaHCO_3$ and brine, then dried over anhydrous sodium sulfate. After rapid column chromatography on silica gel with hexane/ethyl acetate as the eluent, compound **3** was obtained in quantitative yield.

Preparation of **8a**: Triphenylphosphane (0.042 mmol, 11.3 mg) was added to a solution of $[Pd_2(dba)_3]$ (0.01 mmol, 9.2 mg) in THF (1.0 mL) at 25 °C, and the mixture was stirred for 10 min. After the reaction mixture was cooled to 0 °C, benzoyl cyanide (0.5 mmol, 0.066 g) was then added as a solution in THF (0.5 mL), followed by a solution of the *p*-nitrobenzenethiol ester of 7-oxooctanoic acid (1.0 mmol, 0.29 g) in THF (1.0 mL) at 0 °C. A solution of bis(iodozincio)-methane (**1**) in THF (0.45 M, 1.5 mmol, 3.3 mL) was then added dropwise, and the reaction mixture was stirred for a further 1 h at 0 °C. A saturated aqueous solution of ammonium chloride (2.0 mL) was then added, and the mixture was extracted with diethyl ether. The combined organic layers were washed with saturated, aqueous $NaHCO_3$ and brine, and dried over anhydrous sodium sulfate. After rapid column chromatography on silica gel with hexane/ethyl acetate as the eluent, compound **3** was obtained in 92% yield. Triketones **8d** (94%) and **8e** (79%) were obtained in the same way, although P(2-furyl)$_3$ was used instead of PPh_3 in the preparation of **8e**.

8a: ^{1}H NMR (500 MHz, $CDCl_3$): $\delta = 7.8$–8.0 (m, 2H), 7.4–7.6 (m, 3H), 6.17 (s, 1H, enol form), 2.43 (t, $J = 7.5$ Hz, 2H), 2.14 (s, 3H), 1.70 (tt, $J = 5.5$, 5.5 Hz, 2H), 1.62 (tt, $J = 5.5$, 5.5 Hz, 2H), 1.56 (br s, 1H), 1.3–1.41 ppm (m, 2H); ^{13}C NMR (125 MHz, $CDCl_3$): $\delta = 209.0$, 196.7, 183.4, 134.9, 132.2, 128.6, 127.0, 96.1, 43.4, 39.0, 29.9, 28.7, 25.5, 23.4 ppm.

8d: ^{1}H NMR (500 MHz, $CDCl_3$): $\delta = 7.8$–8.0 (m, 2H), 7.4–7.6 (m, 3H), 6.17 (s, 1H, enol form), 3.11 (tq, $J = 7.5$, 7.5 Hz, 1H), 2.93 (dd, $J = 16.0$, 8.0 Hz, 1H), 2.44 (dd, $J = 16.0$, 5.5 Hz, 1H), 2.25 (s, 3H), 1.61 (bs, 1H), 1.18 ppm (d, $J = 5.5$, 5.5 Hz, 3H); ^{13}C NMR (125 MHz, $CDCl_3$): $\delta = 211.0$, 196.6, 181.0, 134.3, 132.3, 128.6, 126.9, 96.7, 42.8, 42.3, 28.5, 16.6 ppm.

8e: ^{1}H NMR (500 MHz, $CDCl_3$): $\delta = 7.8$–8.0 (m, 2H), 7.4–7.6 (m, 3H), 6.23 (s, 1H, enol form), 3.08 (ddq, $J = 8.0$, 7.0, 5.0 Hz, 1H), 3.01 (dd, $J = 18.0$, 8.0 Hz, 1H), 2.50 (dd, $J = 18.0$, 5.0 Hz, 1H), 2.18 (s, 3H), 1.60 (br s, 1H), 1.18 ppm (d, $J = 5.5$, 5.5 Hz, 3H); ^{13}C NMR (125 MHz, $CDCl_3$): $\delta = 206.9$, 201.2, 181.3, 134.4, 132.2, 128.6, 126.9, 95.4, 46.5, 38.7, 30.3, 17.9 ppm.

Received: July 22, 2006
Published online: November 14, 2006

Keywords: chemoselectivity · cross-coupling · enolates · regioselectivity · zinc

 © 2006 Wiley-VCH Verlag GmbH & Co. KGaA, Weinheim

[1] a) S. Matsubara in *Handbook of Functionalized Organometallics, Vol. 2* (Ed.: P. Knochel), Wiley-VCH, Weinheim, **2005**, chap. 8; b) P. Knochel, J.-F. Normant, *Tetrahedron Lett.* **1986**, *27*, 4427; c) P. Knochel, J.-F. Normant, *Tetrahedron Lett.* **1986**, *27*, 4431; d) I. Marek, J.-F. Normant, *Chem. Rev.* **1996**, *96*, 3241; e) S. Matsubara, K. Oshima, K. Utimoto, *J. Organomet. Chem.* **2001**, *617–618*, 39; f) F. Berttini, P. Gasselli, G. Zubiani, G. Cainelli, *Tetrahedron* **1970**, *26*, 1281; g) B. J. J. van de Heisteeg, M. A. Schat, G. Tinga, O. S. Akkerman, F. Bickelhaupt, *Tetrahedron Lett.* **1986**, *27*, 6123; h) E. Nakamura, K. Kubota, G. Sakata, *J. Am. Chem. Soc.* **1997**, *119*, 5457.

[2] a) K. Nomura, K. Oshima, S. Matsubata, *Angew. Chem.* **2005**, *117*, 6010; *Angew. Chem. Int. Ed.* **2005**, *44*, 5860; b) Z. Ikeda, K. Oshima, S. Matsubara, *Org. Lett.* **2005**, *7*, 4859; c) H. Yoshino, N. Toda, M. Kobata, K. Ukai, K. Oshima, K. Utimoto, S. Matsubara, *Chem. Eur. J.* **2005**, *11*, 721.

[3] P. Knochel, H. Leuser, L.-Z. Gong, S. Perrone, F. F. Kneisel in *Handbook of Functionalized Organometallics*, *Vol. 1* (Ed.: P. Knochel), Wiley-VCH, Weinheim, **2005**, chap. 7.

[4] a) S. Matsubara, K. Kawamoto, K. Utimoto, *Synlett* **1998**, 267; b) S. Matsubara, Y. Yamamoto, K. Utimoto, *Synlett*, **1999**, 1471.

[5] a) H. Tokuyama, S. Yokoshima, T. Yamashita, T. Fukuyama, *Tetrahedron Lett.* **1998**, *39*, 3189; b) T. Fukuyama, H. Tokuyama, *Aldrichimica Acta* **2004**, *37*, 87.

[6] a) J. Srogl, W. Liu, D. Marshall, L. S. Liebeskind, *J. Am. Chem. Soc.* **1999**, *121*, 9449; b) W. P. Roberts, I. Ghosh, P. A. Jacobi, *Can. J. Chem.* **2004**, *82*, 279; c) M. E. Angiolelli, A. L. Casalnuovo, T. P. Selby, *Synlett* **2000**, 905.

[7] a) B. W. Fausett, L. S. Liebeskind, *J. Org. Chem.* **2005**, *70*, 4851; b) A. Lengar, C. O. Kappe, *Org. Lett.* **2004**, *6*, 771; c) R. Wittenberg, J. Srogl, M. Egi, L. S. Liebeskind, *Org. Lett.* **2003**, *5*, 3033; d) F.-A. Alphonse, F. Suzenet, A. Keromnes, B. Lebret, G. Guillaumet, *Org. Lett.* **2003**, *5*, 803.

[8] a) M. W. Rathke, *Org. React.* **1975**, *22*, 423; b) A. Fürstner in *Organozinc Reagents* (Eds.: P. Knochel, P. Jones), Oxford University Press, Oxford, **1999**, chap. 14; c) R. D. Rieke, S. J. Uhm, *Synthesis* **1975**, 452; d) E. Vedejes, S. Ahmand, *Tetrahedron Lett.* **1988**, *29*, 2291; e) S. Matsubara, N. Tsubonia, Y. Morizawa, K. Oshima, H. Nozaki, *Bull. Chem. Soc. Jpn.* **1984**, *57*, 3242.

[9] Prepared from a mixed anhydride and a thiol; see: B. Neises, W. Steglich, *Angew. Chem.* **1978**, *90*, 556; *Angew. Chem. Int. Ed. Engl.* **1978**, *17*, 522.

[10] For alkyl zinc reagents with a carbonyl group, see: a) P. Jones, K. C. Reddy, P. Knochel, *Tetrahedron* **1998**, *54*, 1471; b) E. Nakamura, S. Aoki, K. Sekiya, H. Oshino, I. Kuwajima, *J. Am. Chem. Soc.* **1987**, *109*, 8056; c) Y. Tamaru, H. Tanigawa, T. Yamamoto, Z. Yoshida, *Angew. Chem.* **1989**, *101*, 358; *Angew. Chem. Int. Ed. Engl.* **1989**, *28*, 351; d) B. H. Lipshutz, M. R. Wood, R. Tirano, *J. Am. Chem. Soc.* **1995**, *117*, 6126.

[11] The enantiomeric purity of **10** was determined by HPLC (chiralpak AD-H, 0.46 cmϕ × 25 cm (Daicel), hexane/2-propanol (85:15), 1.5 mL cm^{-1}): *R* isomer: 2.89 min, *S* isomer: 4.23 min.

 © 2006 Wiley-VCH Verlag GmbH & Co. KGaA, Weinheim

DOI: 10.1002/anie.200603055

trans Influences on Hypervalent Bonding of Aryl λ^3-Iodanes: Their Stabilities and Isodesmic Reactions of Benziodoxolones and Benziodazolones**

Masahito Ochiai, Takuya Sueda, Kazunori Miyamoto, Paul Kiprof, and Viktor V. Zhdankin*

Aryl λ^3-iodanes ArILL′ (L, L′: heteroatom ligands and others) adopt T-shaped geometries with a nearly linear L–I–L′ triad. It has been generally accepted that electronegative axial ligands stabilize the aryl λ^3-iodanes because of the inherent nature of the linear three-center four-electron (3c–4e) L–I–L′ bonding that places more electron density at the ends (L, L′) than at the center.[1] This idea is in a good agreement with the fact that triphenyl-λ^3-iodane, which decomposes even at −10 °C,[2] is less stable than (diacetoxyiodo)benzene, but not compatible with the labile nature of (dihydroxyiodo)benzene and the derivatives $PhI(OMe)_2$, PhI(OH)OMe,[3] and $PhI(OTf)_2$.[4a] We report herein that mutual ligand influence (*trans* influence) in hypervalent aryl λ^3-iodanes probably plays an important role in their stabilities. The structural *trans* influence of the ligands is responsible for the oxo-bridged polymeric structure of iodosylbenzene as opposed to the monomeric structure of (dihydroxyiodo)benzene,[5] the facile isomerization of phenyl-λ^3-iodanes **6** (L = L′ = NO_3, OTf, ClO_4) to the oxo-bridged dimers,[4] and the smooth rearrangement of some benziodazolones **3a** (L = RO, RCONH) to iminiobenziodoxoles **4**.[6]

The *trans* influence of a ligand in a transition-metal complex is a well-known, much argued phenomenon, defined as the extent to which that ligand weakens the bond *trans* to itself in the equilibrium state of the complex.[7] Therefore, *trans* influence is a thermodynamic concept and directly associated with the stability of the complex. Calculations by Shustorovich and Buslaev indicated that in aryl λ^3-iodanes strengthening of the I–L bond and weakening of the I–L′ bond, which are *trans* to each other, will occur monotonically with increasing donor ability of ligand L.[8] In linear L–I–L′

[*] Prof. M. Ochiai, Dr. T. Sueda, K. Miyamoto
Faculty of Pharmaceutical Sciences
University of Tokushima
1-78 Shomachi, Tokushima 770-8505 (Japan)
Fax: (+81) 88-633-9504
E-mail: mochiai@ph.tokushima-u.ac.jp
Prof. P. Kiprof, Prof. V. V. Zhdankin
Department of Chemistry and Biochemistry
University of Minnesota Duluth
Duluth, MN 55812 (USA)

[**] We gratefully acknowledge the Ministry of Education, Culture, Sports, Science, and Technology of Japan for financial support in the form of a grant.

Supporting information for this article is available on the WWW under http://www.angewandte.org or from the author.

 © 2006 Wiley-VCH Verlag GmbH & Co. KGaA, Weinheim

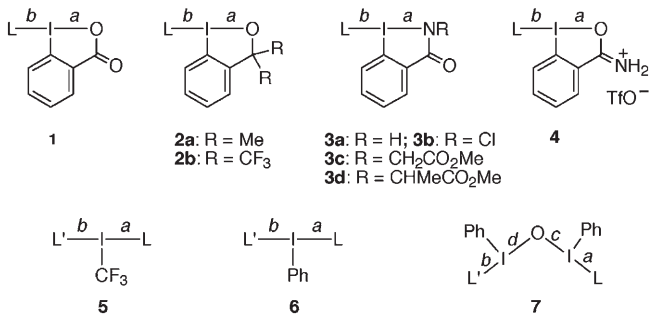

hypervalent bonding in which the central iodine atom retains the $5s^2$ lone pair, the influence of the σ-bonded ligand L is transmitted through the $5p_\sigma$ orbital of the iodine atom, and the resulting *trans* influence is exclusively inductive in nature.

The *trans* influences are experimentally accessible by crystallographic bond-length determination, vibrational (IR) and NMR spectroscopy, and other measurements on stable complexes.[7] In conjunction with the recent increasing use of hypervalent organo-λ^3-iodanes in organic synthesis, a large number of their solid-state structures are available, and this makes it possible to evaluate the magnitude of the *trans* influence of the ligands attached to iodine(III). Comparison of I^{III}–O (N, L, or L′) bond lengths in a variety of organo-λ^3-iodanes **1**–**7** (Tables 1–3) provides an order of structural *trans* influence of the ligands (Scheme 1). For instance, significant differences in the endocyclic I–O bond lengths *a* of **1** (L = Ph, 2.478 Å; L = cyclohexylethynyl, 2.34 Å; L = OH, 2.30 Å; Table 1, entries 2–4) illustrate a quantitative measure of the relative *trans* influence of these groups, which decreases in the order Ph > C≡C-*c*-C_6H_{11} > OH. A similar order (C≡CPh > $OCOC_6H_4$-*m*-Cl > $OCOCF_3$ > NO_3) was reported for platinum(II) hydride complexes.[7b]

Table 1: Selected bond lengths in hypervalent λ^3-iodanes **1**–**4**.

Entry	λ^3-Iodane (L)	Bond *a* [Å]	Bond *b* [Å]	σ_I	Ref.
1	**1** (C(=PPh_3)CO_2Me)	2.484(2)	2.056(3)		[16]
2	**1** (Ph)	2.478(4)	2.105(4)	0.12	[17]
3	**1** (C≡C-*c*-C_6H_{11})	2.34(1)	2.03(2)	0.29	[18]
4	**1** (OH)	2.30	2.00	0.33	[19]
5	**1** (CF_3)	2.283(2)	2.219(4)	0.38	[20]
6	**1** (OMe)	2.22(4)	1.98(4)	0.29	[21]
7	**1** (OO*t*Bu)	2.181(5)	2.039(5)		[13a]
8	**1** ($OOCMe_2C{\equiv}CSiMe_3$)	2.153(7)	2.032(6)		[22]
9	**1** (OAc)	2.13(2)	2.11(2)	0.42	[23]
10	**1** ($OCOC_6H_4$-*m*-Cl)	2.11	2.13		[24]
11	**1** (Cl)	2.091(3)	2.461(1)	0.42	[25]
12	**2a** (Br)	2.050(5)	2.6927(8)	0.45	[26]
13	**2b** (CF_3)	2.2014(15)	2.229(2)	0.38	[20]
14	**2b** (N_3)	2.130(5)	2.182(7)	0.48	[27]
15	**2b** (Br)	2.118(6)	2.5945(11)	0.45	[26]
16	**2b** (Cl)	2.110(5)	2.438(2)	0.42	[25]
17	**3a** (OAc)	2.101(5)	2.234(4)	0.42	[6a]
18	**3b** (Cl)	2.06	2.56	0.42	[12]
19	**3c** (Cl)	2.113	2.563	0.42	[28]
20	**3d** (Ph)	2.455(6)	2.133(7)	0.12	[29]
21	**4** (NHCO*i*Pr)	2.323(3)	2.010(4)	0.21	[6b]
22	**4** (O*i*Pr)	2.271(2)	1.986(2)	0.34	[6a]

Table 2: Selected bond lengths in hypervalent λ^3-iodanes **5** and **6**.

Entry	λ^3-Iodane (L, L′)	Bond *a* [Å]	Bond *b* [Å]	Ref.
1	**5** (OMe, OMe)	2.053[a]	2.053[a]	[30]
2	**5** (OMe, Cl)	1.980[a]	2.579[a]	[30]
3	**5** (Cl, Cl)	2.468[a]	2.468[a]	[31]
4	**5** (Cl, F)	2.412(3)	2.023(6)	[32]
5	**5** (Cl, $OCOCF_3$)	2.398(2)	2.219(6)	[33]
6	**5** (F, F)	1.982(2)	1.982(2)	[34]
7	**5** ($OCOCF_3$, $OCOCF_3$)	2.127[a]	2.127[a]	[35]
8	**6** (Ph, I)	2.099[b]	3.437[b]	[36]
9	**6** (Ph, Br)	2.083[b]	3.250[b]	[36]
10	**6** (Ph, Cl)	2.087[b]	3.085[b]	[36]
11	**6** (Ph, BF_4)	2.03[a]	2.97[a]	[37]
12	**6** ($OCOCF_3$, $OCOCF_3$)	2.162[a]	2.162[a]	[38]

[a] Average. [b] Average in halogen-bridged dimers.

Table 3: Selected bond lengths in hypervalent λ^3-iodanes **7**.

Entry	λ^3-Iodane (L, L′)	Bond *a* [Å]	Bond *b* [Å]	Bond *c* [Å]	Bond *d* [Å]	Ref.
1	**7** ($OCOCF_3$, $OCOCF_3$)	2.273[a]	2.273[a]	2.016[a]	2.016[a]	[39]
2	**7** ($OCOCF_3$, NO_3)	2.264(14)	2.354(15)	2.012(14)	1.999(16)	[40]
3	**7** (NO_3, NO_3)	2.32[a]	2.32[a]	2.01[a]	2.01[a]	[41]

[a] Average.

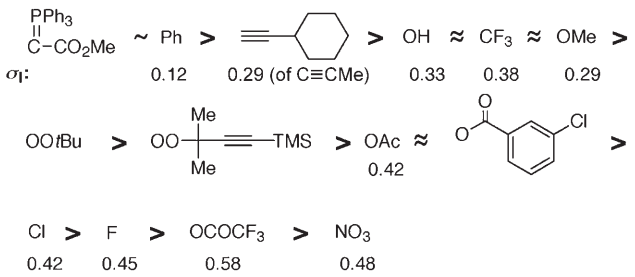

Scheme 1. Ligand order of decreasing *trans* influence in aryl λ^3-iodanes and Hammett inductive constants σ_I. TMS = $SiMe_3$.

The relative *trans* influence of halogens (I > Br ≈ Cl > F) is also determined by comparison of isomorphous pairs of λ^3-iodanes **2b** (L = Br, Cl: Table 1, entries 15 and 16), **5** (L = L′ = Cl and L = Cl, L′ = F: Table 2, entries 3 and 4), and **6** (L = Ph, L′ = I, Br, and Cl: Table 2, entries 8–10) in which the *trans* ligand is the same for both members of each pair. This ordering of halogens is in good agreement with that observed for thiourea complexes of phenyltellurium halides.[8b,9] The order of *trans* influences shown in Scheme 1 seems to correlate with Hammett inductive constants σ_I and to decrease with increasing σ_I, which is in accord with expectations based on the theory.[8] Note that some hypervalent bonds are weak and probably influenced by lattice forces.[9] The intermolecular contacts involving I^{III} centers that are observed frequently in the crystal structures of λ^3-iodanes will also affect the bond lengths.

The phenyl-λ^3-iodanes **6** with two strong *trans*-influencing ligands on iodine(III) (L = L′ = Ph, OH, OMe, OO*t*Bu) are predicted to be labile, because of the unfavorable mutual

 © 2006 Wiley-VCH Verlag GmbH & Co. KGaA, Weinheim

influences of the ligands: in fact, $PhI(OOtBu)_2$ decomposes even at −80 °C in dichloromethane,[10] $PhI(OMe)_2$ decomposes explosively,[11] and $PhI(OH)_2$ has never been synthesized.

The exocyclic I–OAc bond lengths *b* [2.11 Å for **1** (L = OAc) and 2.234 Å for **3a** (L = OAc); Table 1, entries 9 and 17] of five-membered λ^3-iodanyl heterocycles apparently reflect a significantly greater *trans* influence of the benziodazolone group compared to the benziodoxolone ring, as shown in Scheme 2. Furthermore, differences in I–O distances of **1**

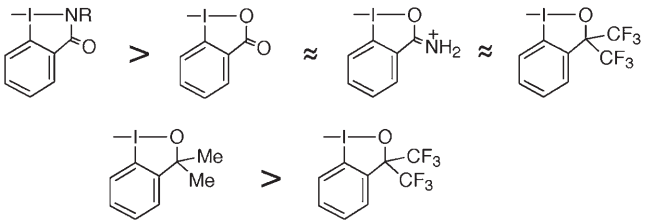

Scheme 2. The *trans* influence in iodazoles and iodoxoles.

(L = MeO) and **4** (L = *i*PrO), and in I–Cl bond lengths of **1** (L = Cl) and **2b** (L = Cl), illustrate that the magnitude of the effects for the iminiobenziodoxole group and the Martin ligand are comparable to that for the benziodoxolone ring (Table 1, entries 6, 22, 11, and 16). As expected, the *trans* influence in the Martin ligand **2b** is smaller than that in the dimethyl analogue (Table 1, entries 12 and 15).

The benziodoxolyl unit in **1**, associated with a moderate *trans* influence, accommodates *trans* ligands L with various degrees of *trans* influence, such as Ph, CCR, OH, CF_3, OMe, OO*t*Bu, OAc, Cl, $OCOCF_3$, OTs, OTf, and so on, and all of these λ^3-iodanes have been synthesized as stable compounds. On the other hand, the benziodazolyl unit in **3a**, with a larger *trans* influence, is applicable only to *trans* ligands L with weak or moderate influence, such as OAc, Cl, OTs, OTf, and so on.[6,12] Thus, alkylperoxy benziodoxolone **1** (L = OO*t*Bu) was prepared from hydroxy-λ^3-iodane **1** (L = OH) through BF_3-catalyzed ligand exchange with *tert*-butyl hydroperoxide under mild conditions,[13] while the attempted ligand exchange of (triflyloxy)benziodazolone **3a** (L = OTf) with *tert*-butyl hydroperoxide in acetonitrile did not afford peroxybenziodazolone **3a** (L = OO*t*Bu) at all, but instead produced the rearranged alkylperoxy iminiobenziodoxole **4** (78%) selectively. The highly *trans*-influencing *t*BuOO ligand probably prefers to bind to iminiobenziodoxolyl units with a moderate influence rather than to benziodazolonyl units. The rearrangement of benziodazolones to iminiobenziodoxoles, probably directed on the basis of a preferred combination of *trans* influences, was originally described by Zhdankin and coworkers in 1997.[6] They reported selective formation of rearranged iminiobenziodoxoles **4** from benziodazolone **3a** (L = TfO) by ligand exchange with the highly *trans*-influencing alkoxyl (MeO and *i*PrO) and amido (EtCONH and *i*PrCONH) groups.

To assess the energetic effect of *trans* influence in benziodoxolones **1** and benziodazolones **3a**, the isodesmic (homodesmic)[14] ligand-exchange reaction energies listed in Table 4 were calculated (see also Table S1 in the Supporting Information). Use of isodesmic reactions helps to eliminate systematic errors in ab initio calculations.[15] Stabilization in this ligand exchange can be taken as an indicator of the

Table 4: Isodesmic reaction energies for ligand exchange between benziodoxolones and benziodazolones in kcal mol^{-1} at the MP2/6-311 + G(2d, p) level of theory.

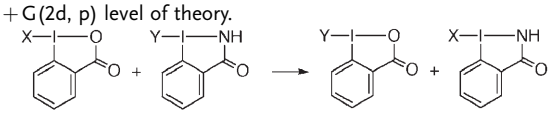

X↓ Y→	OH	OMe	OAc	Cl	F
NO_3	−3.15	−3.24	−1.83	−1.56	−0.80
F	−2.35	−2.44	−1.03	−0.76	
Cl	−1.59	−1.68	−0.27		
OAc	−1.32	−1.42			
OMe	+0.10				

preferred combination, mostly controlled by *trans* influences. Large stabilization energies (> 3 kcal mol^{-1}) were obtained for combinations of a strongly *trans*-influencing group (OH or OMe) that prefers to attach to the benziodoxolone ring with a weaker one (NO_3) that prefers to bind to the benziodazolone ring. Interestingly, the stabilization energy seems to decrease with a decreasing difference in magnitude of the *trans* influences of the ligands; thus, combinations of OH/OMe and OAc/Cl groups showed small isodesmic reaction energies. These isodesmic reaction energies tend to correlate with the differences in inductive parameters σ_I of the two ligands X and Y with a correlation coefficient of $r = 0.91$ (Figure 1), but not with those in electronegativities.

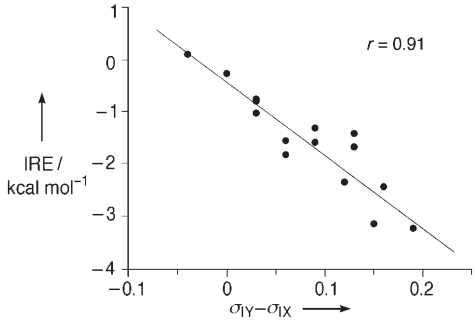

Figure 1. Calculated isodesmic reaction energies (IRE) for ligand exchange between benziodoxolones and benziodazolones versus $\sigma_{IY}-\sigma_{IX}$.

Phenyl-λ^3-iodanes **6** (L = L′ = NO_3, OTf, ClO_4) with two very weakly nucleophilic ligands on iodine(III) are generally labile and extremely moisture-sensitive,[1c,4] probably because of the unfavorable combination of *trans* influences. They have a pronounced tendency to isomerize to the more stable yellow solids of μ-oxo-λ^3-iodanes **7**, which are useful oxidants for alkenes and alkynes. A greater structural *trans* influence of μ-oxo-λ^3-iodanyl groups OI(Ph)L compared to the ligand L (NO_3, OTf, ClO_4) is responsible for this facile dimerization (Scheme 3, left). In fact, the I–$OCOCF_3$ bond lengths *trans* to

 © 2006 Wiley-VCH Verlag GmbH & Co. KGaA, Weinheim

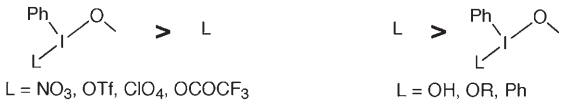

Scheme 3. *trans* influences in μ-oxo-λ^3-iodanyl groups.

the trifluoroacetoxy group of bis(trifluoroacetate) **6** (L = L′ = $OCOCF_3$) and *trans* to the μ-oxo-λ^3-iodanyl group of its μ-oxo analogue **7** are 2.162 and 2.273 Å, respectively, which indicates a greater *trans* influence of $OI(Ph)OCOCF_3$ group than of $OCOCF_3$ (Table 2, entry 12 and Table 3, entry 1). On the other hand, it seems reasonable to assume that the μ-oxo-λ^3-iodanyl group OI(Ph)L shows a reduced *trans* influence compared to the ligand L itself when L (OH, OR, Ph) is a high-*trans*-influence ligand (Scheme 3, right). These considerations seem to account for the fact that iodosylbenzene adopts a μ-oxo-bridged zigzag polymer structure,[5] as opposed to (dihydroxyiodo)benzene, which is monomeric.

In conclusion, we have shown that 3c–4e hypervalent bonding in aryl λ^3-iodanes is greatly affected by *trans* influences, which play an important role in their stability, whereby combinations of ligands with large and small *trans* influences, as in Koser's reagent Ph[I(OH)OTs], or of two moderately *trans*-influencing ligands, as in (diacetoxyiodo)-benzene, are favored.

Received: July 28, 2006
Published online: November 10, 2006

Keywords: hypervalent compounds · iodine · iodosylbenzene · substituent effects · *trans* influence

[1] a) G. F. Koser in *The Chemistry of Halides, Pseudo-halides and Azides, Supplement D* (Eds.: S. Patai, Z. Rappoport), Wiley, New York, **1983**, p. 721; b) A. Varvoglis, *The Organic Chemistry of Polycoordinated Iodine*, VCH, New York, **1992**; c) P. J. Stang, V. V. Zhdankin, *Chem. Rev.* **1996**, *96*, 1123; d) M. Ochiai, *Top. Curr. Chem.* **2003**, *224*, 5.
[2] G. Wittig, K. Clauss, *Justus Liebigs Ann. Chem.* **1952**, *578*, 136.
[3] H. W. Richter, B. R. Cherry, T. D. Zook, G. F. Koser, *J. Am. Chem. Soc.* **1997**, *119*, 9614.
[4] a) N. S. Zefirov, S. O. Safronov, A. A. Kaznacheev, V. V. Zhdankin, *Zh. Org. Khim.* **1989**, *25*, 1807; b) M. Schmeisser, E. Lehmann, D. Naumann, *Chem. Ber.* **1977**, *110*, 2665; c) A. D. Mico, R. Margarita, L. Parlanti, G. Piancatelli, A. Vescovi, *Tetrahedron* **1997**, *53*, 16877.
[5] C. J. Carmalt, J. G. Crossley, J. G. Knight, P. Lightfoot, A. Martin, M. P. Muldowney, N. C. Norman, A. G. Orpen, *J. Chem. Soc. Chem. Commun.* **1994**, 2367.
[6] a) V. V. Zhdankin, R. M. Arbit, M. McSherry, B. Mismash, V. G. Young, *J. Am. Chem. Soc.* **1997**, *119*, 7408; b) V. V. Zhdankin, R. M. Arbit, B. J. Lynch, P. Kiprof, *J. Org. Chem.* **1998**, *63*, 6590.
[7] a) A. Pidcock, R. E. Richards, L. M. Venanzi, *J. Chem. Soc. A* **1966**, 1707; b) T. G. Appleton, H. C. Clark, L. E. Manzer, *Coord. Chem. Rev.* **1973**, *10*, 335; c) G. Henrici-Olivé, S. Olivé, *Coordination and Catalysis*, Verlag Chemie, Weinheim, **1977**; d) K. B. Yatsimirskii, *Pure Appl. Chem.* **1974**, *38*, 341.
[8] a) E. M. Shustorovich, Y. A. Buslaev, *Inorg. Chem.* **1976**, *15*, 1142; b) E. M. Shustorovich, *J. Am. Chem. Soc.* **1978**, *100*, 7513; c) E. M. Shustorovich, Y. A. Buslaev, *Koord. Khim.* **1975**, *1*, 1020.
[9] a) O. Vikane, *Acta Chem. Scand. Ser. A* **1975**, *29*, 787; b) O. Foss, R. Hermansen, K. Maroy, T. Moberg, *Acta Chem. Scand. Ser. A* **1987**, *41*, 130; c) O. Foss, J. Henjum, K. Maartmann-Moe, K. Maroy, *Acta Chem. Scand. Ser. A* **1987**, *41*, 77.
[10] N. A. Milas, B. Plesnicar, *J. Am. Chem. Soc.* **1968**, *90*, 4450.
[11] B. C. Schardt, C. L. Hill, *Inorg. Chem.* **1983**, *22*, 1563.
[12] D. G. Naae, J. Z. Gougoutas, *J. Org. Chem.* **1975**, *40*, 2129.
[13] a) M. Ochiai, T. Ito, Y. Masaki, M. Shiro, *J. Am. Chem. Soc.* **1992**, *114*, 6269; b) M. Ochiai, T. Ito, H. Takahashi, A. Nakanishi, M. Toyonari, T. Sueda, S. Goto, M. Shiro, *J. Am. Chem. Soc.* **1996**, *118*, 7716.
[14] P. George, M. Trachtman, C. W. Bock, A. M. Brett, *J. Chem. Soc. Perkin Trans. 2* **1976**, 1222.
[15] D. D. Zorn, J. A. Boatz, M. S. Gordon, *J. Phys. Chem. B* **2006**, *110*, 11110.
[16] V. V. Zhdankin, O. Maydanovych, J. Herschbach, R. McDonald, R. R. Tykwinski, *J. Am. Chem. Soc.* **2002**, *124*, 11614.
[17] R. J. Batchelor, T. Birchall, J. F. Sawyer, *Inorg. Chem.* **1986**, *25*, 1415.
[18] M. Ochiai, Y. Masaki, M. Shiro, *J. Org. Chem.* **1991**, *56*, 5511.
[19] E. Shefter, W. Wolf, *J. Pharm. Sci.* **1965**, *54*, 104.
[20] P. Eisenberger, S. Gischig, A. Togni, *Chem. Eur. J.* **2006**, *12*, 2579.
[21] M. Etter, *J. Am. Chem. Soc.* **1976**, *98*, 5326.
[22] M. Ochiai, T. Ito, M. Shiro, *J. Chem. Soc. Chem. Commun.* **1993**, 218.
[23] J. Z. Gougoutas, J. C. Clardy, *J. Solid State Chem.* **1972**, *4*, 226.
[24] J. Z. Gougoutas, L. Lessinger, *J. Solid State Chem.* **1974**, *9*, 155.
[25] M. Takahashi, H. Nanba, T. Kitazawa, M. Takeda, Y. Ito, *J. Coord. Chem.* **1996**, *37*, 371.
[26] D. C. Braddock, G. Cansell, S. A. Hermitage, A. J. P. White, *Chem. Commun.* **2006**, 1442.
[27] V. V. Zhdankin, A. P. Krasutsky, C. J. Kuehl, A. J. Simonsen, J. K. Woodward, B. Mismash, J. T. Bolz, *J. Am. Chem. Soc.* **1996**, *118*, 5192.
[28] T. M. Balthazor, D. E. Godar, B. R. Stults, *J. Org. Chem.* **1979**, *44*, 1447.
[29] V. V. Zhdankin, A. Y. Koposov, L. Su, V. V. Boyarskikh, B. C. Netzel, V. G. Young, *Org. Lett.* **2003**, *5*, 1583.
[30] R. Minkwitz, M. Berkei, R. Ludwig, *Eur. J. Inorg. Chem.* **2000**, 2387.
[31] R. Minkwitz, M. Berkei, *Inorg. Chem.* **1999**, *38*, 5041.
[32] R. Minkwitz, M. Berkei, *Inorg. Chem.* **2001**, *40*, 36.
[33] R. Minkwitz, M. Berkei, *Z. Anorg. Allg. Chem.* **2000**, *626*, 2325.
[34] R. Minkwitz, M. Berkei, *Inorg. Chem.* **1998**, *37*, 5247.
[35] R. Minkwitz, M. Berkei, *Z. Naturforsch. B* **2000**, *55*, 718.
[36] N. W. Alcock, R. M. Countryman, *J. Chem. Soc. Dalton Trans.* **1977**, 217.
[37] Y. T. Struchkov, T. L. Khotsyanova, *Izv. Akad. Nauk SSSR Otd. Khim. Nauk* **1960**, 821.
[38] N. W. Alcock, W. D. Harrison, C. Howes, *J. Chem. Soc. Dalton Trans.* **1984**, 1709.
[39] J. Gallos, A. Varvoglis, N. W. Alcock, *J. Chem. Soc. Perkin Trans. 1* **1985**, 757.
[40] G. W. Bushnell, A. Fischer, P. N. Ibrahim, *J. Chem. Soc. Perkin Trans. 2* **1988**, 1281.
[41] N. W. Alcock, R. M. Countryman, *J. Chem. Soc. Dalton Trans.* **1979**, 851.

 © 2006 Wiley-VCH Verlag GmbH & Co. KGaA, Weinheim

Foldamers

DOI: 10.1002/anie.200603084

De Novo Design and Synthesis of Helix–Turn–Helix Structure from Short and Robust Mixed Helices Derived from C-Linked Carbo-β-Amino Acids**

Gangavaram V. M. Sharma, Velaparthi Subash, Kongari Narsimulu, Ampapathi Ravi Sankar, and Ajit C. Kunwar**

Peptides and proteins are molecular devices that adopt specific compact folded and organized structures for performing diverse functions in living systems. The formation of such tertiary and quaternary structures arises from the assembly of stable secondary structures such as helices, sheets, and turns. The development of nonnatural peptides[1–4] with compact and specific conformations is of considerable interest to understand the folding and stabilization and for designing new materials with specific biological functions. In spite of rapid progress made in the design and understanding of foldamers[2a] (mostly from β-amino acids) with a variety of secondary structures, generating distinct tertiary structures from them has so far remained a serious challenge. The helix–turn–helix (HTH) motif,[5] a tertiary structure composed of two helices separated by a turn motif, is one of the simplest functional assemblies and has been implicated in various important functions in DNA-binding proteins. However, attempts to obtain such a structural motif by using β- or γ-amino acids have so far not been successful. Herein, we present the first report on the de novo design of helix–turn and helix–turn–helix motifs in hepta- and undecapeptides, respectively, derived from C-linked carbo-β-amino acids (Caas) and a "turn motif" consisting of β-hGly-D-Pro-Gly-β-hGly (the common name of β-hGly is β-alanine[4]).

We have recently shown that the oligomers of Caas,[6] derived from D-xylose ($Caas_{(x)}$), adopt novel and robust right-as well as left-handed 12/10 helices[7,8] (the 12/10 helices consist of alternating 12- and 10-membered H-bonded pseudo rings[4]), whereas heterogeneous backbone peptides from L-Ala and $Caa_{(x)}$ resulted in unprecedented 11/9 helices.[9] "Alternating chirality"[7,10] of the epimeric $Caa_{(x)}$ (*S* and *R* conformations at C_β) was efficiently used as the design control to successfully identify the mixed helical patterns in as short as tri- and tetrapeptides. Herein, the tetrapeptide β-hGly-D-Pro-Gly-β-hGly is envisioned as a "turn motif",[11,12] which plays a crucial role as the strategic conformation nucleator. Flanking D-Pro-Gly on either side with two units of β-hGly in the tetrapeptide is aimed to provide the necessary continuity for the mixed helices and to provide conformational freedom for accommodating the helical structural elements. The turn motif is linked with tri- and tetrapeptides with mixed helical structures at the N and C termini, respectively, to furnish the HTH structure.

Peptides **1**–**5** (Scheme 1) were prepared by conventional peptide synthesis methods.[13] Alternating sequences of "epimeric" (*R*)- and (*S*)-$Caa_{(l)}$ (from D-mannose) were used in the synthesis of **1** and **2**. Peptide **3** was first condensed with tripeptide **1** to result in a heptapeptide **4**, which upon modification at the C terminus by coupling with **2** gave the undecapeptide **5**. The structural information of these peptides was obtained from extensive NMR spectroscopic, molecular dynamics (MD), and CD studies.[13]

NMR spectroscopic studies on **1**–**5** were carried out at 303 K in 5–10 mM solutions in $CDCl_3$. Peptides **1** and **2**, like our earlier peptides derived from $Caa_{(x)}$,[7] showed the evidence for 12/10-mixed helical structures (see the Supporting Information). The robustness of **1** and **2** is similar to that observed for the corresponding tripeptide and tetrapeptide prepared from $Caa_{(x)}$.[7]

For the turn motif **3**, the ^{1}H NMR spectrum showed an ≈1:24 *cis*/*trans* isomer ratio. The NOE correlations, between the $C_\delta H(2)$ and $C_\alpha H(1)$ protons helped in characterizing the major isomer as the *trans* isomer, whereas the *cis* isomer shows distinctive $C_\alpha H(1)/C_\alpha H(2)$ NOE interactions (for the minor isomer, their small populations did not permit us to obtain structural information[13]). In the major isomer, NH(4) resonated at 7.09 ppm and displayed a small shift in the solvent titration studies, implying its participation in H bonding. The $C_\alpha H(2)/NH(4)$ NOE correlation additionally confirmed the β turn around Pro-Gly. The NOE correlation $C_\alpha H(2)/NH(3)$ was stronger than the $C_\alpha H(2)/NH(4)$, $C_\alpha H_{Pro\text{-}(R)}(3)/NH(4)$, and $C_\alpha H_{(S)\text{-}Pro}(3)/NH(4)$ contacts, suggesting the presence of a type II′ β turn.

In the ^{1}H NMR spectrum of heptapeptide **4**, *cis*/*trans* isomers about the imide bond were observed in an approximate 1:9 ratio. The *trans*-imide bond preceding D-Pro was confirmed with the help of NOE values between $C_\delta H(5)$ and both $C_\alpha H(4)$ protons. Only the major isomer was studied in detail. Wide dispersion of the backbone proton resonances, for amide as well as $C_\alpha H$, suggests that the two structural elements do not destabilize the proposed secondary structure. NH(2), NH(3), and NH(7), in addition to their low-field shifts, display small $\Delta\delta$ values of about −0.01, 0.26, and 0.66 ppm, respectively, in solvent titration studies[14] confirming their participation in intramolecular H bonding. The

[*] Dr. G. V. M. Sharma, V. Subash
D-211, Discovery Laboratory
Organic Chemistry Division III
Indian Institute of Chemical Technology
Hyderabad 500 007 (India)
Fax: (+91) 40-27160387
E-mail: esmvee@iict.res.in
K. Narsimulu, Dr. A. R. Sankar, Dr. A. C. Kunwar
Centre for Nuclear Magnetic Resonance
Indian Institute of Chemical Technology
Hyderabad 500 007 (India)
Fax: (+91) 40-27193108
E-mail: kunwar@iict.res.in

[**] IICT Communication No. 061012. V.S., K.N., and A.R.S. thank CSIR, New Delhi, for financial support.

Supporting information (including NMR spectroscopic details, solvent titration plots, and distance constraints used in molecular dynamics calculations) for this article is available on the WWW under http://www.angewandte.org or from the author.

 © 2006 Wiley-VCH Verlag GmbH & Co. KGaA, Weinheim

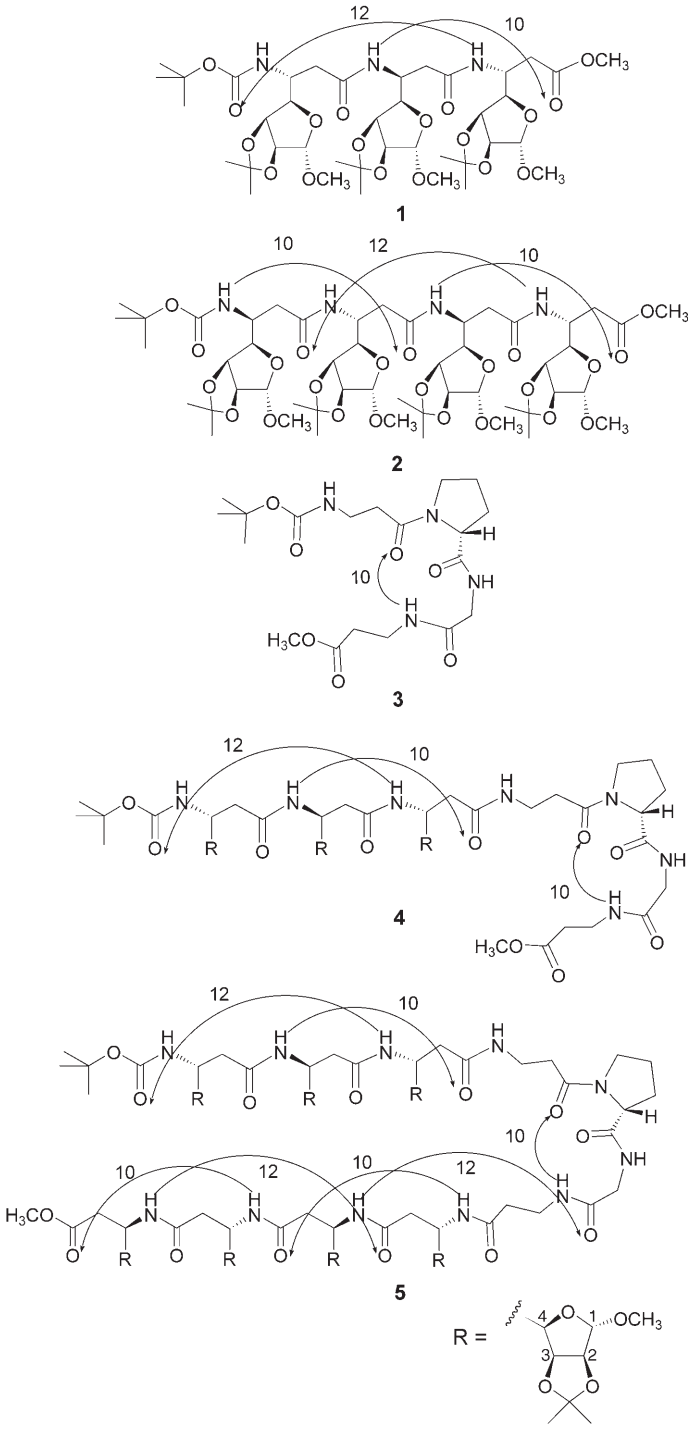

Scheme 1. Structures of peptides **1**–**5** with H-bond interactions shown by arrows.

coupling constants for the first three residues are very similar to that for **1**. Additionally, NOE cross-correlations like $C_\beta H(1)/NH(3)$ and $C_\beta H(1)/C_\alpha H_{Pro\text{-}(R)}(3)$ provide sufficient support for a 12/10-mixed helix involving the first three residues. The presence of $C_\alpha H(5)/NH(6)$ NOE correlations, which are stronger than the $C_\alpha H(5)/NH(7)$, $C_\alpha H_{Pro\text{-}(R)}(6)/NH(7)$, and $C_\alpha H_{Pro\text{-}(S)}(6)/NH(7)$ NOE correlations, in conjunction with the participation of NH(7) in H bonding, show that the last four residues organize into a type II′ β turn. The β-hGly(4) residue has $^3J_{NH\text{-}C_\beta H} = 4.3$ Hz and 8.0 Hz, which corresponds to $|\phi| \approx 120°$. From correlation experiments,[13] it was inferred that the $C_\beta H$ proton (at $\delta = 3.74$ ppm and with large coupling with NH), which is antiperiplanar to the amide proton, has a small coupling with both the $C_\alpha H$ protons, whereas the other $C_\beta H$ proton (at $\delta = 3.32$ ppm) has large coupling with one of the $C_\alpha H$ protons (at $\delta = 2.62$ ppm), therefore suggesting $\theta \approx 60°$. Further support for these observations came from the much smaller intensity of the NOE correlation between $C_\beta H$ ($\delta = 3.32$ ppm) and $C_\alpha H$ ($\delta = 2.62$ ppm) when compared with other $C_\beta H/C_\alpha H$ cross-peaks. These data permitted us to stereospecifically assign the $C_\alpha H$ and $C_\beta H$ protons and further show the $\phi \approx 120°$ and $\theta \approx 60°$ for the fourth residue,[13] which corresponds to further extending of the 12/10 helix in to the turn. These results thus provide generous support for the absence of destabilization of the two structural motifs in **4** when joined by an amide bond. The presence of a super secondary structure of the helix–turn family in heptapeptide **4** is noteworthy and provides credence to our desire to generate a helix–turn–helix tertiary structure de novo.

The ^{1}H NMR spectrum shows that undecapeptide **5** has *cis* and *trans* isomers in an ≈1:6 ratio. For the major isomer, the *trans*-imide bond preceding D-Pro was confirmed by the NOE contacts $C_\alpha H(4)/C_\delta H(5)$, whereas the *cis* isomer shows $C_\alpha H(4)/C_\alpha H(5)$ NOE values. The spectrum displays a large number of amide protons with $\delta > 7$ ppm. Solvent titration studies showed small changes in δNH for eight of the amide protons, confirming their participation in intramolecular H bonding. Typical signatures of a right-handed 12/10-mixed helix discussed for the first three residues of **1** and **4** are distinctly present in the couplings and the NOE data, permitting full characterization of a 12/10 helix for the first three residues in **5**. Similarly, the couplings as well as the characteristic long-range NOE values, $C_\beta H(9)/NH(11)$, $C_\beta H(9)/C_\alpha H_{Pro\text{-}(R)}(11)$, NH(8)/NH(9), and NH(10)/NH(11) provide compelling evidence for the 10/12/10 helical structures arising from the H bonding between NH(8)–CO(9), NH(11)–CO(8), and NH(10)–CO(11) for the last four residues. This validates the use of the tetrapeptide **2** as a helical motif at the C terminus. In addition, observation of $C_\beta H_{Pro\text{-}(R)}(7)/NH(9)$, $C_\beta H_{Pro\text{-}(R)}(7)/C_\alpha H_{Pro\text{-}(R)}(9)$, and involvement of NH(9) in H bonding suggests the presence of an additional 12-membered NH(9)–CO(6) H bond, resulting in an extended 12/10/12/10 helix. Thus, it is evident that the turn-inducing tetrapeptide **3** does not destabilize the robust helices both at the C and the N termini. With these two helical elements firmly in place, it was necessary to look for the distinctive features for a turn involving D-Pro-Gly residues. The NOE cross-correlations (Figure 1), $C_\alpha H(5)/NH(7)$ and NH(6)/NH(7), and involvement of the NH(7) in H bonding provide adequate support for the induction of a β turn. Furthermore, $C_\alpha H(5)/NH(6)$ NOE values, which are stronger than the $C_\alpha H(5)/NH(7)$, $C_\alpha H_{Pro\text{-}(R)}(6)/NH(7)$, and $C_\alpha H_{Pro\text{-}(S)}(6)/NH(7)$, suggests that β-hGly-D-Pro-Gly-β-hGly participates in a type II′ β turn. The fourth residue has $^3J_{NH\text{-}C_\beta H} = 4.0$ and 8.3 Hz, whereas the corresponding values for the seventh residue are 3.8 and 9.3 Hz. Like in **4** for β-hGly(4), the

 © 2006 Wiley-VCH Verlag GmbH & Co. KGaA, Weinheim

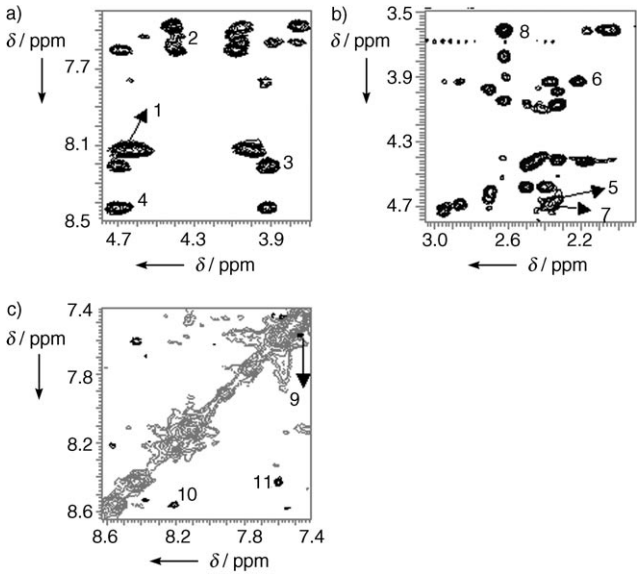

Figure 1. ROESY spectrum of **5**. a) The NOE interactions $C_\beta H(i)/NH(i+2)$ ($i=1$, 7, and 9) are marked as 1, 3, and 4, respectively. $C_\alpha H(5)/NH(7)$ is marked as 2; b) $C_\beta H(i)/C_\alpha H_{Pro\text{-}(R)}(i+2)$ ($i=1$, 7, and 9) are marked as 5, 6, and 7, respectively, and $C_\alpha H(4)/C_\delta H(5)$ (*trans* geometry of D-Pro) is marked as 8; c) $NH(i)/NH(i+1)$ ($i=6$, 8, 10) are marked as 9, 10, and 11, respectively.

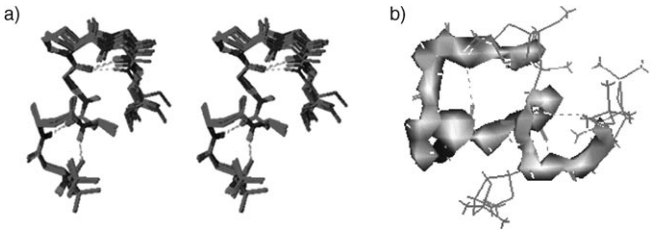

Figure 2. MD structures of **4**. a) Stereoview of 15 superimposed minimum-energy structures (sugar moieties replaced with a methyl groups after the calculations for clarity); b) backbone has been shown as a ribbon for a better display.

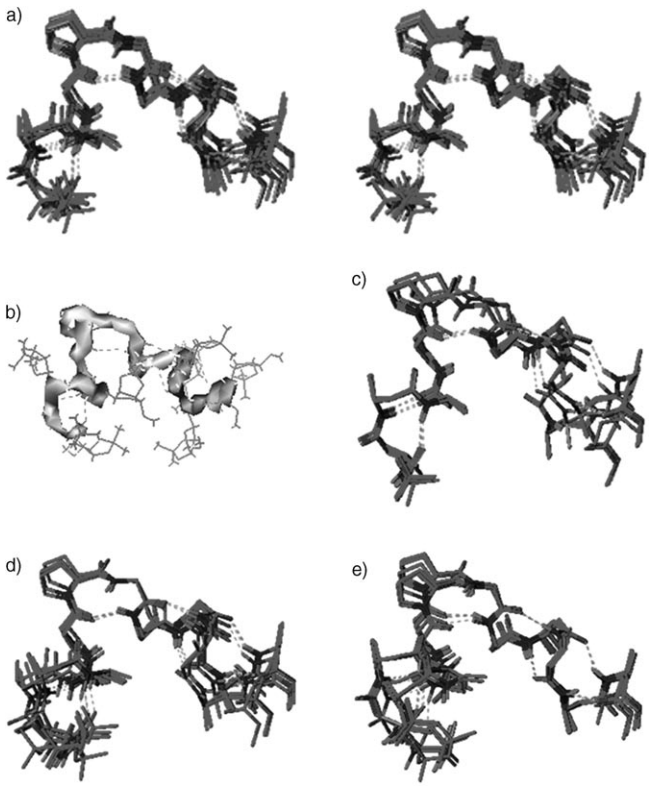

Figure 3. MD structure of undecapeptide **5.** a) Stereoview of 15 superimposed minimum-energy structures (sugar moieties replaced with a methyl groups after the calculations for clarity); b) backbone has been shown as a ribbon for a better display; c) view highlighting helix at the N terminus (only residues 1–4 superimposed); d) view highlighting the turn (only residues 4–7 superimposed); e) view highlighting helix at the C terminus (only residues 7–11 superimposed).

information on $^3J_{C_\alpha H\text{-}C_\beta H}$ and the NOE correlations between the $C_\alpha H$ and $C_\beta H$ permitted us to make stereospecific assignments of $C_\alpha H$ and $C_\beta H$, which in turn showed the predominance of structures with $\phi \approx 120°$ and $\theta \approx 60°$. Similarly for β-hGly(7), ϕ was deduced to be $\approx -120°$ and $\theta \approx 60°$.[13] Observation of strong $C_\alpha H_{Pro\text{-}(R)}(7)/NH(8)$ NOE correlations further support $\psi \approx 120°$. The flanking of D-Pro-Gly with β-hGly generates backbone conformational space, which further extends the two helices into the turn and imparts desired robustness to the structure. All the data presented above provides unequivocal evidence of a HTH tertiary structure in **5**, which contains only 11 amino acid residues.

Except for the first residue, for all Caa residues in **4** and **5**, the $^3J_{C_\beta H\text{-}C_4H} > 9$ Hz implies $\chi 1(C_\beta H\text{-}C_\beta\text{-}C_4\text{-}C_4H) \approx 180°$. However, like earlier observations,[7] the first residue in **1**, **4**, and **5** and the second residue in **2** have $^3J_{C_\beta H\text{-}C_4H} \approx 6$ Hz, suggesting predominance of structures with $|\chi 1| \approx 60°$. The sugar ring couplings of $^3J_{C_1H\text{-}C_2H} \approx 0$ Hz, $^3J_{C_2H\text{-}C_3H} \approx 5.8$ Hz, and $^3J_{C_3H\text{-}C_4H} \approx 3.2$ Hz are in conformity with the $^2T_3$ sugar pucker for the furanose ring.

Fifteen superimposed structures of **4** and **5**, obtained from restrained MD studies are shown in Figures 2 and 3, respectively (the backbones are also represented in ribbon form for better visualization). For peptide **4** (Figure 2), the 12/10 helix as well as the type II′ β turn, characterized from the NMR spectroscopic data, are very clearly visible. The backbone and the heavy-atom root mean square deviation (RMSD) are 0.75 Å and 0.81 Å, respectively. Various views highlighting the two helices and the turn in **5** are presented in Figure 3. The 12/10-mixed helices as well as the type II′ β turn are very well elaborated in these structures. The backbone and the heavy-atom RMSD are 0.45 Å and 0.64 Å, respectively. The premise of using the individual structural elements appears appropriate and resulted in the desired tertiary structure. The two helices, tethered through a turn, are almost orthogonal to each other, with an angle of about 80°, and resemble the ubiquitous protein structural element in DNA-binding motif common to transcription factors and the EF hand of a calcium binding protein.[5,15]

The CD spectra for **1**, **2**, **4**, and **5**[13] correspond to a typical 10/12-mixed helix,[7] with a maximum at 198 nm, whereas that of **3**, on the other hand, showed weak signatures of a turn. The

 © 2006 Wiley-VCH Verlag GmbH & Co. KGaA, Weinheim

characteristics of a turn are not distinctly deciphered in the spectra of **4** and **5**.

In conclusion, the helix–turn–helix motif has been generated de novo with a small peptide containing 11 amino acid residues. The robust individual secondary structures of the oligomers obtained from $Caa_{(l)}$ and the novel turn motif β-hGly-D-Pro-Gly-β-hGly are conserved, resulting in a very well defined HTH tertiary structure with the helices almost orthogonal to each other. These investigations demonstrate that the challenges of assembling higher-order molecular assemblies by using unnatural amino acids can be achieved based on such basic structural units. Availability of the large registry of helical scaffolds in the foldamer domain from the unnatural amino acids would thus permit the creation of a variety of new materials with diverse tertiary structures to understand their implications in biology.

Received: July 30, 2006
Published online: November 17, 2006

Keywords: conformation analysis · foldamers · helical structures · helix–turn–helix motif · peptides

[1] D. J. Hill, M. J. Mio, R. B. Prince, T. S. Hughes, J. S. Moore, *Chem. Rev.* **2001**, *101*, 3893 – 4011.
[2] a) S. H. Gellman, *Acc. Chem. Res.* **1998**, *31*, 173 – 180; b) R. P. Cheng, S. H. Gellman, W. F. DeGrado, *Chem. Rev.* **2001**, *101*, 3219 – 3232.
[3] D. Seebach, J. L. Matthews, *Chem. Commun.* **1997**, 2015 – 2022.
[4] D. Seebach, A. K. Beck, D. J. Bierbaum, *Chem. Biodiversity* **2004**, *1*, 1111 – 1239.
[5] a) S. C. Harrison, A. C. Aggarwal, *Annu. Rev. Biochem.* **1990**, *59*, 993 – 999; b) R. G. Brennan, B. W. Maththews, *J. Biol. Chem.* **1989**, *264*, 1903 – 1906.
[6] G. V. M. Sharma, V. Goverdhan Reddy, A. Subhash Chander, K. Ravinder Reddy, *Tetrahedron: Asymmetry* **2002**, *13*, 21 – 24.
[7] G. V. M. Sharma, K. Ravinder Reddy, P. Radha Krishna, A. Ravi Sankar, K. Narsimulu, S. Kiran Kumar, P. Jayaprakash, B. Jagannadh, A. C. Kunwar, *J. Am. Chem. Soc.* **2003**, *125*, 13670 – 13671.
[8] G. V. M. Sharma, K. Ravinder Reddy, P. Radha Krishna, A. Ravi Sankar, P. Jayaprakash, B. Jagannadh, A. C. Kunwar, *Angew. Chem.* **2004**, *116*, 4051 – 4055; *Angew. Chem. Int. Ed.* **2004**, *43*, 3961 – 3965.
[9] G. V. M. Sharma, P. Nagender, P. Radha Krishna, P. Jayaprakash, K. V. S. Ramakrishna, A. C. Kunwar, *Angew. Chem.* **2005**, *117*, 6028 – 6032; *Angew. Chem. Int. Ed.* **2005**, *44*, 5878 – 5882.
[10] a) K. Mohle, R. Gunther, M. Thormann, N. Sewald, H.-J. Hofmann, *Biopolymers* **1999**, *50*, 167 – 184; b) Y.-D. Wu, D.-P. Wang, *J. Am. Chem. Soc.* **1999**, *121*, 9352 – 9362.
[11] Y. J. Chung, L. A. Christianson, H. E. Stanger, D. R. Powell, S. H. Gellman, *J. Am. Chem. Soc.* **1998**, *120*, 10555 – 10556.
[12] D. Seebach, S. Abele, K. Gademann, B. Jaun, *Angew. Chem.* **1999**, *111*, 1700 – 1703; *Angew. Chem. Int. Ed.* **1999**, *38*, 1595 – 1597.
[13] See the Supporting Information.
[14] Solvent titration studies were carried out by sequentially adding up to 33% of $[D_6]$DMSO to $CDCl_3$ (v/v) solutions of the peptides (600 μL).
[15] Y. Kim, J. T. Welch, K. M. Lindstrom, S. J. Franklin, *J. Biol. Inorg. Chem.* **2001**, *6*, 173 – 181.

 © 2006 Wiley-VCH Verlag GmbH & Co. KGaA, Weinheim

DNA-Binding Peptides

DOI: 10.1002/anie.200603115

Sequence-Specific DNA Binding by Noncovalent Peptide–Tripyrrole Conjugates**

*Juan B. Blanco, Verónica I. Dodero, M. Eugenio Vázquez, Manuel Mosquera, Luis Castedo, and José L. Mascareñas**

The initiation of gene transcription is dependent on the interaction between specific proteins and short DNA sequences that are usually located upstream of the promoter of the gene.[1] In most cases, these proteins are unable to bind DNA as monomeric modules and need to cooperate with other proteins to form high-affinity complexes with specific DNA sequences.[2] Such is the case for the bZIP family of transcription factors, which bind DNA as leucine-zipper-mediated homo- or heterodimers, with an N-terminal basic region (BR) of each monomer inserting into adjacent DNA major grooves.[2,3] Interestingly, in many of these proteins, for example, the yeast transcriptional activator GCN4, the basic region is largely unstructured in the absence of DNA but folds into an α helix upon specific DNA binding.[4] It has been shown that the leucine zipper of bZIP proteins can be replaced by other noncovalent or covalent artificial dimerizing units without considerably compromising the DNA-recognition capabilities of the system.[5,6] However, isolated monovalent bZIP BRs exhibit poor DNA-binding affinities, unless the important DNA-contacting residues are appropriately grafted into a preorganized α helix.[7]

We recently demonstrated that it is possible to promote the DNA binding of such a monomeric bZIP BR upon appropriate cross-linking to a distamycin-like tripyrrole capable of interacting with moderate to good affinity in the

[*] Dr. J. B. Blanco, Dr. V. I. Dodero, Dr. M. E. Vázquez, Prof. Dr. L. Castedo, Prof. Dr. J. L. Mascareñas
Departamento de Química Orgánica
Universidade de Santiago de Compostela
Facultade de Química
15782 Santiago de Compostela (Spain)
Fax: (+34) 981-595-012
E-mail: qojoselm@usc.es
Homepage: http://qoweb.usc.es/jlmgroup/index.htm
Prof. Dr. M. Mosquera
Departamento de Química Física
Universidade de Santiago de Compostela
Facultade de Química
15782 Santiago de Compostela (Spain)

[**] This work was supported by the Spanish MEC (SAF2004-01044). J.B.B. thanks the Spanish M.E.C. for a predoctoral fellowship and M.E.V. thanks the HSFP organization for their support with a Career Development Award (CDA0032/2005-C) and the Spanish MEC for a "Ramon y Cajal" contract. We also thank Prof. J. Benavente for access to radioactivity facilities.

Supporting information (including materials, synthetic procedures, and details of the binding experiments) for this article is available on the WWW under http://www.angewandte.org or from the author.

 WILEY InterScience DISCOVER SOMETHING GREAT

© 2006 Wiley-VCH Verlag GmbH & Co. KGaA, Weinheim

minor groove adjacent to the BR target site.[8] The interaction of hybrids such as **1** to designated composite DNA sites (GTCATAAAA) most probably involves a simultaneous major- and minor-groove interaction (as outlined in Figure 1),

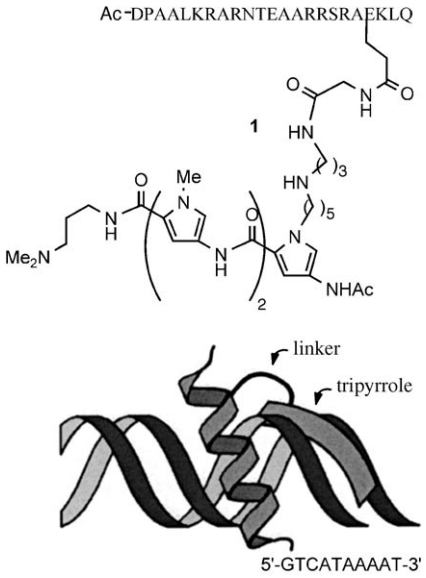

Figure 1. Structure of the tripyrrole–BR hybrid **1** and outline of its hypothetical DNA-binding mode.

and takes place with a K_d in the low nanomolar range at 4 °C. On the basis of this bipartite DNA-binding strategy, we considered it of interest to check whether both DNA-binding units could be connected by means of a noncovalent link so that the interaction would involve the formation of a stable complex among the peptide, the tripyrrole, and the DNA.[9] The feasibility of implementing this type of recognition strategy might open new and interesting opportunities to develop site-specific and ligand-responsive DNA-binding peptides. Herein we demonstrate that the attachment of an adamantyl group at the C terminus of a 23 amino acid peptide derived from a BR bZIP fragment allows its recruitment to a cognate DNA site adjacent to an A/T-rich sequence upon addition of a β-cyclodextrin-containing tripyrrole.[10]

It was not easy to deductively predict the best position of the basic region peptide to link the adamantyl group, and therefore we made peptides in which this unit is either attached to the side chain of amino acid 245 (peptide **2**) or at a C-terminal cysteine (**3a**, **3b**). In the case of peptide **2**, we chose a relatively long tether to connect the adamantane and the BR to ensure a certain degree of flexibility in the system. This peptide was readily prepared by coupling amine **4** with the required basic-region peptide while it was still bound to the resin and fully protected except at glutamic acid 245.[11] A standard TFA-promoted deprotection step led to the desired derivative **2** in good overall yield. Peptides **3a** and **3b** were readily obtained by coupling a fully deprotected basic-region peptide containing a cysteine residue at the C terminus with adamantylmethyl 2-bromoacetate. The cyclodextrin–tripyrrole unit **7a** was prepared from tripyrrole derivative **5** by following the steps indicated in Scheme 1.

As we have already shown for the covalent hybrids,[8] circular dichroism (CD) spectroscopy is a very interesting technique to extract information about the DNA-binding properties of this type of molecules. As shown in Figure 2a, the helicity of peptide **2** is not affected by the presence of 20-

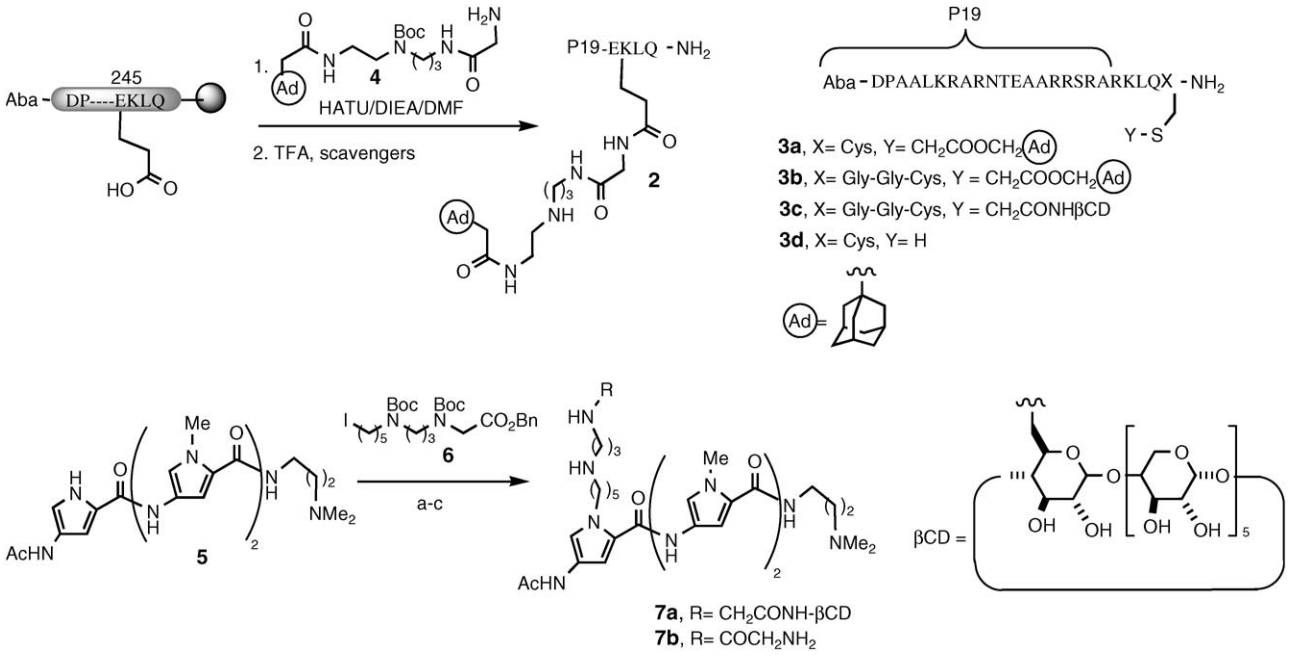

Scheme 1. Synthesis of the adamantyl-containing peptides and the tripyrrole-βCD units. For the synthesis of **7a**: a) K_2CO_3, **6**, DMF/acetone, 60 °C. b) H_2, Pd/C, MeOH. c) 1) i) HATU, DIEA, ii) βCD-NH_2, DMF; 2) TFA. Aba = *p*-acetamidobenzoyl, Boc = *tert*-benzyloxycarbonyl, DIEA = *N*,*N*-diisopropylethylamine, DMF = *N*,*N*-dimethylformamide, HATU = *O*-(7-azabenzotriazol-1-yl)-1,1,3,3-tetramethyluronium hexafluorophosphate, TFA = trifluoroacetic acid.

 © 2006 Wiley-VCH Verlag GmbH & Co. KGaA, Weinheim

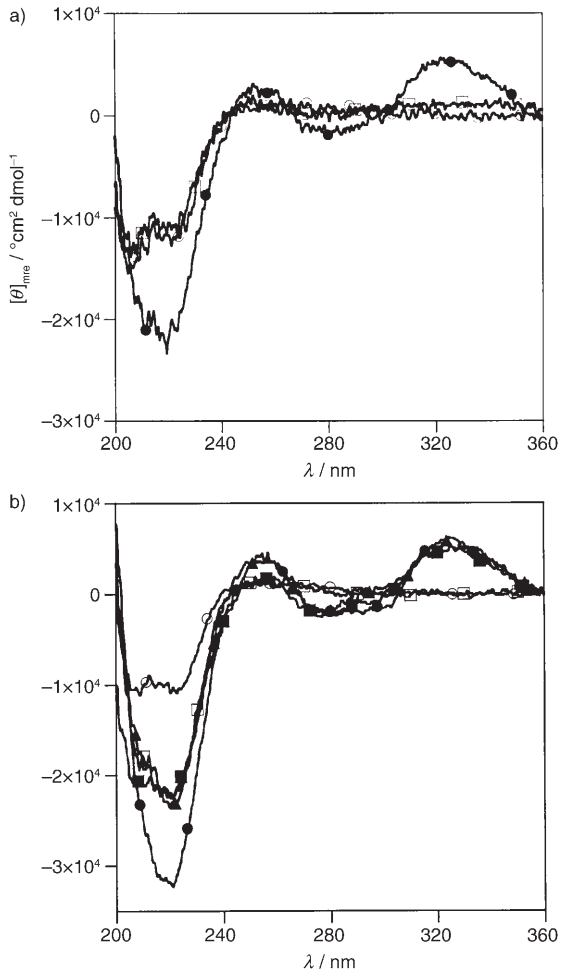

Figure 2. Circular dichroism difference spectra of peptides **2** and **3a**: a) peptide **2**: alone (○), in the presence of CRE^{hs}/A (□), and in the presence CRE^{hs}/A and **7a** (●); b) peptide **3a**: alone (○), in the presence of CRE^{hs}/A (□), in the presence CRE^{hs}/A and **7a** (●), in the presence CRE^{hs}/A and **7b** (■), and in the presence of CRE^{hs}m/A and **7a** (▲). CD spectra were obtained at 4 °C (see the Supporting Information) and are the difference between the spectra of the mixtures and the spectrum of free dsDNA. Sequences of one strand of the ds-oligonucleotides used: CRE^{hs}/A: 5′-d(ACGAACGTCAT*AAAAT*C-CTC)-3′, CRE^{hs}m/A: 5′-d(ACGAACGTCGT*AAAAT*CCTC)-3′. The BR subsite (CRE^{hs}) is shown underlined, and the tripyrrole subsite is shown in italics.

base-pair (bp) duplex oligonucleotide containing the target hybrid DNA sequence (CRE^{hs}/A). However, addition of tripyrrole **7a** to the mixture induces a significant, though not particularly large, increase in the negative intensity of the circular dichroism signal at 222 nm (Figure 2a, ●). Peptide **3a**, which exhibits the natural amino acids of the basic region of GCN4, acquires a notable degree of helicity in the presence of CRE^{hs}/A (Figure 2b, □) but becomes significantly more helicoidal upon addition of the βCD-tripyrrole **7a** (Figure 2b, ●). Peptide **3b** behaved similarly.

Interestingly, the addition of tripyrrole **7b** (that lacks the cyclodextrin unit) in place of **7a** does not promote a change in the helicity of the peptide (Figure 2b, ■). These results are consistent with significant α-helix formation and specific binding of the peptide to the DNA only when the tripyrrole equipped with the βCD (**7a**) is present. In all cases, there is also a positive ellipticity increase at 330 nm, which is consistent with the tripyrrole unit binding in the DNA minor groove. As might be expected, in the presence of the double-stranded (ds) oligonucleotide that features a bp mismatch at the BR-peptide binding subsite (CRE^{hs}m/A), the increase in the magnitude of the negative signal at 222 nm is considerably weaker (Figure 2b, ▲).

The circular dichroism information indicates that the tripyrrole-induced helical transition of peptide **3a** in the presence of the target DNA is considerably higher than for peptide **2**. Therefore, the subsequent DNA-binding studies, based on the use of gel mobility shift experiments (EMSA), were focused on the first peptide, which features the adamantane moiety at a C-terminal cysteine. As expected for an isolated monomeric bZIP BR,[12] we did not observe retard bands upon incubation of peptide **3a** with CRE^{hs}/A, a dsDNA that contains a cognate site for such peptides (Figure 3a, lane 1). However, it was gratifying to see that the addition of increasing amounts of the βCD-tripyrrole unit **7a** leads to the clear formation of a slower migrating band that must correspond to a DNA–peptide–tripyrrole complex (Figure 3a, lanes 2–5).

Interestingly, and in contrast to observations made in the case of covalent BR-peptide–tripyrrole hybrids,[8] a dsDNA molecule mutated at the BR binding site (CRE^{hs}m/A) does not induce the formation of detectable complexation bands (Figure 3a, lanes 6–10). Moreover, we could not detect mobility-shifted bands in the presence of a dsDNA molecule containing the BR-peptide binding subsite but lacking the A-rich sequence (CRE^{hs}, Figure 3a, lanes 11–12). These results are consistent with a very high sequence-specific DNA recognition, much better than in the covalent peptide–tripyrrole hybrids. That the supramolecular assembly is mediated by the host–guest cyclodextrin–adamantane interaction was demonstrated by carrying out control DNA-complexation experiments with the tripyrrole that lacks the βCD unit (**7b**) or with the peptide **3d**, which does not incorporate the adamantane group. As can be deduced from the absence of retard bands in lanes 14 and 15 in Figure 3a, both noncovalent interacting units (the βCD and the adamantane) are required for the formation of the complex between the BR peptide, the tripyrrole, and DNA. It is interesting to compare the gel migration of the above complex with that of the dimer of **3b** and **3c** with a ds-oligonucleotide (CRE) containing a cognate dimeric recognition site (Figure 3a, lane 13).[6] The relative migration is completely consistent with our complexes containing a single peptidic unit.

The specificity of the interaction was further examined by comparing the EMSA results with dsDNA molecules containing specifically designed mutations. As shown in Figure 3b, the introduction of a bp spacing between the consensus recognition sites of the tripyrrole and the BR peptide (CRE^{hs}*cg*/A) leads to a remarkable decrease in affinity (Figure 3b, lanes 6–10), and the presence of an additional bp space almost precludes the formation of the complex (CRE^{hs}*cg*/A, Figure 3b, lanes 11–15). On the other hand, interruption of the adenine (A) sequence in the ds-oligonu-

 © 2006 Wiley-VCH Verlag GmbH & Co. KGaA, Weinheim

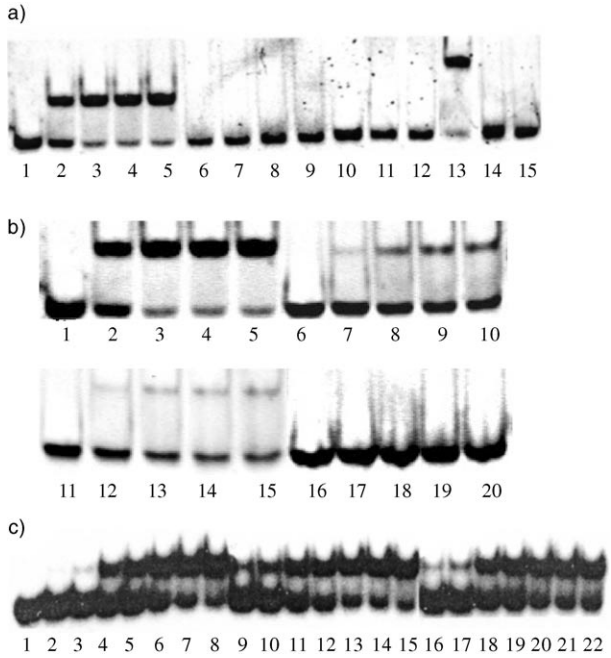

Figure 3. EMSA results showing the binding of peptide **3a** to dsDNA molecules. Experiments for (a) and (b) were analyzed by fluorescent dye staining and those of c) were analyzed by autoradiography. a) [dsDNA] ≈ 30 nM. Lanes 1–5: **7a** in the presence of a mixture of **3a** + CRE^{hs}/A, [**3a**] = 200 nM, [**7a**] = 0, 50, 100, 200, 400 nM; lanes 6–10: **7a** in the presence of a mixture of **3a** + CRE^{hs}m/A, [**3a**] = 200 nM, [**7a**] = 400, 200, 100, 50, 0 nM; lanes 11, 12: **7a** in the presence of a mixture of **3a** + CRE^{hs}, [**3a**] = 5 μM, [**7a**] = 0.5, 1 μM; lane 13: CRE + **3b** + **3c**, [**3b**] = [**3c**] = 500 nM; lane 14: **3a** + CRE^{hs}/A + **7b**, [**3a**] = 2 μM, [**7b**] = 500 nM; lane 15: **3d** + CRE^{hs}/A + **7a**, [**3d**] = 2 μM, [**7a**] = 500 nM. b) [dsDNA] ≈ 30 nM. Lanes 1–5: **7a** in the presence of a mixture of **3a** + CRE^{hs}/A, [**3a**] = 200 nM, [**7a**] = 0, 50, 100, 200, 400 nM; lanes 6–10: **7a** in the presence of a mixture of **3a** + CRE^{hs}*g*/A, [**3a**] = 200 nM, [**7a**] = 0, 50, 100, 200, 400 nM; lanes 11–15: **7a** in the presence of a mixture of **3a** + CRE^{hs}*cg*/A, [**3a**] = 200 nM, [**7a**] = 0, 50, 100, 200, 400 nM; lanes 16–20: **7a** in the presence of a mixture of **3a** + CRE^{hs}*g*/Am, [**3a**] = 200 nM, [**7a**] = 0, 50, 100, 200, 400 nM. c) Autoradiograms with ^{32}P-labeled CRE^{hs}/A (≈ 45 pM of ^{32}P-labeled + 100 nM unlabeled). Lanes 1–8: equimolecular mixture of **3a** and **7a**, [**3a**] = 0, 50, 80, 100, 150, 200, 250, 300 nM; lanes 9–15: **3a** in the presence of a mixture of **7a** + CRE^{hs}/A, [**7a**] = 200 nM, [**3a**] = 50, 80, 100, 150, 200, 250, 300 nM; lanes 16–22: **7a** in the presence of a mixture of CRE^{hs}/A + **3a**, [**3a**] = 200 nM, [**7a**] = 50, 80, 100, 150, 200, 250, 300 nM. Sequences of one strand of the ds-oligonucleotides used: CRE^{hs}: 5′-d(CGAACGTCATCGAAGGTCCT)-3′; CRE: 5′-d(TGGAGATGACGTCATCTCGT)-3′; CRE^{hs}*g*/A: 5′-d(CGAACGTCATG*AAAAT*CCTC)-3′; CRE^{hs}*cg*/A: 5′-d(CGAACGTCATCG*AAAAT*CCT)-3′; CRE^{hs}*g*/Am: 5′-d(CGAACGTCATG*AAA*GTCCTC)-3′. The BR subsite (CRE^{hs}) is shown underlined, and the tripyrrole subsite is shown in italics.

cleotide CRE^{hs}*g*/A completely abolishes the complexation (CRE^{hs}*g*/Am, Figure 3b, lanes 16–20). These data confirm the high specificity of the system and are consistent with the proposed major–minor groove interaction model.

Standard EMSA experiments by using ^{32}P-end-labeled dsDNA molecules revealed that to detect the bands of the complex it is necessary to use larger amounts of the dsDNA than commonly used in this type of assay. Well-known precedents for related systems suggest that such a requirement could probably be a consequence of a relatively high kinetic lability of the peptide–DNA complex, which may partially dissociate under the conditions of the assay.[12] Ensuring the presence of enough dsDNA (> 20 nM), we obtained clear complexation results upon titration of the target DNA with increasing amounts of equimolecular mixtures of **3a** and **7a**, or with fixed concentrations of one of the partners and increasing proportions of the other (Figure 3c). Titration assays in the presence of an excess of the tripyrrole **7a**, therefore ensuring that most of the dsDNA probe is saturated, allowed calculation of an approximate K_d value of **3a** for a DNA·**7a** complex of 63 ± 7 nM (see the Supporting Information). Assuming that the BR monomeric peptide binds DNA with affinities in the range of 1–5 μM,[12] we can infer that the presence of **7a** induces a very important binding improvement.

In conclusion, attachment of complementary noncovalent heterodimerizing units at a side chain of a distamycin-related tripyrrole and at the C terminus of a bZIP BR peptide provides for sequence-specific DNA recognition of relatively long DNA sites (8–9 bp). This strategy, which must involve a major- and minor-groove interaction, allows the DNA binding of very short peptides (23 amino acids) in a highly sequence-specific manner and represents a first step towards the development of small, highly selective and ligand-responsive DNA-binding peptides. Current studies are focused on further characterizing the binding mode, refining the system to obtain more stable complexes, and extending the recognition strategy to other transcription factor fragments.

Experimental Section

Circular dichroism measurements were made in a 2-mm cell at 4 °C. Samples contained 10 mM phosphate-buffered saline solution (pH 7.5), 100 mM NaCl, 5 μM peptide, and 5 μM ds-oligonucleotide when present. The peptide–DNA mixtures were incubated for 5 min before registering. For gel mobility shift assays, binding reactions were performed over 30 min in a binding mixture (20 or 40 μL) containing 18 mM tris(hydroxymethyl)aminomethane (Tris; pH 7.5), 90 mM KCl, 1.8 mM $MgCl_2$, 1.8 mM EDTA, 9% glycerol, 0.11 mg mL^{-1} bovine serum albumin (BSA) and 2.2% NP-40 (nonidet-P40). Products were resolved by PAGE by using a 10% nondenaturing polyacrylamide gel and 0.5XTBE buffer solution (44.5 mM Tris, 44.5 mM boric acid, 1 mM EDTA, pH 8) and analyzed by autoradiography (when radioactivity was used) or by staining with SyBrGold (Molecular Probes: 5 μL in 50 mL of 1XTBE) for 10 min and visualized with fluorescence.

Received: August 1, 2006
Revised: October 13, 2006
Published online: November 17, 2006

Keywords: distamycin · DNA recognition · noncovalent interactions · peptides · proteins

[1] R. J. White, *Gene Transcription, Mechanism and Control*, Blackwell Science, Oxford, **2001**.
[2] a) C. O. Pabo, R. T. Sauer, *Annu. Rev. Biochem.* **1992**, *61*, 1053–1095; b) D. S. Latchman, *Transcriptional Factors: Structural Families and Principles of DNA Recognition*, Academic Press, San Diego, **1998**; c) C. W. Garvie, C. Wolberger, *Mol. Cell* **2001**, *8*, 936–946; d) J. T. Kadonaga, *Cell* **2004**, *116*, 247–257; e) N. M.

 © 2006 Wiley-VCH Verlag GmbH & Co. KGaA, Weinheim

Luscombe, S. E. Austin, H. M. Berman, J. M. Thornton, *Genome Biol.* **2000**, *1*, 1.
[3] a) J. C. Hu, R. T. Sauer, *Nucleic Acids Mol. Biol.* **1992**, *6*, 82–101; b) H. C. Hurst, *Protein Profile* **1995**, *2*, 101–168; c) T. Ellemberger, *Curr. Opin. Struct. Biol.* **1994**, *4*, 12–21.
[4] a) M. A. Weiss, *Biochemistry* **1990**, *29*, 8020–8024; b) K. T. O'Neil, R. H. Hoess, W. F. Degrado, *Science* **1990**, *249*, 774–778.
[5] For covalent dimers, see: a) R. V. Talanian, C. J. McKnight, P. S. Kim, *Science* **1990**, *249*, 769–771; b) B. Cuenoud, A. Shepartz, *Science* **1993**, *259*, 510–513; c) A. M. Caamaño, M. E. Vázquez, J. Martínez-Costas, L. Castedo, J. L. Mascareñas, *Angew. Chem.* **2000**, *112*, 3234–3237; *Angew. Chem. Int. Ed.* **2000**, *39*, 3104–3107; d) T. Morii, Y. Saimei, M. Okagami, K. Makino, Y. Sugiura, *J. Am. Chem. Soc.* **1997**, *119*, 3649–3655.
[6] For noncovalent dimers, see: a) T. Morii, M. Shimomura, M. Morimoto, I. Saito, *J. Am. Chem. Soc.* **1993**, *115*, 1150–1151; b) Y. Aizawa, Y. Sugiura, T. Morii, *Biochemistry* **1999**, *38*, 1626–1632.
[7] a) N. J. Zondlo, A. Schepartz, *J. Am. Chem. Soc.* **1999**, *121*, 6938–6939; b) J. W. Chin, A. Schepartz, *J. Am. Chem. Soc.* **2001**, *123*, 2929–2930; see also: c) D. Stanojevic, G. L. Verdine, *Nat. Struct. Biol.* **1995**, *2*, 450–457.
[8] a) M. E. Vázquez, A. M. Caamaño, J. Martínez-Costas, L. Castedo, J. L. Mascareñas, *Angew. Chem.* **2001**, *113*, 4859–4861; *Angew. Chem. Int. Ed.* **2001**, *40*, 4723–4725; b) J. B. Blanco, M. E. Vázquez, J. Martínez-Costas, L. Castedo, J. L. Mascareñas, *Chem. Biol.* **2003**, *10*, 713–722; c) J. B. Blanco, O. Vázquez, J. Martínez-Costas, L. Castedo, J. L. Mascareñas, *Chem. Eur. J.* **2005**, *11*, 4171–4178; d) J. B. Blanco, M. E. Vázquez, L. Castedo, J. L. Mascareñas, *ChemBioChem* **2005**, *6*, 2173–2177; For a review, see: e) M. E. Vázquez, A. M. Caamaño, J. L. Mascareñas, *Chem. Soc. Rev.* **2003**, *32*, 338–349.
[9] The formation of a cooperative DNA complex between a polyamide and the DNA-binding protein EXD (extradenticle) has been recently disclosed: a) H-D. Arndt, K. E. Hauschild, D. P. Sullivan, K. Lake, P. B. Dervan, A. Z. Ansari, *J. Am. Chem. Soc.* **2003**, *125*, 13322–13323; b) K. E. Hauschild, R. E. Metzler, H.-D. Arndt, R. Moretti, M. Raffaelle, P. B. Dervan, A. Z. Ansari, *Proc. Natl. Acad. Sci. USA* **2005**, *102*, 5008–5013.
[10] We chose a cyclodextrin–adamantane interaction system because it has been successfully used to obtain DNA-binding dimeric BR bZIP peptides, see Ref. [6].
[11] The natural basic region contains an arginine at that position (245), but we changed it to glutamic acid to facilitate its synthetic manipulation (see Ref. [8a]).
[12] a) T. Morii, J. Yamane, Y. Aizawa, K. Makino, Y. Sugiura, *J. Am. Chem. Soc.* **1996**, *118*, 10012–10017; b) M. Zhang, B. Wu, H. Zhao, J. W. Taylor, *J. Pept. Sci.* **2002**, *8*, 125–136; c) D. D. Jones, P. D. Barker *Angew. Chem.* **2005**, *117*, 6495–6499; *Angew. Chem. Int. Ed.* **2005**, *44*, 6337–6341. See also Ref. [7].

 © 2006 Wiley-VCH Verlag GmbH & Co. KGaA, Weinheim

Ligand Effects

DOI: 10.1002/anie.200603139

Inverse Axial-Ligand Effects in the Activation of H_2O_2 and ROOH by an Mn^{III} Corrolazine**

*David E. Lansky, Amy A. Narducci Sarjeant, and David P. Goldberg**

The activation of dioxygen and its two-electron-reduced analogues H_2O_2 and ROOH by both heme- and non-heme-related metal complexes has been the focus of intense efforts because of its relevance to biochemical processes, as well as the potential applications of this chemistry in oxidative catalysis. Heme enzymes such as cytochrome P450, catalases, and peroxidases react with dioxygen and H_2O_2 to give high-valent iron–oxido intermediates such as iron(IV)–oxido π-cation radical ($(porph^{+\cdot})Fe^{IV}=O$), which is presumed to be the critical oxidizing intermediate in cytochrome P450.[1] Delineating the mechanism of formation of these high-valent species, and in particular understanding the O–O-bond cleavage events, remains an important goal. In this regard, many synthetic porphyrin model compounds have been examined to determine the mechanism of O–O-bond cleavage with H_2O_2, ROOH, and organic peracids as oxidants. In these studies, both heterolytic and homolytic cleavage pathways were observed, depending upon the nature of the oxidant and porphyrin employed. However, much remains unknown about what factors (e.g. identity of porphyrin, oxidant, or axial ligand) control the cleavage mechanism.

Herein we describe the reactivity of a manganese(III) corrolazine complex (**1**; Scheme 1) toward H_2O_2 and cumene hydroperoxide (CmOOH). Corrolazines, which are ring-contracted porphyrinoid ligands, have been shown to stabilize

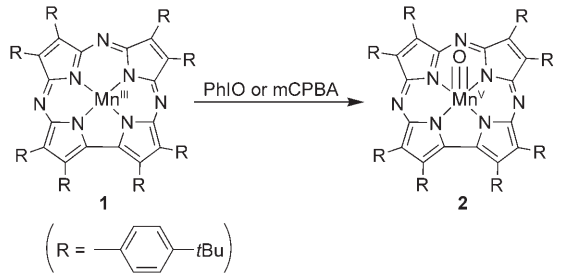

Scheme 1. Synthesis of the stable $Mn^{V}{\equiv}O$ complex **2**.

[*] D. E. Lansky, Dr. A. A. Narducci Sarjeant, Prof. Dr. D. P. Goldberg
Department of Chemistry
Johns Hopkins University
3400 North Charles Street, Baltimore, MD 21218 (USA)
Fax: (+1) 410-516-8420
E-mail: dpg@jhu.edu

[**] This research was supported by the NSF (CHE-0606614).

Supporting information for this article is available on the WWW under http://www.angewandte.org or from the author.

InterScience
© 2006 Wiley-VCH Verlag GmbH & Co. KGaA, Weinheim

high oxidation states of transition metals.[2] For example, treatment of **1** with the oxidants PhIO or *meta*-chloroperoxybenzoic acid (mCPBA) gives a stable $Mn^{V}{\equiv}O$ complex (**2**; Scheme 1), which can be isolated at room temperature.[3] This system is thus ideally suited to test ideas regarding the mechanism of oxidation by H_2O_2 or ROOH, as the expected high-valent metal–oxido porphyrinoid product can be directly identified. In contrast, when working with conventional porphyrins, one usually has to infer the generation of a high-valent metal–oxido species from indirect observations because of their instability. Herein we report that **1** is indeed capable of activating H_2O_2 and CmOOH, and, moreover, there is a remarkable axial-ligand effect upon these reactions. Also, the axially ligated complex $[Et_4N]^+[(TBP_8Cz)Mn^{III}Cl]^-$ (**3**) was structurally characterized, which to our knowledge is the first example of a structurally characterized anionic corrole species.

We speculated that reaction of **1** with H_2O_2 as the oxidizing agent in place of PhIO or mCPBA should give **2**. Surprisingly, this reaction was a failure; when **1** was dissolved in CH_2Cl_2 or benzene and stirred with excess H_2O_2 (30% aqueous solution) at 23 °C, no **2** was produced, as evidenced by TLC and UV/Vis spectroscopy. However, the coordination of axial ligands to **1** caused a dramatic change in reactivity toward H_2O_2. It has been shown previously by UV/Vis spectroscopy that Cl^- forms a 1:1 complex with **1**.[3c] Addition of H_2O_2 to a solution of **1** and Et_4NCl in CH_2Cl_2 led to an immediate color change from the brown of **1** to the deep green of the $Mn^{V}{\equiv}O$ complex (Scheme 2). Analysis of the

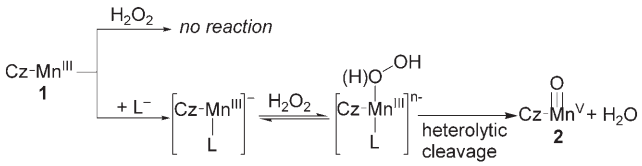

Scheme 2. Activation of H_2O_2 by axially ligated manganese(III) corrolazine.

reaction mixture by UV/Vis spectroscopy and TLC showed that **2** was the major product of this reaction. Isolation after chromatography resulted in a 63% yield of **2**. A likely mechanism for the generation of **2** involves coordination of H_2O_2 to the open site on the Mn center, followed by heterolytic cleavage of the O–O bond ($2e^-$ reduction) to give **2** and OH^-/H_2O. Independent experiments involving addition of Cl^- to **2** show no change in the UV/Vis spectrum, suggesting that once **2** is formed, the Cl^- ion is no longer bound. The strong donation from the triply bonded terminal oxido ligand may discourage binding of negatively charged axial ligands, although we have suggested that a neutral donor (PhIO) may coordinate to **2**.[3b] Some homolytic cleavage may also occur to give a putative Mn^{IV}–O(H) complex that likely rapidly decays.[4] This pathway would account for the less than quantitative yield of **2**.

Definitive proof of axial ligation by Cl^- was obtained by X-ray crystallography (Figure 1).[5] Crystallization of $[Et_4N]^+[(TBP_8Cz)Mn^{III}Cl]^-$ (**3**) was accomplished by vapor diffusion

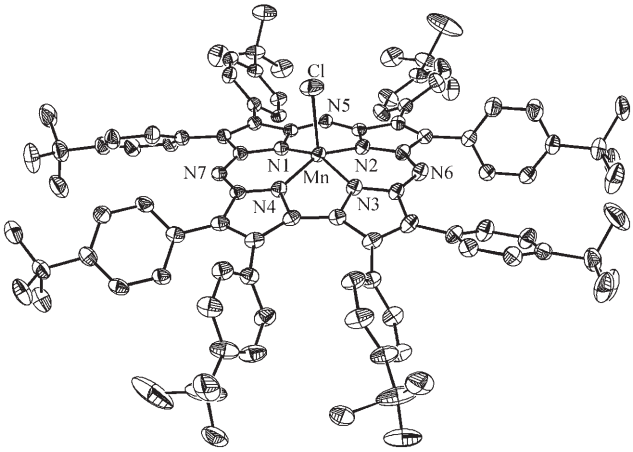

Figure 1. ORTEP diagram of the anion of **3** showing the 50% probability thermal ellipsoids. Hydrogen atoms have been omitted for clarity.

of pentane into a solution of **1**/Et_4NCl in CH_2Cl_2. The Mn ion in **3** is five coordinate with a single axial Cl^- ligand, as expected. The presence of the Et_4N^+ counterion confirms that the complex is negatively charged and the Mn ion is formally in the +3 oxidation state. A UV/Vis spectrum of crystals of **3** redissolved in CH_2Cl_2 matched the spectrum obtained from addition of Et_4NCl to **1** in situ, thus confirming that the complex generated in situ is the same as **3**. The Mn–N and Mn–Cl bond lengths in **3** are normal, and the Mn ion sits significantly further out of the macrocyclic plane (0.6609(7) Å), than in the MeOH adduct $[(TBP_8Cz)Mn^{III}(HOMe)]$[3c] (0.373(2) Å). This large out-of-plane displacement may be due to the steric congestion caused by the large size of the Cl^- ion. The tendency of the corrole to stabilize higher oxidation states appears to make the isolation of negatively charged species rare, whereas corrolazines allow for the isolation of both relatively low- and high-valent complexes.

The strong influence of the axial Cl^- ligand on the H_2O_2 reaction prompted us to examine other potential anionic axial donors. The addition of a series of *para*-substituted arylthiolate donors (p-X-$C_6H_4S^-Na^+$; X = H, OMe, CH_3, Cl, NO_2) had the same general influence as Cl^- on the reactivity of **1** toward H_2O_2: a rapid decay of **1** with concomitant formation of the $Mn^{V}{\equiv}O$ complex. However, a more quantitative comparison made by measuring the rates of reaction of $[\mathbf{1}{-}L]^-$ (L = axial ligand) with H_2O_2 revealed significant differences in the activity of the axial ligands examined. The kinetics were monitored by following the decay of $[\mathbf{1}{-}L]^-$ (absorbance loss at 685 nm; Figure 2). The decay curves were fit to give pseudo-first-order rate constants (k_{obs}), and plots of k_{obs} versus $[H_2O_2]$ showed good linearity; the slopes of these plots yielded the second-order rate constants (k_x''). The observed rate constants include the step involving coordination of H_2O_2 (Scheme 2) and are not a direct measurement of the O–O-bond-cleavage step. However, it is reasonable to assume that the coordination of H_2O_2 is fast and O–O-bond cleavage is the rate-determining step being monitored. Furthermore, the fact that the reaction requires L^- to proceed to any measurable extent suggests that O–O-bond cleavage is

 © 2006 Wiley-VCH Verlag GmbH & Co. KGaA, Weinheim

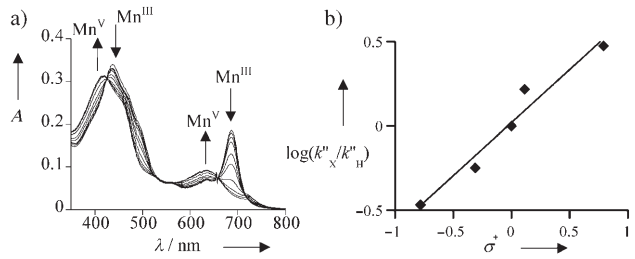

Figure 2. a) Time-dependent UV/Vis spectral changes for **1** + *p*-CH_3-$C_6H_4S^-Na^+$ immediately after addition of H_2O_2. b) Hammett plot for the reaction of $[\mathbf{1}\text{-L}]^- + H_2O_2$ (L = *p*-X-$C_6H_4S^-$).

affected by L^-, because it is unlikely that the coordination of H_2O_2 (or OOH^-) would be strongly enhanced by the formation of $[\mathbf{1}\text{-L}]^-$, a negatively charged complex.

A Hammett analysis of the data (Figure 2) shows that the rate of the H_2O_2 reaction clearly increases with an increase in the electron-withdrawing nature of the arylthiolate ligand ($\rho = 0.63 \pm 0.079$). Assuming this trend arises from an influence on the O–O-bond-cleavage step, this unusual inverse electron demand is opposite to that expected for the normal "push" effect[6] invoked for porphyrin/heme systems such as acylperoxidoiron(III) porphyrins, in which the more electron-donating axial ligand increases the rate of O–O-bond cleavage for both heterolytic and homolytic pathways.[6g,7]

To shed more light on this intriguing axial-ligand effect and obtain a direct measure of the influence of L^- on the mechanism of O–O-bond cleavage, the reaction of cumene hydroperoxide and **1** in the presence of different axial ligands was examined. CmOOH is a useful probe for distinguishing between heterolytic and homolytic cleavage mechanisms, as the former pathway gives 2-phenyl-2-propanol whereas the latter pathway gives acetophenone.[1c,8] The results are summarized in Scheme 3. It is clear that the ratio of

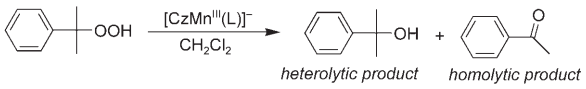

axial ligand:	F^-	Cl^-	Br^-	*p*-NO_2-$C_6H_4S^-$	$C_6H_5S^-$	*p*-MeO-$C_6H_4S^-$
heterol./homol.[a]	2.69	1.15	1.06	2.20	1.78	0.85

[a] mole ratio of alcohol/ketone measured by GC-FID.

Scheme 3. Cleavage pattern of CmOOH + **1** with different axial ligands.

heterolytic versus homolytic cleavage products are strongly influenced by the nature of the axial ligand. There is a dramatic increase in heterolytic cleavage with F^-, which is significantly more electronegative ($F^-_{EN} = 4.2$) than Cl^- ($Cl^-_{EN} = 2.8$) or Br^- ($Br^-_{EN} = 2.7$). Similarly, heterolytic cleavage increases with the electron-withdrawing nature of the *para* substituent of the arylthiolate donors. These trends are in good agreement with the inverse electron demand observed for the reaction of $\mathbf{1} + H_2O_2$ in the presence of axial ligands.

The axial-ligand effect described herein is in stark contrast to the normal push effect observed for both metalloporphyrins and hemoproteins. Interestingly, recent work by Nam et al. describes a similar, unusual inverse electronic effect for certain iron porphyrins, in particular, when H_2O_2 or ROOH is employed as the oxidant.[9] This latter effect appears to be operative when either the electronic properties of the porphyrin ligand itself, or the coordinated axial ligands are varied, and a rationale for these observations has been offered.[9b] We have clearly established that the electronic properties of anionic axial ligands bound to a manganese(III) corrolazine have a strong influence on the mechanism of O–O-bond cleavage for peroxide-type oxidants. Furthermore, this influence is exactly opposite to the expected trend from a classical push effect. In future work it would be of interest to determine if neutral donors (e.g. pyridine, imidazole) show similar trends, and if the origin of these effects can be discerned. These observations should help in understanding the mechanism of O–O-bond cleavage in porphyrinoid systems of both synthetic and biological origin. Moreover, the insights gained regarding the activation of oxidants such as hydrogen peroxide may lead to the design of practical corrolazine-based catalysts that can utilize the highly desirable terminal oxidant H_2O_2, or perhaps even O_2 itself.

Experimental Section

2: H_2O_2 (30% aq, 0.0125 mL, 0.11 mmol) was added to a solution of **1** (15 mg, 11 μmol) and Et_4NCl (2.2 mg, 13 μmol) in CH_2Cl_2, and the reaction mixture was stirred for 1 h. During this time the color changed from the dark brown of **1** to the deep forest green of **2**. The crude product was purified by chromatography (silica gel, CH_2Cl_2) to give **2** as a green solid. Yield: 9.5 mg, (63%).

3: Under aerobic conditions, **1** (5 mg, 3.55 μmol) and Et_4NCl (0.7 mg, 4.26 μmol) were dissolved in CH_2Cl_2 (5 mL) and allowed to stand. Vapor diffusion of pentane into this solution over 7 days yielded green-brown crystals of **3**, which were isolated by decantation and air-dried. UV/Vis spectroscopy (CH_2Cl_2): $\lambda_{max} = 435, 480, 635$ nm. Elemental analysis (%) calcd for $C_{110}H_{138}Cl_3MnN_8$ (**3**·CH_2Cl_2·pentane 1733.6 g mol^{-1}): C 76.21, H, 8.02, N, 6.46; found: C 75.53, H, 8.42, N, 5.95.

Received: August 2, 2006
Published online: November 14, 2006

Keywords: ligand effects · manganese · peroxides · porphyrinoids · reaction mechanisms

[1] a) P. R. Ortiz de Montellano, *Cytochrome P450: Structure, Mechanism, and Biochemistry*, 2nd ed., Plenum, New York, **1995**; b) M. Sono, M. P. Roach, E. D. Coulter, J. H. Dawson, *Chem. Rev.* **1996**, *96*, 2841–2887; c) Y. Watanabe in *The Porphyrin Handbook*, *Vol. 4* (Eds.: K. M. Kadish, K. M. Smith, R. Guilard), Academic Press, New York, **2000**, p. 97; d) B. Meunier, S. P. de Visser, S. Shaik, *Chem. Rev.* **2004**, *104*, 3947–3980.

[2] a) D. T. Gryko, J. P. Fox, D. P. Goldberg, *J. Porphyrins Phthalocyanines* **2004**, *8*, 1091–1105; b) W. D. Kerber, D. P. Goldberg, *J. Inorg. Biochem.* **2006**, *100*, 838–857.

[3] a) B. S. Mandimutsira, B. Ramdhanie, R. C. Todd, H. L. Wang, A. A. Zareba, R. S. Czernuszewicz, D. P. Goldberg, *J. Am. Chem. Soc.* **2002**, *124*, 15170–15171; b) S. H. Wang, B. S. Mandimutsira, R. Todd, B. Ramdhanie, J. P. Fox, D. P. Goldberg, *J. Am. Chem. Soc.* **2004**, *126*, 18–19; c) D. E. Lansky, B. Mandimutsira, B. Ramdhanie, M. Clausén, J. Penner-Hahn, S. A. Zvyagin, J. Telser, J. Krzystek, R. Q. Zhan, Z. P. Ou, K. M. Kadish, L. Zakharov, A. L. Rheingold, D. P. Goldberg, *Inorg. Chem.* **2005**, *44*, 4485–4498.

 © 2006 Wiley-VCH Verlag GmbH & Co. KGaA, Weinheim

[4] D. E. Lansky, D. P. Goldberg, *Inorg. Chem.* **2006**, *45*, 5119 – 5125.
[5] Data collection for **3**·$(CH_2Cl_2)_{2.5}$: $T = 110$ K, $M_r = 1788.82$, crystal dimensions: $0.29 \times 0.24 \times 0.20$ mm^3, triclinic ($P\bar{1}$), $a = 15.2032(13)$, $b = 18.1447(16)$, $c = 21.632(2)$ Å, $\alpha = 69.001(9)$, $\beta = 87.647(8)$, $\gamma = 69.974(8)°$, $V = 5211.4(8)$ Å^3, $Z = 2$, $\rho = 1.140$ g cm^{-3}, $(Mo_{K\alpha}) = 0.328$ mm^{-1}, $Mo_{K\alpha}$ radiation ($\lambda = 0.71073$ Å), $2\theta_{max} = 52.74°$. X-ray diffraction intensities were collected on an Xcalibur3 diffractometer; total number of reflections 104404, independent reflections 21023 [$R_{int} = 0.0277$]. Final R factors [$I > 2\sigma(I)$]: $R1 = 0.0712$, w$R2 = 0.2124$, $GoF = 1.071$. Data were collected, integrated, and corrected for absorption and interframe scaling with the CrysAlis Pro suite of programs (Oxford Diffraction). The structure was solved and refined with the SHELXTL (6.10) suite of programs (G. Sheldrick, Bruker XRD, Madison, WI, **2000**). The structure was solved by using direct methods and completed by subsequent difference Fourier syntheses and refined by full matrix least-squares procedures on F^2. All non-hydrogen atoms were refined with anisotropic displacement coefficients; several additional disordered solvent molecules could not be modeled appropriately. Electronic contributions from these molecules were removed via SQUEEZE (Platon). H atoms were placed in calculated positions and refined by using a riding group model. CCDC-616545 contains the supplementary crystallographic data for this paper. These data can be obtained free of charge from The Cambridge Crystallographic Data Centre via www.ccdc.cam.ac.uk/data_request/cif.
[6] a) J. T. Groves, Y. Watanabe, *Inorg. Chem.* **1986**, *25*, 4808 – 4810; b) J. H. Dawson, *Science* **1988**, *240*, 433 – 439; c) T. G. Traylor, R. Popovitz-Biro, *J. Am. Chem. Soc.* **1988**, *110*, 239 – 243; d) J. T. Groves, Y. Watanabe, *J. Am. Chem. Soc.* **1988**, *110*, 8443 – 8452; e) A. Robert, B. Loock, M. Momenteau, B. Meunier, *Inorg. Chem.* **1991**, *30*, 706 – 711; f) T. Higuchi, K. Shimada, N. Maruyama, M. Hirobe, *J. Am. Chem. Soc.* **1993**, *115*, 7551 – 7552; g) K. Yamaguchi, Y. Watanabe, I. Morishima, *J. Am. Chem. Soc.* **1993**, *115*, 4058 – 4065; h) F. Ogliaro, S. P. de Visser, S. Shaik, *J. Inorg. Biochem.* **2002**, *91*, 554 – 567.
[7] We did not attempt to measure the effects of axial ligands on the reaction of **1** with mCPBA because this reaction is too fast to be studied by conventional UV/Vis methods.
[8] K. U. Ingold, P. A. MacFaul in *Biomimetic Oxidations Catalyzed by Transition Metal Complexes* (Ed.: B. Meunier), Imperial College Press, **2000**, pp. 45 – 89.
[9] a) W. Nam, M. H. Lim, S. Y. Oh, J. H. Lee, H. J. Lee, S. K. Woo, C. Kim, W. Shin, *Angew. Chem.* **2000**, *112*, 3792 – 3795; *Angew. Chem. Int. Ed.* **2000**, *39*, 3646 – 3649; b) W. Nam, H. J. Han, S. Y. Oh, Y. J. Lee, M. H. Choi, S. Y. Han, C. Kim, S. K. Woo, W. Shin, *J. Am. Chem. Soc.* **2000**, *122*, 8677 – 8684; c) W. Nam, M. H. Lim, S. Y. Oh, *Inorg. Chem.* **2000**, *39*, 5572 – 5575.

 © 2006 Wiley-VCH Verlag GmbH & Co. KGaA, Weinheim

C–H Oxidation

DOI: 10.1002/anie.200603321

Polyol Synthesis through Hydrocarbon Oxidation: De Novo Synthesis of L-Galactose**

*Dustin J. Covell, Nicolaas A. Vermeulen, Nathan A. Labenz, and M. Christina White**

Direct oxidation of C–H bonds has the potential to emerge as a powerful approach for introducing oxygen and nitrogen functionality in the synthesis of complex molecules.[1] Functional-group manipulations (FGMs) that are required for carrying oxygenated functionalities throughout a synthetic route may be avoided by installing them directly into the hydrocarbon framework.[2] For a hydrocarbon oxidation strategy to reach its full potential, C–H-oxidation reactions with high levels of chemo-, regio- and stereoselectivity must be identified and developed. We recently described a DMSO-promoted, $Pd(OAc)_2$-catalyzed allylic oxidation reaction that furnishes *E* allylic acetates from α-olefins with high regio- and stereoselectivity, and with outstanding tolerance of functional groups.[3] Herein, we describe advances in this methodology for the oxidation of C–H bonds which enabled the development of a new hydrocarbon oxidation strategy for the rapid assembly of polyol frameworks. This strategy has been validated in an enantioselective, de novo synthesis of differentially protected L-galactose from a commercial, achiral starting material in which all new oxygen functionality has been installed through oxidation reactions of C–H and C=C bonds.

A short hydrocarbon oxidation strategy for the synthesis of chiral polyols is presented in Scheme 1. Key to the efficiency of this strategy is the rapid access to chiral (*E*)-2-butene-1,4-diols such as **2**, which may be directly elaborated to polyol structures through asymmetric dihydroxylation (AD). Compounds like **2** are particularly attractive building

[*] D. J. Covell, N. A. Vermeulen, Prof. M. C. White
Department of Chemistry, Roger Adams Laboratory
University of Illinois
Urbana, IL 61801 (USA)
Fax: (+1) 217-244-8024
E-mail: white@scs.uiuc.edu
N. A. Labenz
Harvard College
Cambridge, MA 02138 (USA)

[**] Financial support was provided by the Henry Dreyfus Foundation, the University of Illinois (UIUC), the Merck Research Laboratories, and the NIH/NIGMS (GM076153). D.J.C. gratefully acknowledges the UIUC for Roger Adams and C. S. Marvel fellowships. We thank Prof. E. N. Jacobsen (Harvard University) and Dr. C. P. Stevenson (Merck) for a gift of oligomeric (*R*,*R*)-[(salen)Co^{III}]OTf catalyst and helpful advice on the Payne rearrangement, respectively. We thank Johnson Matthey for a generous gift of $Pd(OAc)_2$. We are also grateful to M. S. Chen for checking our experimental procedure for the allylic oxidation reaction (Table 1, entry 7).

Supporting information for this article is available on the WWW under http://www.angewandte.org or from the author.

© 2006 Wiley-VCH Verlag GmbH & Co. KGaA, Weinheim

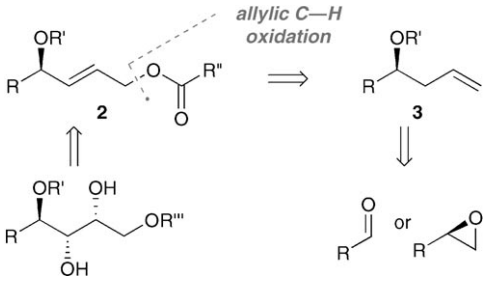

Scheme 1. A hydrocarbon oxidation strategy for the streamlined construction of polyols.

blocks because of their dense functionalization, dissonant relationship between the oxygen atoms,[4] and the ease with which they can be further elaborated through the established oxidation chemistry of olefins. Compounds similar to **2** have been routinely employed as intermediates to install a diverse range of structures in the synthesis of natural products; for example, five- and six-membered mono- and polycyclic ethers,[5] epoxy alcohols,[6] and, most extensively, contiguous polyol structures.[7] Notably, compounds analogous to **2** have been used as intermediates in several stereodivergent syntheses of the hexoses, an important class of polyols (Scheme 2).[8a,9] State-of-the-art syntheses of **2** based on

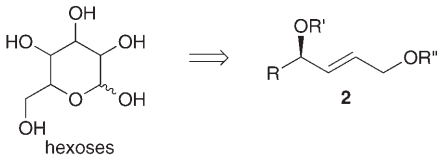

Scheme 2. Chiral (*E*)-2-butene-1,4-diols as key intermediates in stereodivergent hexose syntheses.

Wittig-type olefinations[10] or cross-metathesis reactions[11] suffer from lengthy sequences, in part because of the difficulty in accessing enantioenriched α-hydroxyaldehyde and α-hydroxy olefin starting materials. Alternatively, **2** may be synthesized directly from protected chiral homoallylic alcohols such as **3** through the DMSO/Pd^{II}-promoted allylic oxidation by using the strategy presented in Scheme 1.[2,3a] Homoallylic alcohols **3** are readily accessible from the asymmetric allylation of aldehydes[12,13] or the regioselective vinylation of chiral epoxides (Scheme 1).[14]

4-Methoxybenzoate derivatives of chiral (*E*)-2-butene-1,4-diols **2** are unique among allylic alcohol derivatives in their ability to undergo AD with excellent reagent-controlled diastereoselectivity and minimal acyl transfer.[8] We recently demonstrated that the DMSO/Pd^{II}-promoted linear allylic oxidation of protected chiral homoallylic alcohols with acetic acid furnishes the acetate derivatives of **2** with excellent regio- and stereoselectivities and with no erosion of optical purity.[2] To avoid FGMs, we set out to identify conditions for allylic oxidation of α-olefins using *p*-anisic acid (**5**) to directly generate 4-methoxybenzoate derivatives of **2** from α-olefins (Scheme 1). As shown in Table 1, preliminary studies with α-olefin **4** suggested that acid **5** may be a competent nucleophile

Table 1: Investigation into the linear allylic oxidation reaction to form the hexose precursor **6**.

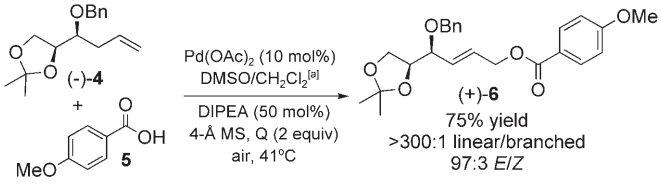

Entry	$DMSO/CH_2Cl_2$ Molarity [M]	Quinone (Q)	Acid **5** (equiv)	Yield [%][c]
1	0.33	BQ	15	23[d]
2	0.33	BQ	15	45
3	0.33	PhBQ	15	55
4	0.6	PhBQ	10	66
5	1.0	PhBQ	5	67
6[b]	2.0	PhBQ	3	75
7[b]	2.0	PhBQ	3	71[e]
8	2.0	PhBQ	3	63[f]
9	3.0	PhBQ	1.5	50

[a] $DMSO/CH_2Cl_2$ (3.2:1). [b] Linear to branched allylic ester and *E*/*Z* ratios were determined by HPLC for the material obtained from entries 6 and 7 on comparison with branched or acetonide-free *E* and *Z* standard compounds: linear/branched > 300:1, *E*/*Z* = 30:1 and 36:1 (for entries 6 and 7, respectively). [c] Yield of isolated product from the reactions carried out on a 1 mmol scale (**4**, 262 mg). Yields and selectivities represent an average of at least 2 runs. [d] With no DIPEA added. [e] $[Pd(CH_3CN)_4](BF_4)_2$ (10 mol%), 13% of **4** was recovered. [f] $Pd(OAc)_2$ (5 mol%). Bn = benzyl, DIPEA = *N*,*N*-diisopropylethylamine, MS = molecular sieves.

in the DMSO/Pd^{II}-promoted linear allylic oxidation reaction to form the hexose precursor **6**, if the challenges associated with high acid loadings and low yields were resolved (15 equiv of **5**, 23% yield, Table 1, entry 1). We were encouraged by the observation that significant amounts of the α-olefin starting material remained at the end of the reaction, thus suggesting that the acid-labile acetonide functionality was tolerant of these conditions. The addition of DIPEA, a noncoordinating base additive, effected a significant increase in yield (45%, Table 1, entry 2). Although the exact role of the base is currently unclear, we hypothesize that it increases concentrations of the benzoate anion. The yield was also increased on switching oxidants from benzoquinone (BQ) to phenylbenzoquinone (PhBQ, 55%, Table 1, entry 3). Finally, on increasing the reaction concentration to 2.0 M, we achieved further increases in yields, and were able to use fewer equivalents of carboxylic acid (2.0 M, 3 equiv **5**, 75% yield, Table 1, entry 6).

The linear allylic oxidation reaction is exceptionally stereo- and regioselective, with the major product formed being the linear *E* isomer (linear/branched > 300:1, *E*/*Z* = 30→36:1, entries 6 and 7, Table 1). The reaction is also preparatively convenient, with all reactions carried out in an air atmosphere with no precautions taken to exclude moisture or O_2. Significantly, with these newly developed conditions, the catalyst loading may be decreased to 5 mol% with only a minor decrease in yield (63%, Table 1, entry 8). Moreover, useful yields are obtained from fragment couplings with 1.5 equivalents of carboxylic acid at 3.0 M concentrations of α-olefin (50%, Table 1, entry 9). The only by-product we

 © 2006 Wiley-VCH Verlag GmbH & Co. KGaA, Weinheim

observed in the reaction using $Pd(OAc)_2$ as the Pd^{II} source was allylic acetate, which can be eliminated by using $[Pd(CH_3CN)_4](BF_4)_2$ (Table 1, entry 7).

We set out to test the efficiency of this overall strategy for polyol construction in the context of a short, de novo synthesis of the differentially protected L-galactose (−)-**11** (Scheme 3). Bulk chemical (*Z*)-2-butene-1,4-diol (**7**) was

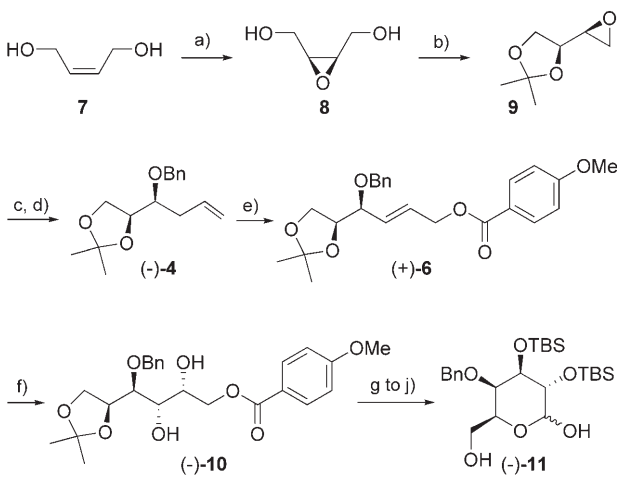

Scheme 3. Total synthesis of differentially protected L-galactose (−)-**11** (see the Supporting Information for full experimental details). a) mCPBA, CH_2Cl_2, 0 °C→RT (74 %); b) oligomeric (R,R)-[(salen)Co^{III}]-OTf (0.05 mol %), CH_3CN; then 2-methoxypropene, *p*-TsOH·H_2O (1 mol %), 0 °C; c) CuBr (10 mol %), CH_2=CHMgBr, THF, −40 °C; d) NaH, TBAI (10 mol %), DMF, 0 °C, BnBr, 0 °C→RT, (54 %, 3 steps from **8**, 99 % ee); e) $[Pd(CH_3CN)_4](BF_4)_2$ (10 mol %), PhBQ (2 equiv), **5** (3 equiv), DIPEA (0.5 equiv), 4-Å MS, DMSO/CH_2Cl_2 (3:1), 41 °C, 72 h (71 %, linear/branched > 300:1, *E*/*Z* = 97:3); f) K_2OsO_4·$2H_2O$ (1 mol %), $(DHQD)_2PHAL$ (5 mol %), $K_3Fe(CN)_6$, K_2CO_3, $MeSO_2NH_2$, *t*BuOH/H_2O, 0 °C (96 %, > 20:1 d.r.); g) TBSOTf, 2,6-lutidine, CH_2Cl_2, 0 °C→RT, (90 %); h) DIBAL, CH_2Cl_2, −78 °C, (98 %); i) $(COCl)_2$, DMSO, NEt_3, −65 °C, (90 %), j) $Zn(NO_3)_2$·$6H_2O$, CH_3CN, 50 °C, (93 %). DHQD = dihydroquinidine, DIBAL = diisobutylaluminum hydride, DMF = *N*,*N*-dimethylformamide, PHAL = phthalazine, TBAI = tetra-*n*-butylammonium iodide, TBS = *tert*-butyldimethylsilyl, Ts = toluene-4-sulfonyl.

epoxidized with *m*-chloroperbenzoic acid (mCPBA) to give the *meso*-epoxide **8** in 74 % yield. The *meso*-epoxide **8** was then desymmetrized by using the enantioselective Payne rearrangement with oligomeric (*R*,*R*)-[(salen)Co^{III}]OTf catalyst (salen = N,N′-bis(salicylidene)ethylenediamine, Tf = trifluoromethanesulfonyl) and subsequently ketalized in situ to give the chiral epoxyketal (*S*,*S*)-**9**.[15,16] Regioselective opening at the terminal position of the epoxyketal with vinylcuprate and subsequent protection of the intermediate alcohol gave the benzyl ether protected homoallylic alcohol (−)-**4** in 54 % overall yield (3 steps, 99 % *ee*).[14,15b] Linear allylic C–H oxidation of (−)-**4** using 10 mol % $[Pd(CH_3CN)_4](BF_4)_2$ in DMSO under the optimized conditions (2 M, PhBQ, 50 mol % DIPEA) with 3 equivalents of *p*-anisic acid **5** furnished the 4-methoxybenzoate-derived (*E*)-2-butene-1,4-diol (+)-**6** in 71 % yield (along with 13 % recovered (−)-**4**) as essentially one isomer (linear/branched = > 300:1; *E*/*Z* = 36:1) and with no erosion of enantiopurity.[17] Alternatively, on using 10 mol % $Pd(OAc)_2$ in DMSO under the same conditions, (+)-**6** was obtained in 75 % yield with around 10 % of the allylic acetate product that was arduous to separate by silica gel chromatography. Asymmetric dihydroxylation of (+)-**6** proceeded smoothly to give the polyoxygenated (−)-**10** in 96 % yield and greater than 20:1 d.r. (^{1}H NMR).[18] Protection of the diol (−)-**10** as the silyl ether, followed by removal of the *p*-methoxybenzoate ester with DIBAL, Swern oxidation of the resulting primary alcohol, and removal of the isopropylidene ketal group with $Zn(NO_3)$·$6H_2O$[19] gave the differentially protected L-galactose (−)-**11** in 74 % yield (over 4 steps).[20] The enantioselective, de novo synthesis of (−)-**11** thus proceeded in a total of 10 linear steps with 20 % overall yield from the commercially available **7**.

Several stereodivergent, de novo syntheses of the hexoses from **7** have employed chiral (*E*)-2-butene-1,4-diols analogous to **6** as intermediates. The C–H-oxidation route to **6** (5 steps, 28 % overall yield) compares favorably, in number of steps and overall yield, with the Wittig olefination routes previously reported (for example: 11 steps, 18 % overall yield,[9] and 9 steps, 16 % overall yield[8a]). The strategy developed herein, along with these previous syntheses, provides access to hexose stereoisomers that are complementary to those obtained through aldol-based approaches.[21]

In summary, we have reported a mild and efficient hydrocarbon oxidation strategy for the preparation of chiral polyols, a process validated by an efficient, enantioselective synthesis of the differentially protected L-galactose (−)-**11**. The synthesis used a highly regio- and stereoselective linear allylic C–H-oxidation reaction that generated 4-methoxybenzoate derivatives of chiral (E)-2-butene-1,4-diols directly from readily available chiral homoallylic alcohols and carboxylic acids. We anticipate that the simple and mild nature of this transformation (that is **2**→**3**, Scheme 1) will render it useful for the synthesis of polyoxygenated motifs in complex molecules.

Experimental Section

Representative procedure for the $Pd(OAc)_2$-catalyzed linear allylic C–H oxidation of (−)-**4** to (+)-**6**: Catalyst $Pd(OAc)_2$ (22.4 mg, 0.1 mmol, 10 mol %), PhBQ (368 mg, 2.0 mmol, 2 equiv), *p*-anisic acid (456 mg, 3.0 mmol, 3 equiv), 4-Å MS (200 mg), (−)-**4** (262 mg, 1 mmol, 1 equiv), DMSO (0.380 mL), CH_2Cl_2 (0.120 mL), DIPEA (0.087 mL, 0.5 mmol, 0.5 equiv), and a teflon stir bar were added sequentially to a borosilicate vial (40 mL). The vial was then capped and the reaction mixture stirred at 41 °C for 72 h. Care was taken to keep all reagents off of the walls of the vial and in maintaining the temperature between 40 °C and 43 °C. After 72 h, the reaction was quenched with saturated aqueous NH_4Cl solution (1 mL), stirred for 30 minutes, and then transferred to a separating funnel, and the vial rinsed with ethyl acetate (10 mL). The mixture was diluted with hexanes (40 mL; causing significant precipitation of phenyldihydroquinone as a black solid that was later removed by filtration). The organic phase was washed with H_2O (50 mL) and aq Na_2CO_3 solution (5 %, 2 × 50 mL). The organic layer was dried ($MgSO_4$), filtered, and concentrated in vacuo. Subsequent transfers were performed using Et_2O to minimize transfer of phenyldihydroquinone. Purification by column chromatography (silica gel, 30 % Et_2O in hexanes) gave (+)-**6** as an amber oil (309 mg, 75 % average yield of 2 runs). The ratios of the linear/branched products (> 300:1) were determined by HPLC on

 © 2006 Wiley-VCH Verlag GmbH & Co. KGaA, Weinheim

comparison with the branched-product standard[22] (Agilent Zobrax Eclipse XDB-C8 column, 35% *i*PrOH in H_2O, 1 mL min^{-1}, t_R(linear) = 15.7 min, t_R(branched, two diastereomers) = 18.0 and 19.0 min). *E*/*Z* ratios (30:1) were determined by HPLC using the *E* and *Z* diols without the acetonide group (Symmetry C-18 column, 40% CH_3CN in H_2O, 1.0 mL min^{-1}, $t_R(E)$ = 10.1 min, $t_R(Z)$ = 11.3 min). The linear acetate product (32 mg, 10%) was also formed in this procedure and was difficult to separate from (+)-**6**.

Representative procedure for the $[Pd(CH_3CN)_4](BF_4)_2$-catalyzed linear allylic C–H oxidation of (−)-**4** to (+)-**6**: Catalyst $[Pd(CH_3CN)_4](BF_4)_2$ (44.4 mg, 0.1 mmol, 10 mol%), PhBQ (368 mg, 2.0 mmol, 2 equiv), *p*-anisic acid (456 mg, 3.0 mmol, 3 equiv), 4-Å MS (200 mg), DMSO (0.380 mL), CH_2Cl_2 (0.120 mL), DIPEA (0.122 mL, 0.7 mmol, 0.7 equiv), and a teflon stir bar were added sequentially to a borosilicate vial (40 mL). The vial was then capped and the reaction mixture stirred at 41 °C for 1 h. The reaction was cooled to room temperature and (−)-**4** (262 mg, 1 mmol, 1 equiv) was added. The vial was capped and stirred at 41 °C for a further 72 h. Care was taken to keep all reagents off of the walls of the vial and in maintaining the temperature between 40 °C and 43 °C. The workup and isolation procedures were identical to those described on using $Pd(OAc)_2$, to give (+)-**6** (71% average yield of 2 runs). Approximately 13% of (−)-**4** was also recovered. Ratios of linear/branched and *E*/*Z* products were determined as described above and found to be similar to those determined for $Pd(OAc)_2$ (linear/branched > 300:1, *E*/*Z* = 36:1).

Received: August 14, 2006
Published online: November 16, 2006

Keywords: allylic oxidation · C–H activation · carbohydrates · enantioselectivity · polyols

[1] a) P. A. Wender, M. K. Hilinski, A. V. W. Mayweg, *Org. Lett.* **2005**, *7*, 79; b) Q. Zhang, J. O. Rich, I. C. Cotterill, D. P. Pantaleone, P. C. Michels, *J. Am. Chem. Soc.* **2005**, *127*, 7286; c) A. Hinman, J. Du Bois, *J. Am. Chem. Soc.* **2003**, *125*, 11510; d) B. D. Dangel, K. Godula, S. W. Youn, B. Sezen, D. Sames, *J. Am. Chem. Soc.* **2002**, *124*, 11856; e) R. Breslow, S. Baldwin, T. Flechter, P. Kalicky, S. Liu, W. Washburn, *J. Am. Chem. Soc.* **1973**, *95*, 3251.

[2] K. J. Fraunhoffer, D. A. Bachovchin, M. C. White, *Org. Lett.* **2005**, *7*, 223.

[3] a) M. S. Chen, M. C. White, *J. Am. Chem. Soc.* **2004**, *126*, 1346; for a related *N*,*N*-dimethylacetamide system, see: b) T. Mitsudome, T. Umetani, N. Nosaka, K. Mori, T. Mizugaki, K. Ebitani, K. Kaneda, *Angew. Chem.* **2006**, *118*, 495; *Angew. Chem. Int. Ed.* **2006**, *45*, 481.

[4] For an explanation of the term dissonant relationship, see: D. A. Evans, G. C. Andrews, *Acc. Chem. Res.* **1974**, *7*, 147.

[5] For example, see: a) L. Jiang, S. D. Burke, *Org. Lett.* **2002**, *4*, 3411; b) A. B. Smith III, Q. Lin, V. A. Doughty, L. Zhuang, M. D. McBriar, J. K. Kerns, C. S. Brook, N. Murase, K. Nakayama, *Angew. Chem.* **2001**, *113*, 202; *Angew. Chem. Int. Ed.* **2001**, *40*, 196.

[6] For example, see: M. T. Crimmins, F. Caussanel, *J. Am. Chem. Soc.* **2006**, *128*, 3128.

[7] For example, see: a) B. M. Trost, S. T. Wrobleski, J. D. Chisholm, P. E. Harrington, M. Jung, *J. Am. Chem. Soc.* **2005**, *127*, 13589; b) N. Ikemoto, S. L. Schreiber, *J. Am. Chem. Soc.* **1992**, *114*, 2524.

[8] a) A. Guzman-Perez, E. J. Corey, *Tetrahedron Lett.* **1997**, *38*, 5941; b) E. J. Corey, A. Guzman-Perez, M. C. Noe, *J. Am. Chem. Soc.* **1995**, *117*, 10805.

[9] a) S. Y. Ko, A. W. M. Lee, S. Masamune, L. A. Reed III, K. B. Sharpless, F. J. Walker, *Science* **1983**, 220, 949; b) S. K. Ko, A. W. M. Lee, S. Masamune, L. A. Reed III, K. B. Sharpless, F. J. Walker, *Tetrahedron* **1990**, *46*, 245.

[10] For example, see: K. Tsuboi, Y. Ichikawa, A. Naganawa, M. Isobe, M. Ubukata, K. Isono, *Tetrahedron* **1997**, *53*, 5083.

[11] a) A. K. Chatterjee, T.-L. Choi, D. P. Sanders, R. H. Grubbs, *J. Am. Chem. Soc.* **2003**, *125*, 11360; b) V. A. Keller, I. Kim, S. D. Burke, *Org. Lett.* **2005**, *7*, 737.

[12] For syntheses of chiral (*E*)-2-buten-1,4-diols with good to moderate enantioselectivities from allylation with chiral (*E*)-γ-(dimethylphenylsilyl)allylboronate reagents followed by epoxidation/Petersen elimination, see: a) W. R. Roush, P. T. Grover, *Tetrahedron Lett.* **1990**, *31*, 7567; b) W. R. Roush, A. N. Pinchuk, G. C. Micalizio, *Tetrahedron Lett.* **2000**, *41*, 9413.

[13] For representative asymmetric allylation reactions, see: a) G. Xia, H. Yamamoto, *J. Am. Chem. Soc.* **2006**, *128*, 2554; b) S. E. Denmark, J. Fu, M. J. Lawler, *J. Org. Chem.* **2006**, *71*, 1523; c) K. Kubota, J. L. Leighton, *Angew. Chem.* **2003**, *115*, 976; *Angew. Chem. Int. Ed.* **2003**, *42*, 946; d) U. S. Racherla, H. C. Brown, *J. Org. Chem.* **1991**, *56*, 401; e) W. R. Roush, A. E. Walts, L. K. Hoong, *J. Am. Chem. Soc.* **1985**, *107*, 8186.

[14] C. Mukai, J. S. Kim, M. Uchiyama, S. Sakamoto, M. Hanaoka, *J. Chem. Soc. Perkin Trans. 1* **1998**, 2903.

[15] a) D. E. White, E. N. Jacobsen, *Tetrahedron: Asymmetry* **2003**, *14*, 3633; b) C. P. Stevenson, PhD thesis, Harvard University (USA) **2005**; c) J. M. Ready, E. N. Jacobsen, *Angew. Chem.* **2002**, *114*, 1432; *Angew. Chem. Int. Ed.* **2002**, *41*, 1374; d) M. H. Wu, K. B. Hansen, E. N. Jacobsen, *Angew. Chem.* **1999**, *111*, 2167; *Angew. Chem. Int. Ed.* **1999**, *38*, 2012.

[16] This reaction was optimized using commercially available (*R*,*R*)-[(salen)Co^{III}]OAc (2 mol%) to give the desired chiral epoxyketal in 50% overall yield (95% *ee*). Lower yields may be attributed to epoxide opening by MeOH during the ketalization step with higher catalyst loadings of the monomeric catalyst. See the Supporting Information for details.

[17] The diastereomer which corresponds to racemization of the allylic center was independently synthesized and was not detected in the HPLC analysis of the products (see the Supporting Information for details).

[18] H. C. Kolb, M. S. VanNieuwenhze, K. B. Sharpless, *Chem. Rev.* **1994**, *94*, 2483.

[19] S. Vijayasaradhi, J. Singh, I. Aidhen, *Synlett* **2000**, 110.

[20] The silyl groups were removed and (−)-**11** was peracetylated to give 1,2,3,6-*O*-tetraacetyl-4-*O*-benzyl-L-galactopyranose, the spectroscopic data of which was found to correspond to those reported for the known compound (see the Supporting Information for details): L. Ermolenko, N. A. Sasaki, *J. Org. Chem.* **2006**, *71*, 693.

[21] A. B. Northrup, D. W. C. MacMillan, *Science* **2004**, *305*, 1752.

[22] a) M. S. Chen, N. Prabagaran, N. Labenz, M. C. White, *J. Am. Chem. Soc.* **2005**, *127*, 6970; b) K. J. Fraunhoffer, N. Prabagaran, L. E. Sirois, M. C. White, *J. Am. Chem. Soc.* **2006**, *128*, 9032.

 © 2006 Wiley-VCH Verlag GmbH & Co. KGaA, Weinheim

Enzyme Catalysis

DOI: 10.1002/anie.200603411

Is the Ferric Hydroperoxy Species Responsible for Sulfur Oxidation in Cytochrome P450s?**

*Max J. Cryle and James J. De Voss**

General research into cytochrome P450 (P450) mediated oxidation has led to a consensus view that the highly active, electrophilic Cpd I is responsible for the vast majority of such oxidations (Scheme 1).[1] The much less reactive Cpd 0 has

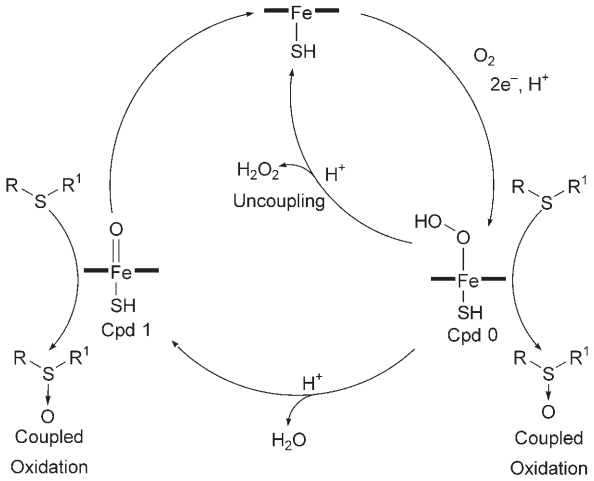

Scheme 1. Abbreviated P450 oxidative cycle of thioethers, indicating possible sources of sulfoxidation and uncoupling.

also been proposed as an oxidant in many P450-catalyzed transformations, including C-H hydroxylation, epoxidation, and sulfoxidation (Scheme 1). To date, however, no reaction has been unambiguously assigned to Cpd 0 and most results suggesting the presence of a second, electrophilic oxidant have been explained by Shaik's two-state reactivity paradigm, in which differing spin states of Cpd I react as different species.[2] However, the possibility remains that substrates containing centers that are much more susceptible to oxidation, such as sulfur, are oxidized by Cpd 0.[1] DFT calculations have suggested that Cpd I is a much more capable oxidant of sulfur than is Cpd 0,[3] and on this basis it was concluded that Cpd I is the major oxidant of thioethers. However, these results do not necessarily preclude Cpd 0 as an active oxidant in wildtype enzymes.

Decreasing the activity of Cpd I through the use of specific threonine-to-alanine active-site mutants has been demonstrated for $P450_{cam}$[4,5] and $P450_{BM3}$,[6,7], among others. These mutants have been used to investigate the oxidation of a wide variety of substrates, including thiothers.[8] Studies of the kinetics of wildtype and mutant $P450_{BM3}$ catalyzed oxidation of a subtrate with both amine or thioether moieties led to the postulate that two separate oxidants affect amine and thioether oxidation; the oxidation of sulfur was greater for the mutant in which Cpd 0 activity is potentiated.[8] An alternative explanation of these results that does not implicate Cpd 0 was proposed in which different spin states of Cpd I masquerade as two different oxidants.[3] Whether Cpd 0 does play a role in wildtype P450 catalyzed sulfoxidation was thus unclear.

Our interest in fatty acid oxidation by P450s[9–14] led us to investigate the use of thiafatty acids as potential mechanistic probes for P450s. Prior, elegant use of thiafatty acids by Buist and Marecak to probe the cryptostereochemistry of dehydrogenase enzymes indicated that these probes yield useful stereochemical data concerning reaction intermediates that are not readily isolatable.[15] We wished to use such probes to reveal the cryptostereochemistry of oxidative carbon–carbon-bond cleavage of fatty acids by $P450_{BioI}$.[11,13,16] Two isolated examples of P450-catalyzed oxidation of analogous thioether- or methylene-containing substrates appeared to indicate that these reactions proceed with the same stereochemical outcome.[17–19] However, we felt it prudent to validate the use of thiafatty acids as stereochemical probes with fatty acid metabolizing P450s for which the stereochemical outcomes were known. Thus, we chose to investigate thiafatty acid oxidation by the widely studied $P450_{BM3}$, a catalytically self-sufficient P450 isolated from *Bacillus megaterium*.[20] The regio- and stereoselectivity of fatty acid oxidation by $P450_{BM3}$ is well known for C_{14} (**1**) and C_{16} (**2**) fatty acids; thus, the thiafatty acids **3** and **4** were chosen as target substrate analogues.[20–23]

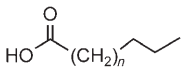

1: $n = 10$
2: $n = 12$

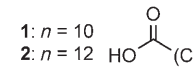

3: $n = 10$, R = SEt
4: $n = 12$, R = SEt
5: $n = 10$, R = S(O)Et
6: $n = 12$, R = S(O)Et

The synthesis of **3** and **4** was trivial and utilized the method of Yin and Pidgeon.[24] The synthesis of nonracemic sulfoxide standards (**5** and **6**) was also clearly important and was accomplished by using two distinct methods to incorporate a sulfoxide of known stereochemistry. Two independent methodologies were used to confirm the stereochemistry of **5** and **6** because of the results of enzymatic oxidation (see below). The first route utilized the displacement of the ethyl sulfinate ester of diacetone glucose, which is available in high diastereomeric ratio with a known diastereomeric preference.[25,26] The second route applied the Kagan oxidation to an alkyl/aryl thioether,[27] followed by Grignard displacement of

[*] Dr. M. J. Cryle, Prof. J. J. De Voss
Department of Chemistry
School of Molecular and Microbial Sciences
University of Queensland
St. Lucia Brisbane 4072 (Australia)
Fax: (+61) 7-3365-4299
E-mail: j.devoss@uq.edu.au

[**] The authors are grateful to Prof. S. Chapman (University of Edinburgh) for the $P450_{BM3}$ clones used in this work.

Supporting information for this article is available on the WWW under http://www.angewandte.org or from the author.

 © 2006 Wiley-VCH Verlag GmbH & Co. KGaA, Weinheim

the *p*-chlorophenyl group.[28] Both routes afforded the same enantiomer, as predicted from previous work and determined by enantioselective HPLC (Chiralcel OB-H).[25–28]

With both product standards in hand, we investigated the $P450_{BM3}$-mediated oxidation of thiafatty acids **3** and **4** (see the Supporting Information for conditions). Analysis of the products of oxidation of **3** and **4** indicated that the presence of the sulfur dramatically alters the regiochemistry of the reaction. The metabolism of fatty acids **1** and **2** yields oxidation products across the three subterminal methylene groups; the highest regiochemical preference in both cases was approximately 50% (Table 1, Scheme 2).[10,20] With **3** and **4**, the relative oxidation at the sulfur atom (ω-2) rose to 99% of the total oxidation, as might be expected after inclusion of a center susceptible to oxidation. Measurement of the stereochemistry of the resultant sulfoxide showed a decrease in enantiomeric purity (ratios change from 99:1 or 98:2 to 75:25). This drop in selectivity may be expected as the more easily oxidized sulfur atom may allow reaction from a greater range of reactive conformations than the more demanding C–H bond.[17–19] Intriguingly, however, the sulfoxides were produced with the opposite enantioselectivity to that observed for comparable fatty acid hydroxylation (*S* sulfoxides versus *R* alcohols).[21,22]

Table 1: $P450_{BM3}$ wildtype (WT) and T268 mutant (TA) oxidation of probes **1–4**.

Substr./ Enzyme	Oxidation Rate[a]	% Coupling[b]	% Oxidation at Site (% Stereochemistry)[c]		
			ω-3	ω-2	ω-1
1/WT	1.0±0.1	88±1	25±2 (74 *R*)	27±2 (98 *R*)	48±2 99 *R*)
3/WT	0.4±0.1	81±9	1±1	99±1 (75 *S*)	0
3/TA	0.4±0.1	88±5	1±1	99±1 (72 *S*)	0
2/WT	1.6±0.5	93±6	24±2 (74 *R*)	53±2 (99 *R*)	23±2 (99 *R*)
2/TA	0.3±0.1	21±5	25±2 (78±4 *R*)[23]	52±2 (92±4 *R*)[23]	23±2 (92±4 *R*)[23]
4/WT	0.9±0.1	81±1	1±1	99±1 (75 *S*)	0
4/TA	0.8±0.1	80±1	1±1	99±1 (75 *S*)	0

[a] Quantified by monitoring the disappearance of NADPH at 340 nm (see the Supporting Information), μmol product formed min^{-1} nmol $heme^{-1}$. [b] Expressed as moles of product formed (GC–MS determination with internal standard) divided by moles of NADPH consumed. [c] Stereochemistry determined by enantiomeric HPLC or GC[23] with isomer identification through comparison with enriched standards (see the Supporting Information).

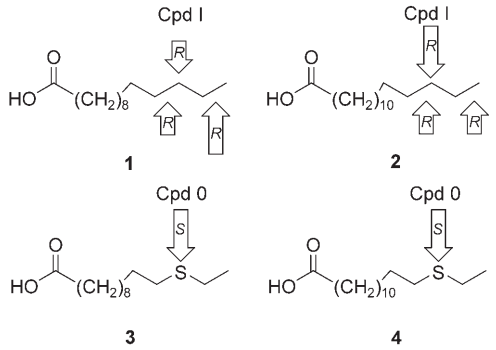

Scheme 2. Comparison of the products of oxidation of fatty acids **1** and **2** and thiafatty acids **3** and **4** by $P450_{BM3}$. The arrows indicate the position and stereochemistry of oxidation.

One explanation for this switch in enantiomeric preference for oxidation **3** and **4** relative to the analogous fatty acids is that they were accessing an unusual binding conformation that allowed the production of the *S* sulfoxide. This appears unlikely, as a range of modified fatty acids appear to undergo uniformly *R* oxidation.[9,22,29] Spectroscopic analysis of binding of **3** and **4** to $P450_{BM3}$ revealed no difference between their interactions and those of **1** and **2**: spectra of $P450_{BM3}$ bound to both fatty acids and thiafatty acids were the same in both the resting-state Fe^{III} and in the reduced Fe^{II} form. Fatty acids and thiafatty acids also afforded the same percentage spin-state change and spectral maximum of the $P450_{BM3}$ upon binding. This result is not suprising, as the replacement of a methylene group with a sulfur atom in the thiafatty acid does not result in a significant alteration in the hydrogen-bonding ability of the substrate and only slightly increases the overall chain length.

An alternative explanation involves sulfoxidation being catalyzed by a different oxidant. This might be either Cpd 0 or again different spin states of Cpd I as suggested by Shaik and co-workers.[3] Cpd 0 is rapidly converted into Cpd I in wildtype P450 enzymes through protonation of the distal oxygen atom of a heme-bound dioxygen intermediate. As this process is less favored than protonation of the proximal oxygen atom, a hydrogen-bonded water network is believed to control the regiochemistry of protonation through interactions with a conserved active-site threonine residue.[1] The TA mutants of both $P450_{cam}$ and $P450_{BM3}$ have reduced Cpd I activity and higher levels of uncoupling, as they lack this network to protonate the dioxgyen intermediate correctly. These mutants, therefore, should exhibit enhanced Cpd 0 activity and decreased Cpd I activity relative to wildtype enzymes.[4–6,22]

Thus, to examine the possibility that a Cpd 0 driven sulfoxidation reaction was occurring with $P450_{BM3}$, the activity of the T268A mutant of $P450_{BM3}$ on the thiafatty acid **4** and the corresponding fatty acid **2** was examined. The poor coupling (moles oxidized product formed/moles of NADPH consumed: see the Supporting Information for details) for oxidation of **2** (approximately 23% of wildtype coupling in our experiments) mirrors the results previously reported for lauric acid with this enzyme.[6,7] The unchanged regiochemistry and poor coupling also parallels the results reported for camphor oxidation by analogous $P450_{cam}$ mutants.[4,5] Importantly, the absolute configuration of the hydroxy fatty acids produced and the enantioselectivity of the $P450_{BM3}$T268A-catalyzed oxidation were unchanged.[23] The results thus support the hypothesis that the formation of Cpd I is slowed in this mutant, thus reducing the overall activity observed for oxidation by this mutant P450. Thus, applying such a mutant to the oxidation of **3** and **4** would

 © 2006 Wiley-VCH Verlag GmbH & Co. KGaA, Weinheim

provide an indication of the oxidative contribution of Cpd I. Turnover of both **3** and **4** with $P450_{BM3}$T268A showed no difference in the coupling, rate, or regio- and enantioselectivity of oxidation relative to that seen with the wildtype enzyme. Thus, the oxidation reactions of **3** and **4** are unaffected by a decrease in the rate of Cpd I formation and represent the only examples, to our knowledge, of P450-catalyzed reactions that are unaffected by mutagenesis of the catalytically important, conserved threonine residue.[4–7,30] This result suggests that a different oxidant is responsible for the sulfur oxidation in both the $P450_{BM3}$T268A mutant and in the wildtype enzyme and implicates Cpd 0 in the oxidation of thioethers. We suggest that the sulfur atom of **3** and **4** reacts rapidly with Cpd 0, thus preventing "incorrect" protonation of Cpd 0 and resultant loss of hydrogen peroxide (uncoupling) (Scheme 1). The results also indicate that an explanation based on differential binding for the observed stereochemical differences between **1** and **2** and **3** and **4** is unlikely. Such an explanation would require that not only do **3** and **4** adopt the same binding orientation, distinct from **1** and **2**, but also that this conformation facilitates the conversion Cpd 0 to Cpd I in the mutant and thus maintains the observed rate and coupling of enzymic oxidation.

In conclusion, care must be exercized in utilizing thioethers to probe the stereochemical outcomes of more energetically demanding reactions catalyzed by P450s, such as C–H oxidation. The two prior reports of comparable P450-mediated sulfur or methylene oxidation suggest that they can proceed with comparable stereochemical outcomes,[17,18,21] but our results demonstrate that this is not universal. The postulate that Cpd 0 is responsible for thioether oxidation in P450s is in harmony with the work of Jones and co-workers that suggests that two different oxidants function in a $P450_{BM3}$-catalyzed oxidation of an amine or thioether.[8] Our proposed mechanism also agrees with earlier work that suggests that a direct oxygen-transfer step operates in P450-mediated thioether oxidation. Additionally, the intermediacy of Cpd 0 may provide a rationale for why amine oxidation, in contrast to thioether oxidation, appears to proceed through an initial electron-transfer step. Although other hypotheses can be advanced to account for the results presented herein, oxidation by Cpd 0 is the simplest one that explains both the observed stereochemical outcome and the efficiency of oxidation by the $P450_{BM3}$T268A mutant. It will be of interest to determine if this process is a general one for the metabolism of sulfur-containing substrates by wildtype P450s.

Received: August 21, 2006
Revised: September 28, 2006
Published online: November 17, 2006

Keywords: cytochromes · enzyme catalysis · oxidation · P450 · sulfur

[1] P. R. Ortiz de Montellano, J. J. De Voss, *Nat. Prod. Rep.* **2002**, *19*, 477.
[2] N. Harris, S. Cohen, M. Filatov, F. Ogliaro, S. Shaik, *Angew. Chem.* **2000**, *112*, 2070; *Angew. Chem. Int. Ed.* **2000**, *39*, 2003.
[3] P. K. Sharma, S. P. De Visser, S. Shaik, *J. Am. Chem. Soc.* **2003**, *125*, 8698.
[4] M. Imai, H. Shimada, Y. Watanabe, Y. Matsushima-Hibiya, R. Makino, H. Koga, T. Horiuchi, Y. Ishimura, *Proc. Natl. Acad. Sci. USA* **1989**, *86*, 7823.
[5] S. A. Martinis, W. M. Atkins, P. S. Stayton, S. G. Sligar, *J. Am. Chem. Soc.* **1989**, *111*, 9252.
[6] H. Yeom, S. G. Sligar, H. Li, T. L. Poulos, A. J. Fulco, *Biochemistry* **1995**, *34*, 14733.
[7] G. Truan, J. A. Peterson, *Arch. Biochem. Biophys.* **1998**, *349*, 53.
[8] T. J. Volz, D. A. Rock, J. P. Jones, *J. Am. Chem. Soc.* **2002**, *124*, 9724.
[9] M. J. Cryle, R. D. Espinoza, S. J. Smith, N. J. Matovic, J. J. De Voss, *Chem. Commun.* **2006**, 2353.
[10] M. J. Cryle, P. R. Ortiz de Montellano, J. J. De Voss, *J. Org. Chem.* **2005**, *70*, 2455.
[11] M. J. Cryle, J. J. De Voss, *Chem. Commun.* **2004**, 86.
[12] M. J. Cryle, J. M. U. Stuthe, P. R. Ortiz de Montellano, J. J. De Voss, *Chem. Commun.* **2004**, 512.
[13] M. J. Cryle, N. J. Matovic, J. J. De Voss, *Org. Lett.* **2003**, *5*, 3341.
[14] X. He, M. J. Cryle, J. J. De Voss, P. R. Ortiz de Montellano, *J. Biol. Chem.* **2005**, *280*, 22697.
[15] P. H. Buist, D. M. Marecak, *J. Am. Chem. Soc.* **1992**, *114*, 5073.
[16] J. E. Stok, J. J. De Voss, *Arch. Biochem. Biophys.* **2000**, *384*, 351.
[17] J. Fruetel, Y.-T. Chang, J. Collins, G. Loew, P. R. Ortiz de Montellano, *J. Am. Chem. Soc.* **1994**, *116*, 11643.
[18] E. Miao, S. Joardar, C. Zuo, N. J. Cloutier, A. Nagahisa, C. Byon, S. R. Wilson, W. H. Orme-Johnson, *Biochemistry* **1995**, *34*, 8415.
[19] D. Filipovic, M. D. Paulsen, P. J. Loida, S. G. Sligar, R. L. Ornstein, *Biochem. Biophys. Res. Commun.* **1992**, *189*, 488.
[20] S. S. Boddupalli, B. C. Pramanik, C. A. Slaughter, R. W. Estabrook, J. A. Peterson, *Arch. Biochem. Biophys.* **1992**, *292*, 20.
[21] M. J. Cryle, N. J. Matovic, J. J. De Voss, *Tetrahedron Lett.* **2006**, in press.
[22] G. Truan, M. R. Komandla, J. R. Falck, J. A. Peterson, *Arch. Biochem. Biophys.* **1999**, *366*, 192.
[23] M. J. Cryle, J. J. De Voss, *Arch. Biochem. Biophys.* **2006**, submitted.
[24] J. Yin, C. Pidgeon, *Tetrahedron Lett.* **1997**, *38*, 5953.
[25] I. Fernandez, N. Khiar, J. M. Llera, F. Alcudia, *J. Org. Chem.* **1992**, *57*, 6789.
[26] I. Fernandez, N. Khiar, A. Roca, A. Benabra, A. Alcudia, J. L. Espartero, F. Alcudia, *Tetrahedron Lett.* **1999**, *40*, 2029.
[27] P. Pitchen, E. Dunach, M. N. Deshmukh, H. B. Kagan, *J. Am. Chem. Soc.* **1984**, *106*, 8188.
[28] M. A. M. Capozzi, C. Cardellicchio, F. Naso, P. Tortorella, *J. Org. Chem.* **2000**, *65*, 2843.
[29] J. H. Capdevila, S. Wei, C. Helvig, J. R. Falck, Y. Belosludtsev, G. Truan, S. E. Graham-Lorence, J. A. Peterson, *J. Biol. Chem.* **1996**, *271*, 22663.
[30] A. D. N. Vaz, D. F. McGinnity, M. J. Coon, *Proc. Natl. Acad. Sci. USA* **1998**, *95*, 3555.

 © 2006 Wiley-VCH Verlag GmbH & Co. KGaA, Weinheim

Supported Catalysts

DOI: 10.1002/anie.200603507

High-Temperature-Stable Catalysts by Hollow Sphere Encapsulation**

*Pablo M. Arnal, Massimiliano Comotti, and Ferdi Schüth**

Dedicated to Professor Klaus Unger on the occasion of his 70th birthday

Supported catalysts play a major role in many fields of chemical production and environmental protection, such as in automobile exhaust treatment.[1] In particular, noble metals are almost always dispersed on support materials of high surface area to expose a high fraction of atoms on the surface of the particles. However, particle growth at high temperatures, accompanied by a corresponding loss of catalytic activity, is a serious problem in many applications.[2–4] This is caused by the increased mobility of the particles on the support at higher temperatures. In spite of the great technological interest, general methods for the stabilization of particles against sintering are lacking, although stabilization of the dispersion has been achieved for special systems by optimizing the interaction with a support material.[5,6] We have now developed a general strategy to address this problem and demonstrate its applicability for the example of Au/ZrO_2 catalysts.

The novel sinter-stable catalyst needs to meet a number of requirements: 1) its components have to be thermally very stable to maintain the integrity of the system; 2) it should present no substantial mass transfer resistance; and 3) it should retain the catalytic activity after high-temperature treatment. The system was realized by combining two complementary technological components. It has been known for a number of years that metal nanoparticles (gold has been studied most often) can be covered by a silica layer.[7–9] In ideal cases, single nanoparticles can be produced in the center of silica shells that are identical in size by a method analogous to the well-known Stöber process. On the other hand, we have recently discovered that monodisperse, hollow, zirconia-based spheres with pores of only a few nanometers in the shells can be synthesized by coating silica with a zirconia shell and subsequent leaching of the silica core.[10] These two methods form the basis for the construction of the sinter-stable catalysts, that is, the production of hollow zirconia shells with exactly one gold nanoparticle in each shell. A related material with a carbon or silica shell was previously obtained by a different route, but no use of this material has been reported.[11] Gold was chosen as a model system, because it is presently one of the most frequently studied catalytic materials with remarkable properties, and several alternative methods for the coating of gold particles with a silica layer have been published.[12–15]

The pathway leading to the catalytic composites is shown schematically in Figure 1, in combination with TEM images of the product after each step. The gold colloid was prepared by following the route described by Enüstün and Turkevich,[16] which relies on reduction by sodium citrate and allows almost monodisperse gold particles to be obtained in the range 15–17 nm. The gold colloids were coated with silica by following essentially the route of Graf et al.[17] However, the amounts of reagents and their concentrations had to be modified to obtain reliable and reproducible results for our purpose. As the growth of the silica shell proceeds under well-controlled conditions that correspond to the Stöber process for the synthesis of monodisperse silica spheres, all particles reach an identical size after this process step, as can be seen in the TEM images in Figure 1. About 95% of the particles synthesized by this pathway contain exactly one gold nanoparticle in the center; occasionally, completely empty silica spheres or spheres containing two gold nanoparticles are observed. However, this small number of defective particles is not critical for the creation of stable catalysts.

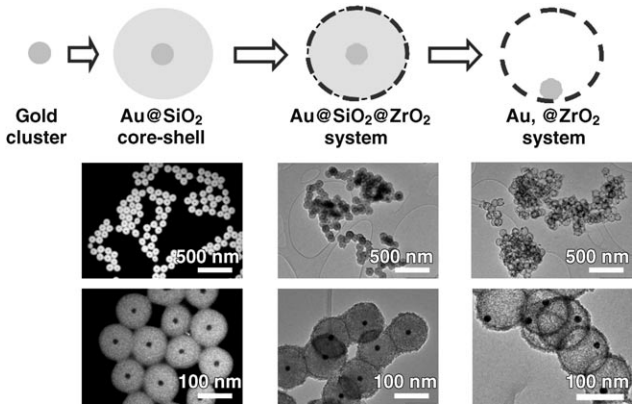

Figure 1. General scheme of the synthetic process and TEM images (left: dark field; middle and right: bright field) of the products obtained after each step. From left to right: in the first step, colloidal gold particles with sizes of approximately 15 nm are synthesized. These colloids are covered with a dense silica layer by a modified Stöber process to form monodisperse silica spheres with one gold particle in the center of each sphere. The spheres are then covered by a thin layer of zirconia particles with pores 3–4 nm in diameter between the individual zirconia particles. Finally, the silica is leached out and loose gold particles, now no longer in the center of the spheres, are obtained. (The formula "Au, @ZrO_2" indicates the presence of free space between the encapsulated gold particle and the mesoporous ZrO_2 shell.)

[*] Dr. P. M. Arnal, M. Comotti, Prof. Dr. F. Schüth
Max-Planck-Institut für Kohlenforschung
45470 Mülheim an der Ruhr (Germany)
Fax: (+49) 208-306-2395
E-mail: schueth@mpi-muelheim.mpg.de

[**] We thank A. Dreier and B. Spliethoff for the TEM analysis. Funding by the DFG through SFB 558 and the Leibniz program, in addition to the basic funding provided by the MPG, is gratefully acknowledged.

Supporting information for this article is available on the WWW under http://www.angewandte.org or from the author.

InterScience
© 2006 Wiley-VCH Verlag GmbH & Co. KGaA, Weinheim

In the next step, the $Au@SiO_2$ spheres are coated with zirconia by following the procedure described by us earlier for pure zirconia spheres.[10] Briefly, after covering the surface with a surfactant (Lutensol AO5), the system is reacted with zirconium butoxide, aged in water, and calcined at 1173 K. As the gold nanoparticles are embedded in the silica, no growth of the gold particles takes place during this step. Next, a shell of tetragonal zirconia, which consists of particles with sizes below 10 nm (and silicon compounds, the exact nature of which is not known at this time), is formed. The pores between the zirconia particles that form the shell are approximately 3–4 nm in size.

Finally, the silica is removed from the composite by treatment with NaOH solution (1N). Some silica remains in the shells, probably in the form of a zirconium silicate which is X-ray amorphous.[10] The TEM images (Figure 1, right) show that after this step, the gold particles are no longer in the center of the spheres because the silica scaffold that fixed the particles has been dissolved. The particles are now deposited somewhere on the inside of the hollow zirconia sphere.

The gold particles are now effectively separated but are highly accessible to gas molecules, which is crucial for application in heterogeneous catalysis, because otherwise mass-transfer limitations will restrict the rates in narrow-pore systems. For mass transfer, the thin, porous zirconia shell with a thickness of only about 20 nm (this can be adjusted to some extent by the parameters of the synthesis) does not provide much resistance, and the rest of the pore system consists of the large voids within the hollow shells. Good performance can therefore be expected in heterogeneous catalytic reactions.

One of the standard reactions investigated over gold catalysts is the oxidation of CO.[12,18,19] Normally, catalysts are highly active only if the particle sizes are smaller than 5 nm. For 15-nm particles, as studied here, only very low activity would be expected. However, as Figure 2 shows, the temperature for half conversion is about 200 °C, which is quite remarkable for this particle size. The high activity may be related to the high-temperature treatment during the synthesis, which leads to faceting of the gold particles.

In particular, during the first calcination step (necessary to achieve the crystallization of zirconia) the presence of silica could modify the gold surface energy, and this may result in the expression of surfaces with different structure than during calcination in air. Furthermore, it has been demonstrated in a previous study that, after calcination at 800 °C, just a small fraction (< 15 %) of the {111} surface area is converted to the less "active" {100} surface, so that the higher-activity surfaces may be retained even after calcination without the silica being present.[20] The development of specific facets and the corresponding presence of special corner and edge sites has been correlated to the surprising activity of gold catalysts before.[21–24]

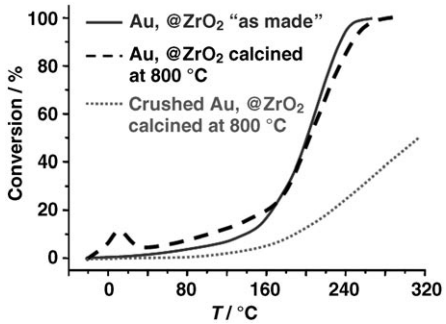

Figure 2. Catalytic performance of the different samples. The activities of the catalysts for the oxidation of CO were measured in a plug-flow reactor using 50 mg of catalyst in a gas mixture of 1 % CO in air (from Air Liquide, 99.997 % purity) at a flow rate of 67 $cm^3 min^{-1}$, which corresponds to a space velocity of 80 000 $cm^3 h^{-1} g_{cat}^{-1}$.

To check whether the encapsulation of the particles within the hollow, porous zirconia spheres is indeed advantageous for the thermal stabilization of the catalysts, a reference sample with nonencapsulated gold particles was prepared. To exclude any other factors that might affect the results, the reference sample was prepared by crushing one of the original samples in a press under a static pressure of 1 GPa. (Previous attempts to destroy the spheres by high-energy ball-milling had proven to be less successful, which demonstrates the excellent mechanical stability of the shells.) Then, both the original and the crushed samples were exposed to a thermal treatment in air. In particular, the samples were heated to 800 °C from room temperature with a heating rate of 2 $K min^{-1}$ and then left in the oven during the cooling step (the total time of treatment was about 12 hours). Figure 3 shows TEM images from before and after this treatment. The $Au,@ZrO_2$ sample is completely unaffected and no growth of the gold particles has taken place, whereas the crushed sample has clearly suffered substantial growth of the gold particles after thermal treatment through a sintering process. This complete absence of sintering for the encapsulated particles can be attributed to the stability of the overall system: the shells stay intact and the pores in the shell are too small to allow the gold particles to pass, so that even if the gold particles are mobile in the shell, they never come into contact with each other to sinter as there is only one particle per shell.

Notably, the zirconia particles in the shells grow somewhat during the heat treatment, as the surface area decreases from about 270 to about 140 $m^2 g^{-1}$, consistent with our previous reports on the pure, hollow zirconia shells.[10] The pore size distribution of the mesoporous shell is only slightly affected by the calcination (shifted to larger sizes). The decrease in surface area is predominantly a result of loss of porosity of the system.

This difference in particle size should also influence the catalytic performance, and, as seen from Figure 2, the conversion over the $Au,@ZrO_2$ sample is unaffected even after treatment at 800 °C, with the exception of a reproducible low-temperature activity in the transient catalytic experiment, the reason for which is presently unclear. The nonencapsulated catalyst, in contrast, suffers a substantial loss in activity, with half conversion reached only at temperatures more than 100 °C higher.

These results clearly show that isolation of metal catalyst particles by hollow sphere encapsulation does indeed allow stabilization of the catalyst against sintering. This method is at present rather expensive and time-consuming, but for technical applications well-controlled properties, such as monodispersity of the spheres, are probably not necessary as long as

 © 2006 Wiley-VCH Verlag GmbH & Co. KGaA, Weinheim

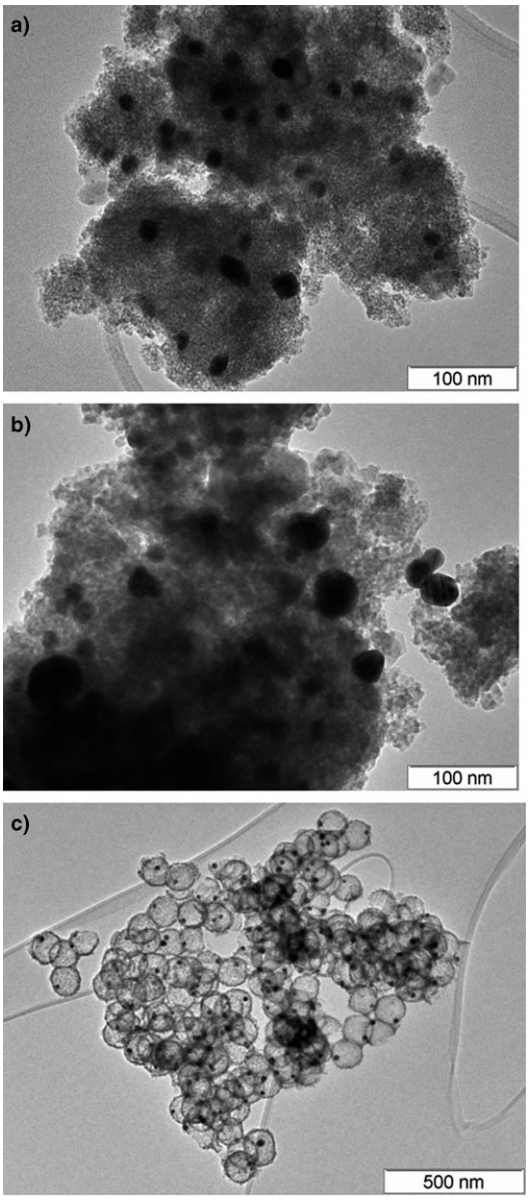

Figure 3. TEM images of encapsulated samples after crushing at a static pressure of 100 MPa (before and after calcination) and comparison with the core–shell system. a) The gold particle size is essentially unchanged compared to that of the core–shell sample before crushing. b) The crushed sample after heat treatment at 800 °C. The gold particle size has appreciably increased. c) The encapsulated sample after heat treatment at 800 °C. All gold particles are still the original size and the hollow shells are still intact. A larger scale was chosen to provide a better overview and prove that no particles had sintered.

the basic principle, full encapsulation of the metals in hollow, thermostable containers, is achieved. The results presented describe the elements of a synthetic platform that is highly flexible. By proper choice of the reaction conditions the size of the silica spheres can be adjusted, the thickness of the zirconia shell can be varied, and the pore sizes of the zirconia shells can be tuned. As has been shown in the literature, other metals can be encapsulated, and also the chemical nature of the shell can be varied.[25] We have already shown that hollow carbon shells can be created, and first results with titania are also promising.[26] It is therefore probable that the route described above provides access to a wide range of different materials systems.

Experimental Section

Catalyst preparation: Millipore water (212.5 mL, 18.2 $M\Omega\,cm^{-2}$) was vigorously stirred under reflux and a $HAuCl_4$ solution (25 mL, 2.54×10^{-3} M; Alfa-Aesar, 99.99%) was added. The resultant solution was stirred until boiling point was reached again. Then, a sodium citrate solution (12.5 mL, 10 $mg\,mL^{-1}$; citric acid trisodium salt dehydrate, 99% purity from ACROS Organics) was added and the system was refluxed for 30 min. Finally, the resultant colloid was cooled to room temperature. Next, a solution of polyvinylpyrrolidone (0.325 mL, 12.8 $mg\,mL^{-1}$), which was freshly prepared by dissolution in Millipore water with ultrasonication (30 min), was added to a previously prepared, cold, colloidal gold solution (240 mL). The resultant mixture was stirred for 24 h to allow complete adsorption of the polymer on the gold surface. After this time, the solution was centrifuged (10000 rpm; 50 min) and the supernatant was removed. The volume of the concentrated colloid was then adjusted to 6 mL by dilution with water. The colloid was vigorously stirred for 5 min, followed by addition of ethanol (18.90 mL) premixed with concentrated ammonia solution (0.84 mL, 28–30% NH_3 in water). Immediately afterwards, a solution of tetraethylorthosilicate (1.19 mL) in ethanol (12.80 mL) was added. The reaction mixture was then stirred for an additional 12 h at room temperature. The resultant colloid was centrifuged (10000 rpm; 30 min) and washed twice with water and twice with absolute ethanol. In between washing and following centrifugation the solid was redispersed by ultrasonication. After washing, the colloid was dispersed in pure ethanol (25 g) in a 100-mL flask, which was sealed with a septum and heated under stirring at 30 °C. Then an aqueous solution (0.125 mL) of Lutensol AO5 (from BASF; 0.43 g dissolved in 11 g MilliQ water) was added to the stirred solution. After 1 h, zirconium butoxide (0.45 mL, 80% w/w in butanol, from Aldrich) was added and the reaction was allowed to proceed overnight. The liquid phase of the colloid was then exchanged for water by centrifugation and redispersion of the solid in water (25 mL) four times. The particles were aged at 20 °C for 3 days. Removal of the organics and crystallization of zirconia were achieved by calcination in air by heating the system from room temperature to 900 °C at a rate of $2\,K\,min^{-1}$. Silica was removed from the composite by treatment with NaOH (1N). Specifically, the sample was kept for 16 h in a NaOH solution under stirring and then the alkaline solution was exchanged with a fresh one and the process was continued for another 12 h at 50 °C. Finally, the core–shell particles were washed five times with water and once with ethyl *tert*-butyl ether.

Ball-milling: A ball-milling experiment was conducted using a Retsch MM2000 apparatus. The sample was milled for 120 min with stainless-steel balls ($\varnothing = 2$ mm) at a frequency of 20 Hz.

Received: August 28, 2006
Revised: September 21, 2006
Published online: November 16, 2006

Keywords: calcination · gold · heterogeneous catalysis · nanoparticles · supported catalysts

[1] *Supported Metals in Catalysis* (Eds.: J. A. Anderson, M. F. Garcia), Imperial College Press, London, **2005**.
[2] E. Lox in *Handbook of Heterogeneous Catalysis* (Eds.: G. Ertl, H. Knözinger, J. Weitkamp), Wiley-VCH, Weinheim, **1997**, pp. 1559–1633.
[3] P. J. F. Harris, *J. Catal.* **1986**, *97*, 527–542.

 © 2006 Wiley-VCH Verlag GmbH & Co. KGaA, Weinheim

[4] R. M. J. Fiedorow, B. S. Chahar, S. E. Wanke, *J. Catal.* **1978**, *51*, 193 – 202.
[5] H. C. Yao, Y. F. Yao, *J. Catal.* **1984**, *86*, 254 – 265.
[6] Y. Nagai, T. Hirabayashi, K. Dohmae, N. Takagi, T. Minami, H. Shinjoh, S. Matsumoto, *J. Catal.* **2006**, *242*, 103 – 109.
[7] L. M. Liz-Marzan, M. Giersig, P. Mulvaney, *Langmuir* **1996**, *12*, 4329 – 4335.
[8] E. Mine, A. Yamada, Y. Kobayashi, M. Konno, L. M. Liz-Marzan, *J. Colloid Interface Sci.* **2003**, *263*, 385 – 390.
[9] R. I. Nooney, T. Dhanasekaran, Y. Chen, R. Josephs, A. E. Ostafin, *Adv. Mater.* **2002**, *14*, 529 – 532.
[10] P. M. Arnal, C. Weidenthaler, F. Schüth, *Chem. Mater.* **2006**, *18*, 2733 – 2739.
[11] J. Y. Kim, S. B. Yoon, J. S. Yu, *Chem. Commun.* **2003**, 790 – 791.
[12] M. Haruta, T. Kobayashi, H. Sano, N. Yamada, *Chem. Lett.* **1987**, 405 – 408.
[13] G. C. Bond, D. T. Thompson, *Catal. Rev. Sci. Eng.* **1999**, *41*, 319 – 388.
[14] Q. Fu, H. Saltsburg, M. Flytzani-Stephanopoulos, *Science* **2003**, *301*, 935 – 938.
[15] M. D. Hughes, Y. J. Xu, P. Jenkins, P. McMorn, P. Landon, D. I. Enache, A. F. Carley, D. A. Attard, G. J. Hutchings, F. King, E. H. Stitt, P. Johnston, K. Griffin, C. J. Kiely, *Nature* **2005**, *437*, 1132 – 1135.
[16] B. V. Enüstün, J. Turkevich, *J. Am. Chem. Soc.* **1963**, *85*, 3317 – 3328.
[17] C. Graf, D. L. J. Vossen, A. Imhof, A. van Blaaderen, *Langmuir* **2003**, *19*, 6693 – 6700.
[18] M. M. Schubert, S. Hackenberg, A. C. van Veen, M. Muhler, V. Plzak, R. J. Behm, *J. Catal.* **2001**, *197*, 113 – 122.
[19] A. Wolf, F. Schüth, *Appl. Catal. A* **2002**, *226*, 1 – 13.
[20] A. S. Barnard, X. M. Lin, L. A. Curtiss, *J. Phys. Chem. B* **2005**, *109*, 24 465 – 24 472.
[21] M. Comotti, W. C. Li, B. Spliethoff, F. Schüth, *J. Am. Chem. Soc.* **2006**, *128*, 917 – 924.
[22] N. Lopez, T. V. W. Janssens, B. S. Clausen, Y. Xu, M. Mavrikakis, T. Bligaard, J. K. Nørskov, *J. Catal.* **2004**, *223*, 232 – 235.
[23] C. Mohr, H. Hofmeister, J. Radnik, P. Claus, *J. Am. Chem. Soc.* **2003**, *125*, 1905 – 1911.
[24] N. Lopez, J. K. Nørskov, *J. Am. Chem. Soc.* **2002**, *124*, 11 262 – 11 263.
[25] J. Li, H. C. Zeng, *Angew. Chem.* **2005**, *117*, 4416 – 4419; *Angew. Chem. Int. Ed.* **2005**, *44*, 4342 – 4345.
[26] P. Arnal, F. Kleitz, F. Schüth, *Chem. Commun.* **2006**, 1203 – 1205.

 © 2006 Wiley-VCH Verlag GmbH & Co. KGaA, Weinheim

Hydrogen Storage

DOI: 10.1002/anie.200600105

Hydrogen Storage in the Giant-Pore Metal–Organic Frameworks MIL-100 and MIL-101**

Michel Latroche, Suzy Surblé, Christian Serre, Caroline Mellot-Draznieks, Philip L. Llewellyn, Jin-Ho Lee, Jong-San Chang, Sung Hwa Jhung, and Gérard Férey*

Nowadays, energetic needs are mainly covered by fossil fuels with concomitant pollutant emissions responsible for global warming. Among the possible solutions to reduce the greenhouse effect, hydrogen has been proposed for energy transportation. Indeed, this gas can be seen as a clean and efficient energy carrier. However, besides the difficulties related to hydrogen production, high-capacity storage is still to be developed. Hydrogen can be stored as a compressed gas, liquefied in tanks, and ab- or adsorbed in solids.[1–3] Many compounds are able to store large amounts of hydrogen. Such solid-state solutions are of interest in terms of safety, global yield, and long-term storage. However, to be suitable for applications, such compounds must have high capacity, good reversibility, fast reactivity, and sustainability. Two different approaches are possible for solid-state storage of hydrogen. In the first, the hydrogen molecule is dissociated and H atoms form chemical bonds with the solid (chemisorption). Such a process allows a very high volumetric density at temperatures and pressures close to ambient conditions. However, storage in metal hydrides has the drawback of low weight capacities, essentially due to the high molar mass of heavy metals such as

[*] Dr. M. Latroche
Laboratoire de Chimie Métallurgique des Terres Rares
CNRS, UPR 209, 94320 Thiais Cedex (France)
Fax: (+33) 149-781-203
E-mail: michel.latroche@iscsa.cnrs.fr

S. Surblé, Dr. C. Serre, Dr. C. Mellot-Draznieks, Prof. G. Férey
Institut Lavoisier
UMR 8180
Université de Versailles—St Quentin en Yvelines
45 Avenue des Etats-Unis, 78035 Versailles Cedex (France)

Dr. P. L. Llewellyn
MADIREL
UMR 6121
Université de Provence-CNRS
Centre de Saint Jérôme
13397 Marseille Cedex 20 (France)

J.-H. Lee, Dr. J.-S. Chang, Dr. S. H. Jhung
Korea Research Institute of Chemical Technology
Jang-dong 100, Yuseong-Gu, 305-600 Daejon (South Korea)

[**] The authors are grateful to Dr. A. Vimont and Pr. M. Daturi (LCS, Caen, France) for the preliminary in situ IR experiments. J.-S.C. would like to thank KRICT for supporting this work under the institutional research program.

Supporting information (Experimental Section) for this article is available on the WWW under http://www.angewandte.org or from the author.

© 2006 Wiley-VCH Verlag GmbH & Co. KGaA, Weinheim

lanthanides and zirconium. This can be overcome by using materials made of much lighter elements such as magnesium or vanadium, which exhibit higher capacities (7.6 wt% for Mg), but high temperatures, typically 300 °C, are required to fully desorb hydrogen[1,4] and the kinetics remain too slow for practical applications. The second approach consists of physisorption of hydrogen on the surface of solids. In this case, there is no chemical dissociation, binding energies are much lower than for chemisorption, and the process has significant capacity but at low temperature, typically that of liquid nitrogen. In the past, exceptionally high storage capacities have been claimed for carbon nanostructures.[5,6] However, these results were not confirmed, and it has been demonstrated that carbon materials cannot store large amounts of hydrogen at room temperature.[7–12] Other porous materials have been investigated, for example, zeolites,[13] but their capacity remains below 1.8 wt% at 77 K. For these microporous materials, many authors have attempted to relate hydrogen capacities to specific areas at low temperature, but Nijkamp et al.[14] concluded that the relation is not straightforward and a better correlation can be found with the micropore volume. This was recently confirmed with the adsorption of hydrogen in ordered nanostructured carbons.[15]

Metal–organic frameworks (MOFs) are a new class of storage materials with low density and high specific area. They are built up by linking inorganic clusters with various organic linkers[16] through strong bonds, and some of them show very promising results for hydrogen adsorption. For example, MOF-5, with large cubic cavities, adsorbs up to 4.7 wt% under 60 bar at 77 K,[17] but the disparity of the results between the various authors[18–20] underlines the importance of careful activation of the sample for good results. We reported hydrogen sorption on the metal terephthalates MIL-53 or $M(OH)[C_6H_4(CO_2)_2]$[21] ($M = Al^{3+}$, Cr^{3+}; MIL: material from Institut Lavoisier), which exhibit one-dimensional (1D) channels with large free diameters of about 8.5 Å. Their hydrogen storage capacities are 3.2 (M = Cr) and 3.8 wt% (M = Al) when loaded at 77 K under 1.6 MPa. In the same system, two chromium carboxylates MIL-100 and MIL-101 with giant pores exist.[22,23] These hybrid solids are built up from carboxylate moieties (benzene-1,3,5-tricarboxylate (btc) for MIL-100; benzene-1,4-dicarboxylate (bdc) for MIL-101) and trimeric chromium(III) octahedral clusters which have removable terminal water molecules and therefore provide potential unsaturated metal sites in the structure. The resulting zeotype architectures (Figure 1) are built by the connection of large hybrid supertetrahedra which further assemble with formation of very large mesopores. The cell volumes are huge (ca. 380000 and ca. 702000 $Å^3$, respectively), and the smaller of the two types of quasispherical cages are delimited by 12 pentagonal faces, and the larger ones by 16 faces (12 pentagonal and four hexagonal). After removal of the guests, the accessible diameters are 25 and 29 Å for MIL-100 and 29 and 34 Å for MIL-101. The as-prepared materials contain water and free carboxylic acid within the pores. Their evacuation prior to gas loading induces significant weight loss without any loss of crystallinity under the given thermal conditions.[24]

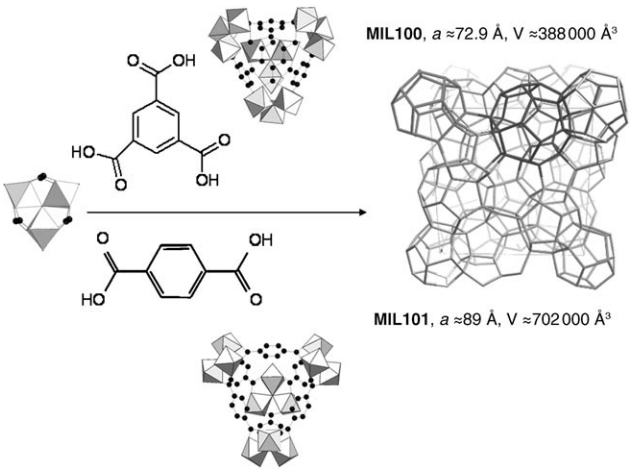

Figure 1. Schematic view of the porous solids MIL-100 and MIL-101. Left: trimers of chromium octahedra which assemble with either btc (MIL-100) or bdc (MIL-101) to form the hybrid supertetrahedra; right: the resulting zeotype architecture (each intersection of cages is occupied by a supertetrahedron).

A powdered sample of MIL-100 outgassed at 220 °C overnight shows a large weight loss of 36.4%, which corresponds to expectation. The density of the outgassed sample, measured with helium gas, is 2.63 $g\,cm^{-1}$, and the Langmuir surface area is close to 2800 $m^2\,g^{-1}$. The hydrogen uptake, measured at 298 and 77 K, shows a very fast adsorption process and thermodynamic equilibrium is reached in a few seconds, as expected for physisorption. At room temperature, the hydrogen gas isotherm curve increases linearly with pressure up to 0.15 wt% under 7.33 MPa (Figure 2). At 77 K, hydrogen adsorption is significant at low pressure, with a maximum capacity of 3.28 wt% under 2.65 MPa. Increasing the pressure to 8.5 MPa leads to a saturation plateau without further hydrogen uptake. The curve, typical of a type-I or Langmuir isotherm profile, shows good reversibility on desorption.

In the case of MIL-101, two different treatments were considered. The first treatment (MIL-101a) consisted, as for

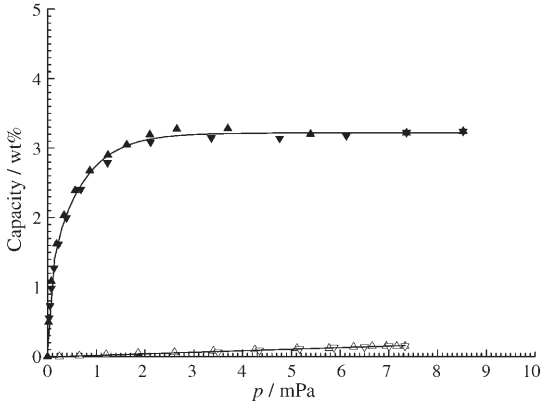

Figure 2. Adsorption (point-up triangles) and desorption (point-down triangles) pressure–composition isotherm (PCI) curves for MIL-100 at 298 (empty symbols) and 77 K (full symbols). Lines are guides to the eye.

 © 2006 Wiley-VCH Verlag GmbH & Co. KGaA, Weinheim

MIL-100, of heating the as-synthesized sample, which contains traces of recrystallized $bdcH_2$ and significant amounts of $bdcH_2$ within the pores, at 220 °C under vacuum overnight. The second sample (MIL-101b) was obtained in the same synthesis conditions as the first but activated by additional treatment steps (see Supporting Information for details). In the latter case, most of the $bdcH_2$ has been evacuated. Preliminary in situ IR experiments showed that this sample contains 10–15 wt % coordinated $bdcH_2$, and therefore only half of the metal sites are poisoned by coordinated $bdcH_2$ molecules. The Langmuir surface areas were close to 4000 (MIL-101a) and 5500 $m^2 g^{-1}$ (MIL-101b). The densities measured after outgassing were 2.26 (a) and 1.74 $g cm^{-1}$ (b). Hydrogen uptake was measured for both MIL-101a and MIL-101b at 298 and at 77 K. Once more, the adsorption/desorption processes are very fast.

At 298 K, MIL-101a shows a linear increase of the adsorption curve up to 0.36 wt % under 8.6 MPa (Figure 3). No saturation is observed, despite a small inflexion of the curve above 6 MPa. Measurement of the desorption branch down to 1.1 MPa shows good reversibility, and the two curves approximately coincide. At 77 K, the isotherm increases rapidly at moderate pressure to reach maximum capacity at 4.5 wt % with a saturation plateau above 4.0 MPa. The curve is reversible on desorption and shows a typical type-I or Langmuir isotherm profile (Figure 3).

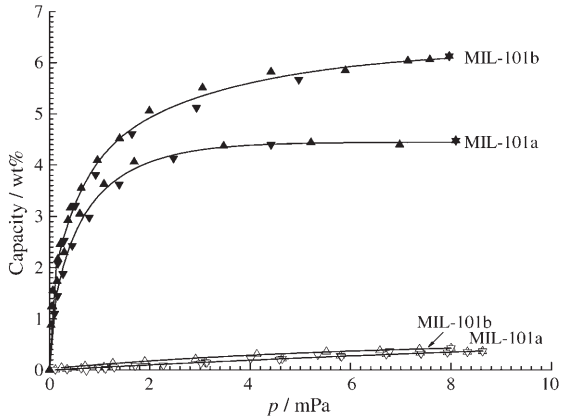

Figure 3. Adsorption (point-up triangles) and desorption (point-down triangles) pressure–composition isotherm (PCI) curves for MIL-101a and MIL-101b at 298 (empty symbols) and 77 K (full symbols). Lines are guides to the eye.

MIL-101b exhibits larger hydrogen uptake at both temperatures. Under ambient conditions, the gain in weight capacity is small (0.43 wt % under 8 MPa) but significant compared to MIL-101a under the same conditions. At 77 K, the capacity increases with pressure up to 6.1 wt % at 8 MPa, but again saturation is almost reached above 4 MPa.

The observed reversible capacities at room temperature for MIL-100 and MIL-101a,b are not negligible and slightly larger than those reported recently by Panella et al.[17] for MOF-5 and $Cu_3(btc)_2$ (0.28 and 0.35 wt %, respectively). However, they are relatively low compared to the values typically reported for metallic hydrides (between 2 and 3 %, depending on metal composition and desorption temperature). Volumetric densities are also low at room temperature (ca. 4–8 $g(H_2) dm^{-3}$), as compared to the 150 $g(H_2) dm^{-3}$ easily achievable with a compound like $LaNi_5$.

At 77 K, MIL-100 and MIL-101b show significant capacities (3.3 and 6.1 wt %, respectively) under moderate pressures. The value for MIL-100 is comparable to those reported for activated carbon and recently published MOFs,[17] while MIL-101b exhibits one of the highest values reported so far for hydrogen physisorption at this temperature (see Table 1). Moreover, preliminary IR spectroscopic experiments indicate that 10–15 wt % of the incorporated $bdcH_2$ still remains trapped in the pores of MIL-101b. Larger capacities are therefore expected if the activation process can be further improved.

For nanostructured carbons hydrogen uptake is reported to be linearly proportional to the specific surface area with a slope of about $(1.5–2) \times 10^{-3}$ wt % $m^{-2} g$.[9,25,26] Accordingly, the very large surface areas developed in MIL-10*X* structures ($X = 0$ or 1) suggest capacities should be very high. However such a relation is not straightforward. The porous chromium terephthalate MIL-53, with 1D empty channels, has a Langmuir surface area close to 1500 $m^2 g^{-1}$ and a reversible capacity of 3.2 wt % at 77 K under 1.6 MPa.[21] In the present studies, the Langmuir surface areas of the samples reach 2700 $m^2 g^{-1}$ (MIL-100) and between 4000 and 5500 $m^2 g^{-1}$ (MIL-101a,b), several times that of MIL-53. Despite these much larger surface areas, the capacity increase of 90 % relative to MIL-53 is smaller than expected. This confirms that surface area is not the only criterion for hydrogen adsorption. Indeed, one would expect that in systems with ultramicropores, that is, pores of up to three times the size of the probe molecule, volume filling should also occur. However, the ratio between capacity uptake and Langmuir surface area is almost constant for the MIL-10*X* compounds, that is, such a relationship is probably valid for compounds having similar structural properties.

Clearly, the very large empty space generated by large cages is useless for gas storage. To retain hydrogen in the tunnels and cages of porous solids, one needs strong interactions between the walls and the H_2 molecules, provided that the pores are sufficiently large to accommodate H_2 molecules. This is supported by recent work by Jhung et al. on nanoporous aluminophosphates showing that small pore size and large micropore volume are beneficial for high hydrogen uptake.[27] A recent neutron-diffraction analysis at 3.5 K on deuterated MOF-5,[28] confirmed later,[29] identified its H_2 adsorption sites. Four positions for hydrogen molecules were reported. Two sites were found to be filled first: one at the center of the three ZnO_3 triangular faces and one on top of the single ZnO_3 triangle. On further loading, two additional adsorption sites are occupied: one above the two oxygen ions and one at the top of the hexagonal linkers. Moreover, the relative binding energies were found to be larger for the three sites around the clusters than for those around the organic linkers. This important result clearly shows that the metal oxide cluster is primarily responsible for adsorption, while the organic linker plays only a secondary role.

 © 2006 Wiley-VCH Verlag GmbH & Co. KGaA, Weinheim

Table 1: Summary of hydrogen adsorption in MOFs at 77 K.

Material[a]	Free apertures[b,c] [Å]	Apparent surface area[d] [$m^2 g^{-1}$]	Pore volume [$cm^3 g^{-1}$][g]	H_2 uptake [wt%]	Conditions	Heat of adsorption [$kJ mol^{-1}$][j–m]	Ref.
$Mn(HCO_2)_2$	3/4.7	297[f]	–	0.9	1 atm	n.a.	[33]
Ni(cyclam)(bpydc)	6.1/7.6	817	0.37	1.1	1 atm	n.a.	[34]
$Zn_2(bdc)_2(dabco)$	7.8/9.5	1450[e]	–	2.0	1 atm	n.a.	[35]
$Ni_2(bpy)_3(NO_3)_4$ (M)	2.4/4.0	–	0.181[h]	0.8	1 atm	n.a.	[36]
$Ni_2(bpy)_3(NO_3)_4$ (E)	2.1/4.2	–	0.149[h]	0.7	1 atm	n.a.	[36]
$Ni_3(btc)_2(3\text{-pic})_6(pd)_3$	8.5/10.7	–	0.63	2.1	14 bar	n.a.	[36]
$Cu_2(pzdc)_2(pyz)$, CPL-1	3.4/5.0	–	–	0.2	1 atm	n.a.	[37]
$Cu_2(bptc)$, MOF-505	6.7/8.3/10.1	1830	0.63	2.48	1 atm	n.a.	[38]
$Sc_2(bdc)_3$	≈5.3	721[e]	0.33	1.5	0.8 bar	n.a.	[39]
$M_3[Co(CN)_6]_2$ M = Mn, Fe, Co, Ni, Cu, Zn	≈2/4.5	720–870[e]	n.a.	1.4–1.8	1 bar	−5.3–7.4[j]	[40]
$Mg_3(ndc)_3$	≈3.5	190[i]	n.a.	0.48	1.17 bar	−7–9.5[j]	[32]
AOH)(bdc), MIL-53(Al)	8.4	1590	0.59	3.8	16 bar	n.a.	[21]
Cr(OH)(bdc), MIL-53(Cr)	8.5	1500	0.56	3.2	16 bar	n.a.	[21]
$Al_3O(OH)(btc)_3$, MIL-96(Al)	≈3/6	–	n.a.	1.7	10 bar	n.a.	[41]
$COF(btc)_2$, MIL-100(Cr)	25/29	2700	1.0	3.3	25 bar	−5.6–6.3[k]	this work
$Cr_3OF(bdc)_3$, MIL-101(Cr)	8.6/29/34	5500	1.9	6.1	60 bar	−9.3–10.0[k]	this work
$Cr_3OF(ntc)_{1.5}$, MIL-102(Cr)	≈4	42	0.12	0.9	10 bar	−5.99[l]	[31]
$Cu_3(btc)_2$, HKUST-1	3.5/9	1958	n.a.	3.6	50 bar	−4.5/−6.8[j]	[17, 42]
$Zn_4O(bdc)_3$, MOF-5 or IRMOF-1	11.2	2296[e]	1.19	4.7	50 bar	−3.8/−4.8[j]	[17, 43, 42]
$Zn_4O(cbbdc)_3$, IRMOF-6	9.3	3300	1.14	4.8	50 bar	n.a.	[44]
$Zn_4O(ndc)_3$, IRMOF-8	12.6	1466	0.52	1.50	40 bar	−6.1[j]	[44, 43]
$Zn_4O(hpdc)_3$, IRMOF-11	9	2340	0.68	3.5	35 bar	−9.1[j]	[44]
$Zn_4O(tmbdc)_3$, IRMOF-18	13.8	1501	0.53	0.89	40 bar	n.a.	[44]
$Zn_4O(ttdc)_3$, IRMOF-20	14	4590	1.53	6.7	70 bar	n.a.	[44]
$Zn_4O(BTB)_2$, MOF-177	11/17	5640	1.59	7.5	70 bar	n.a.	[44]
$Cu_2(bptc)$	6.5	1670[e]	0.68	4.02	20 bar	n.a.	[45]
$Cu_2(tptc)$	7.3	2247[e]	1.08	6.06	20 bar	n.a.	[45]
$Cu_2(qptc)$	8.3	2932[e]	1.14	6.07	20 bar	n.a.	[45]

[a] Abbreviations: bdc = benzene-1,4-dicarboxylate; ndc = naphthalene-2,6-dicarboxylate; hpdc = 4,5,9,10-tetrahydropyrene-2,7-dicarboxylate; tmbdc = 2,3,5,6-tetramethylbenzene-1,4-dicarboxylate; btb = benzene-1,3,5-tribenzoate, cyclam = 1,4,8,11-tetraazacyclotetradecane; bpydc = 2,2′-bipyridyl-5,5′-dicarboxylate; dabco = 1,4-diazabicyclo[2.2.2]octane; bpy = 4,4′-bipyridine; btc = benzene-1,3,5-tricarboxylate; 3-pic = 3-picoline; pd = 1,2-propanediol; ttdc = thieno[3,2-*b*]thiophene-2,5-dicarboxylate; bptc = biphenyl 3,3′:5,5′-tetracarboxylate; tpdc = terphenyl 3,3″:5,5″-tetracarboxylate; qpdc = quaterphenyl 3,3‴:5,5‴-tetracarboxylate. [b] Calculations were performed using the Cerius2 software package. Crystallographic data for the evacuated frameworks were used where available. [c] Free diameters correspond to the largest spheres that can pass through the apertures of the frameworks. [d] Calculated for N_2 adsorption data collected at 77 K using the Langmuir model except where indicated. [e] BET surface area from N_2 at 77 K. [f] BET surface area for CO_2 at 195 K. [g] Calculated from N_2 adsorption data collected at 77 K by using the Dubinin–Radushkevich method, except where indicated. [h] Methanol used as adsorbate. [i] Calculated from O_2 adsorption data collected at 77 K by using the BET model. [j] Values obtained by calculation (from adsorption experiments at different temperatures). [k] Value at low coverage measured directly by microcalorimetric experiments. [l] Values deduced from computer simulation. [m] n.a.: not available.

With this in mind, it is interesting to compare the results obtained with MIL-100 and MIL-101 with those of the metal benzenedicarboxylate MIL-53 or $Cr(OH)(O_2CC_6H_4CO_2)$,[21] which has a very similar composition to MIL-101. MIL-53 does not exhibit any H_2 sorption capacity at room temperature, whereas MIL-100 and MIL-101 do. The presence in MIL-100 or $Cr_3F(H_2O)_2O[C_6H_3(CO_2)_3]_2$ and MIL-101 or $Cr_3F(H_2O)_2O[C_6H_4(CO_2)_2]_3$ of fluorine atoms and of unsaturated chromium sites (i.e., after removal of the terminal water molecules) provides possible sites for strong interaction which may explain the present hydrogen-storage properties observed at 300 K. To understand more deeply the differences in hydrogen adsorption of these large-pore samples, microcalorimetric experiments were performed at 77 K and low pressures (< 1 bar) on both samples with dihydrogen as the gas. Surprisingly, the enthalpy of adsorption in MIL-101b at low coverage is much higher, close to $-10\ kJ\ mol^{-1}$ (range: -9.3 to $-10.0\ kJ\ mol^{-1}$), than that of MIL-100 of around $-6\ kJ\ mol^{-1}$ (range: -5.6 to $-6.3\ kJ\ mol^{-1}$). According to Bathia et al.,[30] the thermodynamic requirement for an adsorbent capable of storing hydrogen at ambient temperature is a heat of adsorption of hydrogen of $15.1\ kJ\ mol^{-1}$. The heats of adsorption reported to date for MOFs are usually in the range 4–7 $kJ\ mol^{-1}$ [17,31] with the highest value of 7.0–9.5 $kJ\ mol^{-1}$ reported for Mg-based MOFs.[32] What could be the nature of the interaction between hydrogen molecules and the framework that gives rise to such high values for MIL-101, the highest so far reported for MOFs? Looking carefully

 © 2006 Wiley-VCH Verlag GmbH & Co. KGaA, Weinheim

at the structures, there could be two possibilities. First, after dehydration both mesosolids have unsaturated metal sites (i.e., five-coordinate chromium sites). However, IR experiments showed that the strongest Lewis metal sites are poisoned in MIL-101 by coordinated $bdcH_2$ moieties, whereas this is not in the case for MIL-100. This observation rules out the possibility of the unsaturated metal sites being the strongest interaction sites for hydrogen in MIL-101. The second possibility might be the presence of strong adsorption sites within the microporous supertetrahedra (ST). If their internal diameters are close to 6.6 and 8.6 Å, respectively, benzene rings of btc moieties in MIL-100 lie at the faces of the STs and leave almost no space for gas molecules to enter the cavities of the STs. On the contrary, in MIL-101, the bdc moieties lie at the edges and leave the STs open to H_2 molecules. Therefore, in our opinion, the most probable hypothesis is that the microporous STs of MIL-101 are the sites of strongest interaction in MIL-101, probably at each corner close to the trimers of chromium octahedra.

In conclusion, the two chromium carboxylates MIL-100 and MIL-101 adsorb large amounts of hydrogen at 77 K, with a capacity close to 6.1 wt% for MIL-101 as well as the highest heat of adsorption reported so far ($10\,kJ\,mol^{-1}$) at low pressure, but relatively low hydrogen uptakes at room temperature. It seems that the small pores in MIL101 play a major role. Indeed the very large empty space generated by large cages leads to very large pores that are not as effective for H_2 storage as small pores. Such criteria must be taken into account in the design of new hybrid solids showing improved hydrogen-storage properties.

Received: January 10, 2006
Revised: September 22, 2006

Keywords: carboxylate ligands · chromium · hydrogen · mesoporous materials · physisorption

[1] L. Schlapbach, A. Züttel, *Nature* **2001**, *414*, 353 – 358.
[2] L. Schlapbach, *MRS Bull.* **2002**, 675 – 676.
[3] A. Züttel, *Mater. Today* **2003**, *September*, 24 – 33.
[4] G. Sandrock, *J. Alloys Compd.* **1999**, *293–295*, 877 – 888.
[5] P. Chen, X. Wu, J. Lin, K. L. Tan, *Science* **1998**, *285*, 91 – 93.
[6] A. Chambers, C. Park, R. T. K. Baker, N. M. Rodriguez, *J. Phys. Chem. B* **1998**, *102*, 4253 – 4256.
[7] M. Hirscher, M. Becher, *J. Nanosci. Nanotechnol.* **2003**, *3*, 3 – 17.
[8] M. Hirscher, M. Becher, M. Haluska, A. Quintel, V. Skakalova, Y.-M. Choi, U. Dettlaff-Weglikowska, S. Roth, I. Stepanek, P. Bernier, *J. Alloys Compd.* **2002**, *330–332*, 654 – 658.
[9] M. Hirscher, M. Becher, M. Haluska, F. von Zeppelin, X. Chen, U. Dettlaff-Weglikowska, S. Roth, *J. Alloys Compd.* **2003**, *356–357*, 433 – 437.
[10] M. Ritschel, M. Uhlemann, O. Gutfleisch, A. Leonhardt, A. Graff, C. Täschner, J. Fink, *Appl. Phys. Lett.* **2002**, *80*, 2985.
[11] G. G. Tibbets, G. P. Meisner, C. H. Olk, *Carbon* **2001**, *39*, 2291.
[12] S. K. Bhatia, A. L. Myers, *Langmuir* **2006**, *22*, 1688 – 1700.
[13] H. W. Langmi, A. Walton, M. M. Al-Mamouri, S. R. Johnson, D. Book, J. D. Speight, P. P. Edwards, I. Gameson, P. A. Anderson, I. R. Harris, *J. Alloys Compd.* **2003**, *356–357*, 710 – 715.
[14] M. G. Nijkamp, J. E. M. J. Raaymakers, A. J. van Dillen, K. P. de Jong, *Appl. Phys. A* **2001**, *72*, 612 – 623.
[15] R. Gadiou, S.-E. Saadallah, T. Piquero, P. David, J. Parmentier, C. Vix-Guterl, *Microporous Mesoporous Mater.* **2005**, *79*, 121 – 128.
[16] O. M. Yaghi, M. O'Keeffe, N. W. Ockwig, H. K. Chae, M. Eddaoui, J. Kim, *Nature* **2003**, *423*, 705.
[17] B. Panella, M. Hirscher, H. Pütter, U. Müller, *Adv. Funct. Mater.* **2006**, *16*, 520 – 524.
[18] N. L. Rosi, J. Eckert, M. Eddaoui, D. T. Vodak, J. Kim, M. O'Keeffe, O. M. Yaghi, *Science* **2003**, *300*, 1127 – 1129.
[19] J. L. C. Rowsell, A. R. Millward, K. S. Park, O. M. Yaghi, *J. Am. Chem. Soc.* **2004**, *126*, 5666 – 5667.
[20] B. Panella, M. Hirscher, *Adv. Mater.* **2005**, *17*, 538 – 540.
[21] G. Férey, M. Latroche, C. Serre, F. Millange, T. Loiseau, A. Percheron-Guegan, *Chem. Commun.* **2003**, *24*, 2976 – 2977.
[22] G. Férey, C. Serre, F. Millange, C. Mellot-Draznieks, S. Surblé, J. Dutour, I. Margiolaki, *Angew. Chem.* **2004**, *116*, 6456; *Angew. Chem. Int. Ed.* **2004**, *43*, 6296.
[23] G. Férey, C. Mellot-Draznieks, C. Serre, F. Millange, J. Dutour, S. Surblé, I. Margiolaki, *Science* **2005**, *309*, 2040.
[24] A. Vimont, J.-M. Goupil, J.-C. Lavalley, M. Daturi, S. Surblé, C. Serre, F. Millange, G. Férey, N. Audebrand, *J. Am. Chem. Soc.* **2006**, *128*, 3218 – 3227.
[25] M. Becher, M. Haluska, M. Hirscher, A. Quintel, V. Skakalova, U. Dettlaff-Weglikovska, X. Chen, M. Hulman, Y. Choi, S. Roth, *C. R. Phys.* **2003**, *4*, 1055 – 1062.
[26] B. Panella, M. Hirscher, S. Roth, *Carbon* **2005**, *43*, 2209 – 2214.
[27] S. H. Jhung, H.-K. Kim, J. W. Yoon, J.-S. Chang, *J. Phys. Chem. B* **2006**, *110*, 9371.
[28] T. Yildirim, M. R. Hartman, *Phys. Rev. Lett.* **2005**, *95*, 215504.
[29] E. C. Spencer, J. A. K. Howard, G. McIntyre, J. L. C. Rowsell, O. M. Yaghi, *Chem. Commun.* **2006**, 278.
[30] S. K. Bathia, A. L. Myers, *Langmuir* **2006**, *22*, 1688.
[31] S. Surblé, C. Serre, F. Millange, T. Düren, M. Latroche, G. Férey, *J. Am. Chem. Soc.* DOI: 10.1021/ja064343u.
[32] M. Dinca, J. R. Long, *J. Am. Chem. Soc.* **2005**, *127*, 9376.
[33] D. N. Dybtsev, H. Chun, S. H. Yoon, D. Kim, *J. Am. Chem. Soc.* **2004**, *126*, 32 – 33.
[34] E. Y. Lee, M. P. Suh, *Angew. Chem.* **2004**, *116*, 2858 – 2861; *Angew. Chem. Int. Ed.* **2004**, *43*, 2798 – 2801.
[35] D. N. Dybtsev, H. Chun, D. Kim, *Angew. Chem.* **2004**, *116*, 5143 – 5146; *Angew. Chem. Int. Ed.* **2004**, *43*, 5033 – 5036.
[36] X. Zhao, B. Xiao, A. J. Fletcher, K. M. Thomas, D. Bradshaw, M. J. Rosseinky, *Science* **2004**, *306*, 1012.
[37] Y. Kubota, M. Takata, R. Matsuda, R. Kitaura, S. Kitagawa, K. Kabo, T. C. Kobayashi, *Angew. Chem.* **2005**, *117*, 942; *Angew. Chem. Int. Ed.* **2005**, *44*, 920.
[38] B. Chen, N. W. Ockwig, A. R. Millard, D. S. Contreras, O. M. Yaghi, *Angew. Chem.* **2005**, *117*, 4823; *Angew. Chem. Int. Ed.* **2005**, *44*, 4745.
[39] J. Perles, M. Iglesias, M.-A. Martin-Luengo, M. A. Monse, C. Ruiz-Valero, N. Snejko, *Chem. Mater.* **2005**, *17*, 5837 – 5842.
[40] S. S. Kaye, J. R. Long, *J. Am. Chem. Soc.* **2006**, *128*, 6506.
[41] T. Loiseau, L. Lecroq, C. Volkringer, J. Marrot, G. Férey, M. Haouas, F. Taulelle, S. Bourrelly, P. L. Llewellyn, M. Latroche, *J. Am. Chem. Soc.* **2006**, *128*, 10223.
[42] J. L. C. Rowsell, O. M. Yaghi, *J. Am. Chem. Soc.* **2006**, *128*, 1304.
[43] A. Dailly, J. J. Vajo, C. C. Ahn, *J. Phys. Chem. B* **2006**, *110*, 1099.
[44] A. G. Wong-Foy, A. J. Matzger, O. M. Yaghi, *J. Am. Chem. Soc.* **2006**, *128*, 3494.
[45] X. Lin, J. Jia, X. Zhao, K. M. Thomas, A. J. Blake, G. S. Walker, N. R. Champness, P. Hubberstey, M. Schröder, *Angew. Chem.*, **2006**, *118*, 7518 – 7524; *Angew. Chem. Int. Ed.*, **2006**, *45*, 7358 – 7364.

 © 2006 Wiley-VCH Verlag GmbH & Co. KGaA, Weinheim

C–H Bond Activation

DOI: 10.1002/anie.200603786

A Versatile Ruthenium Catalyst for C–C Bond Formation by C–H Bond Activation**

Rémi Martinez, Reynald Chevalier, Sylvain Darses, and Jean-Pierre Genet**

Catalytic processes involving C–H bond activation[1] are highly desirable as they allow the functionalization of more-easily available starting materials (atom economy concept[2]) and also because they produce clean reactions (reduced amounts of salts). In the field of C–C bond formation by C–H activation, several catalytic reactions have been developed recently involving mainly low-valent transition metals,[1] such as palladium, rhodium, and particularly ruthenium complexes, which have been extensively used in this field.[3]

The most active catalysts involve low-valent ruthenium complexes with oxidation states 0 or II, such as [Ru(cod)(cot)] (cod = cyclooctadiene, cot = cyclooctatetraene), $[Ru_3(CO)_{12}]$, $[RuH_2(PPh_3)_4]$, and $[RuH_2(CO)(PPh_3)_3]$, because of their high activity both in stoichiometric and catalytic reactions.[3] However, these low-valent catalyst precursors have low activity and/or are generally air- and moisture-sensitive and must therefore be stored under an inert atmosphere at low temperature to prevent their decomposition. Moreover, their synthesis is generally not obvious and requires several preparative and purification steps from commercially available $RuCl_3$. Furthermore, their preparation does not allow the complexation of a large variety of ligands, which limits their scope. The generation of low-valent active ruthenium species in situ under mild conditions would therefore be a highly desirable improvement in terms of simplicity, flexibility, and scope of these catalytic systems.

We tested the feasibility of this approach in one of the most efficient ruthenium(0)-catalyzed processes involving C–H bond activation, namely the Murai reaction.[4] This reaction, and its subsequent variations,[5,6] involves C–H bond activation in the *ortho* position of an electron-withdrawing substituent, such as oxo, imino, or cyano, and subsequent insertion of an alkene. The ruthenium complex $[RuH_2(CO)(PPh_3)_3]$ has been found to be the most active in such processes, along with, in certain cases, $[Ru_3(CO)_{12}]$.[7] No other ruthenium complexes with such high catalytic activity have been found even though several attempts have been made to prepare analogous compounds.[8] One exception concerns the use of the highly reactive and unstable complex $[RuH_2(H_2)(PCy_3)_2]$ (Cy = cyclohexyl) developed by Chaudret et al.[9]

We report herein the generation of low-valent and flexible ruthenium catalysts in situ that are highly active in C–H bond activation, particularly in the Murai reaction. Our initial idea was to generate $\{RuH_2\}$ species as precursors to the ruthenium(0) catalyst[10] from commercial or easily available ruthenium(II) sources by reaction with a hydride donor. The activity of various catalytic systems was evaluated by the reaction of α-tetralone (**1a**) with triethoxyvinylsilane (**2a**) in toluene at 140 °C (Scheme 1).

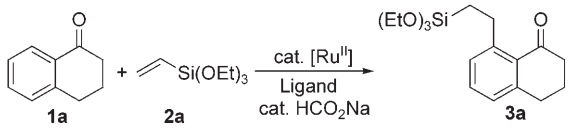

Scheme 1. Use of an in situ generated ruthenium catalyst in the Murai reaction.

We were pleased to find that the reaction between easily available $[\{Ru(p\text{-cymene})Cl_2\}_2]$ and a formate salt generated a highly active catalyst that provided the expected coupling adduct in quantitative yield in the presence of triphenylphosphane as ligand (Table 1, entry 2). Among the various possible counter cations for the formate salts,[11] sodium and thallium were found to be the best as they gave faster initial reaction rates. However, because of the high toxicity of thallium derivatives, only the sodium salt was used in subsequent studies. Thus, reaction of ketone **1a** with tri-

Table 1: Ligand screening in the Murai-type reaction.[a]

Entry	Ligand	Conversion [%][b] after 3 h	after 21 h
1	none	0	0
2	PPh_3	99	100
3	$P(p\text{-tolyl})_3$	3	94
4	$P(m\text{-tolyl})_3$	97	100
5	$P(o\text{-tolyl})_3$	0	0
6	$P(4\text{-}CF_3C_6H_4)_3$	90	93
7	$P(4\text{-}MeOC_6H_4)_3$	54	94
8	$P(2\text{-furyl})_3$	16	55
9	$PCyPh_2$	1	62
10	PCy_2Ph	2	8
11	PCy_3	2	5
12	$P(OEt)_3$	0	0
13	$P(OPh)_3$	0	0
14	dppe	0	0
15	dppf	0	0

[a] Reactions conducted with 1 mmol of **1a**, 2 equiv of **2a**, 2.5 mol% $[\{Ru(p\text{-cymene})Cl_2\}_2]$, and 3 equiv of ligand compared to Ru for monodentate ligands (1 equiv for bidentate ligands), in toluene at 140 °C. [b] Conversion determined by GC. dppe = 1,2-bis(diphenylphosphino)ethane, dppf = 1,1′-bis(diphenylphosphino)ferrocene.

[*] R. Martinez, Dr. R. Chevalier, Dr. S. Darses, Prof. J.-P. Genet
Laboratoire de Synthèse Sélective Organique (UMR 7573, CNRS)
Ecole Nationale Supérieure de Chimie de Paris
11 rue P&M Curie, 75231 Paris cedex 05 (France)
Fax: (+33) 1-4407-1062
E-mail: sylvain-darses@enscp.fr
jean-pierre-genet@enscp.fr

[**] This work was supported by the Centre National de la Recherche Scientifique (CNRS). R.M. thanks the Ministère de l'Education et de la Recherche for a grant. R.C. thanks Rhodia-Silicone for financial support. We thank Dr. Gérard Mignani (Rhodia-Silicone) for fruitful discussions.

Supporting Information for this article is available on the WWW under http://www.angewandte.org or from the author.

InterScience
© 2006 Wiley-VCH Verlag GmbH & Co. KGaA, Weinheim

ethoxyvinylsilane (**2a**) in the presence of 5 mol% [{Ru(*p*-cymene)Cl_2}$_2$], 15 mol% triphenylphosphane, and 30 mol% $NaHCO_2$ in toluene at 140°C afforded the expected product in quantitative yield in less than two hours, a result that compares well with those obtained with the classical complex [$RuH_2(CO)(PPh_3)_3$].

We next decided to conduct a ligand screening to further improve the reactivity of this catalytic system and to demonstrate its versatility (see Table 1 for selected examples). From these results, it appears that only a few ligands are suitable, mainly tri(aryl)phosphanes (Table 1, entries 2–7). The bidentate ligands tested did not produce any catalytic activity (Table 1, entries 14 and 15) and the highest conversions were achieved with triphenylphosphane (Table 1, entry 2). It is also of note that the degree of steric hindrance provided by the phosphane ligand has a strong influence on the reaction course (the reactivity decreases with an increase of the cone angle[12]). Thus, tri(*o*-tolyl)phosphane (Table 1, entry 5) did not allow the formation of the expected adduct, whereas quantitative conversion was achieved under identical conditions with the *meta* or *para* isomers (Table 1, entries 3 and 4). The electronic nature of the ligand also greatly influences the kinetic course of the reaction, with electron-donating substituents retarding the coupling (Table 1, compare entries 6 and 7). Indeed, from these preliminary results it appears that electron-poor and nonhindered tri(aryl)phosphane ligands are the most suitable for this reaction.

We next turned our attention to determining the optimal ratio between the triphenylphosphane ligand and the ruthenium(II) precursor, with α-tetralone (**1a**) as the aromatic ketone (Figure 1a). The reaction conducted with one equivalent of PPh_3 led to partial decomposition of the catalyst and low conversion. At least two equivalents of triphenylphosphane were needed, with optimal reaction rates being achieved with three equivalents of ligand. This result can be compared with that obtained with the most active ruthenium catalyst described for this reaction, namely [$RuH_2(CO)(PPh_3)_3$].[4] Indeed, we have demonstrated that only the triphenylphosphane ligand, in the stoichiometry described above, is a requisite as CO is mainly a spectator ligand in the [$RuH_2(CO)(PPh_3)_3$] catalyst precursor.[13] The stoichiometry of the added ligand compared to ruthenium was further confirmed by the reaction with another aromatic ketone, namely 1-acetonaphthone (**1b**; Figure 1b). Once again, a very fast reaction was achieved with three equivalents of triphenylphosphane, whereas with two equivalents an induction period was observed. It is also of note that ketone **1b** is even more reactive than **1a**—100% conversion was obtained in less than 20 minutes.

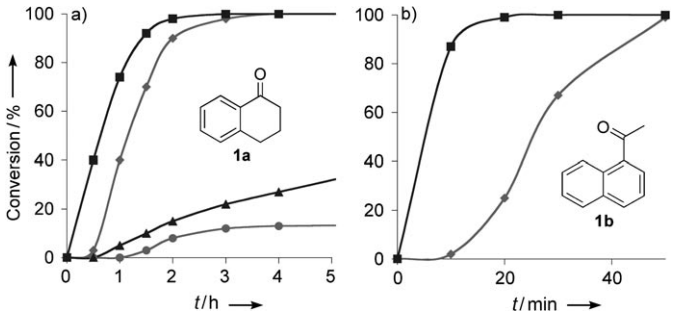

Figure 1. Influence of the amount of triphenylphosphane on the reaction profile for ketones **1a** (a) and **1b** (b). Gray circles: 1 equiv; gray rhombi: 2 equiv; black squares: 3 equiv; black triangles: 4 equiv.

Under these optimal conditions, very high yields of coupling products were achieved for a variety of aromatic methyl ketones (Table 2). All reactions were conducted with two equivalents of alkene, which explains the formation of disubstituted products, but, by careful control of the number of equivalents, it was possible, in many cases, to obtain the mono-substituted acetophenones exclusively. As shown in Table 2, these conditions are compatible with a bromo

Table 2: The Murai reaction with the herein presented in situ generated ruthenium catalyst.[a]

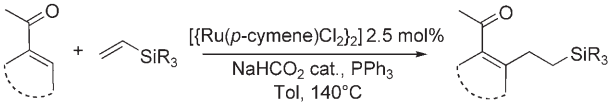

Entry	2	Product	Time [h]	Yield [%][b]
1	a	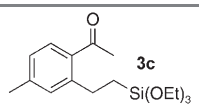 **3c**	1	100 (85/15)
2	a	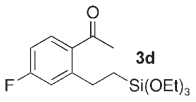 **3d**	2	92 (50/50)
3	a	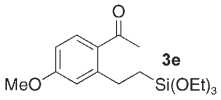 **3e**	0.5	100 (75/25)
4	a	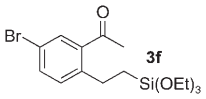 **3f**	20	70[c] (100/0)
5	a	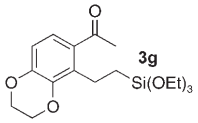 **3g**	1.5	99[d] (100/0)
6	a	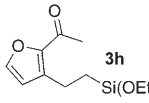 **3h**	4	85
7	a	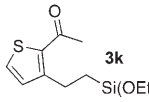 **3k**	2	100
8	b	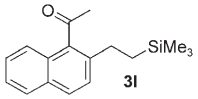 **3l**	5	97
9	c	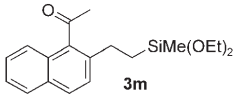 **3m**	20	89

[a] Reactions conducted with 1 mmol of ketone **1**, 2 equiv of vinylsilane **2**, 2.5 mol% [{Ru(*p*-cymene)Cl_2}$_2$], and 15 mol% of PPh_3, in toluene at 140°C. [b] Yields of isolated product, with the percentages of mono- and disubstituted products in parentheses. [c] Regioselectivity 85/15. [d] With 3 equiv of **2a**.

 © 2006 Wiley-VCH Verlag GmbH & Co. KGaA, Weinheim

substituent (Table 2; entry 4, no oxidative addition is observed) and with heterocyclic ketones (Table 2; entries 6 and 7). Moreover, a high regioselectivity was observed with *meta*-substituted acetophenones (Table 2; entries 4 and 5), with a complexing substituent (Table 2; entry 5) or steric effects (Table 2; entry 4) also influencing the regioselectivity.[5] Other alkenylsilanes participated equally well in the reaction (Table 2, entries 8 and 9).

The present reaction conditions are not limited to acetophenones. For example, the α,β-unsaturated amide **4** reacts with vinylsilane **2a** at 120 °C to afford amide **5** in high yield (Scheme 2).[14] The double bond in adduct **5** has been isomerized to the β,γ-position, with an 85/15 isomeric ratio of this bond in favor of the (*E*) isomer.

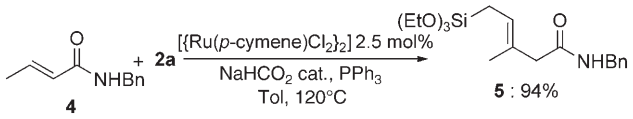

Scheme 2. The Murai reaction with an α,β-unsaturated amide.

The versatility of this in situ generated catalyst was further confirmed by extending the reaction to other substrates, particularly to imine derivatives. Indeed, under standard Murai conditions, that is, with $[RuH_2(CO)(PPh_3)_3]$ as catalyst, aromatic imines fail to react and the use of $[Ru_3(CO)_{12}]$ has proved to be more appropriate.[4,15,16] A rapid screening of substrates revealed that aromatic aldimines react well with our catalytic system. Indeed, reaction of **6** and vinylsilane **2a** in the presence of only one equivalent of triphenylphosphane (instead of the usual three equivalents) compared to ruthenium afforded the expected imine in 100% conversion and, after hydrolysis, the expected aldehyde **7** in quantitative yield (Scheme 3), with the reaction being 10-times faster than with $[Ru_3(CO)_{12}]$ under identical conditions.

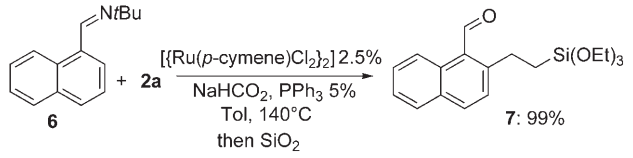

Scheme 3. C–H bond activation of aldimines.

To further demonstrate the versatility of the catalytic system, we turned our attention to the extension of this reaction to other alkenes. As reported previously, one of the main limitations of the Murai reaction is the low number of compatible alkenes and the lack of regioselectivity with other alkenes.[5] For example, the reaction of ketone **1b** with styrene (**8**) affords the coupled product with a 60/40 linear/branched product ratio (l/iso) using our catalyst (with three equivalents of PPh_3).[17] Once again a ligand screening proved to be fruitful, and we were pleased to find that the use of dicyclohexylphenylphosphane instead of triphenylphosphane in the reaction of **1b** with **8** gave the coupled product **9** in 92% yield with high regioselectivity, the anti-Markovnikov adduct being formed for the first time in a 95/5 ratio (Scheme 4).

It is also noteworthy that the reaction can be conducted under solvent-free conditions, which makes it attractive from

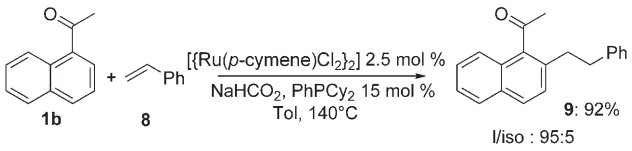

Scheme 4. Coupling with styrene.

an environmental point of view, and it can be scaled-up easily without altering the yields (Scheme 5). Indeed, reaction of 50 mmol of **1b** (7.6 mL) with three equivalents of trimethoxyvinylsilane (**2d**, 23 mL) without any solvent afforded a 45% yield of pure **3n** with only 0.04 mol% of ruthenium (turnover number (TON) = 1125). Adduct **3n** was obtained directly by distillation from the reaction mixture.

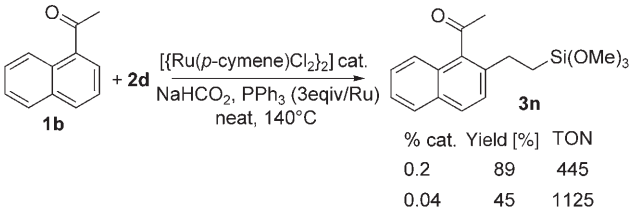

Scheme 5. A large-scale C–H bond activation reaction under solvent-free conditions.

In summary, we have demonstrated for the first time the possibility of generating a highly active ruthenium catalyst for C–H bond activation in situ from stable and easily available ruthenium(II) sources and that this catalyst has a similar or higher activity than the Murai catalyst, depending on the substrates. The versatility of this catalytic system lies in the fact that the electronic and steric properties of the catalyst can be fine-tuned by varying the ligands, thus allowing the functionalization of various substrates. Further work is underway to extend the applications of this catalytic system, and to determine the nature of the active ruthenium species generated under these conditions.

Received: September 14, 2006
Published online: November 16, 2006

Keywords: alkenes · C–H activation · homogeneous catalysis · ketones · ruthenium

[1] Reviews: a) A. E. Shilov, G. B. Shul'pin, *Chem. Rev.* **1997**, *97*, 2879–2932; b) F. Kakiuchi, S. Murai in *Topics in Organometallic Chemistry*, *Vol. 3* (Ed.: S. Murai), Springer, Berlin, **1999**, pp. 47–79; c) G. Dyker, *Angew. Chem.* **1999**, *111*, 1808–1822; *Angew. Chem. Int. Ed.* **1999**, *38*, 1698–1712; d) Y. Guari, S. Sabo-Etienne, B. Chaudret, *Eur. J. Inorg. Chem.* **1999**, 1047–1055; e) C. Jia, T. Kitamura, Y. Fujiwara, *Acc. Chem. Res.* **2001**, *34*, 633–639; f) V. Ritleng, C. Sirlin, M. Pfeffer, *Chem. Rev.* **2002**,

 © 2006 Wiley-VCH Verlag GmbH & Co. KGaA, Weinheim

102, 1731 – 1769; g) F. Kakiuchi, N. Chatani, *Adv. Synth. Catal.* **2003**, *345*, 1077 – 1101; h) A. R. Dick, M. S. Sanford, *Tetrahedron* **2006**, *62*, 2339 – 2463.

[2] a) B. M. Trost, *Science* **1991**, *254*, 1471 – 1477; b) B. M. Trost, *Angew. Chem.* **1995**, *107*, 285 – 307; *Angew. Chem. Int. Ed. Engl.* **1995**, *34*, 259 – 281; c) B. M. Trost, *Acc. Chem. Res.* **2002**, *35*, 695 – 705; d) M. Eissen, R. Mazur, H.-G. Quebbemann, K.-H. Pennemann, *Helv. Chim. Acta* **2004**, *87*, 524 – 535.

[3] a) M. A. Bennett, T. W. Matheson in *Comprehensive Organometallic Chemistry*, *Vol. 4* (Eds.: G. Wilkinson, F. G. A. Stone, E. W. Abel), Pergamon, Oxford, **1982**, p. 931; b) D. F. Shriver, M. I. Bruce in *Comprehensive Organometallic Chemistry II*, *Vol. 7* (Eds.: E. W. Abel, F. G. A. Stone, G. Wilkinson), Pergamon, Oxford, **1995**; c) T. Naota, H. Takaya, S.-I. Murahashi, *Chem. Rev.* **1998**, *98*, 2599 – 2660; d) T. Mitsudo, T. Kondo, *Synlett* **2001**, 309 – 321; e) B. M. Trost, F. D. Toste, A. B. Pinkerton, *Chem. Rev.* **2001**, *101*, 2067 – 2096; f) *Ruthenium in Organic Synthesis* (Ed.: S.-I. Murahashi), Wiley-VCH, Weinheim, **2004**; g) B. M. Trost, M. U. Frederiksen, M. T. Rudd, *Angew. Chem.* **2005**, *117*, 6788 – 6825; *Angew. Chem. Int. Ed.* **2005**, *44*, 6630 – 6666.

[4] S. Murai, F. Kakiuchi, S. Sekine, Y. Tanaka, A. Kamatani, M. Sonoda, N. Chatani, *Nature* **1993**, *366*, 529 – 530.

[5] a) F. Kakiuchi, S. Sekine, Y. Tanaka, A. Kamatani, M. Sonoda, N. Chatani, S. Murai, *Bull. Chem. Soc. Jpn.* **1995**, *68*, 62 – 83; b) M. Sonoda, F. Kakiuchi, N. Chatani, S. Murai, *Bull. Chem. Soc. Jpn.* **1997**, *70*, 3117 – 3128; c) review: F. Kakiuchi, S. Murai, *Acc. Chem. Res.* **2002**, *35*, 826 – 834.

[6] For the ruthenium-catalyzed coupling of aromatic ketones with aryl boronates see: a) F. Kakiuchi, S. Kan, K. Igi, N. Chatani, S. Murai, *J. Am. Chem. Soc.* **2003**, *125*, 1698 – 1699; b) F. Kakiuchi, M. Usui, S. Ueno, N. Chatani, S. Murai, *J. Am. Chem. Soc.* **2004**, *126*, 2706 – 2707.

[7] One rhodium complex has also shown some interesting catalytic activity, see: C. P. Lenges, M. Brookhart, *J. Am. Chem. Soc.* **1999**, *121*, 6616 – 6623.

[8] H. Kawano, R. Tanaka, T. Fujikawa, K. Hiraki, M. Onishi, *Chem. Lett.* **1999**, 401 – 402.

[9] a) Y. Guari, S. Sabo-Etienne, B. Chaudret, *J. Am. Chem. Soc.* **1998**, *120*, 4228 – 4229; b) Y. Guari, A. Castellanos, S. Sabo-Etienne, B. Chaudret, *J. Mol. Catal. A* **2004**, *212*, 77 – 82; c) J. Matthes, S. Gründemann, A. Toner, Y. Guari, B. Donnadieu, J. Spandl, S. Sabo-Etienne, E. Clot, H.-H. Limbach, B. Chaudret, *Organometallics* **2004**, *23*, 1424 – 1433; d) M. Grellier, L. Vendier, B. Chaudret, A. Albinati, S. Rizzato, S. Mason, S. Sabo-Etienne, *J. Am. Chem. Soc.* **2005**, *127*, 17592 – 17593, and references therein.

[10] Studies on the Murai reaction mechanism: a) see ref. [5a]; b) T. Matsubara, N. Koga, D. G. Musaev, K. Morokuma, *J. Am. Chem. Soc.* **1998**, *120*, 12692 – 12693; c) T. Matsubara, N. Koga, D. G. Musaev, K. Morokuma, *Organometallics* **2000**, *19*, 2318 – 2329; d) R. F. R. Jazzar, M. F. Mahon, M. K. Whittlesey, *Organometallics* **2001**, *20*, 3745 – 3751.

[11] Only the zinc, cesium, thallium, and sodium formate salts resulted in complete conversion.

[12] C. A. Tolman, *Chem. Rev.* **1977**, *77*, 313 – 348.

[13] For a discussion on the influence of the CO ligand see: B. M. Trost, K. Imi, I. W. Davies, *J. Am. Chem.Soc.* **1995**, *117*, 5371 – 5372.

[14] C–H bond activation of α,β-unsaturated esters and amides (one example) has already been reported, see ref. [13].

[15] a) F. Kakiuchi, M. Yamauchi, N. Chatani, S. Murai, *Chem. Lett.* **1996**, 111 – 112; b) F. Kakiuchi, T. Sato, T. Tsujimoto, M. Yamauchi, N. Chatani, S. Murai, *Chem. Lett.* **1998**, 1053 – 1054; c) N. Chatani, A. Kamitani, S. Murai, *J. Org. Chem.* **2002**, *67*, 7014 – 7018.

[16] For a related rhodium-catalyzed process see: a) C.-H. Jun, J.-B. Hong, Y.-H. Kim, K.-Y. Chung, *Angew. Chem.* **2000**, *112*, 3582 – 3584; *Angew. Chem. Int. Ed.* **2000**, *39*, 3440 – 3442; b) C.-H. Jun, C. W. Moon, J.-B. Hong, S.-G. Lim, K.-Y. Chung, Y.-H. Kim, *Chem. Eur. J.* **2002**, *8*, 485 – 492; c) S.-G. Lim, J.-A. Ahn, C.-J. Jun, *Org. Lett.* **2004**, *6*, 4687 – 4690; d) R. K. Thalji, J. A. Ellman, R. G. Bergman, *J. Am. Chem. Soc.* **2004**, *126*, 7192 – 7193.

[17] Similar results were obtained with the Murai catalyst $[RuH_2(CO)(PPh_3)_3]$ (l/iso = 70/30): see ref. [5].

 © 2006 Wiley-VCH Verlag GmbH & Co. KGaA, Weinheim

Heterogeneous Catalysis

DOI: 10.1002/anie.200603726

Heterogeneous Copper-in-Charcoal-Catalyzed Click Chemistry**

Bruce H. Lipshutz and Benjamin R. Taft*

Quick inspection of the 2006 literature already turns up nearly 200 papers related to "click" cycloadditions. Click chemistry is clearly on the rise, and for good reason. It offers an almost unlimited array of inert triazole-containing architectures resulting from Huisgen [3+2] cycloadditions,[1] in particular between high-energy organic azides and terminal alkynes, for example, as shown in Equation (1) (Bn = benzyl). This

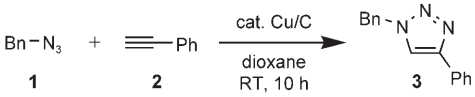

1 2 3 (1)

process is significantly accelerated by Cu^I catalysis, independently discovered and published by the groups of both Sharpless[2] and Meldal[3] in 2002. Recently reviewed,[4] copper(II) sulfate (ca. 1%) in an aqueous medium (e.g. H_2O/*t*BuOH) is typically preferred, where the presence of sodium ascorbate (ca. 10%) serves to generate catalytically active Cu^I in situ. Alternative conditions, such as in situ oxidation of Cu^0 or direct introduction of Cu^I salts (usually CuI), have also been used quite successfully.[5] While both

[*] Prof. Dr. B. H. Lipshutz, B. R. Taft
Department of Chemistry and Biochemistry
University of California, Santa Barbara
Santa Barbara, CA 93106-9510 (USA)
Fax: (+1) 805-893-4120
E-mail: lipshutz@chem.ucsb.edu
Homepage: http://www.chem.ucsb.edu/~lipshutzgroup/

[**] We are grateful to the NSF for financial support. Discussions with Professor Craig Hawker and his group (UCSB) are warmly acknowledged. ICP-AES analyses were conducted by Anthony E. Tomaso (UCSB) and are much appreciated.

Supporting information for this article is available on the WWW under http://www.angewandte.org or from the author.

© 2006 Wiley-VCH Verlag GmbH & Co. KGaA, Weinheim

reaction partners have been individually coupled under solid-phase conditions, (e.g. on polystyrene),[3,6] examples of click chemistry mediated by a source of heterogeneous copper(I) are rare. One report relies on chelation to potentially labile copper by a polystyryl-based benzylic amine.[7a] Only unhindered, low-molecular-weight, and non-basic nitrogen-containing examples were studied therein, without data quantifying losses of copper from the solid support. Other studies are also limited, based on suspensions of unsupported copper clusters.[7b] Herein, we describe the virtues of copper-in-charcoal (Cu/C) as a simple, inexpensive, and especially general and efficient heterogeneous catalyst for use in this emerging area.

Impregnation of activated wood charcoal (Aldrich, 100 mesh, $53.90/kilo)[8] with $Cu(NO_3)_2$ in water using an ultrasonic bath leads, after distillation of water and drying, to nanoparticle-sized Cu/C.[9] As both CuO and Cu_2O have been proposed as the species present within a charcoal matrix,[10] the presence of Cu^I suggested that a reducing agent might not be needed. Indeed, upon mixing benzyl azide (**1**) with phenylacetylene **2** (1:1) in dioxane at room temperature in the presence of 10 mol% Cu/C, cycloaddition was complete within 10 hours. Filtration and solvent evaporation afforded pure triazole **3** regiospecifically and near-quantitatively.

Aromatic alkynes are usually among the more reactive partners, while aliphatic alkynes oftentimes result in significantly slower cycloadditions. Steric hindrance in either substrate can also reduce rates, but with mild heating (60°C) reactions are driven to completion (Scheme 1).

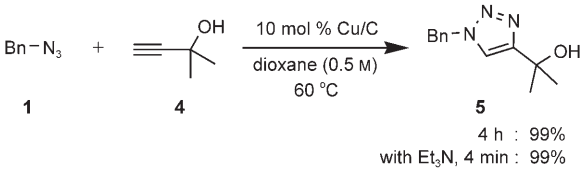

Scheme 1. A representative click reaction under mild heating.

Surprisingly, no bases, ligands,[11] or other additives are required for Cu/C to effectively catalyze these cycloadditions. However, given the likely intermediacy of copper acetylides,[4,5,12] the impact of an amine base was examined. This additive is assumed to aid in both anion formation as well as Cu^I stabilization, thereby significantly increasing rates of triazole formation.[13] Cycloaddition catalyzed by Cu/C in the presence of several different bases led to the unexpected finding, contrary to literature precedent (which encourages use of excess Hünig's base),[14] that one equivalent of Et_3N was particularly effective. Stronger (e.g. 1,8-diazabicyclo-[5.4.0]undec-7-ene (DBU)) and weaker (e.g. pyridine) amine bases had marginal impact (<10% conversion under otherwise identical conditions), while lithium *tert*-butoxide showed no catalytic effect whatsoever. The dramatic role of Et_3N was noted in the case of partners **1** and **4**, for example, where the reaction time leading to product **5** was reduced from 4 h to 4 min (Scheme 1).

Several additional examples were carried out using the same conditions: Cu/C (cat.), Et_3N (1 equiv), dioxane, 60°C (Table 1). Noteworthy features of this process include a) the regiochemistry (1,4-triazole) of addition follows that anticipated for such Cu-catalyzed reactions;[2] b) outstanding functional group tolerance is observed under these heterogeneous

Table 1: Click reactions catalyzed by Cu/C.[a]

Entry	Alkyne	Azide	t [min]	Triazole	Yield [%]
1		Bn-N_3	10		99
2	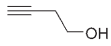	Bn-N_3	20	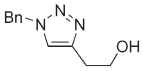	97
3		Bn-N_3	20	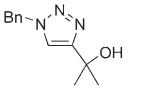	99
4	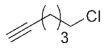	Bn-N_3	20	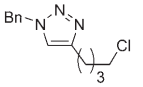	94
5			45	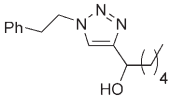	99
6[b]	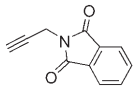	BnN_3	20	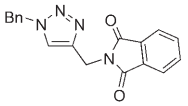	96
7			30	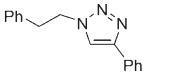	92
8	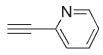		30	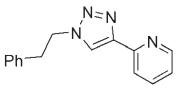	98
9	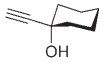		120	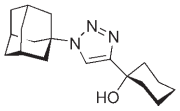	99
10[c]	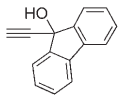		120	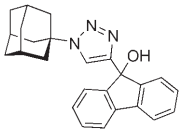	97

[a] Run at 0.5 M in dioxane at 60°C with 5 mol% Cu/C and 1 equivalent Et_3N. [b] Direct comparison to Sharpless' method (88% yield).[2] [c] Product was further purified by silica gel chromatography.

conditions; c) yields are uniformly high; d) generally, reactions are complete within minutes; e) sterically demanding precursors are not precluded from participation; f) heteroaromatics couple smoothly; and g) high-molecular-weight adducts, such as the triazole-containing steroidal derivative **6** ($M_r = 673$), and the precursor to an analogue of coenzyme Q_{10}, **7** ($M_r = 1029$), were both readily formed and isolated in good yields (Figure 1).

Numerous control experiments indicated not only that the Cu^I dispersed within charcoal is essential for catalysis but that Cu/C is also quite robust. Treatment of **1** and **4** with activated charcoal alone, from the same source used to make Cu/C,[8] gave no trace of product **5** (Table 2, entry A). Meticulous drying of these substrates, solvent, and catalyst (including the use of 4-Å molecular sieves) did not noticeably alter the rate

 © 2006 Wiley-VCH Verlag GmbH & Co. KGaA, Weinheim

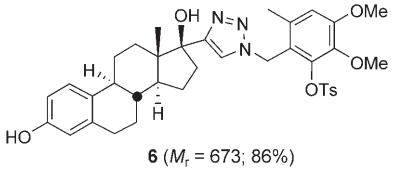

6 (M_r = 673; 86%)

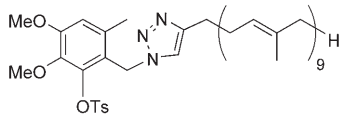

7 (M_r = 1029; 87%)

Figure 1. Examples of higher-molecular-weight adducts. Ts = *para*-toluenesulfonyl.

Table 2: Assessment of catalyst (Cu/C).

1 + **4** $\xrightarrow[Et_3N,\ solvent]{cat.\ Cu/C}$ **5**

Entry	Conditions	Yield [%]
A	charcoal, (no Cu), 60 °C, 1 h	0
B	dry dioxane with 4-Å mol. sieves	99
C	wet, 2:1 dioxane/H_2O	99
D	recycled catalyst in air	99
E	repeat (D), third use in air	99
F	dioxane, room temperature, 6 h	99
G	toluene, room temperature, 2 h	98
H	95 % EtOH, 60 °C, 10 min	98
I	H_2O, 60 °C, 10 min	97

or yield of reaction (Table 2, entry B). At the other extreme, using water as co-solvent, likewise, had no impact (Table 2, entry C). Upon formation of triazole **5**, generated without exclusion of moisture or air, the Cu/C was filtered (in air) and reused in at least two additional cycles without loss of activity (Table 2, entries D and E). In addition to unprocessed dioxane as the medium, other solvents appear to be of equal or even greater potential in these reactions. Toluene led to triazole **5** at room temperature at three times the rate seen in dioxane (entry F vs G, Table 2). Both 95 % EtOH (Table 2, entry H) and even pure water (entry I) are perfectly amenable to heterogeneous Cu/C-catalyzed click reactions, with these cycloadditions reaching completion at 60 °C in less than 10 min.

To further examine the possibility of Cu/C catalysis in the absence of additives (e.g. Et_3N), reactions were exposed to controlled microwave irradiation (Table 3). As expected, the time needed for cycloaddition resulting in triazole **5** was reduced from 4 h to less than 10 min with the reaction temperature being increased from 60 °C to 120 °C. More remarkably, Cu/C quantitatively catalyzed formation of **5** in less than 3 min at 150 °C with no loss of regioselectivity. This flawless 1,4-selectivity suggests that the process is discriminatory towards catalysis by copper (and not driven thermally), which is made all the more apparent when the same reaction in the absence of catalyst afforded no trace of triazole.

Table 3: Microwave irradiation in the absence of base.

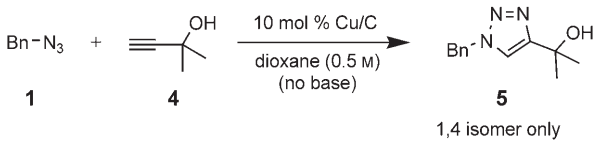

1 **4** **5**

1,4 isomer only

T [°C]	*t*	Yield [%]
conventional heating		
23	48 h	65
60	4 h	99
microwave irradiation		
120	10 min	99
150	3 min	99
150 (no catalyst)	3 min	0

In addition to the simplicity and efficiency of cycloadditions carried out in the presence of Cu/C, product contamination by copper is minimized if not completely averted. Quantitative ICP-AES[15] analyses of triazole products from multiple reactions revealed insignificant copper; indeed, copper concentrations observed were too low for accurate measurement of these millimole-scale reactions. Thus, these data further suggest that Cu/C-catalyzed click cycloadditions take place heterogeneously with negligible leaching of copper into solution, a characteristic that could simplify both preparation and isolation of triazoles for many applications.

Most recently, we have further streamlined the preparation of Cu/C (see Experimental Section) by bypassing the distillation step. To demonstrate utility, a batch of catalyst (> 40 gram) was quickly prepared (Scheme 2) and tested

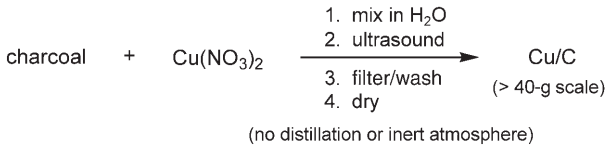

Scheme 2. Simplified, scaled-up preparation of Cu/C.

successfully in the conversion of **1** and **4** into **5**. No noticeable difference in reaction rate or extent of leaching (by ICP-AES) was observed, notwithstanding impregnation of copper(II) nitrate.[16] Assuming catalysis by Cu^I, partial reduction by charcoal could account for the observed activity.

In conclusion, highly efficient click chemistry between organic azides and terminal alkynes can be heterogeneously catalyzed by copper nanoparticles mounted within the pores of activated charcoal.[9] Reactions can be accelerated with stoichiometric Et_3N or by simply increasing the reaction temperature. Under microwave irradiation, triazoles can be formed in minutes at 150 °C. Cycloadditions can be carried out in a purely organic medium, in aqueous solvent mixtures, or in pure water. Solubility issues, copper contamination, and modest yields usually associated with the choice of copper salt are completely averted. External ligands known to accelerate click reactions are not needed. The catalyst appears to be

 © 2006 Wiley-VCH Verlag GmbH & Co. KGaA, Weinheim

unaffected by exposure to air, suggesting a substantial shelf-life. Steric congestion in one or both partners is well-tolerated, and product isolation is notably facile.[17] Further studies that take advantage of Cu/C in several contexts (e.g. kinetic resolutions, mechanistic questions, formation of new triazole-containing ligands, etc.) are ongoing, the results from which will be reported in due course.

Experimental Section

Simplified preparation of Cu/C:[18] Darco KB activated carbon (50.0 g, 100 mesh, 25% H_2O content) was added to a 500-mL round-bottomed flask containing a stir bar. A solution of $Cu(NO_3)_2 \cdot 3H_2O$ (Acros Organics, 11.114 g, 46.0 mmol) in deionized water (100 mL) was added to the flask, and further deionized H_2O (100 mL) was added to wash down the sides of the flask. The flask was loosely capped and stirred under air for 30 min and then submerged in an ultrasonic bath for 7 h. Subsequent washing (toluene) and air drying (3 h) by vacuum filtration yielded about 85 grams of "wet" Cu/C. The catalyst could be used at this stage or further dried in vacuo at 120 °C overnight (41 g yield of "dry" Cu/C).

General procedure for Cu/C-catalyzed "click" reaction: Cu/C (50 mg, 1.01 mmol g^{-1}, ca. 0.05 mmol) is added to a clean 10-mL flask fitted with a stir bar and septum. Dioxane (1–2 mL) is added slowly to the sidewalls of the flask to rinse the catalyst down. While the heterogeneous solution is stirred, triethylamine (1.1 mmol), alkyne (1.1 mmol), and azide (1.0 mmol) are added. The flask is stirred at room temperature (or warmed to 60 °C), and the reaction progress is monitored by TLC until complete consumption of azide has occurred. The mixture is filtered through a pad of celite to remove the catalyst, and the filter cake is further washed with EtOAc to ensure complete transfer. The volatiles are removed in vacuo to give pure triazole.

Received: September 12, 2006
Published online: November 17, 2006

Keywords: click chemistry · copper · cycloaddition · heterogeneous catalysis · microwave irradiation

[1] R. Huisgen, *1,3-Dipolar Cycloaddition Chemistry* (Ed.: A. Padwa), Wiley, New York, **1984**.
[2] K. B. Sharpless, V. V. Fokin, L. G. Green, V. V. Rostovtsev, *Angew. Chem.* **2002**, *114*, 2708; *Angew. Chem. Int. Ed.* **2002**, *41*, 2596.
[3] M. Meldal, C. Christensen, C. W. Tornoe, *J. Org. Chem.* **2002**, *67*, 3057.
[4] J. H. Maarseveen, H. Hiemstra, V. D. Bock, *Eur. J. Org. Chem.* **2006**, 51.
[5] a) K. B. Sharpless, V. V. Fokin, V. V. Rostovtsev, L. Noodleman, R. Hilgraf, T. Lovell, F. Himo, *J. Am. Chem. Soc.* **2005**, *127*, 210; b) C. J. Hawker, T. P. Russell, P. Wu, V. V. Fokin, E. Drockenmuller, K. Schleicher, M. Malkoch, *Macromolecules* **2005**, *38*, 3663.
[6] a) P. Gmeiner, H. Hubner, S. Lober, P.-R. Loaiza, *J. Comb. Chem.* **2006**, *8*, 252; b) M. G. Finn, Q. Wang, J. Kuzelka, S. Punna, *Angew. Chem.* **2005**, *117*, 2255; *Angew. Chem. Int. Ed.* **2005**, *44*, 2215.
[7] a) C. Girard, E. Onen, M. Aufort, S. Beauviere, E. Samson, J. Herscovici, *Org. Lett.* **2006**, *8*, 1689; b) G. Rothenberg, J.-V. Maarseveen, L. D. Pachon, *Adv. Synth. Catal.* **2005**, *347*, 811; see also: A. Ponti, N. Santo, G. Marinoni, C. L. Bianchi, G. Molteni, *New J. Chem.* **2006**, *30*, 1137.
[8] Aldrich Catalogue, #278092. Darko KB, Wet Powder, 100 mesh, contains less than 30% water.
[9] B. H. Lipshutz, B. A. Frieman, A. E. Tomaso, *Angew. Chem.* **2006**, *118*, 1281; *Angew. Chem. Int. Ed.* **2006**, *45*, 1259.
[10] T. Tsoncheva, S. Vankova, D. Mehandjiev, *Fuel* **2003**, *82*, 755.
[11] V. V. Fokin, K. B. Sharpless, R. Hilgraf, T. R. Chan, *Org. Lett.* **2004**, *6*, 2853.
[12] M. G. Finn, V. V. Fokin, V. O. Rodionov, *Angew. Chem.* **2005**, *117*, 2250; *Angew. Chem. Int. Ed.* **2005**, *44*, 2210.
[13] M. R. Ghadiri, C. D. Stout, W. S. Horne, *J. Am. Chem. Soc.* **2003**, *125*, 9372.
[14] C-H. Wong, J. C. Paulson, O. Blixt, M. C. Bryan, F. Fazio, *J. Am. Chem. Soc.* **2002**, *124*, 14397.
[15] ICP-AES: inductively coupled plasma–atomic emission spectroscopy. A. W. Varnes, *Handbook of Instrumental Techniques for Analytical Chemistry* (Ed.: F. Settle), Prentice Hall, Upper Saddle River, NJ, **1997**, p. 395.
[16] For a recent article that describes use of copper(II) salts to catalyze click cycloadditions in water, see: M. L. Kantam, K. Rajgopal, K. R. Reddy, *Synlett* **2006**, 957–959.
[17] Removal of catalyst by filtration followed by evaporation of volatiles gives pure triazole products with little to no copper contamination. See Experimental Section.
[18] Some $Cu(NO_3)_2 \cdot 3H_2O$ remained in the filtrate and was recovered by evaporation of the water. Further optimization of this preparation is ongoing.

 © 2006 Wiley-VCH Verlag GmbH & Co. KGaA, Weinheim

Bismuth Triborate

DOI: 10.1002/anie.200602993

A New Non-Centrosymmetric Modification of BiB_3O_6**

*Johanna S. Knyrim, Petra Becker, Dirk Johrendt, and Hubert Huppertz**

In addition to the applications of many natural borates, the synthesis, structural characterization, and materials processing of new solid-state borates have steadily increased during the past decade. In the field of nonlinear optical (NLO) materials, which are used to generate new lasers with frequencies that cannot be obtained directly, great progress has been made in the last 20 years. Since the discovery of the first effective borate material β-BaB_2O_4 (BBO), which is suitable for frequency conversion, the effectiveness of a large variety of borates has been investigated.[1]

In the system Bi_2O_3/B_2O_3, primarily determined by Levin and McDaniel in 1962,[2] the crystalline compounds $Bi_{12}BO_{20}$ [correctly $Bi_{24}B_2O_{39}$[3] (boron sillenite)], $Bi_4B_2O_9$, $Bi_3B_5O_{12}$, BiB_3O_6, and $Bi_2B_8O_{15}$ were found. Later on, $BiBO_3$ was added to this system as a metastable compound.[4,5] At the moment, the most prominent compound in this system is bismuth triborate (BiB_3O_6,[6–8] BIBO) because of its exceptional nonlinear optical properties,[9] which have raised the interest of many research groups around the world. Meanwhile, BiB_3O_6 is already well-established as a nonlinear optical material with outstanding physical properties and has furthermore been characterized in detail with respect to its piezoelectric, pyroelectric, dielectric, elastic, and thermoelastic properties.[10]

Recently, Li et al. synthesized two new polymorphs of BiB_3O_6.[11] For clarity, the authors renamed bismuth triborate as α-BiB_3O_6 and the two new modifications as β- and γ-BiB_3O_6. In contrast to the α phase, which crystallizes in the non-centrosymmetric, monoclinic space group *C*2, these modifications crystallize in the centrosymmetric space group $P2_1/n$.

[*] J. S. Knyrim, Prof. Dr. D. Johrendt, Dr. H. Huppertz
Department Chemie und Biochemie
Ludwig-Maximilians-Universität München
Butenandtstrasse 5–13, 81377 München (Germany)
Fax: (+49) 89-2180-77806
E-mail: huh@cup.uni-muenchen.de
Dr. P. Becker
Institut für Kristallographie
Universität zu Köln
Zülpicher Strasse 49b, 50674 Köln (Germany)

[**] We would like to thank the Deutsche Forschungsgemeinschaft (HU 966/2-2) for generous support, Dr. P. Mayer for collecting the single-crystal data, T. Miller for the in situ powder diffraction measurements, Dr. L. Bayarjargal for help with powder SHG measurements, and Prof. Dr. L. Bohatý (Universität zu Köln) and Prof. Dr. W. Schnick (LMU München) for the continuous support of these investigations.

Herein, we report the synthesis of a new non-centrosymmetric modification of bismuth triborate (hereafter δ-BiB_3O_6), which was synthesized using a high-pressure/high-temperature reaction at 5.5 GPa and 820 °C in a modified Walker module (multianvil assembly) starting from the oxides Bi_2O_3 and B_2O_3 [Eq. (1)].[12]

$$Bi_2O_3 + 3\,B_2O_3 \xrightarrow[820\,^\circ C]{5.5\,GPa} 2\,\delta\text{-}BiB_3O_6 \quad (1)$$

In the past, we successfully applied the multianvil high-pressure technique to borate chemistry as a versatile tool for the synthesis of new polymorphs and compositions, including new structural features.[13–16] Furthermore, we obtained crystalline compounds by pressure-induced crystallization in systems where only glassy compounds were attainable beforehand (for example, β-SnB_4O_7 in the system Sn/B/O).[17] A similar behavior can be observed in the polymorphs of bismuth triborate. α-BiB_3O_6 tends to solidify as a glass owing to the high viscosity of its melt, which inhibits the initial nucleation of crystals and further limits the growth velocity of crystals in the melt.[8] Furthermore, B_2O_3 evaporates from the melt, leading to severe difficulties in the preparation of a homogenous melt. Even Li et al. had difficulties to crystallize β-BiB_3O_6 and γ-BiB_3O_6, and both structures were determined by powder X-ray diffraction data.[11]

In the current work, high-pressure conditions were applied for the synthesis of δ-BiB_3O_6, thereby leading to a highly crystalline sample. Two factors support the crystallization: the closed sample capsule prevents the evaporation of boron oxide, thus keeping the composition constant, and the high temperature assures high ionic mobility, which enables the reconstructive formation of a denser phase of δ-BiB_3O_6. The importance of an adequate temperature to overcome the kinetic barrier for the transformation into a high-pressure phase is underlined by the fact that Raman spectroscopy studies by Hellwig at room temperature gave no hint to structural changes in α-BiB_3O_6 for pressures up to 18 GPa.[18]

The crystal structure of δ-BiB_3O_6 (Figure 1) was determined on the basis of single-crystal data.[19] The structure is exclusively built up of BO_4 tetrahedra, which share common corners and form layers (light polyhedra in Figure 1). These layers are interconnected through zigzag chains of BO_4 tetrahedra (dark polyhedra), thus forming a network structure with channels of six-membered rings along [010] and ten-membered rings along [001] that contain the metal cations.

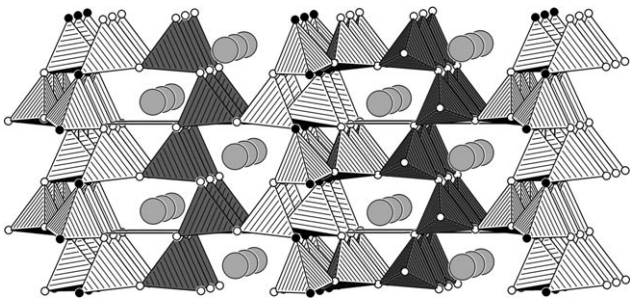

Figure 1. Crystal structure of δ-BiB_3O_6, view along [010]. Gray spheres: Bi^{3+}, light spheres: $O^{[2]}$, black spheres: $O^{[3]}$ (three coordinate).[3]

 © 2006 Wiley-VCH Verlag GmbH & Co. KGaA, Weinheim

Inside of the layers, the black spheres represent three-coordinate oxygen atoms ($O^{[3]}$; $^1/_6$ of all oxygen atoms).

This structure type was recently discovered by us in the high-pressure compounds γ-$Ln(BO_2)_3$ (Ln = La–Nd).[20] Although the topology of the BO_4 tetrahedra is nearly identical, a remarkable difference in the coordination of the metal cations exists. For example, in γ-$Ce(BO_2)_3$ the Ce^{3+} ions are coordinated by 10 oxygen atoms (Ce–O 239–303 pm), while the Bi^{3+} ions in δ-BiB_3O_6 exhibit only a sevenfold coordination [Bi–O 226–273 pm; Figure 2 (left)]. The reason

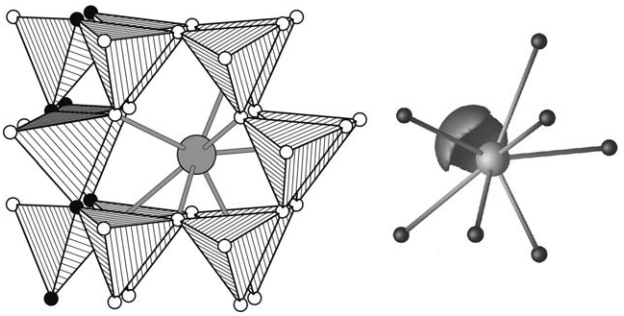

Figure 2. Left: Coordination sphere of bismuth in the crystal structure of δ-BiB_3O_6 (gray spheres: Bi^{3+}, light spheres: $O^{[2]}$, black spheres: $O^{[3]}$ (three coordinate)); right: the lone pair at the Bi^{3+} ion in δ-BiB_3O_6 visualized by the electron localization function (valence ELF; isosurface value ELF = 0.8).

for the different coordination of the Bi^{3+} ions is the sterically active lone pair localized at each Bi^{3+} center. To analyze the conspicuous behavior of the lone pair in δ-BiB_3O_6, we calculated the band structure and the electron-density distribution. Figure 2 (right) displays the coordination of the bismuth atoms in δ-BiB_3O_6, including the ELF isosurface of ELF = 0.8.[21,22] The lone pair at the bismuth atom is clearly visible and points toward the "empty" space above the atom.

A comparison between α-, β-, and γ-BiB_3O_6 shows an increasing density (α: 5.033; β: 5.411; γ: 6.177 $g\,cm^{-3}$), which runs parallel with a transformation of BO_3 into BO_4 groups. In α-BiB_3O_6, the ratio of BO_3/BO_4 is 2:1, and this ratio changes to 1:2 in β-BiB_3O_6, while exclusively BO_4 tetrahedra are present in γ-BiB_3O_6. As expected, the new high-pressure phase δ-BiB_3O_6 exhibits a denser structure (6.378 $g\,cm^{-3}$) than the γ modification prepared under ambient pressure. As the coordination of the oxygen atoms is identical in both structures (fraction of $O^{[3]}$: $^1/_6$), the bismuth coordination was examined. In fact, ECoN calculations (effective coordination numbers, as described by Hoppe)[23] for δ-BiB_3O_6 exhibit sevenfold-coordinated Bi^{3+} ions (Bi–O 226–273 pm) in contrast to sixfold-coordinated Bi^{3+} ions in γ-BiB_3O_6 (216–267 pm).

An ungraded powder sample of δ-BiB_3O_6 was subjected to a qualitative powder second-harmonic-generation (SHG) measurement by using the method reported by Kurtz and Perry.[24] KDP (KDP = KH_2PO_4) (grain size 125–185 μm) was used as a reference material. The observed intensities of the second harmonics generated by δ-BiB_3O_6 and by KDP were nearly equal, thus corroborating the non-centrosymmetry of δ-BiB_3O_6 and signalizing a considerable SHG effect of the measured sample.

Thermoanalytical investigations, using temperature-dependent X-ray powder diffraction patterns of δ-BiB_3O_6, showed that the compound is stable up to 700 °C.[25] Between 700 and 750 °C, the phase transforms into an X-ray-amorphous compound. These results are in agreement with the differential-thermoanalysis/thermogravimetry (DTA/TG) measurements, which exhibit a broad endothermic effect with an onset at 709 °C.[26] Subsequent cooling to room temperature did not succeed in obtaining any crystalline phase under ambient pressure. IR spectroscopic investigations showed strong absorptions of the BO_4 tetrahedra between 800 and 1150 cm^{-1}. Additionally, a strong absorption at 1261 cm^{-1} was observed, which can be assigned to the OB_3 group. Vibrational bands resulting from OH groups or water were not detectable.

Systematic investigations of the minimal pressure for the synthesis of δ-BiB_3O_6 revealed a value of 3 GPa. Thus, it is experimentally possible to grow large single crystals under high-pressure conditions for a detailed characterization of their nonlinear optical properties.

Experimental Section

According to Equation (1), the starting materials for the synthesis of δ-BiB_3O_6 were stoichiometric mixtures of bismuth oxide (Merck, Darmstadt, extra pure) and B_2O_3 (Strem Chemicals, 99.9 %). The mixture was compressed and heated in a multianvil assembly. A precast MgO octahedron (Ceramic Substrates & Components) with an edge length of 18 mm was used as a pressure medium. Eight tungsten carbide cubes (TSM 10, Ceratizit) with a truncation of 11 mm, separated by pyrophyllite gaskets, compressed the octahedron (18/11 assembly). The mixture (ca. 120 mg) was filled into a cylindrical boron nitride crucible that was sealed by a boron nitride plate. Further details of the construction of the assembly can be found in reference [12].

For the synthesis of δ-BiB_3O_6, the assembly was compressed within 120 min to 5.5 GPa and heated to 820 °C in the following 10 min. After holding this temperature for 5 min, the sample was cooled down to 500 °C over another 15 min and after that cooled to room temperature within 1 min. After decompression (6 h), the recovered experimental octahedron was broken apart, and the sample was carefully separated from the surrounding hexagonal boron nitride. The air- and humidity-resistant compound δ-BiB_3O_6 was obtained as a coarsely crystalline, colorless solid.

Received: July 25, 2006
Published online: November 3, 2006

Keywords: bismuth triborate · borates · high-pressure chemistry · nonlinear optics · solid-state structures

[1] P. Becker, *Adv. Mater.* **1998**, *10*, 979.
[2] E. M. Levin, C. L. McDaniel, *J. Am. Ceram. Soc.* **1962**, *45*, 355.
[3] M. Burianek, M. Mühlberg, *Cryst. Res. Technol.* **1997**, *32*, 1023.
[4] M. J. Pottier, *Bull. Soc. Chim. Belg.* **1974**, *83*, 235.
[5] P. Becker, R. Fröhlich, *Z. Naturforsch. B* **2004**, *59*, 256.
[6] J. Liebertz, *Z. Kristallogr.* **1982**, *158*, 319.
[7] R. Fröhlich, L. Bohatý, J. Liebertz, *Acta Crystallogr. Sect. C* **1984**, *40*, 343.
[8] P. Becker, J. Liebertz, L. Bohatý, *J. Cryst. Growth* **1999**, *203*, 149.

 © 2006 Wiley-VCH Verlag GmbH & Co. KGaA, Weinheim

[9] H. Hellwig, J. Liebertz, L. Bohatý, *Solid State Commun.* **1998**, *109*, 249.
[10] S. Haussühl, L. Bohatý, P. Becker, *Appl. Phys. A* **2006**, *82*, 495.
[11] L. Li, G. Li, Y. Wang, F. Liao, J. Lin, *Inorg. Chem.* **2005**, *44*, 8243.
[12] H. Huppertz, *Z. Kristallogr.* **2004**, *219*, 330.
[13] H. Huppertz, B. von der Eltz, *J. Am. Chem. Soc.* **2002**, *124*, 9376.
[14] H. Emme, H. Huppertz, *Chem. Eur. J.* **2003**, *9*, 3623.
[15] H. Huppertz, H. Emme, *J. Phys. Condens. Matter* **2004**, *16*, S1283.
[16] H. Emme, M. Valldor, R. Pöttgen, H. Huppertz, *Chem. Mater.* **2005**, *17*, 2707.
[17] J. S. Knyrim, F. M. Schappacher, R. Pöttgen, J. Schmedt auf der Günne, D. Johrendt, H. Huppertz, *Chem. Mater.* **2006**, *18*, submitted.
[18] H. Hellwig, **2002**, personal communication.
[19] Crystal data for δ-BiB_3O_6: $M_r = 337.4\ g\,mol^{-1}$, colorless block, $0.02 \times 0.03 \times 0.04\ mm^3$, orthorhombic, space group $Pca2_1$, $a = 1844.8(4)$, $b = 444.95(9)$, $c = 428.06(9)$ pm, $V = 0.3514(2)\ nm^3$, $Z = 4$, $\rho_{calcd} = 6.378\ g\,cm^{-3}$, Enraf-Nonius Kappa CCD, $Mo_{K\alpha}$ radiation ($\lambda = 71.073$ pm), graphite monochromator, $F(000) = 584$, $\mu = 50.108$, $T = 293(2)$ K, 6356 measured reflections in the range $4° \le \Theta \le 38°$, 1866 independent reflections ($I > 0\sigma(I)$), multiscan absorption correction, $R_{int} = 0.0605$. Structure solution and parameter refinement (full-matrix least squares against F^2) were performed using the SHELX-97 software suite; 92 refined parameters, $R1 = 0.0276$ and $wR2 = 0.0643$ for $I > 2\sigma(I)$, $R1 = 0.0304$ and $wR2 = 0.0664$ for all data, Flack parameter $= -0.01(2)$, GOF $= 1.057$. Further details on the crystal structure investigations may be obtained from the Fachinformationszentrum Karlsruhe, 76344 Eggenstein-Leopoldshafen, Germany (fax: (+49) 7247-808-666; e-mail: crysdata@fiz-karlsruhe.de), on quoting the depository number CSD-416822.
[20] H. Emme, C. Despotopoulou, H. Huppertz, *Z. Anorg. Allg. Chem.* **2004**, *630*, 2450.
[21] O. K. Andersen, O. Jepsen, TB-LMTO, MPI für Festkörperforschung, Stuttgart, **1994**.
[22] A. D. Becke, K. E. Edgecomb, *J. Chem. Phys.* **1990**, *92*, 5397.
[23] R. Hoppe, *Angew. Chem.* **1970**, *82*, 7; *Angew. Chem. Int. Ed. Engl.* **1970**, *9*, 25.
[24] S. K. Kurtz, T. T. Perry, *J. Appl. Phys.* **1968**, *39*, 3798.
[25] These investigations were performed on an STOE Stadi P powder diffractometer ($Mo_{K\alpha}$) with a computer-controlled STOE furnace. The sample was enclosed in a quartz capillary and heated from room temperature to 500 °C in 100 °C increments and from 500 °C to 1100 °C in 50 °C increments. Afterwards, the sample was cooled down to 500 °C in 50 °C increments, and below 500 °C in 100 °C increments. At each temperature a diffraction pattern was recorded over the angular range $3 \le 2\Theta \le 18°$.
[26] The DTA/TG curve of δ-BiB_3O_6 was recorded between room temperature and 800 °C with a heating rate of $10\ K\,min^{-1}$ using a Setaram TGA 92-2400, combined with a DTA/TG thermobalance.

 © 2006 Wiley-VCH Verlag GmbH & Co. KGaA, Weinheim

Gold Catalysis

DOI: 10.1002/anie.200602484

Gold Catalysts: Nanoporous Gold Foams**

*Volkmar Zielasek, Birte Jürgens, Christian Schulz, Jürgen Biener, Monika M. Biener, Alex V. Hamza, and Marcus Bäumer**

Despite the general inertness of gold, finely dispersed gold nanoparticles on suitable oxide supports can demonstrate remarkable catalytic activity for the epoxidation of propene or the oxidation of CO, for example.[1–7] Gold-based catalysts have potential applications in automotive emission control, because unlike platinum or palladium catalysts, they remain active at low temperatures (room temperature).[8] While various support materials, particle synthesis routes, and deposition techniques have been investigated over the years,[9,10] the mechanisms responsible for the catalytic activity are still under debate, because of the complexity of the particle–support interactions and the reaction pathways. Research to date has shown that the particle size, type of support material, and particle–support contact structure play major roles.[6,11,12]

In contrast to supported gold catalyst systems, unsupported systems, such as gold powder, have not yet drawn much attention, although remarkably high catalytic activity for CO oxidation has been attained with such systems.[13] Moreover, unsupported gold catalysts allow the relevant catalytic mechanisms to be more easily understood and also make new applications accessible. Herein, we demonstrate that high catalytic activity is not necessarily linked to the presence of finely dispersed particles. Nanoporous gold with a spongelike morphology, formed through the selective leaching of silver from a gold–silver alloy,[14–16] has an unexpectedly high catalytic activity for CO oxidation at ambient pressures and temperatures down to −20 °C. Sintering can hamper the catalytic applications of gold particles; in contrast, nanoporous gold has good thermal stability, and its morphology can be easily reproduced.

The spongelike morphology of the nanoporous gold used herein consists of interconnecting ligaments with diameters

[*] Dr. V. Zielasek, B. Jürgens, C. Schulz, Prof. Dr. M. Bäumer
Institut für Angewandte und Physikalische Chemie
Universität Bremen
Leobener Strasse NW2, 28359 Bremen (Germany)
E-mail: mbaeumer@uni-bremen.de
Dr. J. Biener, Dr. M. M. Biener, Dr. A. V. Hamza
Nanoscale Synthesis and Characterization Laboratory
Lawrence Livermore National Laboratory
7000 East Avenue, Livermore, CA 94550 (USA)

[**] We gratefully acknowledge financial support by the Fonds der Chemischen Industrie (FCI). This work was performed in part under the auspices of the U.S. Department of Energy by the University of California, Lawrence Livermore National Laboratory, under contract number W-7405-Eng-48. We are grateful to Prof. Dr. Günter Schulz-Eckloff for helpful discussions.

 © 2006 Wiley-VCH Verlag GmbH & Co. KGaA, Weinheim

on the order of tens of nanometers, as demonstrated by the scanning electron microscopy (SEM) images shown in Figure 1. As evidenced by transmission electron microscopy (TEM), the ligaments are polycrystalline with grain boundaries separated by a few tens of nanometers (for further structural details, see reference [16]). Most importantly, with respect to the role ascribed to low-coordinate gold atoms in the catalytic mechanism, the curved shape of the ligaments implies a high density of low-coordinate surface sites, such as step and kink atoms. For the inner surface of the material, a specific surface area of $3.7\ m^2g^{-1}$ was determined. X-ray photoelectron spectroscopy (XPS) revealed that, in addition to gold, 4.4% metallic silver is present at the surface of the samples used for the catalytic studies described below. However, the total silver content in the bulk of the samples is only 0.7%, as determined by atomic absorption spectroscopy (AAS). Moreover, the XP spectrum reveals only minor surface contamination by carbon and oxygen, even though the surface analysis was carried out after a long deployment of the catalyst (Figure 1, inset).

We studied the catalytic oxidation of CO with synthetic air in a continuous-flow reactor at normal pressure in the temperature range −20 to 50°C. The reactor is illustrated schematically in the inset of Figure 2. An infrared gas analyzer (IRGA) was used to quantify the amount of CO_2 produced during the reaction. In addition, the reaction was followed by detecting the heat evolved during the exothermic oxidation of CO, as the temperature difference ΔT between the catalyst and the reactor (see the Experimental Section for details).

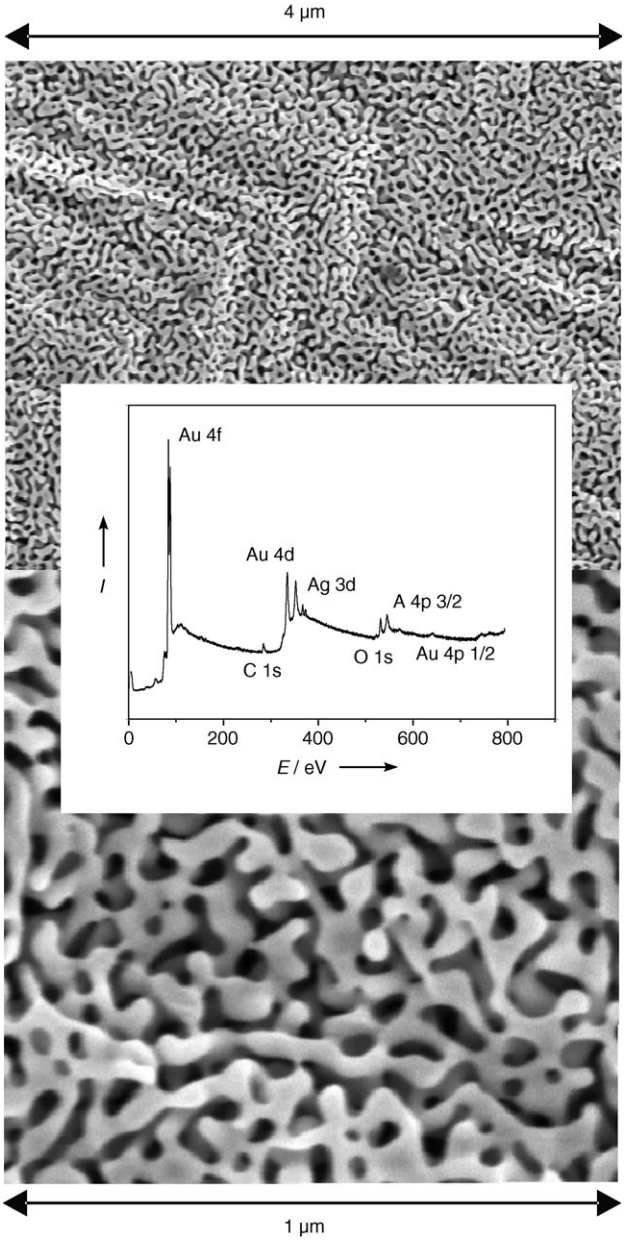

Figure 1. SEM images of the nanoporous gold catalyst reveal a spongelike morphology consisting of ligaments with diameters in the order of several tens of nanometers. Inset: the XP spectrum reveals a silver content of 4.4% and traces of oxygen and carbon at the catalyst surface.

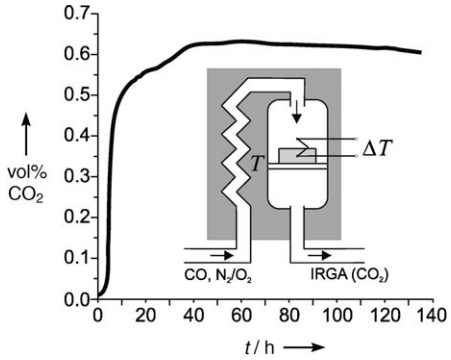

Figure 2. The time dependence of the CO_2 concentration at the reactor outlet reveals the activation phase and long-term activity of a nanoporous gold catalyst (at 50°C). Inset: schematic illustration of the reactor (see text for details).

The amount of CO_2 detected by IRGA for a freshly prepared sample of nanoporous gold is plotted versus time in Figure 2. After an activation phase of approximately 30 min at 50–75°C, an increase in the IRGA signal indicated the onset of catalytic activity. The activity subsequently increased gradually over several hours and then remained at a high level for several days. It is probable that moisture adsorbed in the pores or contaminants stemming from the leaching process are removed during the activation phase. Once activated at elevated temperatures, the samples of nanoporous gold exhibited catalytic activity immediately thereafter, even at lower temperatures.

We used these activated catalysts to study the dependence of the turnover on the concentration of CO admitted to the reactor. The CO_2 concentrations and the ΔT values measured in the reactor at room temperature are shown in Figure 3. The concentration of CO_2 produced clearly increases with the concentration of CO supplied to the reactor. For up to 2 vol% CO, the CO_2 yield corresponds to total conversion. When 8 vol% CO is admitted to the reactor, $^5/_8$ is still converted to CO_2. The fact that the increase in the CO_2 concentration is

 © 2006 Wiley-VCH Verlag GmbH & Co. KGaA, Weinheim

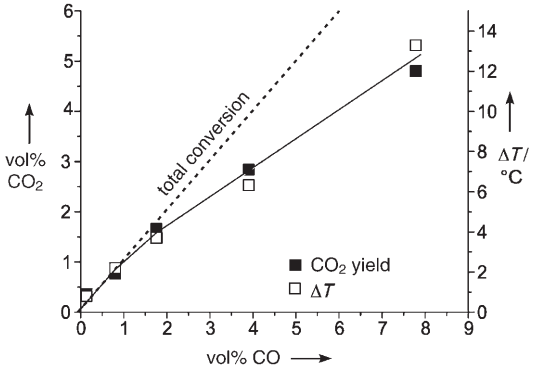

Figure 3. The dependence of the CO_2 concentration at the reactor outlet and the temperature difference ΔT between the catalyst and the reactor on the CO concentration at the inlet (at 23 °C). The similarity of the two curves reveals that the oxidation of CO takes place at the surface of the nanoporous gold catalyst.

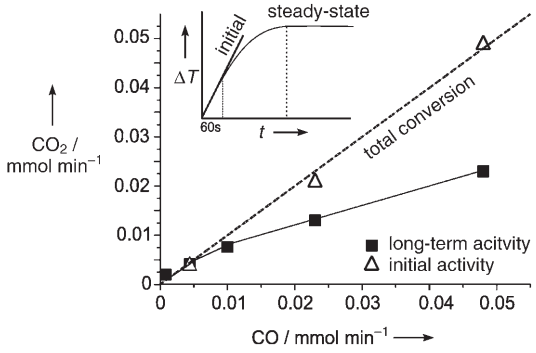

Figure 4. The dependence of the amount of CO_2 produced during 60 s on the amount of CO supplied. The amount of CO_2 detected by IRGA (long-term activity) is compared to that calculated from the initial increase in ΔT (initial activity). Initially, the CO supplied is totally converted, even at concentrations up to 8 vol%. Inset: the general time dependence of ΔT after the start of the CO flow reveals an initial linear increase, followed by saturation once steady-state conditions are reached.

proportional to the increase in ΔT indicates that the reaction occurs at the surface of the nanoporous gold catalyst.

In comparison, in studies on supported gold particles at normal pressure, Haruta found that the total turnover frequency did not depend on the CO concentration in the range 0.1–10 vol%.[11] An interpretation of these findings on the basis of a Langmuir–Hinshelwood mechanism led to the conclusion that the oxidation of CO on the surface is the rate-limiting step. Consequently, the surface should be saturated with oxygen and CO, and the kinetic order of the reaction should be zero. In our experiments, however, we observed a continuous increase in the turnover with CO supply, which indicates that the CO-to-CO_2 conversion rate is limited not by the surface reaction, but rather by gas transport to the surface.

The data in Figures 2 and 3 represent the long-term catalytic activity of the catalyst under steady-state conditions. To determine the initial catalytic activity, ΔT was recorded at the start of the CO flow. As long as the heat exchange between the catalyst and the reactor is negligible, the enthalpy ΔH of the exothermal oxidation of CO is related to ΔT by $\Delta H = c_p \Delta T$, where c_p is the heat capacity of nanoporous gold (we use the value of bulk gold, $c_p = 25.6\ \mathrm{J\,mol^{-1}\,K^{-1}}$). The inset of Figure 4 shows the general dependence of ΔT on time t. For the first 60 s, $d\Delta T/dt$ is nearly constant. On the basis of the measured ΔT values and the calculated enthalpies during the first 60 s after the start of the CO flow, we calculated the amount of CO_2 produced. The results are compared to those from the long-term IRGA measurements in Figure 4. They reveal that even at a CO concentration of 8 vol% the initial activity leads to total conversion. Apparently, reaction-induced processes suppress the turnover after the initial phase of the catalytic reaction.

In Figure 5, the turnover at different CO concentrations and four different reactor temperatures in the range −20–50 °C is shown. This temperature range is particularly interesting for applications of gold catalysts in low-temperature CO oxidation. The long-term activity does not vary significantly in the range 20–50 °C and is reduced by only 10% at 0 °C. Even at −20 °C the turnover at CO concentrations up to 2 vol% is close to total conversion. For higher CO

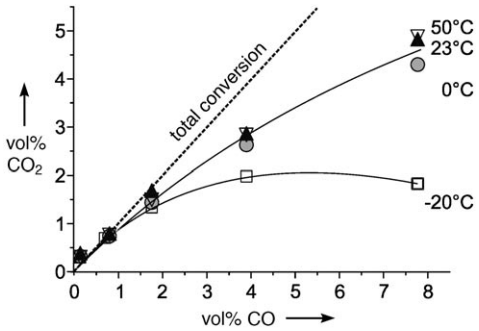

Figure 5. The dependence of the CO_2 concentration at the reactor outlet on the CO concentration at the inlet for four different temperatures in the range −20 to 50 °C. Below 2 vol% CO, nearly total conversion to CO_2 is attained. At temperatures above 0 °C, the conversion rate is approximately $^3/_5$ for 8 vol% CO. At −20 °C, the conversion saturates at approximately 2 vol% CO_2.

concentrations at −20 °C, the turnover saturates at approximately 2 vol% CO_2, which indicates that at low temperatures an elementary step of the reaction, probably the dissociation of O_2, limits the turnover rate.

Finally, the reason for the unexpectedly high catalytic activity of nanoporous gold in the temperatures range 0–50 °C and the underlying mechanism remain to be established. Presumably, the presence of residual silver (see above) plays an important role. Studies on silver-contaminated gold powders[13] and on gold–silver alloy particles on acidic supports[17] suggest that catalytic activity is significantly enhanced by foreign atoms, such as silver. The silver atoms are probably necessary to provide (additional) surface sites for the dissociation of O_2,[18–20] while CO adsorbs preferentially at low-coordinate gold sites.[13] Wang et al. proposed that O_2 molecules on silver sites are activated through electron transfer to the antibonding $2\pi^*$ orbitals, leading to the formation of O_2^- species.[17] In any case, the possibility that the catalytic activity arises from silver sites alone can be excluded. On one hand, silver-based catalysts do not exhibit

 © 2006 Wiley-VCH Verlag GmbH & Co. KGaA, Weinheim

significant CO-to-CO_2 conversion rates at temperatures below 100 °C.[21–23] On the other hand, small amounts of moisture in the reaction gases did not significantly influence the CO turnover for the nanoporous gold catalyst, whereas the formation of a carbonate species has been reported to poison the catalytic activity of silver surfaces.[24] Preliminary results indicate that the catalytic activity of nanoporous gold is independent of the Ag/Au ratio at the catalyst surface. Experiments on samples with similar bulk silver contents but higher surface silver concentrations (20% Ag) exhibited comparable activities to the samples used above.

Although silver is known to segregate to the surface of gold–silver alloys,[17] it is not clear whether the silver forms islands or intermixes with gold on the surface of the nanoporous gold catalyst. However, the distribution of silver could have a strong influence on the catalytic mechanism. In the case of larger silver patches, subsurface oxygen species may form, which have been shown to influence the reactivity of surface oxygen species.[25] When only single silver atoms are present, this subsurface oxygen species does not occur. These considerations may explain why a strong dependence of the catalytic activity on the Au/Ag ratio was observed for gold–silver nanoparticles, because the silver concentration in these systems was significantly higher[17] than that in our nanoporous gold foams, for which no such dependence is observed. More detailed investigations on the catalytic activity of nanoporous gold, in particular concerning its dependence on the silver content and the role of low-coordinate gold sites at the catalyst surface, are in progress to clarify the underlying mechanisms and their structural prerequisites. In this context, foams with smaller pore sizes and bimodal pore size distributions will also be investigated.[26,27] Nanoporous gold is a promising material for catalytic applications, because it is self-supporting, thermally and mechanically stable, and shapeable; as a thin foil it could possibly find use as a membrane catalyst.

Experimental Section

The nanoporous gold catalysts were prepared by dealloying a gold–silver alloy (70% silver) in nitric acid, followed by several cleaning steps in water.[16] The formation of the porous material is a complex process involving the selective leaching of silver, and subsequent large-scale rearrangements of the gold atoms and the resulting vacancies.[15] The silver content of the gold foams was determined by AAS to be less than 1%.

The continuous-flow reactor was fabricated from glass tubing. A silicone oil bath and an NaCl/ice bath allowed the reactions to be carried out at temperatures in the range −20–200 °C. A disk of nanoporous gold (80 mg, thickness 300 μm, diameter ca. 10 mm) was placed on a ceramic frit (diameter 20 mm) inside the reactor. The reactant gas consisted of 1–8 vol% CO in dry synthetic air (80:20 (v:v) N_2/O_2, $c(H_2O) < 5$ ppm) at a flow rate of ca. 15 mL min^{-1}. Note that a fraction of the reactant gas passed the catalyst without contacting it, which could not be avoided for the nanoporous gold samples (in contrast to powder samples). After the gas mixture had passed over the catalyst, the amount of CO_2 produced was quantified by IRGA. The temperature difference between the catalyst and the reactor was measured with one contact of a NiCr–Ni thermocouple applied directly to the gold sample and the reference contact placed 5 mm above the sample in the gas flow. All experiments were carried out on freshly prepared catalysts.

Received: June 20, 2006
Revised: August 15, 2006
Published online: November 13, 2006

Keywords: carbon monoxide · catalysis · gold · nanostructures · surface chemistry

[1] M. Haruta, N. Yamada, T. Kobayashi, S. Iijima, *J. Catal.* **1989**, *115*, 301.
[2] T. Hayashi, K. Tanaka, M. Haruta, *J. Catal.* **1998**, *178*, 566.
[3] K. A. Davis, D. W. Goodman, *J. Phys. Chem. B* **2000**, *104*, 8557.
[4] A. K. Sinha, S. Seelan, S. Tsubota, M. Haruta, *Angew. Chem.* **2004**, *116*, 1572; *Angew. Chem. Int. Ed.* **2004**, *43*, 1546.
[5] T. A. R. Nijhuis, T. Visser, B. M. Weckhuysen, *Angew. Chem.* **2005**, *117*, 1139; *Angew. Chem. Int. Ed.* **2005**, *44*, 1115.
[6] M. Haruta, *Catal. Today* **1997**, *36*, 153.
[7] G. C. Bond, D. T. Thompson, *Catal. Rev. Sci. Eng.* **1999**, *41*, 319.
[8] G. Pattrick, E. van der Lingen, C. W. Corti, R. J. Holliday, D. T. Thompson, *Top. Catal.* **2004**, *30*, 273.
[9] R. Meyer, C. Lemire, S. K. Shaikhutdinov, H.-J. Freund, *Gold Bull.* **2004**, *37*, 72.
[10] M. Haruta, M. Daté, *Appl. Catal. A* **2001**, *222*, 427; M. Haruta, *Chem. Rec.* **2003**, *3*, 75; M. Haruta, *J. New Mater. Electrochem. Syst.* **2004**, *7*, 163.
[11] M. Haruta, *Cattech* **2002**, *6*, 102.
[12] T. V. Choudhary, R. W. Goodman, *Appl. Catal. A* **2005**, *291*, 32.
[13] Y. Iizuka, A. Kawamoto, K. Akita, M. Daté, S. Tsubota, M. Okumura, M. Haruta, *Catal. Lett.* **2004**, *97*, 203.
[14] R. C. Newman, S. G. Corcoran, J. Erlebacher, M. J. Aziz, K. Sieradzki, *MRS Bull.* **1999**, *24*, 24.
[15] J. Erlebacher, M. J. Aziz, A. Karma, N. Dimitrov, K. Sieradzki, *Nature* **2001**, *410*, 450.
[16] A. M. Hodge, J. Biener, L. L. Hsiung, Y. M. Wang, A. V. Hamza, J. H. Satcher, Jr., *J. Mater. Res.* **2005**, *20*, 554.
[17] A.-Q. Wang, J.-H. Liu, S. D. Lin, T.-S. Lin, C.-Y. Mou, *J. Catal.* **2005**, *233*, 186.
[18] A. Nagy, G. Mestl, *Appl. Catal. A* **1999**, *188*, 337.
[19] F. Buatier de Mongeot, A. Cupolillo, M. Rocca, U. Valbusa, *Chem. Phys. Lett.* **1999**, *302*, 302.
[20] V. I. Bukhtiyarov, V. V. Kaichev, I. P. Prosvirin, *J. Chem. Phys.* **1999**, *111*, 2169.
[21] K.-S. Song, S.-K. Kang, S. D. Kim, *Catal. Lett.* **1997**, *49*, 65.
[22] A. M. Venezia, L. F. Liotta, G. Deganello, Z. Schay, D. Horvath, L. Guczi, *Appl. Catal. A* **2001**, *211*, 167.
[23] E. Gulari, C. Güldür, S. Srivannavit, S. Osuwan, *Appl. Catal. A* **1999**, *182*, 147.
[24] V. I. Bukhtiyarov, A. I. Nizovskii, H. Bluhm, M. Hävecker, E. Kleimenov, A. Knop-Gericke, R. Schlögl, *J. Catal.* **2006**, *238*, 260.
[25] P. J. van den Hoek, E. J. Baerends, R. A. van Santen, *J. Phys. Chem.* **1989**, *93*, 9469.
[26] Y. Ding, J. Erlebacher, *J. Am. Chem. Soc.* **2003**, *125*, 7772.
[27] A. M. Hodge, J. R. Hayes, J. A. Caro, J. Biener, A. V. Hamza, *Adv. Eng. Mater.* **2006**, *8*, 853.

 © 2006 Wiley-VCH Verlag GmbH & Co. KGaA, Weinheim

Bond-Stretch Isomers

DOI: 10.1002/anie.200601115

α- and β-$[Fe_2(\mu\text{-}S\textit{t}Bu)_2(S\textit{t}Bu)_4]^{2-}$: Coexistence of Two Bond-Stretch Isomers of a Classical Bitetrahedral Metal Chalcogenolate Compound**

*Bernd Hammann, Changneng Chen, Ulrich Flörke, Ralf Hauptmann, Eckhard Bill, Sebastian Sinnecker, and Gerald Henkel**

Dedicated to Professor Josef Grobe on the occasion of his 75th birthday

Eight years ago, we reported homoleptic binuclear iron(II) thiolate complexes with the coordination number three in which sterically demanding ligands prevented the metal center from adopting the tetrahedral coordination environment typically found with sulfur ligands.[1] Besides these coordinatively unsaturated species, several other structurally related metal(II) chalcogenolate complexes are known which also contain three-coordinate metal centers as a result of the use of bulky ligands.[2]

Homobinuclear thiolate and selenolate complexes of more conventional design, however, are much more numerous. Characterized by four chalcogen donor functions surrounding each metal ion, typical examples include the iron alkane thiolate complexes $[Fe_2(SMe)_6]^{2-}$, $[Fe_2(SEt)_6]^{2-}$, $[Fe_2(S\textit{i}Pr)_6]^{2-}$ and $[Fe_2(S_2\text{-}o\text{-xyl})_3]^{2-}$ (S_2-*o*-xyl = *o*-xylene-α,α′-dithiolate). They consist of two FeS_4 tetrahedra that share a common edge.[3] This architecture leads to a central cyclic Fe_2S_2 unit which is normally planar in the case of monofunctional ligands and which has the form of a rhomb with acute Fe-S-Fe (and obtuse S-Fe-S) angles.

Similar planar M_2E_2 rhombs (E = S, Se) are also present in the binuclear complexes with coordination number three. However, from direct comparison of this unit in $[Fe_2\{SC_6H_3\text{-}2,6\text{-}(SiMe_3)_2\}_4]$ and $[Fe_2(S\textit{i}Pr)_6]^{2-}$, typical examples for three- and four-coordinate complexes, respectively, it became evident that the Fe_2S_2 rhomb within $[Fe_2\{SC_6H_3\text{-}2,6\text{-}(SiMe_3)_2\}_4]$ has acute angles at the iron atoms—in clear contradiction to an expected widening as a result of the trigonal-planar coordination with ideal-typical valence angles of 120°.[1,3b]

Even more surprising, however, are the structural features of the complex $[Fe_2\{SC_6H_3\text{-}2,6\text{-}(SiMe_3)_2\}_4(MeCN)_2]$ which has been obtained by addition of two acetonitrile molecules to $[Fe_2\{SC_6H_3\text{-}2,6\text{-}(SiMe_3)_2\}_4]$.[1] In the course of this reaction, the coordination geometry of the iron centers changed from distorted trigonal planar to distorted tetrahedral resulting in a further lowering of the S-Fe-S angle within the central Fe_2S_2 rhomb from 84.3(1) to 79.8(1)°.

At least as surprising as this extremely small value is that the exocyclic (opposing) S-Fe-N angle does not compensate for this shortening by being larger than the ideal tetrahedral value of 109.5°, but is rather, with 100.3(1)°, significantly smaller.

From these observations it seemed likely that classical binuclear homoleptic chalcogenolate complexes of coordination number four can occur in at least one further conformation not previously observed, which corresponds to a defined minimum on the potential energy surface.

In search for such a conformation, which has clearly been hidden by the metal/ligand combinations used to date, we reexamined various reaction systems. These investigations focused on ligands with highly nucleophilic sulfur donor atoms but that are small enough to allow tetrahedral coordination. Thus, the *tert*-butanethiolate ligand appears to be especially suitable. In our previous studies based on this ligand and its selenium homologue, we were able to synthesize various complexes with completely novel chemical and structural features, for example the bitetrahedral nickel and iron complexes $[Ni_2(S\textit{t}Bu)_6]^{2-}$ and $[Fe_2(S\textit{t}Bu)_5]^{-}$ which show, respectively, the first pair of NiS_4 tetrahedra sharing a common edge and the first pair of FeS_4 tetrahedra sharing a common face.[4] Examination of the reaction system directed towards the synthesis of $[Fe_2(S\textit{t}Bu)_6]^{2-}$ resulted in the discovery of a novel conformation in addition to a species of identical composition but of conventional design, which together represent an unprecedented pair of bond-stretch isomers.

Both isomers form, together with tetramethylammonium cations, a complex salt of composition $[Me_4N]_4\{\alpha\text{-}[Fe_2(S\textit{t}Bu)_6]\}\{\beta\text{-}[Fe_2(S\textit{t}Bu)_6]\}$.[5,6] α-$[Fe_2(S\textit{t}Bu)_6]^{2-}$ (**1a**) is the isomer with the conventional structure (Figure 1). Its centroid is a crystallographic inversion center, and the overall symmetry comes very close to the point group C_{2h} with the 2-fold axis passing through the iron atoms.

Within the central planar Fe_2S_2 unit, the angles at the iron atoms are 95.01(2)° and thus are obtuse, whereas they are acute at the sulfur atoms (84.99(2)°). This geometric feature brings **1a** in line with other alkane thiolate complexes of general formula $[Fe_2(SR)_6]^{2-}$, for example, with R = Me, Et, and *i*Pr the angles at the iron atoms are 104.1(1), 102.3(1), and 99.2(1)°, and at the sulfur atoms 75.9(1), 77.7(1), and 80.8(1)°, respectively. Furthermore, the tendency of these angles to

[*] Dr. B. Hammann, C. Chen,[+] Dr. U. Flörke, Dr. R. Hauptmann,[++] Prof. Dr. G. Henkel
Fakultät für Naturwissenschaften, Department Chemie
Universität Paderborn
Warburger Strasse 100, 33098 Paderborn (Germany)
Fax: (+49) 5251-603423
E-mail: biohenkel@uni-paderborn.de
Dr. E. Bill, Dr. S. Sinnecker
Max-Planck-Institut für Bioanorganische Chemie,
Stiftstrasse 34–36, 45470 Mülheim an der Ruhr (Germany)

[+] Current address:
State Key Laboratory of Structural Chemistry, Fujian Institute of Research on the Structure of Matter, Fuzhou 350002 (China)

[++] Current address:
Eduard-Zintl-Institut für Anorganische und Physikalische Chemie, Technische Universität Darmstadt, Petersenstrasse 18, 64287 Darmstadt (Germany)

[**] This work was supported by the Deutsche Forschungsgemeinschaft (DFG), the Bundesministerium für Bildung, Wissenschaft, Forschung und Technologie (BMBF), and the Fonds der Chemischen Industrie.

 © 2006 Wiley-VCH Verlag GmbH & Co. KGaA, Weinheim

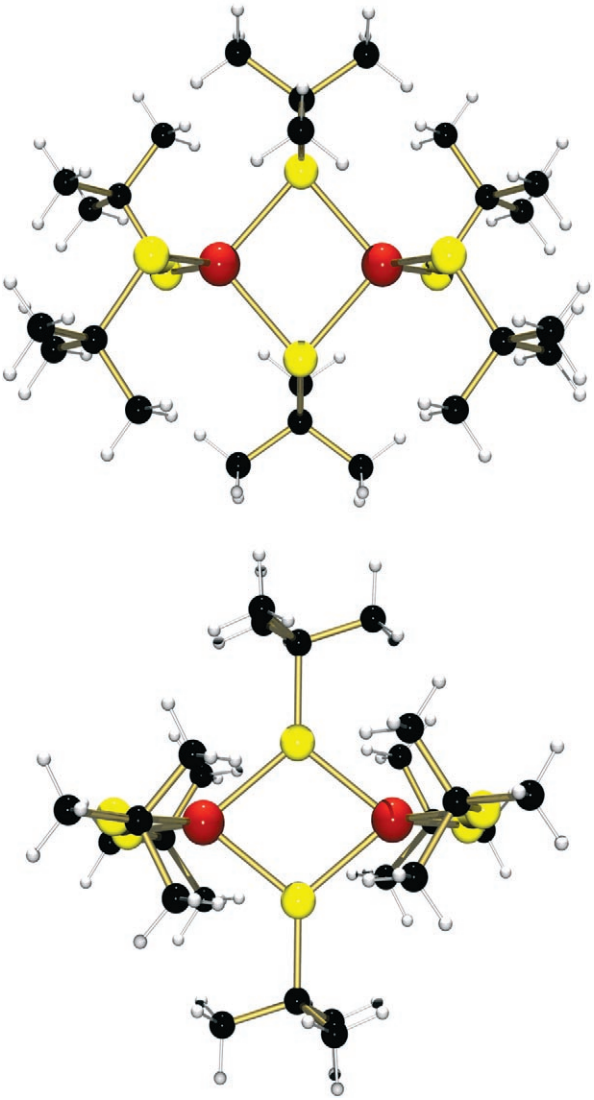

Figure 1. Structures of **1a** (top) and **1b** (bottom); Fe red, S yellow, C black, H white; artificial radii.

approach each other as the bulk of R increases is clearly confirmed. The opposite tendency applies to the correlation between the endo- and the exocyclic S-Fe-S angles, a compression of the ideal sp^3 angle within the Fe_2S_2 rhomb is accompanied by an increase of this angle within the exocyclic part.

The α-carbon atoms of the *tert*-butyl groups lie alternately above and below the Fe_2S_2 plane, so **1a** is best described as the α *anti* isomer. There seems to be no relationship between the distance from the α-carbon atoms to the Fe_2S_2 plane and the spatial demands of the substituents bound to sulfur. They amount to 1.68 Å for R = Me, 1.72 Å for R = Et, 1.65 Å for R = *i*Pr and 1.50 Å for R = *t*Bu.

As for the isomer **1a**, the structure of β-$[Fe_2(S\mathit{t}Bu)_6]^{2-}$ (**1b**, Figure 1) also has a crystallographic inversion center. The point group for the complex anion in its idealized form is also C_{2h}, but in this case the 2-fold axis is perpendicular to the Fe_2S_2 plane. Taking only the $\{Fe_2S_6\}$ core and the α-carbon atoms into account, the symmetry elements of the point group D_{2h} can be recognized with the principle axis now passing through the iron–iron axis.

At a first glance, the isomer **1b** might be seen as a transition state which will be passed through if the *anti* isomer **1a** transforms into its mirror image reflected in the plane containing both iron atoms and the four terminal sulfur atoms. A superposition of the initial and the final state with the structure of **1b** is depicted in Figure 2.

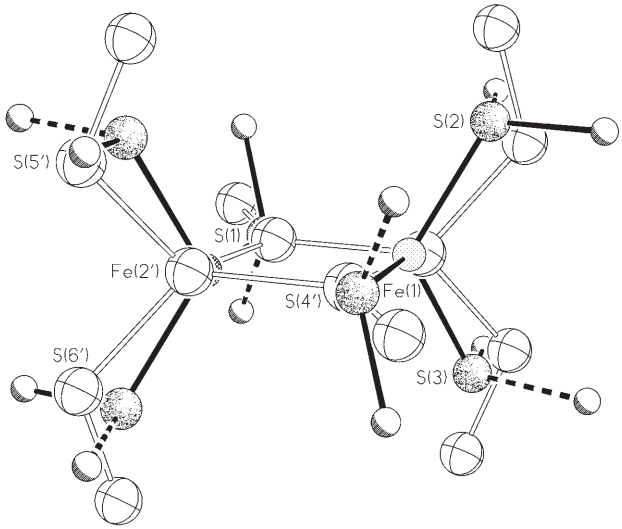

Figure 2. Superposition of **1a** (ball-and-stick model, black bonds, unprimed labels) and its mirror image (ball-and-stick model, dashed bonds to α-carbon atoms after reflection) with **1b** (open bonds, large ORTEP-type spheres, primed labels); methyl groups are omitted.

A comparison of the exo- and endocyclic S-Fe-S angles clearly reflects the fundamental differences between **1a** and **1b**. The central Fe_2S_2 rhomb within isomer **1b** has an extremely acute angle of 76.43° at the iron center which is compressed by approximately 33° compared to the ideal tetrahedral value and by 18.58° compared to the corresponding angle of isomer **1a**.

Thus we find an inverted relationship for the angles of the Fe_2S_2 rhombs of isomers **1a** and **1b**: starting from a square, the geometry found in isomer **1a** is obtained by stretching the diagonal passing through the sulfur atoms, whereas compression of this diagonal leads to the geometry of isomer **1b**. This compression, causes the sulfur atoms approach each other to a distance of 2.914(1) Å, while the Fe-S-Fe angle increases to a value of 103.57(2)°. The distance between the iron atoms increases to 3.701(1) Å and thus approaches the values found in complexes in which FeS_4 tetrahedra share common vertices (3.89(2) Å in $[Fe_4(SEt)_{10}]^{2-}$).[3c]

Further characteristic features of the cyclic $\{Fe_2S_2C_2\}$ core of **1b** are planar $CSFe_2$ fragments caused by the sp^2 hybridized sulfur atoms. This situation allows for extensive S→Fe π-donor interactions between the bridging thiolate ligands and the iron atoms which result in a significant decrease in the Fe–S bond lengths of the central Fe_2S_2 rhomb. Compared with isomer **1a**, this shortening amounts to 0.049 Å, and we regard this feature as being a major

 © 2006 Wiley-VCH Verlag GmbH & Co. KGaA, Weinheim

contribution to the stability of isomer **1b**. π-Donor interactions of similar magnitude also occur in the exocyclic Fe–S bonds, though the shortening of these bonds, compared with isomer **1a** (on average 0.023 Å), is somewhat smaller. The orientation of the *tert*-butyl groups of the nonbridging ligands within **1b** is also compatible with sp^2 hybridized sulfur atoms, their α-carbon atoms lie in the same plane as their sulfur atoms and the iron center. Thus, **1b** is best described as the β in-plane isomer.

A striking feature of **1b** is the unusually small exocyclic S-Fe-S angle, which, at 91.35(2)°, is reminiscent of the angle within the Fe_2S_2 rhomb, and is 26.49° smaller than the corresponding angle of isomer **1a**. We regard **1a** and **1b** as bond-stretch isomers because both complex anions have the same spin state and the differences in their Fe–S bond lengths as well as in their Fe···Fe distances are too great to be the result of crystal packing effects.[7] Their structures are depicted in Figure 1, and selected interatomic distances and angles are in Table 1.[18]

Table 1: Selected interatomic distances [Å] and angles [°] (data without standard errors are average values).

	1a	**1b**
Fe–Fe	3.248(1)	3.701(1)
μS–μS	3.555(1)	2.914(1)
Fe–μS	2.404	2.355
Fe–S_t	2.325	2.302
μS-Fe-μS	95.01(3)	76.43(3)
S_t-Fe-S_t	117.74(3)	91.35(3)
μS-Fe-S_t	110.45	123.30
Fe-μS-Fe	84.99(2)	103.57(2)
X-μS-Y[a]	105.37	119.86

[a] Mean valence angle of the bridging sulfur atom.

Geometry optimizations based on density functional theory (DFT) calculations[8] show that both isomers correspond to a minimum on the potential energy surface. The α isomer appears to be 7 kcal mol^{-1} more stable. However, this value also corresponds approximately to the precision of the calculations.

For both isomers, geometries with planar Fe_2S_2 frameworks are found that differ only negligibly from the experimentally determined geometries. The Fe···Fe distances, for instance, could be reproduced satisfactorily (3.18 Å for isomer **1a** and 3.69 Å for isomer **1b**). According to the results of the DFT calculations, the stabilizing S→Fe π interactions within the $\{Fe_2S_6\}$ core of **1b** involve the $3p_y$ orbitals of the bridging sulfur atoms, the $3p_x$ orbitals of the terminal sulfur atoms, and the $3d_{x^2-y^2}$ orbitals of iron. The energy barrier between both isomers can be estimated, from the more stable variant, to be 32 kcal mol^{-1} by averaging their structures. This value is further proof that **1a** and **1b** have to be classified as different isomers. The borderline between isomers and conformers is drawn by energy barriers of approximately 30 kcal mol^{-1} for a transformation from one geometry into the other.[7a]

The spatial arrangement of the relevant orbitals of isomer **1b** is depicted in Figure 3, top. The corresponding analysis for isomer **1a** (Figure 3, bottom) shows that owing to the unfavorable orientation of the $3p_y$ orbitals of the sulfur atoms, no comparable π interactions within the Fe_2S_2 rhomb are possible, and for the terminal sulfur atoms this orbital situation results in binding σ interactions.

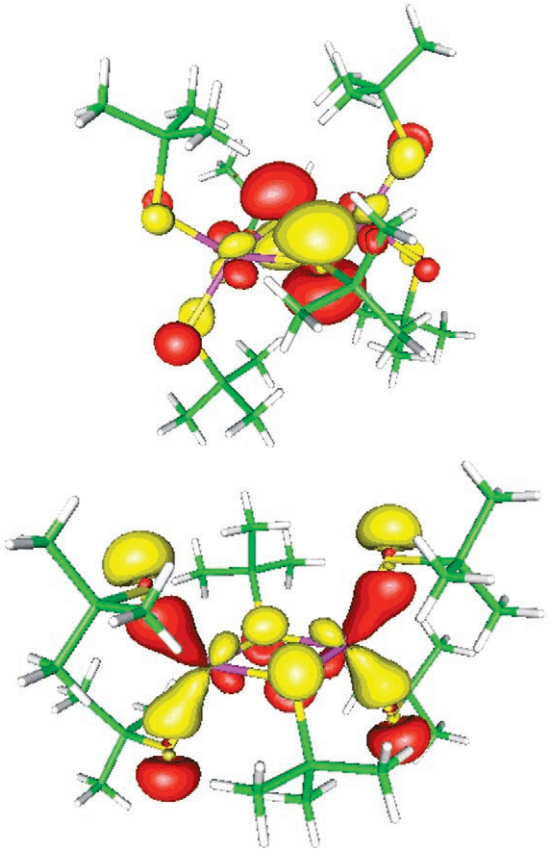

Figure 3. Interactions of the μ-S $3p_x$, S $3p_y$, and Fe $3d_{x^2-y^2}$ orbitals in **1b** (top) and **1a** (bottom); stick model: Fe purple, S yellow, C green, H white.

The zero-field Mössbauer spectrum of the crystalline compound $[Me_4N]_4\{\alpha\text{-}[Fe_2(S\mathit{t}Bu)_6]\}\{\beta\text{-}[Fe_2(S\mathit{t}Bu)_6]\}$ at $T=$ 80 K (Figure 4) consists of the two quadrupol doublets arising from the isomers $\alpha\text{-}[Fe_2(S\mathit{t}Bu)_6]^{2-}$ and $\beta\text{-}[Fe_2(S\mathit{t}Bu)_6]^{2-}$ which are distinctly different. Owing to the pronounced deviation from the ideal tetrahedral geometry, the quadrupole splitting is especially large for **1b**, 3.65 mm s^{-1}. For the less-distorted isomer **1a**, it is 3.16 mm s^{-1}. This value compares well with the corresponding parameter of the (likewise conventionally shaped) complex anion $[Fe_2(SEt)_6]^{2-}$, 3.25 mm s^{-1} for $T=$ 4.2 K and 2.97 mm s^{-1} for $T=100$ K.[9] The corresponding isomer shifts also reflect the effects of the Fe–S bond lengths. The value for the complex anion **1a**, $\delta=0.73$ mm s^{-1}, is clearly larger than that for **1b** ($\delta=0.70$ mm s^{-1}). Interestingly, the isomer shift of the complex anion $[Fe_2(SEt)_6]^{2-}$ was determined to be $\delta=0.70$ mm s^{-1} for $T=4.2$ K and $\delta=0.67$ mm s^{-1} for $T=100$ K. Isomer shifts obtained from our DFT calculations describe the experimentally observed trends correctly:

 © 2006 Wiley-VCH Verlag GmbH & Co. KGaA, Weinheim

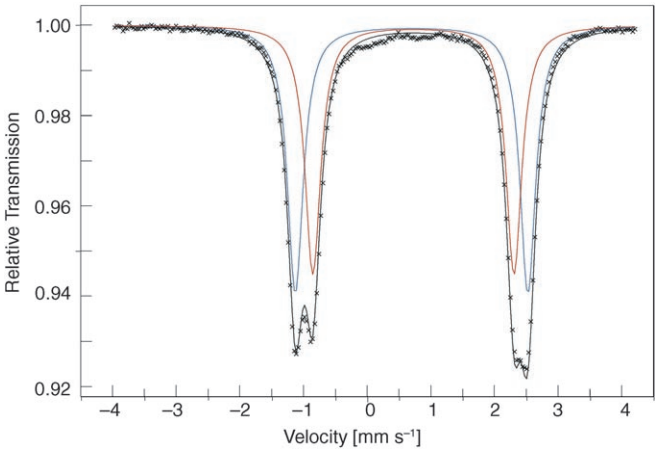

Figure 4. Zero-field Mössbauer spectrum of $[Me_4N]_4\{\alpha\text{-}[Fe_2(S\mathit{t}Bu)_6]\}\text{-}\{\beta\text{-}[Fe_2(S\mathit{t}Bu)_6]\}$ at 80 K. The red and blue curves correspond to the quadrupole doublets assigned to **1a** and **1b**, respectively.

the smaller quadrupole splitting and the larger isomer shift were calculated for isomer **1a** (3.23 and 0.63 $mm\,s^{-1}$, compared to 3.33 and 0.61 $mm\,s^{-1}$ for isomer **1b**).

The results of this work clearly demonstrate that classical coordination chemistry is still capable to produce surprising results. The detection of binuclear bitetrahedral metal thiolate complexes as bond stretch isomers in significantly different stable or metastable conformations raises the question whether we are faced with a special case of an intrinsic phenomenon of polynuclear complexes composed of tetrahedral building blocks linked by common vertices or edges.

At this time we are unable to give conclusive answers to this question. We were able, however, to obtain further indications for such a phenomenon from additional DFT calculations which indicate the possible existence of bond-stretch isomers in the case of the complex anion $[Fe_2(SMe)_6]^{2-}$. If the alkyl group of the ligand is replaced by hydrogen, however, the minimum on the potential energy surface defining the isomer containing sulfur atoms in the sp^2 hybridized state is lost. This result shows how the nature of the substituents on the sulfur atom play an important role in the properties of products formed in reactions with thiolate ligands.

Experimental Section

All manipulations were carried out in a dry nitrogen atmosphere. All solvents were degassed and dried prior to use.

$[Me_4N]_4\{\alpha\text{-}[Fe_2(S\mathit{t}Bu)_6]\}\{\beta\text{-}[Fe_2(S\mathit{t}Bu)_6]\}$: A solution of $FeCl_2$ (130 mg, 1.0 mmol) in dimethylformamide (2 mL) was added dropwise to a stirred solution of Na*S*t*Bu* (400 mg, 3.5 mmol) in methanol (1.5 mL). After stirring for ten minutes, $[NMe_4]Cl$ (170 mg, 1.5 mmol) was added. The reaction mixture was stirred for a further 10 min, then small amounts of an off-white residue were removed by filtration. The mother liquor was divided into two parts each being overlaid with the fourfold volume of diethyl ether in test tubes and stored at −26 °C. After approximately one week, crystals of $[Me_4N]_4\{\alpha\text{-}[Fe_2(S\mathit{t}Bu)_6]\}\{\beta\text{-}[Fe_2(S\mathit{t}Bu)_6]\}$ separated from the solution. Yield 0.18 g (45 % based on Fe)

DFT calculations: Complete geometry optimizations of both isomers **1a** and **1b** were performed by using models based on the X-ray crystal structures employing the density functional BP,[10] in combination with the TZVP basis set for iron and sulfur, and the SV(P) basis set for the remaining elements.[11] Furthermore, the scalar-relativistic zero-order regular approximation (ZORA) approach was used.[12] Broken symmetry DFT was used to describe the antiferromagnetic coupling of the two metal atoms.[13] Mössbauer parameters were calculated employing the same methods and parameters used in a recently published study of mononuclear iron complexes.[14] The B3LYP hybrid functional[15] was employed and the CP(PPP) basis set was used for iron.[16] All calculations were performed with the program package ORCA.[17]

Received: March 21, 2006
Revised: July 13, 2006
Published online: November 10, 2006

Keywords: bond-stretch isomerism · coordination chemistry · iron complexes · S ligands · structure elucidation

[1] R. Hauptmann, R. Kliß, J. Schneider, G. Henkel, *Z. Anorg. Allg. Chem.* **1998**, *624*, 1927 – 1936.

[2] a) P. P. Power, S. C. Shoner, *Angew. Chem.* **1991**, *103*, 308 – 309; *Angew. Chem. Int. Ed. Engl.* **1991**, *30*, 330 – 332; b) K. Ruhlandt-Senge, P. P. Power, *Bull. Soc. Chim. Fr.* **1992**, *129*, 594 – 598; c) R. Hauptmann, R. Kliß, G. Henkel, *Angew. Chem.* **1999**, *111*, 389 – 391; *Angew. Chem. Int. Ed.* **1999**, *38*, 377 – 379; d) P. B. Hitchcock, H. A. Jasim, R. E. Kelly, M. F. Lappert, *J. Chem. Soc. Chem. Commun.* **1985**, 1776 – 1778; e) M. Bochmann, K. J. Webb, M. B. Hursthouse, M. Mazid, *J. Chem. Soc. Dalton Trans.* **1991**, 2317 – 2323; f) W. Wojnowski, B. Becker, L. Walz, K. Peters, E.-M. Peters, H. G. von Schnering, *Polyhedron* **1992**, *11*, 607 – 612; g) H. Grützmacher, M. Steiner, H. Pritzkow, L. Zsolnai, G. Huttner, A. Sebald, *Chem. Ber.* **1992**, *125*, 2199 – 2207; h) M. Bochmann, G. Bwembya, R. Grinter, J. Lu, K. J. Webb, D. J. Williamson, M. B. Hursthouse, M. Mazid, *Inorg. Chem.* **1993**, *32*, 532 – 537; i) M. Bochmann, K. Webb, M. Harman, M. B. Hursthouse, *Angew. Chem.* **1990**, *102*, 703 – 704; *Angew. Chem. Int. Ed. Engl.* **1990**, *29*, 638 – 639; j) K. Ruhlandt-Senge, *Inorg. Chem.* **1995**, *34*, 3499 – 3504.

[3] a) C. Chen, R. Hauptmann, J. Lackmann, G. Henkel, *Z. Kristallogr.* **1999**, *214*, 137 – 138; b) R. Hauptmann, J. Lackmann, C. Chen, G. Henkel, *Acta Crystallogr. Sect. C* **1999**, *55*, 1084 – 1087; c) K. S. Hagen, R. H. Holm, *Inorg. Chem.* **1984**, *23*, 418 – 427; d) G. Henkel, W. Tremel, B. Krebs, *Angew. Chem.* **1983**, *95*, 317 – 318; *Angew. Chem. Int. Ed. Engl.* **1983**, *22*, 319 – 320.

[4] a) G. Henkel, C. Chen, *Inorg. Chem.* **1993**, *32*, 1064 – 1065; b) A. Müller, G. Henkel, *Z. Naturforsch. B* **1995**, *50*, 1464 – 1468.

[5] X-ray structure determination. **1**: $C_{32}H_{78}Fe_2N_2S_6$, $M_r = 795.0$; triclinic, space group $P\bar{1}$; $a = 11.3621(8)$, $b = 11.4852(8)$, $c = 17.205(1)$ Å, $\alpha = 84.621(2)$, $\beta = 85.889(2)$, $\gamma = 85.366(2)°$, $V = 2223.3$ Å^3, $Z = 2$, $\rho_{calcd} = 1.188\,g\,cm^{-3}$, $F(000) = 864$; 25439 reflexions with $1.2 < \theta < 27.9°$, $T = 120$ K, Bruker-AXS SMART APEX CCD diffractometer.[6] $Mo_{K\alpha}$ radiation ($\mu = 0.96\,mm^{-1}$), multi-scan absorption correction (SADABS[6]). Structure solution with direct methods combined with conventional Fourier techniques,[6] refinements[6] based on F^2 with 10558 independent reflections ($R_{int} = 0.055$), 405 parameters, $R1(I > 2\sigma(I)) = 0.043$, $wR2$(all data) = 0.104. Min./max. difference electron density −0.51/0.67 e Å^{-3}. Non-hydrogen atoms with anisotropic temperature factors, H atoms from difference Fourier syntheses and recalculated at idealized positions (riding model, $U_{iso}(H) = 1.5\,U_{eq}(C)$). CCDC-602095 contains the supplementary crystallographic data for this paper. These data can

 © 2006 Wiley-VCH Verlag GmbH & Co. KGaA, Weinheim

be obtained free of charge from The Cambridge Crystallographic Data Centre via www.ccdc.cam.ac.uk/data_request/cif.

[6] Bruker SMART (Ver. 5.62), SAINT (Ver. 6.02), SADABS, SHELXTL (Ver. 6.10). Bruker AXS Inc., Madison, Wisconsin, USA.

[7] a) Y. Jean, A. Lledos, J. K. Burdett, R. Hoffmann, *J. Am. Chem. Soc.* **1988**, *110*, 4506 – 4516; b) W.-D. Stohrer, R. Hoffmann, *J. Am. Chem. Soc.* **1972**, *94*, 779 – 786; c) W.-D. Stohrer, R. Hoffmann, *J. Am. Chem. Soc.* **1972**, *94*, 1661 – 1668; d) G. Parkin, *Chem. Rev.* **1993**, *93*, 887 – 911; e) G. Parkin, R. Hoffmann, *Angew. Chem.* **1994**, *106*, 1530; *Angew. Chem. Int. Ed. Engl.* **1994**, *33*, 1462; f) M.-M. Rohmer, M. Benard, *Chem. Soc. Rev.* **2001**, *30*, 340 – 354.

[8] W. Koch, M. C. Holthausen, *A Chemist's Guide to Density Functional Theory*, Wiley-VCH, Weinheim, **2000**.

[9] a) F. M. MacDonnell, K. Ruhlandt-Senge, J. J. Ellison, R. H. Holm, P. P. Power, *Inorg. Chem.* **1995**, *34*, 1815 – 1822; b) Y. Sanakis, S. J. Yoo, F. Osterloh, R. H. Holm, E. Münck, *Inorg. Chem.* **2002**, *41*, 7081 – 7085.

[10] a) A. D. Becke, *Phys. Rev. A* **1988**, *38*, 3098 – 3100; b) J. P. Perdew, *Phys. Rev. B* **1986**, *34*, 7406; c) J. P. Perdew, *Phys. Rev. B* **1986**, *33*, 8822 – 8824.

[11] a) A. Schäfer, C. Huber, R. Ahlrichs, *J. Chem. Phys.* **1994**, *100*, 5829 – 5835; b) A. Schäfer, H. Horn, R. Ahlrichs, *J. Chem. Phys.* **1992**, *97*, 2571 – 2577.

[12] a) E. van Lenthe, E. J. Baerends, J. G. Snijders, *J. Chem. Phys.* **1993**, *99*, 4597 – 4610; b) E. van Lenthe, E. J. Baerends, J. G. Snijders, *J. Chem. Phys.* **1994**, *101*, 9783 – 9792; c) E. van Lenthe, R. van Leeuwen, E. J. Baerends, J. G. Snijders, *Int. J. Quantum Chem.* **1996**, *57*, 281 – 293.

[13] a) L. Noodleman, *J. Chem. Phys.* **1981**, *74*, 5737 – 5743; b) L. Noodleman, E. R. Davidson, *Chem. Phys.* **1986**, *109*, 131 – 143.

[14] S. Sinnecker, L. D. Slep, E. Bill, F. Neese, *Inorg. Chem.* **2005**, *44*, 2245 – 2254.

[15] a) A. D. Becke, *J. Chem. Phys.* **1993**, *98*, 5648 – 5652; b) C. T. Lee, W. T. Yang, R. G. Parr, *Phys. Rev. B* **1988**, *37*, 785 – 789.

[16] F. Neese, *Inorg. Chim. Acta* **2002**, *337*, 181 – 192.

[17] F. Neese, ORCA—an ab initio, Density Functional and Semiempirical Program Package, Version 2.4. 2004. Mülheim an der Ruhr, Max-Planck-Institut für Bioanorganische Chemie.

[18] Both isomers **1a** and **1b** simultaneously present in $[Me_4N]_4\{\alpha\text{-}[Fe_2(S\mathit{t}Bu)_6]\}\{\beta\text{-}[Fe_2(S\mathit{t}Bu)_6]\}$ can also be obtained separately as tetramethylammonium salts. $[Me_4N]_2\{\beta\text{-}[Fe_2(S\mathit{t}Bu)_6]\}$[19] crystallizes in the monoclinic space group $P2_1/n$ ($a = 11.226(1)$, $b = 10.943(1)$, $c = 18.473(2)$ Å, $\beta = 94.95°$, $T = 120$ K) if cooling is avoided and $[NMe_4]Cl$ is introduced before adding the thiolate solution, whereas $[Me_4N]_2\{\alpha\text{-}[Fe_2(S\mathit{t}Bu)_6]\}$[19] is obtained in form of triclinic crystals (space group $P\bar{1}$, $a = 10.966(1)$, $b = 11.402(1)$, $c = 11.586(1)$ Å, $\alpha = 117.35(1)$, $\beta = 114.24(1)$, $\gamma = 94.43(1)°$, $T = 120$ K) by using $Fe(C_5H_5N)_4Cl_2$ instead of $FeCl_2$. The molecular structures of **1a** and **1b** in these crystals are virtually identical with the corresponding structures described herein.

[19] G. Henkel, B. Hammann, unpublished results.

 © 2006 Wiley-VCH Verlag GmbH & Co. KGaA, Weinheim